

Technical Report

Title: *Analysis of Straddle-Packer Tests in DGR Boreholes*

Document ID: TR-08-32


Authors: Randall Roberts and David Chace,
HydroResolutions LLC,
Richard Beauheim, and
John Avis, Geofirma Engineering Ltd.

Revision: 0

Date: April 12, 2011

DGR Site Characterization Document
Geofirma Engineering Project 08-200



Geofirma Engineering DGR Site Characterization Document		
Title:	Analysis of Straddle-Packer Tests in DGR Boreholes	
Document ID:	TR-08-32	
Revision Number:	0	Date: April 12, 2011
Authors:	Randall Roberts and David Chace, HydroResolutions LLC, Richard Beauheim, and John Avis, Geofirma Engineering Ltd.	
Technical Review:	John Avis, Kenneth Raven, Richard Beauheim; Dylan Luhowy (NWMO)	
QA Review:	John Avis	
Approved by:	 John Avis	

Document Revision History		
Revision	Effective Date	Description of Changes
0	April 12, 2011	Initial release

TABLE OF CONTENTS

1	INTRODUCTION	1
1.1	Background	1
1.2	Hydraulic Testing Activities	4
1.3	Reported Analyses	6
2	EQUIPMENT	7
2.1	Downhole Equipment	7
2.1.1	Packers	8
2.1.2	Shut-In Tool	9
2.1.3	Sediment Trap	9
2.1.4	Sensor Carriers	9
2.1.5	Piston Pulse Generator	9
2.1.6	Slotted Section	9
2.1.7	Centralizers	10
2.1.8	Pressure Transducers	10
2.1.9	Temperature Loggers	10
2.2	Surface Equipment	10
2.2.1	Barometer	11
2.2.2	Pressure-Maintenance Systems	11
2.2.3	Pressure Transducers	11
2.2.4	Data-Acquisition System	11
3	TESTING METHODOLOGY	13
4	ANALYSIS APPROACH	17
4.1	Conceptual Model	17
4.2	Parameters	18
4.3	Tests	20
4.4	Formation Specific Storage - Skin Conductivity - Skin Thickness	20
4.5	Pre-Test Borehole History	22
4.6	Uncertainty Analysis	23
5	PHASE 1 DGR-1 TESTING AND ANALYSIS	25
5.1	294.28-306.28 Salina A2 Carbonate	25
5.2	348.76-360.76 Salina A1 Carbonate	27
5.3	404.37-416.37 Lions Head-Fossil Hill-Cabot Head	29
5.4	Summary of DGR-1 Results	32
6	PHASE 2 DGR-2 ANALYSIS	33
6.1	457.85-488.35 Queenston	34
6.2	487.20-517.70 Queenston	36
6.3	517.50-548.00 Georgian Bay	39
6.4	547.80-578.30 Georgian Bay	41
6.5	578.10-608.60 Georgian Bay	44

6.6	608.40-638.90 Blue Mountain	46
6.7	630.50-661.00 Blue Mountain-Collingwood.....	49
6.8	660.50-691.00 Cobourg	51
6.9	687.60-718.10 Sherman Fall.....	54
6.10	714.50-745.00 Kirkfield	56
6.11	731.60-762.10 Kirkfield	59
6.12	754.50-785.00 Kirkfield-Coboconk	61
6.13	761.50-792.00 Coboconk-Gull River	64
6.14	785.00-815.50 Gull River	66
6.15	801.50-832.00 Gull River	69
6.16	Summary of DGR-2 Results.....	72
7	DGR-3 TESTING AND ANALYSIS.....	78
7.1	210.18-240.92 Salina F-E	79
7.2	240.72-271.46 Salina E-D-C	81
7.3	271.29-302.03 Salina C-B.....	84
7.4	301.81-332.55 Salina B-A2 Carbonate.....	86
7.5	334.99-365.73 Salina A2 Evaporite-A1 Carbonate	89
7.6	346.00-376.74 Salina A1 Carbonate	91
7.7	379.98-410.72 Salina A1 Evaporite-A0-Guelph-Goat Island-Gasport	94
7.8	410.51-441.25 Gasport-Lions Head-Fossil Hill-Cabot Head	96
7.9	441.05-471.79 Cabot Head-Manitoulin-Queenston	99
7.10	471.41-502.15 Queenston.....	101
7.11	501.95-532.69 Queenston-Georgian Bay.....	104
7.12	532.49-563.23 Georgian Bay	106
7.13	563.03-593.77 Georgian Bay	109
7.14	593.57-624.31 Georgian Bay-Blue Mountain	111
7.15	617.63-648.37 Georgian Bay-Blue Mountain	114
7.16	628.00-658.74 Blue Mountain	116
7.17	654.65-685.39 Blue Mountain-Collingwood-Cobourg.....	119
7.18	671.50-702.24 Collingwood-Cobourg-Sherman Fall	121
7.19	710.00-740.74 Sherman Fall-Kirkfield	124
7.20	740.54-771.28 Kirkfield	126
7.21	765.96-796.70 Kirkfield-Coboconk	129
7.22	790.93-821.67 Coboconk-Gull River	131
7.23	815.00-845.74 Gull River	134
7.24	Summary of DGR-3 Results.....	137
8	DGR-4 TESTING AND ANALYSIS.....	143
8.1	190.63-221.37 Salina F	144
8.2	218.13-248.87 Salina F-C	146
8.3	247.00-277.74 Salina C-B.....	149
8.4	261.63-292.37 Salina B.....	151
8.5	284.26-315.00 Salina B-A2 Carbonate.....	154
8.6	296.63-327.37 Salina A2- Upper A1 Carbonate.....	156
8.7	327.26-358.00 Salina A1 Carbonate	159

8.8	350.53-381.27	Salina A1-A0-Guelph-Goat Island	161
8.9	381.08-411.82	Goat Island-Gasport-Lions Head-Fossil Hill	164
8.10	411.51-442.25	Cabot Head-Manitoulin.....	166
8.11	432.00-462.74	Cabot Head - Manitoulin-Queenston	169
8.12	458.23-488.97	Queenston.....	171
8.13	488.77-519.51	Queenston.....	174
8.14	519.10-549.84	Georgian Bay	176
8.15	548.28-579.02	Georgian Bay (a).....	179
8.16	548.28-579.02	Georgian Bay (b).....	181
8.17	577.45-608.19	Georgian Bay	184
8.18	607.79-638.53	Blue Mountain	186
8.19	638.34-669.08	Blue Mountain-Collingwood-Cobourg.....	189
8.20	658.46-689.20	Collingwood - Cobourg.....	191
8.21	687.78-718.52	Cobourg-Sherman Fall-Kirkfield	194
8.22	717.10-747.84	Kirkfield	196
8.23	747.64-778.38	Kirkfield-Coboconk	199
8.24	762.80-793.54	Coboconk-Gull River	201
8.25	793.34-824.08	Gull River	204
8.26		Summary of DGR-4 Results.....	207
9		DGR-5 TESTING AND ANALYSIS.....	213
9.1	477.87-508.13	Manitoulin-Queenston	213
9.2	507.87-538.13	Queenston.....	216
9.3	537.87-568.13	Queenston-Georgian Bay.....	219
9.4	567.87-598.13	Georgian Bay	221
9.5	597.87-628.13	Georgian Bay	224
9.6	627.87-658.13	Georgian Bay-Blue Mountain	226
9.7	657.87-688.13	Blue Mountain	229
9.8	681.07-711.33	Blue Mountain-Collingwood-Cobourg.....	231
9.9	707.24-737.50	Cobourg	234
9.10	737.25-767.51	Sherman Fall.....	236
9.11	767.25-797.51	Kirkfield	239
9.12		Summary of DGR-5 Results.....	242
10		DGR-6 TESTING AND ANALYSIS.....	248
10.1	518.00-528.23	Queenston.....	249
10.2	650.00-660.23	Georgian Bay	251
10.3	678.00-688.23	Georgian Bay-Blue Mountain	254
10.4	700.00-710.23	Blue Mountain	256
10.5	725.00-735.23	Blue Mountain	259
10.6	737.00-747.23	Collingwood.....	261
10.7	764.00-774.23	Cobourg	264
10.8	782.00-792.23	Sherman Fall.....	266
10.9	797.00-807.23	Sherman Fall.....	269
10.10	841.00-851.23	Kirkfield	271
10.11	869.77-880.00	Coboconk.....	274

10.12 880.00-890.23 Coboconk.....	276
10.13 Summary of DGR-6 Results.....	279
11 FORMATION HYDRAULIC CONDUCTIVITY ESTIMATES AND RESULTS COMPARISON	285
12 DATA USE.....	291
13 REFERENCES.....	292

LIST OF APPENDICES

APPENDIX A	DGR-1 Plots
APPENDIX B	DGR-2 Plots
APPENDIX C	DGR-3 Plots
APPENDIX D	DGR-4 Plots
APPENDIX E	DGR-5 Plots
APPENDIX F	DGR-6 Plots

LIST OF TABLES

Table 1-1: Depths of stratigraphic contacts in DGR boreholes.....	3
Table 5-1: Summary of the DGR1_294.28-306.28 testing activities.	25
Table 5-2: Summary of the DGR1_294.28-306.28 parameter estimates.	25
Table 5-3: Summary of the DGR1_348.76-360.76 testing activities.	27
Table 5-4: Summary of the DGR1_348.76-360.76 parameter estimates.	28
Table 5-5: Summary of the DGR1_404.37-416.37 testing activities.	30
Table 5-6: Summary of the DGR1_404.37-416.37 parameter estimates.	30
Table 5-7: Best-fit parameter estimates derived from the DGR-1 analyses	32
Table 6-1: DGR-2 Phase 2 test zones and tests	33
Table 6-2: Summary of the DGR2_457.85-488.35 testing activities.	34
Table 6-3: Summary of the DGR2_457.85-488.35 parameter estimates.	34
Table 6-4: Summary of the DGR2_487.20-517.70 testing activities.	36
Table 6-5: Summary of the DGR2_487.20-517.70 parameter estimates.	37
Table 6-6: Summary of the DGR2_517.50-548.00 testing activities.	39
Table 6-7: Summary of the DGR2_517.50-548.00 parameter estimates.	39
Table 6-8: Summary of the DGR2_547.80-578.30 testing activities.	41
Table 6-9: Summary of the DGR2_547.80-578.30 parameter estimates.	42
Table 6-10: Summary of the DGR2_578.10-608.60 testing activities.	44
Table 6-11: Summary of the DGR2_578.10-608.60 parameter estimates.	44
Table 6-12: Summary of the DGR2_608.40-638.90 testing activities.	46
Table 6-13: Summary of the DGR2_608.40-638.90 parameter estimates.	47
Table 6-14: Summary of the DGR2_630.50-661.00 testing activities.	49
Table 6-15: Summary of the DGR2_630.50-661.00 parameter estimates.	49
Table 6-16: Summary of the DGR2_660.50-691.00 testing activities.	51
Table 6-17: Summary of the DGR2_660.50-691.00 parameter estimates.	52
Table 6-18: Summary of the DGR2_687.60-718.10 testing activities.	54
Table 6-19: Summary of the DGR2_687.60-718.10 parameter estimates.	54
Table 6-20: Summary of the DGR2_714.50-745.00 testing activities.	56
Table 6-21: Summary of the DGR2_714.50-745.00 parameter estimates.	57
Table 6-22: Summary of the DGR2_731.60-762.10 testing activities.	59
Table 6-23: Summary of the DGR2_731.60-762.10 parameter estimates.	59
Table 6-24: Summary of the DGR2_754.50-785.00 testing activities.	61
Table 6-25: Summary of the DGR2_754.50-785.00 parameter estimates.	62
Table 6-26: Summary of the DGR2_761.50-792.00 testing activities.	64
Table 6-27: Summary of the DGR2_761.50-792.00 parameter estimates.	64
Table 6-28: Summary of the DGR2_785.00-815.50 testing activities.	66
Table 6-29: Summary of the DGR2_785.00-815.50 parameter estimates.	67
Table 6-30: Summary of the DGR2_801.50-832.00 testing activities.	69
Table 6-31: Summary of the DGR2_801.50-832.00 parameter estimates.	69
Table 6-32: Best-fit parameter estimates derived from the DGR-2 analyses	72
Table 7-1: DGR-3 test zones and tests.....	78
Table 7-2: Summary of the DGR3_210.18-240.92 testing activities.	79
Table 7-3: Summary of the DGR3_210.18-240.92 parameter estimates.	79
Table 7-4: Summary of the DGR3_240.72 – 271.46 testing activities.....	81
Table 7-5: Summary of the DGR3_240.72 – 271.46 parameter estimates.	82
Table 7-6: Summary of the DGR3_271.29 – 302.03 testing activities.....	84
Table 7-7: Summary of the DGR3_271.29 – 302.03 parameter estimates.	84
Table 7-8: Summary of the DGR3_301.81-332.55 testing activities.	86
Table 7-9: Summary of the DGR3_301.81-332.55 parameter estimates.	87
Table 7-10: Summary of the DGR3_334.99-365.73 testing activities.	89
Table 7-11: Summary of the DGR3_334.99-365.73 parameter estimates.	89
Table 7-12: Summary of the DGR3_346.00-376.74 testing activities.	91
Table 7-13: Summary of the DGR3_346.00-376.74 parameter estimates.	92
Table 7-14: Summary of the DGR3_379.98-410.72 testing activities.	94

Table 7-15: Summary of the DGR3_379.98-410.72 parameter estimates.	94
Table 7-16: Summary of the DGR3_410.51-441.25 testing activities.	96
Table 7-17: Summary of the DGR3_410.51-441.25 parameter estimates.	97
Table 7-18: Summary of the DGR3_441.05-471.79 testing activities.	99
Table 7-19: Summary of the DGR3_441.05-471.79 parameter estimates.	99
Table 7-20: Summary of the DGR3_471.41-502.15 testing activities.	101
Table 7-21: Summary of the DGR3_471.41-502.15 parameter estimates.	102
Table 7-22: Summary of the DGR3_501.95-532.69 testing activities.	104
Table 7-23: Summary of the DGR3_501.95-532.69 parameter estimates.	104
Table 7-24: Summary of the DGR3_532.49-563.23 testing activities.	106
Table 7-25: Summary of the DGR3_532.49-563.23 parameter estimates.	107
Table 7-26: Summary of the DGR3_563.03-593.77 testing activities.	109
Table 7-27: Summary of the DGR3_563.03-593.77 parameter estimates.	109
Table 7-28: Summary of the DGR3_593.57-624.31 testing activities.	111
Table 7-29: Summary of the DGR3_593.57-624.31 parameter estimates.	112
Table 7-30: Summary of the DGR3_617.63-648.37 testing activities.	114
Table 7-31: Summary of the DGR3_617.63-648.37 parameter estimates.	114
Table 7-32: Summary of the DGR3_628.00-658.74 testing activities.	116
Table 7-33: Summary of the DGR3_628.00-658.74 parameter estimates.	117
Table 7-34: Summary of the DGR3_654.65-685.39 testing activities.	119
Table 7-35: Summary of the DGR3_654.65-685.39 parameter estimates.	119
Table 7-36: Summary of the DGR3_671.50-702.24 testing activities.	121
Table 7-37: Summary of the DGR3_671.50-702.24 parameter estimates.	122
Table 7-38: Summary of the DGR3_710.00-740.74 testing activities.	124
Table 7-39: Summary of the DGR3_710.00-740.74 parameter estimates.	124
Table 7-40: Summary of the DGR3_740.54-771.28 testing activities.	126
Table 7-41: Summary of the DGR3_740.54-771.28 parameter estimates.	127
Table 7-42: Summary of the DGR3_765.96-796.70 testing activities.	129
Table 7-43: Summary of the DGR3_765.96-796.70 parameter estimates.	129
Table 7-44: Summary of the DGR3_790.93-821.67 testing activities.	131
Table 7-45: Summary of the DGR3_790.93-821.67 parameter estimates.	132
Table 7-46: Summary of the DGR3_815.00-845.74 testing activities.	134
Table 7-47: Summary of the DGR3_815.00-845.74 parameter estimates.	134
Table 7-48: Best-fit parameter estimates derived from the DGR-3 analyses.	137
Table 8-1: DGR-4 test zones and tests.	143
Table 8-2: Summary of the DGR4_190.63-221.37 testing activities.	144
Table 8-3: Summary of the DGR3_190.63-221.37 parameter estimates.	144
Table 8-4: Summary of the DGR4_218.13-248.87 testing activities.	146
Table 8-5: Summary of the DGR3_218.13-248.87 parameter estimates.	147
Table 8-6: Summary of the DGR4_247.00-277.74 testing activities.	149
Table 8-7: Summary of the DGR3_247.00-277.74 parameter estimates.	149
Table 8-8: Summary of the DGR4_261.63-292.37 testing activities.	151
Table 8-9: Summary of the DGR4_261.63-292.37 parameter estimates.	152
Table 8-10: Summary of the DGR4_284.26-315.00 testing activities.	154
Table 8-11: Summary of the DGR4_284.26-315.00 parameter estimates.	154
Table 8-12: Summary of the DGR4_296.63-327.37 testing activities.	156
Table 8-13: Summary of the DGR4_296.63-327.37 parameter estimates.	157
Table 8-14: Summary of the DGR4_327.26-358.00 testing activities.	159
Table 8-15: Summary of the DGR4_327.26-358.00 parameter estimates.	159
Table 8-16: Summary of the DGR4_350.53-381.27 testing activities.	161
Table 8-17: Summary of the DGR4_350.53-381.27 parameter estimates.	162
Table 8-18: Summary of the DGR4_381.08-411.82 testing activities.	164
Table 8-19: Summary of the DGR4_381.08-411.82 parameter estimates.	164
Table 8-20: Summary of the DGR4_411.51-442.25 testing activities.	166
Table 8-21: Summary of the DGR4_411.51-442.25 parameter estimates.	167
Table 8-22: Summary of the DGR4_432.00-462.74 testing activities.	169

Table 8-23: Summary of the DGR4_432.00-462.74 parameter estimates.	169
Table 8-24: Summary of the DGR4_458.23-488.97 testing activities.	171
Table 8-25: Summary of the DGR4_458.23-488.97 parameter estimates.	172
Table 8-26: Summary of the DGR4_488.77-519.51 testing activities.	174
Table 8-27: Summary of the DGR4_488.77-519.51 parameter estimates.	174
Table 8-28: Summary of the DGR4_519.10-549.84 testing activities.	176
Table 8-29: Summary of the DGR4_519.10-549.84 parameter estimates.	177
Table 8-30: Summary of the DGR4_548.28-579.02 (a) testing activities.	179
Table 8-31: Summary of the DGR4_548.28-579.02 (a) parameter estimates.	179
Table 8-32: Summary of the DGR4_548.28-579.02 (b) testing activities.	181
Table 8-33: Summary of the DGR4_548.28-579.02 (b) parameter estimates.	182
Table 8-34: Summary of the DGR4_577.45-608.19 testing activities.	184
Table 8-35: Summary of the DGR4_577.45-608.19 parameter estimates.	184
Table 8-36: Summary of the DGR4_607.79-638.53 testing activities.	186
Table 8-37: Summary of the DGR4_607.79-638.53 parameter estimates.	187
Table 8-38: Summary of the DGR4_638.34-669.08 testing activities.	189
Table 8-39: Summary of the DGR4_638.34-669.08 parameter estimates.	189
Table 8-40: Summary of the DGR4_658.46-689.20 testing activities.	191
Table 8-41: Summary of the DGR4_658.46-689.20 parameter estimates.	192
Table 8-42: Summary of the DGR4_687.78-718.52 testing activities.	194
Table 8-43: Summary of the DGR4_687.78-718.52 parameter estimates.	194
Table 8-44: Summary of the DGR4_717.10-747.84 testing activities.	196
Table 8-45: Summary of the DGR4_717.10-747.84 parameter estimates.	197
Table 8-46: Summary of the DGR4_747.64-778.38 testing activities.	199
Table 8-47: Summary of the DGR4_747.64-778.38 parameter estimates.	199
Table 8-48: Summary of the DGR4_762.80-793.54 testing activities.	201
Table 8-49: Summary of the DGR4_762.80-793.54 parameter estimates.	202
Table 8-50: Summary of the DGR4_793.34-824.08 testing activities.	204
Table 8-51: Summary of the DGR4_793.34-824.08 parameter estimates.	204
Table 8-52: Best-fit parameter estimates derived from the DGR-4 analyses.	207
Table 9-1: DGR-5 test zones and tests.	213
Table 9-2: Summary of the DGR5_477.87-508.13 testing activities.	214
Table 9-3: Summary of the DGR5_477.87-508.13 parameter estimates.	214
Table 9-4: Summary of the DGR5_507.87-538.13 testing activities.	216
Table 9-5: Summary of the DGR5_507.87-538.13 parameter estimates.	217
Table 9-6: Summary of the DGR5_537.87-568.13 testing activities.	219
Table 9-7: Summary of the DGR5_537.87-568.13 parameter estimates.	219
Table 9-8: Summary of the DGR5_567.87-598.13 testing activities.	221
Table 9-9: Summary of the DGR5_567.87-598.13 parameter estimates.	222
Table 9-10: Summary of the DGR5_597.87-628.13 testing activities.	224
Table 9-11: Summary of the DGR5_597.87-628.13 parameter estimates.	224
Table 9-12: Summary of the DGR5_627.87-658.13 testing activities.	226
Table 9-13: Summary of the DGR5_627.87-658.13 parameter estimates.	227
Table 9-14: Summary of the DGR5_657.87-688.13 testing activities.	229
Table 9-15: Summary of the DGR5_657.87-688.13 parameter estimates.	229
Table 9-16: Summary of the DGR5_681.07-711.33 testing activities.	231
Table 9-17: Summary of the DGR5_681.07-711.33 parameter estimates.	232
Table 9-18: Summary of the DGR5_702.24-737.50 testing activities.	234
Table 9-19: Summary of the DGR5_702.24-737.50 parameter estimates.	234
Table 9-20: Summary of the DGR5_737.25-767.51 testing activities.	236
Table 9-21: Summary of the DGR5_737.25-767.51 parameter estimates.	237
Table 9-22: Summary of the DGR5_767.25-797.51 testing activities.	239
Table 9-23: Summary of the DGR5_767.25-797.51 parameter estimates.	239
Table 9-24: Best-fit parameter estimates derived from the DGR-5 analyses.	242
Table 10-1: DGR-6 test zones and tests.	248
Table 10-2: Summary of the DGR6_518.00-528.23 testing activities.	249

Table 10-3: Summary of the DGR6_518.00-528.23 parameter estimates. 249
Table 10-4: Summary of the DGR6_650.00-660.23 testing activities. 251
Table 10-5: Summary of the DGR6_650.00-660.23 parameter estimates. 252
Table 10-6: Summary of the DGR6_678.00-688.23 testing activities. 254
Table 10-7: Summary of the DGR6_678.00-688.23 parameter estimates. 254
Table 10-8: Summary of the DGR6_700.00-710.23 testing activities. 256
Table 10-9: Summary of the DGR6_678.00-688.23 parameter estimates. 257
Table 10-10: Summary of the DGR6_725.00-735.23 testing activities. 259
Table 10-11: Summary of the DGR6_725.00-735.23 parameter estimates. 259
Table 10-12: Summary of the DGR6_737.00-747.23 testing activities. 261
Table 10-13: Summary of the DGR6_737.00-747.23 parameter estimates. 262
Table 10-14: Summary of the DGR6_764.00-774.23 testing activities. 264
Table 10-15: Summary of the DGR6_764.00-774.23 parameter estimates. 264
Table 10-16: Summary of the DGR6_782.00-792.23 testing activities. 266
Table 10-17: Summary of the DGR6_782.00-792.23 parameter estimates. 267
Table 10-18: Summary of the DGR6_797.00-807.23 testing activities. 269
Table 10-19: Summary of the DGR6_797.00-807.23 parameter estimates. 269
Table 10-20: Summary of the DGR6_841.00-851.23 testing activities. 271
Table 10-21: Summary of the DGR6_841.00-851.23 parameter estimates. 272
Table 10-22: Summary of the DGR6_869.77-880.00 testing activities. 274
Table 10-23: Summary of the DGR6_869.77-880.00 parameter estimates. 274
Table 10-24: Summary of the DGR6_880.00-890.23 testing activities. 276
Table 10-25: Summary of the DGR6_880.00-890.23 parameter estimates. 277
Table 10-26: Best-fit parameter estimates derived from the DGR-6 analyses 279
Table 11-1: Formation horizontal hydraulic conductivity estimates from all DGR borehole analyses. 286

LIST OF FIGURES

Figure 1-1: Reference stratigraphy and drilled depths of DGR-1 and DGR-2 at the Bruce nuclear site. 2
Figure 1-2: Location of DGR-1, DGR-2, DGR-3, DGR-4, DGR-5, and DGR-6 at the Bruce nuclear site. ... 4
Figure 2-1: Schematic of downhole equipment..... 8
Figure 3-1: DGR3_671.50-702.24 test interval and bottom zone response. 15
Figure 4-1: An X-Y-Z scatter plot showing the correlation among skin thickness, skin hydraulic conductivity, and specific storage that can occur in a single-well test. 21
Figure 4-2: Ramey B diagnostic plots showing various combinations of skin factors and formation specific storage. 22
Figure 5-1: Annotated DGR1_294.28-306.28 testing sequence showing best-fit simulation and parameter estimates. 26
Figure 5-2: XY-scatter plot showing estimates of formation hydraulic conductivity and raw static formation pressure derived from the DGR1_294.28-306.28 perturbation analysis. 26
Figure 5-3: DGR1_294.28-306.28 fit value cumulative distribution function. 27
Figure 5-4: Annotated DGR1_348.76-360.76 testing sequence showing best-fit simulation and parameter estimates. 28
Figure 5-5: XY-scatter plot showing estimates of formation hydraulic conductivity and raw static formation pressure derived from the DGR1_348.76-360.76 perturbation analysis. 29
Figure 5-6: DGR1_348.76-360.76 fit value cumulative distribution function. 29
Figure 5-7: Annotated DGR1_404.37-416.37 testing sequence showing best-fit simulation and parameter estimates. 31
Figure 5-8: XY-scatter plot showing estimates of formation hydraulic conductivity and raw static formation pressure derived from the DGR1_404.37-416.37 perturbation analysis. 31
Figure 5-9: DGR1_404.37-416.37 fit value cumulative distribution function. 32
Figure 6-1: Annotated DGR2_457.85-488.35 testing sequence showing best-fit simulation and parameter estimates. 35
Figure 6-2: XY-scatter plot showing estimates of formation hydraulic conductivity and raw static formation pressure derived from the DGR2_457.85-488.35 perturbation analysis. 35
Figure 6-3: DGR2_457.85-488.35 fit value cumulative distribution function. 36

Figure 6-4: Annotated DGR2_487.20-517.70 testing sequence showing best-fit simulation and parameter estimates. 37

Figure 6-5: XY-scatter plot showing estimates of formation hydraulic conductivity and raw static formation pressure derived from the DGR2_487.20-517.70 perturbation analysis. 38

Figure 6-6: DGR2_487.20-517.70 fit value cumulative distribution function. 38

Figure 6-7: Annotated DGR2_517.50-548.00 testing sequence showing best-fit simulation and parameter estimates. 40

Figure 6-8: XY-scatter plot showing estimates of formation hydraulic conductivity and raw static formation pressure derived from the DGR2_517.50-548.00 perturbation analysis. 40

Figure 6-9: DGR2_517.50-548.00 fit value cumulative distribution function. 41

Figure 6-10: Annotated DGR2_547.80-578.30 testing sequence showing best-fit simulation and parameter estimates. 42

Figure 6-11: XY-scatter plot showing estimates of formation hydraulic conductivity and raw static formation pressure derived from the DGR2_547.80-578.30 perturbation analysis. 43

Figure 6-12: DGR2_547.80-578.30 fit value cumulative distribution function. 43

Figure 6-13: Annotated DGR2_578.10-608.60 testing sequence showing best-fit simulation and parameter estimates. 45

Figure 6-14: XY-scatter plot showing estimates of formation hydraulic conductivity and raw static formation pressure derived from the 578.10-608.60 perturbation analysis. 45

Figure 6-15: DGR2_578.10-608.60 fit value cumulative distribution function. 46

Figure 6-16: Annotated DGR2_608.40-638.90 testing sequence showing best-fit simulation and parameter estimates. 47

Figure 6-17: XY-scatter plot showing estimates of formation hydraulic conductivity and raw static formation pressure derived from the 608.40-638.90 perturbation analysis. 48

Figure 6-18: DGR2_608.40-638.90 fit value cumulative distribution function. 48

Figure 6-19: Annotated DGR2_630.50-661.00 testing sequence showing best-fit simulation and parameter estimates. 50

Figure 6-20: XY-scatter plot showing estimates of formation hydraulic conductivity and raw static formation pressure derived from the 630.50-661.00 perturbation analysis. 50

Figure 6-21: DGR2_630.50-661.00 fit value cumulative distribution function. 51

Figure 6-22: Annotated DGR2_660.50-691.00 testing sequence showing best-fit simulation and parameter estimates. 52

Figure 6-23: XY-scatter plot showing estimates of formation hydraulic conductivity and raw static formation pressure derived from the 660.50-691.00 perturbation analysis. 53

Figure 6-24: DGR2_660.50-691.00 fit value cumulative distribution function. 53

Figure 6-25: Annotated DGR2_687.60-718.10 testing sequence showing best-fit simulation and parameter estimates. 55

Figure 6-26: XY-scatter plot showing estimates of formation hydraulic conductivity and raw static formation pressure derived from the 687.60-718.10 perturbation analysis. 55

Figure 6-27: DGR2_687.60-718.10 fit value cumulative distribution function. 56

Figure 6-28: Annotated DGR2_714.50-745.00 testing sequence showing best-fit simulation and parameter estimates. 57

Figure 6-29: XY-scatter plot showing estimates of formation hydraulic conductivity and raw static formation pressure derived from the 714.50-745.00 perturbation analysis. 58

Figure 6-30: DGR2_714.50-745.00 fit value cumulative distribution function. 58

Figure 6-31: Annotated DGR2_731.60-762.10 testing sequence showing best-fit simulation and parameter estimates. 60

Figure 6-32: XY-scatter plot showing estimates of formation hydraulic conductivity and raw static formation pressure derived from the 731.60-762.10 perturbation analysis. 60

Figure 6-33: DGR2_731.60-762.10 fit value cumulative distribution function. 61

Figure 6-34: Annotated DGR2_754.50-785.00 testing sequence showing best-fit simulation and parameter estimates. 62

Figure 6-35: XY-scatter plot showing estimates of formation hydraulic conductivity and raw static formation pressure derived from the 754.50-785.00 perturbation analysis. 63

Figure 6-36: DGR2_754.50-785.00 fit value cumulative distribution function. 63

Figure 6-37: Annotated DGR2_761.50-792.00 testing sequence showing best-fit simulation and parameter estimates..... 65

Figure 6-38: XY-scatter plot showing estimates of formation hydraulic conductivity and raw static formation pressure derived from the 761.50-792.00 perturbation analysis. 65

Figure 6-39: DGR2_761.50-792.00 fit value cumulative distribution function. 66

Figure 6-40: Annotated DGR2_785.00-815.50 testing sequence showing best-fit simulation and parameter estimates..... 67

Figure 6-41: XY-scatter plot showing estimates of formation hydraulic conductivity and raw static formation pressure derived from the 785.00-815.50 perturbation analysis. 68

Figure 6-42: DGR2_785.00-815.50 fit value cumulative distribution function. 68

Figure 6-43: Annotated DGR2_801.50-832.00 testing sequence showing best-fit simulation and parameter estimates..... 70

Figure 6-44: XY-scatter plot showing estimates of formation hydraulic conductivity and raw static formation pressure derived from the 801.50-832.00 perturbation analysis. 70

Figure 6-45: DGR2_801.50-832.00 fit value cumulative distribution function. 71

Figure 6-46: DGR-2 stratigraphic profile of horizontal hydraulic conductivity estimates. 73

Figure 6-47: DGR-2 stratigraphic profile of formation pressure estimates. 74

Figure 6-48: DGR-2 stratigraphic profile of specific storage estimates. 75

Figure 6-49: DGR-2 stratigraphic profile of skin factor estimates. 76

Figure 6-50: DGR-2 stratigraphic profile of test-zone compressibility estimates..... 77

Figure 7-1: Annotated DGR3_210.18-240.92 testing sequence showing best-fit simulation and parameter estimates. 80

Figure 7-2: XY-scatter plot showing estimates of formation hydraulic conductivity and raw static formation pressure derived from the DGR3_210.18-240.92 perturbation analysis. 80

Figure 7-3: DGR3_210.18-240.92 fit value cumulative distribution function. 81

Figure 7-4: Annotated DGR3_240.72-271.46 testing sequence showing best-fit simulation and parameter estimates. 82

Figure 7-5: XY-scatter plot showing estimates of formation hydraulic conductivity and raw static formation pressure derived from the DGR3_240.72-271.46 perturbation analysis. 83

Figure 7-6: DGR3_240.72-271.46 fit value cumulative distribution function. 83

Figure 7-7: Annotated DGR3_271.29-302.03 testing sequence showing best-fit simulation and parameter estimates. 85

Figure 7-8: XY-scatter plot showing estimates of formation hydraulic conductivity and raw static formation pressure derived from the DGR3_271.29-302.03 perturbation analysis. 85

Figure 7-9: DGR3_271.29-302.03 fit value cumulative distribution function. 86

Figure 7-10: Annotated DGR3_301.81-332.55 testing sequence showing best-fit simulation and parameter estimates..... 87

Figure 7-11: XY-scatter plot showing estimates of formation hydraulic conductivity and raw static formation pressure derived from the DGR3_301.81-332.55 perturbation analysis. 88

Figure 7-12: DGR3_301.81-332.55 fit value cumulative distribution function. 88

Figure 7-13: Annotated DGR3_334.99-365.73 testing sequence showing best-fit simulation and parameter estimates..... 90

Figure 7-14: XY-scatter plot showing estimates of formation hydraulic conductivity and raw static formation pressure derived from the DGR3_334.99-365.73 perturbation analysis. 90

Figure 7-15: DGR3_334.99-365.73 fit value cumulative distribution function. 91

Figure 7-16: Annotated DGR3_346.00-376.74 testing sequence showing best-fit simulation and parameter estimates..... 92

Figure 7-17: XY-scatter plot showing estimates of formation hydraulic conductivity and raw static formation pressure derived from the DGR3_346.00-376.74 perturbation analysis. 93

Figure 7-18: DGR3_346.00-376.74 fit value cumulative distribution function. 93

Figure 7-19: Annotated DGR3_379.98-410.72 testing sequence showing best-fit simulation and parameter estimates..... 95

Figure 7-20: XY-scatter plot showing estimates of formation hydraulic conductivity and raw static formation pressure derived from the DGR3_379.98-410.72 perturbation analysis. 95

Figure 7-21: DGR3_379.98-410.72 fit value cumulative distribution function. 96

Figure 7-22: Annotated DGR3_410.51-441.25 testing sequence showing best-fit simulation and parameter estimates..... 97

Figure 7-23: XY-scatter plot showing estimates of formation hydraulic conductivity and raw static formation pressure derived from the DGR3_410.51-441.25 perturbation analysis. 98

Figure 7-24: DGR3_410.51-441.25 fit value cumulative distribution function. 98

Figure 7-25: Annotated DGR3_441.05-471.79 testing sequence showing best-fit simulation and parameter estimates..... 100

Figure 7-26: XY-scatter plot showing estimates of formation hydraulic conductivity and raw static formation pressure derived from the DGR3_441.05-471.79 perturbation analysis. 100

Figure 7-27: DGR3_441.05-471.79 fit value cumulative distribution function. 101

Figure 7-28: Annotated DGR3_471.41-502.15 testing sequence showing best-fit simulation and parameter estimates..... 102

Figure 7-29: XY-scatter plot showing estimates of formation hydraulic conductivity and raw static formation pressure derived from the DGR3_471.41-502.15 perturbation analysis. 103

Figure 7-30: DGR3_471.41-502.15 fit value cumulative distribution function. 103

Figure 7-31: Annotated DGR3_501.95-532.69 testing sequence showing best-fit simulation and parameter estimates..... 105

Figure 7-32: XY-scatter plot showing estimates of formation hydraulic conductivity and raw static formation pressure derived from the DGR3_501.95-532.69 perturbation analysis. 105

Figure 7-33: DGR3_501.95-532.69 fit value cumulative distribution function. 106

Figure 7-34: Annotated DGR3_532.49-563.23 testing sequence showing best-fit simulation and parameter estimates..... 107

Figure 7-35: XY-scatter plot showing estimates of formation hydraulic conductivity and raw static formation pressure derived from the DGR3_532.49-563.23 perturbation analysis. 108

Figure 7-36: DGR3_532.49-563.23 fit value cumulative distribution function. 108

Figure 7-37: Annotated DGR3_563.03-593.77 testing sequence showing best fit simulation and parameter estimates..... 110

Figure 7-38: XY-scatter plot showing estimates of formation hydraulic conductivity and raw static formation pressure derived from the DGR3_563.03-593.77 perturbation analysis. 110

Figure 7-39: DGR3_563.03-593.77 fit value cumulative distribution function. 111

Figure 7-40: Annotated DGR3_593.57-624.31 testing sequence showing best-fit simulation and parameter estimates..... 112

Figure 7-41: XY-scatter plot showing estimates of formation hydraulic conductivity and raw static formation pressure derived from the DGR3_593.57-624.31 perturbation analysis. 113

Figure 7-42: DGR3_593.57-624.31 fit value cumulative distribution function. 113

Figure 7-43: Annotated DGR3_617.63-648.37 testing sequence showing best-fit simulation and parameter estimates..... 115

Figure 7-44: XY-scatter plot showing estimates of formation hydraulic conductivity and raw static formation pressure derived from the DGR3_617.63-648.37 perturbation analysis. 115

Figure 7-45: DGR3_617.63-648.37 fit value cumulative distribution function. 116

Figure 7-46: Annotated DGR3_628.00-658.74 testing sequence showing best-fit simulation and parameter estimates..... 117

Figure 7-47: XY-scatter plot showing estimates of formation hydraulic conductivity and raw static formation pressure derived from the DGR3_628.00-658.74 perturbation analysis. 118

Figure 7-48: DGR3_628.00-658.74 fit value cumulative distribution function. 118

Figure 7-49: Annotated DGR3_654.65-685.39 testing sequence showing best-fit simulation and parameter estimates..... 120

Figure 7-50: XY-scatter plot showing estimates of formation hydraulic conductivity and raw static formation pressure derived from the DGR3_654.65-685.39 perturbation analysis. 120

Figure 7-51: DGR3_654.65-685.39 fit value cumulative distribution function. 121

Figure 7-52: Annotated DGR3_671.50-702.24 testing sequence showing best-fit simulation and parameter estimates..... 122

Figure 7-53: XY-scatter plot showing estimates of formation hydraulic conductivity and raw static formation pressure derived from the DGR3_671.50-702.24 perturbation analysis. 123

Figure 7-54: DGR3_671.50-702.24 fit value cumulative distribution function. 123

Figure 7-55: Annotated DGR3_710.00-740.74 testing sequence showing best-fit simulation and parameter estimates..... 125

Figure 7-56: XY-scatter plot showing estimates of formation hydraulic conductivity and raw static formation pressure derived from the DGR3_710.00-740.74 perturbation analysis. 125

Figure 7-57: DGR3_710.00-740.74 fit value cumulative distribution function. 126

Figure 7-58: Annotated DGR3_740.54-771.28 testing sequence showing best-fit simulation and parameter estimates..... 127

Figure 7-59: XY-scatter plot showing estimates of formation hydraulic conductivity and raw static formation pressure derived from the DGR3_740.54-771.28 perturbation analysis. 128

Figure 7-60: DGR3_740.54-771.28 fit value cumulative distribution function. 128

Figure 7-61: Annotated DGR3_765.96-796.70 testing sequence showing best-fit simulation and parameter estimates..... 130

Figure 7-62: XY-scatter plot showing estimates of formation hydraulic conductivity and raw static formation pressure derived from the DGR3_765.96-796.70 perturbation analysis. 130

Figure 7-63: DGR3_765.96-796.70 fit value cumulative distribution function. 131

Figure 7-64: Annotated DGR3_790.93-821.67 testing sequence showing best-fit simulation and parameter estimates..... 132

Figure 7-65: XY-scatter plot showing estimates of formation hydraulic conductivity and raw static formation pressure derived from the DGR3_790.93-821.67 perturbation analysis. 133

Figure 7-66: DGR3_790.93-821.67 fit value cumulative distribution function. 133

Figure 7-67: Annotated DGR3_815.00-845.74 testing sequence showing best-fit simulation and parameter estimates..... 135

Figure 7-68: XY-scatter plot showing estimates of formation hydraulic conductivity and raw static formation pressure derived from the DGR3_815.00-845.74 perturbation analysis. 135

Figure 7-69: DGR3_815.00-845.74 fit value cumulative distribution function. 136

Figure 7-70: DGR-3 stratigraphic profile of horizontal hydraulic conductivity estimates. 138

Figure 7-71: DGR-3 stratigraphic profile of formation pressure estimates. 139

Figure 7-72: DGR-3 stratigraphic profile of specific storage estimates. 140

Figure 7-73: DGR-3 stratigraphic profile of skin factor estimates. 141

Figure 7-74: DGR-3 stratigraphic profile of test-zone compressibility estimates. 142

Figure 8-1: Annotated DGR4_190.63-221.37 testing sequence showing best-fit simulation and parameter estimates. 145

Figure 8-2: XY-scatter plot showing estimates of formation hydraulic conductivity and raw static formation pressure derived from the DGR4_190.63-221.37 perturbation analysis. 145

Figure 8-3: DGR4_190.63-221.37 fit value cumulative distribution function. 146

Figure 8-4: Annotated DGR4_218.13-248.87 testing sequence showing best-fit simulation and parameter estimates. 147

Figure 8-5: XY-scatter plot showing estimates of formation hydraulic conductivity and raw static formation pressure derived from the DGR4_218.13-248.87 perturbation analysis. 148

Figure 8-6: DGR4_218.13-248.87 fit value cumulative distribution function. 148

Figure 8-7: Annotated DGR4_247.00-277.74 testing sequence showing best-fit simulation and parameter estimates. 150

Figure 8-8: XY-scatter plot showing estimates of formation hydraulic conductivity and raw static formation pressure derived from the DGR4_247.00-277.74 perturbation analysis. 150

Figure 8-9: DGR4_247.00-277.74 fit value cumulative distribution function. 151

Figure 8-10: Annotated DGR4_261.63-292.37 testing sequence showing best-fit simulation and parameter estimates..... 152

Figure 8-11: XY-scatter plot showing estimates of formation hydraulic conductivity and raw static formation pressure derived from the DGR4_261.63-292.37 perturbation analysis. 153

Figure 8-12: DGR4_261.63-292.37 fit value cumulative distribution function. 153

Figure 8-13: Annotated DGR4_284.26-315.00 testing sequence showing best-fit simulation and parameter estimates..... 155

Figure 8-14: XY-scatter plot showing estimates of formation hydraulic conductivity and raw static formation pressure derived from the DGR4_284.26-315.00 perturbation analysis. 155

Figure 8-15: DGR4_284.26-315.00 fit value cumulative distribution function. 156

Figure 8-16: Annotated DGR4_296.63-327.37 testing sequence showing best-fit simulation and parameter estimates..... 157

Figure 8-17: XY-scatter plot showing estimates of formation hydraulic conductivity and raw static formation pressure derived from the DGR4_296.63-327.37 perturbation analysis. 158

Figure 8-18: DGR4_296.63-327.37 fit value cumulative distribution function. 158

Figure 8-19: Annotated DGR4_327.26-358.00 testing sequence showing best-fit simulation and parameter estimates..... 160

Figure 8-20: XY-scatter plot showing estimates of formation hydraulic conductivity and raw static formation pressure derived from the DGR4_327.26-358.00 perturbation analysis. 160

Figure 8-21: DGR4_327.26-358.00 fit value cumulative distribution function. 161

Figure 8-22: Annotated DGR4_350.53-381.27 testing sequence showing best-fit simulation and parameter estimates..... 162

Figure 8-23: XY-scatter plot showing estimates of formation hydraulic conductivity and raw static formation pressure derived from the DGR4_350.53-381.27 perturbation analysis. 163

Figure 8-24: DGR4_350.53-381.27 fit value cumulative distribution function. 163

Figure 8-25: Annotated DGR4_381.08-411.82 testing sequence showing best-fit simulation and parameter estimates..... 165

Figure 8-26: XY-scatter plot showing estimates of formation hydraulic conductivity and raw static formation pressure derived from the DGR4_381.08-411.82 perturbation analysis. 165

Figure 8-27: DGR4_381.08-411.82 fit value cumulative distribution function. 166

Figure 8-28: Annotated DGR4_411.51-442.25 testing sequence showing best-fit simulation and parameter estimates..... 167

Figure 8-29: XY-scatter plot showing estimates of formation hydraulic conductivity and raw static formation pressure derived from the DGR4_411.51-442.25 perturbation analysis. 168

Figure 8-30: DGR4_411.51-442.25 fit value cumulative distribution function. 168

Figure 8-31: Annotated DGR4_432.00-462.74 testing sequence showing best-fit simulation and parameter estimates..... 170

Figure 8-32: XY-scatter plot showing estimates of formation hydraulic conductivity and raw static formation pressure derived from the DGR4_432.00-462.74 perturbation analysis. 170

Figure 8-33: DGR4_432.00-462.74 fit value cumulative distribution function. 171

Figure 8-34: Annotated DGR4_458.23-488.97 testing sequence showing best-fit simulation and parameter estimates..... 172

Figure 8-35: XY-scatter plot showing estimates of formation hydraulic conductivity and raw static formation pressure derived from the DGR4_458.23-488.97 perturbation analysis. 173

Figure 8-36: DGR4_458.23-488.97 fit value cumulative distribution function. 173

Figure 8-37: Annotated DGR4_488.77-519.51 testing sequence showing best-fit simulation and parameter estimates..... 175

Figure 8-38: XY-scatter plot showing estimates of formation hydraulic conductivity and raw static formation pressure derived from the DGR4_488.77-519.51 perturbation analysis. 175

Figure 8-39: DGR4_488.77-519.51 fit value cumulative distribution function. 176

Figure 8-40: Annotated DGR4_519.10-549.84 testing sequence showing best-fit simulation and parameter estimates..... 177

Figure 8-41: XY-scatter plot showing estimates of formation hydraulic conductivity and raw static formation pressure derived from the DGR4_519.10-549.84 perturbation analysis. 178

Figure 8-42: DGR4_519.10-549.84 fit value cumulative distribution function. 178

Figure 8-43: Annotated DGR4_548.28-579.02 (a) testing sequence showing best-fit simulation and parameter estimates..... 180

Figure 8-44: XY-scatter plot showing estimates of formation hydraulic conductivity and raw static formation pressure derived from the DGR4_548.28-579.02 (a) perturbation analysis..... 180

Figure 8-45: DGR4_548.28-579.02 (a) fit value cumulative distribution function. 181

Figure 8-46: Annotated DGR4_548.28-579.02 (b) testing sequence showing best-fit simulation and parameter estimates..... 182

Figure 8-47: XY-scatter plot showing estimates of formation hydraulic conductivity and raw static formation pressure derived from the DGR4_548.28-579.02 (b) perturbation analysis..... 183

Figure 8-48: DGR4_548.28-579.02 (b) fit value cumulative distribution function. 183

Figure 8-49: Annotated DGR4_577.45-608.19 testing sequence showing best-fit simulation and parameter estimates..... 185

Figure 8-50: XY-scatter plot showing estimates of formation hydraulic conductivity and raw static formation pressure derived from the DGR4_577.45-608.19 perturbation analysis. 185

Figure 8-51: DGR4_577.45-608.19 fit value cumulative distribution function. 186

Figure 8-52: Annotated DGR4_607.79-638.53 testing sequence showing best-fit simulation and parameter estimates..... 187

Figure 8-53: XY-scatter plot showing estimates of formation hydraulic conductivity and raw static formation pressure derived from the DGR4_607.79-638.53 perturbation analysis. 188

Figure 8-54: DGR4_607.79-638.53 fit value cumulative distribution function. 188

Figure 8-55: Annotated DGR4_638.34-669.08 testing sequence showing best-fit simulation and parameter estimates..... 190

Figure 8-56: XY-scatter plot showing estimates of formation hydraulic conductivity and raw static formation pressure derived from the DGR4_638.34-669.08 perturbation analysis. 190

Figure 8-57: DGR4_638.34-669.08 fit value cumulative distribution function. 191

Figure 8-58: Annotated DGR4_658.46-689.20 testing sequence showing best-fit simulation and parameter estimates..... 192

Figure 8-59: XY-scatter plot showing estimates of formation hydraulic conductivity and raw static formation pressure derived from the DGR4_658.46-689.20 perturbation analysis. 193

Figure 8-60: DGR4_658.46-689.20 fit value cumulative distribution function. 193

Figure 8-61: Annotated DGR4_687.78-718.52 testing sequence showing best-fit simulation and parameter estimates..... 195

Figure 8-62: XY-scatter plot showing estimates of formation hydraulic conductivity and raw static formation pressure derived from the DGR4_687.78-718.52 perturbation analysis. 195

Figure 8-63: DGR4_687.78-718.52 fit value cumulative distribution function. 196

Figure 8-64: Annotated DGR4_717.10-747.84 testing sequence showing best-fit simulation and parameter estimates..... 197

Figure 8-65: XY-scatter plot showing estimates of formation hydraulic conductivity and raw static formation pressure derived from the DGR4_717.10-747.84 perturbation analysis. 198

Figure 8-66: DGR4_717.10-747.84 fit value cumulative distribution function. 198

Figure 8-67: Annotated DGR4_747.64-778.38 testing sequence showing best-fit simulation and parameter estimates..... 200

Figure 8-68: XY-scatter plot showing estimates of formation hydraulic conductivity and raw static formation pressure derived from the DGR4_747.64-778.38 perturbation analysis. 200

Figure 8-69: DGR4_747.64-778.38 fit value cumulative distribution function. 201

Figure 8-70: Annotated DGR4_762.80-793.54 testing sequence showing best-fit simulation and parameter estimates..... 202

Figure 8-71: XY-scatter plot showing estimates of formation hydraulic conductivity and raw static formation pressure derived from the DGR4_762.80-793.54 perturbation analysis. 203

Figure 8-72: DGR4_762.80-793.54 fit value cumulative distribution function. 203

Figure 8-73: Annotated DGR4_793.34-824.08 testing sequence showing best-fit simulation and parameter estimates..... 205

Figure 8-74: XY-scatter plot showing estimates of formation hydraulic conductivity and raw static formation pressure derived from the DGR4_793.34-824.08 perturbation analysis. 205

Figure 8-75: DGR4_793.34-824.08 fit value cumulative distribution function. Is this cool, or what 206

Figure 8-76: DGR-4 stratigraphic profile of horizontal hydraulic conductivity estimates. 208

Figure 8-77: DGR-4 stratigraphic profile of formation pressure estimates. 209

Figure 8-78: DGR-4 stratigraphic profile of specific storage estimates. 210

Figure 8-79: DGR-4 stratigraphic profile of skin factor estimates. 211

Figure 8-80: DGR-4 stratigraphic profile of test-zone compressibility estimates. 212

Figure 9-1: Annotated DGR5_477.87-508.13 testing sequence showing best-fit simulation and parameter estimates. 215

Figure 9-2: XY-scatter plot showing estimates of formation hydraulic conductivity and raw static formation pressure derived from the DGR5_477.87-508.13 perturbation analysis. 215

Figure 9-3: DGR5_477.87-508.13 fit value cumulative distribution function. 216

Figure 9-4: Annotated DGR5_507.87-538.13 testing sequence showing best-fit simulation and parameter estimates. 217

Figure 9-5: XY-scatter plot showing estimates of formation hydraulic conductivity and raw static formation pressure derived from the DGR5_507.87-538.13 perturbation analysis. 218

Figure 9-6: DGR5_507.87-538.13 fit value cumulative distribution function. 218

Figure 9-7: Annotated DGR5_537.87-568.13 testing sequence showing best-fit simulation and parameter estimates. 220

Figure 9-8: XY-scatter plot showing estimates of formation hydraulic conductivity and raw static formation pressure derived from the DGR5_537.87-568.13 perturbation analysis. 220

Figure 9-9: DGR5_537.87-568.13 fit value cumulative distribution function. 221

Figure 9-10: Annotated DGR5_567.87-598.13 testing sequence showing best-fit simulation and parameter estimates. 222

Figure 9-11: XY-scatter plot showing estimates of formation hydraulic conductivity and raw static formation pressure derived from the DGR5_567.87-598.13 perturbation analysis. 223

Figure 9-12: DGR5_567.87-598.13 fit value cumulative distribution function. 223

Figure 9-13: Annotated DGR5_597.87-628.13 testing sequence showing best-fit simulation and parameter estimates. 225

Figure 9-14: XY-scatter plot showing estimates of formation hydraulic conductivity and raw static formation pressure derived from the DGR5_597.87-628.13 perturbation analysis. 225

Figure 9-15: DGR5_597.87-628.13 fit value cumulative distribution function. 226

Figure 9-16: Annotated DGR5_627.87-658.13 testing sequence showing best-fit simulation and parameter estimates. 227

Figure 9-17: XY-scatter plot showing estimates of formation hydraulic conductivity and raw static formation pressure derived from the DGR5_627.87-658.13 perturbation analysis. 228

Figure 9-18: DGR5_627.87-658.13 fit value cumulative distribution function. 228

Figure 9-19: Annotated DGR5_657.87-688.13 testing sequence showing best-fit simulation and parameter estimates. 230

Figure 9-20: XY-scatter plot showing estimates of formation hydraulic conductivity and raw static formation pressure derived from the DGR5_657.87-688.13 perturbation analysis. 230

Figure 9-21: DGR5_657.87-688.13 fit value cumulative distribution function. 231

Figure 9-22: Annotated DGR5_681.07-711.33 testing sequence showing best-fit simulation and parameter estimates. 232

Figure 9-23: XY-scatter plot showing estimates of formation hydraulic conductivity and raw static formation pressure derived from the DGR5_681.07-711.33 perturbation analysis. 233

Figure 9-24: DGR5_681.07-711.33 fit value cumulative distribution function. 233

Figure 9-25: Annotated DGR5_707.24-737.50 testing sequence showing best-fit simulation and parameter estimates. 235

Figure 9-26: XY-scatter plot showing estimates of formation hydraulic conductivity and raw static formation pressure derived from the DGR5_707.24-737.50 perturbation analysis. 235

Figure 9-27: DGR5_707.24-737.50 fit value cumulative distribution function. 236

Figure 9-28: Annotated DGR5_737.25-767.51 testing sequence showing best-fit simulation and parameter estimates. 237

Figure 9-29: XY-scatter plot showing estimates of formation hydraulic conductivity and raw static formation pressure derived from the DGR5_737.25-767.51 perturbation analysis. 238

Figure 9-30: DGR5_737.25-767.51 fit value cumulative distribution function. 238

Figure 9-31: Annotated DGR5_767.25-797.51 testing sequence showing best-fit simulation and parameter estimates. 240

Figure 9-32: XY-scatter plot showing estimates of formation hydraulic conductivity and raw static formation pressure derived from the DGR5_767.25-797.51 perturbation analysis. 240

Figure 9-33: DGR5_767.25-797.51 fit value cumulative distribution function. 241

Figure 9-34: DGR-5 stratigraphic profile of horizontal hydraulic conductivity estimates. 243

Figure 9-35: DGR-5 stratigraphic profile of formation pressure estimates. 244

Figure 9-36: DGR-5 stratigraphic profile of specific storage estimates. 245

Figure 9-37: DGR-5 stratigraphic profile of skin factor estimates. 246

Figure 9-38: DGR-5 stratigraphic profile of test-zone compressibility estimates. 247

Figure 10-1: Annotated DGR6_518.00-528.23 testing sequence showing best-fit simulation and parameter estimates..... 250

Figure 10-2: XY-scatter plot showing estimates of formation hydraulic conductivity and raw static formation pressure derived from the DGR6_518.00-528.23 perturbation analysis. 250

Figure 10-3: DGR6_518.00-528.23 fit value cumulative distribution function. 251

Figure 10-4: Annotated DGR6_650.00-660.23 testing sequence showing best-fit simulation and parameter estimates..... 252

Figure 10-5: XY-scatter plot showing estimates of formation hydraulic conductivity and raw static formation pressure derived from the DGR6_650.00-660.23 perturbation analysis. 253

Figure 10-6: DGR6_650.00-660.23 fit value cumulative distribution function. 253

Figure 10-7: Annotated DGR6_678.00-688.23 testing sequence showing best-fit simulation and parameter estimates..... 255

Figure 10-8: XY-scatter plot showing estimates of formation hydraulic conductivity and raw static formation pressure derived from the DGR6_678.00-688.23 perturbation analysis. 255

Figure 10-9: DGR6_678.00-688.23 fit value cumulative distribution function. 256

Figure 10-10: Annotated DGR6_700.00-710.23 testing sequence showing best-fit simulation and parameter estimates..... 257

Figure 10-11: XY-scatter plot showing estimates of formation hydraulic conductivity and raw static formation pressure derived from the DGR6_700.00-710.23 perturbation analysis. 258

Figure 10-12: DGR6_700.00-710.23 fit value cumulative distribution function. 258

Figure 10-13: Annotated DGR6_725.00-735.23 testing sequence showing best-fit simulation and parameter estimates..... 260

Figure 10-14: XY-scatter plot showing estimates of formation hydraulic conductivity and raw static formation pressure derived from the DGR6_725.00-735.23 perturbation analysis. 260

Figure 10-15: DGR6_725.00-735.23 fit value cumulative distribution function. 261

Figure 10-16: Annotated DGR6_737.00-747.23 testing sequence showing best-fit simulation and parameter estimates..... 262

Figure 10-17: XY-scatter plot showing estimates of formation hydraulic conductivity and raw static formation pressure derived from the DGR6_737.00-747.23 perturbation analysis. 263

Figure 10-18: DGR6_737.00-747.23 fit value cumulative distribution function. 263

Figure 10-19: Annotated DGR6_764.00-774.23 testing sequence showing best-fit simulation and parameter estimates..... 265

Figure 10-20: XY-scatter plot showing estimates of formation hydraulic conductivity and raw static formation pressure derived from the DGR6_764.00-774.23 perturbation analysis. 265

Figure 10-21: DGR6_764.00-774.23 fit value cumulative distribution function. 266

Figure 10-22: Annotated DGR6_782.00-792.23 testing sequence showing best-fit simulation and parameter estimates..... 267

Figure 10-23: XY-scatter plot showing estimates of formation hydraulic conductivity and raw static formation pressure derived from the DGR6_782.00-792.23 perturbation analysis. 268

Figure 10-24: DGR6_782.00-792.23 fit value cumulative distribution function. 268

Figure 10-25: Annotated DGR6_797.00-807.23 testing sequence showing best-fit simulation and parameter estimates..... 270

Figure 10-26: XY-scatter plot showing estimates of formation hydraulic conductivity and raw static formation pressure derived from the DGR6_797.00-807.23 perturbation analysis. 270

Figure 10-27: DGR6_797.00-807.23 fit value cumulative distribution function. 271

Figure 10-28: Annotated DGR6_841.00-851.23 testing sequence showing best-fit simulation and parameter estimates..... 272

Figure 10-29: XY-scatter plot showing estimates of formation hydraulic conductivity and raw static formation pressure derived from the DGR6_841.00-851.23 perturbation analysis. 273

Figure 10-30: DGR6_841.00-851.23 fit value cumulative distribution function. 273

Figure 10-31: Annotated DGR6_869.77-880.00 testing sequence showing best-fit simulation and parameter estimates..... 275

Figure 10-32: XY-scatter plot showing estimates of formation hydraulic conductivity and raw static formation pressure derived from the DGR6_869.77-880.00 perturbation analysis. 275

Figure 10-33: DGR6_869.77-880.00 fit value cumulative distribution function. 276

Figure 10-34: Annotated DGR6_880.00-890.23 testing sequence showing best-fit simulation and parameter estimates.....	277
Figure 10-35: XY-scatter plot showing estimates of formation hydraulic conductivity and raw static formation pressure derived from the DGR6_880.00-890.23 perturbation analysis.	278
Figure 10-36: DGR6_880.00-890.23 fit value cumulative distribution function.	278
Figure 10-37: DGR-6 stratigraphic profile of horizontal hydraulic conductivity estimates.	280
Figure 10-38: DGR-6 stratigraphic profile of formation pressure estimates.	281
Figure 10-39: DGR-6 stratigraphic profile of specific storage estimates.	282
Figure 10-40: DGR-6 stratigraphic profile of skin factor estimates.	283
Figure 10-41: DGR-6 stratigraphic profile of test-zone compressibility estimates.....	284
Figure 11-1: Comparison of horizontal hydraulic conductivity estimates from DGR boreholes and formation estimates.	287
Figure 11-2: Comparison of fitted specific storage estimates from DGR boreholes.....	288
Figure 11-3: Comparison of test-zone compressibility estimates from DGR boreholes.....	289
Figure 11-4: Comparison of skin factor estimates from DGR boreholes.	290

1 Introduction

The activities described in this Technical Report (TR) constitute one component of the Intera Engineering Ltd. (note that Intera Engineering Ltd changed its name to Geofirma Engineering Ltd in January 2011) Geoscientific Site Characterization Plan (GSCP) for the proposed Deep Geologic Repository (DGR) at the Bruce nuclear site near Tiverton, Ontario, for long-term management of low- and intermediate-level radioactive waste. If approved, the DGR will be constructed at a depth of approximately 680 metres below ground surface (mBGS) in the argillaceous limestone of the Middle Ordovician Cobourg Formation (Figure 1-1).

An important component of the GSCP is the acquisition of in situ estimates of rock mass hydraulic conductivity (K) and other hydrogeologic formation properties including formation pressure (P_f) and specific storage (S_s). A straddle-packer hydraulic test program was designed to acquire representative formation properties in boreholes drilled at the Bruce nuclear site. This report presents the results of analyses performed upon test data collected during the field component of the program.

1.1 Background

The Phase 1 GSCP is described in Intera Engineering Ltd. (2006). Phase 1 work was primarily undertaken in 2007, and consisted of the drilling and testing of two adjacent (40-m separation) vertical boreholes, DGR-1 and DGR-2. DGR-1 was completed with an open bedrock interval from near the top of the Salina Formation F Unit shale (182.9 mBGS) to approximately 15 m into the top of the Queenston Formation (462.87 mBGS). DGR-1 was continuously diamond cored with a nominal diameter of 159 mm, with the upper 182.9 m reamed to accommodate installation of intermediate steel casing to prevent potential cross-contamination of the potable Devonian groundwater resources. DGR-2 was rotary drilled to a depth of 450.7 mBGS to accommodate installation of two intermediate steel casings. DGR-2 was then diamond cored with a nominal diameter of 159 mm and completed with an open bedrock interval from near the top of the Queenston Formation (450.88 mBGS) to approximately 1 m into the Precambrian basement (862.25 m BGS). TR-07-06 (Sterling, 2010) describes the rationale and completion of the drilling and casing of boreholes DGR-1 and DGR-2. Figure 1-1 shows the reference stratigraphy at the Bruce nuclear site and illustrates the drilled depths of DGR-1 and DGR-2. Table 5-1 lists the depths of the stratigraphic contacts in DGR-1 and DGR-2, as well as in the other deep DGR boreholes (Sterling and Melaney, 2011)

Phase 2 GSCP work in 2008 (Intera Engineering Ltd., 2008) consisted of the drilling of two additional boreholes, DGR-3 and DGR-4. Boreholes DGR-3 and DGR-4 were continuously diamond cored with a nominal diameter of 143 mm from bedrock surface to depths of 869.17 and 856.98 mBGS, respectively, into the Cambrian sandstone. The upper 208.5 m of DGR-3 and the upper 188.7 m of DGR-4 were reamed to accommodate installation of intermediate steel casing to the upper Salina F shale. TR-08-13 (Briscoe et al., 2010) describes the drilling and casing installation in boreholes DGR-3 and DGR-4. TR-09-01 (Sterling et al., 2011) describes the drilling and casing installation in boreholes DGR-5 and DGR-6.

Together, boreholes DGR-1/2, DGR-3, and DGR-4, which are spaced approximately 1047 to 1318 m from each other, triangulate the proposed DGR (Figure 1-1) and allow for assessment of the uniformity of bedrock formation thickness, orientation and properties in the vicinity of the DGR. Borehole stratigraphy and nomenclature of DGR boreholes 1 through 4 are described in TR-08-12 (Wigston and Heagle, 2009).

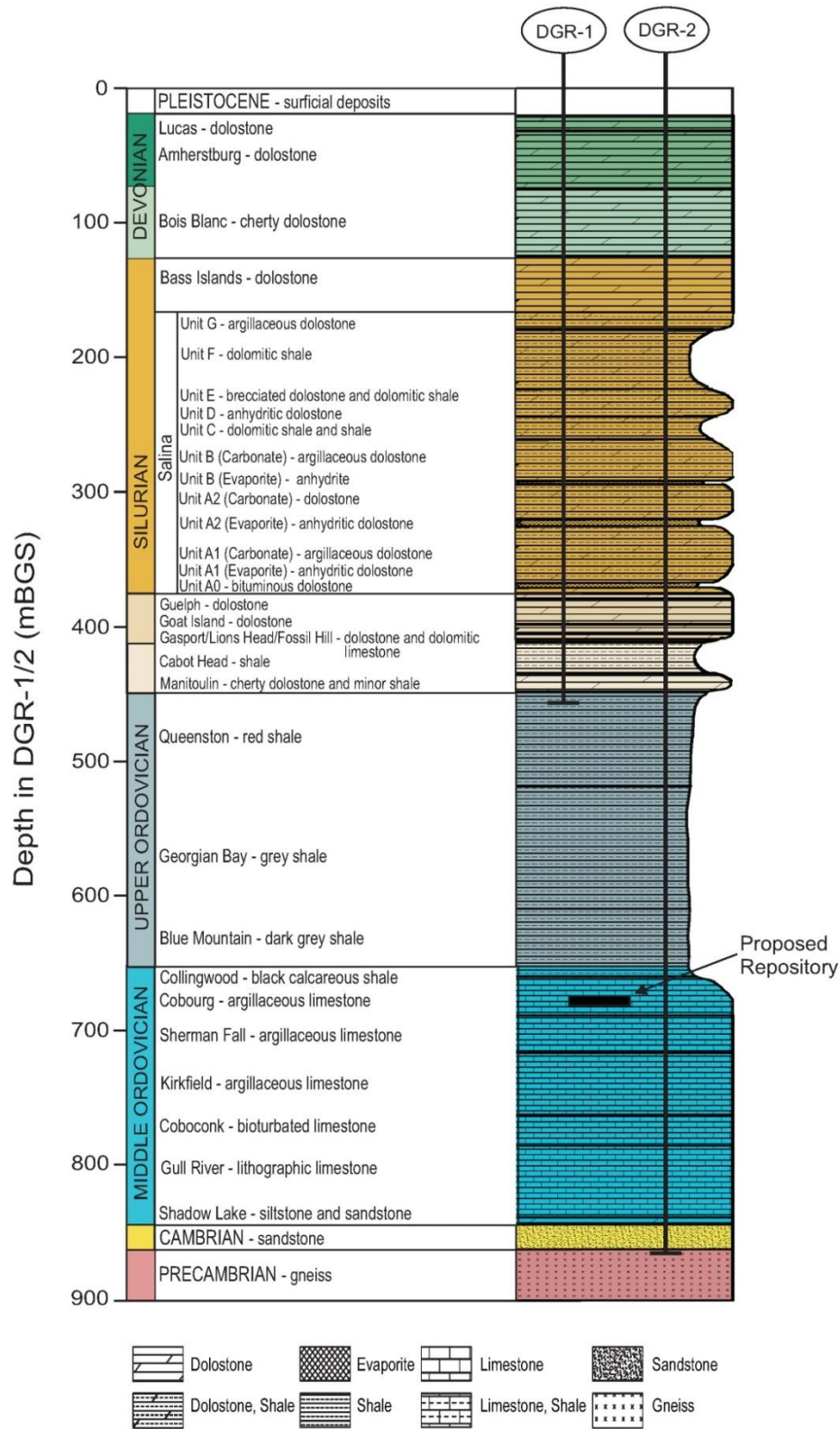


Figure 1-1: Reference stratigraphy and drilled depths of DGR-1 and DGR-2 at the Bruce nuclear site.

Table 1-1: Depths of stratigraphic contacts in DGR boreholes.

<i>Formation, Member, Unit</i>	<i>Top of Formation Length Along Borehole Axis (mLBGS)</i>				
	<i>DGR-1/2</i>	<i>DGR-3</i>	<i>DGR-4</i>	<i>DGR-5</i>	<i>DGR-6</i>
Lucas	20.0	7.9	7.5	22.2	16.9
Amherstburg	30.4	54.5	37.6	33.8	37.0
Bois Blanc	75.0	93.9	76.2	83.2	87.1
Bass Islands	124.0	143.3	126.0	134.8	142.3
Salina G Unit	169.3	187.3	170.1	184.0	193.0
Salina F Unit	178.6	196.5	177.4	192.5	203.0
Salina E Unit	223.0	239.6	221.0	235.2	249.1
Salina D Unit	243.0	263.4	245.5	256.2	268.9
Salina C Unit	244.6	266.0	247.3	257.3	270.0
Salina B Unit – Carbonate	260.3	277.9	262.0	271.2	308.5
Salina B Unit – Evaporite	291.2	303.0	290.8	315.5	333.0
Salina A2 Unit – Carbonate	293.1	304.6	292.5	319.0	337.7
Salina A2 Unit – Evaporite	319.7	333.5	320.9	349.4	367.5
Salina A1 Unit – Carbonate	325.5	338.6	326.1	355.5	371.8
Salina A1 Unit – Evaporite	367.0	379.8	366.8	400.4	418.0
Salina A0 Unit	370.5	384.2	371.8	405.0	423.0
Guelph	374.5	386.8	375.6	408.0	427.3
Goat Island	378.6	392.2	380.5	413.7	431.5
Gasport	397.4	410.5	399.1	433.0	452.2
Lions Head	404.2	417.0	405.6	442.8	461.0
Fossil Hill	408.7	421.5	410.0	445.3	465.0
Cabot Head	411.0	422.8	411.5	447.8	467.9
Manitoulin	434.8	447.5	435.7	473.0	493.6
Queenston	447.6	457.0	446.3	486.6	507.9
Georgian Bay	518.0	531.4	519.3	560.6	583.1
Blue Mountain	608.9	620.1	608.0	653.3	684.7
Collingwood Member	651.6	664.3	653.1	699.9	738.3
Cobourg	659.5	673.0	661.5	708.7	746.1
Sherman Fall	688.1	700.8	689.0	736.5	780.2
Kirkfield	716.1	729.8	717.3	766.5	814.7
Coboconk	762.0	775.6	763.0	-	870.5
Gull River	785.0	799.3	786.8	-	897.2
Shadow Lake	838.6	851.0	839.0	-	-
Cambrian	843.8	855.5	844.1	-	-
Precambrian	860.7	-	-	-	-

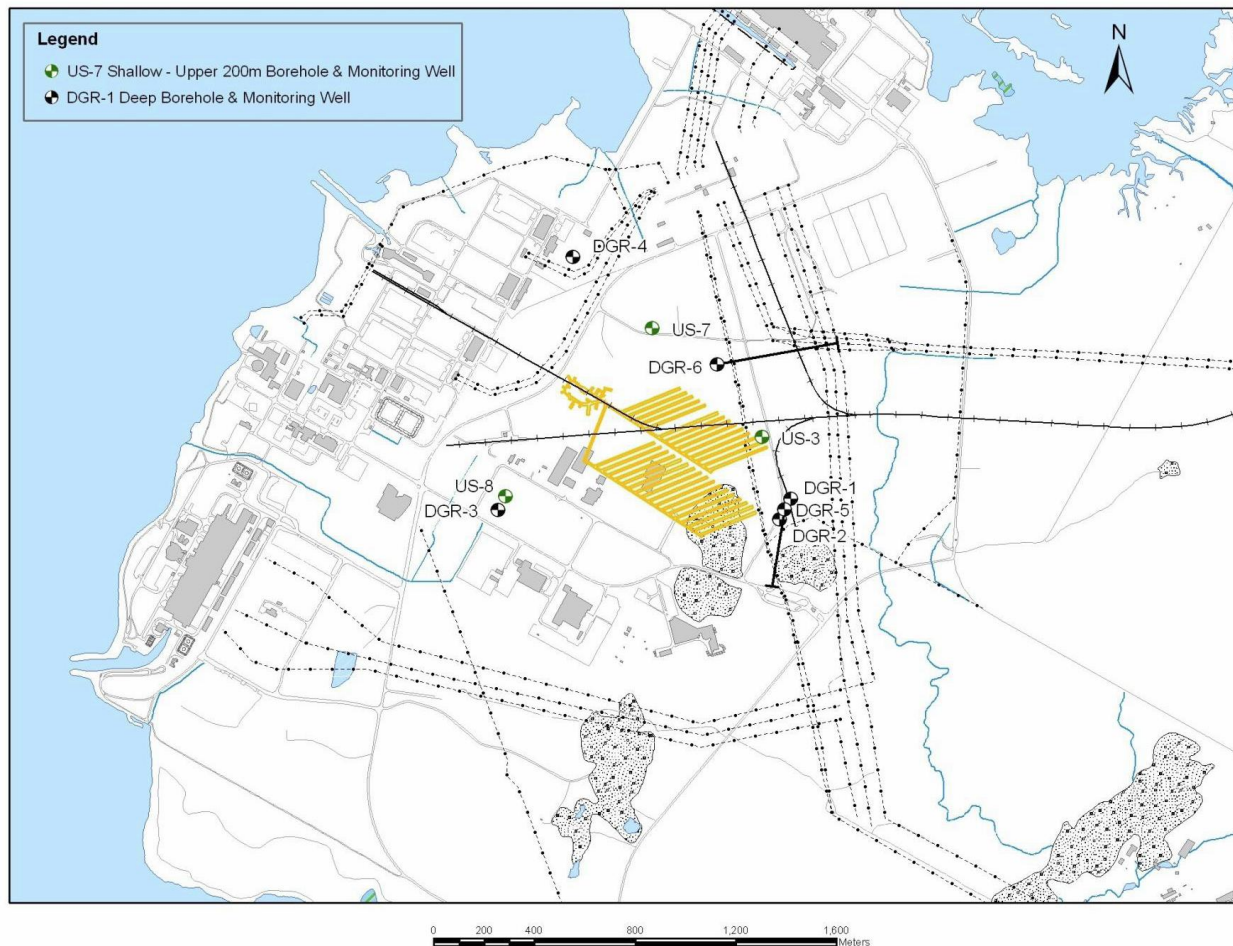


Figure 1-2: Location of DGR-1, DGR-2, DGR-3, DGR-4, DGR-5, and DGR-6 at the Bruce nuclear site.

Boreholes DGR-5 and DGR-6 are inclined boreholes drilled as part of GSCP Phase 2B work in 2009 and 2010 to investigate possible faults identified from seismic surveys, and general vertical structure and permeability within the DGR bedrock. To ensure adequate sampling of possible vertical structure, boreholes DGR-5 and DGR-6 were drilled in approximate orthogonal directions away from the proposed DGR footprint. Borehole DGR-5 was rotary drilled to 188.2 metres length below ground surface (mLBGS) to allow for installation of intermediate steel casing, and then continuously cored to a target depth of 807.15 mLBGS within the bottom of the Kirkfield Formation. Starting and final azimuth/plunge of DGR-5 were 190°/65° and 201°/78°, respectively. Borehole DGR-6 was rotary drilled to 214.8 mLBGS to allow for installation of intermediate steel casing, and then continuously cored to a target depth of 903.16 mLBGS within the top of the Gull River Formation. Starting and final azimuth/plunge of DGR-6 were 80°/60° and 73°/57°, respectively. The completed open hole diameters of both DGR-5 and DGR-6 were nominally 143 mm. TR-09-01 (Sterling et al., 2011) describes the drilling and casing installation in boreholes DGR-5 and DGR-6.

1.2 Hydraulic Testing Activities

Straddle-packer hydraulic testing of boreholes DGR-1 and DGR-2 was specified in the Phase 1 GSCP. A custom test tool and support trailer with a data-acquisition system was developed to address the unique requirements of low-permeability testing in deep boreholes. The test equipment was designed and

constructed by Sandia National Laboratories staff and drew upon many years of experience in testing of low-permeability strata at the Waste Isolation Pilot Plant (WIPP) site in southeastern New Mexico.

The key components of the test tool are two inflatable packers to isolate a test interval within a borehole, a downhole shut-in valve that connects or isolates the test interval from the tubing on which the test tool is suspended in the hole, a hydraulic piston that can be extended or retracted to cause a pressure increase or decrease in the test interval, and pressure transducers that measure the pressure in the test interval, in the bottom of the hole below the lower packer, in the tubing string above the test tool, and in the annulus between the tubing and borehole wall above the upper packer.

DGR-1 and DGR-2 testing was carried out during the summer and fall of 2007 over 11 intervals in DGR-1 (12-m test zone length) and 14 intervals in DGR-2 (28.1-m test zone length). DGR-1 testing was not intended to provide complete formation coverage. These tests were performed under control of test plan TP-06-14 (Beauheim, 2007). Preliminary analyses of these tests indicated relatively low-permeability formations with estimated average hydraulic conductivities of between 10^{-12} and 10^{-11} m/s throughout the Ordovician formations. Additionally, formation pressures were estimated at values consistent with near hydrostatic conditions.

Subsequently, Westbay casing was installed in DGR-2 and a long-term pressure measurement program undertaken. Preliminary results from the Westbay measurements indicated significant underpressures throughout the Ordovician formations.

The straddle-packer test equipment design was refined for Phase 2 work in winter 2008 based on operational experience gained during Phase 1. Testing procedures were also optimized to include additional quality assurance procedures.

Phase 2 hydraulic testing of DGR-3 and DGR-4 was performed from September 2008 through February 2009. This testing was performed according to test plan TP-08-16 (Beauheim, 2008). Twenty-three intervals (30.74-m test zone) in DGR-3 and 24 intervals (30.74-m test zone) in DGR-4 were tested. Preliminary analyses of DGR-3 and DGR-4 tests indicated much lower permeabilities through portions of the Silurian formations and through all Ordovician intervals than had been found during Phase 1 testing. Additionally, the estimated formation pressures in the Ordovician formations were consistent with Westbay-measured pressures from DGR-2.

The inconsistencies in test responses between DGR-2 and DGR-3/ DGR-4 were assessed (Avis and Beauheim, 2009) and the determination made that Phase 1 test results in DGR-2 were systematically compromised by a very small equipment leak, which obscured formation responses in rocks with hydraulic conductivity lower than approximately 10^{-12} m/s. The source and/or location of the leak was unknown and could not be determined. The same assessment was unable to determine if there were similar problems with Phase 1 DGR-1 testing.

Retesting DGR-2 formations with the improved test tool and procedures was recommended as the best approach to resolving the inconsistencies. This testing was undertaken in summer 2009, following test plan TP-09-06 (Beauheim, 2009). Fifteen intervals were tested using a 30.50-m straddle interval.

Phase 2B hydraulic testing of DGR-5 and DGR-6 was performed from February to June 2010. This testing was performed following test plan TP-09-04 (Beauheim, 2010). Eleven intervals (30.26-m test zone) in DGR-5 and 12 intervals (10.23-m test zone) in DGR-6 were tested. The testing in DGR-5 provided continuous coverage of the Ordovician shale and limestone. DGR-6 testing targeted fractured

or suspected permeable intervals and unfractured or tight intervals within the Ordovician shales and limestones with shorter test interval lengths than were used in DGR-2, DGR-3, DGR-4, and DGR-5.

1.3 Reported Analyses

This report summarizes the analyses of Phase 2 straddle-packer hydraulic testing performed in boreholes DGR-2, DGR-3, DGR-4, DGR-5, and DGR-6. Additionally, several Phase 1 DGR-1 tests have been selected for analysis where the shorter straddle interval resulted in greater resolution of properties of thinner formations than are available from DGR-3 and DGR-4 test intervals.

2 Equipment

Low-permeability testing is subject to non-ideal testing conditions that can have significant impact on testing results and suitability of results for analysis. The uncertainty associated with these conditions was minimized through effective equipment design for the DGR testing. The testing equipment used on this program was based on equipment designed to test low-permeability strata at the Waste Isolation Pilot Plant (WIPP) site in New Mexico. Improvements to equipment and test methodology were also made between each phase of activities in the current program.

The majority of tests performed in the DGR boreholes were pulse tests. The pressure response observed during a pulse test is directly proportional to the wellbore storage coefficient of the test interval. The wellbore storage coefficient has two components: the volume of fluid contained within the test zone (V_{tz}) and the compressibility of all the materials within or in contact with the test zone (C_{tz}). V_{tz} includes the volume of fluid between the packers, within any tubing or equipment components below the shut-in valve, and within the feedthrough line connected to the test-zone transducer. C_{tz} is a composite compressibility that includes contributions from the test equipment, the borehole fluid, and the geomechanical response of the borehole wall. To minimize the time required to complete a pulse test, the DGR equipment was carefully designed and selected to minimize both V_{tz} and C_{tz} . During the DGR borehole testing, V_{tz} ranged from 0.17 m³ (DGR-6) to 0.62 m³ (DGR-2). C_{tz} was minimized through use of extremely stiff packers and strong interconnecting components. Most tool feedthroughs and connections were custom-machined stainless steel components.

During pulse tests in low-permeability formations, variations in packer pressures can cause perceptible changes in test-zone pressure that can mask the actual formation response. To minimize variations in packer pressures, pressure accumulators were hydraulically connected to the packers during the DGR testing. Accumulators were hydraulically connected to the shut-in valve and the pulse piston as well.

Another important equipment design feature was to provide remote access to the test data in real time. This allowed for off-site supervision of testing and for continuous monitoring of the test response. Remote access also allowed for near real-time preliminary test analyses. Test supervisors and analysts at remote locations could consult with on-site staff to modify the testing approach if required.

The testing equipment consisted of downhole and surface components. The downhole equipment was connected to surface with four stainless steel hydraulic lines (packer inflate/deflate, piston extend, piston retract, shut-in valve close) and an armoured umbilical cable with transducer power and communication lines. The hydraulic lines and umbilical cable were clamped to the outside of a 2-3/8 inch tubing string that provided the overall mechanical connection between the service rig at surface and the downhole tool.

2.1 Downhole Equipment

The downhole equipment consisted of two inflatable packers, a downhole shut-in valve, a piston-pulse tool, a slotted section, a sediment trap, sensor carriers, and miscellaneous subs and feedthroughs to connect the various pieces (Figure 2-1). Note that the test-zone interval shown in Figure 2-1 is not drawn to scale. The length of the test zone was determined for each of the DGR boreholes based on the testing objectives, and varied from a minimum of 10.23 m to a maximum of 30.74 m. Numerous centralizers were included between tool elements and throughout the tubing string to reduce abrasion as the tool and tubing slid along the boreholes.

The test tool was assembled from individual components as it was lowered into the borehole. An extensive gas and liquid pressure testing program was conducted during tool assembly to eliminate leaks, which can mask the actual hydraulic response of a formation being tested. A final leak test of the fully assembled tool was performed by conducting a pulse test within the surface conductor casing. Note that any undetected leaks within the test equipment would lead to overestimates of hydraulic conductivity.

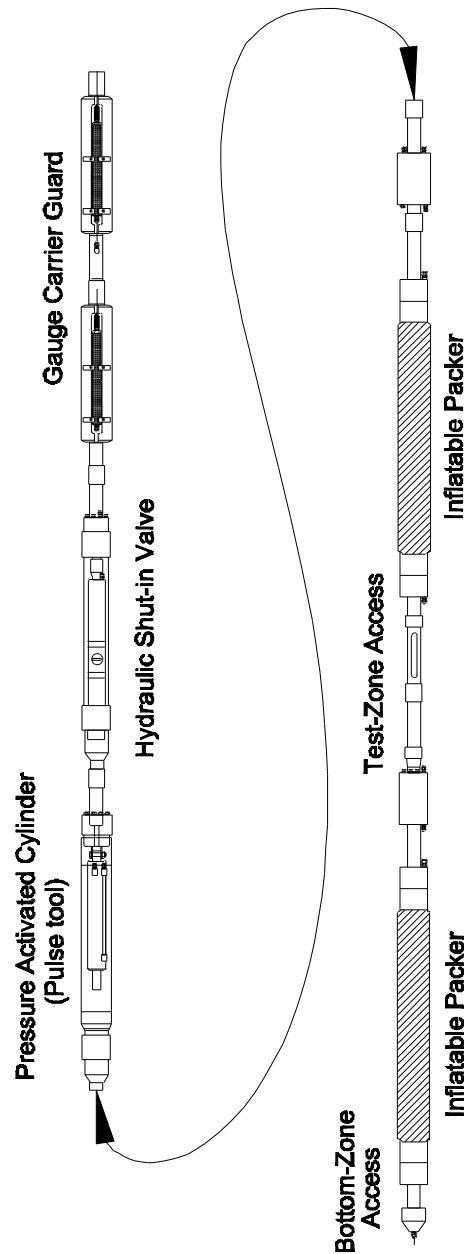


Figure 2-1: Schematic of downhole equipment.

2.1.1 Packers

TAM International 4.25-inch (10.8-cm) external-inflate sliding-end packers were used in the straddle tool for the Phase 1 testing of DGR-1 and DGR-2. The packers had an uninflated diameter of 108 mm and an element length of 1.83 m, providing a seal length of approximately 1.68 m in a 152-mm-diameter hole.

For Phase 2 testing of boreholes DGR-2, DGR-3, DGR-4, DGR-5, and DGR-6, Baski 4.75-inch (12.1-cm) external-inflate sliding-end Fracker packers were used in the straddle tool. The packers had an uninflated diameter of 121 mm and an element length of 1.15 m, providing a seal length of approximately 1.0 m in a 143-mm-diameter hole. All of the packers used were capable of withstanding differential pressures of up to 20.7 MPa. The packers and packer-inflation line were filled with fluid and inflated using a single ¼-inch stainless steel line by pressurizing a fluid reservoir at the surface with compressed nitrogen to 16 to 17 MPa. The packers were oriented so that their fixed ends were up and their sliding ends were down to avoid putting their inflation lines in tension.

2.1.2 Shut-In Tool

A downhole shut-in tool was used to control the connection between the interior of the tubing string above the straddle tool and the test zone between the inflatable packers. The downhole shut-in tool consisted of a Hydraulic Downhole Shut-in Valve (H-DHSIV) manufactured by Inflatable Packers International Pty. Ltd. of Australia. The H-DHSIV used a piston-actuated ball valve to open and close the tool. The valve was set up in a normally open position and hydraulic pressure was applied to push an annular piston down, rotating the ball 90° and closing the valve. A spring pushed the piston up, opening the valve, when the hydraulic pressure was relieved. The ball had a 1.27-cm-diameter opening, and caused no displacement in the test interval when it was actuated.

2.1.3 Sediment Trap

A sediment trap was located between the shut-in valve and the tubing string. The trap was a simple arrangement of tubes that allowed sediment or corrosion particles to settle at the bottom of the tubing string, while preventing particles from entering and potentially fouling the shut-in valve.

2.1.4 Sensor Carriers

The Paroscientific transducers (see Section 1.1.8) used to monitor pressures were mounted in double-pocket sensor carriers that threaded into the tubing string above the packers and enclosed and protected the transducers in the borehole. The double-pocket carriers accommodated two transducers and had an inside diameter of 1.27 cm.

2.1.5 Piston Pulse Generator

For pulse-testing applications, a pressure pulse was created by displacing a known volume of the test zone using a hydraulically actuated piston. The piston used for testing in DGR-1 had a displacement of ~97 cm³, the piston used in DGR-2, DGR-3, DGR-4, and DGR-5 had a displacement of ~164 cm³, and a piston with a displacement of ~48 cm³ was used in DGR-6. These pistons typically produced pulses of 500 to 900 kPa, depending on interval compressibility.

2.1.6 Slotted Section

One section of the tool string between the straddle packers had to allow flow from the straddled test zone into the tool string. A slotted 0.73-ft-long (0.225-m-long) pup joint of 2.5625-inch tubing was used for this purpose.

2.1.7 Centralizers

Centralizers made of ultra high molecular weight polyethylene (UHMWPE) were used to protect the tool components and tubing string from abrasion while running in and out of the slanted DGR-5 and DGR-6 boreholes. The centralizers had multiple fins running lengthwise that held the tool away from the borehole wall. All of the sensor and hydraulic lines were secured in grooves between the fins to keep them from rubbing against the borehole wall or being crushed. Centralizers were placed between major tool components, on every tubing coupling, and in the middle of each tubing joint.

2.1.8 Pressure Transducers

Paroscientific Series 8CB High Pressure Intelligent Depth Sensors, Model 8CB1400-I, were used to monitor pressures in two or three of the zones isolated during hydraulic tests. These transducers have a 0-1400 metres of water range of operation, which corresponds to approximately 0-14000 kPa. They have an accuracy of 0.01% of full scale (approximately 1.4 kPa). The transducers were housed in sensor carriers (described above) positioned above the top packer in the tool string. For the normal straddle-packer tool configuration, one transducer was ported to the interval below the bottom straddle packer, one transducer was ported to the test zone between the packers, and a third transducer was ported to the tubing above the shut-in valve. In DGR-3, the third Paroscientific transducer was not used, and in DGR-4, the third Paroscientific transducer was ported to the annulus between the tubing and borehole wall above the upper packer. These pressure transducers were monitored with the DAS (Section 1.2.3), which recorded the pressure value with time stamp and gauge ID. The conversion from a frequency response at the gauge sensor to an engineering unit was done within the Paroscientific gauge. The Paroscientific transducers were calibrated by Paroscientific, Inc.

In-Situ Level TROLL[®] 700 transducers with a 0 to 100 psia (0 to 689.476 kPa absolute) pressure range were used to monitor the pressure in the annulus between the tubing and borehole wall above the upper packer in DGR-1, DGR-2, and DGR-3, and in the tubing above the shut-in valve in DGR-3 and DGR-4. The Level TROLLs were lowered only a few metres below the surface of the water to avoid tangling with the cables and lines running to the test tool. Level TROLLs could not be deployed in the annulus of the slanted DGR-5 and DGR-6 boreholes. The Level TROLLs were monitored with the DAS (Section 1.2.3), which recorded the pressure values with time stamps and gauge IDs.

2.1.9 Temperature Loggers

The Paroscientific transducers described in Section 1.1.8 also measure temperature, which could be monitored and recorded by the DAS. However, the Paroscientific transducers were above the upper packer and could not, therefore, measure the temperature in the test zone or below the bottom packer. HOBO U12 Stainless Temperature Loggers were placed in the test zone and, in DGR-1, below the bottom packer to monitor temperatures in those intervals. The HOBO loggers were not connected to the DAS, but stored all data internally and were downloaded when the test tool was brought to the surface.

2.2 Surface Equipment

With the exception of reels for the stainless steel hydraulic lines and the umbilical cable for the Paroscientific transducers, all surface equipment was contained within a Mobile Integrated Aquifer Testing and Analysis (MIATA) laboratory designed and constructed by HydroResolutions, LLC. The temperature-controlled MIATA laboratory was enclosed in a customized trailer and was subdivided in two sections: a front section with office, computer, and DAS equipment; and a back section with workbench,

intensifier pumps, and hydraulic line control panel. The surface equipment consisted of a barometer, pressure-maintenance systems, pressure transducers, and the DAS.

2.2.1 Barometer

Barometric pressure was monitored during all hydraulic tests using an Omega PX02K1-16AI-MB electronic barometer. The Omega barometer can measure barometric pressure within a range from 54.2 to 108.4 kPa. The 4-20 mA output of the barometer was monitored by the DAS.

2.2.2 Pressure-Maintenance Systems

If packer-inflation pressure or the hydraulic pressure exerted on the shut-in valve or pulse piston generator changes during a test, the associated change in packer or tool volume will cause a change in the isolated test-zone pressure. The main cause of packer, shut-in valve, and pulse piston generator pressure changes is the daily temperature variations to which their supply reels of stainless steel tubing are subjected: as the reels warm, the internal pressure rises, and as the reels cool, the internal pressure falls. Two pressure-maintenance systems were used to minimize these pressure changes. The pressure-maintenance systems consisted of 2-gallon pressure vessels containing inflatable bladders. The bladders were filled with non-toxic plumbers antifreeze and attached to the hydraulic line(s) of interest. The rest of the pressure vessels were attached to a high-pressure nitrogen source and pressurized to the desired maintenance pressure. As the pressure in the packers and/or hydraulic lines changed as a function of temperature (or as a result of testing activities), fluid moved into or out of the bladder to maintain pressure equilibrium with the surrounding nitrogen. This served to dampen, but not eliminate, the pressure fluctuations in the packers or hydraulic lines and the associated effect on the test-zone pressure.

2.2.3 Pressure Transducers

All hydraulic line pressures, including the packer-inflation pressures, were monitored with Omega Model PX319-3KGI pressure transducers with an operating range of 0-3000 psig (~0-20.7 MPag). The Omega transducers have a 4-20 mA output that was monitored by the DAS.

2.2.4 Data-Acquisition System

The DAS used for the straddle-packer hydraulic testing consisted of an Ethernet I/O server for analog gauges (Omega transducers and barometer) and controls (hydraulic piston), an RS-485 to Ethernet serial device server to communicate with the Paroscientific gauges, an Ethernet switch to connect the servers to the DAS computer, power supplies, and a computer system. All components were off-the-shelf procurements. The Ethernet I/O server was a MOXA ioLogik E2240 with eight analog inputs, two analog outputs, and an LDP1602 LCD module. The RS-485 to Ethernet serial device server was a MOXA NPort 5232. The Ethernet switch was an Atop model EH2006. Allen-Bradley 1606-XLP50E 24V and 1606-XLP50B 12-15V single-phase power supplies provided power to the servers, switch, and Paroscientific gauges.

The primary DAS computer system consisted of a Systemax VLS 1U Hot Swap RAID Server with an Intel Pentium Dual Core E2200 2.2-GHz processor and 1 GB of RAM running Windows XP (Service Pack 2). Data were mirrored onto a Systemax 1U Short Depth Server with an Intel Pentium Dual Core E2200 2.2-GHz processor and 2 GB of RAM for remote real-time access to the data over the internet.

The DAS software consisted of a client application programmed in Borland C++ Builder. The client application stored and retrieved data from a mySQL database. The database was replicated on the remote access server. A human-machine interface (HMI) developed in Borland C++ Builder provided an integrated graphical user interface to the DAS functions and the Paroscientific gauge package. The DAS HMI software displayed the status of all parameters including the valve state, zone pressures, packer pressures, polling frequency, test start time, and test duration. The HMI also provided real-time plotting of any parameter being measured.

3 Testing Methodology

The straddle-packer hydraulic testing in the DGR boreholes was governed by Test Plans (Beauheim, 2007, 2008, 2009, 2010) prepared in accordance with the Intera Engineering Project Quality Plan (Intera Engineering Ltd., 2009). The Test Plans were developed and reviewed before work was started and described testing procedures and associated records to be maintained. They were flexible and could be modified during testing to meet unforeseen eventualities. The Test Plans included a description of Quality Assurance (QA) procedures to be performed before testing commenced. These included leak testing of all tool components as the tool was assembled over the borehole, as well as one or more pulse tests conducted within the steel casing in the upper sections of the borehole to check for leaks in the fully assembled test tool.

Because of the low permeabilities of most of the Silurian and Ordovician strata to be tested, pulse tests were planned for most of the test intervals. Slug tests were performed in higher permeability units such as the Guelph Formation, and drillstem tests (DSTs) were performed in a few intervals found to have intermediate permeability. With few exceptions, two pulse (or other) tests were performed in each interval.

The procedure for pulse testing in each interval was as follows:

- The test tool was lowered into the well on 2.375-inch tubing to its desired position with respect to the interval to be tested. Cable protectors were placed on each tubing coupling as the tool went downhole.
- Once the tool was at the desired depth, all transducers were connected to the DAS and data acquisition was initiated. The shut-in valve was maintained in an open position while the packers were inflated. The packers were inflated to a pressure between 14 and 17 MPa (measured at ground surface).
- The next steps varied depending on the test-zone pressure that was expected based on anticipated formation pressures or, for testing in the later boreholes, pressures measured by the Westbay installations in the earlier boreholes. In most intervals, the test-zone pressure was expected to be below hydrostatic, so the pulse piston was extended to allow testing to begin with a pulse withdrawal. The pressure in the Coboconk and Gull River was expected to be at or greater than hydrostatic, so the pulse piston was left in its retracted position to allow testing to begin with a pulse injection.
- After the pulse piston was in the desired position, the shut-in valve was closed. The test-zone pressure then began to change relative to the annulus pressure (which might change slowly) and the tubing pressure (which should be constant) as the test-zone pressure equilibrated with the pressure of the interval to be tested. The bottomhole pressure typically showed a pressure increase during packer inflation, and then either increased or decreased depending on the natural formation pressure in the interval isolated.
- If the test-zone pressure was expected to be at or below hydrostatic, enough water was swabbed or air-lifted from the tubing to lower the tubing pressure, which should have been similar to the annulus pressure, by ~500 kPa. This provided evidence that the shut-in valve was not leaking during a pulse test. If the test-zone pressure was expected to be above hydrostatic, the tubing was either left as it was or swabbed (or air-lifted). The system was then left to stabilize overnight.
- The next morning, the Test Leader determined either that the test-zone equilibration trend was well-enough defined to allow testing to begin, or that additional equilibration time was required. Once the Test Leader determined that testing could begin, either the pulse piston was extended to initiate a pulse-injection test, or the pulse piston was retracted to initiate a pulse-withdrawal test, depending on the type of test planned.

- The pulse test was then allowed to continue for approximately one day until on-going real-time analysis of the test data indicated that the hydraulic conductivity of the interval had been estimated to within less than an order of magnitude of uncertainty. After the Test Analyst had determined that the available data were adequate for analysis, preparations began for a second test. Three courses of action were possible at this point:
 - If a pulse-withdrawal test had been performed and the test-zone pressure was still above the estimated static formation pressure, the shut-in valve was opened to expose the test zone to the tubing, which was underpressured because of the earlier swabbing. With the shut-in valve open, the pulse piston was extended, after which the shut-in valve was closed. The pulse piston was then retracted to initiate another pulse-withdrawal test.
 - If a pulse-withdrawal test had been performed and the test-zone pressure was below the estimated static formation pressure (or the Test Leader did not want to perform a second pulse-withdrawal test for any reason), the pulse piston was extended to initiate a pulse-injection test.
 - If a pulse-injection test had been performed, the pulse piston was retracted to initiate a pulse-withdrawal test.
- After the second pulse test had continued for approximately one day and on-going real-time analysis of the test data indicated that the hydraulic conductivity of the interval had been estimated to within less than an order of magnitude of uncertainty, the pulse piston was retracted or extended, as appropriate, to verify that the same magnitude pulse was created by piston retraction as was created by piston extension. Monitoring of the response to piston retraction/extension was terminated after at least 10 minutes had elapsed.
- After testing was terminated, the shut-in valve was set to its normal open position, the packers were deflated, and the test tool was moved down to the next interval to be tested in the borehole.

Figure 3-1 shows typical test-zone and bottom-zone responses to a test sequence consisting of a stabilization period followed by two pulse-withdrawal tests (from the DGR3_671.50-702.24 test of the Cobourg Formation, spanning the proposed repository horizon). Each pulse test was approximately one day in duration, with a total testing time of three days (one day of stabilization, followed by two tests at one day each).

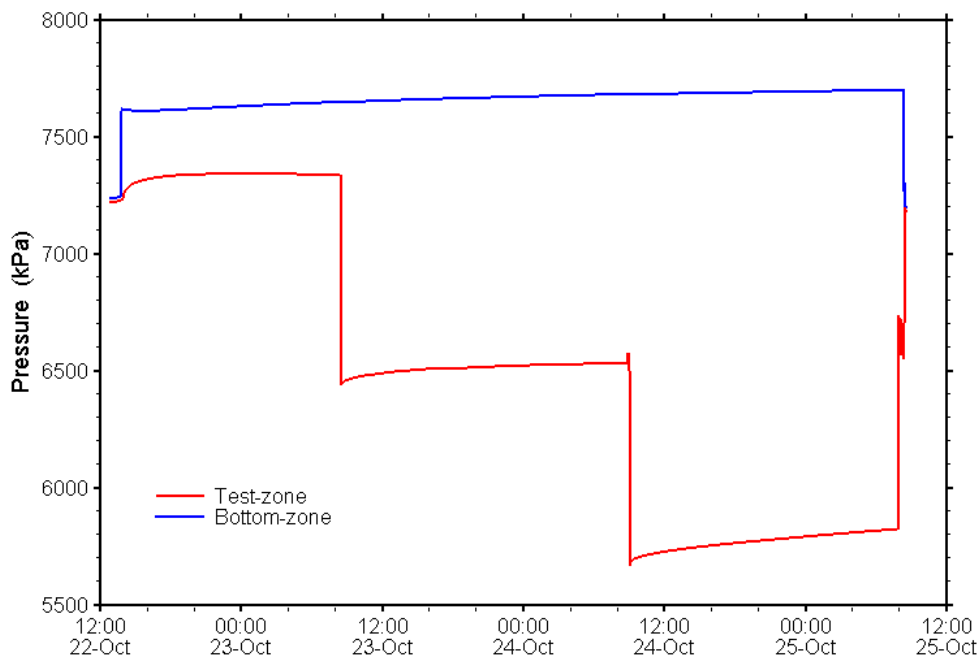


Figure 3-1: DGR3_671.50-702.24 test interval and bottom zone response.

Slug tests and DSTs were performed following procedures similar to those described above for pulse tests, except that the pulse piston was not employed. Water was either added (for a slug-injection test) or removed (for a slug-withdrawal test) from the tubing after the shut-in valve had been closed, and then, after an equilibration period, the shut-in valve was opened to allow the water level in the tubing to equilibrate with the formation pressure. If the rate of equilibration was such that less than 30% recovery had occurred after one hour, the shut-in valve was closed, converting the slug test to a DST.

Different strategies were employed to define test intervals in the different boreholes. In DGR-1, intervals were targeted that had either shown responses during FEC logging (Beauheim and Pedler, 2009) indicative of flow into the borehole (e.g., the interval from 404.37 to 416.37 m BGS) or were considered to be representative portions of sections that did not show indications of flow (e.g., the interval from 348.76 to 360.76 m BGS). For the Phase 2 testing of DGR-2, test intervals were overlapped to provide continuous coverage of the open portion of the borehole to as great a depth as feasible, considering that a bridge plug was set in the lower Gull River Formation at ~837 m BGS. The intervals were designed to cover principally (portions of) single formations, with minimal inclusion of overlying or underlying formations.

A similar strategy of overlapping intervals to provide continuous coverage was employed in the testing of DGR-3 and DGR-4, although multiple formations/units were inevitably grouped in the Silurian test intervals in these holes because of the thinness of the units. Three small gaps in the coverage of the DGR-3 borehole (332.55 to 334.99, 376.74 to 379.98, and 702.24 to 710.00 m BGS) occurred over intervals expected, based on core, to have low permeability. Testing coverage was continuous in DGR-4.

Testing in DGR-5 and DGR-6 was focused on only the Ordovician strata. Overlapping intervals were used in DGR-5 to provide continuous coverage from the lower Manitoulin Formation to the lower Kirkfield Formation. Testing in DGR-6 used a shorter straddle interval (10.23 m) to allow discontinuous, targeted testing of different lithologies within individual formations, as well as to test fractured and unfractured portions of formations. The short straddle interval also allowed the Collingwood Member of the Cobourg

Formation to be tested with minimal contributions from the overlying Blue Mountain and underlying Cobourg Formations, in contrast to the testing in the other deep DGR boreholes.

4 Analysis Approach

Transient pressure data collected during straddle-packer hydraulic testing were analyzed using the Sandia National Laboratories numerical hydraulic-test simulator, nSIGHTS (**n**-dimensional **S**tatistical **I**nverse **G**raphical **H**ydraulic **T**est **S**imulator), a numerical well-test analysis code written in C++ and described in detail in the nSIGHTS 2.40 User's Manual (Nuclear Waste Management Program, 2006). Analysis procedures used in this report are documented in test plan TP-08-18 (Roberts, 2009).

A discussion of the conceptual flow models, descriptions of the types of hydraulic tests performed, definitions of the various fitting parameters, a discussion on borehole pressure history, and an overview of the analysis process, including the uncertainty calculations, are given below.

4.1 Conceptual Model

The term *conceptual model* in this report refers to the mathematical description of the hydrogeologic system. Selecting a conceptual model is the first step in the overall analysis process. The choice of conceptual model, along with the type of hydraulic test(s) performed, determines which parameters will be estimated, i.e., which parameters will be fitting parameters in the analysis process. The primary tool for choosing a conceptual model typically is a diagnostic plot of the transient pressure data collected during testing. The shapes exhibited by the diagnostic plot indicate the flow regime that was encountered during testing, and consequently, the conceptual model that should be used to estimate the properties of that regime. The diagnostic plot shapes reflect not only the pressure responses created by the hydraulic tests, i.e., the pulse and slug tests, but are also affected by pressure transients resulting from drilling and other pre-testing activities. These pre-test pressure transients can persist for months in lower conductivity hydrologic systems like those tested in the DGR boreholes. Given that the pre-testing pressures to which the eventual test zones are subjected prior to installing pressure transducers can only be approximated, their effect on the shapes of the diagnostic plots is unknown to some extent. This uncertainty resulted in the following approach being used to choose the conceptual models for the analyses in this report: the simplest model that would reproduce the measured response and would be reasonable for the geologic setting was selected as the default model – the simplest model being the most defensible.

In a near horizontally layered sedimentary sequence, like that tested in boreholes DGR-1 through DGR-4, where the borehole is drilled approximately perpendicular to the layers, the simplest conceptual model that is generally invoked in well-test analysis is described as an infinite-acting, radial-flow system with wellbore storage and skin. *Infinite-acting* means that the hydraulic parameters controlling the test response, such as transmissivity (T) and storativity (S), are constant within the region affected by the test. The term *radial* indicates horizontal convergent flow toward and/or away from the test zone (depending on the gradient induced during a test). Note that all flow is assumed to be horizontal within the tested layer, i.e., flow with no vertical component. A further assumption made in the conceptual model is that the hydraulic properties of the tested interval do not vary vertically.

DGR-5 and DGR-6 were angled boreholes with test zones that varied from approximately 12.5 to 33.1 degrees from vertical. To interpret the test results from these angled boreholes using nSIGHTS, the geometry of each angled test zone was transformed to that of an equivalent vertical test zone as described in Abbaszadeh and Hegeman (1990). This transformation was accomplished by treating the angled test zone as if it were a vertical cylindrical zone with a diameter equal to the average length of the axes of the ellipse that is created by the intersection of a horizontal plane and the angled test zone. The length of the test zone was assumed to be equal to its vertical thickness. Beauheim et al. (1993) evaluated the conditions under which this equivalent-vertical-borehole approximation was appropriate for

interpretation of hydraulic tests in angled boreholes. They found that the approximation was reasonably accurate when the test zone angle was 30° from vertical or less. When the test zone angle was greater than 30°, the approximation was reasonably accurate if the horizontal/vertical anisotropy was at least 10. In the bedded sedimentary strata tested with boreholes DGR-5 and DGR-6, anisotropy is believed to be at least 10:1.

Wellbore storage is that property of the testing system whereby some portion of the fluid injected/withdrawn during a hydraulic test is taken up by / derived from the test zone (shut-in valve is closed) or the tubing (shut-in valve is open) rather than the formation. During the *wellbore-storage dominated period of a test*, the formation properties of interest have little effect on the observed pressure response, meaning the formation properties are masked to some extent. The *wellbore-storage dominated period of a test* is that period in a test where the total system compressibility acts to mask the formation pressure response by absorbing/producing fluid unrelated to fluid movement in/out of the formation. Ideally, a test will proceed long enough such that the formation-flow component dominates the wellbore-storage component and the formation properties can be reliably estimated. The adequacy of the DGR test durations was determined by real-time analysis. Tests were allowed to run until real-time analysis indicated that the fitting-parameter estimates were being adequately constrained by the pressure data.

An area of altered hydraulic conductivity surrounding the wellbore that results from drilling activities (e.g., mud infiltration, stress relief, etc.) is termed a *skin*. A positive skin is a zone in which *K* has been decreased relative to the unaltered formation *K*. A negative skin is a zone in which *K* near the wellbore has been enhanced.

The diagnostic plot used in the analyses presented in this report is known as a Ramey B plot (Ramey et al., 1975). This plot is useful for determining what type of skin may exist around the borehole and is shown for each analysis in this report that included a pulse and/or slug test (Appendix A). The characteristics of the Ramey B plot are discussed in detail in Section 4.4 below.

4.2 Parameters

Hydraulic conductivity (*K*) [L/T] is a constant of proportionality that was empirically derived by Darcy (1856) expressing the ratio of fluid flux to gradient within a porous medium. Darcy's empirical relationship is generally referred to as Darcy's Law, and can be written as follows:

$$Q = -K \frac{dh}{dl} A \quad \text{Equation 4-1}$$

where:

Q	= flow rate	[L ³ /T]
dh/dl	= hydraulic gradient	[]
A	= flow area	[L ²]

The specific storage (*S_s*) [1/L] of a saturated geologic unit describes the amount of fluid released as a function of both the rock and fluid compressibility per unit decline in hydraulic head per unit volume of rock, and is given as:

$$S_s = \rho g (\alpha + n\beta) \quad \text{Equation 4-2}$$

where:

ρ	= fluid density	$[M/L^3]$
g	= gravity	$[L/T^2]$
α	= rock compressibility	$[LT^2/M]$
n	= porosity	$[]$
β	= fluid compressibility	$[LT^2/M]$

Well-test analysis does not provide estimates of K and S_s , but of their products when multiplied by the test-interval length, transmissivity (T) $[L^2/T]$ and storativity (S) $[-]$. For the analyses presented in this report, K and S_s were calculated by assuming that all test intervals were vertically homogeneous and simply dividing the inferred values of T and S by the test-interval length. The validity of this assumption undoubtedly varies from test interval to test interval; when a test interval is wholly contained within a single formation, vertical homogeneity may be a reasonable assumption. But when a test interval spans portions of several formations, the assumption is less defensible. In such a case, other information must be used to try to infer what portion of the total T (or S) is contributed by the K (or S_s) and thickness of each formation in the test interval. Estimation of individual formation K and S_s values from multiformation tests is discussed in Section 11.

Static formation pressure (P_f) $[M/LT^2]$ is the undisturbed fluid pressure within a formation prior to drilling and testing. Estimates of P_f and K are important for predicting how fluids will move in the presence of an underground repository. "Raw", or uncorrected, formation pressures are those measured by the transducer, which is located some distance above the centre of the test zone. These "raw" numbers are used in the individual test analyses presented in Sections 5 to 10 below. The raw values are subsequently corrected to represent the pressure in the centre of the test interval. Borehole fluid density estimates and measured transducer locations are used in calculating corrections. The corrected values are presented in the test summary tables and the borehole summary tables at the end of each section.

The observed pressure change ($\Delta Pressure$) in the isolated test zone for a given amount of fluid ($\Delta Volume$) that enters/leaves the test zone is controlled by the test-zone compressibility (C_{tz}), defined as follows:

$$C_{tz} = \left(\frac{\Delta Volume}{\frac{TotalVolume}{\Delta Pressure}} \right) \quad \text{Equation 4-3}$$

where: $Total Volume$ = total volume of fluid within the isolated test zone

The skin factor (s) $[]$ is a dimensionless parameter that indicates the relative degree to which skin hydraulic conductivity (K_s) near the borehole differs from the undisturbed formation hydraulic conductivity (K_f) at some distance away from the borehole. The skin factor is defined by Hawkins (1956) as:

$$s = \left(\frac{K_f}{K_s} - 1 \right) \times \ln \left(\frac{(r_w + t_s)}{r_w} \right) \quad \text{Equation 4-4}$$

where:

r_w	= nominal well radius	$[L]$
t_s	= skin thickness	$[L]$

4.3 Tests

A pulse injection (PI) or withdrawal (PW) test is an instantaneous (within the limitations of the equipment) pressure increase/decrease induced in the test zone that is allowed to dissipate back toward static pressure conditions. The rate of pressure decay is used to infer the hydraulic properties of the tested geologic unit. During a pulse test, the test zone is shut-in, i.e., it is isolated from the fluid column in the tubing by closing the shut-in valve. Pulse tests are most suitable for testing formations with hydraulic conductivities less than $1\text{E-}10$ m/s, and were performed in the majority of the test intervals.

Compressibility of the DGR test zones was calculated whenever a pulse test was initiated. The majority of the DGR pulse tests were initiated by rapidly extending or retracting a downhole pulse piston of known volume. The C_{tz} could then be calculated from Equation 4-3 by measuring the initial pressure change, given that the test-zone fluid volume was known. (Note that the test-zone fluid volume comprises the fluid in the borehole between the two packers as well as all fluid contained within the test tool below the shut-in valve.) Several pulse tests were also initiated by first filling the tubing to a level that would produce a specified initial pulse pressure and then quickly opening/closing the downhole shut-in valve. The volume of fluid injected/withdrawn from the test zone could then be calculated from the measured change in the tubing pressure, allowing for an estimate of C_{tz} . In some testing intervals where the initial test-zone pressure was much higher than the expected P_f , two PW tests were performed in relatively rapid succession using a combination of the shut-in valve and the downhole piston. With the first PW lasting only minutes, the two smaller pulses ultimately acted as a single larger PW starting at a pressure closer to the expected P_f . Note that hydraulic parameters such as K cannot be estimated from pulse responses without knowing C_{tz} .

Slug injection (SI) or withdrawal (SW) tests are similar to pulse tests, but the shut-in valve remains open during a slug test and fluid flowing into or out of the formation results in changing water levels within the tubing. Slug tests were initiated by filling the tubing to a desired level while the shut-in valve was closed, and then rapidly opening the shut-in valve. Analogous to C_{tz} in a pulse test, the tubing radius and fluid density controlled the observed pressure change for a given amount of fluid that entered/left the tested formation. The tubing string radius must be known to estimate K from a slug-test response. Slug tests are appropriate for testing formations with hydraulic conductivities in the approximate range of $1\text{E-}6$ to $1\text{E-}9$ m/s. Slug tests were performed in a few intervals in DGR-1, DGR-3, DGR-4, and DGR-6.

The third type of hydraulic test performed in a few intervals was a drillstem test (DST). The initial part of a DST is effectively an abbreviated slug test. As per TP-06-14 (Beauheim, 2007), if 30% of an initial slug had not dissipated after 1 hr, the shut-in valve was closed and the test was converted to a DST. The time during which the shut-in valve was open constitutes the DST flow period and the time after shut-in constitutes the DST buildup period.

4.4 Formation Specific Storage - Skin Conductivity - Skin Thickness

Simultaneously estimating S_s , skin K (K_s), and skin thickness (t_s) values from analysis of single-well data (i.e., no cross-hole response) is complicated by the high degree of correlation among these fitting parameters in the regression process. Figure 4-1 shows 1345 estimates of these three parameters obtained from perturbation analysis (Section 4.6) by matching the DGR-2 457.85-488.35 pulse tests. Note that each of the 1345 solution sets produced effectively equivalent matches (small change in the fit value) to the measured response. The values of K_s and t_s can be simultaneously increased/decreased over a range that results in approximately the same skin factor, s (Equation 4-4).

In addition, S_s and s affect the match to a single-well pressure response in much the same way, so they can be simultaneously changed to produce a series of equivalent matches. Figure 4-2 shows simulated pulse-test responses plotted on a log-log scale as a normalized pressure response and its derivative; a standard well-test diagnostic plot known as a Ramey B plot (Ramey et al., 1975). Various parameter possibilities are simulated to illustrate the difficulty in distinguishing among variations in S_s and s .

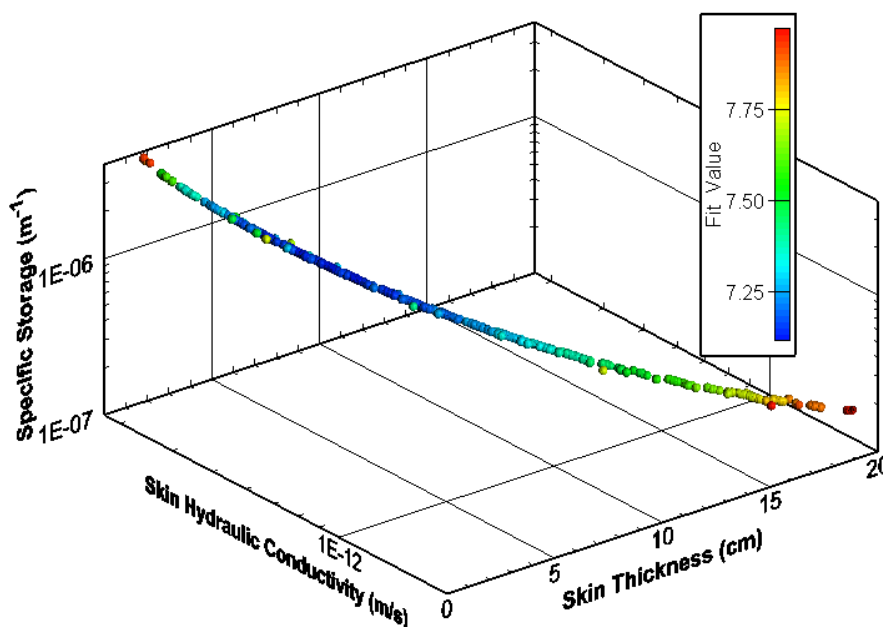


Figure 4-1: An X-Y-Z scatter plot showing the correlation among skin thickness, skin hydraulic conductivity, and specific storage that can occur in a single-well test.

The baseline example shown in red in Figure 4-2 shows simulated responses when the hydraulic properties around the wellbore have not been altered – a condition known as a “zero” skin. Note that S_s for the baseline case is $1E-6 m^{-1}$ and the formation K (K_f) for all examples is constant. When the drilling process results in increased K_s over some distance t_s near the wellbore relative to the unaltered formation K_f , the condition is known as a “negative” skin, plotted as a blue line in Figure 4-2. Notice that the negative skin produces a distinctive downward inflection in that part of the Ramey B derivative that appears as an upward-sloping straight line when no skin is present (timing and magnitude of this inflection depend on the contrast between skin and formation properties). This inflection is observed in many of the DGR pulse responses. A decrease in K_s over some distance t_s around the wellbore is known as a “positive” skin, plotted in green in Figure 4-2. Unlike the negative skin, a positive skin causes no distinct inflection in the Ramey B derivative; it simply changes the slope of the derivative (the pulse recovery is slowed), effectively translating it to the right on the graph relative to the zero-skin case. Shown in magenta and black are two zero-skin examples where S_s has been increased to $1E-5 m^{-1}$ and decreased to $1E-7 m^{-1}$, respectively. As with the positive-skin case, simply changing the value of S_s does not result in a notable inflection in the derivative, it primarily changes the position of the derivative with respect to the baseline case. Figure 4-2 shows that changing K_s or S_s can result in similar responses, and consequently, estimates for each of these parameters can be paired in non-unique combinations to

achieve similar matches to field data. Also note that any small transient changes in test-tool position or packer shape at the start of a pulse or slug test can affect the pressure response in such a way that these non-formation responses resemble a skin effect. The approach used in these analyses for estimating S_s is discussed below in Section 4.6.

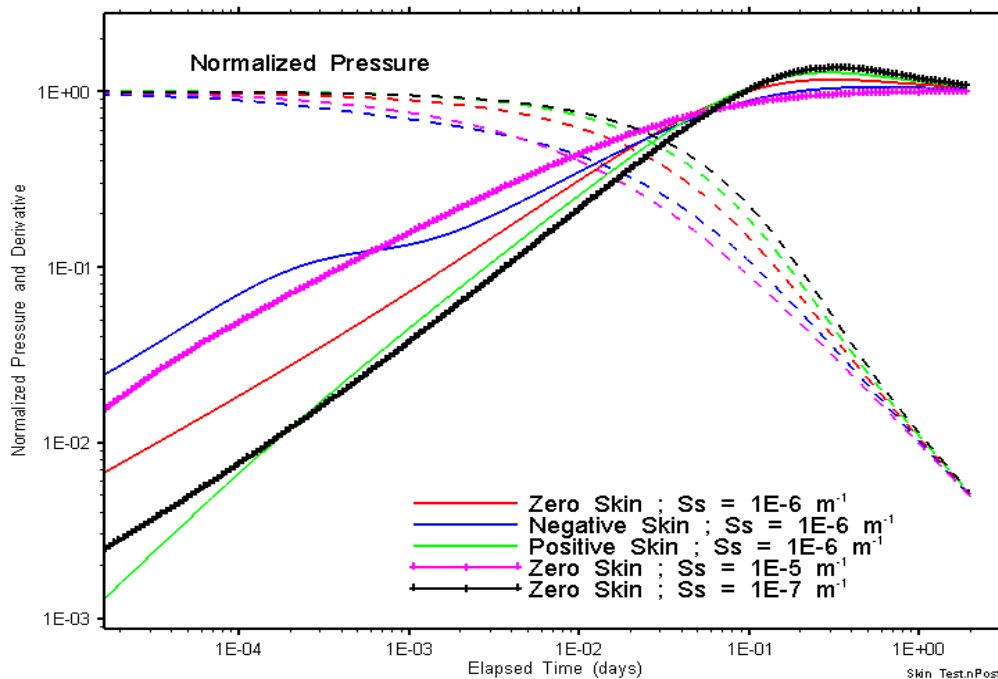


Figure 4-2: Ramey B diagnostic plots showing various combinations of skin factors and formation specific storage.

4.5 Pre-Test Borehole History

The nSIGHTS simulation description includes a detailed specification of the sequence of borehole boundary conditions from the point at which the borehole perturbs the *in situ*, or formation, pressure. The sequence of pressures experienced by a test interval during the period between interception of the interval by drilling and the start of testing is denoted the "pressure history".

Pressure histories were included in the analyses performed for each test interval as specified-pressure boundary conditions at the hole. Part of the pressure history consisted of the calculated pressure (not measured by transducer) at the centre of each test interval from the approximate time of drilling intercept to the time that the pressure at that interval was measured by a pressure transducer. This pressure was calculated using fluid densities recorded during drilling and logging and assumed the borehole was filled to the surface.

Subsequent to the start of straddle-packer testing, pressure histories are extracted from measured pressures in the annulus and bottom zones. For example, due to the overpressured conditions in the formations below the Kirkfield, significant pressure build-ups occurred in the zone beneath the test tool for most tests below the Guelph Formation. These build-ups are then incorporated in the pre-test history when these lower zones are subsequently tested. Plots of pre-test pressure histories for all tests are presented in Appendices.

Specified-pressure boundary conditions are also specified at the early time of PI and PW tests, when the response is dominated by tool compliance effects. For the analyses presented in this report, the first four minutes of each pulse test were specified-pressure histories in the simulations, allowing for some small amount of tool compliance following the pulse initiations. The pressure histories were taken from the measured pressure response during this four minute period.

4.6 Uncertainty Analysis

Preliminary analyses were performed to determine an appropriate conceptual model and obtain a single set of optimized baseline fitting-parameter values for each tested interval. Perturbation analyses were then performed in multiple stages to obtain the final best-fit parameter values and the corresponding uncertainty ranges. Perturbation analysis consists of randomly perturbing the baseline fitting-parameter values a specified number of times and then re-optimizing those perturbed values. This allows multiple minima within the parameter space to be located in the search for the global minimum, i.e., the true optimal solution. To begin, 250 perturbations were performed. At least one subsequent perturbation run then followed where the initial parameter values to be perturbed were updated using the best-fit values obtained from the initial 250 perturbations. If these new best-fit values indicated that the initial baseline parameter values were contained within the global minimum, then a final run of between 500 and 5000 perturbations was performed, with the number of perturbations being dependent upon the complexity of the parameter space. If the initial 250 perturbations indicated that a new global minimum had been found, then another 250 perturbations were run using the new best-fit values as the initial values to be perturbed. This process was repeated until the results indicated that the global minimum had been found and the final perturbation run could be initiated.

After the final perturbation run was completed, a cumulative distribution function (CDF) was calculated using the fit values (measure of the goodness of fit) associated with each perturbation. The characteristics of this fit-value CDF along with a visual assessment of parameter-space plots for each fitting variable and a visual assessment of the fits themselves were all used to determine the value of the "fit discriminant". The fit discriminant is used to reduce the perturbations under consideration to only those within the best-fit minimum, and sufficiently close to be subjectively considered "acceptable" fits. All perturbation results for which the fit value was less than the fit discriminant were deemed acceptable solutions and are included in the final range of reported values for each fitting parameter. The statistics (minimum, maximum, mean, and best fit) for each of the final solution sets are reported in the sections for each test interval. Note that the distribution of values within each solution set is typically not a normal (or log normal) distribution, so it is not unusual for the best-fit value to be different than the mean value. Parameter-space plots showing the fit discriminant value along with the perturbation results for each fitting variable are shown in Appendices A-E.

The conceptual model used for the majority of the analyses in this report was an infinite-acting, homogeneous radial system with wellbore storage and skin, as discussed in Section 4.1. Exceptions to this conceptual model are noted in the individual sections below. For this standard conceptual model, fitting parameters included formation hydraulic conductivity (K_f), specific storage (S_s) (a single value was assumed for both the formation and skin), skin hydraulic conductivity (K_s) and thickness (t_s), and static formation pressure (P_f).

Estimating S_s from single-well tests like those presented in this report can sometimes be confounded by skin effects and tool compliance as discussed in Section 4.4. In addition to these potential problems, estimating S_s can also be complicated by not knowing how much of the tested interval is actually contributing to (controlling) the observed pressure response. Storativity (S), the product of the assumed

contributing formation thickness and S_s , is actually what is estimated during the matching process. Assume, for example, that the estimate of S_s obtained from an analysis is $1\text{E-}8\text{ m}^{-1}$ and the assumed contributing formation thickness is 30 m. The estimate of S in this example would be $3\text{E-}7$; it is this value of S that results in a match to the data. If the true contributing thickness is actually 3 cm, then the estimate of S_s must become $1\text{E-}5\text{ m}^{-1}$ to maintain an S of $3\text{E-}7$ and obtain the same match to the measured response. All of these potential complicating factors can result in perturbation-derived estimates of S_s that are lower than expected values.

At the start of the DGR testing, when perturbation analysis indicated that the best-fit value of S_s was going to be less than $1\text{E-}8\text{ m}^{-1}$, S_s was fixed at a single value in the model. Later in the testing program, it was decided that S_s would be sampled over a range to better convey the corresponding uncertainty in the other fitting parameters, given that the other fitting-parameter estimates may have been correlated with the estimate of S_s . A specified range of log-normally distributed S_s values was sampled and an optimization was performed for each sample to see how the uncertainty in the value of S_s affected the fitting-parameter estimates in the model. Time/budget did not allow the fixed S_s analyses to be redone. Both approaches appear in this report. It can be seen in DGR-6 results (Section 10.13), where both approaches are used, that the sampling approach leads to more variation in estimated K_f and P_f and likely provides a better estimate of uncertainty.

5 Phase 1 DGR-1 Testing And Analysis

As discussed in Section 1.2 and 1.3, testing of DGR-1 was conducted as part of the Phase 1 testing program in 2007. Analyses of DGR-2 results from that program indicated that systemic equipment leakage may have compromised the testing. Due to the improved test equipment and procedures used in Phase 2, only limited analysis of DGR-1 results has been undertaken, specifically where the shorter straddle interval resulted in greater resolution of properties of thinner formations than is available from DGR-3 and DGR-4 test intervals.

The test-zone transducer during DGR-1 testing was located 14.17 m above the middle of the isolated test zone and was hydraulically connected to the test zone via a length of 1/4-in stainless-steel tubing. To determine the P_f values corresponding to the middle of the test zone, the “raw” (as measured by the transducer) P_f estimates were depth-corrected using the offset distance of 14.17 m and an estimated fluid density value of 1050 kg/m^3 . The depth-corrected P_f estimates are given in the tables below whereas the raw P_f estimates are listed in the graph annotations.

Results of each test analysis are discussed below. A summary of DGR-1 testing results is presented in Section 5.4.

5.1 294.28-306.28 Salina A2 Carbonate

The DGR-1 interval from 294.28 to 306.28 m BGS was entirely contained within the Salina A2 Unit carbonate, an argillaceous dolostone. An overview of the testing in this interval is given in Table 5-1 and the corresponding parameter estimates are given in Table 5-2. A pulse-injection test and a DST were performed in this interval.

Table 5-1: Summary of the DGR1_294.28-306.28 testing activities.

Formation / Unit		Top of Test Zone (m BGS)		Bottom of Test Zone (m BGS)	
Salina A2 Carbonate		294.28		306.28	
Test	Initiated	Magnitude (kPa)	Duration	Compressibility (Pa^{-1})	
Shut-in	25-07-07 11:23	N/A		N/A	
PI	25-07-07 16:12	597	18.5 hr	6.3E-10	
DST Flow	26-07-07 10:42	660	1 hr	N/A	
DST Shut-in	26-07-07 11:42	N/A	10.3 hr	N/A	
Borehole Pressure History					
Event		Start		Pressure (kPa)	
Drilling Intercept		30-03-07 16:00		2944	
Density Change		31-03-07 22:00		3385	
FEC Logging		09-05-07 12:00		2929	
Shut-in		25-07-07 11:23		2973	

Table 5-2: Summary of the DGR1_294.28-306.28 parameter estimates.

Parameter	Best Fit	Minimum	Maximum	Mean
K_f (m/s)	1.2E-11	4.4E-12	3.3E-11	1.5E-11
P_f (kPa)	2950	2927	2990	2960
K_s (m/s)	1.3E-10	1.3E-10	1.3E-10	1.3E-10
t_s (cm)	2934	1706	4174	2652
S_s (m^{-1})	2.7E-7	2.6E-7	2.7E-7	2.7E-7

Figure 5-1 shows the measured pressure record from DGR1_294.28-306.28 used in this analysis along with the best-fit simulation and parameter values. The ranges of formation K and raw P_f values estimated from perturbation analysis are shown in Figure 5-2 and the fit value cumulative distribution function is shown in Figure 5-3.

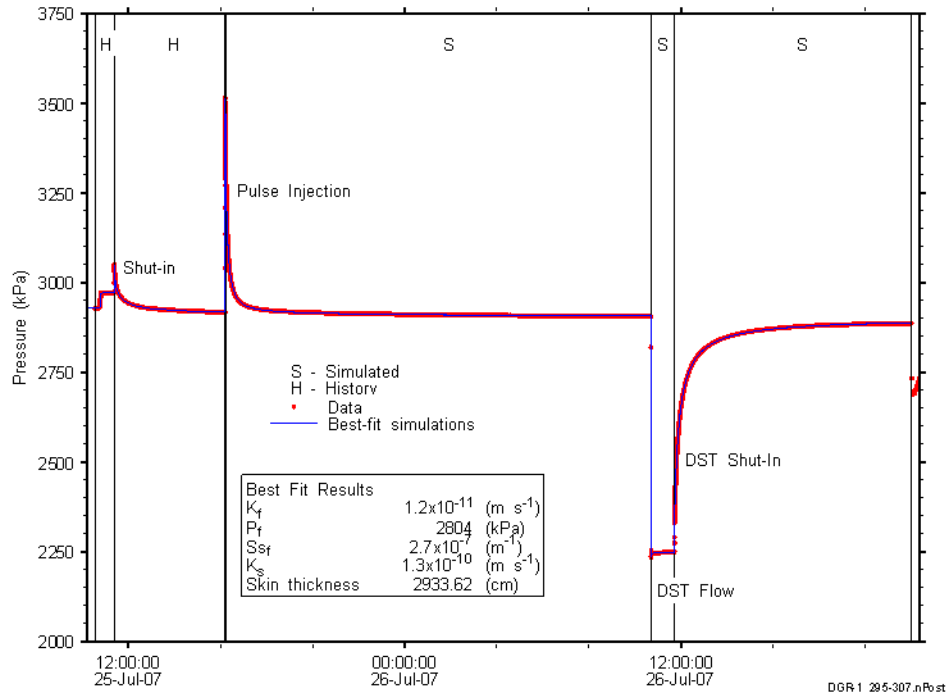


Figure 5-1: Annotated DGR1_294.28-306.28 testing sequence showing best-fit simulation and parameter estimates.

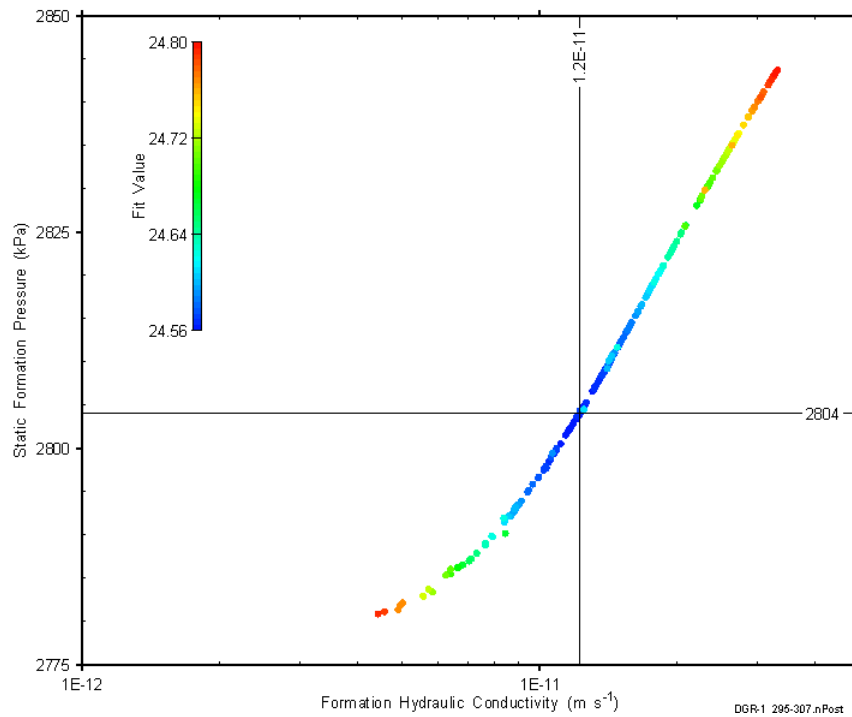


Figure 5-2: XY-scatter plot showing estimates of formation hydraulic conductivity and raw static formation pressure derived from the DGR1_294.28-306.28 perturbation analysis.

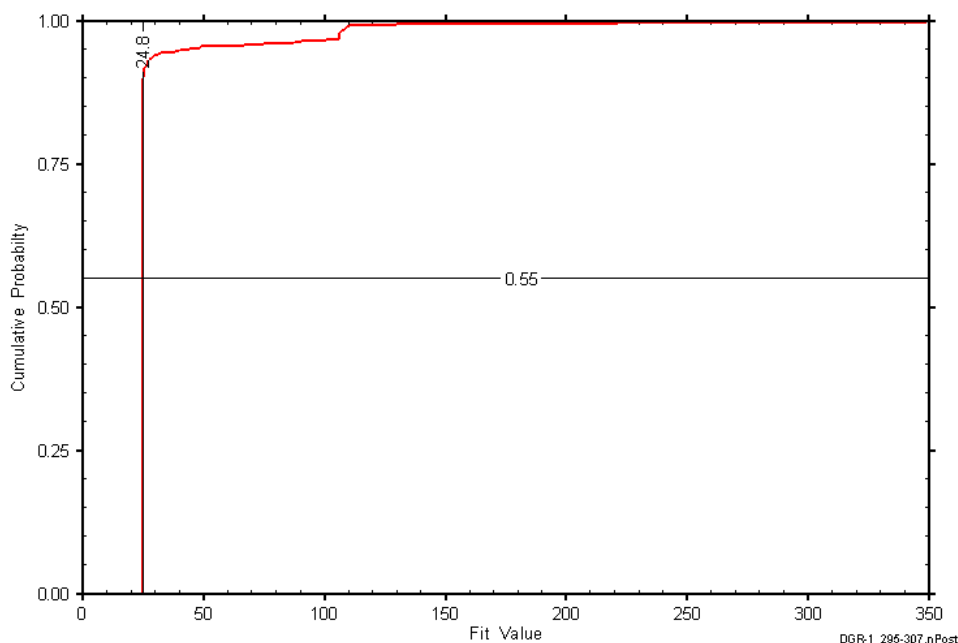


Figure 5-3: DGR1_294.28-306.28 fit value cumulative distribution function.

5.2 348.76-360.76 Salina A1 Carbonate

The DGR-1 interval from 348.76 to 360.76 m BGS was entirely contained within the Salina A1 Unit carbonate, an argillaceous dolostone. An overview of the testing in this interval is given in Table 5-3 and the corresponding parameter estimates are given in Table 5-4. A pulse-injection test and a pulse-withdrawal test were performed in this interval.

Table 5-3: Summary of the DGR1_348.76-360.76 testing activities.

Formation / Unit		Top of Test Zone (m BGS)	Bottom of Test Zone (m BGS)	
Salina A1 Carbonate		348.76	360.76	
Test	Initiated	Magnitude (kPa)	Duration	Compressibility (Pa ⁻¹)
Shut-in	17-07-07 11:47	N/A	20 hr	N/A
PI	18-07-07 08:20	914	50 hr	4.4E-10
PW	20-07-07 10:49	818	20 hr	4.9E-10
Borehole Pressure History				
Event	Start	Pressure (kPa)		
Drilling Intercept	01-04-07 04:00	3483		
Density Change	31-03-07 22:00	4006		
FEC Logging	09-05-07 12:00	3644		
Shut-in	17-07-07 11:47	3777		

Table 5-4: Summary of the DGR1_348.76-360.76 parameter estimates.

Parameter	Best Fit	Minimum	Maximum	Mean
K_f (m/s)	1.8E-12	1.2E-12	5.2E-12	2.4E-12
P_f (kPa)	3867	3844	3884	3871
K_s (m/s)	2.3E-13	1.2E-13	6.4E-13	3.8E-13
t_s (cm)	4.7	1.7	36	14
S_s (m^{-1})	7.5E-7	1.2E-7	1.9E-6	3.4E-7

Figure 5-4 shows the measured pressure record from DGR1_348.76-360.76 used in this analysis along with the best-fit simulation and parameter values. The ranges of formation K and raw P_f values estimated from perturbation analysis are shown in Figure 5-5 and the fit value cumulative distribution function is shown in Figure 5-6.

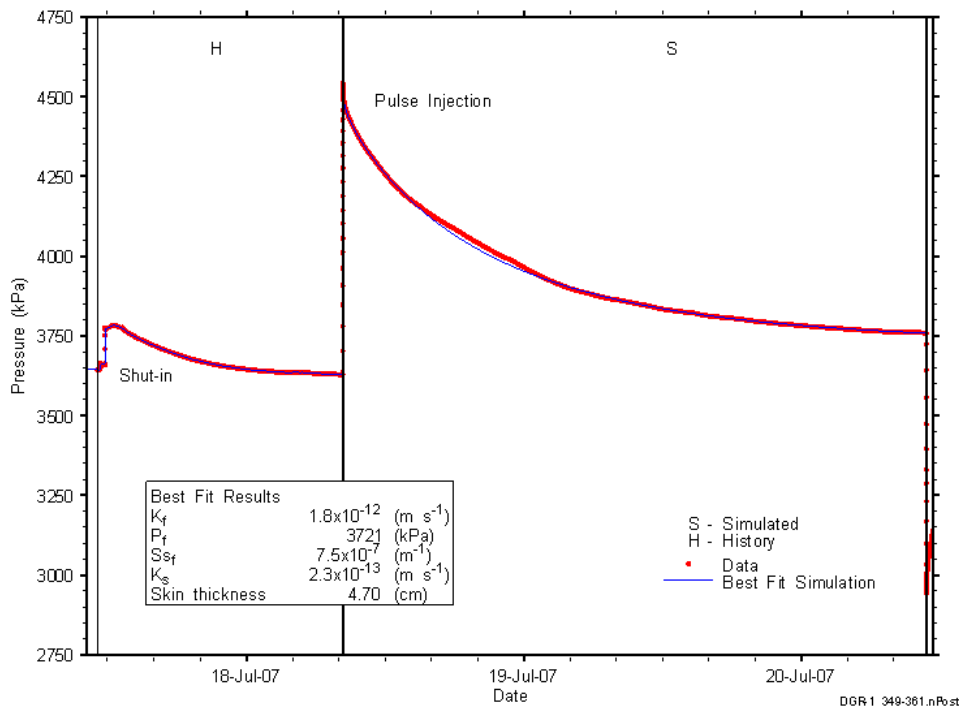


Figure 5-4: Annotated DGR1_348.76-360.76 testing sequence showing best-fit simulation and parameter estimates.

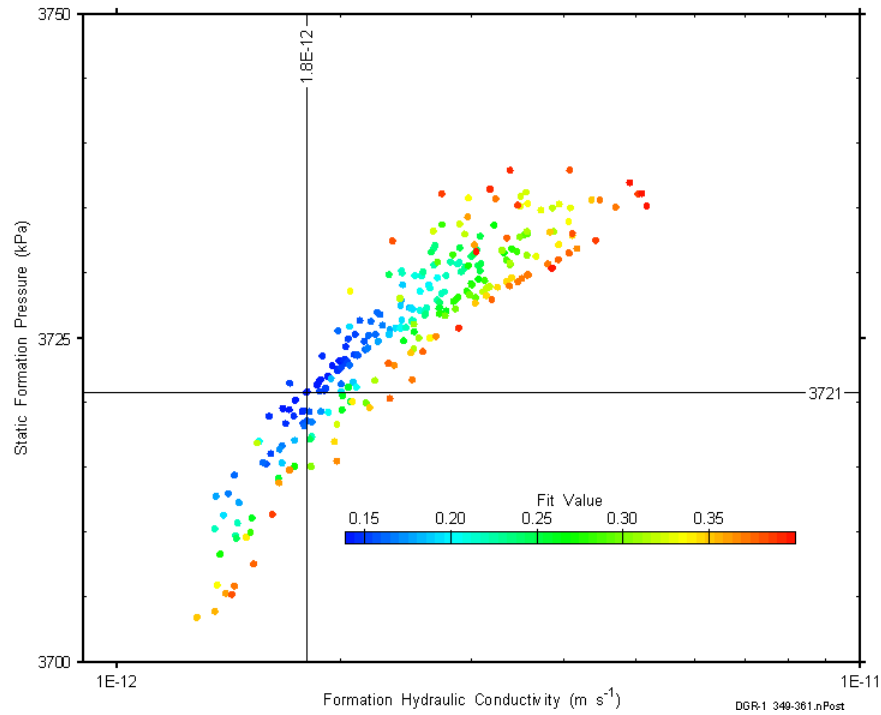


Figure 5-5: XY-scatter plot showing estimates of formation hydraulic conductivity and raw static formation pressure derived from the DGR1_348.76-360.76 perturbation analysis.

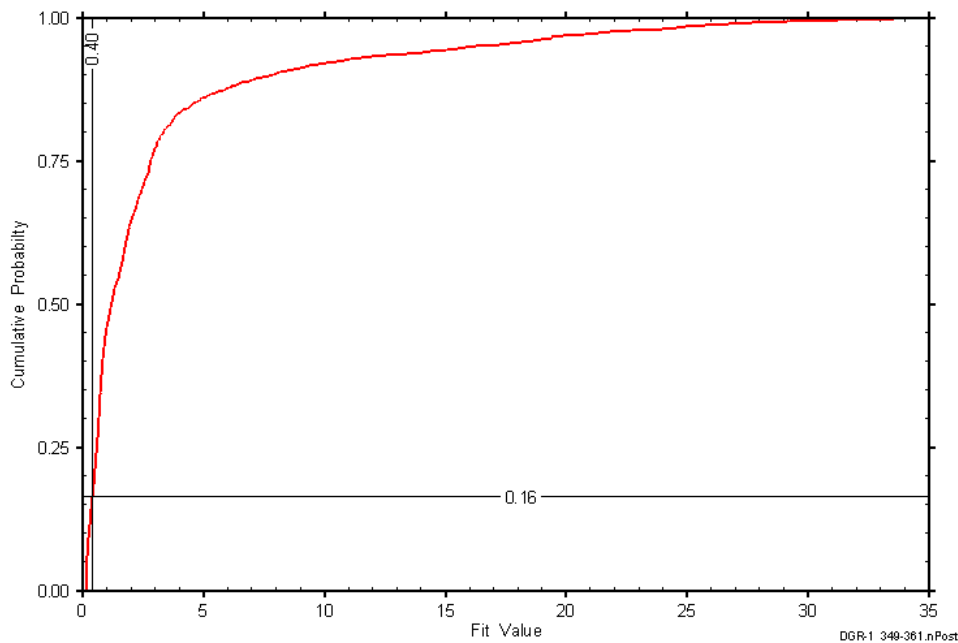


Figure 5-6: DGR1_348.76-360.76 fit value cumulative distribution function.

5.3 404.37-416.37 Lions Head-Fossil Hill-Cabot Head

The DGR-1 interval from 404.37 to 416.37 m BGS contained 4.33 m (all but the upper 0.12 m) of the Lions Head Member of the Amabel Formation, the entire 2.3 m of the Fossil Hill Formation, and the upper 5.37 m of the Cabot Head Formation. The Lions Head and Fossil Hill are dolostones, while the Cabot

Head is a shale. An overview of the testing in this interval is given in Table 5-5 and the corresponding parameter estimates are given in Table 5-6. A DST and pulse-injection test were conducted in this interval.

Table 5-5: Summary of the DGR1_404.37-416.37 testing activities.

Formation / Unit	Top of Test Zone (m BGS)		Bottom of Test Zone (m BGS)	
Lions Head-Fossil Hill-Cabot Head	404.37		416.37	
Test	Initiated	Magnitude (kPa)	Duration	Compressibility (Pa ⁻¹)
Shut-in	22-07-07 11:39	N/A	hr	N/A
DST Flow	23-07-07 13:16	638	1.3 hr	N/A
DST Shut-in	23-07-07 14:35	N/A	20 hr	N/A
PI	24-07-07 10:55	310	21 hr	1.3E-9
Borehole Pressure History				
Event	Start		Pressure (kPa)	
Drilling Intercept	03-04-07 05:00		4024	
Density Change	31-03-07 22:00		4627	
FEC Logging	09-05-07 12:00		4245	
Shut-in	22-07-07 11:39		4335	

Table 5-6: Summary of the DGR1_404.37-416.37 parameter estimates.

Parameter	Best Fit	Minimum	Maximum	Mean
K_f (m/s)	1.8E-11	1.8E-11	1.9E-11	1.8E-11
P_f (kPa)	4991	4987	4995	4990
K_s (m/s)	2.9E-11	2.4E-11	4.3E-11	3.1E-11
t_s (cm)	95	80	146	103
S_s (m ⁻¹)	2.4E-7	6.2E-8	4.3E-7	1.9E-7

Figure 5-7 shows the measured pressure record from DGR1_404.37-416.37 used in this analysis along with the best-fit simulation and parameter values. The ranges of formation K and raw P_f values estimated from perturbation analysis are shown in Figure 5-8 and the fit value cumulative distribution function is shown in Figure 5-9.

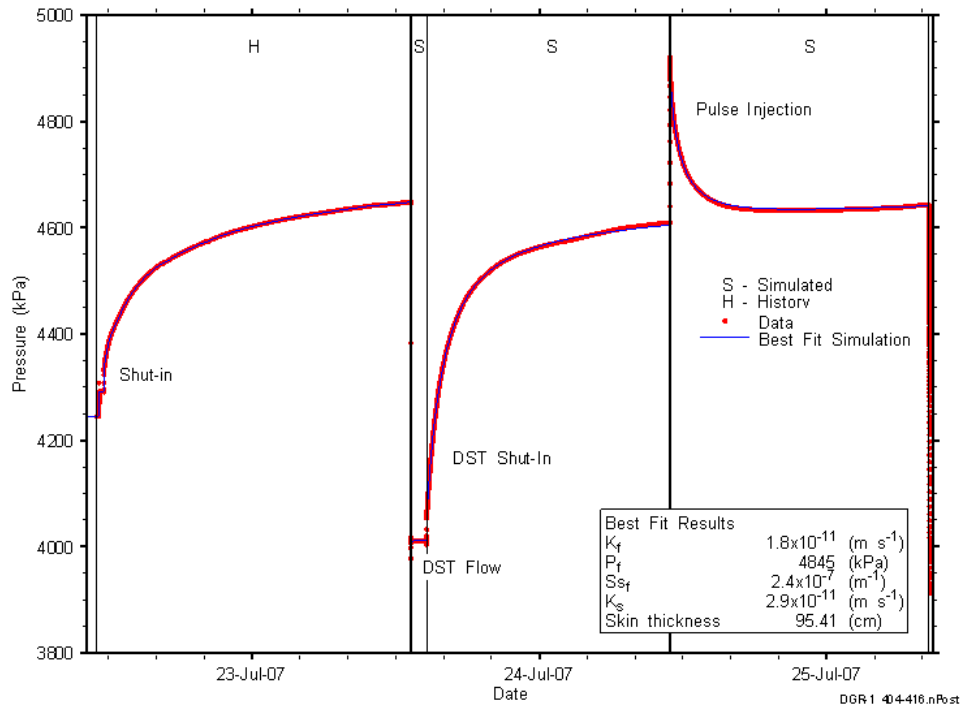


Figure 5-7: Annotated DGR1_404.37-416.37 testing sequence showing best-fit simulation and parameter estimates.

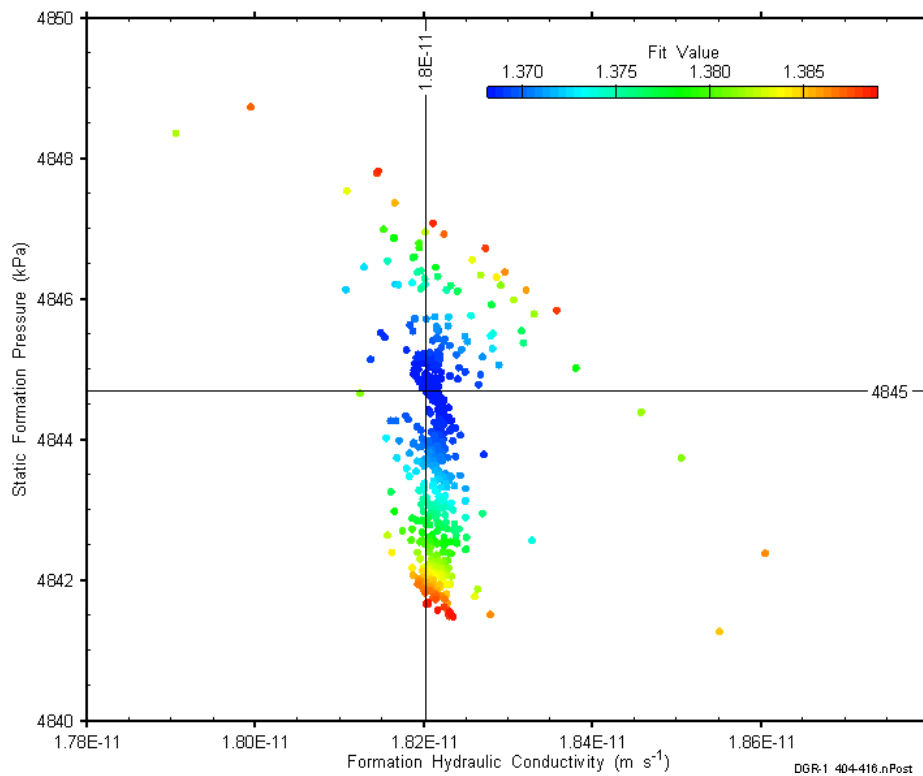


Figure 5-8: XY-scatter plot showing estimates of formation hydraulic conductivity and raw static formation pressure derived from the DGR1_404.37-416.37 perturbation analysis.

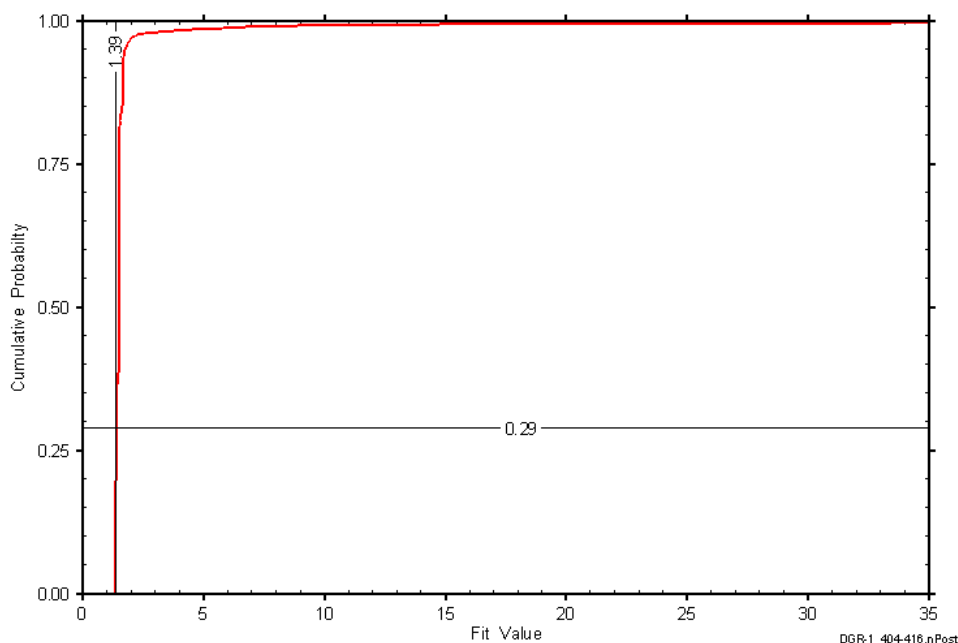


Figure 5-9: DGR1_404.37-416.37 fit value cumulative distribution function.

5.4 Summary of DGR-1 Results

The best-fit parameter estimates derived from the DGR-1 analyses are given in Table 5-7. Stratigraphic profiles of the analysis results for hydraulic conductivity, formation pressure, specific storage, skin factor, and test-zone compressibility are shown combined with the DGR-2 results in Section 4.16.

Table 5-7: Best-fit parameter estimates derived from the DGR-1 analyses

Formation(s)	Top	Bottom	K_f	P_f	S_s	K_s	t_s	s	C_{tz}
	m BGS	m BGS	$m s^{-1}$	kPa	m^{-1}	$m s^{-1}$	cm		Pa^{-1}
Salina A2 Carbonate	294.28	306.28	1.2E-11	2950	2.7E-7	1.3E-10	2934	-5.4	6.3E-10
Salina A1 Carbonate	348.76	360.76	1.8E-12	3867	7.5E-7	2.3E-13	4.7	3.2	4.6E-10
Lions Head-Fossil Hill-Cabot Head	404.37	416.37	1.8E-11	4991	2.4E-7	2.9E-11	95	-0.94	1.3E-9

6 Phase 2 DGR-2 Analysis

As discussed in Section 1.2 and 1.3, initial testing of DGR-2 was conducted as part of the Phase 1 testing program in 2007. Analyses of DGR-2 results from that program indicated that systemic equipment leakage may have compromised the testing. Consequently, DGR-2 was retested during the Phase 2 testing program in 2009. Only the results of the Phase 2 testing are discussed herein.

Phase 2 hydraulic testing in DGR-2 was performed from 30 July until 13 September 2009. Testing with a 30.50-m straddle interval was initiated approximately 10 m below the top of the Queenston Formation and then proceeded down the borehole, with 15 test intervals providing complete test coverage down to the lower Gull River Formation (Table 4-1). The testing in DGR-2 provided coverage of the borehole from 457.85 to 832.00 m BGS. Pulse-withdrawal tests were conducted in all intervals, and pulse-injection tests were conducted in six intervals.

Table 6-1: DGR-2 Phase 2 test zones and tests

Formations / Units	Top of Test Zone (m BGS)	Bottom of Test Zone (m BGS)	Type(s) of Test(s)
Queenston	457.85	488.35	PW
Queenston	487.20	517.70	PW
Georgian Bay	517.50	548.00	PW
Georgian Bay	547.80	578.30	PW
Georgian Bay	578.10	608.60	PW, PI
Blue Mountain	608.40	638.90	PW
Blue Mountain-Collingwood	630.50	661.00	PW
Cobourg	660.50	691.00	PW
Sherman Fall	687.60	718.10	PW
Kirkfield	714.50	745.00	PW
Kirkfield	731.60	762.10	PW, PI
Kirkfield-Coboconk	754.50	785.00	PI, PW
Coboconk-Gull River	761.50	792.00	PI, PW
Gull River	785.00	815.50	PI, PW
Gull River	801.50	832.00	PI, PW
Reference Elevation – Ground Surface	185.84 m above mean sea level		

PW: pulse withdrawal
 PI: pulse injection

The test-zone transducer during Phase 2 DGR-2 testing was located 25.14 m above the middle of the isolated test zone and was hydraulically connected to the test zone via a length of 1/4-in stainless-steel tubing. To determine the P_f values corresponding to the middle of the test zone, the “raw” (as measured by the transducer) P_f estimates were depth-corrected using the offset distance of 25.14 m and the estimated fluid density value for each interval. The depth-corrected P_f estimates are given in the tables below whereas the raw P_f estimates are listed in the graph annotations.

Results of each test analysis are discussed below. A summary of DGR-2 testing results is presented in Section 6.16.

6.1 457.85-488.35 Queenston

The DGR-2 interval from 457.85 to 488.35 m BGS was entirely contained within shale of the Queenston Formation. An overview of the testing in this interval is given in Table 6-2 and the corresponding parameter estimates are given in Table 6-3. A pulse-injection test and a pulse-withdrawal test were conducted in this interval.

Table 6-2: Summary of the DGR2_457.85-488.35 testing activities.

Formation / Unit		Top of Test Zone (m BGS)		Bottom of Test Zone (m BGS)	
Queenston		457.85		488.35	
Test	Initiated	Magnitude (kPa)	Duration	Compressibility (Pa ⁻¹)	
Shut-in	30-07-09 16:17	N/A	16 hr	N/A	
PW1	31-07-09 08:01	336	24 hr	7.7E-10	
PW2 (pt 1)	01-08-09 08:02	214	7 min	N/C	
PW2 (pt 2)	01-08-09 08:09	328	23 hr	7.8E-10	
Borehole Pressure History					
Event		Start		Pressure (kPa)	
Westbay Removal		02-06-09 12:00		4784	
Casing Test		13-07-09		N/A	
Leaking Test		22-07-09		N/A	
Casing Test		29-07-09		N/A	
Shut-in		30-07-09 16:17		5209	

Table 6-3: Summary of the DGR2_457-85-488.35 parameter estimates.

Parameter	Best Fit	Minimum	Maximum	Mean
K_f (m/s)	1.9E-14	1.2E-14	2.5E-14	1.9E-14
P_f (kPa)	4379	4228	4516	4392
K_s (m/s)	5.0E-13	2.7E-13	1.8E-12	6.0E-13
t_s (cm)	5.3	1.8	19	7.0
S_s (m ⁻¹)	1.2E-6	2.1E-7	3.7E-6	9.4E-7

Figure 6-1 shows the measured pressure record from DGR2_457.85-488.35 used in this analysis along with the best-fit simulation and parameter values. The ranges of formation K and raw P_f values estimated from perturbation analysis are shown in Figure 6-2 and the fit value cumulative distribution function is shown in Figure 6-3.

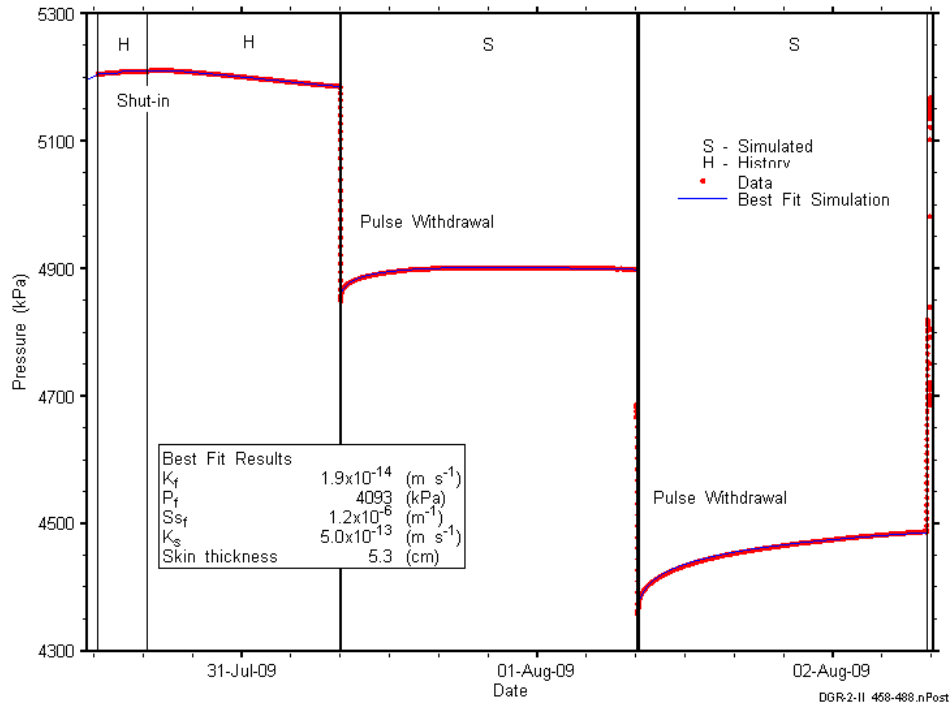


Figure 6-1: Annotated DGR2_457.85-488.35 testing sequence showing best-fit simulation and parameter estimates.

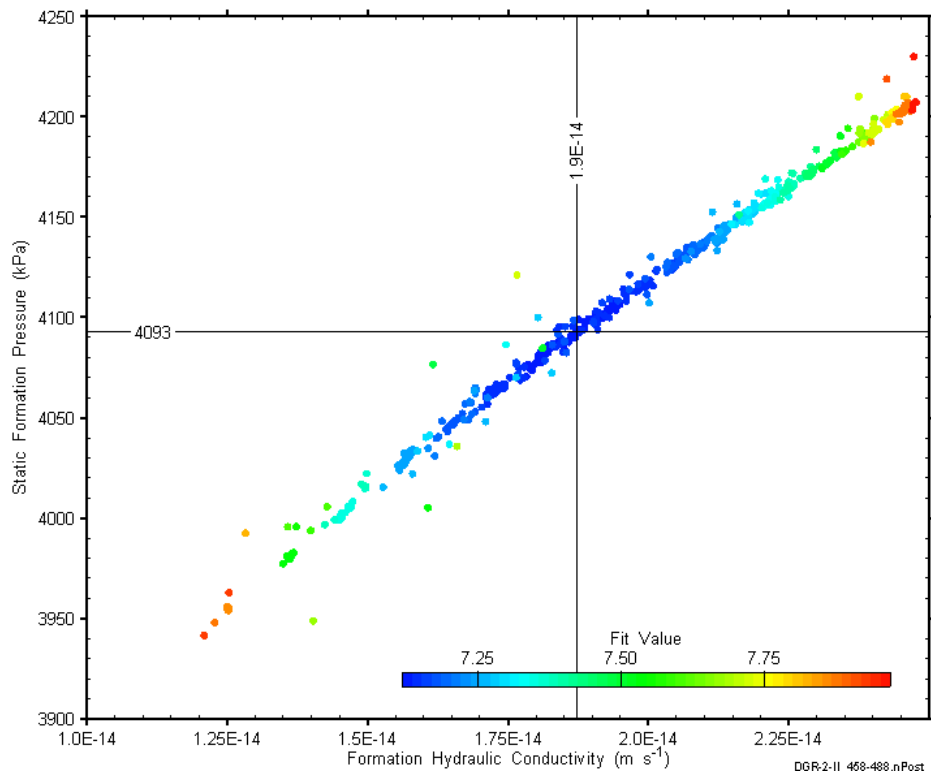


Figure 6-2: XY-scatter plot showing estimates of formation hydraulic conductivity and raw static formation pressure derived from the DGR2_457.85-488.35 perturbation analysis.

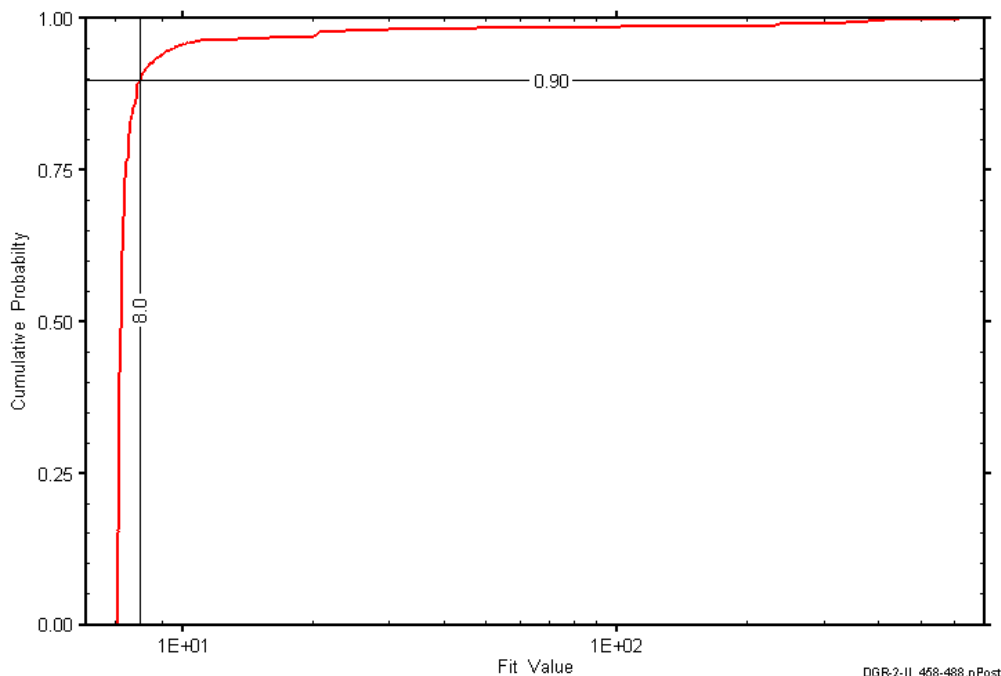


Figure 6-3: DGR2_457.85-488.35 fit value cumulative distribution function.

6.2 487.20-517.70 Queenston

The DGR-2 interval from 487.20 to 517.70 m BGS was entirely contained within shale of the Queenston Formation. An overview of the testing in this interval is given in Table 6-4 and the corresponding parameter estimates are given in Table 6-5. Two pulse-withdrawal tests were conducted in this interval.

Table 6-4: Summary of the DGR2_487.20-517.70 testing activities.

Formation / Unit		Top of Test Zone (m BGS)	Bottom of Test Zone (m BGS)	
Queenston		487.20	517.70	
Test	Initiated	Magnitude (kPa)	Duration	Compressibility (Pa ⁻¹)
Shut-in	02-08-09 14:45	N/A	18 hr	N/A
PW1	03-08-09 08:25	417	23 hr	6.2E-10
PW2 (pt 1)	04-08-09 07:53	74	7 min	N/C
PW2 (pt 2)	04-08-09 08:00	411	24 hr	6.2E-10
Borehole Pressure History				
Event	Start	Pressure (kPa)		
Westbay Removal	02-06-09 12:00	4784		
Casing Test	13-07-09	N/A		
Leaking Test	22-07-09	N/A		
Casing Test	29-07-09	N/A		
Shut-in	02-08-09 14:45	5530		

Table 6-5: Summary of the DGR2_487.20-517.70 parameter estimates.

Parameter	Best Fit	Minimum	Maximum	Mean
K_f (m/s)	3.3E-14	3.1E-14	3.6E-14	3.3E-14
P_f (kPa)	4133	4070	4202	4139
K_s (m/s)	3.8E-12	2.0E-12	8.8E-12	3.2E-12
t_s (cm)	2.2	1.9	2.8	2.3
S_s (m ⁻¹)	1.2E-6	9.5E-7	1.5E-6	1.2E-6

Figure 6-4 shows the measured pressure record from DGR2_457.85-488.35 used in this analysis along with the best-fit simulation and parameter values. The ranges of formation K and raw P_f values estimated from perturbation analysis are shown in Figure 6-5 and the fit value cumulative distribution function is shown in Figure 6-6.

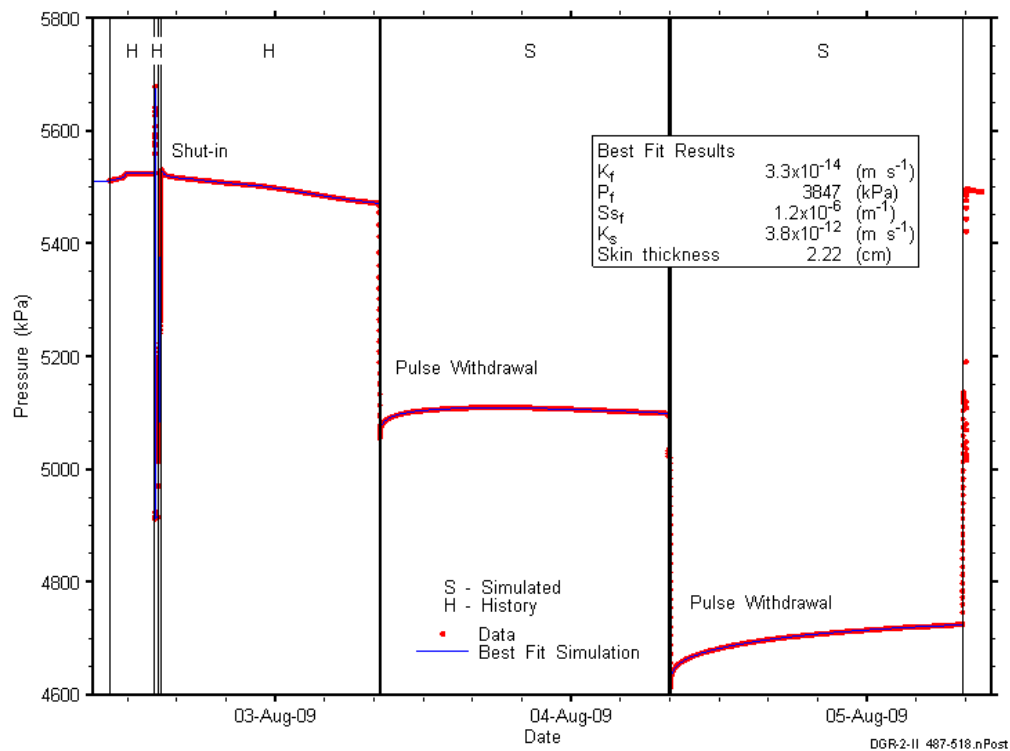


Figure 6-4: Annotated DGR2_487.20-517.70 testing sequence showing best-fit simulation and parameter estimates.

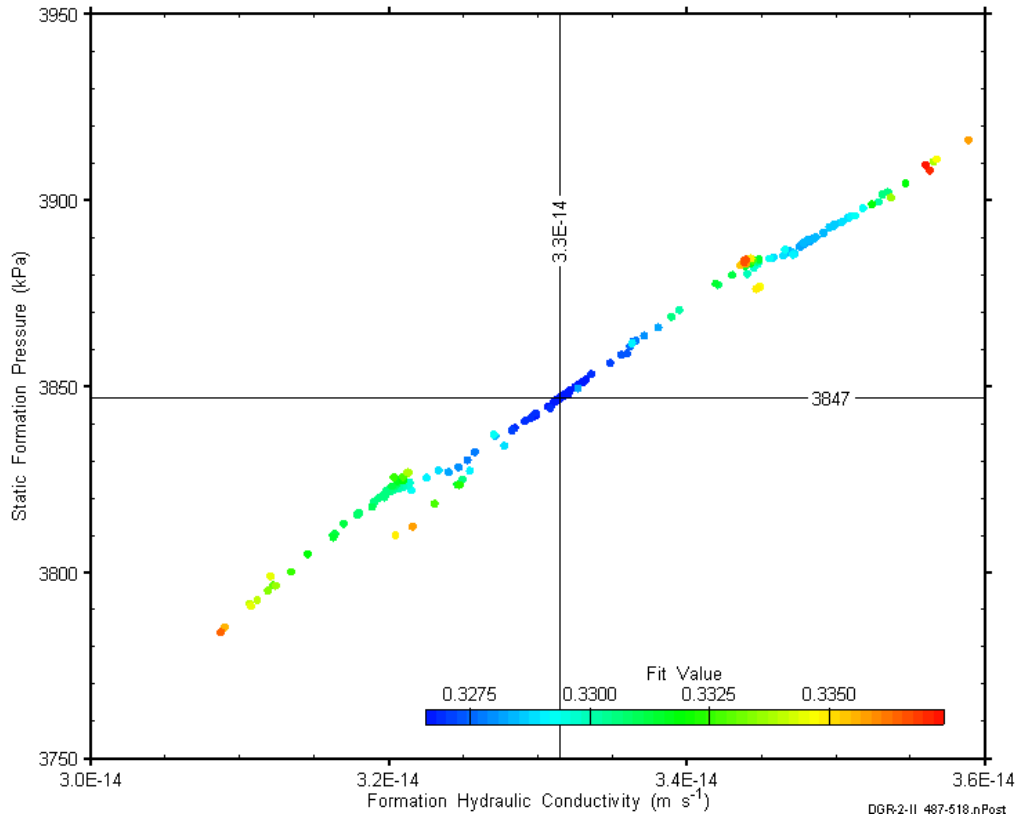


Figure 6-5: XY-scatter plot showing estimates of formation hydraulic conductivity and raw static formation pressure derived from the DGR2_487.20-517.70 perturbation analysis.

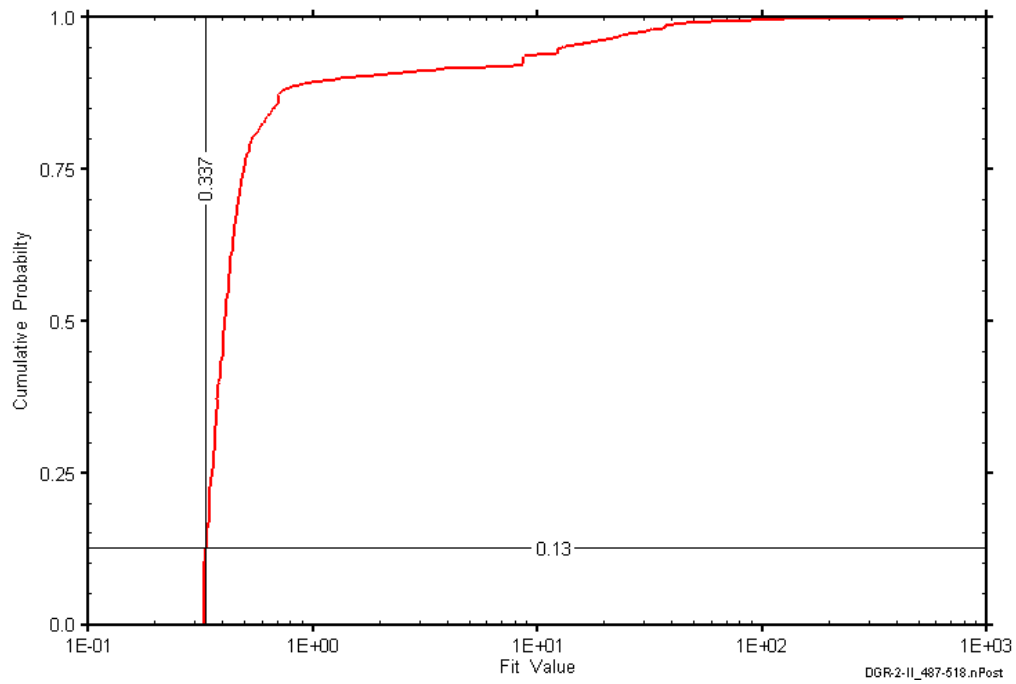


Figure 6-6: DGR2_487.20-517.70 fit value cumulative distribution function.

6.3 517.50-548.00 Georgian Bay

The DGR-2 interval from 517.50 to 548.00 m BGS included the lower 0.5 m of the Queenston Formation while the balance of the interval was the upper Georgian Bay Formation, a shale with limestone, siltstone, and sandstone layers. An overview of the testing in this interval is given in Table 6-6 and the corresponding parameter estimates are given in Table 6-7. Two pulse-withdrawal tests were conducted in this interval.

Table 6-6: Summary of the DGR2_517.50-548.00 testing activities.

Formation / Unit	Top of Test Zone (m BGS)		Bottom of Test Zone (m BGS)	
Georgian Bay	517.50		548.00	
Test	Initiated	Magnitude (kPa)	Duration	Compressibility (Pa ⁻¹)
Shut-in	05-08-09 13:56	N/A	20 hr	N/A
PW1	06-08-09 10:12	581	22 hr	4.5E-10
PW2 (pt 1)	07-08-09 08:00	-41	7 min	N/C
PW2 (pt 2)	07-08-09 08:08	582	23 hr	4.5E-10
Borehole Pressure History				
Event	Start		Pressure (kPa)	
Westbay Removal	02-06-09 12:00		5567	
Casing Test	13-07-09		N/A	
Leaking Test	22-07-09		N/A	
Casing Test	29-07-09		N/A	
Shut-in	05-08-09 13:56		5862	

Table 6-7: Summary of the DGR2_517.50-548.00 parameter estimates.

Parameter	Best Fit	Minimum	Maximum	Mean
K_f (m/s)	4.9E-14	4.6E-14	5.3E-14	5.0E-14
P_f (kPa)	4436	4371	4499	4446
K_s (m/s)	2.5E-12	2.1E-12	3.3E-12	2.6E-12
t_s (cm)	5.9	4.1	9.3	6.6
S_s (m ⁻¹)	4.3E-7	2.5E-7	6.3E-7	3.9E-7

Figure 6-7 shows the measured pressure record from DGR2_517.50-548.00 used in this analysis along with the best-fit simulation and parameter values. The ranges of formation K and raw P_f values estimated from perturbation analysis are shown in Figure 6-8 and the fit value cumulative distribution function is shown in Figure 6-9.

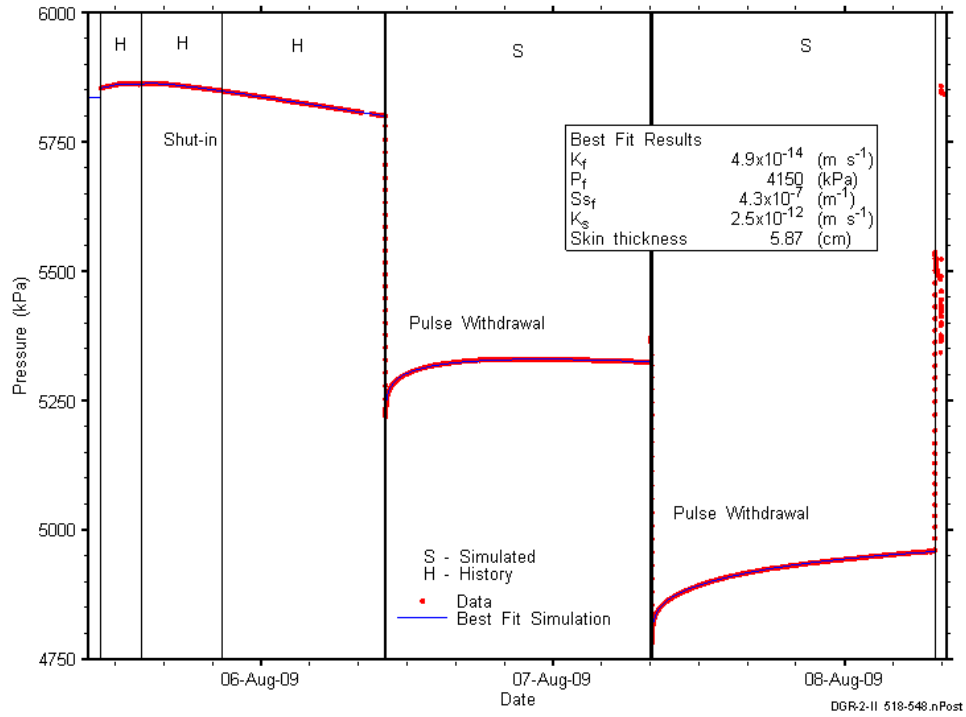


Figure 6-7: Annotated DGR2_517.50-548.00 testing sequence showing best-fit simulation and parameter estimates.

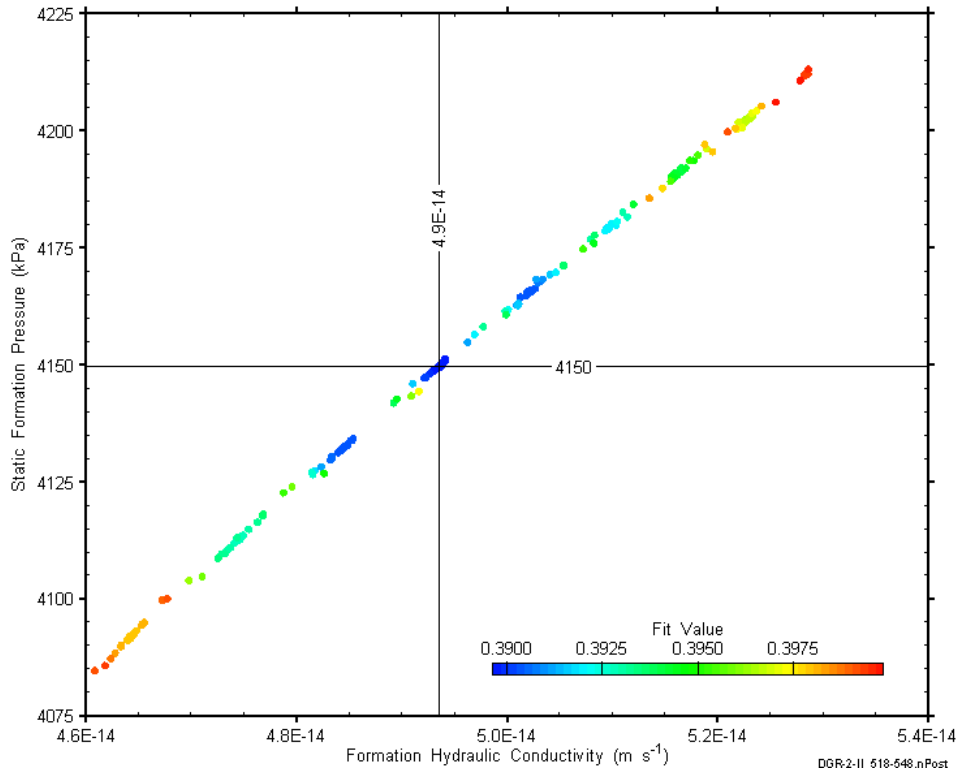


Figure 6-8: XY-scatter plot showing estimates of formation hydraulic conductivity and raw static formation pressure derived from the DGR2_517.50-548.00 perturbation analysis.

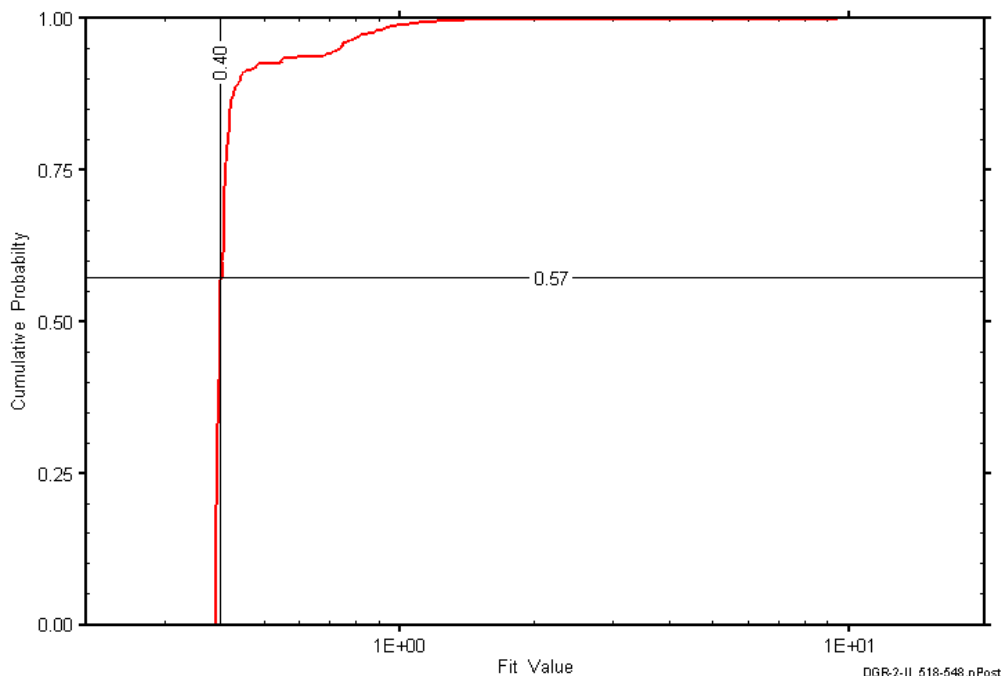


Figure 6-9: DGR2_517.50-548.00 fit value cumulative distribution function.

6.4 547.80-578.30 Georgian Bay

The DGR-2 interval from 547.80 to 578.30 m BGS was entirely contained within the Georgian Bay Formation, a shale with limestone, siltstone, and sandstone layers. An overview of the testing in this interval is given in Table 6-8 and the corresponding parameter estimates are given in Table 6-9. Two pulse-withdrawal tests were conducted in this interval.

Table 6-8: Summary of the DGR2_547.80-578.30 testing activities.

Formation / Unit		Top of Test Zone (m BGS)	Bottom of Test Zone (m BGS)	
Georgian Bay		547.80	578.30	
Test	Initiated	Magnitude (kPa)	Duration	Compressibility (Pa ⁻¹)
Shut-in	08-08-09 13:21	N/A	19 hr	N/A
PW1	09-08-09 07:52	629	23 hr	4.2E-10
PW2 (pt 1)	10-08-09 07:19	-111	8 min	N/C
PW2 (pt 2)	10-08-09 07:27	637	24 hr	4.2E-10
Borehole Pressure History				
Event	Start	Pressure (kPa)		
Westbay Removal	02-06-09 12:00	5915		
Casing Test	13-07-09	N/A		
Leaking Test	22-07-09	N/A		
Casing Test	29-07-09	N/A		
Shut-in	08-08-09 13:21	6215		

Table 6-9: Summary of the DGR2_547.80-578.30 parameter estimates.

Parameter	Best Fit	Minimum	Maximum	Mean
K_f (m/s)	3.4E-14	3.0E-14	3.6E-14	3.3E-14
P_f (kPa)	4563	4463	4620	4542
K_s (m/s)	1.6E-12	7.8E-13	3.4E-12	1.4E-12
t_s (cm)	17	8.0	38	16
S_s (m^{-1})	1.5E-7	4.0E-8	4.3E-7	1.8E-7

Figure 6-10 shows the measured pressure record from DGR2_547.80-578.30 used in this analysis along with the best-fit simulation and parameter values. The ranges of formation K and raw P_f values estimated from perturbation analysis are shown in Figure 6-11 and the fit value cumulative distribution function is shown in Figure 6-12.

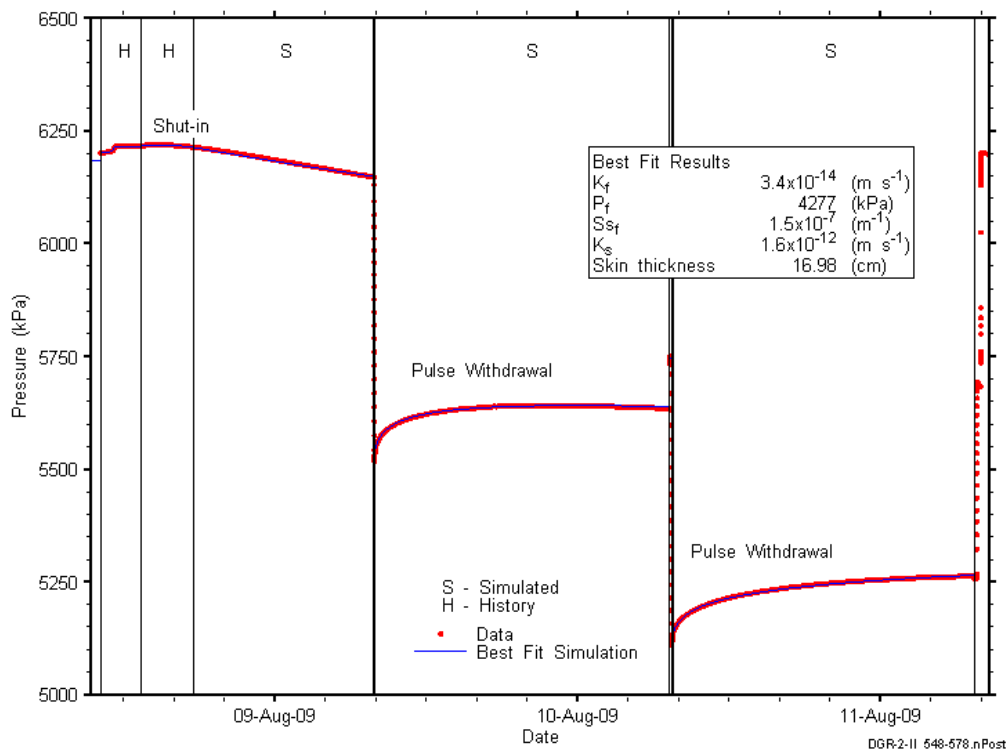


Figure 6-10: Annotated DGR2_547.80-578.30 testing sequence showing best-fit simulation and parameter estimates.

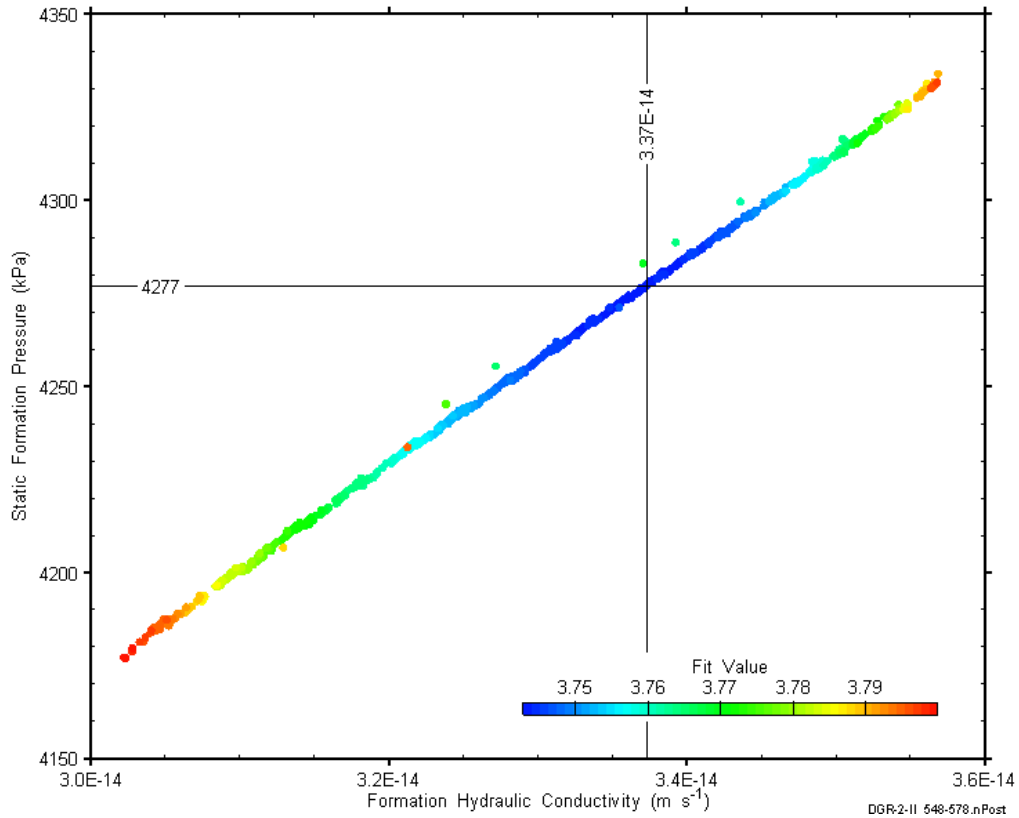


Figure 6-11: XY-scatter plot showing estimates of formation hydraulic conductivity and raw static formation pressure derived from the DGR2_547.80-578.30 perturbation analysis.

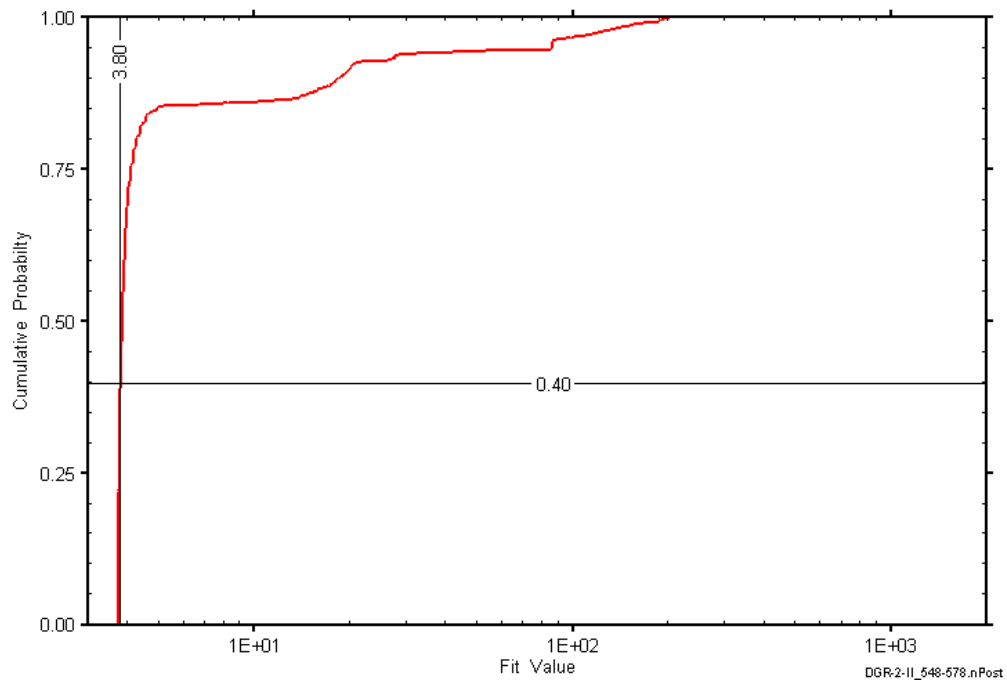


Figure 6-12: DGR2_547.80-578.30 fit value cumulative distribution function.

6.5 578.10-608.60 Georgian Bay

The DGR-2 interval from 578.10 to 608.60 m BGS consisted of the lower third of the Georgian Bay Formation, a shale with fewer limestone, siltstone, and sandstone layers than the overlying portion of the formation. An overview of the testing in this interval is given in Table 6-10 and the corresponding parameter estimates are given in Table 6-11. Two pulse-withdrawal tests and one pulse-injection test were conducted in this interval.

Table 6-10: Summary of the DGR2_578.10-608.60 testing activities.

Formation / Unit	Top of Test Zone (m BGS)		Bottom of Test Zone (m BGS)	
Georgian Bay	578.10		608.60	
Test	Initiated	Magnitude (kPa)	Duration	Compressibility (Pa ⁻¹)
Shut-in	11-08-09 13:19	N/A	2.3 hr	N/A
PW1	11-08-09 15:35	25	29 min	1.1E-8
PW2	11-08-09 16:04	427	16 hr	N/C
PI	12-08-09 08:35	366	22 hr	N/C
Borehole Pressure History				
Event	Start		Pressure (kPa)	
Westbay Removal	02-06-09 12:00		6263	
Casing Test	13-07-09		N/A	
Leaking Test	22-07-09		N/A	
Casing Test	29-07-09		N/A	
Shut-in	11-08-09 13:19		6561	

Table 6-11: Summary of the DGR2_578.10-608.60 parameter estimates.

Parameter	Best Fit	Minimum	Maximum	Mean
K_f (m/s)	4.8E-14	4.7E-14	5.0E-14	4.8E-14
P_f (kPa)	6285	6281	6288	6285
K_s (m/s)	1.9E-10	1.8E-10	2.0E-10	1.9E-10
t_s (cm)	1.4	1.4	1.4	1.4
S_s (m ⁻¹)	6.4E-5	6.3E-5	6.5E-5	6.4E-5

Figure 6-13 shows the measured pressure record from DGR2_578.10-608.60 used in this analysis along with the best-fit simulation and parameter values. The ranges of formation K and raw P_f values estimated from perturbation analysis are shown in Figure 6-14 and the fit value cumulative distribution function is shown in Figure 6-15.

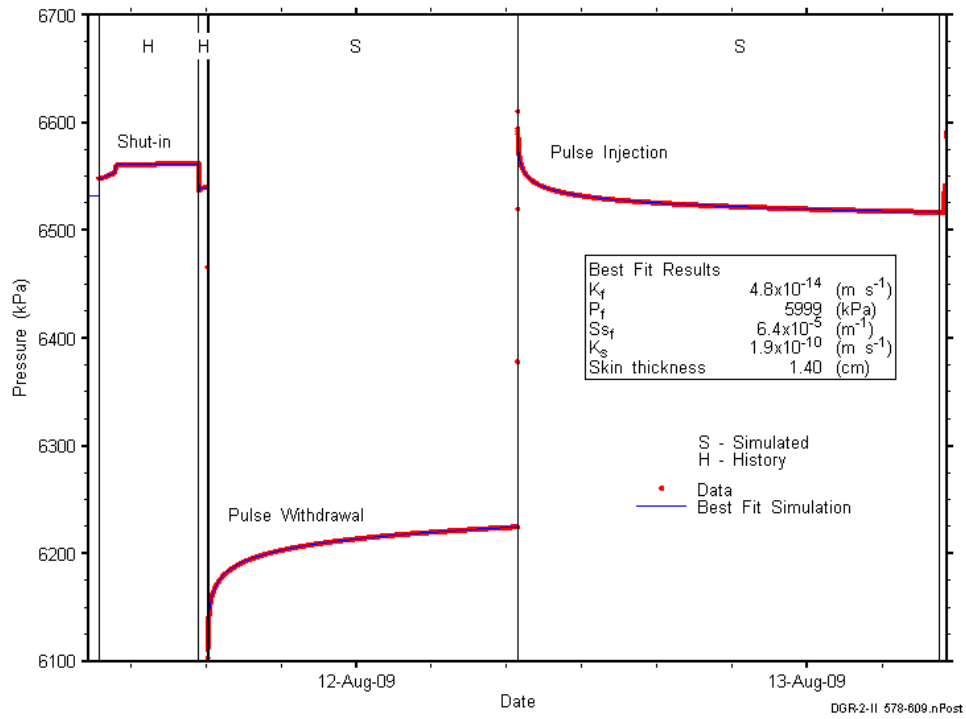


Figure 6-13: Annotated DGR2_578.10-608.60 testing sequence showing best-fit simulation and parameter estimates.

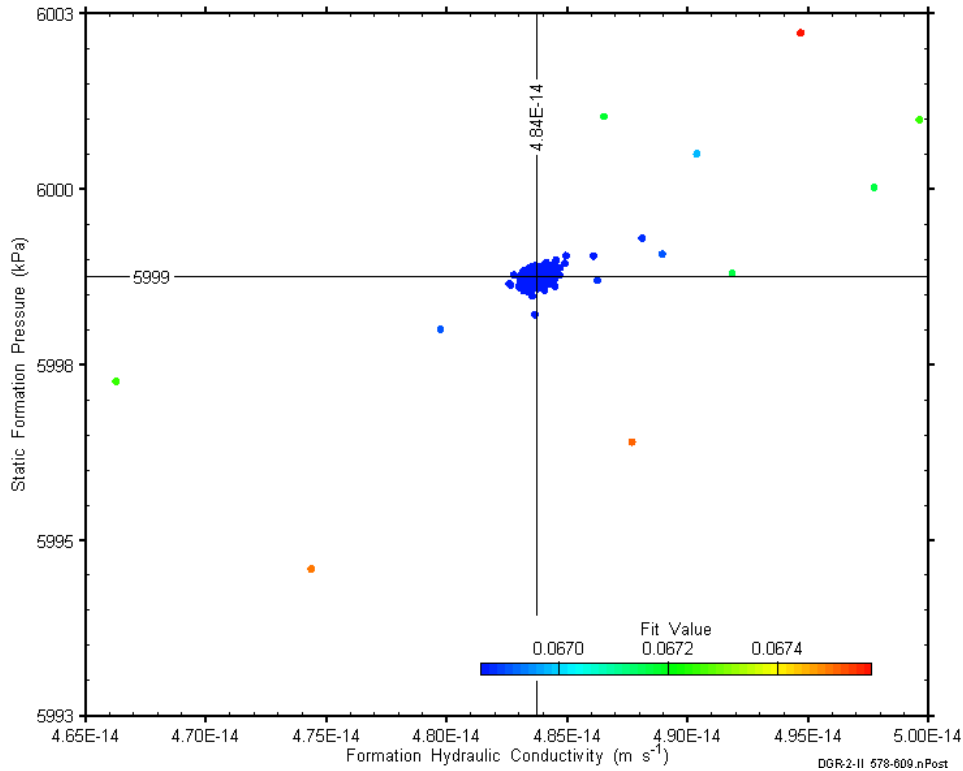


Figure 6-14: XY-scatter plot showing estimates of formation hydraulic conductivity and raw static formation pressure derived from the 578.10-608.60 perturbation analysis.

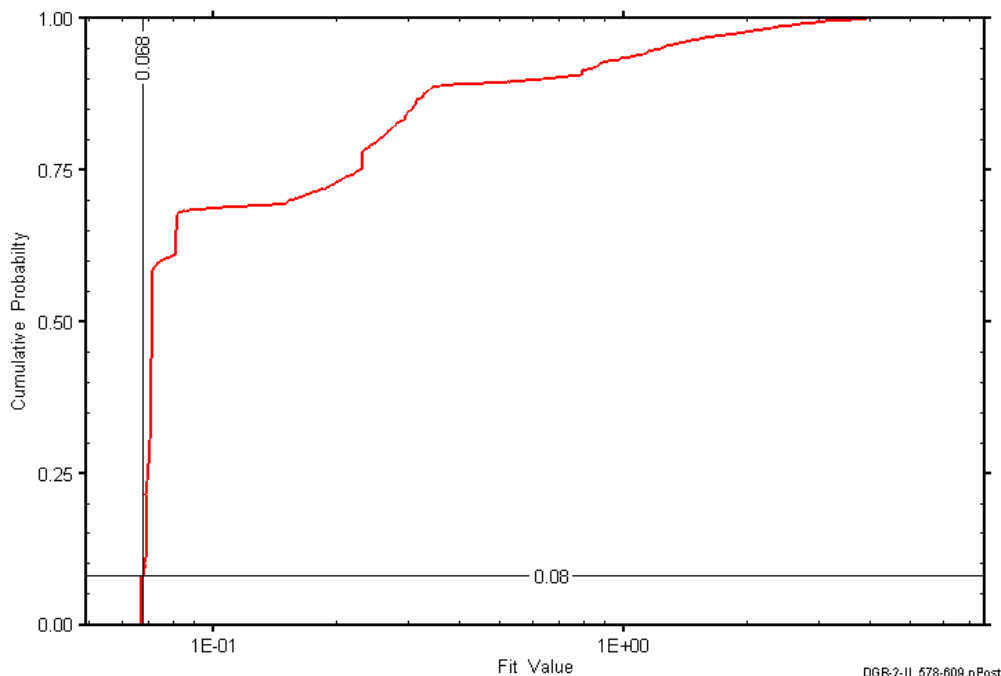


Figure 6-15: DGR2_578.10-608.60 fit value cumulative distribution function.

6.6 608.40-638.90 Blue Mountain

The DGR-2 interval from 608.40 to 638.90 m BGS included the lower 0.5 m of the Georgian Bay Formation while the balance of the interval was the upper 70% of the Blue Mountain Formation, a shale interbedded with siliceous siltstone and sandstone layers and fossiliferous limestone layers. An overview of the testing in this interval is given in Table 6-12 and the corresponding parameter estimates are given in Table 6-13. Two pulse-withdrawal tests were conducted in this interval.

Table 6-12: Summary of the DGR2_608.40-638.90 testing activities.

Formation / Unit		Top of Test Zone (m BGS)	Bottom of Test Zone (m BGS)	
Blue Mountain		608.40	638.90	
Test	Initiated	Magnitude (kPa)	Duration	Compressibility (Pa ⁻¹)
Shut-in	13-08-09 12:46	N/A	19 hr	N/A
PW1	14-08-09 07:52	763	24 hr	3.7E-10
PW2 (Pt 1)	15-08-09 07:37	-231	8 min	N/C
PW2 (Pt 2)	15-08-09 07:45	765	24 hr	3.7E-10
Borehole Pressure History				
Event	Start	Pressure (kPa)		
Westbay Removal	02-06-09 12:00	6545		
Casing Test	13-07-09	N/A		
Leaking Test	22-07-09	N/A		
Casing Test	29-07-09	N/A		
Shut-in	13-08-09 12:46	6935		

Table 6-13: Summary of the DGR2_608.40-638.90 parameter estimates.

Parameter	Best Fit	Minimum	Maximum	Mean
K_f (m/s)	1.2E-14	1.2E-14	1.2E-14	1.2E-14
P_f (kPa)	3213	3082	3315	3212
K_s (m/s)	4.0E-14	3.5E-14	4.9E-14	4.0E-14
t_s (cm)	2.3	1.8	2.9	2.3

Figure 6-16 shows the measured pressure record from DGR2_608.40-638.90 used in this analysis along with the best-fit simulation and parameter values. The S_s value for this analysis was fixed at $1E-6 \text{ m}^{-1}$. The ranges of formation K and raw P_f values estimated from perturbation analysis are shown in Figure 6-17 and the fit value cumulative distribution function is shown in Figure 6-18.

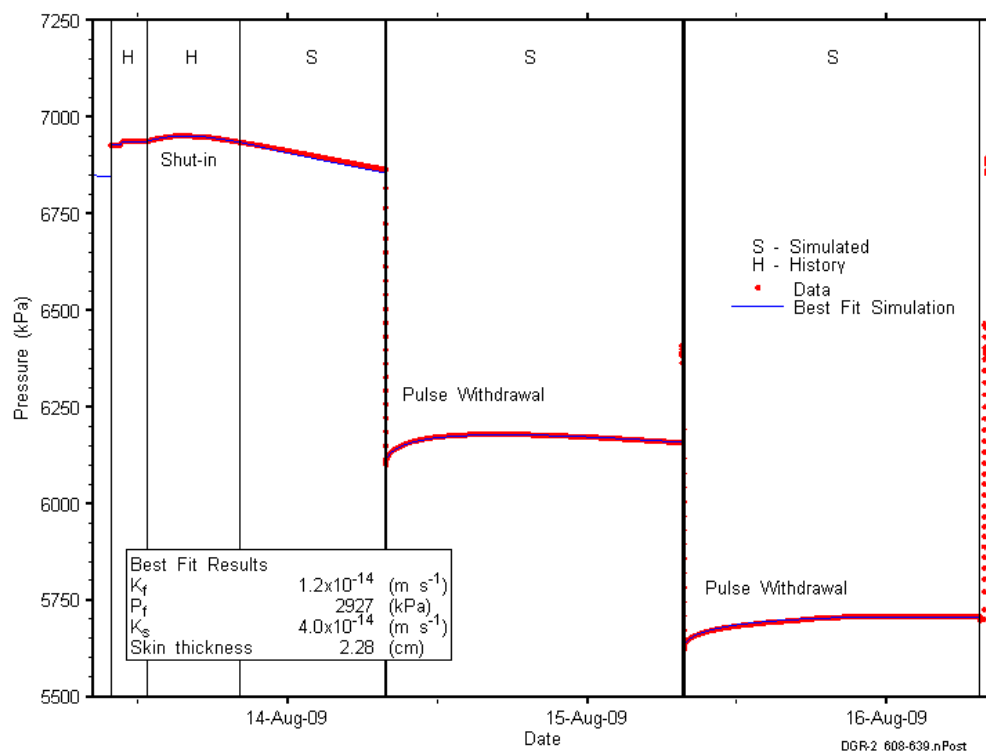


Figure 6-16: Annotated DGR2_608.40-638.90 testing sequence showing best-fit simulation and parameter estimates.

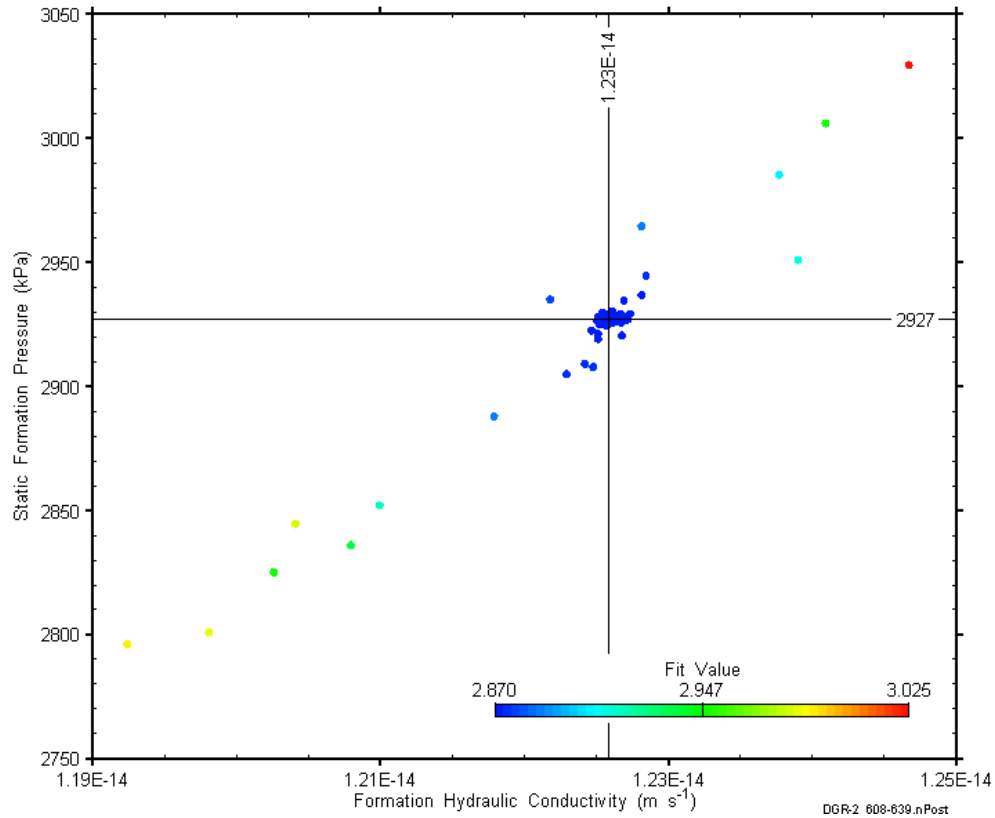


Figure 6-17: XY-scatter plot showing estimates of formation hydraulic conductivity and raw static formation pressure derived from the 608.40-638.90 perturbation analysis.

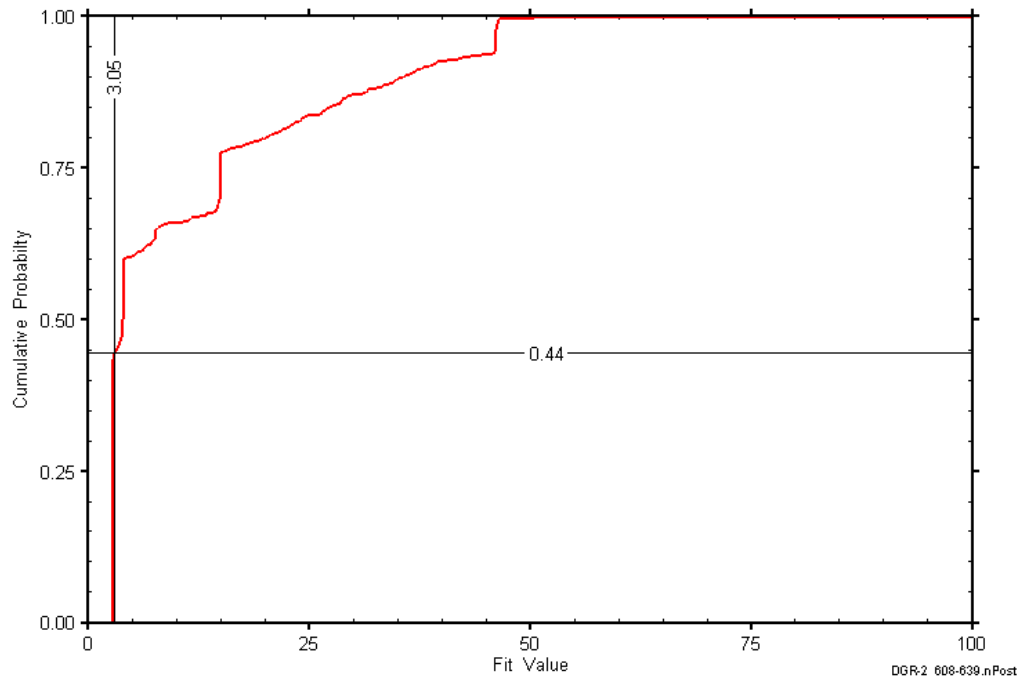


Figure 6-18: DGR2_608.40-638.90 fit value cumulative distribution function.

6.7 630.50-661.00 Blue Mountain-Collingwood

The DGR-2 interval from 630.50 to 661.00 m BGS included the lower 21.1 m of the Blue Mountain Formation, the entire 7.9-m thickness of the Collingwood Member of the Cobourg Formation, and the upper 1.5 m of the Lower Member of the Cobourg Formation. The Blue Mountain is generally a shale interbedded with siliceous siltstone and sandstone layers and fossiliferous limestone layers, although the lower 4+ m is a bed of calcareous shale. The Collingwood is a calcareous shale interbedded with argillaceous limestone layers, while the Lower Member of the Cobourg is an argillaceous limestone. An overview of the testing in this interval is given in Table 6-14 and the corresponding parameter estimates are given in Table 6-15. Two pulse-withdrawal tests were conducted in this interval.

Table 6-14: Summary of the DGR2_630.50-661.00 testing activities.

Formation / Unit		Top of Test Zone (m BGS)	Bottom of Test Zone (m BGS)	
Blue Mountain-Collingwood		630.50	661.00	
Test	Initiated	Magnitude (kPa)	Duration	Compressibility (Pa ⁻¹)
Shut-in	16-08-09 12:28	N/A	20 hr	N/A
PW1	17-08-09 08:20	776	24 hr	3.6E-10
PW2 (Pt 1)	18-08-09 08:05	-221	7 min	N/C
PW2 (Pt 2)	18-08-09 08:12	780	23 hr	3.6E-10
Borehole Pressure History				
Event	Start		Pressure (kPa)	
Westbay Removal	02-06-09 12:00		6877	
Casing Test	13-07-09		N/A	
Leaking Test	22-07-09		N/A	
Casing Test	29-07-09		N/A	
Shut-in	16-08-09 12:28		7162	

Table 6-15: Summary of the DGR2_630.50-661.00 parameter estimates.

Parameter	Best Fit	Minimum	Maximum	Mean
K_f (m/s)	9.4E-15	9.2E-15	9.7E-15	9.4E-15
P_f (kPa)	3764	3696	3865	3764
K_s (m/s)	1.1E-13	9.7E-14	1.2E-13	1.1E-13
t_s (cm)	4.7	4.4	5.0	4.7

Figure 6-19 shows the measured pressure record from DGR2_630.50-661.00 used in this analysis along with the best-fit simulation and parameter values. The S_s value for this analysis was fixed at $3E-7 \text{ m}^{-1}$. The ranges of formation K and raw P_f values estimated from perturbation analysis are shown in Figure 6-20 and the fit value cumulative distribution function is shown in Figure 6-21.

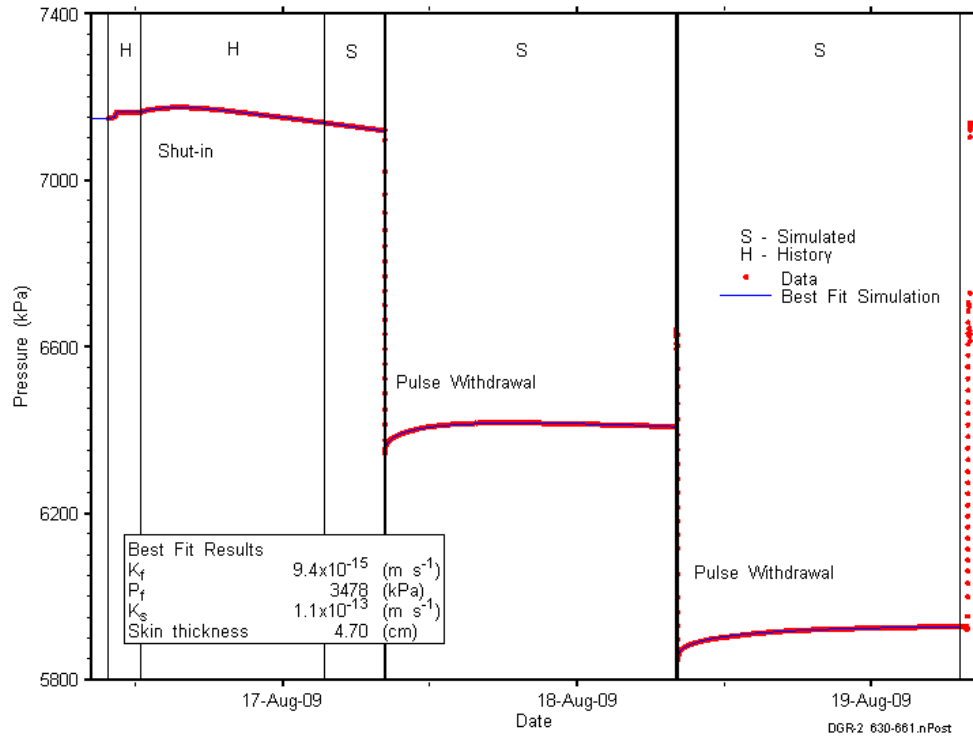


Figure 6-19: Annotated DGR2_630.50-661.00 testing sequence showing best-fit simulation and parameter estimates.

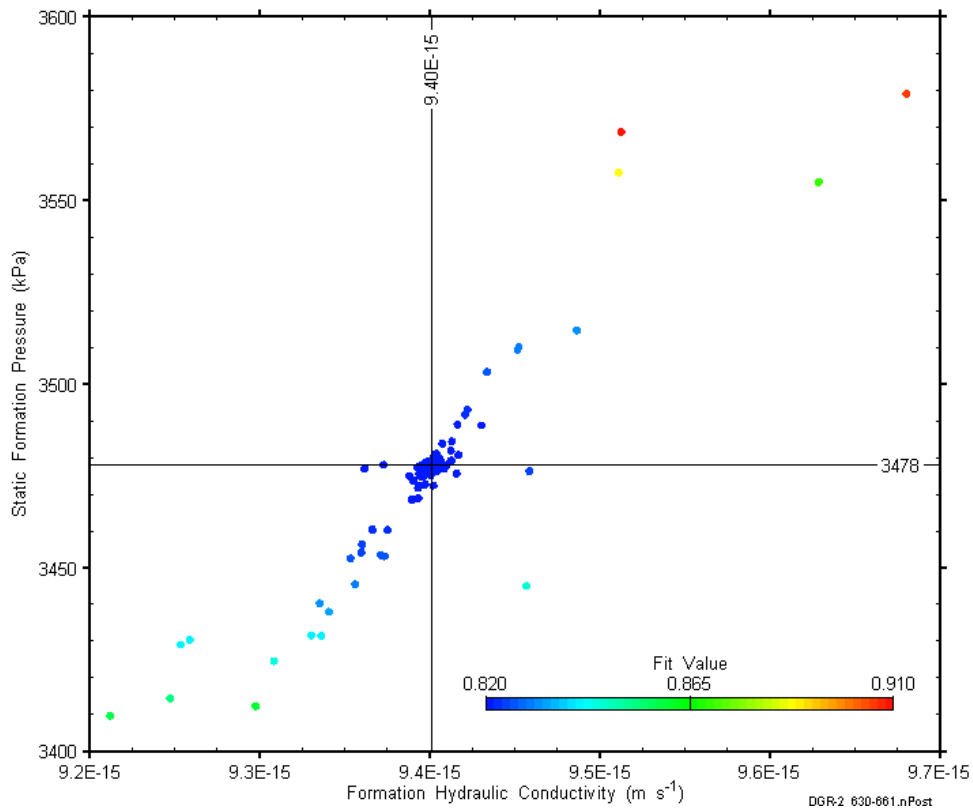


Figure 6-20: XY-scatter plot showing estimates of formation hydraulic conductivity and raw static formation pressure derived from the 630.50-661.00 perturbation analysis.

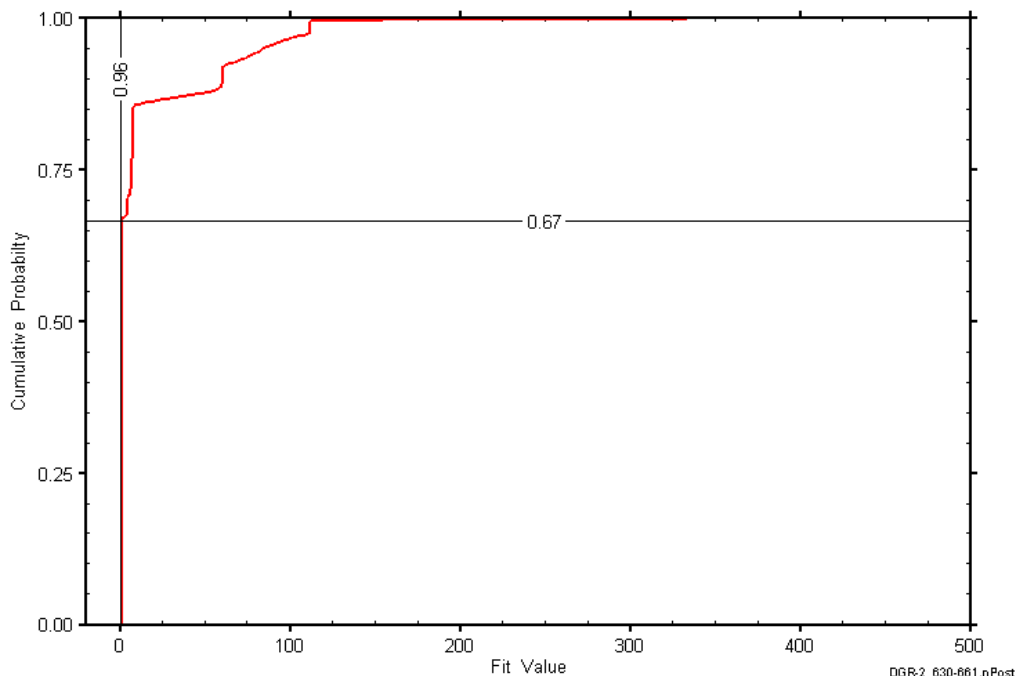


Figure 6-21: DGR2_630.50-661.00 fit value cumulative distribution function.

6.8 660.50-691.00 Cobourg

The DGR-2 interval from 660.50 to 691.00 m BGS included all but the upper 1.0 m of the Lower Member of the Cobourg Formation and the upper 2.9 m of the Sherman Fall Formation. The Lower Member of the Cobourg is an argillaceous limestone, and the upper Sherman Fall is a shaley limestone. An overview of the testing in this interval is given in Table 6-16 and the corresponding parameter estimates are given in Table 6-17. Two pulse-withdrawal tests were conducted in this interval.

Table 6-16: Summary of the DGR2_660.50-691.00 testing activities.

Formation / Unit		Top of Test Zone (m BGS)	Bottom of Test Zone (m BGS)	
Cobourg		660.50	691.00	
Test	Initiated	Magnitude (kPa)	Duration	Compressibility (Pa ⁻¹)
Shut-in	19-08-09 13:00	N/A	20 hr	N/A
PW1	20-08-09 08:23	787	23 hr	3.5E-10
PW2 (Pt 1)	21-08-09 07:56	10	7 min	N/C
PW2 (Pt 2)	21-08-09 08:04	787	46 hr	3.5E-10
Borehole Pressure History				
Event	Start	Pressure (kPa)		
Westbay Removal	02-06-09 12:00	7229		
Casing Test	13-07-09	N/A		
Leaking Test	22-07-09	N/A		
Casing Test	29-07-09	N/A		
Shut-in	19-08-09 13:00	7506		

Table 6-17: Summary of the DGR2_660.50-691.00 parameter estimates.

Parameter	Best Fit	Minimum	Maximum	Mean
K_f (m/s)	3.9E-15	2.3E-15	4.8E-15	3.8E-15
P_f (kPa)	6682	6415	6807	6668
K_s (m/s)	1.4E-13	5.7E-14	6.7E-13	1.6E-13
t_s (cm)	7.2	1.5	37	10
S_s (1/m)	1.2E-7	1.0E-8	5.9E-7	9.9E-8

Figure 6-22 shows the measured pressure record from DGR2_660.50-691.00 used in this analysis along with the best-fit simulation and parameter values. The ranges of formation K and raw P_f values estimated from perturbation analysis are shown in Figure 6-23 and the fit value cumulative distribution function is shown in Figure 6-24.

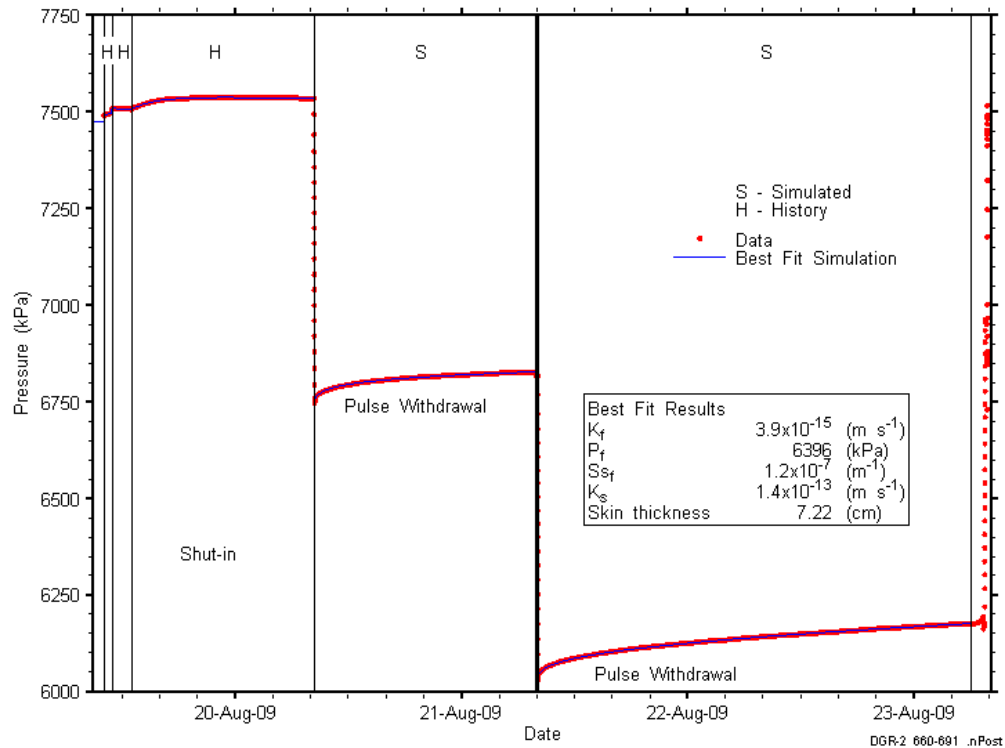


Figure 6-22: Annotated DGR2_660.50-691.00 testing sequence showing best-fit simulation and parameter estimates.

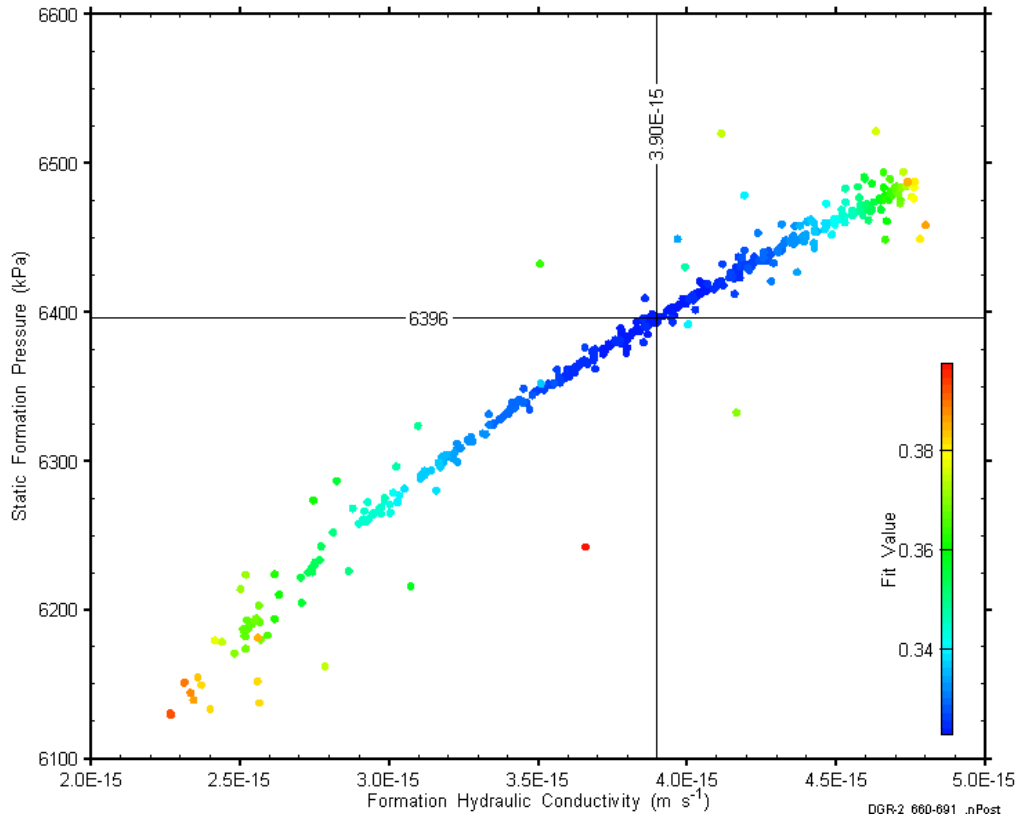


Figure 6-23: XY-scatter plot showing estimates of formation hydraulic conductivity and raw static formation pressure derived from the 660.50-691.00 perturbation analysis.

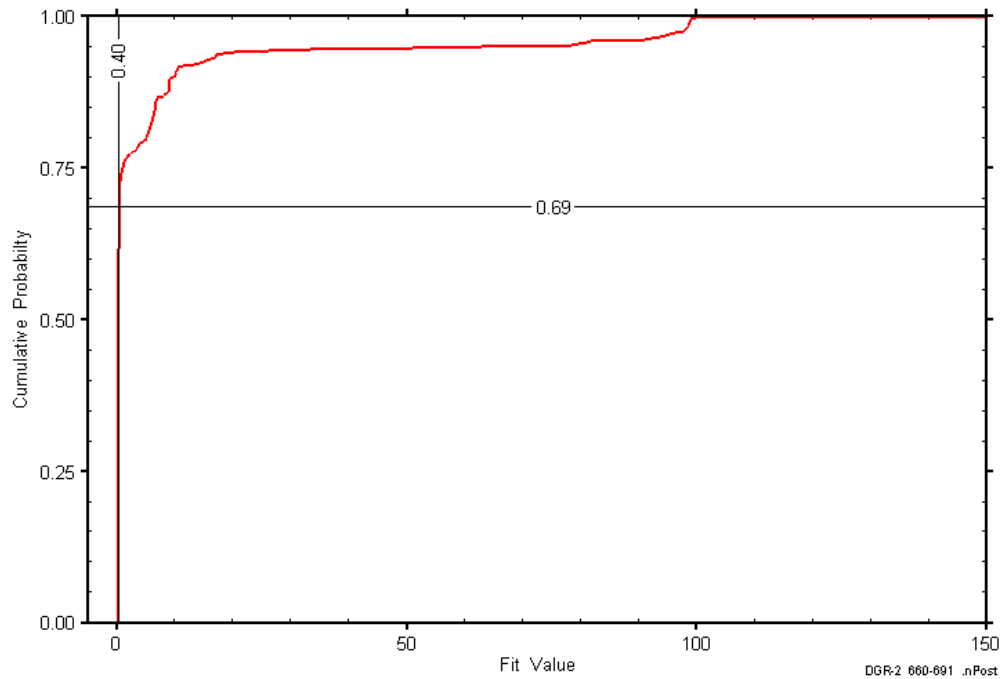


Figure 6-24: DGR2_660.50-691.00 fit value cumulative distribution function.

6.9 687.60-718.10 Sherman Fall

The DGR-2 interval from 687.60 to 718.10 m BGS included the lower 0.5 m of the Cobourg Formation, the entire 28.0-m thickness of the Sherman Fall Formation, and the upper 2.0 m of the Kirkfield Formation. The Lower Member of the Cobourg is an argillaceous limestone, the Sherman Fall is also an argillaceous limestone, and the Kirkfield is an argillaceous limestone with shale interbeds. An overview of the testing in this interval is given in Table 6-18 and the corresponding parameter estimates are given in Table 6-19. Two pulse-withdrawal tests were conducted in this interval.

Table 6-18: Summary of the DGR2_687.60-718.10 testing activities.

Formation / Unit		Top of Test Zone (m BGS)		Bottom of Test Zone (m BGS)	
Sherman Fall		687.60		718.10	
Test	Initiated	Magnitude (kPa)	Duration	Compressibility (Pa ⁻¹)	
Shut-in	23-08-09 13:20	N/A	18 hr	N/A	
PW1	24-08-09 07:38	748	25 hr	3.5E-10	
PW2 (Pt 1)	25-08-09 08:32	65	8 min	N/C	
PW2 (Pt 2)	25-08-09 08:04	748	23 hr	3.5E-10	
Borehole Pressure History					
Event		Start		Pressure (kPa)	
Westbay Removal		02-06-09 12:00		7547	
Casing Test		13-07-09		N/A	
Leaking Test		22-07-09		N/A	
Casing Test		29-07-09		N/A	
Shut-in		23-08-09 13:20		7801	

Table 6-19: Summary of the DGR2_687.60-718.10 parameter estimates.

Parameter	Best Fit	Minimum	Maximum	Mean
K_f (m/s)	2.3E-16	6.3E-17	2.8E-16	1.7E-16
P_f (kPa)	4239	290	4741	3378
K_s (m/s)	1.3E-14	1.3E-14	1.4E-14	1.3E-14
t_s (cm)	2.0	2.0	2.6	2.1
S_s (1/m)	1.3E-6	1.2E-6	1.3E-6	1.3E-6

Figure 6-25 shows the measured pressure record from DGR2_687.60-718.10 used in this analysis along with the best-fit simulation and parameter values. The ranges of formation K and raw P_f values estimated from perturbation analysis are shown in Figure 6-26 and the fit value cumulative distribution function is shown in Figure 6-27.

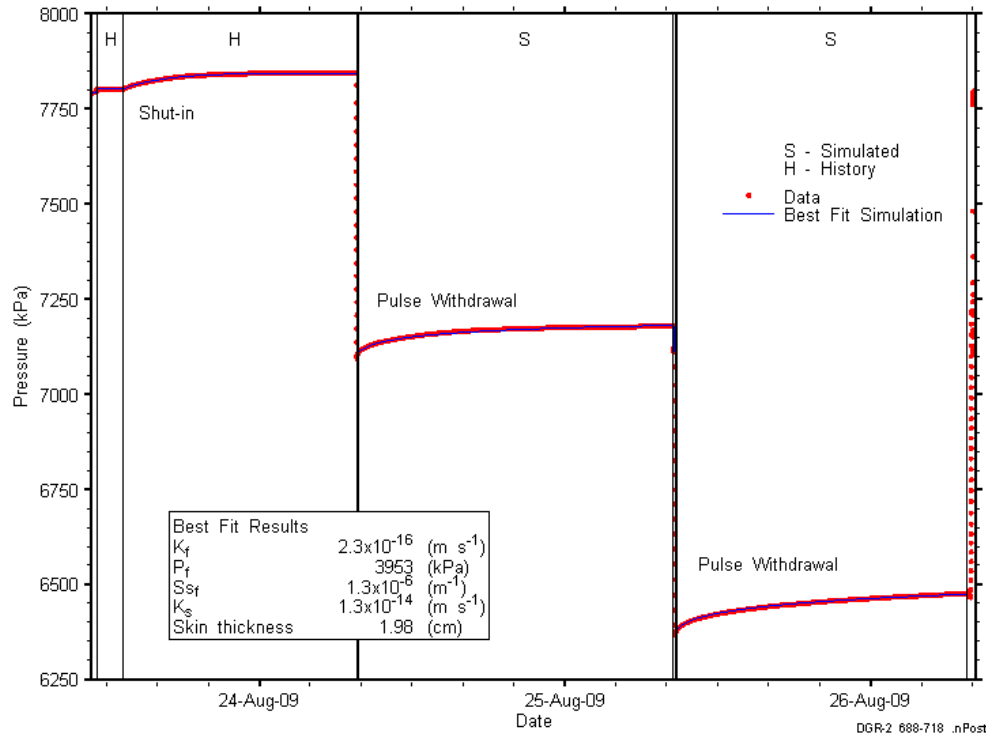


Figure 6-25: Annotated DGR2_687.60-718.10 testing sequence showing best-fit simulation and parameter estimates.

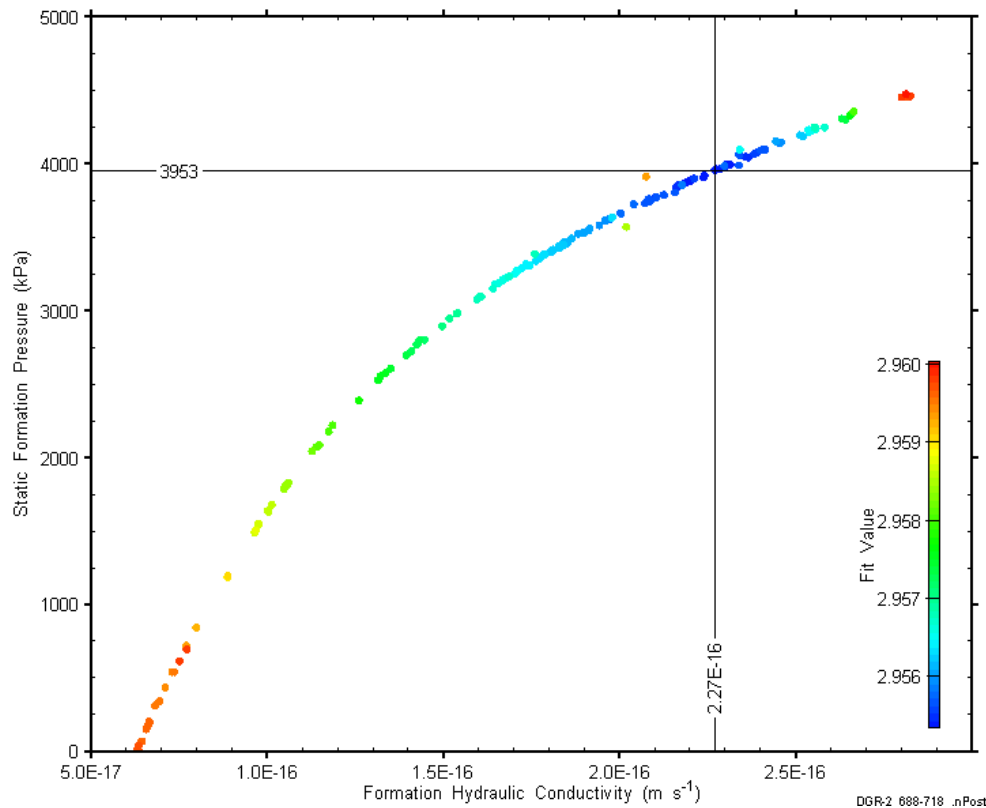


Figure 6-26: XY-scatter plot showing estimates of formation hydraulic conductivity and raw static formation pressure derived from the 687.60-718.10 perturbation analysis.

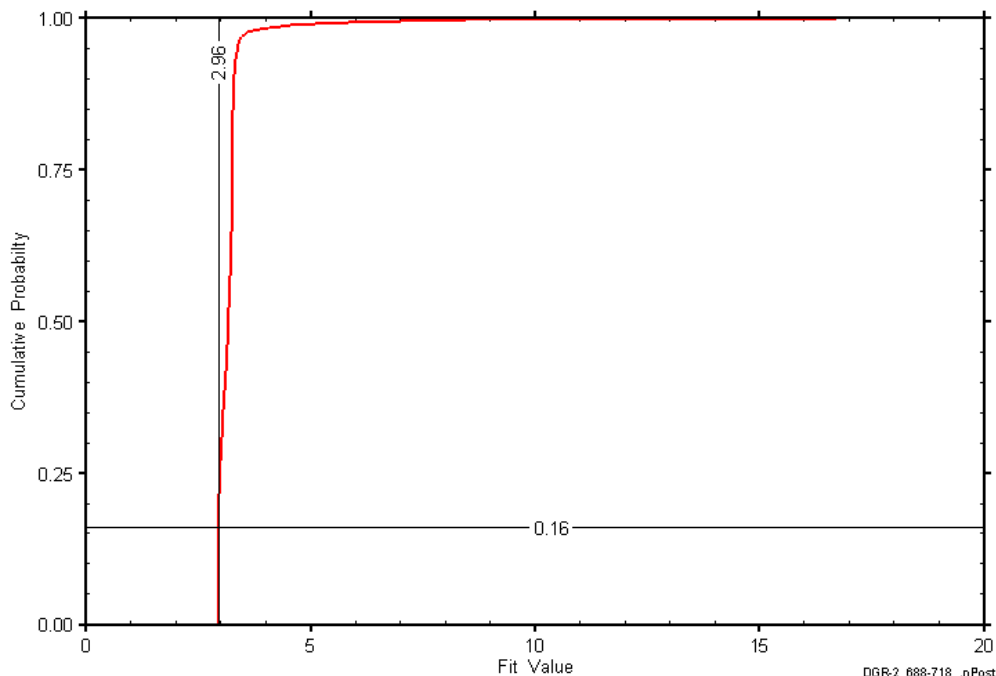


Figure 6-27: DGR2_687.60-718.10 fit value cumulative distribution function.

6.10 714.50-745.00 Kirkfield

The DGR-2 interval from 714.50 to 745.00 m BGS included the lower 1.6 m of the Sherman Fall Formation and the upper 28.9 m of the Kirkfield Formation. The Sherman Fall is an argillaceous limestone, and the Kirkfield is an argillaceous limestone with shale interbeds. An overview of the testing in this interval is given in Table 6-20 and the corresponding parameter estimates are given in Table 6-21. Two pulse-withdrawal tests were conducted in this interval.

Table 6-20: Summary of the DGR2_714.50-745.00 testing activities.

Formation / Unit		Top of Test Zone (m BGS)	Bottom of Test Zone (m BGS)	
Kirkfield		714.50	745.00	
Test	Initiated	Magnitude (kPa)	Duration	Compressibility (Pa ⁻¹)
Shut-in	26-08-09 12:54	N/A	19 hr	N/A
PW1	27-08-09 07:49	731	24 hr	3.6E-10
PW2 (Pt 1)	28-08-09 08:04	32	8 min	N/C
PW2 (Pt 2)	28-08-09 08:13	733	23 hr	3.6E-10
Borehole Pressure History				
Event	Start	Pressure (kPa)		
Westbay Removal	02-06-09 12:00	7857		
Casing Test	13-07-09	N/A		
Leaking Test	22-07-09	N/A		
Casing Test	29-07-09	N/A		
Shut-in	26-08-09 12:54	8108		

Table 6-21: Summary of the DGR2_714.50-745.00 parameter estimates.

Parameter	Best Fit	Minimum	Maximum	Mean
K_f (m/s)	3.6E-16	2.4E-16	3.9E-16	3.3E-16
P_f (kPa)	2621	920	3022	2280
K_s (m/s)	1.1E-13	1.0E-13	1.2E-13	1.1E-13
t_s (cm)	1.1	1.1	1.3	1.2
S_s (1/m)	1.5E-6	1.4E-6	1.5E-6	1.5E-6

Figure 6-28 shows the measured pressure record from DGR2_714.50-745.00 used in this analysis along with the best-fit simulation and parameter values. The ranges of formation K and raw P_f values estimated from perturbation analysis are shown in Figure 6-29 and the fit value cumulative distribution function is shown in Figure 6-30.

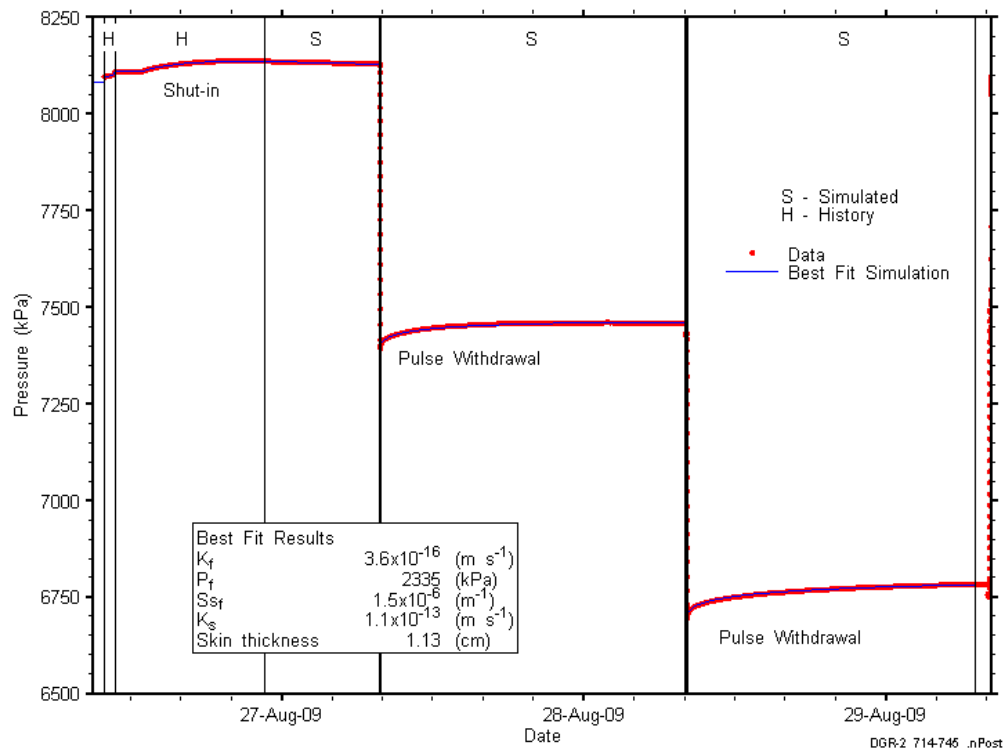


Figure 6-28: Annotated DGR2_714.50-745.00 testing sequence showing best-fit simulation and parameter estimates.

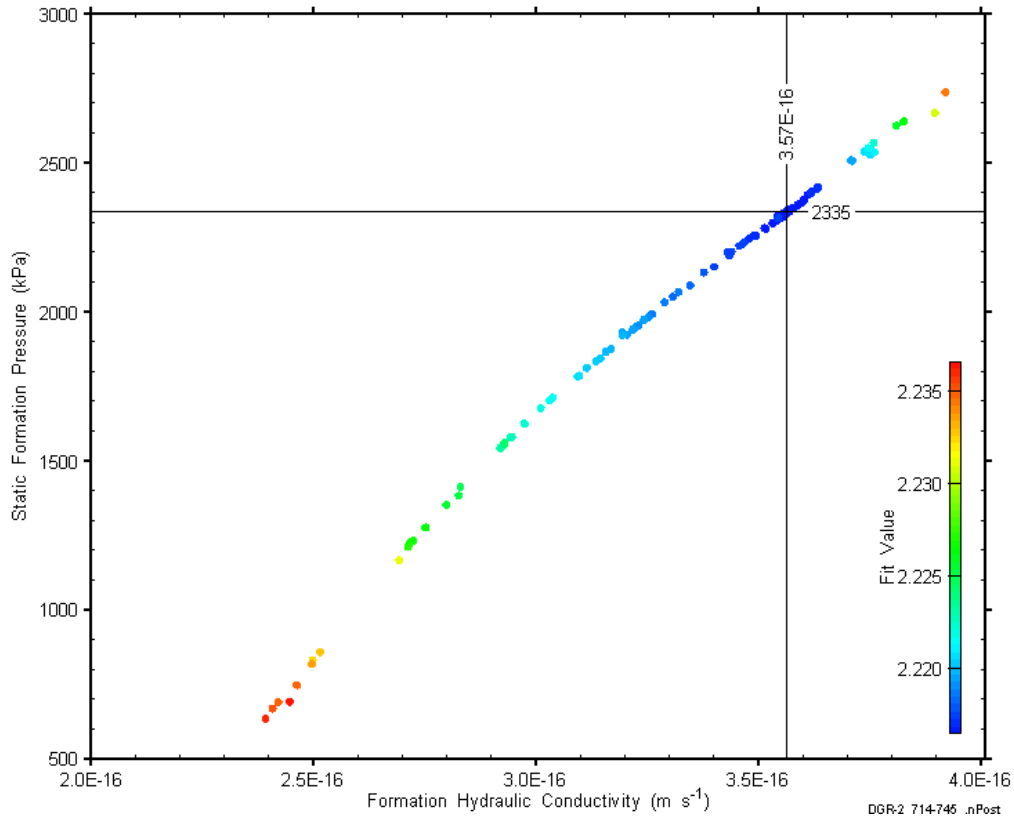


Figure 6-29: XY-scatter plot showing estimates of formation hydraulic conductivity and raw static formation pressure derived from the 714.50-745.00 perturbation analysis.

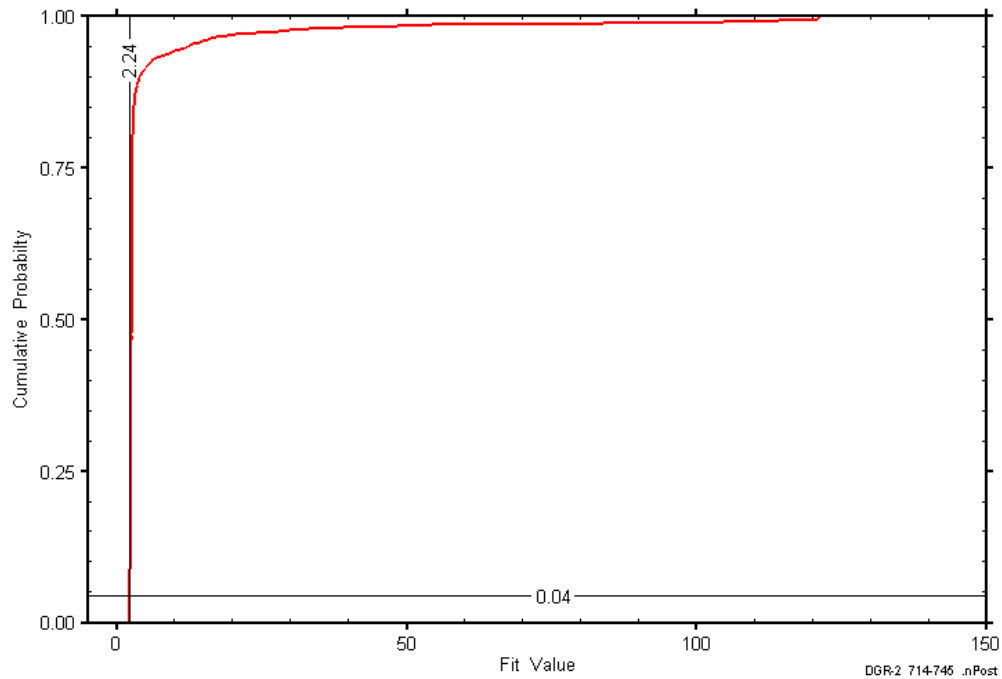


Figure 6-30: DGR2_714.50-745.00 fit value cumulative distribution function.

6.11 731.60-762.10 Kirkfield

The DGR-2 interval from 731.60 to 762.10 m BGS included the lower 30.4 m of the Kirkfield Formation and the upper 0.1 m of the Coboconk Formation. The Kirkfield is an argillaceous limestone with shale interbeds, and the Coboconk is a bioturbated limestone with minor shale interbeds. An overview of the testing in this interval is given in Table 6-22 and the corresponding parameter estimates are given in Table 6-23. Two pulse-withdrawal tests and a short pulse-injection test that was not analyzed were conducted in this interval.

Table 6-22: Summary of the DGR2_731.60-762.10 testing activities.

Formation / Unit		Top of Test Zone (m BGS)		Bottom of Test Zone (m BGS)	
Kirkfield		731.60		762.10	
Test	Initiated	Magnitude (kPa)	Duration	Compressibility (Pa ⁻¹)	
Shut-in	29-08-09 13:58	N/A	18 hr	N/A	
PW1	30-08-09 08:03	752	24 hr	3.6E-10	
PI	31-08-09 08:18	759	1.6 hr	3.6E-10	
PW2 (Pt 1)	31-08-09 09:43	723	6 min	N/C	
PW2 (Pt 2)	31-08-09 09:54	750	21 hr	3.6E-10	
Borehole Pressure History					
Event		Start		Pressure (kPa)	
Westbay Removal		02-06-09 12:00		7857	
Casing Test		13-07-09		N/A	
Leaking Test		22-07-09		N/A	
Casing Test		29-07-09		N/A	
Shut-in		29-08-09 13:58		8290	

Table 6-23: Summary of the DGR2_731.60-762.10 parameter estimates.

Parameter	Best Fit	Minimum	Maximum	Mean
K_f (m/s)	4.8E-16	4.2E-16	5.4E-16	4.8E-16
P_f (kPa)	4035	3581	4430	4049
K_s (m/s)	1.3E-14	1.2E-14	1.4E-14	1.3E-14
t_s (cm)	1.1	1.1	1.2	1.1
S_s (1/m)	1.2E-6	1.1E-6	1.2E-6	1.2E-6

Figure 6-31 shows the measured pressure record from DGR2_731.60-762.10 used in this analysis along with the best-fit simulation and parameter values. The ranges of formation K and raw P_f values estimated from perturbation analysis are shown in Figure 6-32 and the fit value cumulative distribution function is shown in Figure 6-33.

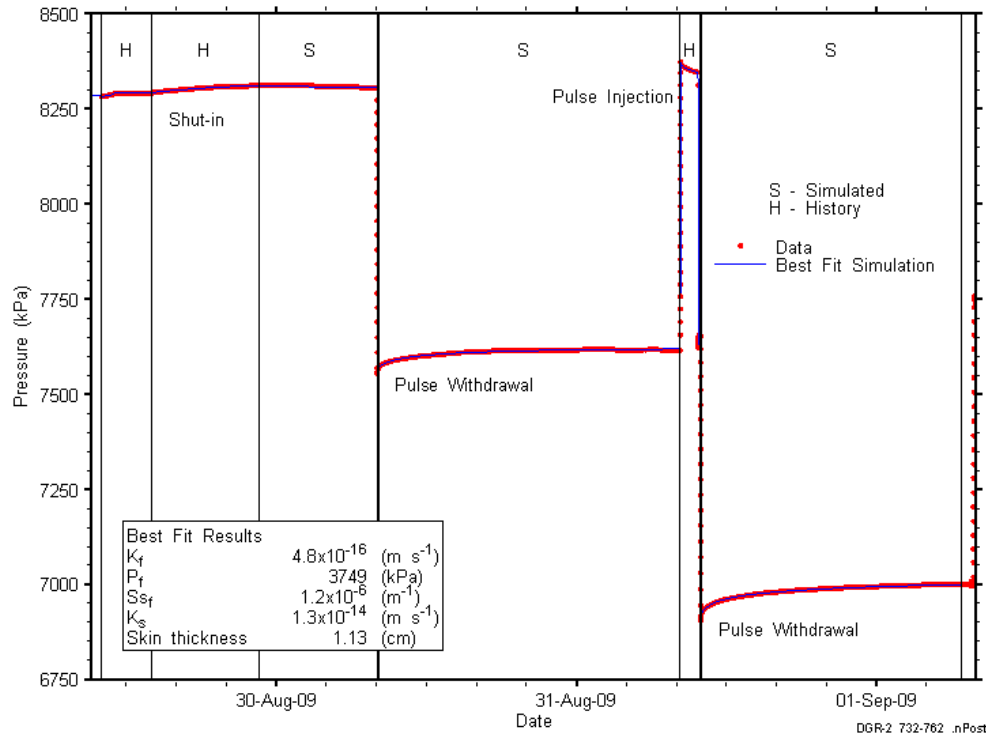


Figure 6-31: Annotated DGR2_731.60-762.10 testing sequence showing best-fit simulation and parameter estimates.

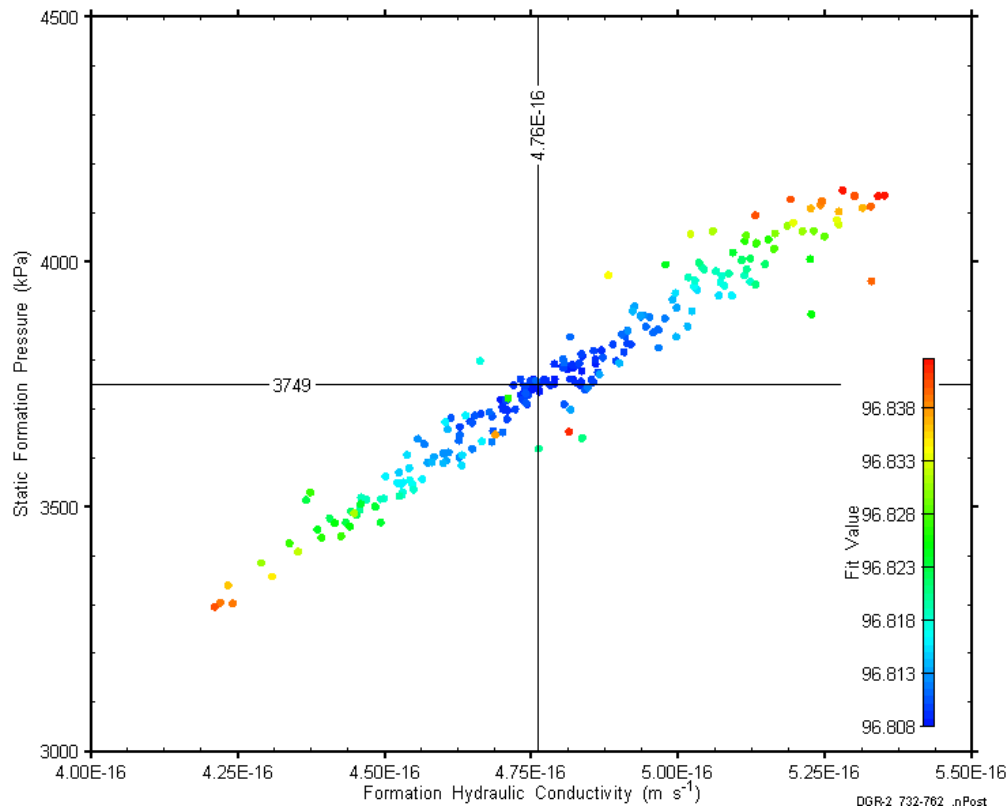


Figure 6-32: XY-scatter plot showing estimates of formation hydraulic conductivity and raw static formation pressure derived from the 731.60-762.10 perturbation analysis.

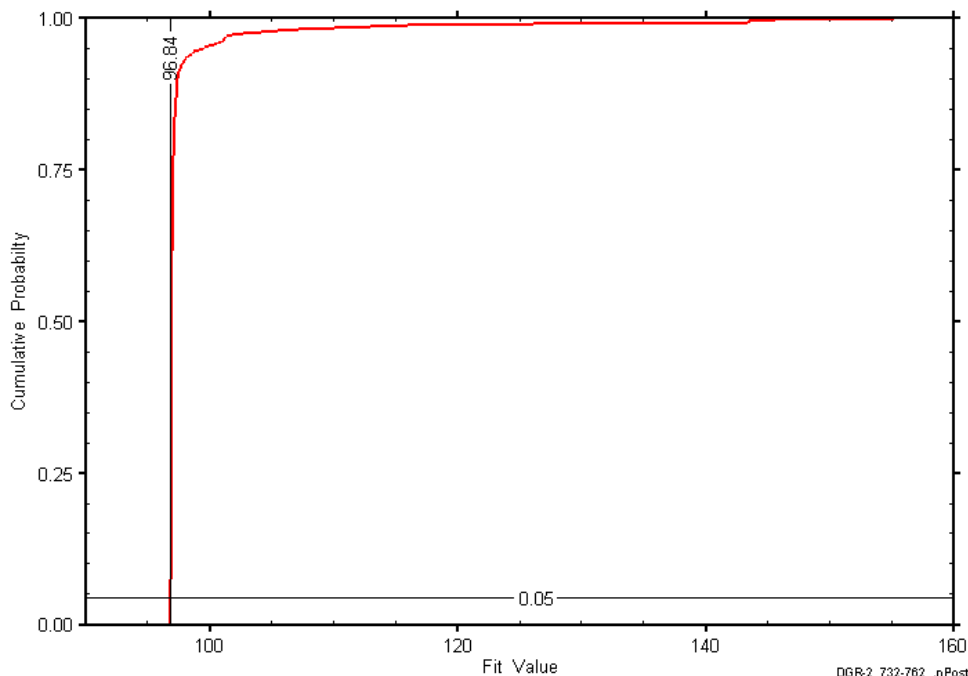


Figure 6-33: DGR2_731.60-762.10 fit value cumulative distribution function.

6.12 754.50-785.00 Kirkfield-Coboconk

The DGR-2 interval from 754.50 to 785.00 m BGS included the lower 7.5 m of the Kirkfield Formation and the entire 23.0-m thickness of the Coboconk Formation. The Kirkfield is an argillaceous limestone with shale interbeds, and the Coboconk is a bioturbated limestone with minor shale interbeds. The upper Coboconk contains a volcanic ash layer approximately 0.12 m thick. The lower half of the Coboconk is petroliferous and contains thin vuggy zones. An overview of the testing in this interval is given in Table 6-24 and the corresponding parameter estimates are given in Table 6-25. A pulse-injection test and a pulse-withdrawal test were conducted in this interval.

Table 6-24: Summary of the DGR2_754.50-785.00 testing activities.

Formation / Unit		Top of Test Zone (m BGS)	Bottom of Test Zone (m BGS)	
Kirkfield-Coboconk		754.50	785.00	
Test	Initiated	Magnitude (kPa)	Duration	Compressibility (Pa ⁻¹)
Shut-in	12-09-09 11:09	N/A	5 hr	N/A
PI	12-09-09 16:17	484	17 hr	4.4E-10
PW	13-09-09 09:03	489	6 hr	4.3E-10
Borehole Pressure History				
Event	Start	Pressure (kPa)		
Westbay Removal	02-06-09 12:00	8312		
Casing Test	13-07-09	N/A		
Leaking Test	22-07-09	N/A		
Casing Test	29-07-09	N/A		
Shut-in	12-09-09 11:09	8551		

Table 6-25: Summary of the DGR2_754.50-785.00 parameter estimates.

Parameter	Best Fit	Minimum	Maximum	Mean
K_f (m/s)	4.0E-11	3.8E-11	4.8E-11	4.0E-11
P_f (kPa)	8858	8856	8859	8858
K_s (m/s)	7.5E-12	6.6E-12	1.8E-11	8.0E-12
t_s (cm)	3.4	2.5	10	3.8
S_s (1/m)	7.5E-5	1.8E-5	1.6E-4	6.6E-5

Figure 6-34 shows the measured pressure record from DGR2_754.50-785.00 used in this analysis along with the best-fit simulation and parameter values. The ranges of formation K and raw P_f values estimated from perturbation analysis are shown in Figure 6-35 and the fit value cumulative distribution function is shown in Figure 6-36.

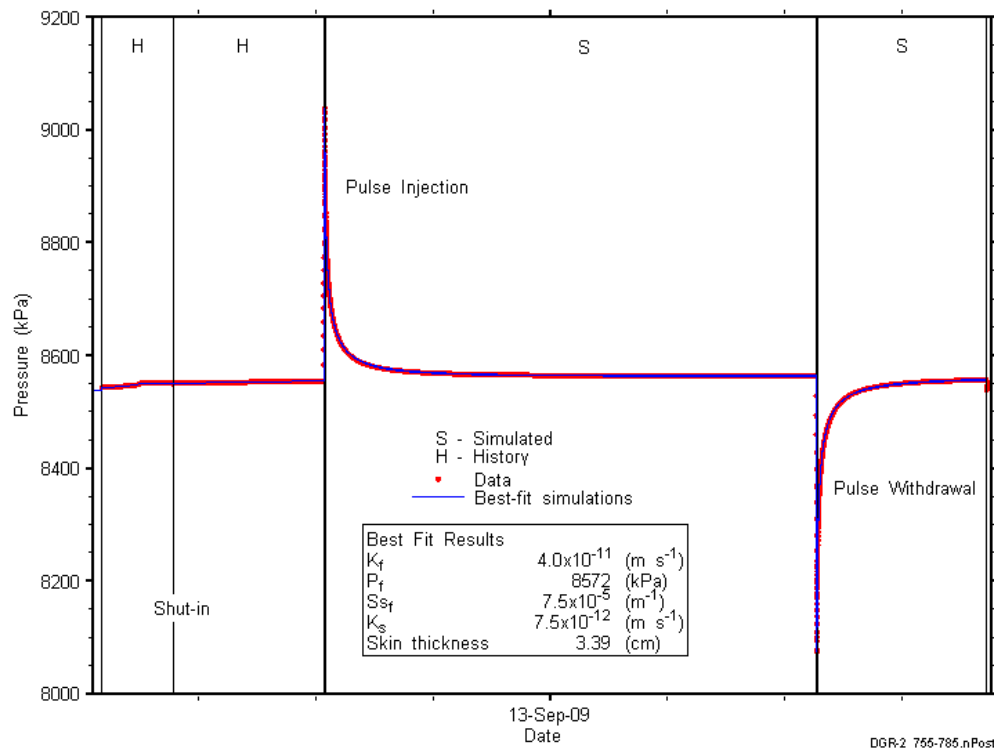


Figure 6-34: Annotated DGR2_754.50-785.00 testing sequence showing best-fit simulation and parameter estimates.

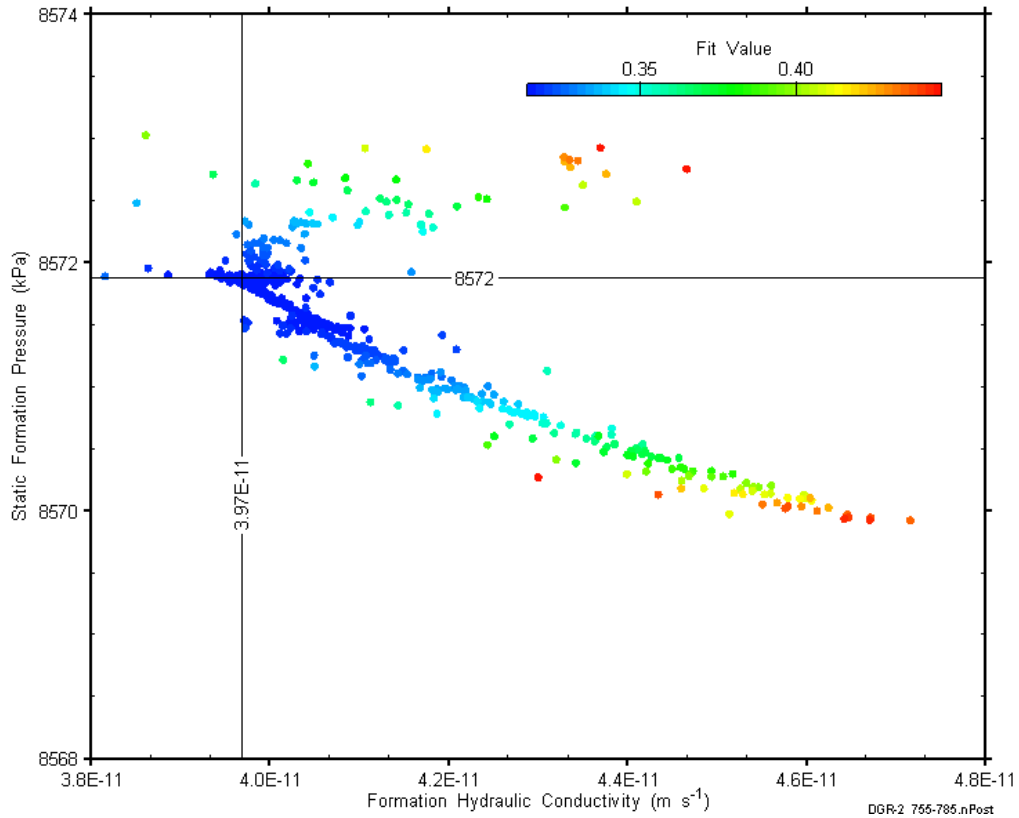


Figure 6-35: XY-scatter plot showing estimates of formation hydraulic conductivity and raw static formation pressure derived from the 754.50-785.00 perturbation analysis.

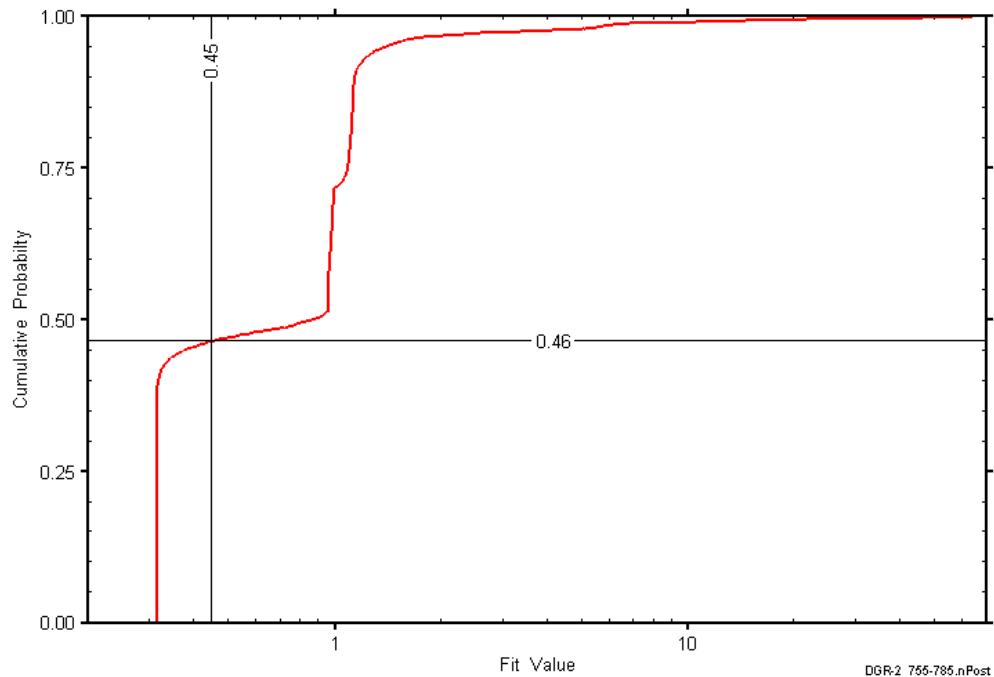


Figure 6-36: DGR2_754.50-785.00 fit value cumulative distribution function.

6.13 761.50-792.00 Coboconk-Gull River

The DGR-2 interval from 761.50 to 792.00 m BGS included the lower 0.5 m of the Kirkfield Formation, the entire 23.0-m thickness of the Coboconk Formation, and the upper 7.0 m of the Gull River Formation. The Kirkfield is an argillaceous limestone with shale interbeds, the Coboconk is a bioturbated limestone with minor shale interbeds, and the Gull River Formation is a fossiliferous limestone/mudstone with thin shale interbeds. The upper Coboconk contains a volcanic ash layer approximately 0.12 m thick. The lower half of the Coboconk is petroliferous and contains thin vuggy zones. An overview of the testing in this interval is given in Table 6-26 and the corresponding parameter estimates are given in Table 6-27. A pulse-injection test and a pulse-withdrawal test were conducted in this interval.

Table 6-26: Summary of the DGR2_761.50-792.00 testing activities.

Formation / Unit		Top of Test Zone (m BGS)	Bottom of Test Zone (m BGS)	
Coboconk-Gull River		761.50	792.00	
Test	Initiated	Magnitude (kPa)	Duration	Compressibility (Pa ⁻¹)
Shut-in	01-09-09 13:20	N/A	19 hr	N/A
PI	02-09-09 07:52	488	24 hr	4.3E-10
PW	03-09-09 08:14	489	23 hr	4.4E-10
Borehole Pressure History				
Event	Start		Pressure (kPa)	
Westbay Removal	02-06-09 12:00		8407	
Casing Test	13-07-09		N/A	
Leaking Test	22-07-09		N/A	
Casing Test	29-07-09		N/A	
Shut-in	01-09-09 13:20		8649	

Table 6-27: Summary of the DGR2_761.50-792.00 parameter estimates.

Parameter	Best Fit	Minimum	Maximum	Mean
K_f (m/s)	4.0E-11	3.8E-11	4.2E-11	4.0E-11
P_f (kPa)	8924	8922	8926	8924
K_s (m/s)	9.7E-12	8.0E-12	1.4E-11	9.7E-12
t_s (cm)	4.5	3.5	6.6	4.6
S_s (1/m)	4.5E-5	2.5E-5	7.5E-5	4.4E-5

Figure 6-37 shows the measured pressure record from DGR2_761.50-792.00 used in this analysis along with the best-fit simulation and parameter values. The ranges of formation K and raw P_f values estimated from perturbation analysis are shown in Figure 6-38 and the fit value cumulative distribution function is shown in Figure 6-39.

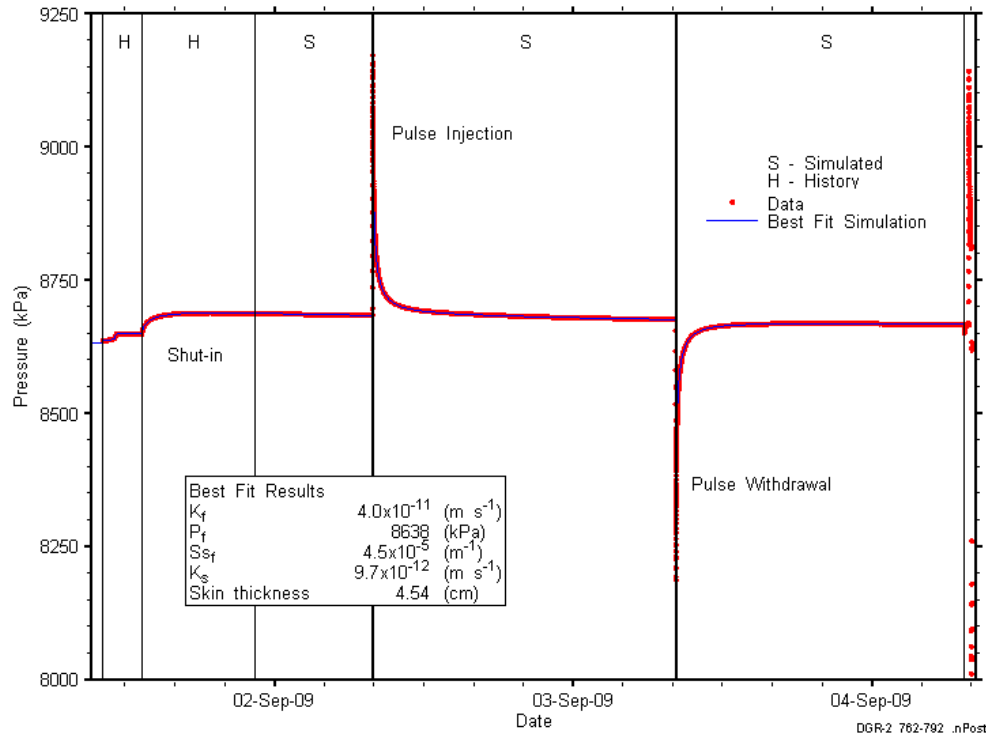


Figure 6-37: Annotated DGR2_761.50-792.00 testing sequence showing best-fit simulation and parameter estimates.

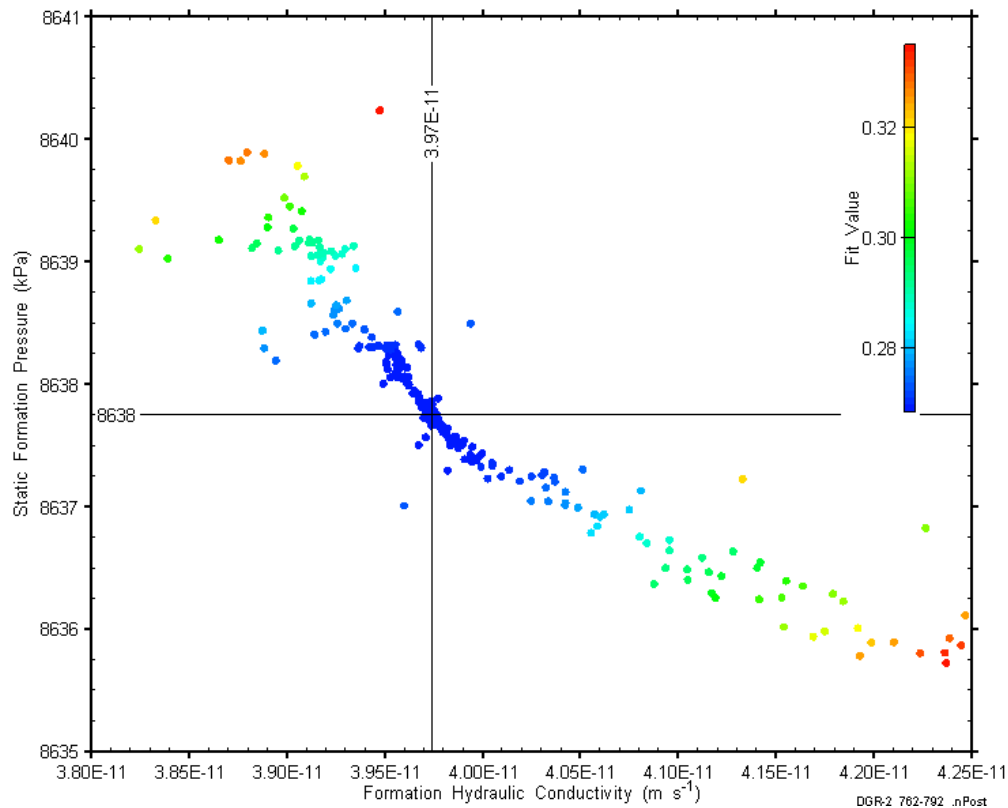


Figure 6-38: XY-scatter plot showing estimates of formation hydraulic conductivity and raw static formation pressure derived from the 761.50-792.00 perturbation analysis.

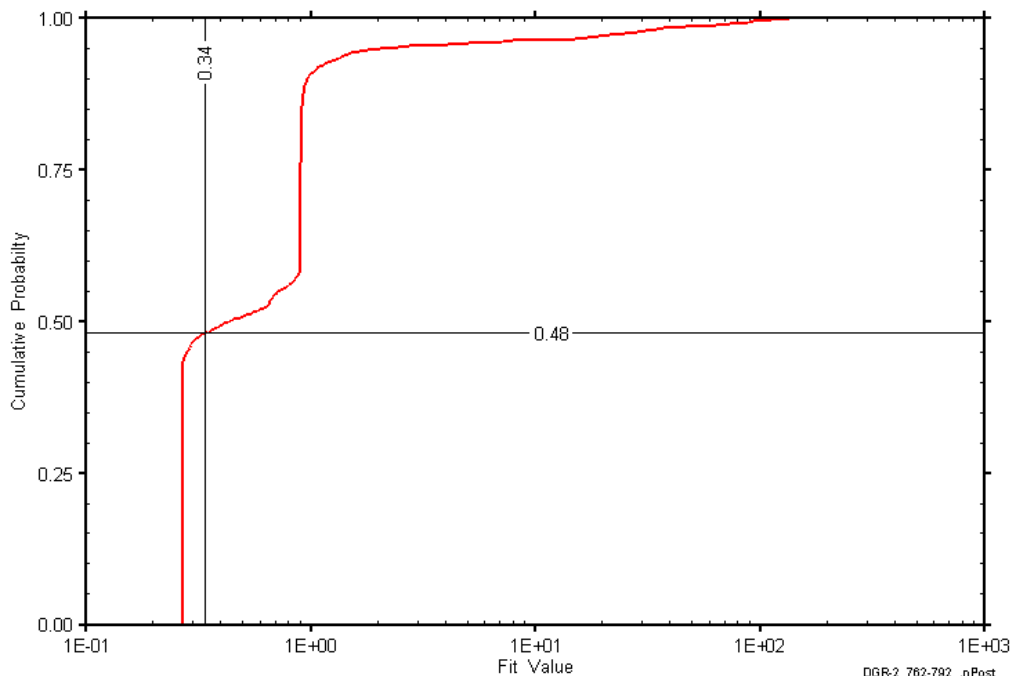


Figure 6-39: DGR2_761.50-792.00 fit value cumulative distribution function.

6.14 785.00-815.50 Gull River

The DGR-2 interval from 785.00 to 815.50 m BGS included the upper 30.5 m of the Gull River Formation. The Gull River is a fossiliferous limestone/mudstone with thin shale interbeds. An overview of the testing in this interval is given in Table 6-28 and the corresponding parameter estimates are given in Table 6-29. A pulse-injection test and a pulse-withdrawal test were conducted in this interval.

Table 6-28: Summary of the DGR2_785.00-815.50 testing activities.

Formation / Unit		Top of Test Zone (m BGS)	Bottom of Test Zone (m BGS)	
Gull River		785.00	815.50	
Test	Initiated	Magnitude (kPa)	Duration	Compressibility (Pa ⁻¹)
Shut-in	04-09-09 13:11	N/A	19 hr	N/A
PI	05-09-09 08:10	794	48 hr	3.5E-10
PW	07-09-09 08:38	807	23 hr	3.4E-10
Borehole Pressure History				
Event	Start	Pressure (kPa)		
Westbay Removal	02-06-09 12:00	8685		
Casing Test	13-07-09	N/A		
Leaking Test	22-07-09	N/A		
Casing Test	29-07-09	N/A		
Shut-in	04-09-09 13:11	8920		

Table 6-29: Summary of the DGR2_785.00-815.50 parameter estimates.

Parameter	Best Fit	Minimum	Maximum	Mean
K_f (m/s)	1.5E-11	1.3E-11	3.2E-11	1.8E-11
P_f (kPa)	9977	9935	9995	9968
K_s (m/s)	7.4E-12	7.3E-12	7.5E-12	7.4E-12
t_s (cm)	645	417	1493	815
S_s (1/m)	1.7E-7	1.6E-7	1.8E-7	1.7E-7

Figure 6-40 shows the measured pressure record from DGR2_785.00-815.50 used in this analysis along with the best-fit simulation and parameter values. The ranges of formation K and raw P_f values estimated from perturbation analysis are shown in Figure 6-41 and the fit value cumulative distribution function is shown in Figure 6-42.

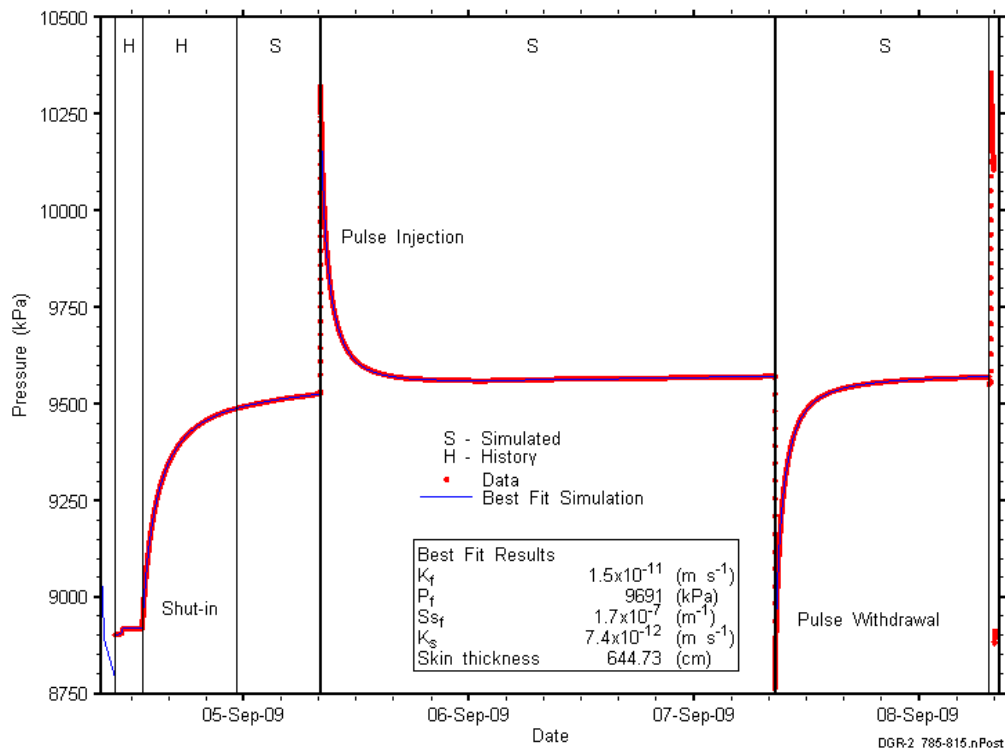


Figure 6-40: Annotated DGR2_785.00-815.50 testing sequence showing best-fit simulation and parameter estimates.

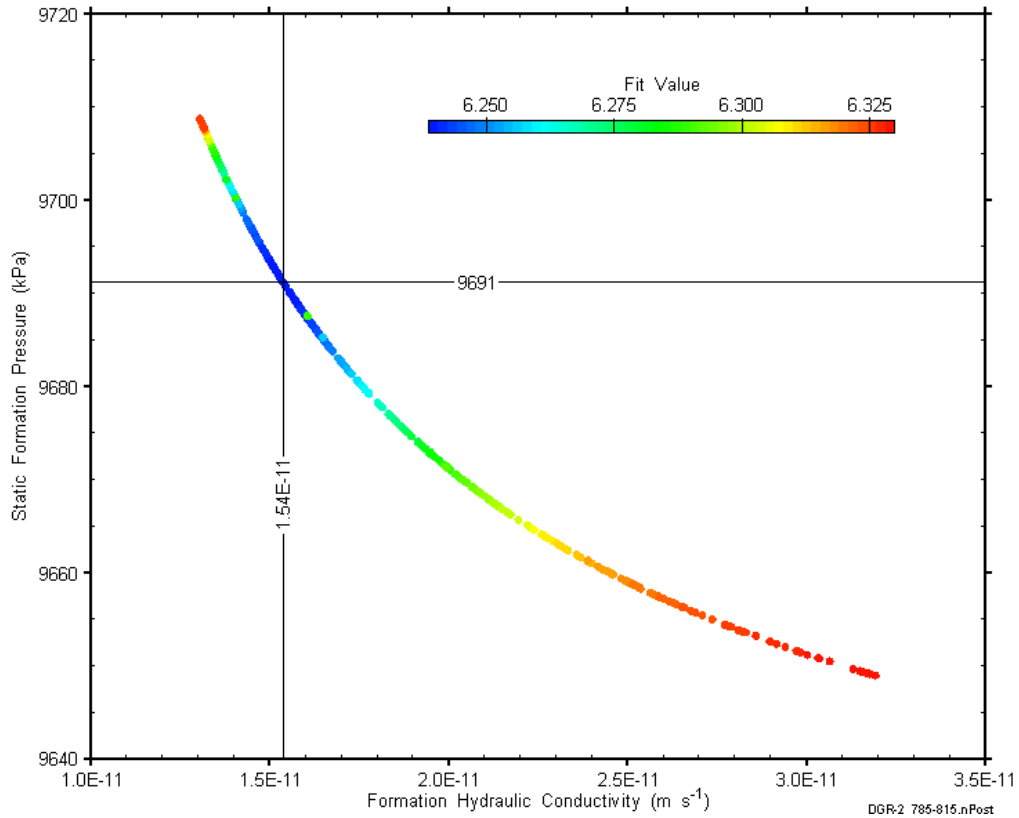


Figure 6-41: XY-scatter plot showing estimates of formation hydraulic conductivity and raw static formation pressure derived from the 785.00-815.50 perturbation analysis.

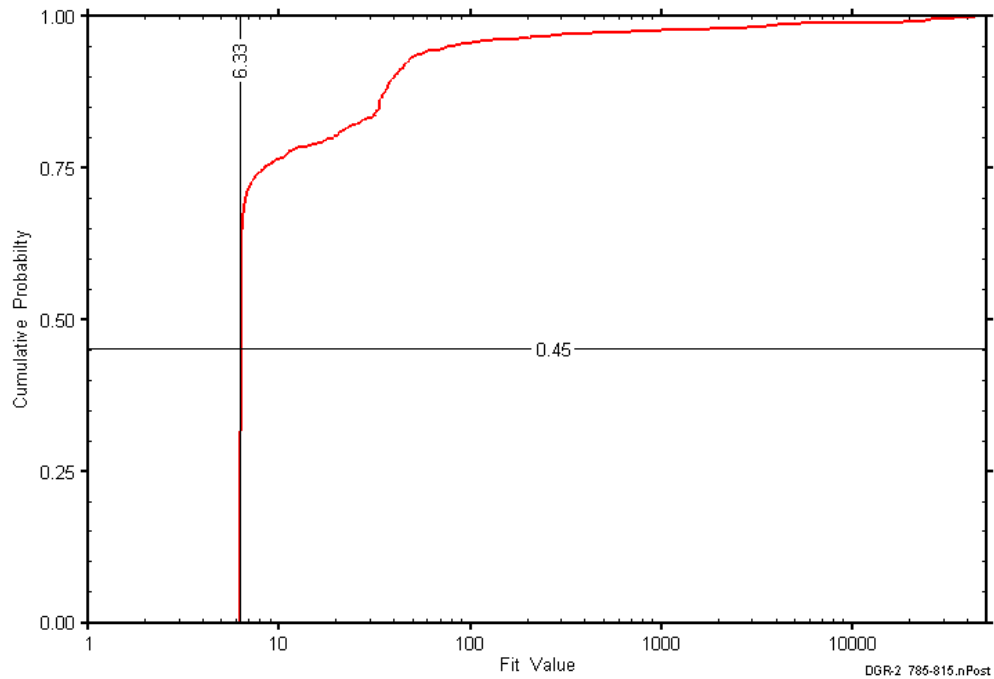


Figure 6-42: DGR2_785.00-815.50 fit value cumulative distribution function.

6.15 801.50-832.00 Gull River

The DGR-2 interval from 801.50 to 832.00 m BGS occupied the middle portion of the Gull River Formation, a fossiliferous limestone/mudstone with thin shale interbeds. An overview of the testing in this interval is given in Table 6-30 and the corresponding parameter estimates are given in Table 6-31. A pulse-injection test and a pulse-withdrawal test were conducted in this interval.

Table 6-30: Summary of the DGR2_801.50-832.00 testing activities.

Formation / Unit		Top of Test Zone (m BGS)		Bottom of Test Zone (m BGS)	
Gull River		801.50		832.00	
Test	Initiated	Magnitude (kPa)	Duration	Compressibility (Pa ⁻¹)	
Shut-in	08-09-09 12:57	N/A	19 hr	N/A	
PI	09-09-09 07:47	788	24 hr	3.5E-10	
PW	10-09-09 07:32	794	24 hr	3.4E-10	
Borehole Pressure History					
Event		Start		Pressure (kPa)	
Westbay Removal		02-06-09 12:00		8883	
Casing Test		13-07-09		N/A	
Leaking Test		22-07-09		N/A	
Casing Test		29-07-09		N/A	
Shut-in		08-09-09 12:57		9120	

Table 6-31: Summary of the DGR2_801.50-832.00 parameter estimates.

Parameter	Best Fit	Minimum	Maximum	Mean
K_f (m/s)	1.3E-11	1.0E-11	1.9E-11	1.3E-11
P_f (kPa)	10161	10133	10176	10161
K_s (m/s)	8.5E-12	4.6E-12	9.4E-12	8.4E-12
t_s (cm)	121	19	346	123
S_s (1/m)	2.1E-7	1.5E-7	6.8E-7	1.7E-7

Figure 6-43 shows the measured pressure record from DGR2_801.50-832.00 used in this analysis along with the best-fit simulation and parameter values. The ranges of formation K and raw P_f values estimated from perturbation analysis are shown in Figure 6-44 and the fit value cumulative distribution function is shown in Figure 6-45.

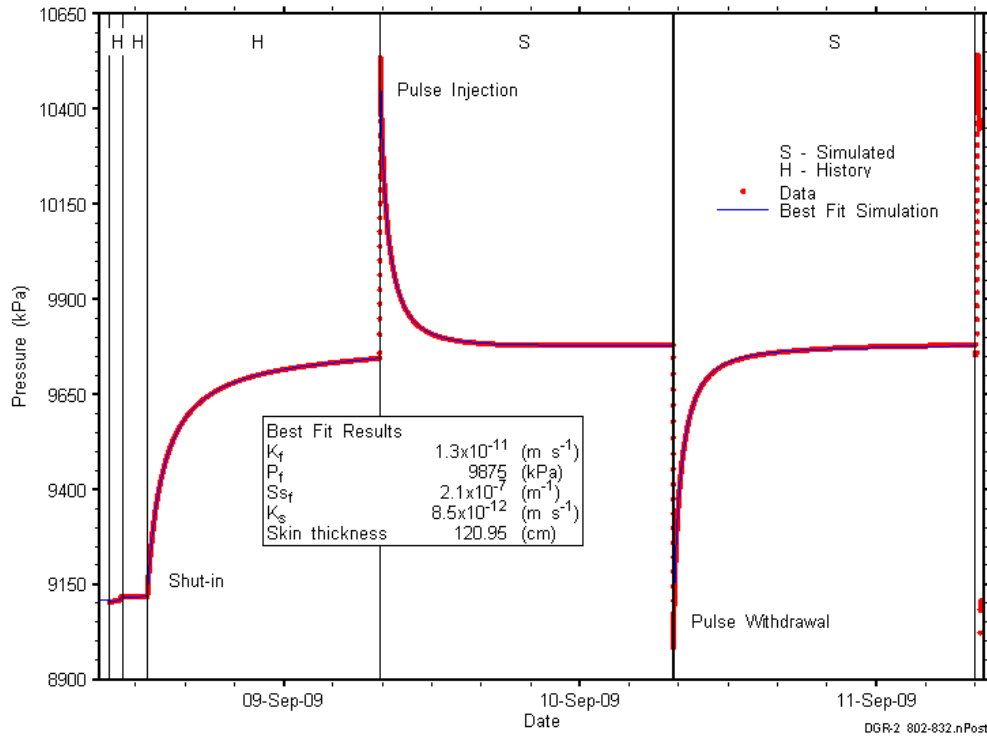


Figure 6-43: Annotated DGR2_801.50-832.00 testing sequence showing best-fit simulation and parameter estimates.

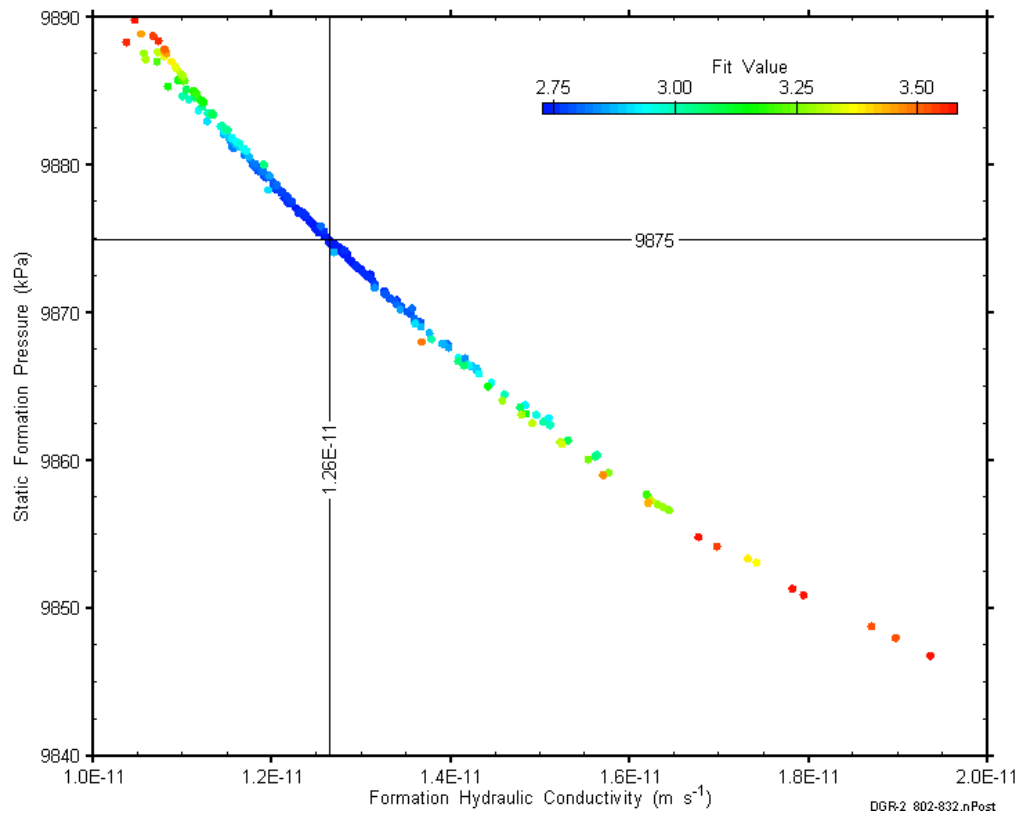


Figure 6-44: XY-scatter plot showing estimates of formation hydraulic conductivity and raw static formation pressure derived from the 801.50-832.00 perturbation analysis.

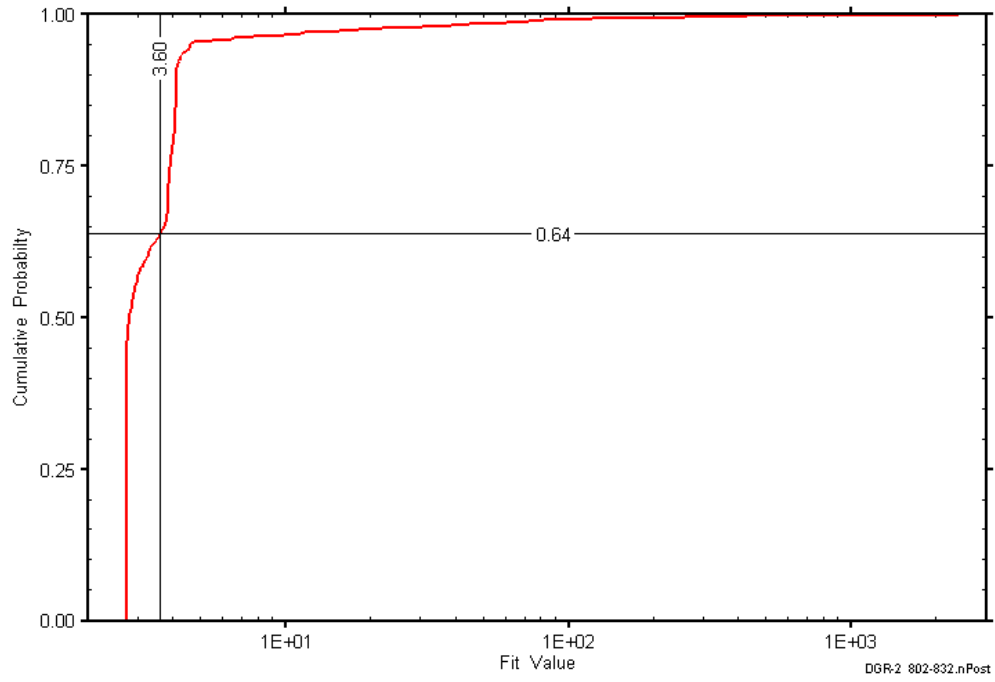


Figure 6-45: DGR2_801.50-832.00 fit value cumulative distribution function.

6.16 Summary of DGR-2 Results

The best-fit parameter estimates derived from the DGR-2 analyses are given in Table 6-32. Figure 6-46 through Figure 6-50 present stratigraphic profiles of the analysis results for hydraulic conductivity, formation pressure, specific storage, skin factor, and test-zone compressibility, respectively, for DGR-2 and for the DGR-1 tests discussed in Section 5.

Table 6-32: Best-fit parameter estimates derived from the DGR-2 analyses

Formation(s)	Top	Bottom	K_f	P_f	S_s	K_s	t_s	s	C_{tz}
	m BGS	m BGS	$m\ s^{-1}$	kPa	m^{-1}	$m\ s^{-1}$	cm		Pa^{-1}
Queenston	457.85	488.35	1.9E-14	4379	1.2E-6	5.0E-13	5.3	-0.49	7.8E-10
Queenston	487.20	517.70	3.3E-14	4133	1.2E-6	3.8E-12	2.2	-0.24	6.3E-10
Georgian Bay	517.50	548.00	4.9E-14	4436	4.3E-7	2.5E-12	5.9	-0.54	4.5E-10
Georgian Bay	547.80	578.30	3.4E-14	4563	1.5E-7	1.6E-12	17	-1.1	4.9E-10
Georgian Bay	578.10	608.60	4.8E-14	6285	6.4E-5	1.9E-10	1.4	-0.16	1.1E-8
Blue Mountain	608.40	638.90	1.2E-14	3213	1E-6*	4.0E-14	2.3	-0.17	3.7E-10
Blue Mountain-Collingwood	630.50	661.00	9.4E-15	3764	3E-7*	1.1E-13	4.7	-0.42	3.6E-10
Cobourg	660.50	691.00	3.9E-15	6682	1.2E-7	1.4E-13	7.2	-0.63	3.5E-10
Sherman Fall	687.60	718.10	2.3E-16	4239	1.3E-6	1.3E-14	2.0	-0.22	3.5E-10
Kirkfield	714.50	745.00	3.6E-16	2621	1.5E-6	1.1E-13	1.1	-0.13	3.6E-10
Kirkfield	731.60	762.10	4.8E-16	4035	1.2E-6	1.3E-14	1.1	-0.13	3.6E-10
Kirkfield-Coboconk	754.50	785.00	4.0E-11	8858	7.5E-5	7.5E-12	3.4	1.5	4.4E-10
Coboconk-Gull River	761.50	792.00	4.0E-11	8924	4.5E-5	9.7E-12	4.5	1.4	3.5E-10
Gull River	785.00	815.5	1.5E-11	9977	1.7E-7	7.4E-12	645	4.7	3.5E-10
Gull River	801.50	832.00	1.3E-11	10161	2.1E-7	8.5E-12	121	1.4	4.4E-10

*: Fixed

As shown in Figure 6-46 and Table 6-32, all but four of the Ordovician test intervals in DGR-2 had K values less than $5E-14$ m/s. The Sherman Fall and Kirkfield had particularly low K values, ranging from $2.3E-16$ to $4.8E-16$ m/s. Significantly higher K estimates were obtained for the Coboconk and Gull River intervals, where K ranged from $1.3E-11$ to $4.0E-11$ m/s. For all tests, uncertainties are well under an order of magnitude.

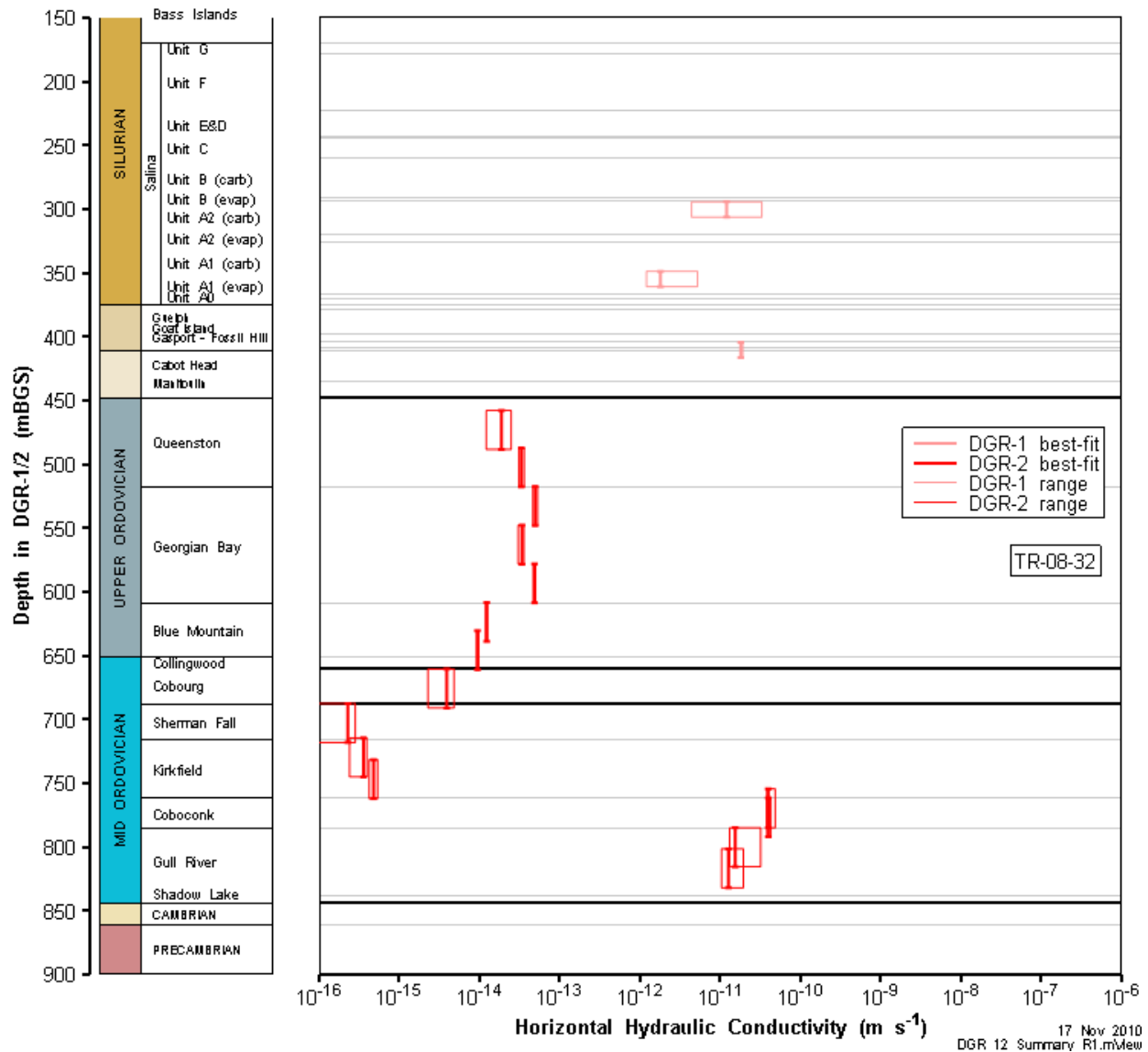


Figure 6-46: DGR-2 stratigraphic profile of horizontal hydraulic conductivity estimates.

As shown in Figure 6-47, the only interval in DGR-2 that was normally pressured relative to a density-compensated hydrostatic condition was the lower Georgian Bay interval from 578.10 to 608.69 mBGS. This interval had the highest test-zone compressibility encountered in the hole, and included a fracture at 585.7 mBGS suspected of containing gas (Sterling, 2010). Apart from the Coboconk and Gull River, which were overpressured, the remaining Ordovician intervals were underpressured to varying degrees.

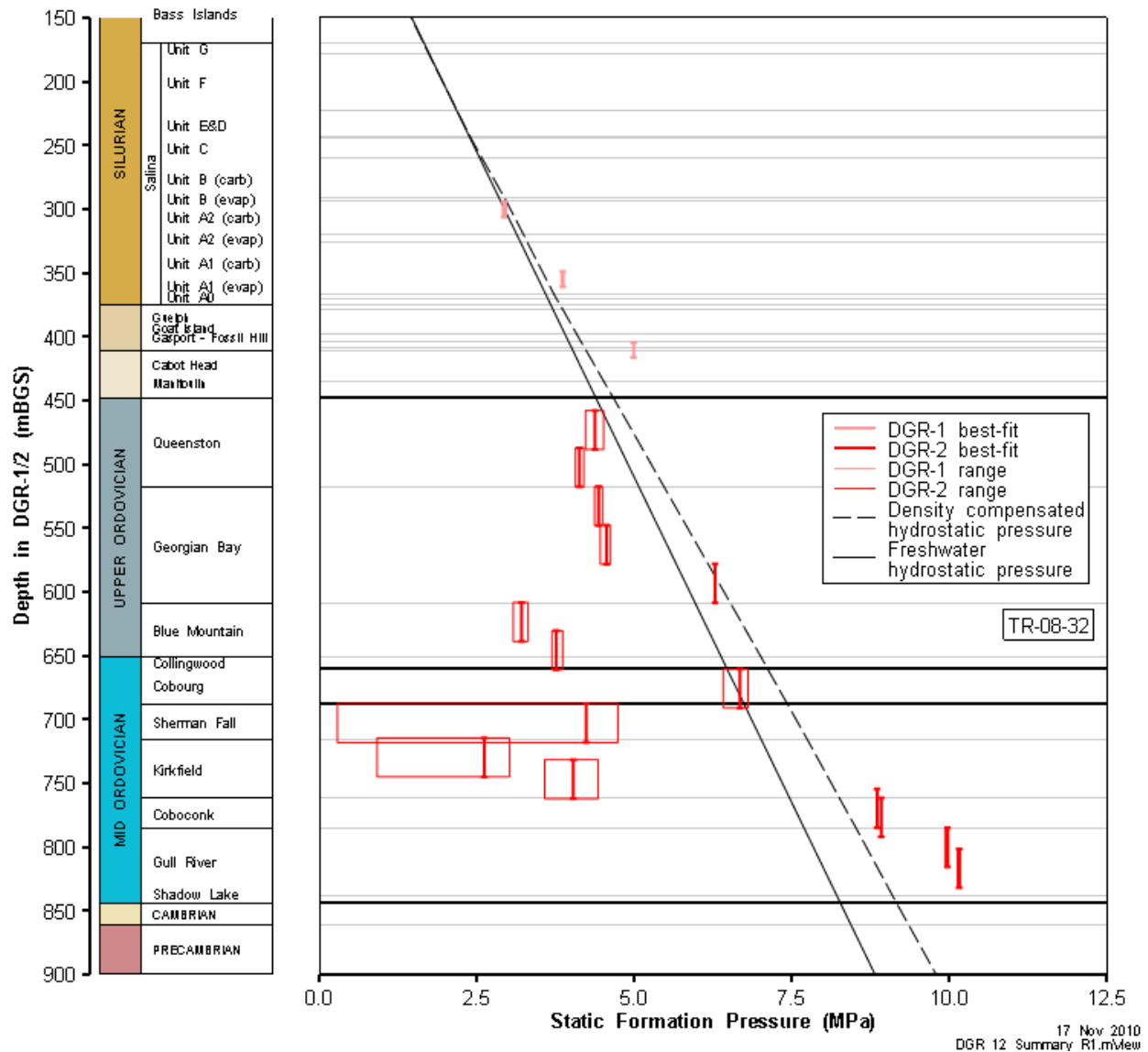


Figure 6-47: DGR-2 stratigraphic profile of formation pressure estimates.

Figure 6-48 shows the S_s values fitted in the simulations for each of the DGR-2 test intervals, along with the uncertainties associated with the fitted values; values that were fixed in the simulations are not shown. The fitted values range from $1.5E-7 \text{ m}^{-1}$ to $7.5E-5 \text{ m}^{-1}$. For some of the test intervals, effectively equivalent fits could be obtained with S_s values ranging over approximately an order of magnitude, or more. This is a consequence of the strong correlation between S_s and skin properties in single-well tests discussed in Section 4.4. For two test intervals, no minimum was found in the S_s fit surface within the range of values thought to be physically reasonable ($1E-7$ to $1E-4 \text{ m}^{-1}$). In those cases, S_s was fixed at $1E-6 \text{ m}^{-1}$ or $3E-7 \text{ m}^{-1}$ to obtain good matches between the observed and simulated test data.

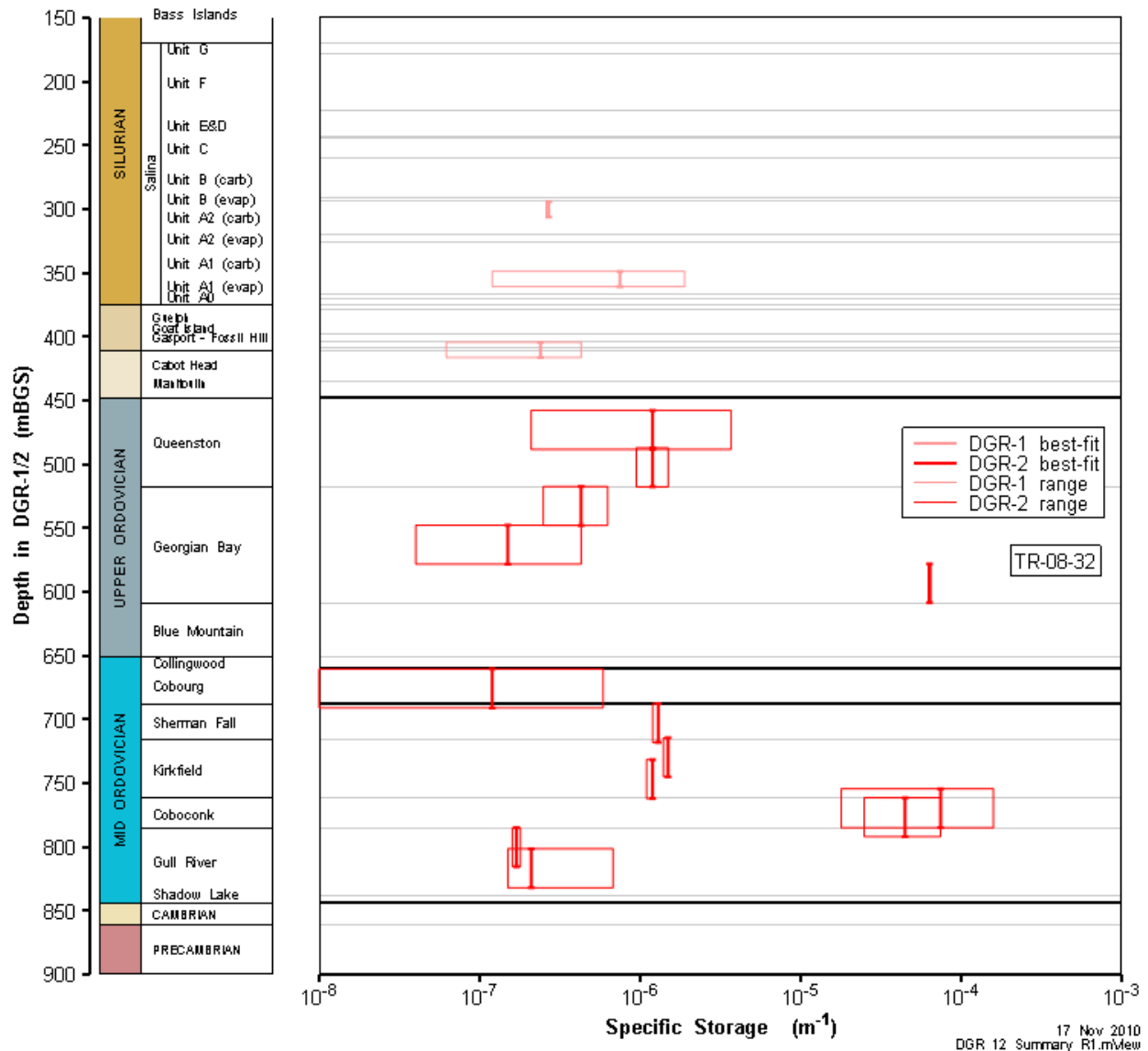


Figure 6-48: DGR-2 stratigraphic profile of specific storage estimates.

Figure 6-49 shows the skin factors obtained from parameter optimization for each of the DGR-2 test intervals. All but four of the test intervals had negative skins, reflecting enhanced permeability around the wellbore. Hydraulically significant fractures are a possible cause of negative skins. Other causes could be enhanced local fracturing caused by stress relief fracturing during drilling. The negative skins in DGR-2 were of low magnitude; the middle Georgian Bay interval had the most negative skin, which was only -1.1 (Table 6-32). The four intervals in the Black River Group (Coboconk and Gull River) limestones all had positive skins associated with decreased permeability around the wellbore. These were also the Ordovician intervals with the highest hydraulic conductivities (Figure 6-46). The most significant skin (4.7) was observed in the upper Gull River test interval.

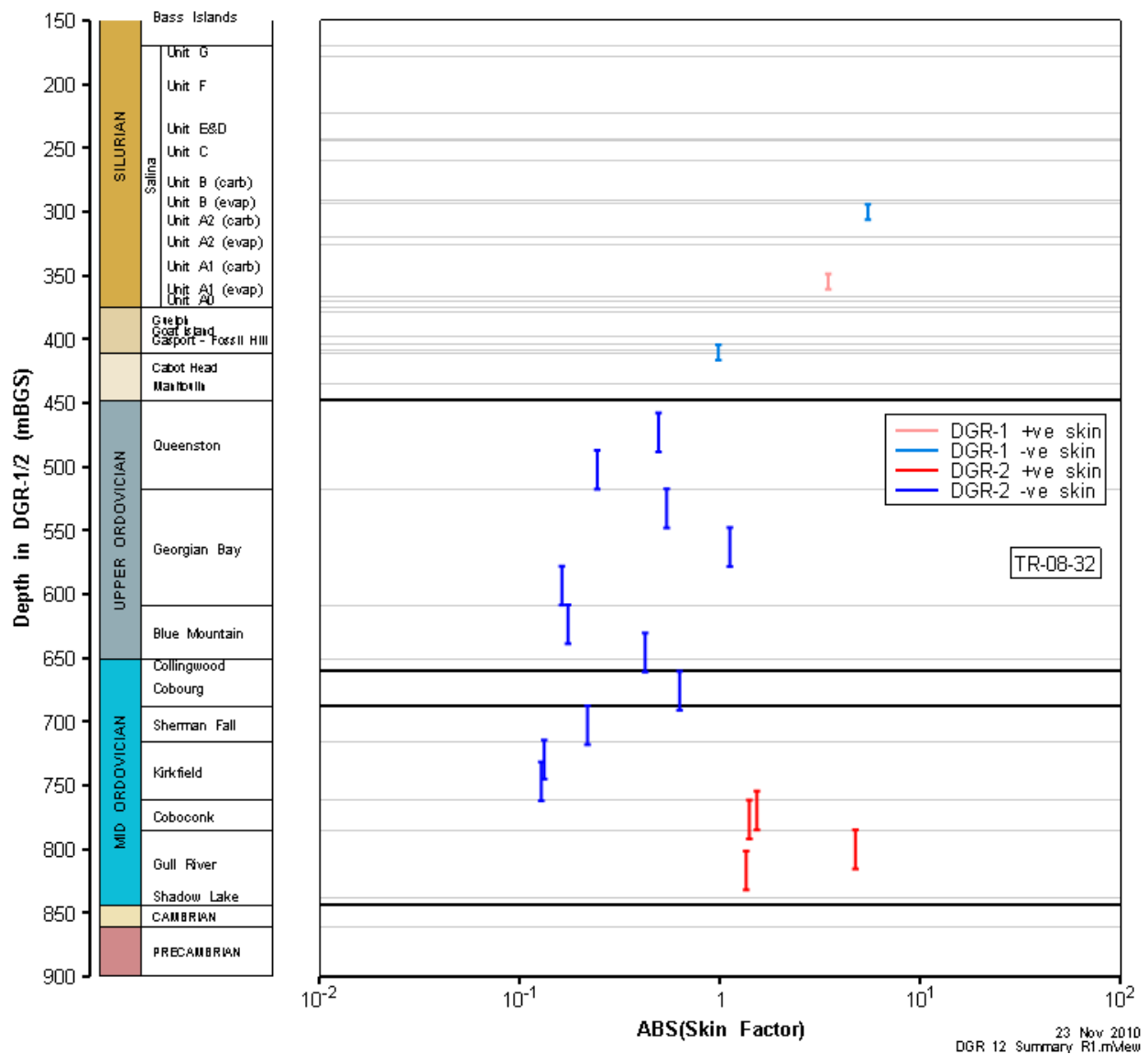


Figure 6-49: DGR-2 stratigraphic profile of skin factor estimates.

As shown in Figure 7-74, of the 15 DGR-2 intervals in which test-zone compressibility was measured, C_{tz} was less than $5E-10 \text{ Pa}^{-1}$ in 12 intervals and less than $8E-10 \text{ Pa}^{-1}$ in 2 more intervals. These values are indicative of water-filled test intervals with typical test-tool compliance. In the lower Georgian Bay interval from 578.1 to 608.6 mBGS, C_{tz} was $1.1E-8 \text{ Pa}^{-1}$. This interval included a fracture at 585.7 mBGS suspected of containing gas (Sterling, 2010). This interval was also the only interval in the Upper Ordovician in DGR-2 that was near normally pressured rather than underpressured (Figure 6-47).

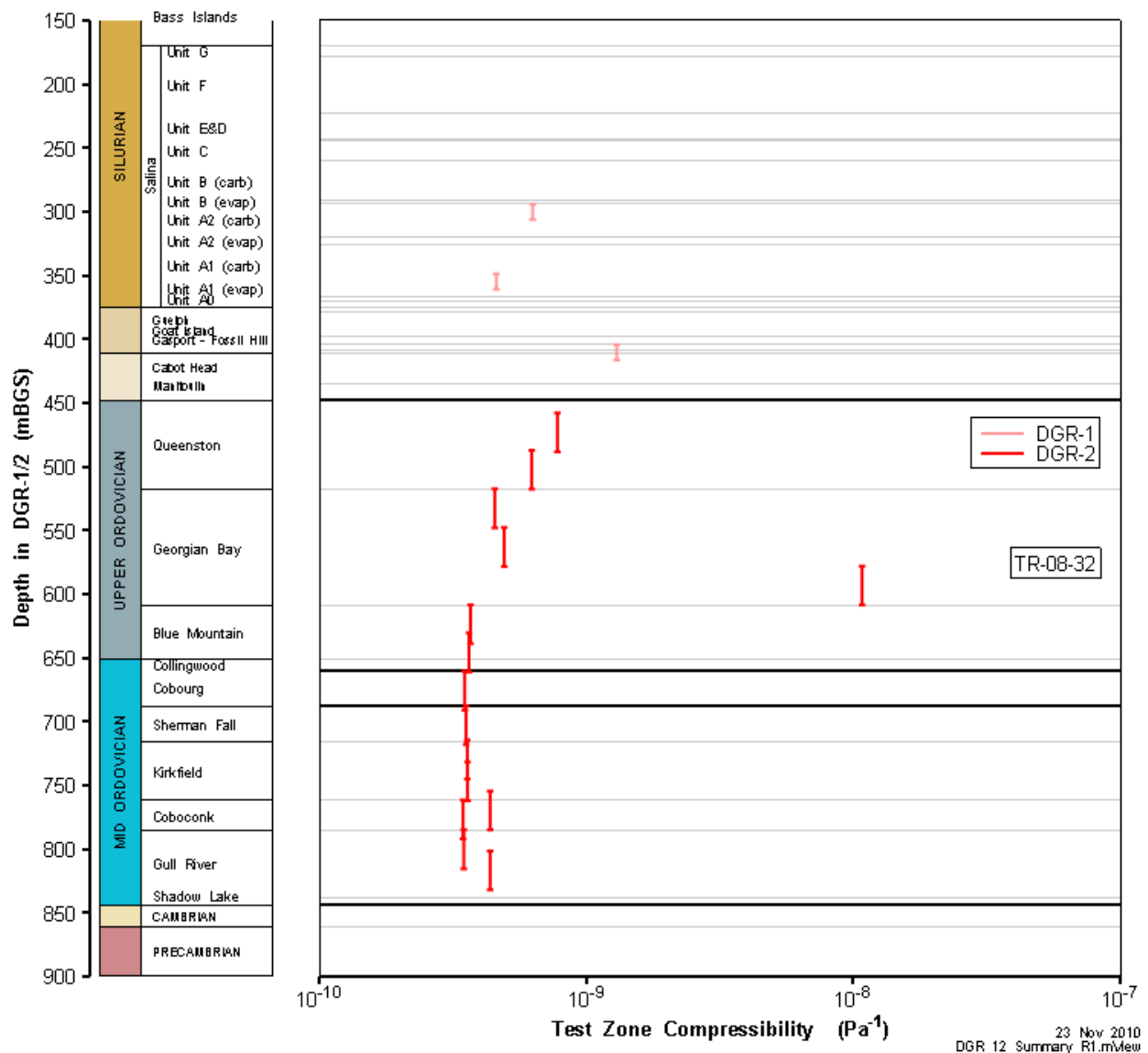


Figure 6-50: DGR-2 stratigraphic profile of test-zone compressibility estimates.

7 DGR-3 Testing and Analysis

Hydraulic testing in DGR-3 was performed from 7 September until 14 November 2008. Testing was initiated at the top of the Salina F unit and then proceeded consecutively down the borehole using a 30.74-m straddle interval, with nearly complete test coverage over all formations. A 7.75m gap at the top of the Sherman Fall formation allowed for more comprehensive testing of individual formation properties within task resource constraints. The testing in DGR-3 provided coverage of the borehole from 210.18 to 845.74 m BGS. Table 7-1 lists the formations and intervals tested, and the type(s) of test(s) performed. Pulse tests were performed in all but two intervals in DGR-3. Slug tests were performed in three intervals and a DST in one.

Table 7-1: DGR-3 test zones and tests

Formations / Units	Top of Test Zone (m BGS)	Bottom of Test Zone (m BGS)	Type(s) of Test(s)
Salina F-E	210.18	240.92	PW, PI
Salina E-D-C	240.72	271.46	PW, PI
Salina C-B	271.29	302.03	PW, PI
Salina B-A2 carbonate	301.81	332.55	PW, SI
Salina A2 evaporite-A1 carbonate	334.99	365.73	SW, DST, SI
Salina A1 carbonate	346.00	376.74	PW, PI
Salina A1 evaporite-A0-Guelph-Goat Island-Gasport	378.98	410.72	SW
Gasport-Lions Head-Fossil Hill-Cabot Head	410.51	441.25	PW, PI
Cabot Head-Manitoulin-Queenston	441.05	471.79	PW
Queenston	471.41	502.15	PW, PI
Queenston-Georgian Bay	501.95	532.69	PW, PI
Georgian Bay	532.49	563.23	PW
Georgian Bay	563.03	593.77	PW
Georgian Bay-Blue Mountain	593.57	624.31	PW
Georgian Bay-Blue Mountain	617.63	648.37	PI
Blue Mountain	628.00	658.74	PW
Blue Mountain-Collingwood-Cobourg	654.65	685.39	PW
Collingwood-Cobourg-Sherman Fall	671.50	702.24	PW
Sherman Fall-Kirkfield	710.00	740.74	PW
Kirkfield	740.54	771.28	PW
Kirkfield-Coboconk	765.96	796.70	PW, PI
Coboconk-Gull River	790.93	821.67	PW, PI
Gull River	815.00	845.74	PI
Reference Elevation – Ground Surface	187.35 m above mean sea level		

PW: pulse withdrawal
 PI: pulse injection
 SI: slug injection
 SW: slug withdrawal
 DST: drillstem test

The test-zone transducer during DGR-3 testing was located 26.64 m above the middle of the isolated test zone and was hydraulically connected to the test zone via a length of 1/4-in stainless-steel tubing. To determine the P_f values corresponding to the middle of the test zone, the “raw” (as measured by the transducer) P_f estimates were depth-corrected using the offset distance of 26.64 m and fluid density values calculated prior to the start of each test. Fluid density was calculated using annulus and test-zone transducer pressure readings and the measured distance between the two transducers. The depth-corrected P_f estimates are given in the tables below whereas the raw P_f estimates are listed in the graph annotations.

Results of each test analysis are discussed below. A summary of DGR-3 testing results is presented in Section 7.24.

7.1 210.18-240.92 Salina F-E

The DGR-3 interval from 210.18 to 240.92 m BGS included the lower 29.42 m of the Salina Unit F and the upper 1.32 m of the Salina Unit E, both of which consist of dolomitic shale and dolostone. An overview of the testing in this interval is given in Table 7-2 and a summary of the corresponding parameter estimates is given in Table 7-3. A pulse-withdrawal test and a short pulse-injection test that was not analyzed were conducted in this interval.

Table 7-2: Summary of the DGR3_210.18-240.92 testing activities.

Formation / Unit		Top of Test Zone (m BGS)		Bottom of Test Zone (m BGS)	
Salina F-E		210.18		240.92	
Test	Initiated	Magnitude (kPa)	Duration	Compressibility (Pa ⁻¹)	
Shut-in	07-09-08 16:38	N/A	21 hr	N/A	
PW	08-09-08 13:08	705	42 hr	4.5E-10	
PI	10-09-08 07:18	716	66 min	4.5E-10	
Borehole Pressure History					
Event		Start		Pressure (kPa)	
Drilling Intercept		02-06-08 04:00		2244	
End of Geophysical Logging		05-08-08		1980	
Prior Testing ¹		12-08-08		N/A	
Shut-in		07-09-08 16:38		2028	

Table 7-3: Summary of the DGR-3_210.18-240.92 parameter estimates.

Parameter	Best Fit	Minimum	Maximum	Mean
K_f (m/s)	4.8E-14	4.4E-14	6.4E-14	5.2E-14
P_f (kPa)	2050	2038	2065	2048
S_s (m ⁻¹)	1.8E-6	7.4E-7	2.1E-6	1.5E-6
K_s (m/s)	6.3E-13	7.4E-14	1E-6	2.5E-10
t_s (cm)	0.6	2E-4	5.9	1.6

Figure 7-1 shows the measured pressure record from DGR3_210.18-240.92 used in this analysis along with the best-fit simulation and parameter values. The ranges of formation K and raw P_f values estimated from perturbation analysis are shown in Figure 7-2 and the fit value cumulative distribution function is shown in Figure 7-3.

¹ . “Prior testing” refers to all data measured by the transducer that is used as part of the borehole pressure history prior to the start of the test being analyzed. The time indicates the start date of data collection.

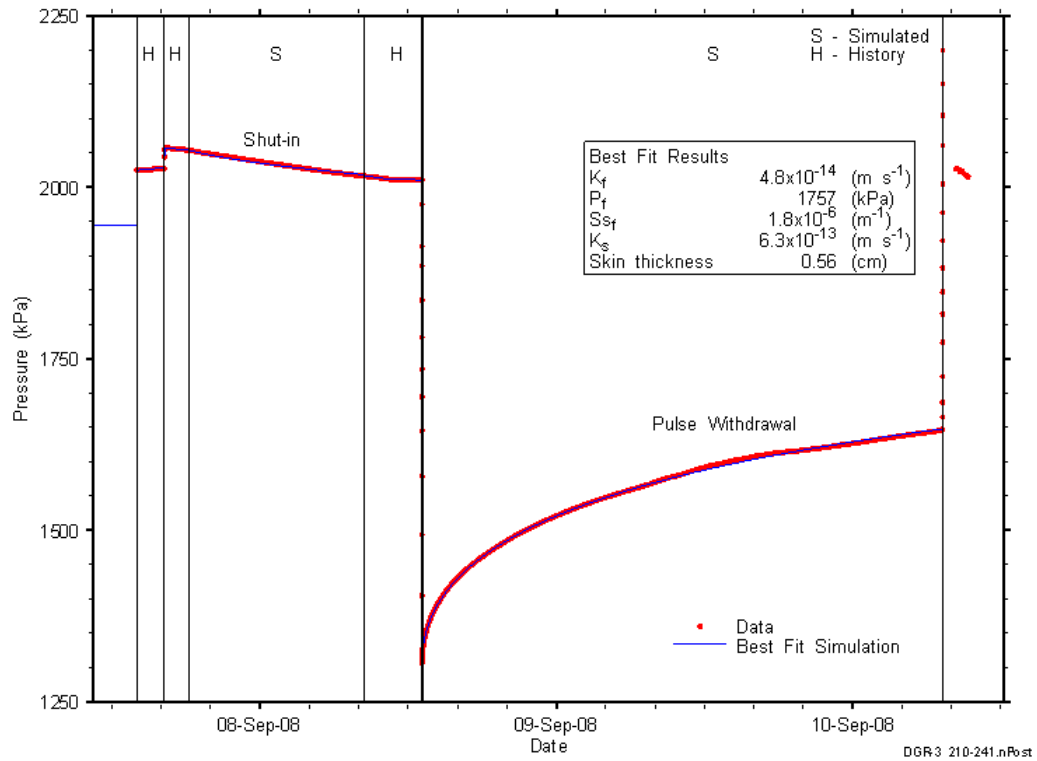


Figure 7-1: Annotated DGR3_210.18-240.92 testing sequence showing best-fit simulation and parameter estimates.

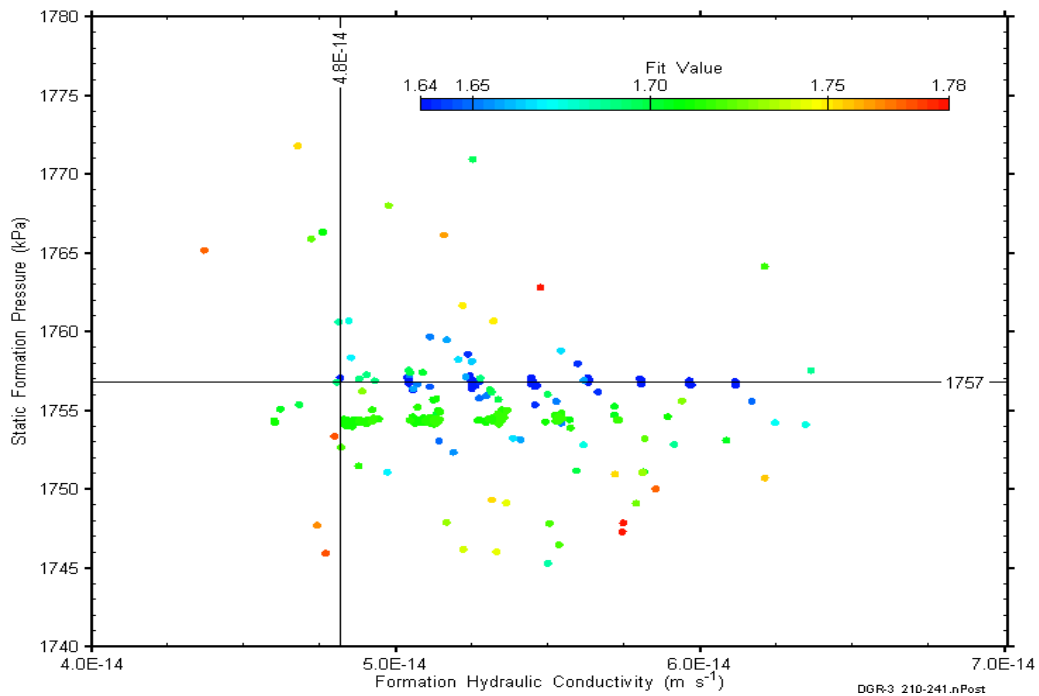


Figure 7-2: XY-scatter plot showing estimates of formation hydraulic conductivity and raw static formation pressure derived from the DGR3_210.18-240.92 perturbation analysis.

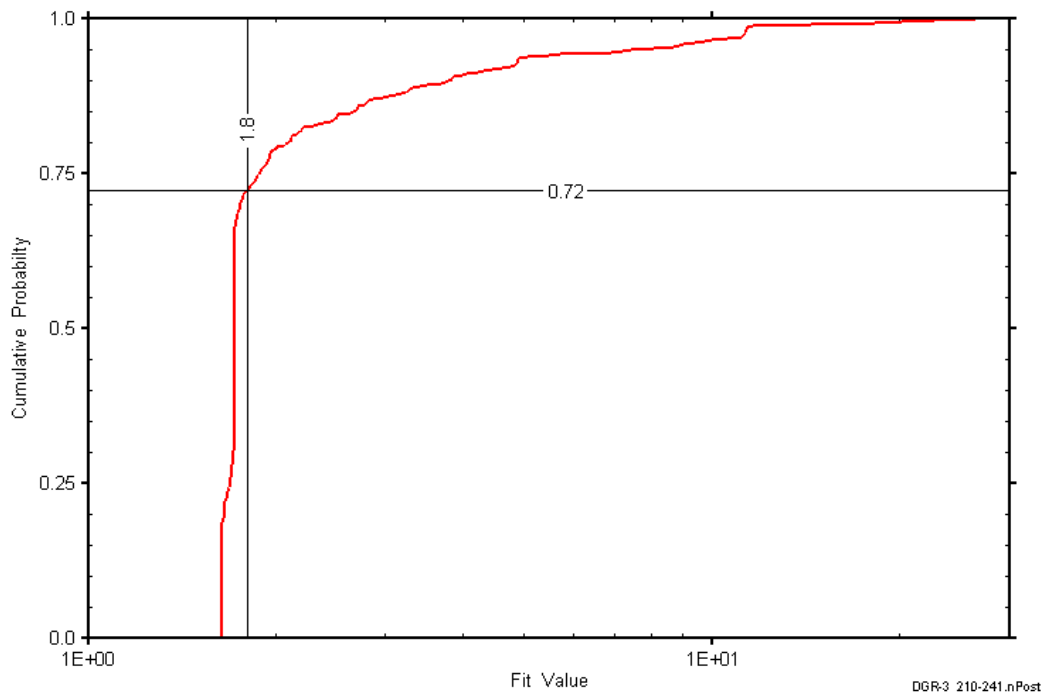


Figure 7-3: DGR3_210.18-240.92 fit value cumulative distribution function.

7.2 240.72-271.46 Salina E-D-C

The DGR-3 interval from 240.72 to 271.46 m BGS included the lower 22.68 m of the Salina Unit E, the entire 2.6-m thickness of the Salina Unit D, and the upper 5.46 m of the Salina Unit C. Unit E consists of dolomitic shale and dolostone with anhydrite, Unit D is an anhydritic dolostone, and Unit C is primarily shale. An overview of the testing in this interval is given in Table 7-4 and a summary of the corresponding parameter estimates is given in Table 7-5. A pulse-withdrawal test and a pulse-injection test were conducted in this interval.

Table 7-4: Summary of the DGR3_240.72 – 271.46 testing activities

Formation / Unit		Top of Test Zone (m BGS)		Bottom of Test Zone (m BGS)	
Salina E-D-C		240.72		271.46	
Test	Initiated	Magnitude (kPa)	Duration	Compressibility (Pa ⁻¹)	
Shut-in	10-09-08 15:34	N/A	24 hr	N/A	
PW	11-09-08 15:13	500	24 hr	6.6E-10	
PI	12-09-08 15:16	538	19 hr	6.1E-10	
PW	13-09-08 10:09	501	26 min	6.6E-10	
Borehole Pressure History					
Event		Start		Pressure (kPa)	
Drilling Intercept		03-06-08 03:00		2573	
End of Geophysical Logging		05-08-08		2370	
Prior Testing		12-08-08		N/A	
Shut-in		10-09-08 15:34		2346	

Table 7-5: Summary of the DGR3_240.72 – 271.46 parameter estimates.

Parameter	Best Fit	Minimum	Maximum	Mean
K_f (m/s)	1.4E-13	4.4E-14	2.0E-13	1.1E-13
P_f (kPa)	1900	1424	2006	1809
S_s (m^{-1})	7.4E-7	6.4E-7	8.5E-7	7.4E-7
K_s (m/s)	9.3E-13	8.7E-13	1.0E-12	9.3E-13
t_s (cm)	56	47	92	63

Figure 7-4 shows the measured pressure record from DGR3_240.72-271.46 used in this analysis along with the best-fit simulation and parameter values. The ranges of formation K and raw P_f values estimated from perturbation analysis are shown in Figure 7-5 and the fit value cumulative distribution function is shown in Figure 7-6.

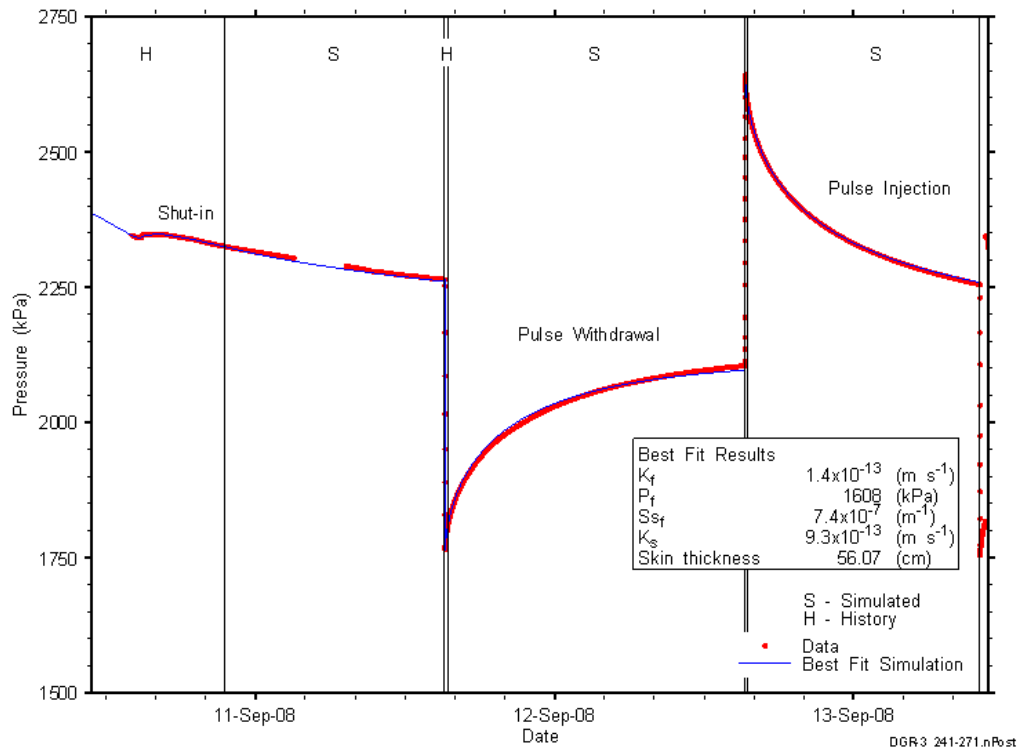


Figure 7-4: Annotated DGR3_240.72-271.46 testing sequence showing best-fit simulation and parameter estimates.

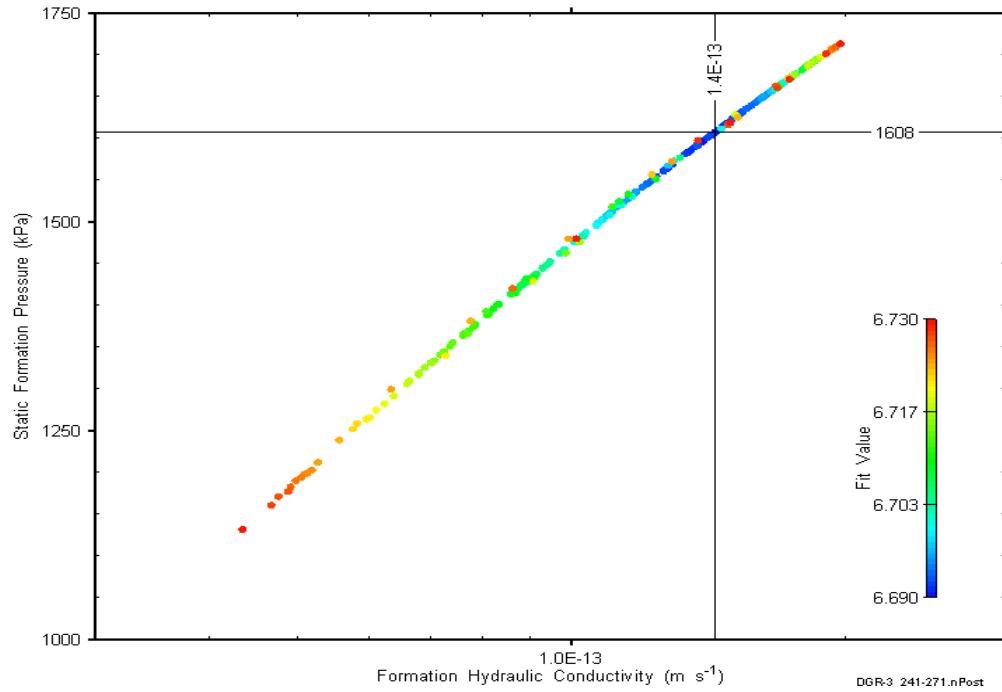


Figure 7-5: XY-scatter plot showing estimates of formation hydraulic conductivity and raw static formation pressure derived from the DGR3_240.72-271.46 perturbation analysis.

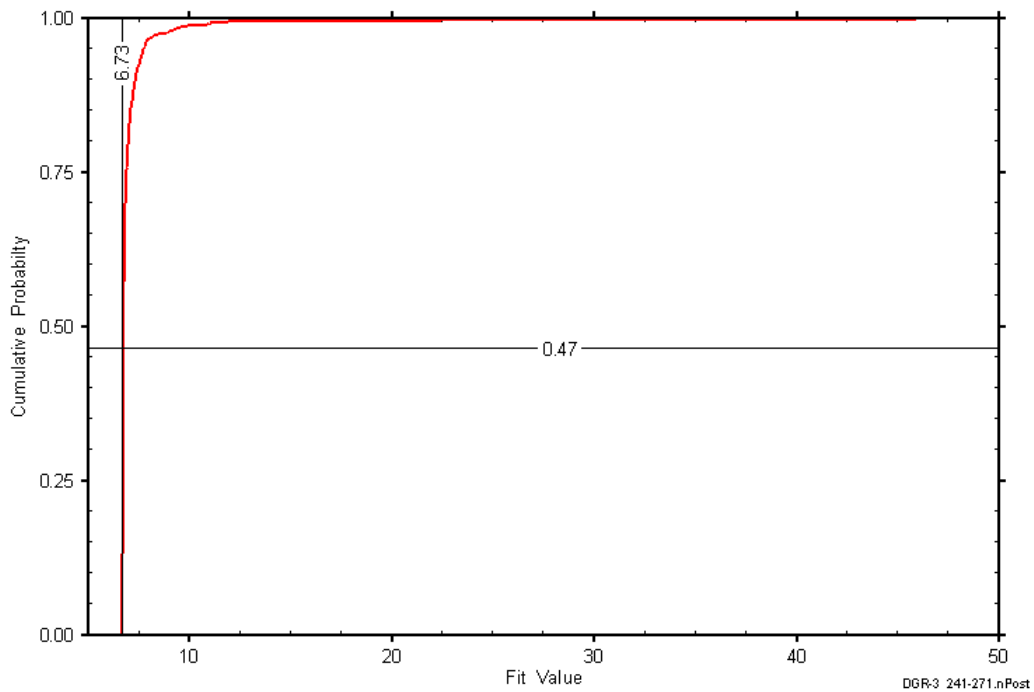


Figure 7-6: DGR3_240.72-271.46 fit value cumulative distribution function.

7.3 271.29-302.03 Salina C-B

The DGR-3 interval from 271.29 to 302.03 m BGS included the lower 6.61 m of the Salina Unit C and all but the lower metre of the Salina Unit B carbonate. This portion of Unit C is a dolomitic shale, and the Unit B carbonate consists of argillaceous dolostone. An overview of the testing in this interval is given in Table 7-6 and the corresponding parameter estimates are given in Table 7-7. A pulse-withdrawal test and a pulse-injection test were conducted in this interval.

Table 7-6: Summary of the DGR3_271.29 – 302.03 testing activities.

Formation / Unit		Top of Test Zone (m BGS)		Bottom of Test Zone (m BGS)	
Salina C-B		271.29		302.03	
Test	Initiated	Magnitude (kPa)	Duration	Compressibility (Pa ⁻¹)	
Shut-in	13-09-08 15:34	N/A	21 hr	N/A	
PW	14-09-08 12:21	128	20 hr	2.0E-9	
PI	15-09-08 08:42	126	22 hr	2.0E-9	
PW	16-09-08 06:53	123	4 min	2.0E-9	
Borehole Pressure History					
Event		Start		Pressure (kPa)	
Drilling Intercept		03-06-08 18:00		2903	
End of Geophysical Logging		05-08-08		2636	
Prior Testing		12-08-08		N/A	
Shut-in		10-09-08 15:34		2667	

Table 7-7: Summary of the DGR3_271.29 – 302.03 parameter estimates.

Parameter	Best Fit	Minimum	Maximum	Mean
K_f (m/s)	3.8E-13	3.5E-13	4.0E-13	3.7E-13
P_f (kPa)	2090	2063	2116	2083
S_s (m ⁻¹)	1.2E-5	9.3E-6	1.6E-5	1.3E-5
K_s (m/s)	2.8E-13	2.3E-13	3.6E-13	2.7E-13
t_s (cm)	4.1	3.6	5.0	4.0

The test-zone compressibility of this interval was high relative to that of most other test intervals for an unknown reason. Specific storage also appeared to be relatively high, although neither K nor P_f were unusually high compared to neighbouring intervals.

Figure 7-7 shows the measured pressure record from DGR3_271.29 – 302.03 used in this analysis along with the best-fit simulation and parameter values. The ranges of formation K and raw P_f values estimated from perturbation analysis are shown in Figure 7-8 and the fit value cumulative distribution function is shown in Figure 7-9.

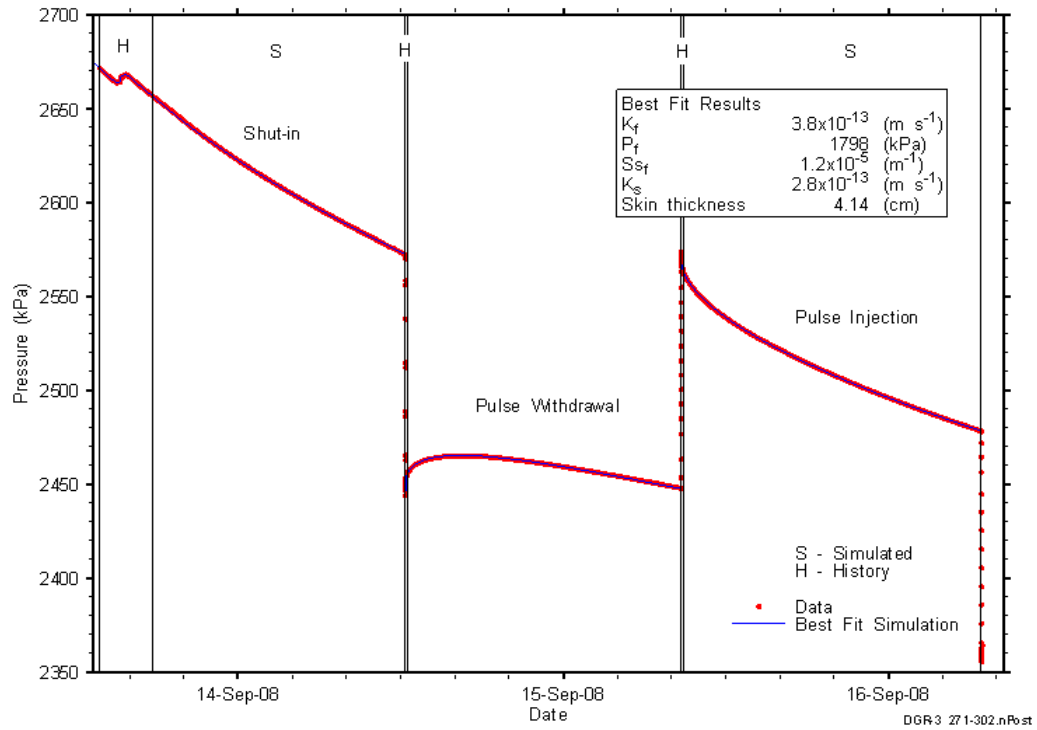


Figure 7-7: Annotated DGR3_271.29-302.03 testing sequence showing best-fit simulation and parameter estimates.

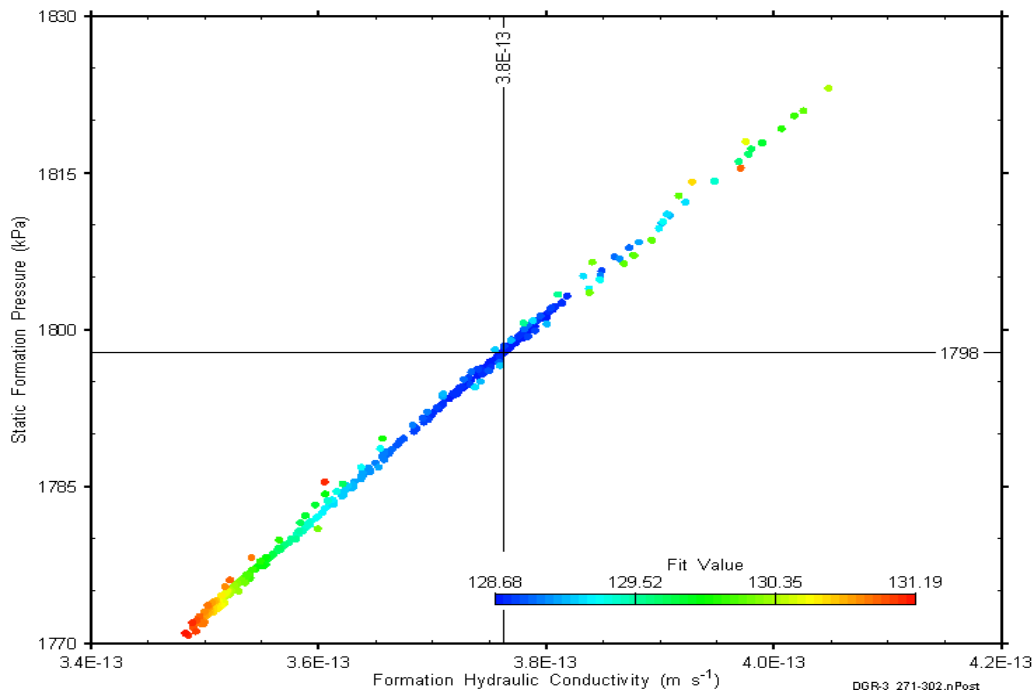


Figure 7-8: XY-scatter plot showing estimates of formation hydraulic conductivity and raw static formation pressure derived from the DGR3_271.29-302.03 perturbation analysis.

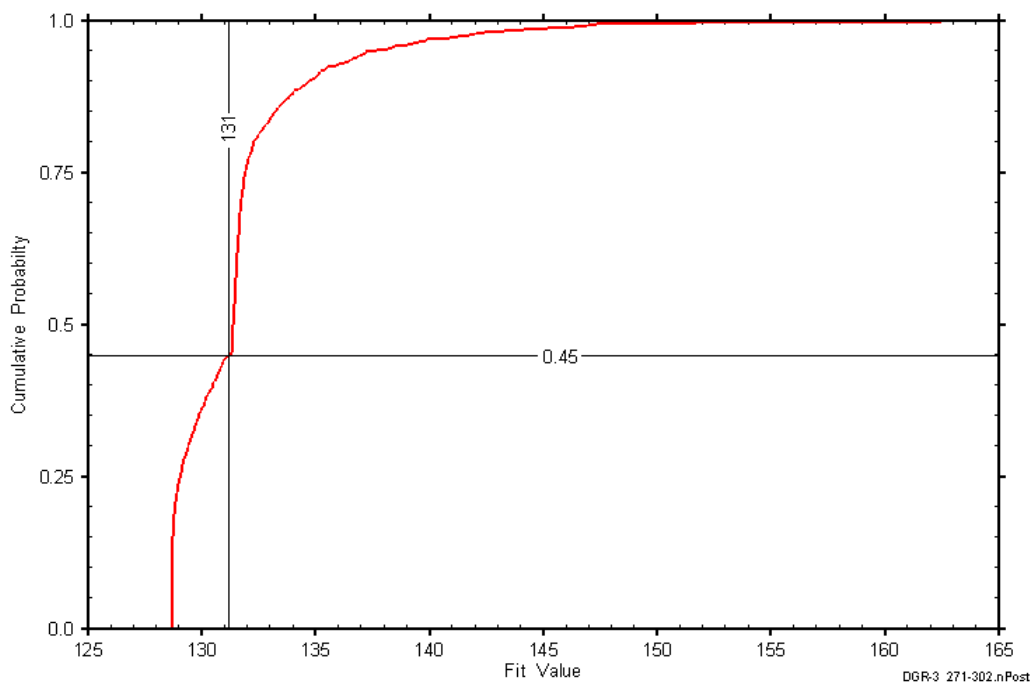


Figure 7-9: DGR3_271.29-302.03 fit value cumulative distribution function.

7.4 301.81-332.55 Salina B-A2 Carbonate

The DGR-3 interval from 301.81 to 332.55 m BGS included the lower 1.19 m of the Salina Unit B carbonate, the 1.6-m-thick Unit B evaporite, and all but the lower metre of the Salina Unit A2 carbonate. The Unit B carbonate consists of argillaceous dolostone, the Unit B evaporite consists of anhydrite with dolostone layers, and the Unit A2 carbonate is argillaceous dolomite and dolostone, dolomitic shale, and anhydritic dolostone. An overview of the testing in this interval is given in Table 7-8 and the corresponding parameter estimates are given in Table 7-9. A short pulse-withdrawal test that was not analyzed and a slug-injection test were performed in this interval.

Table 7-8: Summary of the DGR3_301.81-332.55 testing activities.

Formation / Unit		Top of Test Zone (m BGS)	Bottom of Test Zone (m BGS)	
Salina B-A2 carbonate		301.81	332.55	
Test	Initiated	Magnitude (kPa)	Duration	Compressibility (Pa ⁻¹)
Shut-in	16-09-08 12:30	N/A	3 hr	N/A
PW	16-09-08 15:37	130	1 hr	2.8E-9
SI	16-09-08 16:48	416	15 hr	N/A
Borehole Pressure History				
Event	Start	Pressure (kPa)		
Drilling Intercept	04-06-08 09:00	3232		
End of Geophysical Logging	05-08-08	2971		
Prior Testing	12-08-08	N/A		
Shut-in	16-09-08 12:30	3003		

Table 7-9: Summary of the DGR3_301.81-332.55 parameter estimates.

Parameter	Best Fit	Minimum	Maximum	Mean
K_f (m/s)	3.8E-9	3.8E-9	4.2E-9	4.0E-9
P_f (kPa)	3161	3160	3165	3163
S_s (m^{-1})	7.7E-5	1.9E-6	9.5E-5	2.0E-5
K_s (m/s)	1.5E-15	1E-15	4.5E-10	7.6E-13
t_s (cm)	1.9	1.6	11	3.7

This interval had a high test-zone compressibility ($2.8E-9 Pa^{-1}$) and was sufficiently permeable for a slug test to be the appropriate test to perform. The estimated S_s was also high.

Figure 7-10 shows the measured pressure record from DGR3_301.81-332.55 used in this analysis along with the best-fit simulation and parameter values. The ranges of formation K and raw P_f values estimated from perturbation analysis are shown in Figure 7-11 and the fit value cumulative distribution function is shown in Figure 7-12.

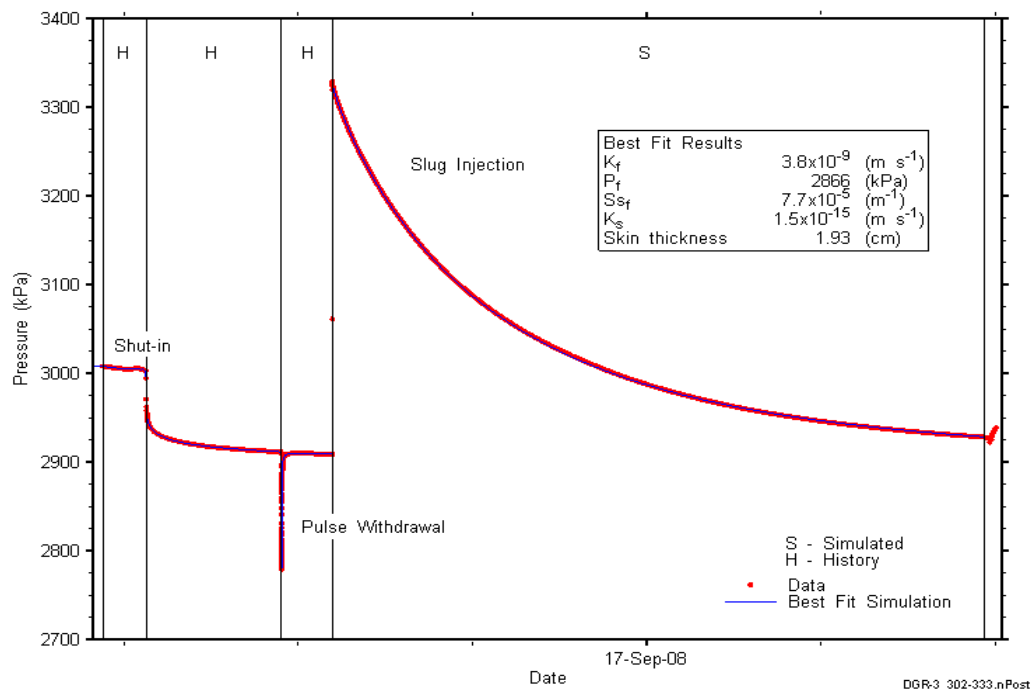


Figure 7-10: Annotated DGR3_301.81-332.55 testing sequence showing best-fit simulation and parameter estimates.

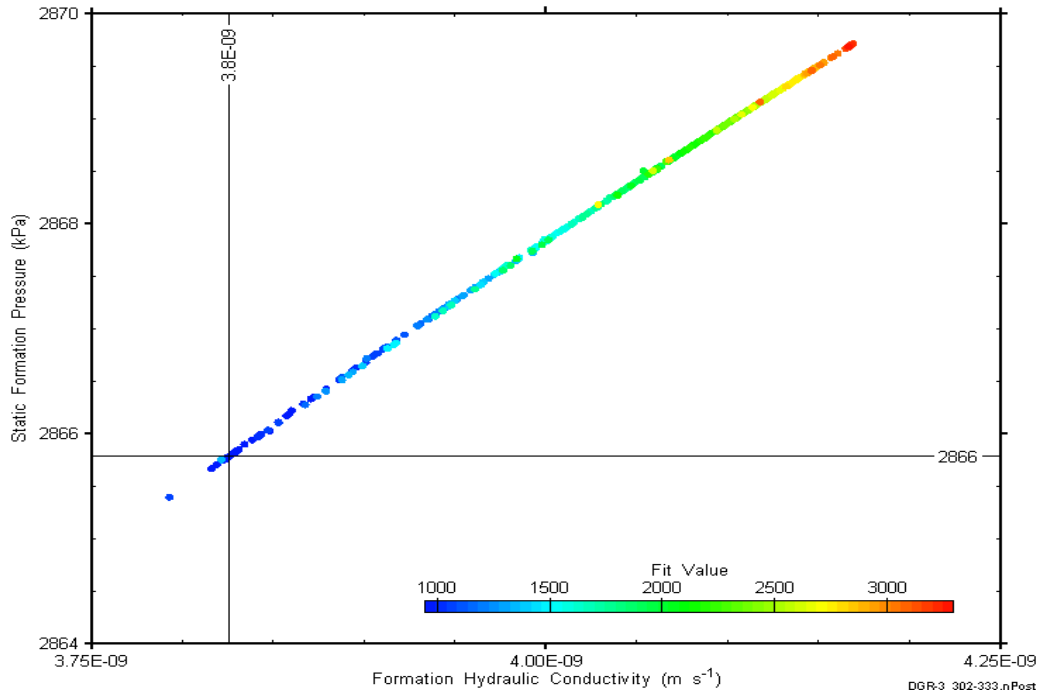


Figure 7-11: XY-scatter plot showing estimates of formation hydraulic conductivity and raw static formation pressure derived from the DGR3_301.81-332.55 perturbation analysis.

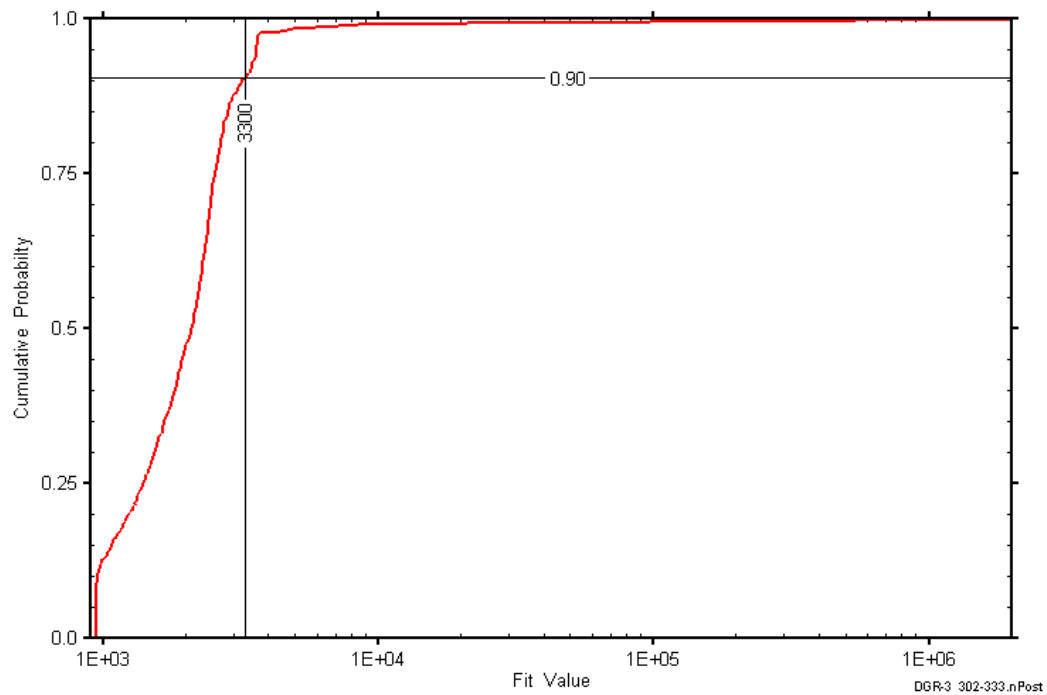


Figure 7-12: DGR3_301.81-332.55 fit value cumulative distribution function.

7.5 334.99-365.73 Salina A2 Evaporite-A1 Carbonate

The DGR-3 interval from 334.99 to 365.73 m BGS included the lower 3.61 m of the Salina Unit A2 evaporite and the upper 27.13 m of the Salina Unit A1 carbonate. The Salina Unit A2 evaporite is anhydritic dolostone to dolomitic anhydrite, and the Unit A1 carbonate is a dolostone with bituminous layers and minor anhydrite layering. The upper 3 to 4 m of the A1 carbonate contains open, vuggy porosity. An overview of the testing in this interval is given in Table 7-10 and the corresponding parameter estimates are given in Table 7-11. A DST and a slug-injection test were conducted in this interval, providing no data to estimate test-zone compressibility. The DST flow period was analyzed as a slug-withdrawal test.

Table 7-10: Summary of the DGR3_334.99-365.73 testing activities.

Formation / Unit		Top of Test Zone (m BGS)		Bottom of Test Zone (m BGS)	
Salina A2 evaporite-A1 carbonate		334.99		365.73	
Test	Initiated	Magnitude (kPa)	Duration	Compressibility (Pa ⁻¹)	
Shut-in	12-11-08 15:26	N/A	18 hr	N/A	
SW	13-11-08 09:03	553	7 hr	N/A	
DST	13-11-08 15:47	N/A	1 hr	N/A	
SI	13-11-08 16:50	610	16 hr	N/A	
Borehole Pressure History					
Event		Start		Pressure (kPa)	
Drilling Intercept		11-06-08 15:00		3490	
End of Geophysical Logging		05-08-08		3262	
Prior Testing		12-08-08		N/A	
Shut-in		12-11-08 15:26		3239	

Table 7-11: Summary of the DGR3_334.99-365.73 parameter estimates.

Parameter	Best Fit	Minimum	Maximum	Mean
K_f (m/s)	1.8E-8	1.8E-8	1.8E-8	1.8E-8
P_f (kPa)	3546	3546	3546	3546
S_{sf} (m ⁻¹)	2.0E-7	1.0E-7	1.5E-5	7.1E-7
K_{s1} (m/s)	1.1E-10	9.8E-11	1.1E-10	1.0E-10
K_{s2} (m/s)	6.3E-11	5.9E-11	7.5E-11	6.2E-11
K_{s3} (m/s)	5.7E-11	5.5E-11	5.8E-11	5.6E-11
S_{ss} (m ⁻¹)	2.0E-7	1E-7	4.4E-6	6.2E-7

Figure 7-13 shows the measured pressure record from DGR3_334.99-365.73 used in this analysis along with the best-fit simulation and parameter values. The specified DGR3_334.99-365.73 conceptual model was an infinite-acting, homogeneous, fully confined, radial system with wellbore storage and a time/test-dependent skin with an assumed thickness of one cm. While the skin K for this test was assumed to vary with the type of test performed, it must be implemented in nSIGHTS as time varying. Initial attempts to match both the SW and SI tests with a single skin K proved unsuccessful. It was thought that the skin K during the SI might decrease somewhat as fluid and suspended drilling fines flowed into the formation. The addition of a time/test-dependent skin to the model resulted in a better match to the observed response. In Table 7-11, K_{s1} represents the skin K during the SW test and K_{s2} and K_{s3} are the estimated skin K values during the early and later time portions of the SI test, respectively. These results indicate that SI skin K was less than the SW skin K , in keeping with the conceptual model assumption. Note that nSIGHTS requires that skin and formation S_s be separate fitting parameters for the time-varying

skin model. Table 7-11 shows that the best-fit values for skin and formation S_s were effectively the same. The ranges of formation K and raw P_f values estimated from DGR3_334.99-365.73 perturbation analysis are shown in Figure 7-14 and the fit value cumulative distribution function is shown in Figure 7-15.

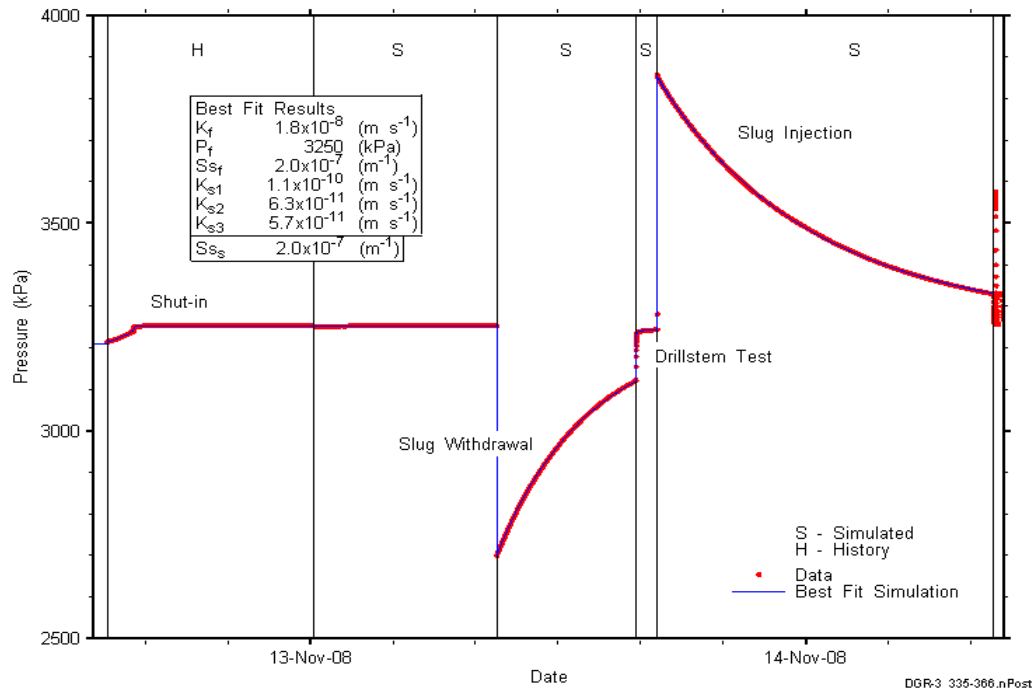


Figure 7-13: Annotated DGR3_334.99-365.73 testing sequence showing best-fit simulation and parameter estimates.

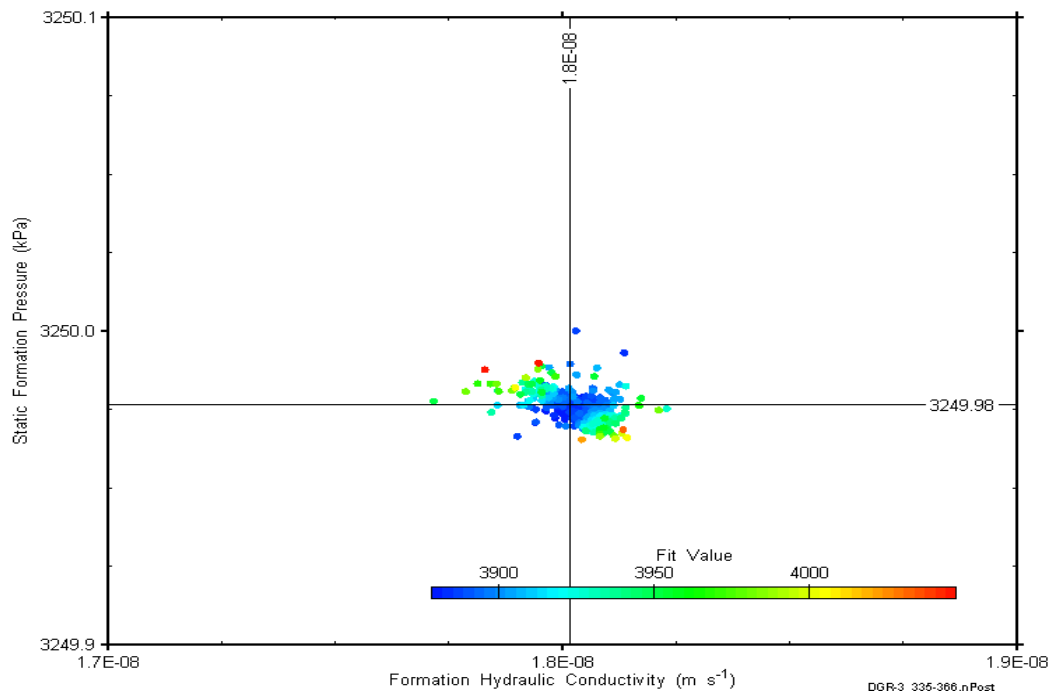


Figure 7-14: XY-scatter plot showing estimates of formation hydraulic conductivity and raw static formation pressure derived from the DGR3_334.99-365.73 perturbation analysis.

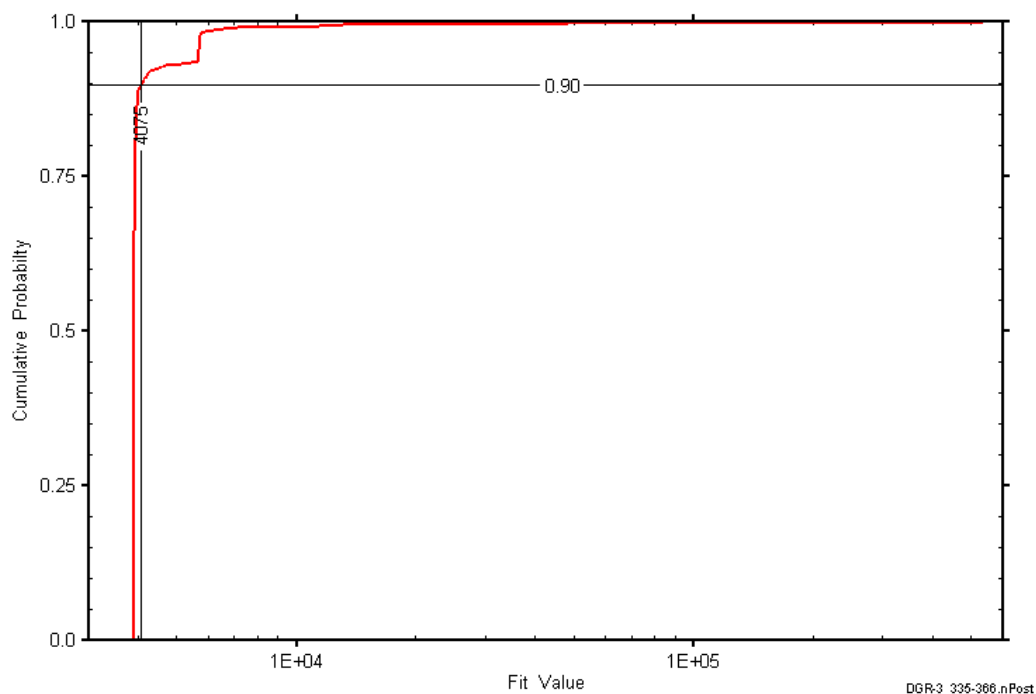


Figure 7-15: DGR3_334.99-365.73 fit value cumulative distribution function.

7.6 346.00-376.74 Salina A1 Carbonate

The DGR-3 interval from 346.00 to 376.74 m BGS was contained entirely within the Salina Unit A1 carbonate, although it did not include the upper vuggy 3-4 m of the unit. The portion of the Salina Unit A1 carbonate that was tested consists of dolostone with bituminous layers and minor anhydrite layering. An overview of the testing in this interval is given in Table 7-12 and the corresponding parameter estimates are given in Table 7-13. Pulse-withdrawal and pulse-injection tests were performed in this interval.

Table 7-12: Summary of the DGR3_346.00-376.74 testing activities.

Formation / Unit		Top of Test Zone (m BGS)	Bottom of Test Zone (m BGS)	
Salina A1 carbonate		346.00	376.74	
Test	Initiated	Magnitude (kPa)	Duration	Compressibility (Pa ⁻¹)
Shut-in	17-09-08 12:04	N/A	4 hr	N/A
PW	17-09-08 16:09	832	16 hr	3.7E-10
PI	18-09-08 07:59	820	4 hr	3.7E-10
Borehole Pressure History				
Event	Start	Pressure (kPa)		
Drilling Intercept	12-06-08 02:00	3708		
End of Geophysical Logging	05-08-08	3438		
Prior Testing	12-08-08	N/A		
Shut-in	17-09-08 12:04	3517		

Table 7-13: Summary of the DGR3_346.00-376.74 parameter estimates.

Parameter	Best Fit	Minimum	Maximum	Mean
K_f (m/s)	4.0E-11	3.6E-11	7.1E-11	5.1E-11
P_f (kPa)	3573	3569	3597	3588
S_s (m^{-1})	7.3E-6	1.6E-8	7.3E-6	1.8E-7
K_s (m/s)	3.0E-12	3.0E-12	4.3E-11	2.1E-11
t_s (cm)	1.1	0.9	192	50

Figure 7-16 shows the measured pressure record from DGR3_346.00-376.74 used in this analysis along with the best-fit simulation and parameter values. The ranges of formation K and raw P_f values estimated from perturbation analysis are shown in Figure 7-17 and the fit value cumulative distribution function is shown in Figure 7-18.

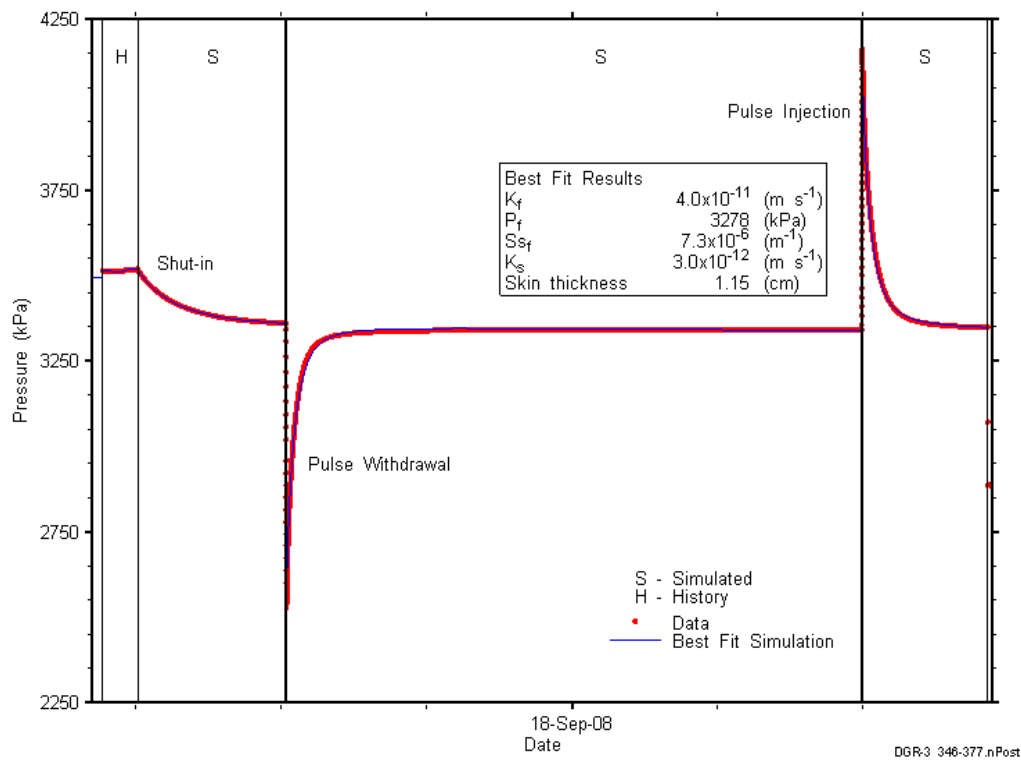


Figure 7-16: Annotated DGR3_346.00-376.74 testing sequence showing best-fit simulation and parameter estimates.

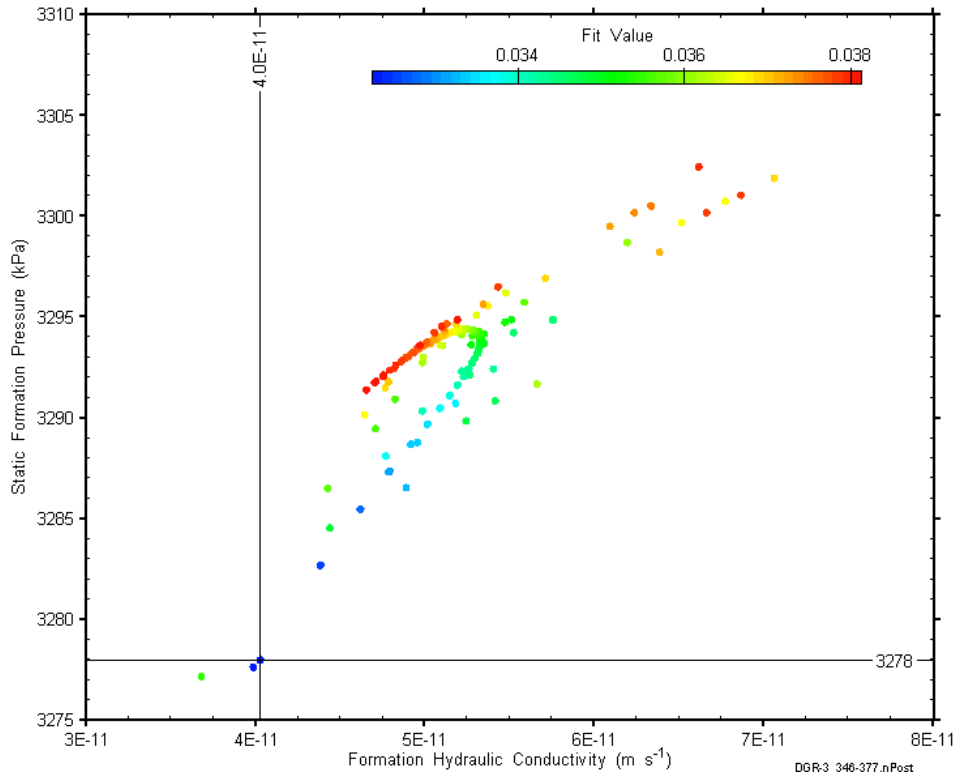


Figure 7-17: XY-scatter plot showing estimates of formation hydraulic conductivity and raw static formation pressure derived from the DGR3_346.00-376.74 perturbation analysis.

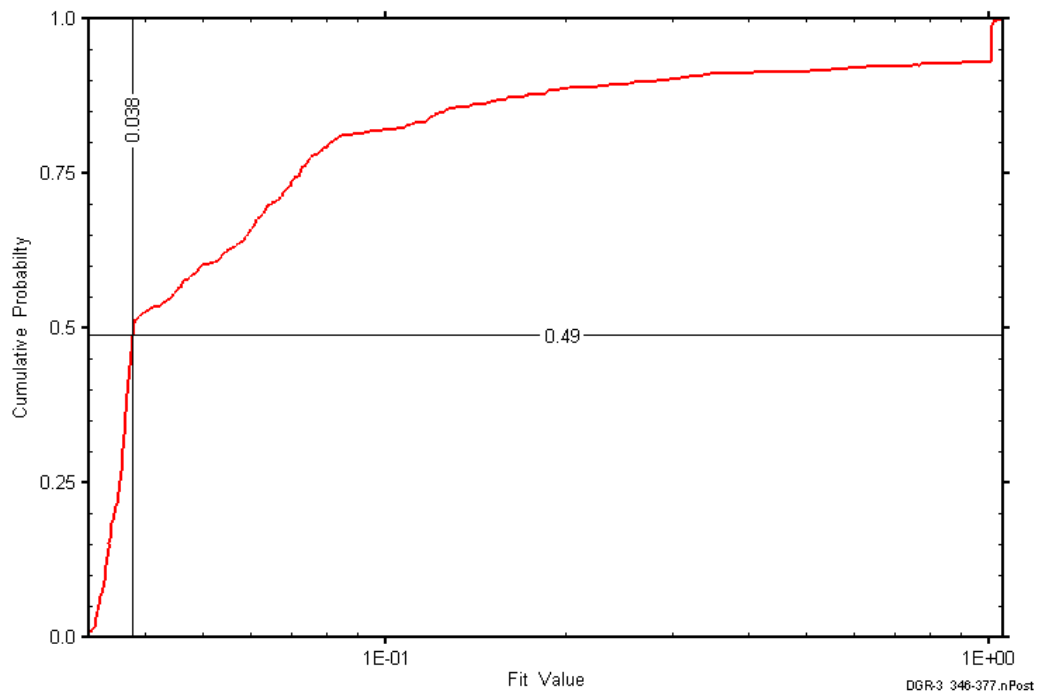


Figure 7-18: DGR3_346.00-376.74 fit value cumulative distribution function.

7.7 379.98-410.72 Salina A1 Evaporite-A0-Guelph-Goat Island-Gasport

The DGR-3 interval from 379.98 to 410.72 m BGS included the lower 3.61 m of the Salina Unit A1 evaporite, the entire 2.6-m thickness of the Salina Unit A0, the entire 5.4-m thickness of the Guelph Formation, the entire 18.3-m thickness of the Goat Island Member of the Lockport Formation, and the upper 0.22 m of the Gasport Member of the Lockport Formation. The Salina Unit A1 evaporite is anhydritic dolostone, the Unit A0 is a bituminous dolostone, the Guelph is vuggy, sucrosic dolostone, the Goat Island is dolostone, and the Gasport is dolomitic limestone. An overview of the testing in this interval is given in Table 7-14 and the corresponding parameter estimates are given in Table 7-15. Only a slug-withdrawal test was performed in this interval, providing no data to estimate test-zone compressibility.

Table 7-14: Summary of the DGR3_379.98-410.72 testing activities.

Formation / Unit		Top of Test Zone (m BGS)	Bottom of Test Zone (m BGS)	
Salina A1 evaporite-A0-Guelph-Goat Island-Gasport		379.98	410.72	
Test	Initiated	Magnitude (kPa)	Duration	Compressibility (Pa ⁻¹)
Shut-in	18-09-08 14:26	N/A	2 hr	N/A
SW	18-09-08 16:39	558	16 hr	N/A
Borehole Pressure History				
Event	Start		Pressure (kPa)	
Drilling Intercept	15-06-08 13:00		4074	
End of Geophysical Logging	05-08-08		3806	
Prior Testing	12-08-08		N/A	
Shut-in	18-09-08 14:26		3844	

Table 7-15: Summary of the DGR3_379.98-410.72 parameter estimates.

Parameter	Best Fit	Minimum	Maximum	Mean
K_f (m/s)	8.9E-9	8.8E-9	9.0E-9	8.9E-9
P_f (kPa)	4224	4222	4224	4224
S_s (m ⁻¹)	2.2E-6	4.2E-7	1.0E-5	1.9E-6
K_s (m/s)	4.3E-6	3.1E-8	1.0E-4	6.2E-6
t_s (cm)	48	20	121	53

Figure 7-19 shows the measured pressure record from DGR3_379.98-410.72 used in this analysis along with the best-fit simulation and parameter values. The ranges of formation K and raw P_f values estimated from perturbation analysis are shown in Figure 7-20 and the fit value cumulative distribution function is shown in Figure 7-21.

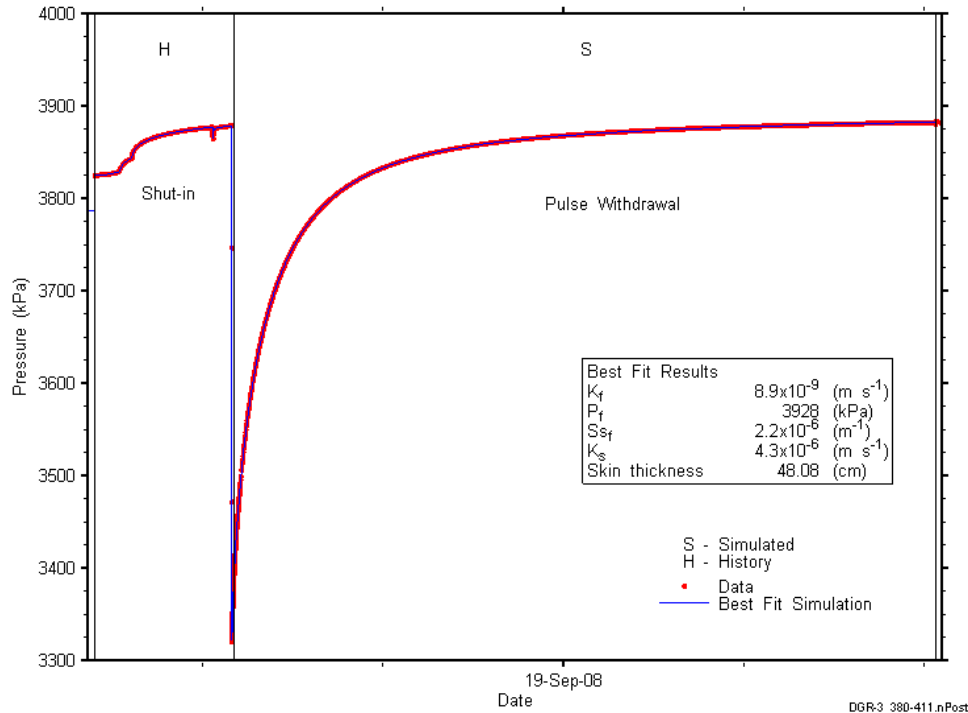


Figure 7-19: Annotated DGR3_379.98-410.72 testing sequence showing best-fit simulation and parameter estimates.

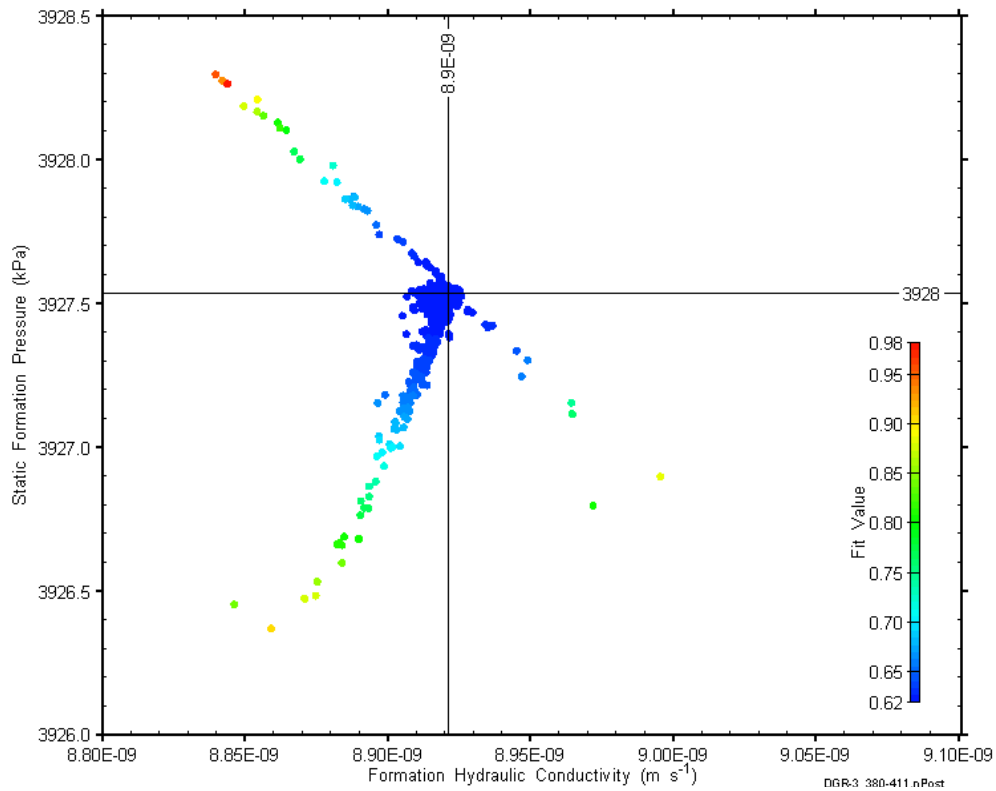


Figure 7-20: XY-scatter plot showing estimates of formation hydraulic conductivity and raw static formation pressure derived from the DGR3_379.98-410.72 perturbation analysis.

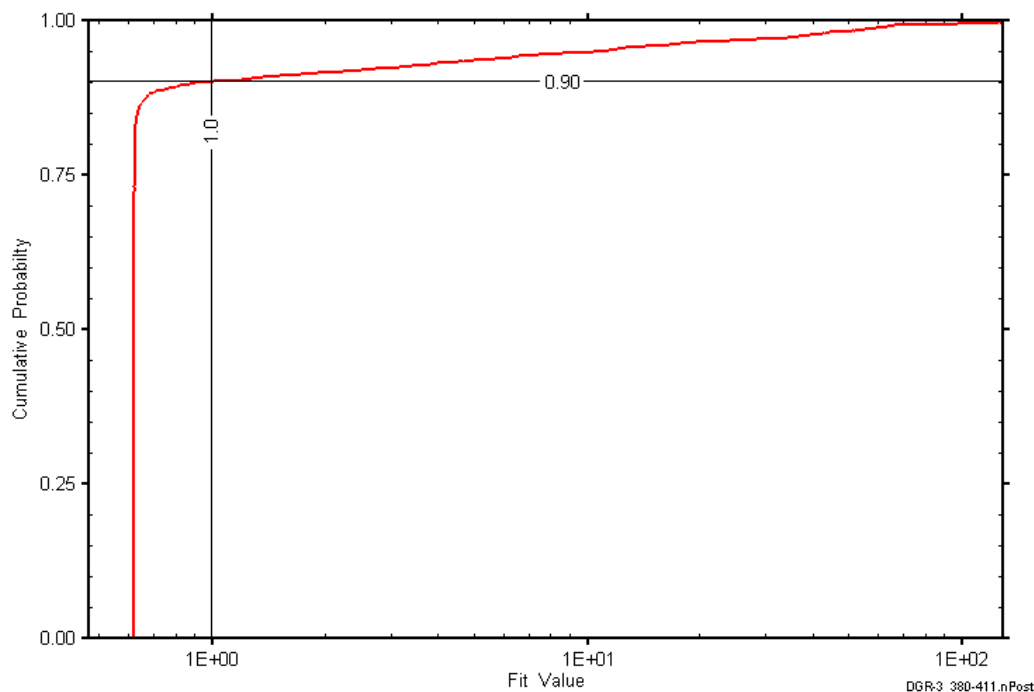


Figure 7-21: DGR3_379.98-410.72 fit value cumulative distribution function.

7.8 410.51-441.25 Gasport-Lions Head-Fossil Hill-Cabot Head

The DGR-3 interval from 410.51 to 441.25 m BGS included the entire 6.5-m thickness of the Gasport Member of the Lockport Formation, the entire 4.5-m thickness of the Lions Head Member of the Amabel Formation, the entire 1.3-m thickness of the Fossil Hill Formation, and the upper 18.45 m of the Cabot Head Formation. The Gasport is dolomitic limestone, the Lions Head and Fossil Hill are dolostones, and the Cabot Head is shale. An overview of the testing in this interval is given in Table 7-16 and the corresponding parameter estimates are given in Table 7-17. Pulse-withdrawal and pulse-injection tests were performed in this interval.

Table 7-16: Summary of the DGR3_410.51-441.25 testing activities.

Formation / Unit		Top of Test Zone (m BGS)	Bottom of Test Zone (m BGS)	
Gasport-Lions Head-Fossil Hill-Cabot Head		410.51	441.25	
Test	Initiated	Magnitude (kPa)	Duration	Compressibility (Pa ⁻¹)
Shut-in	19-09-08 12:17	N/A	20 hr	N/A
PW	20-09-08 08:39	264	23 hr	1.2E-9
PI	21-09-08 07:25	252	24 hr	1.3E-9
Borehole Pressure History				
Event	Start	Pressure (kPa)		
Drilling Intercept	17-06-08 14:30	4403		
End of Geophysical Logging	05-08-08	4084		
Prior Testing	12-08-08	N/A		
Shut-in	19-09-08 12:17	4208		

Table 7-17: Summary of the DGR3_410.51-441.25 parameter estimates.

Parameter	Best Fit	Minimum	Maximum	Mean
K_f (m/s)	3.5E-12	6.6E-13	3.8E-12	3.2E-12
P_f (kPa)	5259	5227	5974	5291
S_s (m^{-1})	2.0E-7	1.1E-7	1.4E-4	2.2E-7
K_s (m/s)	6.6E-12	4.7E-13	7.7E-12	6.5E-12
t_s (cm)	152	3	380	176

This interval had a relatively high test-zone compressibility, and also a high P_f .

Figure 7-22 shows the measured pressure record from DGR3_410.51-441.25 used in this analysis along with the best-fit simulation and parameter values. The ranges of formation K and raw P_f values estimated from perturbation analysis are shown in Figure 7-23 and the fit value cumulative distribution function is shown in Figure 7-24.

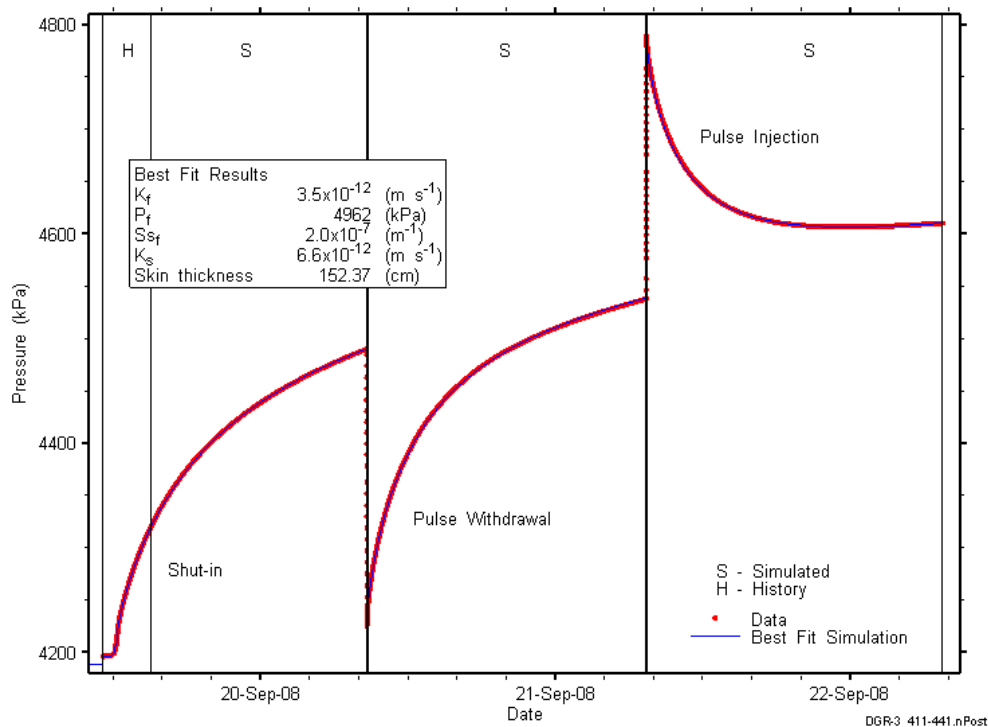


Figure 7-22: Annotated DGR3_410.51-441.25 testing sequence showing best-fit simulation and parameter estimates.

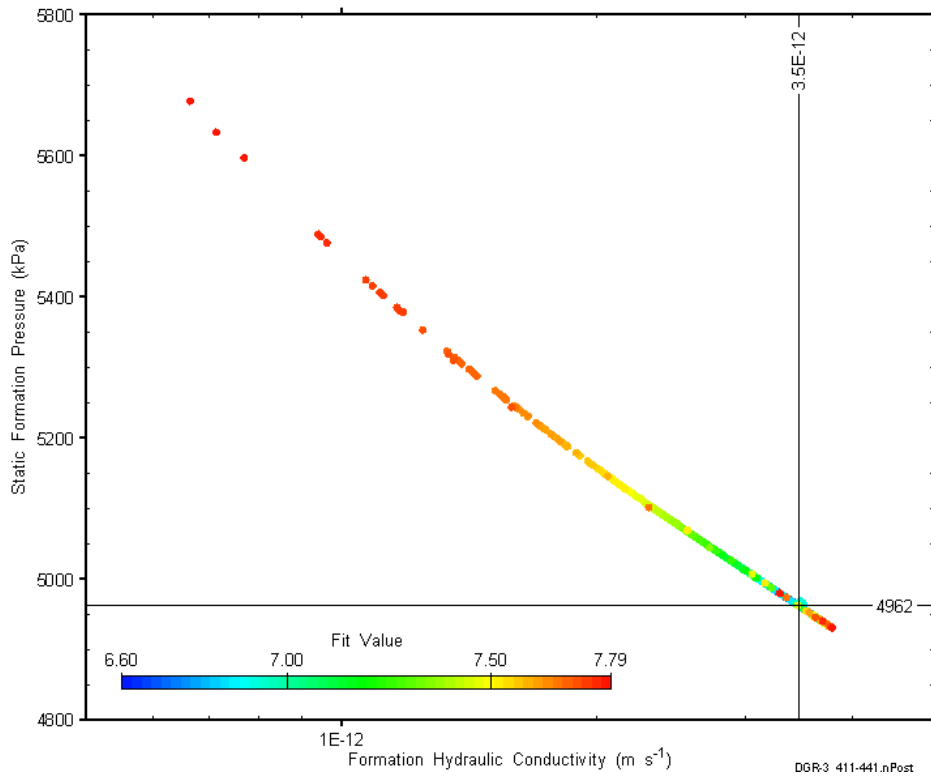


Figure 7-23: XY-scatter plot showing estimates of formation hydraulic conductivity and raw static formation pressure derived from the DGR3_410.51-441.25 perturbation analysis.

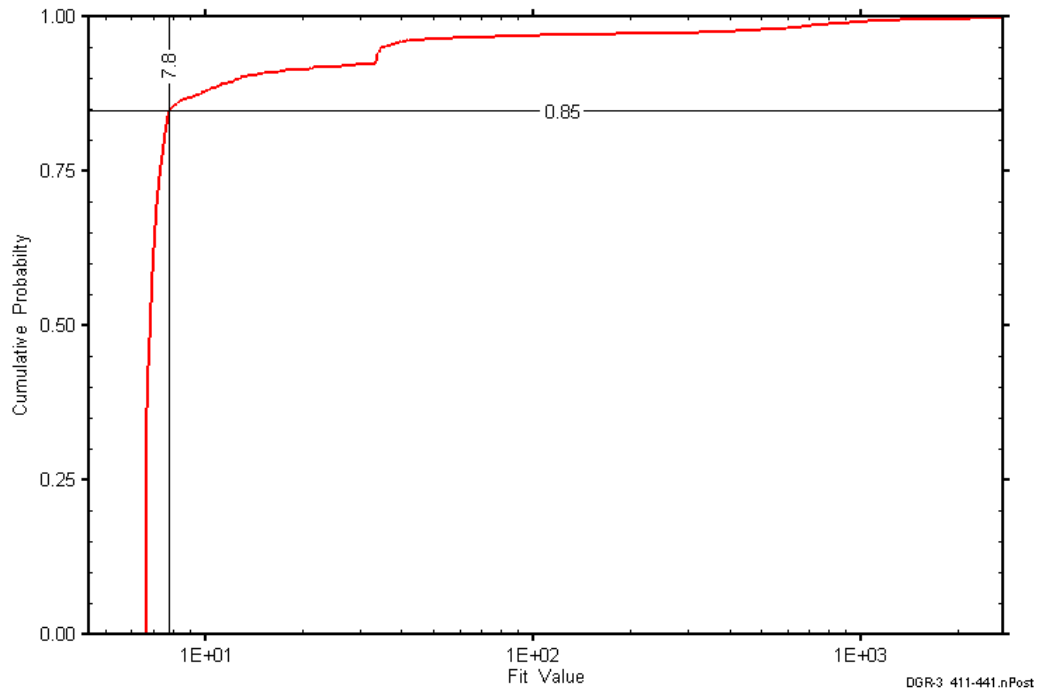


Figure 7-24: DGR3_410.51-441.25 fit value cumulative distribution function.

7.9 441.05-471.79 Cabot Head-Manitoulin-Queenston

The DGR-3 interval from 441.05 to 471.79 m BGS included the lower 6.45 m of the Cabot Head Formation, the entire 9.5-m thickness of the Manitoulin Formation, and the upper 14.79 m of the Queenston Formation. The lower Cabot Head is interbedded dolostone and shale, the Manitoulin is dolostone with minor noncalcareous shale, and the upper Queenston is massive, calcareous shale. An overview of the testing in this interval is given in Table 7-18 and the corresponding parameter estimates are given in Table 7-19. Two pulse-withdrawal tests were performed in this interval.

Table 7-18: Summary of the DGR3_441.05-471.79 testing activities.

Formation / Unit		Top of Test Zone (m BGS)		Bottom of Test Zone (m BGS)	
Cabot Head-Manitoulin-Queenston		441.05		471.79	
Test	Initiated	Magnitude (kPa)	Duration	Compressibility (Pa ⁻¹)	
Shut-in	22-09-08 12:55	N/A	19 hr	N/A	
PW	23-09-08 08:10	50	4 hr	6.6E-9	
PW	23-09-08 11:57	272	45 hr	N/A	
Borehole Pressure History					
Event		Start		Pressure (kPa)	
Drilling Intercept		17-06-08 06:00		4733	
End of Geophysical Logging		05-08-08		4385	
Prior Testing		12-08-08		N/A	
Shut-in		22-09-08 12:55		4566	

Table 7-19: Summary of the DGR3_441.05-471.79 parameter estimates.

Parameter	Best Fit	Minimum	Maximum	Mean
K_f (m/s)	1.6E-13	1.6E-13	1.7E-13	1.6E-13
P_f (kPa)	4138	4137	4139	4138
K_s (m/s)	3.7E-12	3.6E-12	3.9E-12	3.7E-12
t_s (cm)	7.0	7.0	7.0	7.0

This interval had the highest test-zone compressibility encountered in DGR-3, which may be related to fractures observed in the uppermost Queenston at 457.0 and 458.6 m BGS (Briscoe et al., 2010). The fractures did not, however, cause K to be unusually high.

Figure 7-25 shows the measured pressure record from DGR3_441.05-471.79 used in this analysis along with the best-fit simulation and parameter values. The S_s value for this analysis was fixed at $1E-6 \text{ m}^{-1}$. The ranges of formation K and raw P_f values estimated from perturbation analysis are shown in Figure 7-26 and the fit value cumulative distribution function is shown in Figure 7-27.

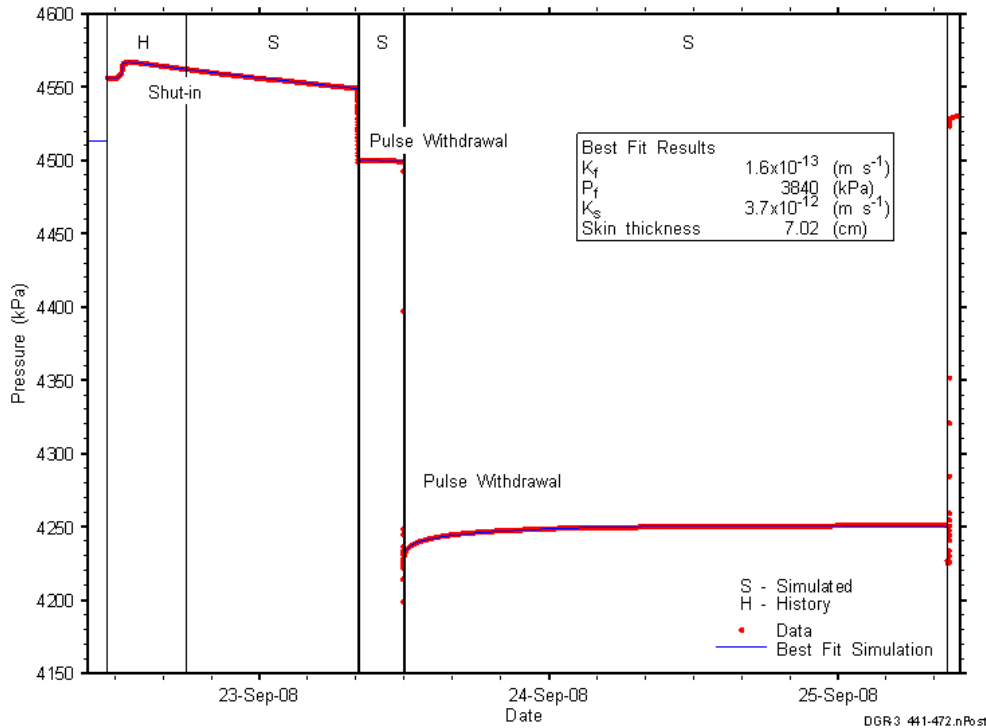


Figure 7-25: Annotated DGR3_441.05-471.79 testing sequence showing best-fit simulation and parameter estimates.

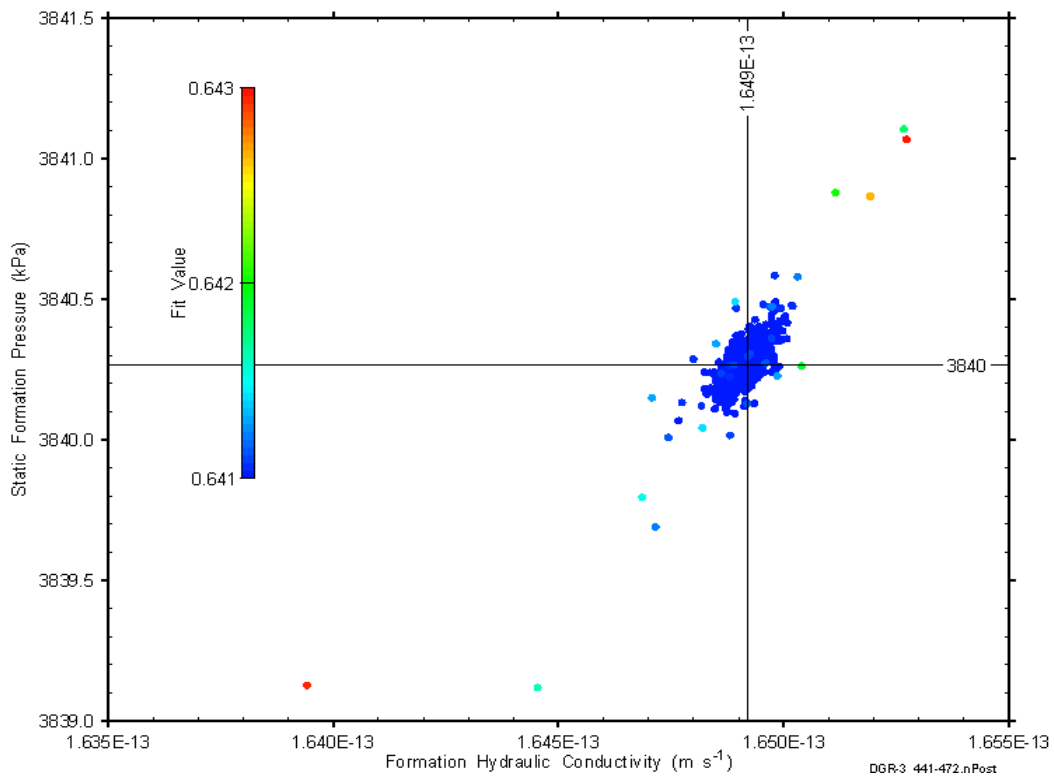


Figure 7-26: XY-scatter plot showing estimates of formation hydraulic conductivity and raw static formation pressure derived from the DGR3_441.05-471.79 perturbation analysis.

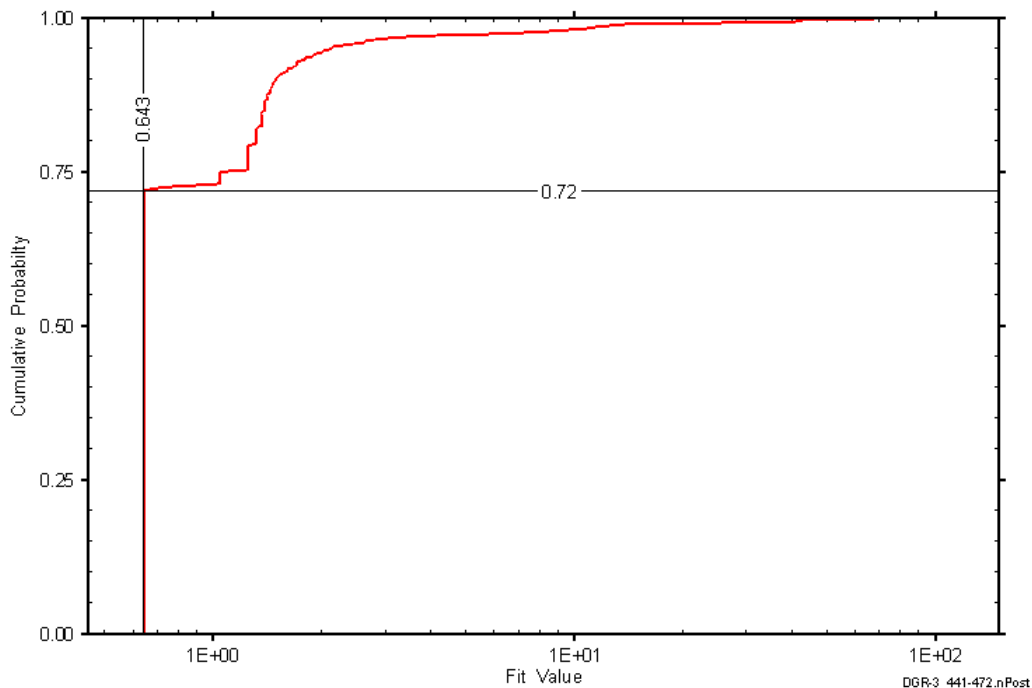


Figure 7-27: DGR3_441.05-471.79 fit value cumulative distribution function.

7.10 471.41-502.15 Queenston

The DGR-3 interval from 471.41 to 502.15 m BGS was entirely contained within the Queenston Formation. This portion of the Queenston consists of shale with carbonate interbeds increasing toward the bottom. An overview of the testing in this interval is given in Table 7-20 and the corresponding parameter estimates are given in Table 7-21. A pulse-withdrawal test and a pulse-injection test were conducted in this interval.

Table 7-20: Summary of the DGR3_471.41-502.15 testing activities.

Formation / Unit		Top of Test Zone (m BGS)	Bottom of Test Zone (m BGS)	
Queenston		471.41	502.15	
Test	Initiated	Magnitude (kPa)	Duration	Compressibility (Pa ⁻¹)
Shut-in	25-09-08 13:00	N/A	19 hr	N/A
PW	26-09-08 07:44	383	30 hr	8.6E-10
PI	27-09-08 14:19	381	21 hr	8.8E-10
Borehole Pressure History				
Event	Start	Pressure (kPa)		
Drilling Intercept	18-06-08 11:00	5060		
End of Geophysical Logging	05-08-08	4770		
Prior Testing	12-08-08	N/A		
Shut-in	25-09-08 13:00	4921		

Table 7-21: Summary of the DGR3_471.41-502.15 parameter estimates.

Parameter	Best Fit	Minimum	Maximum	Mean
K_f (m/s)	1.6E-14	1.1E-14	5.8E-14	2.6E-14
P_f (kPa)	4980	4951	5067	5011
S_s (m^{-1})	7.4E-6	3.2E-7	1.0E-5	3.1E-6
K_s (m/s)	5.1E-14	3.6E-14	1.2E-11	1.0E-13
t_s (cm)	0.3	0.3	9.1	1.8

Figure 7-28 shows the measured pressure record from DGR3_471.41-502.15 used in this analysis along with the best-fit simulation and parameter values. The ranges of formation K and raw P_f values estimated from perturbation analysis are shown in Figure 7-29 and the fit value cumulative distribution function is shown in Figure 7-30.

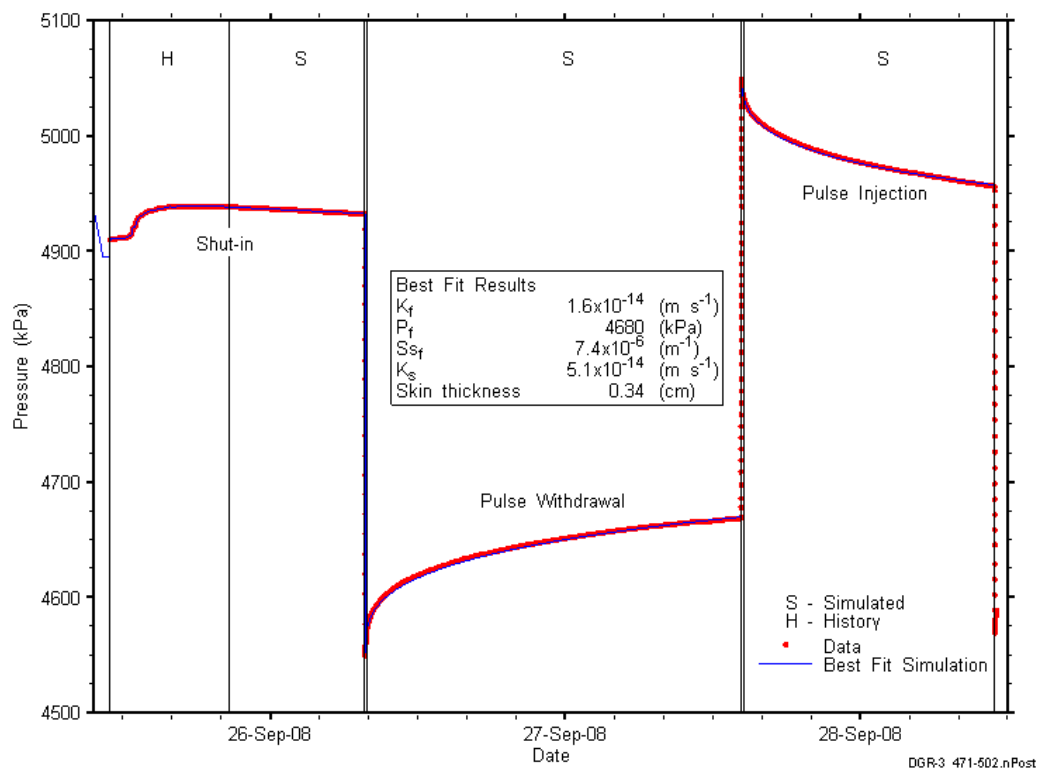


Figure 7-28: Annotated DGR3_471.41-502.15 testing sequence showing best-fit simulation and parameter estimates.

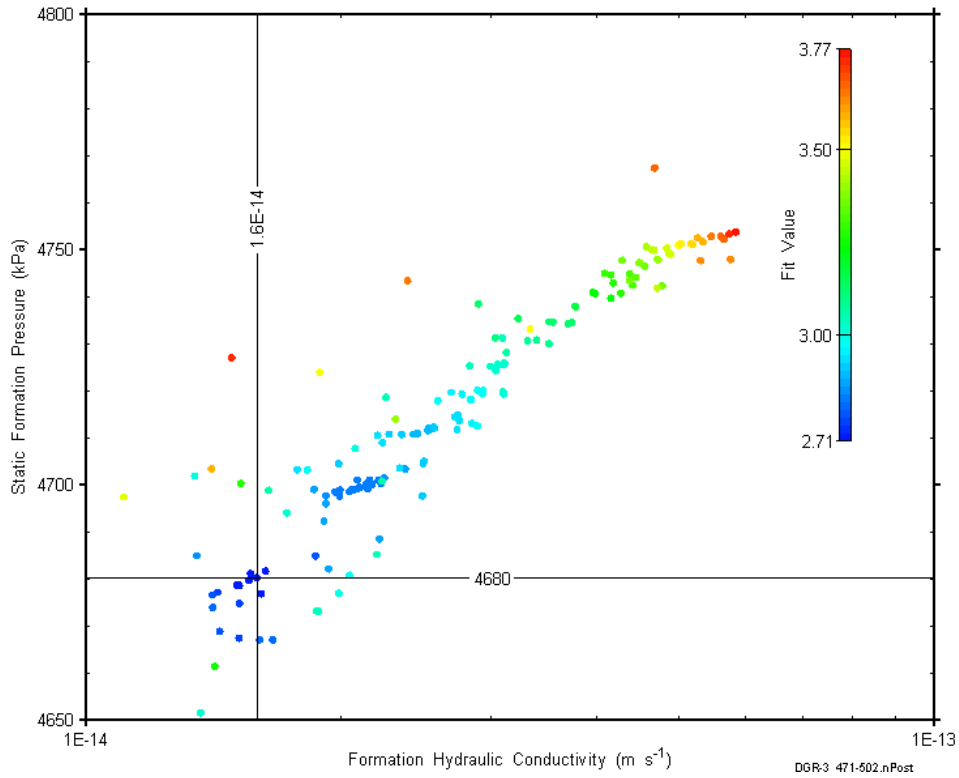


Figure 7-29: XY-scatter plot showing estimates of formation hydraulic conductivity and raw static formation pressure derived from the DGR3_471.41-502.15 perturbation analysis.

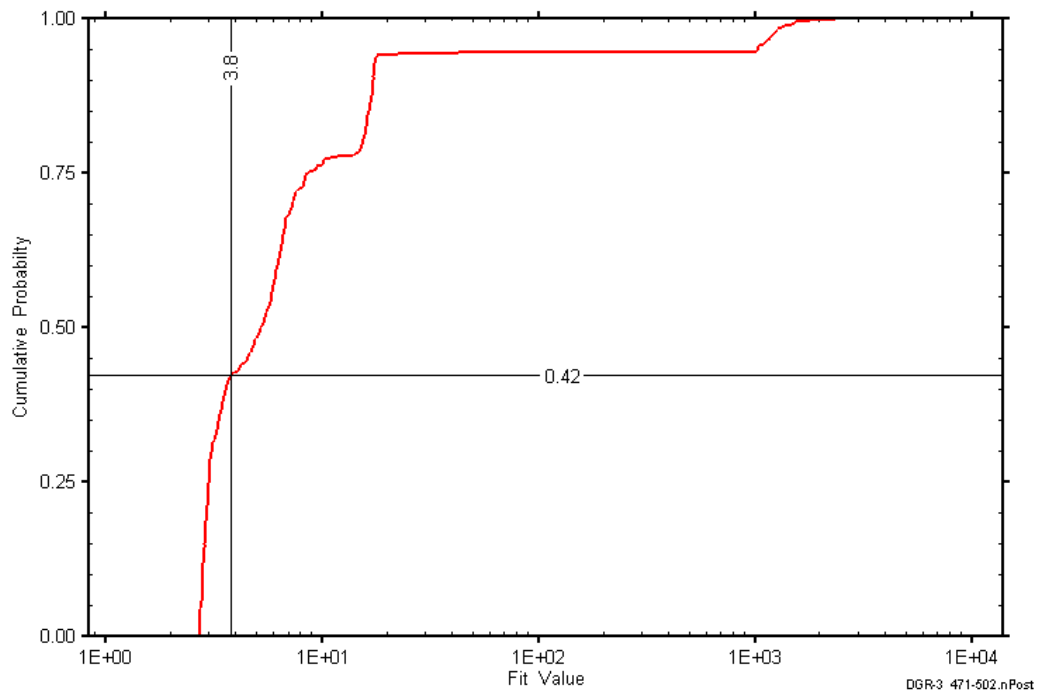


Figure 7-30: DGR3_471.41-502.15 fit value cumulative distribution function.

7.11 501.95-532.69 Queenston-Georgian Bay

The DGR-3 interval from 501.95 to 532.69 m BGS included the lower 29.45 m of the Queenston Formation and the upper 1.29 m of the Georgian Bay Formation. This portion of the Queenston consists of interbedded shale and limestone, with mostly shale over the lower ~11 m, and the uppermost Georgian Bay consists of interbedded shale and limestone. An overview of the testing in this interval is given in Table 7-22 and the corresponding parameter estimates are given in Table 7-23. A pulse-withdrawal test and a pulse-injection test were conducted in this interval.

Table 7-22: Summary of the DGR3_501.95-532.69 testing activities.

Formation / Unit		Top of Test Zone (m BGS)		Bottom of Test Zone (m BGS)	
Queenston-Georgian Bay		501.95		532.69	
Test	Initiated	Magnitude (kPa)	Duration	Compressibility (Pa ⁻¹)	
Shut-in	28-09-08 15:15	N/A	18 hr	N/A	
PW	29-09-08 09:14	724	24 hr	4.4E-10	
PI	30-09-08 08:50	730	23 hr	4.4E-10	
Borehole Pressure History					
Event		Start		Pressure (kPa)	
Drilling Intercept		19-06-08 15:00		5390	
End of Geophysical Logging		05-08-08		5094	
Prior Testing		12-08-08		N/A	
Shut-in		28-09-08 15:15		5280	

Table 7-23: Summary of the DGR3_501.95-532.69 parameter estimates.

Parameter	Best Fit	Minimum	Maximum	Mean
K_f (m/s)	1.4E-14	1.3E-14	1.7E-14	1.4E-14
P_f (kPa)	3834	3757	3926	3834
S_s (m ⁻¹)	2.3E-6	1.8E-6	2.5E-6	2.3E-6
K_s (m/s)	5.8E-14	4.7E-14	4.8E-11	7.3E-14
t_s (cm)	0.1	5E-5	1.6	0.4

Figure 7-31 shows the measured pressure record from DGR3_501.95-532.69 used in this analysis along with the best-fit simulation and parameter values. The ranges of formation K and raw P_f values estimated from perturbation analysis are shown in Figure 7-32 and the fit value cumulative distribution function is shown in Figure 7-33.

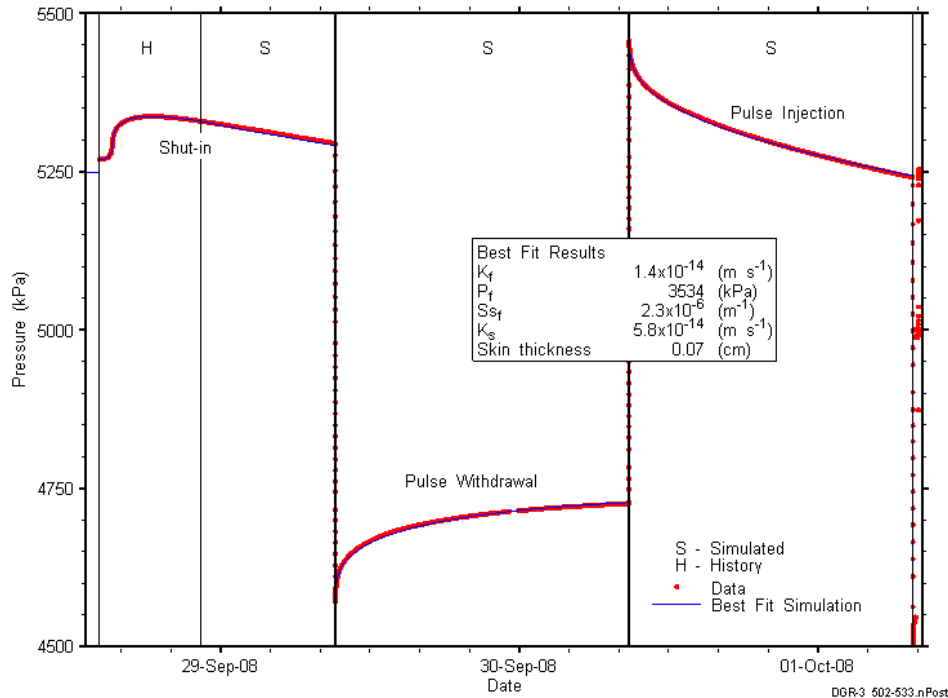


Figure 7-31: Annotated DGR3_501.95-532.69 testing sequence showing best-fit simulation and parameter estimates.

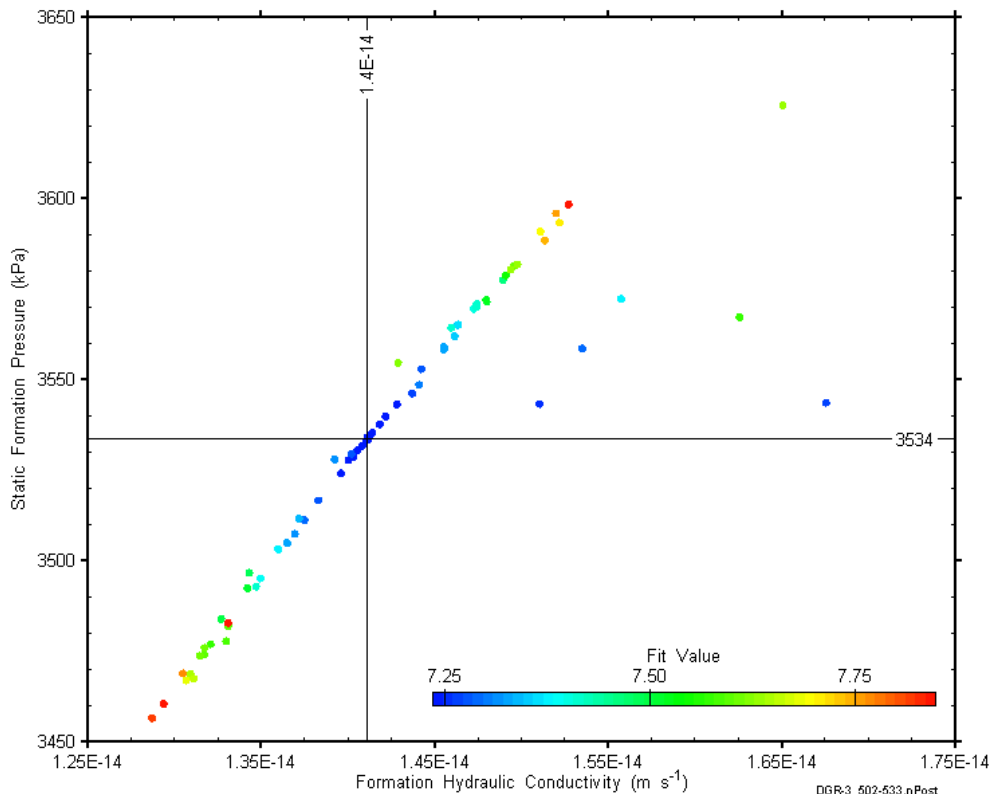


Figure 7-32: XY-scatter plot showing estimates of formation hydraulic conductivity and raw static formation pressure derived from the DGR3_501.95-532.69 perturbation analysis.

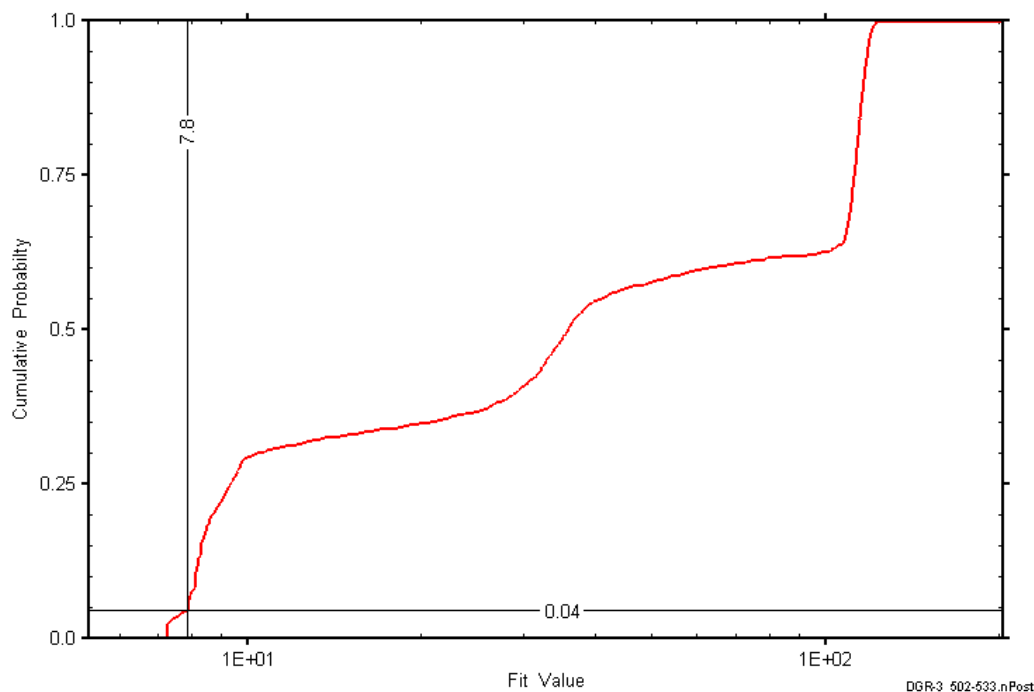


Figure 7-33: DGR3_501.95-532.69 fit value cumulative distribution function.

7.12 532.49-563.23 Georgian Bay

The DGR-3 interval from 532.49 to 563.23 m BGS was entirely contained within a section of the Georgian Bay Formation consisting of shale interbedded with limestone and siltstone layers. An overview of the testing in this interval is given in Table 7-24 and the corresponding parameter estimates are given in Table 7-25. Two pulse-withdrawal tests were conducted in this interval.

Table 7-24: Summary of the DGR3_532.49-563.23 testing activities.

Formation / Unit		Top of Test Zone (m BGS)	Bottom of Test Zone (m BGS)	
Georgian Bay		532.49	563.23	
Test	Initiated	Magnitude (kPa)	Duration	Compressibility (Pa ⁻¹)
Shut-in	01-10-08 12:08	N/A	20 hr	N/A
PW	02-10-08 07:59	519	27 hr	6.2E-10
PW	03-10-08 10:26	554	22 hr	5.9E-10
Borehole Pressure History				
Event	Start	Pressure (kPa)		
Drilling Intercept	20-06-08 15:00	5719		
End of Geophysical Logging	05-08-08	5443		
Prior Testing	12-08-08	N/A		
Shut-in	01-10-08 12:08	5640		

Table 7-25: Summary of the DGR3_532.49-563.23 parameter estimates.

Parameter	Best Fit	Minimum	Maximum	Mean
K_f (m/s)	1.2E-14	1.0E-14	1.3E-14	1.2E-14
P_f (kPa)	3741	3586	3886	3742
S_s (m^{-1})	5.9E-6	5.3E-6	6.7E-6	5.9E-6
K_s (m/s)	1.5E-13	1.3E-13	1.7E-13	1.5E-13
t_s (cm)	0.6	0.6	0.6	0.6

Figure 7-34 shows the measured pressure record from DGR3_532.49-563.23 used in this analysis along with the best-fit simulation and parameter values. The ranges of formation K and raw P_f values estimated from perturbation analysis are shown in Figure 7-35 and the fit value cumulative distribution function is shown in Figure 7-36.

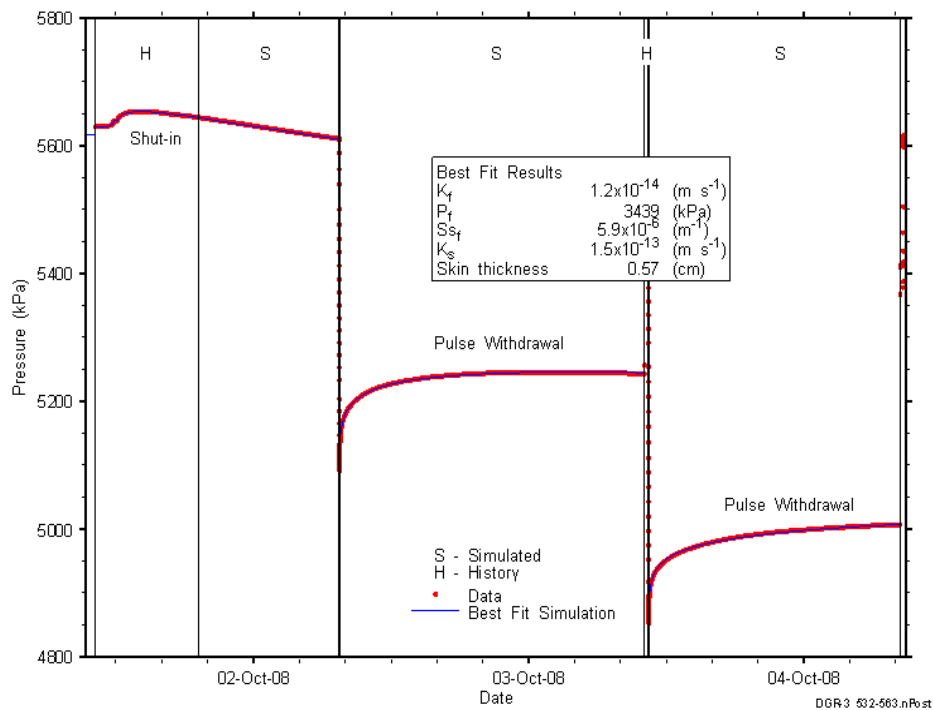


Figure 7-34: Annotated DGR3_532.49-563.23 testing sequence showing best-fit simulation and parameter estimates.

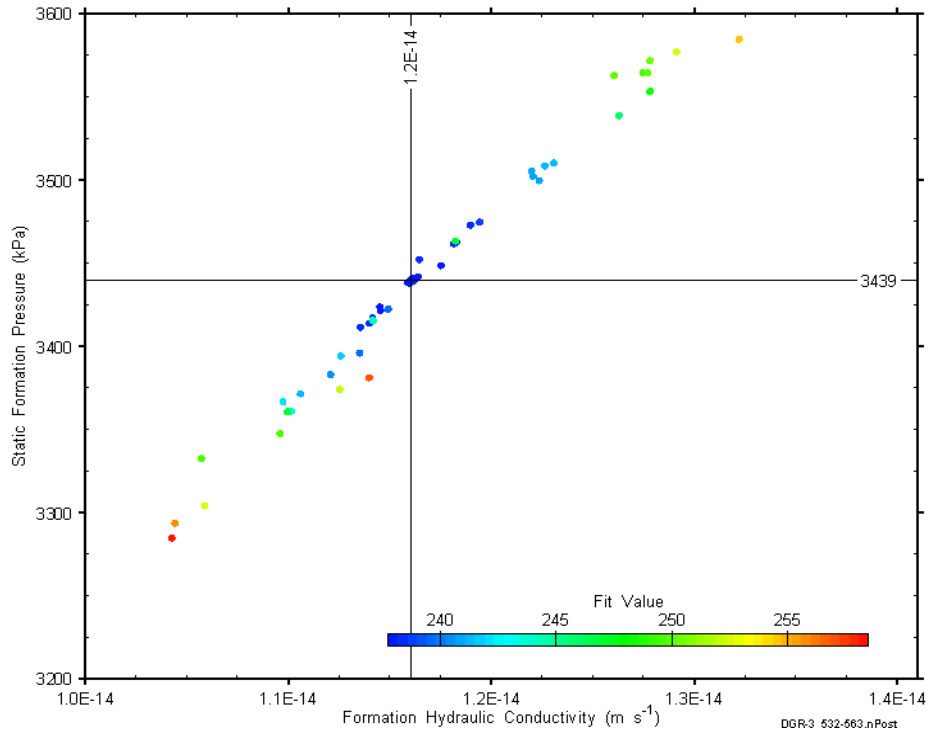


Figure 7-35: XY-scatter plot showing estimates of formation hydraulic conductivity and raw static formation pressure derived from the DGR3_532.49-563.23 perturbation analysis.

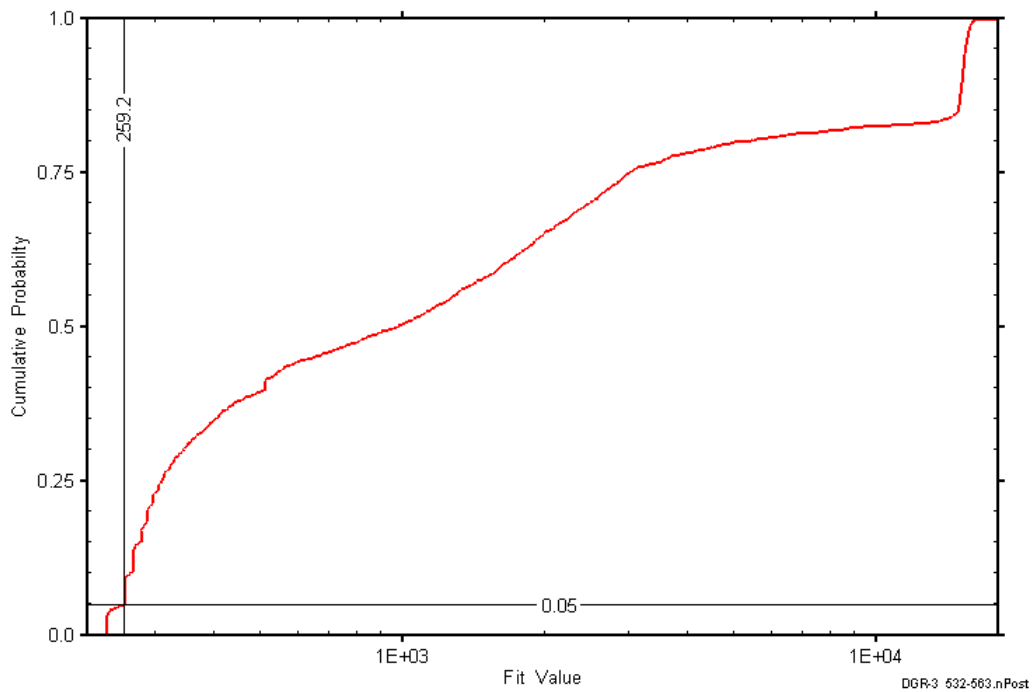


Figure 7-36: DGR3_532.49-563.23 fit value cumulative distribution function.

7.13 563.03-593.77 Georgian Bay

The DGR-3 interval from 563.03 to 593.77 m BGS was entirely contained within a section of the Georgian Bay Formation consisting of shale with trace to minor interbeds of limestone and siltstone. An overview of the testing in this interval is given in Table 7-26 and the corresponding parameter estimates are given in Table 7-27. Two pulse-withdrawal tests were conducted in this interval.

Table 7-26: Summary of the DGR3_563.03-593.77 testing activities.

Formation / Unit		Top of Test Zone (m BGS)		Bottom of Test Zone (m BGS)	
Georgian Bay		563.03		593.77	
Test	Initiated	Magnitude (kPa)	Duration	Compressibility (Pa ⁻¹)	
Shut-in	04-10-08 11:22	N/A	21 hr	N/A	
PW	05-10-08 08:00	605	24 hr	5.4E-10	
PW	06-10-08 08:06	630	24 hr	5.2E-10	
Borehole Pressure History					
Event		Start		Pressure (kPa)	
Drilling Intercept		21-06-08 10:00		6048	
End of Geophysical Logging		05-08-08		5793	
Prior Testing		12-08-08		N/A	
Shut-in		04-10-08 11:22		5997	

Table 7-27: Summary of the DGR3_563.03-593.77 parameter estimates.

Parameter	Best Fit	Minimum	Maximum	Mean
K_f (m/s)	1.2E-14	1.1E-14	1.3E-14	1.2E-14
P_f (kPa)	2559	2338	2768	2555
S_s (m ⁻¹)	3.5E-6	3.1E-6	4.0E-6	3.5E-6
K_s (m/s)	1.1E-13	9.1E-14	1.2E-13	1.1E-13
t_s (cm)	0.6	0.1	0.7	0.1

Figure 7-37 shows the measured pressure record from DGR3_563.03-593.77 used in this analysis along with the best-fit simulation and parameter values. The ranges of formation K and raw P_f values estimated from perturbation analysis are shown in Figure 7-38 and the fit value cumulative distribution function is shown in Figure 7-39.

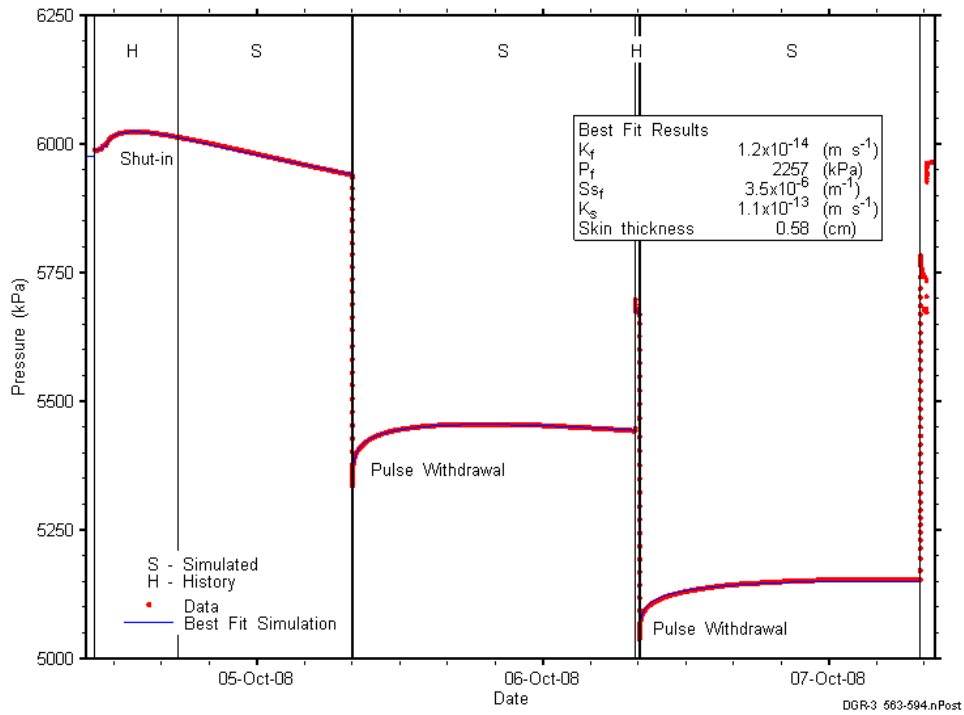


Figure 7-37: Annotated DGR3_563.03-593.77 testing sequence showing best fit simulation and parameter estimates.

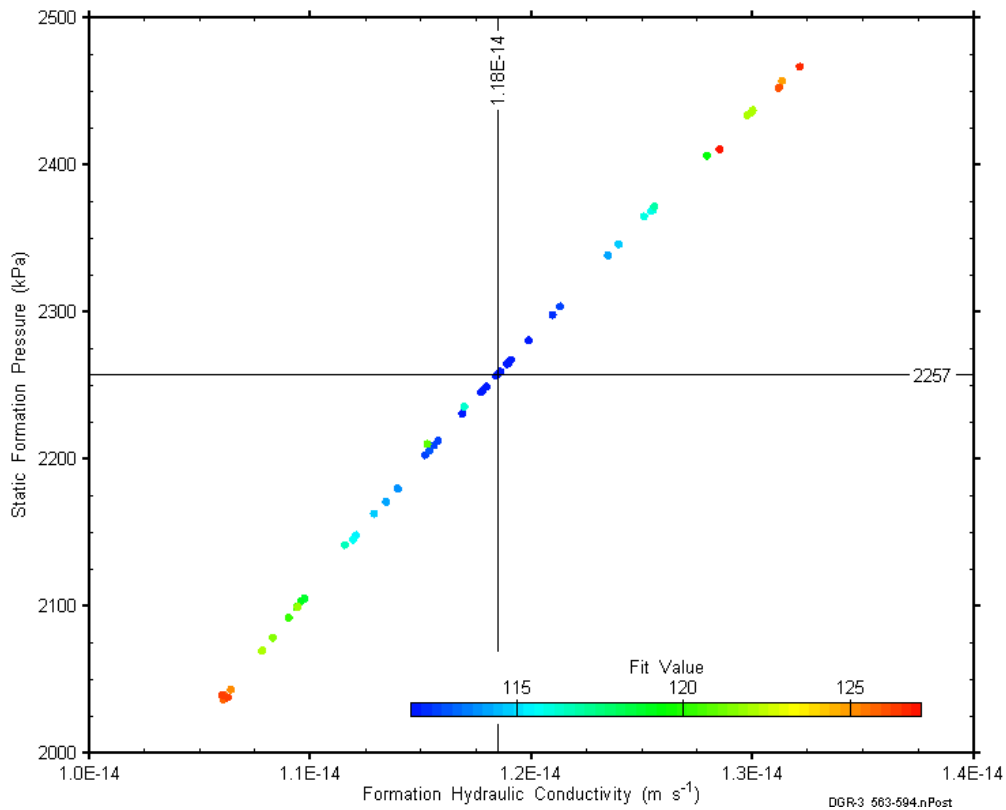


Figure 7-38: XY-scatter plot showing estimates of formation hydraulic conductivity and raw static formation pressure derived from the DGR3_563.03-593.77 perturbation analysis.

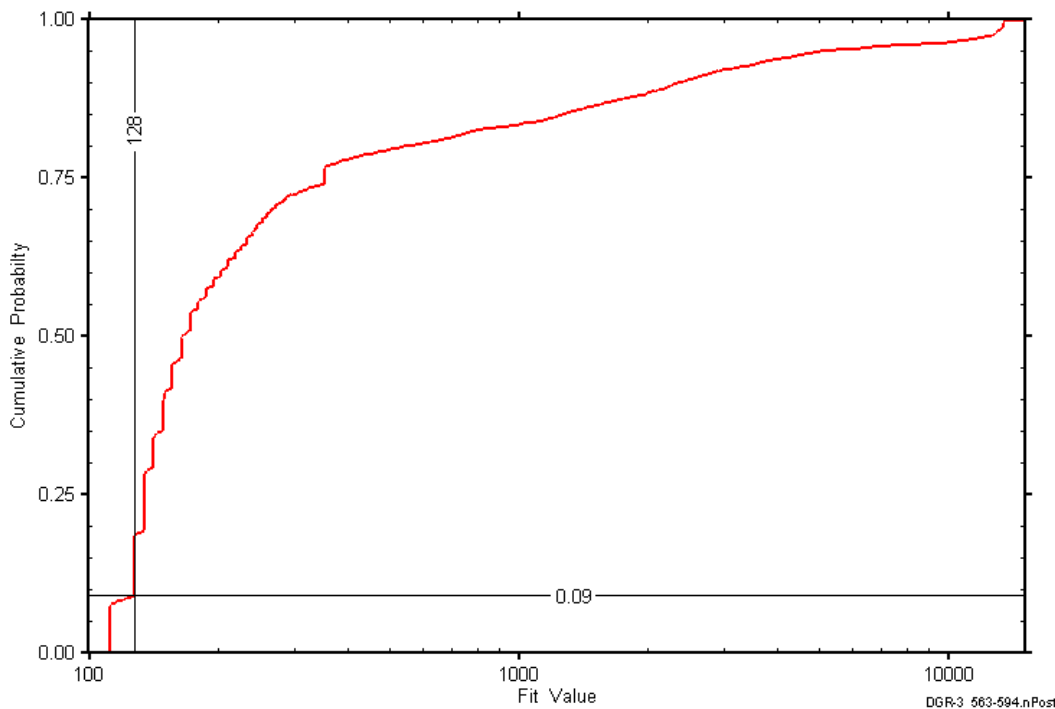


Figure 7-39: DGR3_563.03-593.77 fit value cumulative distribution function.

7.14 593.57-624.31 Georgian Bay-Blue Mountain

The DGR-3 interval from 593.57 to 624.31 m BGS included the lower 26.53 m of the Georgian Bay Formation and the upper 4.21 m of the Blue Mountain Formation. This portion of the Georgian Bay consists of shale, petroliferous in sections, with trace interbeds of limestone and siltstone, and the uppermost Blue Mountain consists of shale with limestone and siltstone interbeds. An overview of the testing in this interval is given in Table 7-28 and the corresponding parameter estimates are given in Table 7-29. Two pulse-withdrawal tests were conducted in this interval.

Table 7-28: Summary of the DGR3_593.57-624.31 testing activities.

Formation / Unit		Top of Test Zone (m BGS)	Bottom of Test Zone (m BGS)	
Georgian Bay-Blue Mountain		593.57	624.31	
Test	Initiated	Magnitude (kPa)	Duration	Compressibility (Pa ⁻¹)
Shut-in	07-10-08 11:52	N/A	20 hr	N/A
PW	08-10-08 07:38	395	24 hr	7.5E-10
PW	09-10-08 07:42	387	24 hr	7.5E-10
Borehole Pressure History				
Event	Start	Pressure (kPa)		
Drilling Intercept	22-06-08 05:00	6377		
End of Geophysical Logging	05-08-08	6130		
Prior Testing	12-08-08	N/A		
Shut-in	07-10-08 11:52	6347		

Table 7-29: Summary of the DGR3_593.57-624.31 parameter estimates.

Parameter	Best Fit	Minimum	Maximum	Mean
K_f (m/s)	3.3E-14	2.9E-14	3.9E-14	3.3E-14
P_f (kPa)	3358	3201	3595	3375
S_s (m^{-1})	2.8E-5	2.3E-5	3.3E-5	2.8E-5
K_s (m/s)	2.4E-13	1.9E-13	3.1E-13	2.4E-13
t_s (cm)	0.4	0.4	0.4	0.4

Figure 7-40 shows the measured pressure record from DGR3_593.57-624.31 used in this analysis along with the best-fit simulation and parameter values. The ranges of formation K and raw P_f values estimated from perturbation analysis are shown in Figure 7-41 and the fit value cumulative distribution function is shown in Figure 7-42.

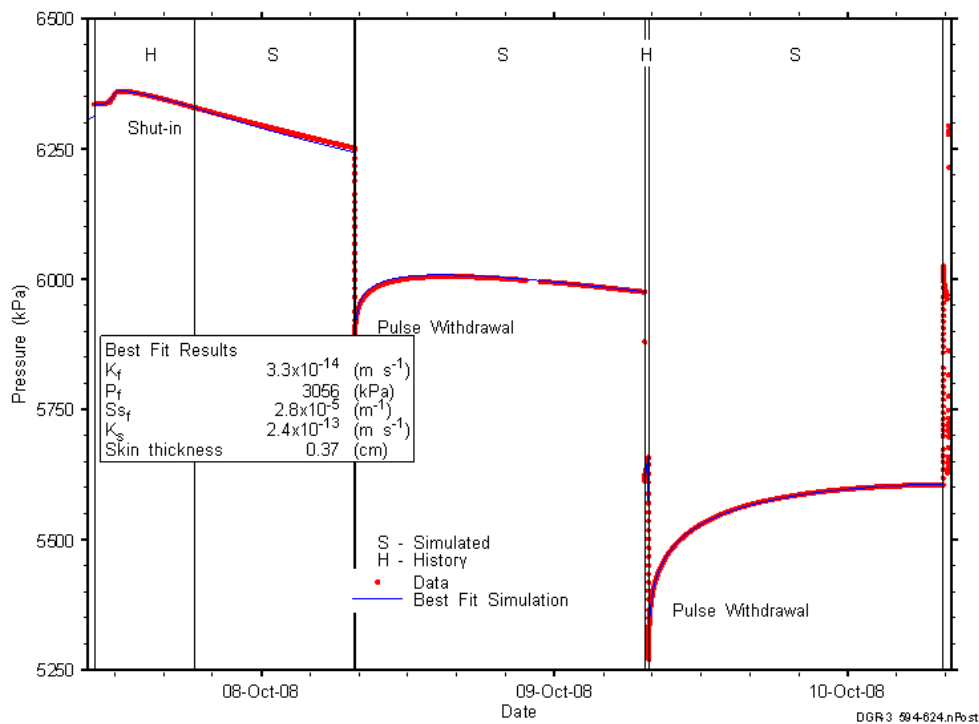


Figure 7-40: Annotated DGR3_593.57-624.31 testing sequence showing best-fit simulation and parameter estimates.

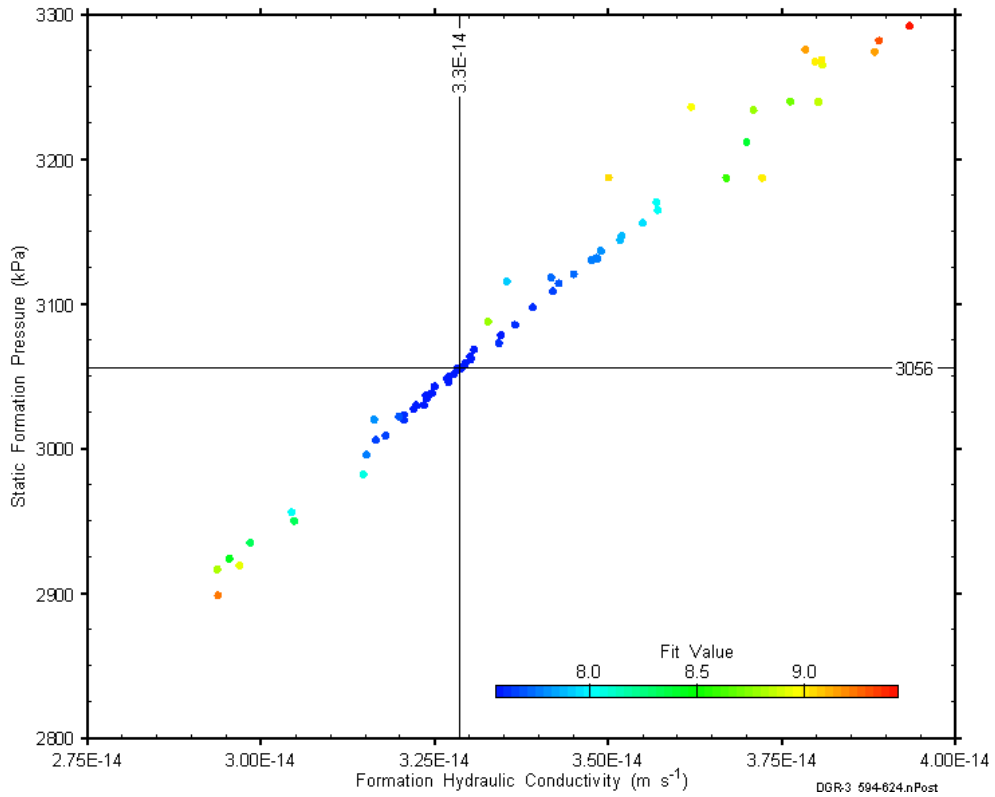


Figure 7-41: XY-scatter plot showing estimates of formation hydraulic conductivity and raw static formation pressure derived from the DGR3_593.57-624.31 perturbation analysis.

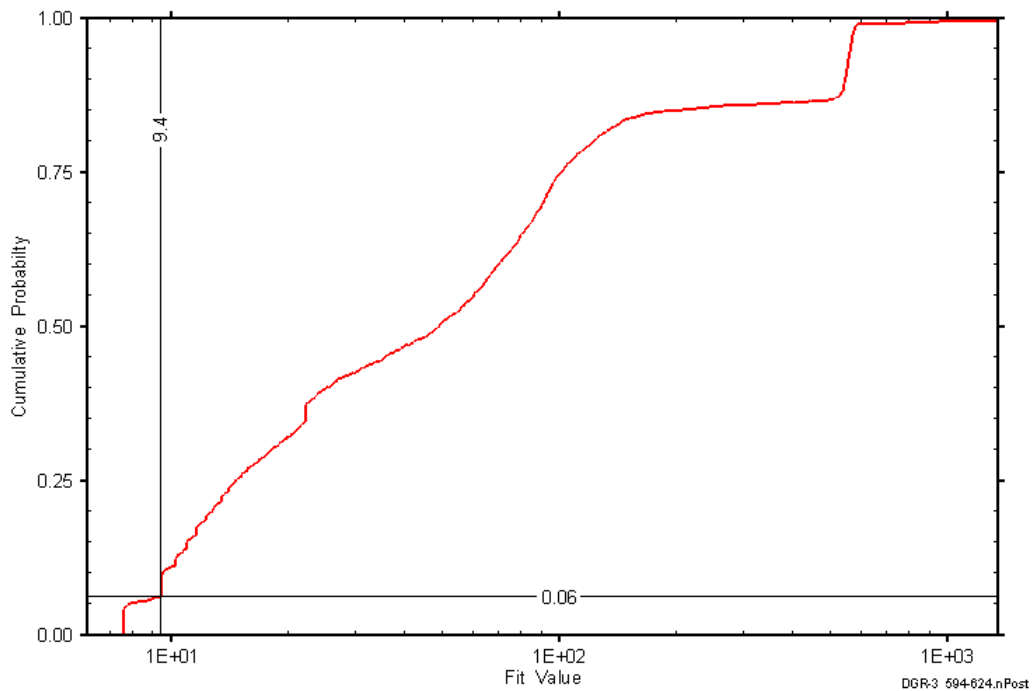


Figure 7-42: DGR3_593.57-624.31 fit value cumulative distribution function.

7.15 617.63-648.37 Georgian Bay-Blue Mountain

The DGR-3 interval from 617.63 to 648.37 m BGS included the lower 2.47 m of the Georgian Bay Formation and the upper 40.37 m of the Blue Mountain Formation. This portion of the Georgian Bay consists of shale, petroliferous in sections, with trace interbeds of limestone and siltstone, and the upper Blue Mountain consists of shale with some limestone and siltstone interbeds. An overview of the testing in this interval is given in Table 7-30 and the corresponding parameter estimates are given in Table 7-31.

This second test on the Georgian Bay - Blue Mountain formations was undertaken after completion of other tests in DGR-3 as the test tool was being withdrawn from the borehole. The goal of the test was to fill a gap in the testing of the Blue Mountain and further characterize the source of the relatively higher formation pressure and test-zone compressibility determined in the preliminary analyses of the 628.00-658.74 Blue Mountain interval described below in Section 7.16. Both intervals contained fractured sections of the Blue Mountain. The test was planned as a single PI, which was felt to be the best approach to confirm the previously obtained P_f estimate.

Table 7-30: Summary of the DGR3_617.63-648.37 testing activities.

Formation / Unit		Top of Test Zone (m BGS)		Bottom of Test Zone (m BGS)	
Georgian Bay-Blue Mountain 2		617.63		648.37	
Test	Initiated	Magnitude (kPa)	Duration	Compressibility (Pa ⁻¹)	
Shut-in	09-11-08 14:13	N/A	19 hr	N/A	
PI	10-11-08 09:33	148	47 hr	2.2E-9	
Borehole Pressure History					
Event		Start		Pressure (kPa)	
Drilling Intercept		23-06-08 01:00		6537	
End of Geophysical Logging		05-08-08		6408	
Prior Testing		12-08-08		N/A	
Shut-in		09-11-08 14:13		3976	

Table 7-31: Summary of the DGR3_617.63-648.37 parameter estimates.

Parameter	Best Fit	Minimum	Maximum	Mean
K_f (m/s)	1.3E-13	1.3E-13	1.4E-13	1.3E-13
P_f (kPa)	6657	6648	6668	6657
K_s (m/s)	3.8E-12	3.2E-12	4.7E-12	3.8E-12
t_s (cm)	7.5	7.4	7.6	7.5

Figure 7-43 shows the measured pressure record from DGR3_617.63-648.37 used in this analysis along with the best-fit simulation and parameter values. The S_s value for this analysis was fixed at $1E-6 \text{ m}^{-1}$, a value estimated from perturbation analysis. The ranges of formation K and raw P_f values estimated from perturbation analysis are shown in Figure 7-44 and the fit value cumulative distribution function is shown in Figure 7-45.

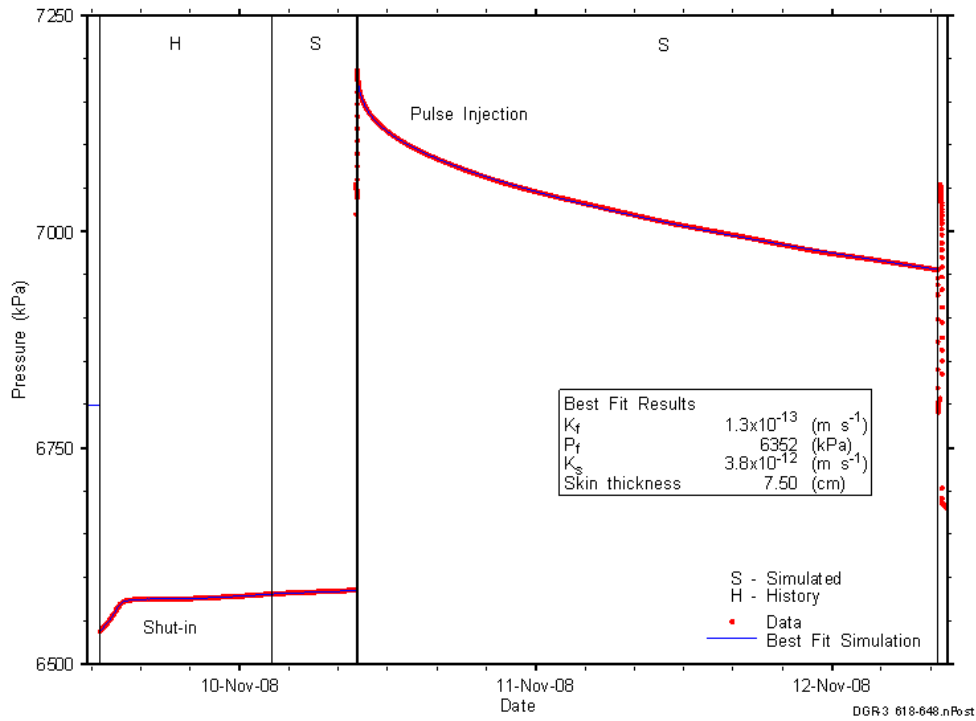


Figure 7-43: Annotated DGR3_617.63-648.37 testing sequence showing best-fit simulation and parameter estimates.

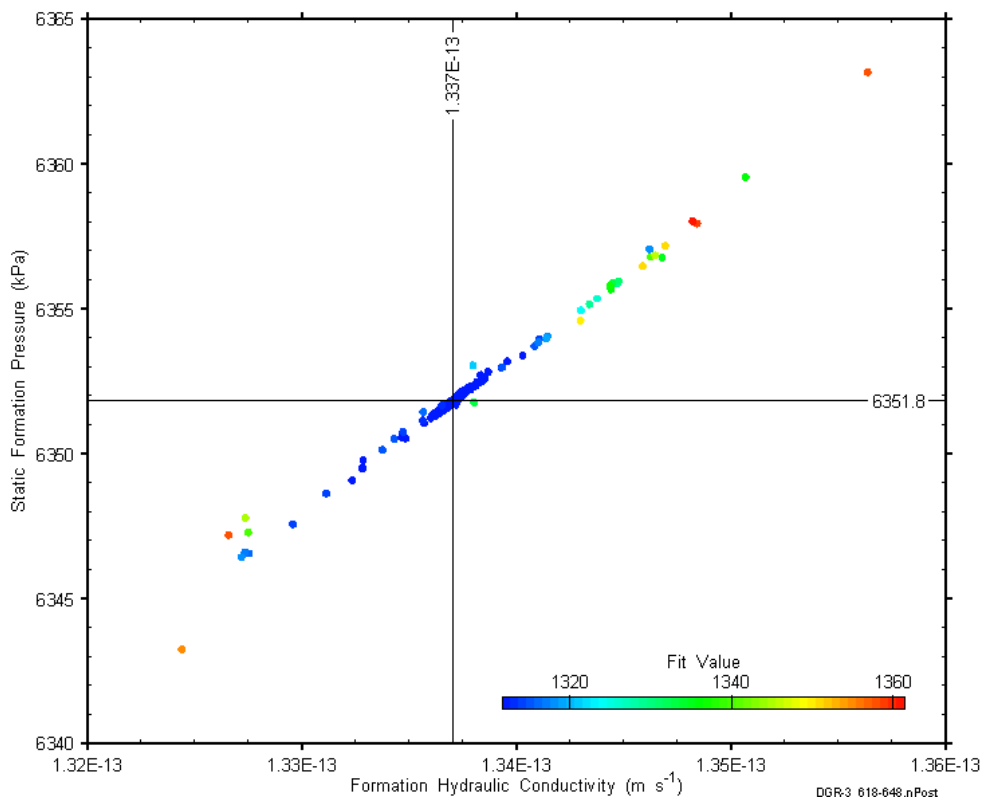


Figure 7-44: XY-scatter plot showing estimates of formation hydraulic conductivity and raw static formation pressure derived from the DGR3_617.63-648.37 perturbation analysis.

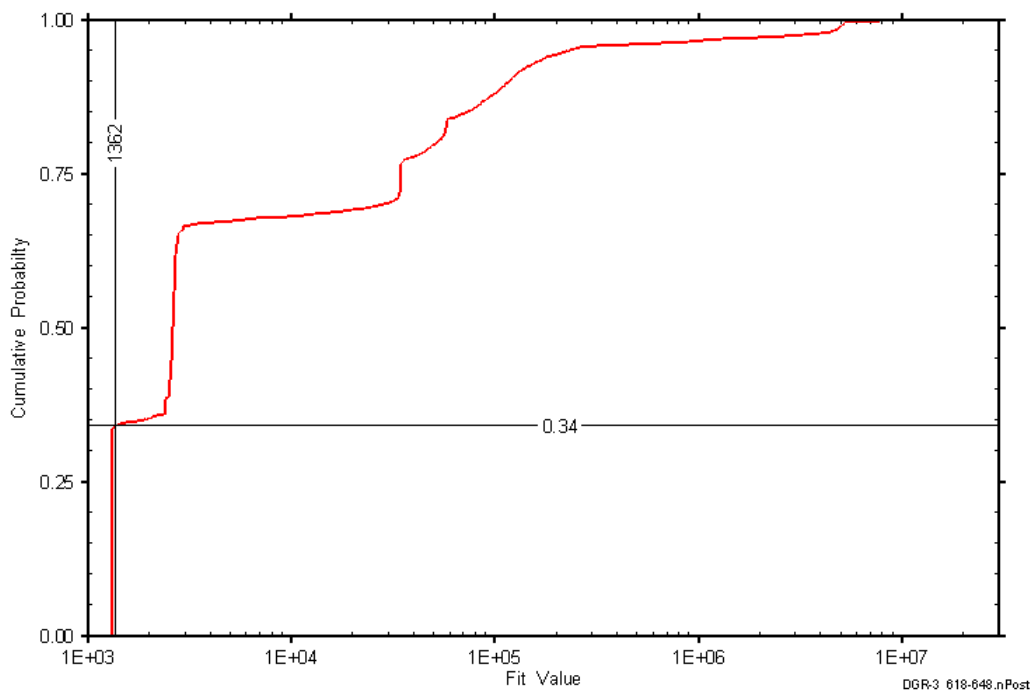


Figure 7-45: DGR3_617.63-648.37 fit value cumulative distribution function.

7.16 628.00-658.74 Blue Mountain

The DGR-3 interval from 628.00 to 658.74 m BGS was entirely contained within a section of the Blue Mountain Formation consisting of shale, with trace to minor interbeds of limestone and siltstone in the upper half of the interval. The entire core over the test interval had a petroliferous odour, and the core run from 637.38 to 640.43 m BGS contained abundant subvertical, calcite-filled hairline fractures (Briscoe et al., 2010). An overview of the testing in this interval is given in Table 7-32 and the corresponding parameter estimates are given in Table 7-33. A single pulse-withdrawal test was conducted in this interval. The test was terminated prematurely due to an equipment failure when communication with the probe was lost. However, there were sufficient data to perform an analysis.

Table 7-32: Summary of the DGR3_628.00-658.74 testing activities.

Formation / Unit		Top of Test Zone (m BGS)	Bottom of Test Zone (m BGS)	
Blue Mountain		628.00	658.74	
Test	Initiated	Magnitude (kPa)	Duration	Compressibility (Pa ⁻¹)
Shut-in	10-10-08 11:57	N/A	21 hr	N/A
PW	11-10-08 08:52	175	12 hr	1.8E-9
Borehole Pressure History				
Event	Start	Pressure (kPa)		
Drilling Intercept	23-06-08 08:00	6748		
End of Geophysical Logging	05-08-08	6527		
Prior Testing	12-08-08	N/A		
Shut-in	10-10-08 11:57	6718		

Table 7-33: Summary of the DGR3_628.00-658.74 parameter estimates.

Parameter	Best Fit	Minimum	Maximum	Mean
K_f (m/s)	3.5E-13	3.4E-13	3.7E-13	3.5E-13
P_f (kPa)	7655	7623	7683	7656
K_s (m/s)	9.6E-12	8.2E-12	1.2E-11	9.7E-12
t_s (cm)	7.6	7.4	7.7	7.6

Both test-zone compressibility and P_f were relatively high in this test interval.

Figure 7-46 shows the measured pressure record from DGR3_628.00-658.74 used in this analysis along with the best-fit simulation and parameter values. The S_s value for this analysis was fixed at $1E-6 \text{ m}^{-1}$, a value estimated from perturbation analysis. The ranges of formation K and raw P_f values estimated from perturbation analysis are shown in Figure 7-47 and the fit value cumulative distribution function is shown in Figure 7-48.

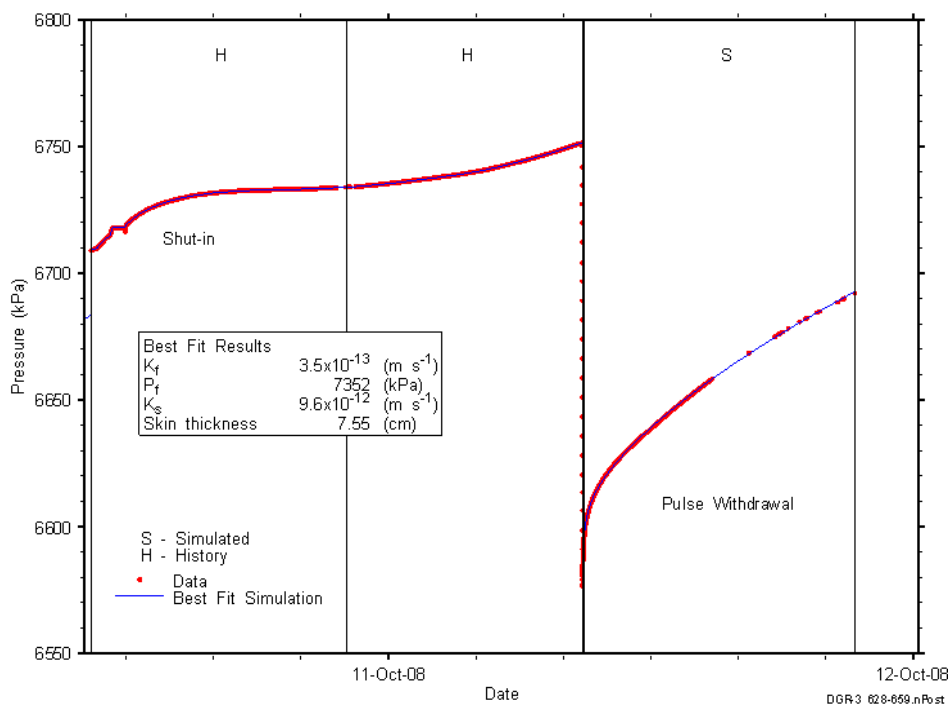


Figure 7-46: Annotated DGR3_628.00-658.74 testing sequence showing best-fit simulation and parameter estimates.

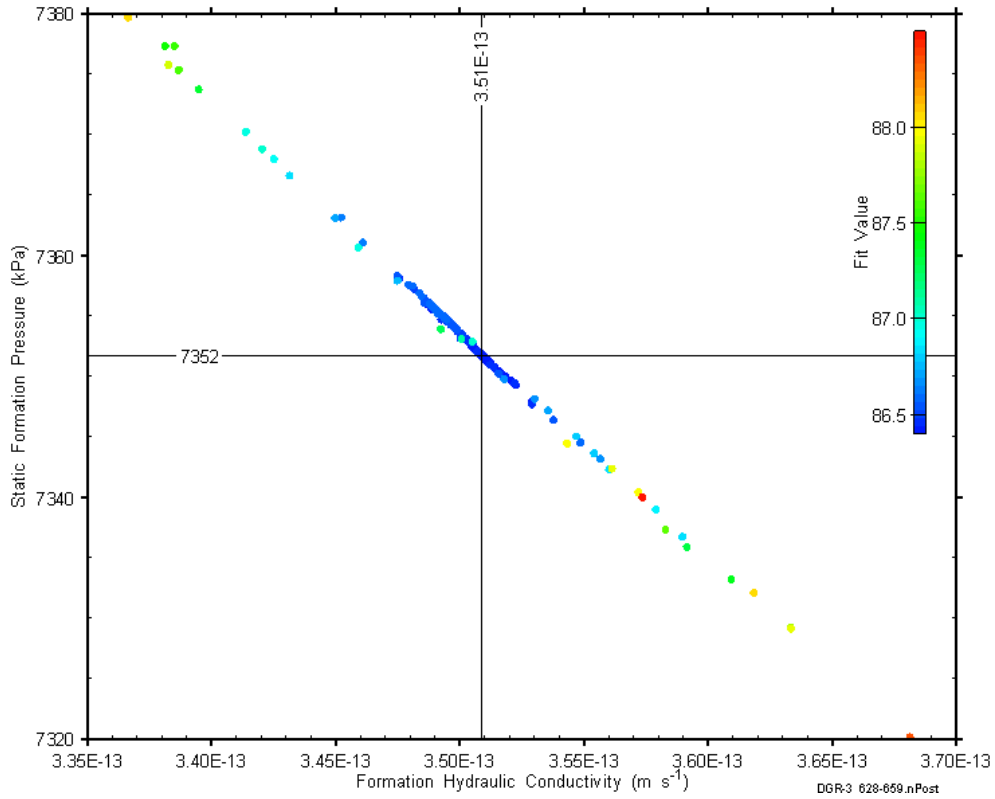


Figure 7-47: XY-scatter plot showing estimates of formation hydraulic conductivity and raw static formation pressure derived from the DGR3_628.00-658.74 perturbation analysis.

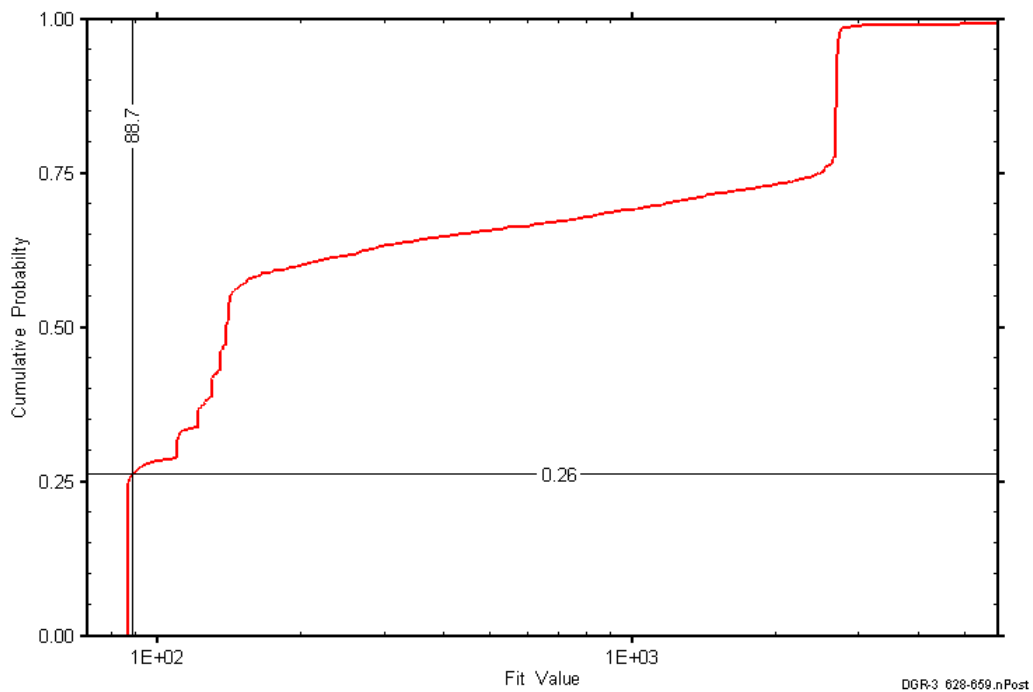


Figure 7-48: DGR3_628.00-658.74 fit value cumulative distribution function.

7.17 654.65-685.39 Blue Mountain-Collingwood-Cobourg

The DGR-3 interval from 654.65 to 685.39 m BGS included the lower 9.65 m of the Blue Mountain Formation, the entire 8.7-m thickness of the Collingwood Member of the Cobourg Formation, and the upper 12.39 m of the Lower Member of the Cobourg Formation. The lower Blue Mountain is shale, the Collingwood is interbedded shale and argillaceous limestone, and the Lower Member of the Cobourg is argillaceous limestone. An overview of the testing in this interval is given in Table 7-34 and the corresponding parameter estimates are given in Table 7-35. Two pulse-withdrawal tests were performed in this interval.

Table 7-34: Summary of the DGR3_654.65-685.39 testing activities.

Formation / Unit		Top of Test Zone (m BGS)		Bottom of Test Zone (m BGS)	
Blue Mountain-Collingwood-Cobourg		654.65		685.39	
Test	Initiated	Magnitude (kPa)	Duration	Compressibility (Pa ⁻¹)	
Shut-in	18-10-08 14:30	N/A	18 hr	N/A	
PW	19-10-08 08:11	916	25 hr	3.7E-10	
PW	20-10-08 09:09	913	23 hr	3.7E-10	
Borehole Pressure History					
Event		Start		Pressure (kPa)	
Drilling Intercept		24-06-08 04:00		6936	
End of Geophysical Logging		05-08-08		6843	
Prior Testing		12-08-08		N/A	
Shut-in		18-10-08 14:30		7323	

Table 7-35: Summary of the DGR3_654.65-685.39 parameter estimates.

Parameter	Best Fit	Minimum	Maximum	Mean
K_f (m/s)	2.4E-14	2.4E-14	2.4E-14	2.4E-14
P_f (kPa)	5241	5232	5246	5241
K_s (m/s)	1.4E-13	1.3E-13	1.8E-13	1.4E-13
t_s (cm)	3.1	2.9	3.1	3.1

Figure 7-49 shows the measured pressure record from DGR3_654.65-685.39 used in this analysis along with the best-fit simulation and parameter values. The S_s value in this analysis was fixed at $1E-7 \text{ m}^{-1}$, a value estimated from perturbation analysis. The ranges of formation K and raw P_f values estimated from perturbation analysis are shown in Figure 7-50 and the fit value cumulative distribution function is shown in Figure 7-51.

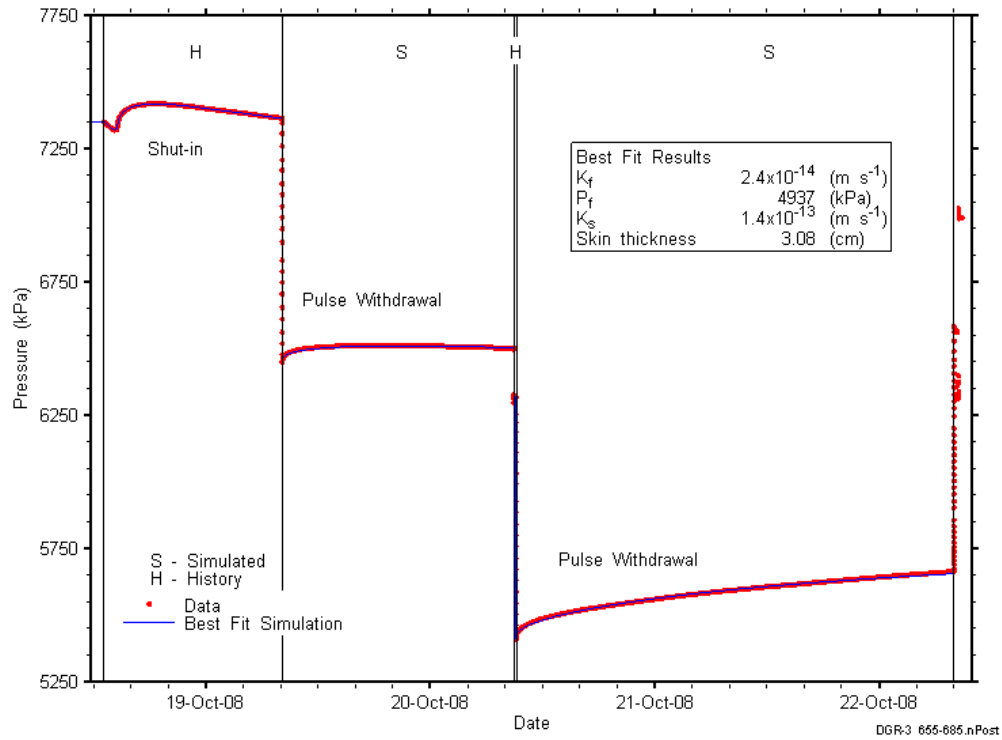


Figure 7-49: Annotated DGR3_654.65-685.39 testing sequence showing best-fit simulation and parameter estimates.

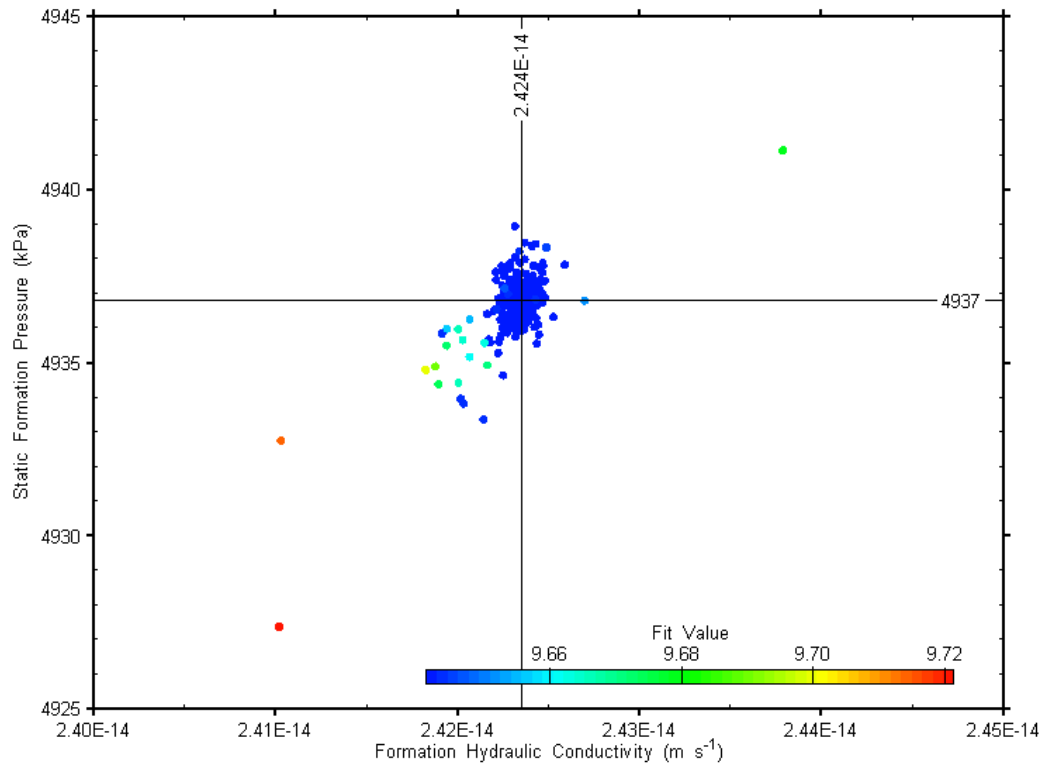


Figure 7-50: XY-scatter plot showing estimates of formation hydraulic conductivity and raw static formation pressure derived from the DGR3_654.65-685.39 perturbation analysis.

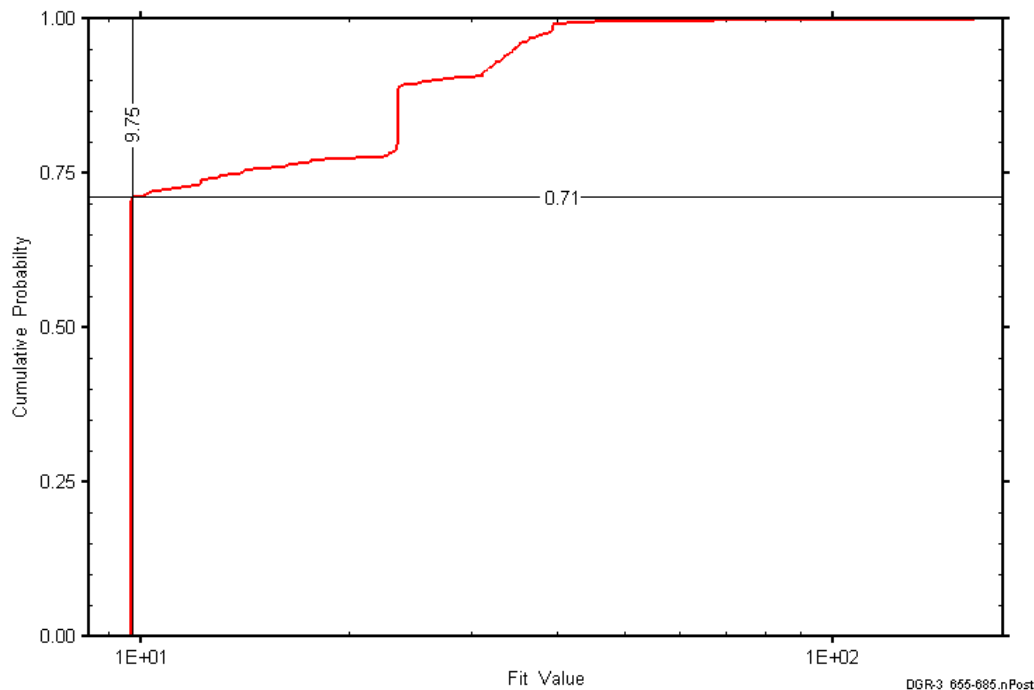


Figure 7-51: DGR3_654.65-685.39 fit value cumulative distribution function.

7.18 671.50-702.24 Collingwood-Cobourg-Sherman Fall

The DGR-3 interval from 671.50 to 702.24 m BGS included the lower 1.5 m of the Collingwood Member of the Cobourg Formation, the entire 27.8-m thickness of the Lower Member of the Cobourg Formation, and the upper 1.44 m of the Sherman Fall Formation. The entire interval consisted of argillaceous limestone. An overview of the testing in this interval is given in Table 7-36 and the corresponding parameter estimates are given in Table 7-37. Two pulse-withdrawal tests were performed in this interval.

Table 7-36: Summary of the DGR3_671.50-702.24 testing activities.

Formation / Unit		Top of Test Zone (m BGS)	Bottom of Test Zone (m BGS)	
Collingwood-Cobourg-Sherman Fall		671.50	702.24	
Test	Initiated	Magnitude (kPa)	Duration	Compressibility (Pa ⁻¹)
Shut-in	22-10-08 13:55	N/A	19 hr	N/A
PW	23-10-08 08:30	898	25 hr	3.7E-10
PW	24-10-08 09:02	912	23 hr	3.6E-10
Borehole Pressure History				
Event	Start	Pressure (kPa)		
Drilling Intercept	24-06-08 22:00	7117		
End of Geophysical Logging	05-08-08	7287		
Prior Testing	12-08-08	N/A		
Shut-in	22-10-08 13:55	7232		

Table 7-37: Summary of the DGR3_671.50-702.24 parameter estimates.

Parameter	Best Fit	Minimum	Maximum	Mean
K_f (m/s)	1.3E-14	1.2E-14	1.3E-14	1.3E-14
P_f (kPa)	5694	5654	5724	5694
K_s (m/s)	9.4E-14	7.2E-14	1.4E-13	9.4E-14
t_s (cm)	1.6	1.6	1.6	1.6

Figure 7-52 shows the measured pressure record from DGR3_671.50-702.24 used in this analysis along with the best-fit simulation and parameter values. The S_s value for this analysis was fixed at $2E-7 \text{ m}^{-1}$, a value estimated from perturbation analysis. The ranges of formation K and raw P_f values estimated from perturbation analysis are shown in Figure 7-53 and the fit value cumulative distribution function is shown in Figure 7-54.

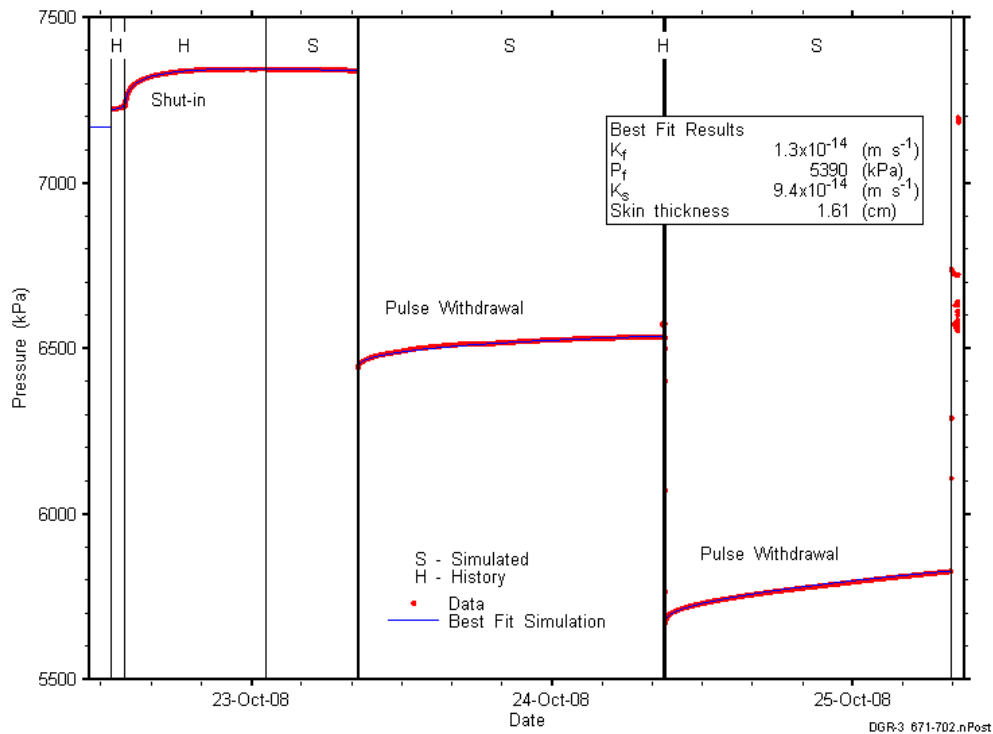


Figure 7-52: Annotated DGR3_671.50-702.24 testing sequence showing best-fit simulation and parameter estimates.

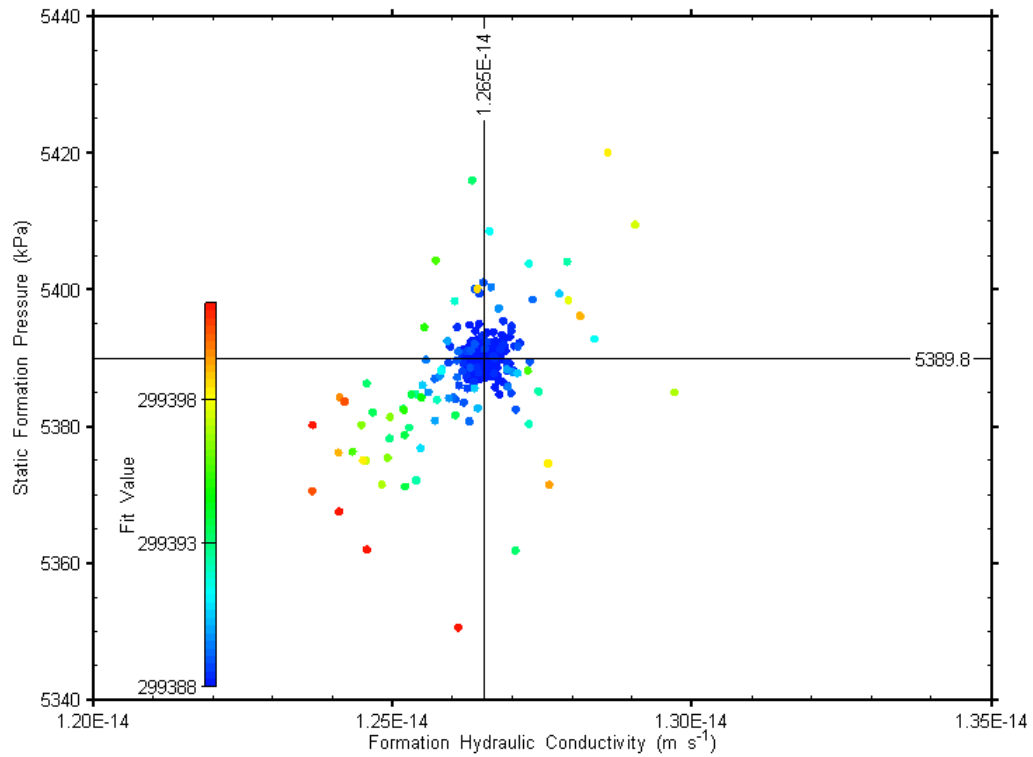


Figure 7-53: XY-scatter plot showing estimates of formation hydraulic conductivity and raw static formation pressure derived from the DGR3_671.50-702.24 perturbation analysis.

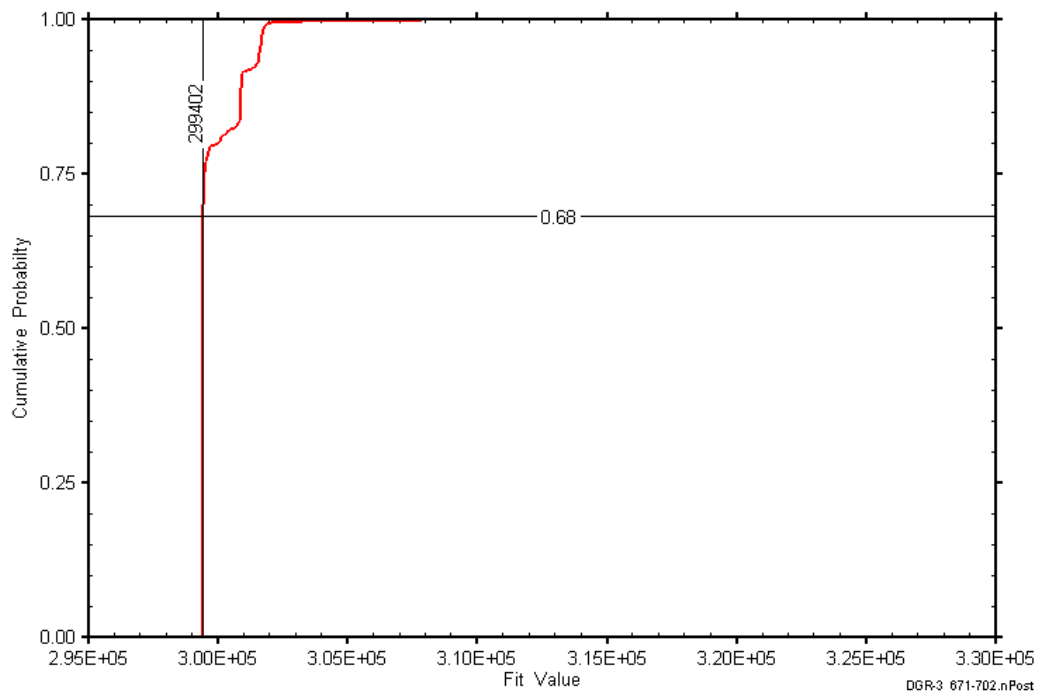


Figure 7-54: DGR3_671.50-702.24 fit value cumulative distribution function.

7.19 710.00-740.74 Sherman Fall-Kirkfield

The DGR-3 interval from 710.00 to 740.74 m BGS included the lower 19.8 m of the Sherman Fall Formation and the upper 10.94 m of the Kirkfield Formation. The entire interval consisted of interbedded argillaceous limestone and shale. An overview of the testing in this interval is given in Table 7-38 and the corresponding parameter estimates are given in Table 7-39. Two pulse-withdrawal tests were conducted in this interval.

Table 7-38: Summary of the DGR3_710.00-740.74 testing activities.

Formation / Unit		Top of Test Zone (m BGS)		Bottom of Test Zone (m BGS)	
Sherman Fall-Kirkfield		710.00		740.74	
Test	Initiated	Magnitude (kPa)	Duration	Compressibility (Pa ⁻¹)	
Shut-in	25-10-08 12:19	N/A	20 hr	N/A	
PW	26-10-08 08:11	864	25 hr	3.7E-10	
PW	27-10-08 08:42	866	24 hr	3.7E-10	
Borehole Pressure History					
Event		Start		Pressure (kPa)	
Drilling Intercept		05-07-08 10:00		7532	
End of Geophysical Logging		05-08-08		7057	
Prior Testing		12-08-08		N/A	
Shut-in		25-10-08 12:19		7716	

Table 7-39: Summary of the DGR3_710.00-740.74 parameter estimates.

Parameter	Best Fit	Minimum	Maximum	Mean
K _f (m/s)	1.3E-14	1.3E-14	1.3E-14	1.3E-14
P _f (kPa)	7064	7062	7066	7064
K _s (m/s)	7.3E-14	7.0E-14	7.6E-14	7.3E-14
t _s (cm)	1.4	1.4	1.4	1.4

Figure 7-55 shows the measured pressure record from DGR3_710.00-740.74 used in this analysis along with the best-fit simulation and parameter values. The S_s value for this analysis was fixed at 3E-7 m⁻¹, a value estimated from perturbation analysis. The ranges of formation K and raw P_f values estimated from perturbation analysis are shown in Figure 7-56 and the fit value cumulative distribution function is shown in Figure 7-57.

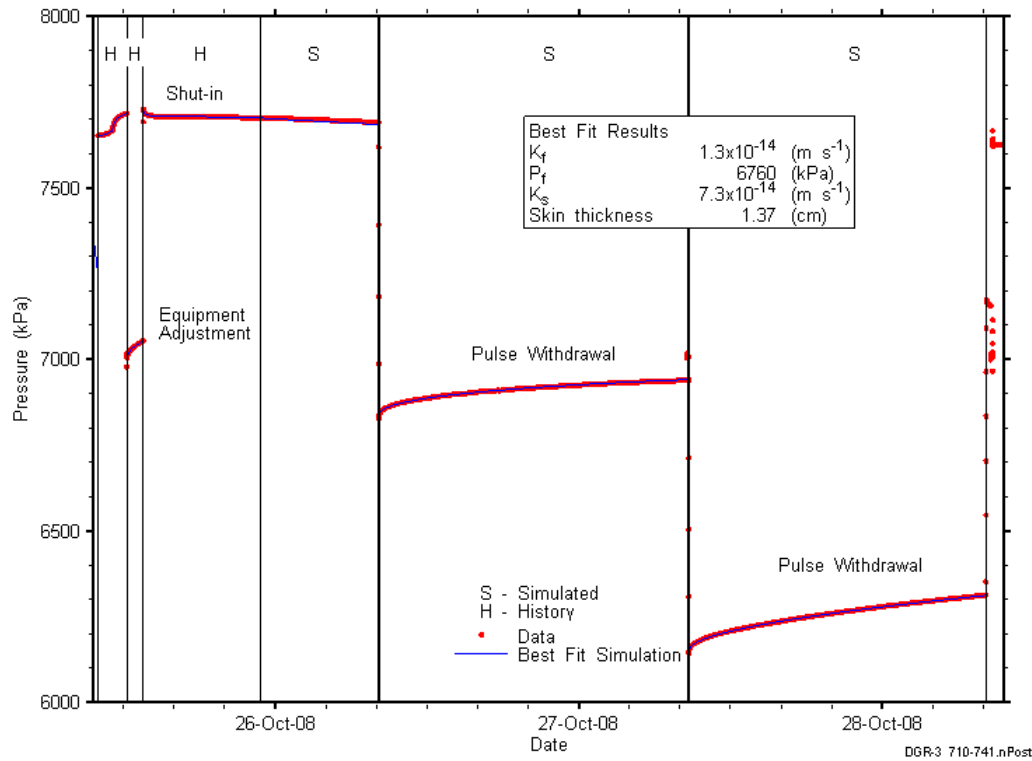


Figure 7-55: Annotated DGR3_710.00-740.74 testing sequence showing best-fit simulation and parameter estimates.

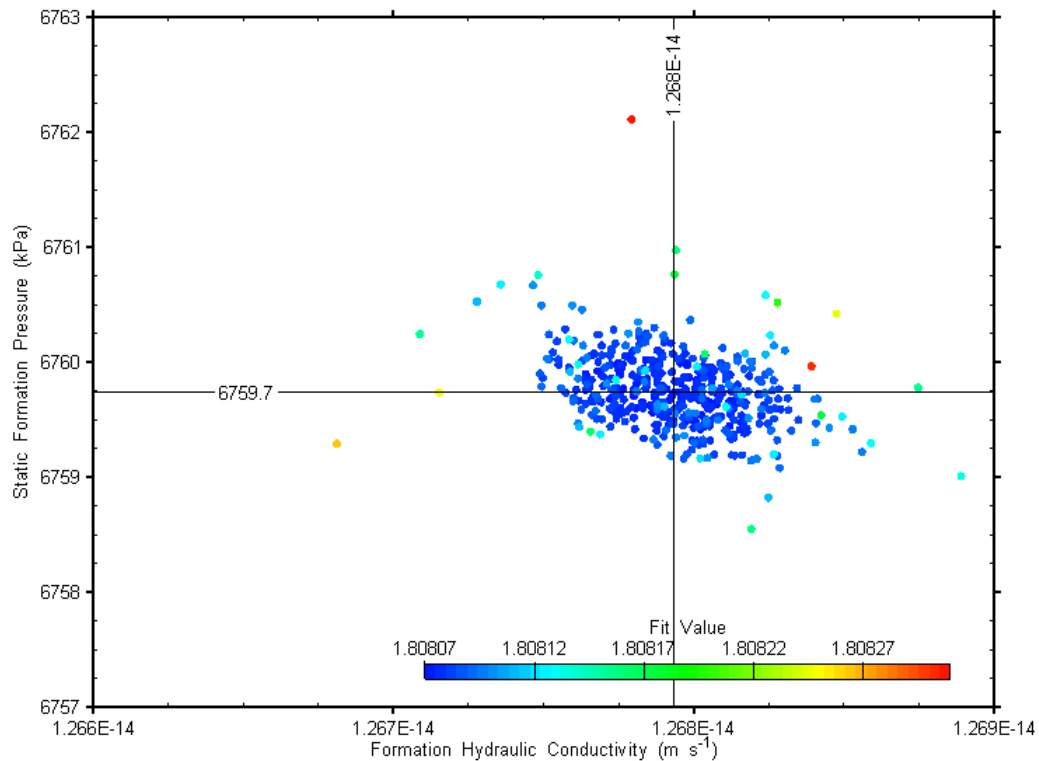


Figure 7-56: XY-scatter plot showing estimates of formation hydraulic conductivity and raw static formation pressure derived from the DGR3_710.00-740.74 perturbation analysis.

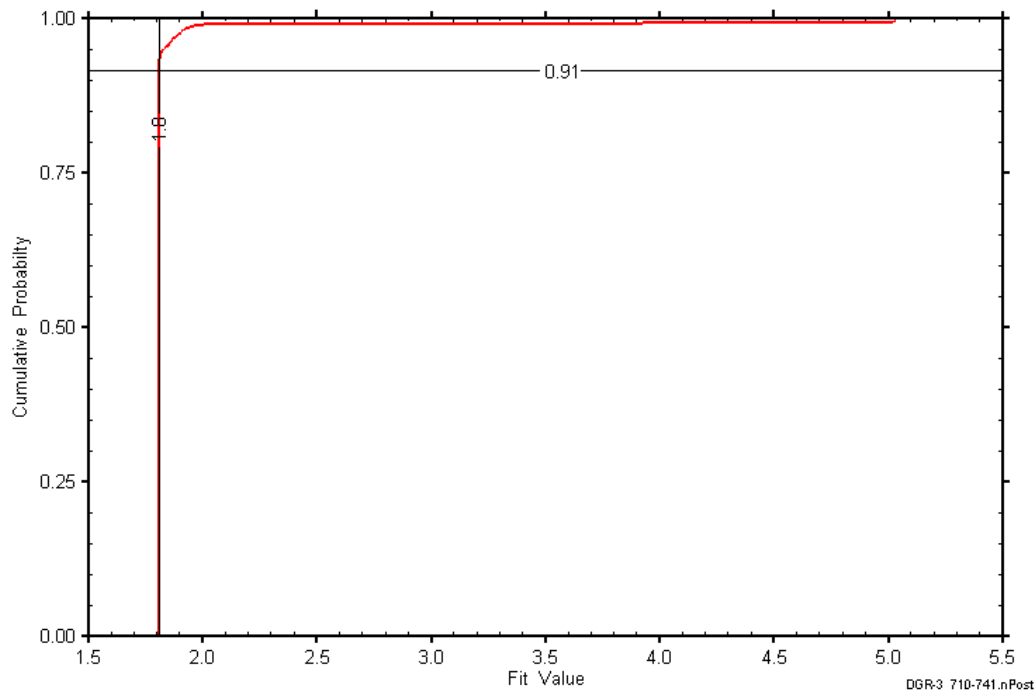


Figure 7-57: DGR3_710.00-740.74 fit value cumulative distribution function.

7.20 740.54-771.28 Kirkfield

The DGR-3 interval from 740.54 to 771.28 m BGS was entirely contained within a section of the Kirkfield Formation consisting of interbedded argillaceous limestone and shale. An overview of the testing in this interval is given in Table 7-40 and the corresponding parameter estimates are given in Table 7-41. Two pulse-withdrawal tests were conducted in this interval.

Table 7-40: Summary of the DGR3_740.54-771.28 testing activities.

Formation / Unit		Top of Test Zone (m BGS)	Bottom of Test Zone (m BGS)	
Kirkfield		740.54	771.28	
Test	Initiated	Magnitude (kPa)	Duration	Compressibility (Pa ⁻¹)
Shut-in	28-10-08 11:19	N/A	21 hr	N/A
PW	29-10-08 08:08	877	24 hr	3.7E-10
PW	30-10-08 07:46	875	24 hr	3.8E-10
Borehole Pressure History				
Event	Start	Pressure (kPa)		
Drilling Intercept	07-07-08 18:00	7867		
End of Geophysical Logging	05-08-08	7743		
Prior Testing	12-08-08	N/A		
Shut-in	28-10-08 11:19	8005		

Table 7-41: Summary of the DGR3_740.54-771.28 parameter estimates.

Parameter	Best Fit	Minimum	Maximum	Mean
K_f (m/s)	1.7E-14	1.7E-14	1.7E-14	1.7E-14
P_f (kPa)	6850	6846	6855	6850
K_s (m/s)	3.2E-13	2.7E-13	3.7E-13	3.2E-13
t_s (cm)	4.4	4.4	4.5	4.4

Figure 7-58 shows the measured pressure record from DGR3_740.54-771.28 used in this analysis along with the best-fit simulation and parameter values. The S_s value for this analysis was fixed at $1E-7 \text{ m}^{-1}$, a value estimated from perturbation analysis. The ranges of formation K and raw P_f values estimated from perturbation analysis are shown in Figure 7-59 and the fit value cumulative distribution function is shown in Figure 7-60.

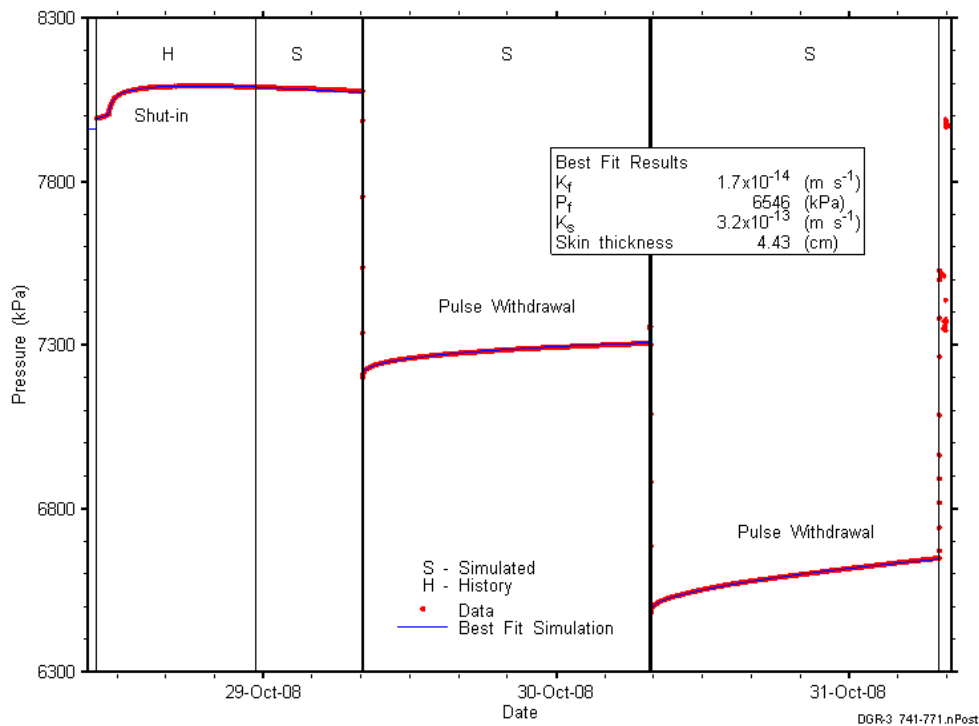


Figure 7-58: Annotated DGR3_740.54-771.28 testing sequence showing best-fit simulation and parameter estimates.

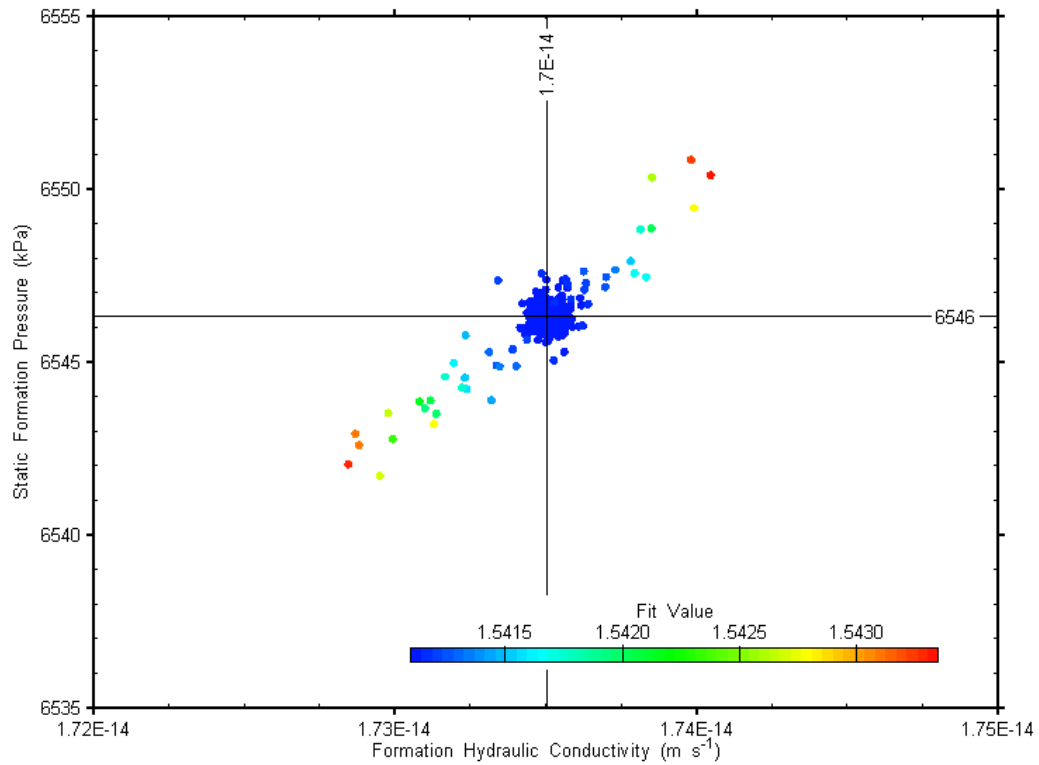


Figure 7-59: XY-scatter plot showing estimates of formation hydraulic conductivity and raw static formation pressure derived from the DGR3_740.54-771.28 perturbation analysis.

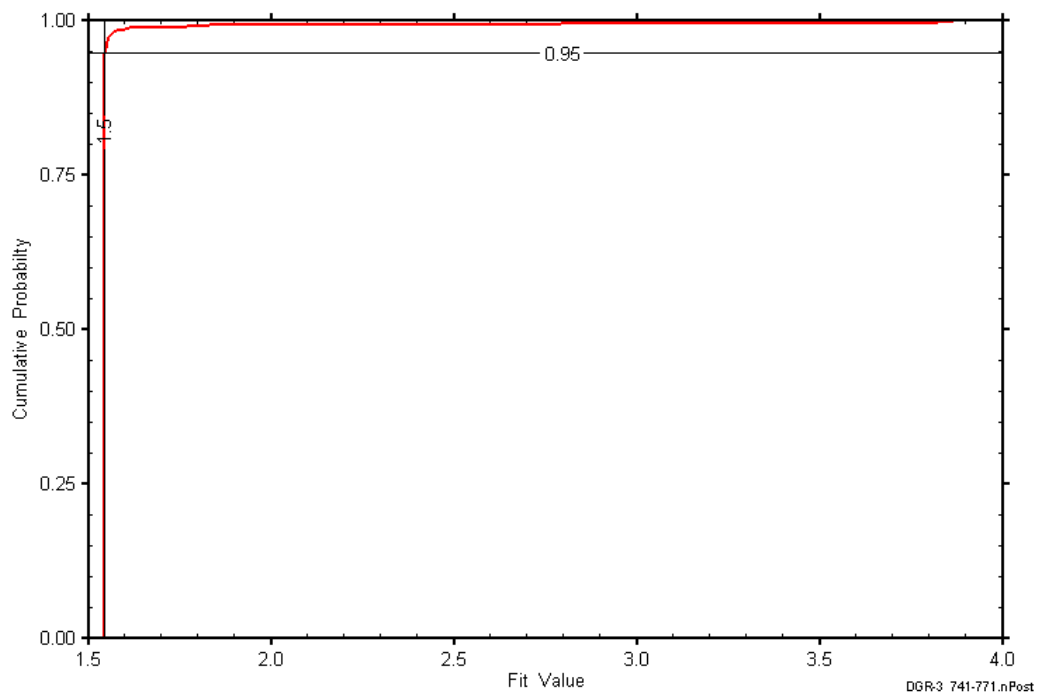


Figure 7-60: DGR3_740.54-771.28 fit value cumulative distribution function.

7.21 765.96-796.70 Kirkfield-Coboconk

The DGR-3 interval from 765.96 to 796.70 m BGS included the lower 9.64 m of the Kirkfield Formation and the upper 21.1 m of the Coboconk Formation. The Kirkfield consists of interbedded argillaceous limestone and shale, and the Coboconk consists of limestone with bituminous argillaceous laminae. Both the 0.1-m-thick volcanic ash layer and a 0.1-m-thick dolostone layer typically observed in the Coboconk were included in the test interval. An overview of the testing in this interval is given in Table 7-42 and the corresponding parameter estimates are given in Table 7-43. A pulse-withdrawal test and a pulse-injection test were conducted in this interval.

Table 7-42: Summary of the DGR3_765.96-796.70 testing activities.

Formation / Unit		Top of Test Zone (m BGS)	Bottom of Test Zone (m BGS)	
Kirkfield-Coboconk		765.96	796.70	
Test	Initiated	Magnitude (kPa)	Duration	Compressibility (Pa ⁻¹)
Shut-in	31-10-08 10:43	N/A	21 hr	N/A
PW	01-11-08 07:45	821	25 hr	4.1E-10
PI	02-11-08 09:11	821	23 hr	4.1E-10
Borehole Pressure History				
Event	Start		Pressure (kPa)	
Drilling Intercept	08-07-08 18:30		8136	
End of Geophysical Logging	05-08-08		8054	
Prior Testing	12-08-08		N/A	
Shut-in	31-10-08 10:43		8291	

Table 7-43: Summary of the DGR3_765.96-796.70 parameter estimates.

Parameter	Best Fit	Minimum	Maximum	Mean
K_f (m/s)	1.0E-12	9.8E-13	1.0E-12	1.0E-12
P_f (kPa)	8827	8827	8828	8827
K_s (m/s)	5.7E-14	5.3E-14	6.3E-14	5.7E-14
t_s (cm)	2.0	1.8	2.2	2.0
S_s (m ⁻¹)	8.4E-6	6.5E-6	1.1E-5	8.4E-6

Figure 7-61 shows the measured pressure record from DGR3_765.96-796.70 used in this analysis along with the best-fit simulation and parameter values. The ranges of formation K and raw P_f values estimated from perturbation analysis are shown in Figure 7-62 and the fit value cumulative distribution function is shown in Figure 7-63.

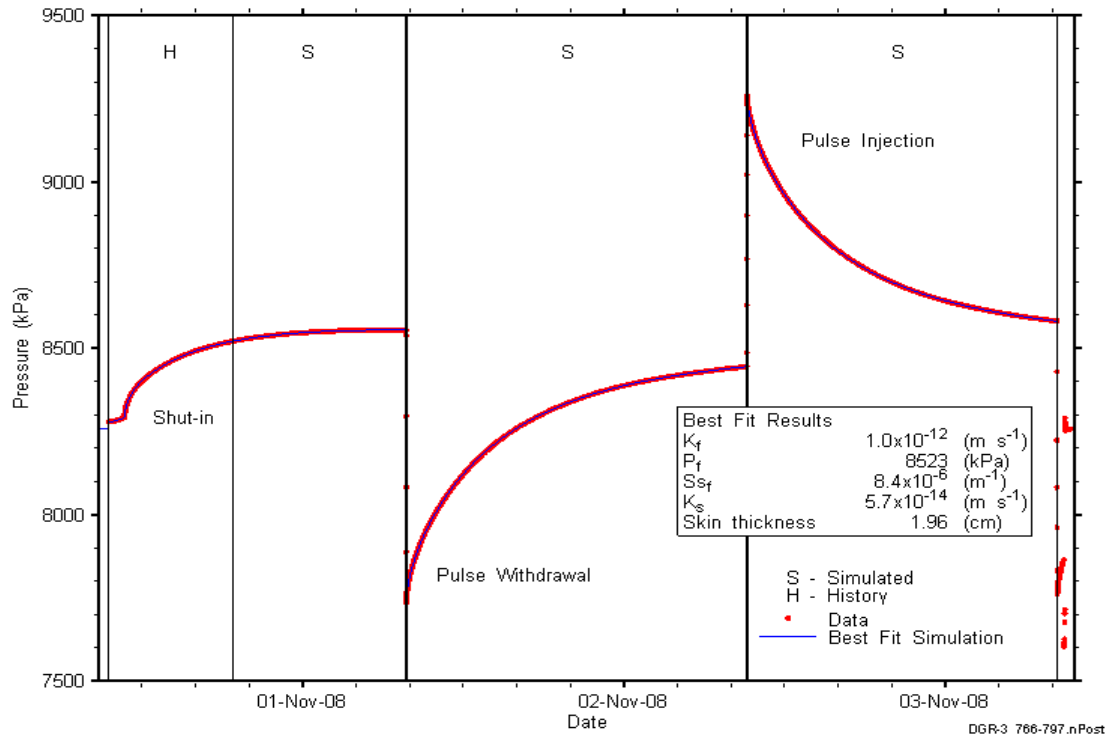


Figure 7-61: Annotated DGR3_765.96-796.70 testing sequence showing best-fit simulation and parameter estimates.

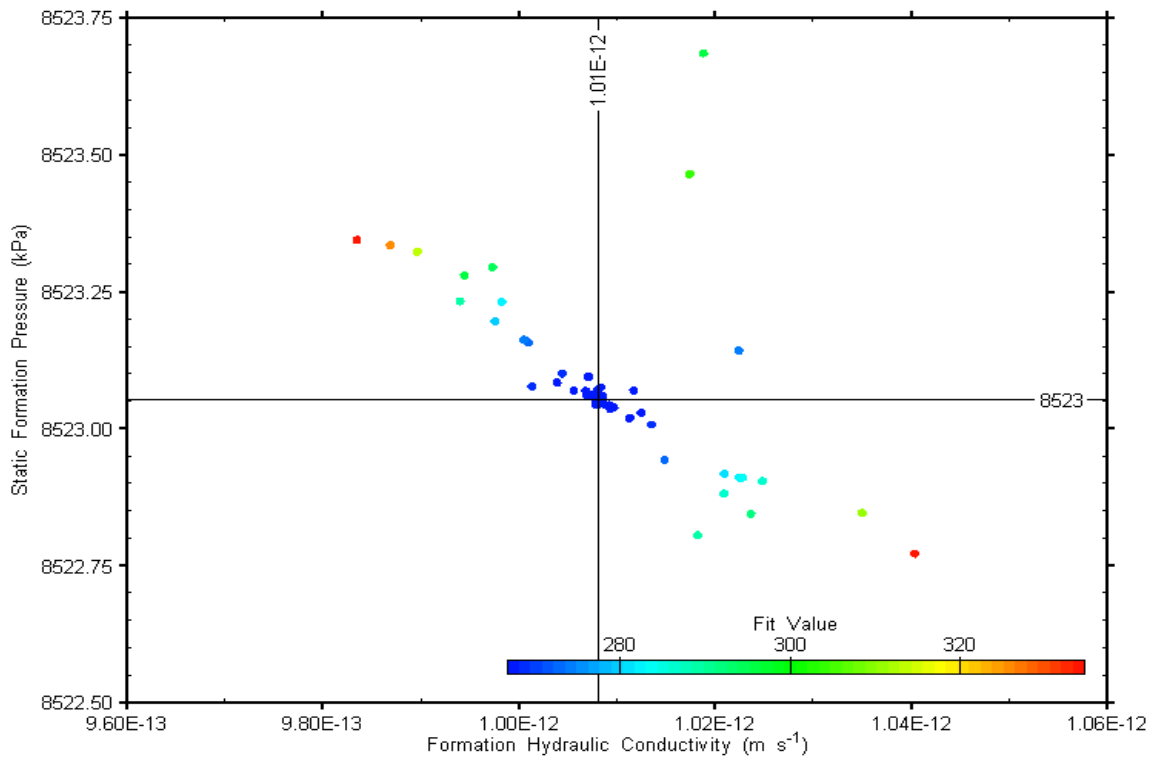


Figure 7-62: XY-scatter plot showing estimates of formation hydraulic conductivity and raw static formation pressure derived from the DGR3_765.96-796.70 perturbation analysis.

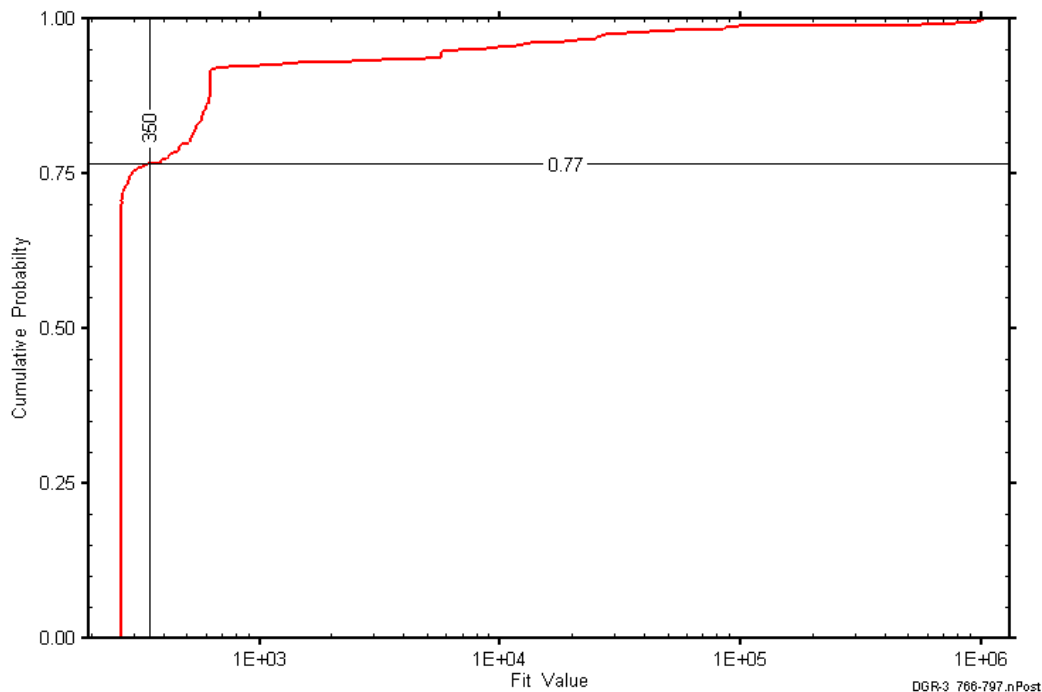


Figure 7-63: DGR3_765.96-796.70 fit value cumulative distribution function.

7.22 790.93-821.67 Coboconk-Gull River

The DGR-3 interval from 790.93 to 821.67 m BGS included the lower 8.37 m of the Coboconk Formation and the upper 22.37 m of the Gull River Formation. The Coboconk consists of limestone with bituminous argillaceous laminae, and the upper Gull River consists of limestone with shale laminae and interbeds. Neither the 0.1-m-thick volcanic ash layer nor the 0.1-m-thick dolostone layer typically observed in the Coboconk were included in the test interval, although a vuggy interval near the bottom of the Coboconk was included. An overview of the testing in this interval is given in Table 7-44 and the corresponding parameter estimates are given in Table 7-45. A pulse-withdrawal test and a pulse-injection test were conducted in this interval.

Table 7-44: Summary of the DGR3_790.93-821.67 testing activities.

Formation / Unit		Top of Test Zone (m BGS)	Bottom of Test Zone (m BGS)	
Coboconk-Gull River		790.93	821.67	
Test	Initiated	Magnitude (kPa)	Duration	Compressibility (Pa ⁻¹)
Shut-in	03-11-08 12:01	N/A	20 hr	N/A
PW	04-11-08 08:23	901	24 hr	3.7E-10
PI	05-11-08 08:45	909	24 hr	3.7E-10
Borehole Pressure History				
Event	Start	Pressure (kPa)		
Drilling Intercept	09-07-08 18:00	8405		
End of Geophysical Logging	05-08-08	8334		
Prior Testing	12-08-08	N/A		
Shut-in	03-11-08 12:01	8572		

Table 7-45: Summary of the DGR3_790.93-821.67 parameter estimates.

Parameter	Best Fit	Minimum	Maximum	Mean
K_f (m/s)	1.5E-13	1.4E-13	1.7E-13	1.5E-13
P_f (kPa)	9531	9519	9541	9531
K_s (m/s)	2.0E-14	1.8E-14	2.4E-14	2.0E-14
t_s (cm)	1.8	1.6	2.0	1.8
S_s (m^{-1})	2.8E-6	2.0E-6	3.7E-6	2.8E-6

Figure 7-64 shows the measured pressure record from DGR3_790.93-821.67 used in this analysis along with the best-fit simulation and parameter values. The ranges of formation K and raw P_f values estimated from the DGR3_790.93-821.67 perturbation analysis are shown in Figure 7-65 and the fit value cumulative distribution function is shown in Figure 7-66.

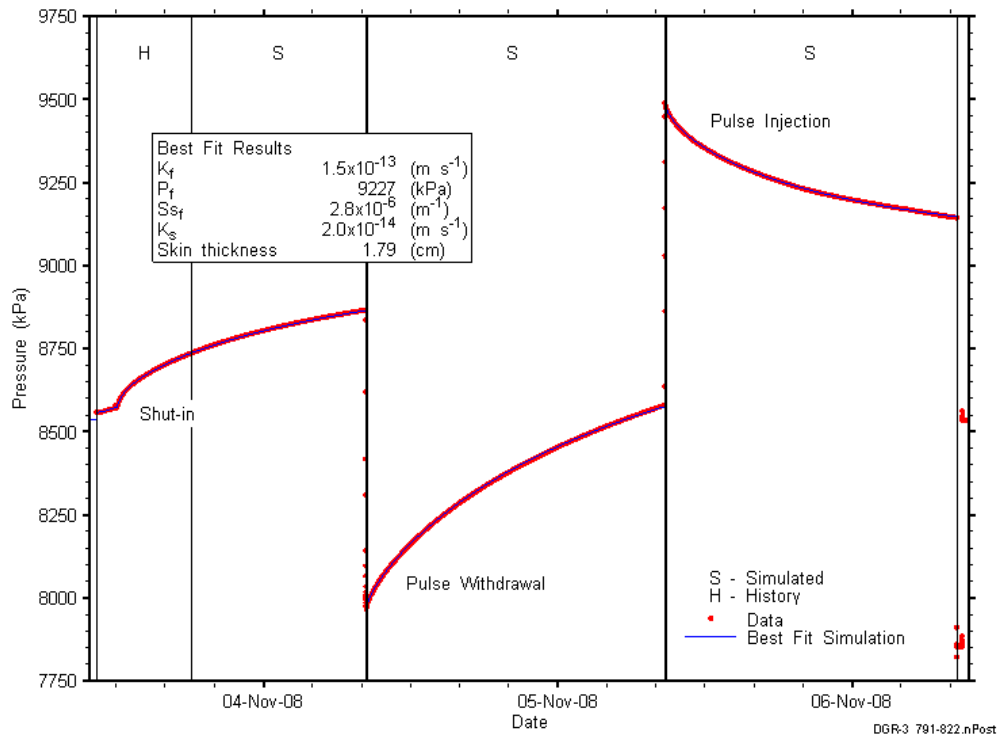


Figure 7-64: Annotated DGR3_790.93-821.67 testing sequence showing best-fit simulation and parameter estimates.

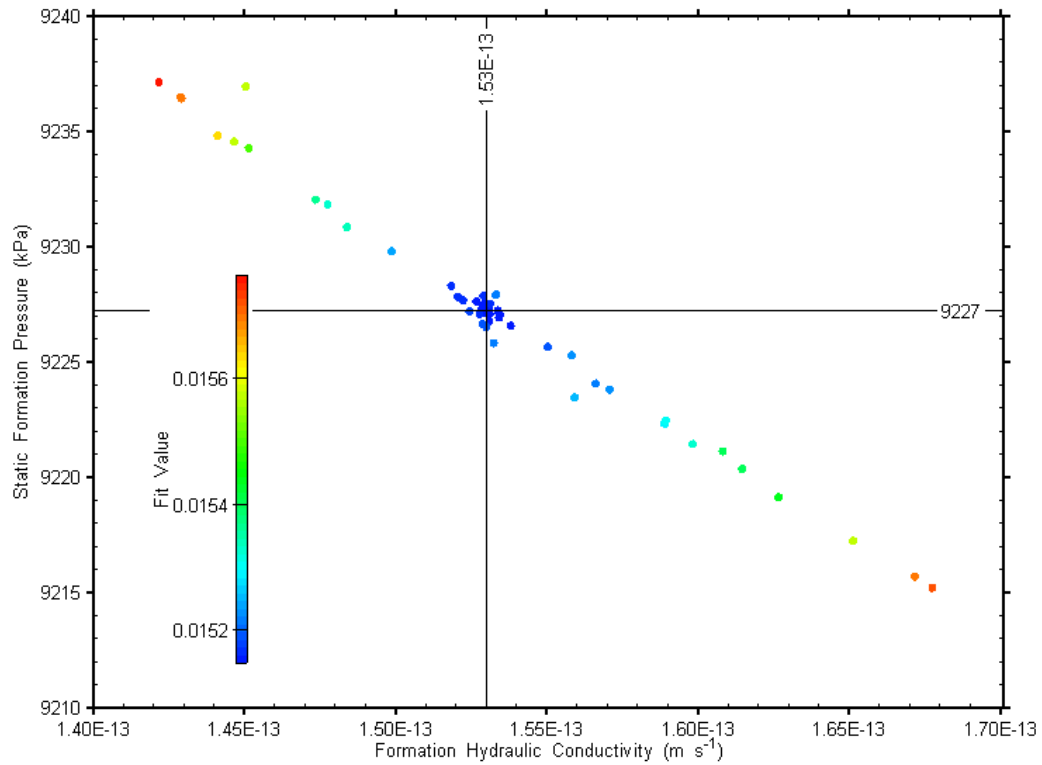


Figure 7-65: XY-scatter plot showing estimates of formation hydraulic conductivity and raw static formation pressure derived from the DGR3_790.93-821.67 perturbation analysis.

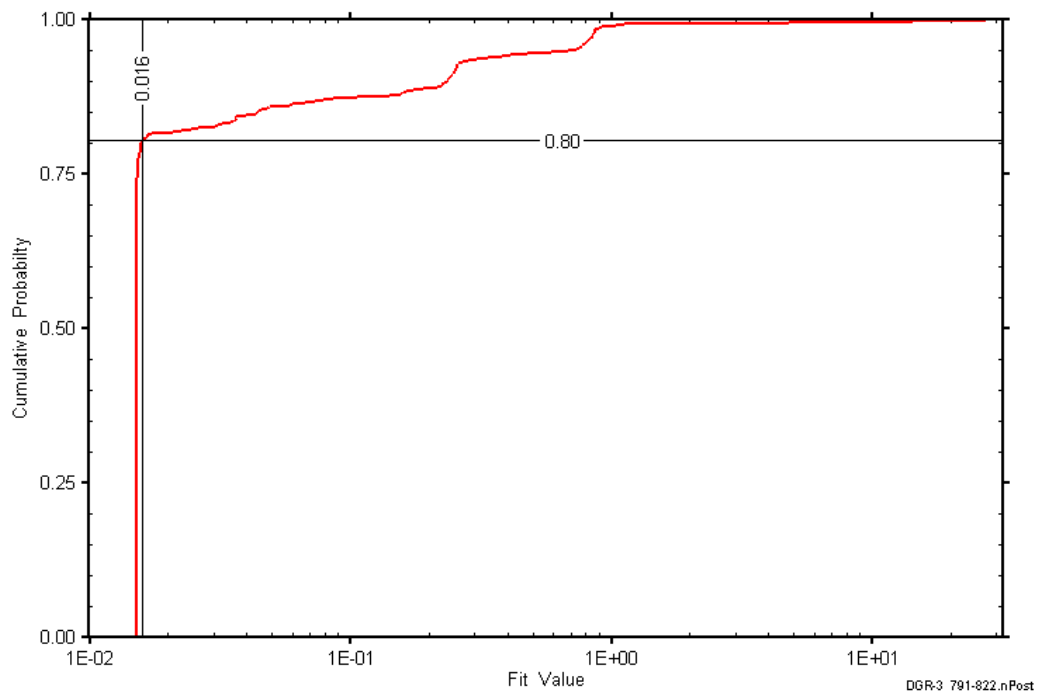


Figure 7-66: DGR3_790.93-821.67 fit value cumulative distribution function.

7.23 815.00-845.74 Gull River

The DGR-3 interval from 815.00 to 845.74 m BGS was entirely contained within a section of the Gull River Formation consisting of limestone with shale laminae and interbeds, and two dolostone layers 0.6 to 1.0 m thick (Briscoe et al., 2010). An overview of the testing in this interval is given in Table 7-46 and the corresponding parameter estimates are given in Table 7-47. A single pulse-injection test was conducted in this interval.

Table 7-46: Summary of the DGR3_815.00-845.74 testing activities.

Formation / Unit		Top of Test Zone (m BGS)		Bottom of Test Zone (m BGS)	
Gull River		815.00		845.74	
Test	Initiated	Magnitude (kPa)	Duration	Compressibility (Pa ⁻¹)	
Shut-in	06-11-08 14:01	N/A	18 hr	N/A	
PI	07-11-08 07:48	906	25 hr	3.8E-10	
Borehole Pressure History					
Event		Start		Pressure (kPa)	
Drilling Intercept		10-07-08 16:00		8664	
End of Geophysical Logging		05-08-08		8608	
Prior Testing		12-08-08		N/A	
Shut-in		06-11-08 14:01		8850	

Table 7-47: Summary of the DGR3_815.00-845.74 parameter estimates.

Parameter	Best Fit	Minimum	Maximum	Mean
K_f (m/s)	3.7E-13	3.6E-13	3.7E-13	3.7E-13
P_f (kPa)	10523	10518	10527	10523
K_s (m/s)	4.7E-14	4.5E-14	4.9E-14	4.7E-14
t_s (cm)	2.5	2.4	2.6	2.5
S_s (m ⁻¹)	4.9E-6	4.5E-6	5.3E-6	4.9E-6

Figure 7-67 shows the measured pressure record from DGR3_815.00-845.74 used in this analysis along with the best-fit simulation and parameter values. The ranges of formation K and raw P_f values estimated from perturbation analysis are shown in Figure 7-68 and the fit value cumulative distribution function is shown in Figure 7-69.

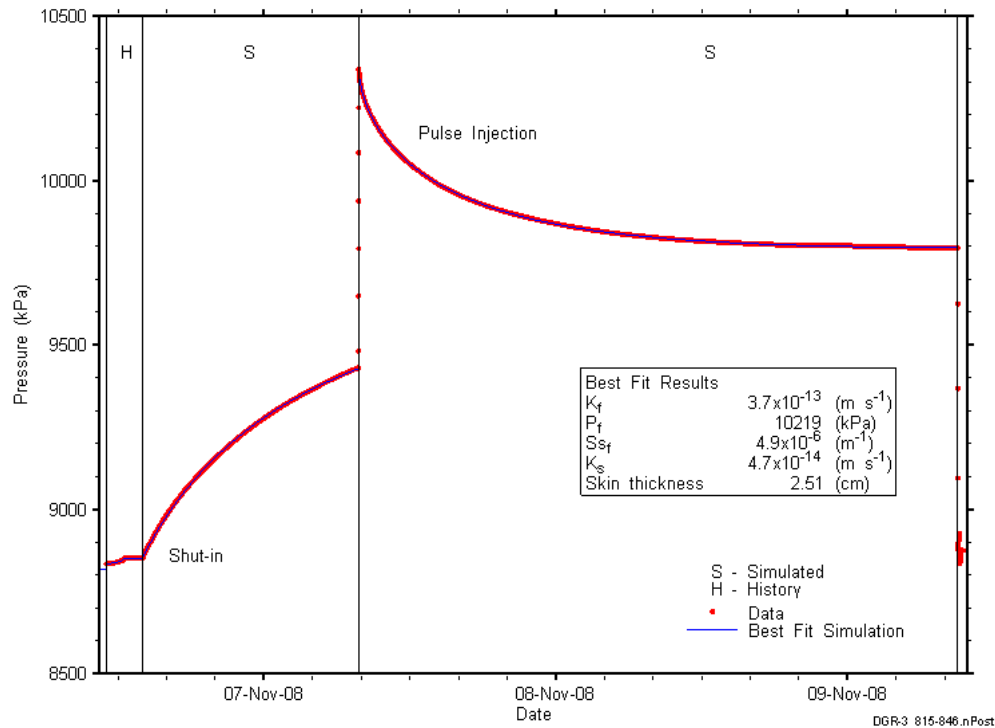


Figure 7-67: Annotated DGR3_815.00-845.74 testing sequence showing best-fit simulation and parameter estimates.

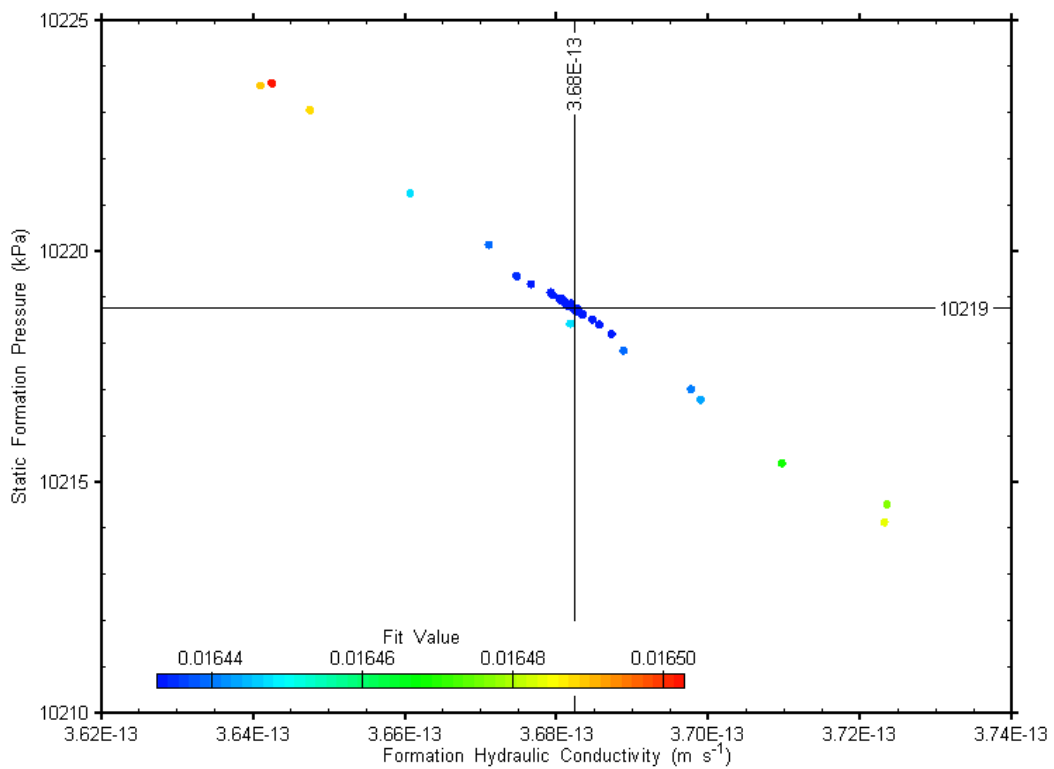


Figure 7-68: XY-scatter plot showing estimates of formation hydraulic conductivity and raw static formation pressure derived from the DGR3_815.00-845.74 perturbation analysis.

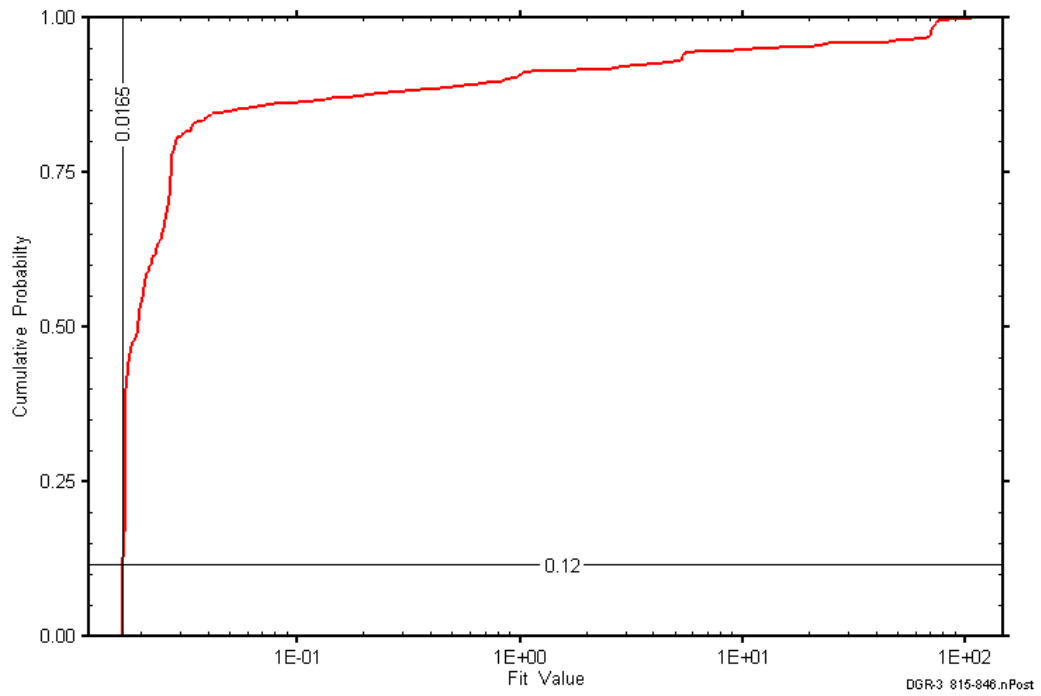


Figure 7-69: DGR3_815.00-845.74 fit value cumulative distribution function.

7.24 Summary of DGR-3 Results

The best-fit parameter estimates derived from the DGR-3 analyses are given in Table 7-48. Figure 7-70 through Figure 7-74 present stratigraphic profiles of the analysis results for hydraulic conductivity, formation pressure, specific storage, skin factor, and test-zone compressibility, respectively.

Table 7-48: Best-fit parameter estimates derived from the DGR-3 analyses

Formation(s) Tested	Top	Bottom	K_f	P_f	S_s	K_s	t_s	s	C_{tz}
	mBGS	m BGS	$m\ s^{-1}$	kPa	m^{-1}	$m\ s^{-1}$	cm		Pa^{-1}
Salina F-E	210.18	240.92	4.8E-14	2050	1.8E-6	6.3E-13	0.6	-7.0E-02	4.5E-10
Salina E-D-C	240.72	271.46	1.4E-13	1900	7.4E-7	9.3E-13	56	-1.8E+00	6.4E-10
Salina C-B	271.29	302.03	3.8E-13	2090	1.2E-5	2.8E-13	4.1	1.5E-01	2.0E-9
Salina B-A2 carbonate	301.81	332.55	3.8E-9	3161	7.7E-5	1.5E-15	1.9	5.9E+05	2.8E-9
Salina A2 evaporite- A1 carbonate	334.99	365.73	1.8E-8	3546	2.0E-7	7.3E-11**	n/a	n/a	n/c
Salina A1 carbonate	346.00	376.74	4.0E-11	3573	7.3E-6	3.0E-12	1.1	1.8E+00	3.7E-10
Salina A1 evaporite- A0-Guelph-Goat Island-Gasport	379.98	410.72	8.9E-9	4224	2.2E-6	4.3E-6	48	-2.0E+00	n/c
Gasport-Lions Head- Fossil Hill-Cabot Head	410.51	441.25	3.5E-12	5259	2.0E-7	6.6E-12	152	-1.5E+00	1.3E-9
Cabot Head- Manitoulin-Queenston	441.05	471.79	1.6E-13	4138	1.0E-6*	3.7E-12	7.0	-6.5E-01	6.6E-9
Queenston	471.41	502.15	1.6E-14	4980	7.4E-6	5.1E-14	0.3	-3.2E-02	8.7E-10
Queenston-Georgian Bay	501.95	532.69	1.4E-14	3834	2.3E-6	5.8E-14	0.1	-7.0E-03	4.4E-10
Georgian Bay	532.49	563.23	1.2E-14	3741	5.9E-6	1.5E-13	0.6	-7.1E-02	6.0E-10
Georgian Bay	563.03	593.77	1.2E-14	2559	3.5E-6	1.1E-13	0.6	-6.9E-02	5.3E-10
Georgian Bay-Blue Mountain	593.57	624.31	3.3E-14	3358	2.8E-5	2.4E-13	0.4	-4.4E-02	7.5E-10
Georgian Bay-Blue Mountain	617.63	648.37	1.3E-13	6657	1.0E-6*	3.8E-12	7.5	-6.9E-01	2.1E-9
Blue Mountain	628.00	658.74	3.5E-13	7655	1.0E-6*	9.6E-12	7.6	-7.0E-01	1.8E-9
Blue Mountain- Collingwood-Cobourg	654.65	685.39	2.4E-14	5241	1.0E-7*	1.4E-13	3.1	-3.0E-01	3.7E-10
Collingwood- Cobourg-Sherman Fall	671.50	702.24	1.3E-14	5694	2.0E-7*	9.4E-14	1.6	-1.8E-01	3.6E-10
Sherman Fall-Kirkfield	710.00	740.74	1.3E-14	7064	3.0E-7*	7.3E-14	1.4	-1.4E-01	3.7E-10
Kirkfield	740.54	771.28	1.7E-14	6850	1.0E-7*	3.2E-13	4.4	-4.6E-01	3.7E-10
Kirkfield-Coboconk	765.96	796.70	1.0E-12	8827	8.4E-6	5.7E-14	2.0	4.0E+00	4.1E-10
Coboconk-Gull River	790.93	821.67	1.5E-13	9531	2.8E-6	2.0E-14	1.8	1.5E+00	3.7E-10
Gull River	815.00	845.74	3.7E-13	10523	4.9E-6	4.7E-14	2.5	2.1E+00	3.8E-10

n/a: not applicable

n/c: not calculated

*: fixed ** Geometric mean of all skins

As shown in Figure 7-70 and Table 7-48, all of the Ordovician test intervals and all but five of the Silurian test intervals in DGR-3 had K values between $1E-14$ and $1E-12$ m/s. The Salina A1 carbonate interval had an average K of $4.0E-11$ m/s and the Gasport-Lions Head-Fossil Hill-Cabot Head interval had an overall average K of $3.5E-12$ m/s. Significantly higher K values were found in the Salina B-A2 carbonate interval ($3.8E-9$ m/s), the Salina A2 evaporite-A1 carbonate interval ($1.8E-8$ m/s), and the Salina A1 evaporite-Salina A0-Guelph-Goat Island-Gasport interval ($8.9E-9$ m/s). The principal contributors of permeability in these three intervals are believed to be the Salina A2 carbonate, the upper Salina A1 carbonate, and the Guelph, respectively. The Ordovician shales, except for the Blue Mountain, and Trenton Group (Cobourg, Sherman Fall, and Kirkfield) limestones had K values between $1.2E-14$ and $3.3E-14$ m/s. The test intervals that included the fractured region in the Blue Mountain Formation (approximately 637 to 640 m BGS) had K values of $1.3E-13$ to $3.5E-13$ m/s. The Black River Group (Coboconk and Gull River) limestones had some of the highest hydraulic conductivities in the Ordovician section, $1.5E-13$ to $1.0E-12$ m/s.

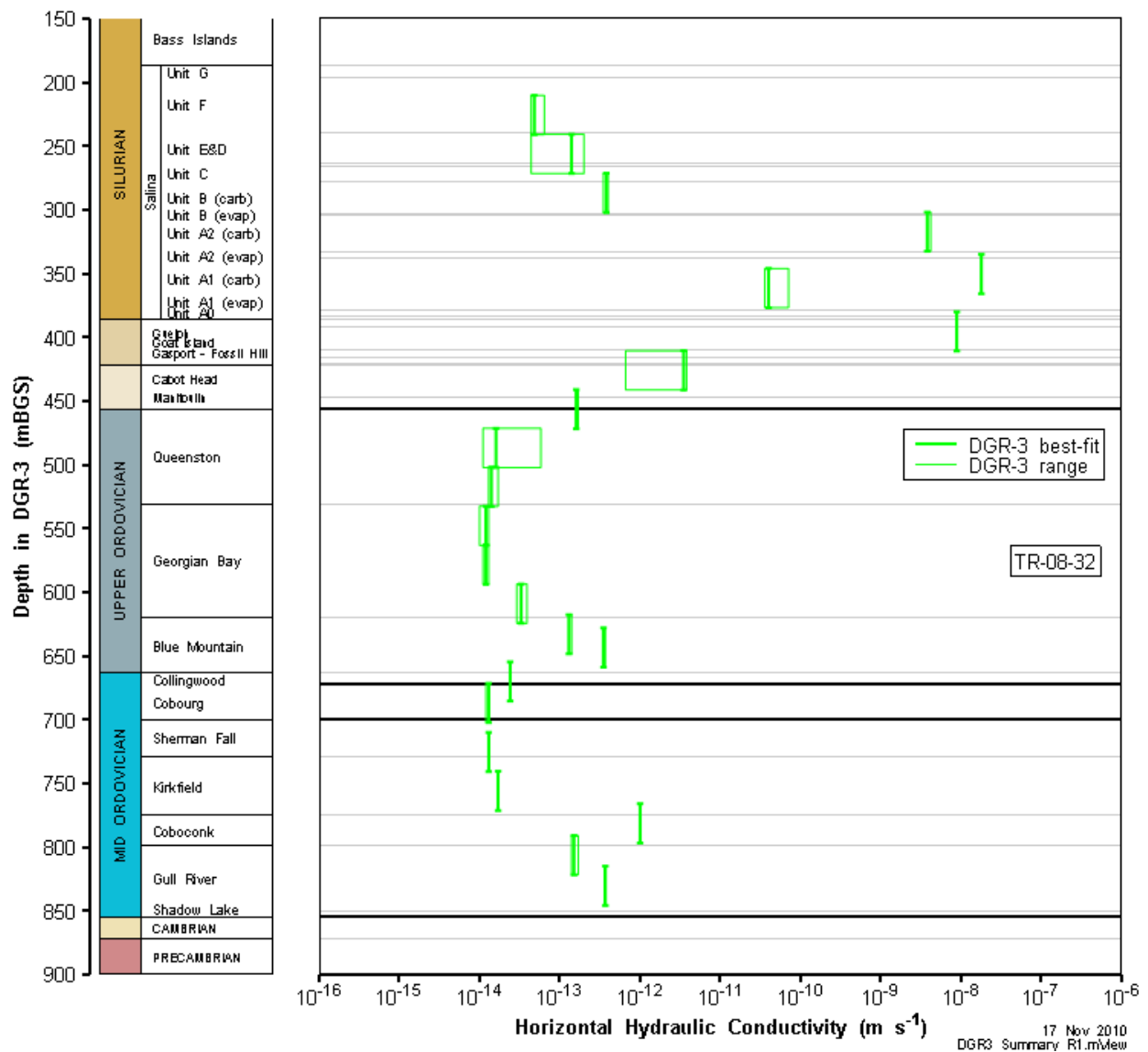


Figure 7-70: DGR-3 stratigraphic profile of horizontal hydraulic conductivity estimates.

As shown in Figure 7-71, the P_f values approximately followed a density-compensated hydrostatic gradient through the Silurian section of DGR-3, with the exception of underpressures in the Salina E-D-C interval and the Salina C-B interval and overpressure in the Gasport-Lions Head-Fossil Hill-Cabot Head interval. Larger deviations from a hydrostatic gradient were observed in the Ordovician section, with pronounced underpressures observed in the lower Queenston interval, all Georgian Bay intervals, the Blue Mountain-Collingwood-Cobourg interval, and the Cobourg interval, while overpressures were observed in the Blue Mountain interval from 628.00 to 658.74 m BGS and in the Coboconk-Gull River and Gull River intervals. The Gasport-Lions Head-Fossil Hill-Cabot Head and Blue Mountain overpressures are associated with high test-zone compressibilities.

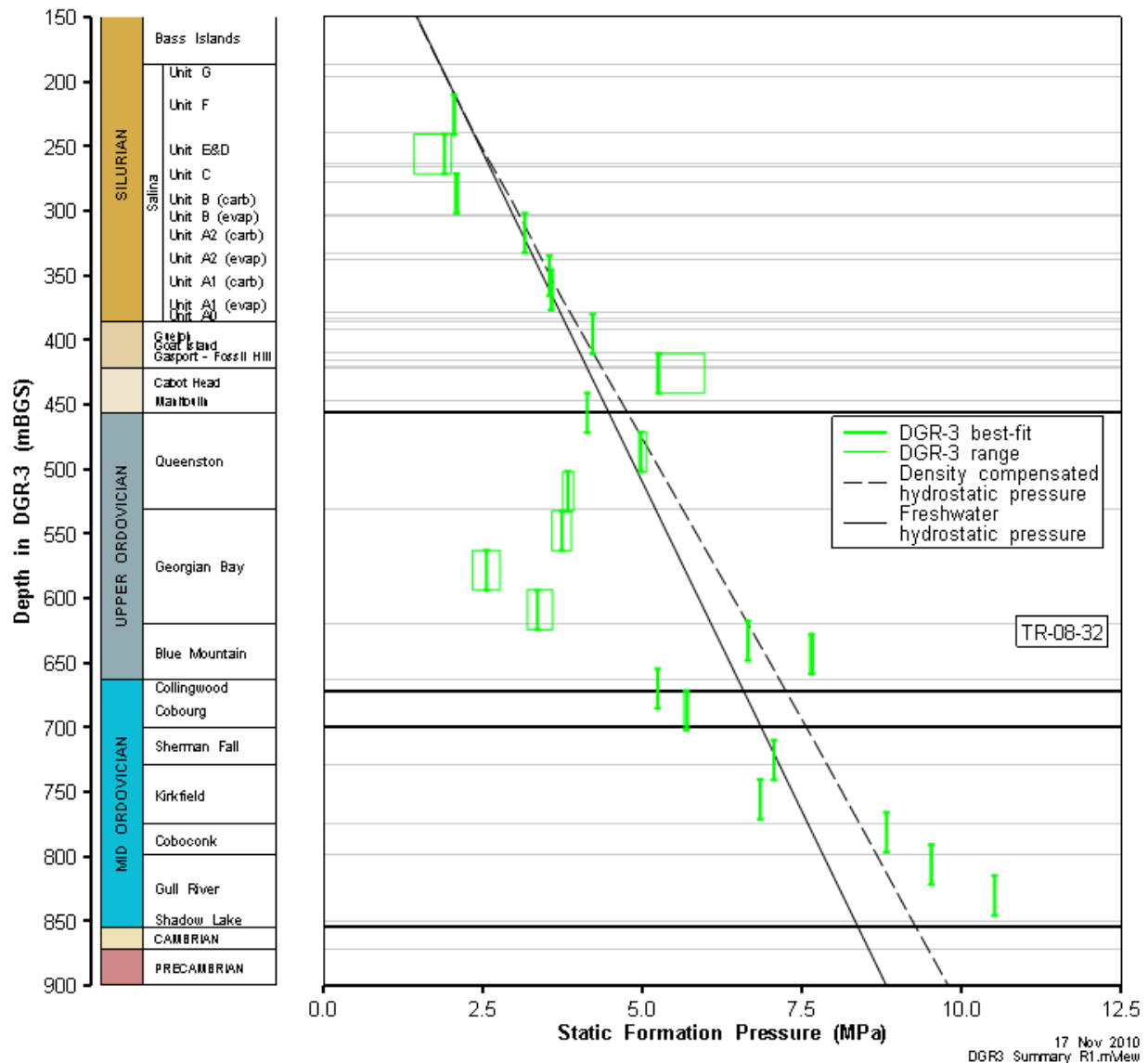


Figure 7-71: DGR-3 stratigraphic profile of formation pressure estimates.

Figure 7-72 shows the S_s values fitted in the simulations for each of the DGR-3 test intervals, along with the uncertainties associated with the fitted values; values that were fixed in the simulations are not shown. The fitted values range from $2E-7 \text{ m}^{-1}$ to nearly $8E-5 \text{ m}^{-1}$. For a number of the Silurian and one of the Ordovician test intervals, effectively equivalent fits could be obtained with S_s values ranging over as much as two orders of magnitude. This is a consequence of the strong correlation between S_s and skin properties in single-well tests discussed in Section 4.4. For seven test intervals, no minimum was found in the S_s fit surface within the range of values thought to be physically reasonable ($1E-7$ to $1E-4 \text{ m}^{-1}$). In those cases, S_s was fixed preferably at $1E-6 \text{ m}^{-1}$, or as low as $1E-7 \text{ m}^{-1}$, if necessary to obtain good matches between the observed and simulated test data.

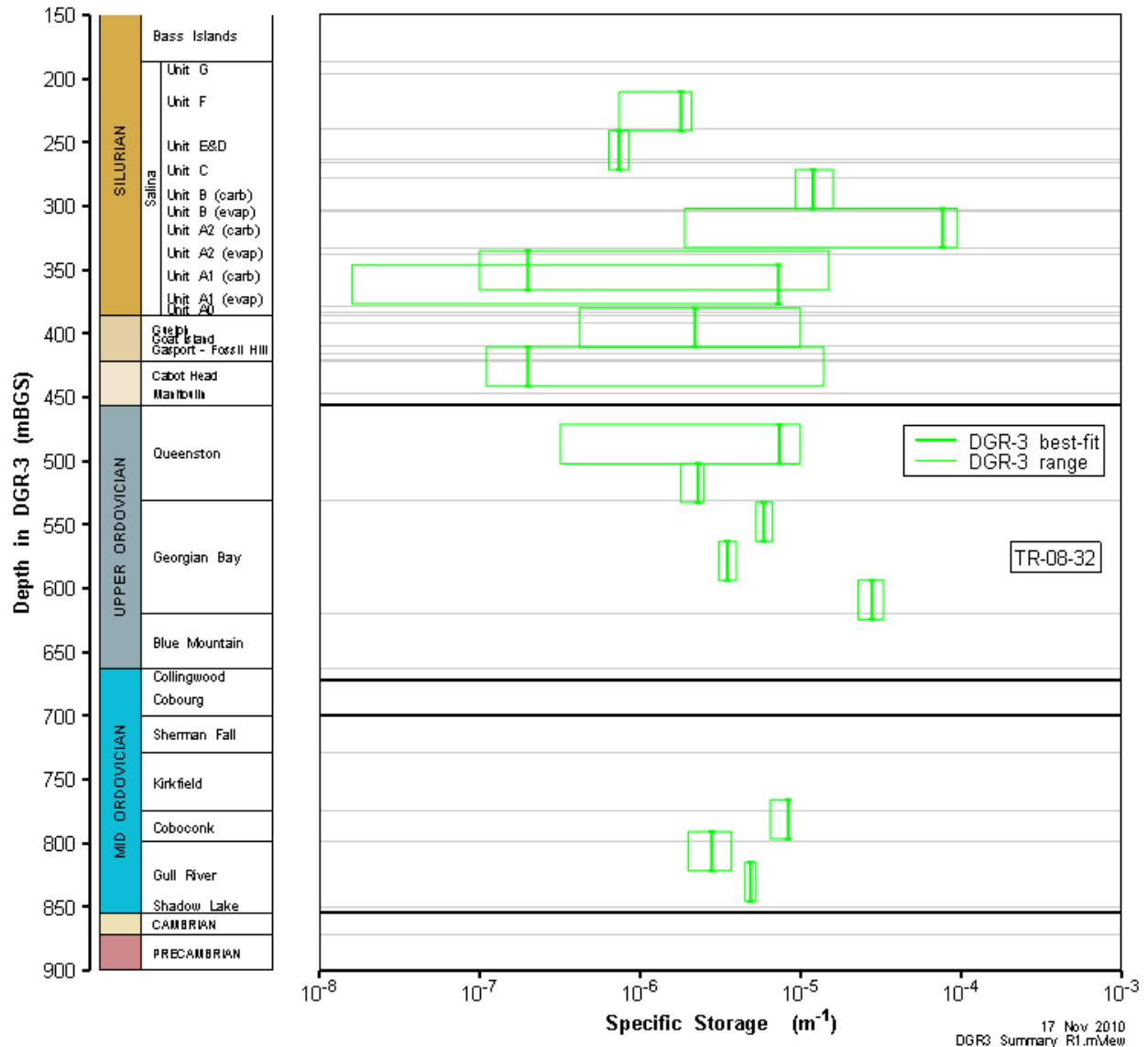


Figure 7-72: DGR-3 stratigraphic profile of specific storage estimates.

Figure 7-73 shows the skin factors obtained from parameter optimization for each of the DGR-3 test intervals. All but six of the test intervals had negative skins, reflecting enhanced permeability around the wellbore. Hydraulically significant fractures are a possible cause of negative skins. Other causes could be enhanced local fracturing caused by stress relief fracturing during drilling. The negative skins in DGR-3 were generally of low magnitude; the Salina A1 evaporite-Salina A0-Guelph-Goat Island-Gasport interval had the most negative skin, which was only -2.04 (Table 7-48). Six intervals had positive skins associated with decreased permeability around the wellbore. As was the case in DGR-2 (Figure 6-49), all of the Black River Group (Coboconk and Gull River) test intervals had positive skins. By far, the most significant skin was that observed in the Salina B-A2 carbonate test interval (6E5). This also happened to be the test interval with the highest fitted S_s value and the second highest measured C_{tz} (Table 7-48).

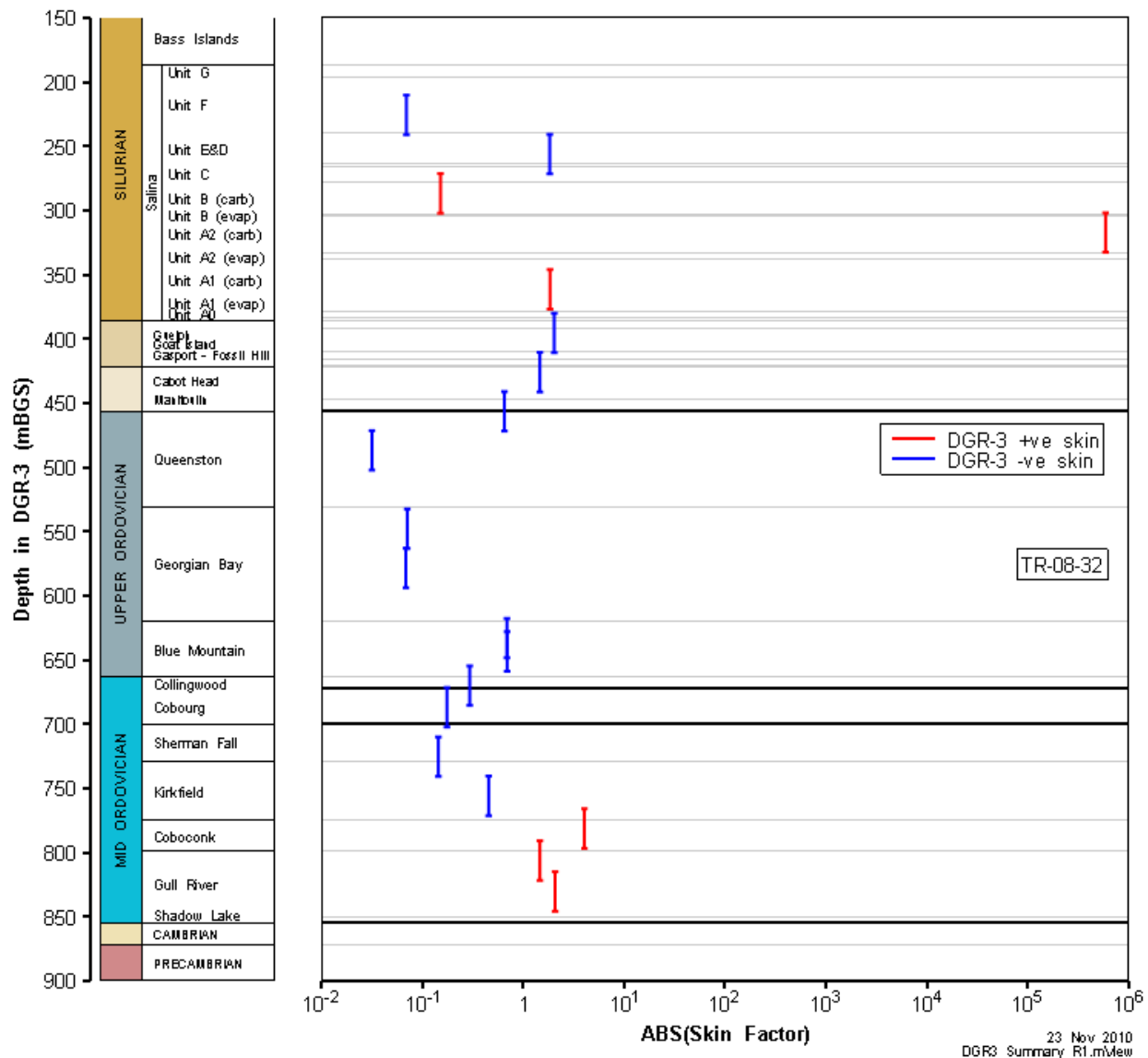


Figure 7-73: DGR-3 stratigraphic profile of skin factor estimates.

As shown in Figure 7-74, of the 21 intervals in which test-zone compressibility was measured, C_{tz} was less than $5E-10 \text{ Pa}^{-1}$ in 10 intervals and less than $9E-10 \text{ Pa}^{-1}$ in 5 more intervals. These values are indicative of water-filled test intervals with typical test-tool compliance. In the remaining 6 intervals, C_{tz} ranged from $1.3E-9$ to $6.6E-9 \text{ Pa}^{-1}$. Higher test-zone compressibilities may be due to a higher rock compressibility for the associated formation or may be suggestive of a relatively small amount of gas in the test zone but, as mentioned above, no direct evidence of gas is available.

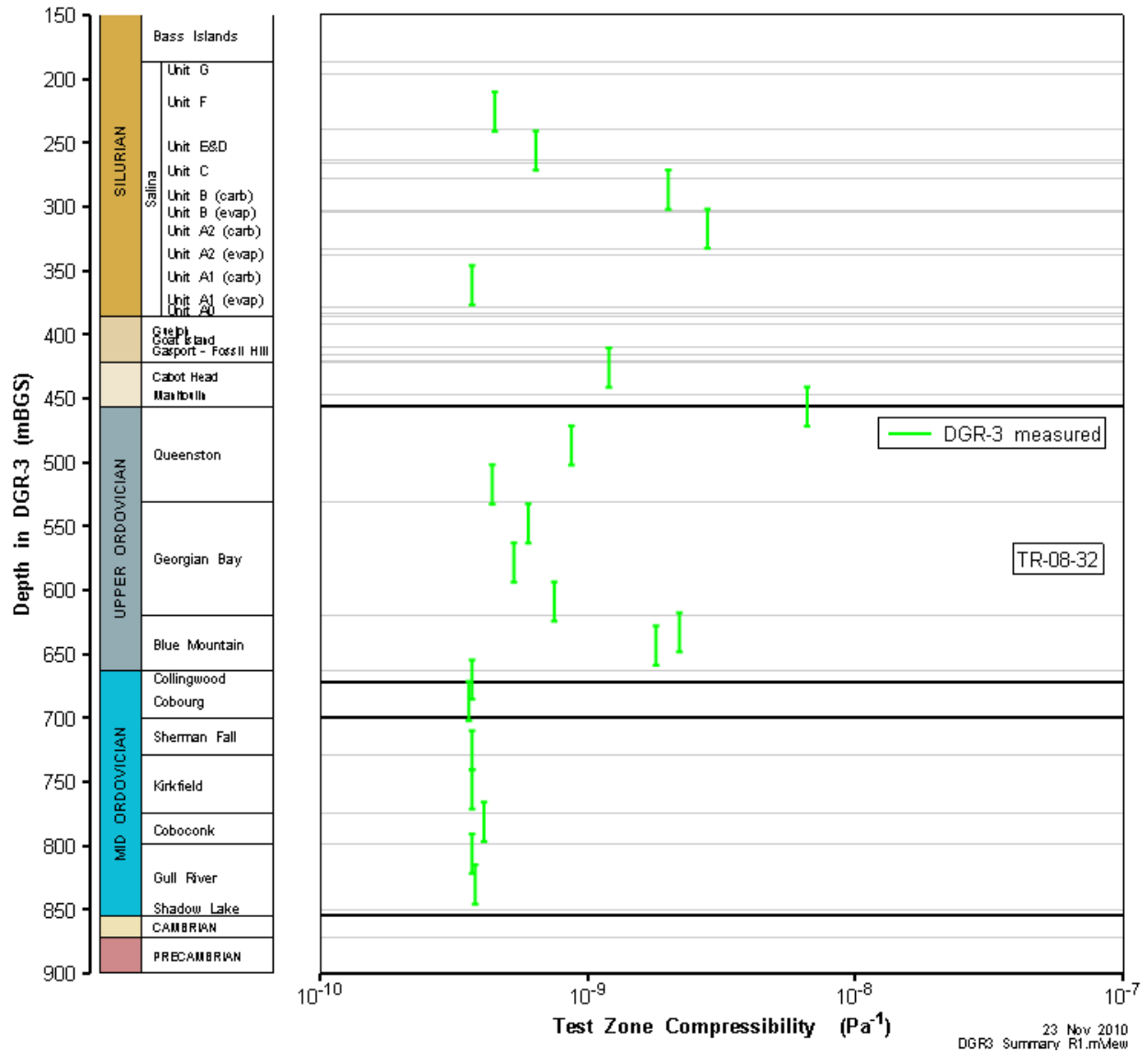


Figure 7-74: DGR-3 stratigraphic profile of test-zone compressibility estimates.

8 DGR-4 Testing And Analysis

Hydraulic testing in DGR-4 was performed from 25 November 2008 until 22 February 2009. Testing was initiated at the top of the Salina F unit and then proceeded consecutively down the borehole using a 30.74-m straddle interval, providing continuous coverage of the borehole from 190.63 to 824.08 m BGS. Table 8-1 lists the formations and intervals tested and the types of tests performed. Pulse tests were performed in all but three intervals in DGR-4. Slug tests were performed in four intervals.

Table 8-1: DGR-4 test zones and tests

Formations / Units/Member	Top of Test Zone (m BGS)	Bottom of Test Zone (m BGS)	Type(s) of Test(s)
Salina F	190.63	221.37	PW, PI
Salina E-D	218.13	248.87	PI, PW
Salina C-B	247.00	277.74	PI, PW
Salina B	261.63	292.37	PW
Salina B-A2 carbonate	284.26	315.00	SW
Salina A2-A1 carbonate	296.63	327.37	SW, SI
Salina A1 carbonate	327.26	358.00	PW, SW, SI
Salina A1-A0-Guelph	350.53	381.27	SW, SI
Goat Island-Gasport-Lions Head-Fossil Hill	381.08	411.82	PW, PI
Cabot Head-Manitoulin	411.51	442.25	PW, PI
Manitoulin-Queenston	432.00	462.74	PW
Queenston	458.23	488.97	PW
Queenston	488.77	519.51	PW
Georgian Bay	519.10	549.84	PW
Georgian Bay (a & b)	548.28	579.02	PW
Georgian Bay	577.45	608.19	PW
Blue Mountain	607.79	638.53	PW
Blue Mountain-Collingwood-Cobourg	638.34	669.08	PW
Cobourg	658.46	689.20	PW
Sherman Fall	687.78	718.52	PW
Kirkfield	717.10	747.84	PW
Kirkfield-Coboconk	747.64	778.38	PW, PI
Coboconk-Gull River	762.80	793.54	PI, PW
Gull River	793.34	824.08	PI, PW
Reference Elevation – Ground Surface	181.60 m above mean sea level		

PW: pulse withdrawal

PI: pulse injection

SW: slug withdrawal

SI: slug injection

The test-zone transducer during DGR-4 testing was located 26.64 m above the middle of the isolated test zone and was hydraulically connected to the test zone via a length of 1/4-in stainless-steel tubing. To determine the P_f values corresponding to the middle of the test zone, the “raw” (as measured by the transducer) P_f estimates were depth-corrected using the offset distance of 26.64 m and fluid density values calculated prior to the start of each test. Fluid density was calculated using annulus-transducer pressure readings and the measured height of the annulus fluid column. The depth-corrected P_f estimates are given in the tables below whereas the raw P_f estimates are listed in the graph annotations.

Results of each test analysis are discussed below. A summary of DGR-4 testing results is presented in Section 8.26.

8.1 190.63-221.37 Salina F

The DGR-4 interval from 190.63 to 221.37 m BGS included the lower 30.37 m of the Salina Unit F and the upper 0.37 m of the Salina Unit E, both of which consist of dolomitic shale and dolostone. An overview of the testing in this interval is given in Table 8-2 and the corresponding parameter estimates are given in Table 8-3. A pulse-withdrawal test and a short pulse-injection test that was not analyzed were conducted in this interval.

Table 8-2: Summary of the DGR4_190.63-221.37 testing activities.

Formation / Unit		Top of Test Zone (m BGS)		Bottom of Test Zone (m BGS)	
Salina F		190.63		221.37	
Test	Initiated	Magnitude (kPa)	Duration	Compressibility (Pa ⁻¹)	
Shut-in	25-11-08 14:25	N/A	18.5 hr	N/A	
PW	26-11-08 08:57	731	24 hr	4.5E-10	
PI	27-11-08 09:23	758	23 hr	4.3E-10	
Borehole Pressure History					
Event		Start		Pressure (kPa)	
Drilling Intercept		09-09-08 16:40		2034	
End of Geophysical Logging		30-10-08 12:00		1766	
Prior Testing		N/A		N/A	
Shut-in		25-11-08 14:25		1823	

Table 8-3: Summary of the DGR3_190.63-221.37 parameter estimates.

Parameter	Best Fit	Minimum	Maximum	Mean
K_f (m/s)	5.6E-14	3.6E-16	6.1E-14	5.0E-14
P_f (kPa)	1563	1454	1583	1534
K_s (m/s)	9.3E-14	8.8E-14	9.8E-13	9.2E-14
t_s (cm)	17	14	31	20
S_s (m ⁻¹)	9.9E-7	9.3E-7	1.1E-6	9.9E-7

Figure 8-1 shows the measured pressure record from DGR4_190.63-221.37 used in this analysis along with the best-fit simulation and parameter values. The ranges of formation K and raw P_f values estimated from perturbation analysis are shown in Figure 8-2 and the fit value cumulative distribution function is shown in Figure 8-3.

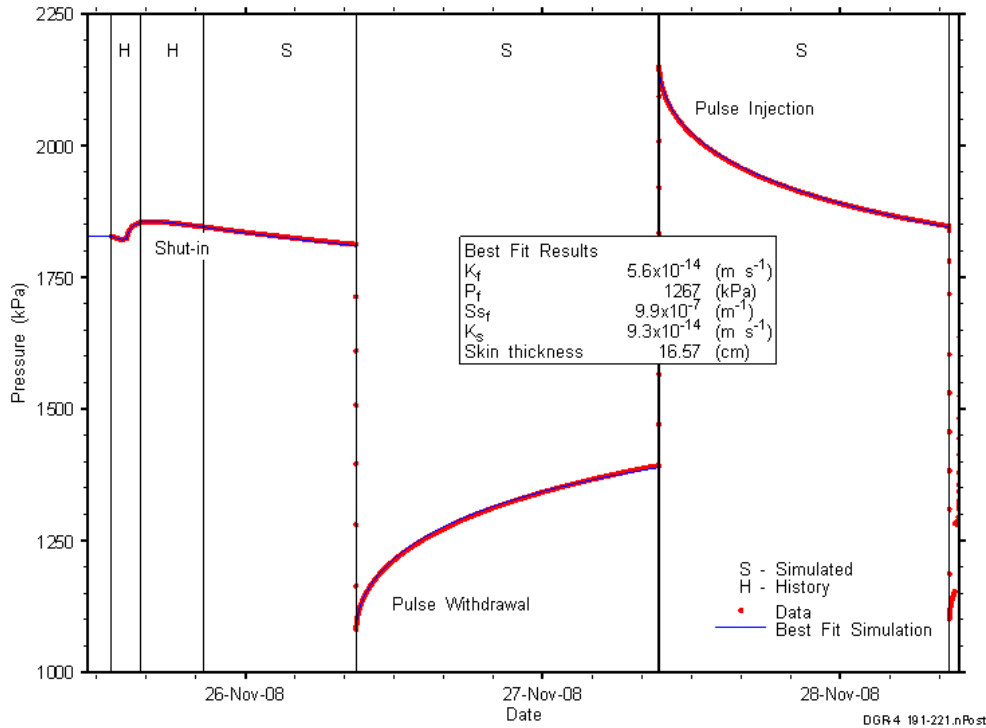


Figure 8-1: Annotated DGR4_190.63-221.37 testing sequence showing best-fit simulation and parameter estimates.

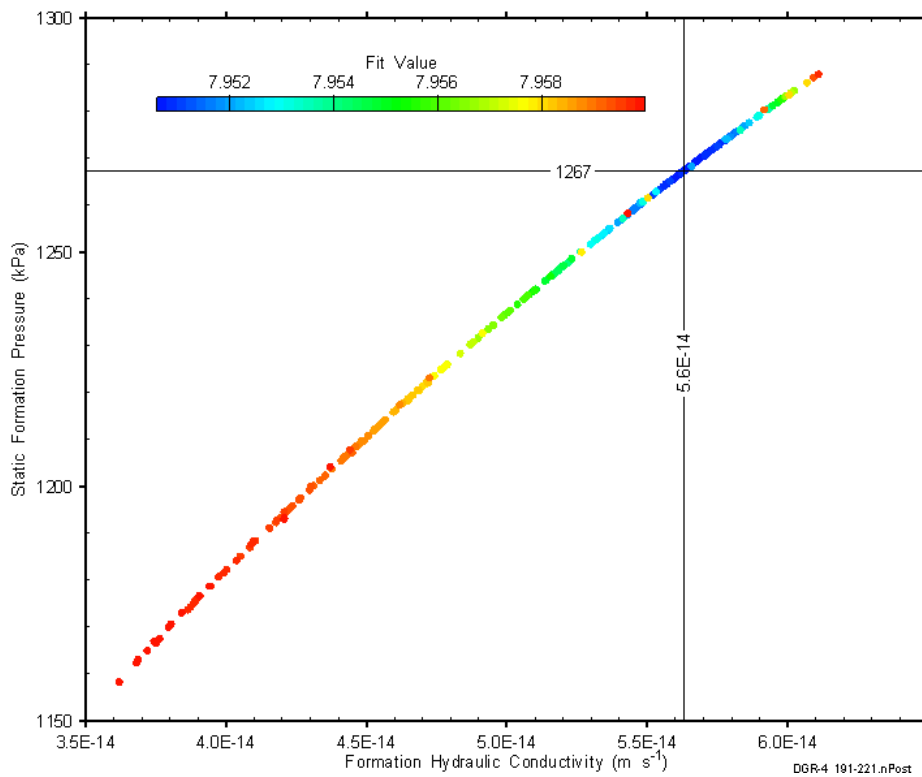


Figure 8-2: XY-scatter plot showing estimates of formation hydraulic conductivity and raw static formation pressure derived from the DGR4_190.63-221.37 perturbation analysis.

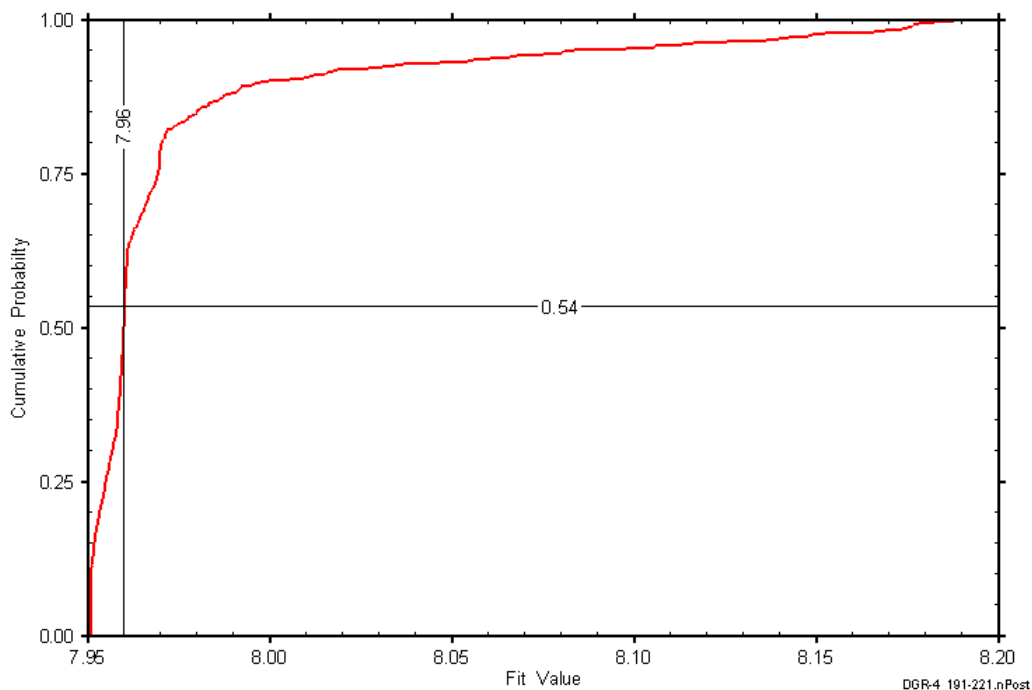


Figure 8-3: DGR4_190.63-221.37 fit value cumulative distribution function.

8.2 218.13-248.87 Salina F-C

The DGR-4 interval from 218.13 to 248.87 m BGS included the lower 2.87 m of the Salina F Unit, the entire 24.5-m thickness of the Salina Unit E, the entire 1.8-m thickness of the Salina Unit D, and the upper 1.57 m of the Salina Unit C. The lowermost Unit F consists of dolomitic shale and dolostone, Unit E consists of dolomitic shale and dolostone with anhydrite, Unit D is an anhydritic dolostone and dolomitic shale, and the upper part of Unit C is primarily dolomitic shale. An overview of the testing in this interval is given in Table 8-4 and the corresponding parameter estimates are given in Table 8-5. A pulse-injection test and a pulse-withdrawal test were conducted in this interval.

Table 8-4: Summary of the DGR4_218.13-248.87 testing activities.

Formation / Unit		Top of Test Zone (m BGS)	Bottom of Test Zone (m BGS)	
Salina F-C		218.13	248.87	
Test	Initiated	Magnitude (kPa)	Duration	Compressibility (Pa ⁻¹)
Shut-in	28-11-08 12:52	N/A	20 hr	N/A
PI	29-11-08 08:49	779	24 hr	4.2E-10
PW	30-11-08 09:19	765	23 hr	4.3E-10
Borehole Pressure History				
Event	Start		Pressure (kPa)	
Drilling Intercept	10-09-08 17:00		2330	
End of Geophysical Logging	30-10-08 12:00		2063	
Prior Testing	25-11-08 13:12		N/A	
Shut-in	28-11-08 12:52		2086	

Table 8-5: Summary of the DGR3_218.13-248.87 parameter estimates.

Parameter	Best Fit	Minimum	Maximum	Mean
K_f (m/s)	4.1E-13	3.9E-13	4.2E-13	4.1E-13
P_f (kPa)	1945	1933	1954	1946
K_s (m/s)	1.1E-12	5.6E-13	2.7E-12	1.2E-12
t_s (cm)	26	15	74	29
S_s (m^{-1})	1.2E-7	1.4E-8	3.6E-7	9.8E-8

Figure 8-4 shows the measured pressure record from DGR4_218.13-248.87 used in this analysis along with the best-fit simulation and parameter values. The ranges of formation K and raw P_f values estimated from perturbation analysis are shown in Figure 8-5 and the fit value cumulative distribution function is shown in Figure 8-6.

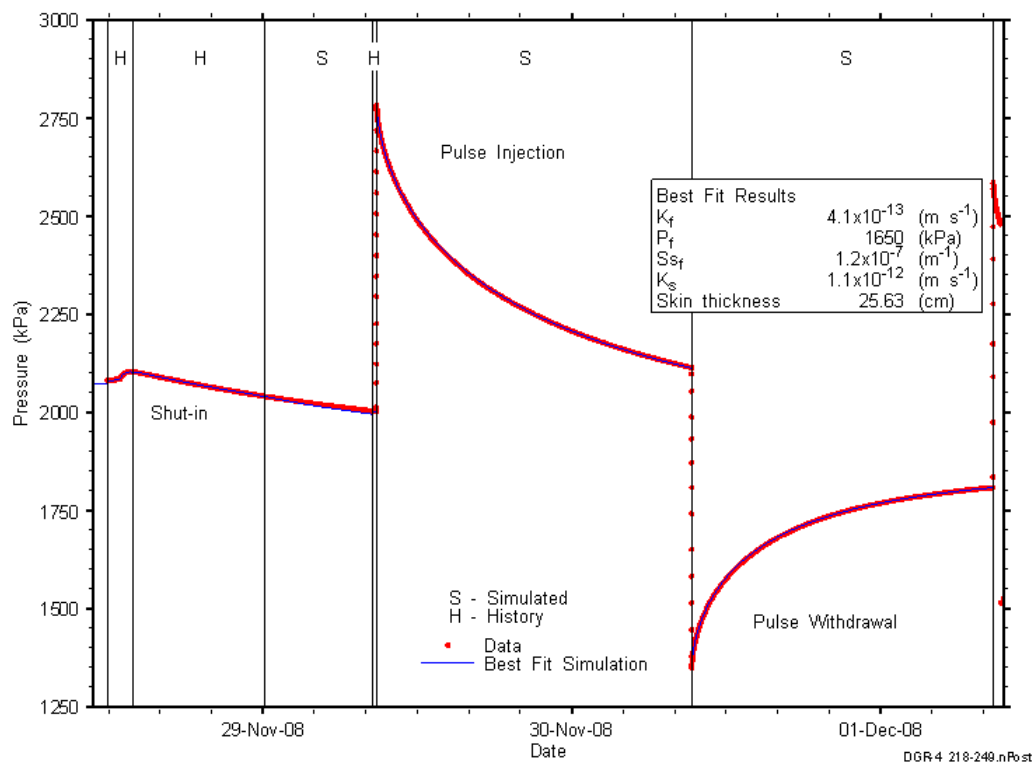


Figure 8-4: Annotated DGR4_218.13-248.87 testing sequence showing best-fit simulation and parameter estimates.

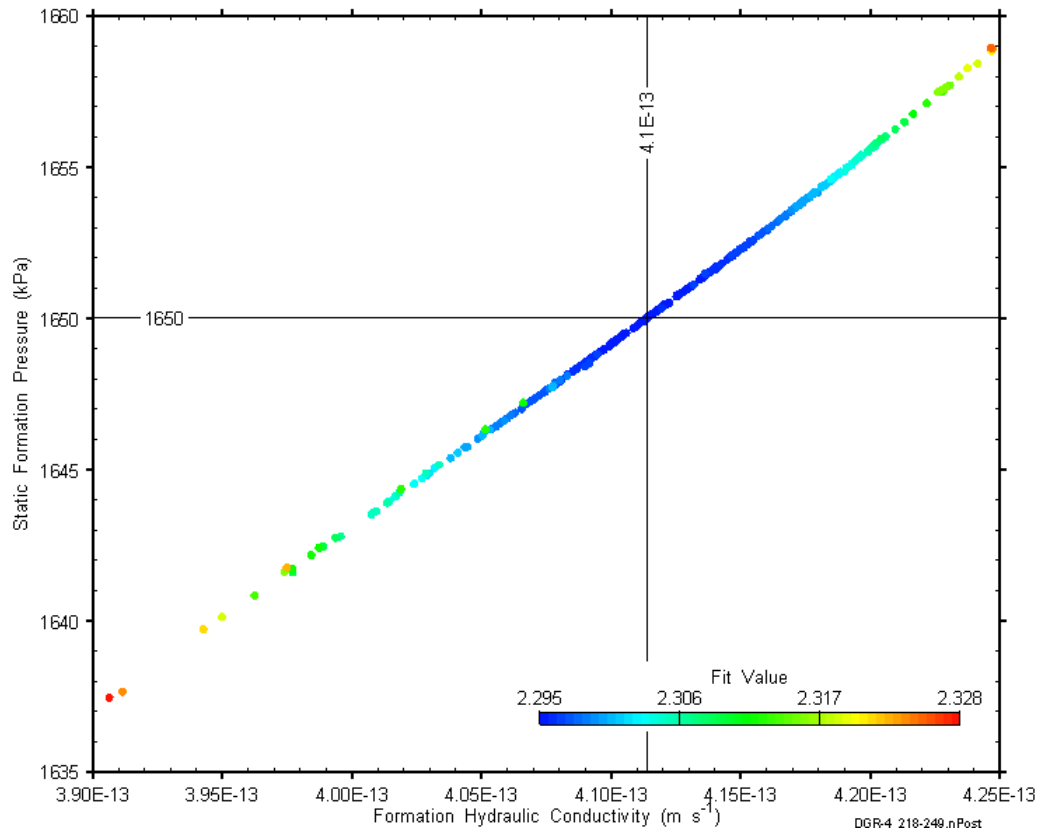


Figure 8-5: XY-scatter plot showing estimates of formation hydraulic conductivity and raw static formation pressure derived from the DGR4_218.13-248.87 perturbation analysis.

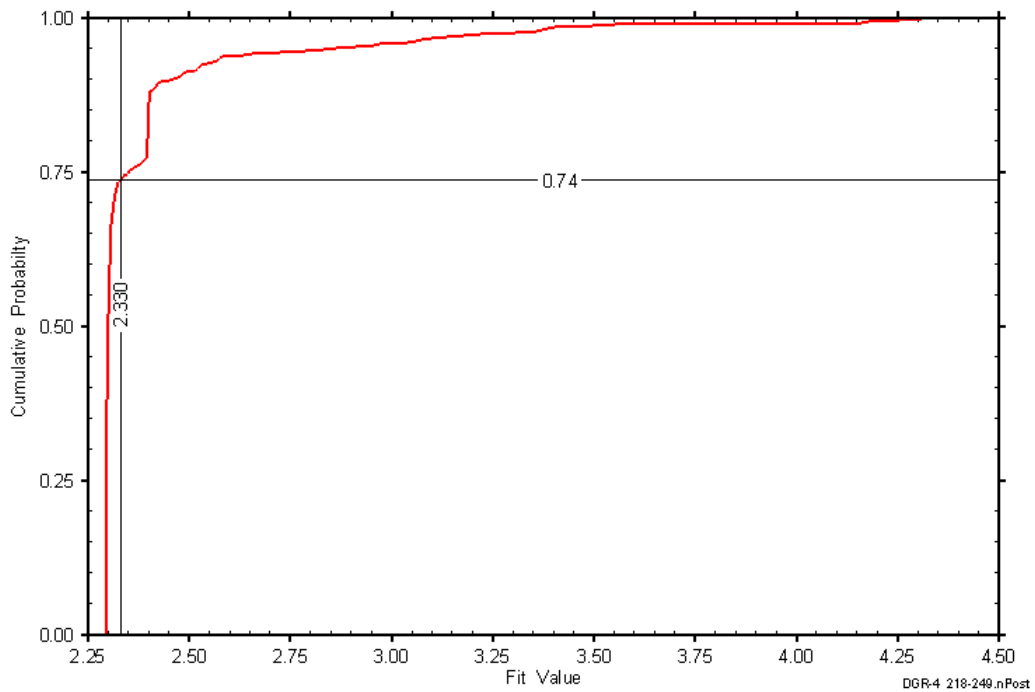


Figure 8-6: DGR4_218.13-248.87 fit value cumulative distribution function.

8.3 247.00-277.74 Salina C-B

The DGR-4 interval from 247.00 to 277.74 m BGS included the lower 0.3 m of the Salina Unit D, the entire 14.7-m thickness of Salina Unit C, and the upper 15.74 m of the Salina Unit B carbonate. The lowermost Unit D consists of dolomitic shale and dolostone, Unit C is dolomitic shale and dolostone, and the Unit B carbonate consists of anhydritic dolostone and dolomitic shale. An overview of the testing in this interval is given in Table 8-6 and the corresponding parameter estimates are given in Table 8-7. A pulse-injection test and a pulse-withdrawal test were conducted in this interval.

Table 8-6: Summary of the DGR4_247.00-277.74 testing activities.

Formation / Unit		Top of Test Zone (m BGS)		Bottom of Test Zone (m BGS)	
Salina C-B		247.00		277.74	
Test	Initiated	Magnitude (kPa)	Duration	Compressibility (Pa ⁻¹)	
Shut-in	01-12-08 13:46	N/A	19 hr	N/A	
PI	02-12-08 08:30	246	24 hr	1.1E-9	
PW (pt 1)	03-12-08 09:03	317	13 min	N/A	
PW (pt 2)	03-12-08 09:17	199	24	1.4E-9	
Borehole Pressure History					
Event		Start		Pressure (kPa)	
Drilling Intercept		11-09-08 08:13		2641	
End of Geophysical Logging		30-10-08 12:00		2374	
Prior Testing		25-11-08 13:12		N/A	
Shut-in		01-12-08 13:46		2379	

Table 8-7: Summary of the DGR3_247.00-277.74 parameter estimates.

Parameter	Best Fit	Minimum	Maximum	Mean
K_f (m/s)	4.7E-13	4.7E-13	4.7E-13	4.7E-13
P_f (kPa)	1975	1975	1975	1975
S_s (m ⁻¹)	4.7E-6	4.7E-6	4.7E-6	4.7E-6

Figure 8-7 shows the measured pressure record from DGR4_247.00-277.74 used in this analysis along with the best-fit simulation and parameter values. The ranges of formation K and raw P_f values estimated from perturbation analysis are shown in Figure 8-8 and the fit value cumulative distribution function is shown in Figure 8-9.

Preliminary analysis showed that including a skin in the DGR4_247.00-277.74 conceptual model resulted in orders-of-magnitude uncertainty in the fitting parameters for very little improvement in the fit. This suggested that including a borehole skin resulted in an over-parameterized model, so a skin was not included in the final analysis.

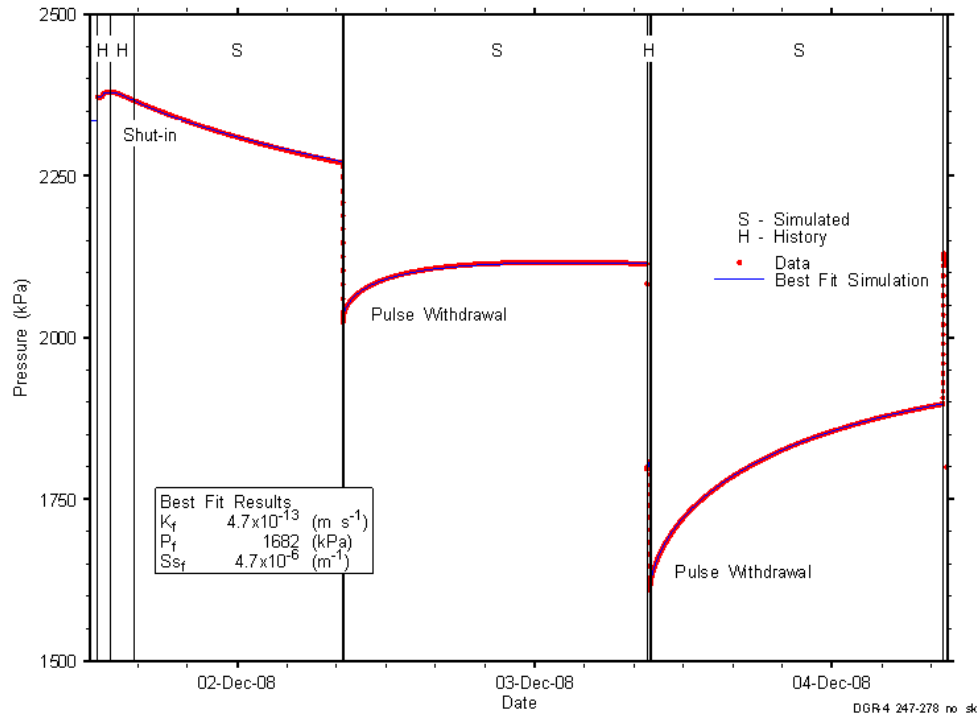


Figure 8-7: Annotated DGR4_247.00-277.74 testing sequence showing best-fit simulation and parameter estimates.

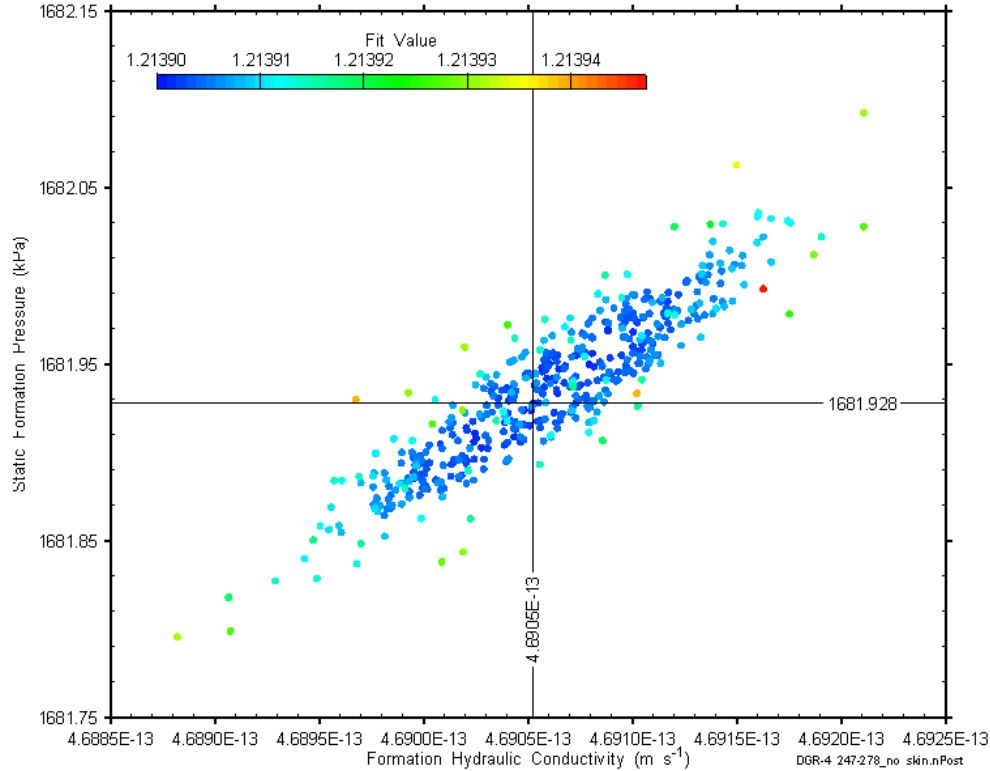


Figure 8-8: XY-scatter plot showing estimates of formation hydraulic conductivity and raw static formation pressure derived from the DGR4_247.00-277.74 perturbation analysis.

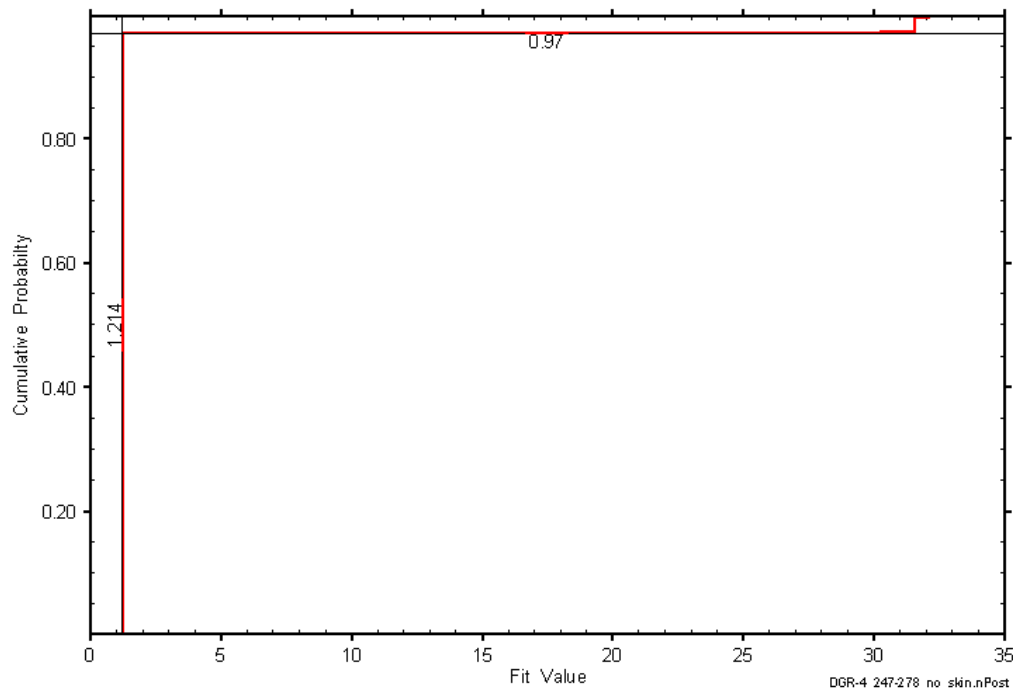


Figure 8-9: DGR4_247.00-277.74 fit value cumulative distribution function.

8.4 261.63-292.37 Salina B

The DGR-4 interval from 261.63 to 292.37 m BGS included the lower 0.37 m of the Salina Unit C, the entire 28.8-m thickness of the Unit B carbonate, and all but the lower 0.13 m of the 1.7-m thickness of the Salina Unit B evaporite. The lowermost Unit C carbonate consists of dolomitic shale, the Unit B carbonate consists of anhydritic dolostone and dolomitic shale, and the Unit B evaporite consists of anhydritic and dolomitic shale. An overview of the testing in this interval is given in Table 8-4 and the corresponding parameter estimates are given in Table 8-5. Two pulse-withdrawal tests were performed in this interval.

Table 8-8: Summary of the DGR4_261.63-292.37 testing activities.

Formation / Unit		Top of Test Zone (m BGS)	Bottom of Test Zone (m BGS)	
Salina B		261.63	292.37	
Test	Initiated	Magnitude (kPa)	Duration	Compressibility (Pa ⁻¹)
Shut-in	04-12-08 14:24	N/A	19 hr	N/A
PW1	05-12-08 09:01	314	24 hr	9.5E-10
PW2 (pt 1)	06-12-08 09:29	548	17 min	N/C
PW2 (pt 2)	06-12-08 09:47	245	47 hr	1.2E-09
Borehole Pressure History				
Event	Start	Pressure (kPa)		
Drilling Intercept	11-09-08 12:53	2799		
End of Geophysical Logging	30-10-08 12:00	2532		
Prior Testing	25-11-08 13:12	N/A		
Shut-in	04-12-08 14:24	2569		

Table 8-9: Summary of the DGR4_261.63-292.37 parameter estimates.

Parameter	Best Fit	Minimum	Maximum	Mean
K_f (m/s)	3.1E-13	2.7E-13	3.1E-13	3.0E-13
P_f (kPa)	1919	1865	1934	1917
K_s (m/s)	2.2E-12	5.4E-13	6.3E-12	2.2E-12
t_s (cm)	26	5.1	127	30
S_s (m ⁻¹)	2.0E-7	1.1E-8	1.6E-6	1.9E-7

Figure 8-10 shows the measured pressure record from DGR4_261.63-292.37 used in this analysis along with the best-fit simulation and parameter values. The ranges of formation K and raw P_f values estimated from perturbation analysis are shown in Figure 8-11 and the fit value cumulative distribution function is shown in Figure 8-12.

Test-zone compressibility (C_{tz}) was assumed to be pressure-dependent in this analysis. Pressure-dependent C_{tz} has been observed in other testing programs using similar testing equipment when the system pressure dropped below 2000 kPa (Beauheim et al., 1993). Test-zone compressibility was assumed to vary linearly between the two values listed in Table 8-8. Including pressure-dependent C_{tz} was necessary to obtain reasonable fits to both pulses with a single parameter set.

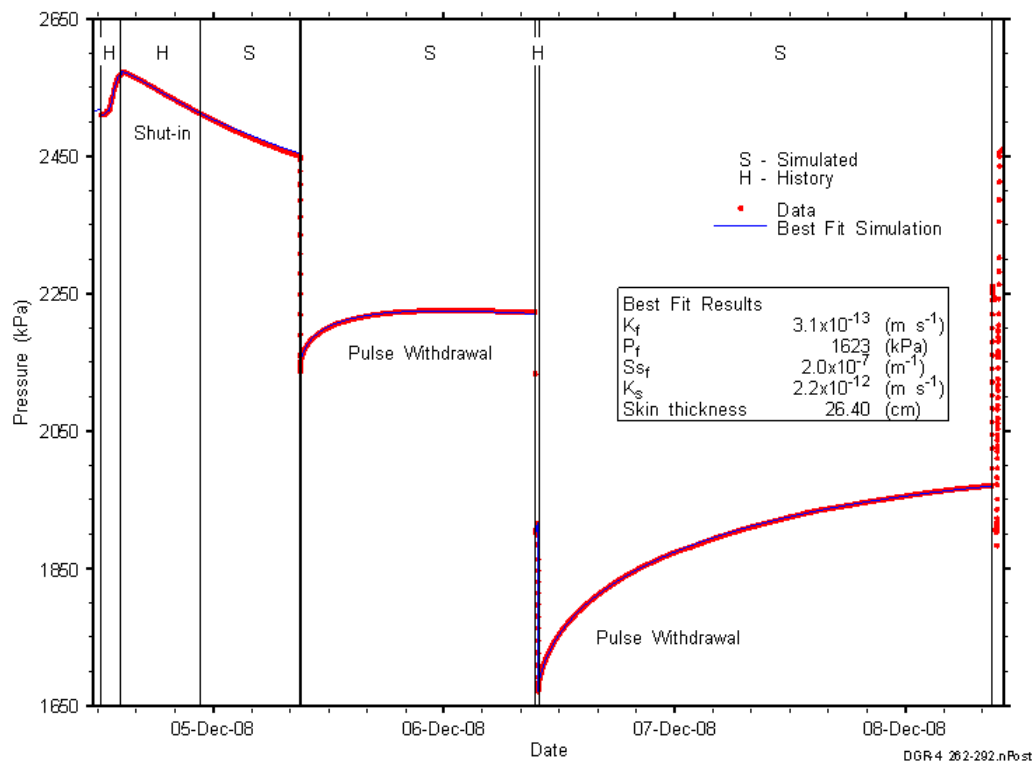


Figure 8-10: Annotated DGR4_261.63-292.37 testing sequence showing best-fit simulation and parameter estimates.

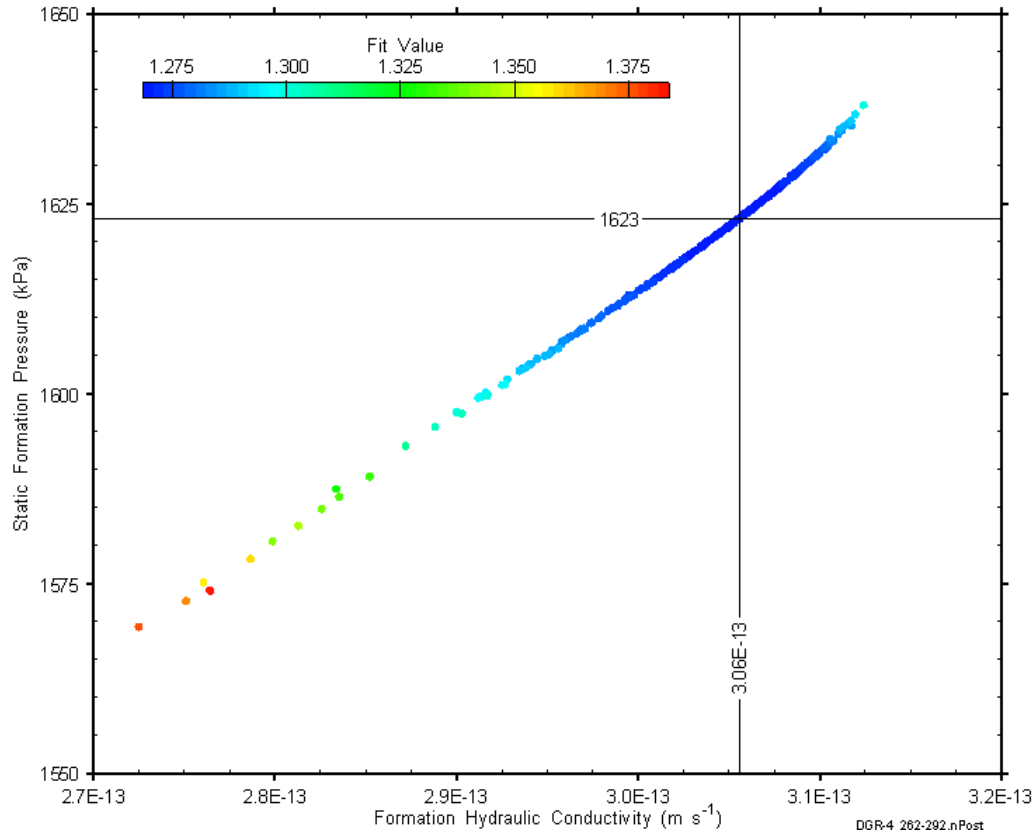


Figure 8-11: XY-scatter plot showing estimates of formation hydraulic conductivity and raw static formation pressure derived from the DGR4_261.63-292.37 perturbation analysis.

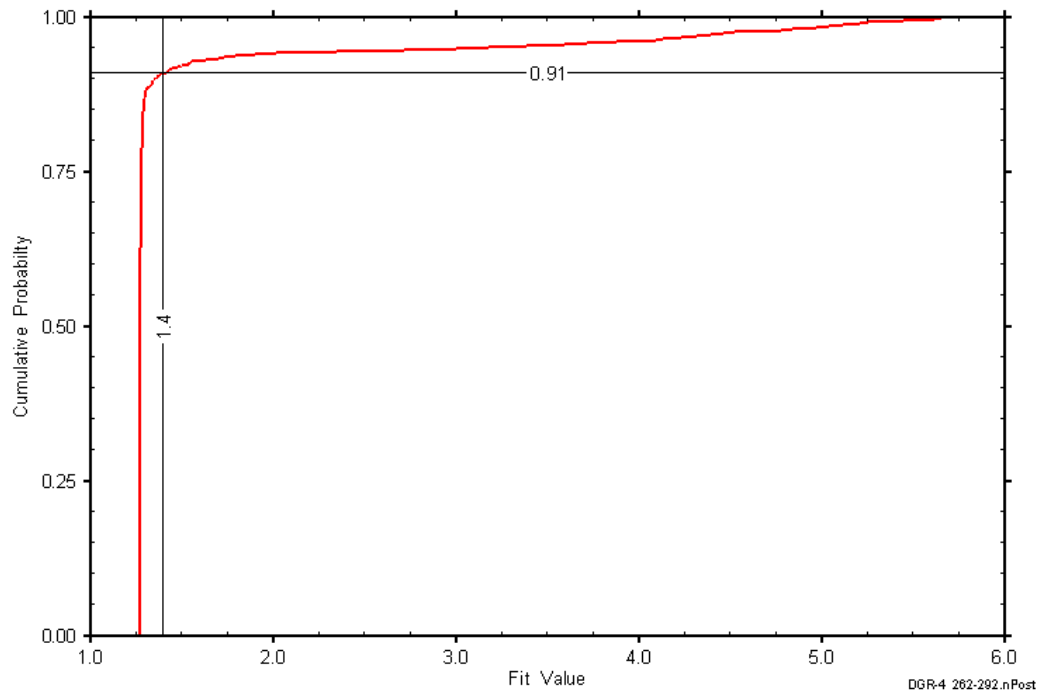


Figure 8-12: DGR4_261.63-292.37 fit value cumulative distribution function.

8.5 284.26-315.00 Salina B-A2 Carbonate

The DGR-4 interval from 284.26 to 315.00 m BGS included the lower 1.19 m of the Salina Unit B carbonate, the 1.7-m-thick Unit B evaporite, and the upper 22.5 m of the Salina Unit A2 carbonate. The Unit B carbonate consists of anhydritic dolostone and dolomitic shale, the Unit B evaporite consists of anhydritic and dolomitic shale, and the Unit A2 carbonate is argillaceous dolomite and dolostone, dolomitic shale, and anhydritic dolostone. An overview of the testing in this interval is given in Table 8-10 and the corresponding parameter estimates are given in Table 8-11. A slug test was performed in this interval, so no data are available to estimate test-zone compressibility. A slug-withdrawal test was performed in this interval.

Table 8-10: Summary of the DGR4_284.26-315.00 testing activities.

Formation / Unit		Top of Test Zone (m BGS)	Bottom of Test Zone (m BGS)	
Salina B-A2 carbonate		284.26	315.00	
Test	Initiated	Magnitude (kPa)	Duration	Compressibility (Pa ⁻¹)
Shut-in	21-02-09 14:28	N/A	2.7 hr	N/A
SW	21-02-09 17:11	506	16 hr	N/A
Borehole Pressure History				
Event	Start		Pressure (kPa)	
Drilling Intercept	12-09-08 02:36		3043	
End of Geophysical Logging	30-10-08 12:00		2775	
Prior Testing	25-11-08 13:12		N/A	
Shut-in	21-02-09 14:28		2627	

Table 8-11: Summary of the DGR4_284.26-315.00 parameter estimates.

Parameter	Best Fit	Minimum	Maximum	Mean
K_f (m/s)	4.5E-10	1.4E-10	3.5E-9	4.2E-10
P_f (kPa)	3182	3000	3668	3255
K_s (m/s)	6.4E-11	4.0E-11	1.6E-10	7.7E-11
t_s (cm)	5.9	2.7	24	8.4
S_s (1/m)	8.5E-5	1.9E-5	1E-4	5.8E-5

Figure 8-13 shows the measured pressure record from DGR4_284.26-315.00 used in this analysis along with the best-fit simulation and parameter values. The ranges of formation K and raw P_f values estimated from perturbation analysis are shown in Figure 8-14 and the fit value cumulative distribution function is shown in Figure 8-15.

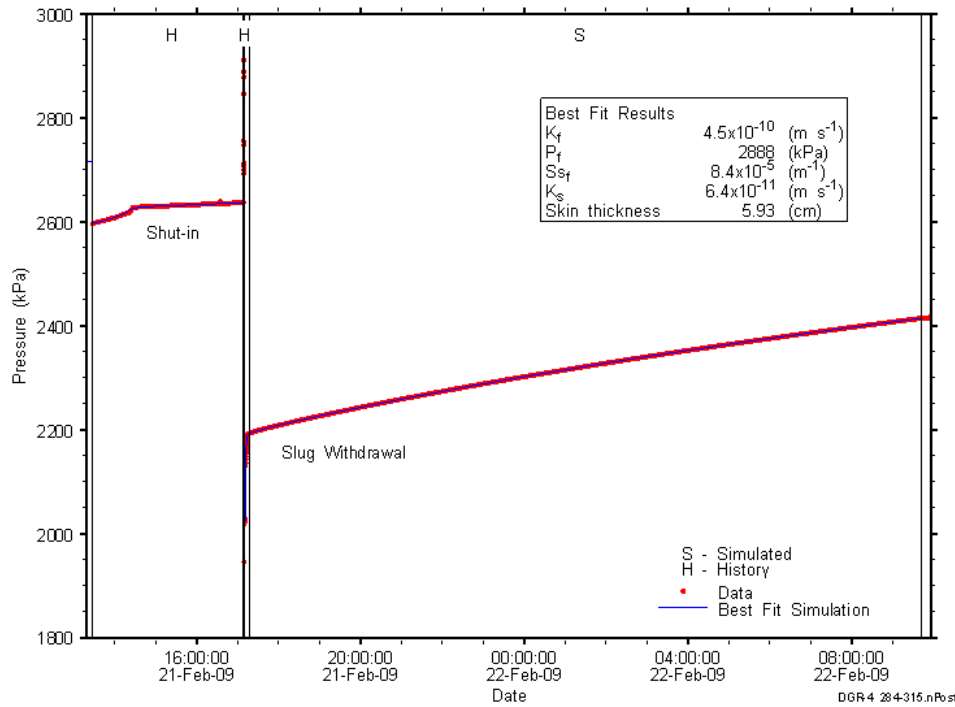


Figure 8-13: Annotated DGR4_284.26-315.00 testing sequence showing best-fit simulation and parameter estimates.

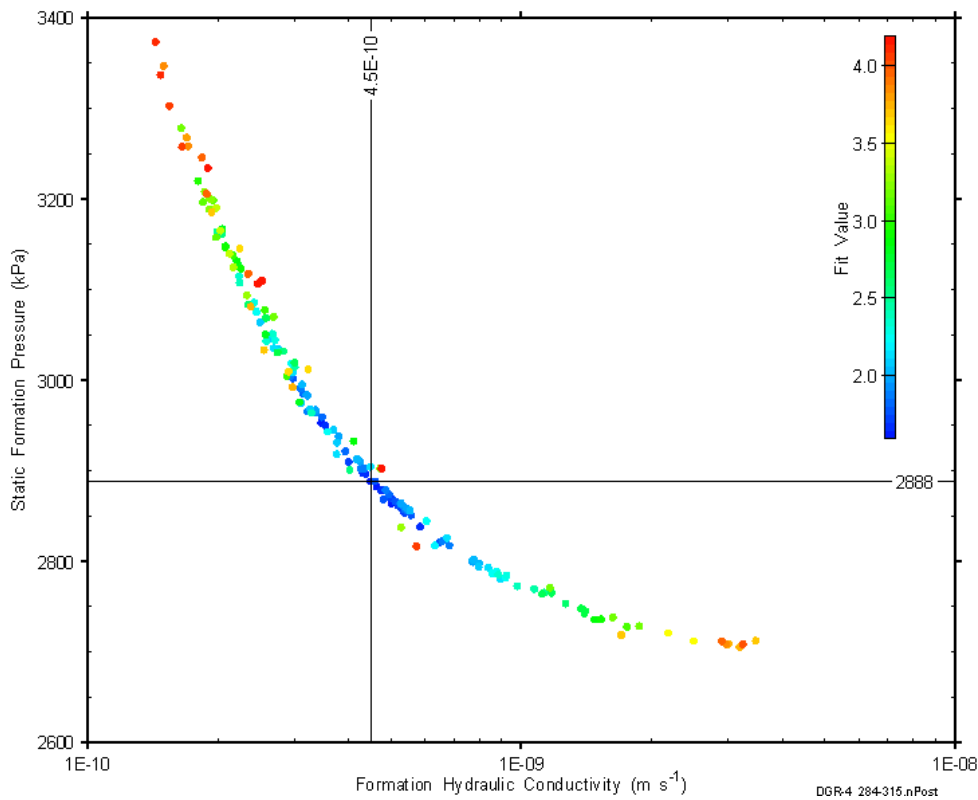


Figure 8-14: XY-scatter plot showing estimates of formation hydraulic conductivity and raw static formation pressure derived from the DGR4_284.26-315.00 perturbation analysis.

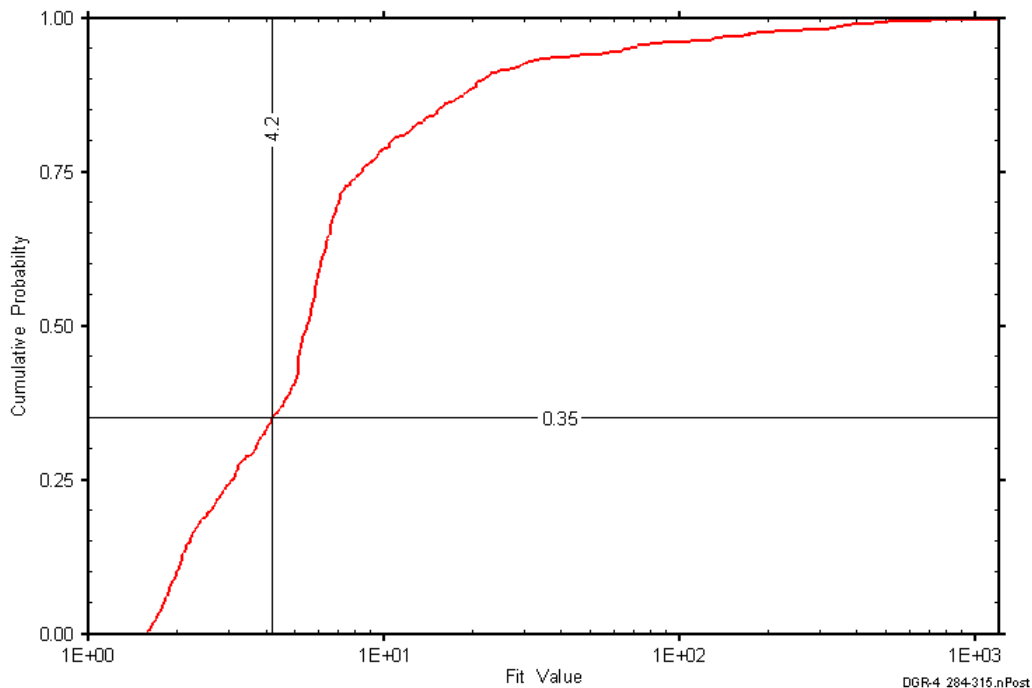


Figure 8-15: DGR4_284.26-315.00 fit value cumulative distribution function.

8.6 296.63-327.37 Salina A2- Upper A1 Carbonate

The DGR-4 interval from 296.63 to 327.37 m BGS included the lower 24.27 m of the Salina Unit A2 carbonate, the entire 5.2-m thickness of the Unit A2 evaporite, and the upper 1.27 m of the Salina Unit A1 carbonate. The Salina Unit A2 carbonate is argillaceous dolomite and dolostone, dolomitic shale, and anhydritic dolostone, and is locally fractured. The A2 evaporite is anhydritic and argillaceous dolostone and dolomitic shale, and the upper Unit A1 carbonate is a vuggy dolostone interbedded with dolomitic shale. An overview of the testing in this interval is given in Table 8-12 and the corresponding parameter estimates are given in Table 8-13. Slug-withdrawal and slug-injection tests were performed in this interval, providing no data to estimate test-zone compressibility.

Table 8-12: Summary of the DGR4_296.63-327.37 testing activities.

Formation / Unit		Top of Test Zone (m BGS)	Bottom of Test Zone (m BGS)	
Salina A2 carbonate		296.63	327.37	
Test	Initiated	Magnitude (kPa)	Duration	Compressibility (Pa ⁻¹)
Shut-in	08-12-08 15:37	N/A	2.4 hr	N/A
SW	08-12-08 18:03	666	15 hr	N/A
SI	09-12-08 09:32	517	4 hr	N/A
Borehole Pressure History				
Event	Start	Pressure (kPa)		
Drilling Intercept	12-09-08 10:37	3176		
End of Geophysical Logging	30-10-08 12:00	2909		
Prior Testing	25-11-08 13:12	N/A		
Shut-in	08-12-08 15:37	2221		

Table 8-13: Summary of the DGR4_296.63-327.37 parameter estimates.

Parameter	Best Fit	Minimum	Maximum	Mean
K_f (m/s)	1.7E-8	1.7E-8	1.7E-8	1.7E-8
P_f (kPa)	3197	3197	3197	3197
K_s (m/s)	8.0E-9	4.3E-9	9.2E-9	7.9E-9
t_s (cm)	56	13	104	58

Figure 8-16 shows the measured pressure record from DGR4_296.63-327.37 used in this analysis along with the best-fit simulation and parameter values. The S_s value for this analysis was fixed at $1E-6 m^{-1}$, a value estimated from preliminary perturbation analysis. The ranges of formation K and raw P_f values estimated from perturbation analysis are shown in Figure 8-17 and the fit value cumulative distribution function is shown in Figure 8-18.

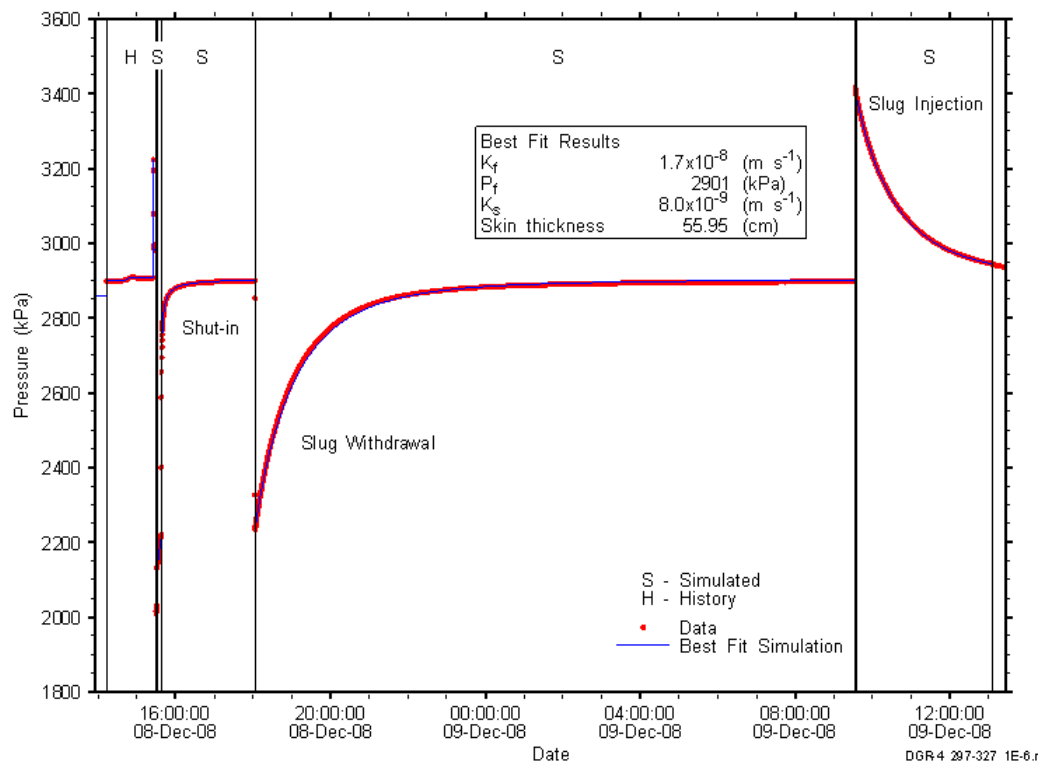


Figure 8-16: Annotated DGR4_296.63-327.37 testing sequence showing best-fit simulation and parameter estimates.

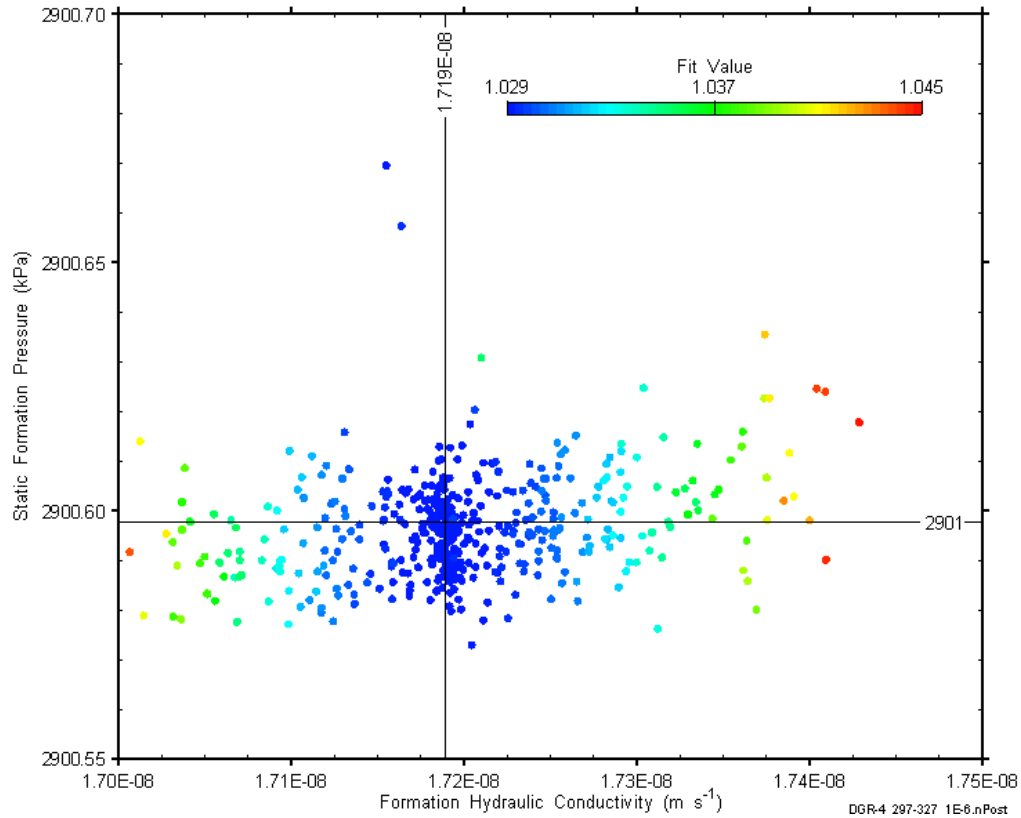


Figure 8-17: XY-scatter plot showing estimates of formation hydraulic conductivity and raw static formation pressure derived from the DGR4_296.63-327.37 perturbation analysis.

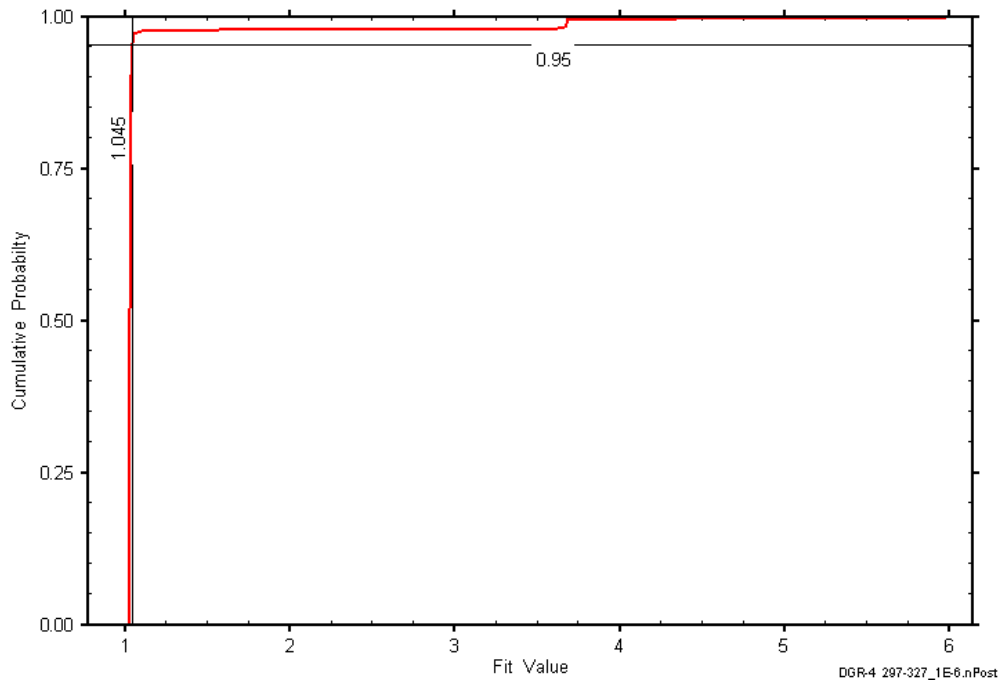


Figure 8-18: DGR4_296.63-327.37 fit value cumulative distribution function.

8.7 327.26-358.00 Salina A1 Carbonate

The DGR-4 interval from 327.26 to 358.00 m BGS was contained entirely within the Salina Unit A1 carbonate, although it did not include the upper 1.16 m of the unit. The portion of the Salina Unit A1 carbonate that was tested consists of dolostone that is locally argillaceous or anhydritic. The upper few metres of the dolostone are vuggy. An overview of the testing in this interval is given in Table 8-14 and the corresponding parameter estimates are given in Table 8-15. Pulse-withdrawal, slug-withdrawal, and slug-injection tests were conducted in this interval.

Table 8-14: Summary of the DGR4_327.26-358.00 testing activities.

Formation / Unit		Top of Test Zone (m BGS)		Bottom of Test Zone (m BGS)	
Salina A2E-A1C		327.26		358.00	
Test	Initiated	Magnitude (kPa)	Duration	Compressibility (Pa ⁻¹)	
Shut-in	09-12-08 16:44	N/A	16 hr	N/A	
PW	10-12-08 08:46	285	1 hr	5.2E-10	
SW	10-12-08 09:41	743	23 hr	N/A	
SI	11-12-08 09:44	608	22 hr	N/A	
Borehole Pressure History					
Event		Start		Pressure (kPa)	
Drilling Intercept		17-09-08 02:19		3506	
End of Geophysical Logging		30-10-08 12:00		3239	
Prior Testing		25-11-08 13:12		N/A	
Shut-in		09-12-08 16:44		3284	

Table 8-15: Summary of the DGR4_327.26-358.00 parameter estimates.

Parameter	Best Fit	Minimum	Maximum	Mean
K _f (m/s)	4.4E-8	3.2E-8	6.7E-8	4.4E-8
P _f (kPa)	3484	3483	3485	3484
K _s (m/s)	3.7E-10	3.6E-10	3.8E-10	3.7E-10
t _s (cm)	50	46	54	50

Figure 8-19 shows the measured pressure record from DGR4_327.26-358.00 used in this analysis along with the best-fit simulation and parameter values. The S_s value for this analysis was fixed at 1E-6 m⁻¹, a value estimated from preliminary perturbation analysis. The ranges of formation K and raw P_f values estimated from perturbation analysis are shown in Figure 8-20 and the fit value cumulative distribution function is shown in Figure 8-21.

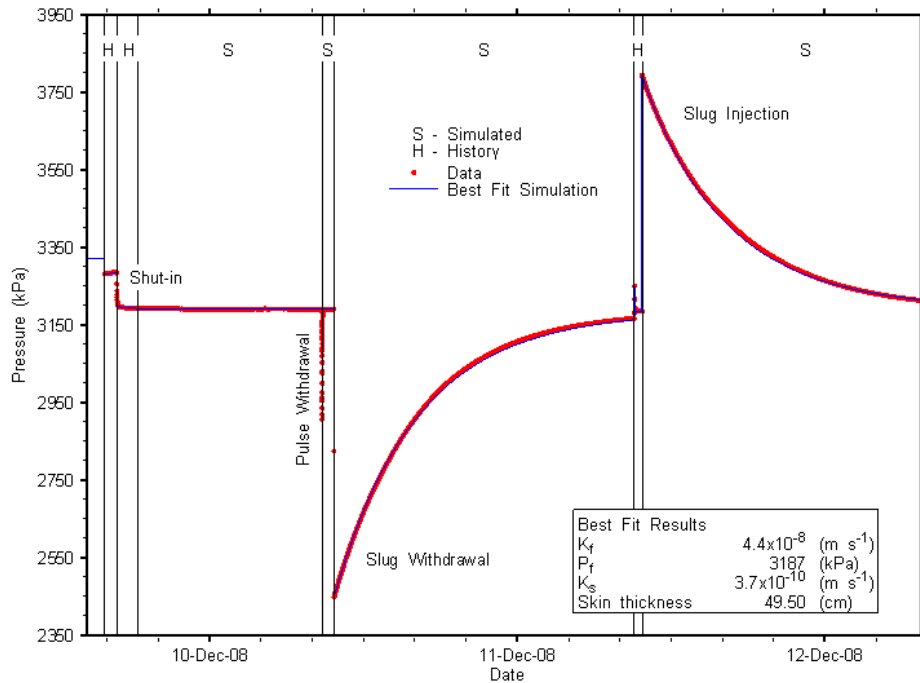


Figure 8-19: Annotated DGR4_327.26-358.00 testing sequence showing best-fit simulation and parameter estimates.

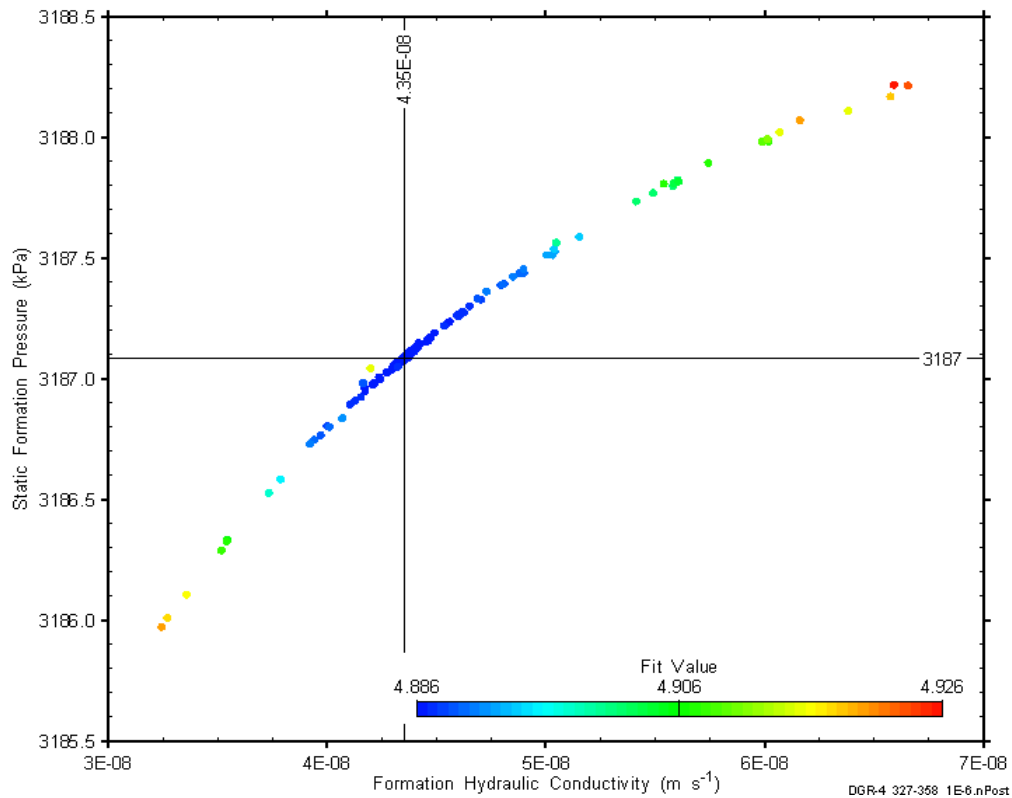


Figure 8-20: XY-scatter plot showing estimates of formation hydraulic conductivity and raw static formation pressure derived from the DGR4_327.26-358.00 perturbation analysis.

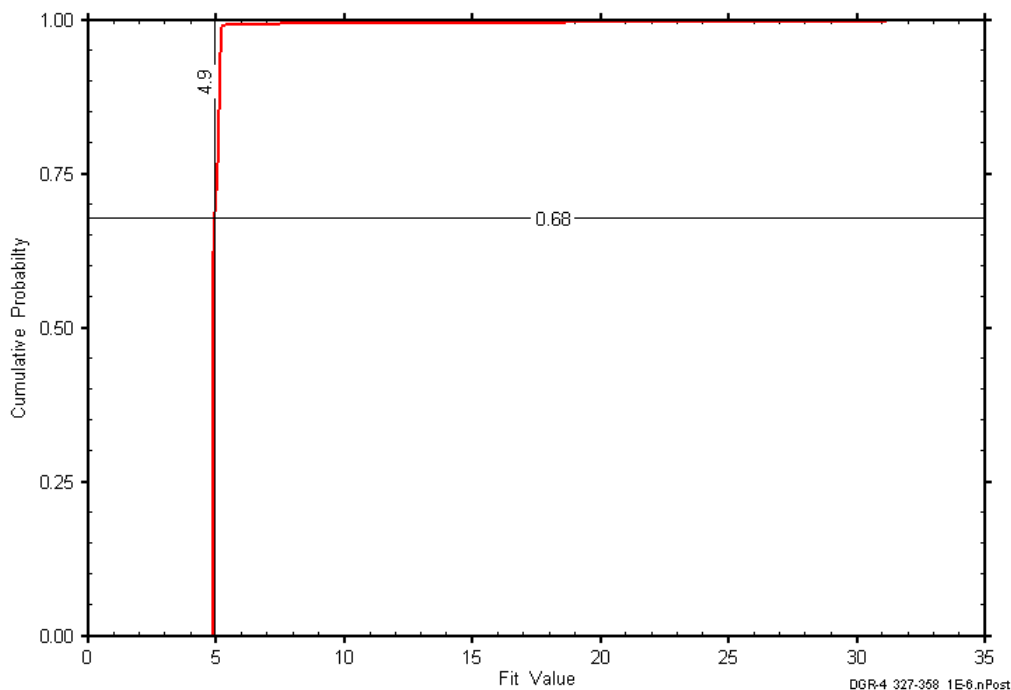


Figure 8-21: DGR4_327.26-358.00 fit value cumulative distribution function.

8.8 350.53-381.27 Salina A1-A0-Guelph-Goat Island

The DGR-4 interval from 350.53 to 381.27 m BGS included the lower 16.27 m of the Salina Unit A1 carbonate, the entire 5.0-m thickness of the Unit A1 evaporite, the entire 3.8-m thickness of the Salina Unit A0, the entire 4.9-m thickness of the Guelph Formation, and the upper 0.77 m of the Goat Island Member of the Lockport Formation. The Salina Unit A1 carbonate is argillaceous dolostone, the Unit A1 evaporite is anhydritic dolostone, the Unit A0 is a bituminous dolostone, the Guelph is vuggy, sucrosic dolostone, and the uppermost Goat Island is dolostone. An overview of the testing in this interval is given in Table 8-16 and the corresponding parameter estimates are given in Table 8-17. Only slug-withdrawal and slug-injection tests were performed in this interval, providing no data to estimate test-zone compressibility.

Table 8-16: Summary of the DGR4_350.53-381.27 testing activities.

Formation / Unit		Top of Test Zone (m BGS)	Bottom of Test Zone (m BGS)	
Salina A1-Guelph		350.53	381.27	
Test	Initiated	Magnitude (kPa)	Duration	Compressibility (Pa ⁻¹)
Shut-in	12-12-08 11:48	N/A	4.7 hr	N/A
SW	12-12-08 16:28	867	17 hr	N/A
SI	13-12-08 09:36	407	23 hr	N/A
Borehole Pressure History				
Event	Start		Pressure (kPa)	
Drilling Intercept	17-09-08 13:41		3757	
End of Geophysical Logging	30-10-08 12:00		3490	
Prior Testing	25-11-08 13:12		N/A	
Shut-in	12-12-08 11:48		3566	

Table 8-17: Summary of the DGR4_350.53-381.27 parameter estimates.

Parameter	Best Fit	Minimum	Maximum	Mean
K_f (m/s)	3.0E-9	3.0E-9	3.0E-9	3.0E-9
P_f (kPa)	3935	3934	3935	3935
K_s (m/s)	4.0E-8	1.8E-8	9.5E-5	1.1E-7
t_s (cm)	109	67	154	100

Figure 8-22 shows the measured pressure record from DGR4_350.53-381.27 used in this analysis along with the best-fit simulation and parameter values. The S_s value for this analysis was fixed at $1E-6\text{ m}^{-1}$, a value estimated from preliminary perturbation analysis. The ranges of formation K and raw P_f values estimated from perturbation analysis are shown in Figure 8-23 and the fit value cumulative distribution function is shown in Figure 8-24.

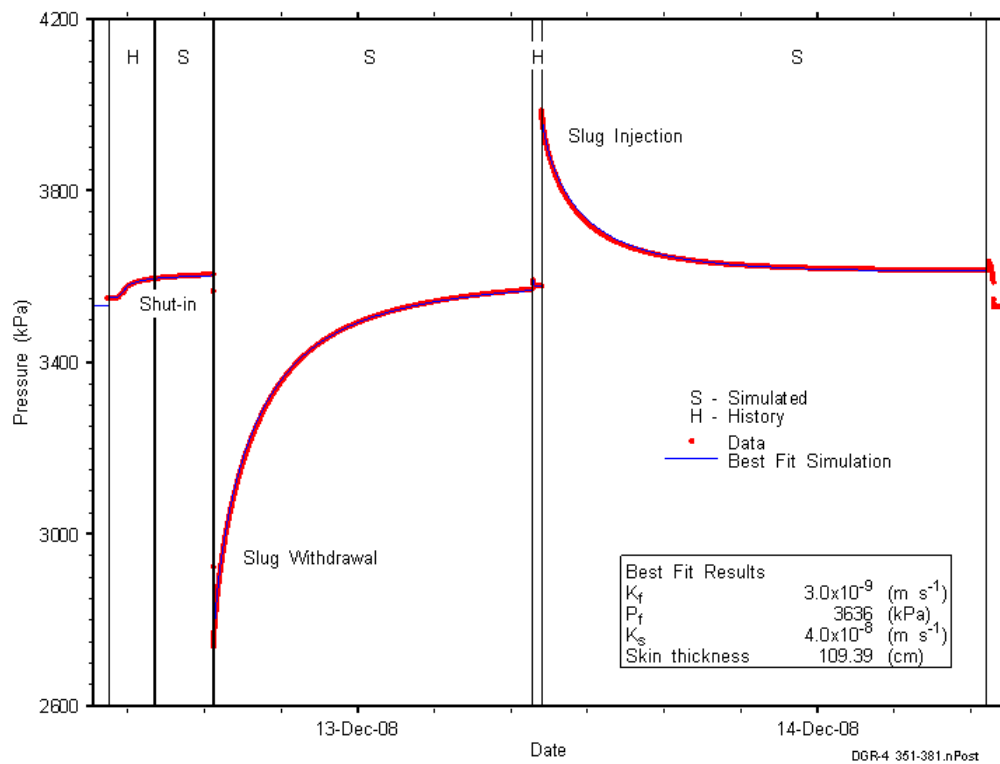


Figure 8-22: Annotated DGR4_350.53-381.27 testing sequence showing best-fit simulation and parameter estimates.

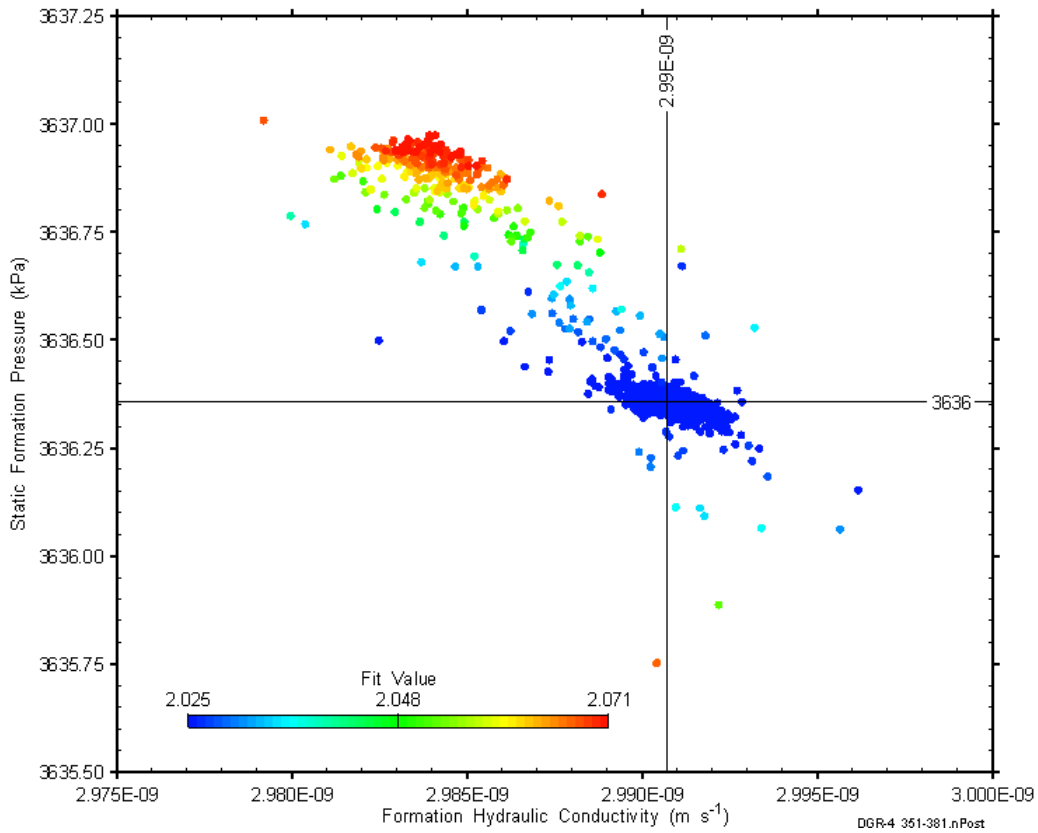


Figure 8-23: XY-scatter plot showing estimates of formation hydraulic conductivity and raw static formation pressure derived from the DGR4_350.53-381.27 perturbation analysis.

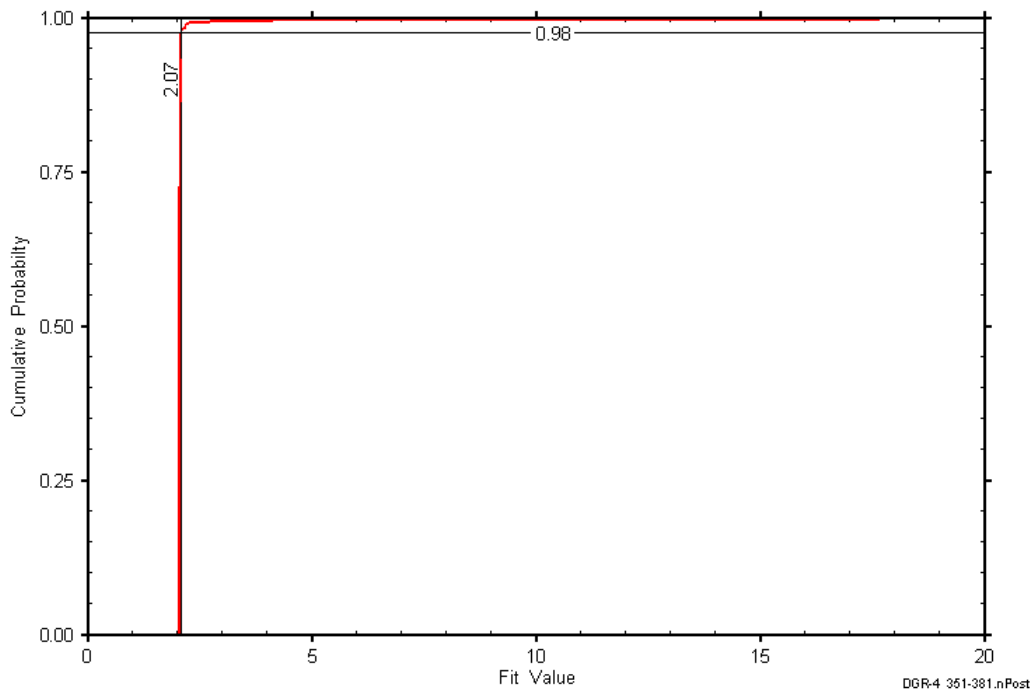


Figure 8-24: DGR4_350.53-381.27 fit value cumulative distribution function.

8.9 381.08-411.82 Goat Island-Gasport-Lions Head-Fossil Hill

The DGR-4 interval from 381.08 to 411.82 m BGS included the lower 18.02 m of the Goat Island Member of the Lockport Formation, the entire 6.5-m thickness of the Gasport Member of the Lockport Formation, the entire 4.4-m thickness of the Lions Head Member of the Amabel Formation, the entire 1.5-m thickness of the Fossil Hill Formation, and the upper 0.32 m of the Cabot Head Formation. The Goat Island is dolostone with argillaceous laminae, the Gasport is dolomitic limestone, the Lions Head and Fossil Hill are dolostones, and the uppermost Cabot Head is shale. An overview of the testing in this interval is given in Table 8-18 and the corresponding parameter estimates are given in Table 8-19. Pulse-withdrawal and pulse-injection tests were performed in this interval.

Table 8-18: Summary of the DGR4_381.08-411.82 testing activities.

Formation / Unit		Top of Test Zone (m BGS)	Bottom of Test Zone (m BGS)	
Goat Island-Gasport-Lions Head-Fossil Hill		381.08	411.82	
Test	Initiated	Magnitude (kPa)	Duration	Compressibility (Pa ⁻¹)
Shut-in	14-12-08 11:43	N/A	22 hr	N/A
PW	15-12-08 09:41	244	24 hr	1.4E-9
PI	16-12-08 09:36	220	22 hr	1.5E-9
Borehole Pressure History				
Event	Start		Pressure (kPa)	
Drilling Intercept	22-09-08 22:15		4087	
End of Geophysical Logging	30-10-08 12:00		3819	
Prior Testing	25-11-08 13:12		N/A	
Shut-in	14-12-08 11:43		3921	

Table 8-19: Summary of the DGR4_381.08-411.82 parameter estimates.

Parameter	Best Fit	Minimum	Maximum	Mean
K_f (m/s)	1.6E-12	1.2E-12	1.7E-12	1.6E-12
P_f (kPa)	5067	5042	5158	5070
K_s (m/s)	4.2E-12	5.0E-13	1.0E-11	3.8E-12
t_s (cm)	31	1E-4	74	32
S_s (1/m)	8.4E-7	1.1E-7	1.3E-5	8.7E-7

Figure 8-25 shows the measured pressure record from DGR4_381.08-411.82 used in this analysis along with the best-fit simulation and parameter values. The ranges of formation K and raw P_f values estimated from perturbation analysis are shown in Figure 8-26 and the fit value cumulative distribution function is shown in Figure 8-27.

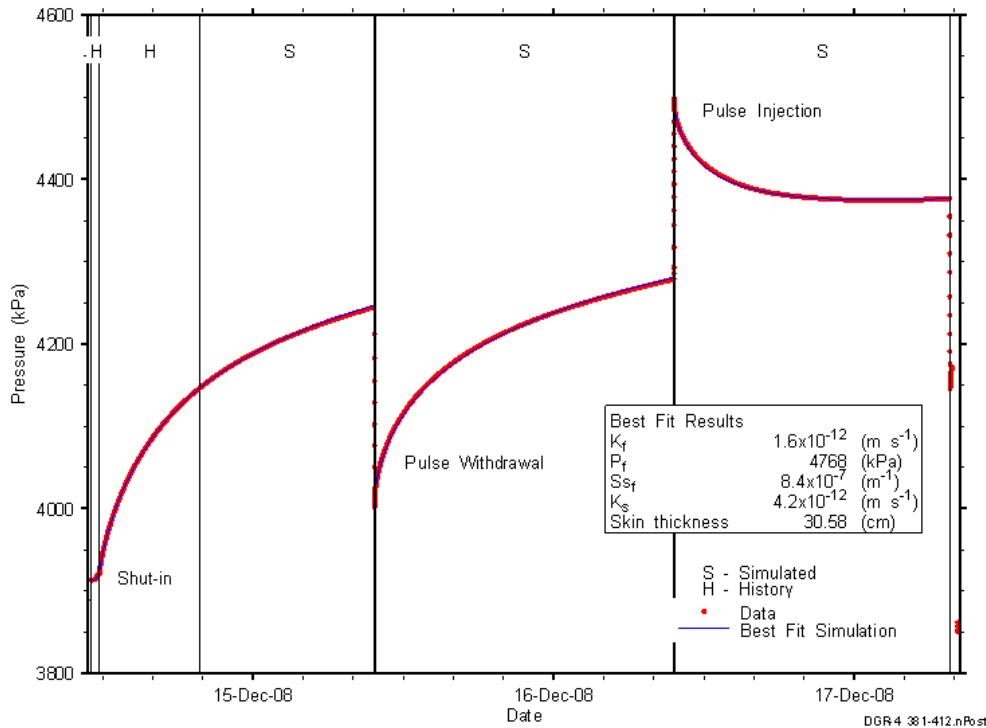


Figure 8-25: Annotated DGR4_381.08-411.82 testing sequence showing best-fit simulation and parameter estimates.

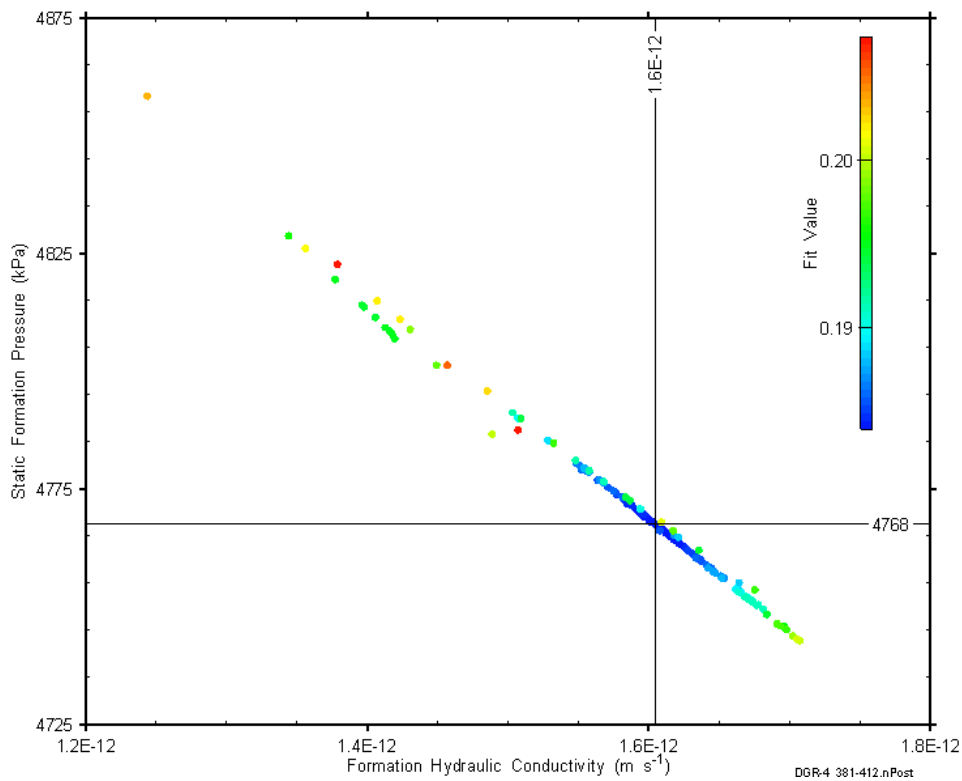


Figure 8-26: XY-scatter plot showing estimates of formation hydraulic conductivity and raw static formation pressure derived from the DGR4_381.08-411.82 perturbation analysis.

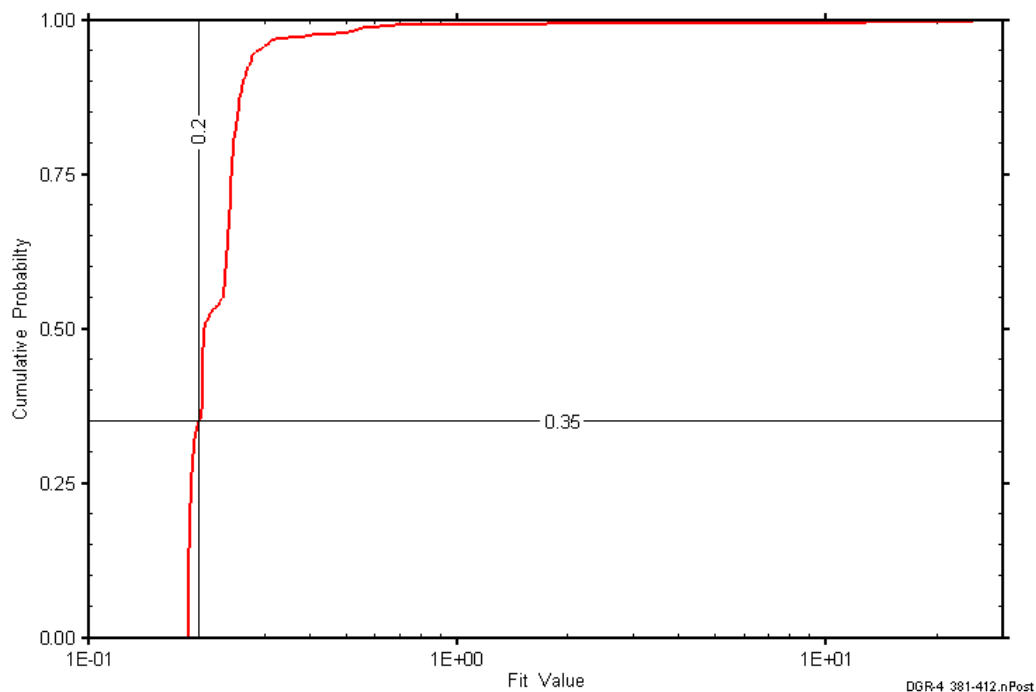


Figure 8-27: DGR4_381.08-411.82 fit value cumulative distribution function.

8.10 411.51-442.25 Cabot Head-Manitoulin

The DGR-4 interval from 411.51 to 442.25 m BGS included the entire 24.2 m of the Cabot Head Formation and the upper 6.55 m of the Manitoulin Formation. The Cabot Head is shale interbedded with limestone and dolostone and the Manitoulin is interbedded dolostone/limestone and shale. An overview of the testing in this interval is given in Table 8-20 and the corresponding parameter estimates are given in Table 8-21. A pulse-withdrawal test and a pulse-injection test were performed in this interval.

Table 8-20: Summary of the DGR4_411.51-442.25 testing activities.

Formation / Unit		Top of Test Zone (m BGS)	Bottom of Test Zone (m BGS)	
Cabot Head-Manitoulin		411.51	442.25	
Test	Initiated	Magnitude (kPa)	Duration	Compressibility (Pa ⁻¹)
Shut-in	17-12-08 12:00	N/A	22 hr	N/A
PW	18-12-08 09:44	839	23 hr	4.0E-10
PI	19-12-08 09:18	829	23 hr	4.0E-10
Borehole Pressure History				
Event	Start	Pressure (kPa)		
Drilling Intercept	23-09-08 20:58	4415		
End of Geophysical Logging	30-10-08 12:00	4147		
Prior Testing	25-11-08 13:12	N/A		
Shut-in	17-12-08 12:00	4253		

Table 8-21: Summary of the DGR4_411.51-442.25 parameter estimates.

Parameter	Best Fit	Minimum	Maximum	Mean
K_f (m/s)	4.4E-14	2.8E-14	6.2E-14	4.1E-14
P_f (kPa)	4594	4593	4604	4596
K_s (m/s)	1.2E-13	5.5E-14	6.3E-13	1.2E-13
t_s (cm)	2.6	0.5	16	2.9
S_s (1/m)	7.8E-7	1.0E-7	2.0E-6	8.4E-7

Figure 8-28 shows the measured pressure record from DGR4_411.51-442.25 used in this analysis along with the best-fit simulation and parameter values. The ranges of formation K and raw P_f values estimated from perturbation analysis are shown in Figure 8-29 and the fit value cumulative distribution function is shown in Figure 8-30.

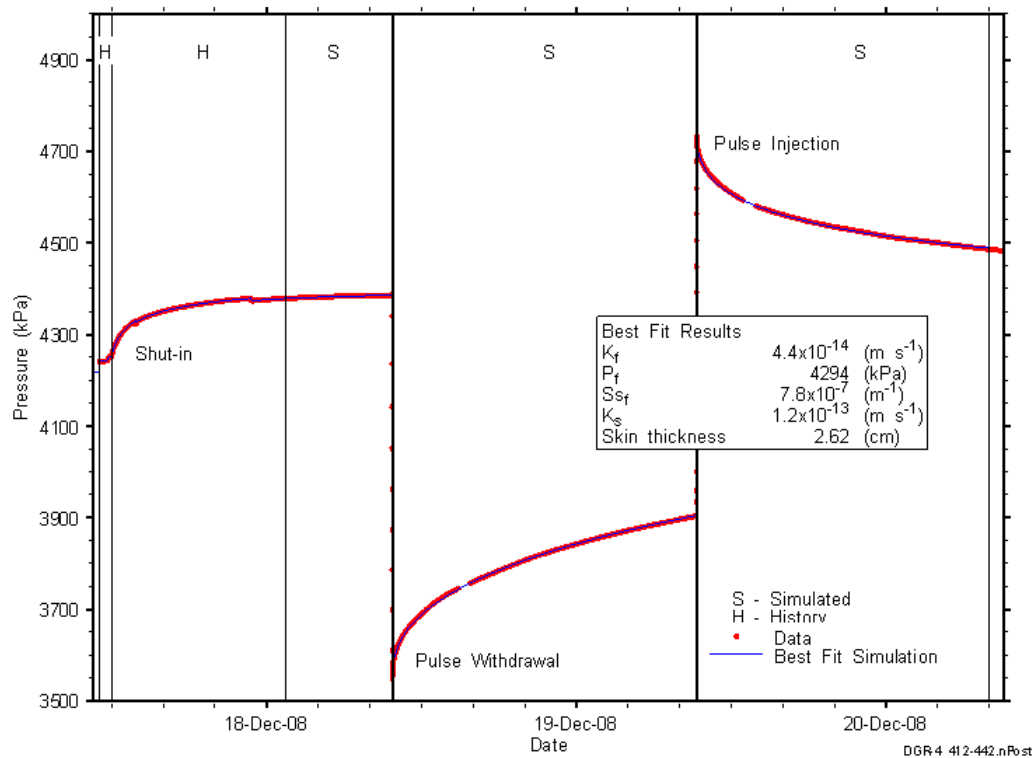


Figure 8-28: Annotated DGR4_411.51-442.25 testing sequence showing best-fit simulation and parameter estimates.

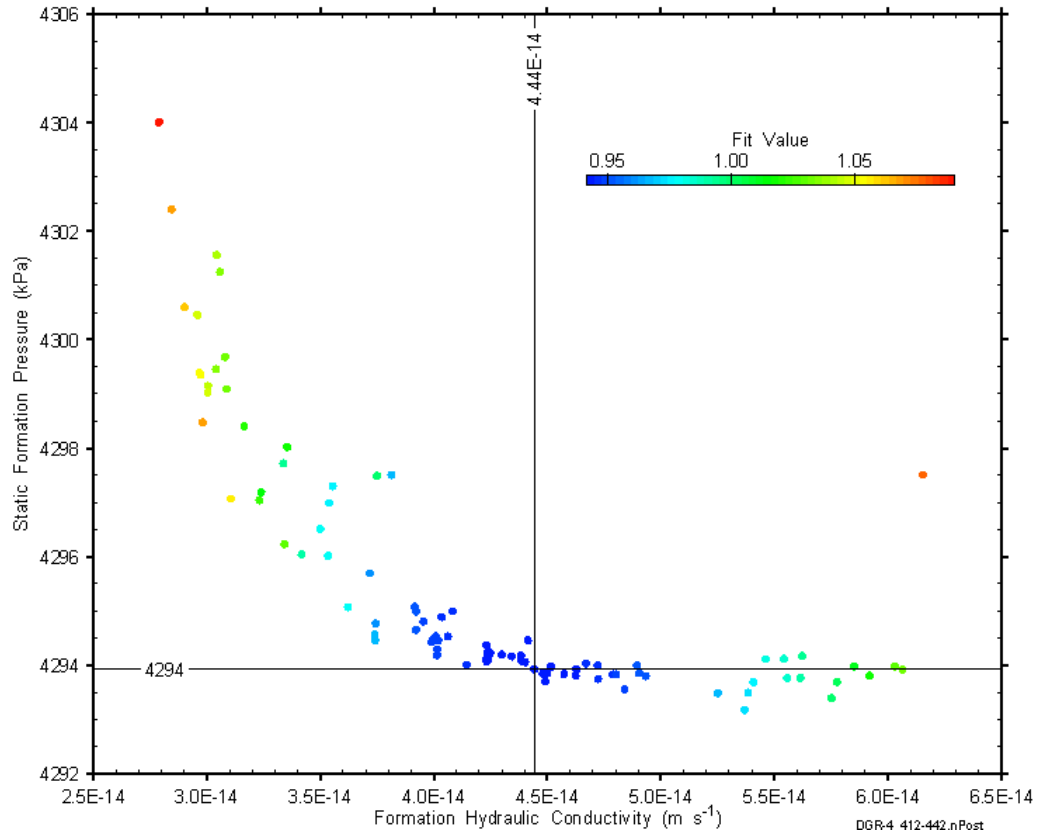


Figure 8-29: XY-scatter plot showing estimates of formation hydraulic conductivity and raw static formation pressure derived from the DGR4_411.51-442.25 perturbation analysis.

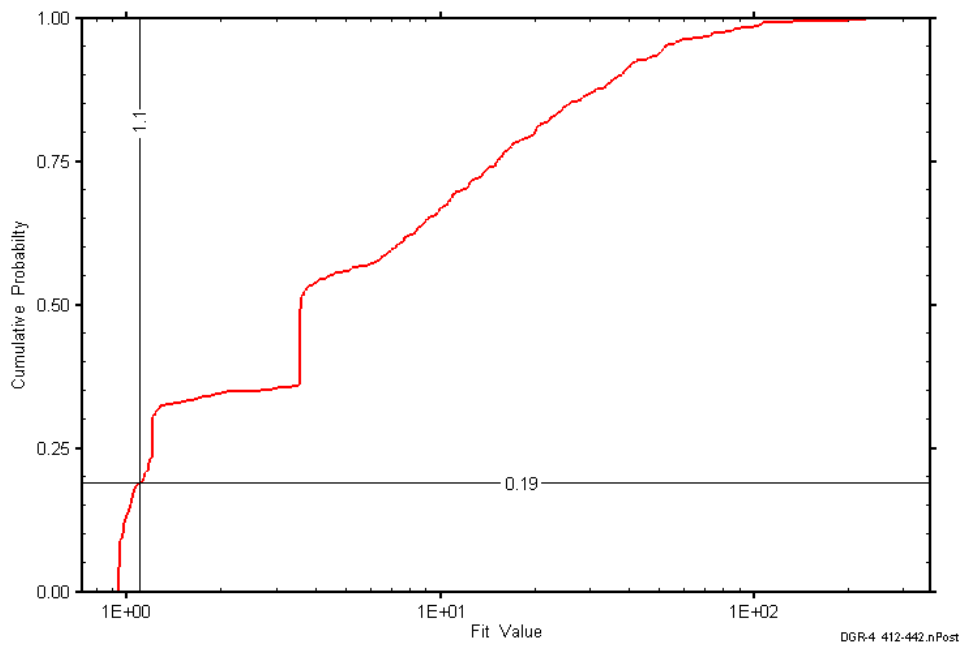


Figure 8-30: DGR4_411.51-442.25 fit value cumulative distribution function.

8.11 432.00-462.74 Cabot Head - Manitoulin-Queenston

The DGR-4 interval from 432.00 to 462.74 m BGS included the lower 3.7 m of the Cabot Head Formation, the entire 10.6-m thickness of the Manitoulin Formation, and the upper 16.44 m of the Queenston Formation. The lower Cabot Head is shale interbedded with limestone and dolostone, the Manitoulin is interbedded dolostone/limestone and shale, and the upper Queenston is massive, calcareous shale. An overview of the testing in this interval is given in Table 8-22 and the corresponding parameter estimates are given in Table 8-23. Two pulse-withdrawal tests were performed in this interval.

Table 8-22: Summary of the DGR4_432.00-462.74 testing activities.

Formation / Unit		Top of Test Zone (m BGS)		Bottom of Test Zone (m BGS)	
Manitoulin-Queenston		432.00		462.74	
Test	Initiated	Magnitude (kPa)	Duration	Compressibility (Pa ⁻¹)	
Shut-in	06-01-09 14:55	N/A	18 hr	N/A	
PW1	07-01-09 09:07	33.7	24 hr	1.0E-8	
PW2 (pt 1)	08-01-09 09:08	829	8 min	N/C	
PW2 (pt 2)	08-01-09 09:16	33.1	24 hr	1.0E-8	
Borehole Pressure History					
Event		Start		Pressure (kPa)	
Drilling Intercept		24-09-08 23:16		4635	
End of Geophysical Logging		30-10-08 12:00		4368	
Prior Testing		25-11-08 13:12		N/A	
Shut-in		06-01-09 14:55		4500	

Table 8-23: Summary of the DGR4_432.00-462.74 parameter estimates.

Parameter	Best Fit	Minimum	Maximum	Mean
K_f (m/s)	1.9E-12	3.6E-13	1.8E-11	2.6E-12
P_f (kPa)	2271	1427	3941	2337
K_s (m/s)	1.1E-11	2.1E-12	1.2E-10	1.6E-11
t_s (cm)	25	4.7	223	42
S_s (1/m)	7.9E-7	1.0E-7	4.0E-6	5.6E-7

Figure 8-31 shows the measured pressure record from DGR4_432.00-462.74 used in this analysis along with the best-fit simulation and parameter values. The ranges of formation K and raw P_f values estimated from perturbation analysis are shown in Figure 8-32 and the fit value cumulative distribution function is shown in Figure 8-33.

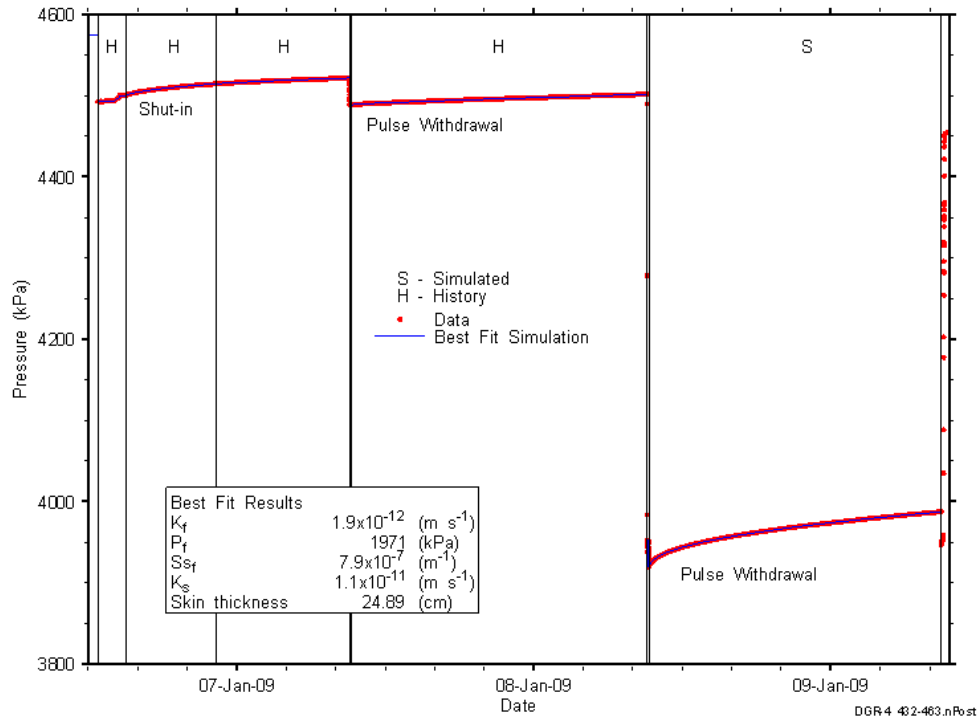


Figure 8-31: Annotated DGR4_432.00-462.74 testing sequence showing best-fit simulation and parameter estimates.

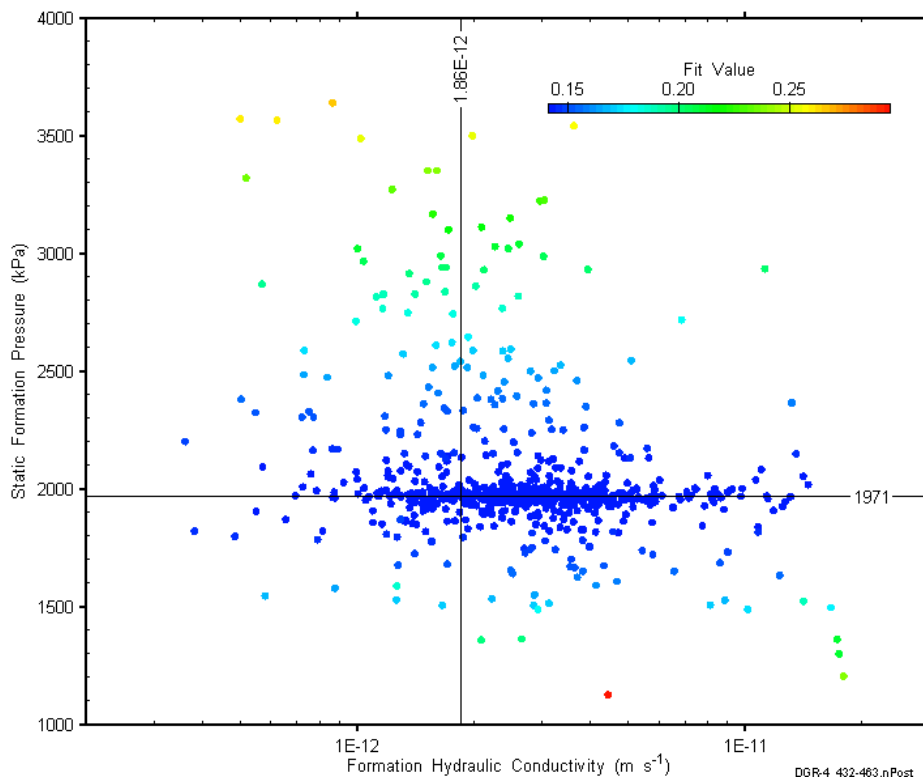


Figure 8-32: XY-scatter plot showing estimates of formation hydraulic conductivity and raw static formation pressure derived from the DGR4_432.00-462.74 perturbation analysis.

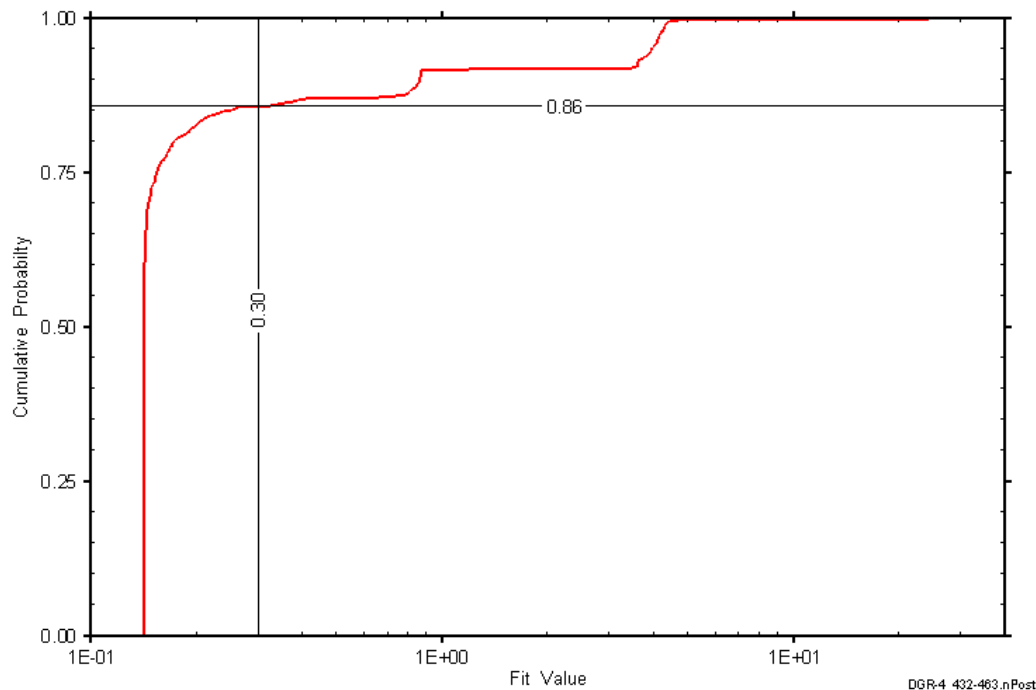


Figure 8-33: DGR4_432.00-462.74 fit value cumulative distribution function.

8.12 458.23-488.97 Queenston

The DGR-4 interval from 458.23 to 488.97 m BGS was entirely contained within the Queenston Formation. This portion of the Queenston consists of shale with carbonate interbeds increasing toward the bottom. An overview of the testing in this interval is given in Table 8-24 and the corresponding parameter estimates are given in Table 8-25. A pulse-withdrawal test was conducted in this interval.

Table 8-24: Summary of the DGR4_458.23-488.97 testing activities.

Formation / Unit		Top of Test Zone (m BGS)	Bottom of Test Zone (m BGS)	
Queenston		458.23	488.97	
Test	Initiated	Magnitude (kPa)	Duration	Compressibility (Pa ⁻¹)
Shut-in	09-01-09 12:09	N/A	21 hr	N/A
PW (pt 1)	10-01-09 09:35	736	2 min	4.5E-10
PW (pt 2)	10-01-09 09:42	746	48 hr	4.5E-10
Borehole Pressure History				
Event	Start	Pressure (kPa)		
Drilling Intercept	25-09-08 01:59	4918		
End of Geophysical Logging	30-10-08 12:00	4651		
Prior Testing	25-11-08 13:12	N/A		
Shut-in	09-01-09 12:09	4798		

Table 8-25: Summary of the DGR4_458.23-488.97 parameter estimates.

Parameter	Best Fit	Minimum	Maximum	Mean
K_f (m/s)	2.3E-14	2.3E-14	2.3E-14	2.3E-14
P_f (kPa)	3647	3645	3650	3647
K_s (m/s)	1.7E-13	1.7E-13	1.9E-13	1.7E-13
t_s (cm)	2.3	2.3	2.3	2.3

Figure 8-34 shows the measured pressure record from DGR4_458.23-488.97 used in this analysis along with the best-fit simulation and parameter values. The S_s value for this analysis was fixed at $1E-6 m^{-1}$, a value estimated from preliminary perturbation analysis. The ranges of formation K and raw P_f values estimated from perturbation analysis are shown in Figure 8-35 and the fit value cumulative distribution function is shown in Figure 8-36.

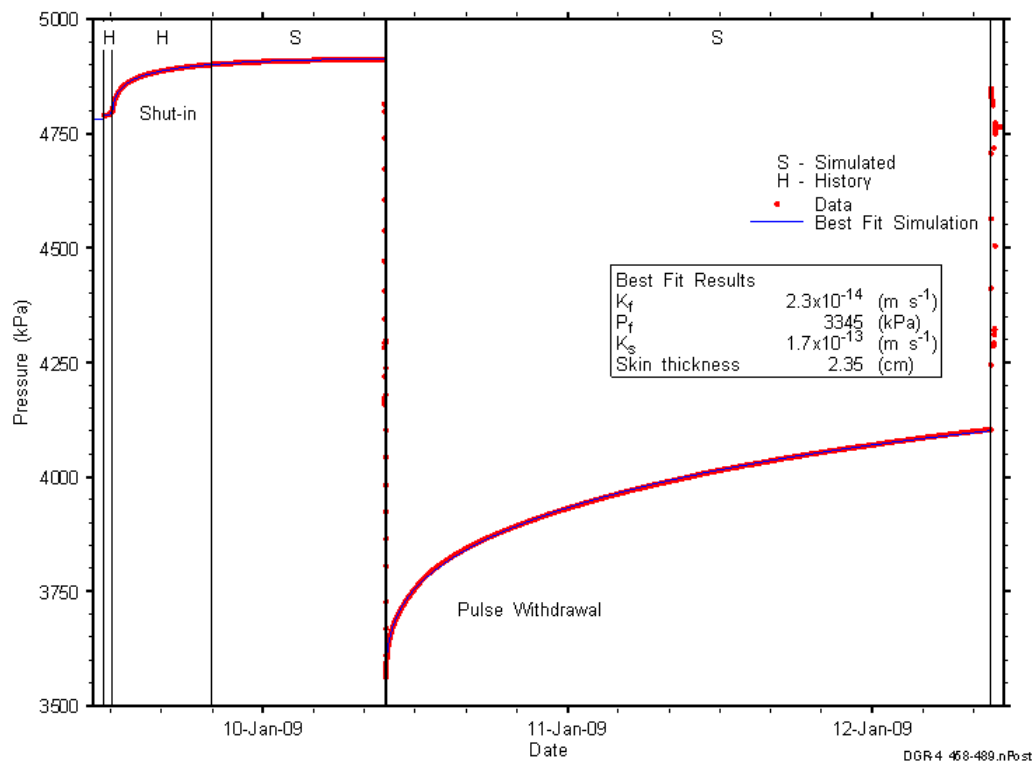


Figure 8-34: Annotated DGR4_458.23-488.97 testing sequence showing best-fit simulation and parameter estimates.

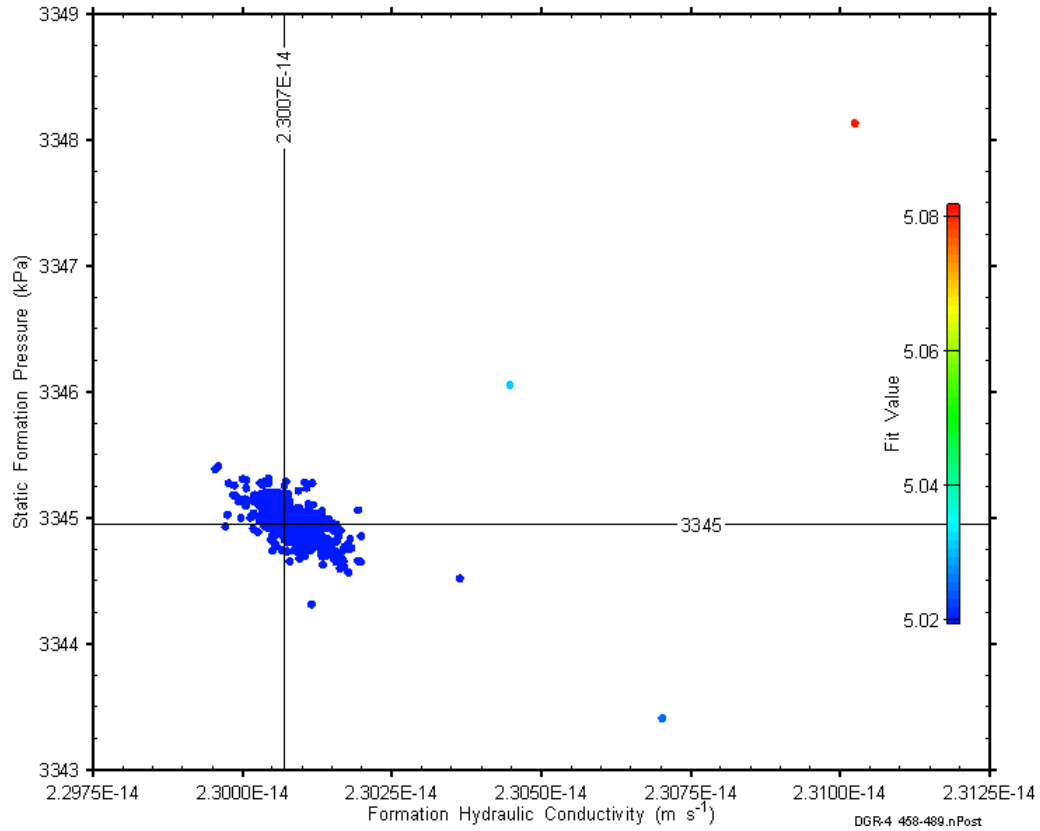


Figure 8-35: XY-scatter plot showing estimates of formation hydraulic conductivity and raw static formation pressure derived from the DGR4_458.23-488.97 perturbation analysis.

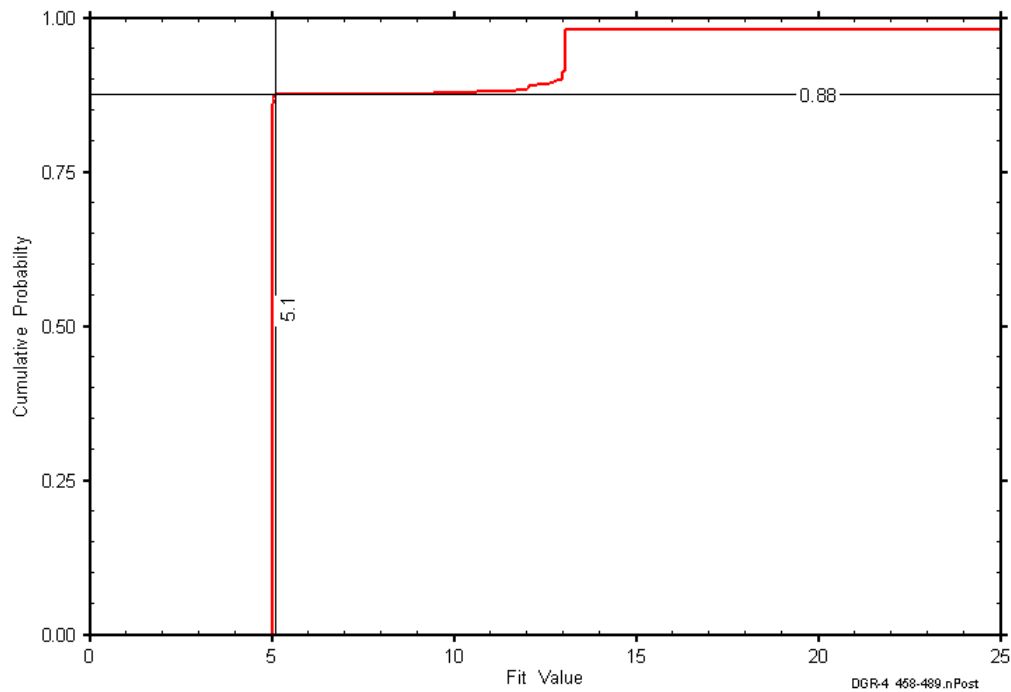


Figure 8-36: DGR4_458.23-488.97 fit value cumulative distribution function.

8.13 488.77-519.51 Queenston

The DGR-4 interval from 488.77 to 519.51 m BGS was entirely contained within the Queenston Formation. This portion of the Queenston consists of approximately 20 m of interbedded shale and limestone, underlain by calcareous shale. An overview of the testing in this interval is given in Table 8-26 and the corresponding parameter estimates are given in Table 8-27. A pulse-withdrawal test was conducted in this interval.

Table 8-26: Summary of the DGR4_488.77-519.51 testing activities.

Formation / Unit		Top of Test Zone (m BGS)		Bottom of Test Zone (m BGS)	
Queenston		488.77		519.51	
Test	Initiated	Magnitude (kPa)	Duration	Compressibility (Pa ⁻¹)	
Shut-in	12-01-09 12:53	N/A	20 hr	N/A	
PW (pt 1)	13-01-09 09:18	404	11 min	N/C	
PW (pt 2)	13-01-09 09:29	494	46 hr	6.8E-10	
Borehole Pressure History					
Event		Start		Pressure (kPa)	
Drilling Intercept		25-09-08 20:22		5247	
End of Geophysical Logging		30-10-08 12:00		4980	
Prior Testing		25-11-08 13:12		N/A	
Shut-in		12-01-09 12:53		5164	

Table 8-27: Summary of the DGR4_488.77-519.51 parameter estimates.

Parameter	Best Fit	Minimum	Maximum	Mean
K_f (m/s)	2.2E-14	1.4E-14	3.2E-14	2.3E-14
P_f (kPa)	3474	3042	3783	3519
K_s (m/s)	2.2E-13	9.5E-14	6.3E-13	2.5E-13
t_s (cm)	2.4	0.9	8.4	3.3
S_s (1/m)	9.7E-7	2.5E-7	2.3E-6	7.9E-7

Figure 8-37 shows the measured pressure record from DGR4_488.77-519.51 used in this analysis along with the best-fit simulation and parameter values. The ranges of formation K and raw P_f values estimated from perturbation analysis are shown in Figure 8-38 and the fit value cumulative distribution function is shown in Figure 8-39.

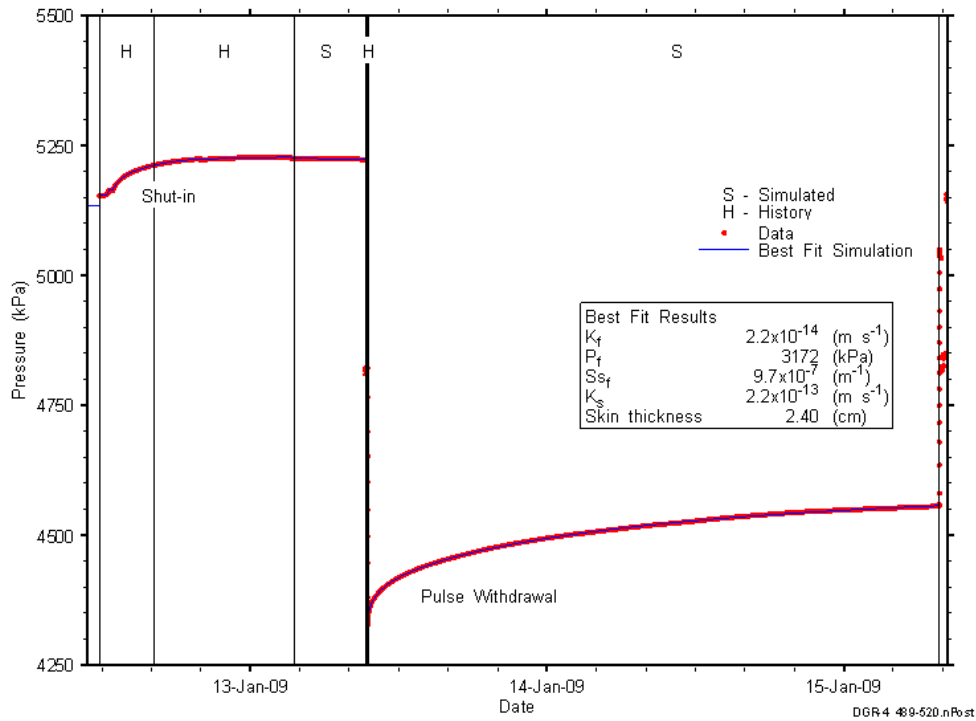


Figure 8-37: Annotated DGR4_488.77-519.51 testing sequence showing best-fit simulation and parameter estimates.

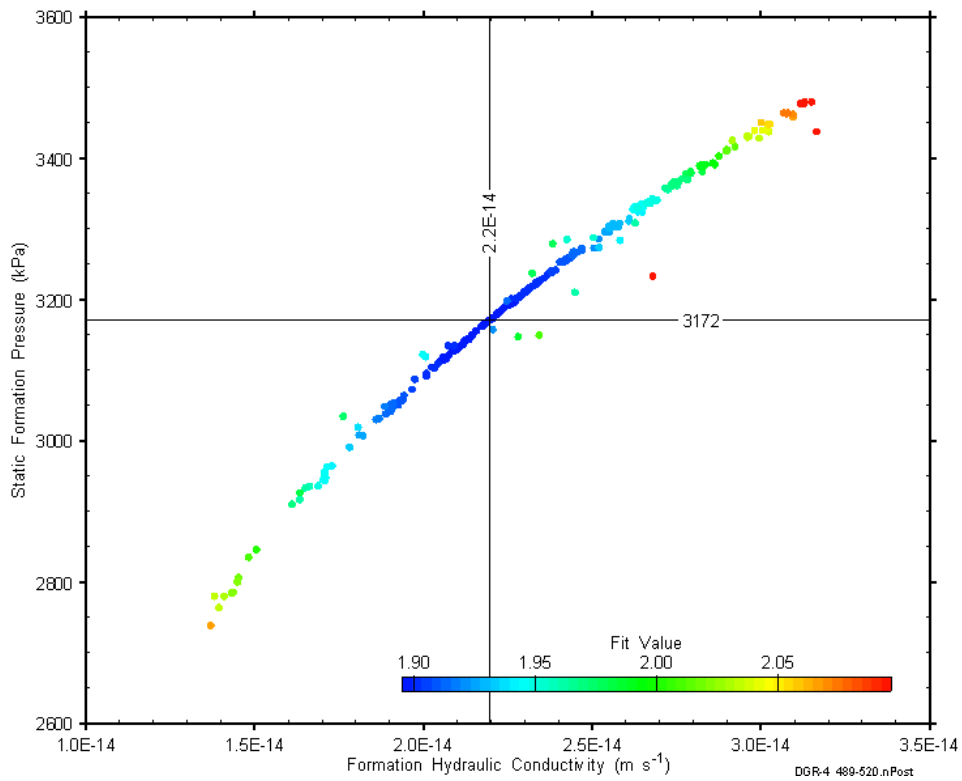


Figure 8-38: XY-scatter plot showing estimates of formation hydraulic conductivity and raw static formation pressure derived from the DGR4_488.77-519.51 perturbation analysis.

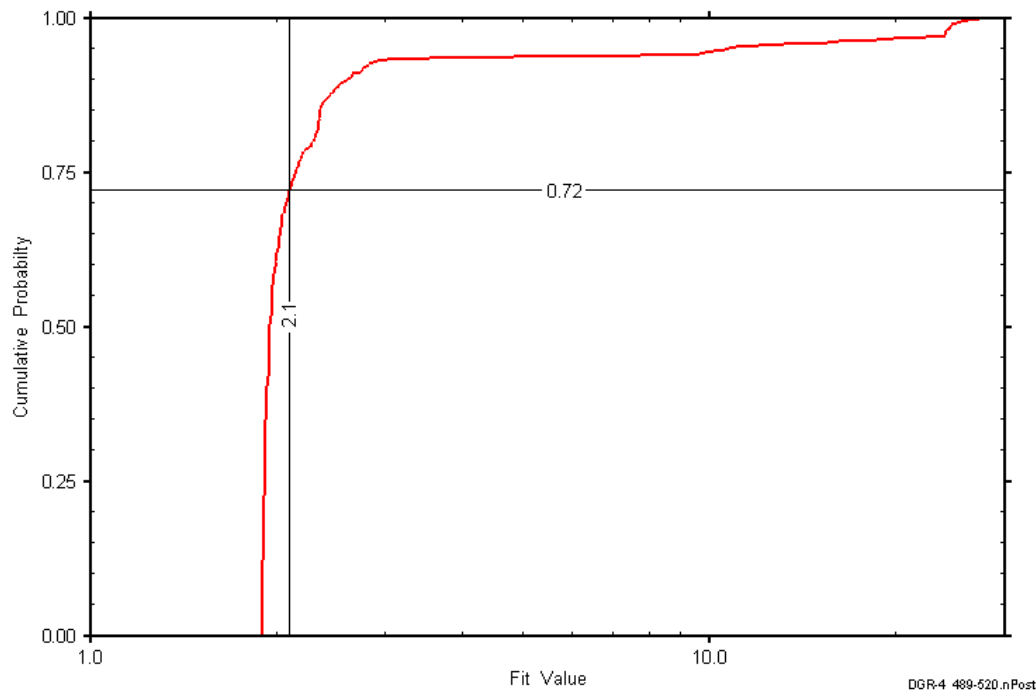


Figure 8-39: DGR4_488.77-519.51 fit value cumulative distribution function.

8.14 519.10-549.84 Georgian Bay

The DGR-4 interval from 519.10 to 549.84 m BGS included the lower 0.2 m of the Queenston Formation and the upper 30.54 m of the Georgian Bay Formation. The lowermost Queenston consists of calcareous shale, and the upper Georgian Bay consists of interbedded shale and limestone/siltstone. An overview of the testing in this interval is given in Table 8-28 and the corresponding parameter estimates are given in Table 8-29. One pulse-withdrawal test was conducted in this interval.

Table 8-28: Summary of the DGR4_519.10-549.84 testing activities.

Formation / Unit		Top of Test Zone (m BGS)	Bottom of Test Zone (m BGS)	
Georgian Bay		519.10	549.84	
Test	Initiated	Magnitude (kPa)	Duration	Compressibility (Pa ⁻¹)
Shut-in	15-01-09 16:35	N/A	16 hr	N/A
PW (pt 1)	16-01-09 08:34	437	9 min	N/C
PW (pt 2)	16-01-09 08:44	616	48 hr	5.3E-10
Borehole Pressure History				
Event	Start		Pressure (kPa)	
Drilling Intercept	26-09-08 15:26		5575	
End of Geophysical Logging	30-10-08 12:00		5307	
Prior Testing	25-11-08 13:12		N/A	
Shut-in	15-01-09 16:35		5541	

Table 8-29: Summary of the DGR4_519.10-549.84 parameter estimates.

Parameter	Best Fit	Minimum	Maximum	Mean
K_f (m/s)	5.2E-15	4.8E-15	5.6E-15	5.2E-15
P_f (kPa)	1130	1013	1250	1131
K_s (m/s)	3.2E-14	2.9E-14	3.5E-14	3.2E-14
t_s (cm)	0.5	0.5	0.5	0.5
S_s (1/m)	4.5E-6	4.2E-6	4.8E-6	4.5E-6

Figure 8-40 shows the measured pressure record from DGR4_519.10-549.84 used in this analysis along with the best-fit simulation and parameter values. The ranges of formation K and raw P_f values estimated from perturbation analysis are shown in Figure 8-41 and the fit value cumulative distribution function is shown in Figure 8-42.

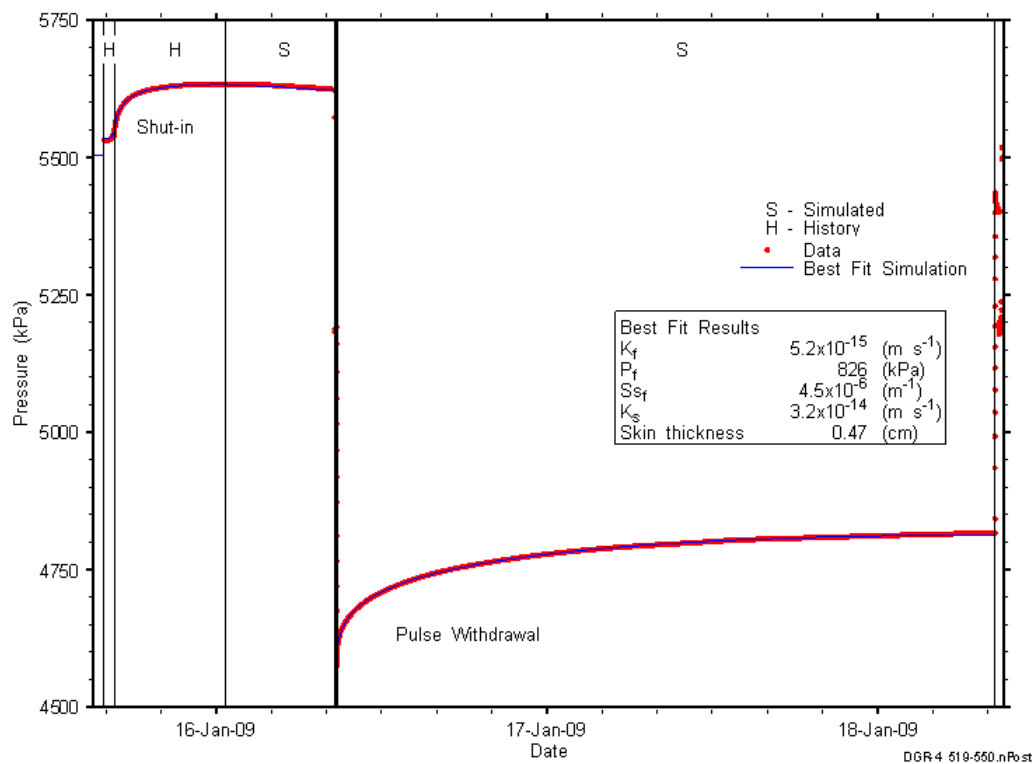


Figure 8-40: Annotated DGR4_519.10-549.84 testing sequence showing best-fit simulation and parameter estimates.

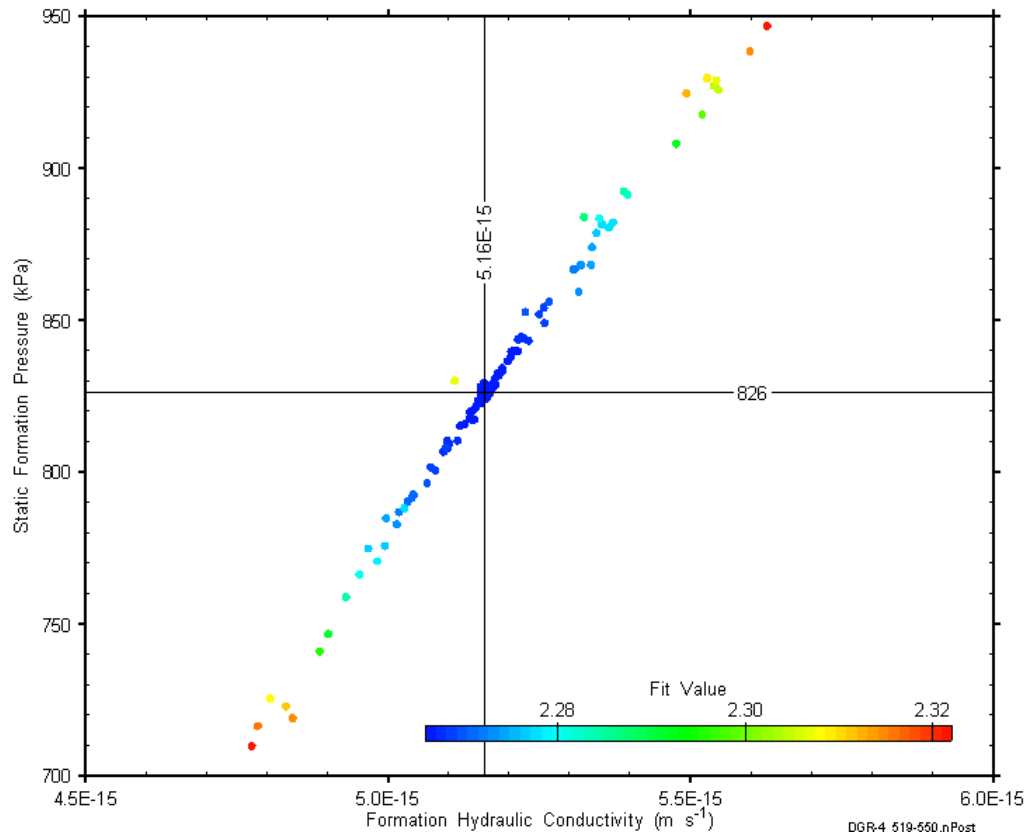


Figure 8-41: XY-scatter plot showing estimates of formation hydraulic conductivity and raw static formation pressure derived from the DGR4_519.10-549.84 perturbation analysis.

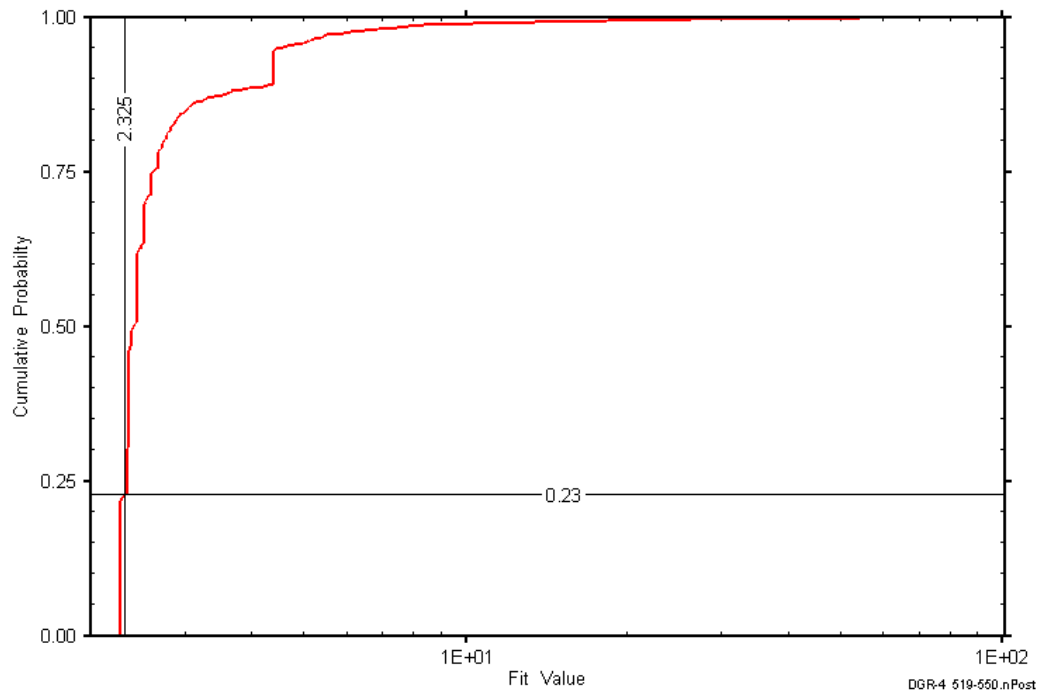


Figure 8-42: DGR4_519.10-549.84 fit value cumulative distribution function.

8.15 548.28-579.02 Georgian Bay (a)

The DGR-4 interval from 548.28 to 579.02 m BGS was entirely contained within the Georgian Bay Formation, a shale with limestone, siltstone, and sandstone layers. An overview of the testing in this interval is given in Table 8-30 and the corresponding parameter estimates are given in Table 8-31. Note that this interval was tested twice with approximately 30 days between the two tests. The first and second tests are referenced as (a) and (b), respectively. One pulse-withdrawal test was conducted in this interval.

Table 8-30: Summary of the DGR4_548.28-579.02 (a) testing activities.

Formation / Unit		Top of Test Zone (m BGS)		Bottom of Test Zone (m BGS)	
Georgian Bay (a)		548.28		579.02	
Test	Initiated	Magnitude (kPa)	Duration	Compressibility (Pa ⁻¹)	
Shut-in	18-01-09 12:51	N/A	19.7 hr	N/A	
PW (pt 1)	19-01-09 08:34	N/A	9 min	NC	
PW (pt 2)	19-01-09 08:43	781	72 hr	3.9E-10	
Borehole Pressure History					
Event		Start		Pressure (kPa)	
Drilling Intercept		28-09-08 10:15		5889	
End of Geophysical Logging		30-10-08 12:00		5622	
Prior Testing		25-11-08 13:12		N/A	
Shut-in		18-01-09 12:51		5872	

Table 8-31: Summary of the DGR4_548.28-579.02 (a) parameter estimates.

Parameter	Best Fit	Minimum	Maximum	Mean
K_f (m/s)	2.8E-14	2.5E-14	3.2E-14	2.8E-14
P_f (kPa)	875	489	1270	922
K_s (m/s)	2.5E-13	1.9E-13	6.5E-13	2.8E-13
t_s (cm)	5.9	3.5	22	7.6
S_s (m ⁻¹)	4.6E-7	7.7E-8	7.8E-7	3.6E-7

Figure 8-43 shows the measured pressure record from DGR4_519.10-549.84 (a) used in this analysis along with the best-fit simulation and parameter values. The ranges of formation K and raw P_f values estimated from perturbation analysis are shown in Figure 8-44 and the fit value cumulative distribution function is shown in Figure 8-45.

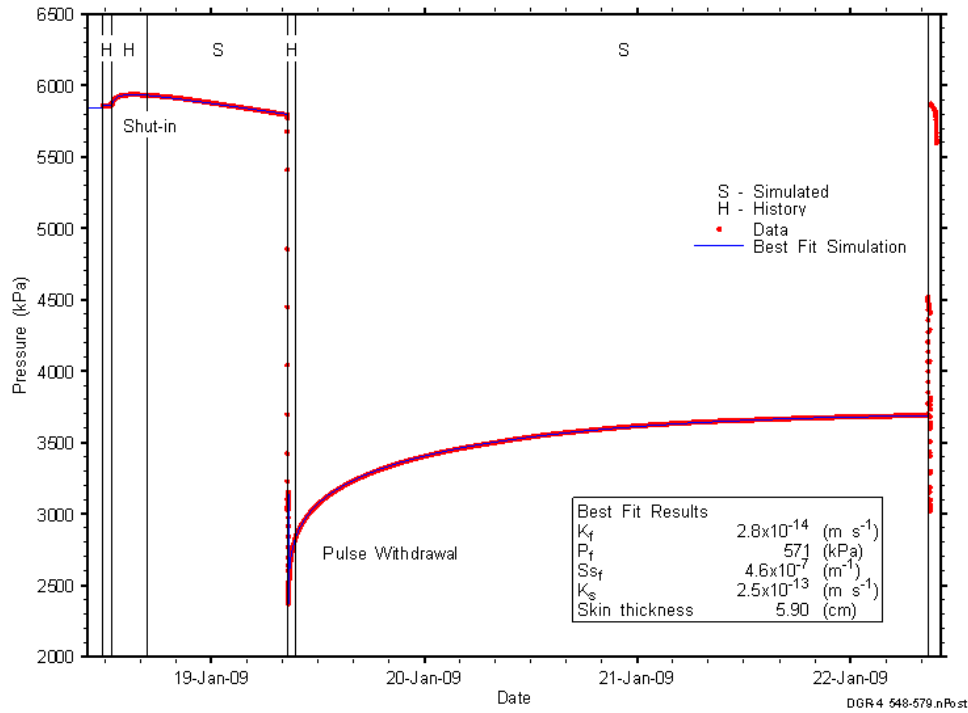


Figure 8-43: Annotated DGR4_548.28-579.02 (a) testing sequence showing best-fit simulation and parameter estimates.

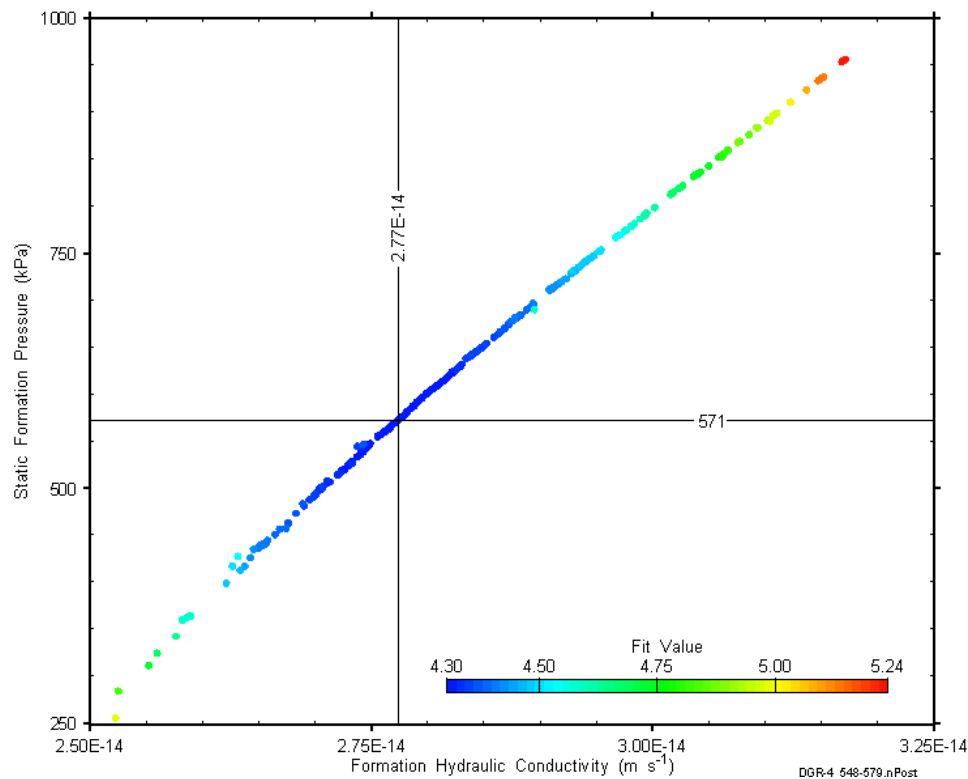


Figure 8-44: XY-scatter plot showing estimates of formation hydraulic conductivity and raw static formation pressure derived from the DGR4_548.28-579.02 (a) perturbation analysis.

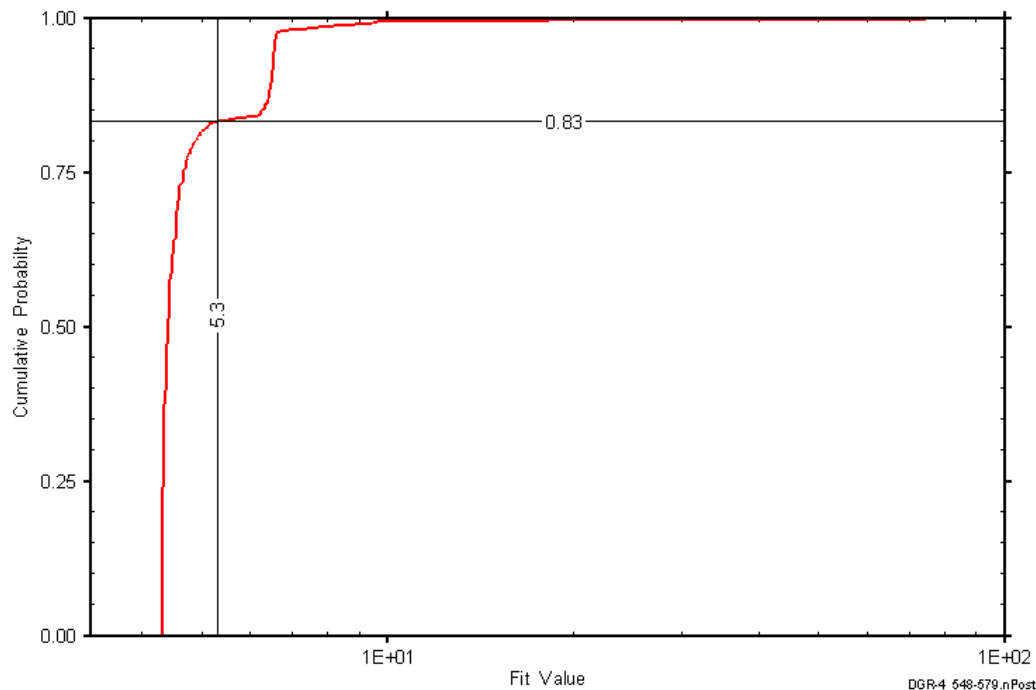


Figure 8-45: DGR4_548.28-579.02 (a) fit value cumulative distribution function.

8.16 548.28-579.02 Georgian Bay (b)

The DGR-4 interval from 548.28 to 579.02 m BGS was entirely contained within the Georgian Bay Formation, a shale with limestone, siltstone, and sandstone layers. An overview of the testing in this interval is given in Table 8-32 and the corresponding parameter estimates are given in Table 8-33. Note that this interval was tested twice with approximately 30 days between the two tests. The first and second tests are referenced as (a) and (b), respectively. One pulse-injection test was conducted in this interval.

Table 8-32: Summary of the DGR4_548.28-579.02 (b) testing activities.

Formation / Unit		Top of Test Zone (m BGS)	Bottom of Test Zone (m BGS)	
Georgian Bay (b)		548.28	579.02	
Test	Initiated	Magnitude (kPa)	Duration	Compressibility (Pa ⁻¹)
Shut-in	18-02-09 15:40	N/A	18 hr	N/A
PI	19-02-09 09:39	823	47 hr	3.9E-10
Borehole Pressure History				
Event	Start		Pressure (kPa)	
Drilling Intercept	28-09-08 10:15		5889	
End of Geophysical Logging	30-10-08 12:00		5622	
Prior Testing	25-11-08 13:12		N/A	
Shut-in	18-02-09 15:40		5774	

Table 8-33: Summary of the DGR4_548.28-579.02 (b) parameter estimates.

Parameter	Best Fit	Minimum	Maximum	Mean
K_f (m/s)	4.6E-14	3.0E-14	5.5E-14	3.9E-14
P_f (kPa)	3926	3229	4163	3672
K_s (m/s)	1.3E-12	4.1E-13	5.0E-12	8.1E-13
t_s (cm)	5.9	1.7	23	3.9
S_s (m ⁻¹)	2.6E-7	3.7E-8	9.8E-7	4.7E-7

Figure 8-46 shows the measured pressure record from DGR4_548.28-579.02 (b) used in this analysis along with the best-fit simulation and parameter values. The ranges of formation K and raw P_f values estimated from perturbation analysis are shown in Figure 8-47 and the fit value cumulative distribution function is shown in Figure 8-48.

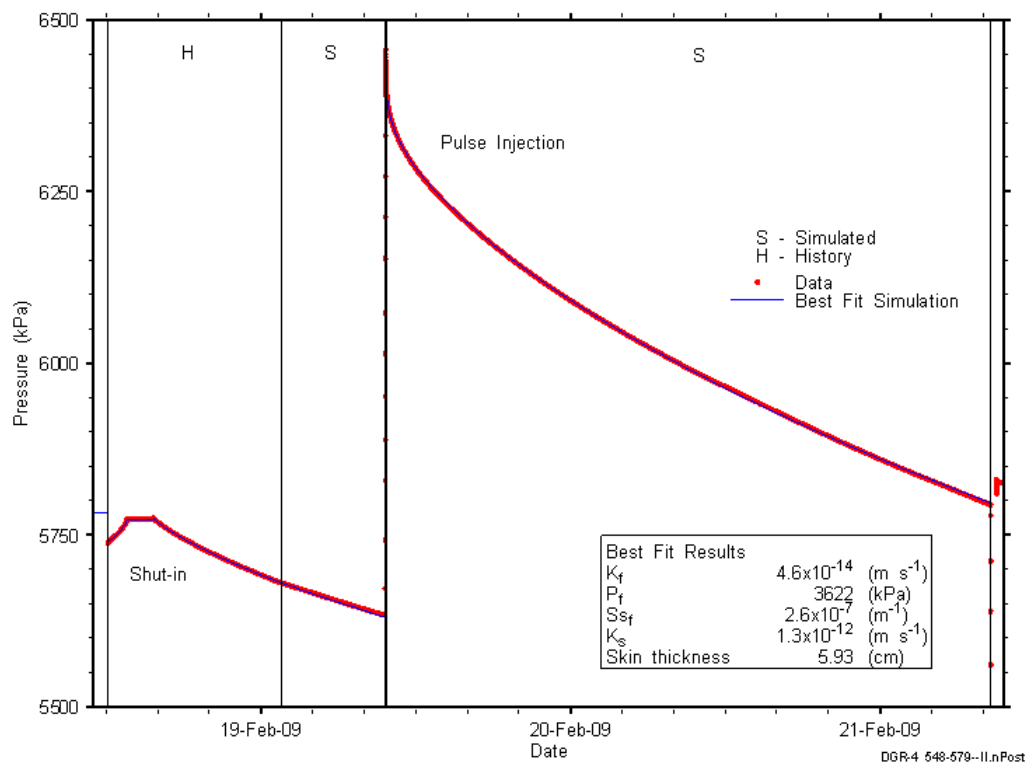


Figure 8-46: Annotated DGR4_548.28-579.02 (b) testing sequence showing best-fit simulation and parameter estimates.

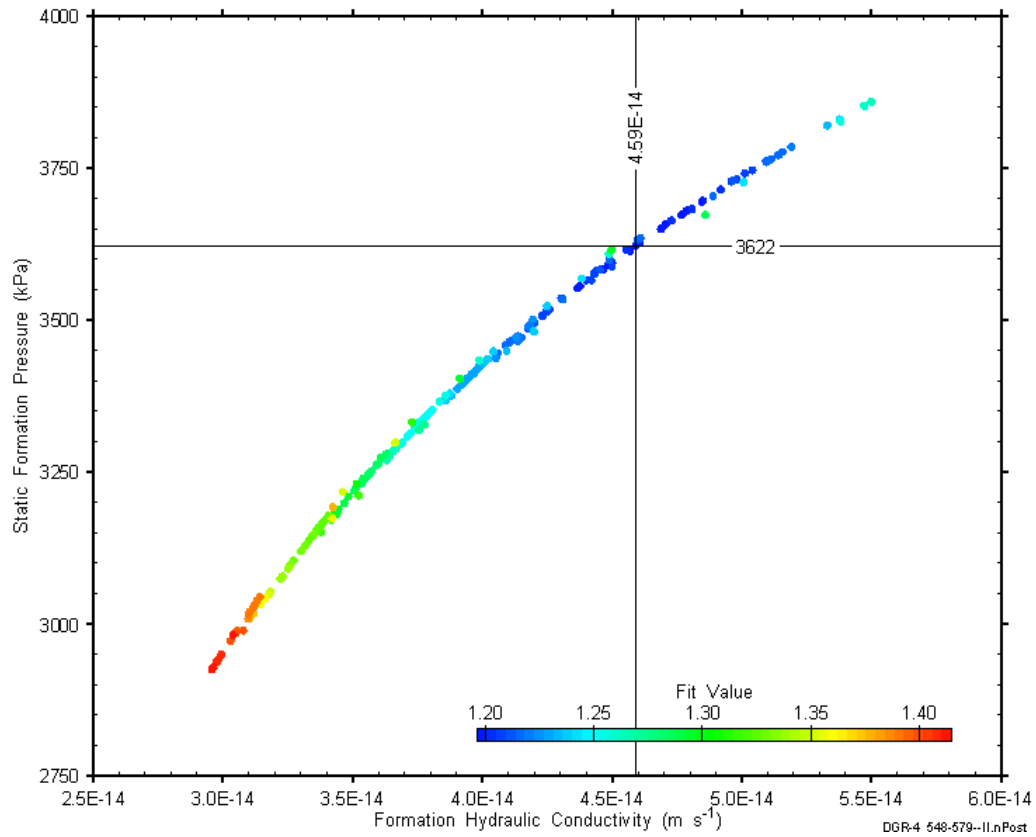


Figure 8-47: XY-scatter plot showing estimates of formation hydraulic conductivity and raw static formation pressure derived from the DGR4_548.28-579.02 (b) perturbation analysis.

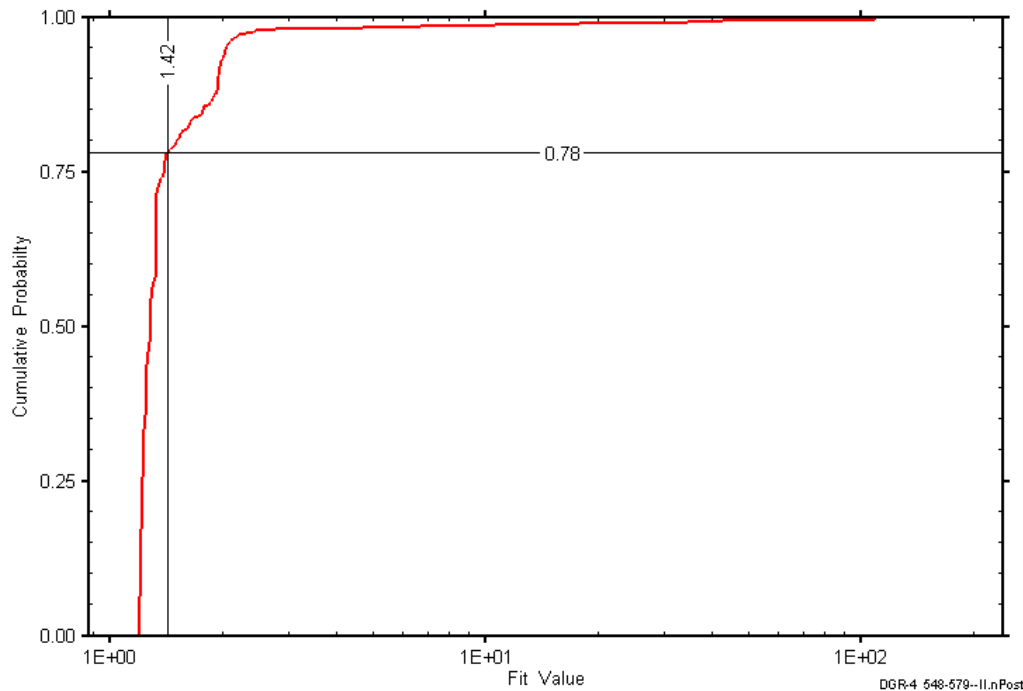


Figure 8-48: DGR4_548.28-579.02 (b) fit value cumulative distribution function.

8.17 577.45-608.19 Georgian Bay

The DGR-4 interval from 577.45 to 608.19 m BGS consisted of the lower third of the Georgian Bay Formation and the upper 0.19 m of the Blue Mountain Formation. This portion of the Georgian Bay is a shale with fewer limestone, siltstone, and sandstone layers than the overlying portion of the formation. The uppermost Blue Mountain is shale. An overview of the testing in this interval is given in Table 8-34 and the corresponding parameter estimates are given in Table 8-35. Two pulse-withdrawal tests were conducted in this interval.

Table 8-34: Summary of the DGR4_577.45-608.19 testing activities.

Formation / Unit		Top of Test Zone (m BGS)		Bottom of Test Zone (m BGS)	
Georgian Bay		577.45		608.19	
Test	Initiated	Magnitude (kPa)	Duration	Compressibility (Pa ⁻¹)	
Shut-in	22-01-09 14:58	N/A	18 hr	N/A	
PW 1	23-01-09 08:54	123	24 hr	2.7E-9	
PW 2 (pt 1)	24-01-09 09:04	N/A	5.6 min	NC	
PW 2 (pt 2)	24-01-09 09:10	117	23 hr	2.7E-9	
Borehole Pressure History					
Event		Start		Pressure (kPa)	
Drilling Intercept		30-09-08 10:20		6203	
End of Geophysical Logging		30-10-08 12:00		5936	
Prior Testing		25-11-08 13:12		N/A	
Shut-in		22-01-09 14:58		6047	

Table 8-35: Summary of the DGR4_577.45-608.19 parameter estimates.

Parameter	Best Fit	Minimum	Maximum	Mean
K_f (m/s)	9.4E-14	9.1E-14	9.7E-14	9.4E-14
P_f (kPa)	5210	5162	5218	5206
K_s (m/s)	1.9E-11	9.3E-12	7.1E-11	2.2E-11
t_s (cm)	9.2	9.1	9.9	9.3

Figure 8-49 shows the measured pressure record from DGR4_577.45-608.19 used in this analysis along with the best-fit simulation and parameter values. The S_s value for this analysis was fixed at $1E-6 \text{ m}^{-1}$, a value estimated from preliminary perturbation analysis. The ranges of formation K and raw P_f values estimated from perturbation analysis are shown in Figure 8-50 and the fit value cumulative distribution function is shown in Figure 8-51.

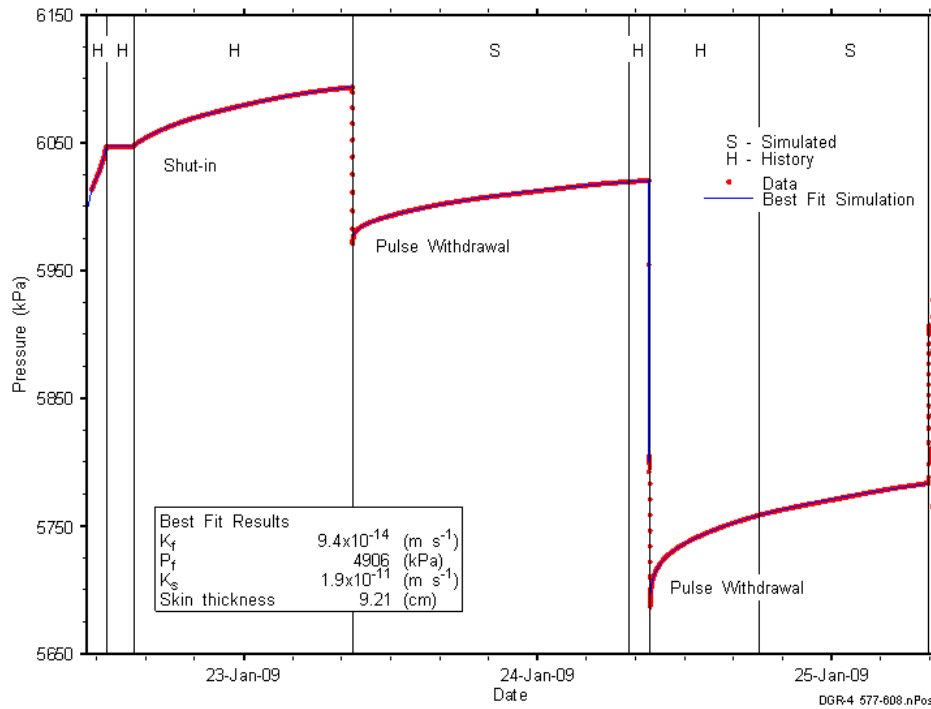


Figure 8-49: Annotated DGR4_577.45-608.19 testing sequence showing best-fit simulation and parameter estimates.

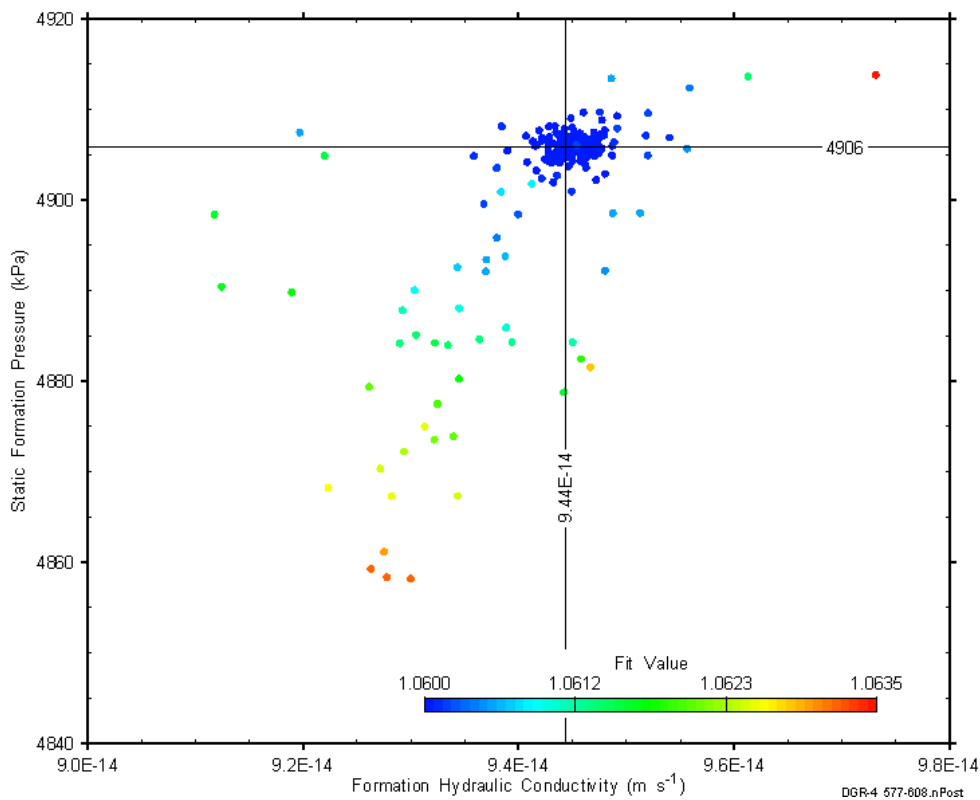


Figure 8-50: XY-scatter plot showing estimates of formation hydraulic conductivity and raw static formation pressure derived from the DGR4_577.45-608.19 perturbation analysis.

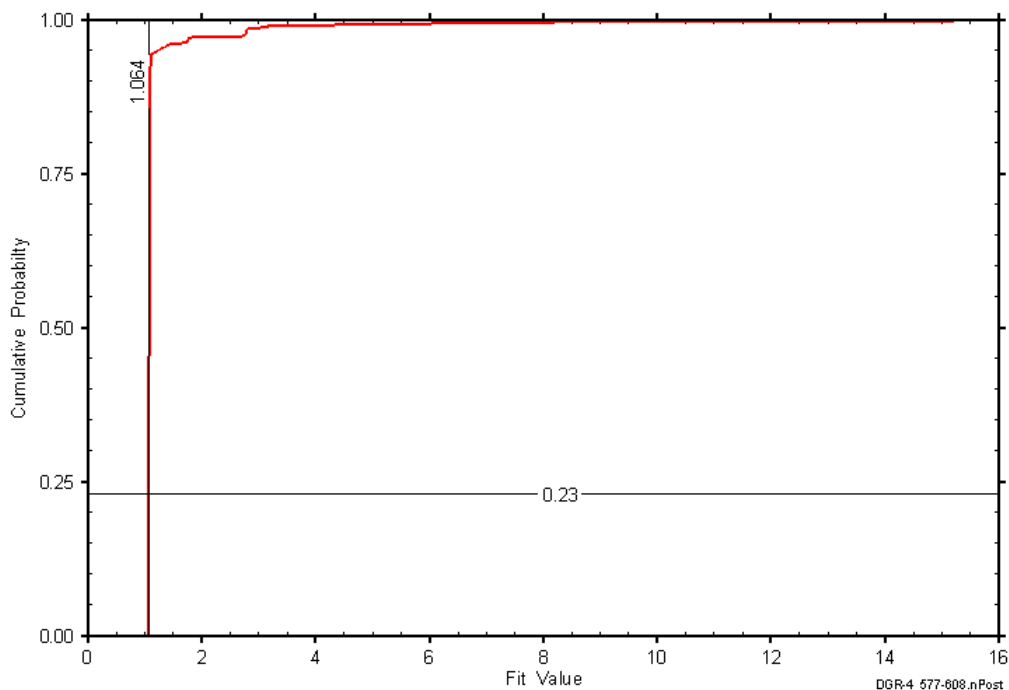


Figure 8-51: DGR4_577.45-608.19 fit value cumulative distribution function.

8.18 607.79-638.53 Blue Mountain

The DGR-4 interval from 607.79 to 638.53 m BGS included the lower 0.21 m of the Georgian Bay Formation while the balance of the interval was the upper 68% of the Blue Mountain Formation, a shale interbedded with siliceous siltstone and sandstone layers and fossiliferous limestone layers. An overview of the testing in this interval is given in Table 8-36 and the corresponding parameter estimates are given in Table 8-37. Two pulse-withdrawal tests were conducted in this interval.

Table 8-36: Summary of the DGR4_607.79-638.53 testing activities.

Formation / Unit		Top of Test Zone (m BGS)	Bottom of Test Zone (m BGS)	
Blue Mountain		607.79	638.53	
Test	Initiated	Magnitude (kPa)	Duration	Compressibility (Pa ⁻¹)
Shut-in	25-01-09 13:31	N/A	19 hr	N/A
PW 1	26-01-09 08:31	872	24 hr	3.8E-10
PW 2	27-01-09 08:50	882	24 hr	3.8E-10
Borehole Pressure History				
Event	Start		Pressure (kPa)	
Drilling Intercept	02-10-08 12:44		6530	
End of Geophysical Logging	30-10-08 12:00		6263	
Prior Testing	25-11-08 13:12		N/A	
Shut-in	25-01-09 13:31		6550	

Table 8-37: Summary of the DGR4_607.79-638.53 parameter estimates.

Parameter	Best Fit	Minimum	Maximum	Mean
K_f (m/s)	1.2E-14	1.1E-14	1.5E-14	1.3E-14
P_f (kPa)	1026	809	1732	1336
K_s (m/s)	2.3E-14	2.2E-14	3.4E-14	2.7E-14
t_s (cm)	0.5	0.3	1.9	1.0
S_s (m^{-1})	1.8E-6	1.0E-6	2.1E-6	1.5E-6

Figure 8-52 shows the measured pressure record from DGR4_607.79-638.53 used in this analysis along with the best-fit simulation and parameter values. The ranges of formation K and raw P_f values estimated from perturbation analysis are shown in Figure 8-53 and the fit value cumulative distribution function is shown in Figure 8-54.

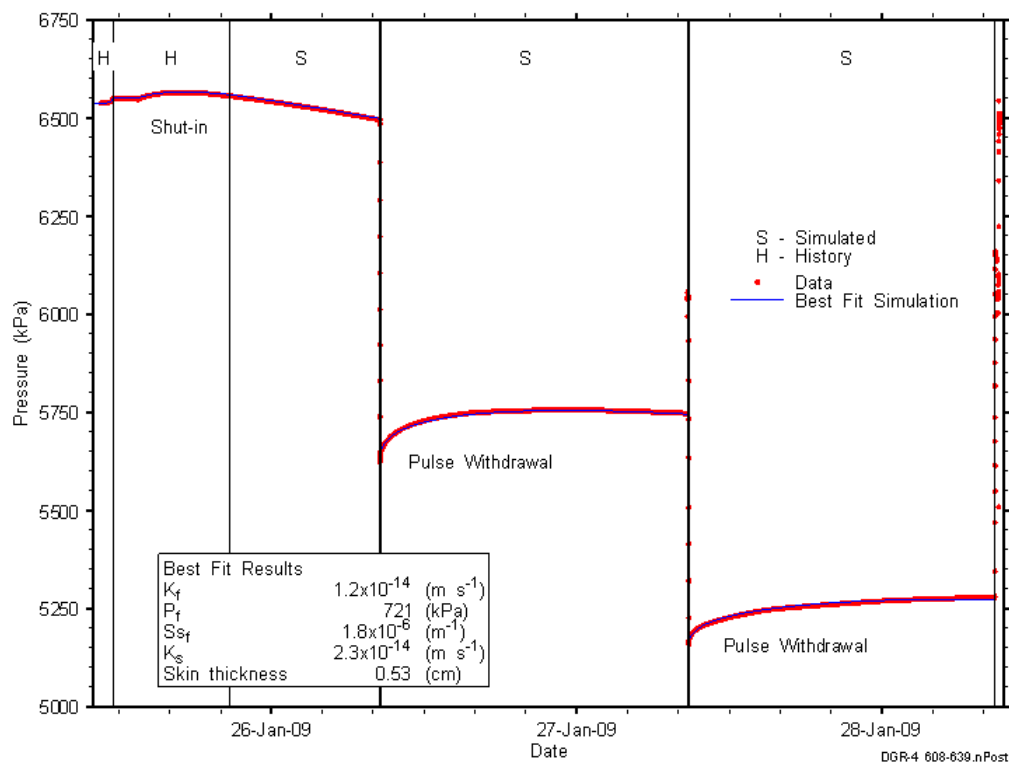


Figure 8-52: Annotated DGR4_607.79-638.53 testing sequence showing best-fit simulation and parameter estimates.

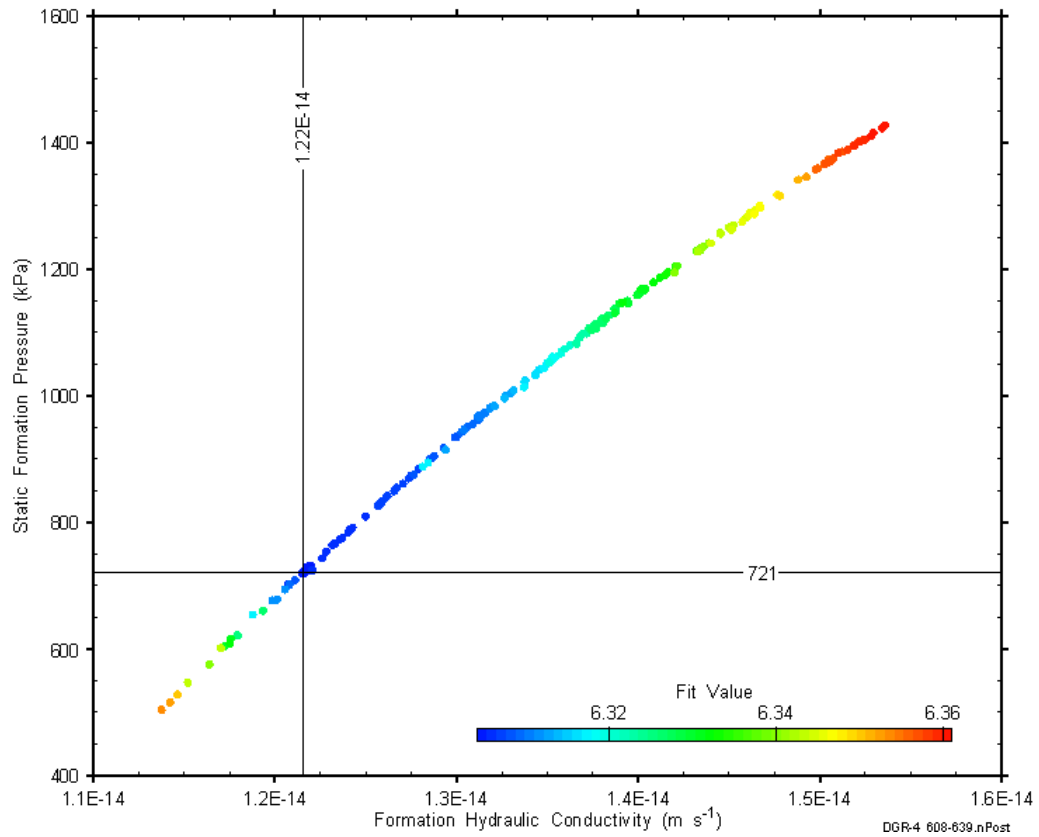


Figure 8-53: XY-scatter plot showing estimates of formation hydraulic conductivity and raw static formation pressure derived from the DGR4_607.79-638.53 perturbation analysis.

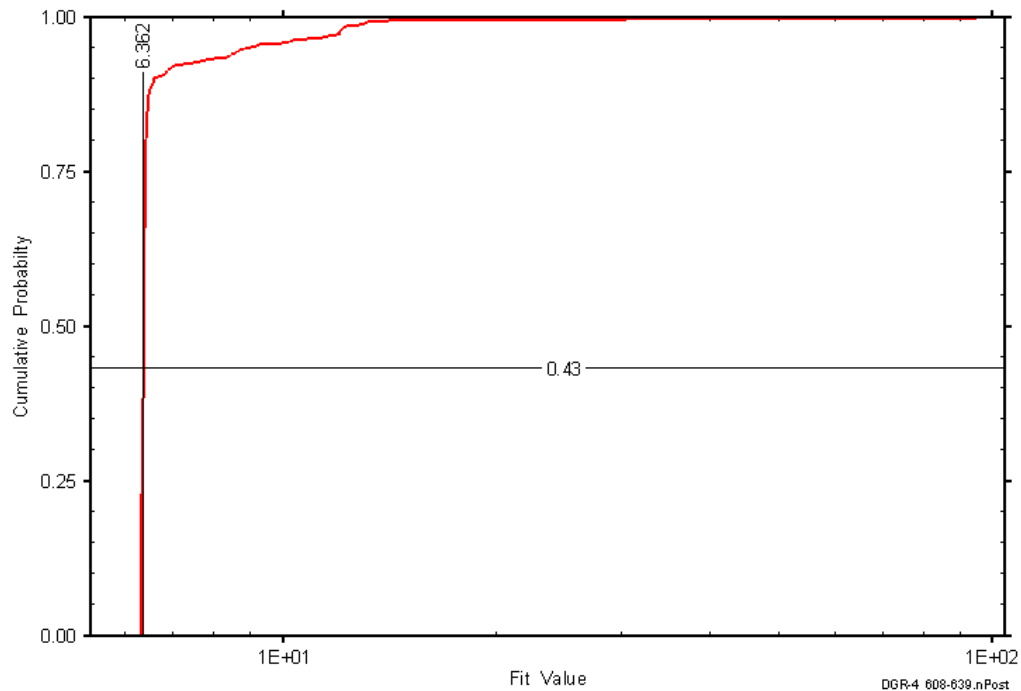


Figure 8-54: DGR4_607.79-638.53 fit value cumulative distribution function.

8.19 638.34-669.08 Blue Mountain-Collingwood-Cobourg

The DGR-4 interval from 638.34 to 669.08 m BGS included the lower 14.76 m of the Blue Mountain Formation, the entire 8.4-m thickness of the Collingwood Member of the Cobourg Formation, and the upper 7.58 m of the Lower Member of the Cobourg Formation. The lower Blue Mountain is shale, the Collingwood is interbedded shale and argillaceous limestone, and the Lower Member of the Cobourg is argillaceous limestone. An overview of the testing in this interval is given in Table 8-38 and the corresponding parameter estimates are given in Table 8-39. One pulse-withdrawal test was performed in this interval.

Table 8-38: Summary of the DGR4_638.34-669.08 testing activities.

Formation / Unit		Top of Test Zone (m BGS)		Bottom of Test Zone (m BGS)	
Blue Mountain-Collingwood-Cobourg		638.34		669.08	
Test	Initiated	Magnitude (kPa)	Duration	Compressibility (Pa ⁻¹)	
Shut-in	28-01-09 14:22	N/A	20 hr	N/A	
PW 1	29-01-09 10:23	899	46 hr	3.7E-10	
Borehole Pressure History					
Event		Start		Pressure (kPa)	
Drilling Intercept		05-10-08 09:18		6860	
End of Geophysical Logging		30-10-08 12:00		6592	
Prior Testing		25-11-08 13:12		N/A	
Shut-in		28-01-09 14:22		6893	

Table 8-39: Summary of the DGR4_638.34-669.08 parameter estimates.

Parameter	Best Fit	Minimum	Maximum	Mean
K_f (m/s)	1.3E-14	1.2E-14	1.3E-14	1.3E-14
P_f (kPa)	3325	3247	3401	3324
K_s (m/s)	2.0E-13	1.9E-13	2.2E-13	2.0E-13
t_s (cm)	0.4	0.4	0.4	0.4
S_s (m ⁻¹)	1.2E-6	1.1E-6	1.3E-6	1.2E-6

Figure 8-55 shows the measured pressure record from DGR4_638.34-669.08 used in this analysis along with the best-fit simulation and parameter values. The ranges of formation K and raw P_f values estimated from perturbation analysis are shown in Figure 8-56 and the fit value cumulative distribution function is shown in Figure 8-57.

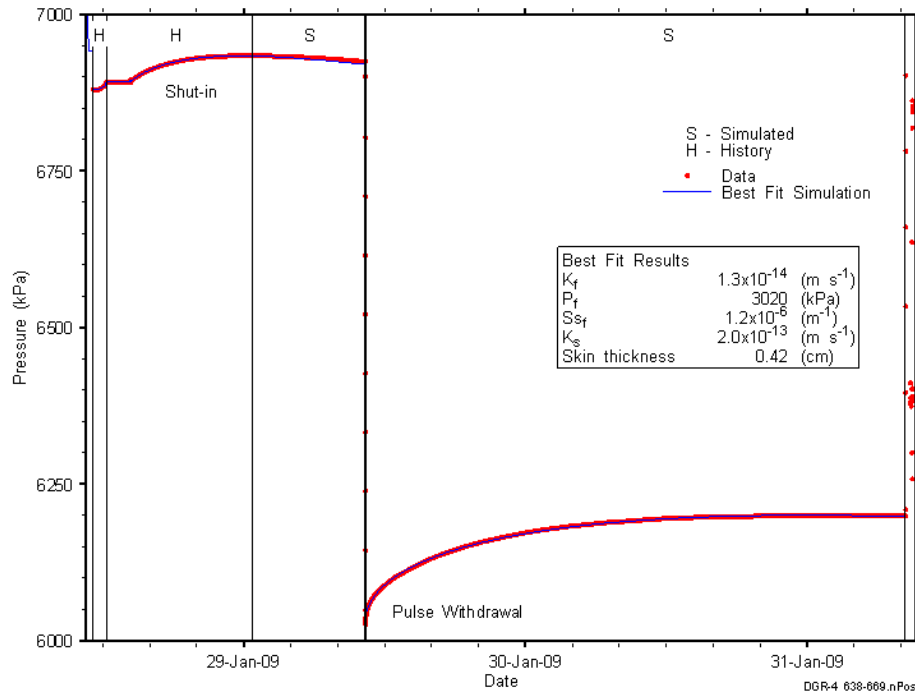


Figure 8-55: Annotated DGR4_638.34-669.08 testing sequence showing best-fit simulation and parameter estimates.

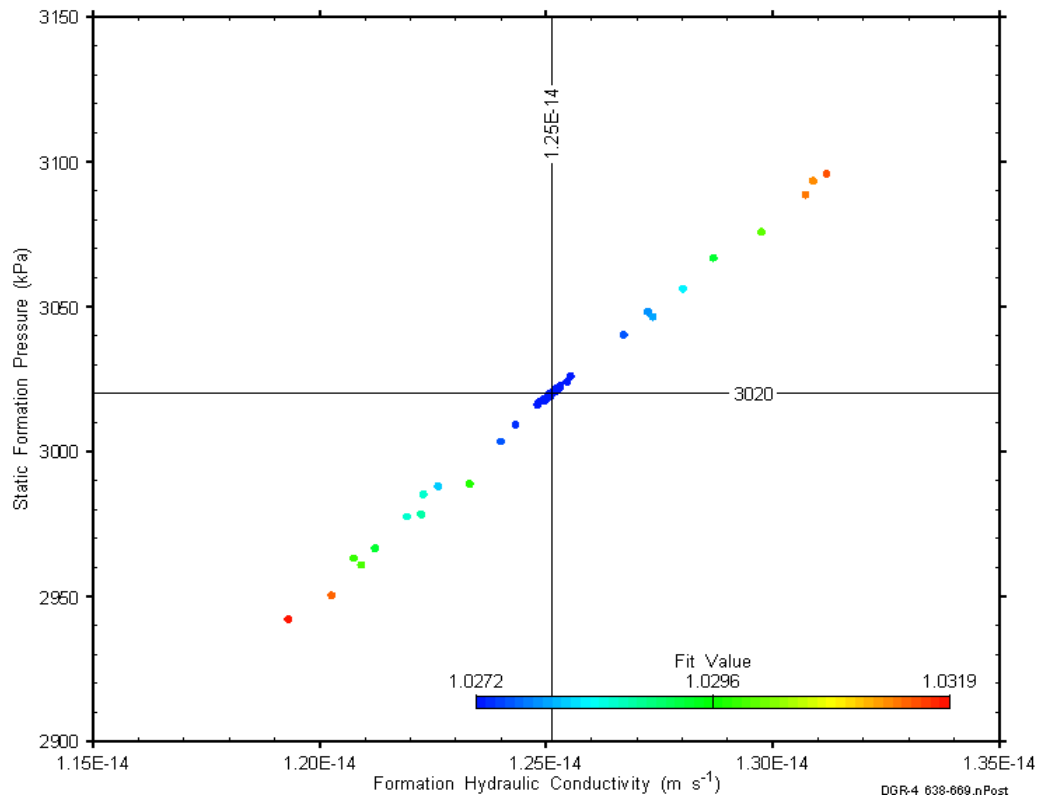


Figure 8-56: XY-scatter plot showing estimates of formation hydraulic conductivity and raw static formation pressure derived from the DGR4_638.34-669.08 perturbation analysis.

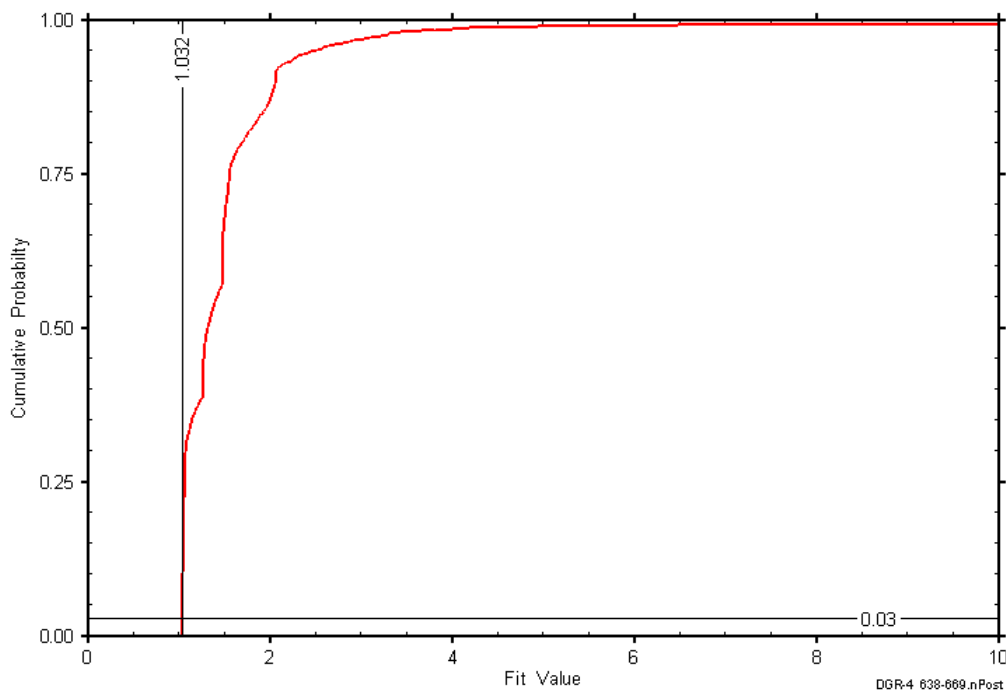


Figure 8-57: DGR4_638.34-669.08 fit value cumulative distribution function.

8.20 658.46-689.20 Collingwood - Cobourg

The DGR-4 interval from 658.46 to 689.20 m BGS included the lower 3.04 m of the Collingwood Member of the Cobourg Formation, the entire 27.5-m thickness of the Lower Member of the Cobourg Formation, and the upper 0.2 m of the Sherman Fall Formation. The entire interval consisted of argillaceous limestone. An overview of the testing in this interval is given in Table 8-40 and the corresponding parameter estimates are given in Table 8-41. Two pulse-withdrawal tests were performed in this interval.

Table 8-40: Summary of the DGR4_658.46-689.20 testing activities.

Formation / Unit		Top of Test Zone (m BGS)	Bottom of Test Zone (m BGS)	
Cobourg		658.46	689.20	
Test	Initiated	Magnitude (kPa)	Duration	Compressibility (Pa ⁻¹)
Shut-in	31-01-09 14:03	N/A	19 hr	N/A
PW 1	01-02-09 09:23	872	24 hr	3.7E-10
PW 2 (pt 1)	02-02-09 09:20	N/A	13 min	N/C
PW 2 (pt 2)	02-02-09 09:33	876	23 hr	3.7E-10
Borehole Pressure History				
Event	Start	Pressure (kPa)		
Drilling Intercept	06-10-08 15:57	7077		
End of Geophysical Logging	30-10-08 12:00	6809		
Prior Testing	25-11-08 13:12	N/A		
Shut-in	31-01-09 14:03	7117		

Table 8-41: Summary of the DGR4_658.46-689.20 parameter estimates.

Parameter	Best Fit	Minimum	Maximum	Mean
K_f (m/s)	2.4E-14	1.7E-14	1.1E-13	3.6E-14
P_f (kPa)	5912	5600	6458	6088
K_s (m/s)	6.6E-15	6.6E-15	6.7E-15	6.6E-15
t_s (cm)	10	7.5	22	13

Figure 8-58 shows the measured pressure record from DGR4_658.46-689.20 used in this analysis along with the best-fit simulation and parameter values. The S_s value for this analysis was fixed at $1E-6 \text{ m}^{-1}$, a value estimated from preliminary perturbation analysis. The ranges of formation K and raw P_f values estimated from perturbation analysis are shown in Figure 8-59 and the fit value cumulative distribution function is shown in Figure 8-60.

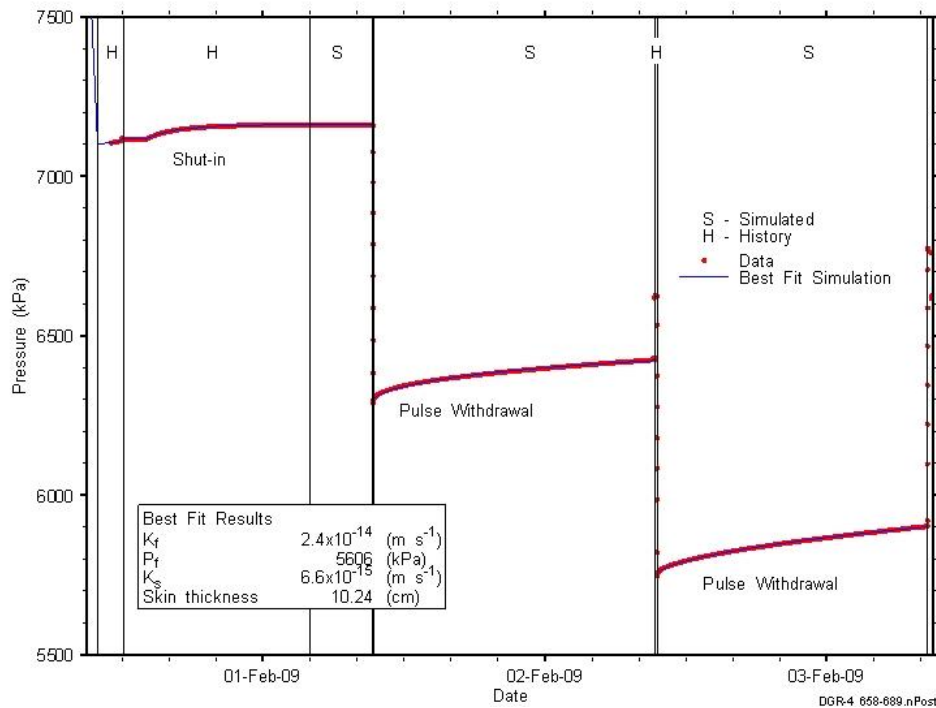


Figure 8-58: Annotated DGR4_658.46-689.20 testing sequence showing best-fit simulation and parameter estimates.

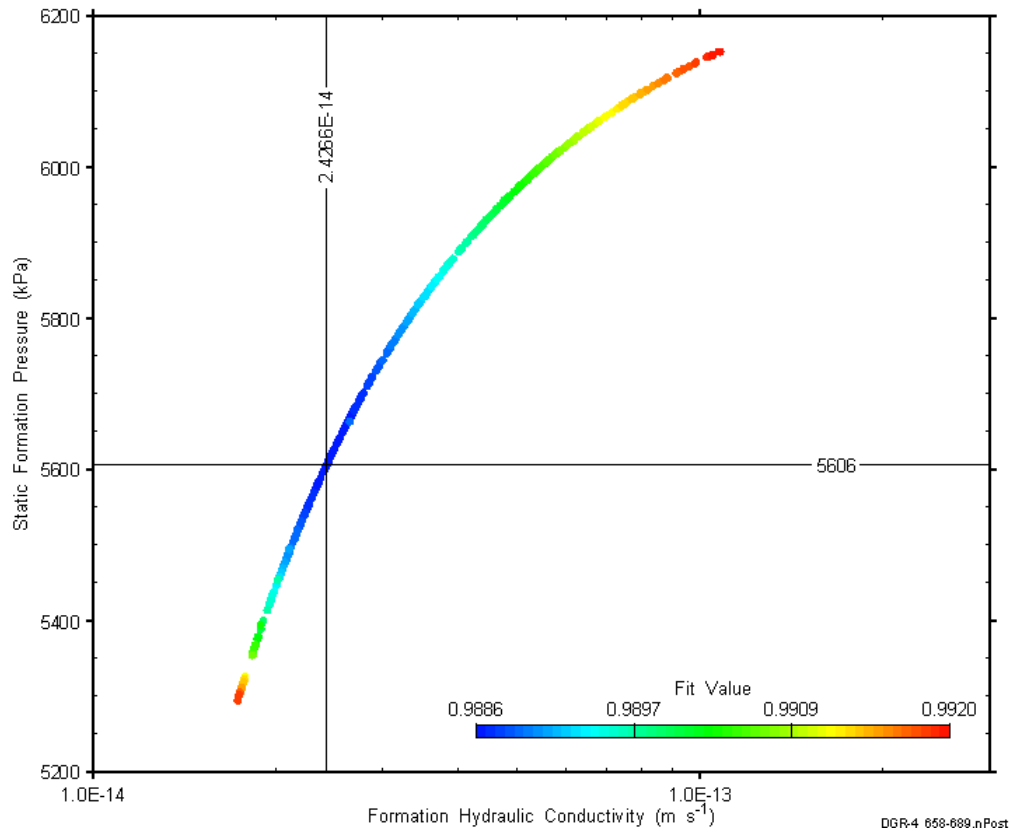


Figure 8-59: XY-scatter plot showing estimates of formation hydraulic conductivity and raw static formation pressure derived from the DGR4_658.46-689.20 perturbation analysis.

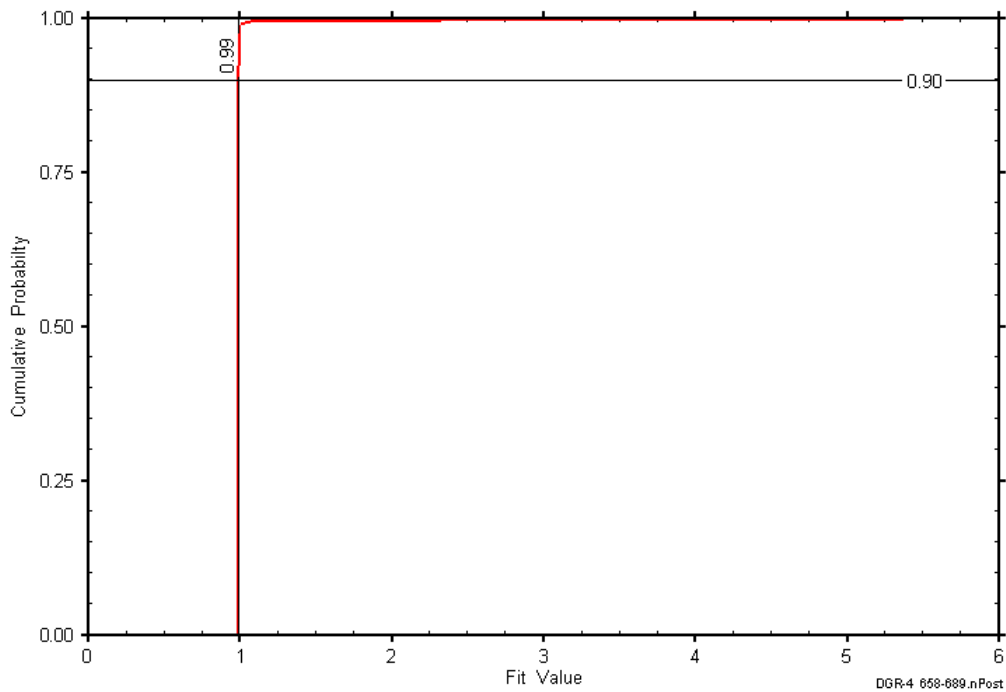


Figure 8-60: DGR4_658.46-689.20 fit value cumulative distribution function.

8.21 687.78-718.52 Cobourg-Sherman Fall-Kirkfield

The DGR-4 interval from 687.78 to 718.52 m BGS included the lower 1.22 m of the Cobourg Formation, the entire 28.3-m thickness of the Sherman Fall Formation, and the upper 1.22 m of the Kirkfield Formation. The entire interval consisted of interbedded argillaceous limestone and shale. An overview of the testing in this interval is given in Table 8-42 and the corresponding parameter estimates are given in Table 8-43. Two pulse-withdrawal tests were conducted in this interval.

Table 8-42: Summary of the DGR4_687.78-718.52 testing activities.

Formation / Unit	Top of Test Zone (m BGS)		Bottom of Test Zone (m BGS)	
Sherman Fall	687.78		718.52	
Test	Initiated	Magnitude (kPa)	Duration	Compressibility (Pa ⁻¹)
Shut-in	03-02-09 14:39	N/A	19 hr	N/A
PW 1	04-02-09 09:38	807	24 hr	3.8E-10
PW 2 (pt 1)	05-02-09 09:27	N/A	21 min	NC
PW 2 (pt 2)	05-02-09 09:48	810	23 hr	3.8E-10
Borehole Pressure History				
Event	Start		Pressure (kPa)	
Drilling Intercept	07-10-08 18:06		7393	
End of Geophysical Logging	30-10-08 12:00		7125	
Prior Testing	25-11-08 13:12		N/A	
Shut-in	03-02-09 14:39		7464	

Table 8-43: Summary of the DGR4_687.78-718.52 parameter estimates.

Parameter	Best Fit	Minimum	Maximum	Mean
K_f (m/s)	8.7E-15	8.6E-15	8.8E-15	8.7E-15
P_f (kPa)	3695	3688	3705	3695
K_s (m/s)	4.1E-14	3.0E-14	4.8E-14	4.1E-14
t_s (cm)	0.3	5E-5	0.3	0.2

Figure 8-61 shows the measured pressure record from DGR4_687.78-718.52 used in this analysis along with the best-fit simulation and parameter values. The S_s value for this analysis was fixed at $1E-6 \text{ m}^{-1}$, a value estimated from preliminary perturbation analysis. The ranges of formation K and raw P_f values estimated from perturbation analysis are shown in Figure 8-62 and the fit value cumulative distribution function is shown in Figure 8-63.

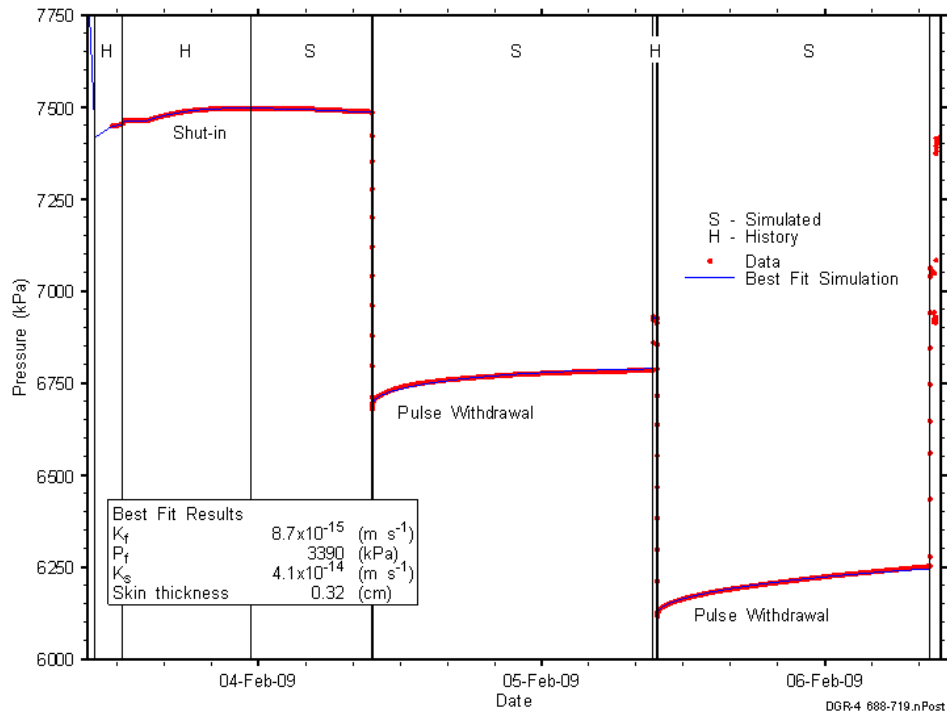


Figure 8-61: Annotated DGR4_687.78-718.52 testing sequence showing best-fit simulation and parameter estimates.

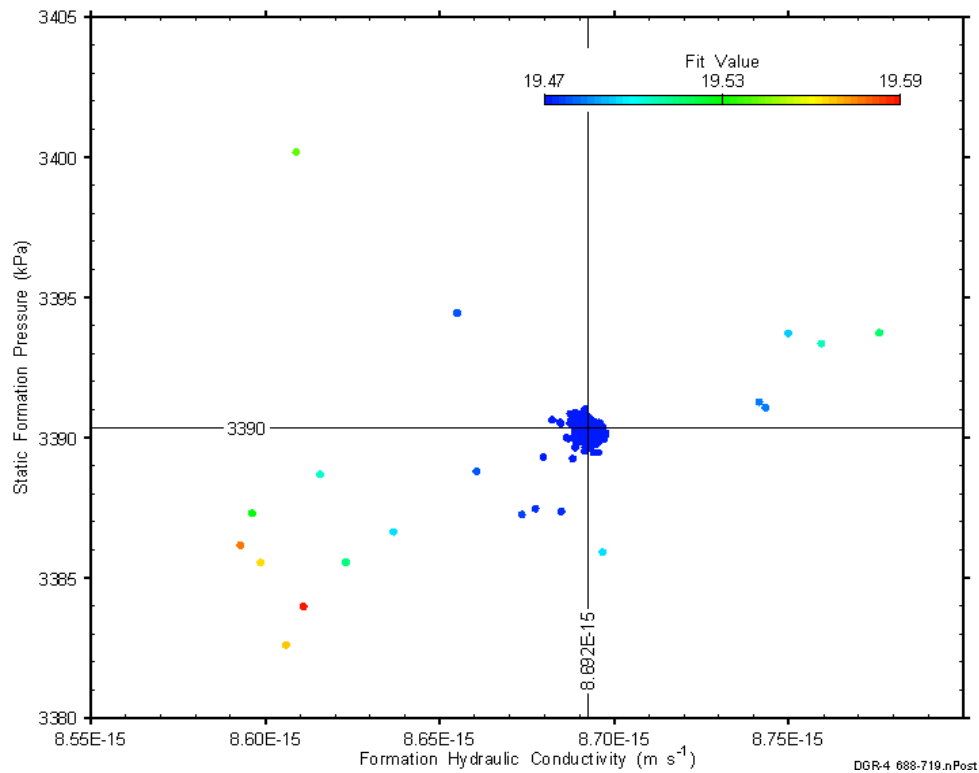


Figure 8-62: XY-scatter plot showing estimates of formation hydraulic conductivity and raw static formation pressure derived from the DGR4_687.78-718.52 perturbation analysis.

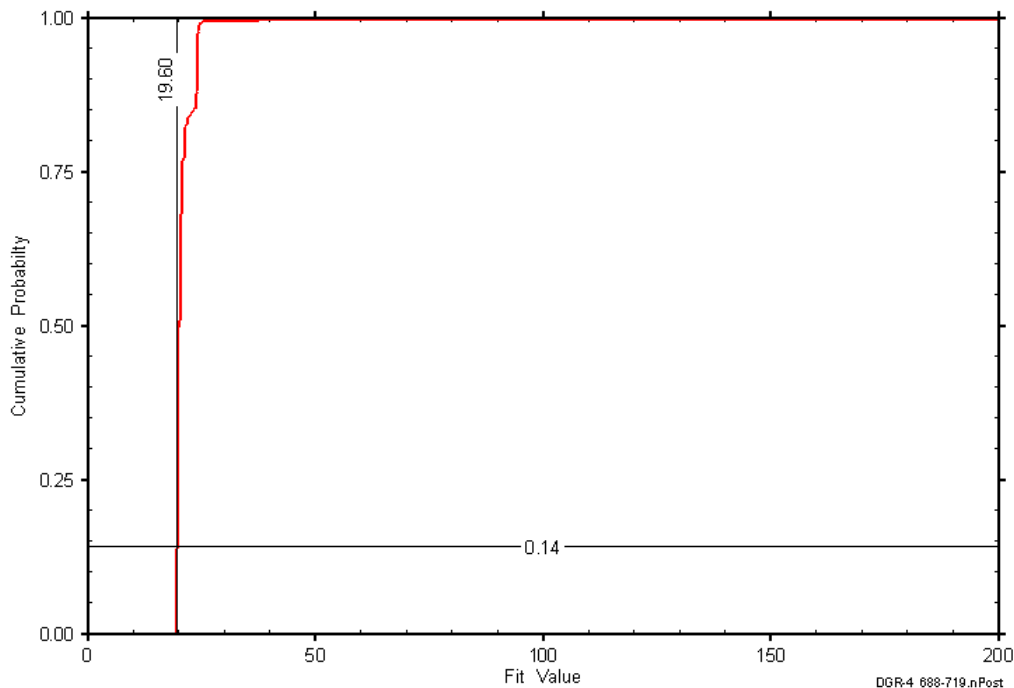


Figure 8-63: DGR4_687.78-718.52 fit value cumulative distribution function.

8.22 717.10-747.84 Kirkfield

The DGR-4 interval from 717.10 to 747.84 m BGS included the lower 0.2 m of the Sherman Fall Formation and the upper 30.54 m of the Kirkfield Formation. The entire interval consisted of interbedded argillaceous limestone and shale. An overview of the testing in this interval is given in Table 8-44 and the corresponding parameter estimates are given in Table 8-45. Two pulse-withdrawal tests were conducted in this interval.

Table 8-44: Summary of the DGR4_717.10-747.84 testing activities.

Formation / Unit		Top of Test Zone (m BGS)	Bottom of Test Zone (m BGS)	
Kirkfield		717.10	747.84	
Test	Initiated	Magnitude (kPa)	Duration	Compressibility (Pa ⁻¹)
Shut-in	06-02-09 14:55	N/A	19 hr	N/A
PW 1	07-02-09 09:30	819	24 hr	3.7E-10
PW 2 (pt 1)	08-02-09 09:13	N/A	13 min	NC
PW 2 (pt 2)	08-02-09 09:26	822	23 hr	3.7E-10
Borehole Pressure History				
Event	Start	Pressure (kPa)		
Drilling Intercept	08-10-08 22:34	7709		
End of Geophysical Logging	30-10-08 12:00	7442		
Prior Testing	25-11-08 13:12	N/A		
Shut-in	06-02-09 14:55	7790		

Table 8-45: Summary of the DGR4_717.10-747.84 parameter estimates.

Parameter	Best Fit	Minimum	Maximum	Mean
K_f (m/s)	4.1E-15	3.9E-15	4.3E-15	4.1E-15
P_f (kPa)	5729	5177	5648	5424
K_s (m/s)	1.5E-14	1.4E-14	1.6E-14	1.5E-14
t_s (cm)	1.8	1.5	2.1	1.8

Figure 8-64 shows the measured pressure record from DGR4_717.10-747.84 used in this analysis along with the best-fit simulation and parameter values. The S_s value for this analysis was fixed at $1E-6 \text{ m}^{-1}$, a value estimated from preliminary perturbation analysis. The ranges of formation K and raw P_f values estimated from perturbation analysis are shown in Figure 8-65 and the fit value cumulative distribution function is shown in Figure 8-66.

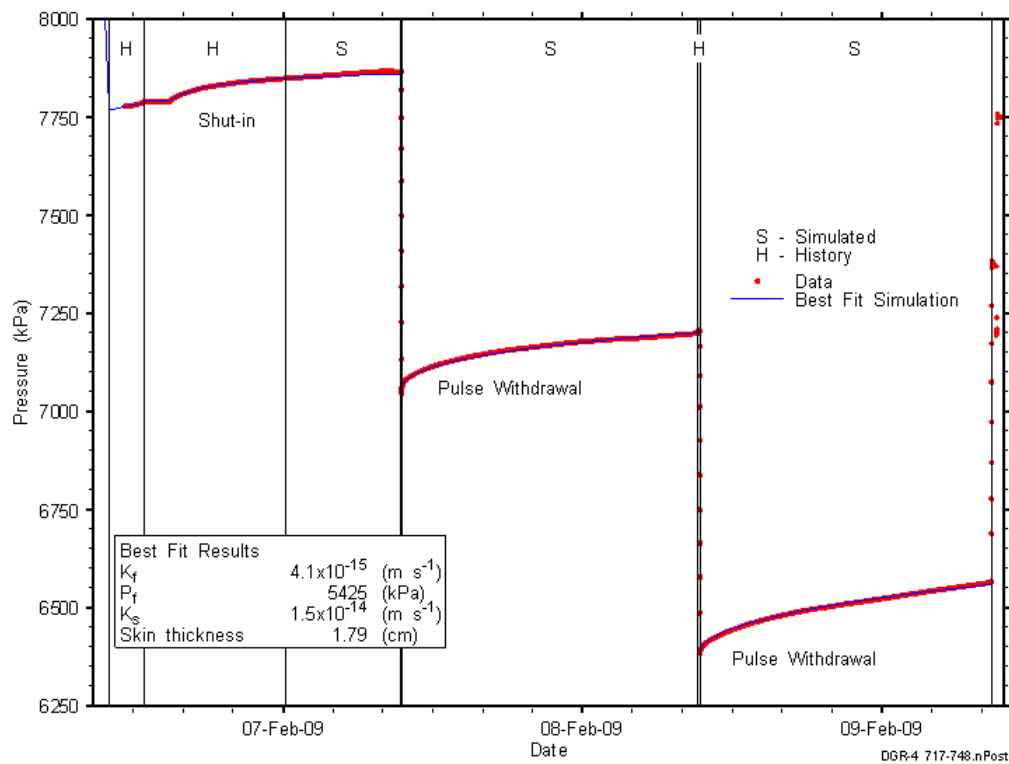


Figure 8-64: Annotated DGR4_717.10-747.84 testing sequence showing best-fit simulation and parameter estimates.

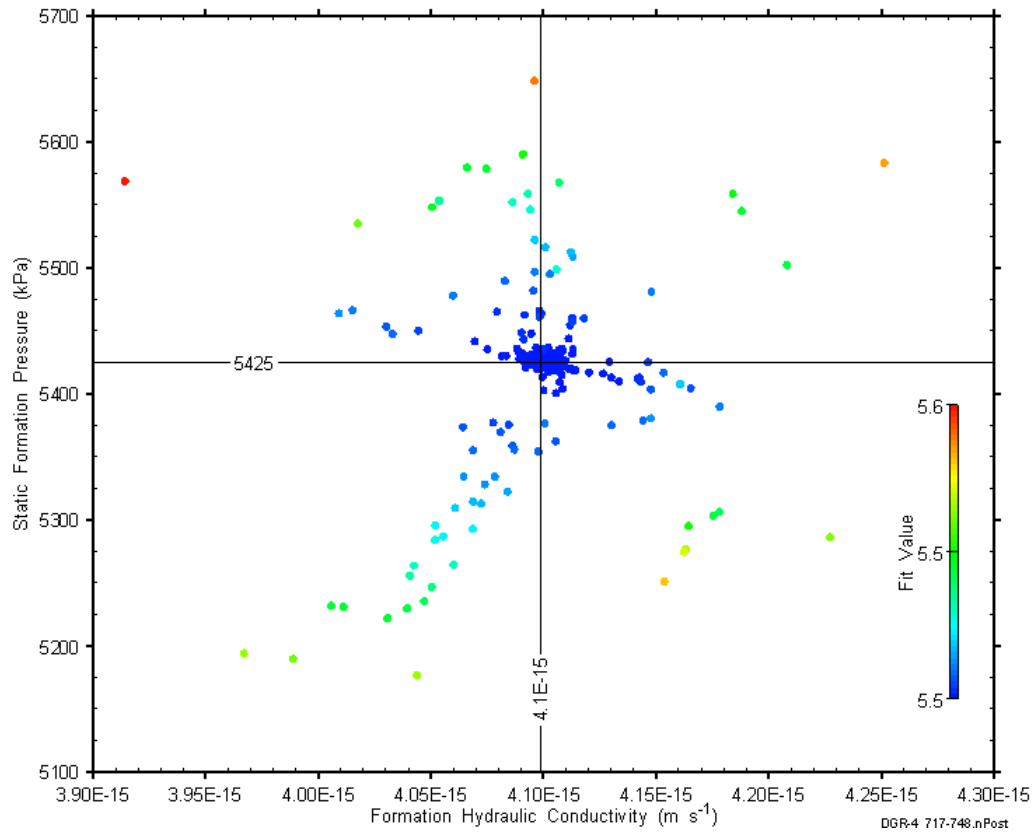


Figure 8-65: XY-scatter plot showing estimates of formation hydraulic conductivity and raw static formation pressure derived from the DGR4_717.10-747.84 perturbation analysis.

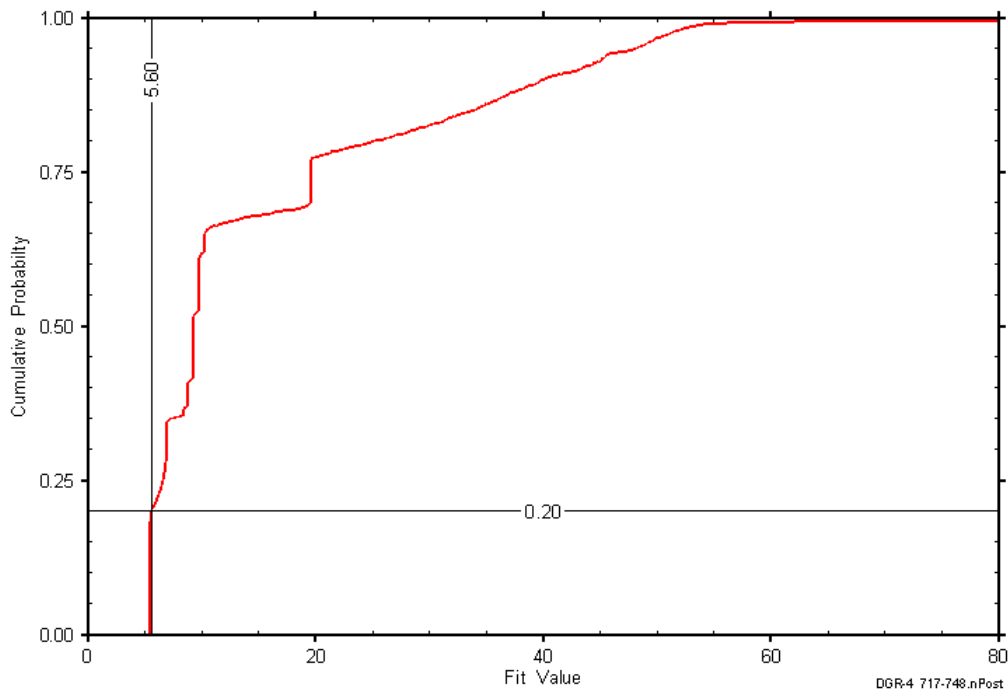


Figure 8-66: DGR4_717.10-747.84 fit value cumulative distribution function.

8.23 747.64-778.38 Kirkfield-Coboconk

The DGR-4 interval from 747.64 to 778.38 m BGS included the lower 15.36 m of the Kirkfield Formation and the upper 15.38 m of the Coboconk Formation. The Kirkfield consists of interbedded argillaceous limestone and shale, and the Coboconk consists of limestone with bituminous argillaceous laminae. Both the 0.1-m-thick volcanic ash layer and a 0.1-m-thick dolostone layer typically observed in the Coboconk were included in the test interval. An overview of the testing in this interval is given in Table 8-46 and the corresponding parameter estimates are given in Table 8-47. A pulse-withdrawal test and a pulse-injection test were conducted in this interval.

Table 8-46: Summary of the DGR4_747.64-778.38 testing activities.

Formation / Unit		Top of Test Zone (m BGS)	Bottom of Test Zone (m BGS)	
Kirkfield-Coboconk		747.64	778.38	
Test	Initiated	Magnitude (kPa)	Duration	Compressibility (Pa ⁻¹)
Shut-in	09-02-09 15:02	N/A	19 hr	N/A
PW	10-02-09 09:37	831	23 hr	3.8E-10
PI	11-02-09 09:02	827	24 hr	3.8E-10
Borehole Pressure History				
Event	Start		Pressure (kPa)	
Drilling Intercept	18-10-08 16:24		8038	
End of Geophysical Logging	30-10-08 12:00		7771	
Prior Testing	25-11-08 13:12		N/A	
Shut-in	09-02-09 15:02		8133	

Table 8-47: Summary of the DGR4_747.64-778.38 parameter estimates.

Parameter	Best Fit	Minimum	Maximum	Mean
K_f (m/s)	4.7E-12	4.4E-12	5.0E-12	4.7E-12
P_f (kPa)	8816	8808	8824	8816
K_s (m/s)	2.8E-13	2.2E-13	4.1E-13	2.8E-13
t_s (cm)	3.3	2.6	4.6	3.3
S_s (m ⁻¹)	1.9E-6	1.0E-6	2.9E-6	1.9E-6

Figure 8-67 shows the measured pressure record from DGR4_747.64-778.38 used in this analysis along with the best-fit simulation and parameter values. The ranges of formation K and raw P_f values estimated from perturbation analysis are shown in Figure 8-68 and the fit value cumulative distribution function is shown in Figure 8-69.

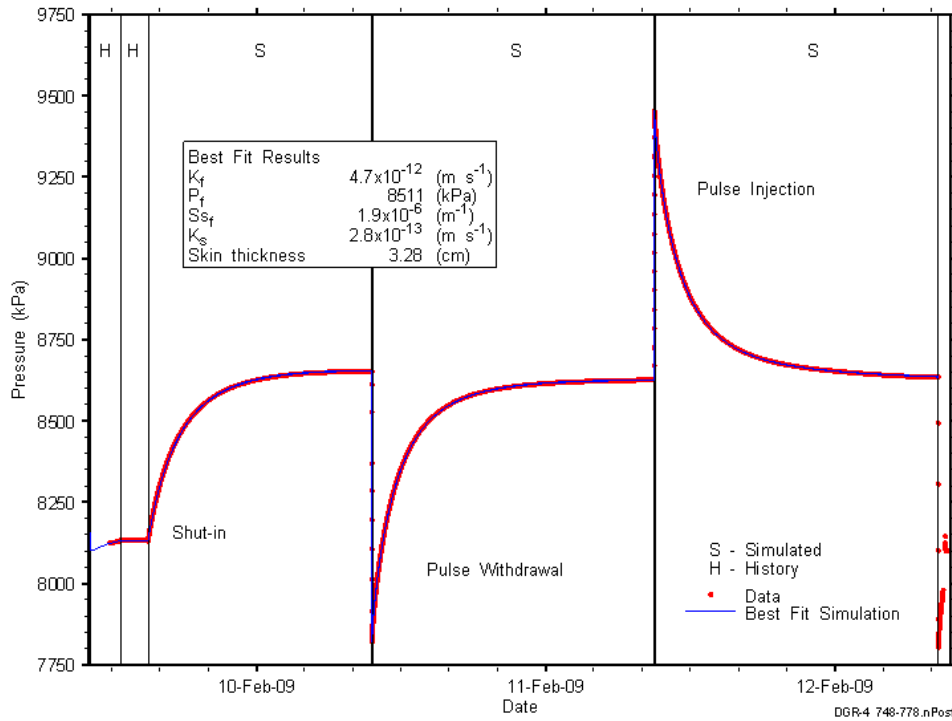


Figure 8-67: Annotated DGR4_747.64-778.38 testing sequence showing best-fit simulation and parameter estimates.

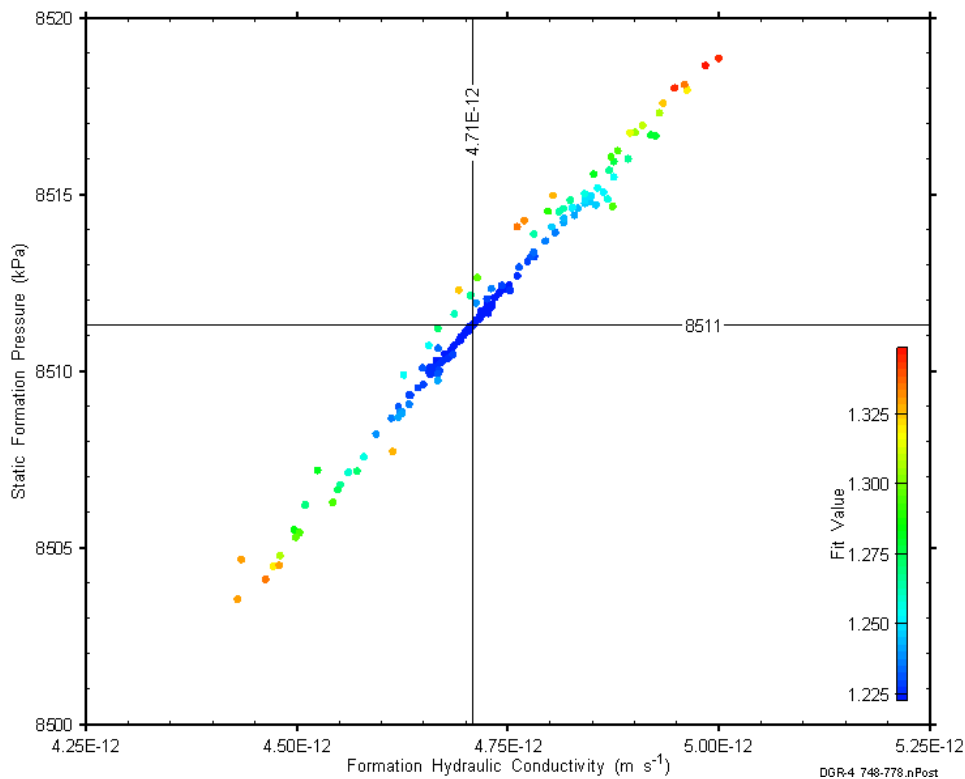


Figure 8-68: XY-scatter plot showing estimates of formation hydraulic conductivity and raw static formation pressure derived from the DGR4_747.64-778.38 perturbation analysis.

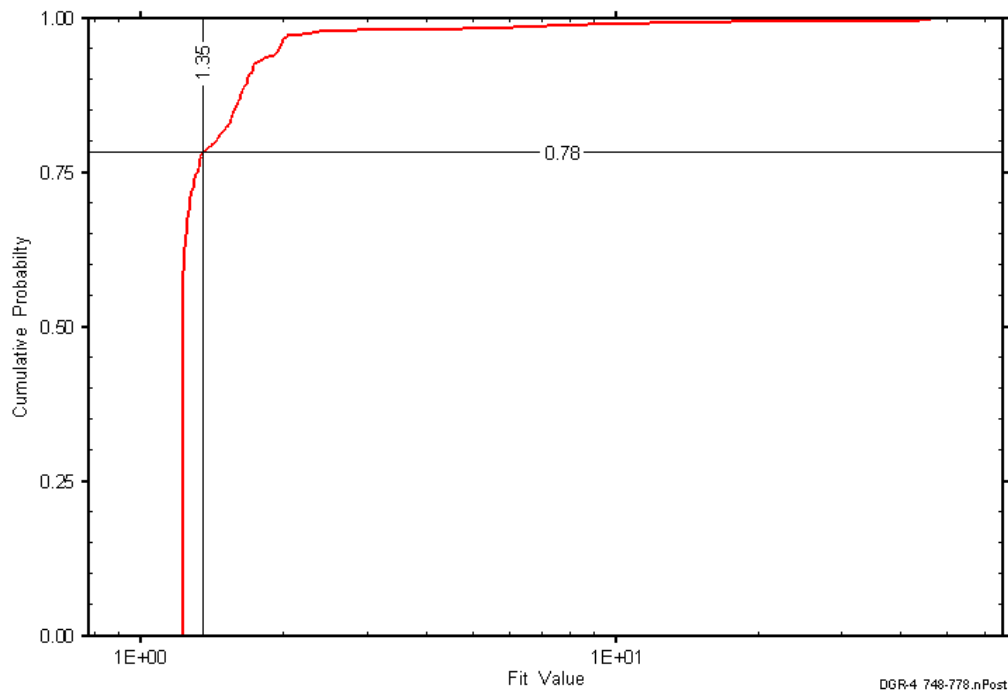


Figure 8-69: DGR4_747.64-778.38 fit value cumulative distribution function.

8.24 762.80-793.54 Coboconk-Gull River

The DGR-4 interval from 762.80 to 793.54 m BGS included the lower 0.2 m of the Kirkfield Formation, the entire 23.8- m thickness of the Coboconk Formation, and the upper 6.74 m of the Gull River Formation. The lowermost Kirkfield consists of interbedded argillaceous limestone and shale, the Coboconk consists of limestone with bituminous argillaceous laminae, and the upper Gull River consists of limestone with shale laminae and interbeds. Both the 0.1-m-thick volcanic ash layer and the 0.1-m-thick dolostone layer typically observed in the Coboconk were included in the test interval. An overview of the testing in this interval is given in Table 8-48 and the corresponding parameter estimates are given in Table 8-49. A pulse-injection test and a pulse-withdrawal test were conducted in this interval.

Table 8-48: Summary of the DGR4_762.80-793.54 testing activities.

Formation / Unit		Top of Test Zone (m BGS)	Bottom of Test Zone (m BGS)	
Coboconk-Gull River		762.80	793.54	
Test	Initiated	Magnitude (kPa)	Duration	Compressibility (Pa ⁻¹)
Shut-in	12-02-09 14:20	N/A	19 hr	N/A
PI	13-02-09 09:04	870	24 hr	3.8E-10
PW	14-02-09 08:56	874	24 hr	3.8E-10
Borehole Pressure History				
Event	Start	Pressure (kPa)		
Drilling Intercept	19-10-08 09:25	8201		
End of Geophysical Logging	30-10-08 12:00	7934		
Prior Testing	25-11-08 13:12	N/A		
Shut-in	12-02-09 14:20	8304		

Table 8-49: Summary of the DGR4_762.80-793.54 parameter estimates.

Parameter	Best Fit	Minimum	Maximum	Mean
K_f (m/s)	9.6E-12	8.5E-12	1.1E-11	9.6E-12
P_f (kPa)	8967	8954	8982	8967
K_s (m/s)	6.6E-13	5.4E-13	7.5E-13	6.6E-13
t_s (cm)	11	8.0	15	11

Figure 8-70 shows the measured pressure record from DGR4_762.80-793.54 used in this analysis along with the best-fit simulation and parameter values. The S_s value for this analysis was fixed at $1E-6 \text{ m}^{-1}$, a value estimated from preliminary perturbation analysis. The ranges of formation K and raw P_f values estimated from perturbation analysis are shown in Figure 8-71 and the fit value cumulative distribution function is shown in Figure 8-72.

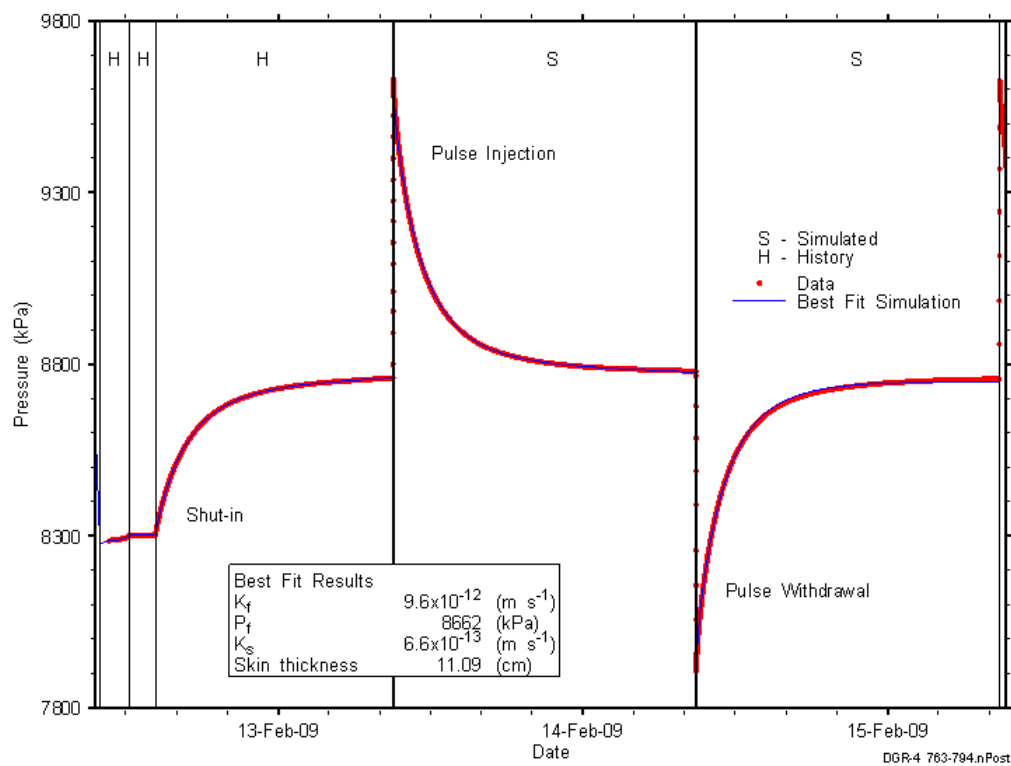


Figure 8-70: Annotated DGR4_762.80-793.54 testing sequence showing best-fit simulation and parameter estimates.

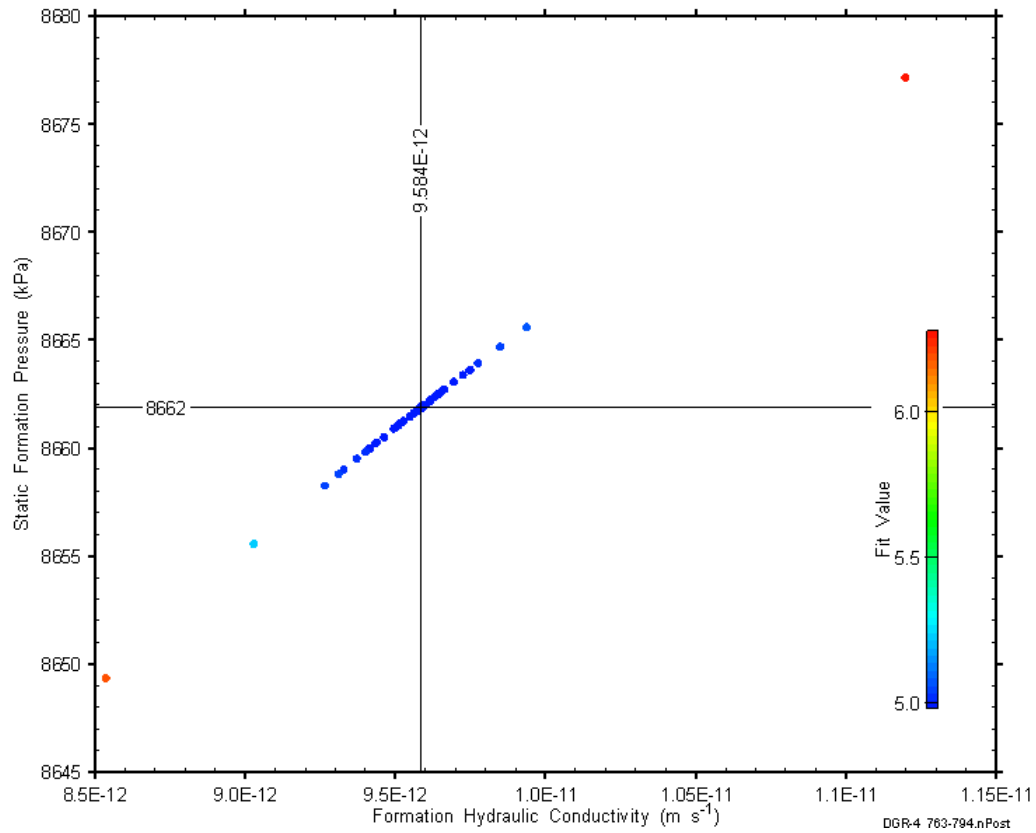


Figure 8-71: XY-scatter plot showing estimates of formation hydraulic conductivity and raw static formation pressure derived from the DGR4_762.80-793.54 perturbation analysis.

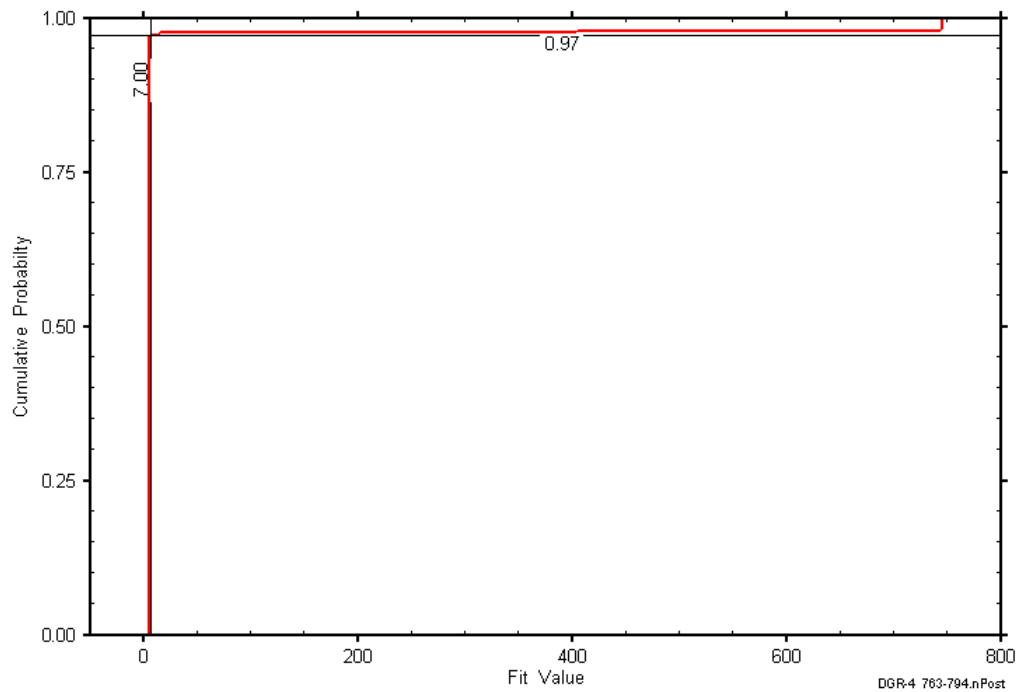


Figure 8-72: DGR4_762.80-793.54 fit value cumulative distribution function.

8.25 793.34-824.08 Gull River

The DGR-4 interval from 793.34 to 824.08 m BGS was entirely contained within a section of the Gull River Formation consisting of limestone with shale laminae and interbeds, a dolostone layer 0.6 m thick, and a dolomitic limestone layer over the bottom 0.65 m of the interval (Briscoe et al., 2010). An overview of the testing in this interval is given in Table 8-50 and the corresponding parameter estimates are given in Table 8-51. A pulse-injection test and a pulse-withdrawal test were conducted in this interval.

Table 8-50: Summary of the DGR4_793.34-824.08 testing activities.

Formation / Unit		Top of Test Zone (m BGS)		Bottom of Test Zone (m BGS)	
Gull River		793.34		824.08	
Test	Initiated	Magnitude (kPa)	Duration	Compressibility (Pa ⁻¹)	
Shut-in	15-02-09 12:51	N/A	21 hr	N/A	
PI	16-02-09 09:44	924	24 hr	3.7E-10	
PW	17-02-09 09:21	933	23 hr	3.7E-10	
Borehole Pressure History					
Event		Start		Pressure (kPa)	
Drilling Intercept		20-10-08 21:01		8531	
End of Geophysical Logging		30-10-08 12:00		8263	
Prior Testing		25-11-08 13:12		N/A	
Shut-in		15-02-09 12:51		8662	

Table 8-51: Summary of the DGR4_793.34-824.08 parameter estimates.

Parameter	Best Fit	Minimum	Maximum	Mean
K _f (m/s)	5.5E-12	5.5E-12	5.6E-12	5.5E-12
P _f (kPa)	10190	10189	10190	10190
K _s (m/s)	6.3E-13	6.2E-13	6.5E-13	6.3E-13
t _s (cm)	8.5	8.3	8.9	8.5

Figure 8-73 shows the measured pressure record from DGR4_793.34-824.08 used in this analysis along with the best-fit simulation and parameter values. The S_s value for this analysis was fixed at 1E-6 m⁻¹, a value estimated from preliminary perturbation analysis. The ranges of formation K and raw P_f values estimated from perturbation analysis are shown in Figure 8-74 and the fit value cumulative distribution function is shown in Figure 8-75.

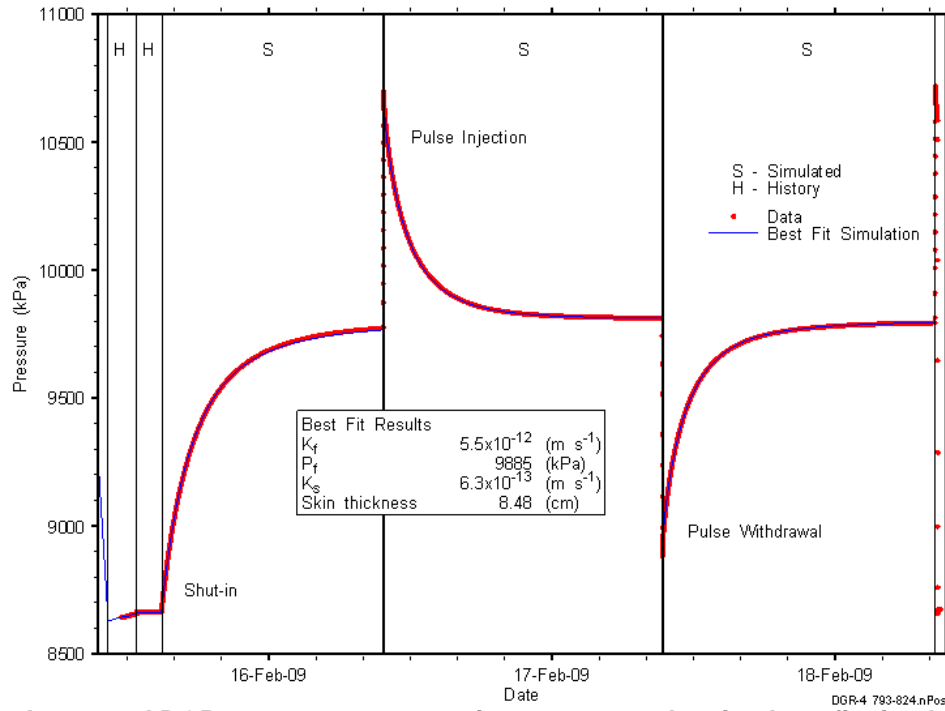


Figure 8-73: Annotated DGR4_793.34-824.08 testing sequence showing best-fit simulation and parameter estimates.

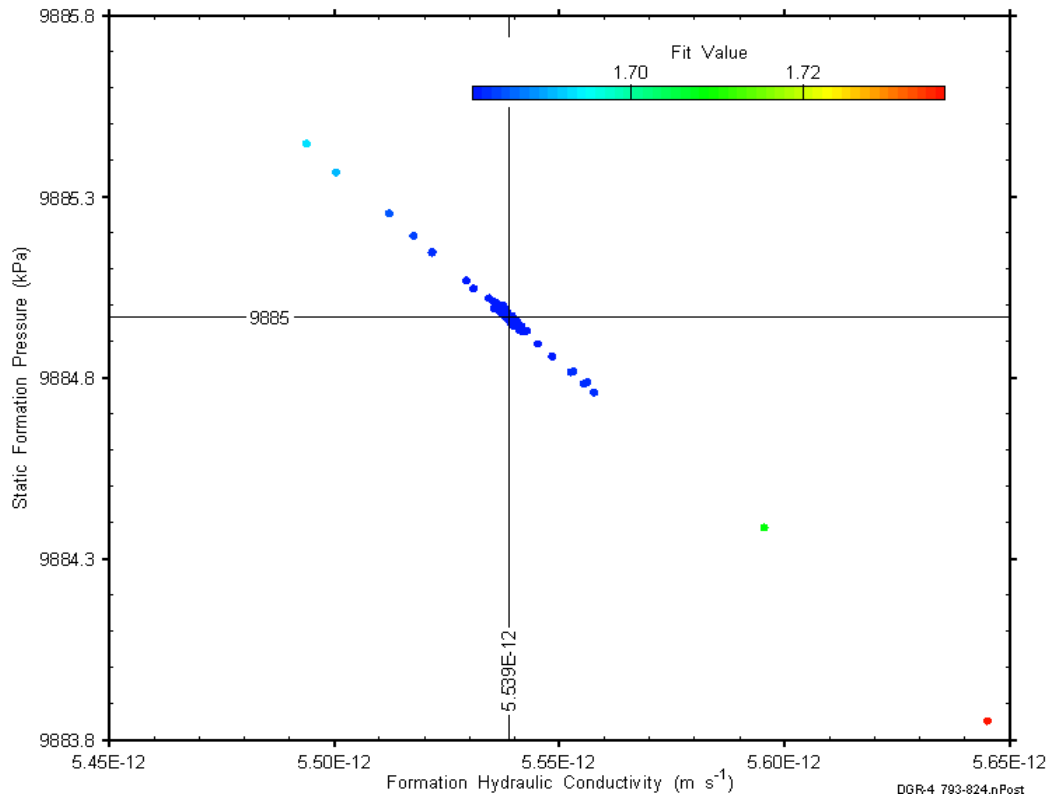


Figure 8-74: XY-scatter plot showing estimates of formation hydraulic conductivity and raw static formation pressure derived from the DGR4_793.34-824.08 perturbation analysis.

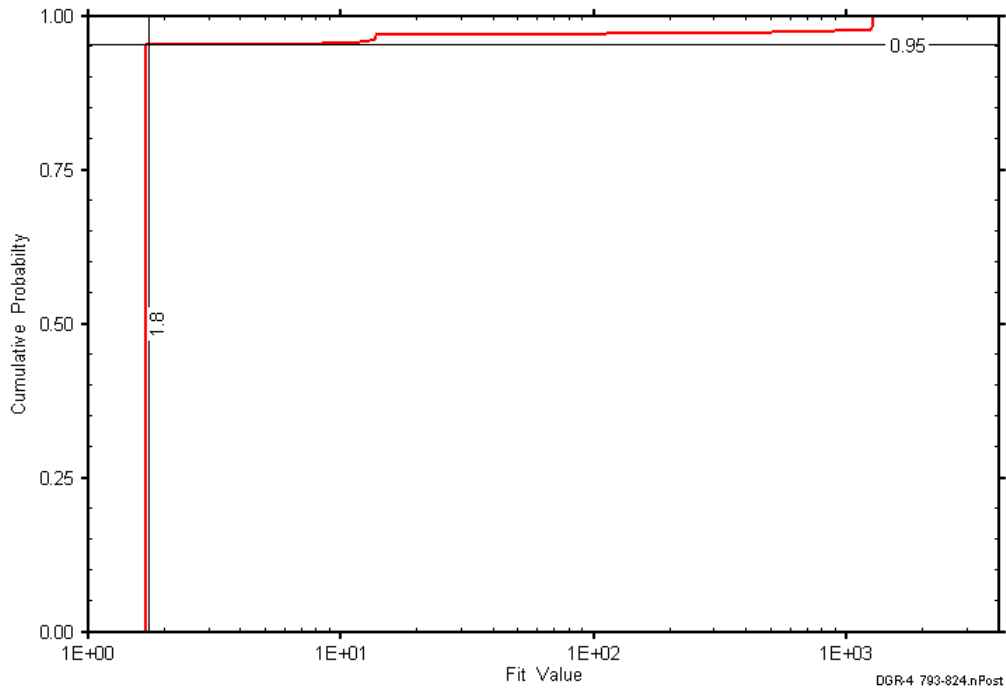


Figure 8-75: DGR4_793.34-824.08 fit value cumulative distribution function. Is this cool, or what

8.26 Summary of DGR-4 Results

The best-fit parameter estimates derived from the DGR-4 analyses are given in Table 8-52. Figure 8-76 through Figure 8-80 present stratigraphic profiles of the analysis results for hydraulic conductivity, formation pressure, specific storage, skin factor, and test-zone compressibility respectively.

Table 8-52: Best-fit parameter estimates derived from the DGR-4 analyses

Formation(s) Tested	Top	Bottom	K_f	P_f	S_s	K_s	t_s	s	C_{tz}
	m BGS	m BGS	$m s^{-1}$	kPa	m^{-1}	$m s^{-1}$	cm		Pa^{-1}
Salina F	190.63	221.37	5.6E-14	1563	9.9E-7	9.3E-14	17	-0.47	4.4E-10
Salina F-C	218.13	248.87	4.1E-13	1945	1.2E-7	1.1E-12	26	-0.96	4.2E-10
Salina C-B	247.00	277.74	4.7E-13	1975	4.7E-6	n/a	n/a	n/a	1.2E-9
Salina B	261.63	292.37	3.1E-13	1919	2.0E-7	2.2E-12	26	-1.3	1.1E-9
Salina B-A2 carbonate	284.26	315.00	4.5E-10	3182	8.5E-5	6.4E-11	5.9	3.6	n/c
Salina A2-A1 carbonate	296.63	327.37	1.7E-8	3197	1.0E-6*	8.0E-9	56	2.5	n/c
Salina A1 carbonate	327.26	358.00	4.4E-8	3484	1.0E-6*	3.7E-10	50	240	5.2E-10
Salina A1-A0- Guelph	350.53	381.27	3.0E-9	3935	1.0E-6*	4.0E-8	109	-2.6	n/c
Goat Island- Gasport-Lions Head-Fossil Hill	381.08	411.82	1.6E-12	5067	8.4E-7	4.2E-12	31	-1.0	1.4E-9
Cabot Head- Manitoulin	411.51	442.25	4.4E-14	4594	7.8E-7	1.2E-13	2.6	-0.20	4.0E-10
Manitoulin- Queenston	432.00	462.74	1.9E-12	2271	7.9E-7	1.1E-11	25	-1.3	1.0E-8
Queenston	458.23	488.97	2.3E-14	3647	1.0E-6*	1.7E-13	2.3	-0.25	4.5E-10
Queenston	488.77	519.51	2.2E-14	3474	9.7E-7	2.2E-13	2.4	-0.26	6.8E-10
Georgian Bay	519.10	549.84	5.2E-15	1130	4.5E-6	3.2E-14	0.5	-0.053	5.4E-10
Georgian Bay (a)	548.28	579.02	2.8E-14	875	4.6E-7	2.5E-13	5.9	-0.53	3.9E-10
Georgian Bay (b)	548.28	579.02	4.6E-14	3926	2.6E-7	1.3E-12	5.9	-0.58	3.9E-10
Georgian Bay	577.45	608.19	9.4E-14	5210	1.0E-6*	1.9E-11	9.2	-0.82	2.7E-9
Blue Mountain	607.79	638.53	1.2E-14	1026	1.8E-6	2.3E-14	0.5	-0.034	3.8E-10
Blue Mountain- Collingwood- Cobourg	638.34	669.08	1.3E-14	3325	1.2E-6	2.0E-13	0.4	-0.054	3.7E-10
Cobourg	658.46	689.20	2.4E-14	5912	1.0E-6*	6.6E-15	10	2.4	3.7E-10
Sherman Fall	687.78	718.52	8.7E-15	3695	1.0E-6*	4.1E-14	0.3	-0.035	3.8E-10
Kirkfield	717.10	747.84	4.1E-15	5729	1.0E-6*	1.5E-14	1.8	-0.16	3.7E-10
Kirkfield- Coboconk	747.64	778.38	4.7E-12	8816	1.9E-6	2.8E-13	3.3	6.0	3.8E-10
Coboconk-Gull River	762.80	793.54	9.6E-12	8967	1.0E-6*	6.6E-13	11	13	3.8E-10
Gull River	793.34	824.08	5.5E-12	10190	1.0E-6*	6.3E-13	8.5	6.1	3.7E-10

n/a: not applicable

n/c: not calculated

*: fixed

As shown in Figure 8-76 and Table 8-52, all but four of the Silurian test intervals in DGR-4 had K values between approximately $4E-14$ and $2E-12$ m/s. Significantly higher K values were found in the Salina B-A2 carbonate interval ($4.5E-10$ m/s), the Upper Salina A1 carbonate interval ($1.7E-8$ m/s), the Salina A1 carbonate interval ($4.4E-8$ m/s), and the Salina A1-Salina A0-Guelph interval ($3.0E-9$ m/s). The principal contributors of permeability in these four intervals are believed to be the Salina A2 carbonate, the upper Salina A1 carbonate, and/or the Guelph. All but three of the Ordovician test intervals had K values less than or equal to $1E-13$ m/s. Significantly higher K values ($4.7E-12$ to $9.6E-12$ m/s) were found in the intervals that included the Black River Group (Coboconk and Gull River) limestones.

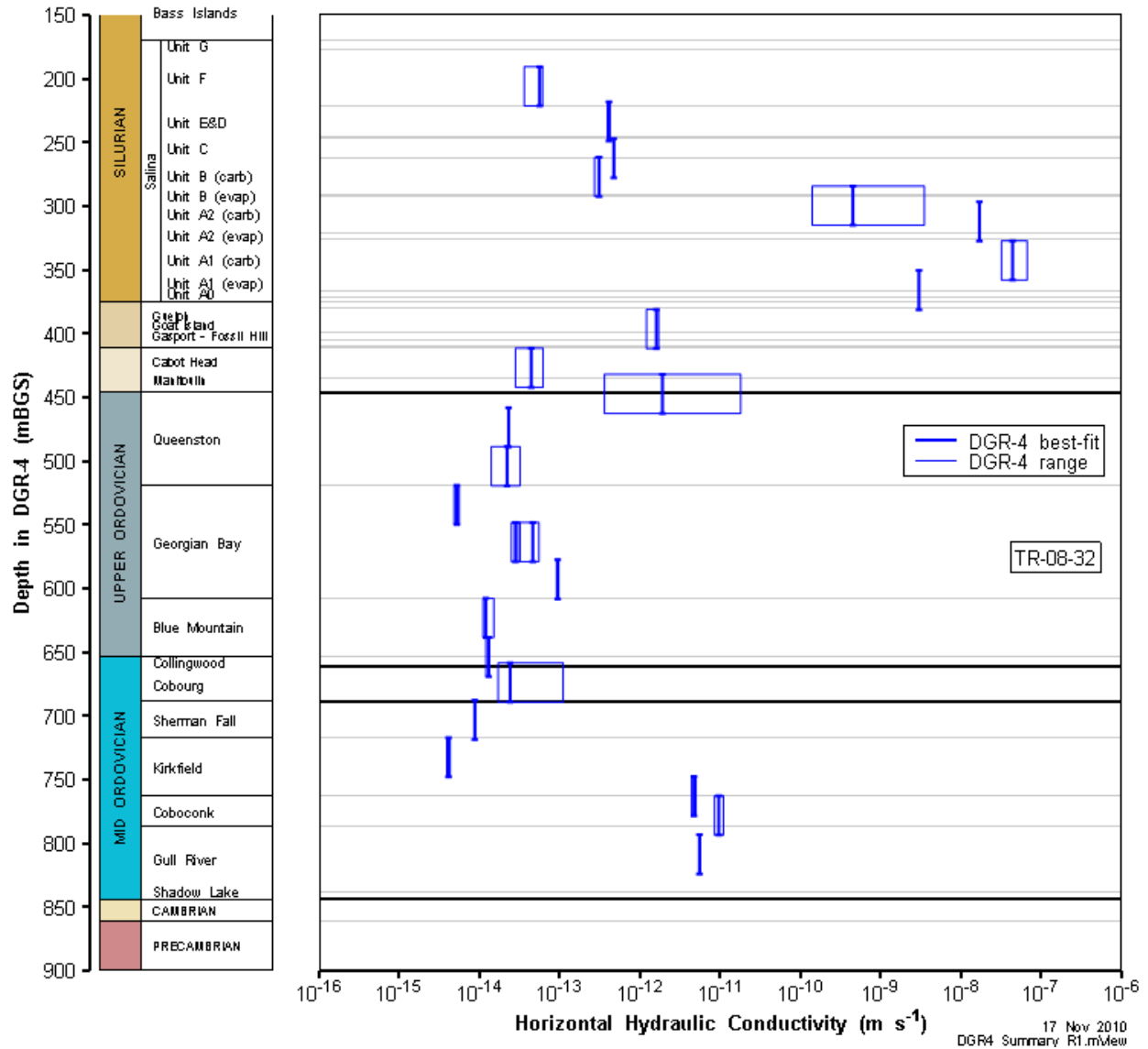


Figure 8-76: DGR-4 stratigraphic profile of horizontal hydraulic conductivity estimates.

As shown in Figure 8-77, the P_f values approximately followed a density-compensated hydrostatic gradient through the Silurian section of DGR-4, with the exception of underpressures in the Salina F through B intervals and overpressure in the Goat Island-Gasport-Lions Head-Fossil Hill interval. The Goat Island-Gasport-Lions Head-Fossil Hill overpressure is associated with high test-zone compressibility. Larger deviations from a hydrostatic gradient were observed in the Ordovician section, with pronounced, although not uniform, underpressures observed everywhere except in the Coboconk and Gull River Formations, where overpressures are observed. The lowermost Georgian Bay interval had less underpressure and much higher test-zone compressibility than the adjacent intervals.

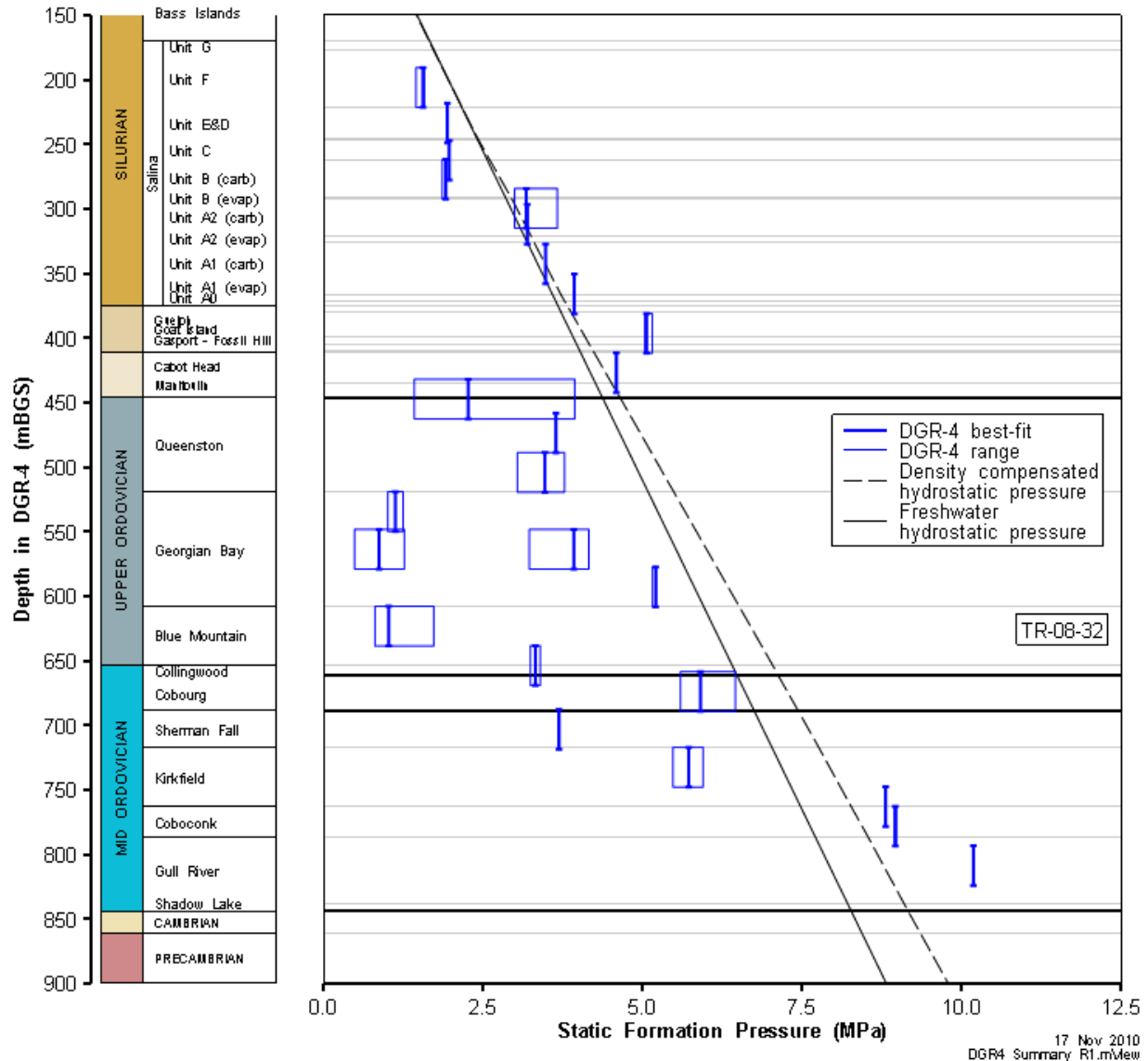


Figure 8-77: DGR-4 stratigraphic profile of formation pressure estimates.

Figure 8-78 shows the S_s values fitted in the simulations for each of the DGR-4 test intervals, along with the uncertainties associated with the fitted values; values that were fixed in the simulations are not shown. The fitted values range from $1.2E-7 \text{ m}^{-1}$ to $8.5E-5 \text{ m}^{-1}$. For some of the test intervals, effectively equivalent fits could be obtained with S_s values ranging over as much as two orders of magnitude. This is a consequence of the strong correlation between S_s and skin properties in single-well tests discussed in Section 4.4. For ten test intervals, no minimum was found in the S_s fit surface within the range of values thought to be physically reasonable ($1E-7$ to $1E-4 \text{ m}^{-1}$). In those cases, S_s was fixed at $1E-6 \text{ m}^{-1}$ (Table 8-52).

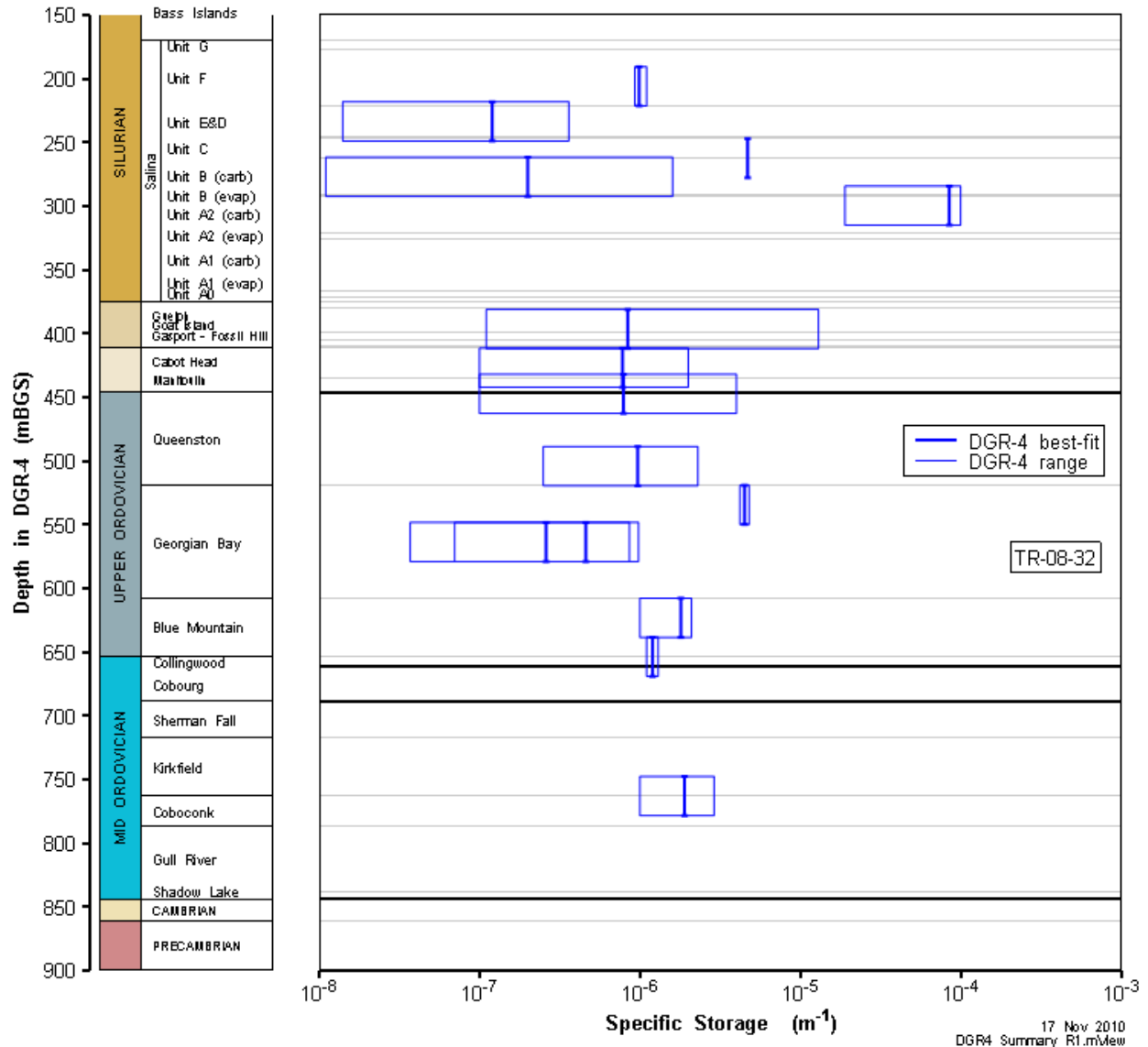


Figure 8-78: DGR-4 stratigraphic profile of specific storage estimates.

Figure 8-79 shows the skin factors obtained from parameter optimization for each of the DGR-4 test intervals. All but seven of the test intervals had negative skins, reflecting enhanced permeability around the wellbore. Hydraulically significant fractures are a possible cause of negative skins. Other causes could be enhanced local fracturing caused by stress relief fracturing during drilling. The negative skins in DGR-4 were generally of low magnitude; the Salina A1-Salina A0-Guelph interval had the most negative skin, which was only -3.73 (Table 8-52). Seven intervals had positive skins associated with decreased permeability around the wellbore. As was the case in DGR-2 and DGR-3 (Figure 7-73 and Figure 7-73), all of the Black River Group (Coboconk and Gull River) test intervals had positive skins. By far, the most significant positive skin (157) was that observed in the Salina A1 carbonate test interval.

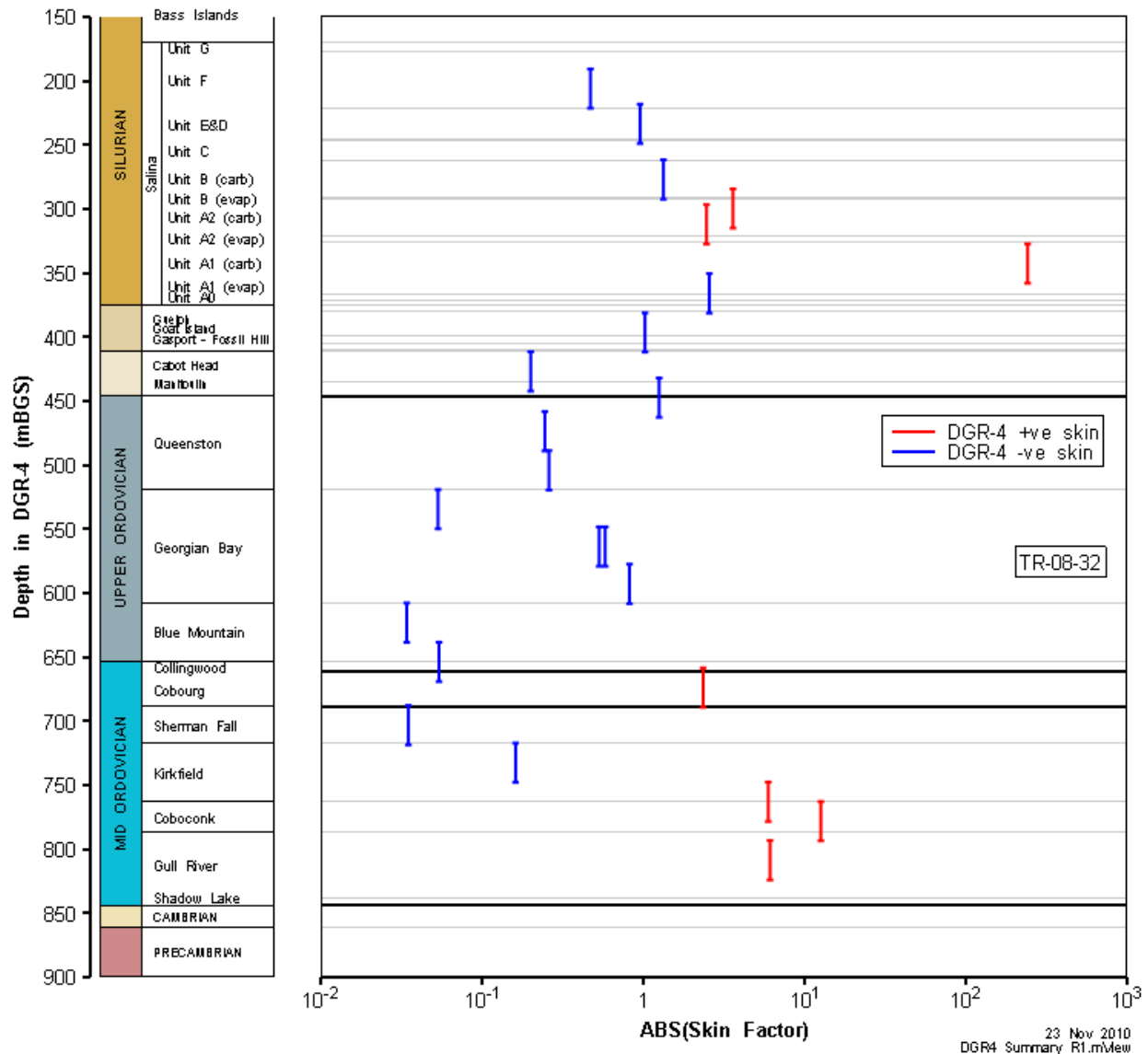


Figure 8-79: DGR-4 stratigraphic profile of skin factor estimates.

As shown in Figure 8-80, of the 22 intervals in which test-zone compressibility was measured in DGR-4, C_{tz} was less than $5E-10 \text{ Pa}^{-1}$ in 14 intervals and less than $7E-10 \text{ Pa}^{-1}$ in 3 more intervals. These values are indicative of water-filled test intervals with typical test-tool compliance. In the remaining 5 intervals, C_{tz} ranged from $1.1E-9$ to $1.0E-8 \text{ Pa}^{-1}$. Higher test-zone compressibilities such as these (particularly $1.0E-8 \text{ Pa}^{-1}$) are suggestive of a relatively small amount of gas in the test zone, but no direct evidence of gas is available. The highest C_{tz} mentioned above was measured in the Manitoulin-Queenston interval, which was also more underpressured than adjacent zones (Figure 8-77). Fractures were observed in the lowermost Manitoulin core from DGR-4 (Briscoe et al., 2010), which may be related to the high C_{tz} and low P_f .

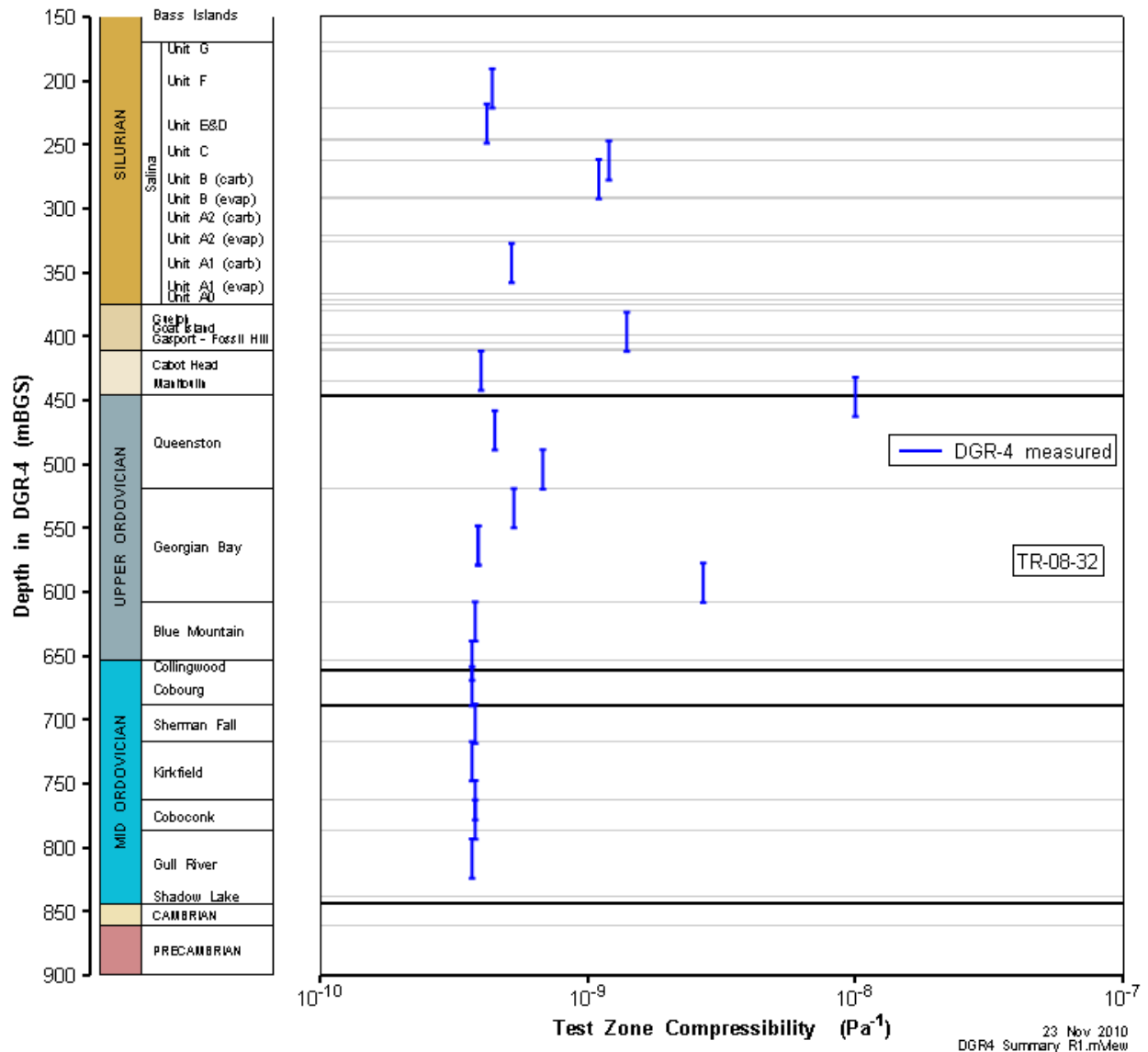


Figure 8-80: DGR-4 stratigraphic profile of test-zone compressibility estimates.

9 DGR-5 Testing and Analysis

Hydraulic testing in the slanted borehole DGR-5 was performed from 7 February until 13 March 2010. Testing was conducted using a 30.26-m straddle interval over 11 test zones extending from the middle of the Silurian Manitoulin Formation to the middle of the Ordovician Kirkfield Formation. The testing in DGR-5 provided complete coverage of the borehole from 477.87 to 797.51 m LBGS. Table 9-1 lists the formations and intervals tested, and the type(s) of test(s) performed. Pulse-withdrawal tests were performed in all of the DGR-5 intervals, and pulse-injection tests were performed in two intervals.

Table 9-1: DGR-5 test zones and tests

Formations / Units	Top of Test Zone (m LBGS)	Bottom of Test Zone (m LBGS)	Type(s) of Test(s)
Manitoulin-Queenston	477.87	508.13	PW, PI
Queenston	507.87	538.13	PW
Queenston-Georgian Bay	537.87	568.13	PW
Georgian Bay	567.87	598.13	PW
Georgian Bay	597.87	628.13	PW
Georgian Bay-Blue Mountain	627.87	658.13	PW, PI
Blue Mountain	657.87	688.13	PW
Blue Mountain-Collingwood-Cobourg	681.07	711.33	PW
Cobourg	707.24	737.50	PW
Sherman Fall	737.25	767.51	PW
Kirkfield	767.25	797.51	PW
Reference Elevation – Ground Surface	185.70 m above mean sea level		

PW: pulse withdrawal
 PI: pulse injection

The test-zone transducer during DGR-5 testing was located 29.01 m above the middle of the isolated test zone as measured along the length of the test tool and was hydraulically connected to the test zone via a length of 1/4-in stainless-steel tubing. To determine the P_f values corresponding to the middle of the test zone, the “raw” (as measured by the transducer) P_f estimates were depth-corrected using the estimated fluid density value for each interval and the offset distance of 29.01 m corrected to vertical using the test interval angle. The depth-corrected P_f estimates are given in the tables below whereas the raw P_f estimates are listed in the graph annotations.

Results of each test analysis are discussed below. A summary of DGR-5 testing results is presented in Section 9.12.

9.1 477.87-508.13 Manitoulin-Queenston

The DGR-5 interval from 477.87 to 508.13 m LBGS included the lower 8.73-m thickness of the Manitoulin Formation and the upper 21.53 m of the Queenston Formation, measured along the slant of the hole. The Manitoulin is cherty dolostone and interbedded shale and dolostone, and the upper Queenston is massive, calcareous shale. Information on the angle and vertical extent of the test interval is given in Table 9-2. An overview of the testing in this interval is given in Table 9-2 and the corresponding parameter estimates are given in Table 9-3. A pulse-withdrawal test and a pulse-injection test were performed in this interval.

Table 9-2: Summary of the DGR5_477.87-508.13 testing activities.

Formation / Unit		Top of Test Zone (m LBGS)	Bottom of Test Zone (m LBGS)	
Manitoulin-Queenston		477.87	508.13	
Test Interval Angle (degrees from vertical)		Vertical Top of Test Zone (m BGS)	Vertical Bottom of Test Zone (m BGS)	
19.05		437.94	466.55	
Test	Initiated	Magnitude (kPa)	Duration	Compressibility (Pa ⁻¹)
Shut-in	07-02-10 14:32	N/A	18 hr	N/A
PW	08-02-10 08:39	66	25 hr	4.6E-09
PI	09-02-10 09:24	66	31 hr	4.6E-09
Borehole Pressure History				
Event		Start	Pressure (kPa)	
Drilling Intercept		07-10-09	4680	
Open Hole		08-11-09	N/A	
Prior Testing		02-02-10	N/A	

Table 9-3: Summary of the DGR5_477.87-508.13 parameter estimates.

Parameter	Best Fit	Minimum	Maximum	Mean
K_f (m/s)	2.7E-13	2.5E-13	2.7E-13	2.6E-13
P_f (kPa)	4105	4055	4111	4095
K_s (m/s)	2.0E-10	5.0E-11	7.5E-10	1.5E-10
t_s (cm)	125	20	125	68
S_s (1/m)	1.0E-8	1.0E-08	2.6E-07	3.7E-08

Figure 9-1 shows the measured pressure record from DGR5_477.87-508.13 used in this analysis along with the best-fit simulation and parameter values. Attempts to match the shut-in, pulse withdrawal, and pulse injection responses with a single parameter set were not successful. It was decided to use only the shut-in and PW pressures to estimate hydraulic parameters. The ranges of formation K and raw P_f values estimated from perturbation analysis are shown in Figure 9-2 and the fit value cumulative distribution function is shown in Figure 9-3.

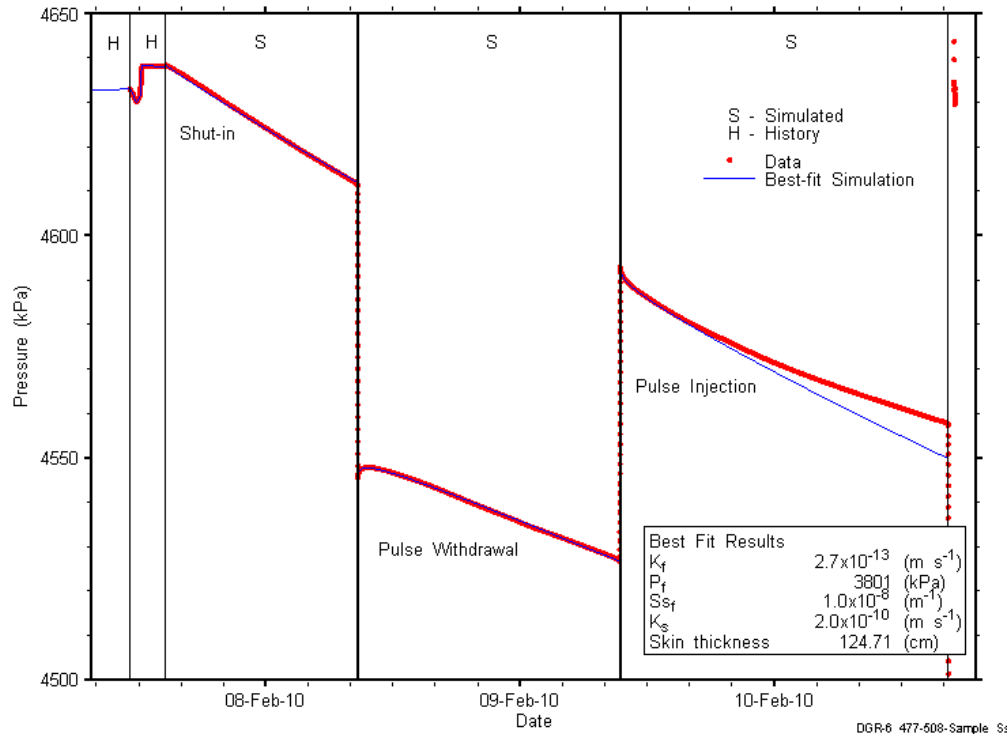


Figure 9-1: Annotated DGR5_477.87-508.13 testing sequence showing best-fit simulation and parameter estimates.

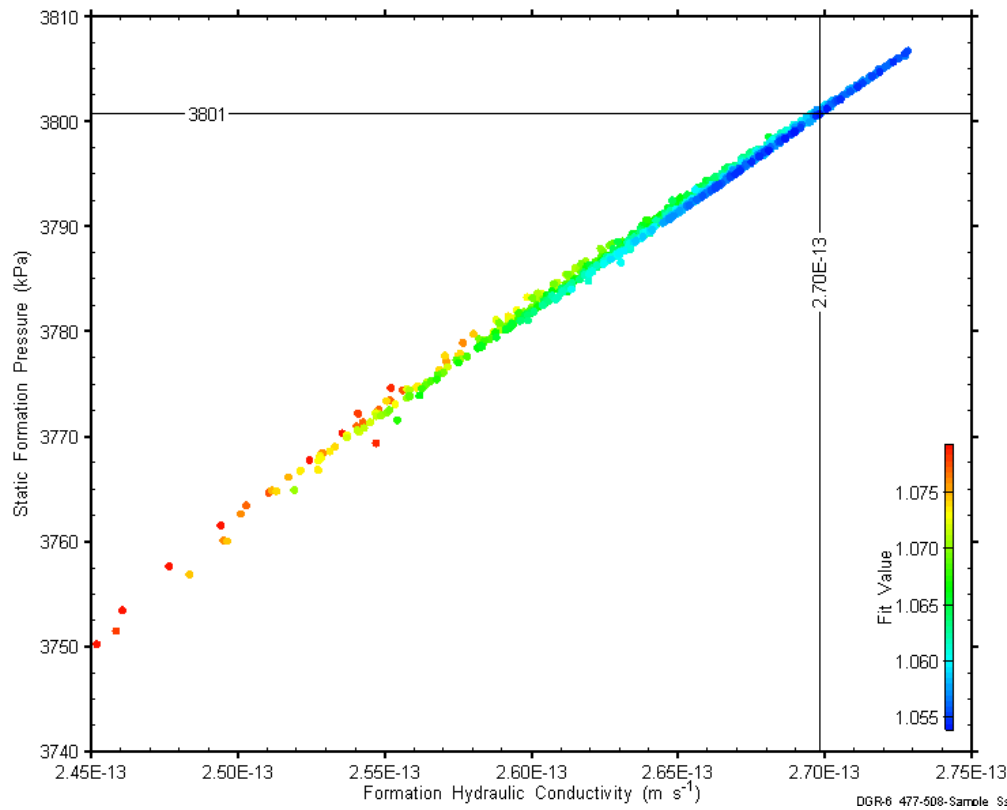


Figure 9-2: XY-scatter plot showing estimates of formation hydraulic conductivity and raw static formation pressure derived from the DGR5_477.87-508.13 perturbation analysis.

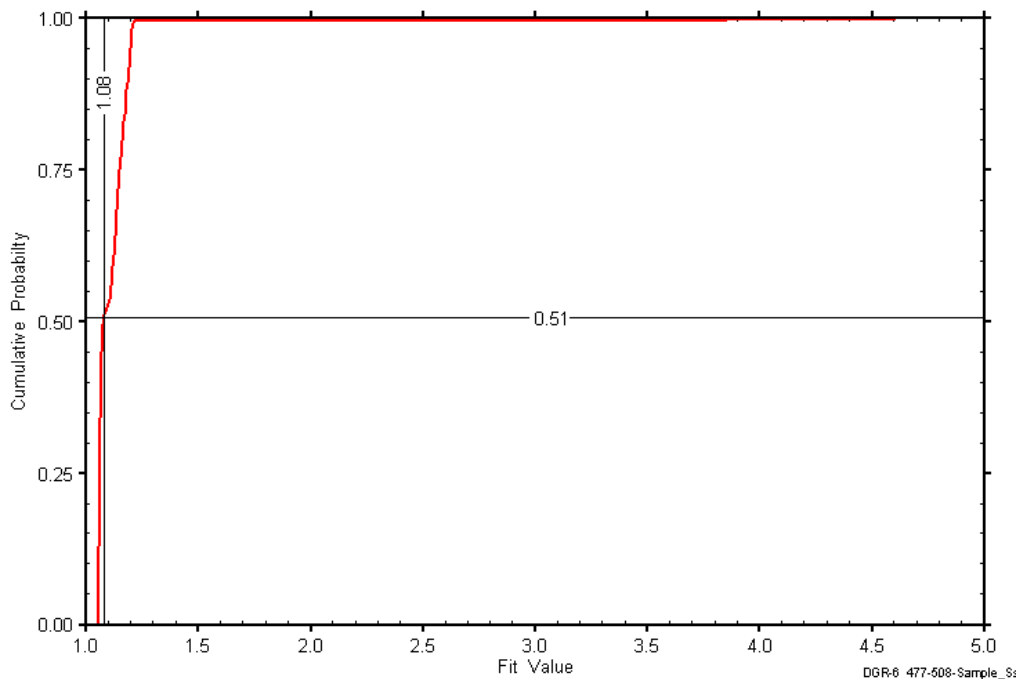


Figure 9-3: DGR5_477.87-508.13 fit value cumulative distribution function.

9.2 507.87-538.13 Queenston

The DGR-5 interval from 507.87 to 538.13 m LBGS was entirely contained within the Queenston Formation. This portion of the Queenston consists of approximately 14.1 m of calcareous shale underlain by approximately 16.1 m of interbedded shale and limestone, as measured along the slant of the hole. Information on the angle and vertical extent of the test interval is given in Table 9-4. An overview of the testing in this interval is given in Table 9-4 and the corresponding parameter estimates are given in Table 9-5. Two pulse-withdrawal tests were performed in this interval.

Table 9-4: Summary of the DGR5_507.87-538.13 testing activities.

Formation / Unit		Top of Test Zone (m LBGS)	Bottom of Test Zone (m LBGS)	
Queenston		507.87	538.13	
Test Interval Angle (degrees from vertical)		Vertical Top of Test Zone (m BGS)	Vertical Bottom of Test Zone (m BGS)	
18.07		466.30	495.07	
Test	Initiated	Magnitude (kPa)	Duration	Compressibility (Pa ⁻¹)
Shut-in	11-02-10 17:42	N/A	18 hr	N/A
PW1	12-02-10 11:59	301	22 hr	1.0E-09
PW2 (Pt 1)	13-02-10 10:05	306	14 min	N/C
PW2 (Pt 2)	13-02-10 10:19	298	22 hr	1.0E-09
Borehole Pressure History				
Event		Start	Pressure (kPa)	
Drilling Intercept		14-10-09	4958	
Open Hole		08-11-09	N/A	
Prior Testing		02-02-10	N/A	
Shut-in		11-02-10	N/A	

Table 9-5: Summary of the DGR5_507.87-538.13 parameter estimates.

Parameter	Best Fit	Minimum	Maximum	Mean
K_f (m/s)	1.4E-13	1.2E-13	1.4E-13	1.3E-13
P_f (kPa)	4856	4800	4857	4840
K_s (m/s)	2.3E-11	2.6E-12	1.0E-09	1.0E-11
t_s (cm)	70	5.95	73.11	25.43
S_s (1/m)	1.0E-8	1.0E-08	4.4E-07	7.8E-08

Figure 9-4 shows the measured pressure record from DGR5_507.87-538.13 used in this analysis along with the best-fit simulation and parameter values. The ranges of formation K and raw P_f values estimated from perturbation analysis are shown in Figure 9-5 and the fit value cumulative distribution function is shown in Figure 9-6.

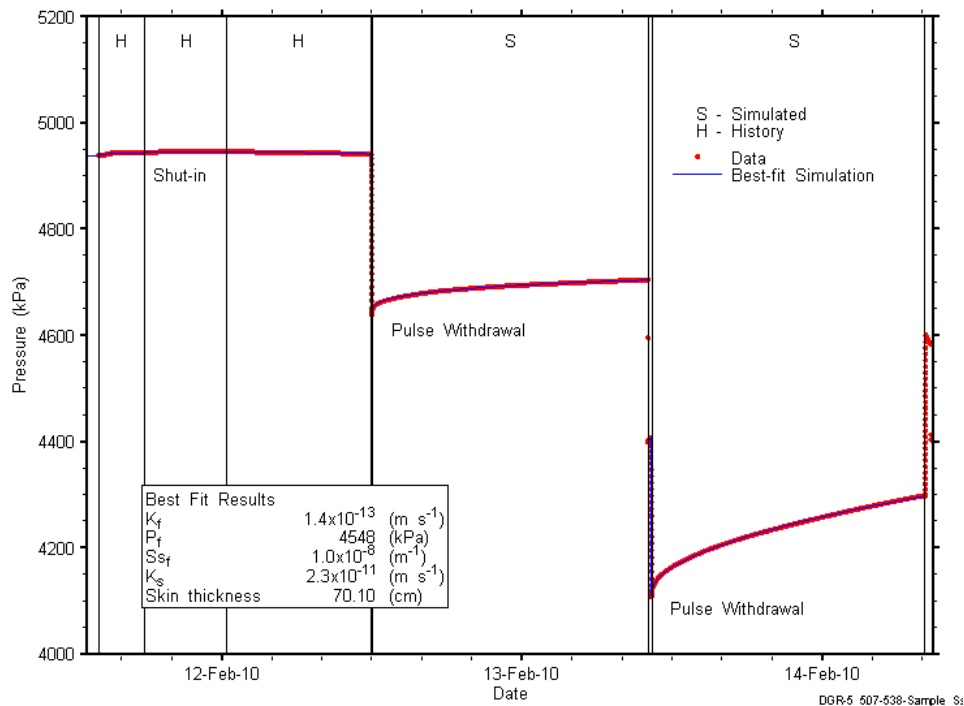


Figure 9-4: Annotated DGR5_507.87-538.13 testing sequence showing best-fit simulation and parameter estimates.

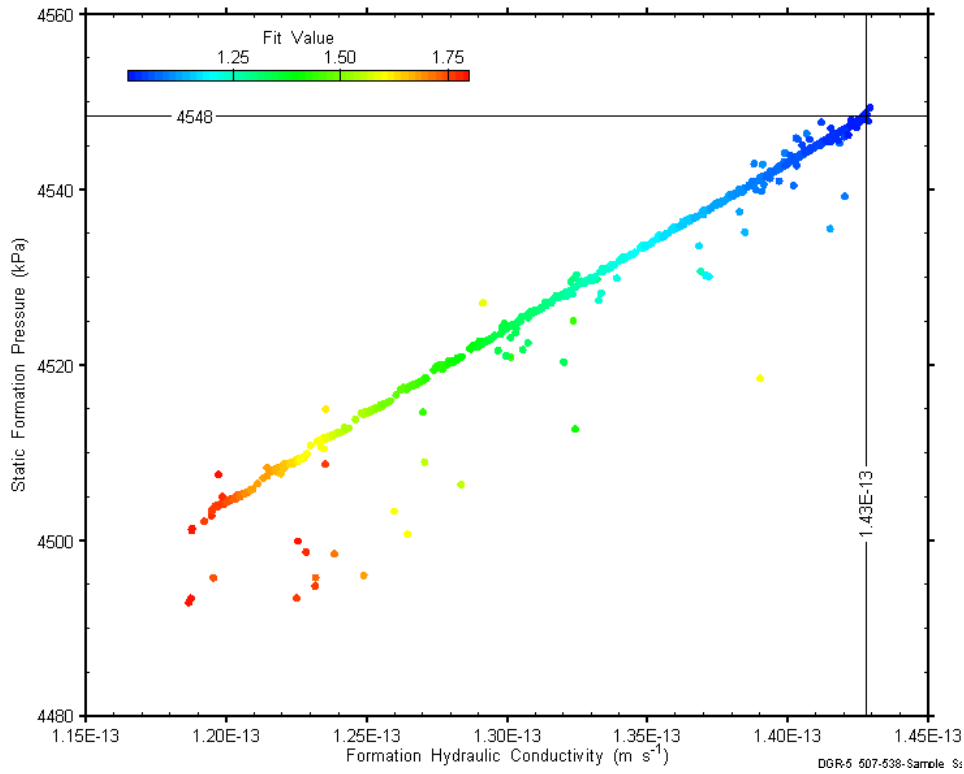


Figure 9-5: XY-scatter plot showing estimates of formation hydraulic conductivity and raw static formation pressure derived from the DGR5_507.87-538.13 perturbation analysis.

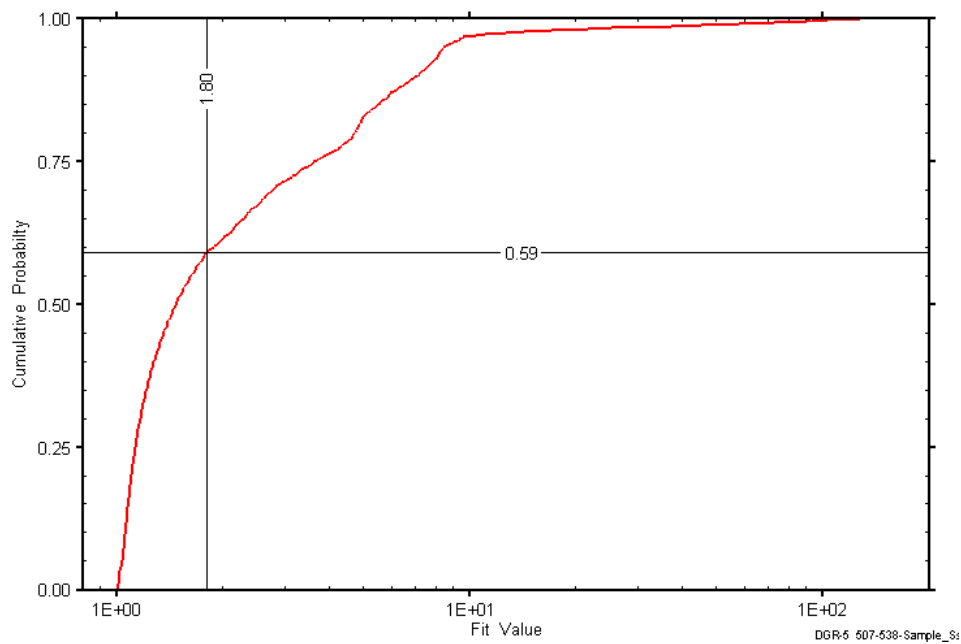


Figure 9-6: DGR5_507.87-538.13 fit value cumulative distribution function.

9.3 537.87-568.13 Queenston-Georgian Bay

The DGR-5 interval from 537.87 to 568.13 m LBGS included the lower 22.73 m of the Queenston Formation and the upper 7.53 m of the Georgian Bay Formation, measured along the slant of the hole. The portion of the Queenston tested consists of approximately 11.4 m of interbedded shale and limestone underlain by approximately 11.3 m of calcareous shale. The upper Georgian Bay is interbedded shale and limestone with siltstone interbeds over the lower 2 m. Information on the angle and vertical extent of the test interval is given in Table 9-6. An overview of the testing in this interval is given in Table 9-6 and the corresponding parameter estimates are given in Table 9-7. Two pulse-withdrawal tests were performed in this interval.

Table 9-6: Summary of the DGR5_537.87-568.13 testing activities.

Formation / Unit		Top of Test Zone (m LBGS)	Bottom of Test Zone (m LBGS)	
Queenston-Georgian Bay		537.87	568.13	
Test Interval Angle (degrees from vertical)		Vertical Top of Test Zone (m BGS)	Vertical Bottom of Test Zone (m BGS)	
17.60		494.82	523.66	
Test	Initiated	Magnitude (kPa)	Duration	Compressibility (Pa ⁻¹)
Shut-in	14-02-10 16:18	N/A	18 hr	N/A
PW1	15-02-10 11:07	653	22 hr	4.8E-10
PW2 (Pt 1)	16-02-10 09:19	70	10 min	N/C
PW2 (Pt 2)	16-02-10 09:29	658	23 hr	4.8E-10
Borehole Pressure History				
Event		Start	Pressure (kPa)	
Drilling Intercept		16-10-09	5292	
Open Hole		08-11-09	N/A	
Prior Testing		02-02-10	N/A	
Shut-in		14-02-10	N/A	

Table 9-7: Summary of the DGR5_537.87-568.13 parameter estimates.

Parameter	Best Fit	Minimum	Maximum	Mean
K_f (m/s)	9.4E-13	4.4E-13	3.9E-11	3.9E-11
P_f (kPa)	4949	4808	5086	4981
K_s (m/s)	7.8E-14	3.6E-14	1.1E-13	8.0E-14
t_s (cm)	6.4	2.15	11.92	7.51
S_s (1/m)	1.1E-06	6.8E-07	3.0E-06	1.1E-06

Figure 9-7 shows the measured pressure record from DGR5_537.87-568.13 used in this analysis along with the best-fit simulation and parameter values. The ranges of formation K and raw P_f values estimated from perturbation analysis are shown in Figure 9-8 and the fit value cumulative distribution function is shown in Figure 9-9.

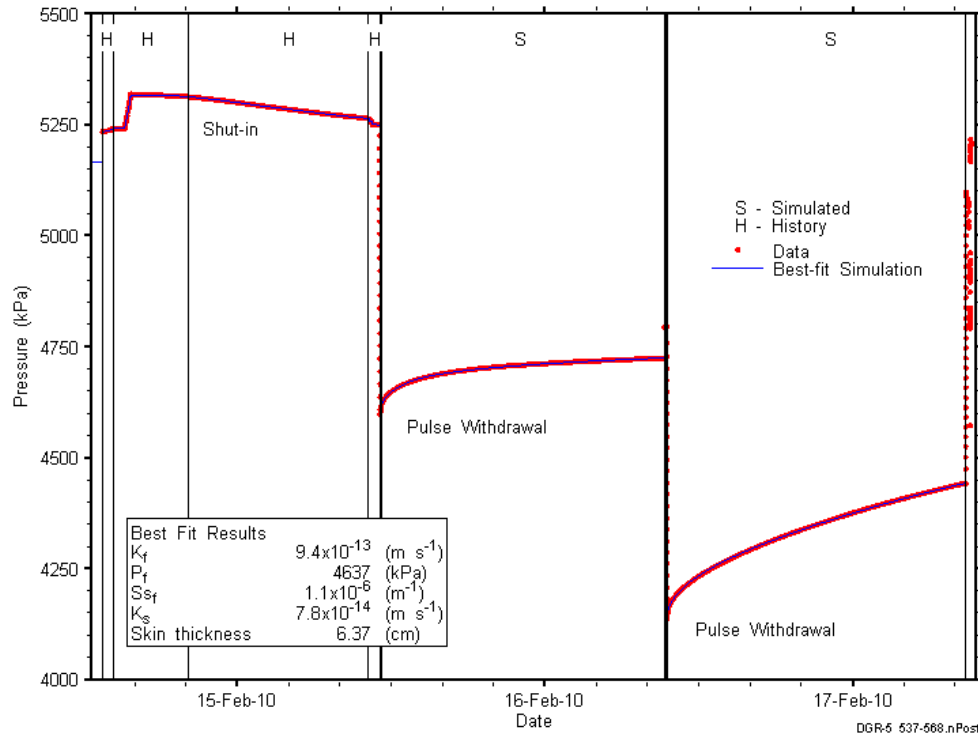


Figure 9-7: Annotated DGR5_537.87-568.13 testing sequence showing best-fit simulation and parameter estimates.

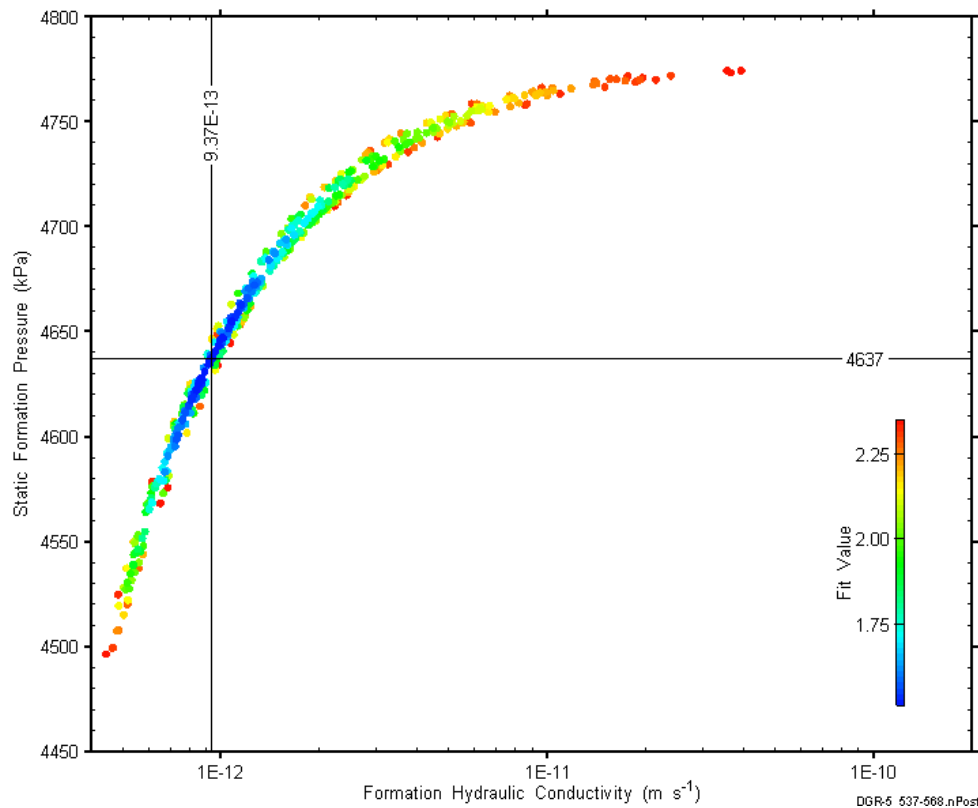


Figure 9-8: XY-scatter plot showing estimates of formation hydraulic conductivity and raw static formation pressure derived from the DGR5_537.87-568.13 perturbation analysis.

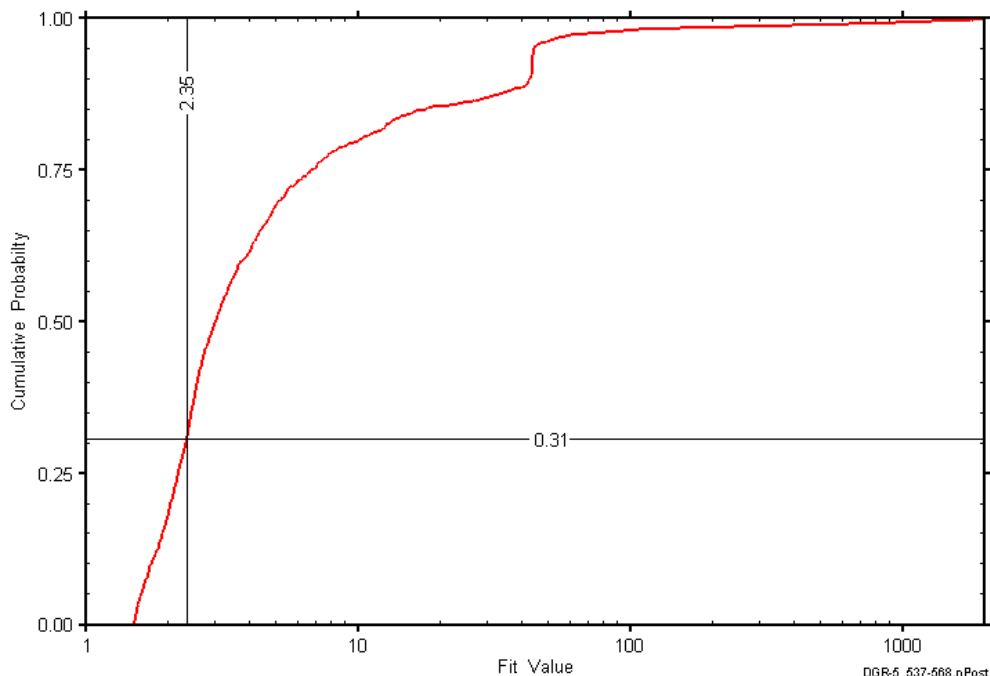


Figure 9-9: DGR5_537.87-568.13 fit value cumulative distribution function.

9.4 567.87-598.13 Georgian Bay

The DGR-5 interval from 567.87 to 598.13 m LBGS was entirely contained within the Georgian Bay Formation. This portion of the Georgian Bay consists of approximately 19.7 m of interbedded shale and limestone/siltstone underlain by approximately 10.5 m of shale with some laminae to thin beds of limestone/siltstone. Information on the angle and vertical extent of the test interval is given in Table 9-8. An overview of the testing in this interval is given in Table 9-9 and the corresponding parameter estimates are given in Table 9-9. Two pulse-withdrawal tests were performed in this interval.

Table 9-8: Summary of the DGR5_567.87-598.13 testing activities.

Formation / Unit		Top of Test Zone (m LBGS)	Bottom of Test Zone (m LBGS)	
Georgian Bay		567.87	598.13	
Test Interval Angle (degrees from vertical)		Vertical Top of Test Zone (m BGS)	Vertical Bottom of Test Zone (m BGS)	
17.27		523.42	552.31	
Test	Initiated	Magnitude (kPa)	Duration	Compressibility (Pa ⁻¹)
Shut-in	17-02-10 15:43	N/A	18 hr	N/A
PW1	18-02-10 09:38	632	23 hr	5.0E-10
PW2 (Pt 1)	19-02-10 09:01	99	9 min	N/C
PW2 (Pt 2)	19-02-10 09:10	664	22 hr	4.8E-10
Borehole Pressure History				
Event		Start	Pressure (kPa)	
Drilling Intercept		17-10-09	5600	
Open Hole		08-11-09	N/A	
Prior Testing		02-02-10	N/A	
Shut-in		17-02-10	N/A	

Table 9-9: Summary of the DGR5_567.87-598.13 parameter estimates.

Parameter	Best Fit	Minimum	Maximum	Mean
K_f (m/s)	3.3E-13	1.7E-13	1.9E-11	7.4E-13
P_f (kPa)	4782	4368	5322	5002
K_s (m/s)	3.2E-14	1.2E-14	1.2E-13	4.8E-14
t_s (cm)	1.3	0.4	7.7	3.0
S_s (1/m)	5.7E-06	1.2E-06	1.8E-05	3.5E-06

Figure 9-10 shows the measured pressure record from DGR5_567.87-598.13 used in this analysis along with the best-fit simulation and parameter values. The ranges of formation K and raw P_f values estimated from perturbation analysis are shown in Figure 9-11 and the fit value cumulative distribution function is shown in Figure 9-12.

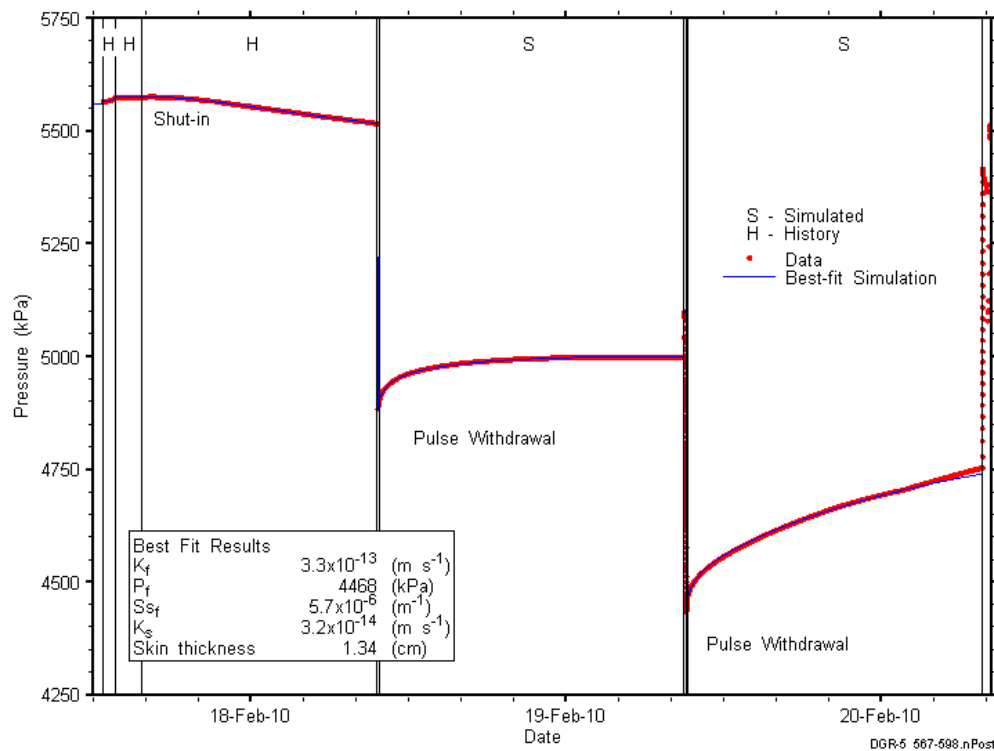


Figure 9-10: Annotated DGR5_567.87-598.13 testing sequence showing best-fit simulation and parameter estimates.

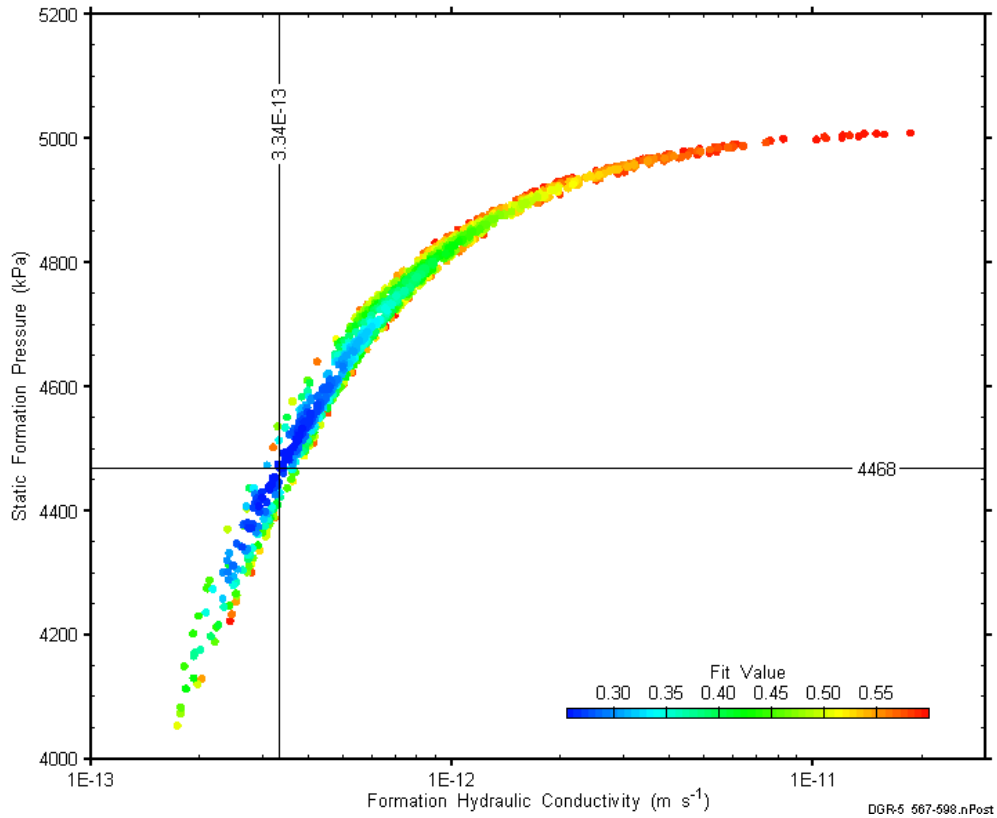


Figure 9-11: XY-scatter plot showing estimates of formation hydraulic conductivity and raw static formation pressure derived from the DGR5_567.87-598.13 perturbation analysis.

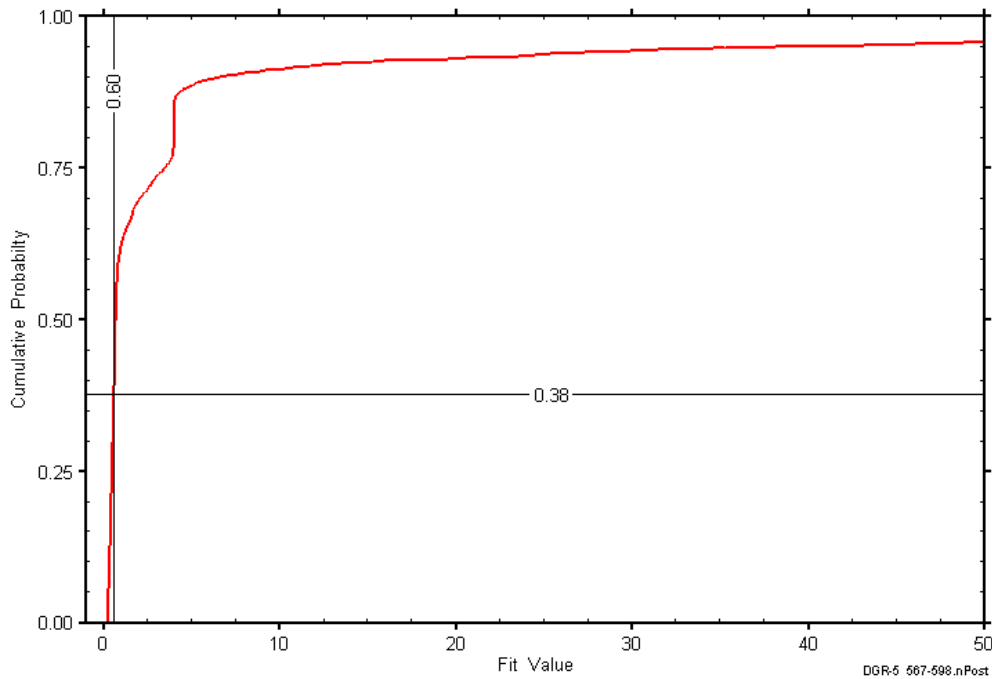


Figure 9-12: DGR5_567.87-598.13 fit value cumulative distribution function.

9.5 597.87-628.13 Georgian Bay

The DGR-5 interval from 597.87 to 628.13 m LBGS was entirely contained within the Georgian Bay Formation. This portion of the Georgian Bay consists of shale with trace laminae to thin interbeds of limestone/siltstone. Information on the angle and vertical extent of the test interval is given in Table 9-10. An overview of the testing in this interval is given in Table 9-10 and the corresponding parameter estimates are given in Table 9-11. Two pulse-withdrawal tests were performed in this interval.

Table 9-10: Summary of the DGR5_597.87-628.13 testing activities.

Formation / Unit		Top of Test Zone (m LBGS)		Bottom of Test Zone (m LBGS)	
Georgian Bay		597.87		628.13	
Test Interval Angle (degrees from vertical)		Vertical Top of Test Zone (m BGS)		Vertical Bottom of Test Zone (m BGS)	
16.95		552.06		581.01	
Test	Initiated	Magnitude (kPa)	Duration	Compressibility (Pa ⁻¹)	
Shut-in	20-02-10 15:44	N/A	17 hr	N/A	
PW1	21-02-10 08:42	729	24 hr	4.2E-10	
PW2 (Pt 1)	22-02-10 08:56	155	7 min	N/C	
PW2 (Pt 2)	22-02-10 09:03	730	23 hr	4.2E-10	
Borehole Pressure History					
Event		Start		Pressure (kPa)	
Drilling Intercept		19-10-09		5908	
Open Hole		08-11-09		N/A	
Prior Testing		02-02-10		N/A	
Shut-in		20-02-10		N/A	

Table 9-11: Summary of the DGR5_597.87-628.13 parameter estimates.

Parameter	Best Fit	Minimum	Maximum	Mean
K _f (m/s)	2.9E-15	2.3E-15	4.3E-15	2.9E-15
P _f (kPa)	344	317	2518	1082
K _s (m/s)	2.8E-12	2.1E-13	3.8E-12	4.5E-13
t _s (cm)	92	4.9	92	18
S _s (1/m)	1.0E-08	1.0E-08	8.6E-07	2.9E-07

Figure 9-13 shows the measured pressure record from DGR5_597.87-628.13 used in this analysis along with the best-fit simulation and parameter values. The ranges of formation K and raw P_f values estimated from perturbation analysis are shown in Figure 9-14 and the fit value cumulative distribution function is shown in Figure 9-15.

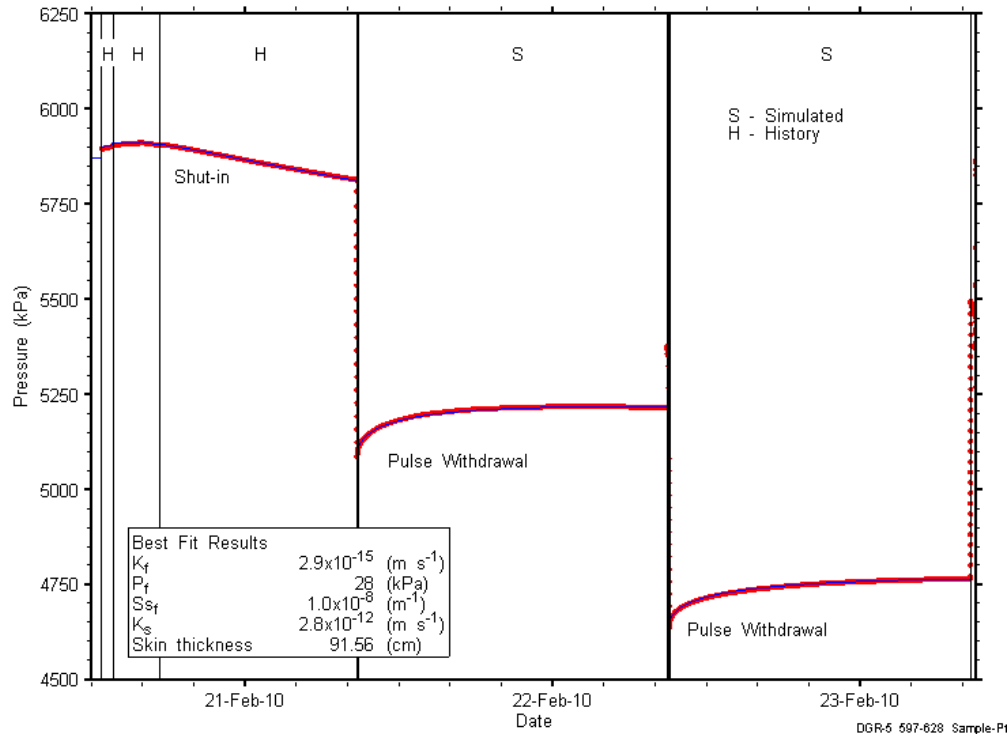


Figure 9-13: Annotated DGR5_597.87-628.13 testing sequence showing best-fit simulation and parameter estimates.

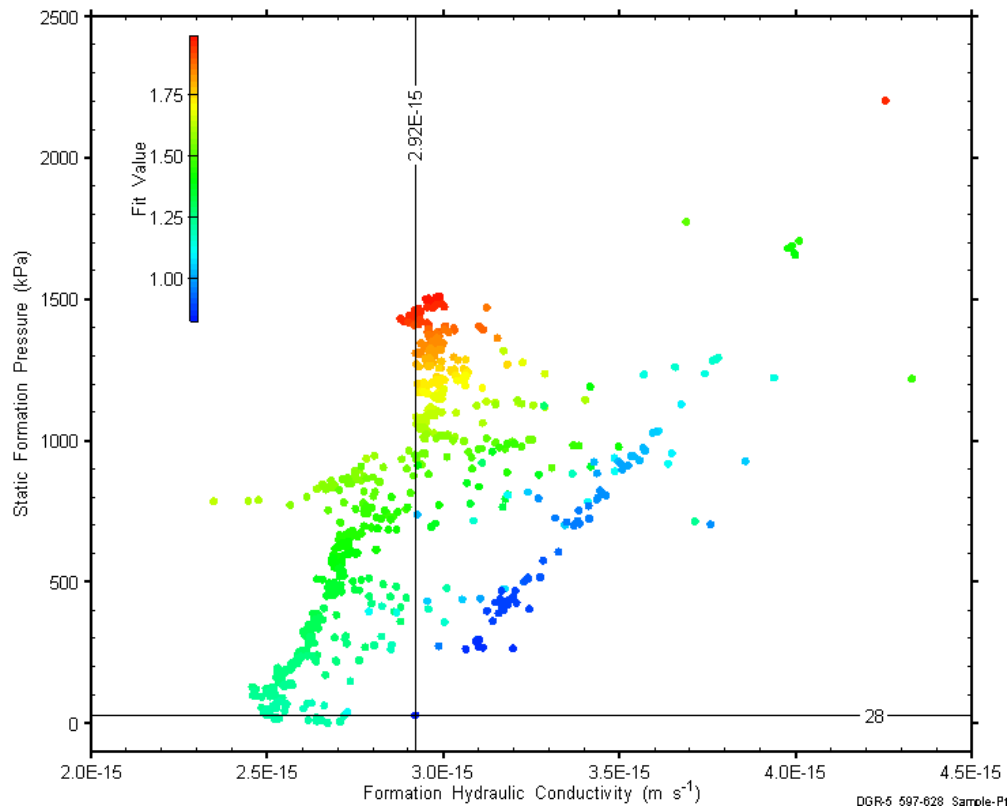


Figure 9-14: XY-scatter plot showing estimates of formation hydraulic conductivity and raw static formation pressure derived from the DGR5_597.87-628.13 perturbation analysis.

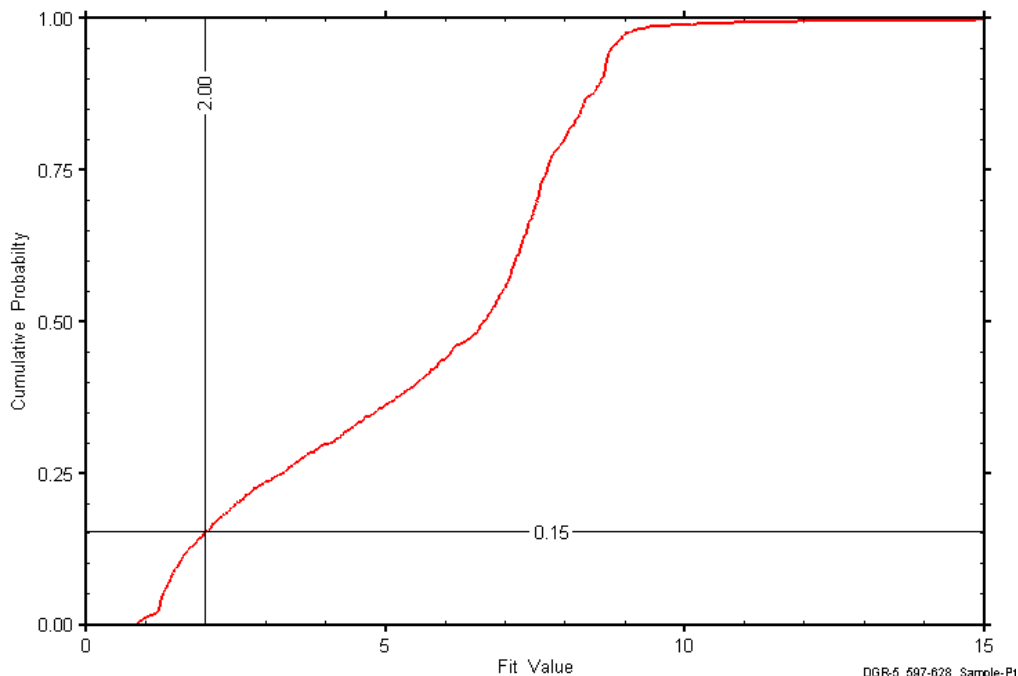


Figure 9-15: DGR5_597.87-628.13 fit value cumulative distribution function.

9.6 627.87-658.13 Georgian Bay-Blue Mountain

The DGR-5 interval from 627.87 to 658.13 m LBGS included the lower 25.43 m of the Georgian Bay Formation and the upper 4.83 m of the Blue Mountain Formation, measured along the slant of the hole. The entire test interval consisted of shale with trace laminae to thin interbeds of limestone/siltstone. Information on the angle and vertical extent of the test interval is given in Table 9-12. An overview of the testing in this interval is given in Table 9-12 and the corresponding parameter estimates are given in Table 9-13. A pulse-withdrawal test and a pulse-injection test were performed in this interval.

Table 9-12: Summary of the DGR5_627.87-658.13 testing activities.

Formation / Unit		Top of Test Zone (m LBGS)	Bottom of Test Zone (m LBGS)	
Georgian Bay-Blue Mountain		627.87	658.13	
Test Interval Angle (degrees from vertical)		Vertical Top of Test Zone (m BGS)	Vertical Bottom of Test Zone (m BGS)	
16.30		580.76	609.80	
Test	Initiated	Magnitude (kPa)	Duration	Compressibility (Pa ⁻¹)
Shut-in	23-02-10 15:30	N/A	17 hr	N/A
PW	24-02-10 08:26	92	30 hr	3.2E-09
PI (Pt 1)	25-02-10 14:34	91	6 min	3.2E-09
PI (Pt 2)	25-02-10 14:40	304	18 hr	N/C
Borehole Pressure History				
Event		Start	Pressure (kPa)	
Drilling Intercept		21-10-09	6217	
Open Hole		08-11-09	N/A	
Prior Testing		02-02-10	N/A	
Shut-in		23-02-10	N/A	

Table 9-13: Summary of the DGR5_627.87-658.13 parameter estimates.

Parameter	Best Fit	Minimum	Maximum	Mean
K_f (m/s)	3.2E-14	1.6E-14	6.4E-14	4.6E-14
P_f (kPa)	7946	7578	8337	7749
K_s (m/s)	6.0E-13	1.7E-13	1.6E-12	9.2E-13
t_s (cm)	0.4	0.2	1.2	0.8
S_s (1/m)	2.2E-05	8.3E-06	5.1E-05	1.3E-05

Figure 9-16 shows the measured pressure record from DGR5_627.87-658.13 used in this analysis along with the best-fit simulation and parameter values. The ranges of formation K and raw P_f values estimated from perturbation analysis are shown in Figure 9-17 and the fit value cumulative distribution function is shown in Figure 9-18.

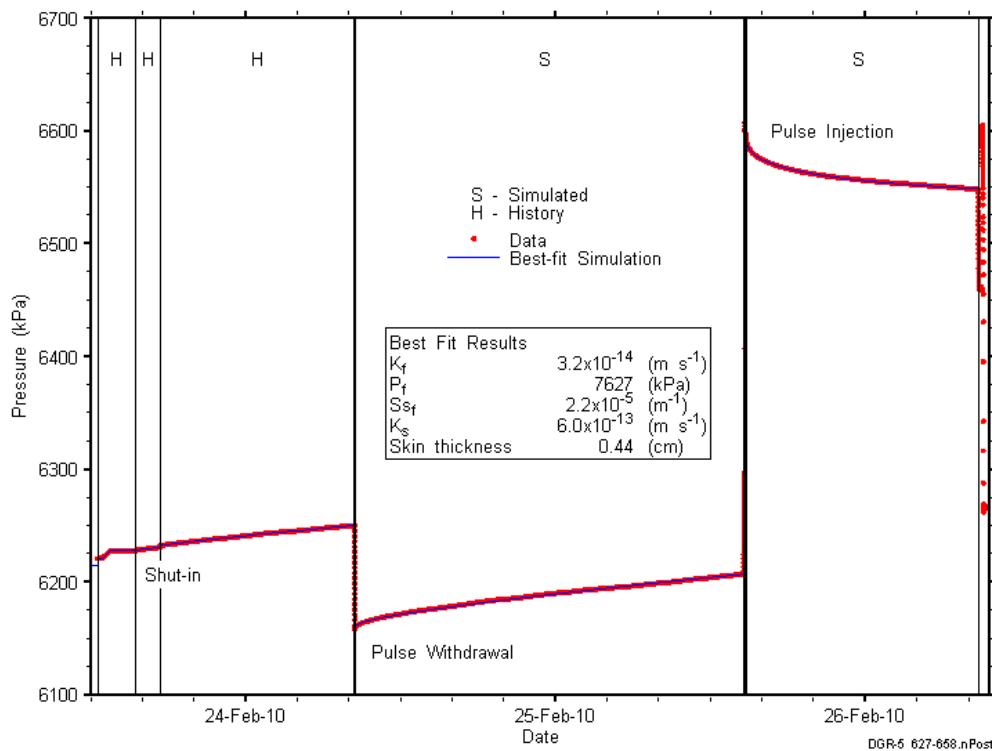


Figure 9-16: Annotated DGR5_627.87-658.13 testing sequence showing best-fit simulation and parameter estimates.

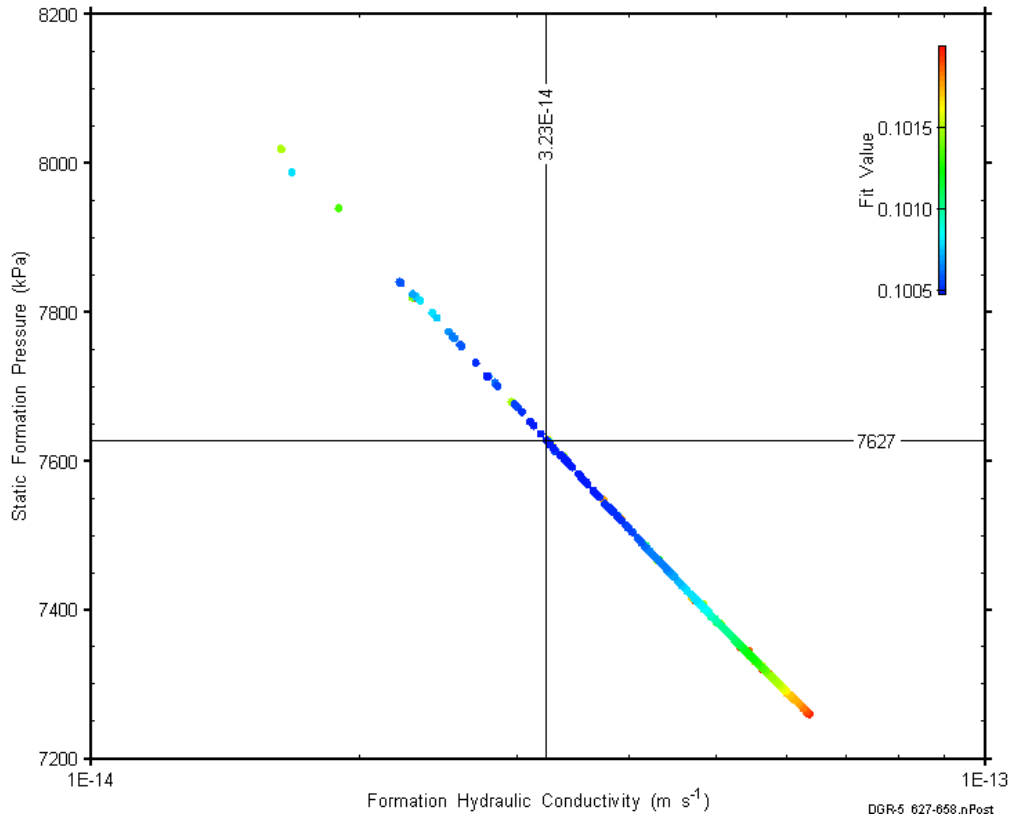


Figure 9-17: XY-scatter plot showing estimates of formation hydraulic conductivity and raw static formation pressure derived from the DGR5_627.87-658.13 perturbation analysis.

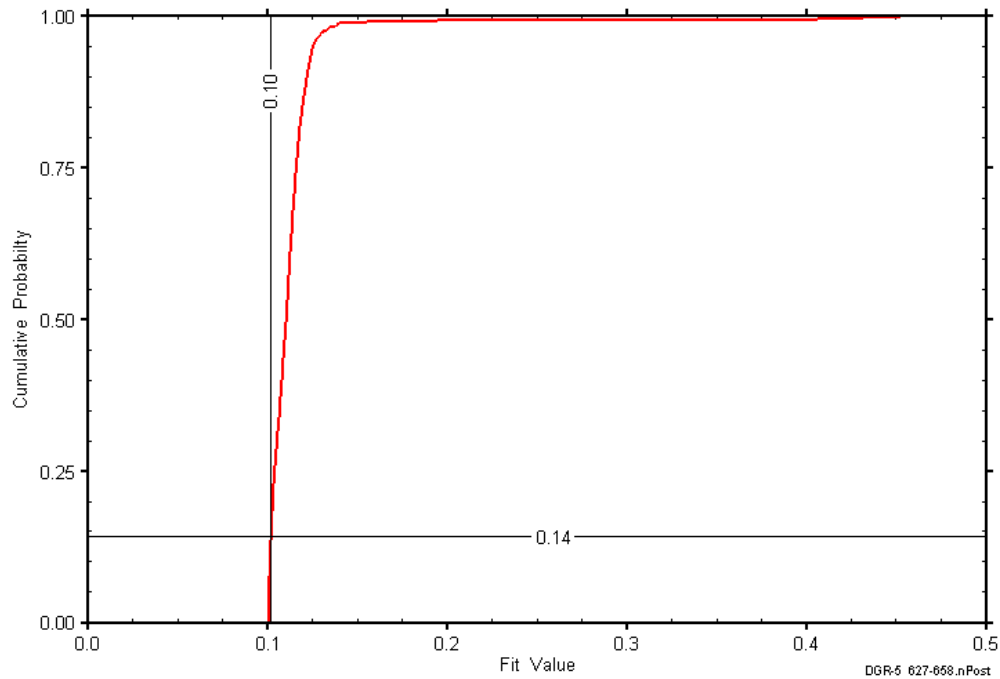


Figure 9-18: DGR5_627.87-658.13 fit value cumulative distribution function.

9.7 657.87-688.13 Blue Mountain

The DGR-5 interval from 657.87 to 688.13 m LBGS was entirely contained within the Blue Mountain Formation. This portion of the Blue Mountain consists of massively bedded shale with trace laminae to thin interbeds of limestone/siltstone in the upper approximately 25 m. Information on the angle and vertical extent of the test interval is given in Table 9-14. An overview of the testing in this interval is given in Table 9-14 and the corresponding parameter estimates are given in Table 9-15. Two pulse-withdrawal tests were performed in this interval.

Table 9-14: Summary of the DGR5_657.87-688.13 testing activities.

Formation / Unit		Top of Test Zone (m LBGS)		Bottom of Test Zone (m LBGS)	
Blue Mountain		657.87		688.13	
Test Interval Angle (degrees from vertical)		Vertical Top of Test Zone (m BGS)		Vertical Bottom of Test Zone (m BGS)	
14.89		609.55		638.80	
Test	Initiated	Magnitude (kPa)	Duration	Compressibility (Pa ⁻¹)	
Shut-in	26-02-10 15:27	N/A	17 hr	N/A	
PW1	27-02-10 08:05	688	25 hr	4.3E-10	
PW2 (Pt 1)	28-02-10 09:04	31	5 min	N/C	
PW2 (Pt 2)	28-02-10 09:09	687	23 hr	4.3E-10	
Borehole Pressure History					
Event		Start		Pressure (kPa)	
Drilling Intercept		22-10-09		6527	
Open Hole		08-11-09		N/A	
Prior Testing		02-02-10		N/A	
Shut-in		26-02-10		N/A	

Table 9-15: Summary of the DGR5_657.87-688.13 parameter estimates.

Parameter	Best Fit	Minimum	Maximum	Mean
K_f (m/s)	3.1E-14	2.0E-14	4.9E-14	3.2E-14
P_f (kPa)	3892	3176	4526	3938
K_s (m/s)	9.3E-14	4.8E-14	6.9E-13	1.1E-13
t_s (cm)	1.8	0.4	15	2.6
S_s (1/m)	1.7E-06	1.7E-07	3.9E-06	1.4E-06

Figure 9-19 shows the measured pressure record from DGR5_657.87-688.13 used in this analysis along with the best-fit simulation and parameter values. The ranges of formation K and raw P_f values estimated from perturbation analysis are shown in Figure 9-20 and the fit value cumulative distribution function is shown in Figure 9-21.

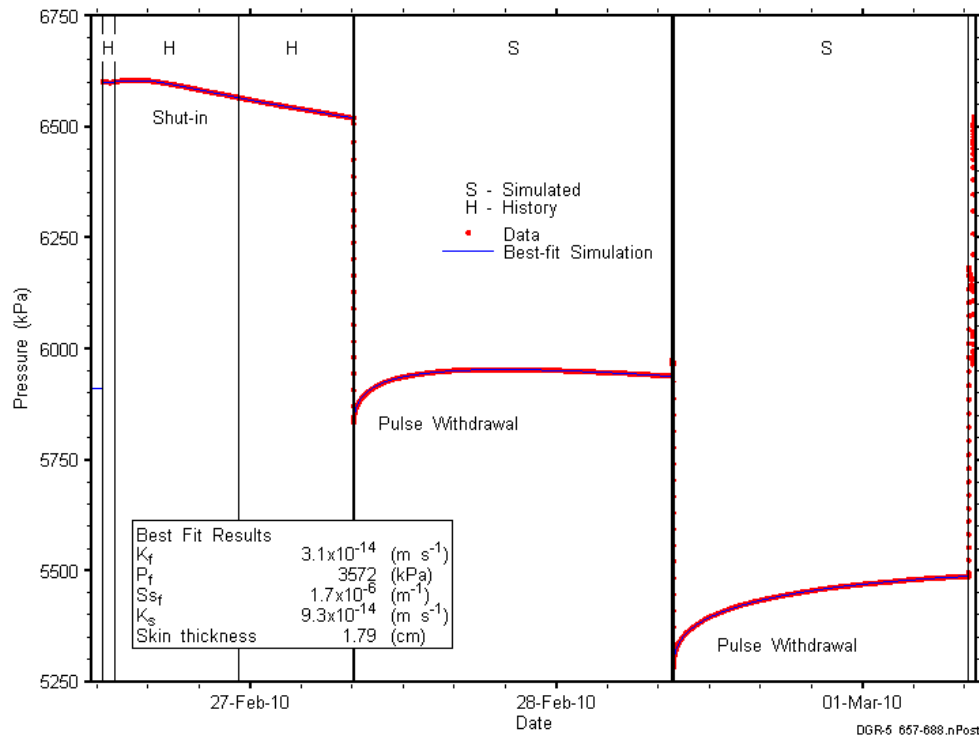


Figure 9-19: Annotated DGR5_657.87-688.13 testing sequence showing best-fit simulation and parameter estimates.

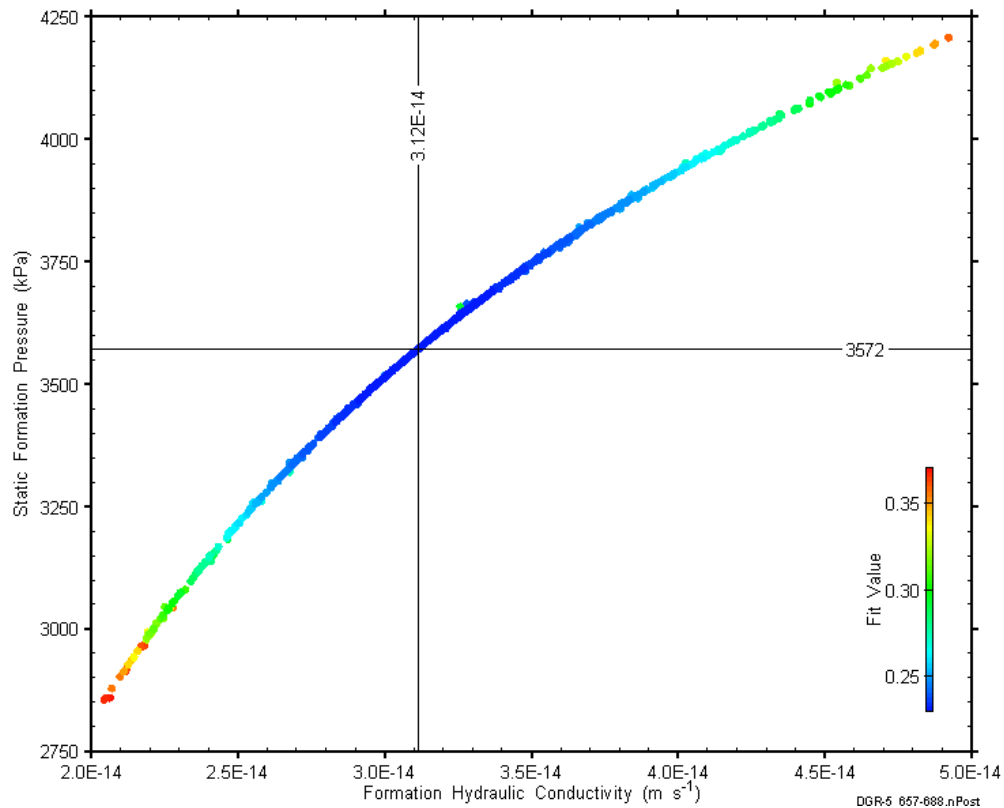


Figure 9-20: XY-scatter plot showing estimates of formation hydraulic conductivity and raw static formation pressure derived from the DGR5_657.87-688.13 perturbation analysis.

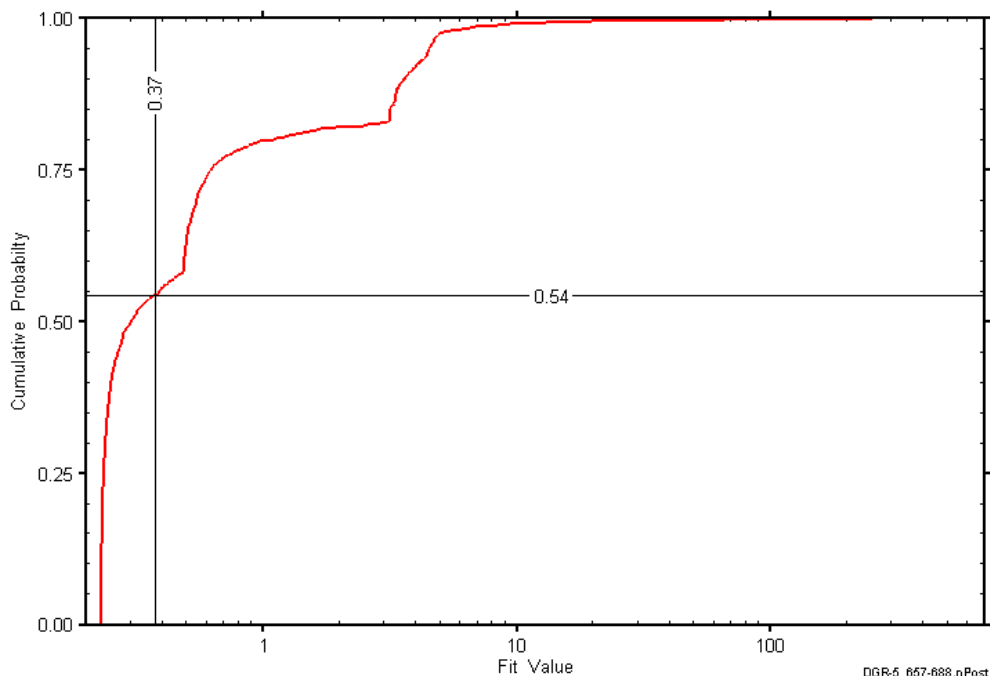


Figure 9-21: DGR5_657.87-688.13 fit value cumulative distribution function.

9.8 681.07-711.33 Blue Mountain-Collingwood-Cobourg

The DGR-5 interval from 681.07 to 711.33 m LBGs included the lower 18.83 m of the Blue Mountain Formation, the entire 8.80-m thickness of the Collingwood Member of the Cobourg Formation, and the upper 2.63 m of the Lower Member of the Cobourg Formation, measured along the slant of the hole. The lower Blue Mountain is shale, the Collingwood is interbedded shale and argillaceous limestone, and the Lower Member of the Cobourg is argillaceous limestone. Information on the angle and vertical extent of the test interval is given in Table 9-16. An overview of the testing in this interval is given in Table 9-16 and the corresponding parameter estimates are given in Table 9-17. Two pulse-withdrawal tests were performed in this interval.

Table 9-16: Summary of the DGR5_681.07-711.33 testing activities.

Formation / Unit		Top of Test Zone (m LBGs)	Bottom of Test Zone (m LBGs)	
Blue Mountain-Collingwood-Cobourg		681.07	711.33	
Test Interval Angle (degrees from vertical)		Vertical Top of Test Zone (m BGS)	Vertical Bottom of Test Zone (m BGS)	
13.43		631.95	661.38	
Test	Initiated	Magnitude (kPa)	Duration	Compressibility (Pa ⁻¹)
Shut-in	01-03-10 15:01	N/A	18 hr	N/A
PW1	02-03-10 08:54	825	24 hr	3.8E-10
PW2 (Pt 1)	03-03-10 08:31	193	23 min	N/C
PW2 (Pt 2)	03-03-10 08:54	825	24 hr	3.8E-10
Borehole Pressure History				
Event		Start	Pressure (kPa)	
Drilling Intercept		23-10-09	6768	

Open Hole	08-11-09	N/A
Prior Testing	02-02-10	N/A
Shut-in	01-03-10	N/A

Table 9-17: Summary of the DGR5_681.07-711.33 parameter estimates.

Parameter	Best Fit	Minimum	Maximum	Mean
K_f (m/s)	3.0E-14	2.7E-14	3.6E-14	3.1E-14
P_f (kPa)	5056	4837	5286	5074
K_s (m/s)	2.2E-13	1.3E-13	1.4E-12	2.6E-13
t_s (cm)	4.3	1.8	37	5.8
S_s (1/m)	2.3E-07	1.2E-08	4.4E-07	1.9E-07

Figure 9-22 shows the measured pressure record from DGR5_681.07-711.33 used in this analysis along with the best-fit simulation and parameter values. The ranges of formation K and raw P_f values estimated from perturbation analysis are shown in Figure 9-23 and the fit value cumulative distribution function is shown in Figure 9-24.

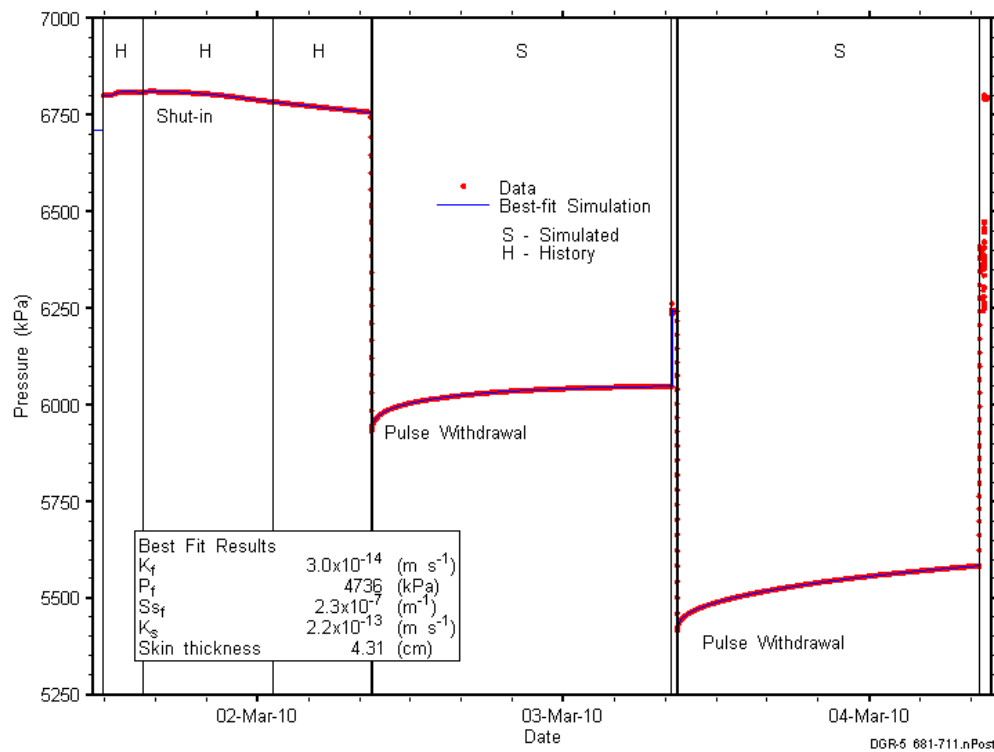


Figure 9-22: Annotated DGR5_681.07-711.33 testing sequence showing best-fit simulation and parameter estimates.

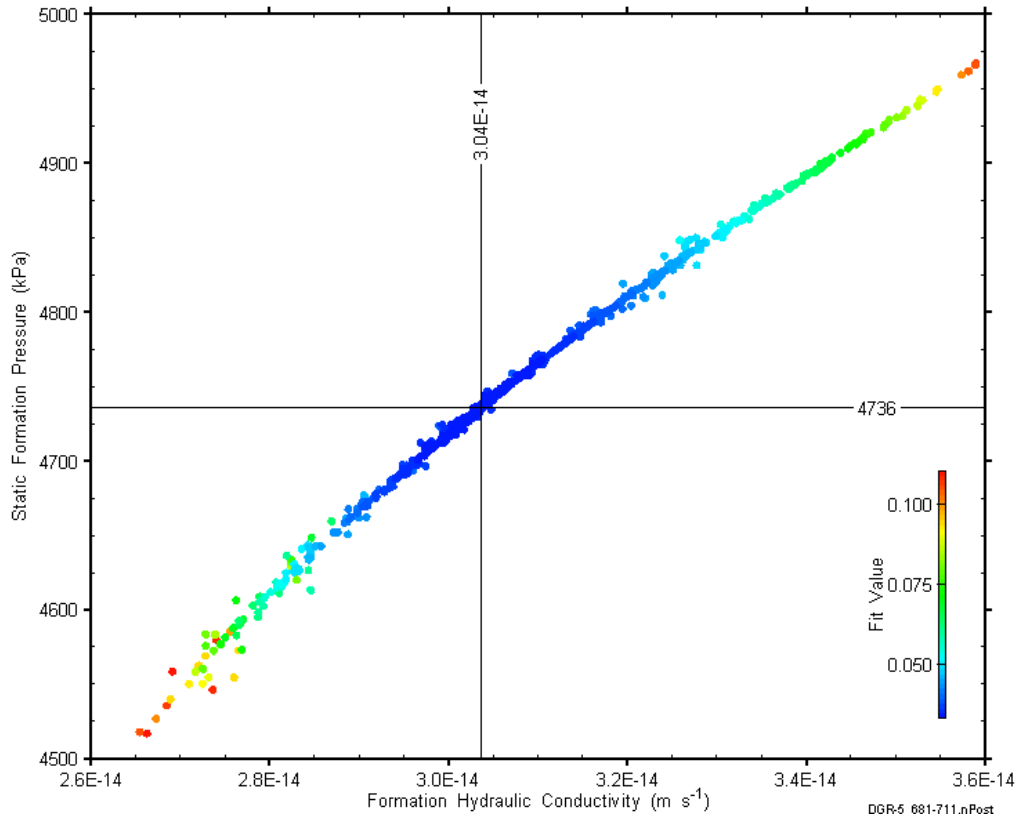


Figure 9-23: XY-scatter plot showing estimates of formation hydraulic conductivity and raw static formation pressure derived from the DGR5_681.07-711.33 perturbation analysis.

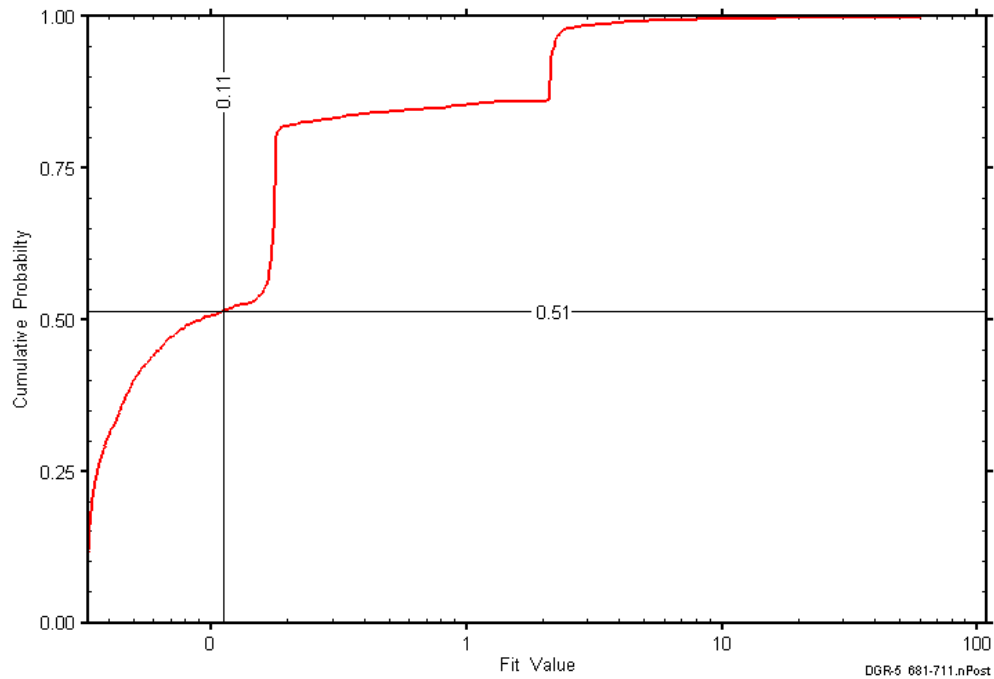


Figure 9-24: DGR5_681.07-711.33 fit value cumulative distribution function.

9.9 707.24-737.50 Cobourg

The DGR-5 interval from 707.24 to 737.50 m LBGs included the lower 1.46 m of the Collingwood Member of the Cobourg Formation, the entire 27.80-m thickness of the Lower Member of the Cobourg Formation, and the upper 1.0 m of the Sherman Fall Formation, measured along the slant of the hole. The Collingwood is interbedded shale and argillaceous limestone, and the Lower Member of the Cobourg and upper Sherman Fall are both argillaceous limestone. Information on the angle and vertical extent of the test interval is given in Table 9-18. An overview of the testing in this interval is given in Table 9-18 and the corresponding parameter estimates are given in Table 9-19. Two pulse-withdrawal tests were performed in this interval.

Table 9-18: Summary of the DGR5_702.24-737.50 testing activities.

Formation / Unit		Top of Test Zone (m LBGs)	Bottom of Test Zone (m LBGs)	
Cobourg		707.24	737.50	
Test Interval Angle (degrees from vertical)		Vertical Top of Test Zone (m BGS)	Vertical Bottom of Test Zone (m BGS)	
12.74		657.39	686.91	
Test	Initiated	Magnitude (kPa)	Duration	Compressibility (Pa ⁻¹)
Shut-in	04-03-10 14:27	N/A	18 hr	N/A
PW1	05-03-10 08:11	930	24 hr	3.6E-10
PW2 (Pt 1)	06-03-10 08:36	159	9 min	N/C
PW2 (Pt 2)	06-03-10 08:45	933	24 hr	3.6E-10
Borehole Pressure History				
Event		Start	Pressure (kPa)	
Drilling Intercept		24-10-09	7041	
Open Hole		08-11-09	N/A	
Prior Testing		02-02-10	N/A	
Shut-in		04-03-10	N/A	

Table 9-19: Summary of the DGR5_707.24-737.50 parameter estimates.

Parameter	Best Fit	Minimum	Maximum	Mean
K_f (m/s)	1.1E-14	7.7E-15	1.2E-14	9.7E-15
P_f (kPa)	6429	5989	6564	6276
K_s (m/s)	1.3E-12	1.2E-13	2.5E-12	3.6E-13
t_s (cm)	27	2.2	31	7.9
S_s (1/m)	1.2E-08	1.0E-08	3.0E-07	8.8E-08

Figure 9-25 shows the measured pressure record from DGR5_707.24-737.50 used in this analysis along with the best-fit simulation and parameter values. The ranges of formation K and raw P_f values estimated from perturbation analysis are shown in Figure 9-26 and the fit value cumulative distribution function is shown in Figure 9-27.

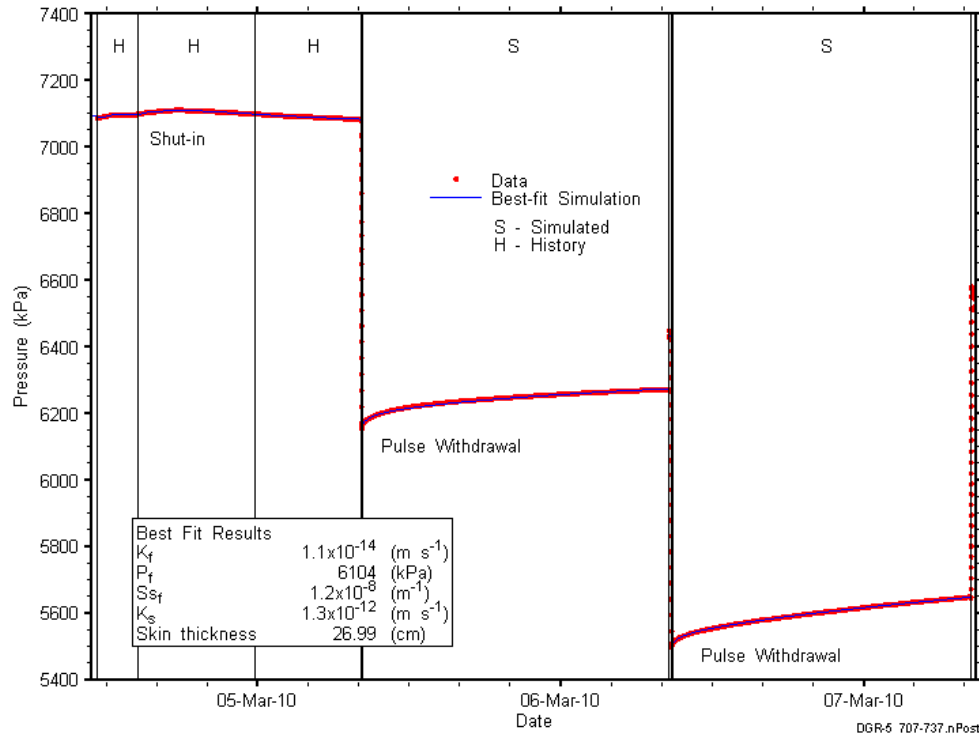


Figure 9-25: Annotated DGR5_707.24-737.50 testing sequence showing best-fit simulation and parameter estimates.

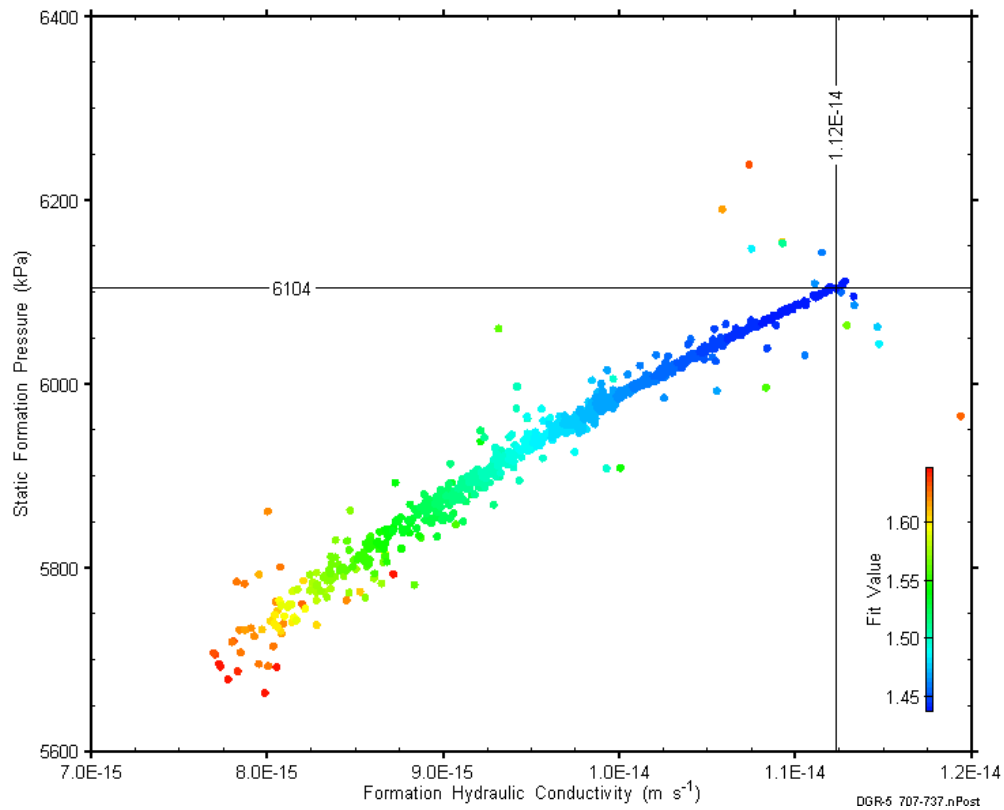


Figure 9-26: XY-scatter plot showing estimates of formation hydraulic conductivity and raw static formation pressure derived from the DGR5_707.24-737.50 perturbation analysis.

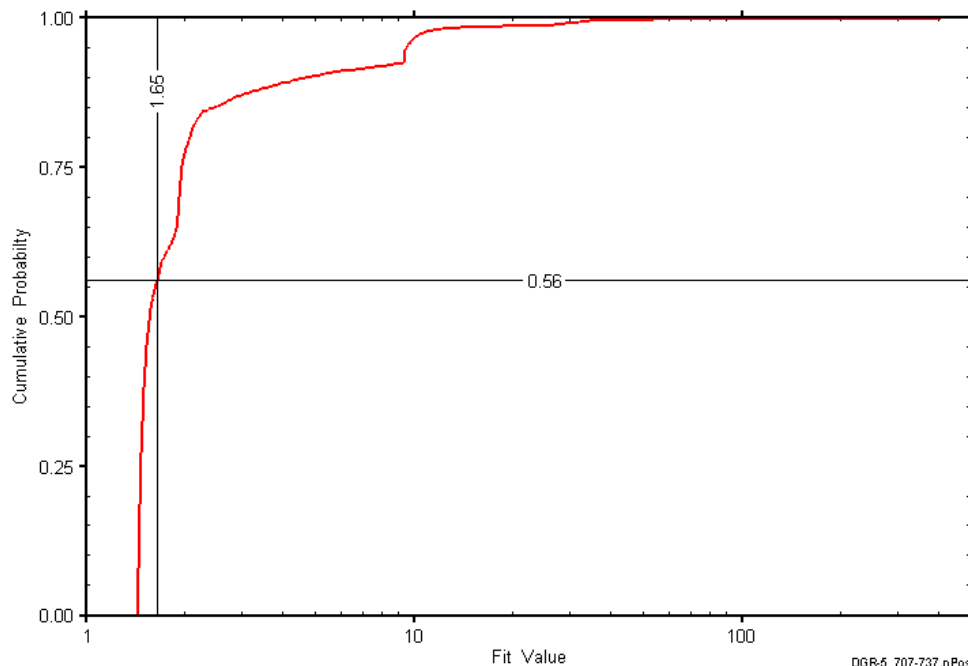


Figure 9-27: DGR5_707.24-737.50 fit value cumulative distribution function.

9.10 737.25-767.51 Sherman Fall

The DGR-5 interval from 737.25 to 767.51 m LBGS contained all but the upper 0.75 m of the 30.0-m-thick Sherman Fall Formation along with the upper 1.0 m of the Kirkfield Formation, measured along the slant of the hole. The upper 15.0-m portion of the Sherman Fall tested consists of argillaceous limestone, while the lower Sherman Fall and upper Kirkfield are both interbedded argillaceous limestone and shale. Information on the angle and vertical extent of the test interval is given in Table 9-20. An overview of the testing in this interval is given in Table 9-20 and the corresponding parameter estimates are given in Table 9-21. Two pulse-withdrawal tests were performed in this interval.

Table 9-20: Summary of the DGR5_737.25-767.51 testing activities.

Formation / Unit		Top of Test Zone (m LBGS)	Bottom of Test Zone (m LBGS)	
Sherman Fall		737.25	767.51	
Test Interval Angle (degrees from vertical)		Vertical Top of Test Zone (m BGS)	Vertical Bottom of Test Zone (m BGS)	
12.58		686.66	716.20	
Test	Initiated	Magnitude (kPa)	Duration	Compressibility (Pa ⁻¹)
Shut-in	07-03-10 14:31	N/A	19 hr	N/A
PW1	08-03-10 09:11	940	23 hr	3.7E-10
PW2 (Pt 1)	09-03-10 08:26	100	7 min	N/C
PW2 (Pt 2)	09-03-10 08:33	942	24 hr	3.6E-10
Borehole Pressure History				
Event	Start	Pressure (kPa)		
Drilling Intercept	26-10-09	7356		
Open Hole	08-11-09	N/A		
Prior Testing	02-02-10	N/A		
Shut-in	07-03-10	N/A		

Table 9-21: Summary of the DGR5_737.25-767.51 parameter estimates.

Parameter	Best Fit	Minimum	Maximum	Mean
K_f (m/s)	1.6E-14	1.3E-14	2.0E-14	1.7E-14
P_f (kPa)	5561	5250	5835	5637
K_s (m/s)	2.1E-13	1.1E-13	1.3E-12	3.1E-13
t_s (cm)	4.6	2.0	34	8.1
S_s (1/m)	1.7E-07	1.1E-08	3.8E-07	1.0E-07

Figure 9-28 shows the measured pressure record from DGR5_737.25-767.51 used in this analysis along with the best-fit simulation and parameter values. The ranges of formation K and raw P_f values estimated from perturbation analysis are shown in Figure 9-29 and the fit value cumulative distribution function is shown in Figure 9-30.

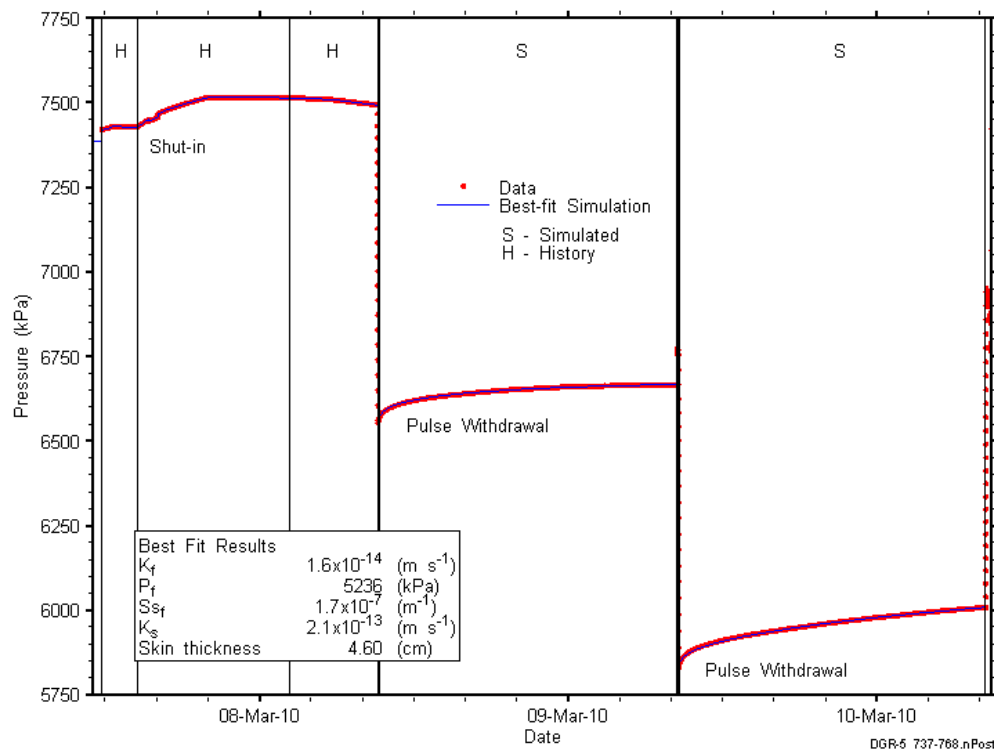


Figure 9-28: Annotated DGR5_737.25-767.51 testing sequence showing best-fit simulation and parameter estimates.

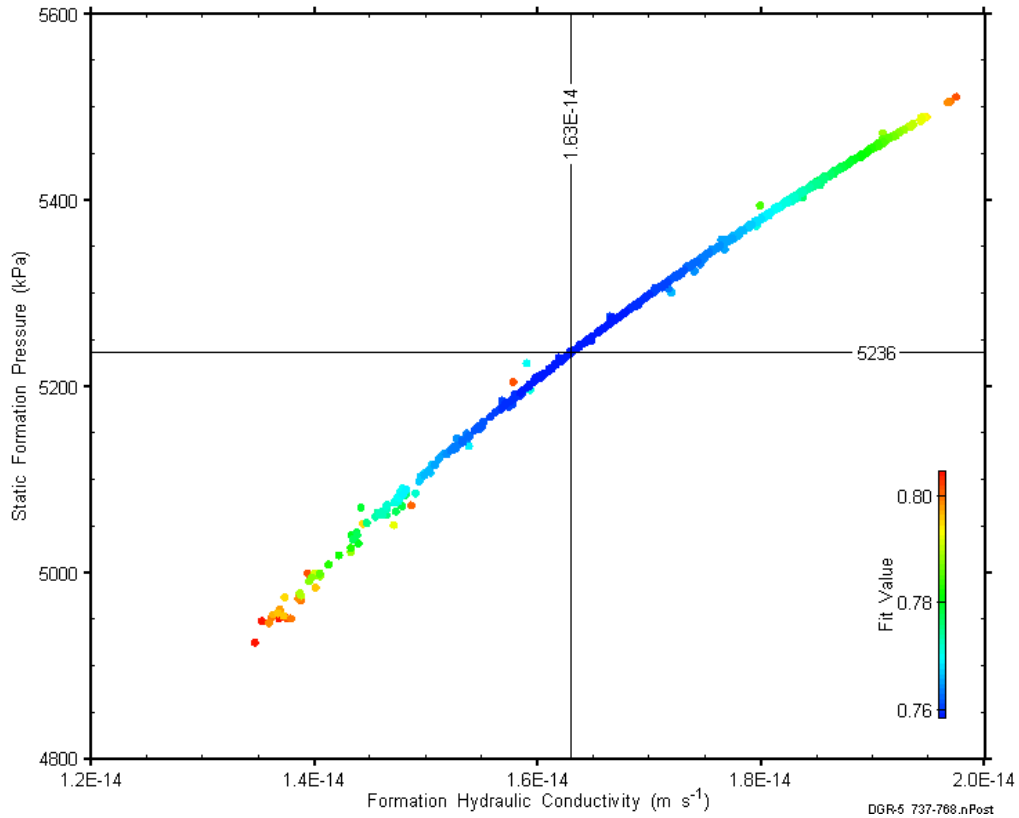


Figure 9-29: XY-scatter plot showing estimates of formation hydraulic conductivity and raw static formation pressure derived from the DGR5_737.25-767.51 perturbation analysis.

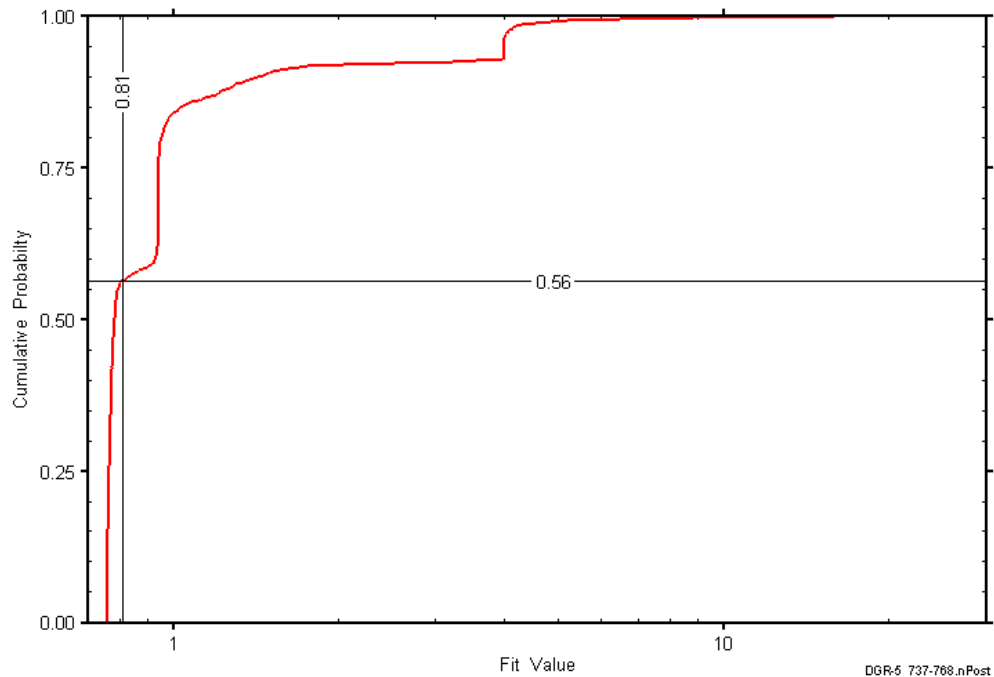


Figure 9-30: DGR5_737.25-767.51 fit value cumulative distribution function.

9.11 767.25-797.51 Kirkfield

The DGR-5 interval from 767.25 to 797.51 m LBGS was entirely contained within the Kirkfield Formation. This portion of the Kirkfield consists of interbedded argillaceous limestone and shale. Information on the angle and vertical extent of the test interval is given in Table 9-22. An overview of the testing in this interval is given in Table 9-22 and the corresponding parameter estimates are given in Table 9-23. Two pulse-withdrawal tests were performed in this interval.

Table 9-22: Summary of the DGR5_767.25-797.51 testing activities.

Formation / Unit		Top of Test Zone (m LBGS)		Bottom of Test Zone (m LBGS)	
Kirkfield		767.25		797.51	
Test Interval Angle (degrees from vertical)		Vertical Top of Test Zone (m BGS)		Vertical Bottom of Test Zone (m BGS)	
12.54		715.94		745.48	
Test	Initiated	Magnitude (kPa)	Duration	Compressibility (Pa ⁻¹)	
Shut-in	10-03-10 14:45	N/A	18 hr	N/A	
PW1	11-03-10 08:31	960	24 hr	3.6E-10	
PW2 (Pt 1)	12-03-10 08:51	206	7 min	N/C	
PW2 (Pt 2)	12-03-10 08:58	975	24 hr	3.5E-10	
Borehole Pressure History					
Event		Start		Pressure (kPa)	
Drilling Intercept		26-10-09		7672	
Open Hole		08-11-09		N/A	
Prior Testing		02-02-10		N/A	
Shut-in		10-03-10		N/A	

Table 9-23: Summary of the DGR5_767.25-797.51 parameter estimates.

Parameter	Best Fit	Minimum	Maximum	Mean
K_f (m/s)	2.3E-14	1.7E-14	2.4E-14	2.1E-14
P_f (kPa)	6152	5487	6189	5963
K_s (m/s)	3.6E-13	1.1E-13	3.3E-07	9.9E-13
t_s (cm)	27	1.5	39	10
S_s (1/m)	1.0E-08	1.0E-08	2.8E-07	5.5E-08

Figure 9-31 shows the measured pressure record from DGR5_767.25-797.51 used in this analysis along with the best-fit simulation and parameter values. The ranges of formation K and raw P_f values estimated from perturbation analysis are shown in Figure 9-32 and the fit value cumulative distribution function is shown in Figure 9-33.

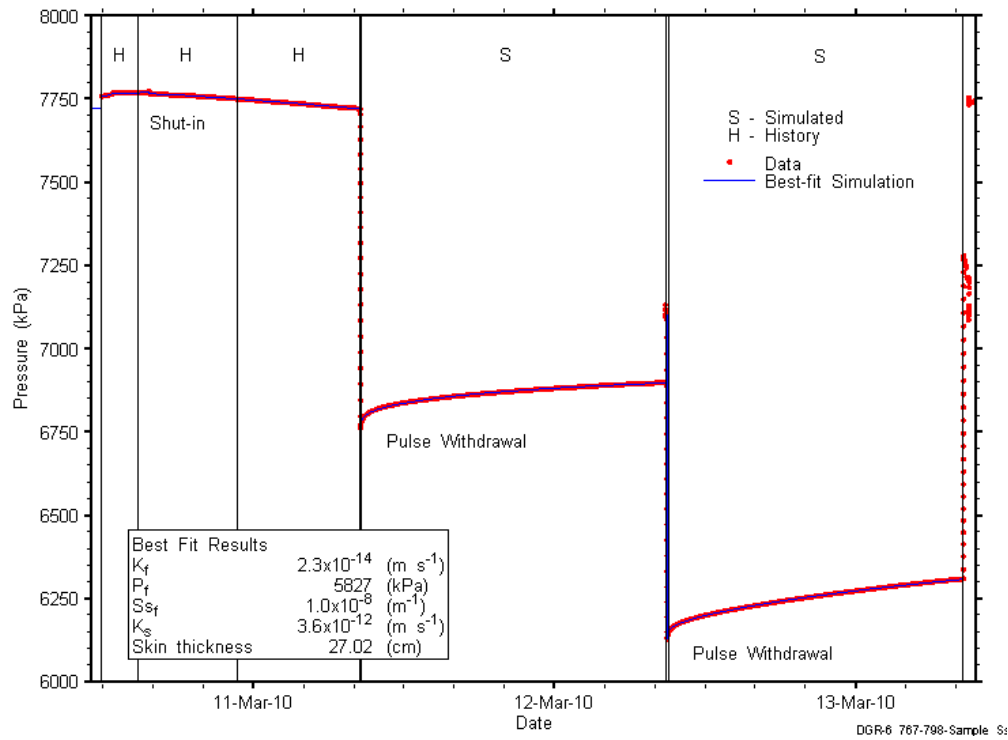


Figure 9-31: Annotated DGR5_767.25-797.51 testing sequence showing best-fit simulation and parameter estimates.

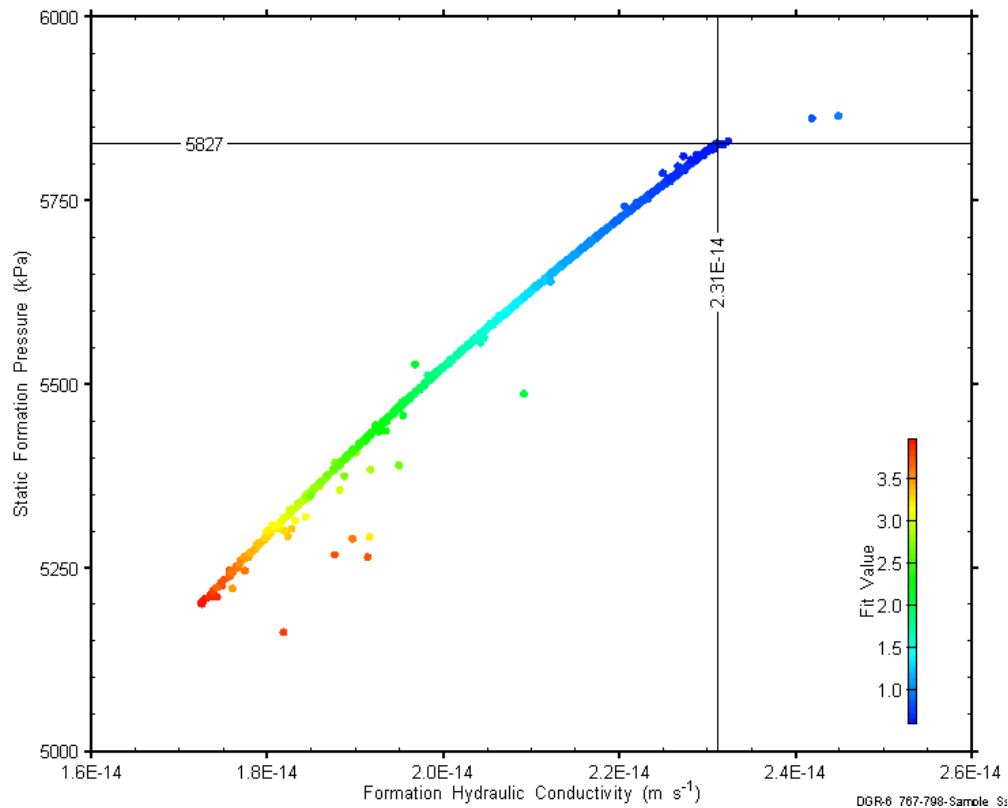


Figure 9-32: XY-scatter plot showing estimates of formation hydraulic conductivity and raw static formation pressure derived from the DGR5_767.25-797.51 perturbation analysis.

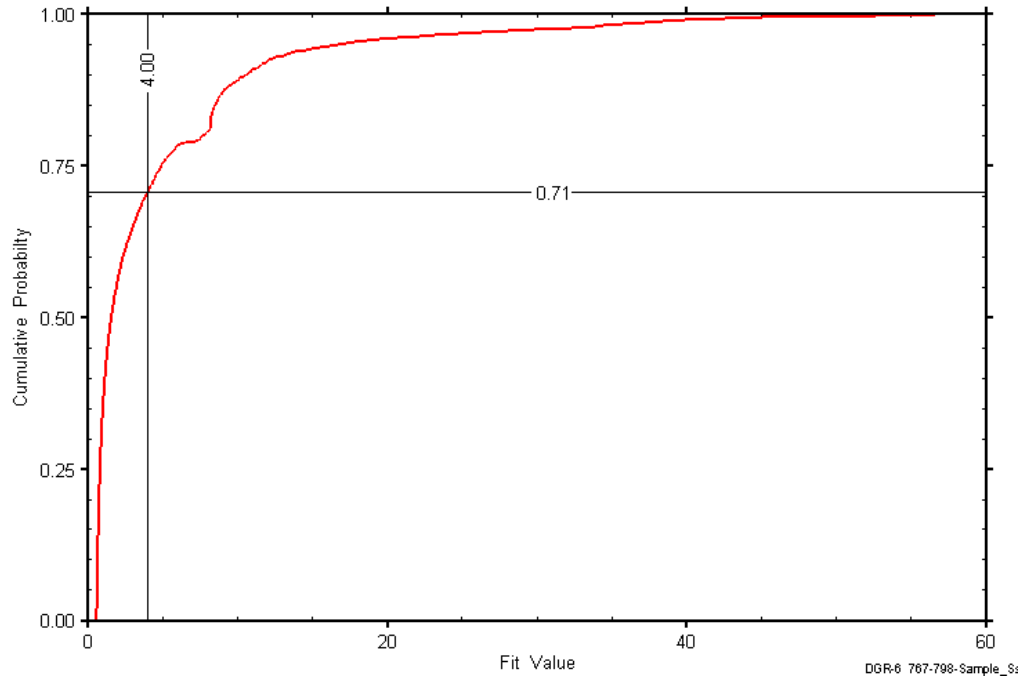


Figure 9-33: DGR5_767.25-797.51 fit value cumulative distribution function.

9.12 Summary of DGR-5 Results

The best-fit parameter estimates derived from the DGR-5 analyses are given in Table 9-24. Note that the vertical depths, rather than the depths along the slanted borehole, are given for the test intervals. Figure 9-34 through Figure 9-38 present stratigraphic profiles of the analysis results for hydraulic conductivity, formation pressure, specific storage, skin factor, and test-zone compressibility respectively.

Table 9-24: Best-fit parameter estimates derived from the DGR-5 analyses

Formation(s) Tested	Top	Bottom	K_f	P_f	S_s	K_s	t_s	s	C_{tz}
	m BGS	m BGS	$m\ s^{-1}$	kPa	m^{-1}	$m\ s^{-1}$	cm		Pa^{-1}
Manitoulin-Queenston	437.94	466.55	2.7E-13	4105	1.0E-8*	2.0E-10	125	-2.8	4.6E-9
Queenston	466.30	495.07	1.4E-13	4856	1.0E-8*	2.3E-11	70	-2.3	1.0E-9
Queenston-Georgian Bay	494.82	523.66	9.4E-13	4949	1.1E-6	7.8E-14	6.4	6.7	4.8E-10
Georgian Bay	523.42	552.31	3.3E-13	4782	5.7E-6	3.2E-14	1.3	1.5	4.9E-10
Georgian Bay	552.06	581.01	2.9E-15	344	1.0E-8*	2.8E-12	92	-2.5	4.2E-10
Georgian Bay-Blue Mountain	580.76	609.80	3.2E-14	7946	2.2E-5	6.0E-13	0.4	-0.051	3.2E-9
Blue Mountain	609.55	638.80	3.1E-14	3892	1.7E-6	9.3E-14	1.8	-0.14	4.3E-10
Blue Mountain-Collingwood-Cobourg	631.95	661.38	3.0E-14	5056	2.3E-7	2.2E-13	4.3	-0.39	3.8E-10
Cobourg	657.39	686.91	1.1E-14	6429	1.2E-8*	1.3E-12	27	-1.5	3.6E-10
Sherman Fall	686.66	716.20	1.6E-14	5561	1.7E-7	2.1E-13	4.6	-0.45	3.6E-10
Kirkfield	715.94	745.48	2.3E-14	6152	1.0E-8*	3.6E-12	27	-1.5	3.6E-10

*: sampled

As shown in Figure 9-34 and Table 9-24, six of the Ordovician test intervals in DGR-5 had K values between 1.1E-14 and 3.2E-14 m/s. The middle Georgian Bay interval had a lower K of 2.9E-15 m/s. Higher K values of 1.5E-13 to 9.4E-13 m/s were found in the Manitoulin-Queenston, Queenston, Queenston-Georgian Bay, and upper Georgian Bay intervals. Uncertainty in hydraulic conductivity was generally well under an order of magnitude, except in the Queenston-Georgian Bay and upper Georgian Bay intervals.

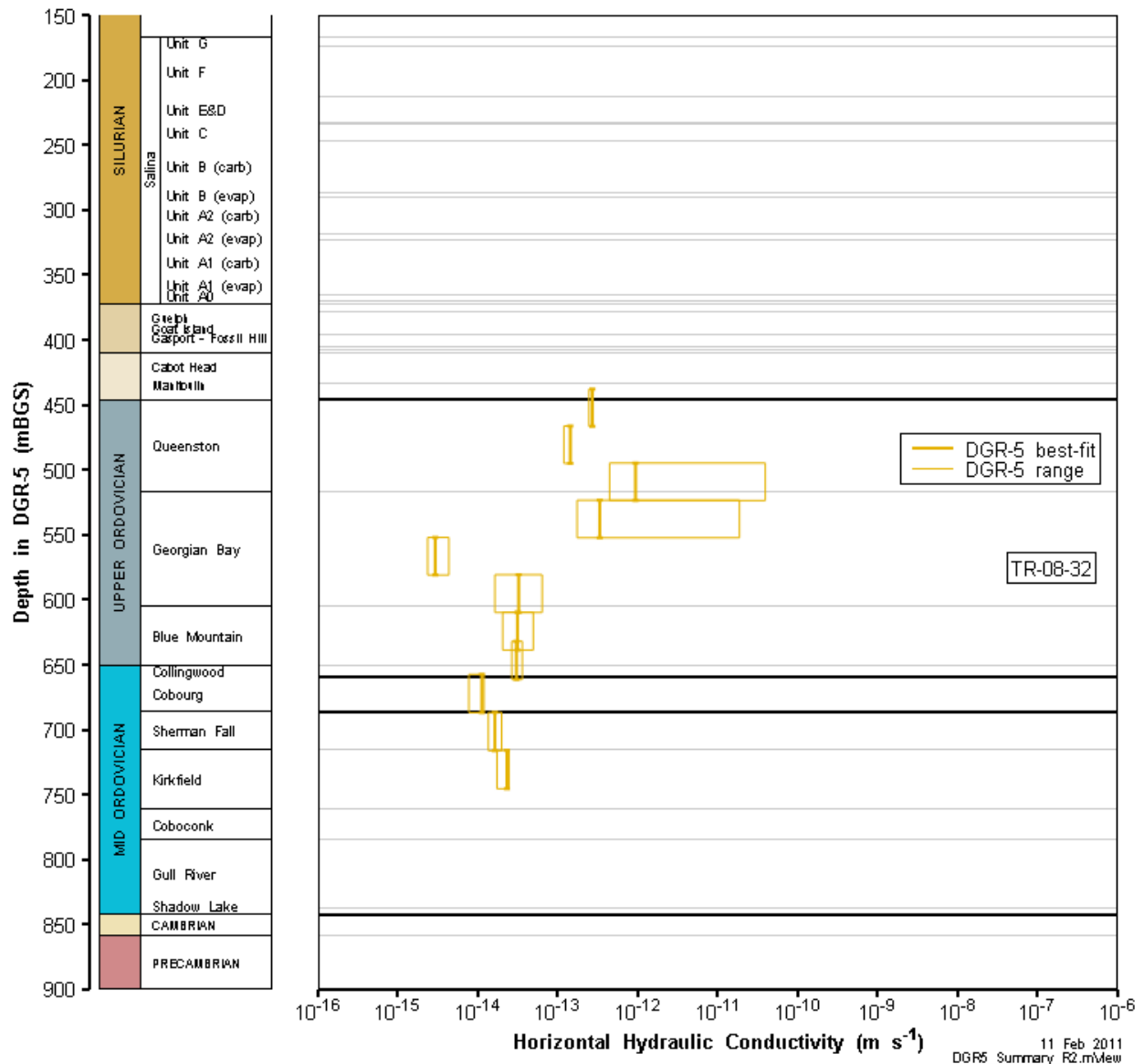


Figure 9-34: DGR-5 stratigraphic profile of horizontal hydraulic conductivity estimates.

As shown in Figure 9-35, the majority of the test intervals in DGR-5 were underpressured relative to a density-compensated hydrostatic condition. The interval in the middle of the Queenston was nearly normally pressured, while the Georgian Bay-Blue Mountain interval was the only overpressured interval. This interval also had a high test-zone compressibility (Table 9-24). The intervals in the middle Georgian Bay and Blue Mountain adjacent to this overpressured interval were the most underpressured intervals tested.

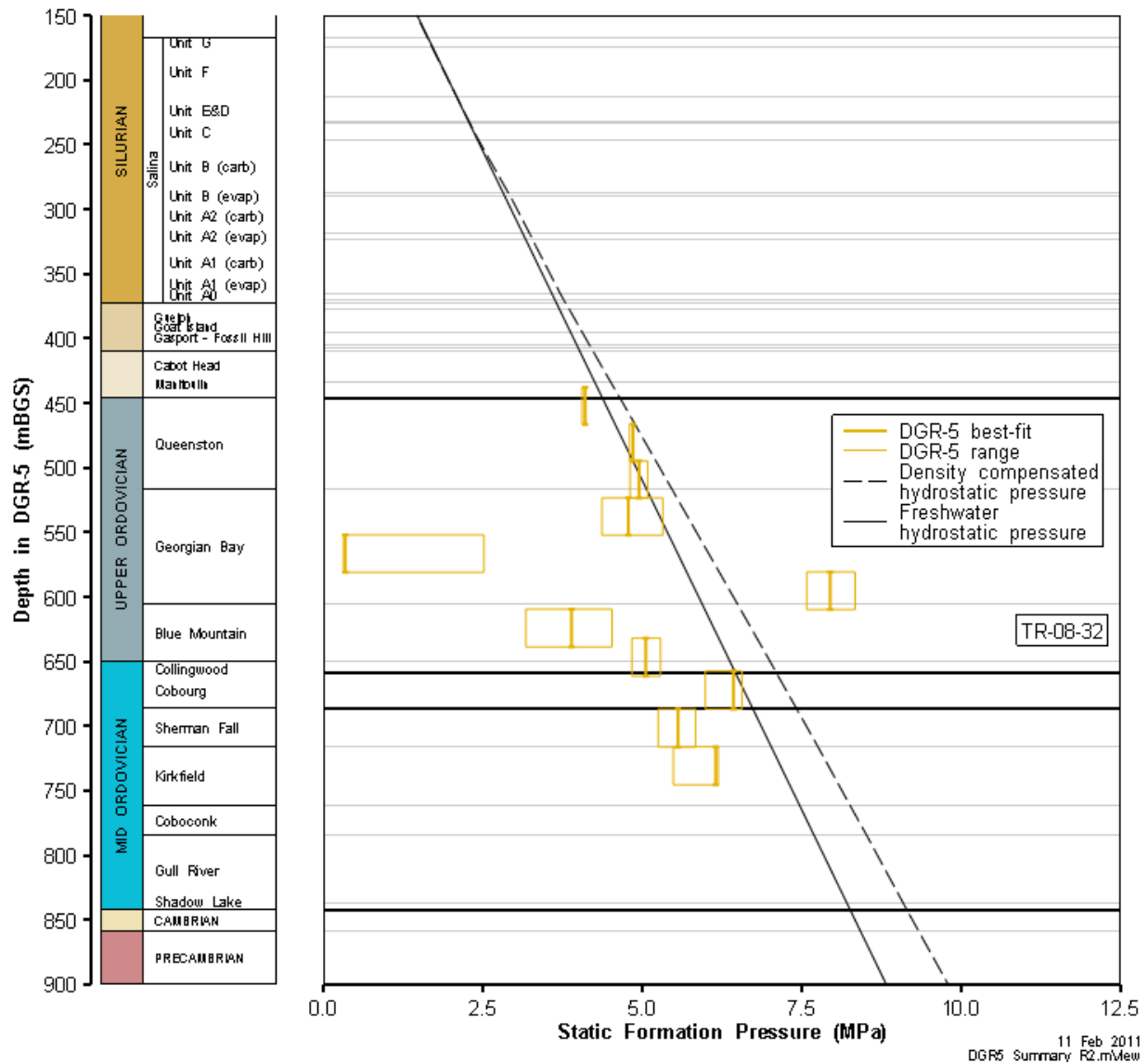


Figure 9-35: DGR-5 stratigraphic profile of formation pressure estimates.

Figure 9-36 shows the S_s values fitted in the simulations for each of the DGR-5 test intervals, along with the uncertainties associated with the fitted values. The fitted values range from $1.7E-7 \text{ m}^{-1}$ to $2.2E-5 \text{ m}^{-1}$. For many of the test intervals, effectively equivalent fits could be obtained with S_s values ranging over more than an order of magnitude. This is a consequence of the strong correlation between S_s and skin properties in single-well tests discussed in Section 4.4. For five test intervals, no minimum was found in the S_s fit surface within the range of values thought to be physically reasonable ($1E-8$ to $1E-4 \text{ m}^{-1}$); the best fit was always found at the lowest S_s value allowed. In those cases, S_s was sampled over a range extending down to $1E-8 \text{ m}^{-1}$, and the best fit was generally found at that value. The sampled values are not shown in Figure 9-36, but are given in Table 9-24.

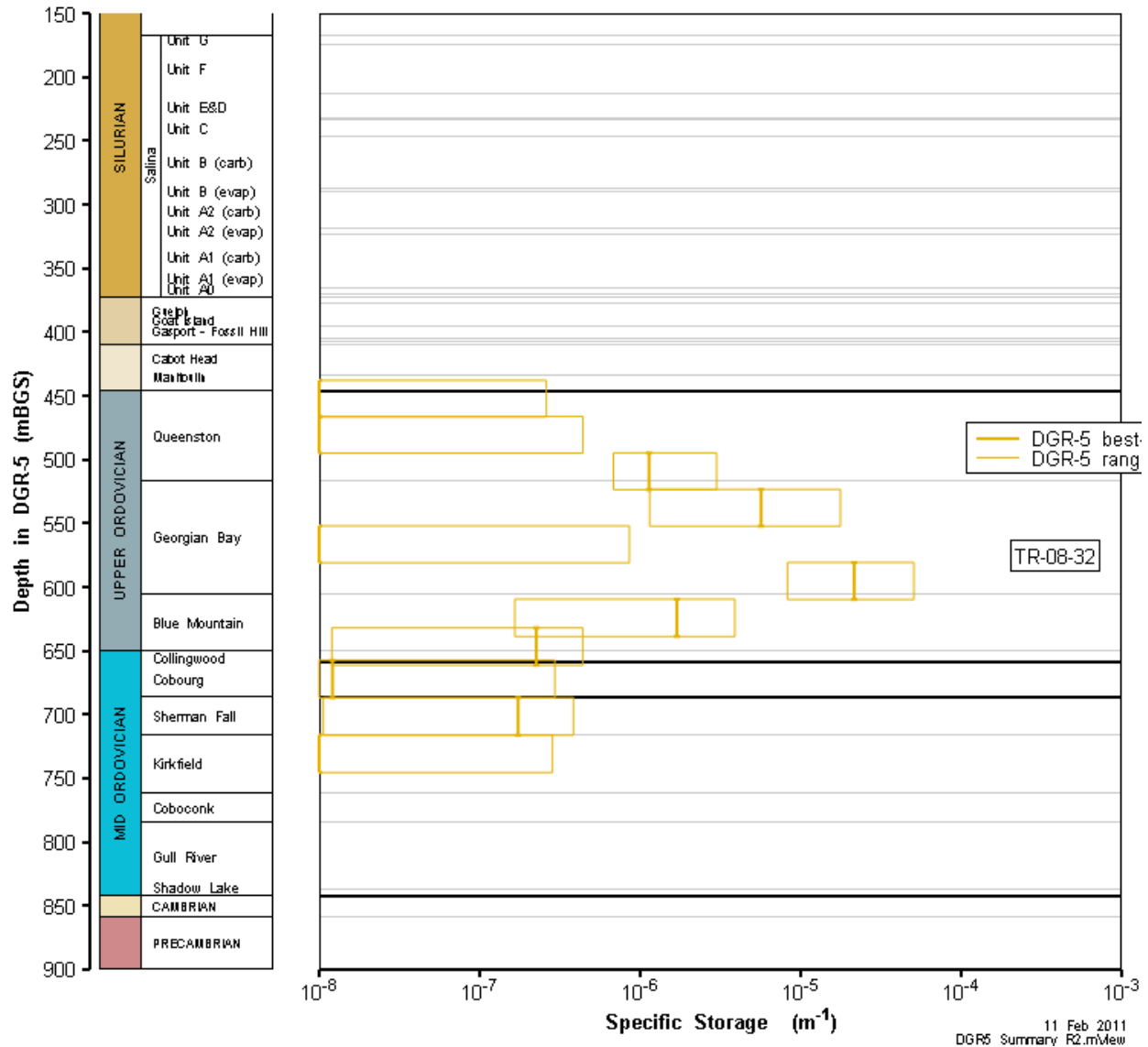


Figure 9-36: DGR-5 stratigraphic profile of specific storage estimates.

Figure 9-37 shows the skin factors obtained from parameter optimization for each of the DGR-5 test intervals. All but two of the test intervals had negative skins, reflecting enhanced permeability around the wellbore. Hydraulically significant fractures are a possible cause of negative skins. Other causes could be enhanced local fracturing caused by stress relief fracturing during drilling. The negative skins in DGR-5 were generally of low magnitude; the Manitoulin-Queenston interval had the most negative skin, which was only -2.8 (Table 9-24). Two intervals had positive skins associated with decreased permeability around the wellbore, the most significant of which was the skin of 6.7 for the Queenston-Georgian Bay interval.

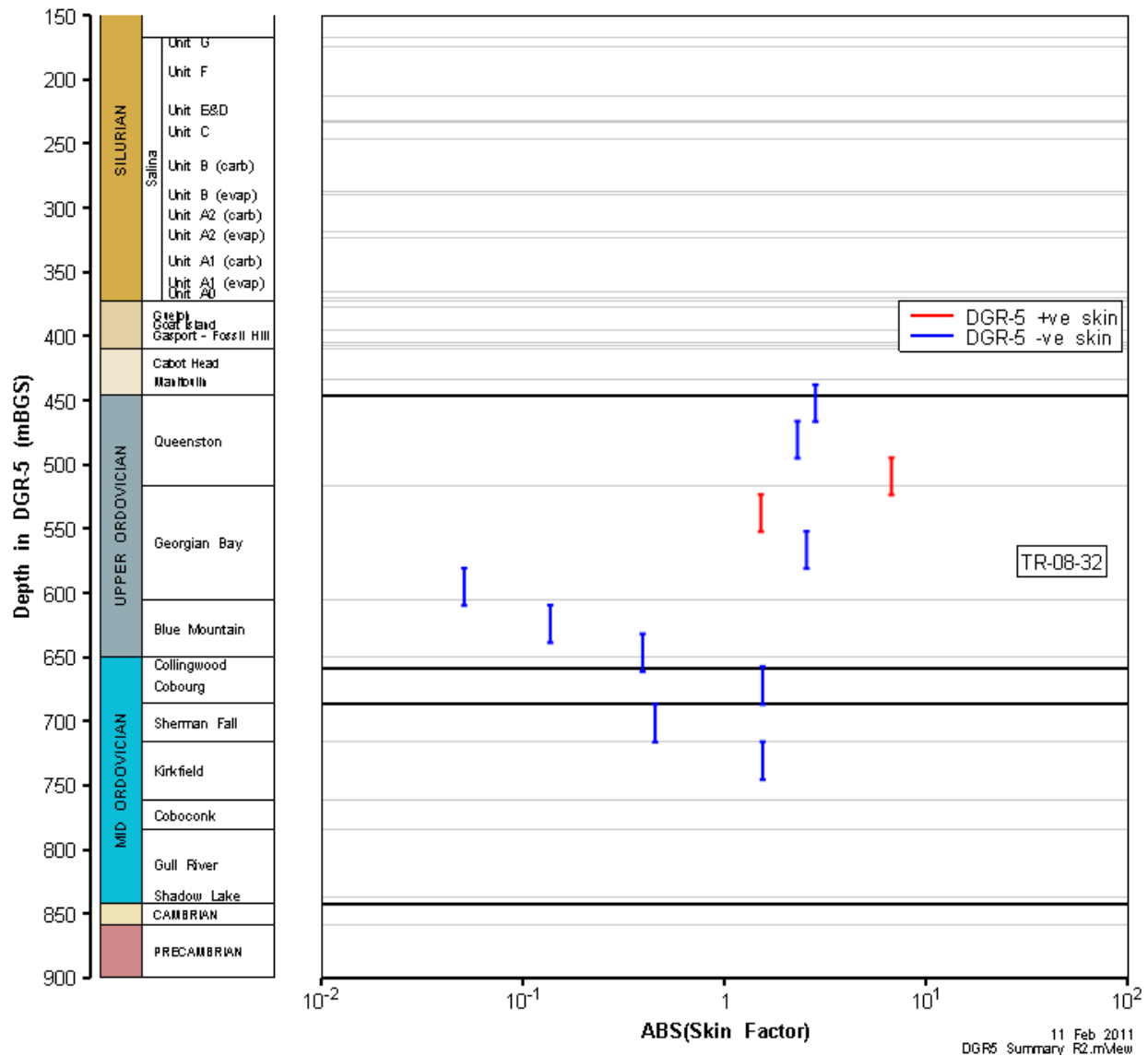


Figure 9-37: DGR-5 stratigraphic profile of skin factor estimates.

As shown in Figure 9-38, of the 11 DGR-5 intervals in which test-zone compressibility was measured, C_{tz} was less than $5E-10 \text{ Pa}^{-1}$ in 8 intervals. These values are indicative of water-filled test intervals with typical test-tool compliance. In the remaining 3 intervals, C_{tz} ranged from $1.0E-9$ to $4.6E-9 \text{ Pa}^{-1}$. Higher test-zone compressibilities such as these (particularly $4.6E-9 \text{ Pa}^{-1}$) are suggestive of a relatively small amount of gas in the test zone, but no direct evidence of gas is available. The highest C_{tz} mentioned above was measured in the Manitoulin-Queenston interval, which was also slightly underpressured (Figure 9-35). Fractures were observed in core from the upper Queenston in DGR-5 (Sterling et al., 2011), which may be related to the high C_{tz} and low P_f .

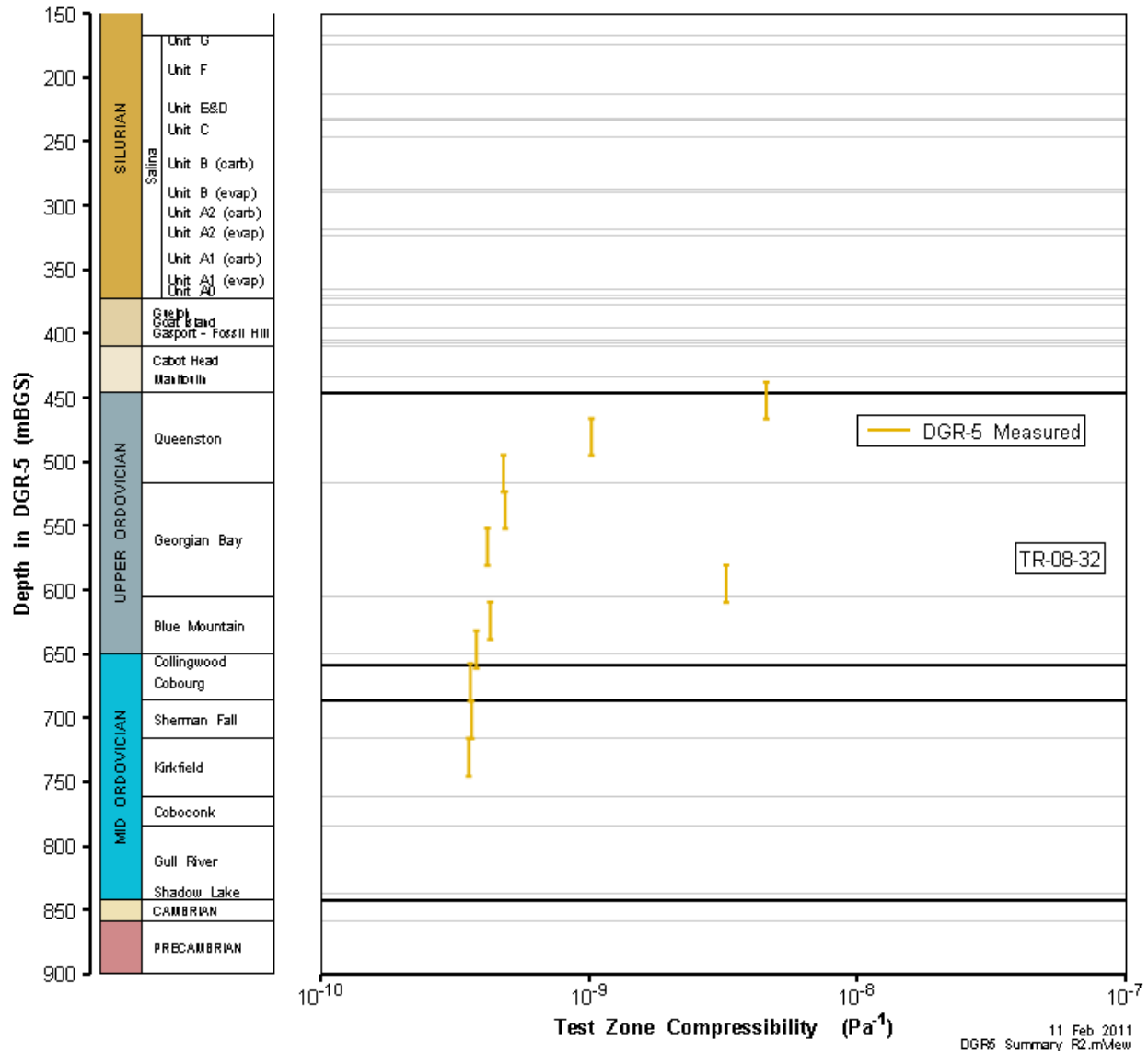


Figure 9-38: DGR-5 stratigraphic profile of test-zone compressibility estimates.

10 DGR-6 Testing and Analysis

Hydraulic testing in the slanted borehole DGR-6 was performed from 30 April until 24 June 2010. Twelve intervals were tested using a 10.23-m straddle. The intervals were selected to allow testing of different lithologies within individual formations, as well as to test fractured and unfractured portions of formations. The short straddle interval also allowed the Collingwood Member of the Cobourg Formation to be tested with minimal contributions from the overlying Blue Mountain and underlying Cobourg Formations, in contrast to the testing in the other deep DGR boreholes. The testing in DGR-6 provided intermittent coverage of the borehole from 518.00 to 890.23 m LBGS. Table 10-1 lists the formations and intervals tested, and the type(s) of test(s) performed. Pulse tests were performed in all DGR-6 intervals, slug tests were performed in three intervals, and a DST was performed in one.

Table 10-1: DGR-6 test zones and tests

Formations / Units	Top of Test Zone (m LBGS)	Bottom of Test Zone (m LBGS)	Type(s) of Test(s)
Queenston	518.00	528.23	PW, PI
Georgian Bay	650.00	660.23	PW, PI, SI, SW
Georgian Bay-Blue Mountain	678.00	688.23	PW, SW, SI
Blue Mountain	700.00	710.23	PW, SI
Blue Mountain	725.00	735.23	PW
Collingwood	737.00	747.23	PW
Cobourg	764.00	774.23	PW
Sherman Fall	782.00	792.23	PW
Sherman Fall	797.00	807.23	PW
Kirkfield	841.00	851.23	PW
Coboconk	869.77	880.00	PW
Coboconk	880.00	890.23	PW, DST
Reference Elevation – Ground Surface	183.50 m above mean sea level		

PW: pulse withdrawal
 PI: pulse injection
 SI: slug injection
 SW: slug withdrawal
 DST: drillstem test

The test-zone transducer during DGR-6 testing was located 20.23 m above the middle of the isolated test zone as measured along the length of the test tool and was hydraulically connected to the test zone via a length of 1/4-in stainless-steel tubing. To determine the P_f values corresponding to the middle of the test zone, the “raw” (as measured by the transducer) P_f estimates were depth-corrected using the estimated fluid density value for each interval and the offset distance of 20.23 m corrected to vertical using the test interval angle. The depth-corrected P_f estimates are given in the tables below whereas the raw P_f estimates are listed in the graph annotations.

Results of each test analysis are discussed below. A summary of DGR-6 testing results is presented in Section 10.13.

10.1 518.00-528.23 Queenston

The DGR-6 interval from 518.00 to 528.23 m LBGS was entirely contained within the Queenston Formation. This portion of the Queenston consists of massively bedded shale. Information on the angle and vertical extent of the test interval is given in Table 10-2. An overview of the testing in this interval is given in Table 10-2 and the corresponding parameter estimates are given in Table 10-3. A pulse-withdrawal test and a pulse-injection test were performed in this interval.

Table 10-2: Summary of the DGR6_518.00-528.23 testing activities.

Formation / Unit		Top of Test Zone (m LBGS)		Bottom of Test Zone (m LBGS)	
Queenston		518.00		528.23	
Test Interval Angle (degrees from vertical)		Vertical Top of Test Zone (m BGS)		Vertical Bottom of Test Zone (m BGS)	
21.76		453.30		462.80	
Test	Initiated	Magnitude (kPa)	Duration	Compressibility (Pa ⁻¹)	
Shut-in	30-04-10 11:14	N/A	20 hr	N/A	
PW	01-05-10 07:31	716	25 hr	3.7E-10	
PI	02-05-10 08:58	713	22 hr	3.8E-10	
Borehole Pressure History					
Event		Start		Pressure (kPa)	
Drilling Intercept		24-11-09		5038	
Open Hole		25-01-10		N/A	
Prior Testing		19-04-10		N/A	
Shut-in		30-04-10		N/A	

Table 10-3: Summary of the DGR6_518.00-528.23 parameter estimates.

Parameter	Best Fit	Minimum	Maximum	Mean
K_f (m/s)	1.2E-13	1.0E-13	1.2E-13	1.1E-13
P_f (kPa)	5034	5033	5044	5038
K_s (m/s)	2.4E-12	5.7E-13	2.8E-12	1.3E-12
t_s (cm)	45	7.73	44.51	21.94
S_s (m ⁻¹)	1.0E-8	1.0E-08	1.3E-07	3.7E-08

Figure 10-1 shows the measured pressure record from DGR6_518.00-528.23 used in this analysis along with the best-fit simulation and parameter values. The ranges of formation K and raw P_f values estimated from perturbation analysis are shown in Figure 10-2 and the fit value cumulative distribution function is shown in Figure 10-3.

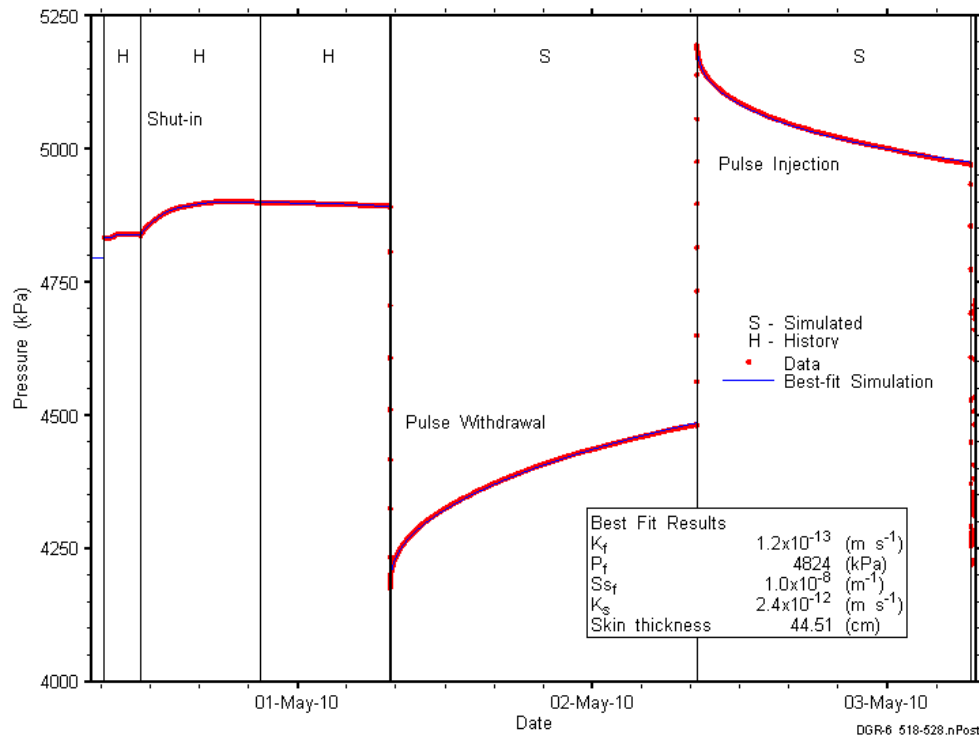


Figure 10-1: Annotated DGR6_518.00-528.23 testing sequence showing best-fit simulation and parameter estimates.

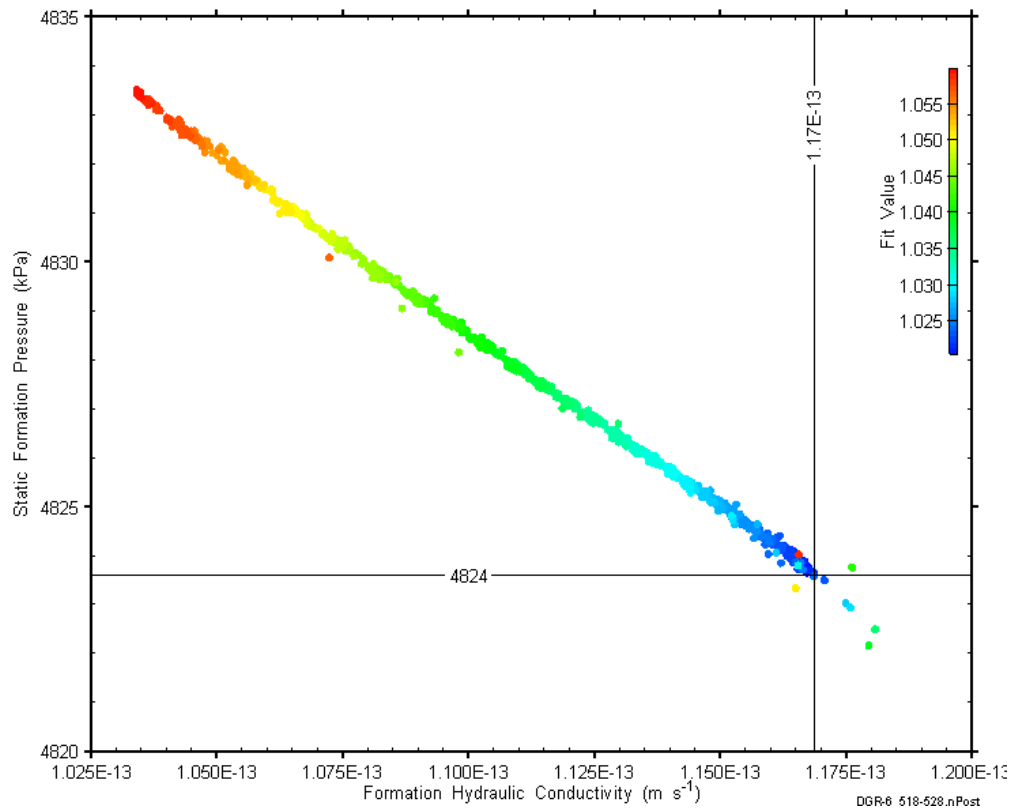


Figure 10-2: XY-scatter plot showing estimates of formation hydraulic conductivity and raw static formation pressure derived from the DGR6_518.00-528.23 perturbation analysis.

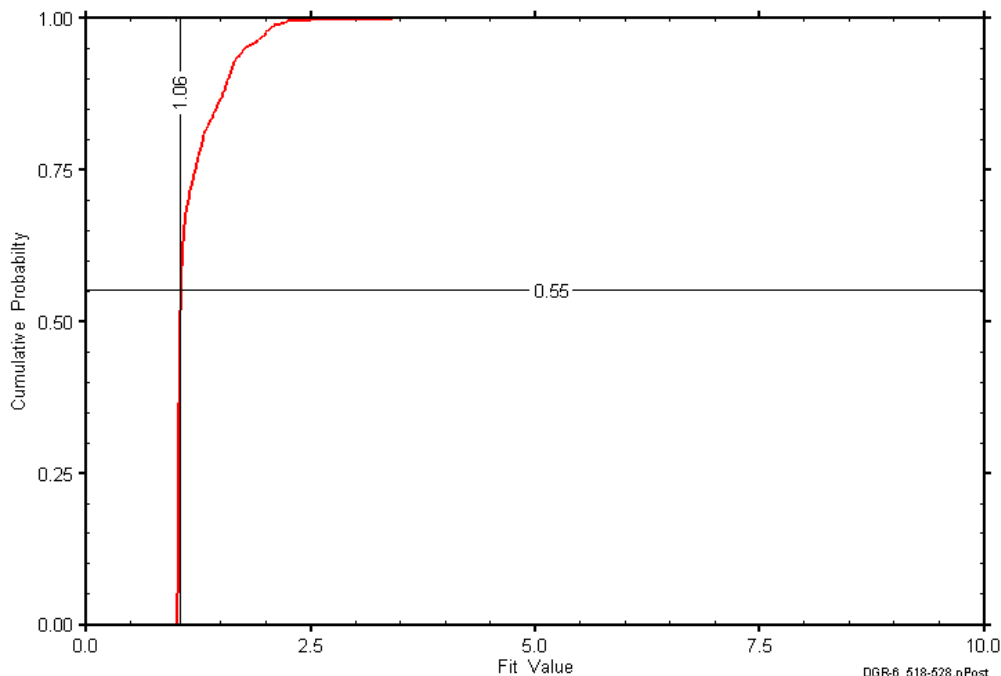


Figure 10-3: DGR6_518.00-528.23 fit value cumulative distribution function.

10.2 650.00-660.23 Georgian Bay

The DGR-6 interval from 650.00 to 660.23 m LBGS was entirely contained within the Georgian Bay Formation. This portion of the Georgian Bay consists of shale with trace laminae to thin interbeds of limestone/siltstone. Fractures infilled with halite or calcite were observed in core from this interval (Sterling et al., 2011). Information on the angle and vertical extent of the test interval is given in Table 10-4. An overview of the testing in this interval is given in Table 10-4 and the corresponding parameter estimates are given in Table 10-5. Two pulse-withdrawal tests, two pulse-injection tests, a slug-injection test, and a slug-withdrawal test were performed in this interval.

Table 10-4: Summary of the DGR6_650.00-660.23 testing activities.

Formation / Unit		Top of Test Zone (m LBGS)	Bottom of Test Zone (m LBGS)	
Georgian Bay		650.00	660.23	
Test Interval Angle (degrees from vertical)		Vertical Top of Test Zone (m BGS)	Vertical Bottom of Test Zone (m BGS)	
32.47		572.46	581.09	
Test	Initiated	Magnitude (kPa)	Duration	Compressibility (Pa ⁻¹)
Shut-in	03-05-10 17:00	N/A	16 hr	N/A
PW1	04-05-10 09:18	40	4 hr	6.4E-09
PW2	04-05-10 12:55	731	18 hr	N/C
PI1	05-05-10 07:19	43	96 min	7.2E-09
PI2	05-05-10 08:54	774	7 hr	N/C
SI	05-05-10 15:27	109	16 hr	N/C
SW	06-05-10 09:13	996	22 hr	N/C

Borehole Pressure History		
Event	Start	Pressure (kPa)
Drilling Intercept	07-01-10	6318
Open Hole	25-01-10	N/A
Prior Testing	19-04-10	N/A
Shut-in	03-05-10	N/A

Table 10-5: Summary of the DGR6_650.00-660.23 parameter estimates.

Parameter	Best Fit	Minimum	Maximum	Mean
K_f (m/s)	3.6E-14	1.5E-14	5.8E-14	3.5E-14
P_f (kPa)	5773	4896	7677	6041
K_s (m/s)	1.1E-07	5.1E-09	2.3E-06	2.3E-07
t_s (cm)	3.3	2.3	8.9	4.9
S_s (m ⁻¹)	7.2E-05	2.2E-05	9.0E-05	4.9E-05

Figure 10-4 shows the measured pressure record from DGR6_650.00-660.23 used in this analysis along with the best-fit simulation and parameter values. Preliminary analysis of the DGR6_650.00-660.23 response resulted in distinctly different K_f estimates for the withdrawal and injection tests (pulse and slug), with the injection K_f estimates being lower than withdrawal K_f estimates. It is believed that mud in the borehole fluid was affecting the injection tests, so only the withdrawal tests were matched for the final analysis. The ranges of formation K and raw P_f values estimated from perturbation analysis are shown in Figure 10-5 and the fit value cumulative distribution function is shown in Figure 10-6.

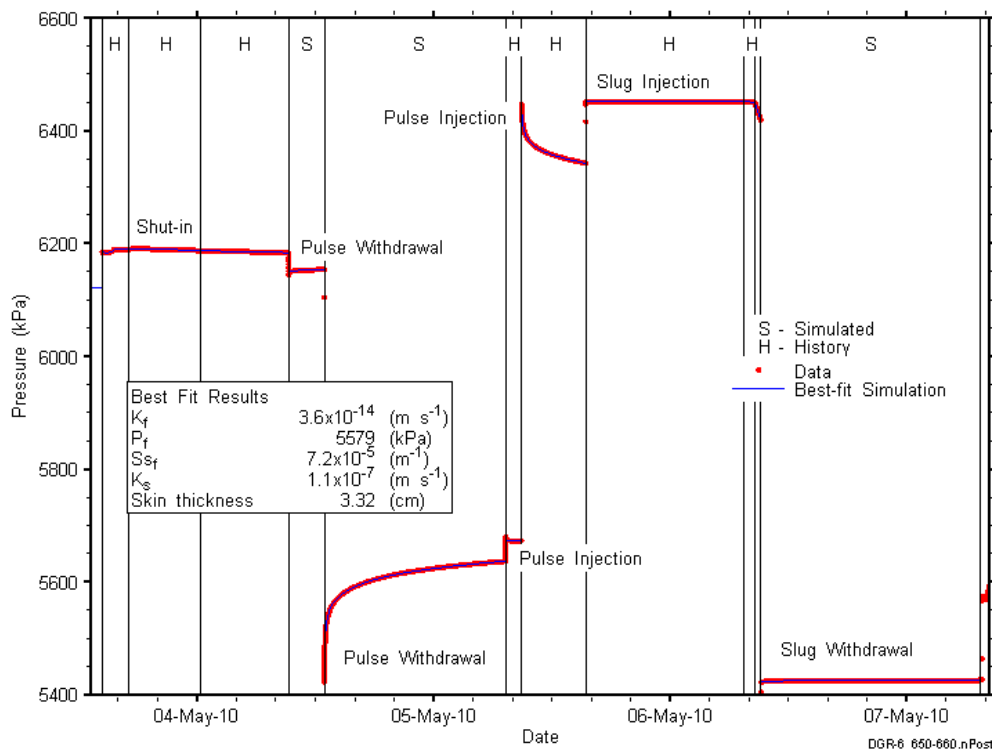


Figure 10-4: Annotated DGR6_650.00-660.23 testing sequence showing best-fit simulation and parameter estimates.

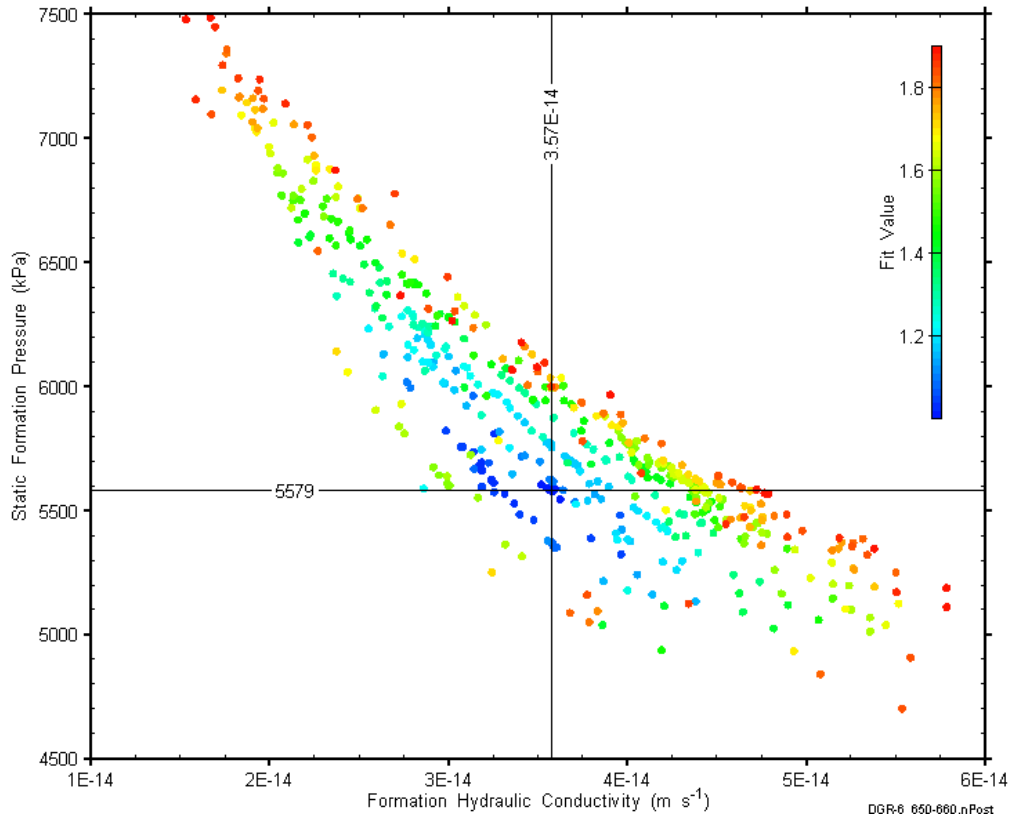


Figure 10-5: XY-scatter plot showing estimates of formation hydraulic conductivity and raw static formation pressure derived from the DGR6_650.00-660.23 perturbation analysis.

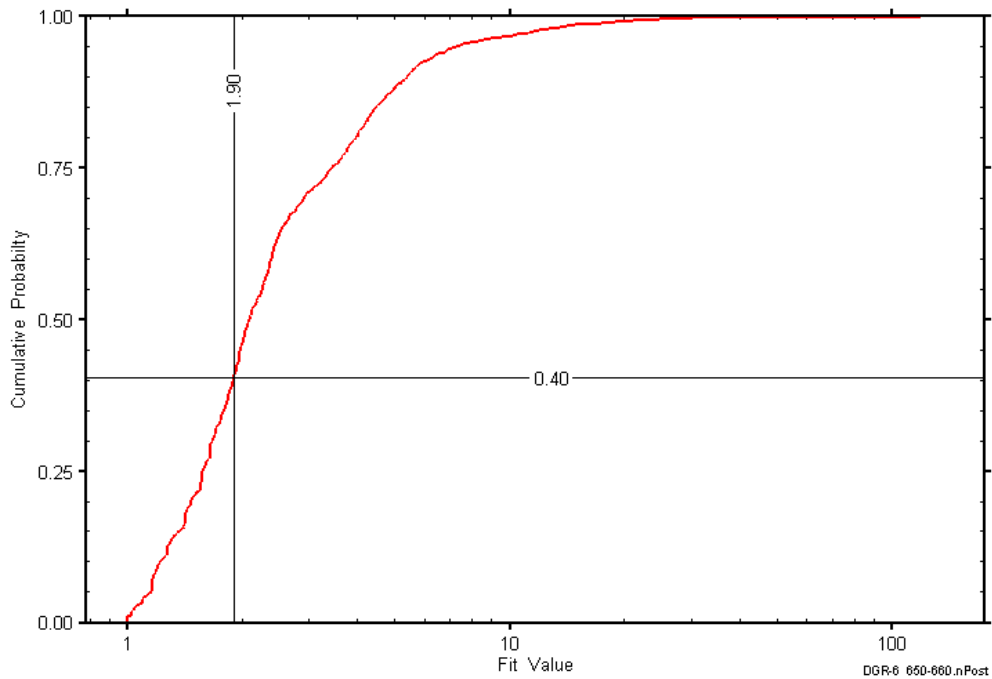


Figure 10-6: DGR6_650.00-660.23 fit value cumulative distribution function.

10.3 678.00-688.23 Georgian Bay-Blue Mountain

The DGR-6 interval from 678.00 to 688.23 m LBGS included the lower 6.7 m of the Georgian Bay Formation and the upper 3.53 m of the Blue Mountain Formation, measured along the slant of the hole. The entire test interval consisted of shale with trace laminae to thin interbeds of limestone/siltstone. A 7.5-mm-thick fracture filled with halite was observed in the core at 680.3 m LBGS (Sterling et al., 2011). Information on the angle and vertical extent of the test interval is given in Table 10-6. An overview of the testing in this interval is given in Table 10-6 and the corresponding parameter estimates are given in Table 10-7. A pulse-withdrawal test, a slug-withdrawal test, and a slug-injection test were performed in this interval.

Table 10-6: Summary of the DGR6_678.00-688.23 testing activities.

Formation / Unit		Top of Test Zone (m LBGS)	Bottom of Test Zone (m LBGS)	
Georgian Bay-Blue Mountain		678.00	688.23	
Test Interval Angle (degrees from vertical)		Vertical Top of Test Zone (m BGS)	Vertical Bottom of Test Zone (m BGS)	
32.93		596.02	604.60	
Test	Initiated	Magnitude (kPa)	Duration	Compressibility (Pa ⁻¹)
Shut-in	08-05-10 14:28	N/A	18 hr	N/A
PW	09-05-10 08:34	10	71 min	2.5E-08
SW	09-05-10 09:46	919	22 hr	N/C
SI	10-05-10 08:35	1208	22 hr	N/C
Borehole Pressure History				
Event	Start		Pressure (kPa)	
Drilling Intercept	11-01-10		6571	
Open Hole	25-01-10		N/A	
Prior Testing	19-04-10		N/A	
Shut-in	08-05-10		N/A	

Table 10-7: Summary of the DGR6_678.00-688.23 parameter estimates.

Parameter	Best Fit	Minimum	Maximum	Mean
K_f (m/s)	1.5E-12	5.3E-13	2.5E-12	1.4E-12
P_f (kPa)	5046	4389	5612	5051
K_s (m/s)	2.8E-06	6.1E-10	1.0E-03	5.4E-06
t_s (cm)	285	4.2	614	154
S_s (m ⁻¹)	4.3E-08	1.0E-08	2.6E-05	1.8E-07

Figure 10-7 shows the measured pressure record from DGR6_678.00-688.23 used in this analysis along with the best-fit simulation and parameter values. Preliminary analysis of the DGR6_678.00-688.23 response resulted in distinctly different K_f estimates for the SW and SI tests, with the SI K_f estimate being lower than that obtained from the SW analysis. It is believed that mud in the borehole fluid was affecting the SI test, so only the SW test was matched for the final analysis. The ranges of formation K and raw P_f values estimated from perturbation analysis are shown in Figure 10-8 and the fit value cumulative distribution function is shown in Figure 10-9.

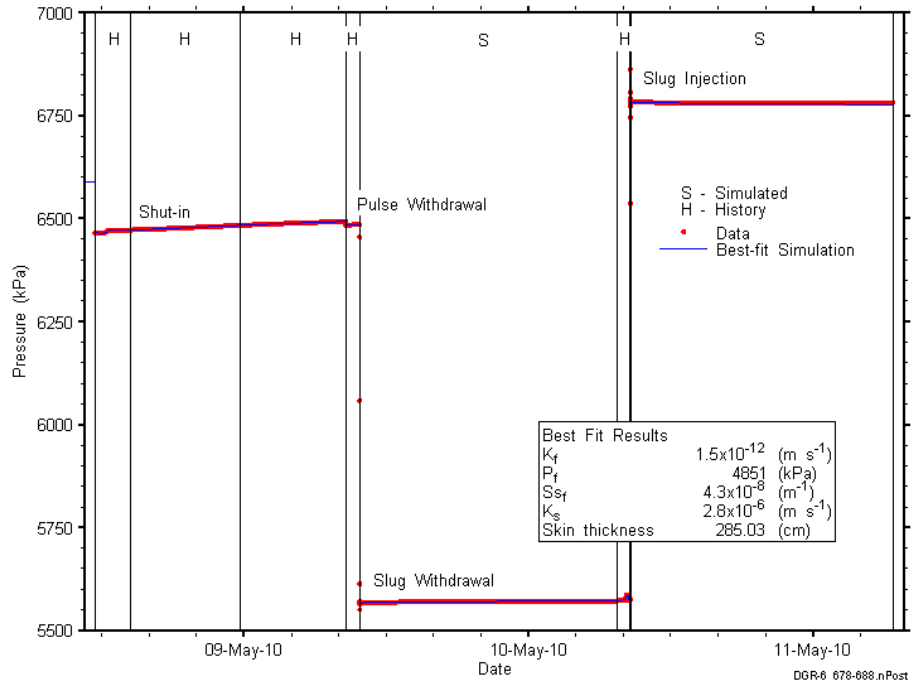


Figure 10-7: Annotated DGR6_678.00-688.23 testing sequence showing best-fit simulation and parameter estimates.

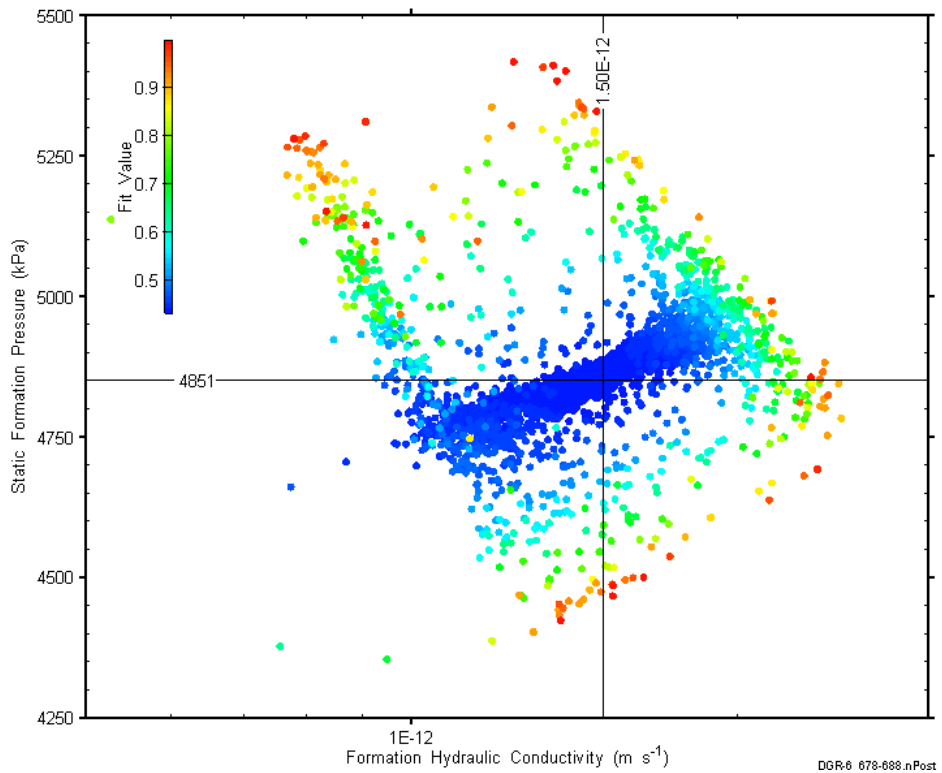


Figure 10-8: XY-scatter plot showing estimates of formation hydraulic conductivity and raw static formation pressure derived from the DGR6_678.00-688.23 perturbation analysis.

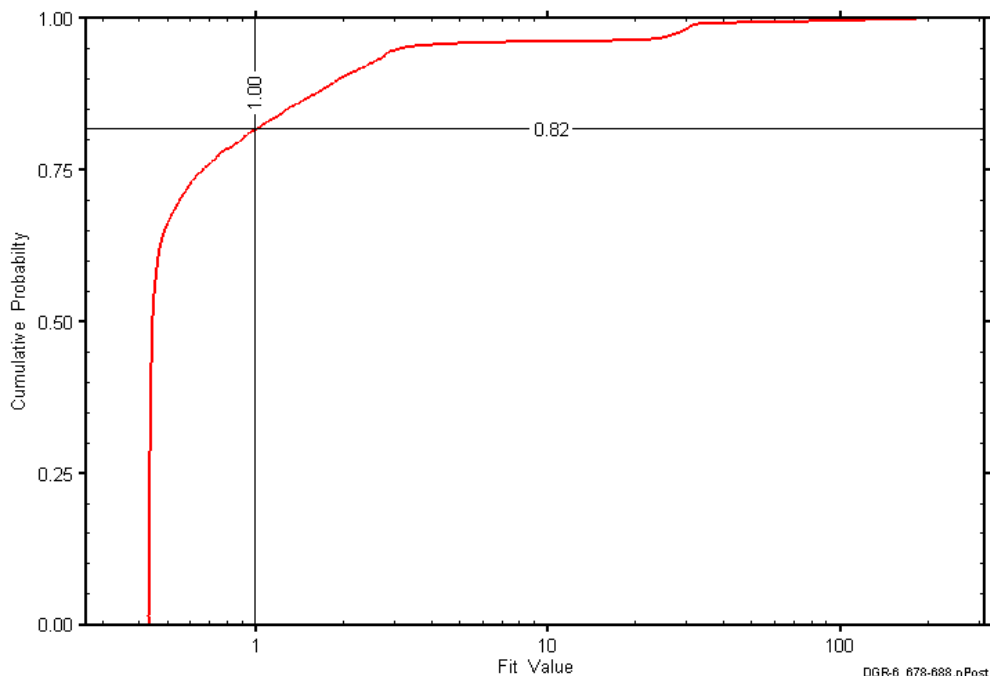


Figure 10-9: DGR6_678.00-688.23 fit value cumulative distribution function.

10.4 700.00-710.23 Blue Mountain

The DGR-6 interval from 700.00 to 710.23 m LBGS was entirely contained within the Blue Mountain Formation. This portion of the Blue Mountain consists of massively bedded shale with trace laminae to thin interbeds of limestone/siltstone. Seven filled fractures were logged in the core from this interval (Sterling et al., 2011). Information on the angle and vertical extent of the test interval is given in Table 10-8. An overview of the testing in this interval is given in Table 10-9 and the corresponding parameter estimates are given in Table 10-9. Two pulse-withdrawal tests and a slug-injection test were performed in this interval.

Table 10-8: Summary of the DGR6_700.00-710.23 testing activities.

Formation / Unit		Top of Test Zone (m LBGS)	Bottom of Test Zone (m LBGS)	
Blue Mountain		700.00	710.23	
Test Interval Angle (degrees from vertical)		Vertical Top of Test Zone (m BGS)	Vertical Bottom of Test Zone (m BGS)	
32.26		614.49	623.14	
Test	Initiated	Magnitude (kPa)	Duration	Compressibility (Pa ⁻¹)
Shut-in	11-05-10 12:07	N/A	3 hr	N/A
PW	11-05-10 14:46	163	17 hr	1.6E-09
PW2 (Part 1)	12-05-10 08:07	787	4 min	N/C
PW2 (Part 2)	12-05-10 08:10	149	23 hr	1.6E-09
SI	13-05-10 16:11	1187	15 hr	N/C
Borehole Pressure History				
Event		Start	Pressure (kPa)	
Drilling Intercept		14-01-10	6587	

Open Hole	25-01-10	N/A
Prior Testing	19-04-10	N/A
Shut-in	11-05-10	N/A

Table 10-9: Summary of the DGR6_678.00-688.23 parameter estimates.

Parameter	Best Fit	Minimum	Maximum	Mean
K_f (m/s)	1.0E-14	5.4E-15	1.8E-14	1.1E-14
P_f (kPa)	3419	2002	3924	3420
K_s (m/s)	4.4E-11	2.4E-11	5.4E-11	3.4E-11
t_s (cm)	1.2	1.1	2.5	1.6
S_s (m ⁻¹)	1.8E-05	8.3E-06	1.9E-05	1.4E-05

Figure 10-10 shows the measured pressure record from DGR6_700.00-710.23 used in this analysis along with the best-fit simulation and parameter values. The pressure response while the tubing was being filled prior to the SI indicated that the shut-in valve had not completely closed when the second PW was initiated. Problems with the shut-in valve do not affect the SI response, but mud that was later discovered in the borehole fluid likely did affect the SI. For this reason, only the first PW test was analyzed for this interval. The ranges of formation K and raw P_f values estimated from perturbation analysis are shown in Figure 10-11 and the fit value cumulative distribution function is shown in Figure 10-12.

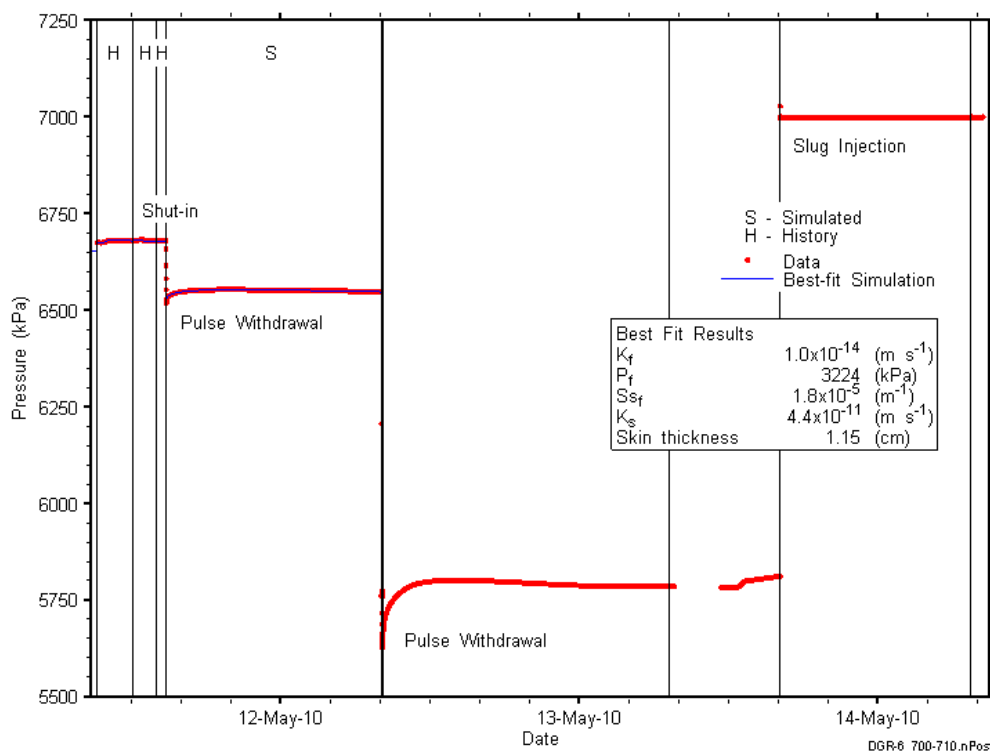


Figure 10-10: Annotated DGR6_700.00-710.23 testing sequence showing best-fit simulation and parameter estimates.

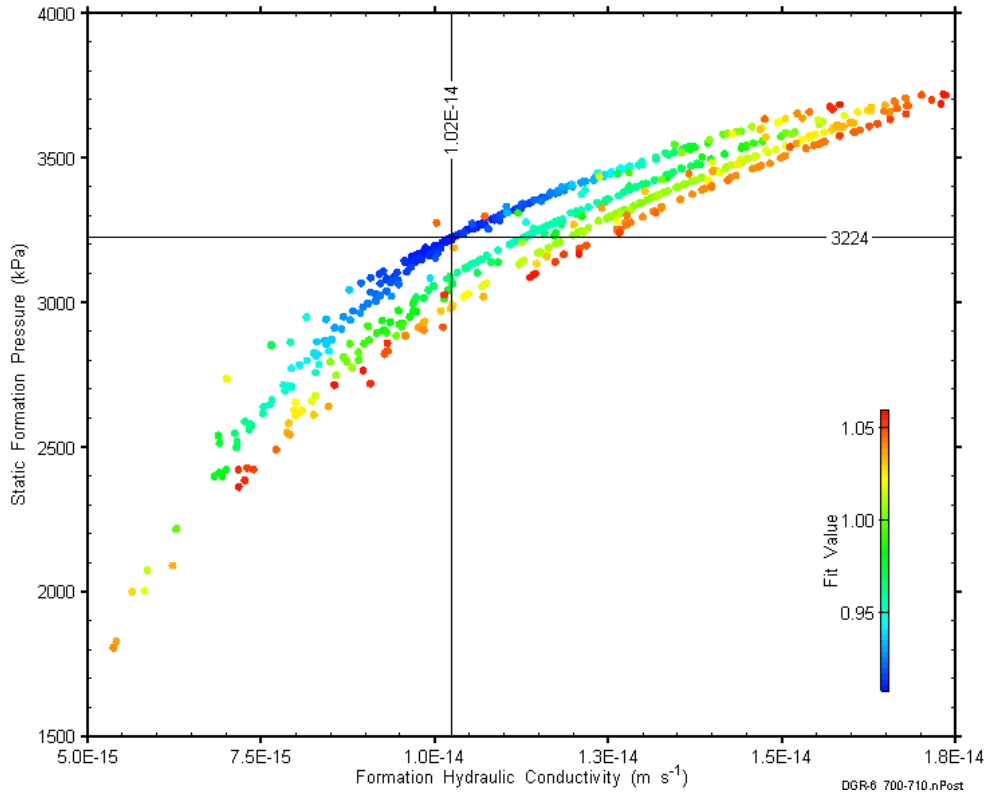


Figure 10-11: XY-scatter plot showing estimates of formation hydraulic conductivity and raw static formation pressure derived from the DGR6_700.00-710.23 perturbation analysis.

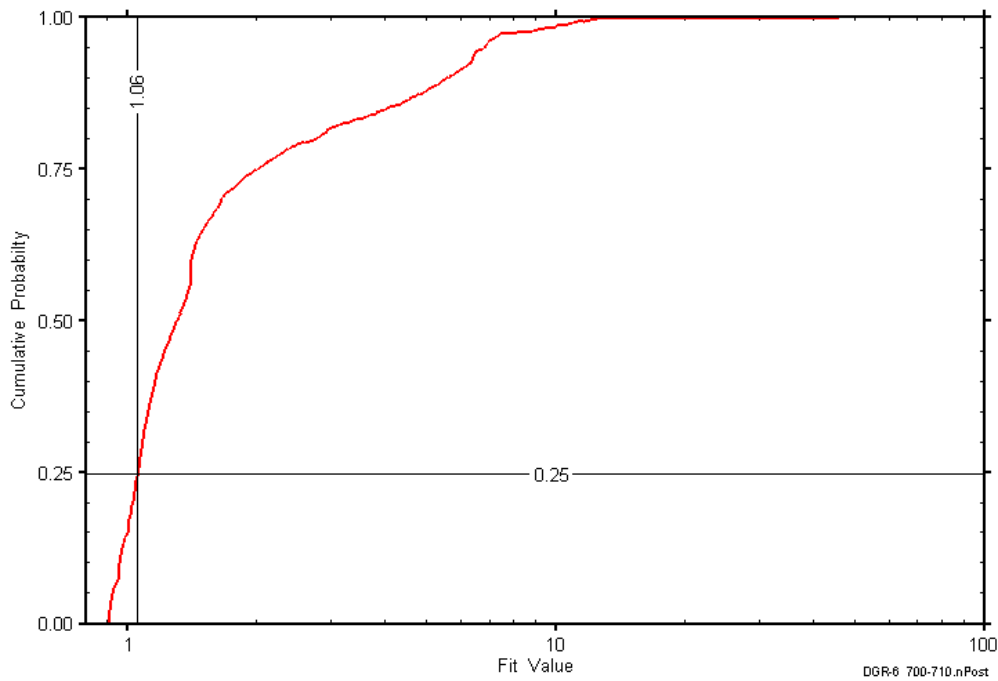


Figure 10-12: DGR6_700.00-710.23 fit value cumulative distribution function.

10.5 725.00-735.23 Blue Mountain

The DGR-6 interval from 725.00 to 735.23 m LBGS was entirely contained within the Blue Mountain Formation. This portion of the Blue Mountain consists of massively bedded, unfractured shale. Information on the angle and vertical extent of the test interval is given in Table 10-10. An overview of the testing in this interval is given in Table 10-10 and the corresponding parameter estimates are given in Table 10-11. Two pulse-withdrawal tests were performed in this interval.

Table 10-10: Summary of the DGR6_725.00-735.23 testing activities.

Formation / Unit		Top of Test Zone (m LBGS)		Bottom of Test Zone (m LBGS)	
Blue Mountain		725.00		735.23	
Test Interval Angle (degrees from vertical)		Vertical Top of Test Zone (m BGS)		Vertical Bottom of Test Zone (m BGS)	
32.69		635.61		644.22	
Test	Initiated	Magnitude (kPa)	Duration	Compressibility (Pa ⁻¹)	
Shut-in	01-06-10 11:31	N/A	20 hr	N/A	
PW1	02-06-10 07:34	736	24 hr	3.6E-10	
PW2	03-06-10 08:26	737	23 hr	3.6E-10	
Borehole Pressure History					
Event		Start		Pressure (kPa)	
Drilling Intercept		16-01-10		6998	
Open Hole		25-01-10		N/A	
Prior Testing		19-04-10		N/A	
Shut-in		01-06-10		N/A	

Table 10-11: Summary of the DGR6_725.00-735.23 parameter estimates.

Parameter	Best Fit	Minimum	Maximum	Mean
K_f (m/s)	6.6E-14	6.0E-14	6.7E-14	6.4E-14
P_f (kPa)	6289	6200	6309	6259
K_s (m/s)	2.8E-12	7.0E-13	9.0E-12	1.6E-12
t_s (cm)	38	6.1	40	18
S_s (m ⁻¹)	1.0E-08	1.0E-08	1.3E-07	3.6E-08

Figure 10-13 shows the measured pressure record from DGR6_725.00-735.23 used in this analysis along with the best-fit simulation and parameter values. The ranges of formation K and raw P_f values estimated from perturbation analysis are shown in Figure 10-14 and the fit value cumulative distribution function is shown in Figure 10-15.

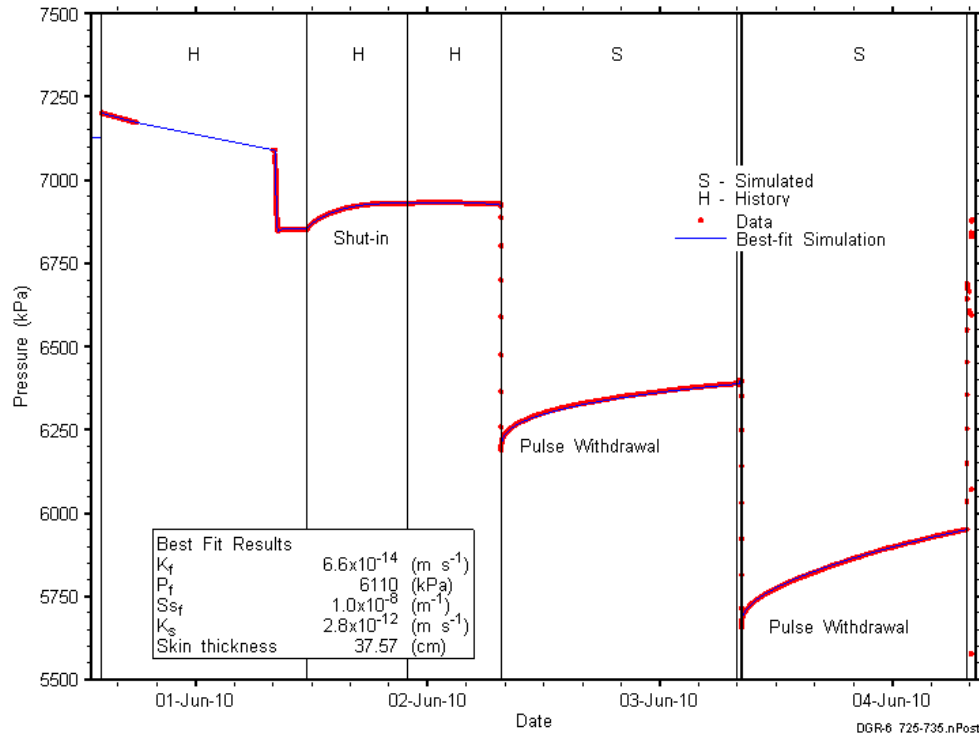


Figure 10-13: Annotated DGR6_725.00-735.23 testing sequence showing best-fit simulation and parameter estimates.

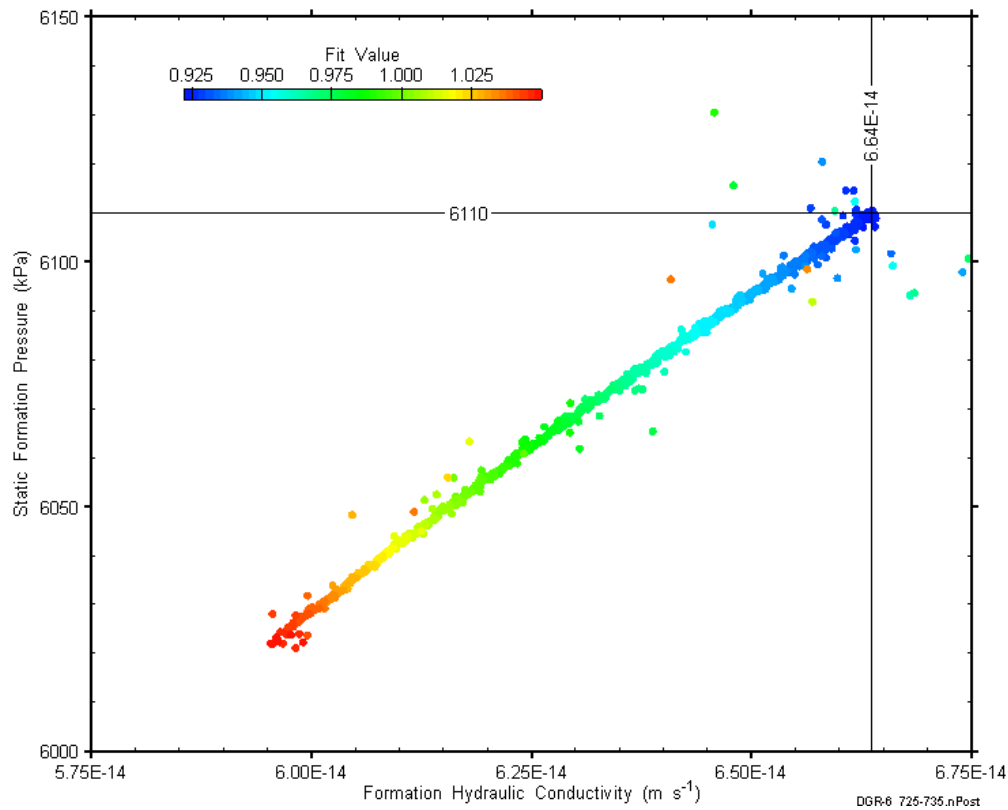


Figure 10-14: XY-scatter plot showing estimates of formation hydraulic conductivity and raw static formation pressure derived from the DGR6_725.00-735.23 perturbation analysis.

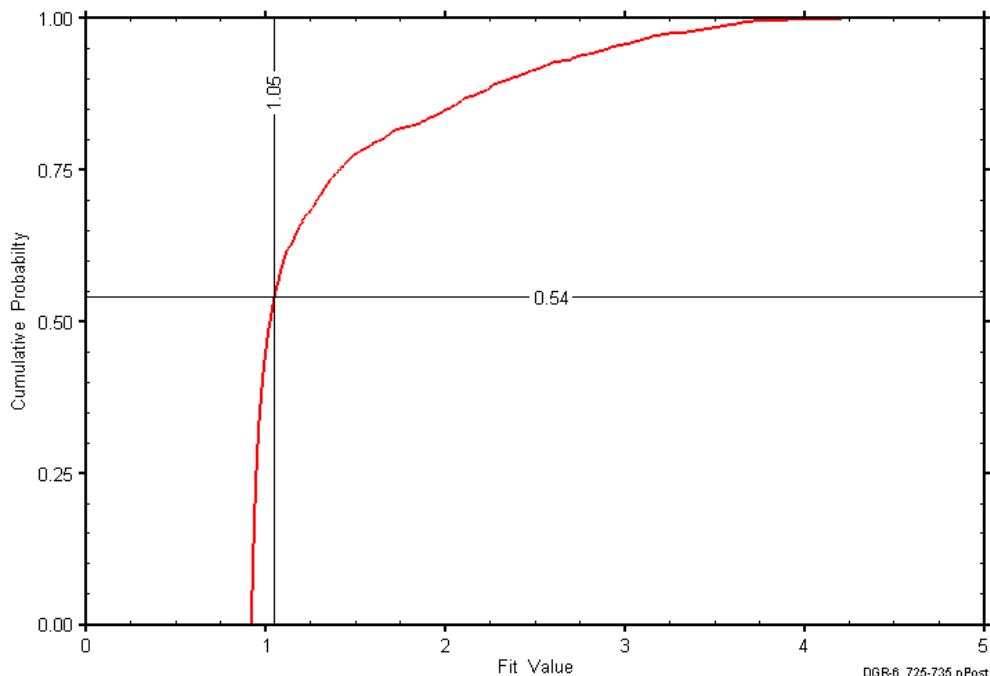


Figure 10-15: DGR6_725.00-735.23 fit value cumulative distribution function.

10.6 737.00-747.23 Collingwood

The DGR-6 interval from 737.00 to 747.23 m LBGS included the lower 1.3 m of the Blue Mountain Formation, the entire 7.8-m thickness of the Collingwood Member of the Cobourg Formation, and the upper 1.13 m of the Lower Member of the Cobourg Formation, measured along the slant of the hole. The lower Blue Mountain is shale, the Collingwood is interbedded shale and argillaceous limestone, and the Lower Member of the Cobourg is argillaceous limestone. Information on the angle and vertical extent of the test interval is given in Table 10-12. An overview of the testing in this interval is given in Table 10-12 and the corresponding parameter estimates are given in Table 10-13. Two pulse-withdrawal tests were performed in this interval.

Table 10-12: Summary of the DGR6_737.00-747.23 testing activities.

Formation / Unit		Top of Test Zone (m LBGS)	Bottom of Test Zone (m LBGS)	
Collingwood		737.00	747.23	
Test Interval Angle (degrees from vertical)		Vertical Top of Test Zone (m BGS)	Vertical Bottom of Test Zone (m BGS)	
32.79		645.71	654.31	
Test	Initiated	Magnitude (kPa)	Duration	Compressibility (Pa ⁻¹)
Shut-in	04-06-10 14:01	N/A	18 hr	N/A
PW1	05-06-10 08:05	736	24 hr	3.4E-10
PW2	06-06-10 08:04	737	23 hr	3.4E-10
Borehole Pressure History				
Event		Start	Pressure (kPa)	
Drilling Intercept		16-01-10	6924	
Open Hole		25-01-10	N/A	
Prior Testing		19-04-10	N/A	
Shut-in		04-06-10	N/A	

Table 10-13: Summary of the DGR6_737.00-747.23 parameter estimates.

Parameter	Best Fit	Minimum	Maximum	Mean
K_f (m/s)	4.0E-14	3.9E-14	4.1E-14	4.0E-14
P_f (kPa)	7302	7253	7338	7302
K_s (m/s)	9.5E-13	5.7E-13	2.0E-12	9.5E-13
t_s (cm)	5.1	5.0	5.3	5.1

Figure 10-16 shows the measured pressure record from DGR6_737.00-747.23 used in this analysis along with the best-fit simulation and parameter values. The S_s value for this analysis was fixed at $1E-7 \text{ m}^{-1}$, a value estimated from perturbation analysis. The ranges of formation K and raw P_f values estimated from perturbation analysis are shown in Figure 10-17 and the fit value cumulative distribution function is shown in Figure 10-18.

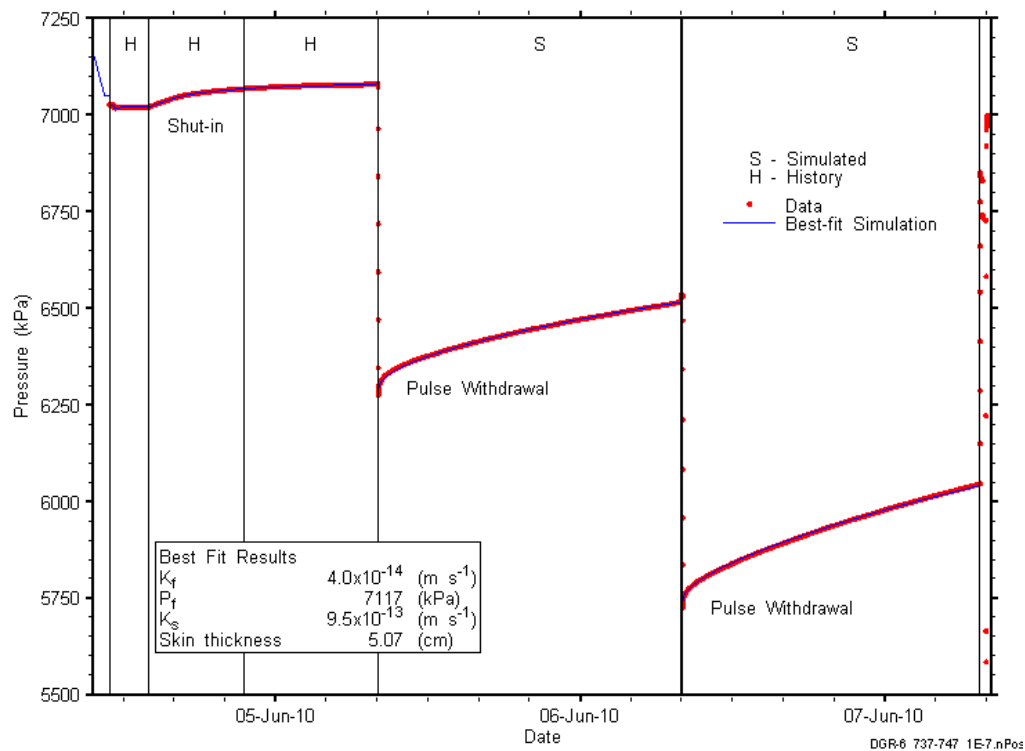


Figure 10-16: Annotated DGR6_737.00-747.23 testing sequence showing best-fit simulation and parameter estimates.

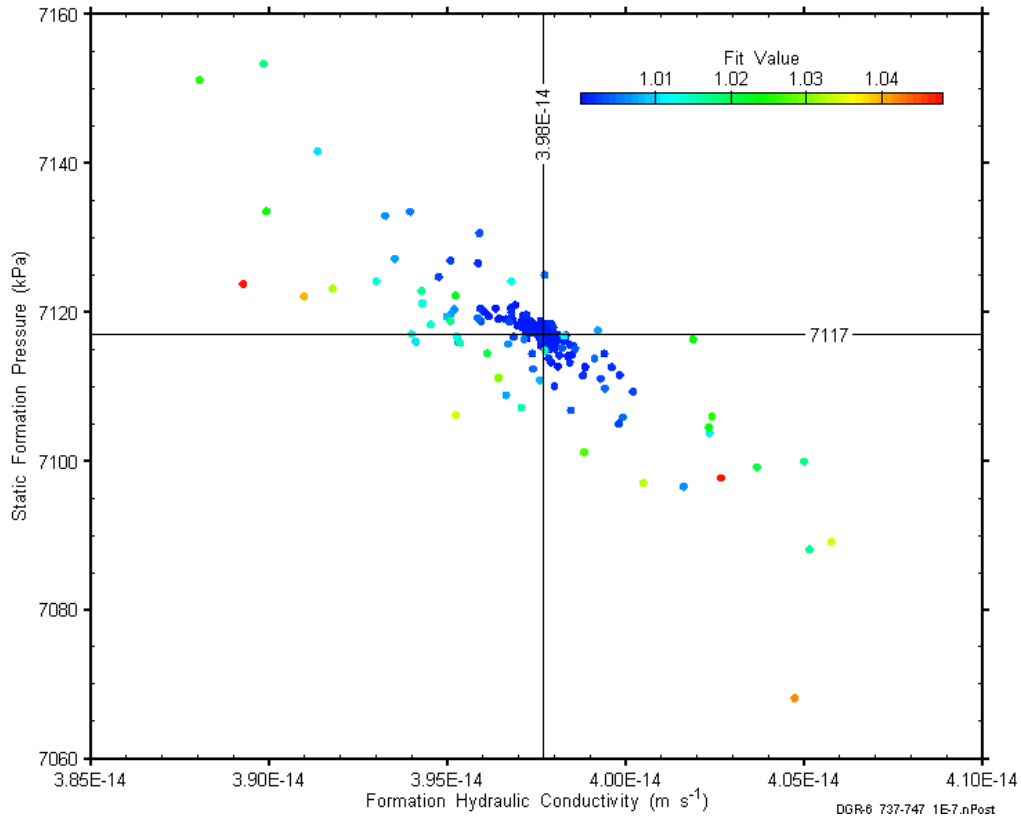


Figure 10-17: XY-scatter plot showing estimates of formation hydraulic conductivity and raw static formation pressure derived from the DGR6_737.00-747.23 perturbation analysis.

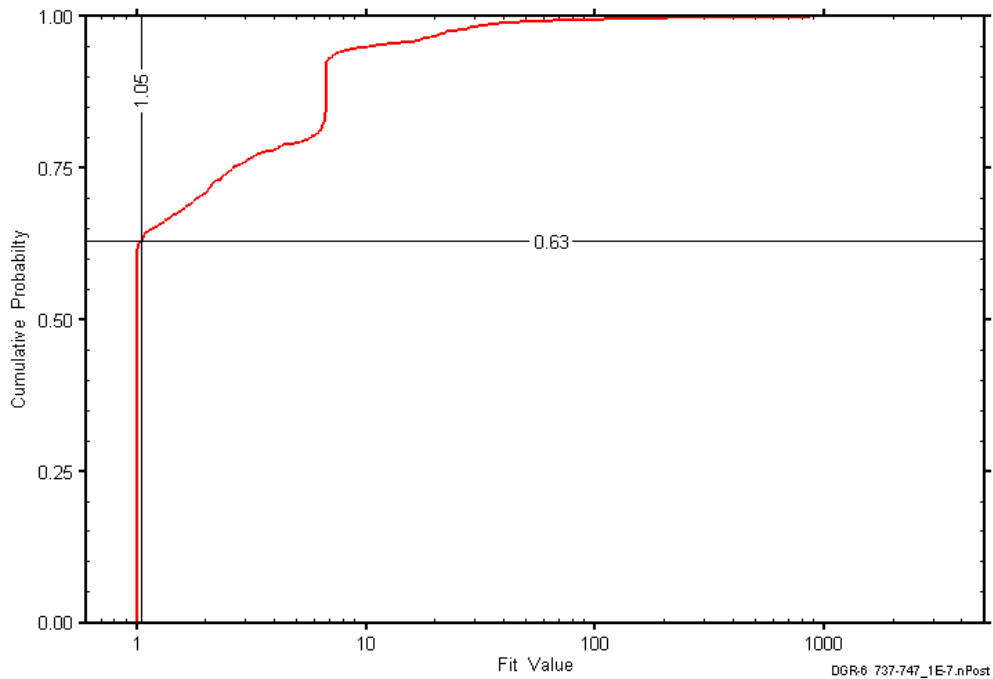


Figure 10-18: DGR6_737.00-747.23 fit value cumulative distribution function.

10.7 764.00-774.23 Cobourg

The DGR-6 interval from 764.00 to 774.23 m LBGs was entirely contained within the Lower Member of the Cobourg Formation. This portion of the Cobourg consists of argillaceous limestone. Information on the angle and vertical extent of the test interval is given in Table 10-14. An overview of the testing in this interval is given in Table 10-14 and the corresponding parameter estimates are given in Table 10-15. Two pulse-withdrawal tests were performed in this interval.

Table 10-14: Summary of the DGR6_764.00-774.23 testing activities.

Formation / Unit		Top of Test Zone (m LBGs)		Bottom of Test Zone (m LBGs)	
Cobourg		764.00		774.23	
Test Interval Angle (degrees from vertical)		Vertical Top of Test Zone (m BGS)		Vertical Bottom of Test Zone (m BGS)	
33.25		668.34		676.89	
Test	Initiated	Magnitude (kPa)	Duration	Compressibility (Pa ⁻¹)	
Shut-in	07-06-10 14:07	N/A	17 hr	N/A	
PW1	08-06-10 07:36	736	25 hr	3.4E-10	
PW2	09-06-10 08:27	737	23 hr	3.4E-10	
Borehole Pressure History					
Event		Start		Pressure (kPa)	
Drilling Intercept		16-01-10		7168	
Open Hole		25-01-10		N/A	
Prior Testing		19-04-10		N/A	
Shut-in		07-06-10		N/A	

Table 10-15: Summary of the DGR6_764.00-774.23 parameter estimates.

Parameter	Best Fit	Minimum	Maximum	Mean
K_f (m/s)	3.1E-14	2.1E-14	3.3E-14	2.5E-14
P_f (kPa)	8296	8209	8971	8639
K_s (m/s)	1.5E-11	3.4E-12	8.5E-10	3.3E-11
t_s (cm)	24	7.6	30	17
S_s (m ⁻¹)	1.1E-8	1.0E-08	6.0E-08	2.3E-08

Figure 10-19 shows the measured pressure record from DGR6_764.00-774.23 used in this analysis along with the best-fit simulation and parameter values. Temperature induced packer-pressure changes affected the first PW test-zone response to such a degree that it was deemed unsuitable for analysis. Only the second PW test in this interval was analyzed. The ranges of formation K and raw P_f values estimated from perturbation analysis are shown in Figure 10-20 and the fit value cumulative distribution function is shown in Figure 10-21.

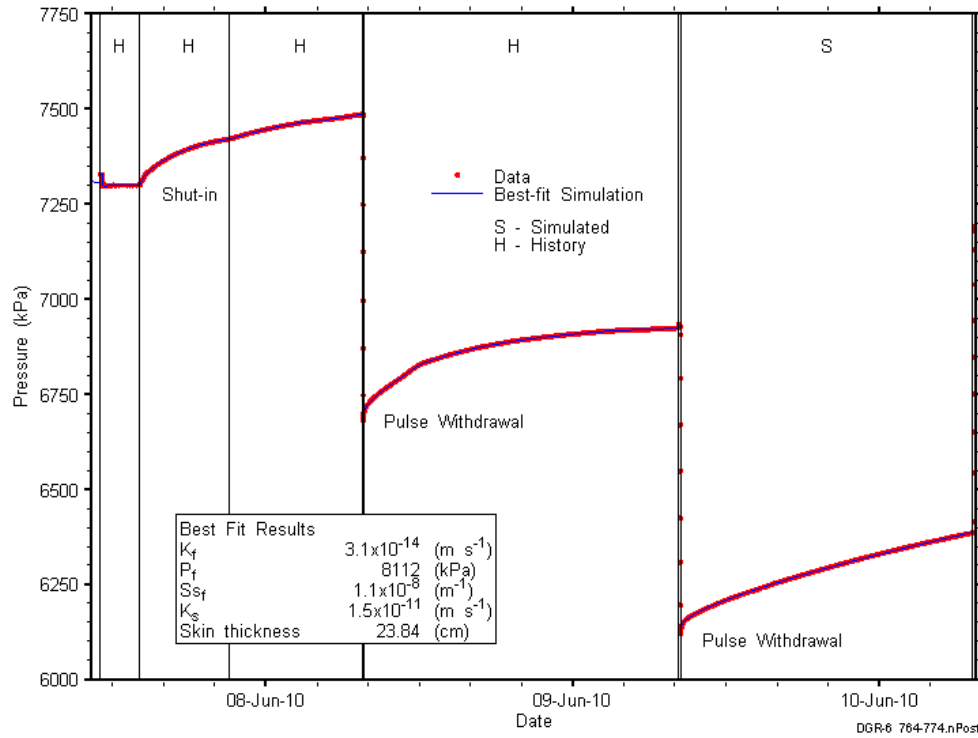


Figure 10-19: Annotated DGR6_764.00-774.23 testing sequence showing best-fit simulation and parameter estimates.

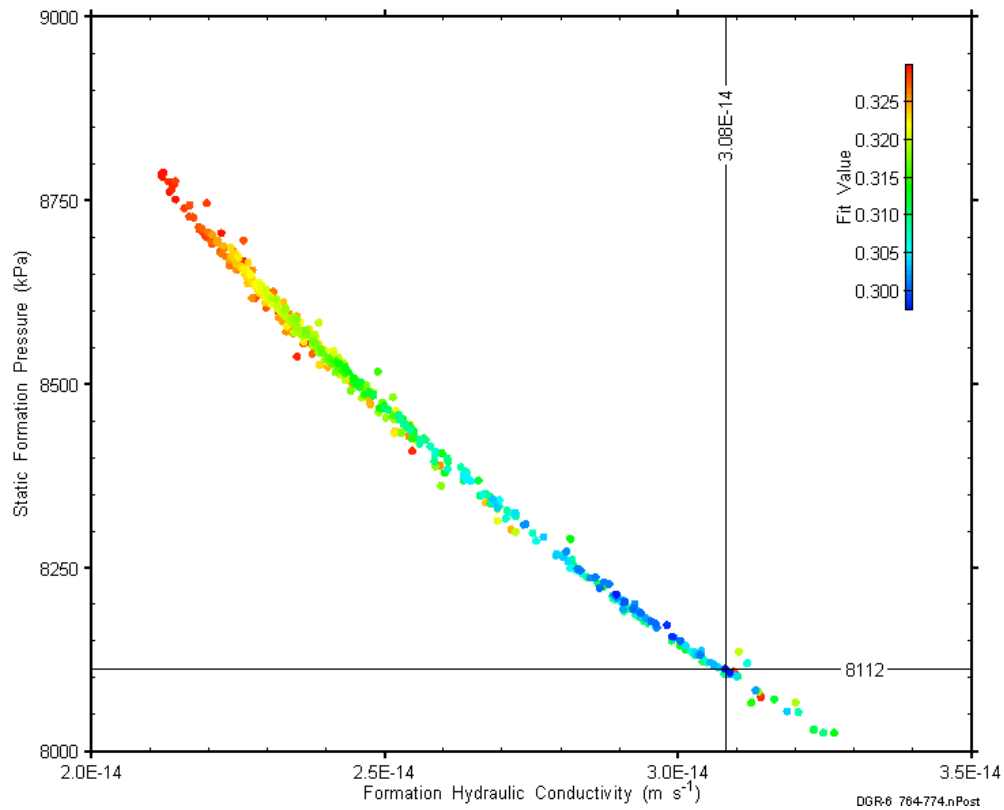


Figure 10-20: XY-scatter plot showing estimates of formation hydraulic conductivity and raw static formation pressure derived from the DGR6_764.00-774.23 perturbation analysis.

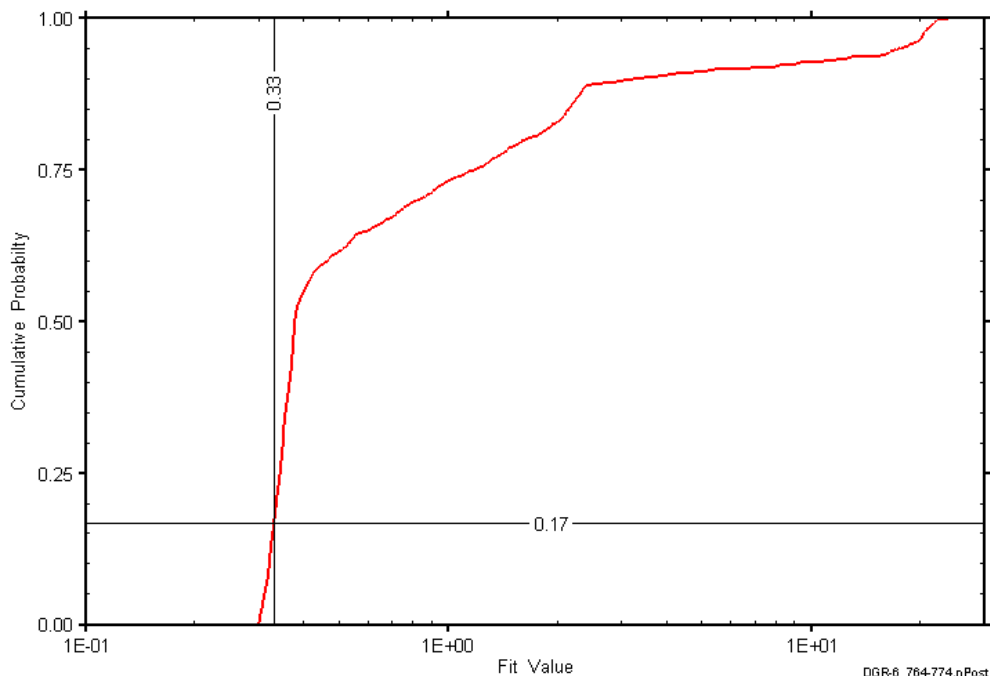


Figure 10-21: DGR6_764.00-774.23 fit value cumulative distribution function.

10.8 782.00-792.23 Sherman Fall

The DGR-6 interval from 782.00 to 792.23 m LBGS was entirely contained within the Sherman Fall Formation. This portion of the Sherman Fall consists of interbedded argillaceous limestone and shale. Information on the angle and vertical extent of the test interval is given in Table 10-16. An overview of the testing in this interval is given in Table 10-16 and the corresponding parameter estimates are given in Table 10-17. Two pulse-withdrawal tests were performed in this interval.

Table 10-16: Summary of the DGR6_782.00-792.23 testing activities.

Formation / Unit		Top of Test Zone (m LBGS)	Bottom of Test Zone (m LBGS)	
Sherman Fall		782.00	792.23	
Test Interval Angle (degrees from vertical)		Vertical Top of Test Zone (m BGS)	Vertical Bottom of Test Zone (m BGS)	
33.23		683.39	691.94	
Test	Initiated	Magnitude (kPa)	Duration	Compressibility (Pa ⁻¹)
Shut-in	10-06-10 13:14	N/A	19 hr	N/A
PW1	11-06-10 08:04	809	24 hr	3.3E-10
PW2	12-06-10 07:56	804	23 hr	3.3E-10
Borehole Pressure History				
Event		Start	Pressure (kPa)	
Drilling Intercept		18-01-10	7331	
Open Hole		25-01-10	N/A	
Prior Testing		19-04-10	N/A	
Shut-in		10-06-10	N/A	

Table 10-17: Summary of the DGR6_782.00-792.23 parameter estimates.

Parameter	Best Fit	Minimum	Maximum	Mean
K_f (m/s)	4.5E-14	4.4E-14	4.6E-14	4.5E-14
P_f (kPa)	7484	7463	7502	7484
K_s (m/s)	1.4E-12	9.5E-13	2.7E-12	1.5E-12
t_s (cm)	4.7	4.7	4.9	4.7

Figure 10-22 shows the measured pressure record from DGR6_782.00-792.23 used in this analysis along with the best-fit simulation and parameter values. The S_s value for this analysis was fixed at $1E-7 \text{ m}^{-1}$, a value estimated from perturbation analysis. The ranges of formation K and raw P_f values estimated from perturbation analysis are shown in Figure 10-23 and the fit value cumulative distribution function is shown in Figure 10-24.

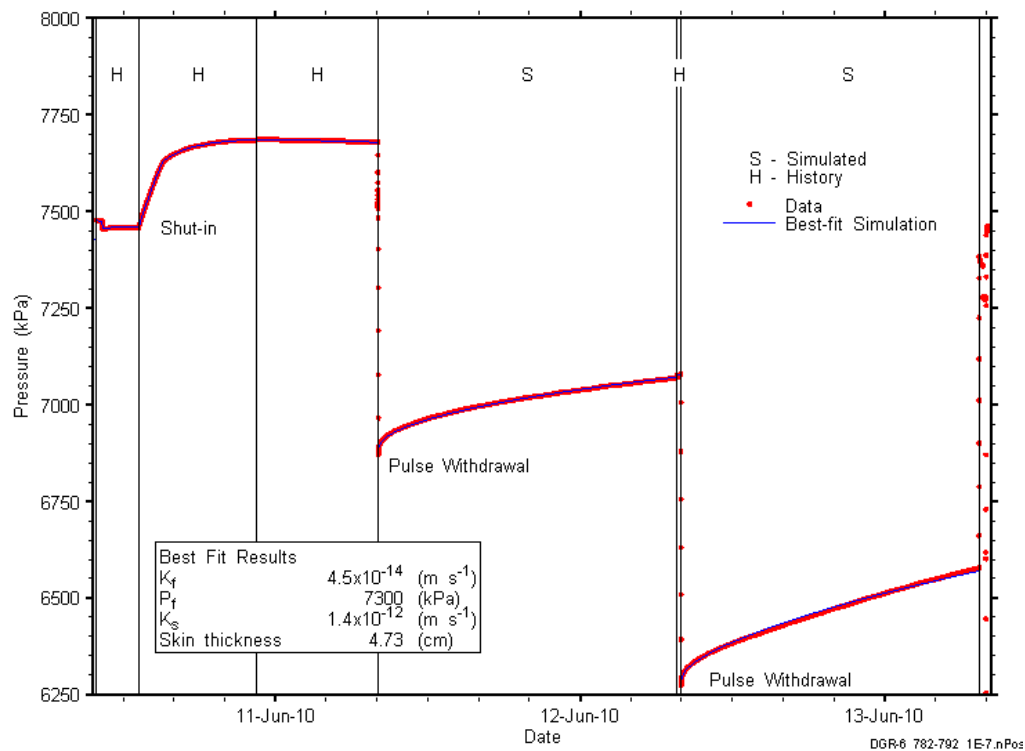


Figure 10-22: Annotated DGR6_782.00-792.23 testing sequence showing best-fit simulation and parameter estimates.

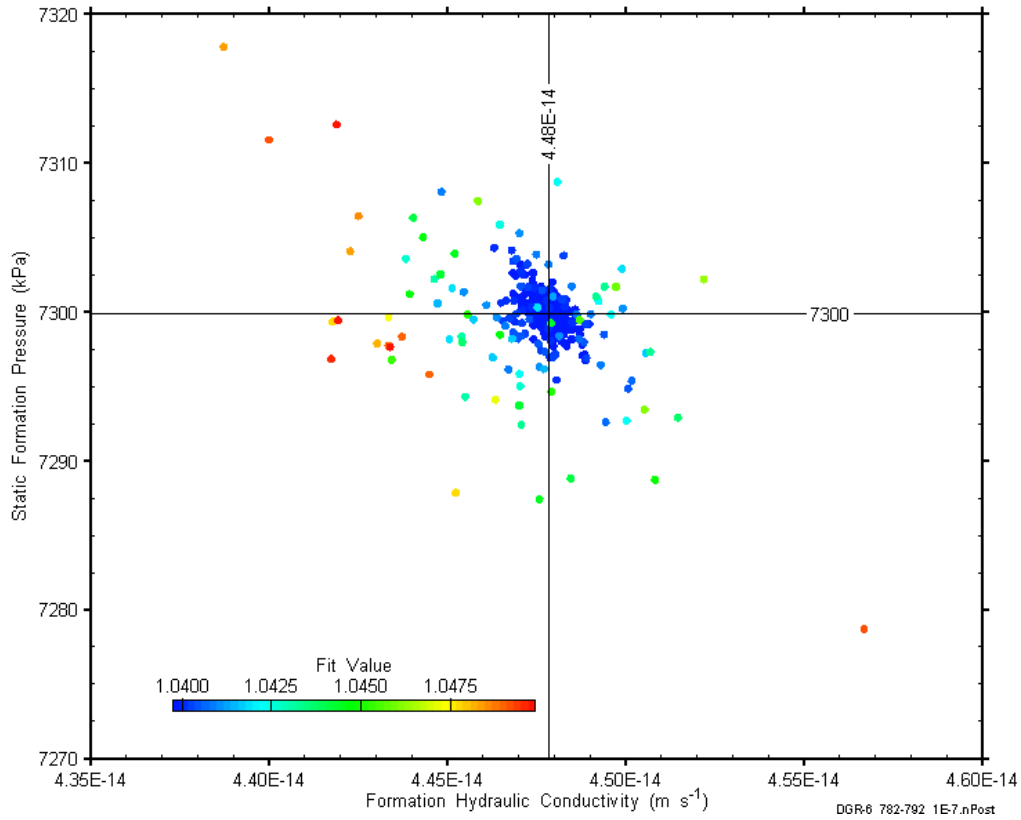


Figure 10-23: XY-scatter plot showing estimates of formation hydraulic conductivity and raw static formation pressure derived from the DGR6_782.00-792.23 perturbation analysis.

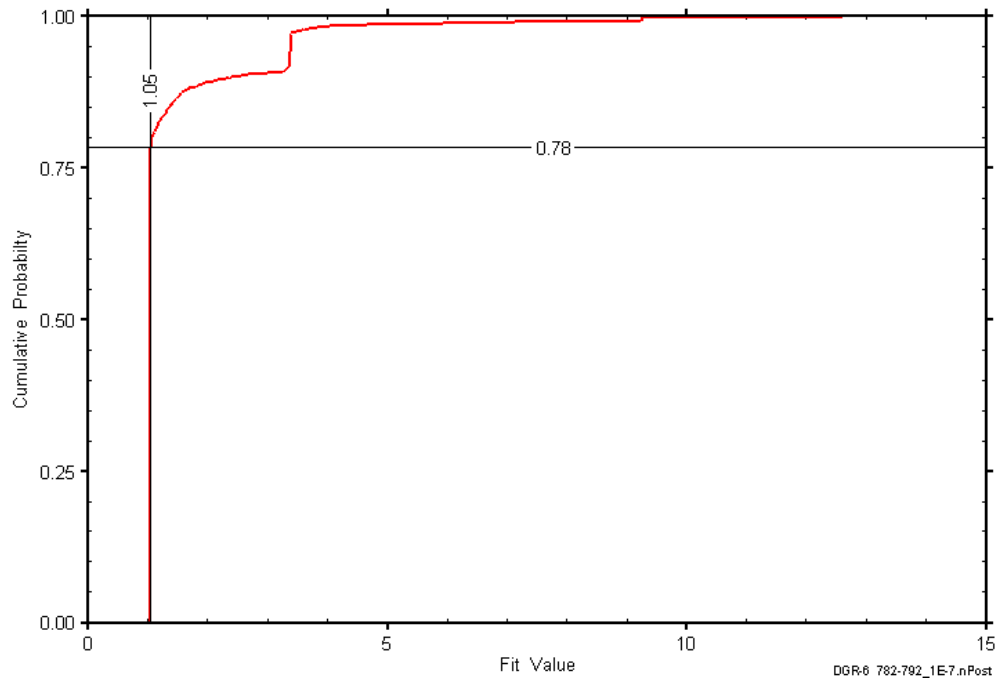


Figure 10-24: DGR6_782.00-792.23 fit value cumulative distribution function.

10.9 797.00-807.23 Sherman Fall

The DGR-6 interval from 797.00 to 807.23 m LBGS was entirely contained within the Sherman Fall Formation. This portion of the Sherman Fall consists of interbedded argillaceous limestone and shale with a few fractures. Information on the angle and vertical extent of the test interval is given in Table 10-18. An overview of the testing in this interval is given in Table 10-18 and the corresponding parameter estimates are given in Table 10-19. Two pulse-withdrawal tests were performed in this interval.

Table 10-18: Summary of the DGR6_797.00-807.23 testing activities.

Formation / Unit		Top of Test Zone (m LBGS)		Bottom of Test Zone (m LBGS)	
Sherman Fall		797.00		807.23	
Test Interval Angle (degrees from vertical)		Vertical Top of Test Zone (m BGS)		Vertical Bottom of Test Zone (m BGS)	
33.08		695.94		704.51	
Test	Initiated	Magnitude (kPa)	Duration	Compressibility (Pa ⁻¹)	
Shut-in	13-06-10 12:54	N/A	19 hr	N/A	
PW1	14-06-10 07:41	805	24 hr	3.4E-10	
PW2	15-06-10 08:45	805	23 hr	3.4E-10	
Borehole Pressure History					
Event		Start		Pressure (kPa)	
Drilling Intercept		18-01-10		7466	
Open Hole		25-01-10		N/A	
Prior Testing		19-04-10		N/A	
Shut-in		13-06-10		N/A	

Table 10-19: Summary of the DGR6_797.00-807.23 parameter estimates.

Parameter	Best Fit	Minimum	Maximum	Mean
K _f (m/s)	2.6E-14	2.5E-14	2.6E-14	2.6E-14
P _f (kPa)	8258	8244	8287	8258
K _s (m/s)	7.6E-13	5.9E-13	1.0E-12	7.6E-13
t _s (cm)	6.1	5.9	6.3	6.1

Figure 10-25 shows the measured pressure record from DGR6_797.00-807.23 used in this analysis along with the best-fit simulation and parameter values. The S_s value for this analysis was fixed at 1E-7 m⁻¹, a value estimated from perturbation analysis. The ranges of formation K and raw P_f values estimated from perturbation analysis are shown in Figure 10-26 and the fit value cumulative distribution function is shown in Figure 10-27.

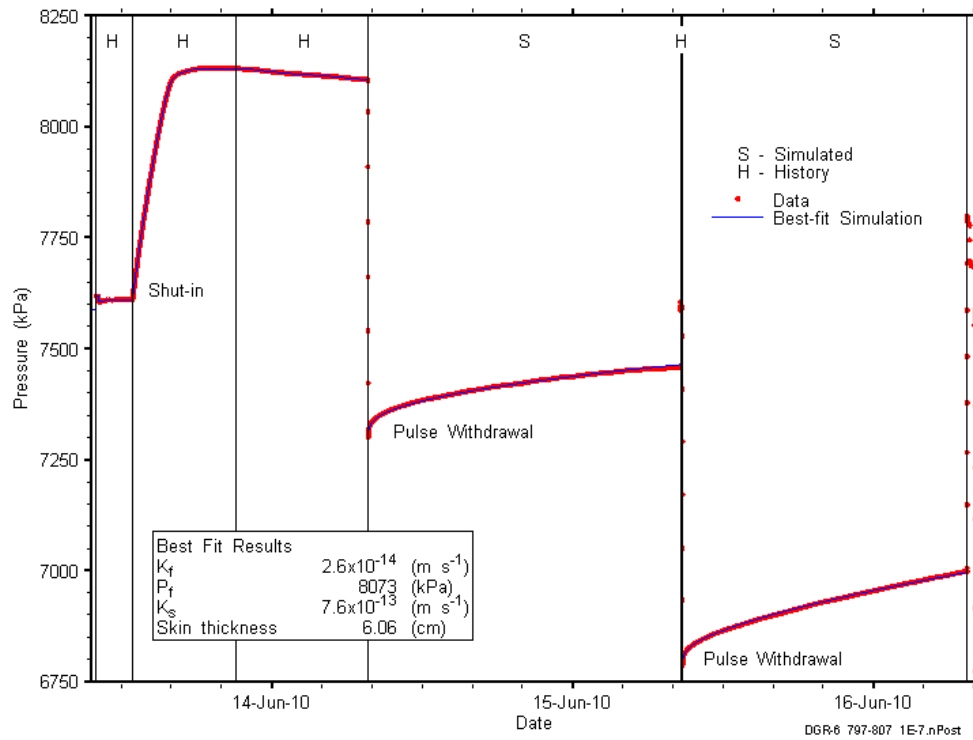


Figure 10-25: Annotated DGR6_797.00-807.23 testing sequence showing best-fit simulation and parameter estimates.

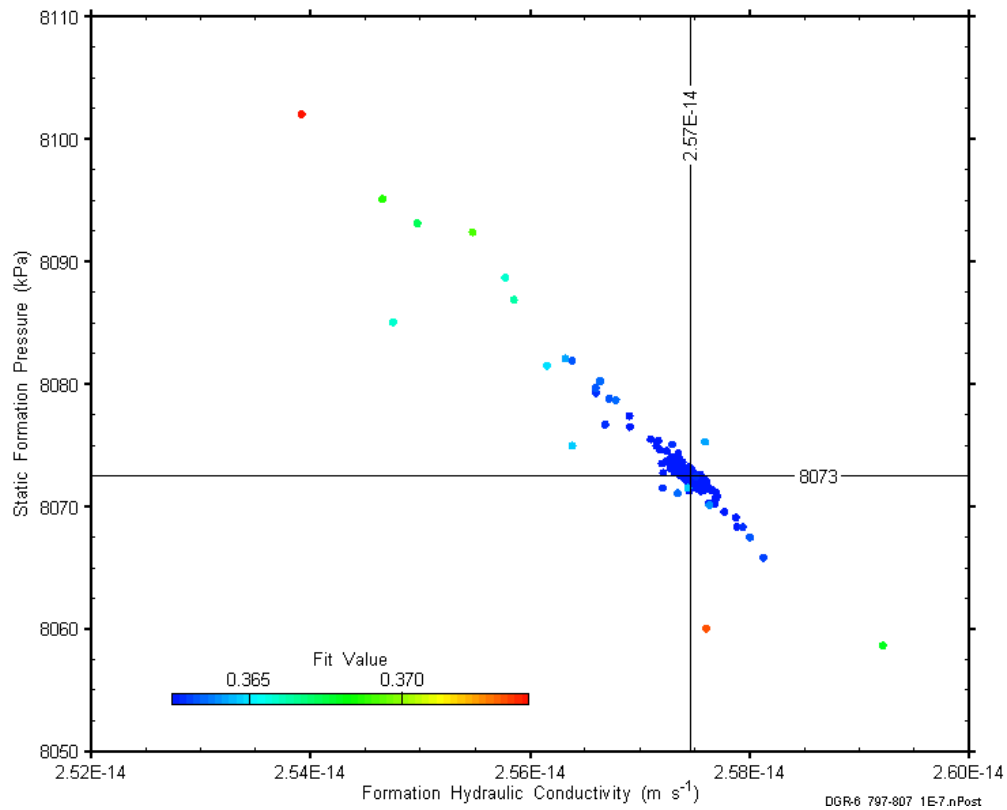


Figure 10-26: XY-scatter plot showing estimates of formation hydraulic conductivity and raw static formation pressure derived from the DGR6_797.00-807.23 perturbation analysis.

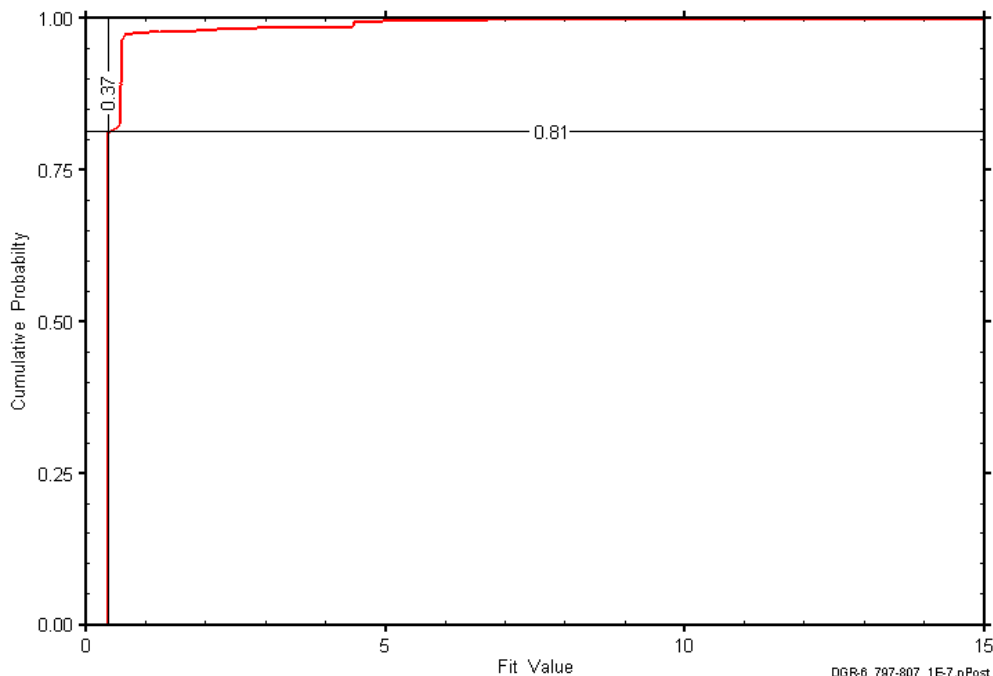


Figure 10-27: DGR6_797.00-807.23 fit value cumulative distribution function.

10.10 841.00-851.23 Kirkfield

The DGR-6 interval from 841.00 to 851.23 m LBGs was entirely contained within the Kirkfield Formation. This portion of the Kirkfield consists of interbedded argillaceous limestone and shale. Information on the angle and vertical extent of the test interval is given in Table 10-20. An overview of the testing in this interval is given in Table 10-20 and the corresponding parameter estimates are given in Table 10-21. Two pulse-withdrawal tests were performed in this interval.

Table 10-20: Summary of the DGR6_841.00-851.23 testing activities.

Formation / Unit		Top of Test Zone (m LBGs)	Bottom of Test Zone (m LBGs)	
Kirkfield		841.00	851.23	
Test Interval Angle (degrees from vertical)		Vertical Top of Test Zone (m BGS)	Vertical Bottom of Test Zone (m BGS)	
32.83		732.76	741.35	
Test	Initiated	Magnitude (kPa)	Duration	Compressibility (Pa ⁻¹)
Shut-in	16-06-10 14:44	N/A	17 hr	N/A
PW1	17-06-10 07:40	810	24 hr	3.4E-10
PW2	18-06-10 07:45	814	23 hr	3.4E-10
Borehole Pressure History				
Event	Start	Pressure (kPa)		
Drilling Intercept	20-01-10	7863		
Open Hole	25-01-10	N/A		
Prior Testing	19-04-10	N/A		
Shut-in	16-06-10	N/A		

Table 10-21: Summary of the DGR6_841.00-851.23 parameter estimates.

Parameter	Best Fit	Minimum	Maximum	Mean
K_f (m/s)	2.9E-14	1.3E-14	3.0E-14	2.5E-14
P_f (kPa)	9574	9483	11410	9857
K_s (m/s)	2.3E-12	1.5E-13	2.9E-12	1.1E-12
t_s (cm)	24	2.0	31	15
S_s (m^{-1})	1.5E-8	1.0E-08	3.6E-07	4.0E-08

Figure 10-28 shows the measured pressure record from DGR6_841.00-851.23 used in this analysis along with the best-fit simulation and parameter values. Temperature induced packer-pressure changes affected the first PW test-zone response to such a degree that it was deemed unsuitable for analysis. Only the second PW test in this interval was analyzed. The ranges of formation K and raw P_f values estimated from perturbation analysis are shown in Figure 10-29 and the fit value cumulative distribution function is shown in Figure 10-30.

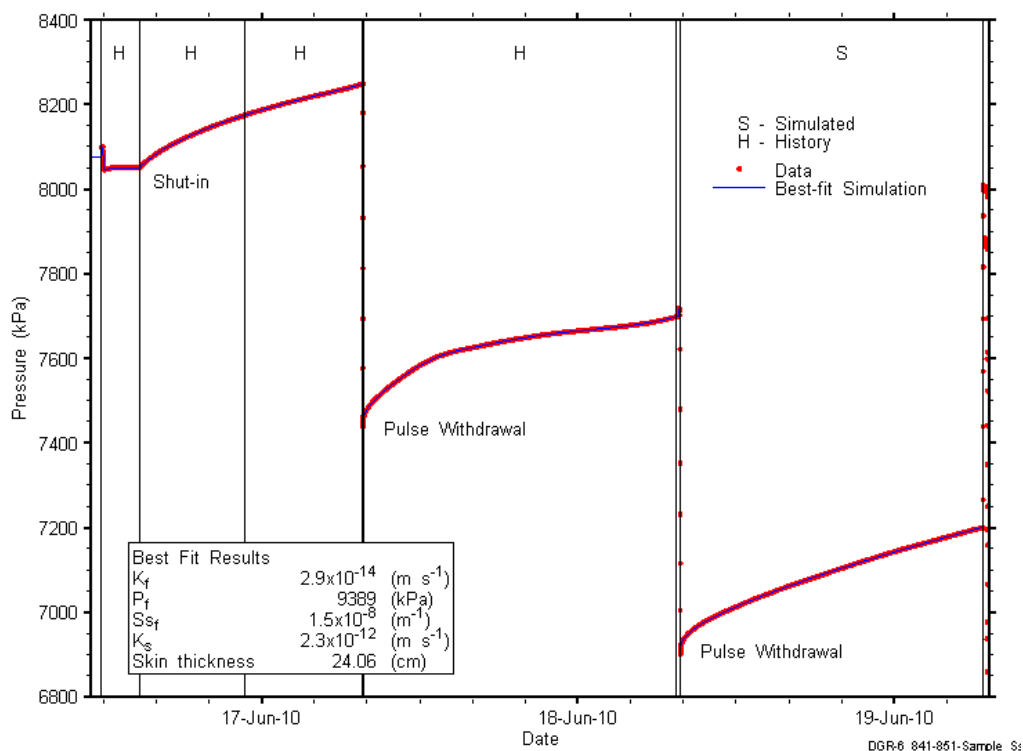


Figure 10-28: Annotated DGR6_841.00-851.23 testing sequence showing best-fit simulation and parameter estimates.

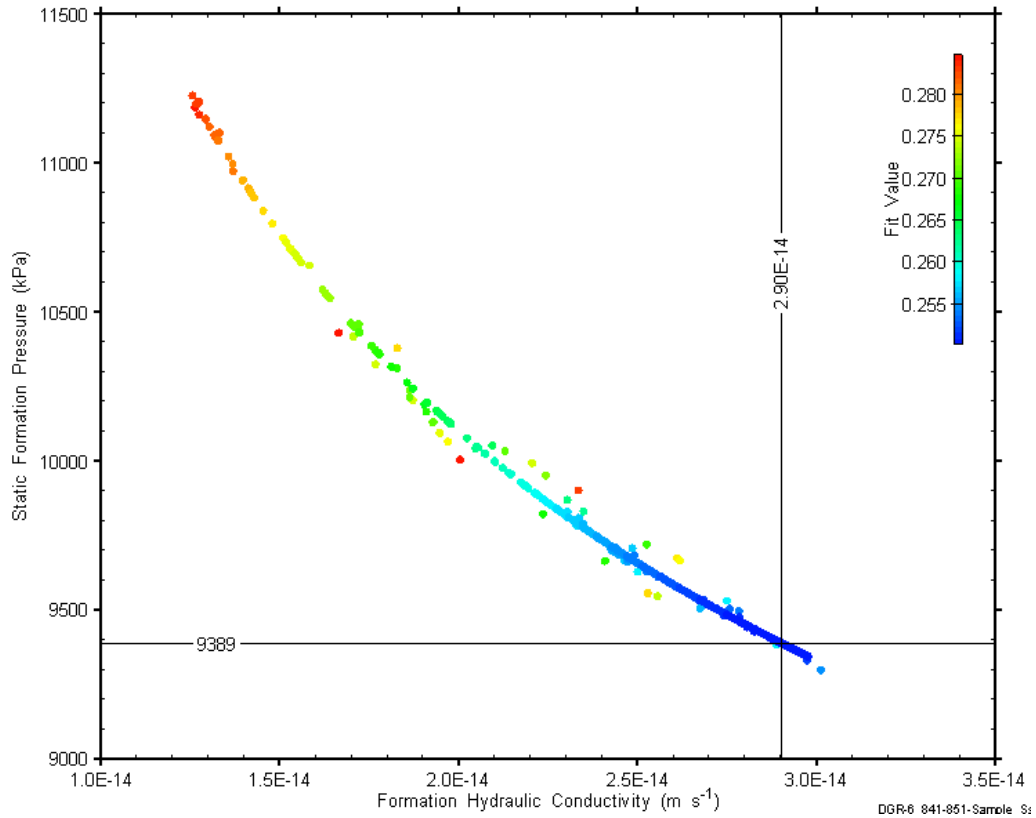


Figure 10-29: XY-scatter plot showing estimates of formation hydraulic conductivity and raw static formation pressure derived from the DGR6_841.00-851.23 perturbation analysis.

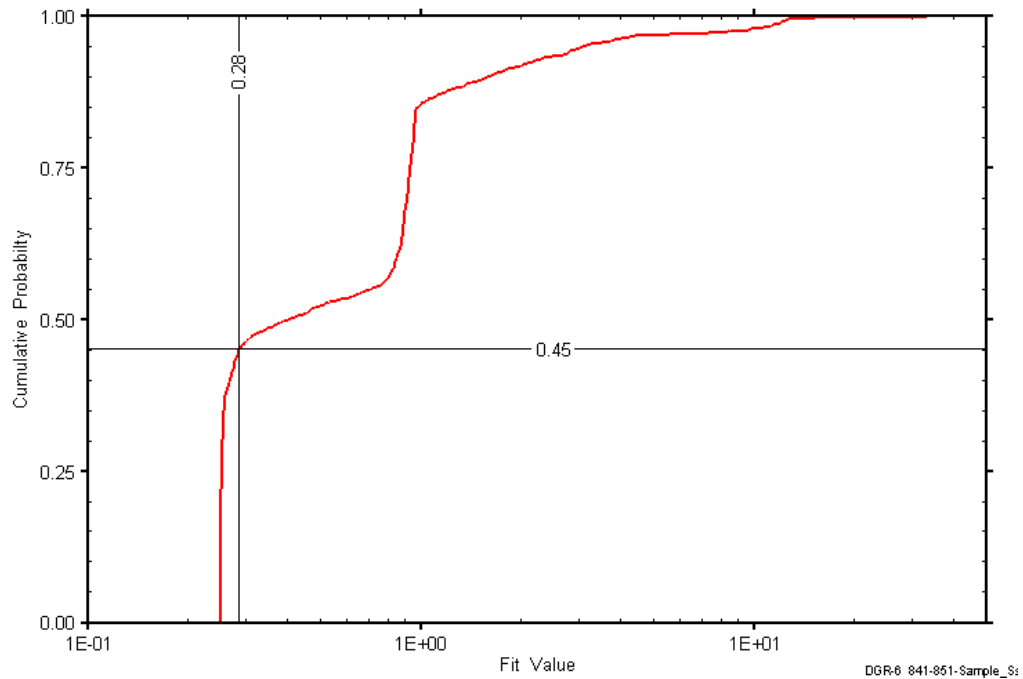


Figure 10-30: DGR6_841.00-851.23 fit value cumulative distribution function.

10.11 869.77-880.00 Coboconk

The DGR-6 interval from 869.77 to 880.00 m LBGS included the lower 0.73 m of the Kirkfield Formation and the upper 9.5 m of the Coboconk Formation. The lowermost Kirkfield consists of interbedded argillaceous limestone and shale, and the upper Coboconk consists of limestone with shale laminae. The portion of the Coboconk tested included the 0.14-m-thick volcanic ash layer observed in all the DGR boreholes, but not the deeper dolostone marker bed or the vuggy lower portion of the unit. Information on the angle and vertical extent of the test interval is given in Table 10-22. An overview of the testing in this interval is given in Table 10-22 and the corresponding parameter estimates are given in Table 10-23. Two pulse-withdrawal tests were performed in this interval.

Table 10-22: Summary of the DGR6_869.77-880.00 testing activities.

Formation / Unit		Top of Test Zone (m LBGS)	Bottom of Test Zone (m LBGS)	
Coboconk		869.77	880.00	
Test Interval Angle (degrees from vertical)		Vertical Top of Test Zone (m BGS)	Vertical Bottom of Test Zone (m BGS)	
32.53		756.93	765.55	
Test	Initiated	Magnitude (kPa)	Duration	Compressibility (Pa ⁻¹)
Shut-in	19-06-10 12:46	N/A	19 hr	N/A
PW1	20-06-10 07:26	714	24 hr	3.8E-10
PW2	21-06-10 07:41	724	23 hr	3.9E-10
Borehole Pressure History				
Event	Start		Pressure (kPa)	
Drilling Intercept	21-01-10		8123	
Open Hole	25-01-10		N/A	
Prior Testing	19-04-10		N/A	
Shut-in	19-06-10		N/A	

Table 10-23: Summary of the DGR6_869.77-880.00 parameter estimates.

Parameter	Best Fit	Minimum	Maximum	Mean
K_f (m/s)	1.4E-14	1.2E-14	1.6E-14	1.4E-14
P_f (kPa)	12022	11711	12427	12010
K_s (m/s)	1.0E-13	9.4E-14	1.2E-13	1.0E-13
t_s (cm)	0.5	0.40	0.63	0.47
S_s (m ⁻¹)	2.4E-6	1.9E-06	2.8E-06	2.4E-06

Figure 10-31 shows the measured pressure record from DGR6_869.77-880.00 used in this analysis along with the best-fit simulation and parameter values. The ranges of formation K and raw P_f values estimated from perturbation analysis are shown in Figure 10-32 and the fit value cumulative distribution function is shown in Figure 10-33.

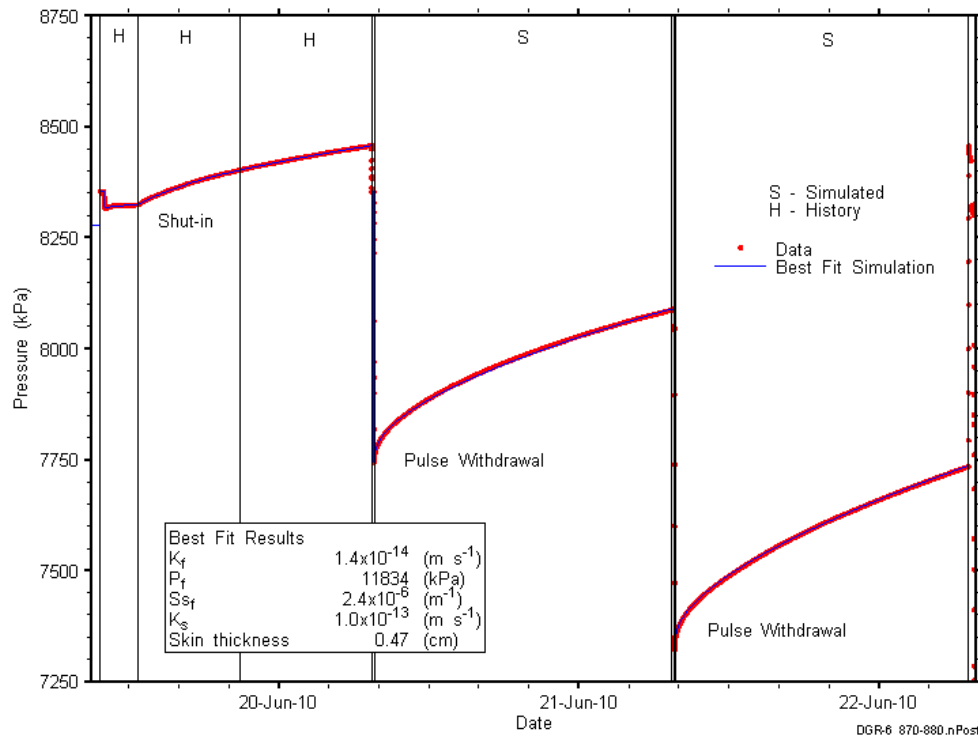


Figure 10-31: Annotated DGR6_869.77-880.00 testing sequence showing best-fit simulation and parameter estimates.

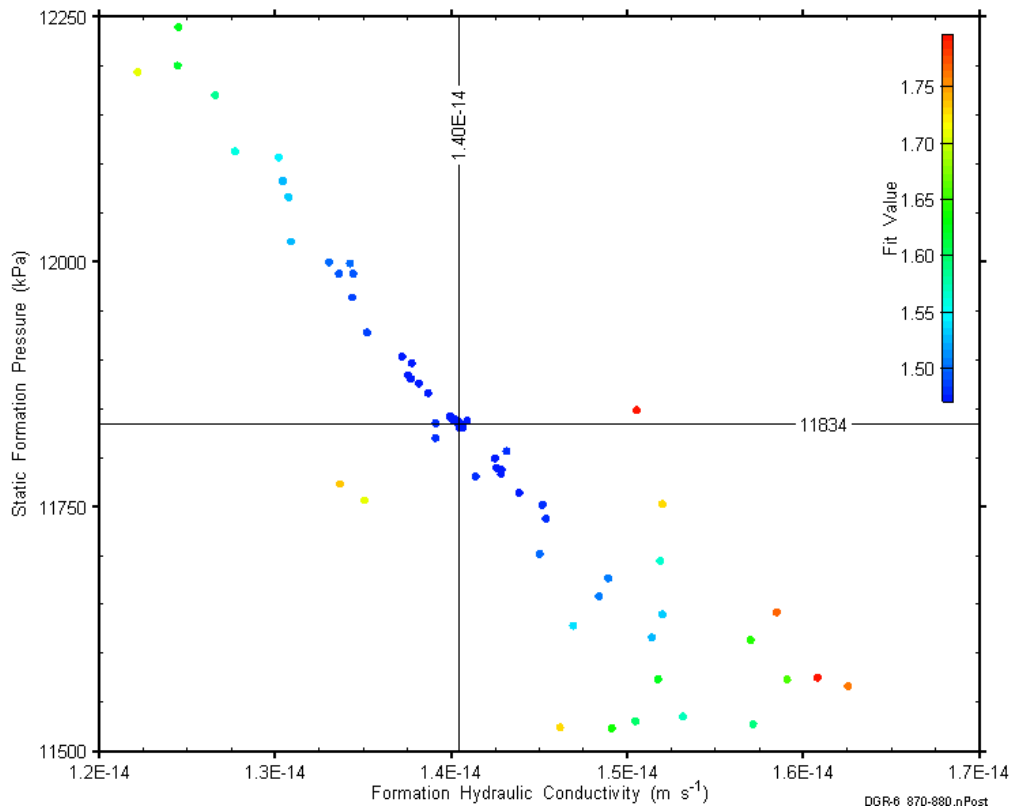


Figure 10-32: XY-scatter plot showing estimates of formation hydraulic conductivity and raw static formation pressure derived from the DGR6_869.77-880.00 perturbation analysis.

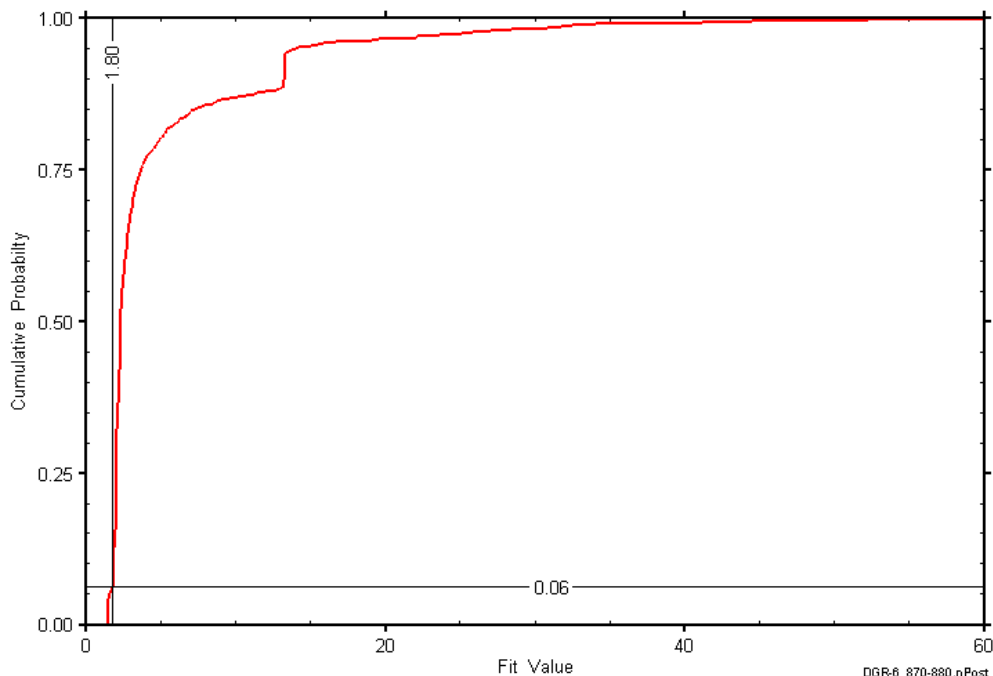


Figure 10-33: DGR6_869.77-880.00 fit value cumulative distribution function.

10.12 880.00-890.23 Coboconk

The DGR-6 interval from 880.00 to 890.23 m LBGS was contained entirely within the Coboconk Formation. The portion of the Coboconk tested consists of limestone with shale laminae and vugs, and included the 0.1-m-thick dolostone marker bed observed in all the DGR boreholes, but not the volcanic ash layer that was included in the immediately overlying test interval. Information on the angle and vertical extent of the test interval is given in Table 10-24. An overview of the testing in this interval is given in Table 10-24 and the corresponding parameter estimates are given in Table 10-25. One pulse-withdrawal test and a DST were performed in this interval.

Table 10-24: Summary of the DGR6_880.00-890.23 testing activities.

Formation / Unit		Top of Test Zone (m LBGS)	Bottom of Test Zone (m LBGS)	
Coboconk		880.00	890.23	
Test Interval Angle (degrees from vertical)		Vertical Top of Test Zone (m BGS)	Vertical Bottom of Test Zone (m BGS)	
31.92		765.55	774.24	
Test	Initiated	Magnitude (kPa)	Duration	Compressibility (Pa ⁻¹)
Shut-in	22-06-10 12:41	N/A	19 hr	N/A
PW	23-06-10 07:36	692	2 hr	3.9E-10
DST Flow Period	23-06-10 09:31	889	7 hr	N/C
DST Shut In	23-06-10 16:52	N/A	14 hr	N/A
Borehole Pressure History				
Event	Start	Pressure (kPa)		
Drilling Intercept	23-01-10	8216		
Open Hole	25-01-10	N/A		
Prior Testing	19-04-10	N/A		
Shut-in	22-06-10	N/A		

Table 10-25: Summary of the DGR6_880.00-890.23 parameter estimates.

Parameter	Best Fit	Minimum	Maximum	Mean
K_f (m/s)	2.4E-10	2.24E-10	2.87E-10	2.45E-10
P_f (kPa)	8943	8931	8951	8943
K_s (m/s)	6.6E-11	4.14E-11	8.41E-11	6.55E-11
t_s (cm)	101	34	261	109
S_s (m ⁻¹)	1.0E-6	4.2E-07	3.1E-06	1.0E-06

Figure 10-34 shows the measured pressure record from DGR6_880.00-890.23 used in this analysis along with the best-fit simulation and parameter values. The ranges of formation K and raw P_f values estimated from perturbation analysis are shown in Figure 10-35 and the fit value cumulative distribution function is shown in Figure 10-36.

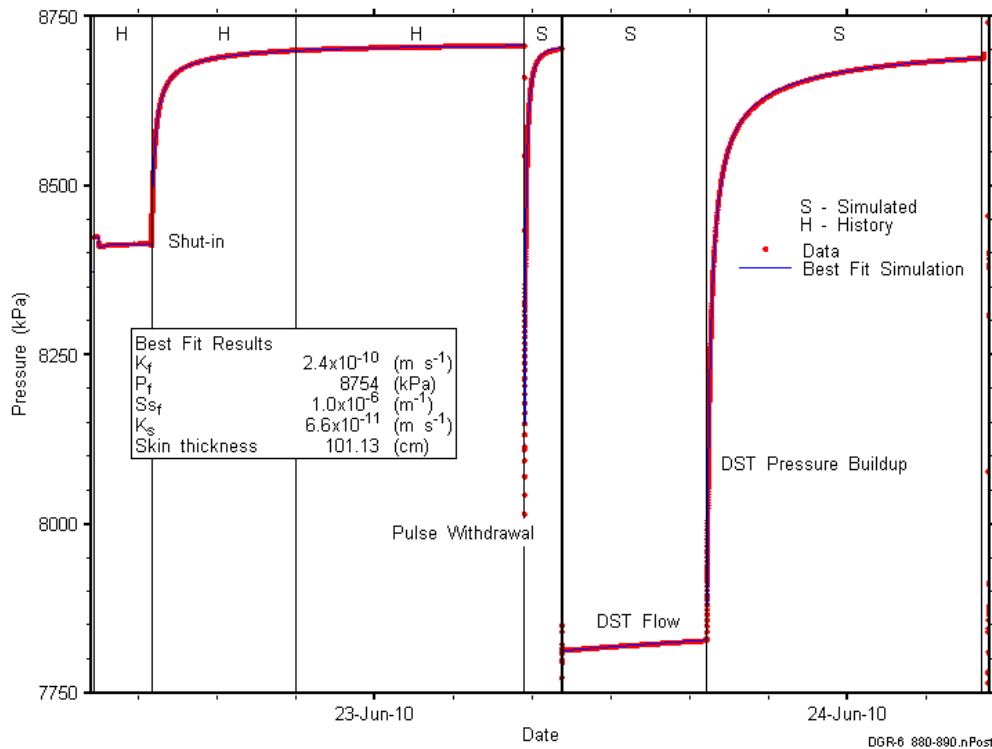


Figure 10-34: Annotated DGR6_880.00-890.23 testing sequence showing best-fit simulation and parameter estimates.

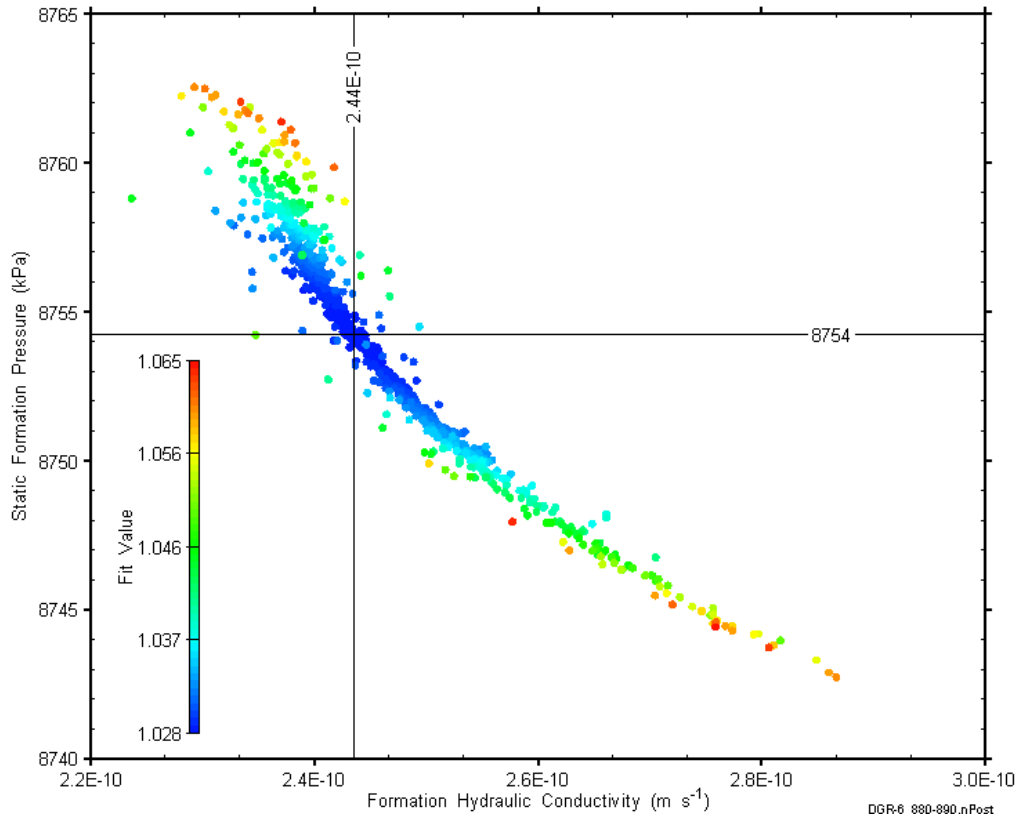


Figure 10-35: XY-scatter plot showing estimates of formation hydraulic conductivity and raw static formation pressure derived from the DGR6_880.00-890.23 perturbation analysis.

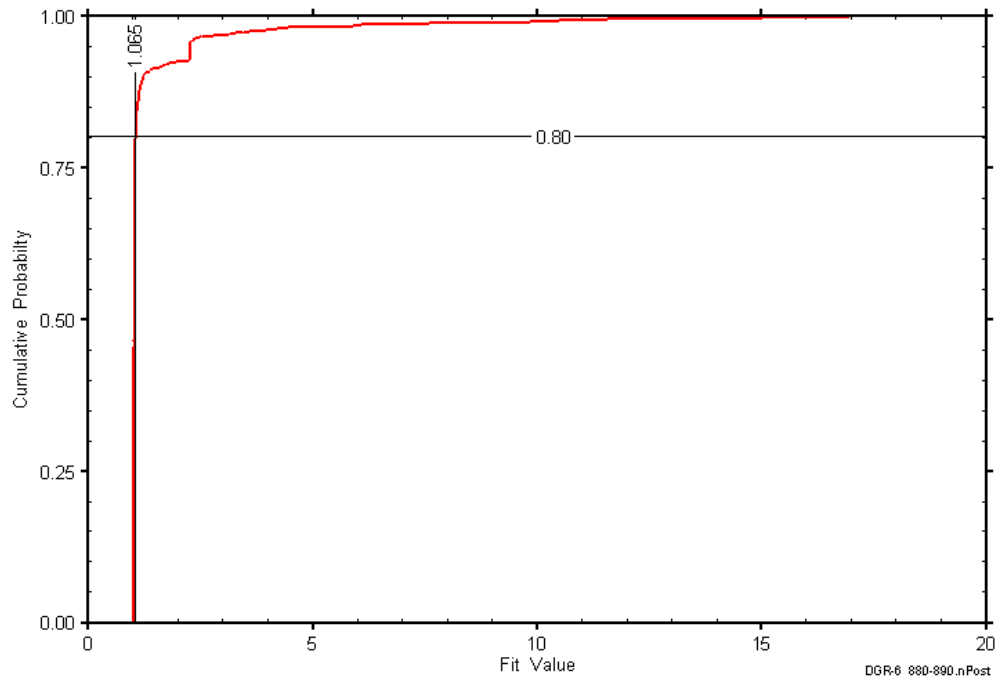


Figure 10-36: DGR6_880.00-890.23 fit value cumulative distribution function.

10.13 Summary of DGR-6 Results

The best-fit parameter estimates derived from the DGR-6 analyses are given in Table 10-26. Note that the vertical depths, rather than the depths along the slanted borehole, are given for the test intervals. Figure 10-37 through Figure 10-41 present stratigraphic profiles of the analysis results for hydraulic conductivity, formation pressure, specific storage, skin factor, and test-zone compressibility, respectively.

Table 10-26: Best-fit parameter estimates derived from the DGR-6 analyses

Formation(s) Tested	Top	Bottom	K_f	P_f	S_s	K_s	t_s	s	C_{tz}
	m BGS	m BGS	$m\ s^{-1}$	kPa	m^{-1}	$m\ s^{-1}$	cm		Pa^{-1}
Queenston	453.30	462.80	1.2E-13	5034	1.0E-8*	2.4E-12	45	-1.82	3.7E-10
Georgian Bay	572.46	581.09	3.6E-14	5773	7.2E-5	1.1E-07	3.3	-0.34	6.4E-9
Georgian Bay- Blue Mountain	596.02	604.60	1.5E-12	5046	4.3E-8	2.8E-06	285	-3.58	2.5E-8
Blue Mountain	614.49	623.14	1.0E-14	3419	1.8E-5	4.4E-11	1.2	-0.13	1.6E-9
Blue Mountain	635.61	644.22	6.6E-14	6289	1.0E-8*	2.8E-12	38	-1.69	3.6E-10
Collingwood	645.71	654.31	4.0E-14	7302	1E-7**	9.5E-13	5.1	-0.47	3.4E-10
Cobourg	668.34	676.89	3.1E-14	8296	1.1E-8*	1.5E-11	24	-1.37	3.4E-10
Sherman Fall	683.39	691.94	4.5E-14	7484	1E-7**	1.4E-12	4.7	-0.44	3.3E-10
Sherman Fall	695.94	704.51	2.6E-14	8258	1E-7**	7.6E-13	6.1	-0.54	3.4E-10
Kirkfield	732.76	741.35	2.9E-14	9574	1.5E-8	2.3E-12	24	-1.37	3.4E-10
Coboconk	756.93	765.55	1.4E-14	12022	2.4E-6	1.0E-13	0.5	-0.05	3.9E-10
Coboconk	765.55	774.24	2.4E-10	8943	1.0E-6	6.6E-11	101	7.23	3.9E-10

*: sampled

** : fixed

As shown in Figure 10-37 and Table 10-26, all but two of the Ordovician test intervals in DGR-6 had K values between approximately $1E-14$ and $1E-13$ m/s. The Coboconk test interval from 869.77 to 880.00 m LBGS that included the ash layer seen in all DGR boreholes had one of the lower K values encountered. Significantly higher K estimates were obtained for the Georgian Bay-Blue Mountain interval ($1.5E-12$ m/s) and the lower Coboconk interval that included the dolostone marker bed and vuggy zone ($2.4E-10$ m/s). The principal contributor of permeability in the Georgian Bay-Blue Mountain interval is believed to be thin siltstone, sandstone, and dolostone layers in the lower Georgian Bay, rather than the fracture observed at a depth of 680.3 m LBGS, which is filled with halite. The volcanic ash layer in the upper Coboconk test interval did not appear to cause high hydraulic conductivity. The uncertainty ranges on the DGR-6 hydraulic conductivity estimates all span less than an order of magnitude.

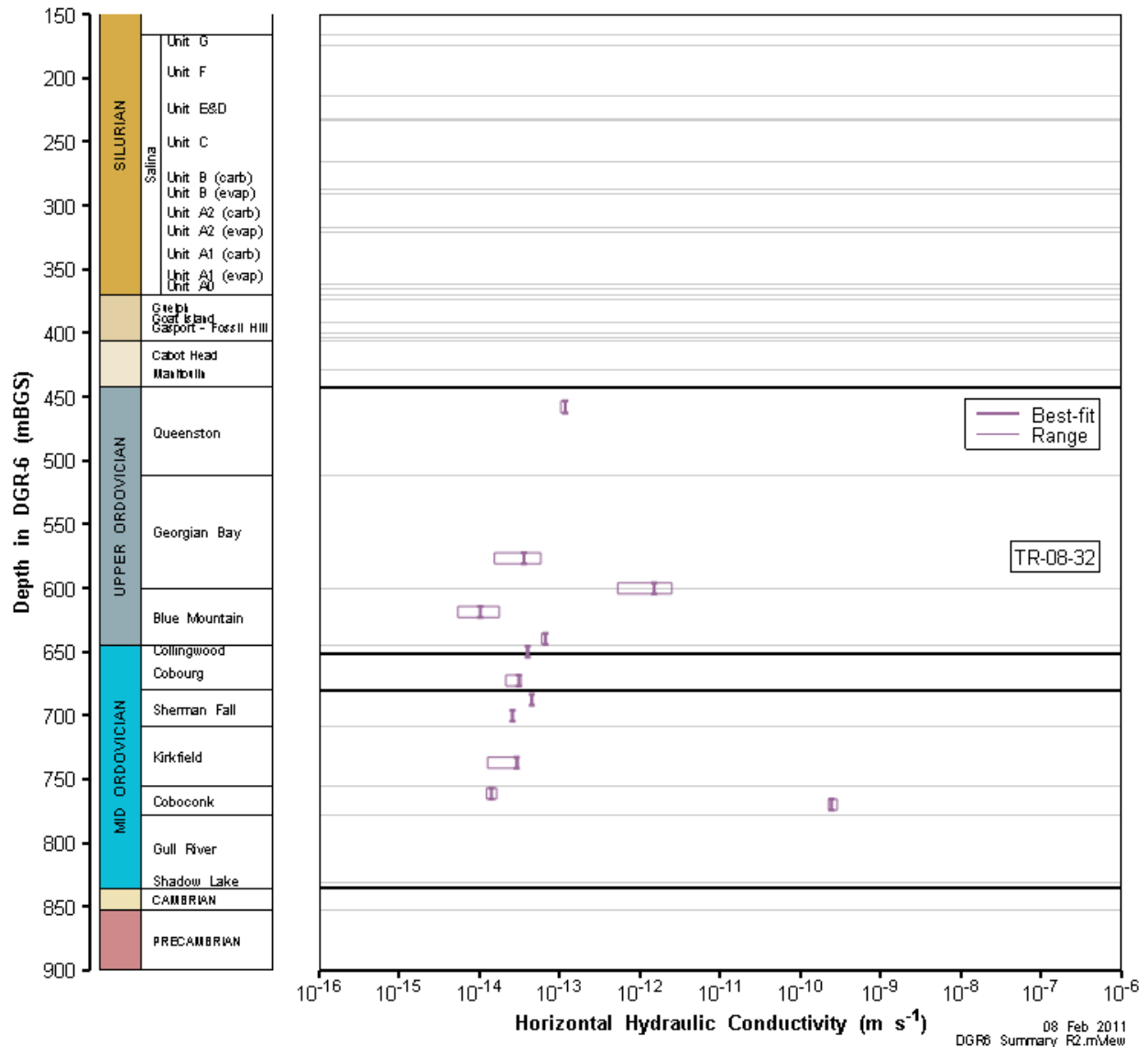


Figure 10-37: DGR-6 stratigraphic profile of horizontal hydraulic conductivity estimates.

As shown in Figure 10-38, the Ordovician intervals in DGR-6 were less underpressured than was observed in the other DGR boreholes (cf. Figure 6-47, Figure 7-71, Figure 8-77, Figure 9-35). Relative to the density-compensated hydrostatic pressure line shown on Figure 10-38, only the Georgian Bay, Georgian Bay-Blue Mountain, and both Blue Mountain intervals were underpressured. The upper Sherman Fall interval was near normally pressured, the Queenston and Collingwood intervals were slightly overpressured, and the lower Sherman Fall and lower Coboconk intervals were more overpressured, but by less than 1 MPa. The Cobourg, Kirkfield, and especially upper Coboconk intervals were overpressured by more than 1 MPa. Interestingly, the higher permeability lower Coboconk interval was less overpressured than the lower permeability upper Coboconk interval.

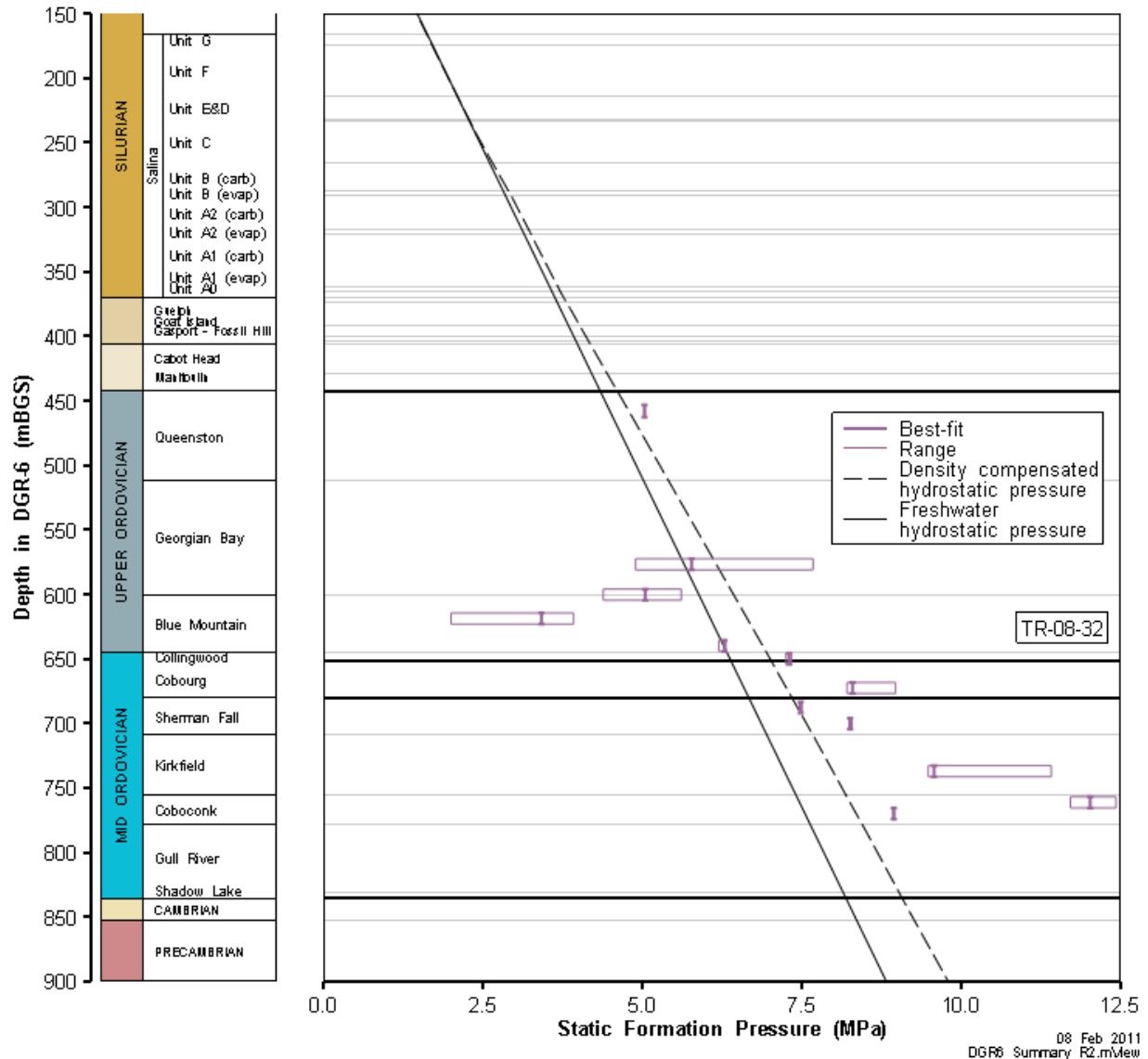


Figure 10-38: DGR-6 stratigraphic profile of formation pressure estimates.

Figure 10-39 shows the S_s values fitted in the simulations for each of the DGR-6 test intervals, along with the uncertainties associated with the fitted values. The fitted values range from $1.5E-8 \text{ m}^{-1}$ to $7.2E-5 \text{ m}^{-1}$. For some of the test intervals, effectively equivalent fits could be obtained with S_s values ranging over one or more orders of magnitude. This is a consequence of the strong correlation between S_s and skin properties in single-well tests discussed in Section 4.4. For three test intervals, no minimum was found in the S_s fit surface within the range of values thought to be physically reasonable ($1E-7$ to $1E-4 \text{ m}^{-1}$). In those cases, S_s was fixed at $1E-7 \text{ m}^{-1}$ (Table 10-26). For three other test intervals where no S_s minimum could be found, S_s was sampled over a range extending down to $1E-8 \text{ m}^{-1}$, and the best fit was generally found at that value. The fixed and sampled values are not shown in Figure 10-39, but are given in Table 10-26.

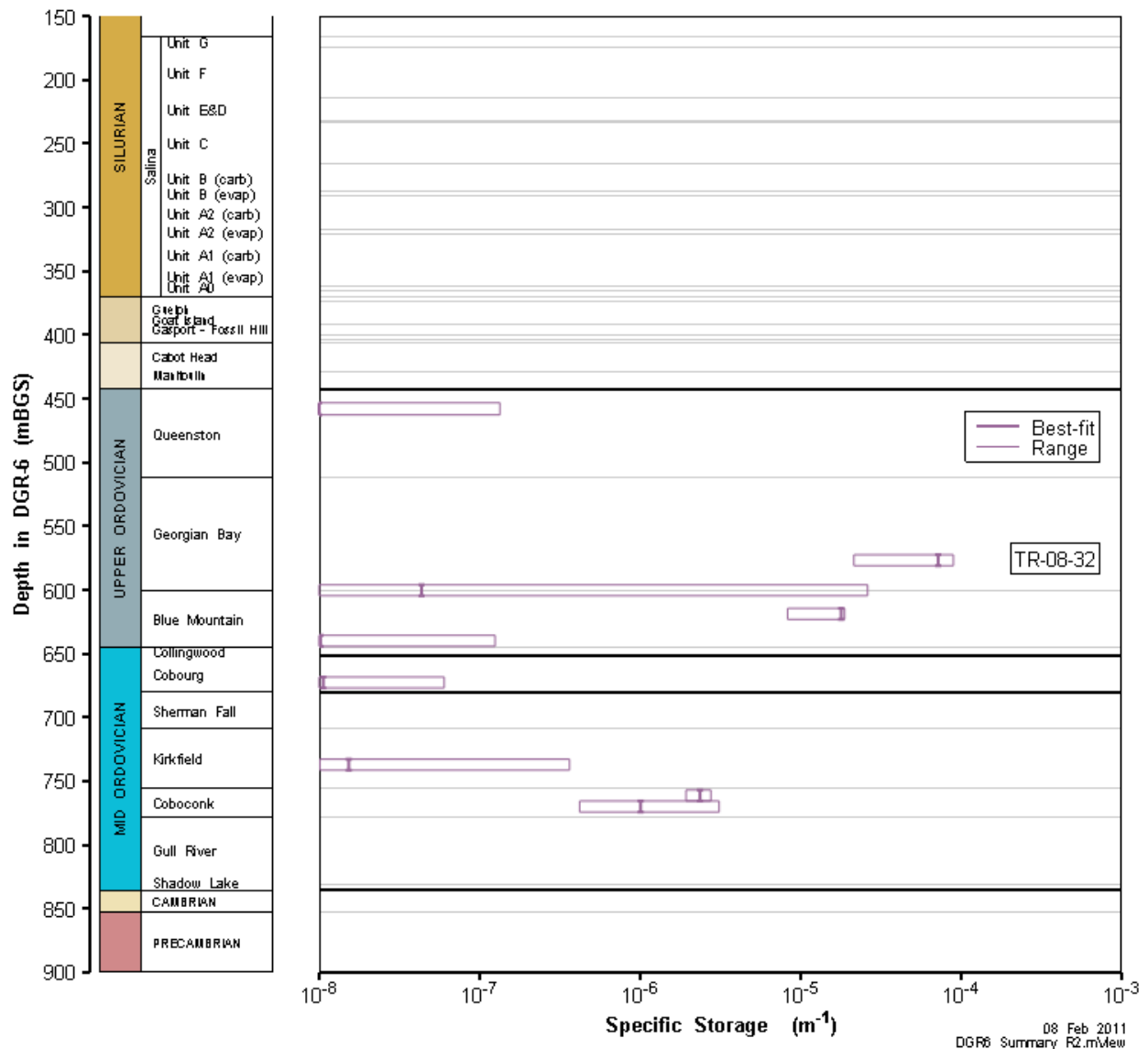


Figure 10-39: DGR-6 stratigraphic profile of specific storage estimates.

Figure 10-40 shows the skin factors obtained from parameter optimization for each of the DGR-6 test intervals. All but the lower Coboconk test interval had negative skins, reflecting enhanced permeability around the wellbore. Hydraulically significant fractures are a possible and the most likely cause of negative skins. Other causes could be enhanced local fracturing caused by stress relief fracturing during drilling. The negative skins in DGR-6 were generally of low magnitude; the Georgian Bay-Blue Mountain interval had the most negative skin, which was -3.58 (Table 10-26) The lower Coboconk interval, which had the highest hydraulic conductivity, also had the most significant, and only positive, skin, which was 7.23.

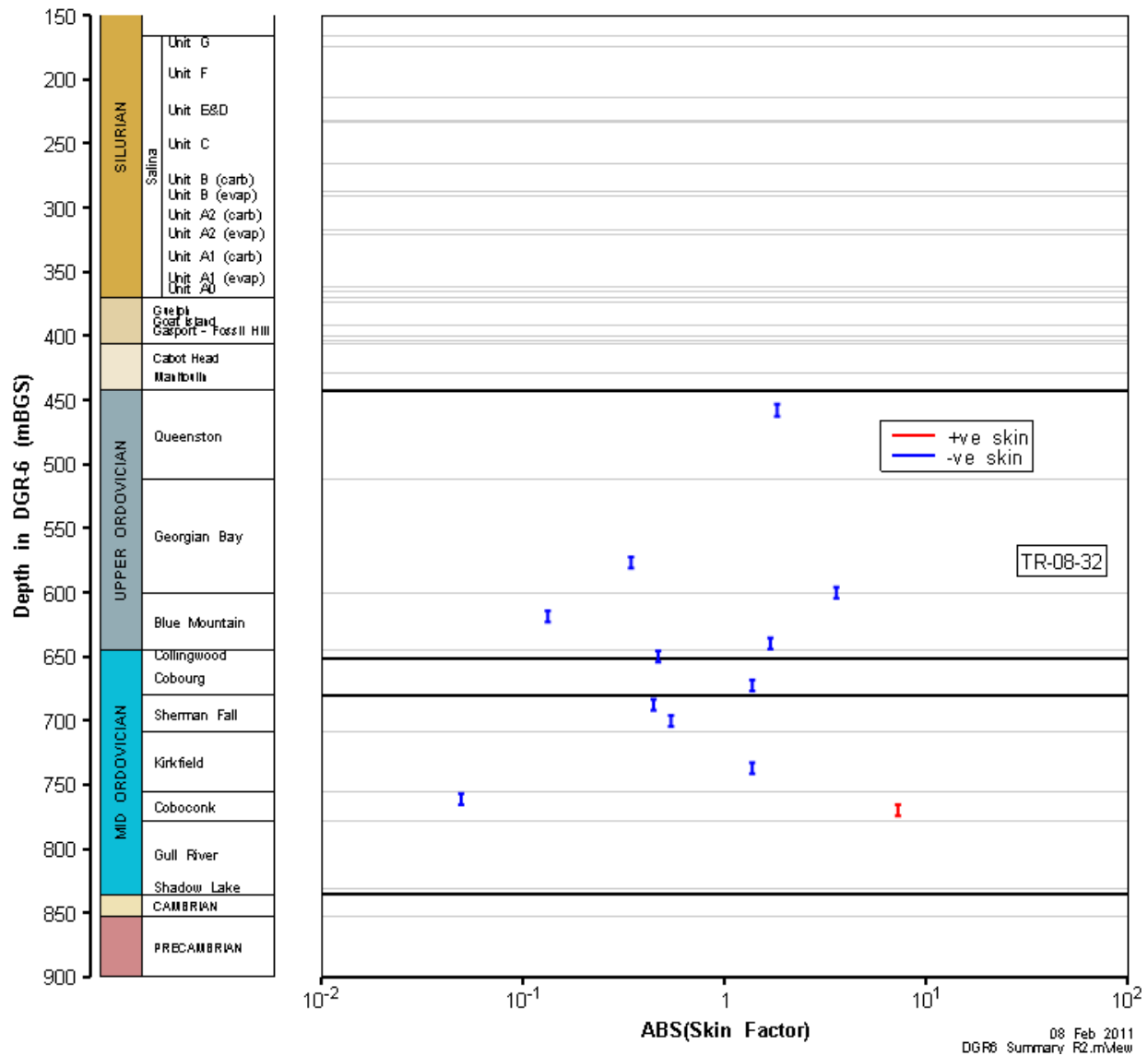


Figure 10-40: DGR-6 stratigraphic profile of skin factor estimates.

As shown in Figure 10-41, of the 12 DGR-6 intervals in which test-zone compressibility was measured, C_{tz} was less than $4E-10 \text{ Pa}^{-1}$ in 9 of the intervals. These values are indicative of water-filled test intervals with typical test-tool compliance. In the remaining 3 intervals, C_{tz} ranged from $1.6E-9$ to $2.5E-8 \text{ Pa}^{-1}$. Higher test-zone compressibilities such as these (particularly $2.5E-8 \text{ Pa}^{-1}$) are suggestive of a relatively small amount of gas in the test zone, but no direct evidence of gas is available. The highest C_{tz} mentioned above was measured in the Georgian Bay-Blue Mountain interval, which was also the second-most permeable interval tested (Figure 10-37) and the interval with the most negative skin (Figure 10-40). All of these observations are consistent with one or more fractures in the test interval, but the only fracture noted (at 680.3 m LBGs) was filled with halite (Sterling et al., 2011).

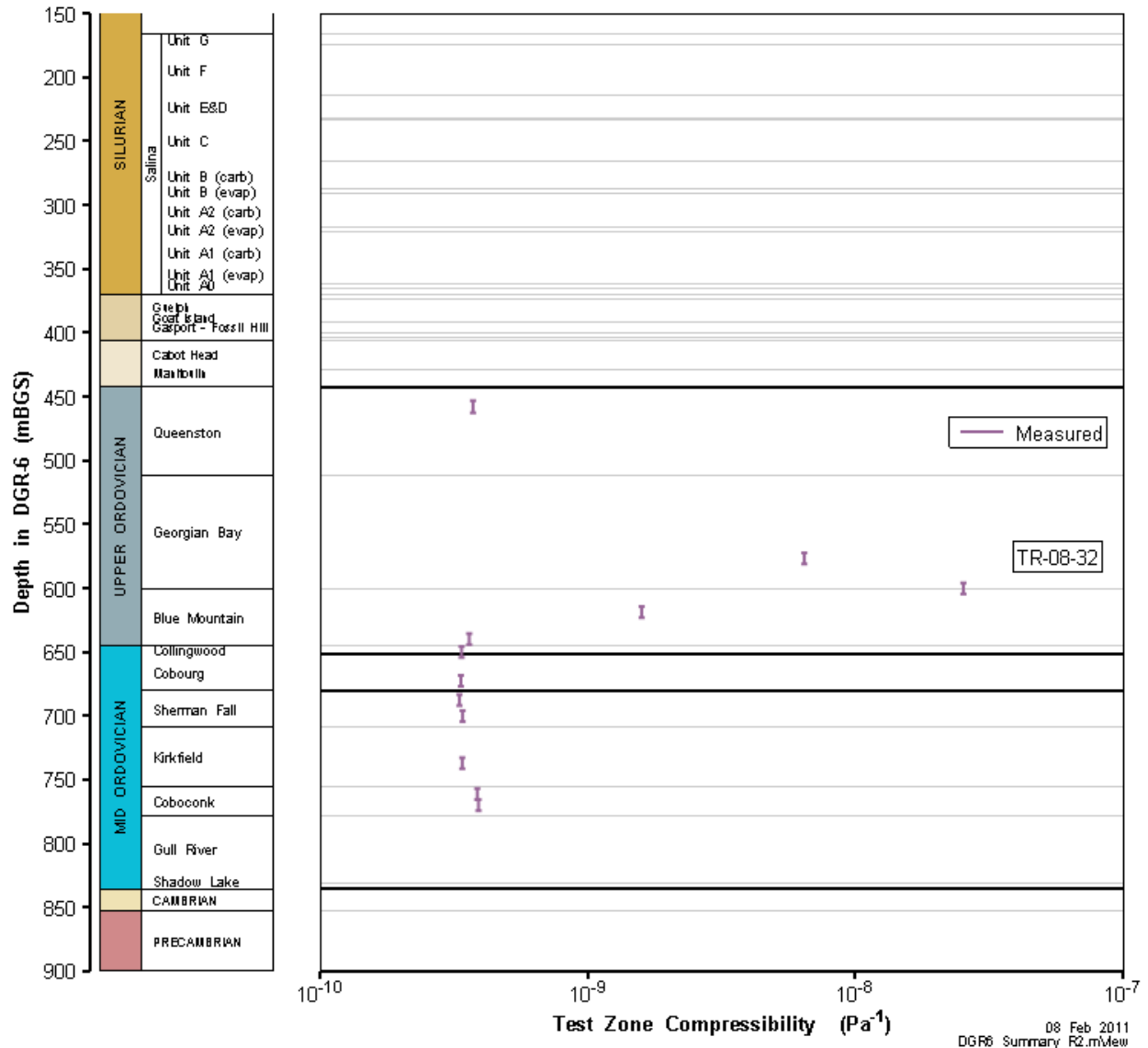


Figure 10-41: DGR-6 stratigraphic profile of test-zone compressibility estimates.

11 Formation Hydraulic Conductivity Estimates And Results Comparison

This section presents estimates of formation horizontal hydraulic conductivity based on straddle-packer testing results and presents comparisons of hydraulic conductivity, specific storage, test-zone compressibility, and skin factor for available tests.

The values presented in Table 11-1 represent the authors' consensus on appropriate values of horizontal formation hydraulic conductivity to be used in numerical modelling or other applications where formation-specific hydraulic conductivity values are required.

The values presented are the geometric mean of the best-fit values for all hydraulic tests for which the formation in question comprised a significant portion of the test interval, rounded to a single decimal place. Tests which also include high-conductivity intervals are not included in the geometric mean of adjacent lower conductivity intervals. Additionally, anomalous results which reflected localized response in a single borehole were not included. Examples of these are primarily Ordovician formation tests with high test zone compressibility. For higher-conductivity formations, specifically the Upper Salina A1 carbonate and Guelph, the geometric mean is scaled by the interval length divided by the average formation thickness, resulting in multipliers of 9.0 and 6.0 respectively.

The Silurian evaporite intervals (Salina B evaporite, Salina A2 evaporite, Salina A1 evaporite) are all relatively thin and are expected to be low conductivity based on observation of cores. Similarly, the Salina A0 dolostone is very thin, massive, and expected to be low-permeability based on core observations. Individual tests straddling these intervals give results indicative of the higher conductivity formations within the test interval. The lowest conductivity test (DGR4_261.63-292.37) that includes an evaporite has been selected as representative of all untested and low permeability Silurian formations. The actual hydraulic conductivity of the intervals may be lower.

Table 11-1: Formation horizontal hydraulic conductivity estimates from all DGR borehole analyses.

Formation/Unit	DGR-1	DGR-2	DGR-3	DGR-4	DGR-5	DGR-6	Estimate
Salina F			4.8E-14	5.6E-14			5E-14
Salina E			1.4E-13	4.1E-13			2E-13
Salina D			1.4E-13	4.1E-13			2E-13
Salina C			3.7E-13	4.7E-13			4E-13
Salina B			3.7E-13	4.7E-13 3.1E-13 4.5E-10			4E-13
Salina B evaporite			3.8E-9	3.1E-13 4.5E-10			3E-13
Salina A2 (carbonate)	1.2E-11		3.8E-9	4.5E-10 1.7E-8			3E-10
Salina A2 (evaporite)			x	x			3E-13
Salina A1 Upper (carbonate)			1.8E-8	1.7E-8 4.4E-8			2E-7
Salina A1 (carbonate)	1.8E-12		1.8E-8 4.0E-11	4.4E-8 3.0E-9			9E-12
Salina A1 (evaporite)			x	x			3E-13
Salina A0			x	x			3E-13
Guelph			8.9E-9	3.0E-9			3E-8
Goat Island			8.9E-9	1.6E-12			2E-12
Gasport			3.5E-12	1.6E-12			2E-12
Lions Head	1.8E-11		3.5E-12	1.6E-12			5E-12
Fossil Hill	1.8E-11		3.5E-12	1.6E-12			5E-12
Cabot Head	1.8E-11		3.5E-12 1.6E-13	4.4E-14			9E-14
Manitoulin			1.6E-13	4.4E-14 1.9E-12	2.7E-13		1E-13
Queenston		1.9E-14 3.3E-14	1.6E-13 1.6E-14 1.4E-14	1.9E-12 2.3E-14 2.2E-14	2.7E-13 1.5E-13 9.4E-13	1.2E-13	3E-14
Georgian Bay		4.9E-14 3.4E-14 4.8E-14	1.2E-14 1.2E-14 1.3E-13	5.2E-14 2.8E-14 4.6E-14 9.4E-14	9.4E-13 3.3E-13 2.9E-15 3.2E-14	3.6E-14 1.5E-12	3E-14
Blue Mountain		1.2E-14	1.3E-13 3.5E-13	1.2E-14 1.3E-14	3.1E-14	1.0E-14 6.6E-14	3E-14
Collingwood		9.4E-15	2.4E-14	1.3E-14	3.0E-14	4.0E-14	2E-14
Cobourg		3.9E-15	1.3E-14	2.4E-14	1.1E-14	3.1E-14	1E-14
Sherman Fall		2.3E-16	1.3E-14 1.3E-14	8.7E-15	1.6E-14	4.5E-14 2.6E-14	9E-15
Kirkfield		3.6E-16 4.8E-16	1.7E-14 1.0E-12	4.1E-15 4.7E-12	2.3E-14	2.9E-14	4E-15
Coboconk		4.0E-11	1.0E-12 1.5E-13	4.7E-12 9.6E-12		1.4E-14 2.4E-10	2E-11
Gull River		1.5E-11 1.3E-11	1.5E-13 3.7E-13	5.5E-12			2E-12

X.XE-YY - not used in formation estimate

Figure 11-1 presents estimated formation hydraulic conductivities compared to test interval results, plotted against DGR-1 and DGR-2 stratigraphy. DGR-3, DGR-4, DGR-5, and DGR-6 test intervals are adjusted so that interval extents are in the same relative position within each formation.

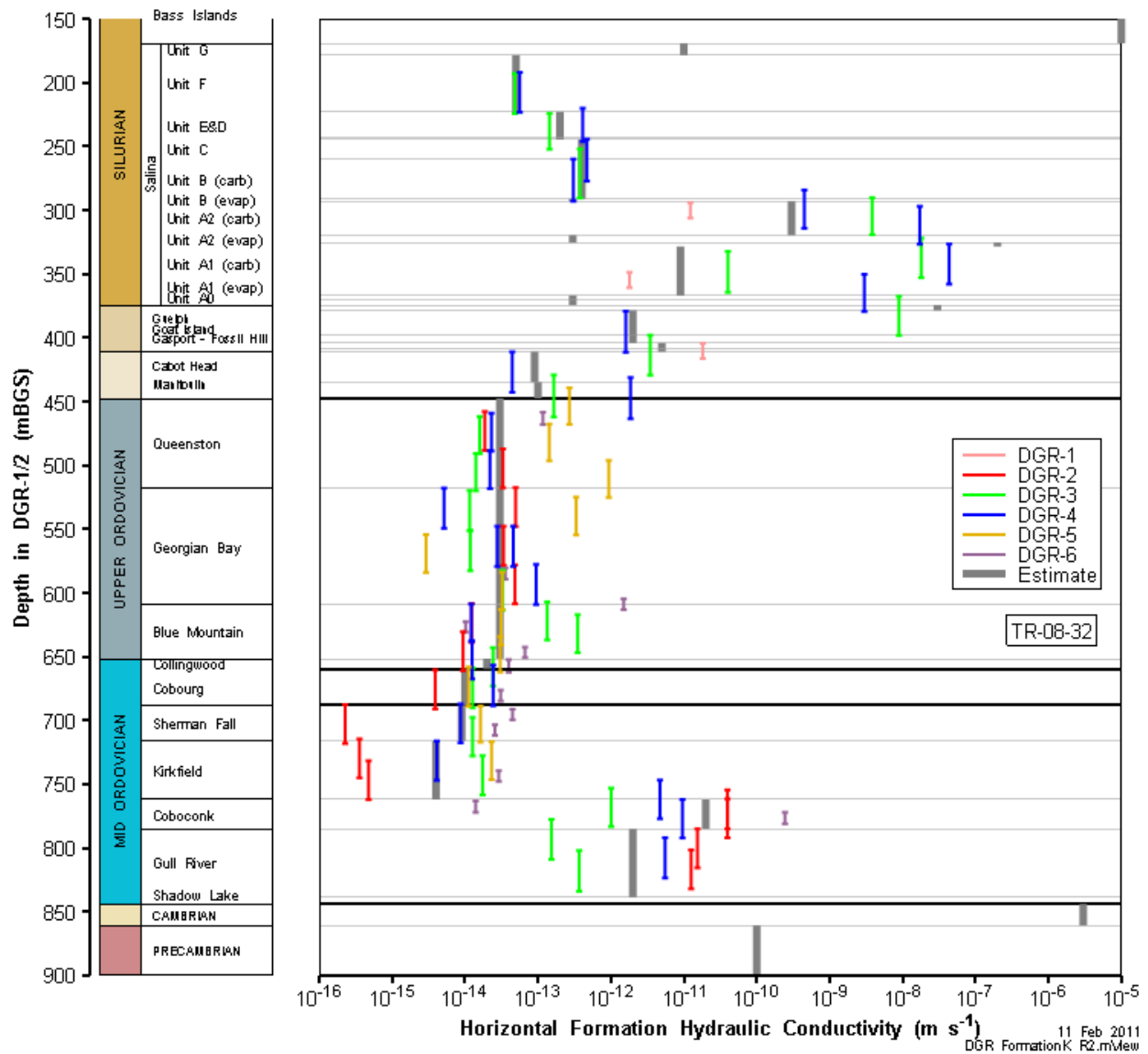


Figure 11-1: Comparison of horizontal hydraulic conductivity estimates from DGR boreholes and formation estimates.

Figure 11-2 compares best-fit specific storage values with associated uncertainty ranges from all tests in the DGR boreholes where specific storage was a fitting parameter. Significant uncertainty and variation are observed within most formations/units, which probably reflects the difficulty in obtaining a good S_s estimate from single-well tests because of its strong correlation with skin properties (Section 4.4).

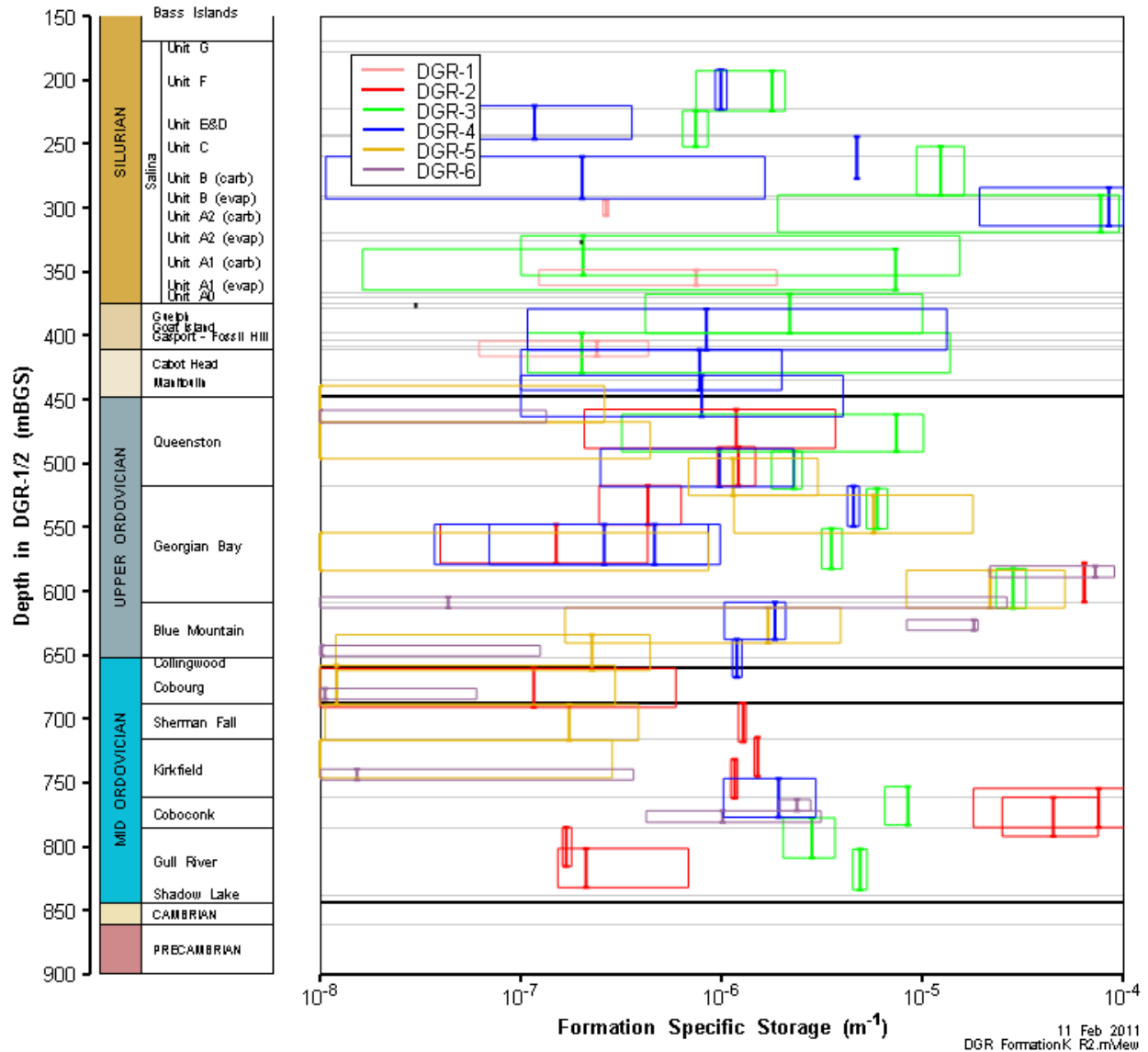


Figure 11-2: Comparison of fitted specific storage estimates from DGR boreholes.

Figure 11-3 compares calculated test-zone compressibilities for all intervals where pulse tests were conducted. The consistency of low values within the Middle Ordovician limestones is noteworthy. Also, consistently high values are observed in test intervals including the Lions Head and Fossil Hill, across the Manitoulin-Queenston contact, and in the lower Georgian Bay Formation. Significant variation is observed between intervals and boreholes in the Blue Mountain Formation.

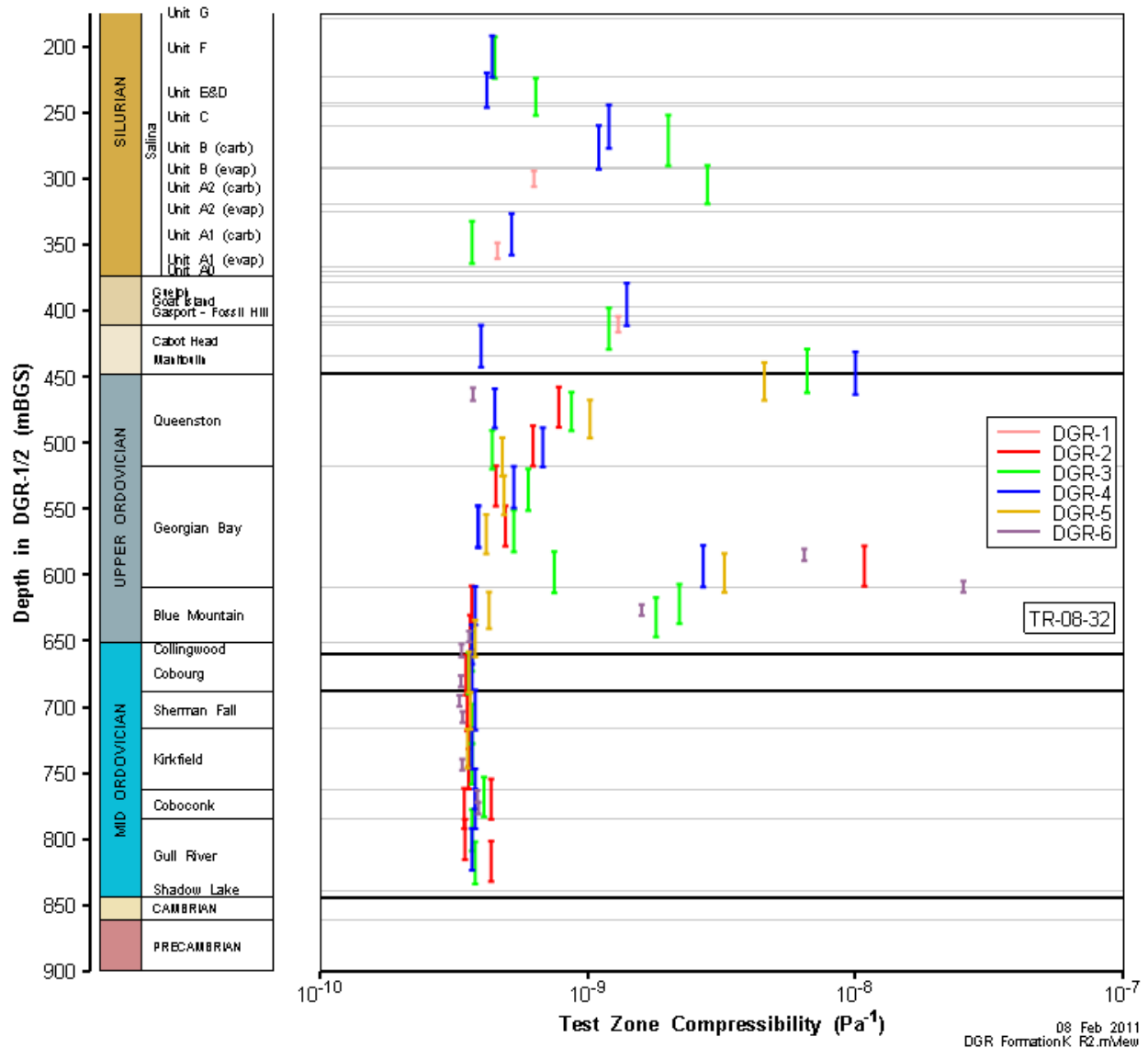


Figure 11-3: Comparison of test-zone compressibility estimates from DGR boreholes.

Figure 11-4 compares skin factor estimates for all test intervals. Most intervals had consistently negative skins, albeit of low magnitude. Test intervals including the Salina Unit A2 and A1 carbonates typically had positive skins, in some cases quite high. Black River Group (Coboconk and Gull River) test intervals also had consistently positive skins. With some exceptions, the intervals showing positive skins tended to be intervals with higher hydraulic conductivity. Intervals including the Guelph, however, had consistently negative skins.

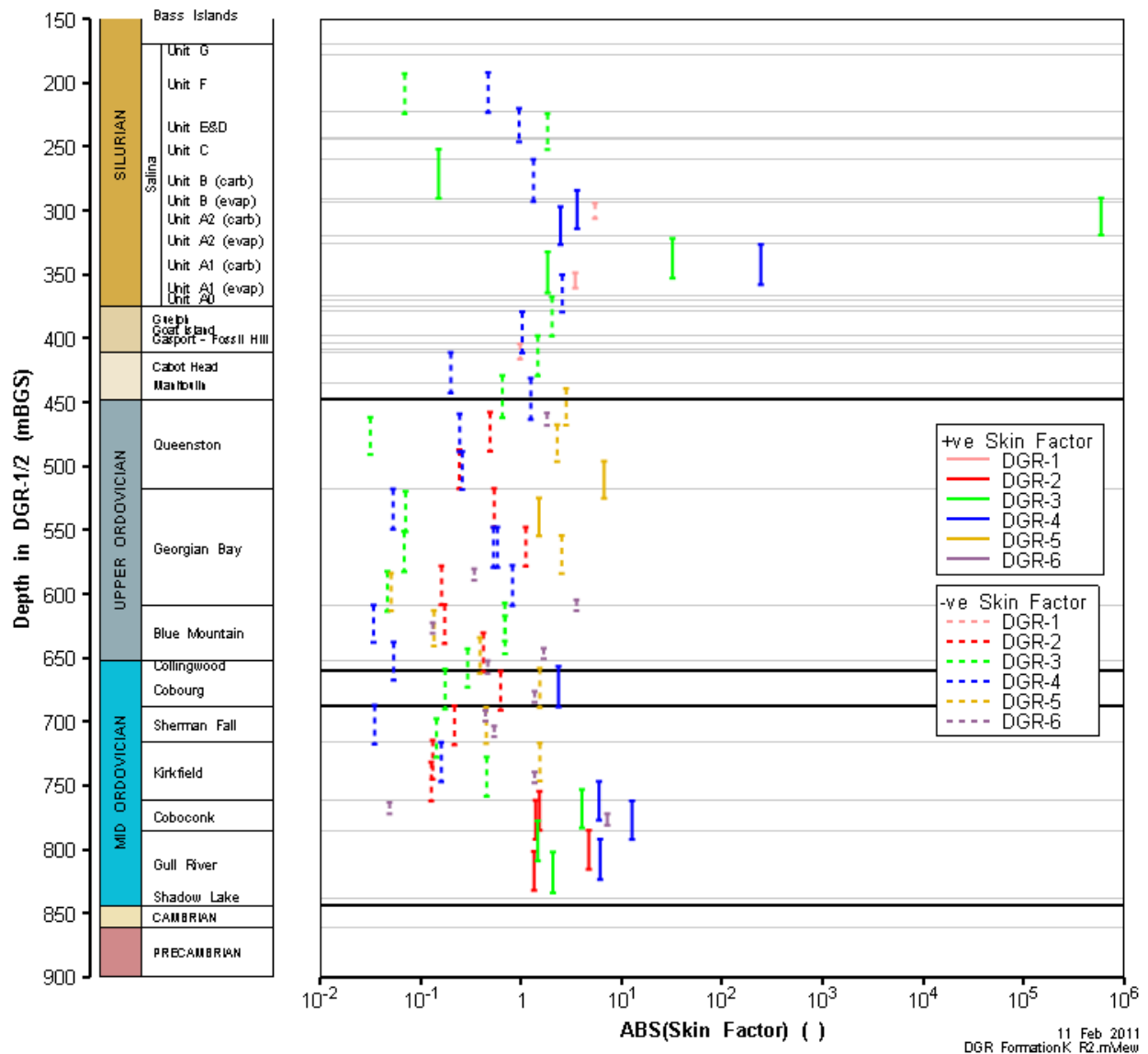


Figure 11-4: Comparison of skin factor estimates from DGR boreholes.

12 Data Use

Hydraulic conductivity values estimated from straddle-packer analyses presented in this report are assumed to represent only the horizontal hydraulic conductivity of the tested interval and provide no information regarding the vertical hydraulic conductivity of the system. In addition, formation parameter values reported represent the average values over the entire test-zone length for each test. Actual values of discrete intervals within the complete test-zone length may differ from the average values derived from analysis.

13 References

Abbaszadeh, M., and P.S. Hegeman. 1990. "Pressure-Transient Analysis for a Slanted Well in a Reservoir With Vertical Pressure Support." *SPE Formation Evaluation*, 5(3), 277-284.

Avis, J.A., and R.L. Beauheim. 2009. Reliability of Phase 1 DGR-1 and DGR-2 hydraulic testing results. Memorandum to Mark Jensen, NWMO, February 18.

Beauheim, R.L. 2007. Test Plan, DGR-1 and 2 Straddle-Packer Hydraulic Testing, TP-06-14, Revision 2, September 21, Intera Engineering Ltd., Ottawa.

Beauheim, R.L. 2008. Test Plan, DGR-3 and 4 Straddle-Packer Hydraulic Testing, TP-08-16, Revision 1, November 21, Intera Engineering Ltd., Ottawa.

Beauheim, R.L. 2009. Test Plan, Phase 2 DGR-2 Straddle-Packer Hydraulic Testing, TP-09-06, Revision 1, August 12, Intera Engineering Ltd., Ottawa.

Beauheim, R.L. 2010. Test Plan, DGR-5 and DGR-6 Straddle-Packer Hydraulic Testing, TP-09-04, Revision 1, April 15, Intera Engineering Ltd., Ottawa.

Beauheim, R.L., and W.H. Pedler. 2009. Technical Report: Fluid Electrical Conductivity Logging in Borehole DGR-1, TR-07-14, Revision 2, February 5, Intera Engineering Ltd., Ottawa

Beauheim, R.L., R.M. Roberts, T.F. Dale, M.D. Fort, and W.A. Stensrud. 1993. Hydraulic Testing of Salado Formation Evaporites at the Waste Isolation Pilot Plant Site: Second Interpretive Report. SAND92-0533. Albuquerque, NM: Sandia National Laboratories.

Briscoe, G., A. Wigston, and M. Melaney. 2010. Technical Report: Drilling, Logging and Sampling of DGR-3 and DGR-4, TR-08-13, Revision 0, February 11, Intera Engineering Ltd., Ottawa.

Darcy, H. 1856. *Les fontaines publiques de la ville de Dijon*. Victor Dalmont, Paris

Hawkins, M.F., Jr. 1956. "A Note on the Skin Effect." Technical Note 389, *Petroleum Transactions*, AIME. 207, 356-357.

Intera Engineering Ltd. 2006. Geoscientific Site Characterization Plan, OPG's Deep Geologic Repository for Low & Intermediate Level Waste. OPG Report 00216-REP-03902-00002-R00, April.

Intera Engineering Ltd. 2008. Phase 2 Geoscientific Site Characterization Plan, OPG's Deep Geologic Repository for Low and Intermediate Level Waste. OPG Report # 00216-REP-03902-00006-R00, April.

Intera Engineering Ltd., 2009. Project Quality Plan, DGR Site Characterization, Revision 4, August 14, Ottawa.

Nuclear Waste Management Program. 2006. nSIGHTS 2.40 User Manual Version 2.1. ERMS #530161. April 12, Carlsbad, NM: Sandia National Laboratories.

Ramey, H.J., Jr., R.G. Agarwal, and I. Martin. 1975. "Analysis of 'Slug Test' or DST Flow Period Data." *Journal of Canadian Petroleum Technology* 14(3), 37-47.

Roberts, R.M. 2009. Test Plan, DGR-3 and DGR-4 nSIGHTS Well-Test Analyses, TP-08-18, Revision 0, April 30, Intera Engineering Ltd., Ottawa.

Sterling, S. 2010. Technical Report: Drilling Logging and Sampling of DGR-1 and DGR-2, TR-07-06, Revision 1, June 17, Intera Engineering Ltd., Ottawa.

Sterling, S., and M. Melaney. 2011. Technical Report: Bedrock Formations in DGR-1 to DGR-6, TR-09-11, Revision 0, April 7, Geofirma Engineering Ltd., Ottawa.

Sterling, S., G. Briscoe and M. Melaney. 2011. Technical Report: Drilling, Logging and Sampling of DGR-5 and DGR-6, TR-09-01, Revision 0, April 6, Geofirma Engineering Ltd., Ottawa.

Wigston, A., and D. Heagle. 2009. Technical Report: Bedrock Formations in DGR-1, DGR-2, DGR-3 and DGR-4, TR-08-12, Revision 1, March 25, Intera Engineering Ltd., Ottawa.

Appendix A. - DGR-1 Plots

Various plots of results from the DGR-1 analyses are shown below. These plots include XY-scatter plots of the fitting-parameter estimates, linear and log-log horsetail plots of the simulated pressure responses showing field-data matches, K_f , P_f , and S_s cumulative distribution functions, and parameter-space plots showing the characteristics of the minima for each of the fitting parameters.

A.1 294.28-306.28 Salina A2

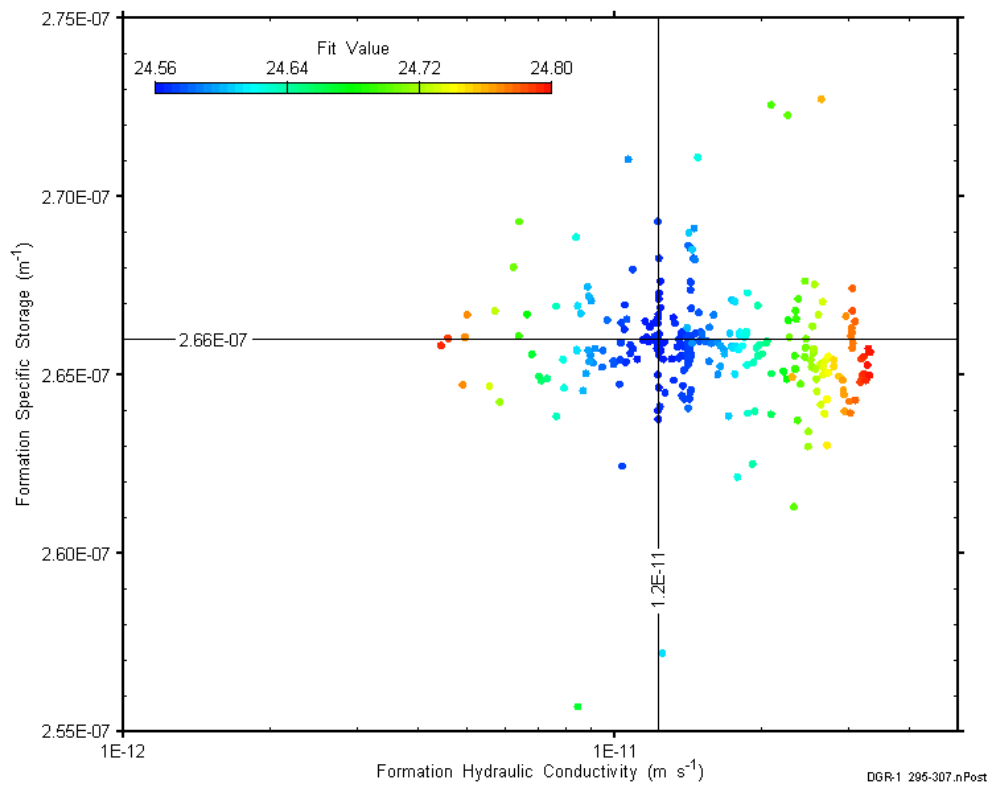


Figure A-1 XY-scatter plot showing estimates of formation hydraulic conductivity and formation specific storage derived from the DGR1_294.28-306.28 perturbation analysis.

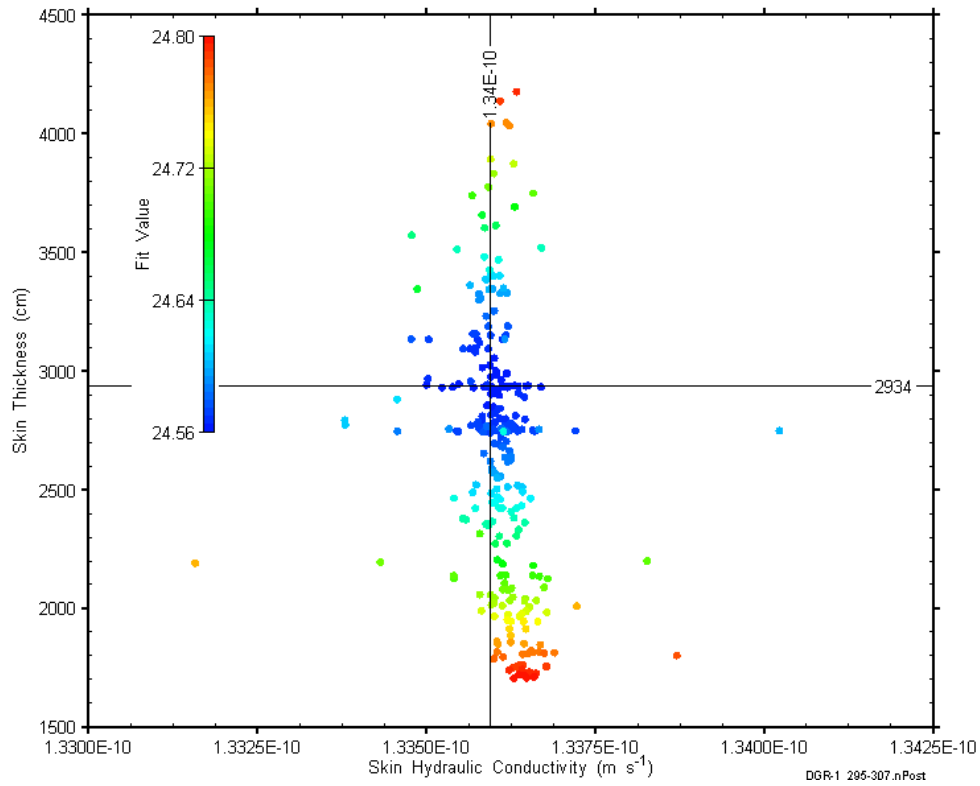


Figure A-2 XY-scatter plot showing estimates of skin hydraulic conductivity and skin thickness derived from the DGR1_294.28-306.28 perturbation analysis.

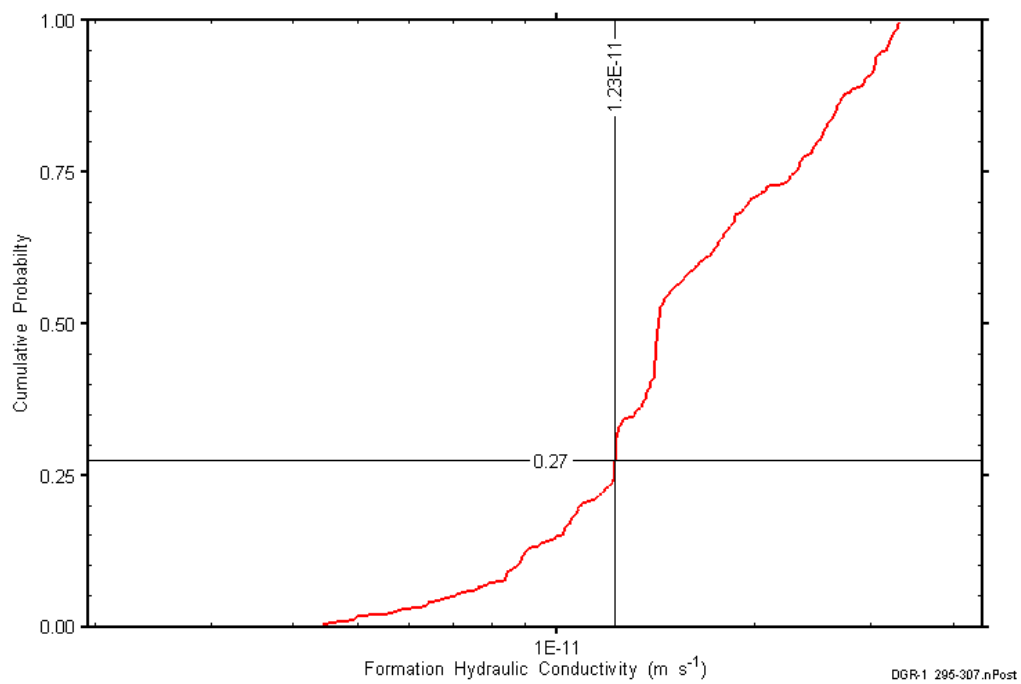


Figure A-3: DGR1_294.28-306.28 formation hydraulic conductivity cumulative distribution function.

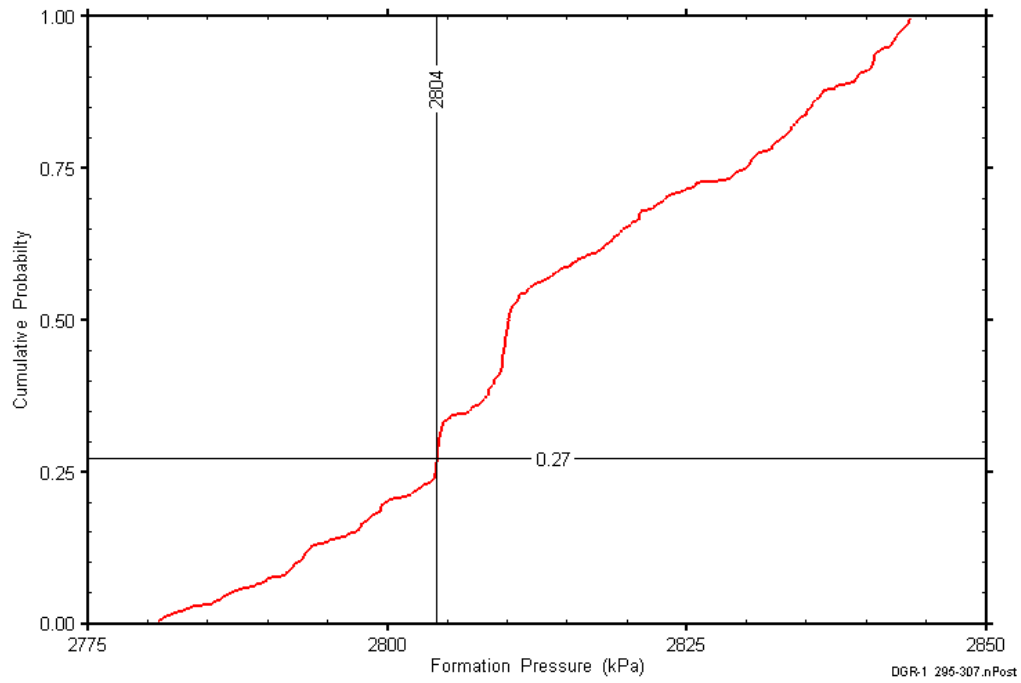


Figure A-4: DGR1_294.28-306.28 static formation pressure cumulative distribution function.

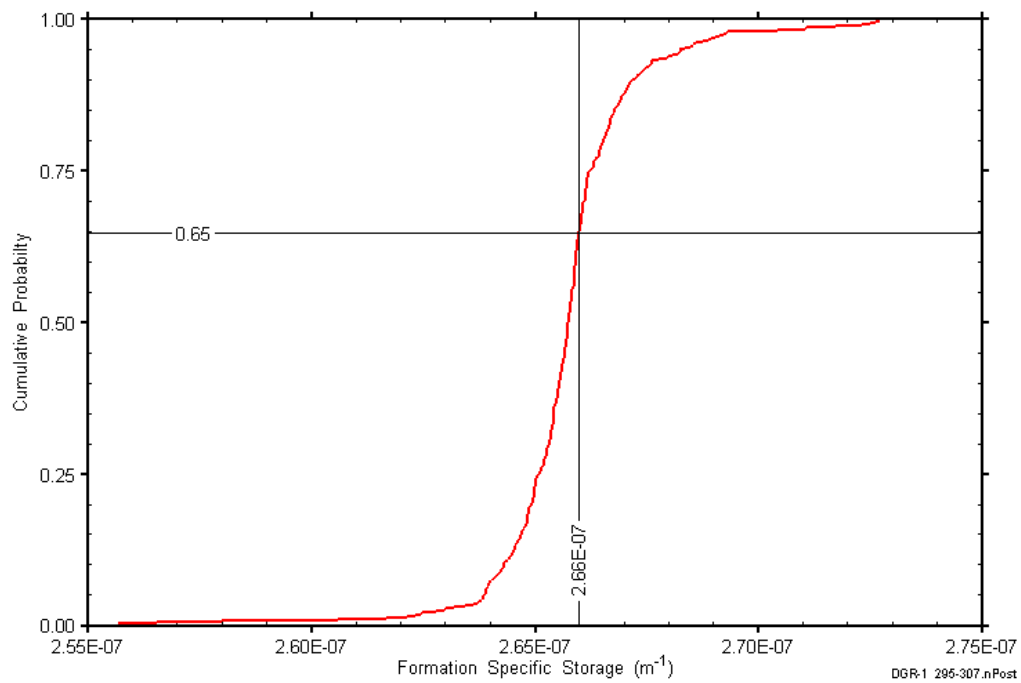


Figure A-5: DGR1_294.28-306.28 formation specific storage cumulative distribution function.

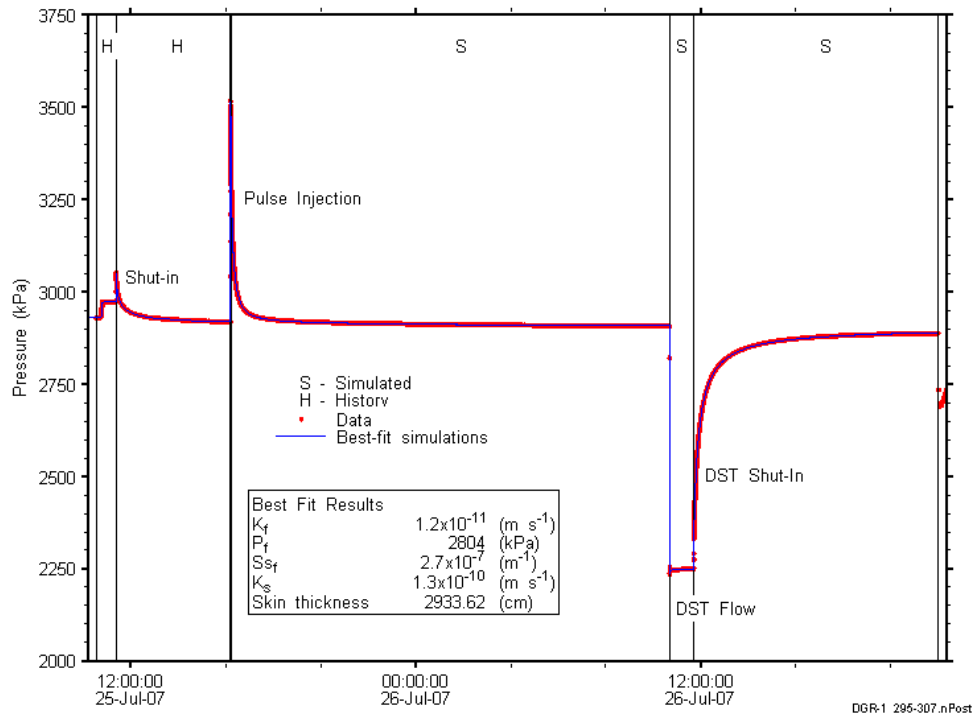


Figure A-6: Linear plot showing details of simulations of the DGR1_294.28-306.28 pressure response.

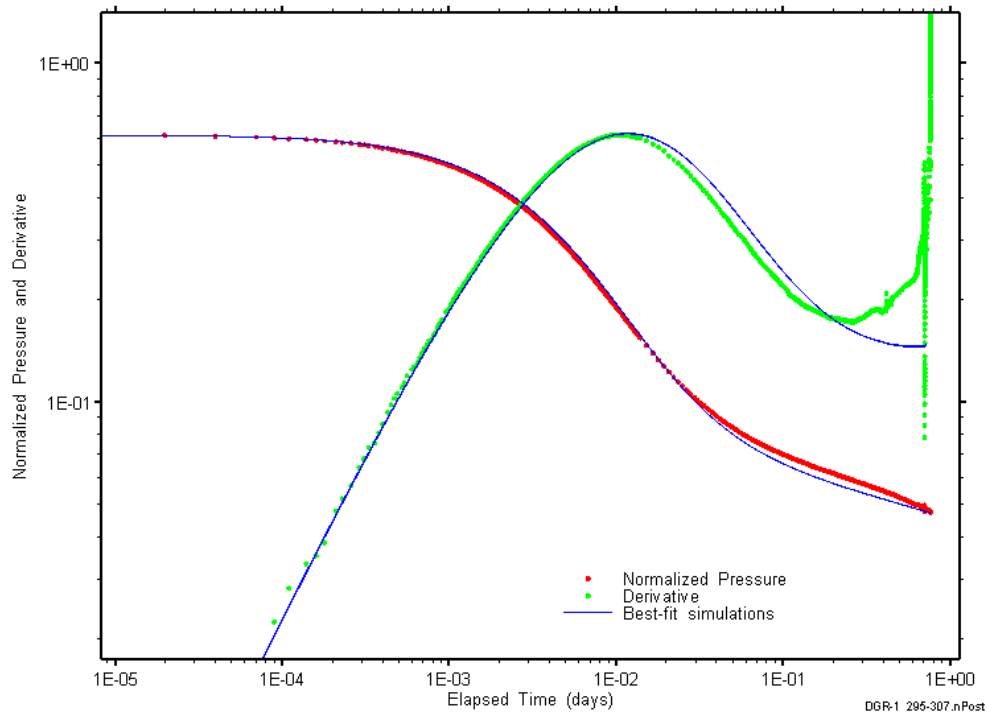


Figure A-7: Log-log plot showing simulations of the DGR1_294.28-306.28 pulse withdrawal Ramey B and derivative response.

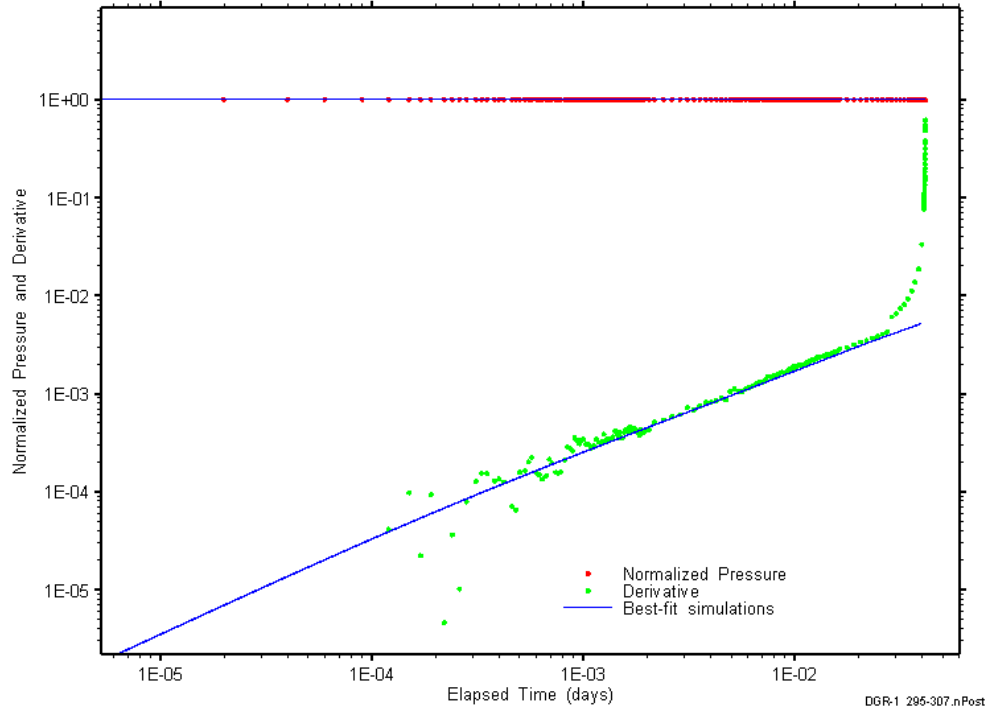


Figure A-8: Log-log plot showing simulations of the DGR1_294.28-306.28 DST flow period Ramey B and derivative response.

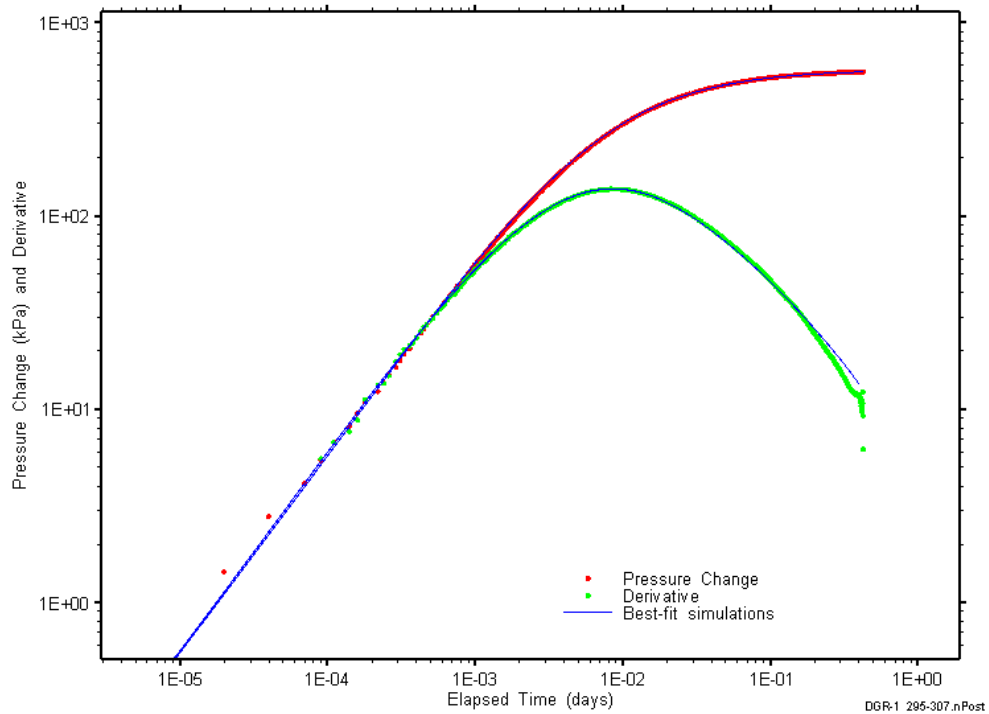


Figure A-9: Log-log plot showing simulations of the DGR1_294.28-306.28 DST shut-in pressure change and derivative response.

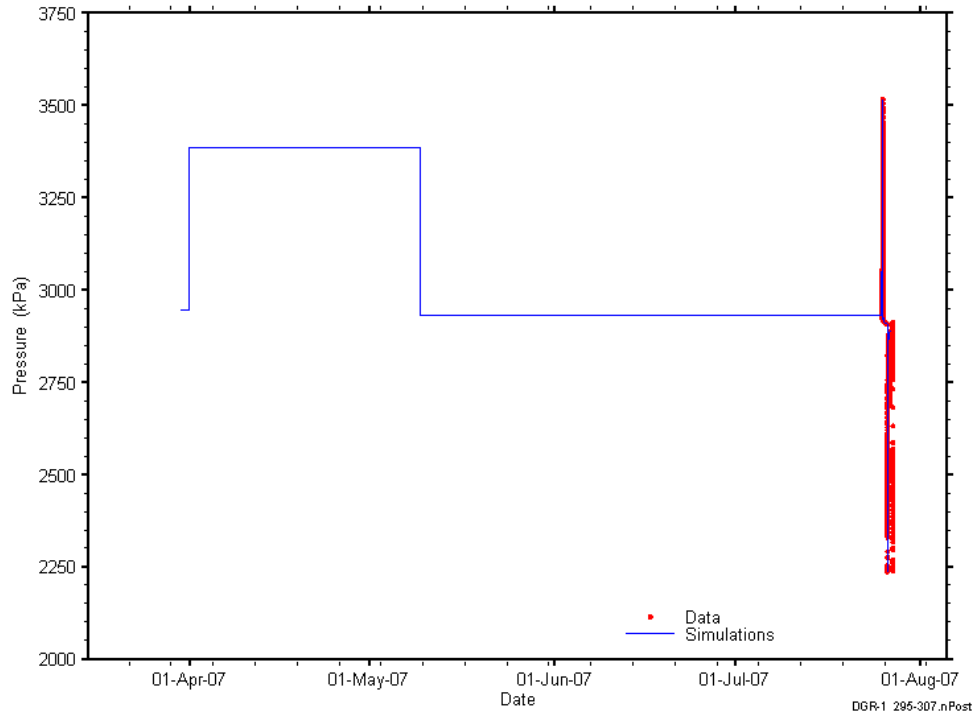


Figure A-10: Linear plot showing simulations of the DGR1_294.28-306.28 pressure response, including pre-test pressure history.

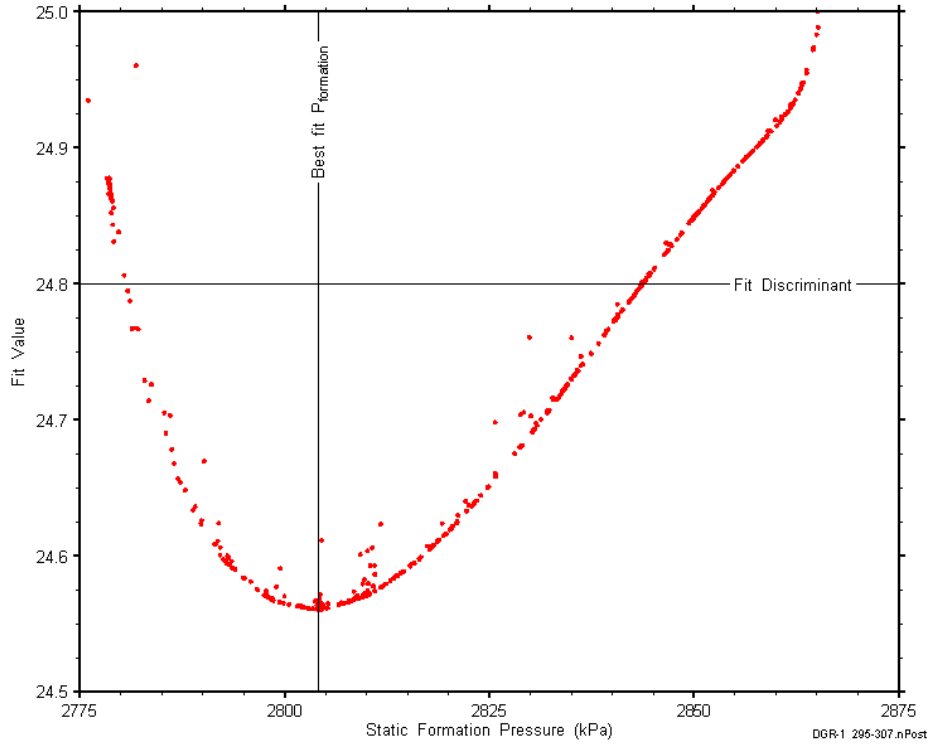


Figure A-11: XY-scatter plot showing the static formation pressure parameter space derived from DGR1_294.28-306.28 perturbation analysis along with the fit discriminant and best fit values.

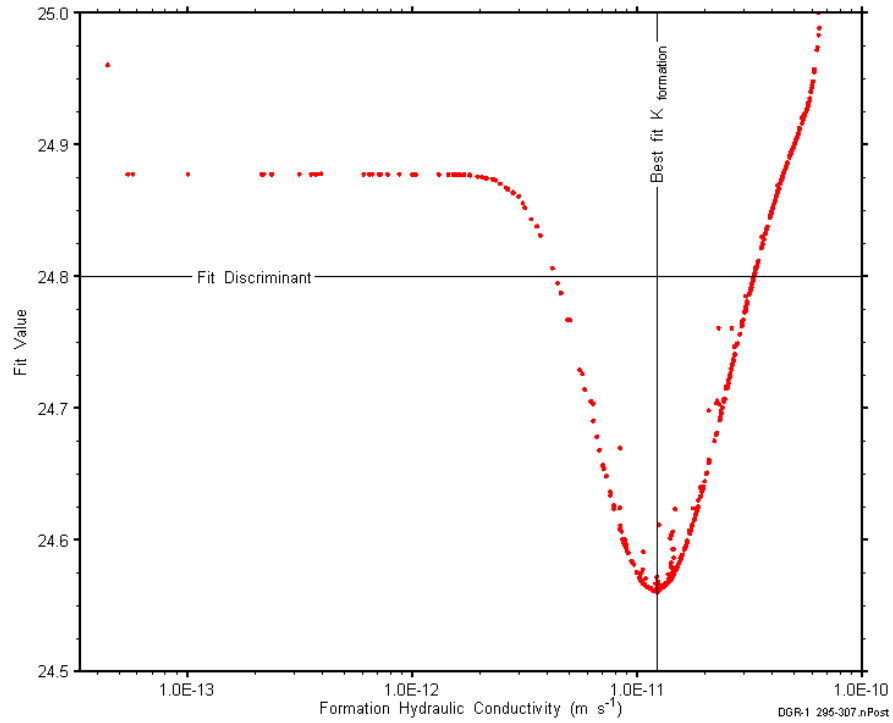


Figure A-12: XY-scatter plot showing the formation hydraulic conductivity parameter space derived from DGR1_294.28-306.28 perturbation analysis along with the fit discriminant and best fit values.

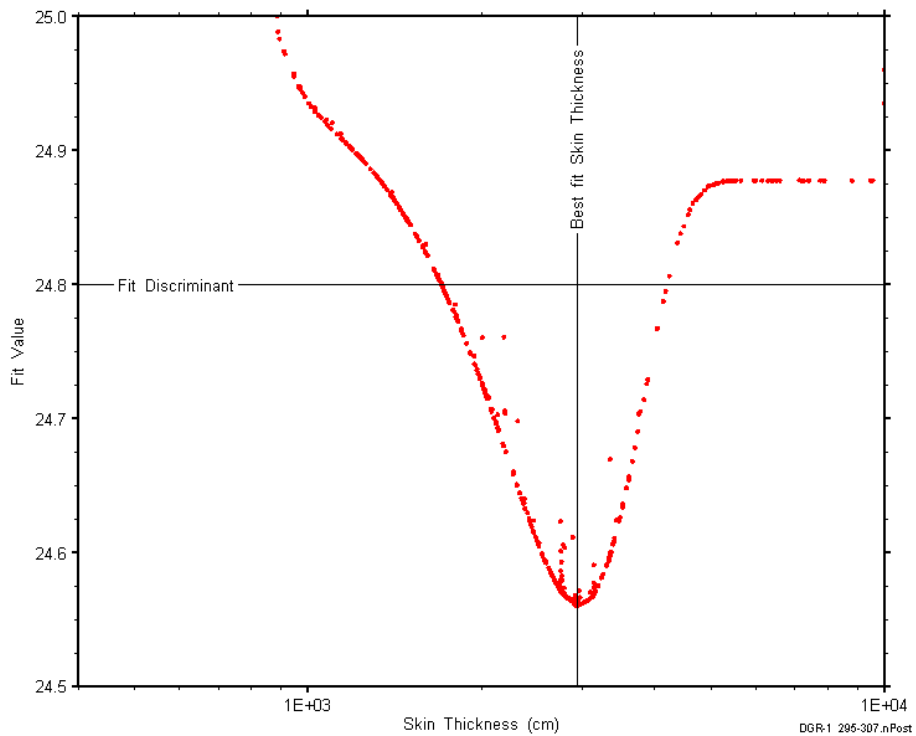


Figure A-13: XY-scatter plot showing the skin-thickness parameter space derived from DGR1_294.28-306.28 perturbation analysis along with the fit discriminant and best fit values.

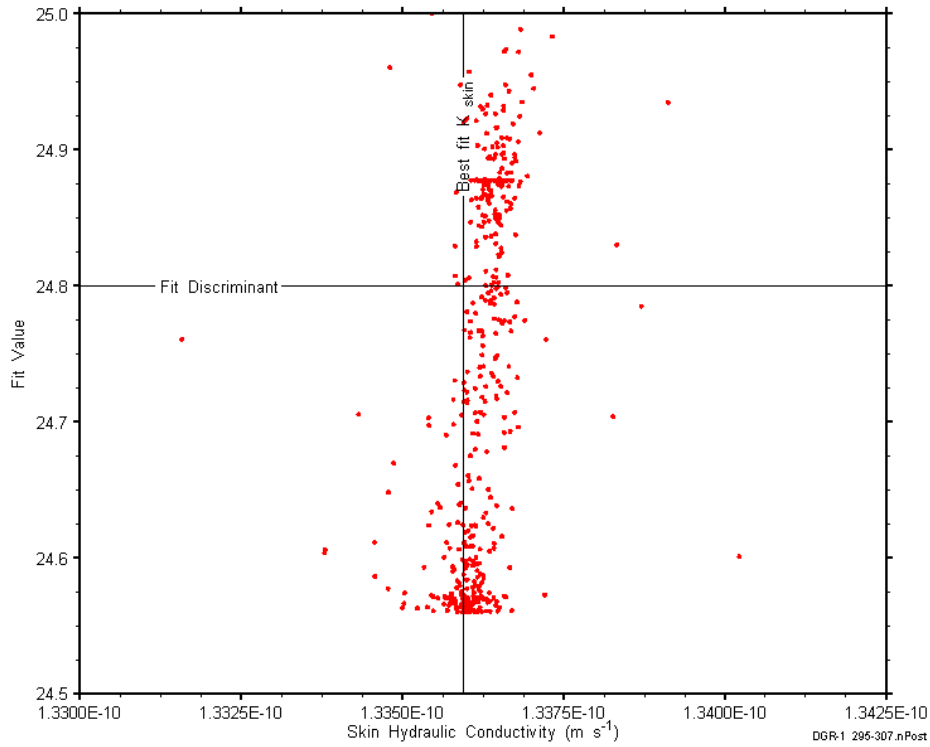


Figure A-14: XY-scatter plot showing the skin hydraulic conductivity parameter space derived from DGR1_294.28-306.28 perturbation analysis along with the fit discriminant and best fit values.

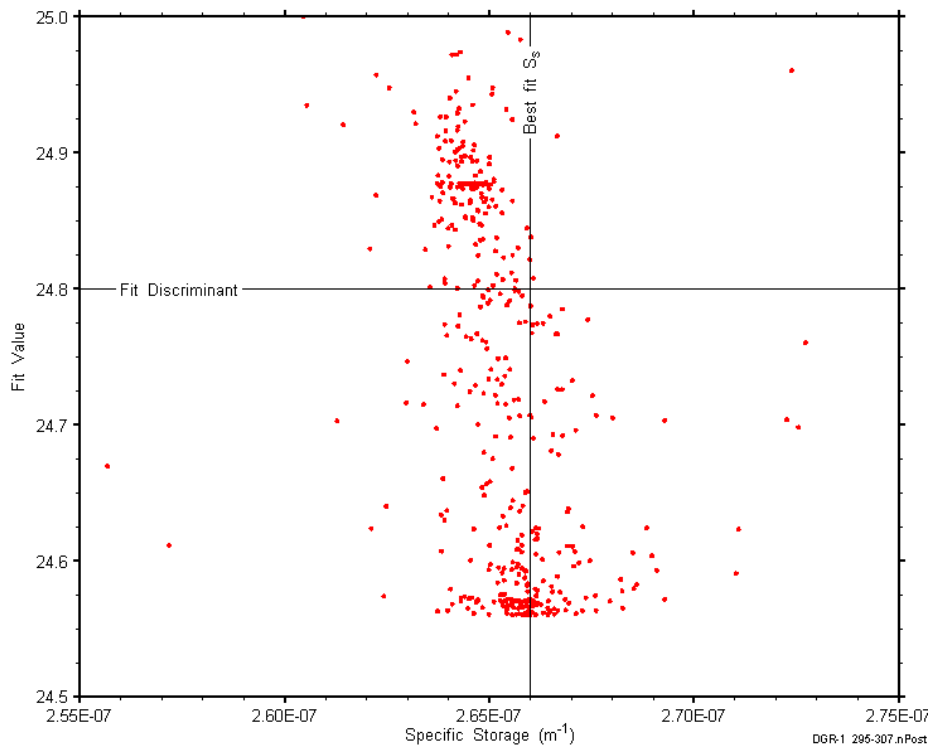


Figure A-15: XY-scatter plot showing the formation specific storage parameter space derived from DGR1_294.28-306.28 perturbation analysis along with the fit discriminant and best fit values.

A.2 348.76-360.76 Salina A1

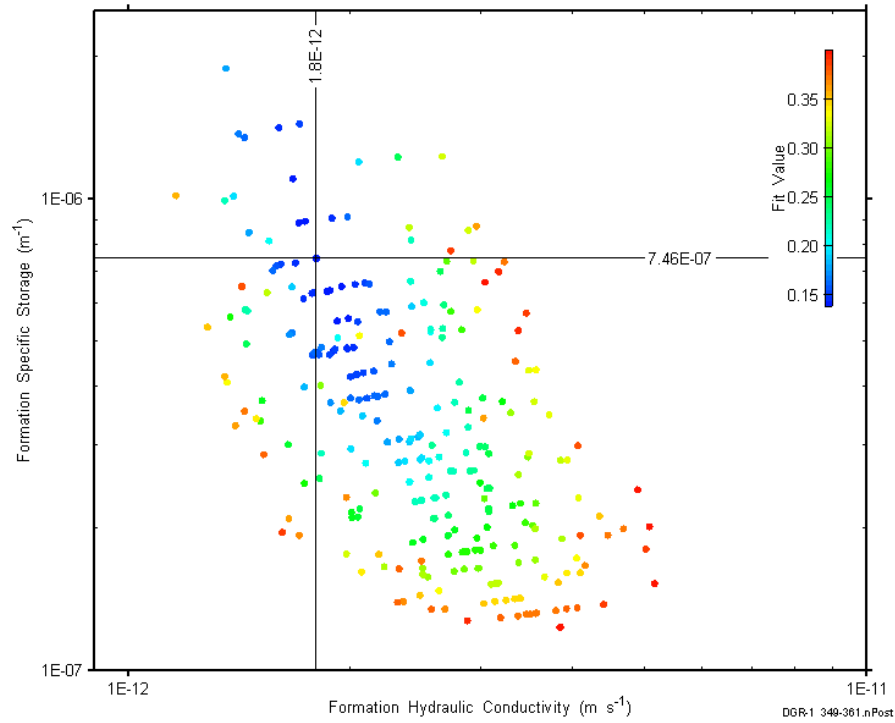


Figure A-16: XY-scatter plot showing estimates of formation hydraulic conductivity and formation specific storage derived from the DGR1_348.76-360.76 perturbation analysis.

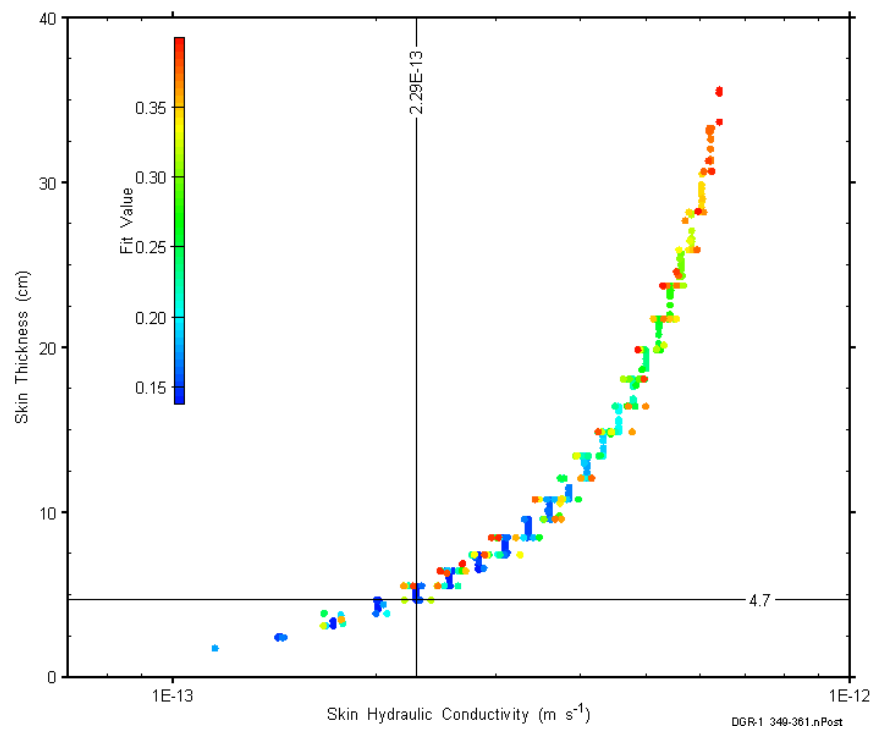


Figure A-17: XY-scatter plot showing estimates of skin hydraulic conductivity and skin thickness derived from the DGR1_348.76-360.76 perturbation analysis.

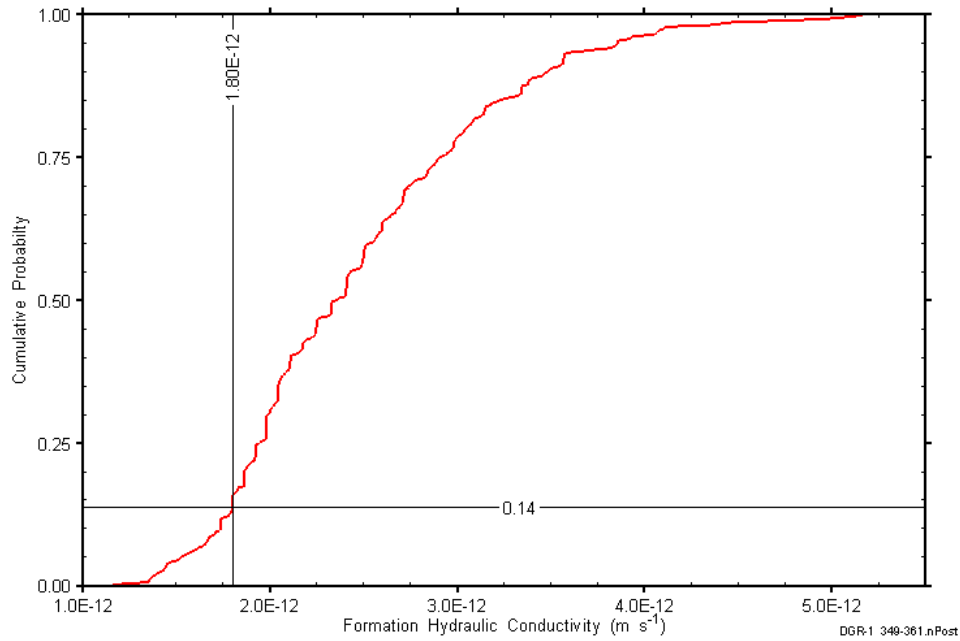


Figure A-18: DGR1_348.76-360.76 formation hydraulic conductivity cumulative distribution function.

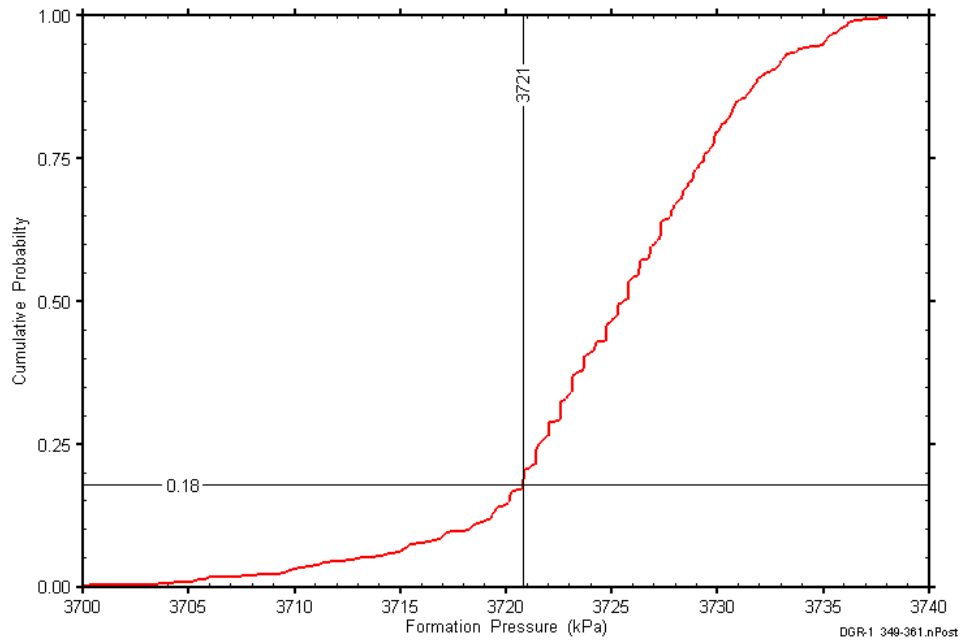


Figure A-19: DGR1_348.76-360.76 static formation pressure cumulative distribution function.

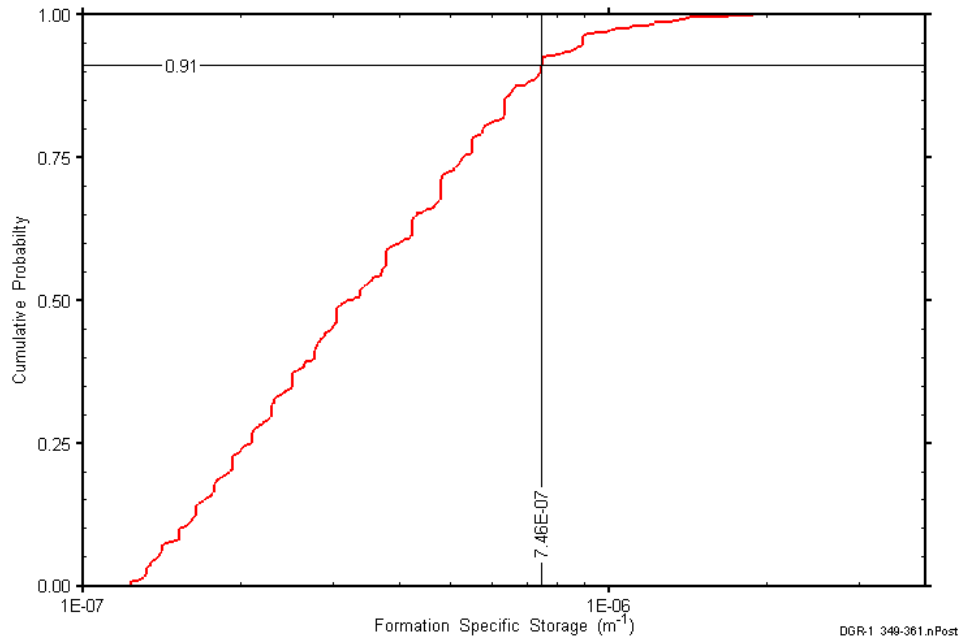


Figure A-20: DGR1_348.76-360.76 formation specific storage cumulative distribution function.

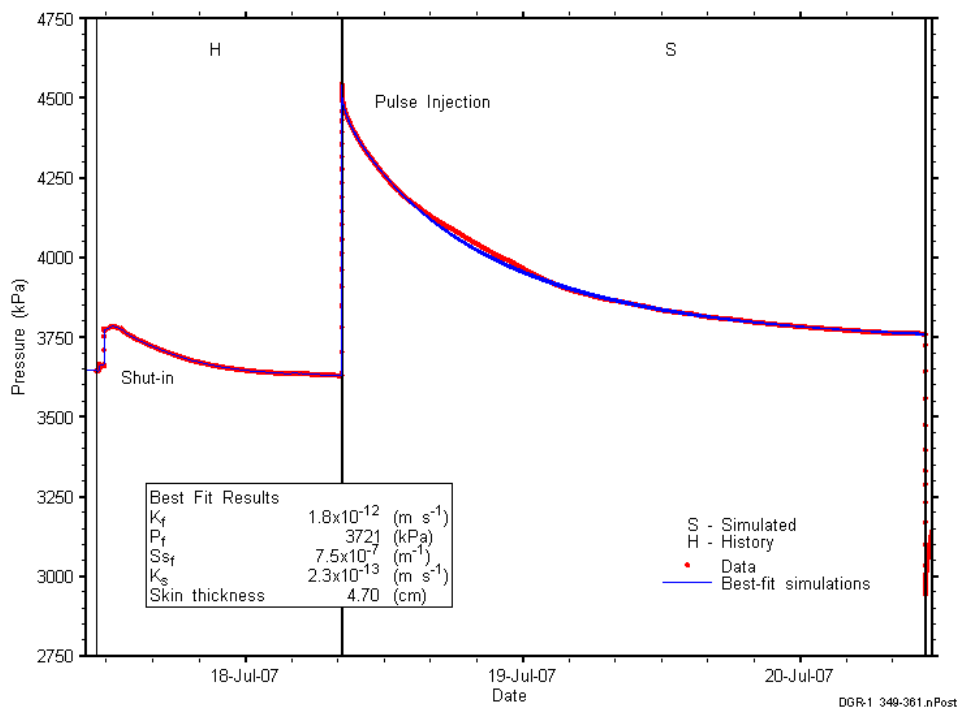


Figure A-21: Linear plot showing details of simulations of the DGR1_348.76-360.76 pressure response.

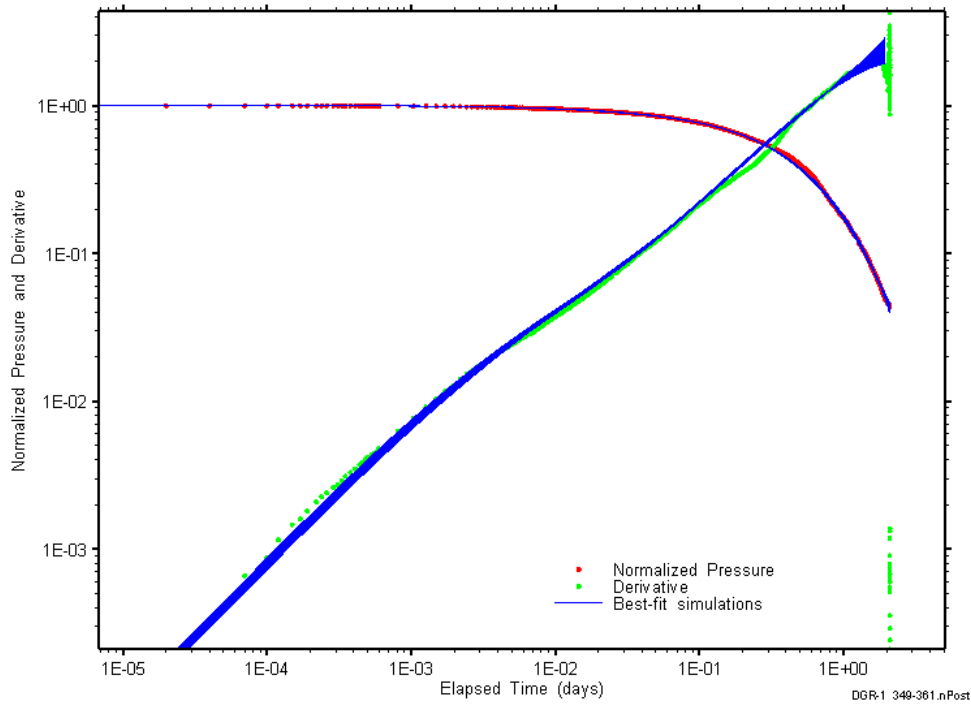


Figure A-22: Log-log plot showing simulations of the DGR1_348.76-360.76 pulse withdrawal Ramey B and derivative response.

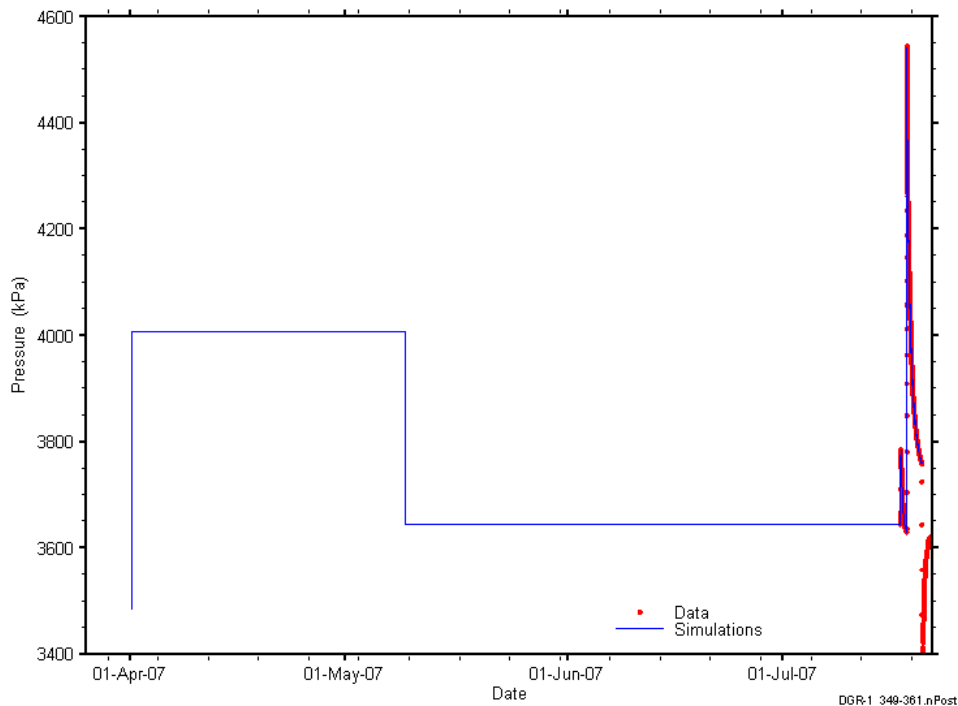


Figure A-23: Linear plot showing simulations of the DGR1_348.76-360.76 pressure response, including pre-test pressure history.

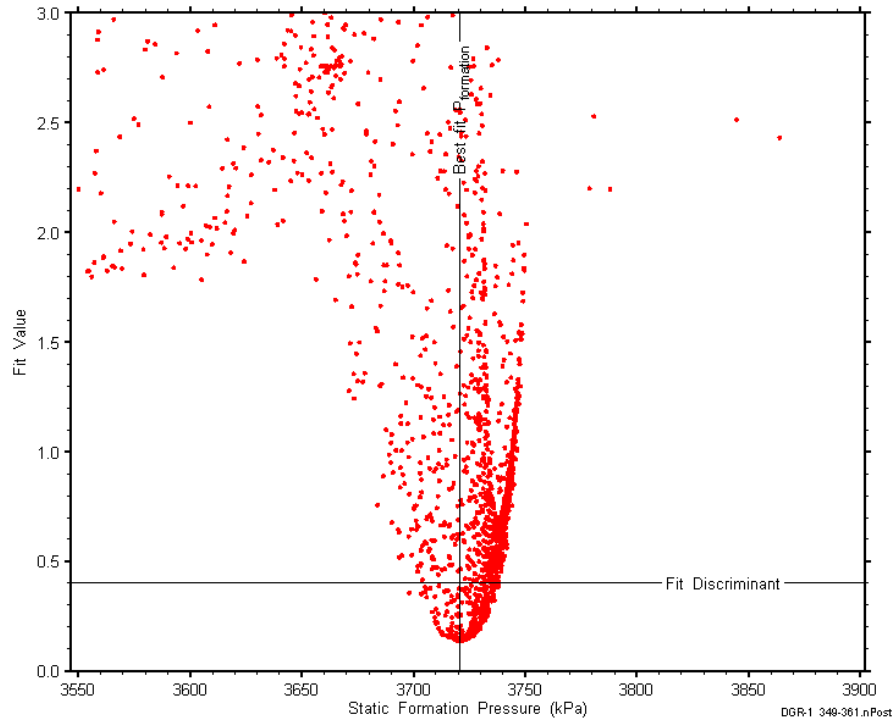


Figure A-24: XY-scatter plot showing the static formation pressure parameter space derived from DGR1_348.76-360.76 perturbation analysis along with the fit discriminant and best fit values.

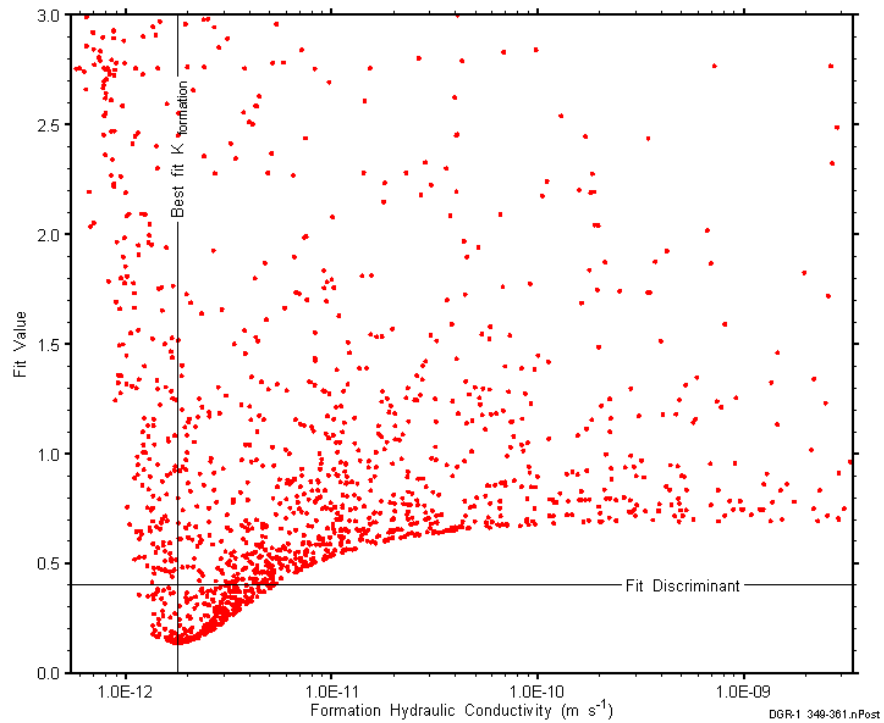


Figure A-25: XY-scatter plot showing the formation hydraulic conductivity parameter space derived from DGR1_348.76-360.76 perturbation analysis along with the fit discriminant and best fit values.

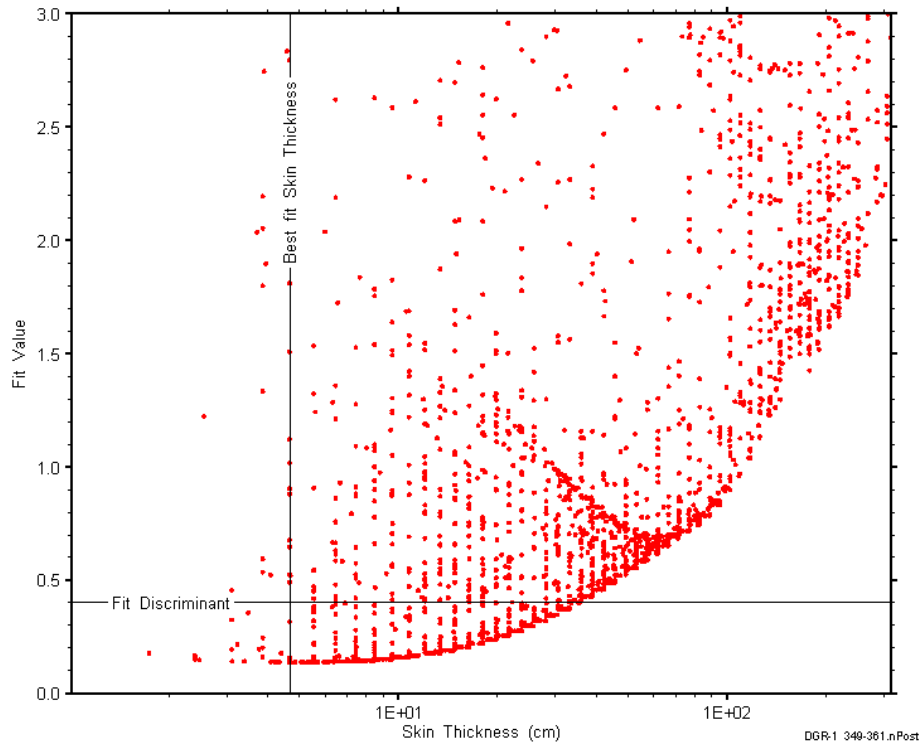


Figure A-26: XY-scatter plot showing the skin-thickness parameter space derived from DGR1_348.76-360.76 perturbation analysis along with the fit discriminant and best fit values.

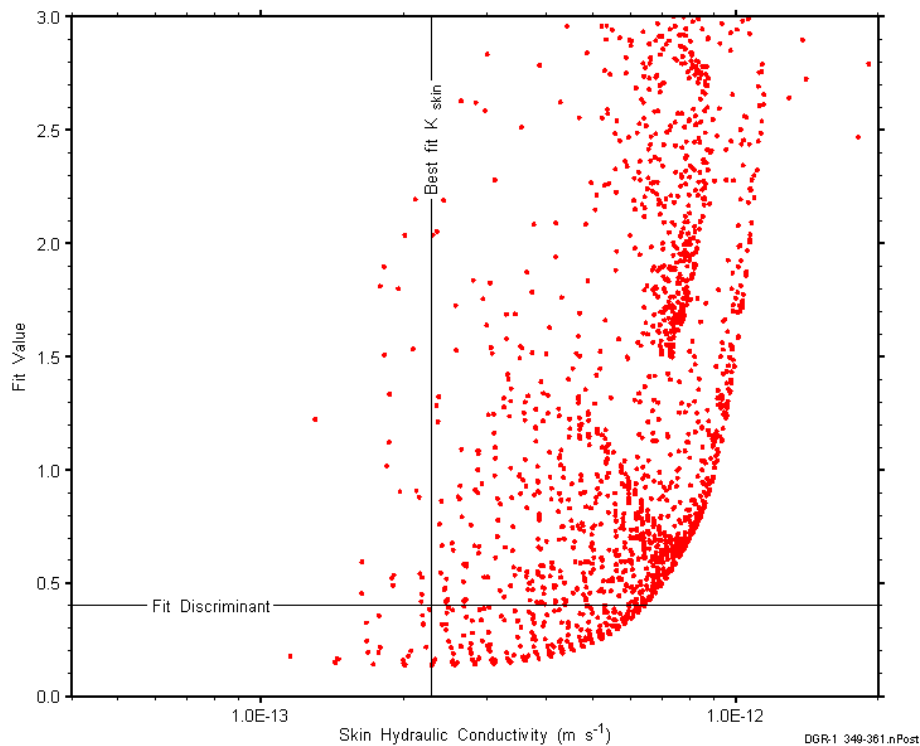


Figure A-27: XY-scatter plot showing the skin hydraulic conductivity parameter space derived from DGR1_348.76-360.76 perturbation analysis along with the fit discriminant and best fit values.

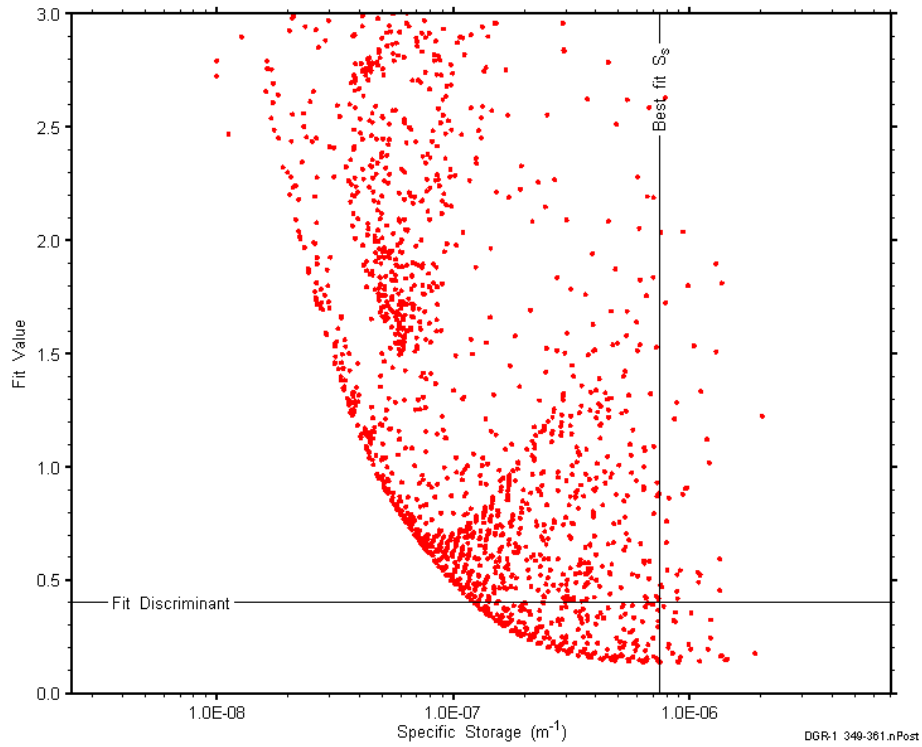


Figure A-28: XY-scatter plot showing the formation specific storage parameter space derived from DGR1_294.28-306.28 perturbation analysis along with the fit discriminant and best fit values.

A.3 404.37-416.37 Lions Head-Fossil Hill-Cabot Head

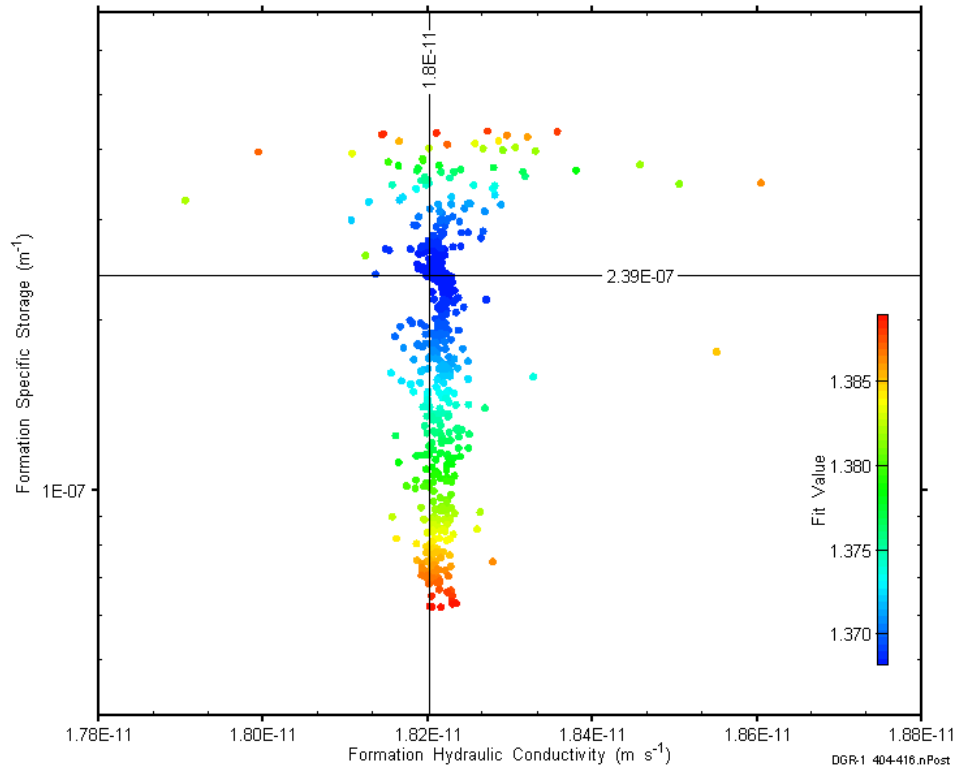


Figure A-29: XY-scatter plot showing estimates of formation hydraulic conductivity and formation specific storage derived from the DGR1_404.37-416.37 perturbation analysis.

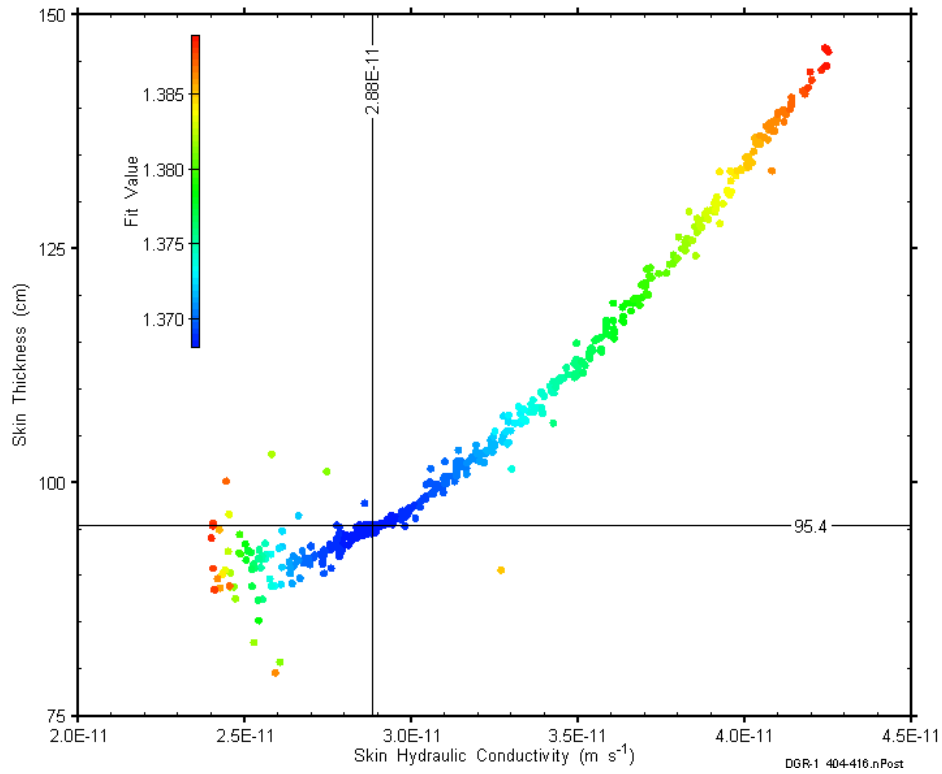


Figure A-30: XY-scatter plot showing estimates of skin hydraulic conductivity and skin thickness derived from the DGR1_404.37-416.37 perturbation analysis.

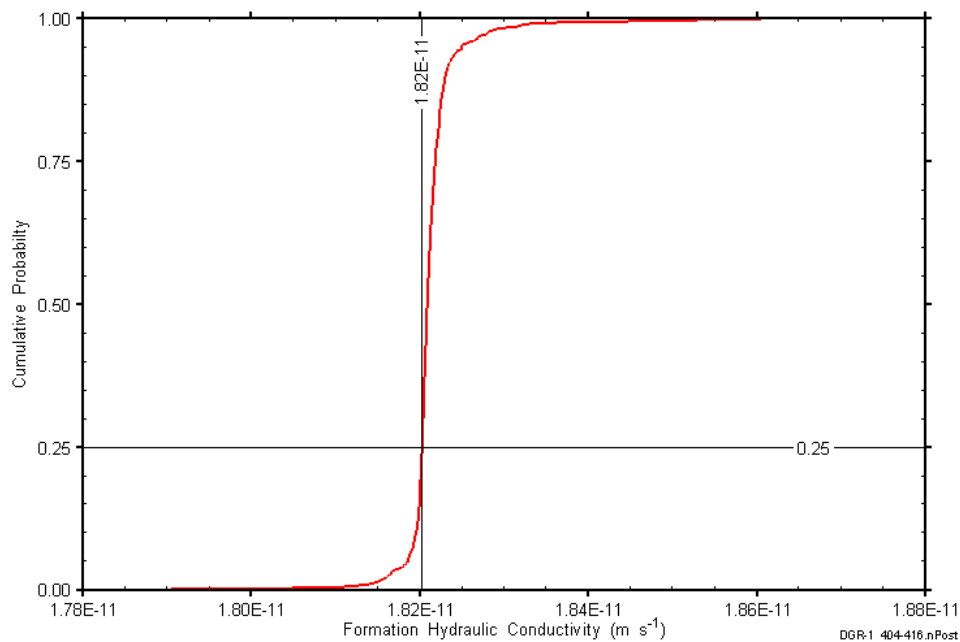


Figure A-31: DGR1_404.37-416.37 formation hydraulic conductivity cumulative distribution function.

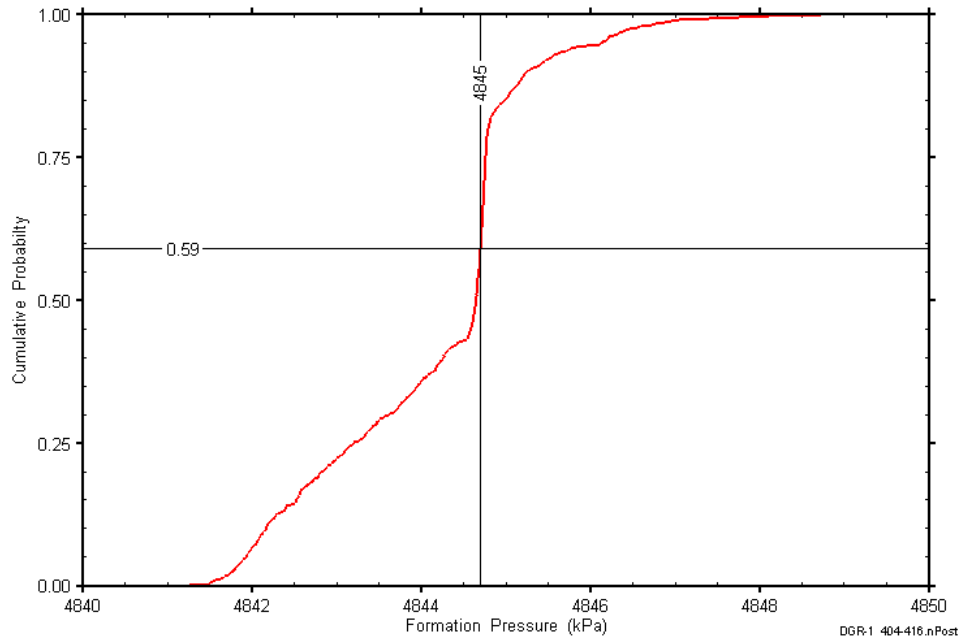


Figure A-32: DGR1_404.37-416.37 static formation pressure cumulative distribution function.

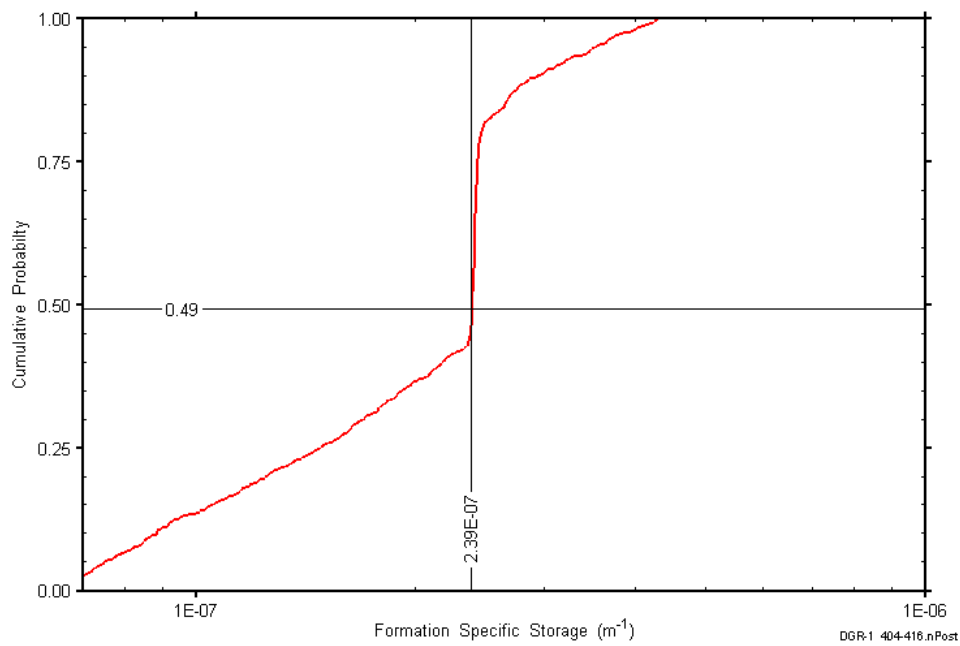


Figure A-33: DGR1_404.37-416.37 formation specific storage cumulative distribution function.

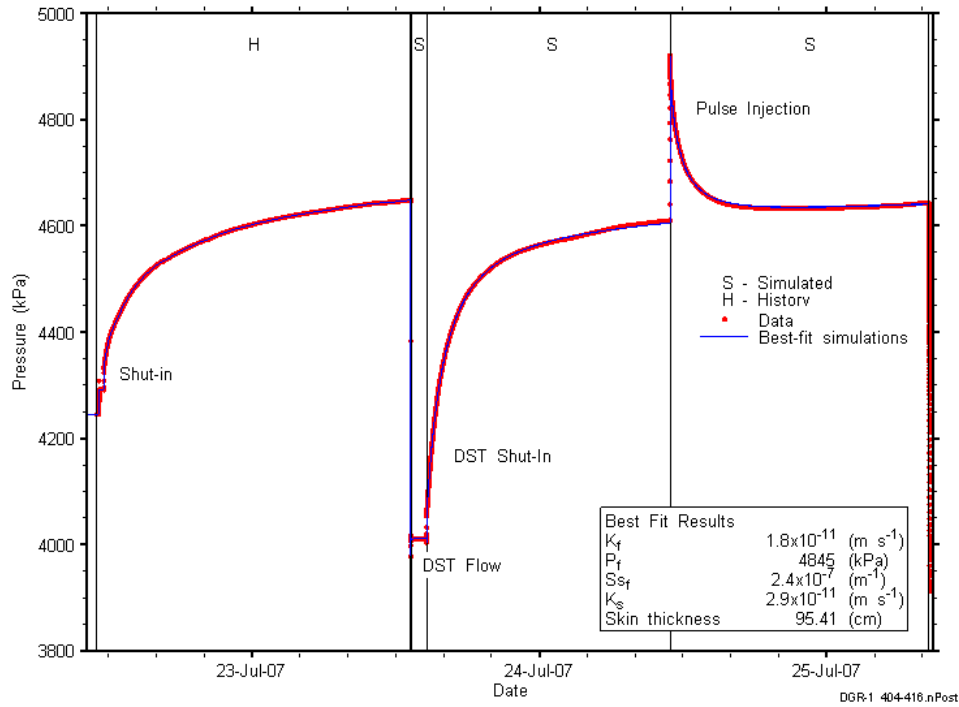


Figure A-34: Linear plot showing details of simulations of the DGR1_404.37-416.37 pressure response.

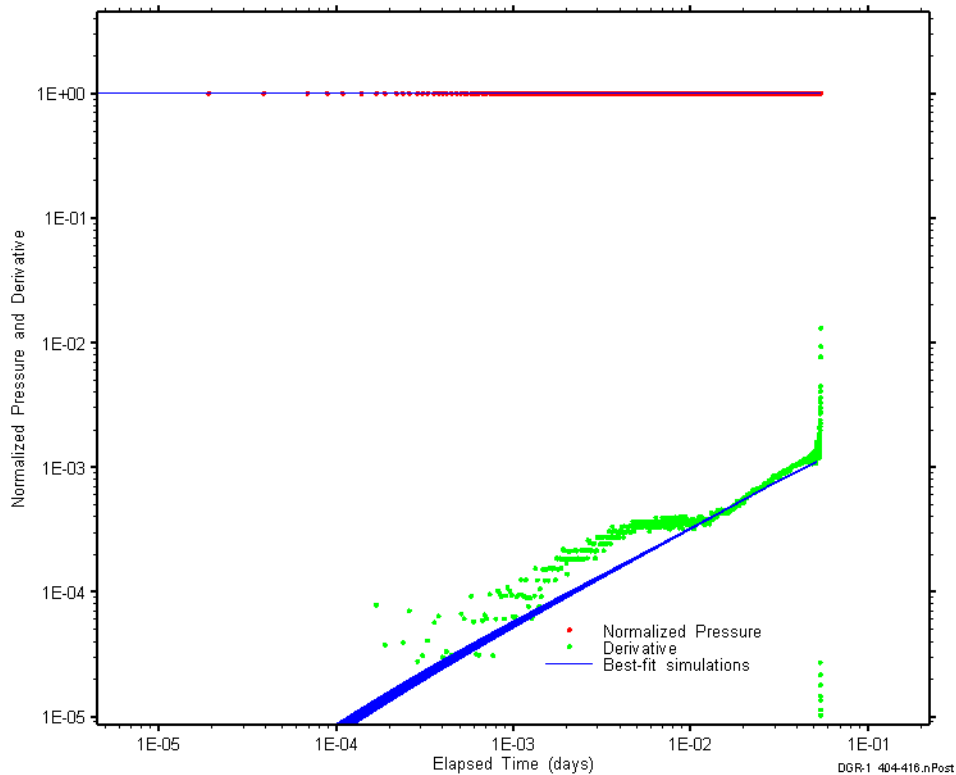


Figure A-35: Log-log plot showing simulations of the DGR1_404.37-416.37 DST flow period Ramey B and derivative response.

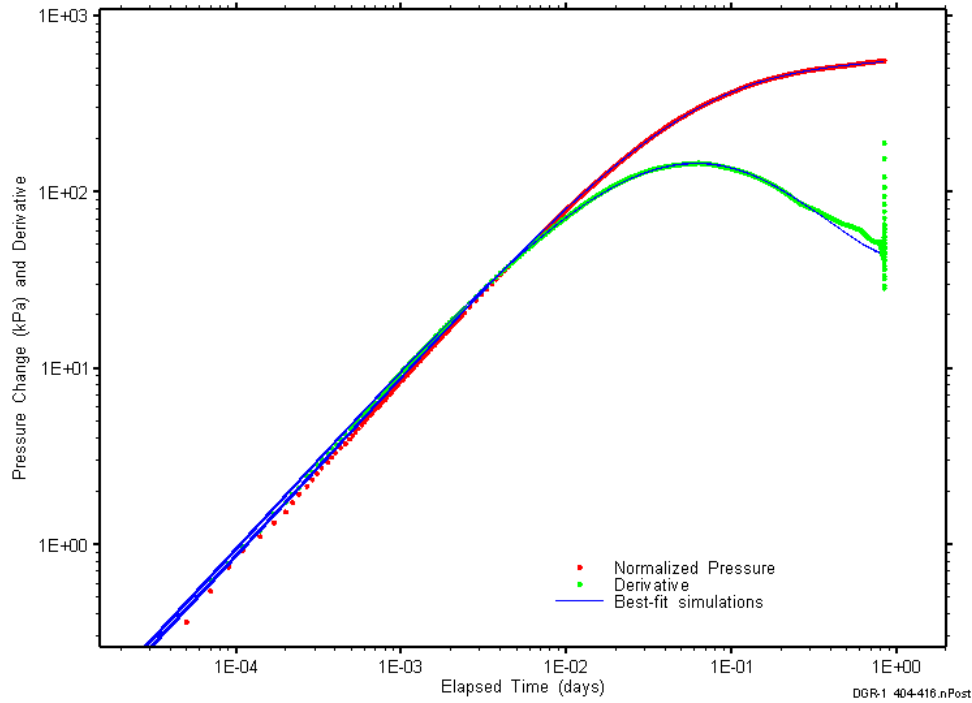


Figure A-36: Log-log plot showing simulations of the DGR1_404.37-416.37 DST shut-in pressure change and derivative response.

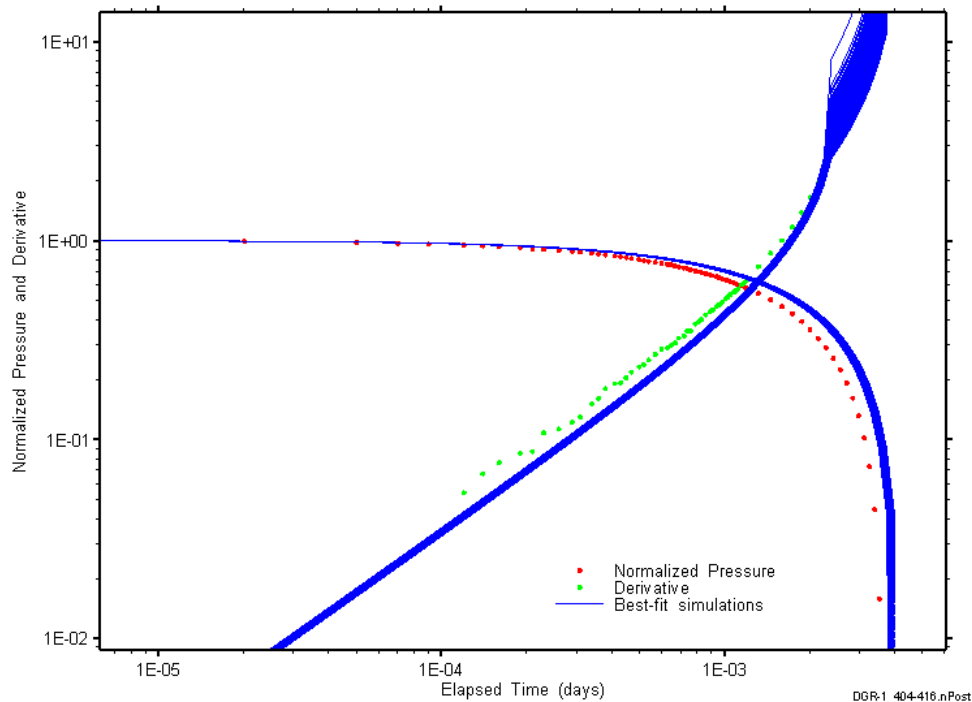


Figure A-37: Log-log plot showing simulations of the DGR1_404.37-416.37 pulse withdrawal Ramey B and derivative response.

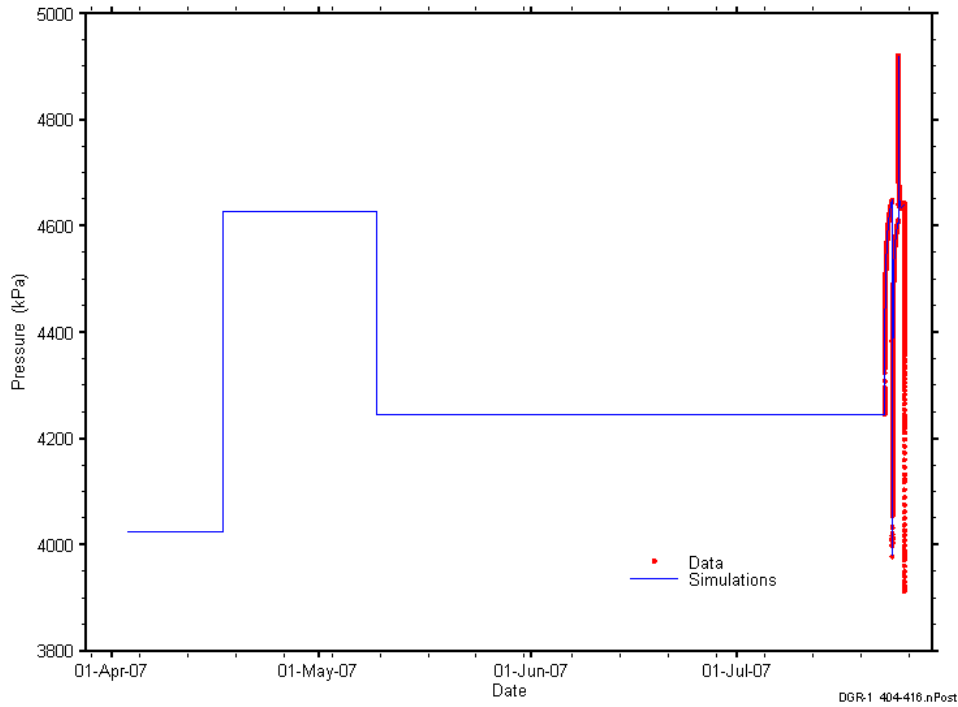


Figure A-38: Linear plot showing simulations of the DGR1_404.37-416.37 pressure response, including pre-test pressure history.

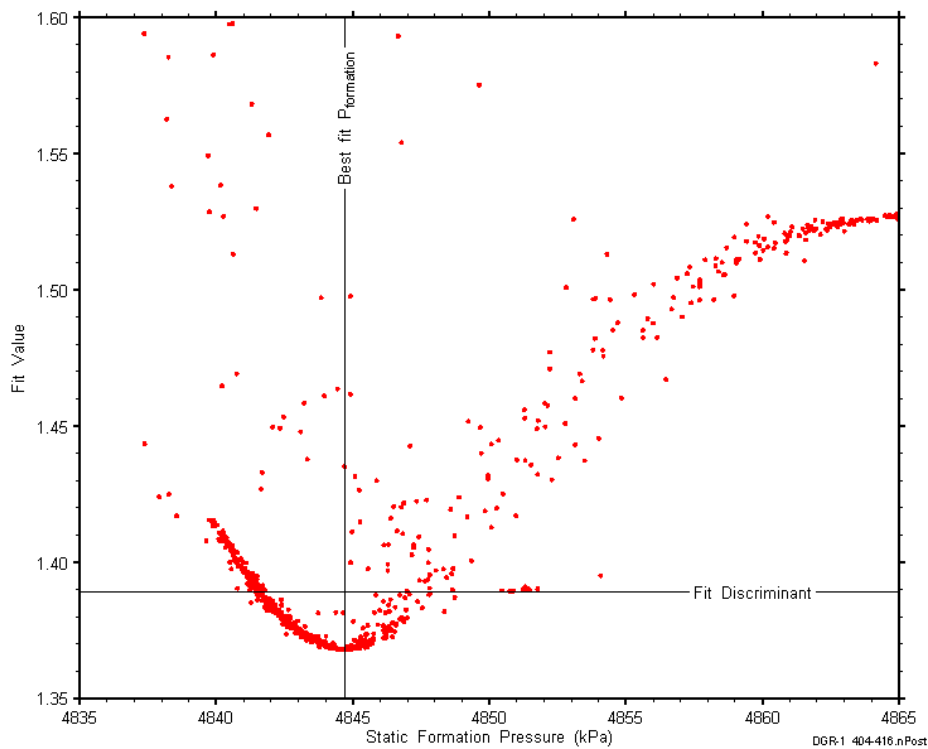


Figure A-39: XY-scatter plot showing the static formation pressure parameter space derived from DGR1_404.37-416.37 perturbation analysis along with the fit discriminant and best fit values.

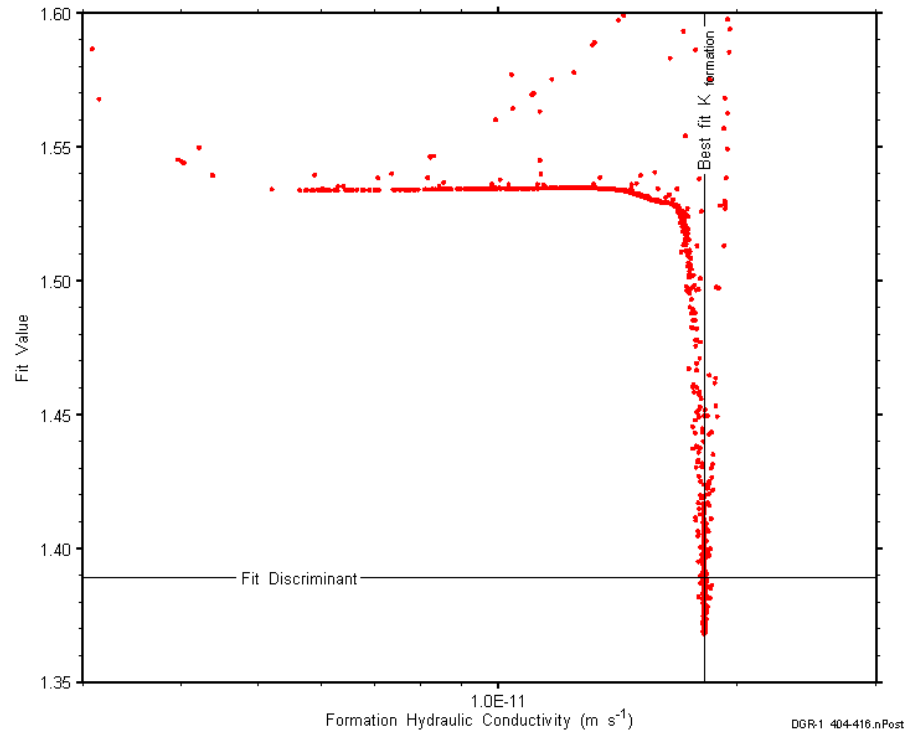


Figure A-40: XY-scatter plot showing the formation hydraulic conductivity parameter space derived from DGR1_404.37-416.37 perturbation analysis along with the fit discriminant and best fit values.

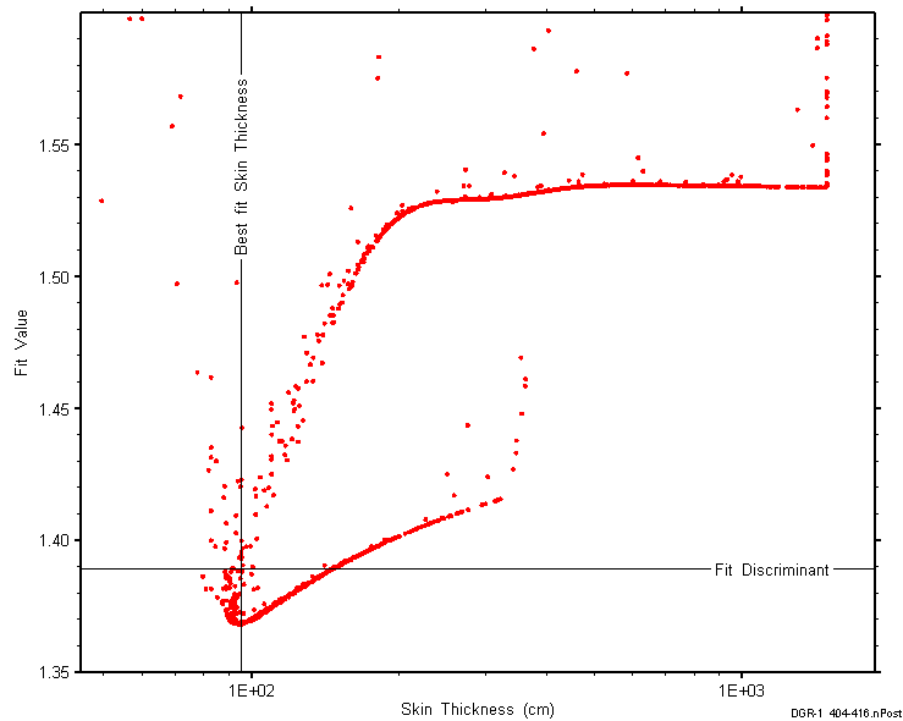


Figure A-41: XY-scatter plot showing the skin-thickness parameter space derived from DGR1_404.37-416.37 perturbation analysis along with the fit discriminant and best fit values.

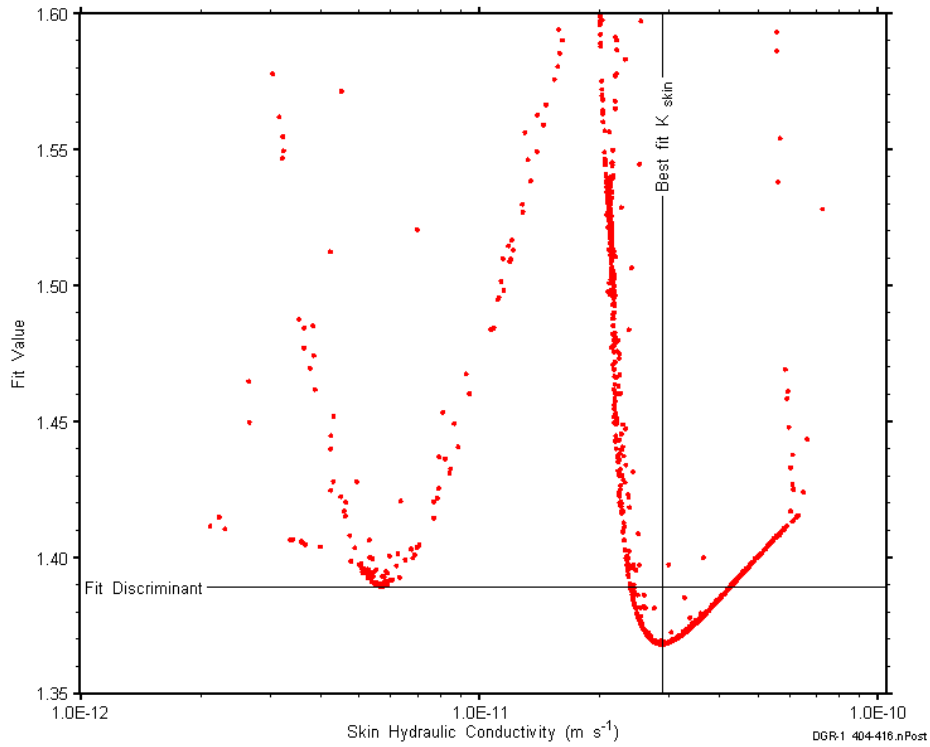


Figure A-42: XY-scatter plot showing the skin hydraulic conductivity parameter space derived from DGR1_404.37-416.37 perturbation analysis along with the fit discriminant and best fit values.

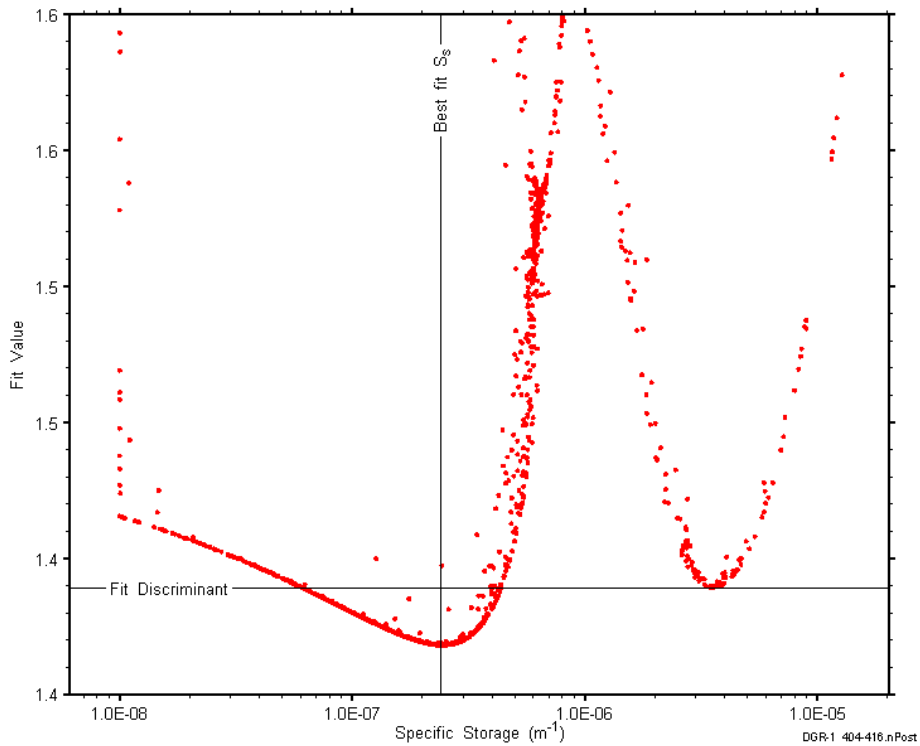


Figure A-43: XY-scatter plot showing the formation specific storage parameter space derived from DGR1_404.37-416.37 perturbation analysis along with the fit discriminant and best fit values.

Appendix B. - DGR-2 Plots

Various plots of results from the DGR-2 analyses are shown below. These plots include XY-scatter plots of the fitting-parameter estimates, linear and log-log horsetail plots of the simulated pressure responses showing field-data matches, K_f , P_f , and S_s cumulative distribution functions, and parameter-space plots showing the characteristics of the minima for each of the fitting parameters.

B.1 457.85-488.35 Queenston

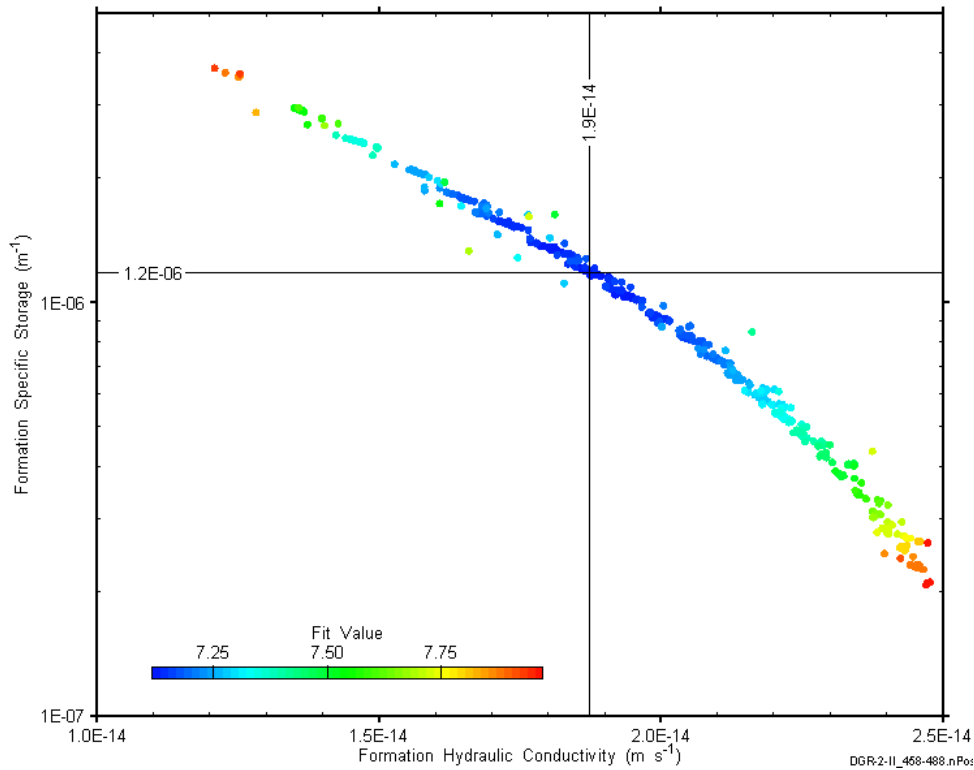


Figure B-1: XY-scatter plot showing estimates of formation hydraulic conductivity and formation specific storage derived from the DGR2_457.85-488.35 perturbation analysis.

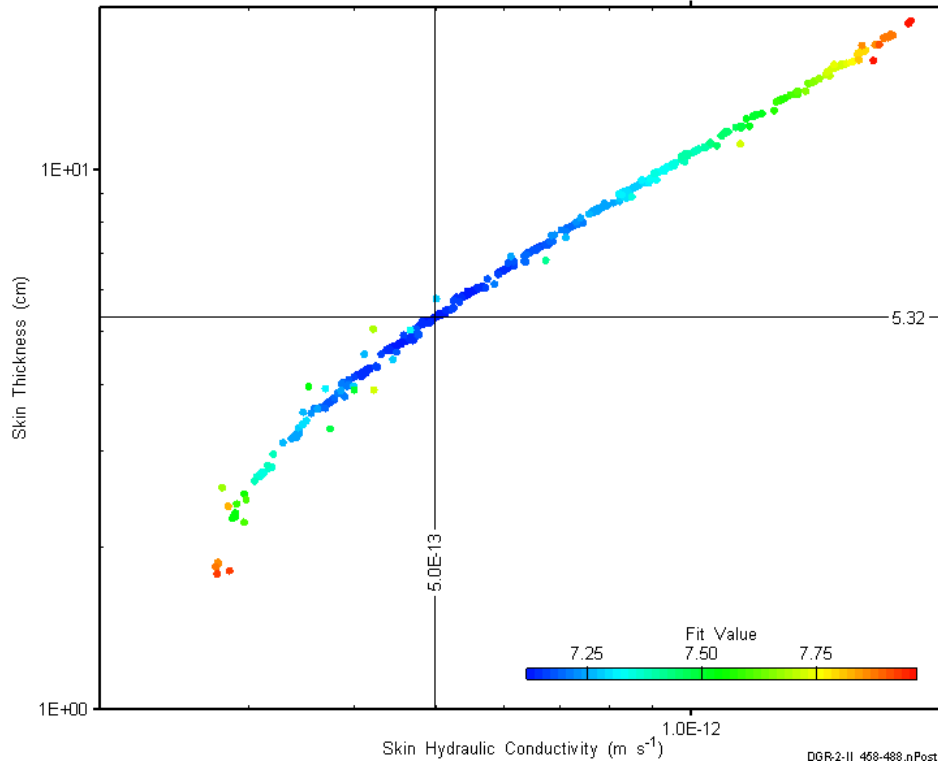


Figure B-2: XY-scatter plot showing estimates of skin hydraulic conductivity and skin thickness derived from the DGR2_457.85-488.35 perturbation analysis.

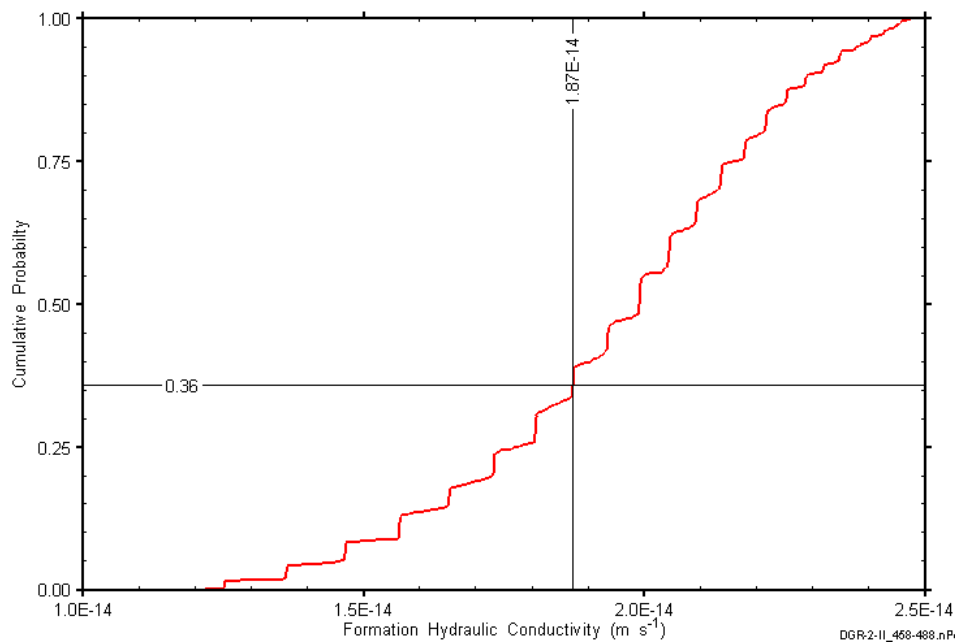


Figure B-3: DGR2_457.85-488.35 formation hydraulic conductivity cumulative distribution function.

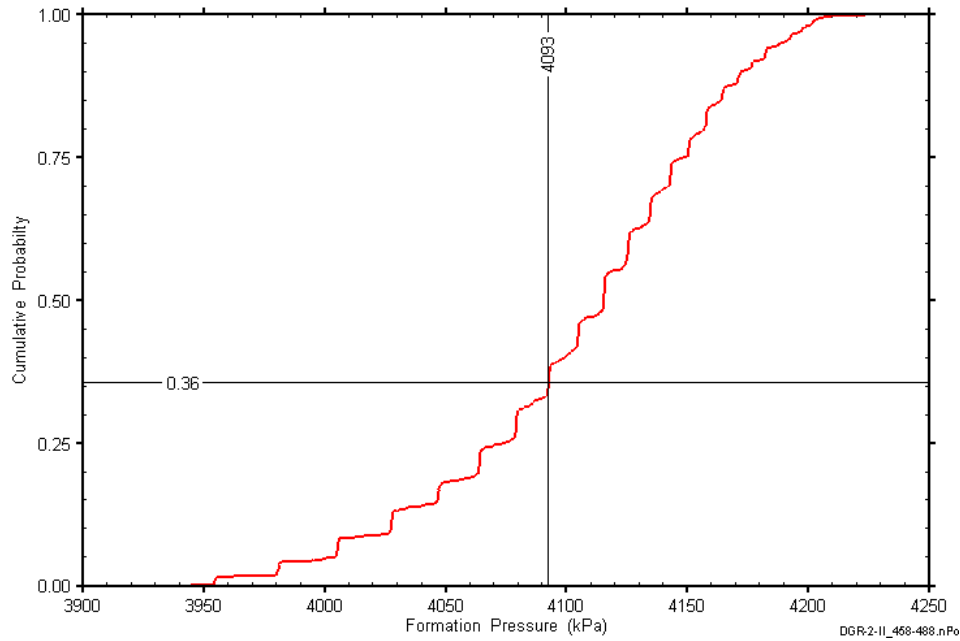


Figure B-4: DGR2_457.85-488.35 static formation pressure cumulative distribution function.

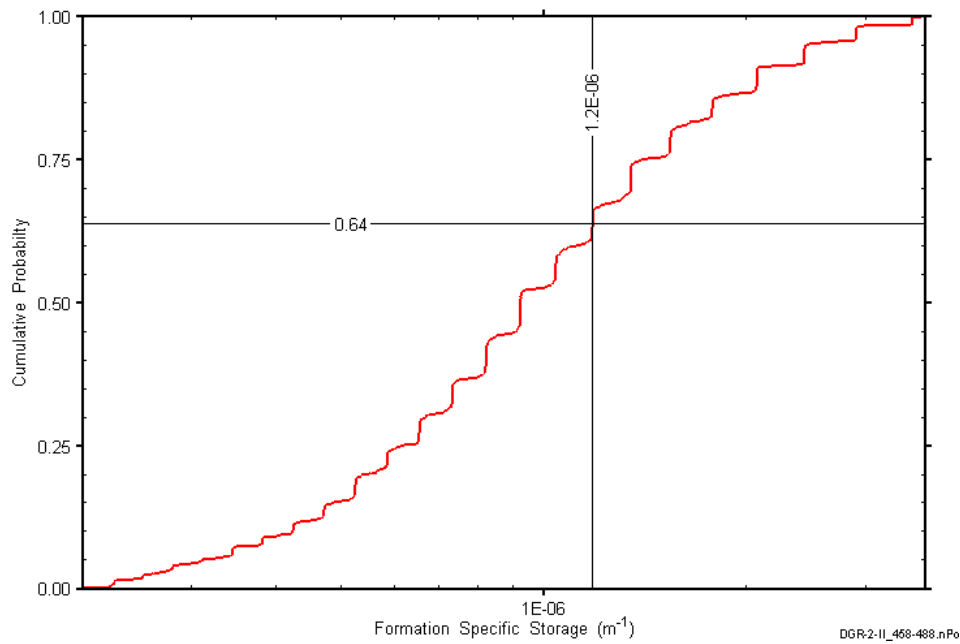


Figure B-5: DGR2_457.85-488.35 formation specific storage cumulative distribution function.

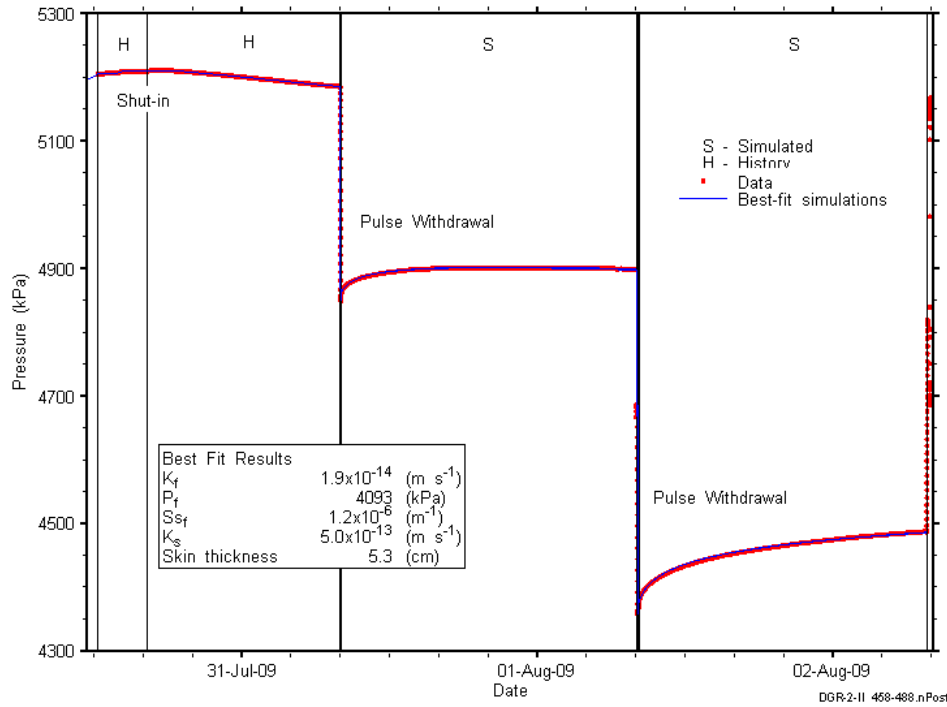


Figure B-6: Linear plot showing details of simulations of the DGR2_457.85-488.35 pressure response.

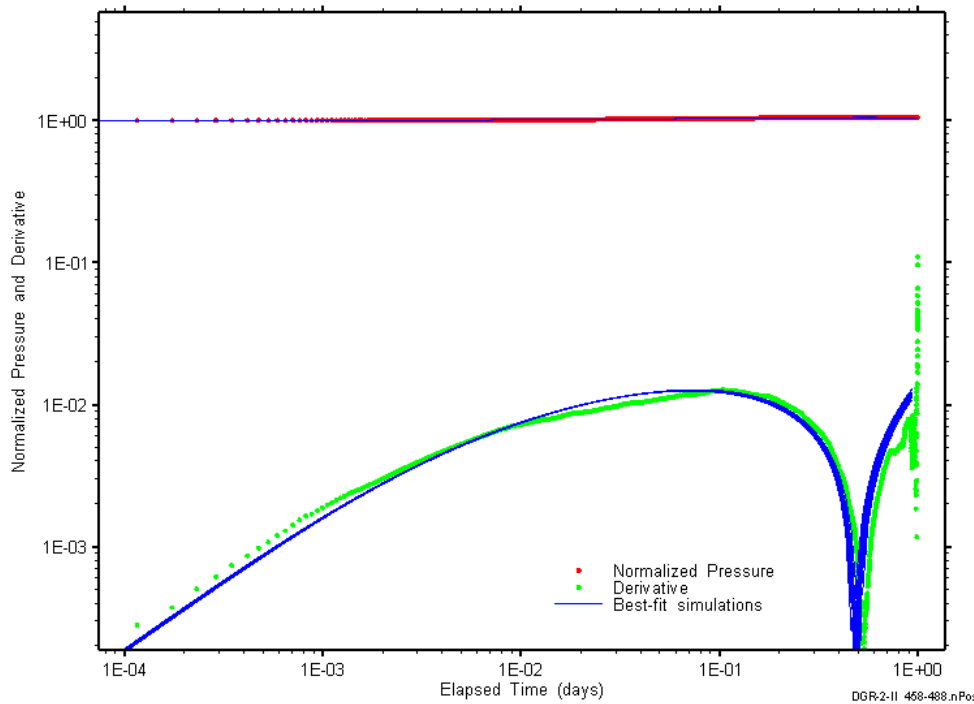


Figure B-7: Log-log plot showing simulations of the DGR2_457.85-488.35 PW1 Ramey B and derivative response.

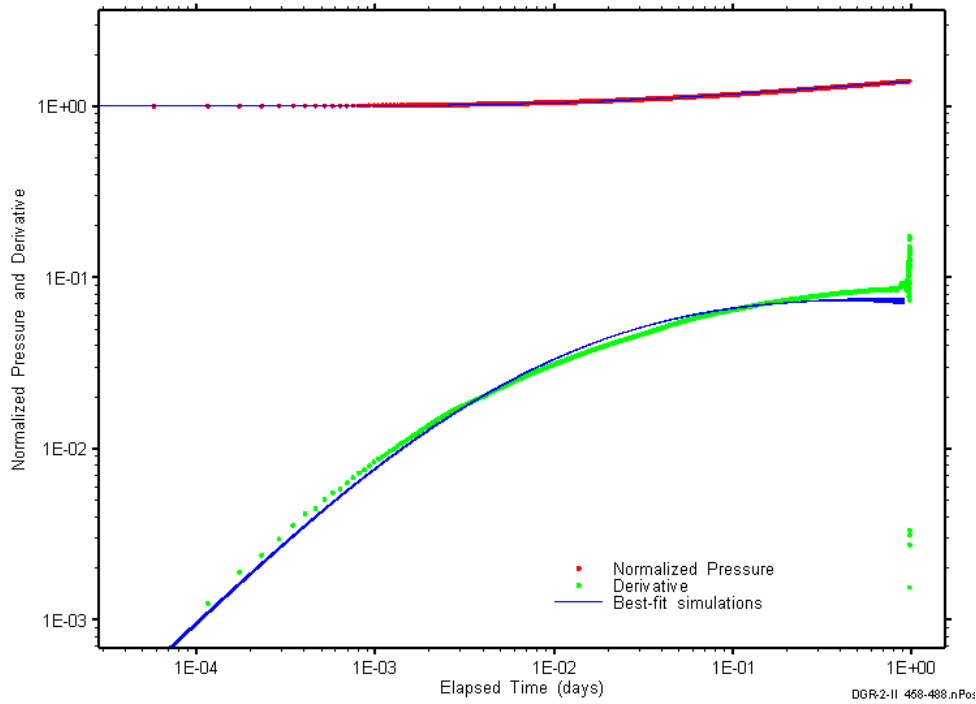


Figure B-8: Log-log plot showing simulations of the DGR2_457.85-488.35 PW2 Ramey B and derivative response.

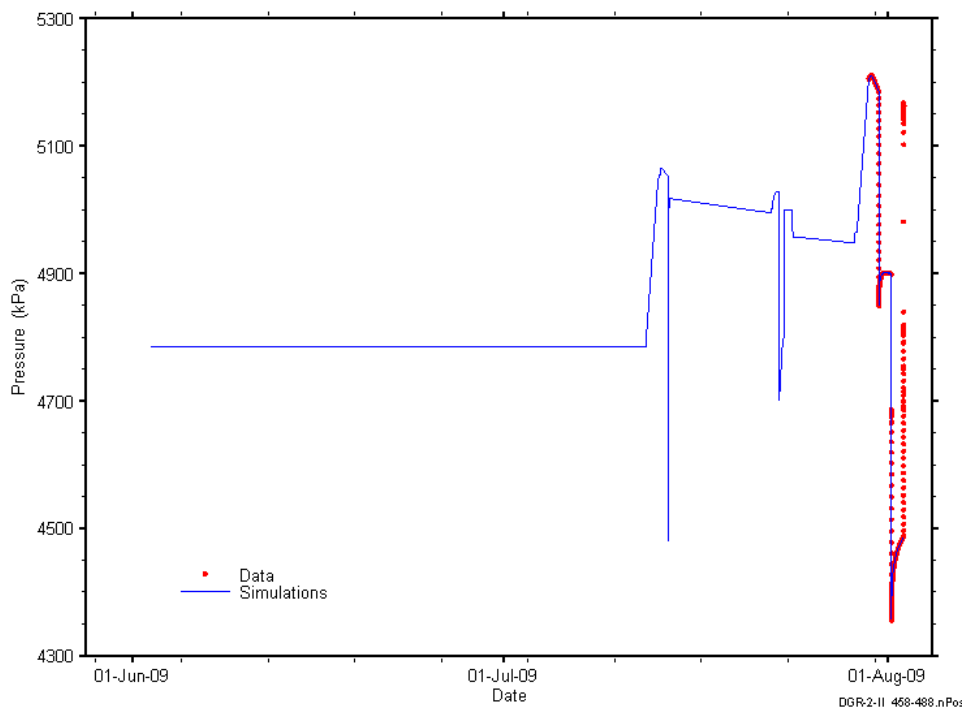


Figure B-9: Linear plot showing simulations of the DGR2_457.85-488.35 pressure response, including pre-test pressure history.

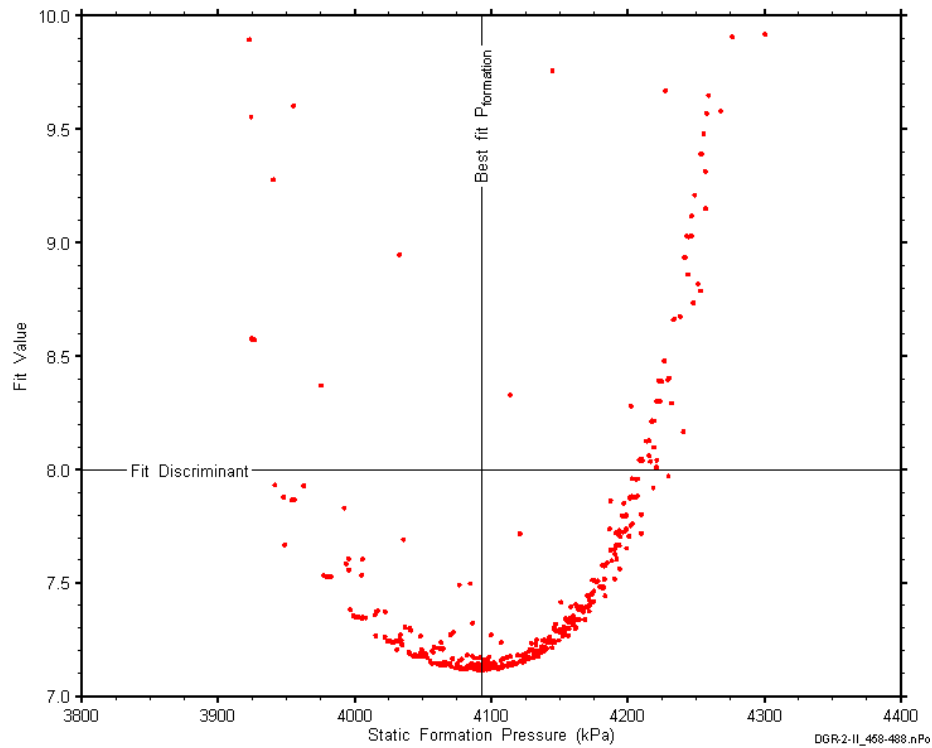


Figure B-10: XY-scatter plot showing the static formation pressure parameter space derived from DGR2_457.85-488.35 perturbation analysis along with the fit discriminant and best fit values.

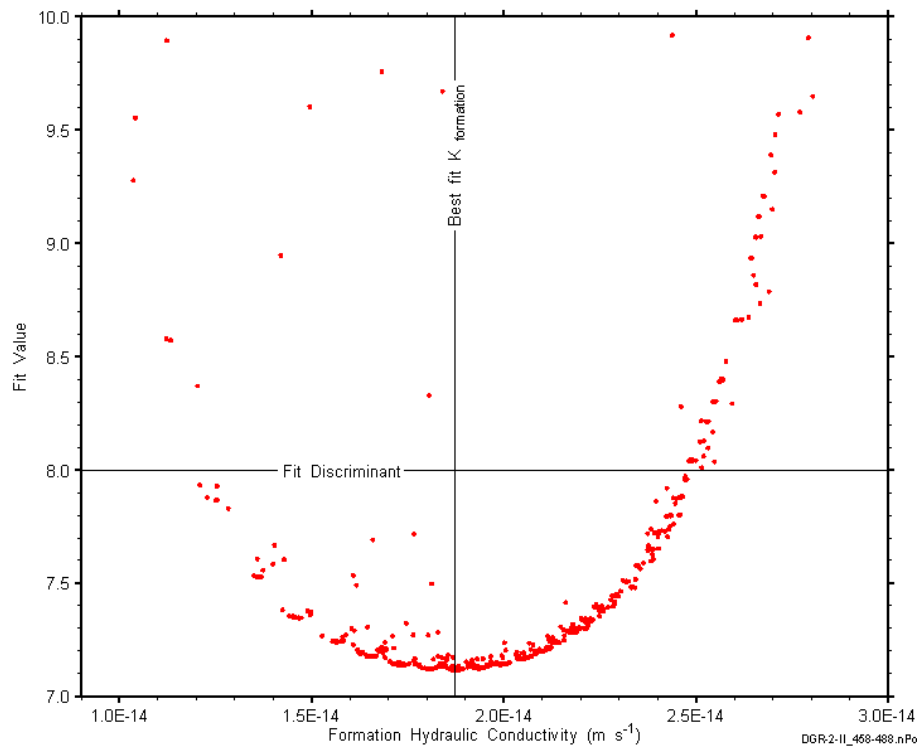


Figure B-11: XY-scatter plot showing the formation hydraulic conductivity parameter space derived from DGR2_457.85-488.35 perturbation analysis along with the fit discriminant and best fit values.

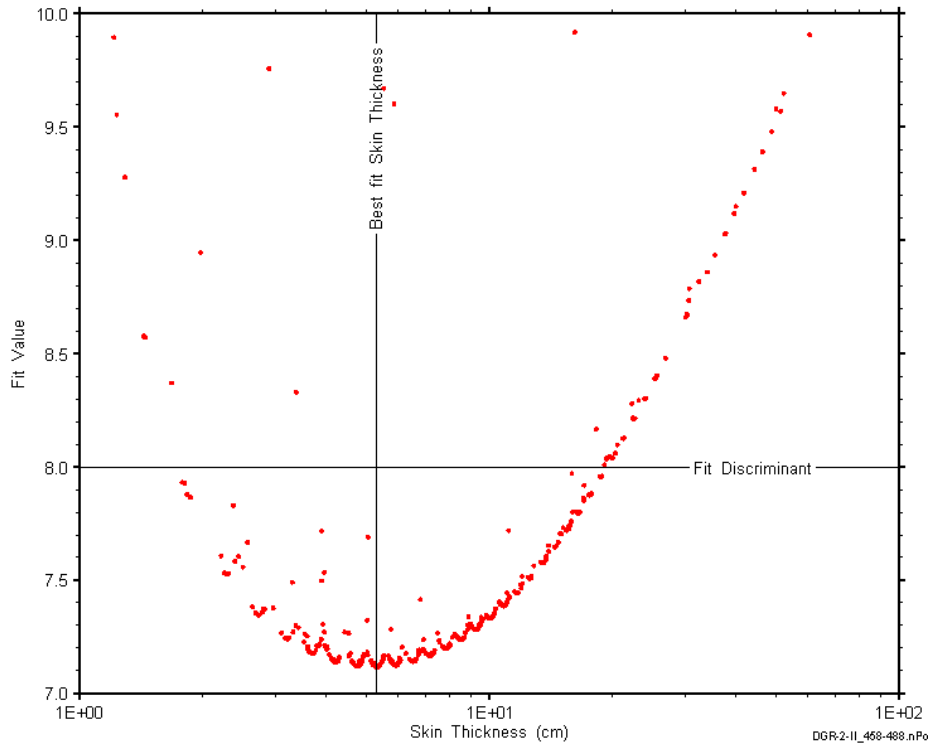


Figure B-12: XY-scatter plot showing the skin-thickness parameter space derived from DGR2_457.85-488.35 perturbation analysis along with the fit discriminant and best fit values.

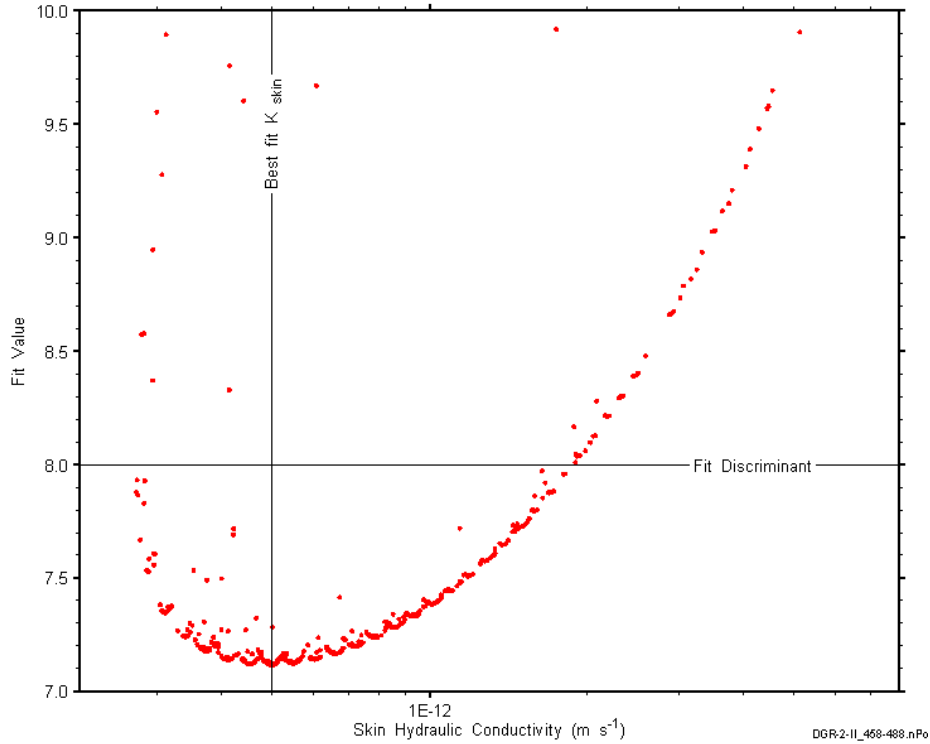


Figure B-13: XY-scatter plot showing the skin hydraulic conductivity parameter space derived from DGR2_457.85-488.35 perturbation analysis along with the fit discriminant and best fit values.

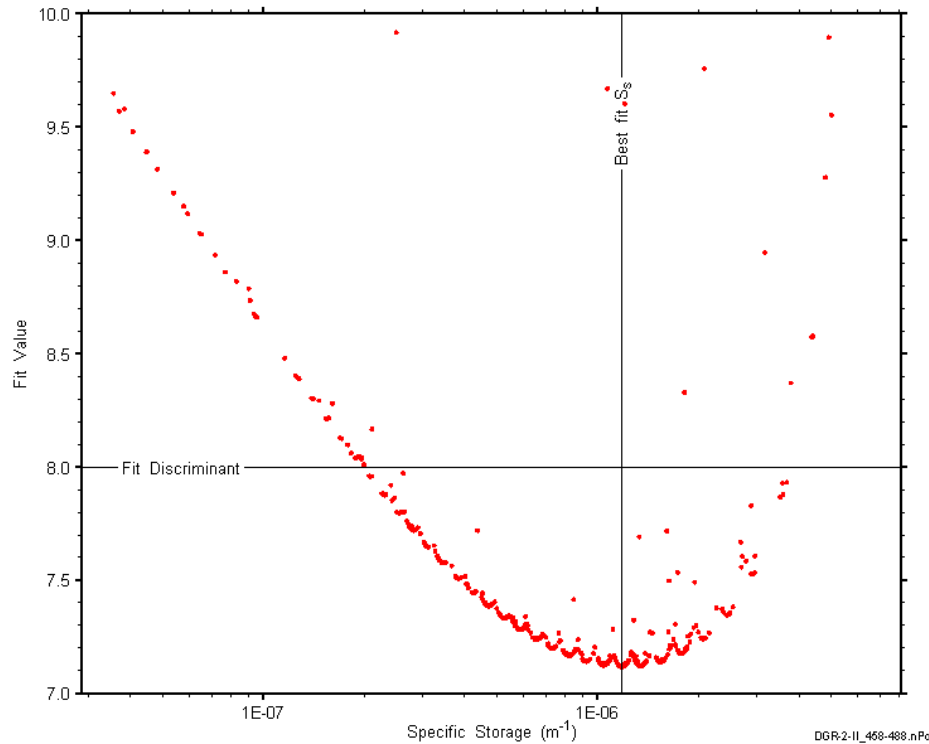


Figure B-14: XY-scatter plot showing the formation specific storage parameter space derived from DGR2_457.85-488.35 perturbation analysis along with the fit discriminant and best fit values.

B.2 487.20-517.70 Queenston

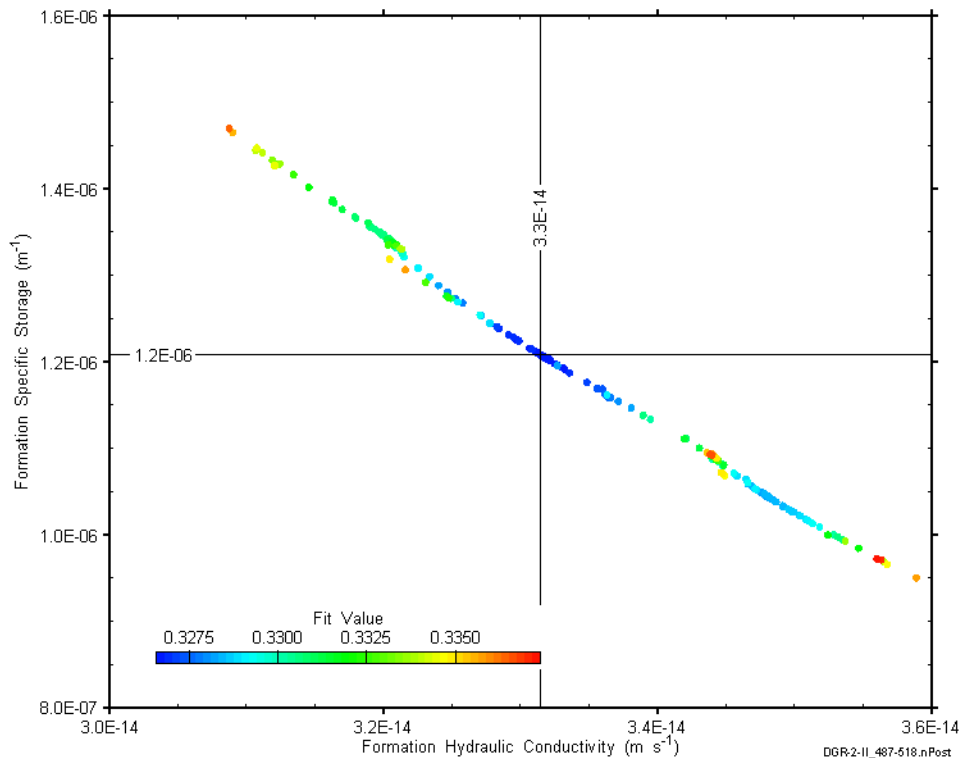


Figure B-15: XY-scatter plot showing estimates of formation hydraulic conductivity and formation specific storage derived from the DGR2_487.20-517.70 perturbation analysis.

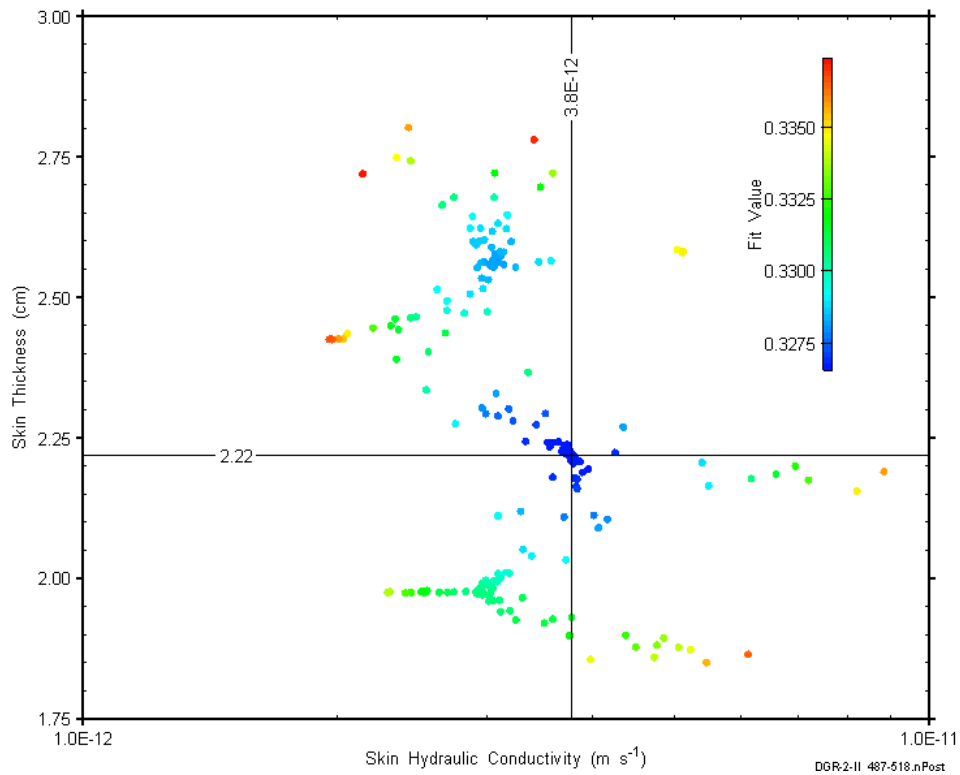


Figure B-16: XY-scatter plot showing estimates of skin hydraulic conductivity and skin thickness derived from the DGR2_487.20-517.70 perturbation analysis.

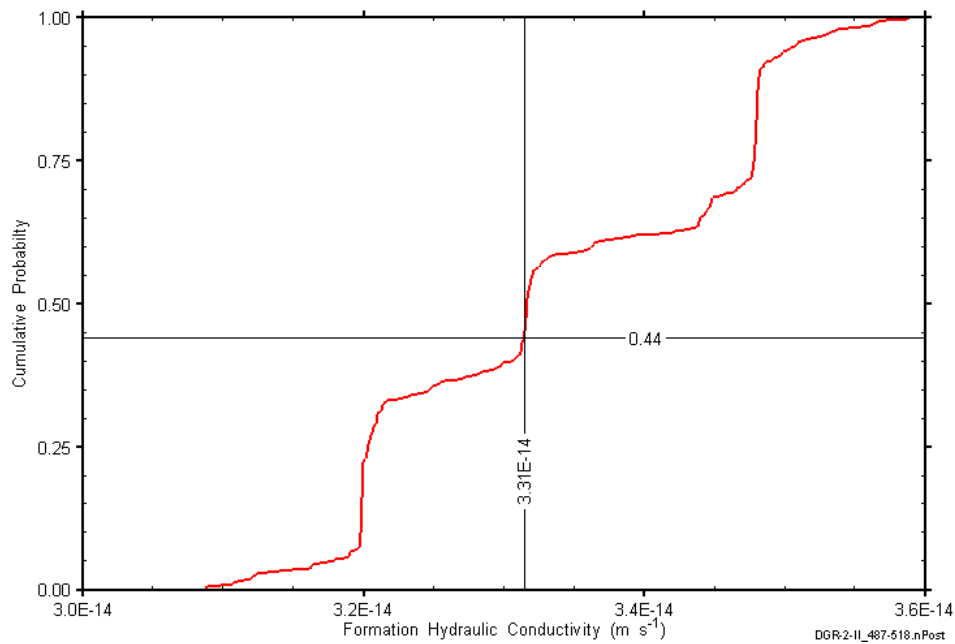


Figure B-17: DGR2_487.20-517.70 formation hydraulic conductivity cumulative distribution function.

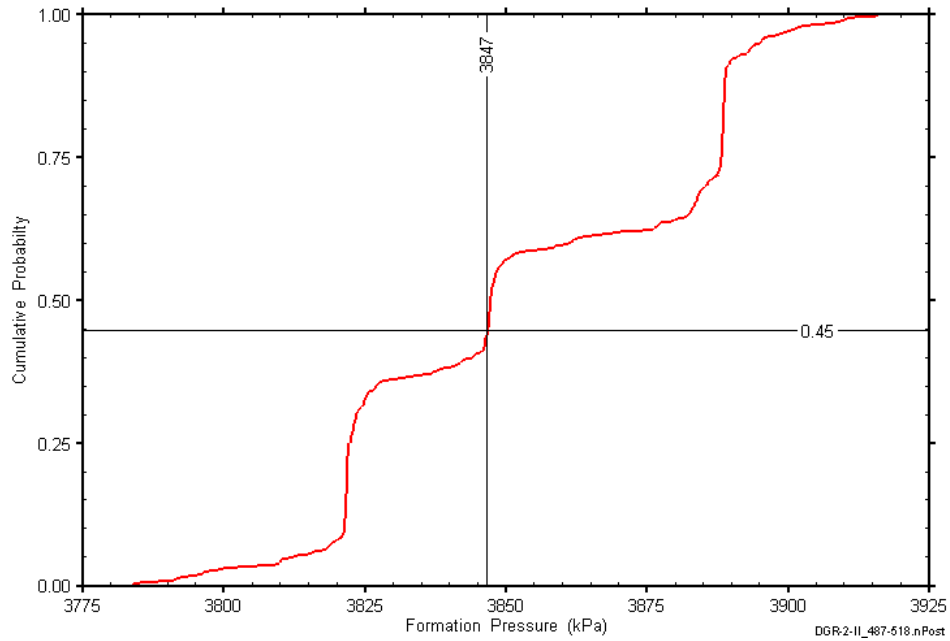


Figure B-18: DGR2_487.20-517.70 static formation pressure cumulative distribution function.

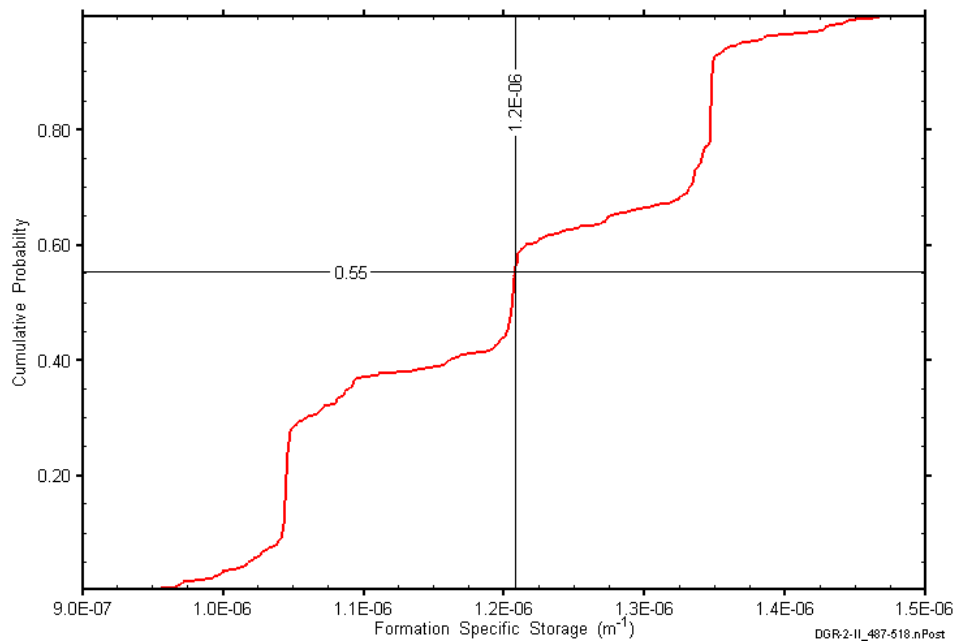


Figure B-19: DGR2_487.20-517.70 formation specific storage cumulative distribution function.

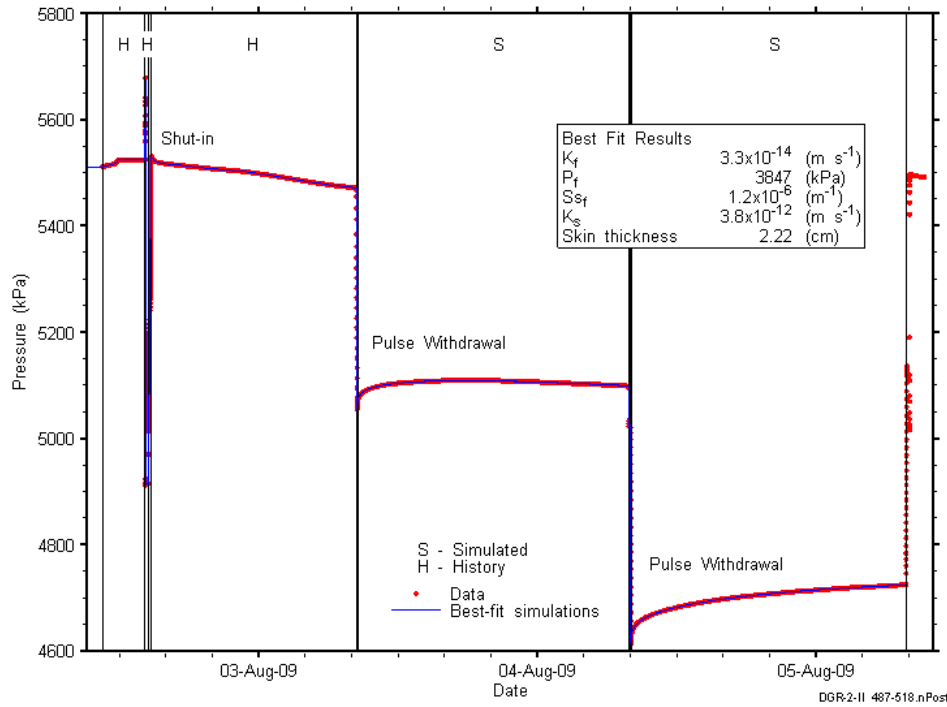


Figure B-20: Linear plot showing details of simulations of the DGR2_487.20-517.70 pressure response.

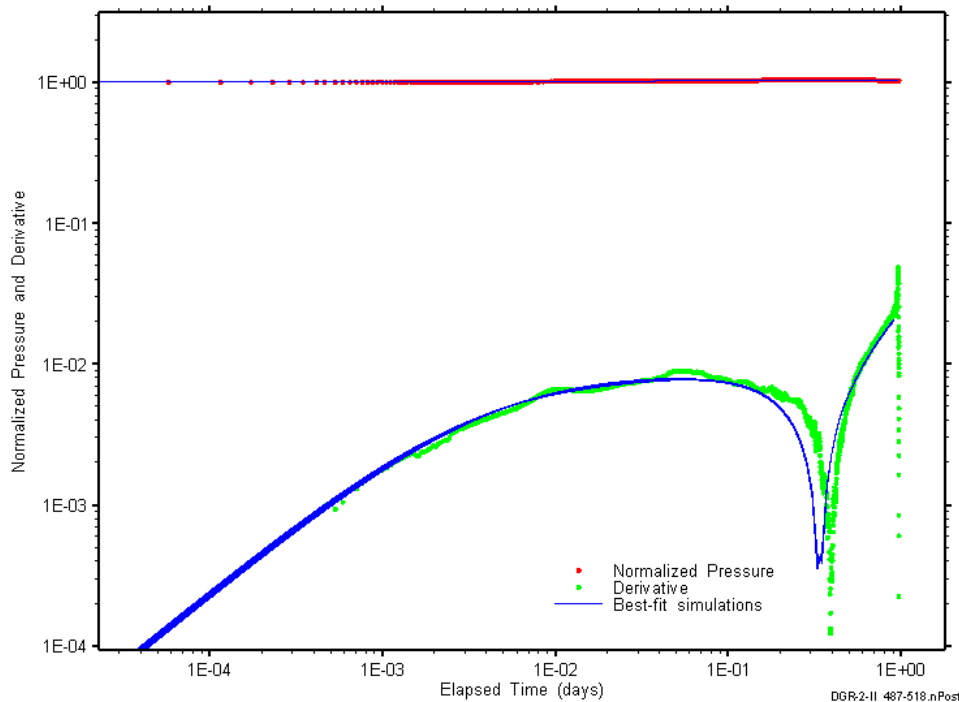


Figure B-21: Log-log plot showing simulations of the DGR2_487.20-517.70 PW1 Ramey B and derivative response.

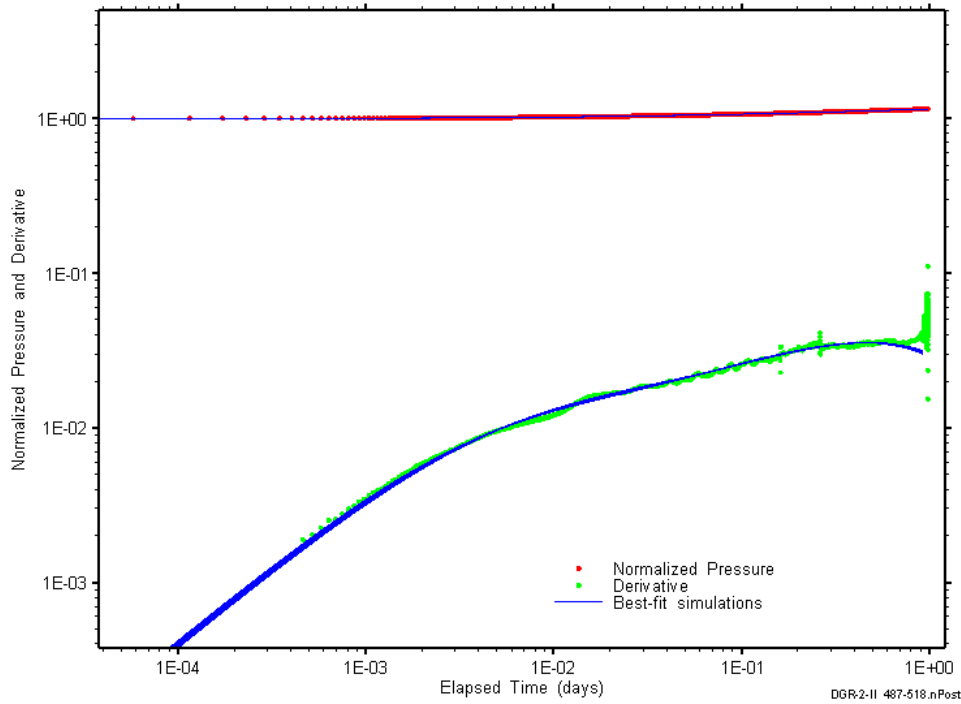


Figure B-22: Log-log plot showing simulations of the DGR2_487.20-517.70 PW2 Ramey B and derivative response.

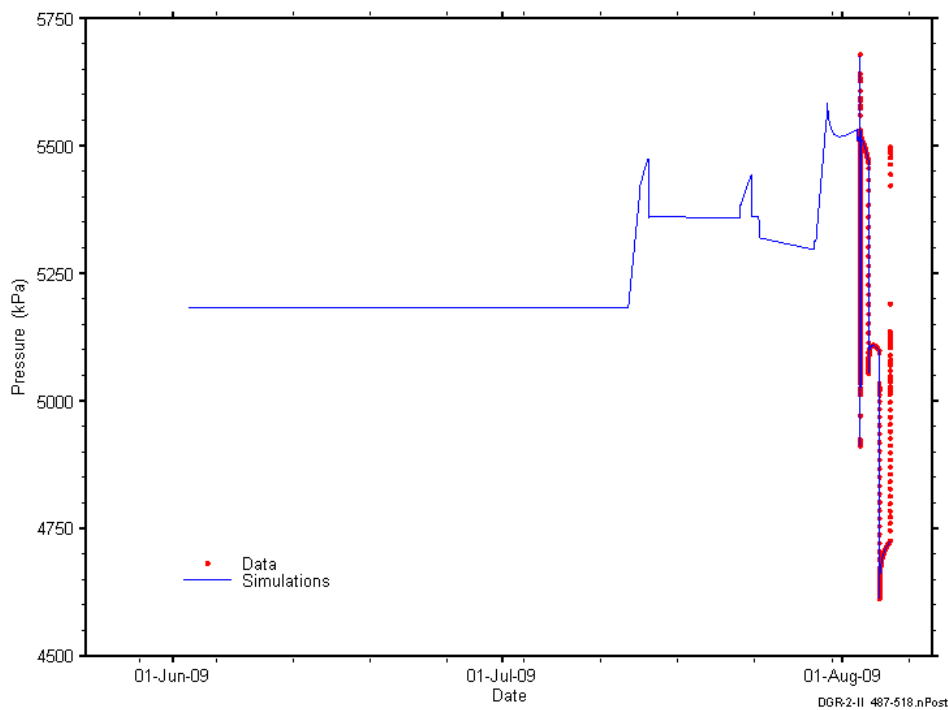


Figure B-23: Linear plot showing simulations of the DGR2_487.20-517.70 pressure response, including pre-test pressure history.

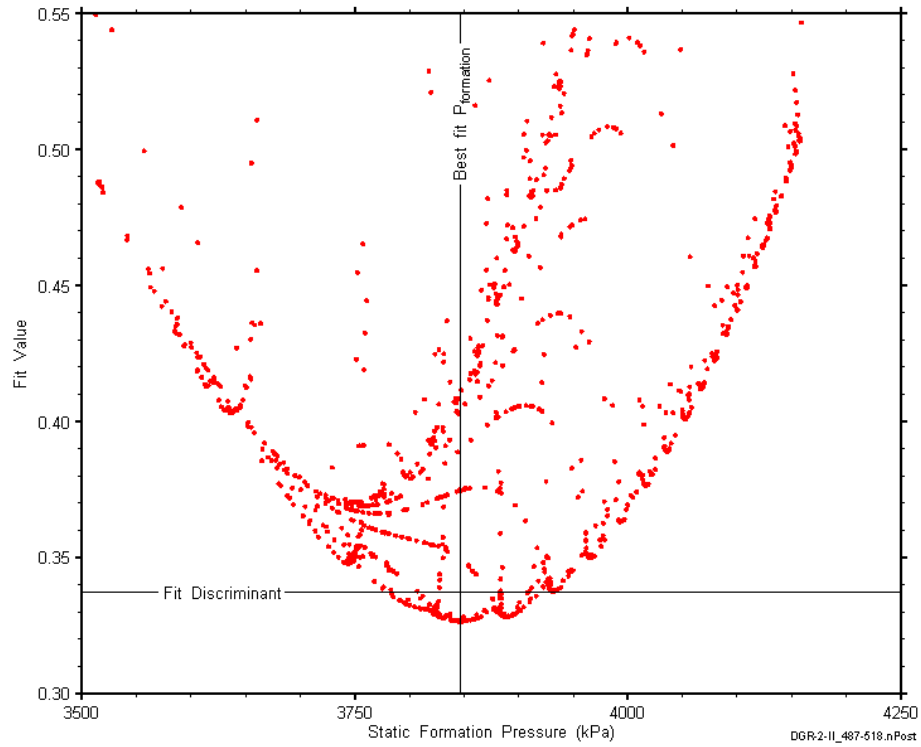


Figure B-24: XY-scatter plot showing the static formation pressure parameter space derived from DGR2_487.20-517.70 perturbation analysis along with the fit discriminant and best fit values.

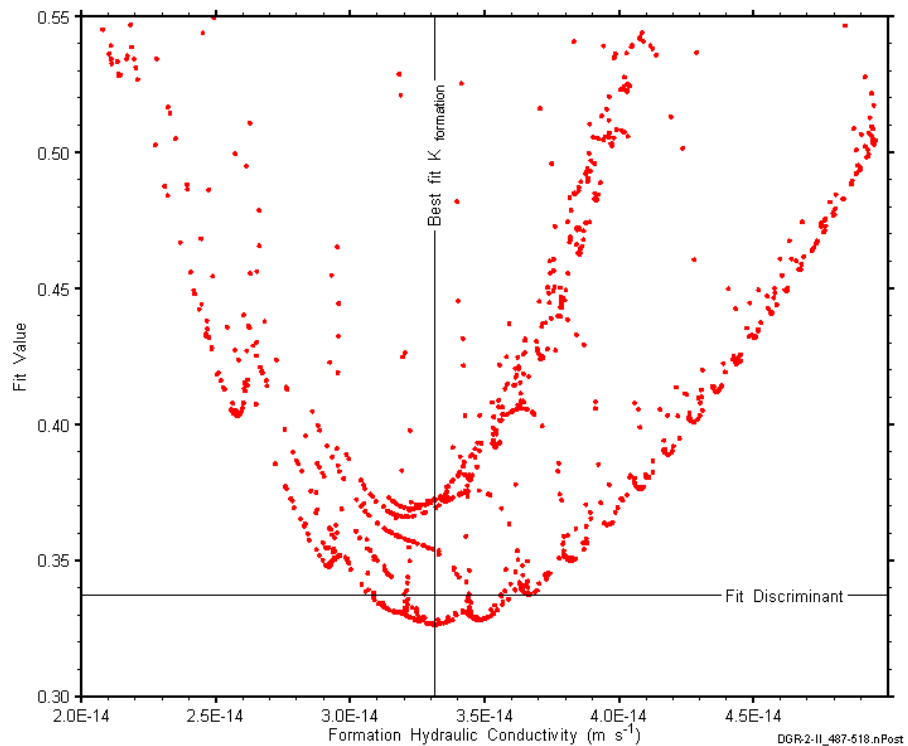


Figure B-25: XY-scatter plot showing the formation hydraulic conductivity parameter space derived from DGR2_487.20-517.70 perturbation analysis along with the fit discriminant and best fit values.

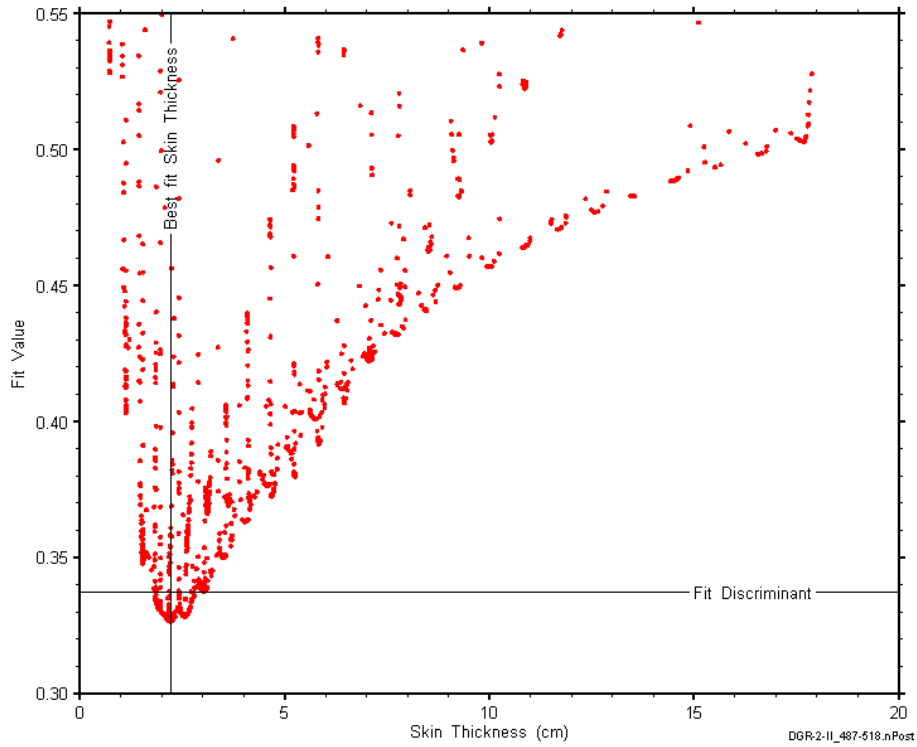


Figure B-26: XY-scatter plot showing the skin-thickness parameter space derived from DGR2_487.20-517.70 perturbation analysis along with the fit discriminant and best fit values.

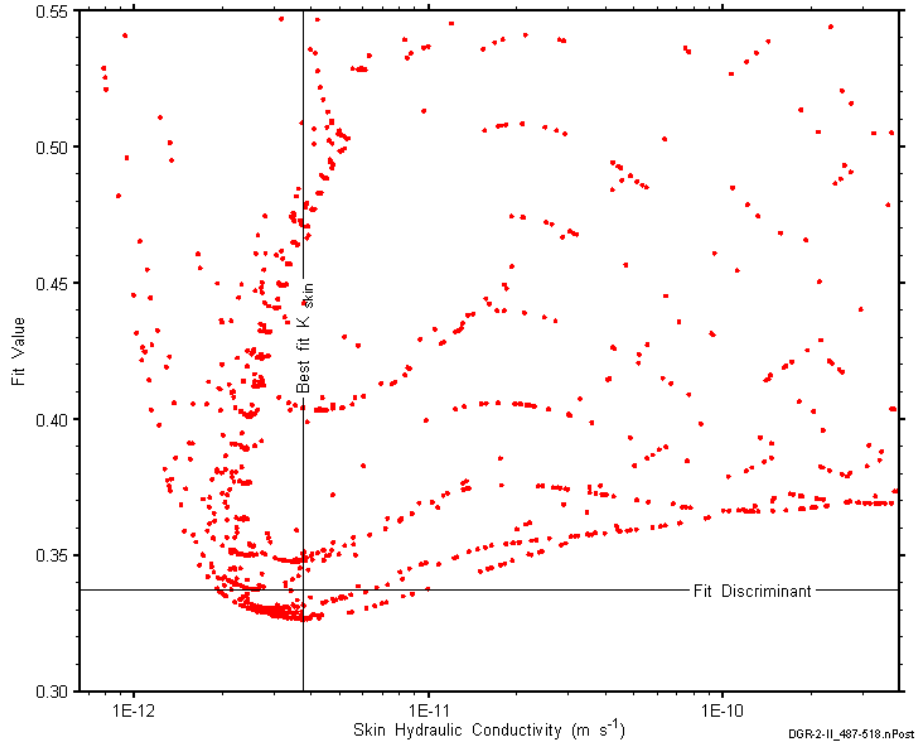


Figure B-27: XY-scatter plot showing the skin hydraulic conductivity parameter space derived from DGR2_487.20-517.70 perturbation analysis along with the fit discriminant and best fit values.

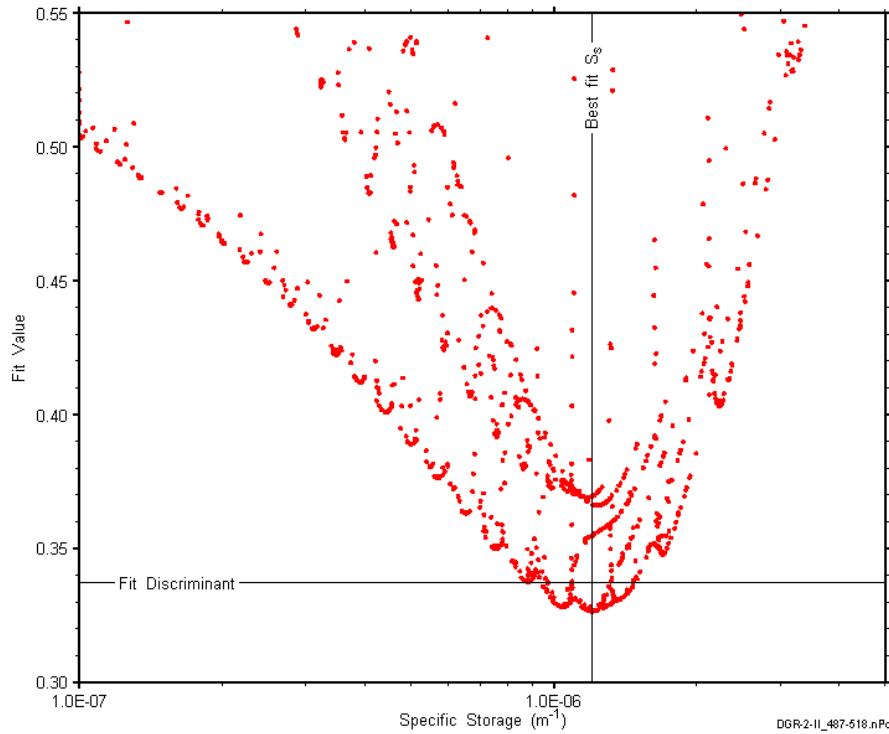


Figure B-28: XY-scatter plot showing the formation specific storage parameter space derived from DGR2_487.20-517.70 perturbation analysis along with the fit discriminant and best fit values.

B.3 517.50-548.00 Georgian Bay

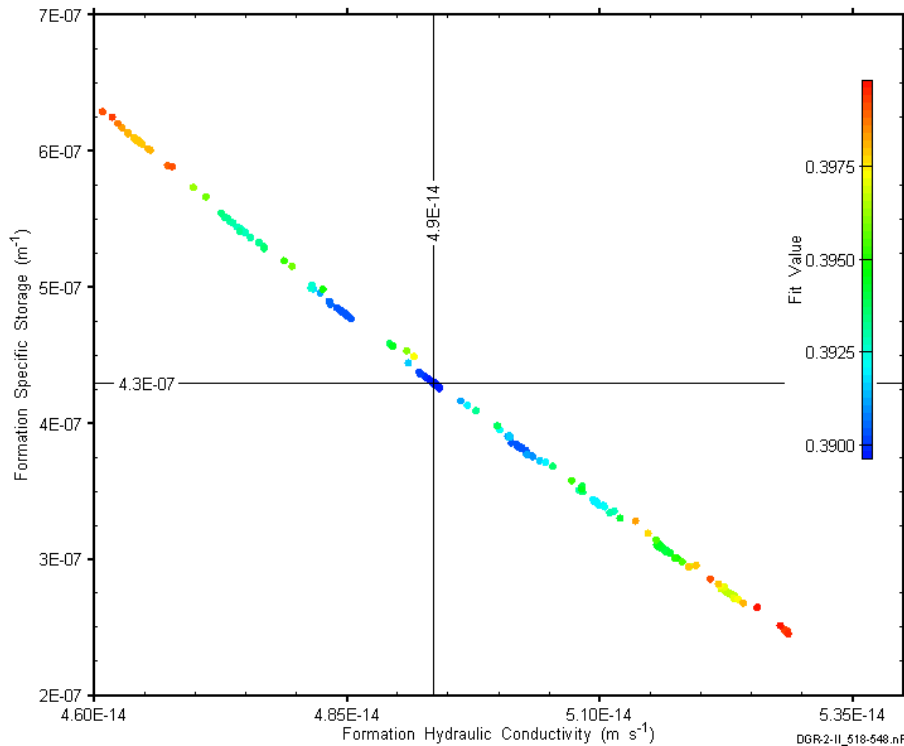


Figure B-29: XY-scatter plot showing estimates of formation hydraulic conductivity and formation specific storage derived from the DGR2_517.50-548.00 perturbation analysis.

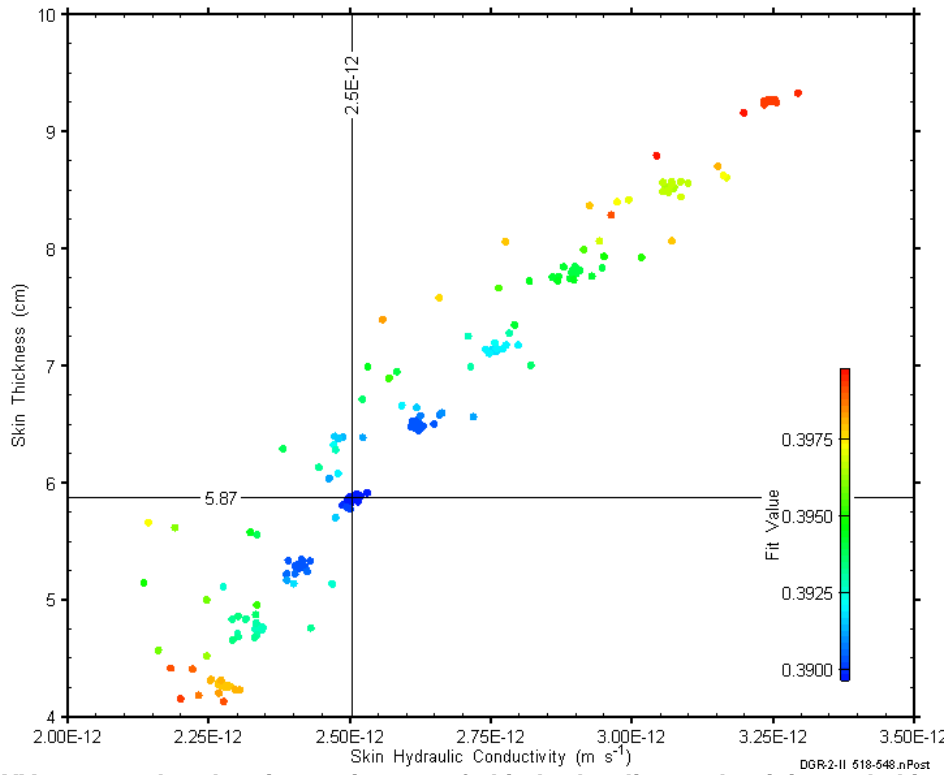


Figure B-30: XY-scatter plot showing estimates of skin hydraulic conductivity and skin thickness derived from the DGR2_517.50-548.00 perturbation analysis.

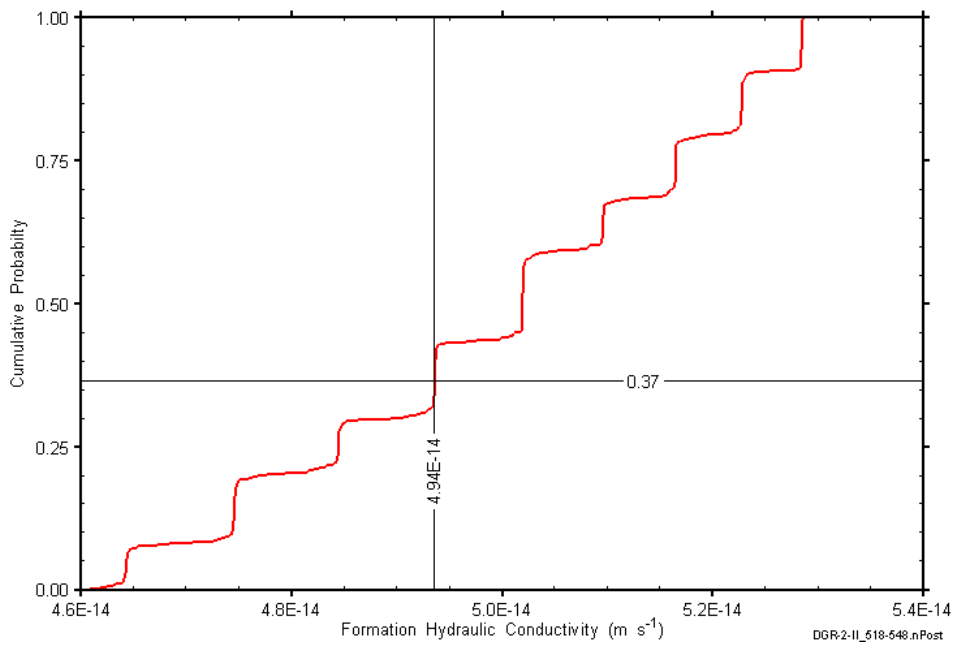


Figure B-31: DGR2_517.50-548.00 formation hydraulic conductivity cumulative distribution function.

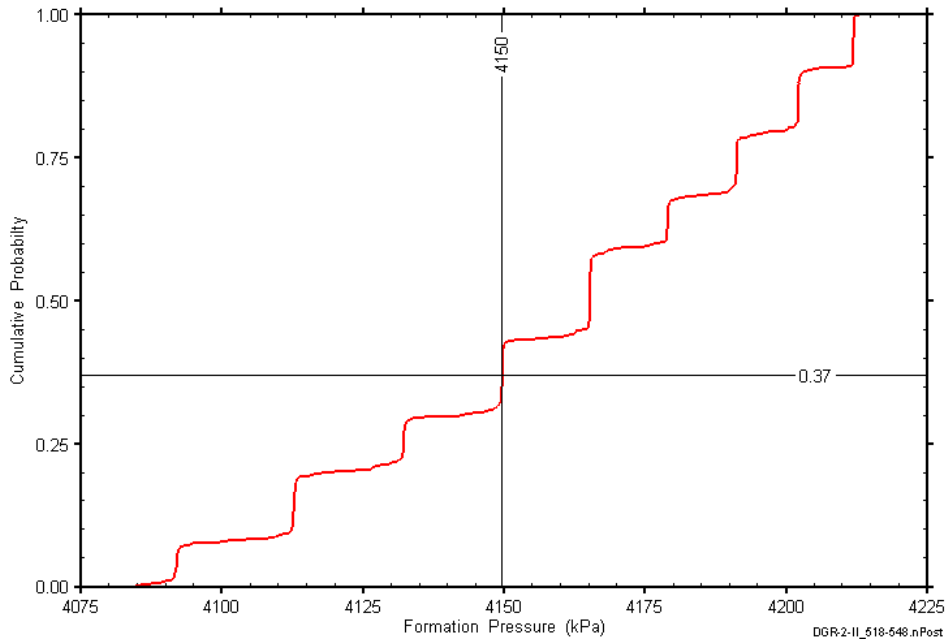


Figure B-32: DGR2_517.50-548.00 static formation pressure cumulative distribution function.

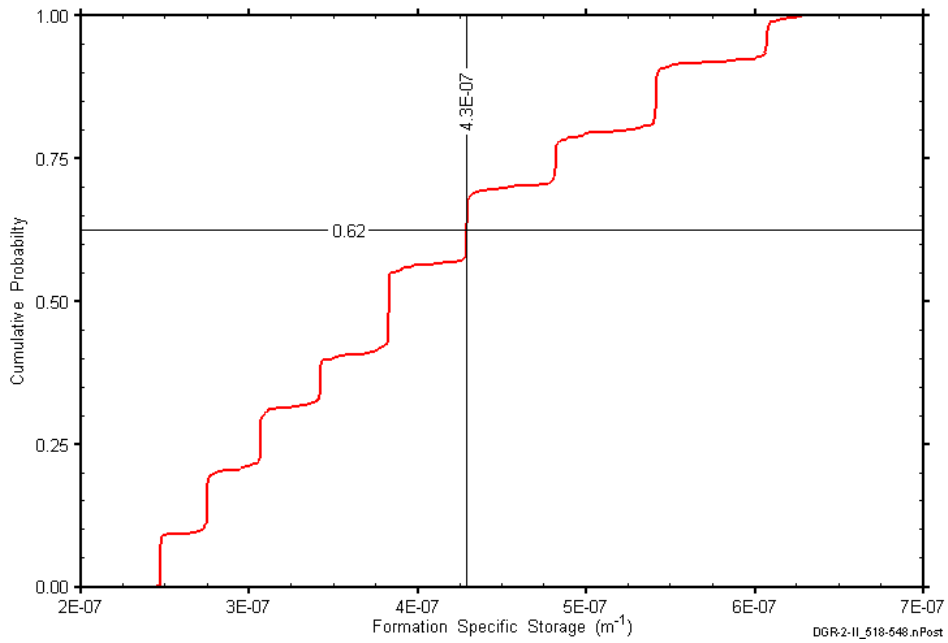


Figure B-33: DGR2_517.50-548.00 formation specific storage cumulative distribution function.

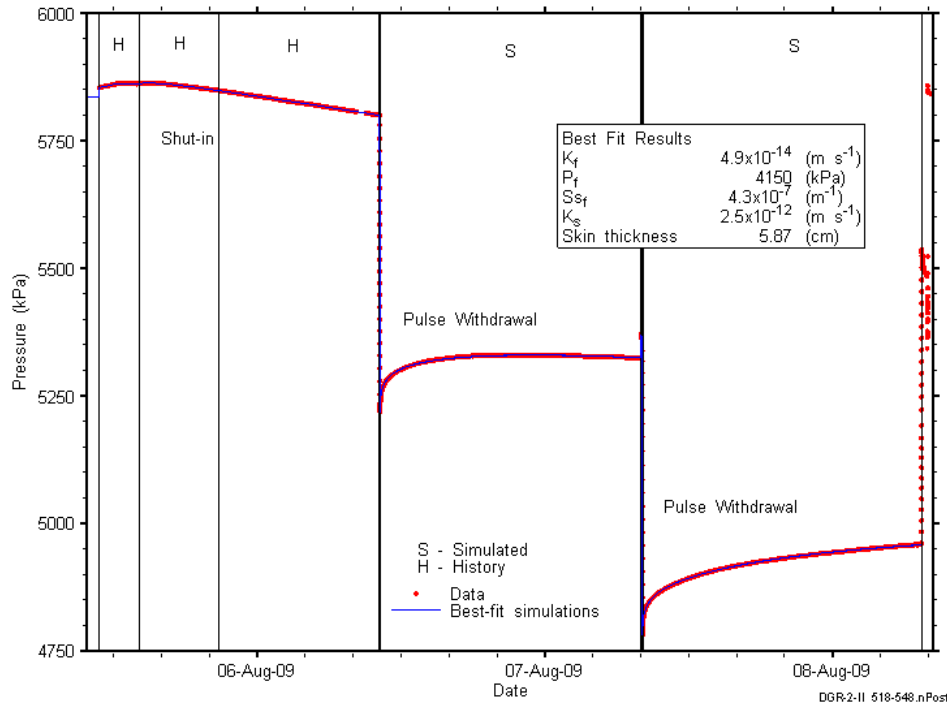


Figure B-34: Linear plot showing details of simulations of the DGR2_517.50-548.00 pressure response.

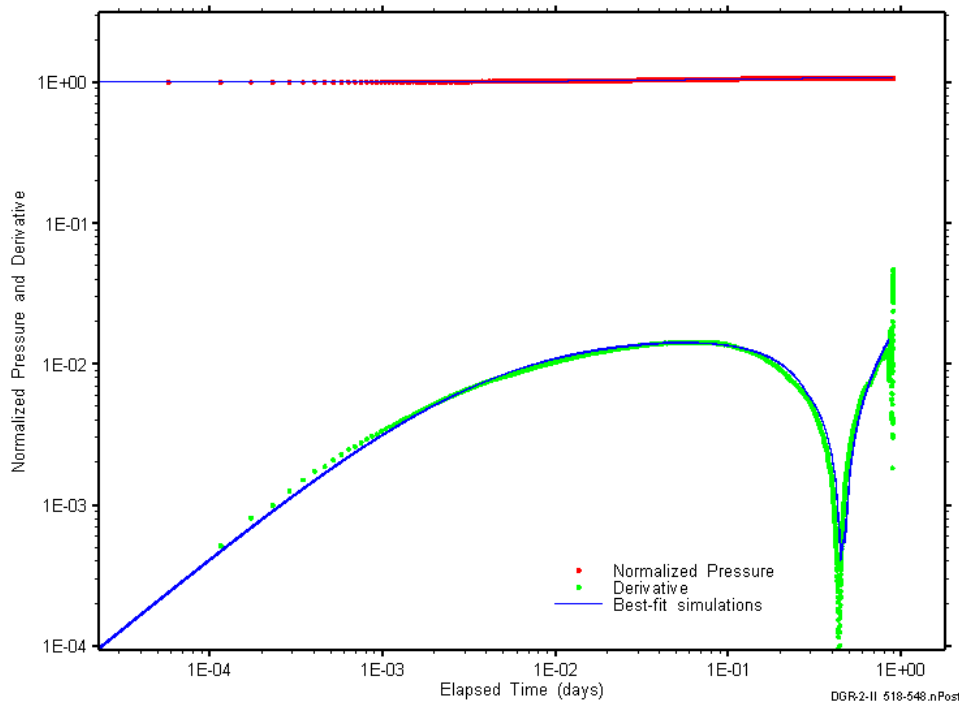


Figure B-35: Log-log plot showing simulations of the DGR2_517.50-548.00 PW1 Ramey B and derivative response.

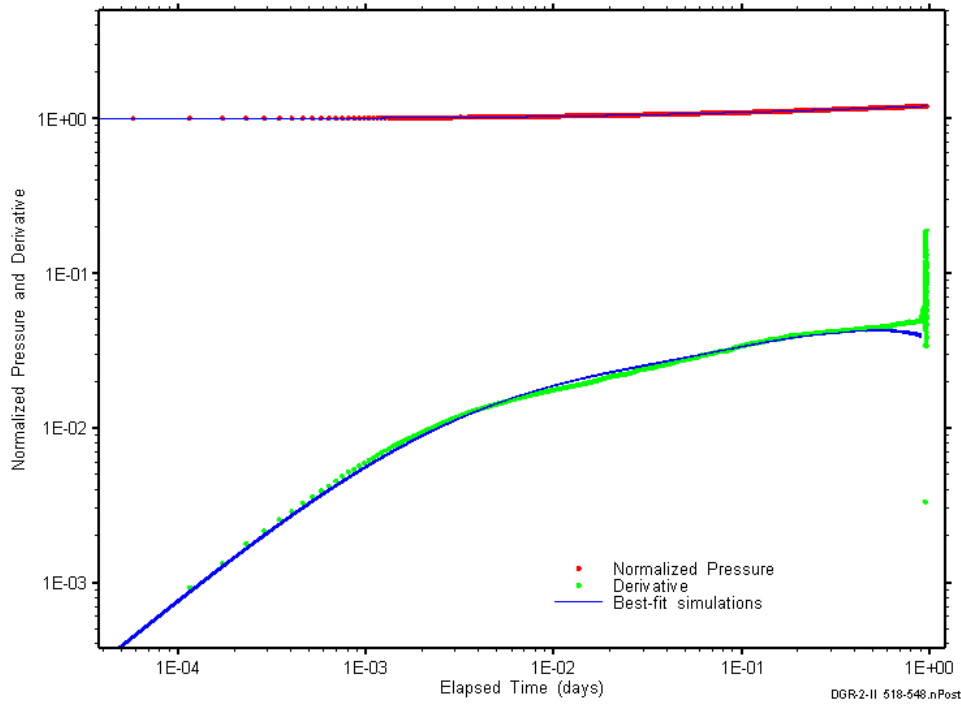


Figure B-36: Log-log plot showing simulations of the DGR2_517.50-548.00 PW2 Ramey B and derivative response.

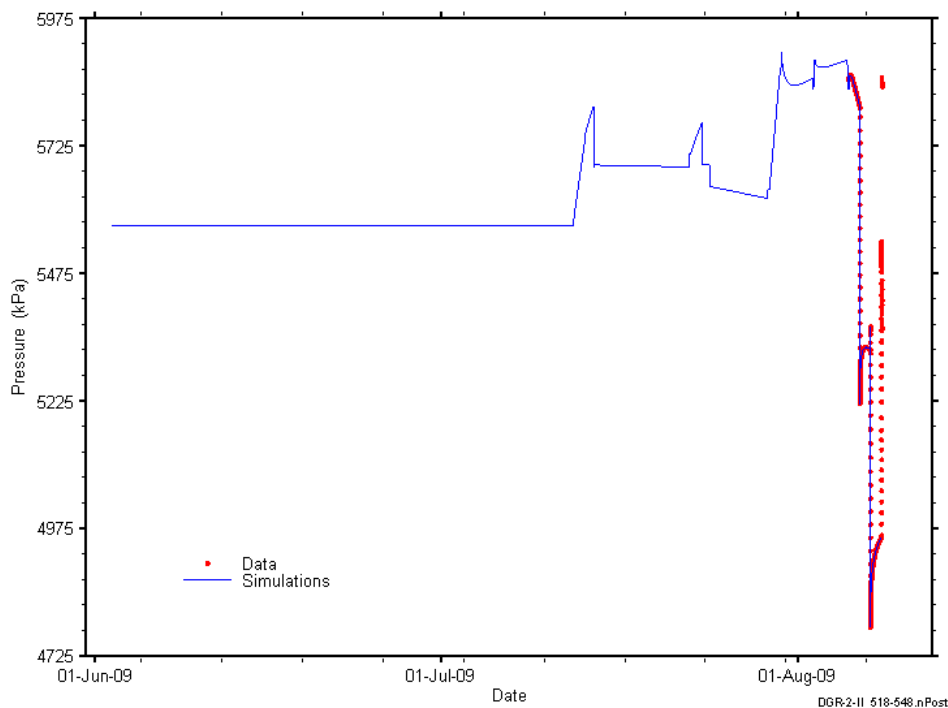


Figure B-37: Linear plot showing simulations of the DGR2_517.50-548.00 pressure response, including pre-test pressure history.

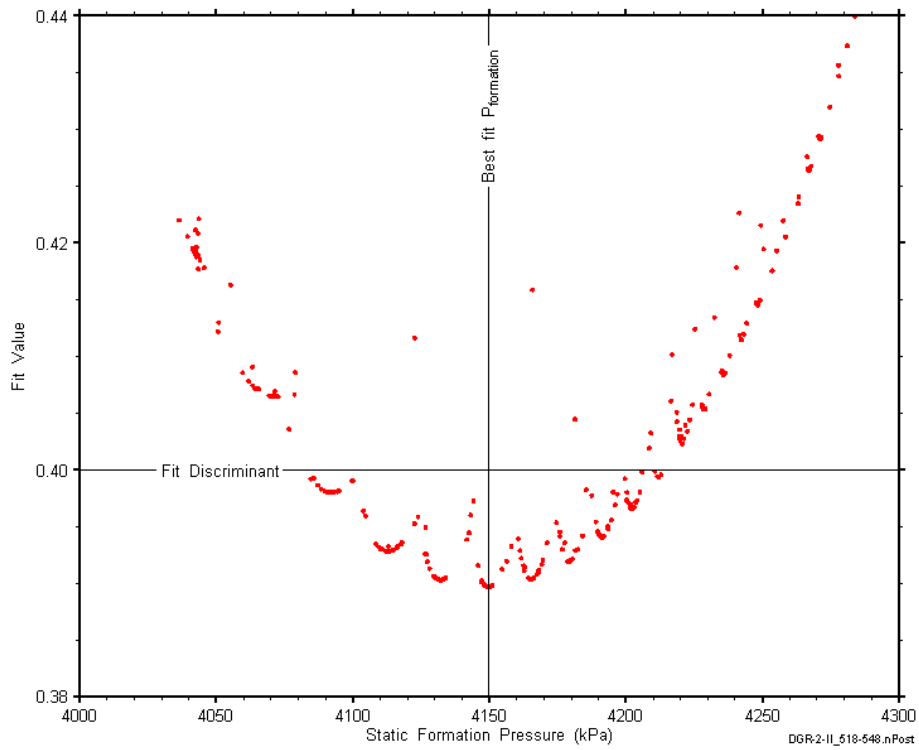


Figure B-38: XY-scatter plot showing the static formation pressure parameter space derived from DGR2_517.50-548.00 perturbation analysis along with the fit discriminant and best fit values.

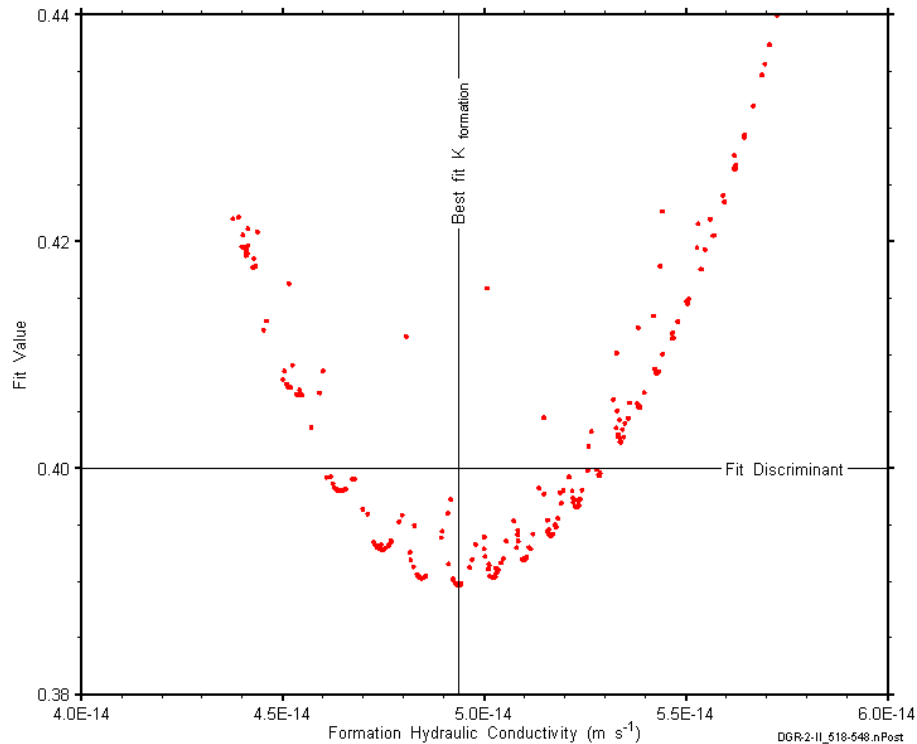


Figure B-39: XY-scatter plot showing the formation hydraulic conductivity parameter space derived from DGR2_517.50-548.00 perturbation analysis along with the fit discriminant and best fit values.

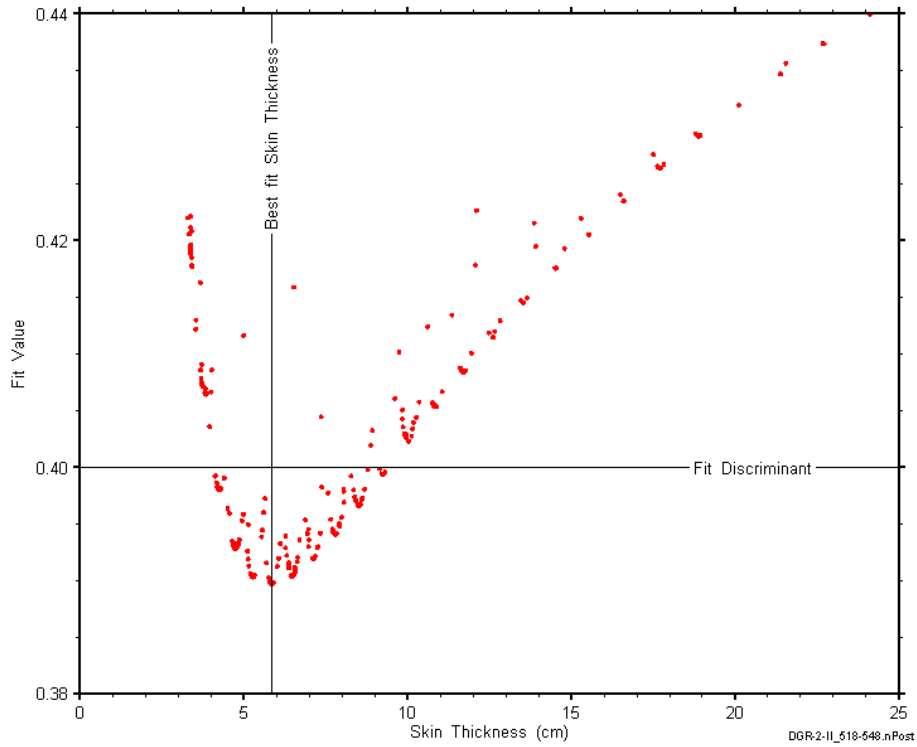


Figure B-40: XY-scatter plot showing the skin-thickness parameter space derived from DGR2_517.50-548.00 perturbation analysis along with the fit discriminant and best fit values.

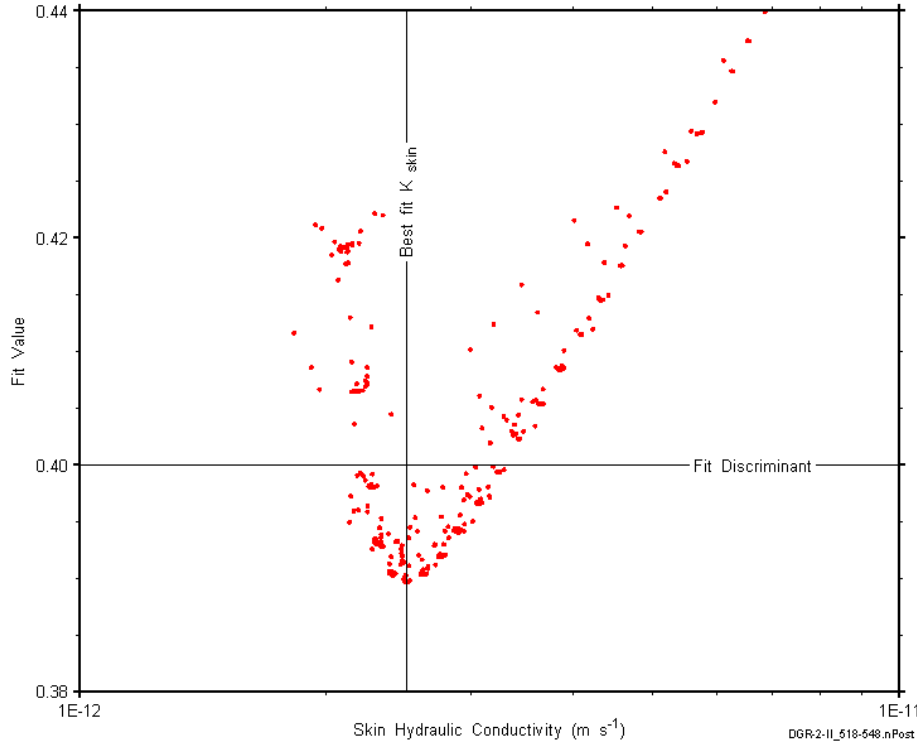


Figure B-41: XY-scatter plot showing the skin hydraulic conductivity parameter space derived from DGR2_517.50-548.00 perturbation analysis along with the fit discriminant and best fit values.

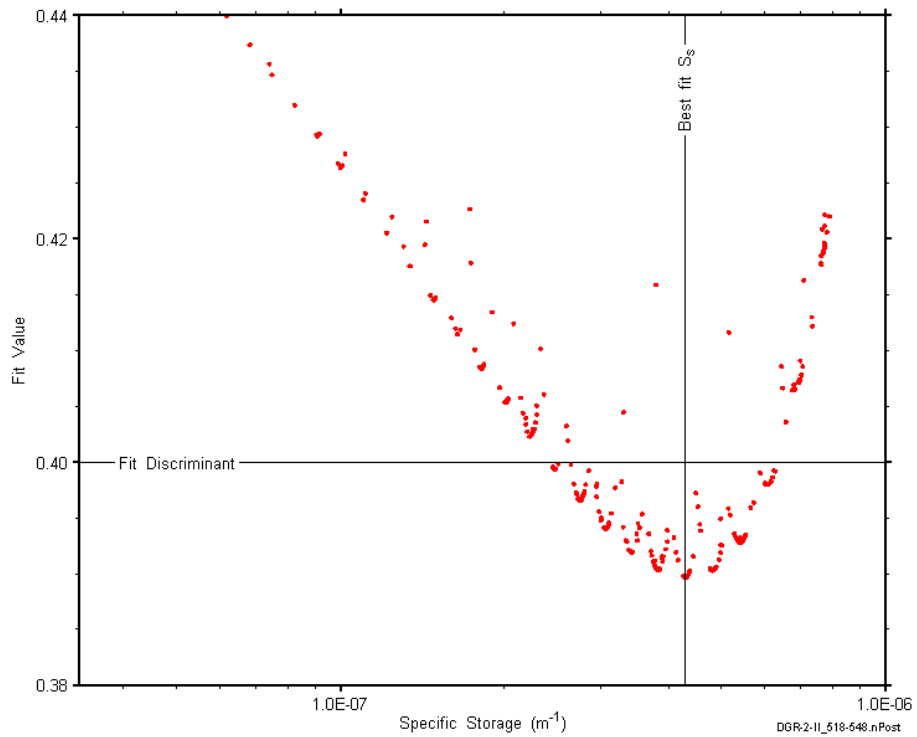


Figure B-42: XY-scatter plot showing the formation specific storage parameter space derived from DGR2_517.50-548.00 perturbation analysis along with the fit discriminant and best fit values.

B.4 547.80-578.30 Georgian Bay

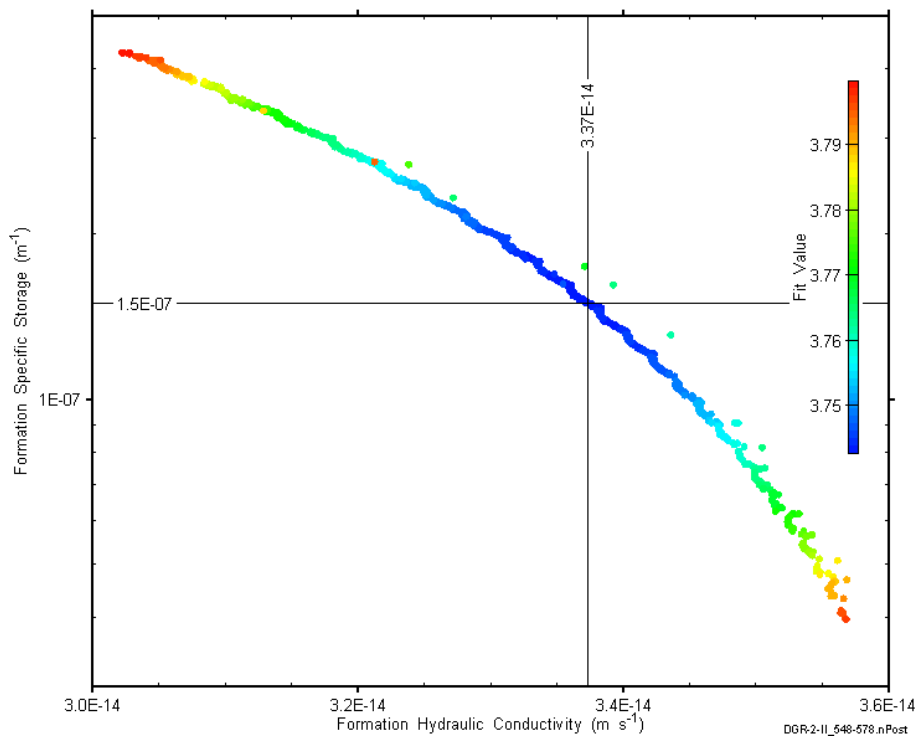


Figure B-43: XY-scatter plot showing estimates of formation hydraulic conductivity and formation specific storage derived from the DGR2_547.80-578.30 perturbation analysis.

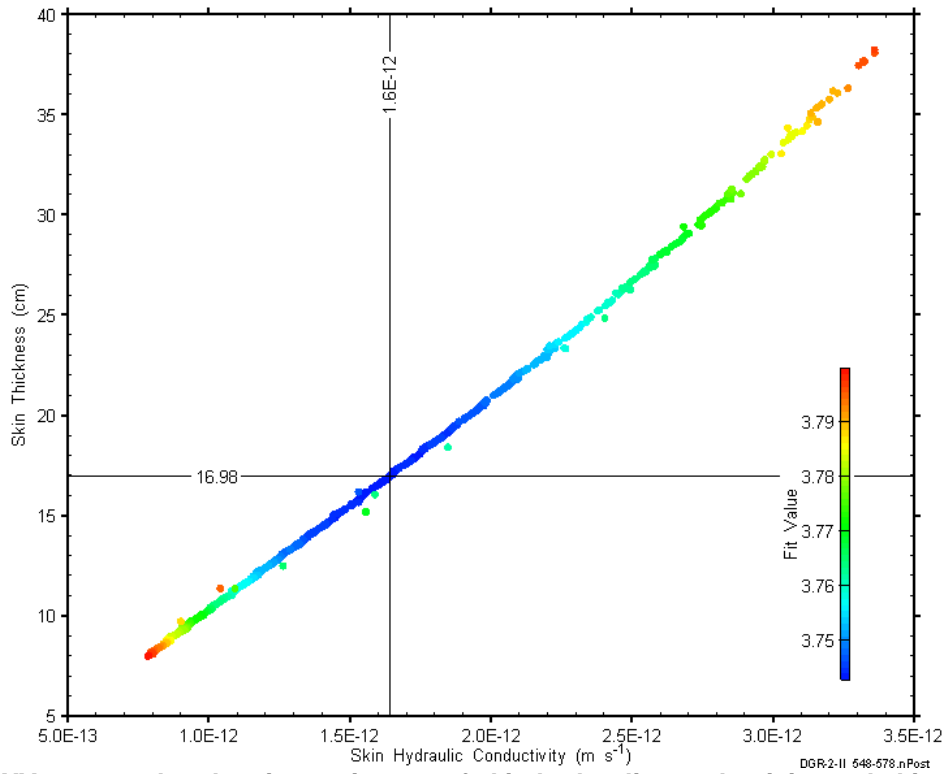


Figure B-44: XY-scatter plot showing estimates of skin hydraulic conductivity and skin thickness derived from the DGR2_547.80-578.30 perturbation analysis.

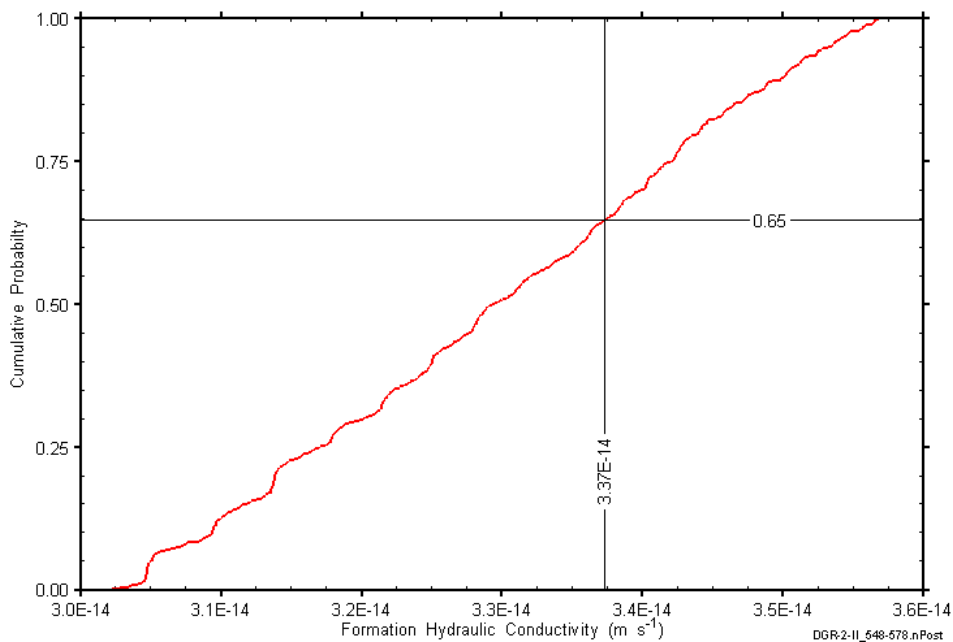


Figure B-45: DGR2_547.80-578.30 formation hydraulic conductivity cumulative distribution function.

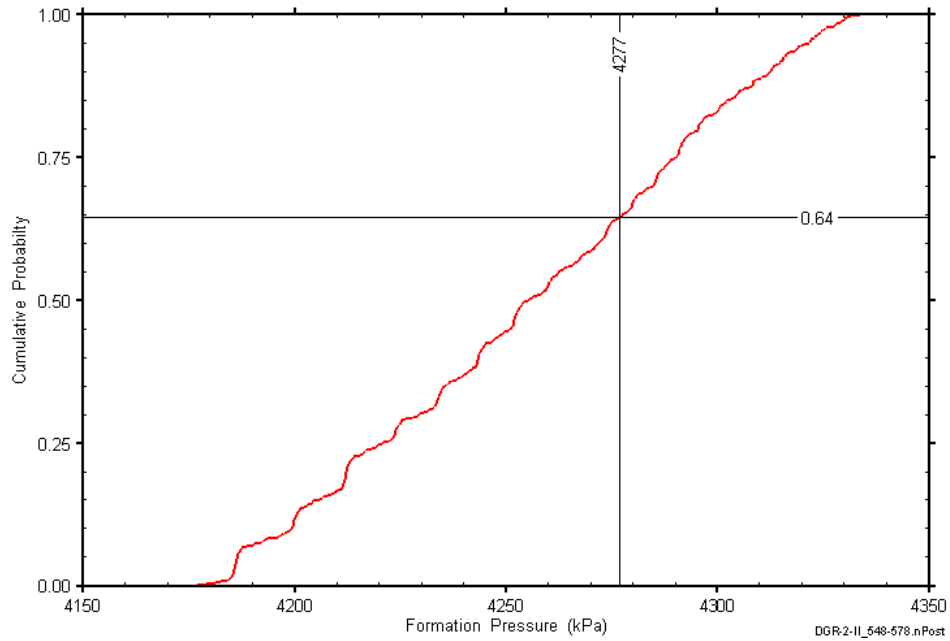


Figure B-46: DGR2_547.80-578.30 static formation pressure cumulative distribution function.

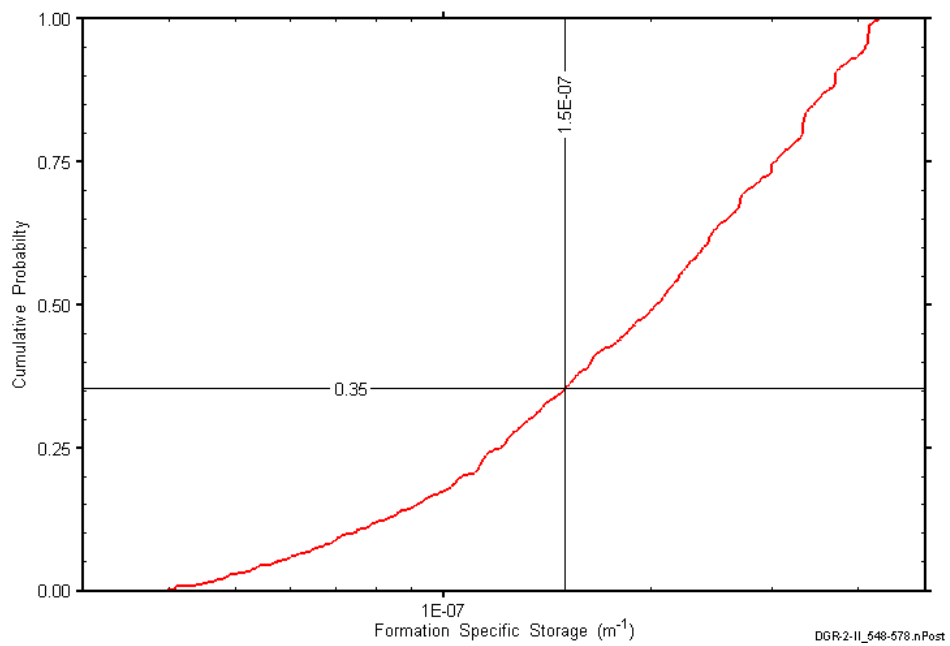


Figure B-47: DGR2_547.80-578.30 formation specific storage cumulative distribution function.

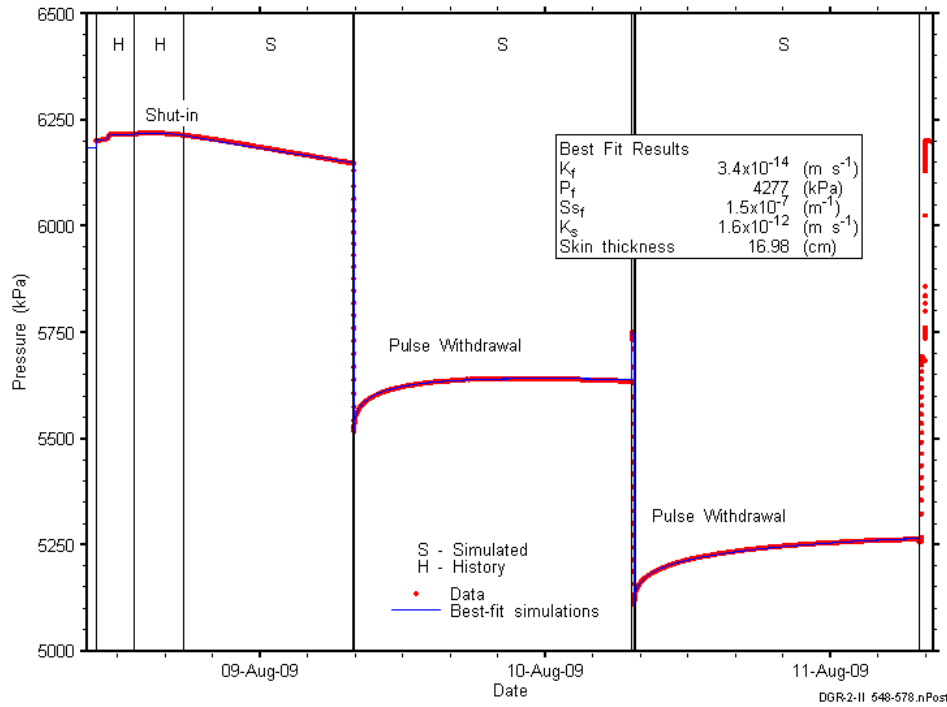


Figure B-48: Linear plot showing details of simulations of the DGR2_547.80-578.30 pressure response.

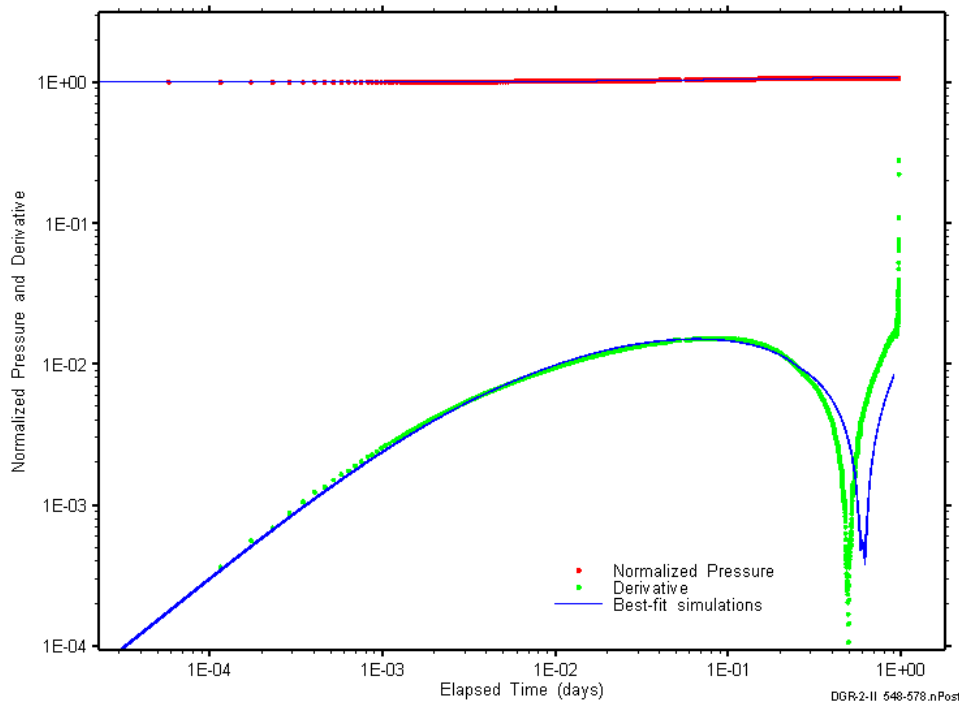


Figure B-49: Log-log plot showing simulations of the DGR2_547.80-578.30 PW1 Ramey B and derivative response.

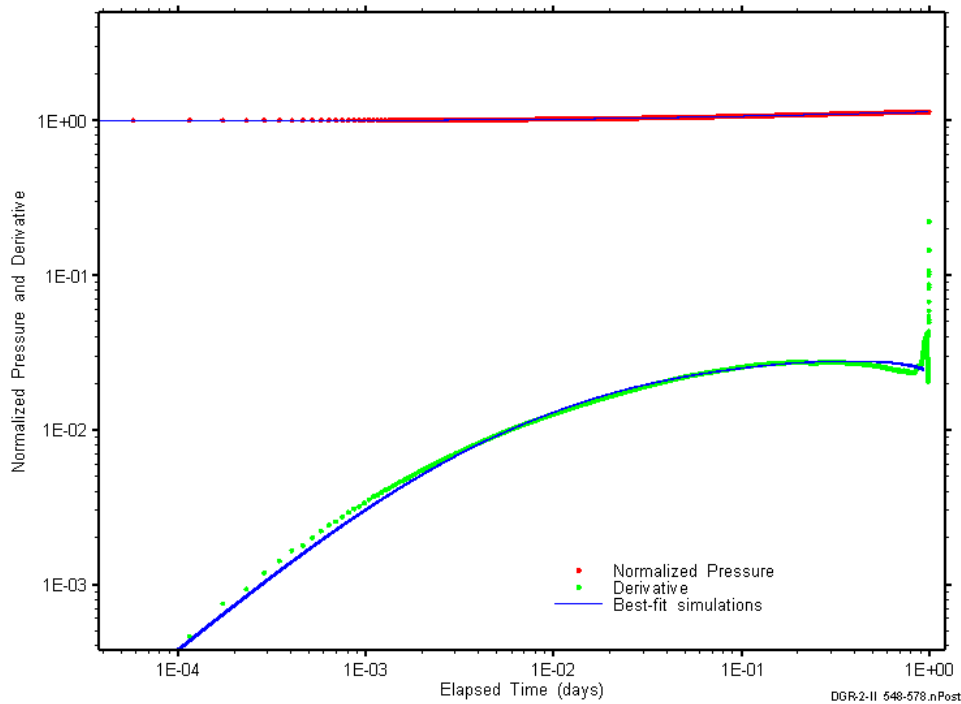


Figure B-50: Log-log plot showing simulations of the DGR2_547.80-578.30 PW2 Ramey B and derivative response.

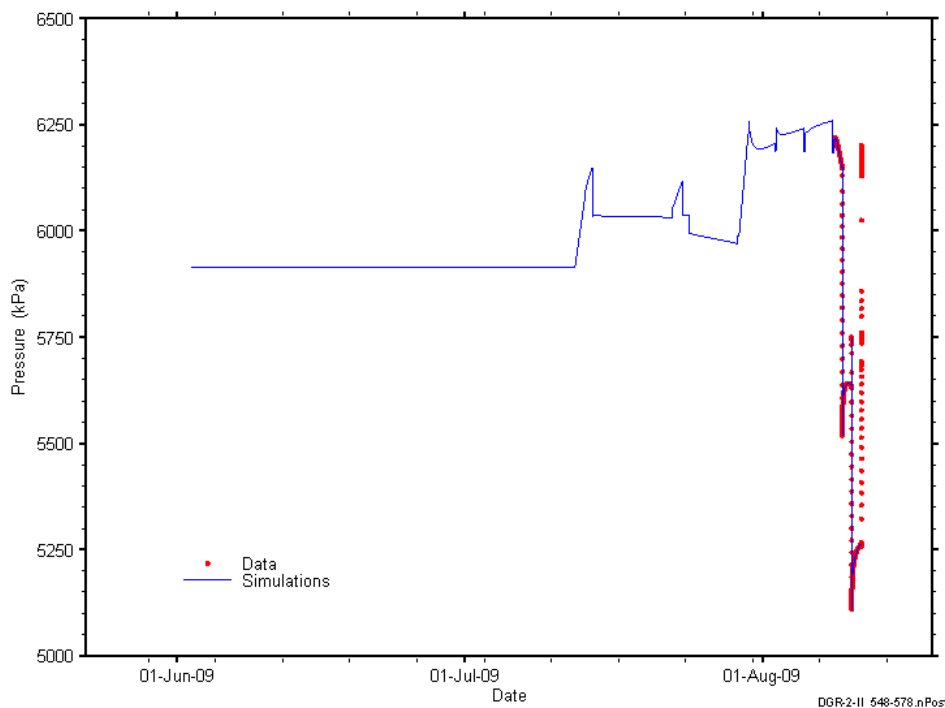


Figure B-51: Linear plot showing simulations of the DGR2_547.80-578.30 pressure response, including pre-test pressure history.

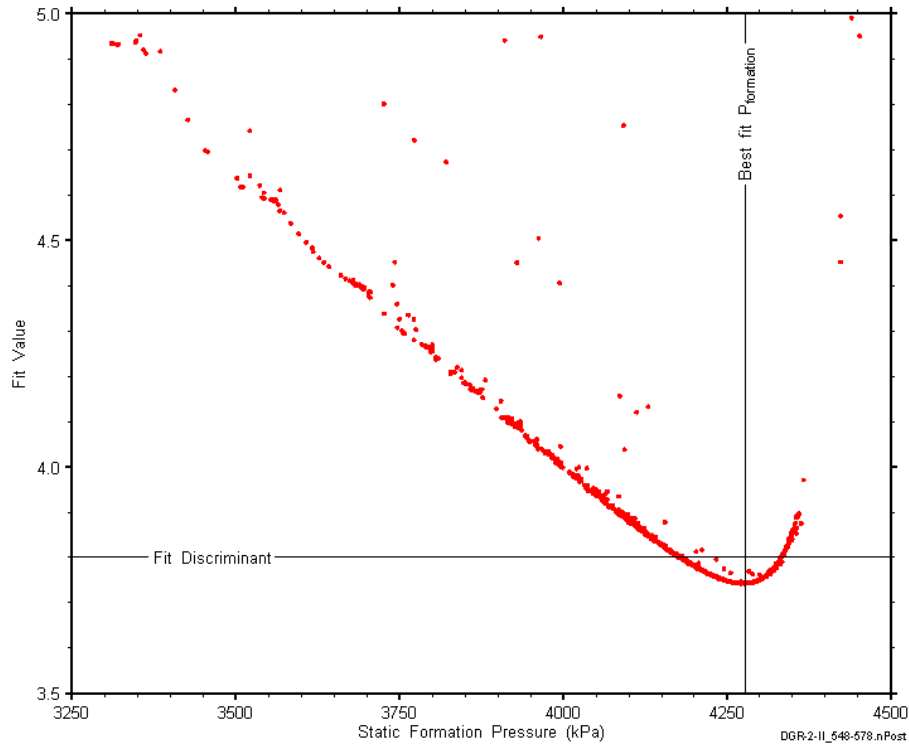


Figure B-52: XY-scatter plot showing the static formation pressure parameter space derived from DGR2_547.80-578.30 perturbation analysis along with the fit discriminant and best fit values.

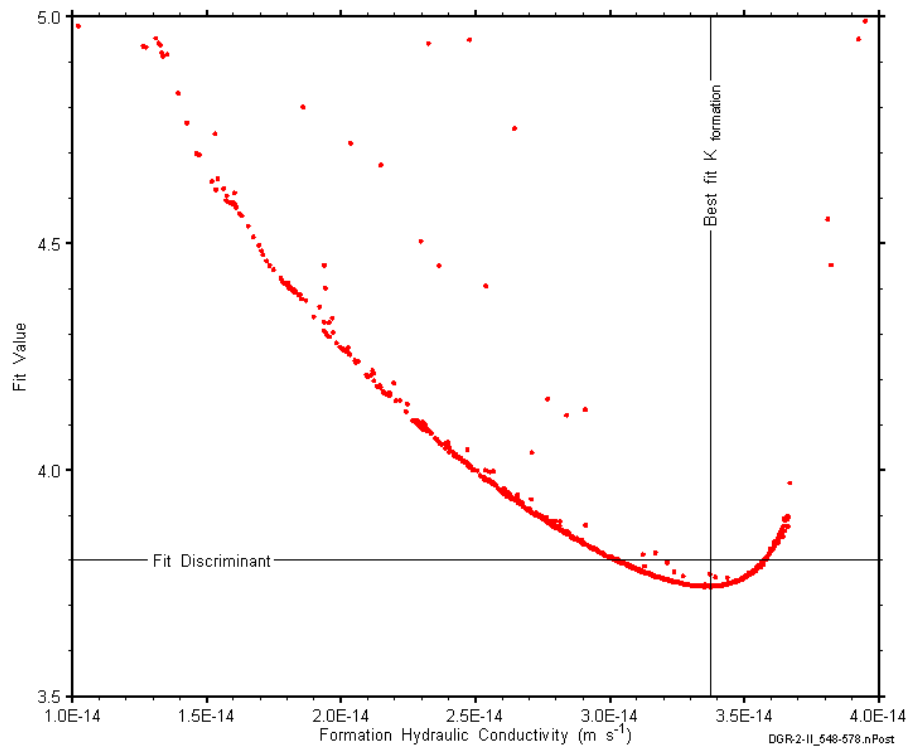


Figure B-53: XY-scatter plot showing the formation hydraulic conductivity parameter space derived from DGR2_547.80-578.30 perturbation analysis along with the fit discriminant and best fit values.

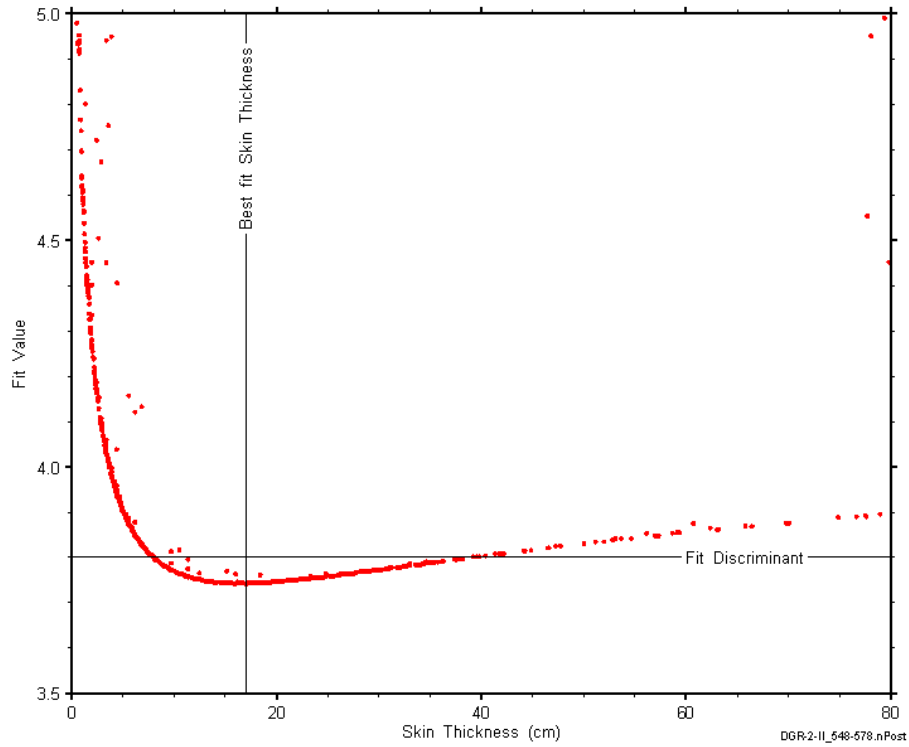


Figure B-54: XY-scatter plot showing the skin-thickness parameter space derived from DGR2_547.80-578.30 perturbation analysis along with the fit discriminant and best fit values.

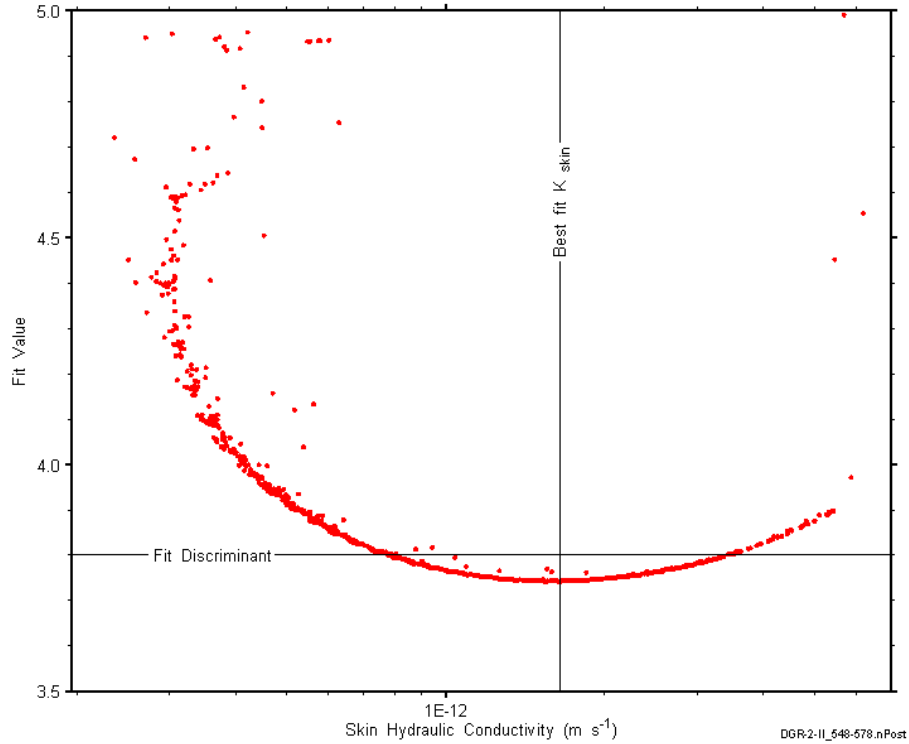


Figure B-55: XY-scatter plot showing the skin hydraulic conductivity parameter space derived from DGR2_547.80-578.30 perturbation analysis along with the fit discriminant and best fit values.

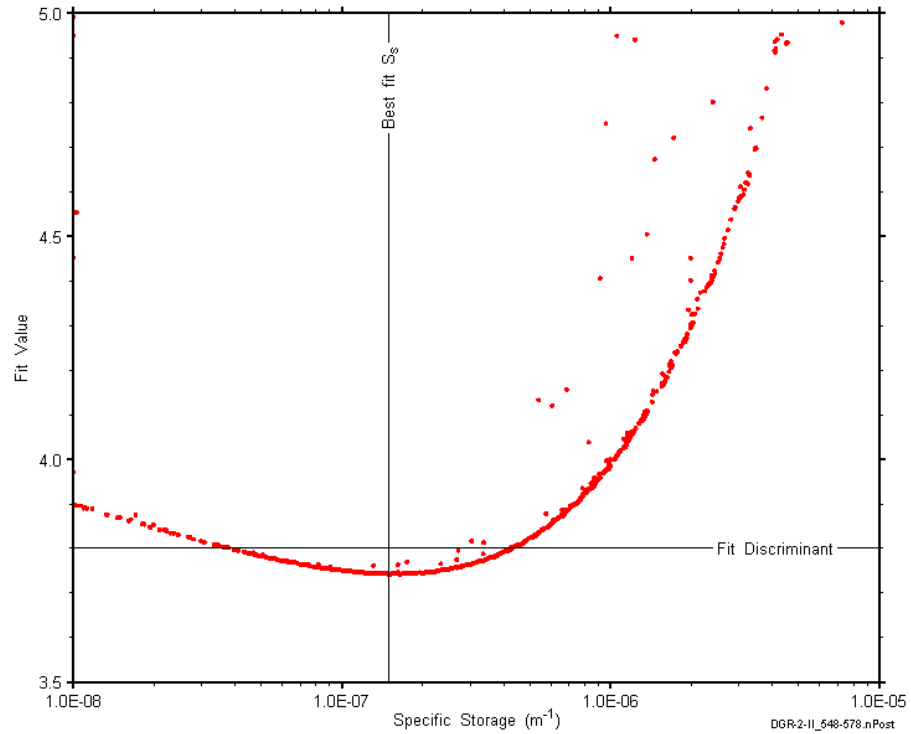


Figure B-56: XY-scatter plot showing the formation specific storage parameter space derived from DGR2_547.80-578.30 perturbation analysis along with the fit discriminant and best fit values.

B.5 578.10-608.60 Georgian Bay

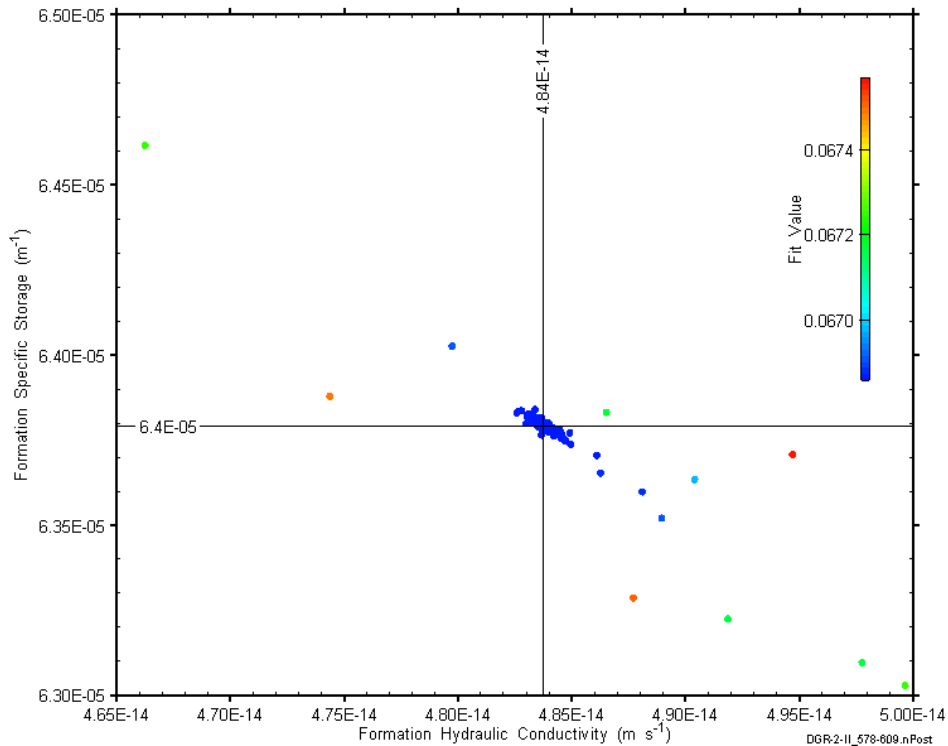


Figure B-57: XY-scatter plot showing estimates of formation hydraulic conductivity and formation specific storage derived from the DGR2_578.10-608.60 perturbation analysis.

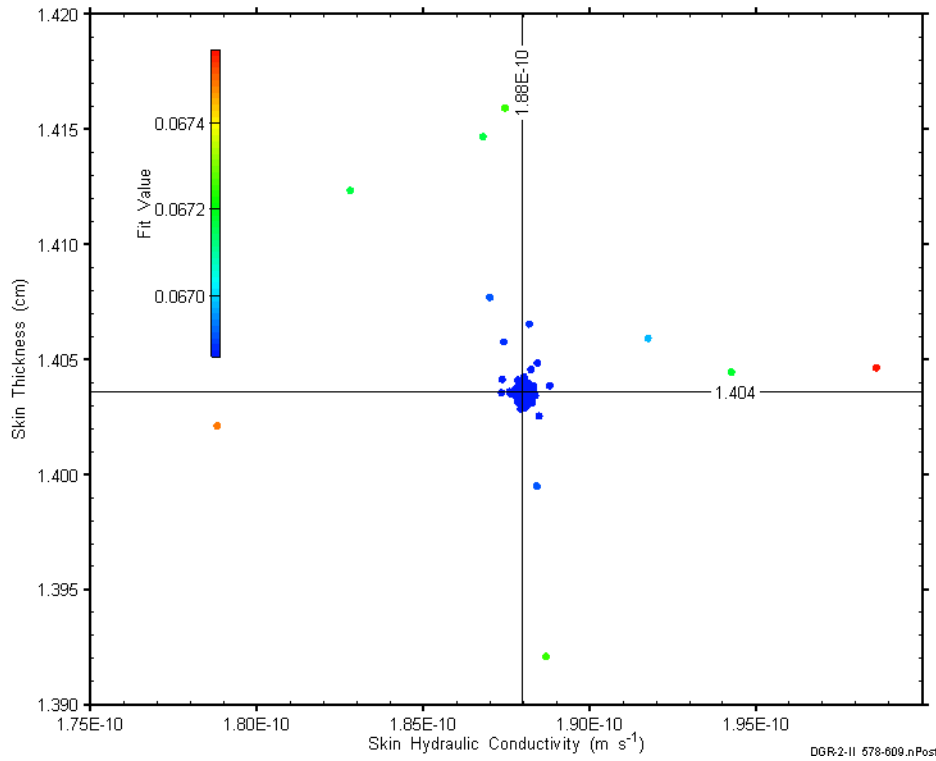


Figure B-58: XY-scatter plot showing estimates of skin hydraulic conductivity and skin thickness derived from the DGR2_578.10-608.60 perturbation analysis.

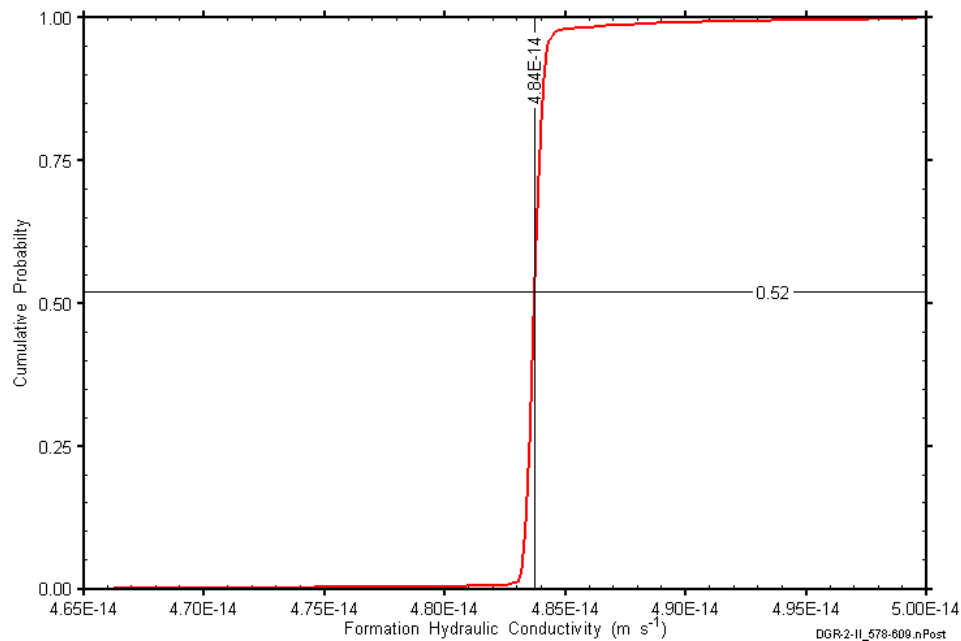


Figure B-59: DGR2_578.10-608.60 formation hydraulic conductivity cumulative distribution function.

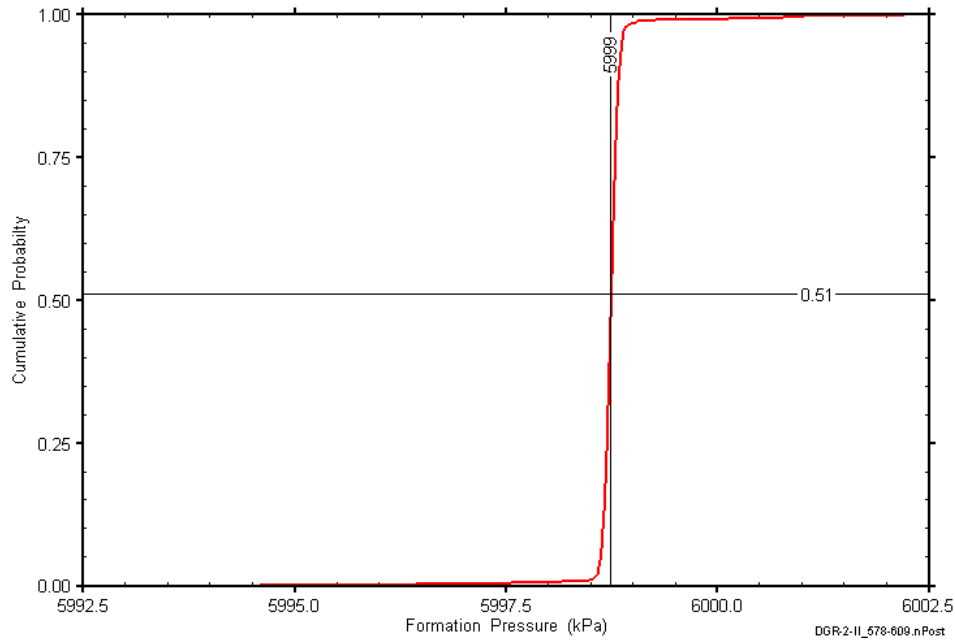


Figure B-60: DGR2_578.10-608.60 static formation pressure cumulative distribution function.

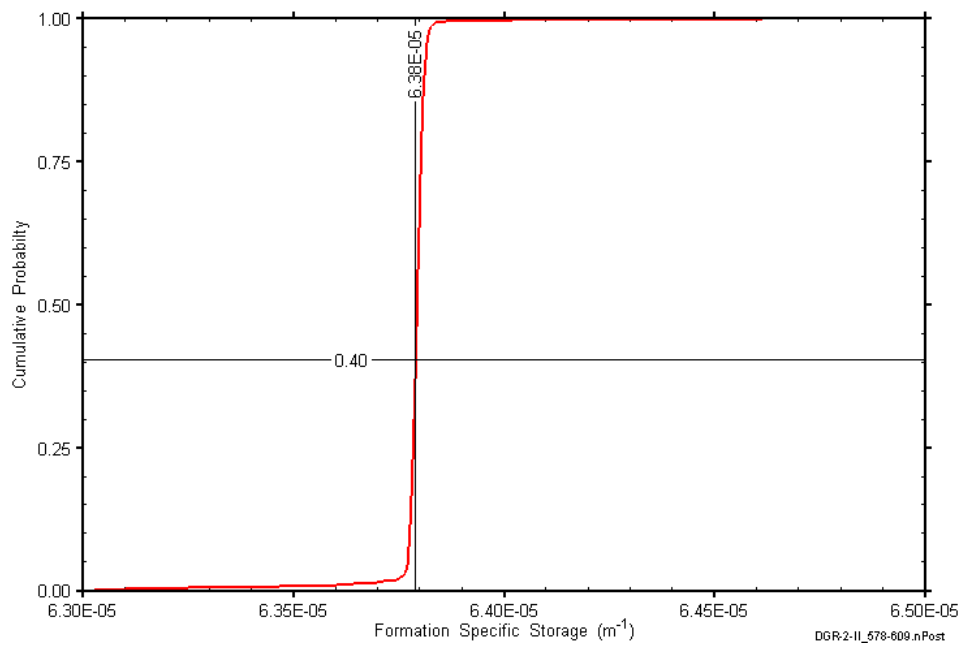


Figure B-61: DGR2_578.10-608.60 formation specific storage cumulative distribution function.

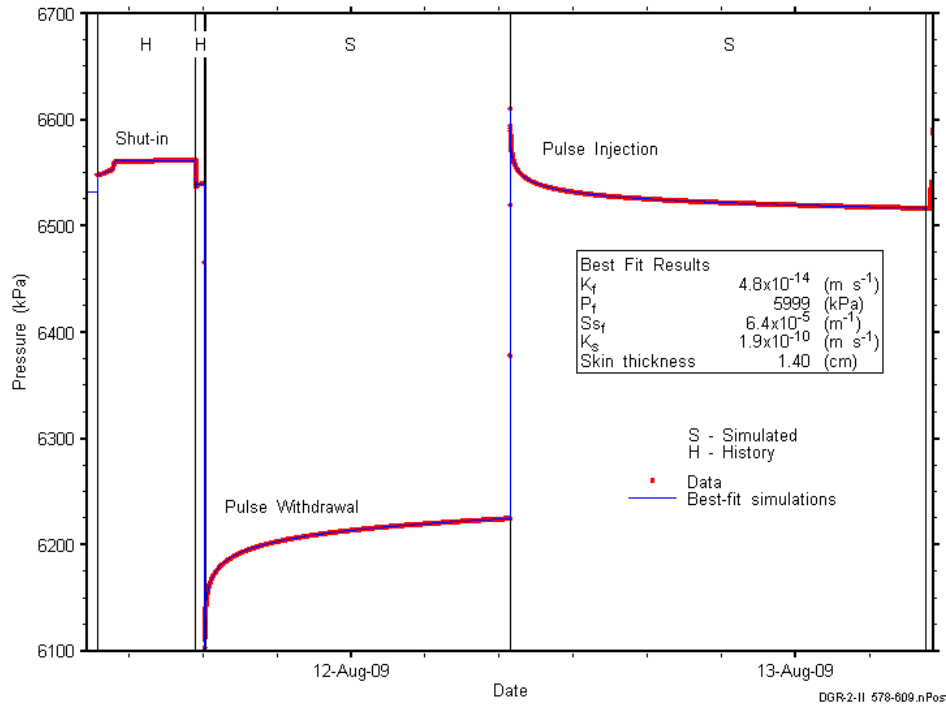


Figure B-62: Linear plot showing details of simulations of the DGR2_578.10-608.60 pressure response.

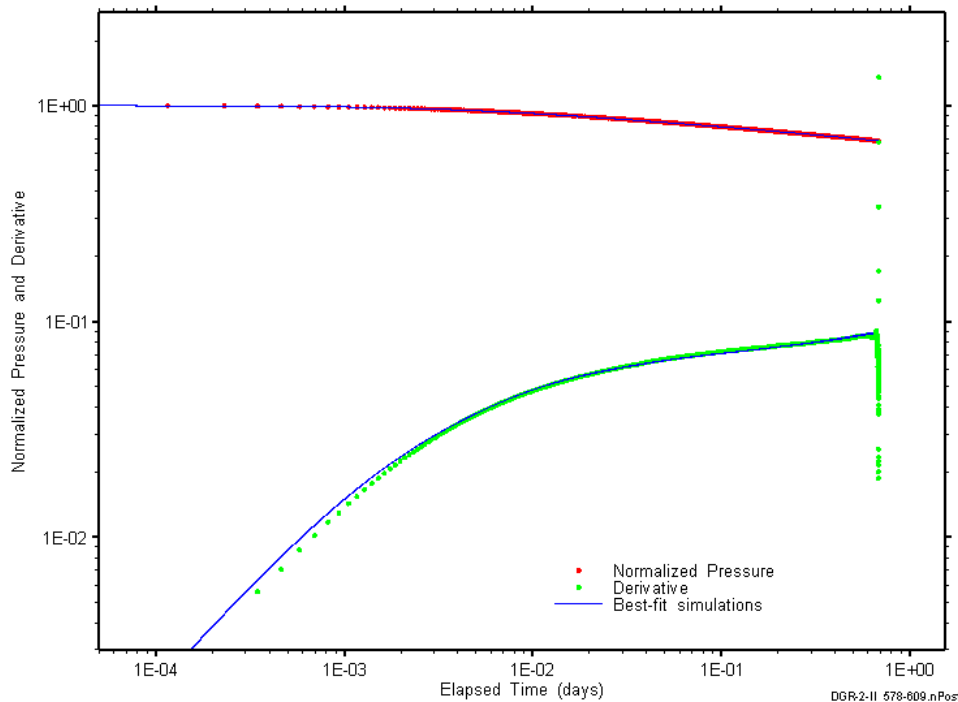


Figure B-63: Log-log plot showing simulations of the DGR2_578.10-608.60 PW Ramey B and derivative response.

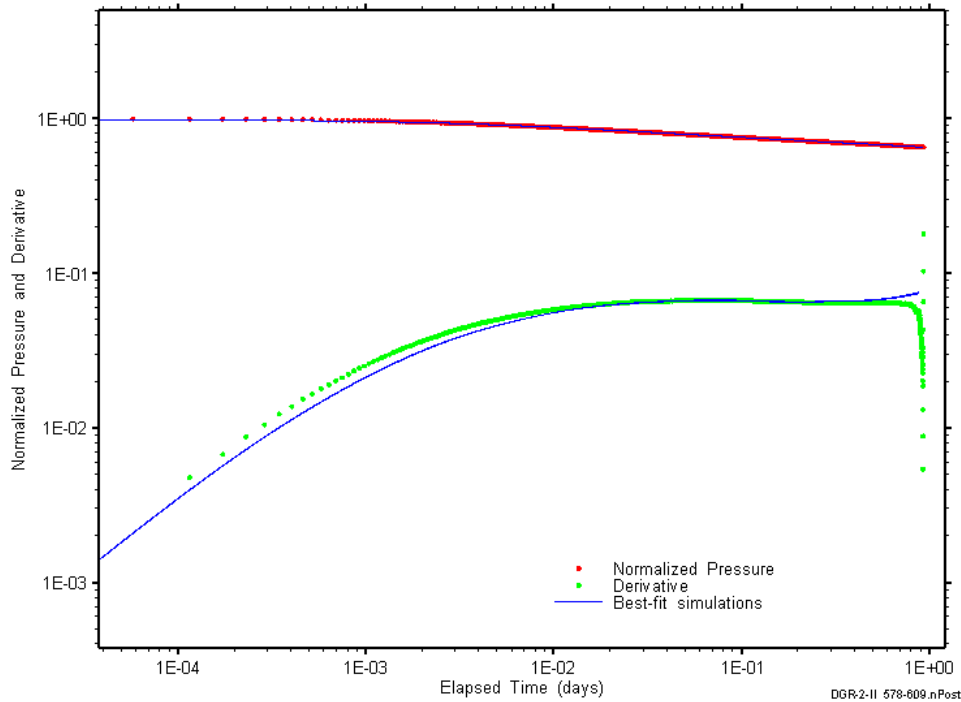


Figure B-64: Log-log plot showing simulations of the DGR2_578.10-608.60 PI Ramey B and derivative response.

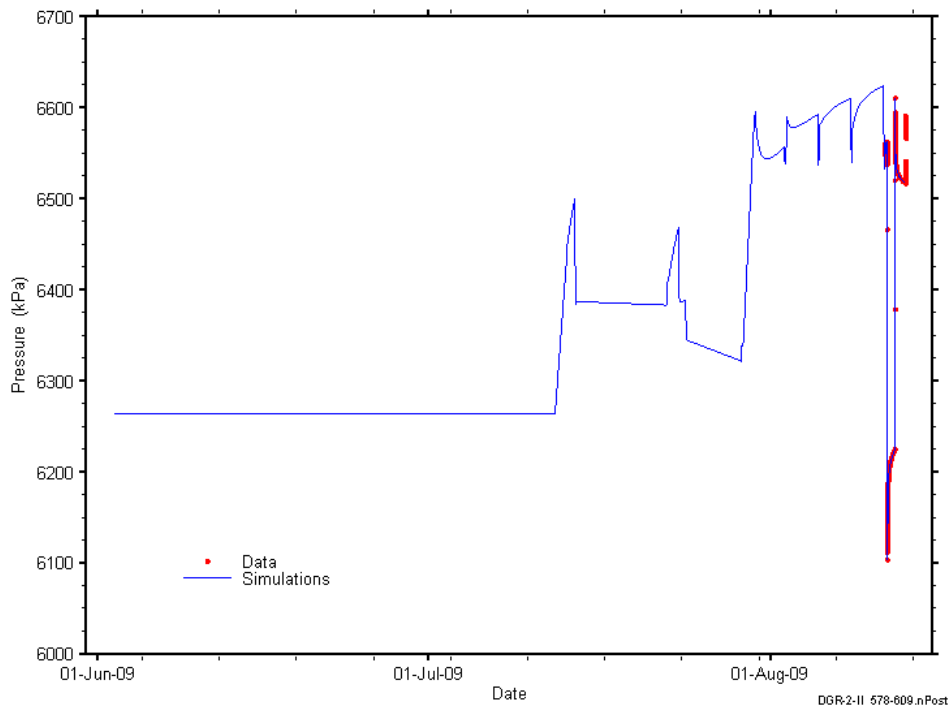


Figure B-65: Linear plot showing simulations of the DGR2_578.10-608.60 pressure response, including pre-test pressure history.

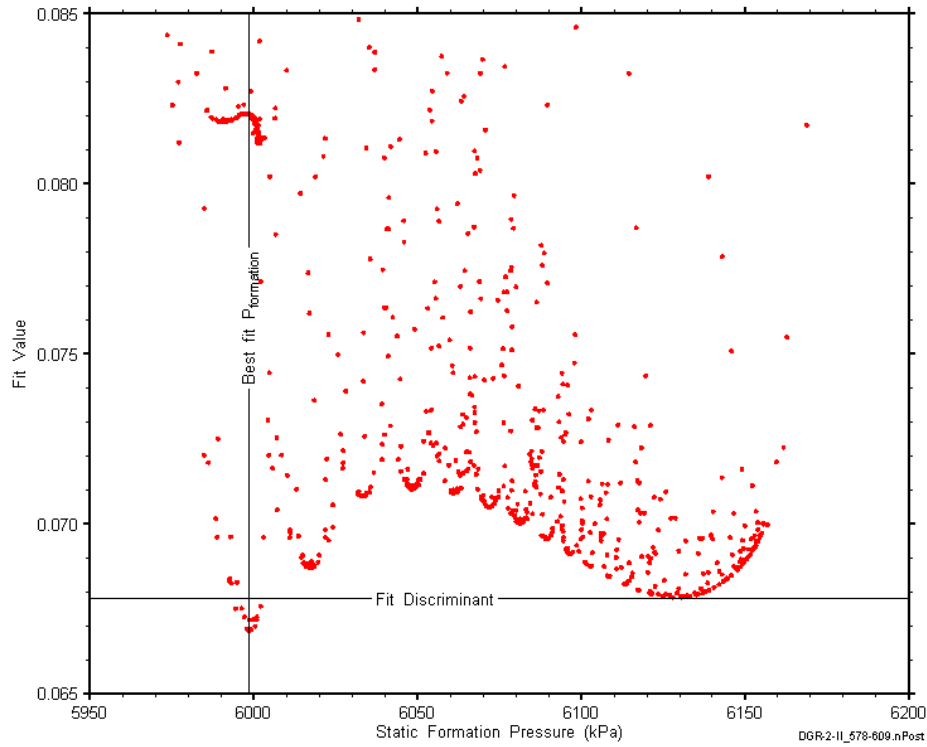


Figure B-66: XY-scatter plot showing the static formation pressure parameter space derived from DGR2_578.10-608.60 perturbation analysis along with the fit discriminant and best fit values.

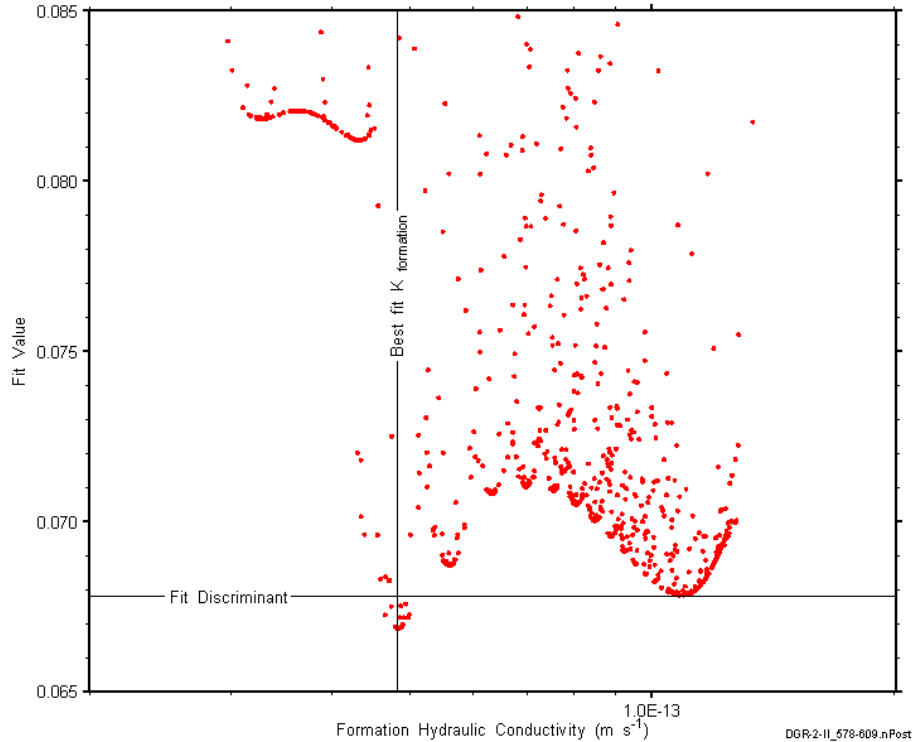


Figure B-67: XY-scatter plot showing the formation hydraulic conductivity parameter space derived from DGR2_578.10-608.60 perturbation analysis along with the fit discriminant and best fit values.

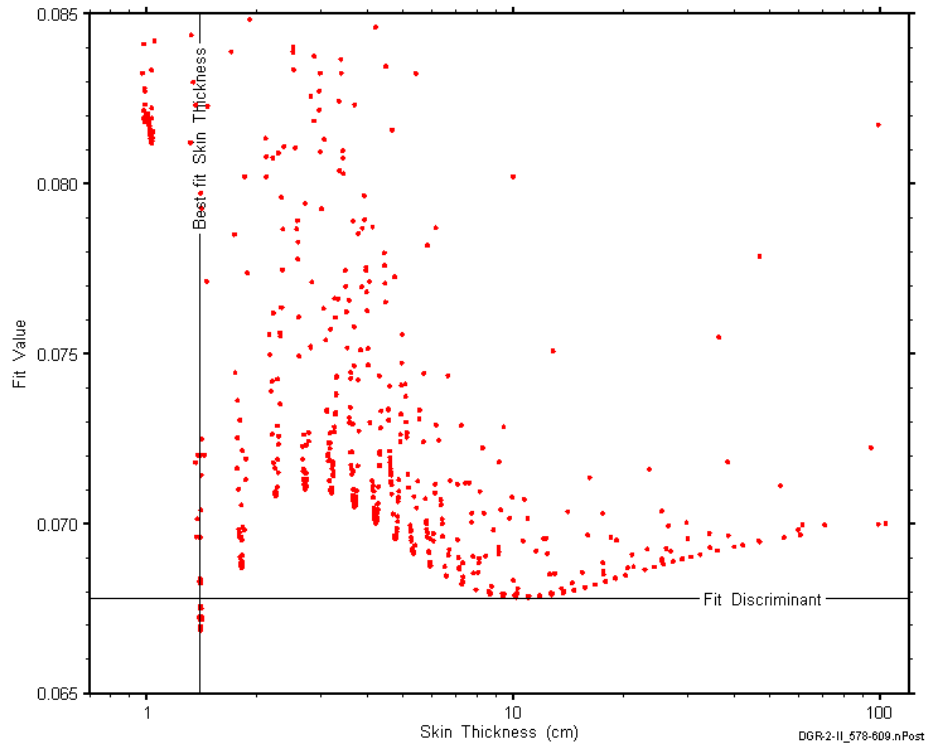


Figure B-68: XY-scatter plot showing the skin-thickness parameter space derived from DGR2_578.10-608.60 perturbation analysis along with the fit discriminant and best fit values.

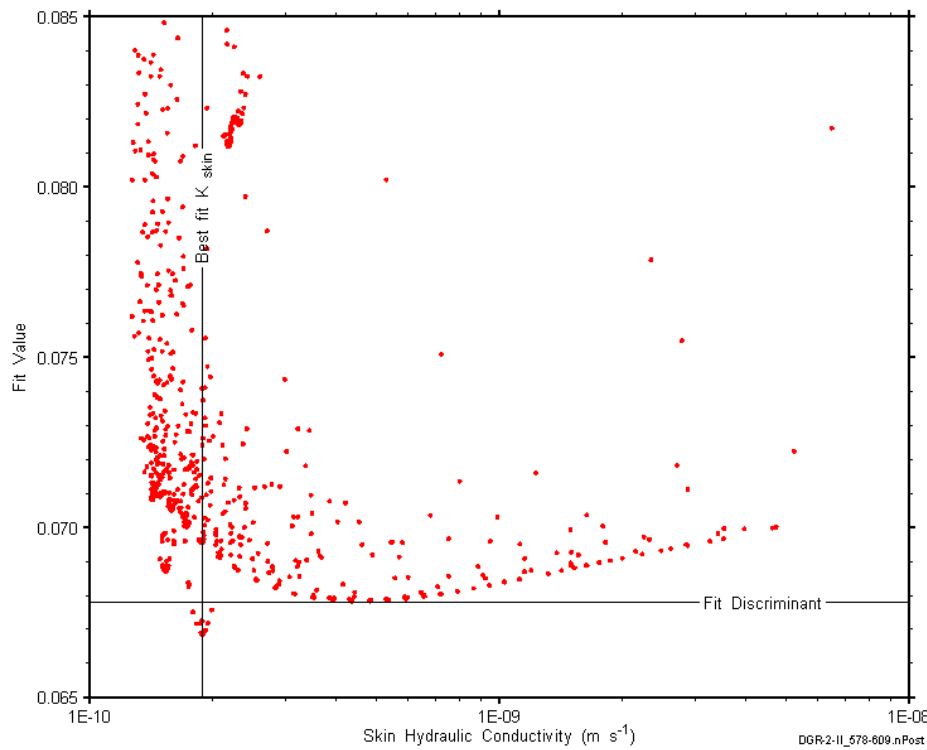


Figure B-69: XY-scatter plot showing the skin hydraulic conductivity parameter space derived from DGR2_578.10-608.60 perturbation analysis along with the fit discriminant and best fit values.

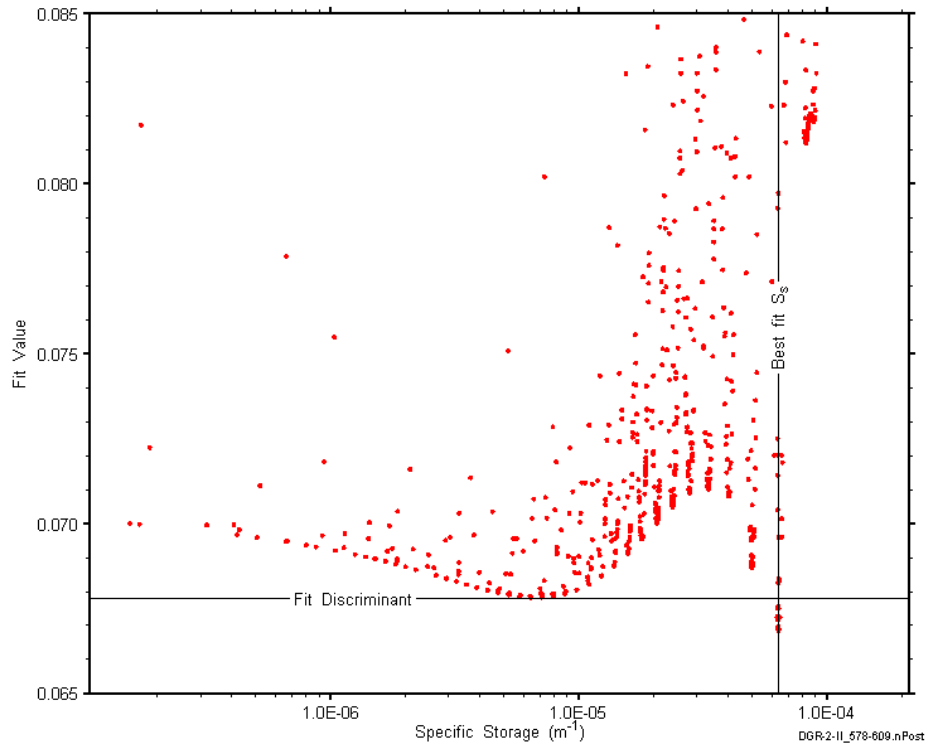


Figure B-70: XY-scatter plot showing the formation specific storage parameter space derived from DGR2_578.10-608.60 perturbation analysis along with the fit discriminant and best fit values.

B.6 608.40-638.90 Blue Mountain

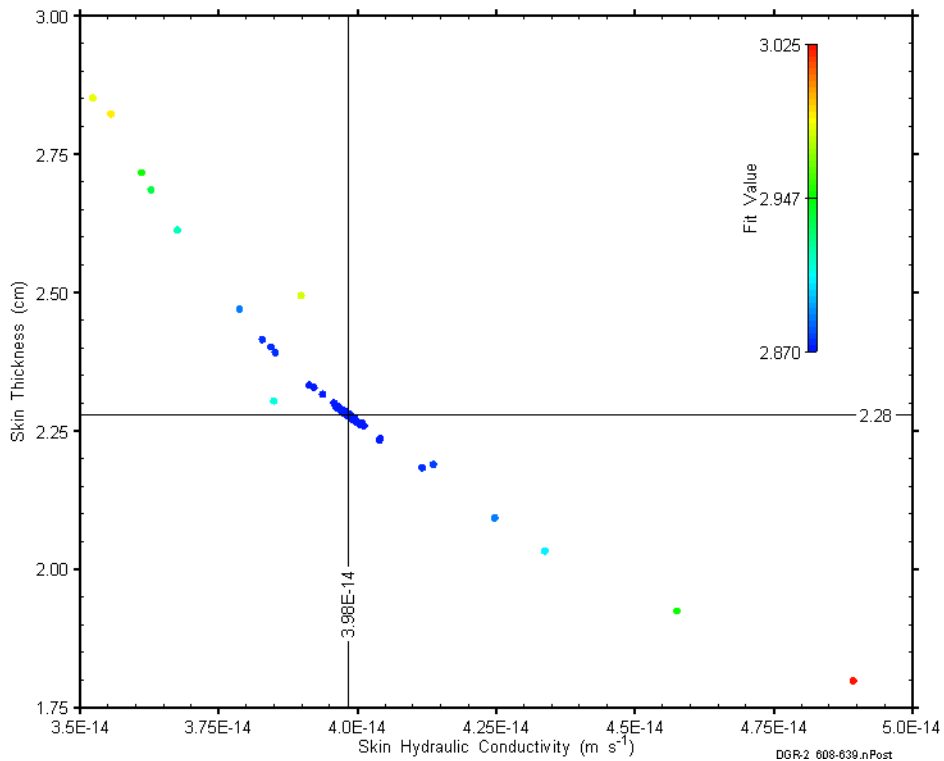


Figure B-71: XY-scatter plot showing estimates of skin hydraulic conductivity and skin thickness derived from the DGR2_608.40-638.90 perturbation analysis.

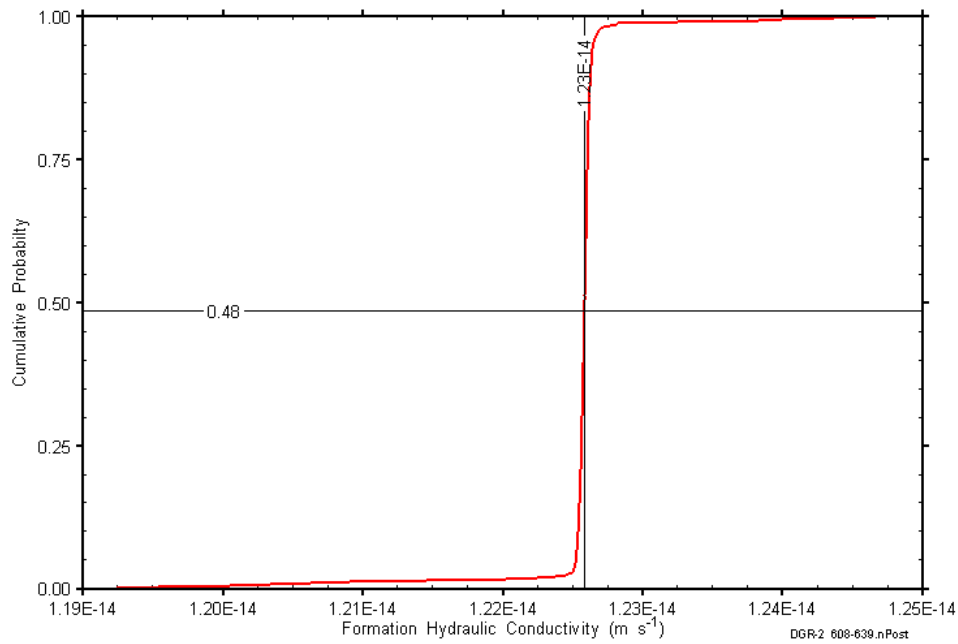


Figure B-72: DGR2_608.40-638.90 formation hydraulic conductivity cumulative distribution function.

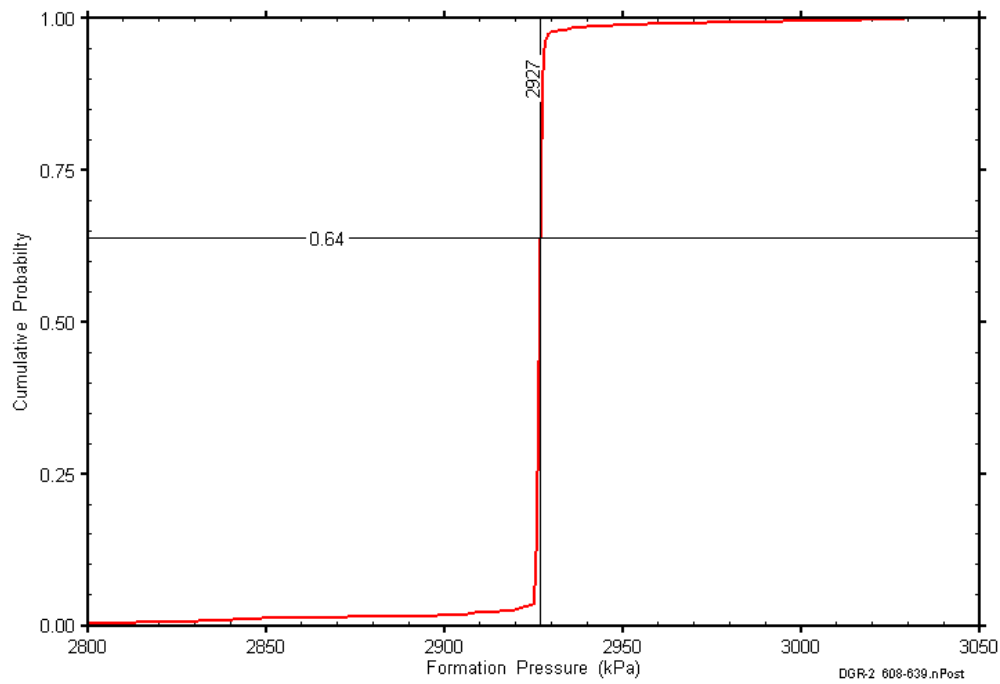


Figure B-73: DGR2_608.40-638.90 static formation pressure cumulative distribution function.

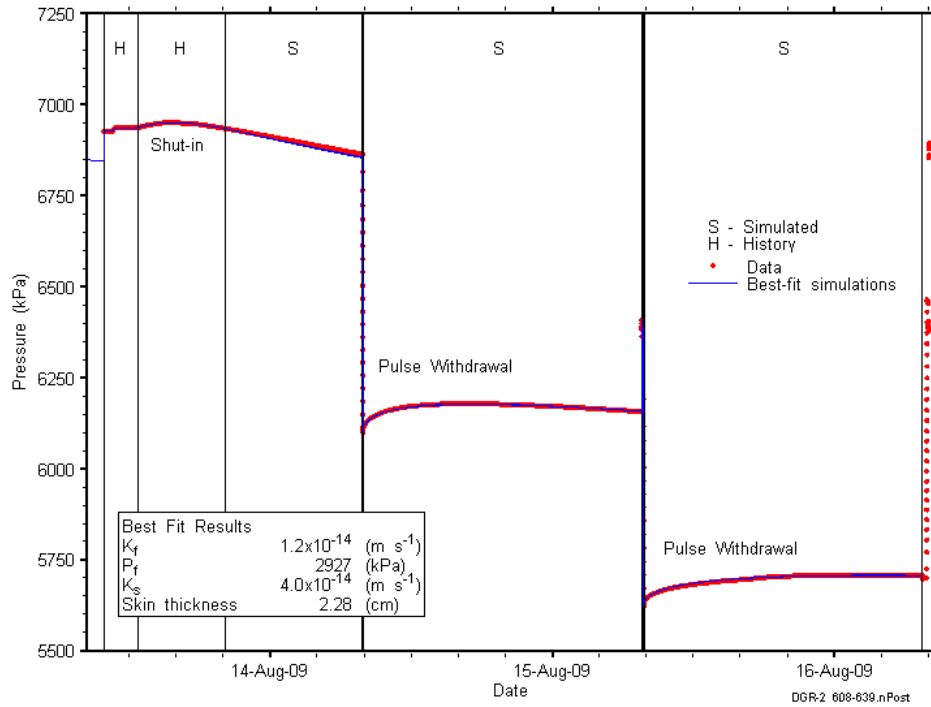


Figure B-74: Linear plot showing details of simulations of the DGR2_608.40-638.90 pressure response.

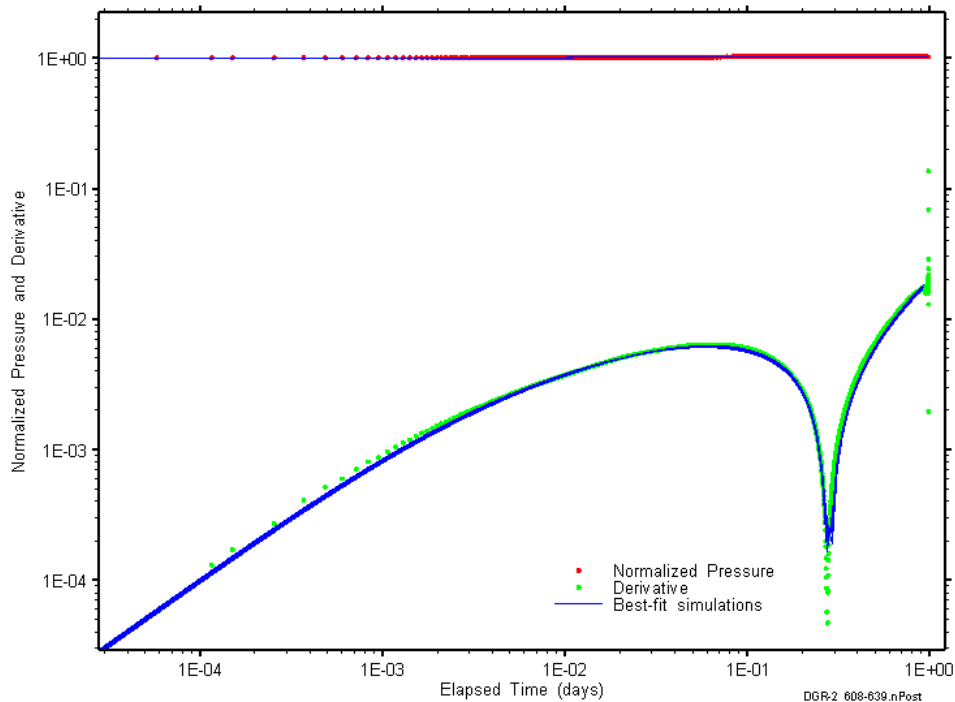


Figure B-75: Log-log plot showing simulations of the DGR2_608.40-638.90 PW1 Ramey B and derivative response.

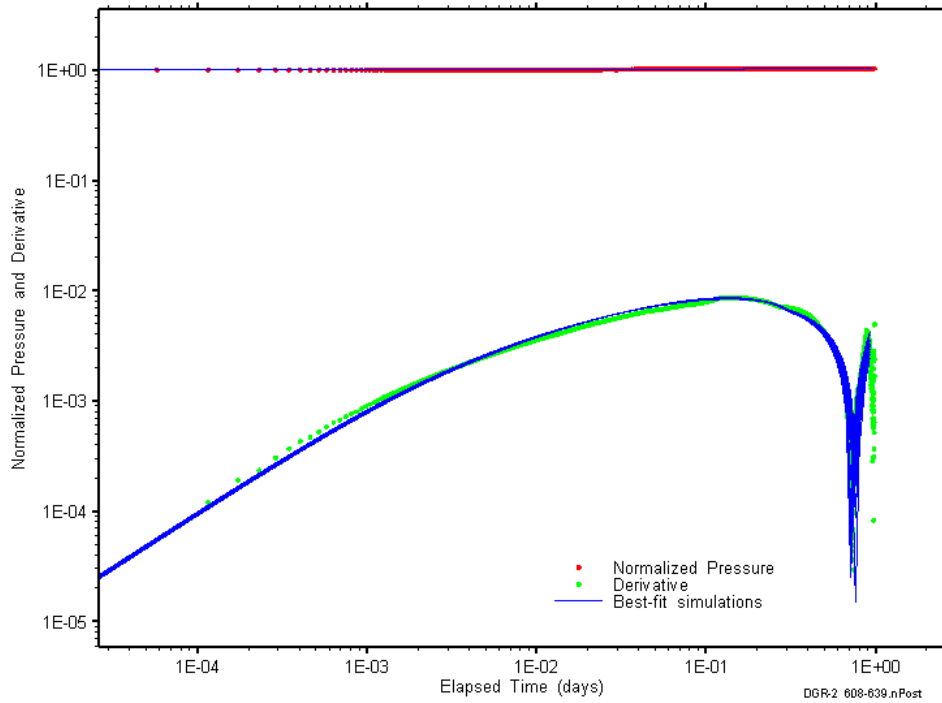


Figure B-76: Log-log plot showing simulations of the DGR2_608.40-638.90 PW2 Ramey B and derivative response.

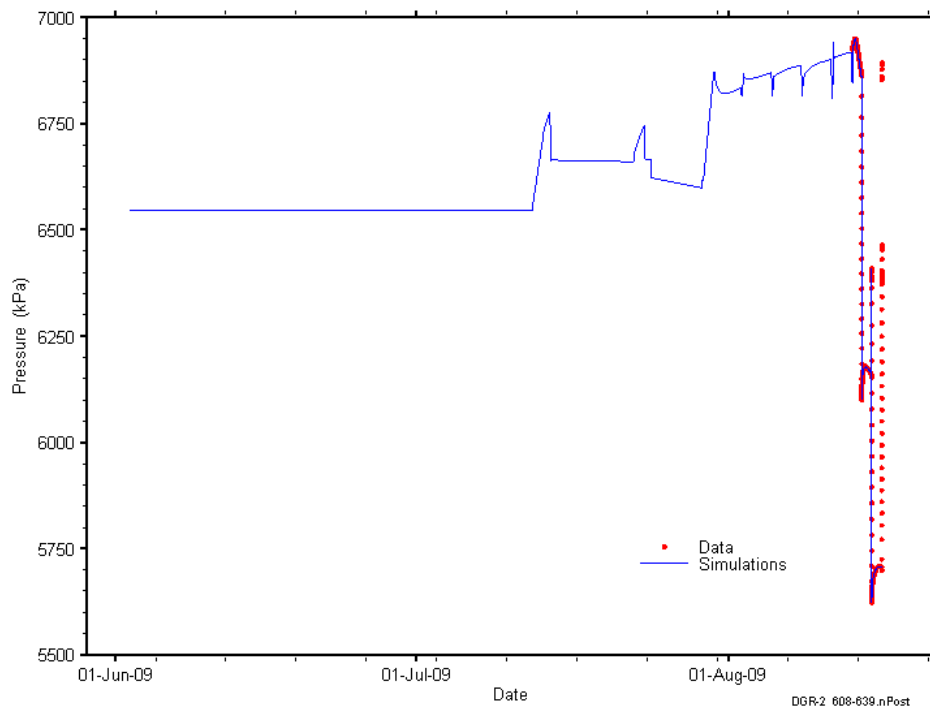


Figure B-77: Linear plot showing simulations of the DGR2_608.40-638.90 pressure response, including pre-test pressure history.

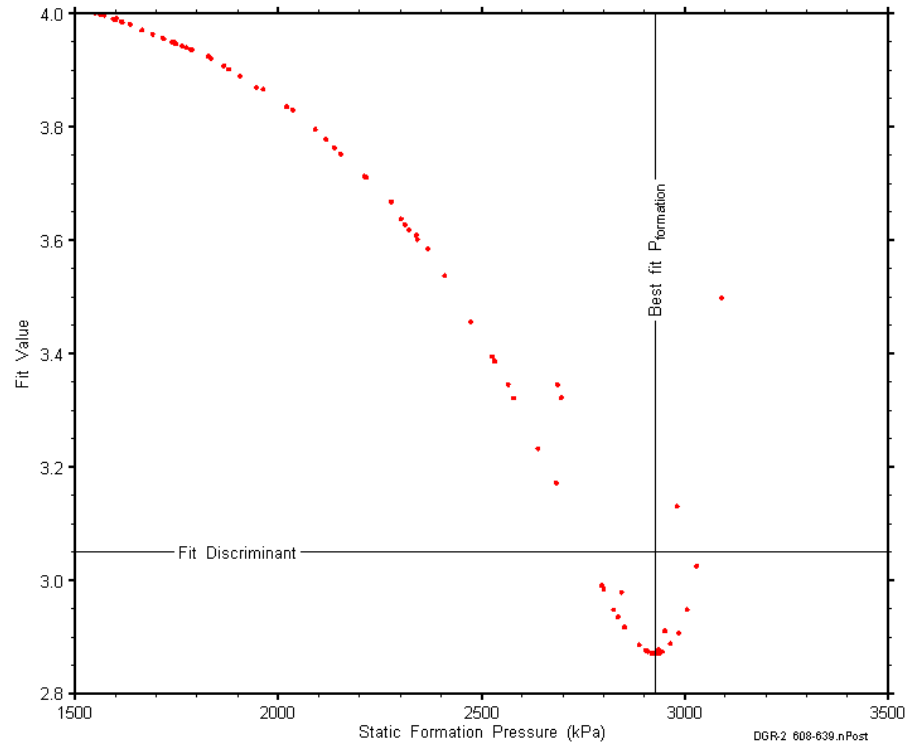


Figure B-78: XY-scatter plot showing the static formation pressure parameter space derived from DGR2_608.40-638.90 perturbation analysis along with the fit discriminant and best fit values.

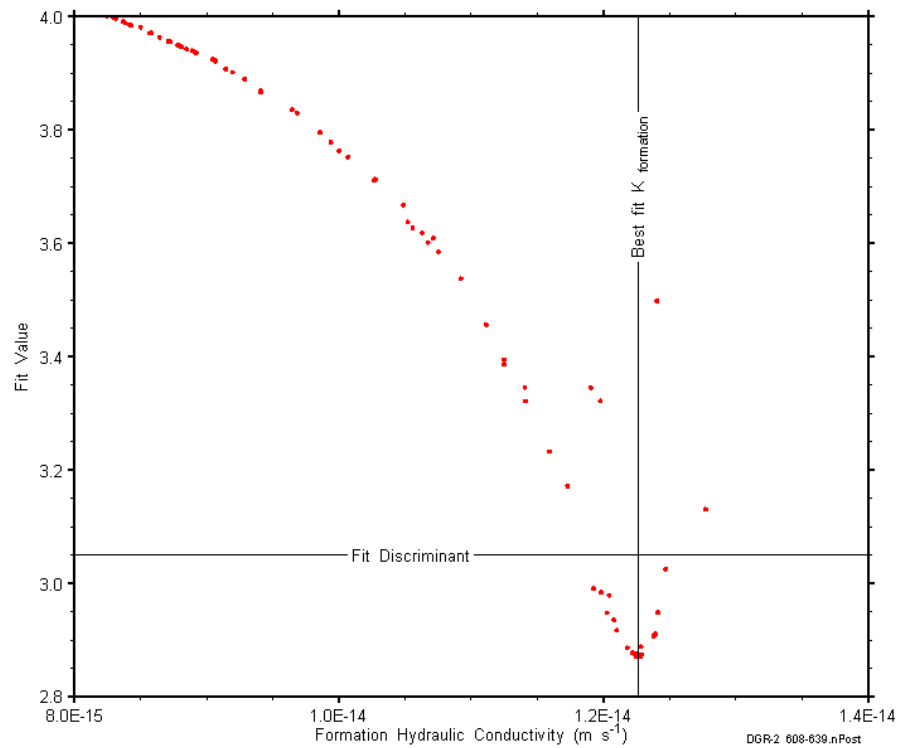


Figure B-79: XY-scatter plot showing the formation hydraulic conductivity parameter space derived from DGR2_608.40-638.90 perturbation analysis along with the fit discriminant and best fit values.

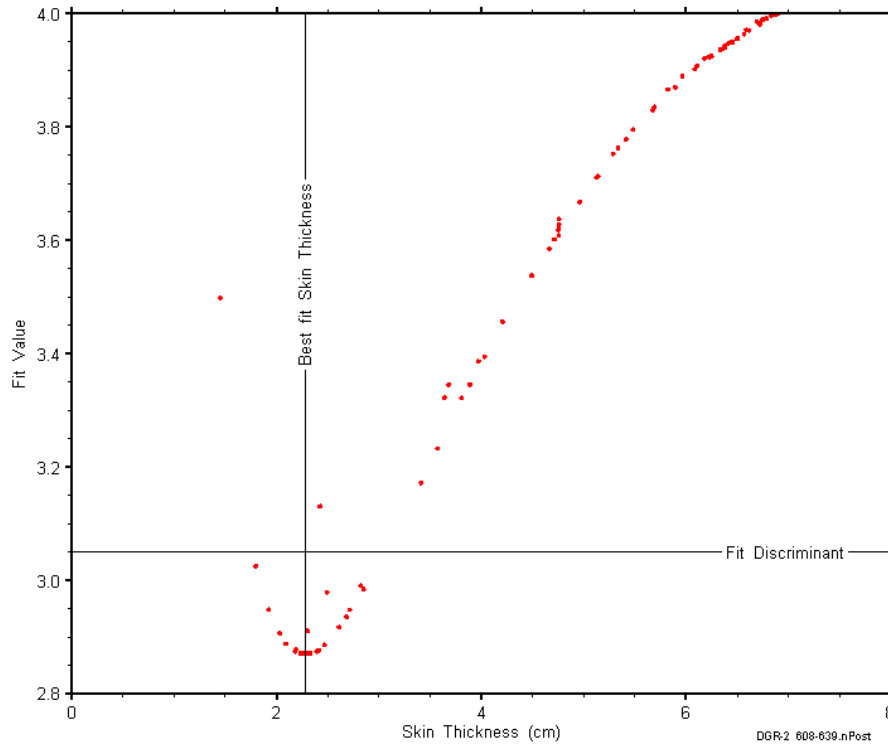


Figure B-80: XY-scatter plot showing the skin-thickness parameter space derived from DGR2_608.40-638.90 perturbation analysis along with the fit discriminant and best fit values.

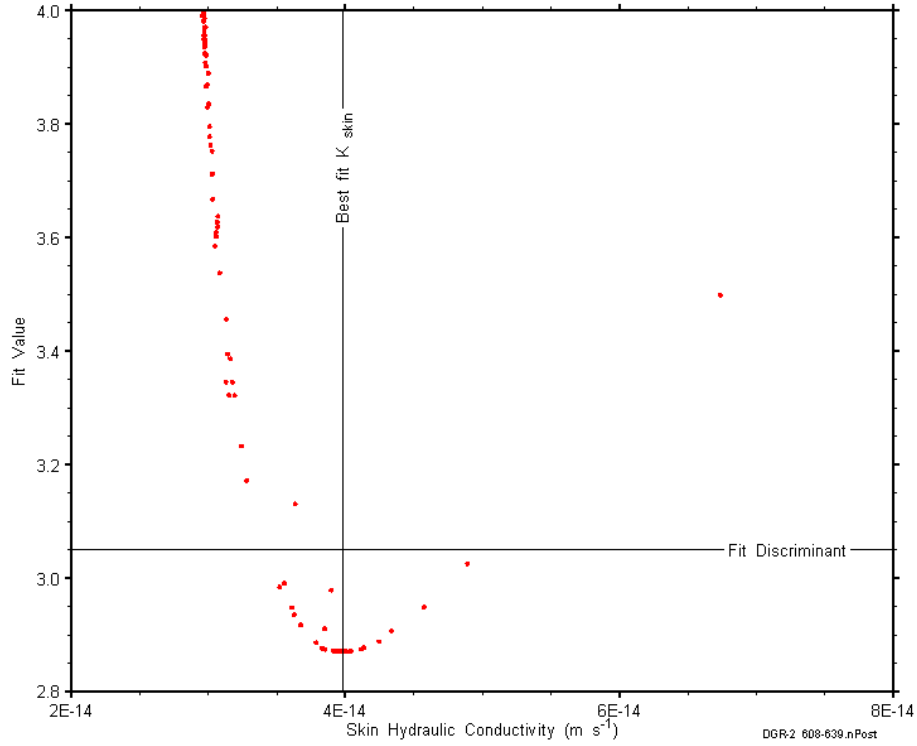


Figure B-81: XY-scatter plot showing the skin hydraulic conductivity parameter space derived from DGR2_608.40-638.90 perturbation analysis along with the fit discriminant and best fit values.

B.7 630.50-661.00 Collingwood

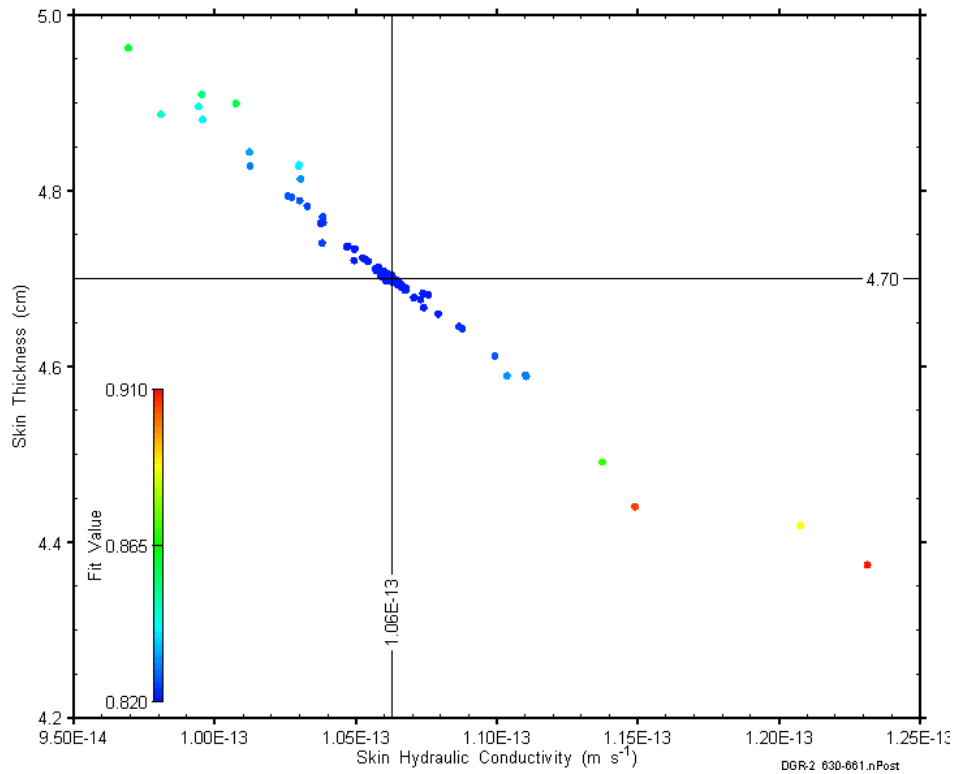


Figure B-82: XY-scatter plot showing estimates of skin hydraulic conductivity and skin thickness derived from the DGR2_630.50-661.00 perturbation analysis.

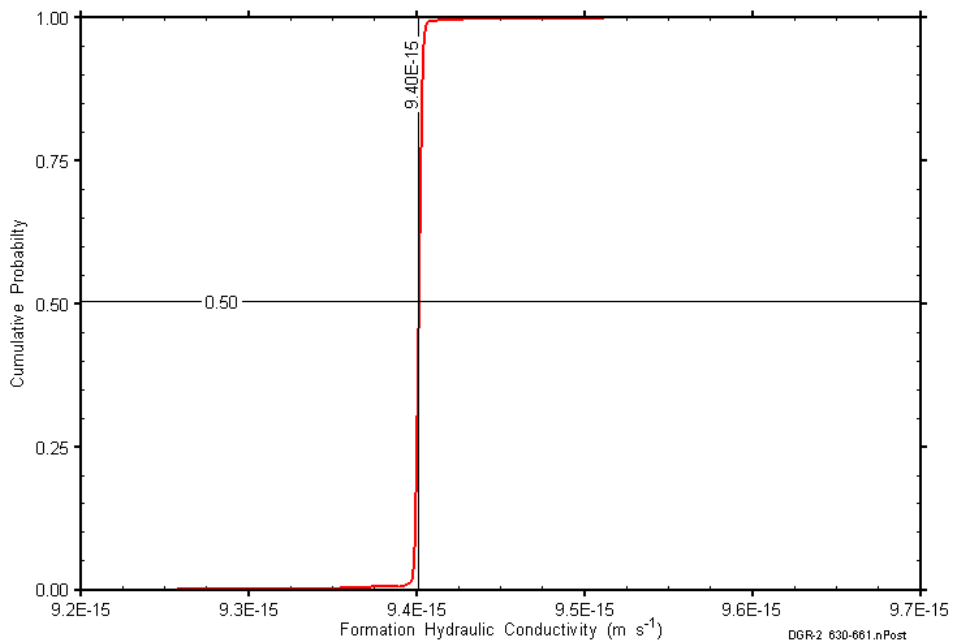


Figure B-83: DGR2_630.50-661.00 formation hydraulic conductivity cumulative distribution function.

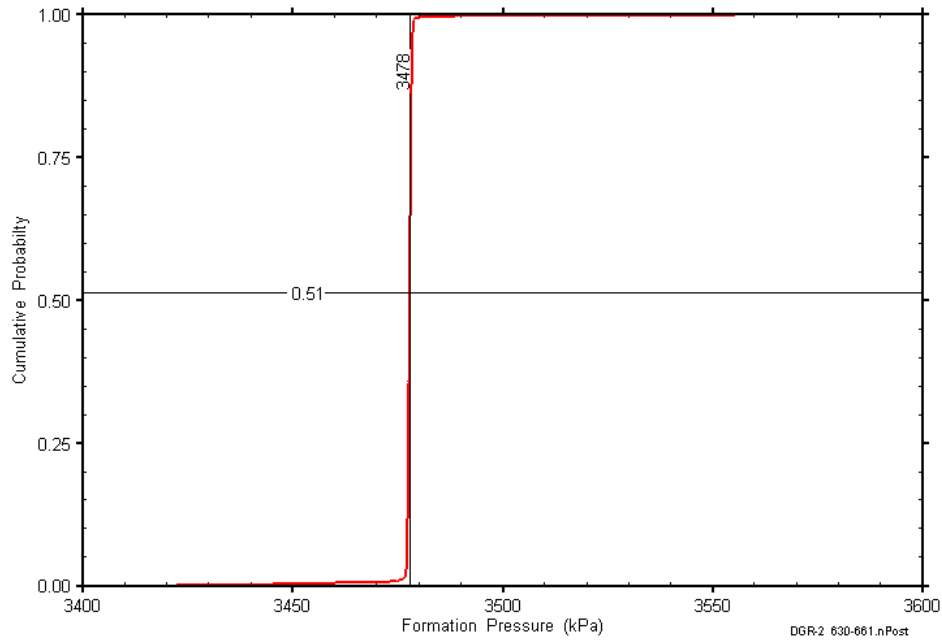


Figure B-84: DGR2_630.50-661.00 static formation pressure cumulative distribution function.

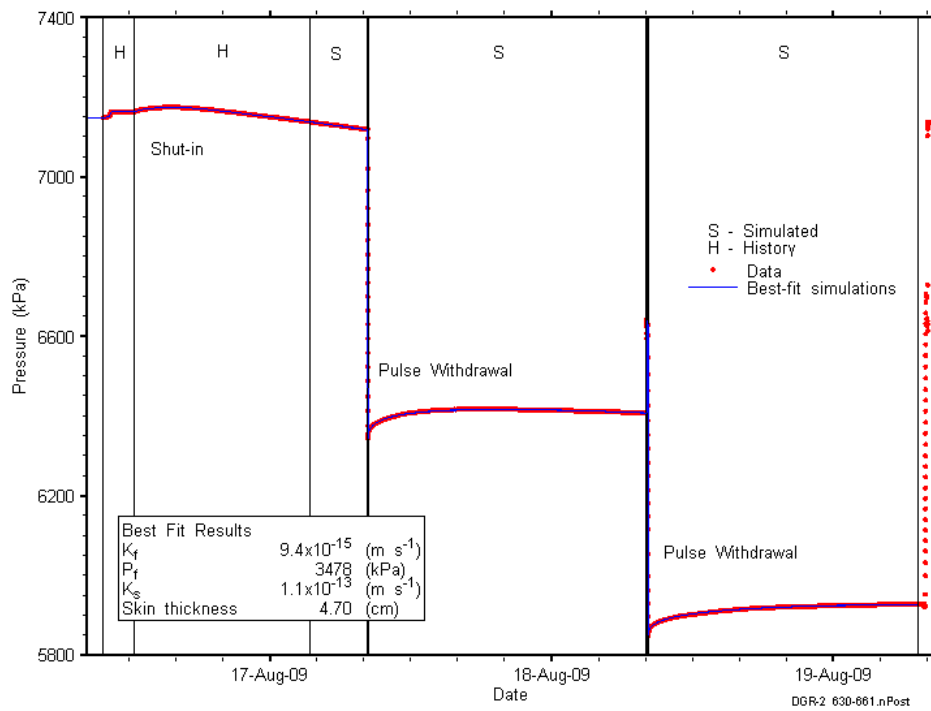


Figure B-85: Linear plot showing details of simulations of the DGR2_630.50-661.00 pressure response.

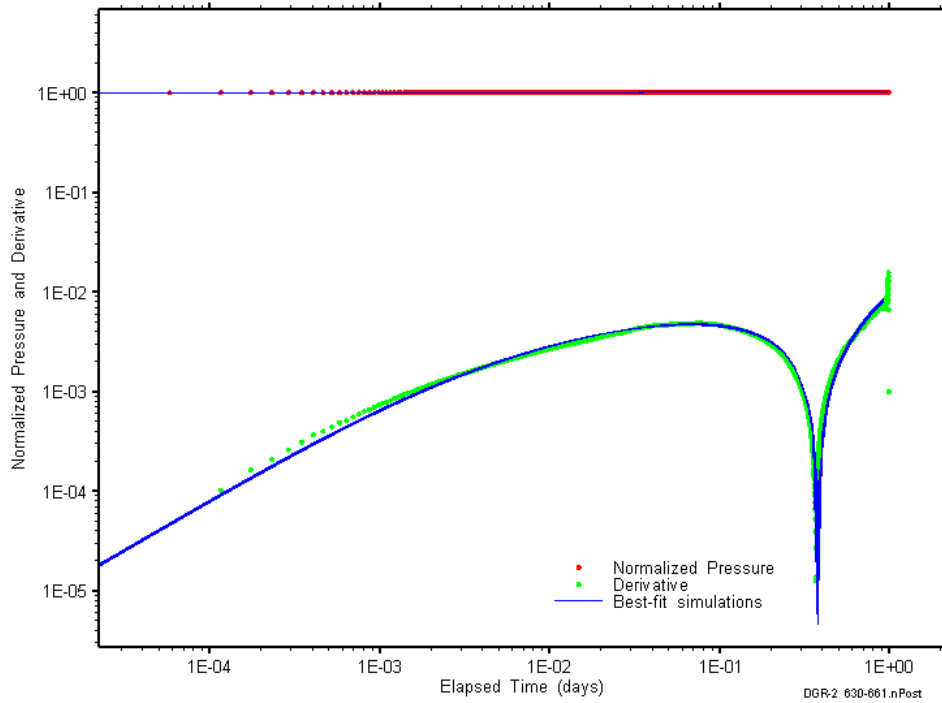


Figure B-86: Log-log plot showing simulations of the DGR2_630.50-661.00 PW1 Ramey B and derivative response.

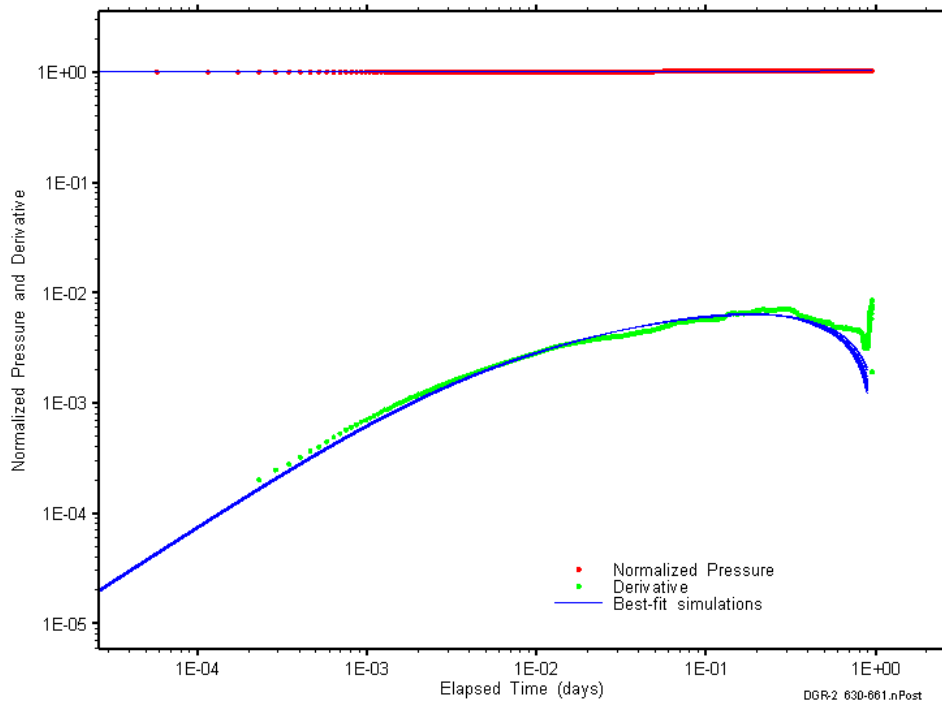


Figure B-87: Log-log plot showing simulations of the DGR2_630.50-661.00 PW2 Ramey B and derivative response.

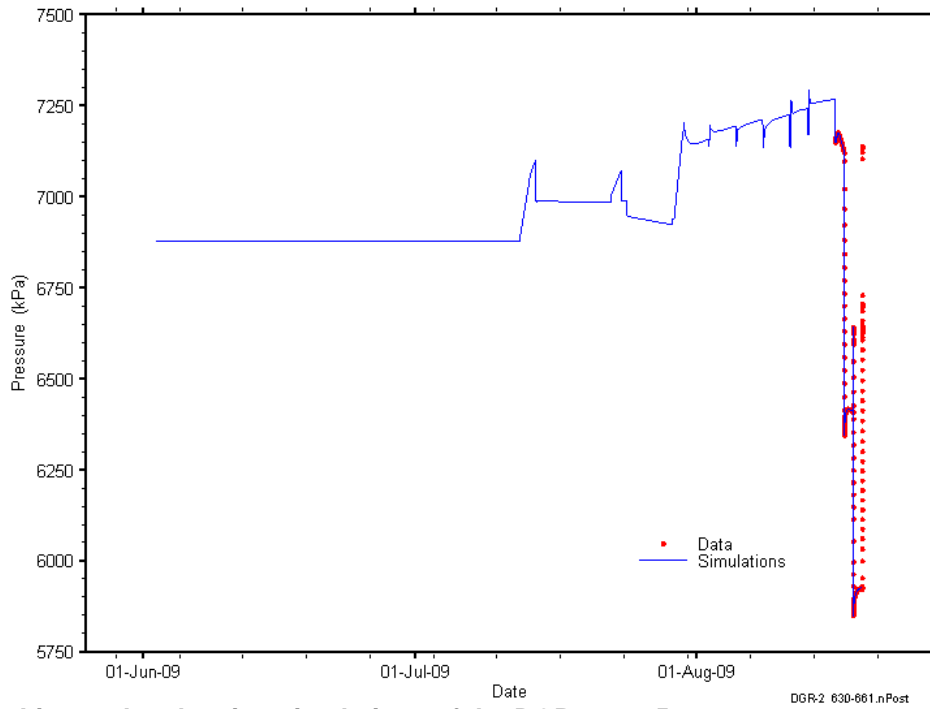


Figure B-88: Linear plot showing simulations of the DGR2_630.50-661.00 pressure response, including pre-test pressure history.

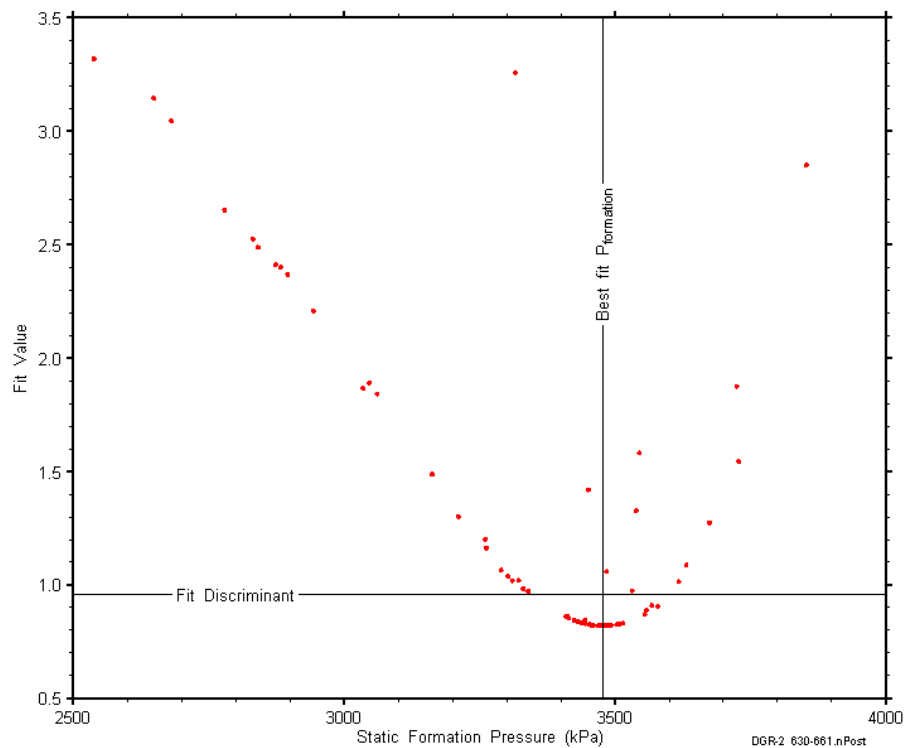


Figure B-89: XY-scatter plot showing the static formation pressure parameter space derived from DGR2_630.50-661.00 perturbation analysis along with the fit discriminant and best fit values.

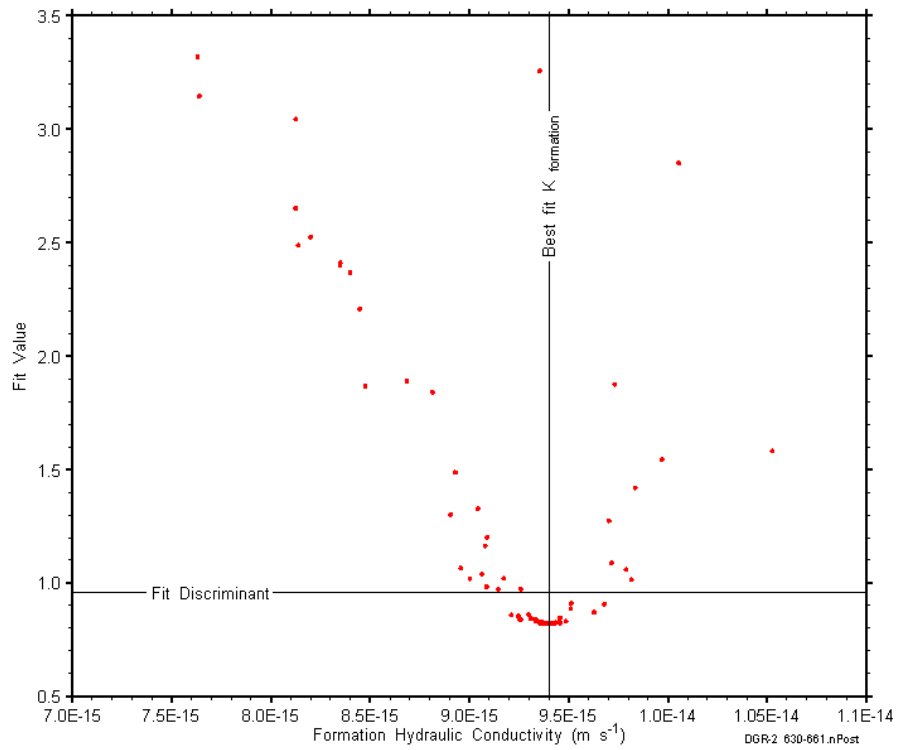


Figure B-90: XY-scatter plot showing the formation hydraulic conductivity parameter space derived from DGR2_630.50-661.00 perturbation analysis along with the fit discriminant and best fit values.

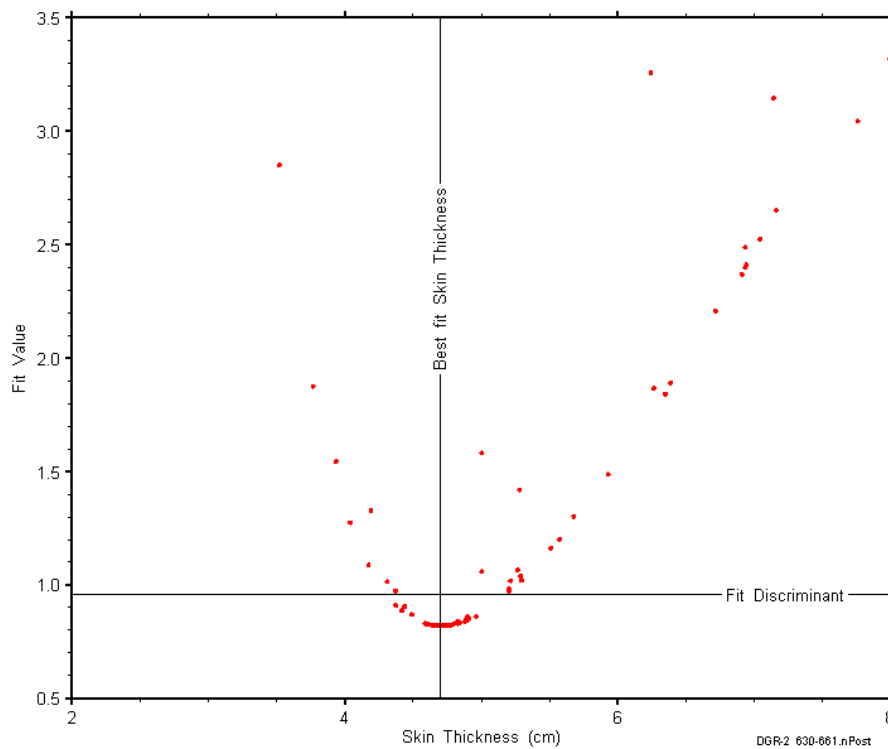


Figure B-91: XY-scatter plot showing the skin-thickness parameter space derived from DGR2_630.50-661.00 perturbation analysis along with the fit discriminant and best fit values.

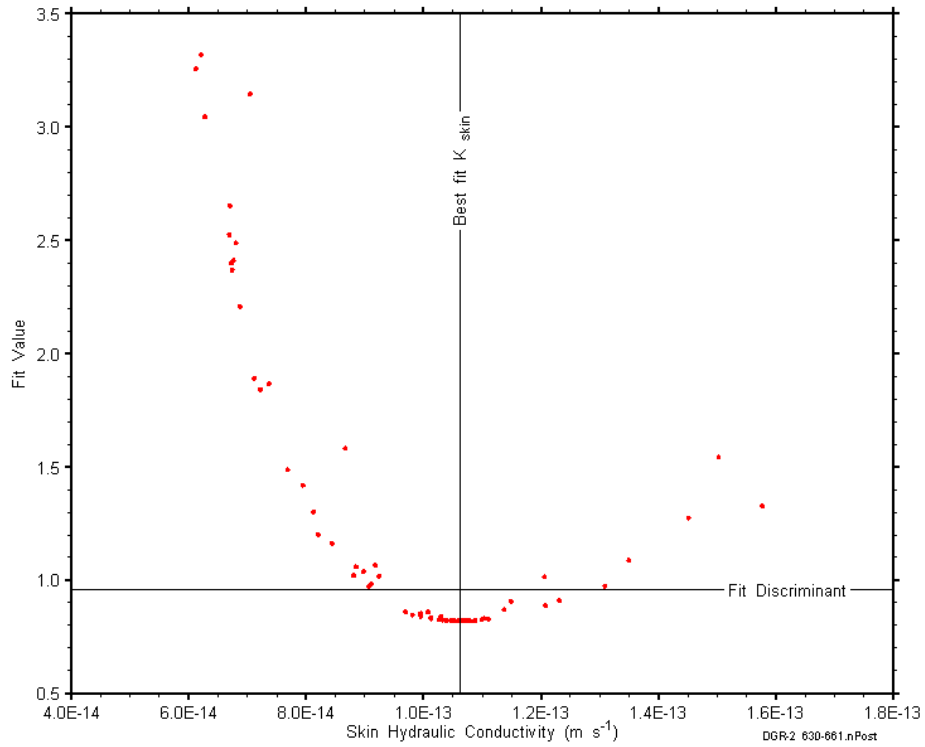


Figure B-92: XY-scatter plot showing the skin hydraulic conductivity parameter space derived from DGR2_630.50-661.00 perturbation analysis along with the fit discriminant and best fit values.

B.8 660.50-691.00 Cobourg

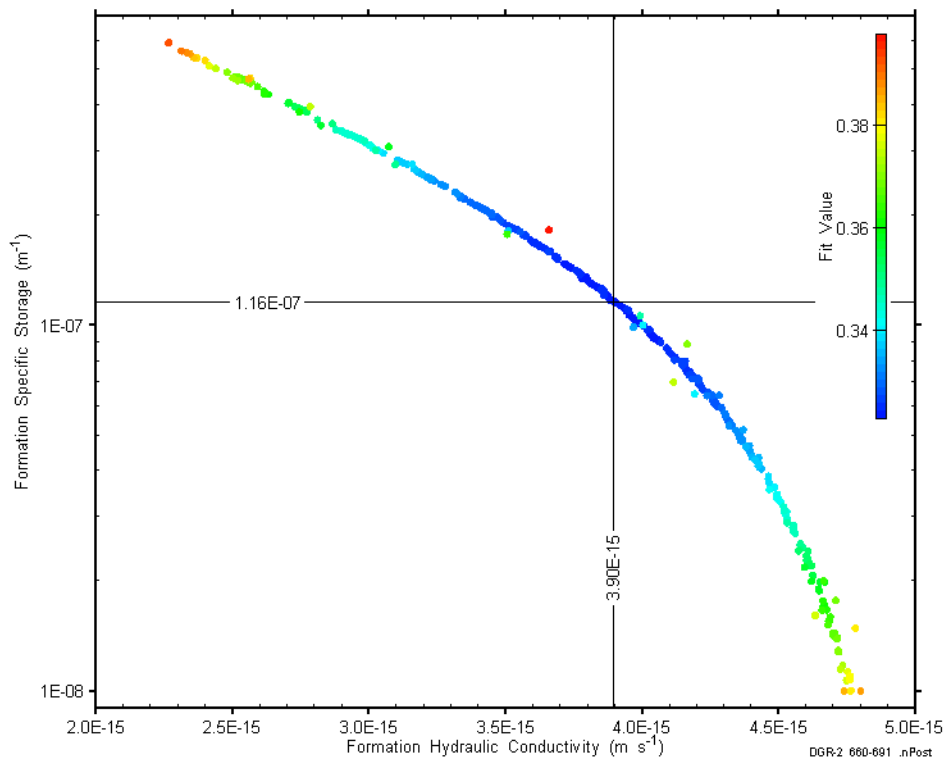


Figure B-93: XY-scatter plot showing estimates of formation hydraulic conductivity and formation specific storage derived from the DGR2_660.50-691.00 perturbation analysis.

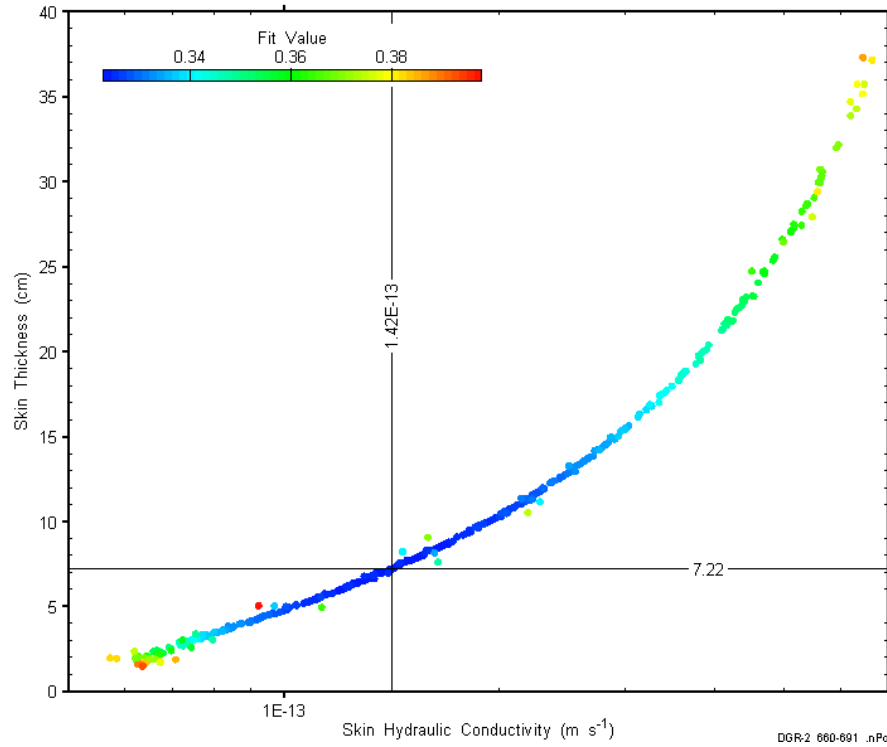


Figure B-94: XY-scatter plot showing estimates of skin hydraulic conductivity and skin thickness derived from the DGR2_660.50-691.00 perturbation analysis.

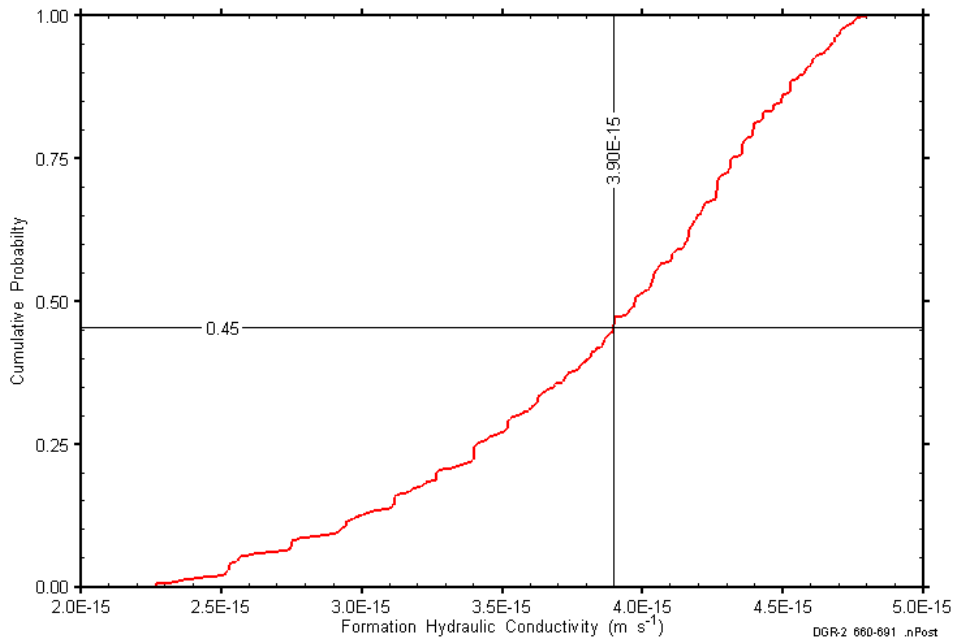


Figure B-95: DGR2_660.50-691.00 formation hydraulic conductivity cumulative distribution function.

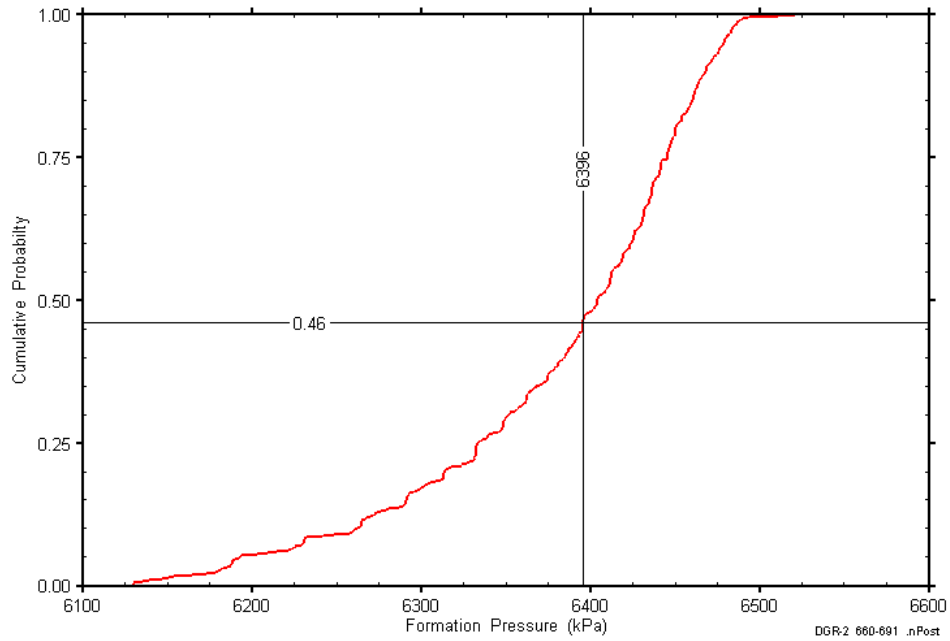


Figure B-96: DGR2_660.50-691.00 static formation pressure cumulative distribution function.

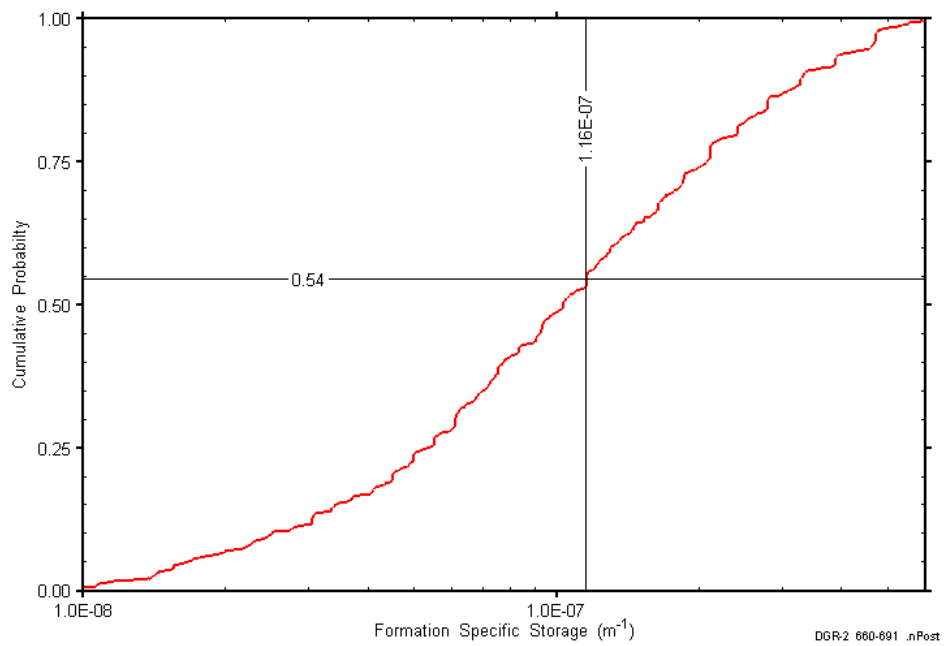


Figure B-97: DGR2_660.50-691.00 formation specific storage cumulative distribution function.

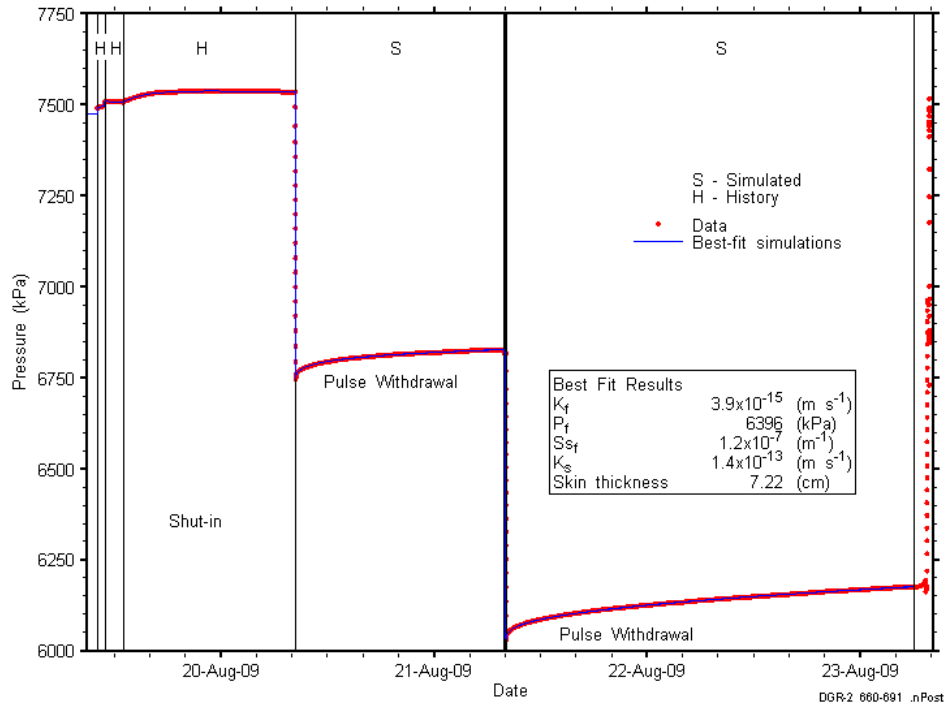


Figure B-98: Linear plot showing details of simulations of the DGR2_660.50-691.00 pressure response.

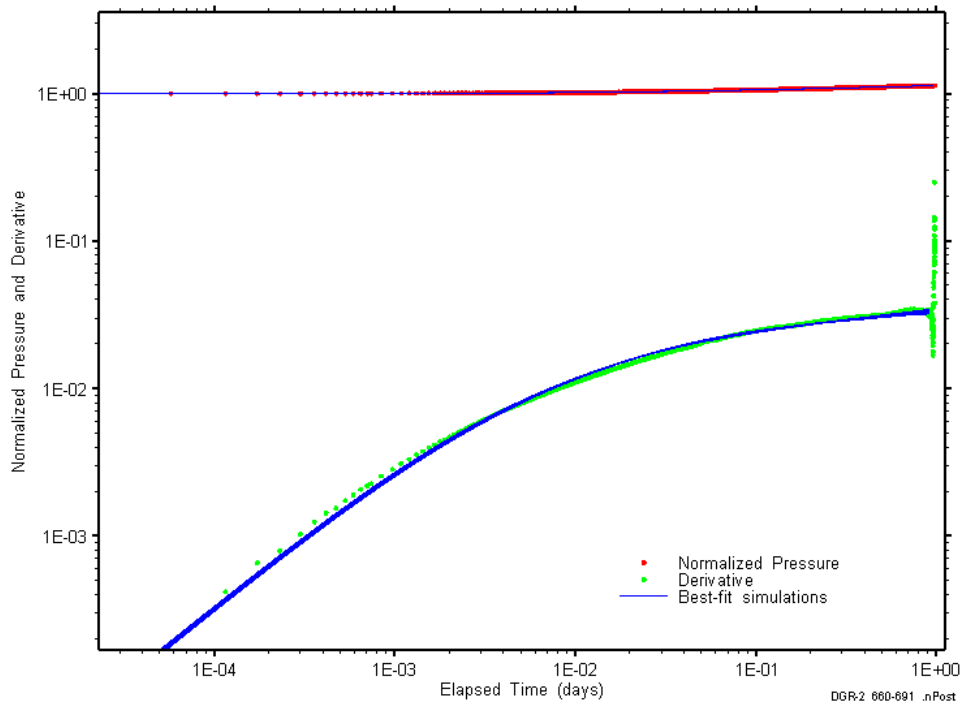


Figure B-99: Log-log plot showing simulations of the DGR2_660.50-691.00 PW1 Ramey B and derivative response.

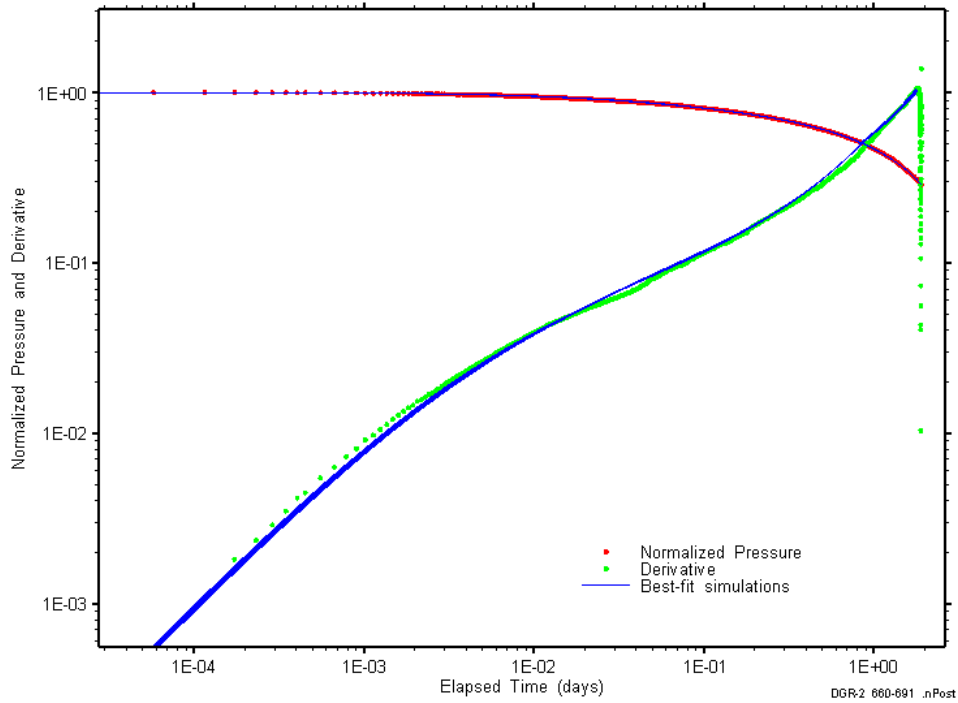


Figure B-100: Log-log plot showing simulations of the DGR2_660.50-691.00 PW2 Ramey B and derivative response.

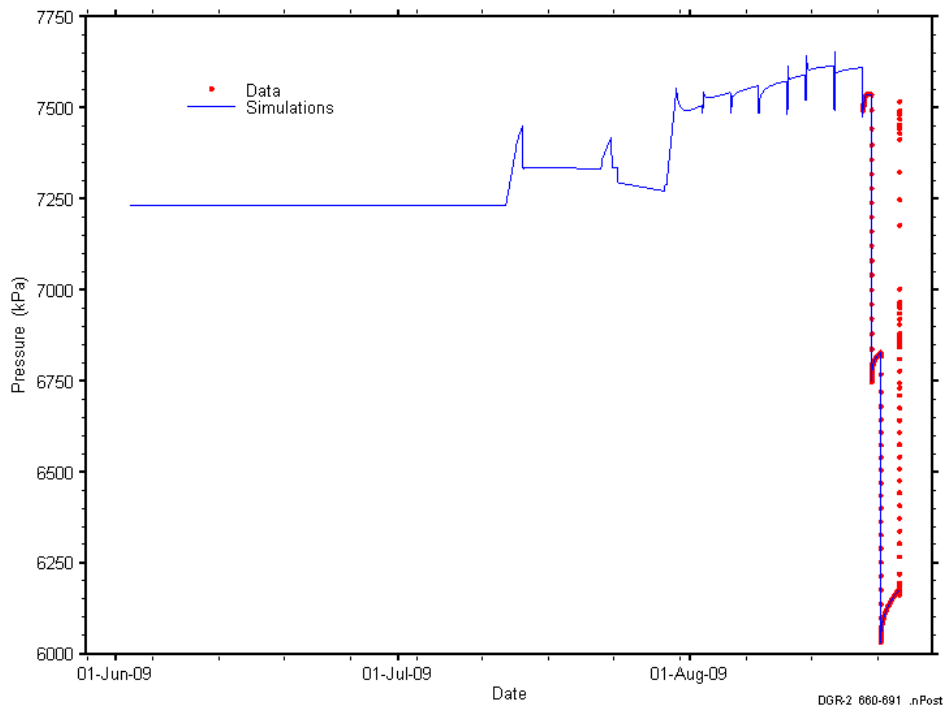


Figure B-101: Linear plot showing simulations of the DGR2_660.50-691.00 pressure response, including pre-test pressure history.

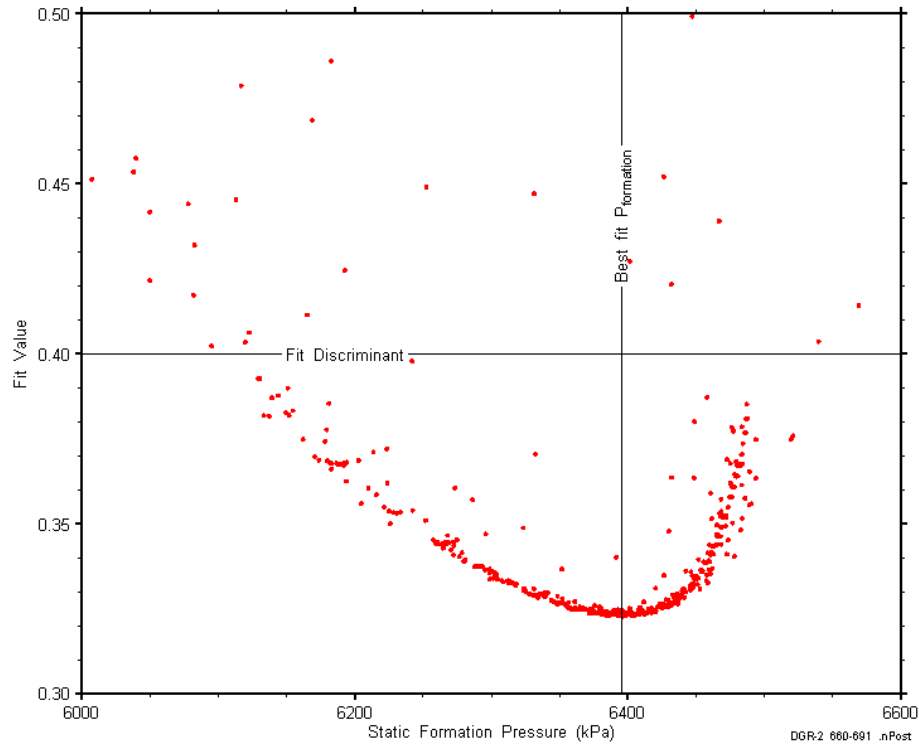


Figure B-102: XY-scatter plot showing the static formation pressure parameter space derived from DGR2_660.50-691.00 perturbation analysis along with the fit discriminant and best fit values.

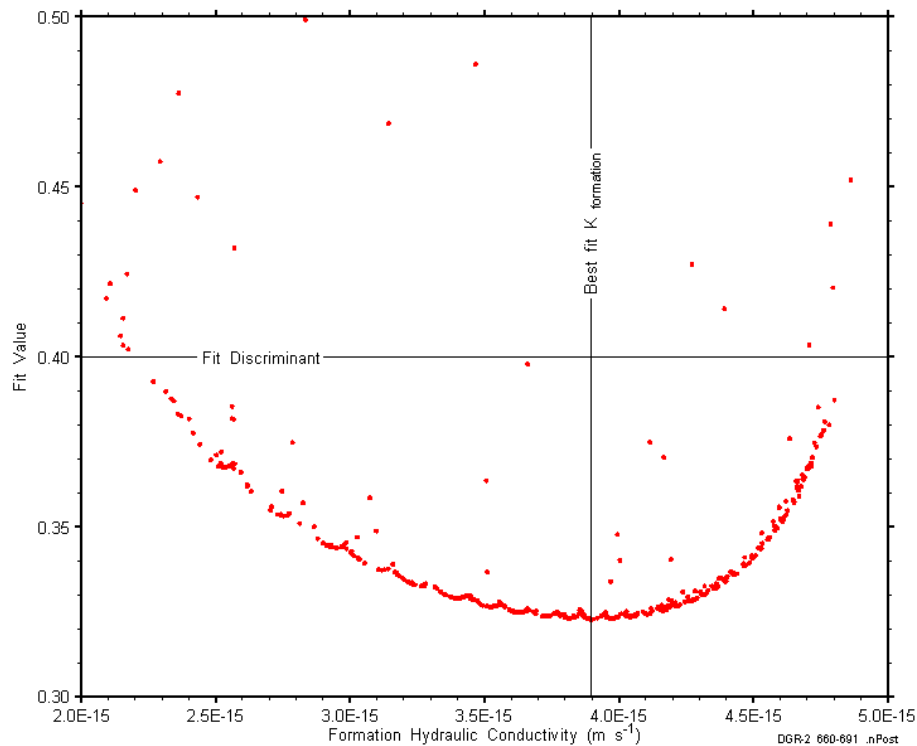


Figure B-103: XY-scatter plot showing the formation hydraulic conductivity parameter space derived from DGR2_660.50-691.00 perturbation analysis along with the fit discriminant and best fit values.

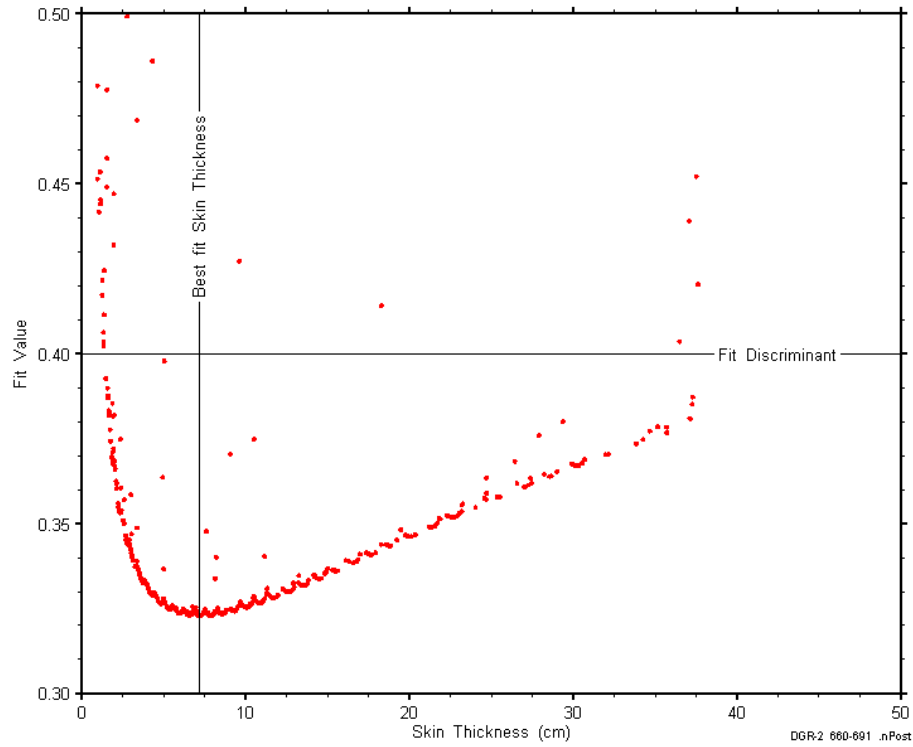


Figure B-104: XY-scatter plot showing the skin-thickness parameter space derived from DGR2_660.50-691.00 perturbation analysis along with the fit discriminant and best fit values.

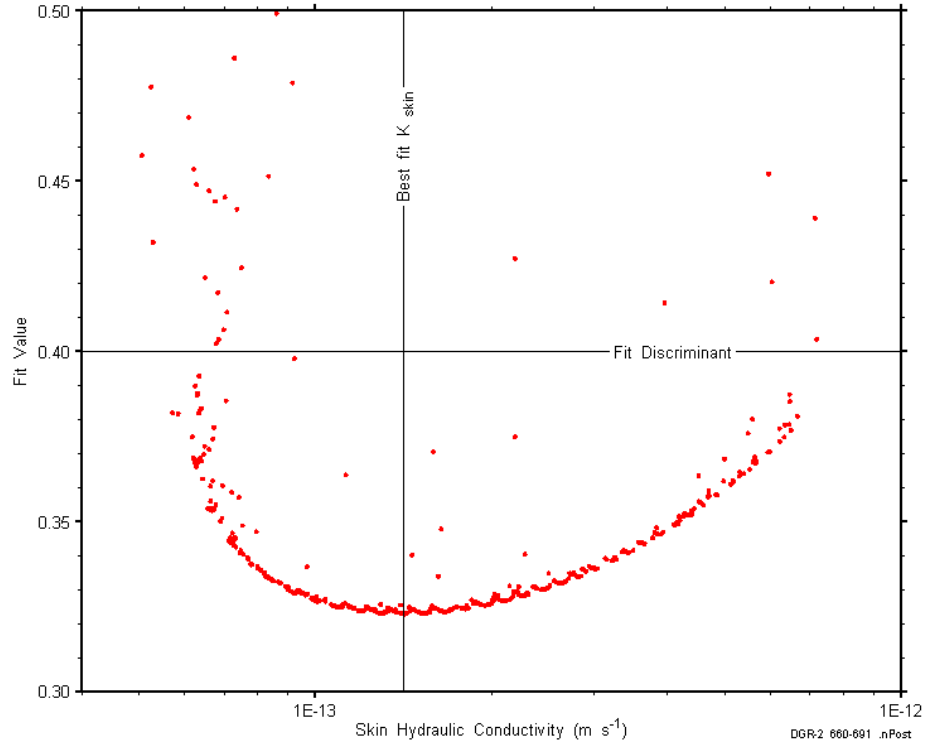


Figure B-105: XY-scatter plot showing the skin hydraulic conductivity parameter space derived from DGR2_660.50-691.00 perturbation analysis along with the fit discriminant and best fit values.

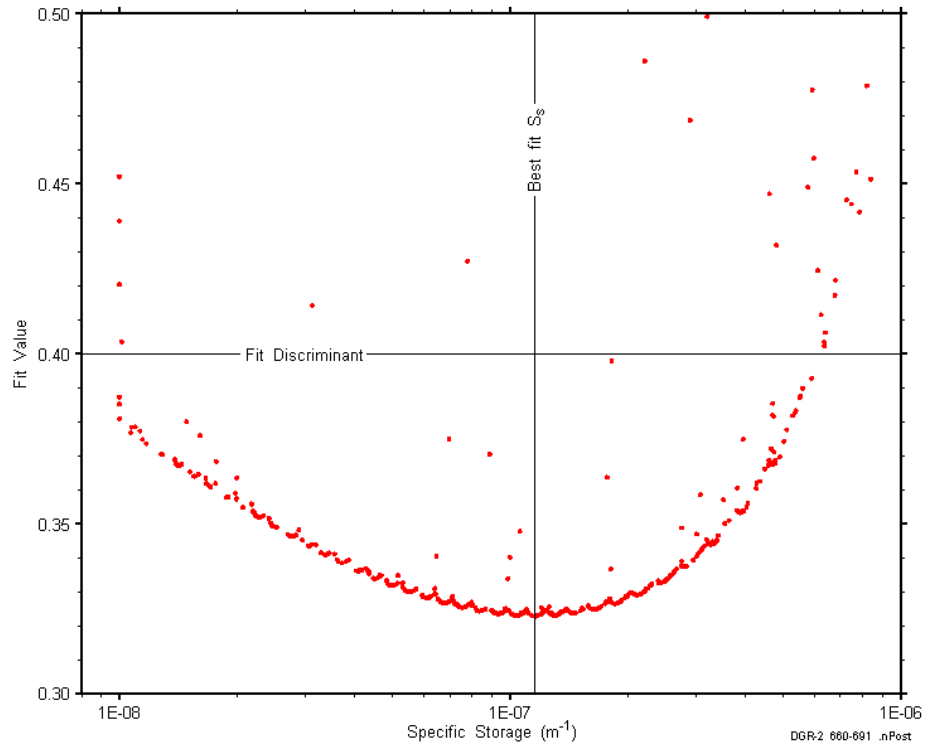


Figure B-106: XY-scatter plot showing the formation specific storage parameter space derived from DGR2_660.50-691.00 perturbation analysis along with the fit discriminant and best fit values.

B.9 687.60-718.10 Sherman Fall

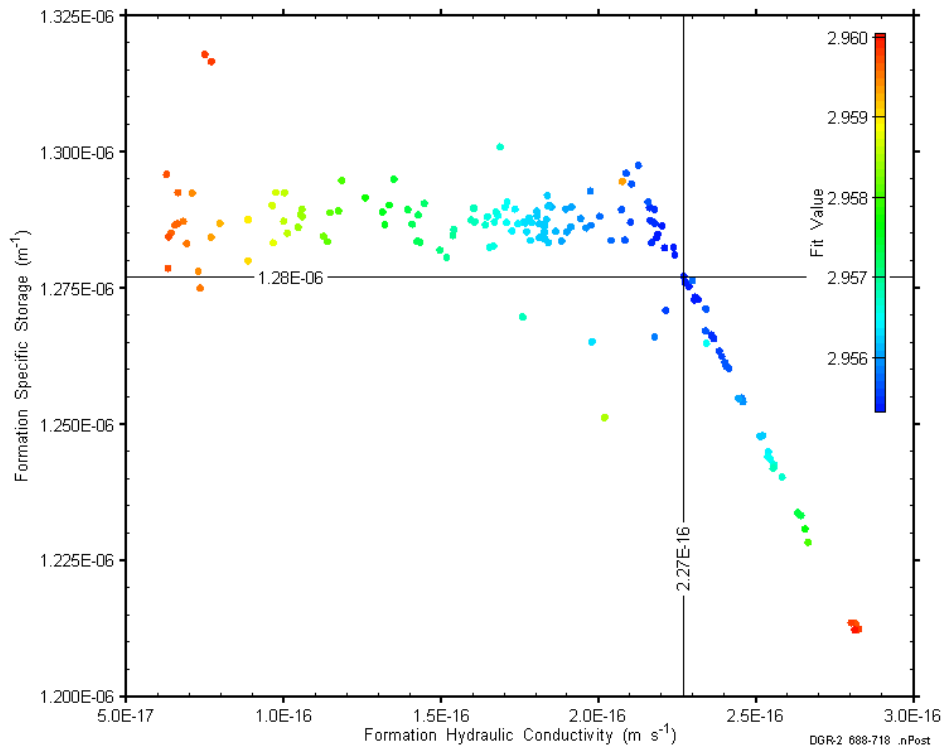


Figure B-107: XY-scatter plot showing estimates of formation hydraulic conductivity and formation specific storage derived from the DGR2_687.60-718.10 perturbation analysis.

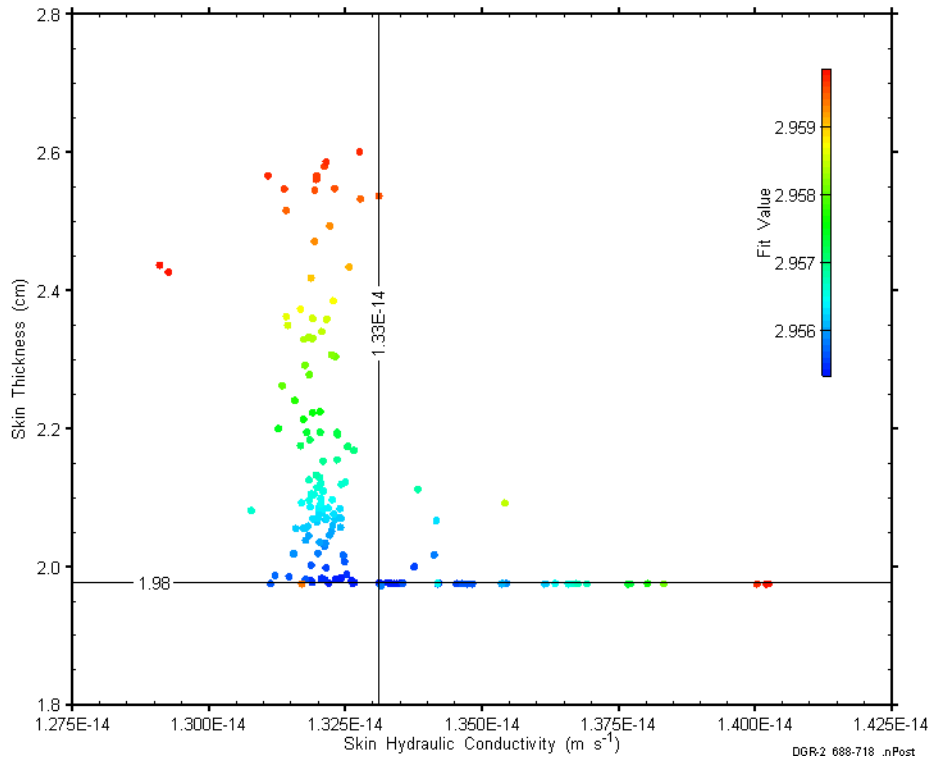


Figure B-108: XY-scatter plot showing estimates of skin hydraulic conductivity and skin thickness derived from the DGR2_687.60-718.10 perturbation analysis.

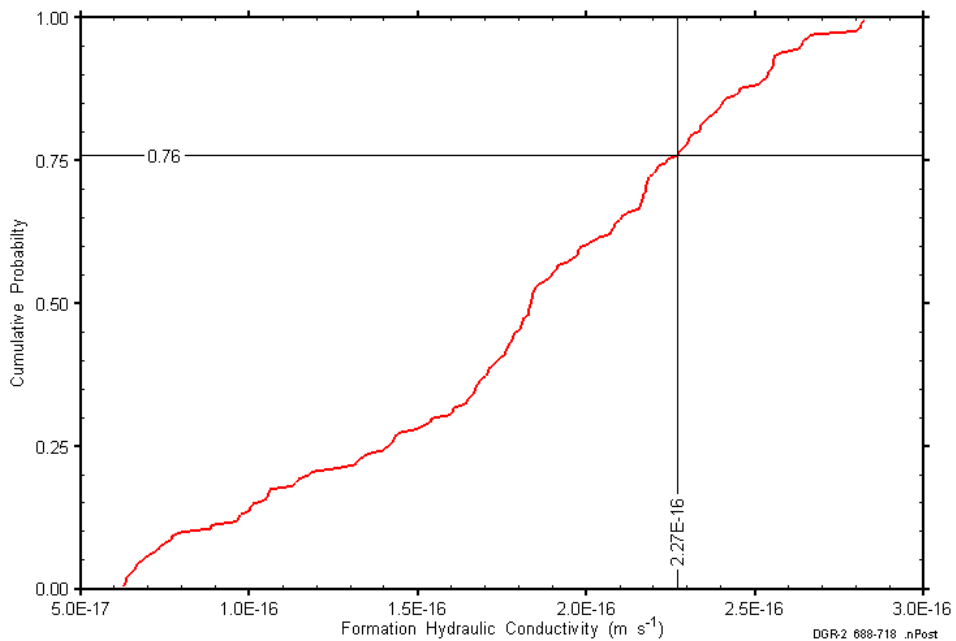


Figure B-109: DGR2_687.60-718.10 formation hydraulic conductivity cumulative distribution function.

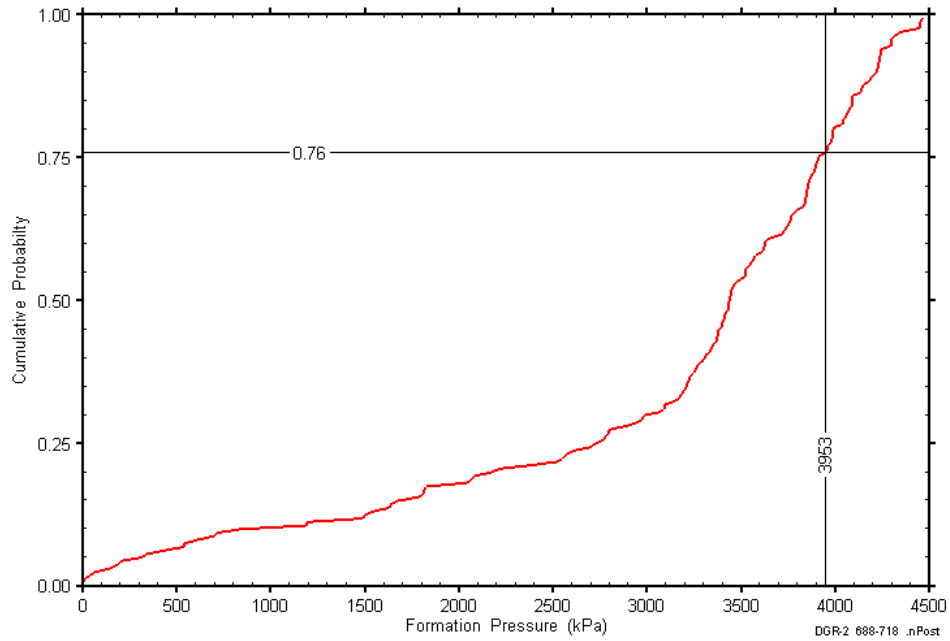


Figure B-110: DGR2_687.60-718.10 static formation pressure cumulative distribution function.

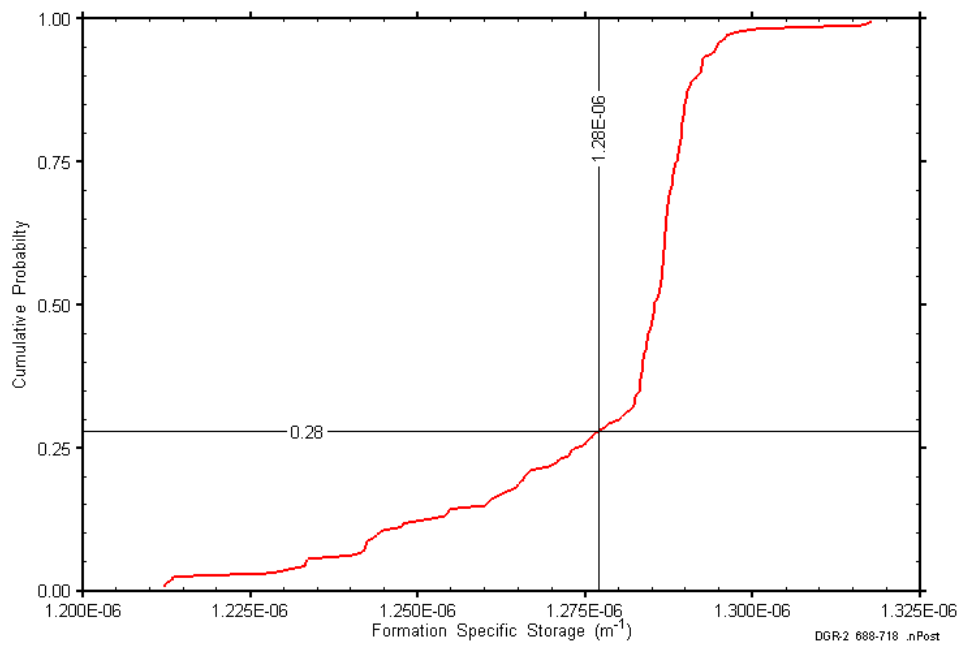


Figure B-111: DGR2_687.60-718.10 formation specific storage cumulative distribution function.

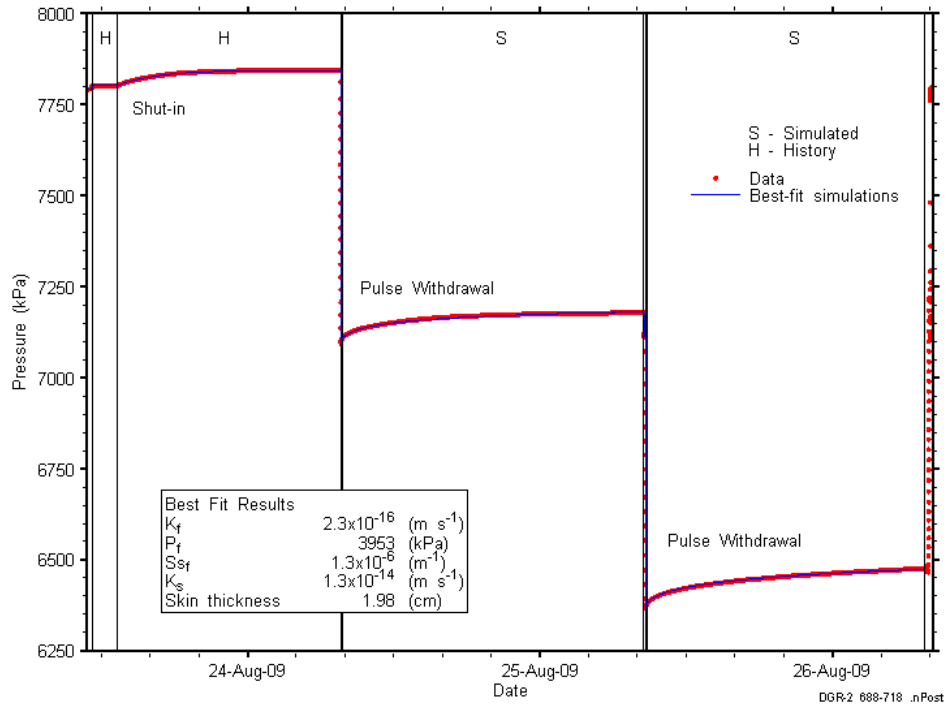


Figure B-112: Linear plot showing details of simulations of the DGR2_687.60-718.10 pressure response.

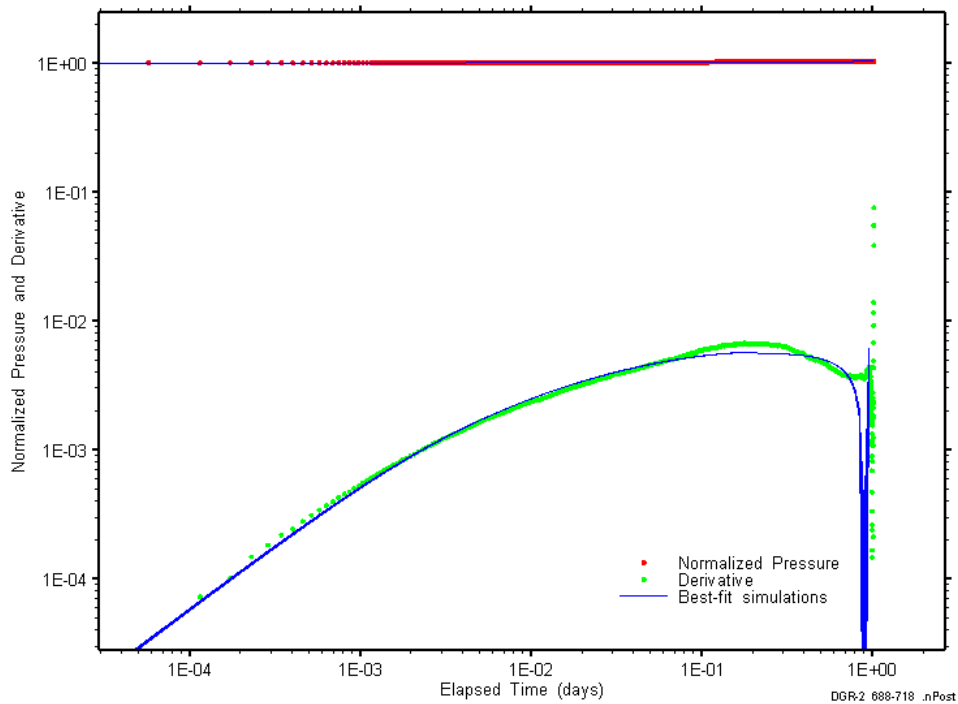


Figure B-113: Log-log plot showing simulations of the DGR2_687.60-718.10 PW1 Ramey B and derivative response.

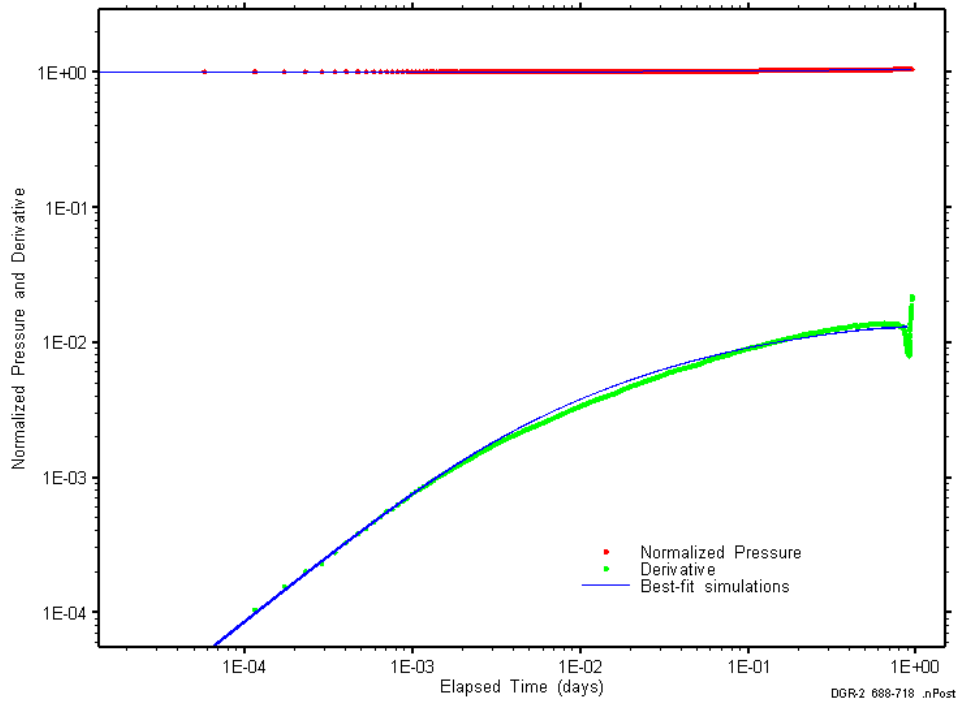


Figure B-114: Log-log plot showing simulations of the DGR2_687.60-718.10 PW2 Ramey B and derivative response.

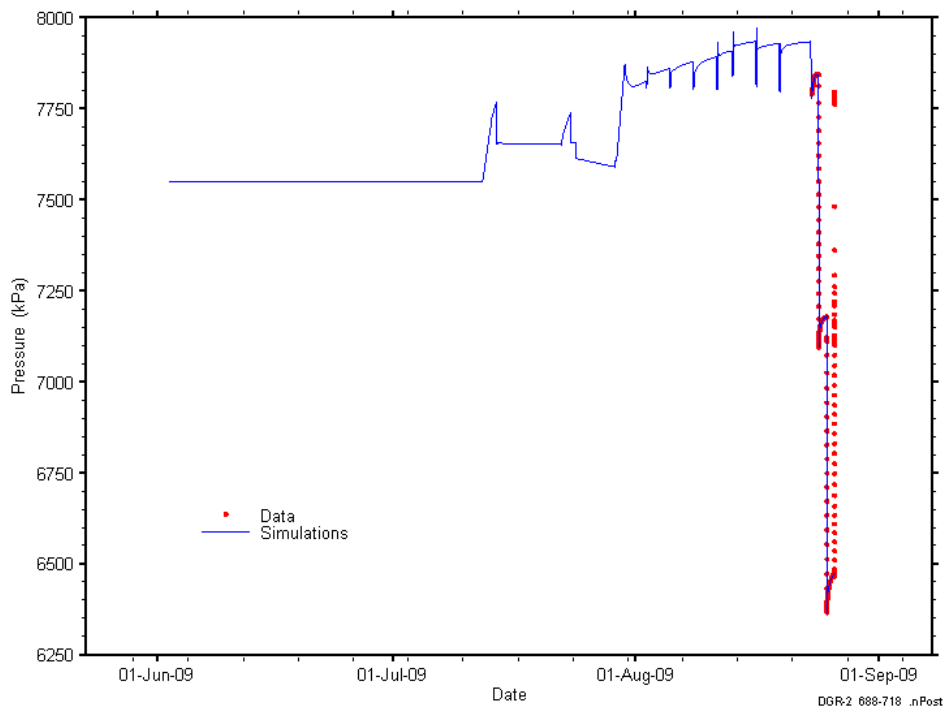


Figure B-115: Linear plot showing simulations of the DGR2_687.60-718.10 pressure response, including pre-test pressure history.

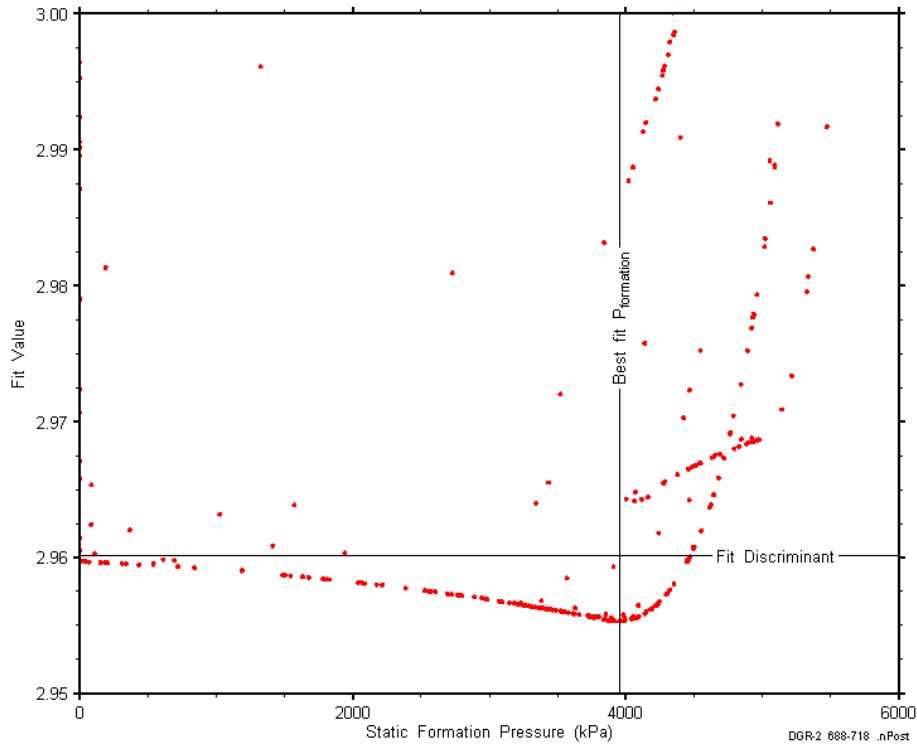


Figure B-116: XY-scatter plot showing the static formation pressure parameter space derived from DGR2_687.60-718.10 perturbation analysis along with the fit discriminant and best fit values.

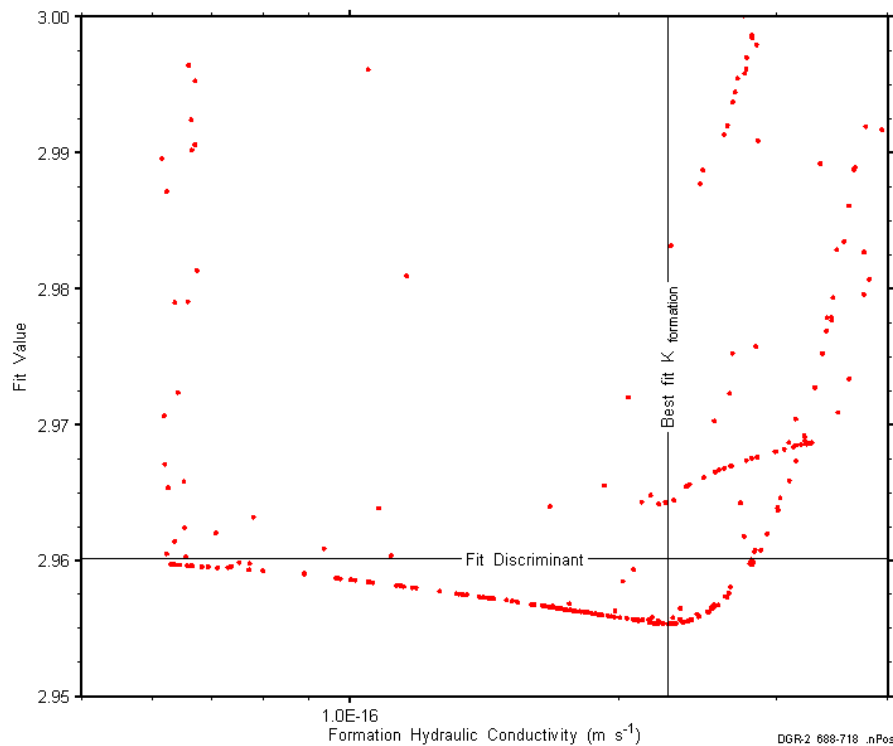


Figure B-117: XY-scatter plot showing the formation hydraulic conductivity parameter space derived from DGR2_687.60-718.10 perturbation analysis along with the fit discriminant and best fit values.

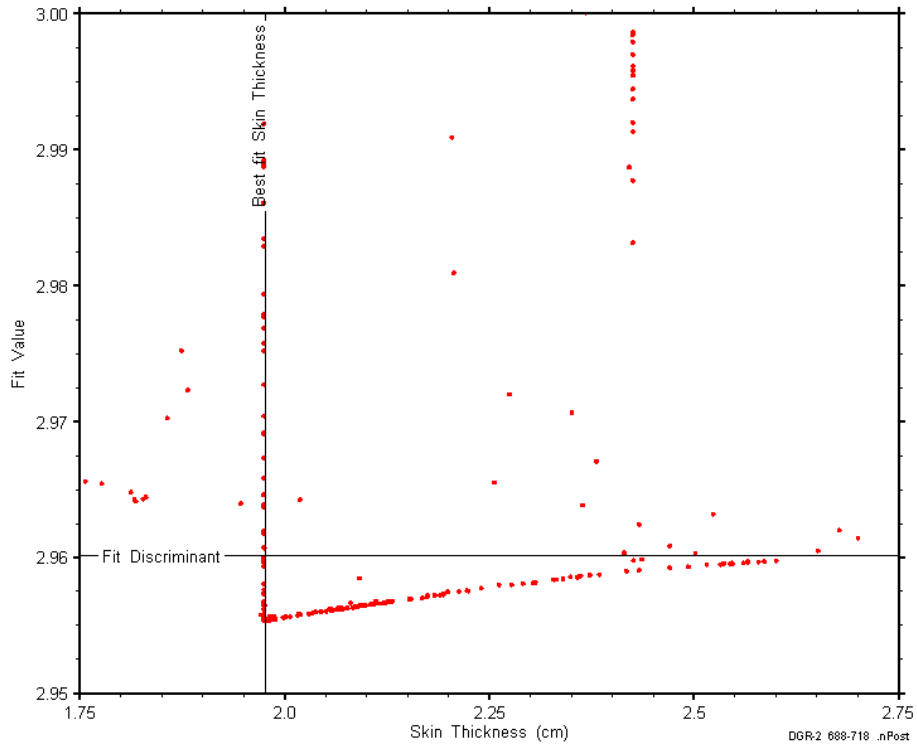


Figure B-118: XY-scatter plot showing the skin-thickness parameter space derived from DGR2_687.60-718.10 perturbation analysis along with the fit discriminant and best fit values.

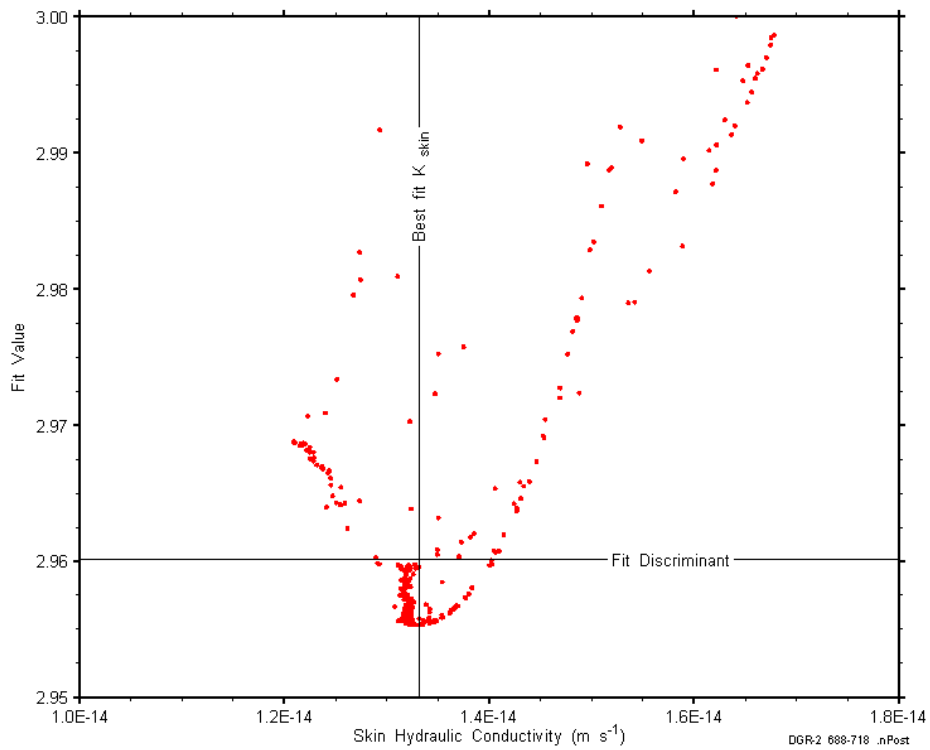


Figure B-119: XY-scatter plot showing the skin hydraulic conductivity parameter space derived from DGR2_687.60-718.10 perturbation analysis along with the fit discriminant and best fit values.

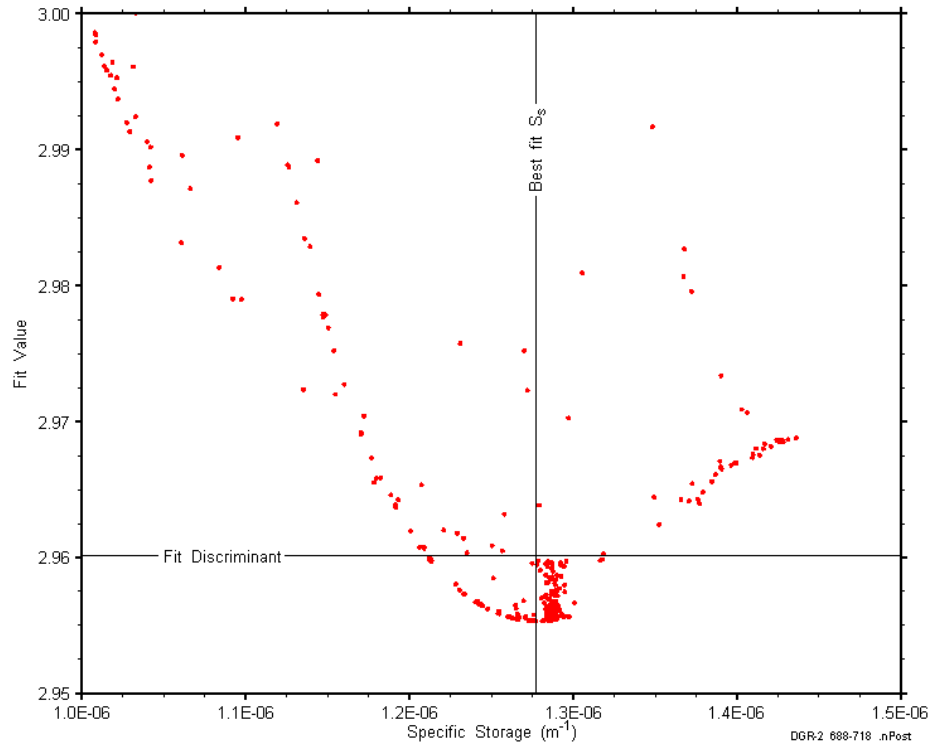


Figure B-120: XY-scatter plot showing the formation specific storage parameter space derived from DGR2_687.60-718.10 perturbation analysis along with the fit discriminant and best fit values.

B.10 714.50-745.00 Kirkfield

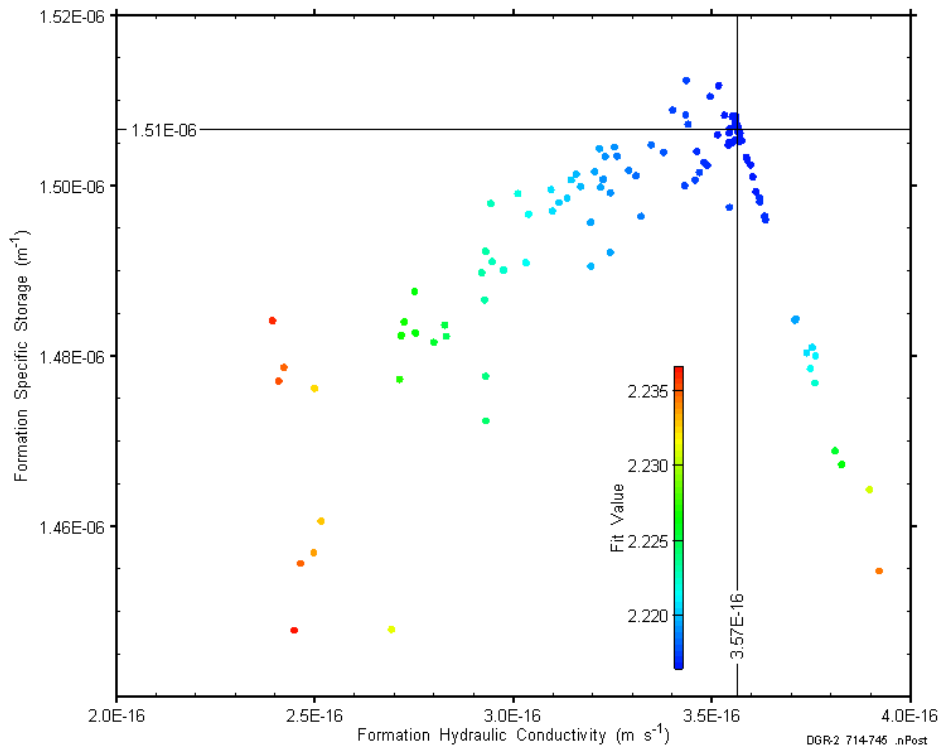


Figure B-121: XY-scatter plot showing estimates of formation hydraulic conductivity and formation specific storage derived from the DGR2_714.50-745.00 perturbation analysis.

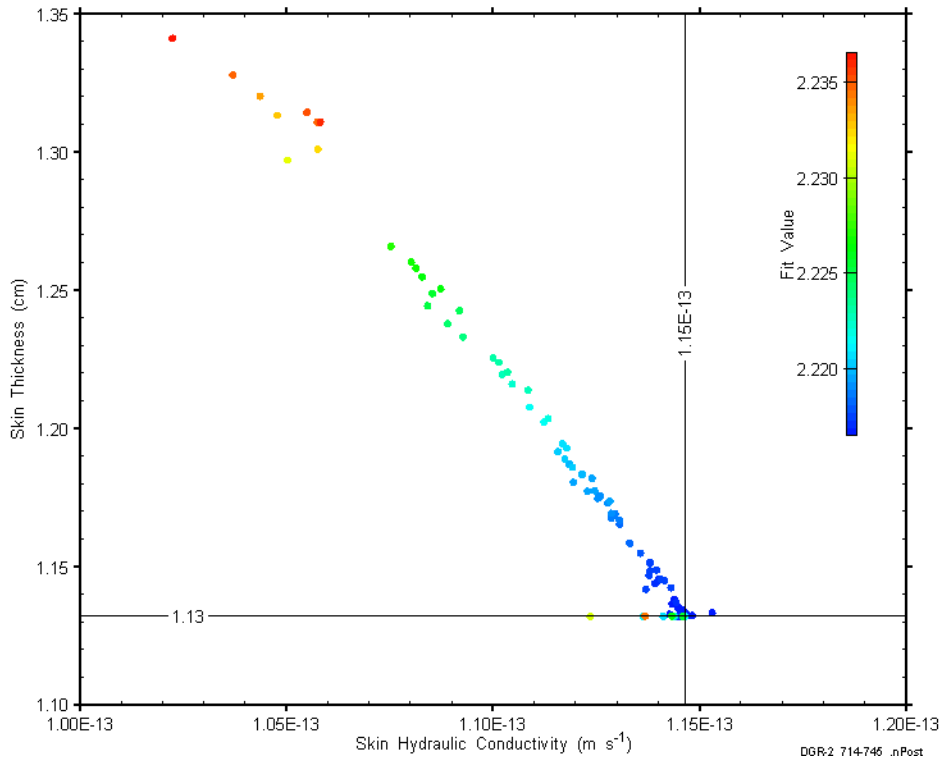


Figure B-122: XY-scatter plot showing estimates of skin hydraulic conductivity and skin thickness derived from the DGR2_714.50-745.00 perturbation analysis.

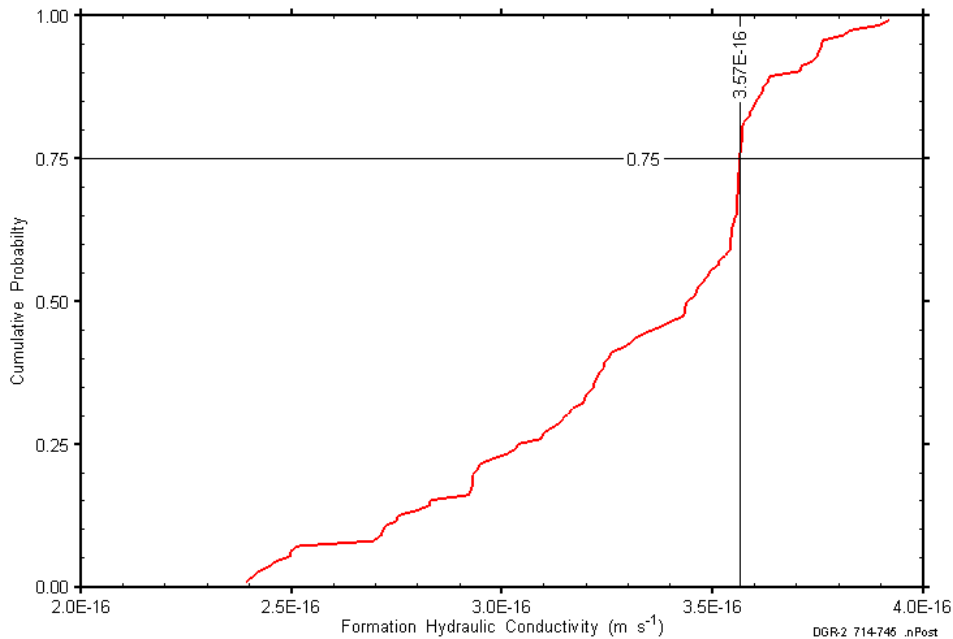


Figure B-123: DGR2_714.50-745.00 formation hydraulic conductivity cumulative distribution function.

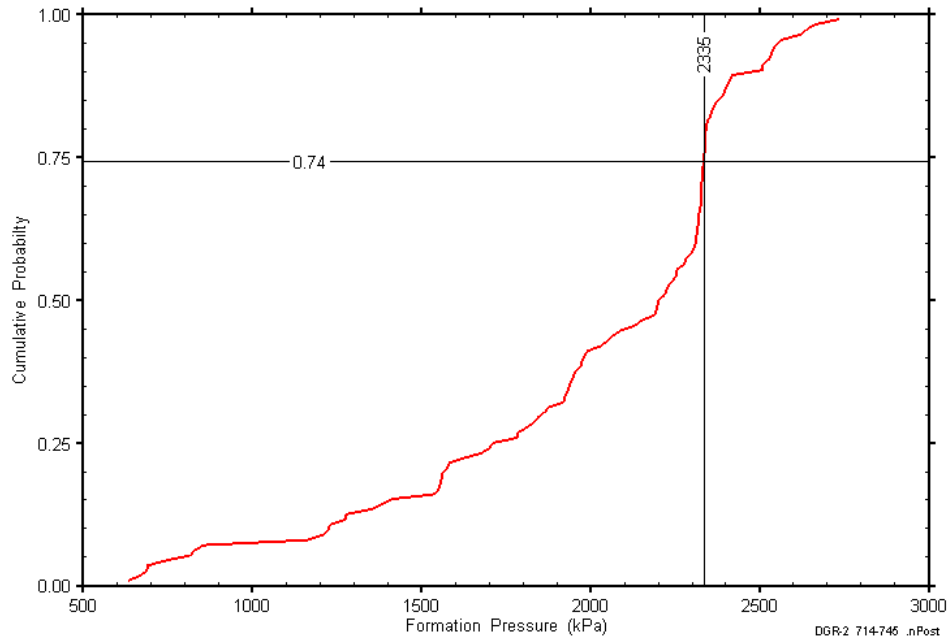


Figure B-124: DGR2_714.50-745.00 static formation pressure cumulative distribution function.

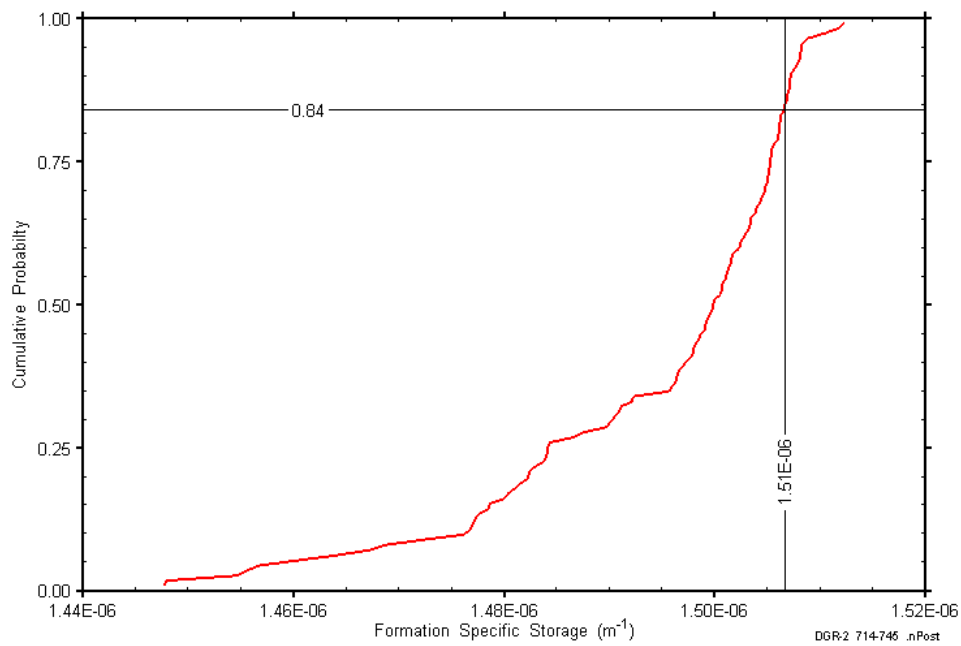


Figure B-125: DGR2_714.50-745.00 formation specific storage cumulative distribution function.

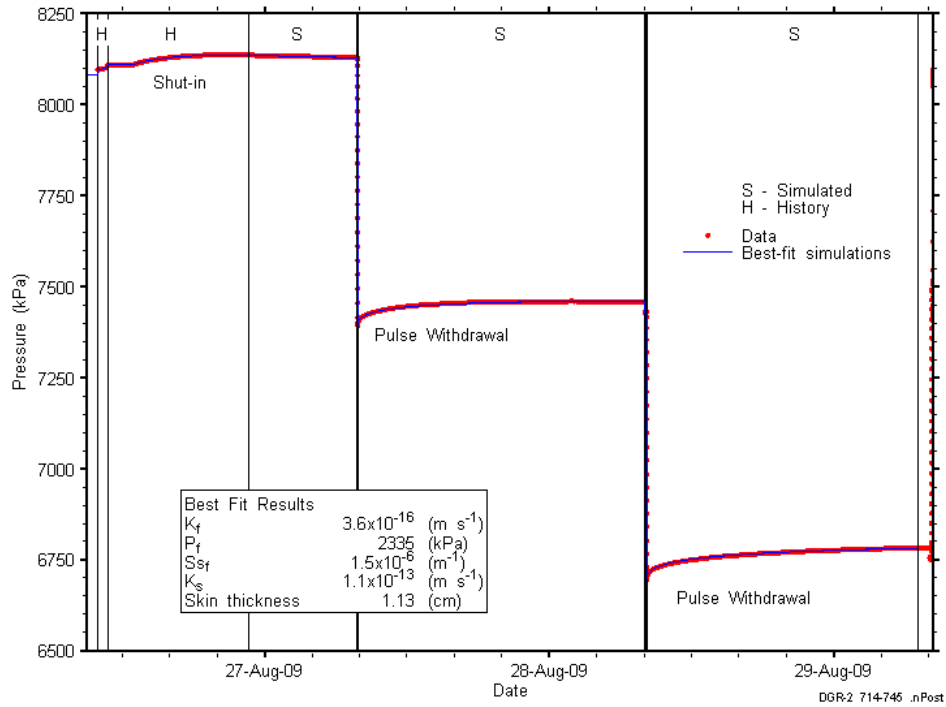


Figure B-126: Linear plot showing details of simulations of the DGR2_714.50-745.00 pressure response.

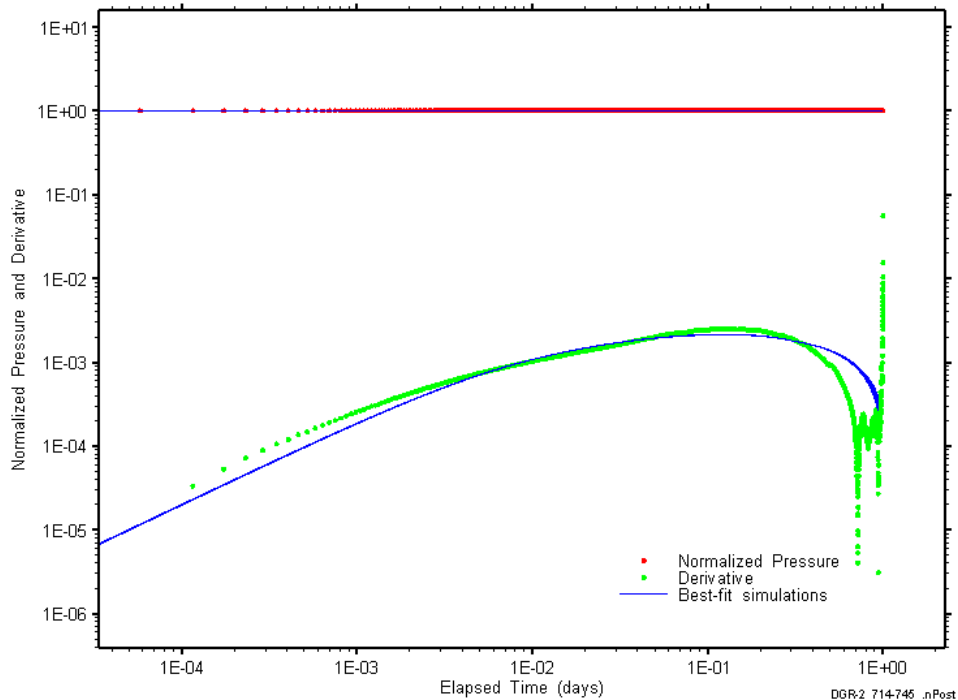


Figure B-127: Log-log plot showing simulations of the DGR2_714.50-745.00 PW1 Ramey B and derivative response.

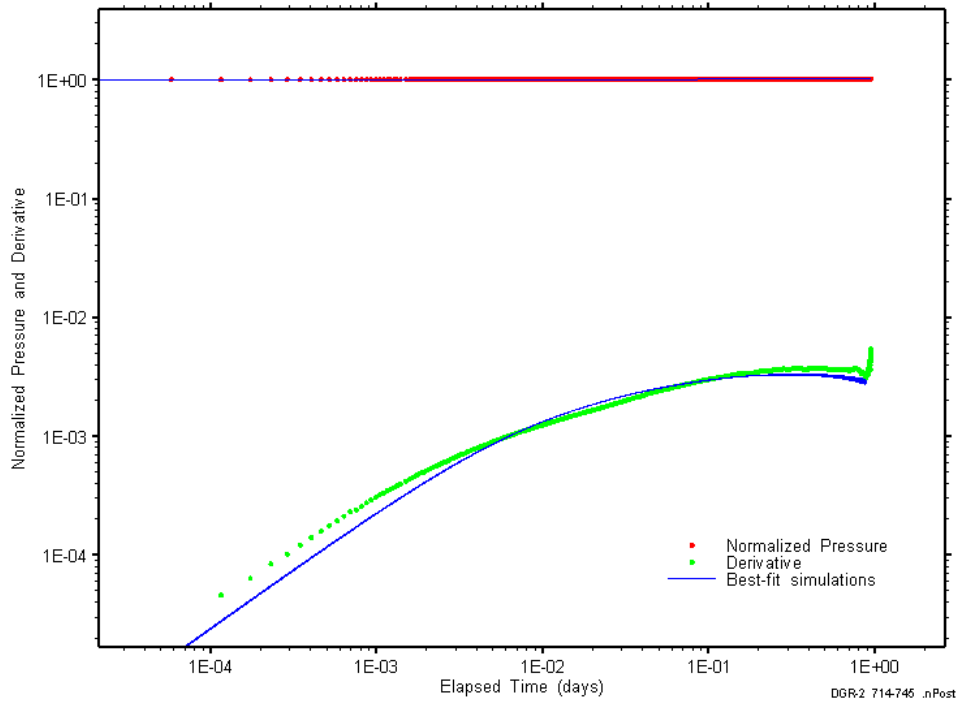


Figure B-128: Log-log plot showing simulations of the DGR2_714.50-745.00 PW2 Ramey B and derivative response.

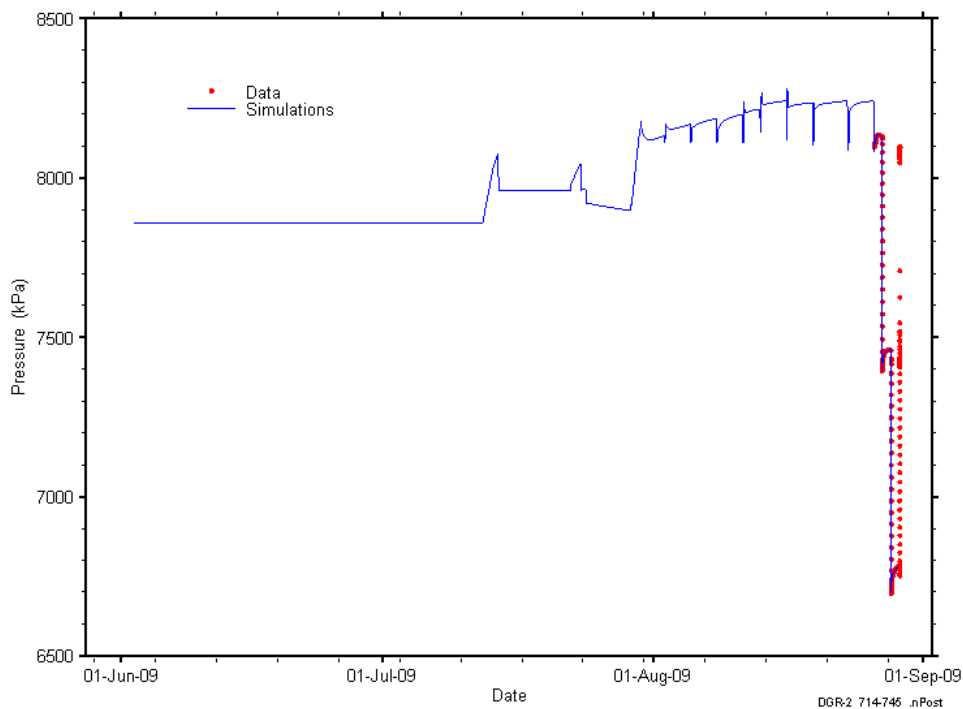


Figure B-129: Linear plot showing simulations of the DGR2_714.50-745.00 pressure response, including pre-test pressure history.

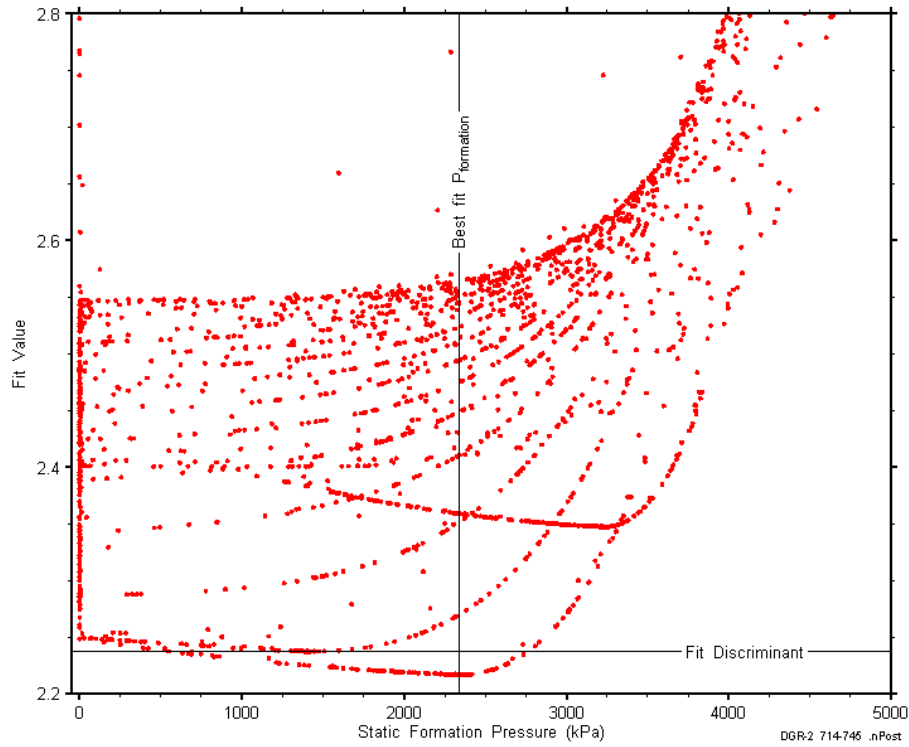


Figure B-130: XY-scatter plot showing the static formation pressure parameter space derived from DGR2_714.50-745.00 perturbation analysis along with the fit discriminant and best fit values.

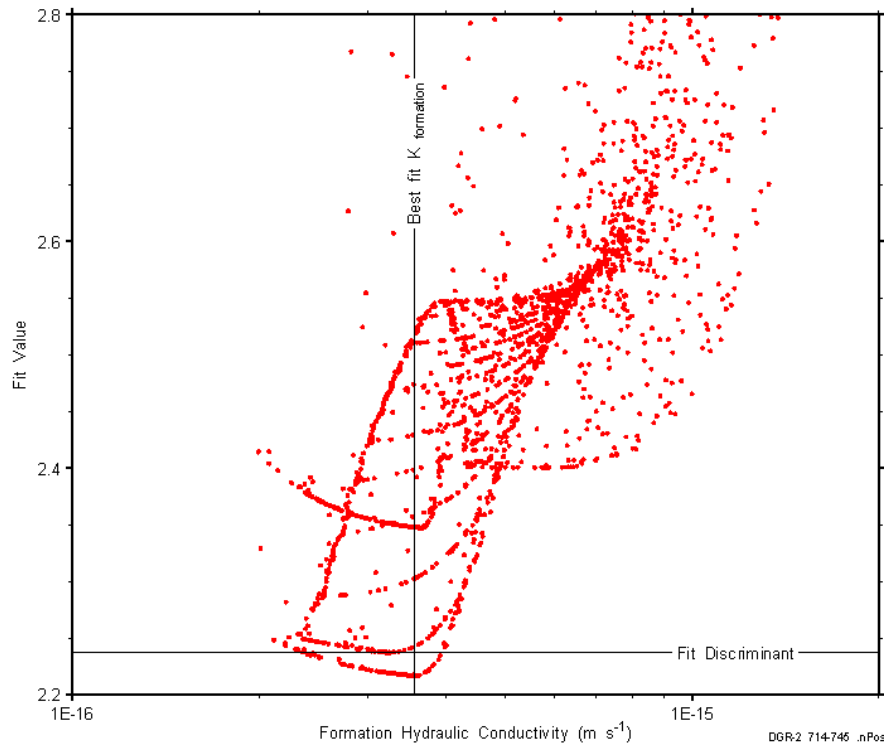


Figure B-131: XY-scatter plot showing the formation hydraulic conductivity parameter space derived from DGR2_714.50-745.00 perturbation analysis along with the fit discriminant and best fit values.

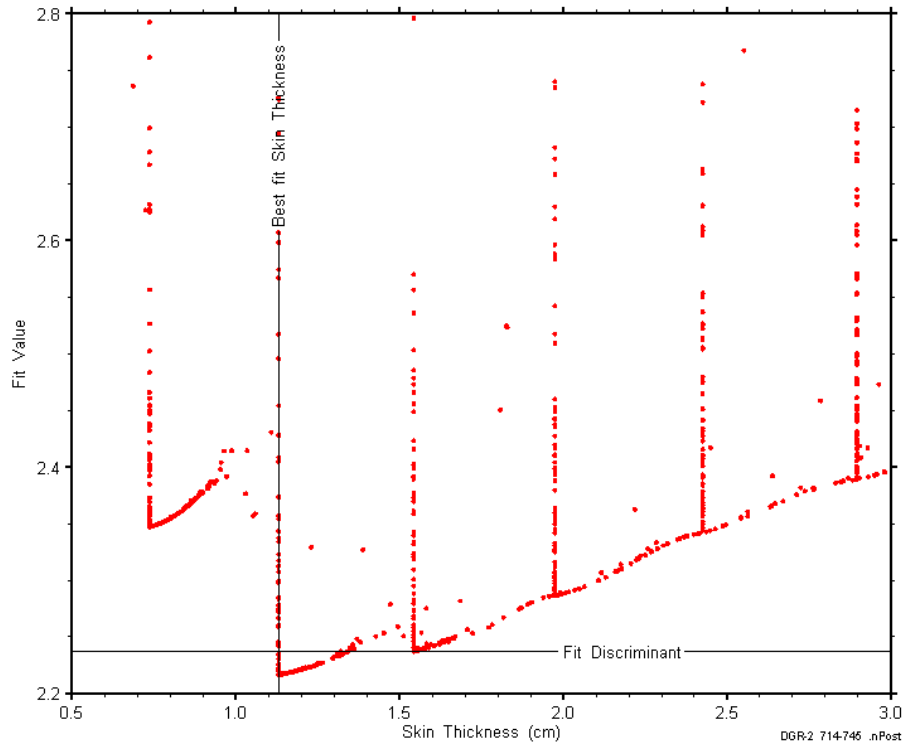


Figure B-132: XY-scatter plot showing the skin-thickness parameter space derived from DGR2_714.50-745.00 perturbation analysis along with the fit discriminant and best fit values.

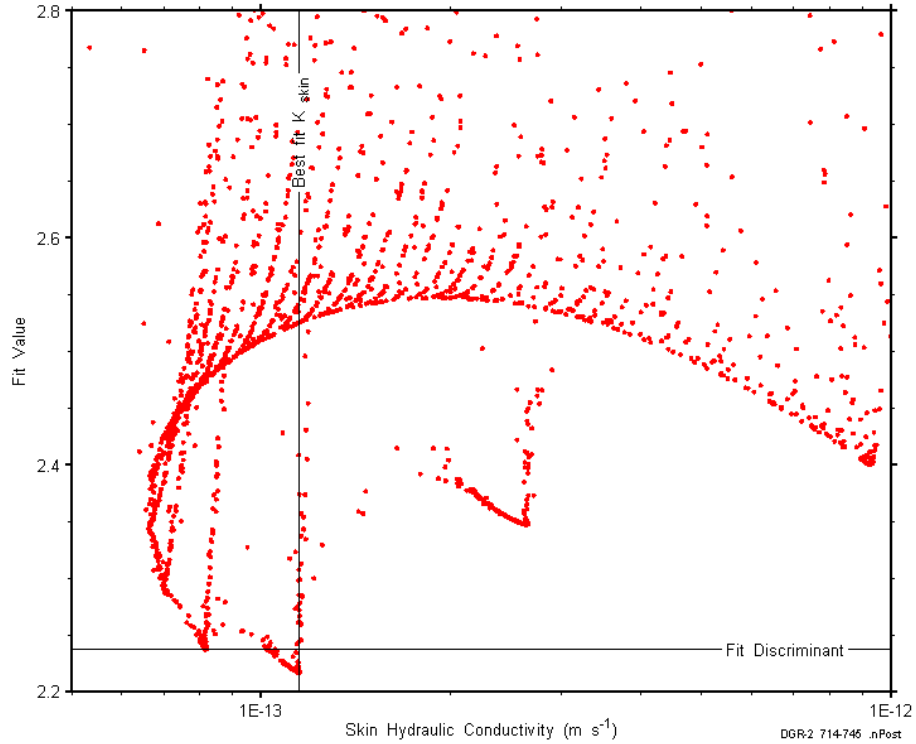


Figure B-133: XY-scatter plot showing the skin hydraulic conductivity parameter space derived from DGR2_714.50-745.00 perturbation analysis along with the fit discriminant and best fit values.

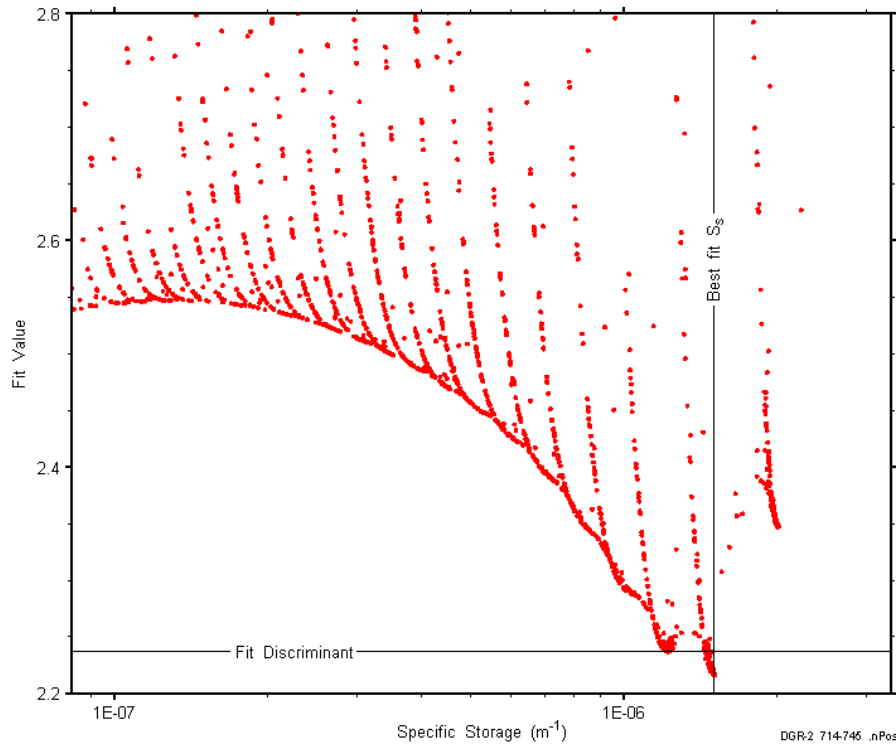


Figure B-134: XY-scatter plot showing the formation specific storage parameter space derived from DGR2_714.50-745.00 perturbation analysis along with the fit discriminant and best fit values.

B.11 731.60-762.10 Kirkfield

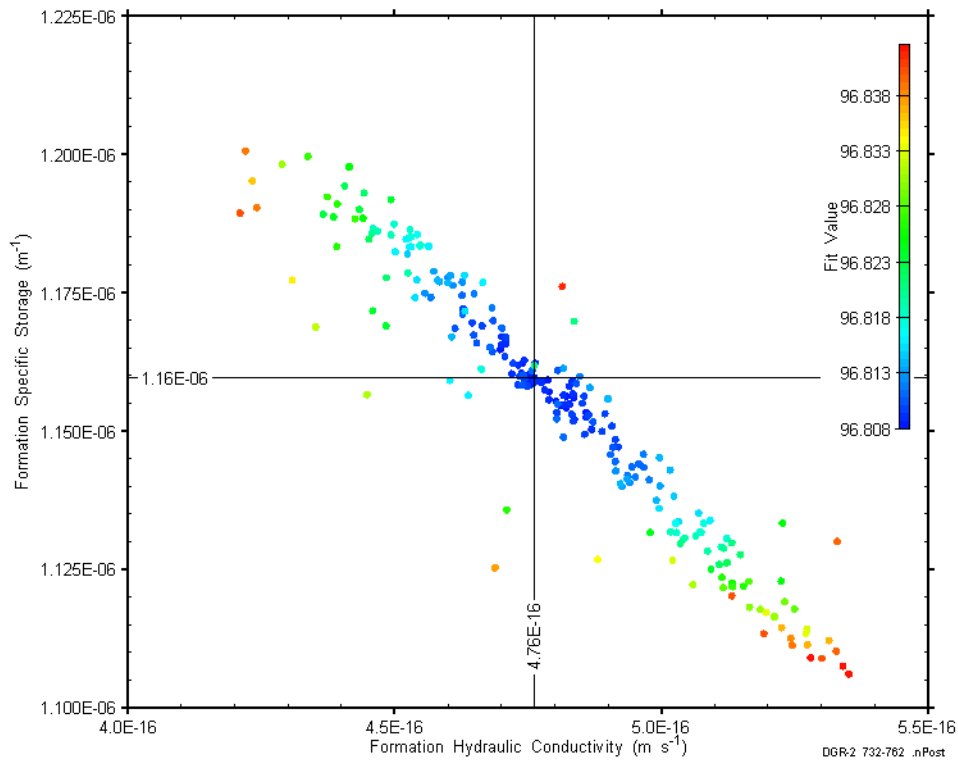


Figure B-135: XY-scatter plot showing estimates of formation hydraulic conductivity and formation specific storage derived from the DGR2_731.60-762.10 perturbation analysis.

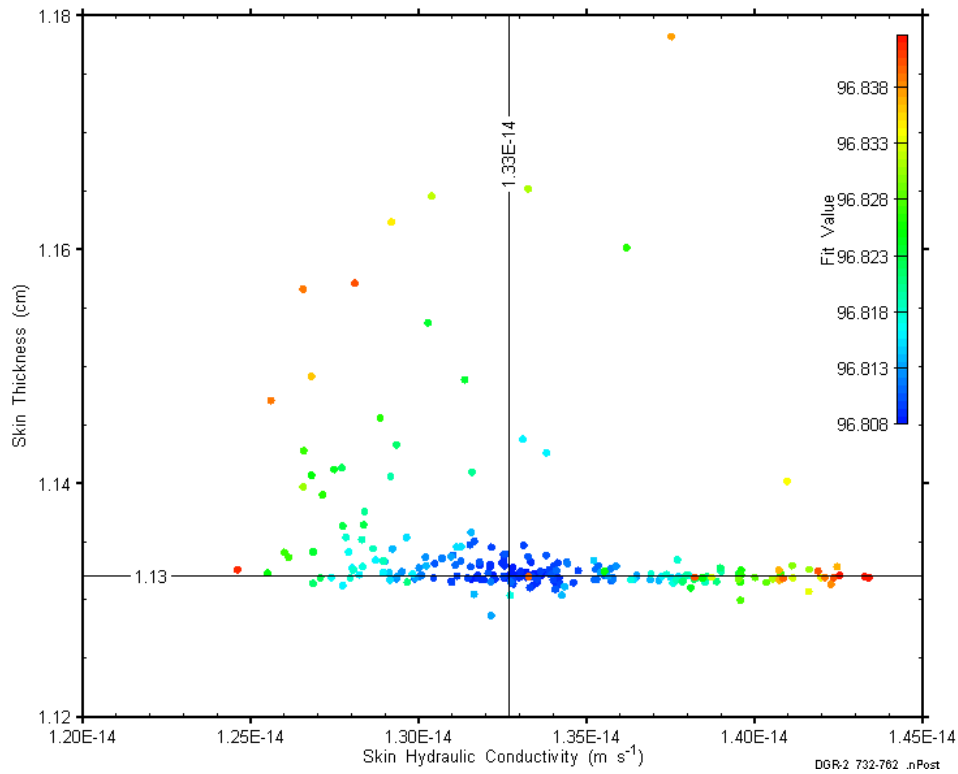


Figure B-136: XY-scatter plot showing estimates of skin hydraulic conductivity and skin thickness derived from the DGR2_731.60-762.10 perturbation analysis.

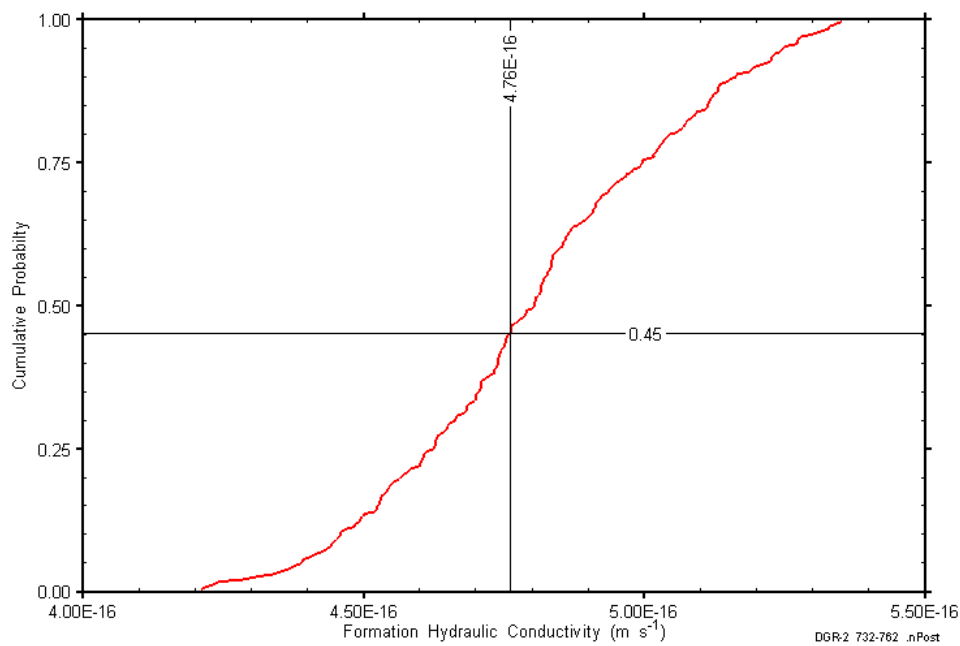


Figure B-137: DGR2_731.60-762.10 formation hydraulic conductivity cumulative distribution function.

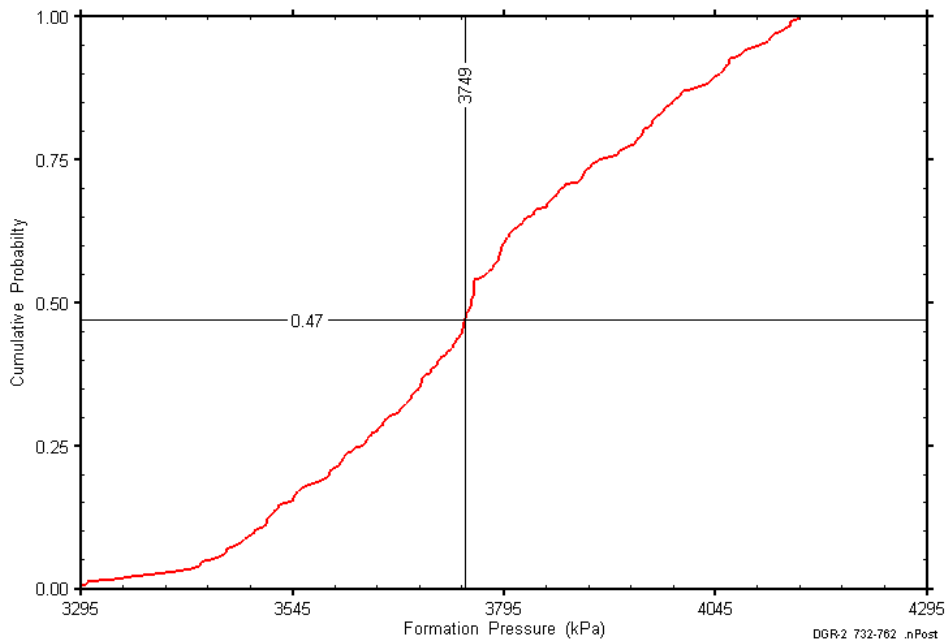


Figure B-138: DGR2_731.60-762.10 static formation pressure cumulative distribution function.

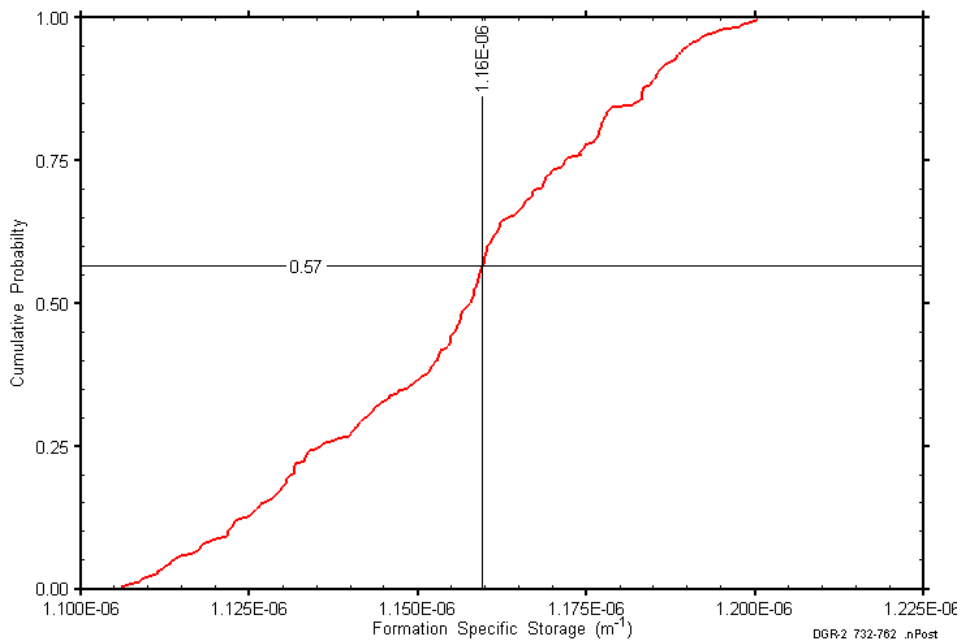


Figure B-139: DGR2_731.60-762.10 formation specific storage cumulative distribution function.

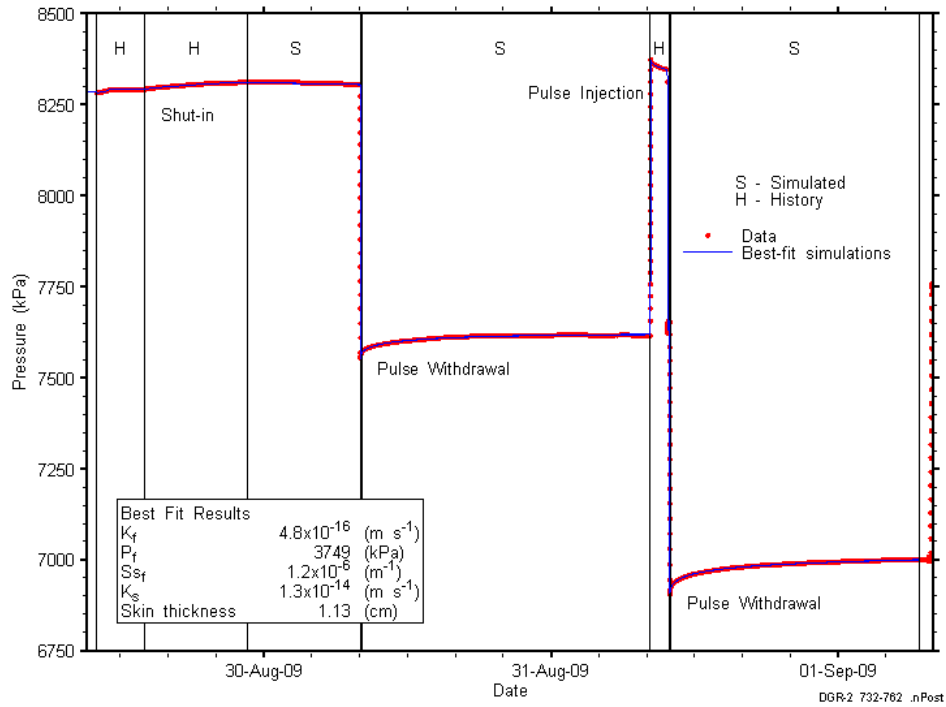


Figure B-140: Linear plot showing details of simulations of the DGR2_731.60-762.10 pressure response.

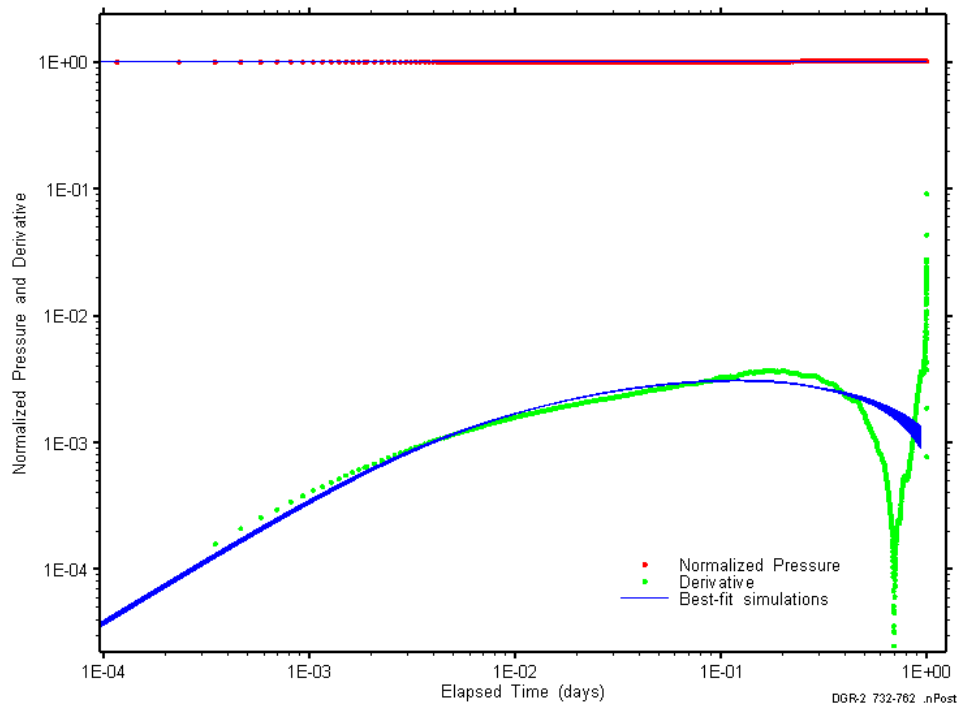


Figure B-141: Log-log plot showing simulations of the DGR2_731.60-762.10 PW1 Ramey B and derivative response.

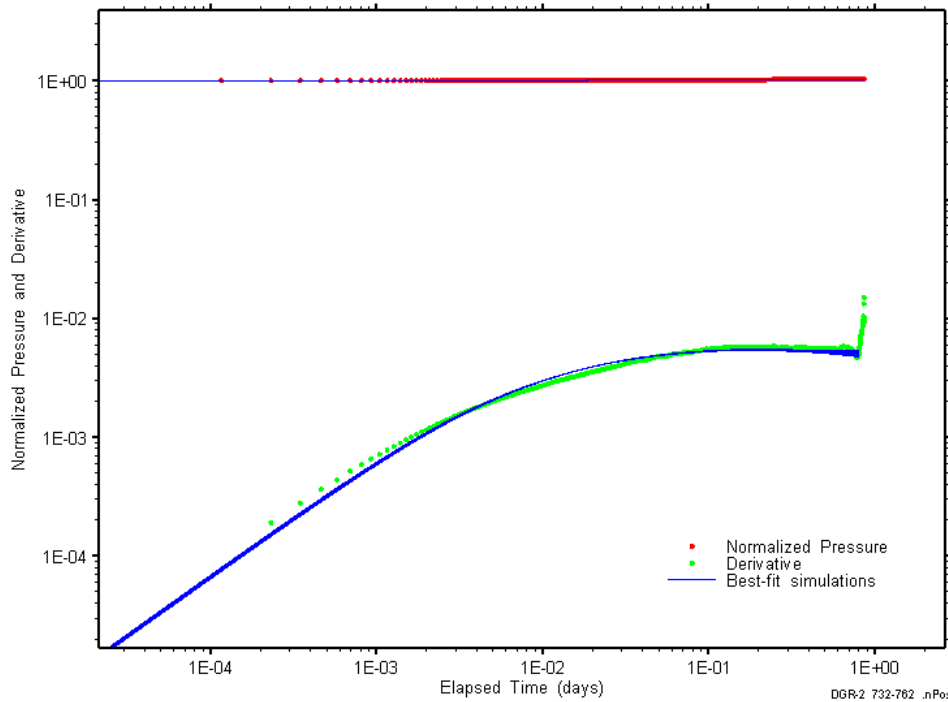


Figure B-142: Log-log plot showing simulations of the DGR2_731.60-762.10 PW2 Ramey B and derivative response.

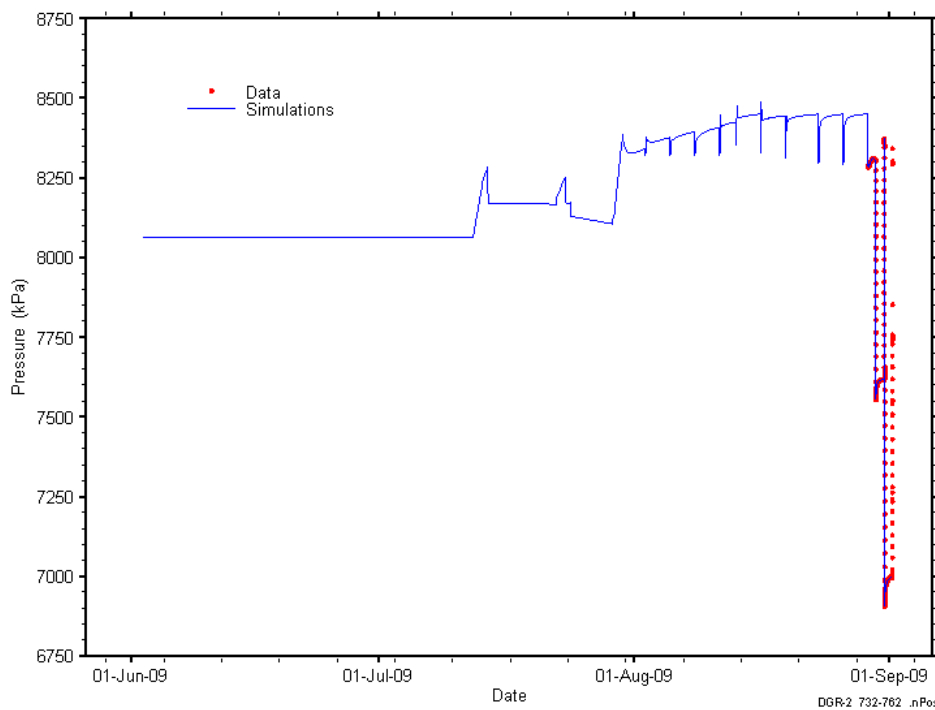


Figure B-143: Linear plot showing simulations of the DGR2_731.60-762.10 pressure response, including pre-test pressure history.

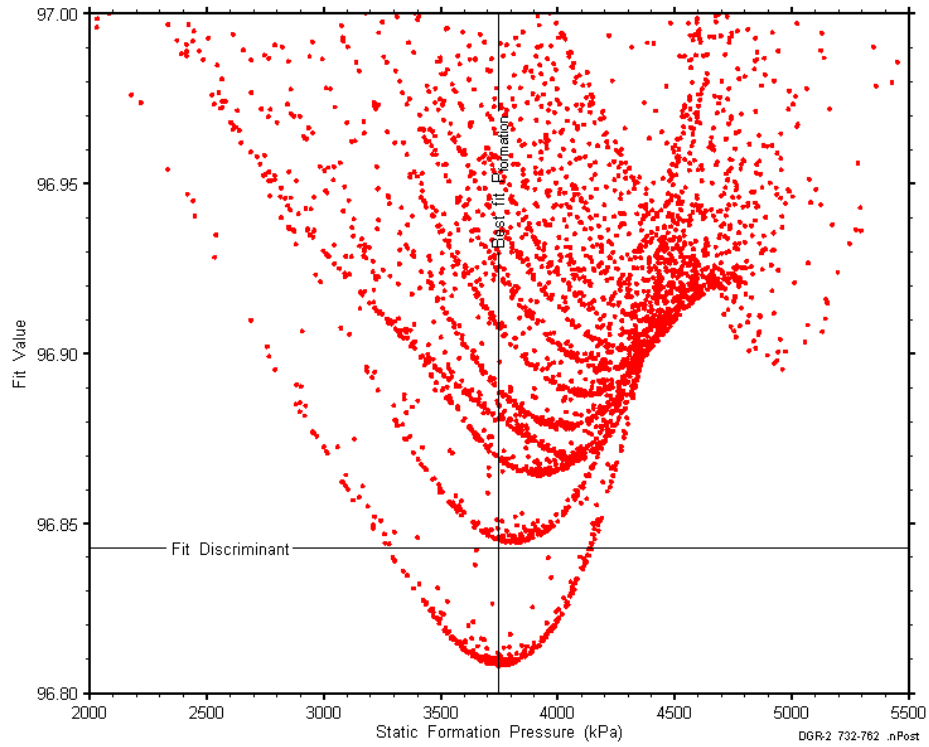


Figure B-144: XY-scatter plot showing the static formation pressure parameter space derived from DGR2_731.60-762.10 perturbation analysis along with the fit discriminant and best fit values.

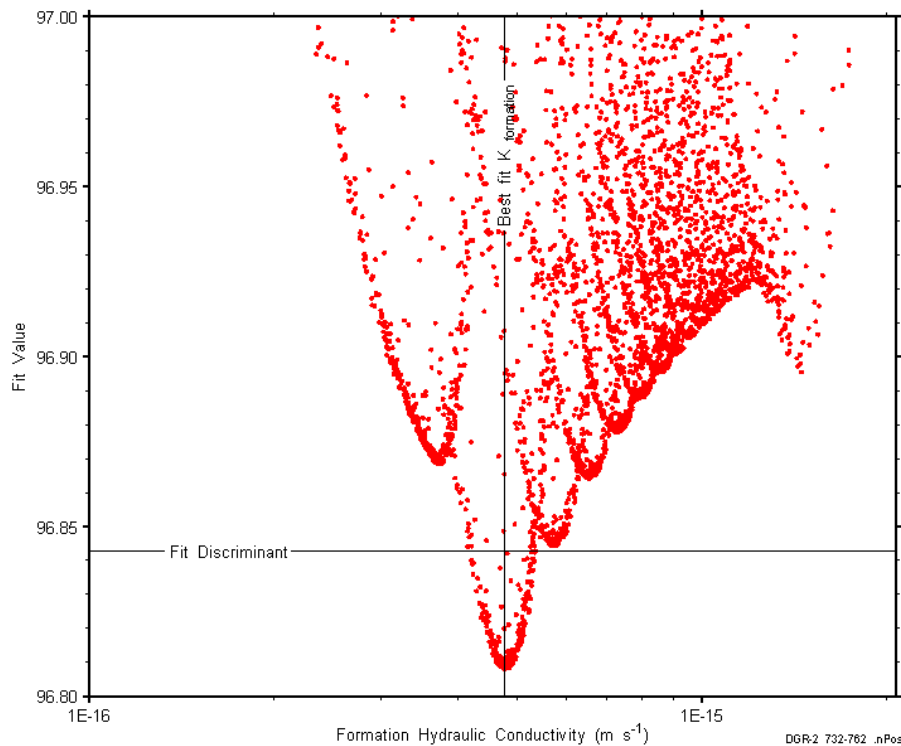


Figure B-145: XY-scatter plot showing the formation hydraulic conductivity parameter space derived from DGR2_731.60-762.10 perturbation analysis along with the fit discriminant and best fit values.

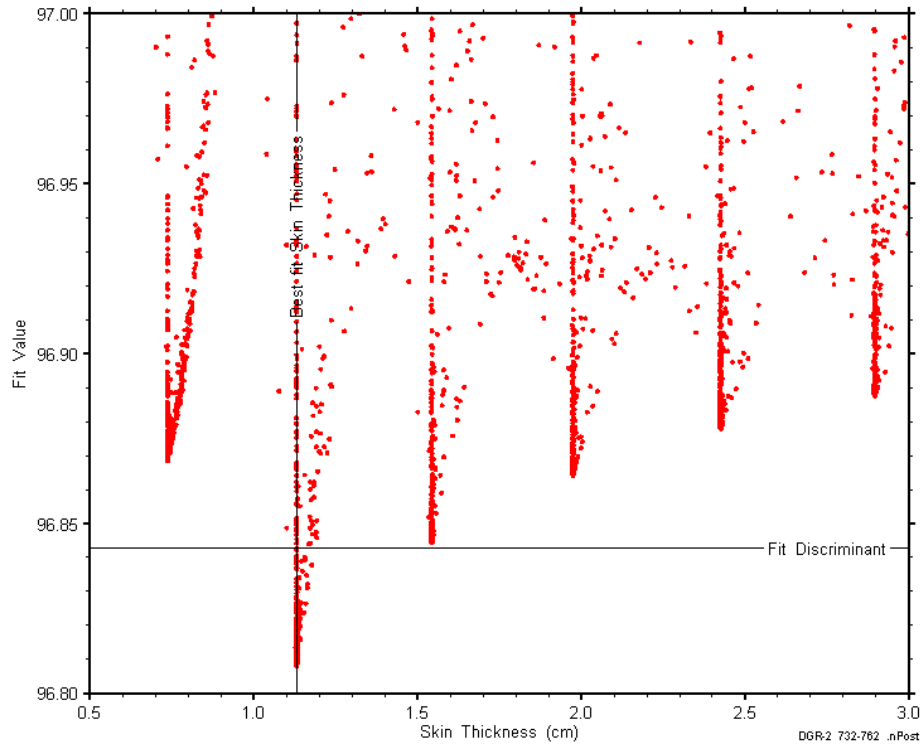


Figure B-146: XY-scatter plot showing the skin-thickness parameter space derived from DGR2_731.60-762.10 perturbation analysis along with the fit discriminant and best fit values.

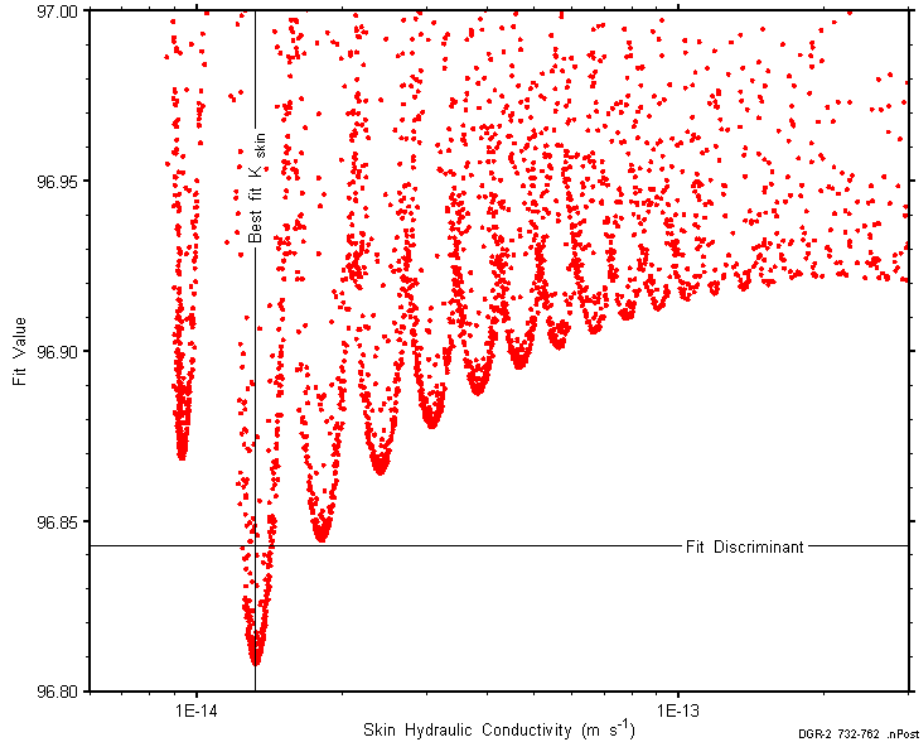


Figure B-147: XY-scatter plot showing the skin hydraulic conductivity parameter space derived from DGR2_731.60-762.10 perturbation analysis along with the fit discriminant and best fit values.

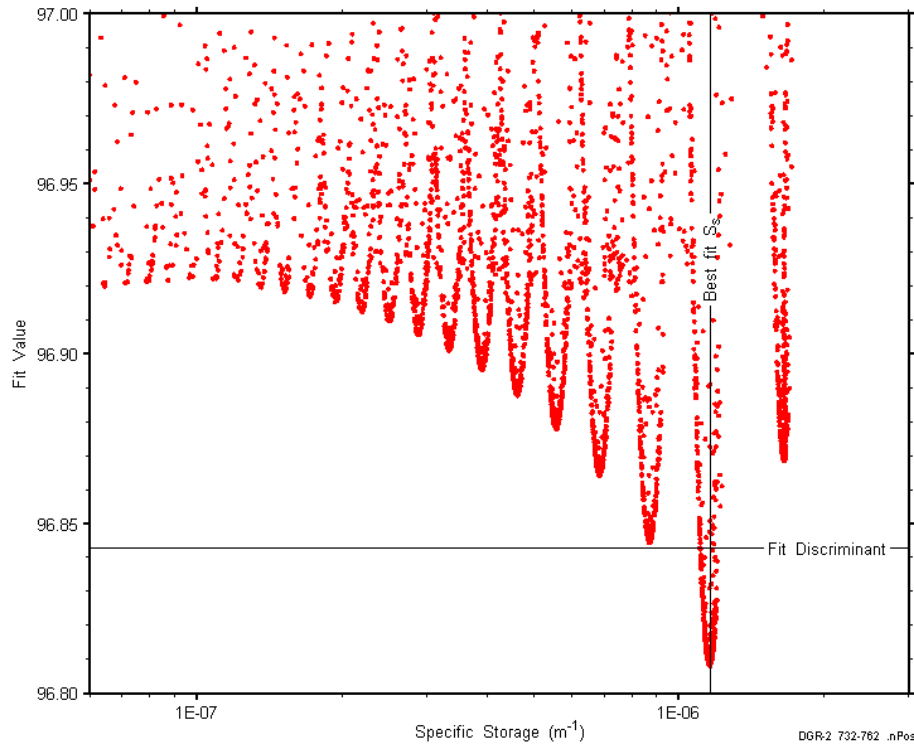


Figure B-148: XY-scatter plot showing the formation specific storage parameter space derived from DGR2_731.60-762.10 perturbation analysis along with the fit discriminant and best fit values.

B.12 754.50-785.00 Kirkfield-Coboconk

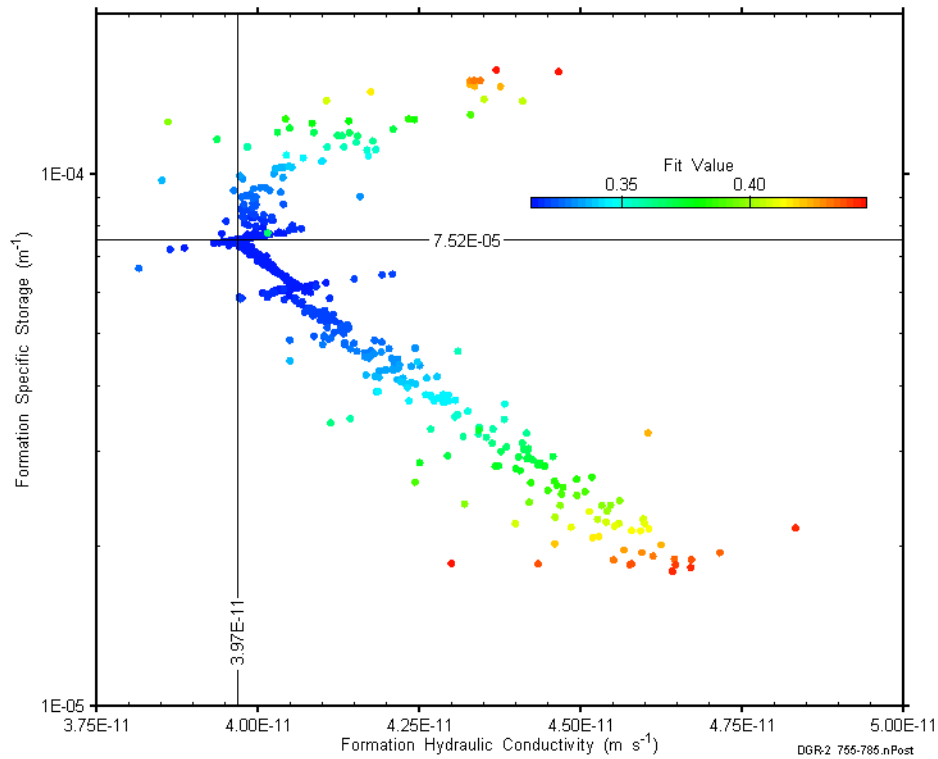


Figure B-149: XY-scatter plot showing estimates of formation hydraulic conductivity and formation specific storage derived from the DGR2_754.50-785.00 perturbation analysis.

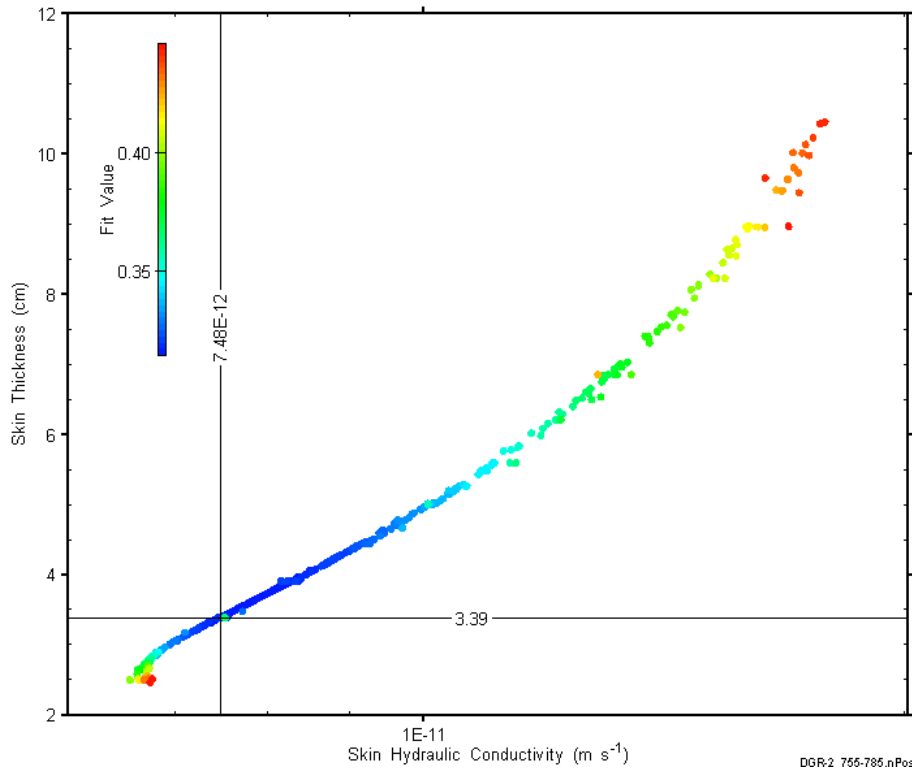


Figure B-150: XY-scatter plot showing estimates of skin hydraulic conductivity and skin thickness derived from the DGR2_754.50-785.00 perturbation analysis.

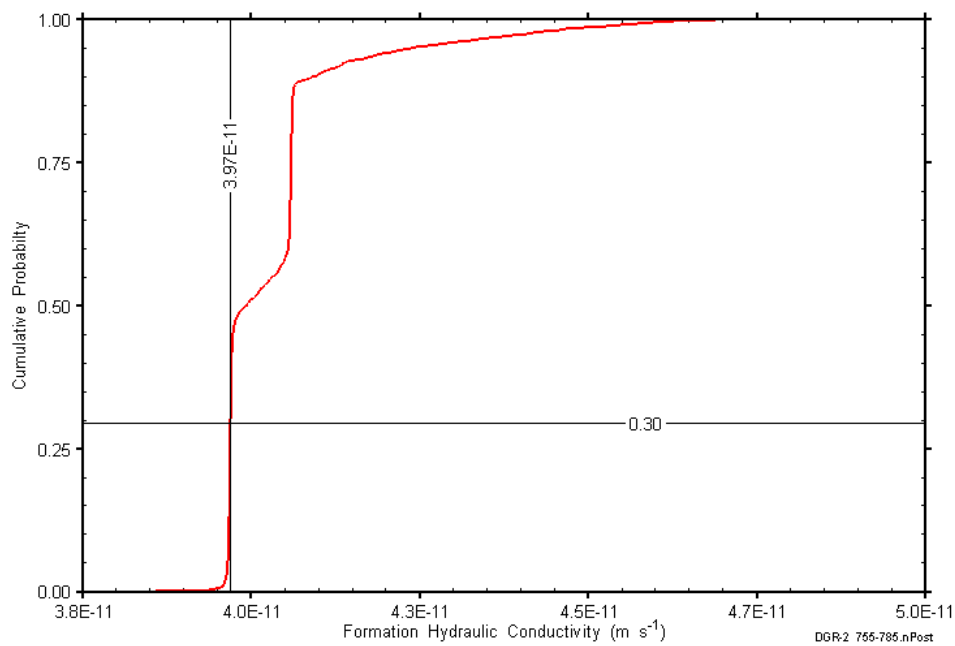


Figure B-151: DGR2_754.50-785.00 formation hydraulic conductivity cumulative distribution function.

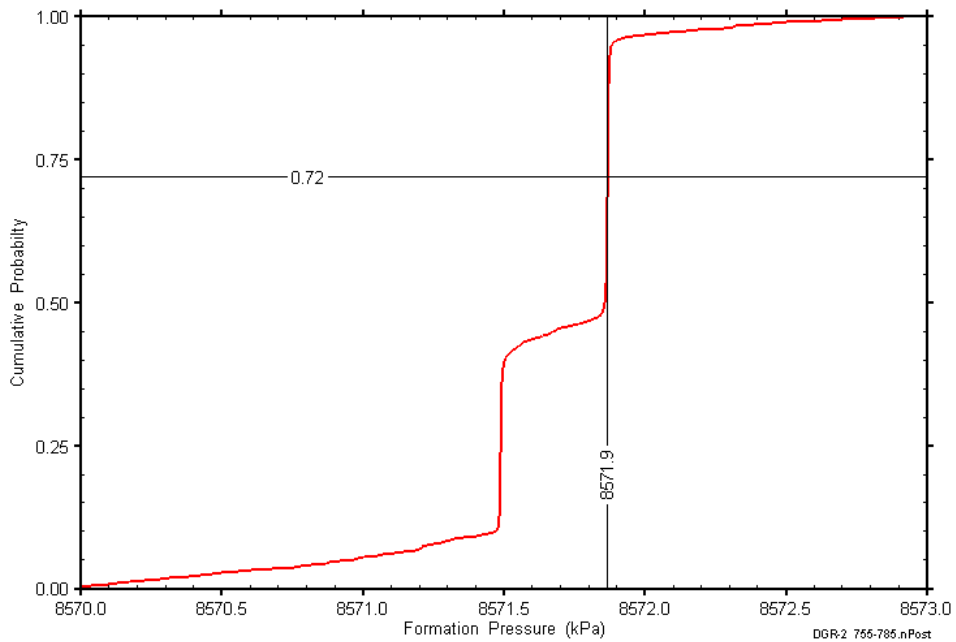


Figure B-152: DGR2_754.50-785.00 static formation pressure cumulative distribution function.

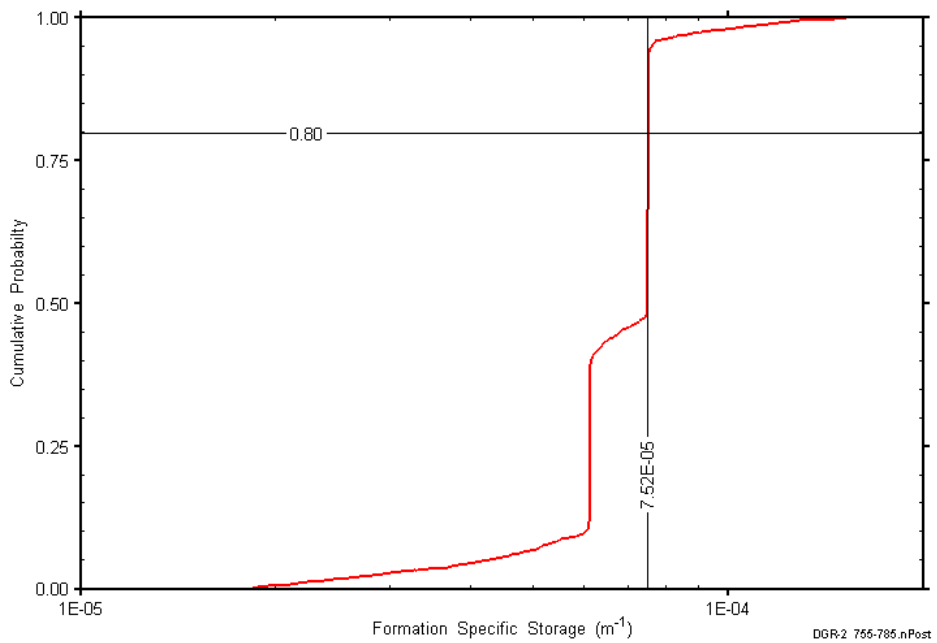


Figure B-153: DGR2_754.50-785.00 formation specific storage cumulative distribution function.

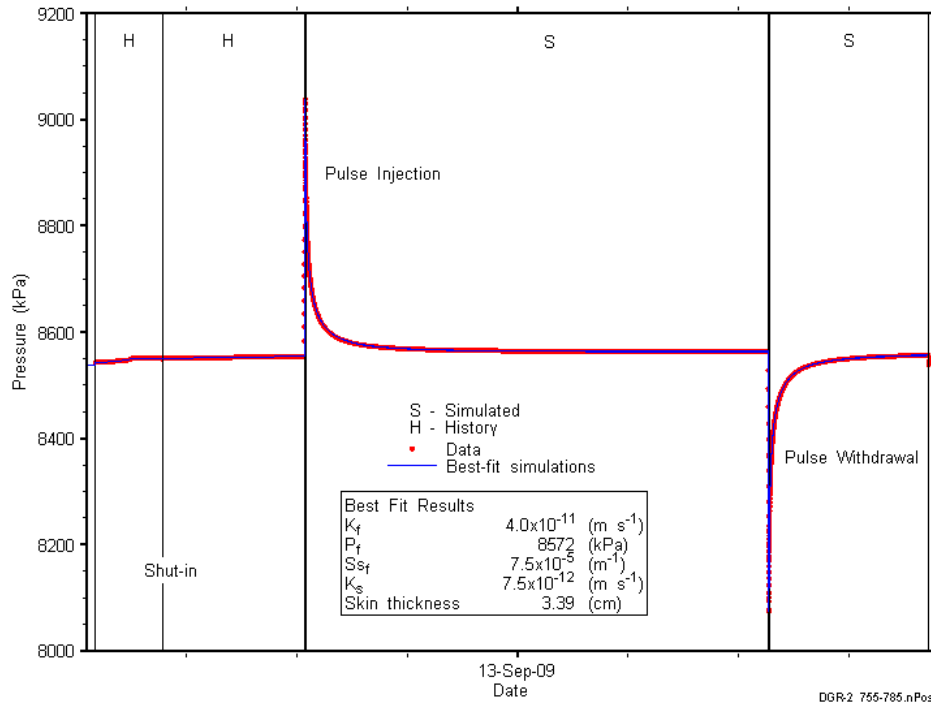


Figure B-154: Linear plot showing details of simulations of the DGR2_754.50-785.00 pressure response.

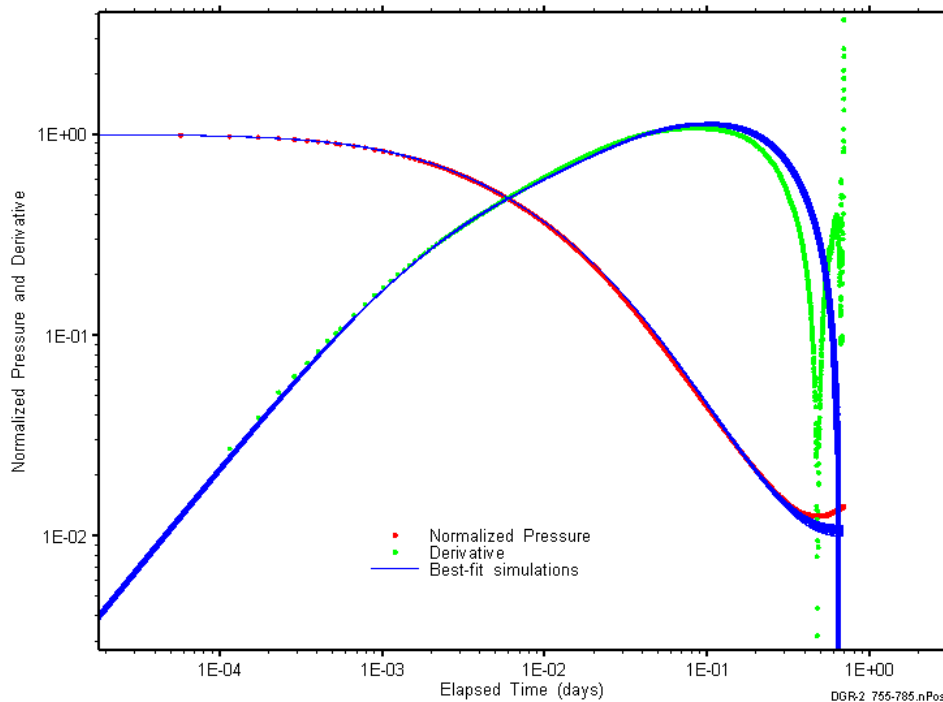


Figure B-155: Log-log plot showing simulations of the DGR2_754.50-785.00 PI Ramey B and derivative response.

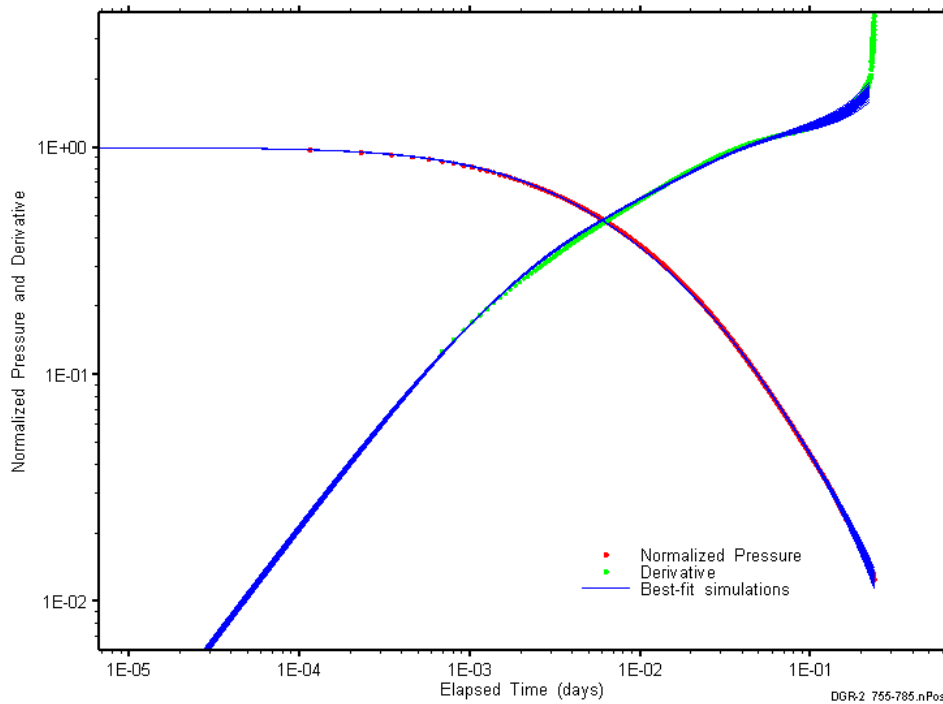


Figure B-156: Log-log plot showing simulations of the DGR2_754.50-785.00 PW Ramey B and derivative response.

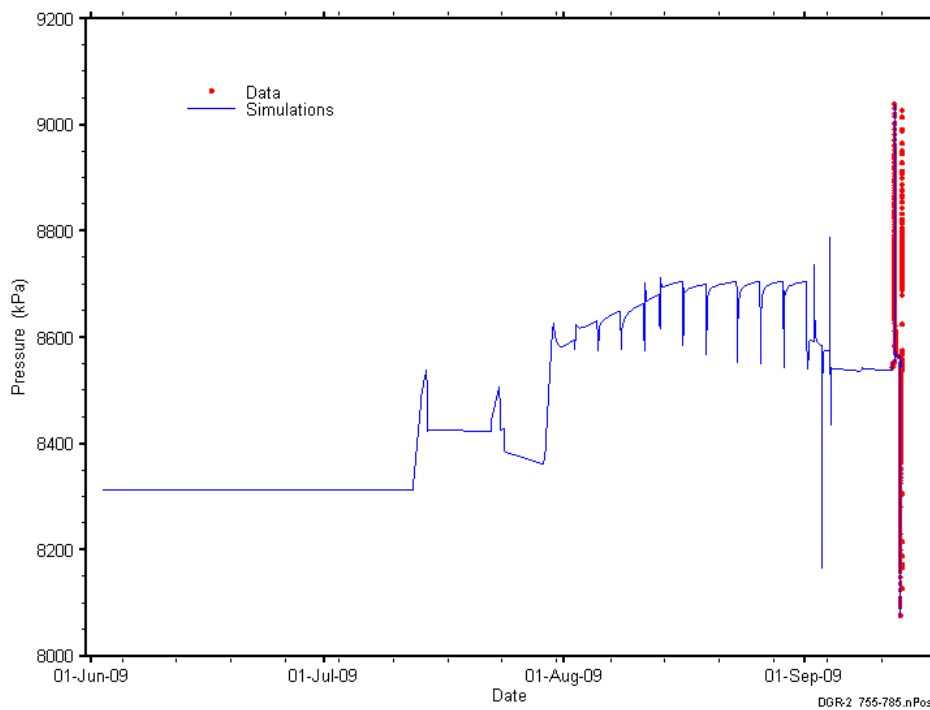


Figure B-157: Linear plot showing simulations of the DGR2_754.50-785.00 pressure response, including pre-test pressure history.

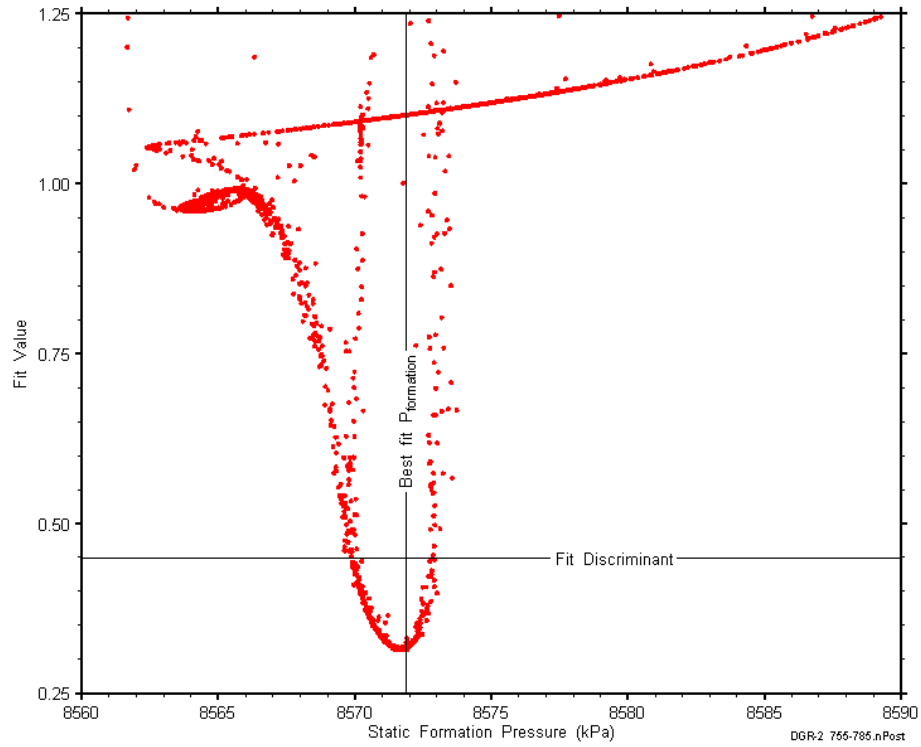


Figure B-158: XY-scatter plot showing the static formation pressure parameter space derived from DGR2_754.50-785.00 perturbation analysis along with the fit discriminant and best fit values.

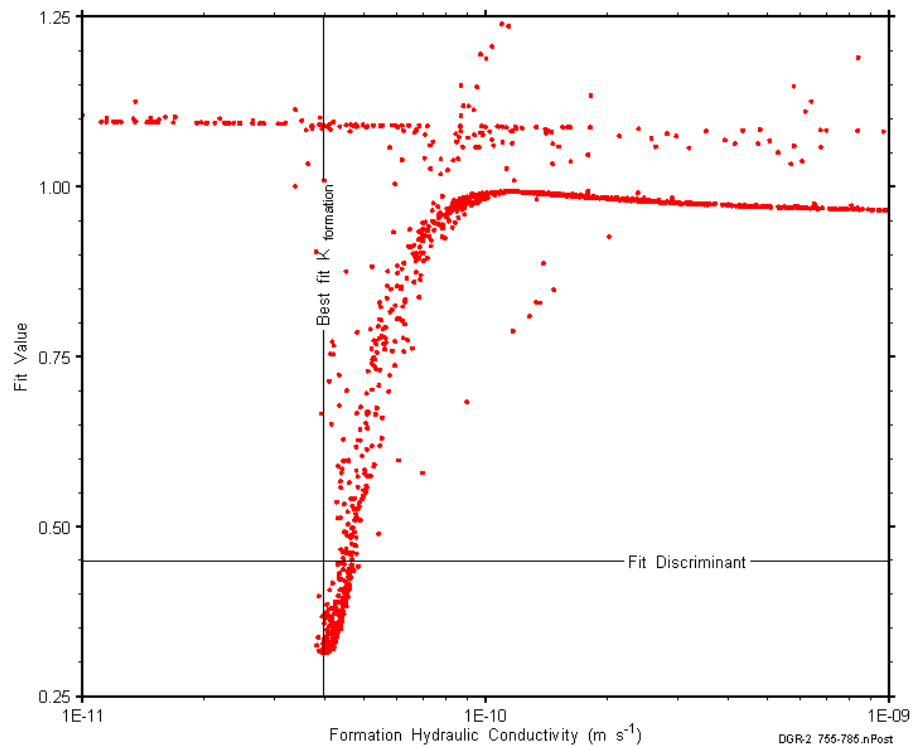


Figure B-159: XY-scatter plot showing the formation hydraulic conductivity parameter space derived from DGR2_754.50-785.00 perturbation analysis along with the fit discriminant and best fit values.

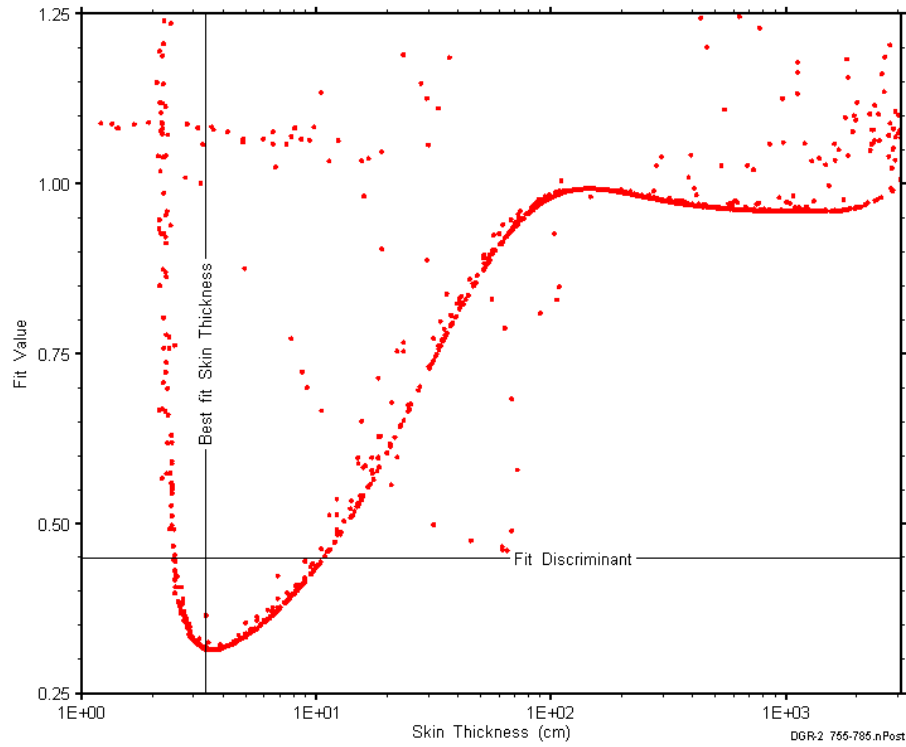


Figure B-160: XY-scatter plot showing the skin-thickness parameter space derived from DGR2_754.50-785.00 perturbation analysis along with the fit discriminant and best fit values.

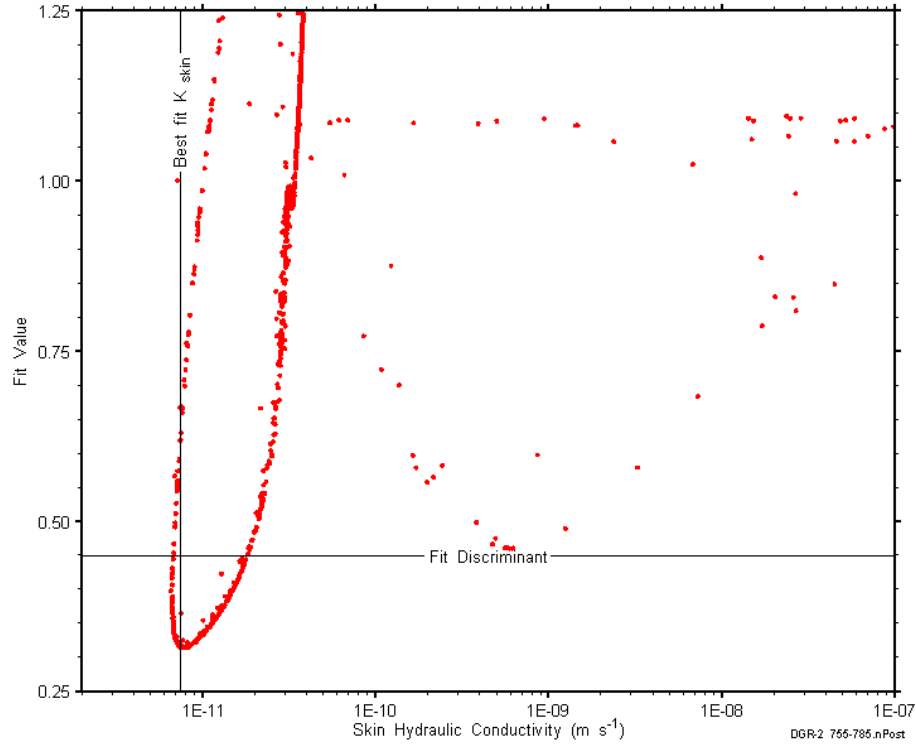


Figure B-161: XY-scatter plot showing the skin hydraulic conductivity parameter space derived from DGR2_754.50-785.00 perturbation analysis along with the fit discriminant and best fit values.

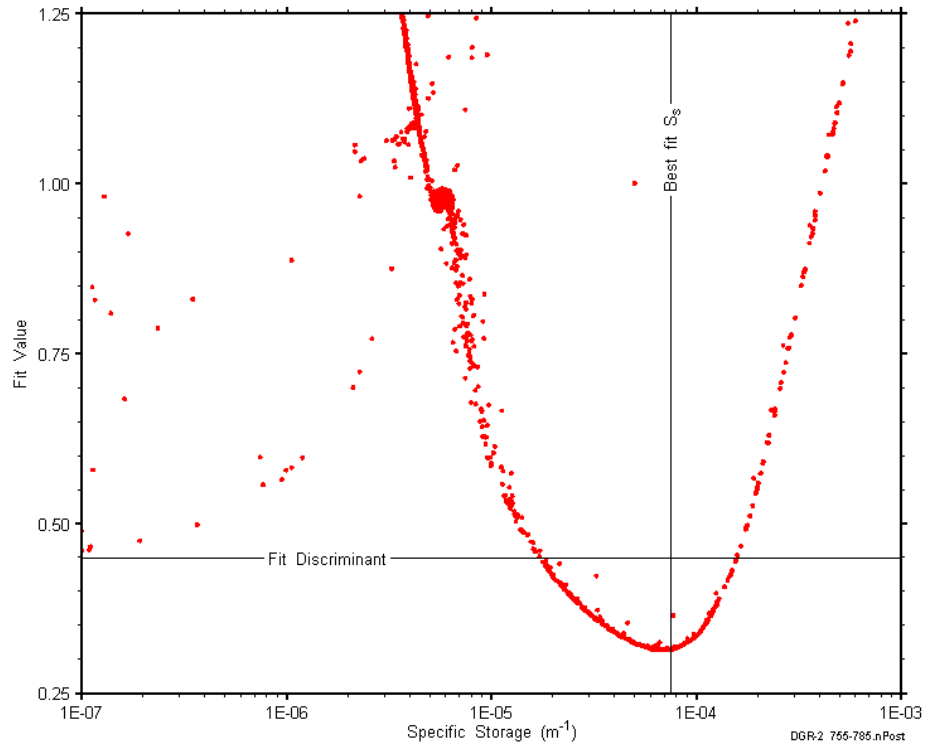


Figure B-162: XY-scatter plot showing the formation specific storage parameter space derived from DGR2_754.50-785.00 perturbation analysis along with the fit discriminant and best fit values.

B.13 761.50-792.00 Coboconk

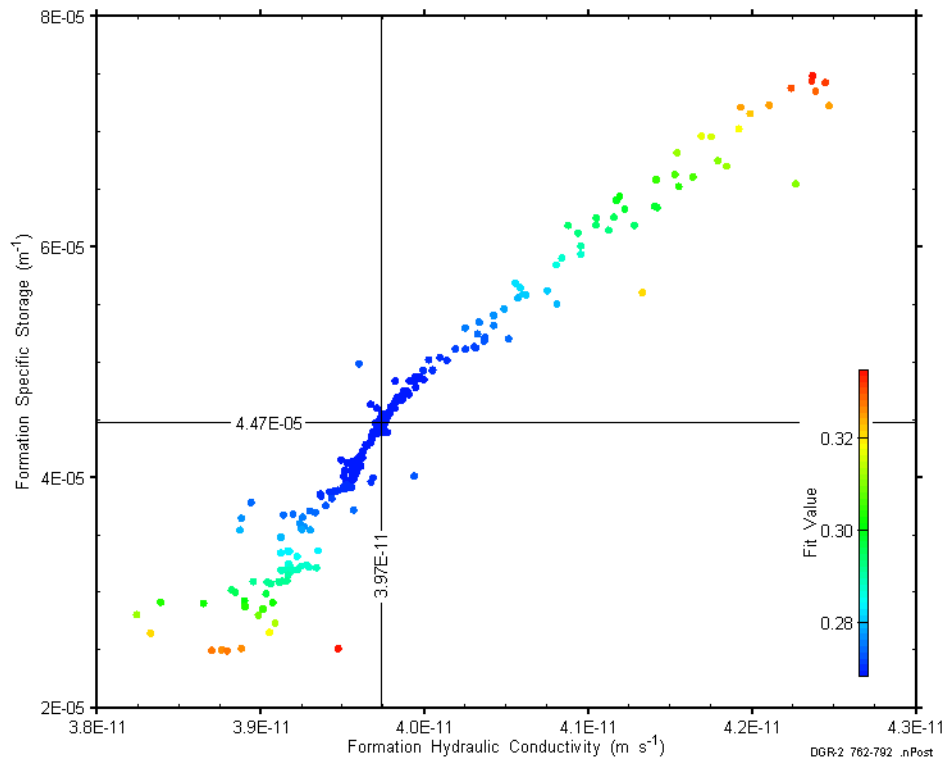


Figure B-163: XY-scatter plot showing estimates of formation hydraulic conductivity and formation specific storage derived from the DGR2_761.50-792.00 perturbation analysis.

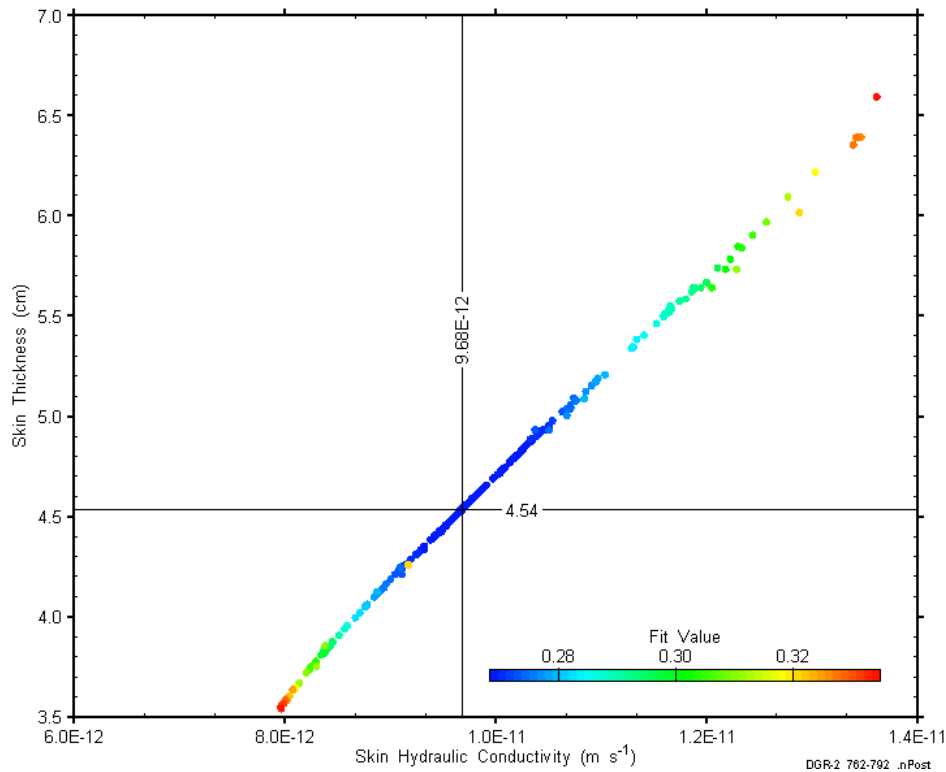


Figure B-164: XY-scatter plot showing estimates of skin hydraulic conductivity and skin thickness derived from the DGR2_761.50-792.00 perturbation analysis.

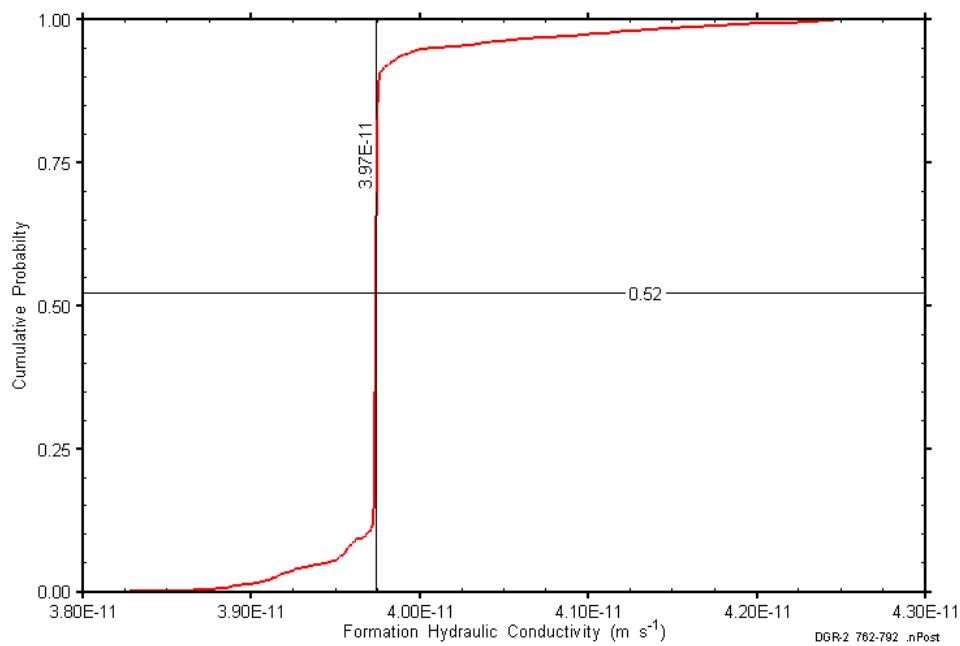


Figure B-165: DGR2_761.50-792.00 formation hydraulic conductivity cumulative distribution function.

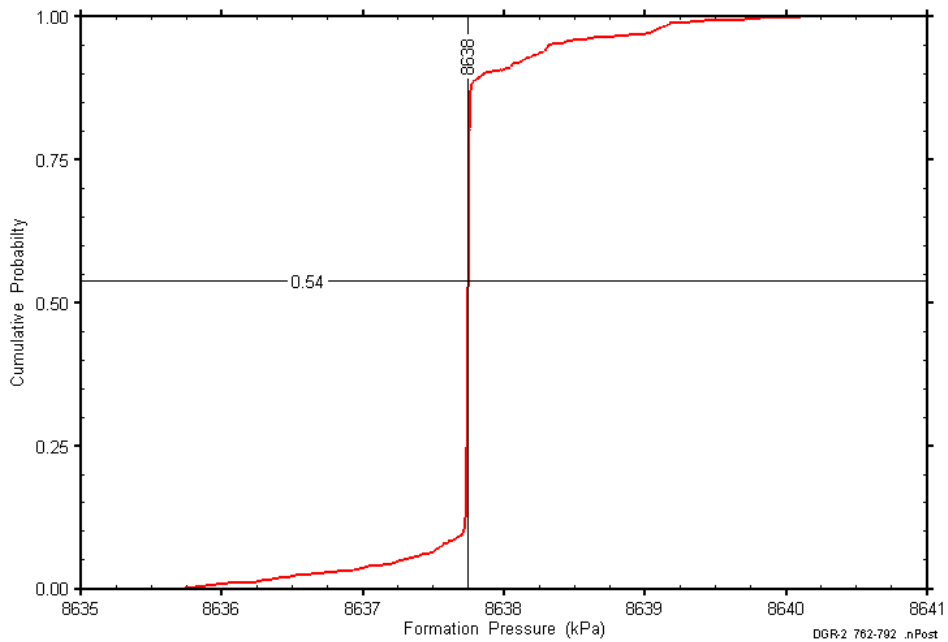


Figure B-166: DGR2_761.50-792.00 static formation pressure cumulative distribution function.

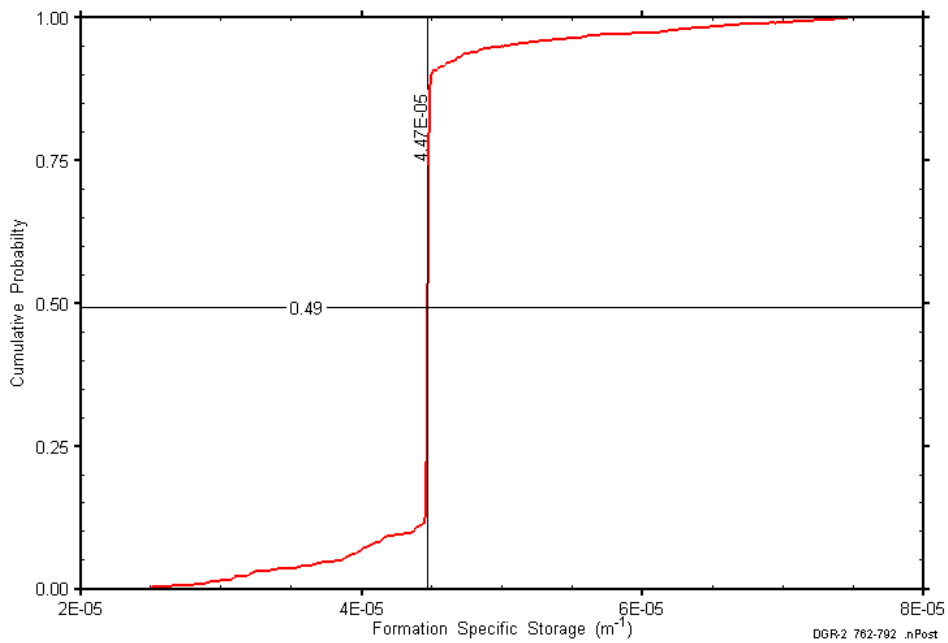


Figure B-167: DGR2_761.50-792.00 formation specific storage cumulative distribution function.

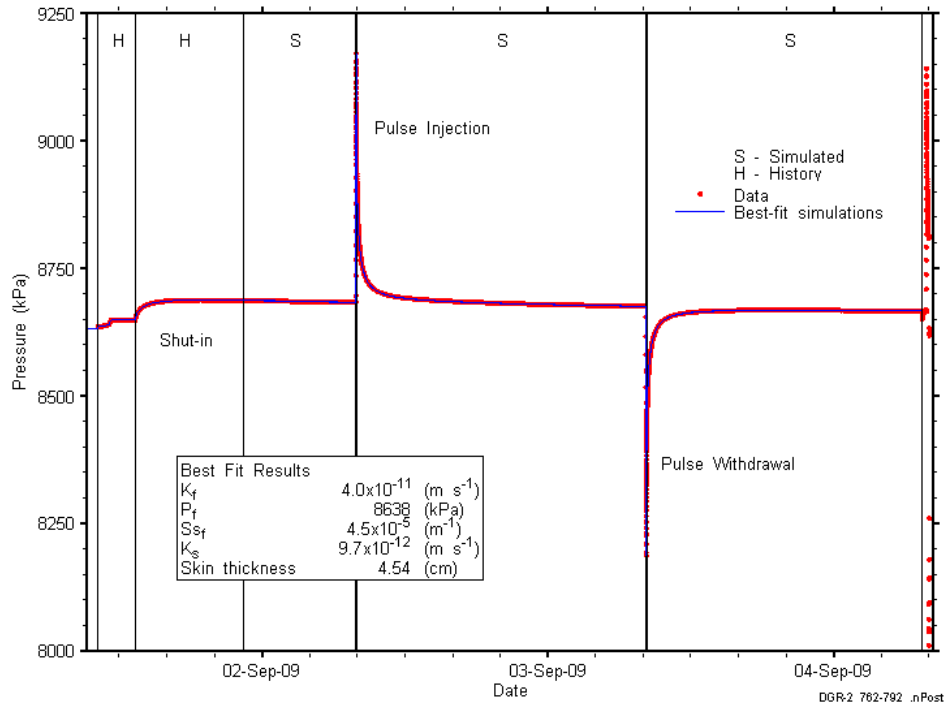


Figure B-168: Linear plot showing details of simulations of the DGR2_761.50-792.00 pressure response.

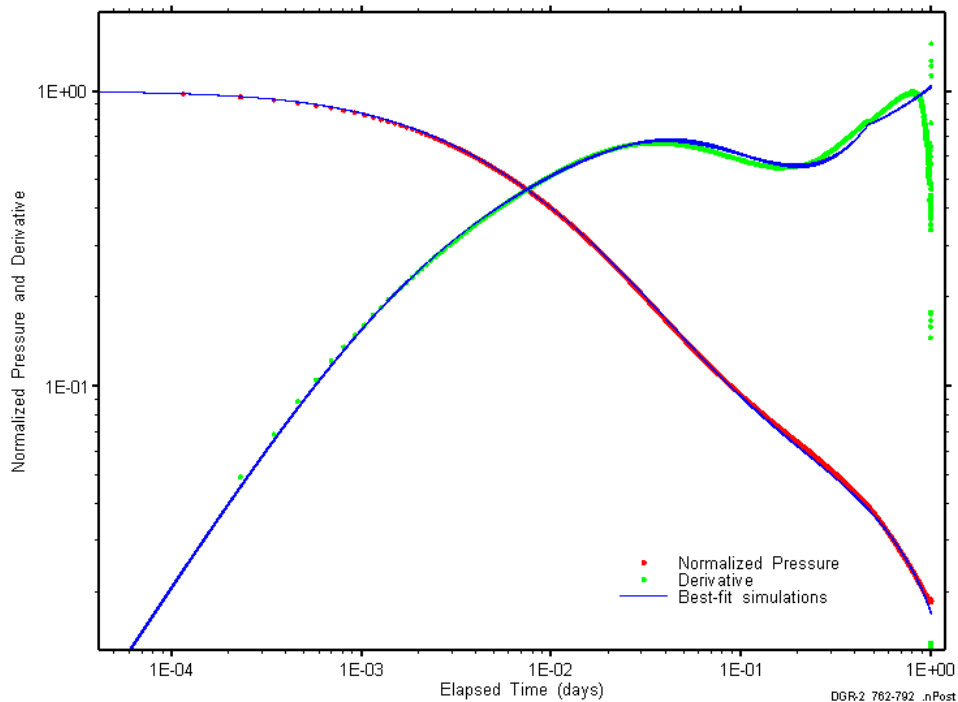


Figure B-169: Log-log plot showing simulations of the DGR2_761.50-792.00 PI Ramey B and derivative response.

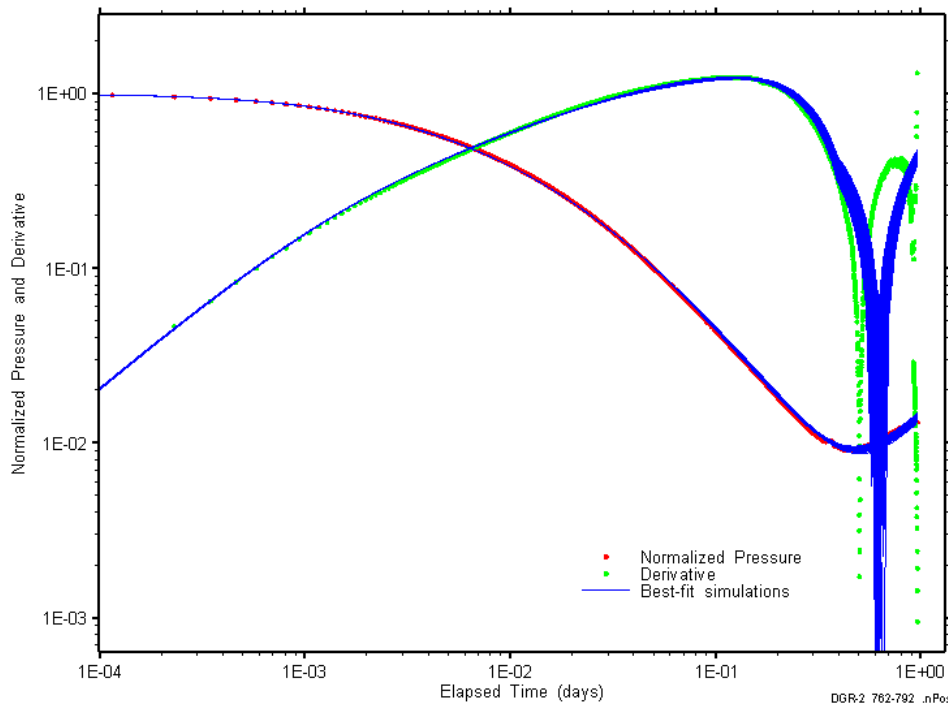


Figure B-170: Log-log plot showing simulations of the DGR2_761.50-792.00 PW Ramey B and derivative response.

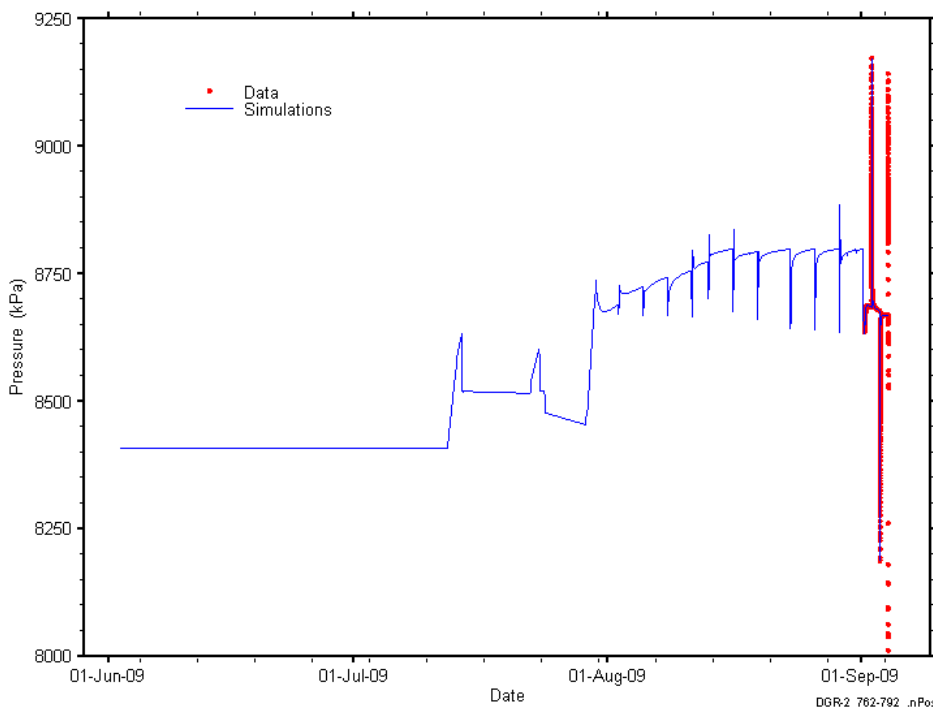


Figure B-171: Linear plot showing simulations of the DGR2_761.50-792.00 pressure response, including pre-test pressure history.

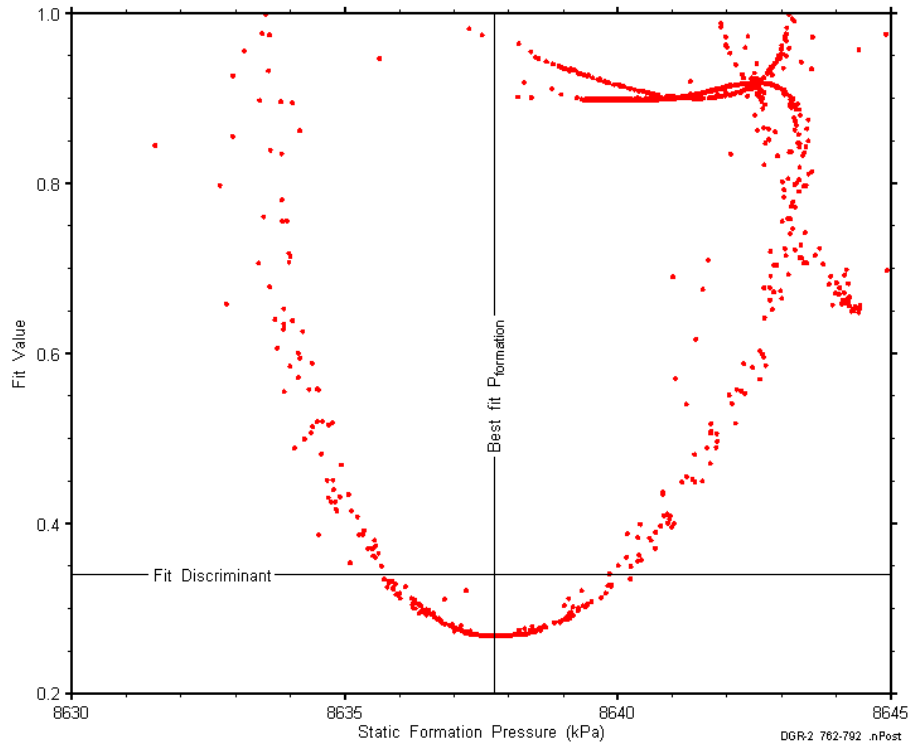


Figure B-172: XY-scatter plot showing the static formation pressure parameter space derived from DGR2_761.50-792.00 perturbation analysis along with the fit discriminant and best fit values.

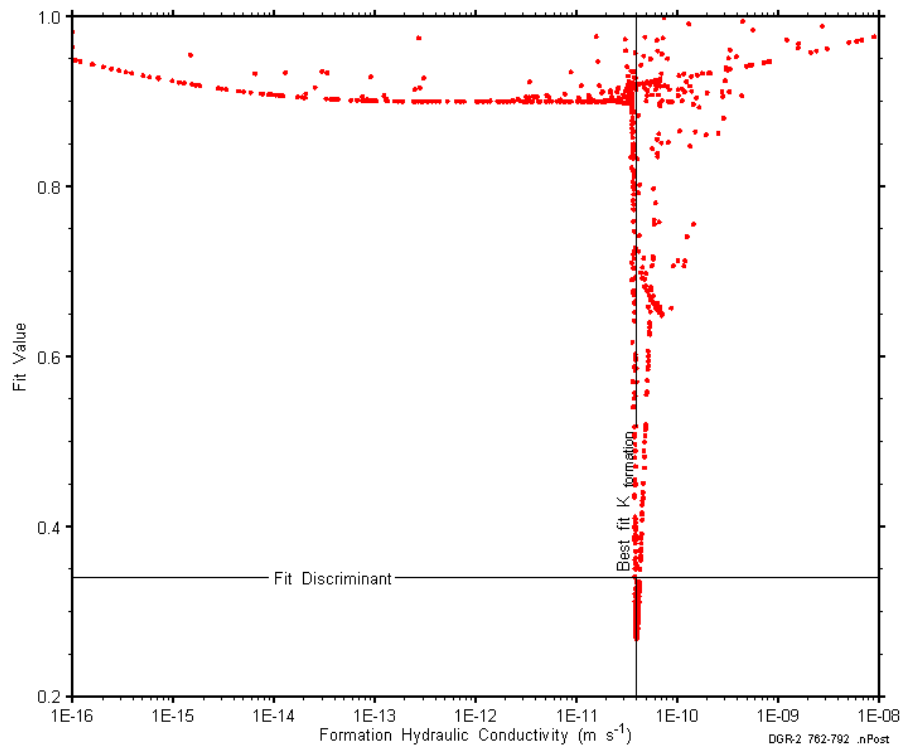


Figure B-173: XY-scatter plot showing the formation hydraulic conductivity parameter space derived from DGR2_761.50-792.00 perturbation analysis along with the fit discriminant and best fit values.

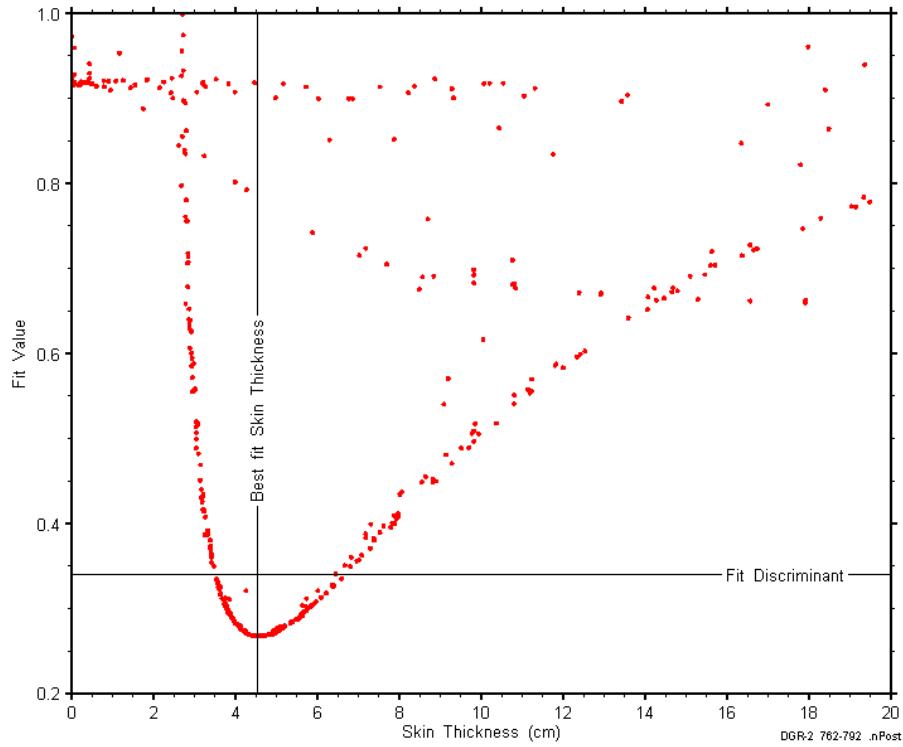


Figure B-174: XY-scatter plot showing the skin-thickness parameter space derived from DGR2_761.50-792.00 perturbation analysis along with the fit discriminant and best fit values.

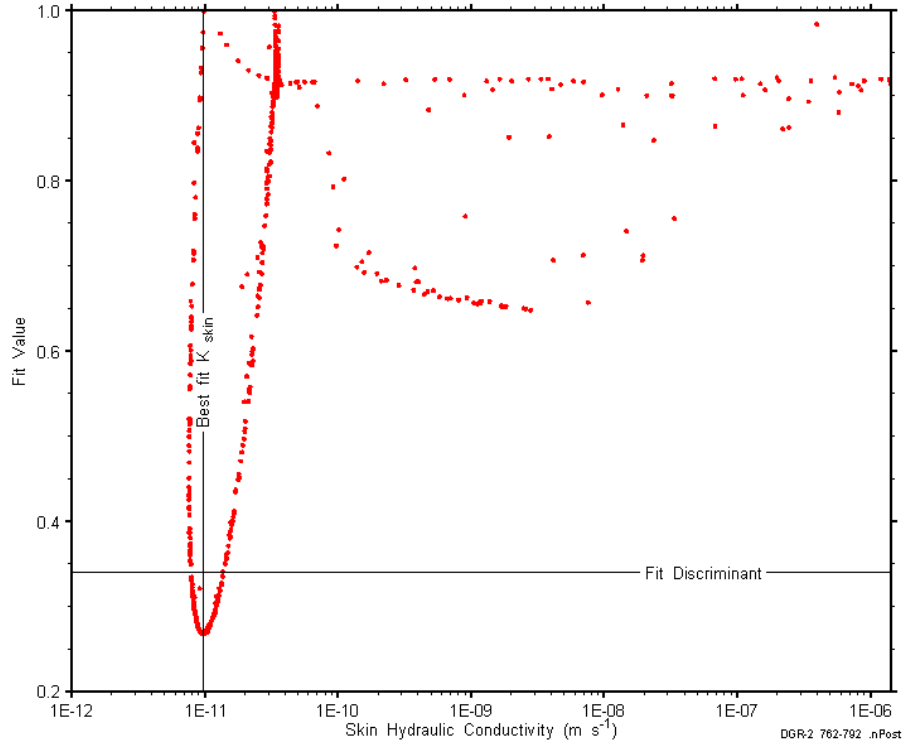


Figure B-175: XY-scatter plot showing the skin hydraulic conductivity parameter space derived from DGR2_761.50-792.00 perturbation analysis along with the fit discriminant and best fit values.

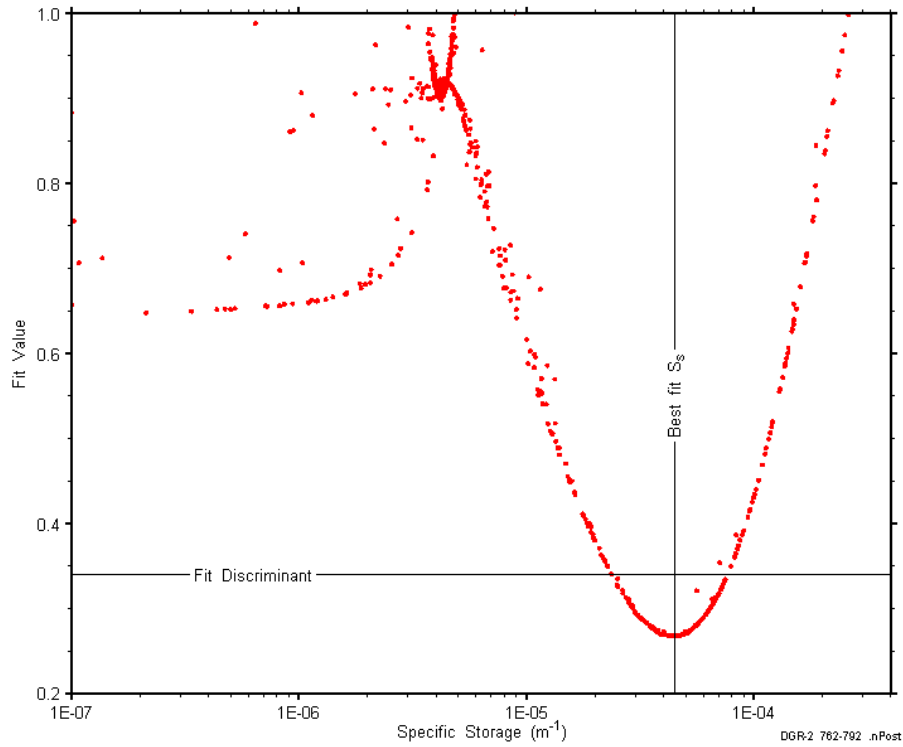


Figure B-176: XY-scatter plot showing the formation specific storage parameter space derived from DGR2_761.50-792.00 perturbation analysis along with the fit discriminant and best fit values.

B.14 785.00-815.50 Gull River

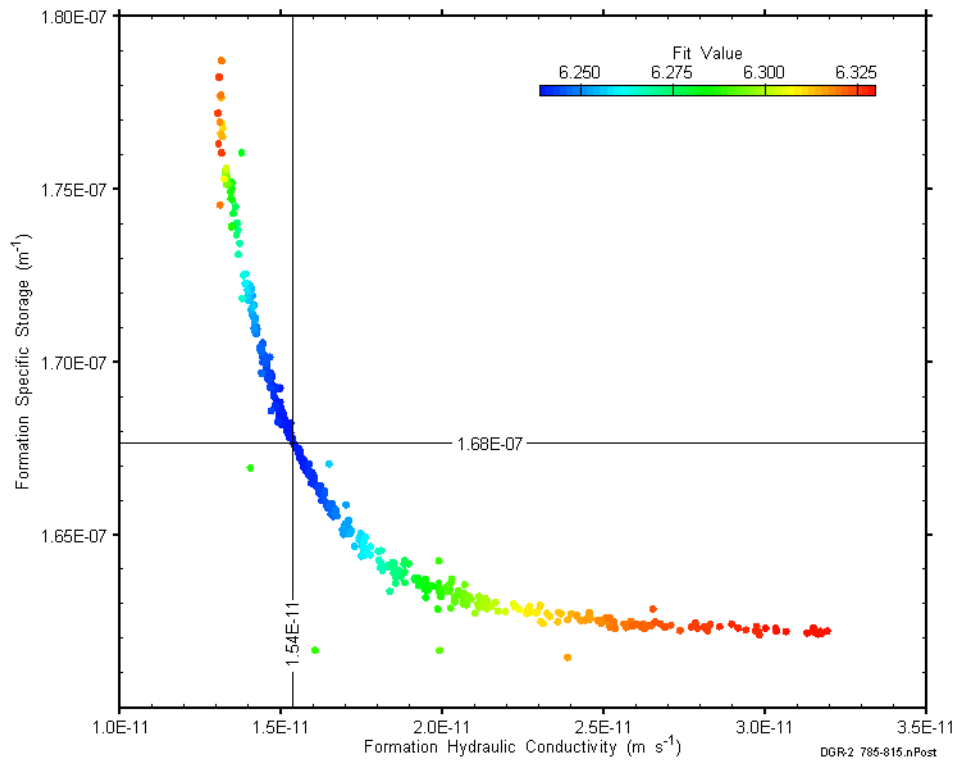


Figure B-177: XY-scatter plot showing estimates of formation hydraulic conductivity and formation specific storage derived from the DGR2_785.00-815.50 perturbation analysis.

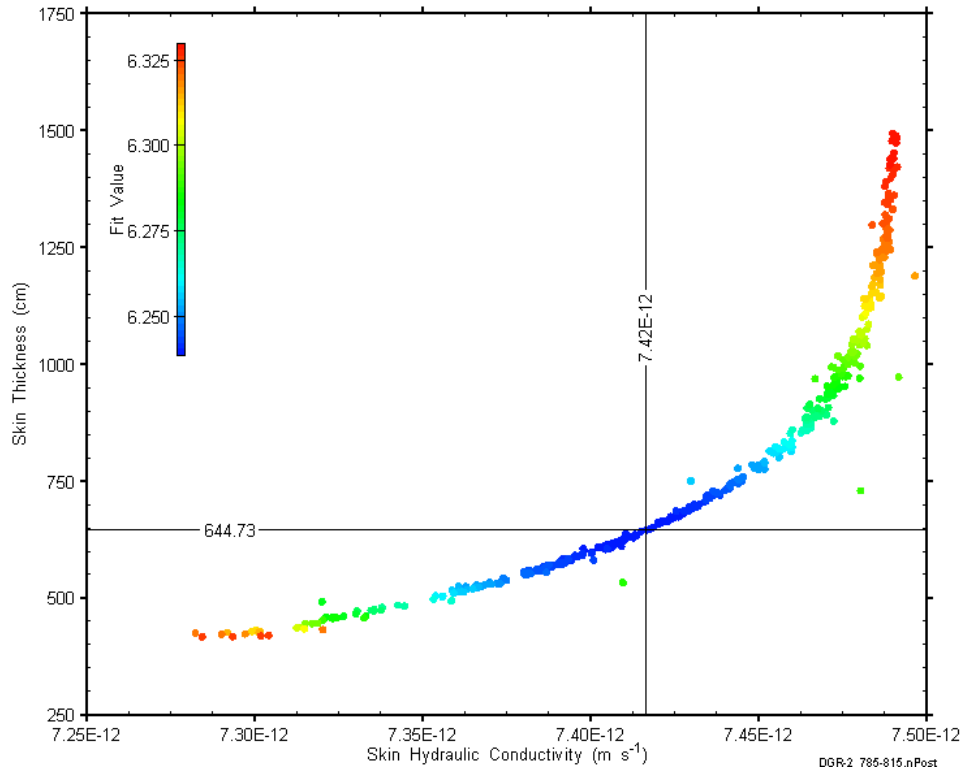


Figure B-178: XY-scatter plot showing estimates of skin hydraulic conductivity and skin thickness derived from the DGR2_785.00-815.50 perturbation analysis.

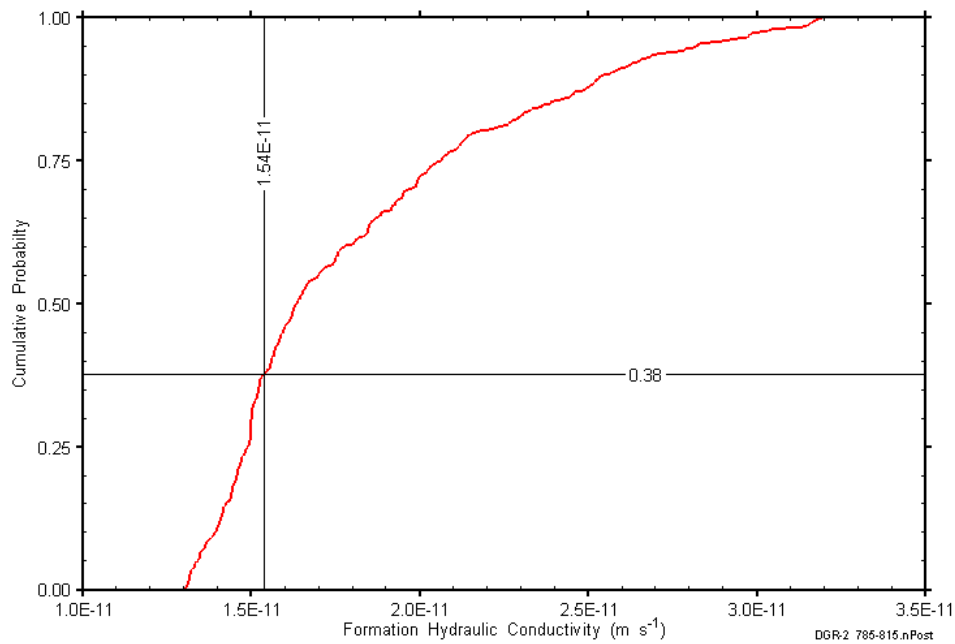


Figure B-179: DGR2_785.00-815.50 formation hydraulic conductivity cumulative distribution function.

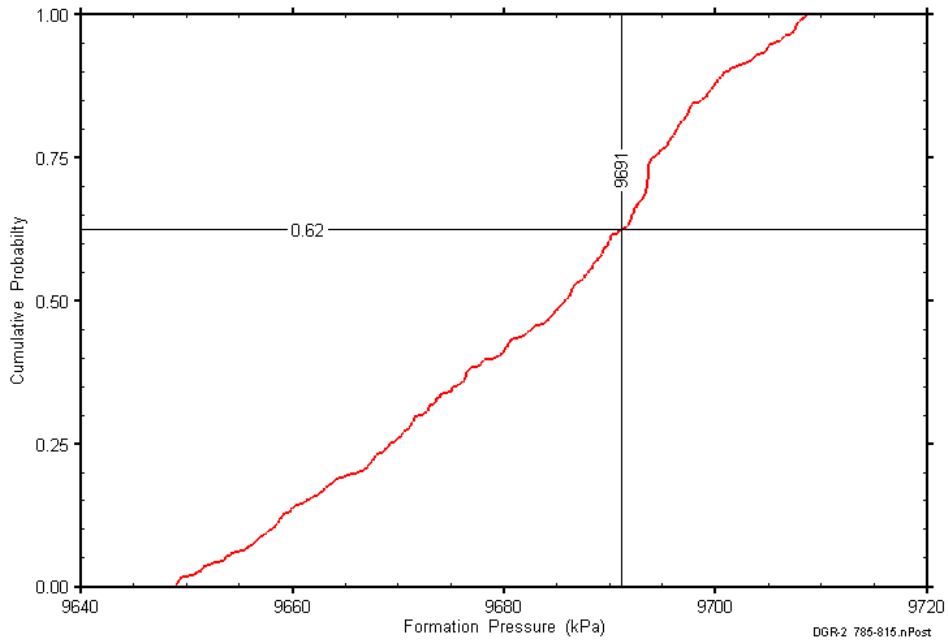


Figure B-180: DGR2_785.00-815.50 static formation pressure cumulative distribution function.

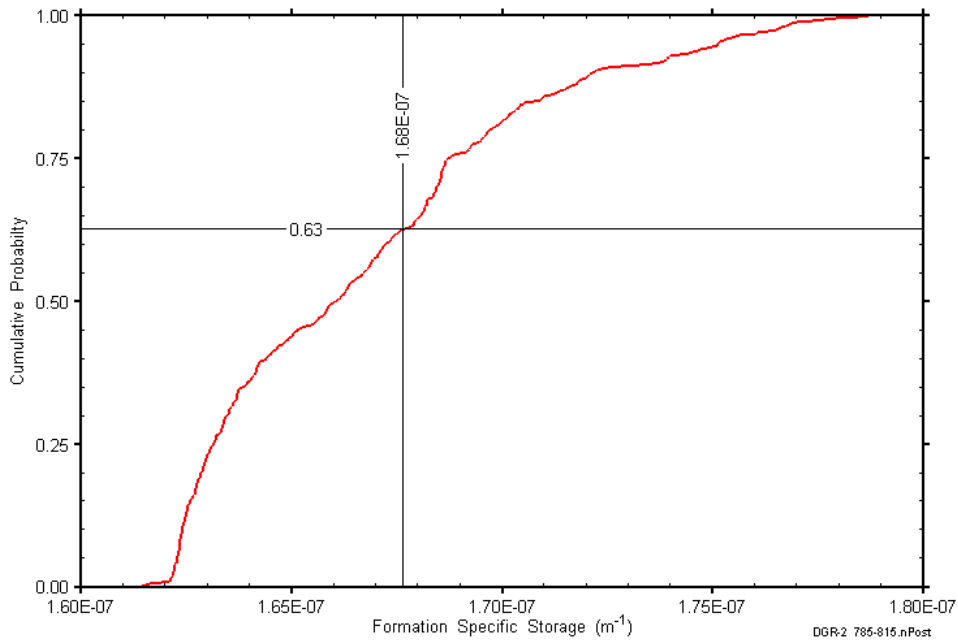


Figure B-181: DGR2_785.00-815.50 formation specific storage cumulative distribution function.

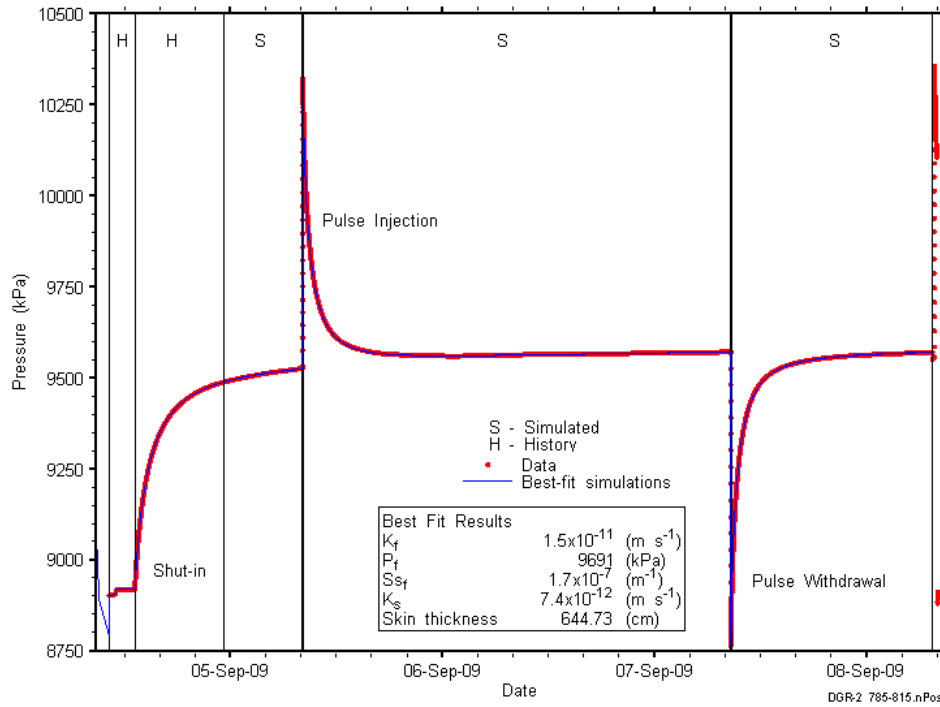


Figure B-182: Linear plot showing details of simulations of the DGR2_785.00-815.50 pressure response.

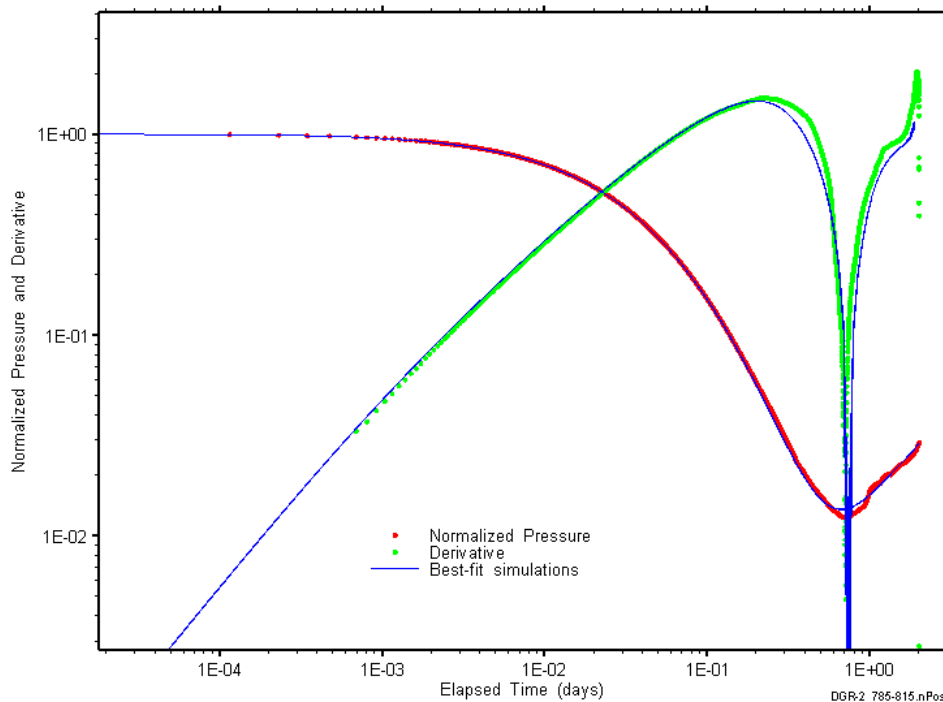


Figure B-183: Log-log plot showing simulations of the DGR2_785.00-815.50 PI Ramey B and derivative response.

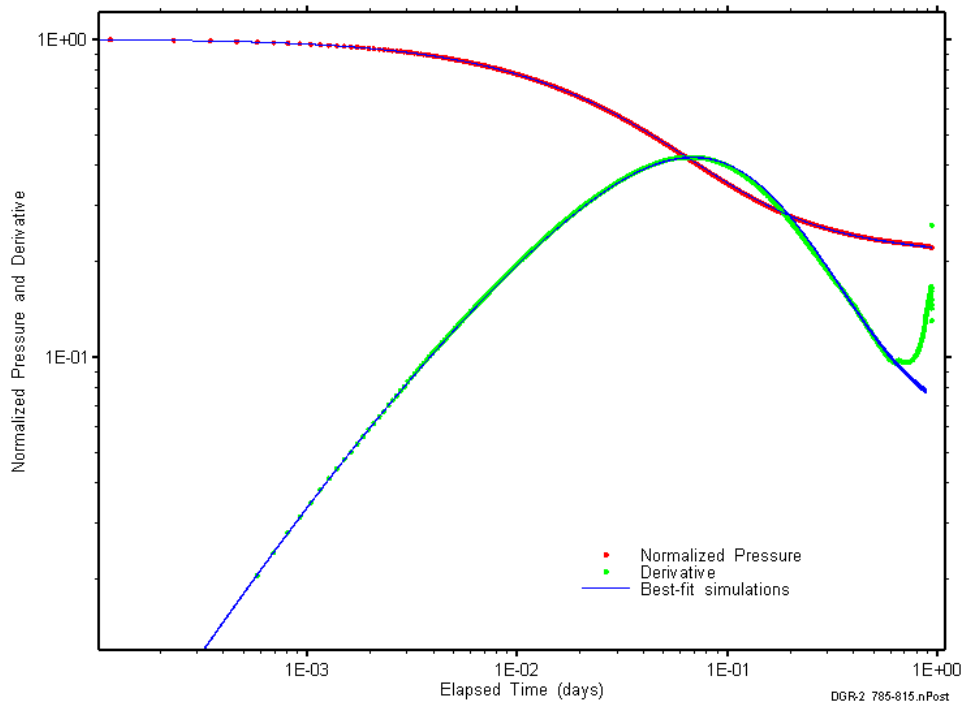


Figure B-184: Log-log plot showing simulations of the DGR2_785.00-815.50 PW Ramey B and derivative response.

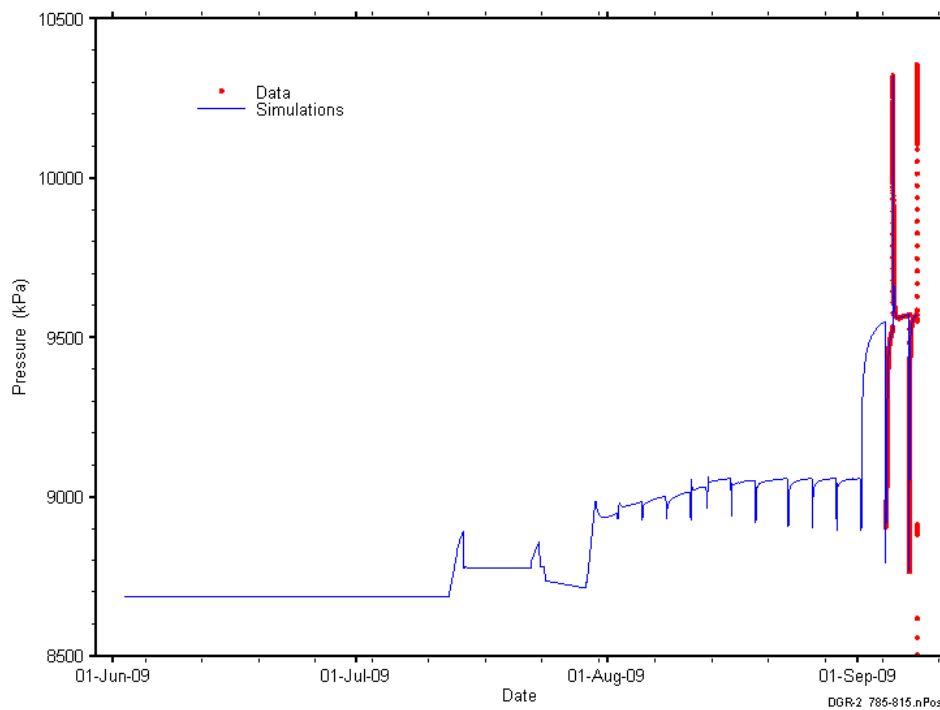


Figure B-185: Linear plot showing simulations of the DGR2_785.00-815.50 pressure response, including pre-test pressure history.

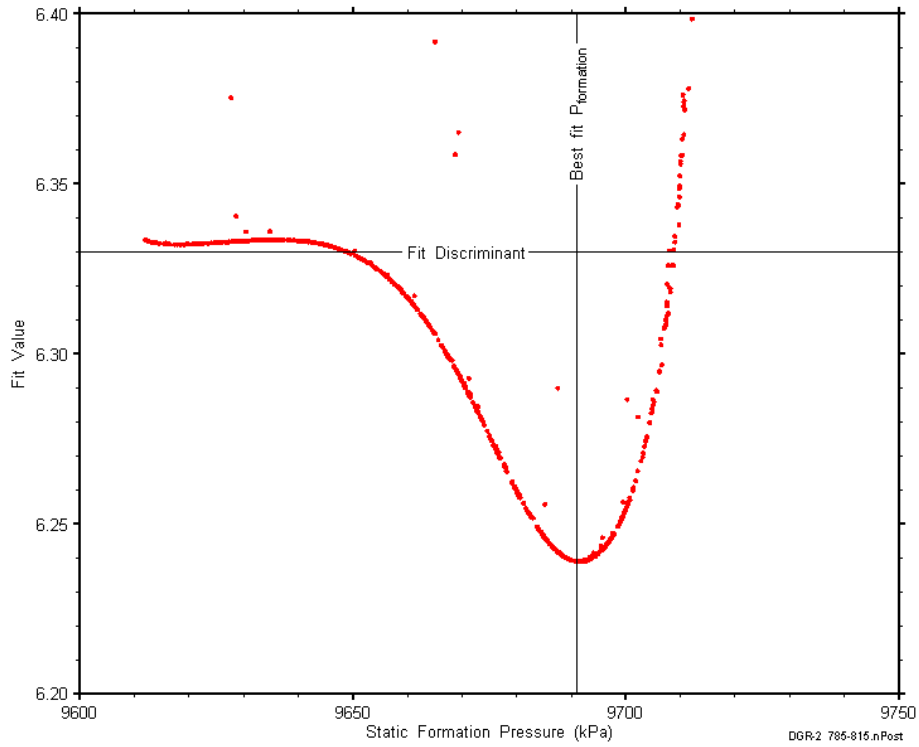


Figure B-186: XY-scatter plot showing the static formation pressure parameter space derived from DGR2_785.00-815.50 perturbation analysis along with the fit discriminant and best fit values.

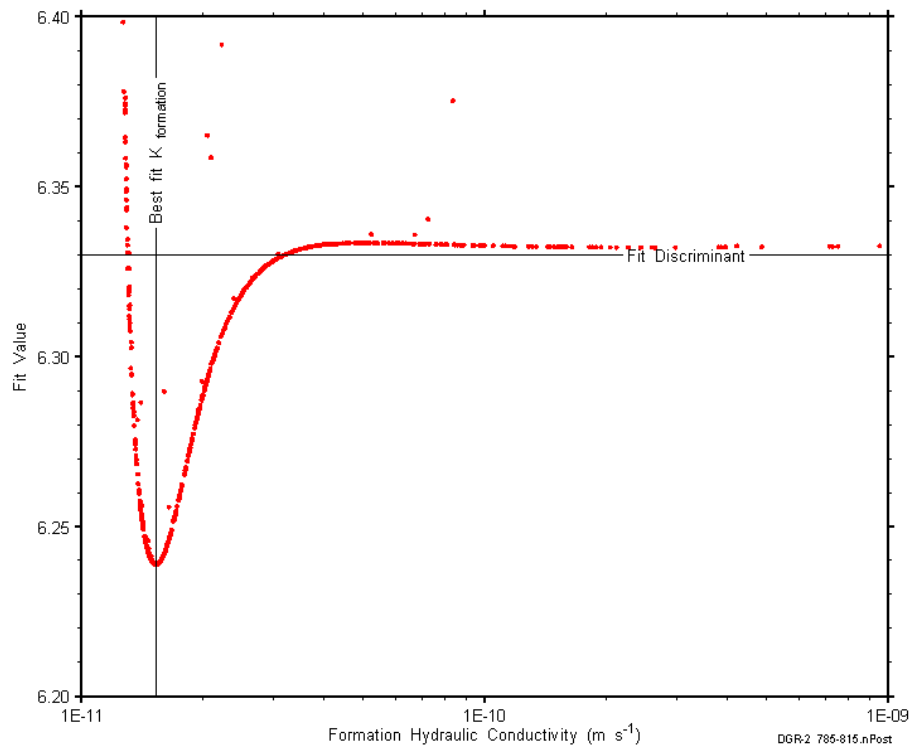


Figure B-187: XY-scatter plot showing the formation hydraulic conductivity parameter space derived from DGR2_785.00-815.50 perturbation analysis along with the fit discriminant and best fit values.

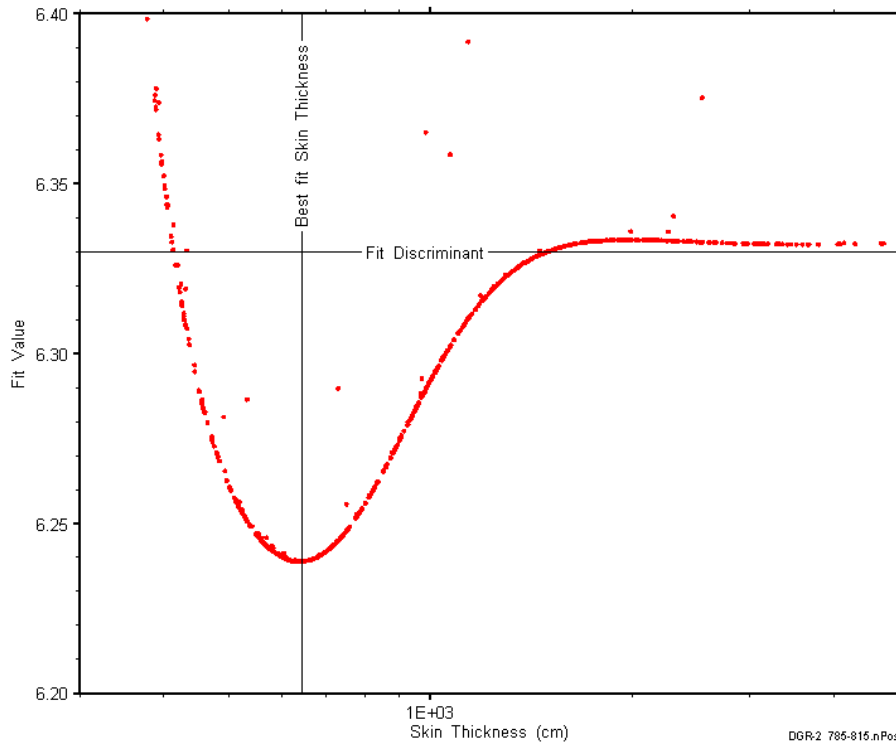


Figure B-188: XY-scatter plot showing the skin-thickness parameter space derived from DGR2_785.00-815.50 perturbation analysis along with the fit discriminant and best fit values.

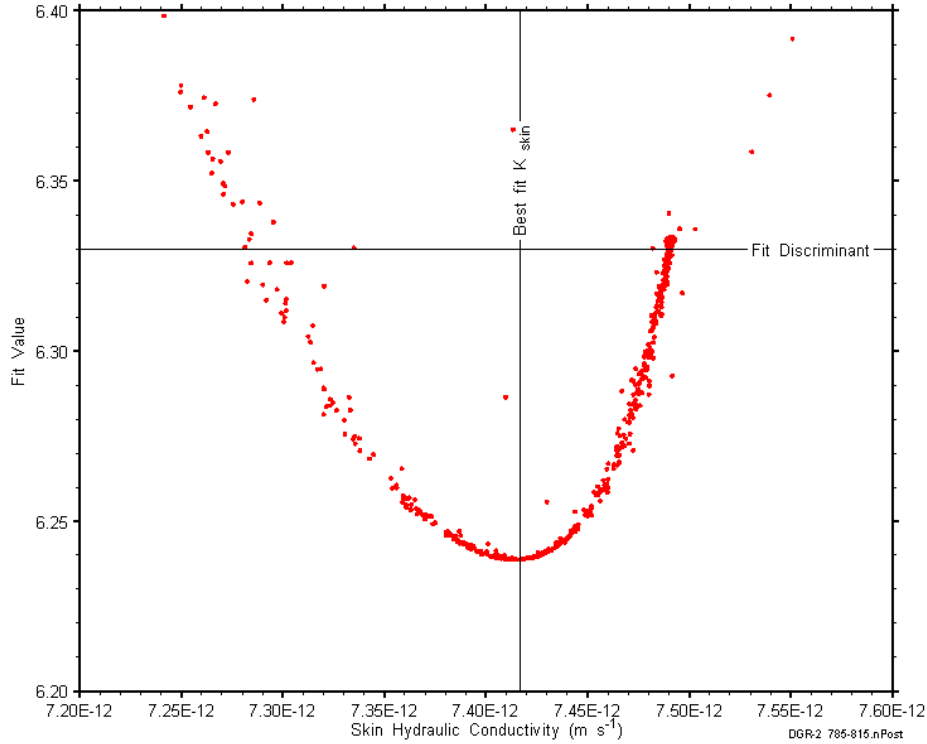


Figure B-189: XY-scatter plot showing the skin hydraulic conductivity parameter space derived from DGR2_785.00-815.50 perturbation analysis along with the fit discriminant and best fit values.

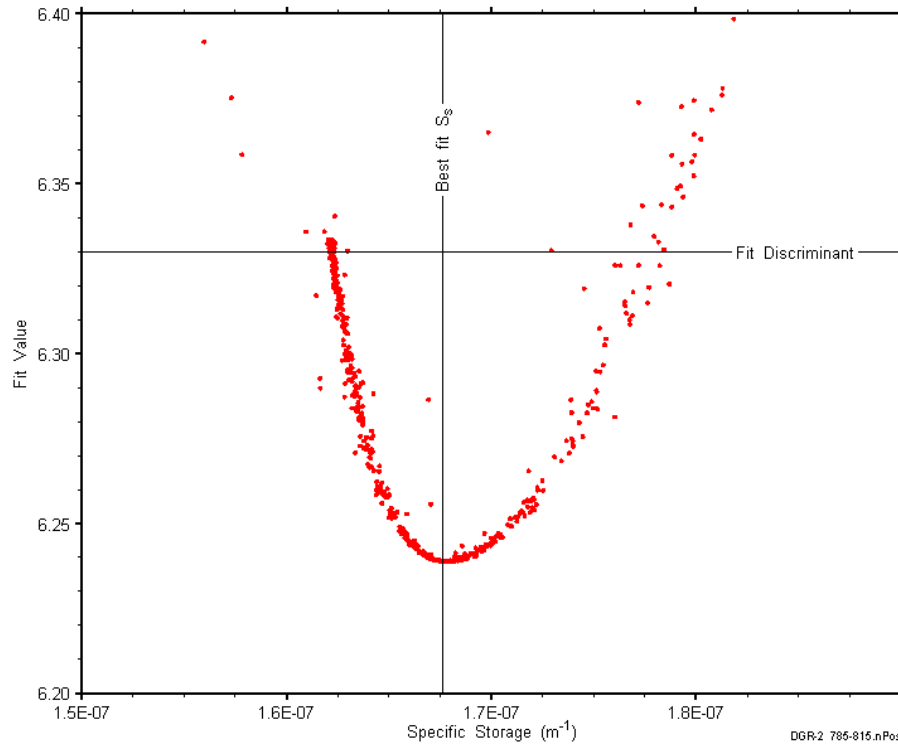


Figure B-190: XY-scatter plot showing the formation specific storage parameter space derived from DGR2_785.00-815.50 perturbation analysis along with the fit discriminant and best fit values.

B.15 801.50-832.00 Gull River

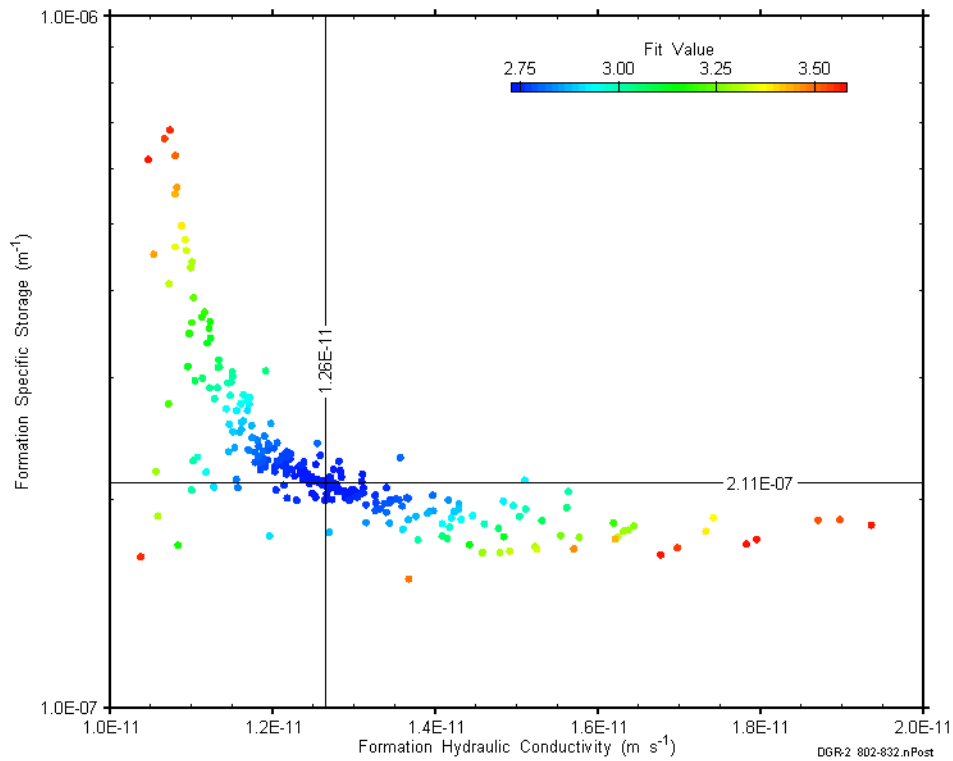


Figure B-191: XY-scatter plot showing estimates of formation hydraulic conductivity and formation specific storage derived from the DGR2_801.50-832.00 perturbation analysis.

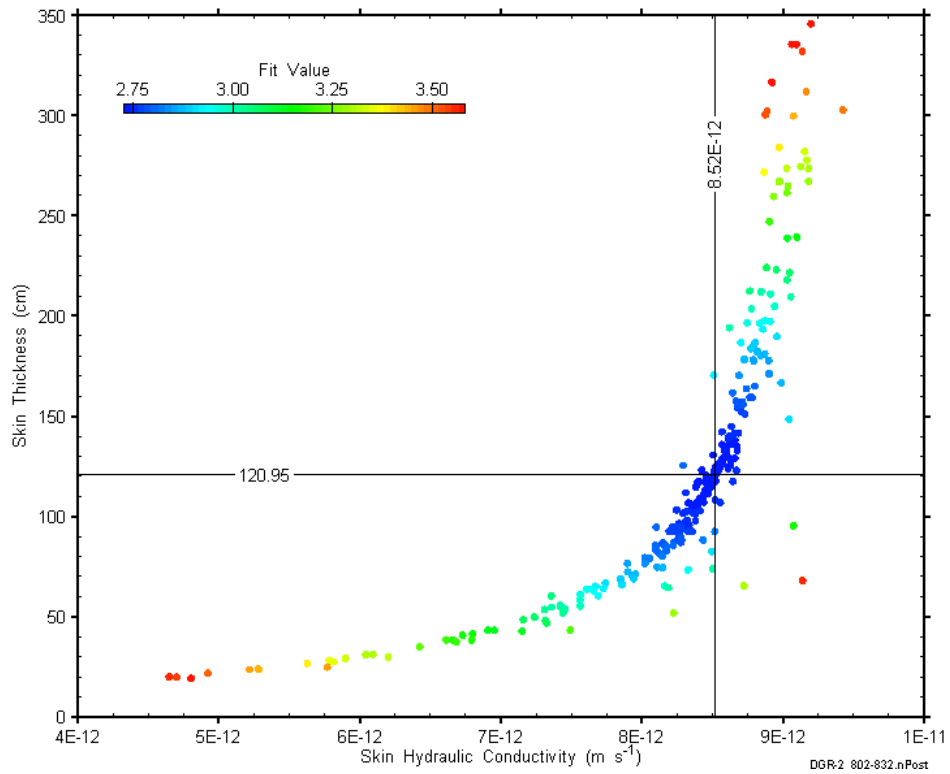


Figure B-192: XY-scatter plot showing estimates of skin hydraulic conductivity and skin thickness derived from the DGR2_801.50-832.00 perturbation analysis.

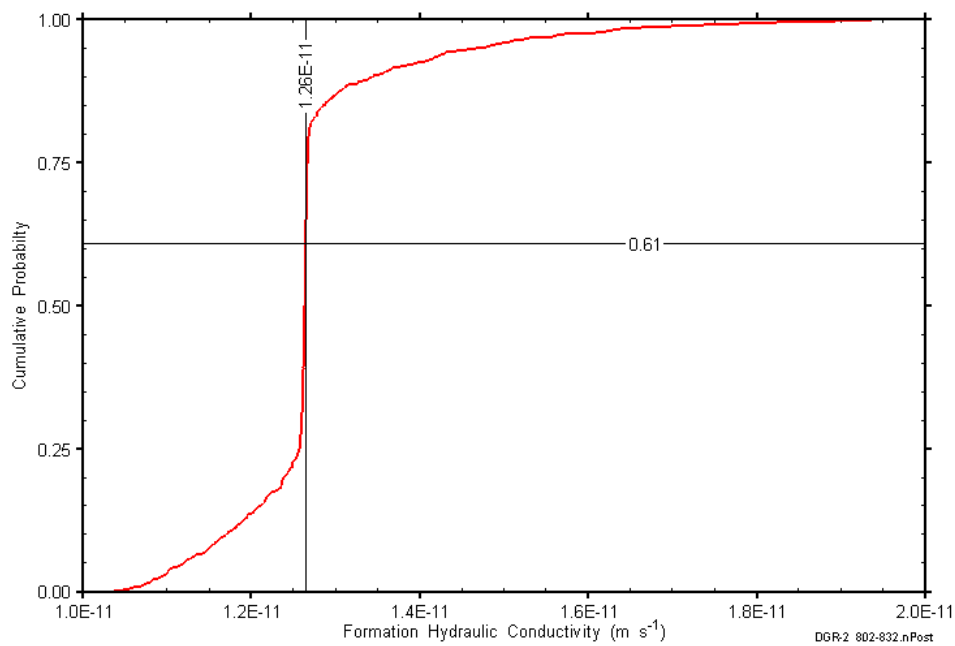


Figure B-193: DGR2_801.50-832.00 formation hydraulic conductivity cumulative distribution function.

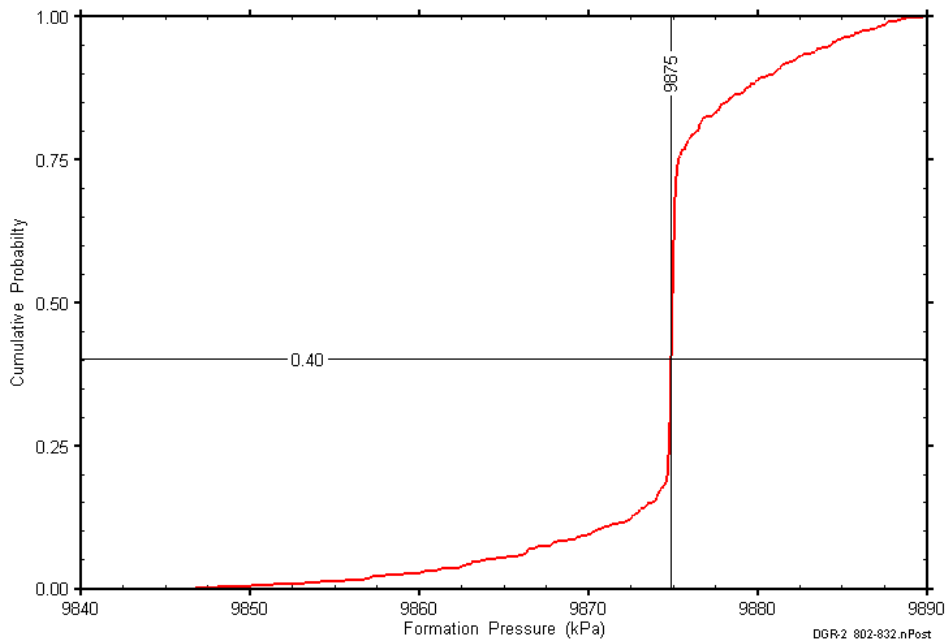


Figure B-194: DGR2_801.50-832.00 static formation pressure cumulative distribution function.

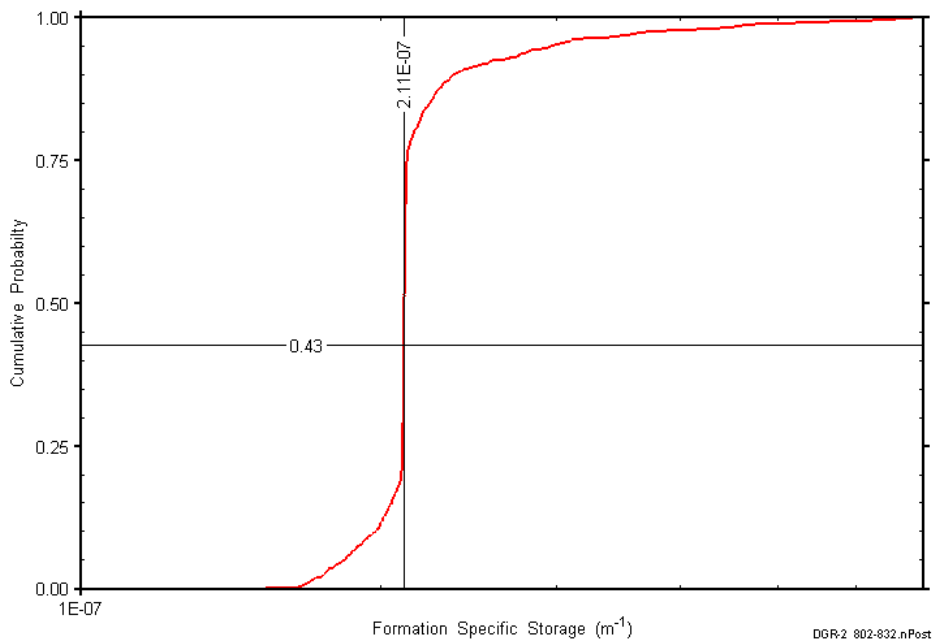


Figure B-195: DGR2_801.50-832.00 formation specific storage cumulative distribution function.

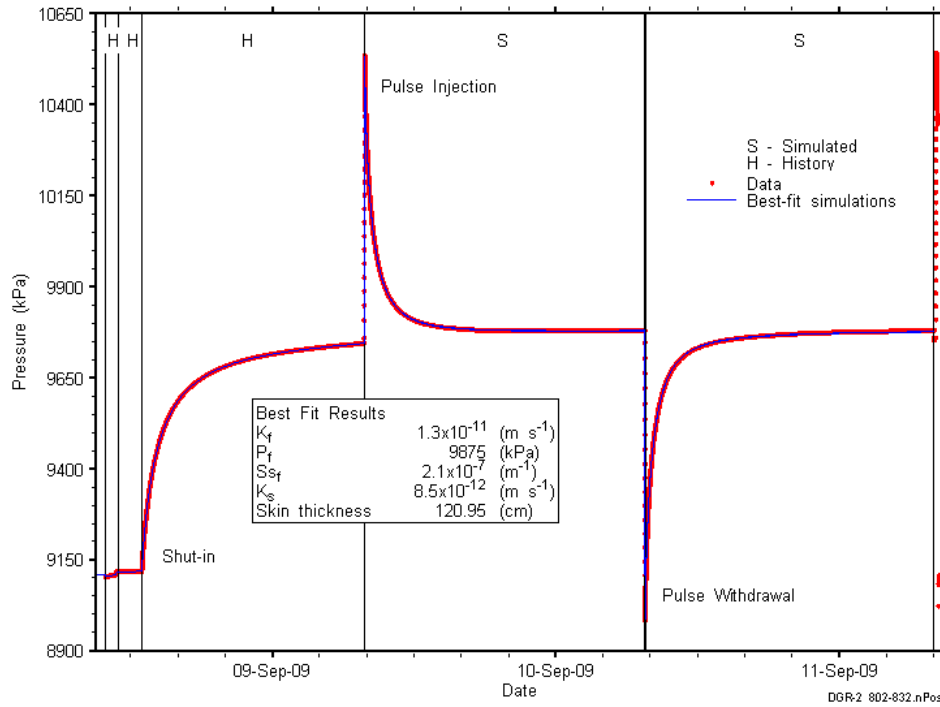


Figure B-196: Linear plot showing details of simulations of the DGR2_801.50-832.00 pressure response.

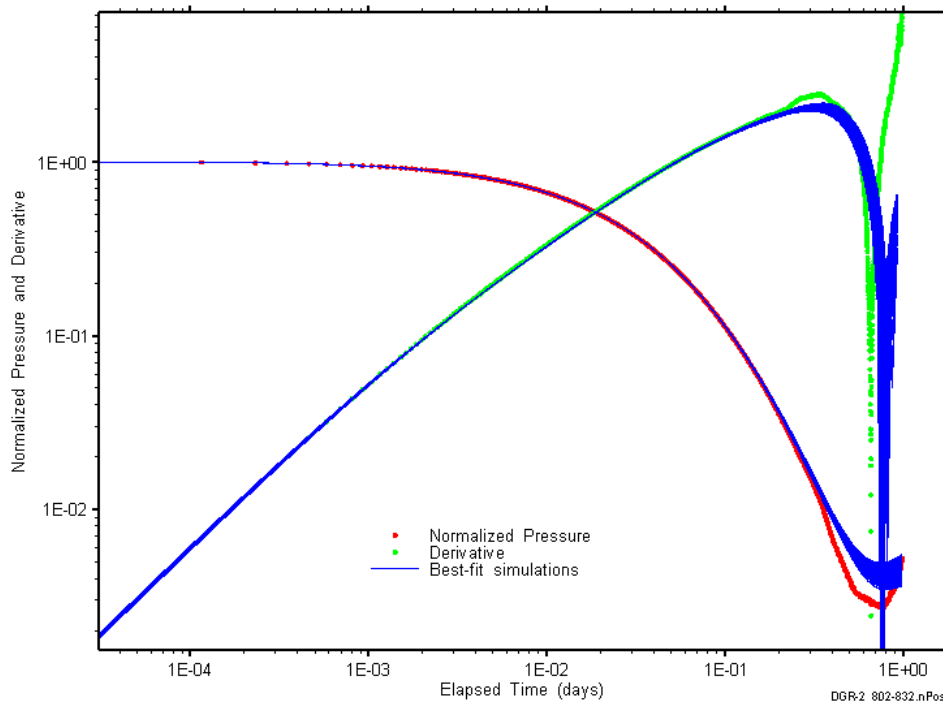


Figure B-197: Log-log plot showing simulations of the DGR2_801.50-832.00 PI Ramey B and derivative response.

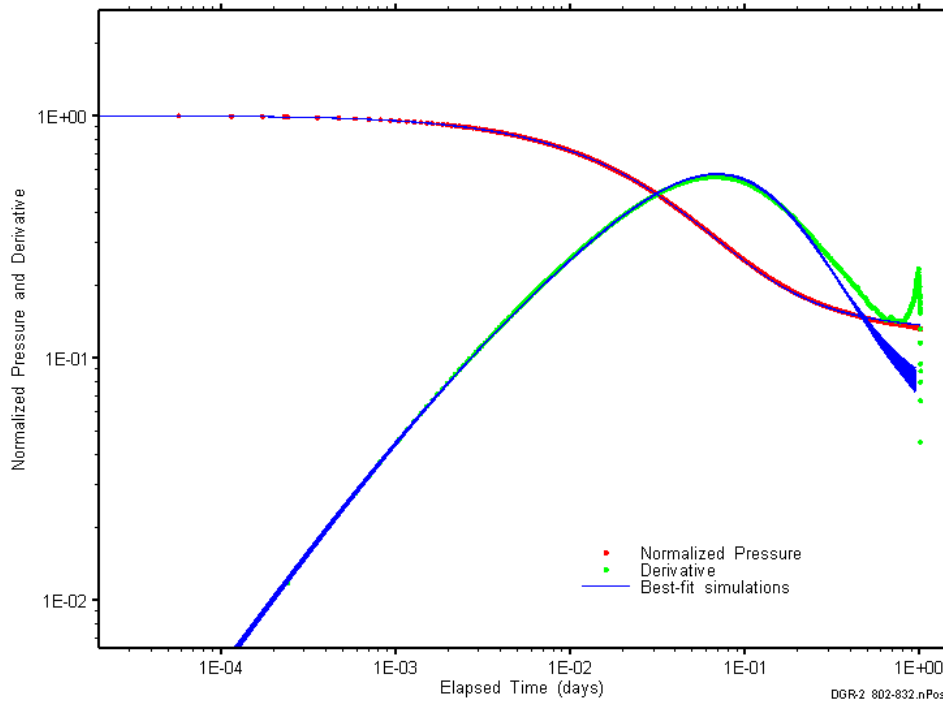


Figure B-198: Log-log plot showing simulations of the DGR2_801.50-832.00 PW Ramey B and derivative response.

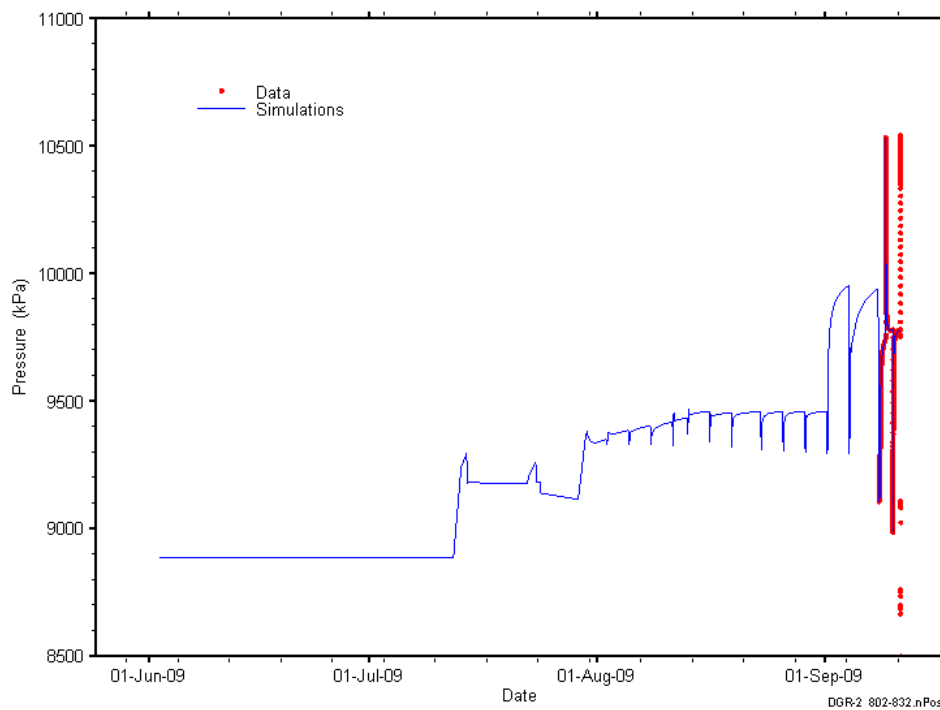


Figure B-199: Linear plot showing simulations of the DGR2_801.50-832.00 pressure response, including pre-test pressure history.

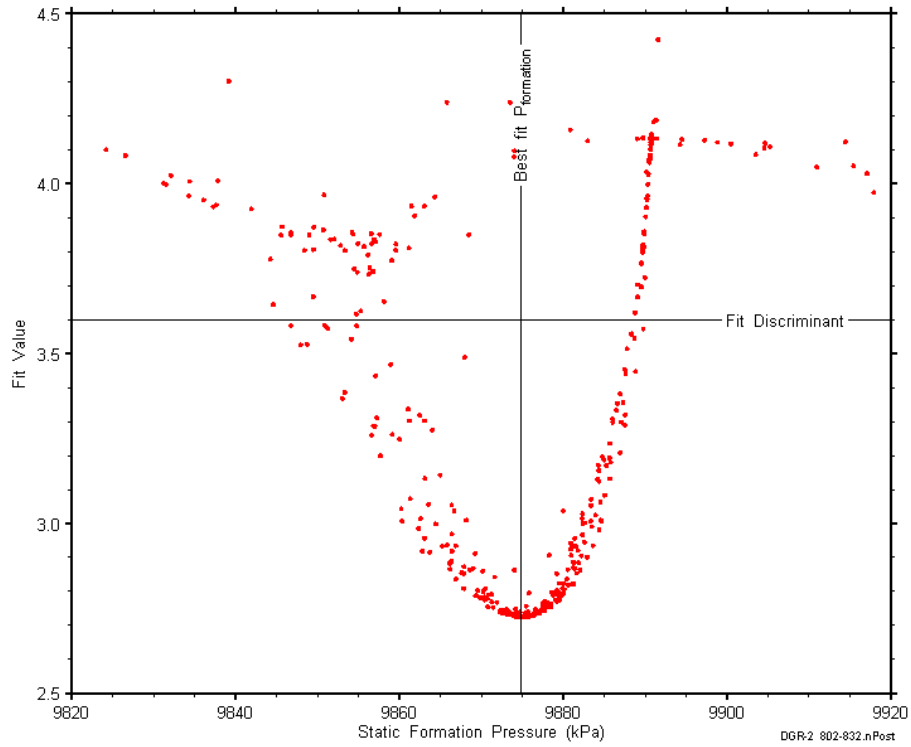


Figure B-200: XY-scatter plot showing the static formation pressure parameter space derived from DGR2_801.50-832.00 perturbation analysis along with the fit discriminant and best fit values.

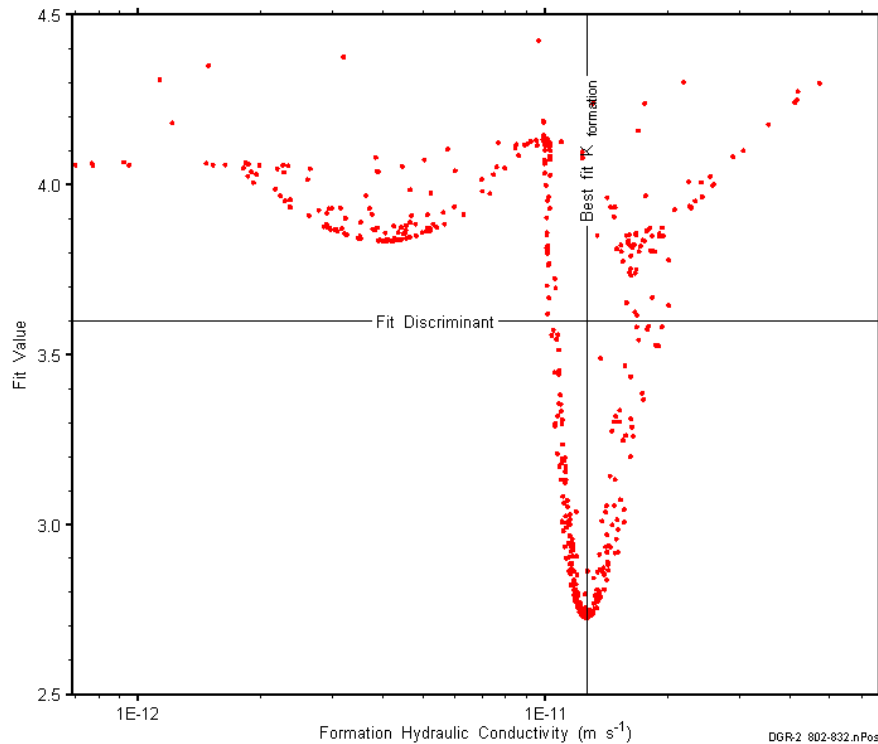


Figure B-201: XY-scatter plot showing the formation hydraulic conductivity parameter space derived from DGR2_801.50-832.00 perturbation analysis along with the fit discriminant and best fit values.

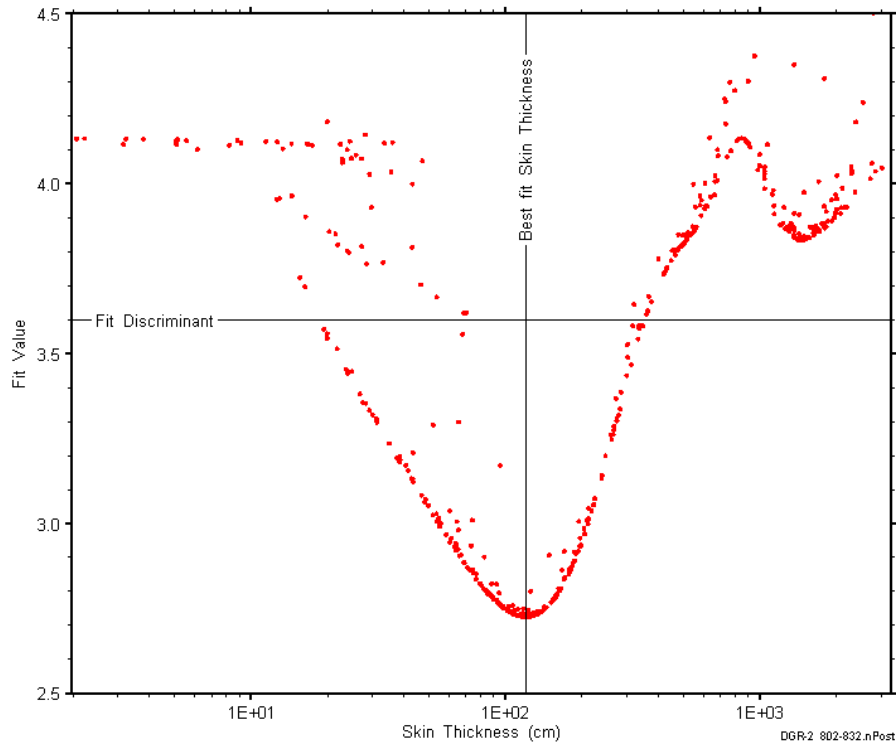


Figure B-202: XY-scatter plot showing the skin-thickness parameter space derived from DGR2_801.50-832.00 perturbation analysis along with the fit discriminant and best fit values.

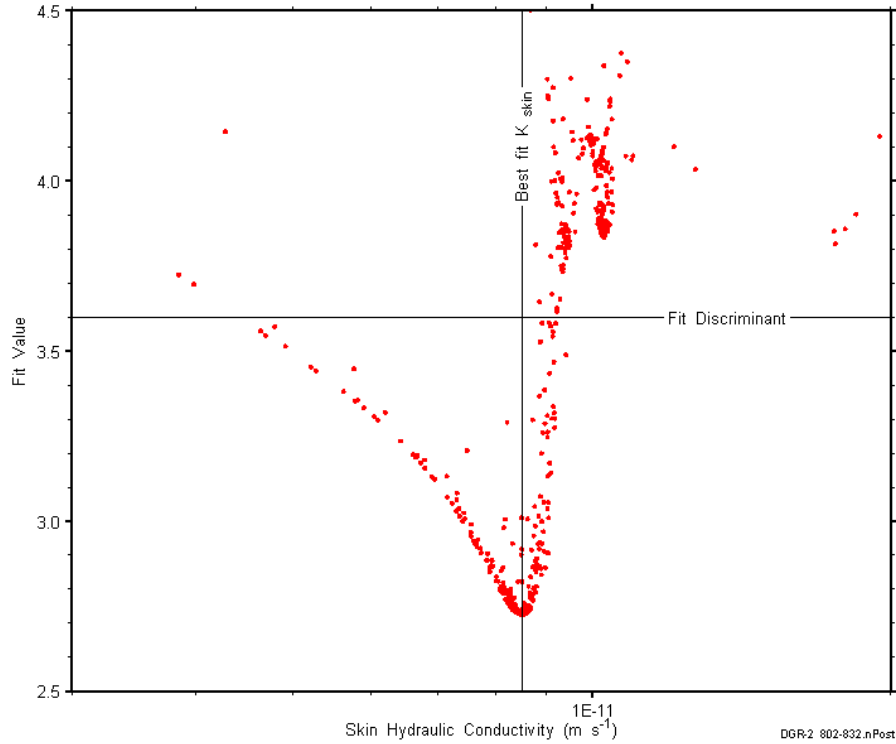


Figure B-203: XY-scatter plot showing the skin hydraulic conductivity parameter space derived from DGR2_801.50-832.00 perturbation analysis along with the fit discriminant and best fit values.

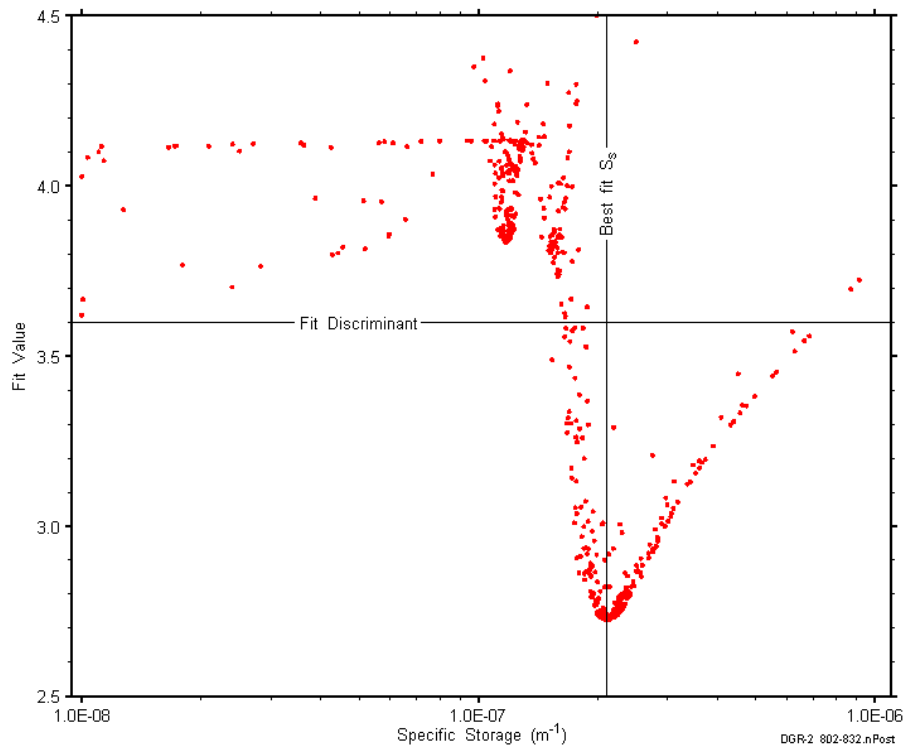


Figure B-204: XY-scatter plot showing the formation specific storage parameter space derived from DGR2_801.50-832.00 perturbation analysis along with the fit discriminant and best fit values.

Appendix C. DGR-3 Plots

Various plots of results from the DGR-3 analyses are shown below. These plots include XY-scatter plots of the fitting-parameter estimates, linear and log-log horsetail plots of the simulated pressure responses showing field-data matches, K_f , P_{fi} and S_s cumulative distribution functions, and parameter-space plots showing the characteristics of the minima for each of the fitting parameters.

C.1 210.18-240.92 Salina F-E

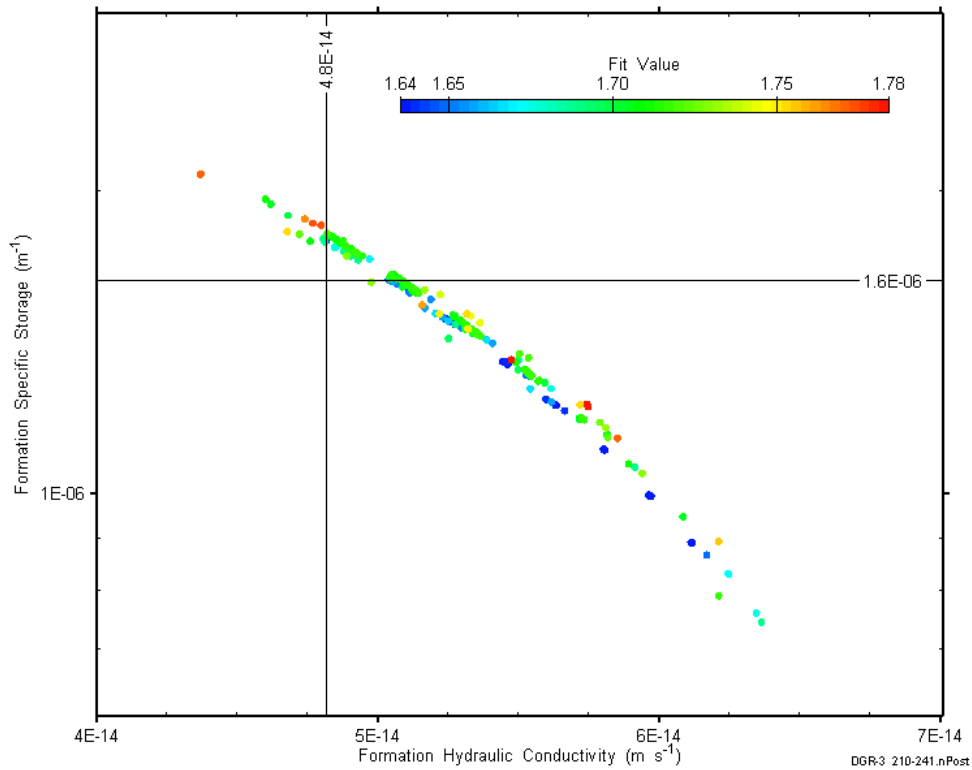


Figure C-1: XY-scatter plot showing estimates of formation hydraulic conductivity and formation specific storage derived from the DGR3_210.18-240.92 perturbation analysis.

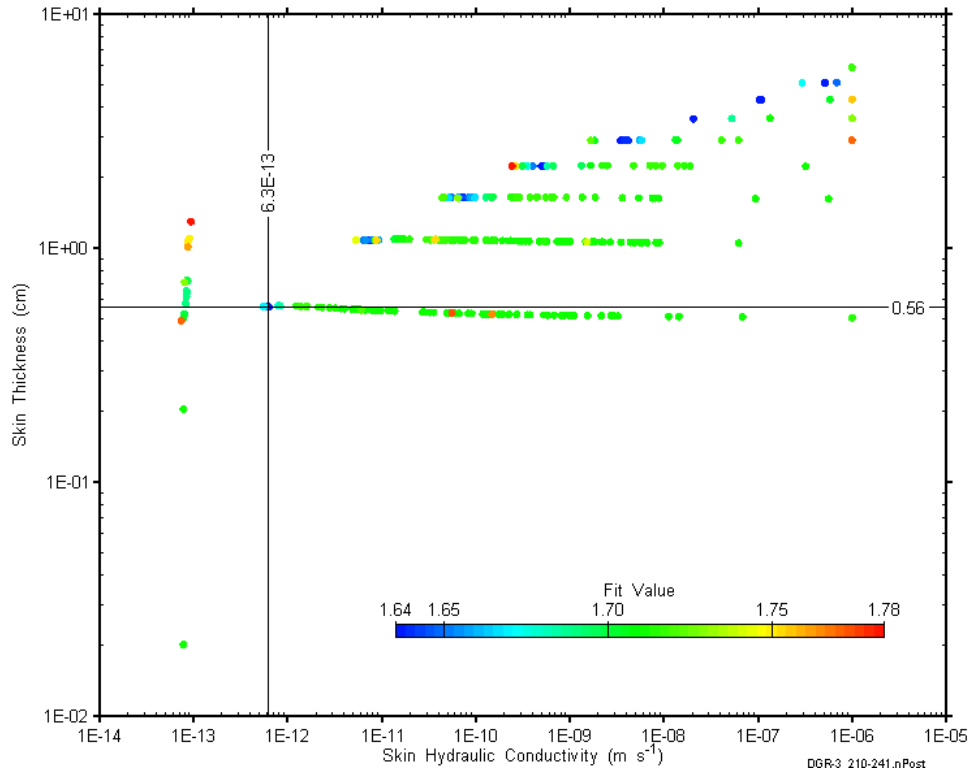


Figure C-2: XY-scatter plot showing estimates of skin hydraulic conductivity and skin thickness derived from the DGR3_210.18-240.92 perturbation analysis.

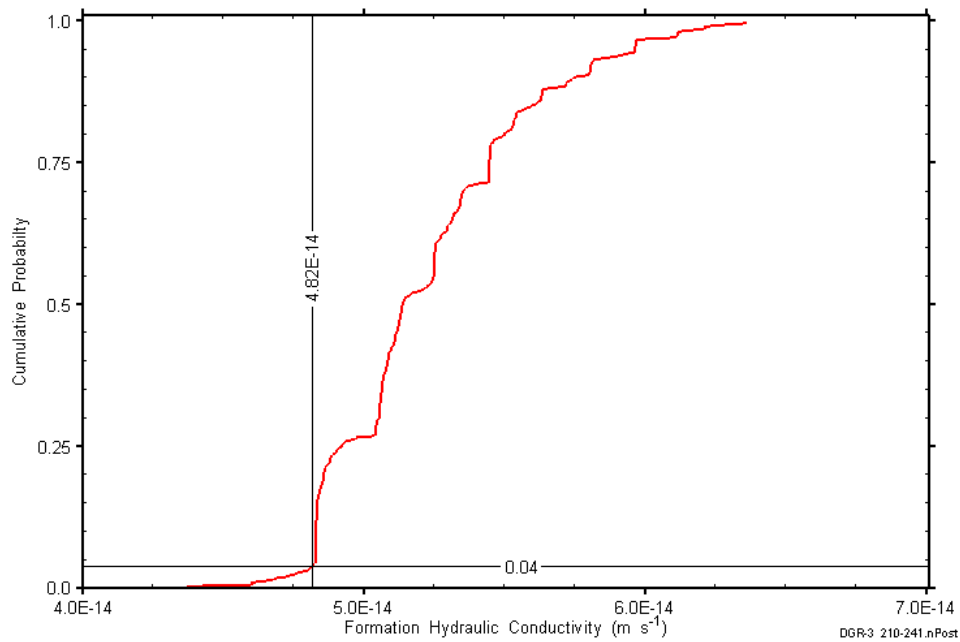


Figure C-3: DGR3_210.18-240.92 formation hydraulic conductivity cumulative distribution function.

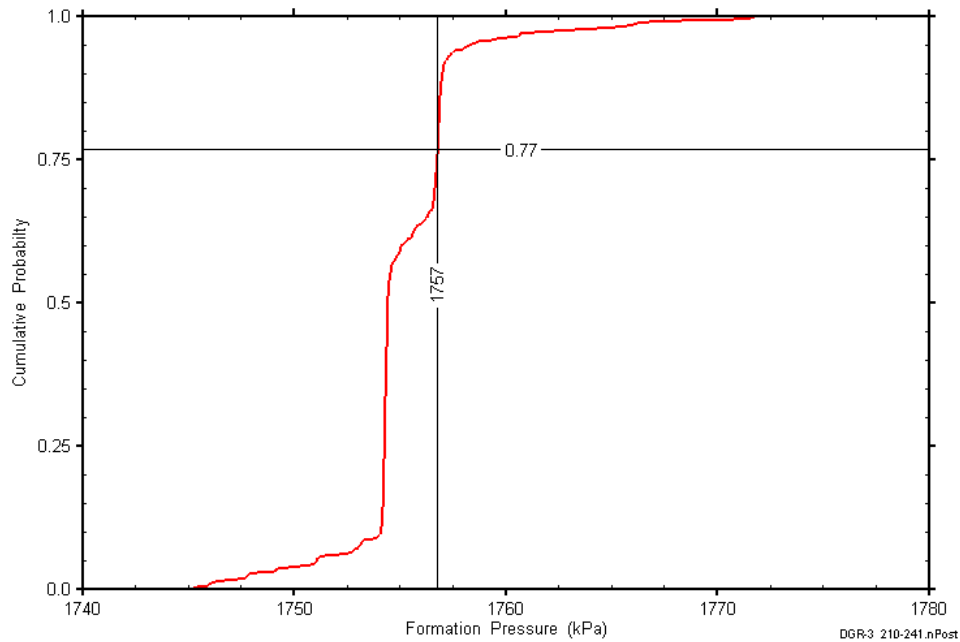


Figure C-4: DGR3_210.18-240.92 static formation pressure cumulative distribution function.

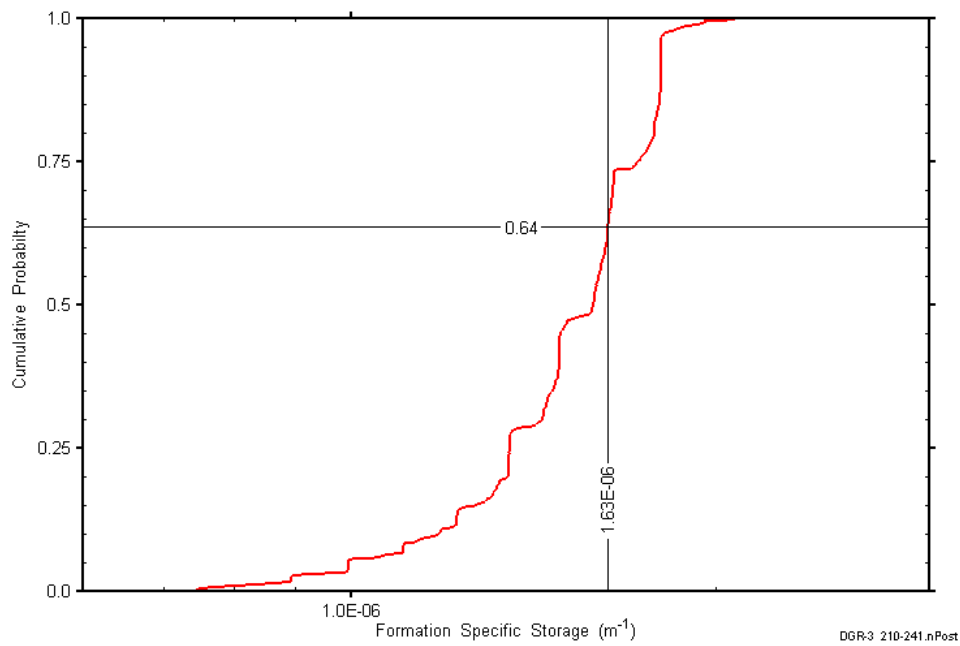


Figure C-5: DGR3_210.18-240.92 formation specific storage cumulative distribution function.

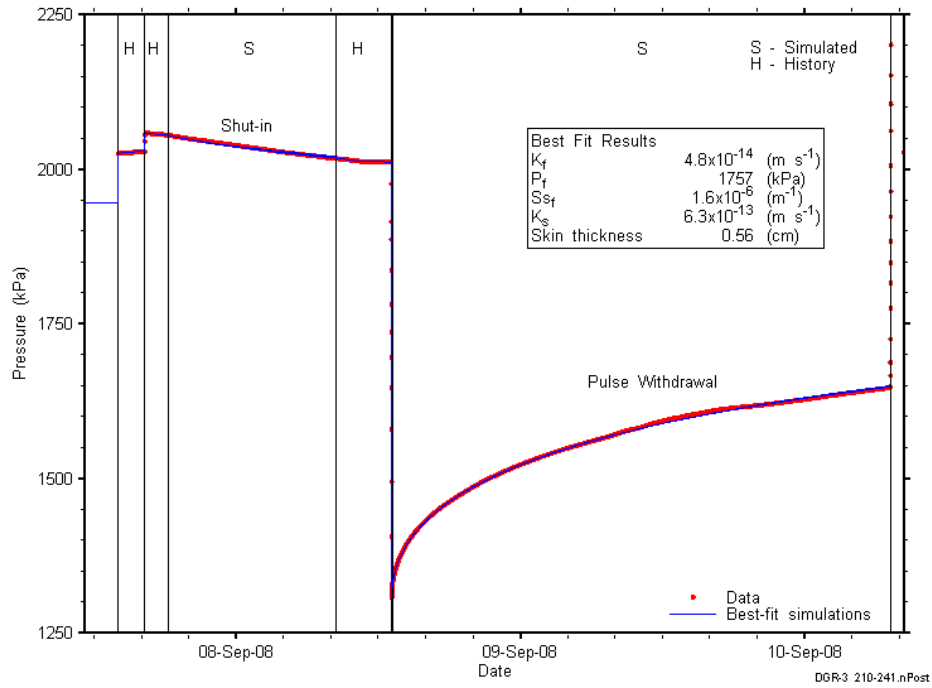


Figure C-6: Linear plot showing details of simulations of the DGR3_210.18-240.92 pressure response.

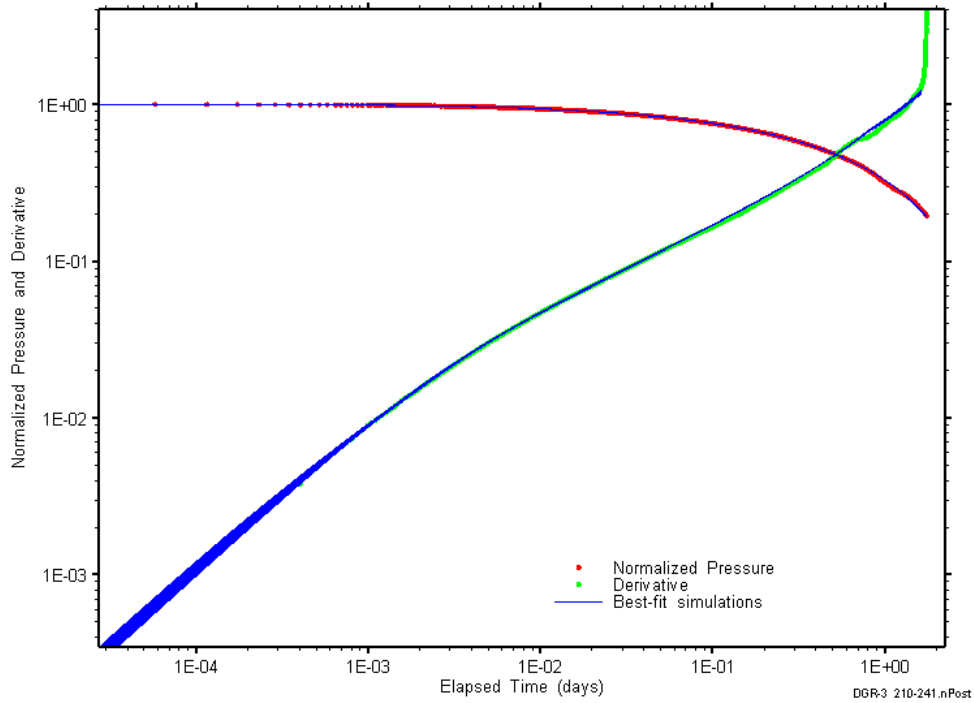


Figure C-7: Log-log plot showing 361 simulations of the DGR2_806.16-834.26 pulse withdrawal Ramey B and derivative response.

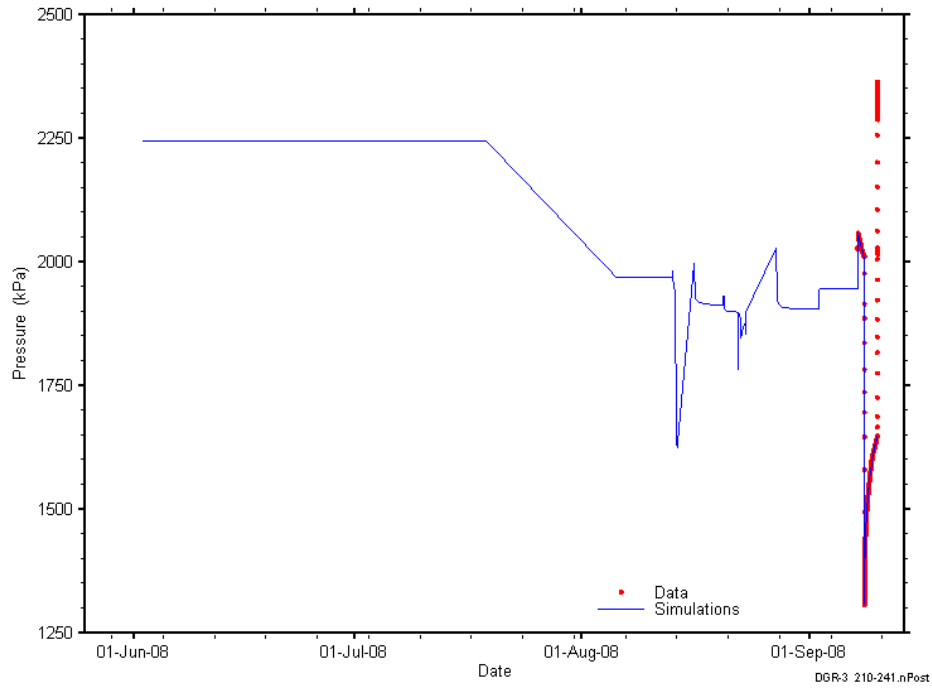


Figure C-8: Linear plot showing simulations of the DGR3_210.18-240.92 pressure response, including pre-test pressure history.

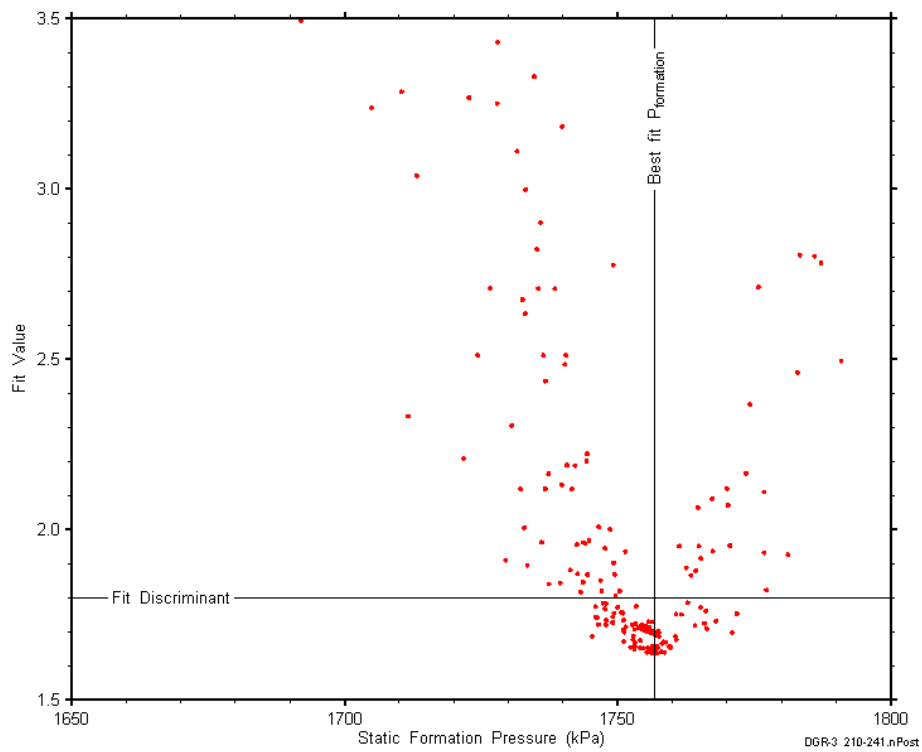


Figure C-9: XY-scatter plot showing the static formation pressure parameter space derived from DGR3_210.18-240.92 perturbation analysis along with the fit discriminant and best fit values.

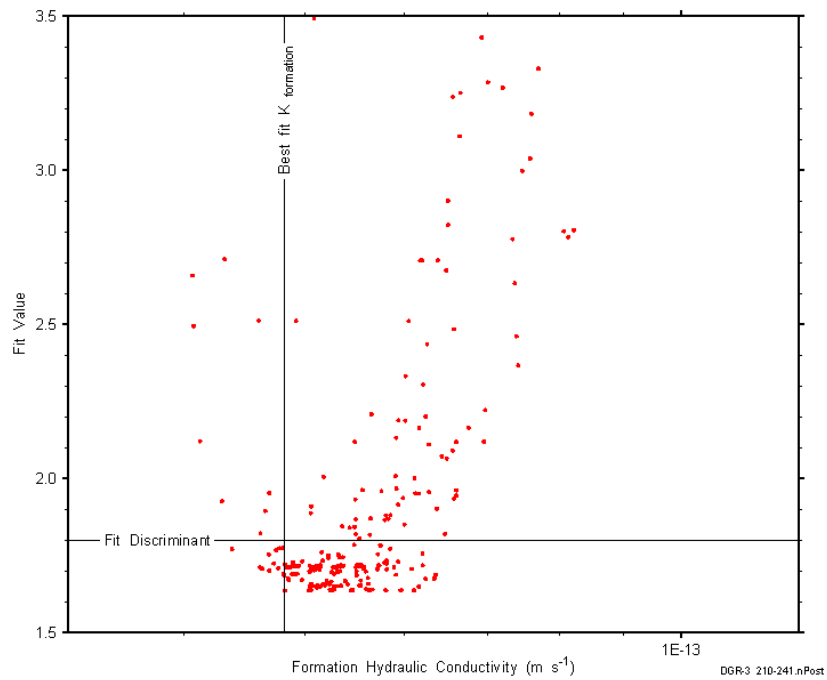


Figure C-10: XY-scatter plot showing the formation hydraulic conductivity parameter space derived from DGR3_210.18-240.92 perturbation analysis along with the fit discriminant and best fit values.

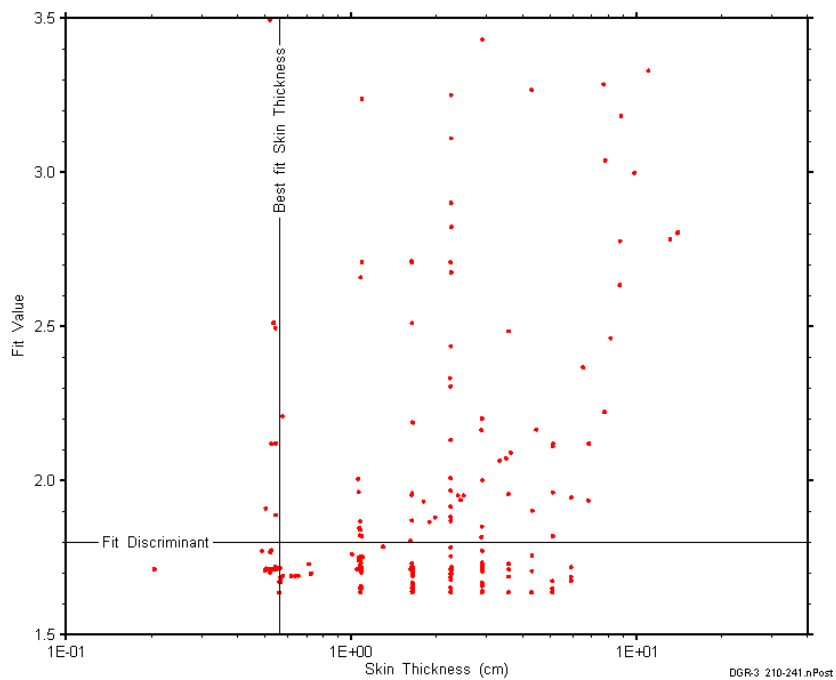


Figure C-11: XY-scatter plot showing the skin-thickness parameter space derived from DGR3_210.18-240.92 perturbation analysis along with the fit discriminant and best fit values.

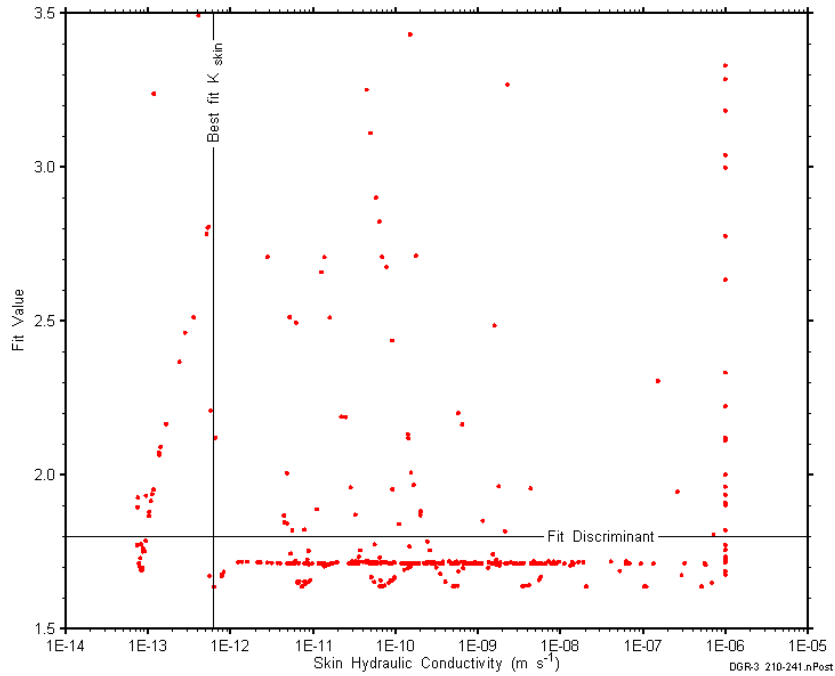


Figure C-12: XY-scatter plot showing the skin hydraulic conductivity parameter space derived from DGR3_210.18-240.92 perturbation analysis along with the fit discriminant and best fit values.

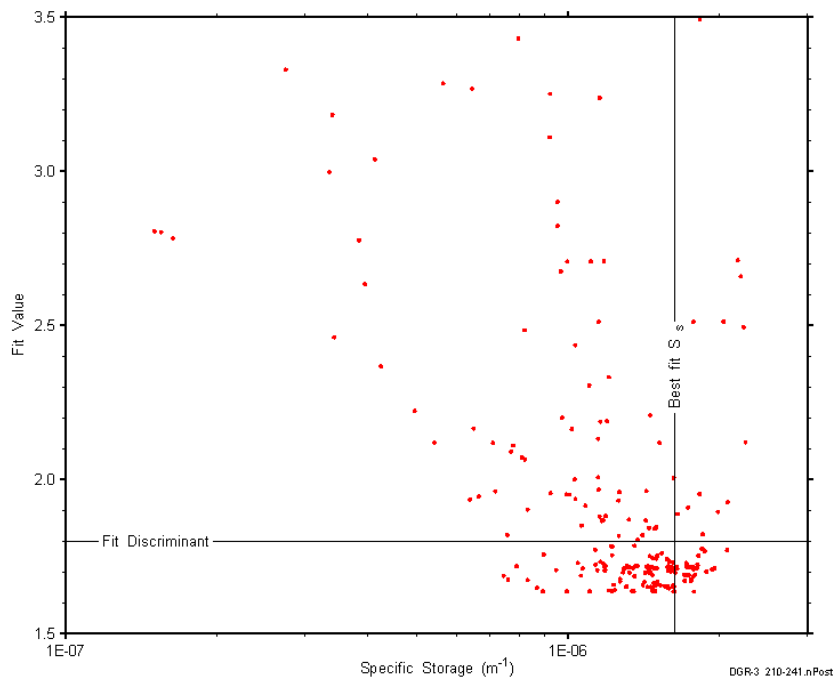


Figure C-13: XY-scatter plot showing the formation specific storage parameter space derived from DGR3_210.18-240.92 perturbation analysis along with the fit discriminant and best fit values.

C.2 240.72-271.46 Salina E-D-C

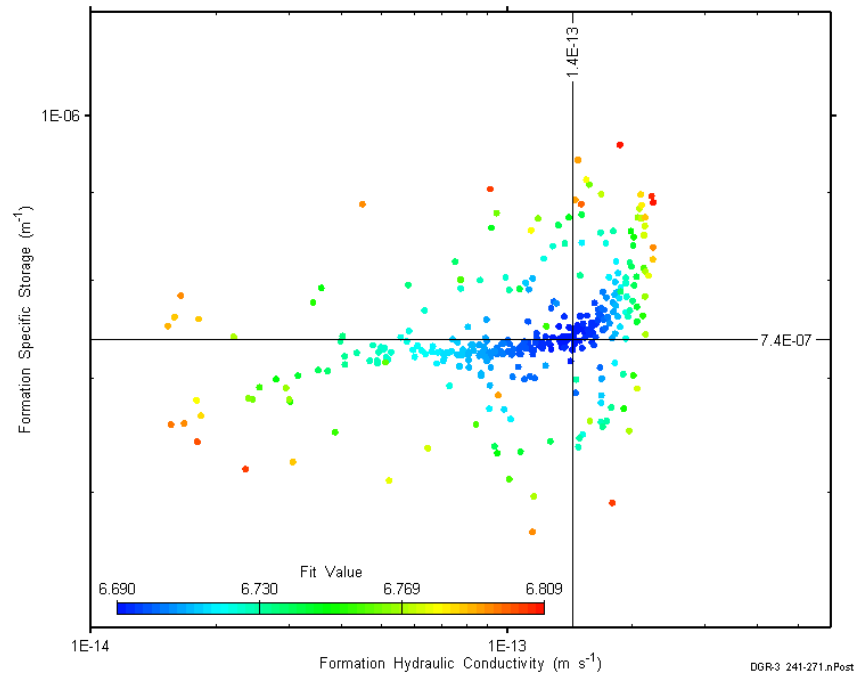


Figure C-14: XY-scatter plot showing estimates of formation hydraulic conductivity and formation specific storage derived from the DGR3_240.72-271.46 perturbation analysis.

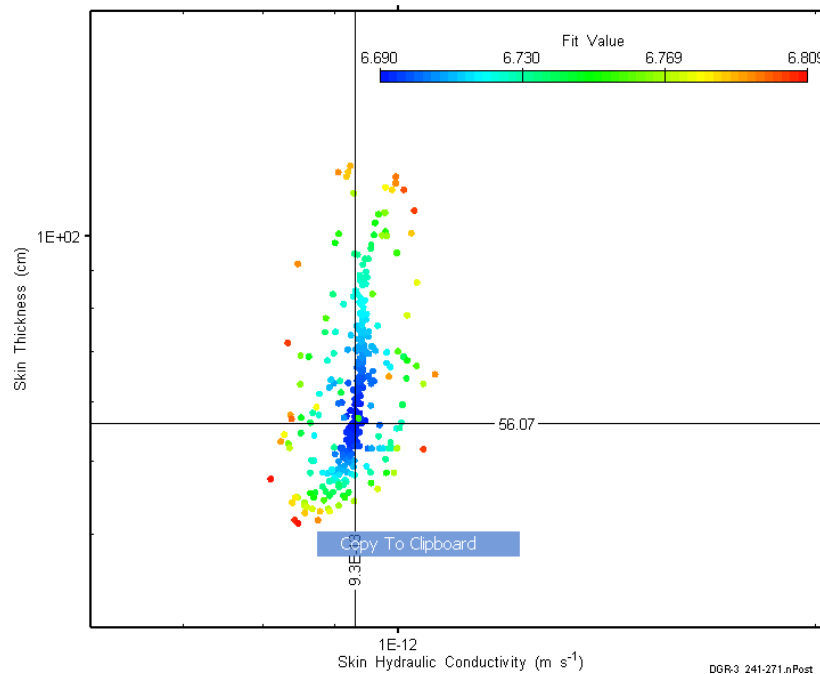


Figure C-15: XY-scatter plot showing estimates of skin hydraulic conductivity and skin thickness derived from the DGR3_240.72-271.46 perturbation analysis.

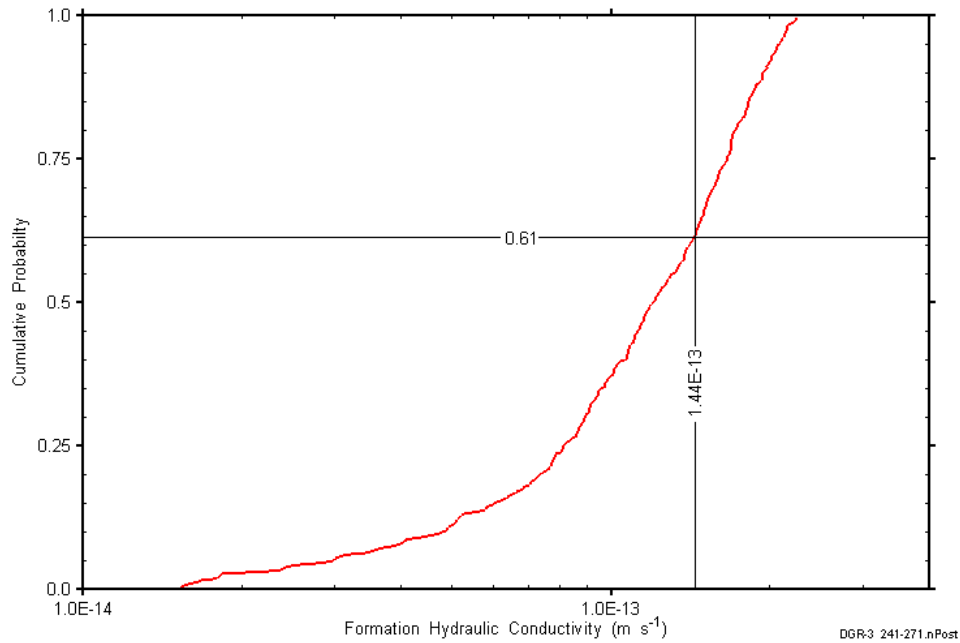


Figure C-16: DGR3_240.72-271.46 formation hydraulic conductivity cumulative distribution function.

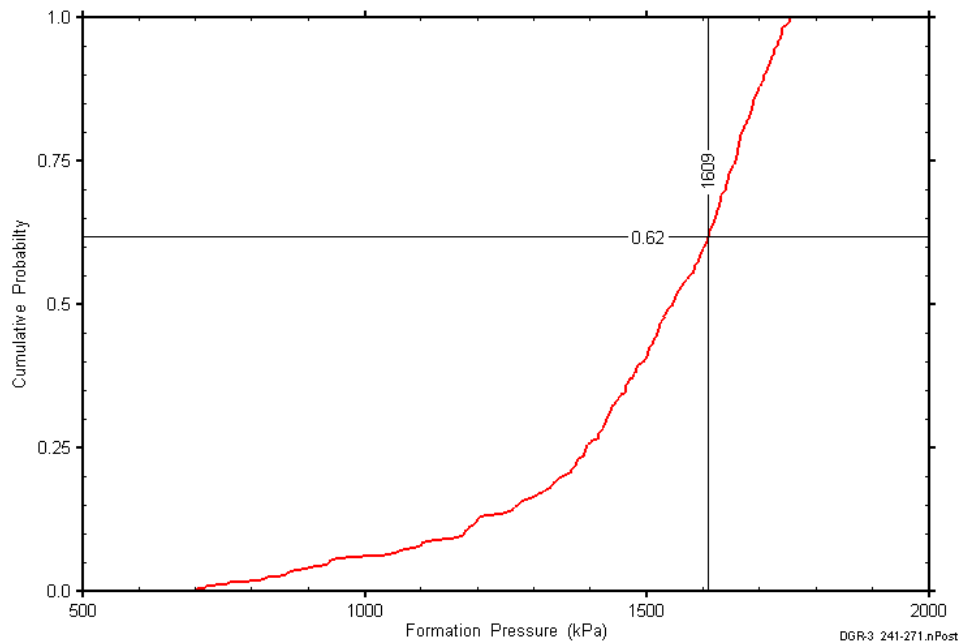


Figure C-17: DGR3_240.72-271.46 static formation pressure cumulative distribution function.

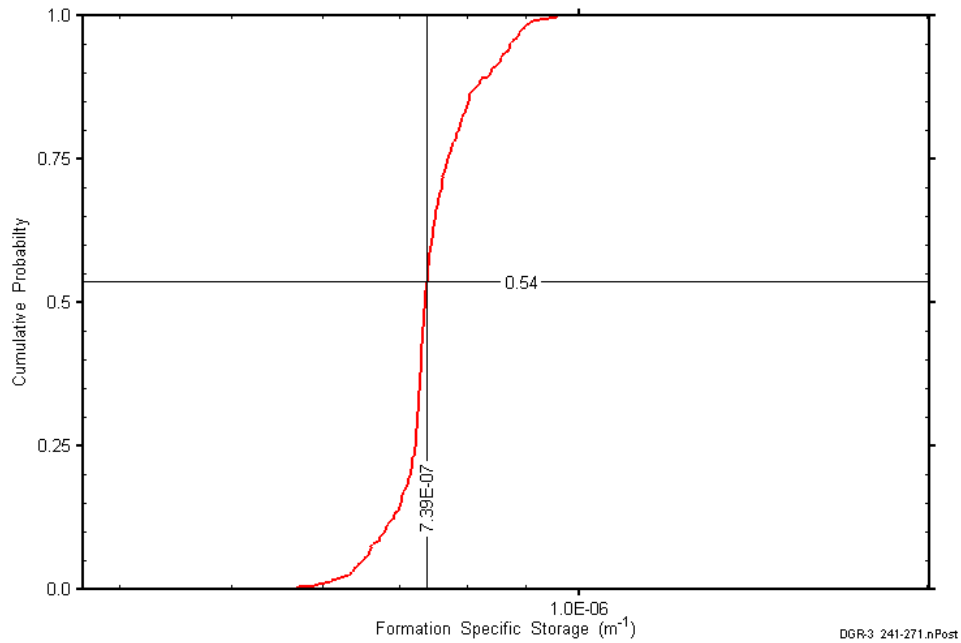


Figure C-18: DGR3_240.72-271.46 formation specific storage cumulative distribution function.

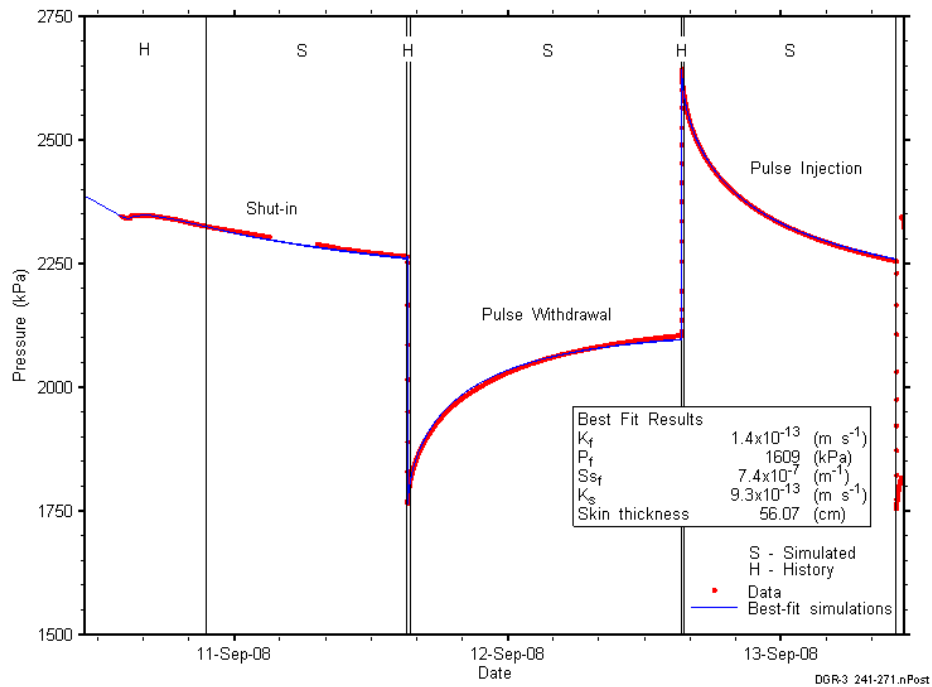


Figure C-19: Linear plot showing simulations of the DGR3_240.72-271.46 pressure response.

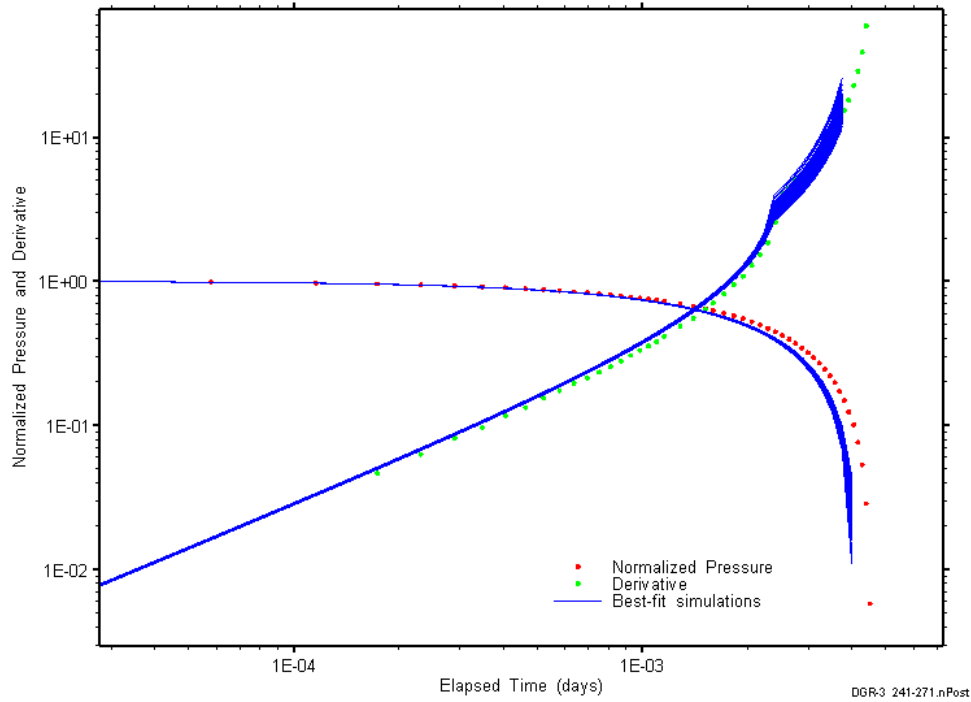


Figure C-20: Log-log plot showing simulations of the DGR3_240.72–271.46 pulse withdrawal Ramey B and derivative response.

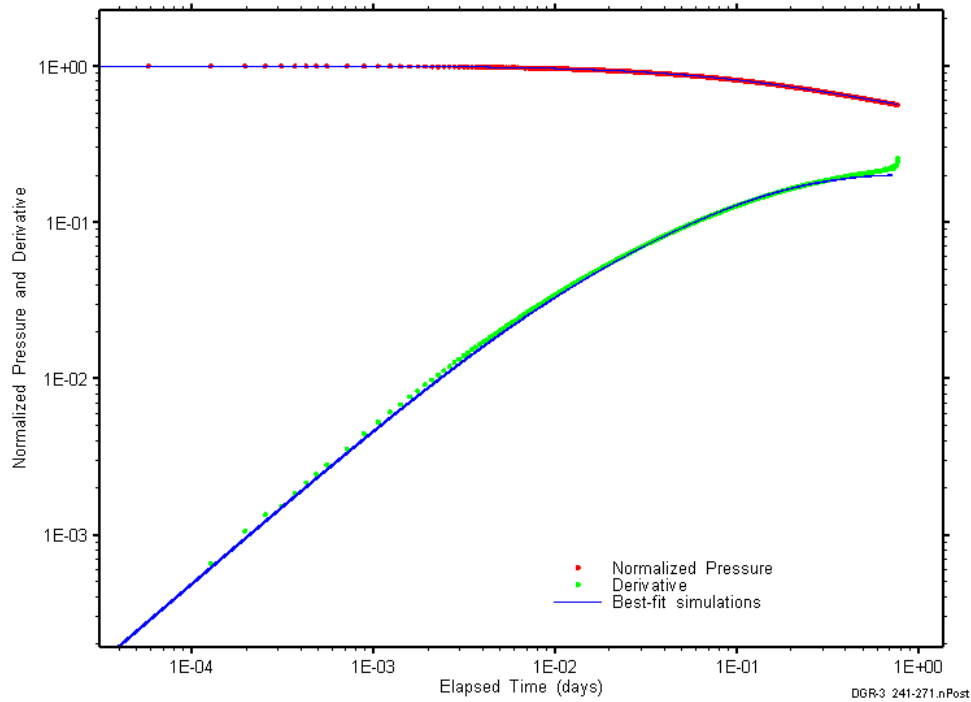


Figure C-21: Log-log plot showing simulations of the DGR3_240.72–271.46 pulse injection Ramey B and derivative response.

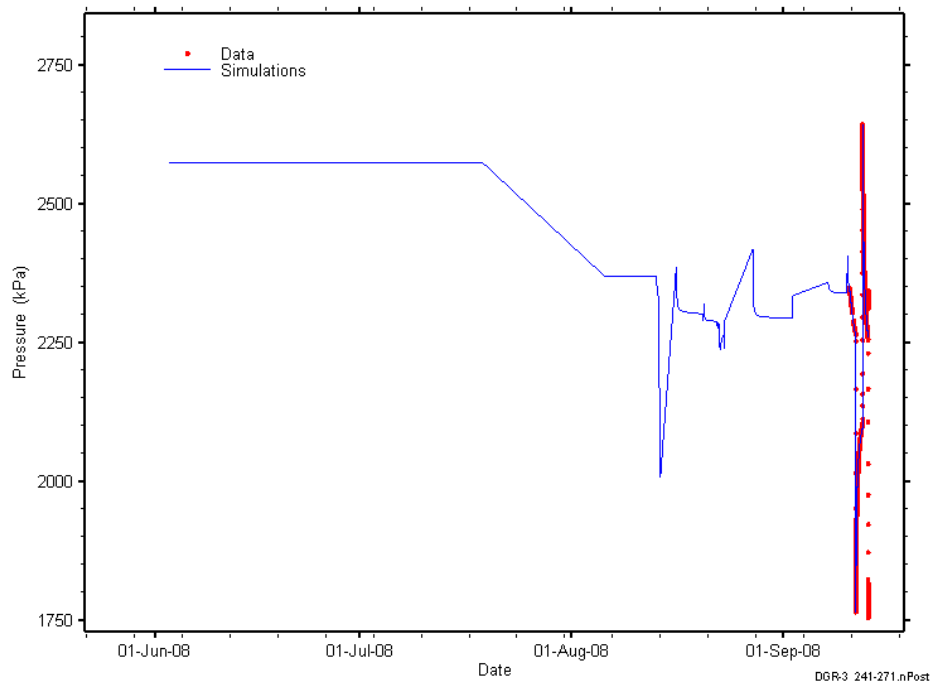


Figure C-22: Linear plot showing simulations of the DGR3_240.72-271.46 pressure response, including pre-test pressure history.

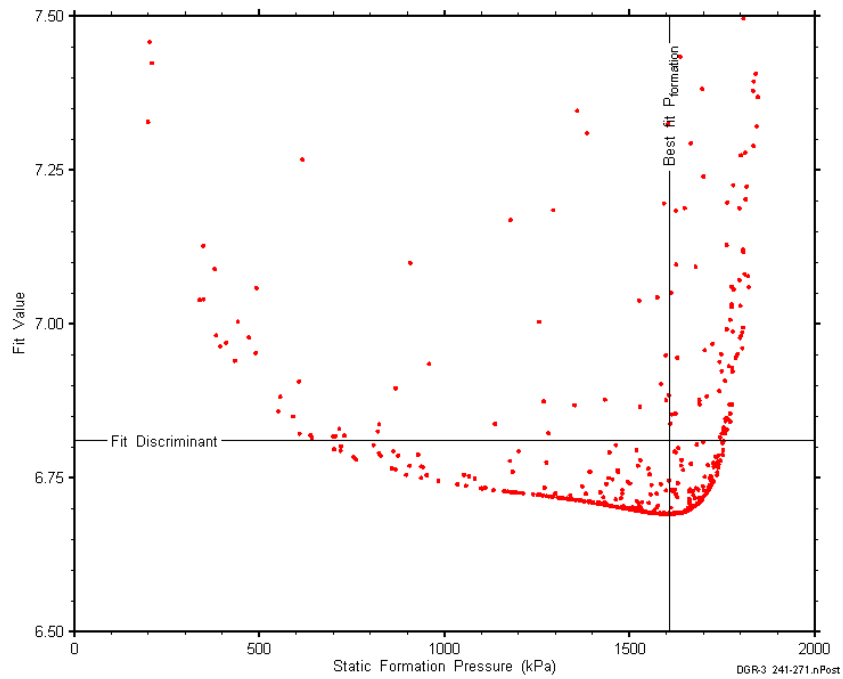


Figure C-23: XY-scatter plot showing the static formation pressure parameter space derived from DGR3_240.72-271.46 perturbation analysis along with the fit discriminant and best fit values.

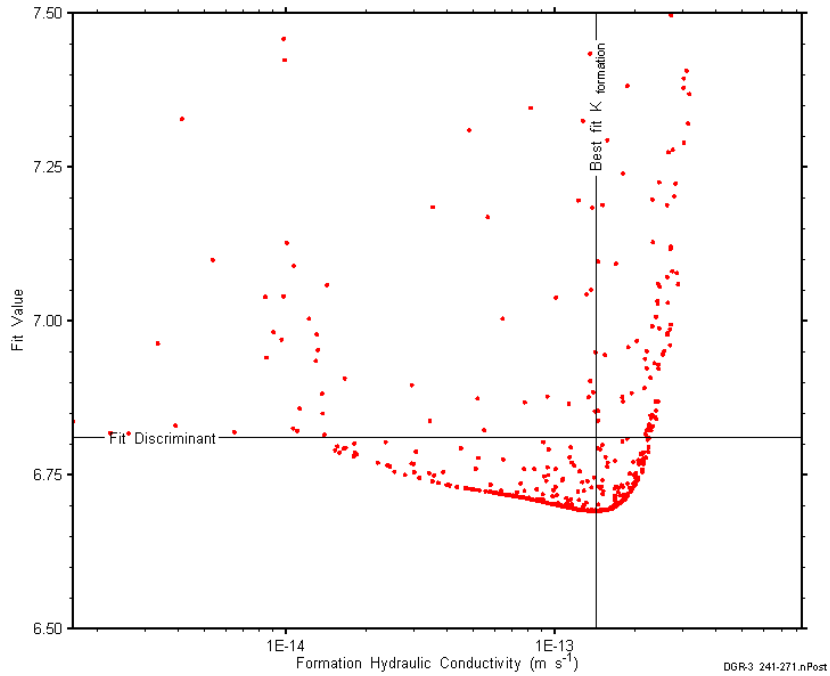


Figure C-24: XY-scatter plot showing the formation hydraulic conductivity parameter space derived from DGR3_240.72-271.46 perturbation analysis along with the fit discriminant and best fit values.

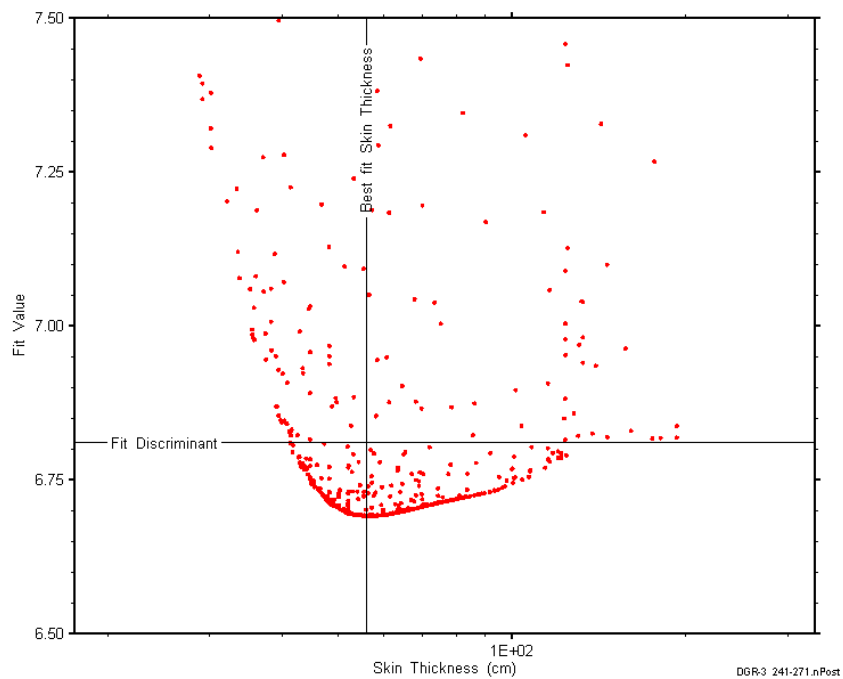


Figure C-25: XY-scatter plot showing the skin-thickness parameter space derived from DGR3_240.72-271.46 perturbation analysis along with the fit discriminant and best fit values.

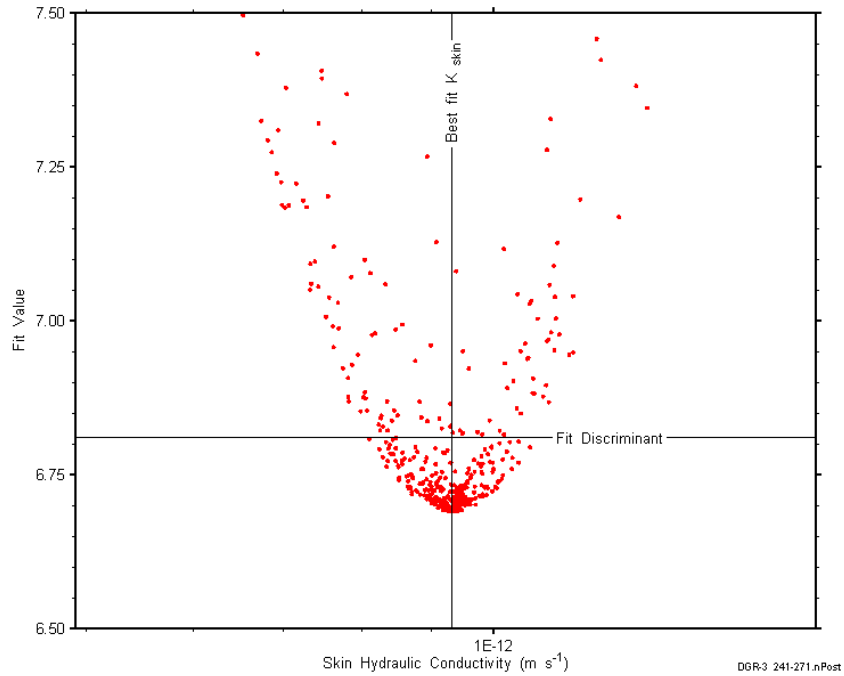


Figure C-26: XY-scatter plot showing the skin hydraulic conductivity parameter space derived from DGR3_240.72-271.46 perturbation analysis along with the fit discriminant and best fit values.

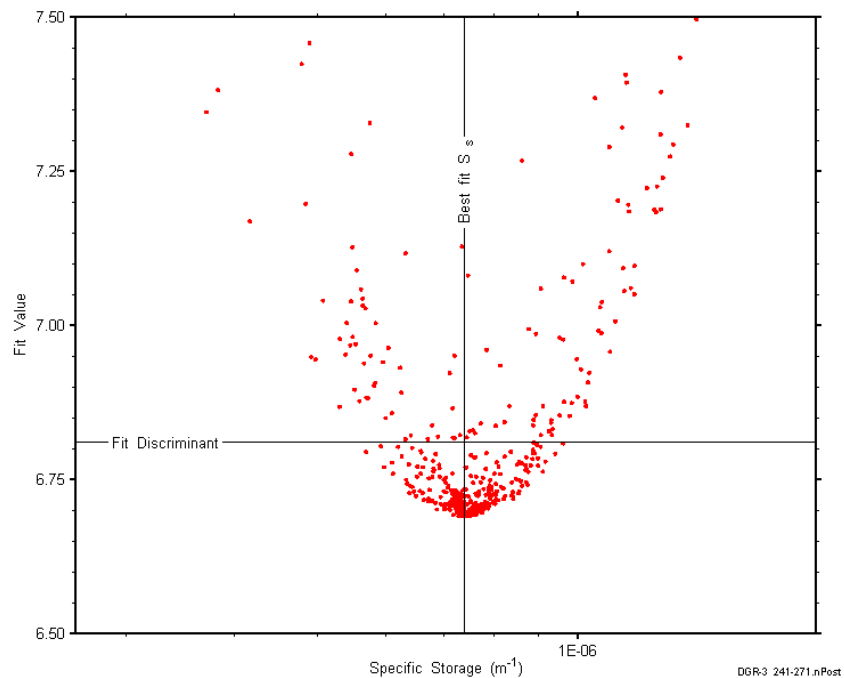


Figure C-27: XY-scatter plot showing the formation specific storage parameter space derived from DGR3_240.72-271.46 perturbation analysis along with the fit discriminant and best fit values.

C.3 271.29-302.03 Salina C-B

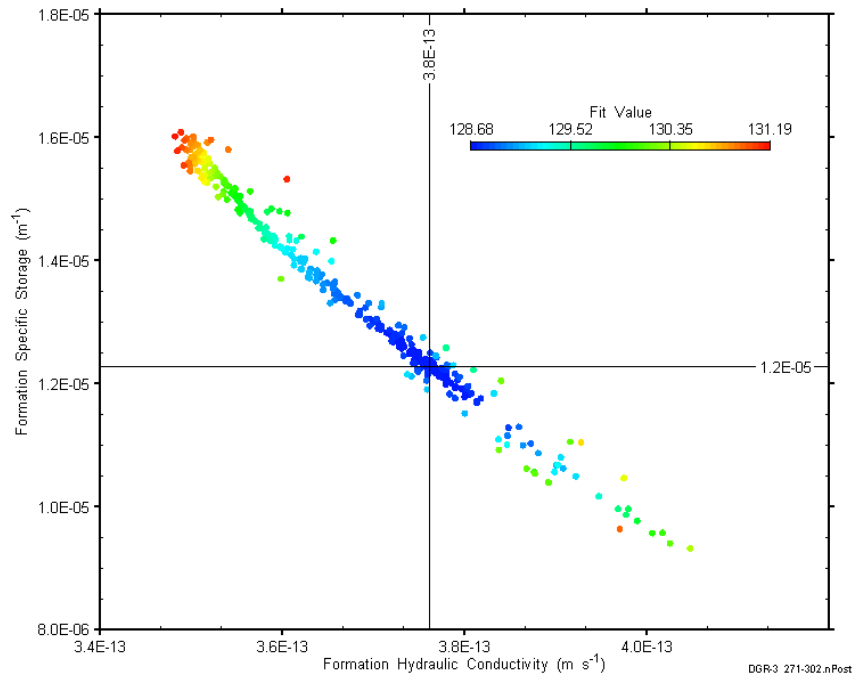


Figure C-28: XY-scatter plot showing estimates of formation hydraulic conductivity and formation specific storage derived from the DGR3_271.29-302.03 perturbation analysis.

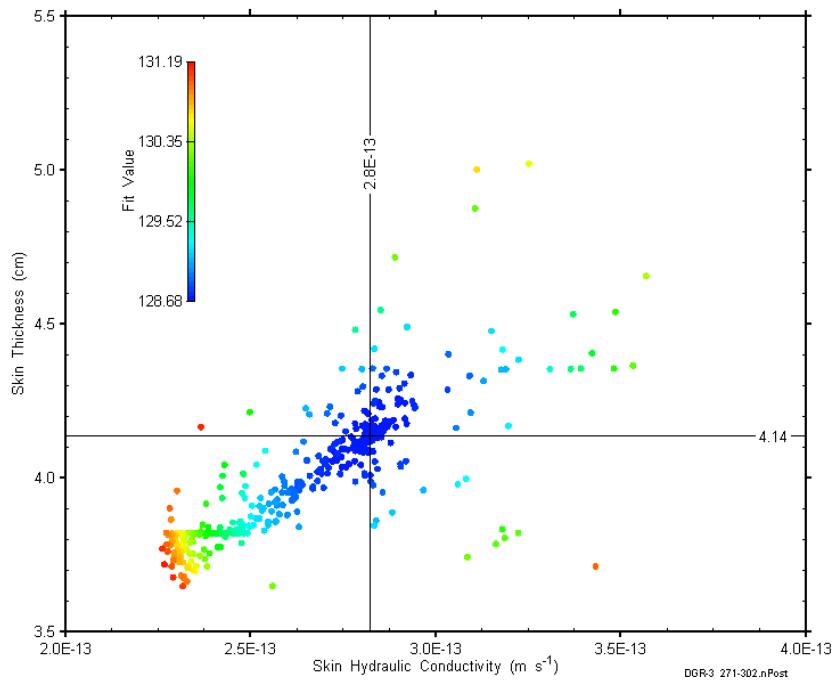


Figure C-29: XY-scatter plot showing estimates of skin hydraulic conductivity and skin thickness derived from the DGR3_271.29-302.03 perturbation analysis.

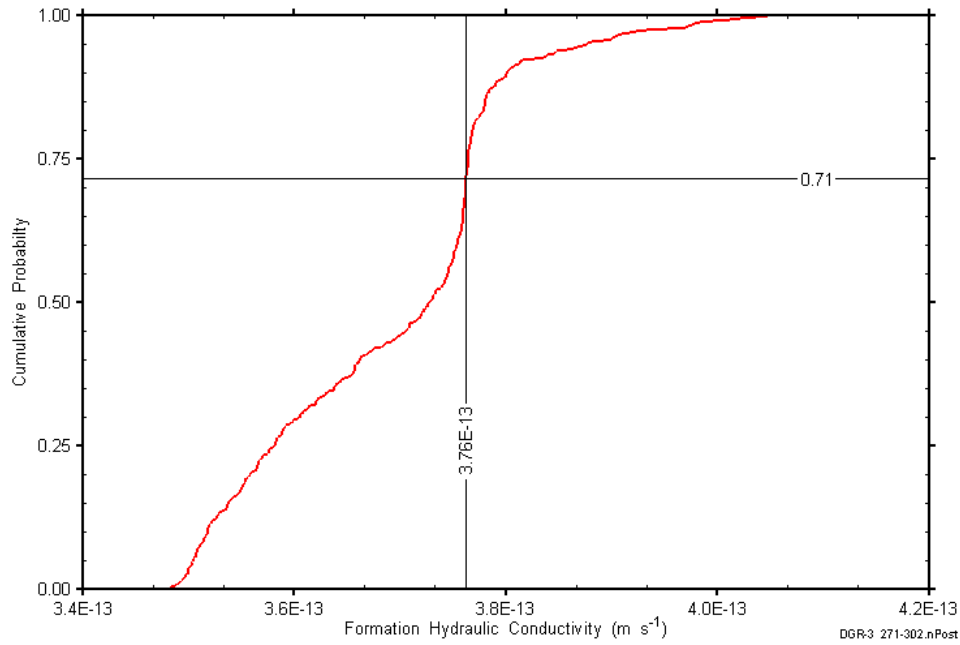


Figure C-30: DGR3_271.29-302.03 formation hydraulic conductivity cumulative distribution function.

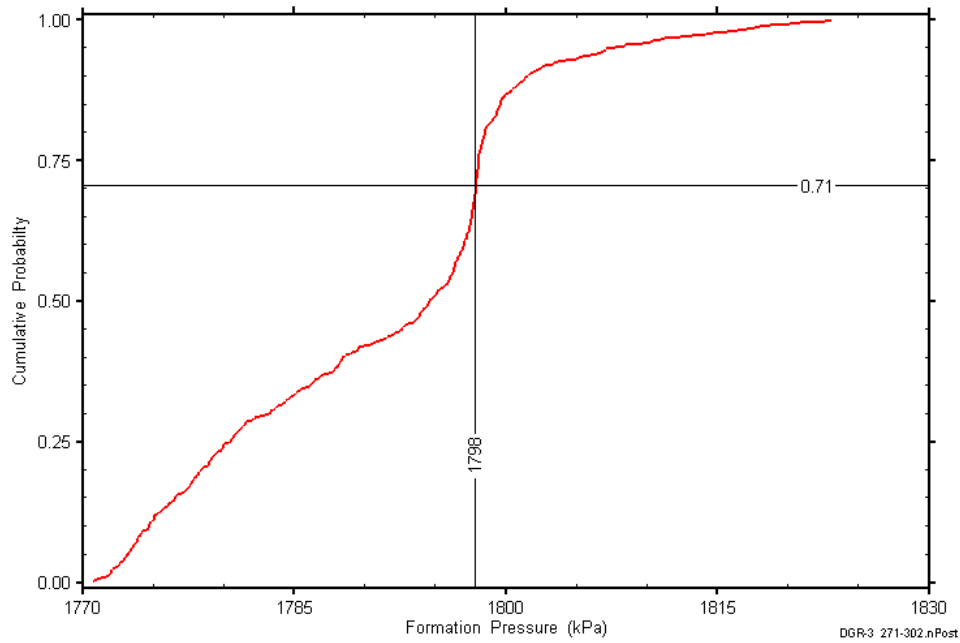


Figure C-31: DGR3_271.29-302.03 static formation pressure cumulative distribution function.

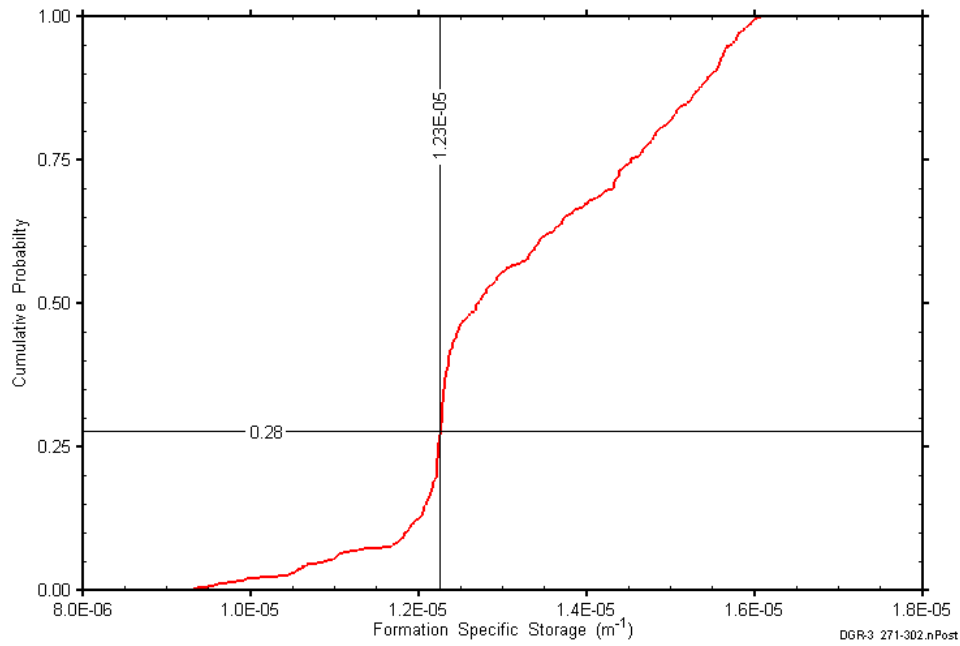


Figure C-32: DGR3_271.29-302.03 formation specific storage cumulative distribution function.

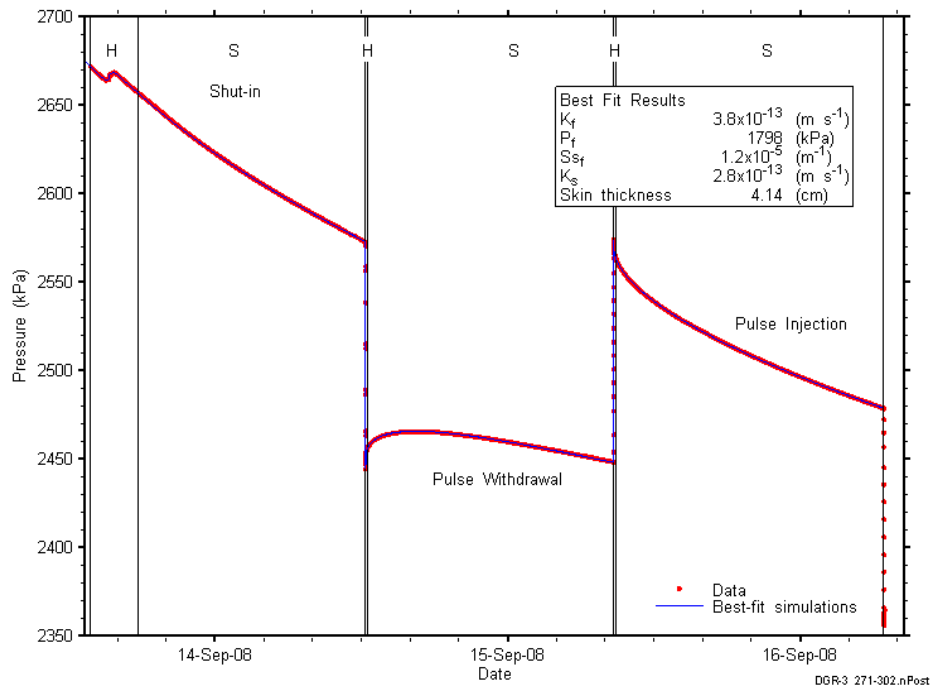


Figure C-33: Linear plot showing simulations of the DGR3_271.29-302.03 pressure response.

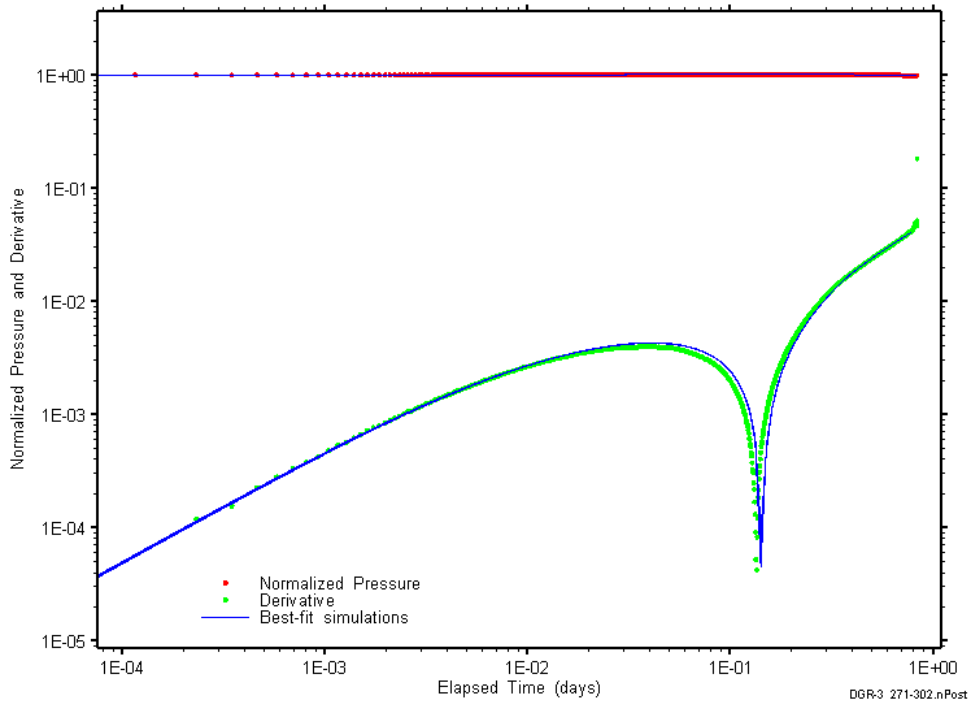


Figure C-34: Log-log plot showing simulations of the DGR3_271.29–302.03 pulse withdrawal Ramey B and derivative response.

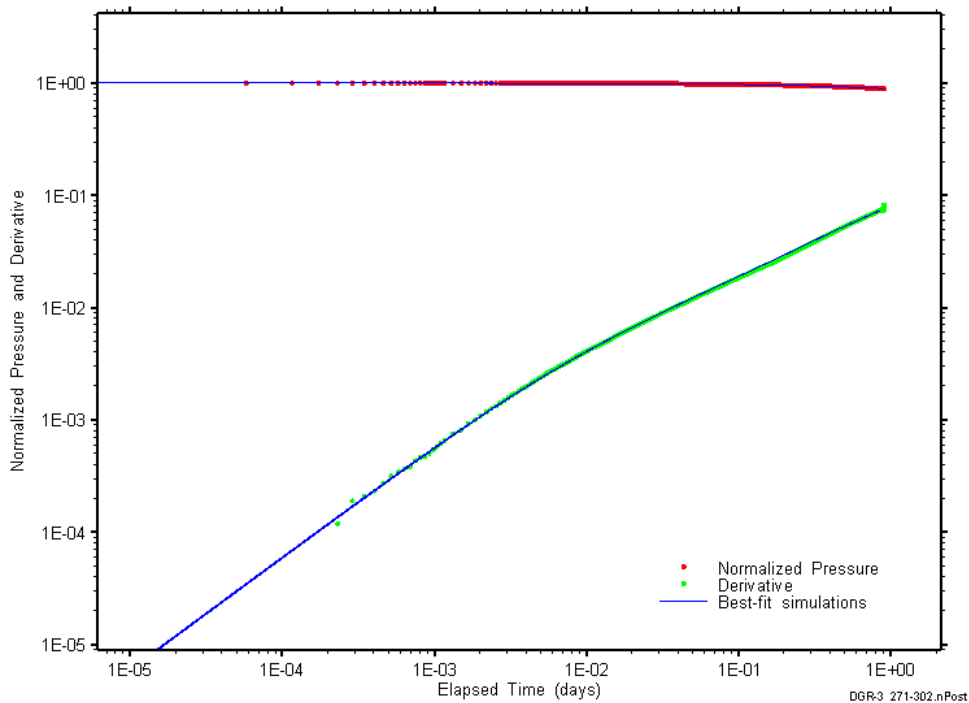


Figure C-35: Log-log plot showing simulations of the DGR3_271.29–302.03 pulse injection Ramey B and derivative response.

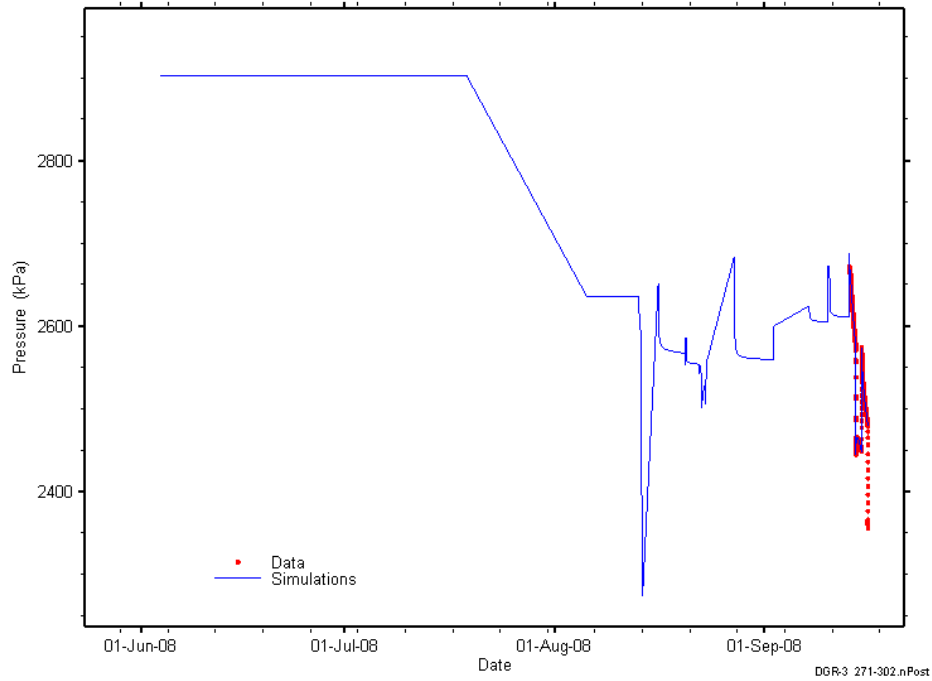


Figure C-36: Linear plot showing simulations of the DGR3_271.29-302.03 pressure response, including pre-test pressure history.

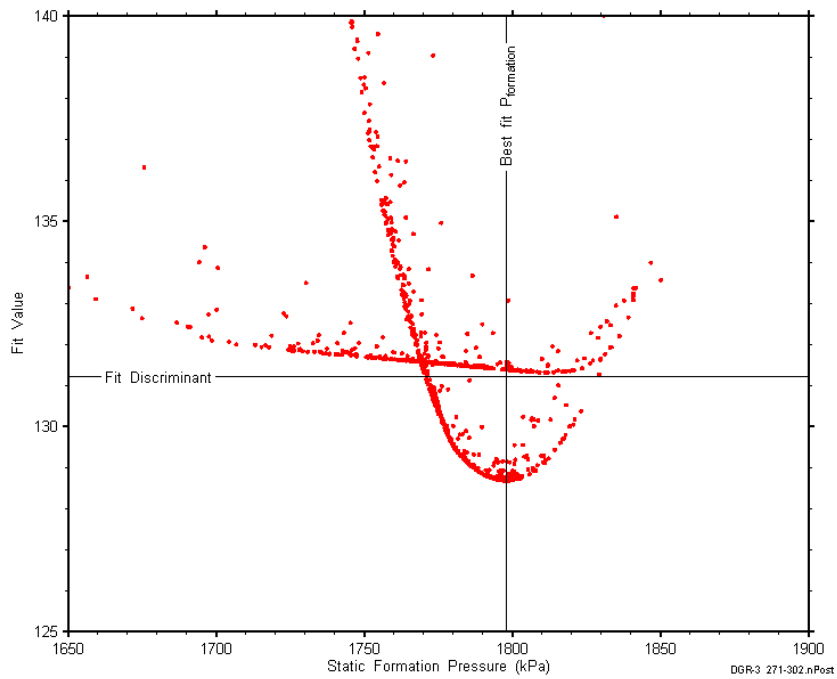


Figure C-37: XY-scatter plot showing the static formation pressure parameter space derived from DGR3_271.29-302.03 perturbation analysis along with the fit discriminant and best fit values.

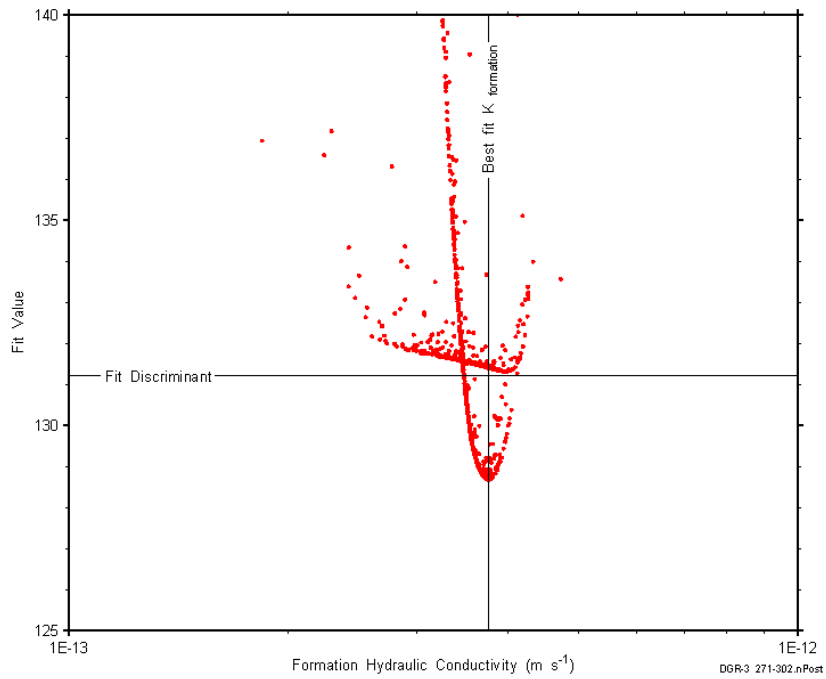


Figure C-38: XY-scatter plot showing the formation hydraulic conductivity parameter space derived from DGR3_271.29-302.03 perturbation analysis along with the fit discriminant and best fit values.

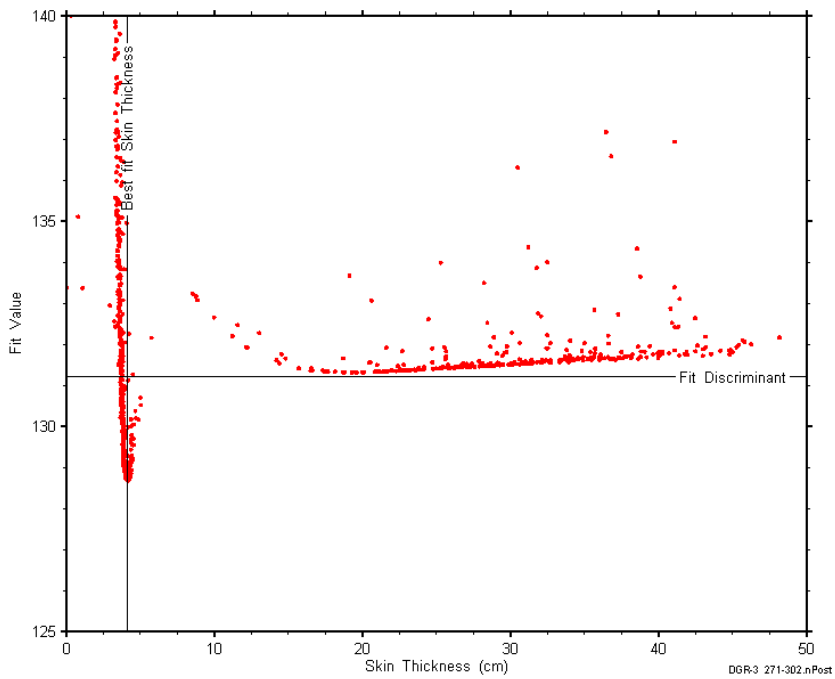


Figure C-39: XY-scatter plot showing the skin-thickness parameter space derived from DGR3_271.29-302.03 perturbation analysis along with the fit discriminant and best fit values.

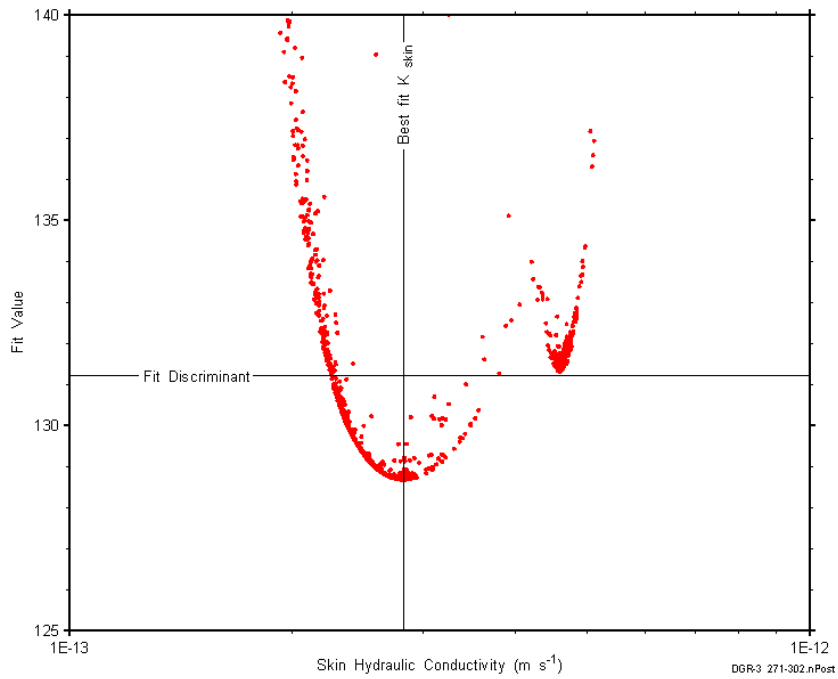


Figure C-40: XY-scatter plot showing the skin hydraulic conductivity parameter space derived from DGR3_271.29-302.03 perturbation analysis along with the fit discriminant and best fit values.

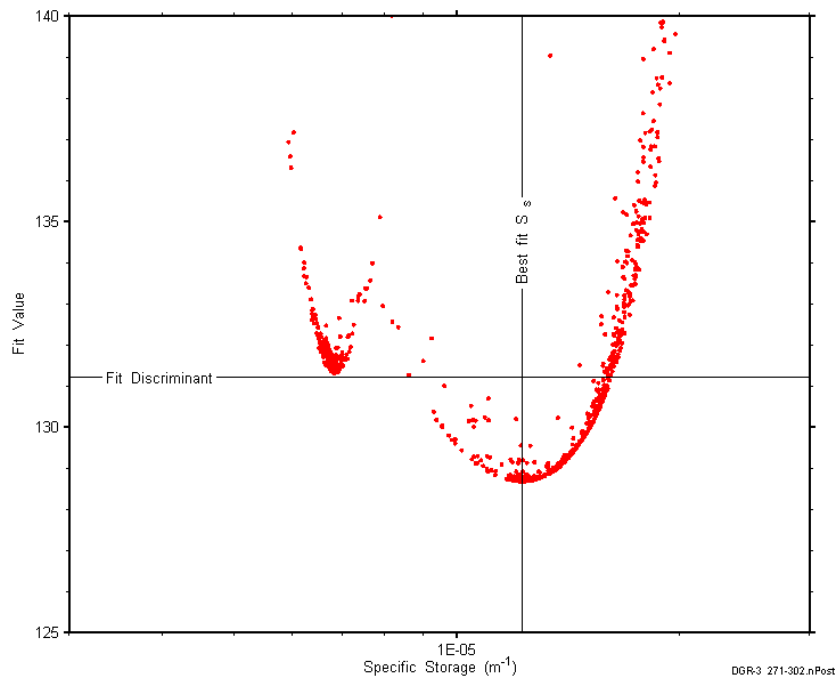


Figure C-41: XY-scatter plot showing the formation specific storage parameter space derived from DGR3_271.29-302.03 perturbation analysis along with the fit discriminant and best fit values.

C.4 301.81-332.55 Salina B-A2 carbonate

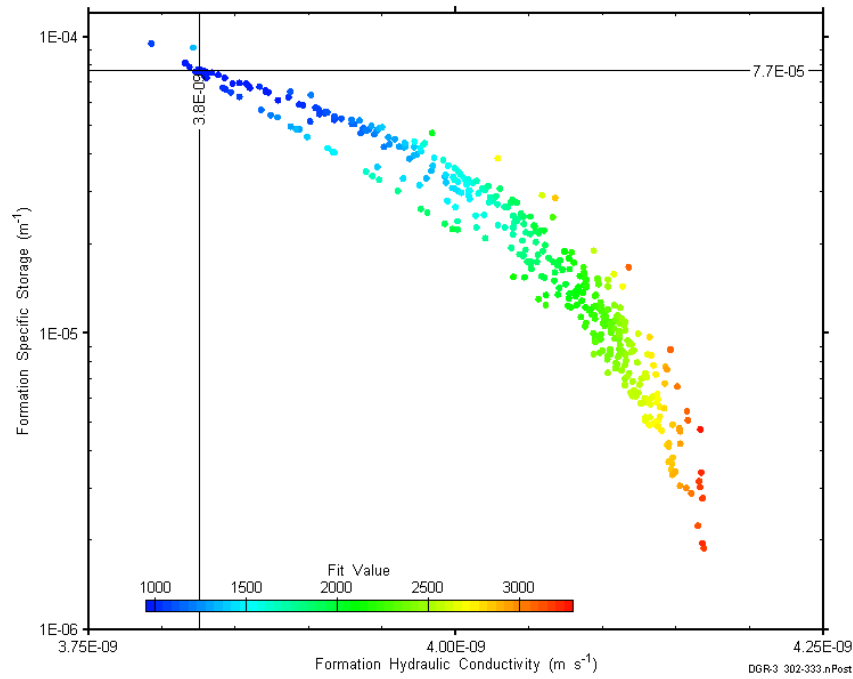


Figure C-42: XY-scatter plot showing estimates of formation hydraulic conductivity and formation specific storage derived from the DGR3_301.81-332.55 perturbation analysis.

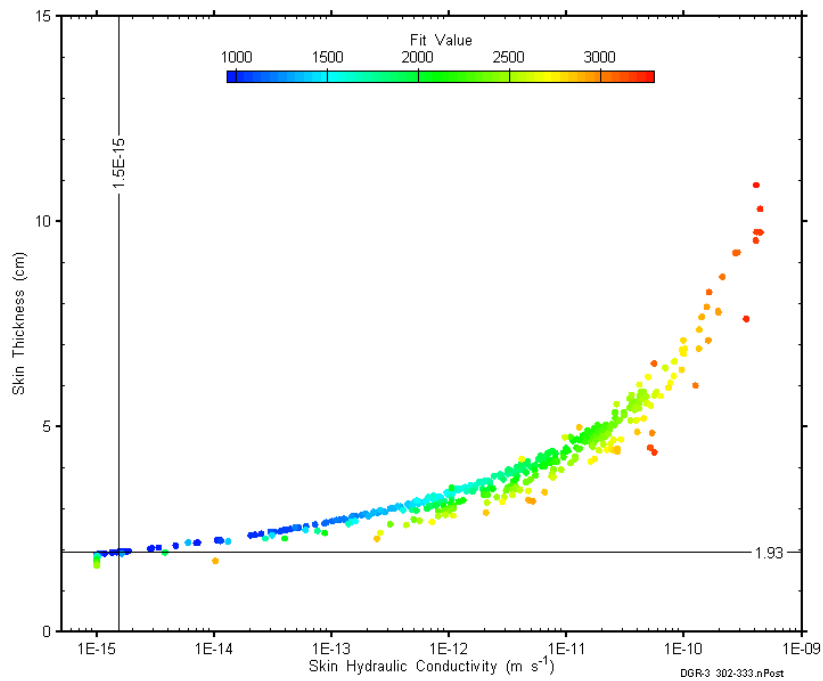


Figure C-43: XY-scatter plot showing estimates of skin hydraulic conductivity and skin thickness derived from the DGR3_301.81-332.55 perturbation analysis.

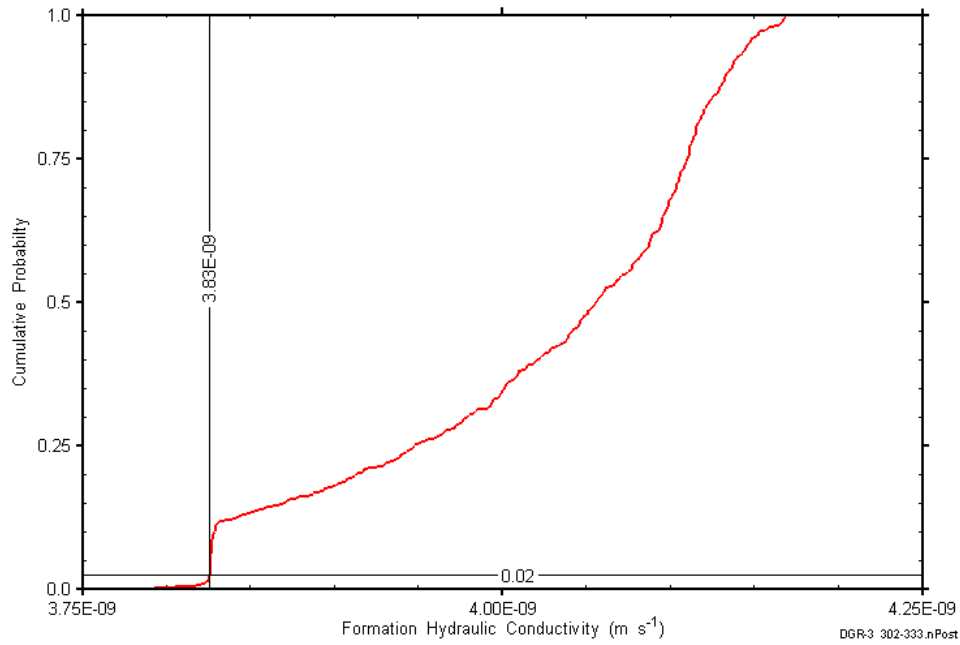


Figure C-44: DGR3_301.81-332.55 formation hydraulic conductivity cumulative distribution function.

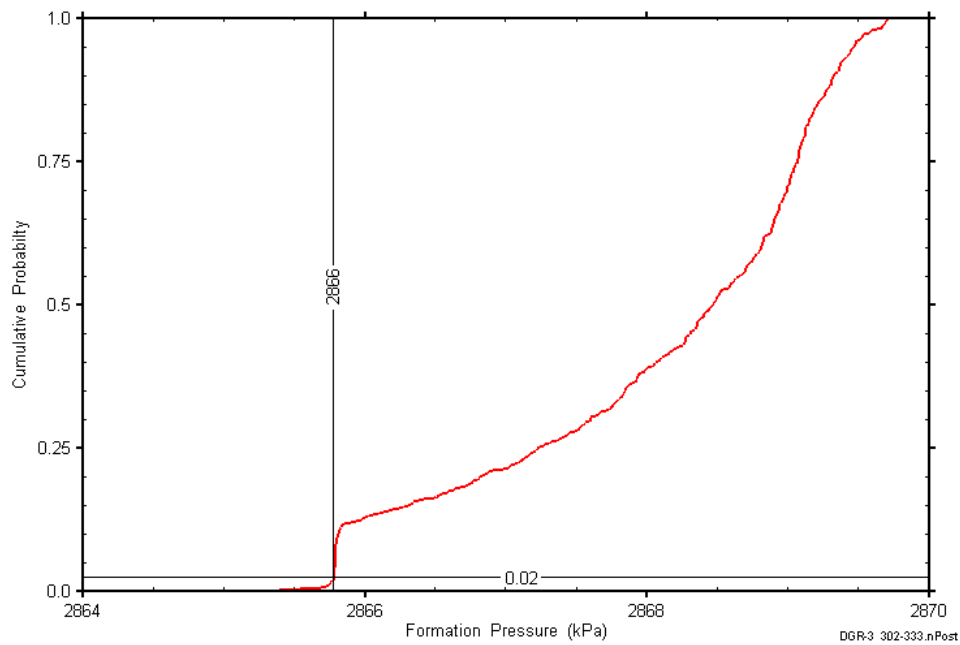


Figure C-45: DGR3_301.81-332.553 static formation pressure cumulative distribution function.

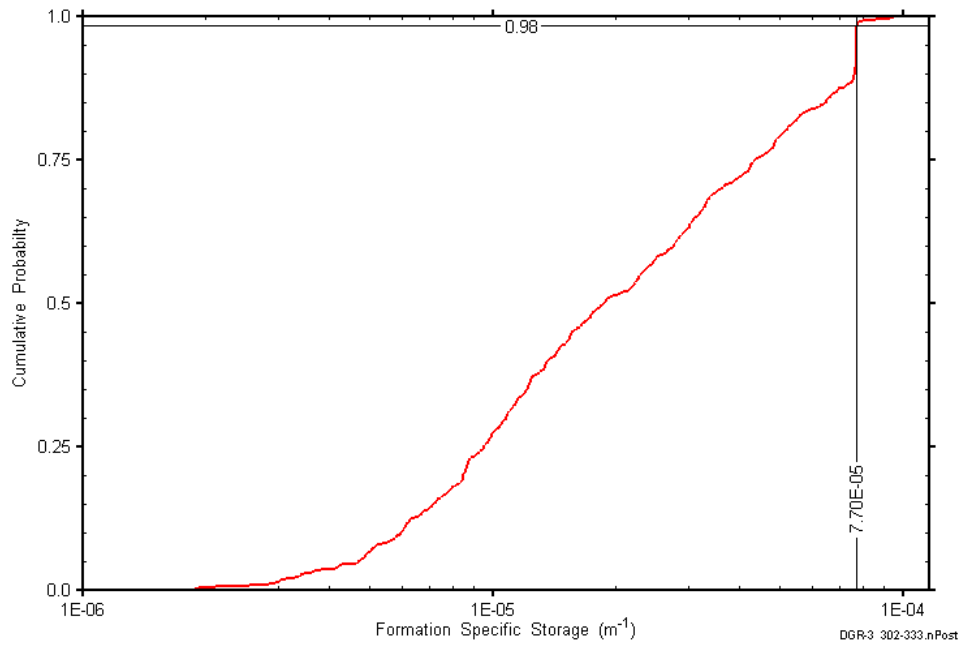


Figure C-46: DGR3_301.81-332.55 formation specific storage cumulative distribution function.

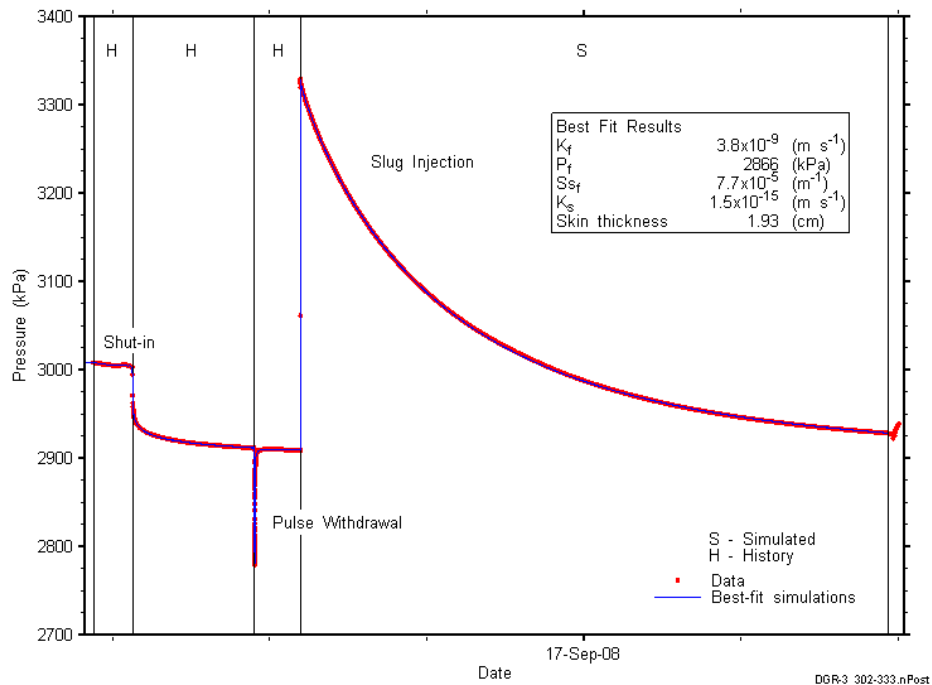


Figure C-47: Linear plot showing simulations of the DGR3_301.81-332.55 pressure response.

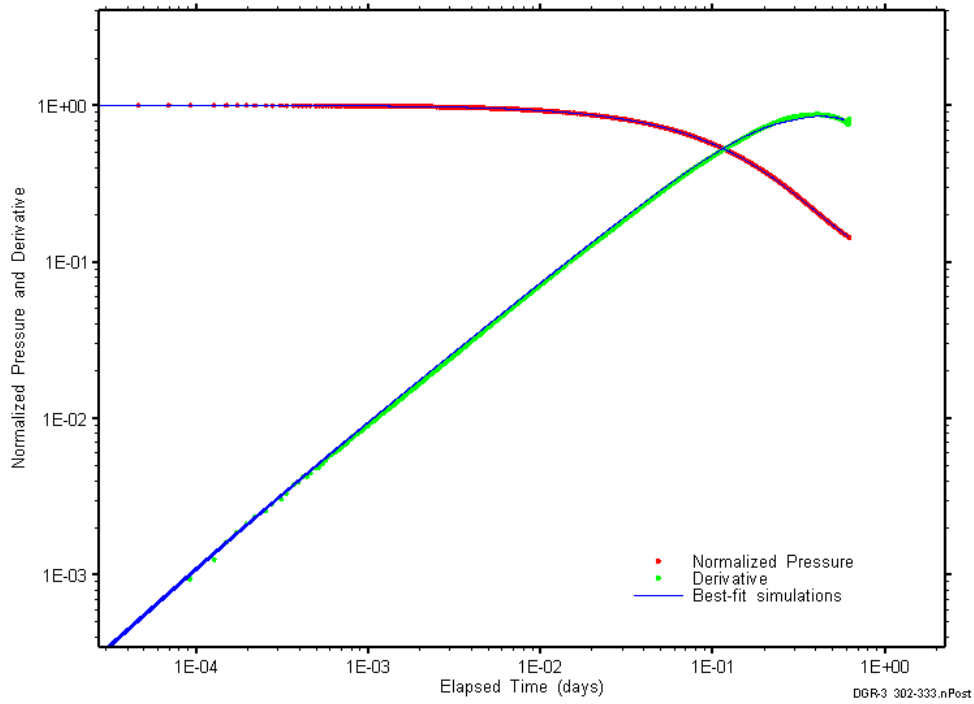


Figure C-48: Log-log plot showing simulations of the DGR3_301.81–332.55 shut-in period Ramey B and derivative response.

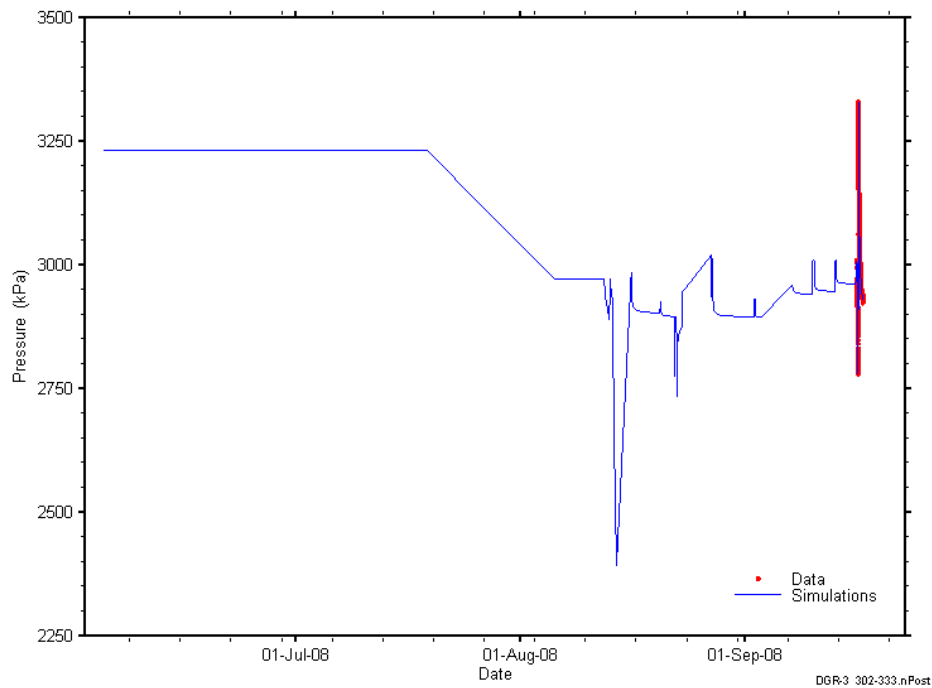


Figure C-49: Linear plot showing simulations of the DGR3_301.81-332.55 pressure response, including pre-test pressure history.

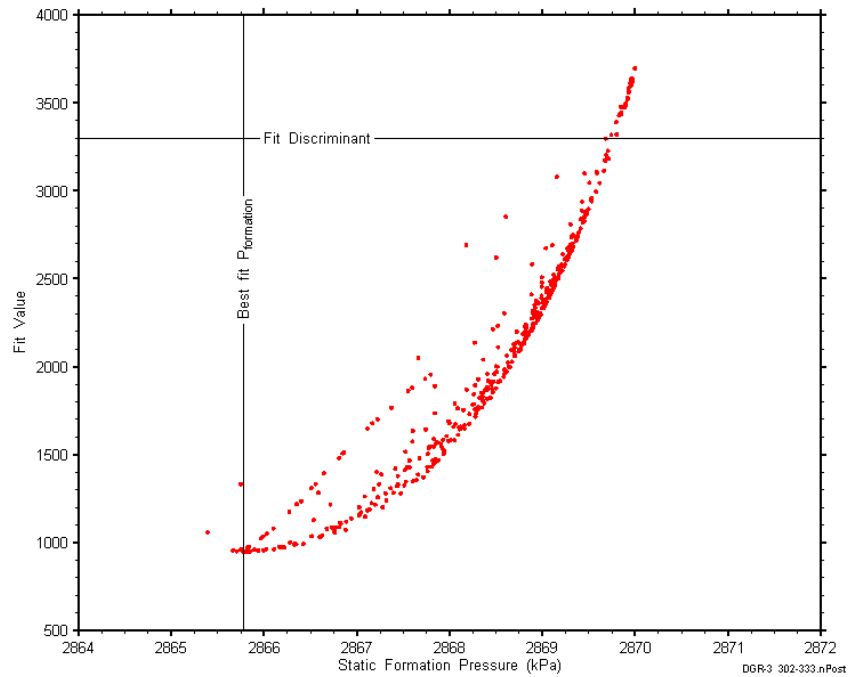


Figure C-50: XY-scatter plot showing the static formation pressure parameter space derived from DGR3_301.81-332.55 perturbation analysis along with the fit discriminant and best fit values.

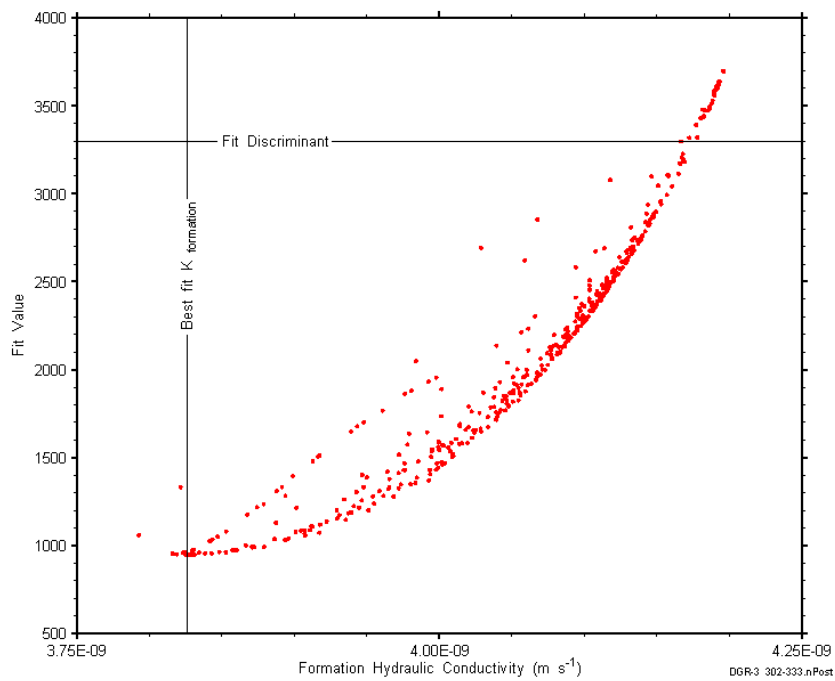


Figure C-51: XY-scatter plot showing the formation hydraulic conductivity parameter space derived from DGR3_301.81-332.55 perturbation analysis along with the fit discriminant and best fit values.

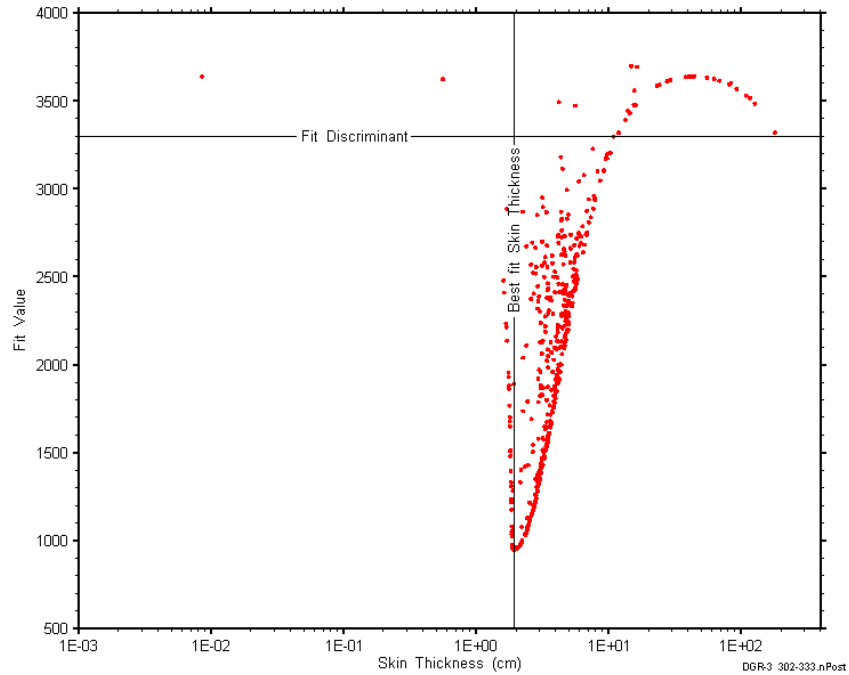


Figure C-52: XY-scatter plot showing the skin-thickness parameter space derived from DGR3_301.81-332.55 perturbation analysis along with the fit discriminant and best fit values.

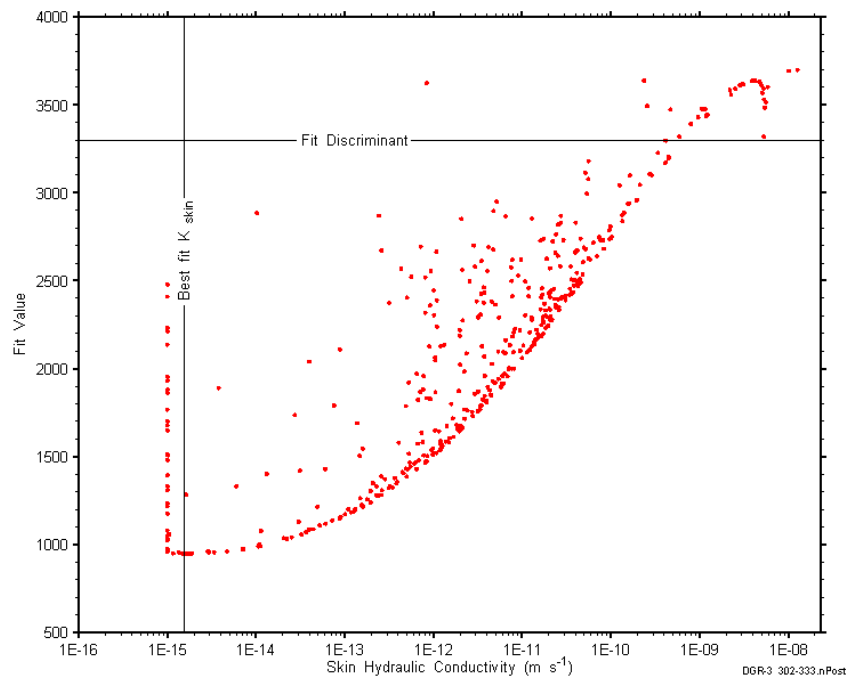


Figure C-53: XY-scatter plot showing the skin hydraulic conductivity parameter space derived from DGR3_301.81-332.55 perturbation analysis along with the fit discriminant and best fit values.

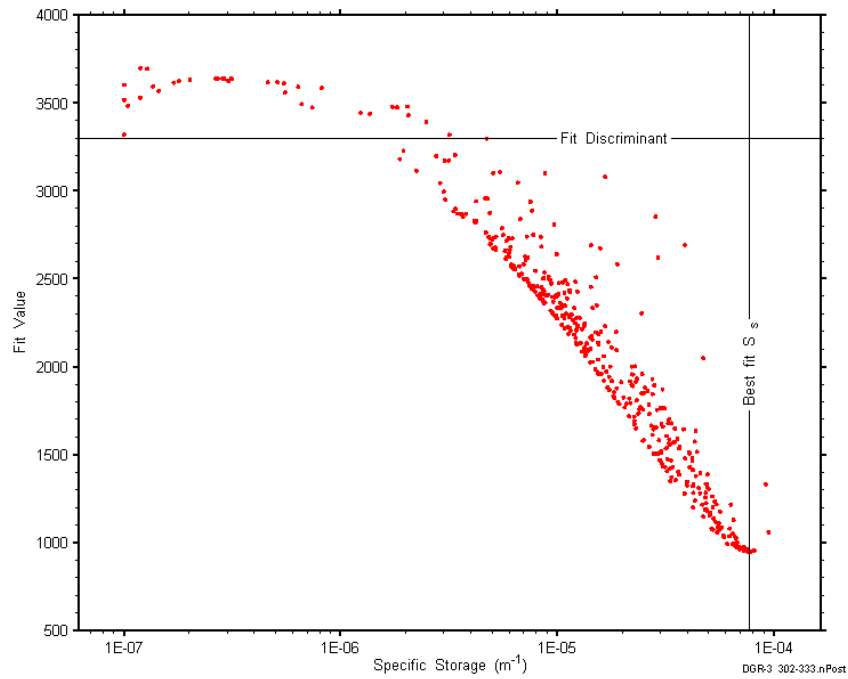


Figure C-54: XY-scatter plot showing the formation specific storage parameter space derived from DGR3_301.81-332.55 perturbation analysis along with the fit discriminant and best fit values.

C.5 334.99-365.73 Salina A2 evaporite-A1 carbonate

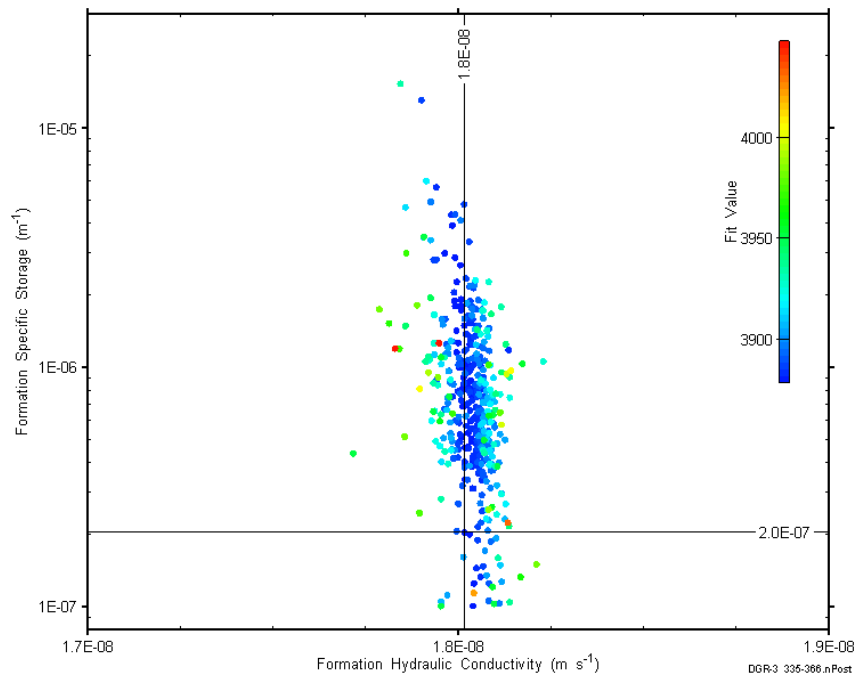


Figure C-55: XY-scatter plot showing estimates of formation hydraulic conductivity and formation specific storage derived from the DGR3_334.99-365.73 perturbation analysis.

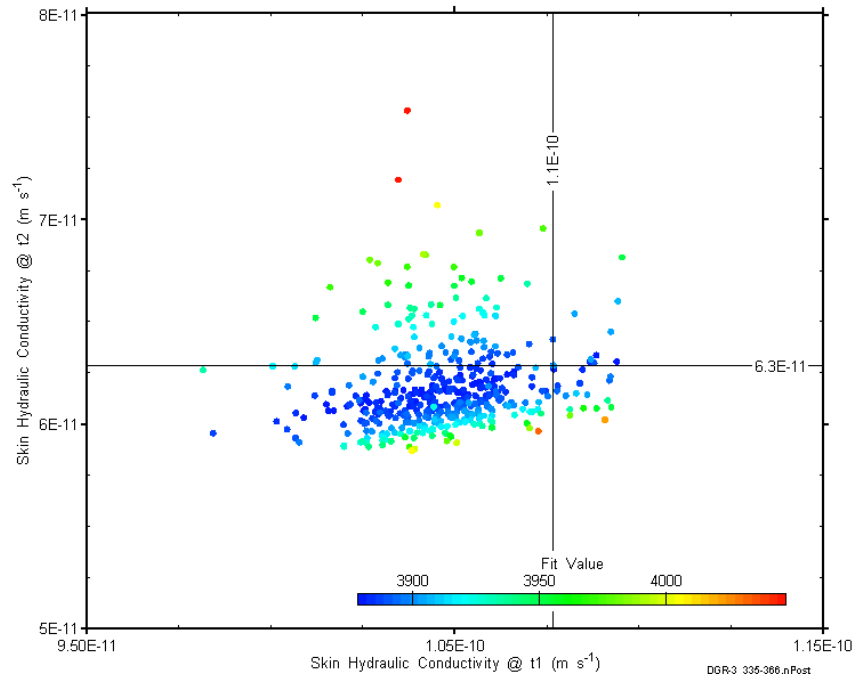


Figure C-56: XY-scatter plot showing estimates of skin hydraulic conductivity at time t1 and skin hydraulic conductivity at time t2 derived from the DGR3_334.99-365.73 perturbation analysis.

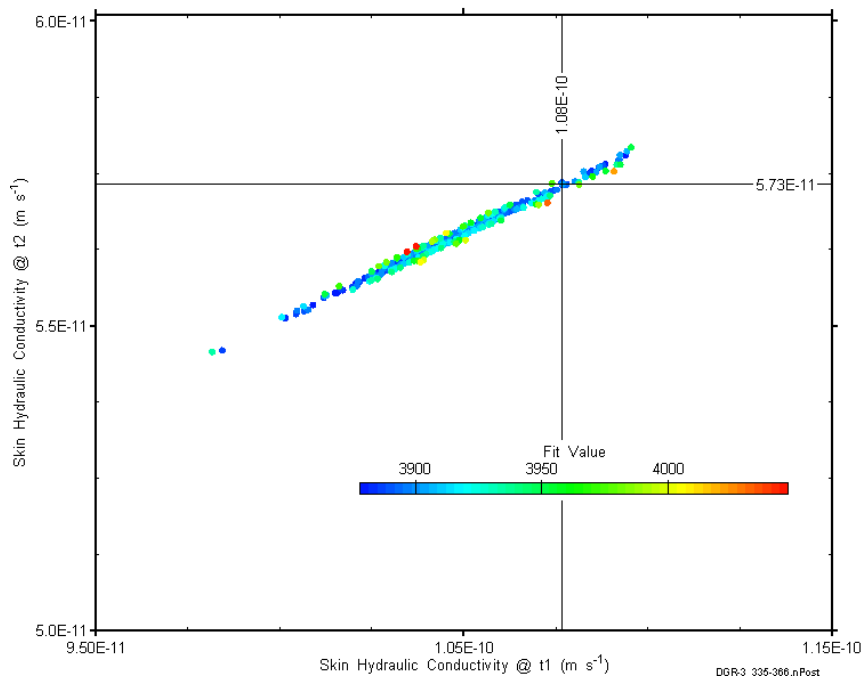


Figure C-57: XY-scatter plot showing estimates of skin hydraulic conductivity at time t1 and skin hydraulic conductivity at time t3 derived from the DGR3_334.99-365.73 perturbation analysis.

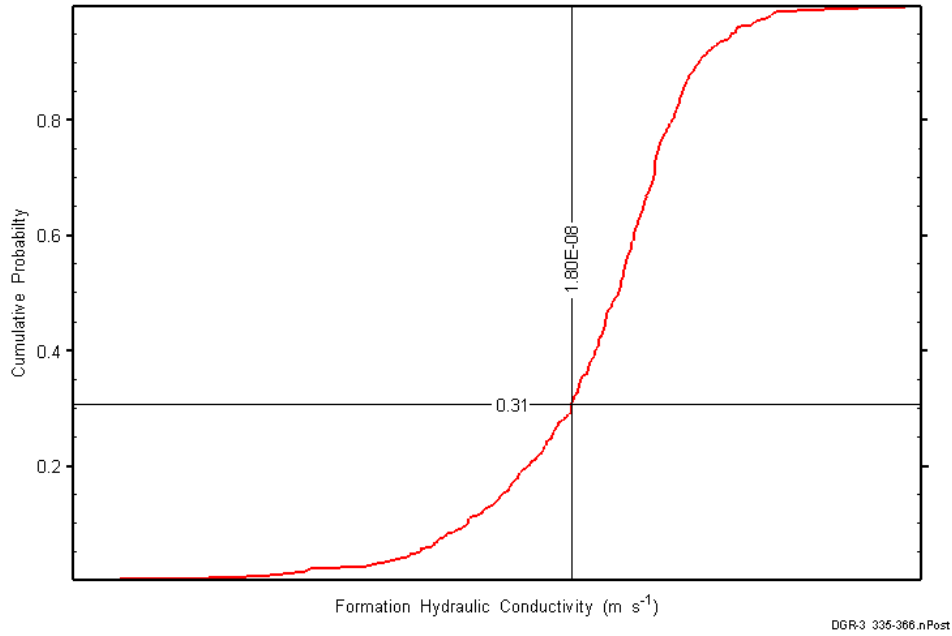


Figure C-58: DGR3_334.99-365.73 formation hydraulic conductivity cumulative distribution function.

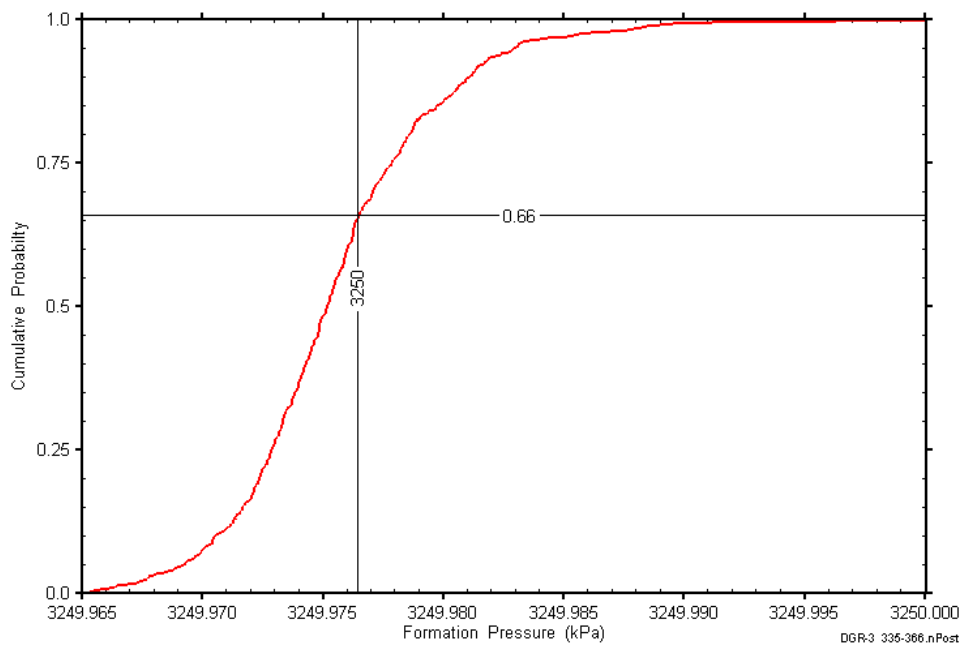


Figure C-59: DGR3_334.99-365.73 static formation pressure cumulative distribution function.

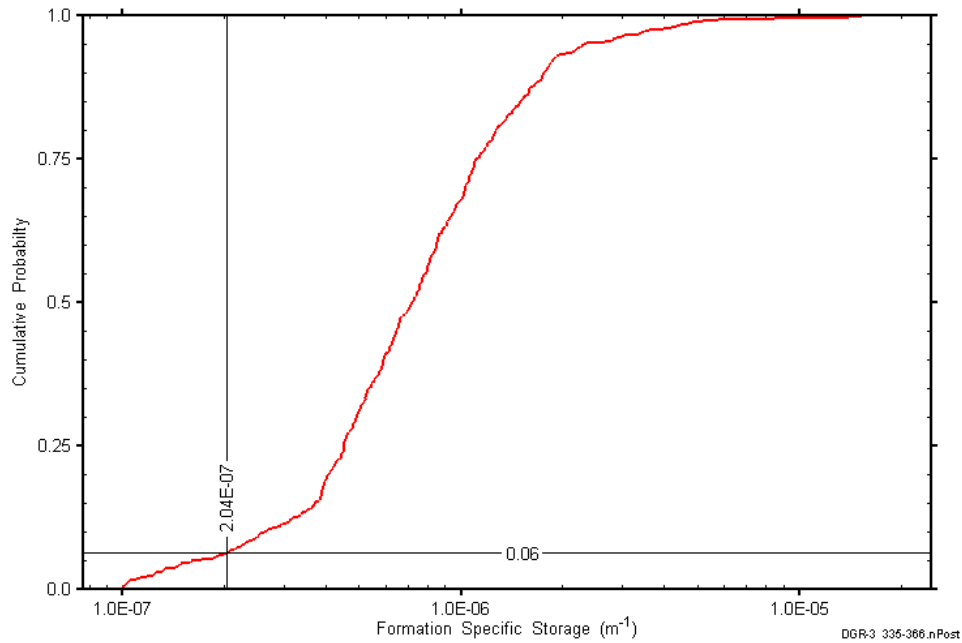


Figure C-60: DGR3_334.99-365.73 formation specific storage cumulative distribution function.

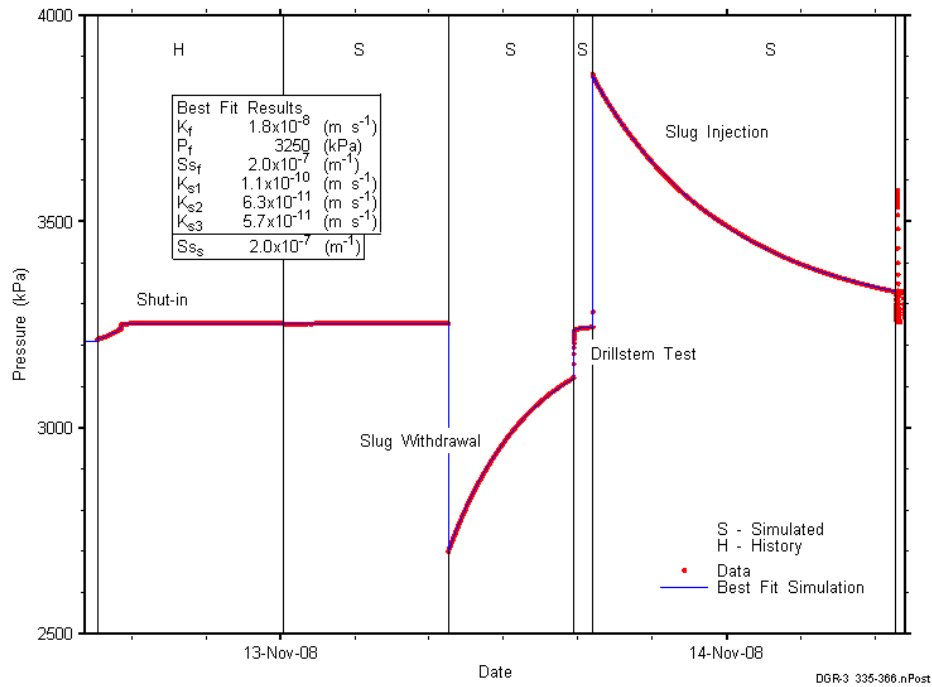


Figure C-61: Linear plot showing simulations of the DGR3_334.99-365.73 pressure response.

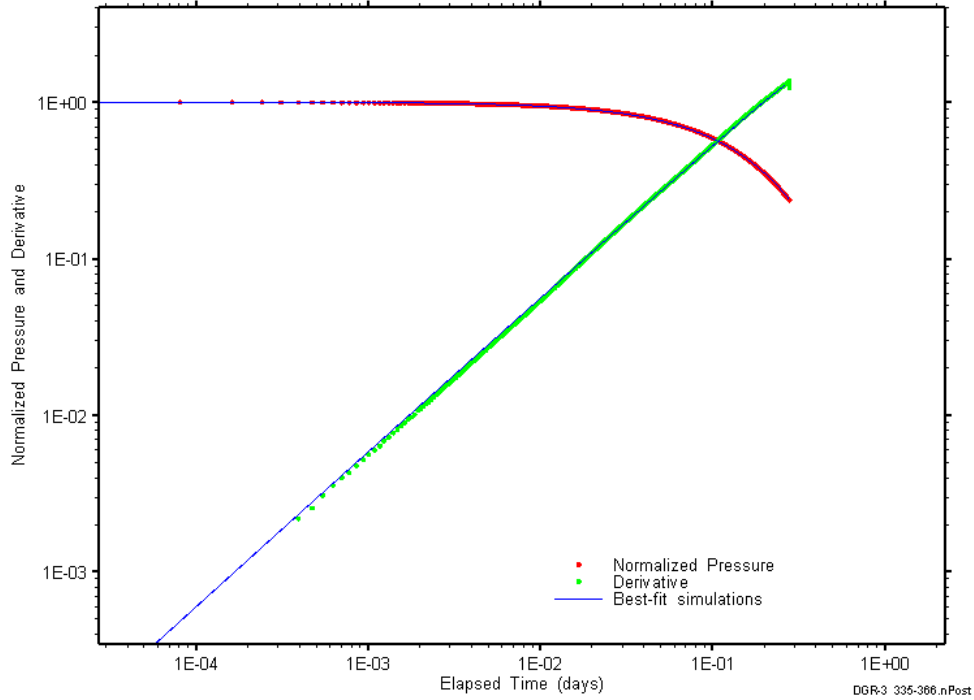


Figure C-62: Log-log plot showing simulations of the DGR3_334.99–365.73 slug withdrawal Ramey B and derivative response.

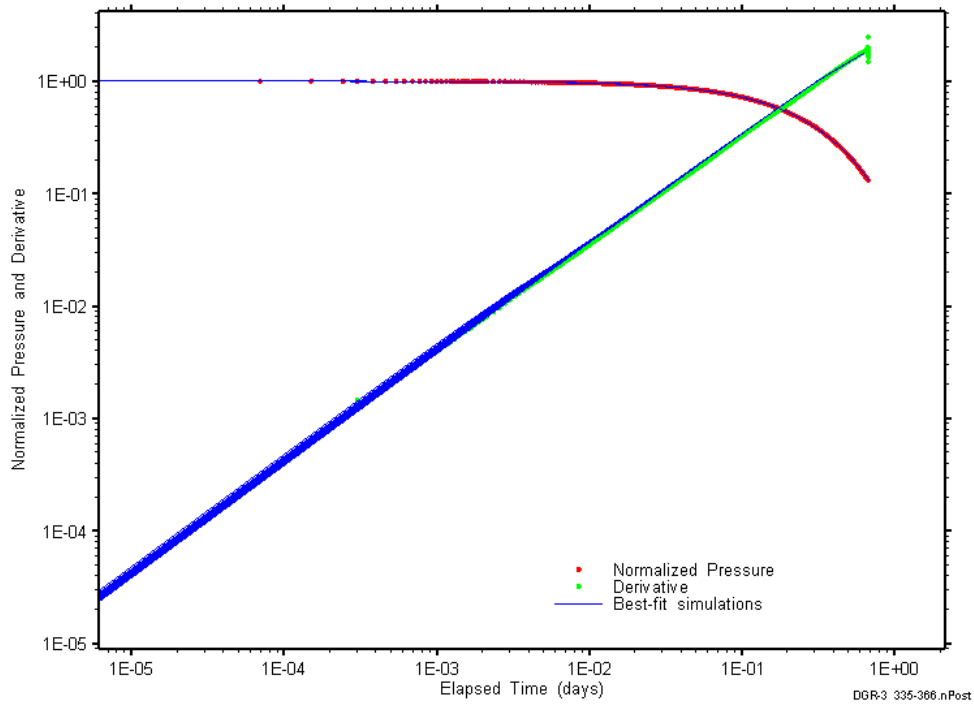


Figure C-63: Log-log plot showing simulations of the DGR3_334.99–365.73 slug injection Ramey B and derivative response.

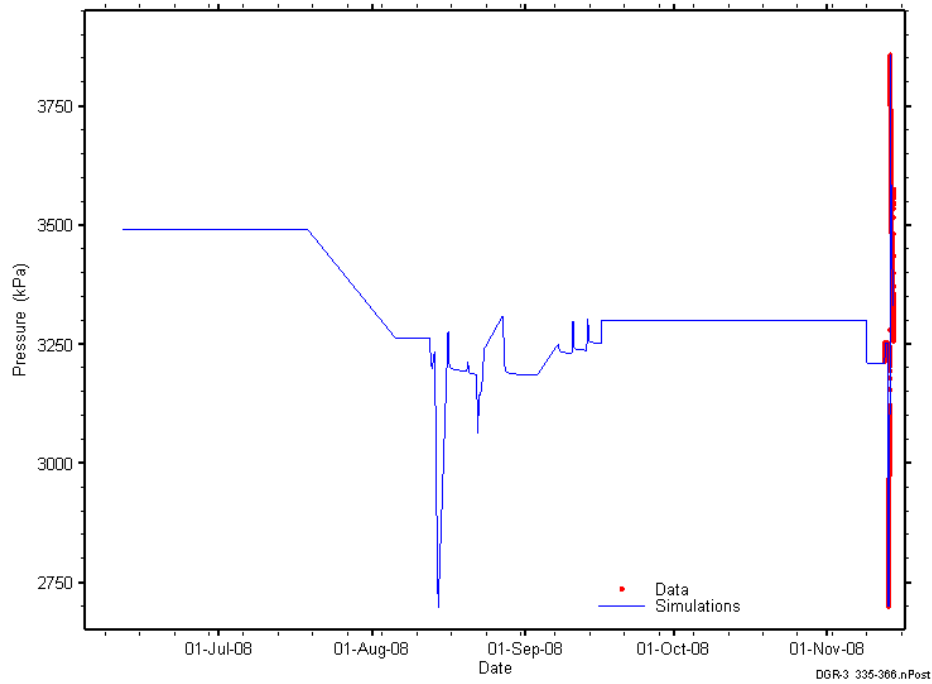


Figure C-64: Linear plot showing simulations of the DGR3_334.99-365.73 pressure response, including pre-test pressure history.

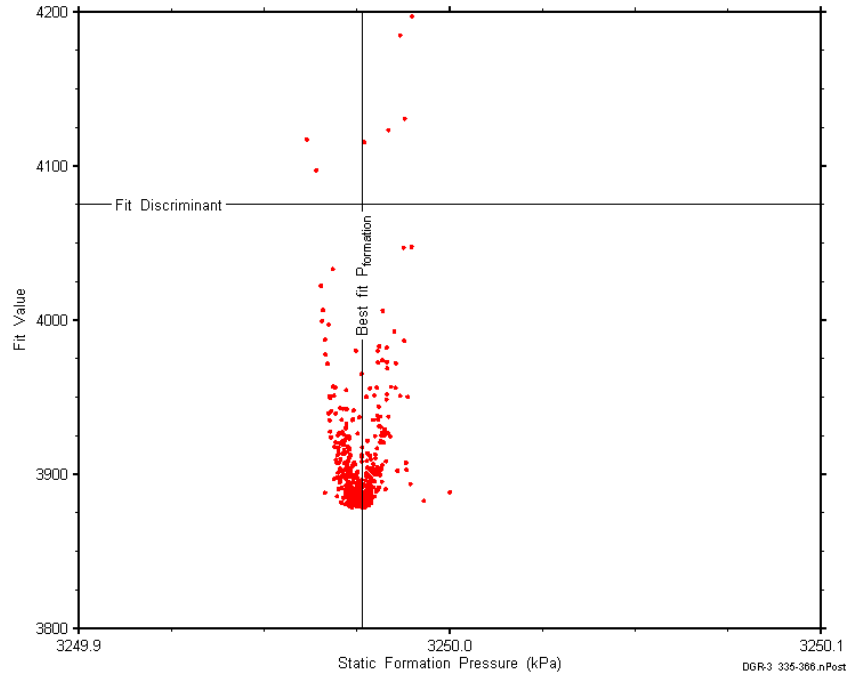


Figure C-65: XY-scatter plot showing the static formation pressure parameter space derived from DGR3_334.99-365.73 perturbation analysis along with the fit discriminant and best fit values.

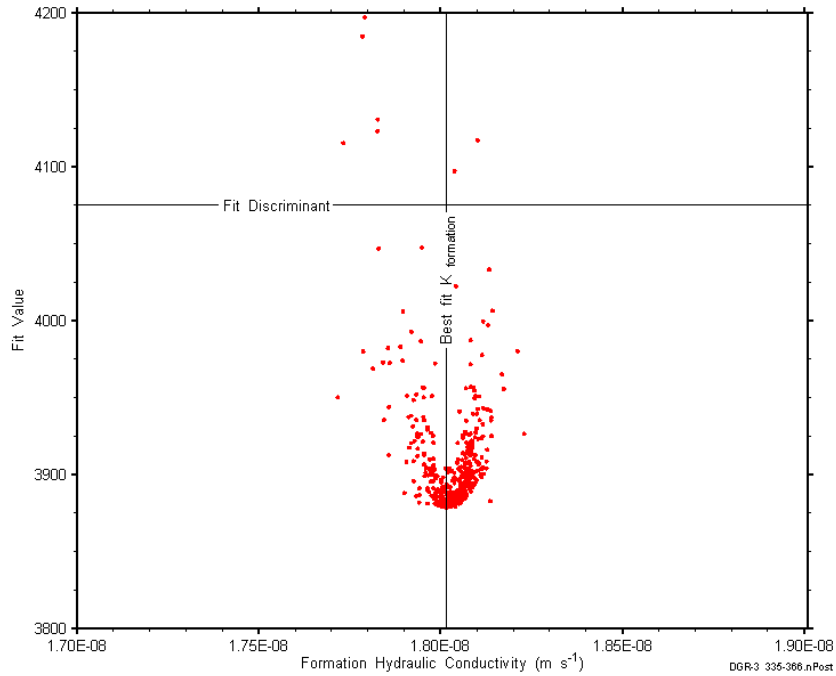


Figure C-66: XY-scatter plot showing the formation hydraulic conductivity parameter space derived from DGR3_334.99-365.73 perturbation analysis along with the fit discriminant and best fit values.

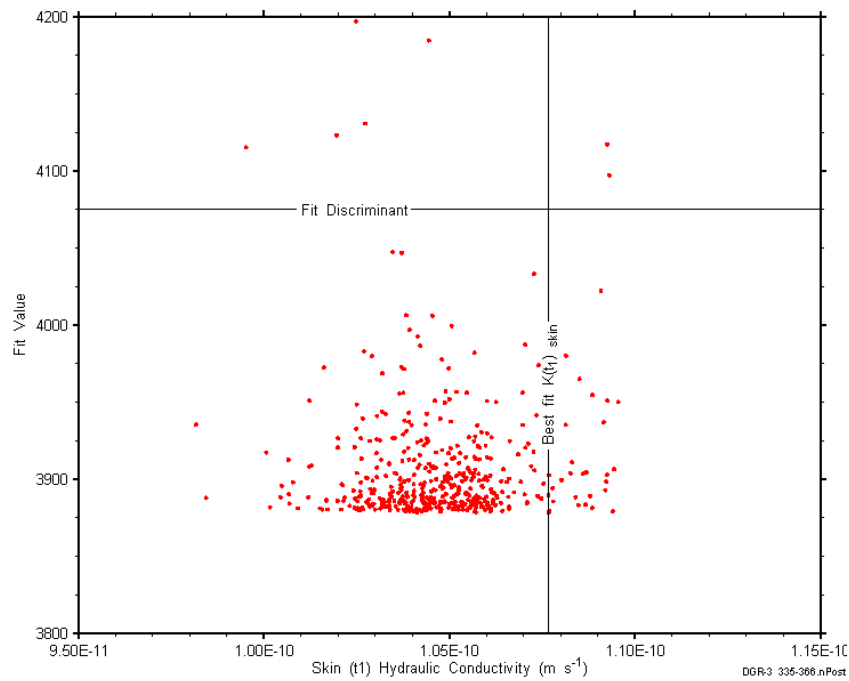


Figure C-67: XY-scatter plot showing the skin hydraulic conductivity at time t1 parameter space derived from DGR3_334.99-365.73 perturbation analysis along with the fit discriminant and best fit values.

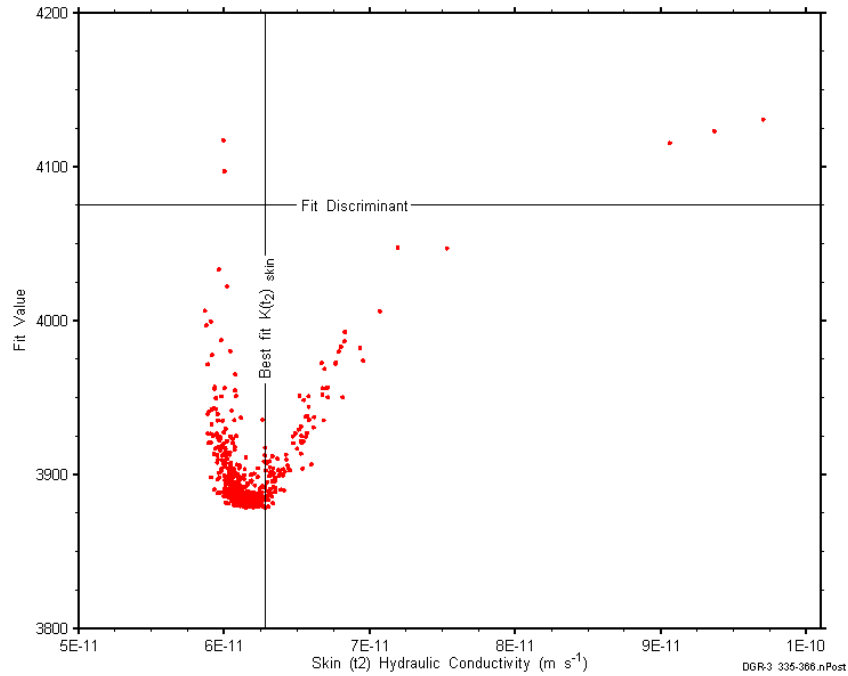


Figure C-68: XY-scatter plot showing the skin hydraulic conductivity at time t_2 parameter space derived from DGR3_334.99-365.73 perturbation analysis along with the fit discriminant and best fit values.

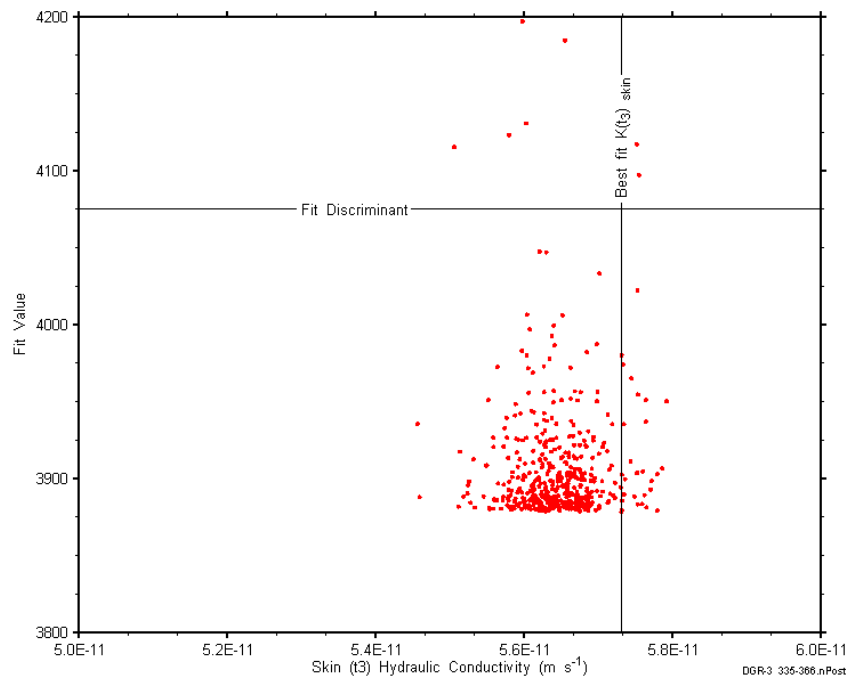


Figure C-69: XY-scatter plot showing the skin hydraulic conductivity at time t_3 parameter space derived from DGR3_334.99-365.73 perturbation analysis along with the fit discriminant and best fit values.

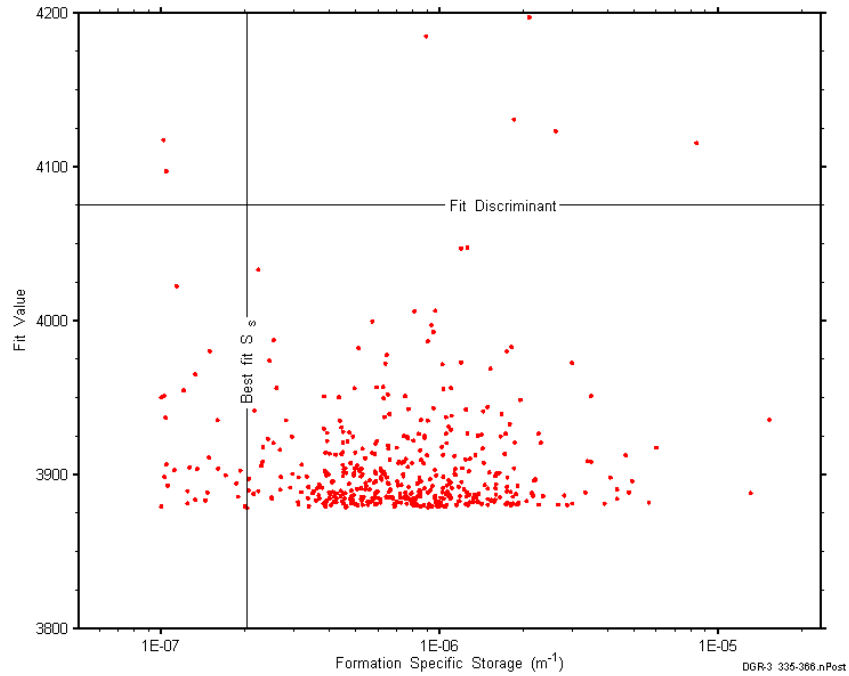


Figure C-70: XY-scatter plot showing the formation specific storage parameter space derived from DGR3_334.99-365.73 perturbation analysis along with the fit discriminant and best fit values.

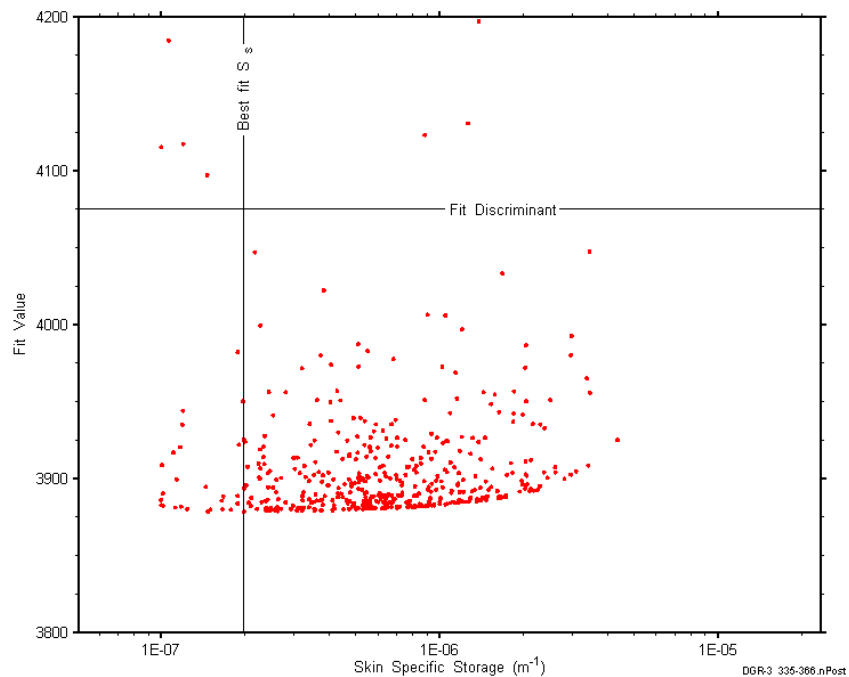


Figure C-71: XY-scatter plot showing the skin specific storage parameter space derived from DGR3_334.99-365.73 perturbation analysis along with the fit discriminant and best fit values.

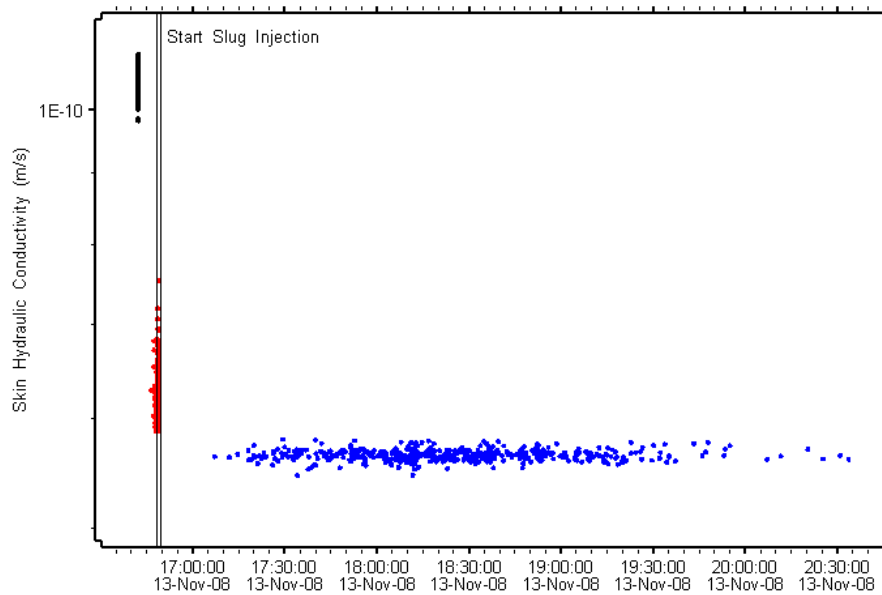


Figure C-72: XY-scatter plot showing the skin hydraulic conductivity parameter as a function of time derived from DGR3_334.99-365.73 perturbation analysis.

C.6 346.00-376.74 Salina A1 carbonate

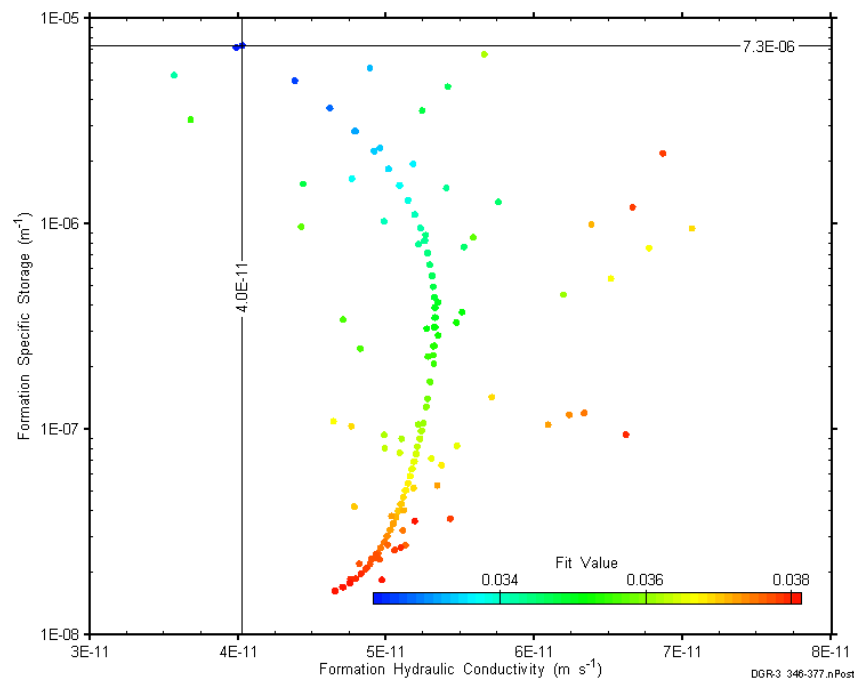


Figure C-73: XY-scatter plot showing estimates of formation hydraulic conductivity and formation specific storage derived from the DGR3_346.00-376.74 perturbation analysis.

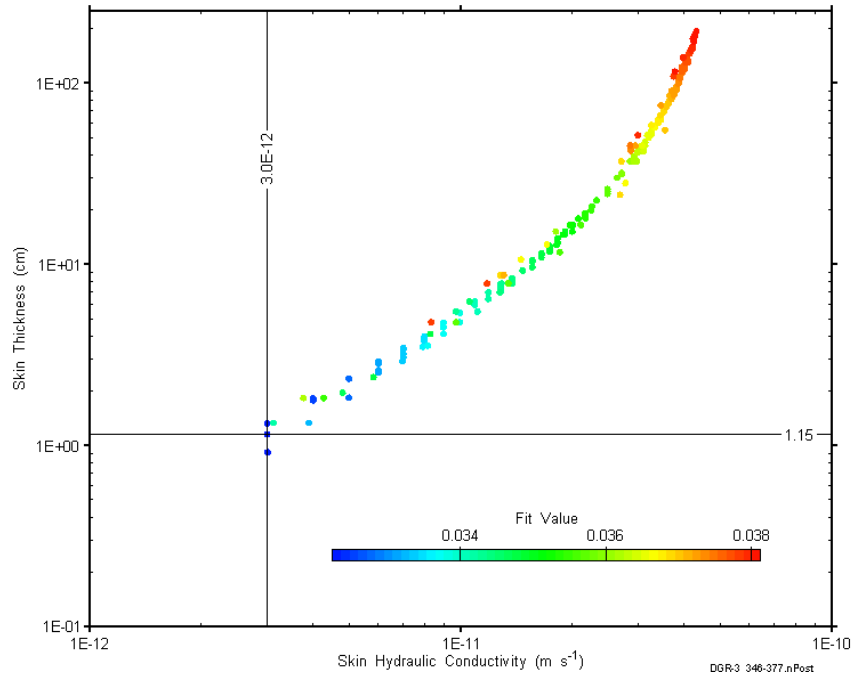


Figure C-74: XY-scatter plot showing estimates of skin hydraulic conductivity and skin thickness derived from the DGR3_346.00-376.74 perturbation analysis.

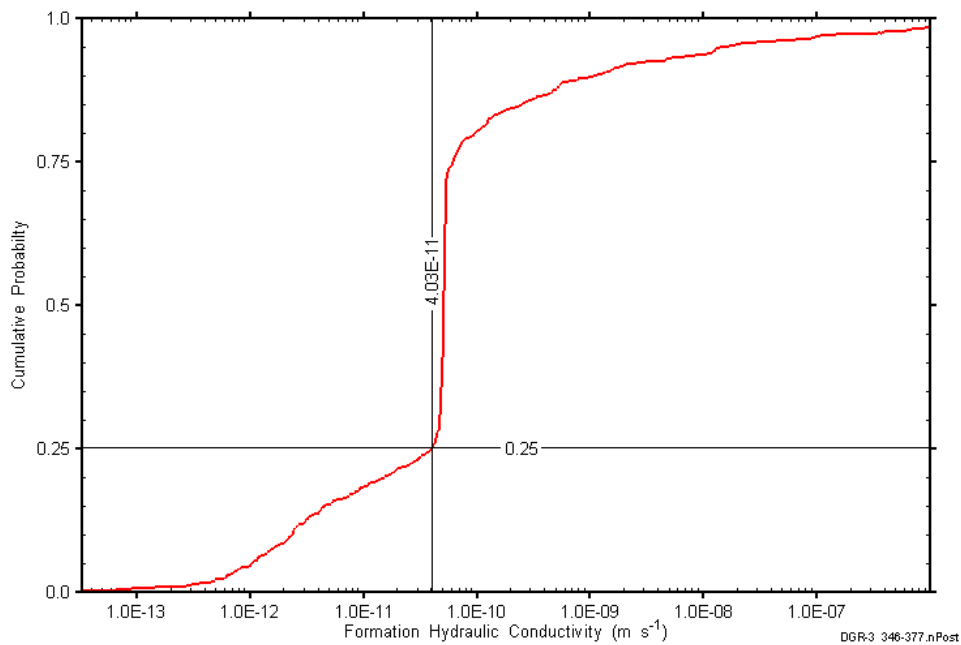


Figure C-75: DGR3_346.00-376.74 formation hydraulic conductivity cumulative distribution function.

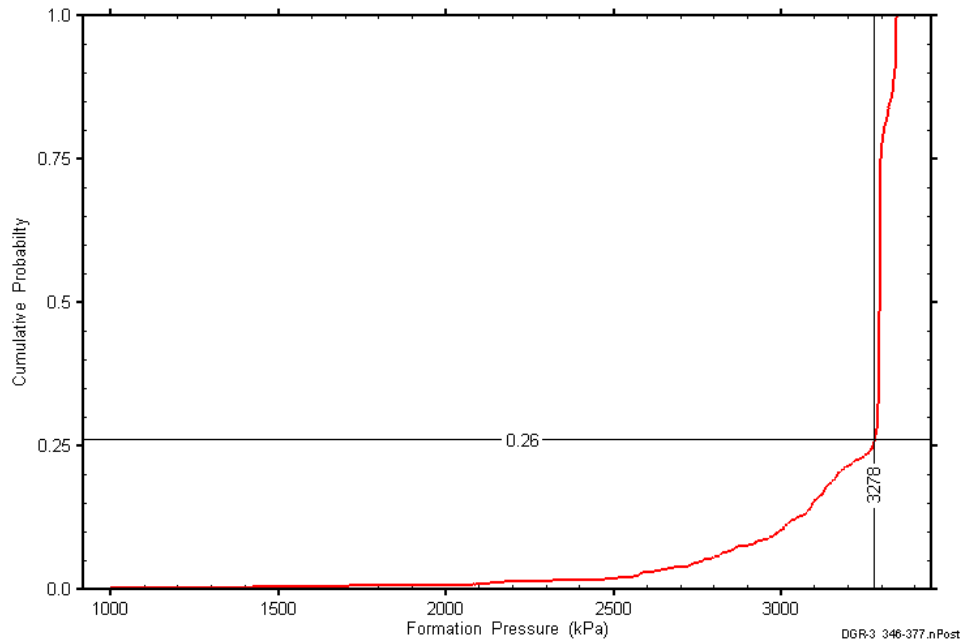


Figure C-76: DGR3_346.00-376.74 static formation pressure cumulative distribution function

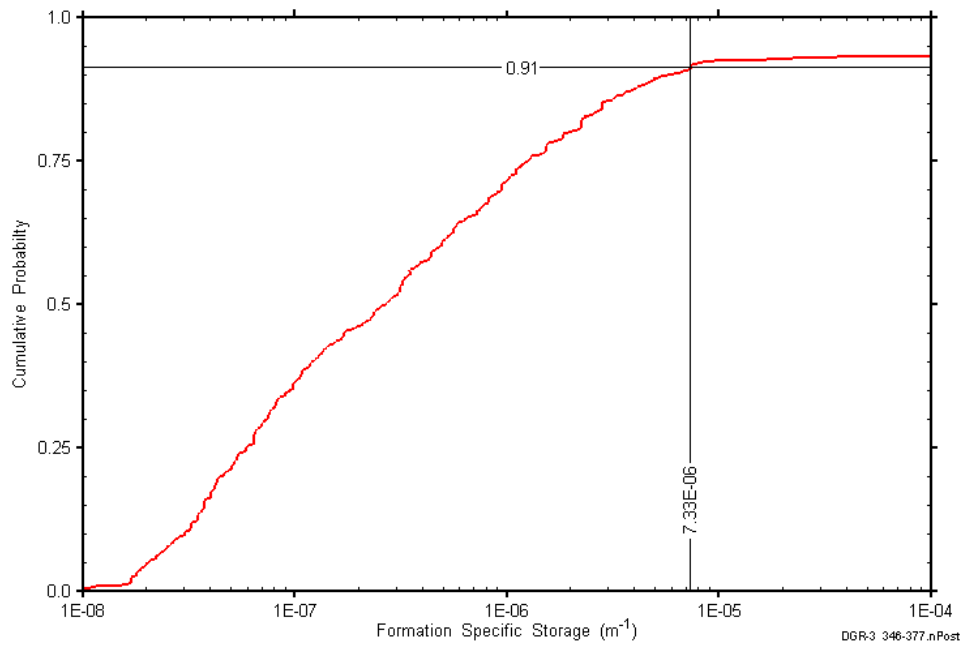


Figure C-77: DGR3_346.00-376.74 formation specific storage cumulative distribution function.

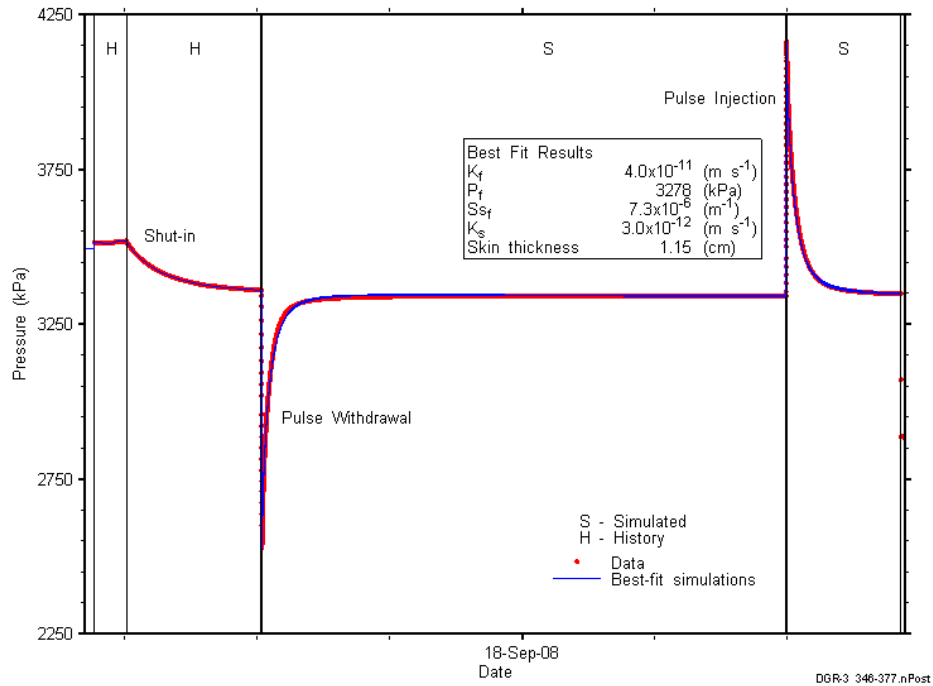


Figure C-78: Linear plot showing simulations of the DGR3_346.00-376.74 pressure response.

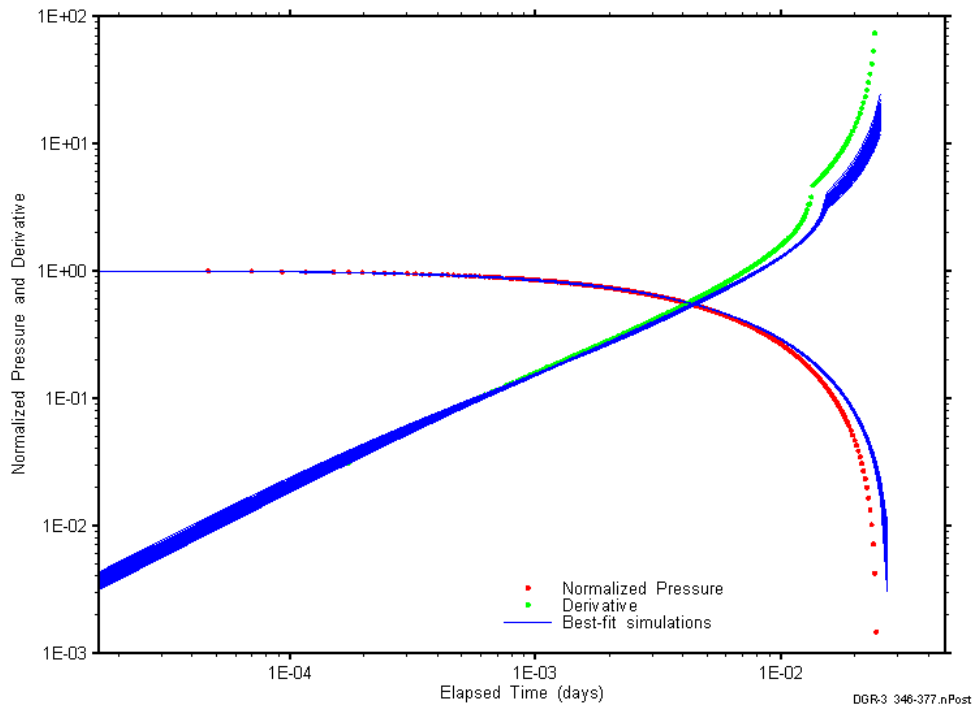


Figure C-79: Log-log plot showing simulations of the DGR3_346.00-376.74 pulse withdrawal Ramey B and derivative response.

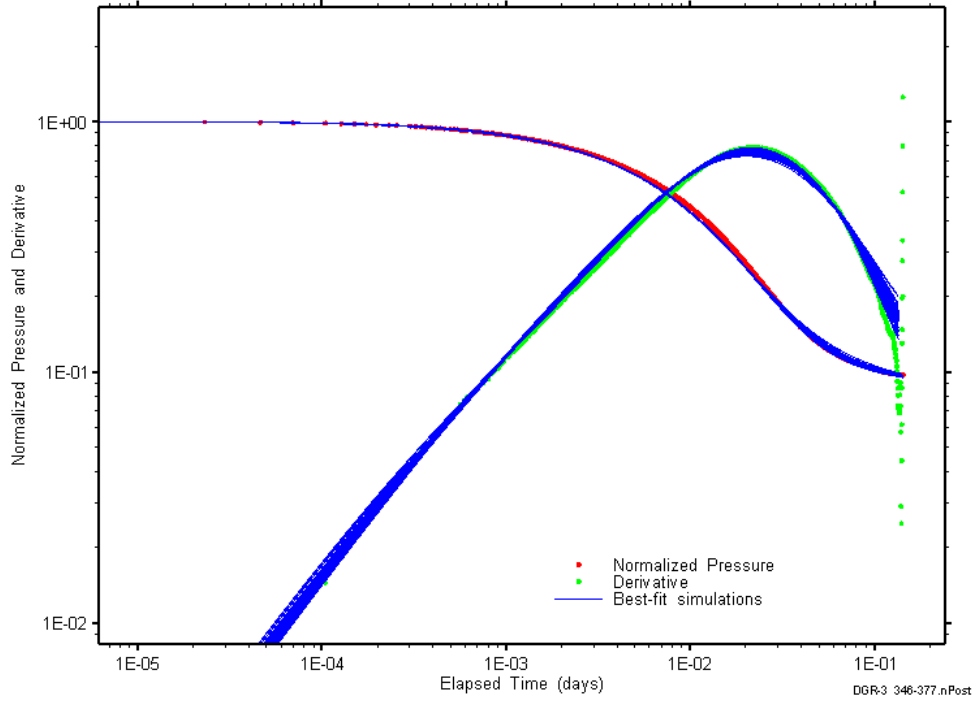


Figure C-80: Log-log plot showing simulations of the DGR3_346.00–376.74 pulse injection Ramey B and derivative response.

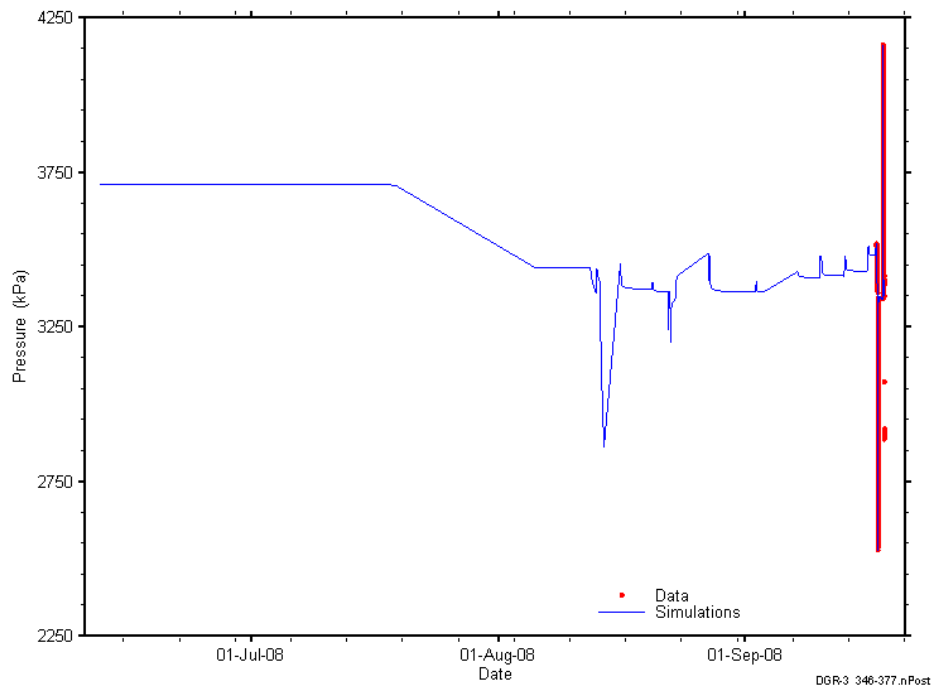


Figure C-81: Linear plot showing simulations of the DGR3_346.00-376.74 pressure response, including pre-test pressure history.

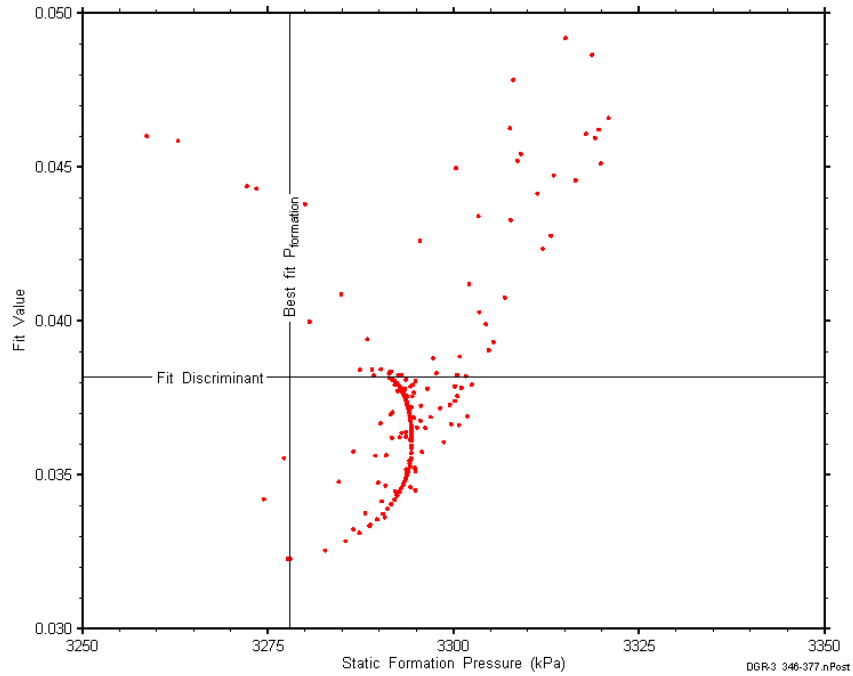


Figure C-82: XY-scatter plot showing the static formation pressure parameter space derived from DGR3_346.00-376.74 perturbation analysis along with the fit discriminant and best fit values.

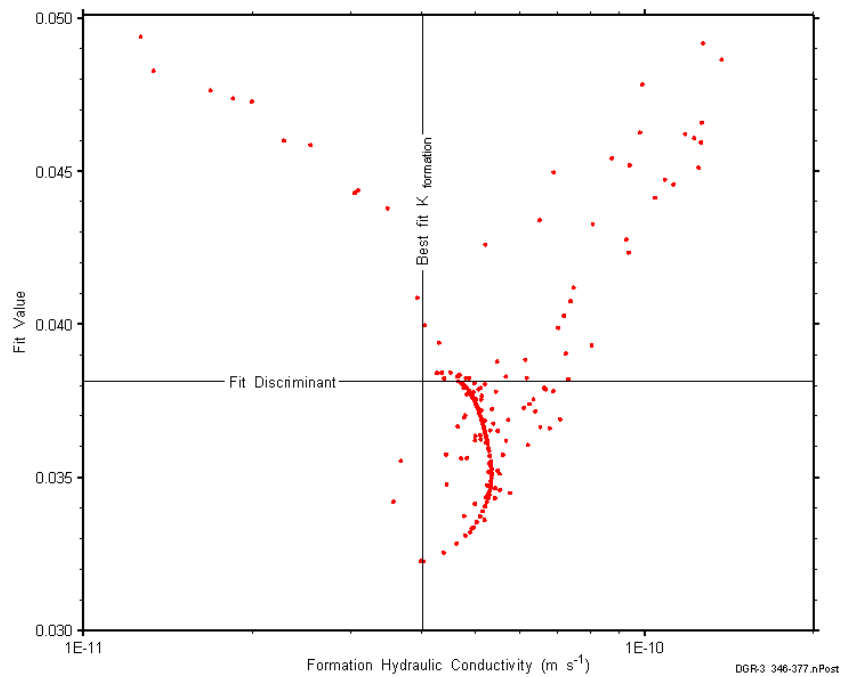


Figure C-83: XY-scatter plot showing the formation hydraulic conductivity parameter space derived from DGR3_346.00-376.74 perturbation analysis along with the fit discriminant and best fit values.

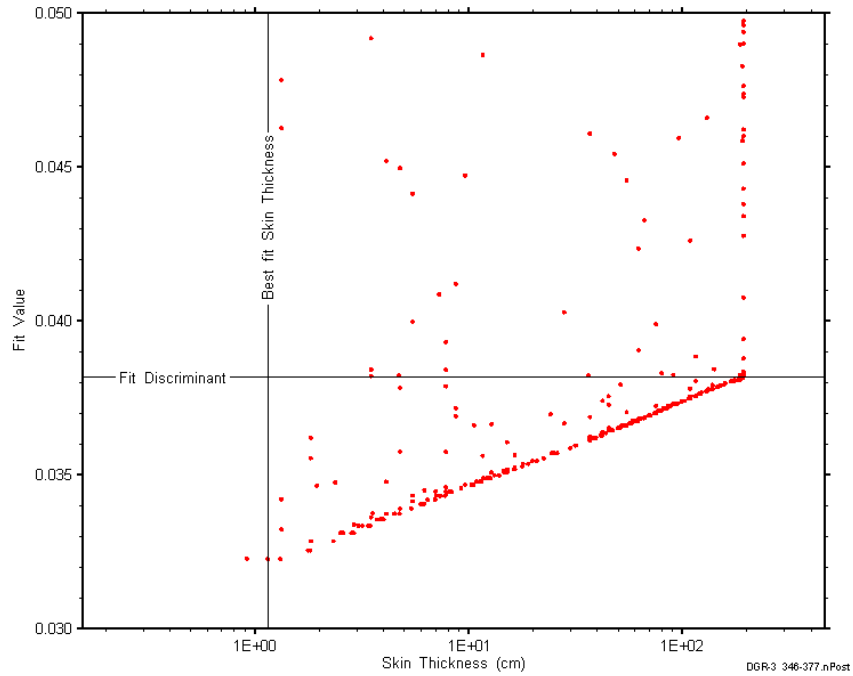


Figure C-84: XY-scatter plot showing the skin-thickness parameter space derived from DGR3_346.00-376.74 perturbation analysis along with the fit discriminant and best fit values.

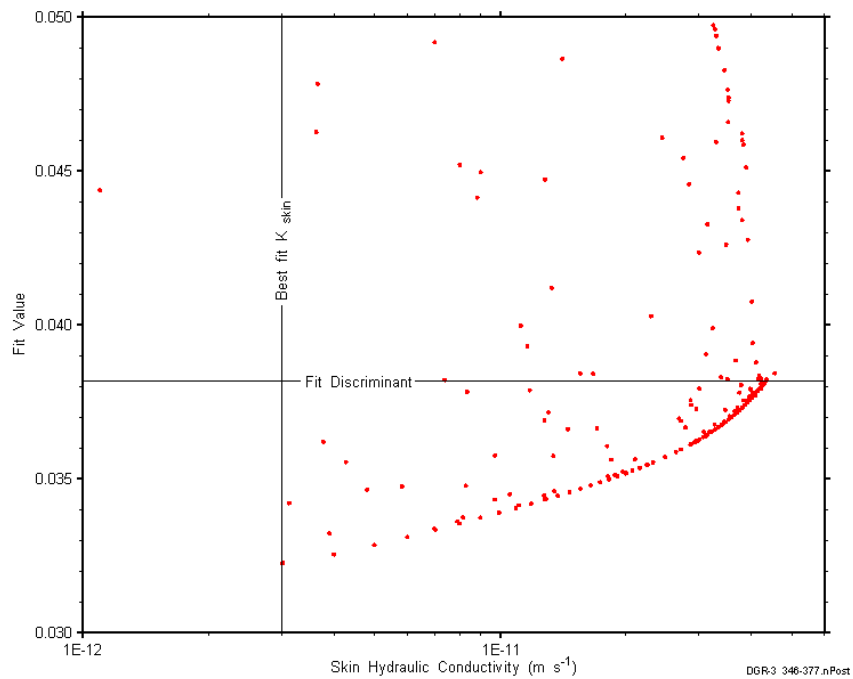


Figure C-85: XY-scatter plot showing the skin hydraulic conductivity parameter space derived from DGR3_346.00-376.74 perturbation analysis along with the fit discriminant and best fit values.

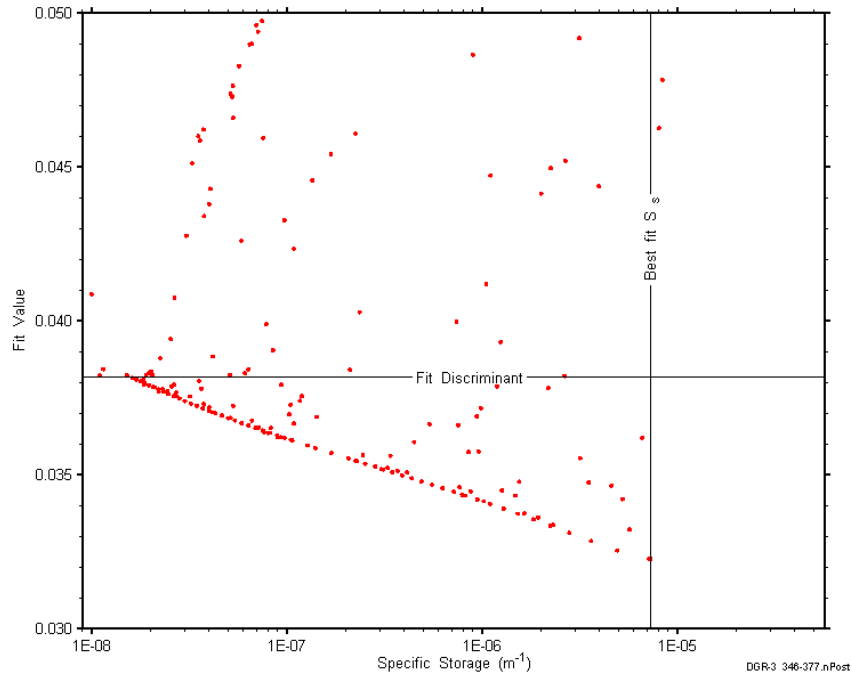


Figure C-86: XY-scatter plot showing the formation specific storage parameter space derived from DGR3_346.00-376.74 perturbation analysis along with the fit discriminant and best fit values.

C.7 378.98-410.72 Salina A1 evaporite-A0-Guelph-Goat Island-Gasport

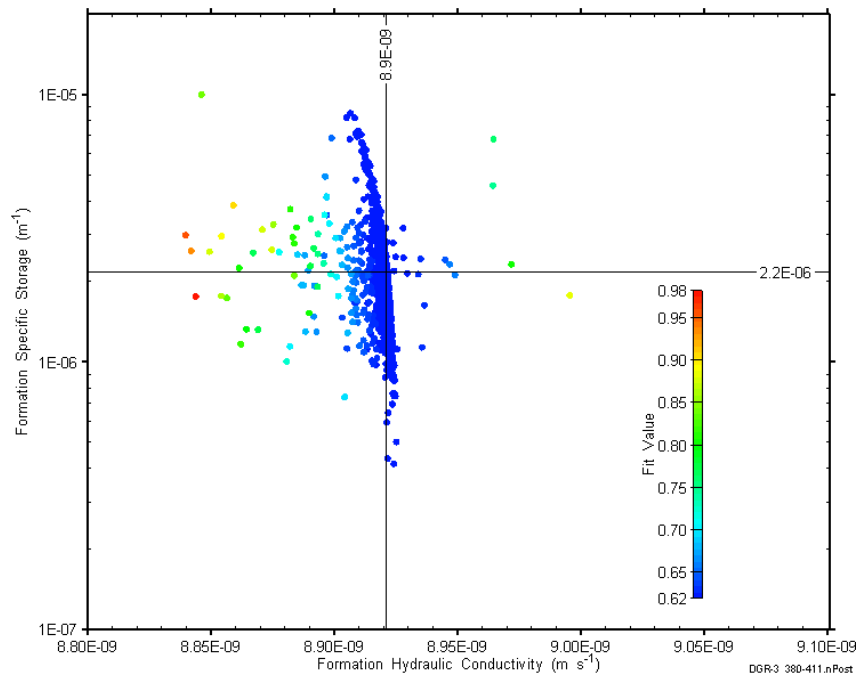


Figure C-87: XY-scatter plot showing estimates of formation hydraulic conductivity and formation specific storage derived from the DGR3_378.98-410.72 perturbation analysis.

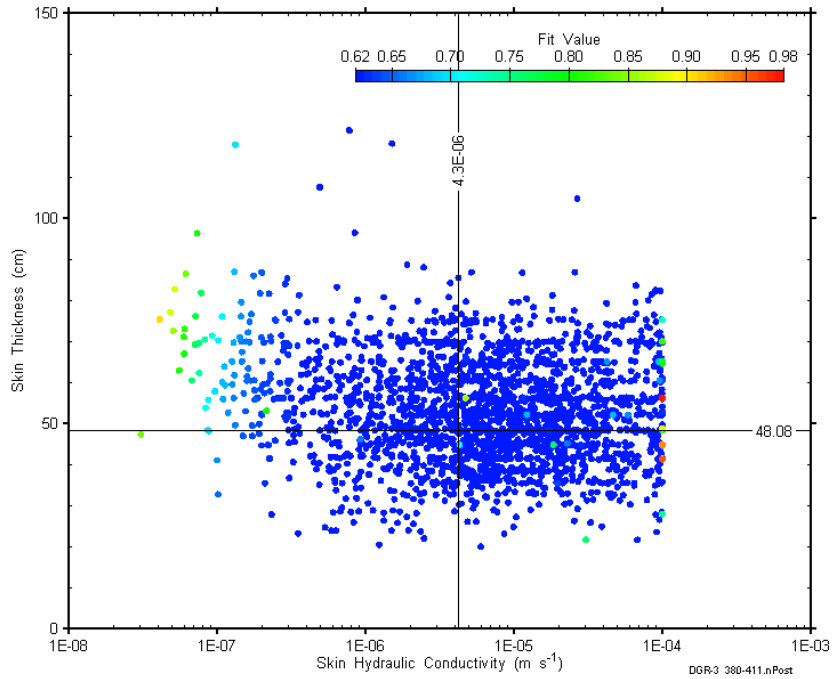


Figure C-88: XY-scatter plot showing estimates of skin hydraulic conductivity and skin thickness derived from the DGR3_378.98-410.72 perturbation analysis.

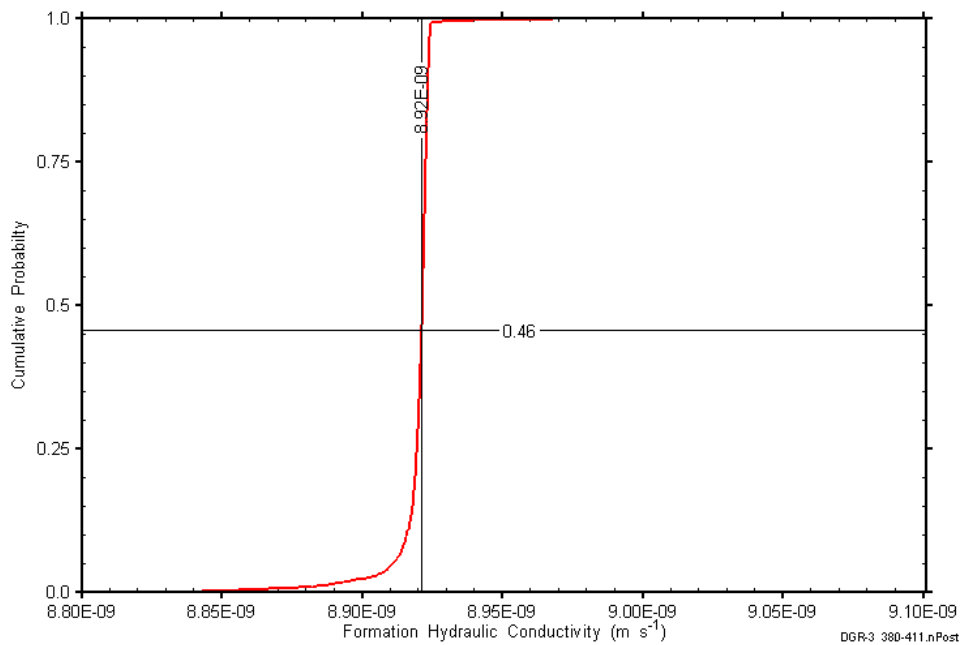


Figure C-89: DGR3_378.98-410.72 formation hydraulic conductivity cumulative distribution function.

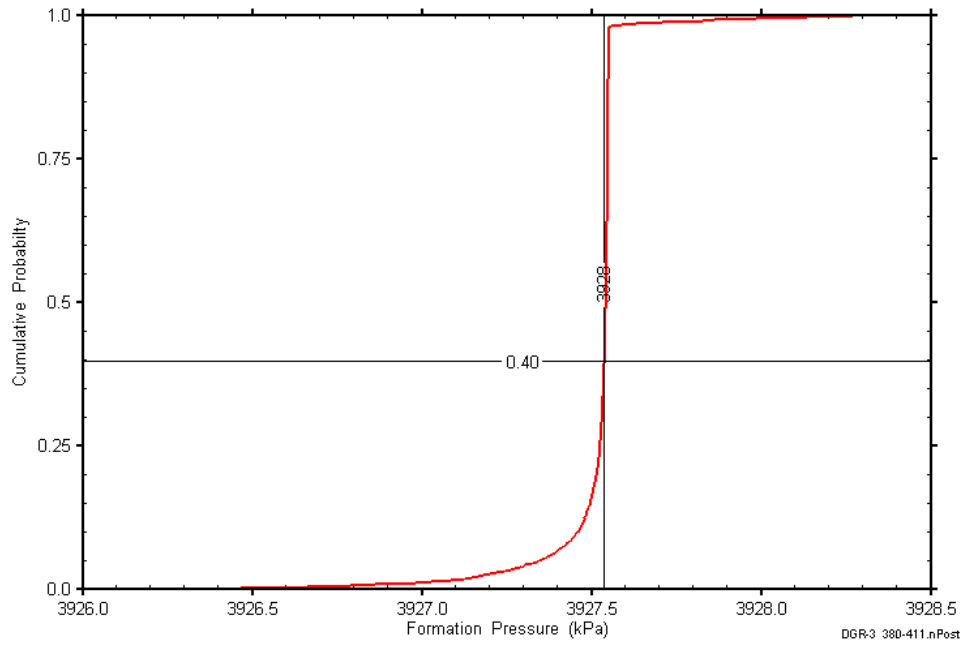


Figure C-90: DGR3_378.98-410.72 static formation pressure cumulative distribution function.

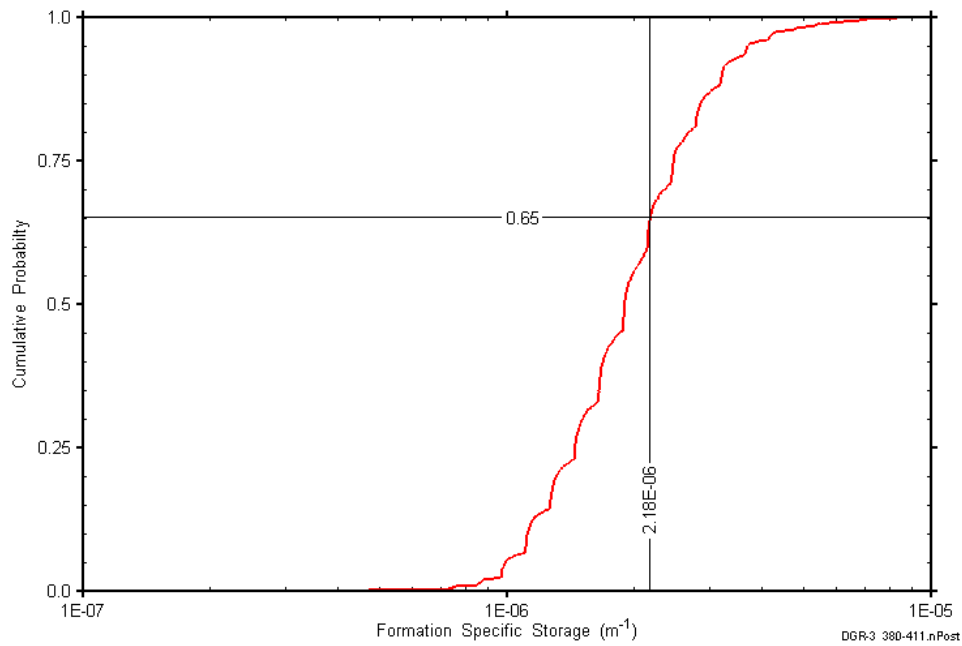


Figure C-91: DGR3_378.98-410.72 formation specific storage cumulative distribution function.

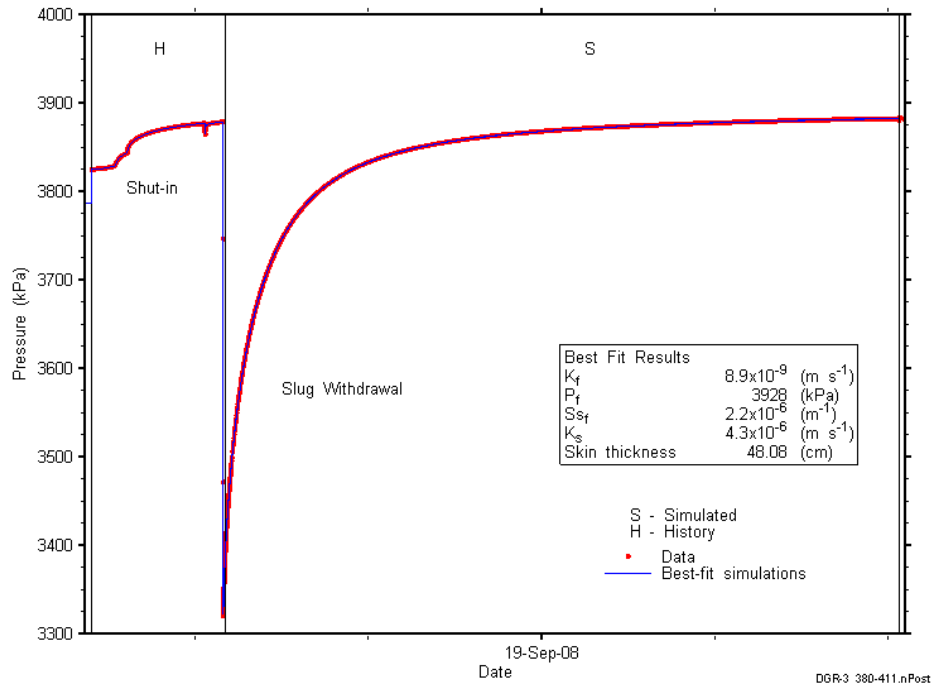


Figure C-92: Linear plot showing simulations of the DGR3_378.98-410.72 pressure response.

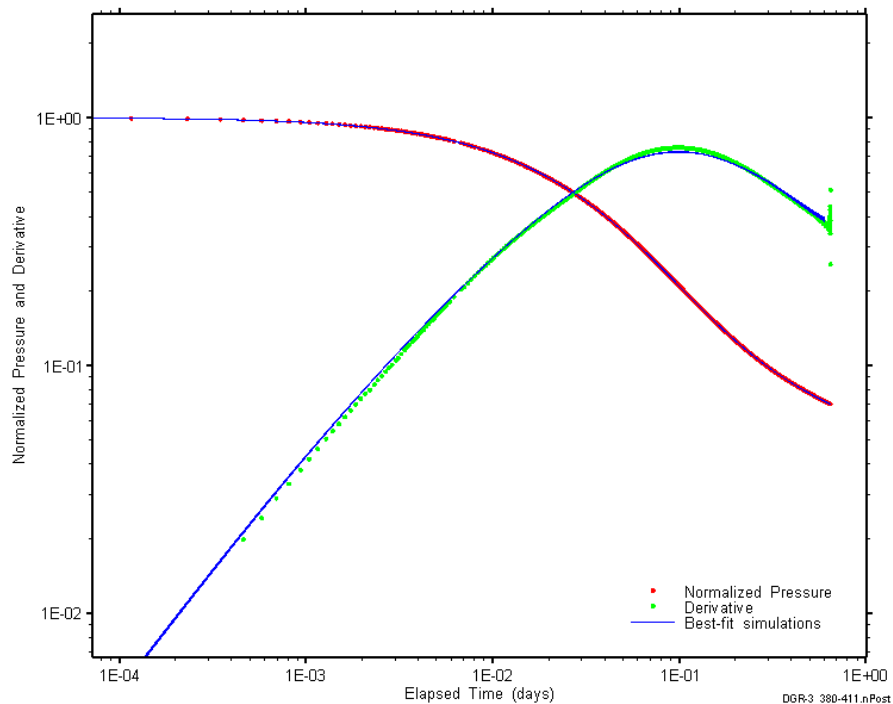


Figure C-93: Log-log plot showing simulations of the DGR3_378.98-410.72 slug withdrawal Ramey B and derivative response.

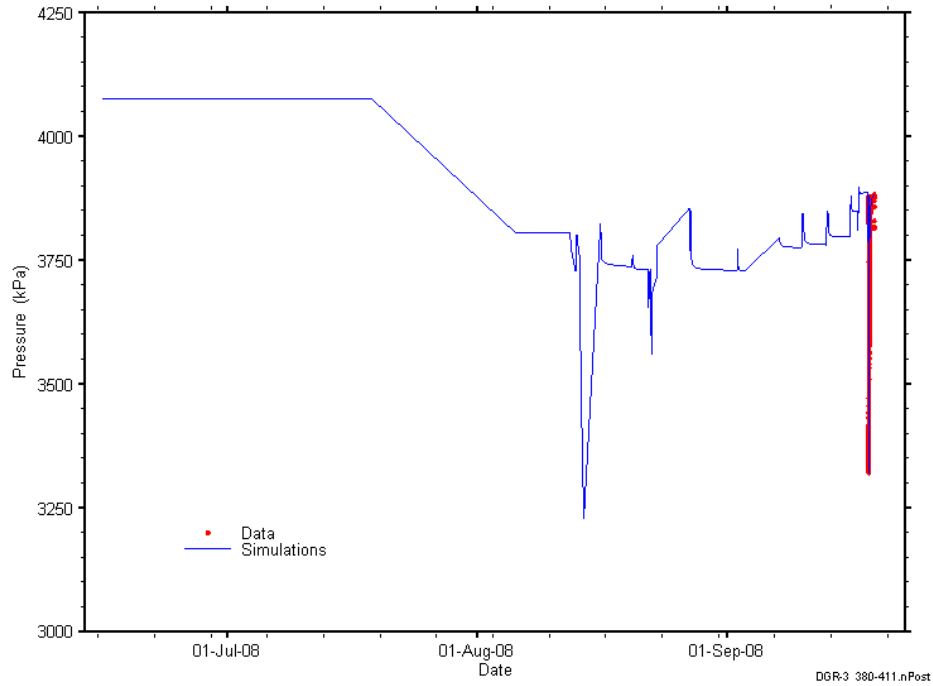


Figure C-94: Linear plot showing simulations of the DGR3_378.98-410.72 pressure response, including pre-test pressure history.

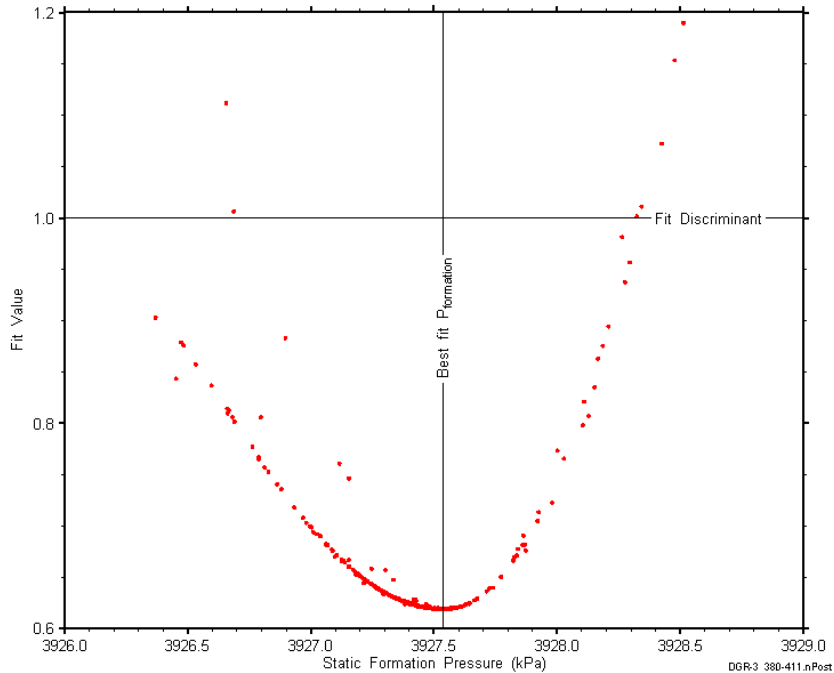


Figure C-95: XY-scatter plot showing the static formation pressure parameter space derived from DGR3_378.98-410.72 perturbation analysis along with the fit discriminant and best fit values.

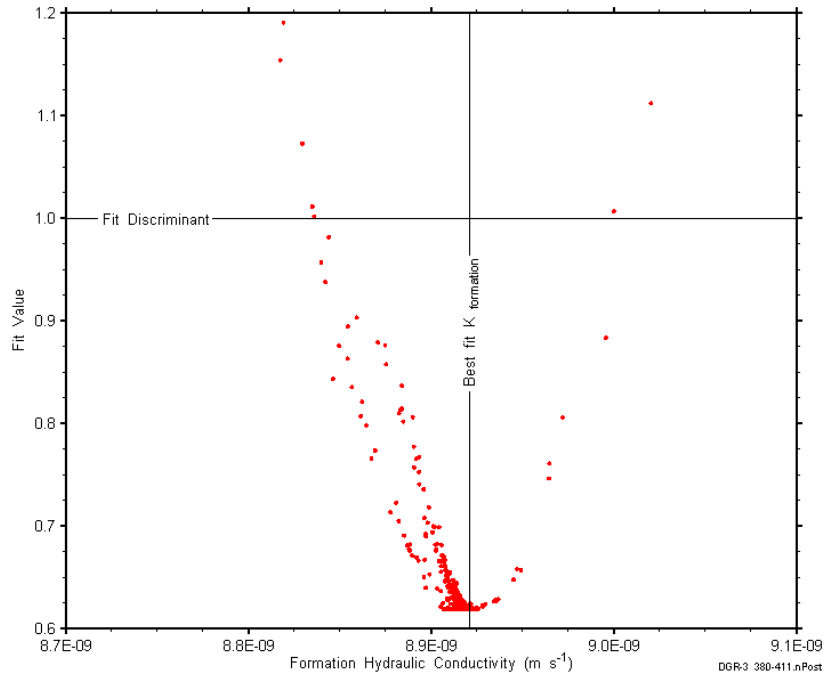


Figure C-96: XY-scatter plot showing the formation hydraulic conductivity parameter space derived from DGR3_378.98-410.72 perturbation analysis along with the fit discriminant and best fit values.

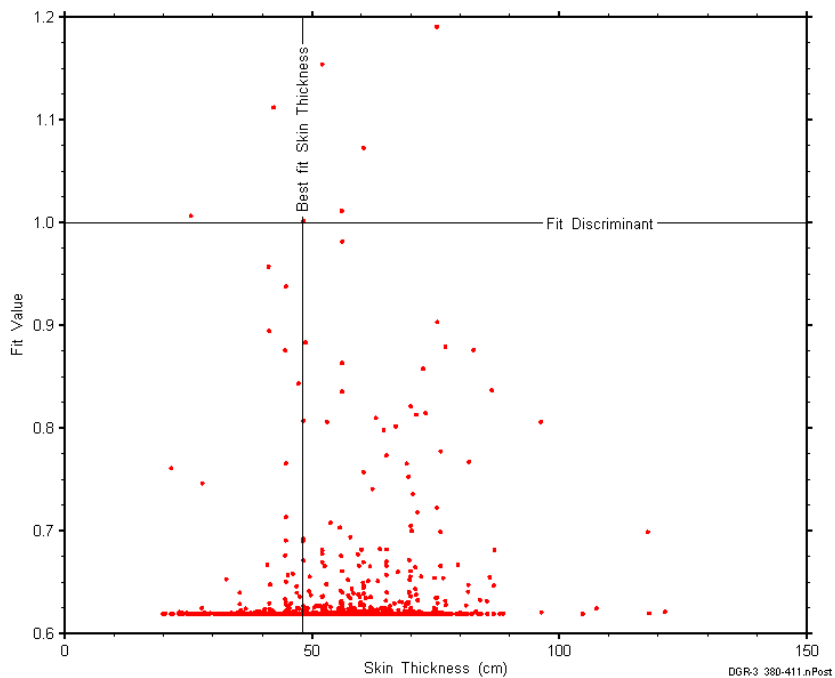


Figure C-97: XY-scatter plot showing the skin-thickness parameter space derived from DGR3_378.98-410.72 perturbation analysis along with the fit discriminant and best fit values.

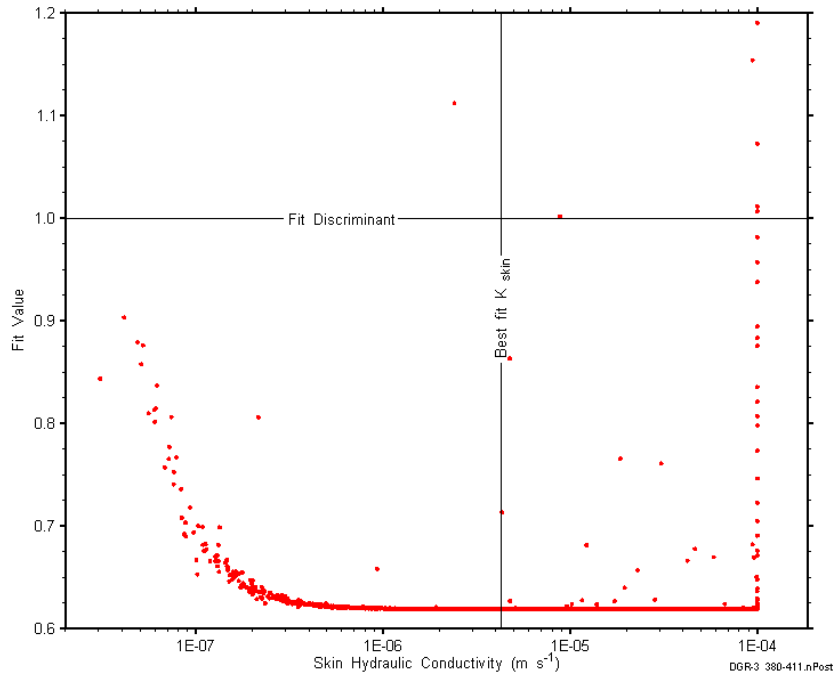


Figure C-98: XY-scatter plot showing the skin hydraulic conductivity parameter space derived from DGR3_378.98-410.72 perturbation analysis along with the fit discriminant and best fit values.

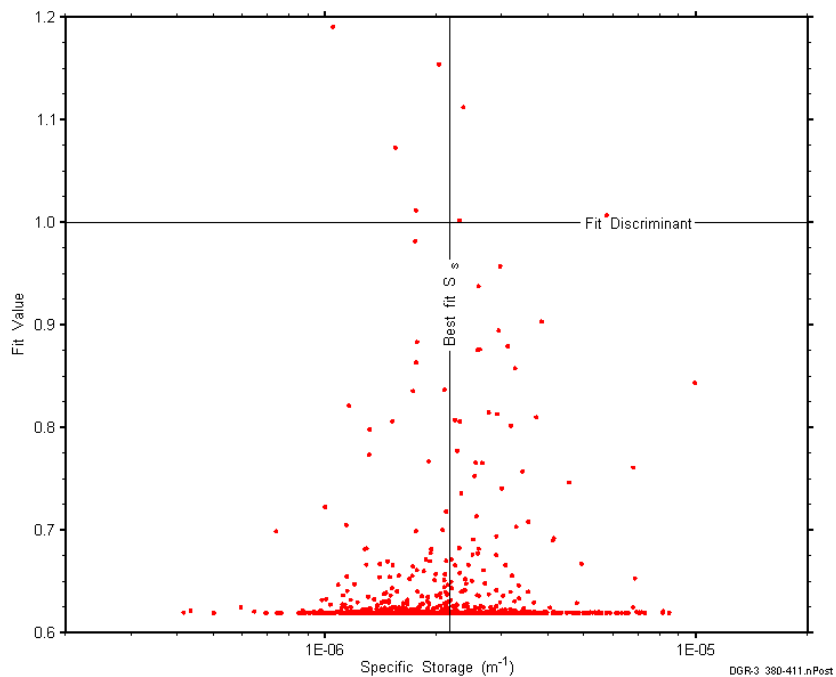


Figure C-99: XY-scatter plot showing the formation specific storage parameter space derived from DGR3_378.98-410.72 perturbation analysis along with the fit discriminant and best fit values.

C.8 410.51-441.25 Gasport-Lions Head-Fossil Hill-Cabot Head

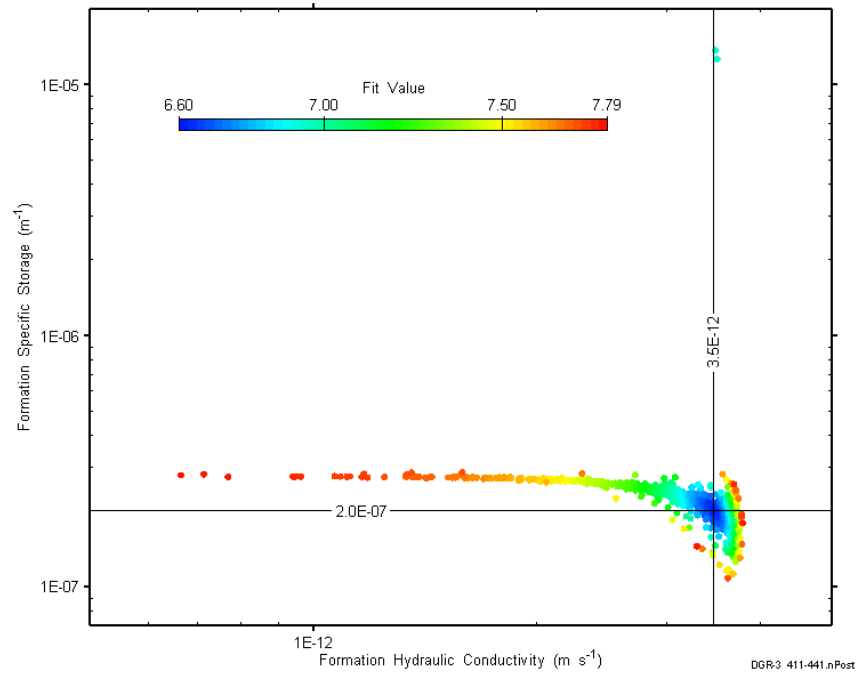


Figure C-100: XY-scatter plot showing estimates of formation hydraulic conductivity and formation specific storage derived from the DGR3_410.51-441.25 perturbation analysis.

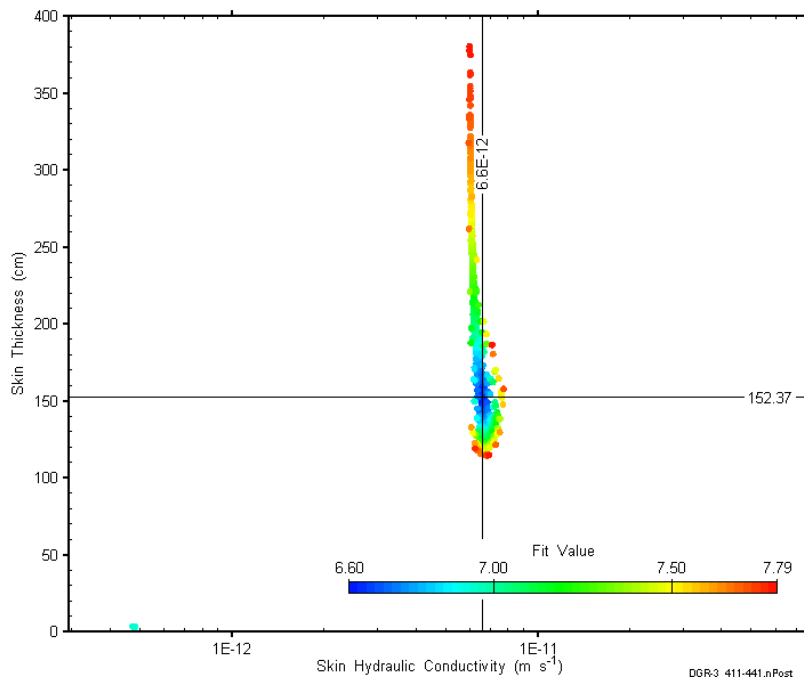


Figure C-101: XY-scatter plot showing estimates of skin hydraulic conductivity and skin thickness derived from the DGR3_410.51-441.25 perturbation analysis.

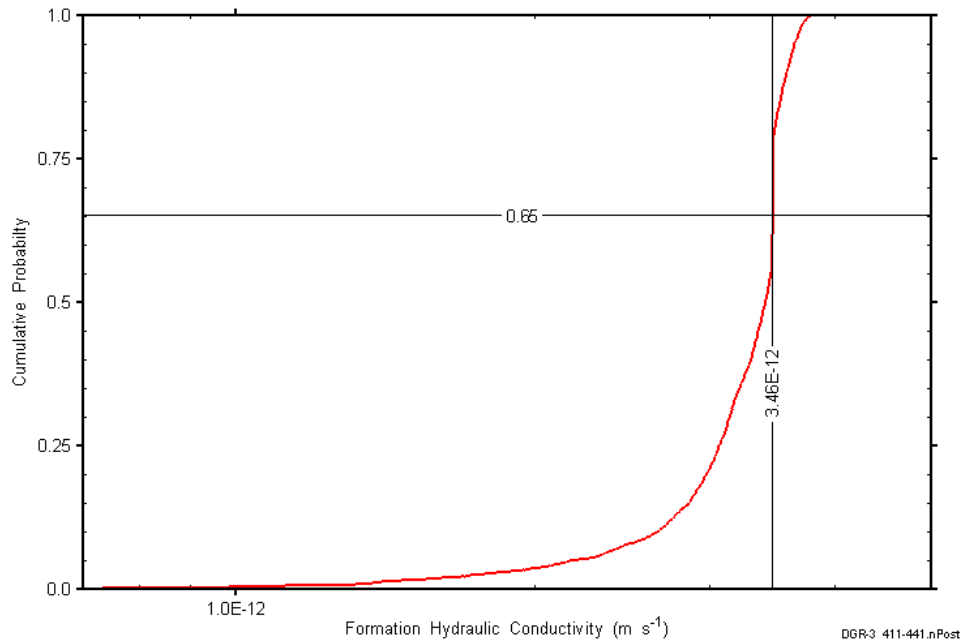


Figure C-102: DGR3_410.51-441.25 formation hydraulic conductivity cumulative distribution function.

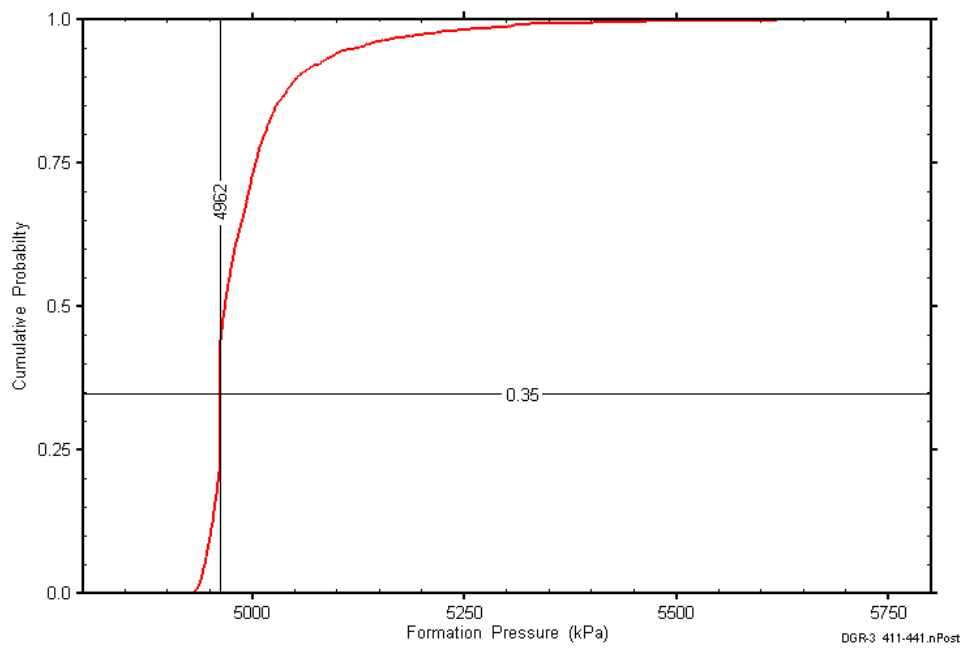


Figure C-103: DGR3_410.51-441.25 static formation pressure cumulative distribution function.

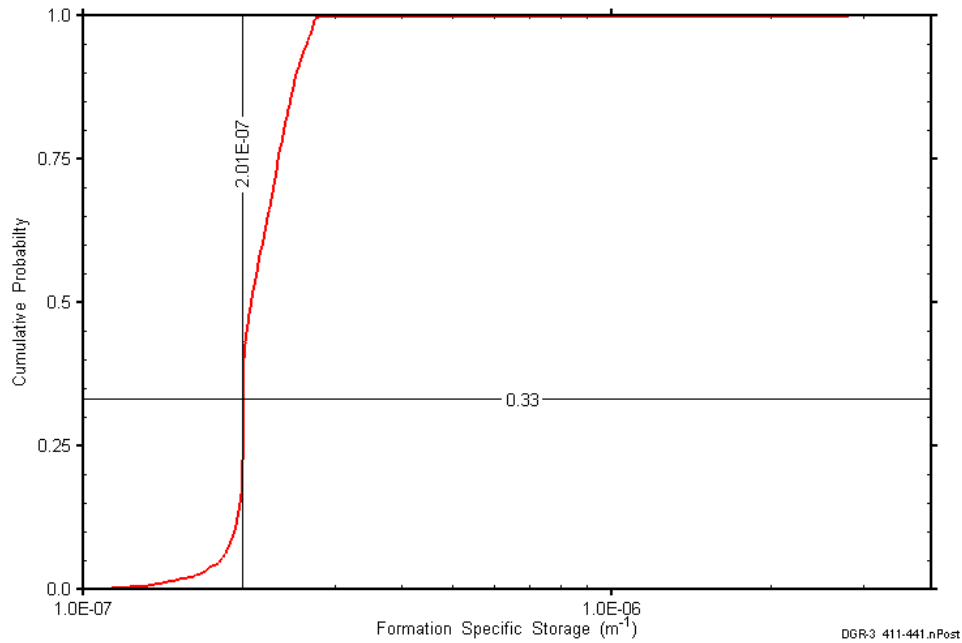


Figure C-104: DGR3_410.51-441.25 formation specific storage cumulative distribution function.

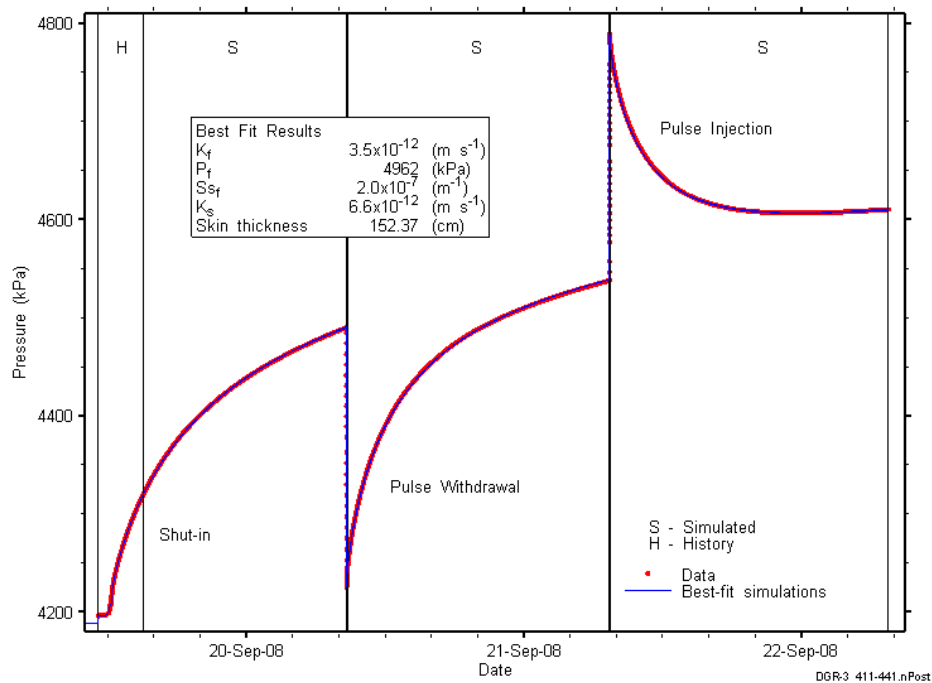


Figure C-105: Linear plot showing simulations of the DGR3_410.51-441.25 pressure response.

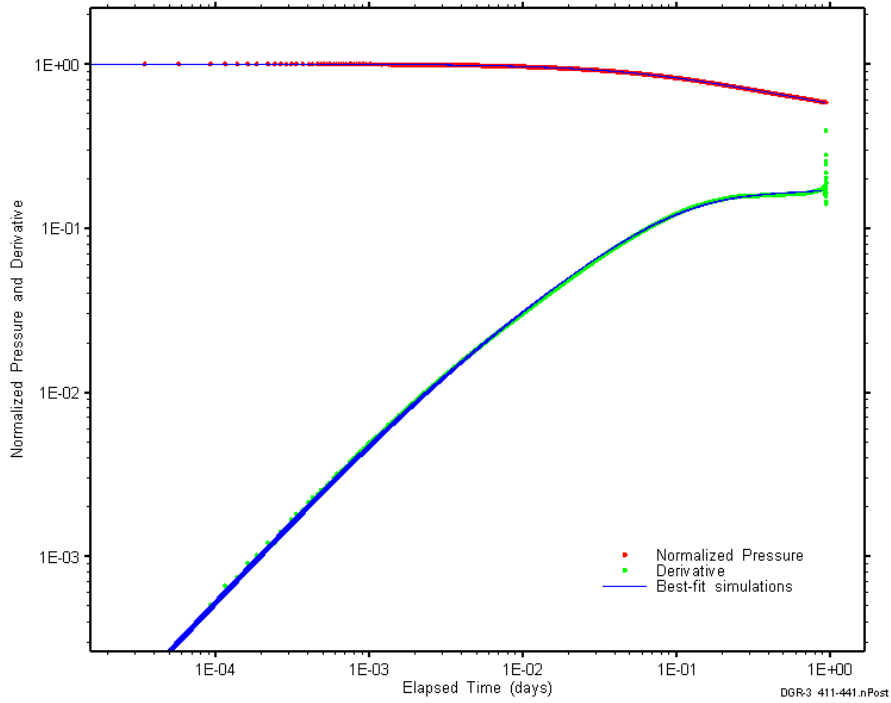


Figure C-106: Log-log plot showing simulations of the DGR3_410.51–441.25 pulse withdrawal Ramey B and derivative response.

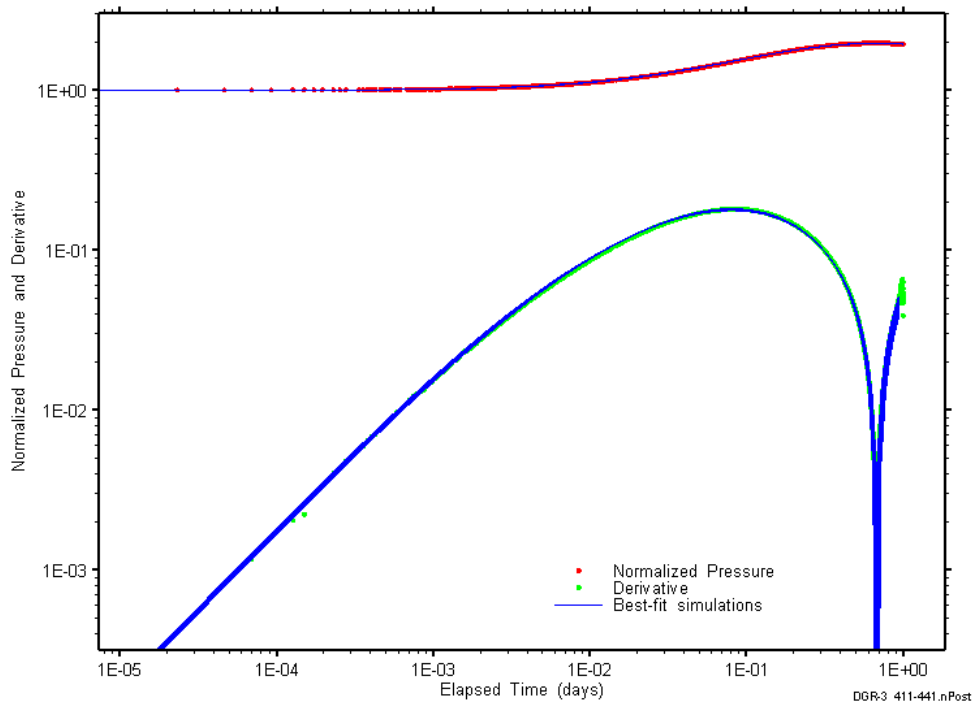


Figure C-107: Log-log plot showing simulations of the DGR3_410.51–441.25 pulse injection Ramey B and derivative response.

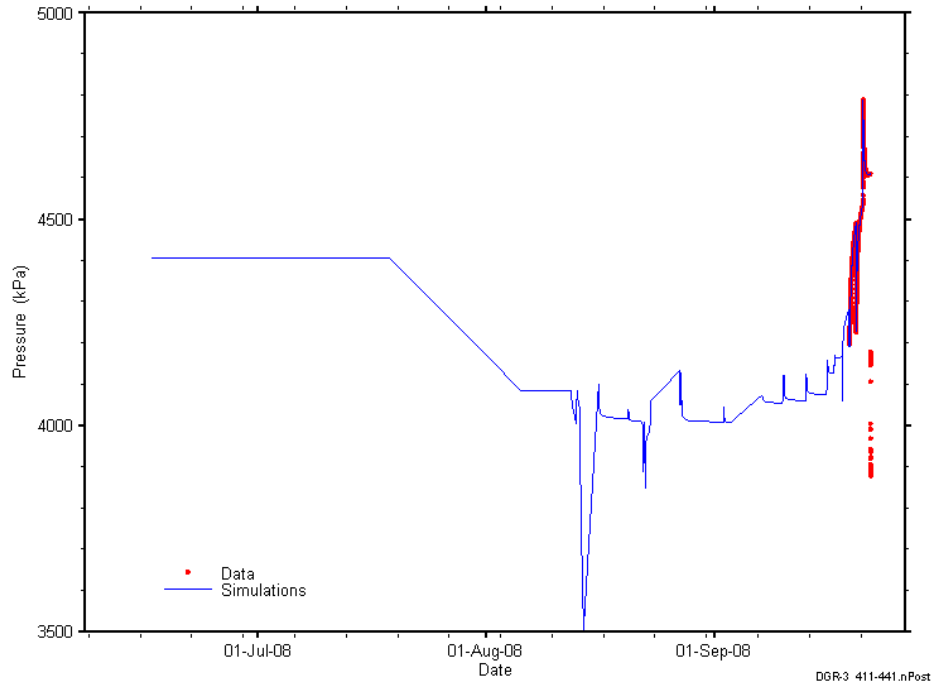


Figure C-108: Linear plot showing simulations of the DGR3_410.51-441.25 pressure response, including pre-test pressure history.

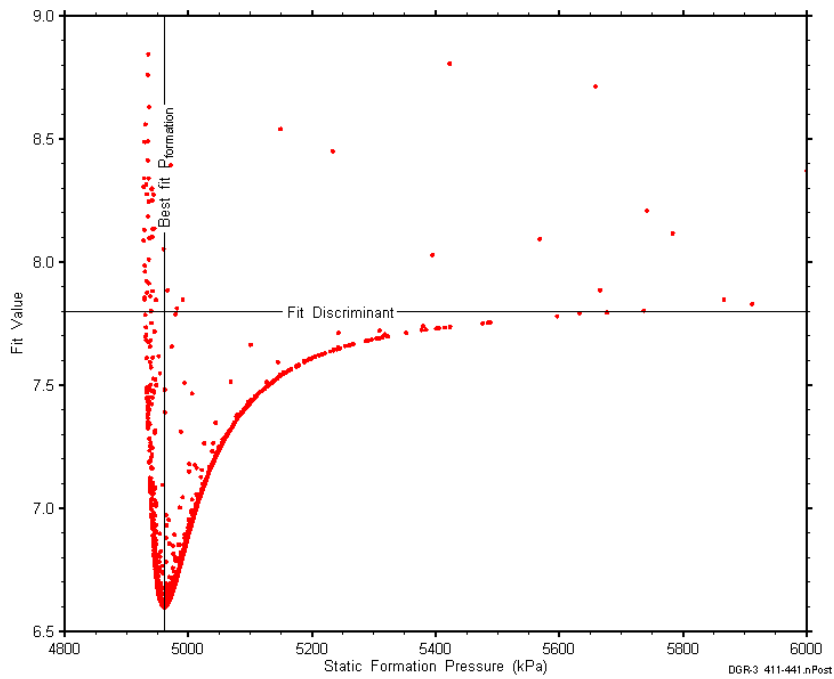


Figure C-109: XY-scatter plot showing the static formation pressure parameter space derived from DGR3_410.51-441.25 perturbation analysis along with the fit discriminant and best fit values.

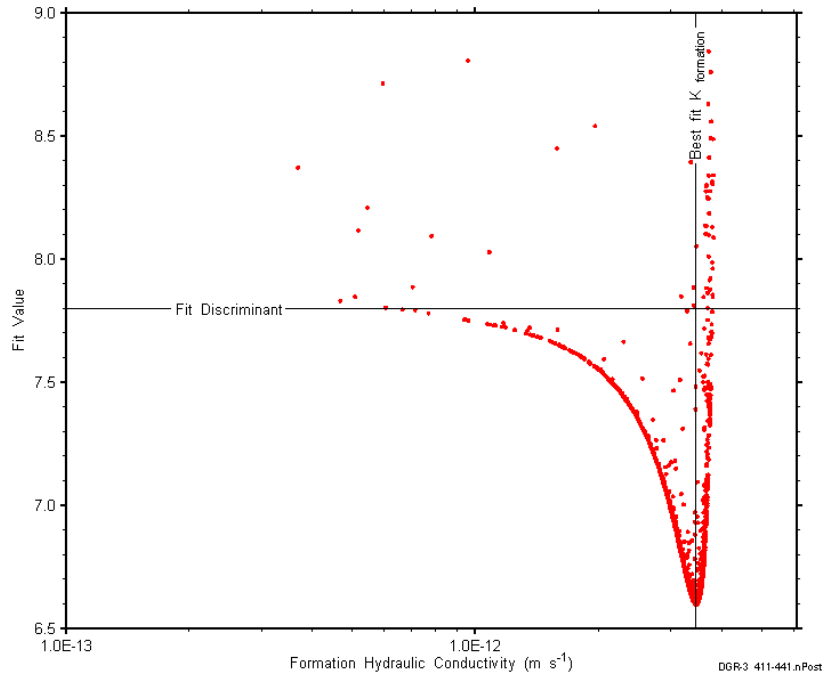


Figure C-110: XY-scatter plot showing the formation hydraulic conductivity parameter space derived from DGR3_410.51-441.25 perturbation analysis along with the fit discriminant and best fit values.

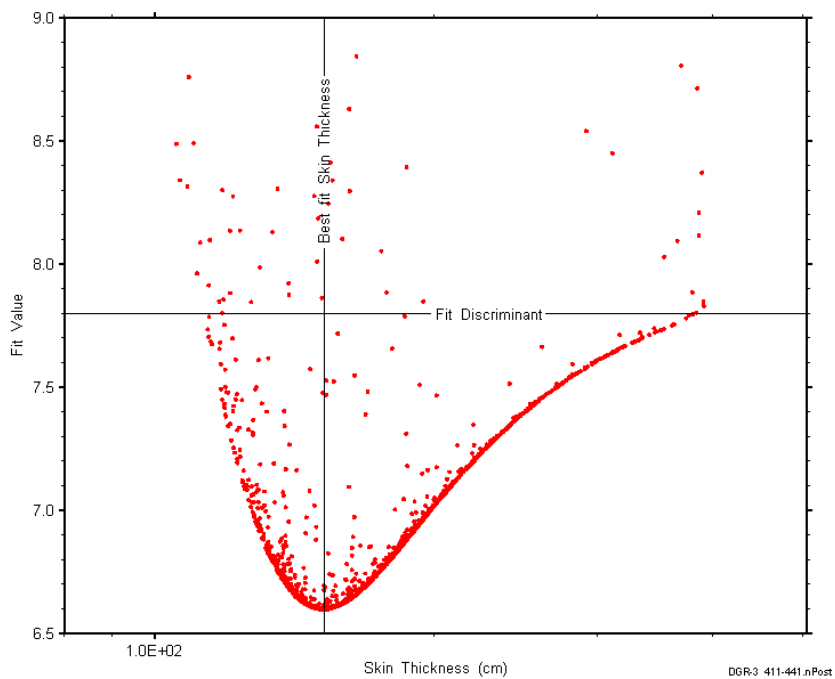


Figure C-111: XY-scatter plot showing the skin-thickness parameter space derived from DGR3_410.51-441.25 perturbation analysis along with the fit discriminant and best fit values.

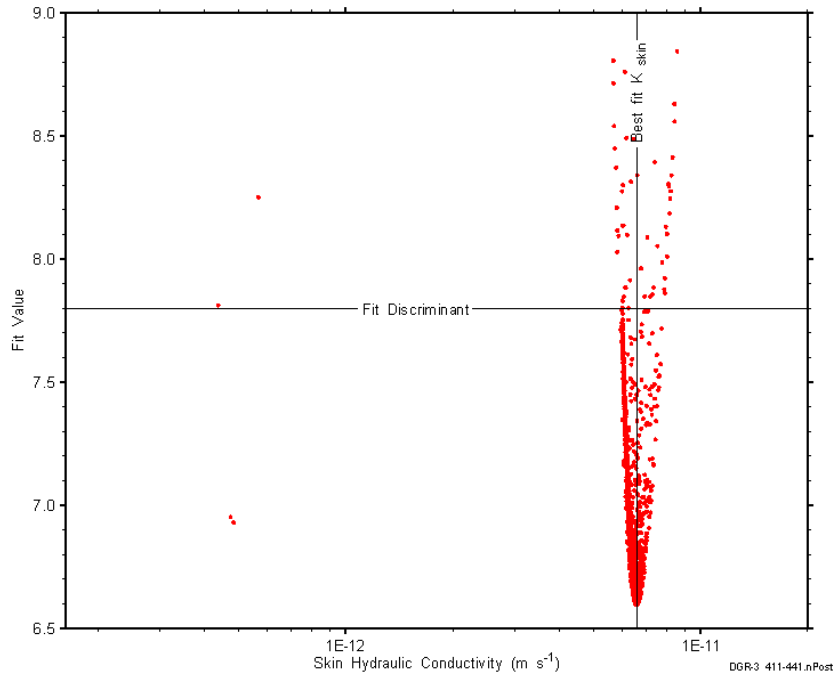


Figure C-112: XY-scatter plot showing the skin hydraulic conductivity parameter space derived from DGR3_410.51-441.25 perturbation analysis along with the fit discriminant and best fit values.

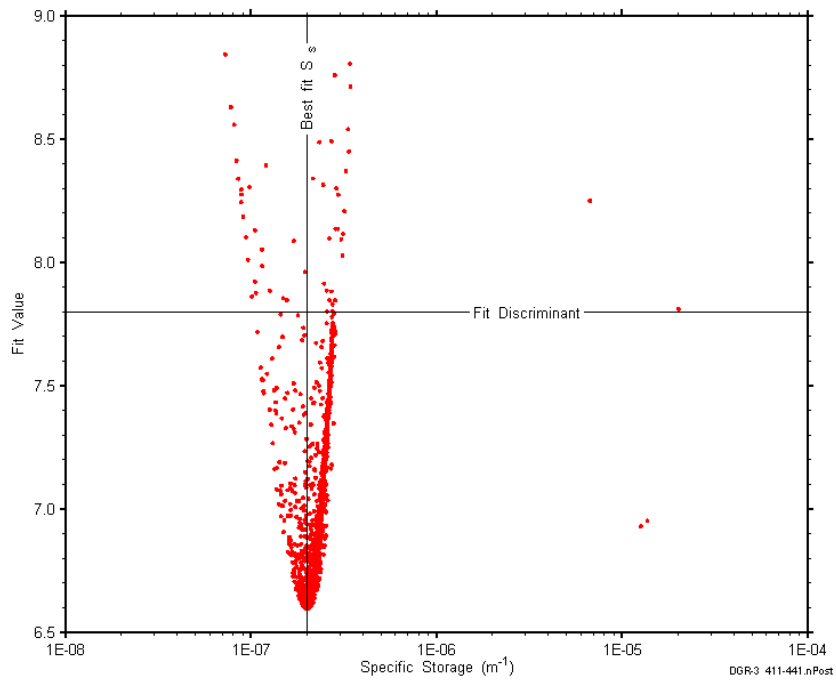


Figure C-113: XY-scatter plot showing the formation specific storage parameter space derived from DGR3_410.51-441.25 perturbation analysis along with the fit discriminant and best fit values.

C.9 441.05-471.79 Cabot Head-Manitoulin-Queenston

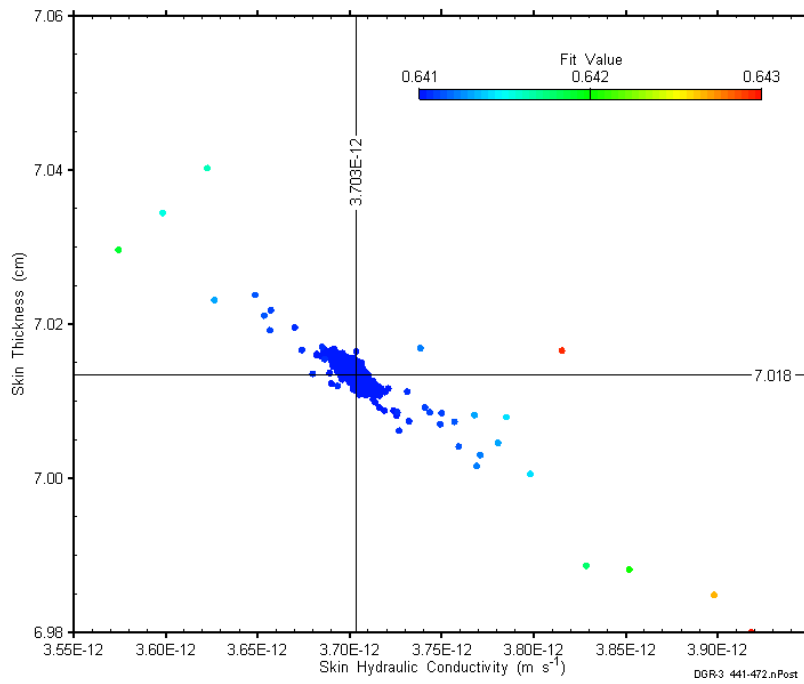


Figure C-114: XY-scatter plot showing estimates of skin hydraulic conductivity and skin thickness derived from the DGR3_441.05-471.79 perturbation analysis.

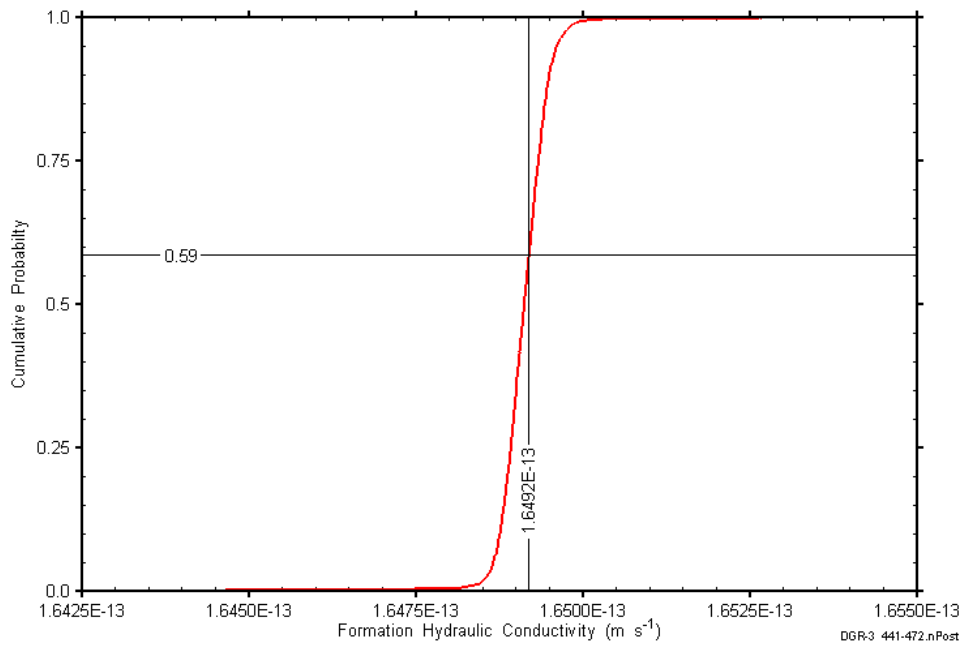


Figure C-115: DGR3_441.05-471.79 formation hydraulic conductivity cumulative distribution function.

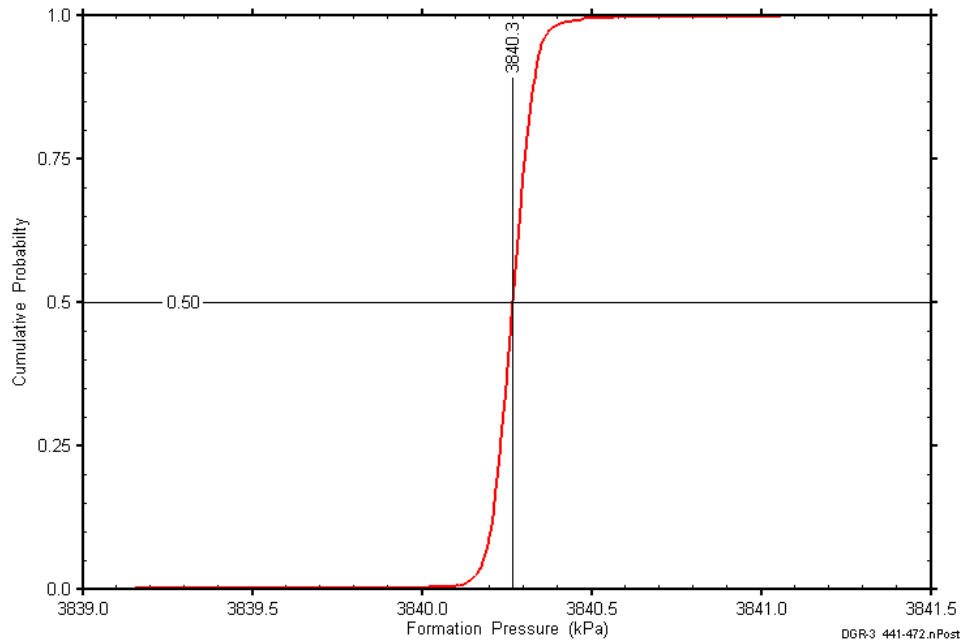


Figure C-116: DGR3_441.05-471.79 static formation pressure cumulative distribution function.

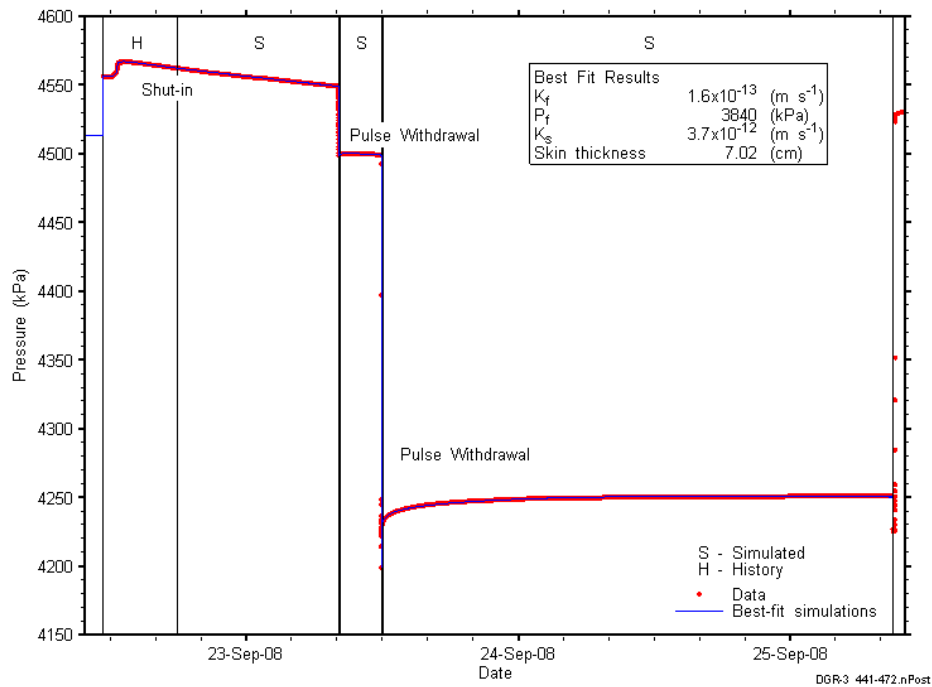


Figure C-117: Linear plot showing simulations of the DGR3_441.05-471.79 pressure response.

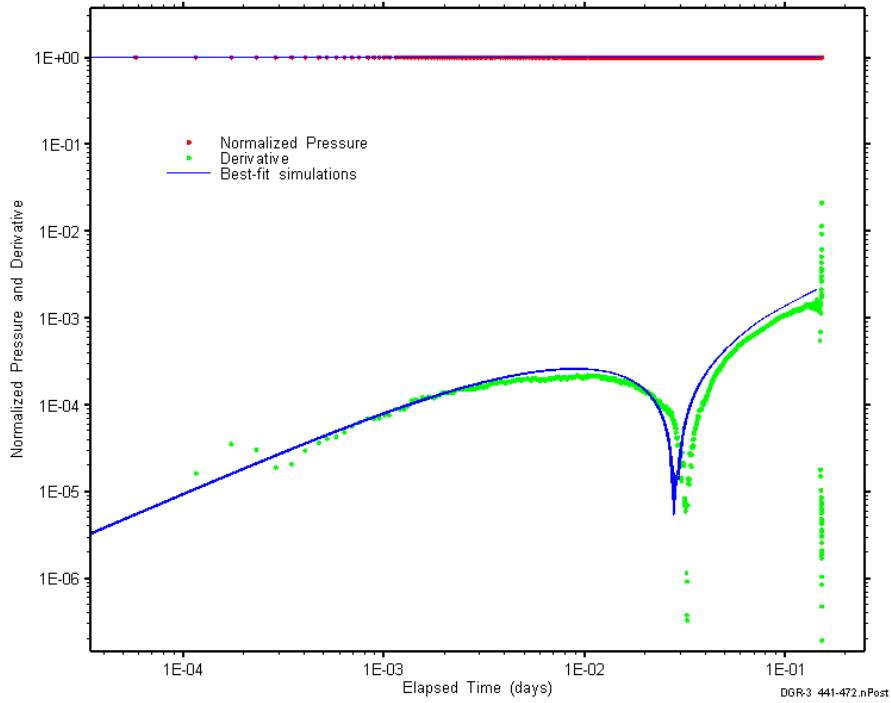


Figure C-118: Log-log plot showing simulations of the DGR3_441.05–471.79 pulse withdrawal #1 Ramey B and derivative response.

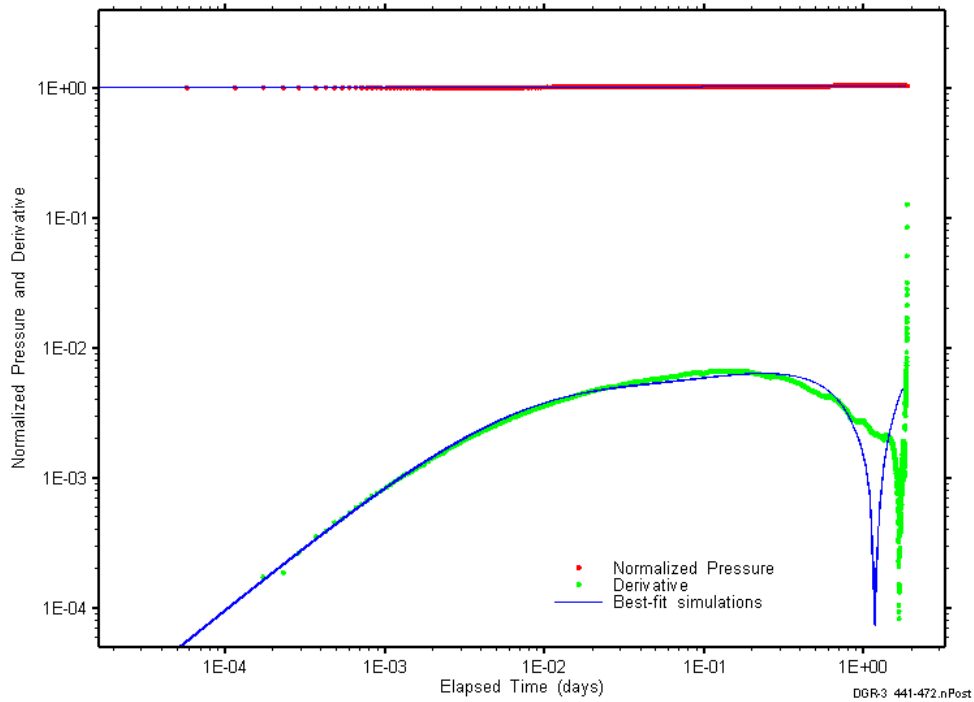


Figure C-119: Log-log plot showing simulations of the DGR3_441.05–471.79 pulse withdrawal #2 Ramey B and derivative response.

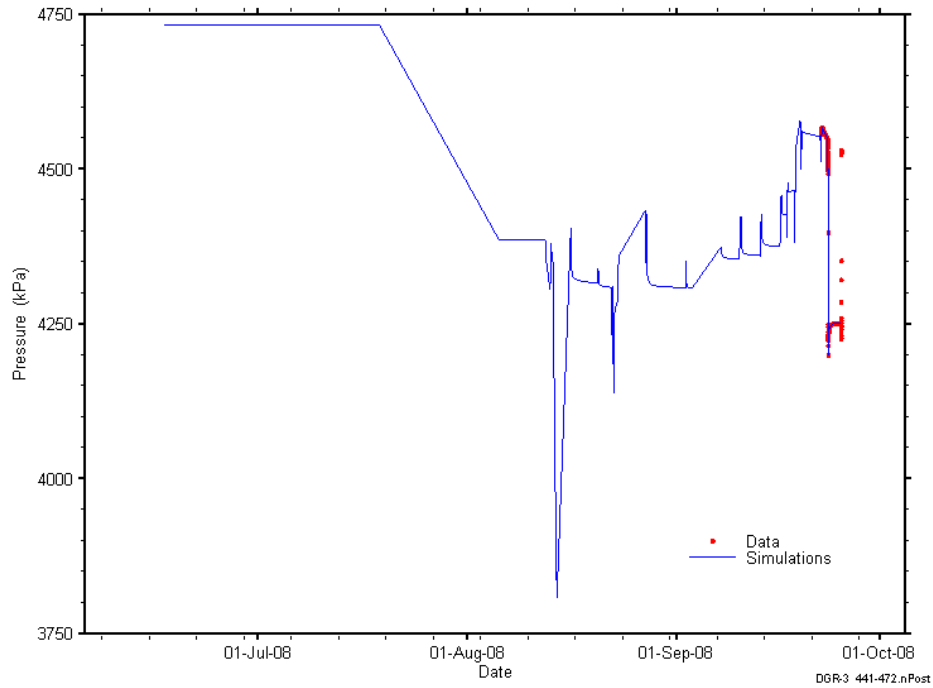


Figure C-120: Linear plot showing simulations of the DGR3_441.05-471.79 pressure response, including pre-test pressure history.

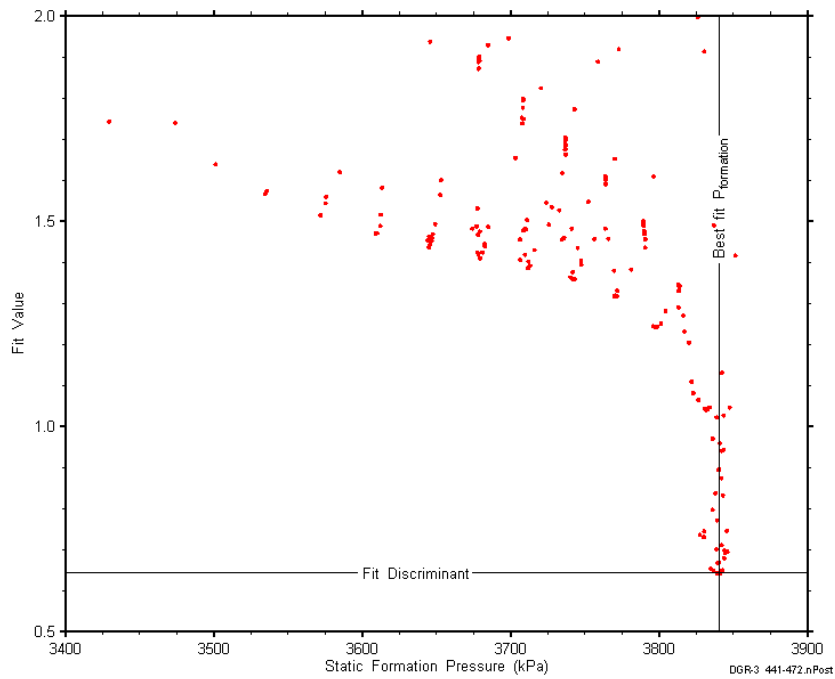


Figure C-121: XY-scatter plot showing the static formation pressure parameter space derived from DGR3_441.05-471.79 perturbation analysis along with the fit discriminant and best fit values.

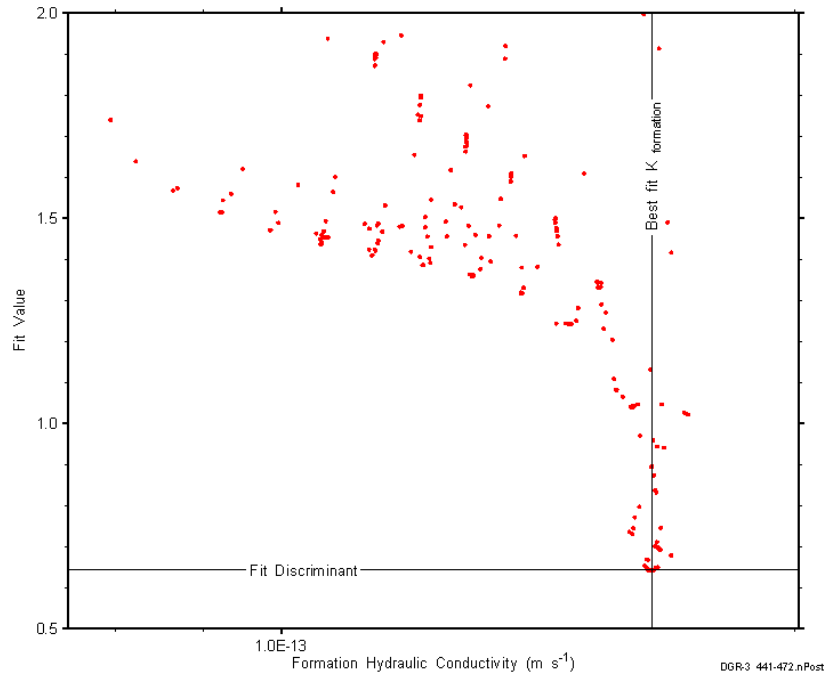


Figure C-122: XY-scatter plot showing the formation hydraulic conductivity parameter space derived from DGR3_441.05-471.79 perturbation analysis along with the fit discriminant and best fit values.

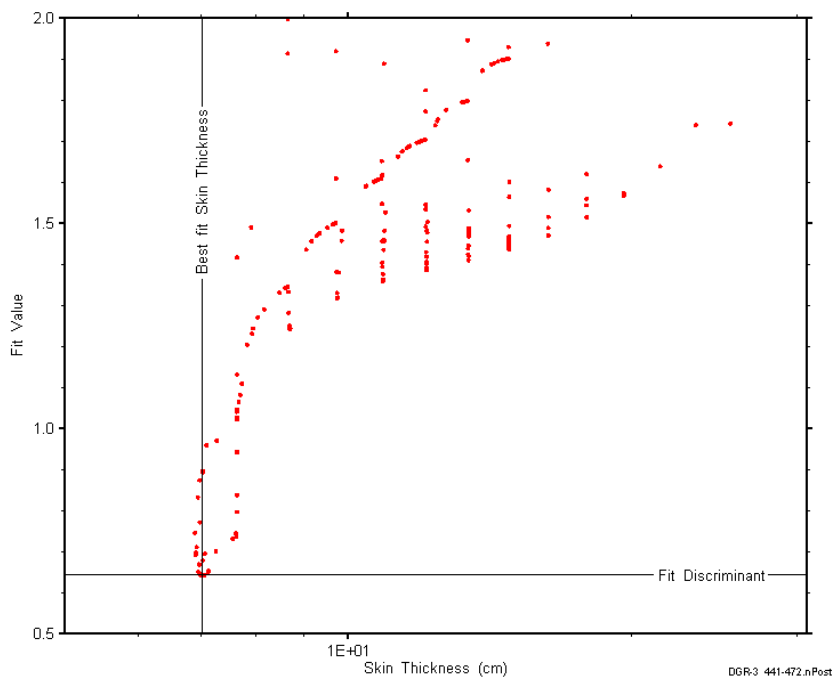


Figure C-123: XY-scatter plot showing the skin-thickness parameter space derived from DGR3_441.05-471.79 perturbation analysis along with the fit discriminant and best fit values.

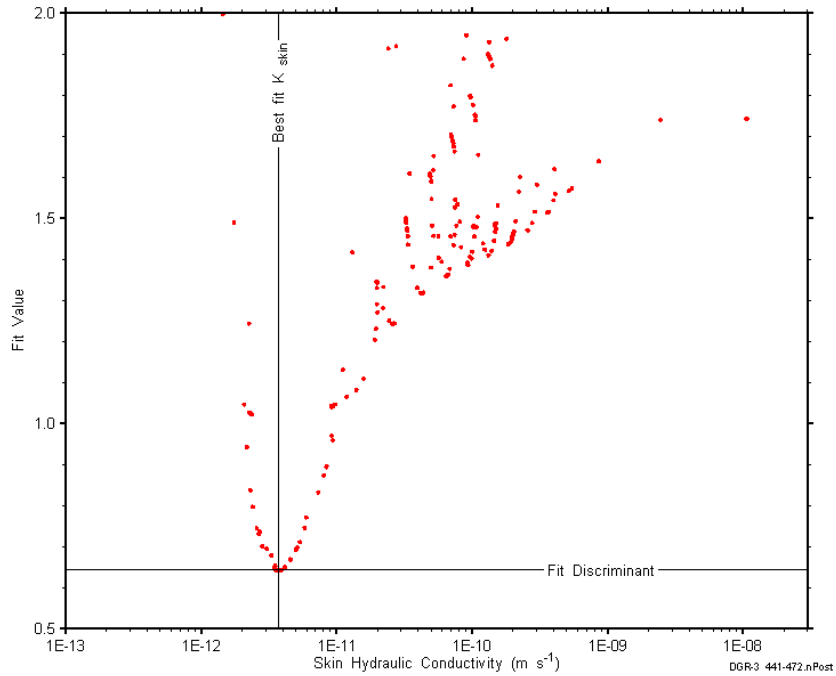


Figure C-124: XY-scatter plot showing the skin hydraulic conductivity parameter space derived from DGR3_441.05-471.79 perturbation analysis along with the fit discriminant and best fit values.

C.10 471.41-502.15 Queenston

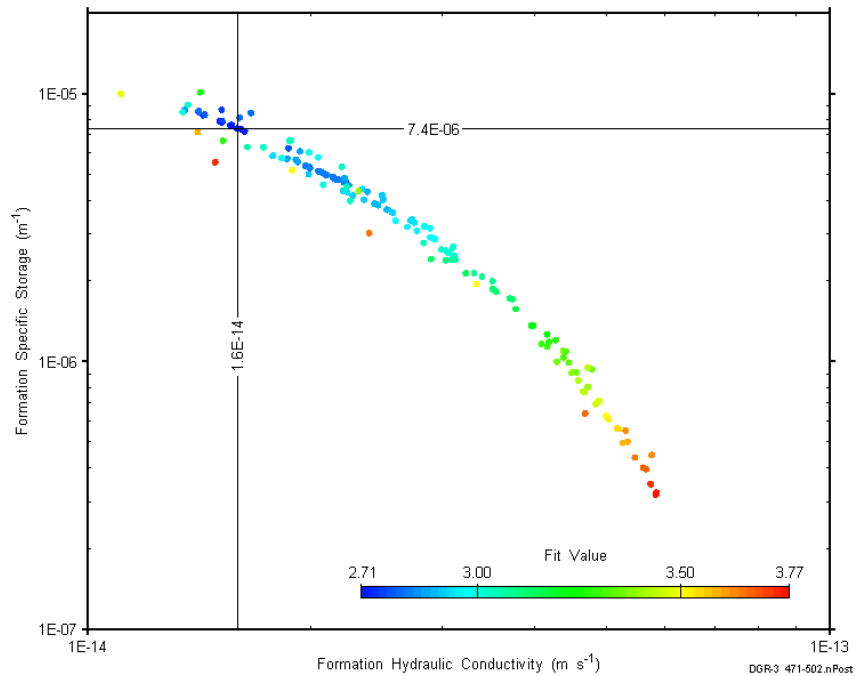


Figure C-125: XY-scatter plot showing estimates of formation hydraulic conductivity and formation specific storage derived from the DGR3_471.41-502.15 perturbation analysis.

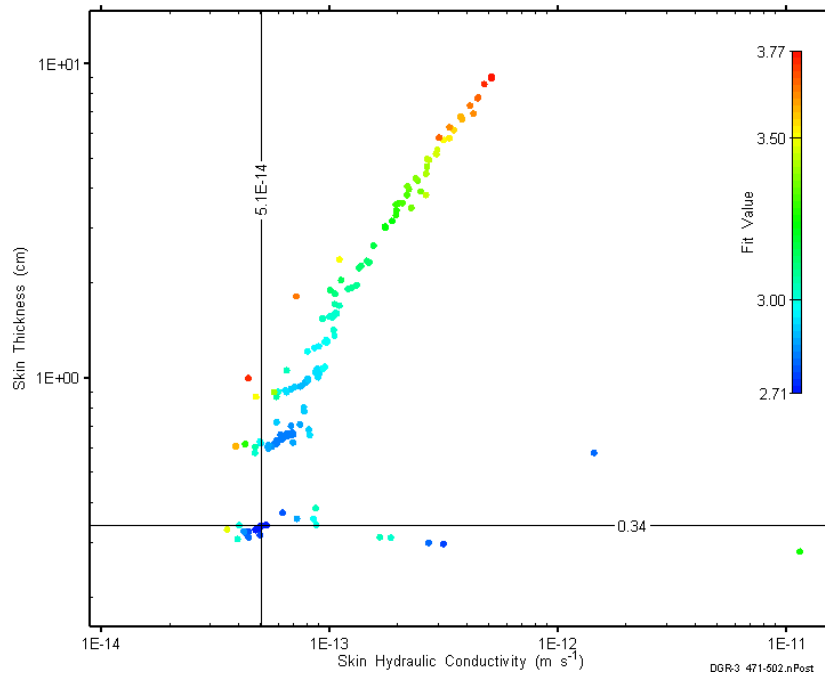


Figure C-126: XY-scatter plot showing estimates of skin hydraulic conductivity and skin thickness derived from the DGR3_471.41-502.15 perturbation analysis.

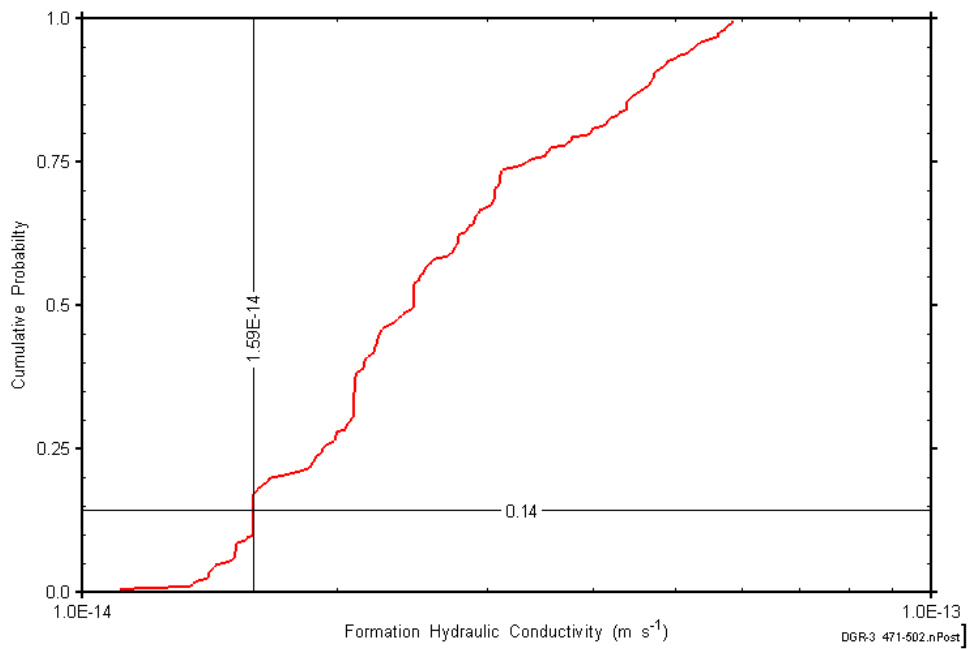


Figure C-127: DGR3_471.41-502.15 formation hydraulic conductivity cumulative distribution function.

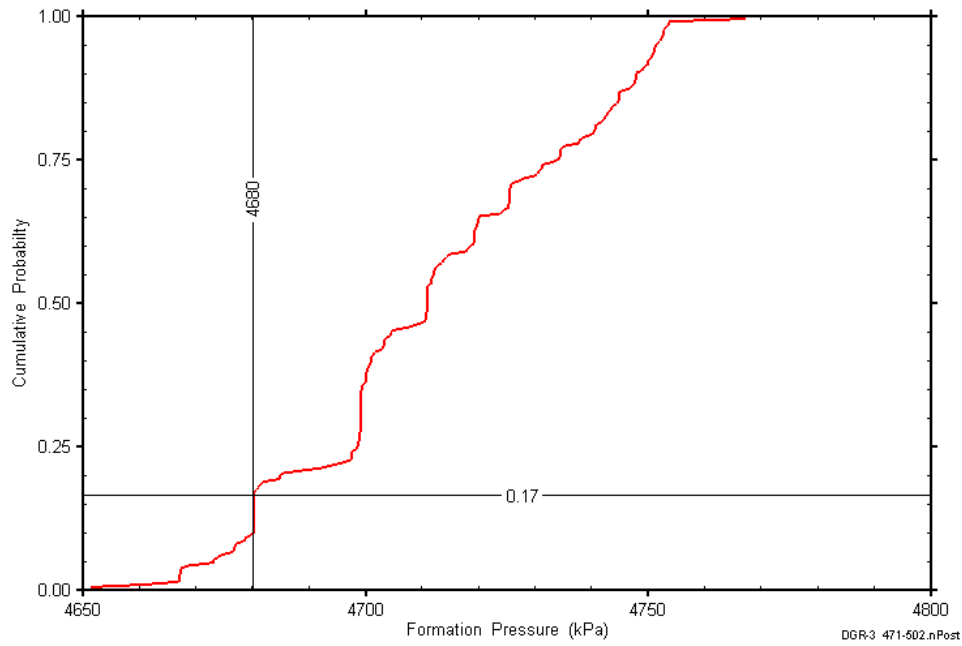


Figure C-128: DGR3_471.41-502.15 static formation pressure cumulative distribution function.

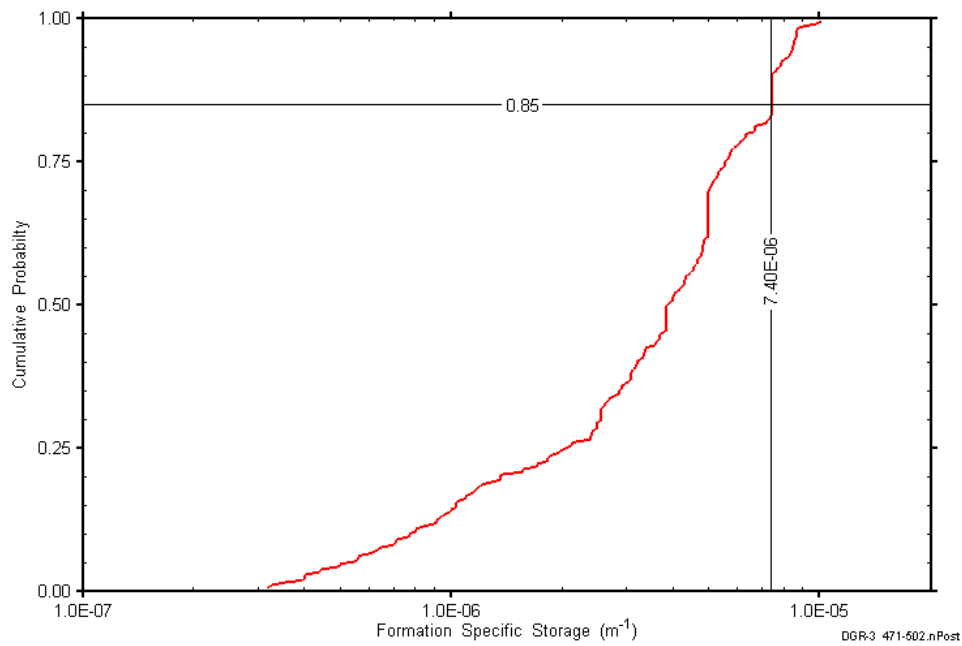


Figure C-129: DGR3_471.41-502.15 formation specific storage cumulative distribution function.

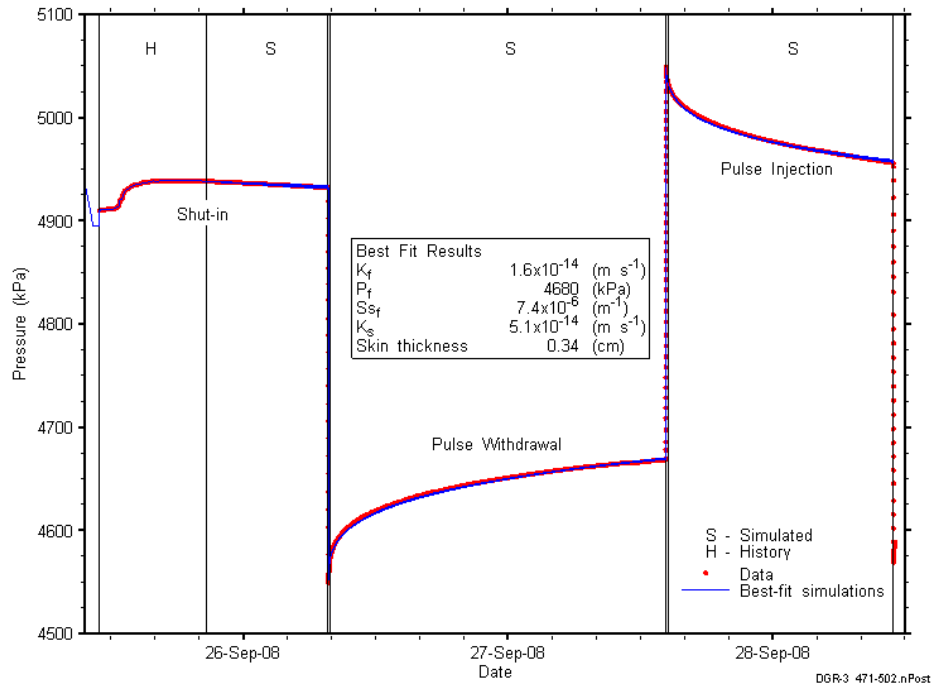


Figure C-130: Linear plot showing simulations of the DGR3_471.41-502.15 pressure response.

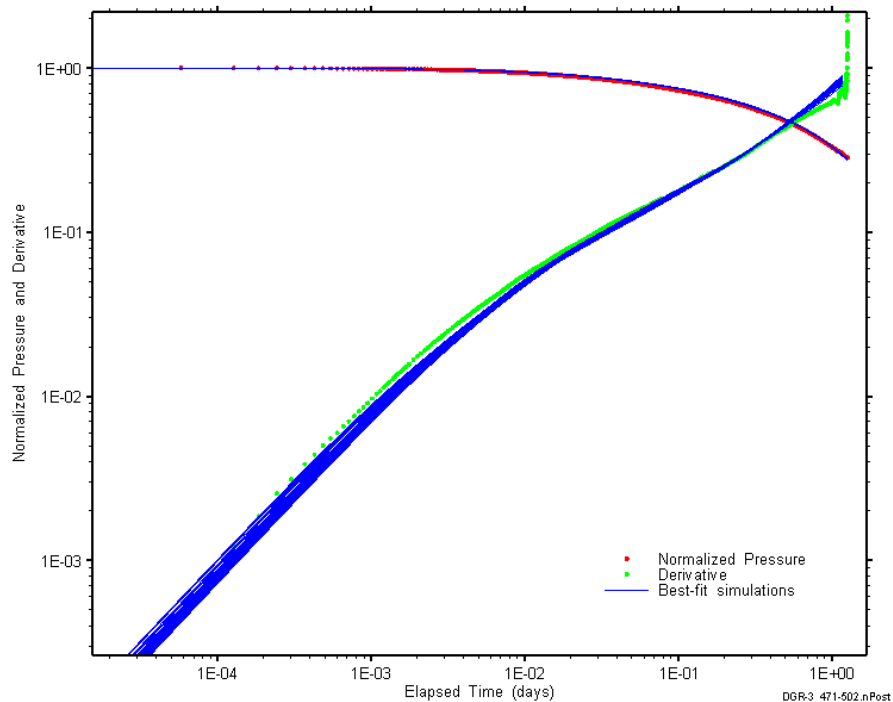


Figure C-131: Log-log plot showing simulations of the DGR3_471.41-502.15 pulse withdrawal Ramey B and derivative response.

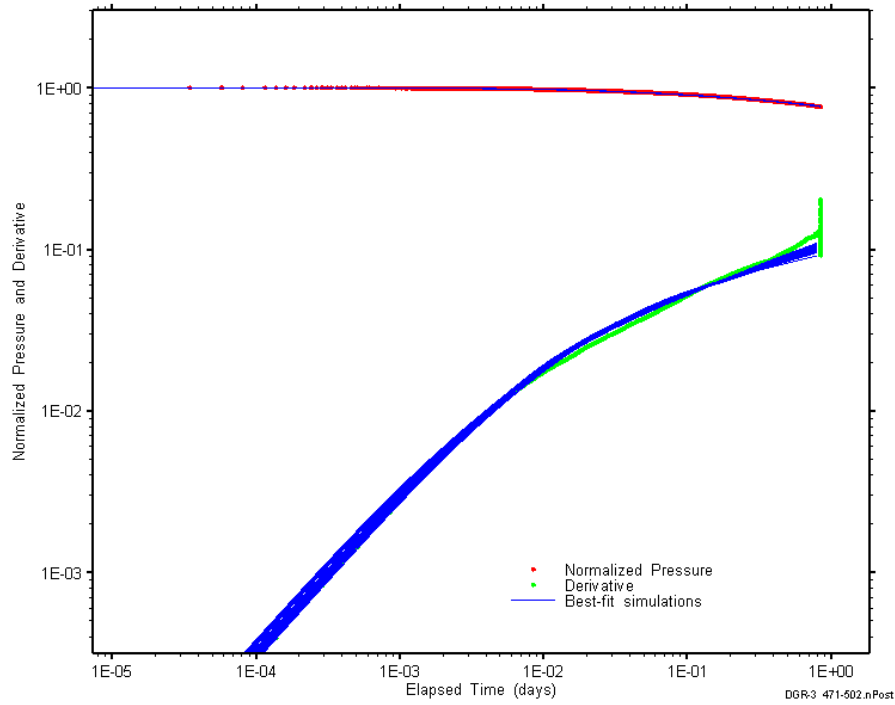


Figure C-132: Log-log plot showing simulations of the DGR3_471.41–502.15 pulse injection Ramey B and derivative response.

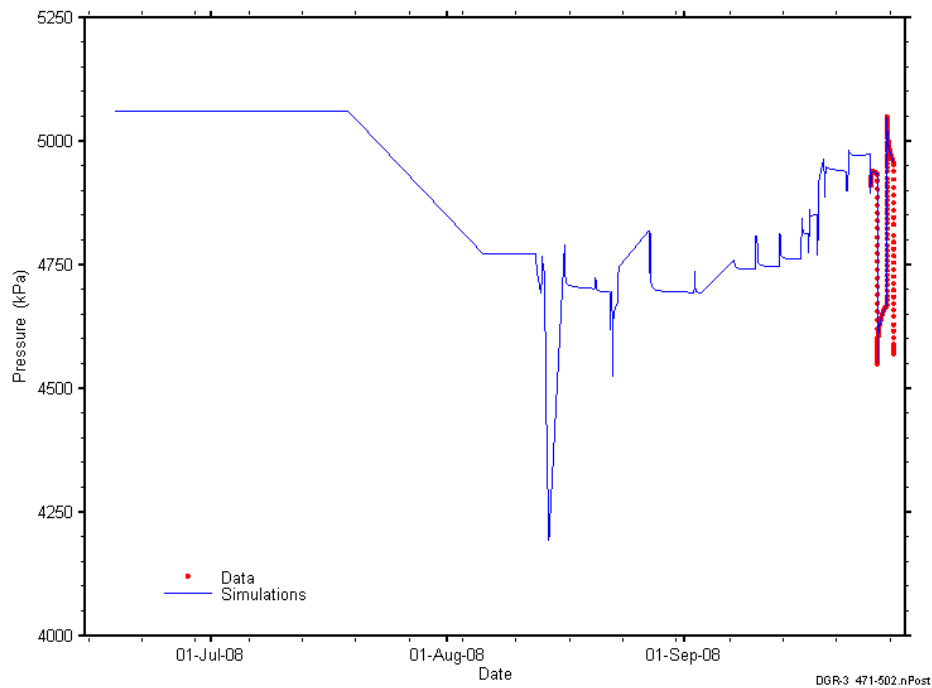


Figure C-133: Linear plot showing simulations of the DGR3_471.41-502.15 pressure response, including pre-test pressure history.

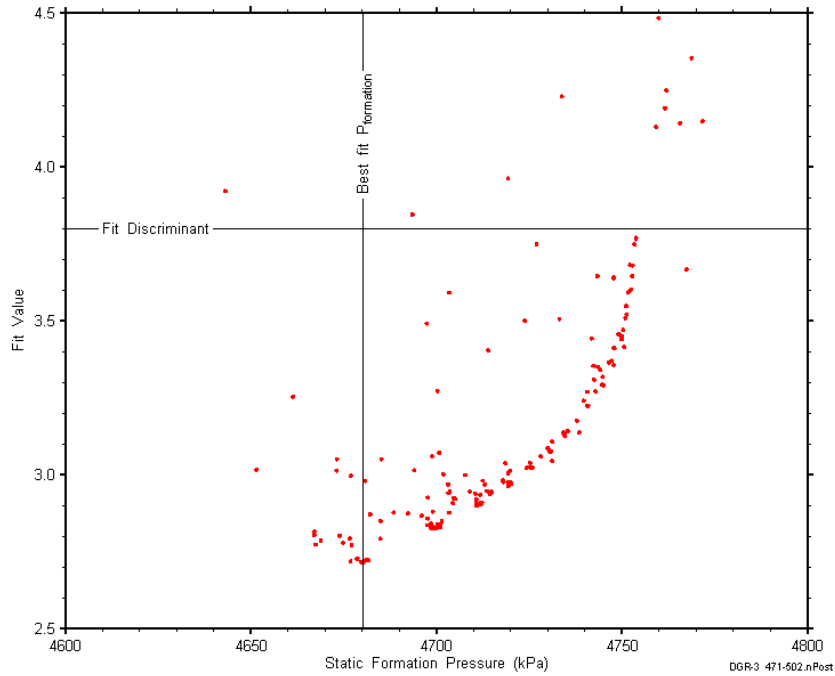


Figure C-134: XY-scatter plot showing the static formation pressure parameter space derived from DGR3_471.41-502.15 perturbation analysis along with the fit discriminant and best fit values.

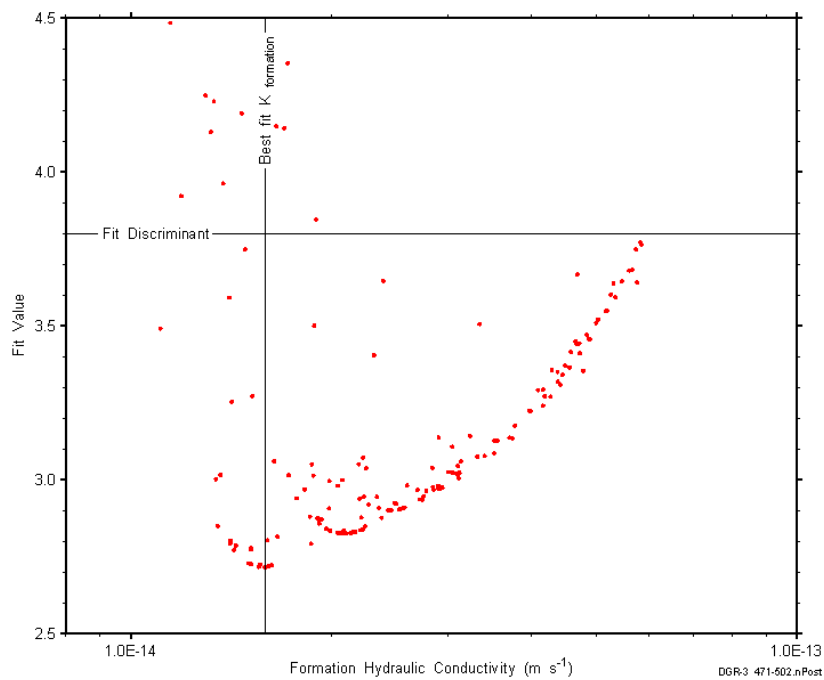


Figure C-135: XY-scatter plot showing the formation hydraulic conductivity parameter space derived from DGR3_471.41-502.15 perturbation analysis along with the fit discriminant and best fit values.

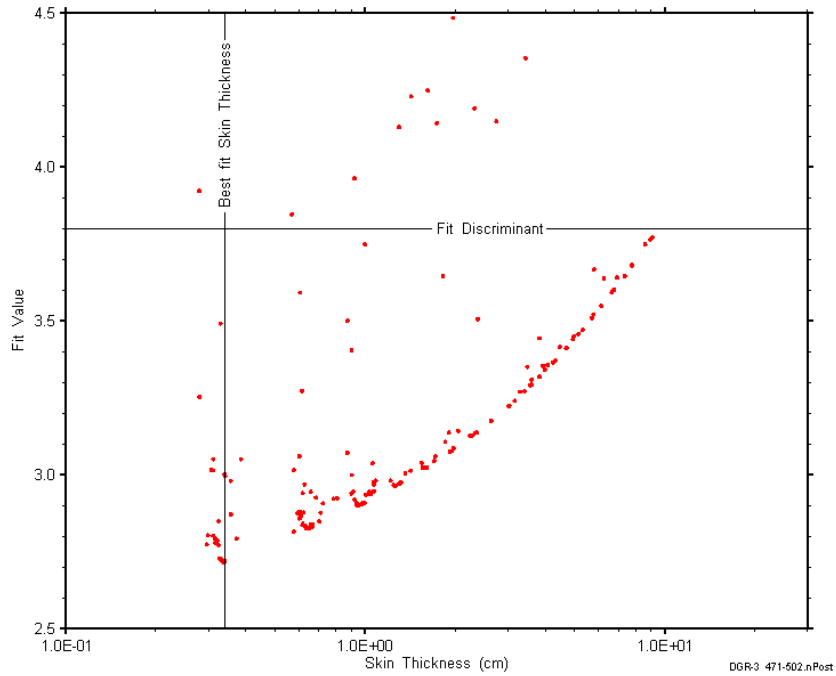


Figure C-136: XY-scatter plot showing the skin-thickness parameter space derived from DGR3_471.41-502.15 perturbation analysis along with the fit discriminant and best fit values.

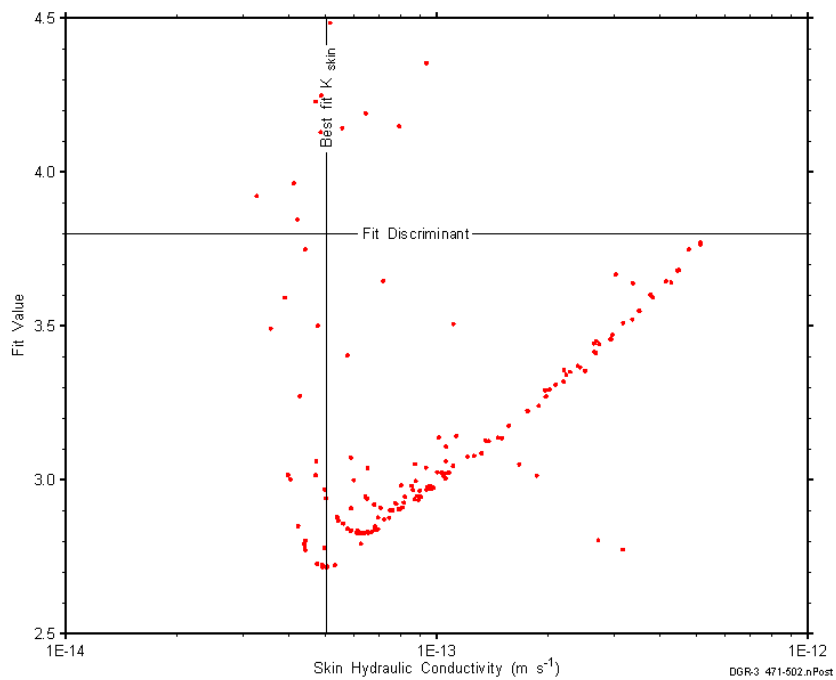


Figure C-137: XY-scatter plot showing the skin hydraulic conductivity parameter space derived from DGR3_471.41-502.15 perturbation analysis along with the fit discriminant and best fit values.

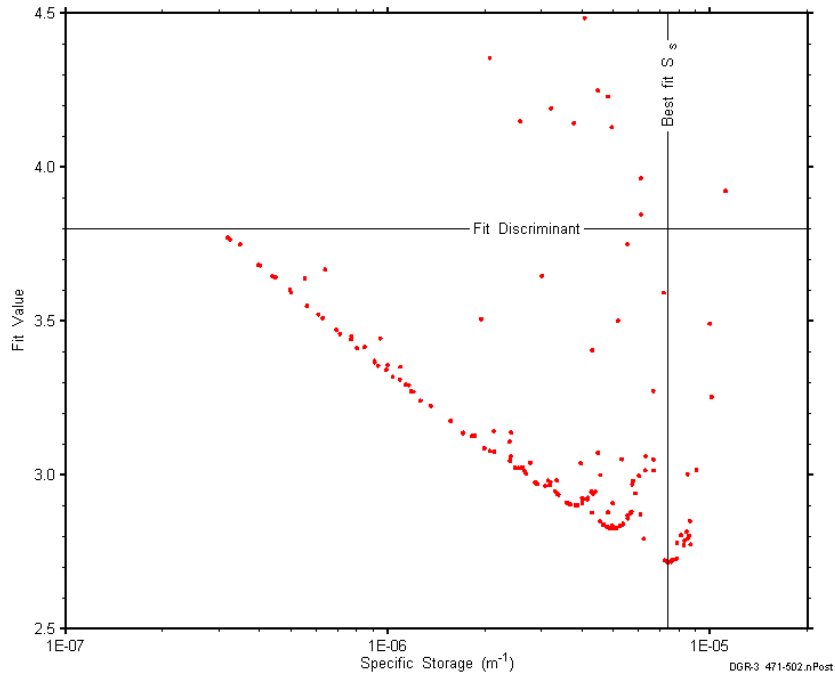


Figure C-138: XY-scatter plot showing the formation specific storage parameter space derived from DGR3_471.41-502.15 perturbation analysis along with the fit discriminant and best fit values.

C.11 501.95-532.69 Queenston-Georgian Bay

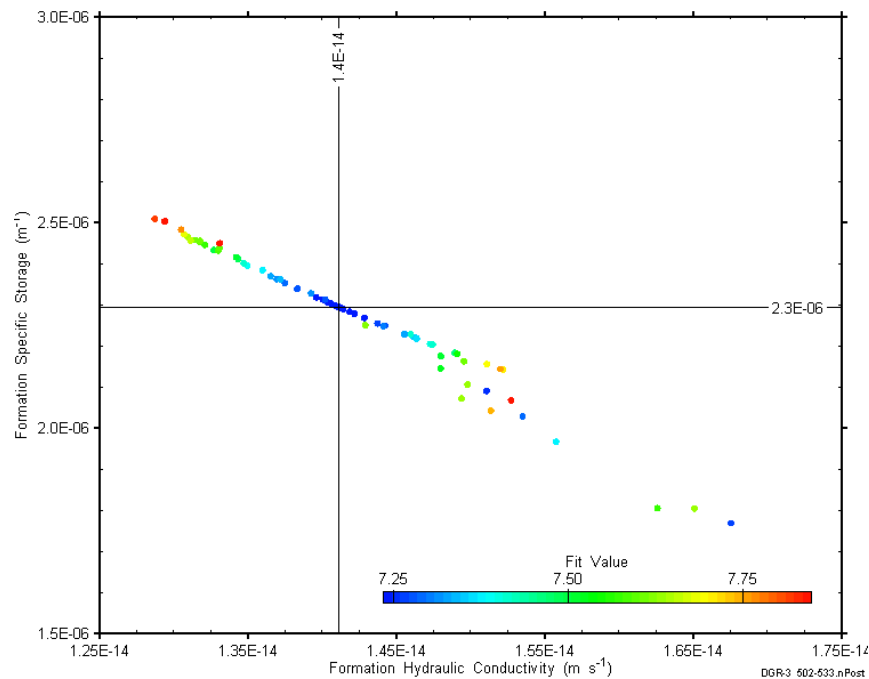


Figure C-139: XY-scatter plot showing estimates of formation hydraulic conductivity and formation specific storage derived from the DGR3_501.95-532.69 perturbation analysis.

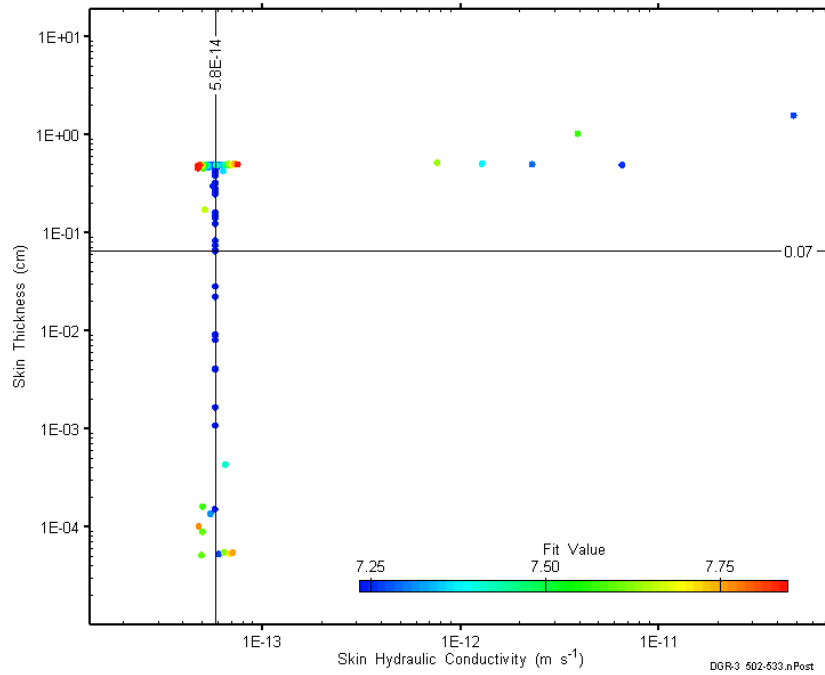


Figure C-140: XY-scatter plot showing estimates of skin hydraulic conductivity and skin thickness derived from the DGR3_501.95-532.69 perturbation analysis.

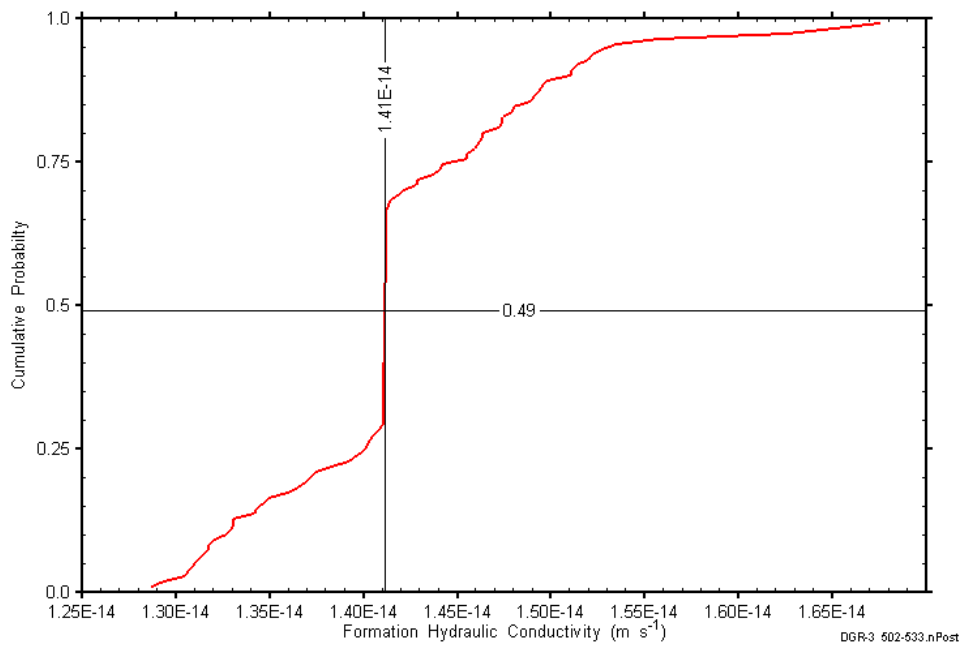


Figure C-141: DGR3_501.95-532.69 formation hydraulic conductivity cumulative distribution function.

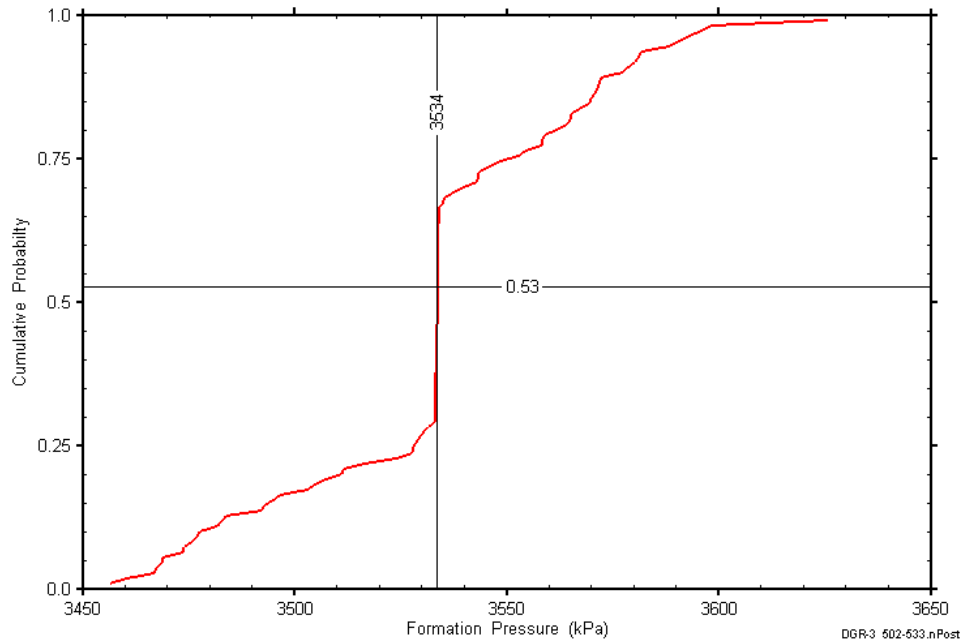


Figure C-142: DGR3_501.95-532.69 static formation pressure cumulative distribution function.

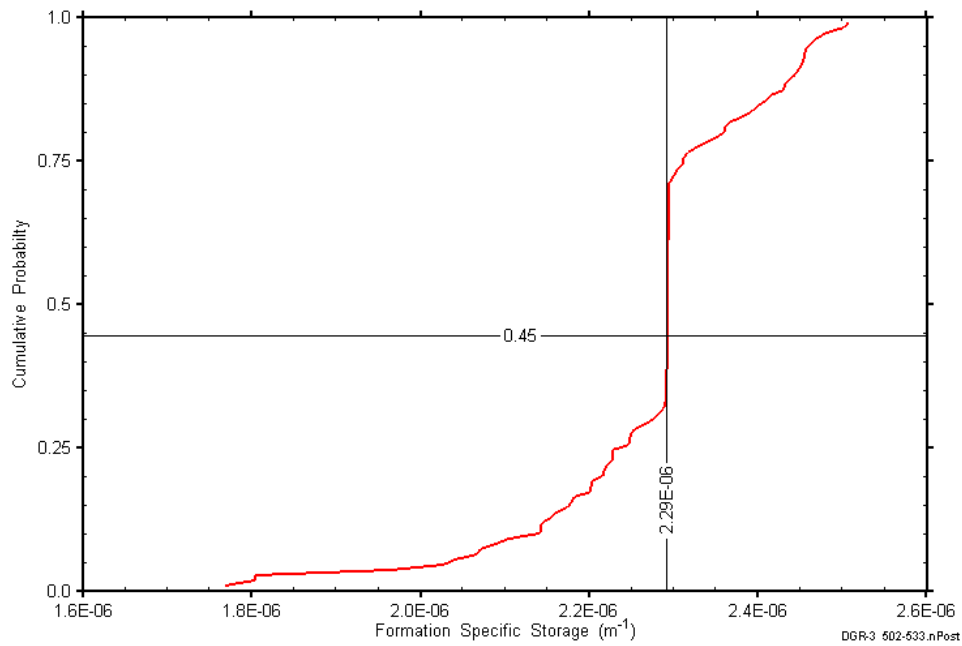


Figure C-143: DGR3_501.95-532.69 formation specific storage cumulative distribution function.

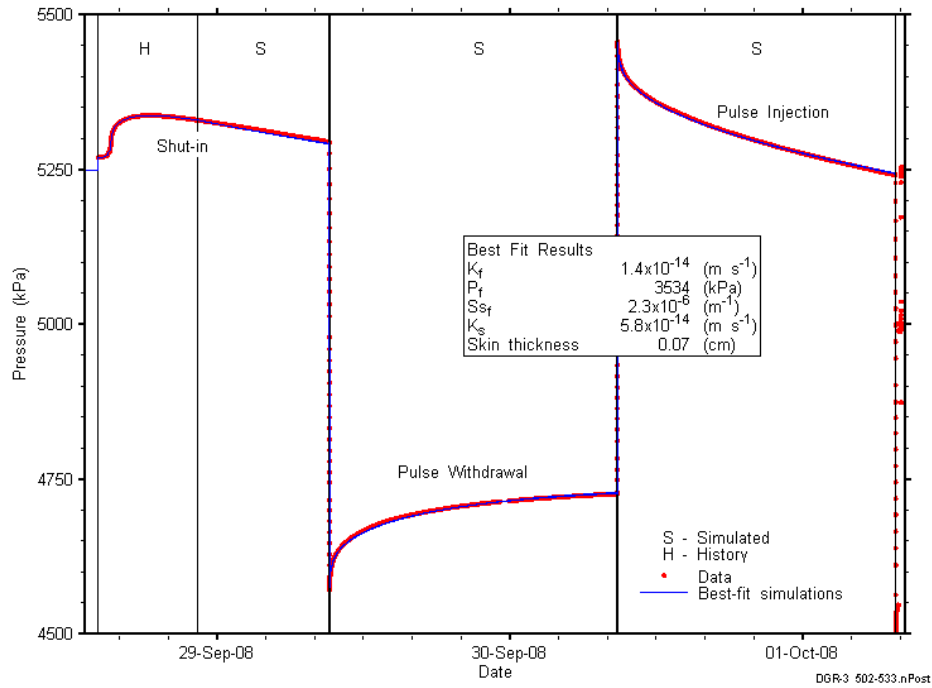


Figure C-144: Linear plot showing simulations of the DGR3_501.95-532.69 pressure response.

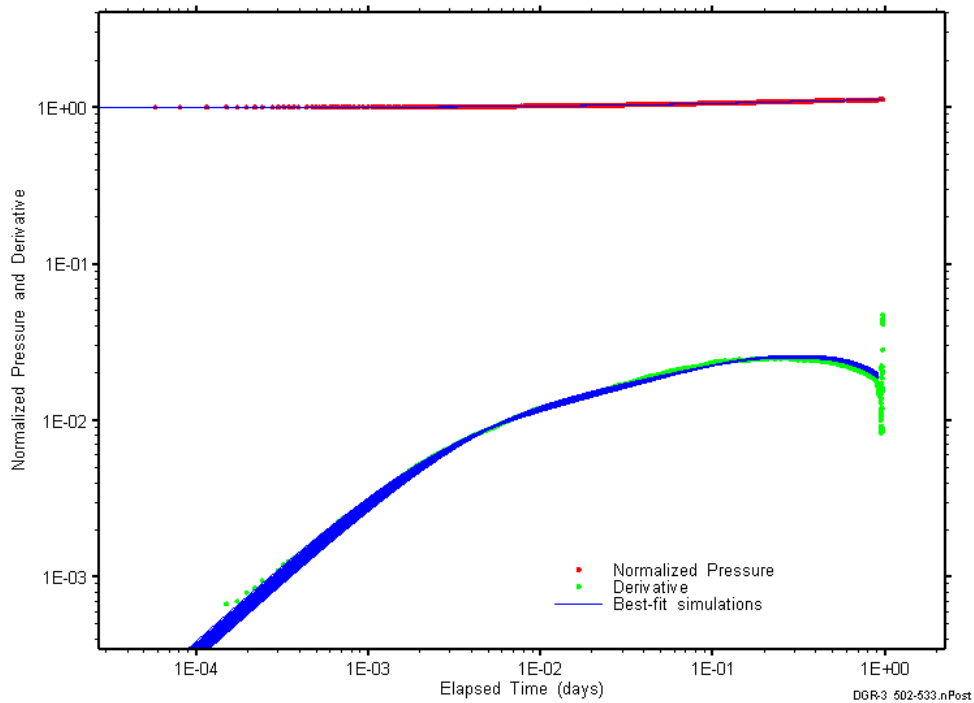


Figure C-145: Log-log plot showing simulations of the DGR3_501.95-532.69 pulse withdrawal Ramey B and derivative response.

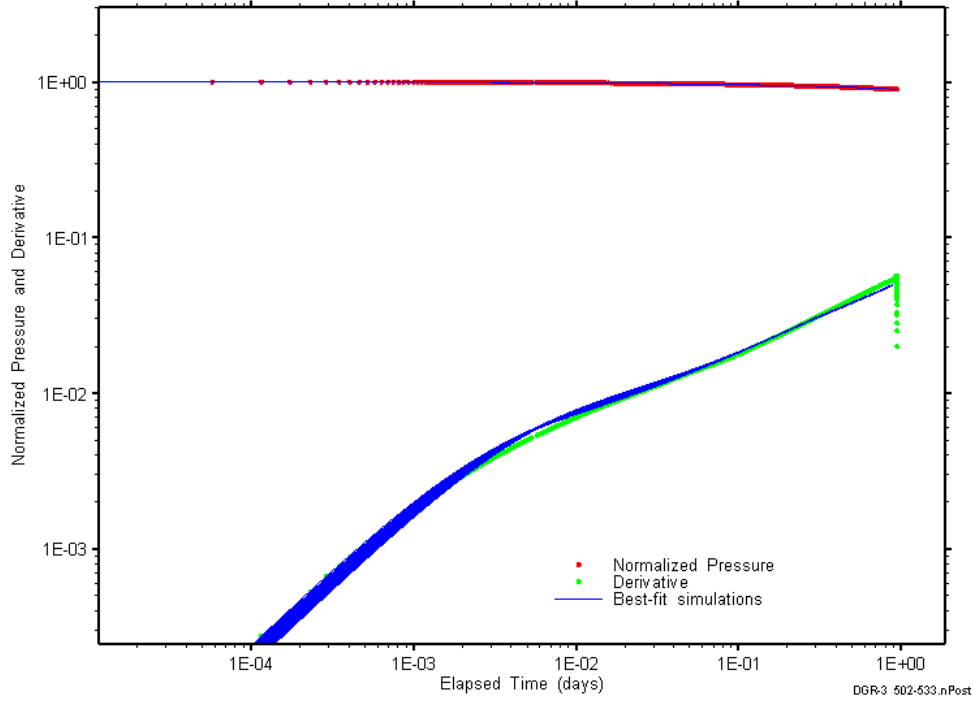


Figure C-146: Log-log plot showing simulations of the DGR3_501.95–532.69 pulse injection Ramey B and derivative response.

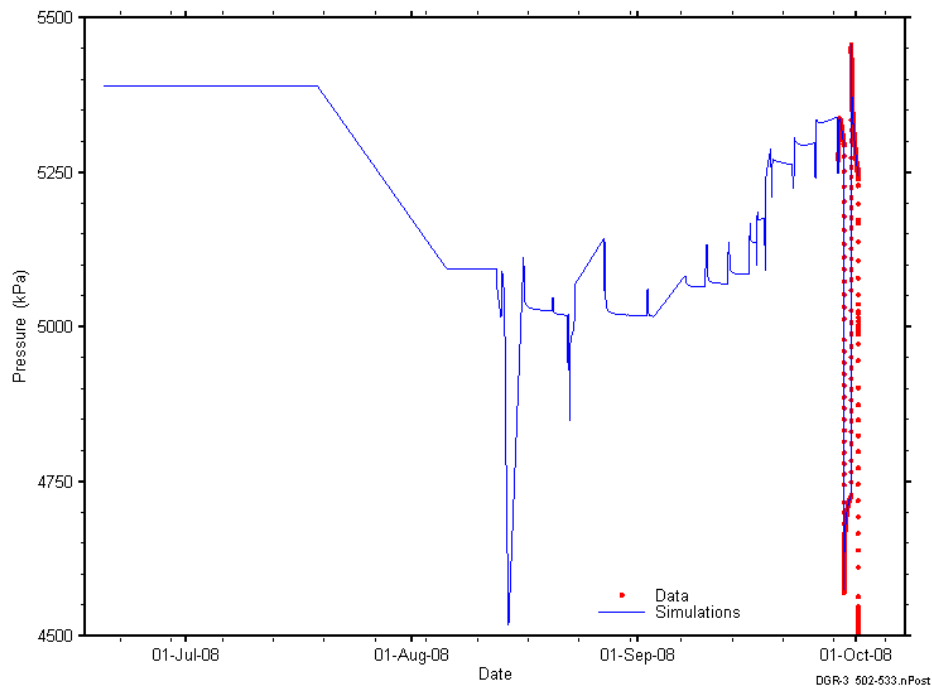


Figure C-147: Linear plot showing simulations of the DGR3_501.95-532.69 pressure response, including pre-test pressure history.

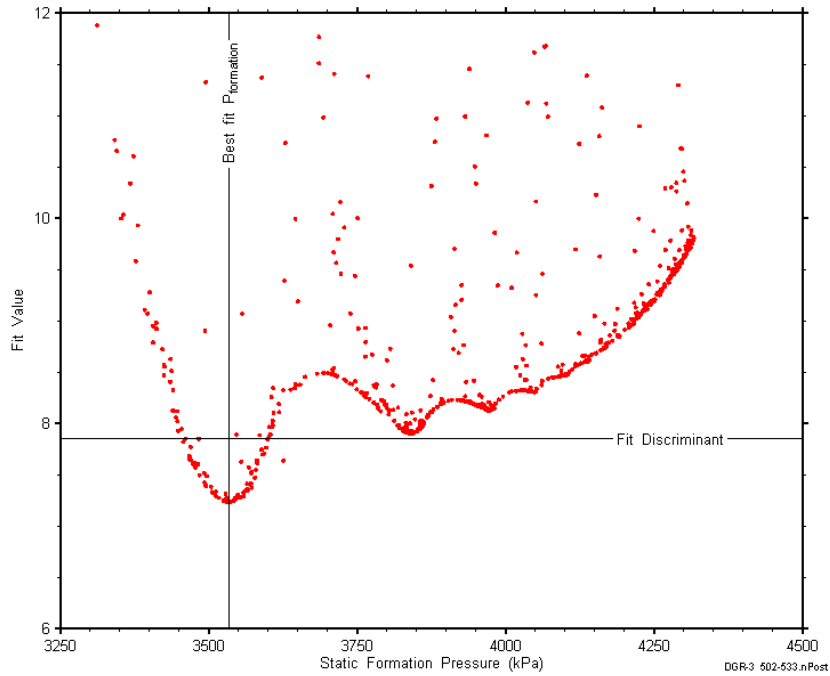


Figure C-148: XY-scatter plot showing the static formation pressure parameter space derived from DGR3_501.95-532.69 perturbation analysis along with the fit discriminant and best fit values.

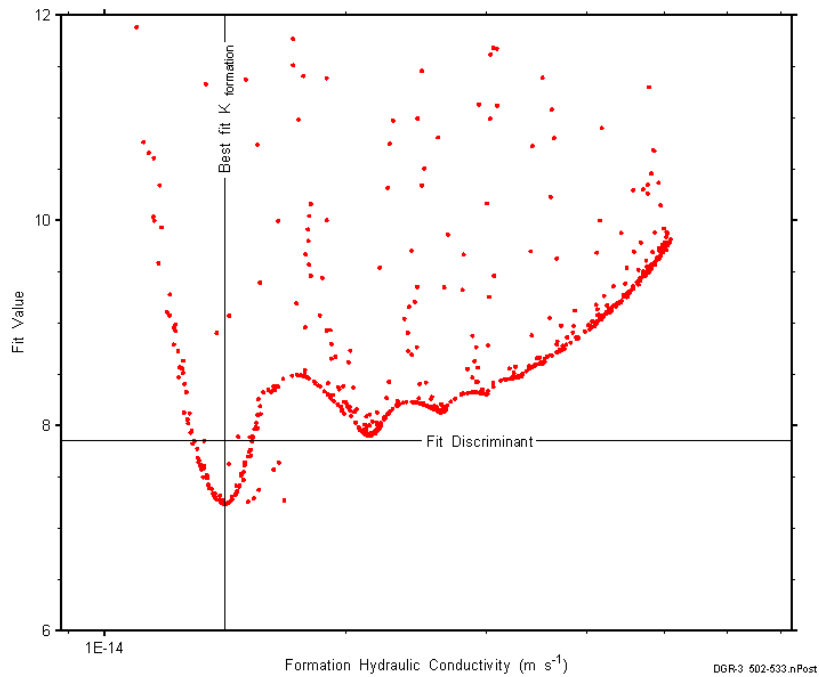


Figure C-149: XY-scatter plot showing the formation hydraulic conductivity parameter space derived from DGR3_501.95-532.69 perturbation analysis along with the fit discriminant and best fit values.

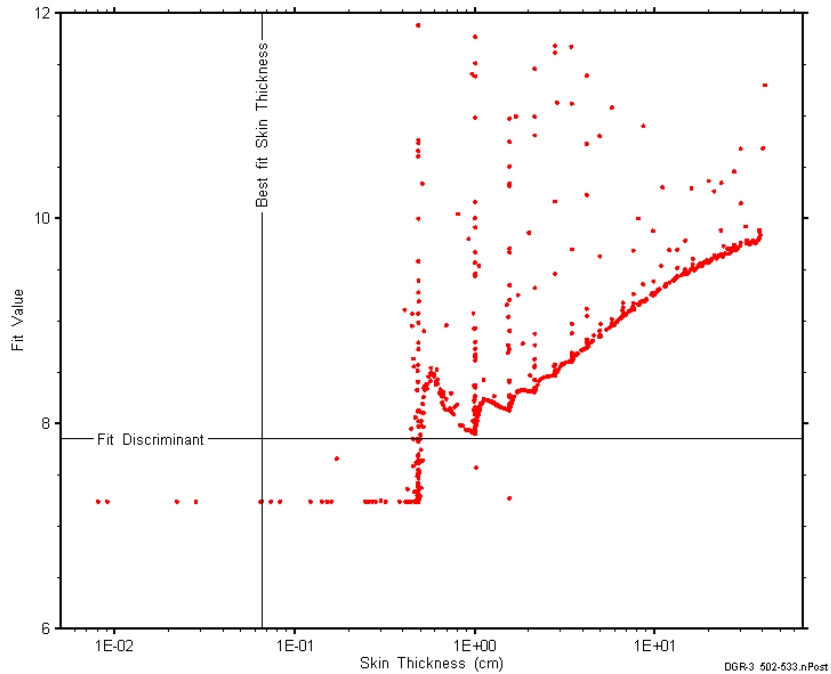


Figure C-150: XY-scatter plot showing the skin-thickness parameter space derived from DGR3_501.95-532.69 perturbation analysis along with the fit discriminant and best fit values.

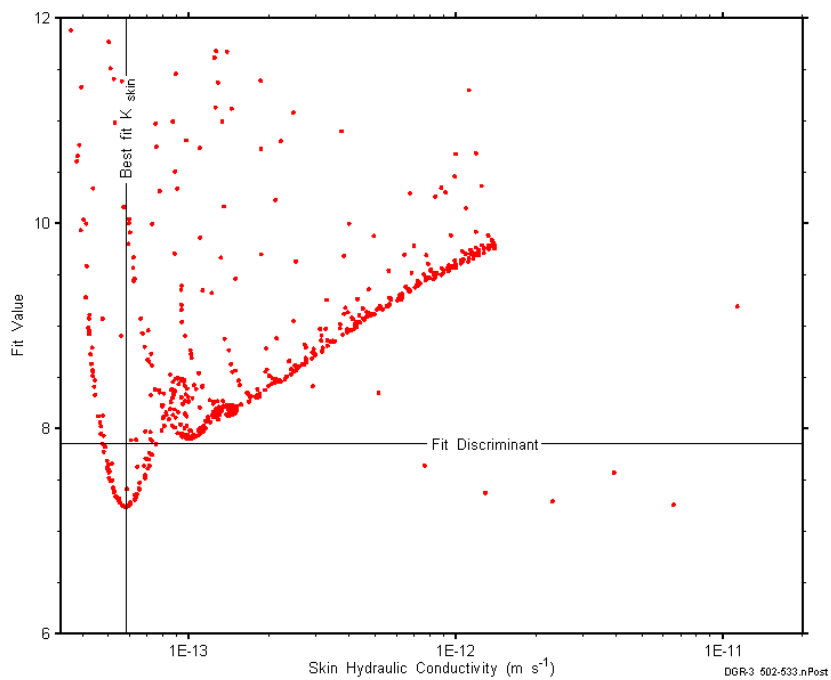


Figure C-151: XY-scatter plot showing the skin hydraulic conductivity parameter space derived from DGR3_501.95-532.69 perturbation analysis along with the fit discriminant and best fit values.

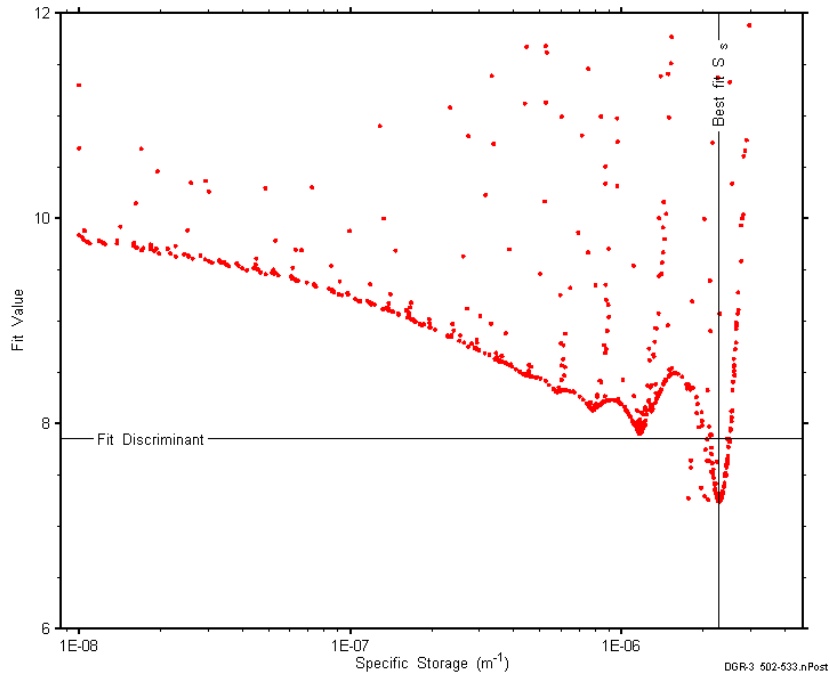


Figure C-152: XY-scatter plot showing the formation specific storage parameter space derived from DGR3_501.95-532.69 perturbation analysis along with the fit discriminant and best fit values.

C.12 532.49-563.23 Georgian Bay

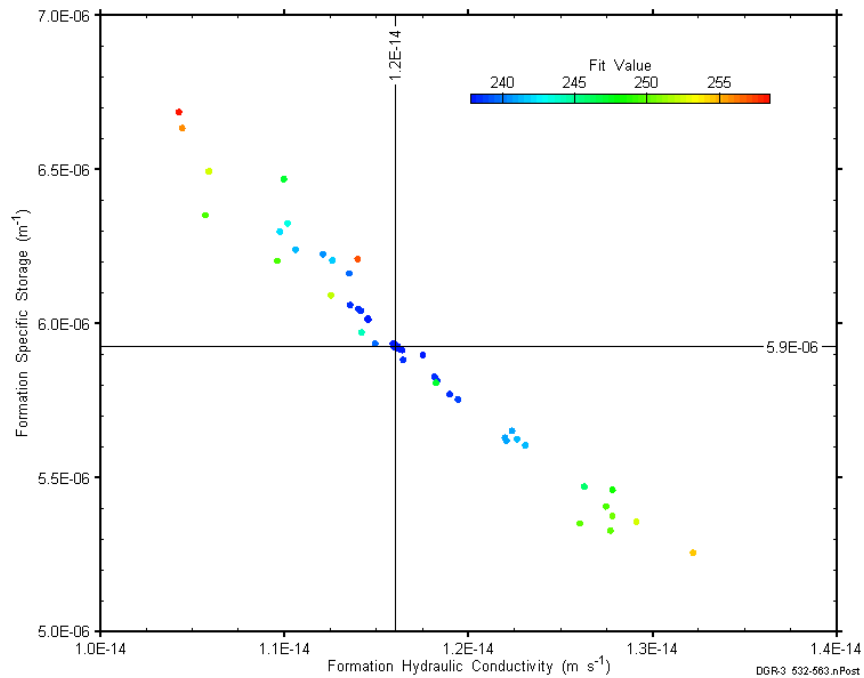


Figure C-153: XY-scatter plot showing estimates of formation hydraulic conductivity and formation specific storage derived from the DGR3_532.49-563.23 perturbation analysis.

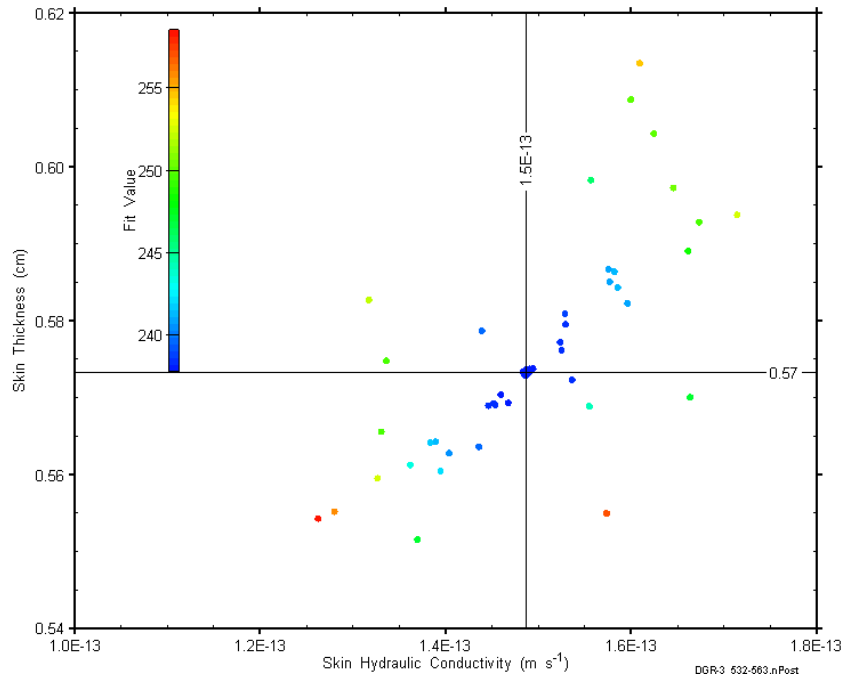


Figure C-154: XY-scatter plot showing estimates of skin hydraulic conductivity and skin thickness derived from the DGR3_532.49-563.23 perturbation analysis.

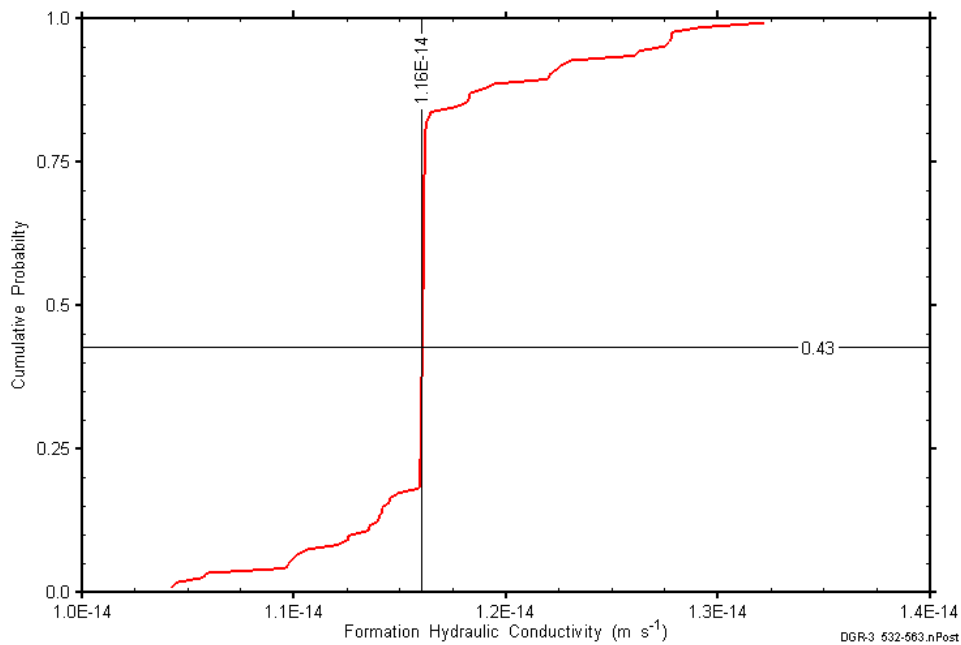


Figure C-155: DGR3_532.49-563.23 formation hydraulic conductivity cumulative distribution function.

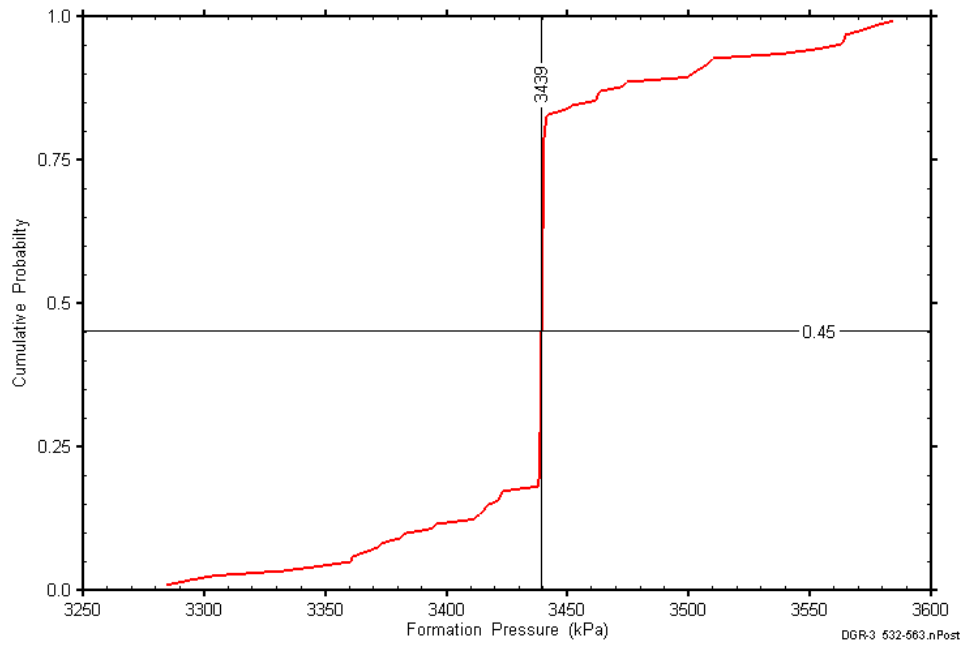


Figure C-156: DGR3_532.49-563.23 static formation pressure cumulative distribution function.

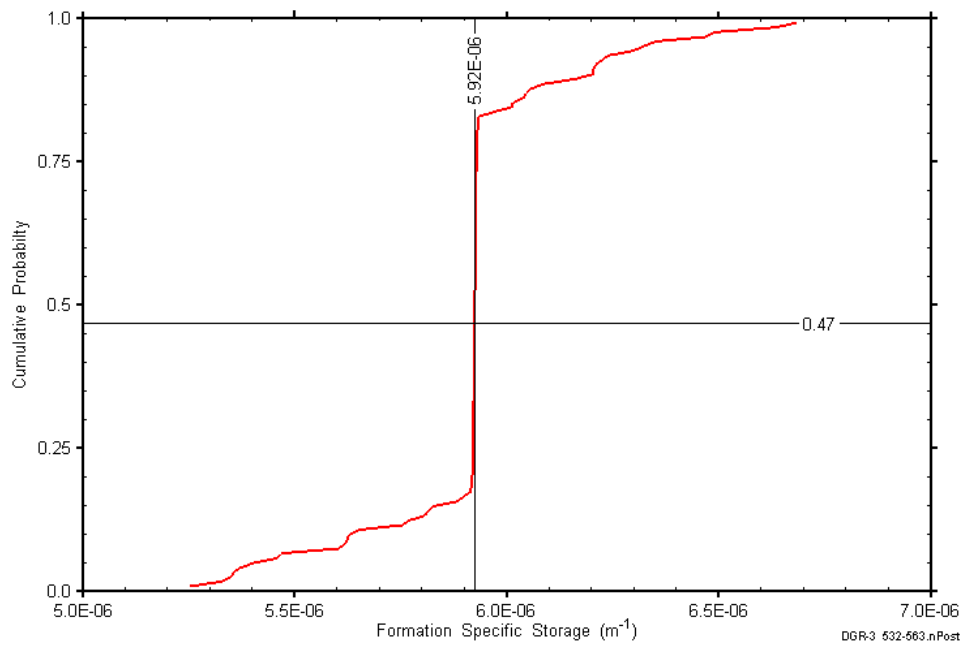


Figure C-157: DGR3_532.49-563.23 formation specific storage cumulative distribution function.

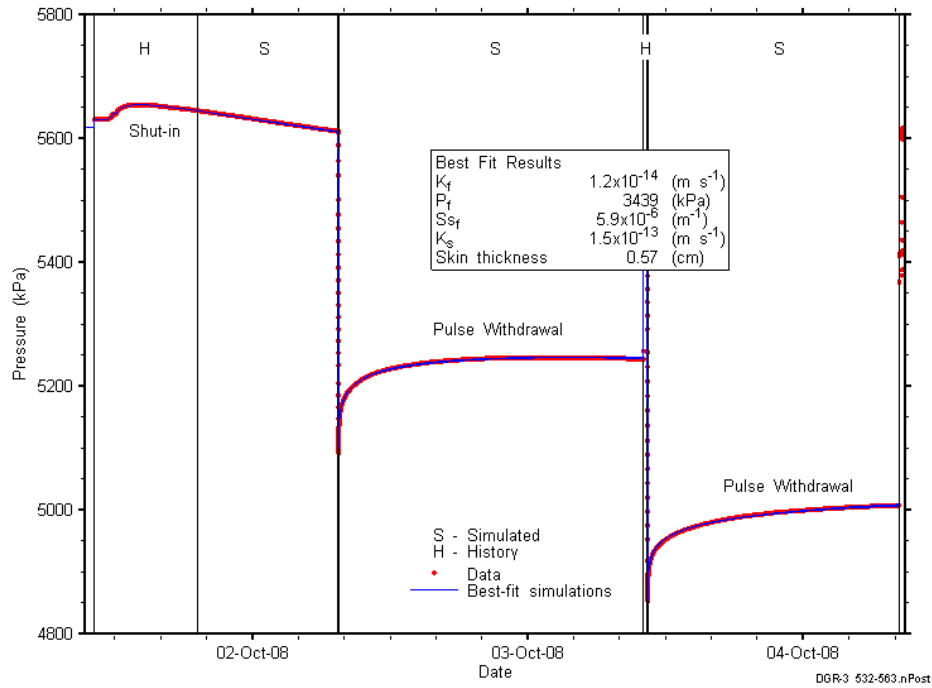


Figure C-158: Linear plot showing simulations of the DGR3_532.49-563.23 pressure response.

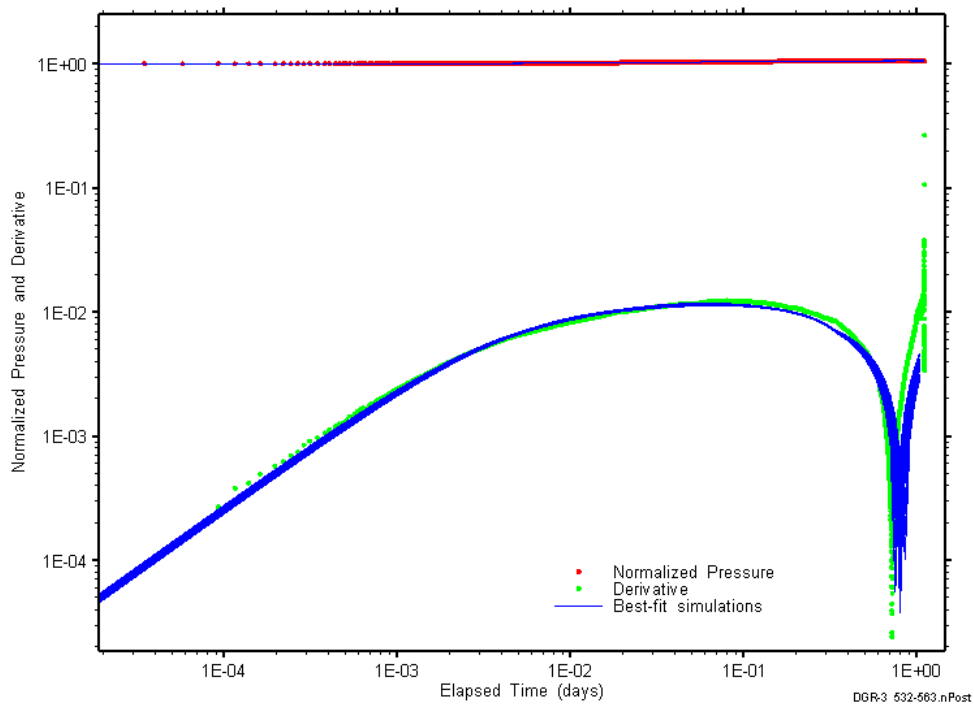


Figure C-159: Log-log plot showing simulations of the DGR3_532.49-563.23 pulse withdrawal #1 Ramey B and derivative response.

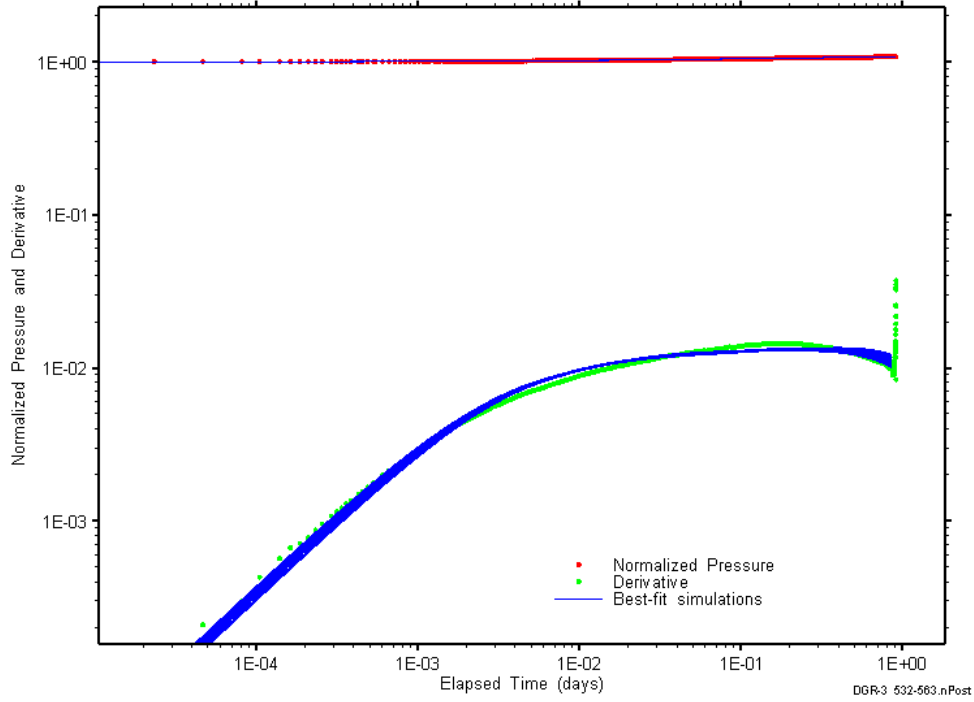


Figure C-160: Log-log plot showing simulations of the DGR3_532.49–563.23 pulse withdrawal #2 Ramey B and derivative response.

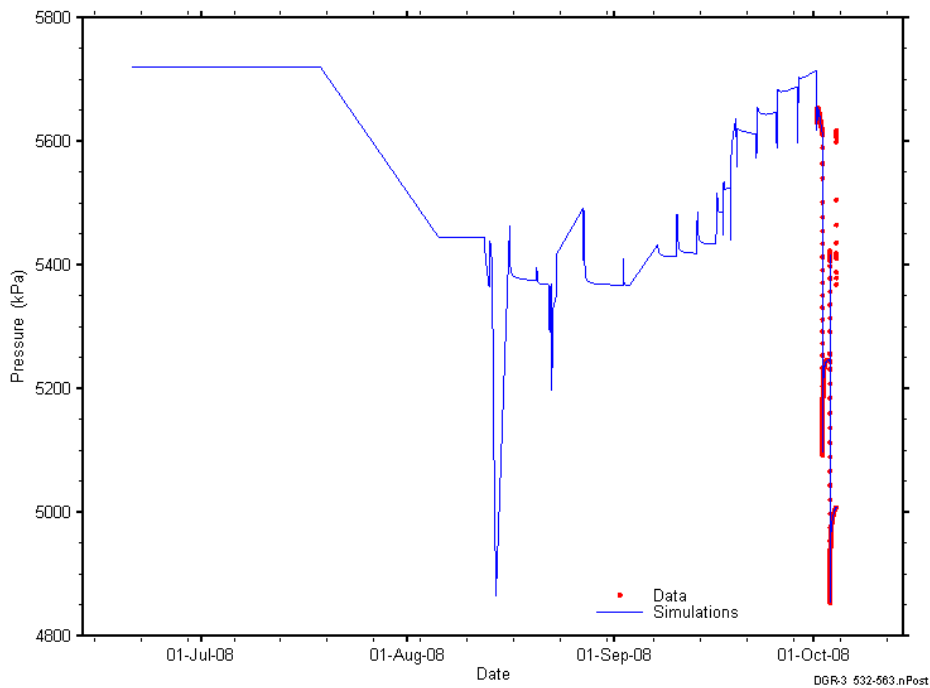


Figure C-161: Linear plot showing simulations of the DGR3_532.49-563.23 pressure response, including pre-test pressure history.

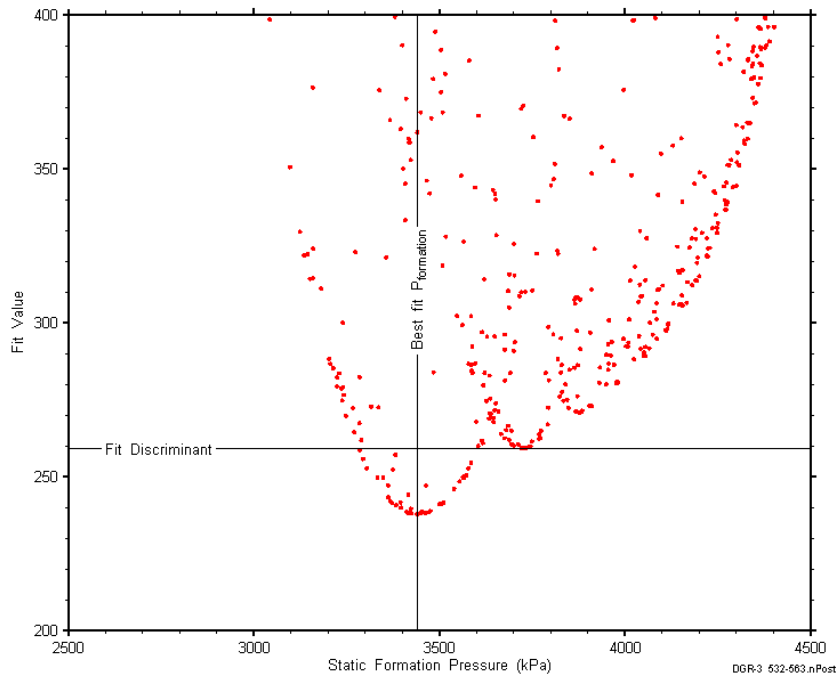


Figure C-162: XY-scatter plot showing the static formation pressure parameter space derived from DGR3_532.49-563.23 perturbation analysis along with the fit discriminant and best fit values.

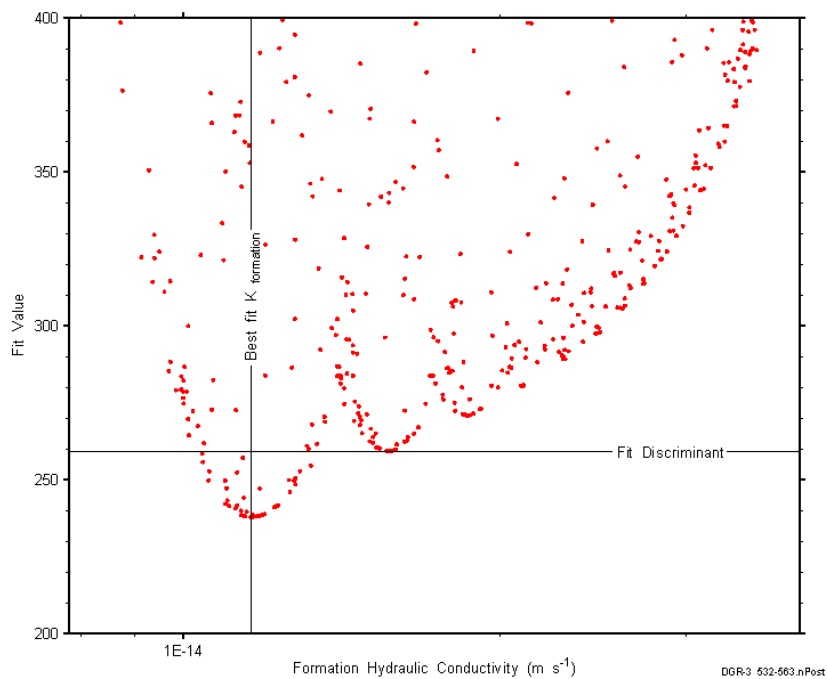


Figure C-163: XY-scatter plot showing the formation hydraulic conductivity parameter space derived from DGR3_532.49-563.23 perturbation analysis along with the fit discriminant and best fit values.

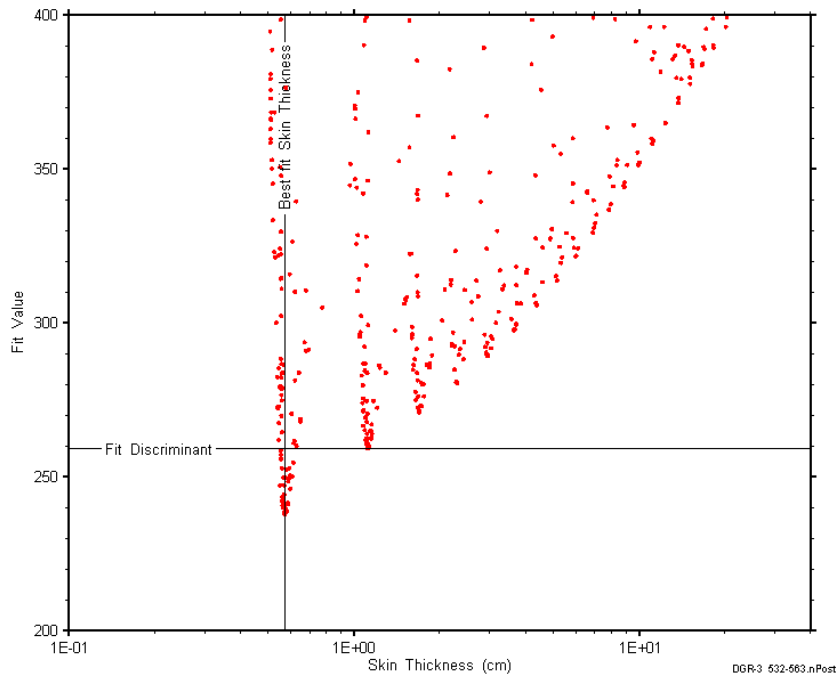


Figure C-164: XY-scatter plot showing the skin-thickness parameter space derived from DGR3_532.49-563.23 perturbation analysis along with the fit discriminant and best fit values.

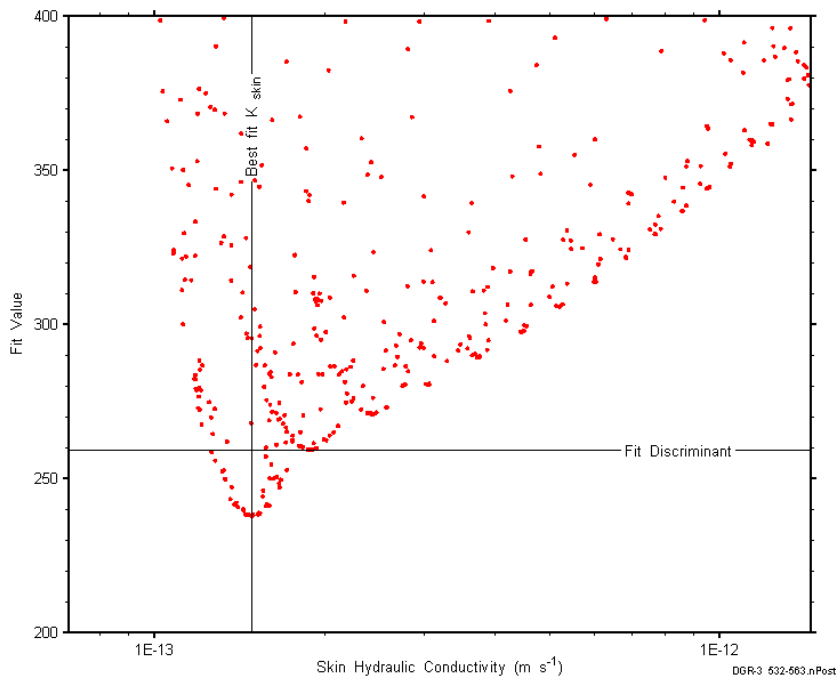


Figure C-165: XY-scatter plot showing the skin hydraulic conductivity parameter space derived from DGR3_532.49-563623 perturbation analysis along with the fit discriminant and best fit values.

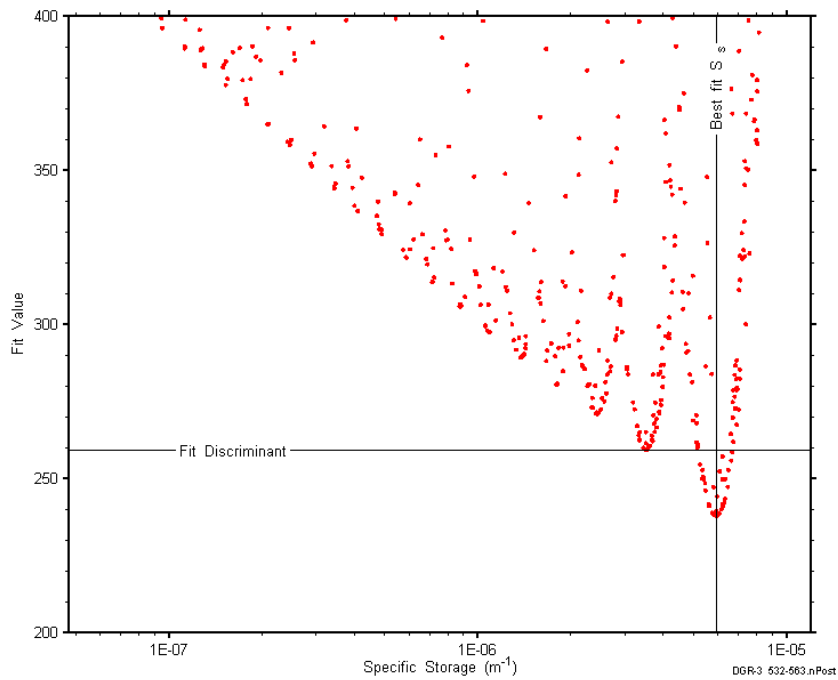


Figure C-166: XY-scatter plot showing the formation specific storage parameter space derived from DGR3_532.49-563.23 perturbation analysis along with the fit discriminant and best fit values.

C.13 563.03-593.77 Georgian Bay

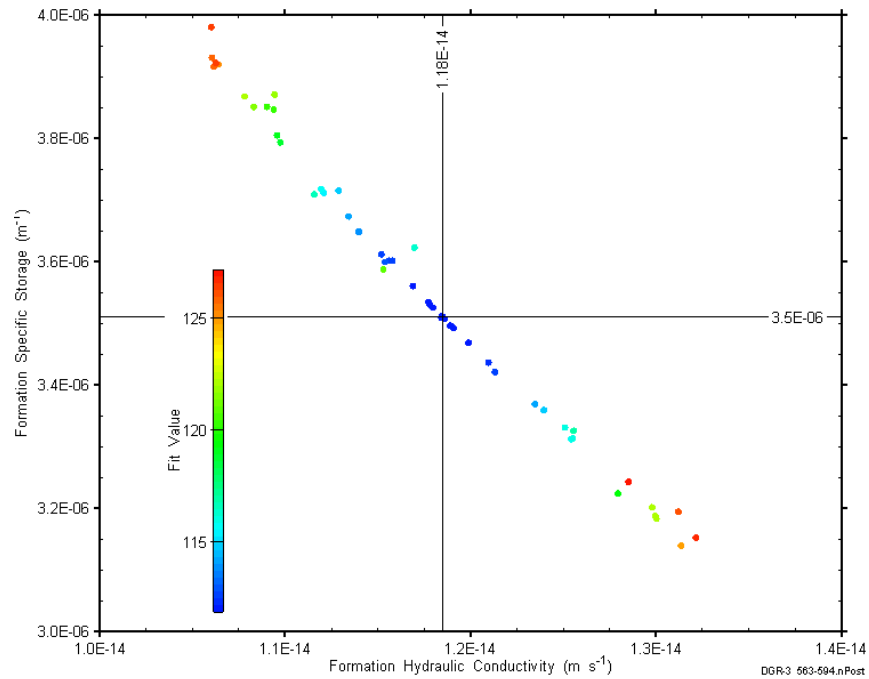


Figure C-167: XY-scatter plot showing estimates of formation hydraulic conductivity and formation specific storage derived from the DGR3_563.03-593.77 perturbation analysis.

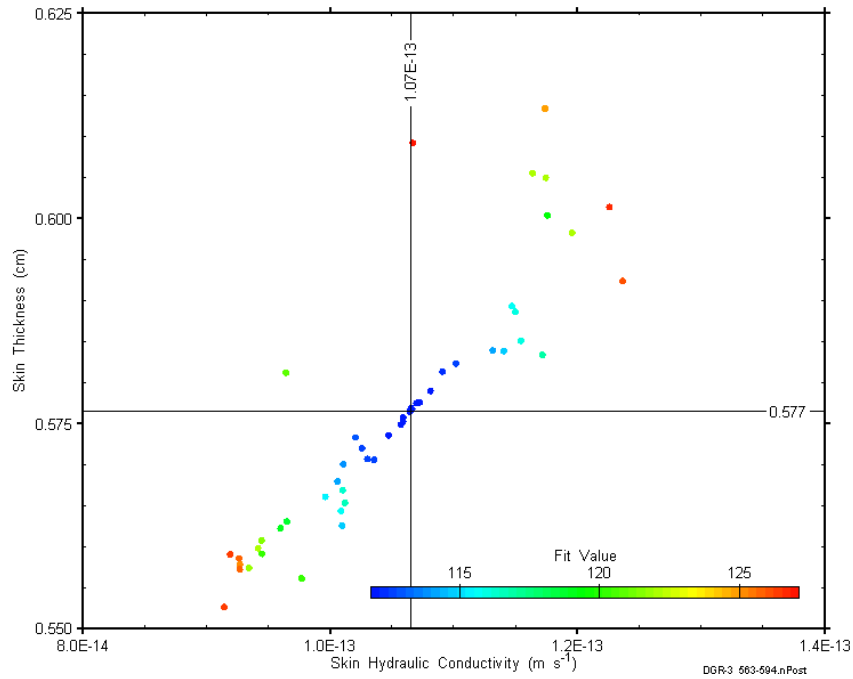


Figure C-168: XY-scatter plot showing estimates of skin hydraulic conductivity and skin thickness derived from the DGR3_563.03-593.77 perturbation analysis.

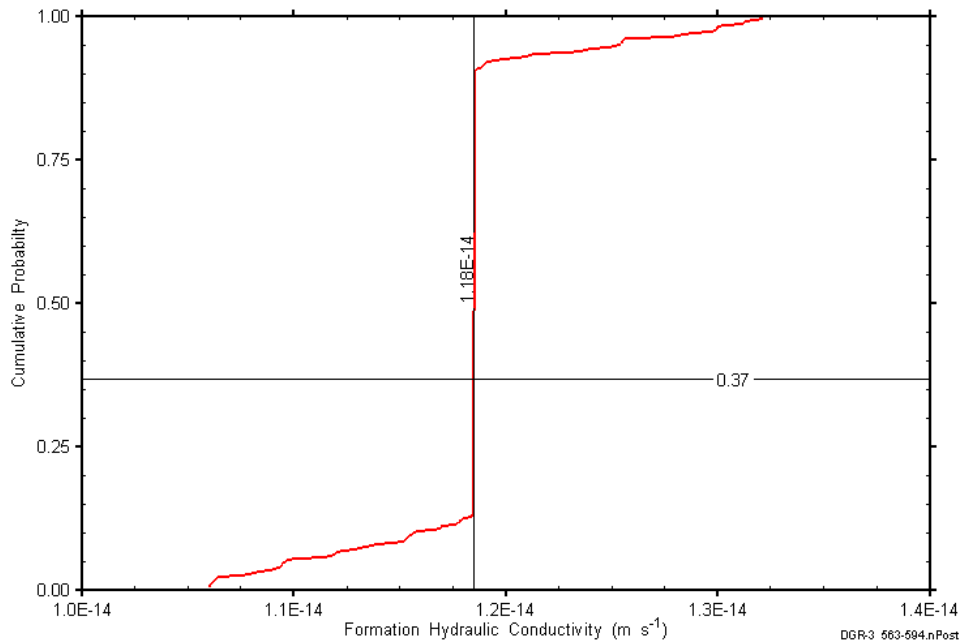


Figure C-169: DGR3_563.03-593.77 formation hydraulic conductivity cumulative distribution function.

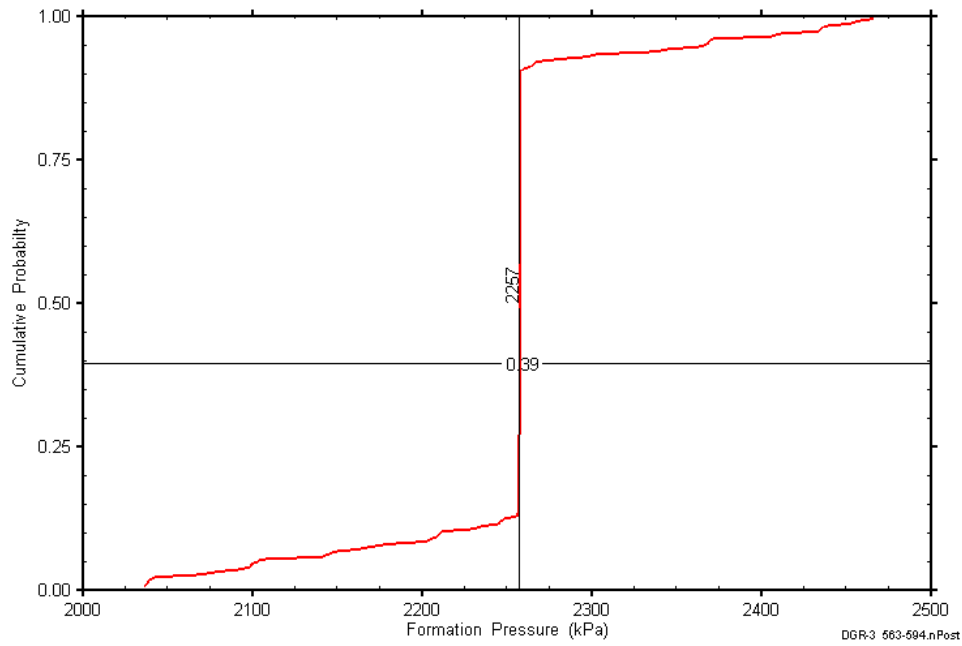


Figure C-170: DGR3_563.03-593.77 static formation pressure cumulative distribution function.

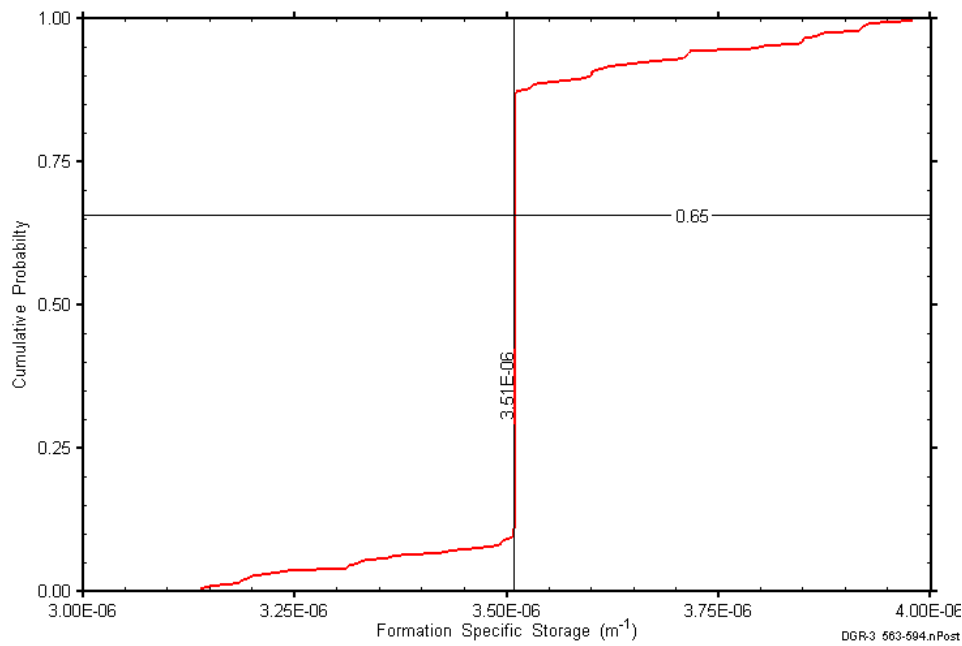


Figure C-171: DGR3_563.03-593.77 formation specific storage cumulative distribution function.

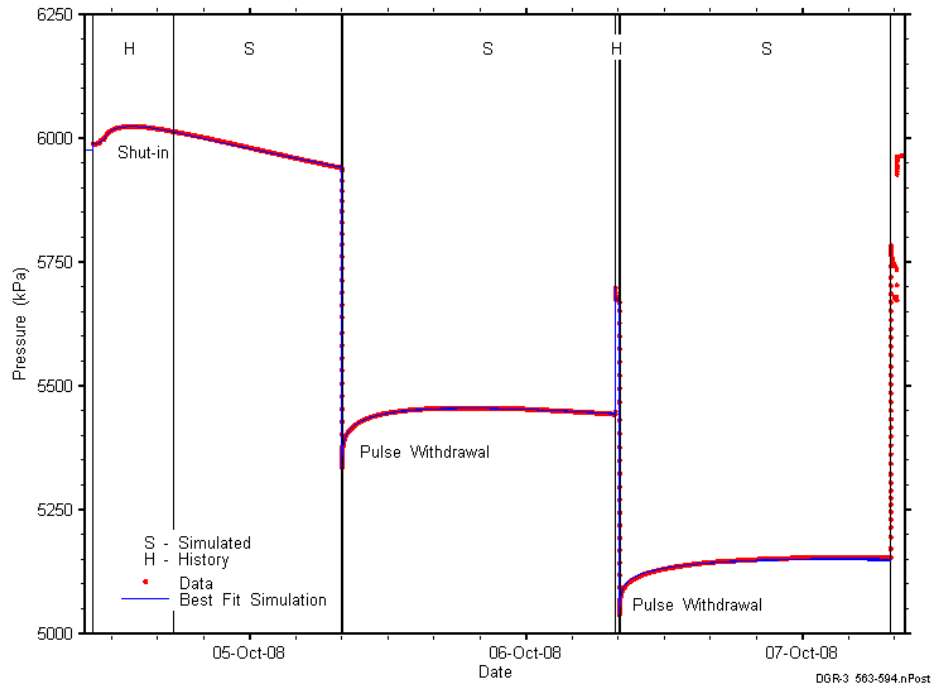


Figure C-172: Linear plot showing simulations of the DGR3_563.03-593.77 pressure response.

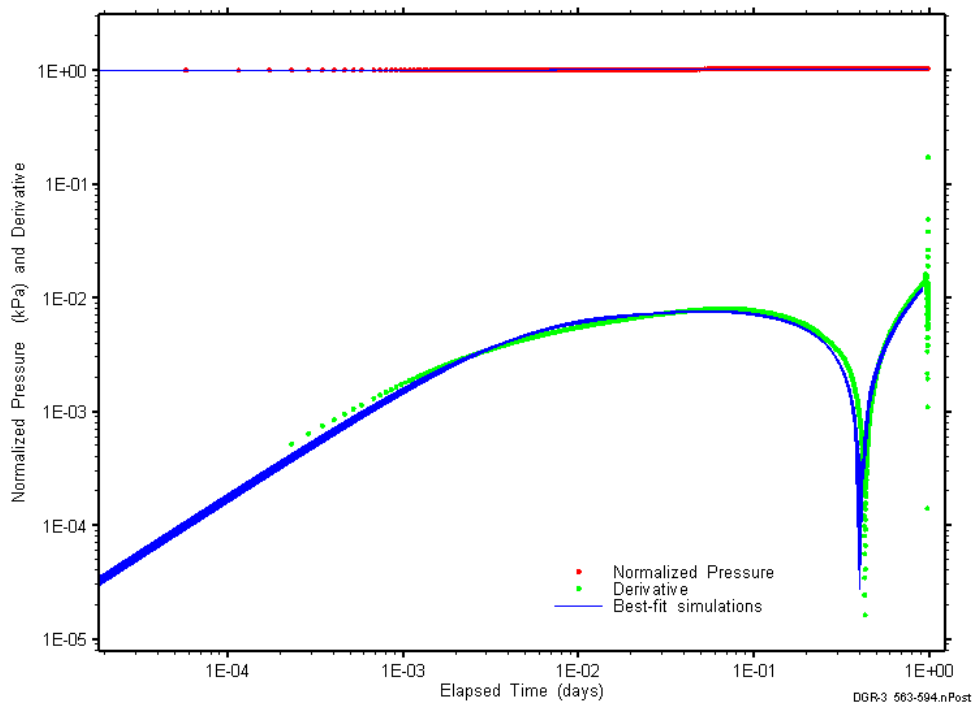


Figure C-173: Log-log plot showing simulations of the DGR3_563.03-593.77 pulse withdrawal #1 Ramey B and derivative response.

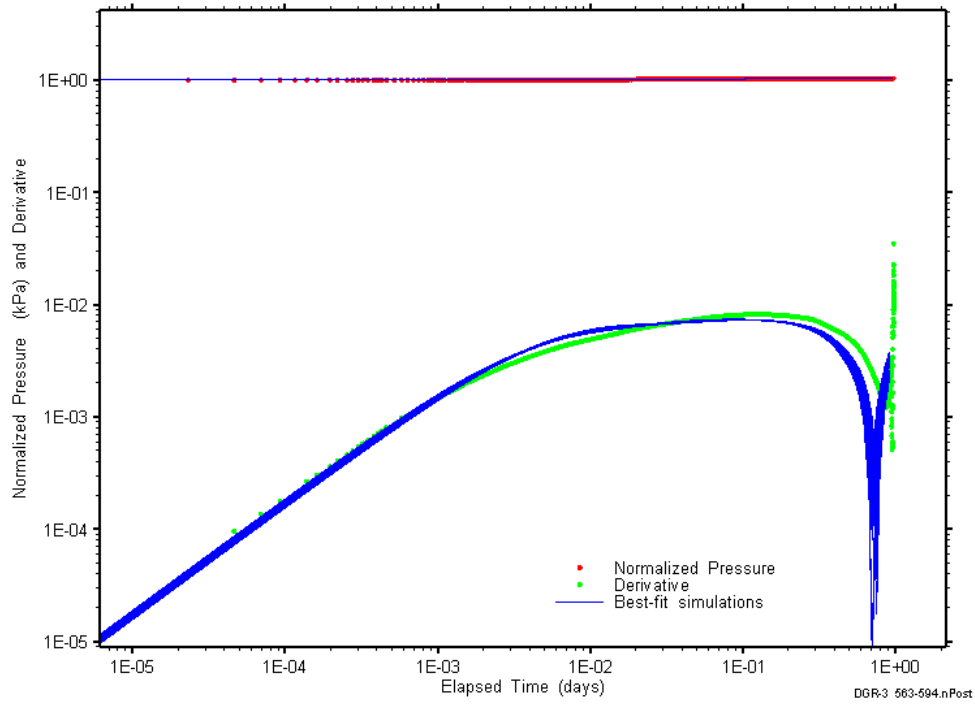


Figure C-174: Log-log plot showing simulations of the DGR3_563.03–593.77 pulse withdrawal #2 Ramey B and derivative response.

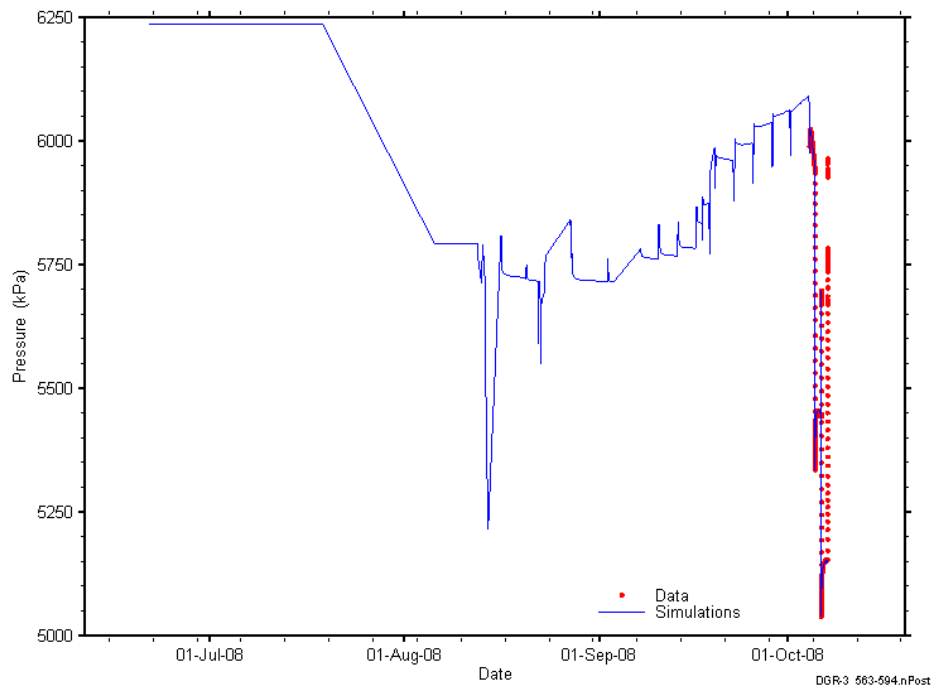


Figure C-175: Linear plot showing simulations of the DGR3_563.03–593.77 pressure response, including pre-test pressure history.

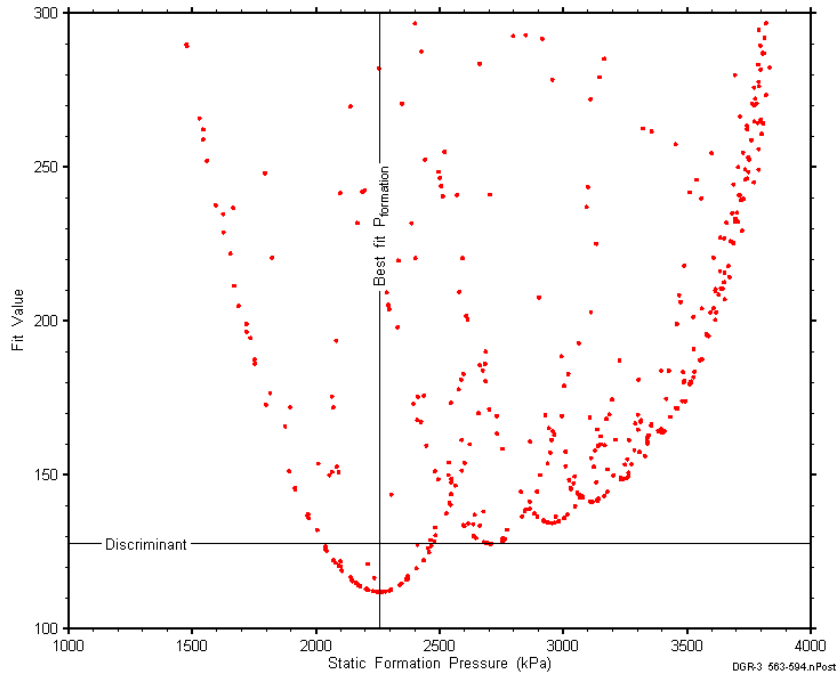


Figure C-176: XY-scatter plot showing the static formation pressure parameter space derived from DGR3_563.03-593.77 perturbation analysis along with the fit discriminant and best fit values.

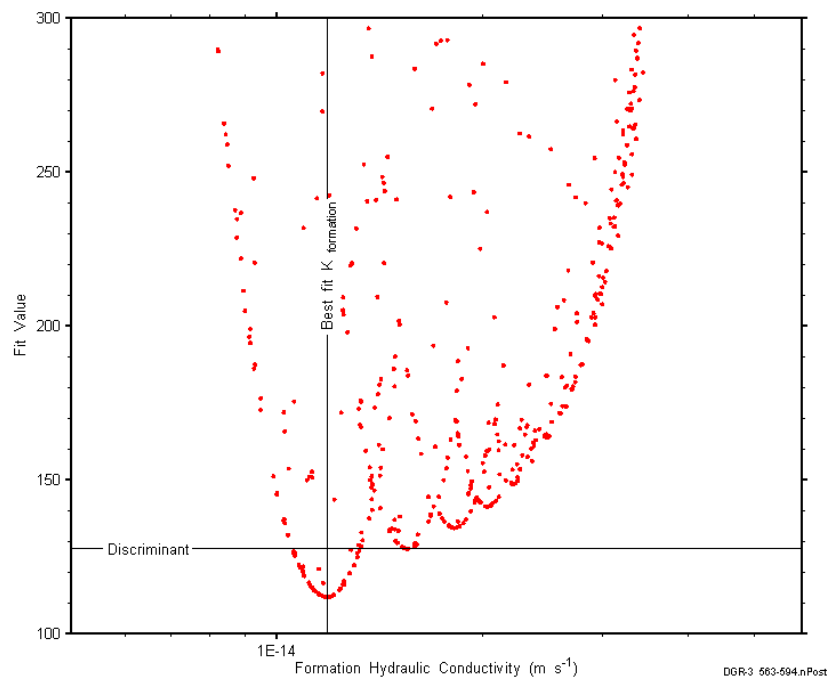


Figure C-177: XY-scatter plot showing the formation hydraulic conductivity parameter space derived from DGR3_563.03-593.77 perturbation analysis along with the fit discriminant and best fit values.

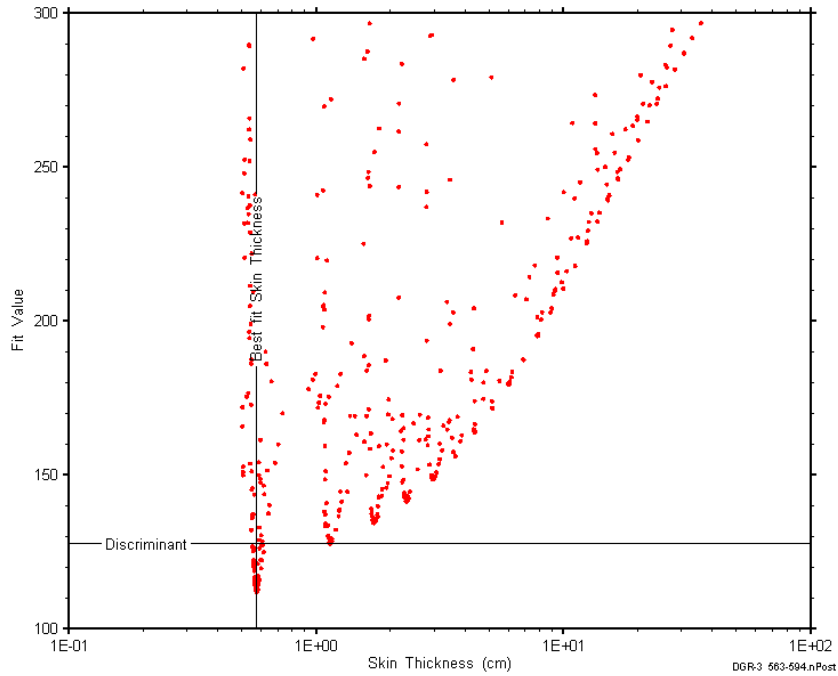


Figure C-178: XY-scatter plot showing the skin-thickness parameter space derived from DGR3_563.03-593.77 perturbation analysis along with the fit discriminant and best fit values.

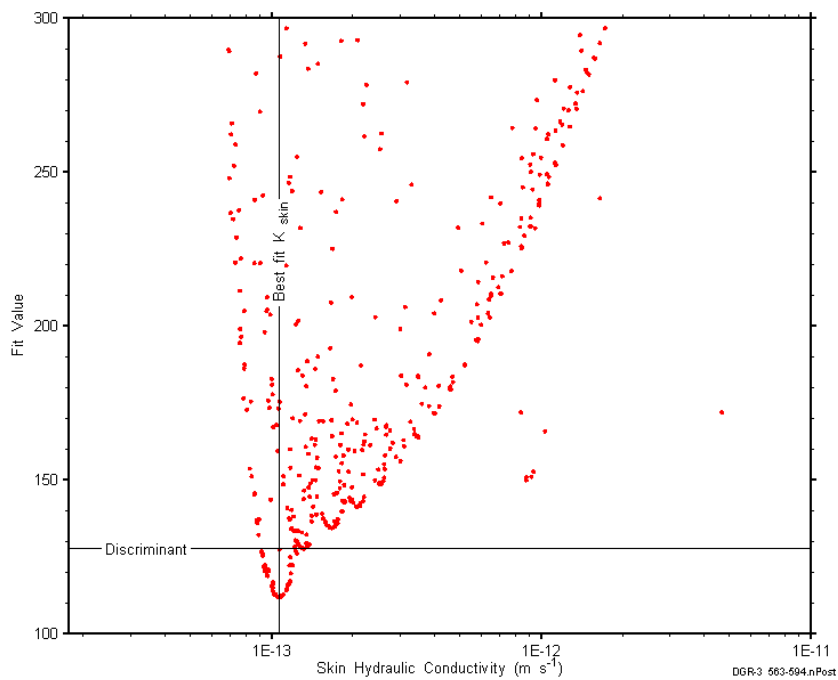


Figure C-179: XY-scatter plot showing the skin hydraulic conductivity parameter space derived from DGR3_563.03-593677 perturbation analysis along with the fit discriminant and best fit values.

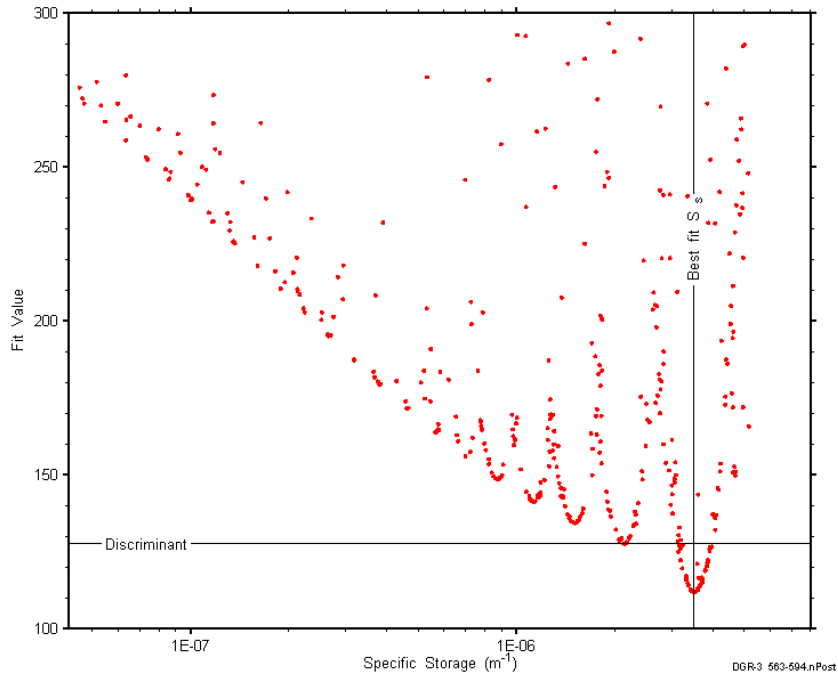


Figure C-180: XY-scatter plot showing the formation specific storage parameter space derived from DGR3_563.03-593.77 perturbation analysis along with the fit discriminant and best fit values.

C.14 593.57-624.31 Georgian Bay-Blue Mountain

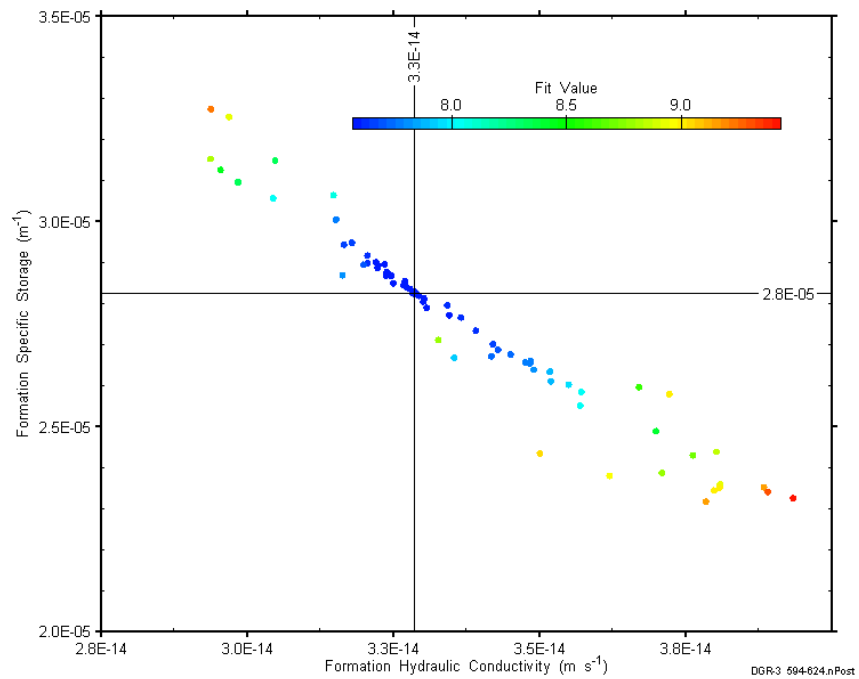


Figure C-181: XY-scatter plot showing estimates of formation hydraulic conductivity and formation specific storage derived from the DGR3_593.57-624.31 perturbation analysis.

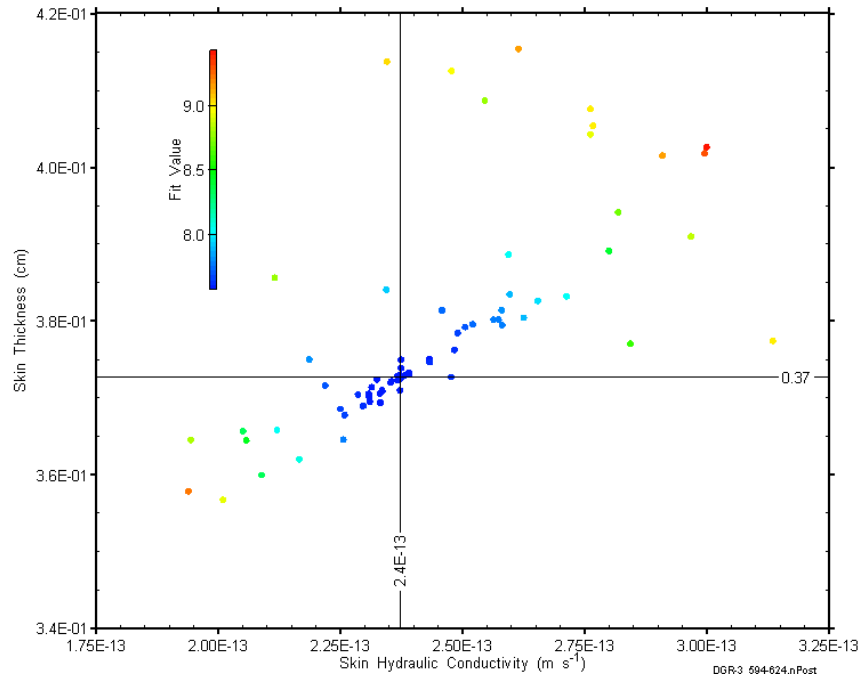


Figure C-182: XY-scatter plot showing estimates of skin hydraulic conductivity and skin thickness derived from the DGR3_593.57-624.31 perturbation analysis.

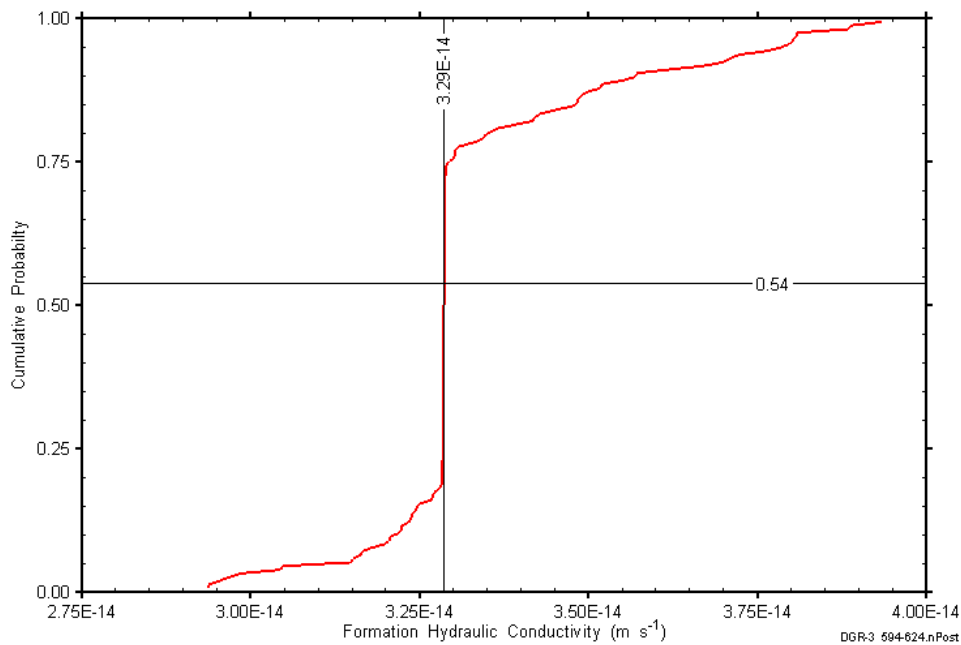


Figure C-183: DGR3_593.57-624.31 formation hydraulic conductivity cumulative distribution function.

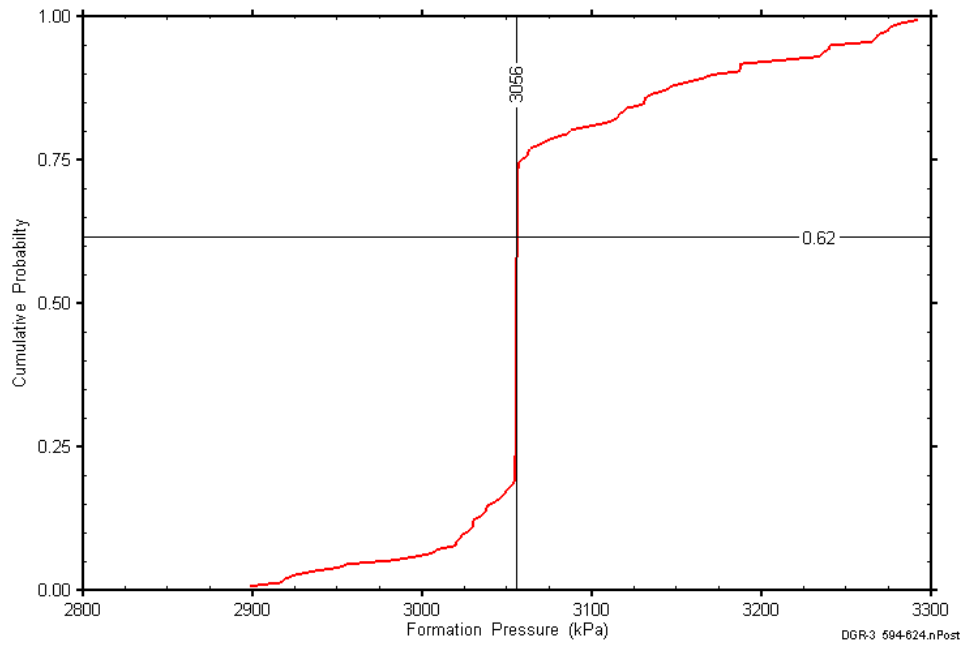


Figure C-184: DGR3_593.57-624.31 static formation pressure cumulative distribution function.

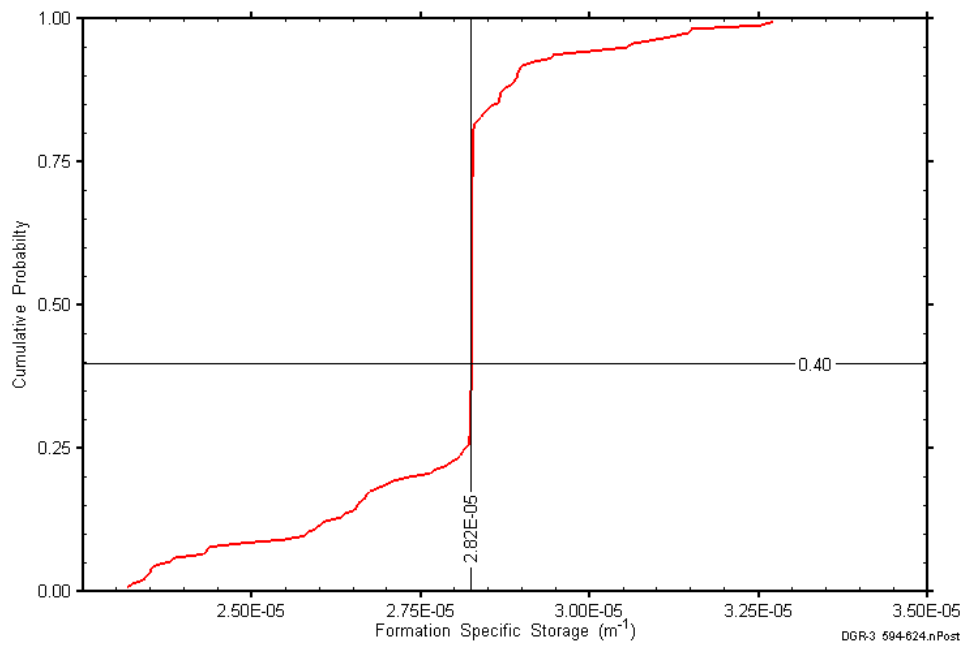


Figure C-185: DGR3_593.57-624.31 formation specific storage cumulative distribution function.

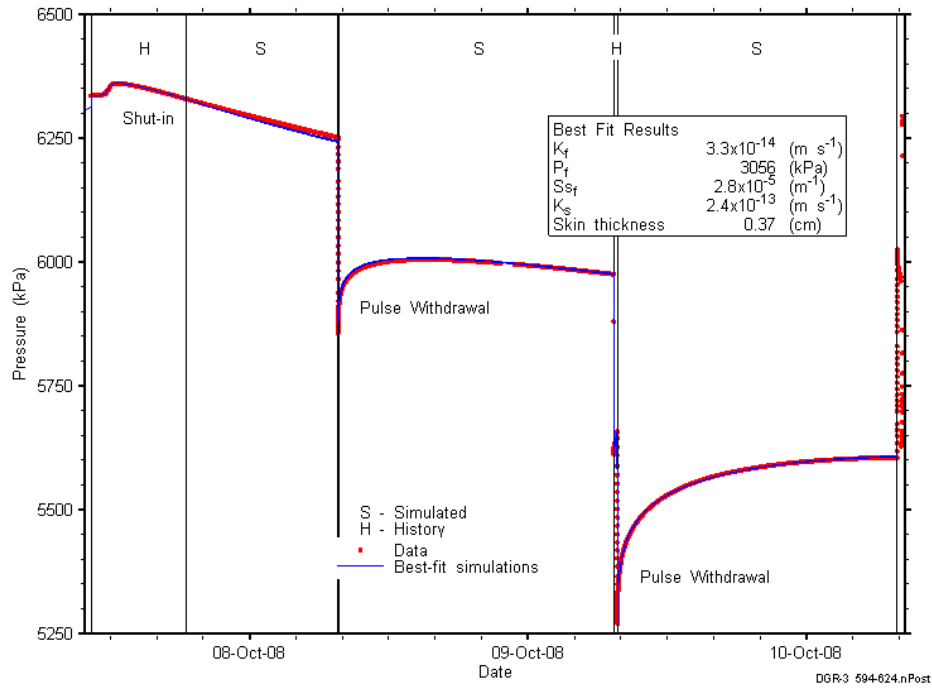


Figure C-186: Linear plot showing simulations of the DGR3_593.57-624.31 pressure response.

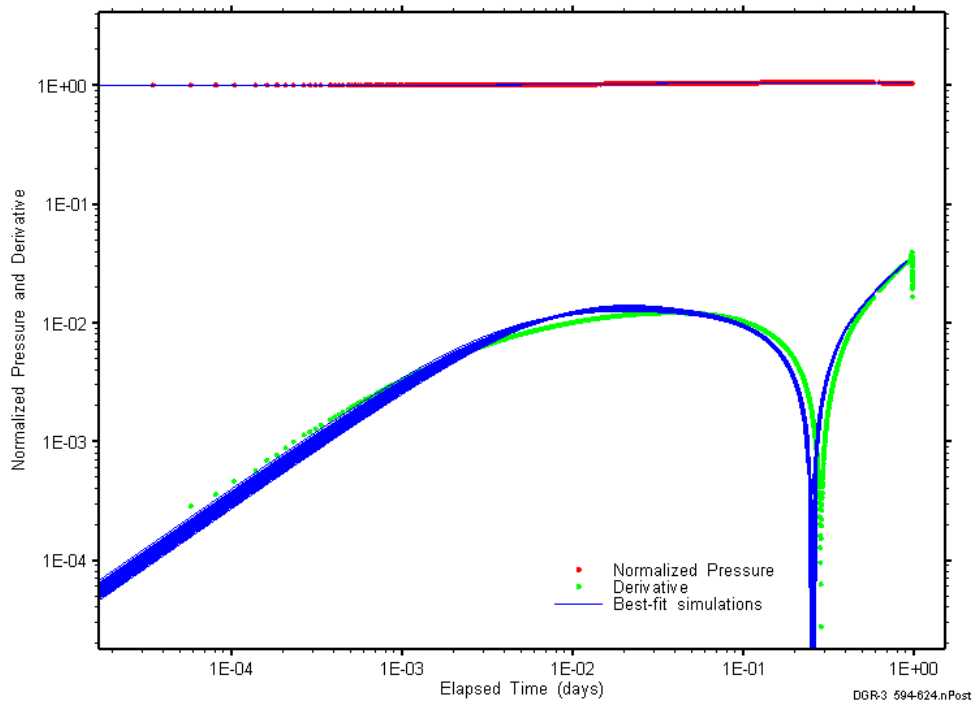


Figure C-187: Log-log plot showing simulations of the DGR3_593.57-624.31 pulse withdrawal #1 Ramey B and derivative response.

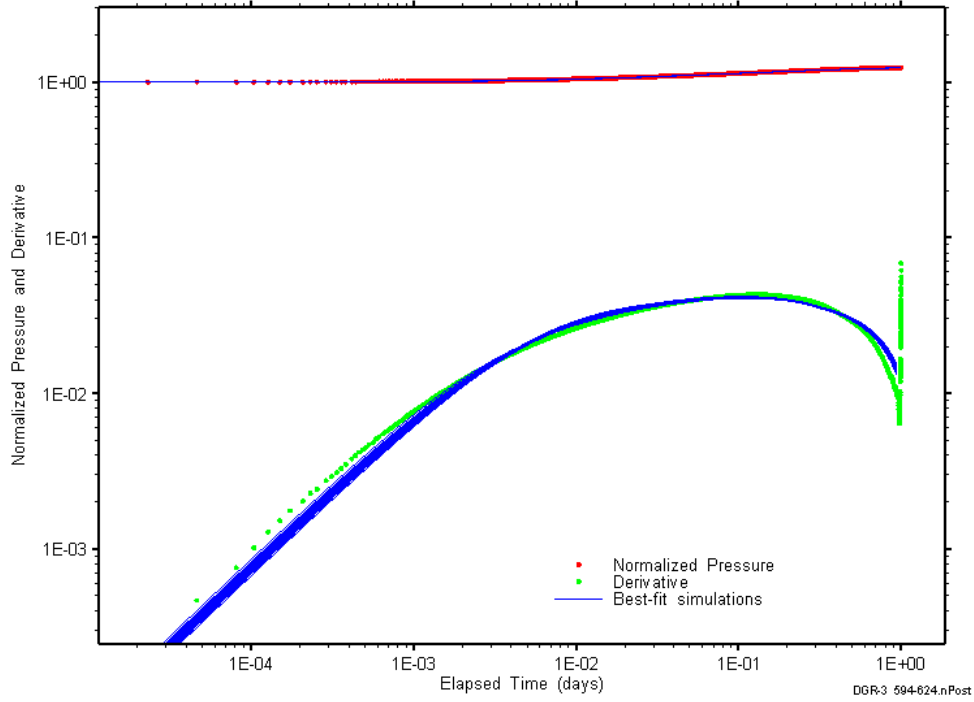


Figure C-188: Log-log plot showing simulations of the DGR3_593.57–624.31 pulse withdrawal #2 Ramey B and derivative response.

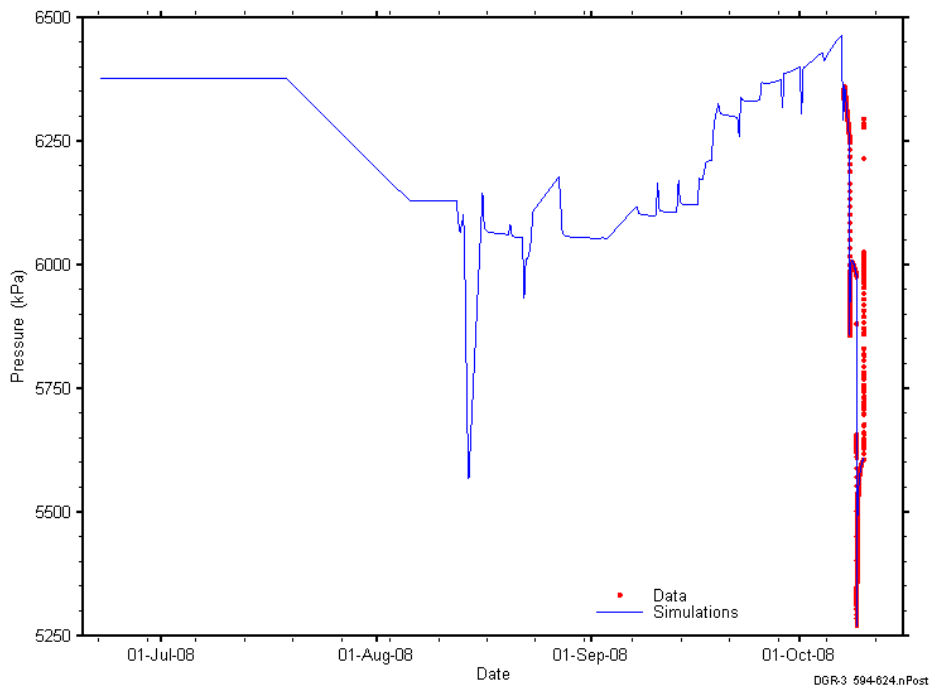


Figure C-189: Linear plot showing simulations of the DGR3_593.57–624.31 pressure response, including pre-test pressure history.

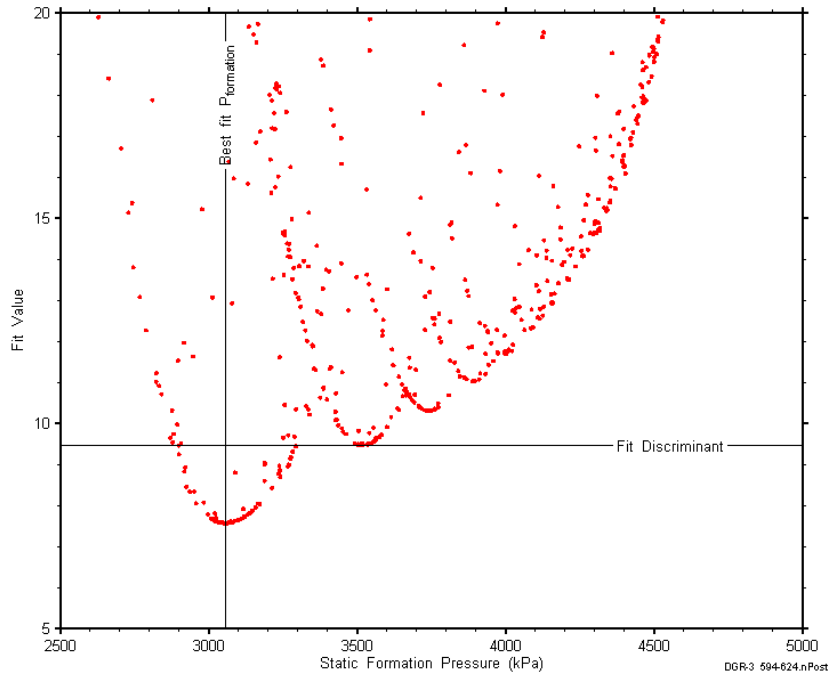


Figure C-190: XY-scatter plot showing the static formation pressure parameter space derived from DGR3_593.57-624.31 perturbation analysis along with the fit discriminant and best fit values.

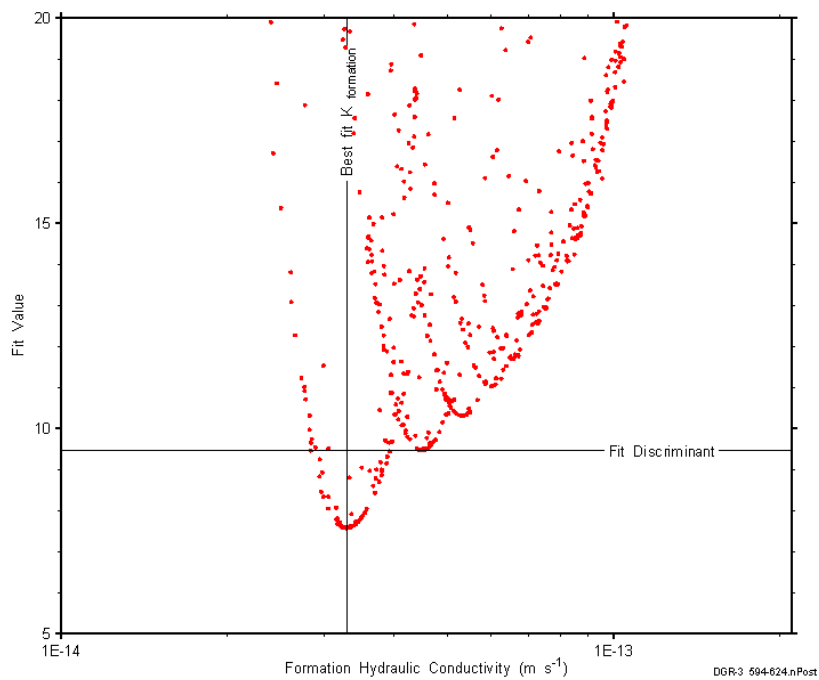


Figure C-191: XY-scatter plot showing the formation hydraulic conductivity parameter space derived from DGR3_593.57-624.31 perturbation analysis along with the fit discriminant and best fit values.

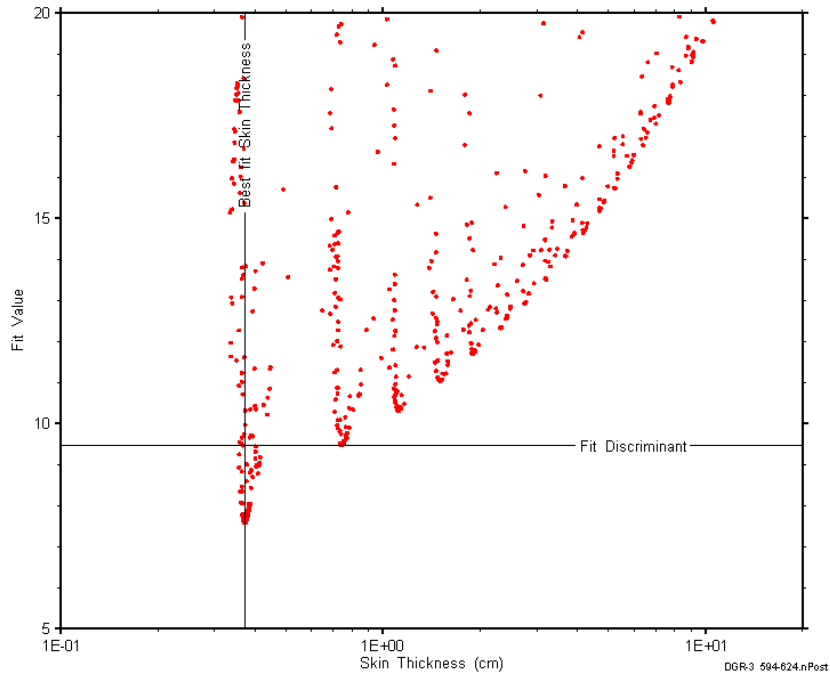


Figure C-192: XY-scatter plot showing the skin-thickness parameter space derived from DGR3_593.57-624.31 perturbation analysis along with the fit discriminant and best fit values.

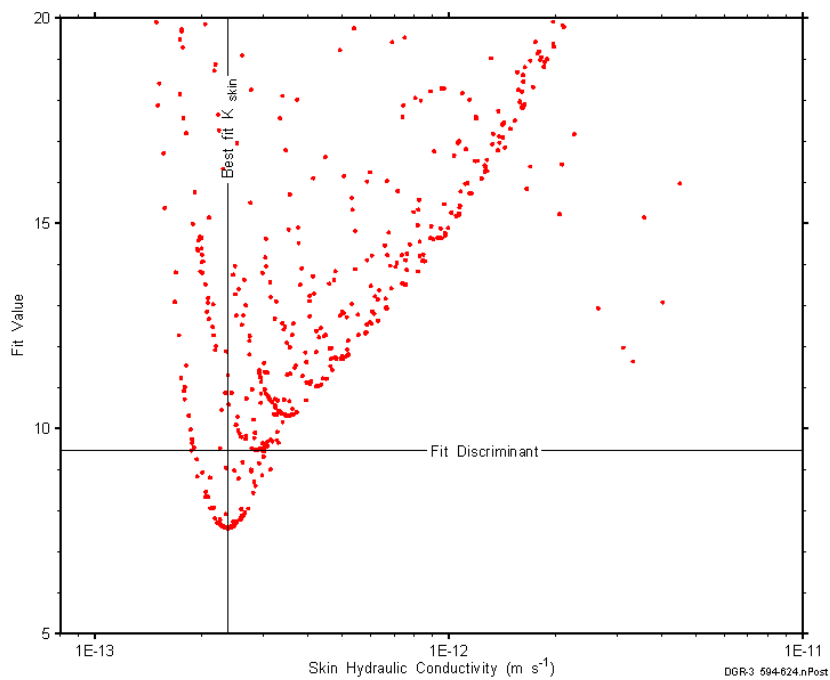


Figure C-193: XY-scatter plot showing the skin hydraulic conductivity parameter space derived from DGR3_593.57-624.631 perturbation analysis along with the fit discriminant and best fit values.

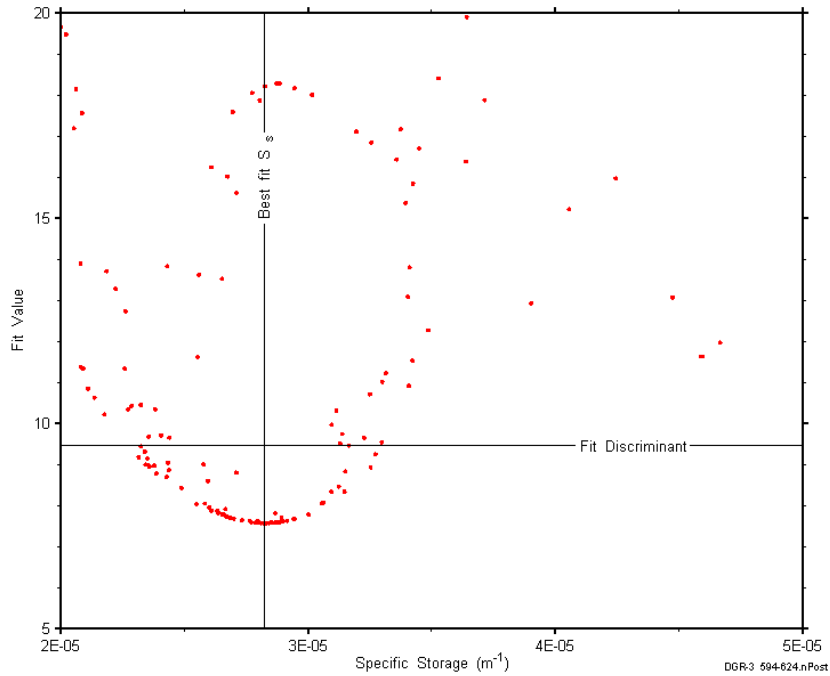


Figure C-194: XY-scatter plot showing the formation specific storage parameter space derived from DGR3_593.57-624.31 perturbation analysis along with the fit discriminant and best fit values.

C.15 617.63-648.37 Georgian Bay-Blue Mountain

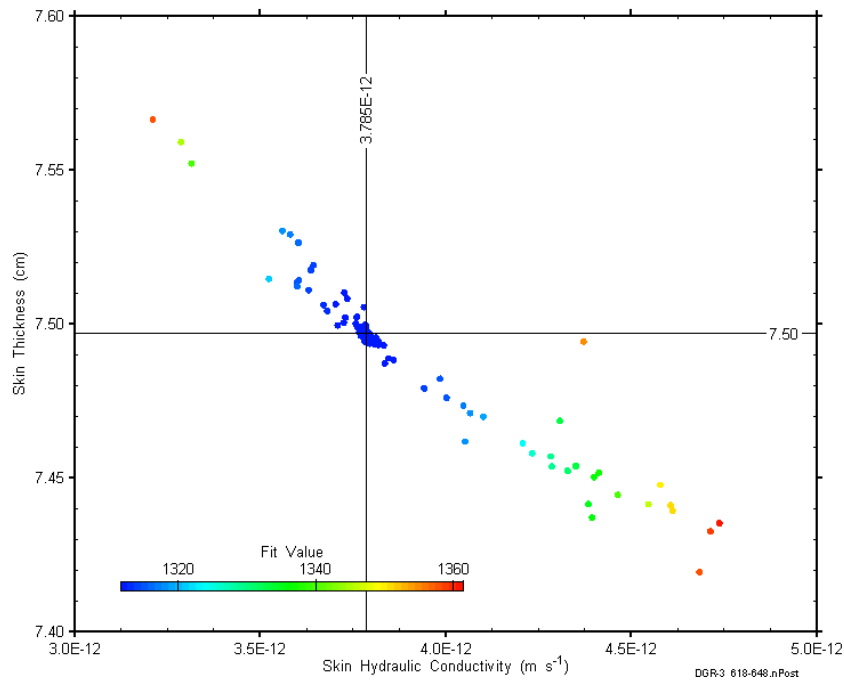


Figure C-195: XY-scatter plot showing estimates of skin hydraulic conductivity and skin thickness derived from the DGR3_617.63-648.37 perturbation analysis.

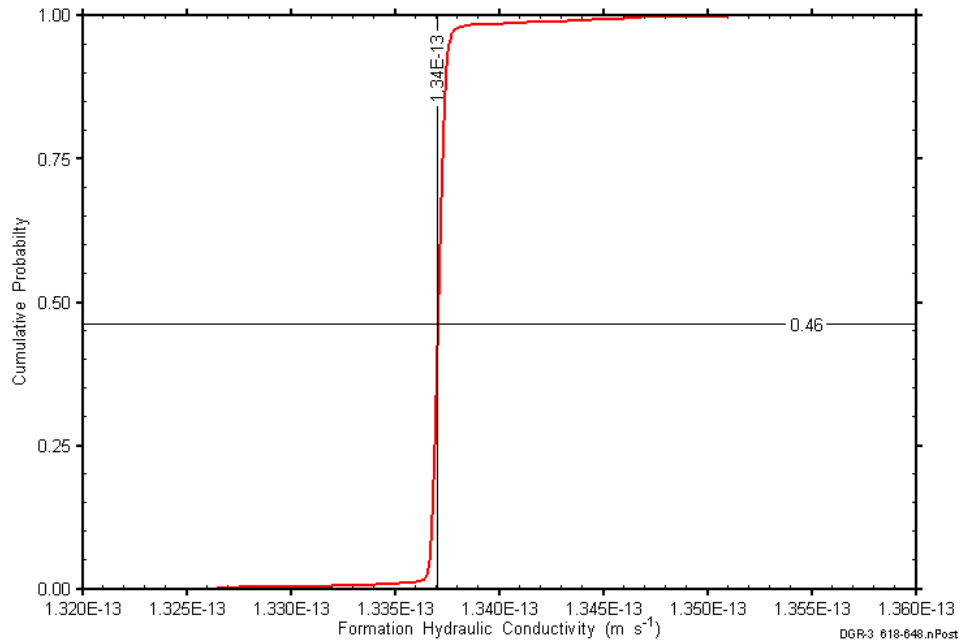


Figure C-196: DGR3_617.63-648.37 formation hydraulic conductivity cumulative distribution function.

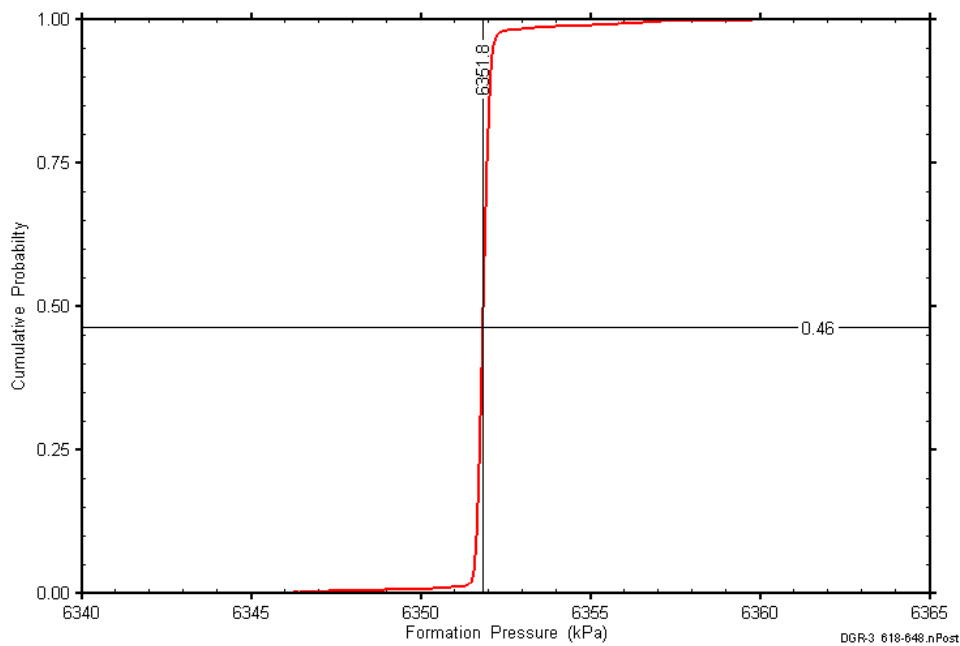


Figure C-197: DGR3_617.63-648.37 static formation pressure cumulative distribution function.

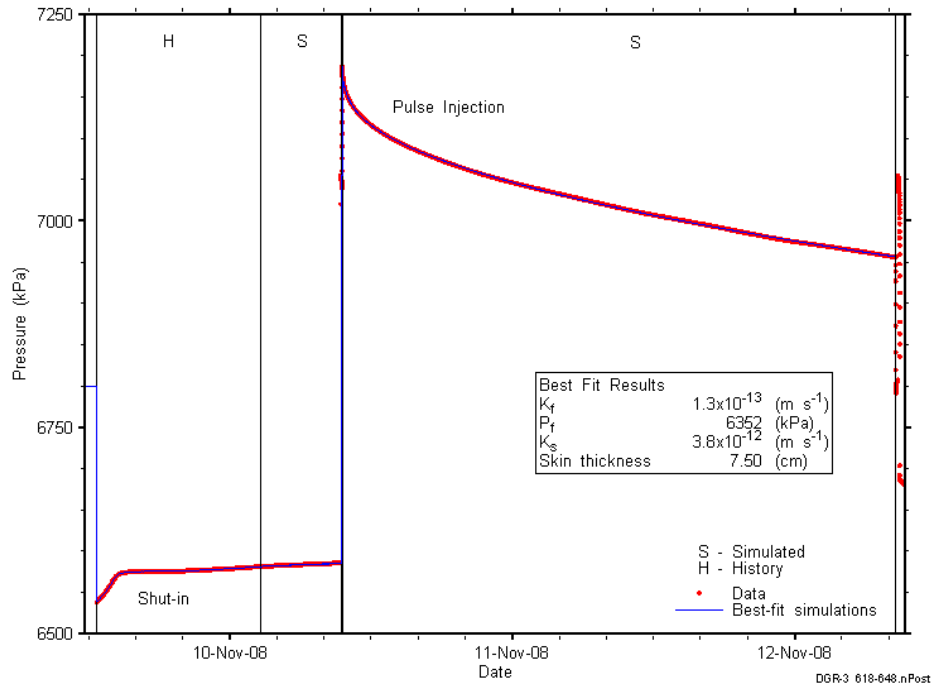


Figure C-198: Linear plot showing simulations of the DGR3_617.63-648.37 pressure response.

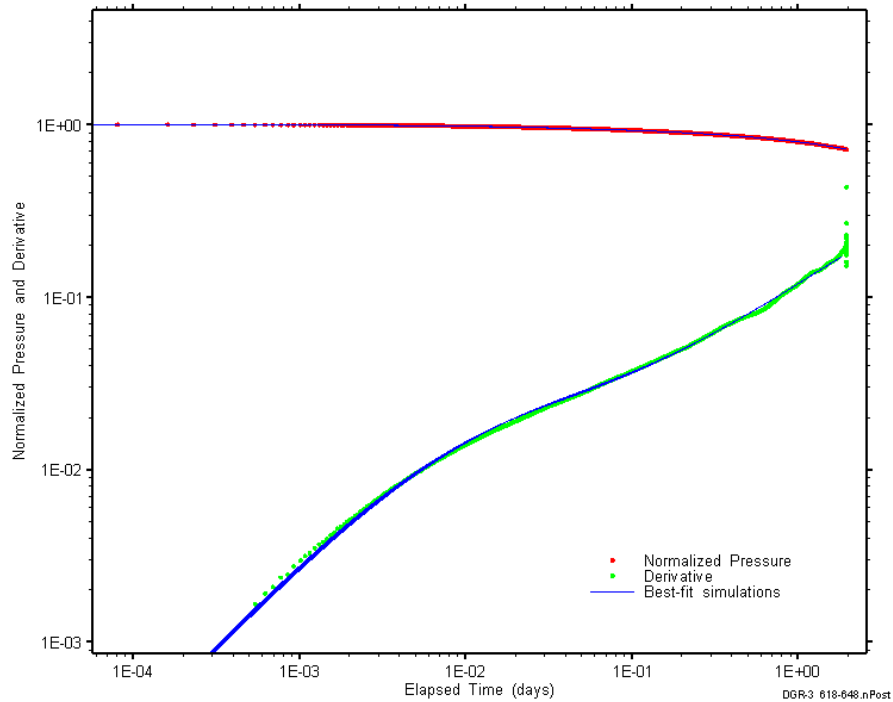


Figure C-199: Log-log plot showing simulations of the DGR3_617.63-648.37 pulse injection Ramey B and derivative response.

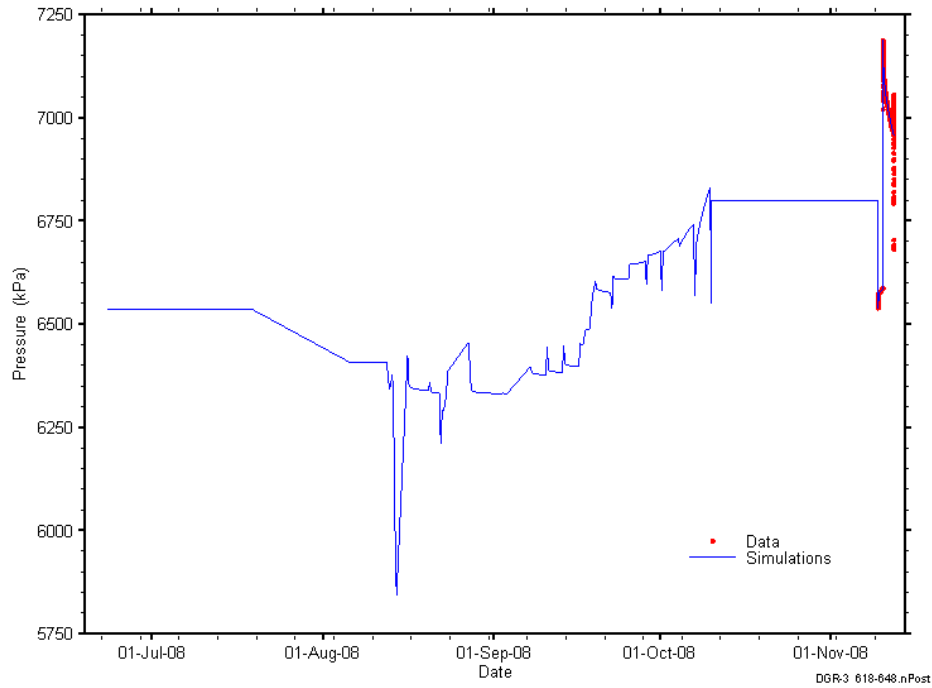


Figure C-200: Linear plot showing simulations of the DGR3_617.63-648.37 pressure response, including pre-test pressure history.

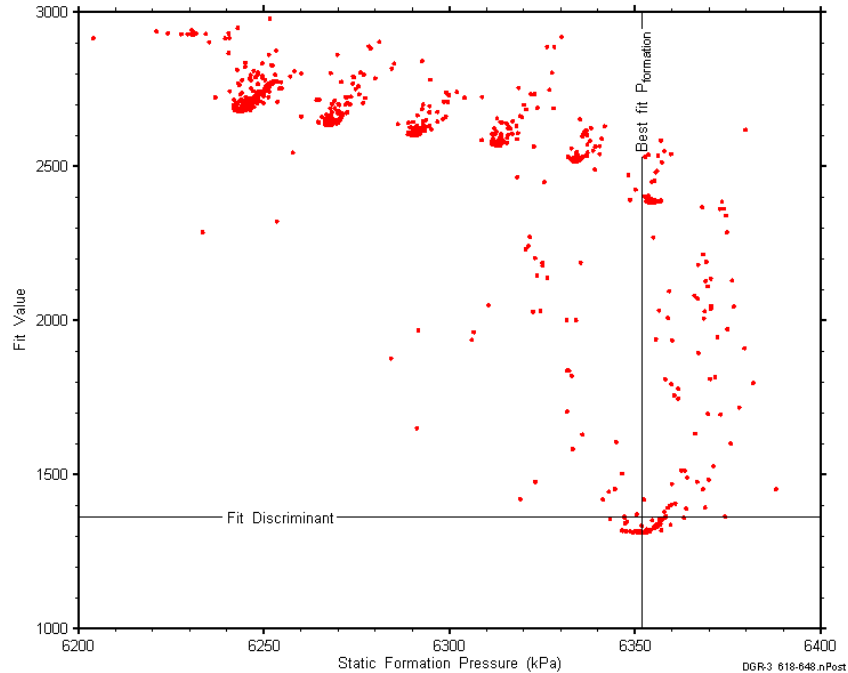


Figure C-201: XY-scatter plot showing the static formation pressure parameter space derived from DGR3_617.63-648.37 perturbation analysis along with the fit discriminant and best fit values.

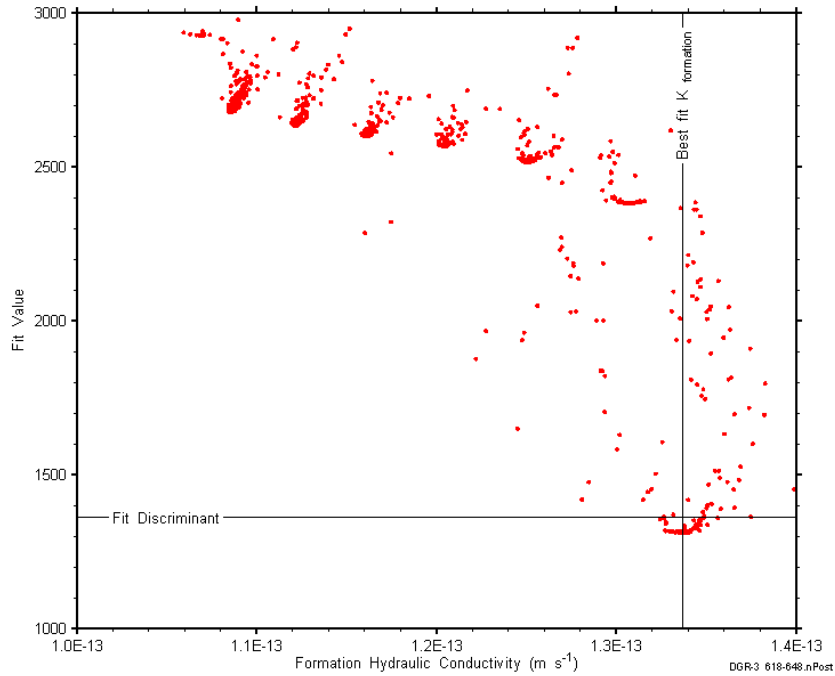


Figure C-202: XY-scatter plot showing the formation hydraulic conductivity parameter space derived from DGR3_617.63-648.37 perturbation analysis along with the fit discriminant and best fit values.

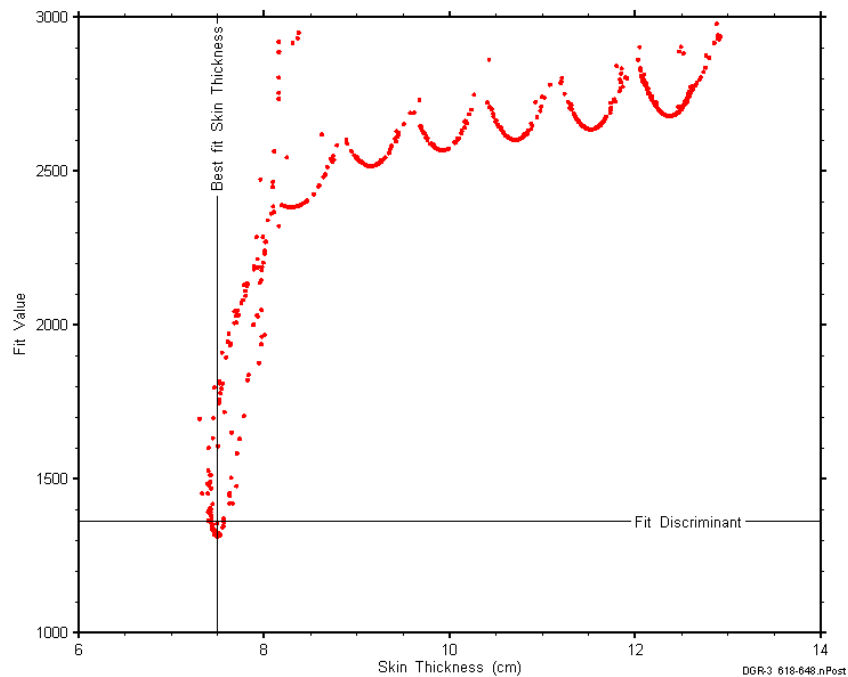


Figure C-203: XY-scatter plot showing the skin-thickness parameter space derived from DGR3_617.63-648.37 perturbation analysis along with the fit discriminant and best fit values.

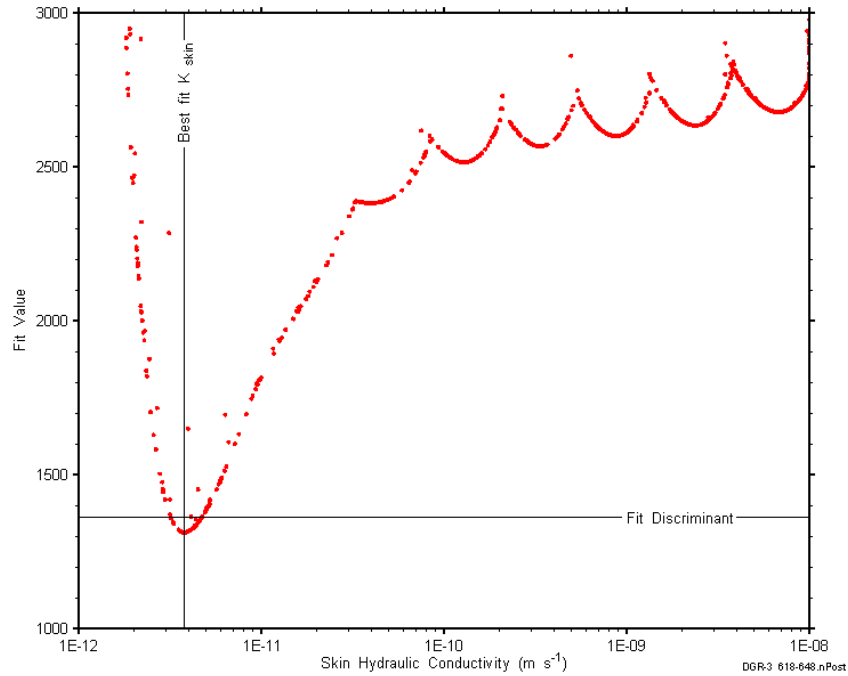


Figure C-204: XY-scatter plot showing the skin hydraulic conductivity parameter space derived from DGR3_617.63-648.37 perturbation analysis along with the fit discriminant and best fit values.

C.16 628.00-658.74 Blue Mountain

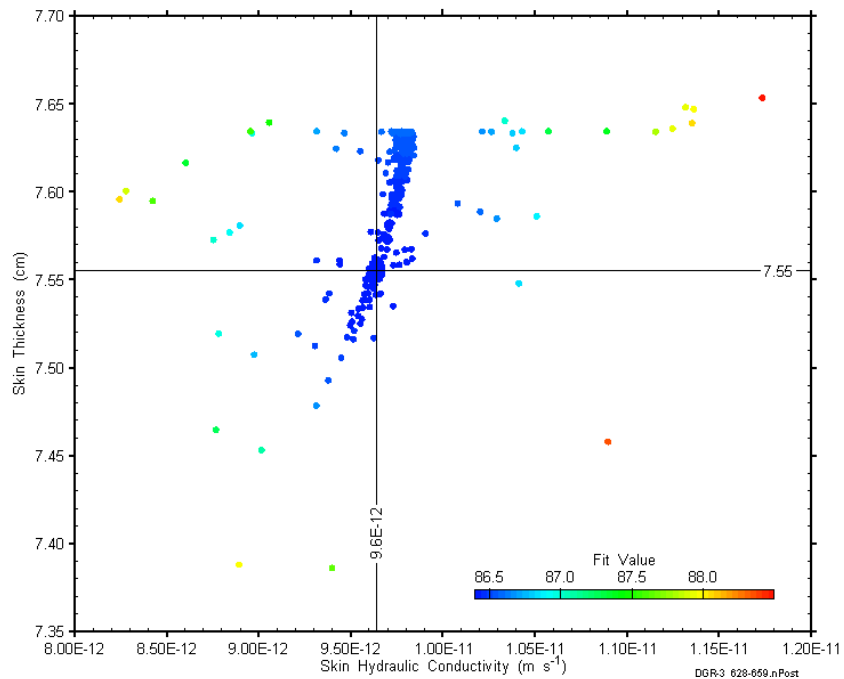


Figure C-205: XY-scatter plot showing estimates of skin hydraulic conductivity and skin thickness derived from the DGR3_628.00-658.74 perturbation analysis.

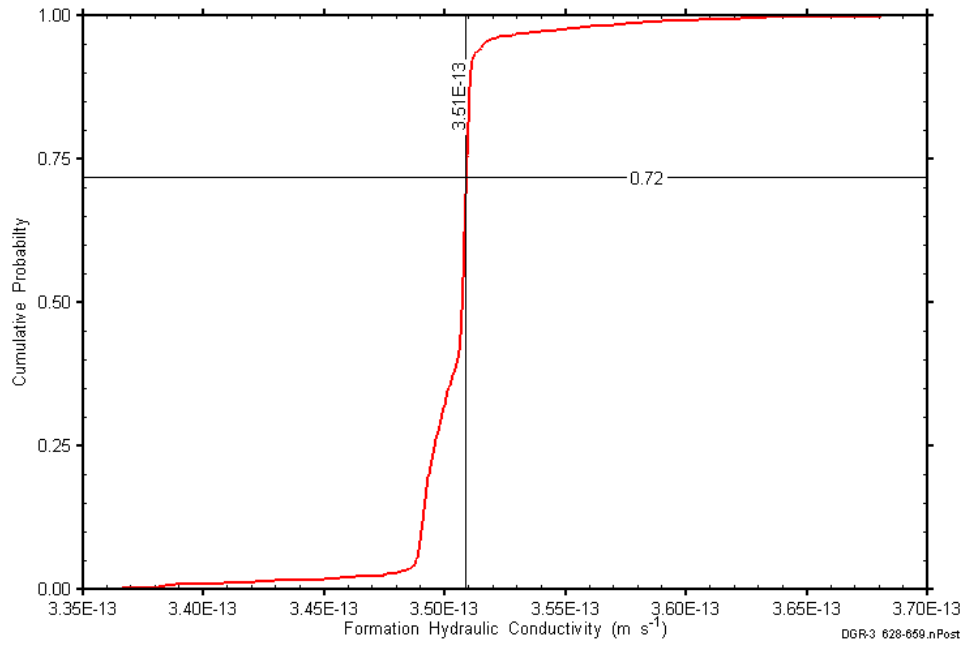


Figure C-206: DGR3_628.00-658.74 formation hydraulic conductivity cumulative distribution function.

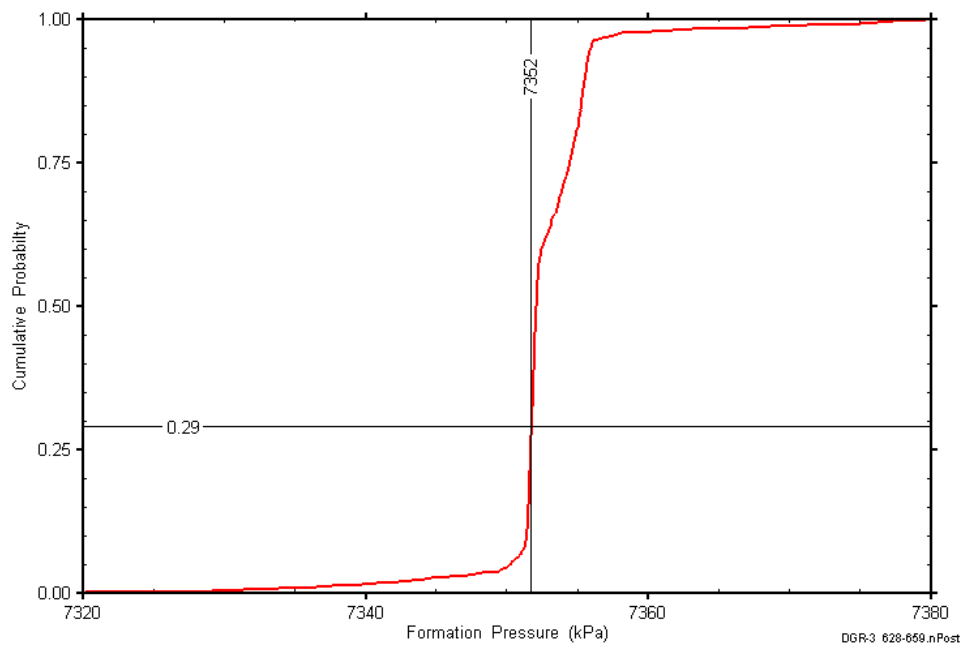


Figure C-207: DGR3_628.00-658.74 static formation pressure cumulative distribution function.

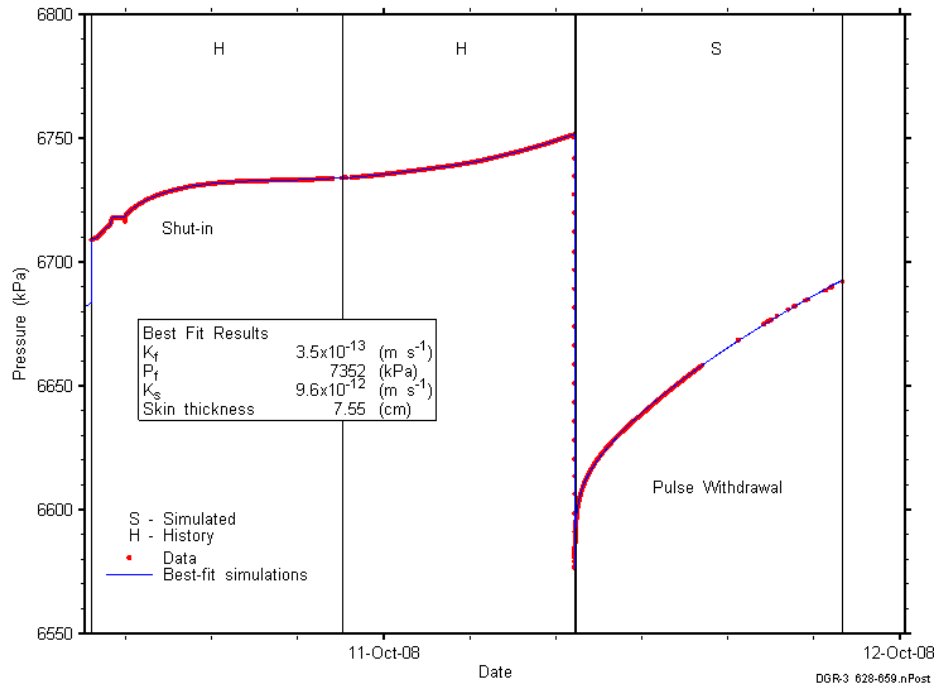


Figure C-208: Linear plot showing simulations of the DGR3_628.00-658.74 pressure response.

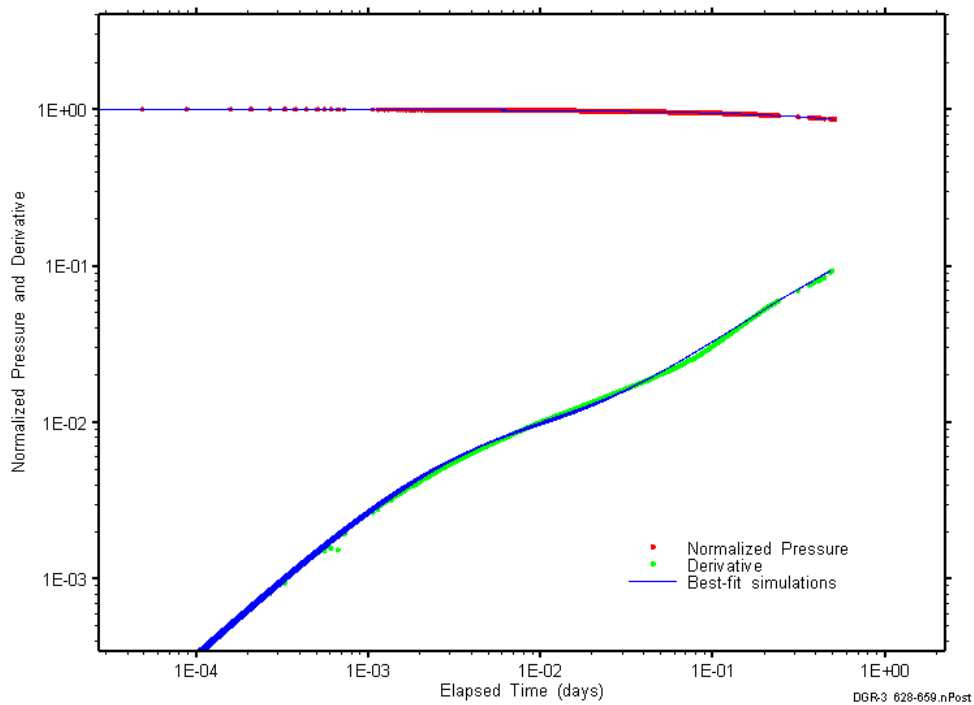


Figure C-209: Log-log plot showing simulations of the DGR3_628.00-658.74 pulse withdrawal Ramey B and derivative response.

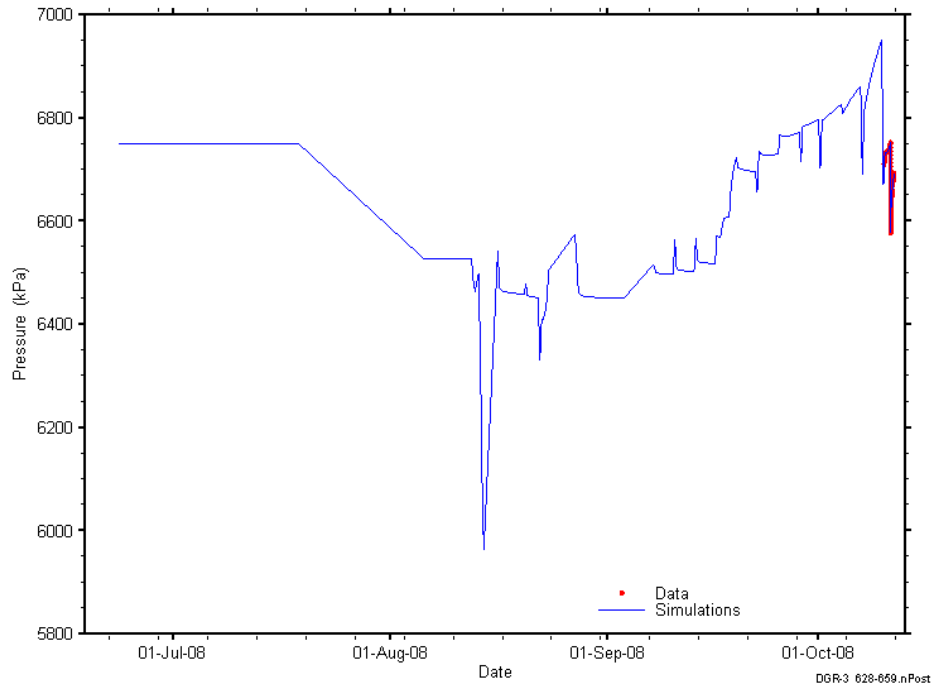


Figure C-210: Linear plot showing details of simulations of the DGR3_628.00-658.74 pressure response, including pre-test pressure history.

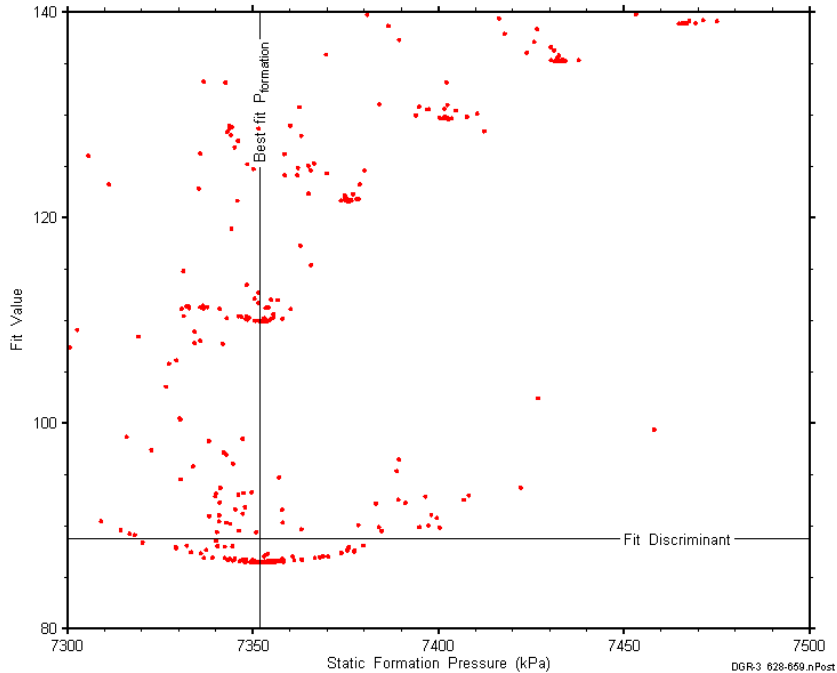


Figure C-211: XY-scatter plot showing the static formation pressure parameter space derived from DGR3_628.00-658.74 perturbation analysis along with the fit discriminant and best fit values.

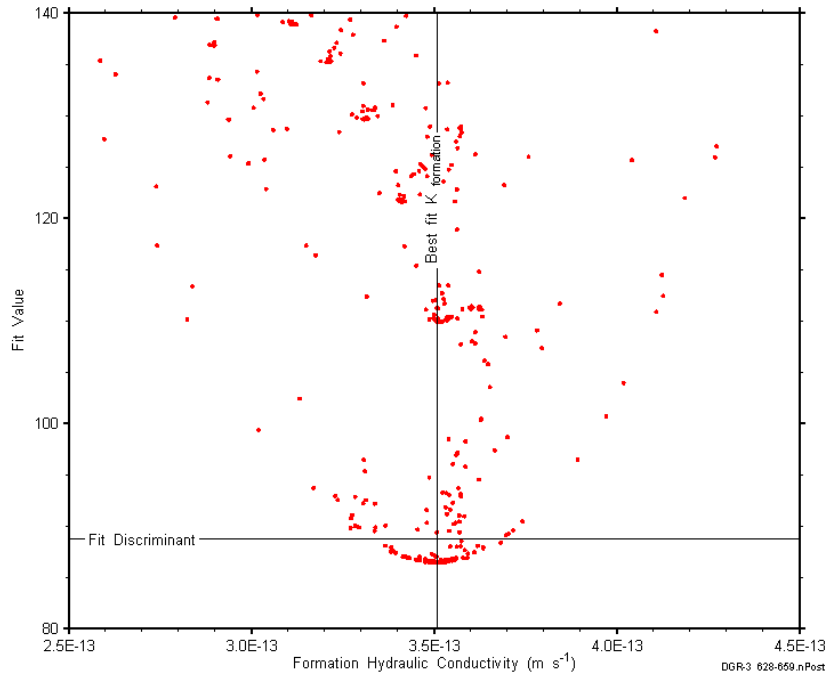


Figure C-212: XY-scatter plot showing the formation hydraulic conductivity parameter space derived from DGR3_628.00-658.74 perturbation analysis along with the fit discriminant and best fit values.

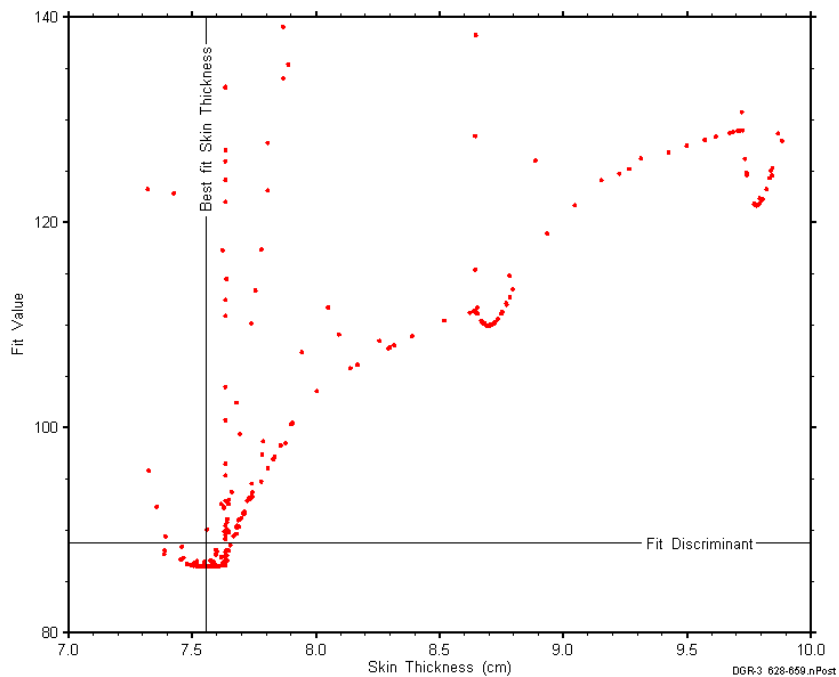


Figure C-213: XY-scatter plot showing the skin-thickness parameter space derived from DGR3_628.00-658.74 perturbation analysis along with the fit discriminant and best fit values.

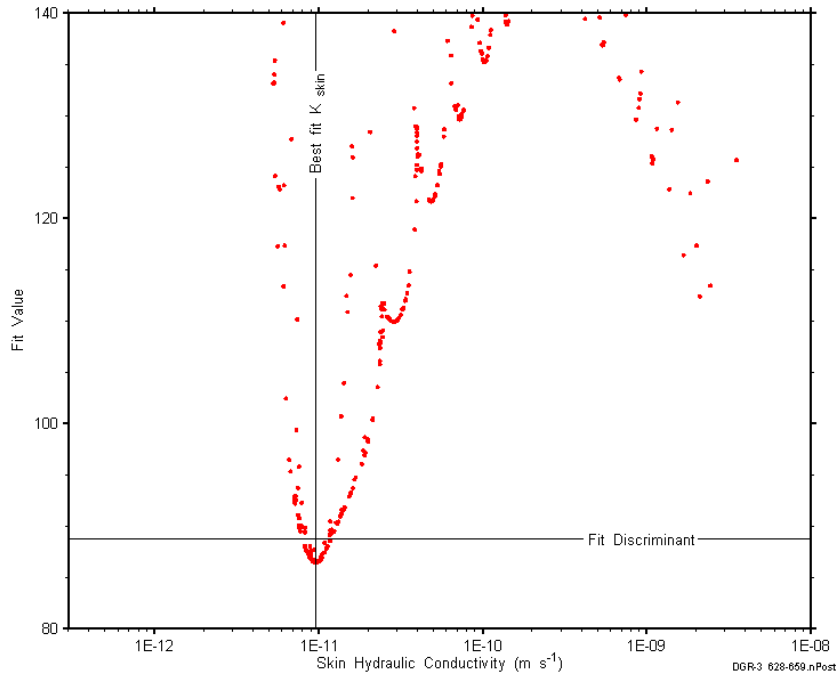


Figure C-214: XY-scatter plot showing the skin hydraulic conductivity parameter space derived from DGR3_628.00-658.74 perturbation analysis along with the fit discriminant and best fit values.

C.17 654.65-685.39 Blue Mountain-Collingwood-Coburg

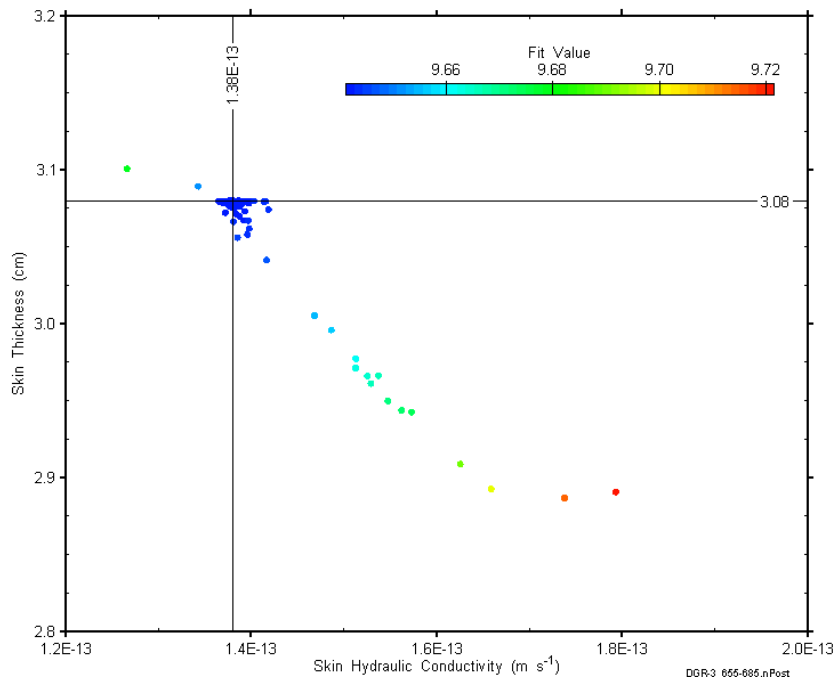


Figure C-215: XY-scatter plot showing estimates of skin hydraulic conductivity and skin thickness derived from the DGR3_654.65-685.39 perturbation analysis.

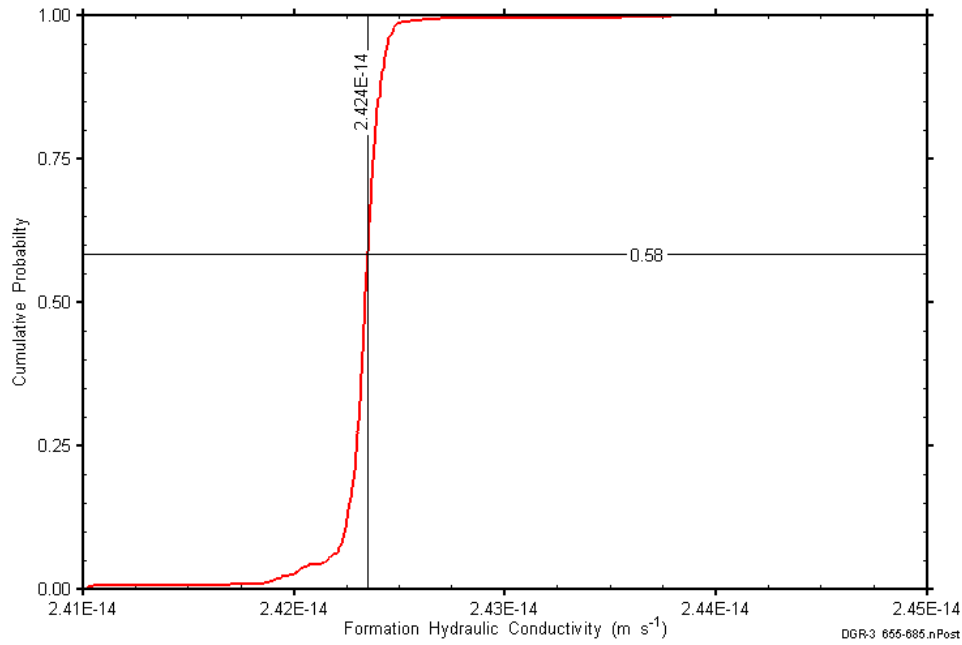


Figure C-216: DGR3_654.65-685.39 formation hydraulic conductivity cumulative distribution function.

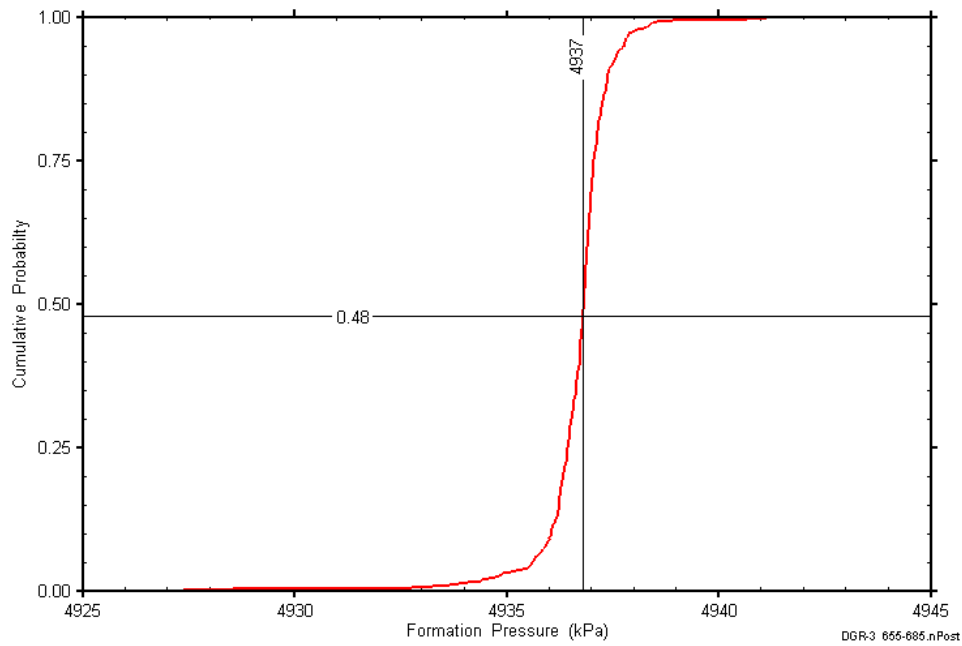


Figure C-217: DGR3_654.65-685.39 static formation pressure cumulative distribution function.

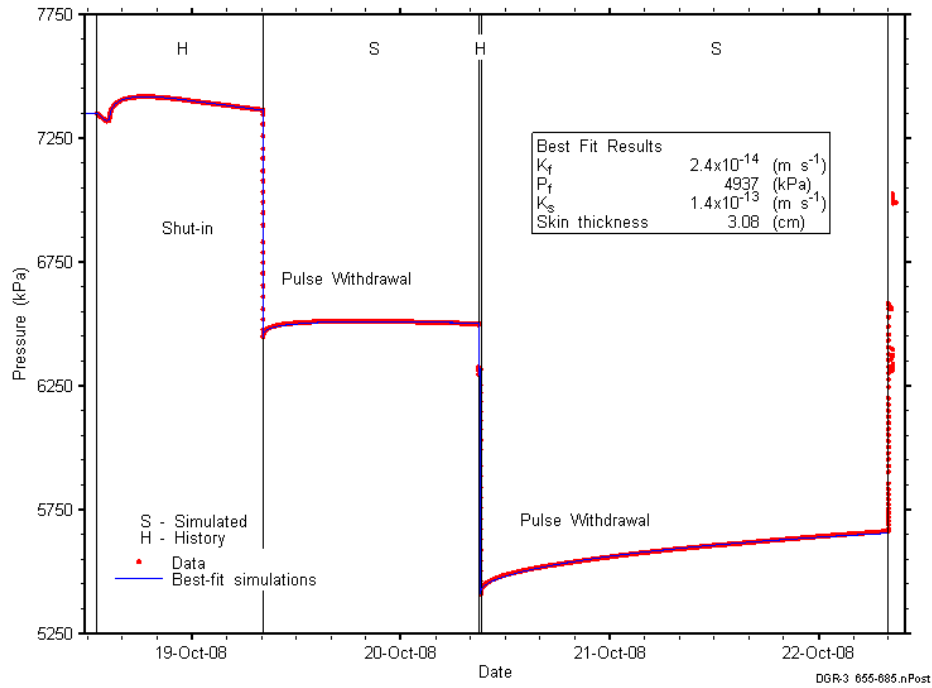


Figure C-218: Linear plot showing simulations of the DGR3_654.65-685.39 pressure response.

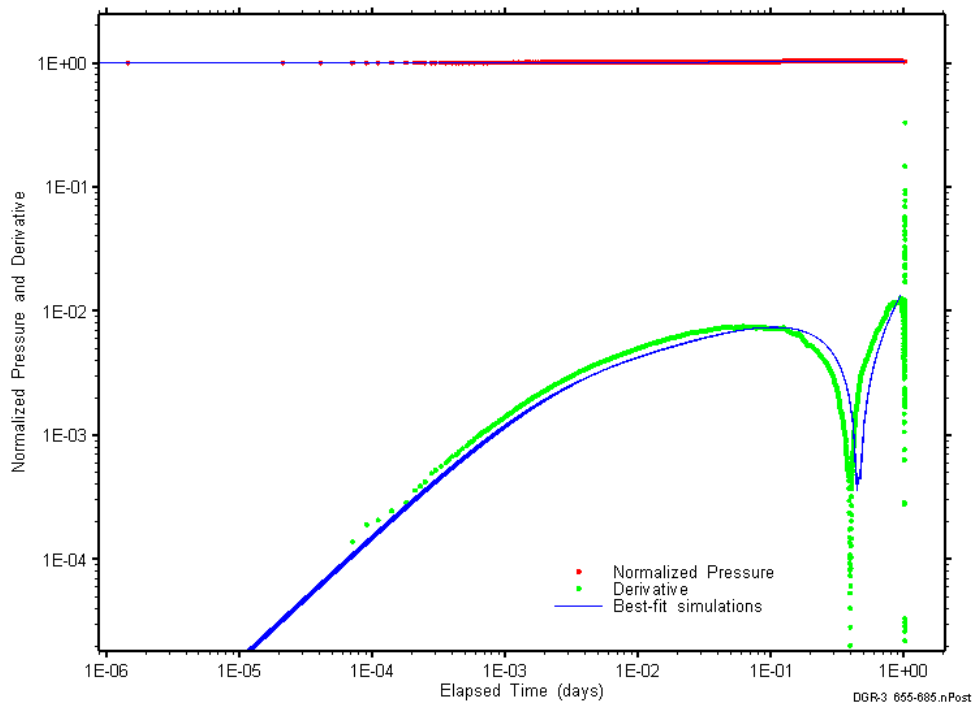


Figure C-219: Log-log plot showing simulations of the DGR3_654.65-685.39 pulse withdrawal #1 Ramey B and derivative response.

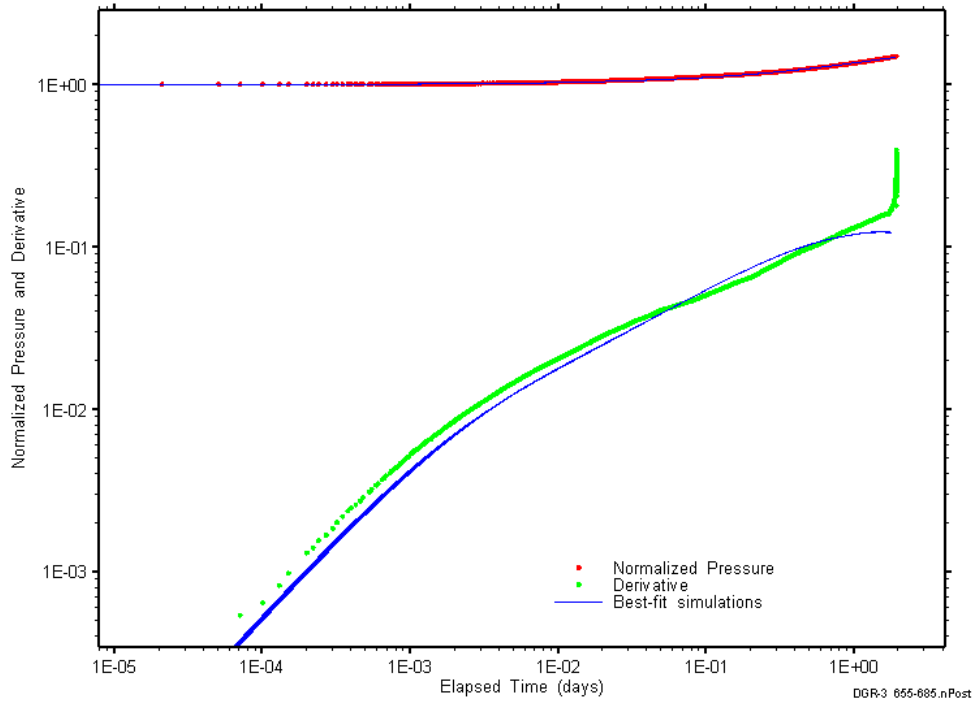


Figure C-220: Log-log plot showing simulations of the DGR3_654.65–685.39 pulse withdrawal #2 Ramey B and derivative response.

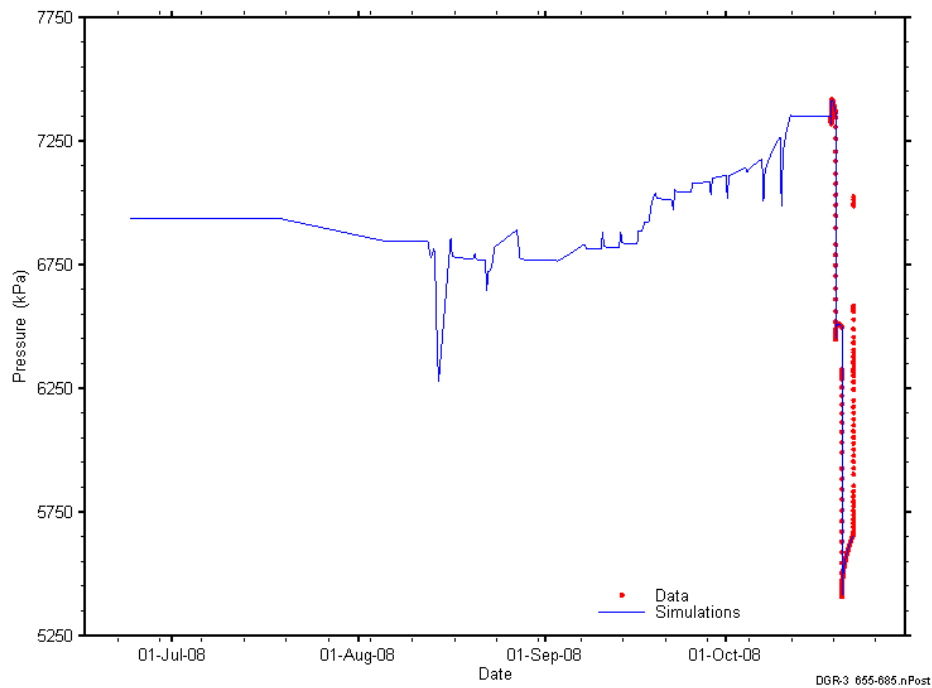


Figure C-221: Linear plot showing simulations of the DGR3_654.65–685.39 pressure response, including pre-test pressure history.

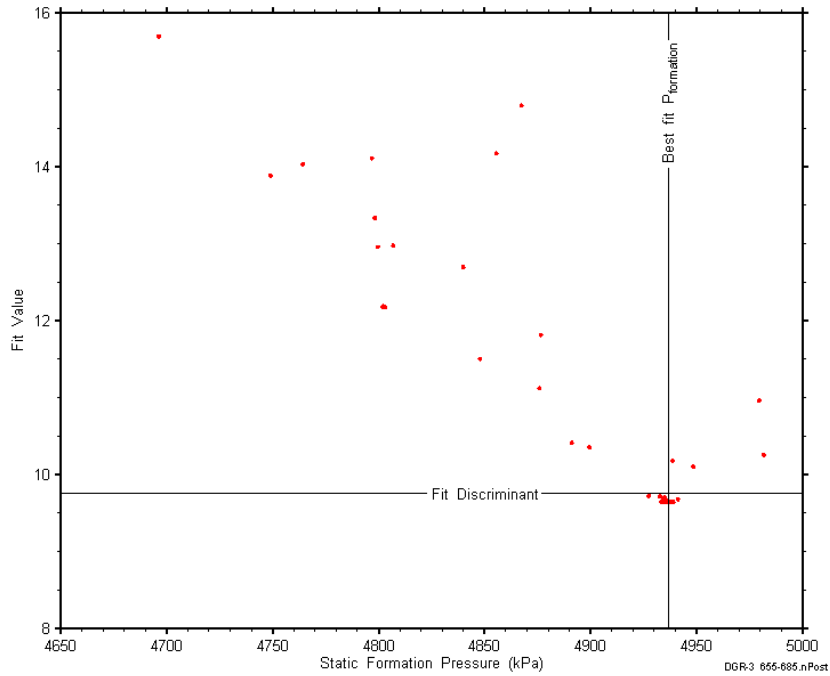


Figure C-222: XY-scatter plot showing the static formation pressure parameter space derived from DGR3_654.65-685.39 perturbation analysis along with the fit discriminant and best fit values.

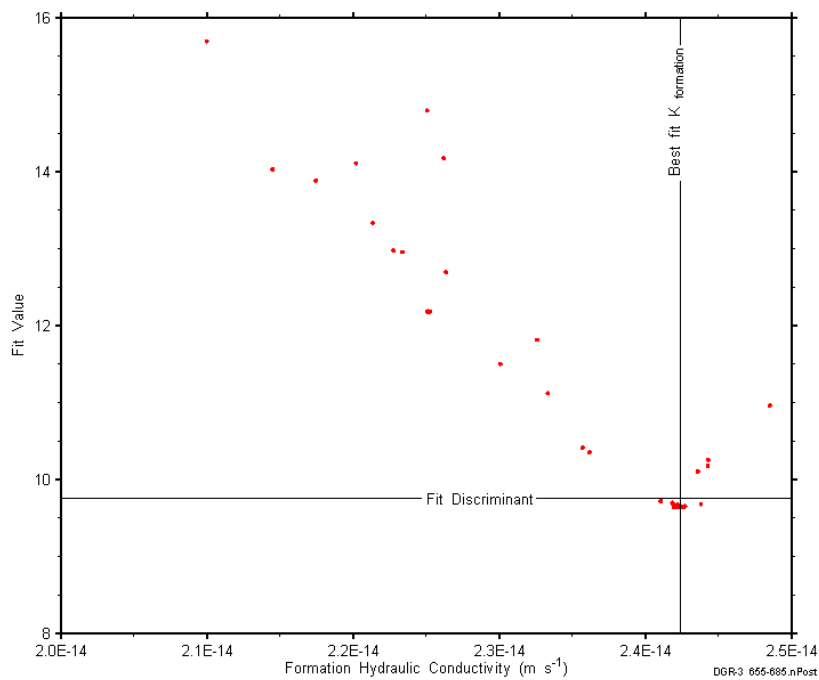


Figure C-223: XY-scatter plot showing the formation hydraulic conductivity parameter space derived from DGR3_654.65-685.39 perturbation analysis along with the fit discriminant and best fit values.

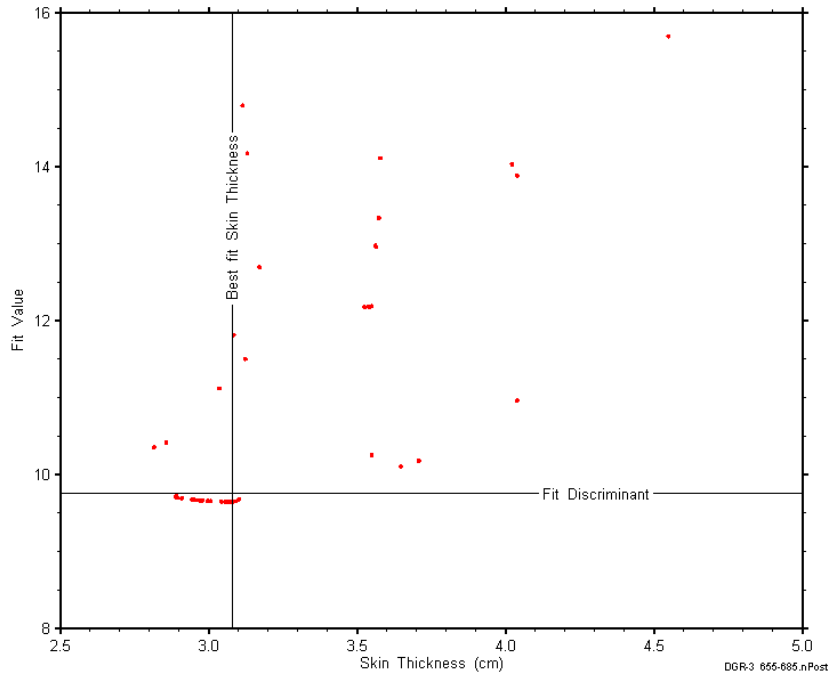


Figure C-224: XY-scatter plot showing the skin-thickness parameter space derived from DGR3_654.65-685.39 perturbation analysis along with the fit discriminant and best fit values.

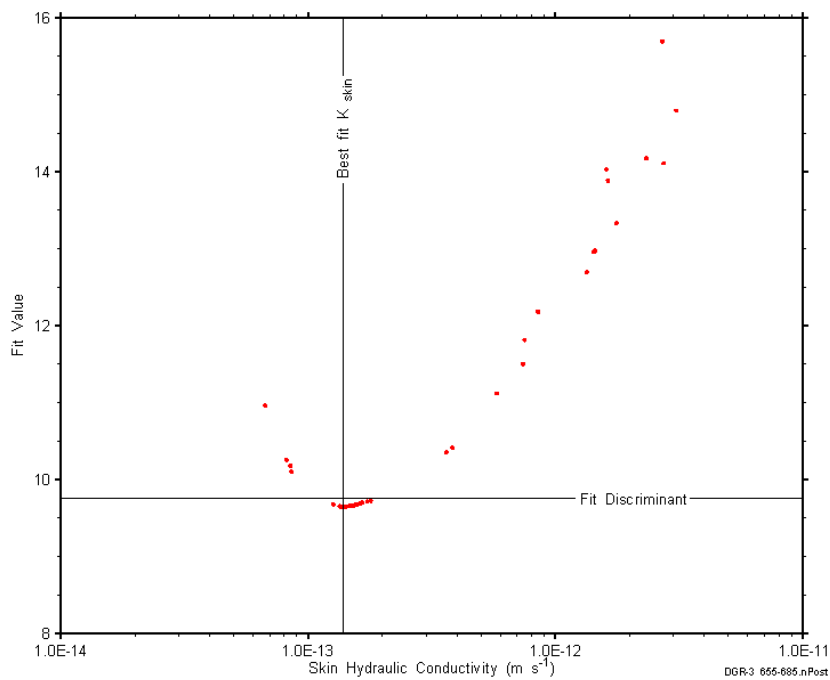


Figure C-225: XY-scatter plot showing the skin hydraulic conductivity parameter space derived from DGR3_654.65-685.39 perturbation analysis along with the fit discriminant and best fit values.

C.18 671.50-702.24 Collingwood-Coburg-Sherman Fall

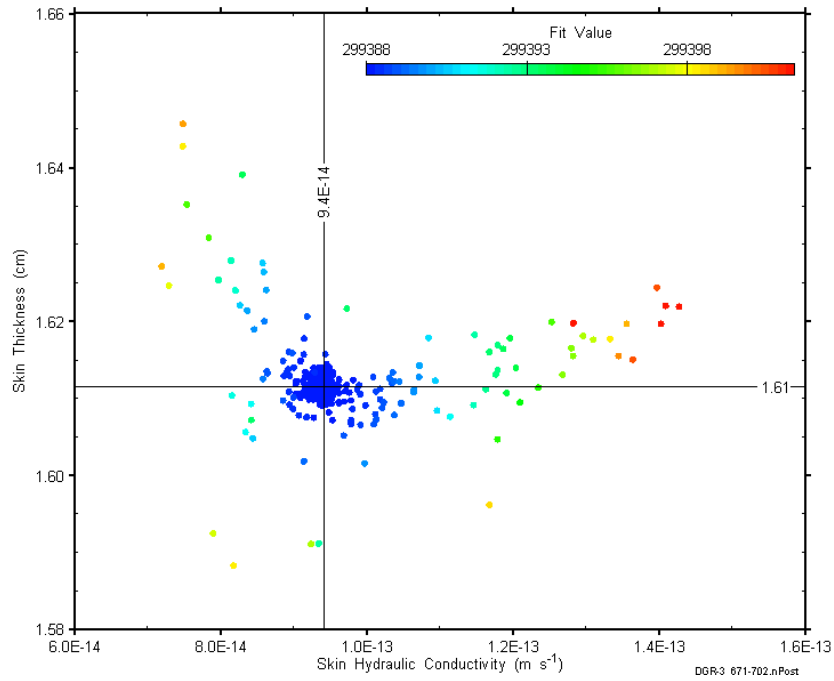


Figure C-226: XY-scatter plot showing estimates of skin hydraulic conductivity and skin thickness derived from the DGR3_671.50-702.24 perturbation analysis.

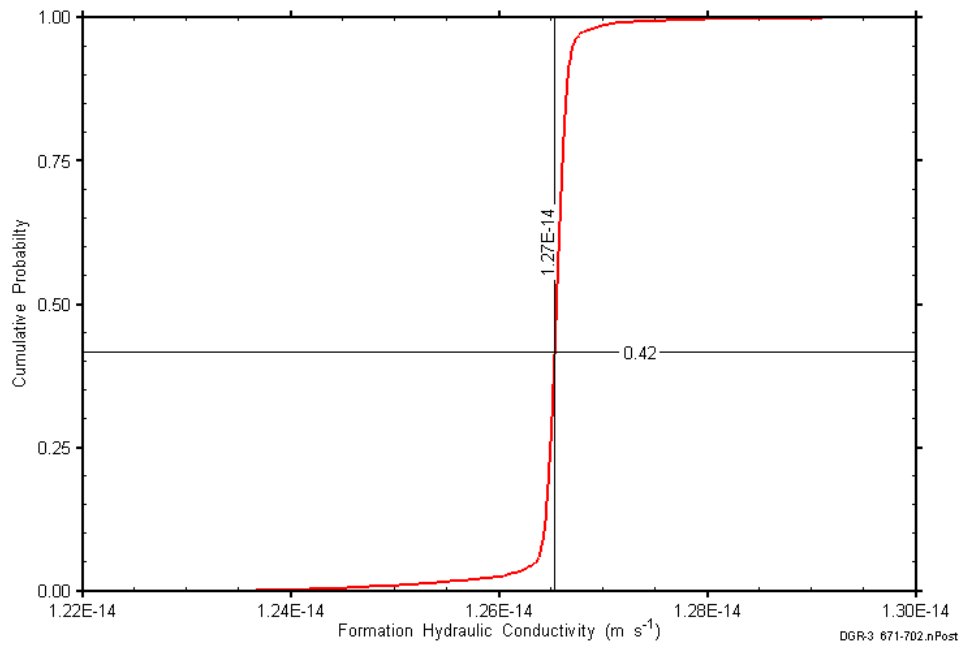


Figure C-227: DGR3_671.50-702.24 formation hydraulic conductivity cumulative distribution function.

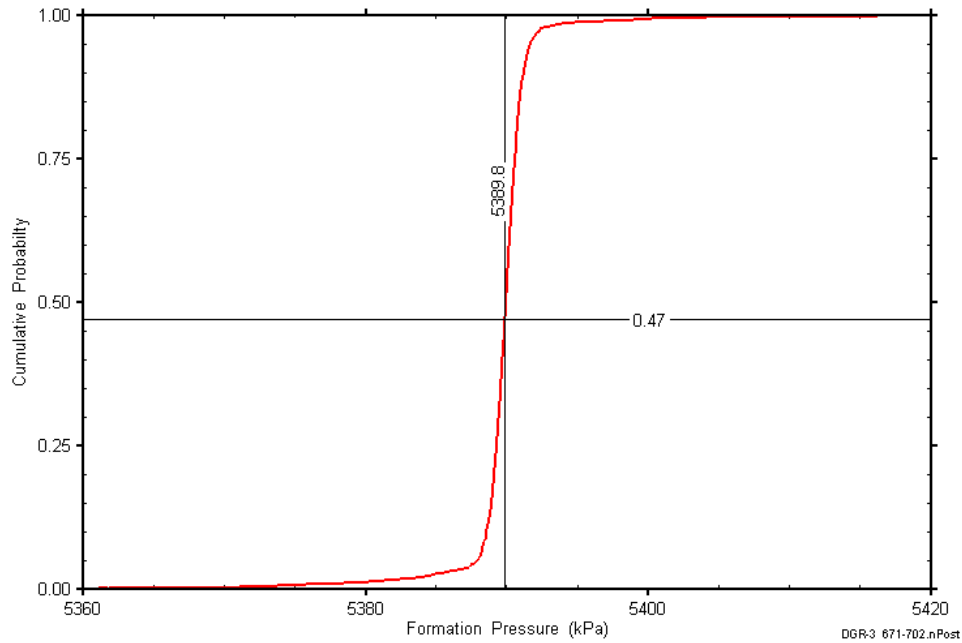


Figure C-228: DGR3_671.50-702.24 static formation pressure cumulative distribution function.

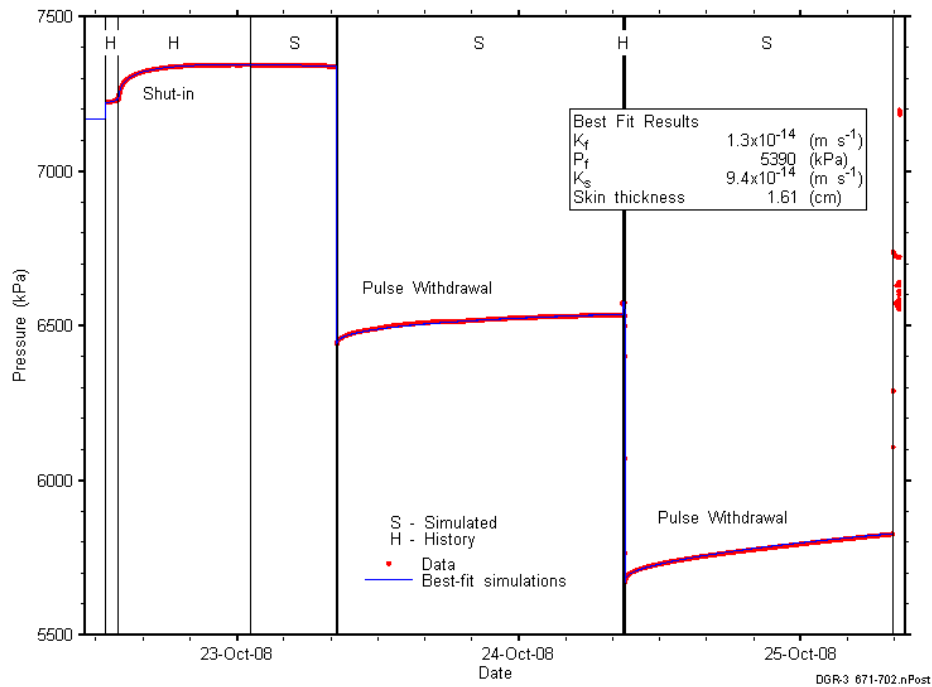


Figure C-229: Linear plot showing simulations of the DGR3_671.50-702.24 pressure response.

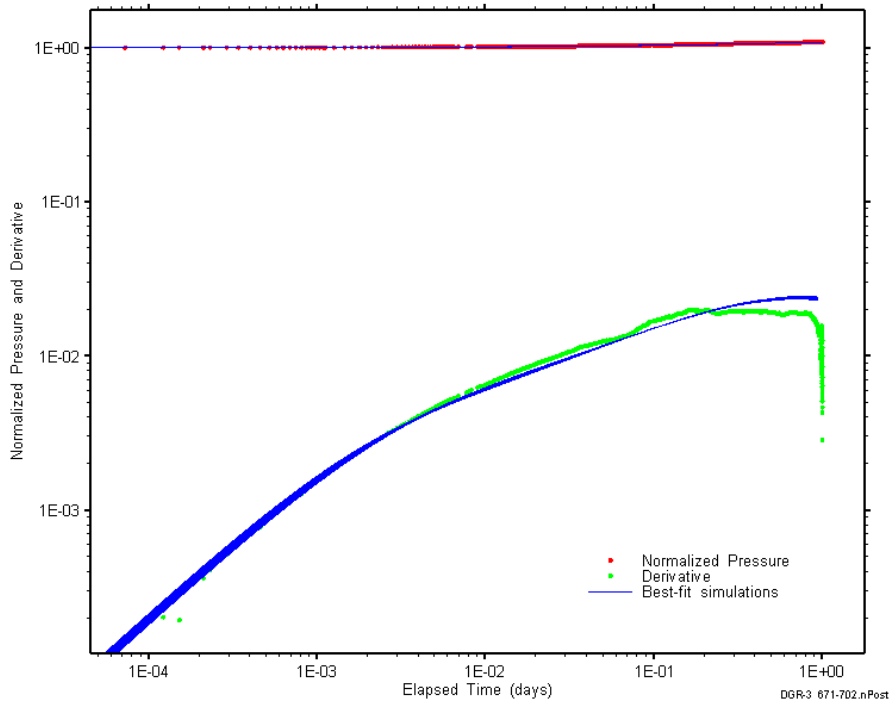


Figure C-230: Log-log plot showing simulations of the DGR3_671.50–702.24 pulse withdrawal #1 Ramey B and derivative response.

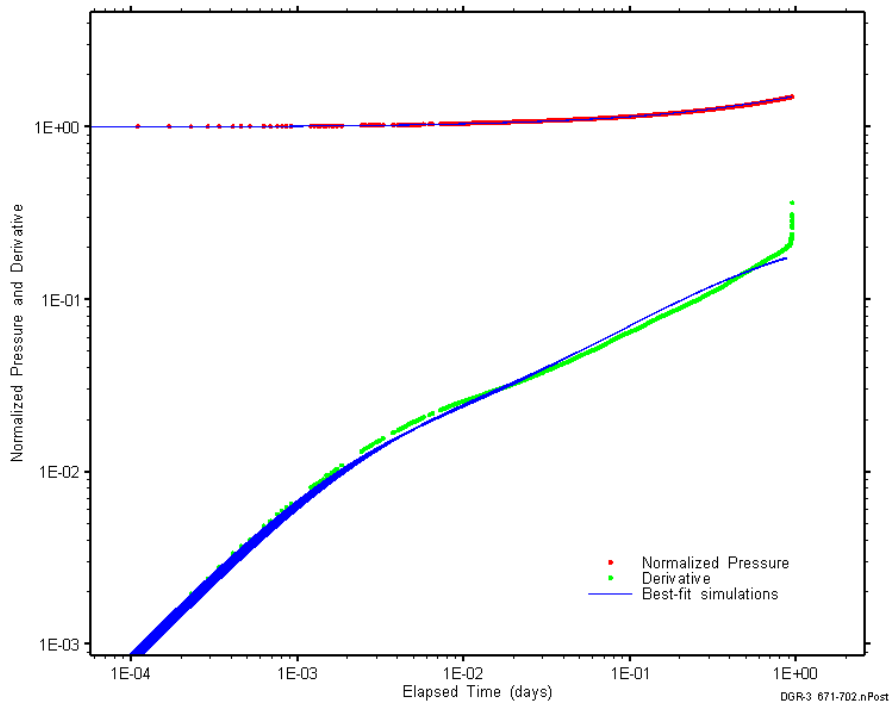


Figure C-231: Log-log plot showing simulations of the DGR3_671.50–702.24 pulse withdrawal #2 Ramey B and derivative response.

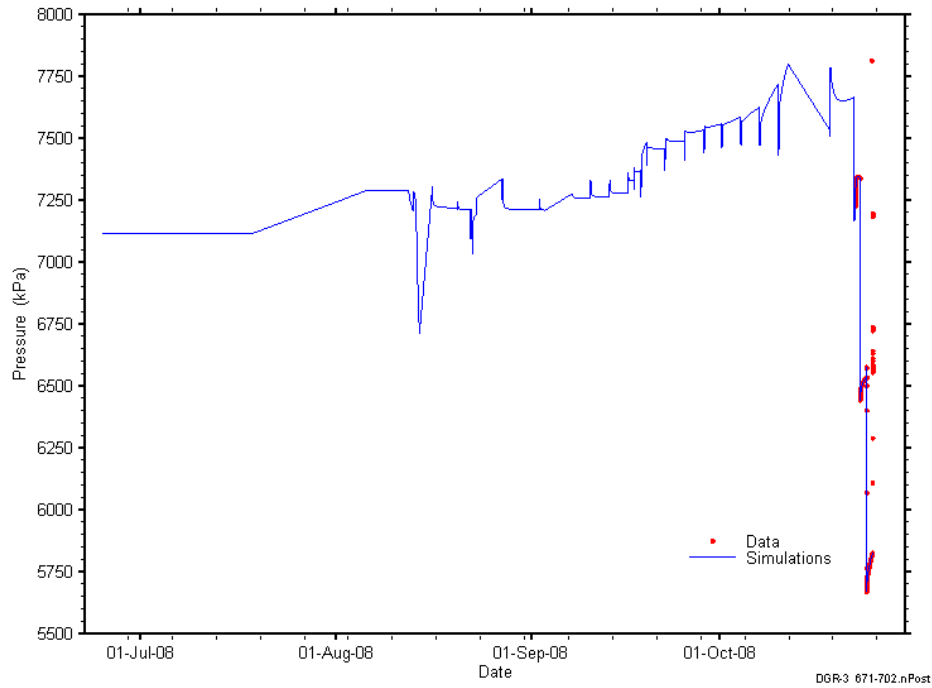


Figure C-232: Linear plot showing simulations of the DGR3_671.50-702.24 pressure response, including pre-test pressure history.

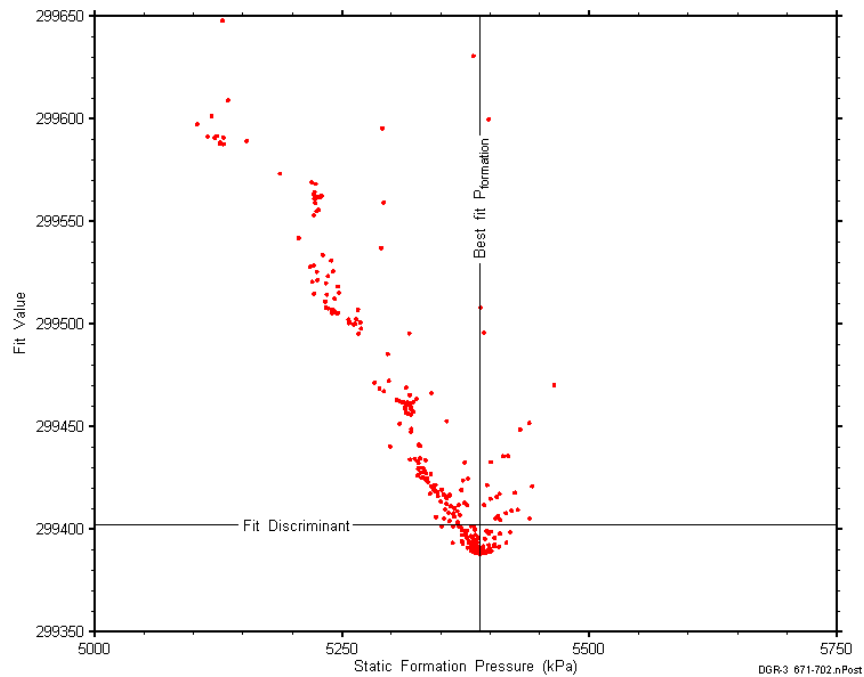


Figure C-233: XY-scatter plot showing the static formation pressure parameter space derived from DGR3_671.50-702.24 perturbation analysis along with the fit discriminant and best fit values.

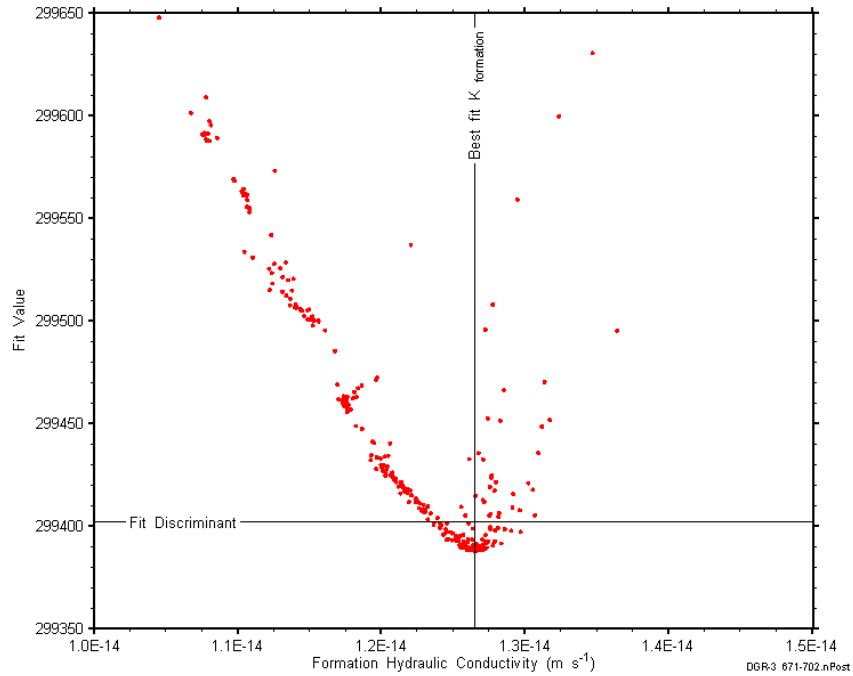


Figure C-234: XY-scatter plot showing the formation hydraulic conductivity parameter space derived from DGR3_671.50-702.24 perturbation analysis along with the fit discriminant and best fit values.

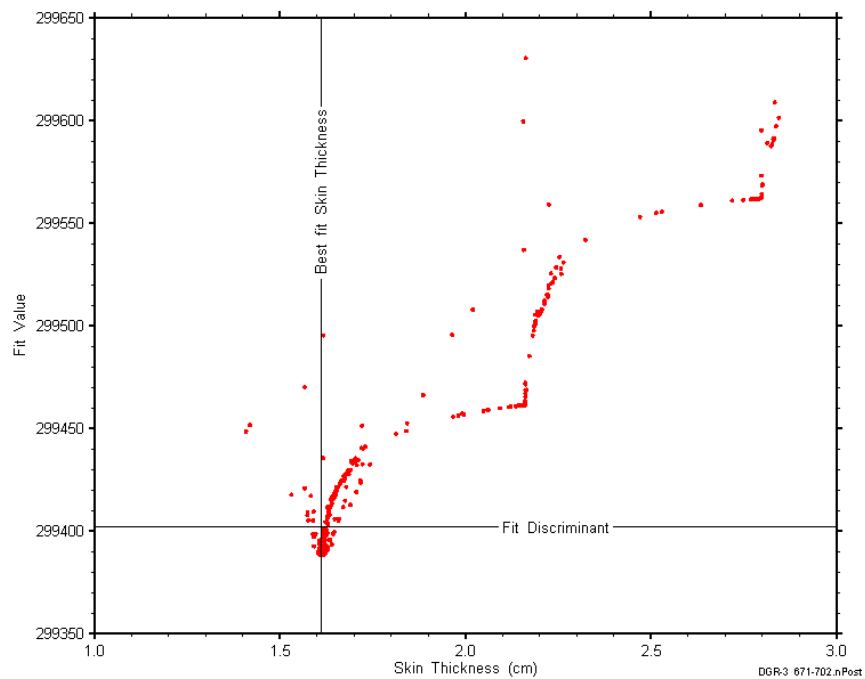


Figure C-235: XY-scatter plot showing the skin-thickness parameter space derived from DGR3_671.50-702.24 perturbation analysis along with the fit discriminant and best fit values.

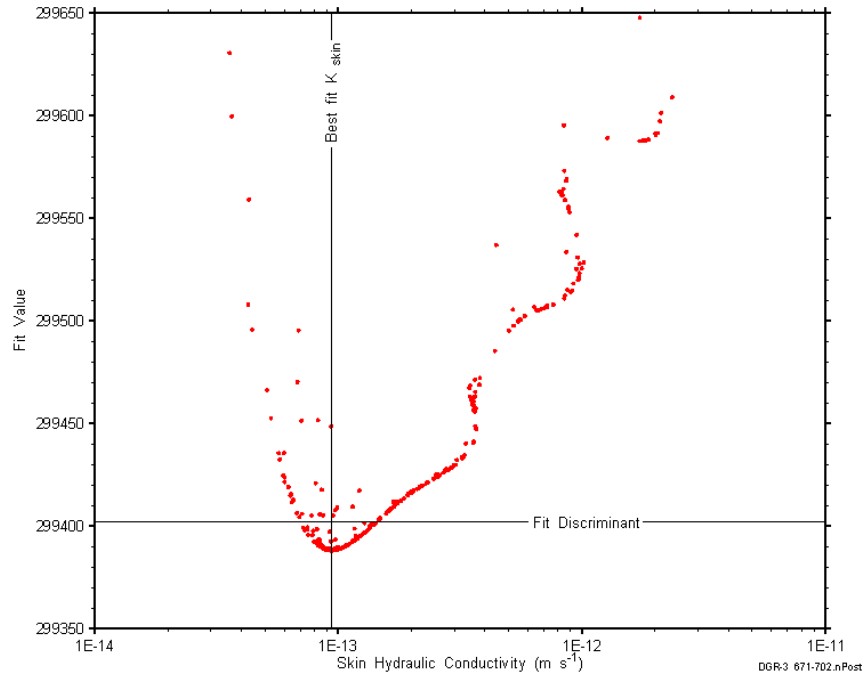


Figure C-236: XY-scatter plot showing the skin hydraulic conductivity parameter space derived from DGR3_671.50-702.24 perturbation analysis along with the fit discriminant and best fit values.

C.19 710.00-740.74 Sherman Fall-Kirkfield

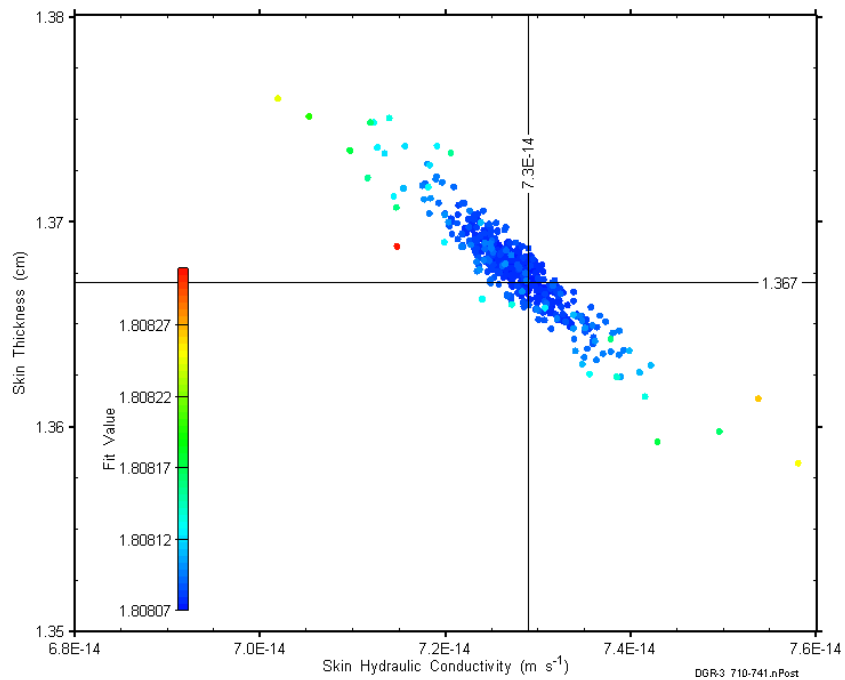


Figure C-237: XY-scatter plot showing estimates of skin hydraulic conductivity and skin thickness derived from the DGR3_710.00-740.74 perturbation analysis.

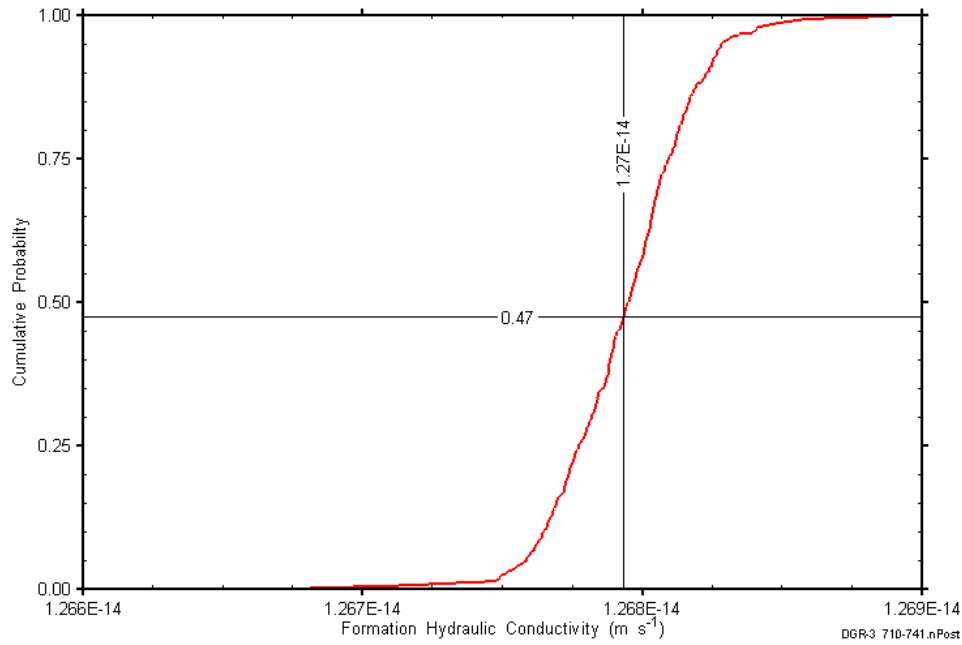


Figure C-238: DGR3_710.00-740.74 formation hydraulic conductivity cumulative distribution function.

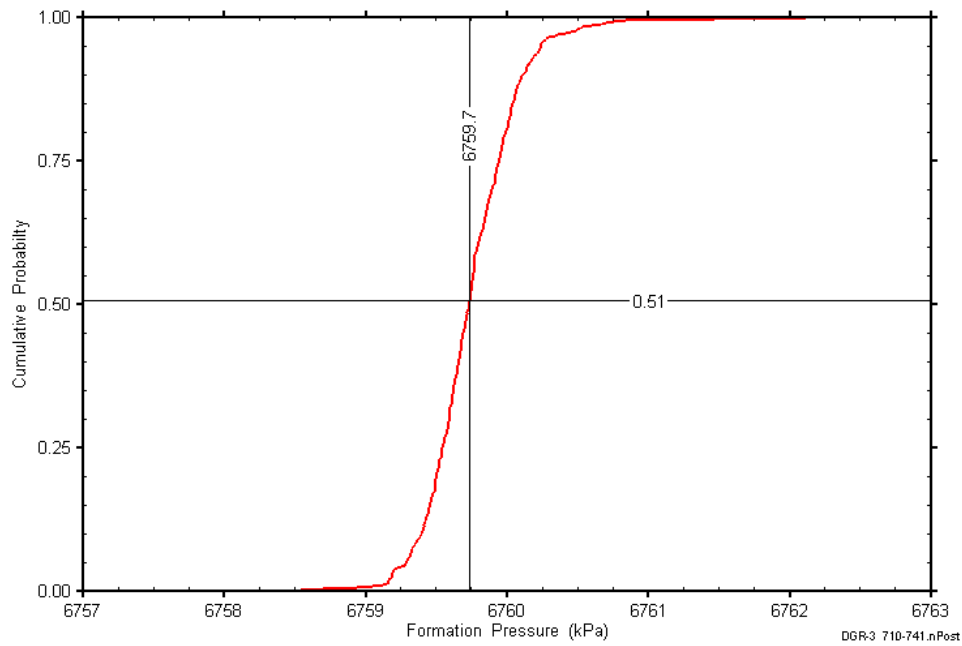


Figure C-239: DGR3_710.00-740.74 static formation pressure cumulative distribution function.

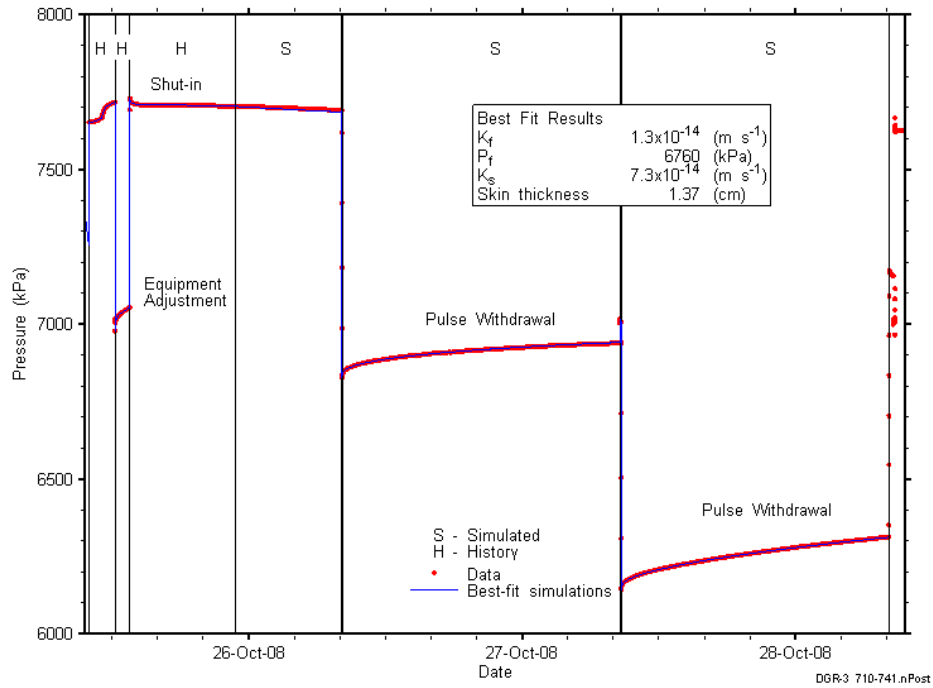


Figure C-240: Linear plot showing simulations of the DGR3_710.00-740.74 pressure response.

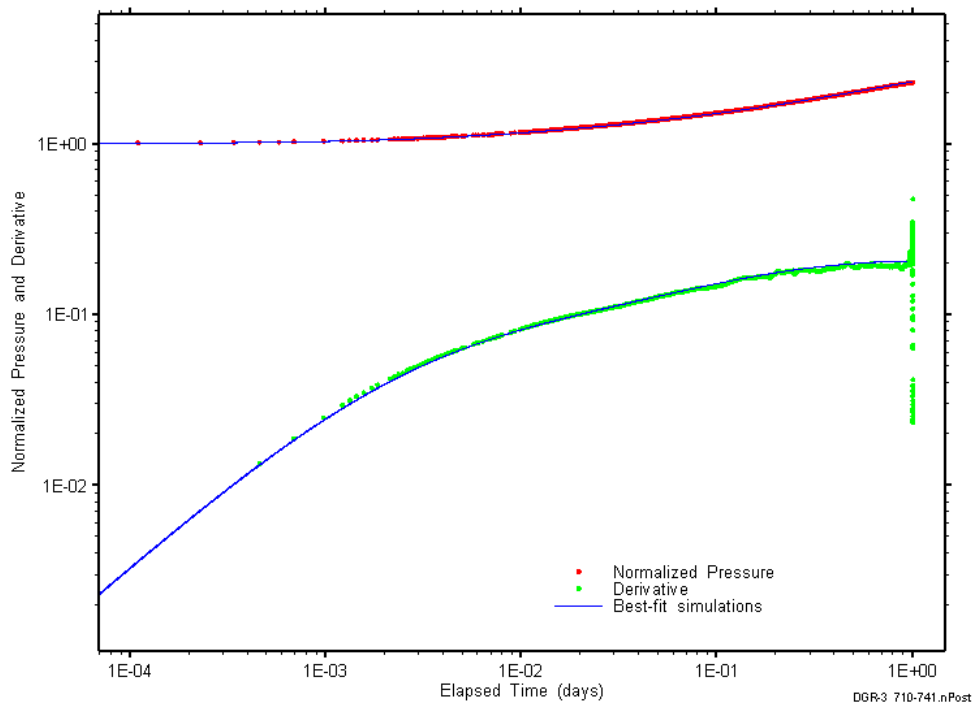


Figure C-241: Log-log plot showing simulations of the DGR3_710.00-740.24 pulse withdrawal #1 Ramey B and derivative response.

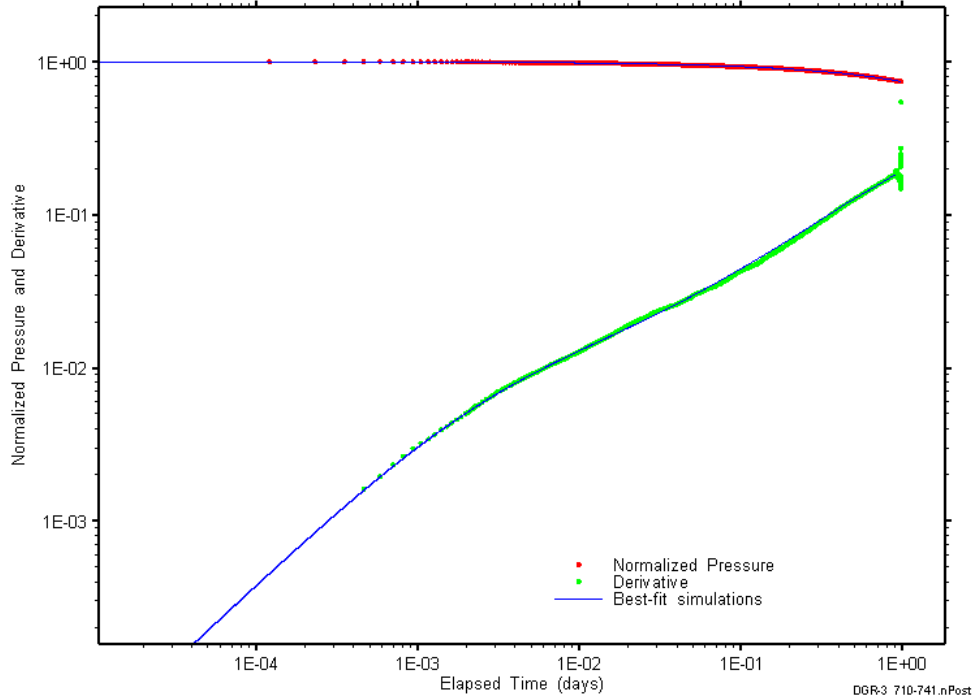


Figure C-242: Log-log plot showing simulations of the DGR3_710.00–740.24 pulse withdrawal #2 Ramey B and derivative response.

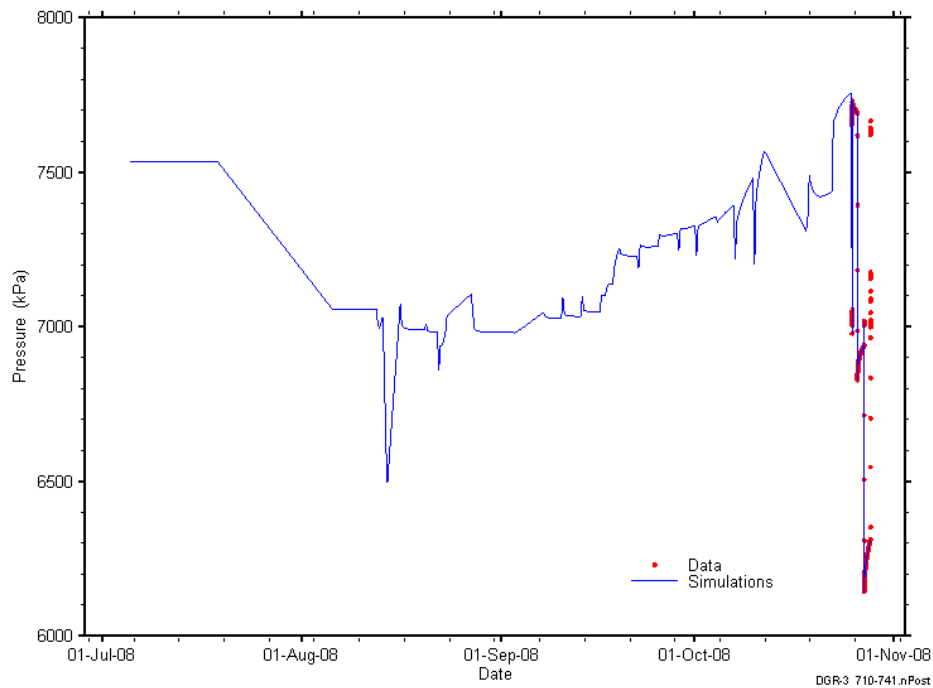


Figure C-243: Linear plot showing simulations of the DGR3_710.00-740.74 pressure response, including pre-test pressure history.

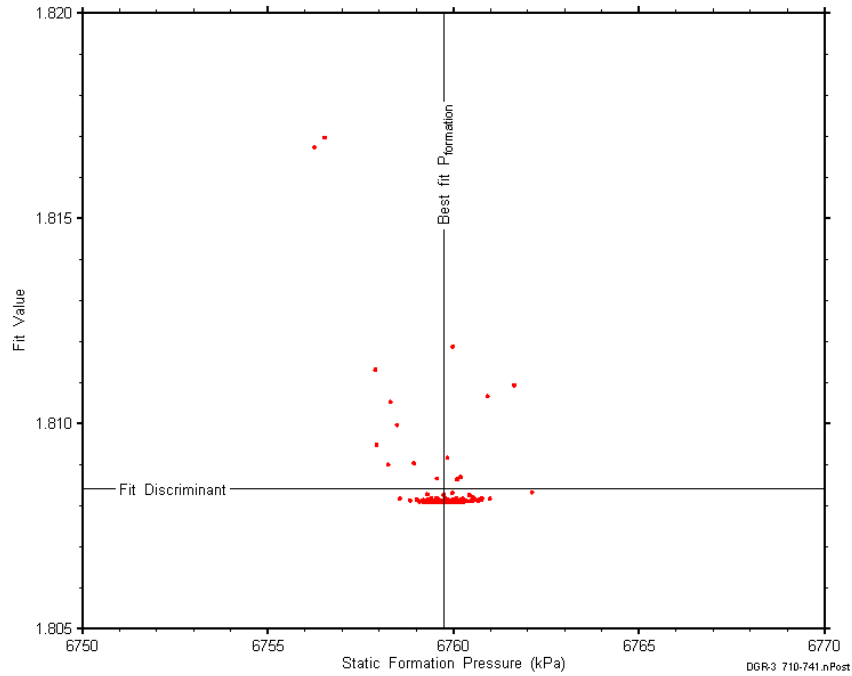


Figure C-244: XY-scatter plot showing the static formation pressure parameter space derived from DGR3_710.00-740.74 perturbation analysis along with the fit discriminant and best fit values.

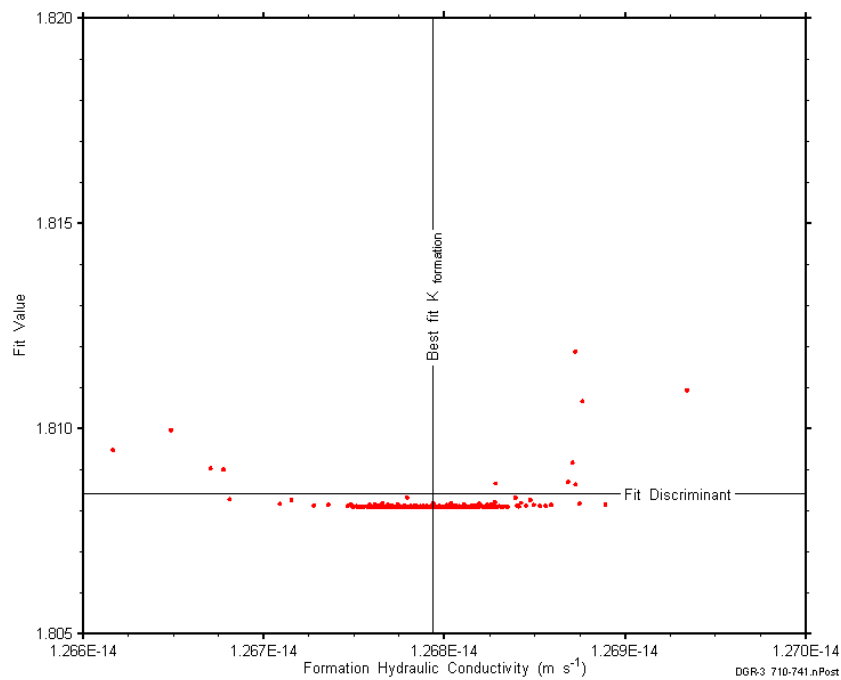


Figure C-245: XY-scatter plot showing the formation hydraulic conductivity parameter space derived from DGR3_710.00-740.74 perturbation analysis along with the fit discriminant and best fit values.

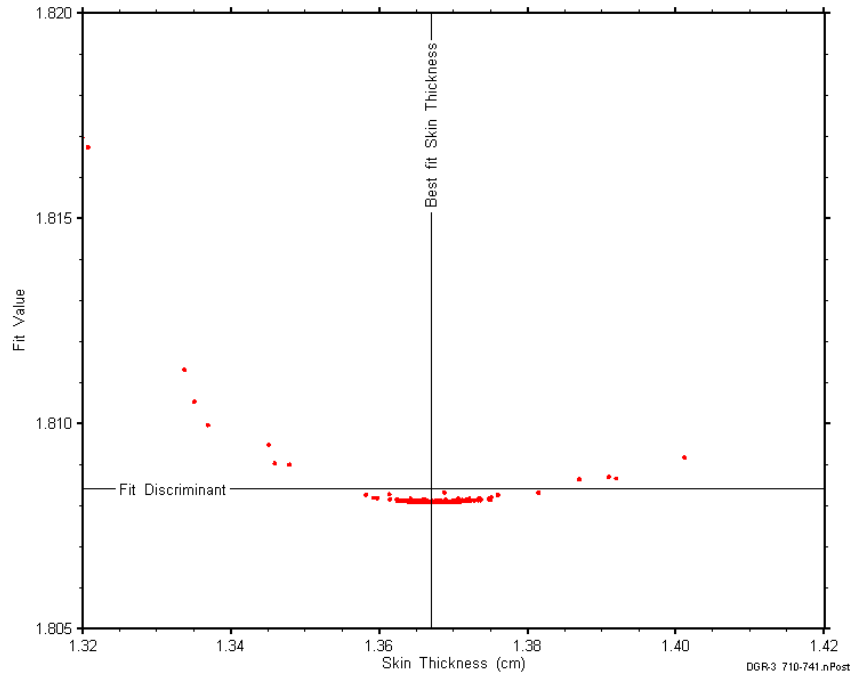


Figure C-246: XY-scatter plot showing the skin-thickness parameter space derived from DGR3_710.00-740.74 perturbation analysis along with the fit discriminant and best fit values.

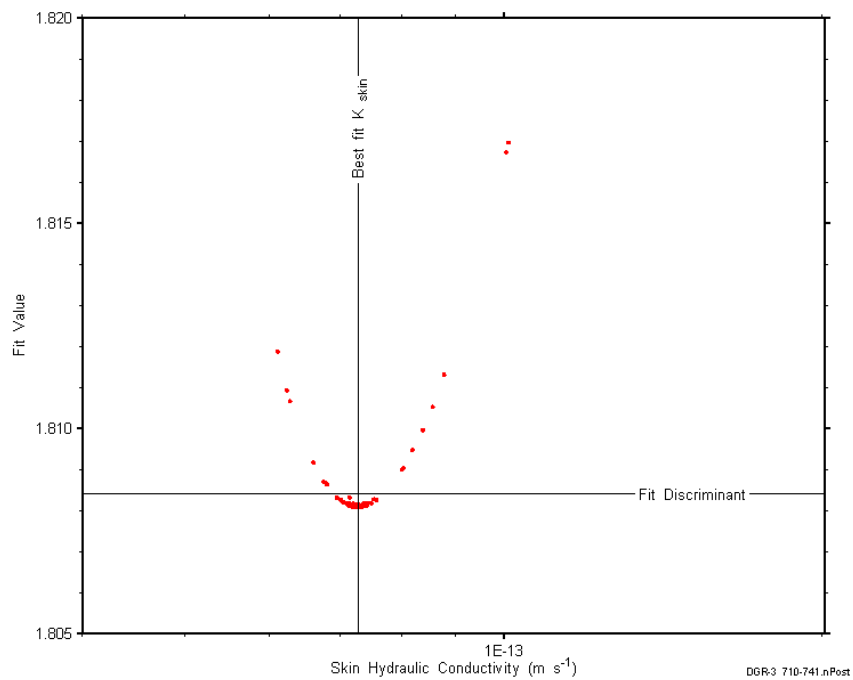


Figure C-247: XY-scatter plot showing the skin hydraulic conductivity parameter space derived from DGR3_710.00-740.74 perturbation analysis along with the fit discriminant and best fit values.

C.20 741.54-771.28 Kirkfield

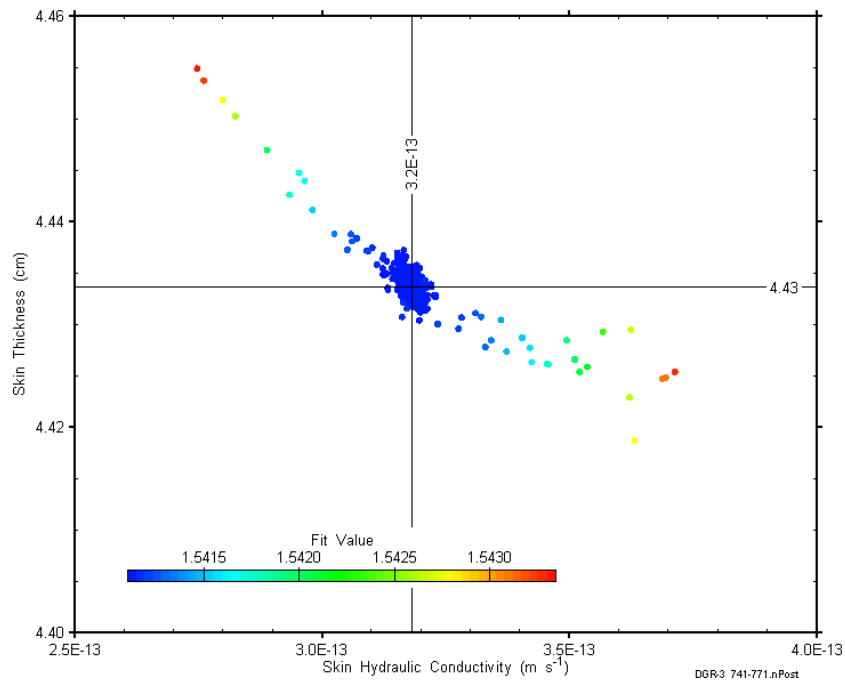


Figure C-248: XY-scatter plot showing estimates of skin hydraulic conductivity and skin thickness derived from the DGR3_741.54-771.28 perturbation analysis.

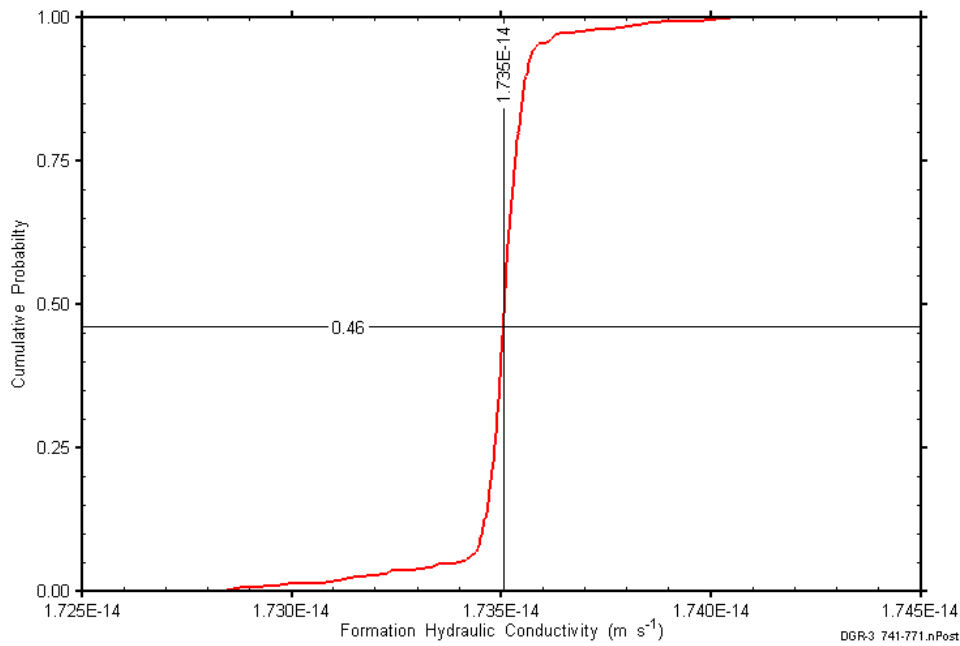


Figure C-249: DGR3_741.54-771.28 formation hydraulic conductivity cumulative distribution function.

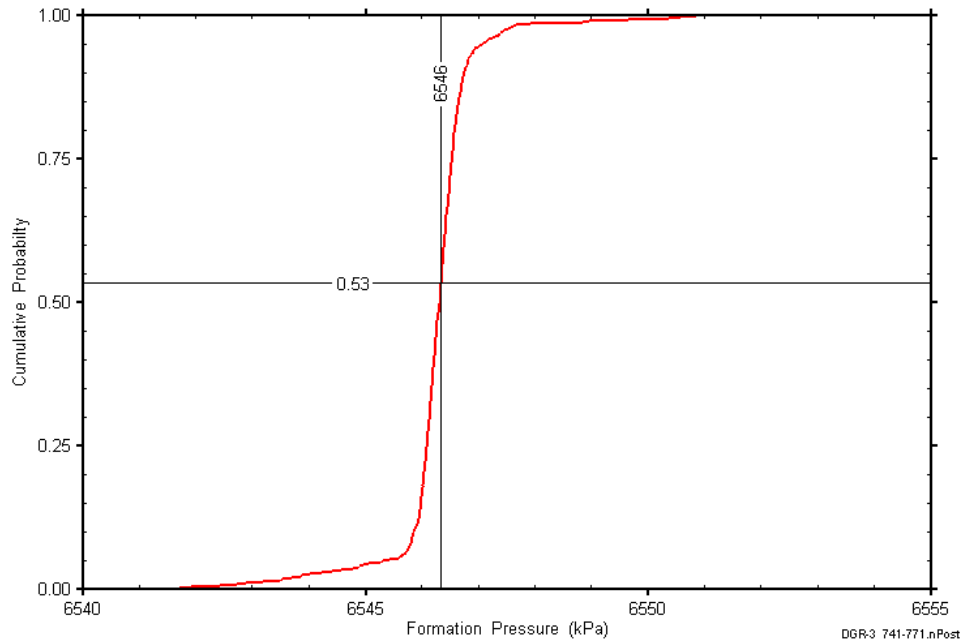


Figure C-250: DGR3_741.54-771.28 static formation pressure cumulative distribution function.

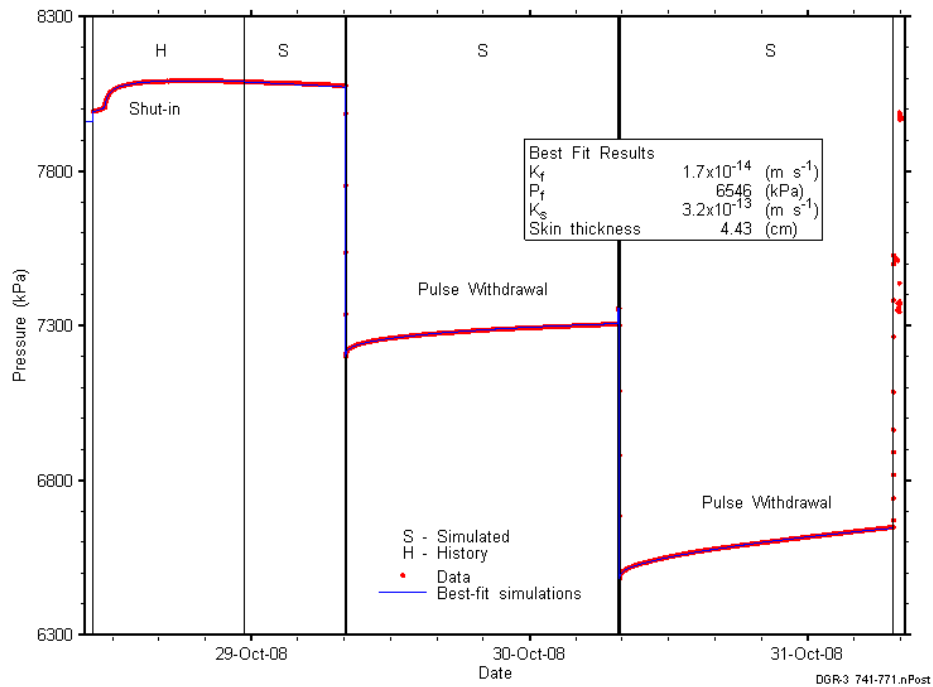


Figure C-251: Linear plot showing simulations of the DGR3_741.54-771.28 pressure response.

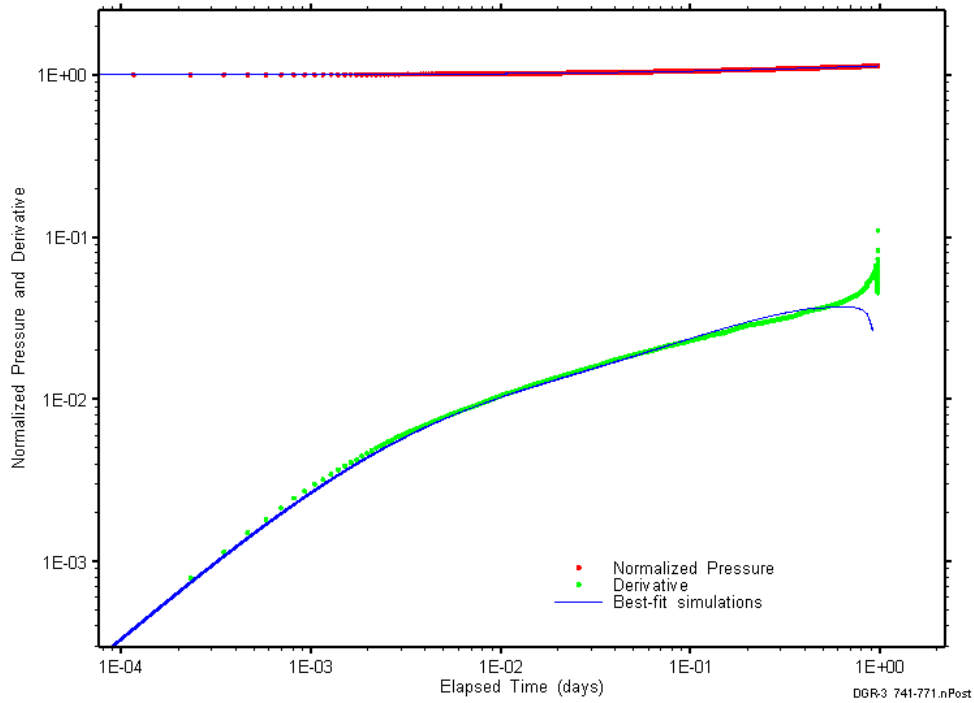


Figure C-252: Log-log plot showing simulations of the DGR3_741.54–771.28 pulse withdrawal #1 Ramey B and derivative response.

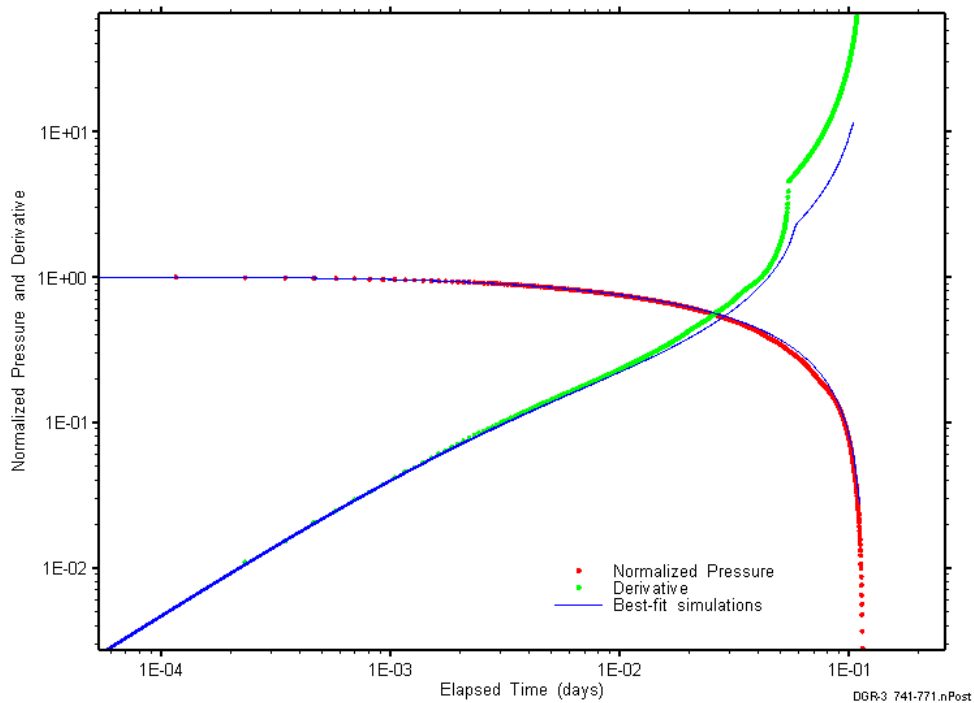


Figure C-253: Log-log plot showing simulations of the DGR3_741.54–771.28 pulse withdrawal #2 Ramey B and derivative response.

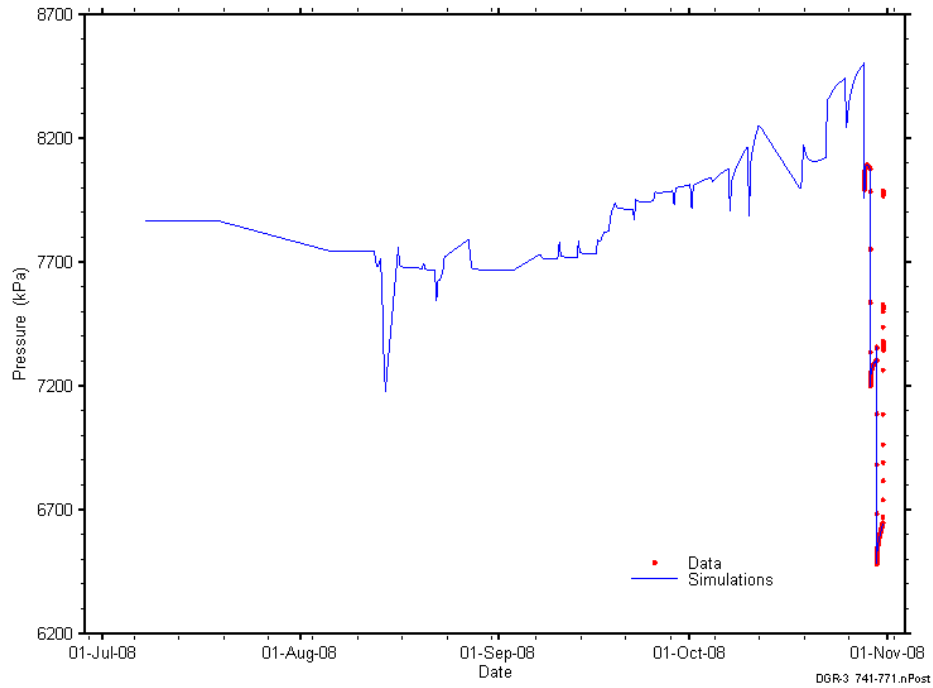


Figure C-254: Linear plot showing simulations of the DGR3_741.54-771.28 pressure response, including pre-test pressure history.

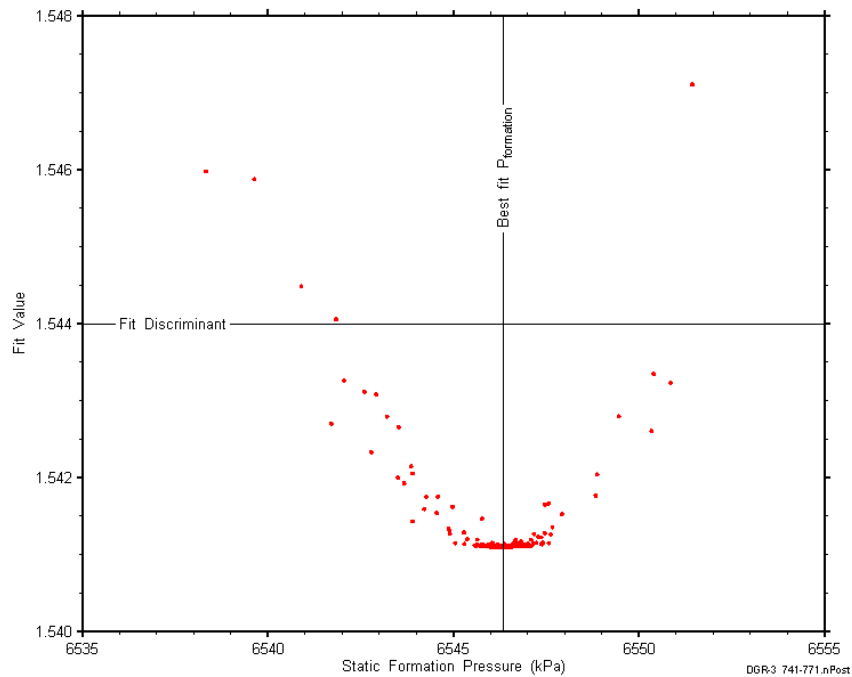


Figure C-255: XY-scatter plot showing the static formation pressure parameter space derived from DGR3_741.54-771.28 perturbation analysis along with the fit discriminant and best fit values.

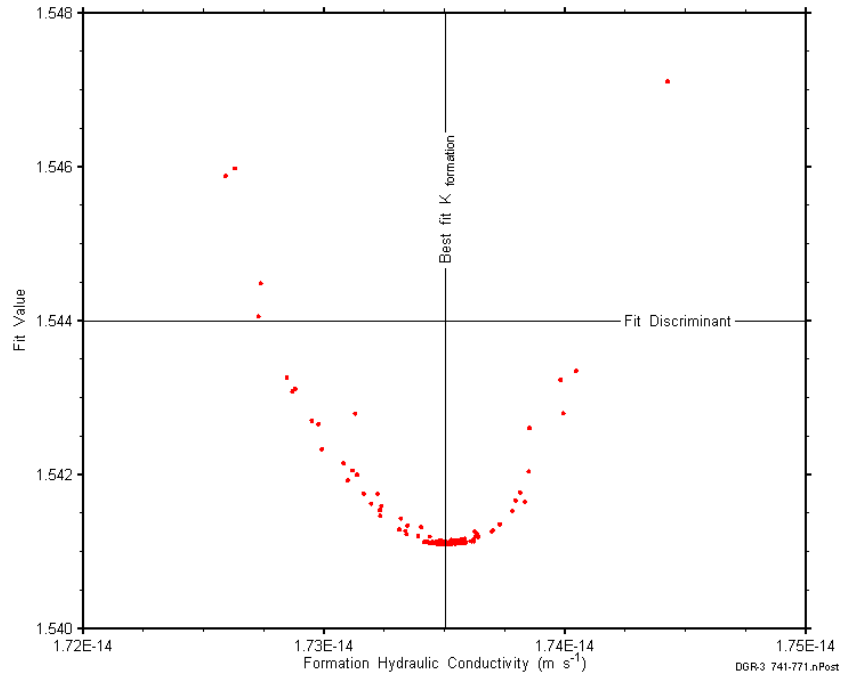


Figure C-256: XY-scatter plot showing the formation hydraulic conductivity parameter space derived from DGR3_741.54-771.28 perturbation analysis along with the fit discriminant and best fit values.

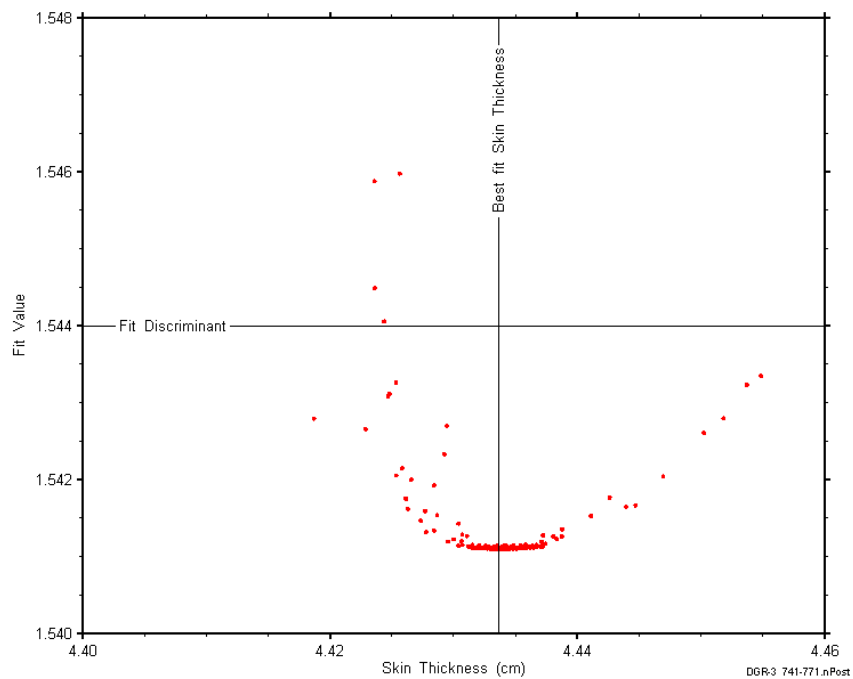


Figure C-257: XY-scatter plot showing the skin-thickness parameter space derived from DGR3_741.54-771.28 perturbation analysis along with the fit discriminant and best fit values.

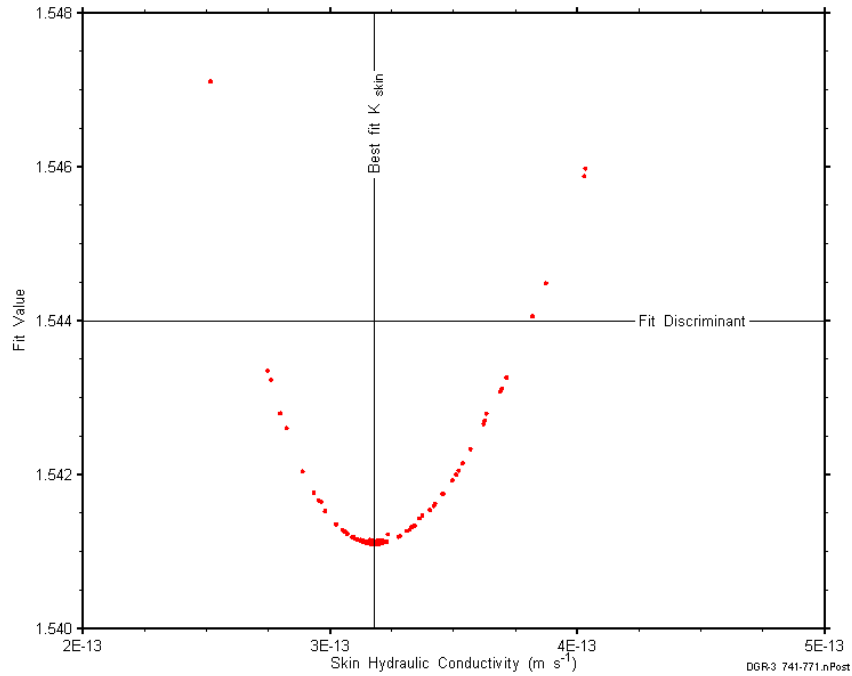


Figure C-258: XY-scatter plot showing the skin hydraulic conductivity parameter space derived from DGR3_741.54-771.28 perturbation analysis along with the fit discriminant and best fit values.

C.21 765.96-796-70 Kirkfield-Coboconk

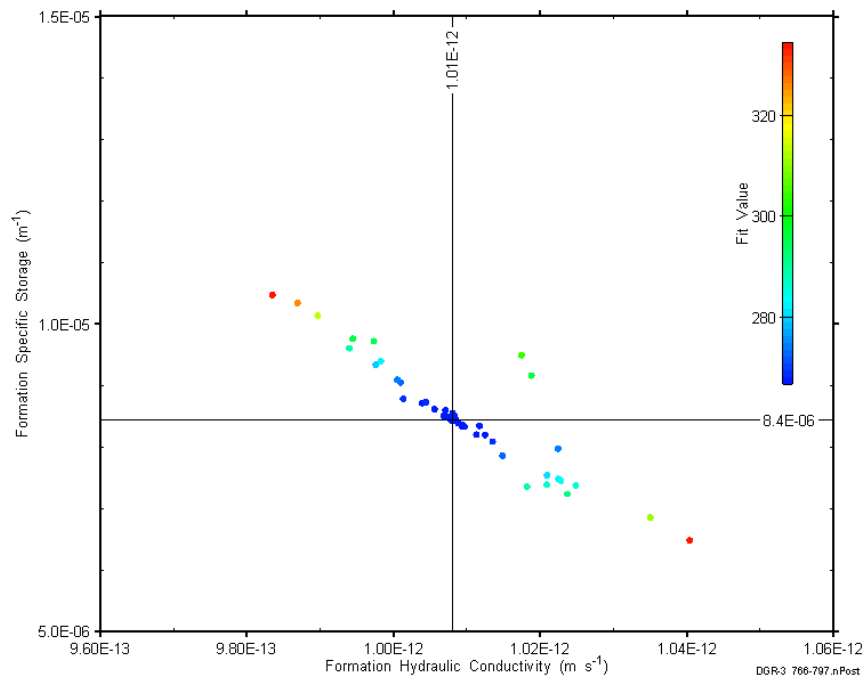


Figure C-259: XY-scatter plot showing estimates of formation hydraulic conductivity and formation specific storage derived from the DGR3_765.96-796.70 perturbation analysis.

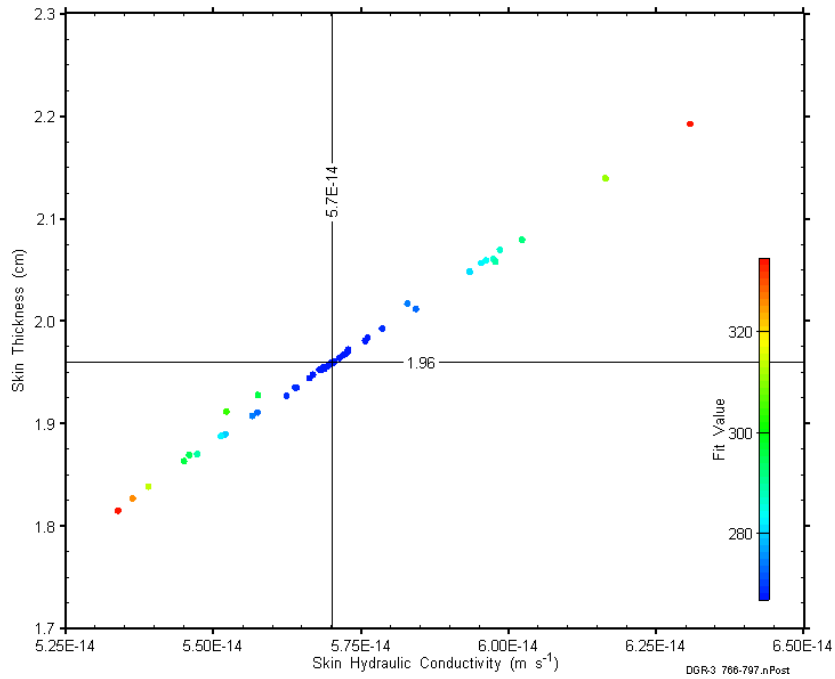


Figure C-260: XY-scatter plot showing estimates of skin hydraulic conductivity and skin thickness derived from the DGR3_765.96-796.70 perturbation analysis.

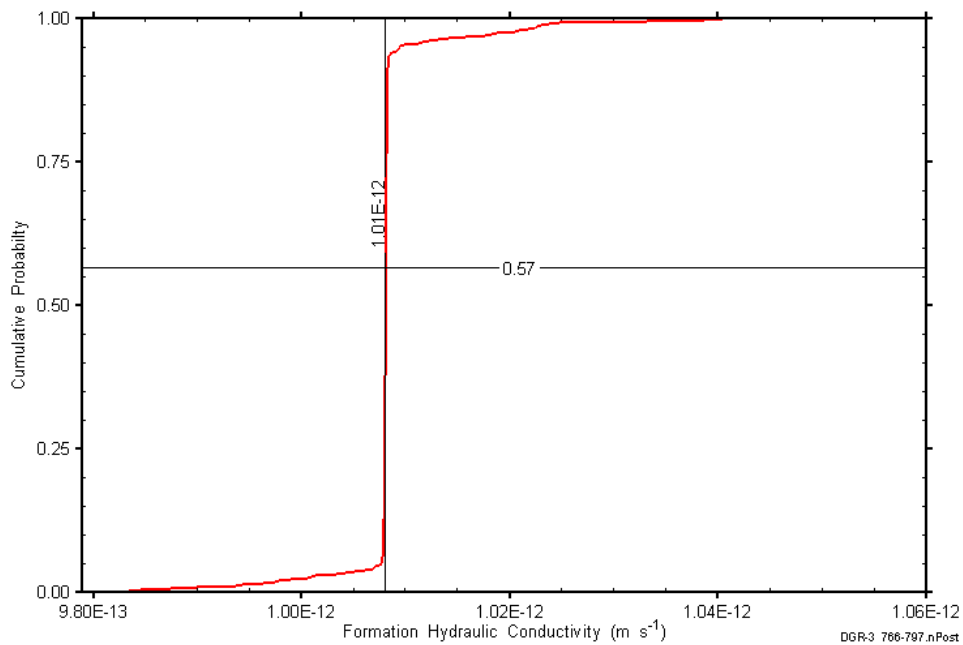


Figure C-261: DGR3_765.96-796.70 formation hydraulic conductivity cumulative distribution function.

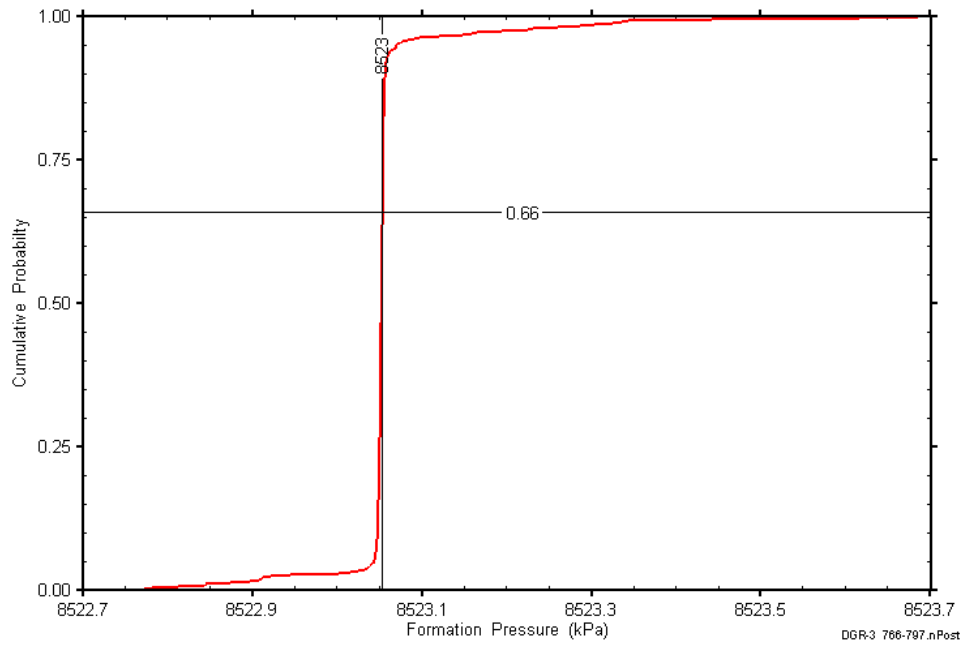


Figure C-262: DGR3_765.96-796.70 static formation pressure cumulative distribution function.

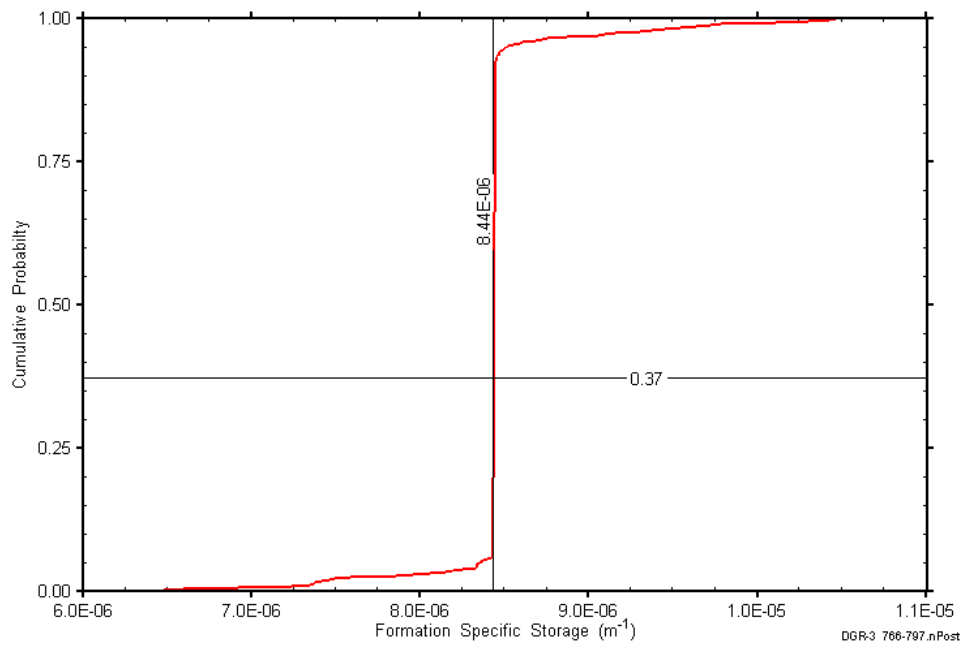


Figure C-263: DGR3_765.96-796.70 formation specific storage cumulative distribution function.

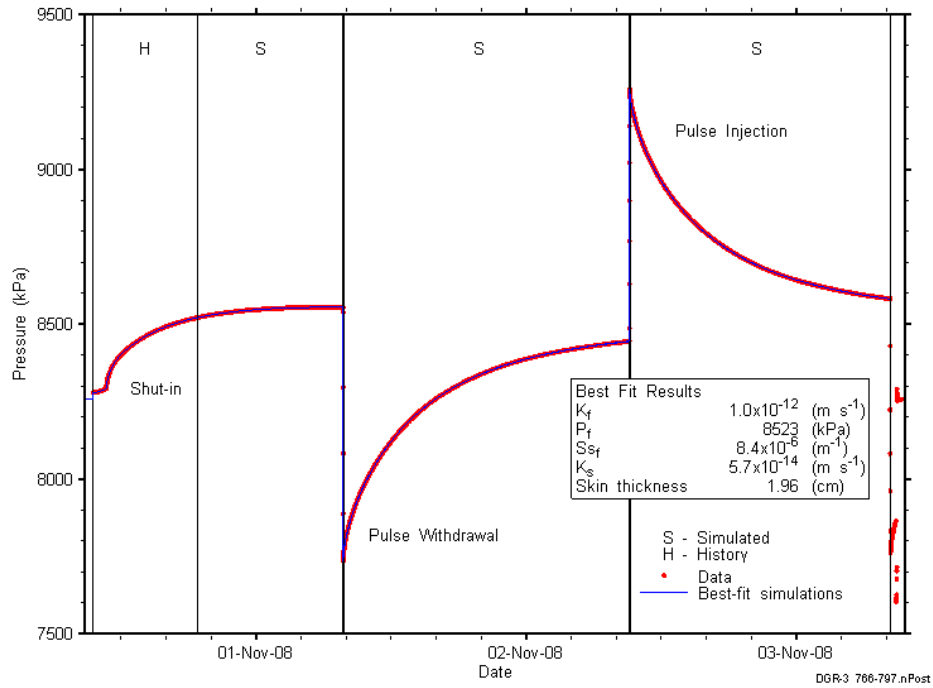


Figure C-264: Linear plot showing simulations of the DGR3_765.96-796.70 pressure response.

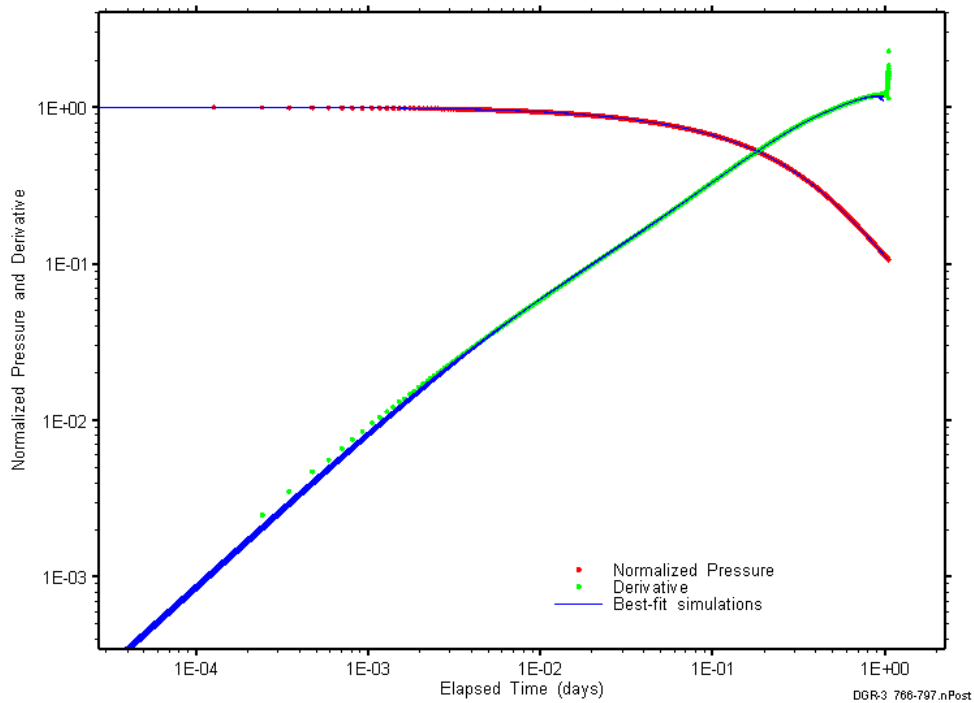


Figure C-265: Log-log plot showing simulations of the DGR3_765.96-796.70 pulse withdrawal Ramey B and derivative response.

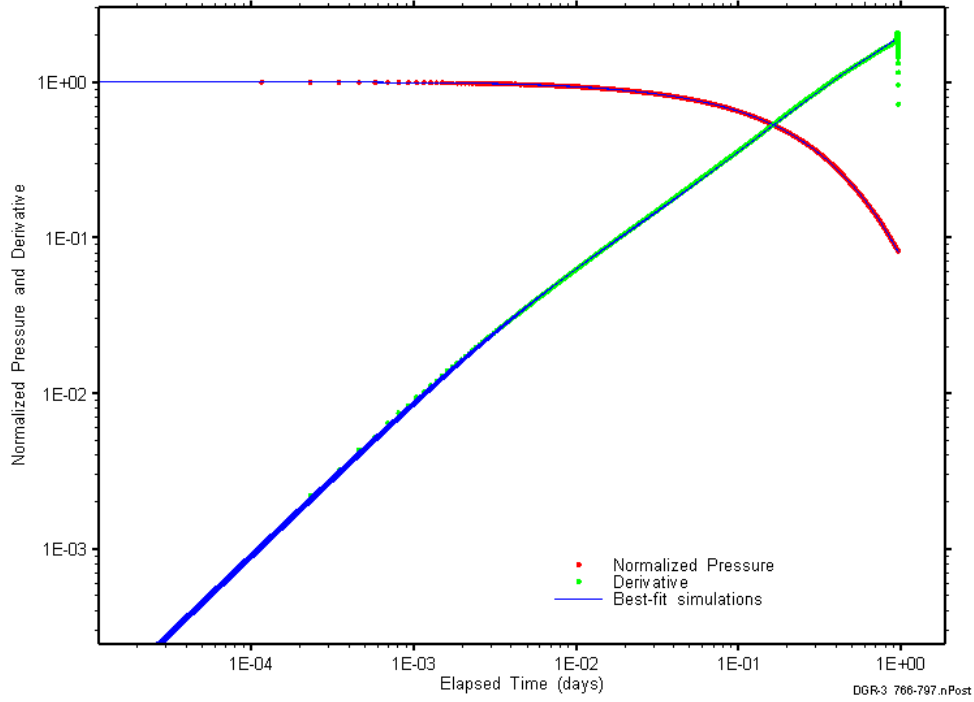


Figure C-266: Log-log plot showing simulations of the DGR3_765.96–796.70 pulse injection Ramey B and derivative response.

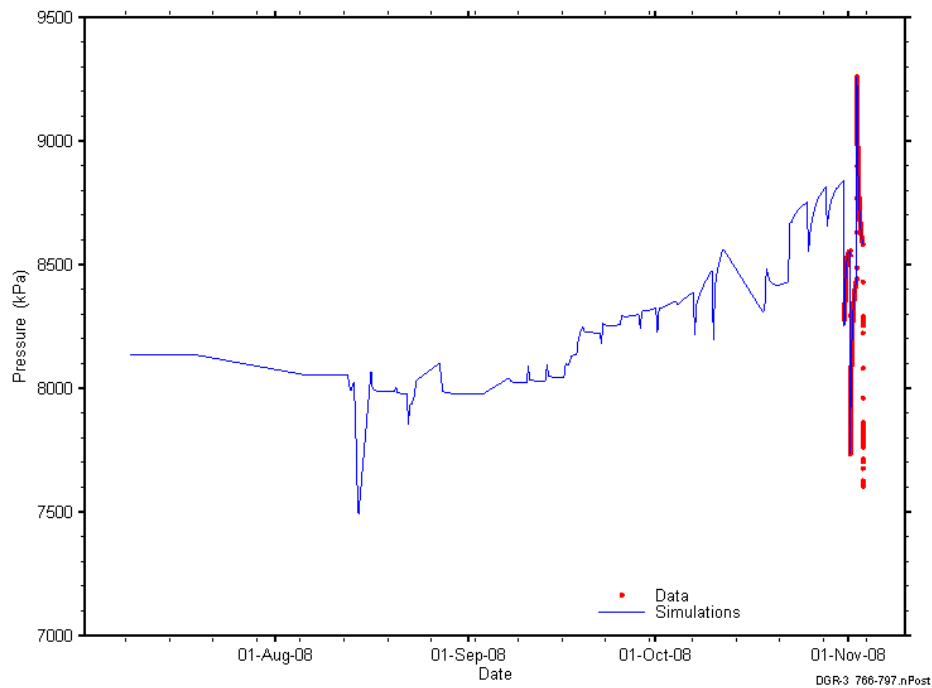


Figure C-267: Linear plot showing simulations of the DGR3_765.96–796.70 pressure response, including pre-test pressure history.

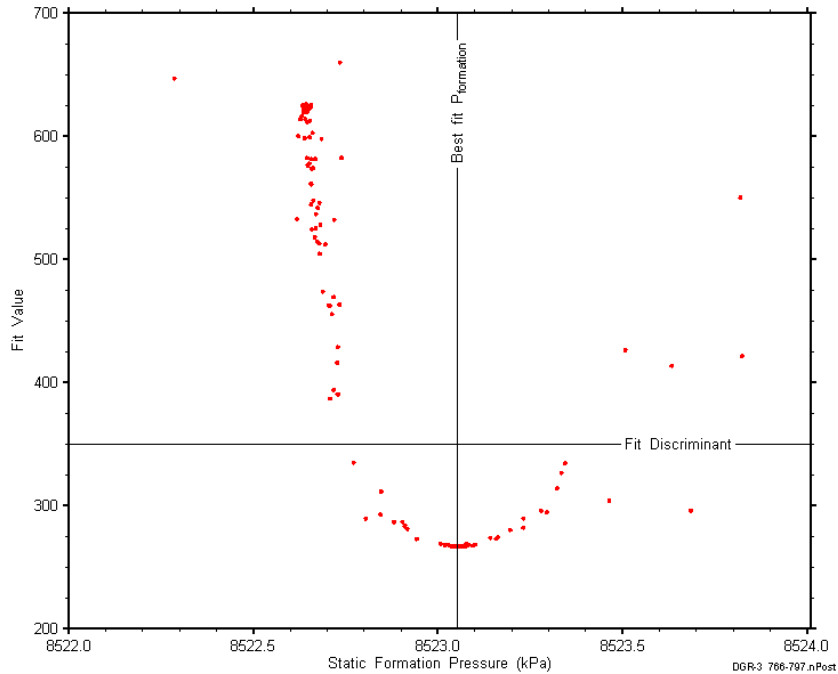


Figure C-268: XY-scatter plot showing the static formation pressure parameter space derived from DGR3_765.96-796.70 perturbation analysis along with the fit discriminant and best fit values.

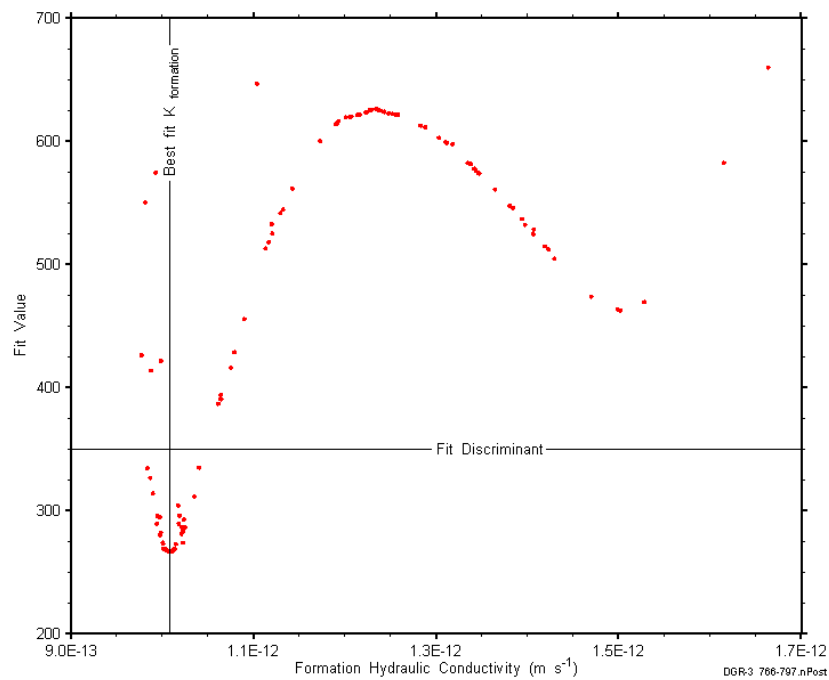


Figure C-269: XY-scatter plot showing the formation hydraulic conductivity parameter space derived from DGR3_765.96-796.70 perturbation analysis along with the fit discriminant and best fit values.

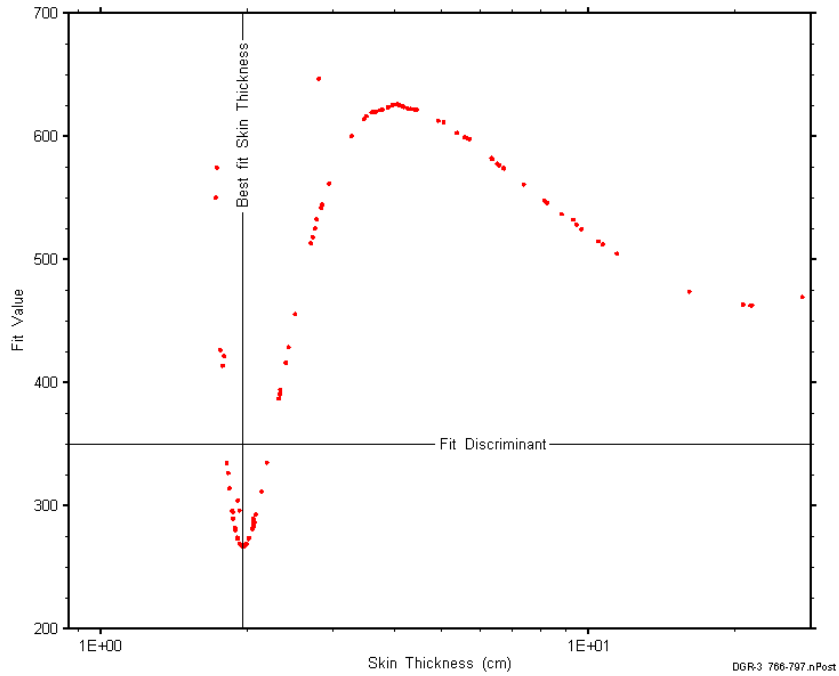


Figure C-270: XY-scatter plot showing the skin-thickness parameter space derived from DGR3_765.96-796.70 perturbation analysis along with the fit discriminant and best fit values.

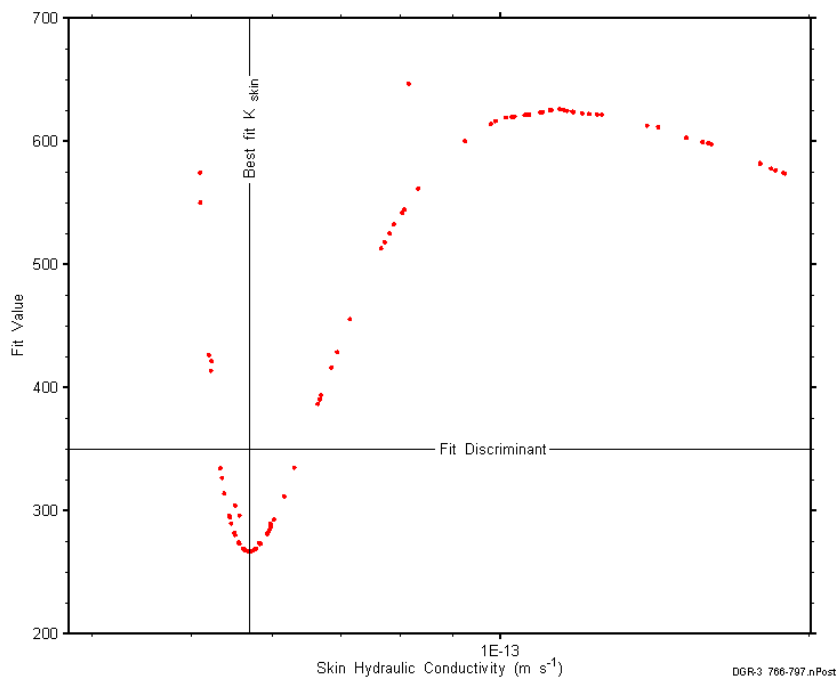


Figure C-271: XY-scatter plot showing the skin hydraulic conductivity parameter space derived from DGR3_765.96-796.70 perturbation analysis along with the fit discriminant and best fit values.

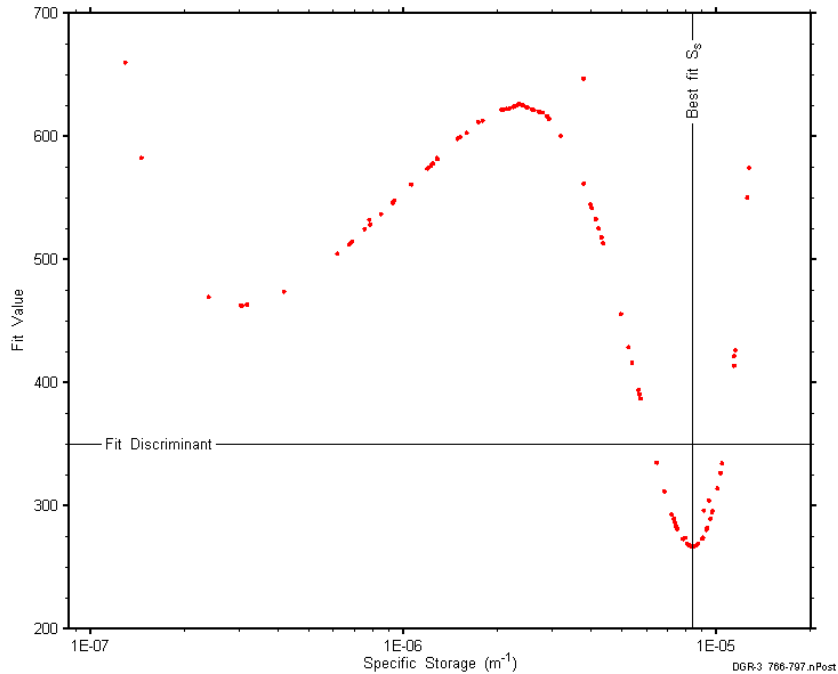


Figure C-272: XY-scatter plot showing the formation specific storage parameter space derived from DGR3_765.96-796.70 perturbation analysis along with the fit discriminant and best fit values.

C.22 790.93-821.67 Coboconk-Gull River

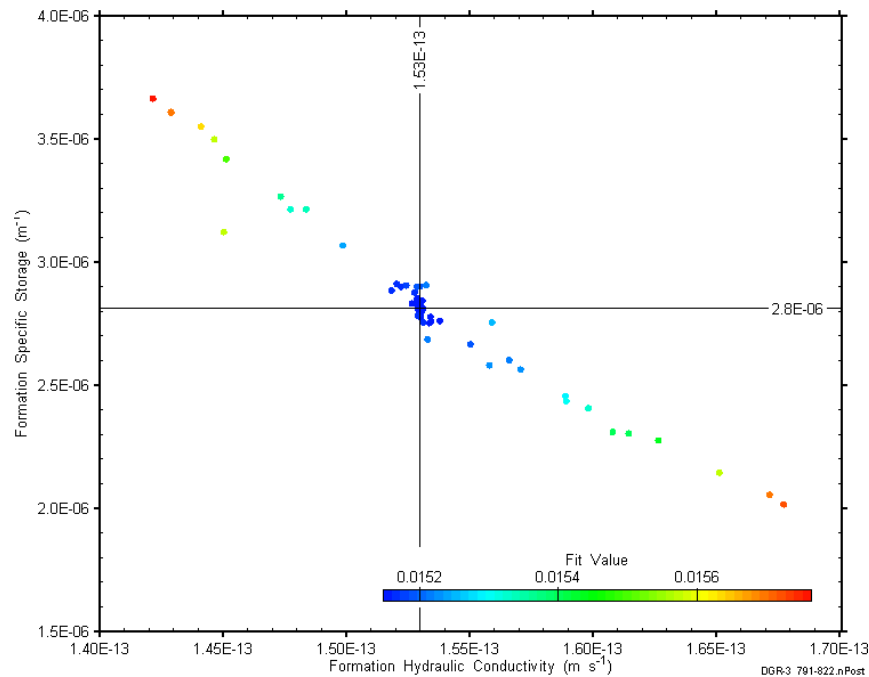


Figure C-273: XY-scatter plot showing estimates of formation hydraulic conductivity and formation specific storage derived from the DGR3_790.93-821.67 perturbation analysis.

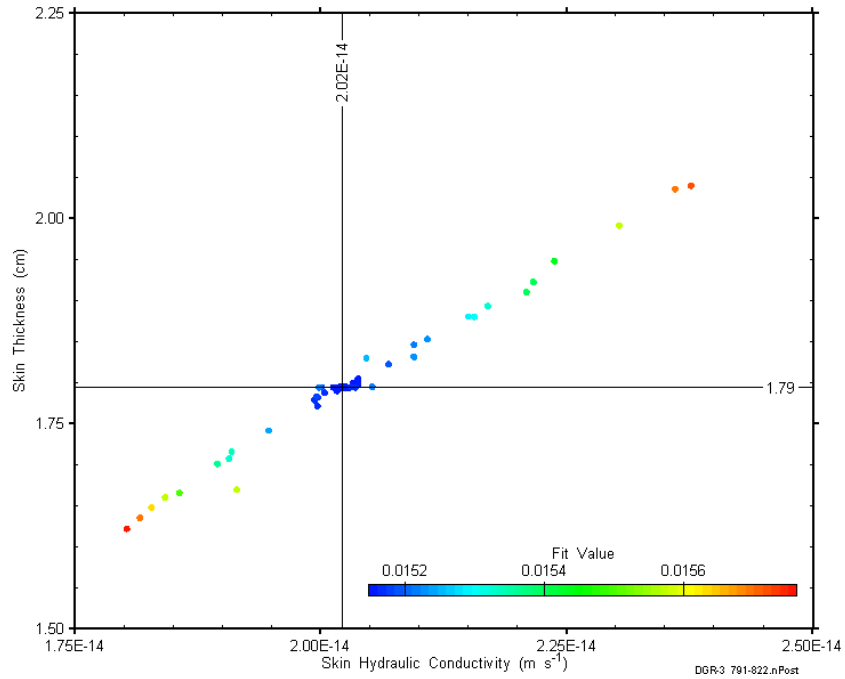


Figure C-274: XY-scatter plot showing estimates of skin hydraulic conductivity and skin thickness derived from the DGR3_790.93-821.67 perturbation analysis.

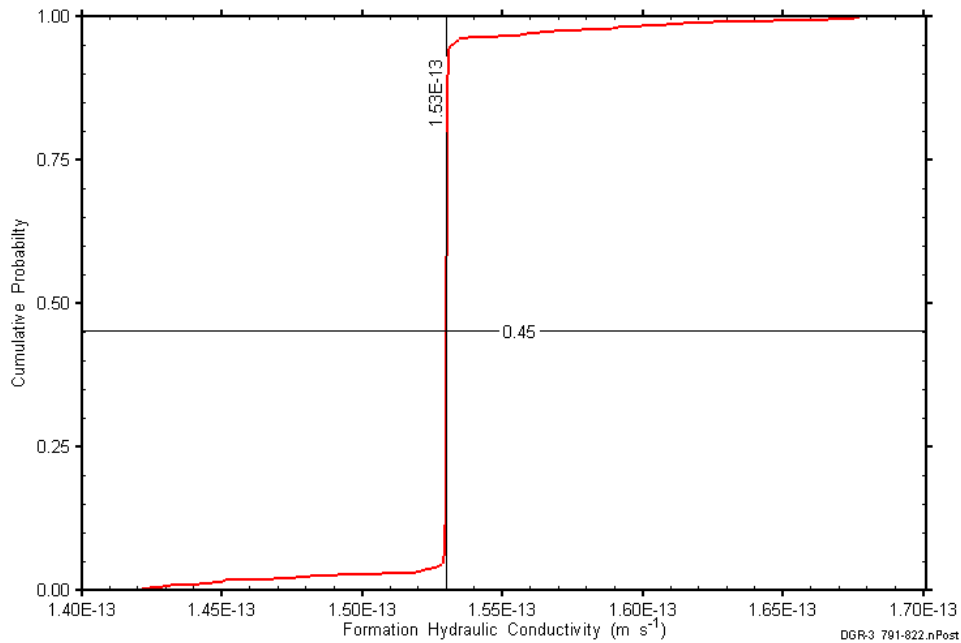


Figure C-275: DGR3_790.93-821.67 formation hydraulic conductivity cumulative distribution function.

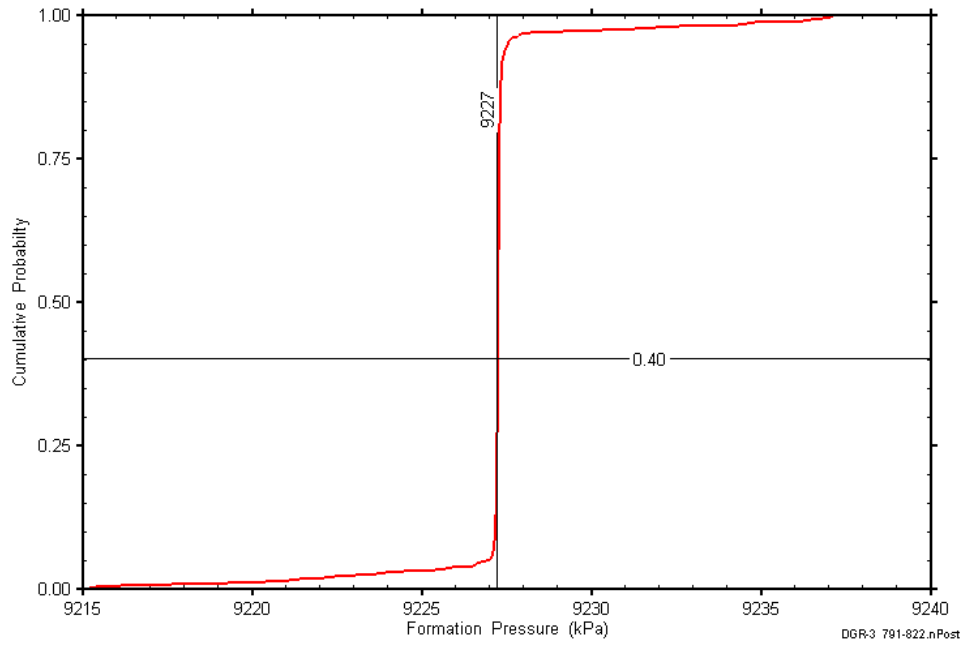


Figure C-276: DGR3_790.93-821.67 static formation pressure cumulative distribution function.

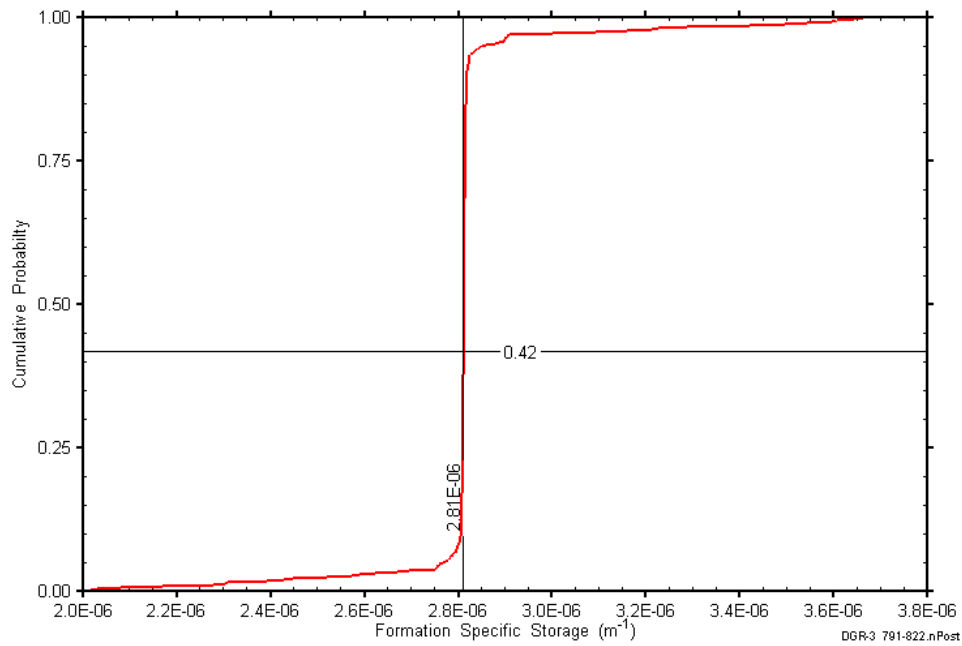


Figure C-277: DGR3_790.93-821.67 formation specific storage cumulative distribution function.

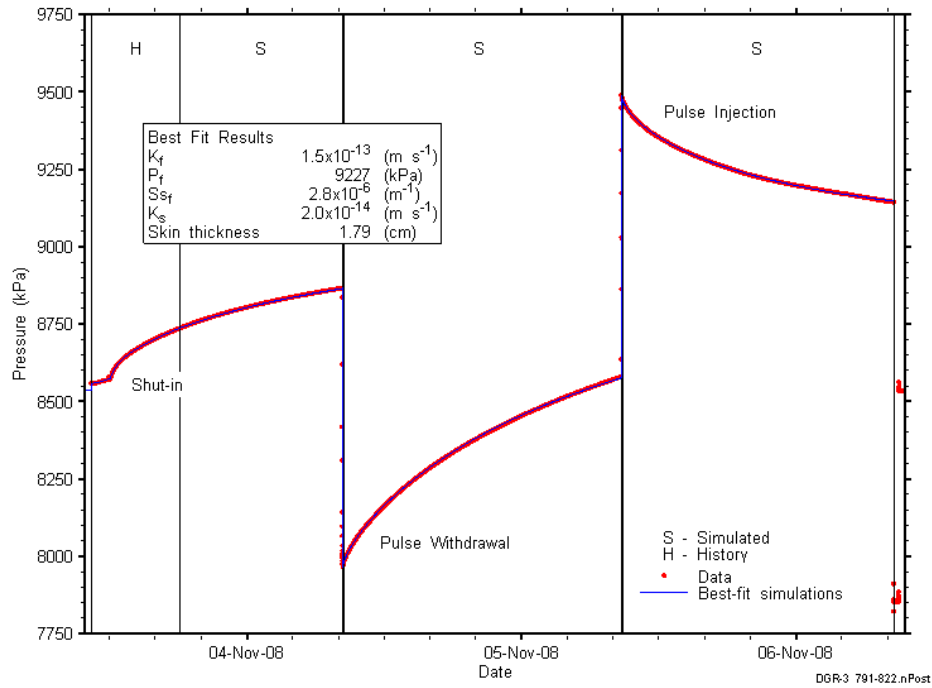


Figure C-278: Linear plot showing simulations of the DGR3_790.93-821.67 pressure response.

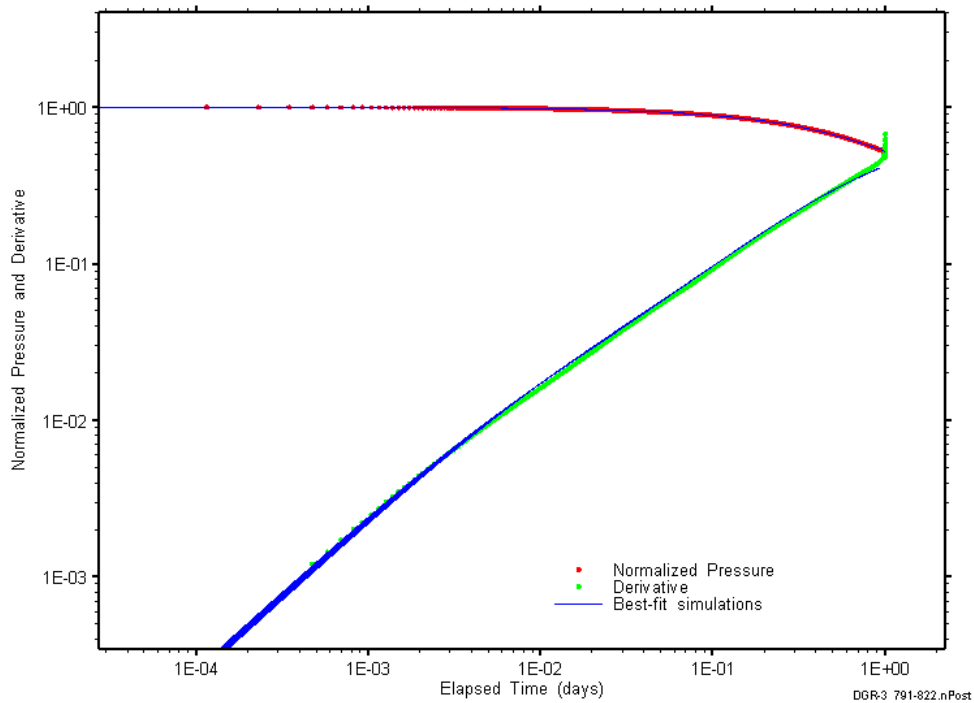


Figure C-279: Log-log plot showing simulations of the DGR3_790.93-821.67 pulse withdrawal Ramey B and derivative response.

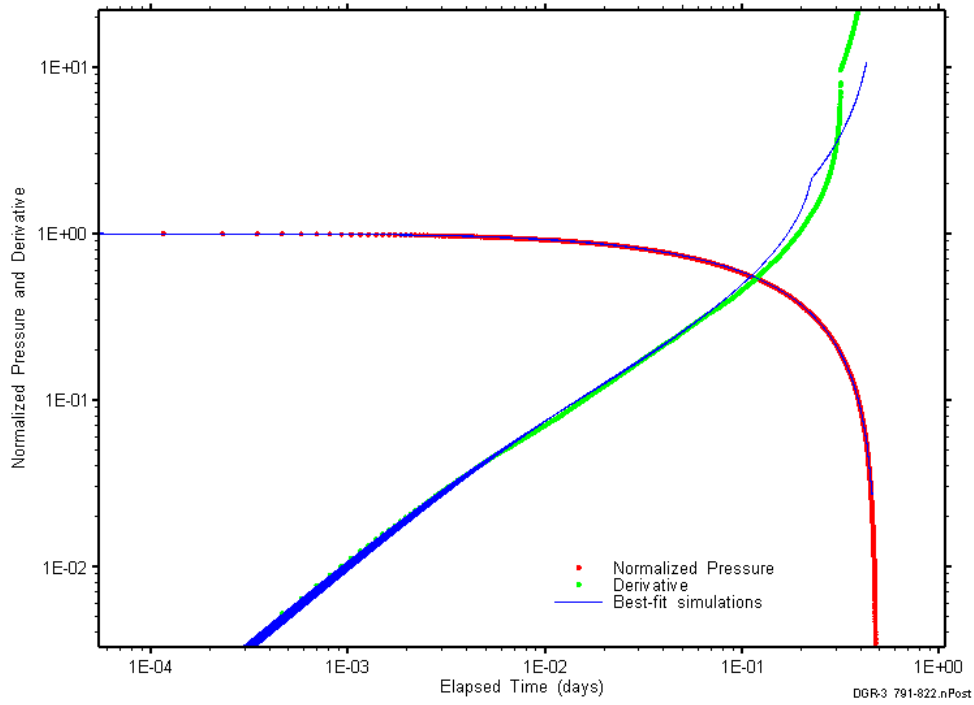


Figure C-280: Log-log plot showing simulations of the DGR3_790.93–821.67 pulse injection Ramey B and derivative response.

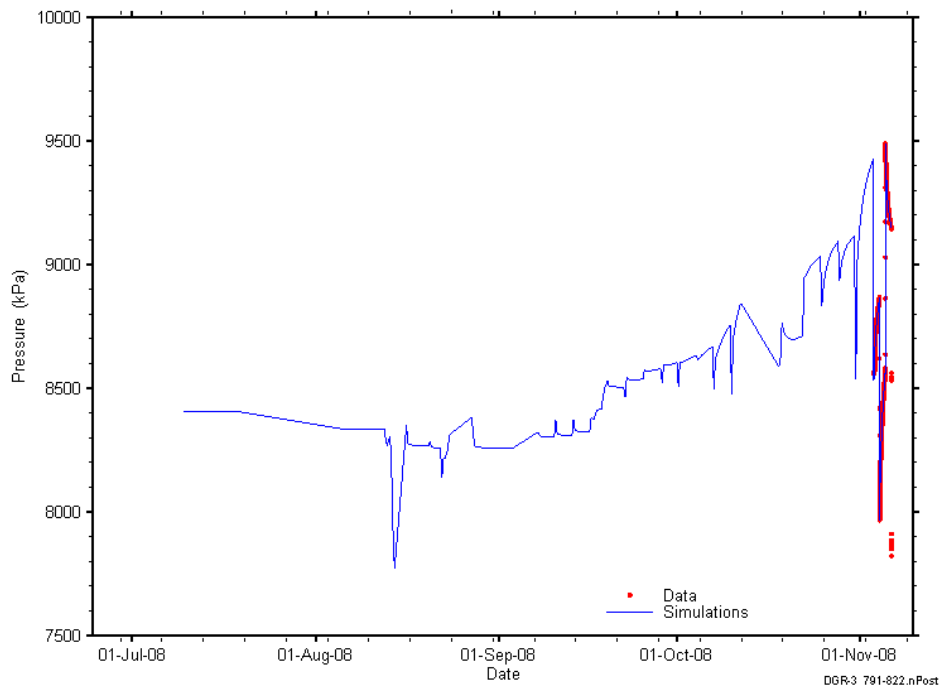


Figure C-281: Linear plot showing simulations of the DGR3_790.93–821.67 pressure response, including pre-test pressure history.

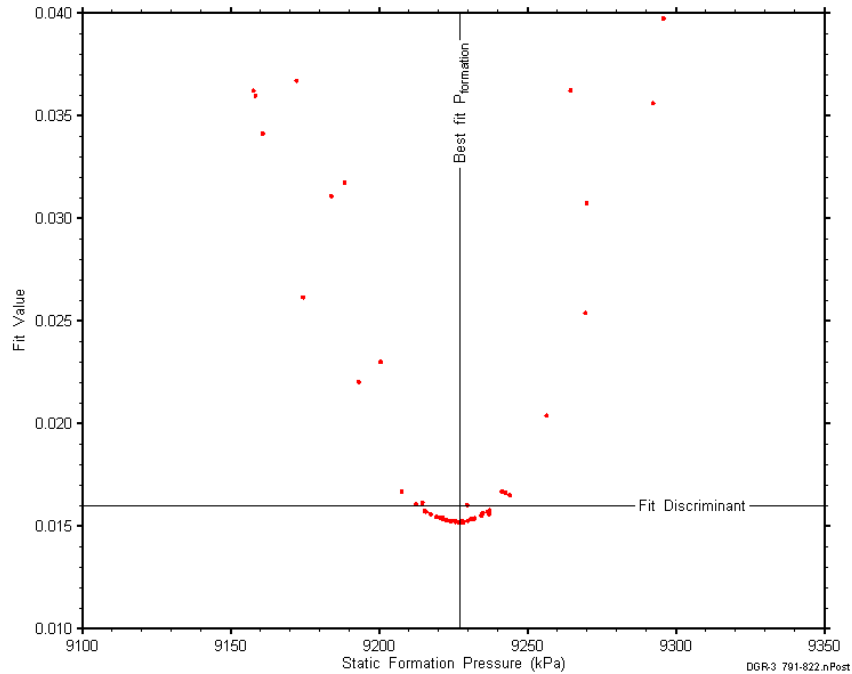


Figure C-282: XY-scatter plot showing the static formation pressure parameter space derived from DGR3_790.93-821.67 perturbation analysis along with the fit discriminant and best fit values.

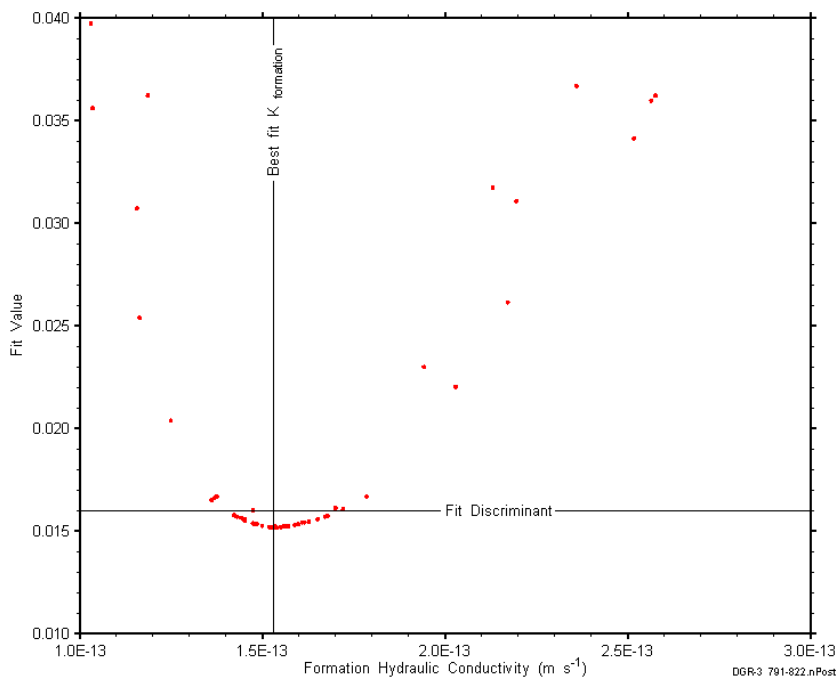


Figure C-283: XY-scatter plot showing the formation hydraulic conductivity parameter space derived from DGR3_790.93-821.67 perturbation analysis along with the fit discriminant and best fit values.

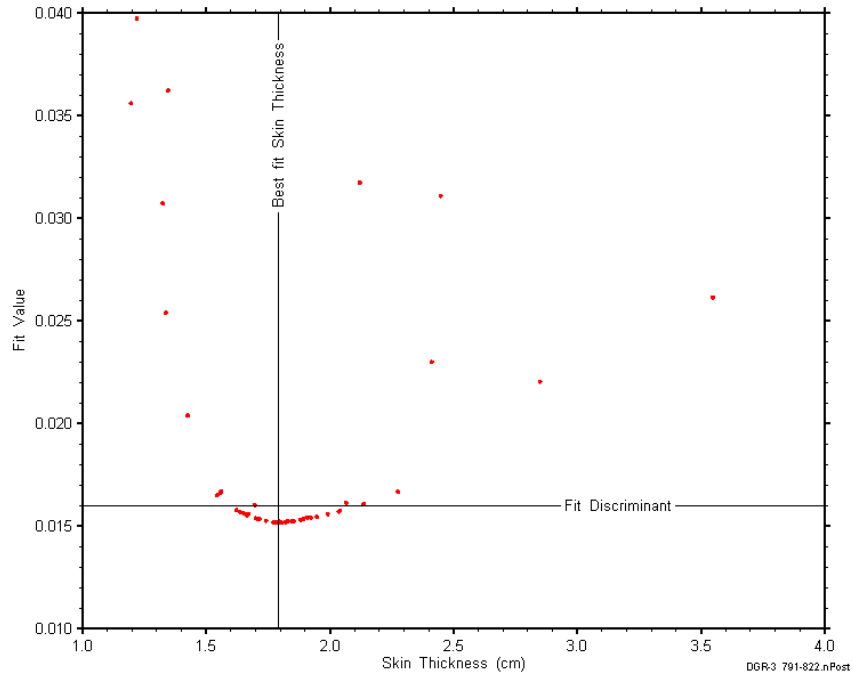


Figure C-284: XY-scatter plot showing the skin-thickness parameter space derived from DGR3_790.93-821.67 perturbation analysis along with the fit discriminant and best fit values.

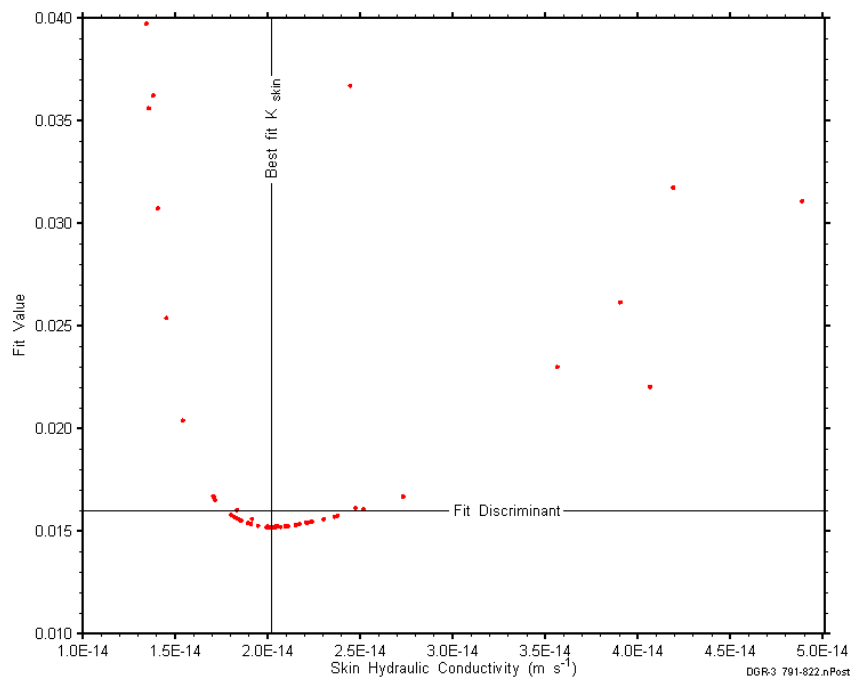


Figure C-285: XY-scatter plot showing the skin hydraulic conductivity parameter space derived from DGR3_790.93-821.67 perturbation analysis along with the fit discriminant and best fit values.

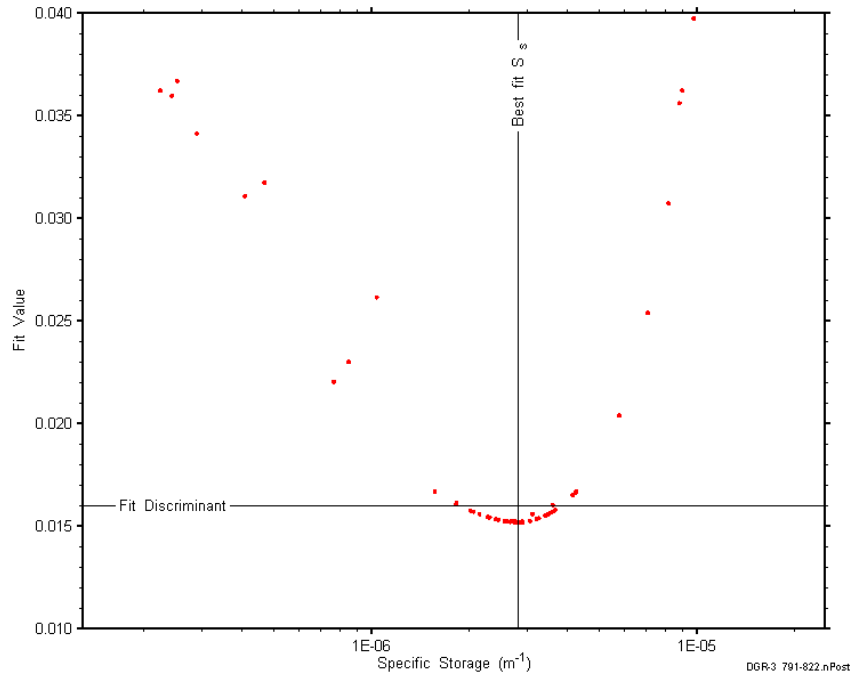


Figure C-286: XY-scatter plot showing the formation specific storage parameter space derived from DGR3_790.93-821.67 perturbation analysis along with the fit discriminant and best fit values.

C.23 815.00-845.74 Gull River

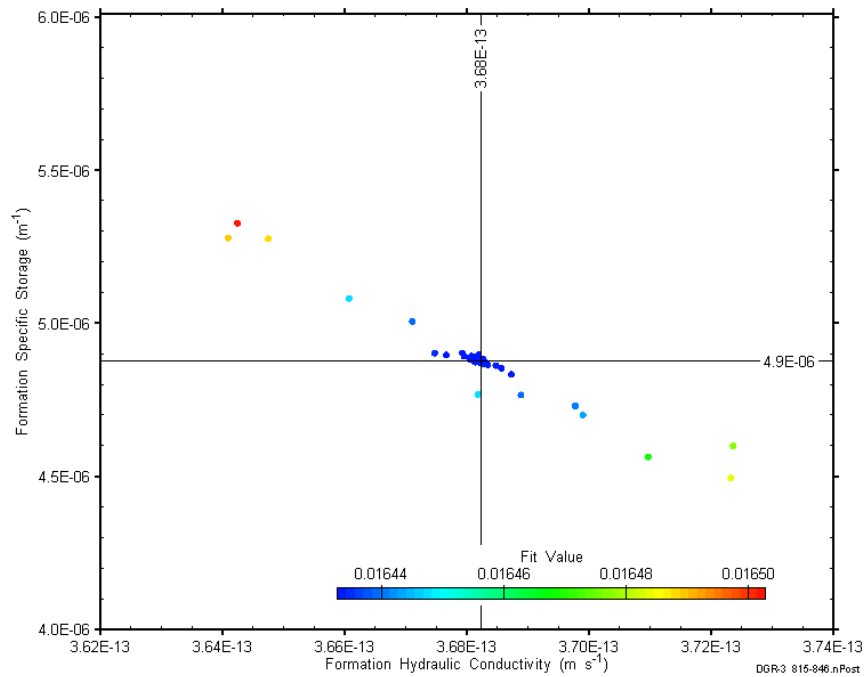


Figure C-287: XY-scatter plot showing estimates of formation hydraulic conductivity and formation specific storage derived from the DGR3_815.00-845.74 perturbation analysis.

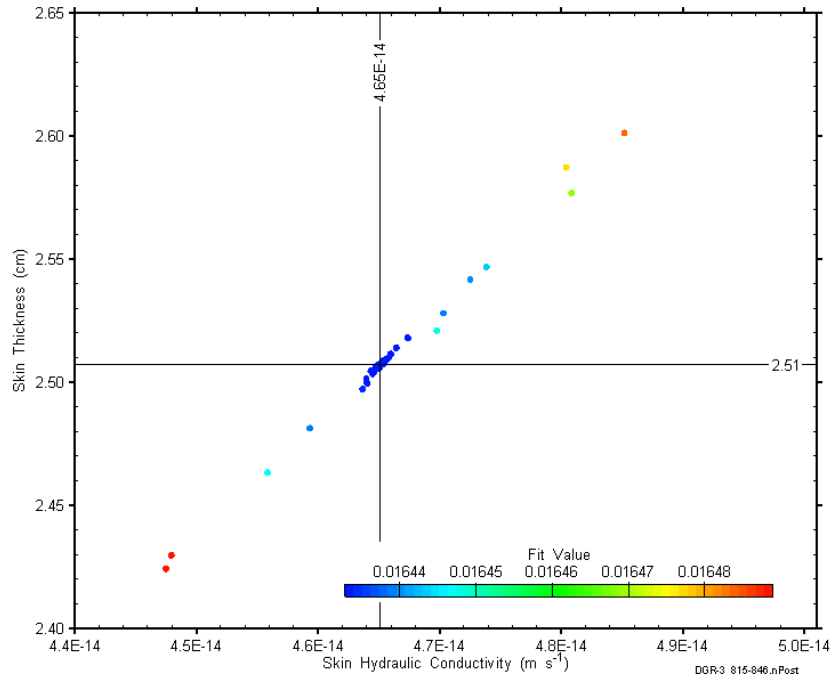


Figure C-288: XY-scatter plot showing estimates of skin hydraulic conductivity and skin thickness derived from the DGR3_815.00-845.74 perturbation analysis.

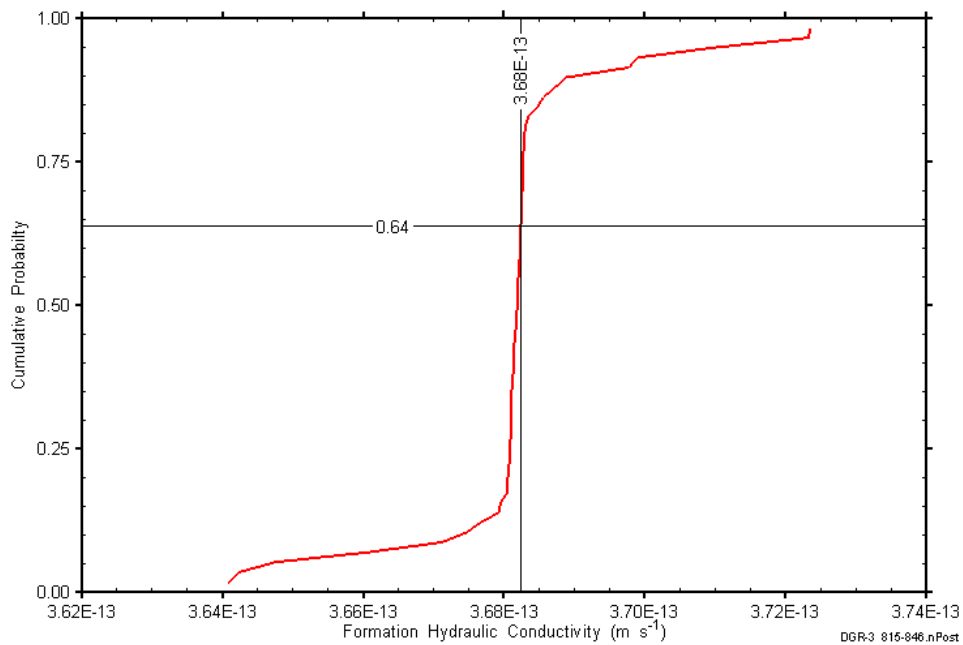


Figure C-289: DGR3_815.00-845.74 formation hydraulic conductivity cumulative distribution function.

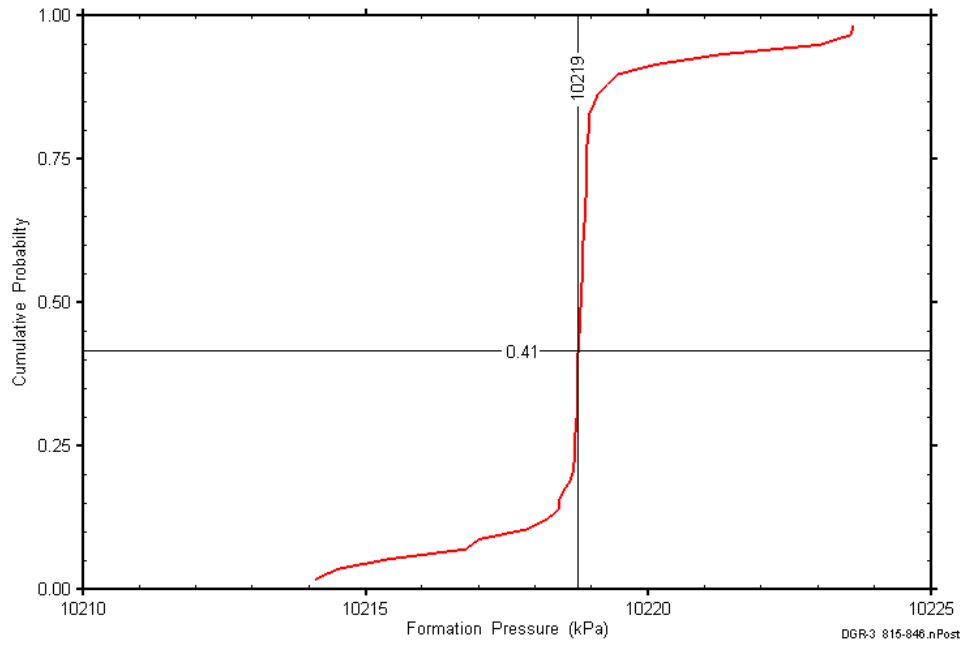


Figure C-290: DGR3_815.00-845.74 static formation pressure cumulative distribution function.

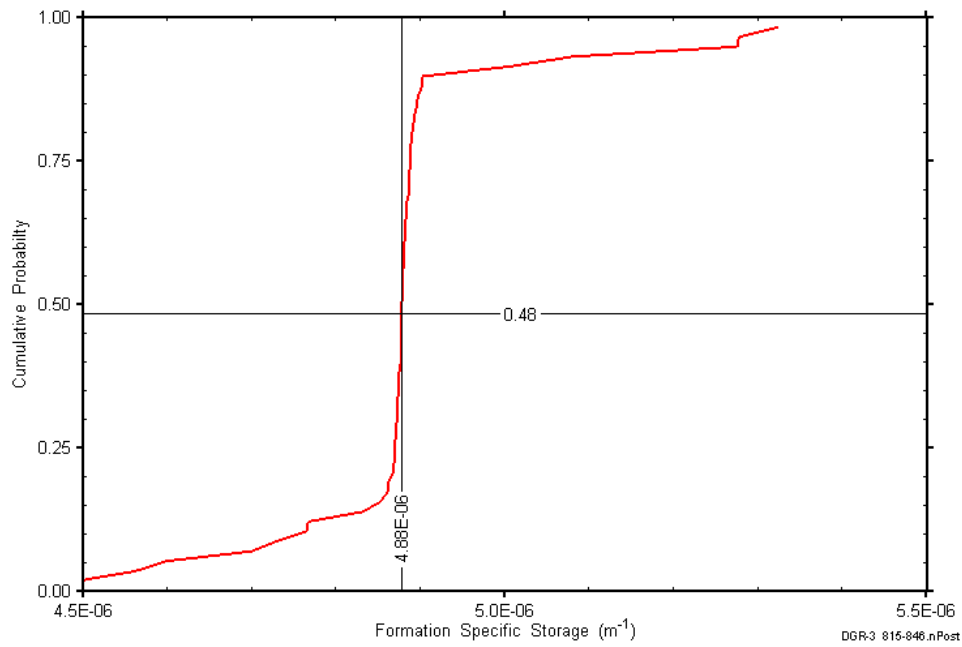


Figure C-291: DGR3_815.00-845.74 formation specific storage cumulative distribution function.

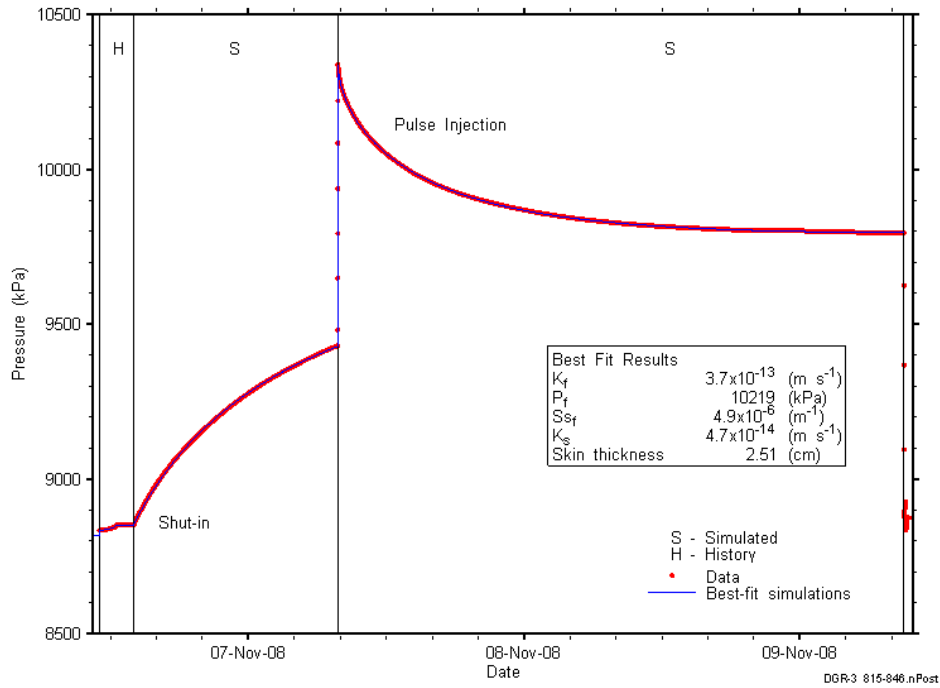


Figure C-292: Linear plot showing simulations of the DGR3_815.00-845.74 pressure response.

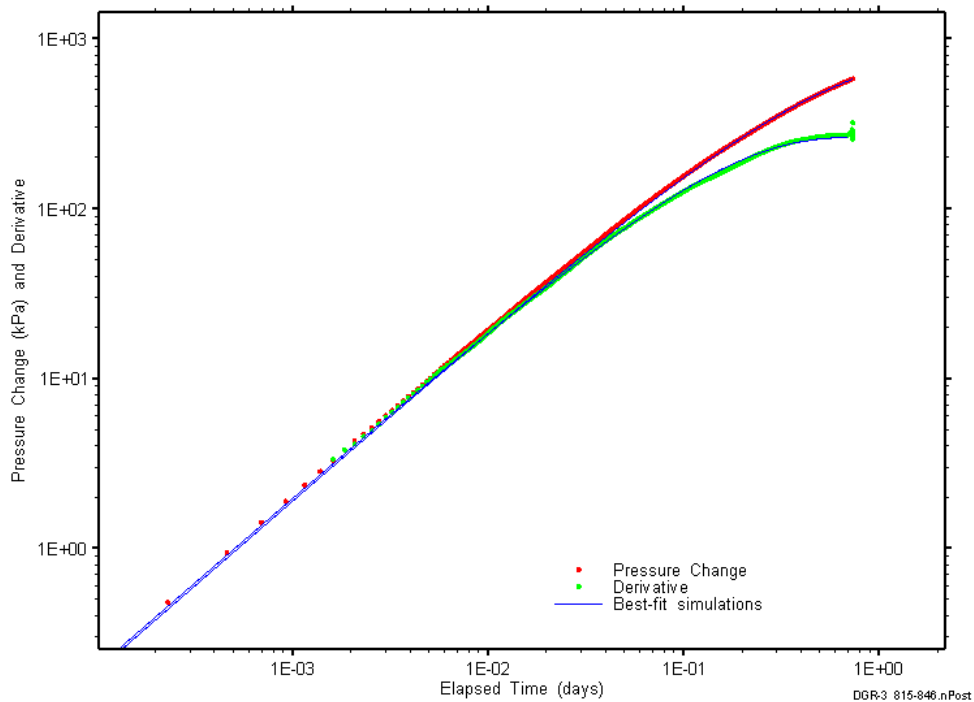


Figure C-293: Log-log plot showing simulations of the DGR3_815.00-845.74 shut-in period Ramey B and derivative response.

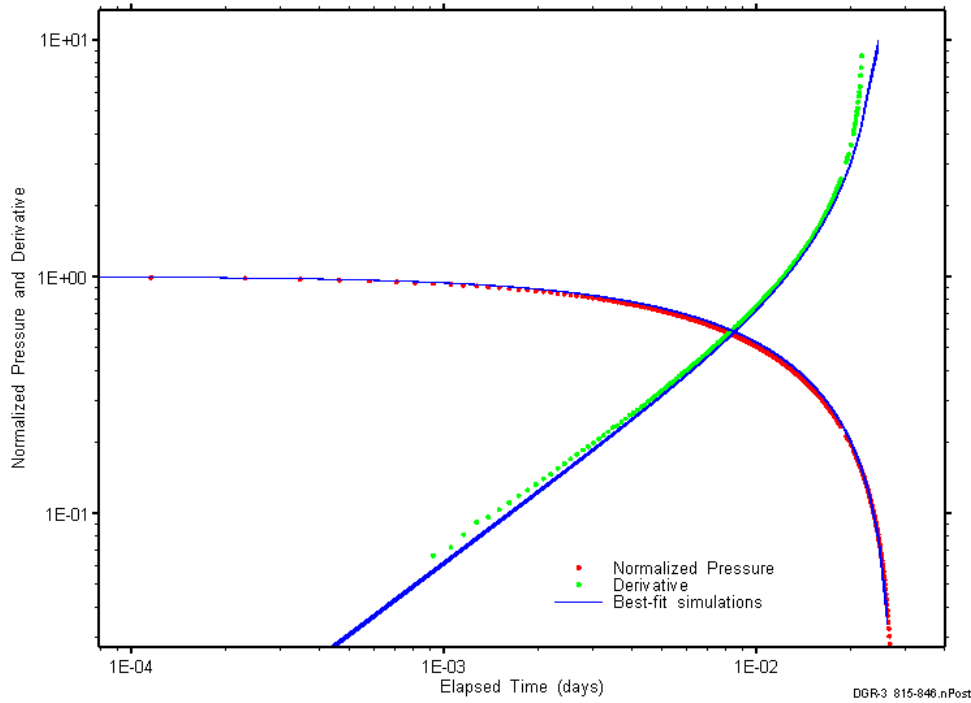


Figure C-294: Log-log plot showing simulations of the DGR3_815.00–845.74 pulse injection Ramey B and derivative response.

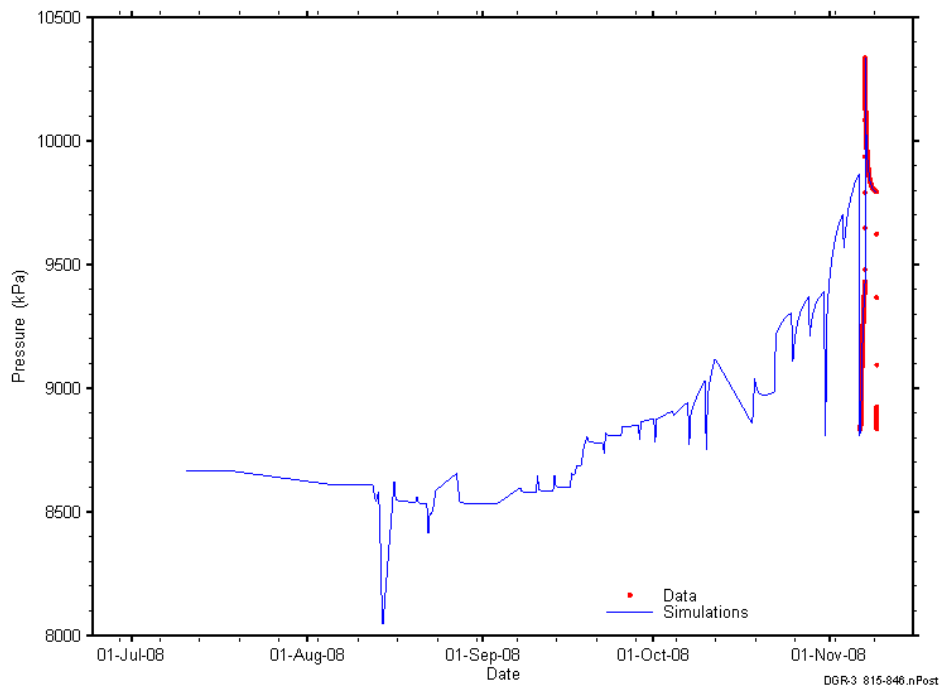


Figure C-295: Linear plot showing simulations of the DGR3_815.00–845.74 pressure response, including pre-test pressure history.

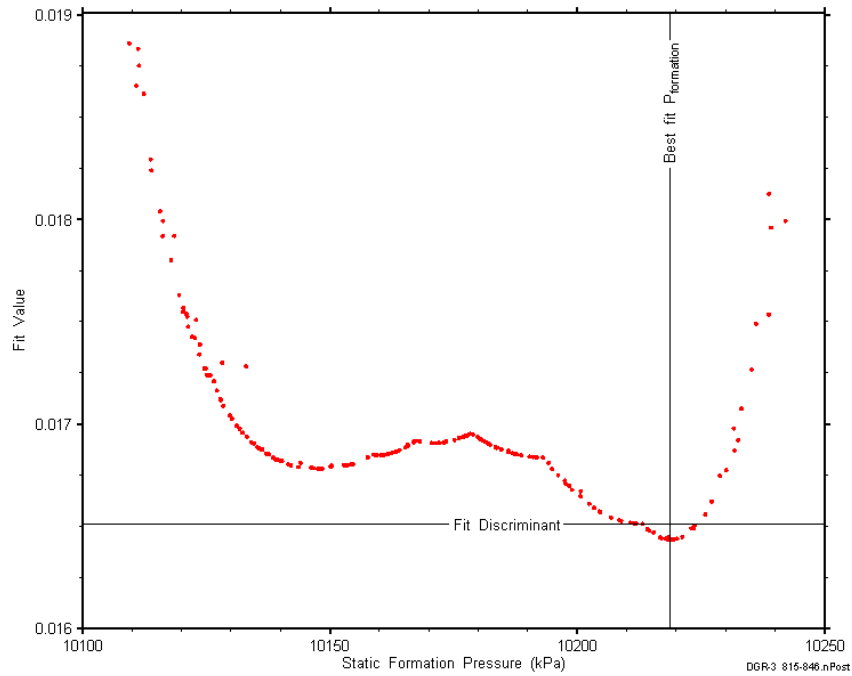


Figure C-296: XY-scatter plot showing the static formation pressure parameter space derived from DGR3_815.00-845.74 perturbation analysis along with the fit discriminant and best fit values.

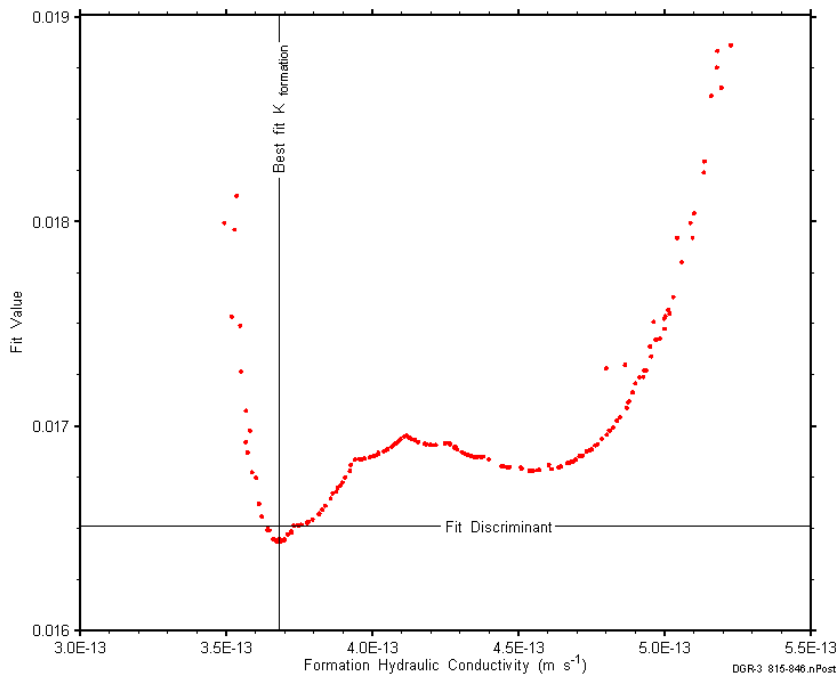


Figure C-297: XY-scatter plot showing the formation hydraulic conductivity parameter space derived from DGR3_815.00-845.74 perturbation analysis along with the fit discriminant and best fit values.

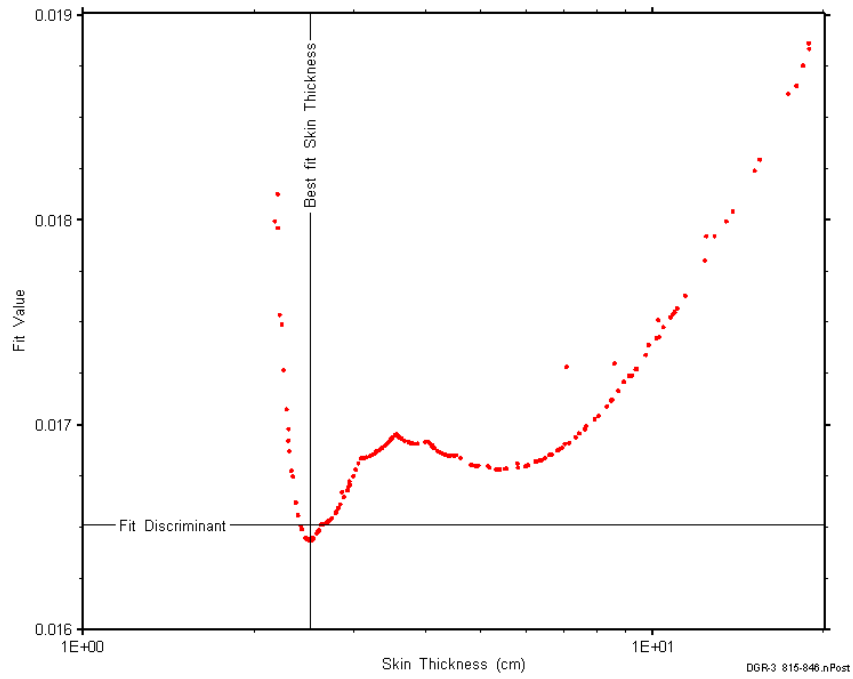


Figure C-298: XY-scatter plot showing the skin-thickness parameter space derived from DGR3_815.00-845.74 perturbation analysis along with the fit discriminant and best fit values.

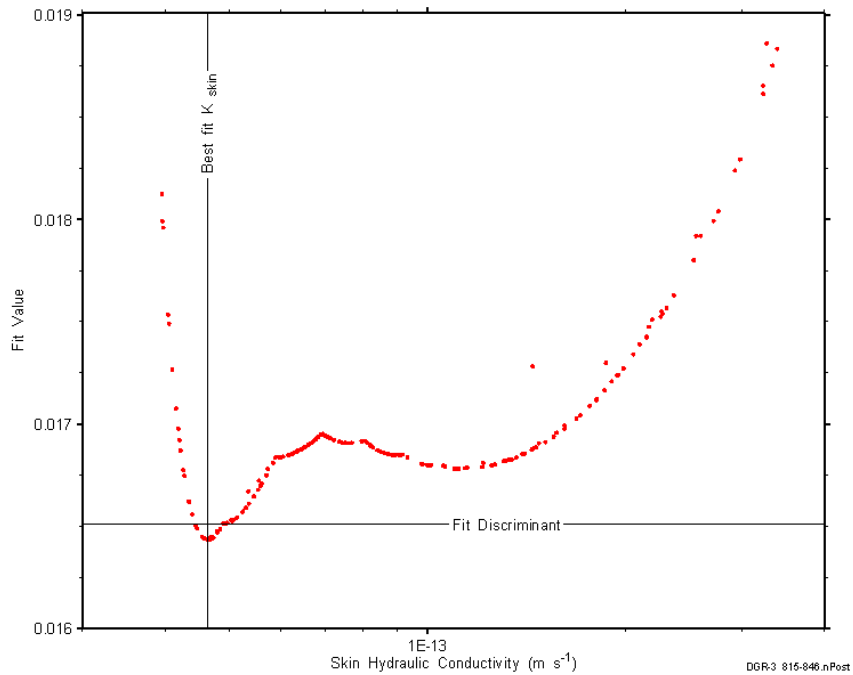


Figure C-299: XY-scatter plot showing the skin hydraulic conductivity parameter space derived from DGR3_815.00-845.74 perturbation analysis along with the fit discriminant and best fit values.

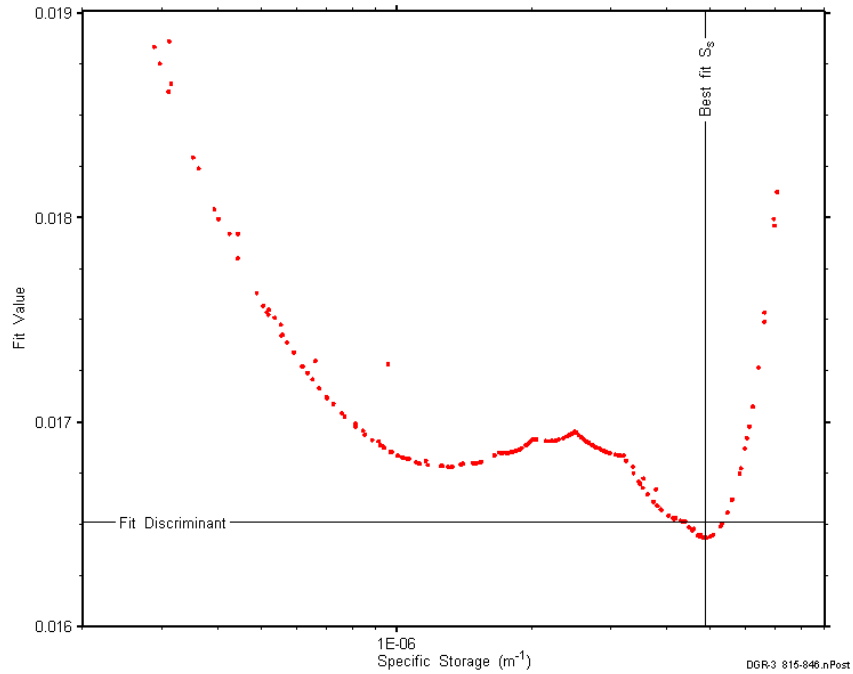


Figure C-300: XY-scatter plot showing the formation specific storage parameter space derived from DGR3_815.00-845.74 perturbation analysis along with the fit discriminant and best fit values.

Appendix D. DGR-4 PLOTS

Various plots showing results from the DGR-4 analyses are shown below. These plots include XY-scatter plots of the fitting-parameter estimates, linear and log-log horsetail plots of the simulated pressure responses showing field-data matches, Kf, Pf, and Ss cumulative distribution functions, and parameter-space plots showing the characteristics of the minima for each of the fitting parameters.

D.1 190.63-221.37 Salina F

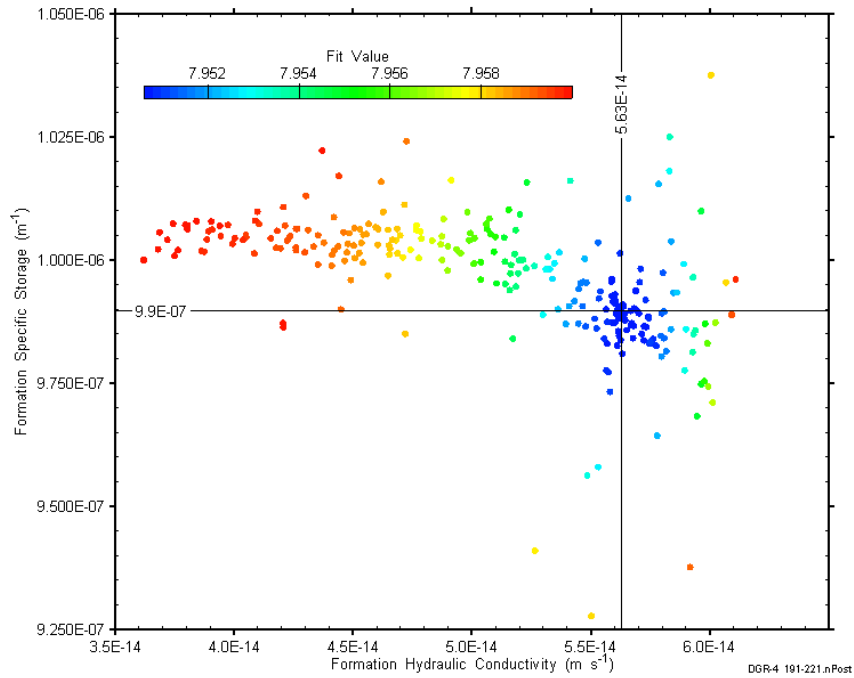


Figure D-1: XY-scatter plot showing estimates of formation hydraulic conductivity and formation specific storage derived from the DGR4_190.63-221.37 perturbation analysis.

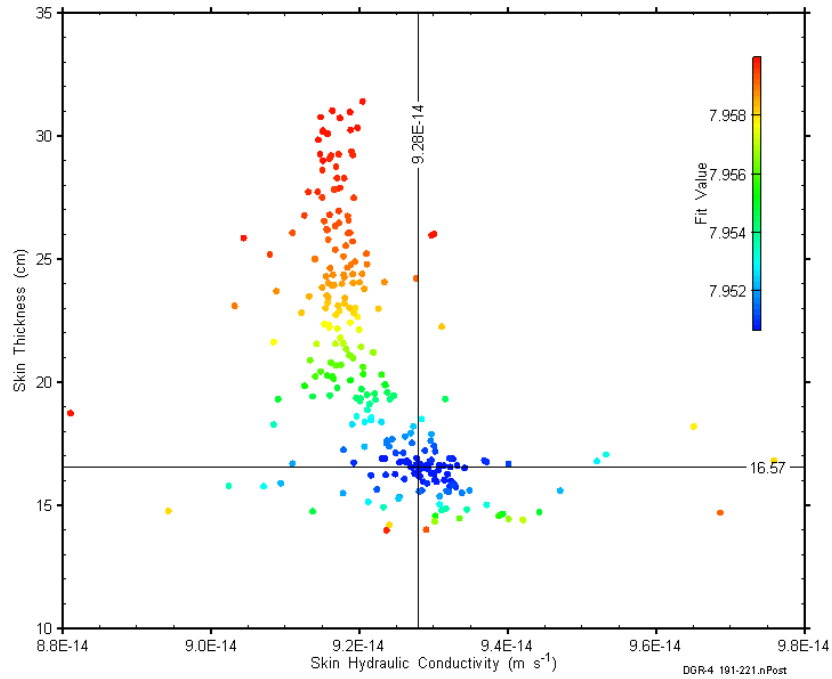


Figure D-2: XY-scatter plot showing estimates of skin hydraulic conductivity and skin thickness derived from the DGR4_190.63-221.37 perturbation analysis.

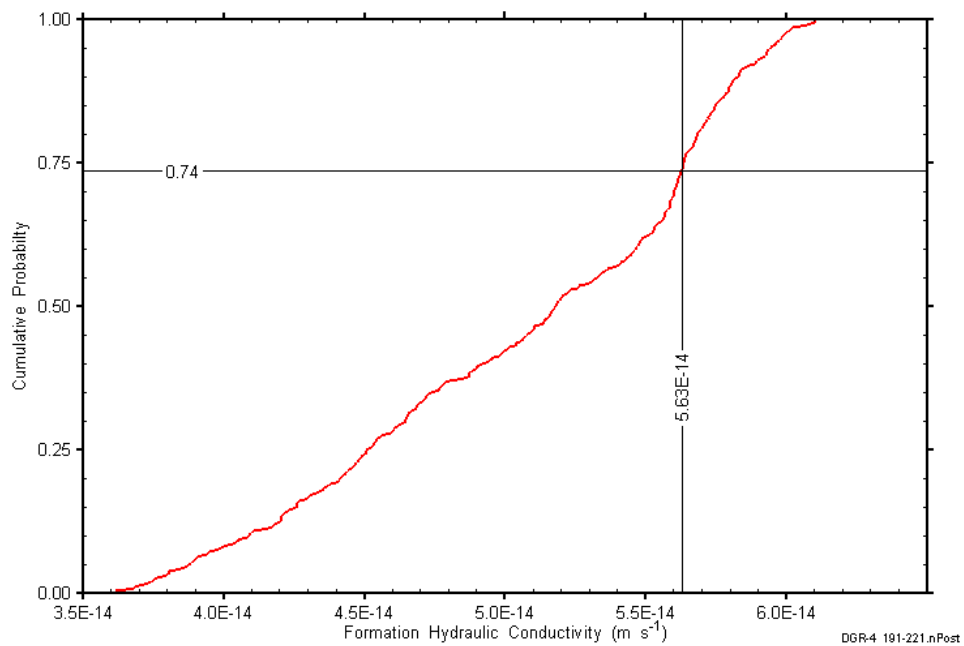


Figure D-3: DGR4_190.63-221.37 formation hydraulic conductivity cumulative distribution function.

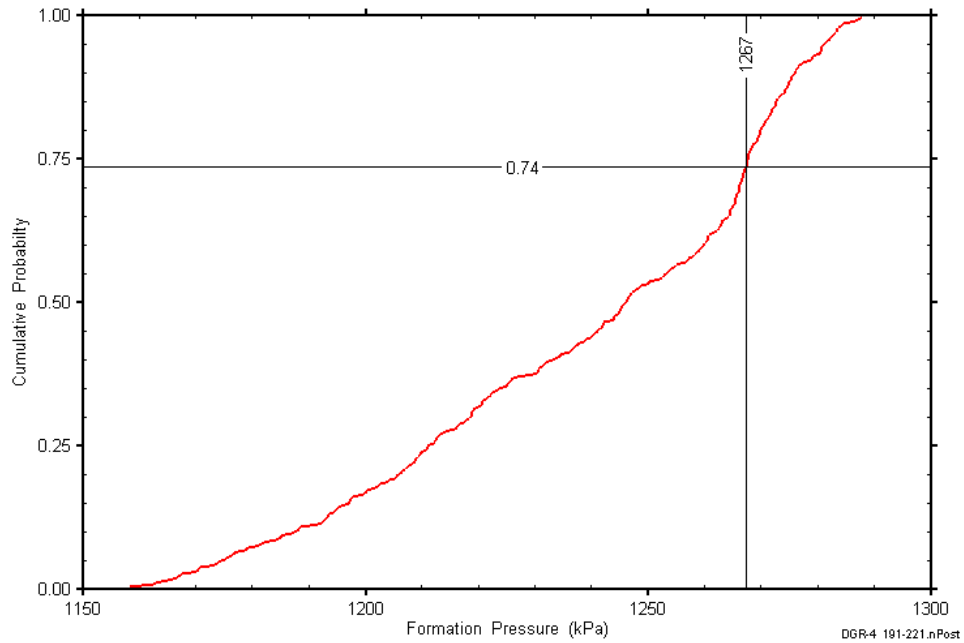


Figure D-4: DGR4_190.63-221.37 static formation pressure cumulative distribution function.

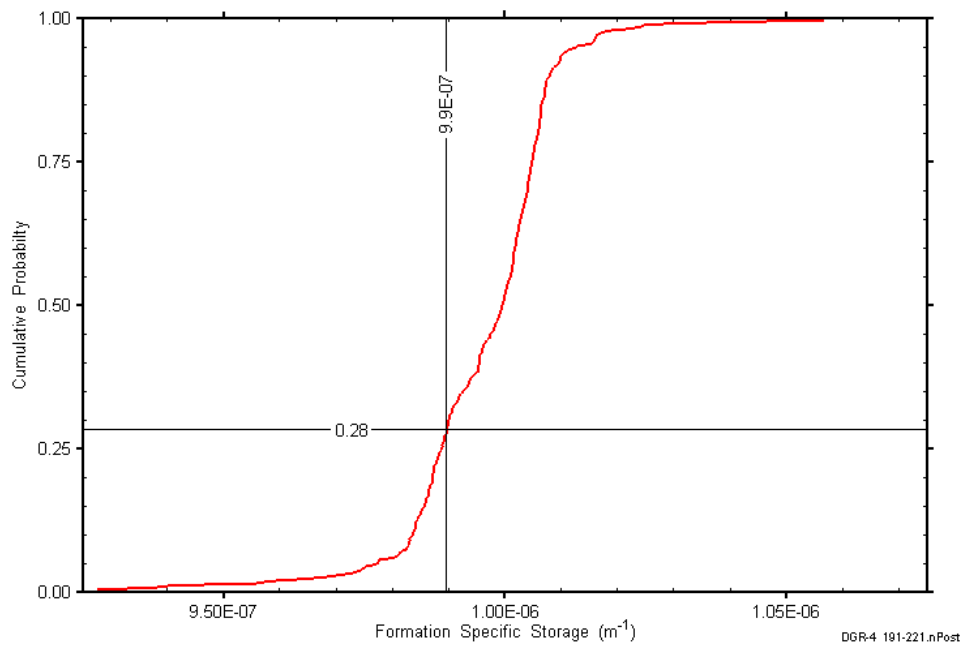


Figure D-5: DGR4_190.63-221.37 formation specific storage cumulative distribution function.

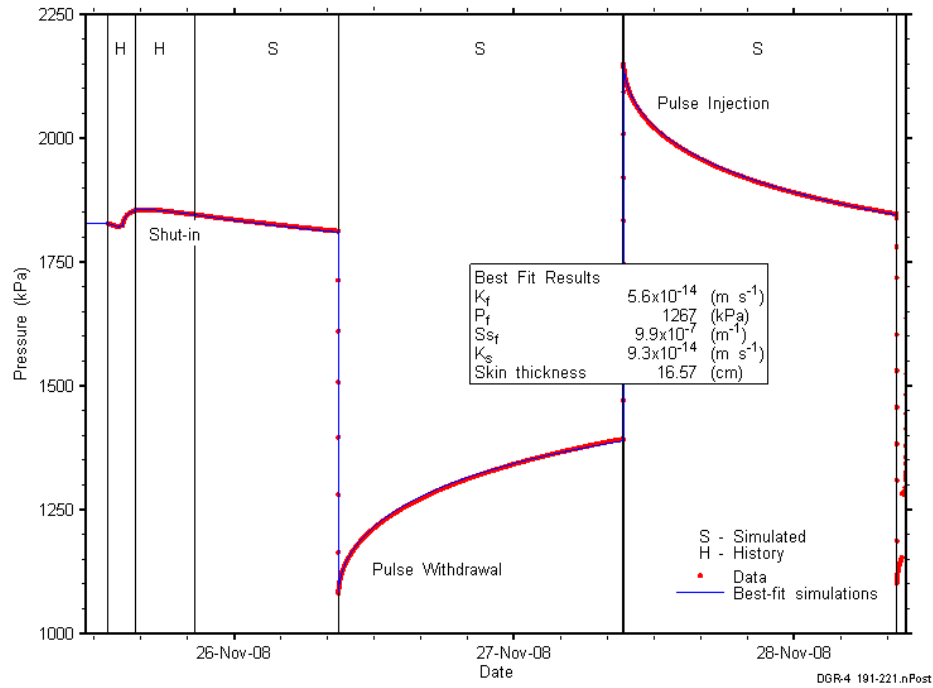


Figure D-6: Linear plot showing simulations of the DGR4_190.63-221.37 pressure response.

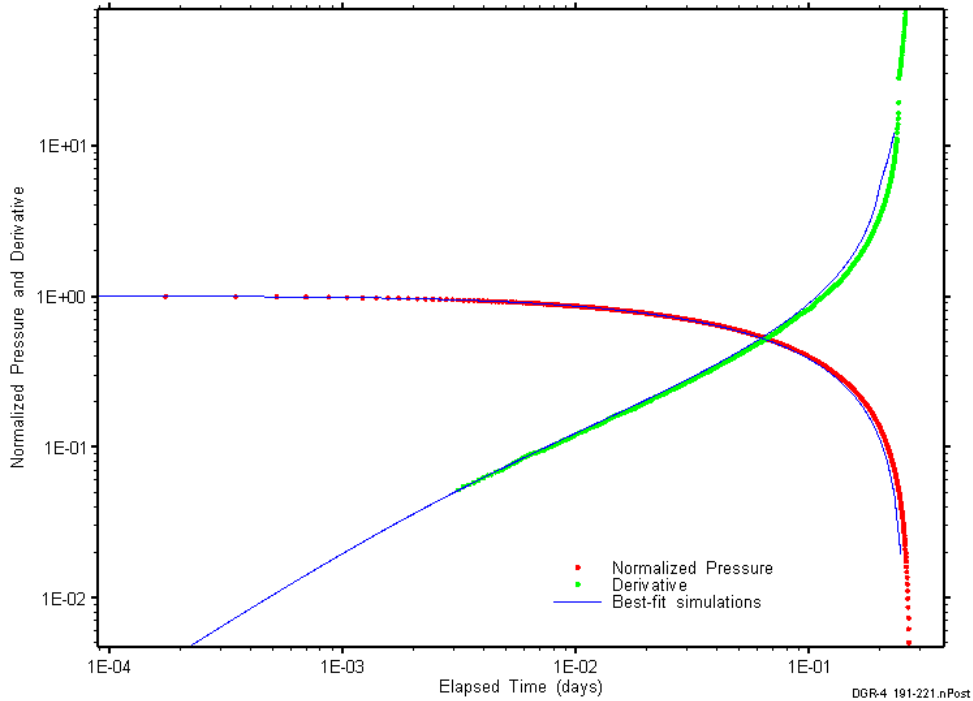


Figure D-7: Log-log plot showing simulations of the DGR4_190.63–221.37 pulse withdrawal Ramey B and derivative response.

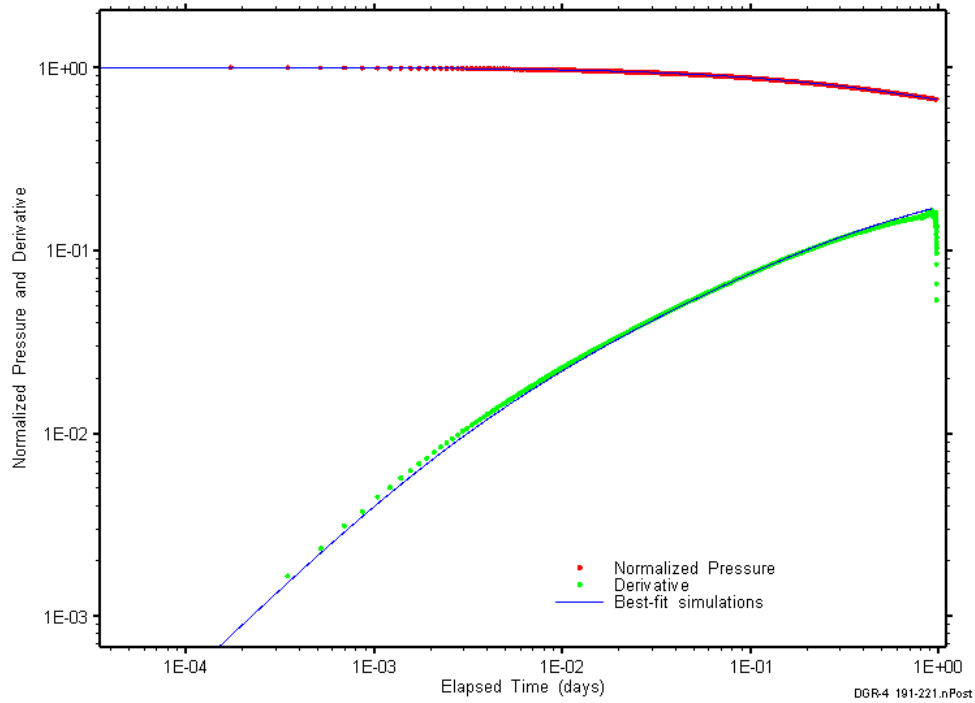


Figure D-8: Log-log plot showing simulations of the DGR4_190.63–221.37 pulse injection Ramey B and derivative response.

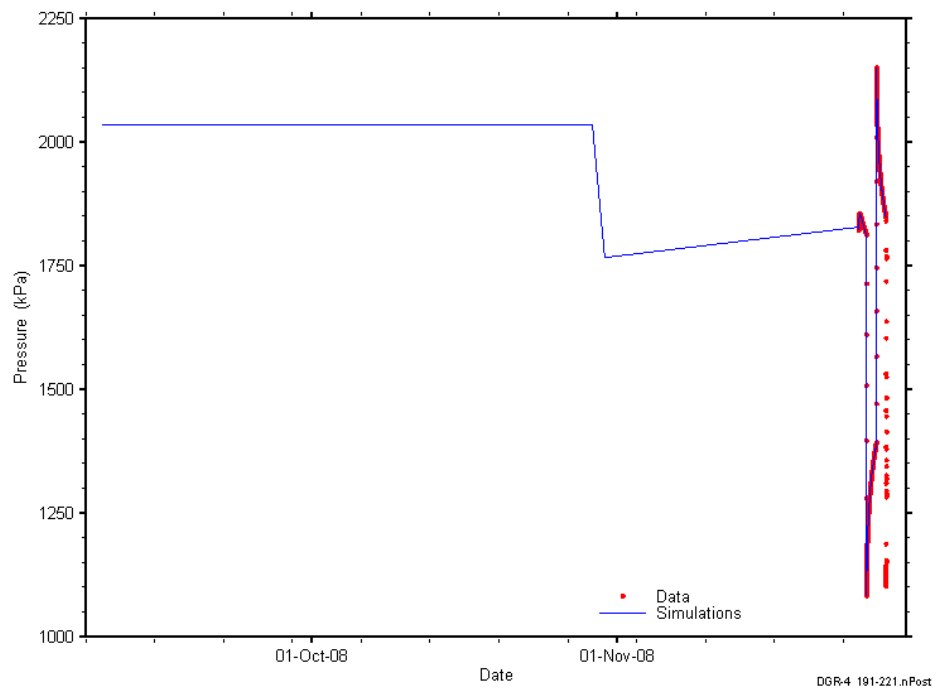


Figure D-9: Linear plot showing simulations of the DGR4_190.63-221.37 pressure response, including pre-test pressure history.

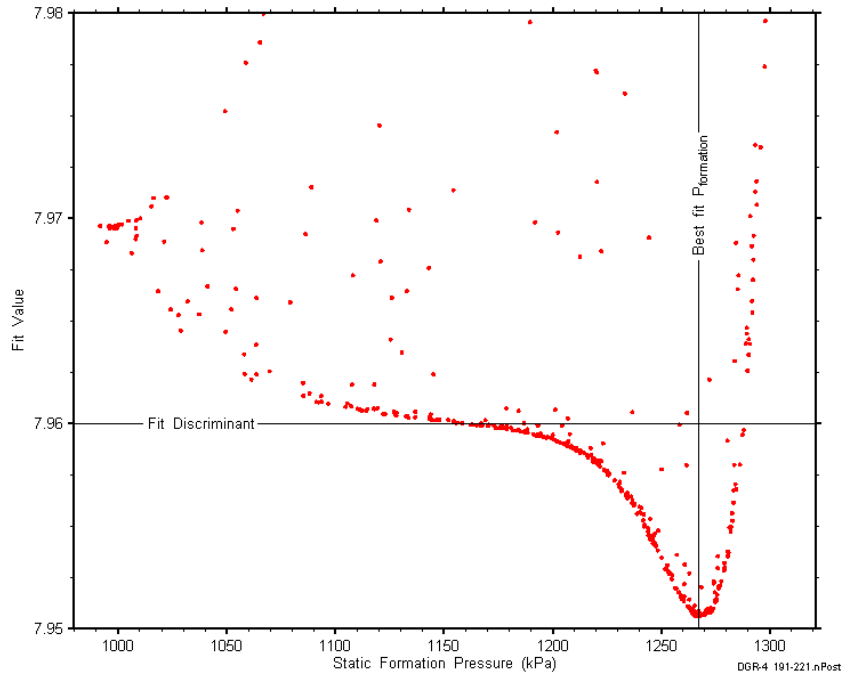


Figure D-10: XY-scatter plot showing the static formation pressure parameter space derived from DGR4_190.63-221.37 perturbation analysis along with the fit discriminant and best fit values.

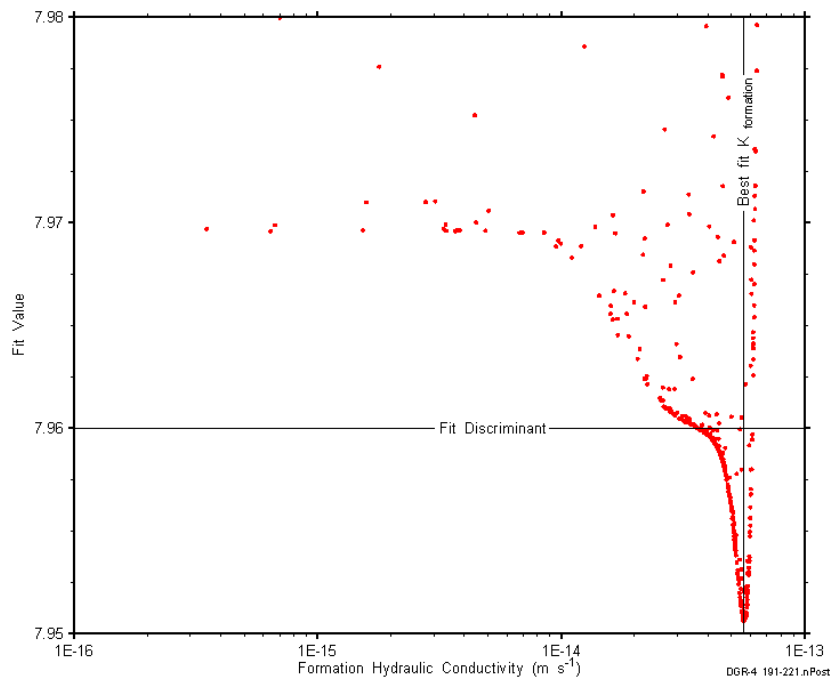


Figure D-11: XY-scatter plot showing the formation hydraulic conductivity parameter space derived from DGR4_190.63-221.37 perturbation analysis along with the fit discriminant and best fit values.

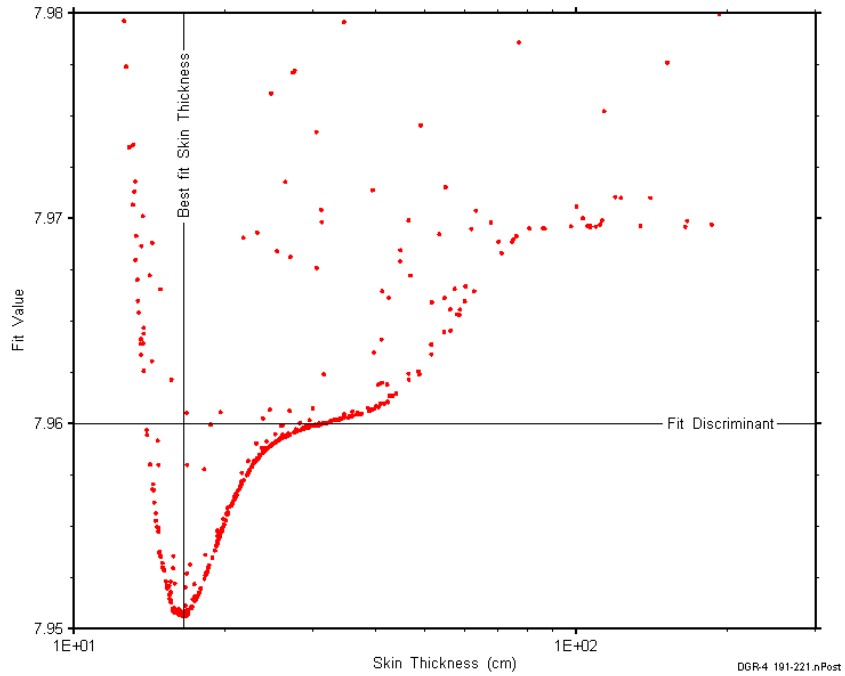


Figure D-12: XY-scatter plot showing the skin-thickness parameter space derived from DGR4_190.63-221.37 perturbation analysis along with the fit discriminant and best fit values.

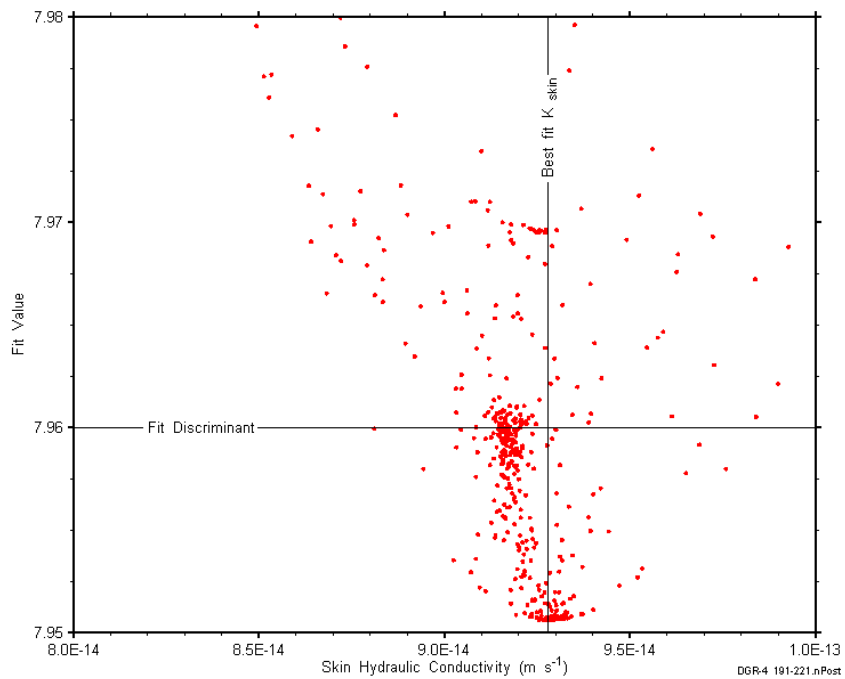


Figure D-13: XY-scatter plot showing the skin hydraulic conductivity parameter space derived from DGR4_190.63-221.37 perturbation analysis along with the fit discriminant and best fit values.

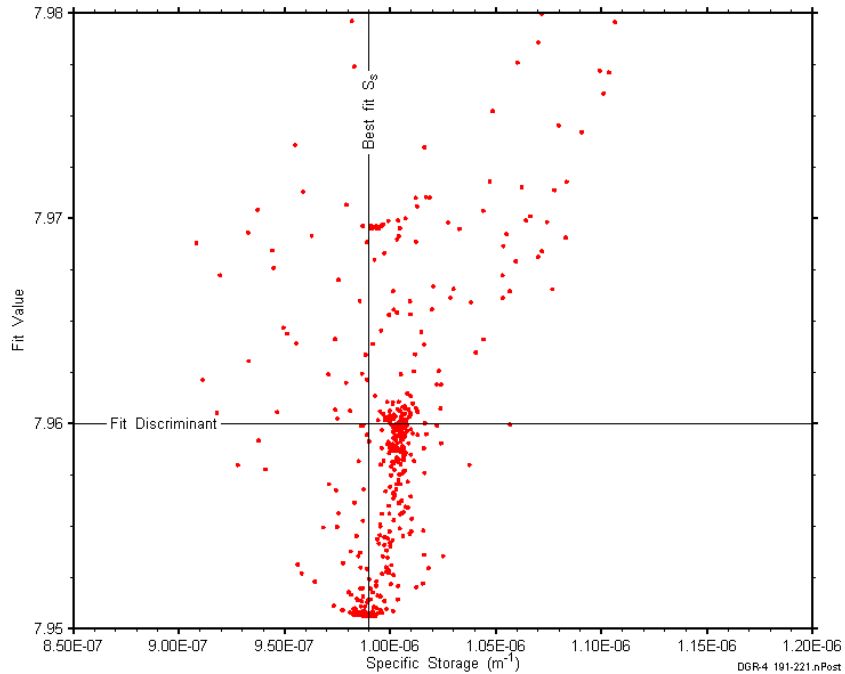


Figure D-14: XY-scatter plot showing the formation specific storage parameter space derived from DGR4_190.63-221.37 perturbation analysis along with the fit discriminant and best fit values.

D.2 218.13-248.87 Salina E-D

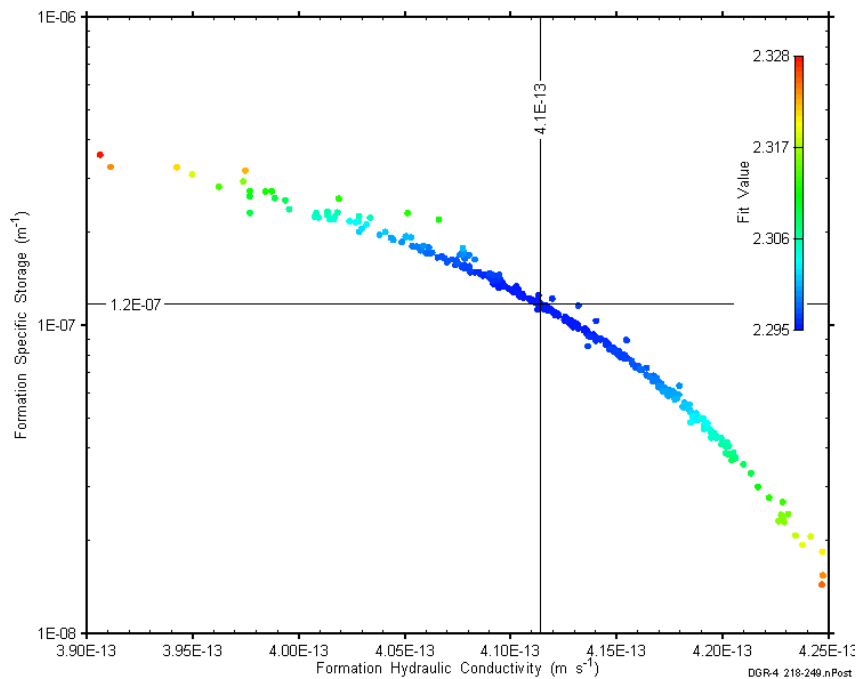


Figure D-15: XY-scatter plot showing estimates of formation hydraulic conductivity and formation specific storage derived from the DGR4_218.13-248.87 perturbation analysis.

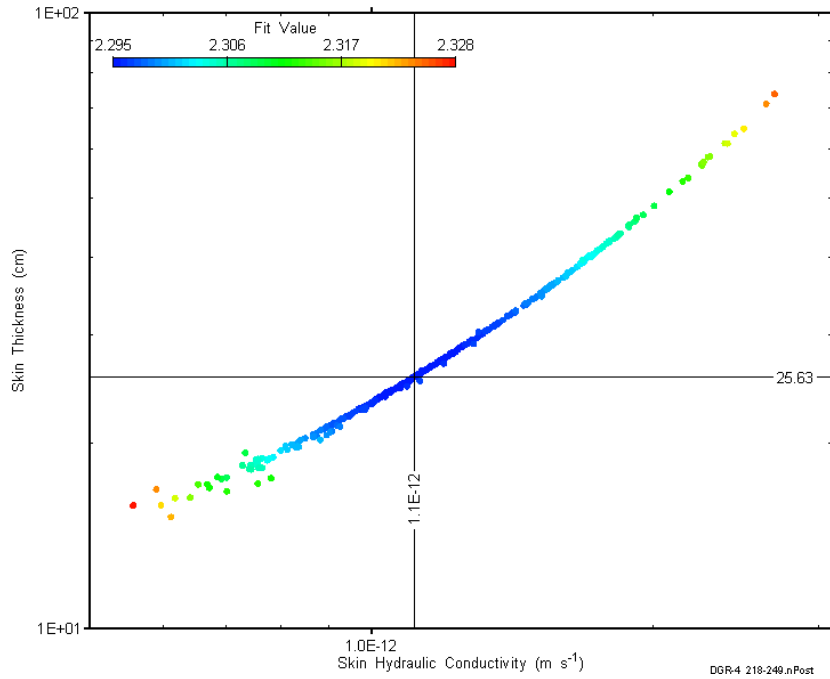


Figure D-16: XY-scatter plot showing estimates of skin hydraulic conductivity and skin thickness derived from the DGR4_218.13-248.87 perturbation analysis.

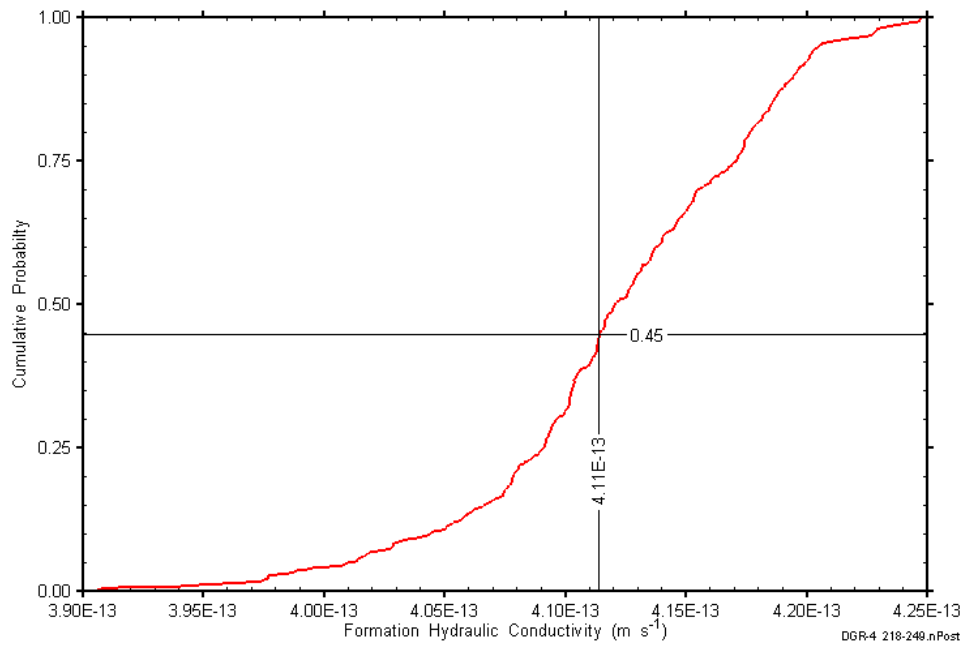


Figure D-17: DGR4_218.13-248.87 formation hydraulic conductivity cumulative distribution function.

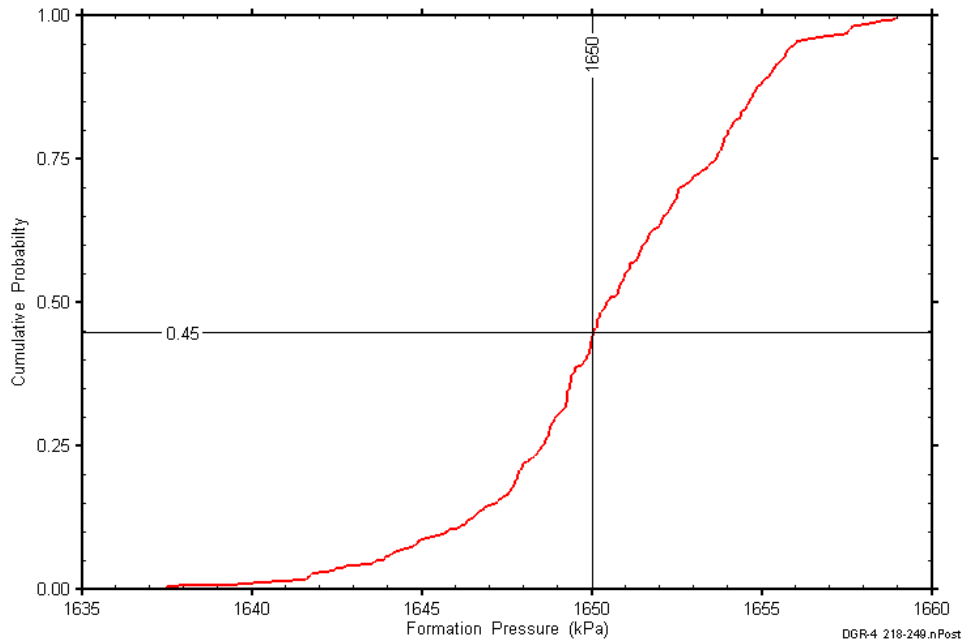


Figure D-18: DGR4_218.13-248.87 static formation pressure cumulative distribution function.

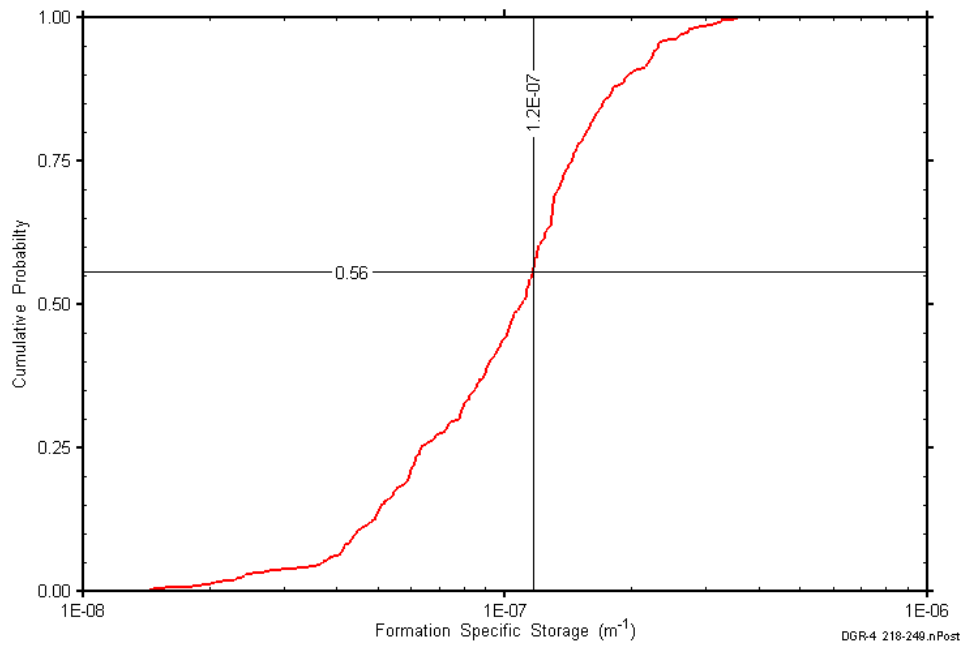


Figure D-19: DGR4_218.13-248.87 formation specific storage cumulative distribution function.

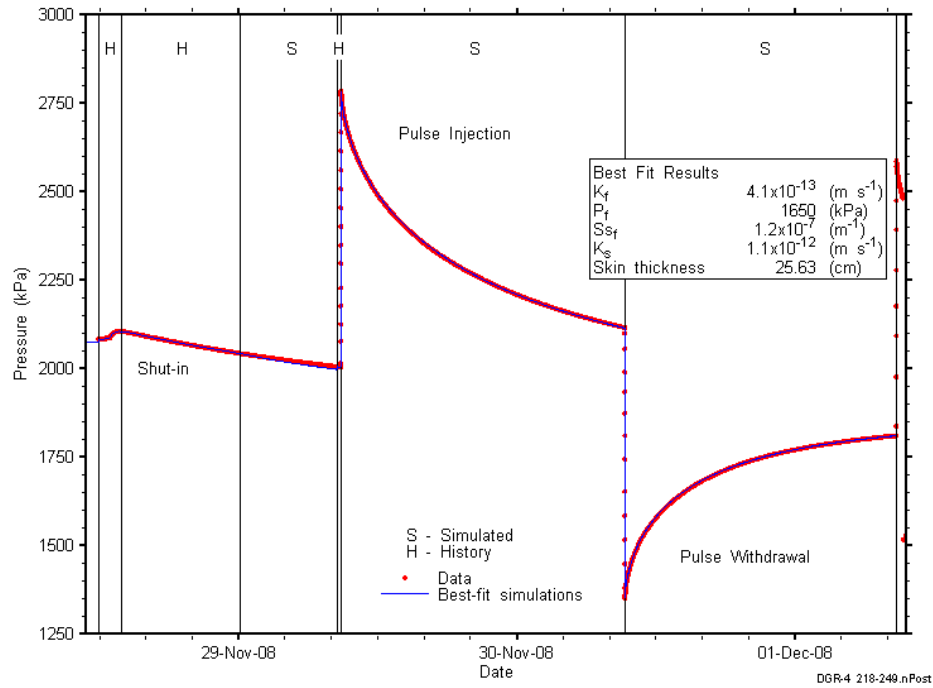


Figure D-20: Linear plot showing simulations of the DGR4_218.13-248.87 pressure response.

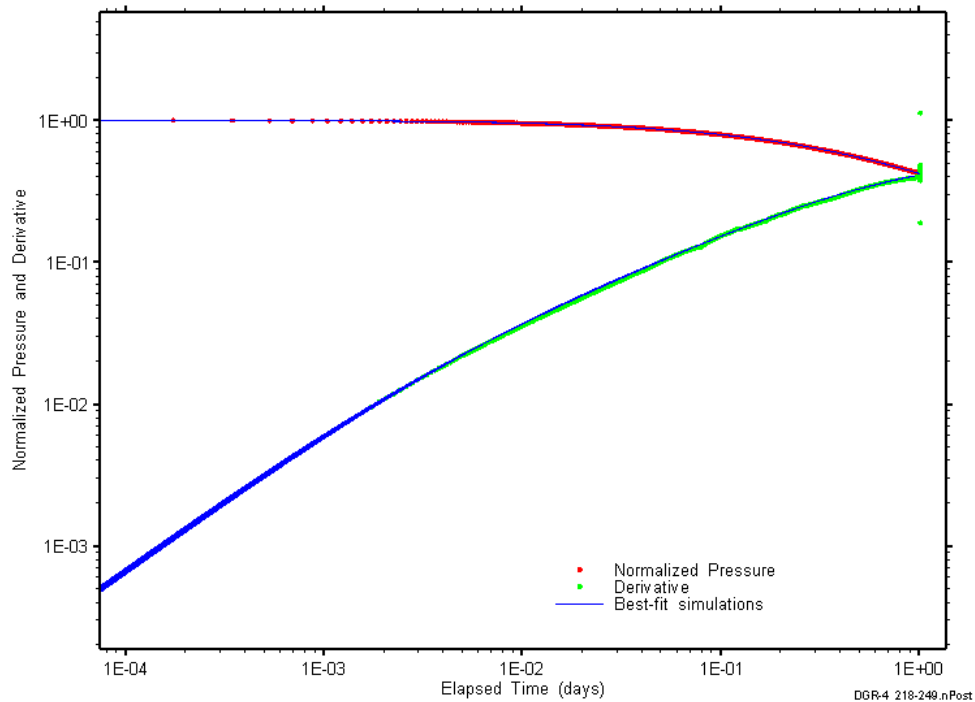


Figure D-21: Log-log plot showing simulations of the DGR4_218.13–248.87 pulse injection Ramey B and derivative response.

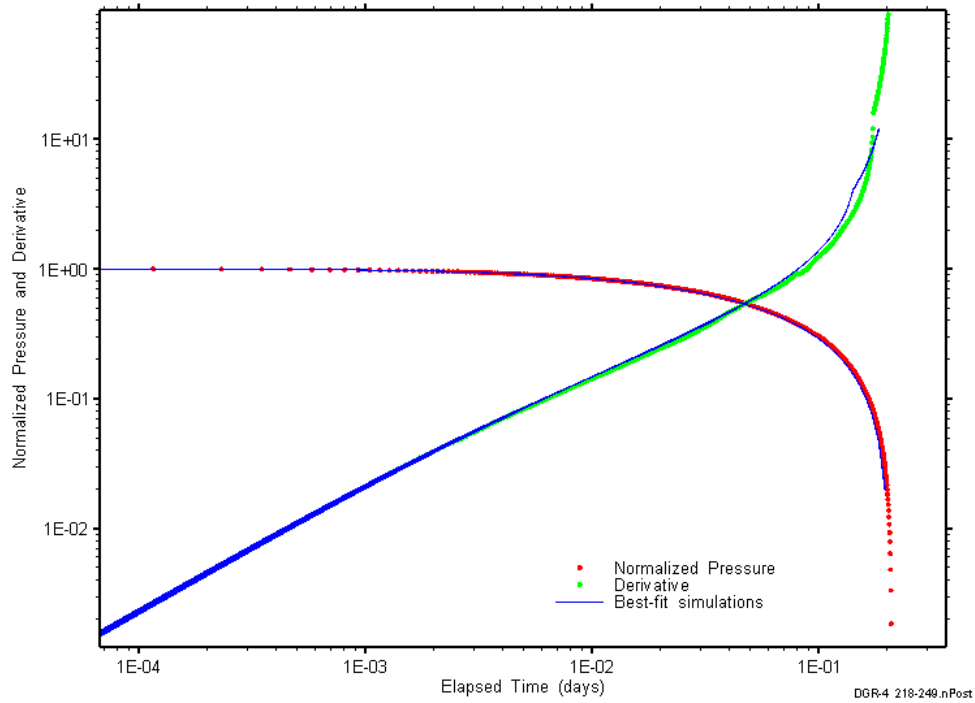


Figure D-22: Log-log plot showing simulations of the DGR4_218.13–248.87 pulse withdrawal Ramey B and derivative response.

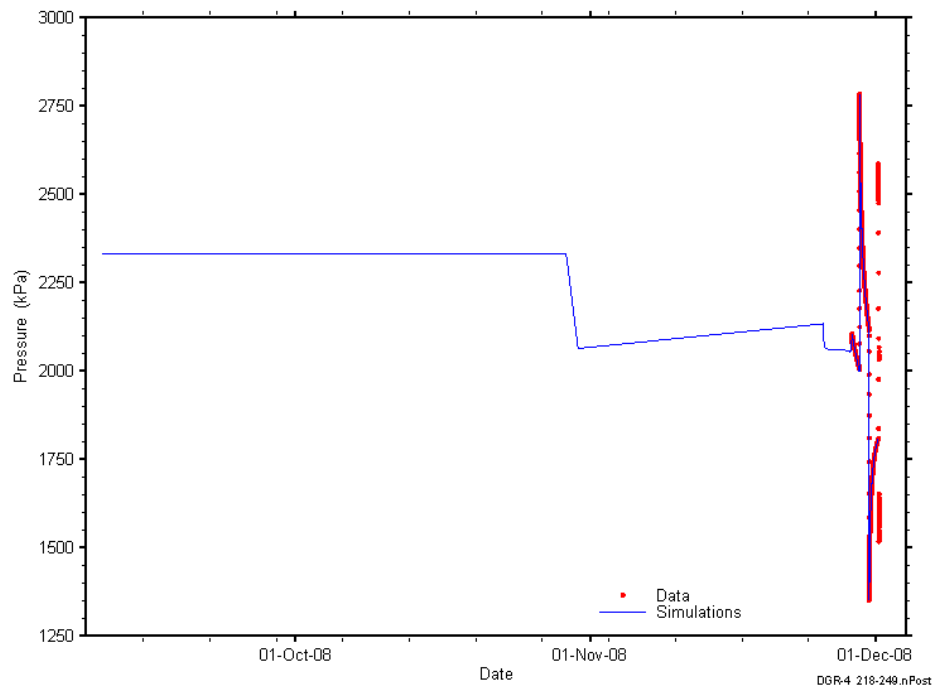


Figure D-23: Linear plot showing simulations of the DGR4_218.13-248.87 pressure response, including pre-test pressure history.

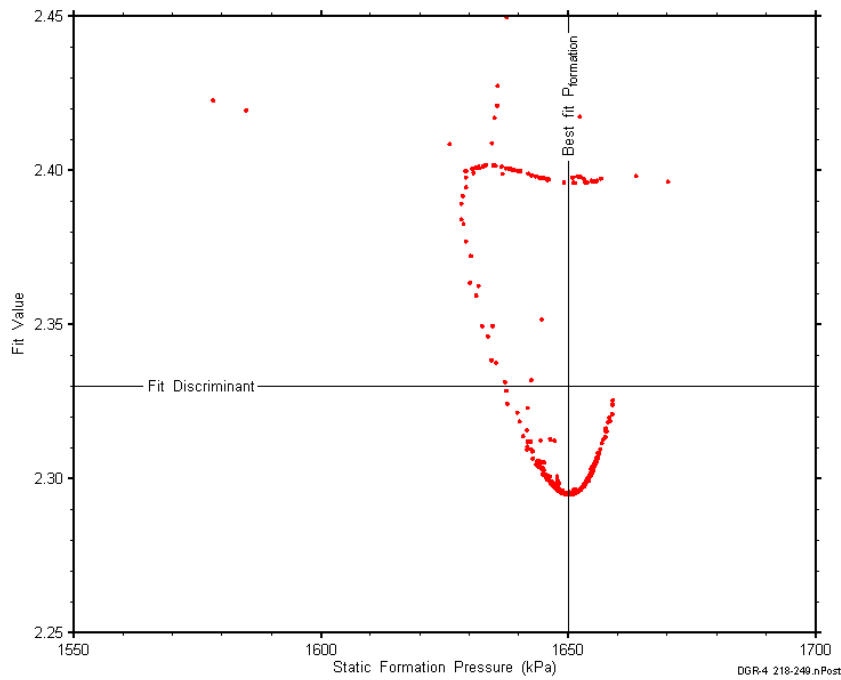


Figure D-24: XY-scatter plot showing the static formation pressure parameter space derived from DGR4_218.13-248.87 perturbation analysis along with the fit discriminant and best fit values.

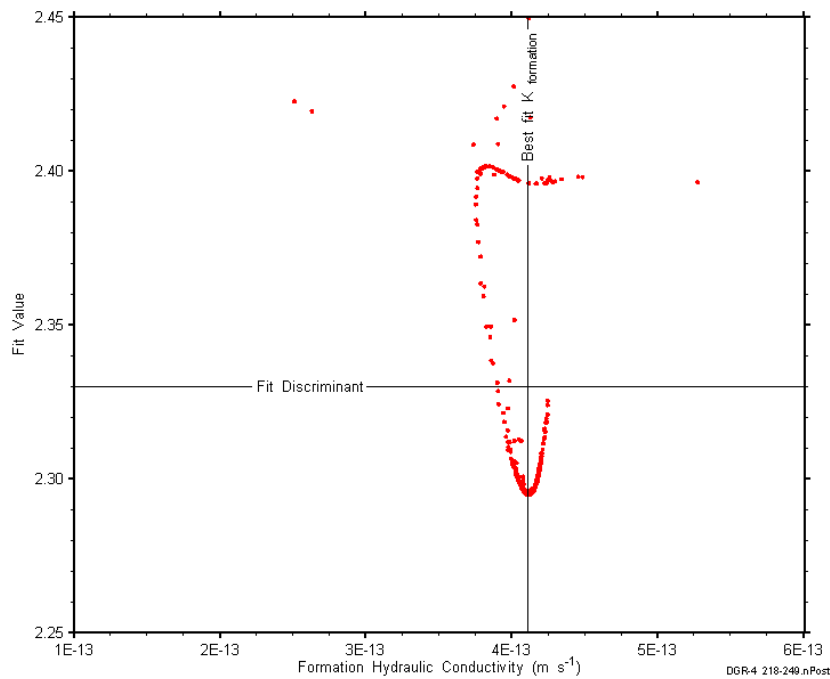


Figure D-25: XY-scatter plot showing the formation hydraulic conductivity parameter space derived from DGR4_218.13-248.87 perturbation analysis along with the fit discriminant and best fit values.

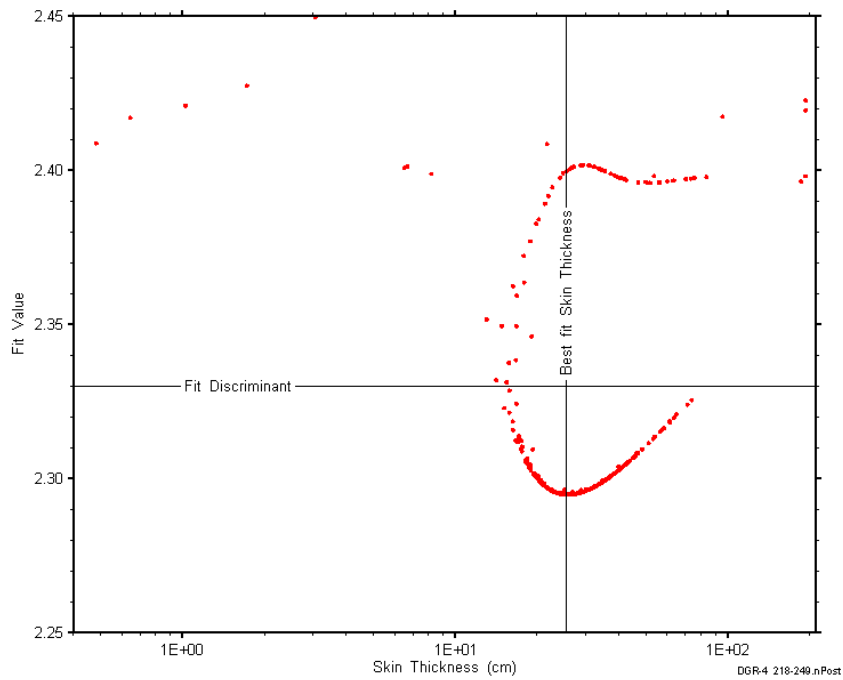


Figure D-26: XY-scatter plot showing the skin-thickness parameter space derived from DGR4_218.13-248.87 perturbation analysis along with the fit discriminant and best fit values.

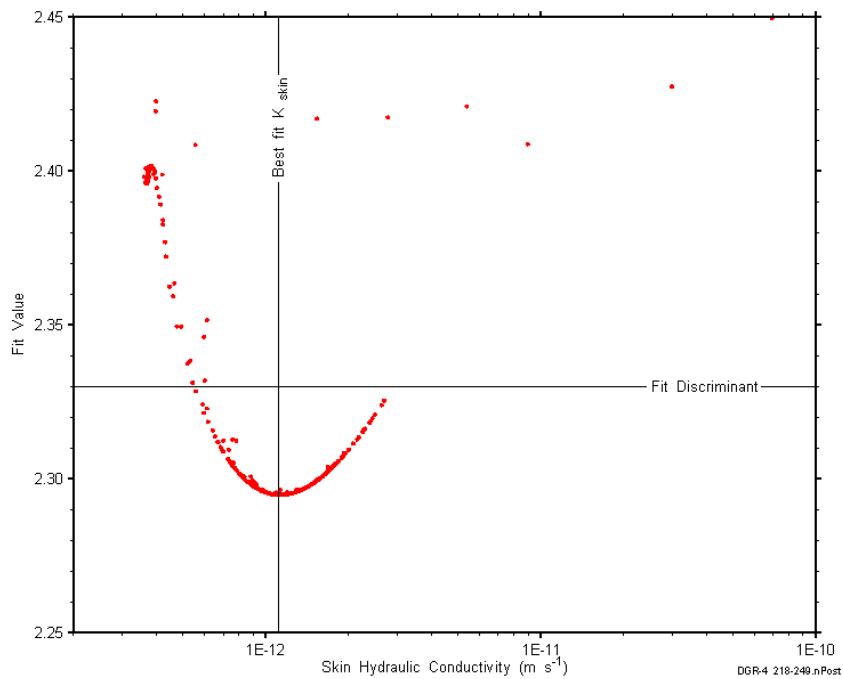


Figure D-27: XY-scatter plot showing the skin hydraulic conductivity parameter space derived from DGR4_218.13-248.87 perturbation analysis along with the fit discriminant and best fit values.

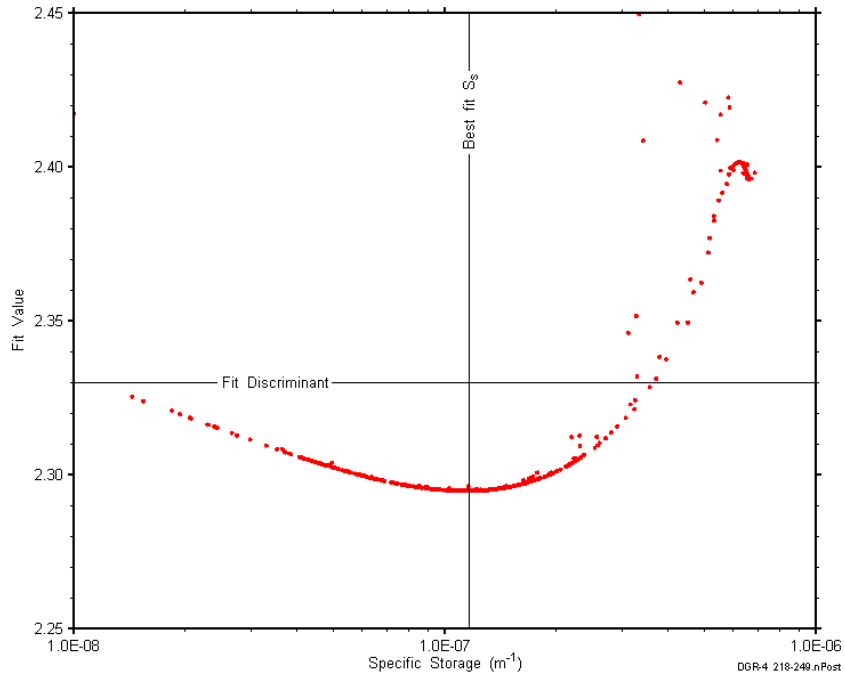


Figure D-28: XY-scatter plot showing the formation specific storage parameter space derived from DGR4_218.13-248.87 perturbation analysis along with the fit discriminant and best fit values.

D.3 247.00-277.74 Salina C-B

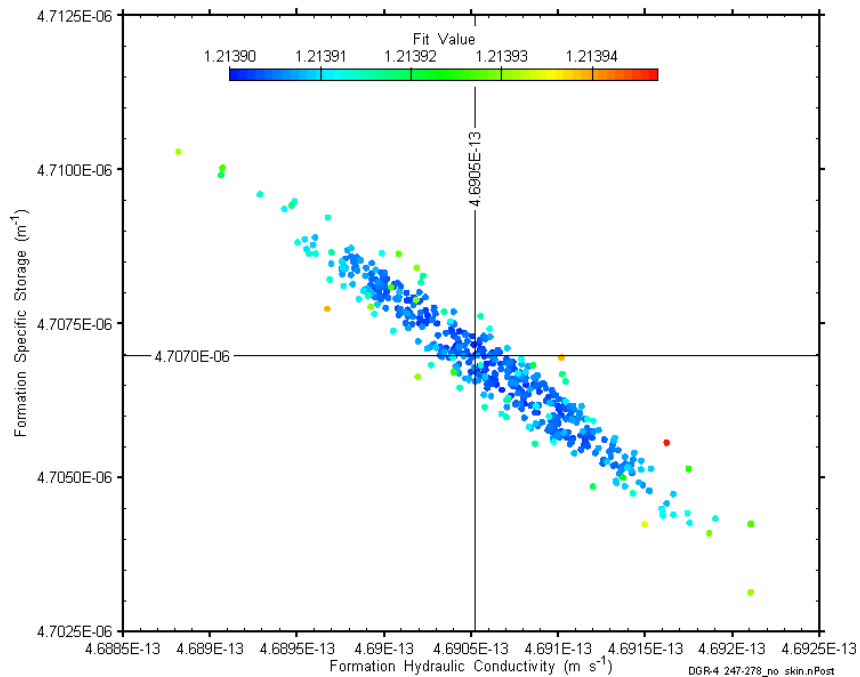


Figure D-29: XY-scatter plot showing estimates of formation hydraulic conductivity and formation specific storage derived from the DGR4_247.00-277.74 perturbation analysis.

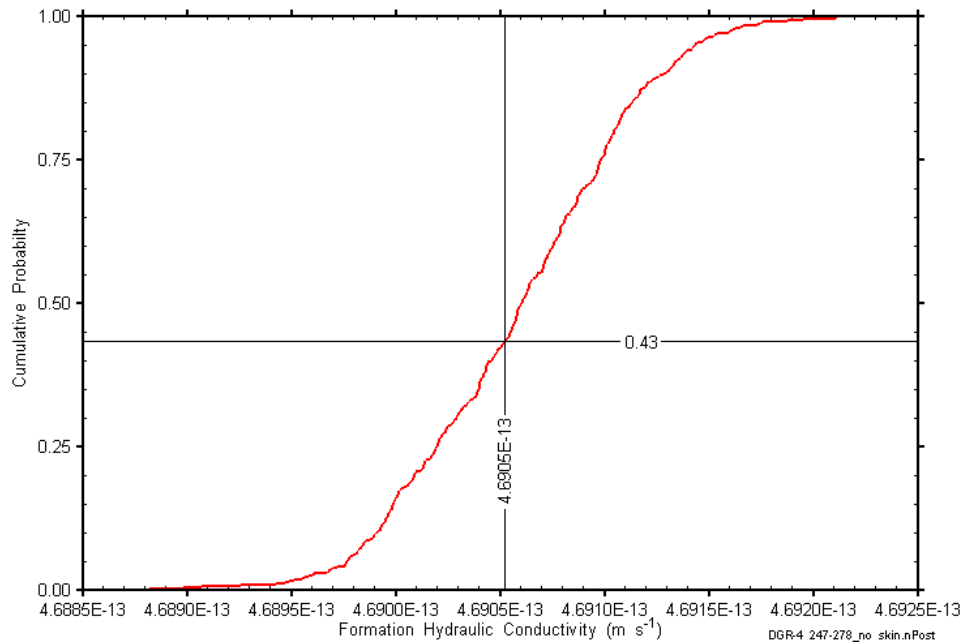


Figure D-30: DGR4_247.00-277.74 formation hydraulic conductivity cumulative distribution function.

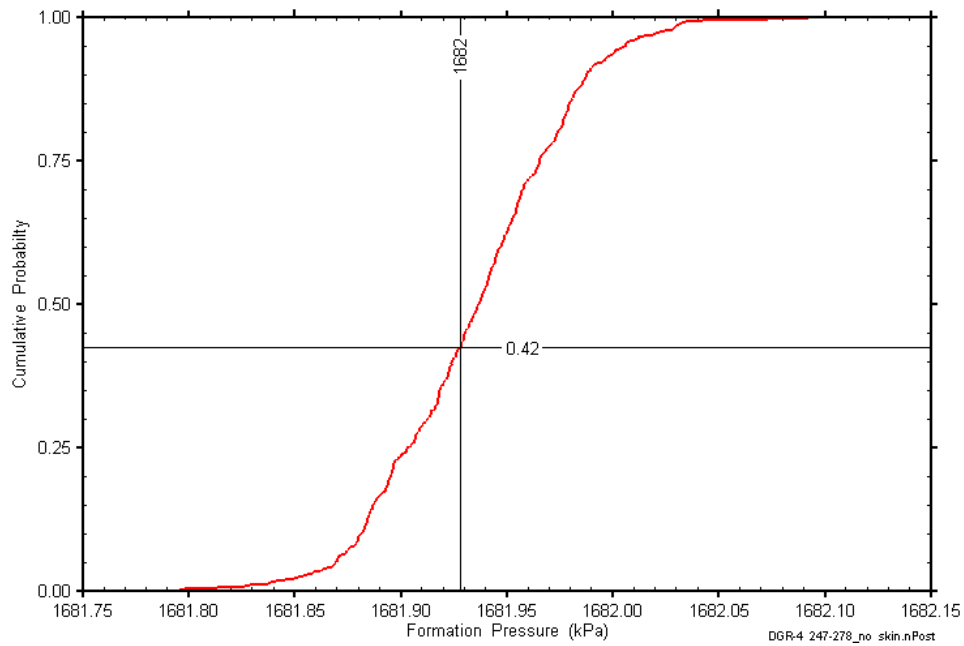


Figure D-31: DGR4_247.00-277.74 static formation pressure cumulative distribution function.

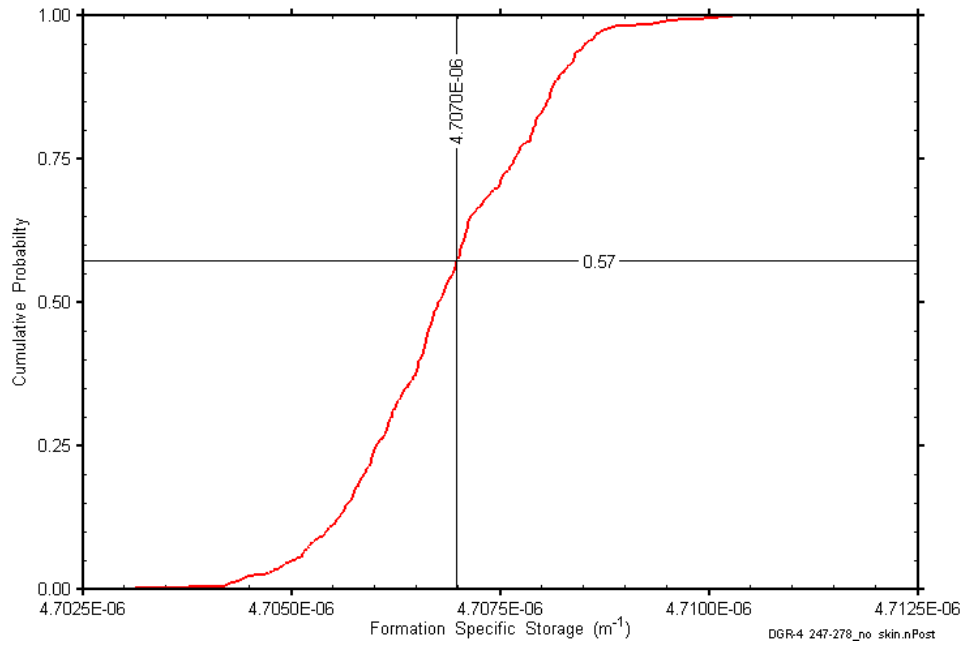


Figure D-32: DGR4_247.00-277.74 formation specific storage cumulative distribution function.

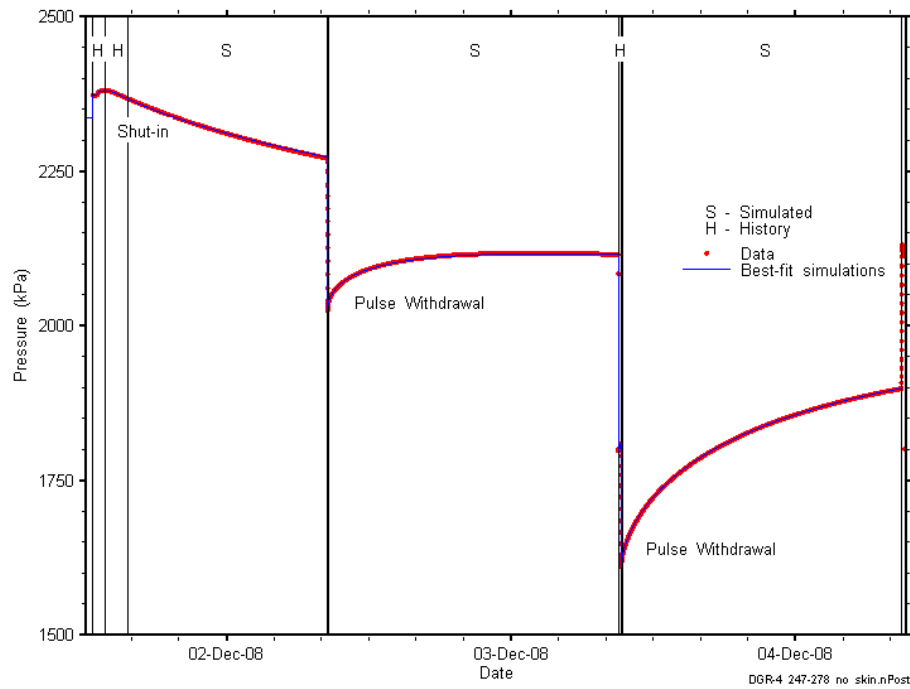


Figure D-33: Linear plot showing simulations of the DGR4_247.00-277.74 pressure response.

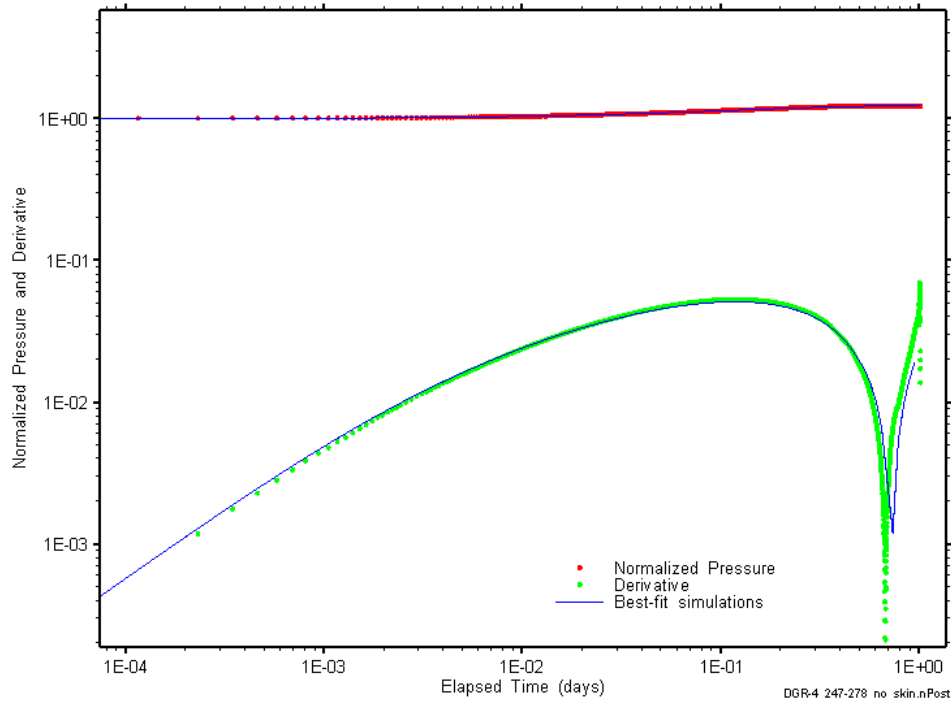


Figure D-34: Log-log plot showing simulations of the DGR4_247.00–277.74 pulse withdrawal #1 Ramey B and derivative response.

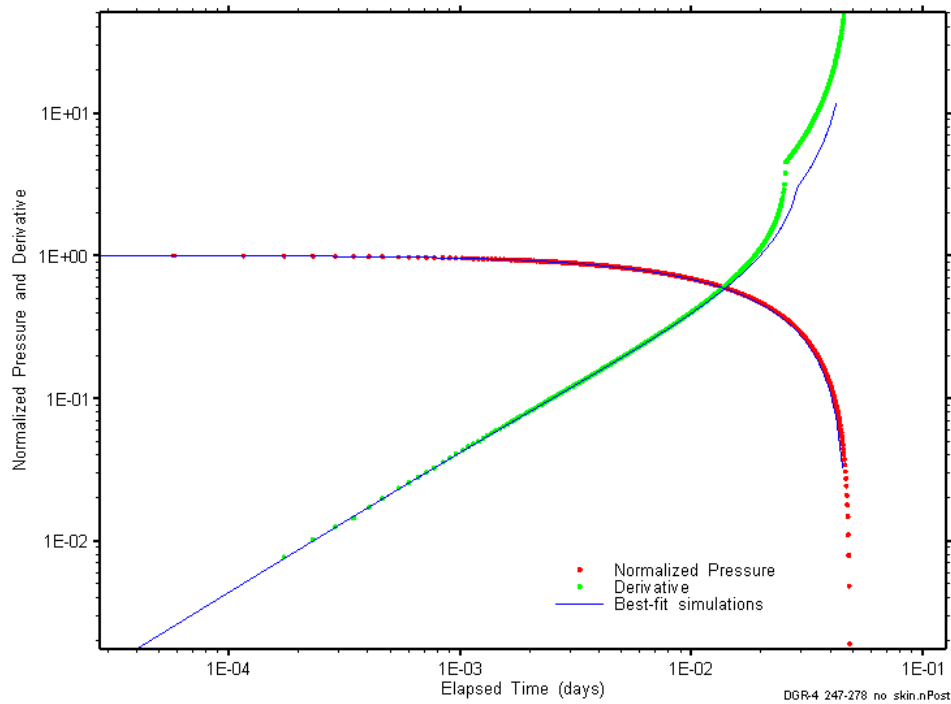


Figure D-35: Log-log plot showing simulations of the DGR4_247.00–277.74 pulse withdrawal #2 Ramey B and derivative response.

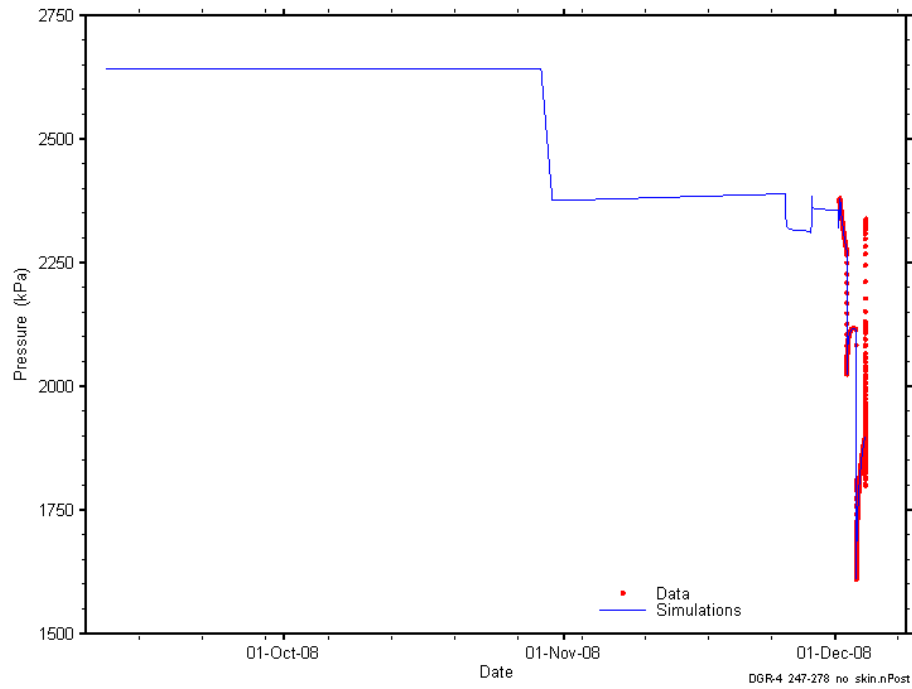


Figure D-36: Linear plot showing simulations of the DGR4_247.00-277.74 pressure response, including pre-test pressure history.

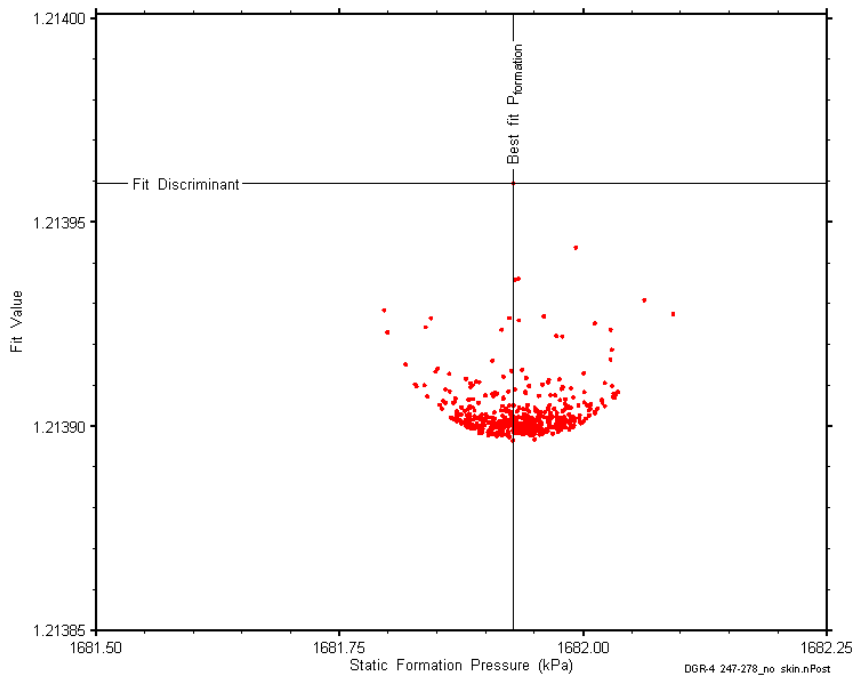


Figure D-37: XY-scatter plot showing the static formation pressure parameter space derived from DGR4_247.00-277.74 perturbation analysis along with the fit discriminant and best fit values.

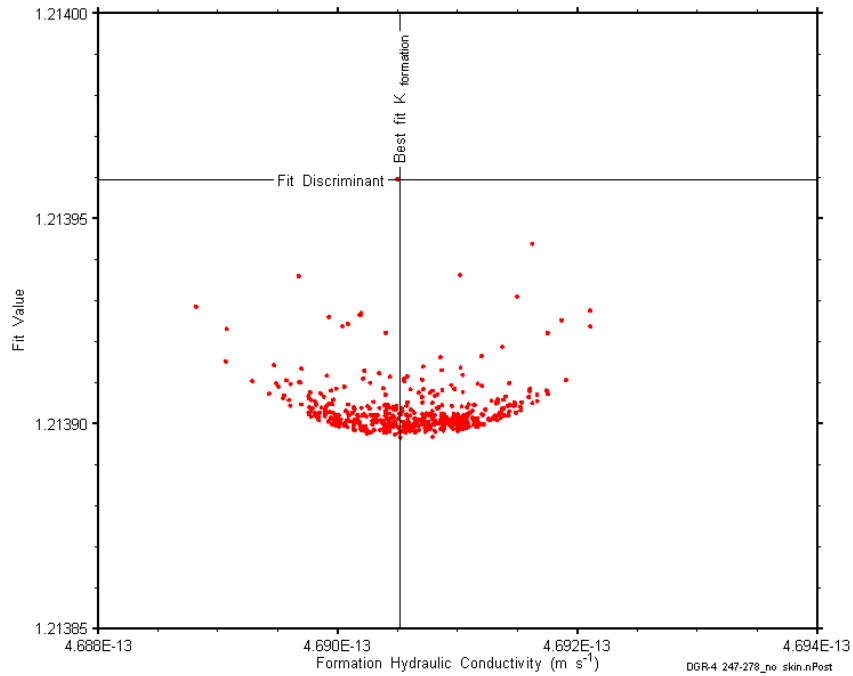


Figure D-38: XY-scatter plot showing the formation hydraulic conductivity parameter space derived from DGR4_247.00-277.74 perturbation analysis along with the fit discriminant and best fit values.

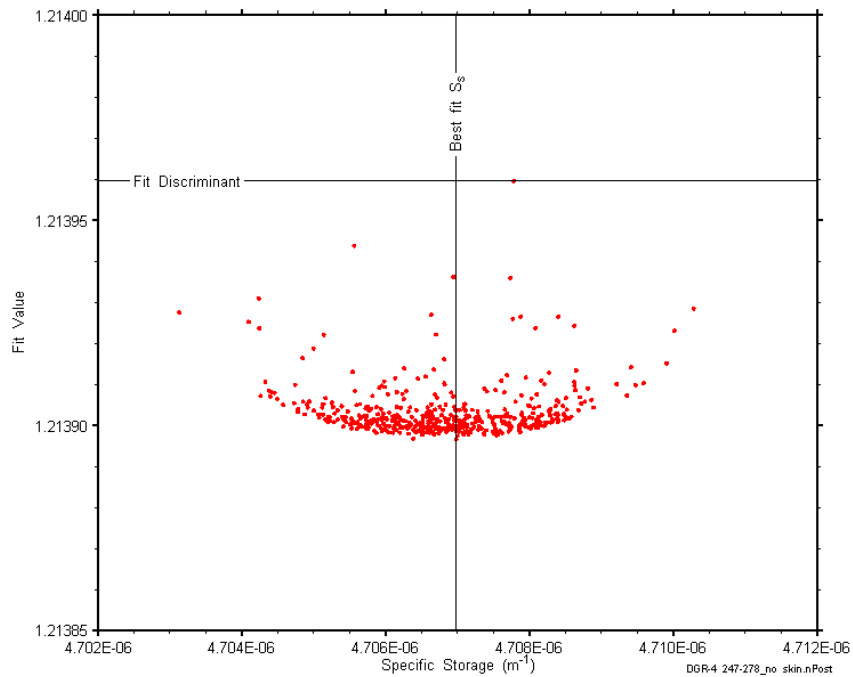


Figure D-39: XY-scatter plot showing the formation specific storage parameter space derived from DGR4_247.00-277.74 perturbation analysis along with the fit discriminant and best fit values.

D.4 261.63-292.37 Salina B

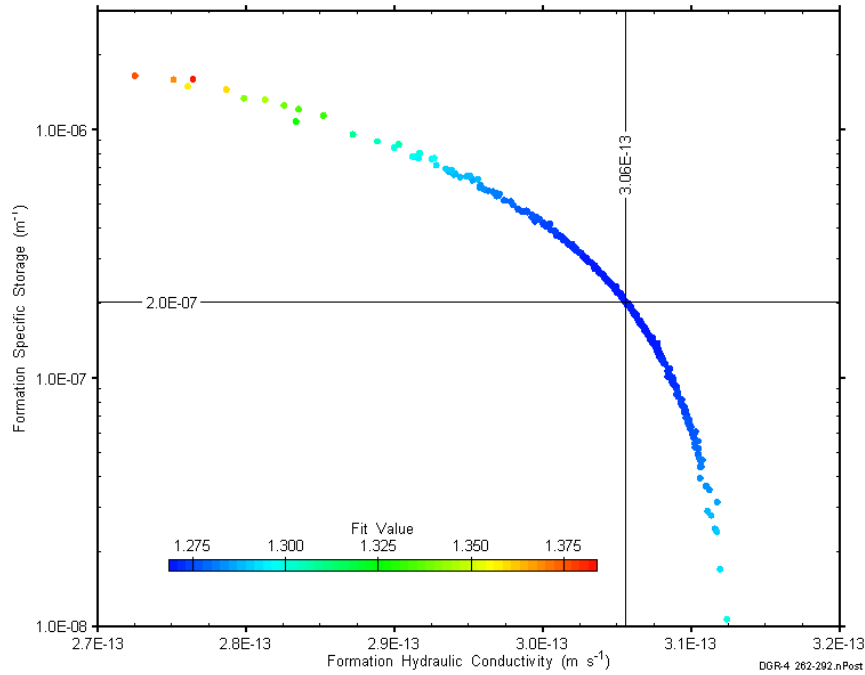


Figure D-40: XY-scatter plot showing estimates of formation hydraulic conductivity and formation specific storage derived from the DGR4_261.63-292.37 perturbation analysis.

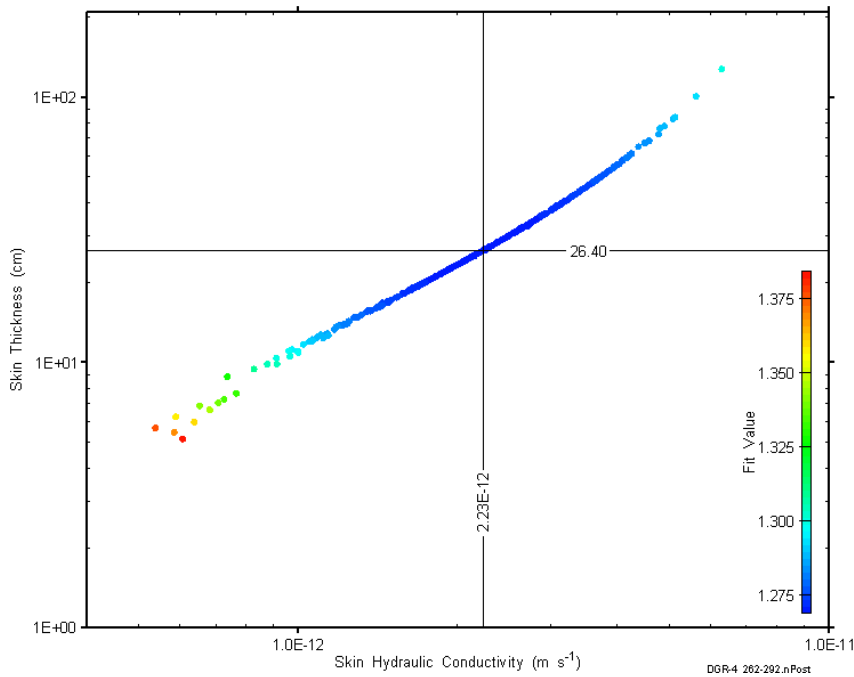


Figure D-41: XY-scatter plot showing estimates of skin hydraulic conductivity and skin thickness derived from the DGR4_261.63-292.37 perturbation analysis.

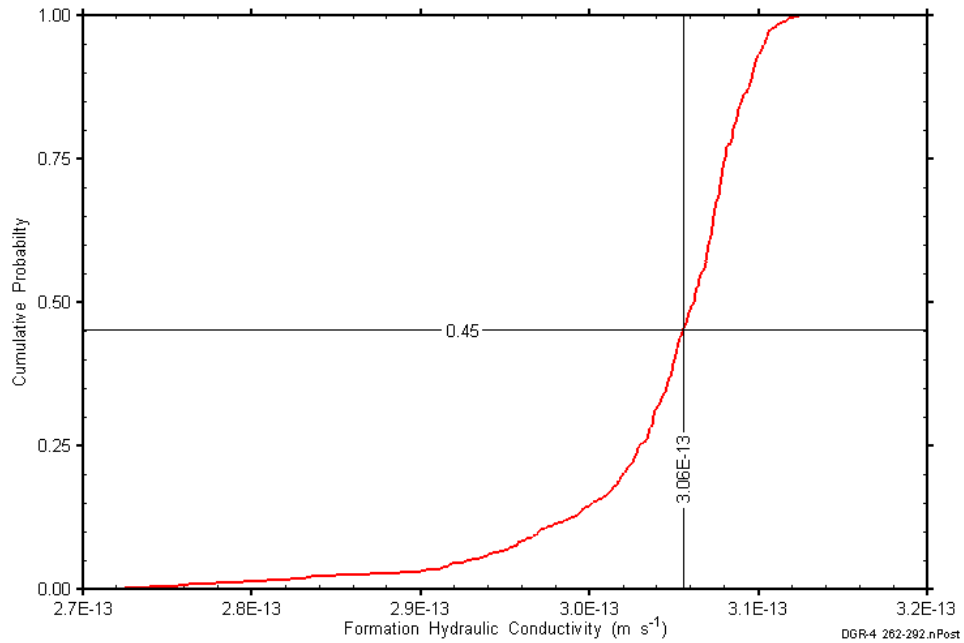


Figure D-42: DGR4_261.63-292.37 formation hydraulic conductivity cumulative distribution function.

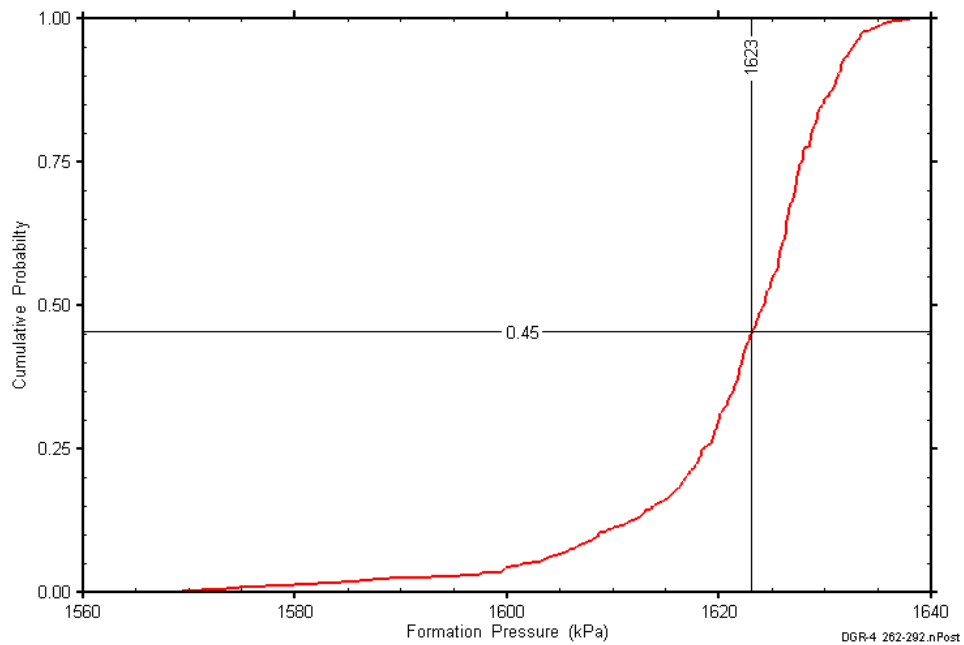


Figure D-43: DGR4_261.63-292.37 static formation pressure cumulative distribution function.

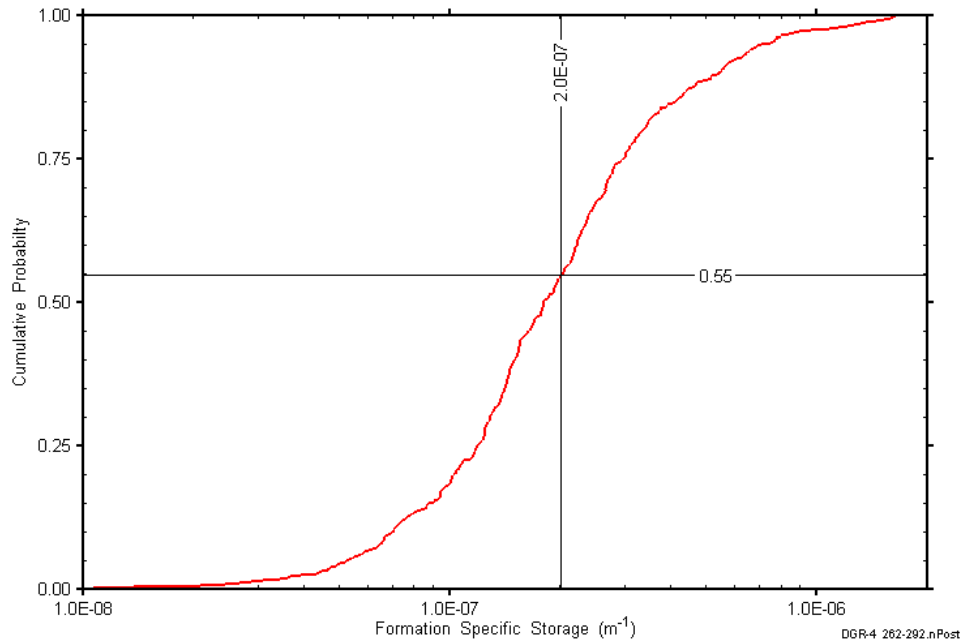


Figure D-44: DGR4_261.63-292.37 formation specific storage cumulative distribution function.

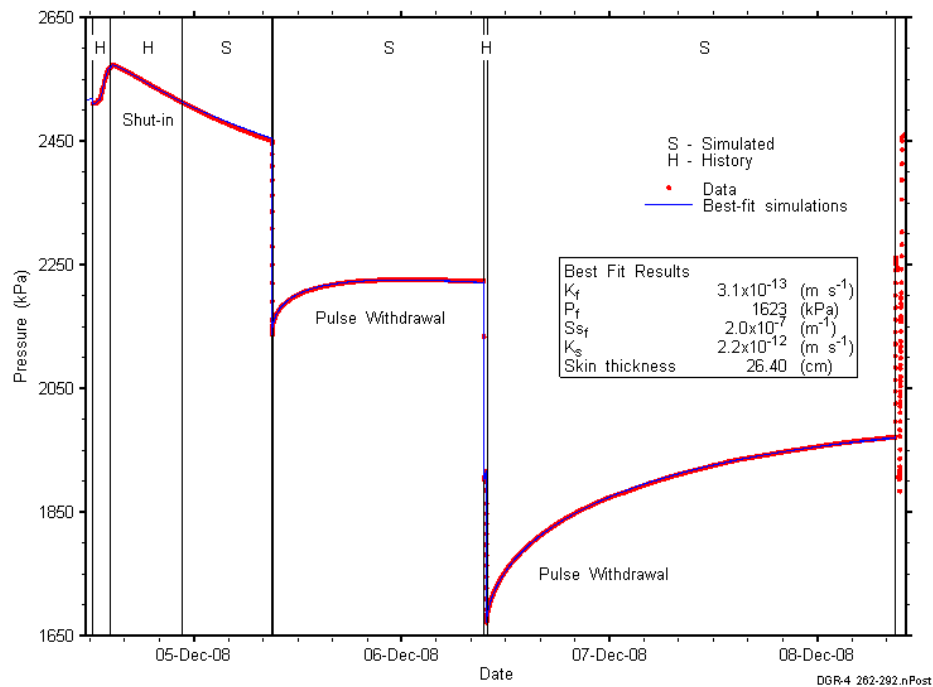


Figure D-45: Linear plot showing simulations of the DGR4_261.63-292.37 pressure response.

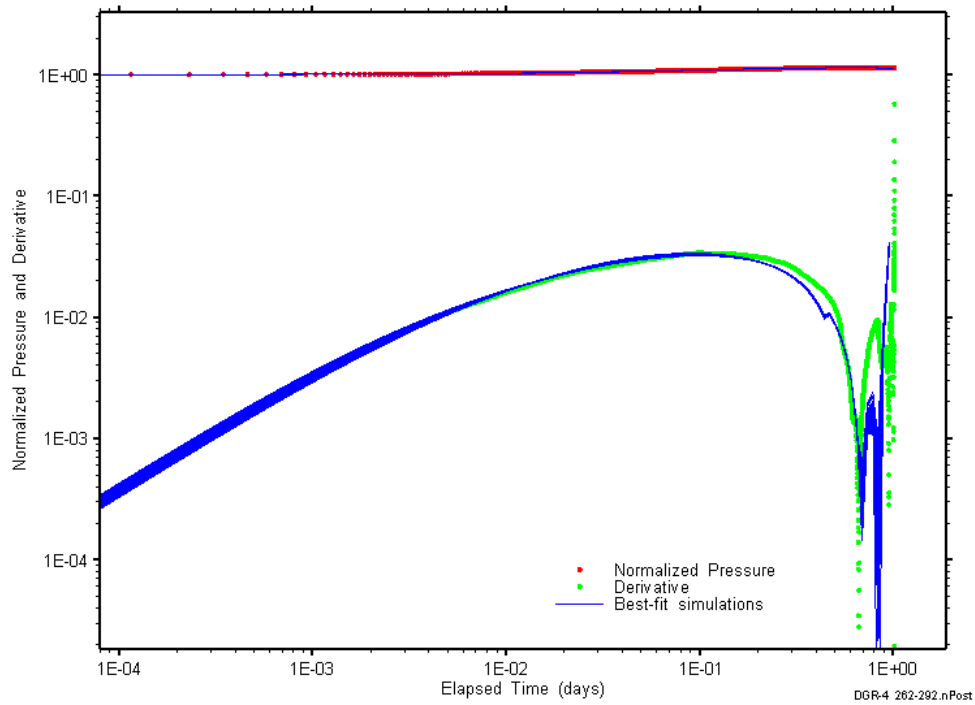


Figure D-46: Log-log plot showing simulations of the DGR4_261.63–292.37 pulse withdrawal #1 Ramey B and derivative response.

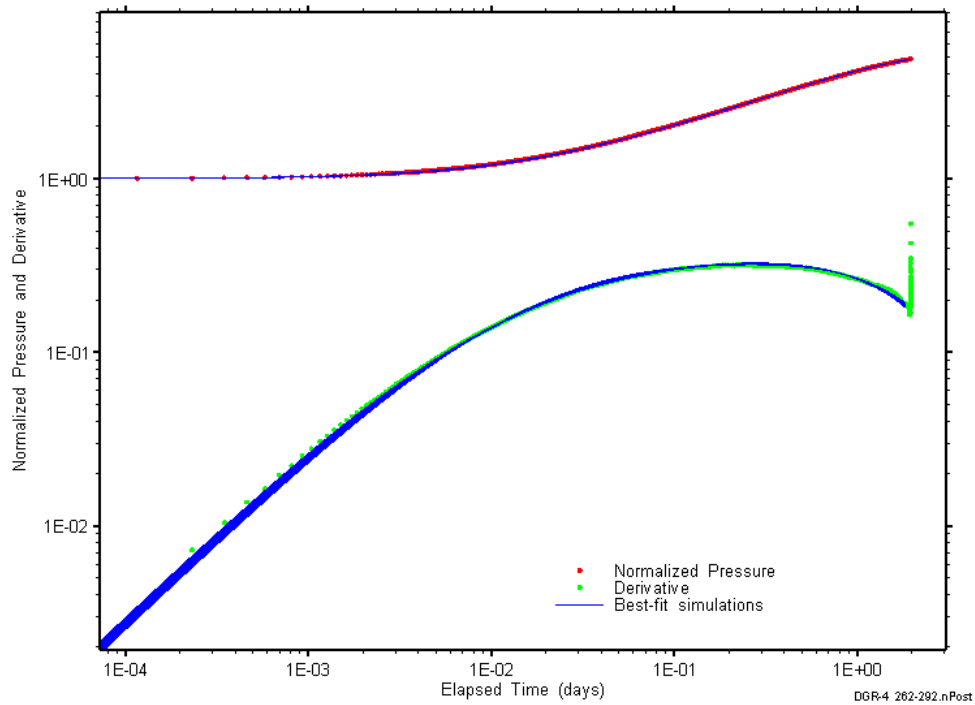


Figure D-47: Log-log plot showing simulations of the DGR4_261.63–292.37 pulse withdrawal #2 Ramey B and derivative response.

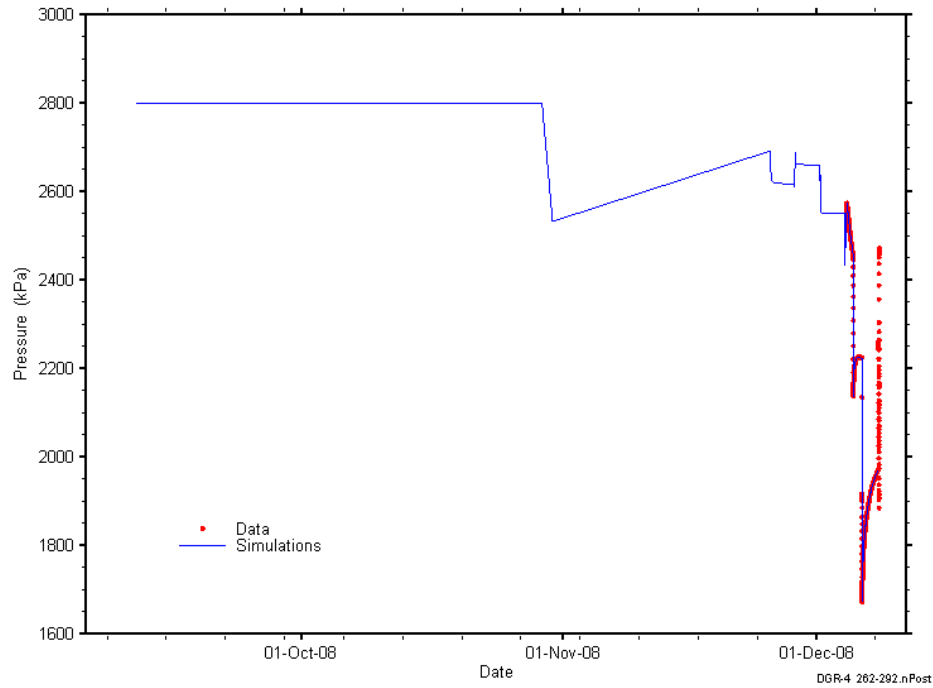


Figure D-48: Linear plot showing simulations of the DGR4_261.63-292.37 pressure response, including pre-test pressure history.

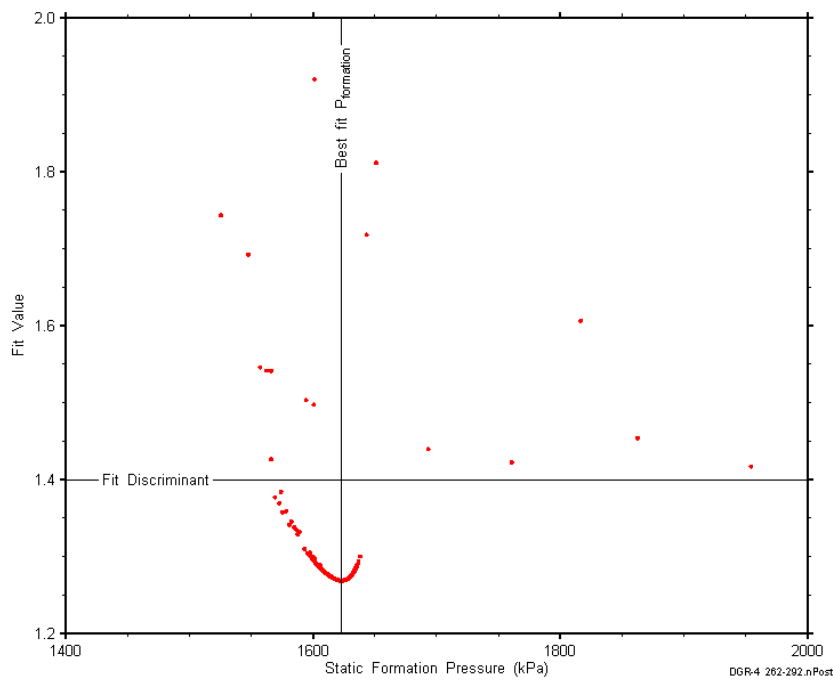


Figure D-49: XY-scatter plot showing the static formation pressure parameter space derived from DGR4_261.63-292.37 perturbation analysis along with the fit discriminant and best fit values.

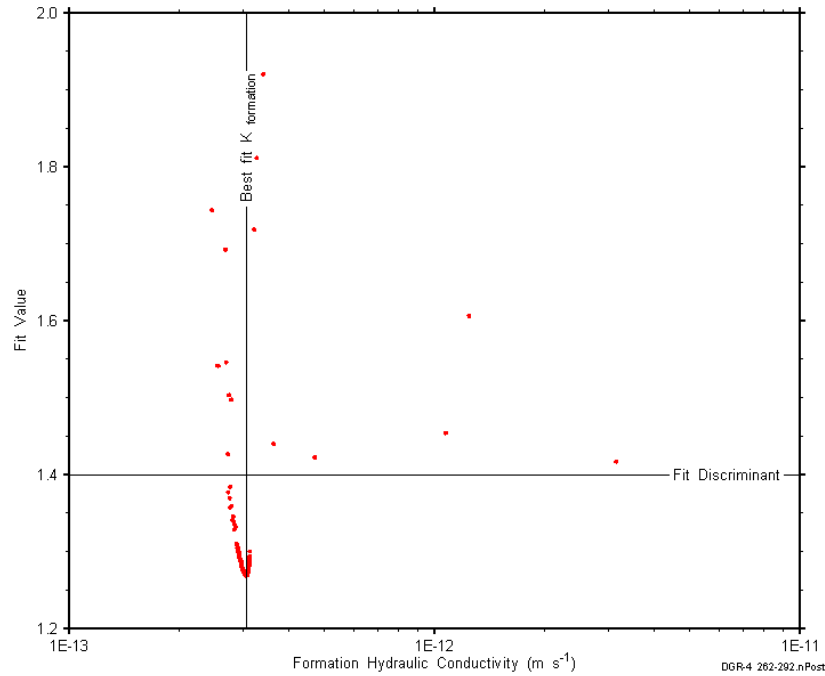


Figure D-50: XY-scatter plot showing the formation hydraulic conductivity parameter space derived from DGR4_261.63-292.37 perturbation analysis along with the fit discriminant and best fit values.

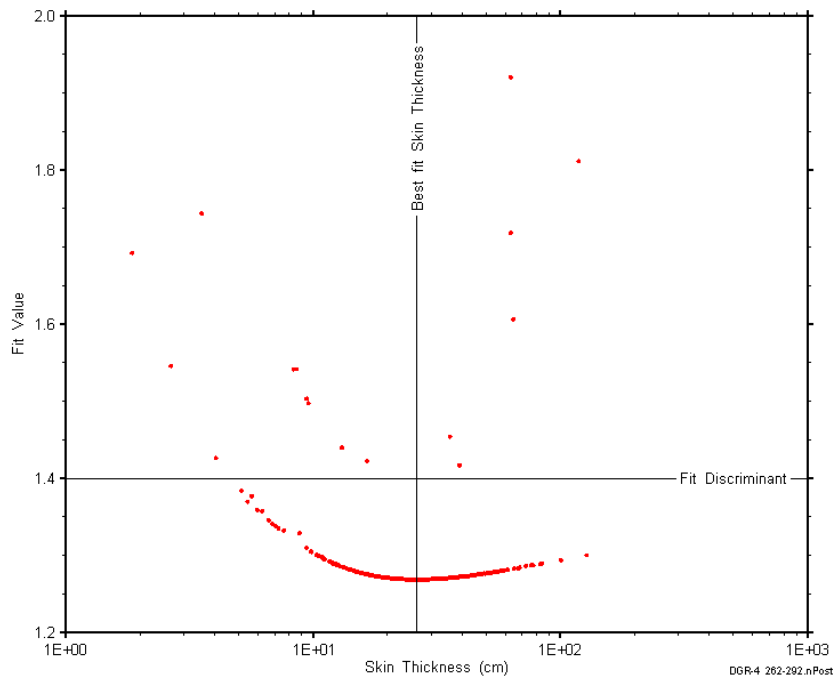


Figure D-51: XY-scatter plot showing the skin-thickness parameter space derived from DGR4_261.63-292.37 perturbation analysis along with the fit discriminant and best fit values.

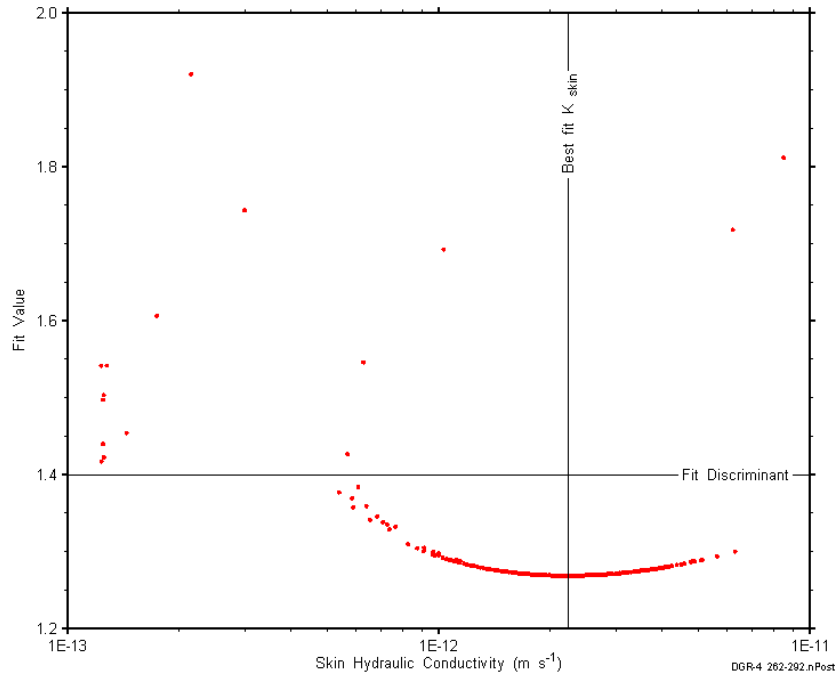


Figure D-52: XY-scatter plot showing the skin hydraulic conductivity parameter space derived from DGR4_261.63-292.37 perturbation analysis along with the fit discriminant and best fit values.

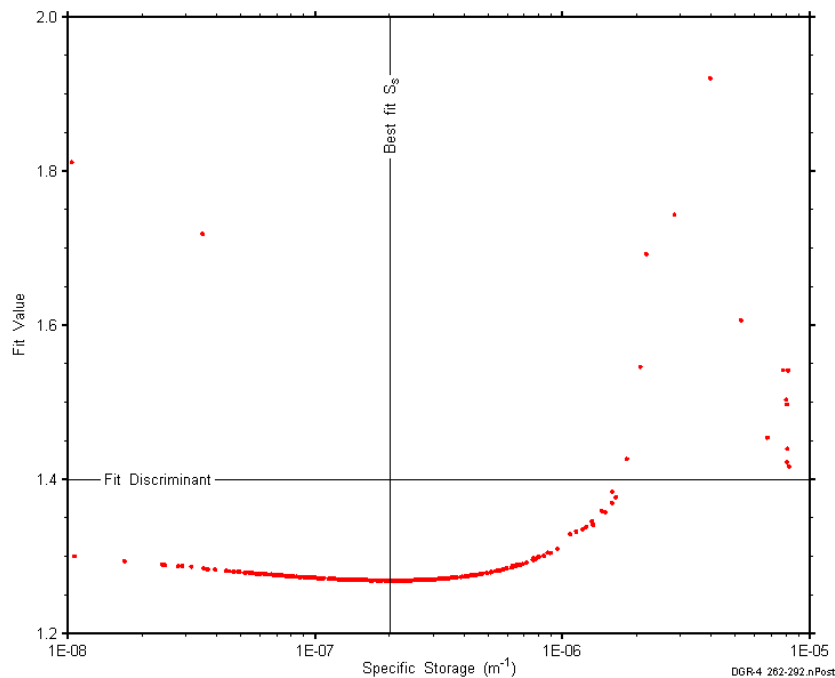


Figure D-53: XY-scatter plot showing the formation specific storage parameter space derived from DGR4_261.63-292.37 perturbation analysis along with the fit discriminant and best fit values.

D.5 284.26-315.00 Salina B-A2 carbonate

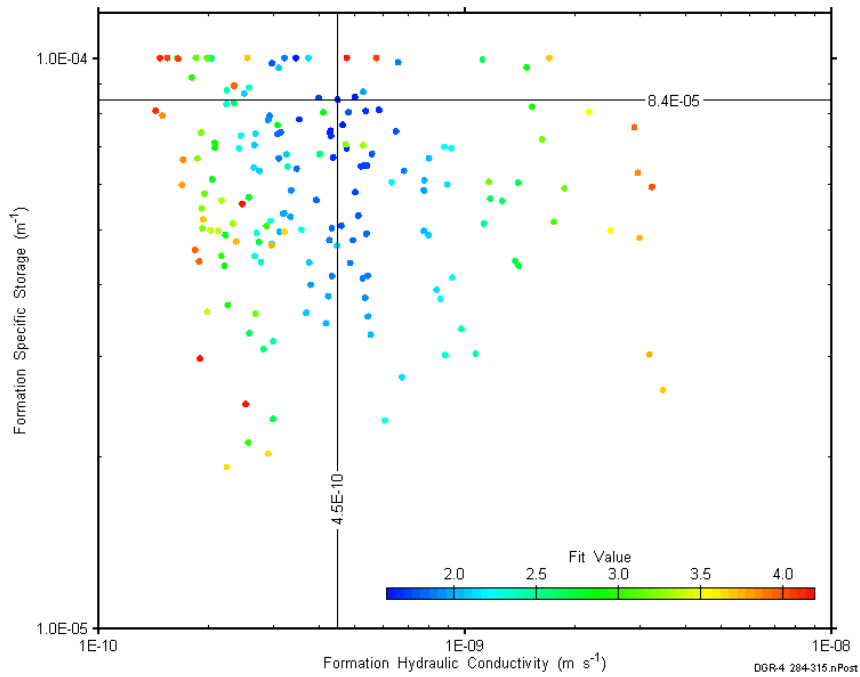


Figure D-54: XY-scatter plot showing estimates of formation hydraulic conductivity and formation specific storage derived from the DGR4_284.26-315.00 perturbation analysis.

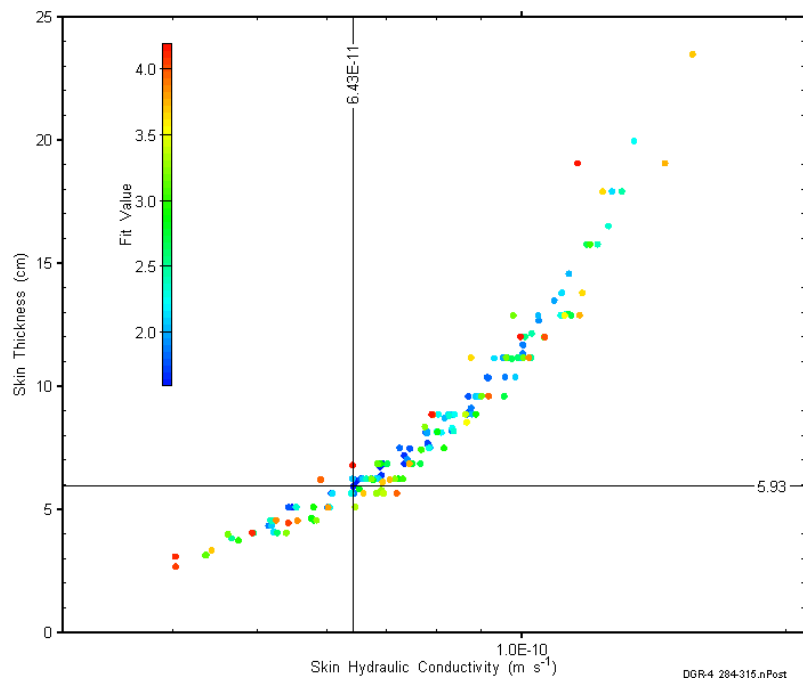


Figure D-55: XY-scatter plot showing estimates of skin hydraulic conductivity and skin thickness derived from the DGR4_284.26-315.00 perturbation analysis.

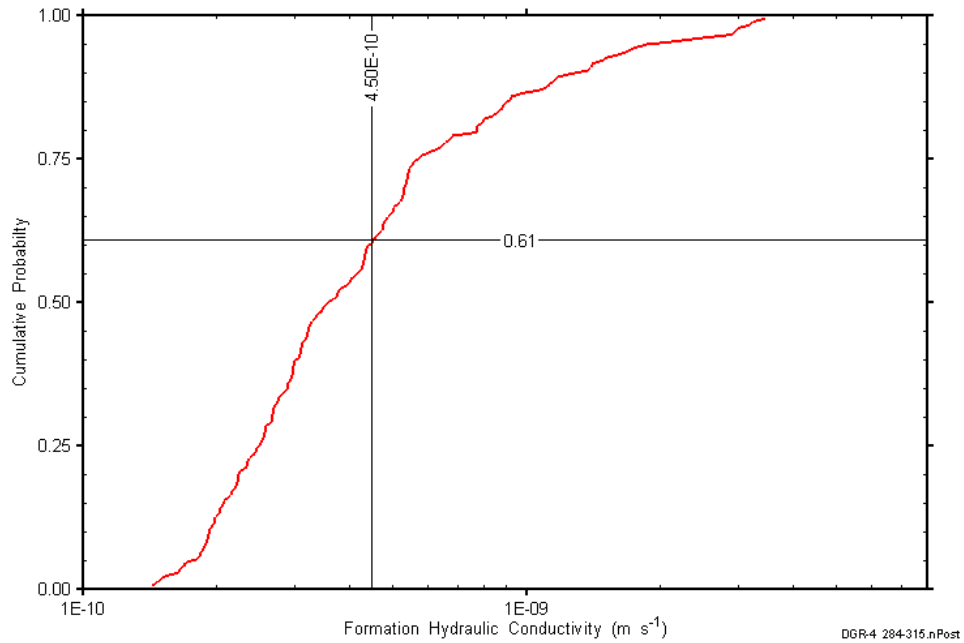


Figure D-56: DGR4_284.26-315.00 formation hydraulic conductivity cumulative distribution function.

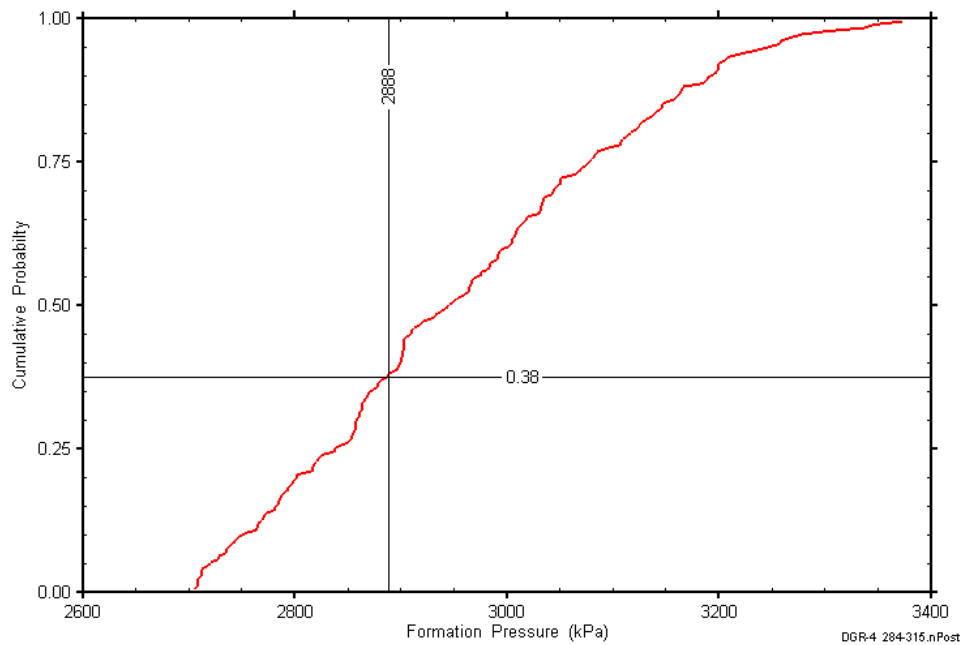


Figure D-57: DGR4_284.26-315.00 static formation pressure cumulative distribution function.

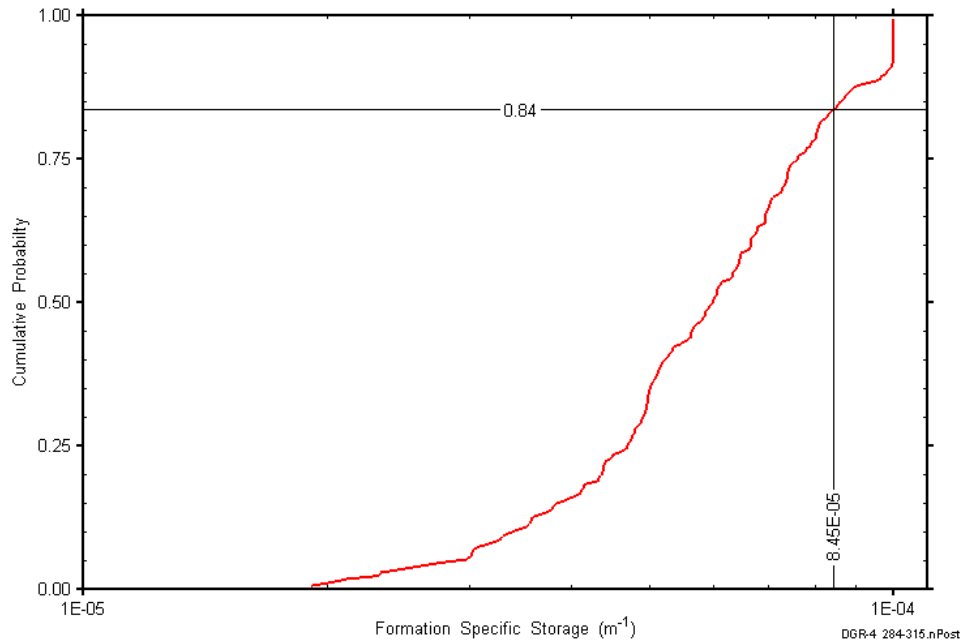


Figure D-58: DGR4_284.26-315.00 formation specific storage cumulative distribution function.

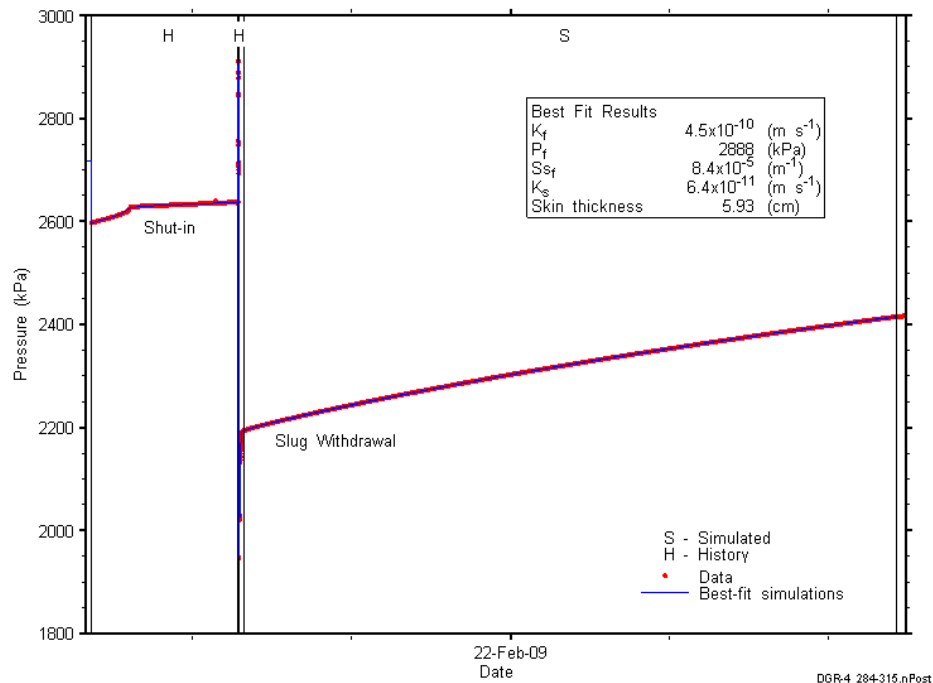


Figure D-59: Linear plot showing simulations of the DGR4_284.26-315.00 pressure response.

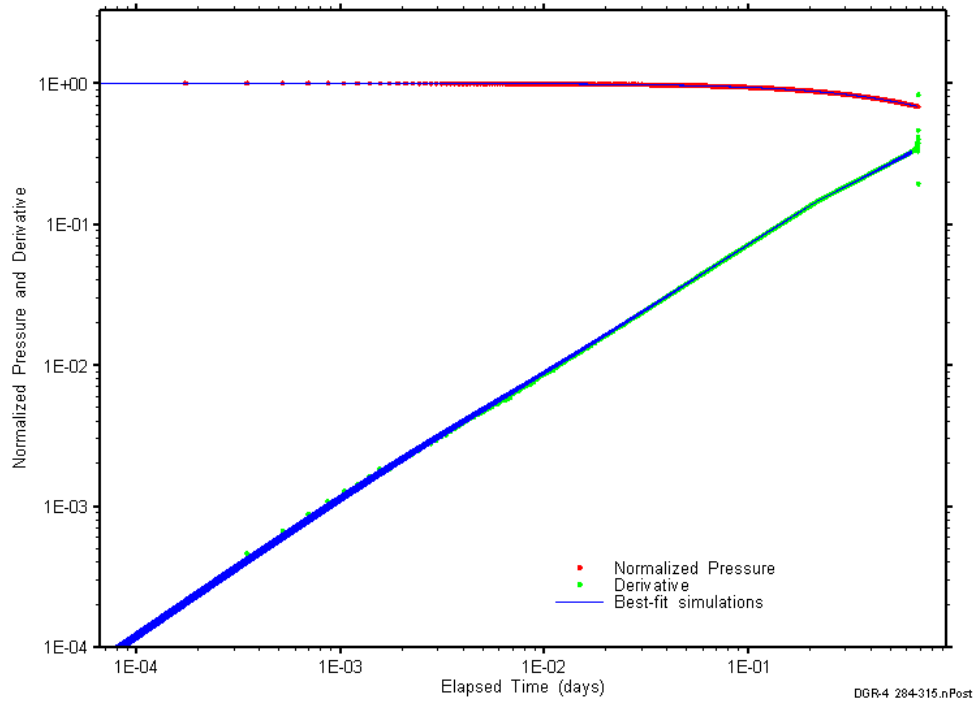


Figure D-60: Log-log plot showing simulations of the DGR4_284.26–315.00 slug withdrawal Ramey B and derivative response.

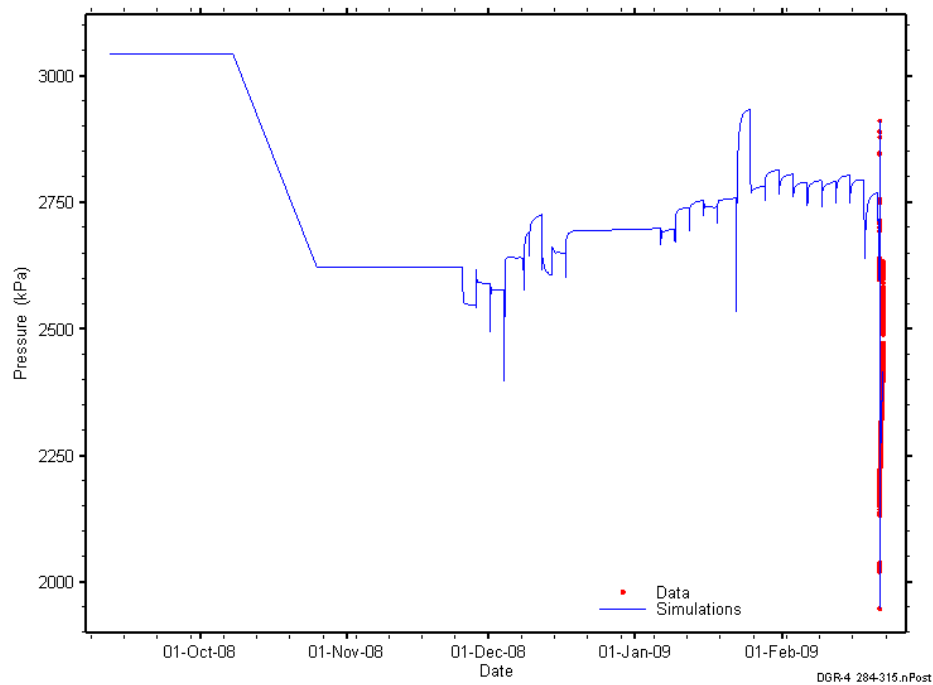


Figure D-61: Linear plot showing simulations of the DGR4_284.26-315.00 pressure response, including pre-test pressure history.

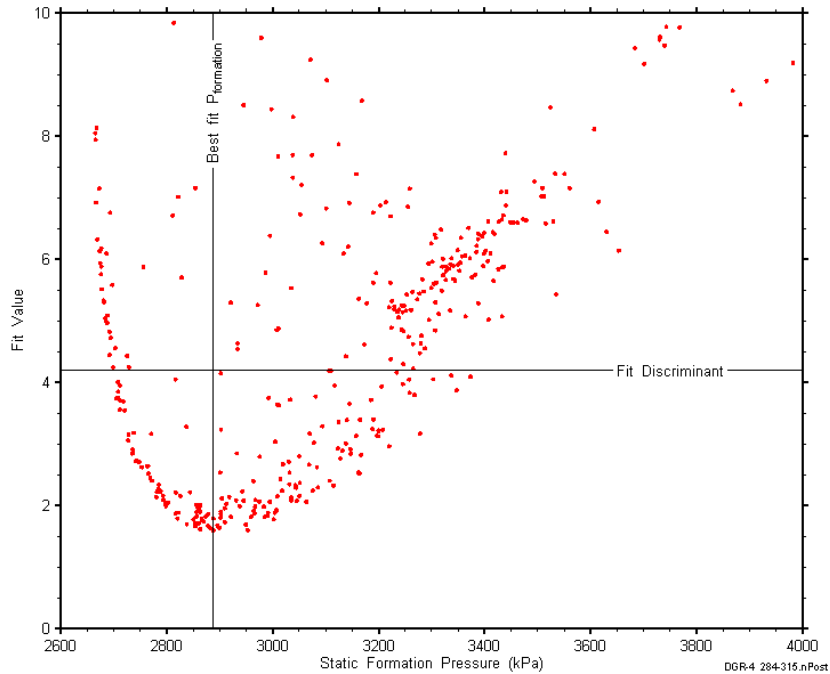


Figure D-62: XY-scatter plot showing the static formation pressure parameter space derived from DGR4_284.26-315.00 perturbation analysis along with the fit discriminant and best fit values.

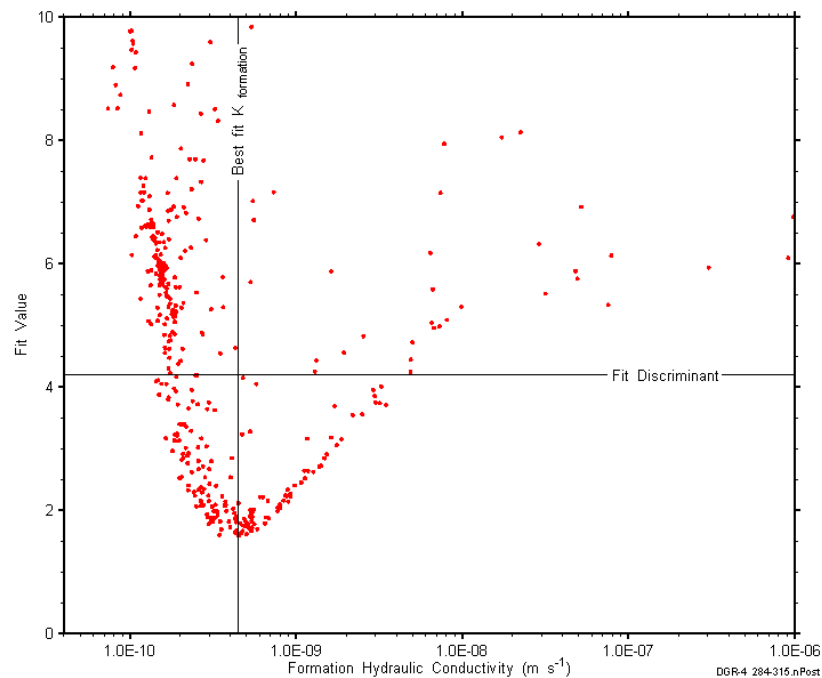


Figure D-63: XY-scatter plot showing the formation hydraulic conductivity parameter space derived from DGR4_284.26-315.00 perturbation analysis along with the fit discriminant and best fit values.

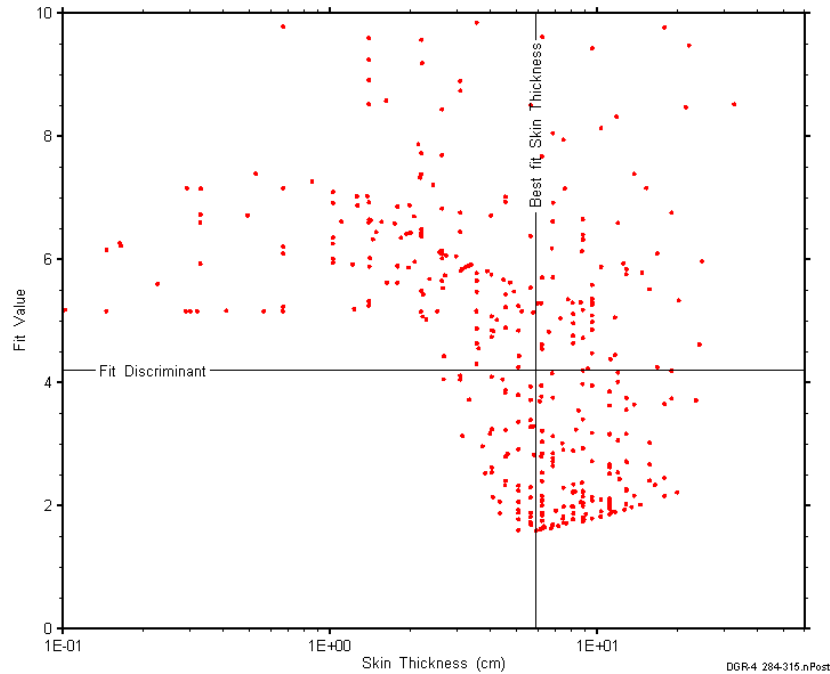


Figure D-64: XY-scatter plot showing the skin-thickness parameter space derived from DGR4_284.26-315.00 perturbation analysis along with the fit discriminant and best fit values.

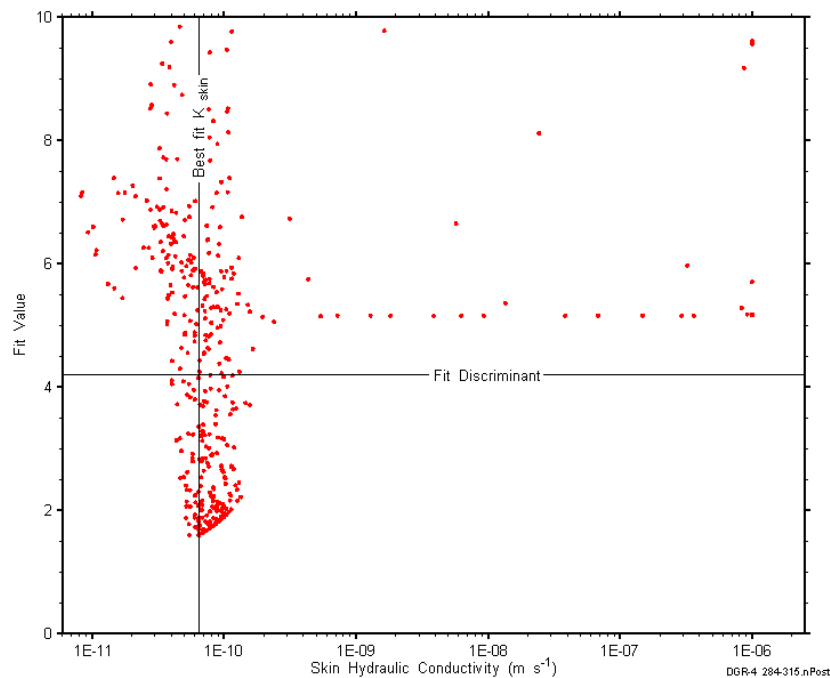


Figure D-65: XY-scatter plot showing the skin hydraulic conductivity parameter space derived from DGR4_284.26-315.00 perturbation analysis along with the fit discriminant and best fit values.

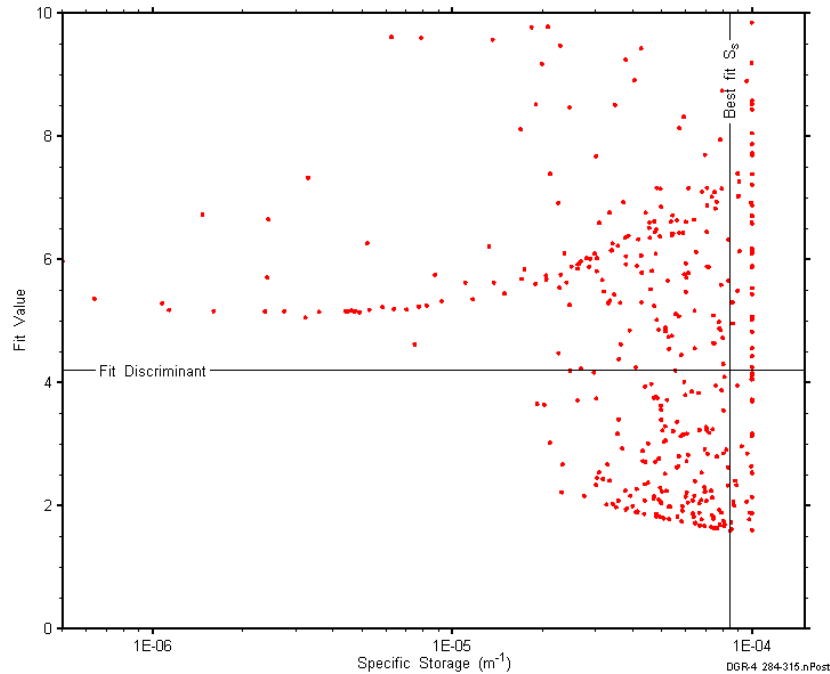


Figure D-66: XY-scatter plot showing the formation specific storage parameter space derived from DGR4_284.26-315.00 perturbation analysis along with the fit discriminant and best fit values.

D.6 296.63-327.37 Salina A2-A1 carbonate

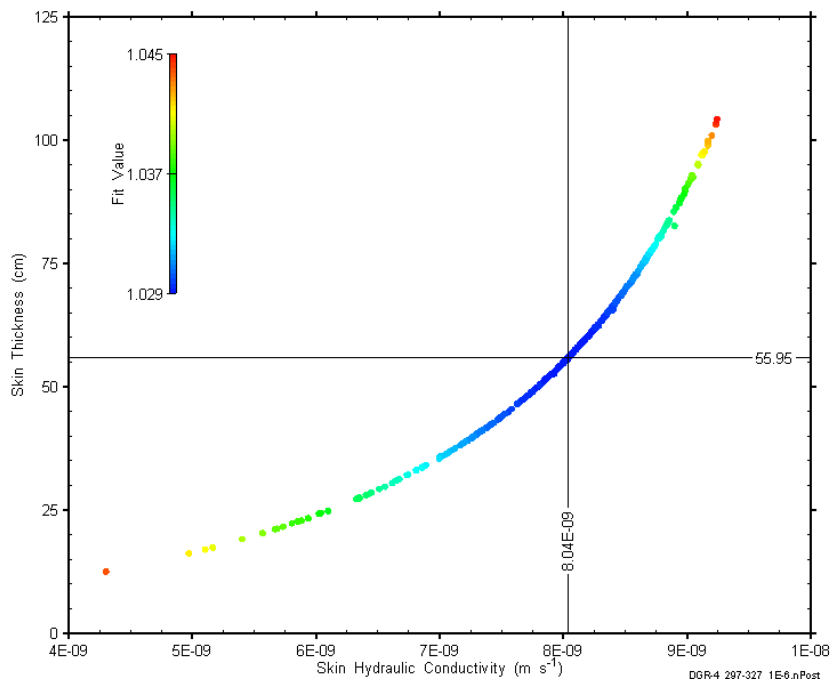


Figure D-67: XY-scatter plot showing estimates of skin hydraulic conductivity and skin thickness derived from the DGR4_296.63-327.37 perturbation analysis.

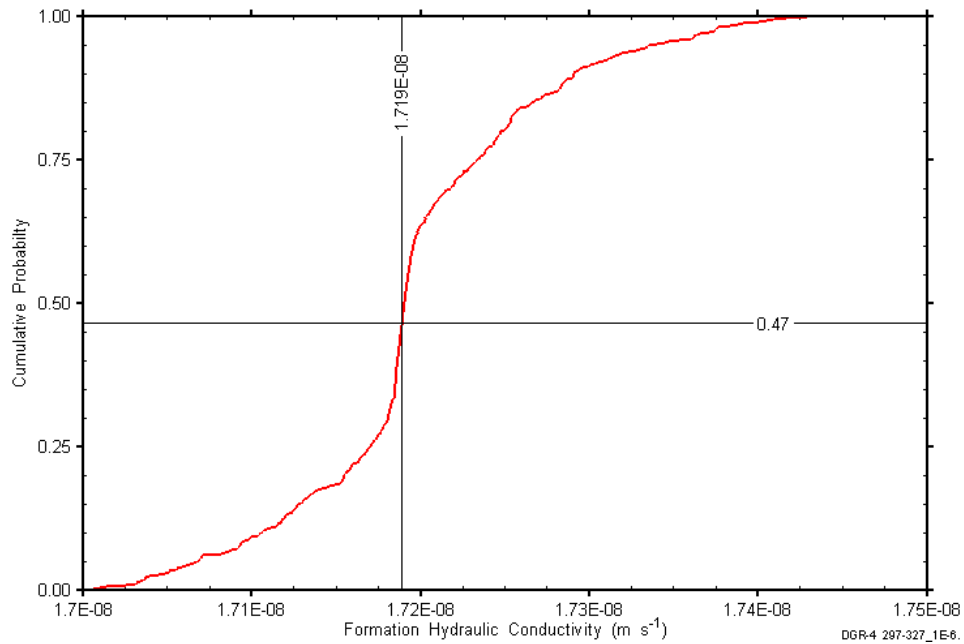


Figure D-68: DGR4_296.63-327.37 formation hydraulic conductivity cumulative distribution function.

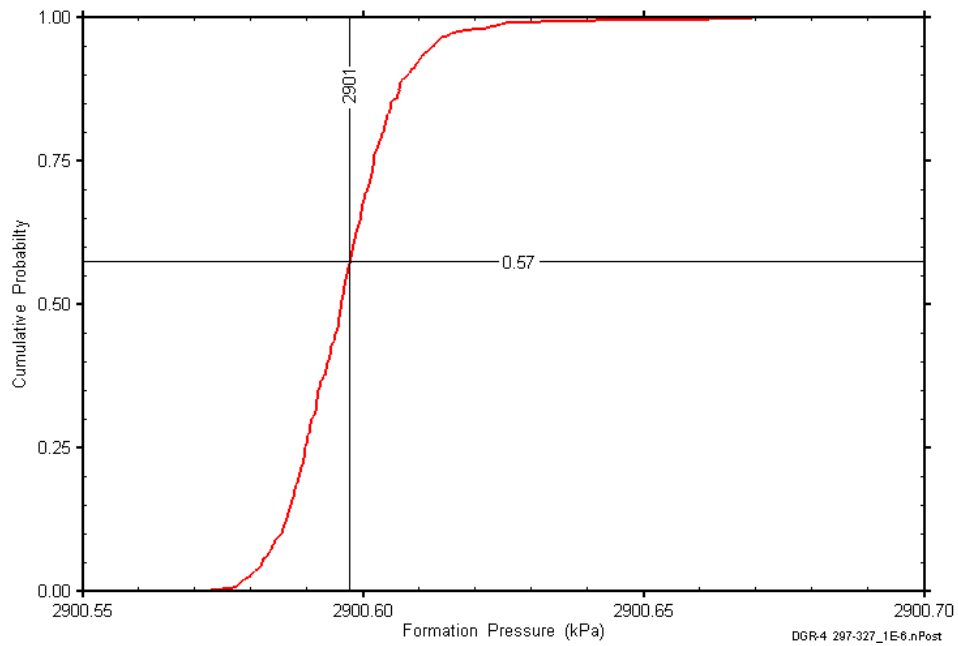


Figure D-69: DGR4_296.63-327.37 static formation pressure cumulative distribution function.

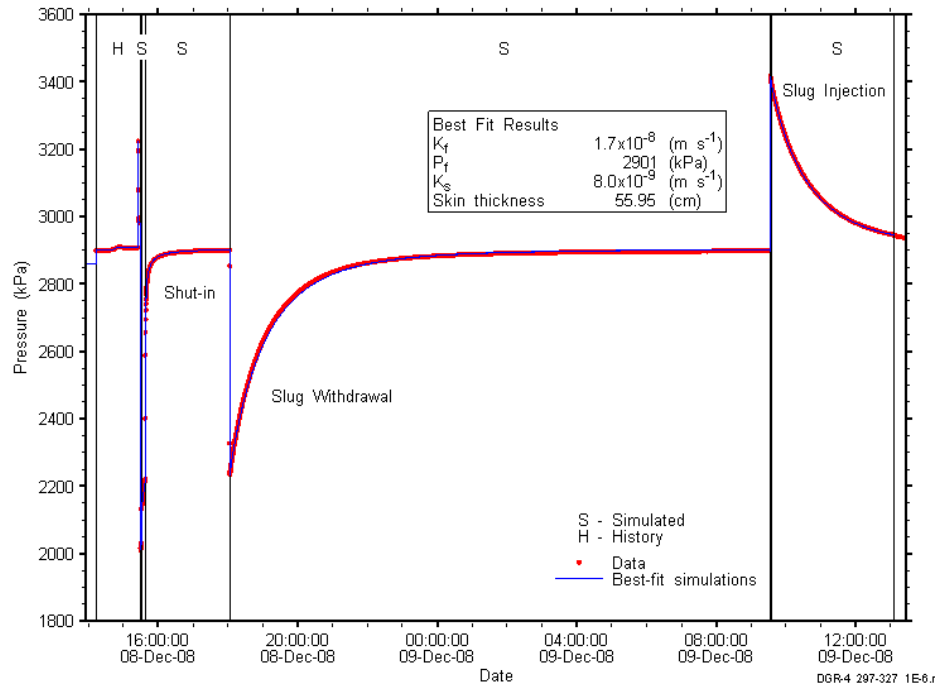


Figure D-70: Linear plot showing simulations of the DGR4_296.63-327.37 pressure response.

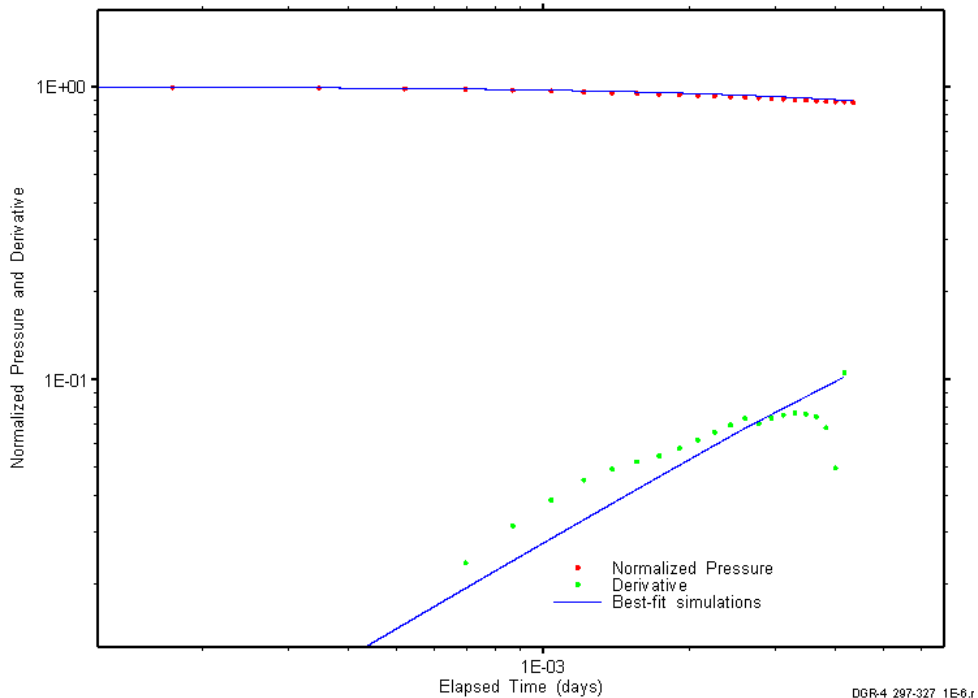


Figure D-71: Log-log plot showing simulations of the DGR4_296.63-327.37 slug withdrawal #1 Ramey B and derivative response.

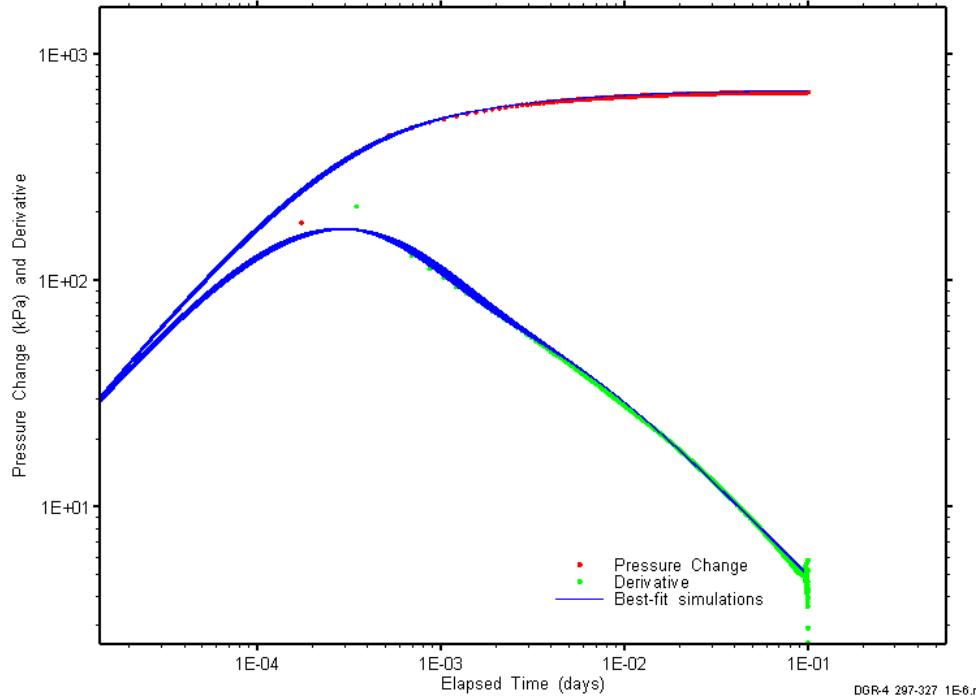


Figure D-72: Log-log plot showing simulations of the DGR4_296.63–327.37 shut-in period diagnostic and derivative response.

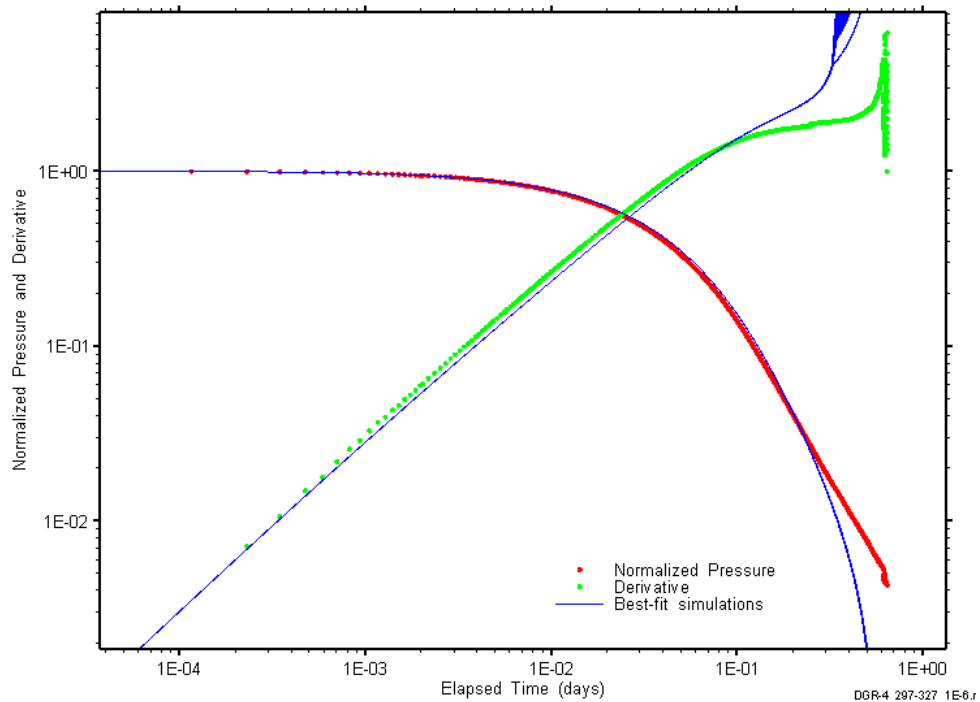


Figure D-73: Log-log plot showing simulations of the DGR4_296.63–327.37 slug withdrawal #2 Ramey B and derivative response.

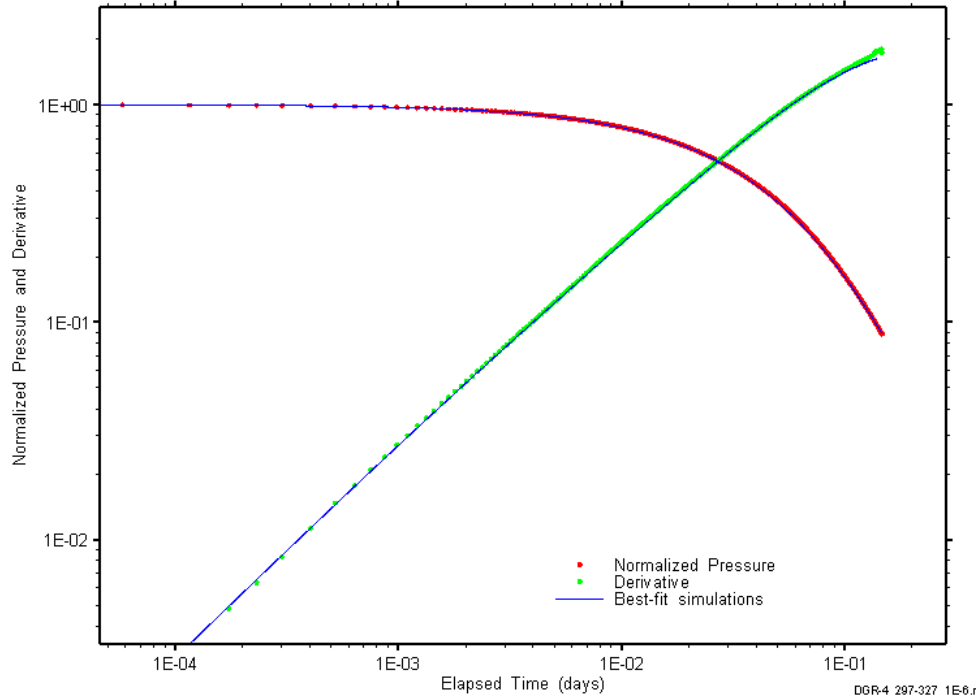


Figure D-74: Log-log plot showing simulations of the DGR4_296.63–327.37 slug injection Ramey B and derivative response.

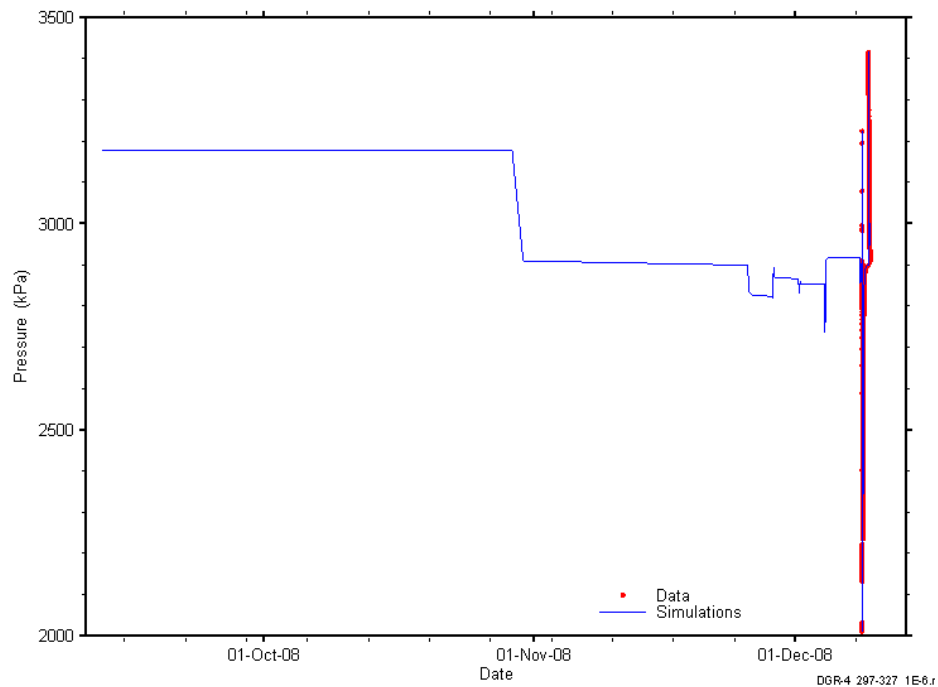


Figure D-75: Linear plot showing simulations of the DGR4_296.63-327.37 pressure response, including pre-test pressure history.

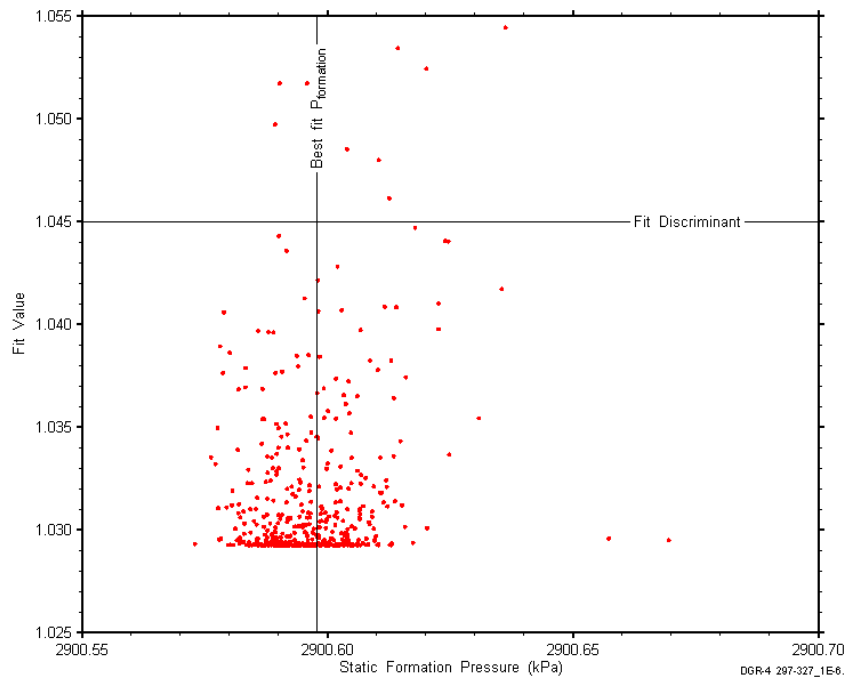


Figure D-76: XY-scatter plot showing the static formation pressure parameter space derived from DGR4_296.63-327.37 perturbation analysis along with the fit discriminant and best fit values.

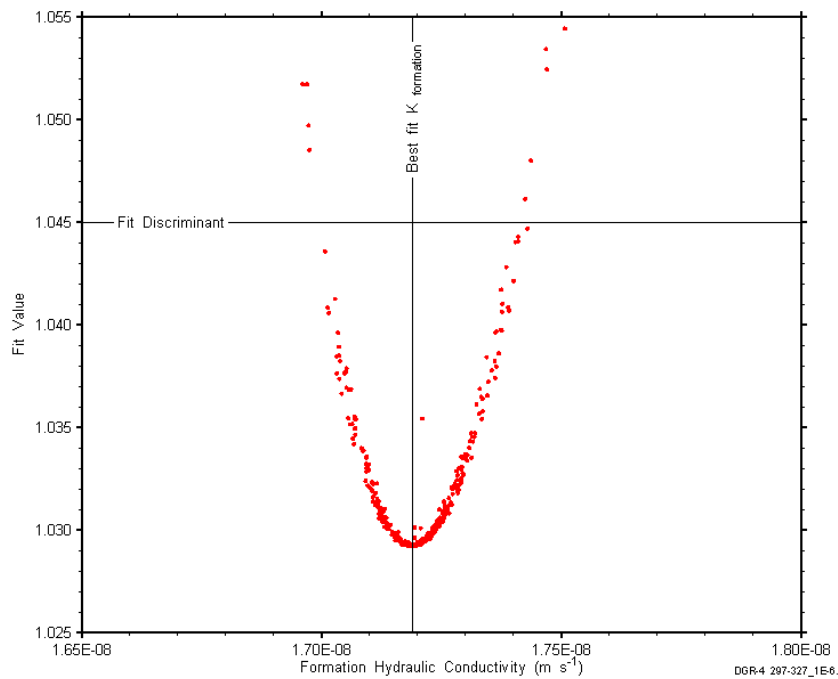


Figure D-77: XY-scatter plot showing the formation hydraulic conductivity parameter space derived from DGR4_296.63-327.37 perturbation analysis along with the fit discriminant and best fit values.

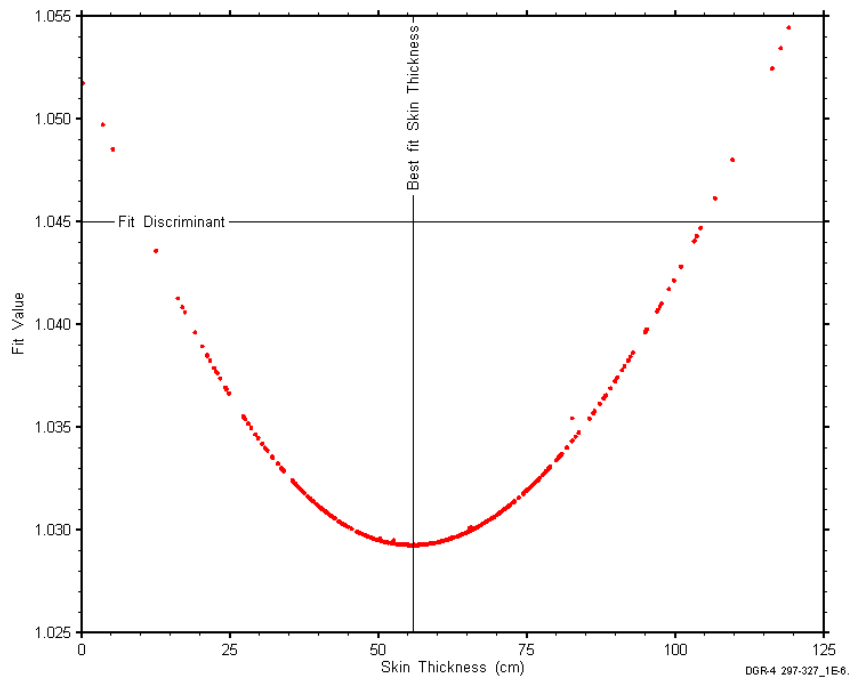


Figure D-78: XY-scatter plot showing the skin-thickness parameter space derived from DGR4_296.63-327.37 perturbation analysis along with the fit discriminant and best fit values.

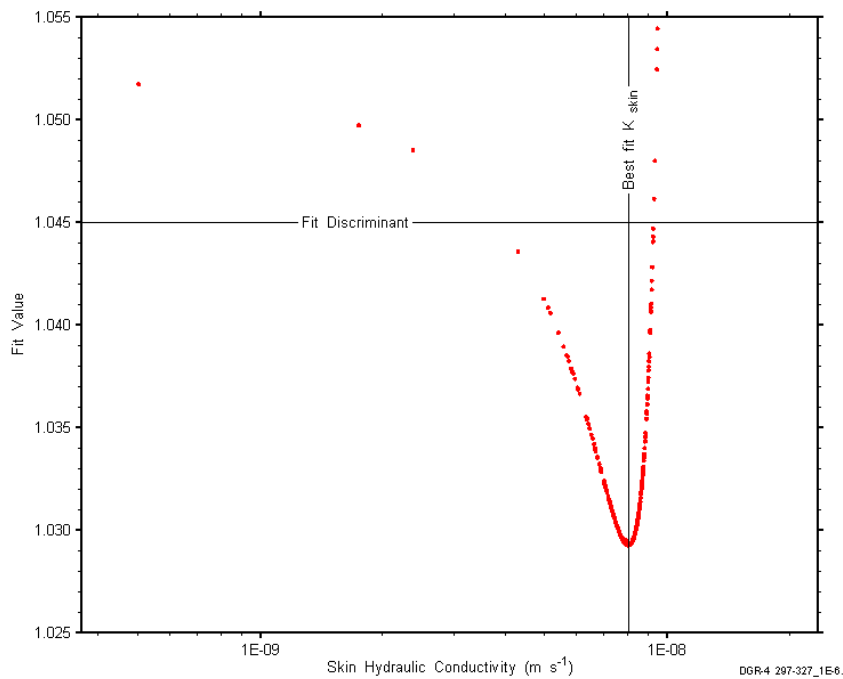


Figure D-79: XY-scatter plot showing the skin hydraulic conductivity parameter space derived from DGR4_296.63-327.37 perturbation analysis along with the fit discriminant and best fit values.

D.7 327.26-358.00 Salina A1 carbonate

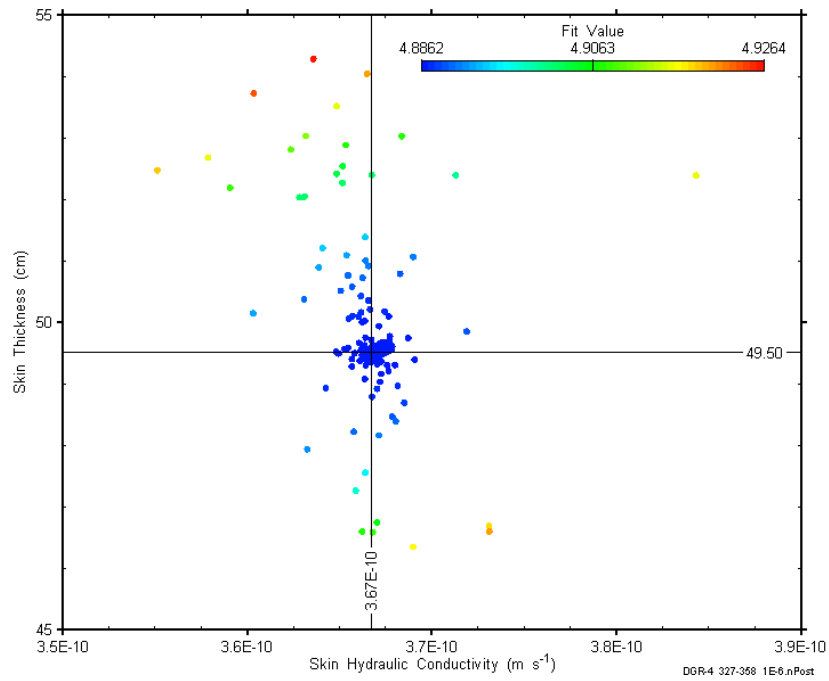


Figure D-80: XY-scatter plot showing estimates of skin hydraulic conductivity and skin thickness derived from the DGR4_327.26-358.00 perturbation analysis.

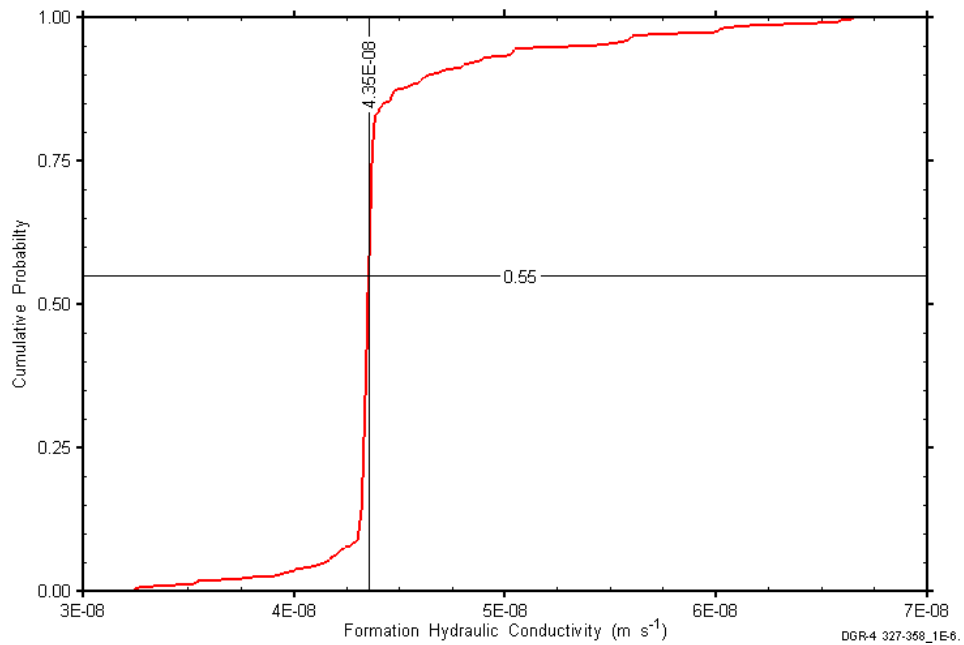


Figure D-81: DGR4_327.26-358.00 formation hydraulic conductivity cumulative distribution function.

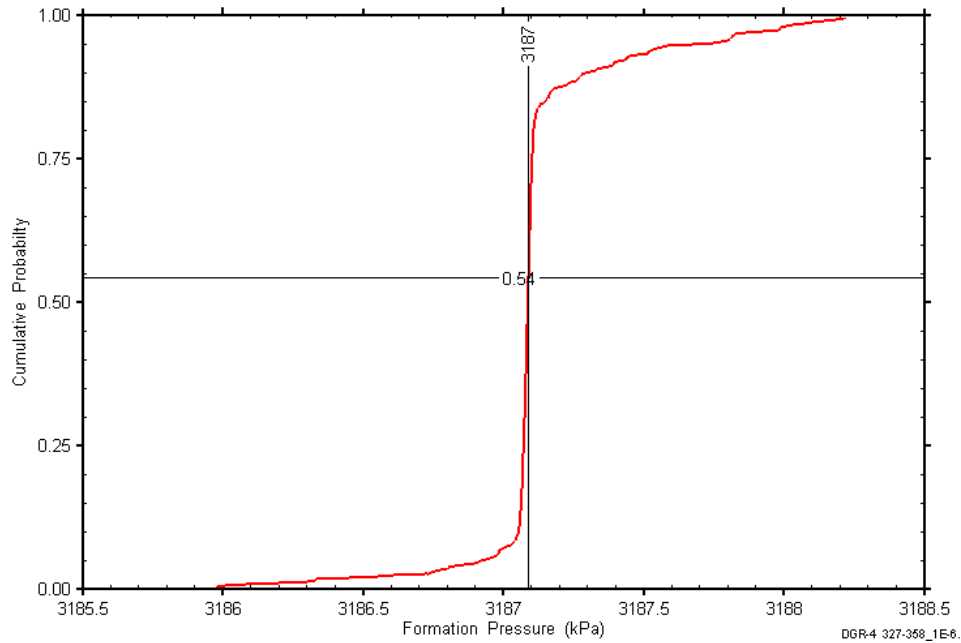


Figure D-82: DGR4_327.26-358.74 static formation pressure cumulative distribution function.

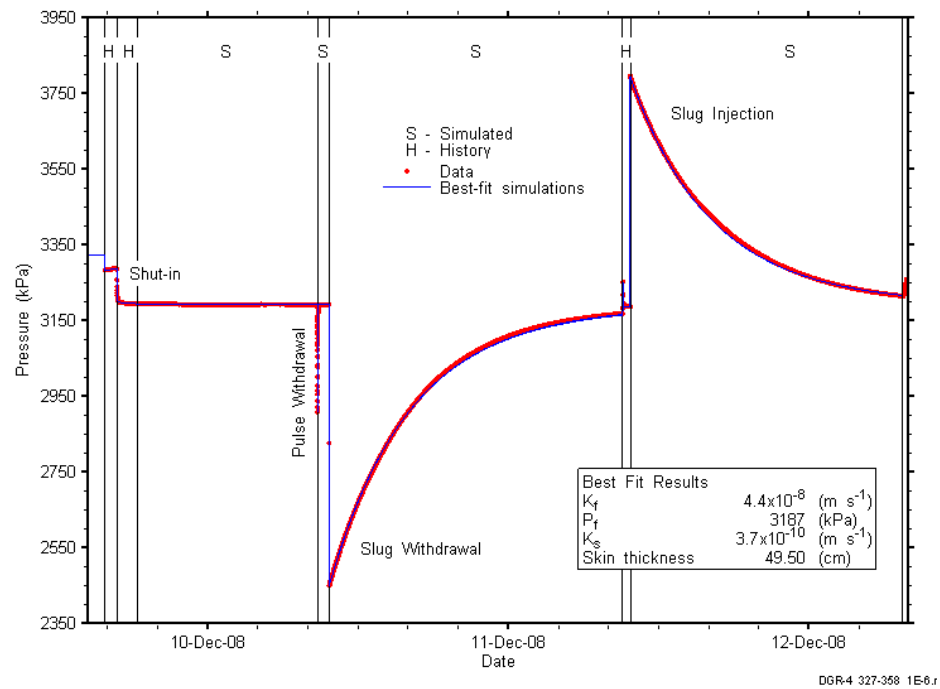


Figure D-83: Linear plot showing simulations of the DGR4_327.26-358.00 pressure response.

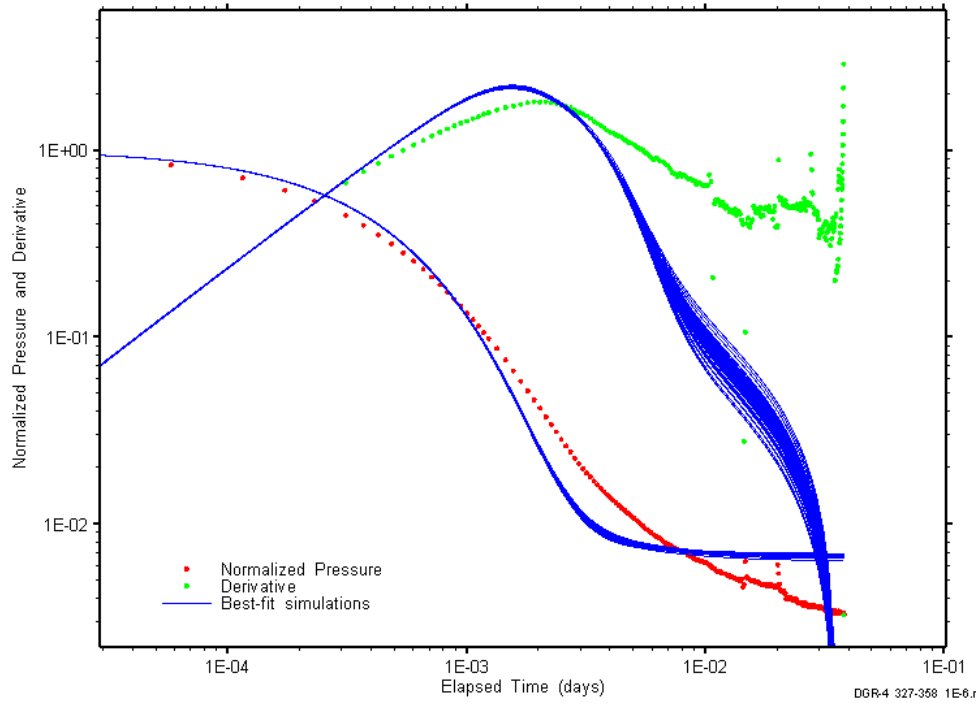


Figure D-84: Log-log plot showing simulations of the DGR4_327.26–358.00 pulse withdrawal Ramey B and derivative response.

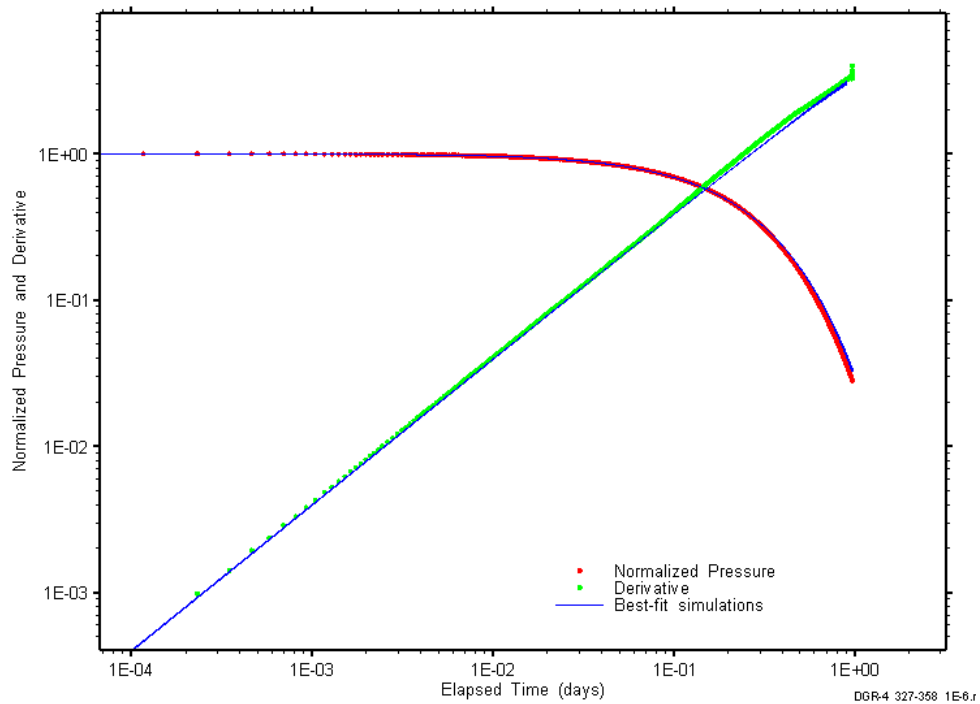


Figure D-85: Log-log plot showing simulations of the DGR4_327.26–358.00 slug withdrawal Ramey B and derivative response.

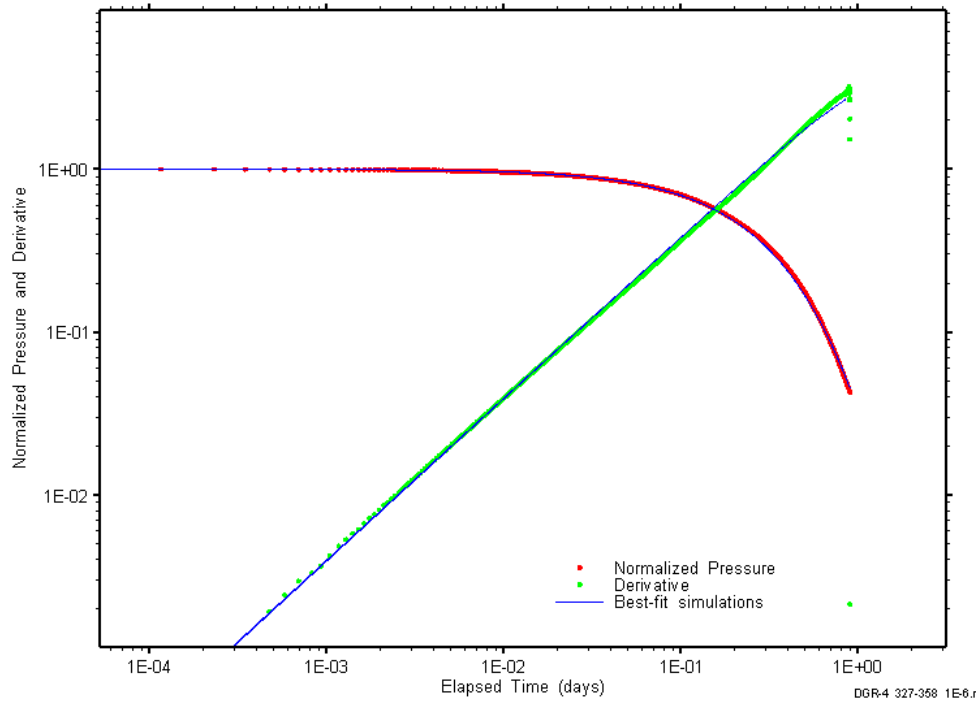


Figure D-86: Log-log plot showing simulations of the DGR4_327.26–358.00 slug injection Ramey B and derivative response.

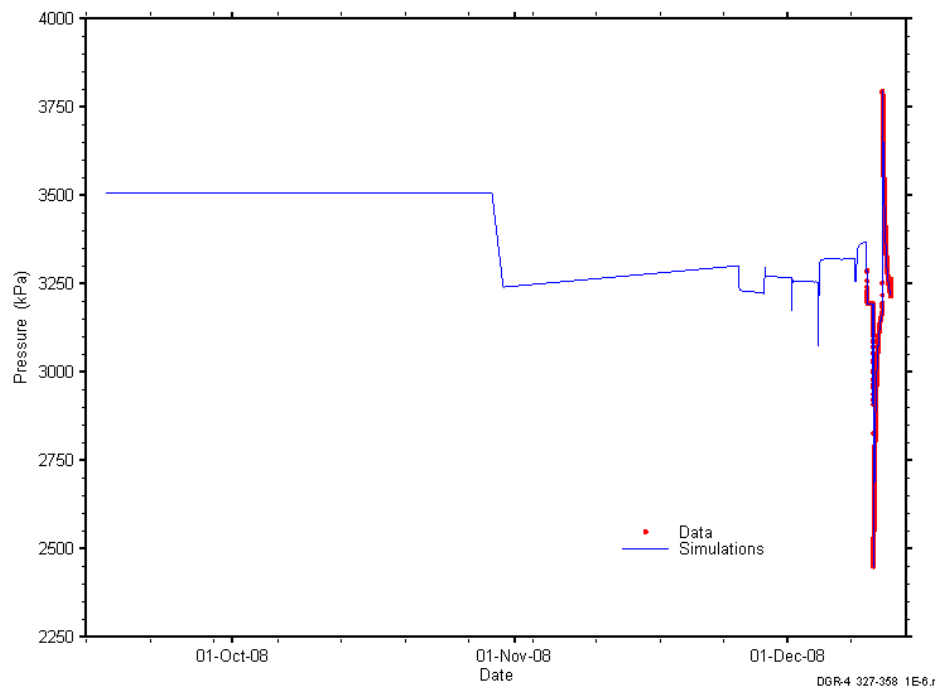


Figure D-87: Linear plot showing simulations of the DGR4_327.26-358.00 pressure response, including pre-test pressure history.

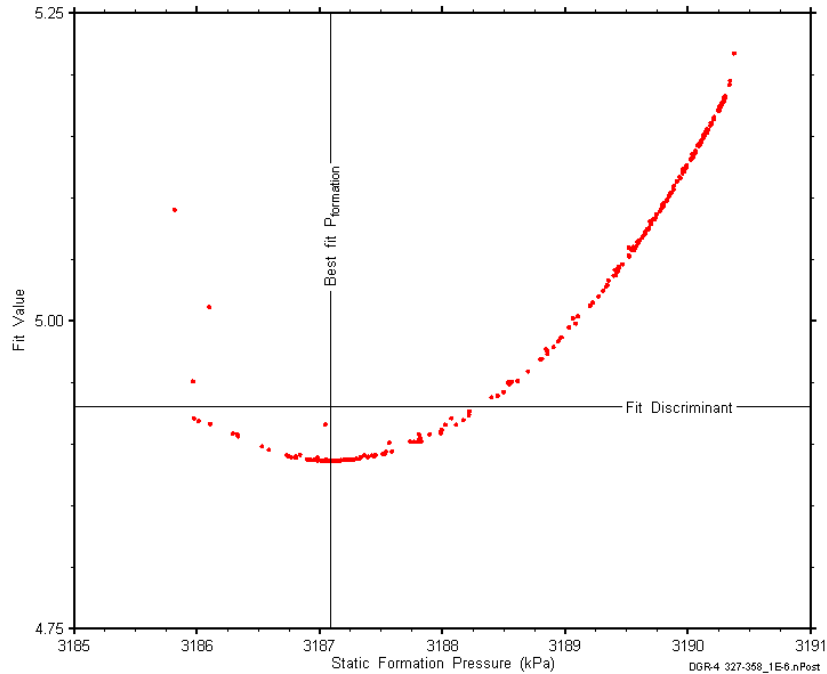


Figure D-88: XY-scatter plot showing the static formation pressure parameter space derived from DGR4_327.26-358.00 perturbation analysis along with the fit discriminant and best fit values.

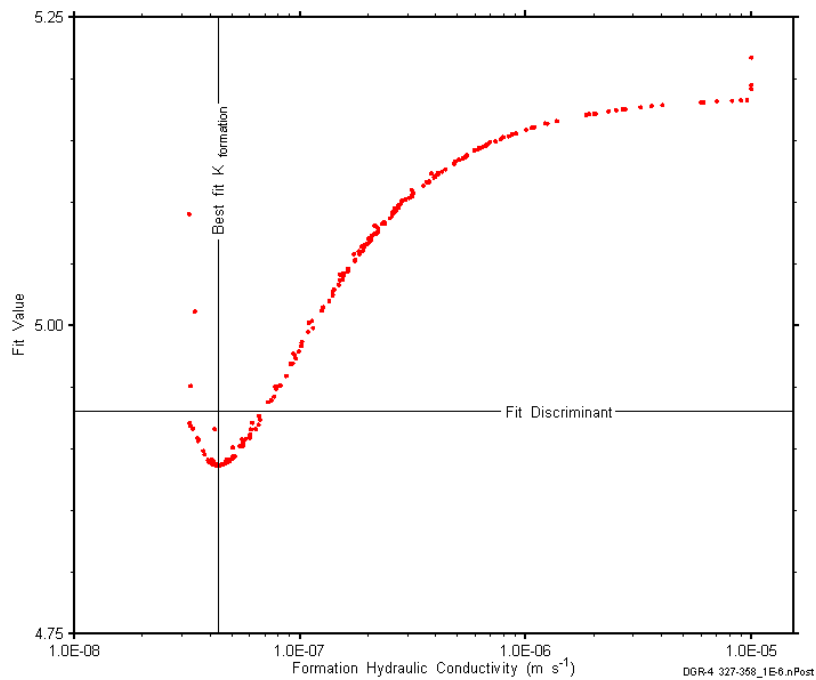


Figure D-89: XY-scatter plot showing the formation hydraulic conductivity parameter space derived from DGR4_327.26-358.00 perturbation analysis along with the fit discriminant and best fit values.

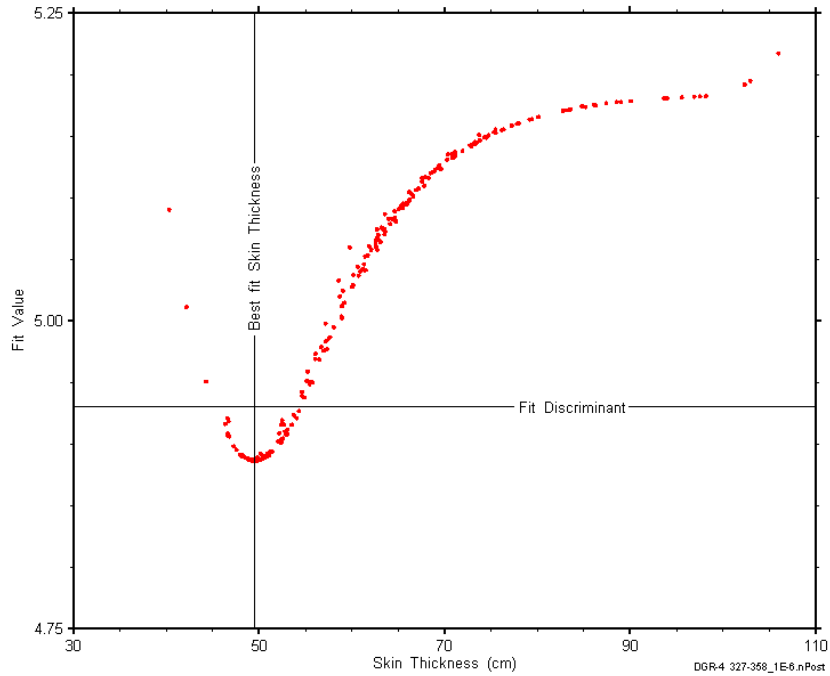


Figure D-90: XY-scatter plot showing the skin-thickness parameter space derived from DGR4_327.26-358.00 perturbation analysis along with the fit discriminant and best fit values.

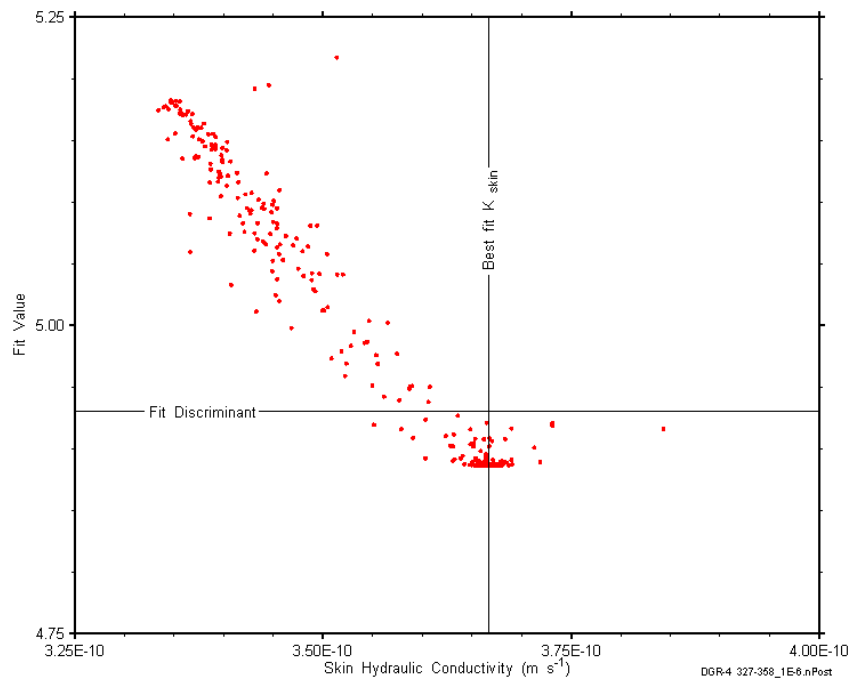


Figure D-91: XY-scatter plot showing the skin hydraulic conductivity parameter space derived from DGR4_327.26-358.00 perturbation analysis along with the fit discriminant and best fit values.

D.8 350.53-381.27 Salina A1-A0-Guelph

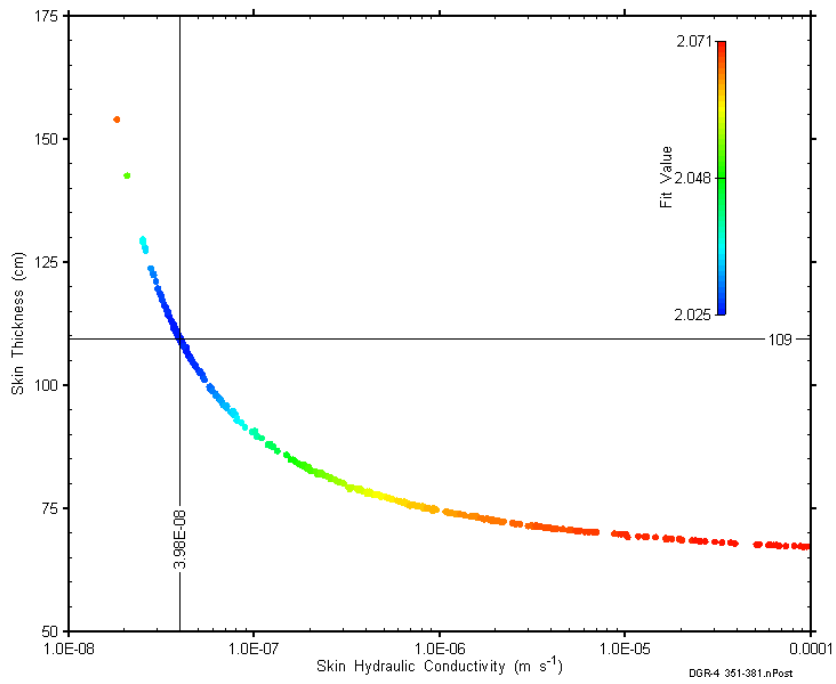


Figure D-92: XY-scatter plot showing estimates of skin hydraulic conductivity and skin thickness derived from the DGR4_350.53-381.27 perturbation analysis.

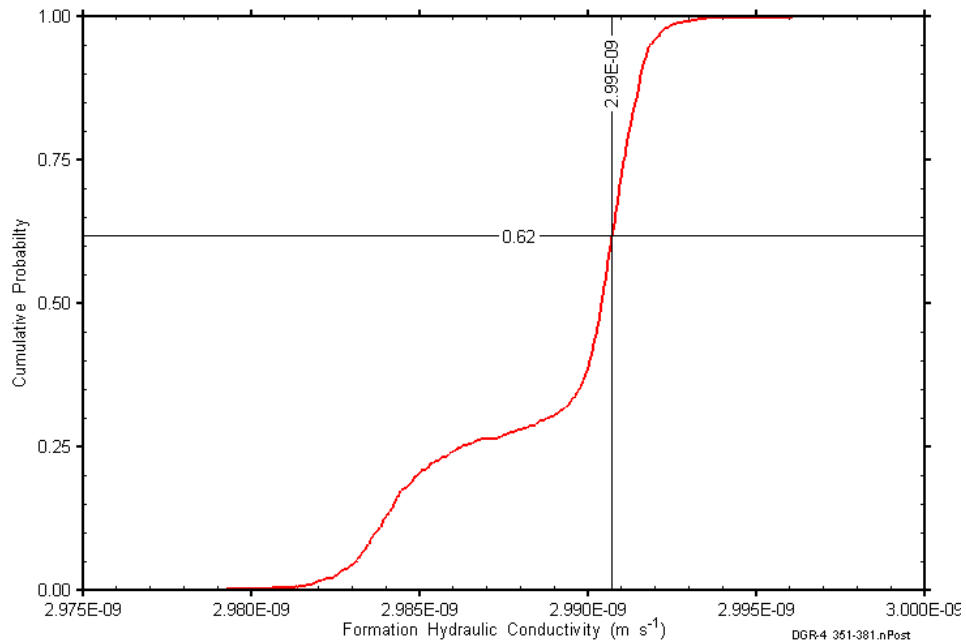


Figure D-93: DGR4_350.53-381.27 formation hydraulic conductivity cumulative distribution function.

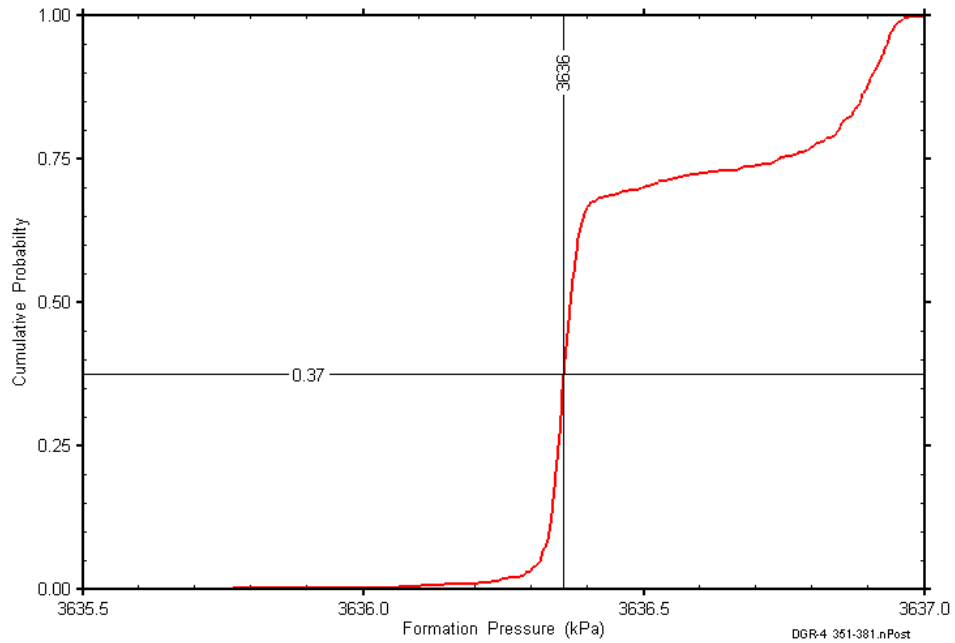


Figure D-94: DGR4_350.53-381.27 static formation pressure cumulative distribution function.

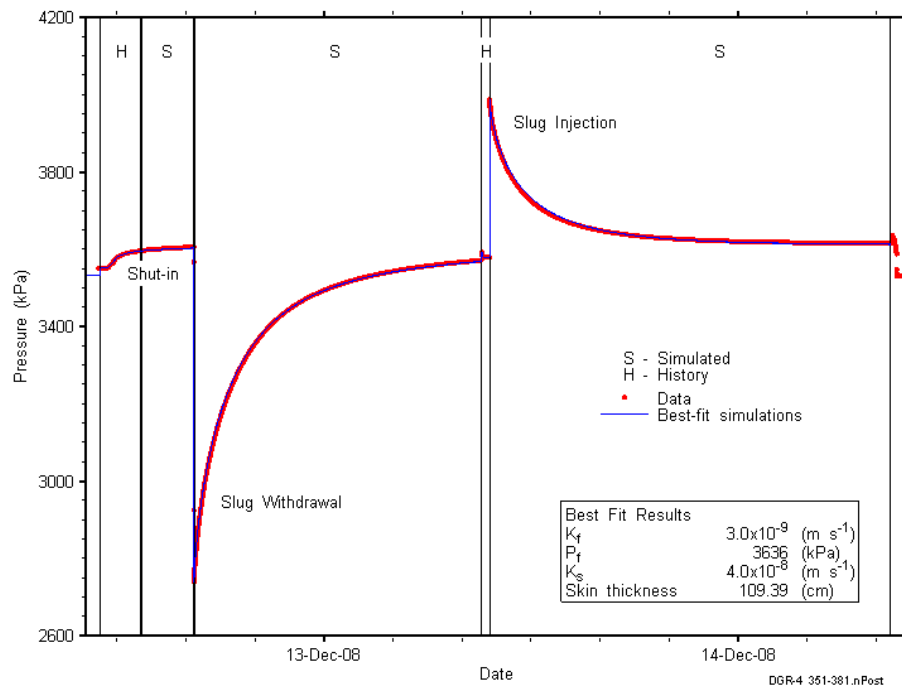


Figure D-95: Linear plot showing simulations of the DGR4_350.53-381.27 pressure response.

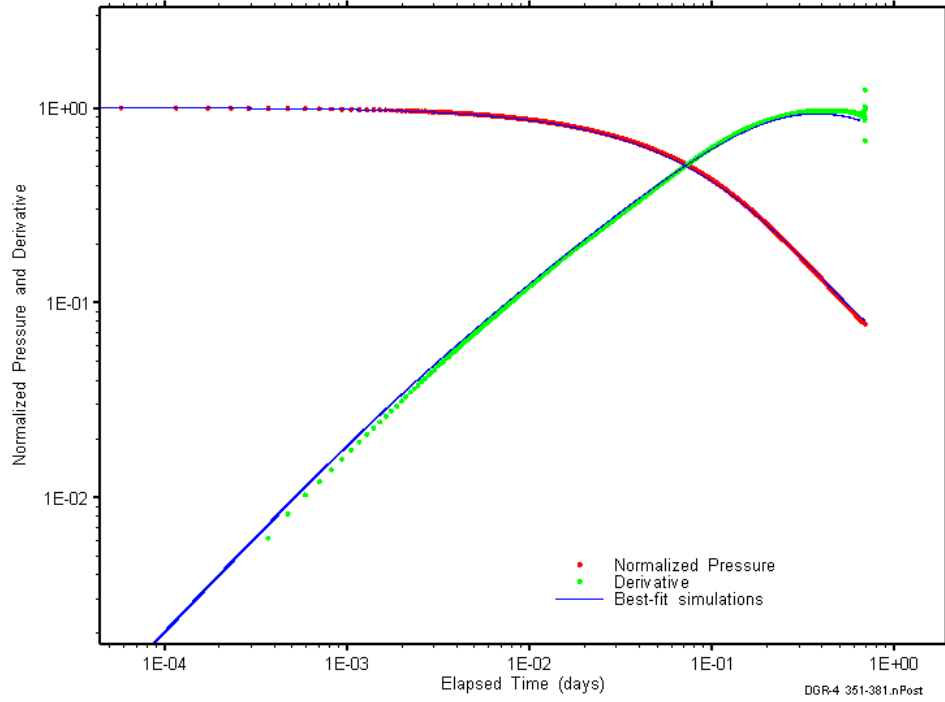


Figure D-96: Log-log plot showing simulations of the DGR4_350.53–381.27 slug withdrawal Ramey B and derivative response.

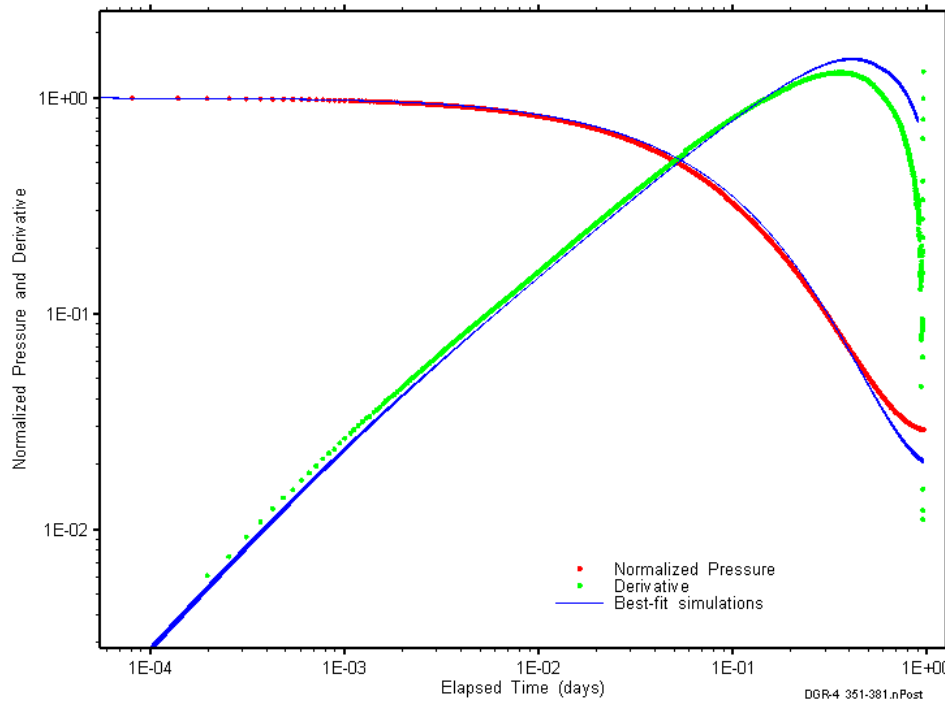


Figure D-97: Log-log plot showing simulations of the DGR4_350.53–381.27 slug injection Ramey B and derivative response.

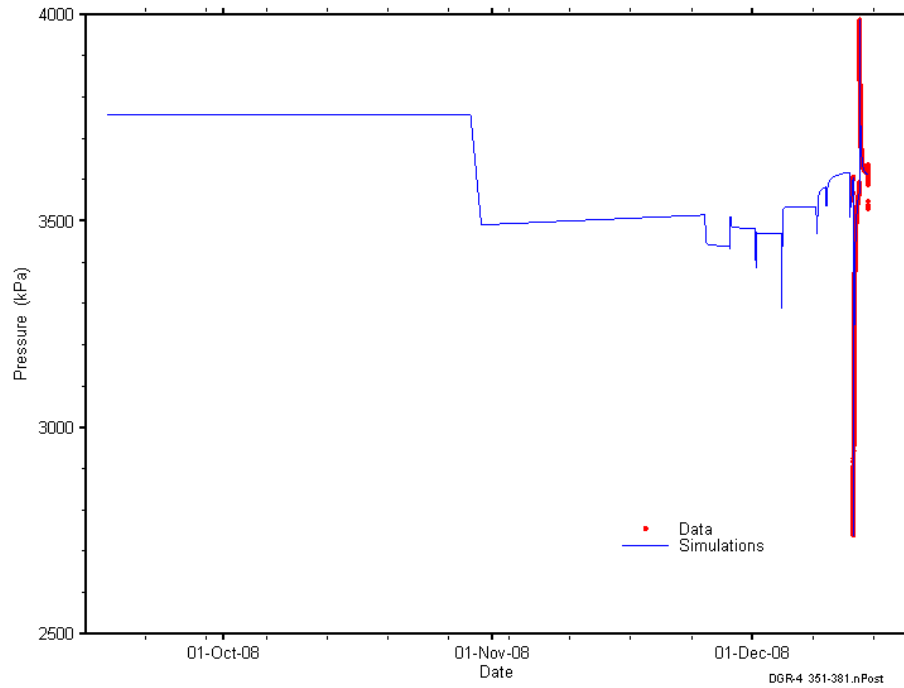


Figure D-98: Linear plot showing simulations of the DGR4_350.53-381.27 pressure response, including pre-test pressure history.

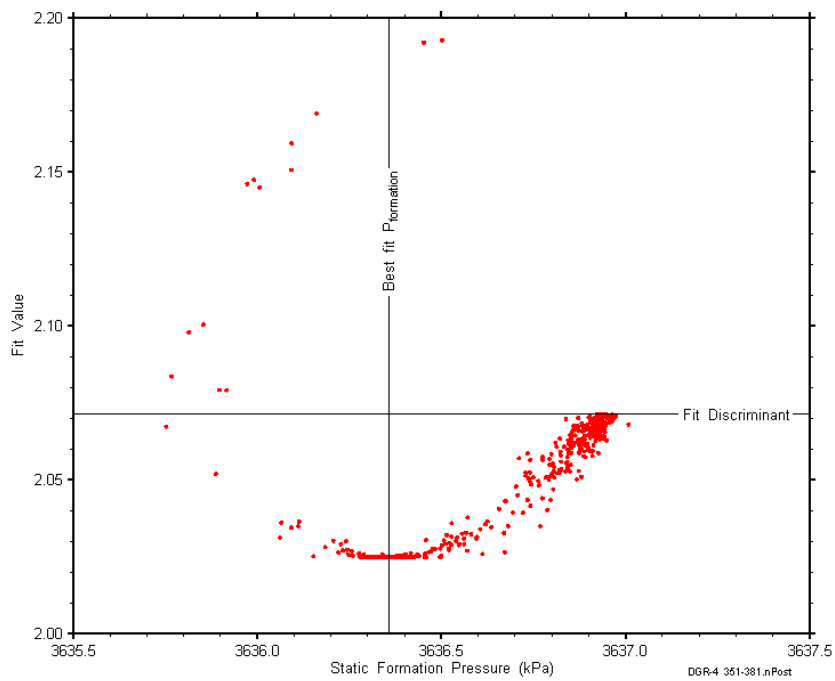


Figure D-99: XY-scatter plot showing the static formation pressure parameter space derived from DGR4_350.53-381.27 perturbation analysis along with the fit discriminant and best fit values.

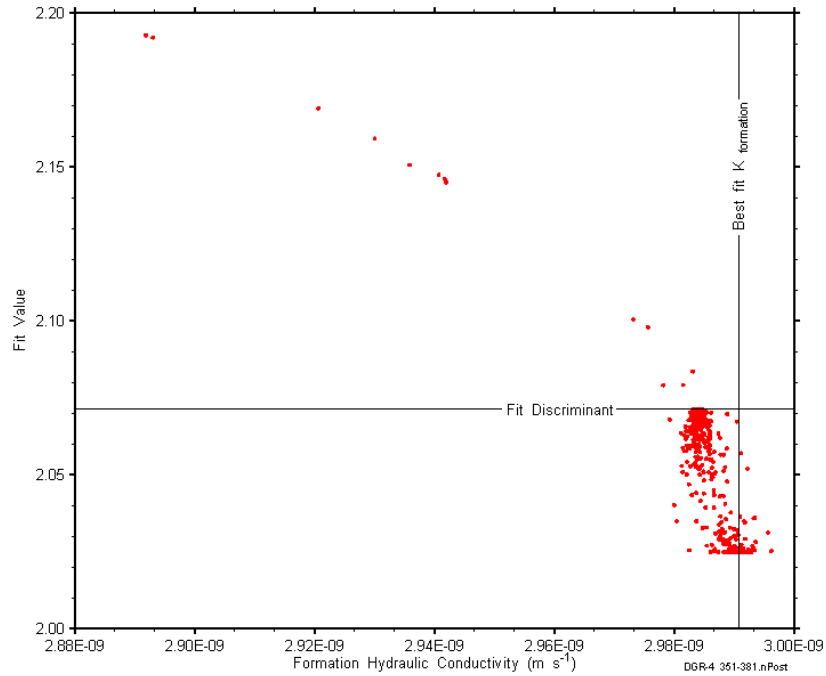


Figure D-100: XY-scatter plot showing the formation hydraulic conductivity parameter space derived from DGR4_350.53-381.27 perturbation analysis along with the fit discriminant and best fit values.

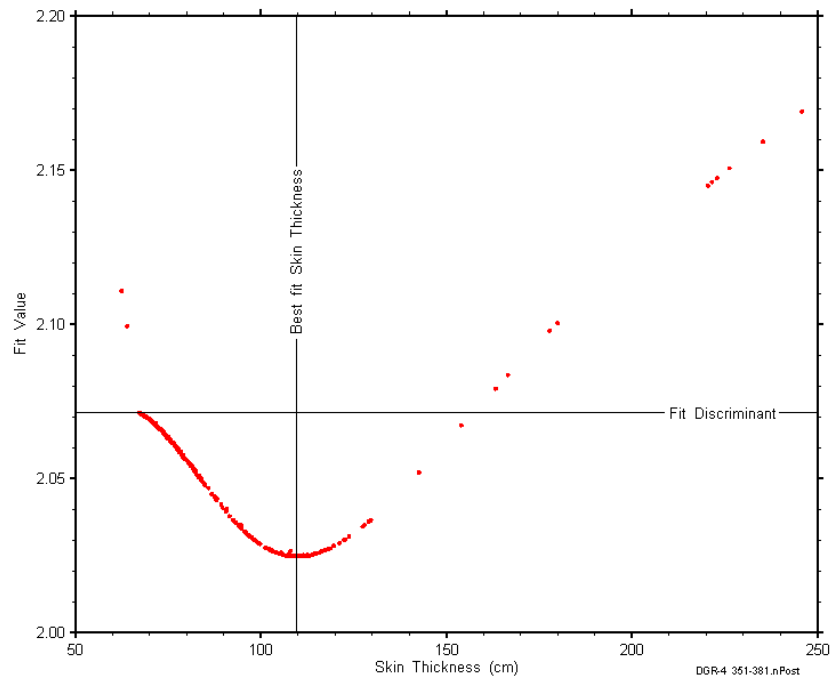


Figure D-101: XY-scatter plot showing the skin-thickness parameter space derived from DGR4_350.53-381.27 perturbation analysis along with the fit discriminant and best fit values.

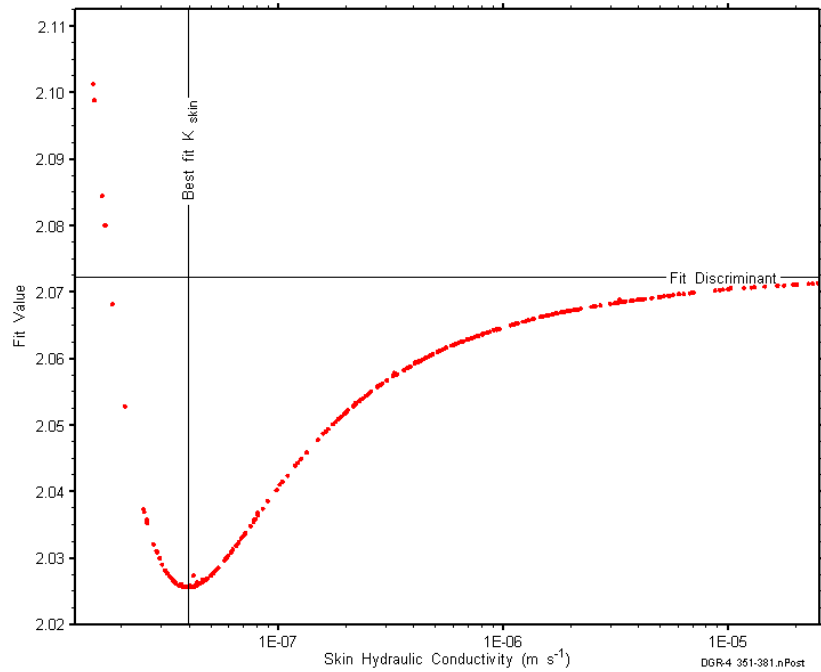


Figure D-102: XY-scatter plot showing the skin hydraulic conductivity parameter space derived from DGR4_350.53-381.27 perturbation analysis along with the fit discriminant and best fit values.

D.9 381.08-411.82 Goat Island-Gasport-Lions Head-Fossil Hill

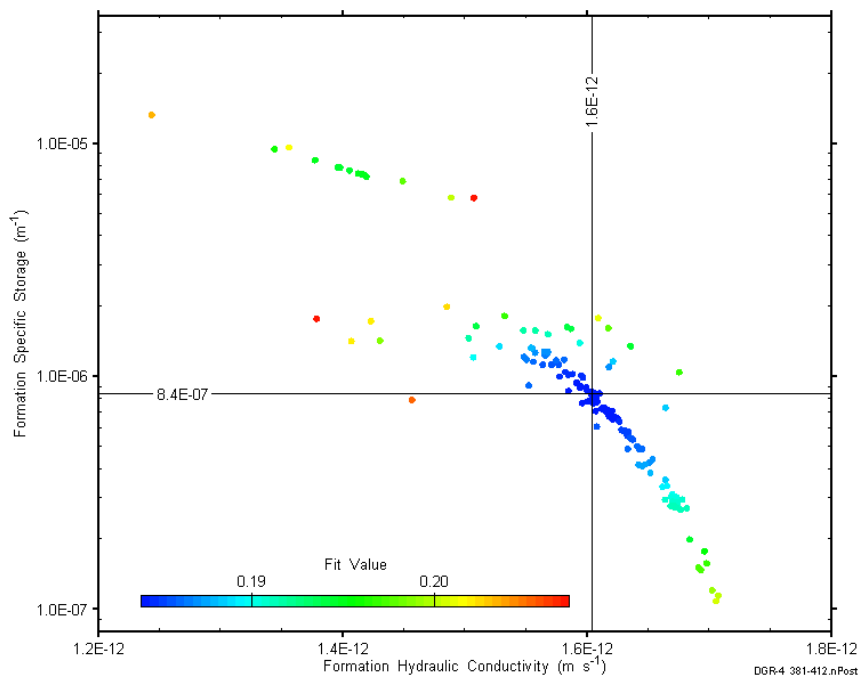


Figure D-103: XY-scatter plot showing estimates of formation hydraulic conductivity and formation specific storage derived from the DGR4_381.08-411.82 perturbation analysis.

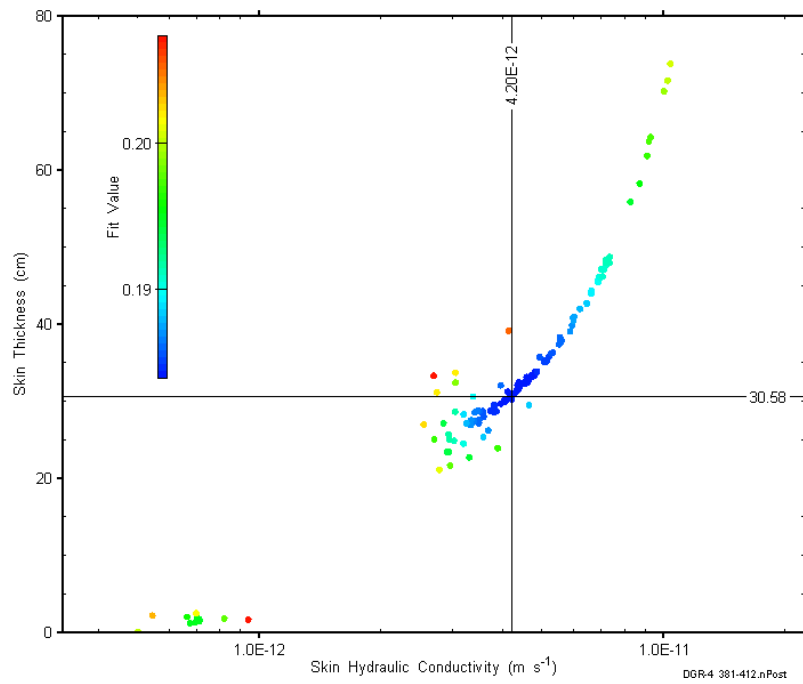


Figure D-104: XY-scatter plot showing estimates of skin hydraulic conductivity and skin thickness derived from the DGR4_381.08-411.82 perturbation analysis.

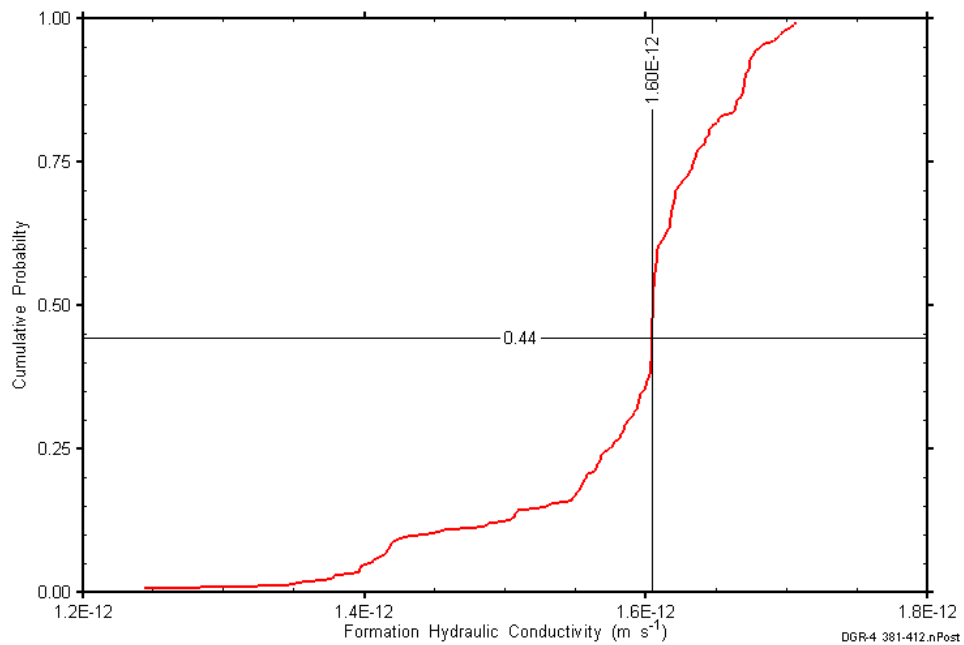


Figure D-105: DGR4_381.08-411.82 formation hydraulic conductivity cumulative distribution function.

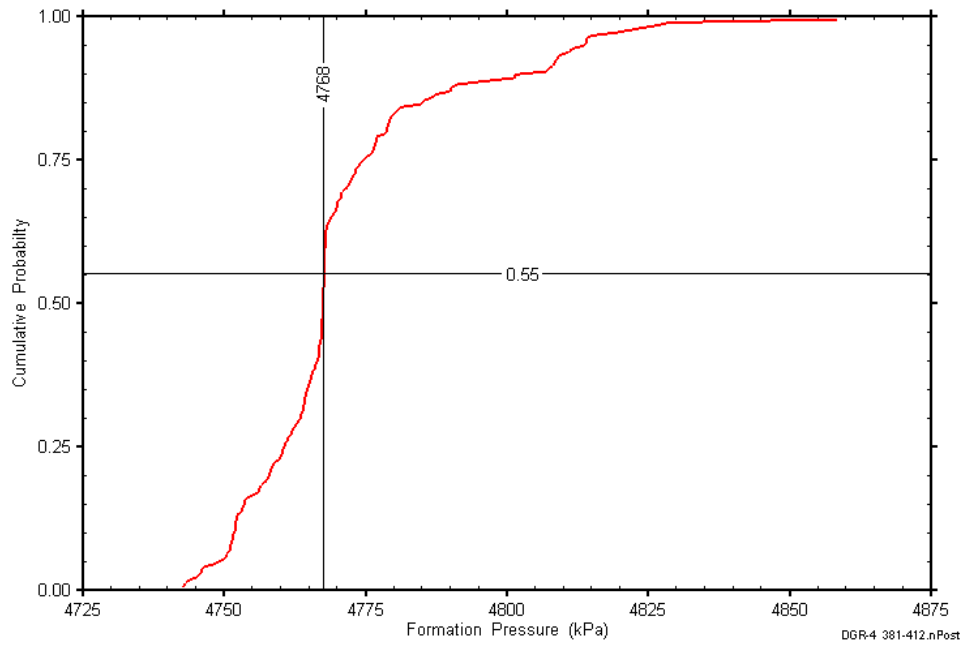


Figure D-106: DGR4_381.08-411.82 static formation pressure cumulative distribution function.

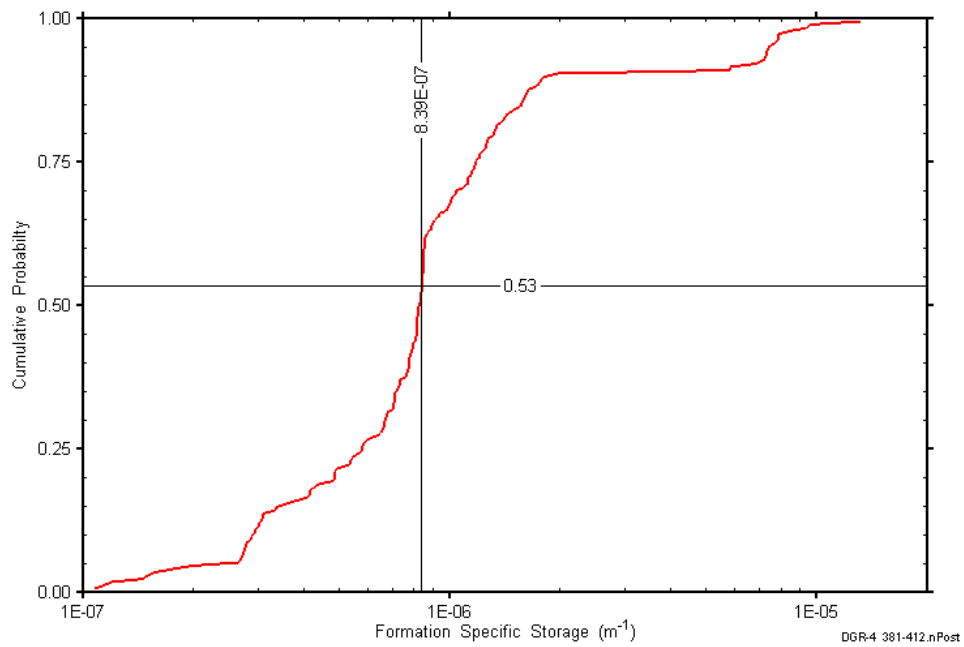


Figure D-107: DGR4_381.08-411.82 formation specific storage cumulative distribution function.

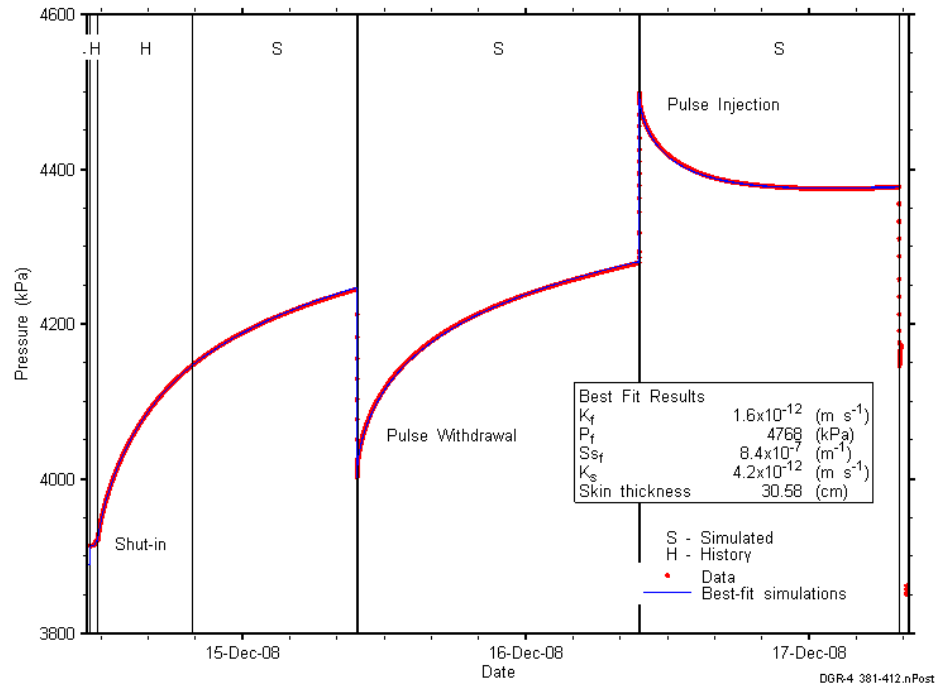


Figure D-108: Linear plot showing simulations of the DGR4_381.08-411.82 pressure response.

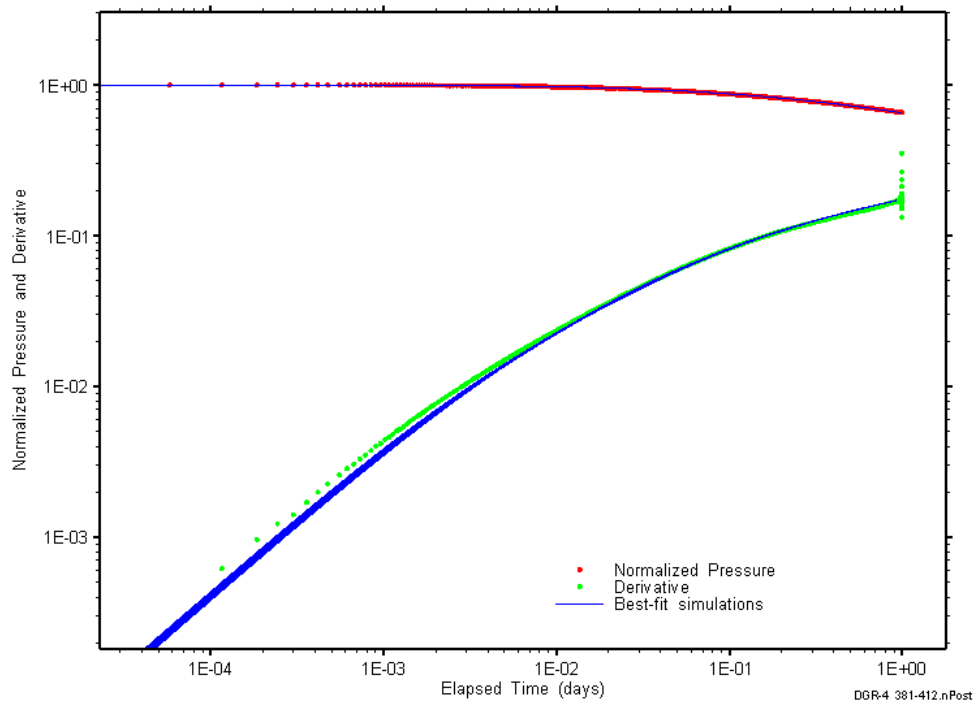


Figure D-109: Log-log plot showing simulations of the DGR4_381.08-411.82 pulse withdrawal Ramey B and derivative response.

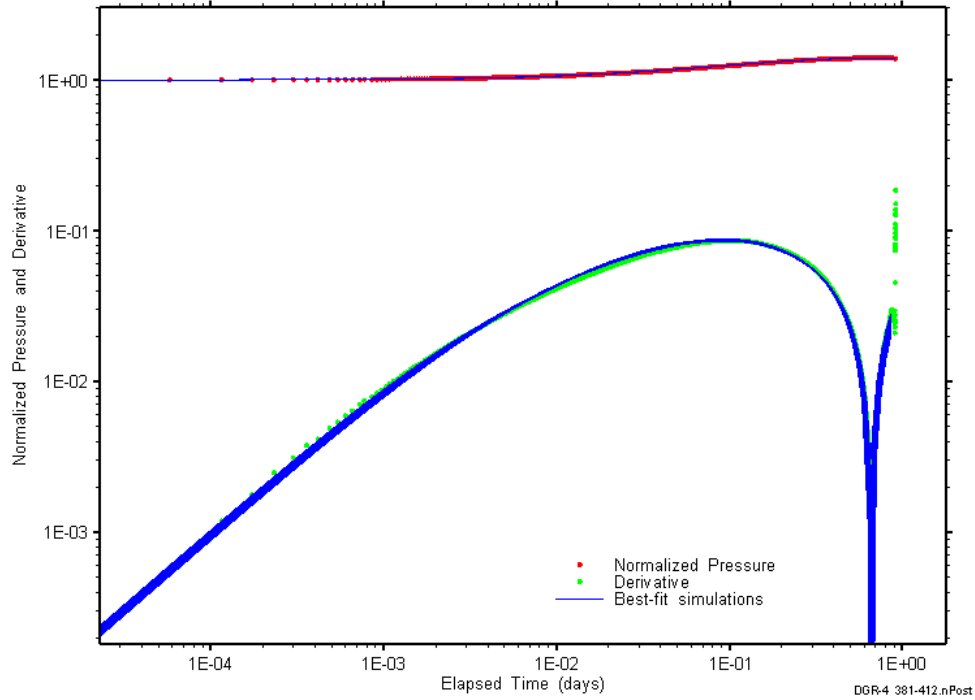


Figure D-110: Log-log plot showing simulations of the DGR4_381.08–411.82 pulse injection Ramey B and derivative response.

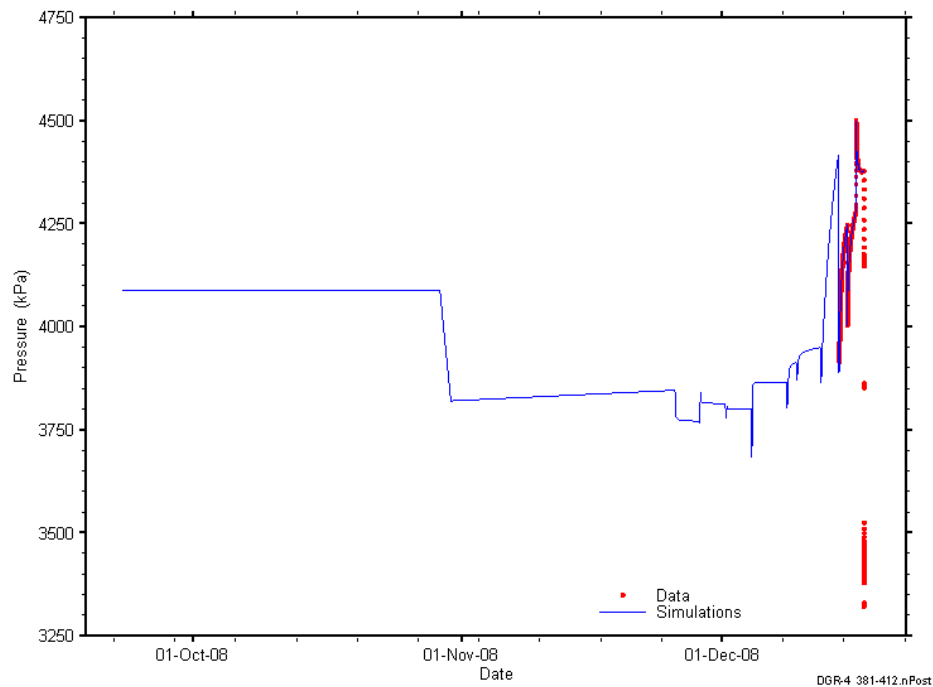


Figure D-111: Linear plot showing details of simulations of the DGR4_381.08-411.82 pressure response, including pre-test pressure history.

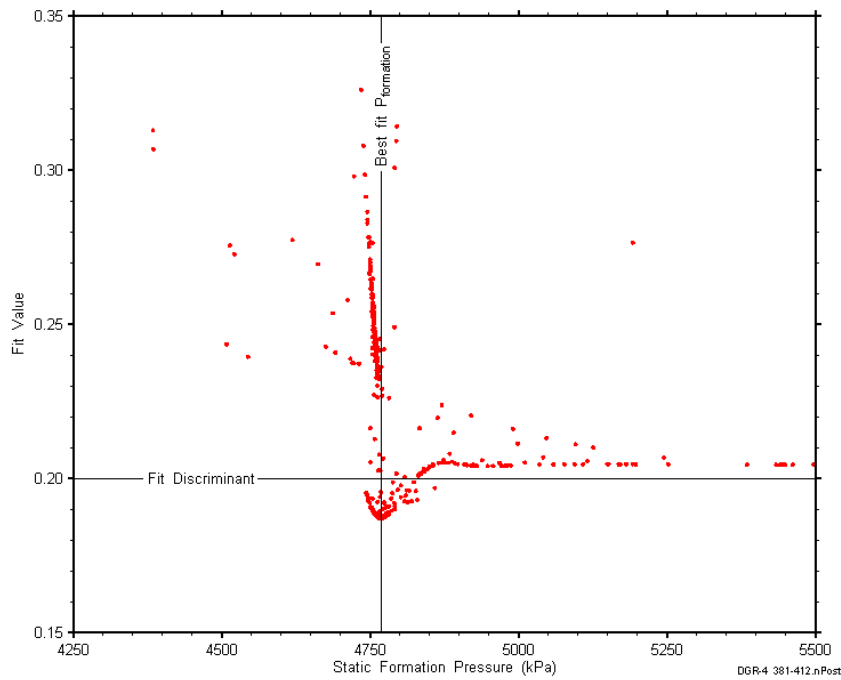


Figure D-112: XY-scatter plot showing the static formation pressure parameter space derived from DGR4_381.08-411.82 perturbation analysis along with the fit discriminant and best fit values.

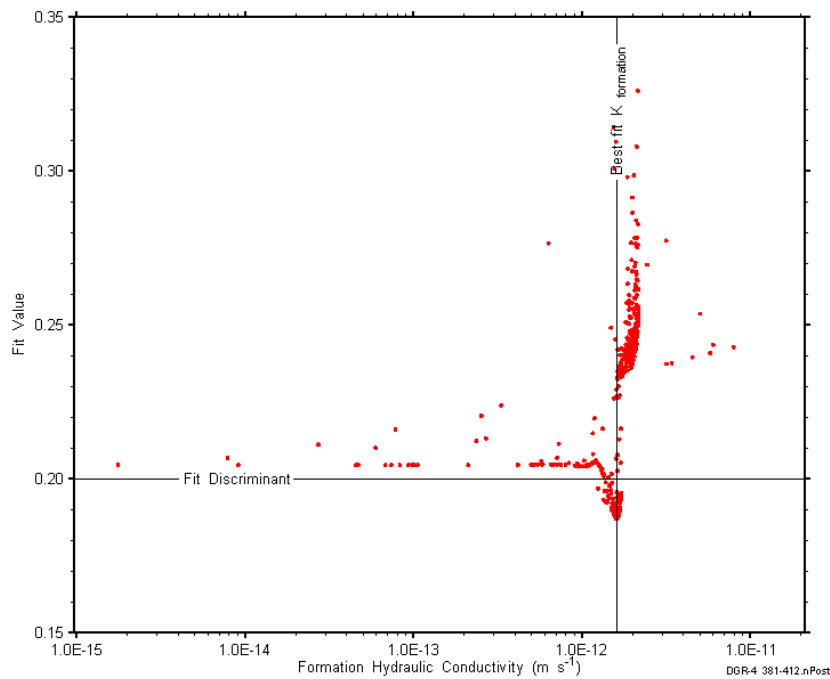


Figure D-113: XY-scatter plot showing the formation hydraulic conductivity parameter space derived from DGR4_381.08-411.82 perturbation analysis along with the fit discriminant and best fit values.

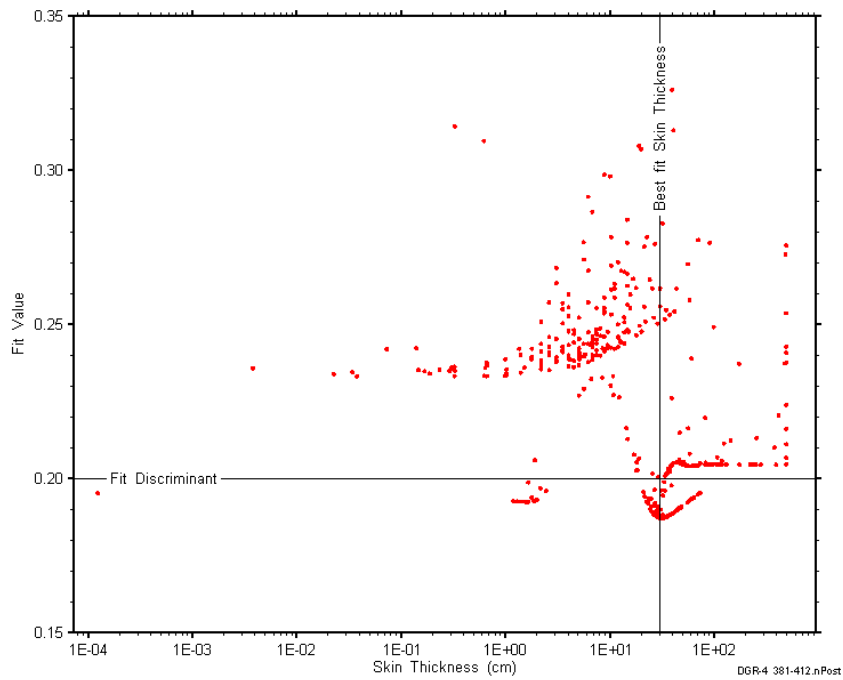


Figure D-114: XY-scatter plot showing the skin-thickness parameter space derived from DGR4_381.08-411.82 perturbation analysis along with the fit discriminant and best fit values.

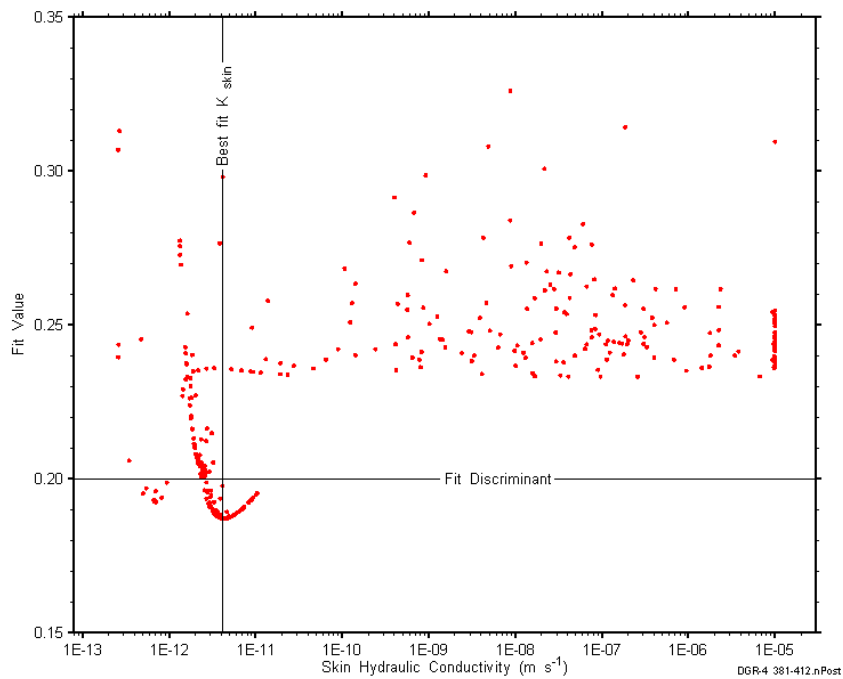


Figure D-115: XY-scatter plot showing the skin hydraulic conductivity parameter space derived from DGR4_381.08-411.82 perturbation analysis along with the fit discriminant and best fit values.

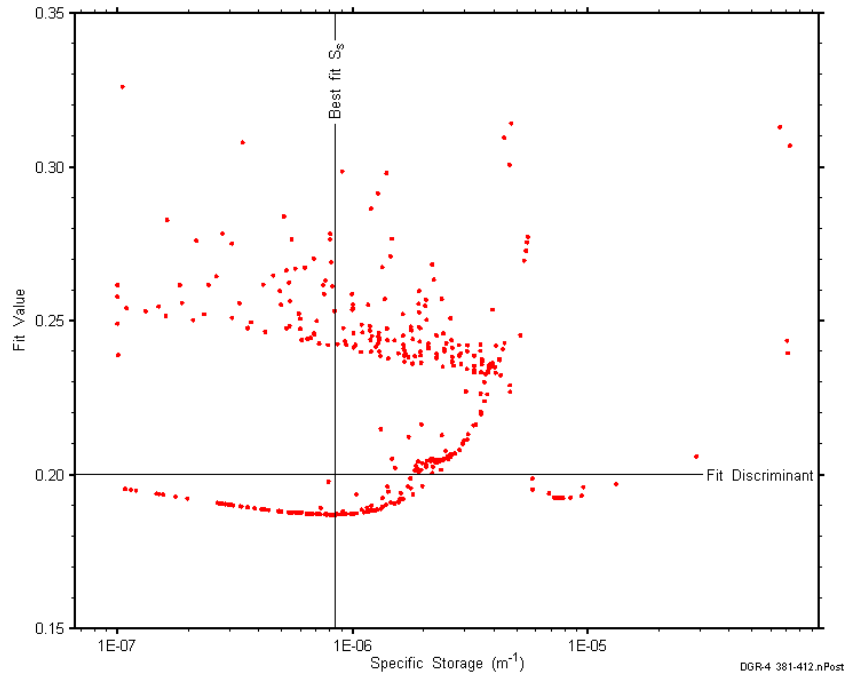


Figure D-116: XY-scatter plot showing the formation specific storage parameter space derived from DGR4_381.08-411.82 perturbation analysis along with the fit discriminant and best fit values.

D.10 411.51-442.25 Cabot Head-Manitoulin

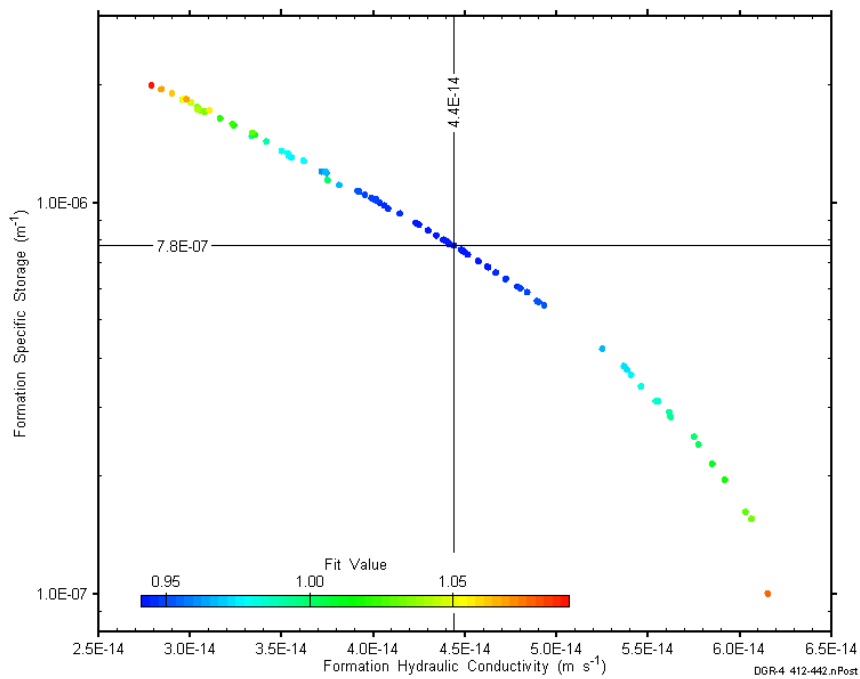


Figure D-117: XY-scatter plot showing estimates of formation hydraulic conductivity and formation specific storage derived from the DGR4_411.51-442.25 perturbation analysis.

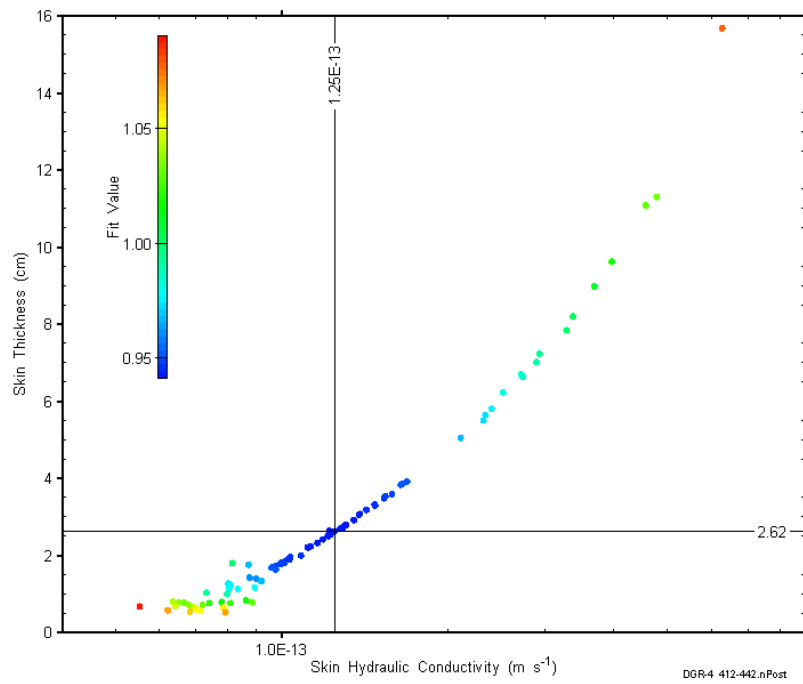


Figure D-118: XY-scatter plot showing estimates of skin hydraulic conductivity and skin thickness derived from the DGR4_411.51-442.25 perturbation analysis.

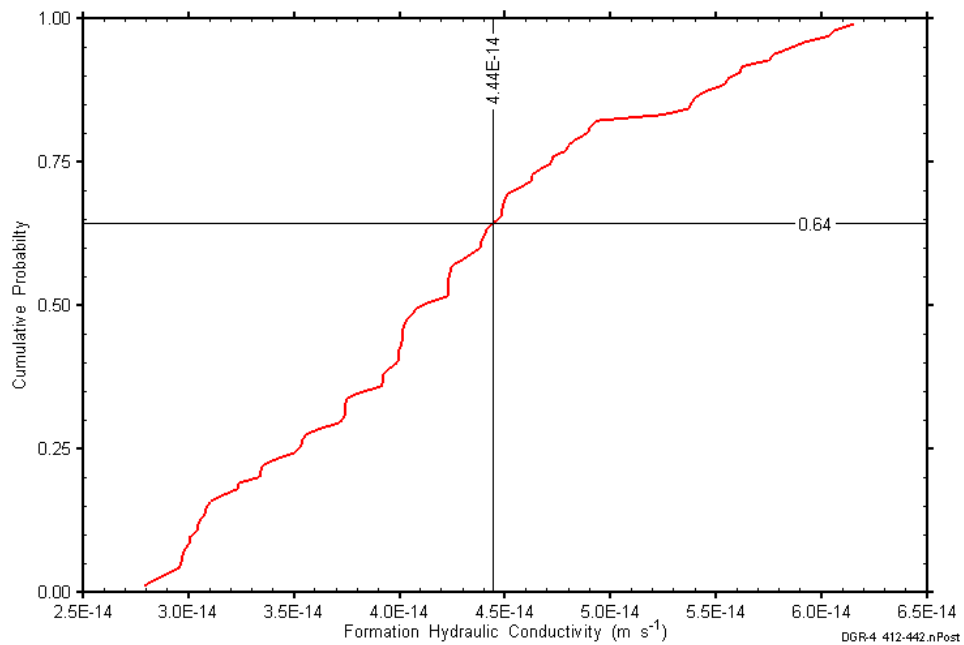


Figure D-119: DGR4_411.51-442.25 formation hydraulic conductivity cumulative distribution function.

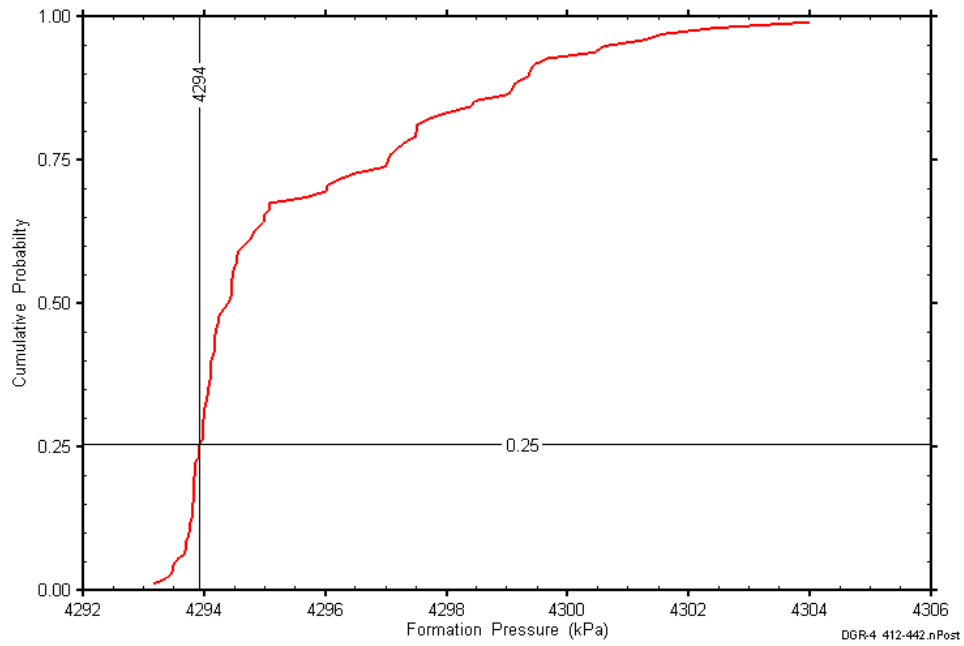


Figure D-120: DGR4_411.51-442.25 static formation pressure cumulative distribution function.

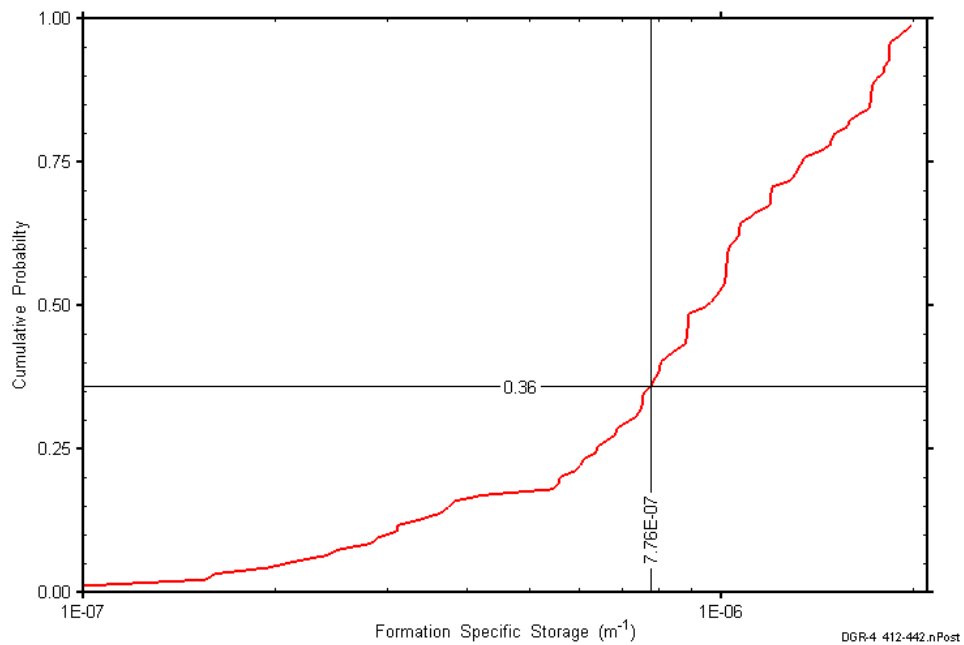


Figure D-121: DGR4_411.51-442.25 formation specific storage cumulative distribution function.

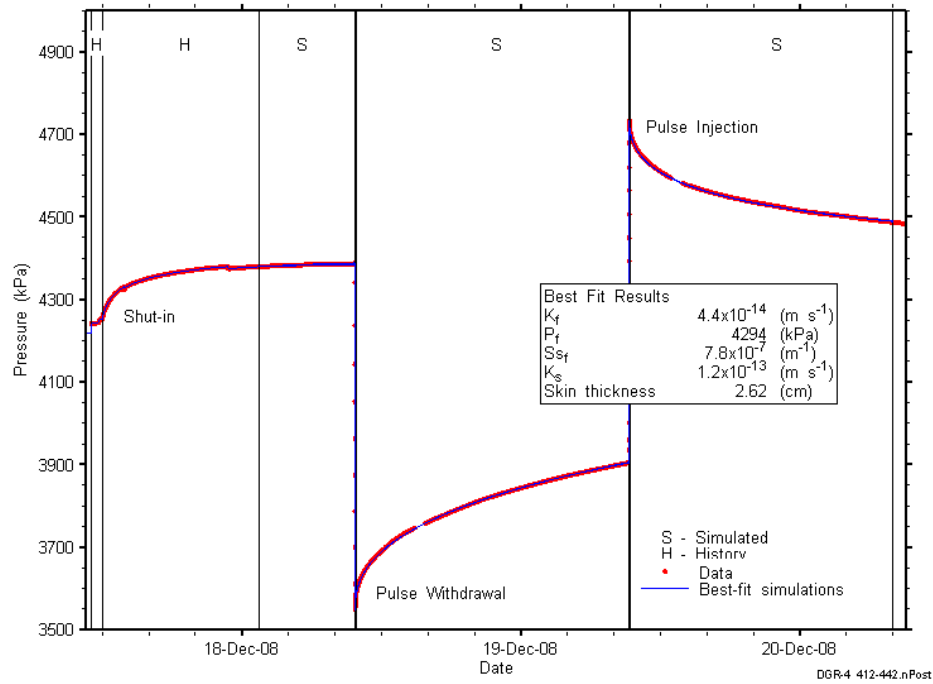


Figure D-122: Linear plot showing simulations of the DGR4_411.51-442.25 pressure response.

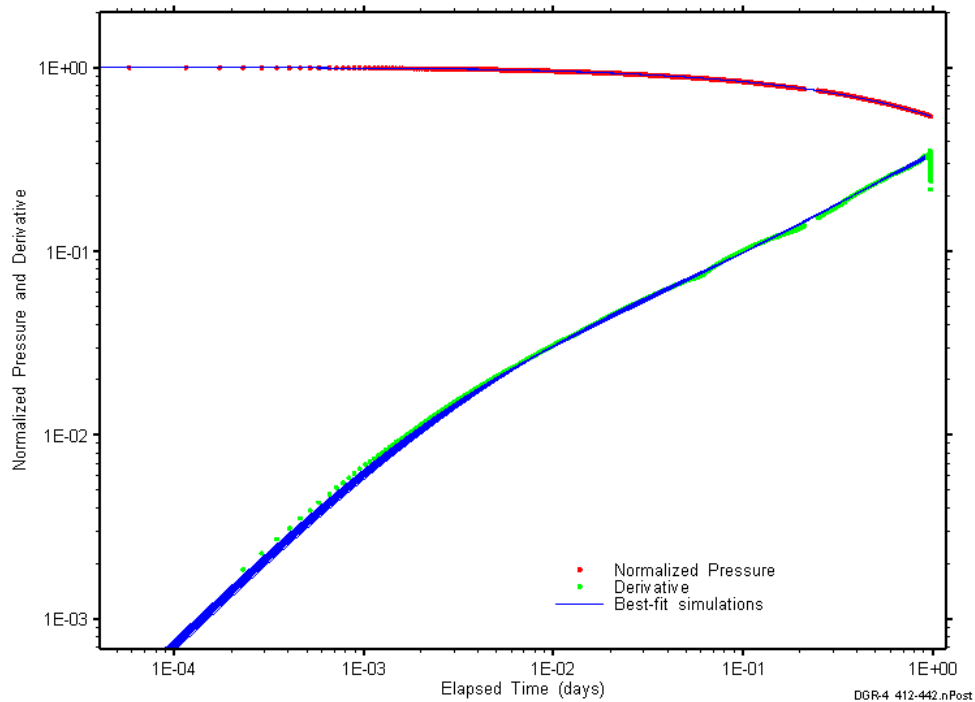


Figure D-123: Log-log plot showing simulations of the DGR4_411.51-442.25 pulse withdrawal Ramey B and derivative response.

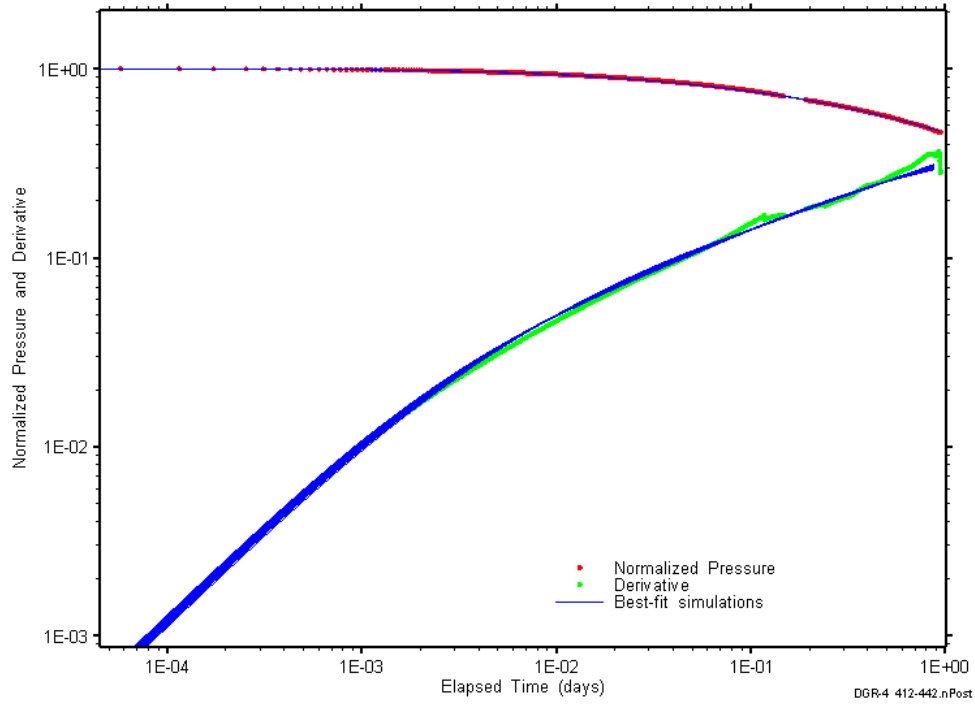


Figure D-124: Log-log plot showing simulations of the DGR4_411.51–442.25 pulse injection Ramey B and derivative response.

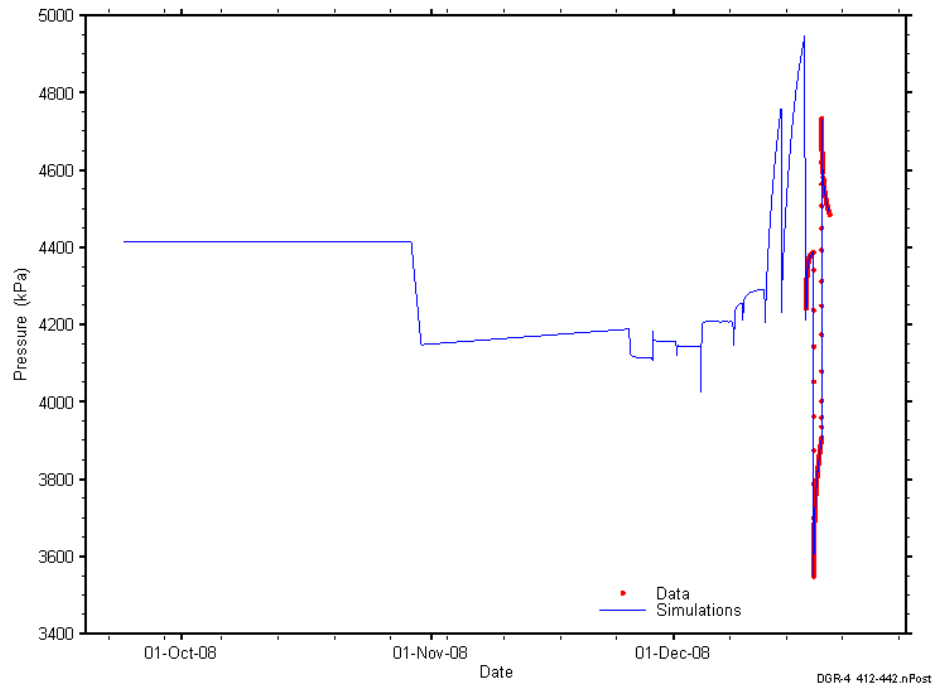


Figure D-125: Linear plot showing simulations of the DGR4_411.51–442.25 pressure response, including pre-test pressure history.

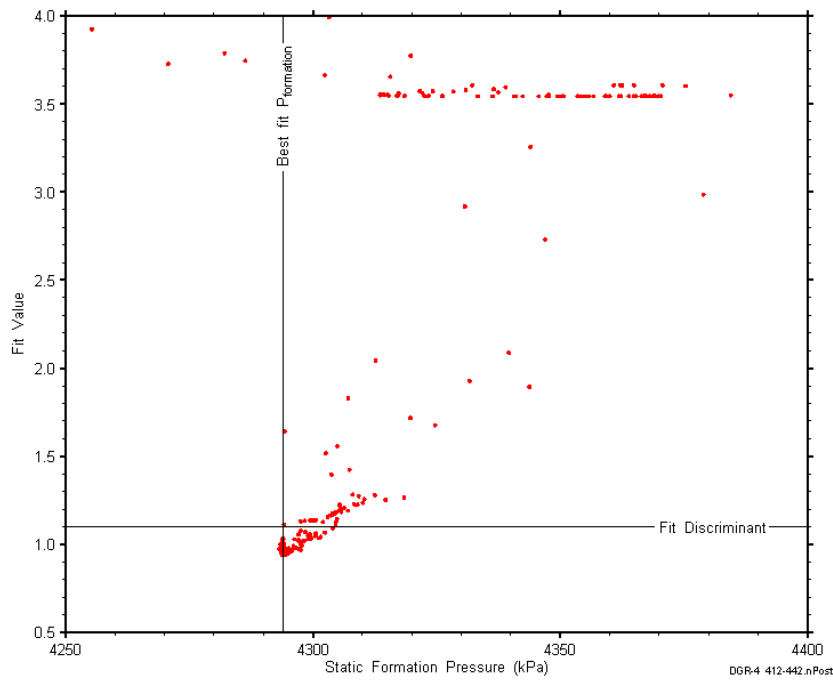


Figure D-126: XY-scatter plot showing the static formation pressure parameter space derived from DGR4_411.51-442.25 perturbation analysis along with the fit discriminant and best fit values.

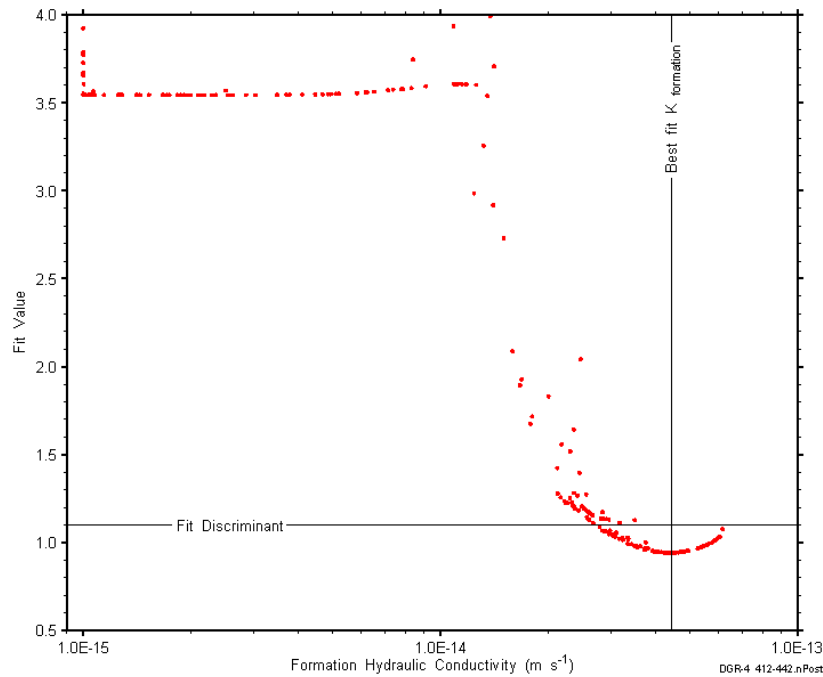


Figure D-127: XY-scatter plot showing the formation hydraulic conductivity parameter space derived from DGR4_411.51-442.25 perturbation analysis along with the fit discriminant and best fit values.

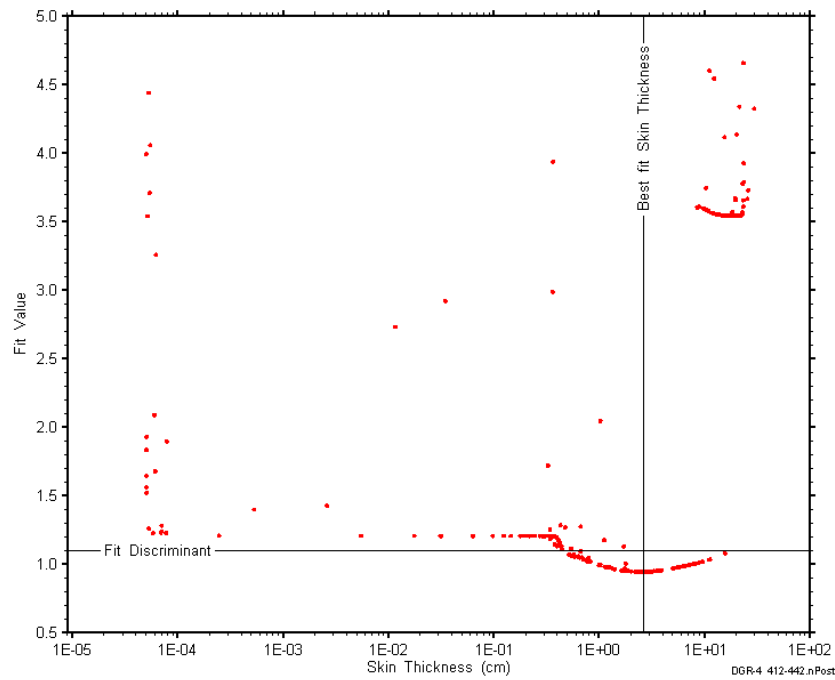


Figure D-128: XY-scatter plot showing the skin-thickness parameter space derived from DGR4_411.51-442.25 perturbation analysis along with the fit discriminant and best fit values.

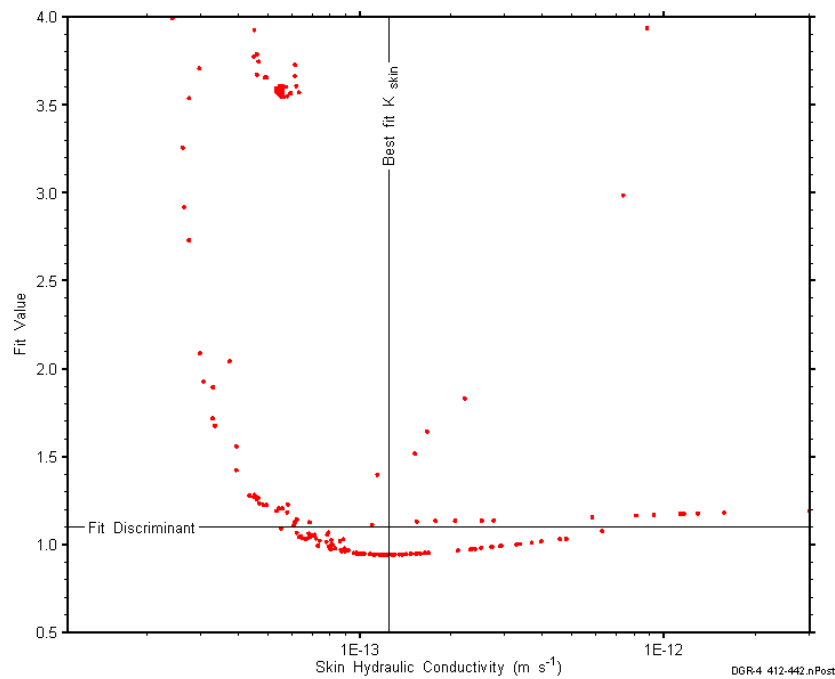


Figure D-129: XY-scatter plot showing the skin hydraulic conductivity parameter space derived from DGR4_411.51-442.25 perturbation analysis along with the fit discriminant and best fit values.

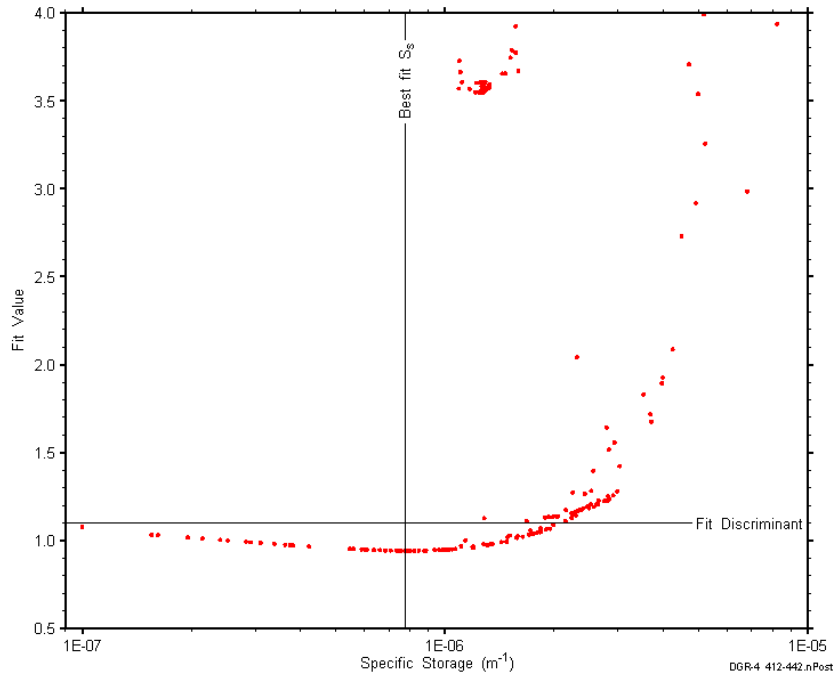


Figure D-130: XY-scatter plot showing the formation specific storage parameter space derived from DGR4_411.51-442.25 perturbation analysis along with the fit discriminant and best fit values.

D.11 432.00-462.74 Manitoulin-Queenston

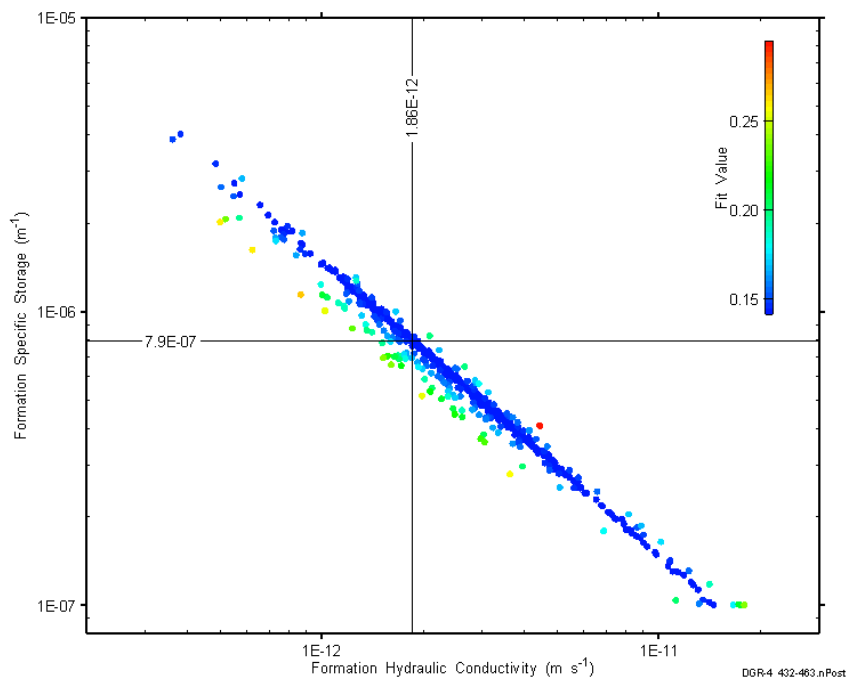


Figure D-131: XY-scatter plot showing estimates of formation hydraulic conductivity and formation specific storage derived from the DGR4_432.00-462.74 perturbation analysis.

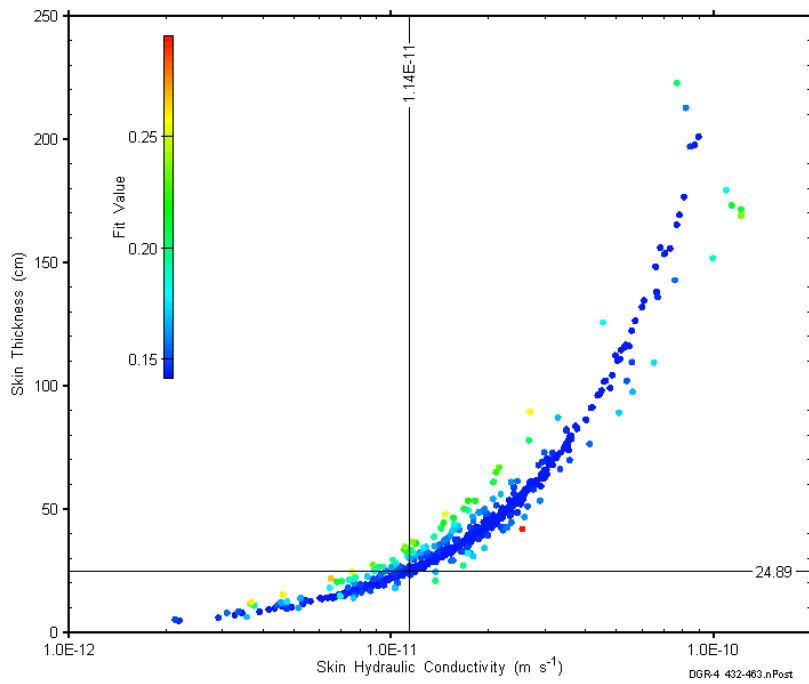


Figure D-132: XY-scatter plot showing estimates of skin hydraulic conductivity and skin thickness derived from the DGR4_432.00-462.74 perturbation analysis.

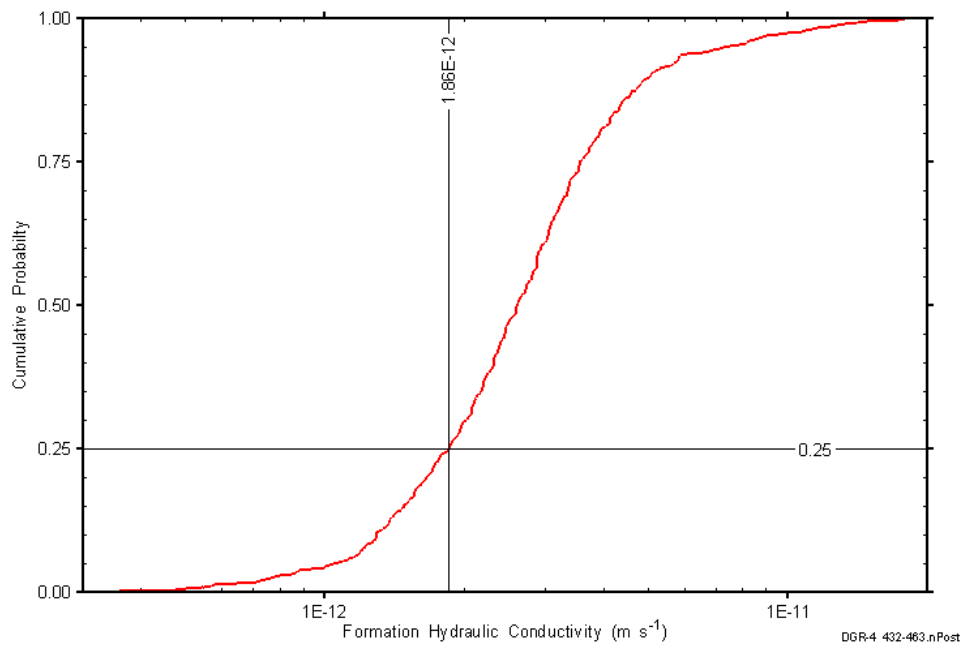


Figure D-133: DGR4_432.00-462.74 formation hydraulic conductivity cumulative distribution function.

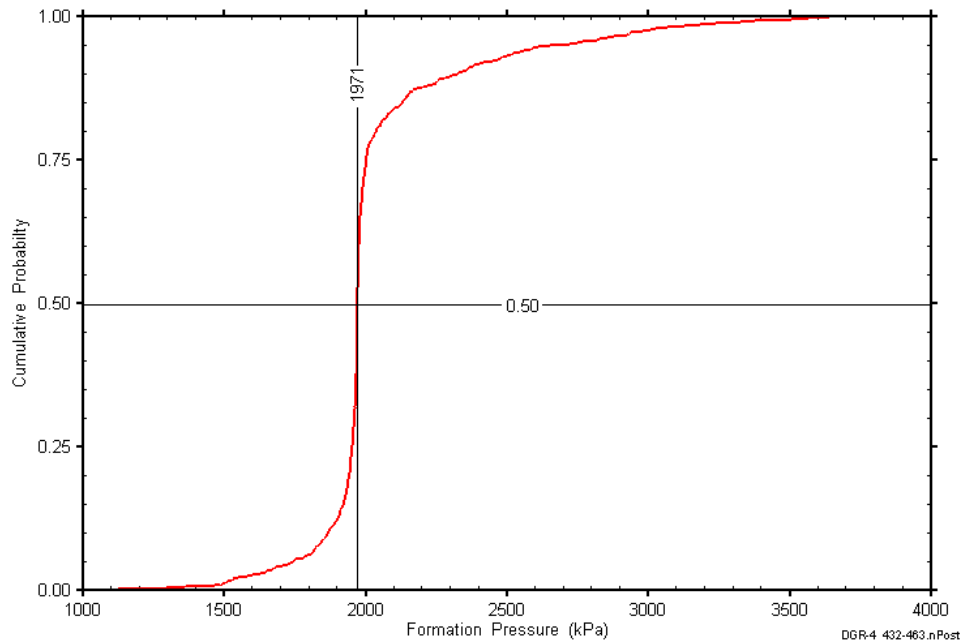


Figure D-134: DGR4_432.00-462.74 static formation pressure cumulative distribution function.

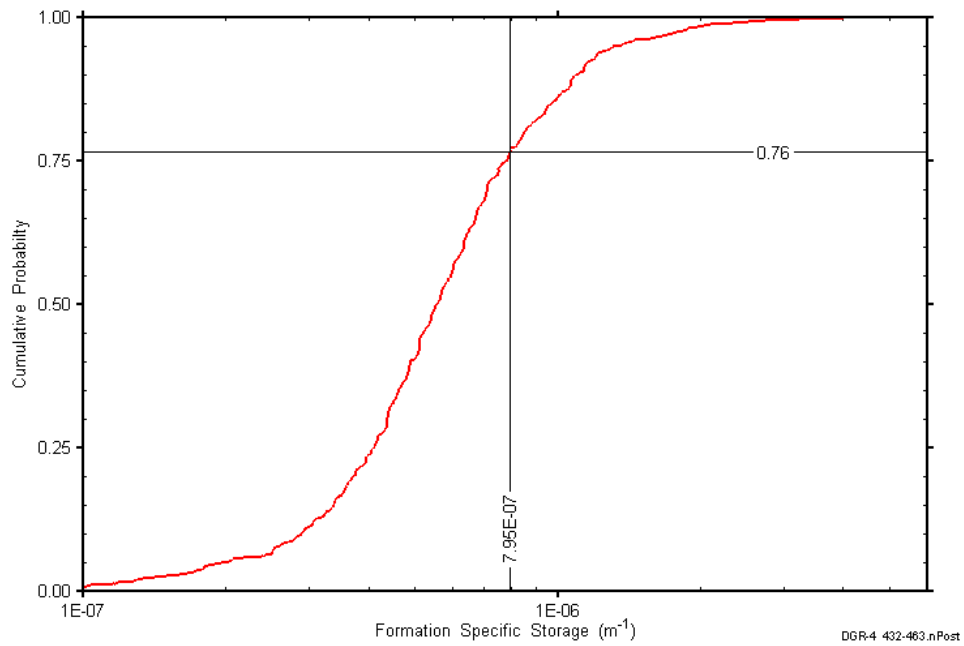


Figure D-135: DGR4_432.00-462.74 formation specific storage cumulative distribution function.

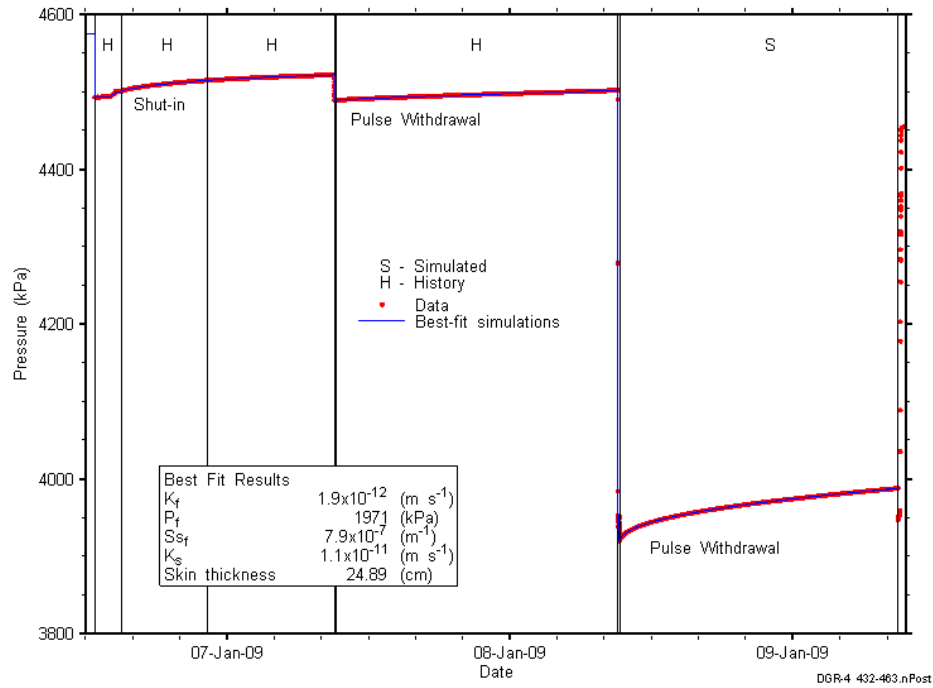


Figure D-136: Linear plot showing simulations of the DGR4_432.00-462.74 pressure response.

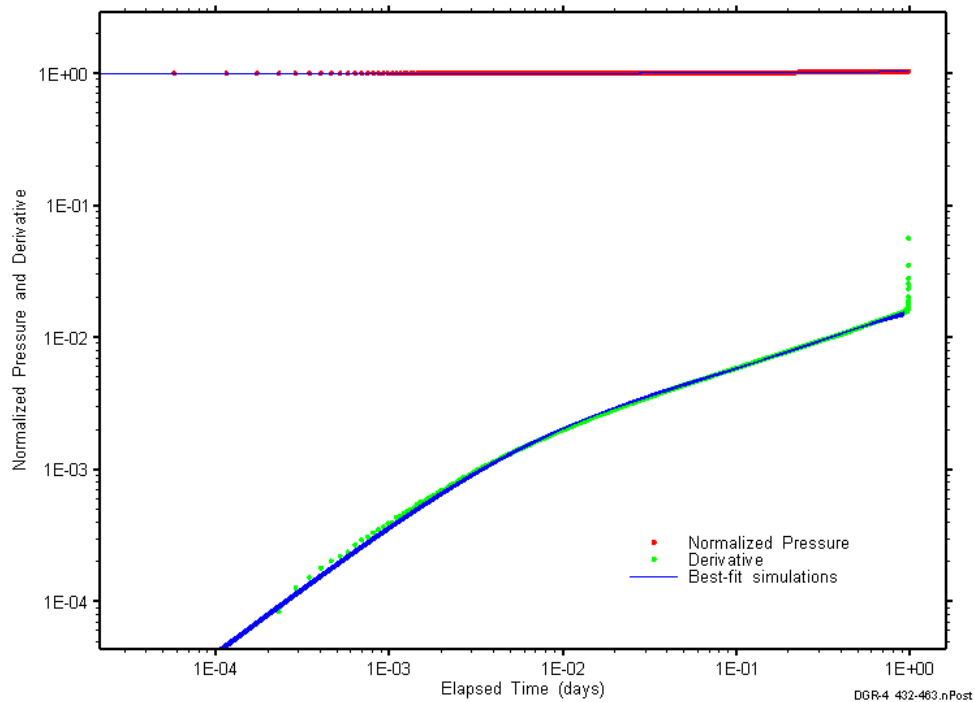


Figure D-137: Log-log plot showing simulations of the DGR4_432.00-462.74 pulse withdrawal Ramey B and derivative response.

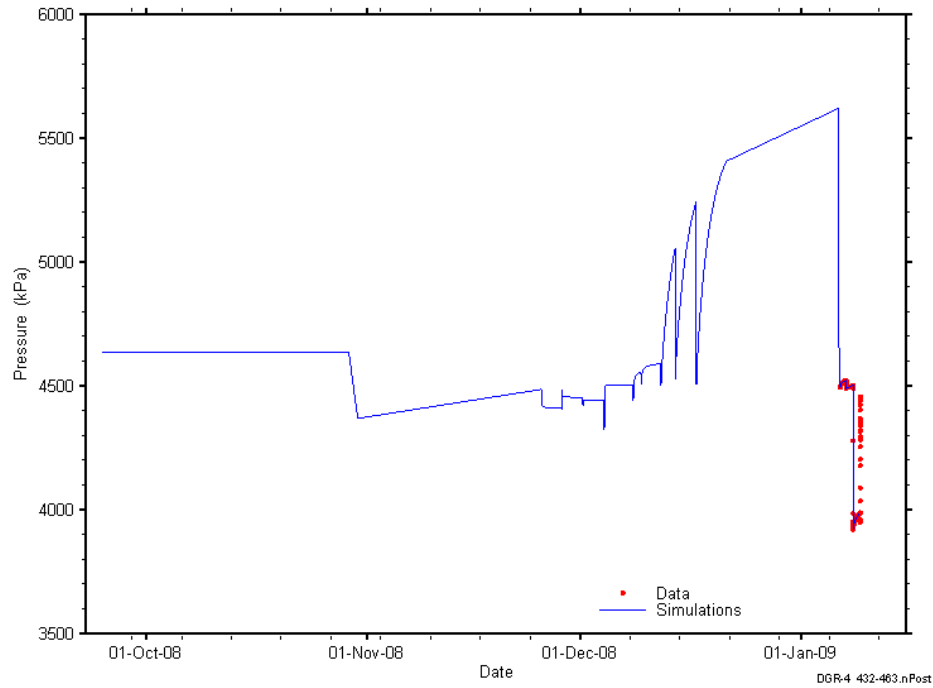


Figure D-138: Linear plot showing simulations of the DGR4_432.00-462.74 pressure response, including pre-test pressure history.

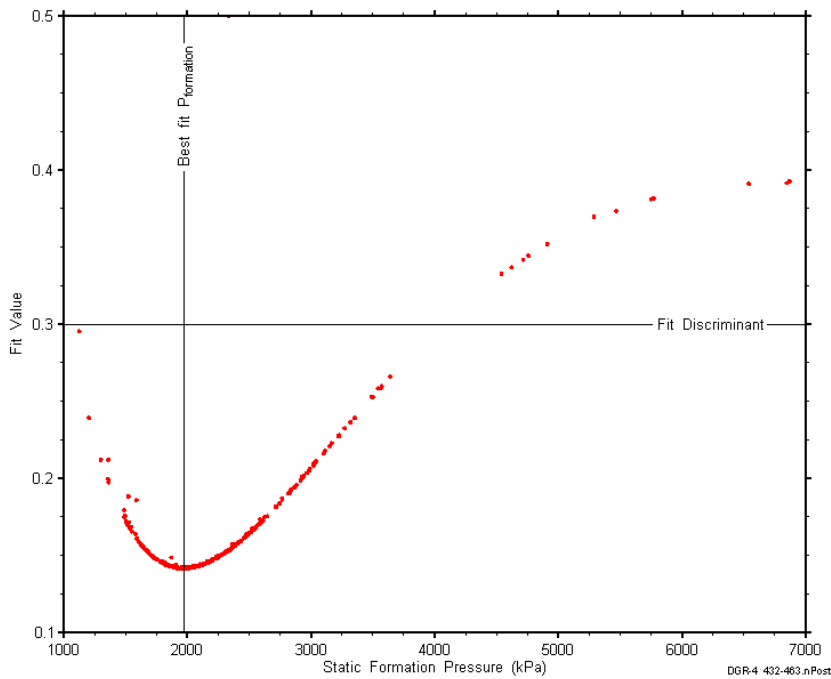


Figure D-139: XY-scatter plot showing the static formation pressure parameter space derived from DGR4_432.00-462.74 perturbation analysis along with the fit discriminant and best fit values.

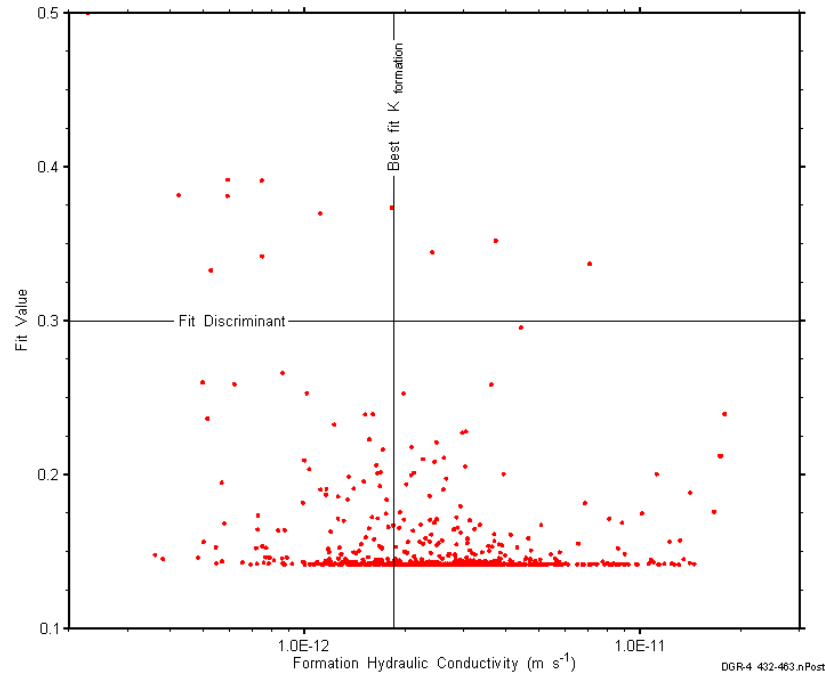


Figure D-140: XY-scatter plot showing the formation hydraulic conductivity parameter space derived from DGR4_432.00-462.74 perturbation analysis along with the fit discriminant and best fit values.

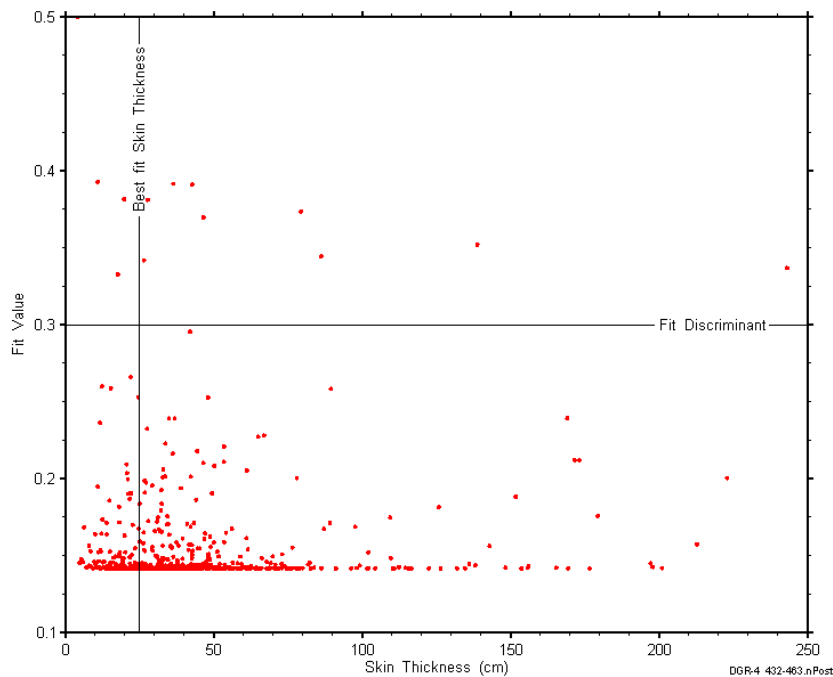


Figure D-141: XY-scatter plot showing the skin-thickness parameter space derived from DGR4_432.00-462.74 perturbation analysis along with the fit discriminant and best fit values.

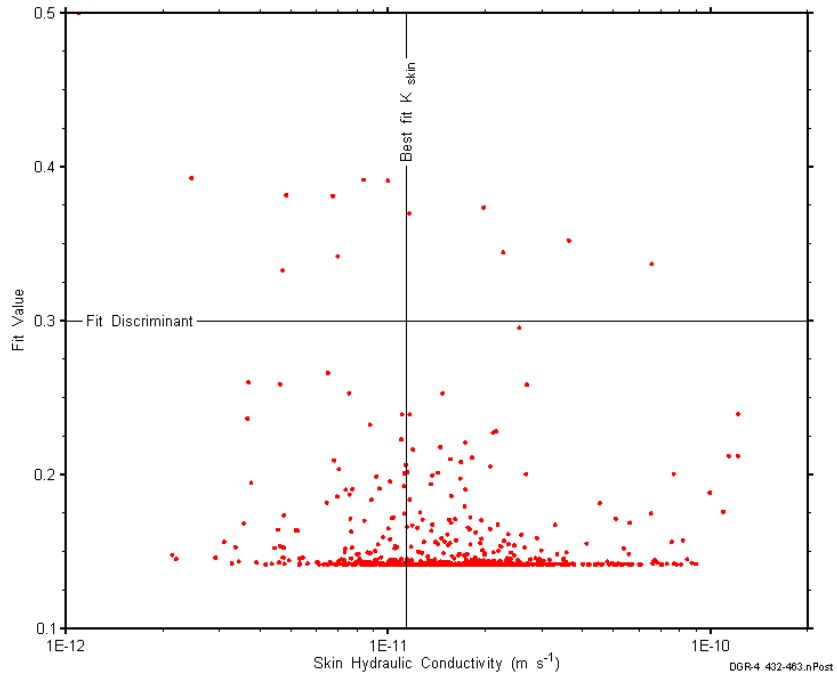


Figure D-142: XY-scatter plot showing the skin hydraulic conductivity parameter space derived from DGR4_432.00-462.74 perturbation analysis along with the fit discriminant and best fit values.

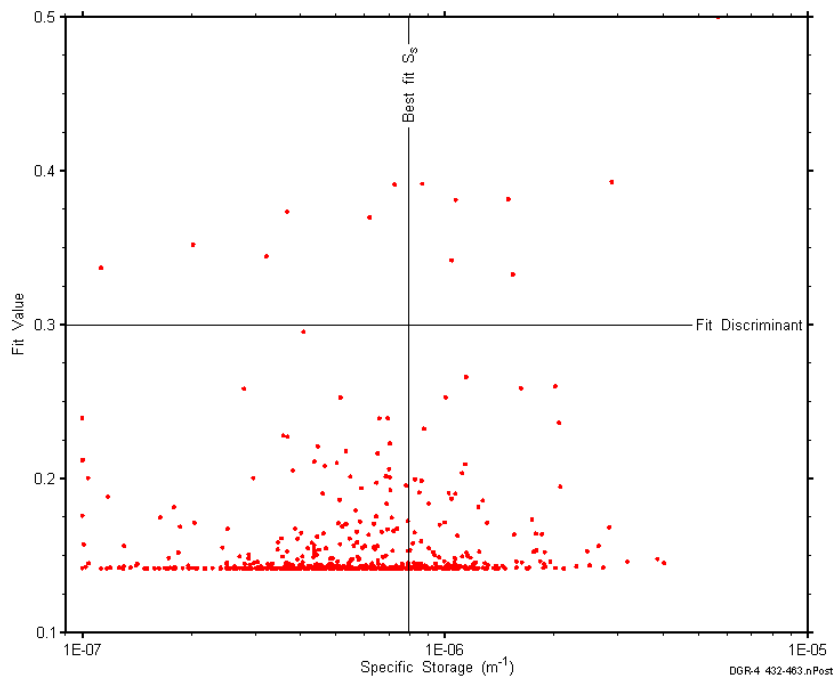


Figure D-143: XY-scatter plot showing the formation specific storage parameter space derived from DGR4_432.00-462.74 perturbation analysis along with the fit discriminant and best fit values.

D.12 458.23-488.97 Queenston 1

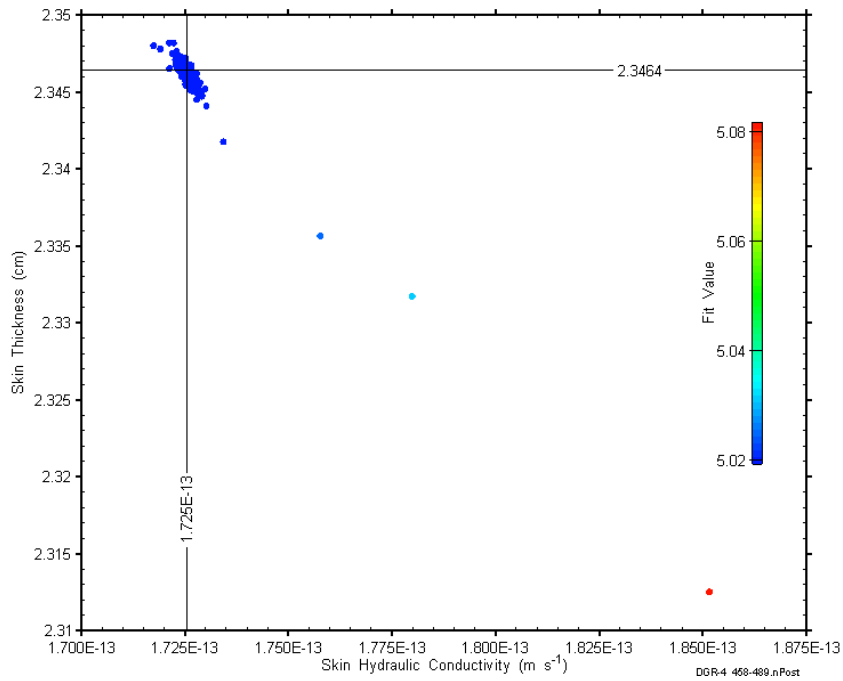


Figure D-144: XY-scatter plot showing estimates of skin hydraulic conductivity and skin thickness derived from the DGR4_458.23-488.97 perturbation analysis.

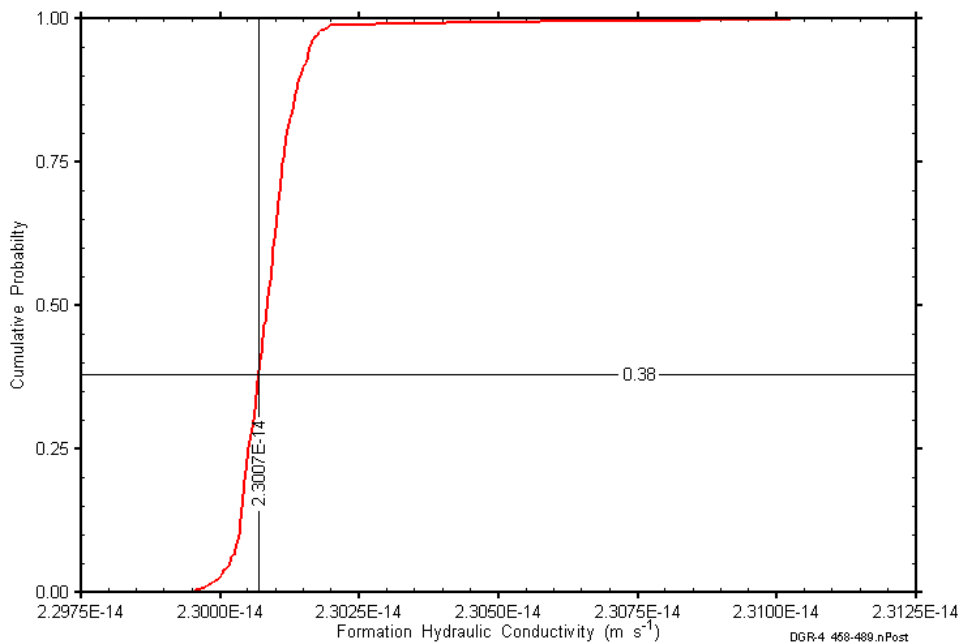


Figure D-145: DGR4_458.23-488.97 formation hydraulic conductivity cumulative distribution function.

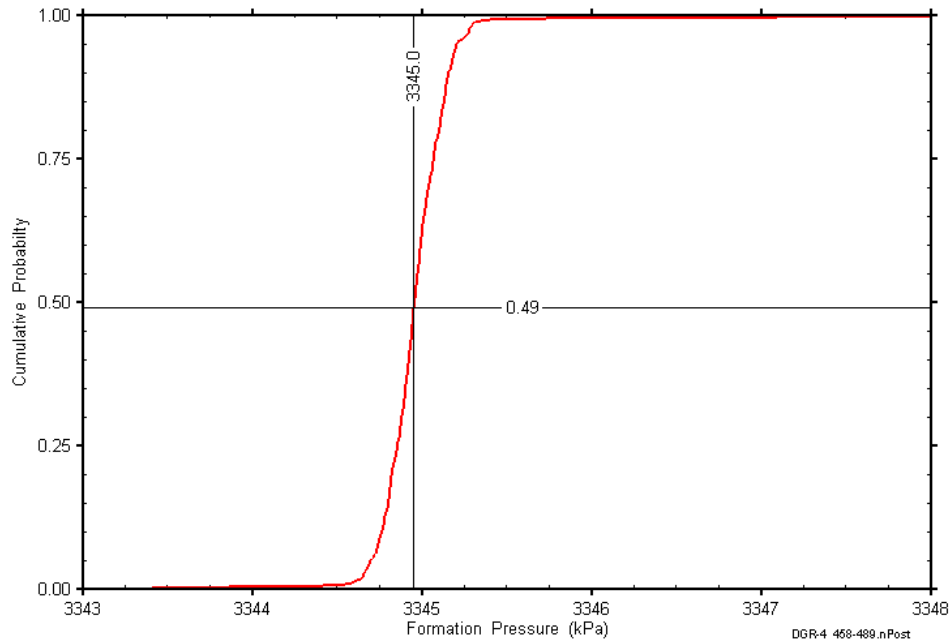


Figure D-146: DGR4_458.23-488.97 static formation pressure cumulative distribution function.

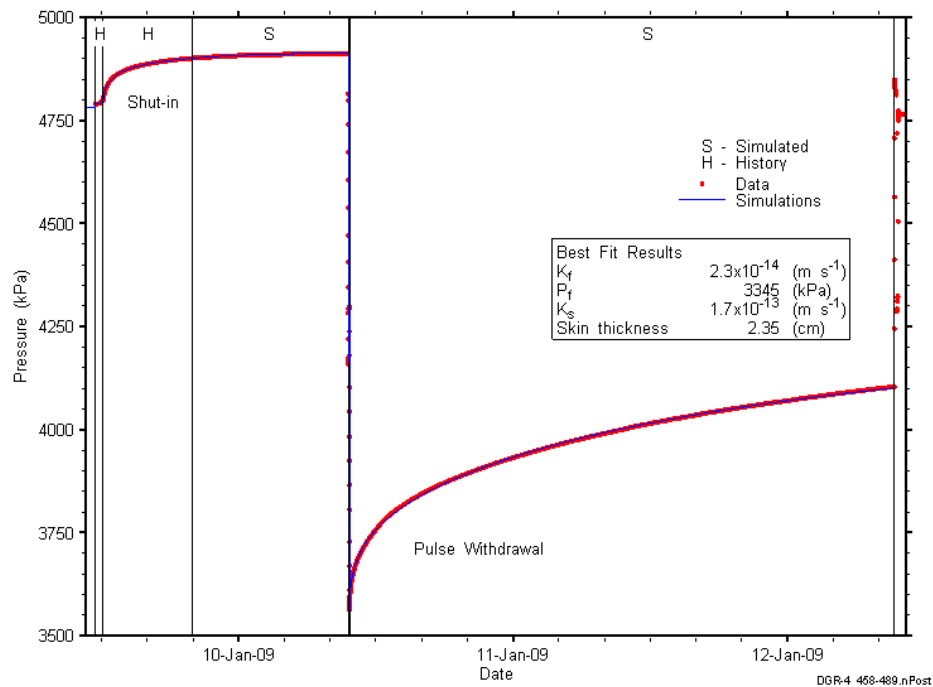


Figure D-147: Linear plot showing simulations of the DGR4_458.23-488.97 pressure response.

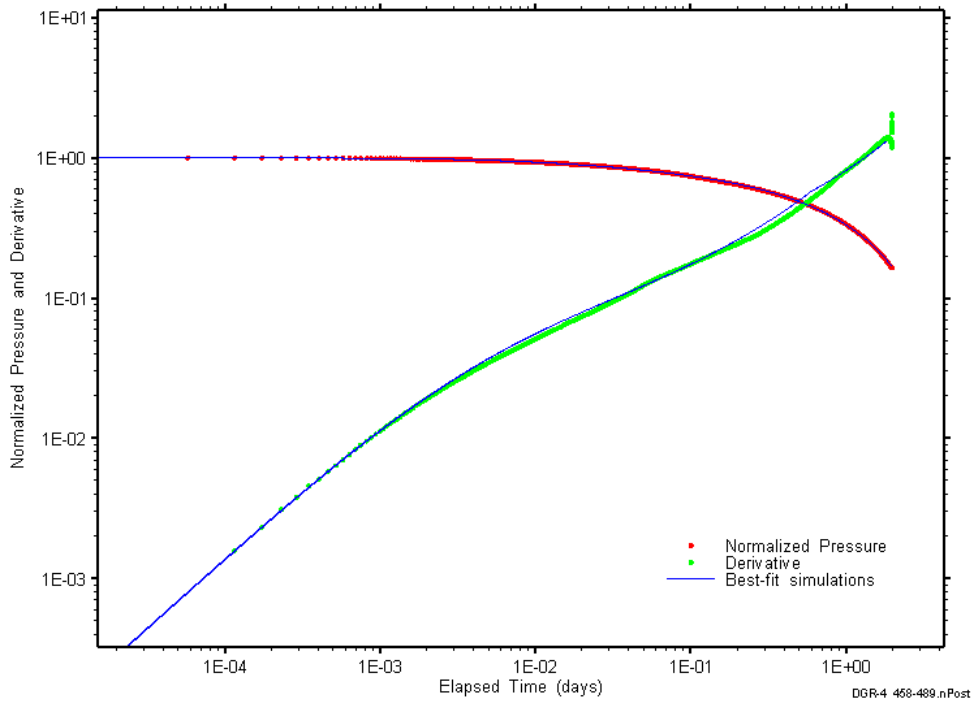


Figure D-148: Log-log plot showing simulations of the DGR4_458.23–488.97 pulse withdrawal Ramey B and derivative response.

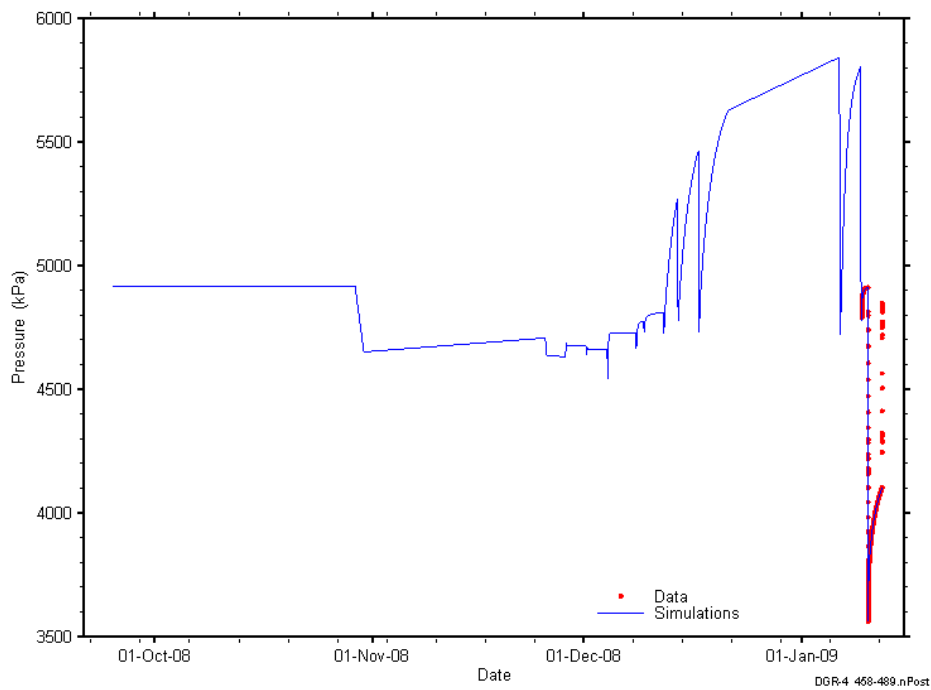


Figure D-149: Linear plot showing simulations of the DGR4_458.23-488.97 pressure response, including pre-test pressure history.

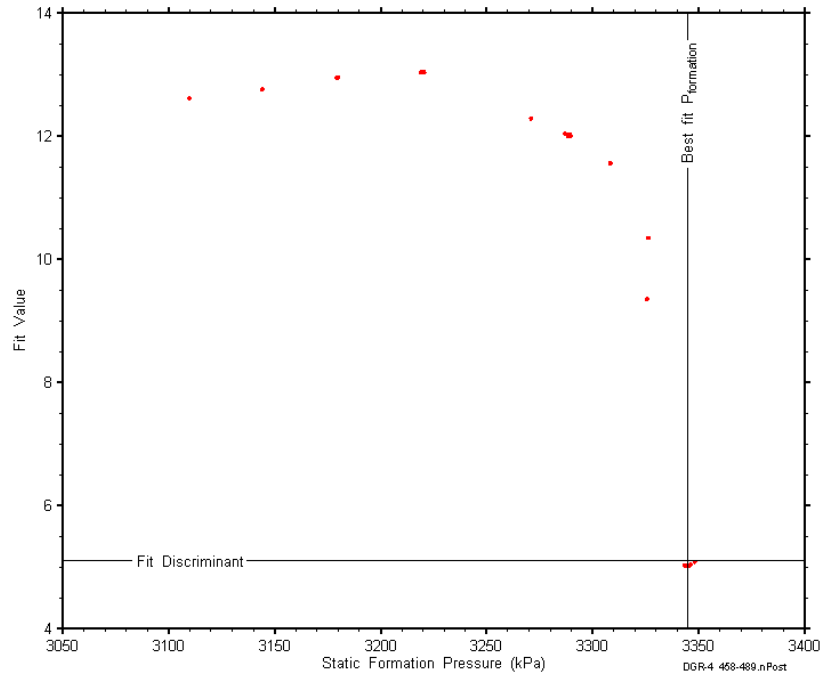


Figure D-150: XY-scatter plot showing the static formation pressure parameter space derived from DGR4_458.23-488.97 perturbation analysis along with the fit discriminant and best fit values.

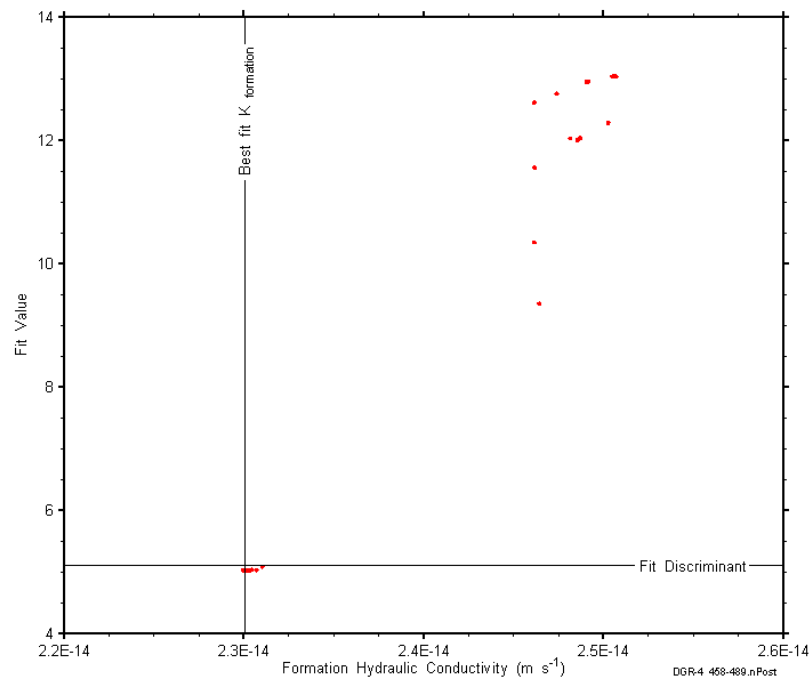


Figure D-151: XY-scatter plot showing the formation hydraulic conductivity parameter space derived from DGR4_458.23-488.97 perturbation analysis along with the fit discriminant and best fit values.

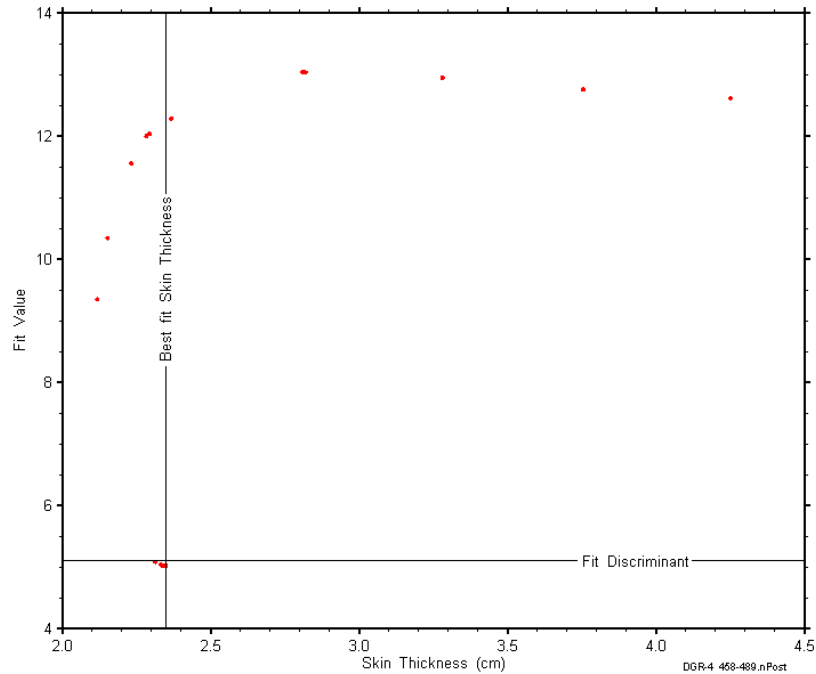


Figure D-152: XY-scatter plot showing the skin-thickness parameter space derived from DGR4_458.23-488.97 perturbation analysis along with the fit discriminant and best fit values.

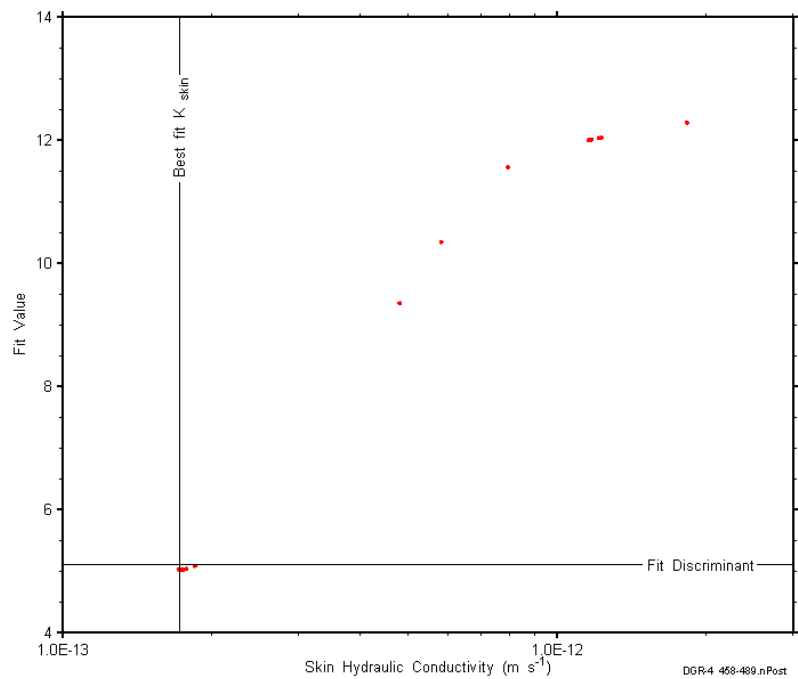


Figure D-153: XY-scatter plot showing the skin hydraulic conductivity parameter space derived from DGR4_458.23-488.97 perturbation analysis along with the fit discriminant and best fit values.

D.13 488.77-519.51 Queenston 2

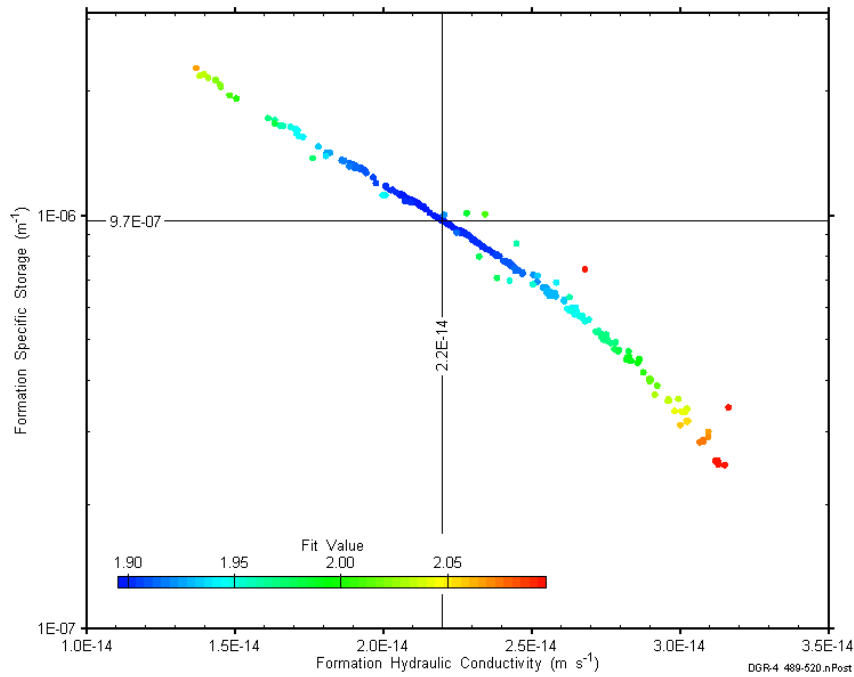


Figure D-154: XY-scatter plot showing estimates of formation hydraulic conductivity and formation specific storage derived from the DGR4_488.77-519.51 perturbation analysis.

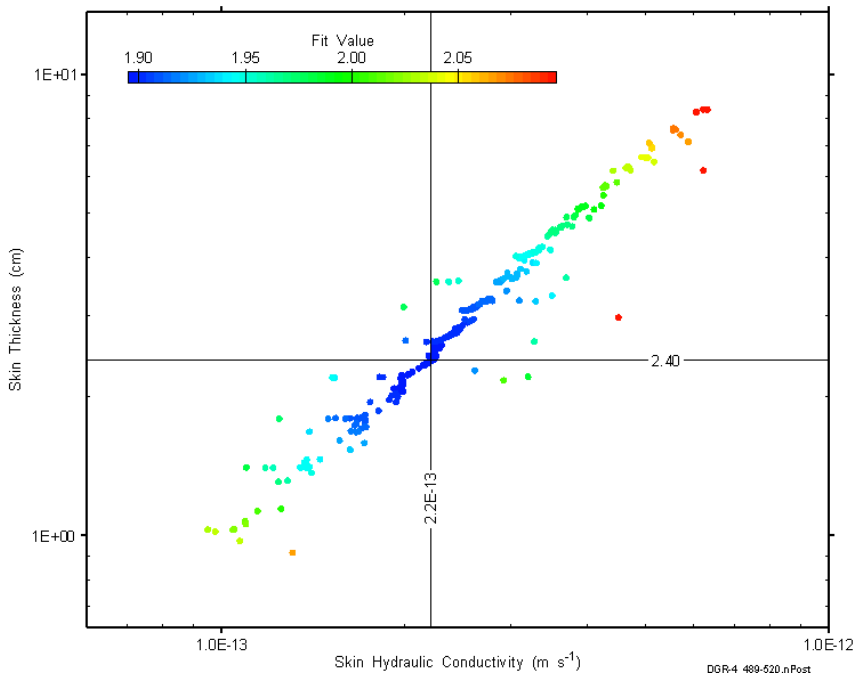


Figure D-155: XY-scatter plot showing estimates of skin hydraulic conductivity and skin thickness derived from the DGR4_488.77-519.51 perturbation analysis.

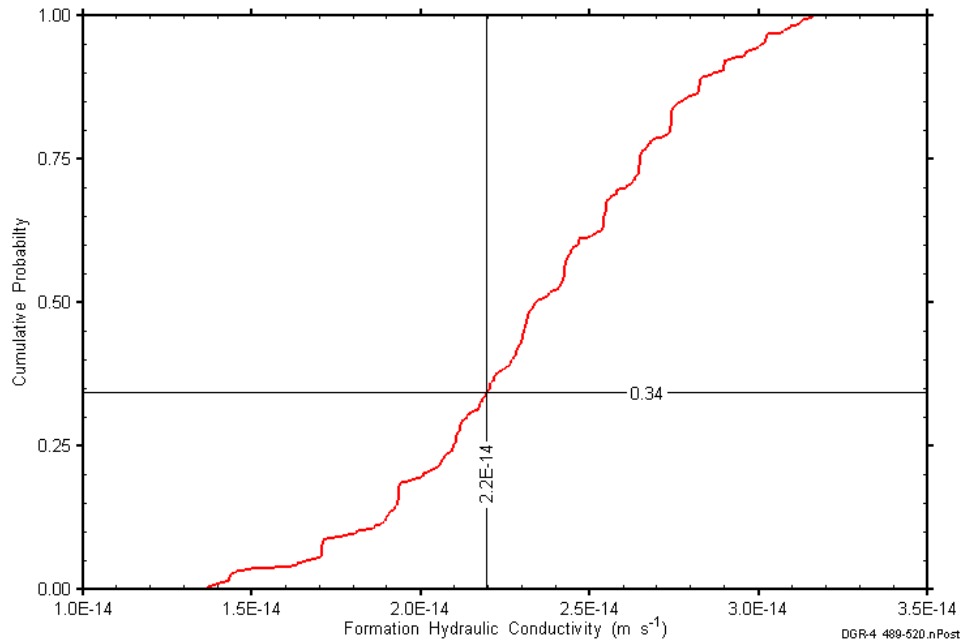


Figure D-156: DGR4_488.77-519.51 formation hydraulic conductivity cumulative distribution function.

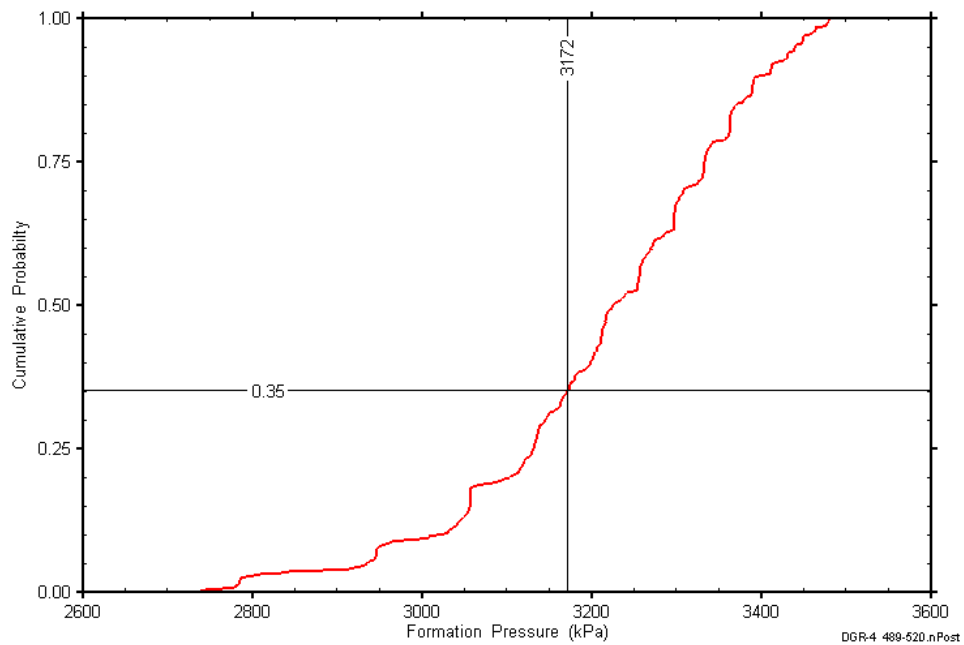


Figure D-157: DGR4_488.77-519.51 static formation pressure cumulative distribution function.

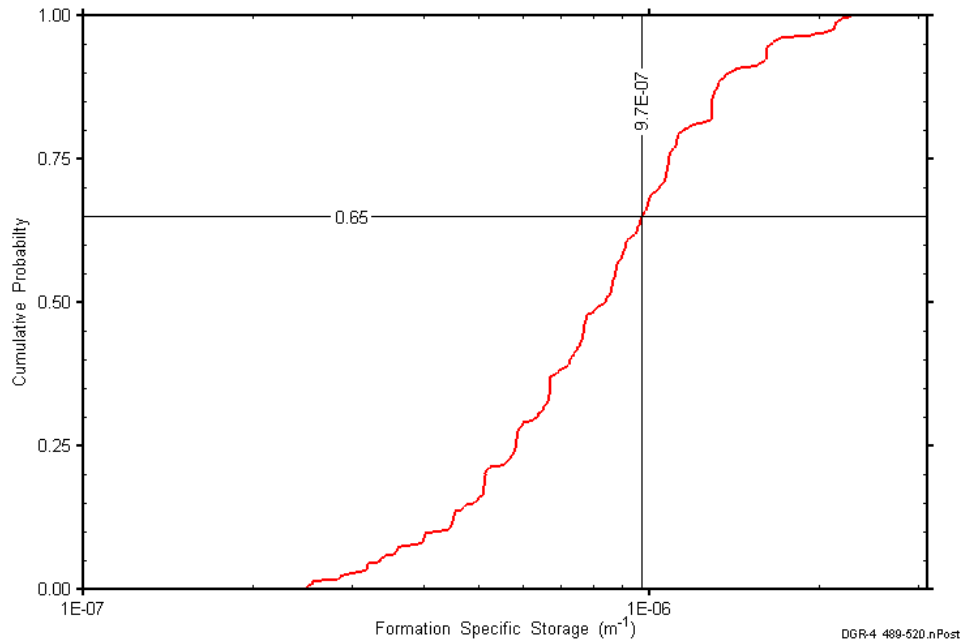


Figure D-158: DGR4_488.77-519.51 formation specific storage cumulative distribution function.

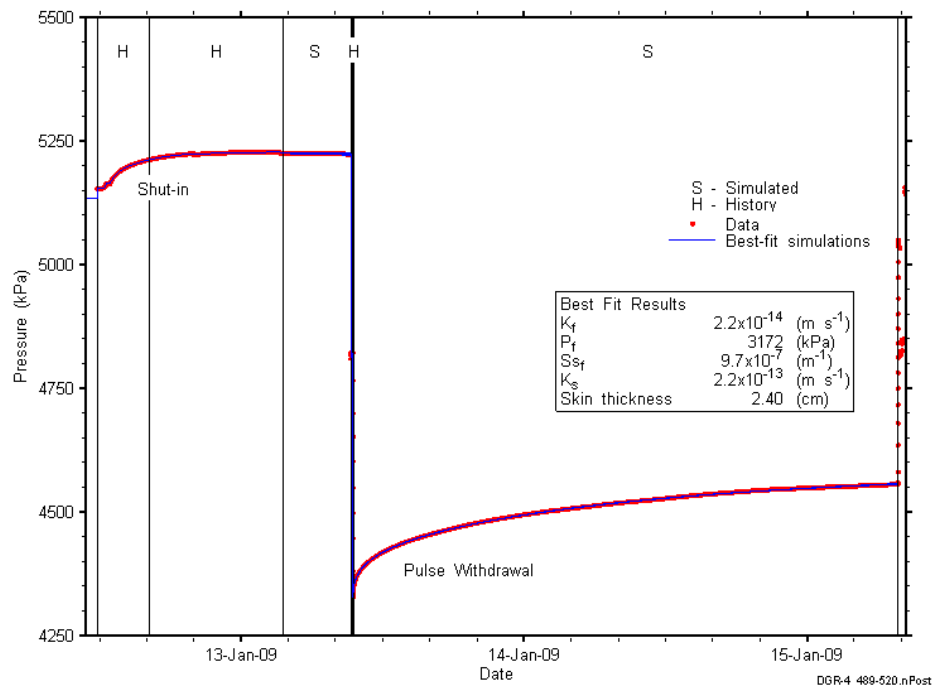


Figure D-159: Linear plot showing simulations of the DGR4_488.77-519.51 pressure response.

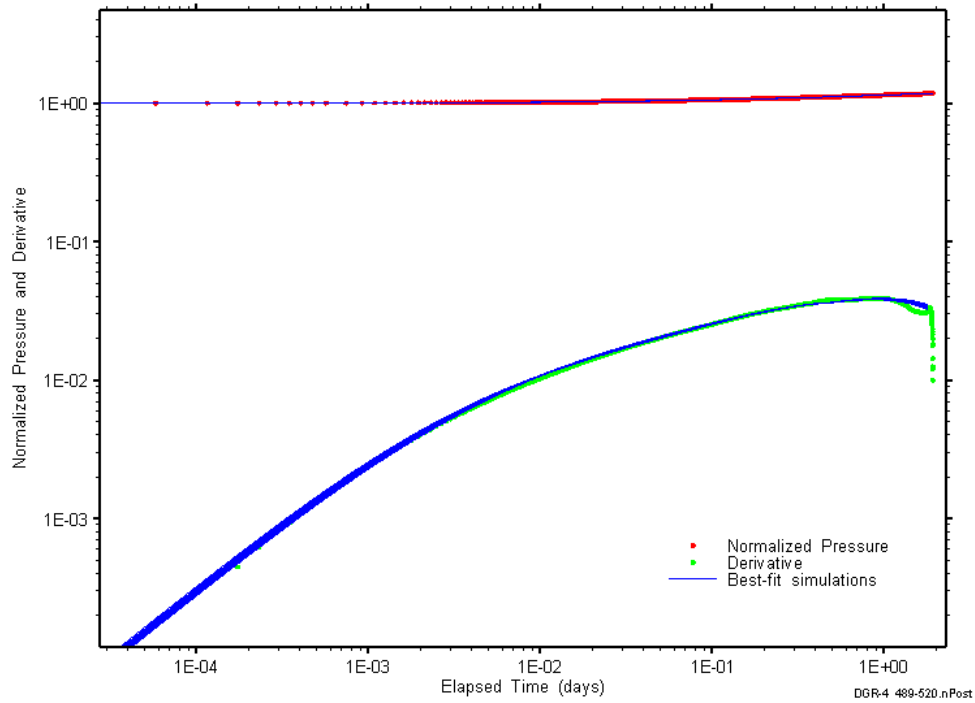


Figure D-160: Log-log plot showing simulations of the DGR4_488.77–519.51 pulse withdrawal Ramey B and derivative response.

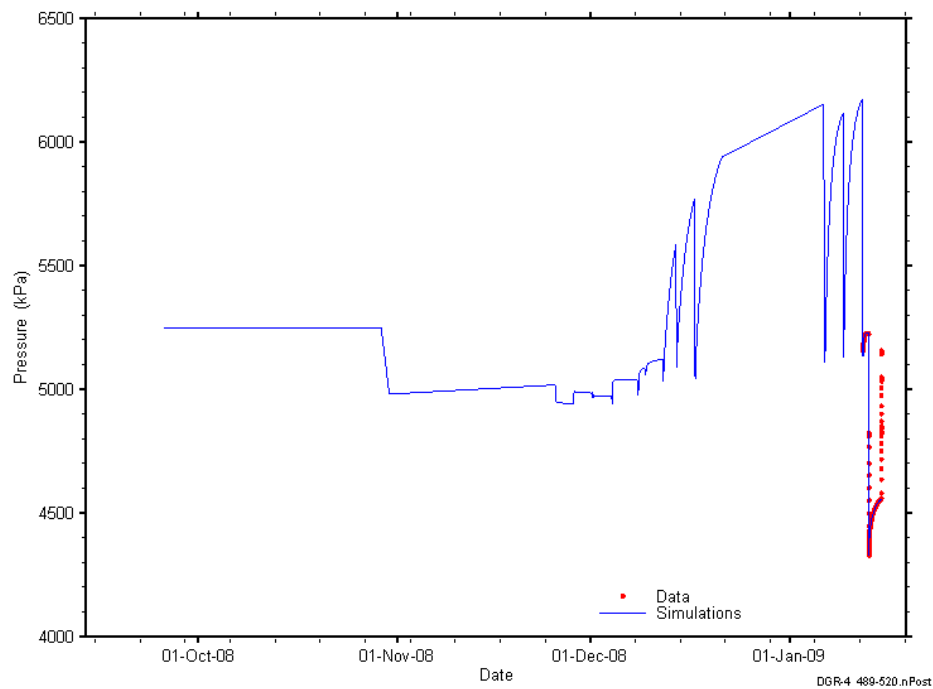


Figure D-161: Linear plot showing simulations of the DGR4_488.77–519.51 pressure response, including pre-test pressure history.

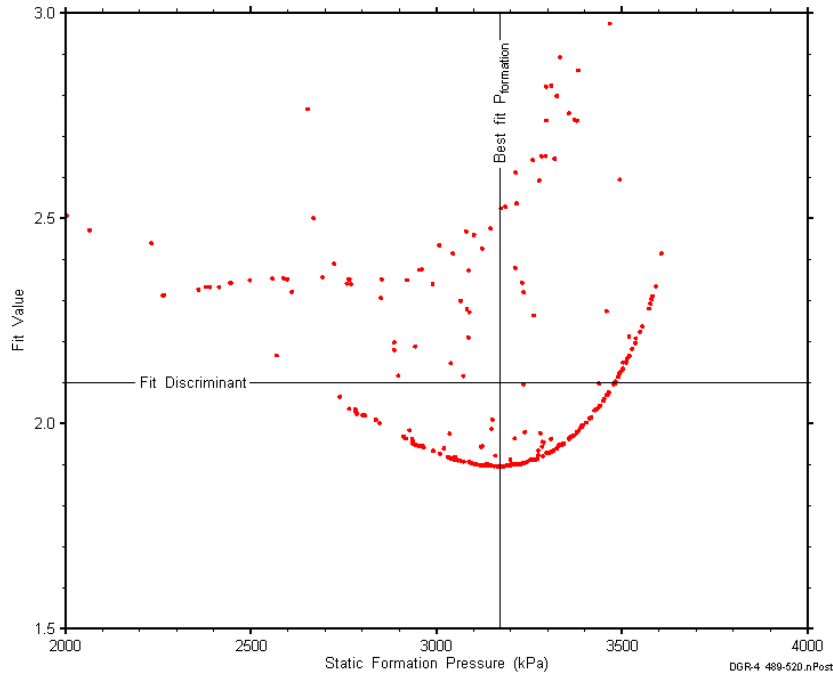


Figure D-162: XY-scatter plot showing the static formation pressure parameter space derived from DGR4_488.77-519.51 perturbation analysis along with the fit discriminant and best fit values.

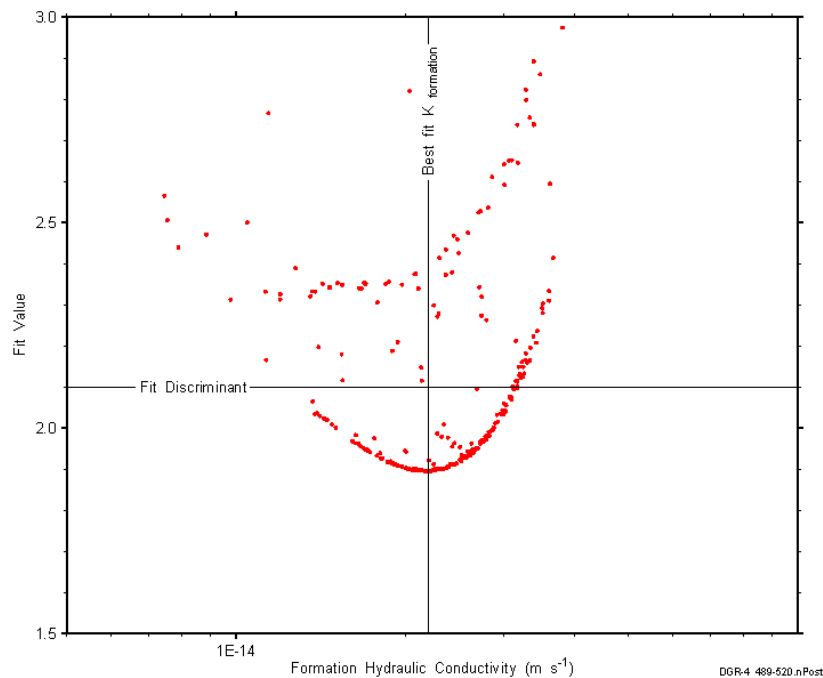


Figure D-163: XY-scatter plot showing the formation hydraulic conductivity parameter space derived from DGR4_488.77-519.51 perturbation analysis along with the fit discriminant and best fit values.

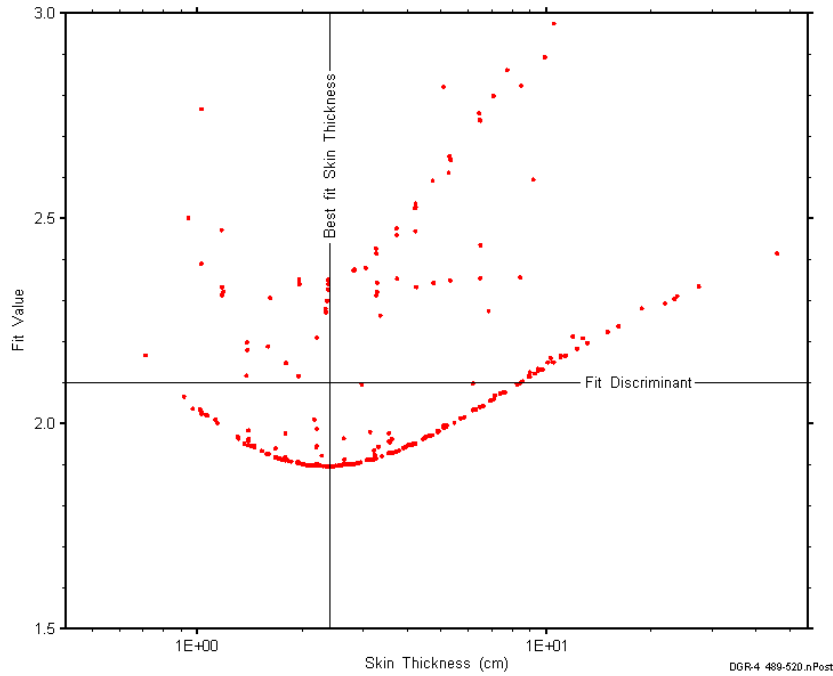


Figure D-164: XY-scatter plot showing the skin-thickness parameter space derived from DGR4_488.77-519.51 perturbation analysis along with the fit discriminant and best fit values.

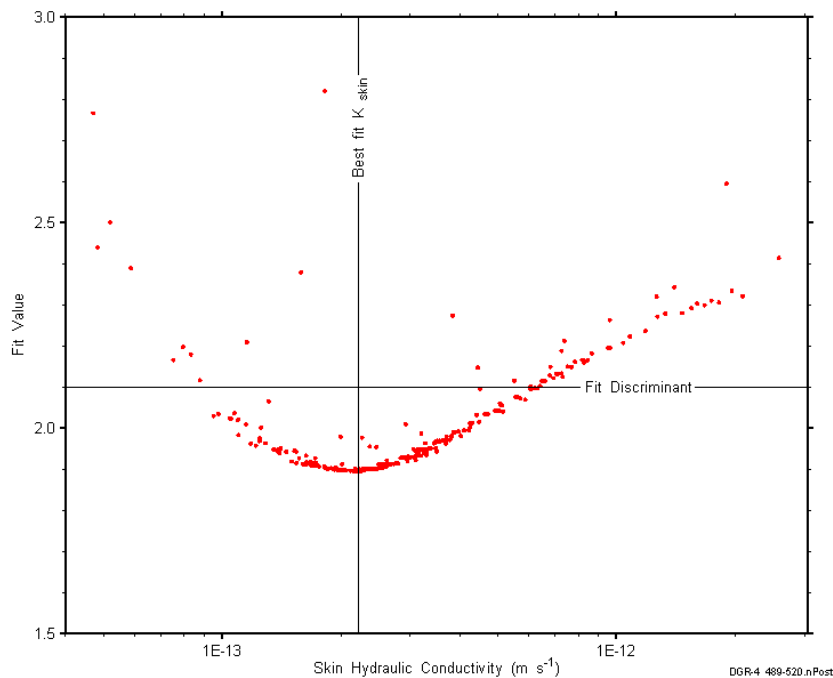


Figure D-165: XY-scatter plot showing the skin hydraulic conductivity parameter space derived from DGR4_488.77-519.51 perturbation analysis along with the fit discriminant and best fit values.

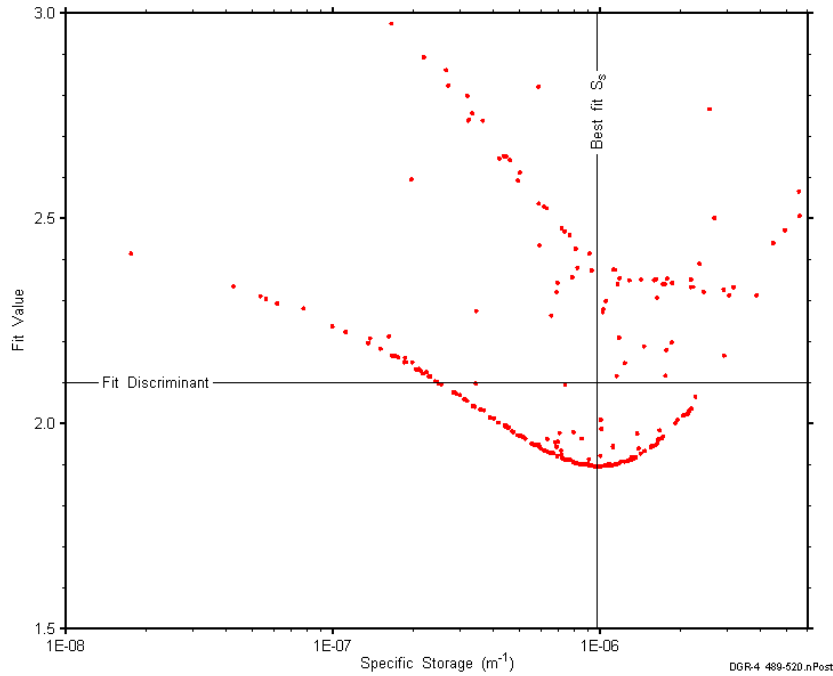


Figure D-166: XY-scatter plot showing the formation specific storage parameter space derived from DGR4_488.77-519.51 perturbation analysis along with the fit discriminant and best fit values.

D.14 519.10-549.84 Georgian Bay 1

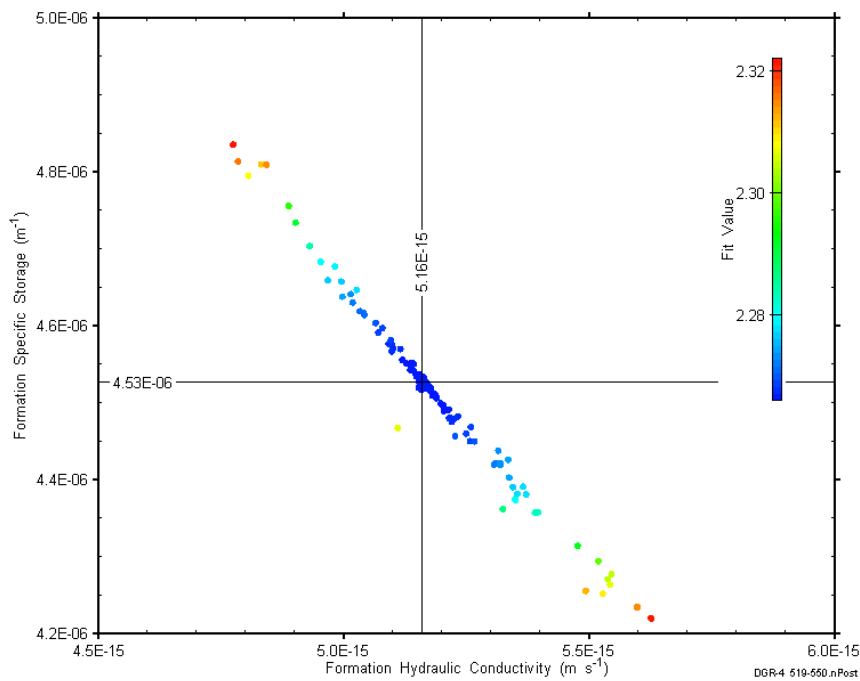


Figure D-167: XY-scatter plot showing estimates of formation hydraulic conductivity and formation specific storage derived from the DGR4_519.10-549.84 perturbation analysis.

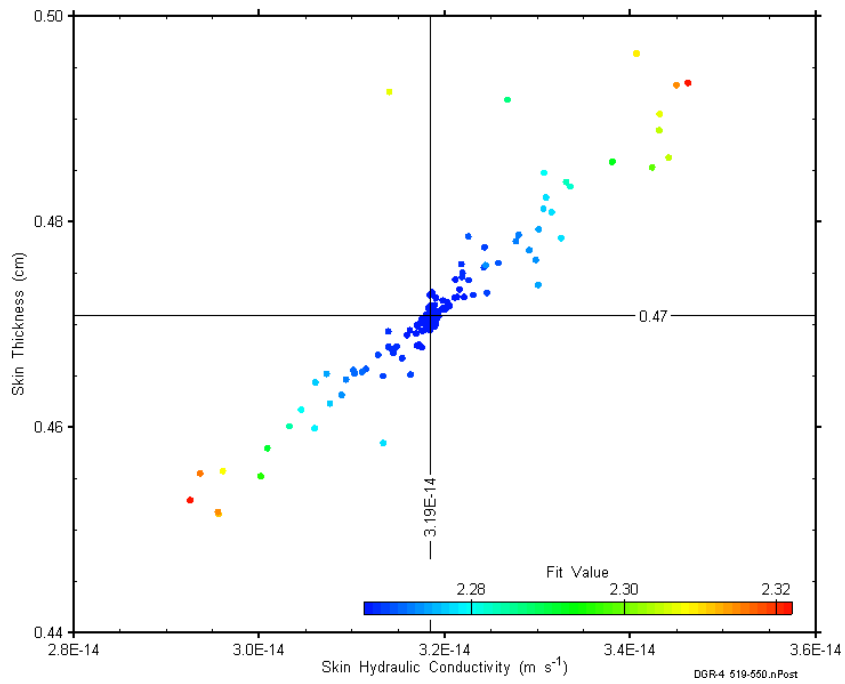


Figure D-168: XY-scatter plot showing estimates of skin hydraulic conductivity and skin thickness derived from the DGR4_519.10-549.84 perturbation analysis.

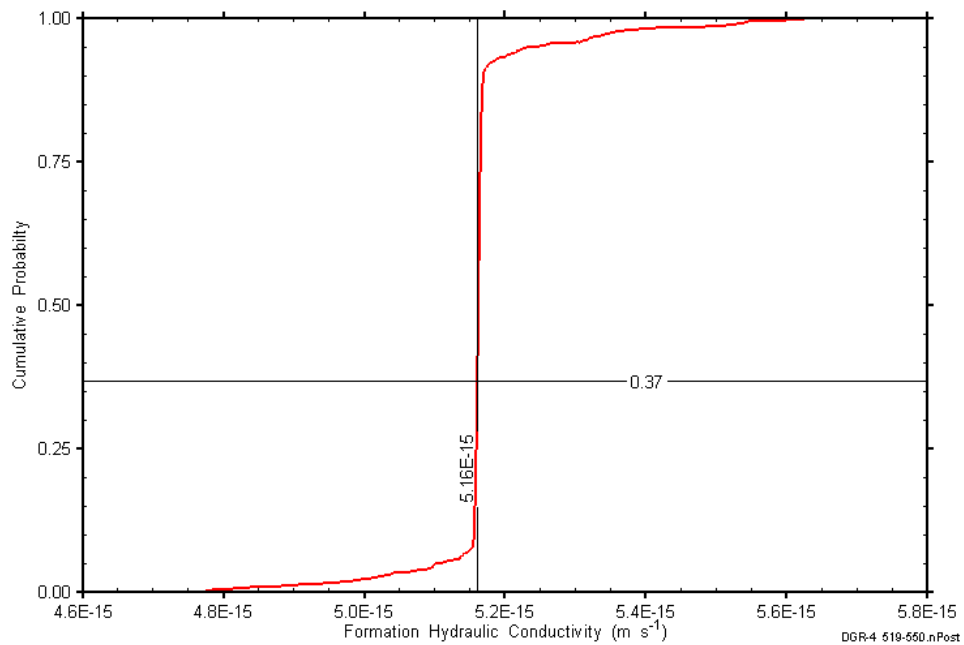


Figure D-169: DGR4_519.10-549.84 formation hydraulic conductivity cumulative distribution function.

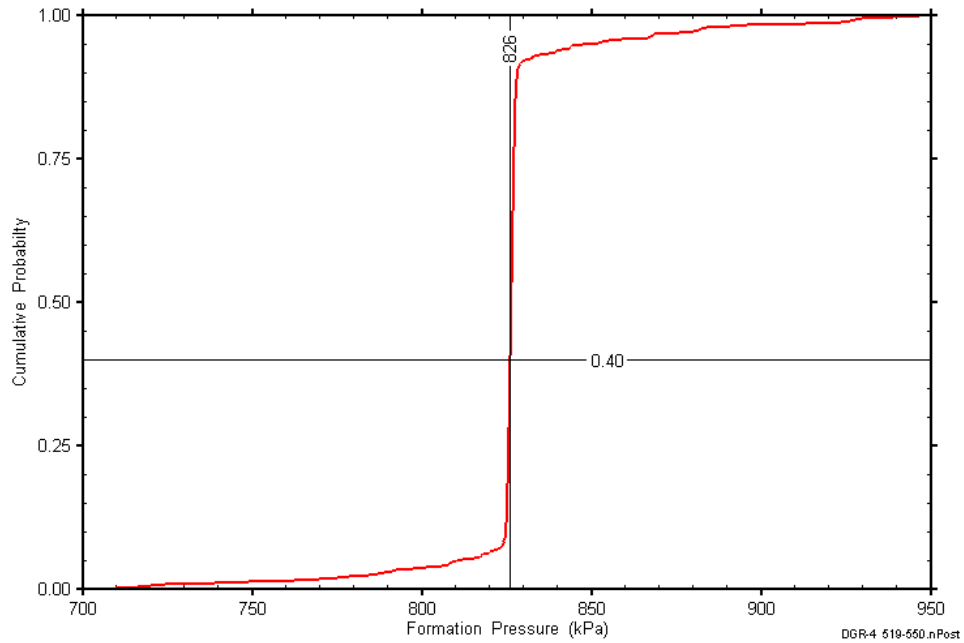


Figure D-170: DGR4_519.10-549.84 static formation pressure cumulative distribution function.

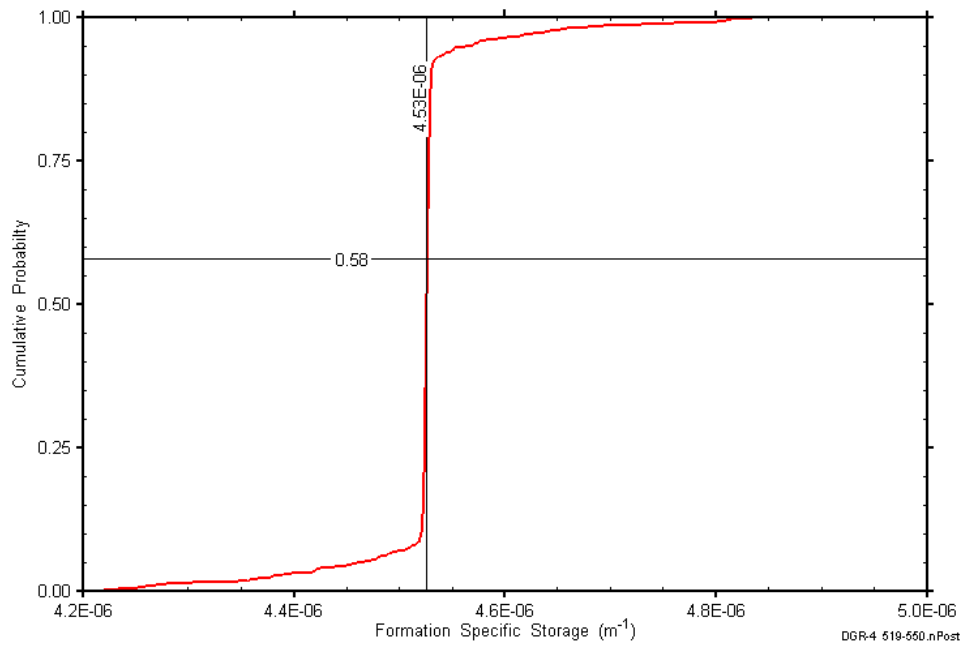


Figure D-171: DGR4_519.10-549.84 formation specific storage cumulative distribution function.

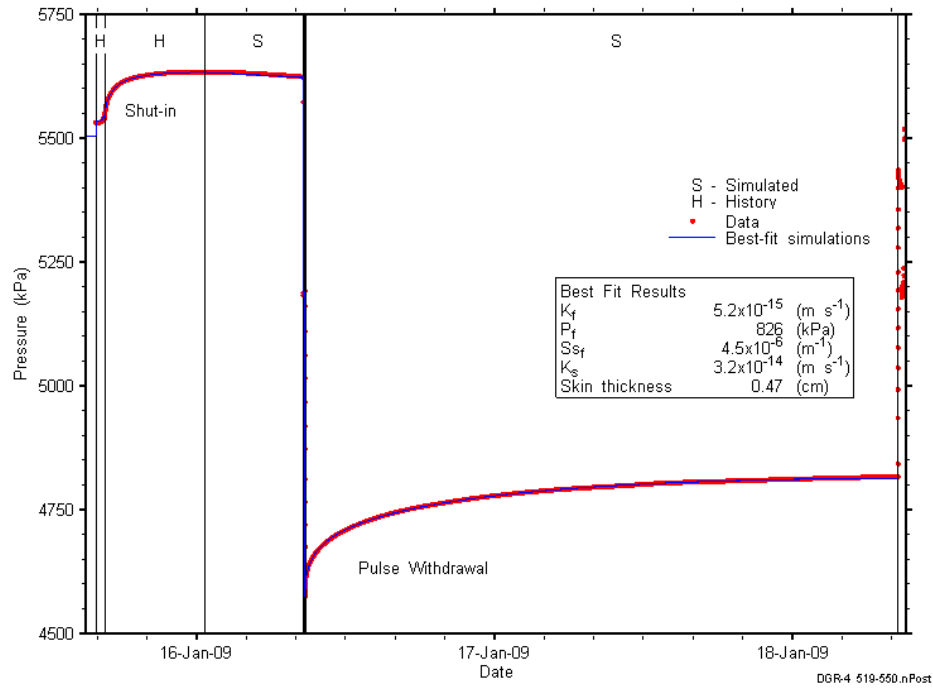


Figure D-172: Linear plot showing simulations of the DGR4_519.10-549.84 pressure response.

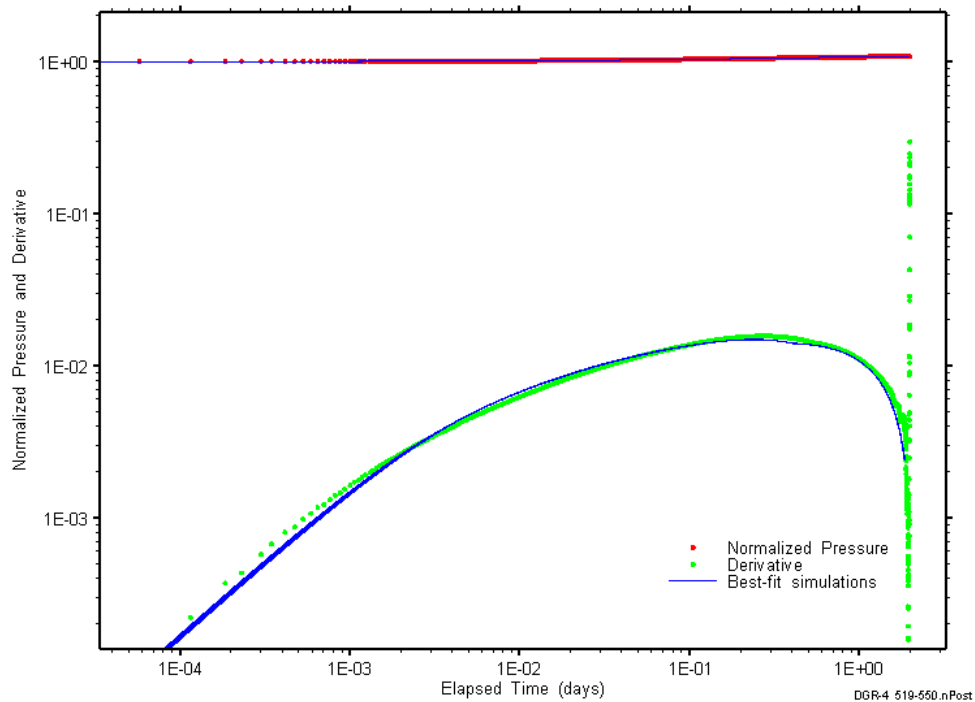


Figure D-173: Log-log plot showing simulations of the DGR4_519.10-549.84 pulse withdrawal Ramey B and derivative response.

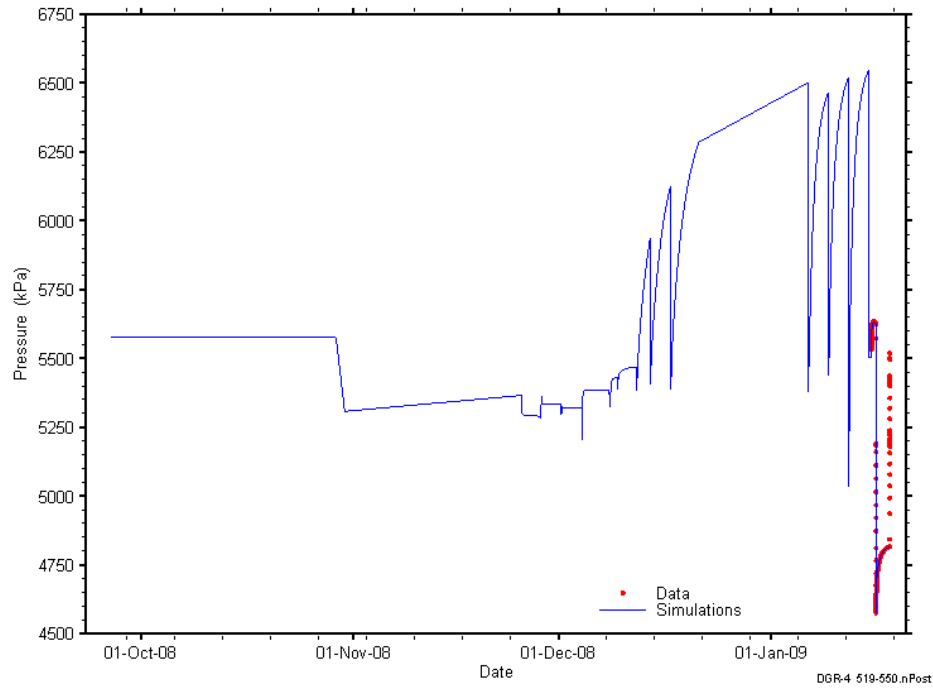


Figure D-174: Linear plot showing simulations of the DGR4_519.10-549.84 pressure response, including pre-test pressure history.

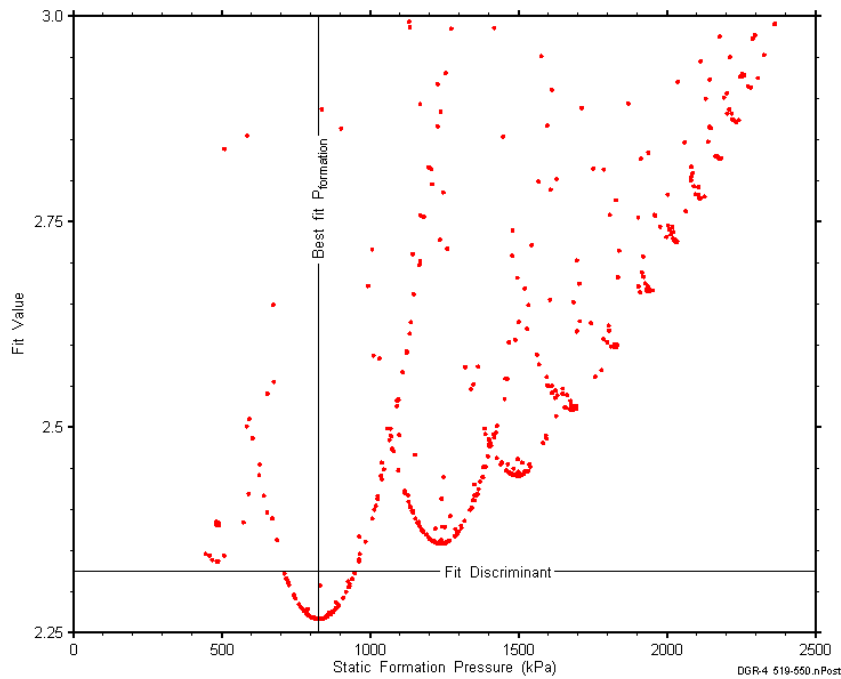


Figure D-175: XY-scatter plot showing the static formation pressure parameter space derived from DGR4_519.10-549.84 perturbation analysis along with the fit discriminant and best fit values.

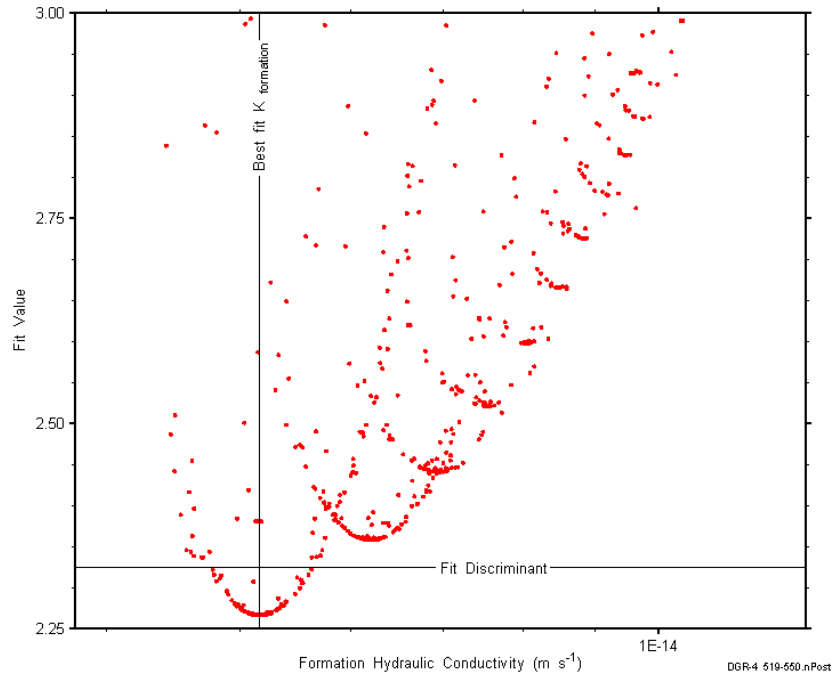


Figure D-176: XY-scatter plot showing the formation hydraulic conductivity parameter space derived from DGR4_519.10-549.84 perturbation analysis along with the fit discriminant and best fit values.

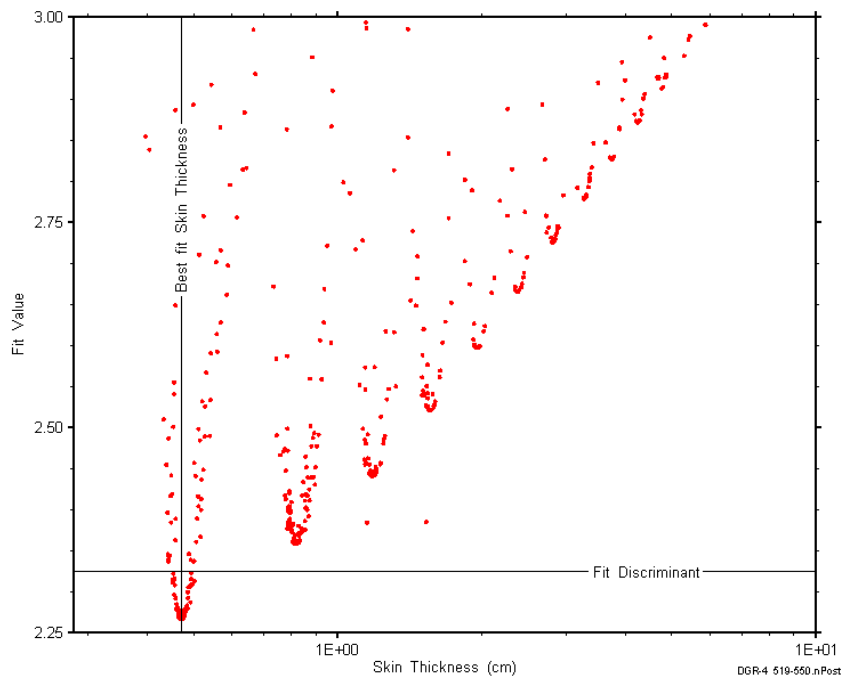


Figure D-177: XY-scatter plot showing the skin-thickness parameter space derived from DGR4_519.10-549.84 perturbation analysis along with the fit discriminant and best fit values.

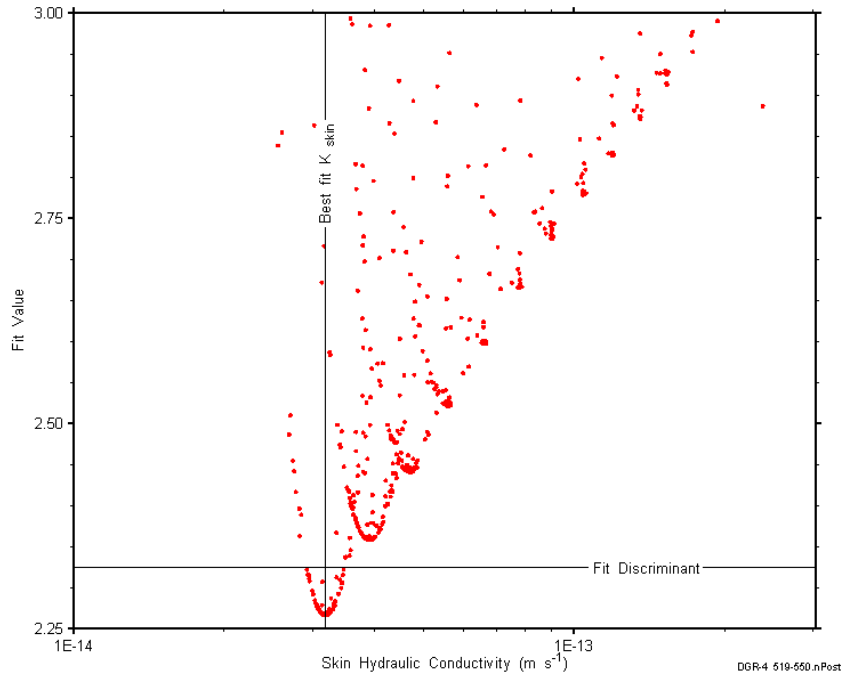


Figure D-178: XY-scatter plot showing the skin hydraulic conductivity parameter space derived from DGR4_519.10-549.84 perturbation analysis along with the fit discriminant and best fit values.

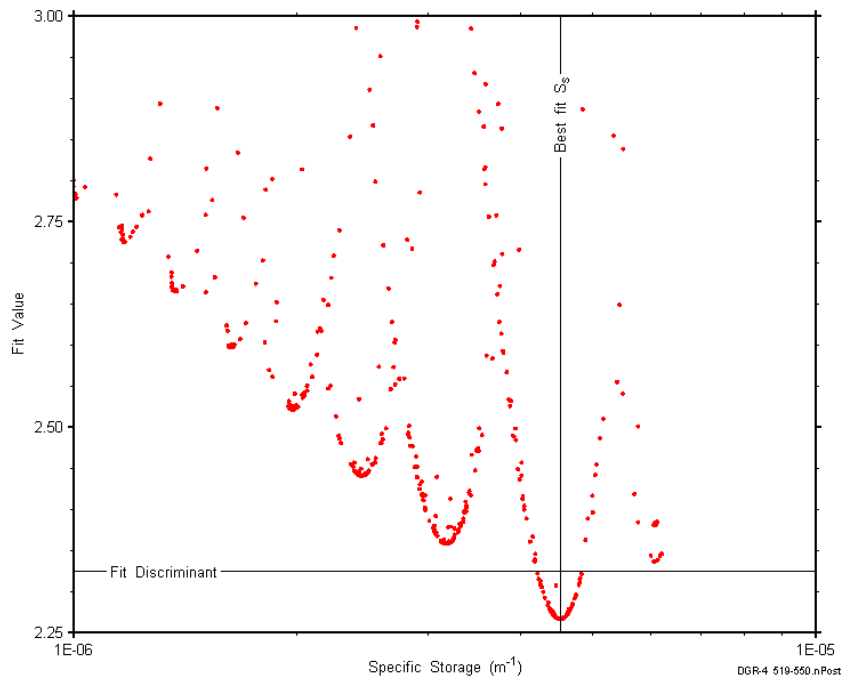


Figure D-179: XY-scatter plot showing the formation specific storage parameter space derived from DGR4_519.10-549.84 perturbation analysis along with the fit discriminant and best fit values.

D.15 548.28-579.02 Georgian Bay 2 (a & b)

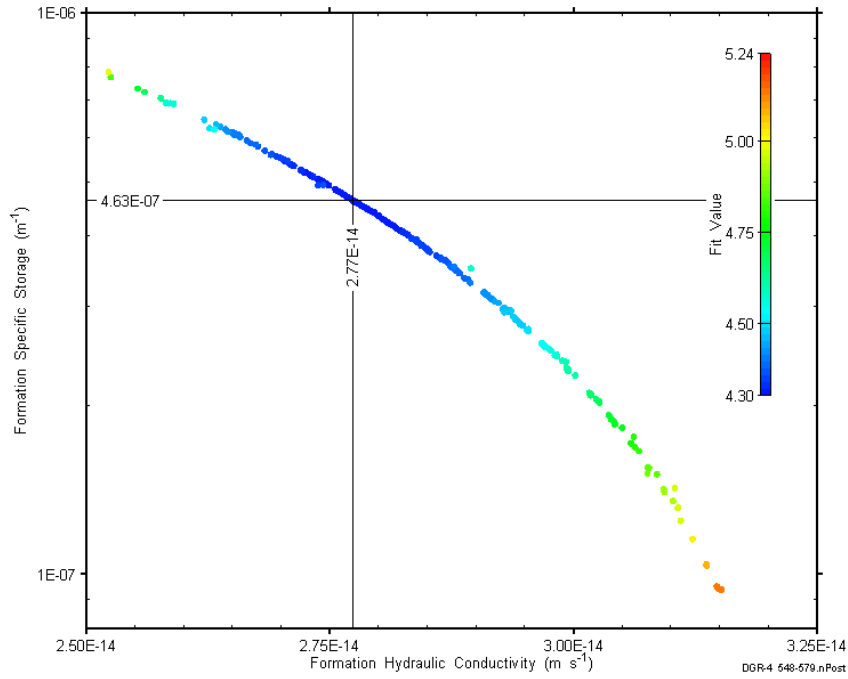


Figure D-180: XY-scatter plot showing estimates of formation hydraulic conductivity and formation specific storage derived from the DGR4_548.28-579.02 (a) perturbation analysis.

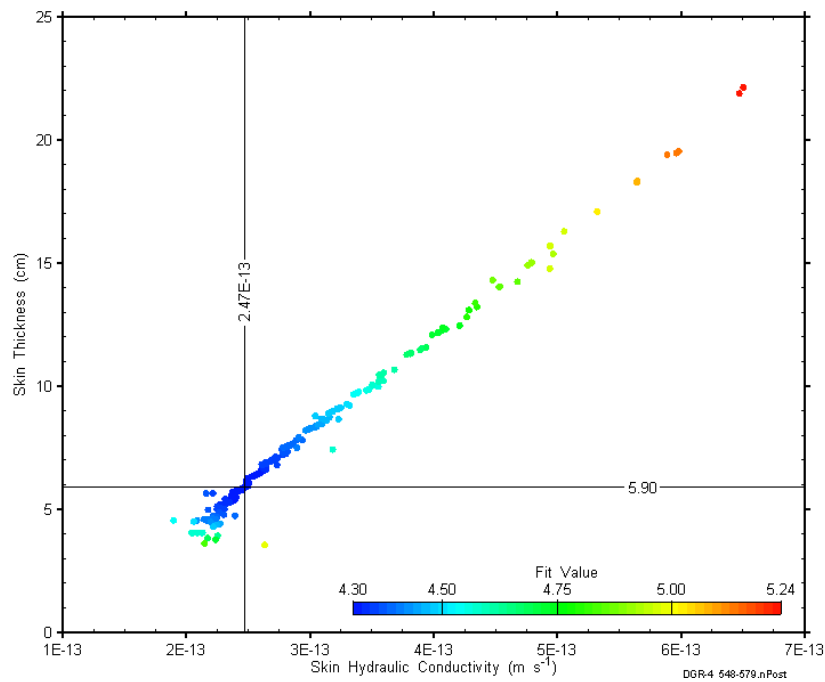


Figure D-181: XY-scatter plot showing estimates of skin hydraulic conductivity and skin thickness derived from the DGR4_548.28-579.02 (a) perturbation analysis.

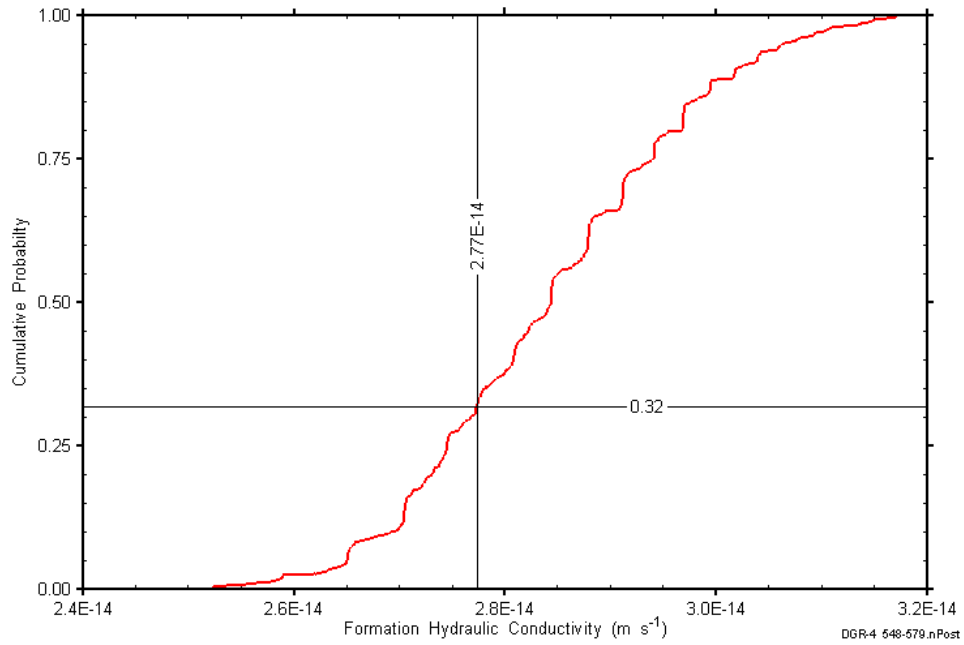


Figure D-182: DGR4_548.28-579.02 (a) formation hydraulic conductivity cumulative distribution function.

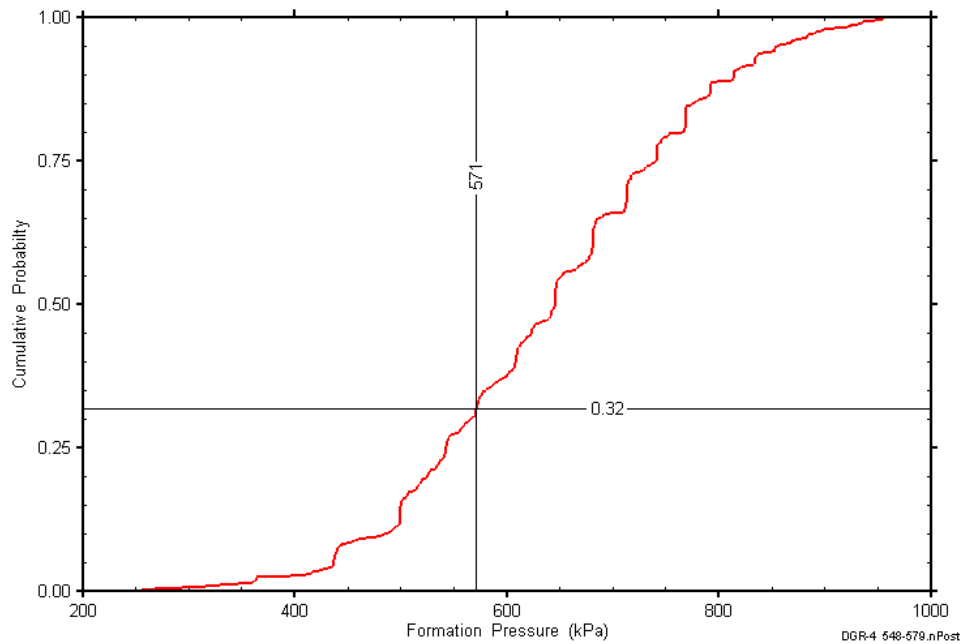


Figure D-183: DGR4_548.28-549.02 (a) static formation pressure cumulative distribution function.

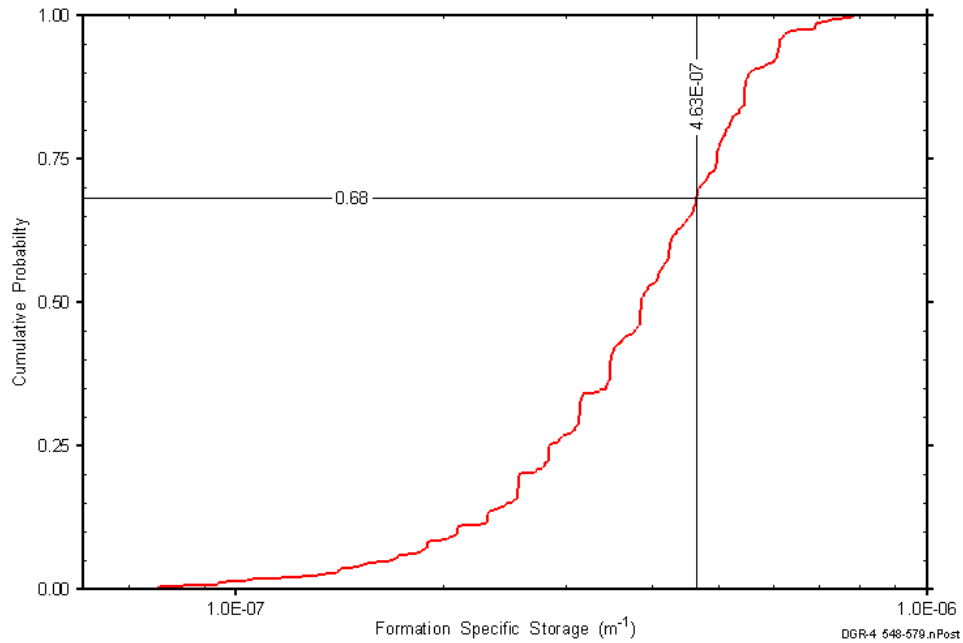


Figure D-184: DGR4_548.28-579.02 (a) formation specific storage cumulative distribution function.

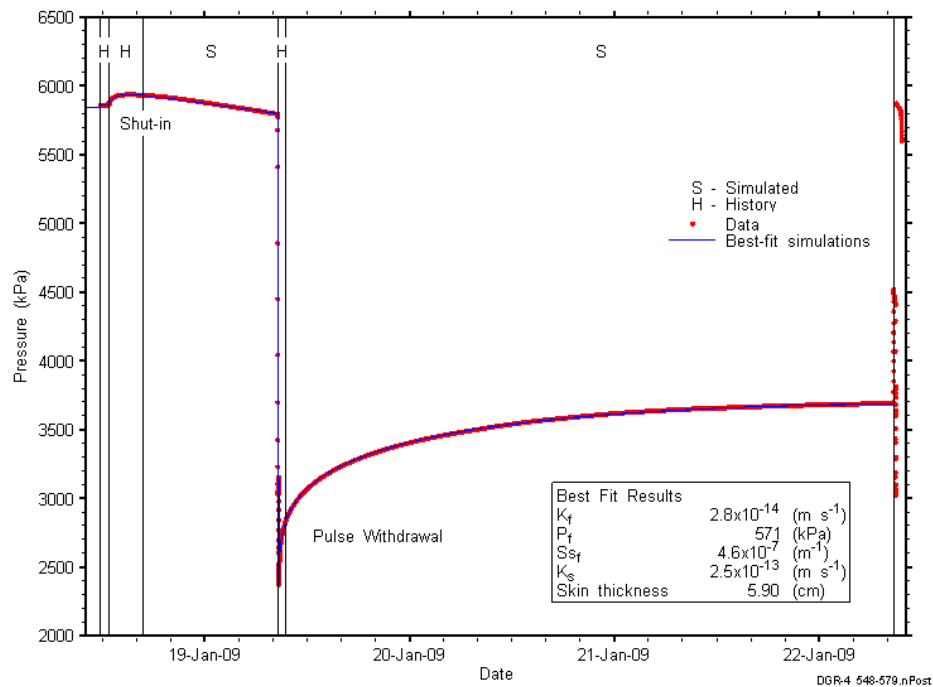


Figure D-185: Linear plot showing simulations of the DGR4_548.28-579.02 (a) pressure response.

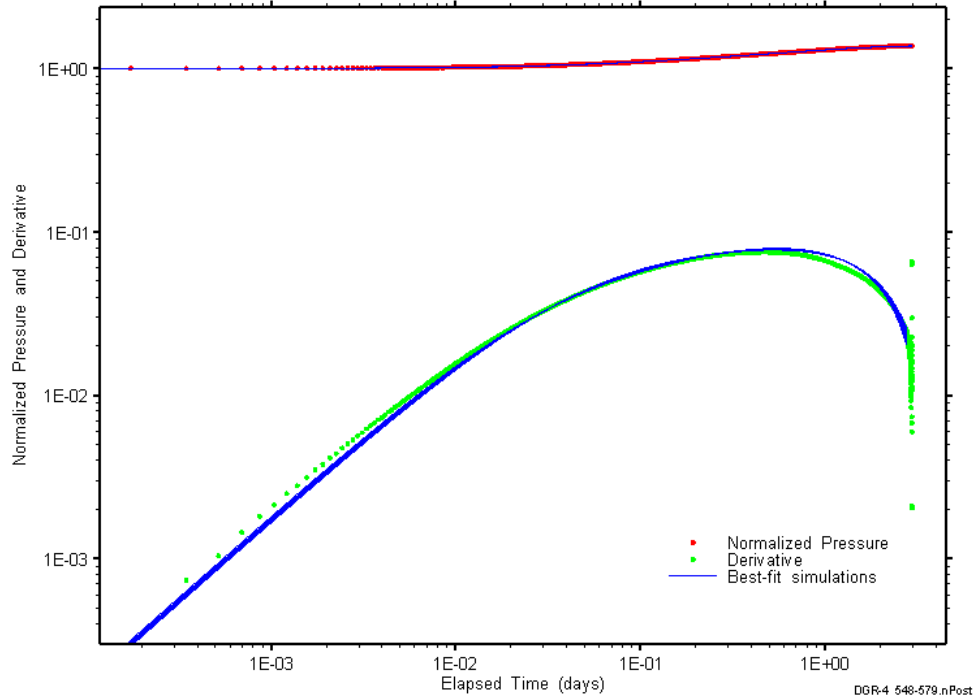


Figure D-186: Log-log plot showing simulations of the DGR4_548.28–579.02 (a) pulse withdrawal Ramey B and derivative response.

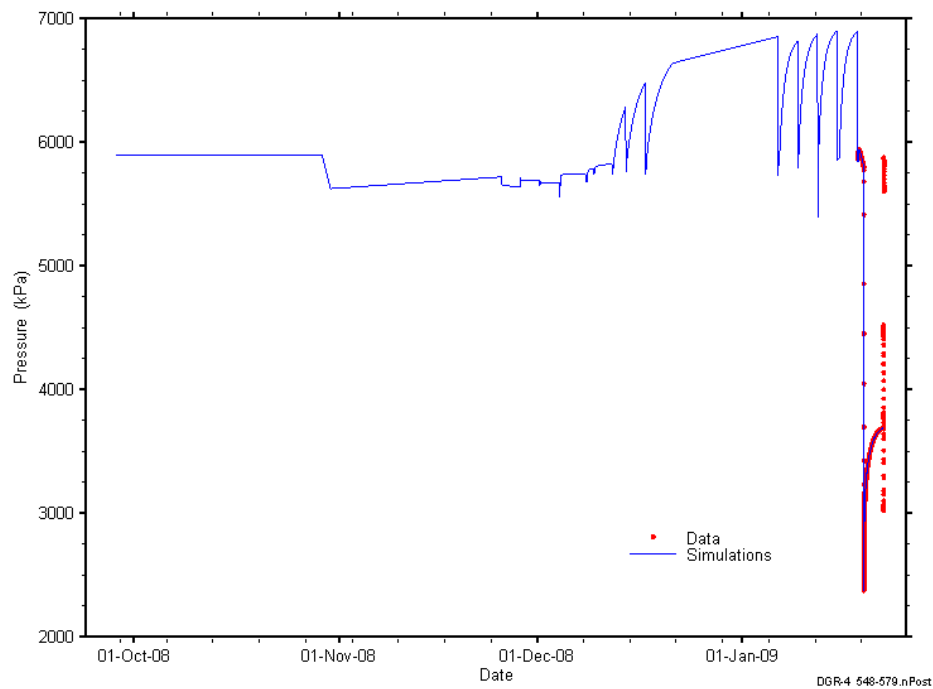


Figure D-187: Linear plot showing simulations of the DGR4_548.28-579.02 (a) pressure response, including pre-test pressure history.

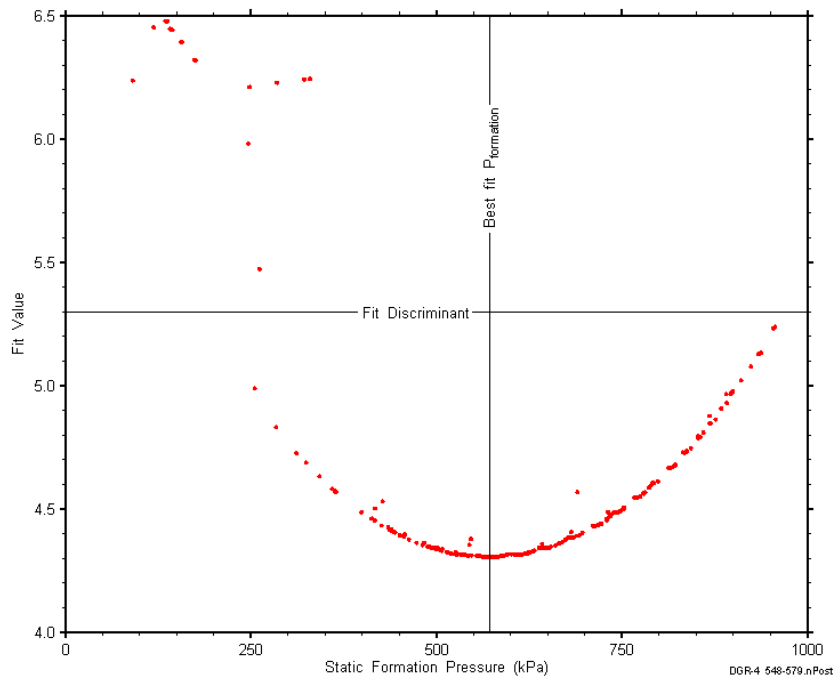


Figure D-188: XY-scatter plot showing the static formation pressure parameter space derived from DGR4_548.28-579.02 (a) perturbation analysis along with the fit discriminant and best fit values.

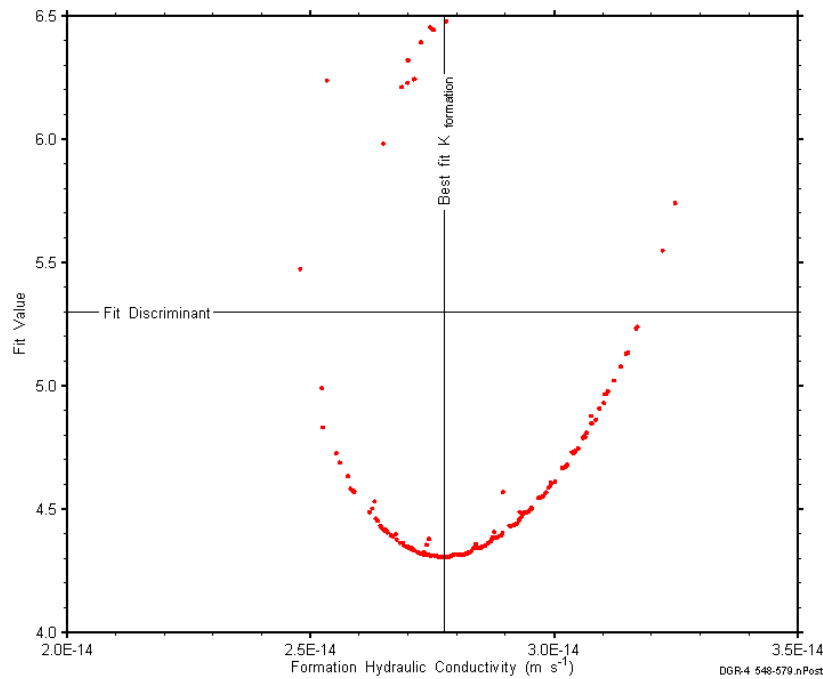


Figure D-189: XY-scatter plot showing the formation hydraulic conductivity parameter space derived from DGR4_548.28-579.02 (a) perturbation analysis along with the fit discriminant and best fit values.

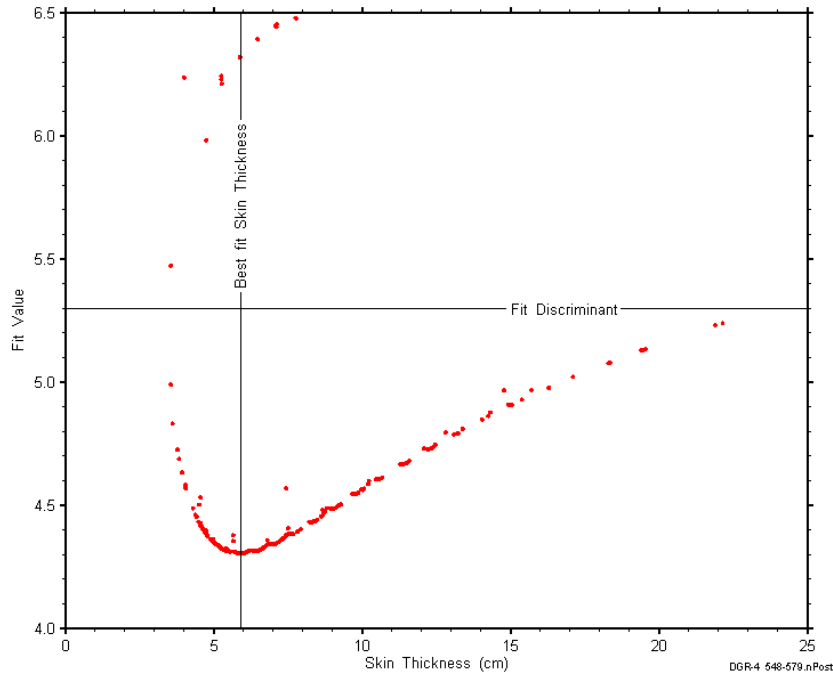


Figure D-190: XY-scatter plot showing the skin-thickness parameter space derived from DGR4_548.28-579.02 (a) perturbation analysis along with the fit discriminant and best fit values.

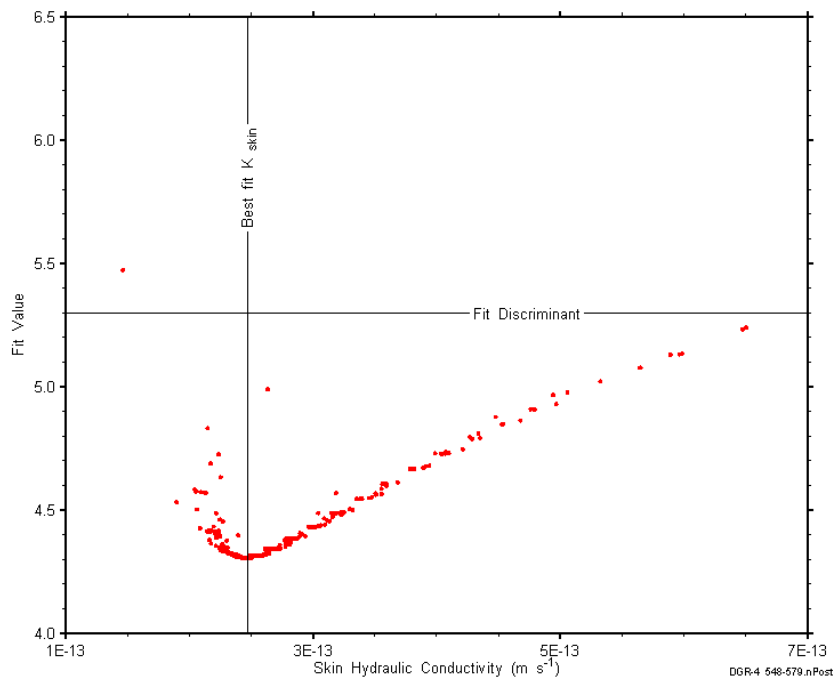


Figure D-191: XY-scatter plot showing the skin hydraulic conductivity parameter space derived from DGR4_548.28-579.02 (a) perturbation analysis along with the fit discriminant and best fit values.

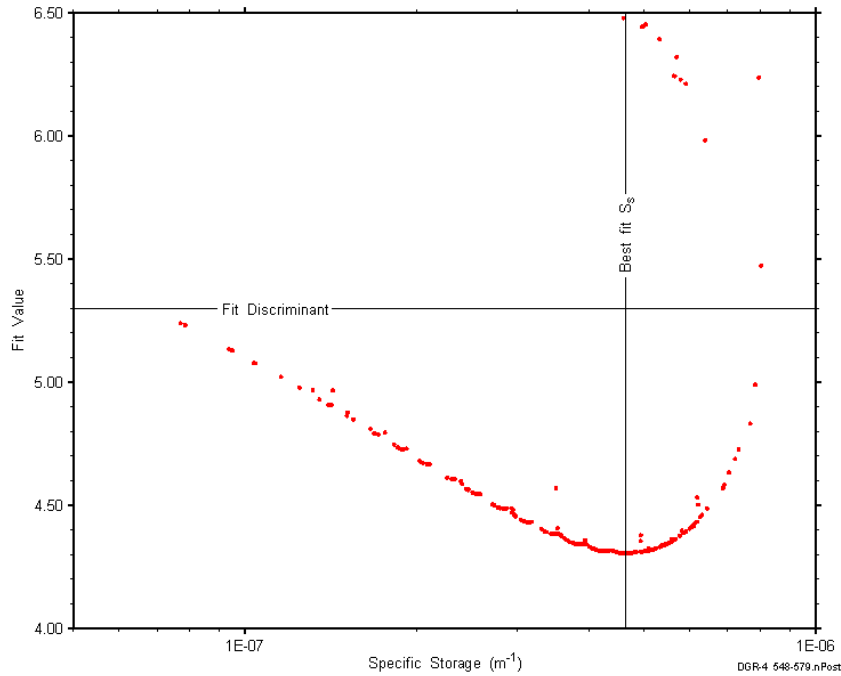


Figure D-192: XY-scatter plot showing the formation specific storage parameter space derived from DGR4_548.28-579.02 (a) perturbation analysis along with the fit discriminant and best fit values.

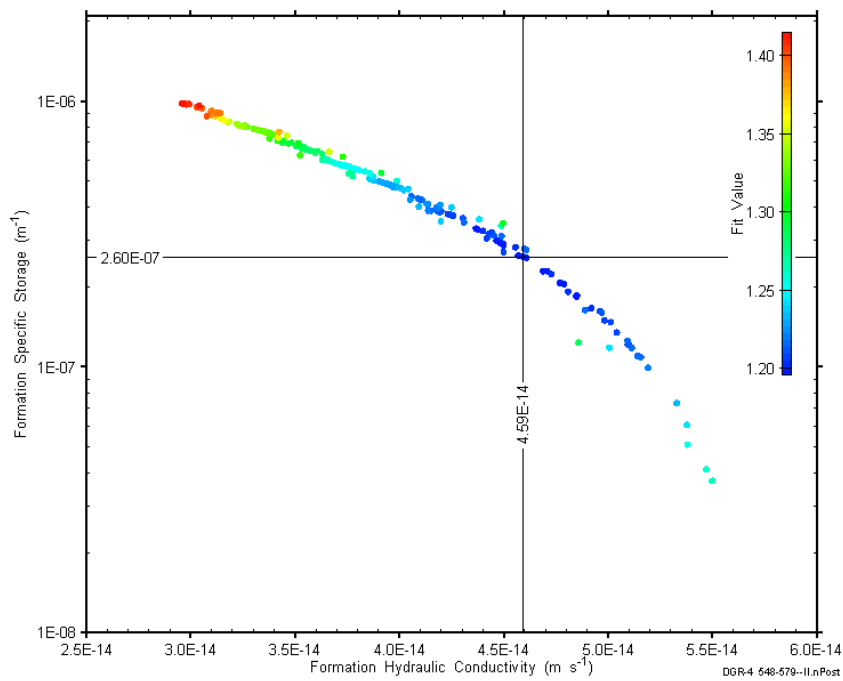


Figure D-193: XY-scatter plot showing estimates of formation hydraulic conductivity and formation specific storage derived from the DGR4_548.28-579.02 (b) perturbation analysis.

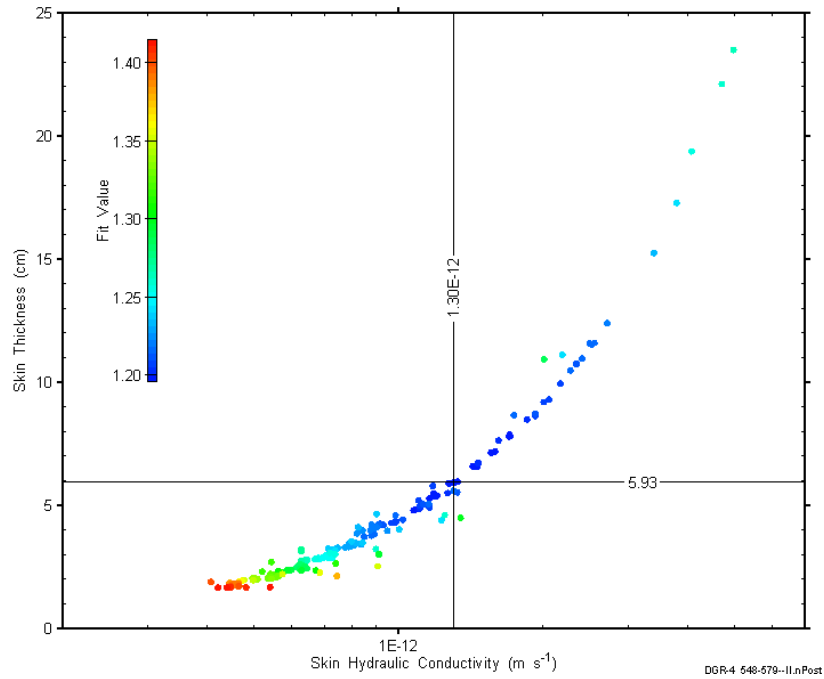


Figure D-194: XY-scatter plot showing estimates of skin hydraulic conductivity and skin thickness derived from the DGR4_548.28-579.02 (b) perturbation analysis.

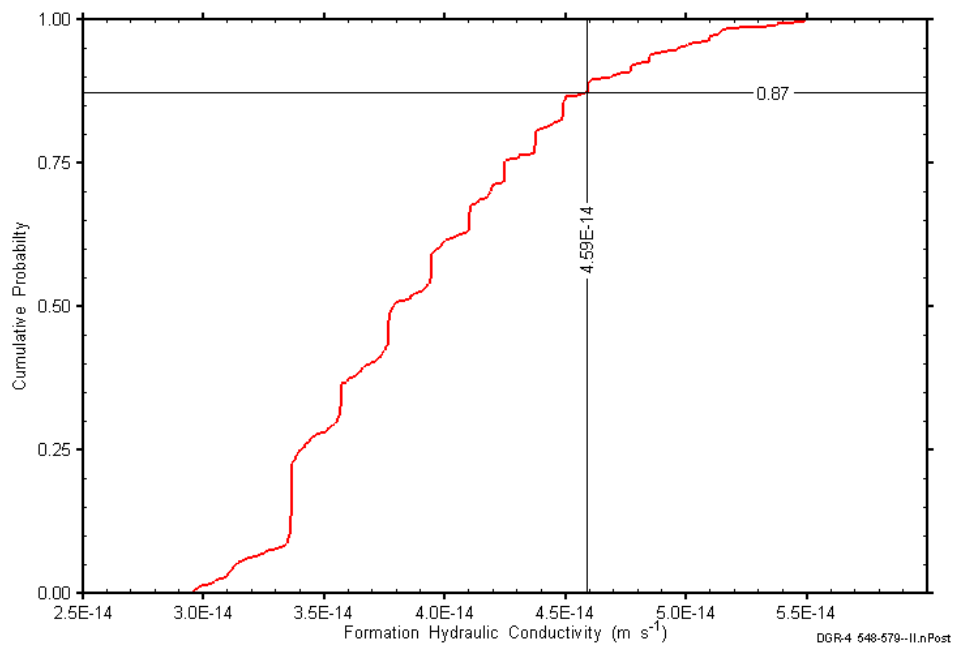


Figure D-195: DGR4_548.28-579.02 (b) formation hydraulic conductivity cumulative distribution function.

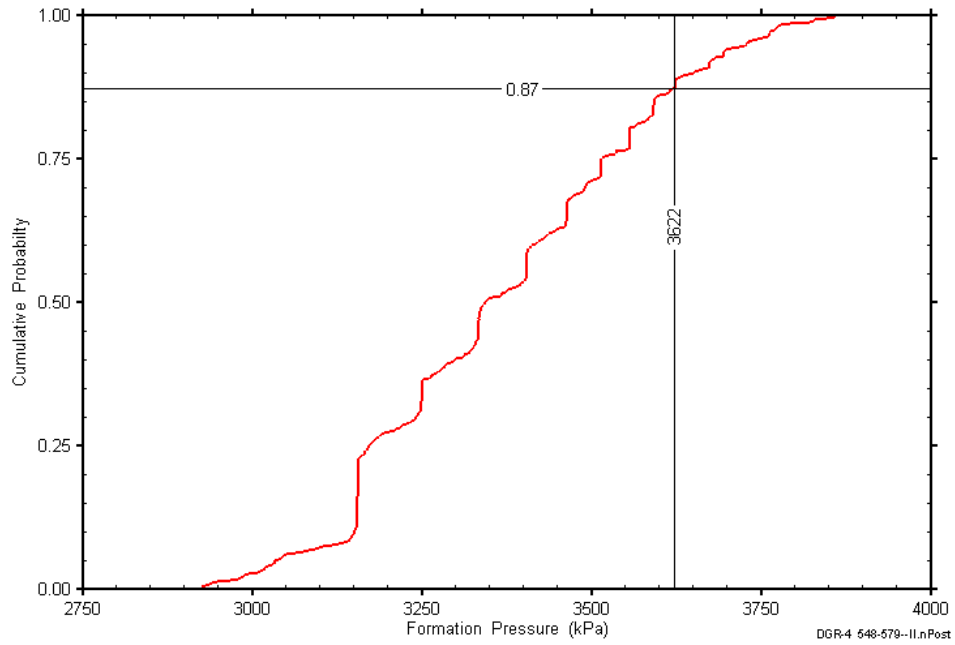


Figure D-196: DGR4_548.28-549.02 (b) static formation pressure cumulative distribution function.

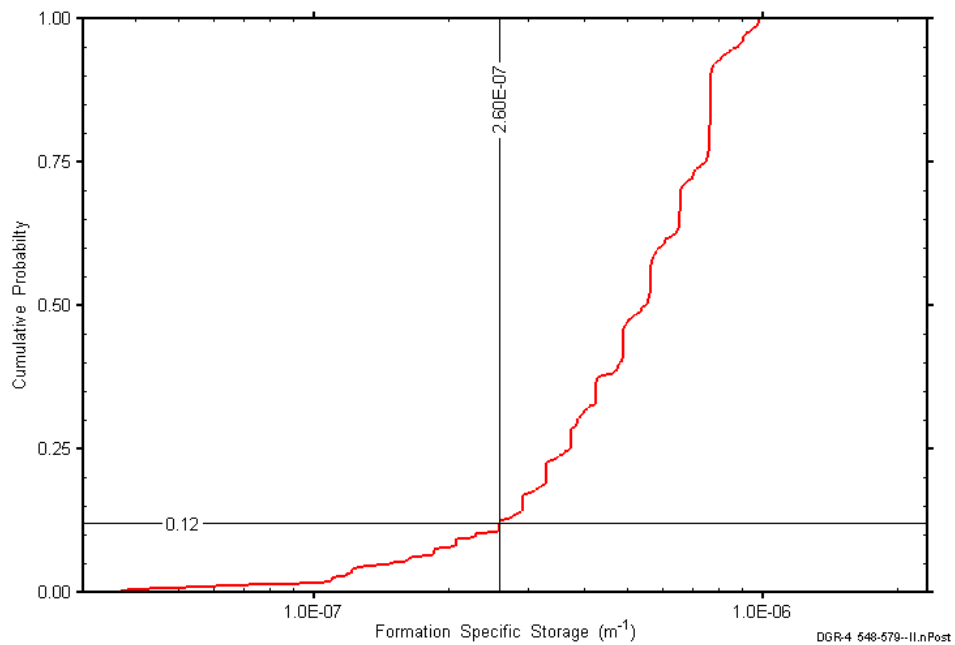


Figure D-197: DGR4_548.28-579.02 (b) formation specific storage cumulative distribution function.

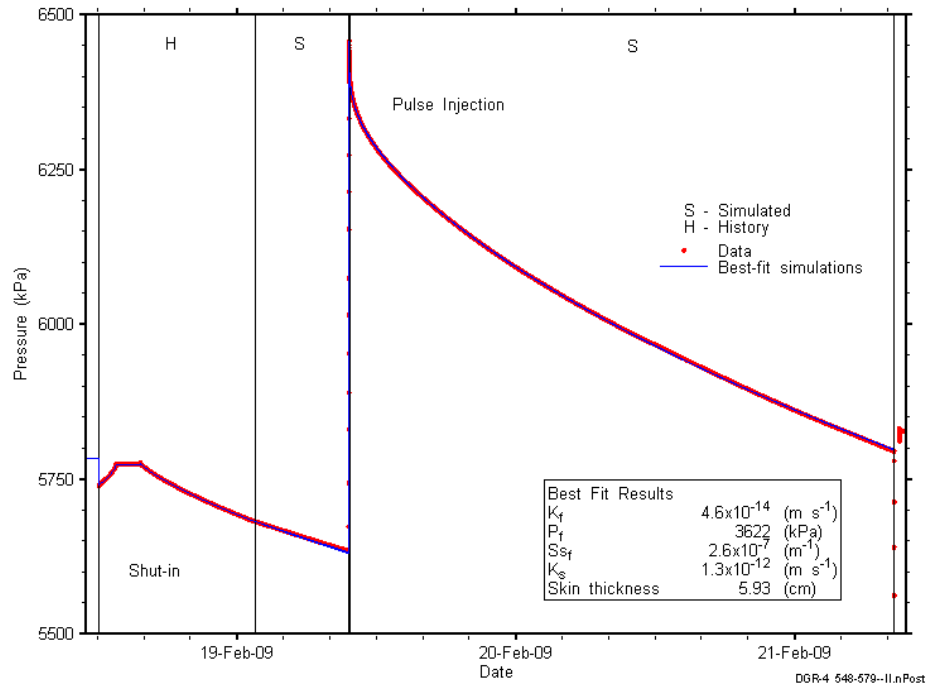


Figure D-198: Linear plot showing simulations of the DGR4_548.28-579.02 (b) pressure response.

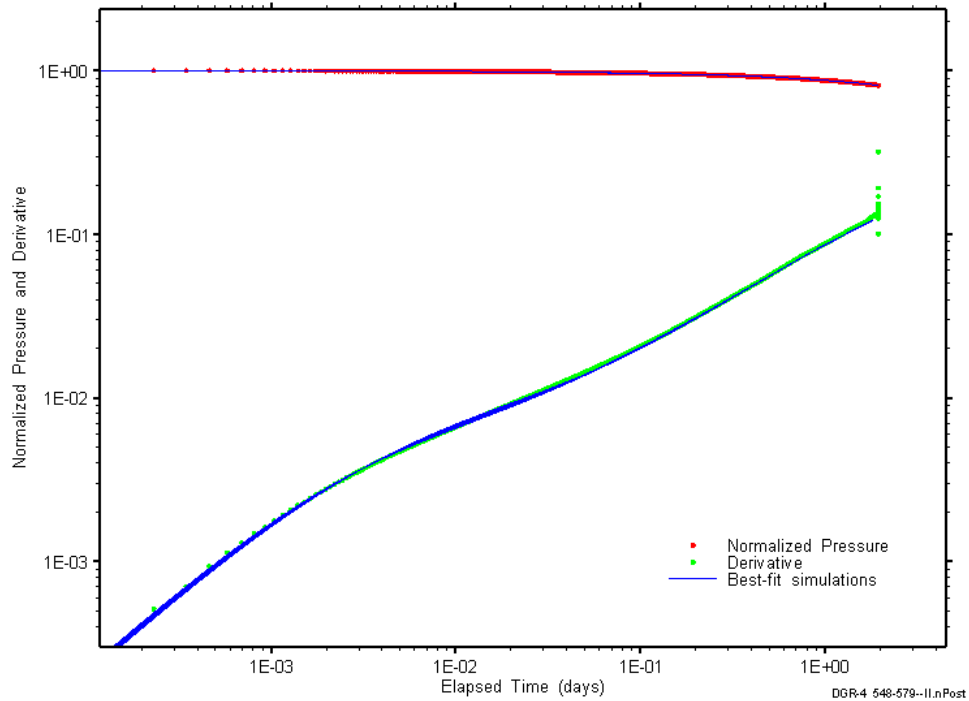


Figure D-199: Log-log plot showing simulations of the DGR4_548.28-579.02 (b) pulse withdrawal Ramey B and derivative response.

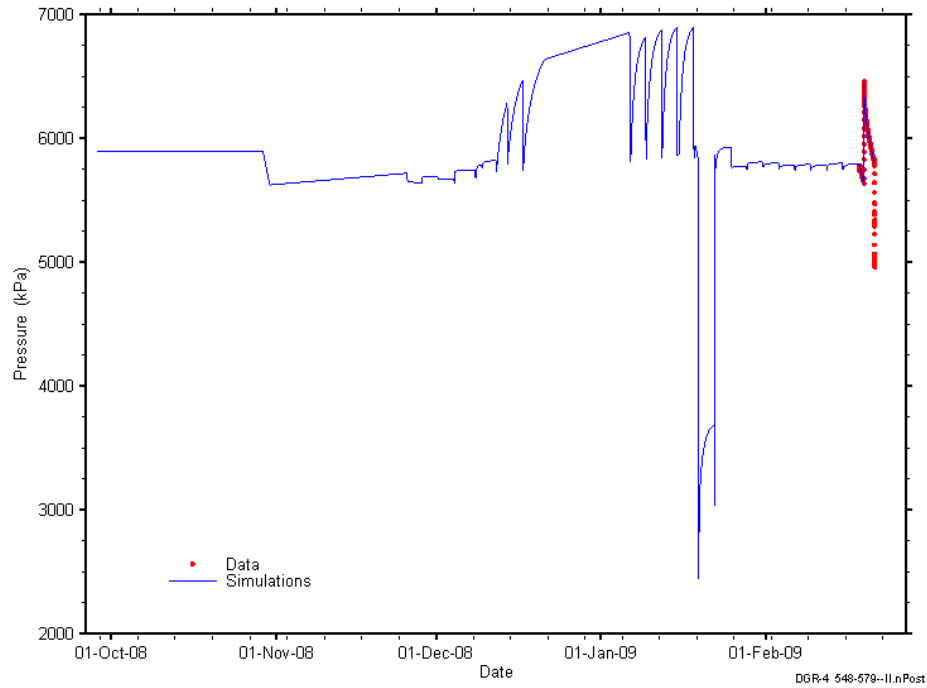


Figure D-200: Linear plot showing simulations of the DGR4_548.28-579.02 (b) pressure response, including pre-test pressure history.

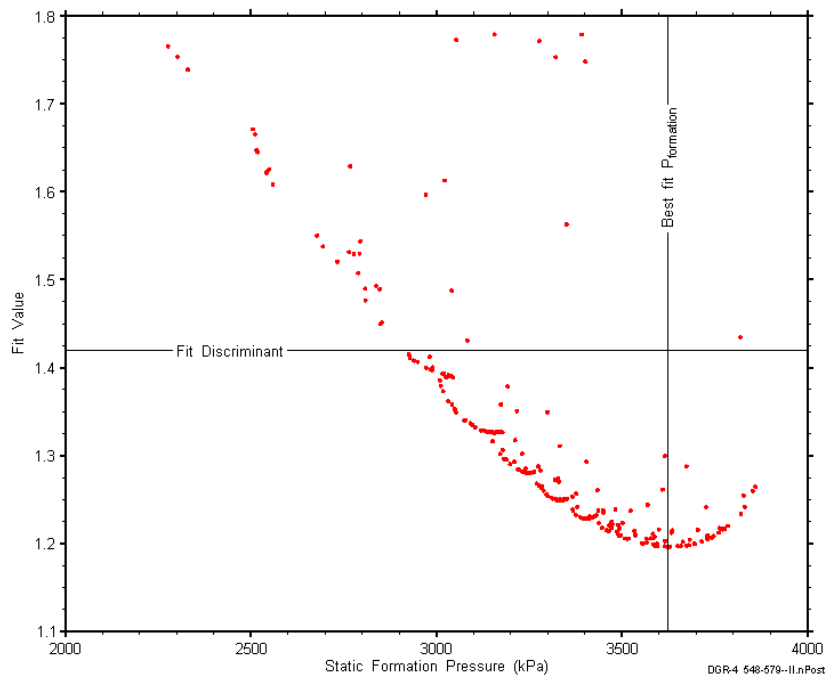


Figure D-201: XY-scatter plot showing the static formation pressure parameter space derived from DGR4_548.28-579.02 (b) perturbation analysis along with the fit discriminant and best fit values.

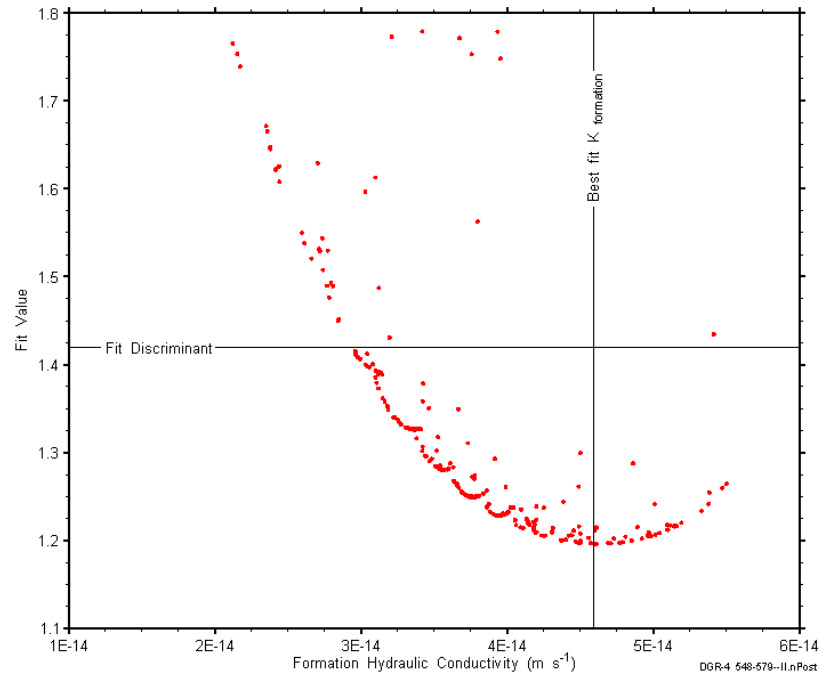


Figure D-202: XY-scatter plot showing the formation hydraulic conductivity parameter space derived from DGR4_548.28-579.02 (b) perturbation analysis along with the fit discriminant and best fit values.

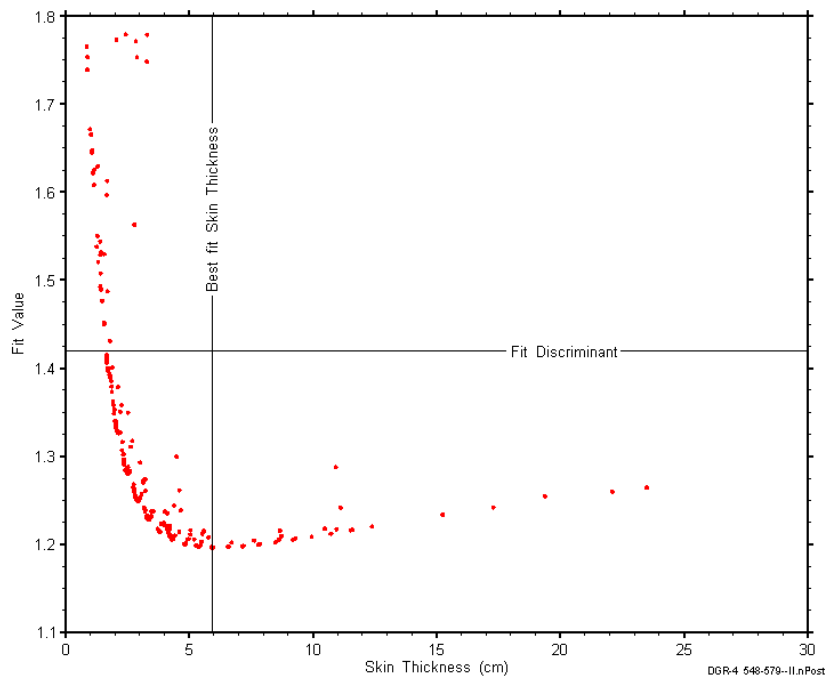


Figure D-203: XY-scatter plot showing the skin-thickness parameter space derived from DGR4_548.28-579.02 (b) perturbation analysis along with the fit discriminant and best fit values.

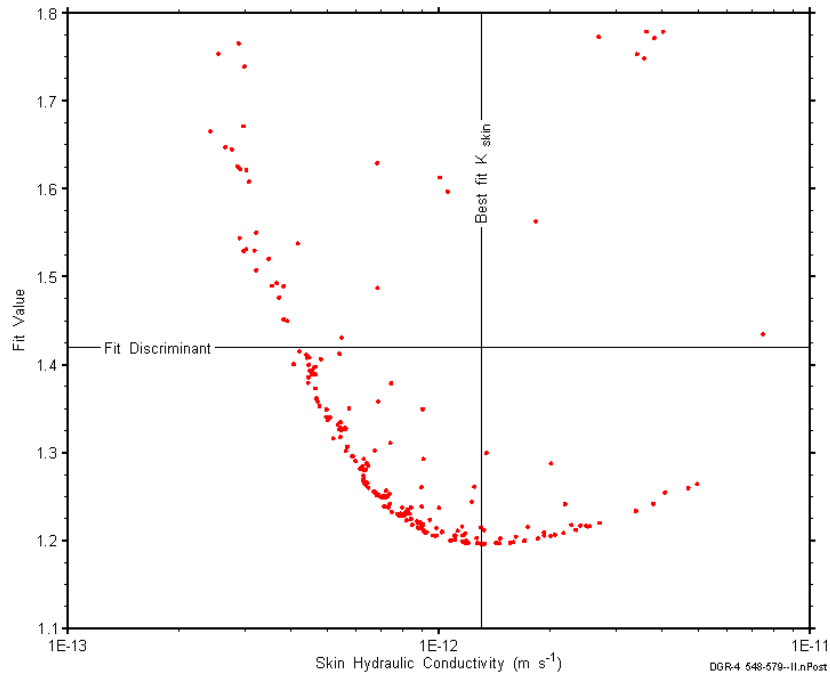


Figure D-204: XY-scatter plot showing the skin hydraulic conductivity parameter space derived from DGR4_548.28-579.02 (b) perturbation analysis along with the fit discriminant and best fit values.

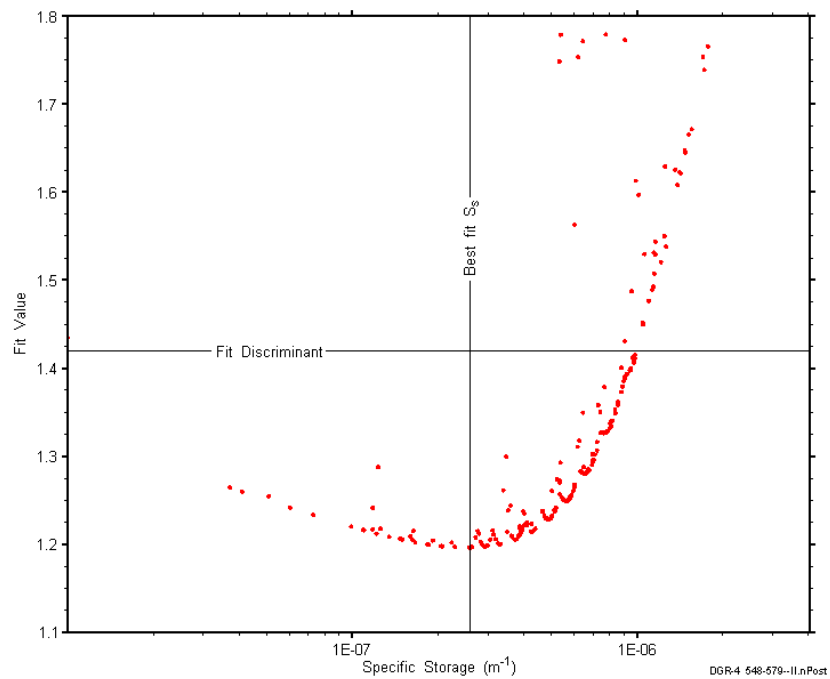


Figure D-205: XY-scatter plot showing the formation specific storage parameter space derived from DGR4_548.28-579.02 (b) perturbation analysis along with the fit discriminant and best fit values.

D.16 577.45-608.19 Georgian Bay 3

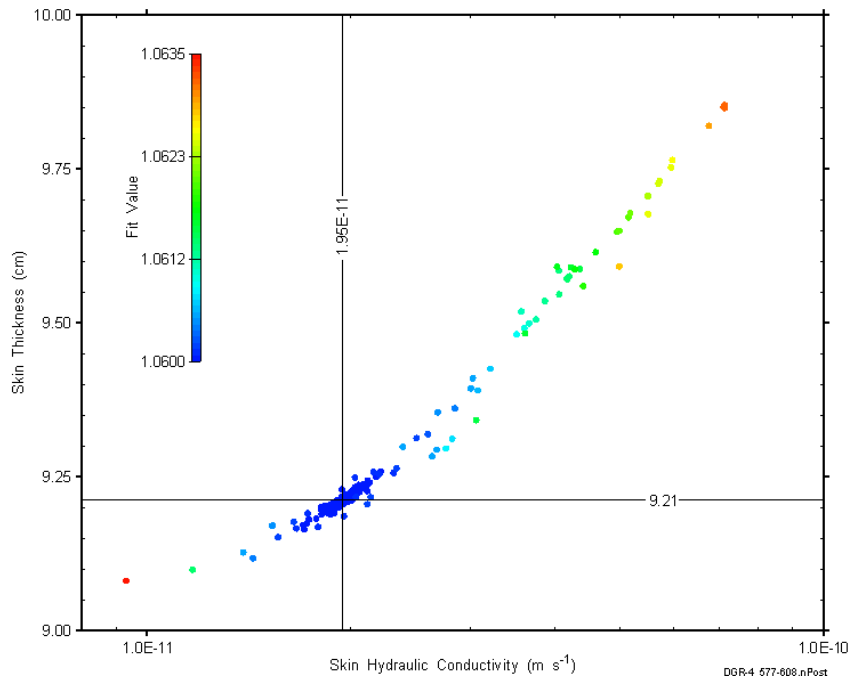


Figure D-206: XY-scatter plot showing estimates of skin hydraulic conductivity and skin thickness derived from the DGR4_577.45-608.19 perturbation analysis.

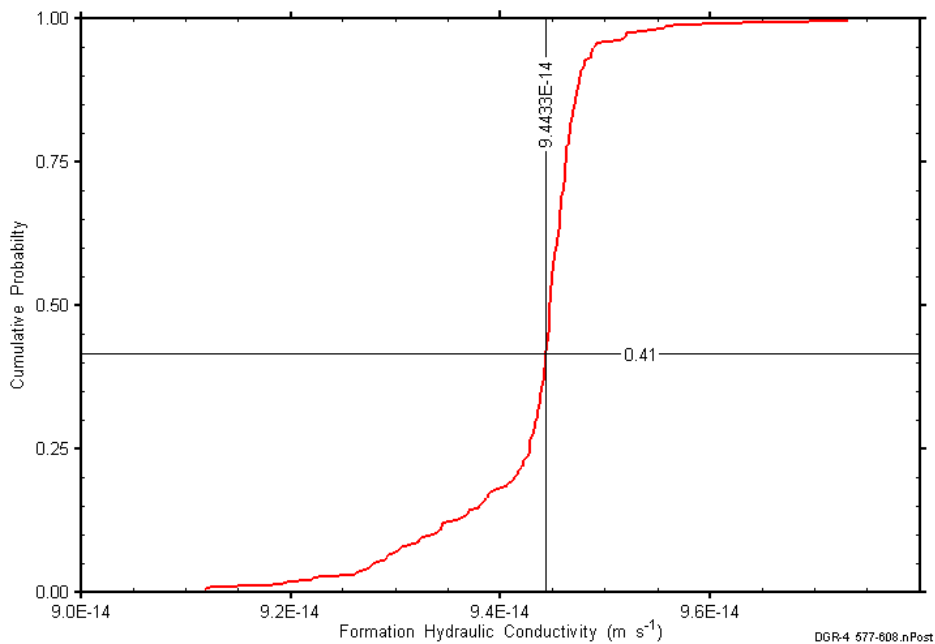


Figure D-207: DGR4_577.45-608.19 formation hydraulic conductivity cumulative distribution function.

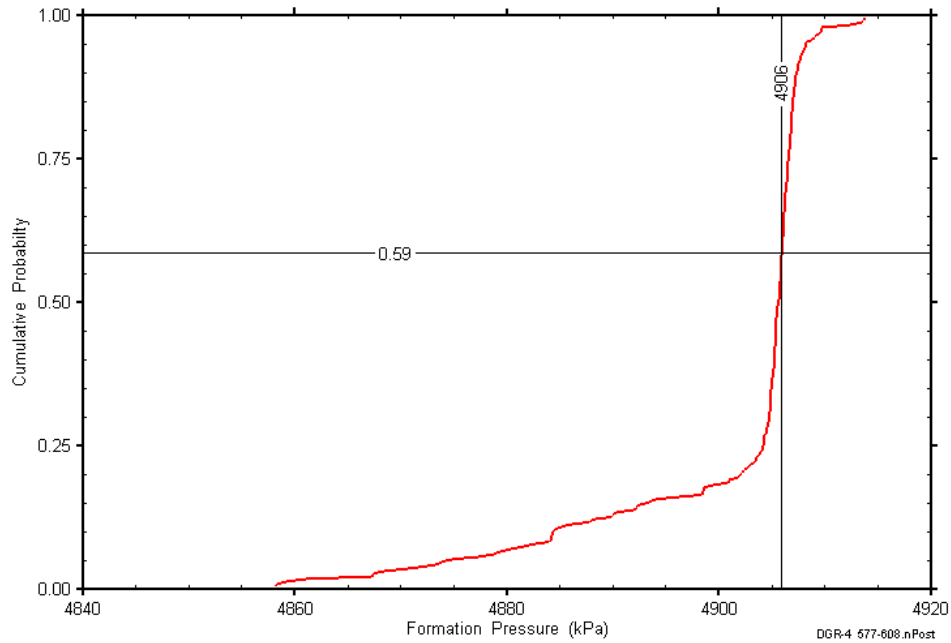


Figure D-208: DGR4_577.45-608.19 static formation pressure cumulative distribution function.

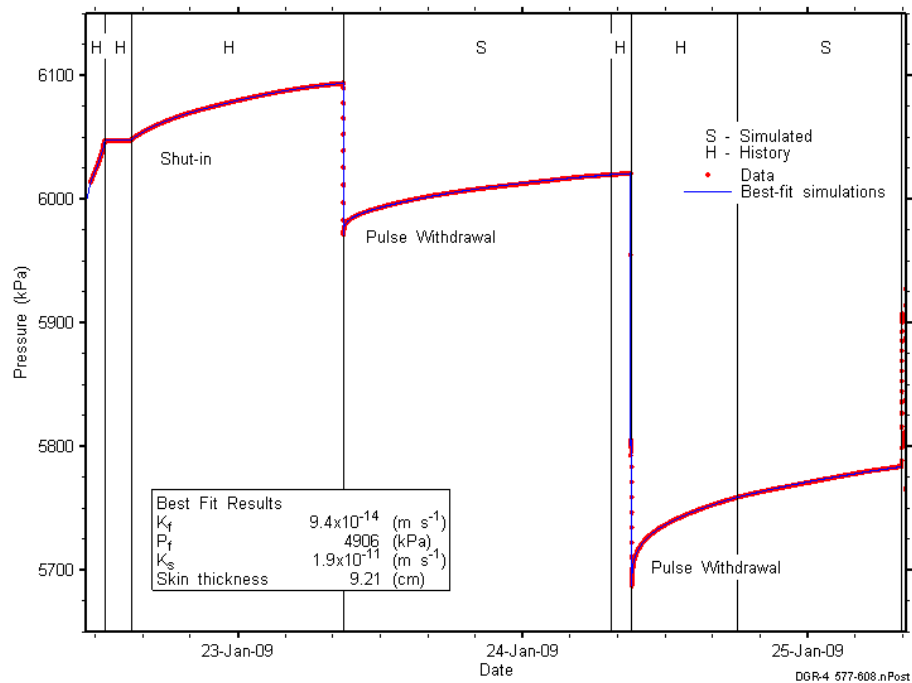


Figure D-209: Linear plot showing simulations of the DGR4_577.45-608.19 pressure response.

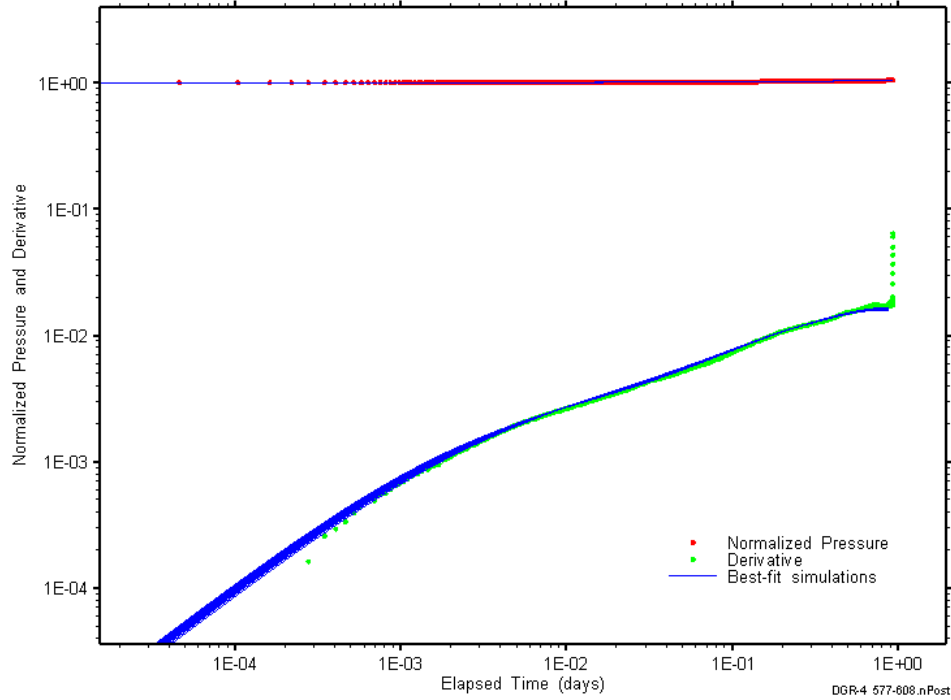


Figure D-210: Log-log plot showing simulations of the DGR4_577.45–608.19 pulse withdrawal #1 Ramey B and derivative response.

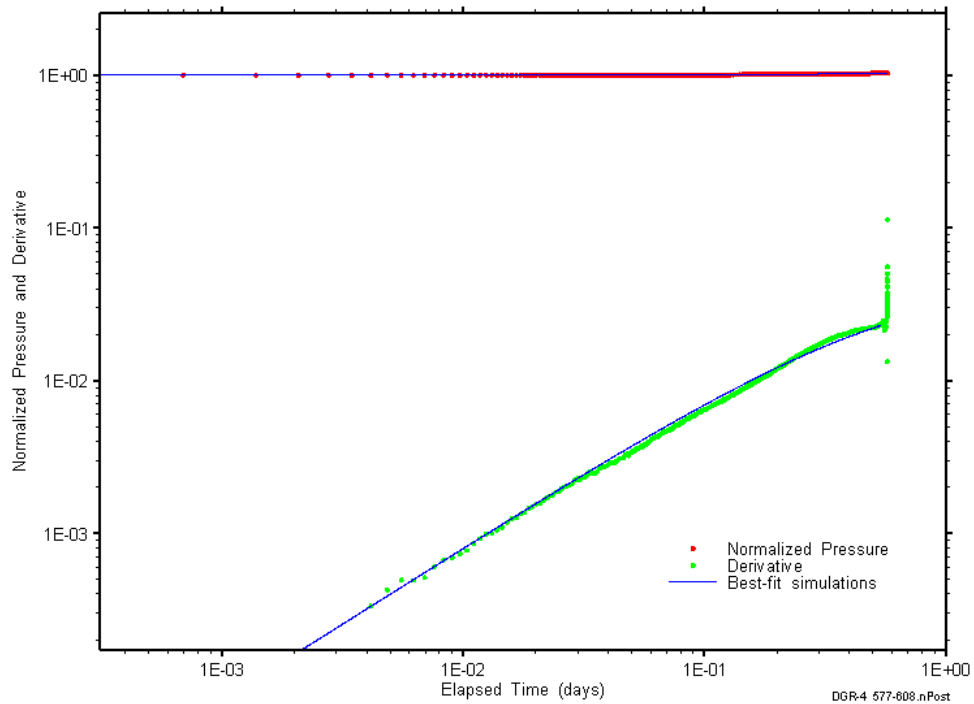


Figure D-211: Log-log plot showing simulations of the DGR4_577.45–608.19 pulse withdrawal #2 Ramey B and derivative response.

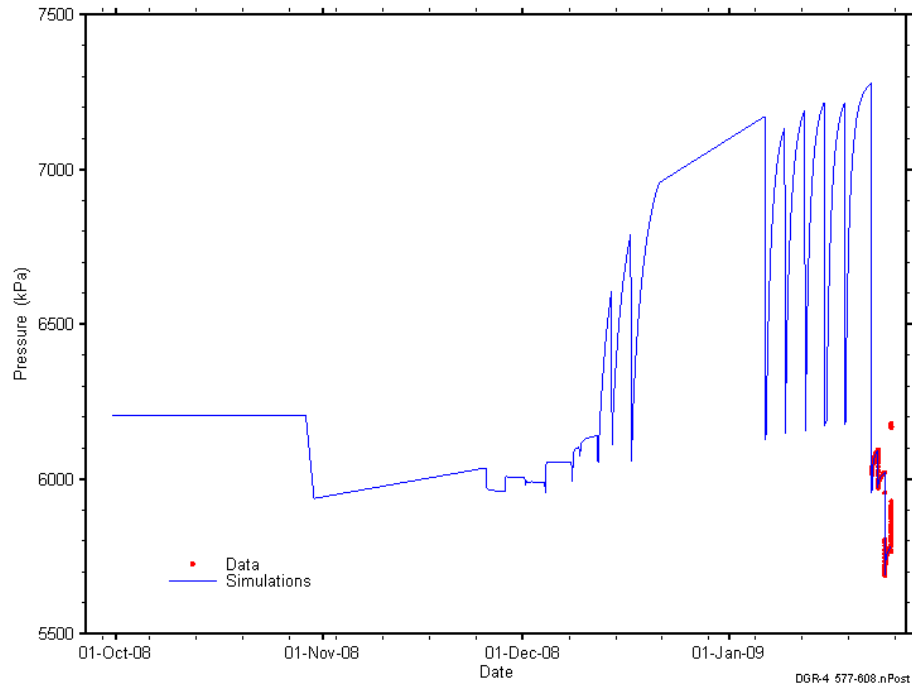


Figure D-212: Linear plot showing simulations of the DGR4_577.45-608.19 pressure response, including pre-test pressure history.

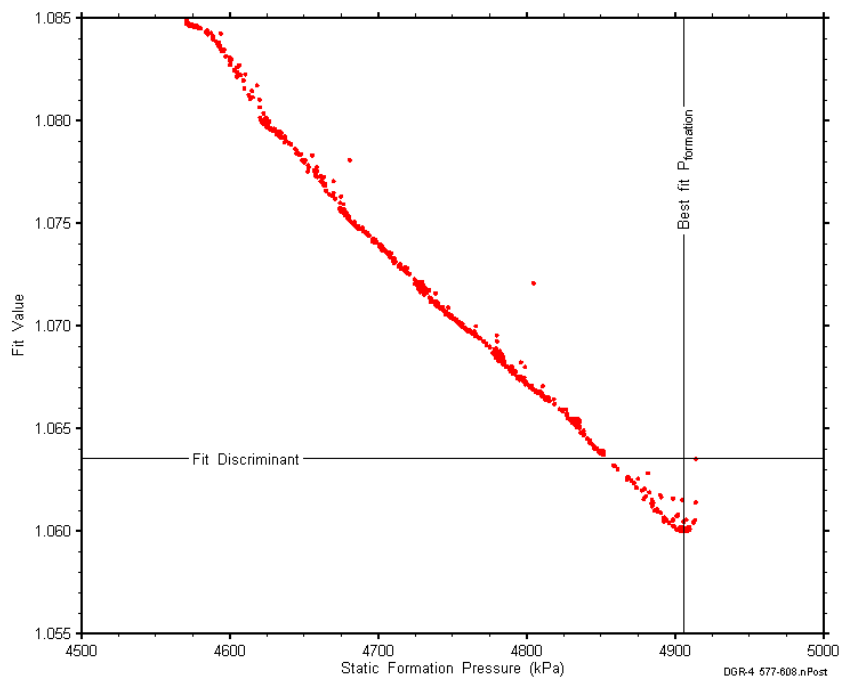


Figure D-213: XY-scatter plot showing the static formation pressure parameter space derived from DGR4_577.45-608.19 perturbation analysis along with the fit discriminant and best fit values.

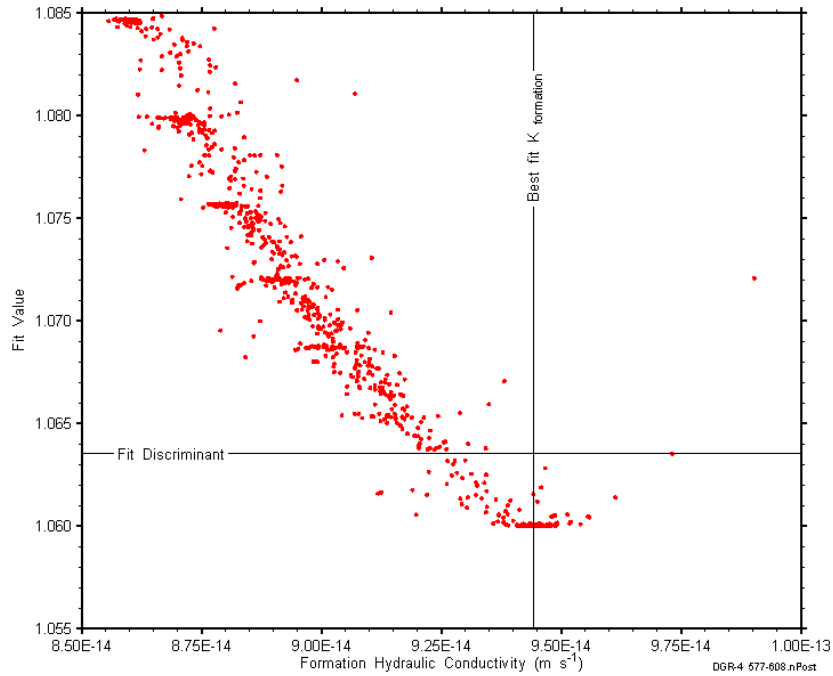


Figure D-214: XY-scatter plot showing the formation hydraulic conductivity parameter space derived from DGR4_577.45-608.19 perturbation analysis along with the fit discriminant and best fit values.

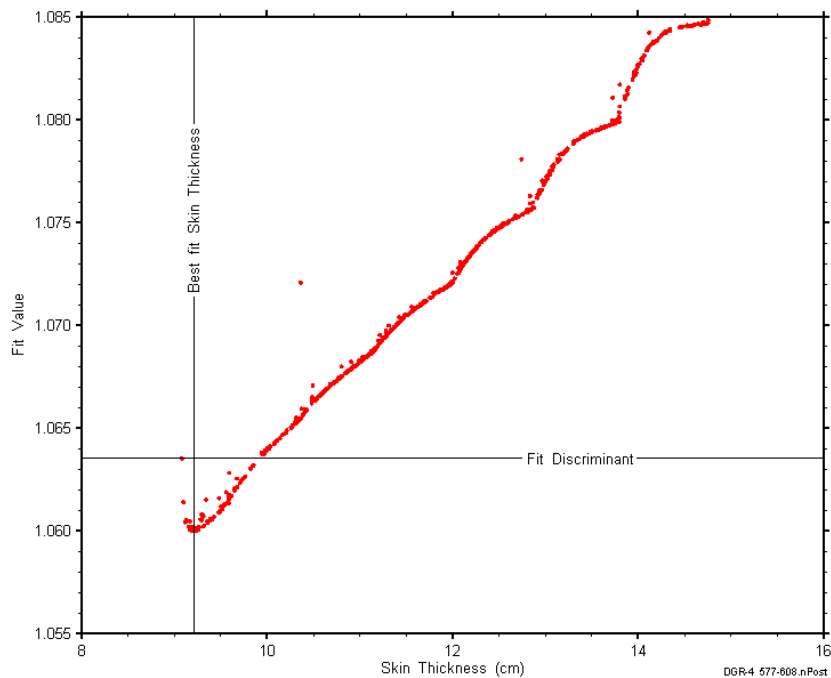


Figure D-215: XY-scatter plot showing the skin-thickness parameter space derived from DGR4_577.45-608.19 perturbation analysis along with the fit discriminant and best fit values.

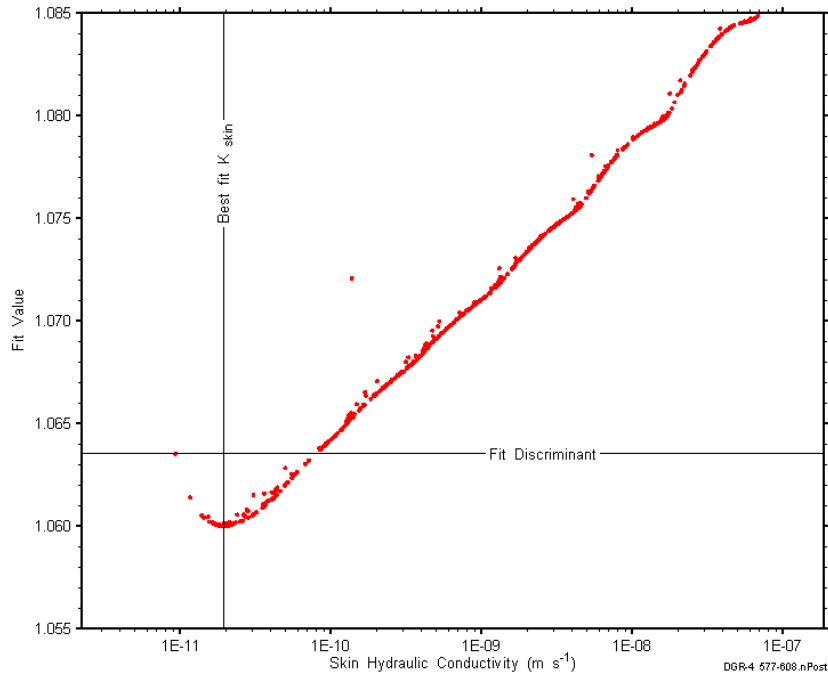


Figure D-216: XY-scatter plot showing the skin hydraulic conductivity parameter space derived from DGR4_577.45-608.19 perturbation analysis along with the fit discriminant and best fit values.

D.17 607.79-638.53 Blue Mountain

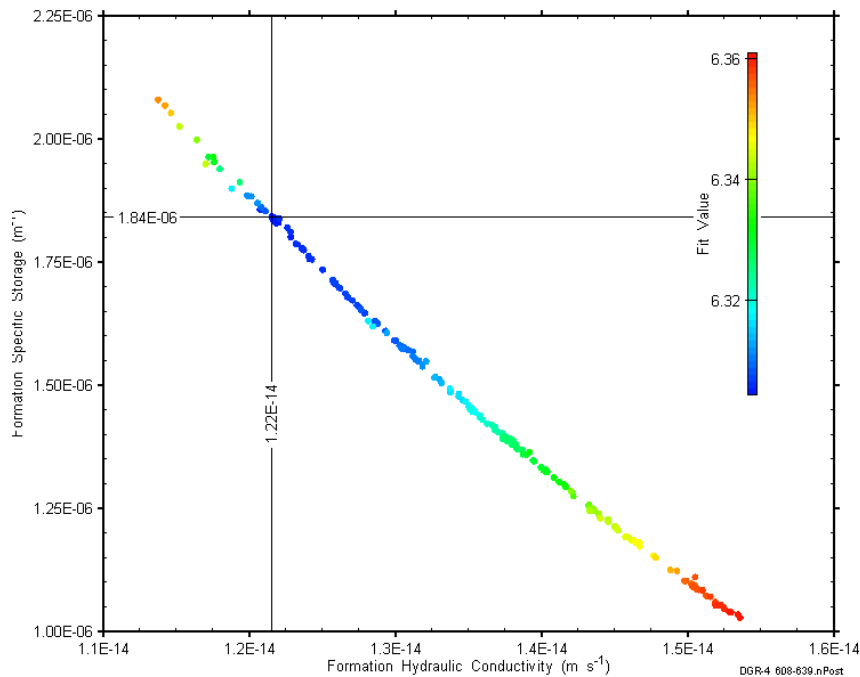


Figure D-217: XY-scatter plot showing estimates of formation hydraulic conductivity and formation specific storage derived from the DGR4_607.79-638.53 perturbation analysis.

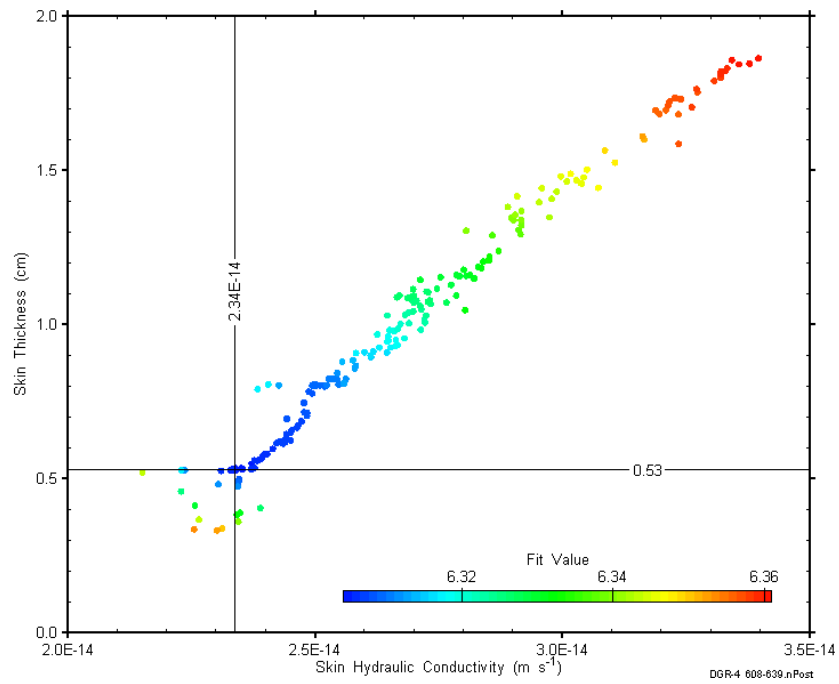


Figure D-218: XY-scatter plot showing estimates of skin hydraulic conductivity and skin thickness derived from the DGR4_607.79-638.53 perturbation analysis.

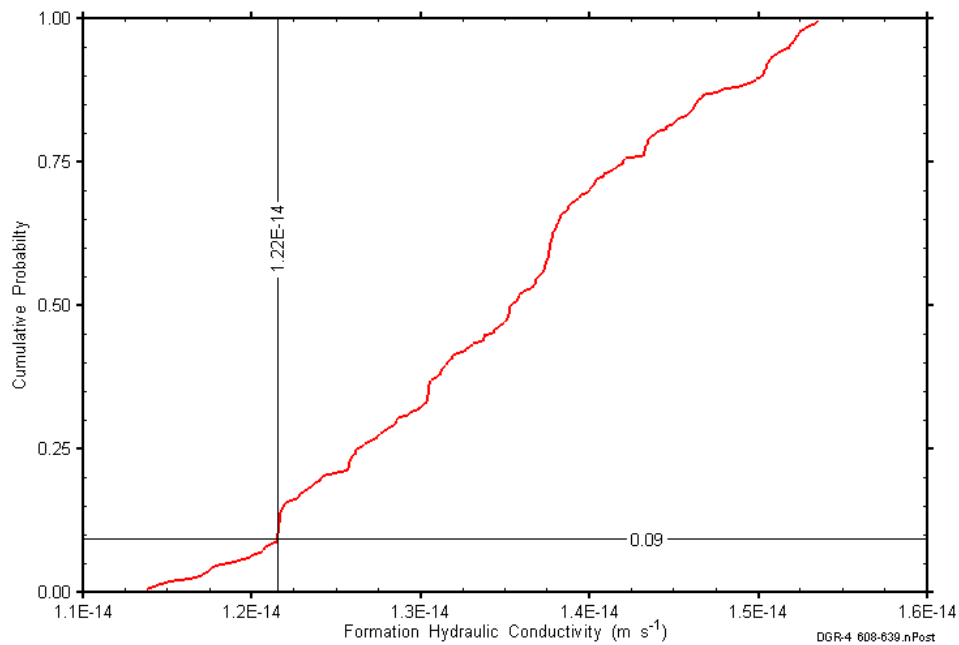


Figure D-219: DGR4_607.79-638.53 formation hydraulic conductivity cumulative distribution function.

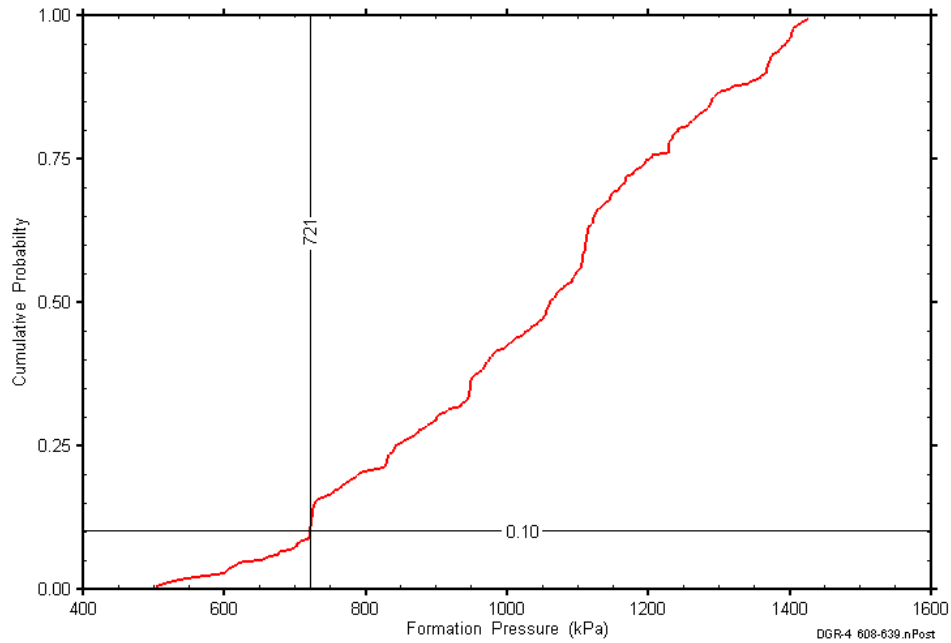


Figure D-220: DGR4_607.79-638.53 static formation pressure cumulative distribution function.

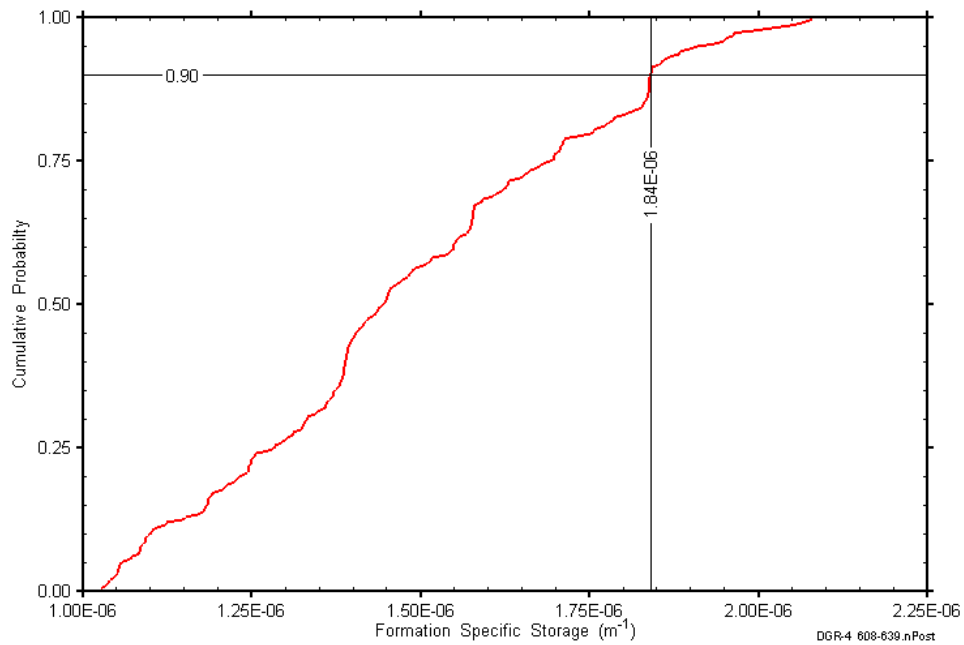


Figure D-221: DGR4_607.79-638.53 formation specific storage cumulative distribution function.

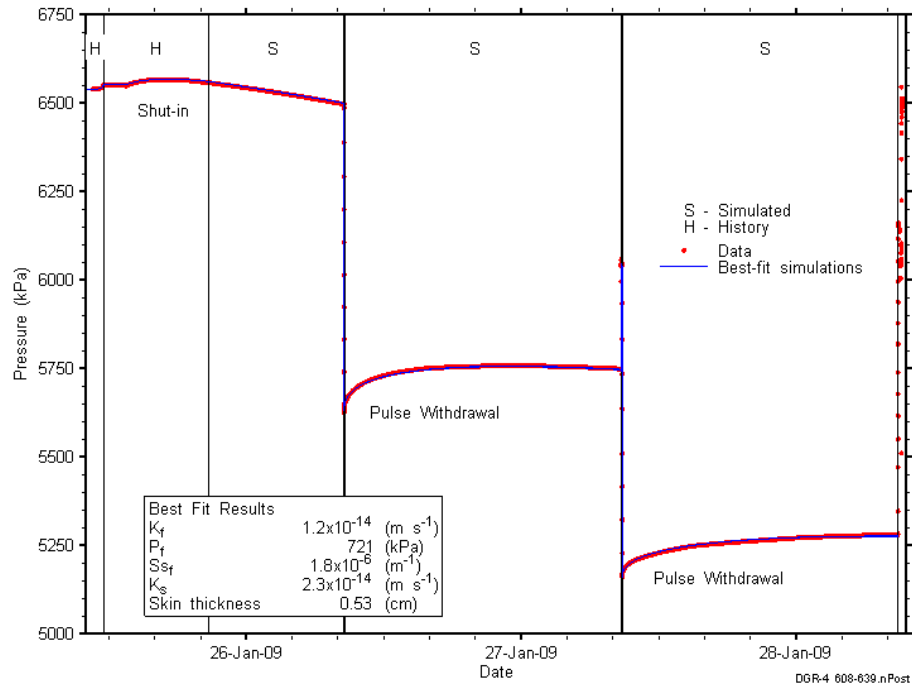


Figure D-222: Linear plot showing simulations of the DGR4_607.79-638.53 pressure response.

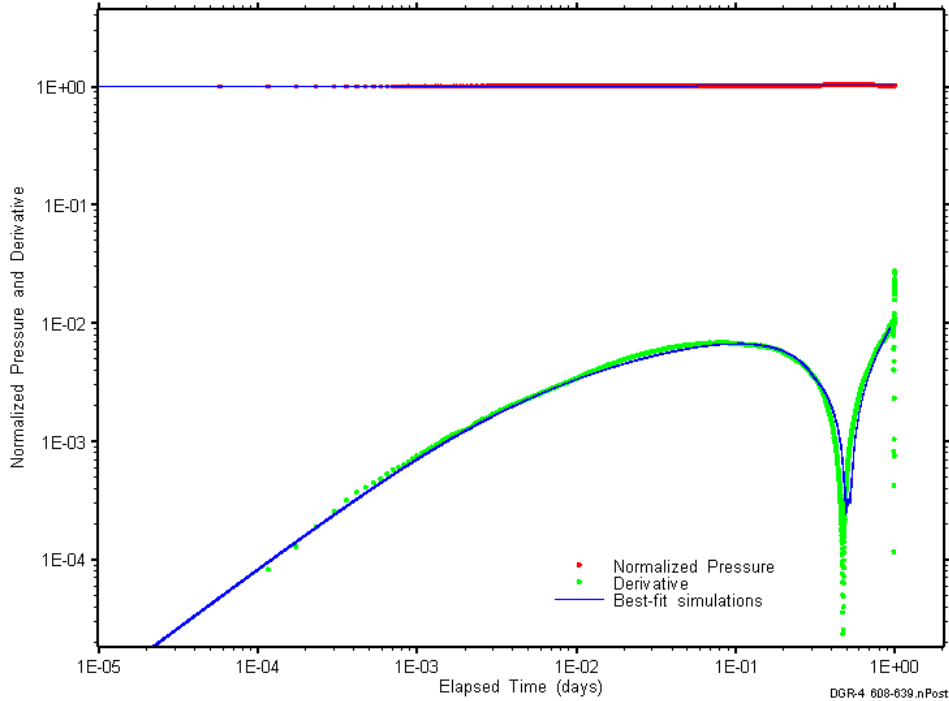


Figure D-223: Log-log plot showing simulations of the DGR4_607.79-638.53 pulse withdrawal #1 Ramey B and derivative response.

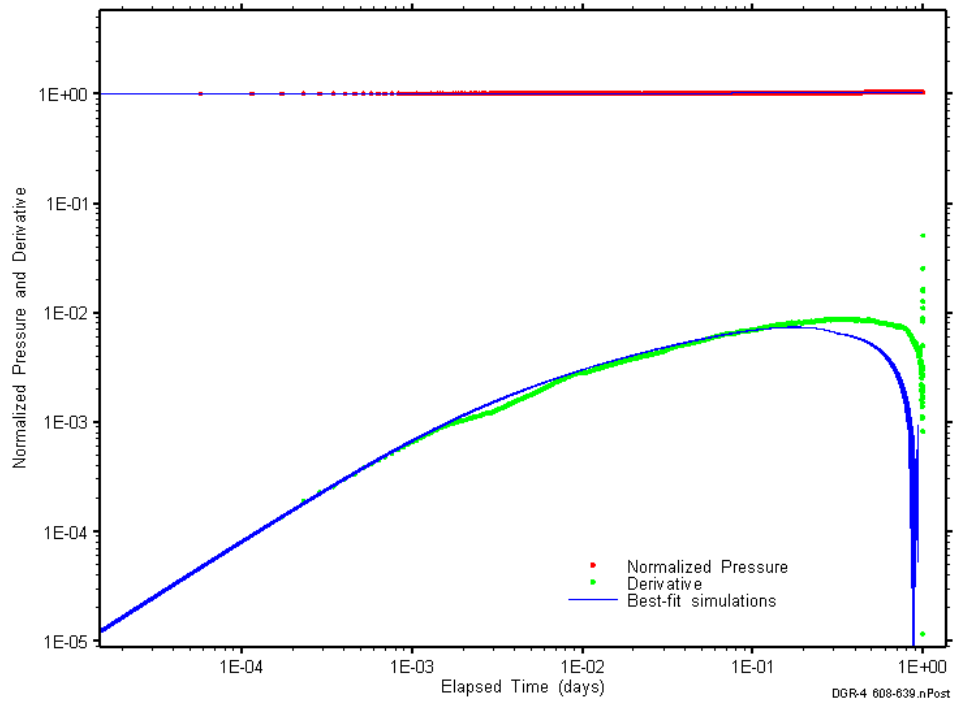


Figure D-224: Log-log plot showing simulations of the DGR4_607.79–638.53 pulse withdrawal #2 Ramey B and derivative response.

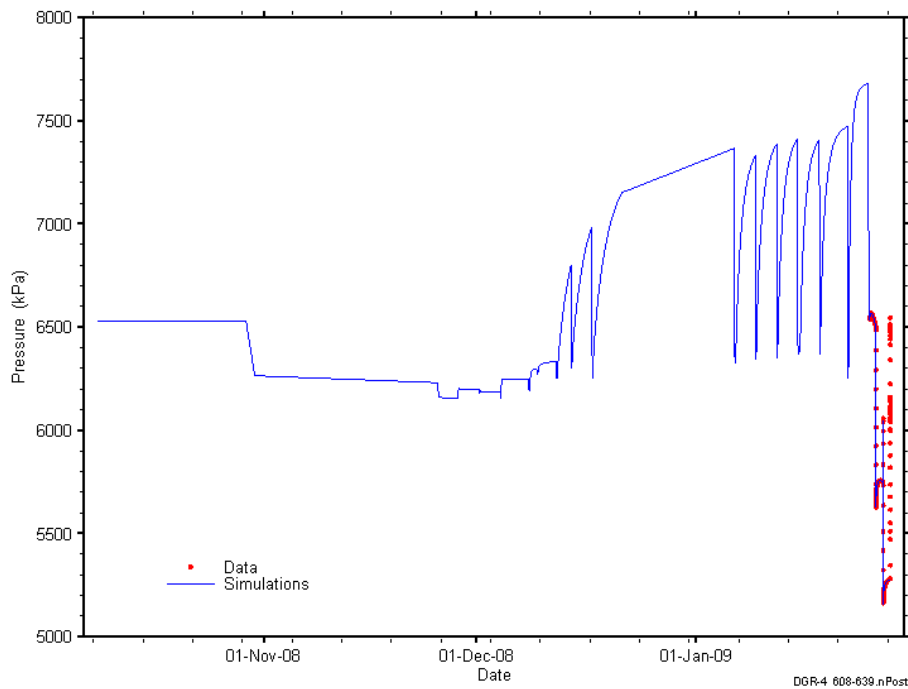


Figure D-225: Linear plot showing simulations of the DGR4_607.79–638.53 pressure response, including pre-test pressure history.

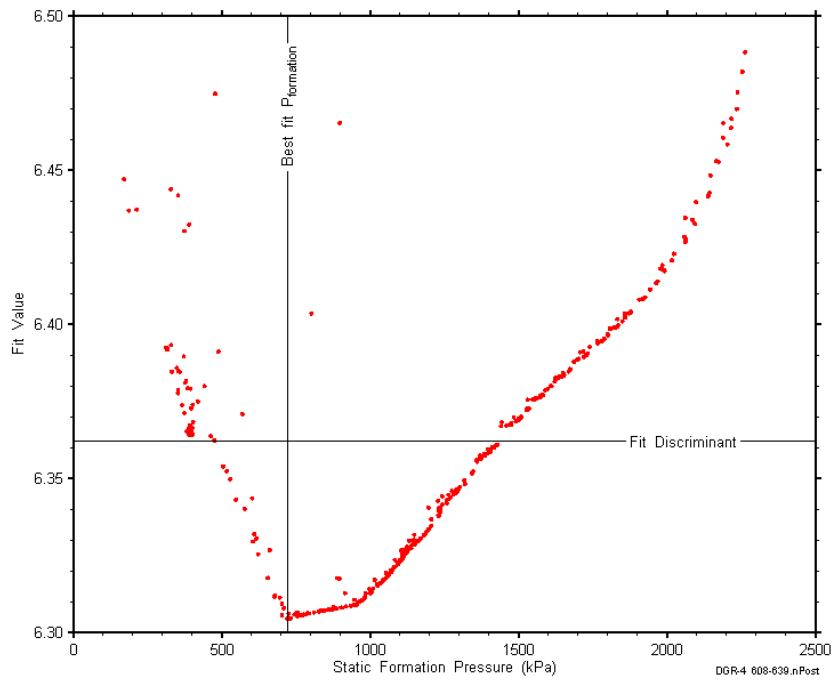


Figure D-226: XY-scatter plot showing the static formation pressure parameter space derived from DGR4_607.79-638.53 perturbation analysis along with the fit discriminant and best fit values.

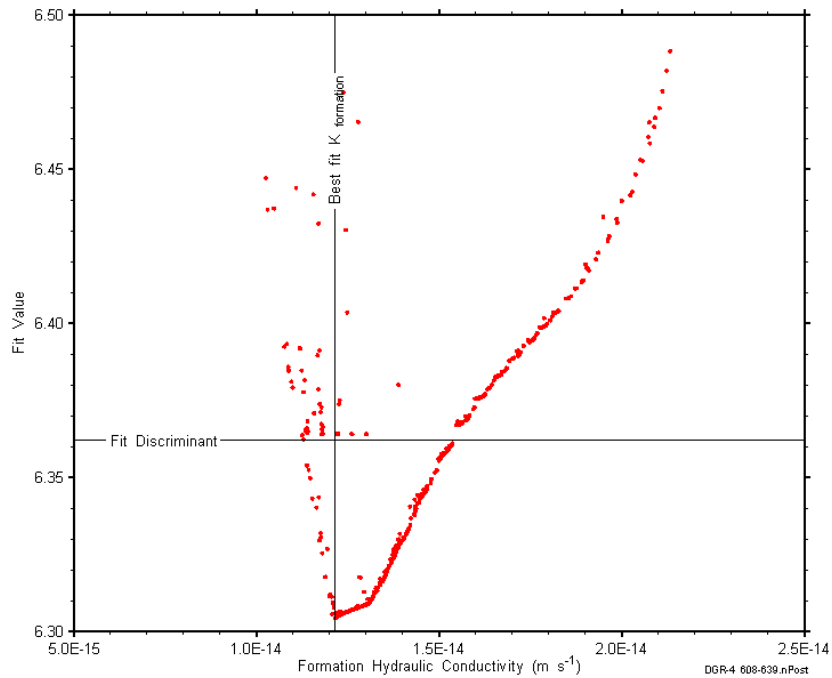


Figure D-227: XY-scatter plot showing the formation hydraulic conductivity parameter space derived from DGR4_607.79-638.53 perturbation analysis along with the fit discriminant and best fit values.

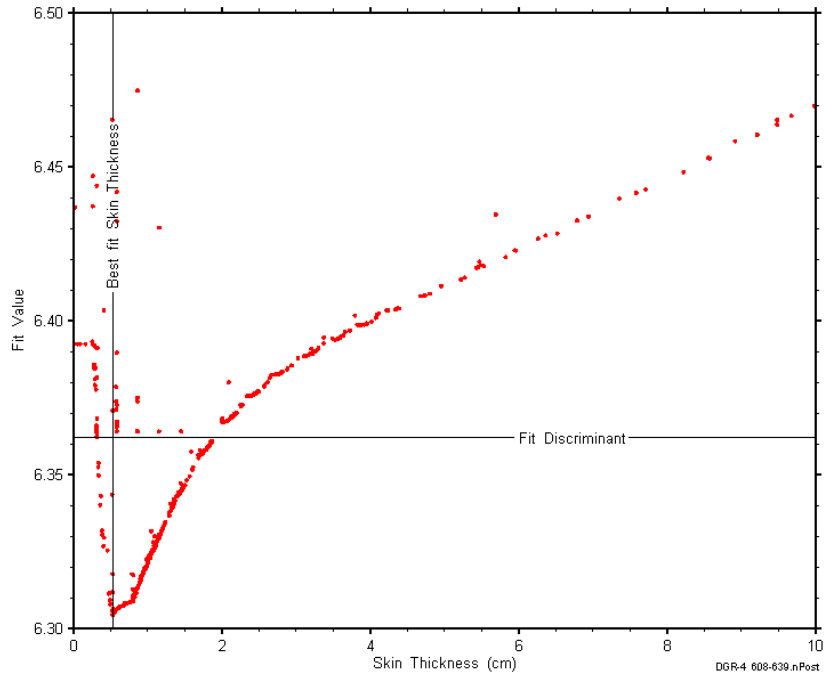


Figure D-228: XY-scatter plot showing the skin-thickness parameter space derived from DGR4_607.79-638.53 perturbation analysis along with the fit discriminant and best fit values.

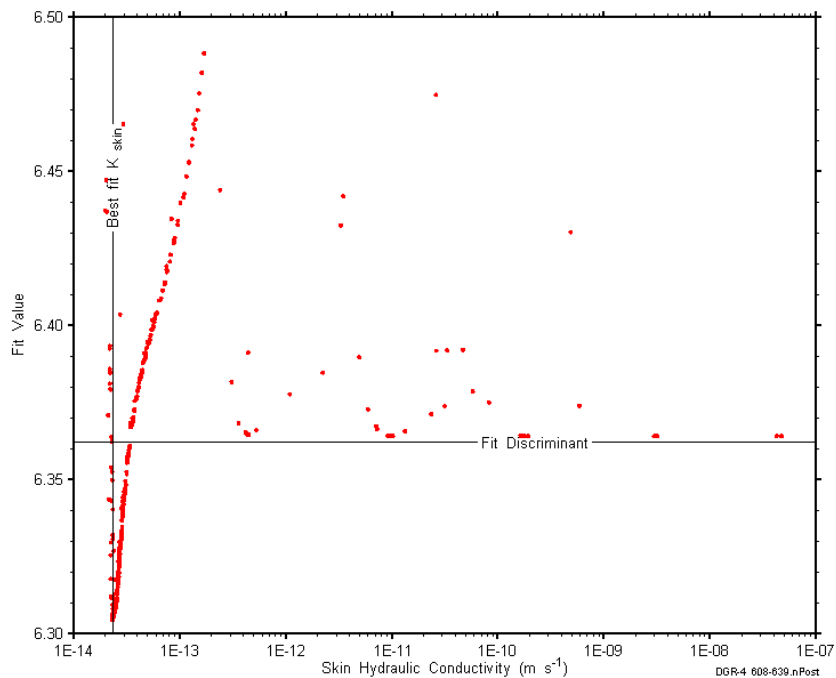


Figure D-229: XY-scatter plot showing the skin hydraulic conductivity parameter space derived from DGR4_607.79-638.53 perturbation analysis along with the fit discriminant and best fit values.

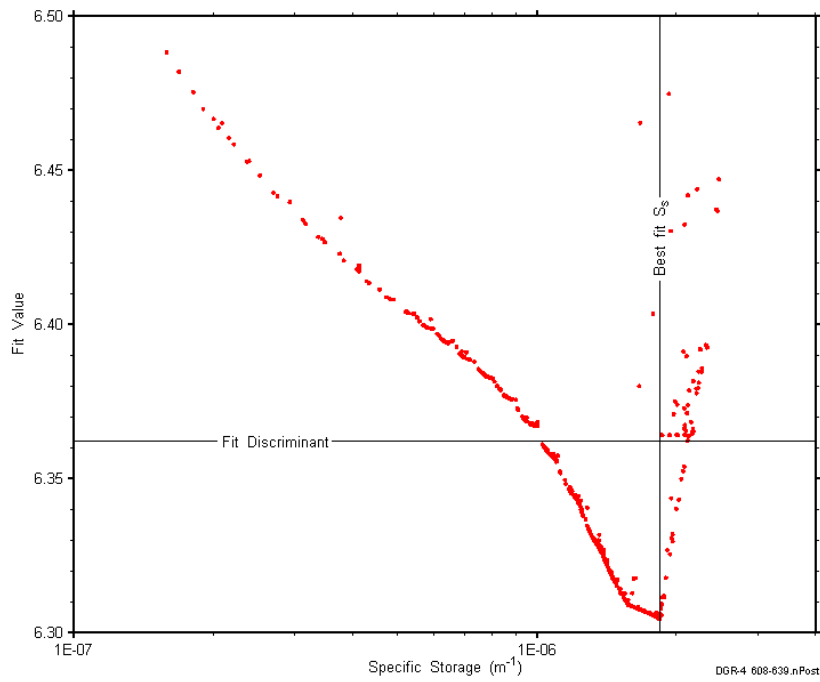


Figure D-230: XY-scatter plot showing the formation specific storage parameter space derived from DGR4_607.79-638.53 perturbation analysis along with the fit discriminant and best fit values.

D.18 638.34-669.08 Blue Mountain-Collinwood-Coburg

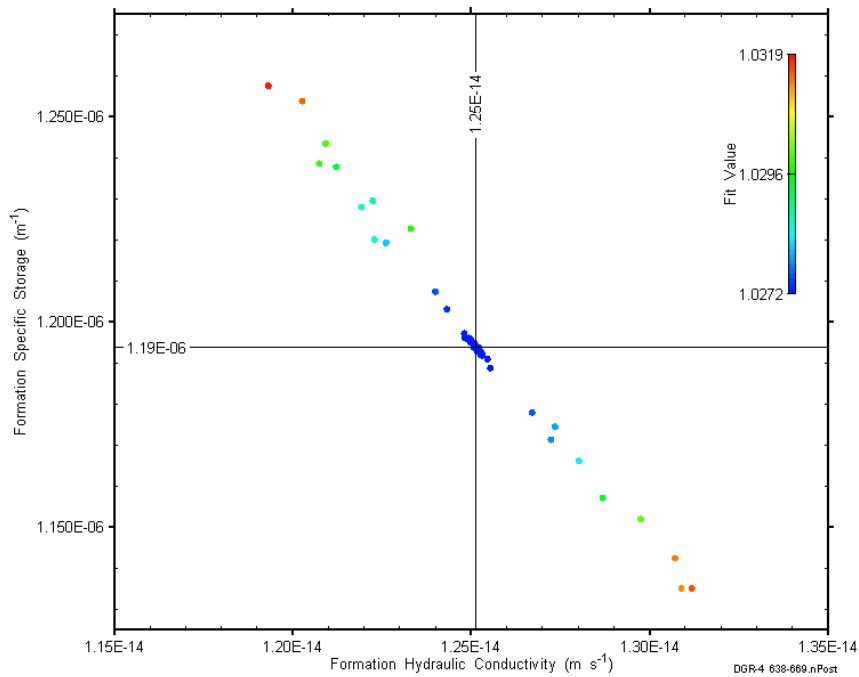


Figure D-231: XY-scatter plot showing estimates of formation hydraulic conductivity and formation specific storage derived from the DGR4_638.34-669.08 perturbation analysis.

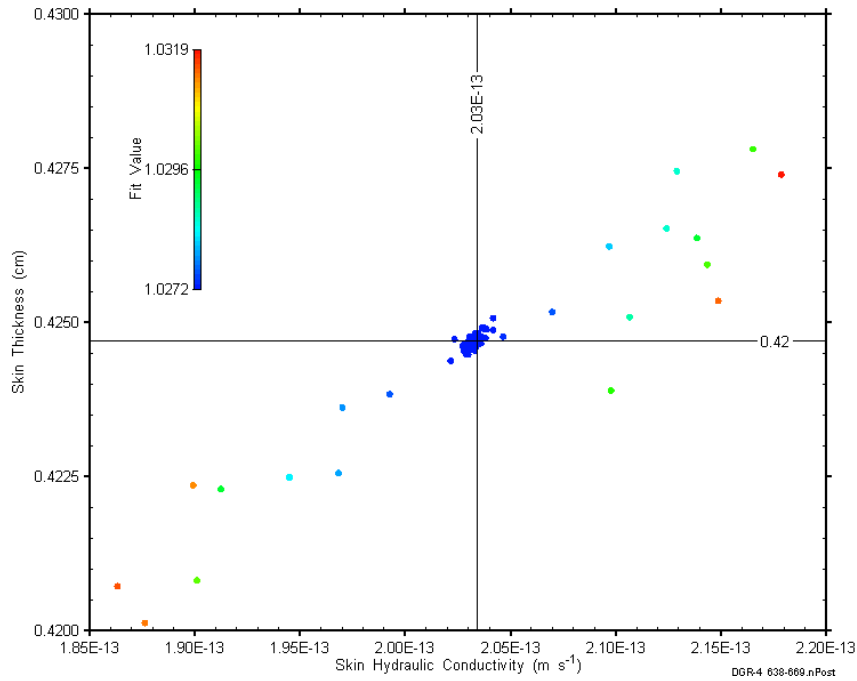


Figure D-232: XY-scatter plot showing estimates of skin hydraulic conductivity and skin thickness derived from the DGR4_638.34-669.08 perturbation analysis.

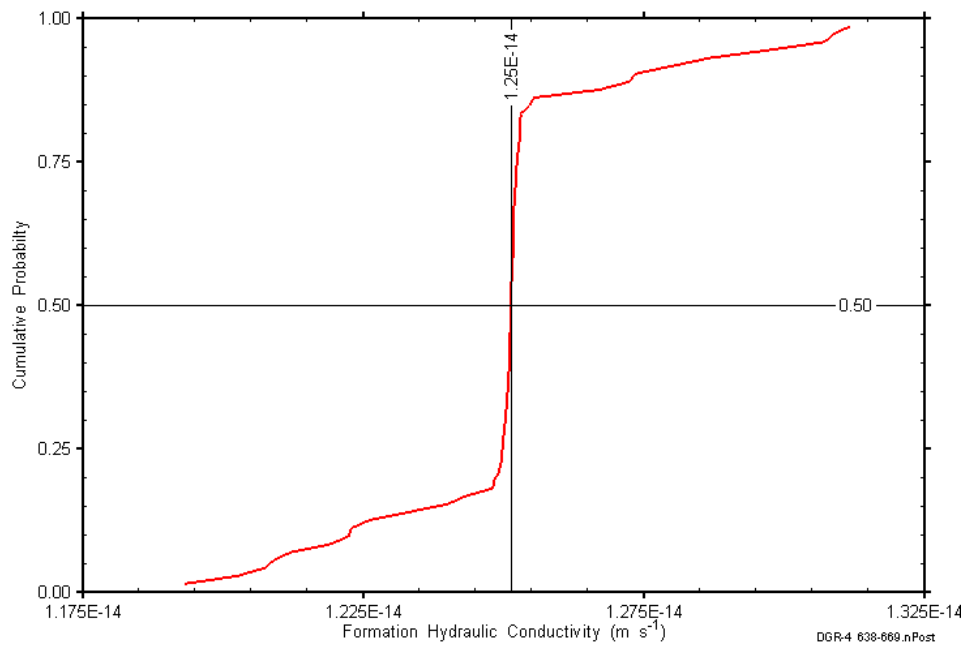


Figure D-233: DGR4_638.34-669.08 formation hydraulic conductivity cumulative distribution function.

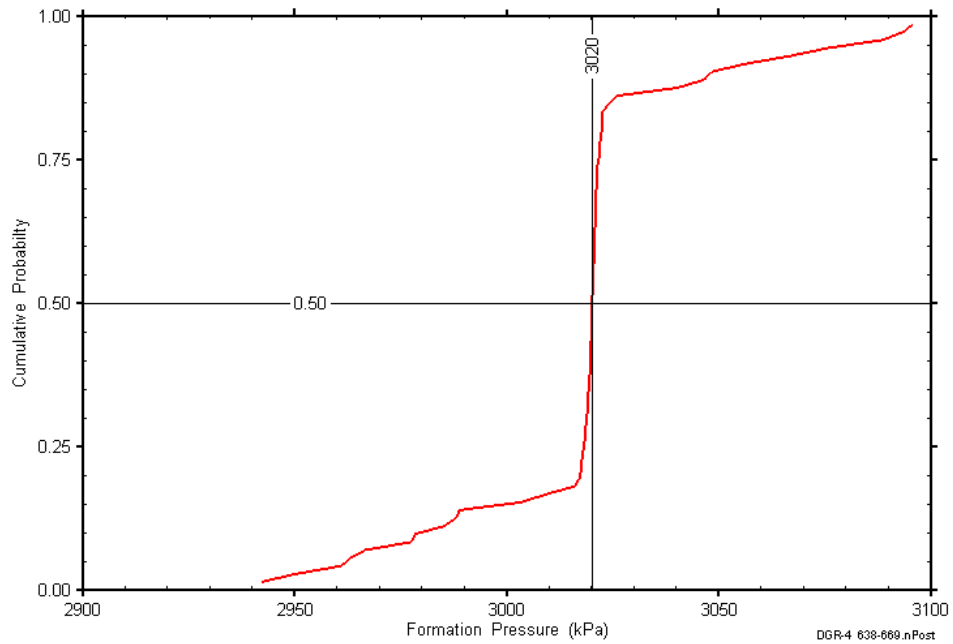


Figure D-234: DGR4_638.34-669.08 static formation pressure cumulative distribution function.

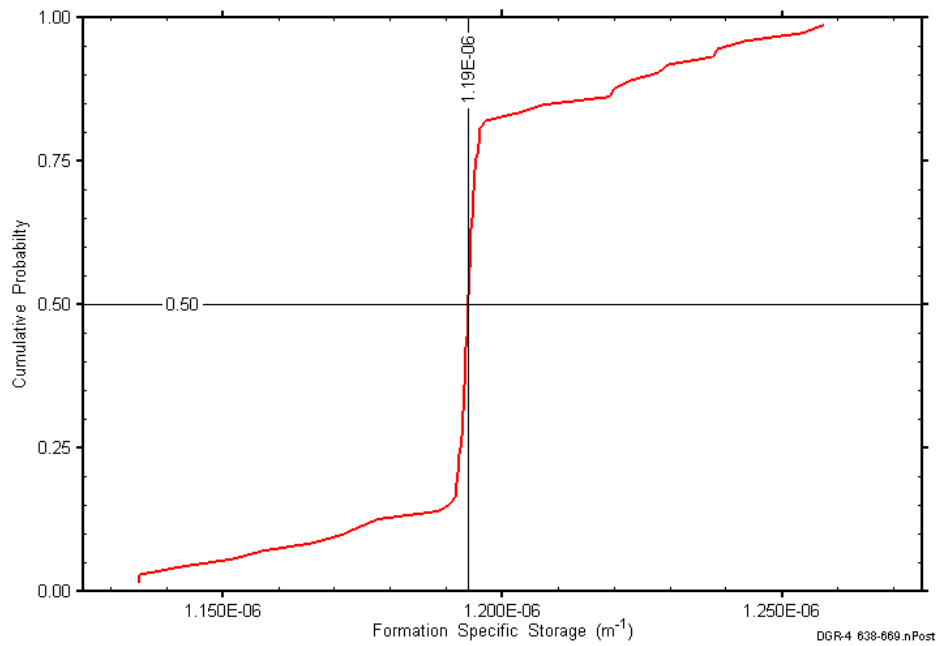


Figure D-235: DGR4_638.34-669.08 formation specific storage cumulative distribution function.

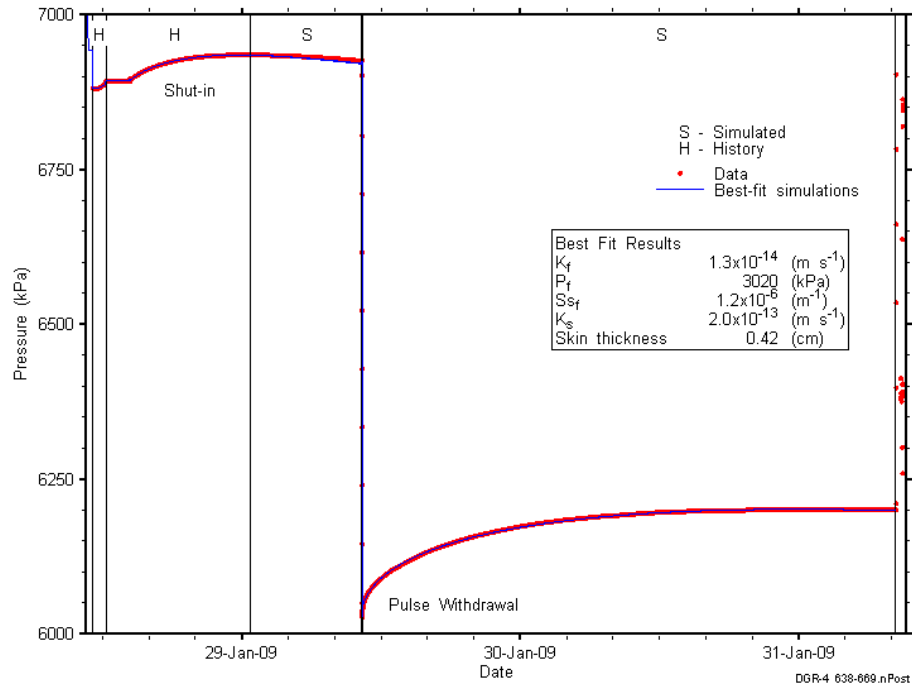


Figure D-236: Linear plot showing simulations of the DGR4_638.34-669.08 pressure response.

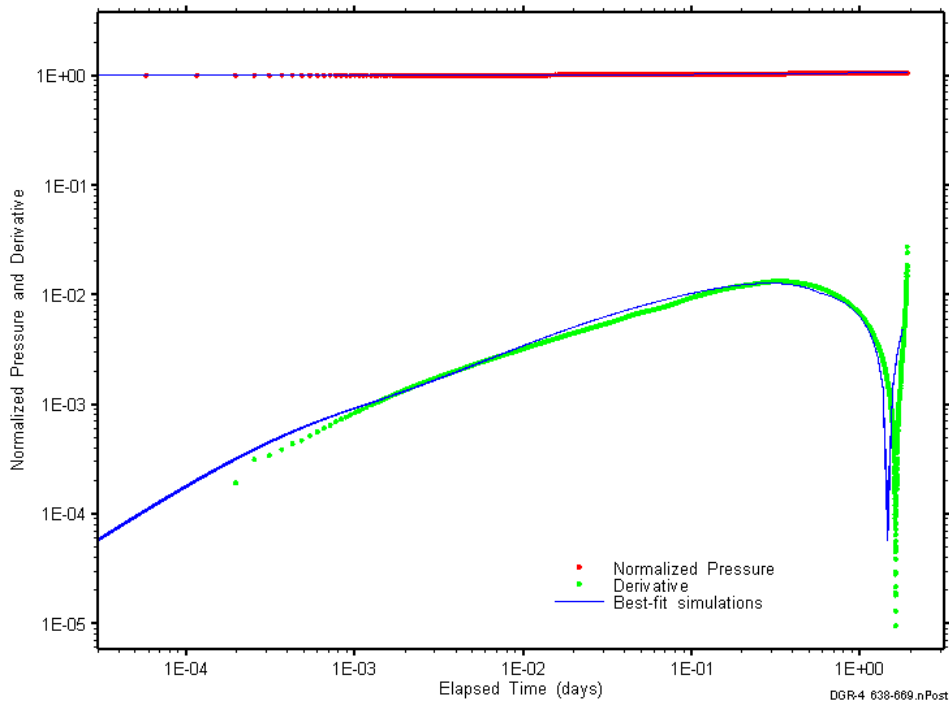


Figure D-237: Log-log plot showing simulations of the DGR4_638.34-669.08 pulse withdrawal Ramey B and derivative response.

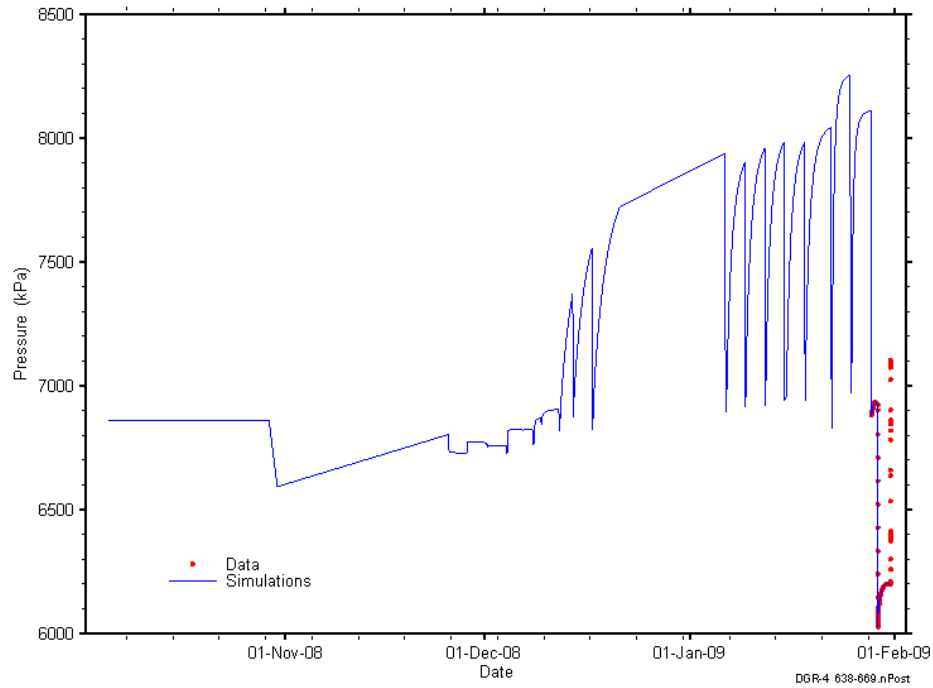


Figure D-238: Linear plot showing simulations of the DGR4_638.34-669.08 pressure response, including pre-test pressure history.

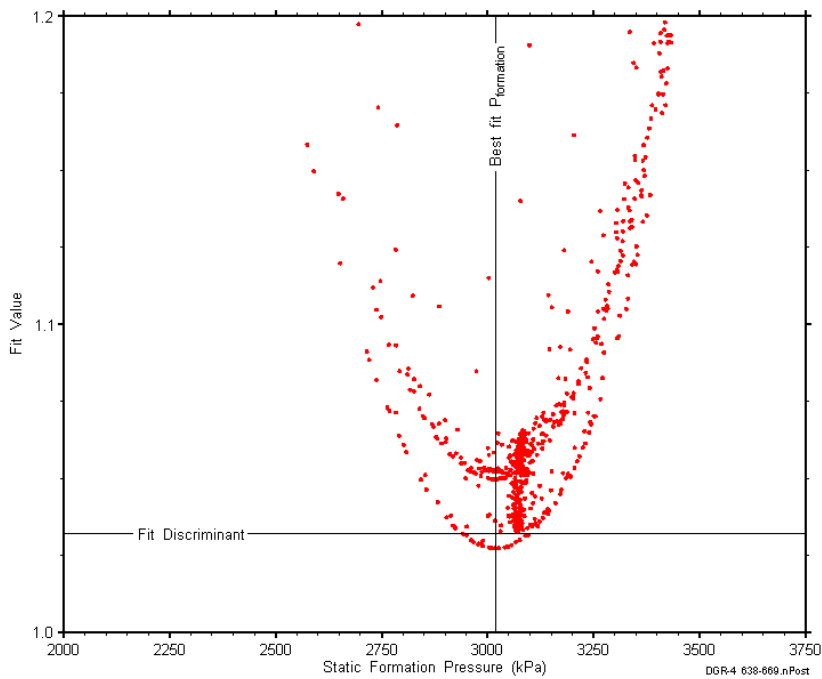


Figure D-239: XY-scatter plot showing the static formation pressure parameter space derived from DGR4_638.34-669.08 perturbation analysis along with the fit discriminant and best fit values.

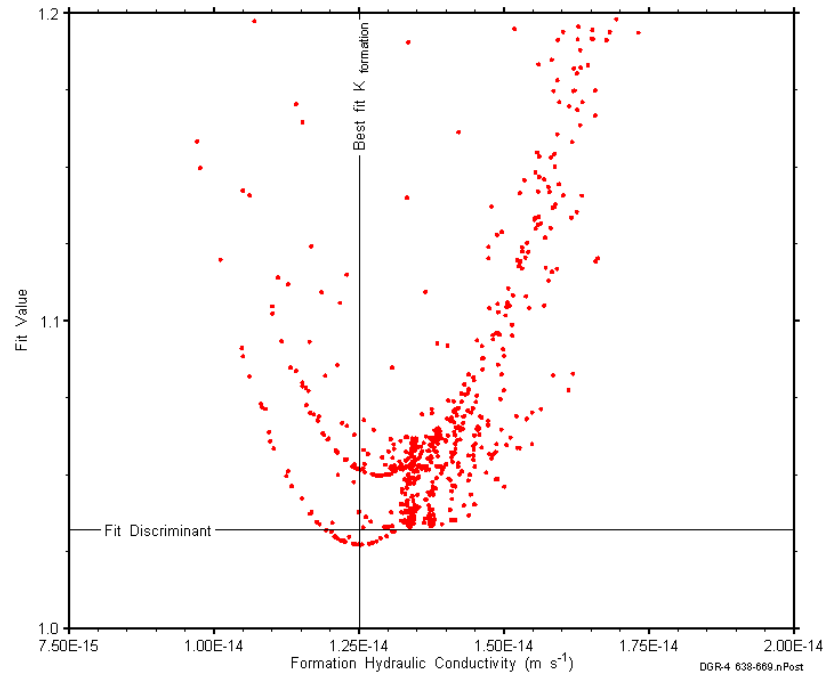


Figure D-240: XY-scatter plot showing the formation hydraulic conductivity parameter space derived from DGR4_638.34-669.08 perturbation analysis along with the fit discriminant and best fit values.

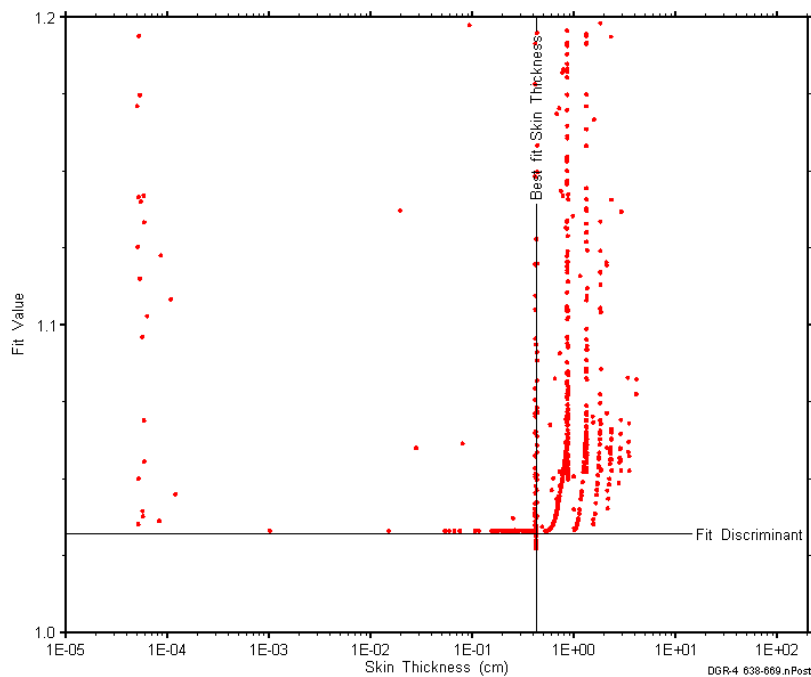


Figure D-241: XY-scatter plot showing the skin-thickness parameter space derived from DGR4_638.34-669.08 perturbation analysis along with the fit discriminant and best fit values.

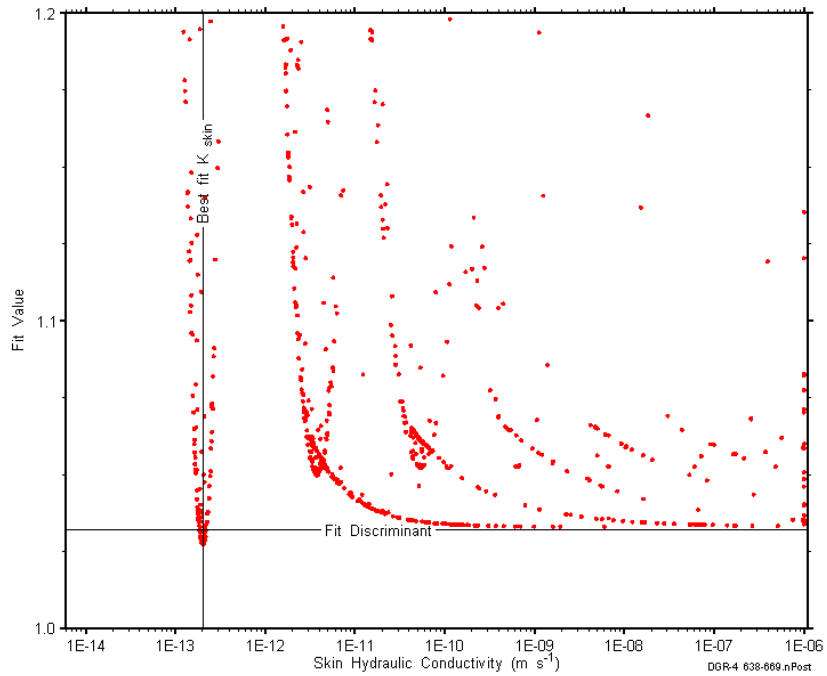


Figure D-242: XY-scatter plot showing the skin hydraulic conductivity parameter space derived from DGR4_638.34-669.08 perturbation analysis along with the fit discriminant and best fit values.

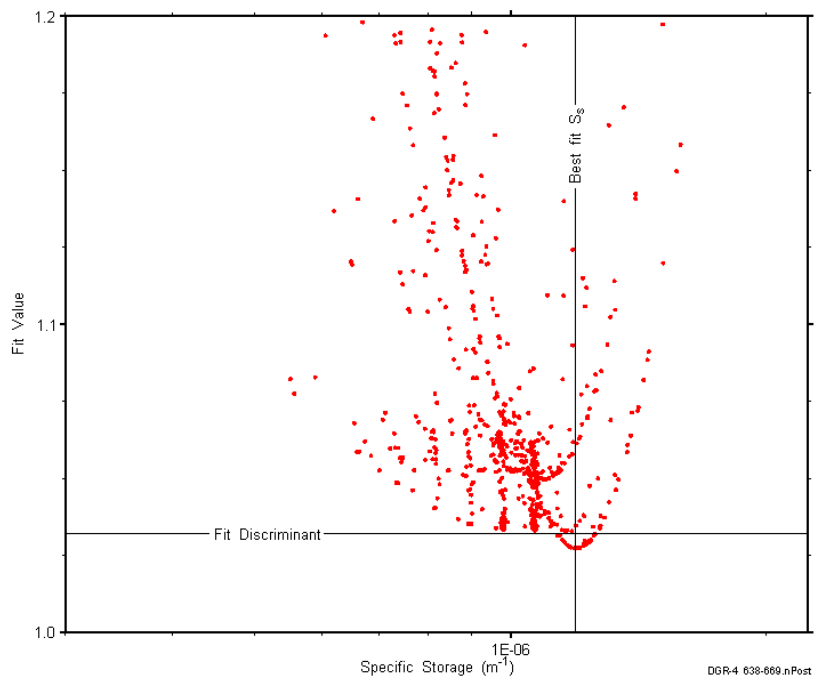


Figure D-243: XY-scatter plot showing the formation specific storage parameter space derived from DGR4_638.34-669.08 perturbation analysis along with the fit discriminant and best fit values.

D.19 658.46-689.20 Coburg

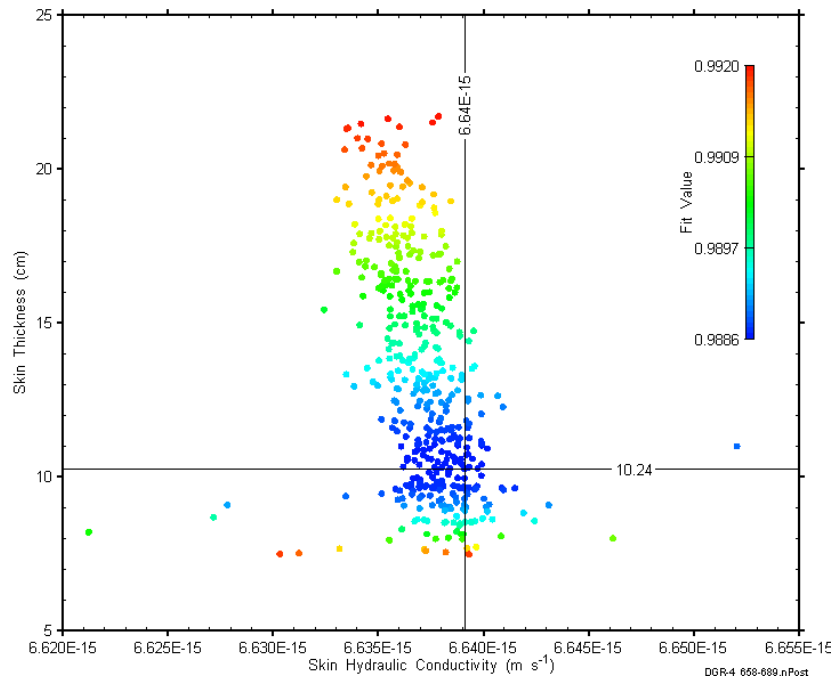


Figure D-244: XY-scatter plot showing estimates of skin hydraulic conductivity and skin thickness derived from the DGR4_635.46-689.20 perturbation analysis.

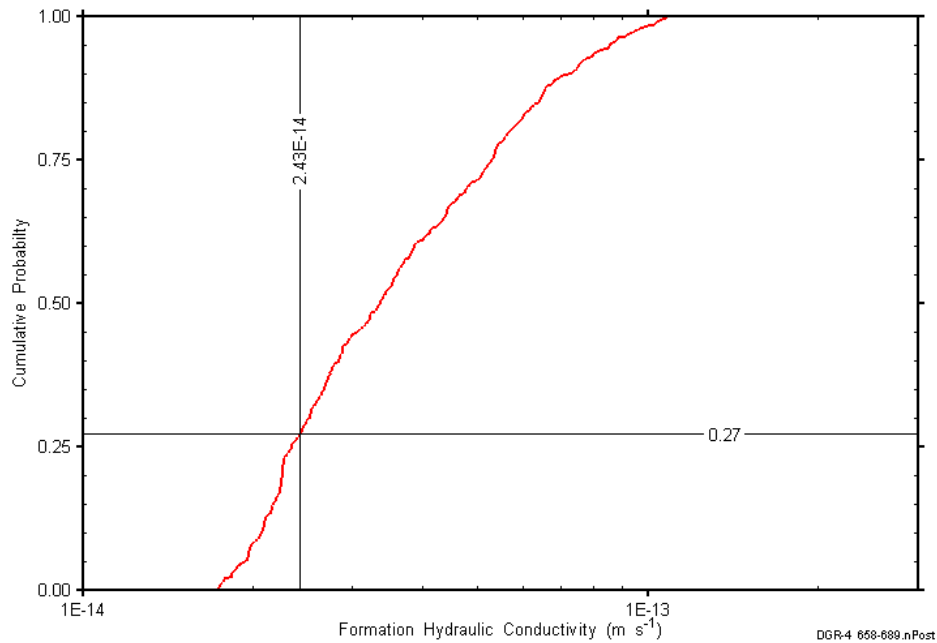


Figure D-245: DGR4_658.46-689.20 formation hydraulic conductivity cumulative distribution function.

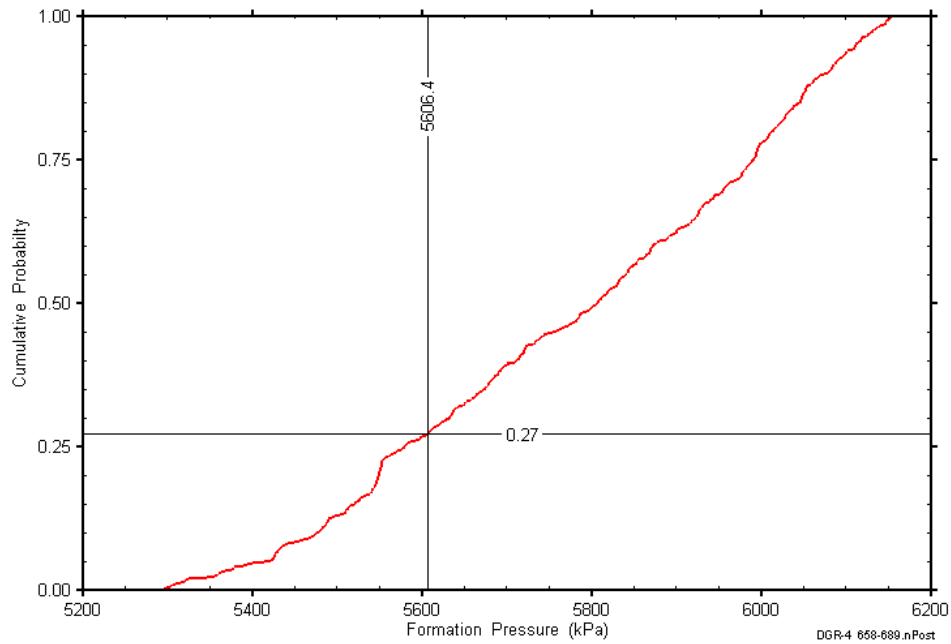


Figure D-246: DGR4_658.46-689.20 static formation pressure cumulative distribution function.

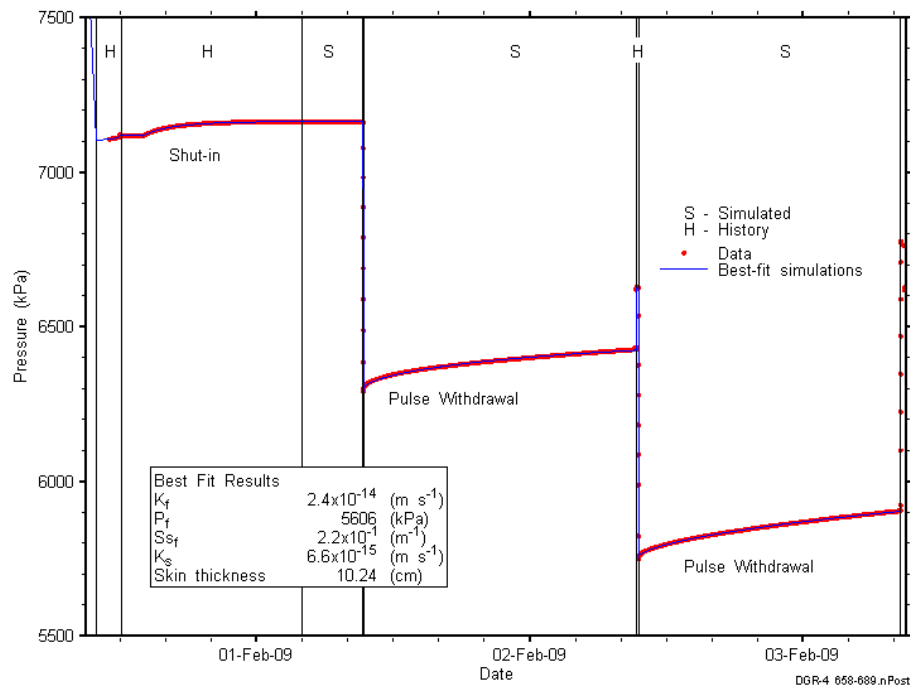


Figure D-247: Linear plot showing simulations of the DGR4_658.46-689.20 pressure response.

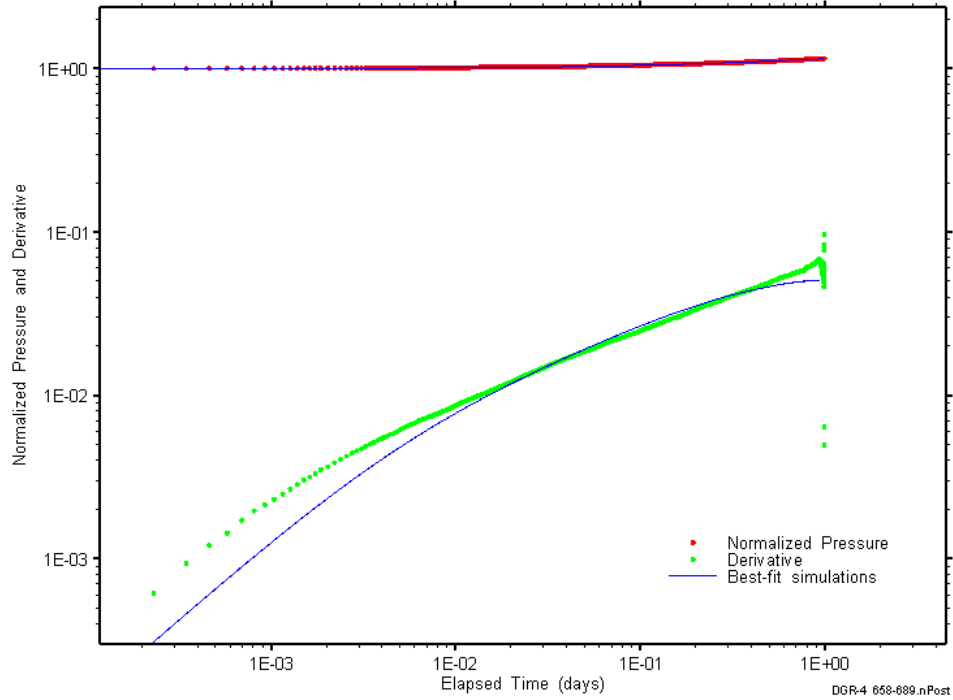


Figure D-248: Log-log plot showing simulations of the DGR4_658.46–689.20 pulse withdrawal #1 Ramey B and derivative response.

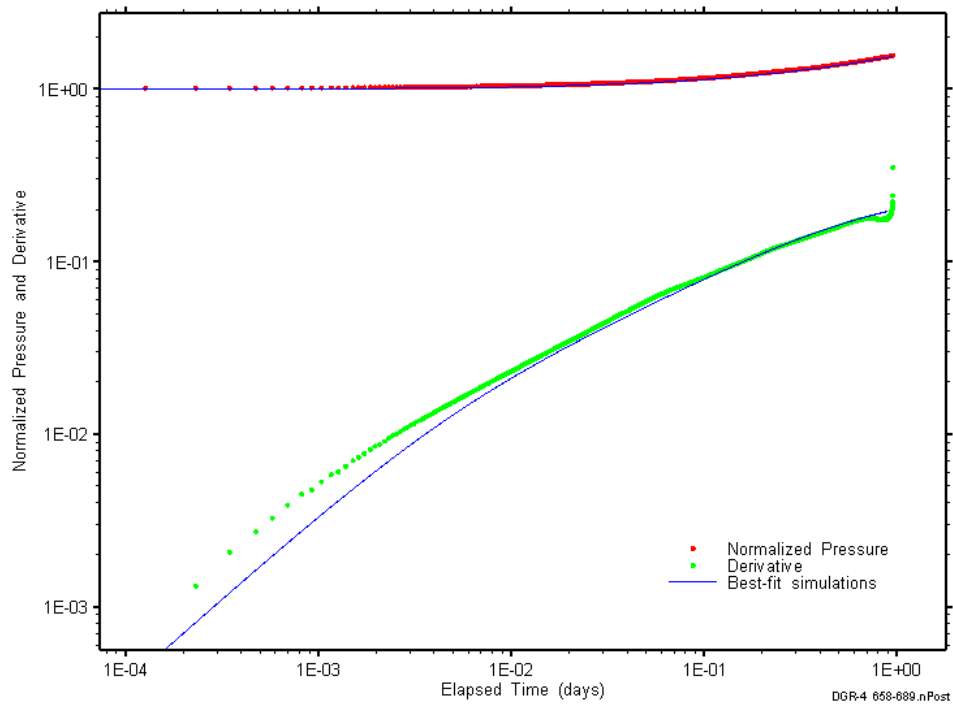


Figure D-249: Log-log plot showing simulations of the DGR4_658.46–689.20 pulse withdrawal #2 Ramey B and derivative response.

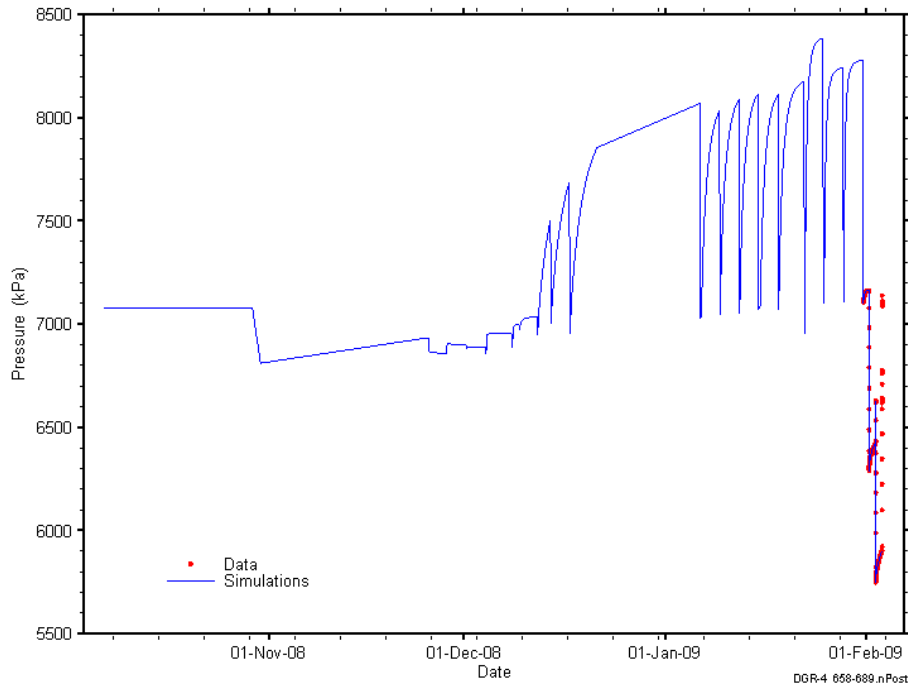


Figure D-250: Linear plot showing simulations of the DGR4_658.46-689.20 pressure response, including pre-test pressure history.

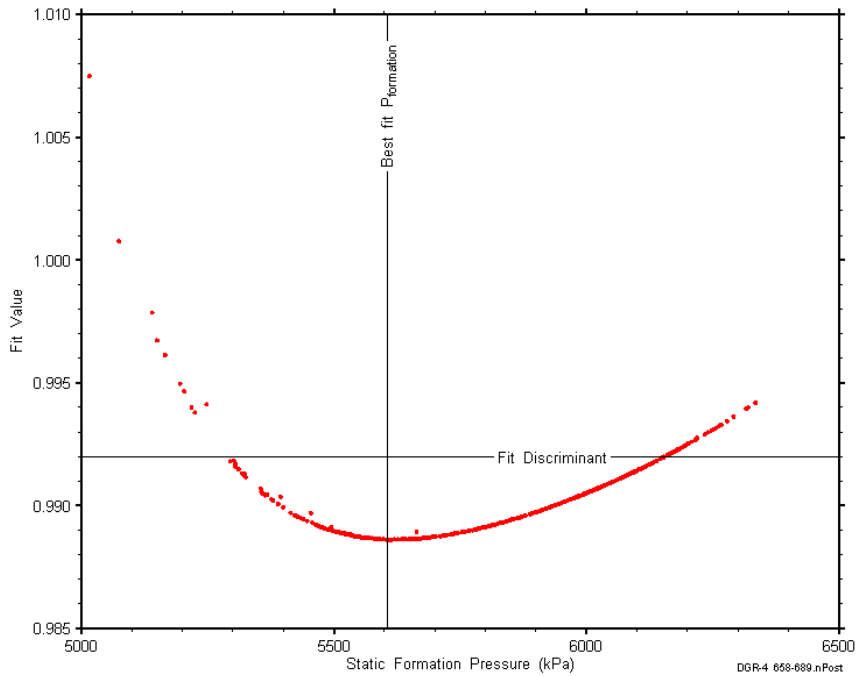


Figure D-251: XY-scatter plot showing the static formation pressure parameter space derived from DGR4_658.46-689.20 perturbation analysis along with the fit discriminant and best fit values.

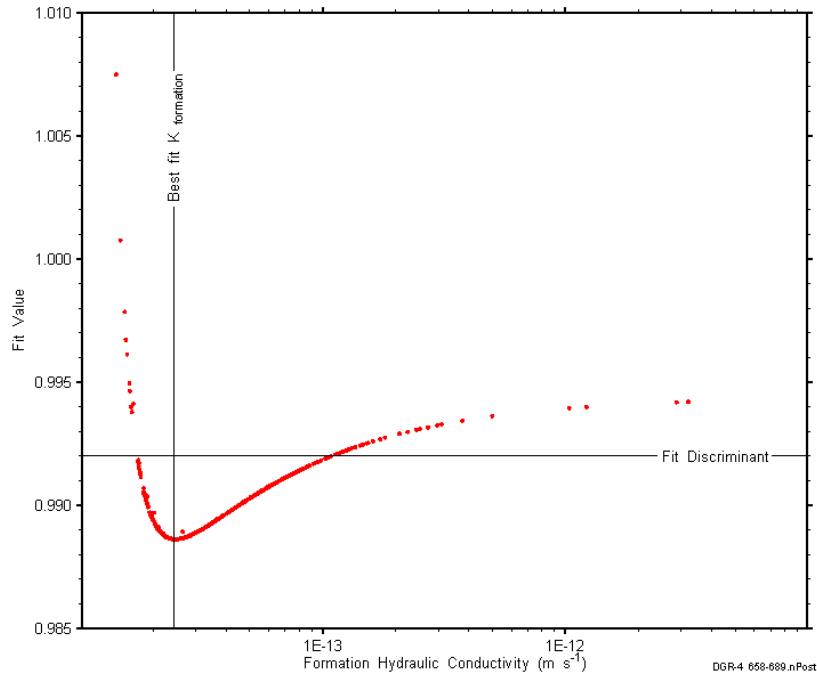


Figure D-252: XY-scatter plot showing the formation hydraulic conductivity parameter space derived from DGR4_658.46-689.20 perturbation analysis along with the fit discriminant and best fit values.

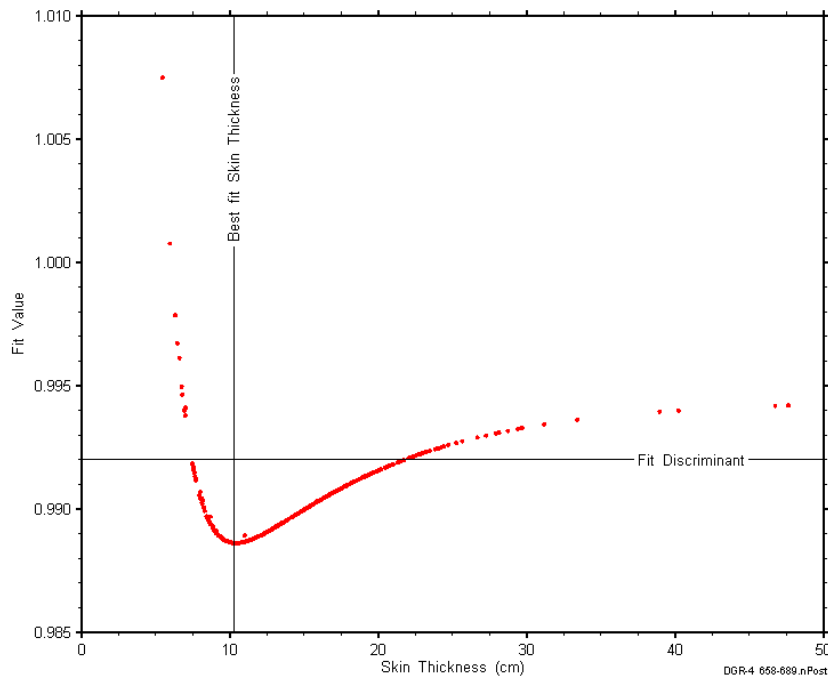


Figure D-253: XY-scatter plot showing the skin-thickness parameter space derived from DGR4_658.46-689.20 perturbation analysis along with the fit discriminant and best fit values.

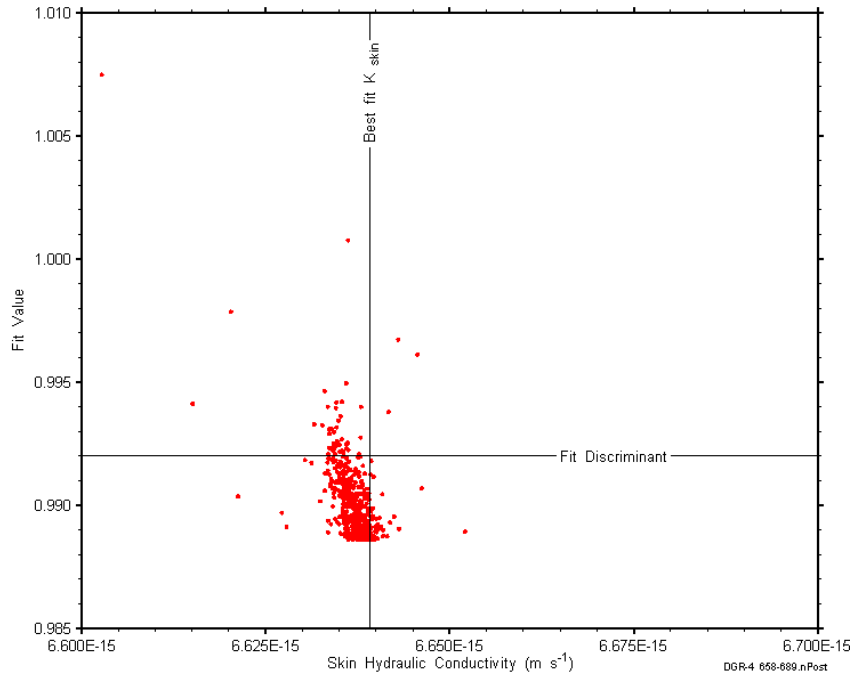


Figure D-254: XY-scatter plot showing the skin hydraulic conductivity parameter space derived from DGR4_658.46-689.20 perturbation analysis along with the fit discriminant and best fit values.

D.20 687.78-718.52 Sherman Fall

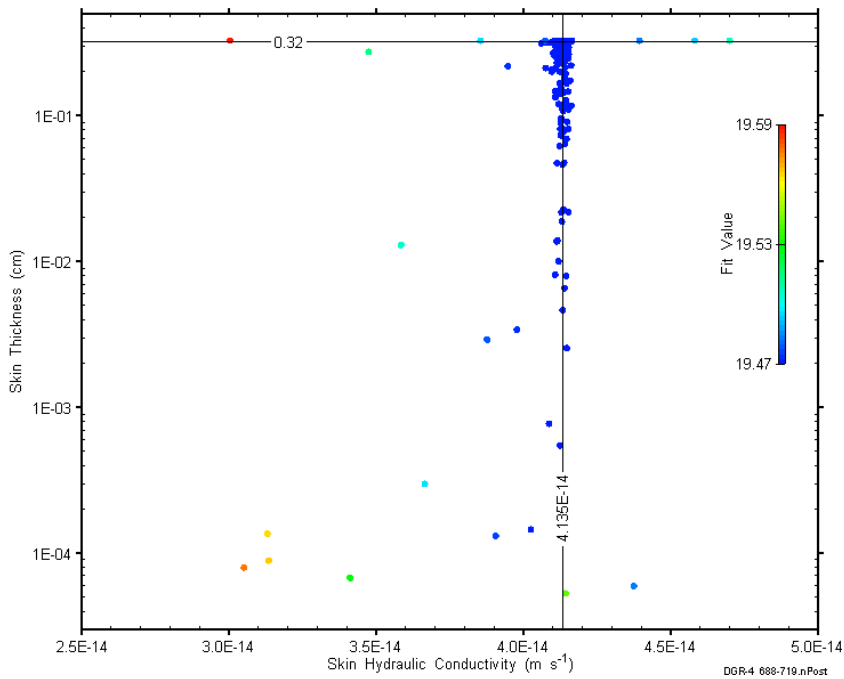


Figure D-255: XY-scatter plot showing estimates of skin hydraulic conductivity and skin thickness derived from the DGR4_687.78-718.52 perturbation analysis.

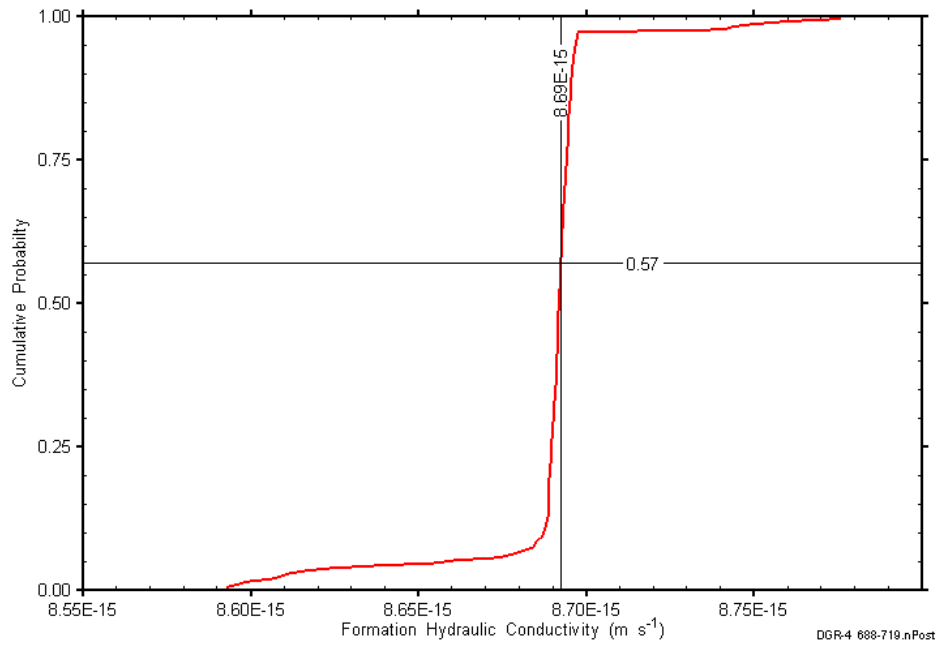


Figure D-256: DGR4_687.78-718.52 formation hydraulic conductivity cumulative distribution function.

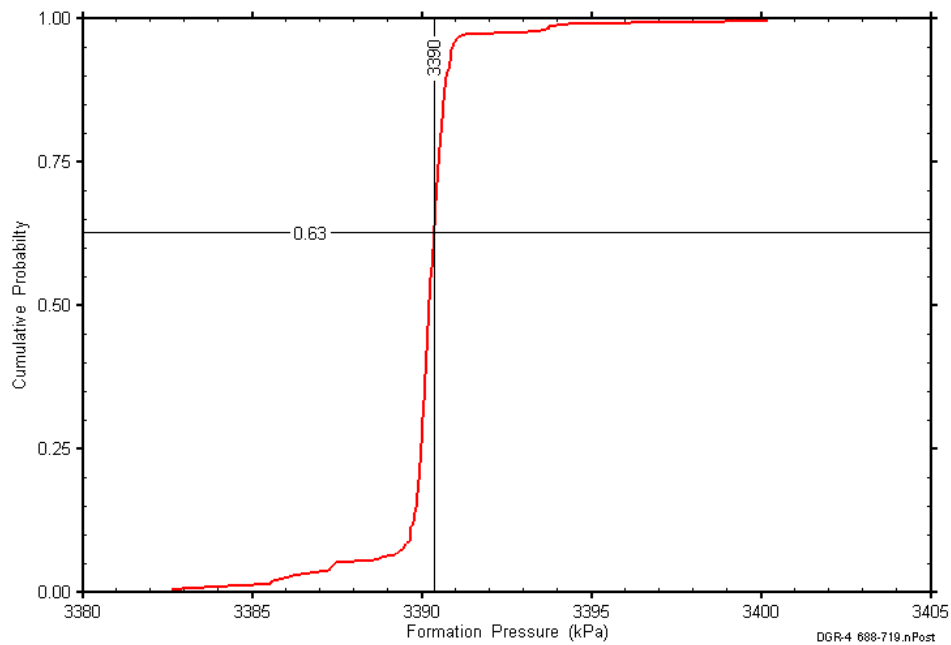


Figure D-257: DGR4_687.78-718.52 static formation pressure cumulative distribution function.

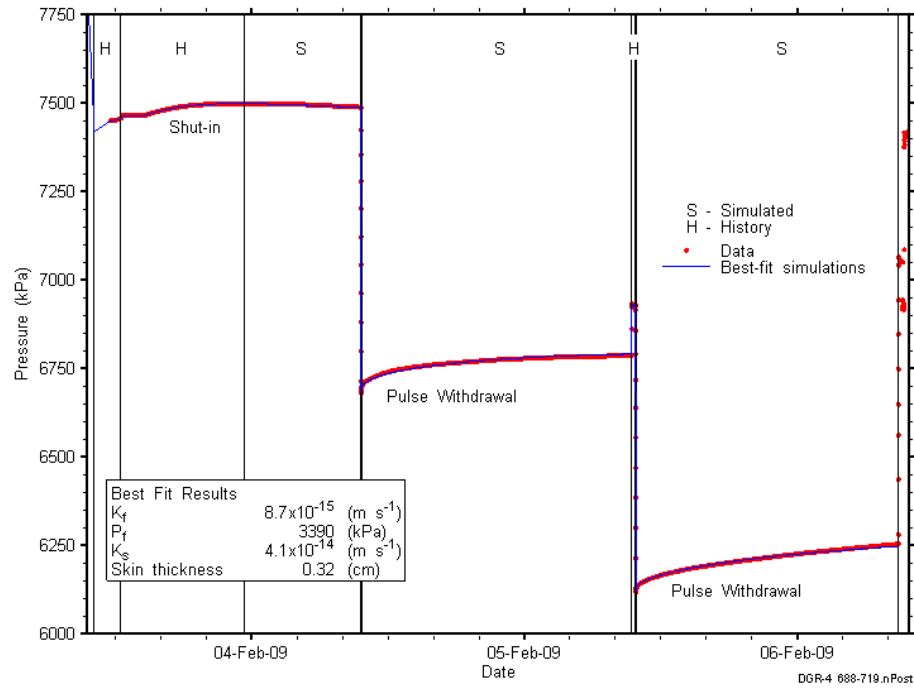


Figure D-258: Linear plot showing simulations of the DGR4_687.78-718.52 pressure response.

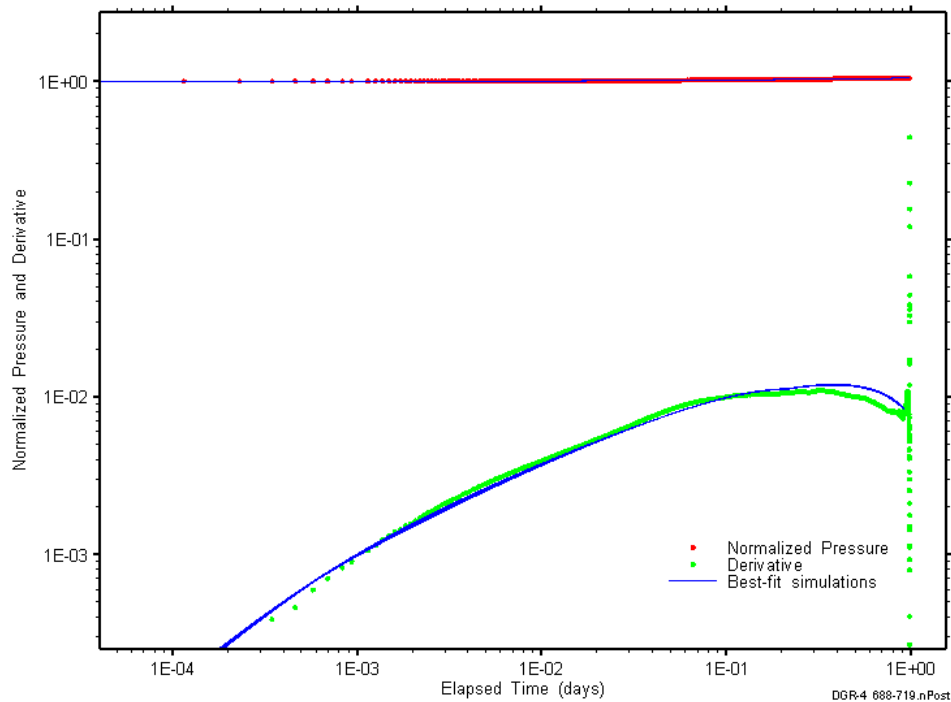


Figure D-259: Log-log plot showing simulations of the DGR4_687.78-718.52 pulse withdrawal #1 Ramey B and derivative response.

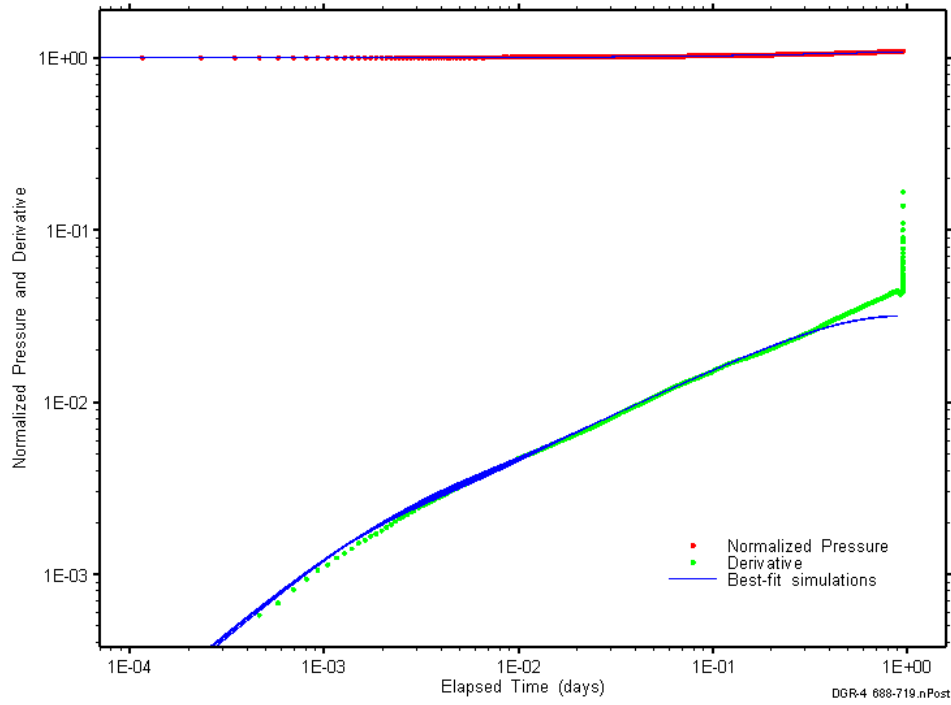


Figure D-260: Log-log plot showing simulations of the DGR4_687.78–718.52 pulse withdrawal #2 Ramey B and derivative response.

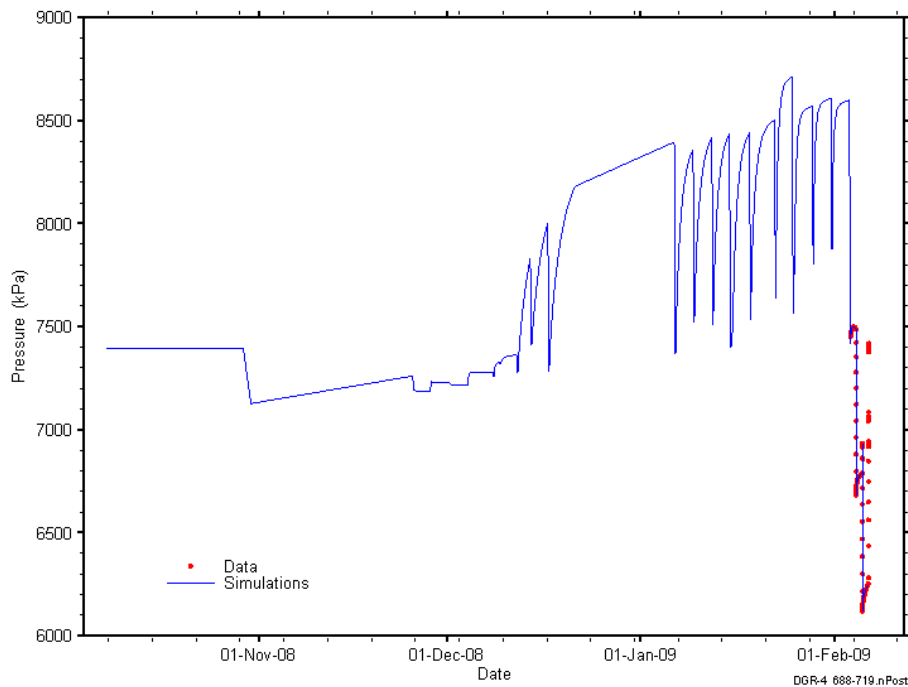


Figure D-261: Linear plot showing simulations of the DGR4_687.78-718.52 pressure response, including pre-test pressure history.

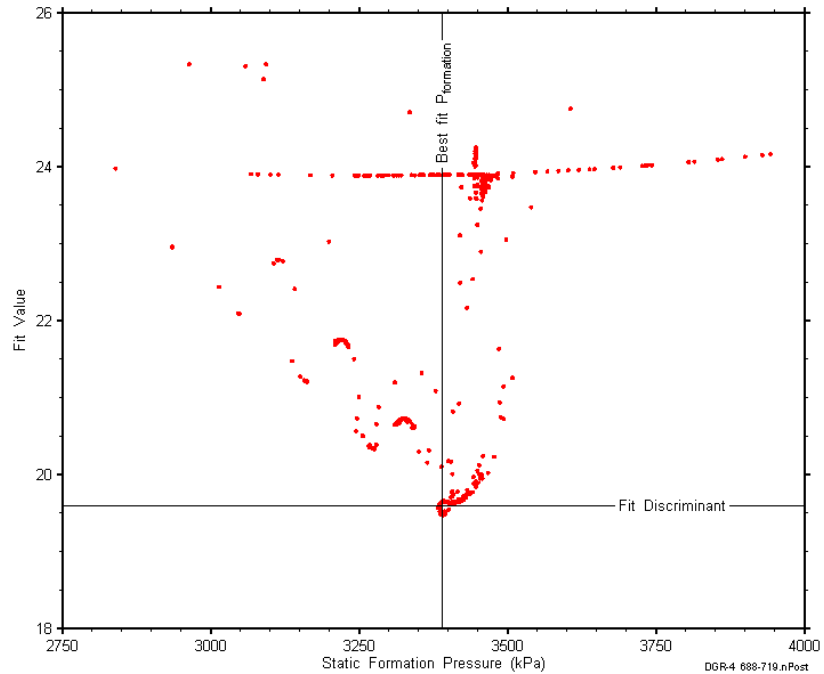


Figure D-262: XY-scatter plot showing the static formation pressure parameter space derived from DGR4_687.78-718.52 perturbation analysis along with the fit discriminant and best fit values.

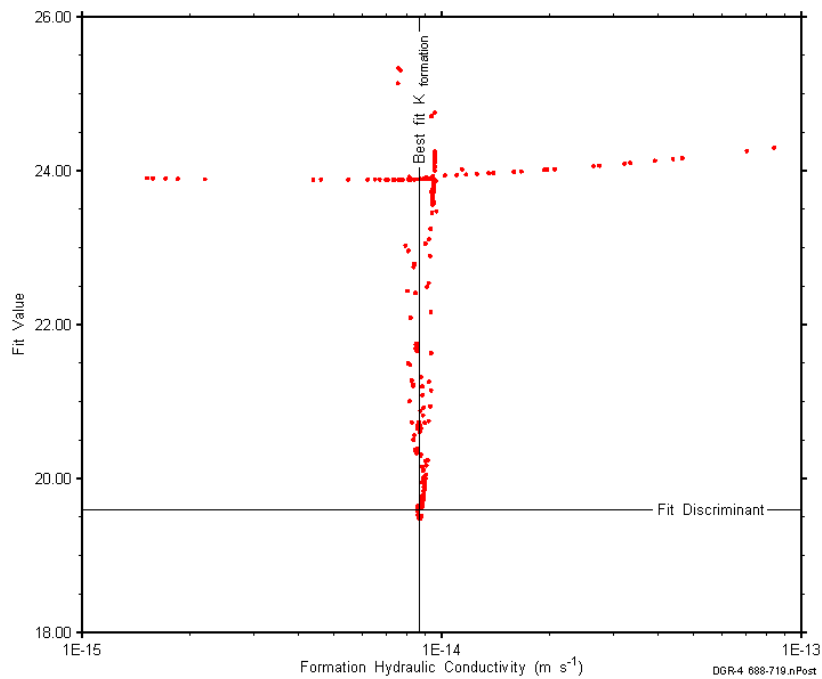


Figure D-263: XY-scatter plot showing the formation hydraulic conductivity parameter space derived from DGR4_687.78-718.52 perturbation analysis along with the fit discriminant and best fit values.

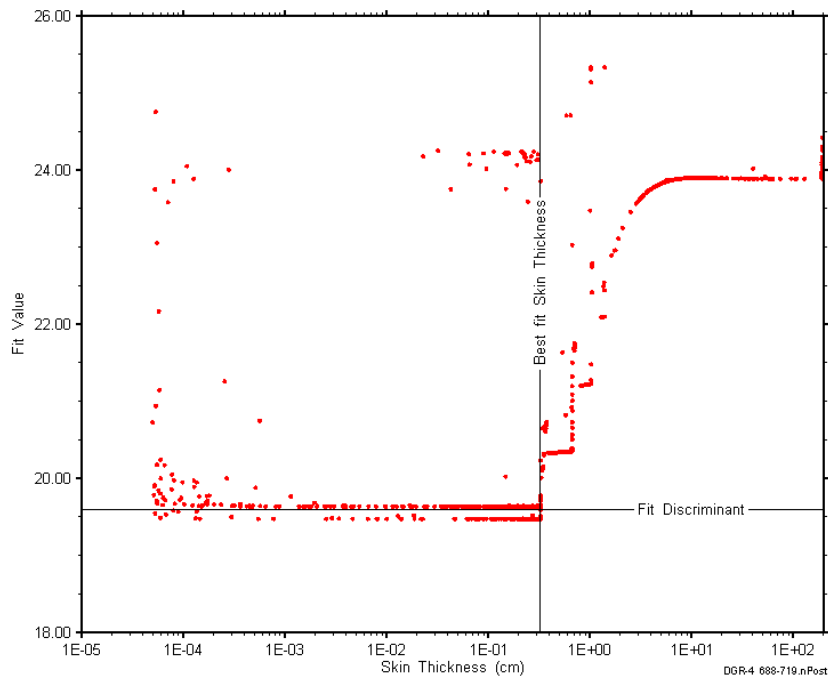


Figure D-264: XY-scatter plot showing the skin-thickness parameter space derived from DGR4_687.78-718.52 perturbation analysis along with the fit discriminant and best fit values.

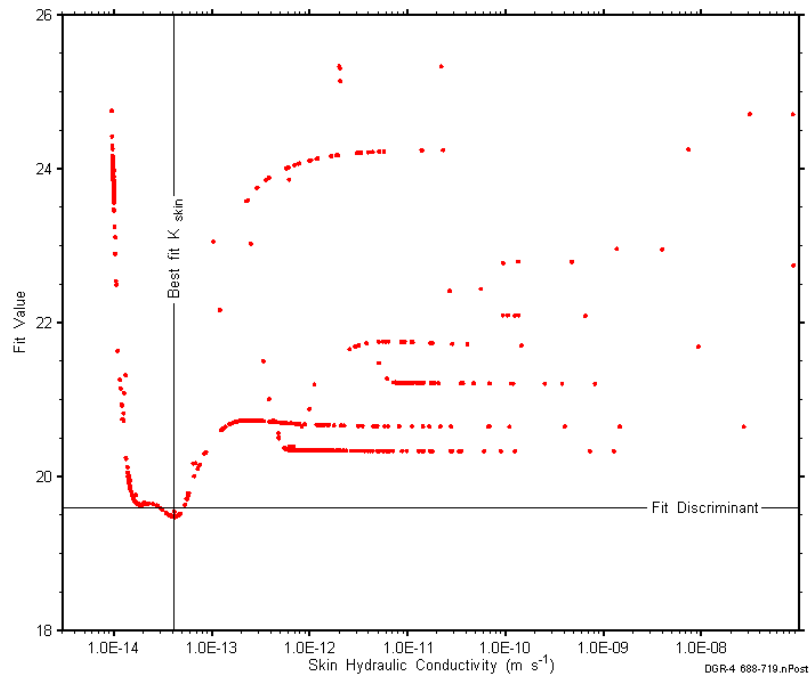


Figure D-265: XY-scatter plot showing the skin hydraulic conductivity parameter space derived from DGR4_687.78-718.52 perturbation analysis along with the fit discriminant and best fit values.

D.21 717.10-747.84 Kirkfield

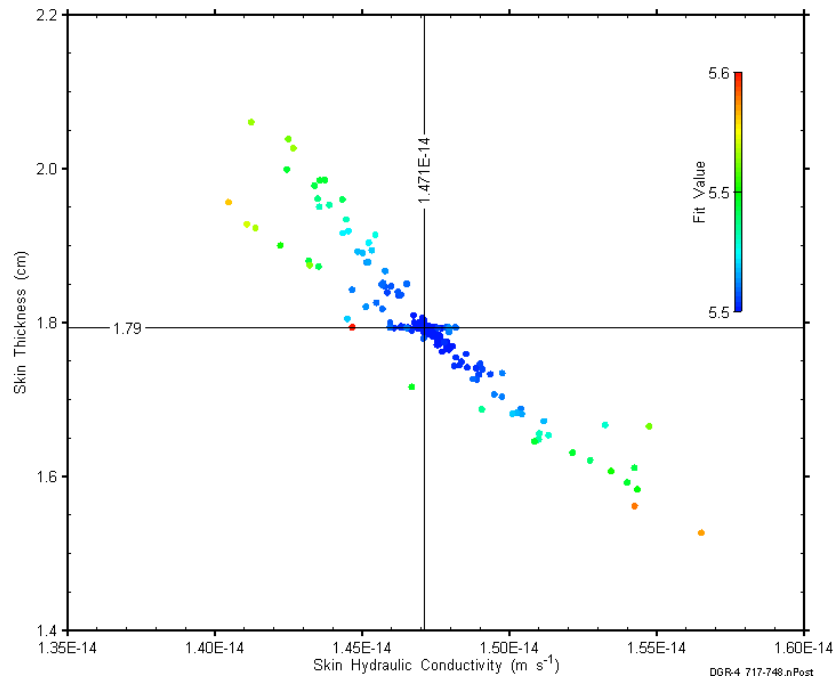


Figure D-266: XY-scatter plot showing estimates of skin hydraulic conductivity and skin thickness derived from the DGR4_717.10-747.84 perturbation analysis.

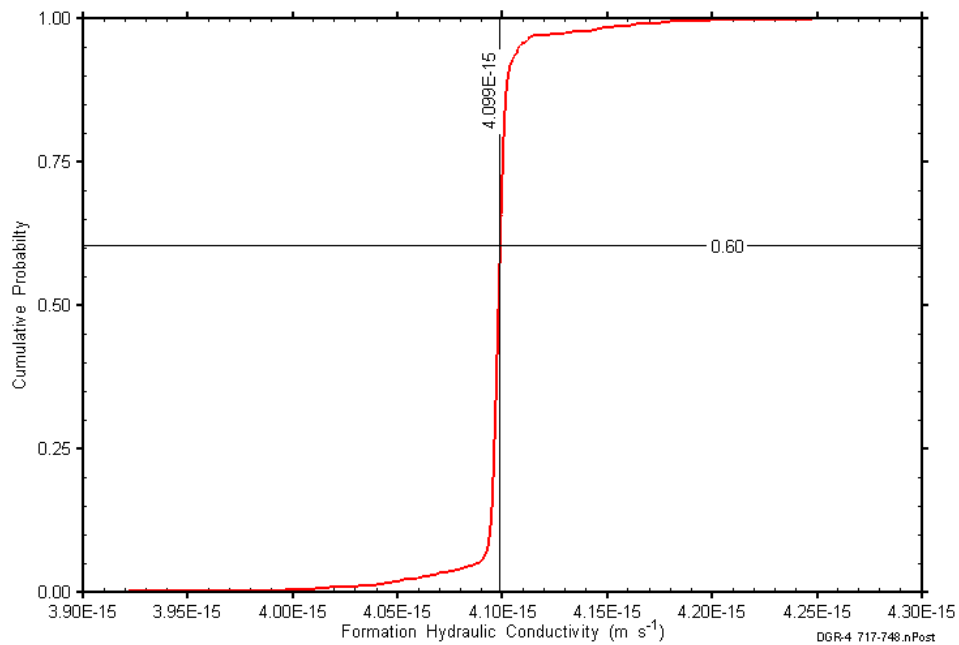


Figure D-267: DGR4_717.10-747.84 formation hydraulic conductivity cumulative distribution function.

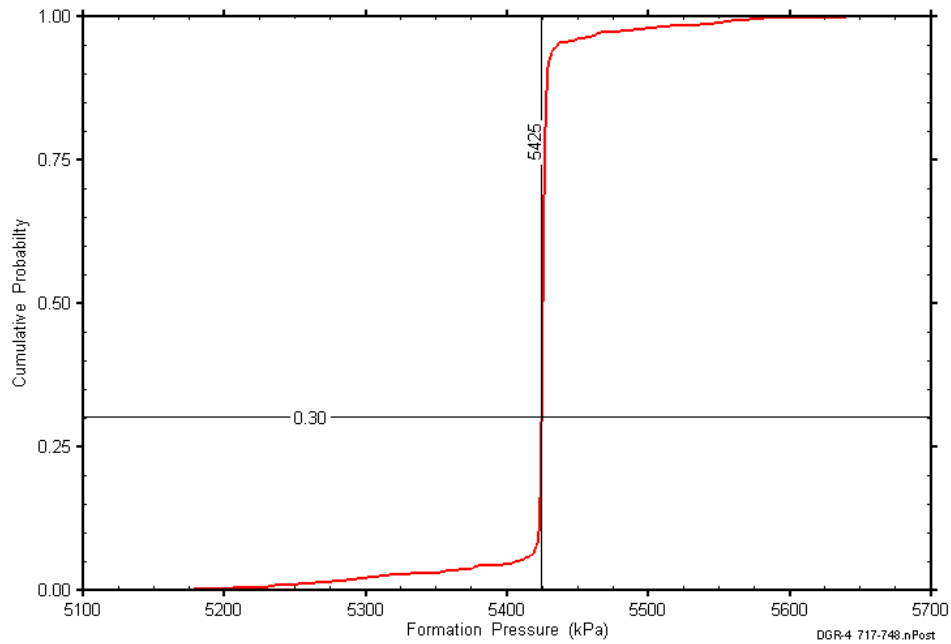


Figure D-268: DGR4_717.10-747.84 static formation pressure cumulative distribution function.

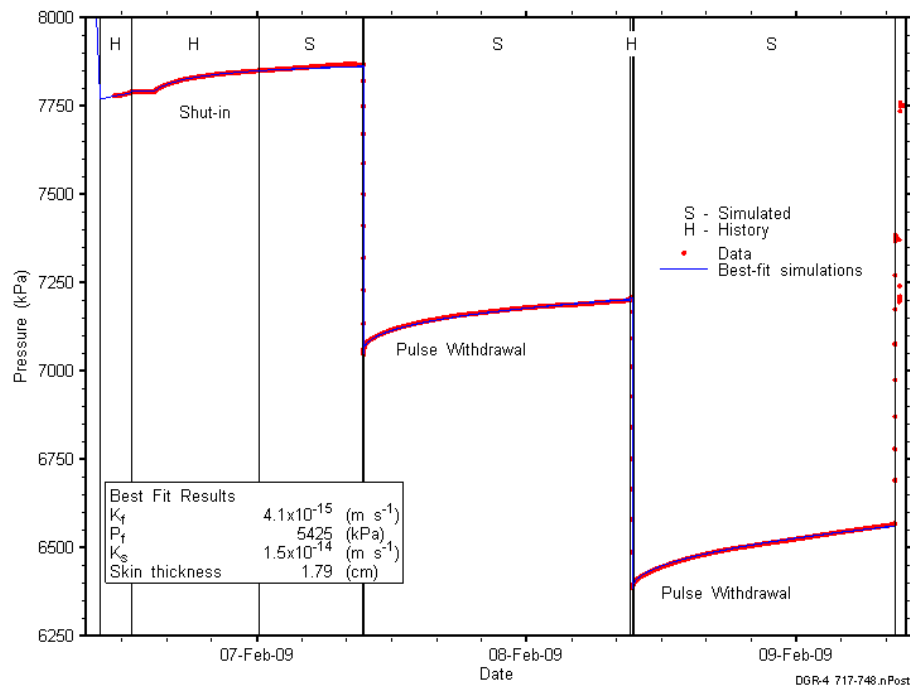


Figure D-269: Linear plot showing simulations of the DGR4_717.10-747.84 pressure response.

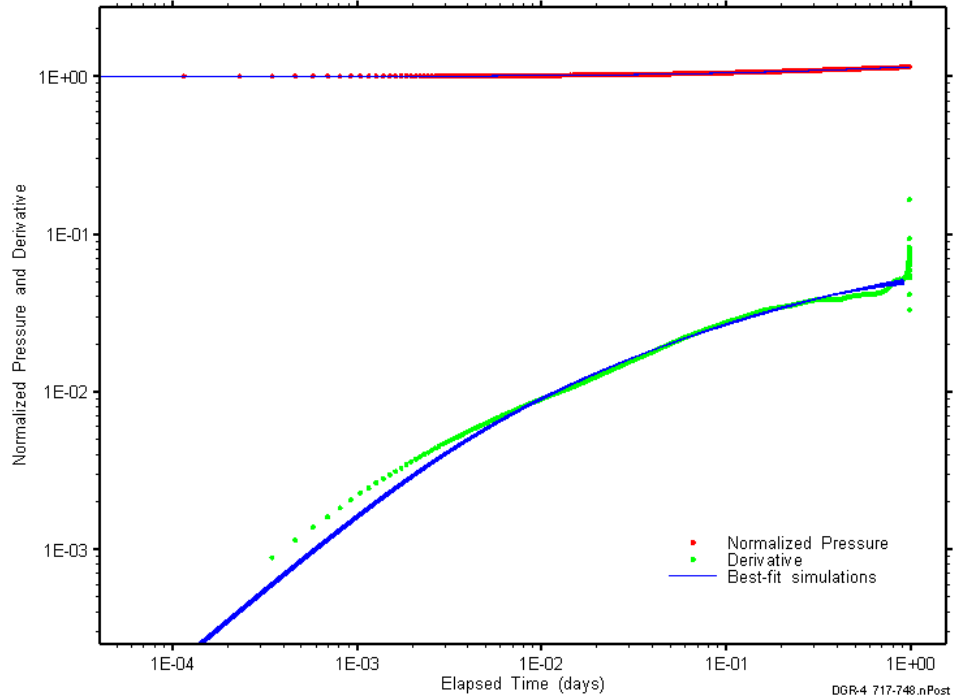


Figure D-270: Log-log plot showing simulations of the DGR4_717.10–747.84 pulse withdrawal #1 Ramey B and derivative response.

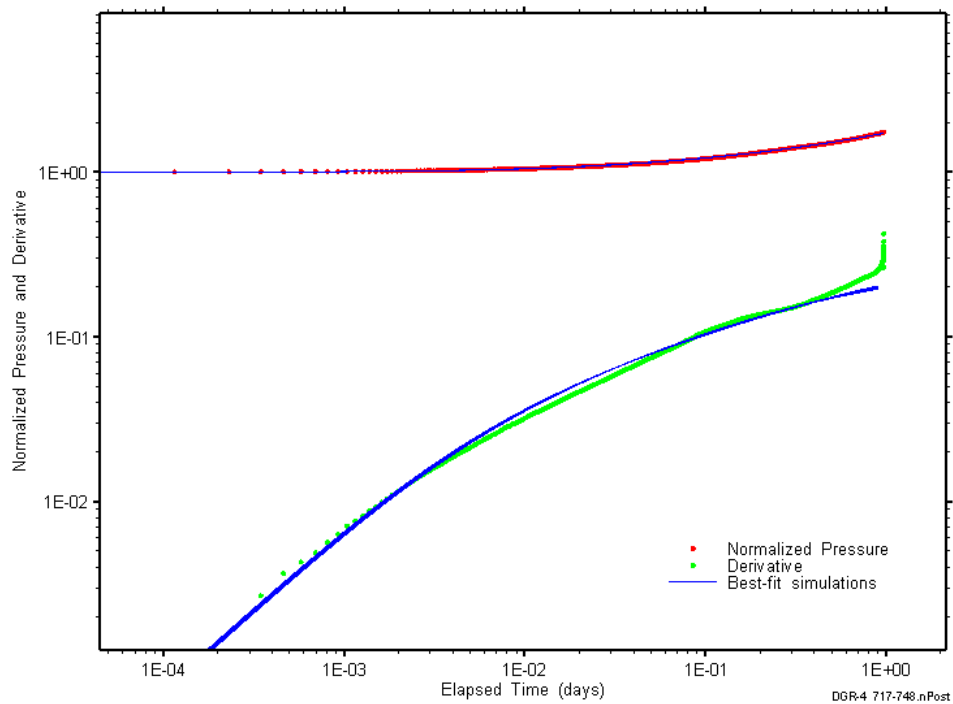


Figure D-271: Log-log plot showing simulations of the DGR4_717.10–747.84 pulse withdrawal #2 Ramey B and derivative response.

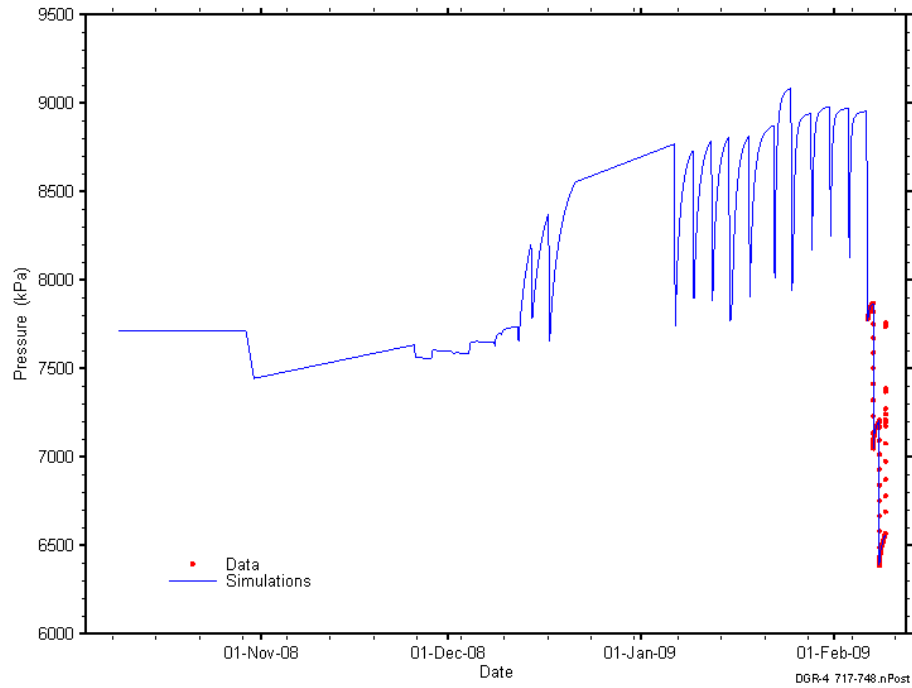


Figure D-272: Linear plot showing simulations of the DGR4_717.10-747.84 pressure response, including pre-test pressure history.

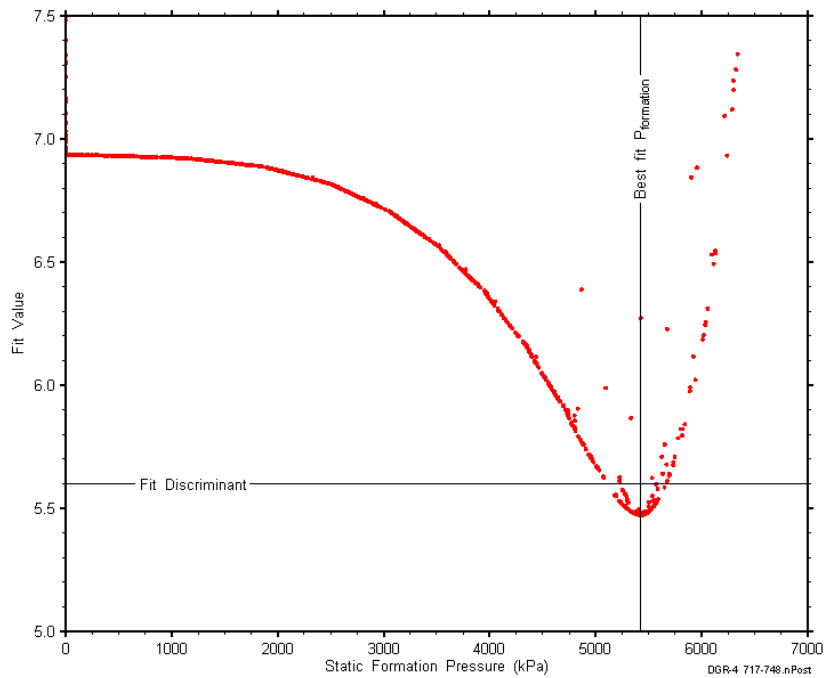


Figure D-273: XY-scatter plot showing the static formation pressure parameter space derived from DGR4_717.10-747.84 perturbation analysis along with the fit discriminant and best fit values.

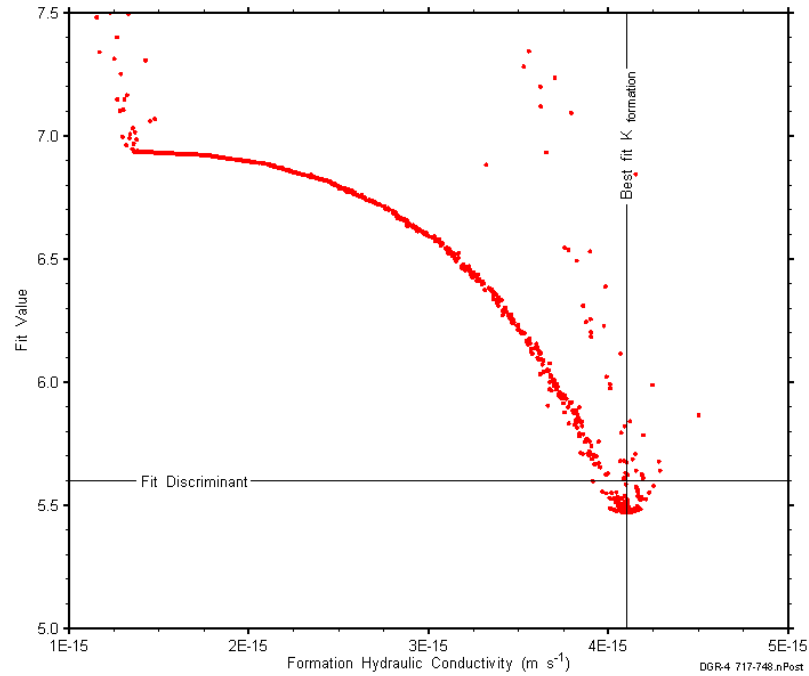


Figure D-274: XY-scatter plot showing the formation hydraulic conductivity parameter space derived from DGR4_717.10-747.84 perturbation analysis along with the fit discriminant and best fit values.

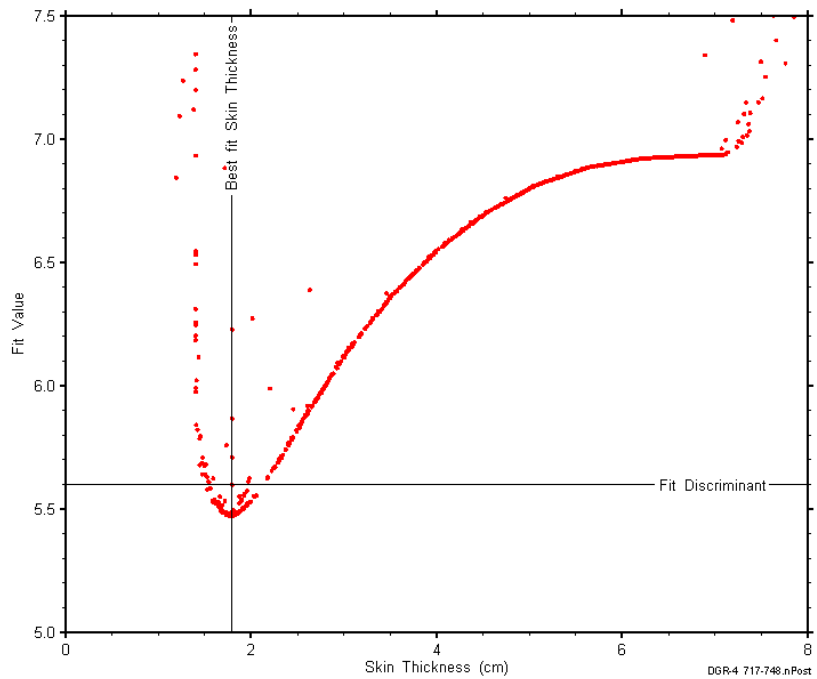


Figure D-275: XY-scatter plot showing the skin-thickness parameter space derived from DGR4_717.10-747.84 perturbation analysis along with the fit discriminant and best fit values.

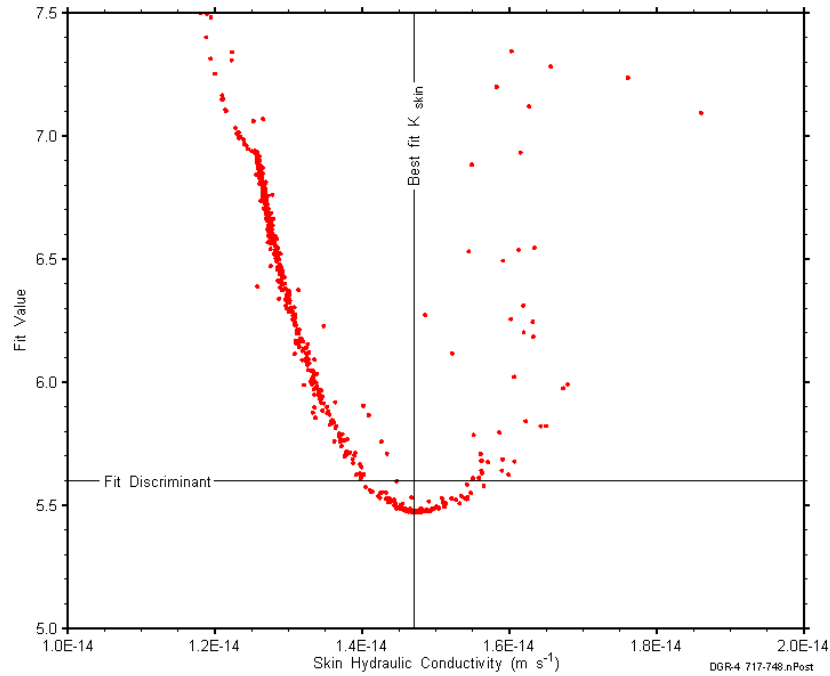


Figure D-276: XY-scatter plot showing the skin hydraulic conductivity parameter space derived from DGR4_717.10-747.84 perturbation analysis along with the fit discriminant and best fit values.

D.22 747.64-778.38 Kirkfield-Coboconk

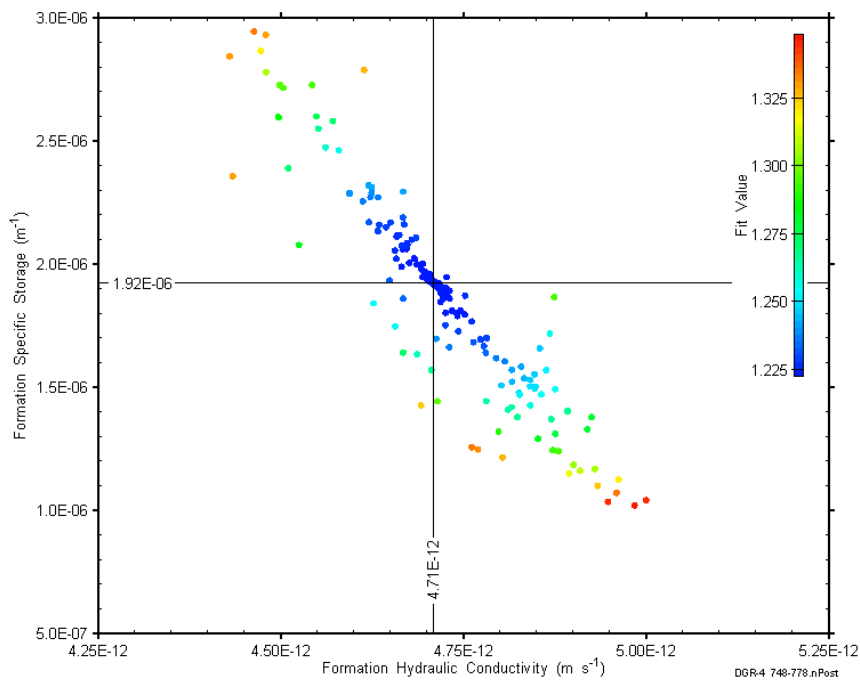


Figure D-277: XY-scatter plot showing estimates of formation hydraulic conductivity and formation specific storage derived from the DGR4_747.64-778.38 perturbation analysis.

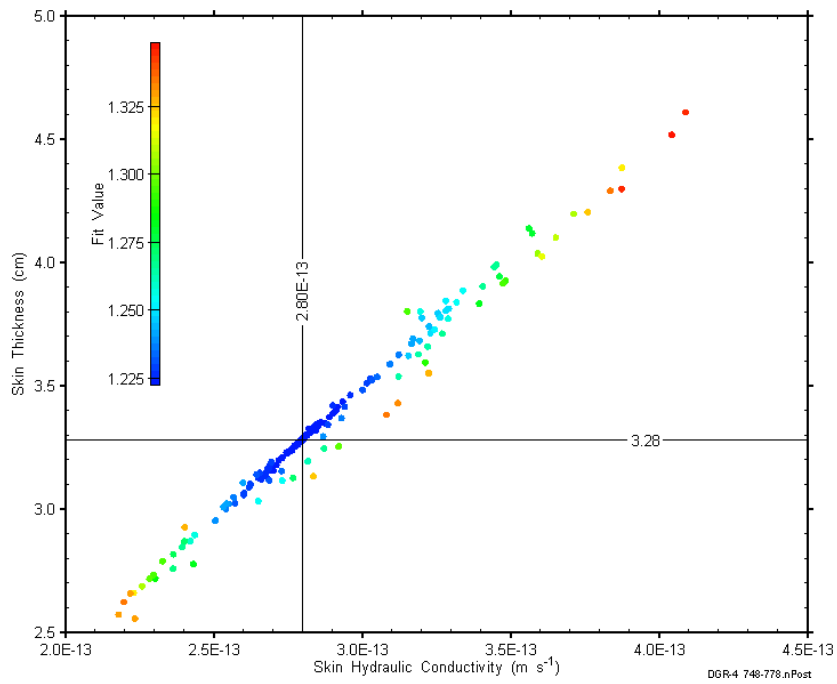


Figure D-278: XY-scatter plot showing estimates of skin hydraulic conductivity and skin thickness derived from the DGR4_747.64-778.38 perturbation analysis.

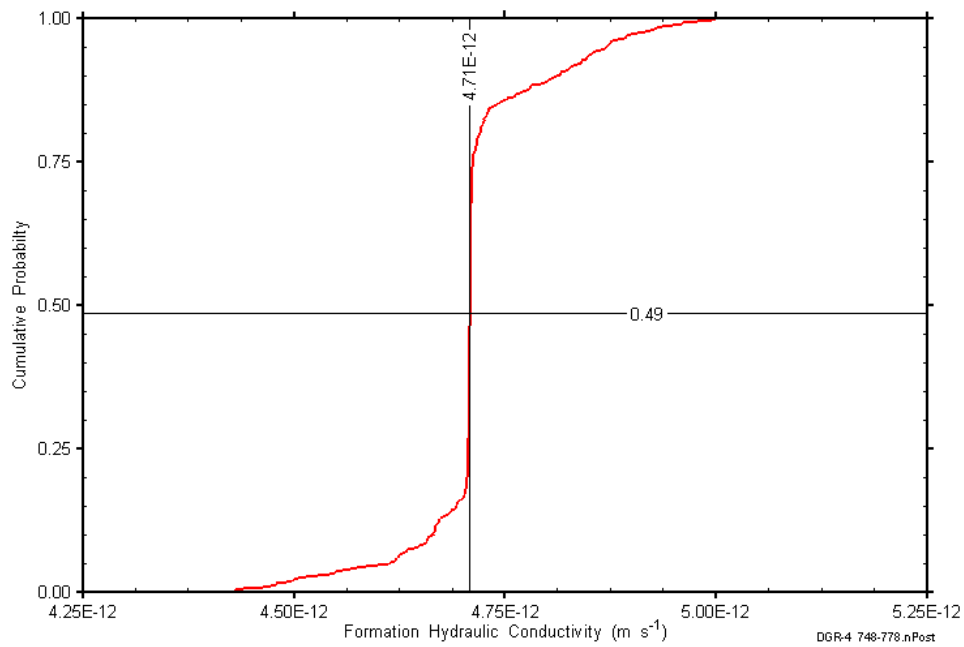


Figure D-279: DGR4_747.64-778.38 formation hydraulic conductivity cumulative distribution function.

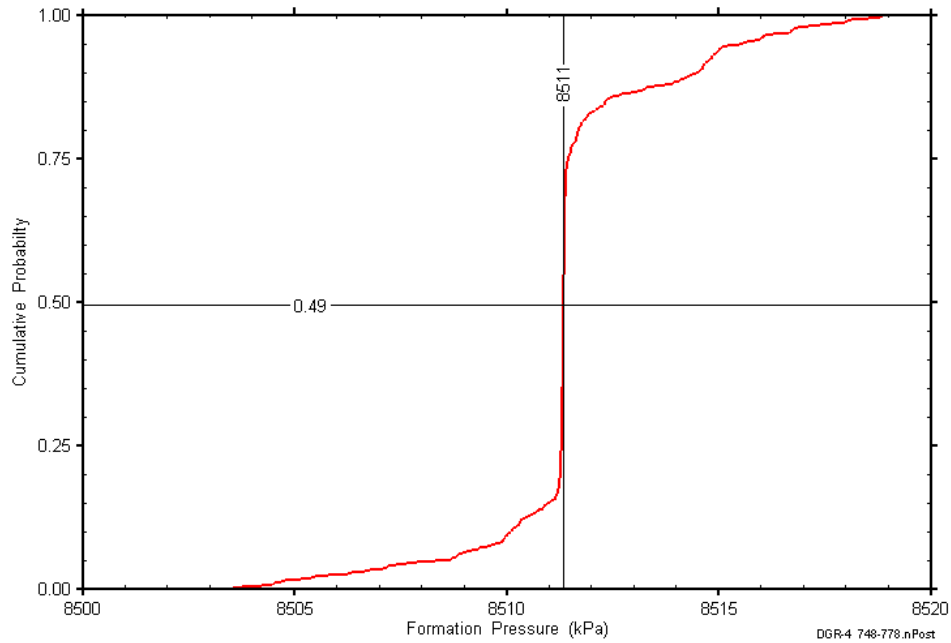


Figure D-280: DGR4_747.64-778.38 static formation pressure cumulative distribution function.

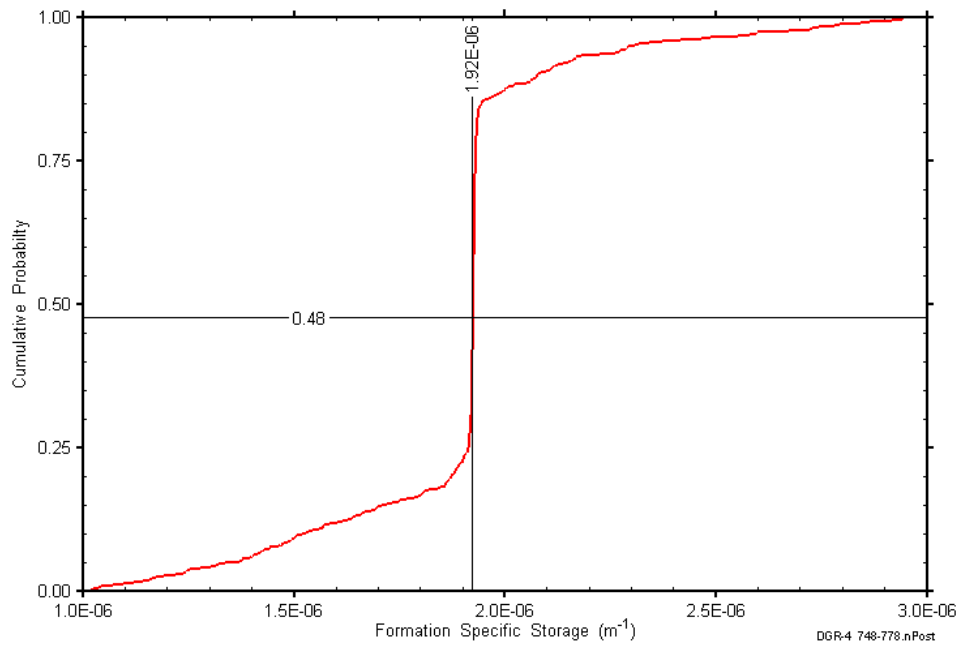


Figure D-281: DGR4_747.64-778.38 formation specific storage cumulative distribution function.

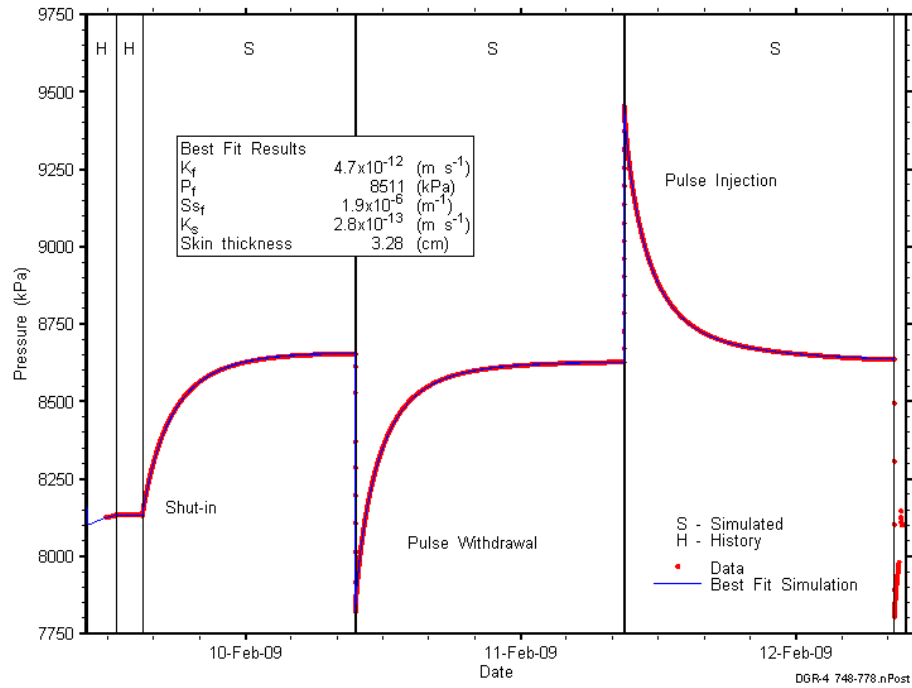


Figure D-282: Linear plot showing simulations of the DGR4_747.64-778.38 pressure response.

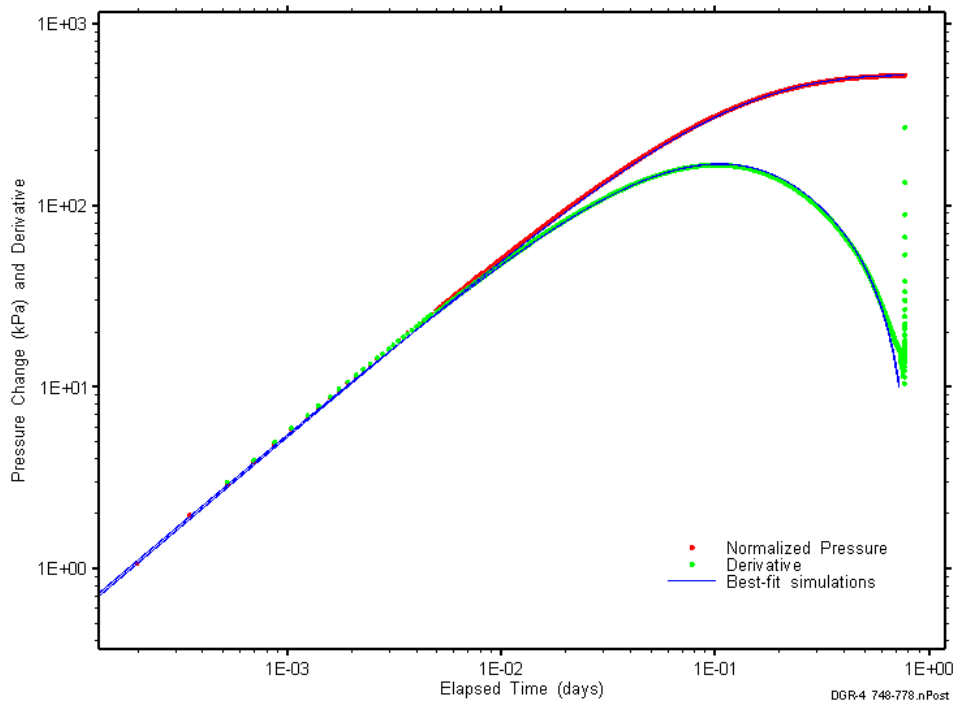


Figure D-283: Log-log plot showing simulations of the DGR4_747.64-778.38 shut-in period Ramey B and derivative response.

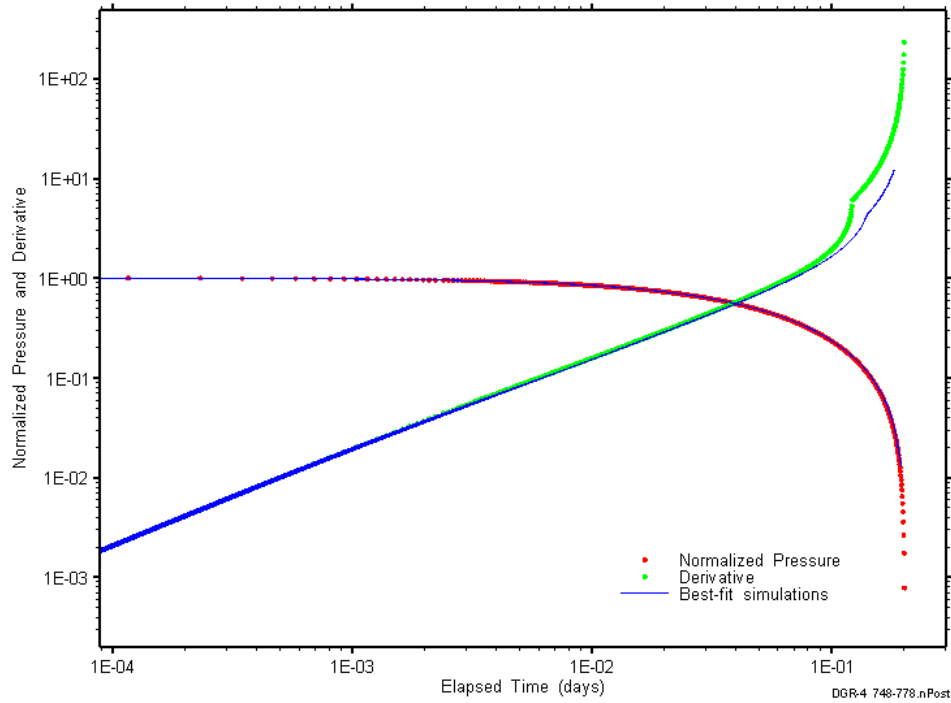


Figure D-284: Log-log plot showing simulations of the DGR4_747.64–778.38 pulse withdrawal Ramey B and derivative response.

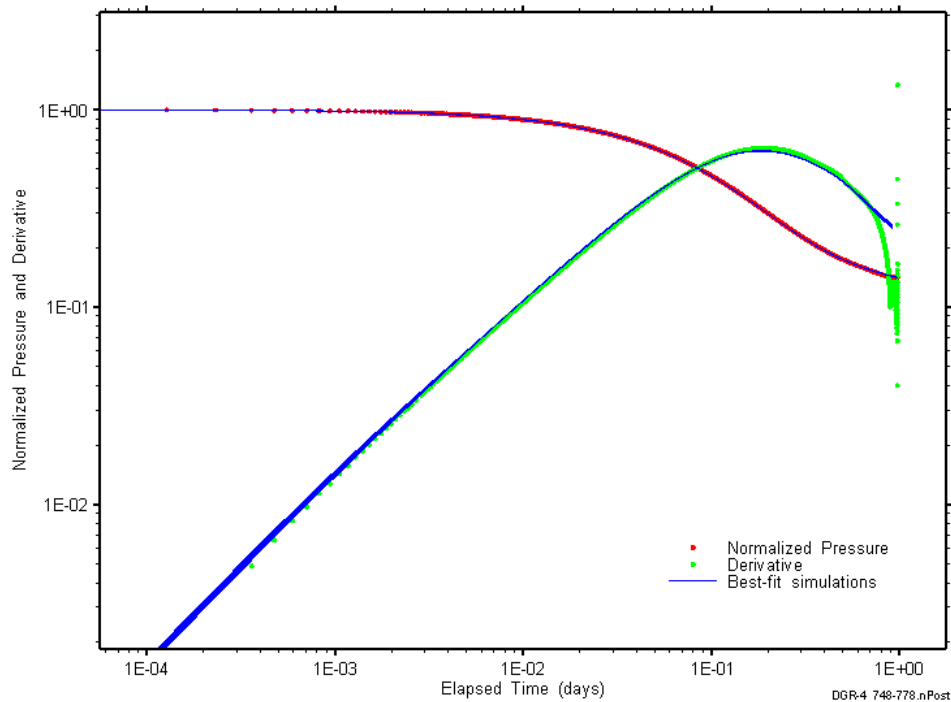


Figure D-285: Log-log plot showing simulations of the DGR4_747.64–778.38 pulse injection Ramey B and derivative response.

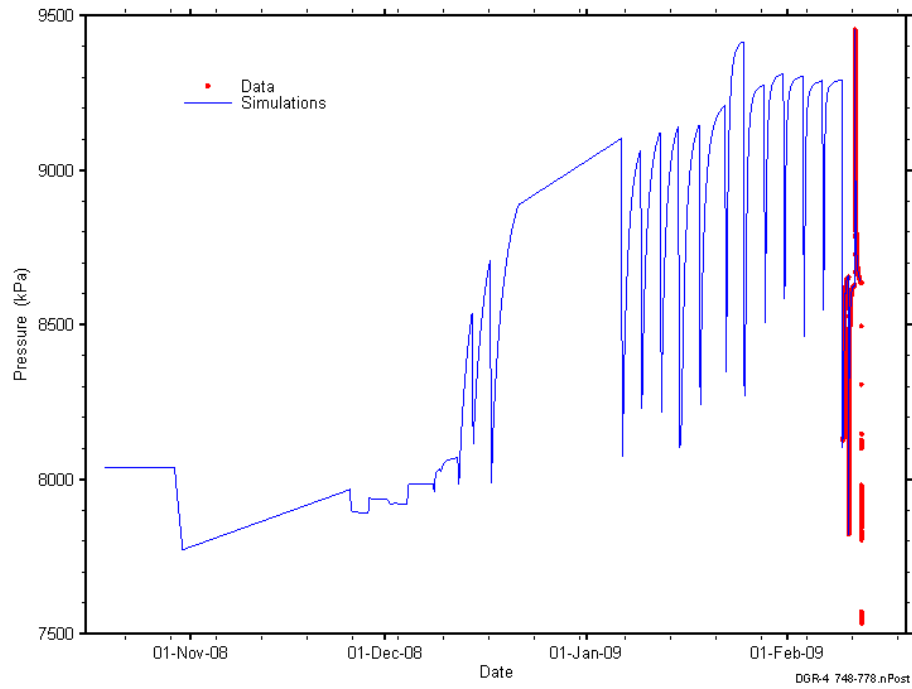


Figure D-286: Linear plot showing simulations of the DGR4_747.64-778.38 pressure response, including pre-test pressure history.

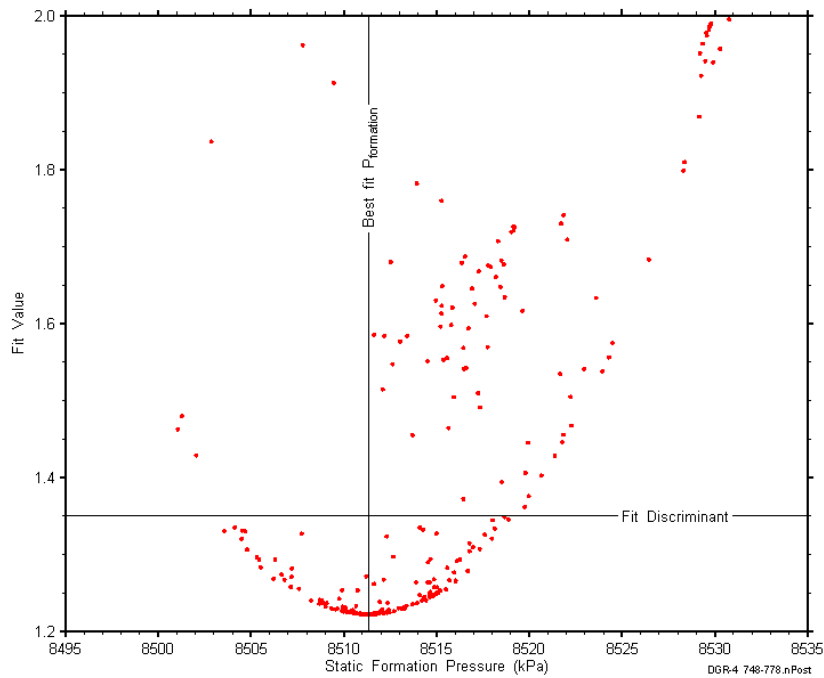


Figure D-287: XY-scatter plot showing the static formation pressure parameter space derived from DGR4_747.64-778.38 perturbation analysis along with the fit discriminant and best fit values.

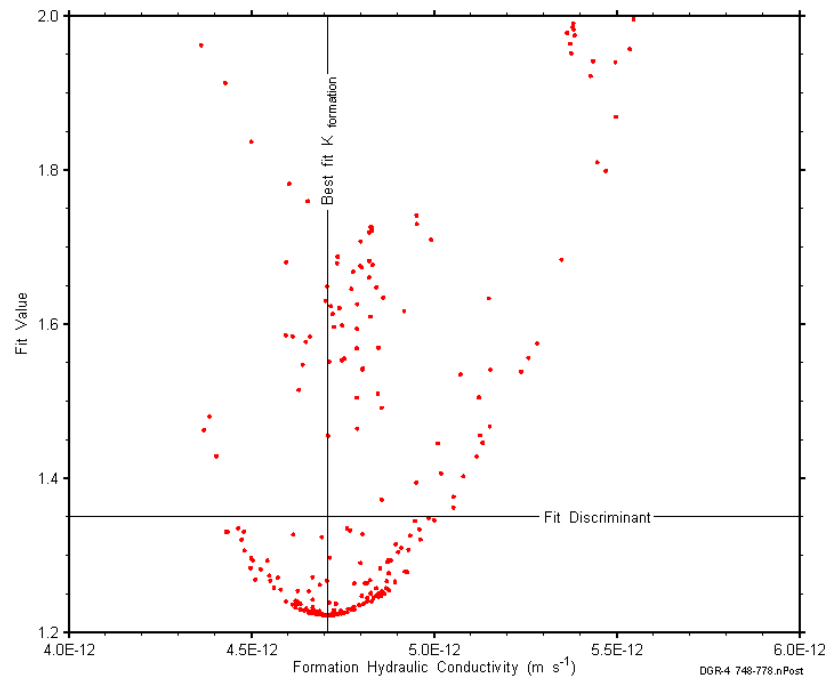


Figure D-288: XY-scatter plot showing the formation hydraulic conductivity parameter space derived from DGR4_747.64-778.38 perturbation analysis along with the fit discriminant and best fit values.

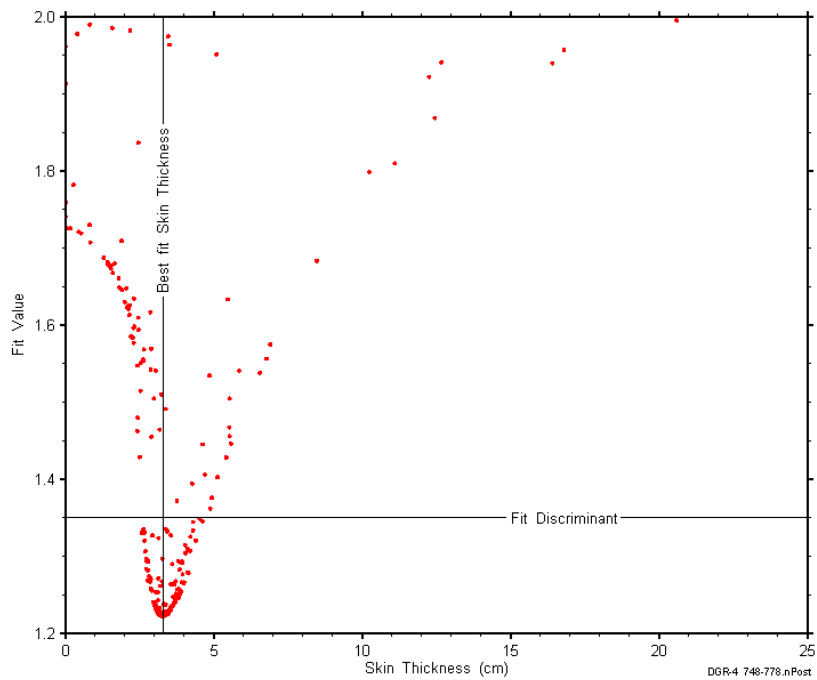


Figure D-289: XY-scatter plot showing the skin-thickness parameter space derived from DGR4_747.64-778.38 perturbation analysis along with the fit discriminant and best fit values.

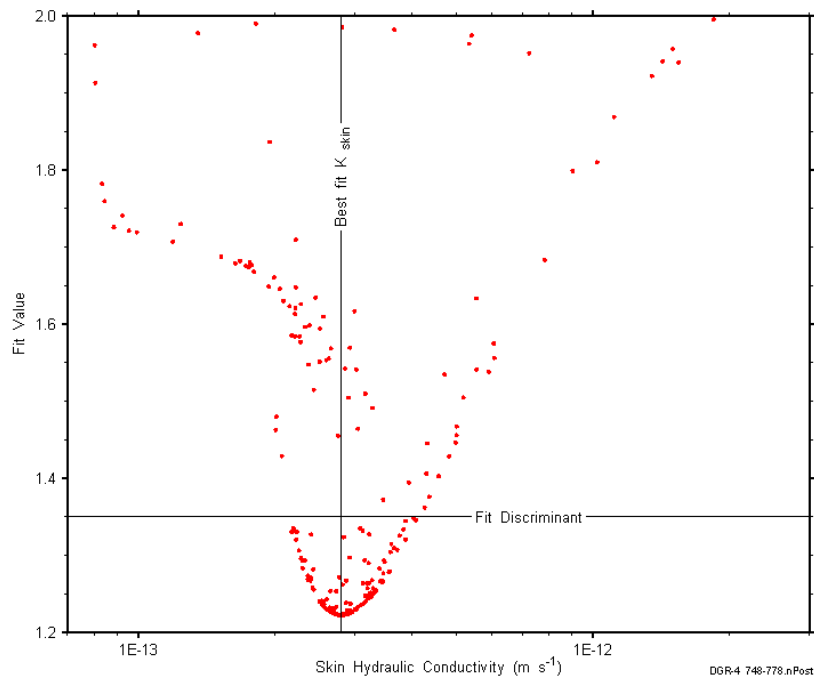


Figure D-290: XY-scatter plot showing the skin hydraulic conductivity parameter space derived from DGR4_747.64-778.38 perturbation analysis along with the fit discriminant and best fit values.

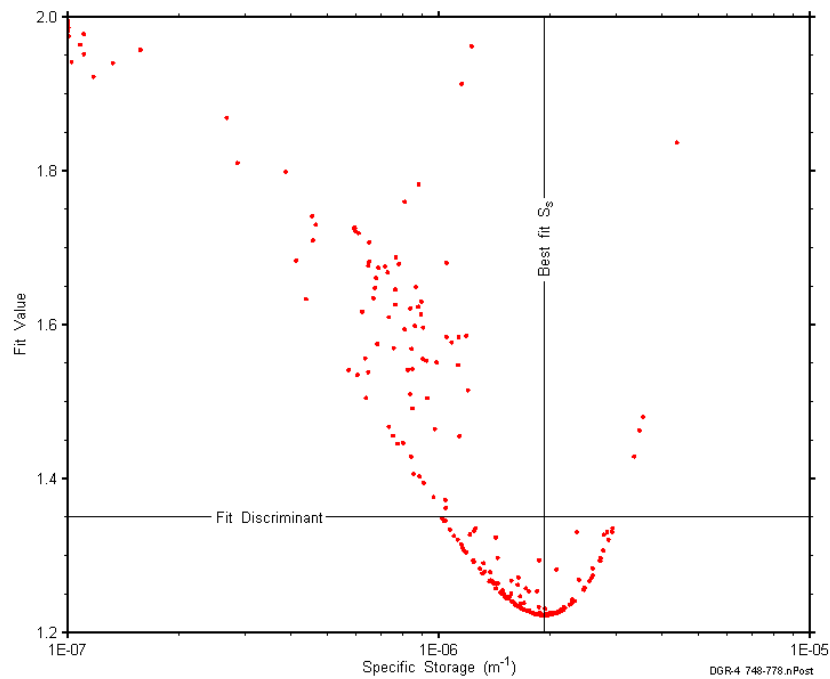


Figure D-291: XY-scatter plot showing the formation specific storage parameter space derived from DGR4_747.64-778.38 perturbation analysis along with the fit discriminant and best fit values.

D.23 762.80-793.54 Coboconk-Gull River

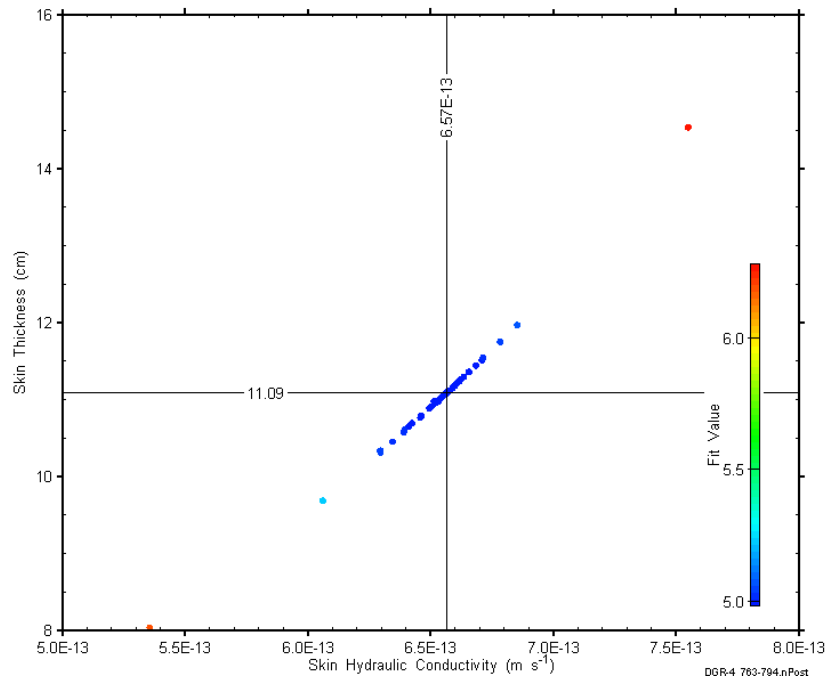


Figure D-292: XY-scatter plot showing estimates of skin hydraulic conductivity and skin thickness derived from the DGR4_762.80-793.54 perturbation analysis.

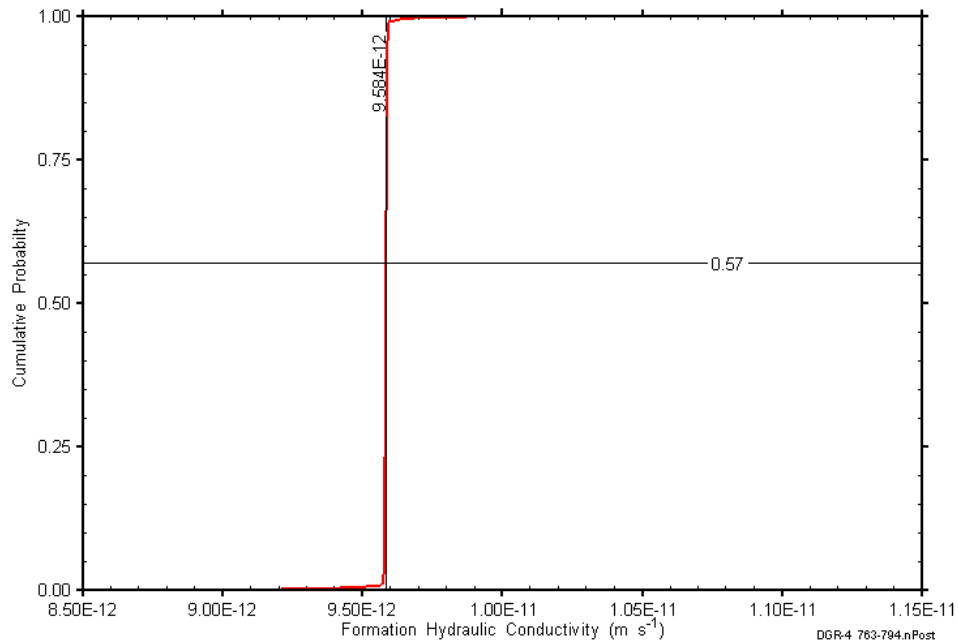


Figure D-293: DGR4_762.80-793.54 formation hydraulic conductivity cumulative distribution function.

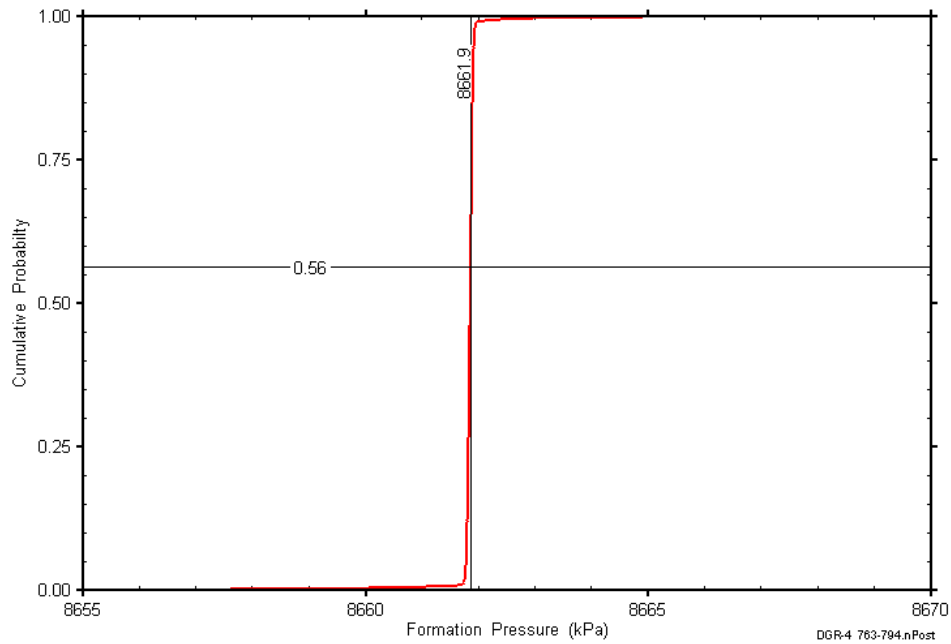


Figure D-294: DGR4_762.80-793.54 static formation pressure cumulative distribution function.

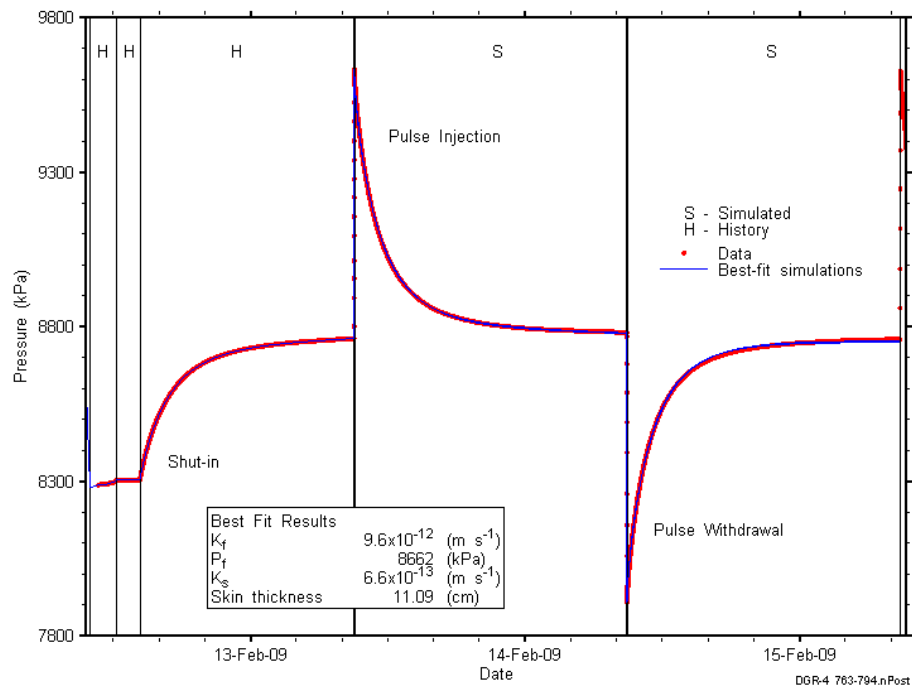


Figure D-295: Linear plot showing simulations of the DGR4_762.80-793.54 pressure response.

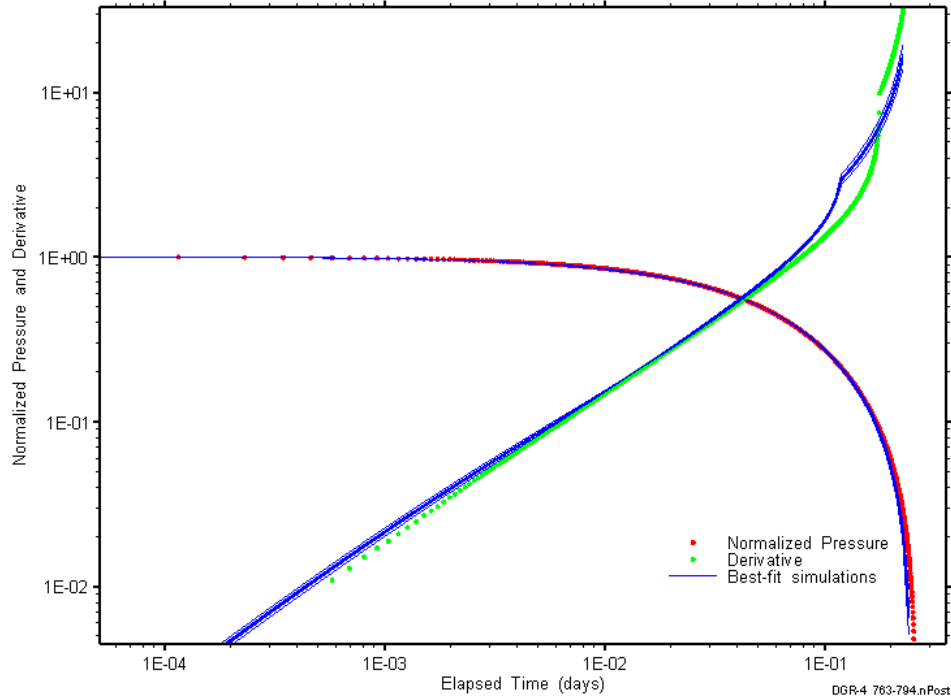


Figure D-296: Log-log plot showing simulations of the DGR4_762.80–793.54 pulse injection Ramey B and derivative response.

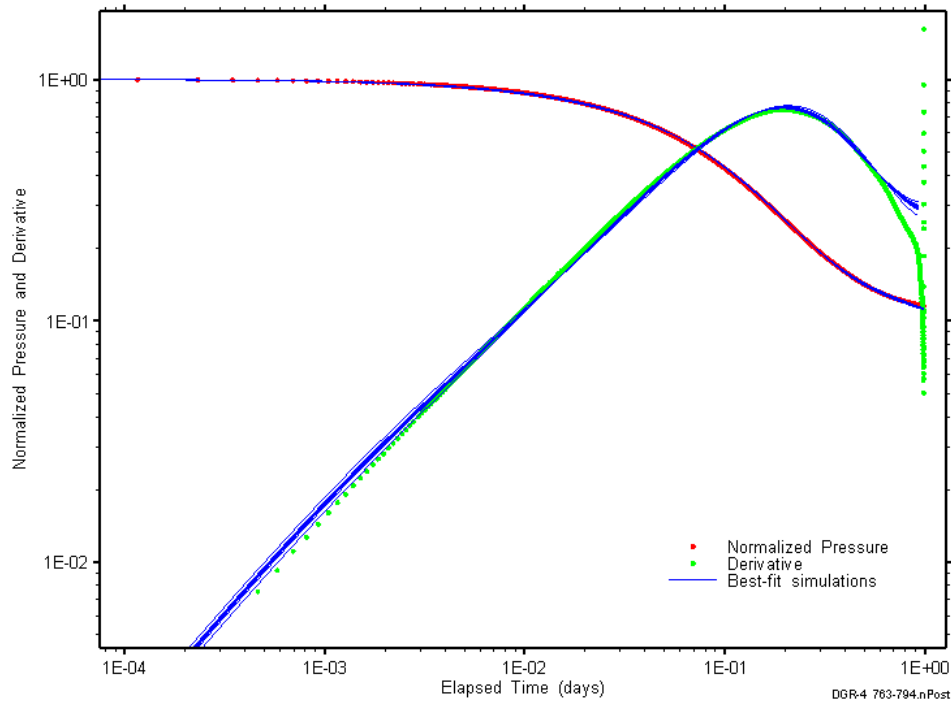


Figure D-297: Log-log plot showing simulations of the DGR4_762.80–793.54 pulse withdrawal Ramey B and derivative response.

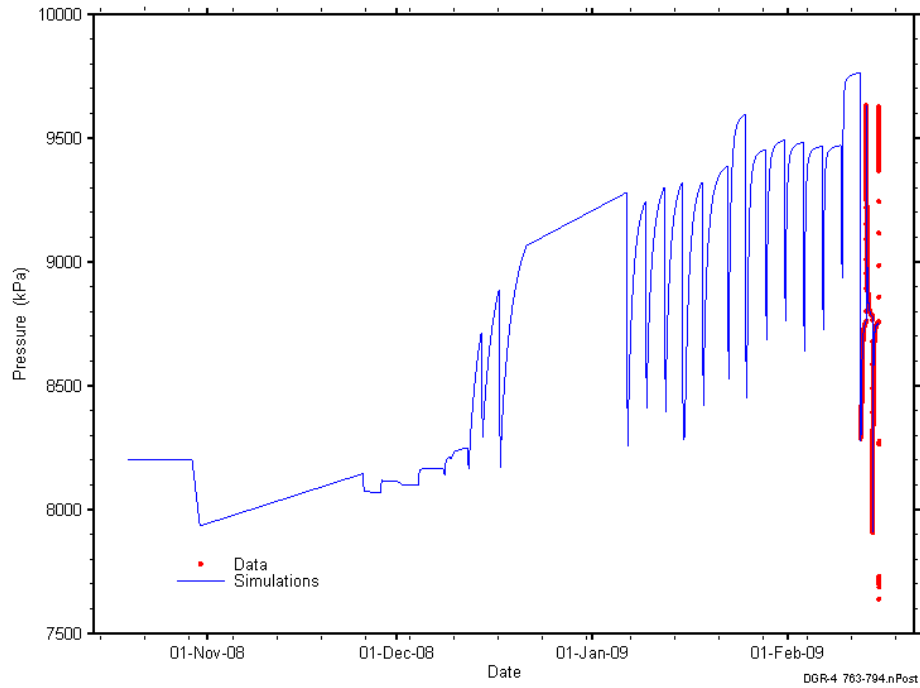


Figure D-298: Linear plot showing simulations of the DGR4_762.80-793.54 pressure response, including pre-test pressure history.

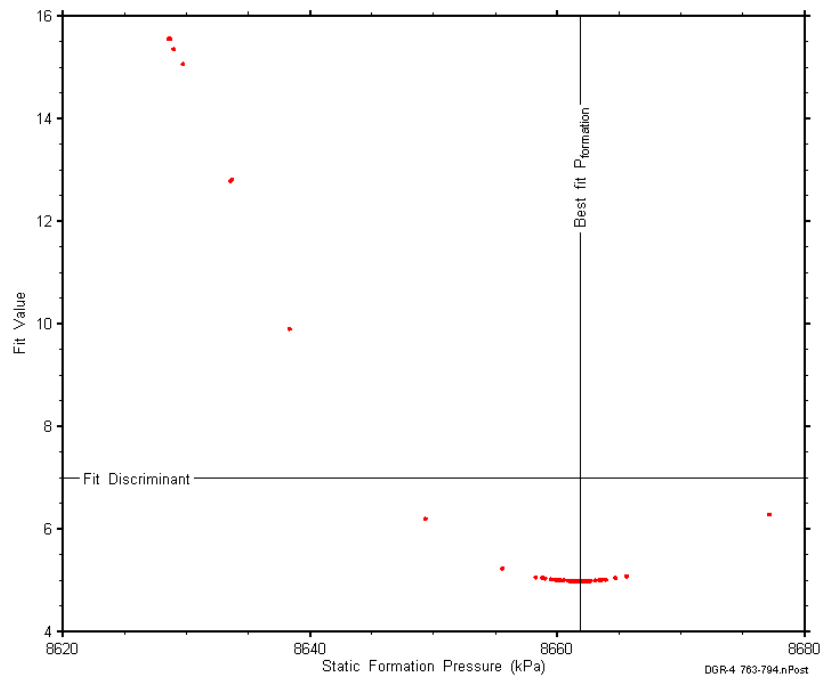


Figure D-299: XY-scatter plot showing the static formation pressure parameter space derived from DGR4_762.80-793.54 perturbation analysis along with the fit discriminant and best fit values.

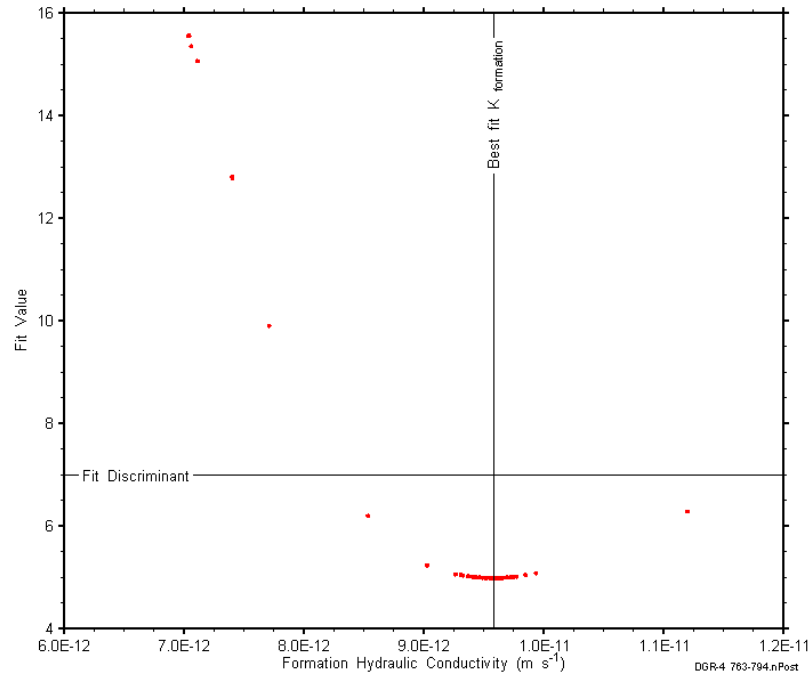


Figure D-300: XY-scatter plot showing the formation hydraulic conductivity parameter space derived from DGR4_762.80-793.54 perturbation analysis along with the fit discriminant and best fit values.

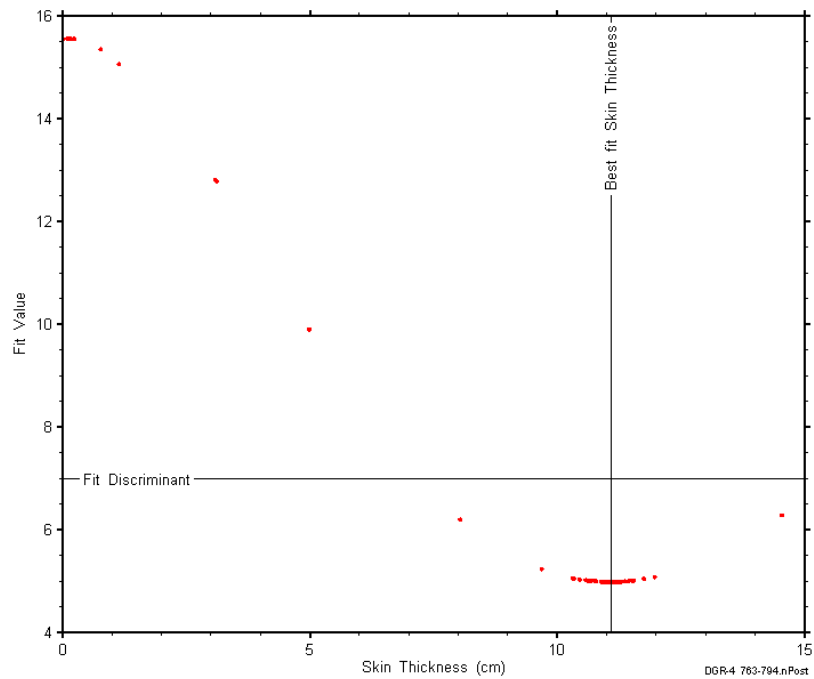


Figure D-301: XY-scatter plot showing the skin-thickness parameter space derived from DGR4_762.80-793.54 perturbation analysis along with the fit discriminant and best fit values.

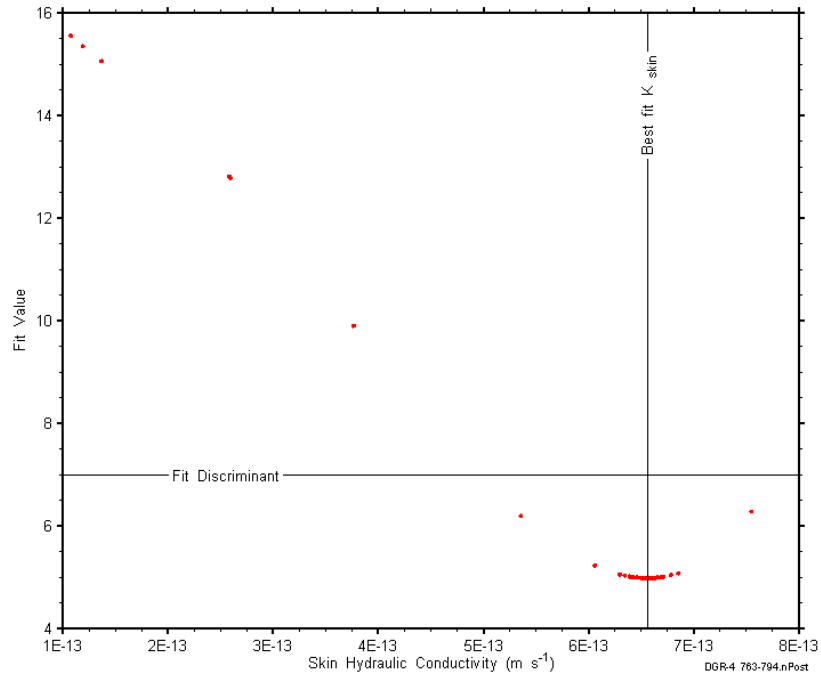


Figure D-302: XY-scatter plot showing the skin hydraulic conductivity parameter space derived from DGR4_762.80-793.54 perturbation analysis along with the fit discriminant and best fit values.

D.24 793.34-824.08 Gull River

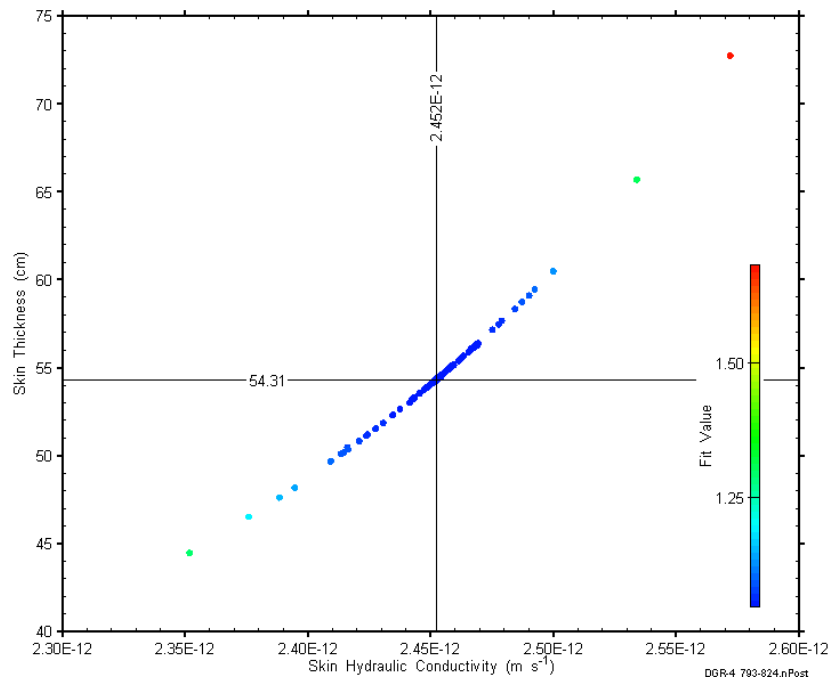


Figure D-303: XY-scatter plot showing estimates of skin hydraulic conductivity and skin thickness derived from the DGR4_793.34-824.08 perturbation analysis.

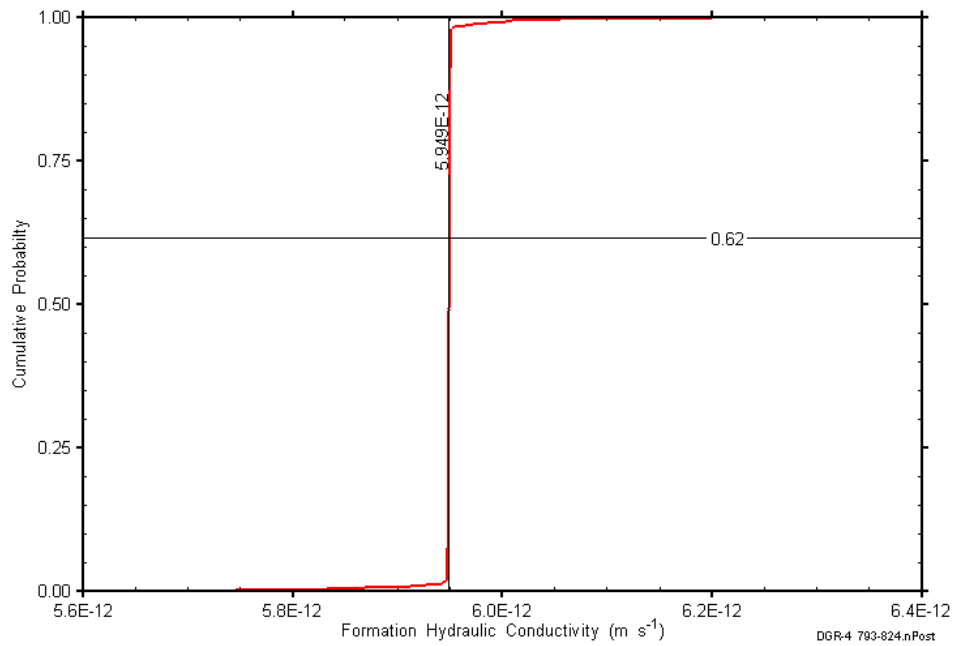


Figure D-304: DGR4_793.34-824.08 formation hydraulic conductivity cumulative distribution function.

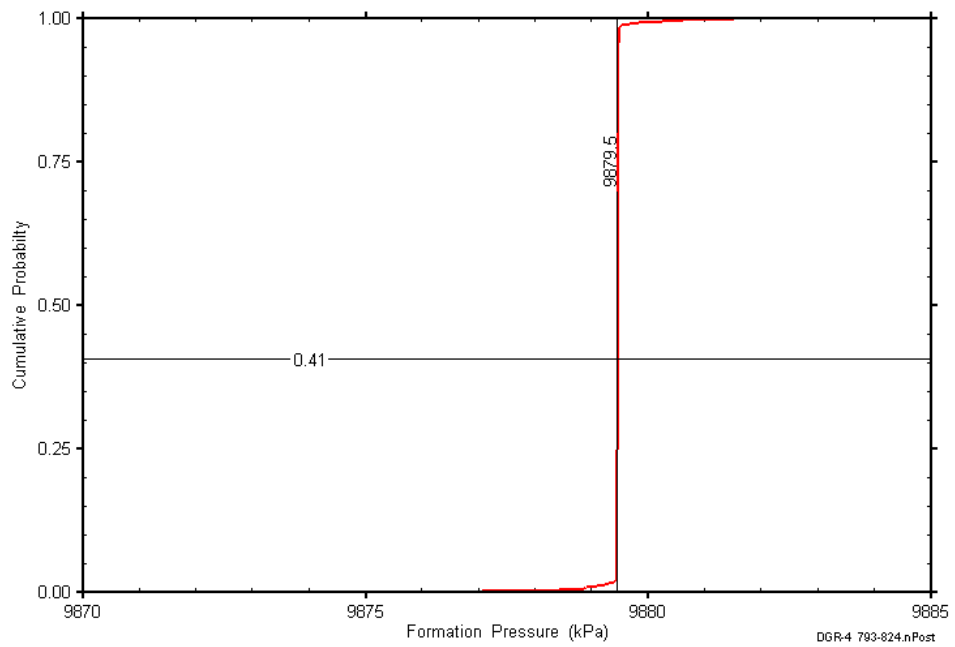


Figure D-305: DGR4_793.34-824.08 static formation pressure cumulative distribution function.

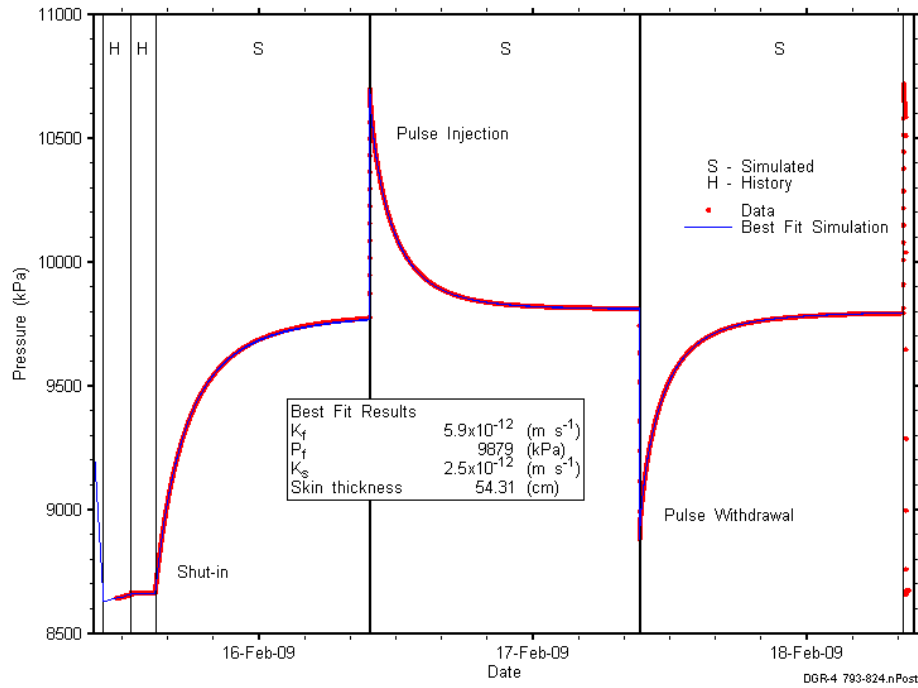


Figure D-306: Linear plot showing simulations of the DGR4_793.34-824.08 pressure response.

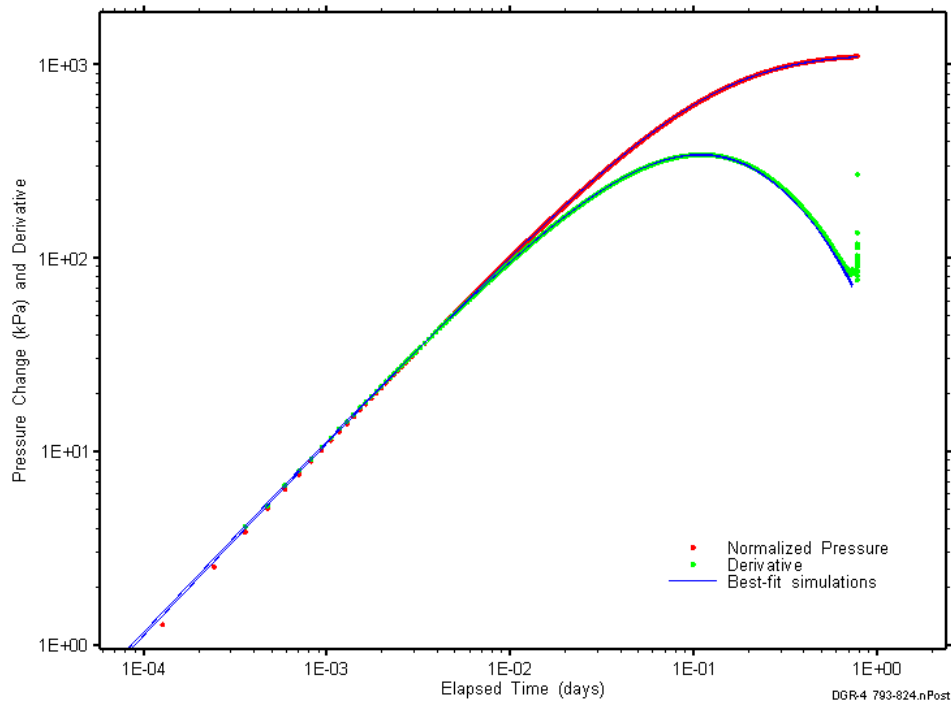


Figure D-307: Log-log plot showing simulations of the DGR4_793.34-824.08 shut-in period Ramey B and derivative response.

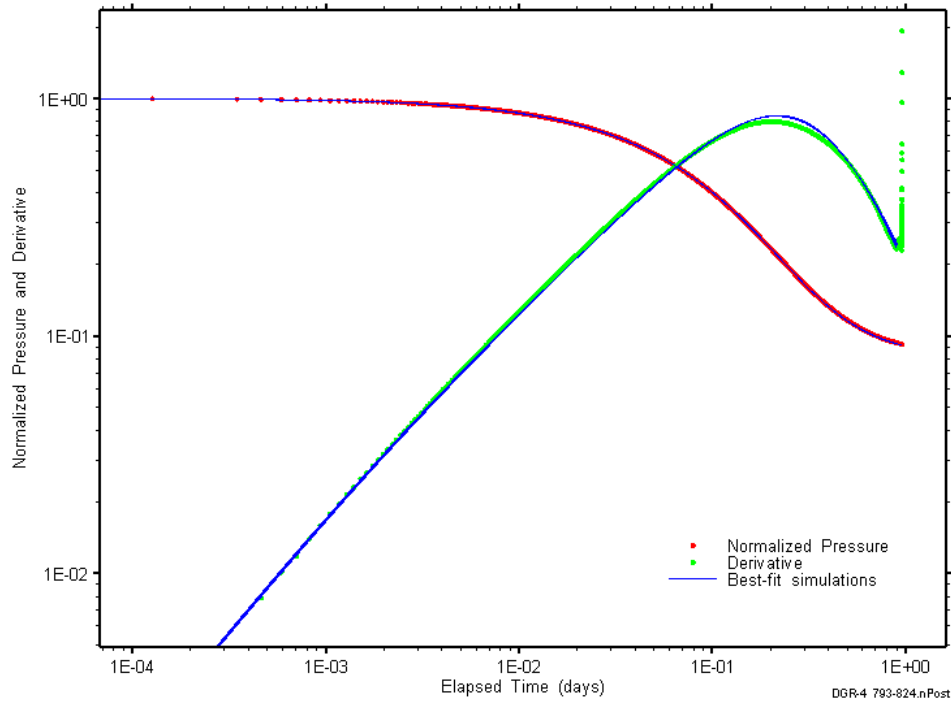


Figure D-308: Log-log plot showing simulations of the DGR4_793.34–824.08 pulse injection Ramey B and derivative response.

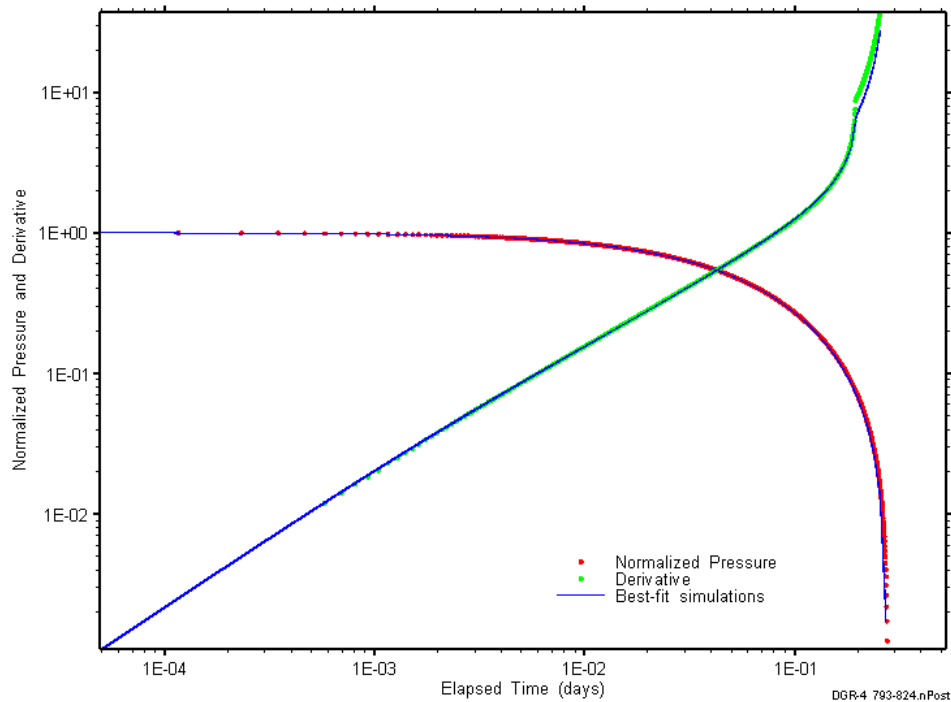


Figure D-309: Log-log plot showing simulations of the DGR4_793.34–824.08 pulse withdrawal Ramey B and derivative response.

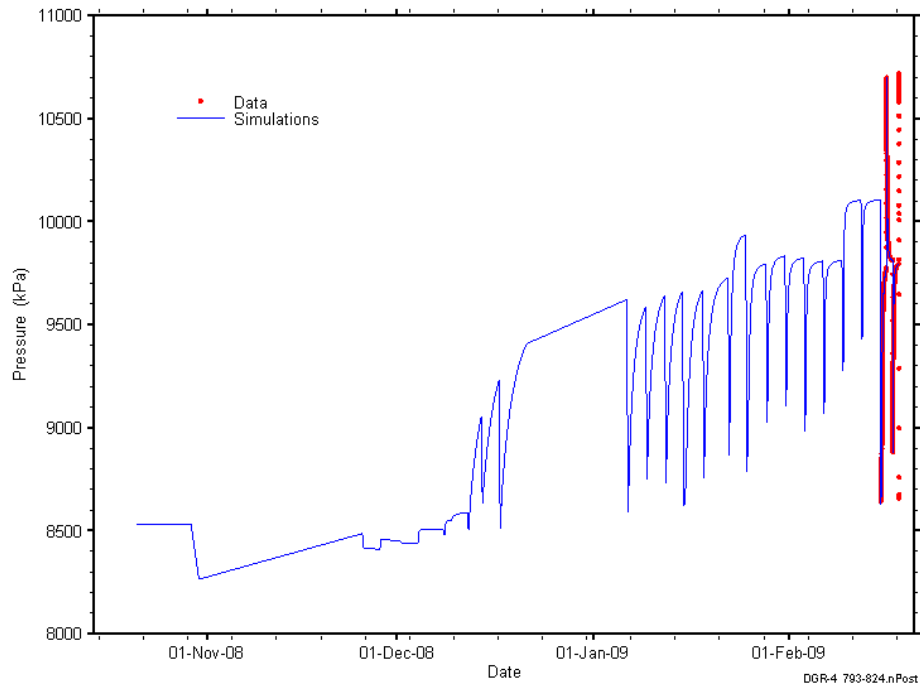


Figure D-310: Linear plot showing simulations of the DGR4_793.34-824.08 pressure response, including pre-test pressure history.

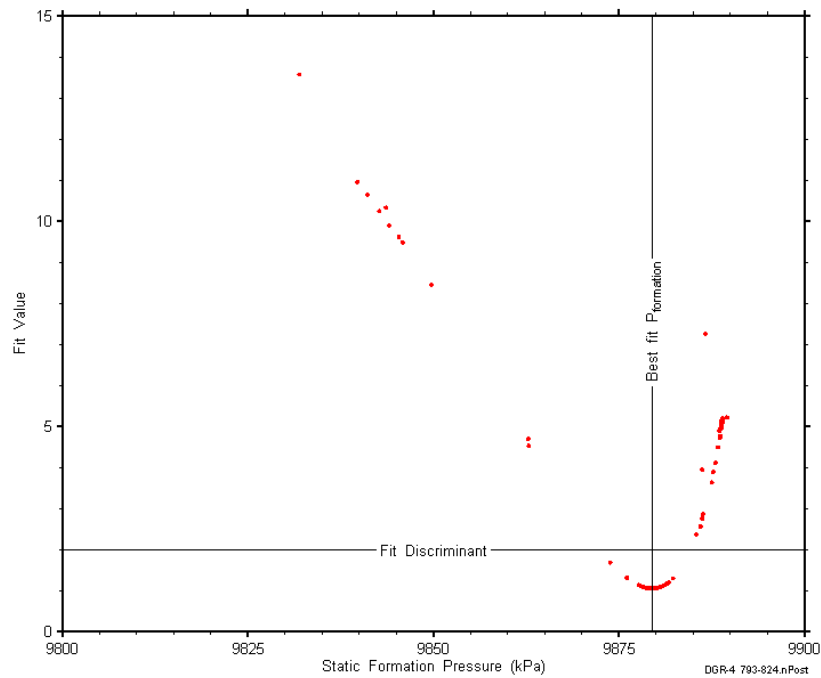


Figure D-311: XY-scatter plot showing the static formation pressure parameter space derived from DGR4_793.34-824.08 perturbation analysis along with the fit discriminant and best fit values.

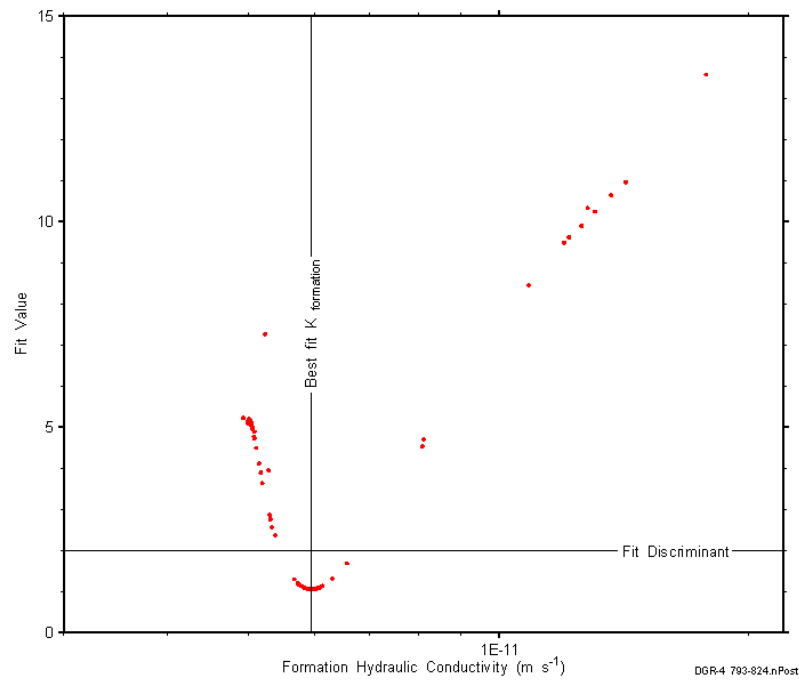


Figure D-312: XY-scatter plot showing the formation hydraulic conductivity parameter space derived from DGR4_793.34-824.08 perturbation analysis along with the fit discriminant and best fit values.

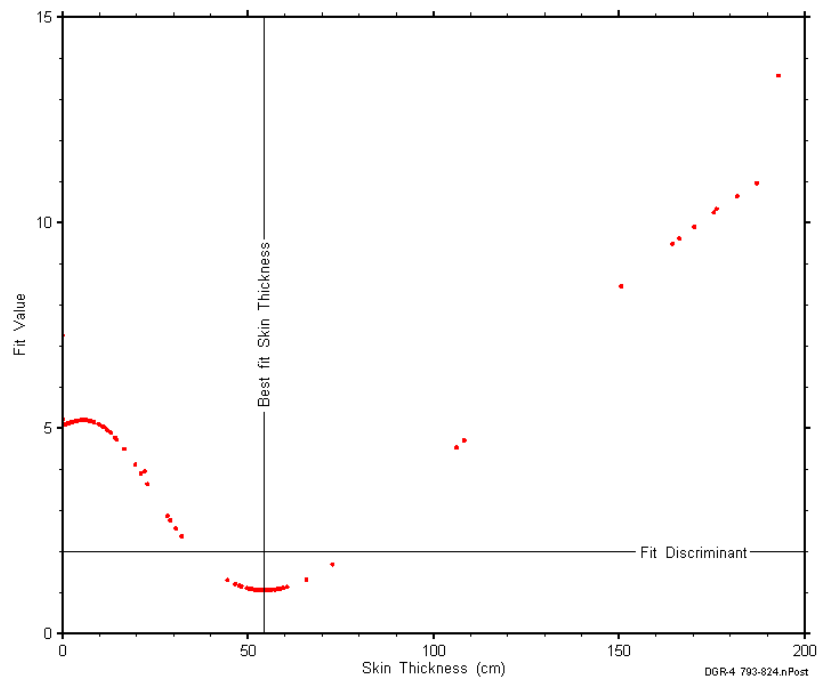


Figure D-313: XY-scatter plot showing the skin-thickness parameter space derived from DGR4_793.34-824.08 perturbation analysis along with the fit discriminant and best fit values.

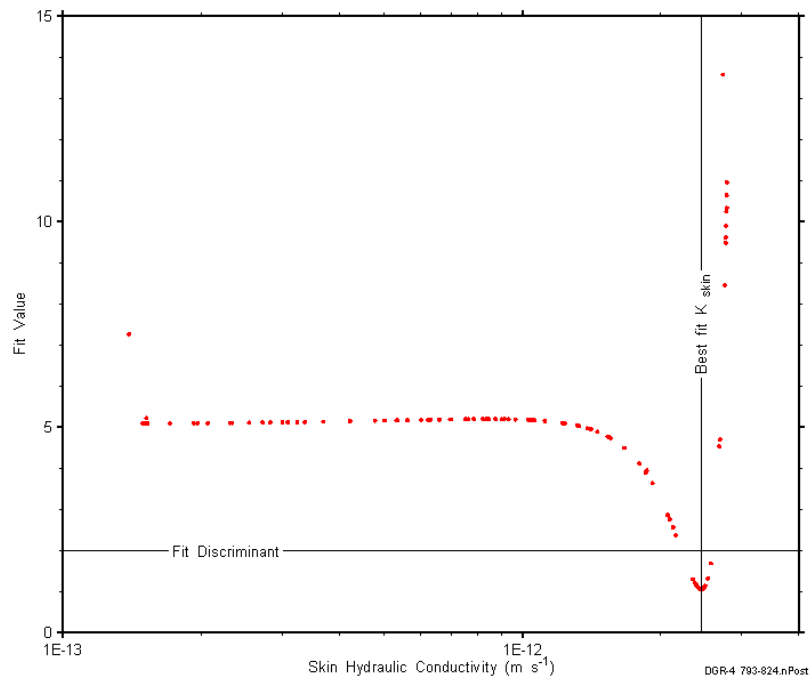


Figure D-314: XY-scatter plot showing the skin hydraulic conductivity parameter space derived from DGR4_793.34-824.08 perturbation analysis along with the fit discriminant and best fit values.

Appendix E. DGR-5 Plots

Various plots of results from the DGR-5 analyses are shown below. These plots include XY-scatter plots of the fitting-parameter estimates, linear and log-log horsetail plots of the simulated pressure responses showing field-data matches, K_f , P_f , and S_s cumulative distribution functions, and parameter-space plots showing the characteristics of the minima for each of the fitting parameters.

E.1 437.94-466.55 Manitoulin-Queenston

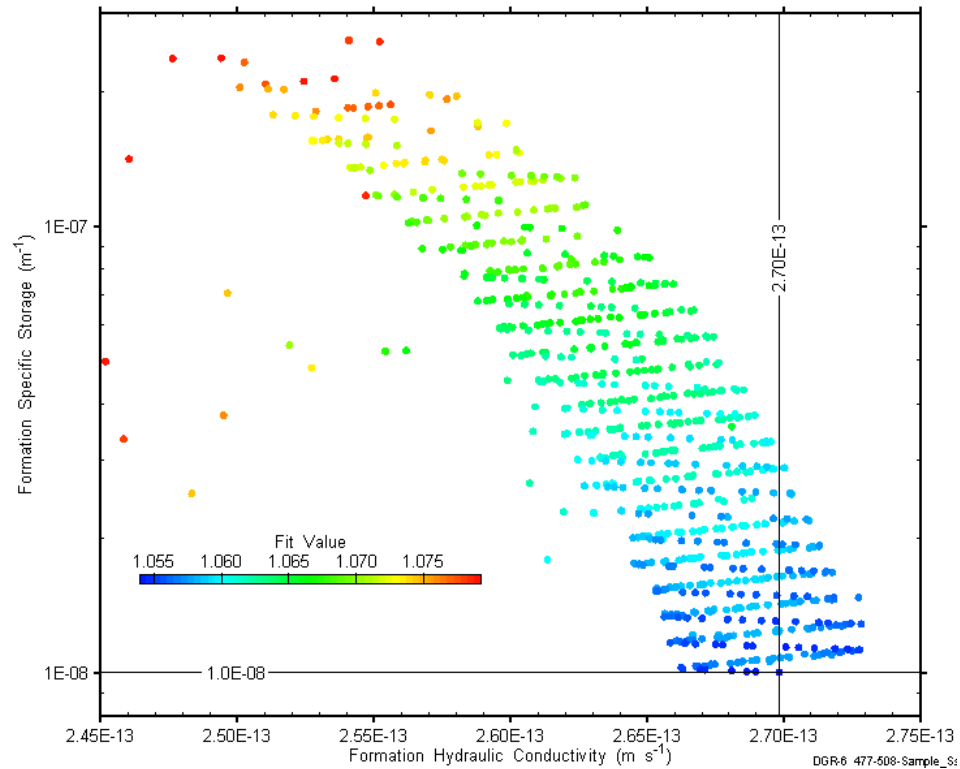


Figure E-1: XY-scatter plot showing estimates of formation hydraulic conductivity and formation specific storage derived from the DGR5_437.94-466.55 perturbation analysis.

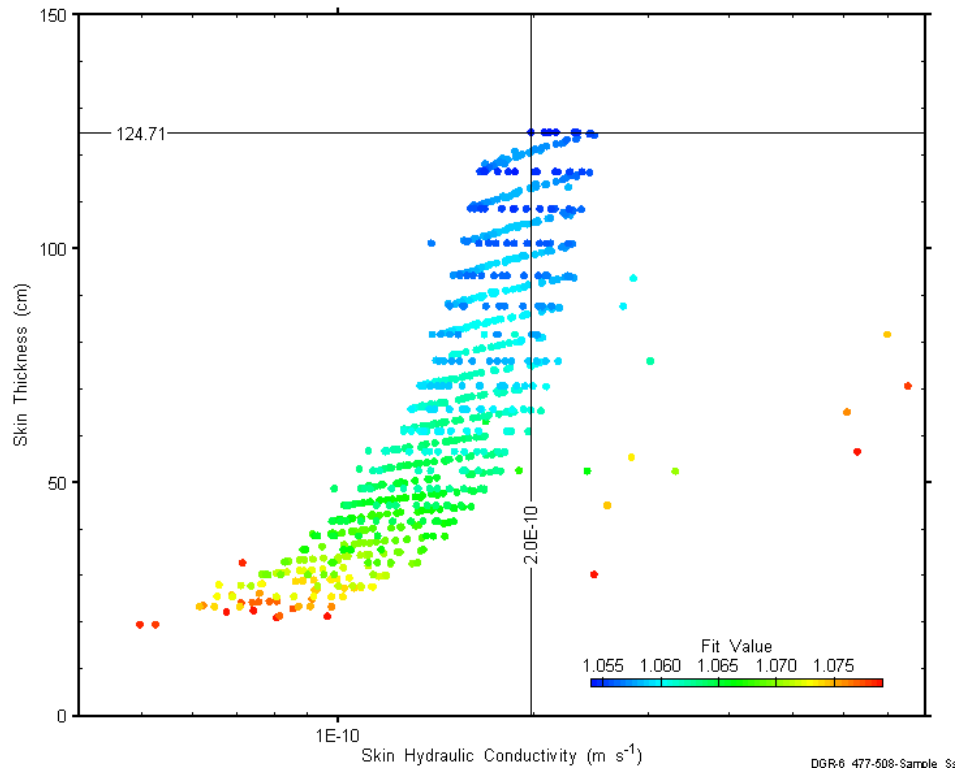


Figure E-2: XY-scatter plot showing estimates of skin hydraulic conductivity and skin thickness derived from the DGR5_437.94-466.55 perturbation analysis.

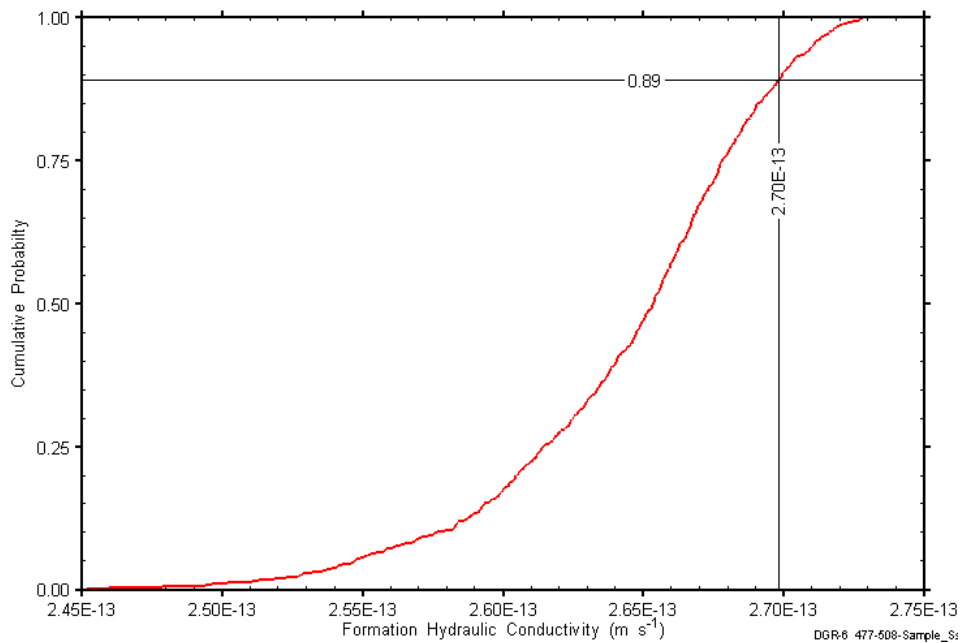


Figure E-3: DGR5_437.94-466.55 formation hydraulic conductivity cumulative distribution function.

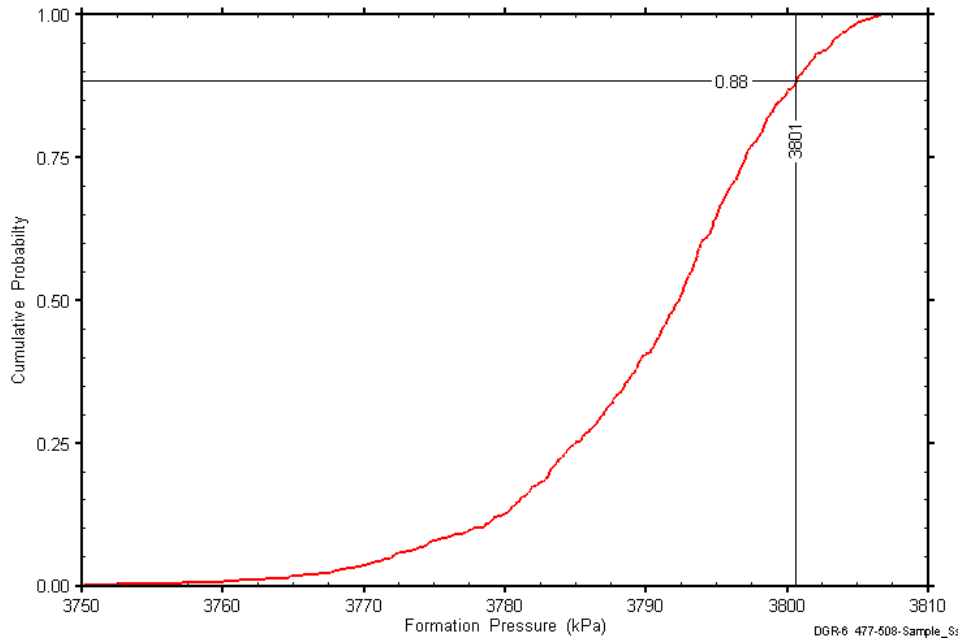


Figure E-4: DGR5_437.94-466.55 static formation pressure cumulative distribution function.

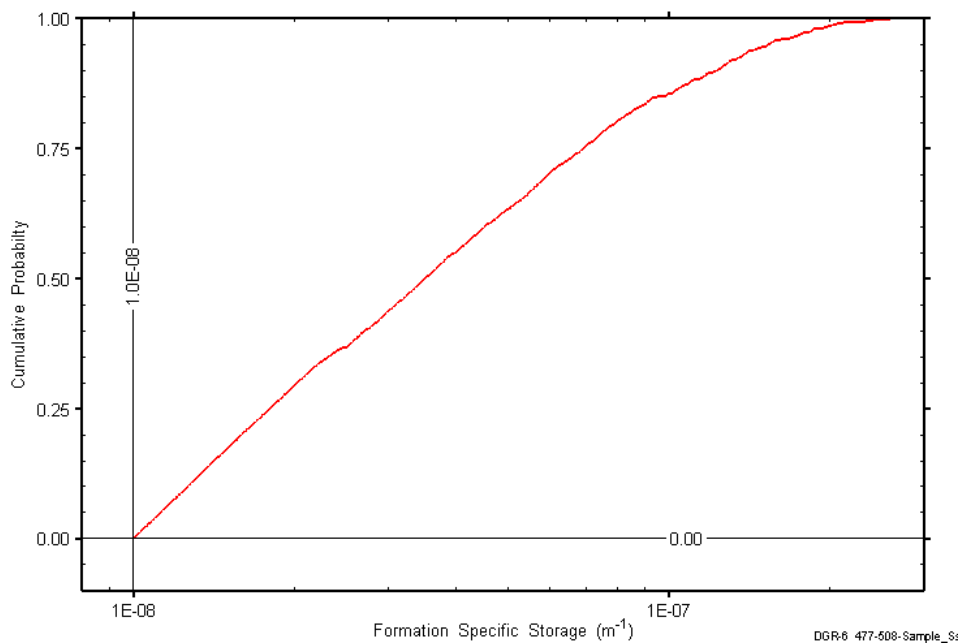


Figure E-5: DGR5_437.94-466.55 formation specific storage cumulative distribution function.

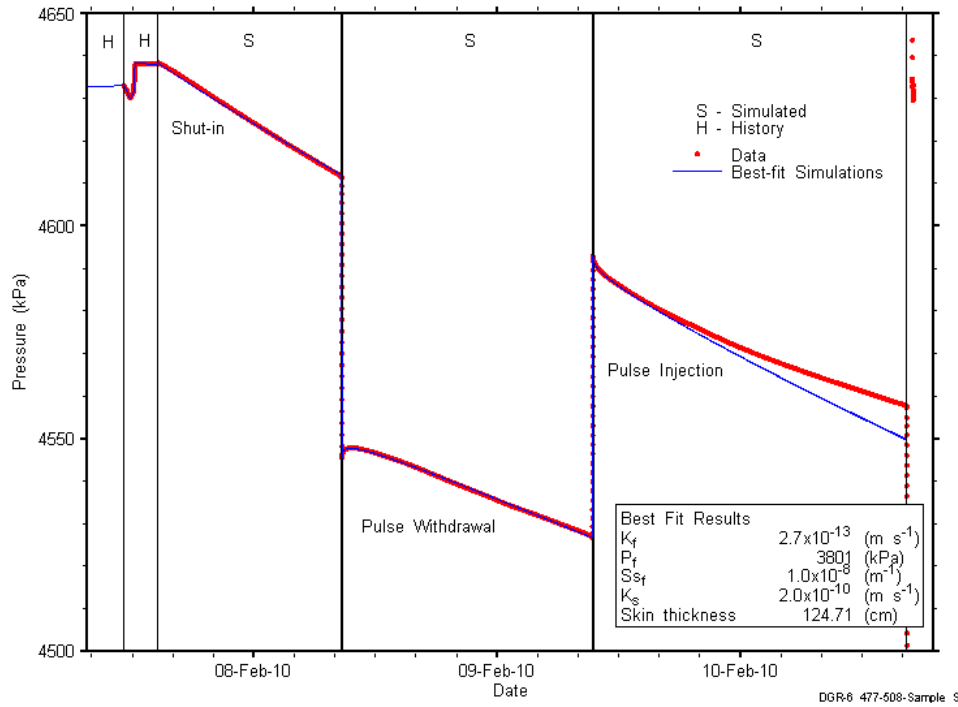


Figure E-6: Linear plot showing simulations of the DGR5_437.94-466.55 pressure response.

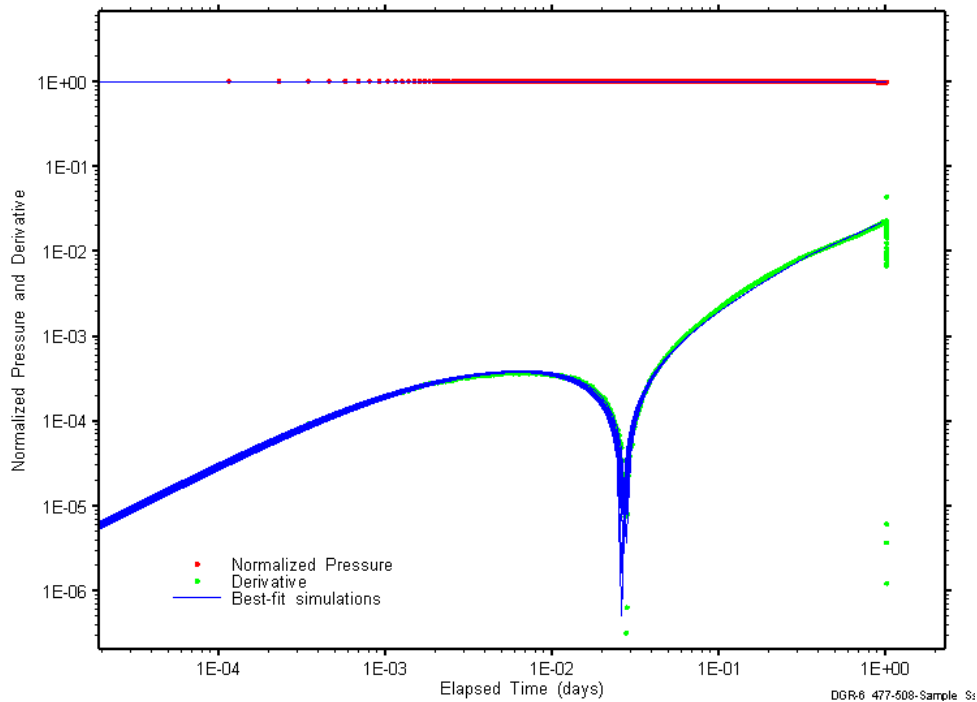


Figure E-7: Log-log plot showing simulations of the DGR5_437.94-466.55 PW Ramey B and derivative response.

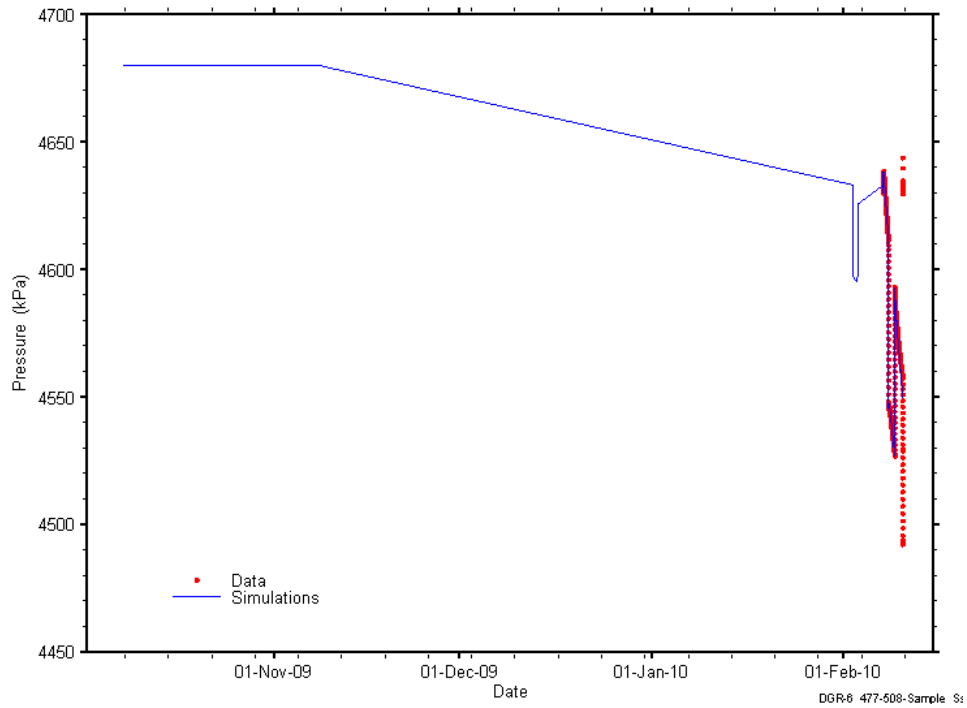


Figure E-8: Linear plot showing simulations of the DGR5_437.94-466.55 pressure response, including pre-test pressure history.

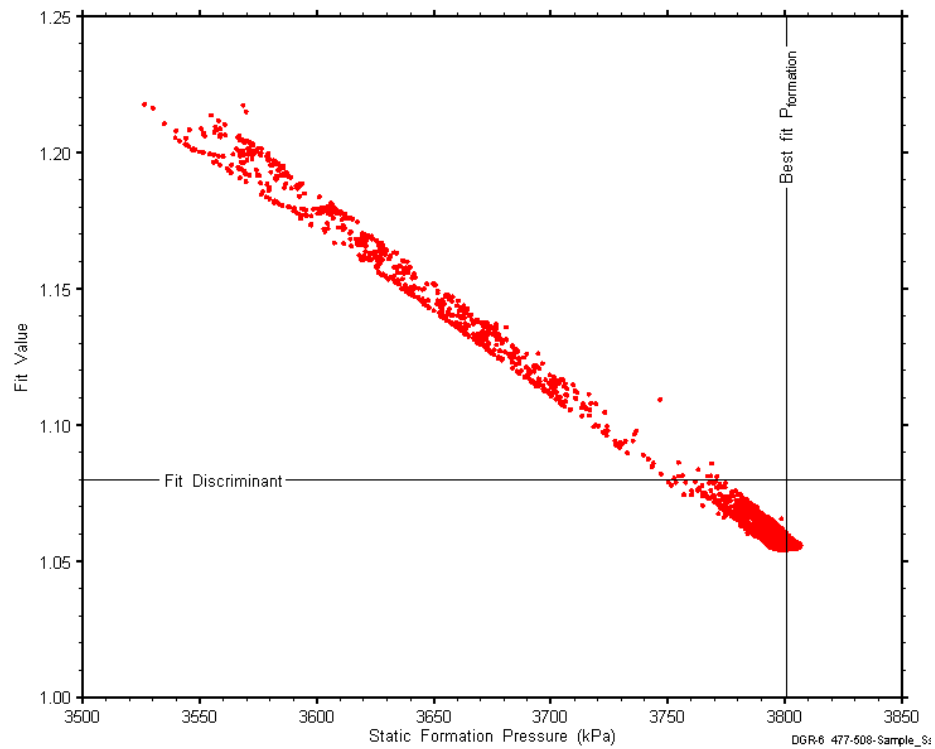


Figure E-9: XY-scatter plot showing the static formation pressure parameter space derived from DGR5_437.94-466.55 perturbation analysis along with the fit discriminant and best fit values.

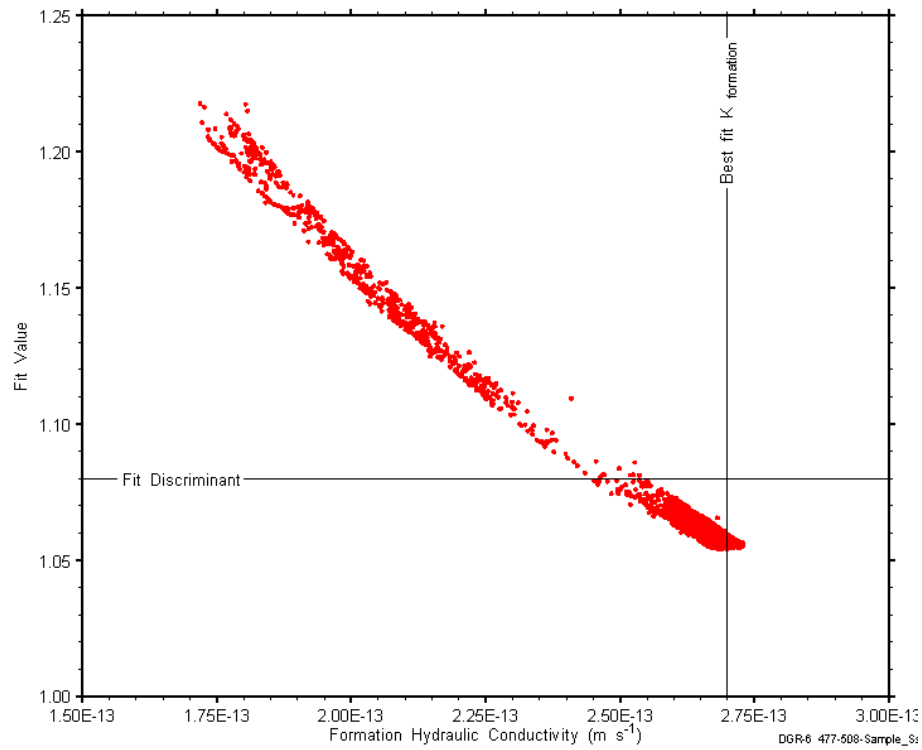


Figure E-10: XY-scatter plot showing the formation hydraulic conductivity parameter space derived from DGR5_437.94-466.55 perturbation analysis along with the fit discriminant and best fit values.

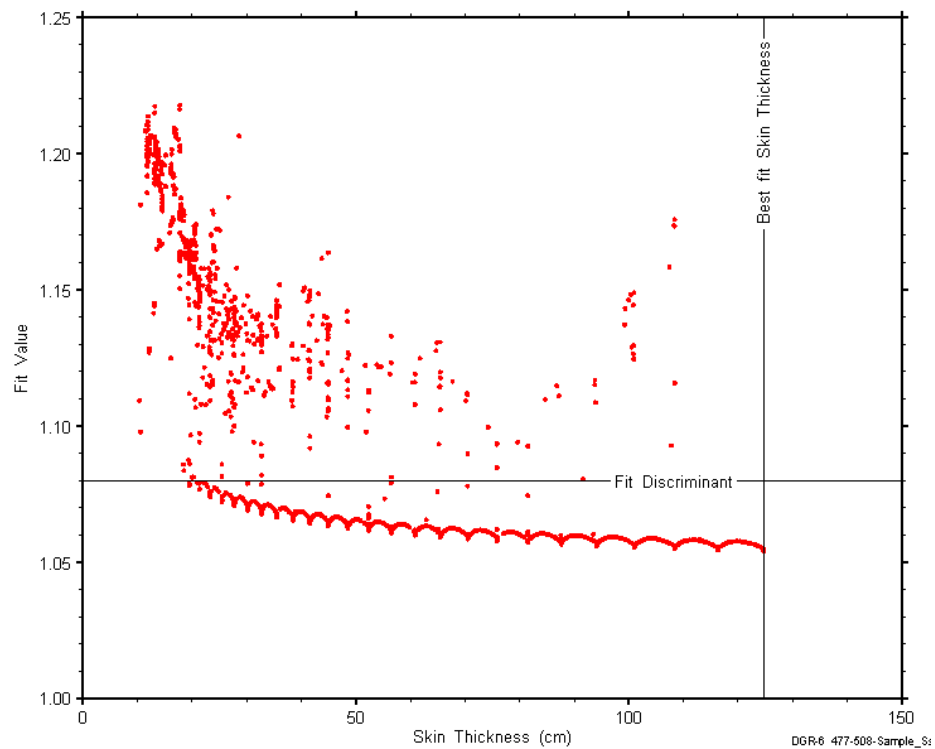


Figure E-11: XY-scatter plot showing the skin-thickness parameter space derived from DGR5_437.94-466.55 perturbation analysis along with the fit discriminant and best fit values.

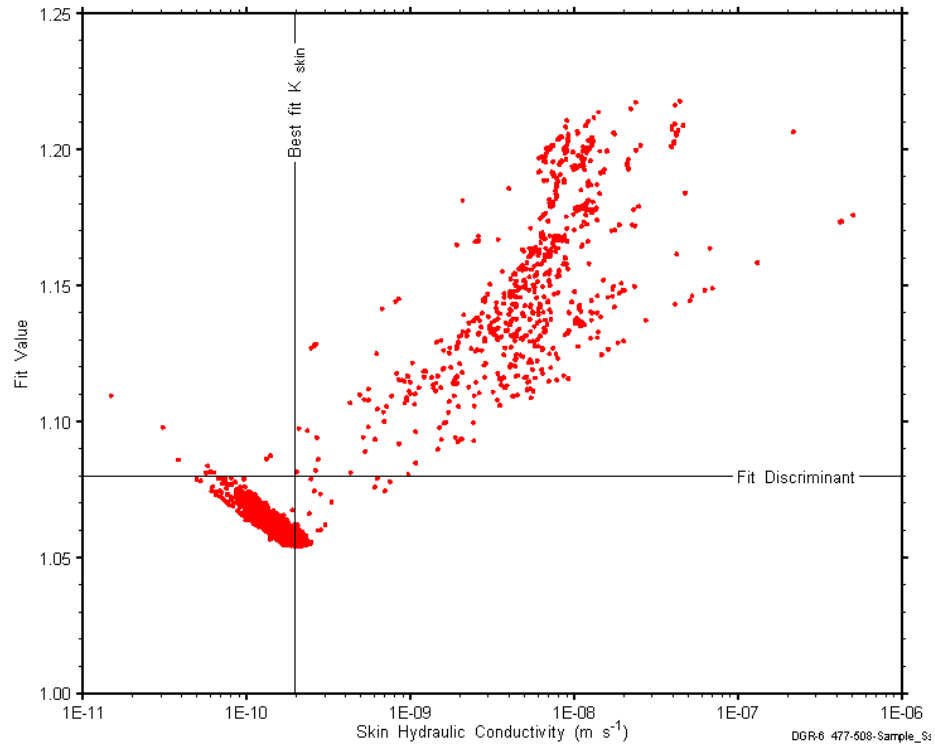


Figure E-12: XY-scatter plot showing the skin hydraulic conductivity parameter space derived from DGR5_437.94-466.55 perturbation analysis along with the fit discriminant and best fit values.

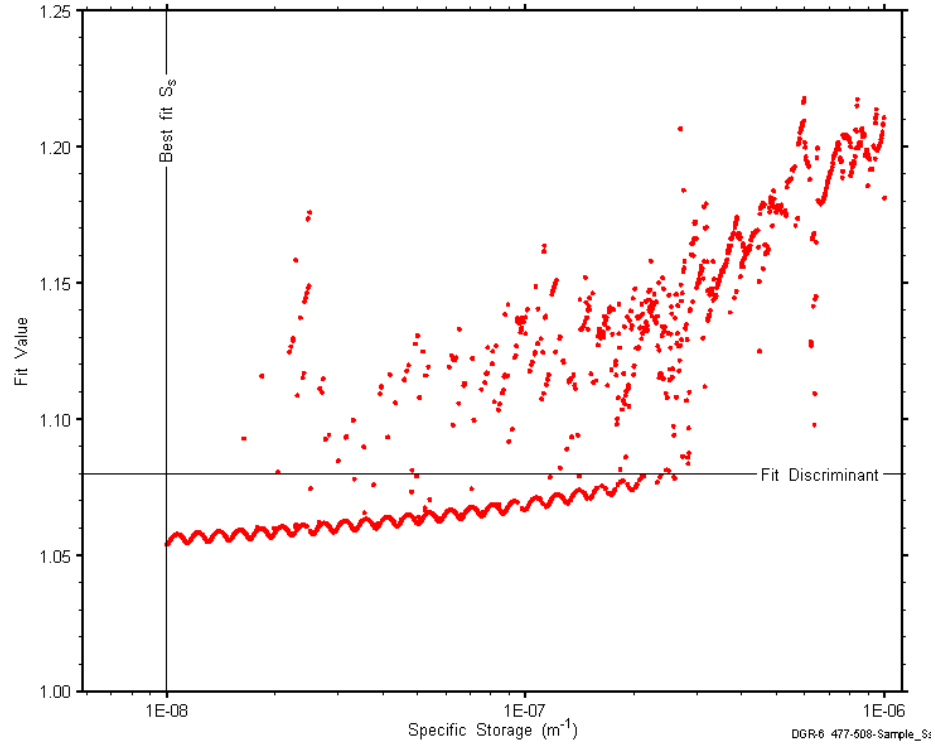


Figure E-13: XY-scatter plot showing the formation specific storage parameter space derived from DGR5_437.94-466.55 perturbation analysis along with the fit discriminant and best fit values.

E.2 466.30-495.07 Queenston

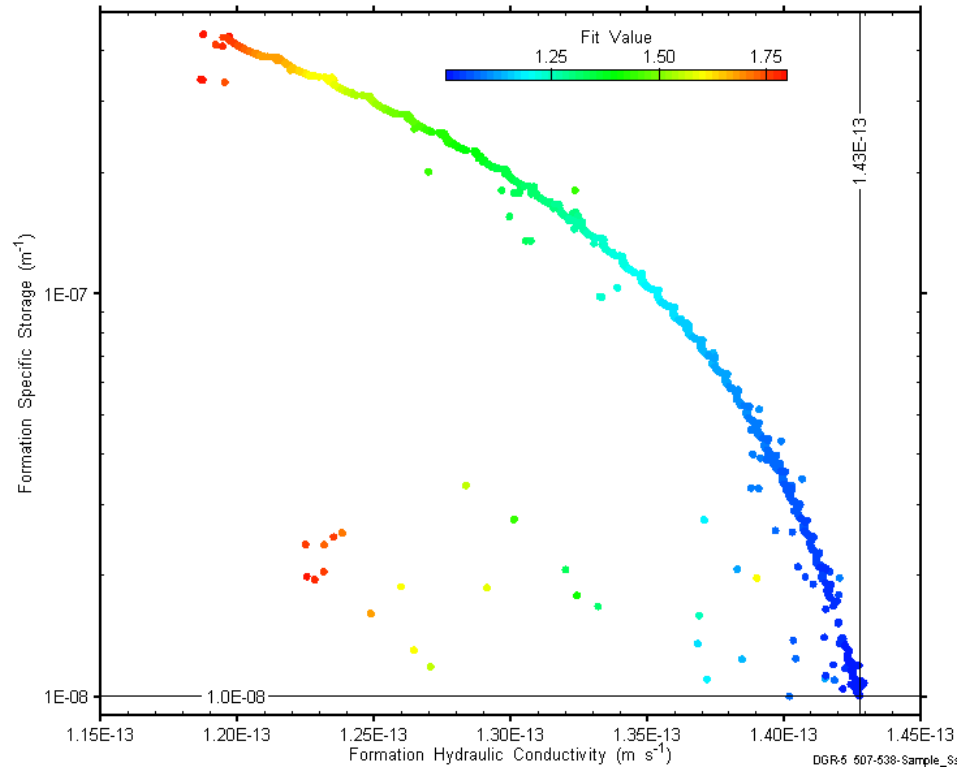


Figure E-14: XY-scatter plot showing estimates of formation hydraulic conductivity and formation specific storage derived from the DGR5_466.30-495.07 perturbation analysis.

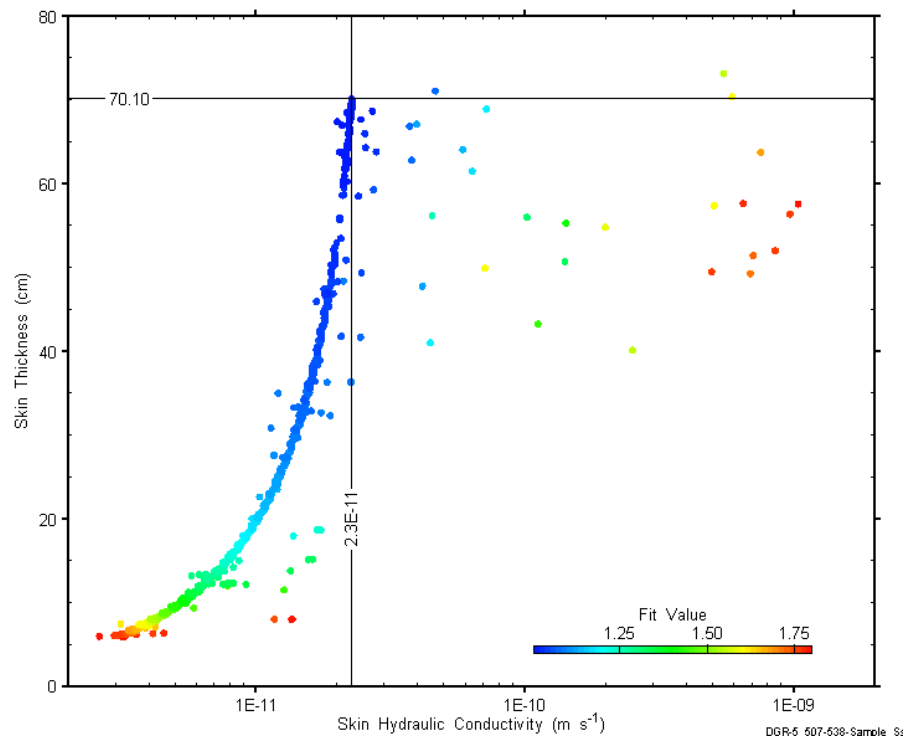


Figure E-15: XY-scatter plot showing estimates of skin hydraulic conductivity and skin thickness derived from the DGR5_466.30-495.07 perturbation analysis.

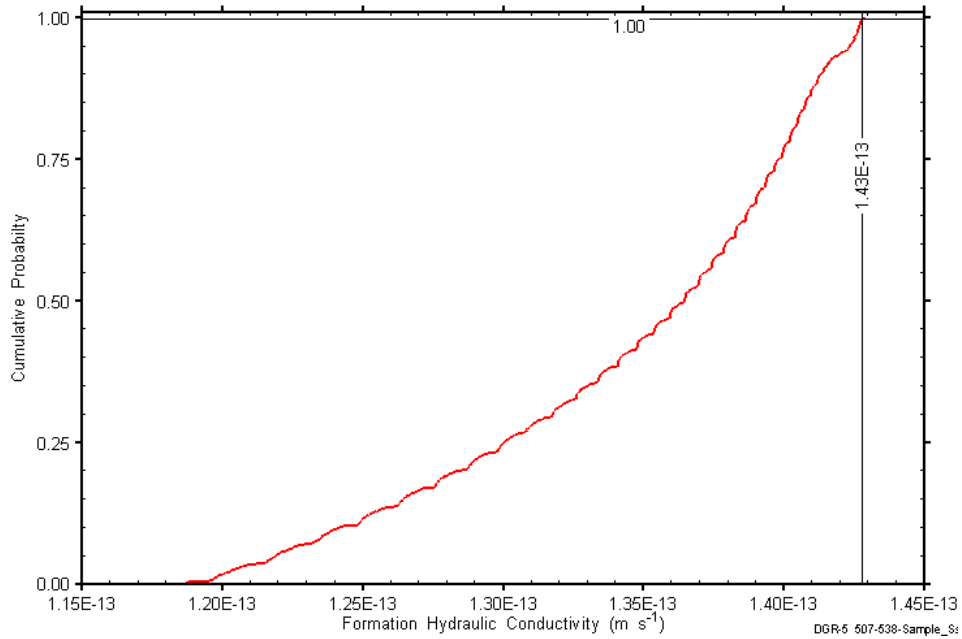


Figure E-16: DGR5_466.30-495.07 formation hydraulic conductivity cumulative distribution function.

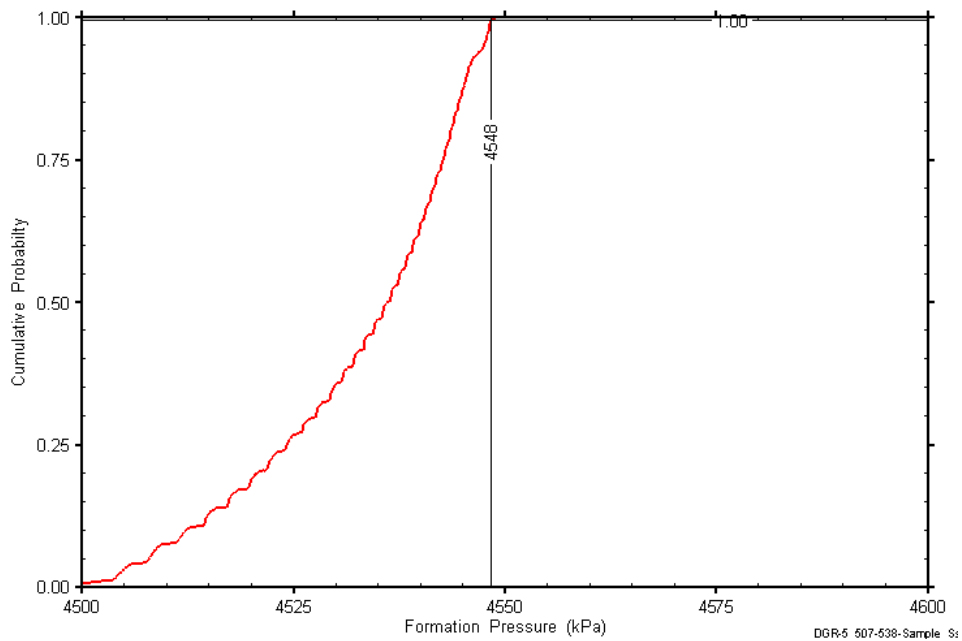


Figure E-17: DGR5_466.30-495.07 static formation pressure cumulative distribution function.

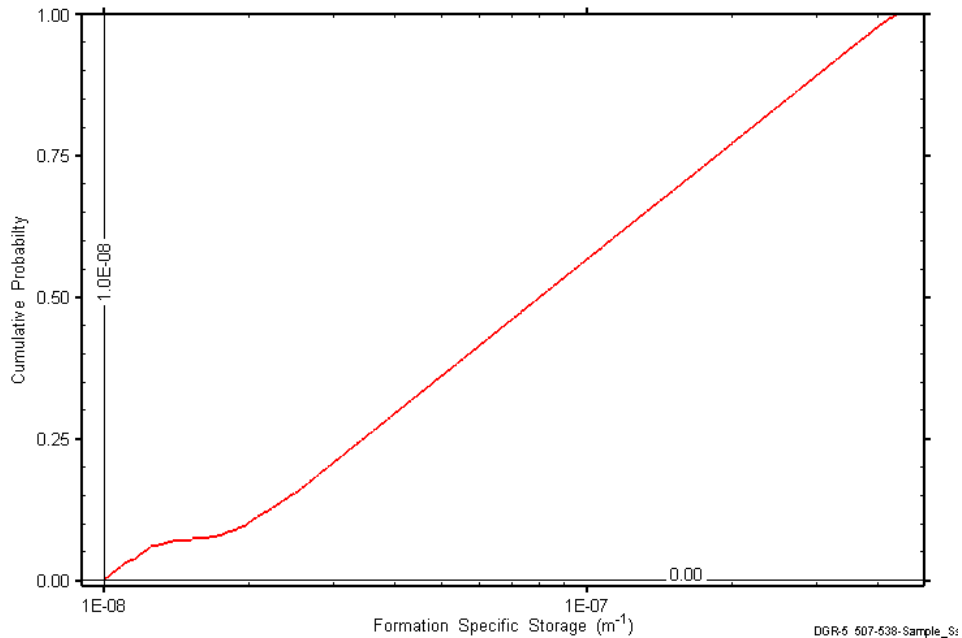


Figure E-18: DGR5_466.30-495.07 formation specific storage cumulative distribution function.

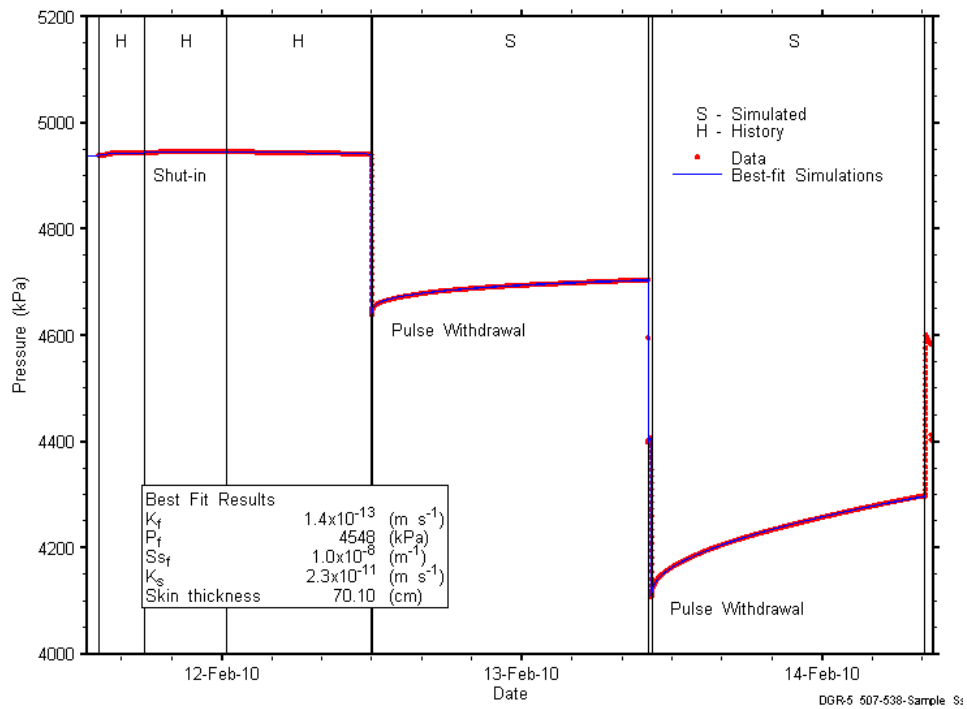


Figure E-19: Linear plot showing simulations of the DGR5_466.30-495.07 pressure response.

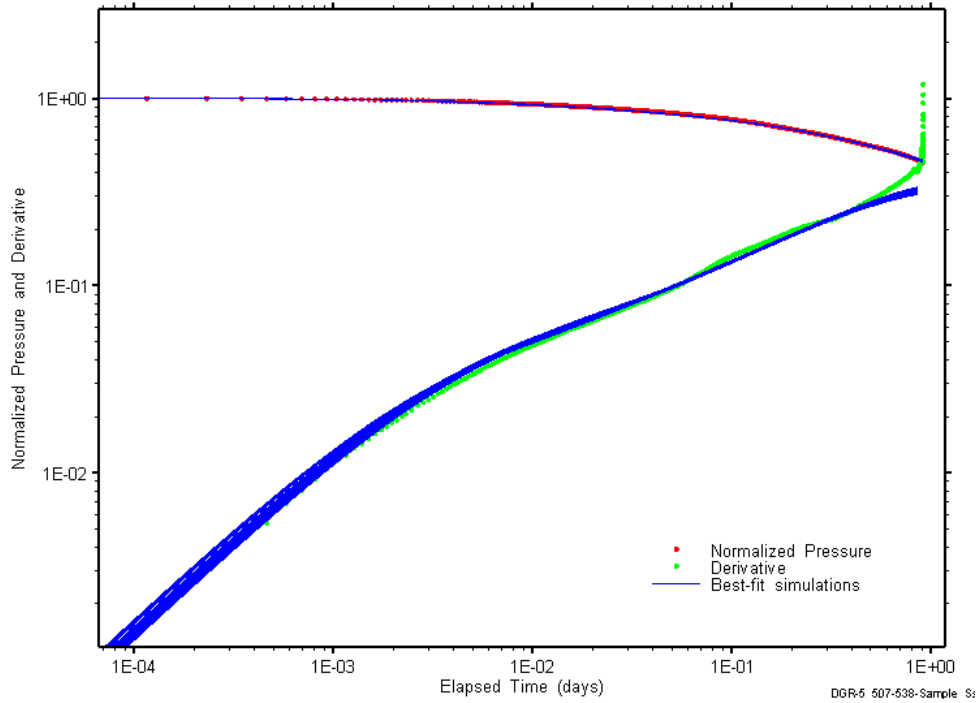


Figure E-20: Log-log plot showing simulations of the DGR5_466.30-495.07 PW1 Ramey B and derivative response.

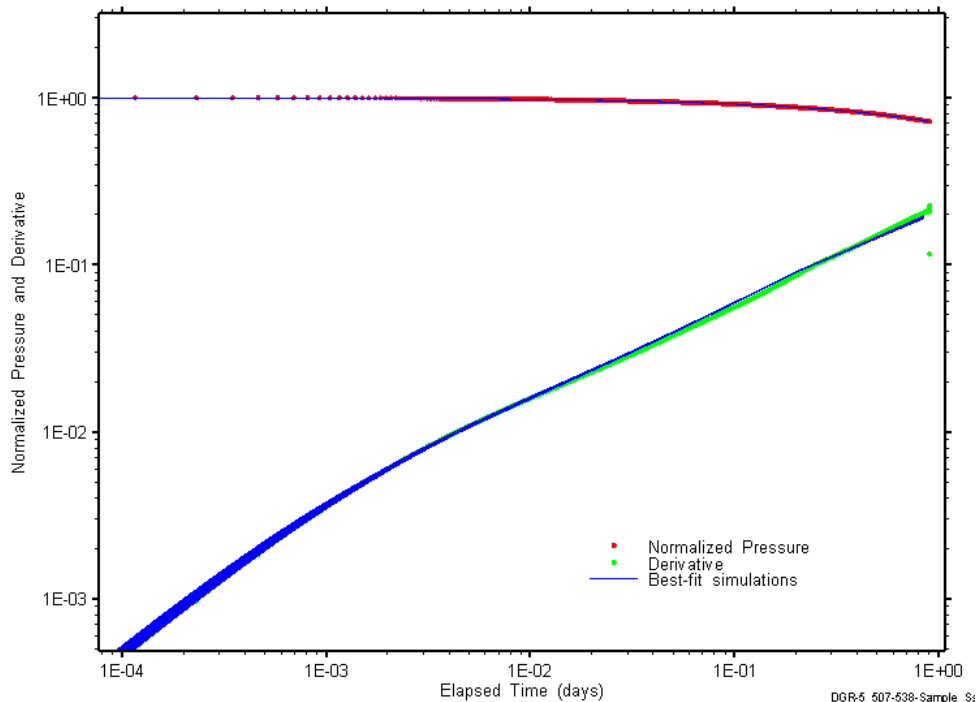


Figure E-21: Log-log plot showing simulations of the DGR5_466.30-495.07 PW2 Ramey B and derivative response.

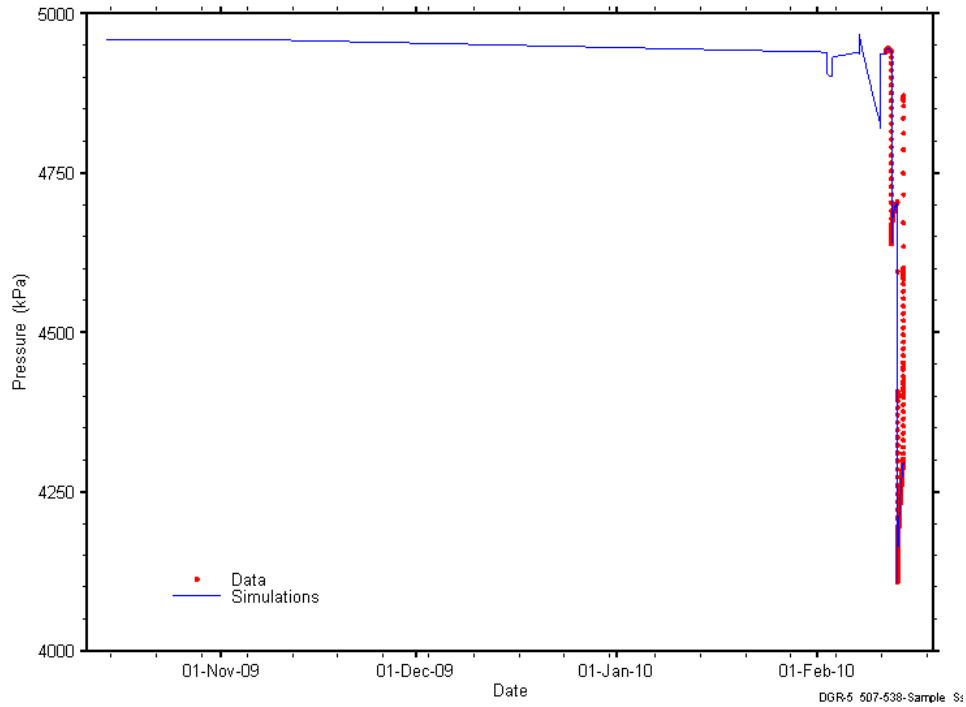


Figure E-22: Linear plot showing simulations of the DGR5_466.30-495.07 pressure response, including pre-test pressure history.

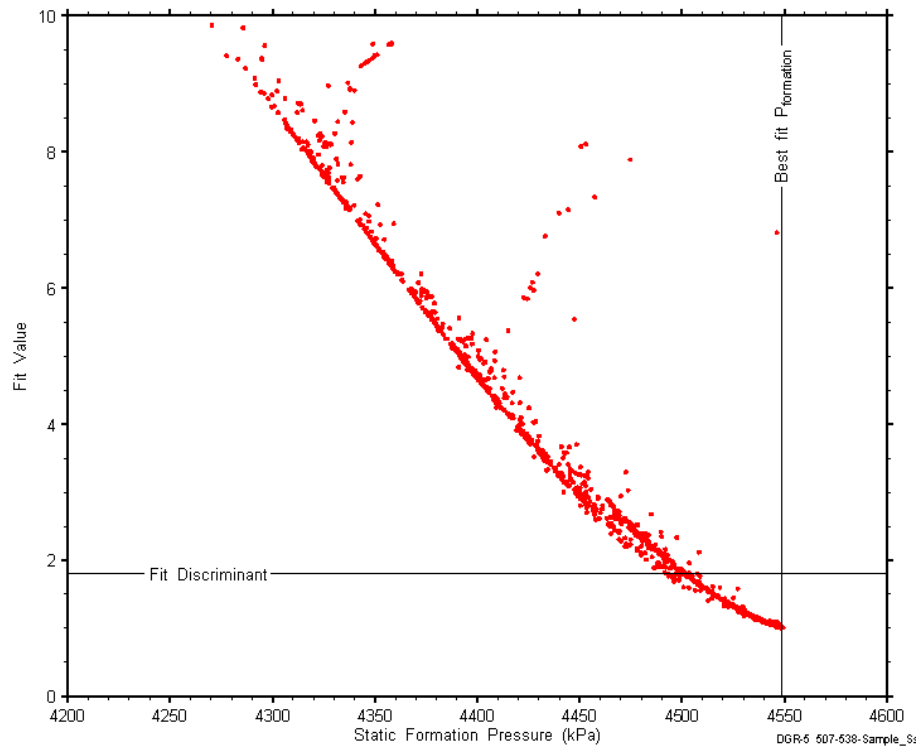


Figure E-23: XY-scatter plot showing the static formation pressure parameter space derived from DGR5_466.30-495.07 perturbation analysis along with the fit discriminant and best fit values.

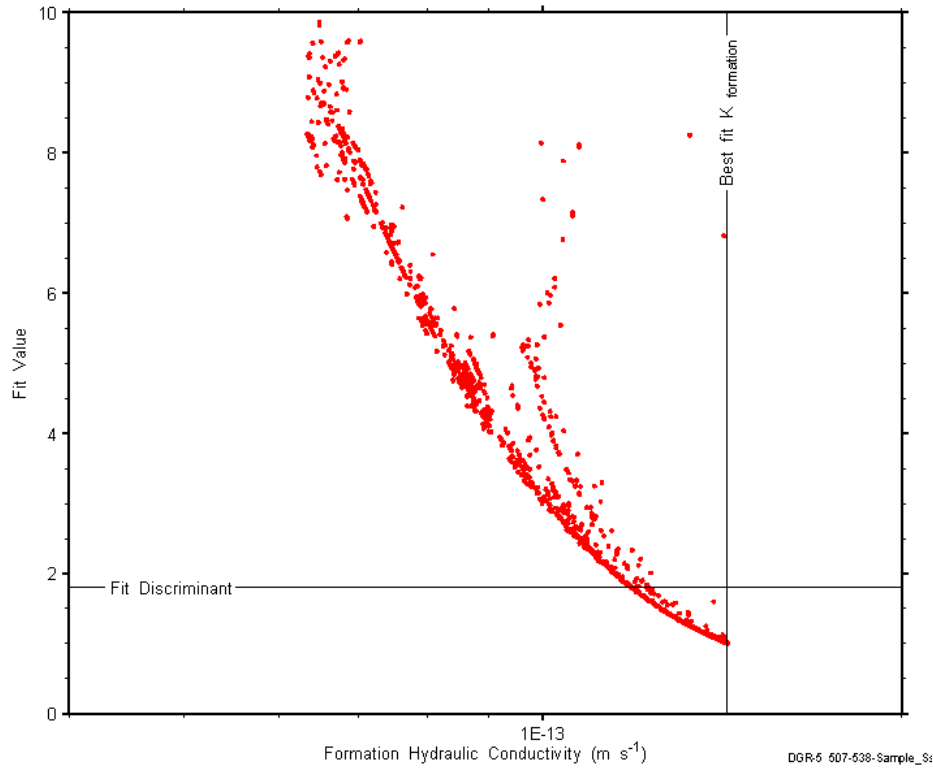


Figure E-24: XY-scatter plot showing the formation hydraulic conductivity parameter space derived from DGR5_466.30-495.07 perturbation analysis along with the fit discriminant and best fit values.

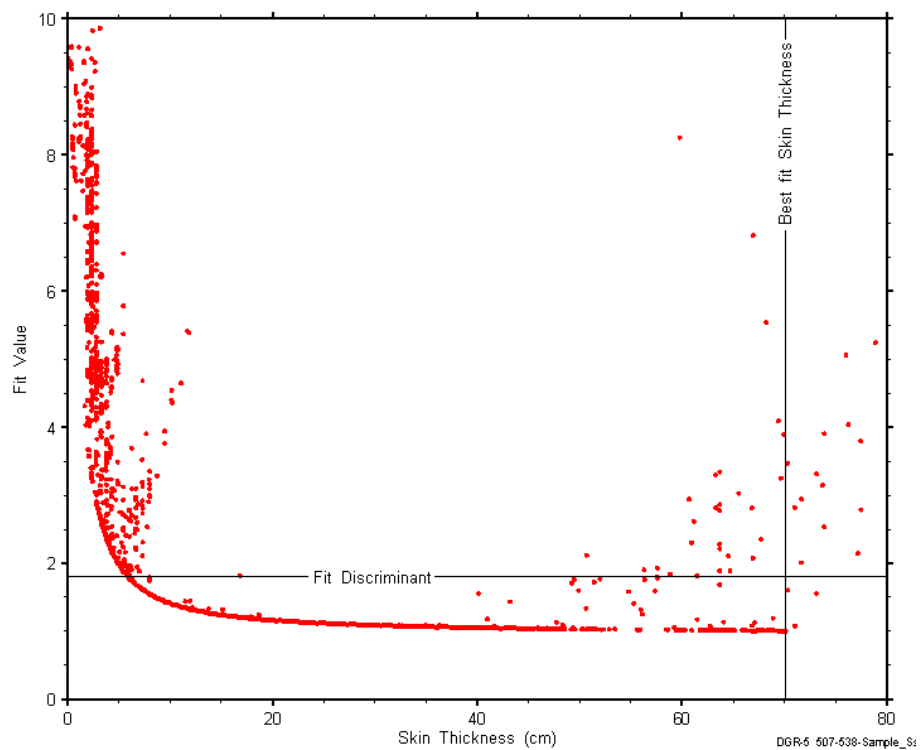


Figure E-25: XY-scatter plot showing the skin-thickness parameter space derived from DGR5_466.30-495.07 perturbation analysis along with the fit discriminant and best fit values.

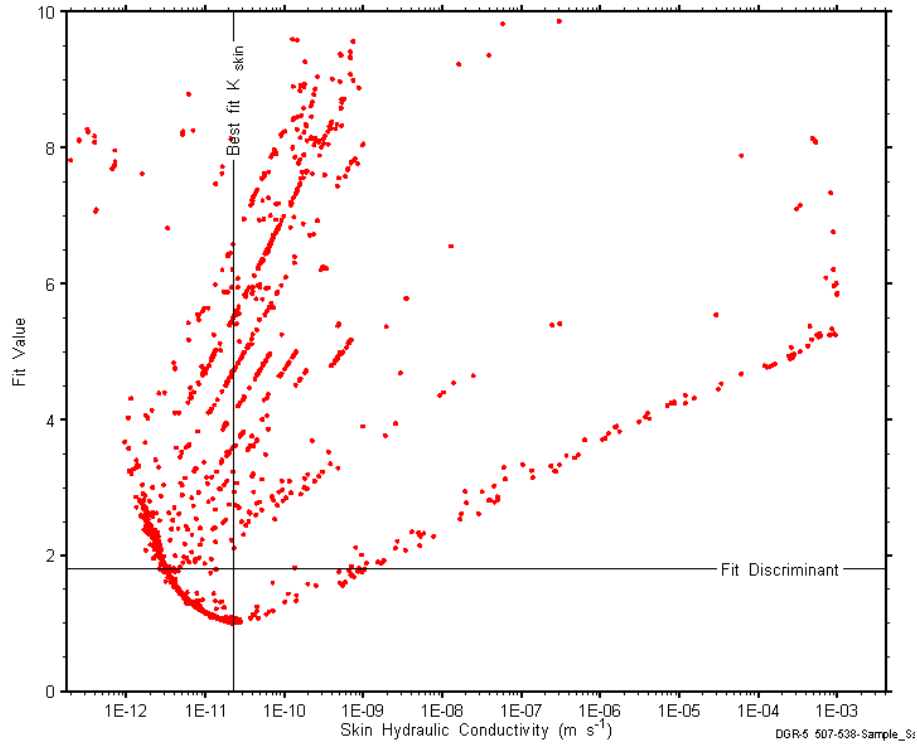


Figure E-26: XY-scatter plot showing the skin hydraulic conductivity parameter space derived from DGR5_466.30-495.07 perturbation analysis along with the fit discriminant and best fit values.

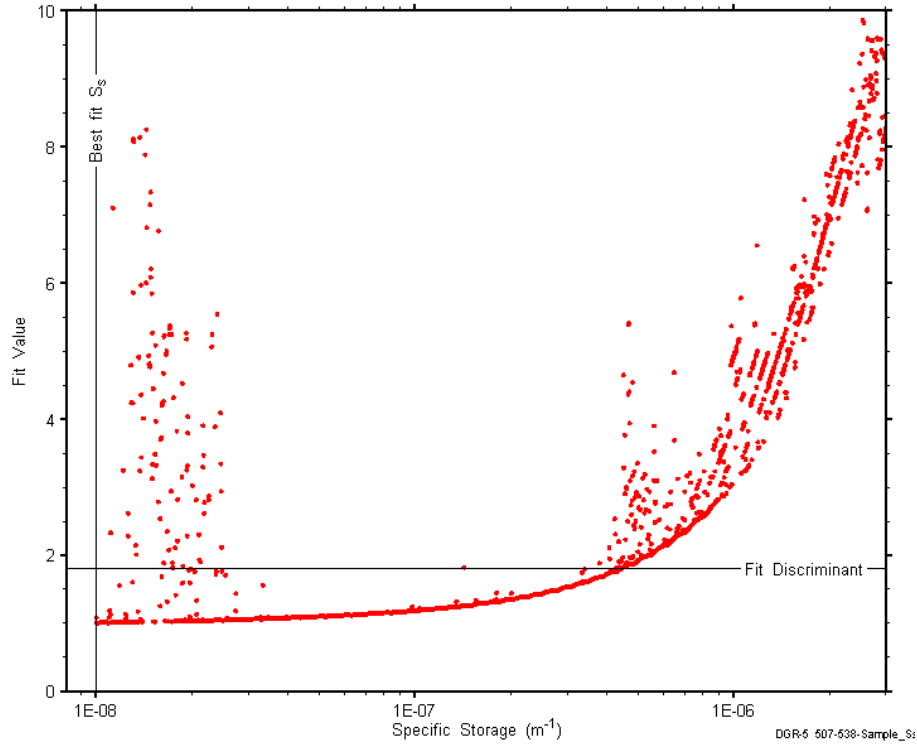


Figure E-27: XY-scatter plot showing the formation specific storage parameter space derived from DGR5_466.30-495.07 perturbation analysis along with the fit discriminant and best fit values.

E.3 494.82-523.66 Queenston-Georgian Bay

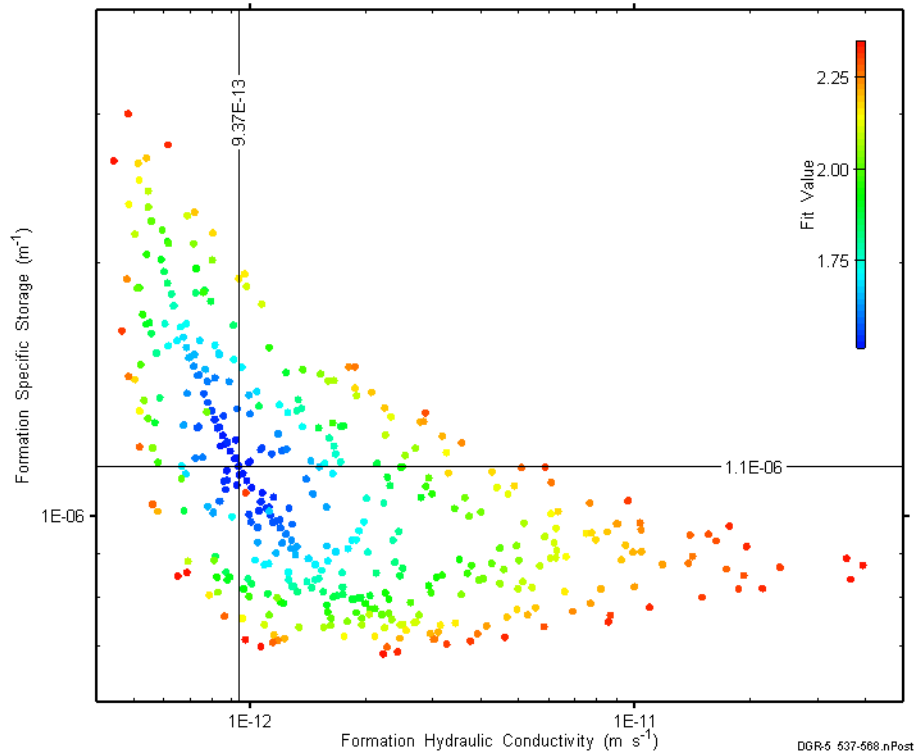


Figure E-28: XY-scatter plot showing estimates of formation hydraulic conductivity and formation specific storage derived from the DGR5_494.82-523.66 perturbation analysis.

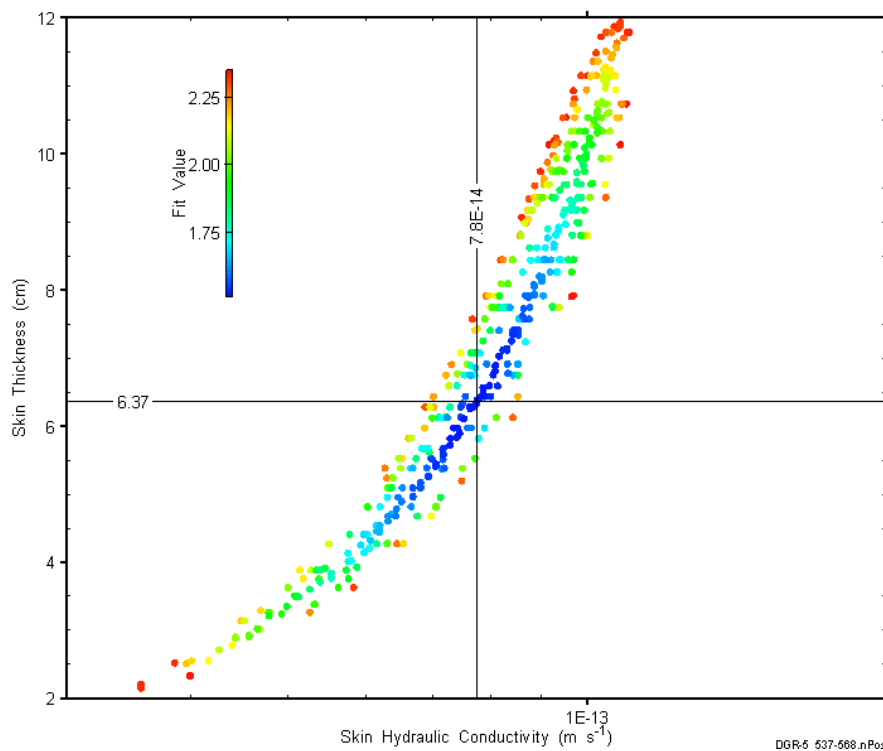


Figure E-29: XY-scatter plot showing estimates of skin hydraulic conductivity and skin thickness derived from the DGR5_494.82-523.66 perturbation analysis.

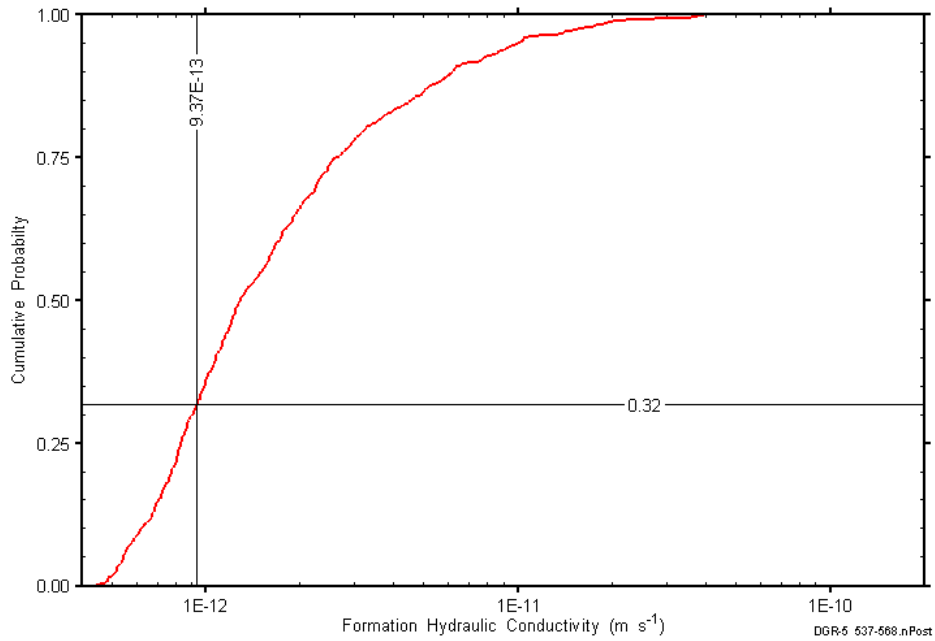


Figure E-30: DGR5_494.82-523.66 formation hydraulic conductivity cumulative distribution function.

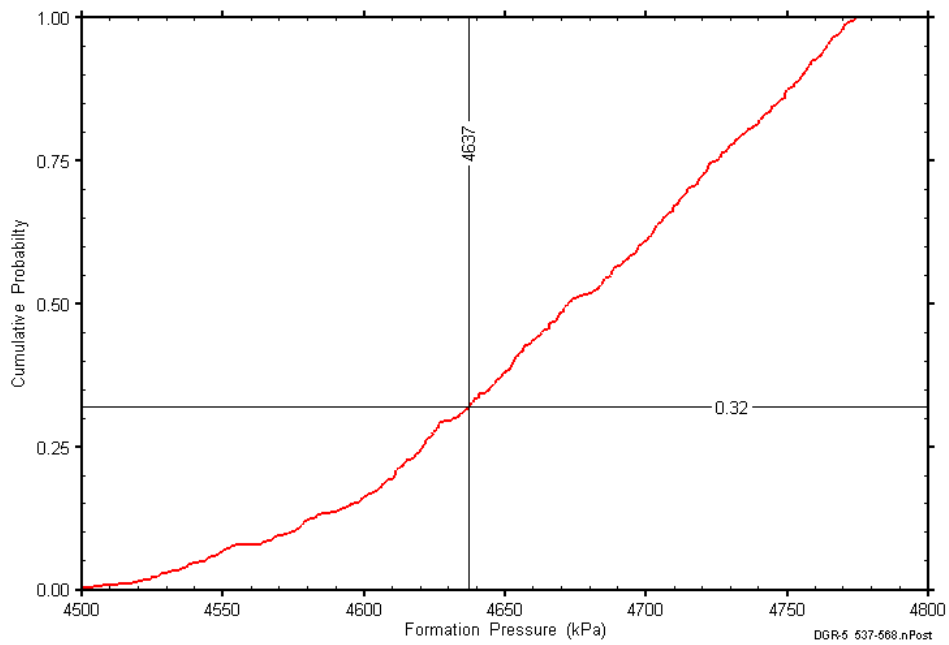


Figure E-31: DGR5_494.82-523.66 static formation pressure cumulative distribution function.

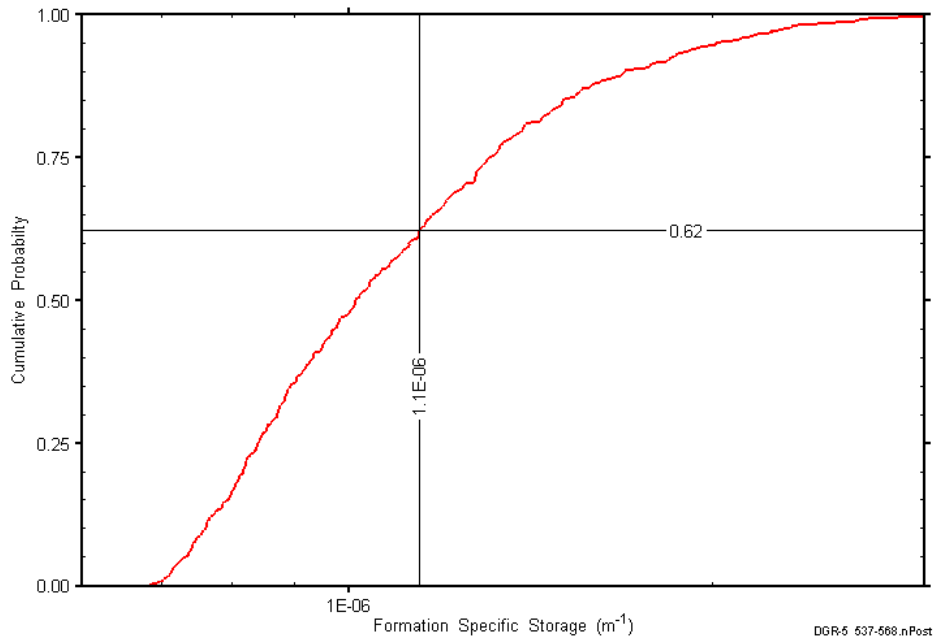


Figure E-32: DGR5_494.82-523.66 formation specific storage cumulative distribution function.

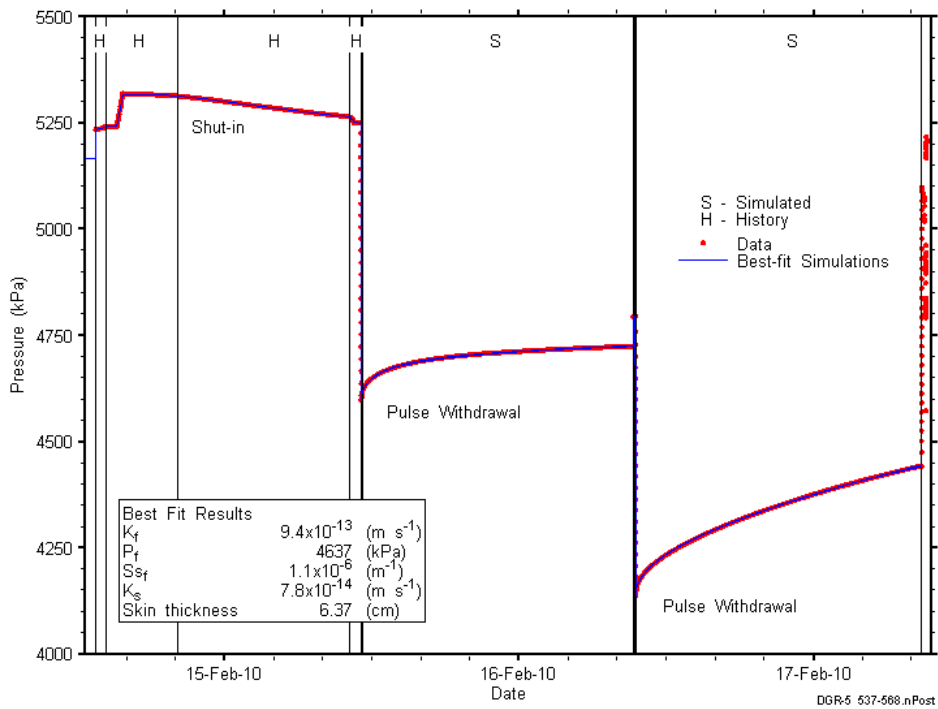


Figure E-33: Linear plot showing simulations of the DGR5_494.82-523.66 pressure response.

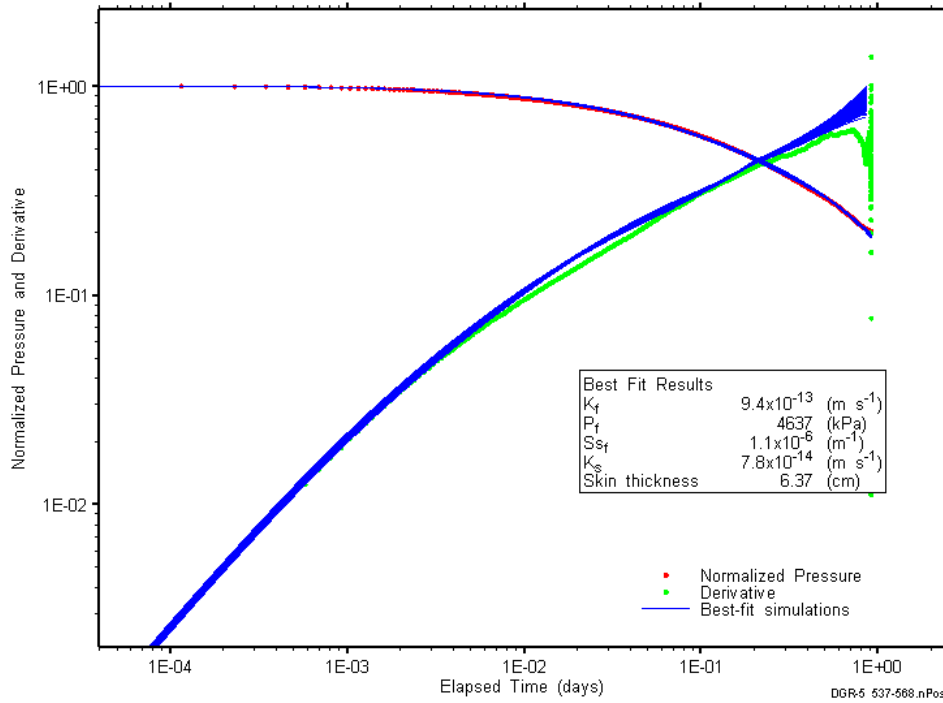


Figure E-34: Log-log plot showing simulations of the DGR5_494.82-523.66 PW1 Ramey B and derivative response.

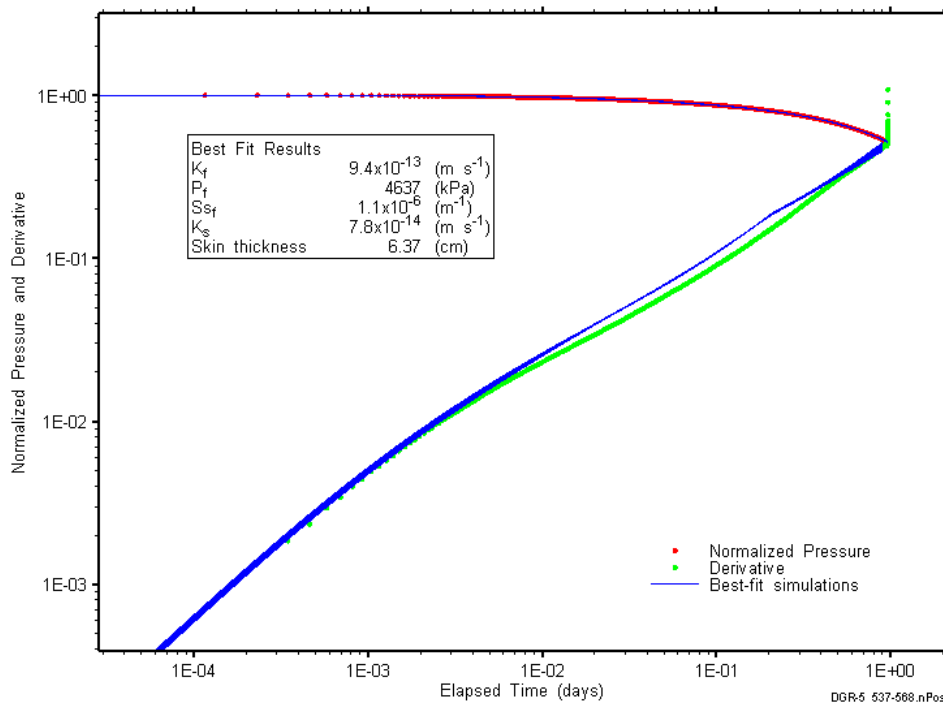


Figure E-35: Log-log plot showing simulations of the DGR5_494.82-523.66 PW2 Ramey B and derivative response.

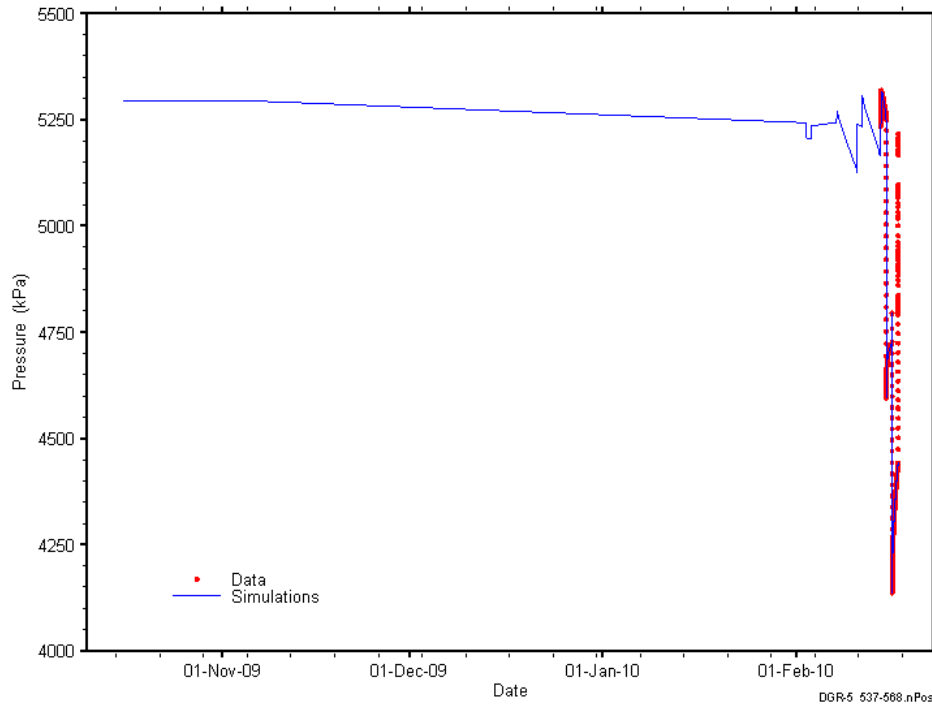


Figure E-36: Linear plot showing simulations of the DGR5_494.82-523.66 pressure response, including pre-test pressure history.

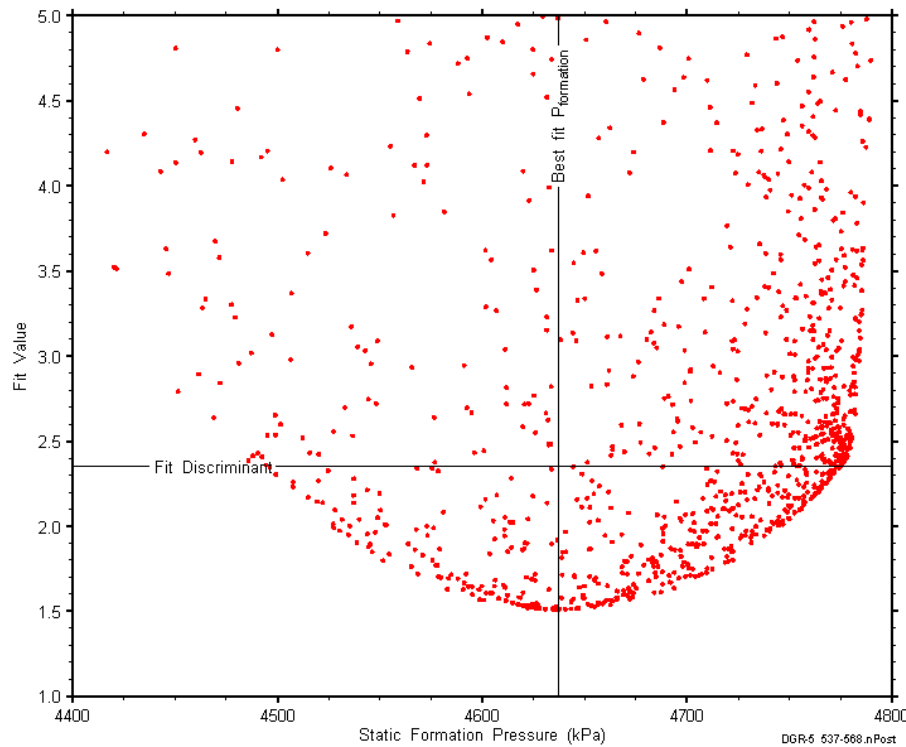


Figure E-37: XY-scatter plot showing the static formation pressure parameter space derived from DGR5_494.82-523.66 perturbation analysis along with the fit discriminant and best fit values.

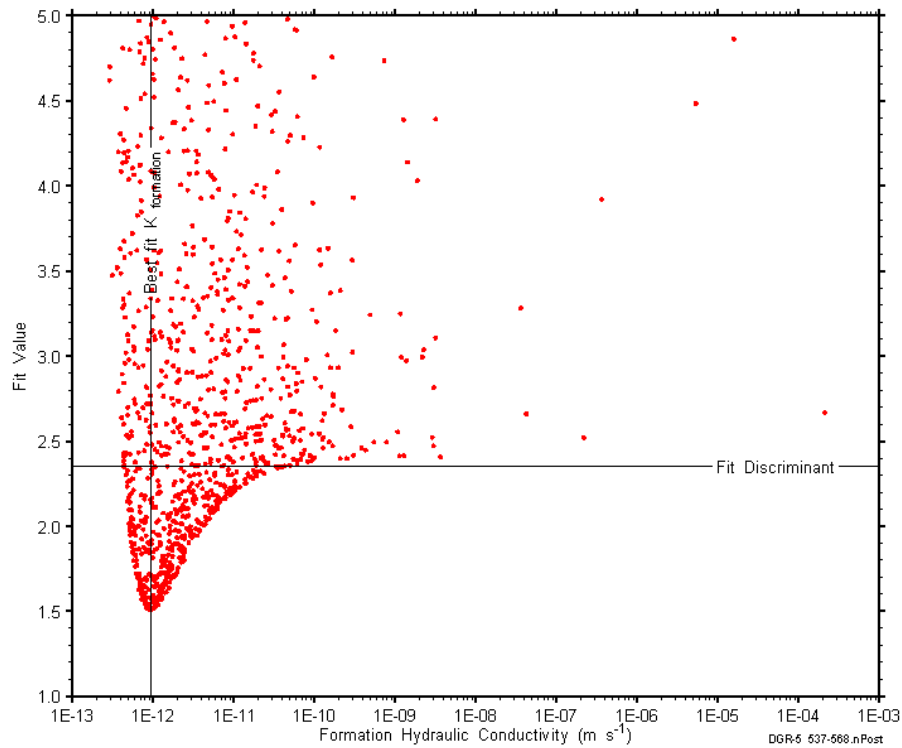


Figure E-38: XY-scatter plot showing the formation hydraulic conductivity parameter space derived from DGR5_494.82-523.66 perturbation analysis along with the fit discriminant and best fit values.

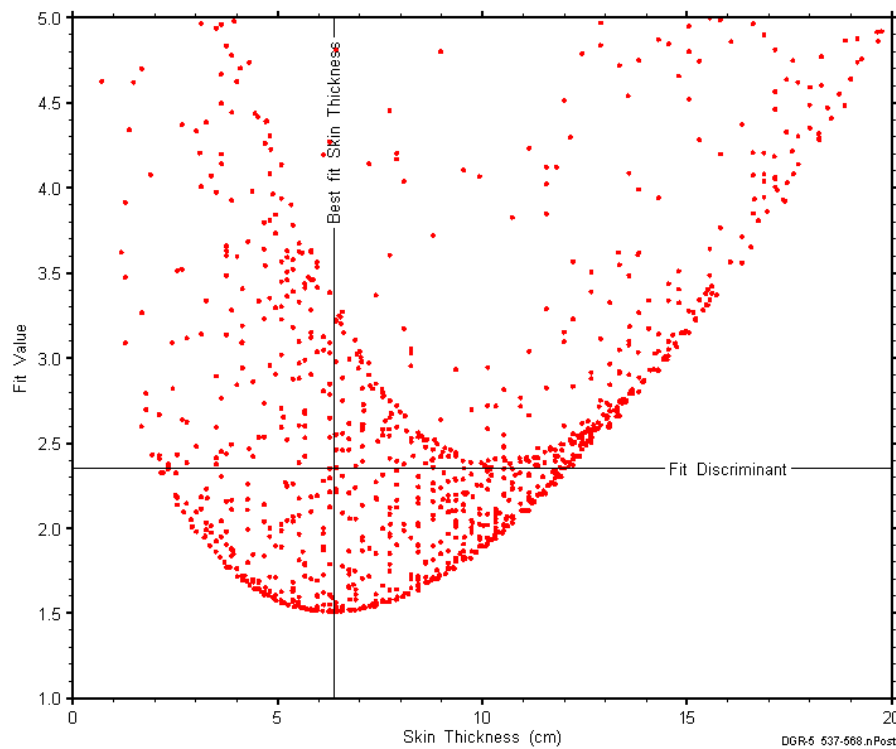


Figure E-39: XY-scatter plot showing the skin-thickness parameter space derived from DGR5_494.82-523.66 perturbation analysis along with the fit discriminant and best fit values.

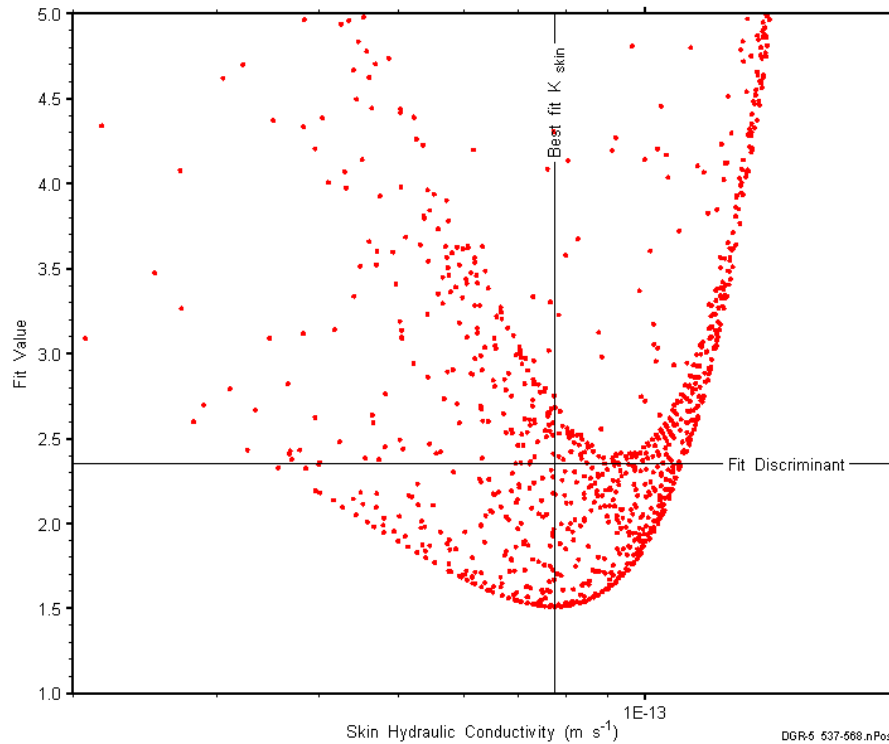


Figure E-40: XY-scatter plot showing the skin hydraulic conductivity parameter space derived from DGR5_494.82-523.66 perturbation analysis along with the fit discriminant and best fit values.

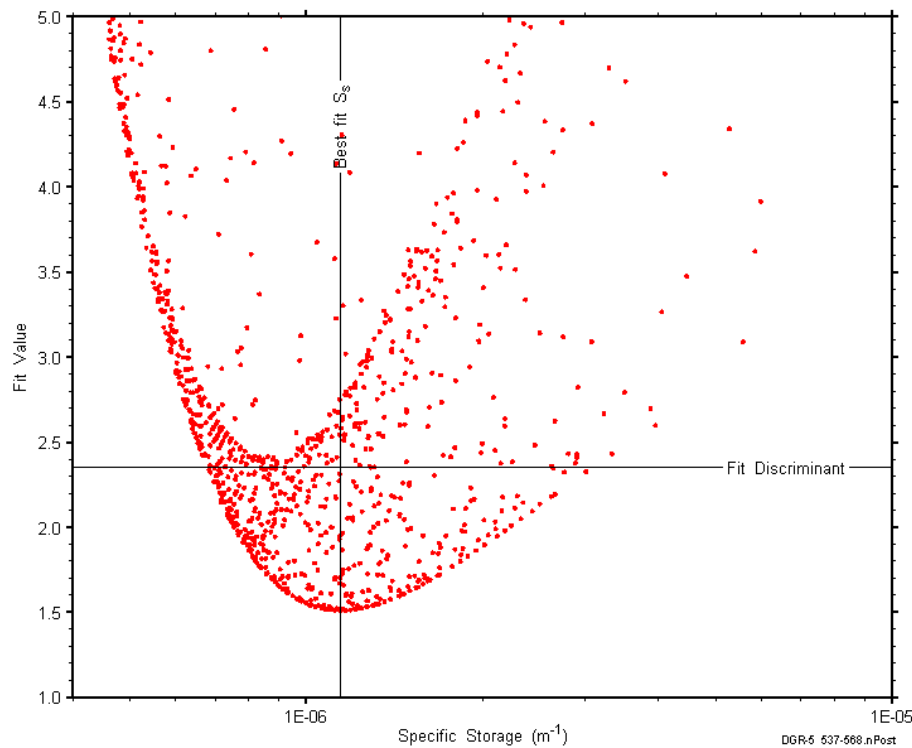


Figure E-41: XY-scatter plot showing the formation specific storage parameter space derived from DGR5_494.82-523.66 perturbation analysis along with the fit discriminant and best fit values.

E.4 523.42-552.31 Georgian Bay

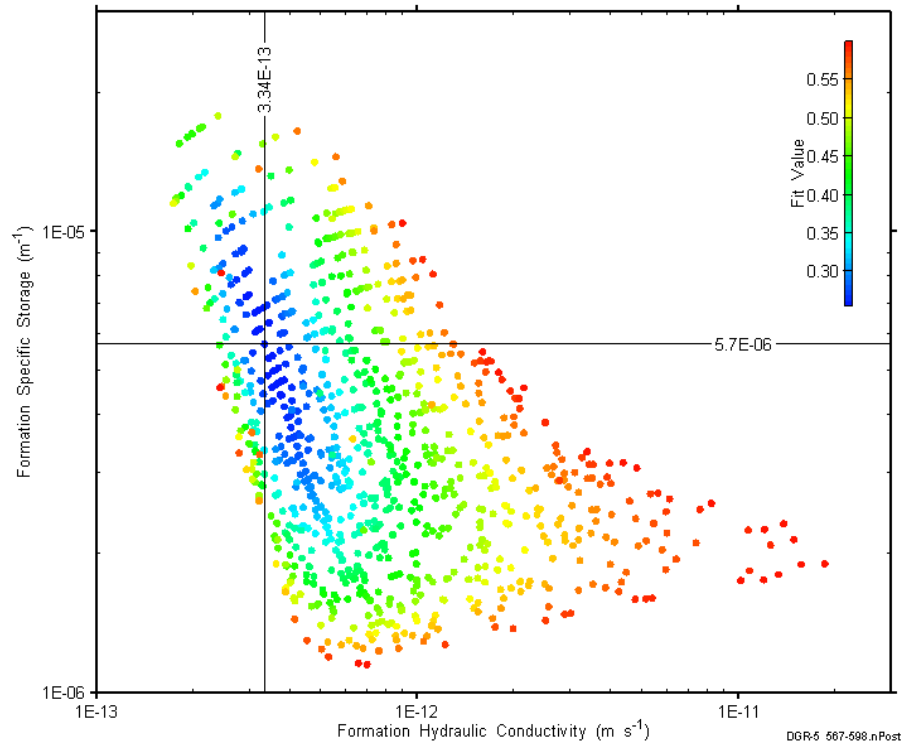


Figure E-42: XY-scatter plot showing estimates of formation hydraulic conductivity and formation specific storage derived from the DGR5_523.42-552.31 perturbation analysis.

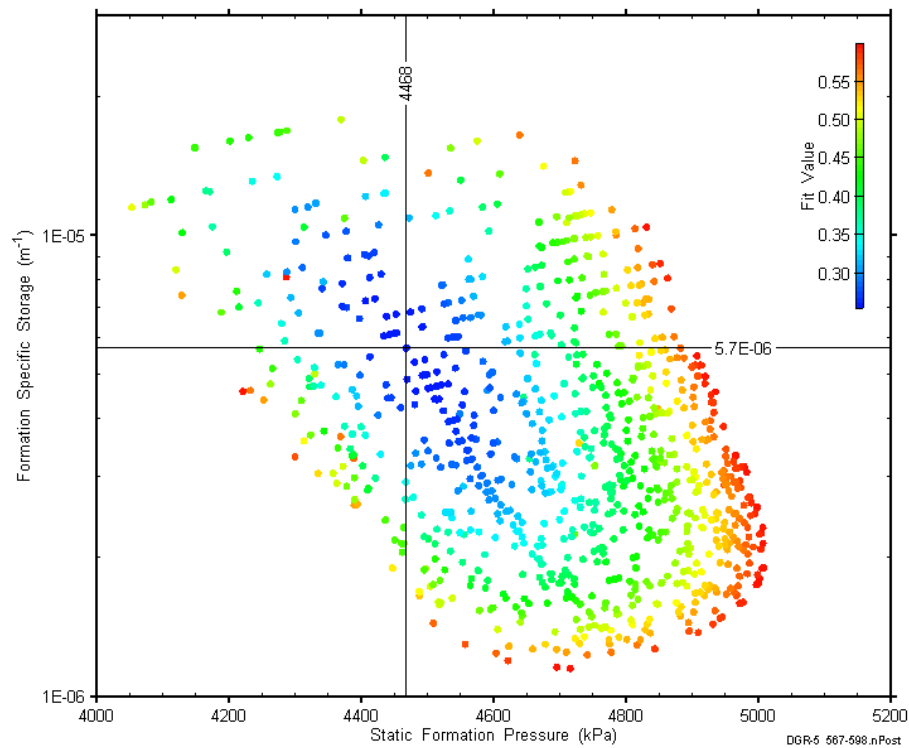


Figure E-43: XY-scatter plot showing estimates of static formation pressure and formation specific storage derived from the DGR5_523.42-552.31 perturbation analysis.

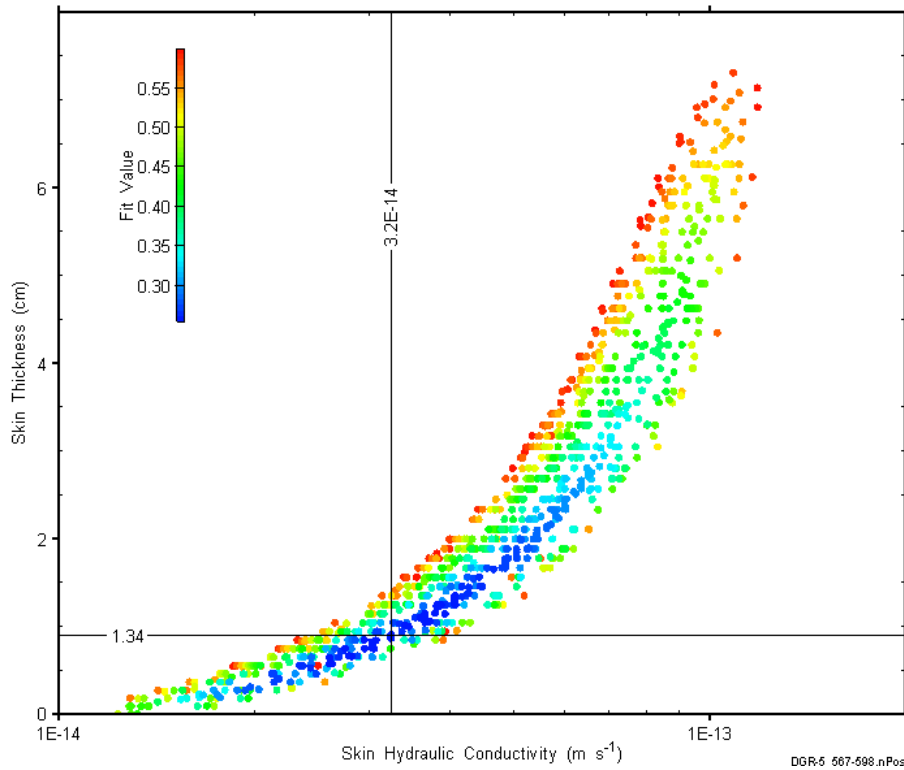


Figure E-44: XY-scatter plot showing estimates of skin hydraulic conductivity and skin thickness derived from the DGR5_523.42-552.31 perturbation analysis.

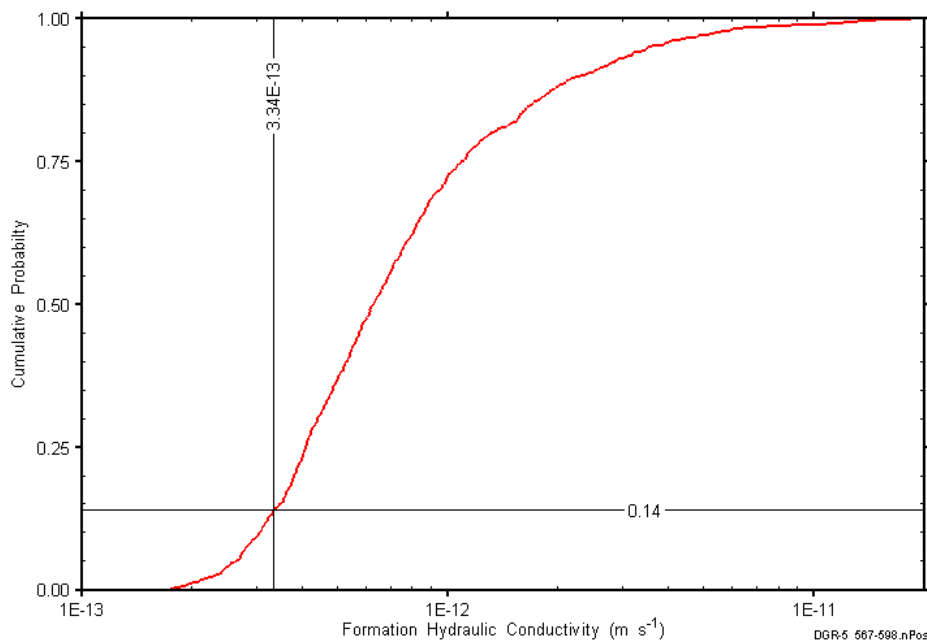


Figure E-45: DGR5_523.42-552.31 formation hydraulic conductivity cumulative distribution function.

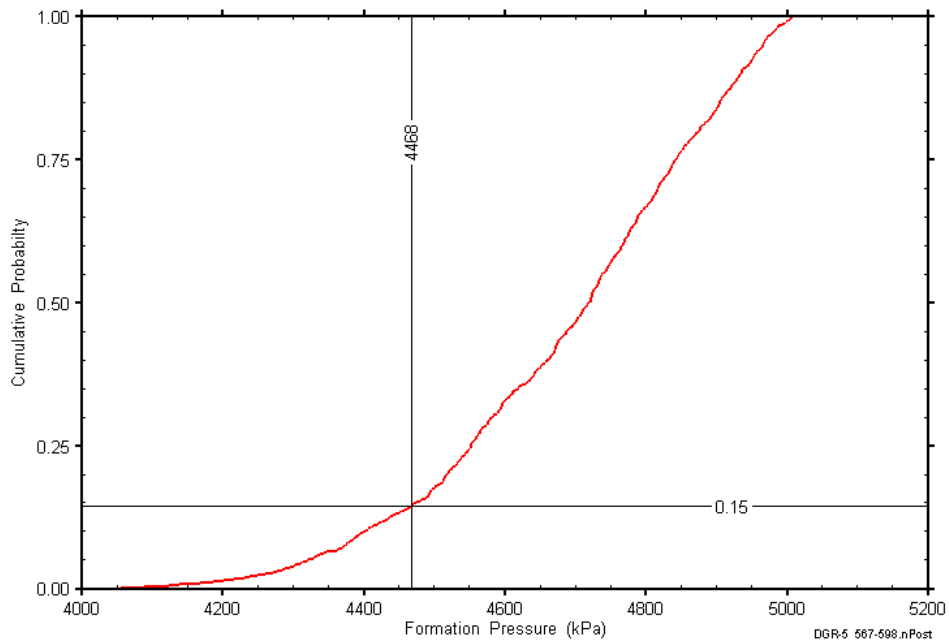


Figure E-46: DGR5_523.42-552.31 static formation pressure cumulative distribution function.

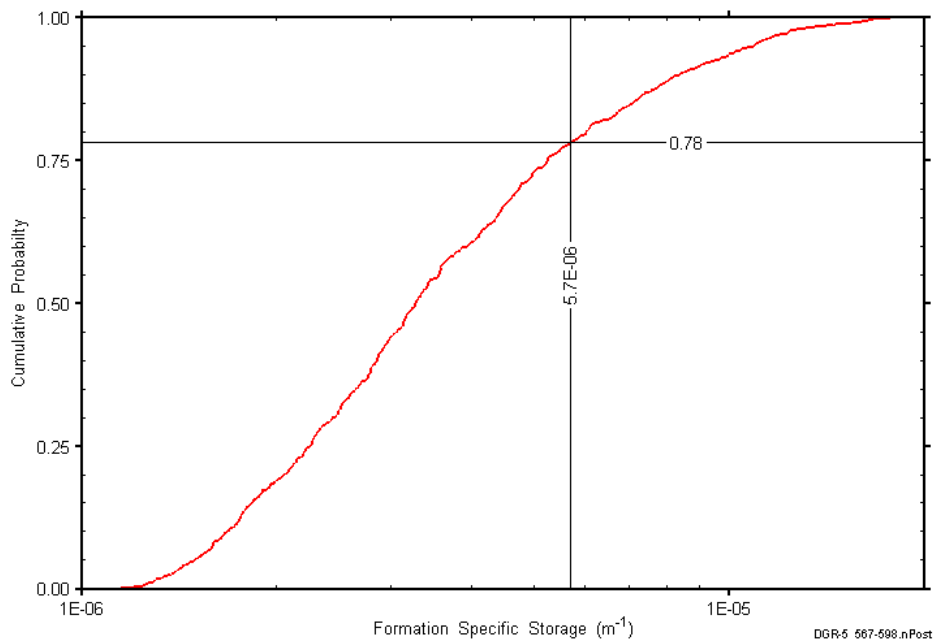


Figure E-47: DGR5_523.42-552.31 formation specific storage cumulative distribution function.

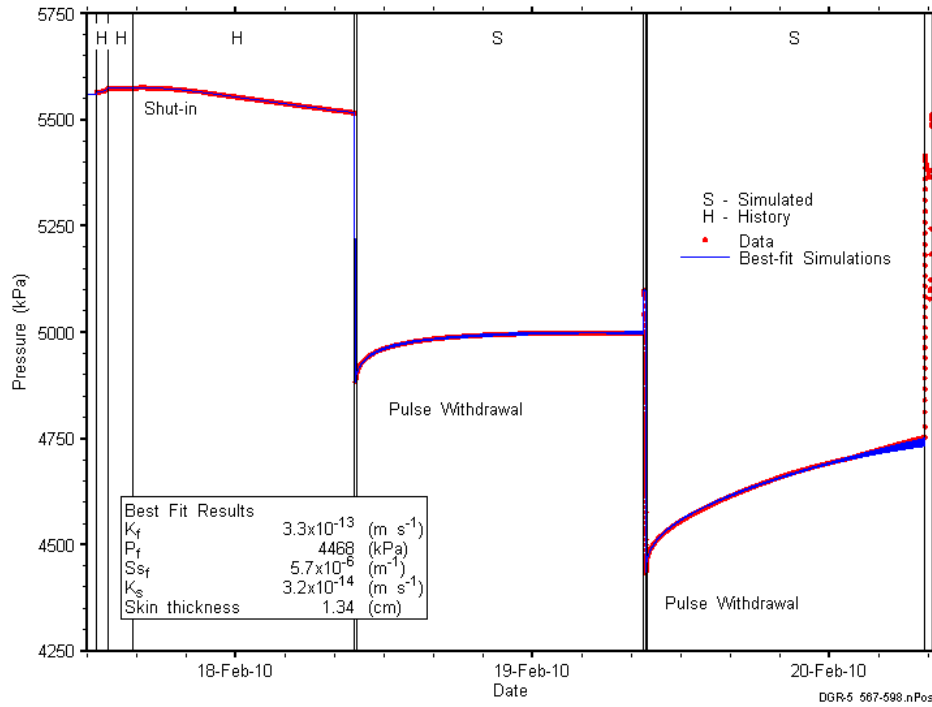


Figure E-48: Linear plot showing simulations of the DGR5_523.42-552.31 pressure response.

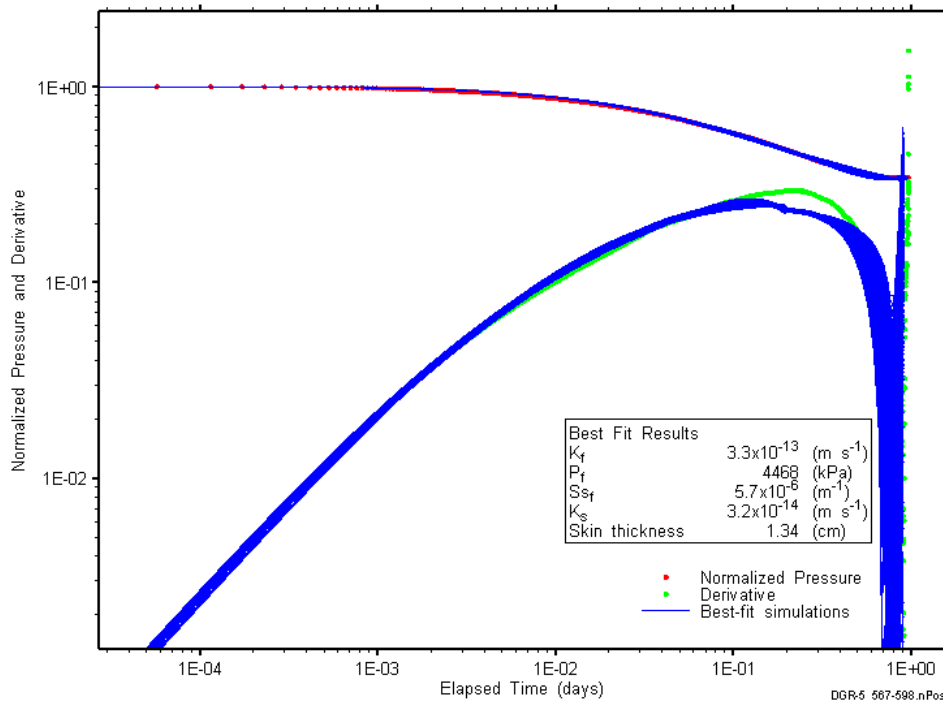


Figure E-49 Log-log plot showing simulations of the DGR5_523.42-552.31 PW1 Ramey B and derivative response.

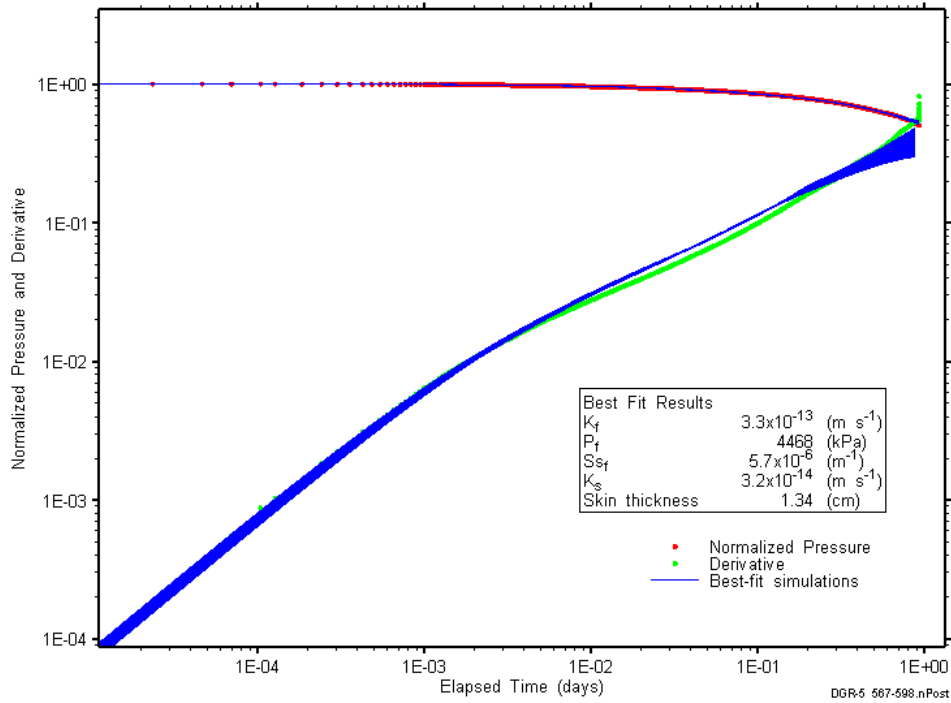


Figure E-50: Log-log plot showing simulations of the DGR5_523.42-552.31 PW2 Ramey B and derivative response.

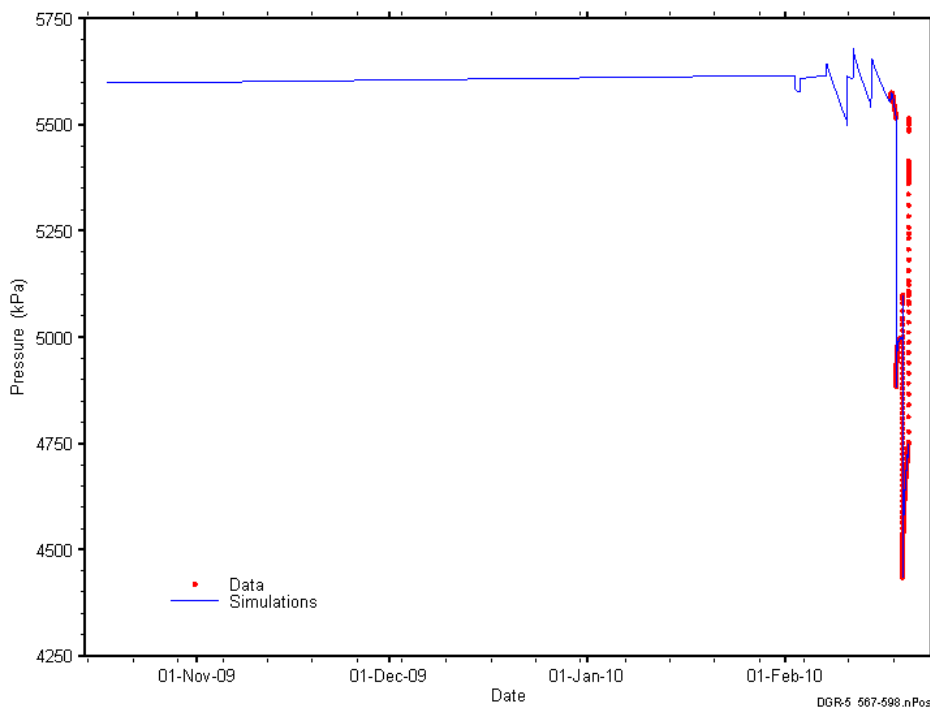


Figure E-51: Linear plot showing simulations of the DGR5_523.42-552.31 pressure response, including pre-test pressure history.

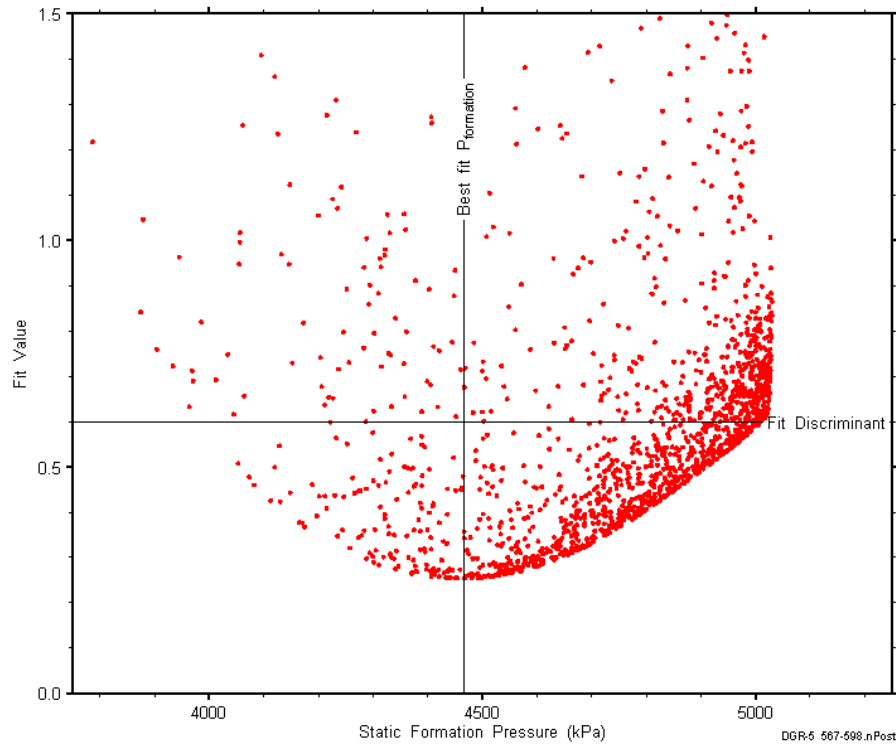


Figure E-52: XY-scatter plot showing the static formation pressure parameter space derived from DGR5_523.42-552.31 perturbation analysis along with the fit discriminant and best fit values.

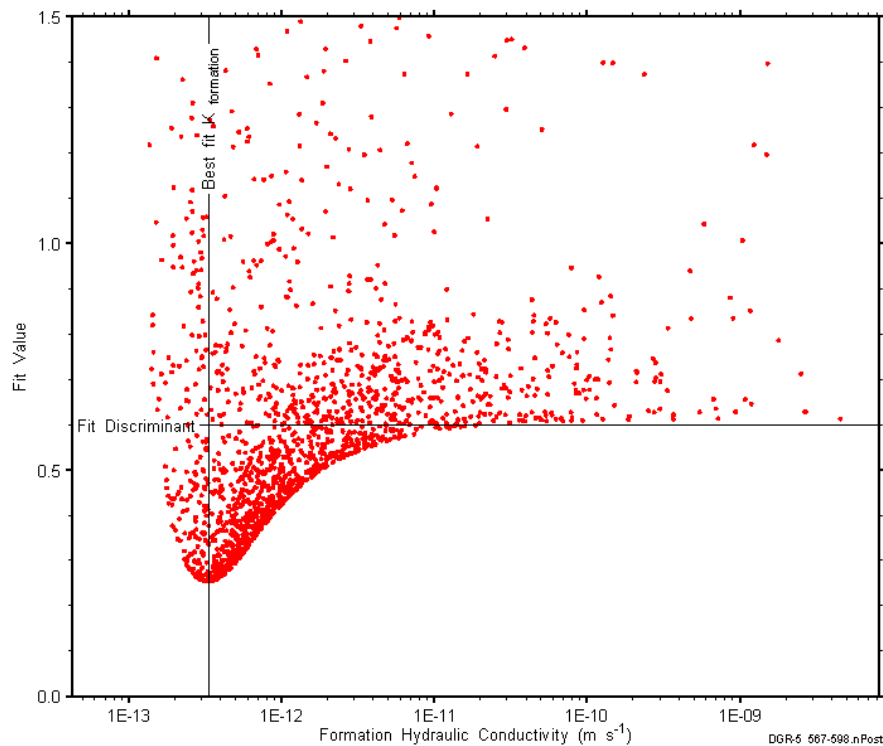


Figure E-53: XY-scatter plot showing the formation hydraulic conductivity parameter space derived from DGR5_523.42-552.31 perturbation analysis along with the fit discriminant and best fit values.

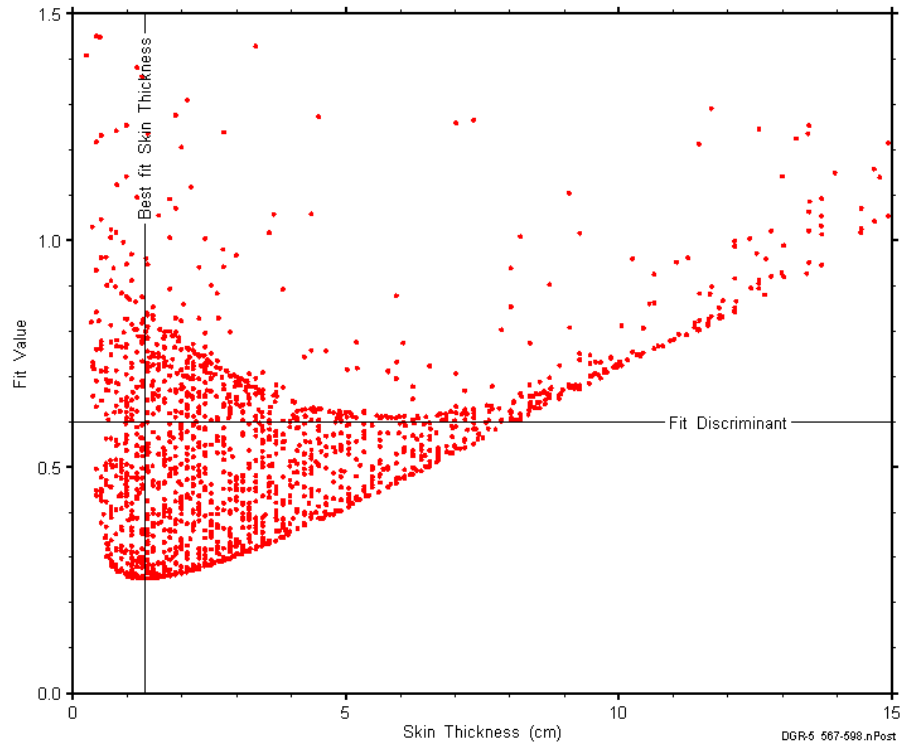


Figure E-54: XY-scatter plot showing the skin-thickness parameter space derived from DGR5_523.42-552.31 perturbation analysis along with the fit discriminant and best fit values.

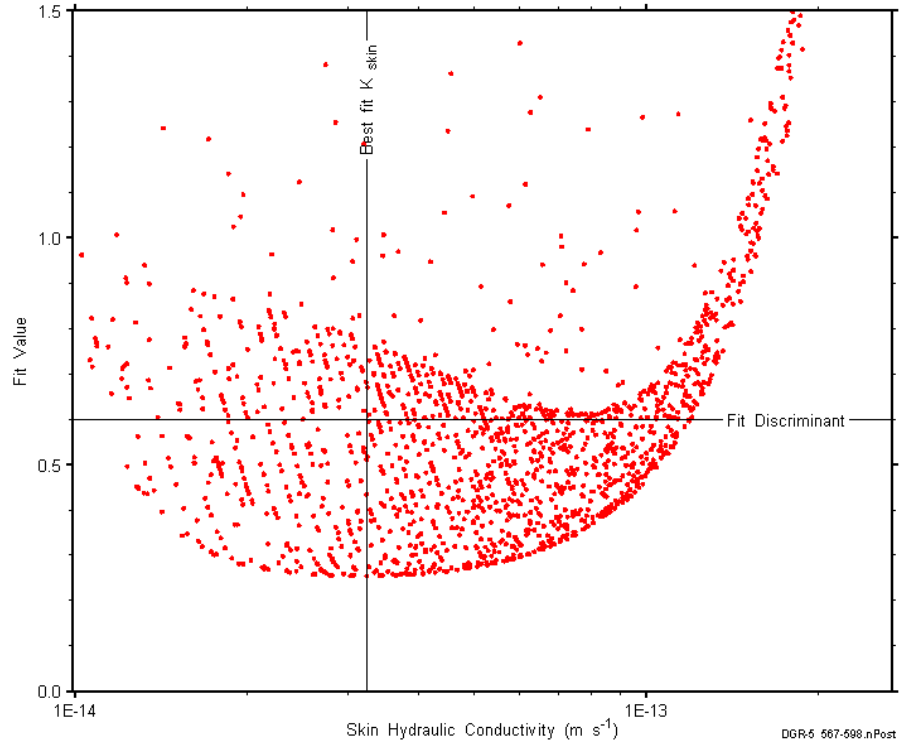


Figure E-55: XY-scatter plot showing the skin hydraulic conductivity parameter space derived from DGR5_523.42-552.31 perturbation analysis along with the fit discriminant and best fit values.

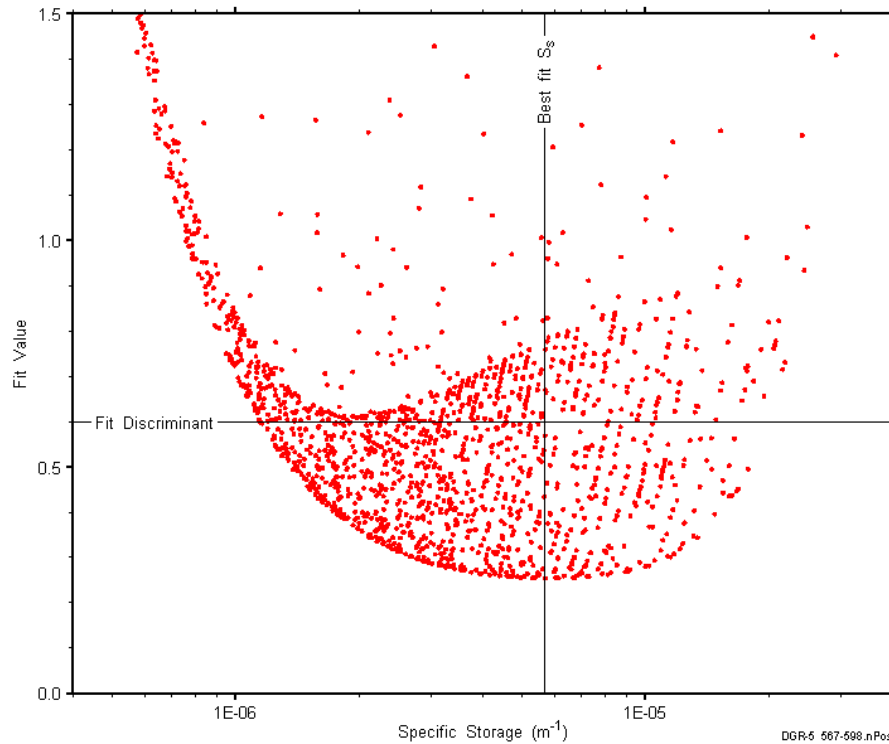


Figure E-56: XY-scatter plot showing the formation specific storage parameter space derived from DGR5_523.42-552.31 perturbation analysis along with the fit discriminant and best fit values.

E.5 552.06-581.01 Georgian Bay

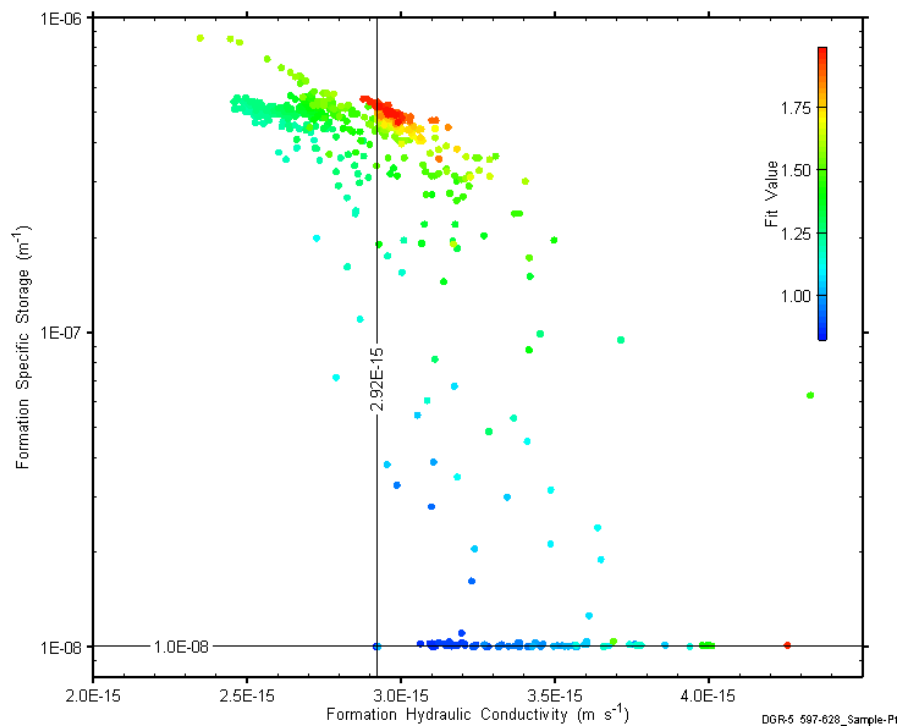


Figure E-57: XY-scatter plot showing estimates of formation hydraulic conductivity and formation specific storage derived from the DGR5_552.06-581.01 perturbation analysis.

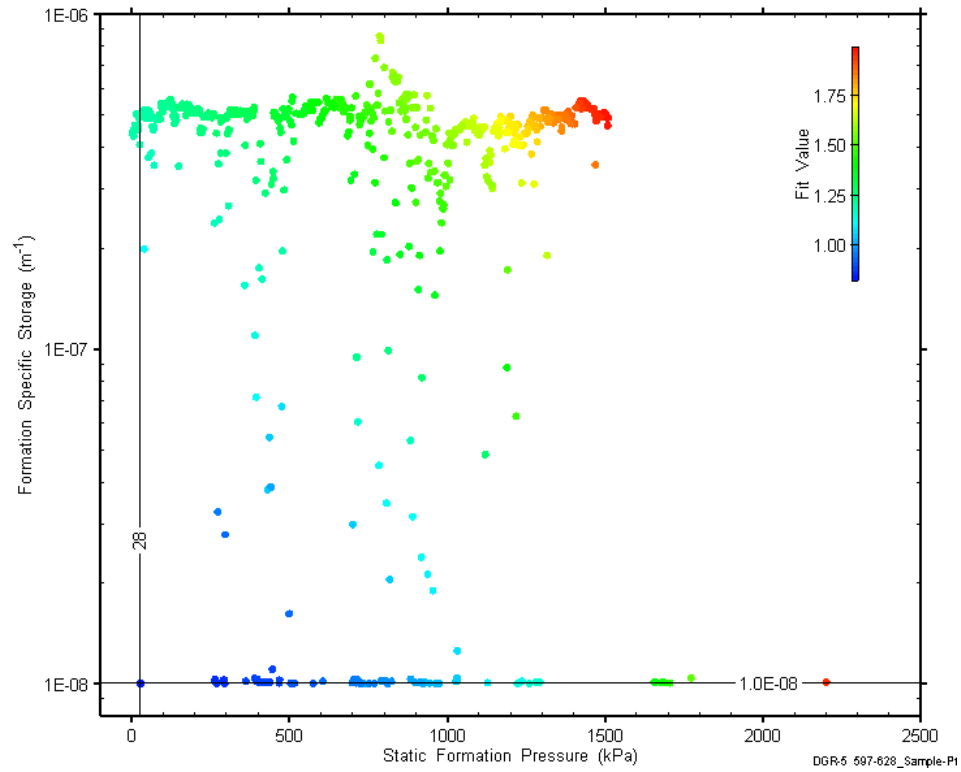


Figure E-58: XY-scatter plot showing estimates of static formation pressure and formation specific storage derived from the 552.06-581.01 perturbation analysis.

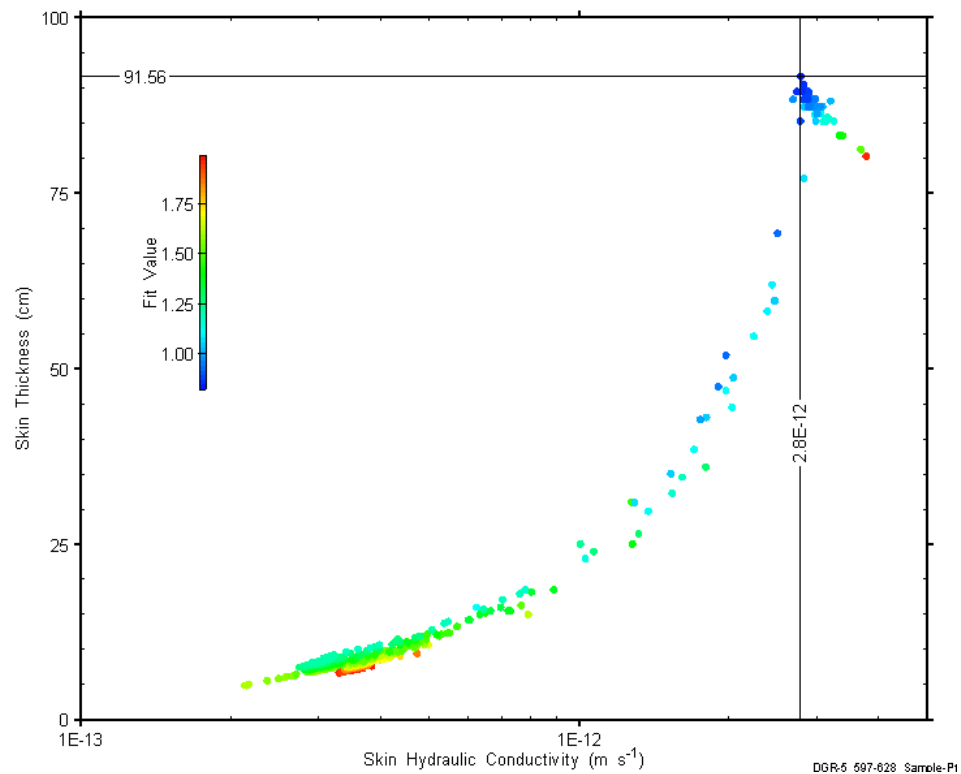


Figure E-59: XY-scatter plot showing estimates of skin hydraulic conductivity and skin thickness derived from the DGR5_552.06-581.01 perturbation analysis.

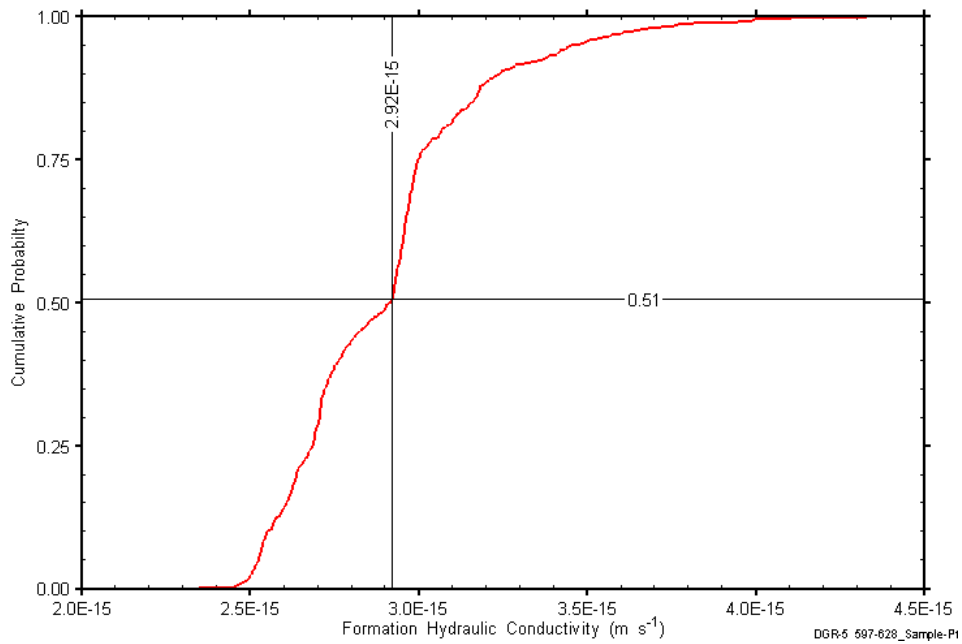


Figure E-60: DGR5_552.06-581.01 formation hydraulic conductivity cumulative distribution function.

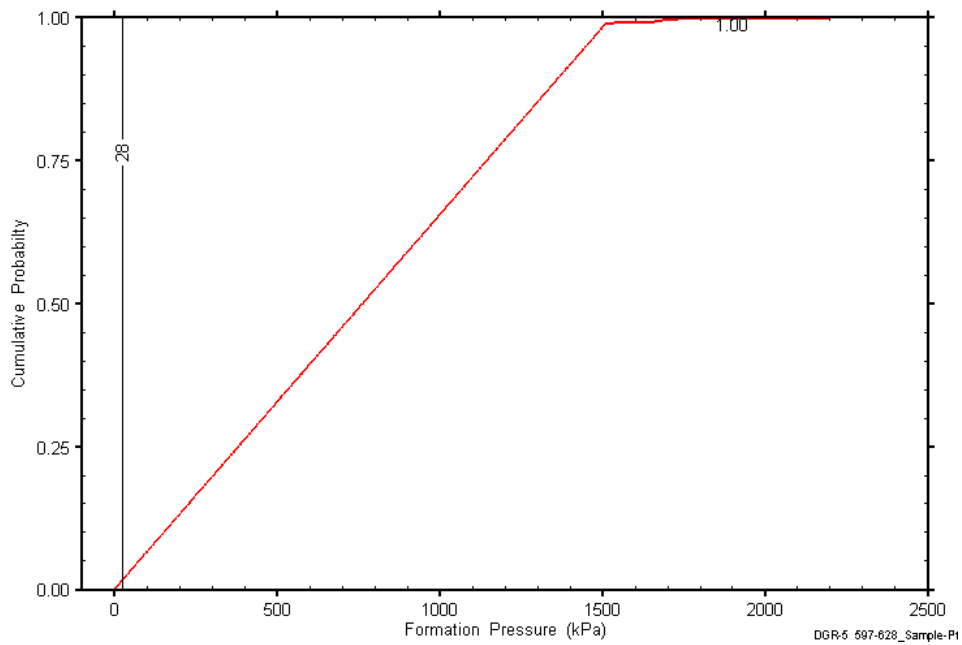


Figure E-61: DGR5_552.06-581.01 static formation pressure cumulative distribution function.

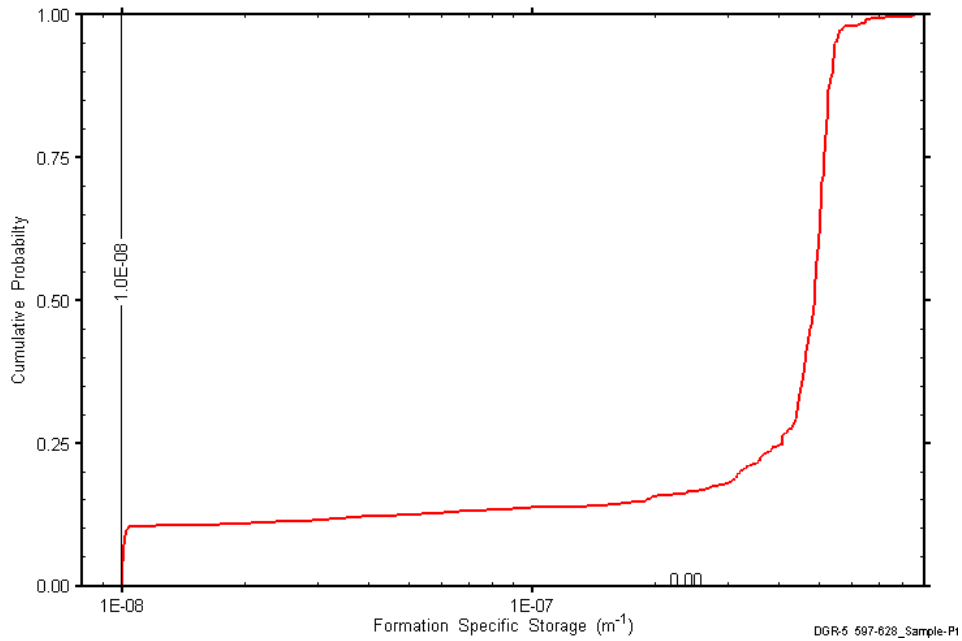


Figure E-62: DGR5_552.06-581.01 formation specific storage cumulative distribution function.

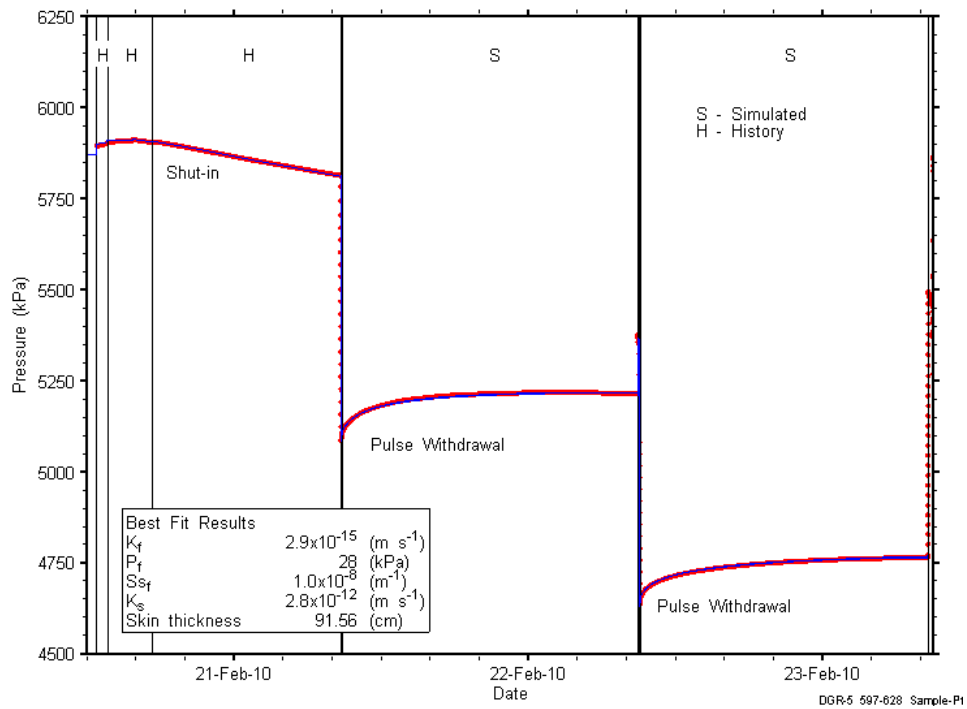


Figure E-63: Linear plot showing simulations of the DGR5_552.06-581.01 pressure response.

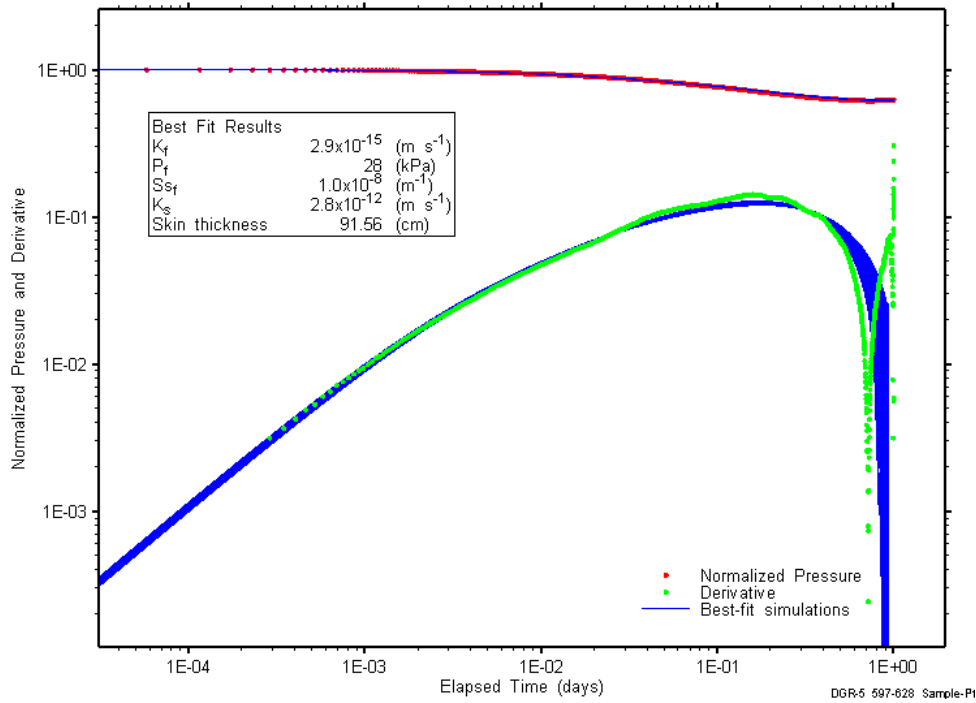


Figure E-64: Log-log plot showing simulations of the DGR5_552.06-581.01 PW1 Ramey B and derivative response.

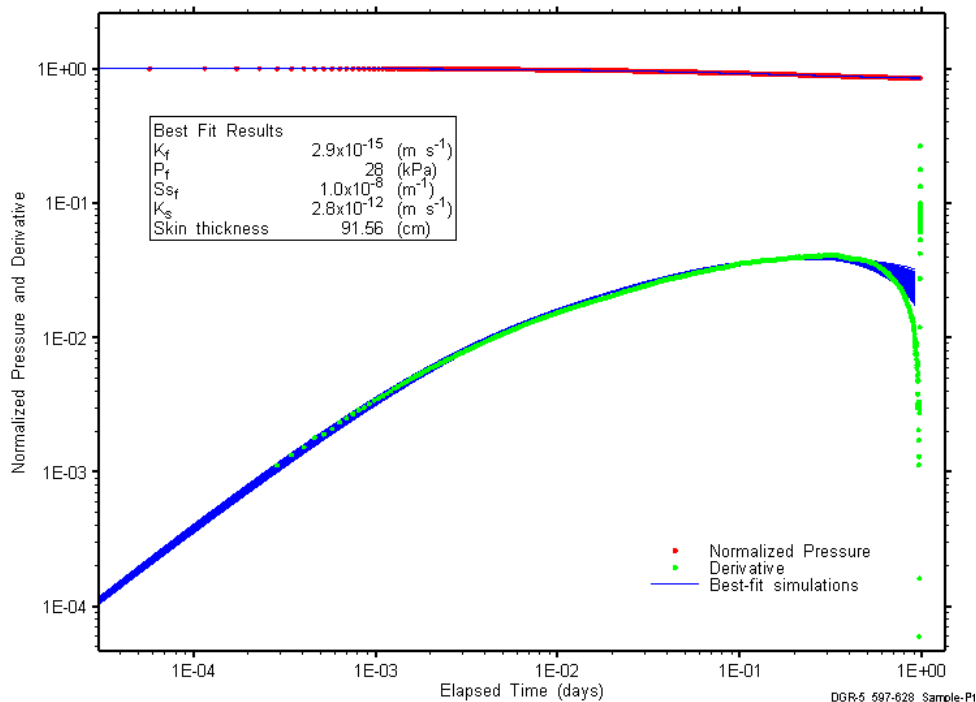


Figure E-65: Log-log plot showing simulations of the DGR5_552.06-581.01 PW2 Ramey B and derivative response.

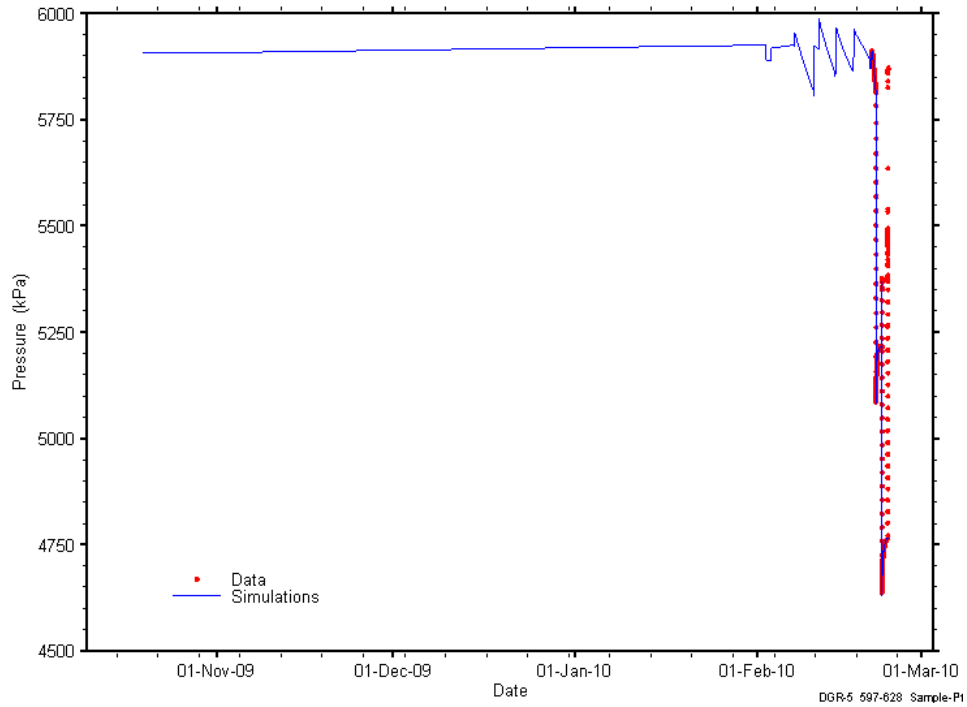


Figure E-66: Linear plot showing simulations of the DGR5_552.06-581.01 pressure response, including pre-test pressure history.

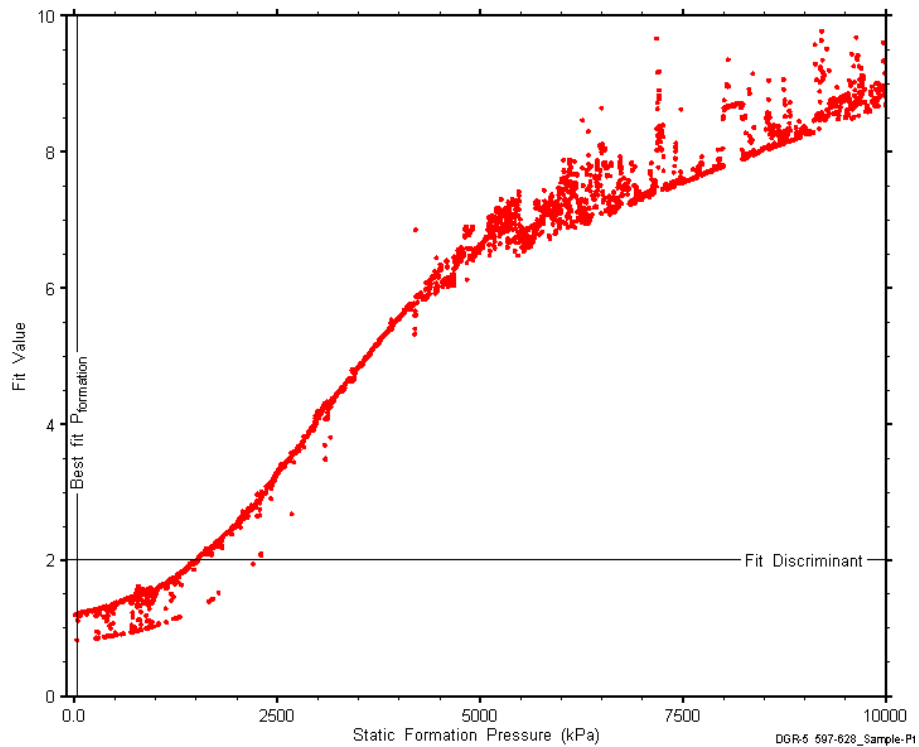


Figure E-67: XY-scatter plot showing the static formation pressure parameter space derived from DGR5_552.06-581.01 perturbation analysis along with the fit discriminant and best fit values.

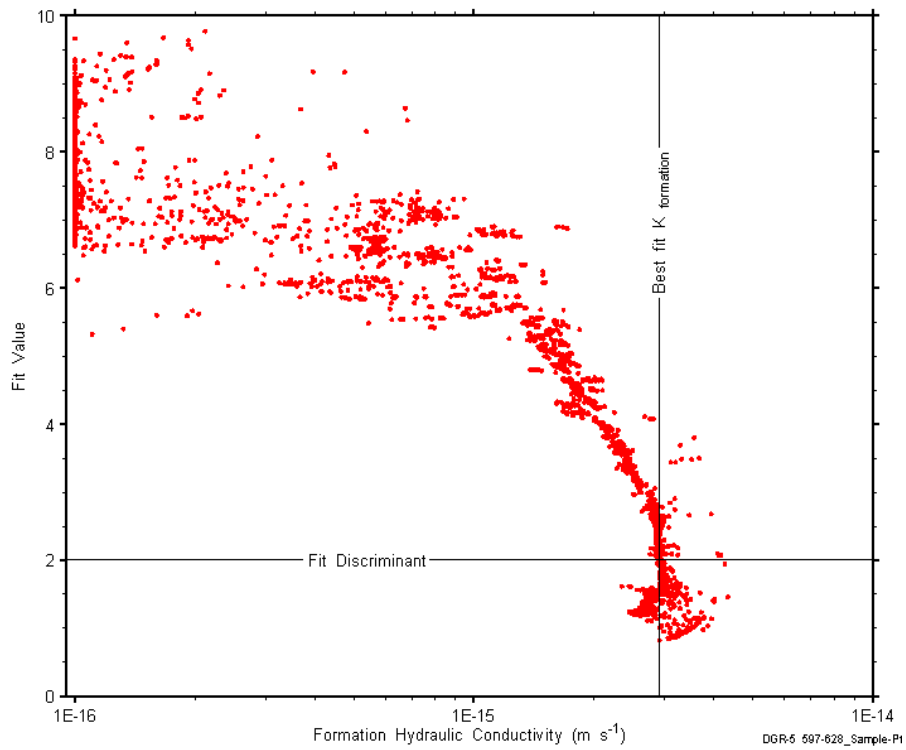


Figure E-68: XY-scatter plot showing the formation hydraulic conductivity parameter space derived from DGR5_552.06-581.01 perturbation analysis along with the fit discriminant and best fit values.

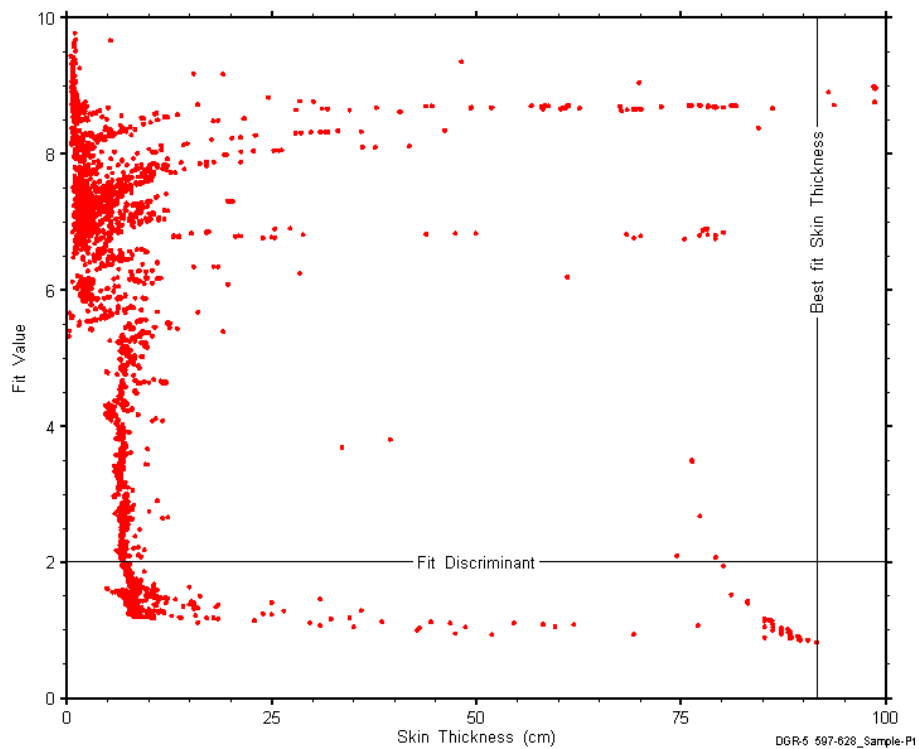


Figure E-69: XY-scatter plot showing the skin-thickness parameter space derived from DGR5_552.06-581.01 perturbation analysis along with the fit discriminant and best fit values.

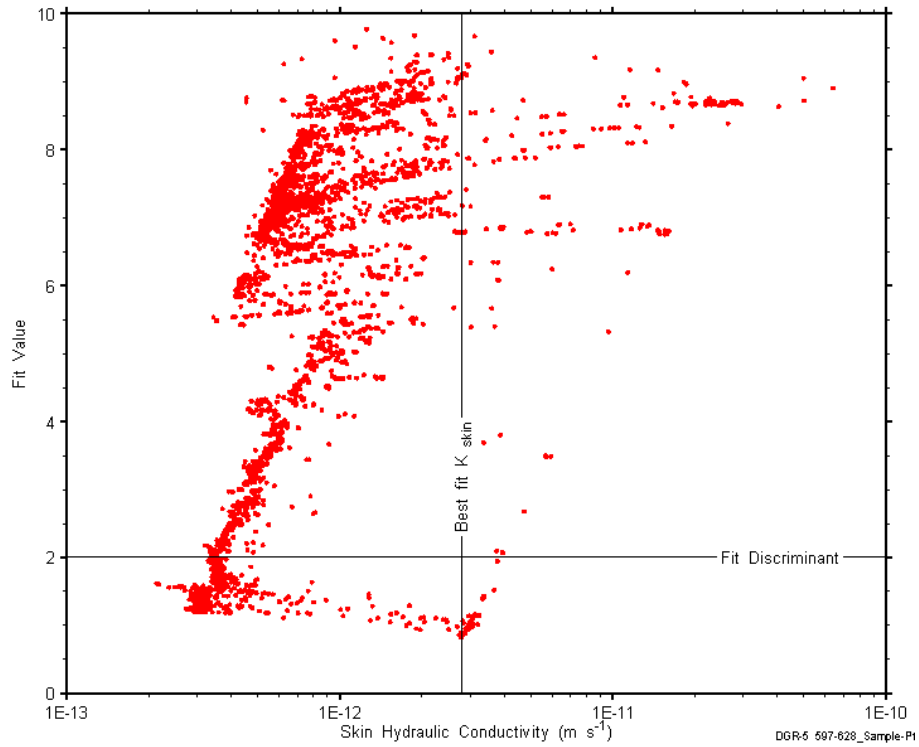


Figure E-70: XY-scatter plot showing the skin hydraulic conductivity parameter space derived from DGR5_552.06-581.01 perturbation analysis along with the fit discriminant and best fit values.

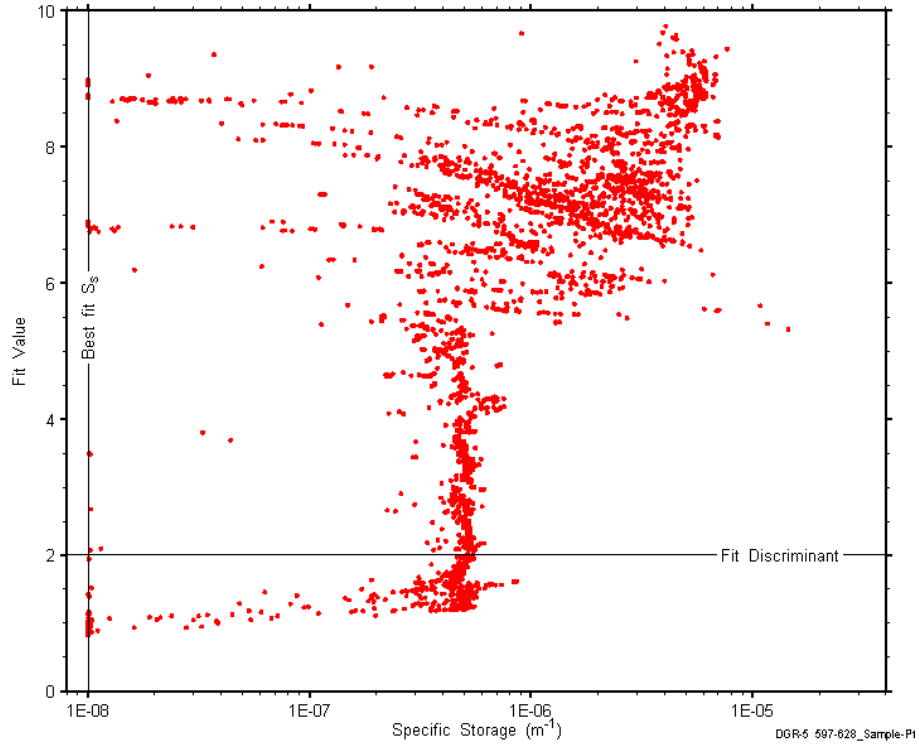


Figure E-71: XY-scatter plot showing the formation specific storage parameter space derived from DGR5_552.06-581.01 perturbation analysis along with the fit discriminant and best fit values.

E.6 580.76-609.80 Georgian Bay

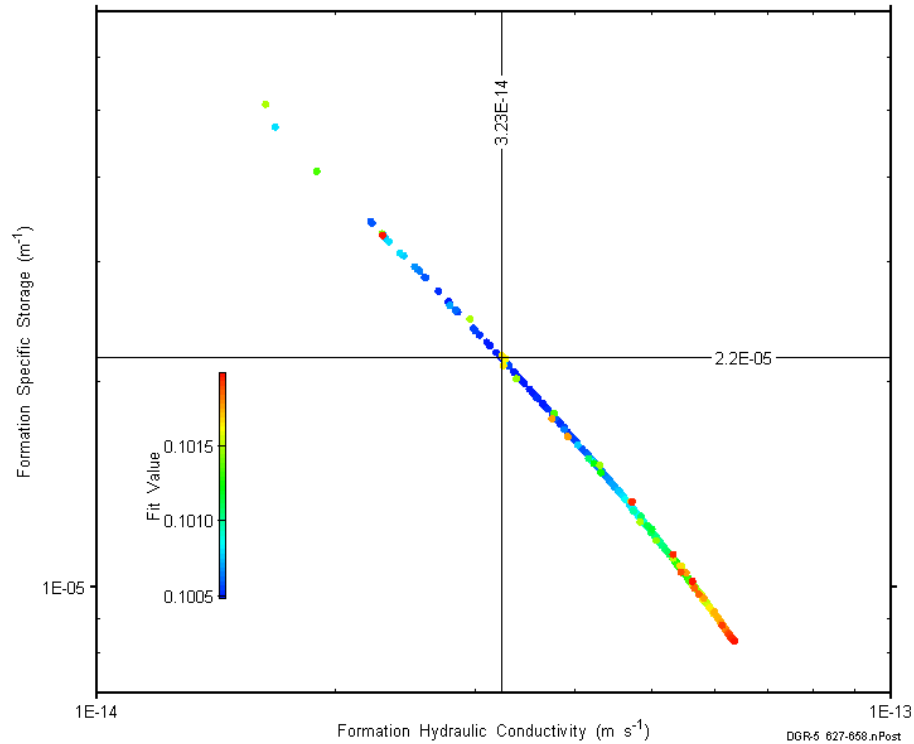


Figure E-72: XY-scatter plot showing estimates of formation hydraulic conductivity and formation specific storage derived from the DGR5_580.76-609.80 perturbation analysis.

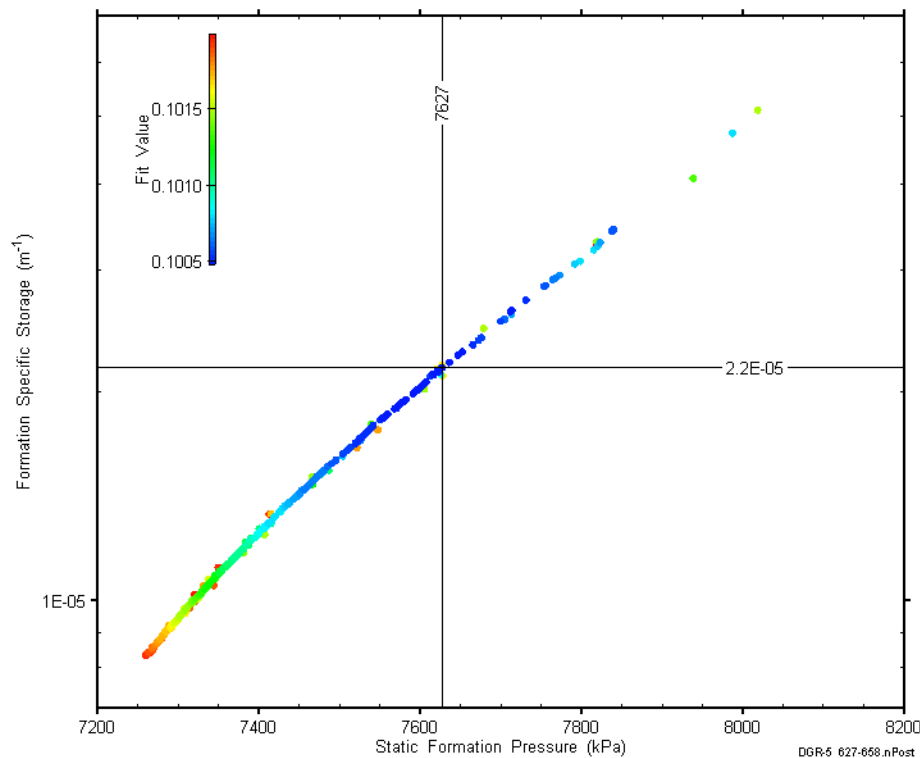


Figure E-73: XY-scatter plot showing estimates of static formation pressure and formation specific storage derived from the DGR5_580.76-609.80 perturbation analysis.

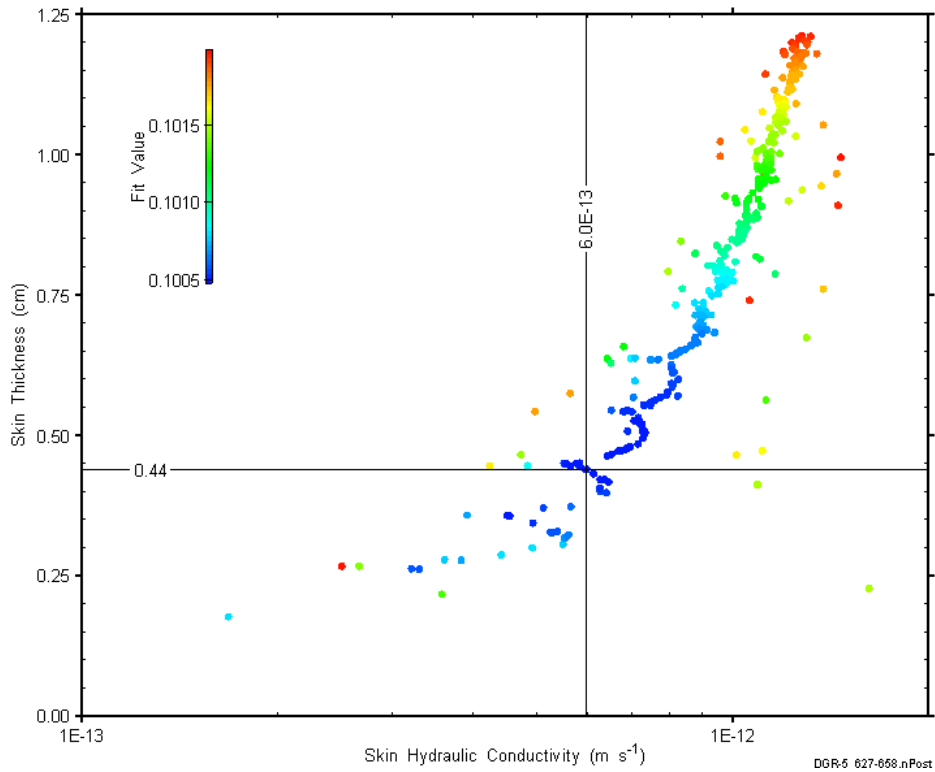


Figure E-74: XY-scatter plot showing estimates of skin hydraulic conductivity and skin thickness derived from the DGR5_580.76-609.80 perturbation analysis.

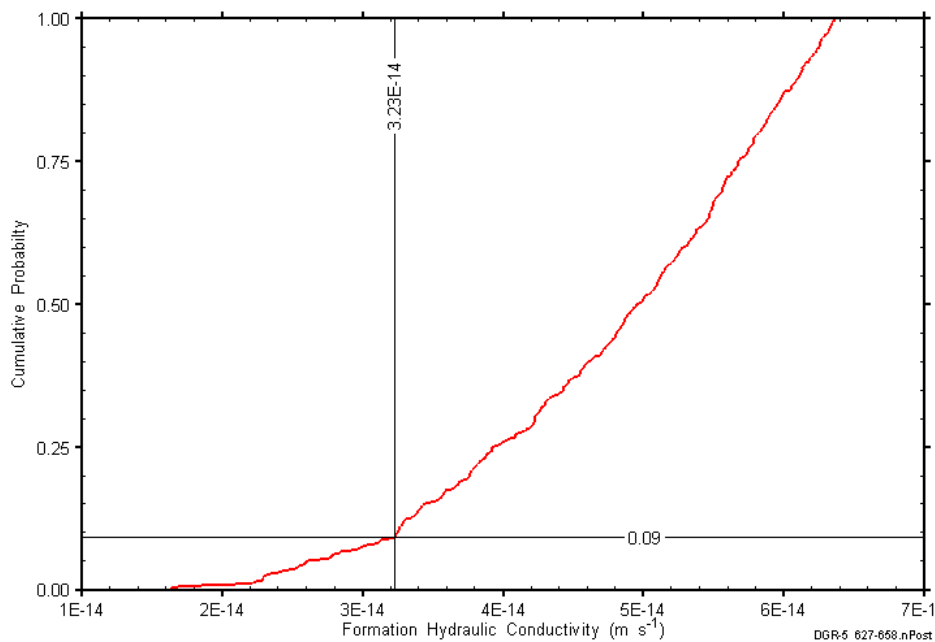


Figure E-75: DGR5_580.76-609.80 formation hydraulic conductivity cumulative distribution function.

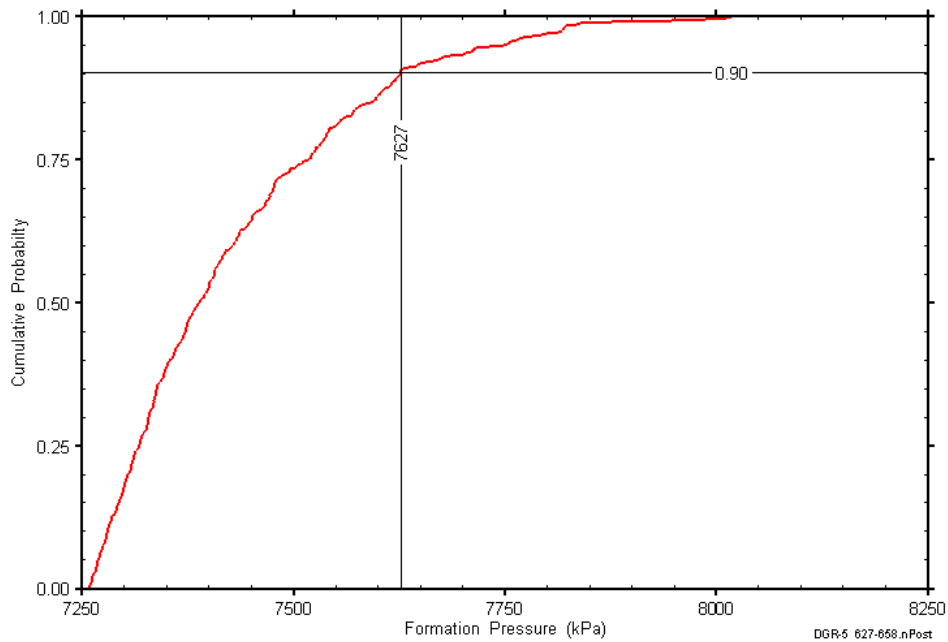


Figure E-76: DGR5_580.76-609.80 static formation pressure cumulative distribution function.

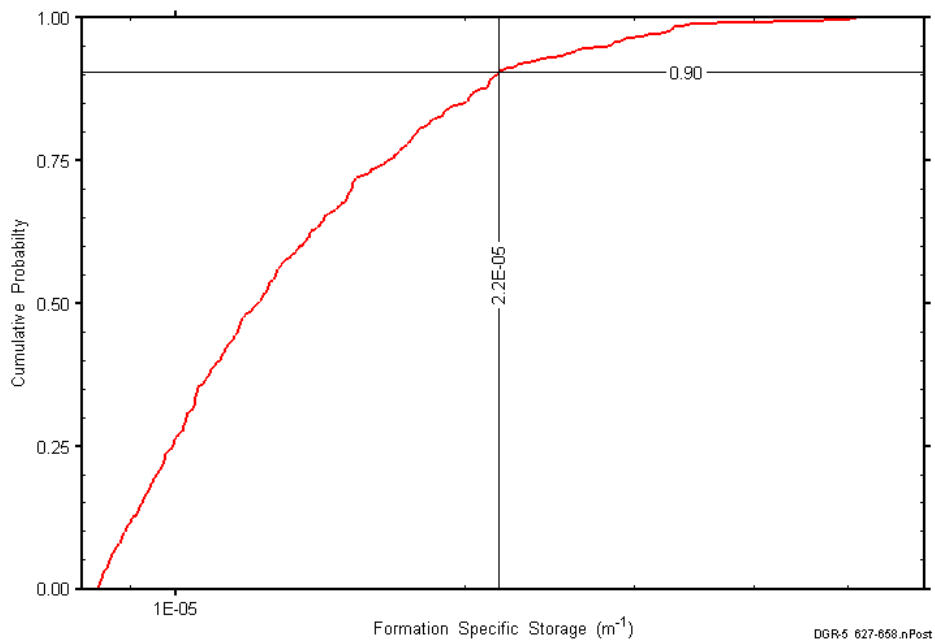


Figure E-77: DGR5_580.76-609.80 formation specific storage cumulative distribution function.

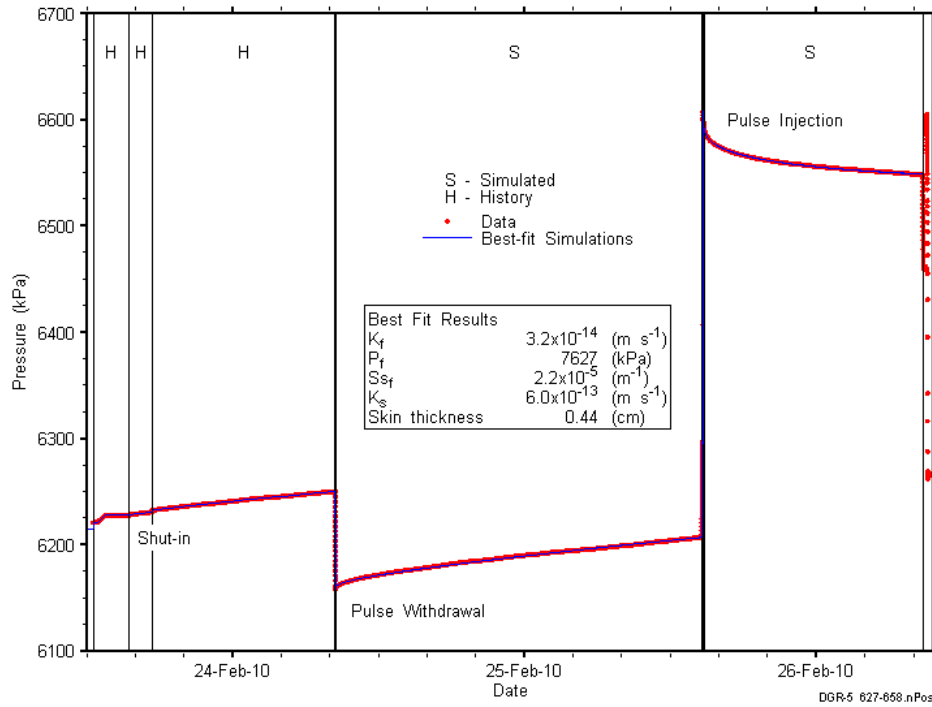


Figure E-78: Linear plot showing simulations of the DGR5_580.76-609.80 pressure response.

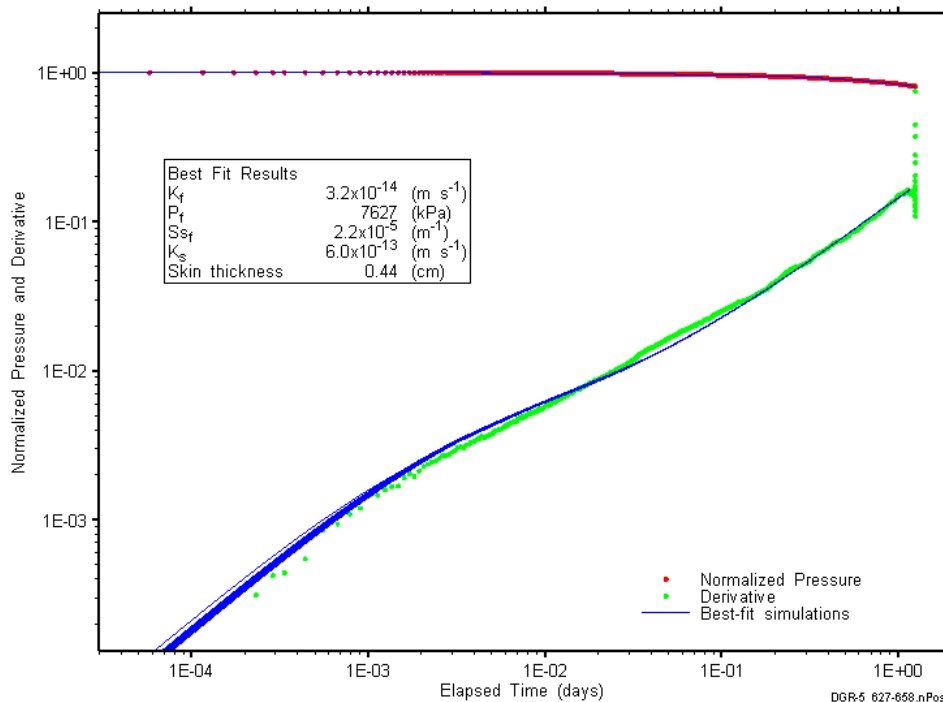


Figure E-79: Log-log plot showing simulations of the DGR5_580.76-609.80 PW Ramey B and derivative response.

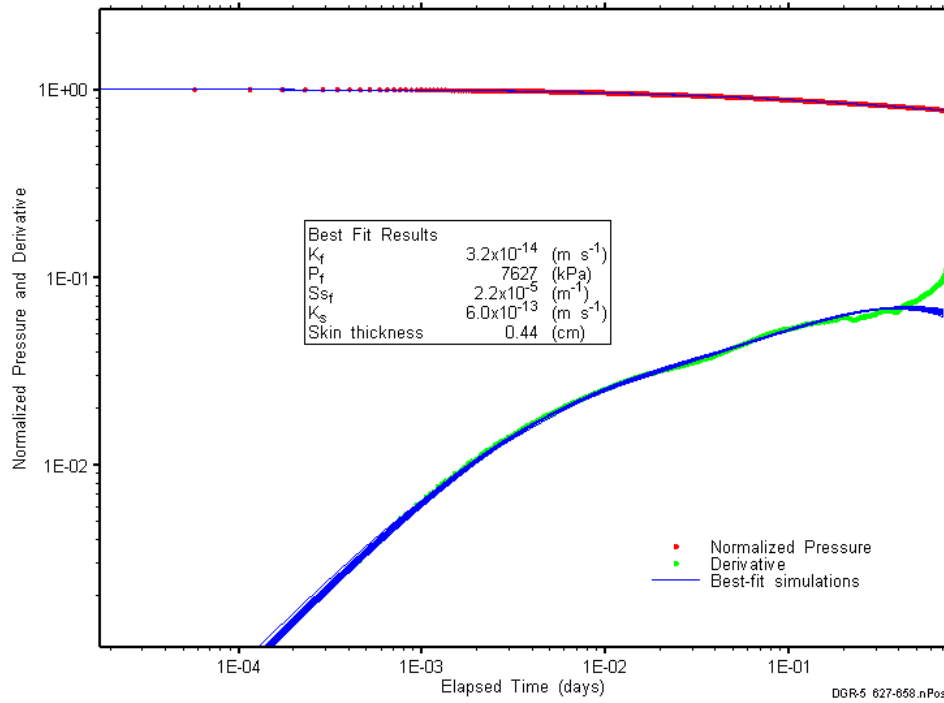


Figure E-80: Log-log plot showing simulations of the DGR5_580.76-609.80 PI Ramey B and derivative response.

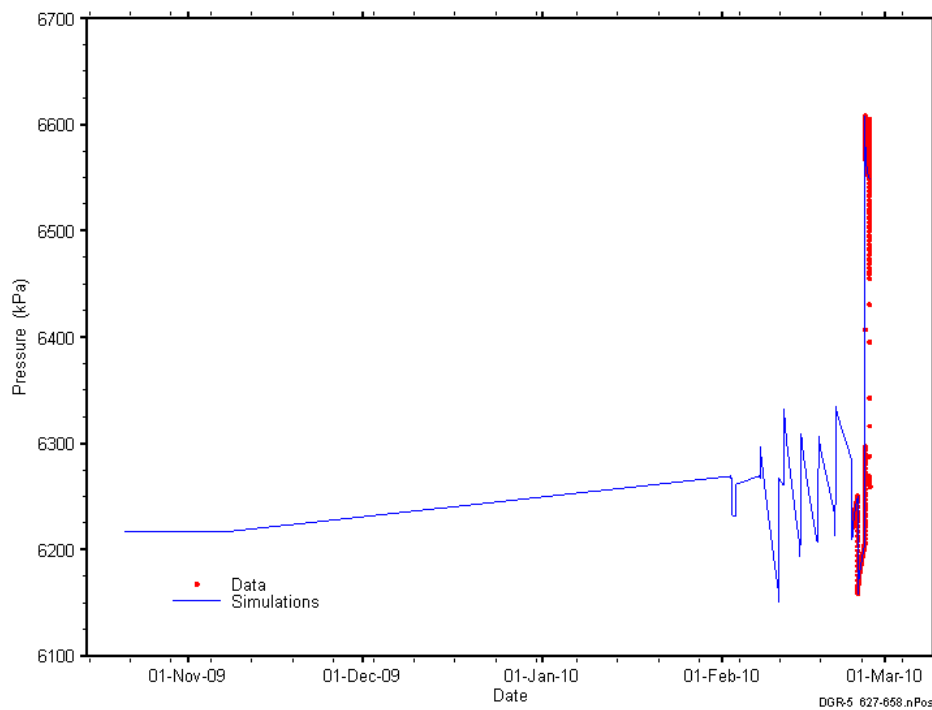


Figure E-81: Linear plot showing simulations of the DGR5_580.76-609.80 pressure response, including pre-test pressure history.

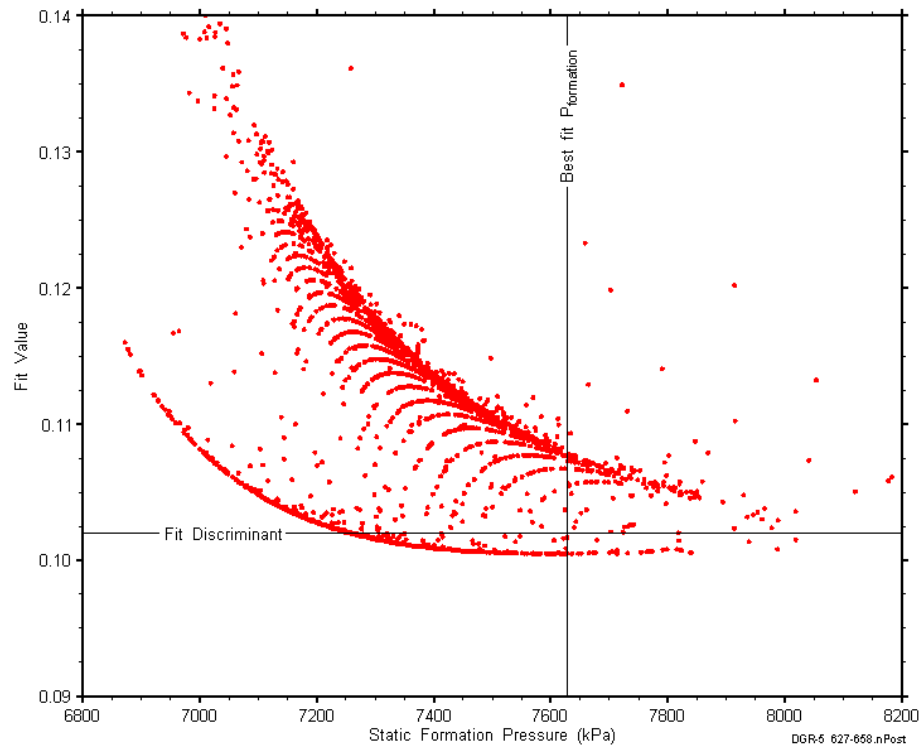


Figure E-82: XY-scatter plot showing the static formation pressure parameter space derived from DGR5_580.76-609.80 perturbation analysis along with the fit discriminant and best fit values.

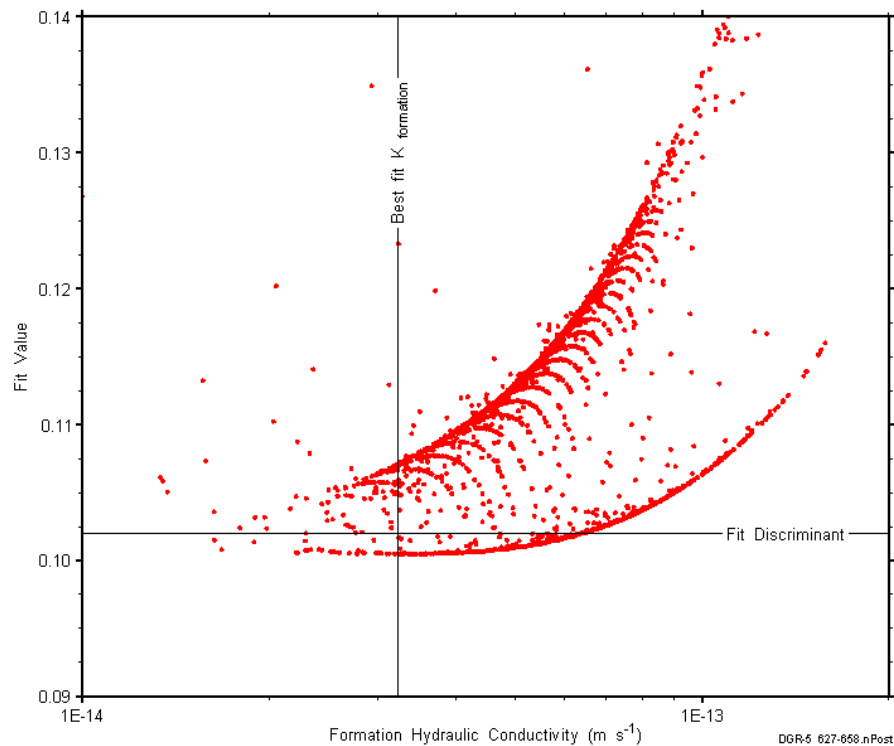


Figure E-83: XY-scatter plot showing the formation hydraulic conductivity parameter space derived from DGR5_580.76-609.80 perturbation analysis along with the fit discriminant and best fit values.

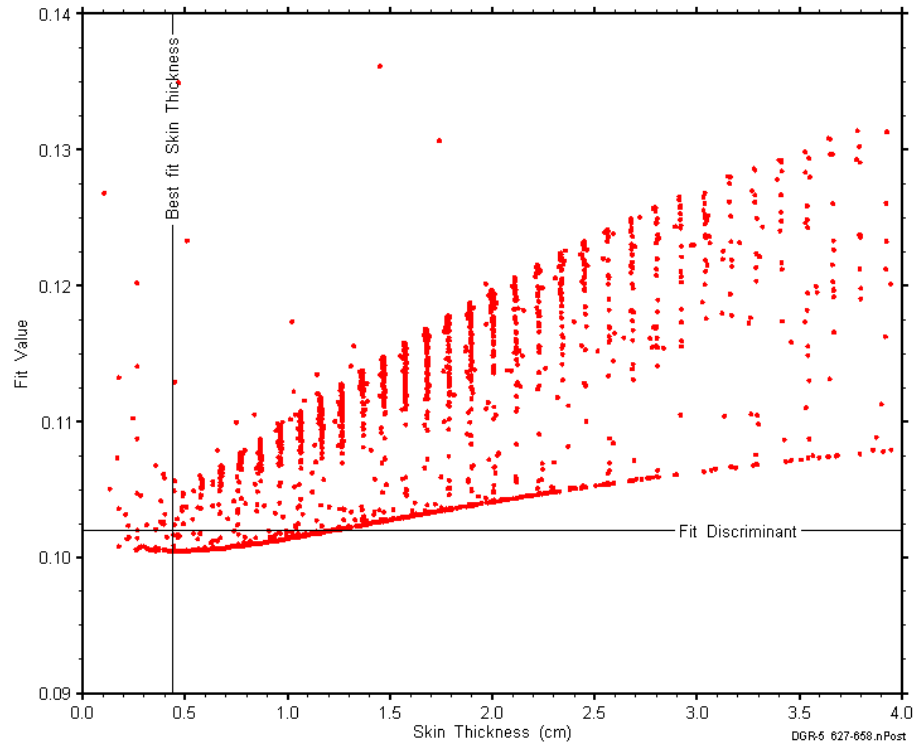


Figure E-84: XY-scatter plot showing the skin-thickness parameter space derived from DGR5_580.76-609.80 perturbation analysis along with the fit discriminant and best fit values.

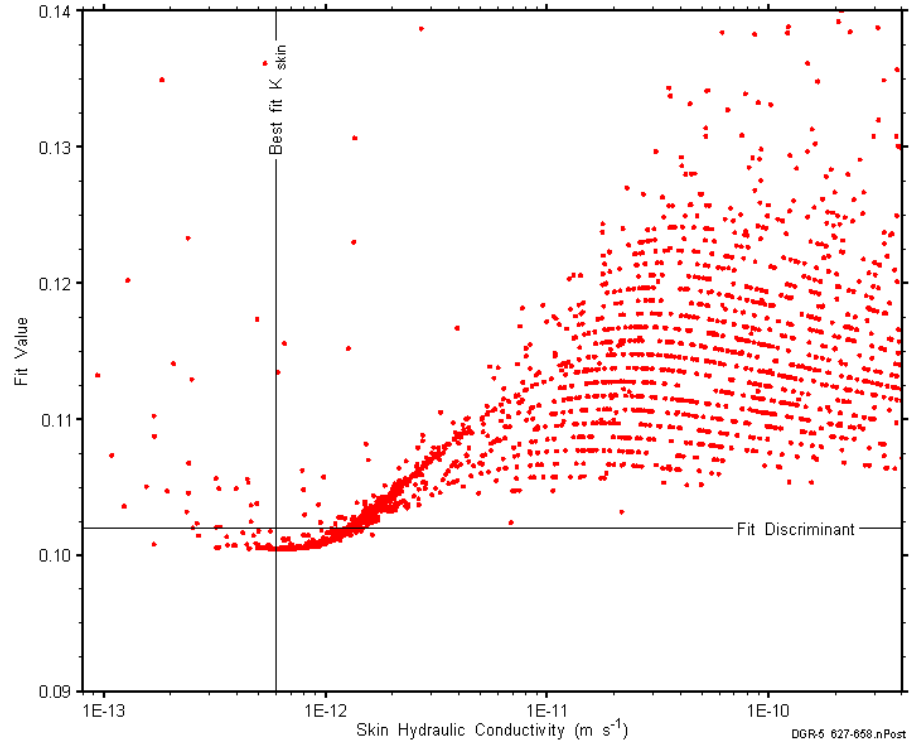


Figure E-85: XY-scatter plot showing the skin hydraulic conductivity parameter space derived from DGR5_580.76-609.80 perturbation analysis along with the fit discriminant and best fit values.

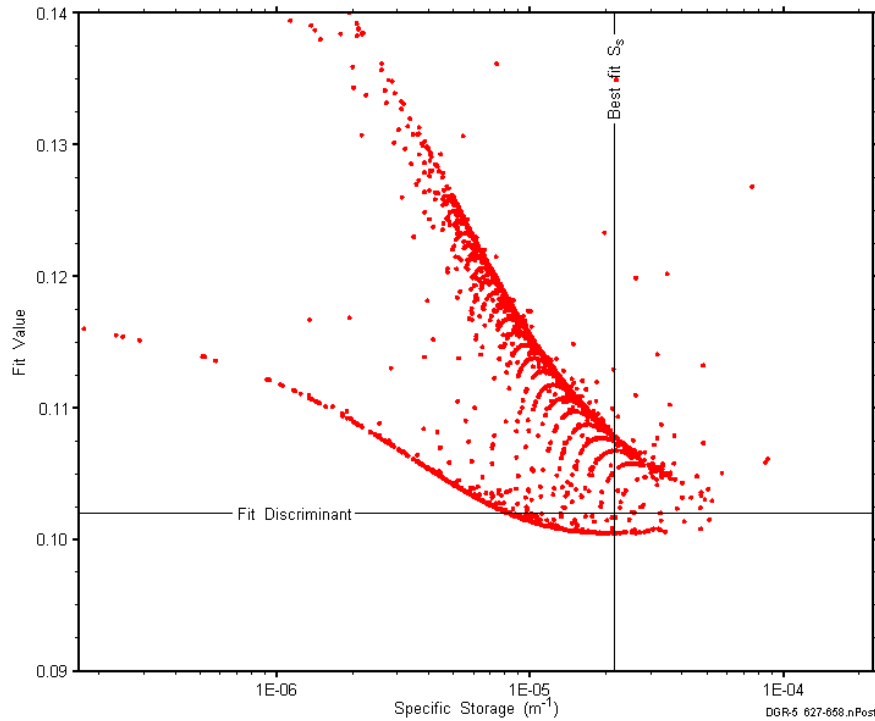


Figure E-86: XY-scatter plot showing the formation specific storage parameter space derived from DGR5_580.76-609.80 perturbation analysis along with the fit discriminant and best fit values.

E.7 609.55-638.80 Blue Mountain

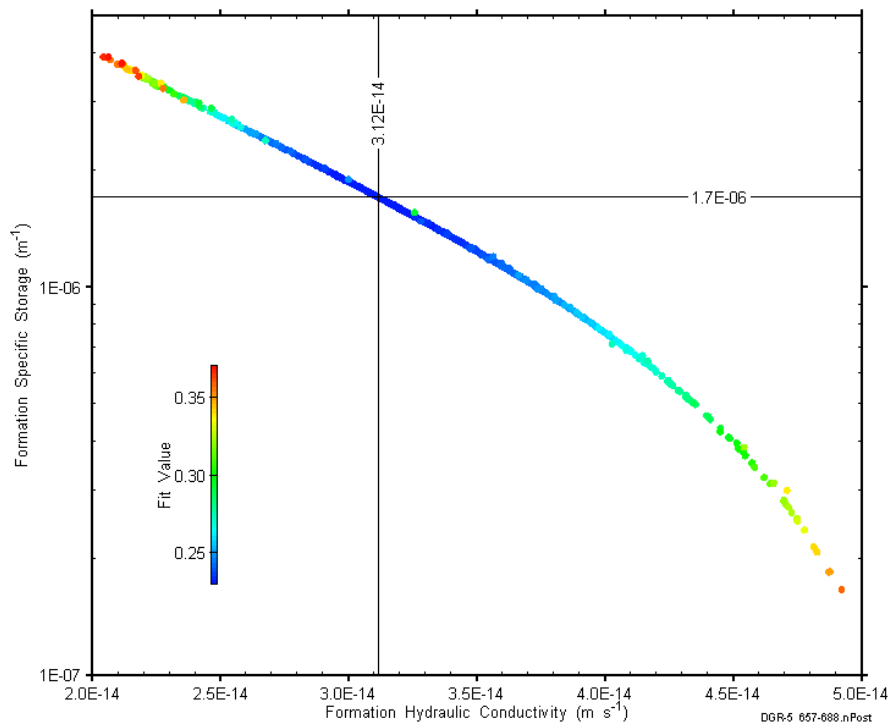


Figure E-87: XY-scatter plot showing estimates of formation hydraulic conductivity and formation specific storage derived from the DGR5_609.55-638.80 perturbation analysis.

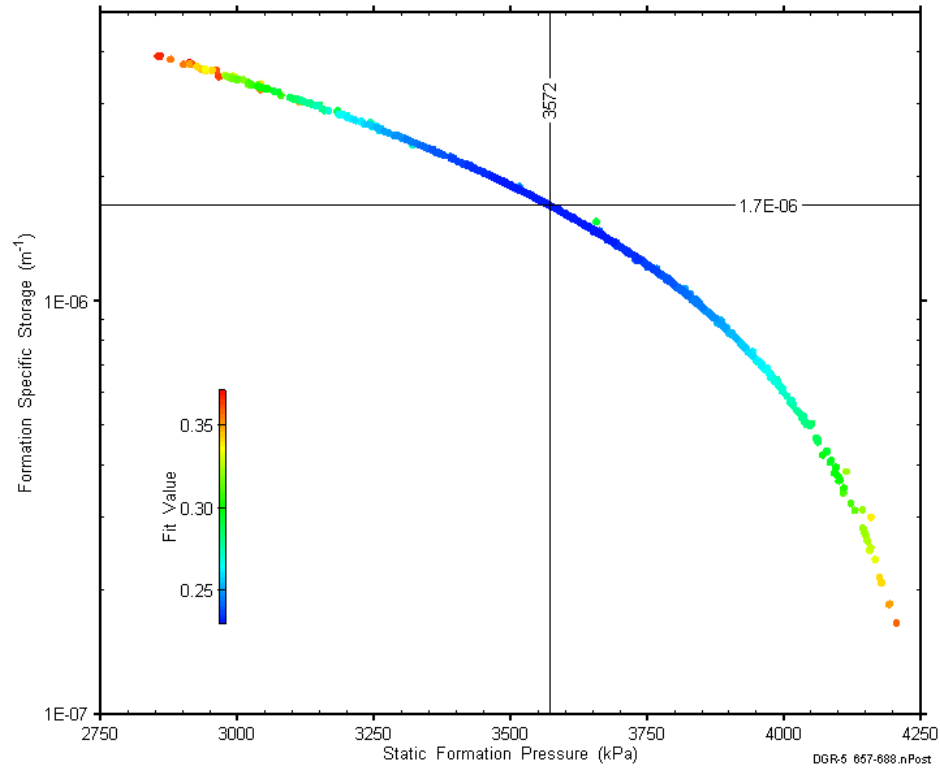


Figure E-88: XY-scatter plot showing estimates of static formation pressure and formation specific storage derived from the DGR5_609.55-638.80 perturbation analysis.

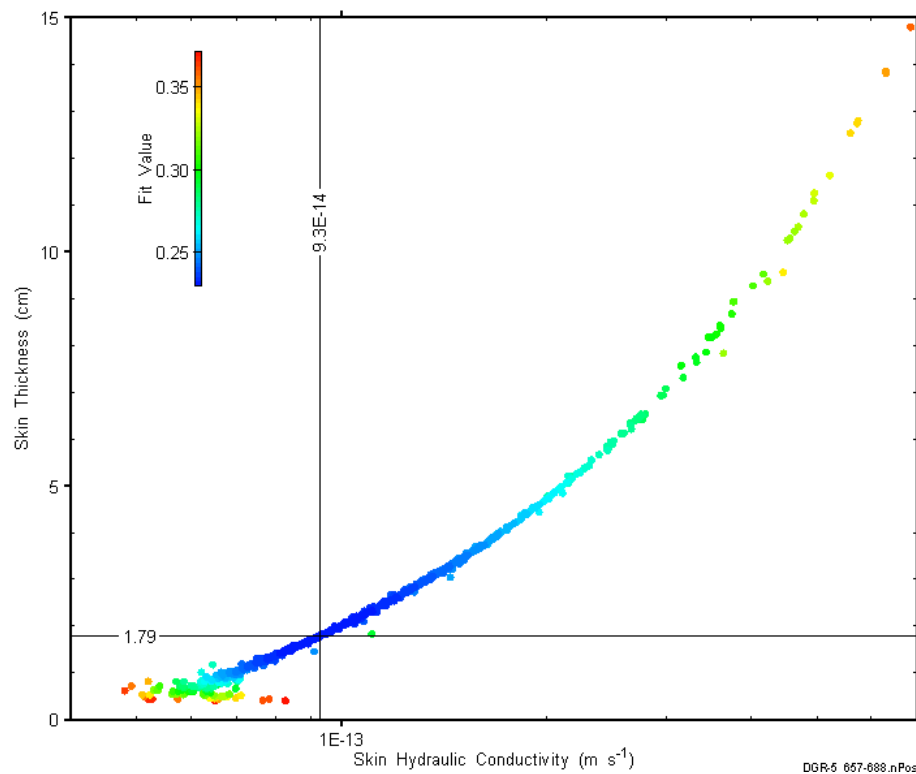


Figure E-89: XY-scatter plot showing estimates of skin hydraulic conductivity and skin thickness derived from the DGR5_609.55-638.80 perturbation analysis.

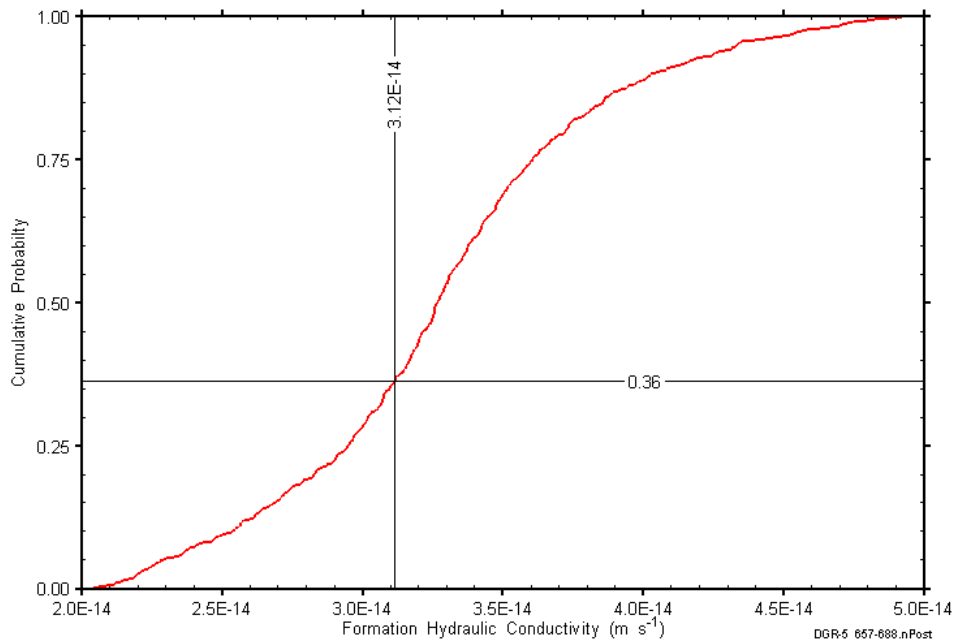


Figure E-90: DGR5_609.55-638.80 formation hydraulic conductivity cumulative distribution function.

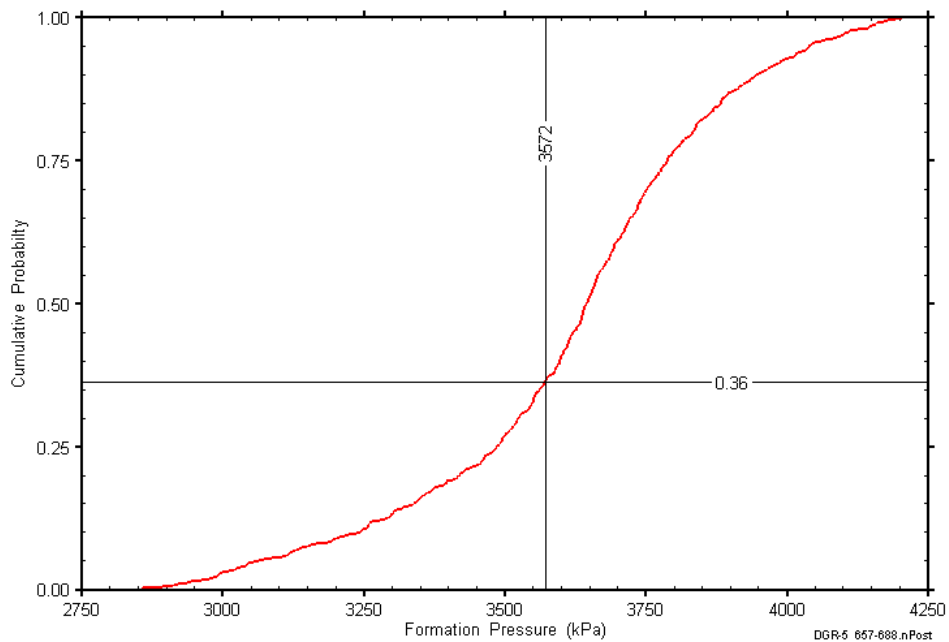


Figure E-91: DGR5_609.55-638.80 static formation pressure cumulative distribution function.

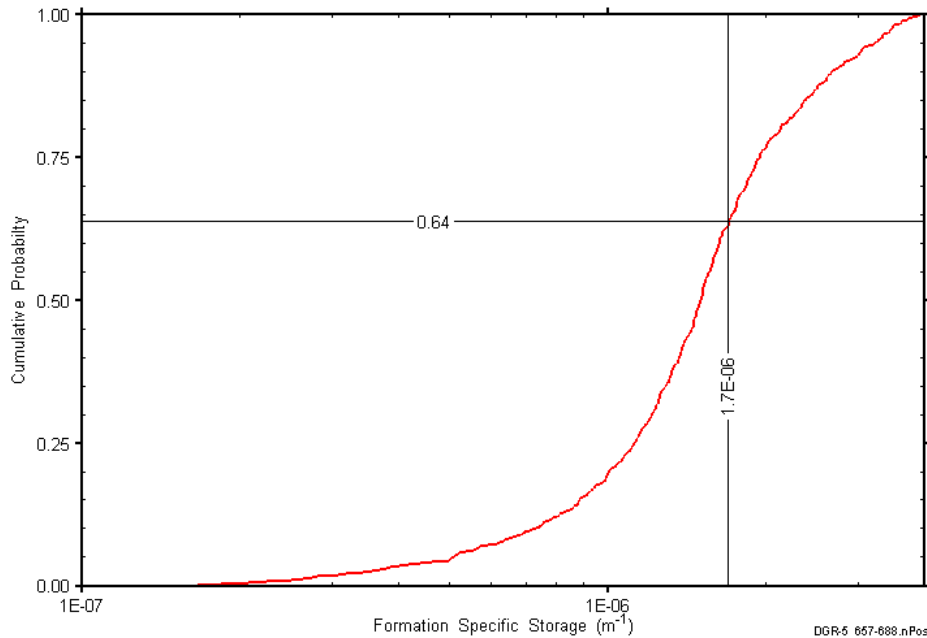


Figure E-92: DGR5_609.55-638.80 formation specific storage cumulative distribution function.

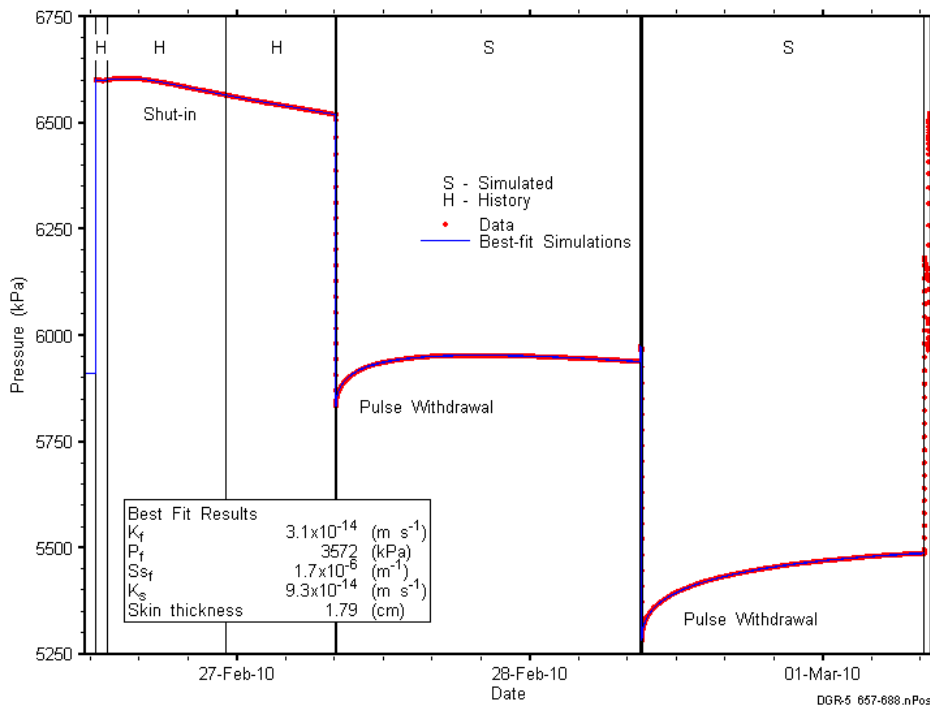


Figure E-93: Linear plot showing simulations of the DGR5_609.55-638.80 pressure response.

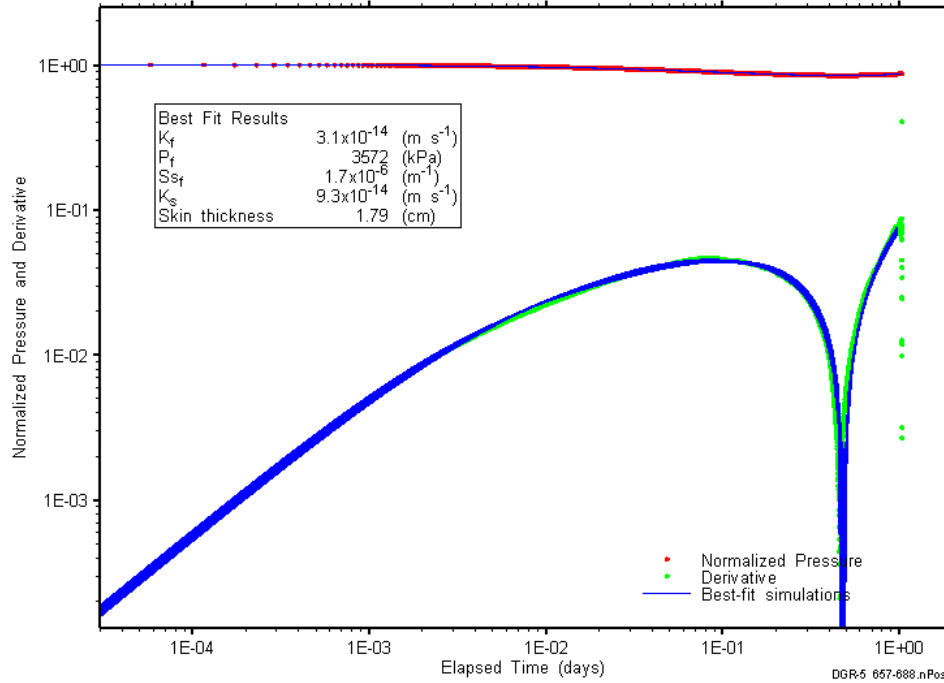


Figure E-94: Log-log plot showing simulations of the DGR5_609.55-638.80 PW1 Ramey B and derivative response.

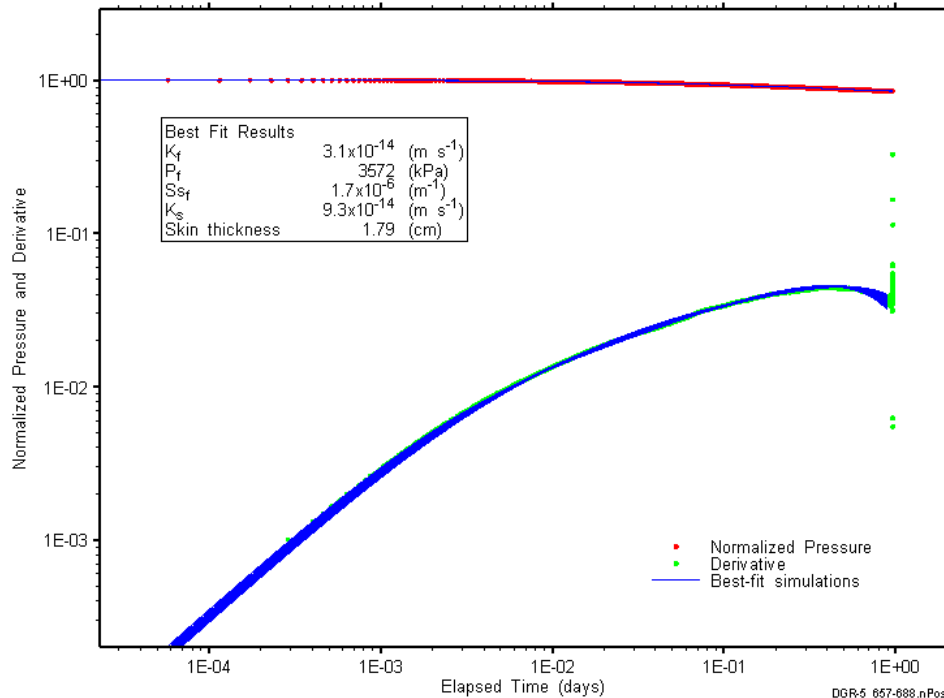


Figure E-95: Log-log plot showing simulations of the DGR5_609.55-638.80 PW2 Ramey B and derivative response.

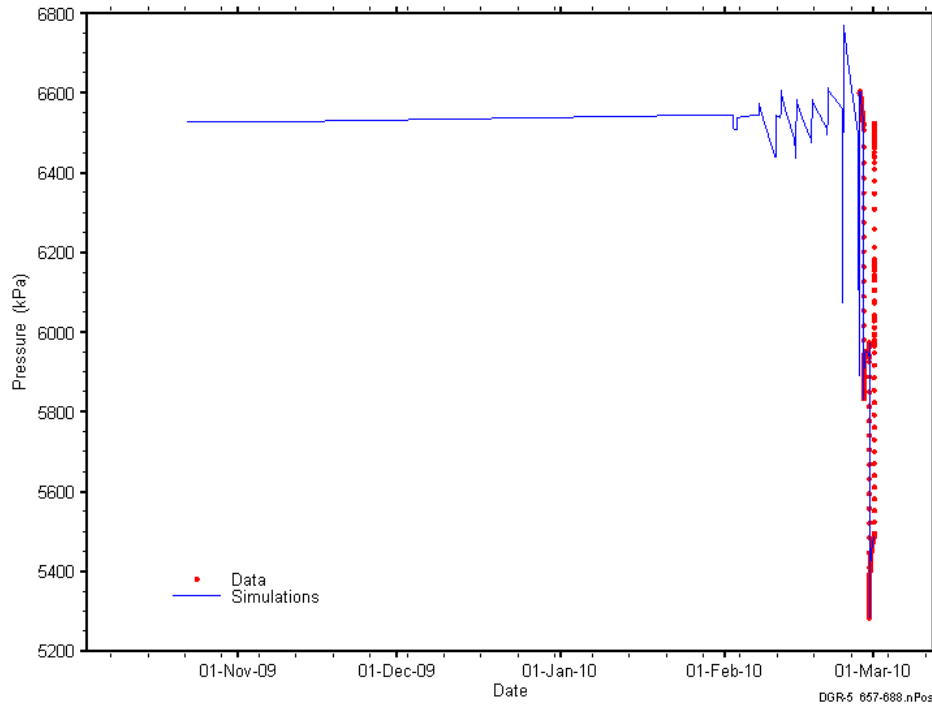


Figure E-96: Linear plot showing simulations of the DGR5_609.55-638.80 pressure response, including pre-test pressure history.

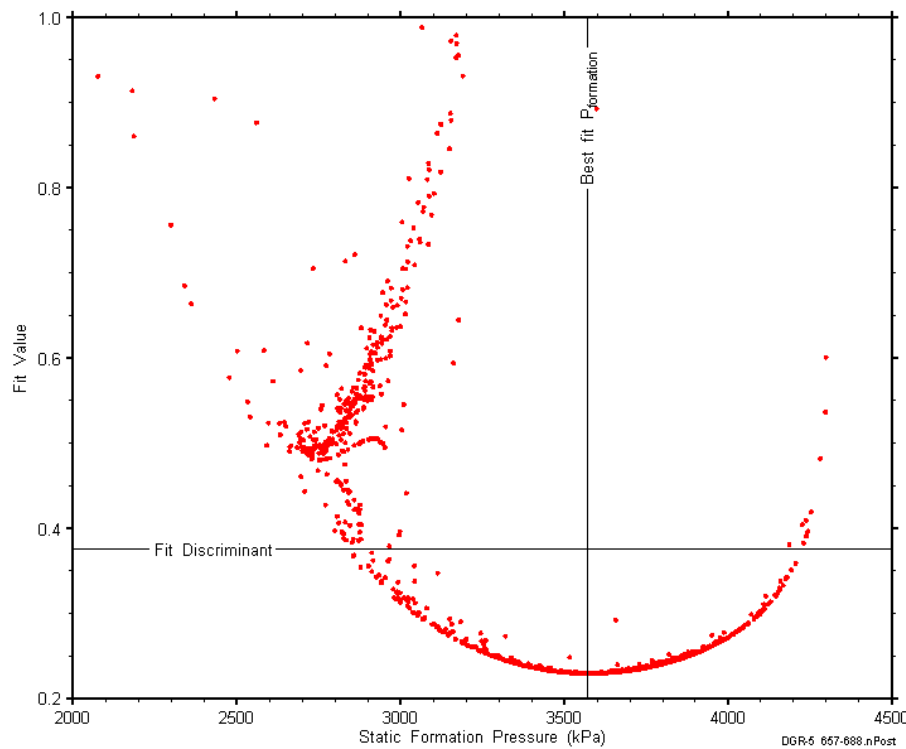


Figure E-97: XY-scatter plot showing the static formation pressure parameter space derived from DGR5_609.55-638.80 perturbation analysis along with the fit discriminant and best fit values.

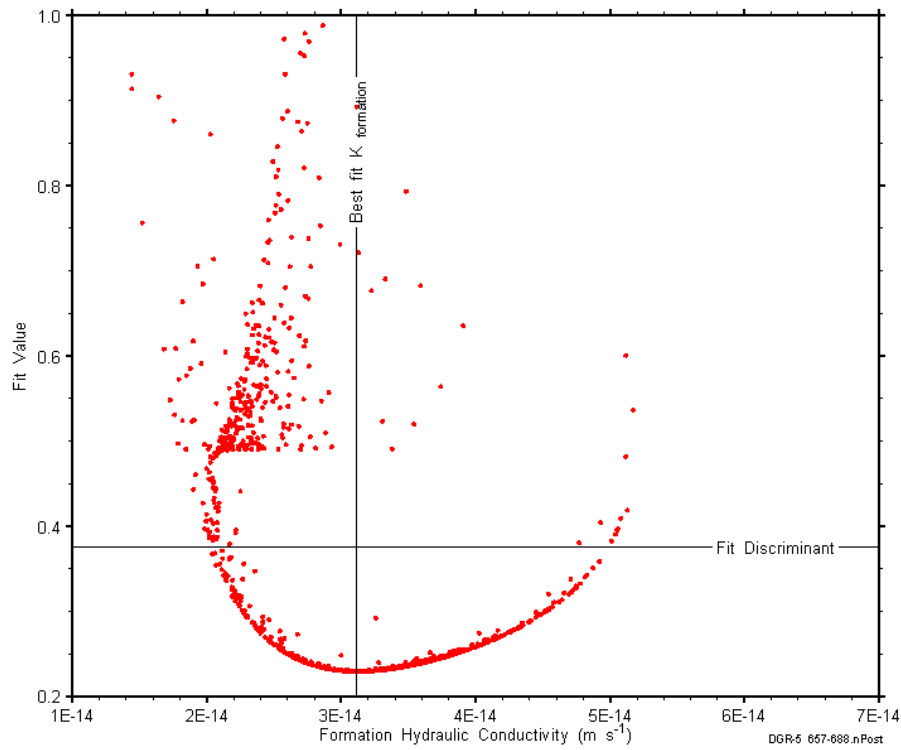


Figure E-98: XY-scatter plot showing the formation hydraulic conductivity parameter space derived from DGR5_609.55-638.80 perturbation analysis along with the fit discriminant and best fit values.

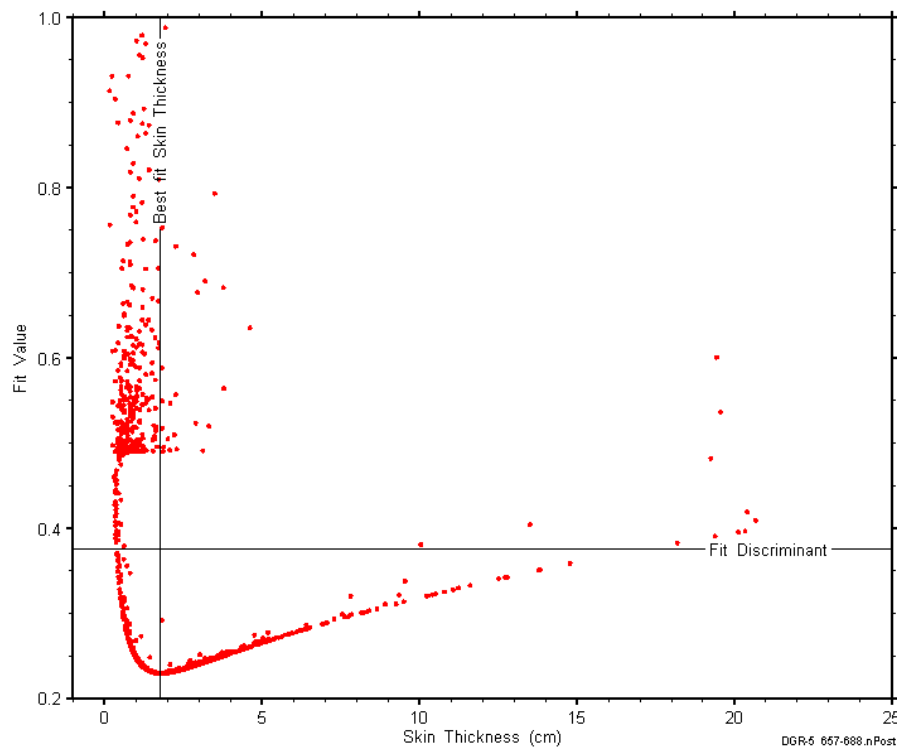


Figure E-99: XY-scatter plot showing the skin-thickness parameter space derived from DGR5_609.55-638.80 perturbation analysis along with the fit discriminant and best fit values.

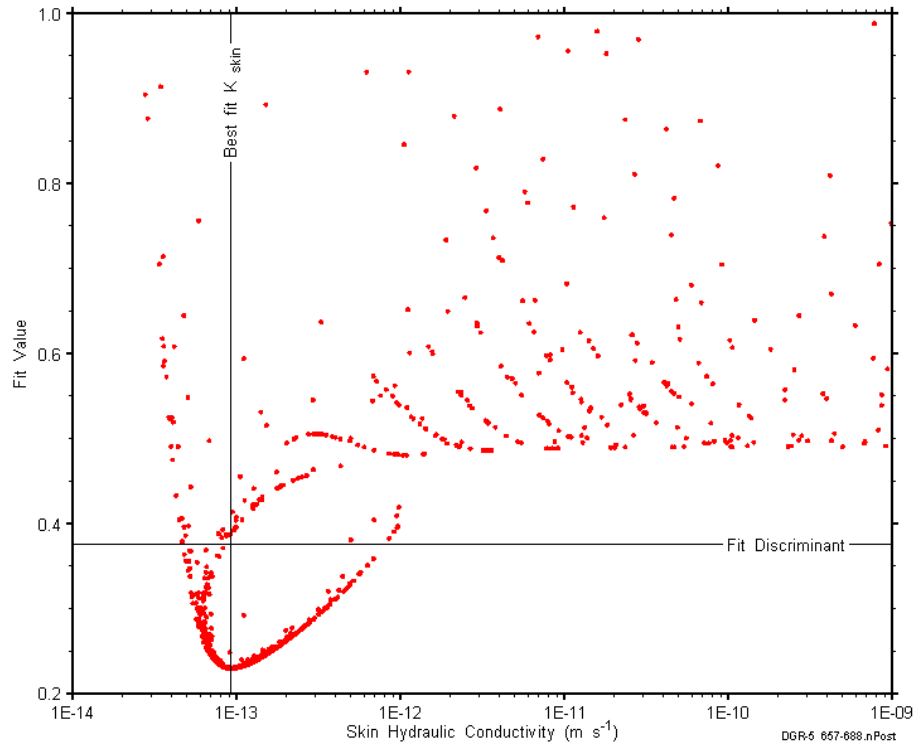


Figure E-100: XY-scatter plot showing the skin hydraulic conductivity parameter space derived from DGR5_609.55-638.80 perturbation analysis along with the fit discriminant and best fit values.

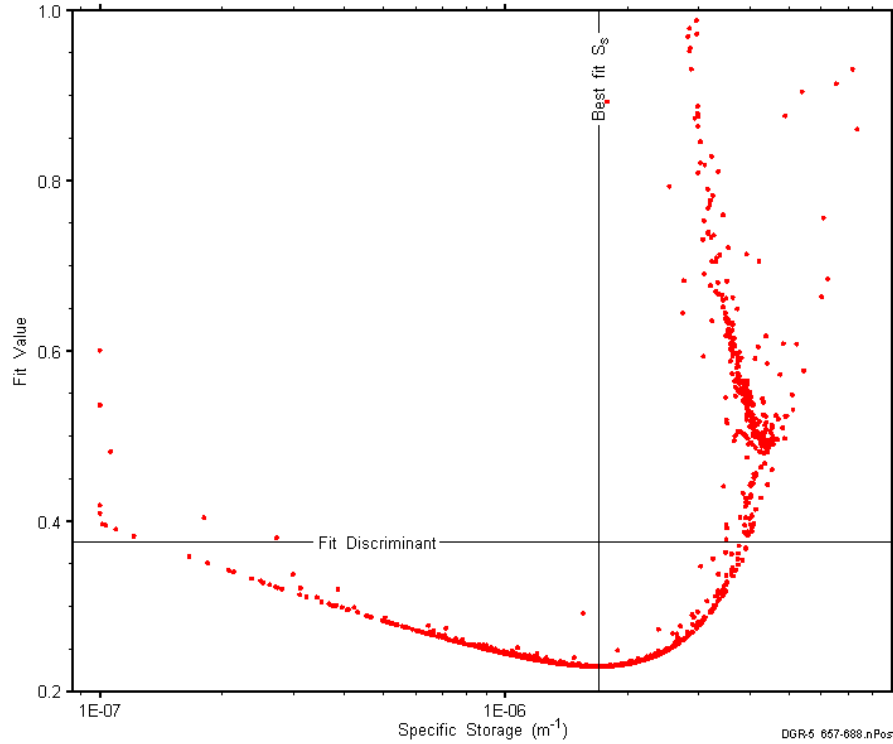


Figure E-101: XY-scatter plot showing the formation specific storage parameter space derived from DGR5_609.55-638.80 perturbation analysis along with the fit discriminant and best fit values.

E.8 631.95-661.38 Blue Mountain-Cobourg

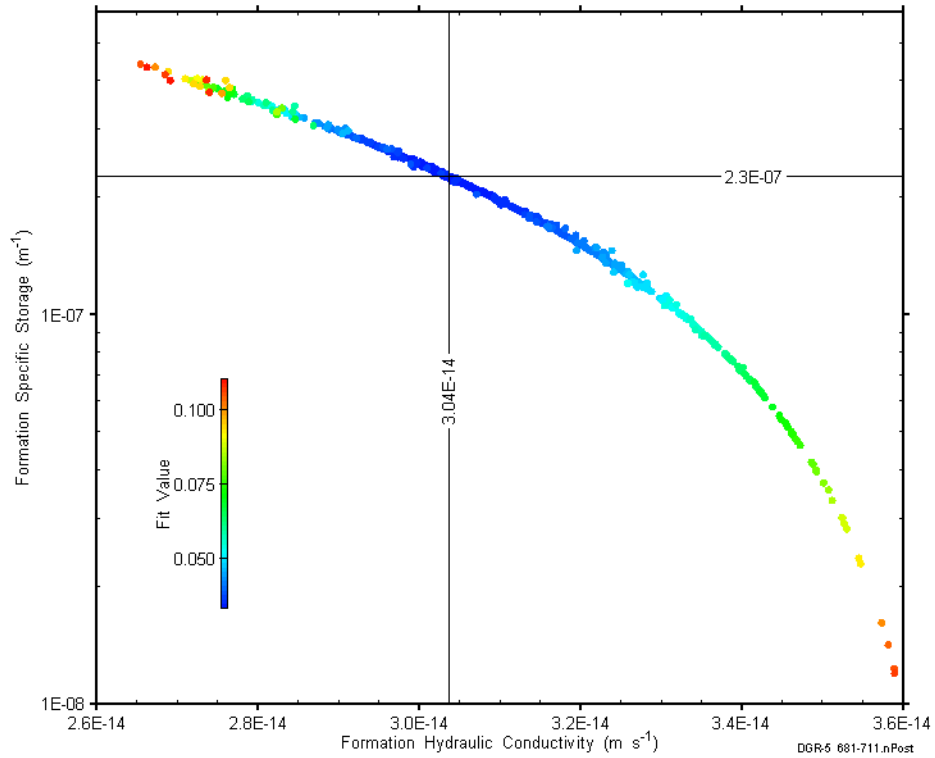


Figure E-102: XY-scatter plot showing estimates of formation hydraulic conductivity and formation specific storage derived from the DGR5_631.95-661.38 perturbation analysis.

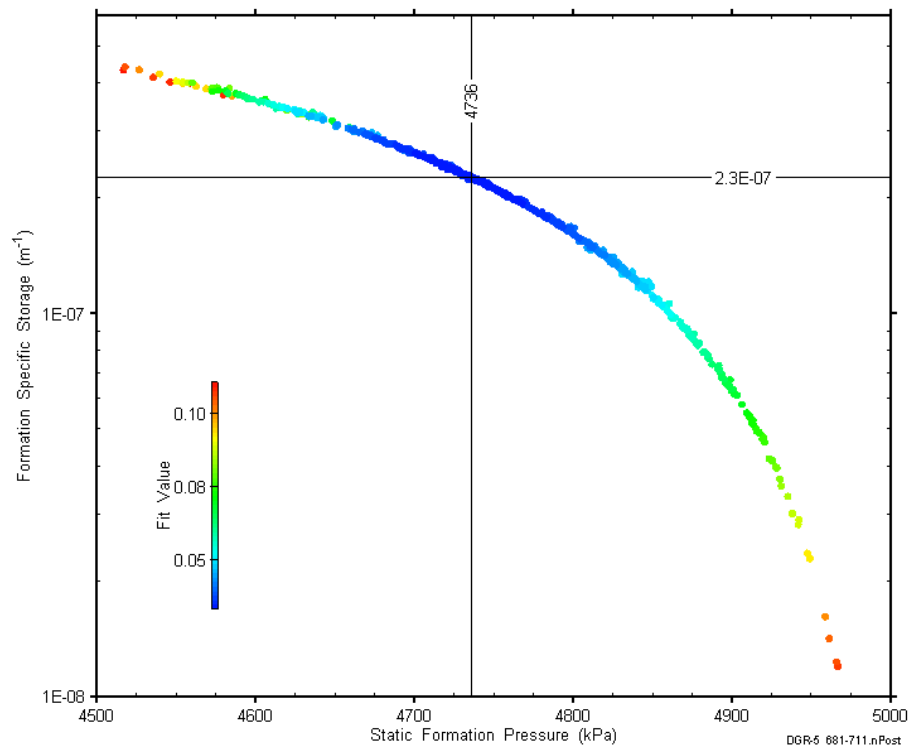


Figure E-103: XY-scatter plot showing estimates of static formation pressure and formation specific storage derived from the DGR5_631.95-661.38 perturbation analysis.

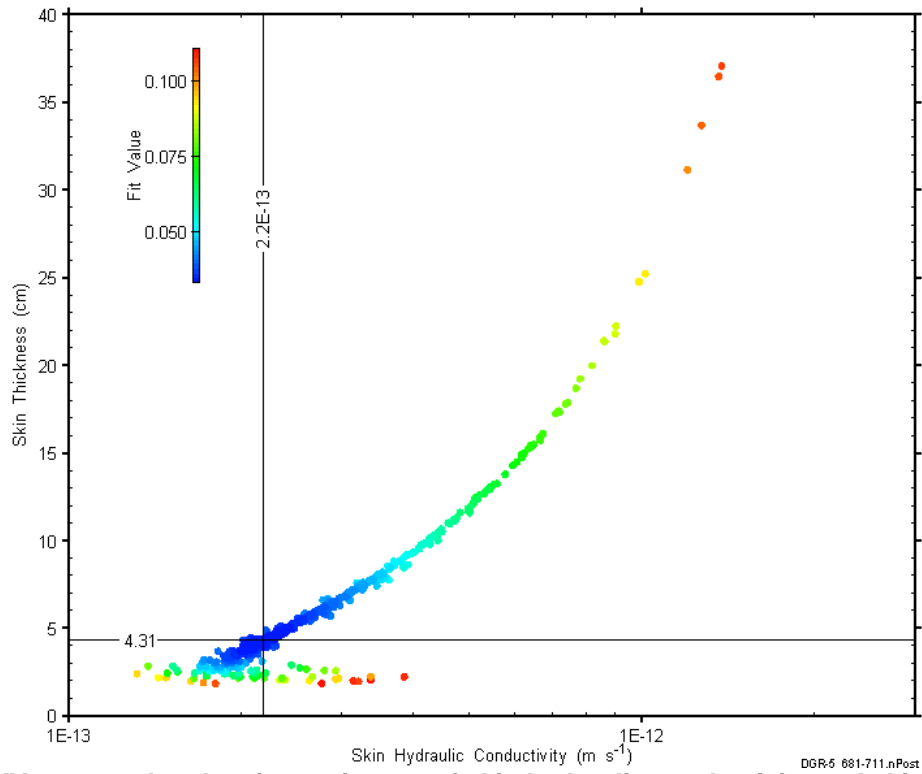


Figure E-104: XY-scatter plot showing estimates of skin hydraulic conductivity and skin thickness derived from the DGR5_631.95-661.38 perturbation analysis.

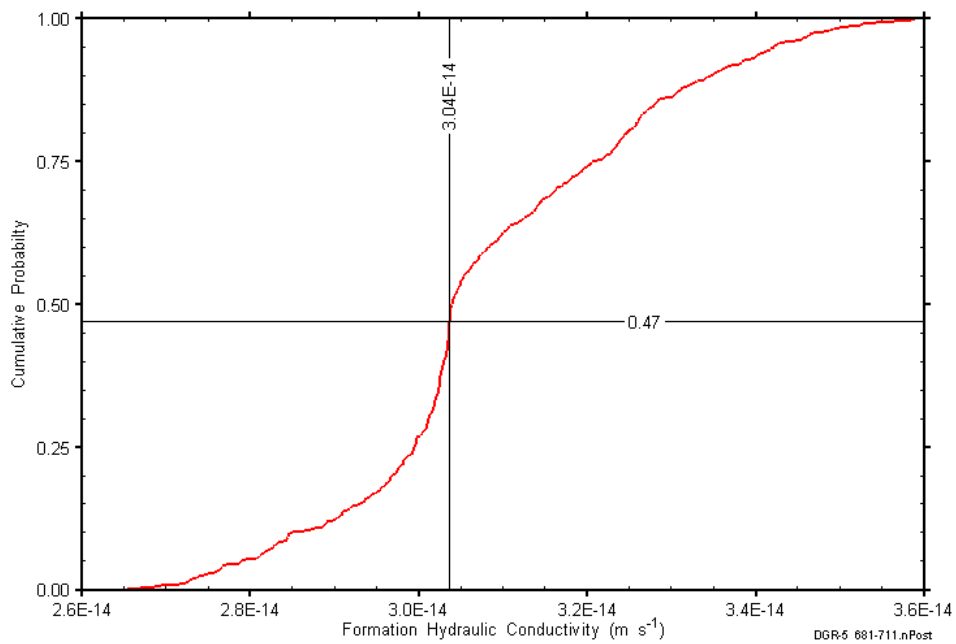


Figure E-105: DGR5_631.95-661.38 formation hydraulic conductivity cumulative distribution function.

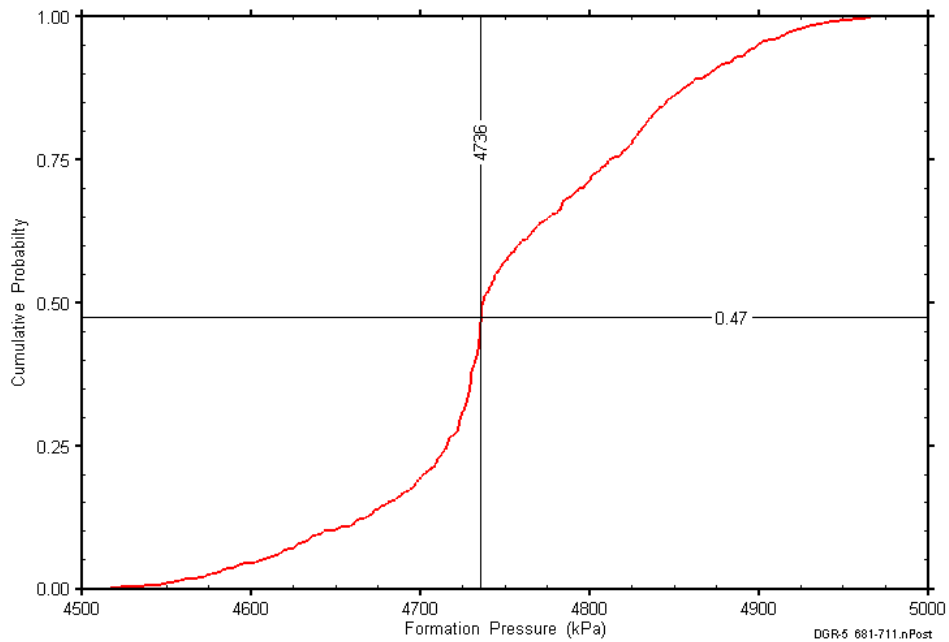


Figure E-106: DGR5_631.95-661.38 static formation pressure cumulative distribution function.

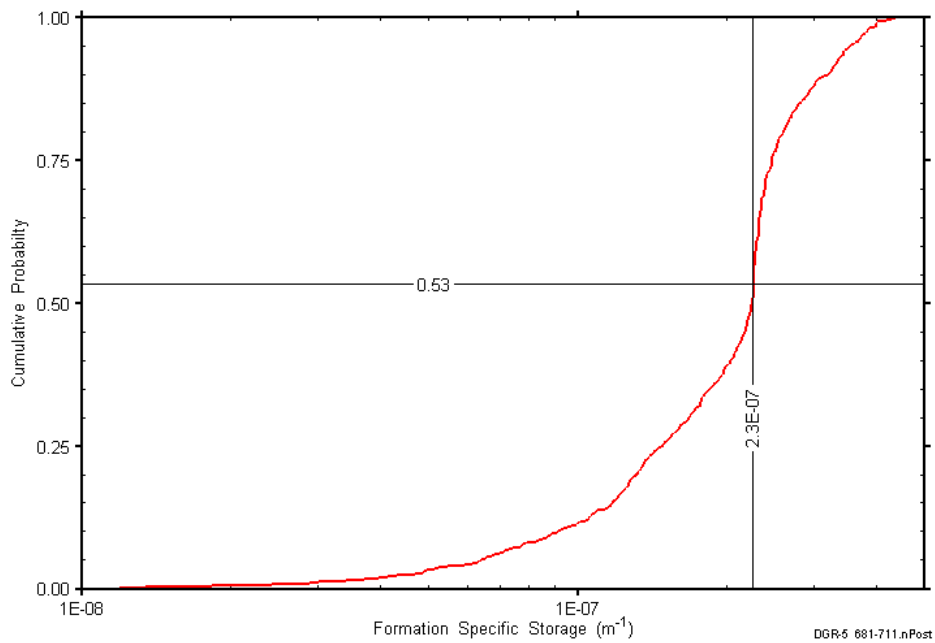


Figure E-107: DGR5_631.95-661.38 formation specific storage cumulative distribution function.

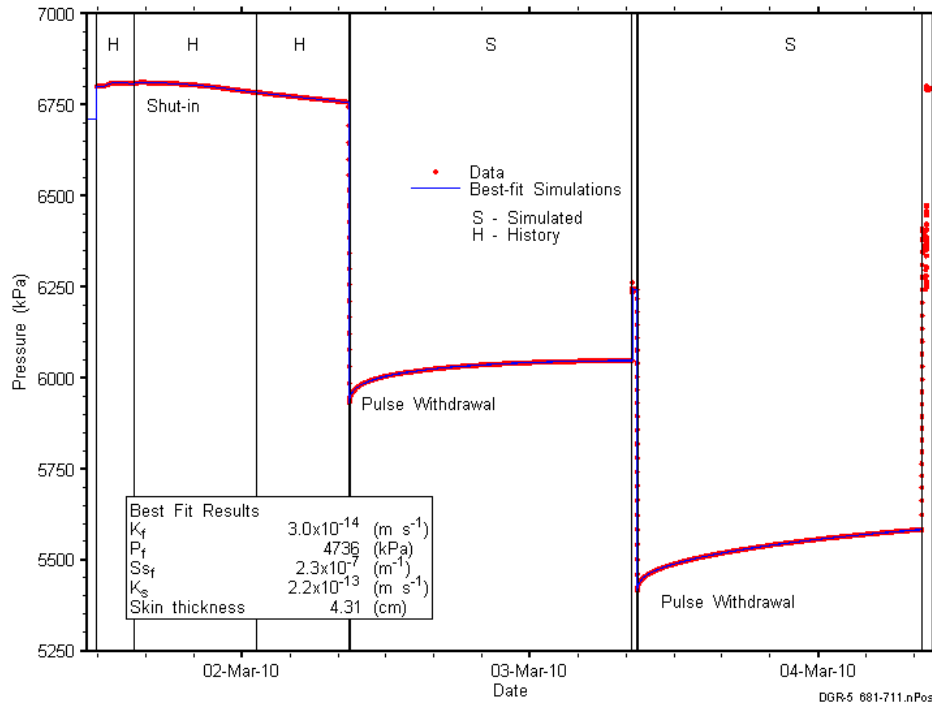


Figure E-108: Linear plot showing simulations of the DGR5_631.95-661.38 pressure response.

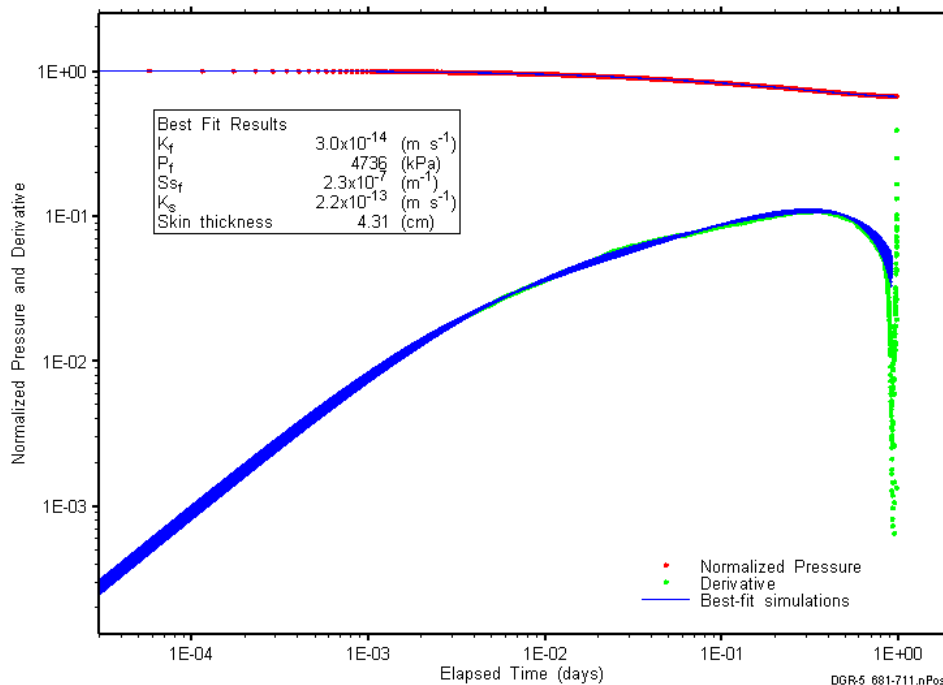


Figure E-109: Log-log plot showing simulations of the DGR5_631.95-661.38 PW1 Ramey B and derivative response.

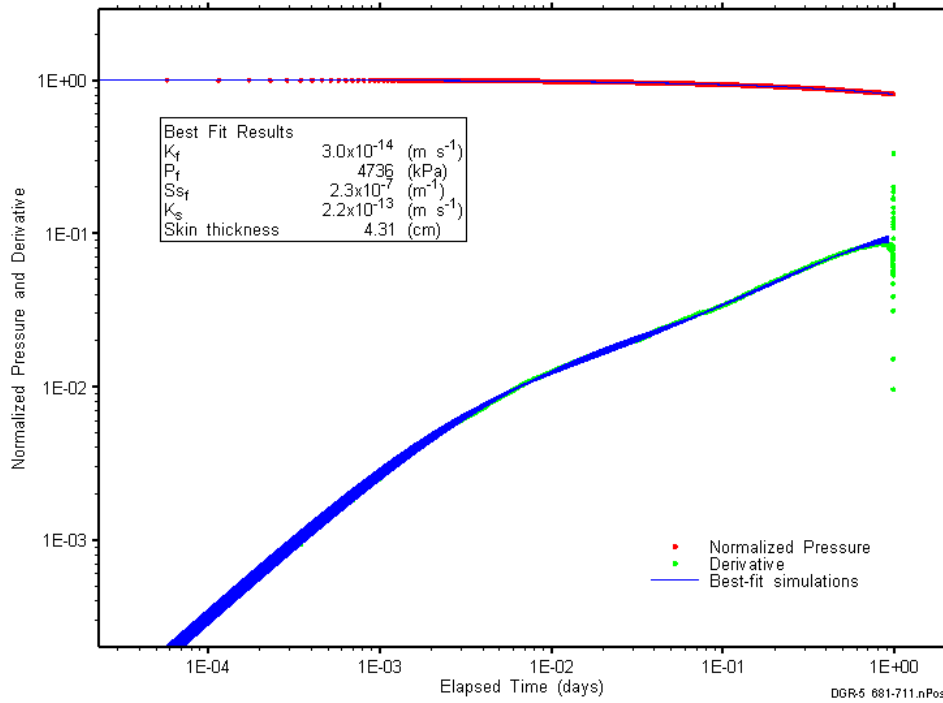


Figure E-110: Log-log plot showing simulations of the DGR5_631.95-661.38 PW2 Ramey B and derivative response.

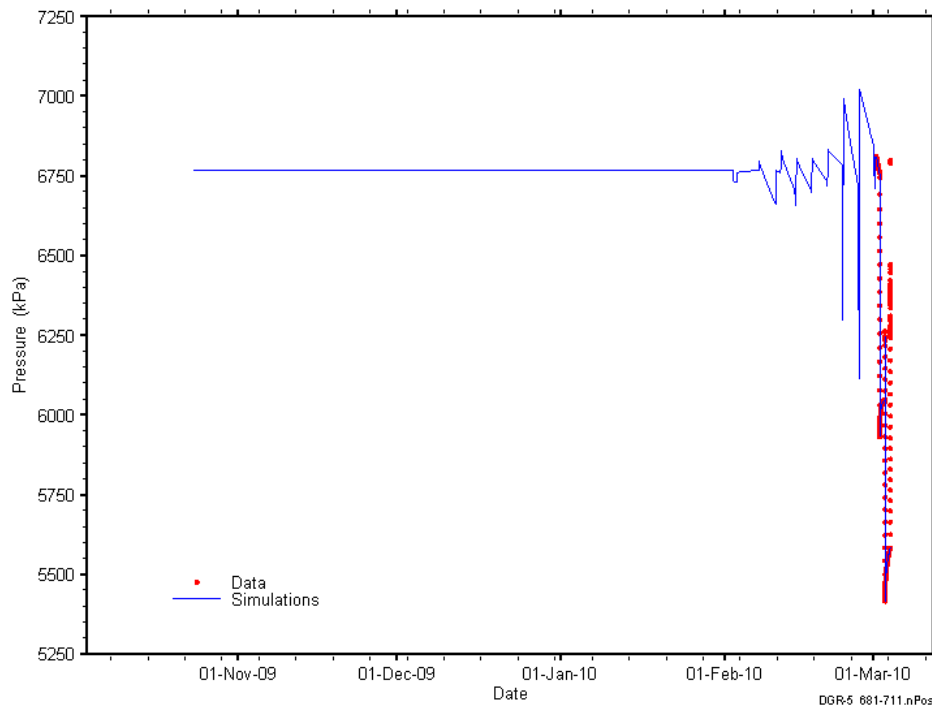


Figure E-111: Linear plot showing simulations of the DGR5_631.95-661.38 pressure response, including pre-test pressure history.

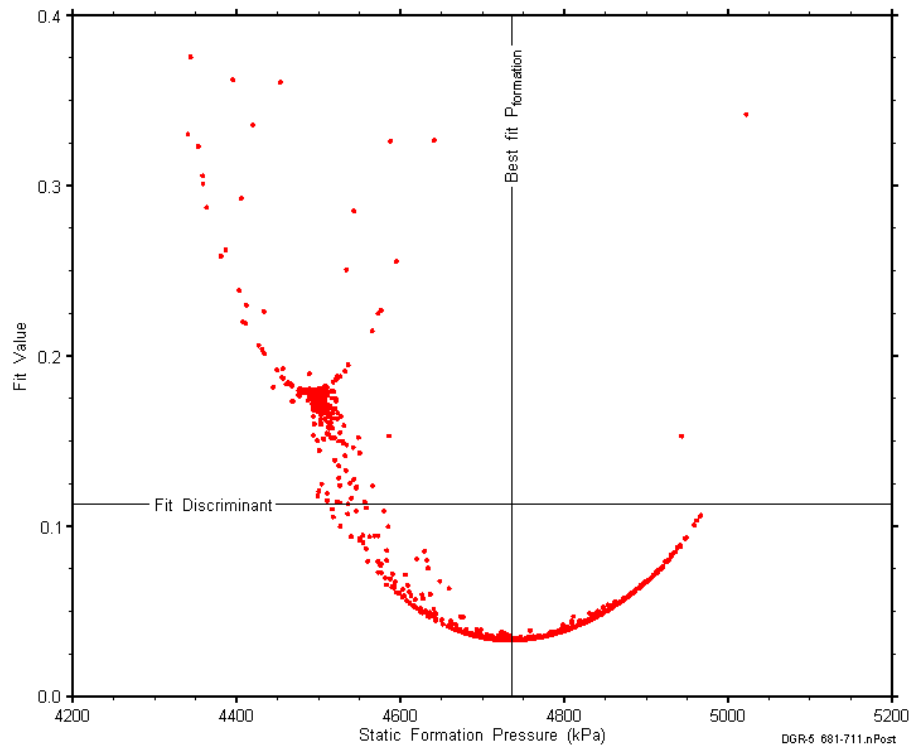


Figure E-112: XY-scatter plot showing the static formation pressure parameter space derived from DGR5_631.95-661.38 perturbation analysis along with the fit discriminant and best fit values.

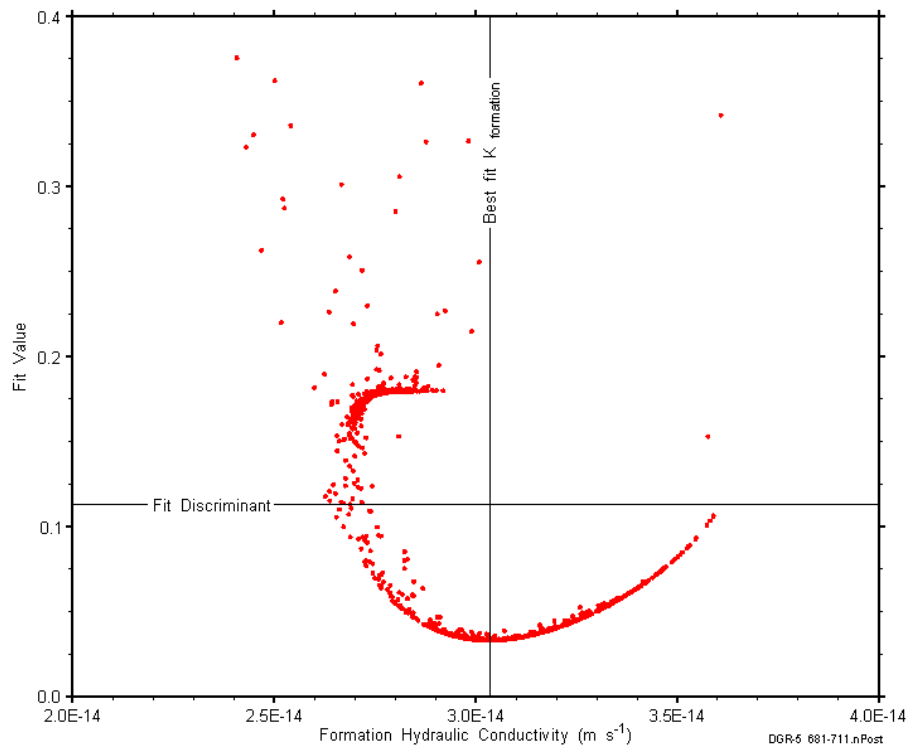


Figure E-113: XY-scatter plot showing the formation hydraulic conductivity parameter space derived from DGR5_631.95-661.38 perturbation analysis along with the fit discriminant and best fit values.

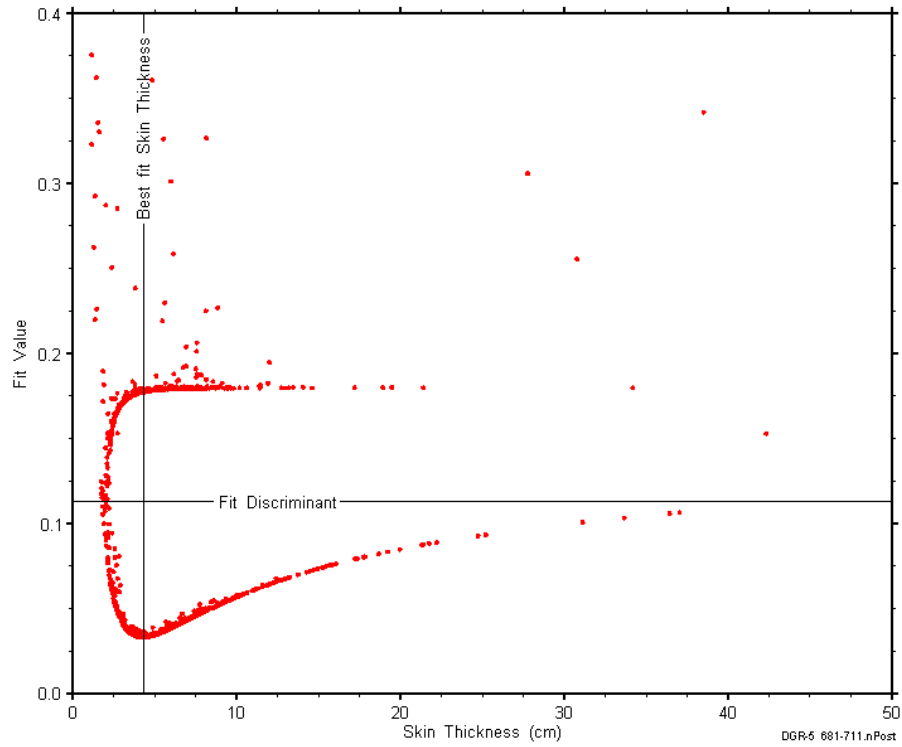


Figure E-114: XY-scatter plot showing the skin-thickness parameter space derived from DGR5_631.95-661.38 perturbation analysis along with the fit discriminant and best fit values.

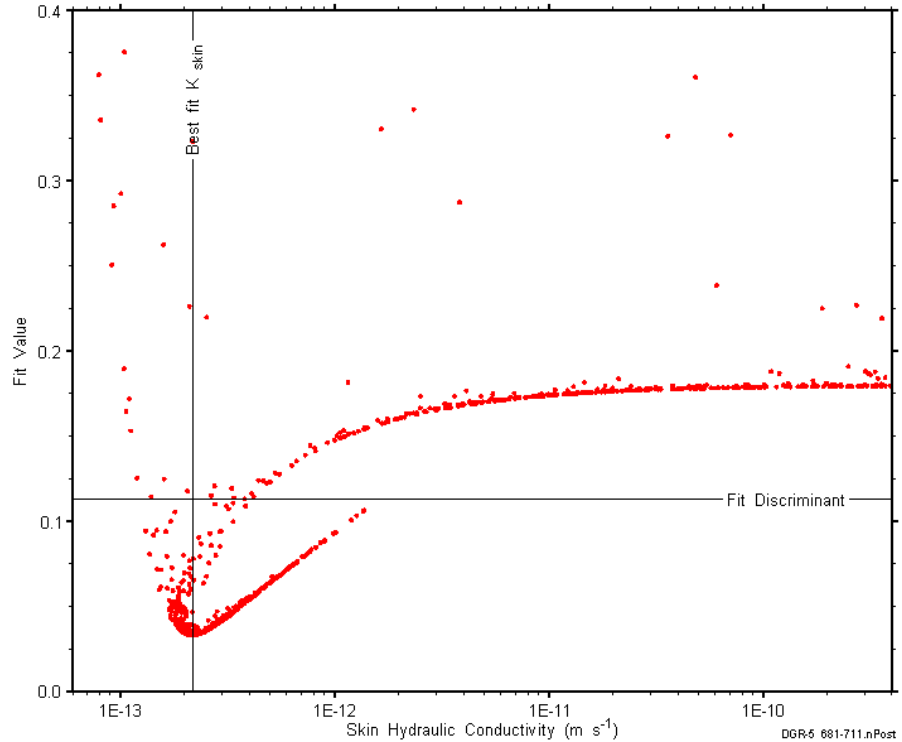


Figure E-115: XY-scatter plot showing the skin hydraulic conductivity parameter space derived from DGR5_631.95-661.38 perturbation analysis along with the fit discriminant and best fit values.

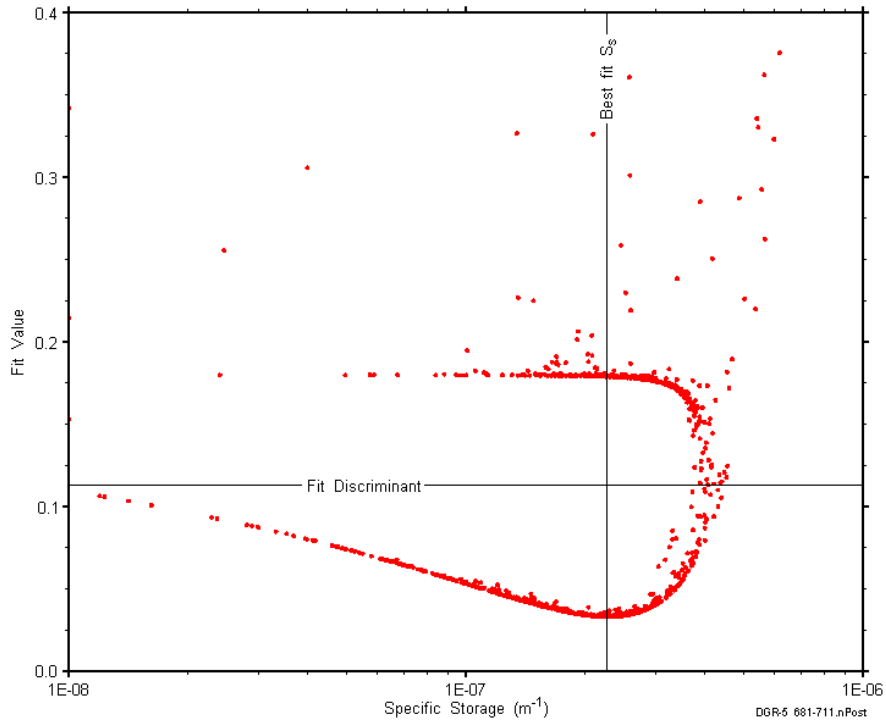


Figure E-116: XY-scatter plot showing the formation specific storage parameter space derived from DGR5_631.95-661.38 perturbation analysis along with the fit discriminant and best fit values.

E.9 657.39-686.91 Cobourg

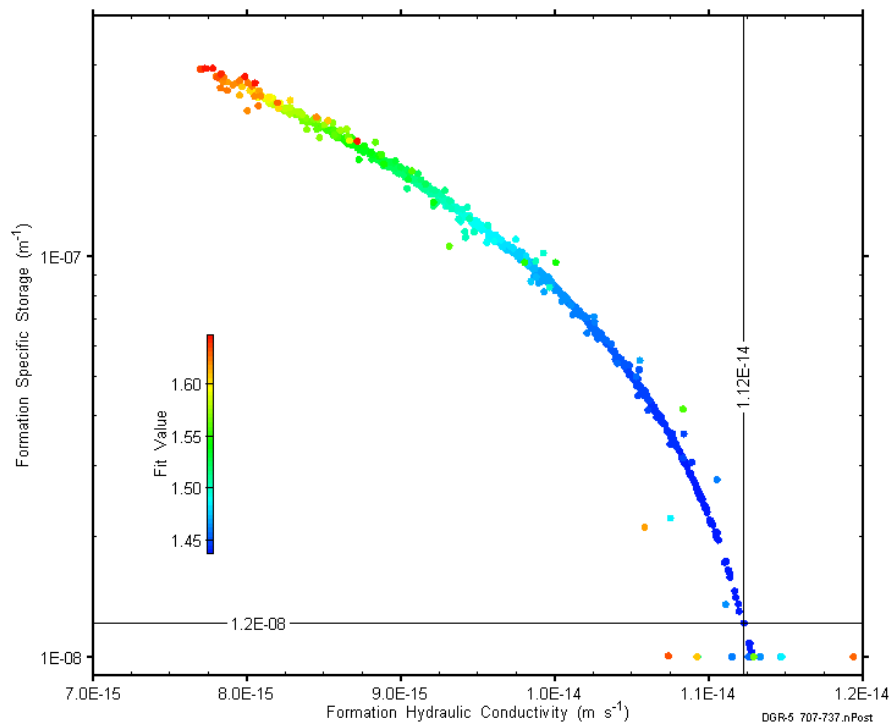


Figure E-117: XY-scatter plot showing estimates of formation hydraulic conductivity and formation specific storage derived from the DGR5_657.39-686.91 perturbation analysis.

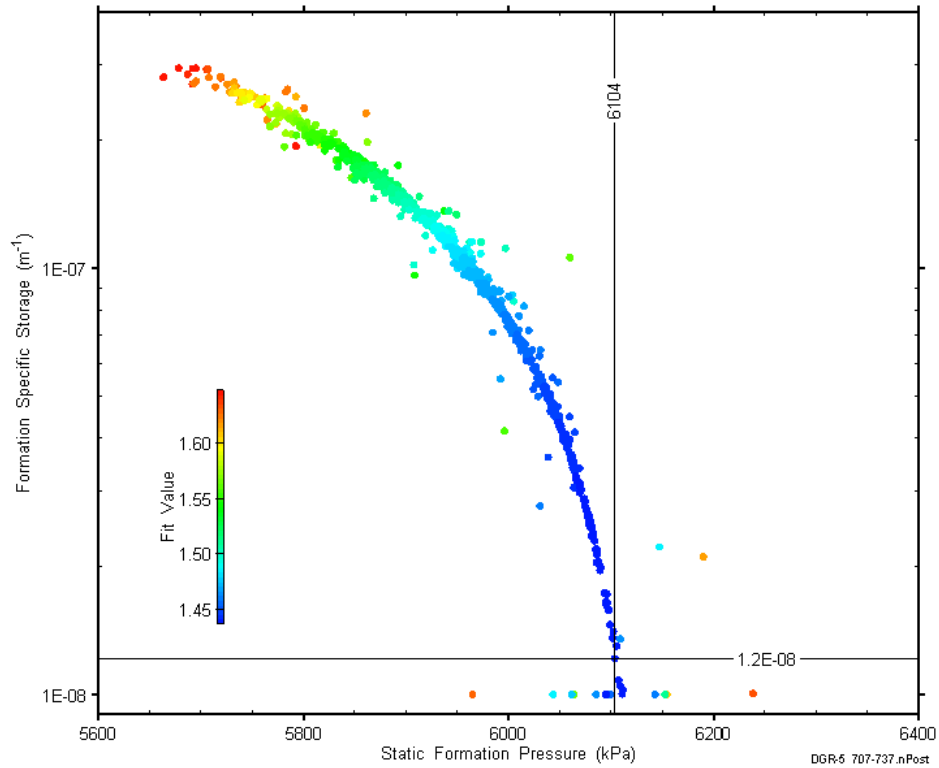


Figure E-118: XY-scatter plot showing estimates of static formation pressure and formation specific storage derived from the DGR5_657.39-686.91 perturbation analysis.

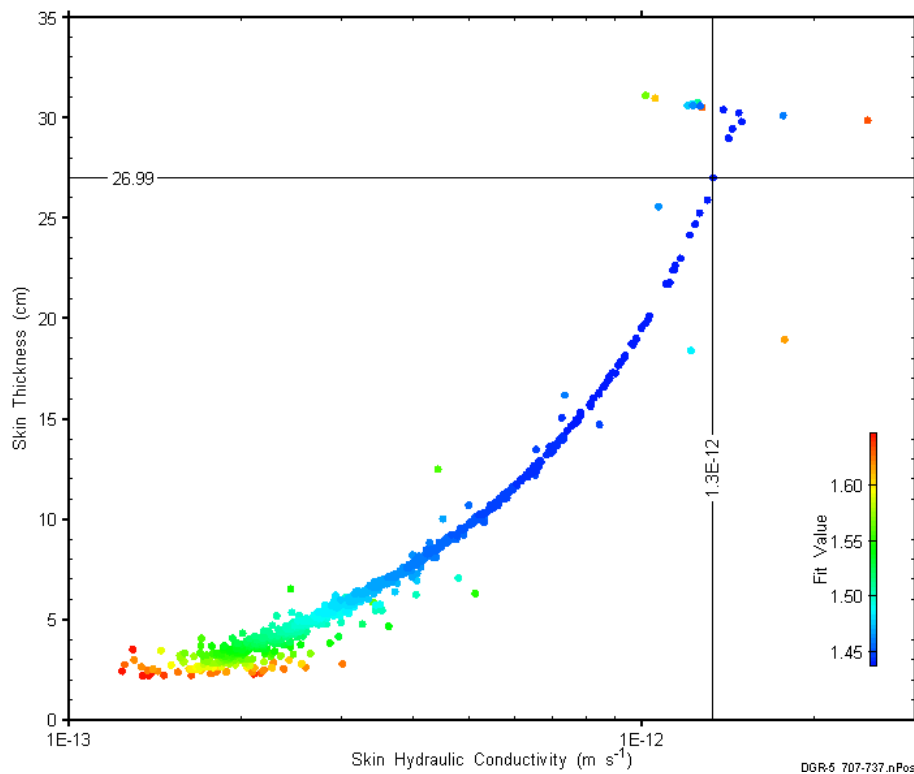


Figure E-119: XY-scatter plot showing estimates of skin hydraulic conductivity and skin thickness derived from the DGR5_657.39-686.91 perturbation analysis.

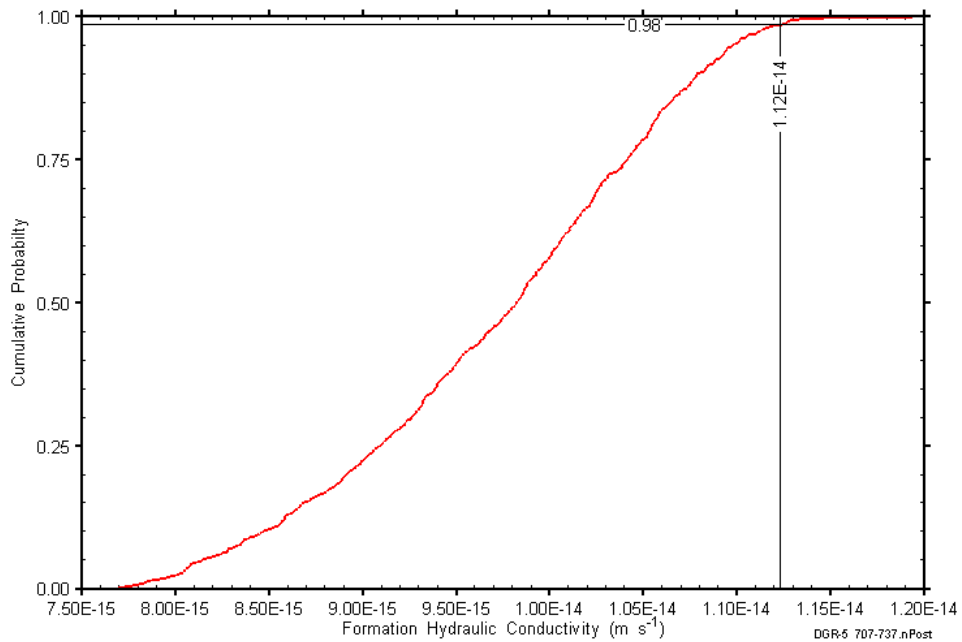


Figure E-120: DGR5_657.39-686.91 formation hydraulic conductivity cumulative distribution function.

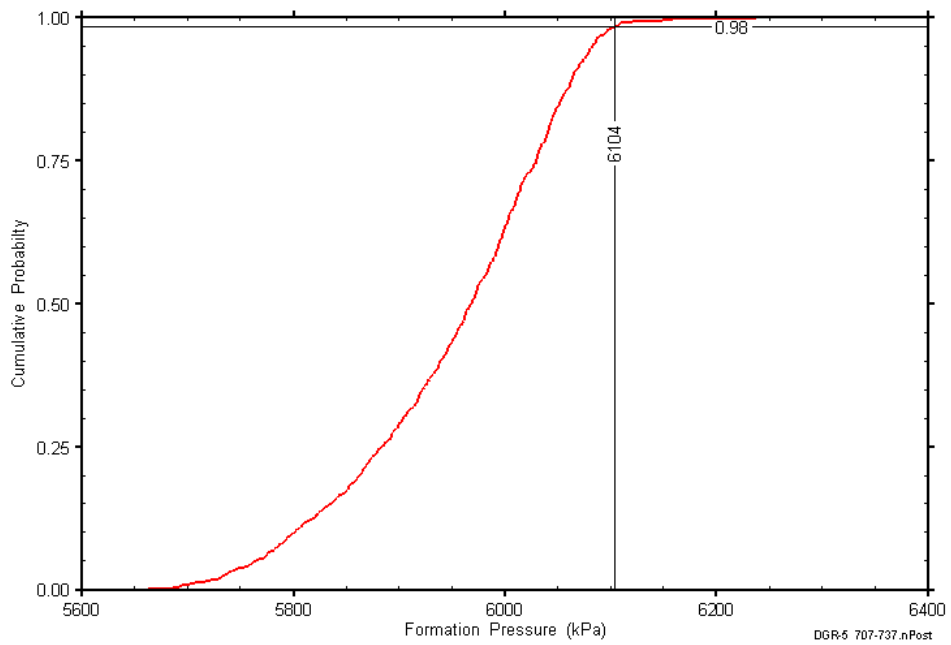


Figure E-121: DGR5_657.39-686.91 static formation pressure cumulative distribution function.

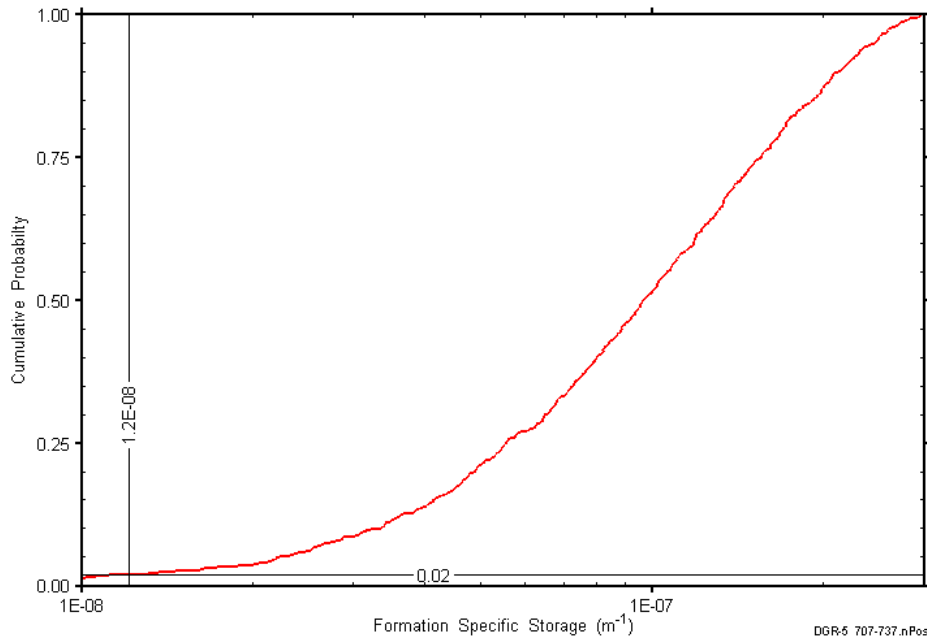


Figure E-122: DGR5_657.39-686.91 formation specific storage cumulative distribution function.

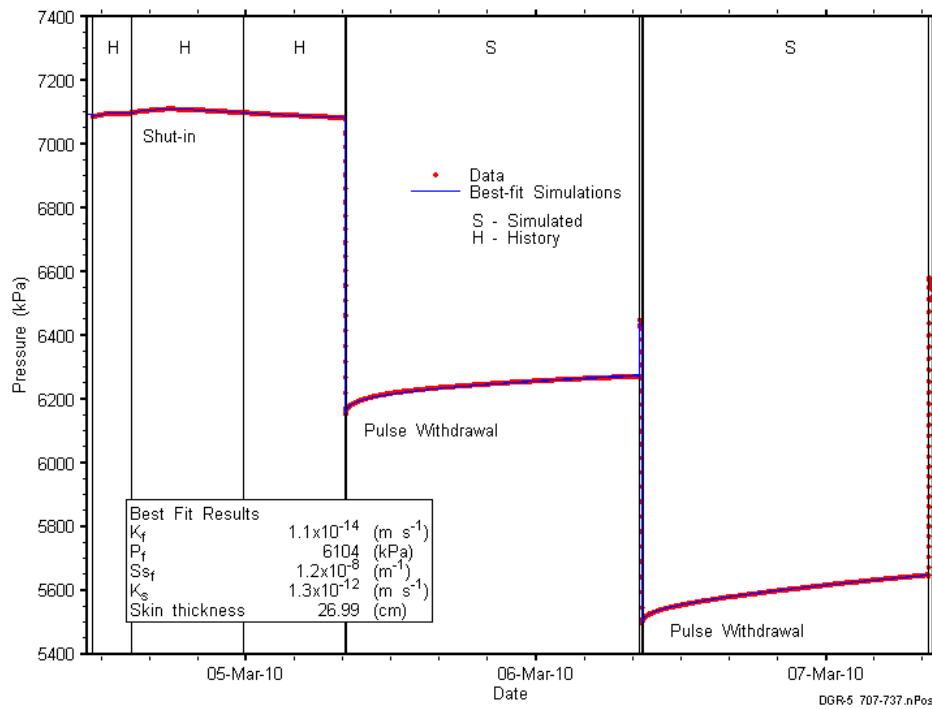


Figure E-123: Linear plot showing simulations of the DGR5_657.39-686.91 pressure response.

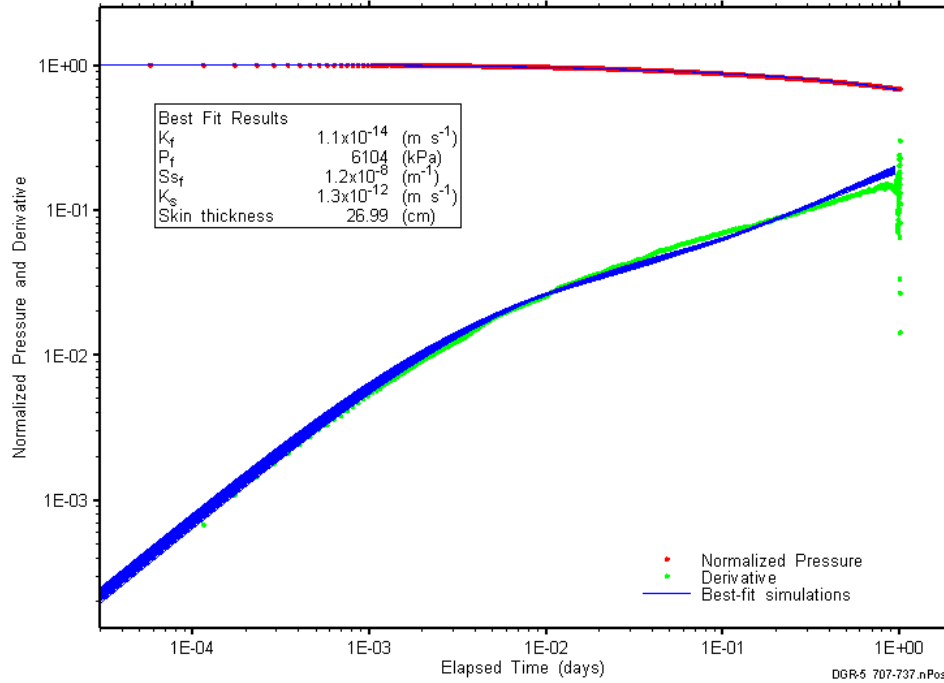


Figure E-124: Log-log plot showing simulations of the DGR5_657.39-686.91 PW1 Ramey B and derivative response.

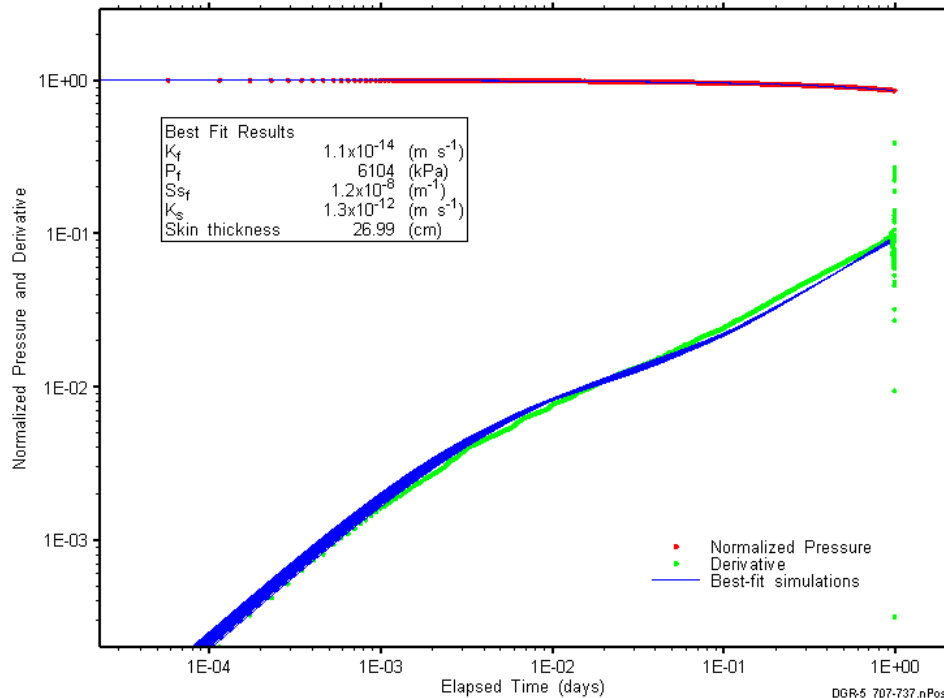


Figure E-125: Log-log plot showing simulations of the DGR5_657.39-686.91 PW2 Ramey B and derivative response.

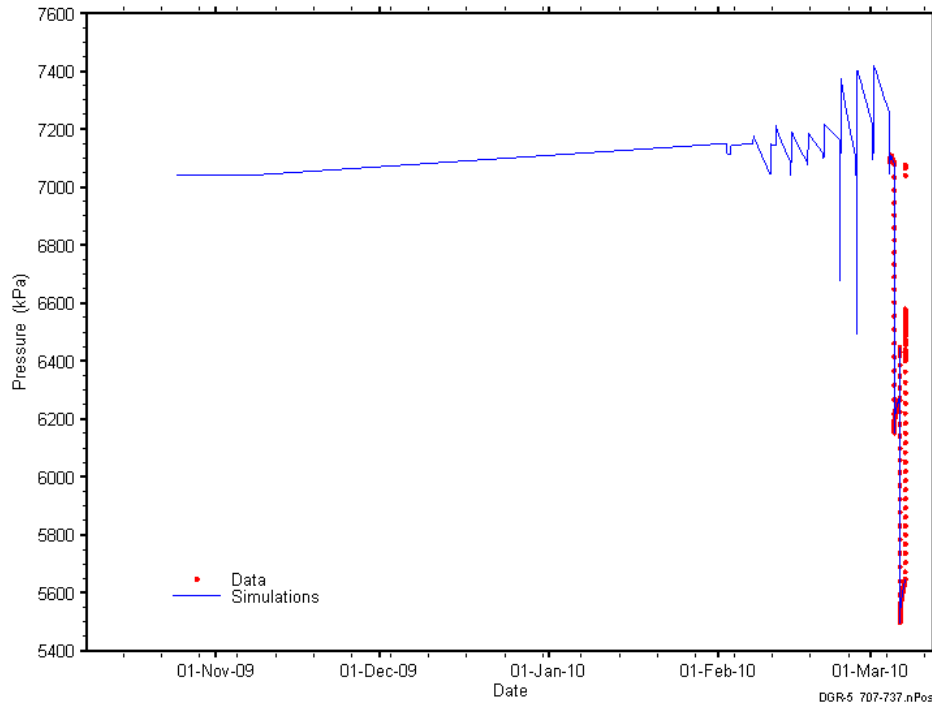


Figure E-126: Linear plot showing simulations of the DGR5_657.39-686.91 pressure response, including pre-test pressure history.

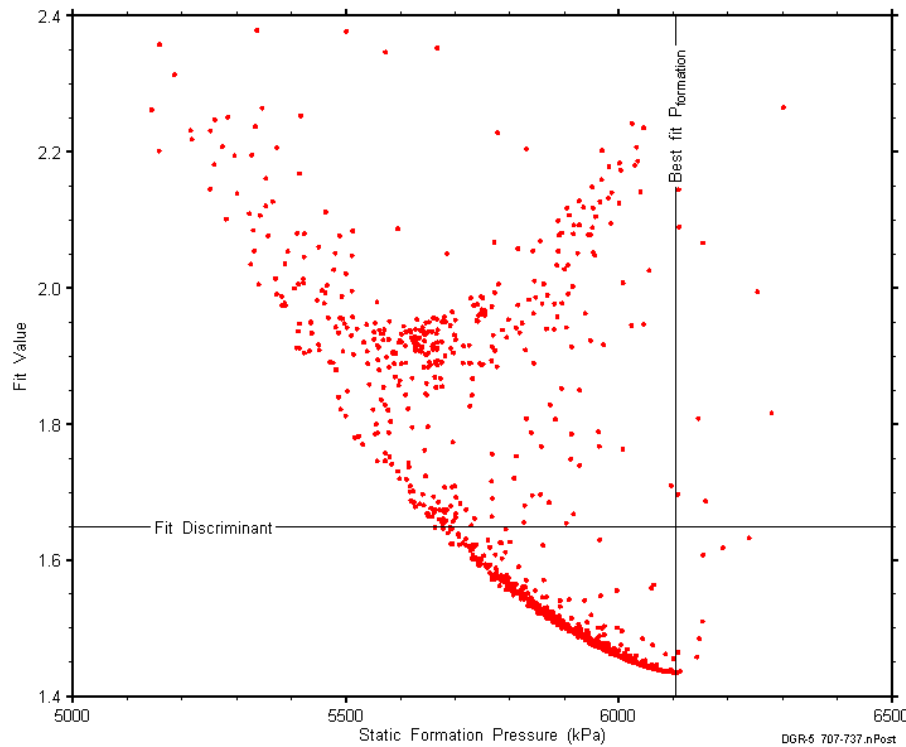


Figure E-127: XY-scatter plot showing the static formation pressure parameter space derived from DGR5_657.39-686.91 perturbation analysis along with the fit discriminant and best fit values.

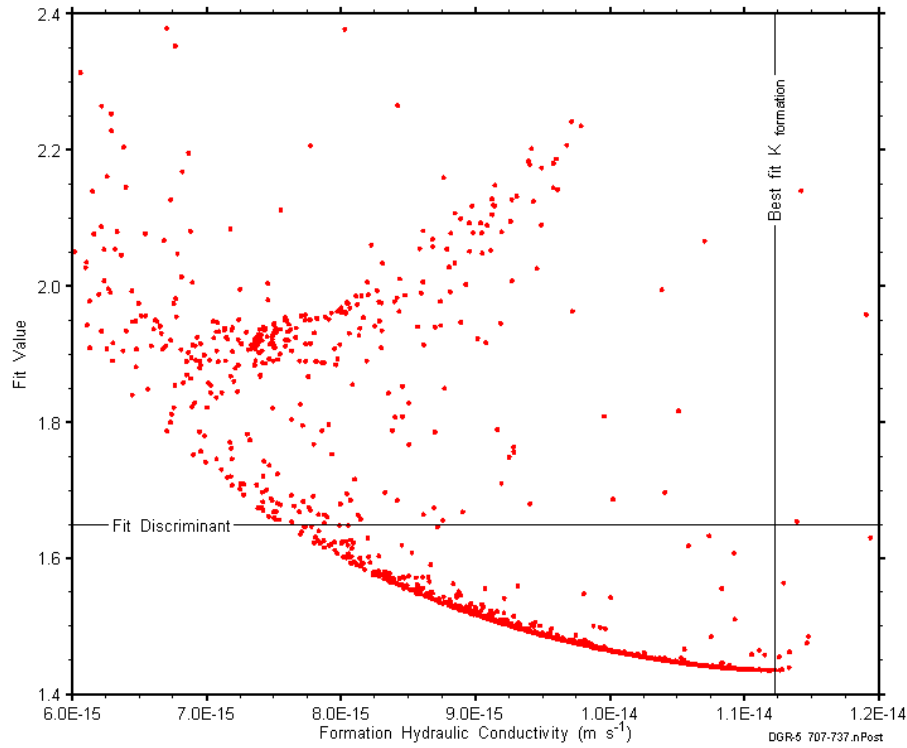


Figure E-128: XY-scatter plot showing the formation hydraulic conductivity parameter space derived from DGR5_657.39-686.91 perturbation analysis along with the fit discriminant and best fit values.

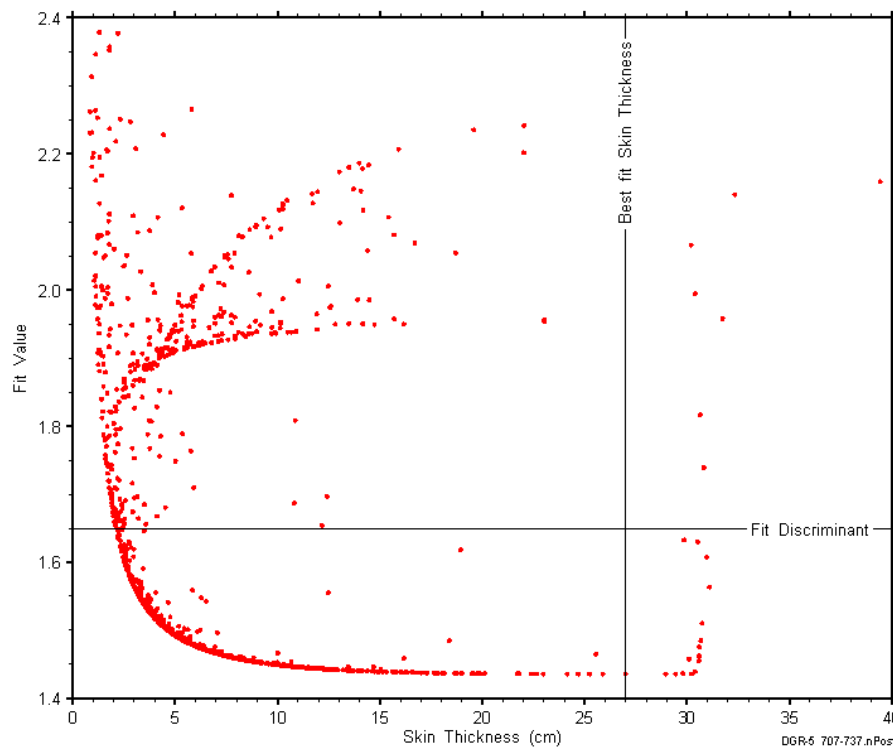


Figure E-129: XY-scatter plot showing the skin-thickness parameter space derived from DGR5_657.39-686.91 perturbation analysis along with the fit discriminant and best fit values.

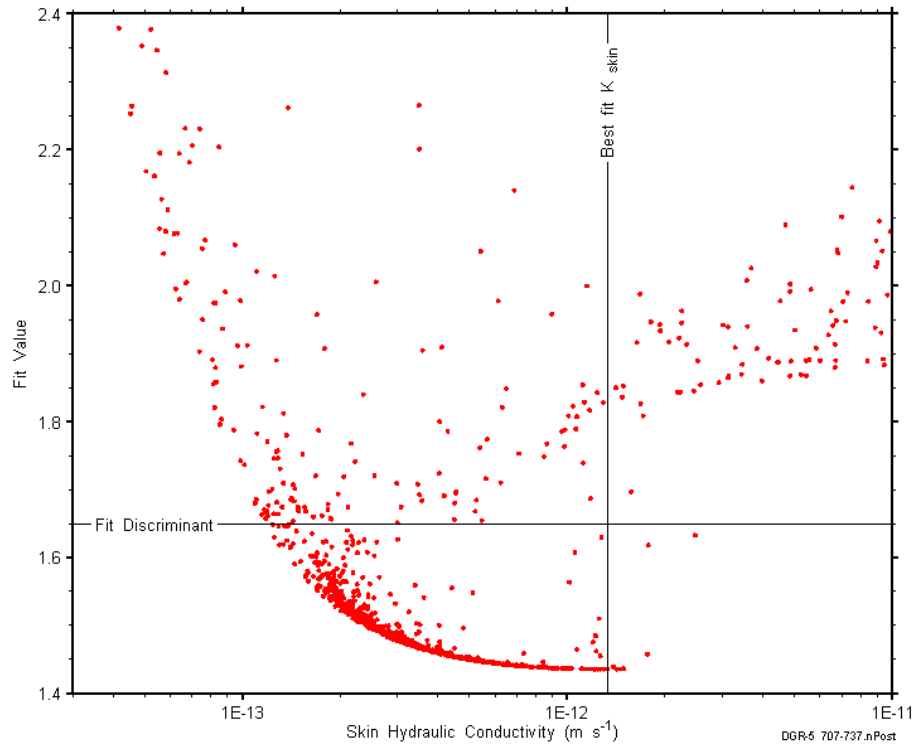


Figure E-130: XY-scatter plot showing the skin hydraulic conductivity parameter space derived from DGR5_657.39-686.91 perturbation analysis along with the fit discriminant and best fit values.

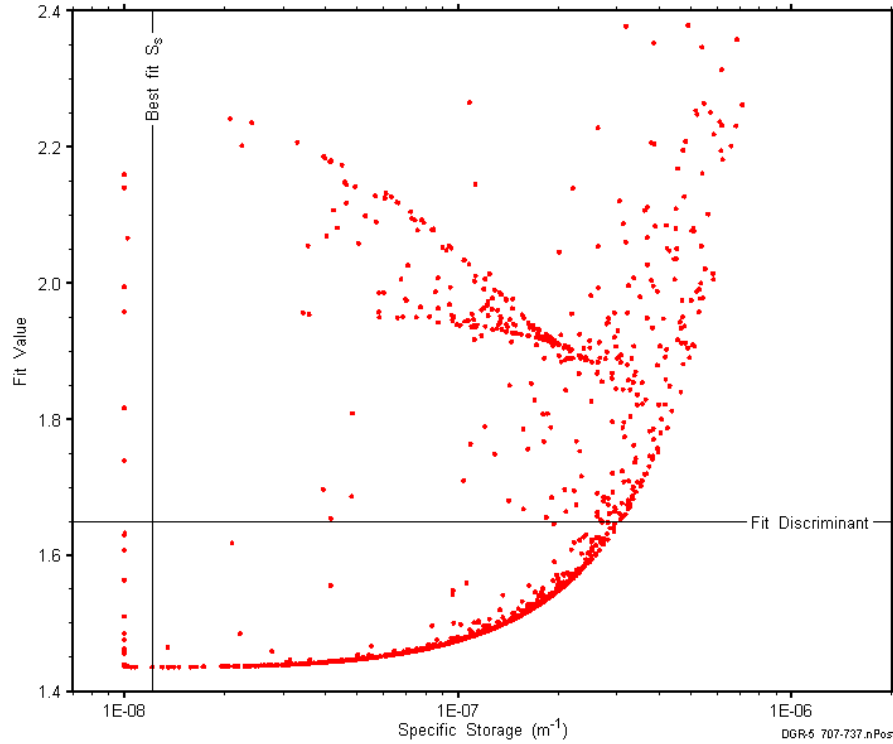


Figure E-131: XY-scatter plot showing the formation specific storage parameter space derived from DGR5_657.39-686.91 perturbation analysis along with the fit discriminant and best fit values.

E.10 686.66-716.20 Sherman Fall

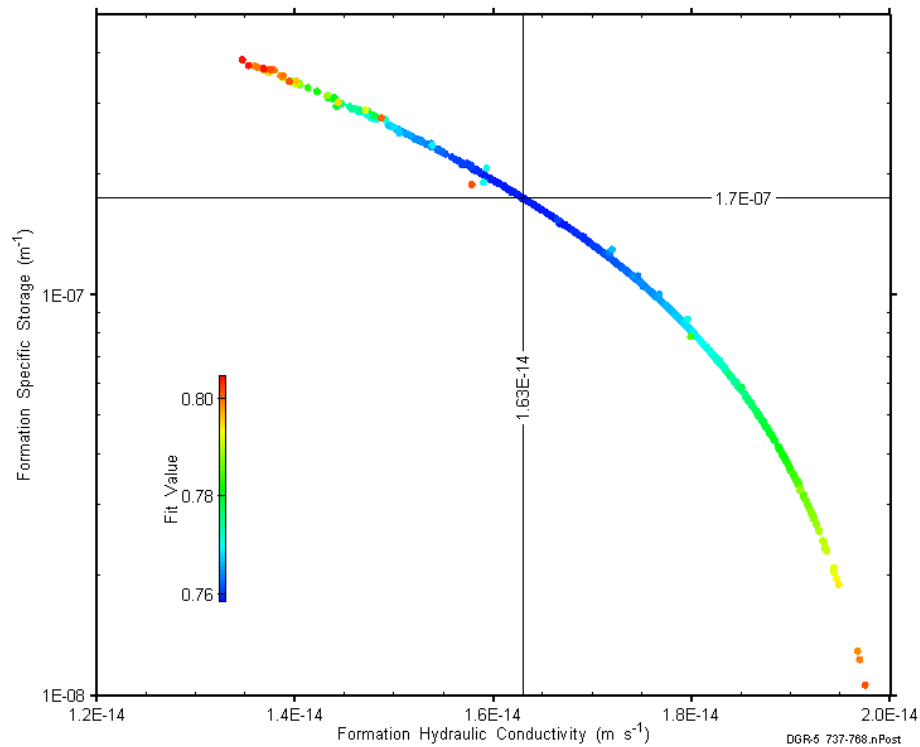


Figure E-132: XY-scatter plot showing estimates of formation hydraulic conductivity and formation specific storage derived from the DGR5_686.66-716.20 perturbation analysis.

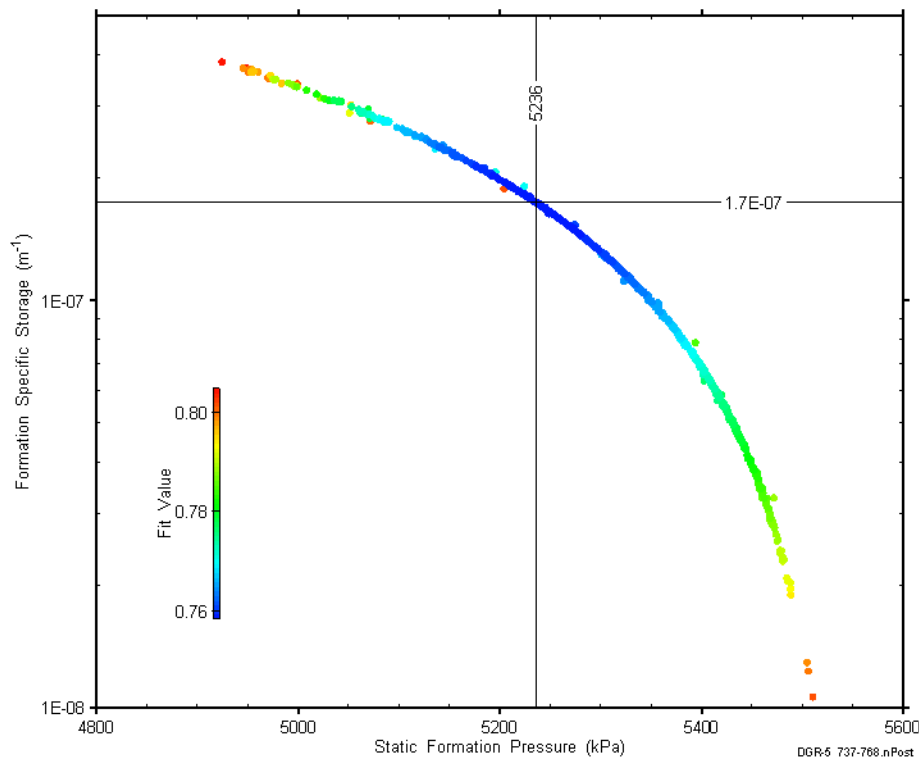


Figure E-133: XY-scatter plot showing estimates of static formation pressure and formation specific storage derived from the DGR5_686.66-716.20 perturbation analysis.

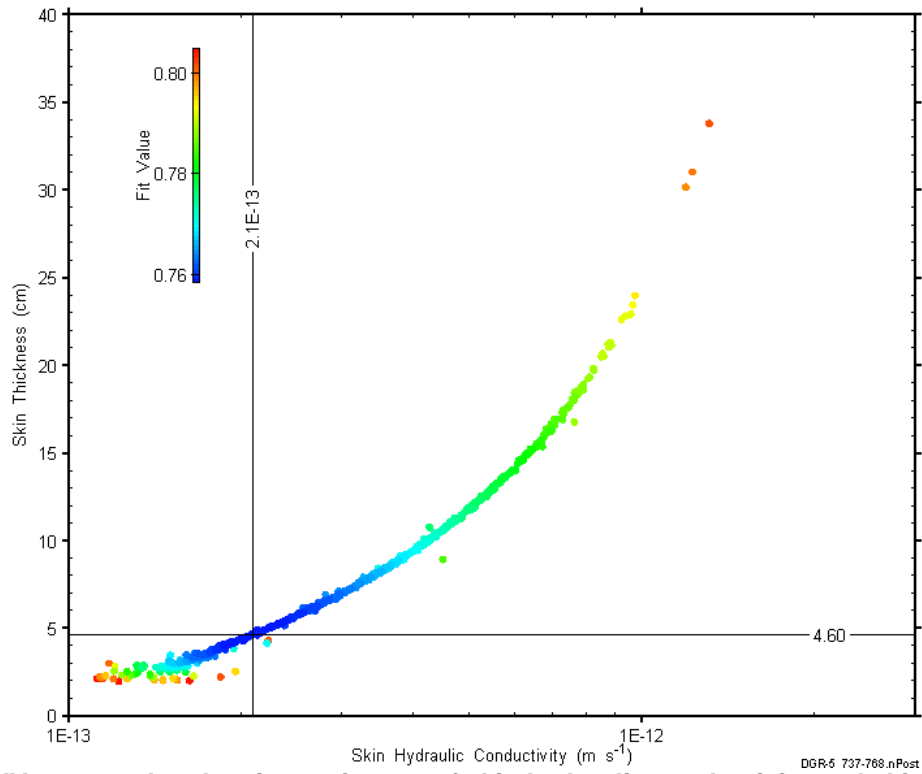


Figure E-134: XY-scatter plot showing estimates of skin hydraulic conductivity and skin thickness derived from the DGR5_686.66-716.20 perturbation analysis.

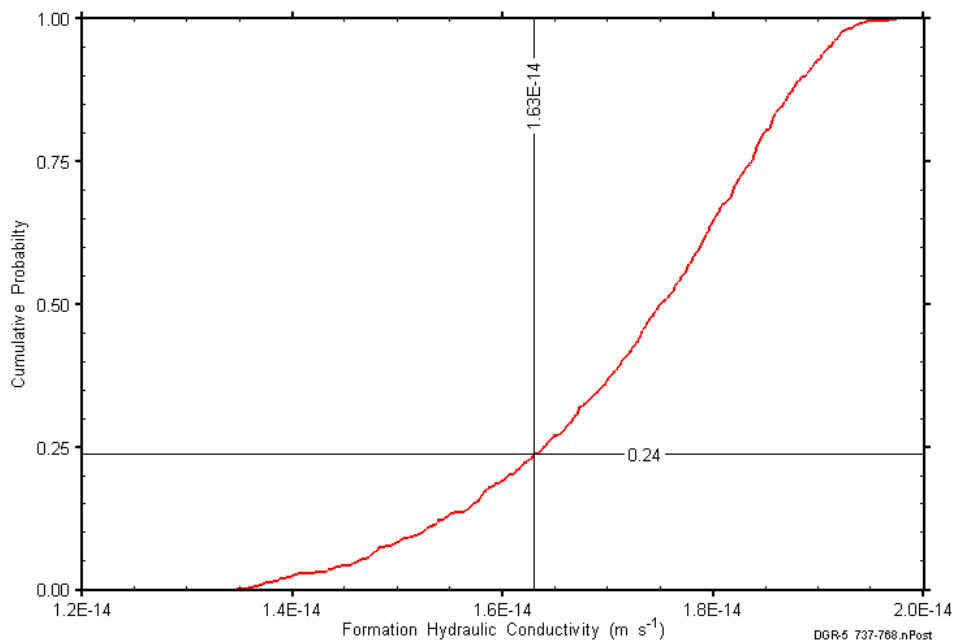


Figure E-135: DGR5_686.66-716.20 formation hydraulic conductivity cumulative distribution function.

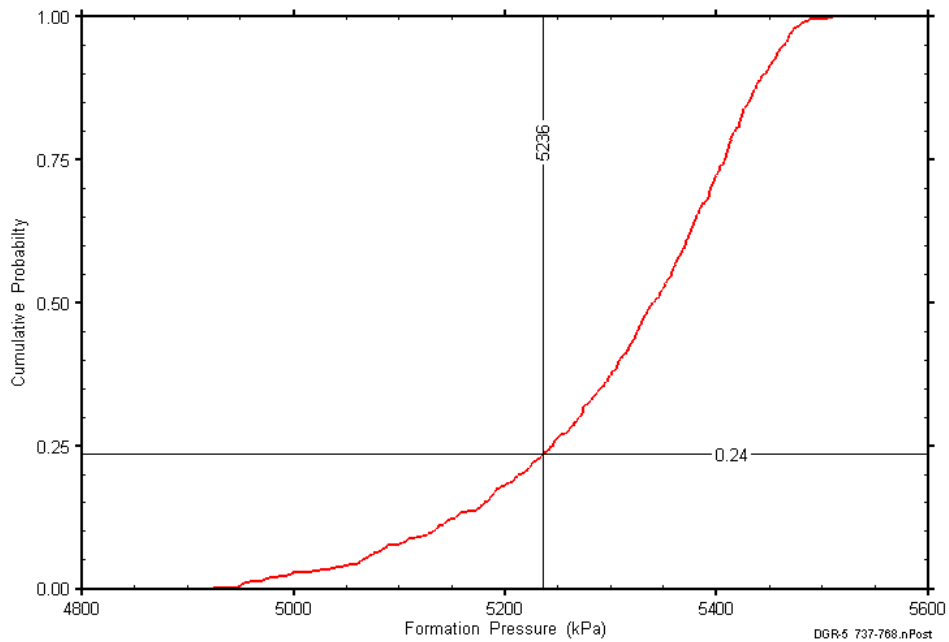


Figure E-136: DGR5_686.66-716.20 static formation pressure cumulative distribution function.

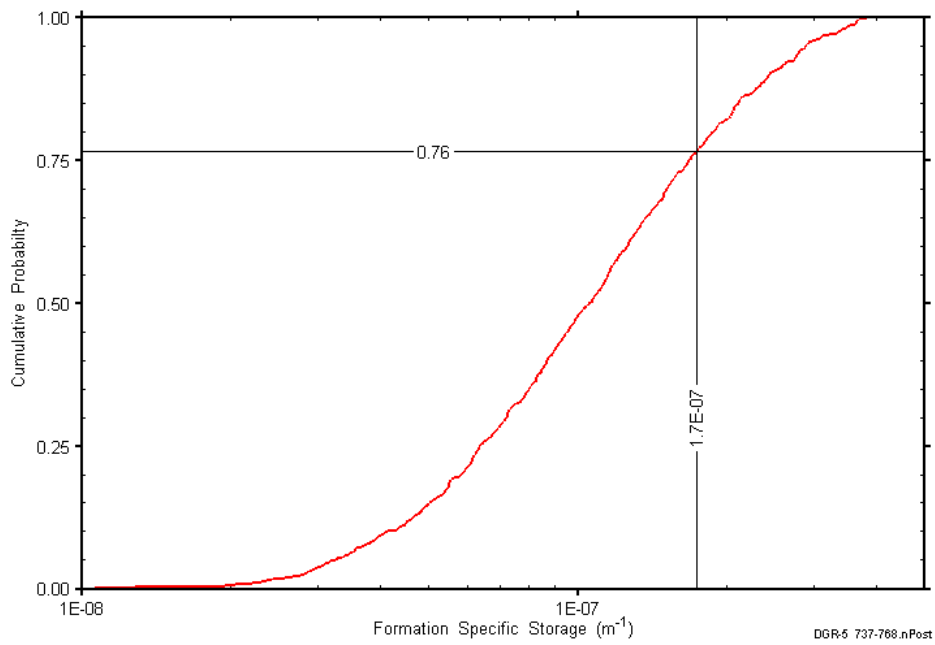


Figure E-137: DGR5_686.66-716.20 formation specific storage cumulative distribution function.

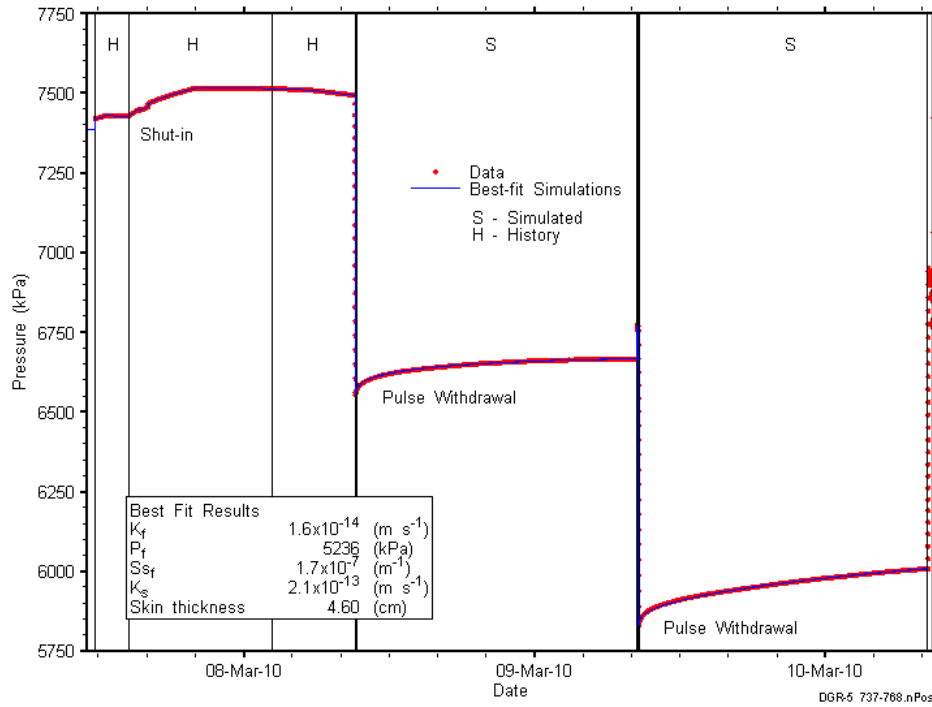


Figure E-138: Linear plot showing simulations of the DGR5_686.66-716.20 pressure response.

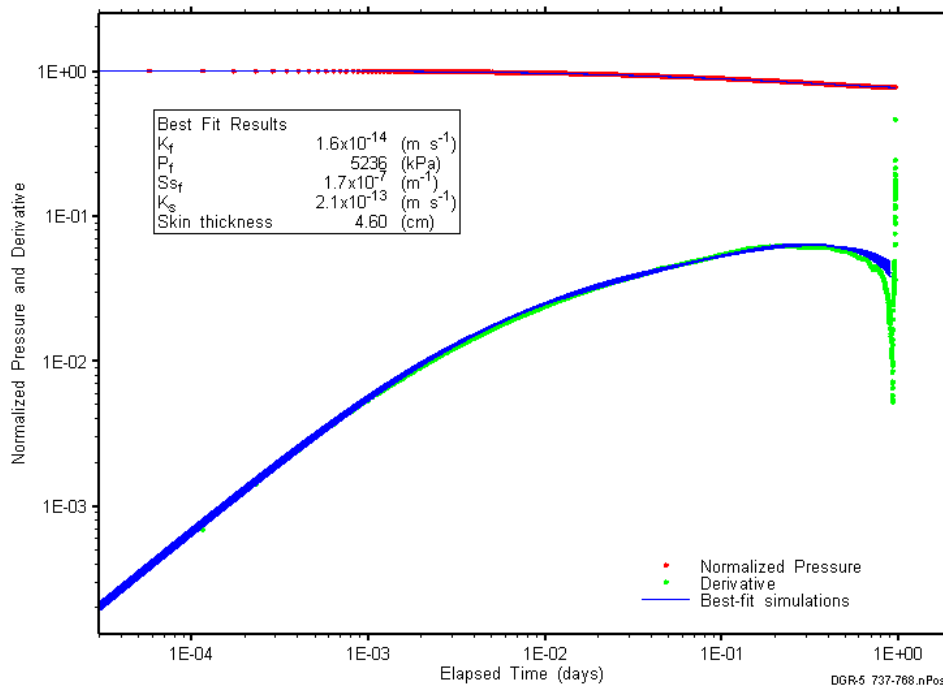


Figure E-139: Log-log plot showing simulations of the DGR5_686.66-716.20 PW1 Ramey B and derivative response.

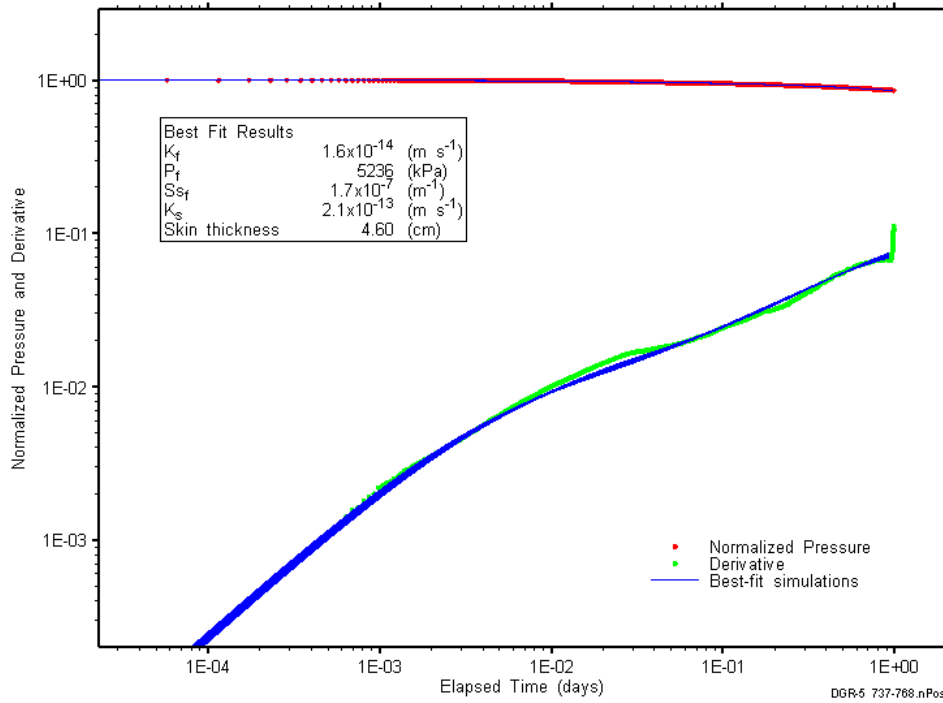


Figure E-140: Log-log plot showing simulations of the DGR5_686.66-716.20 PW Ramey B and derivative response.

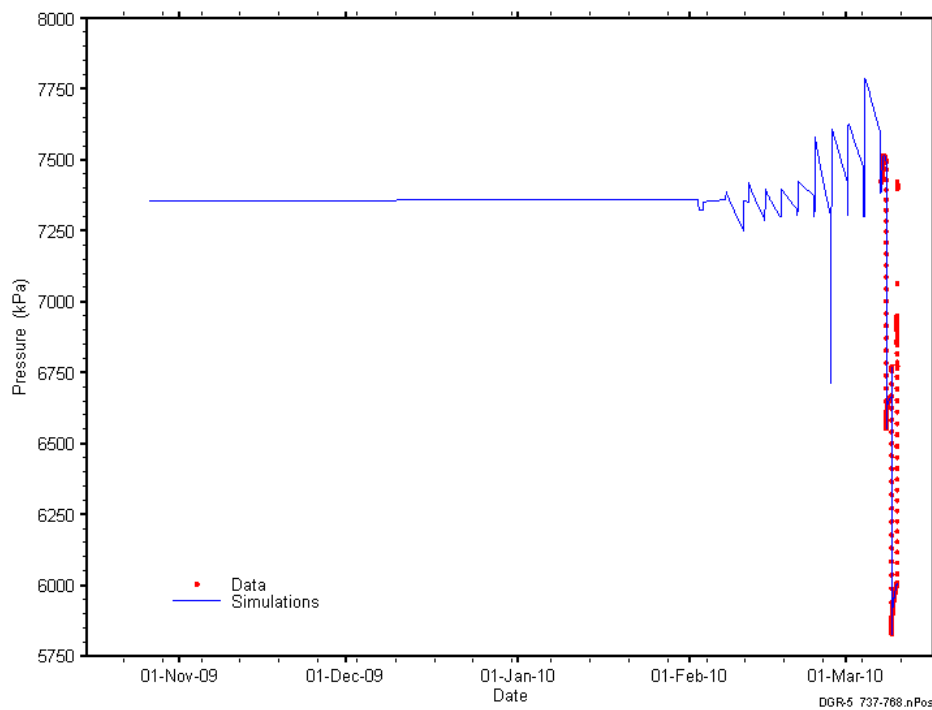


Figure E-141: Linear plot showing simulations of the DGR5_686.66-716.20 pressure response, including pre-test pressure history.

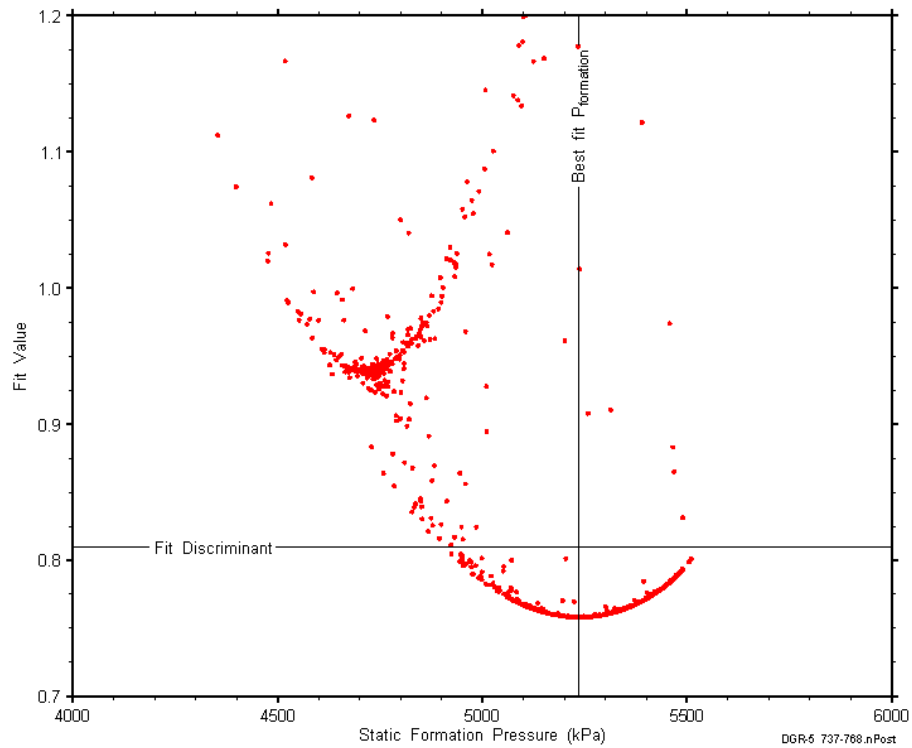


Figure E-142: XY-scatter plot showing the static formation pressure parameter space derived from DGR5_686.66-716.20 perturbation analysis along with the fit discriminant and best fit values.

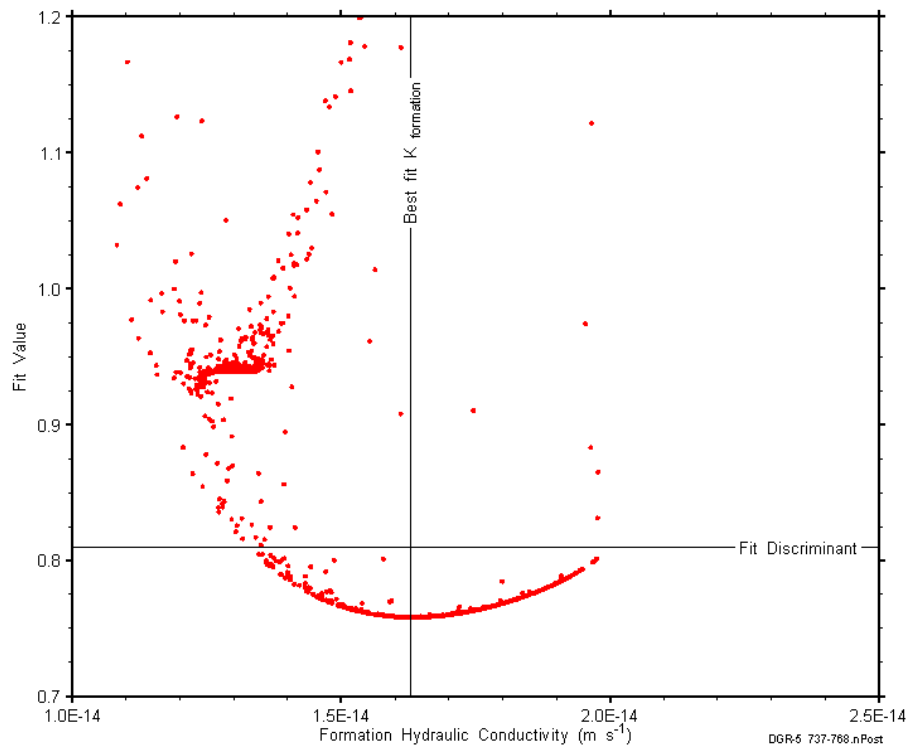


Figure E-143: XY-scatter plot showing the formation hydraulic conductivity parameter space derived from DGR5_686.66-716.20 perturbation analysis along with the fit discriminant and best fit values.

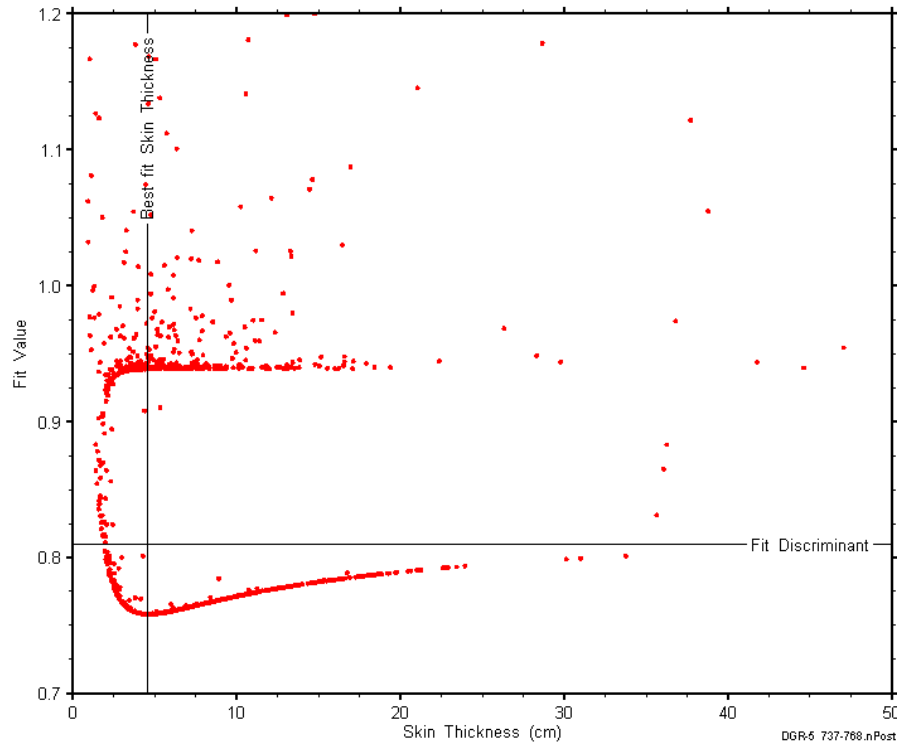


Figure E-144: XY-scatter plot showing the skin-thickness parameter space derived from DGR5_686.66-716.20 perturbation analysis along with the fit discriminant and best fit values.

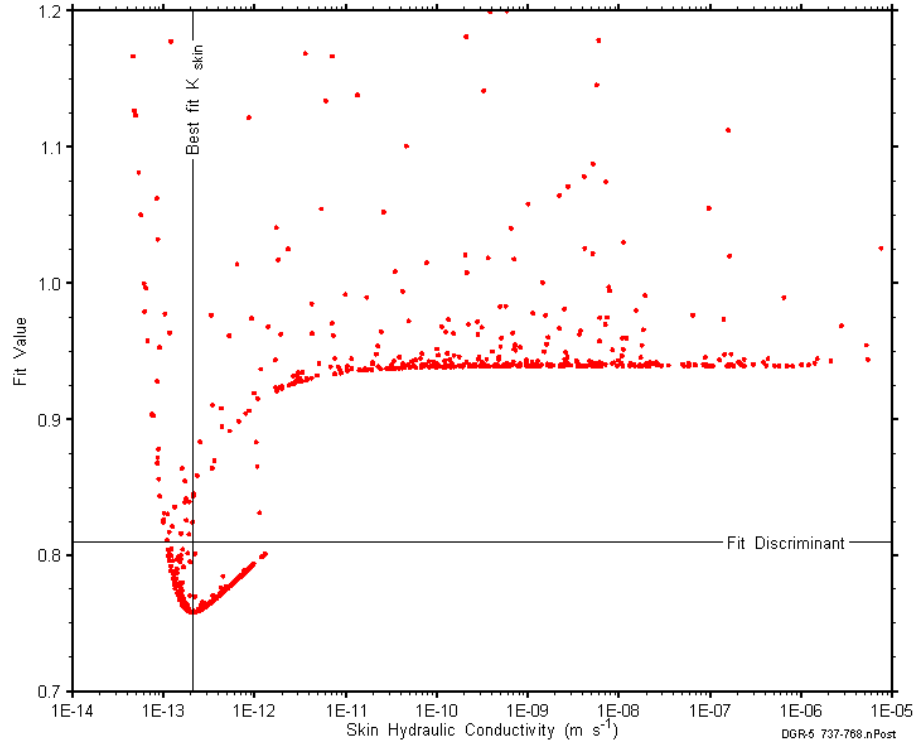


Figure E-145: XY-scatter plot showing the skin hydraulic conductivity parameter space derived from DGR5_686.66-716.20 perturbation analysis along with the fit discriminant and best fit values.

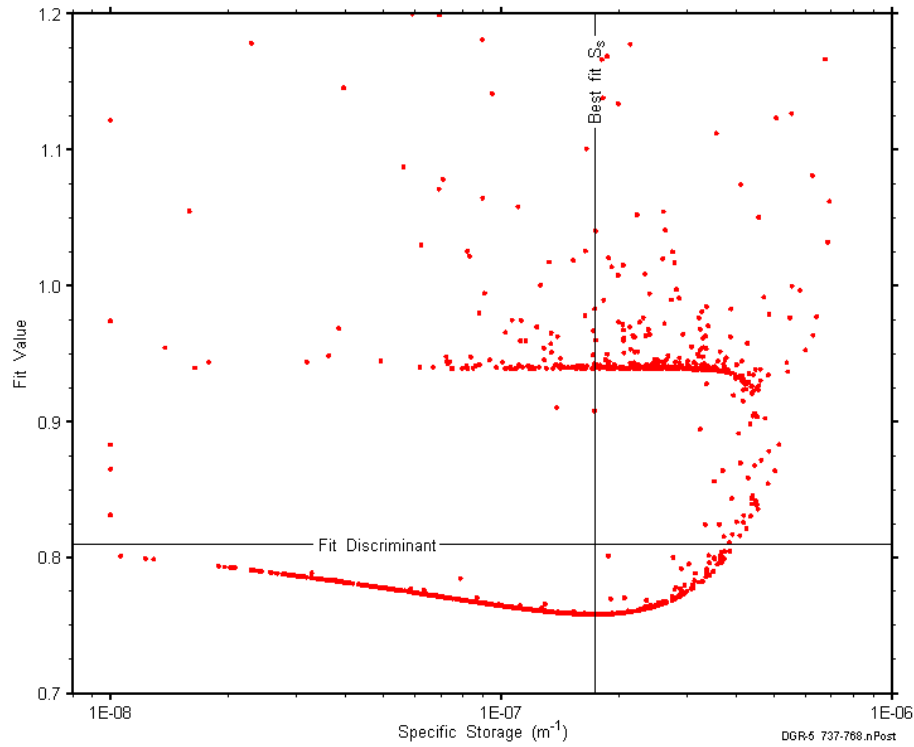


Figure E-146: XY-scatter plot showing the formation specific storage parameter space derived from DGR5_686.66-716.20 perturbation analysis along with the fit discriminant and best fit values.

E.11 715.94-745.48 Kirkfield

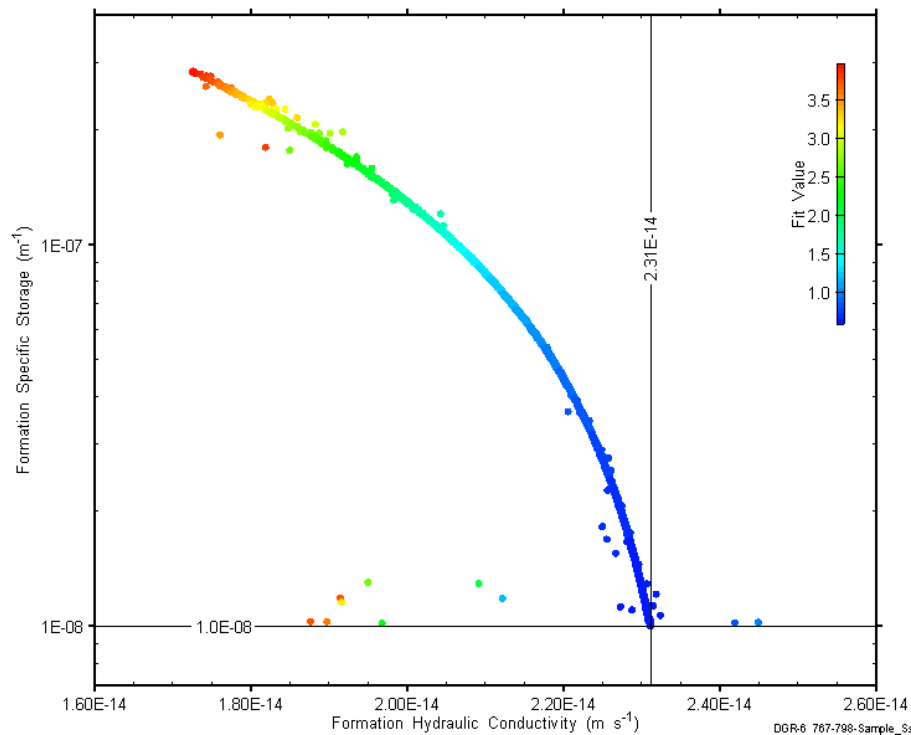


Figure E-147: XY-scatter plot showing estimates of formation hydraulic conductivity and formation specific storage derived from the DGR5_715.94-745.48 perturbation analysis.

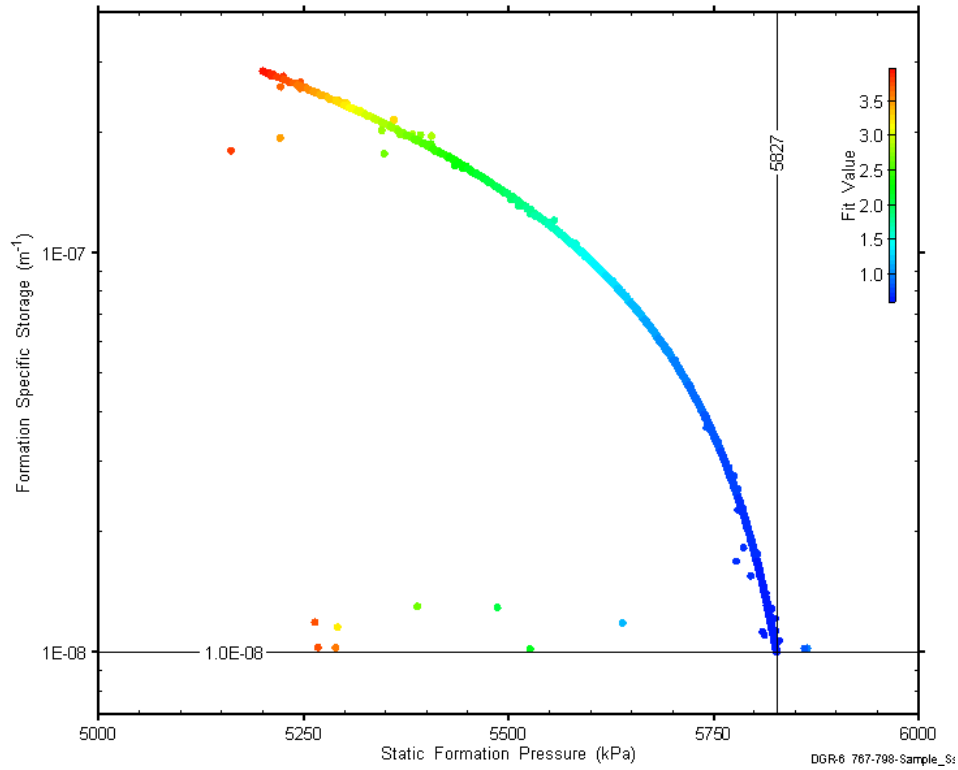


Figure E-148: XY-scatter plot showing estimates of static formation pressure and formation specific storage derived from the DGR5_715.94-745.48 perturbation analysis.

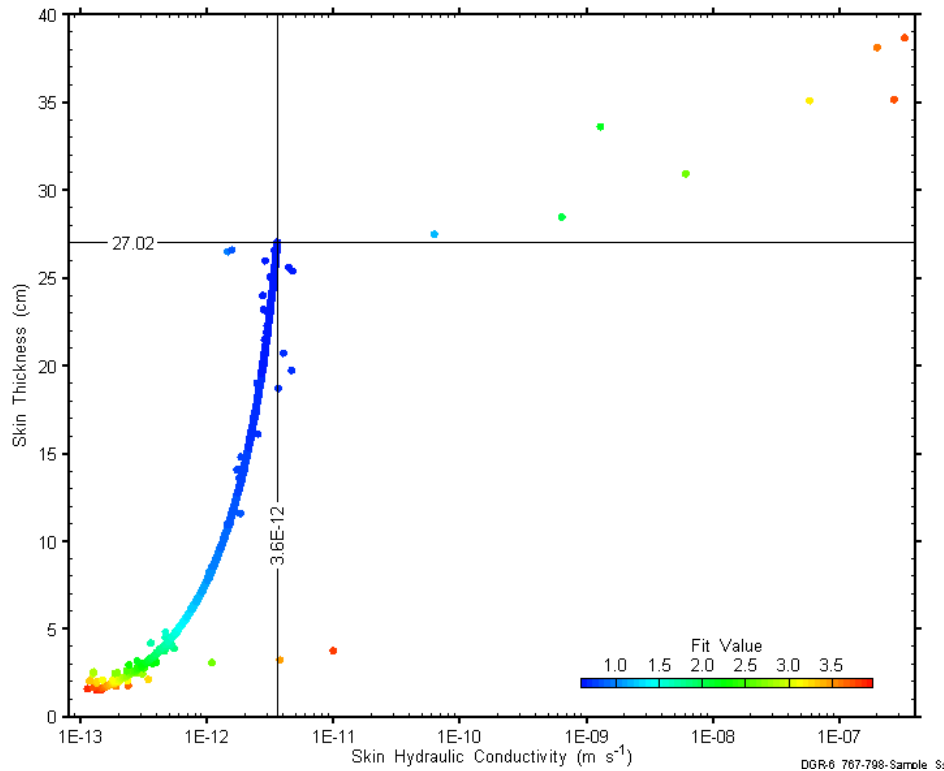


Figure E-149: XY-scatter plot showing estimates of skin hydraulic conductivity and skin thickness derived from the DGR5_715.94-745.48 perturbation analysis.

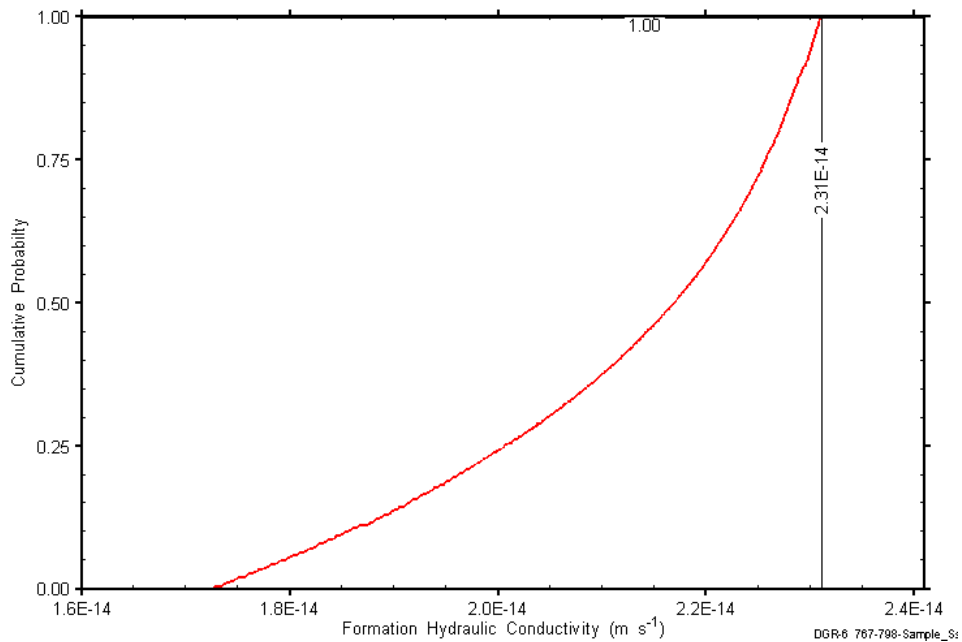


Figure E-150: DGR5_715.94-745.48 formation hydraulic conductivity cumulative distribution function.

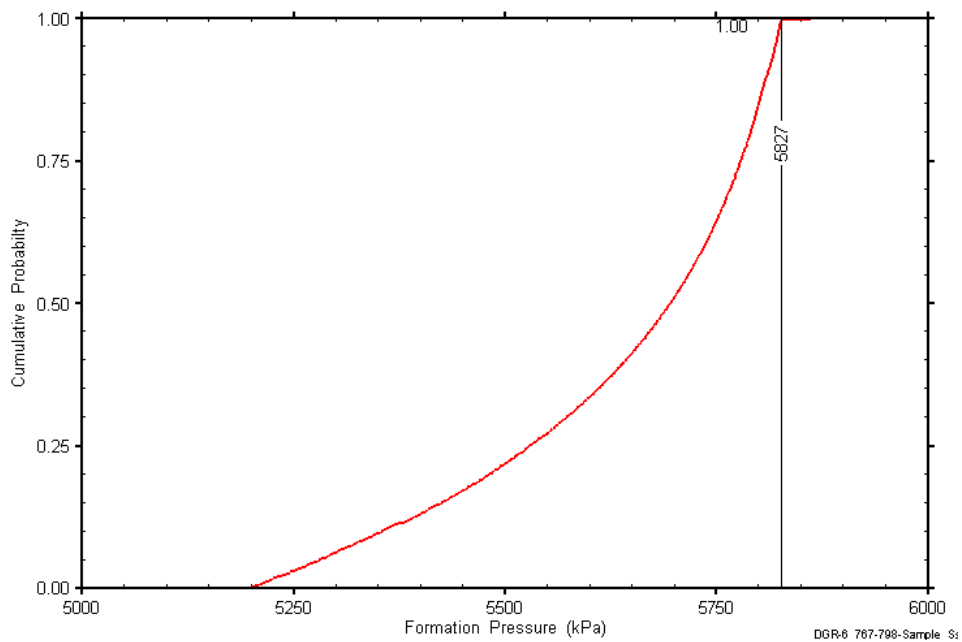


Figure E-151: DGR5_715.94-745.48 static formation pressure cumulative distribution function.

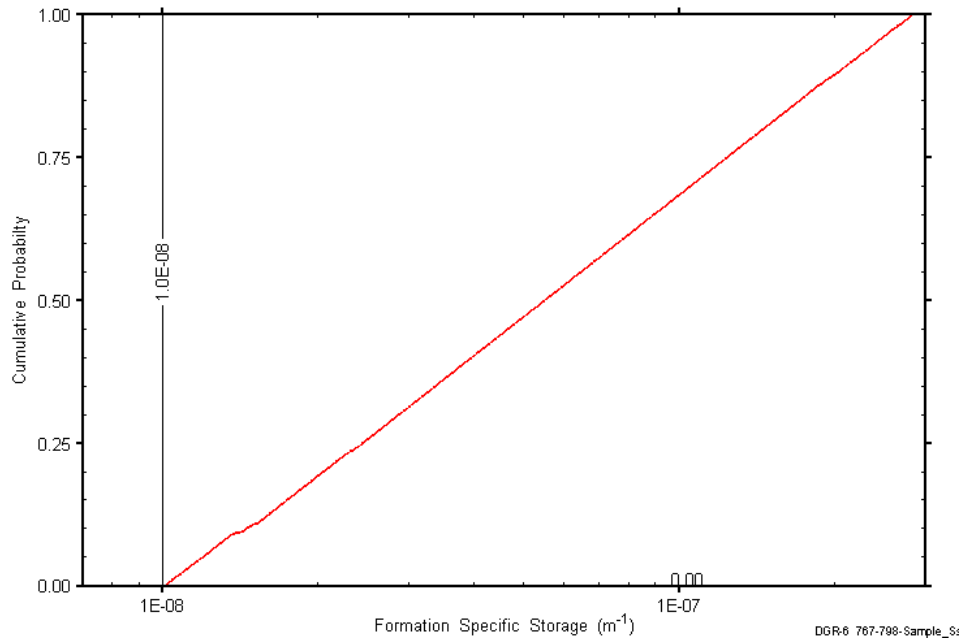


Figure E-152: DGR5_715.94-745.48 formation specific storage cumulative distribution function.

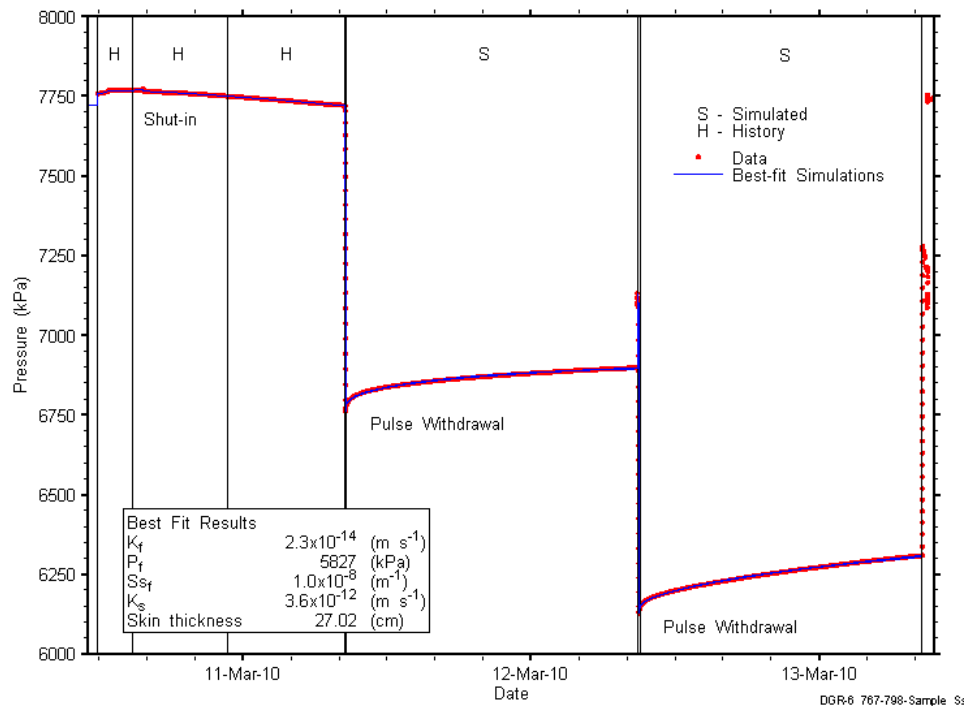


Figure E-153: Linear plot showing simulations of the DGR5_715.94-745.48 pressure response.

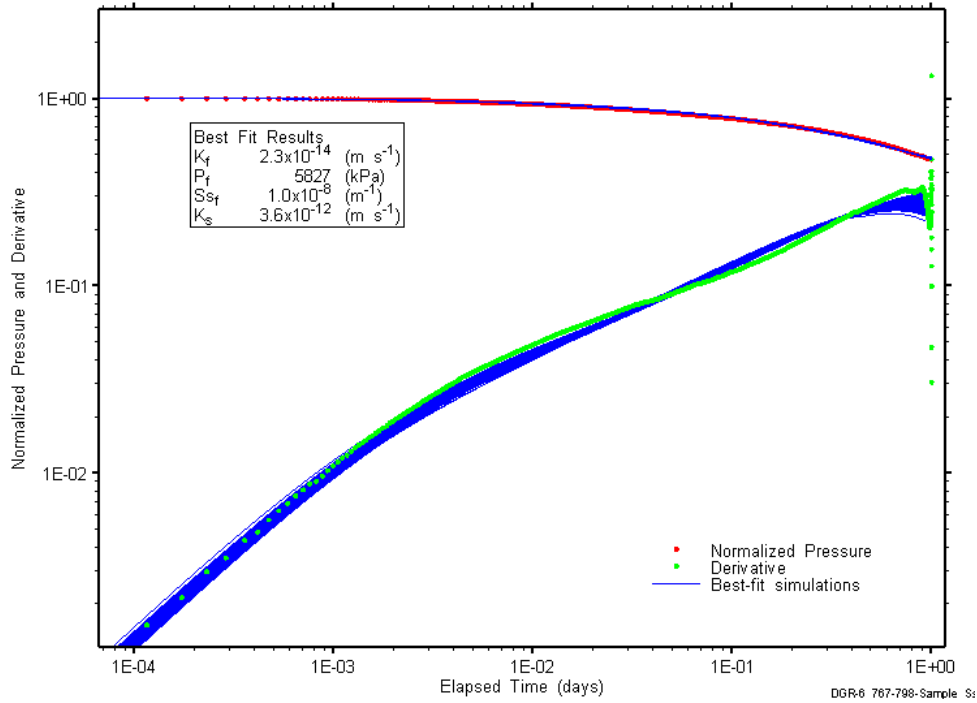


Figure E-154: Log-log plot showing simulations of the DGR5_715.94-745.48 PW1 Ramey B and derivative response.

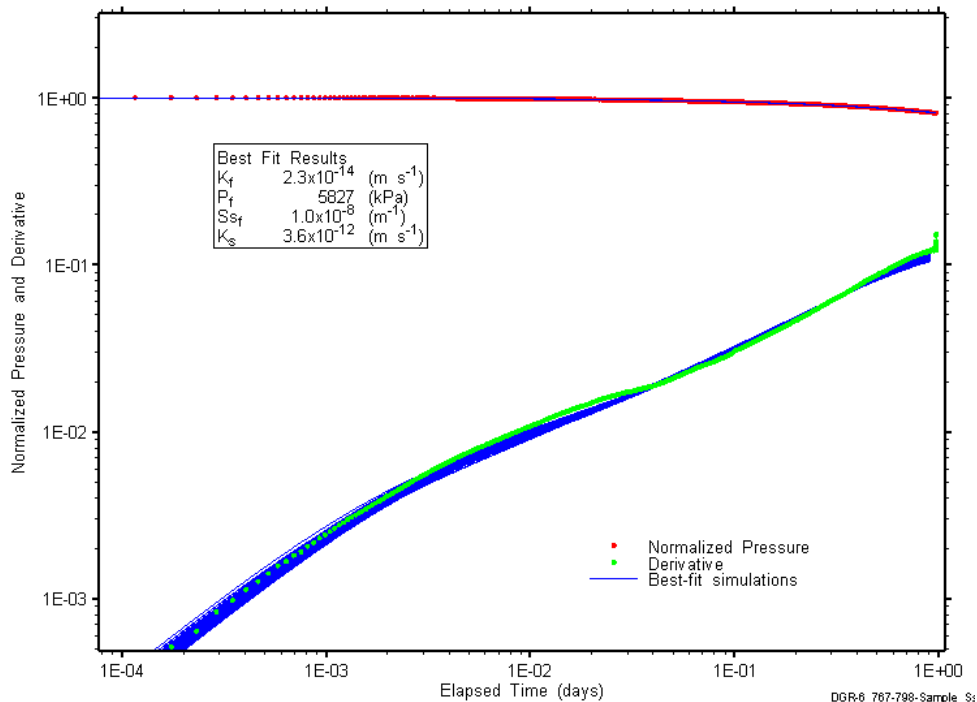


Figure E-155: Log-log plot showing simulations of the DGR5_715.94-745.48 PW2 Ramey B and derivative response.

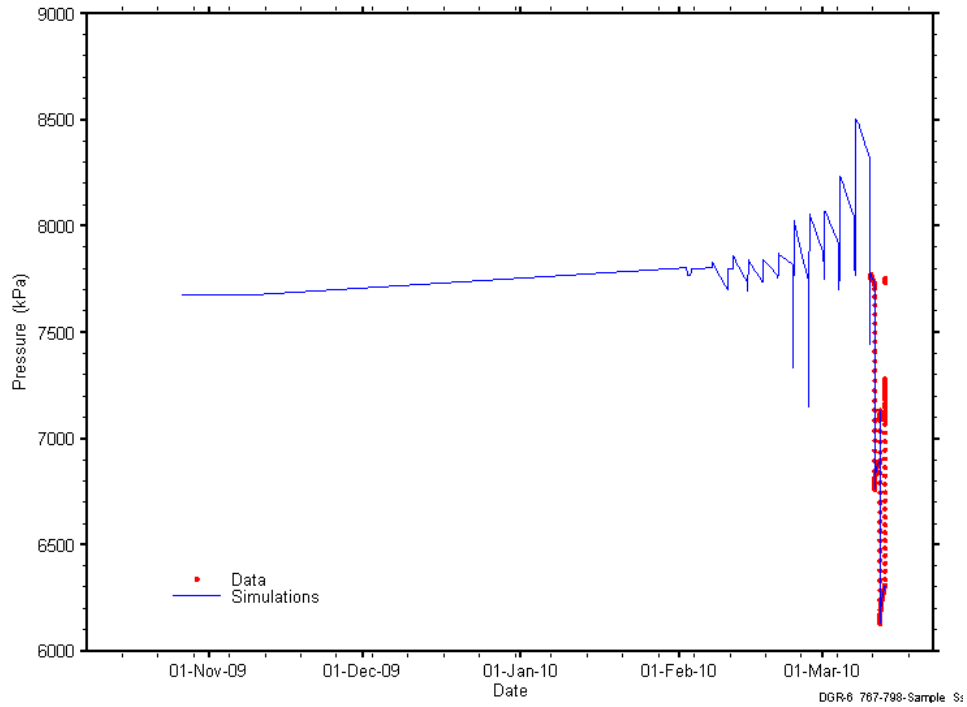


Figure E-156: Linear plot showing simulations of the DGR5_715.94-745.48 pressure response, including pre-test pressure history.

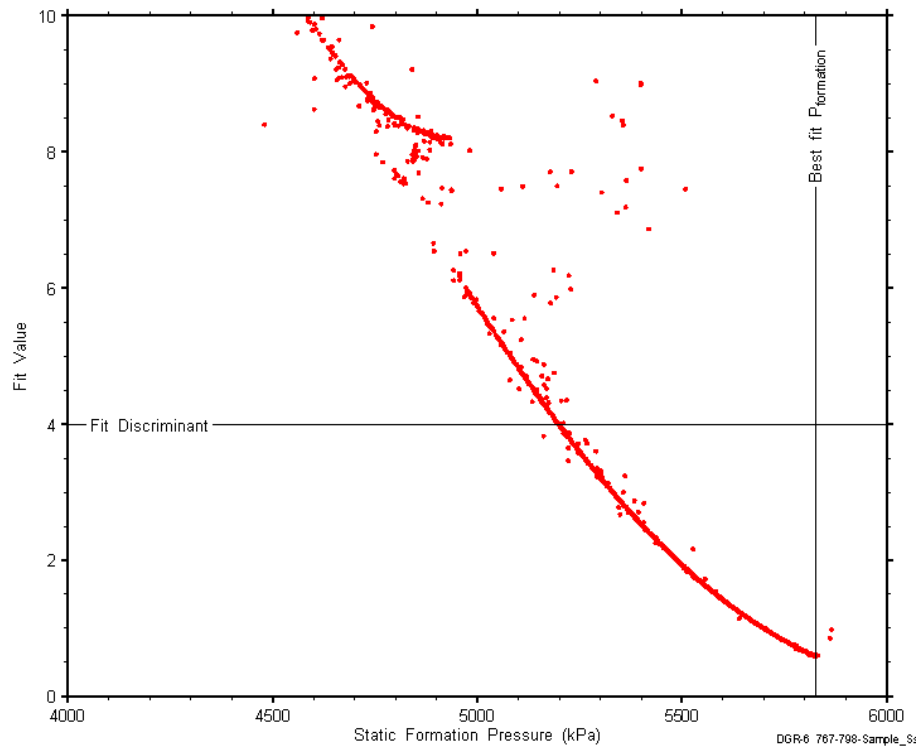


Figure E-157: XY-scatter plot showing the static formation pressure parameter space derived from DGR5_715.94-745.48 perturbation analysis along with the fit discriminant and best fit values.

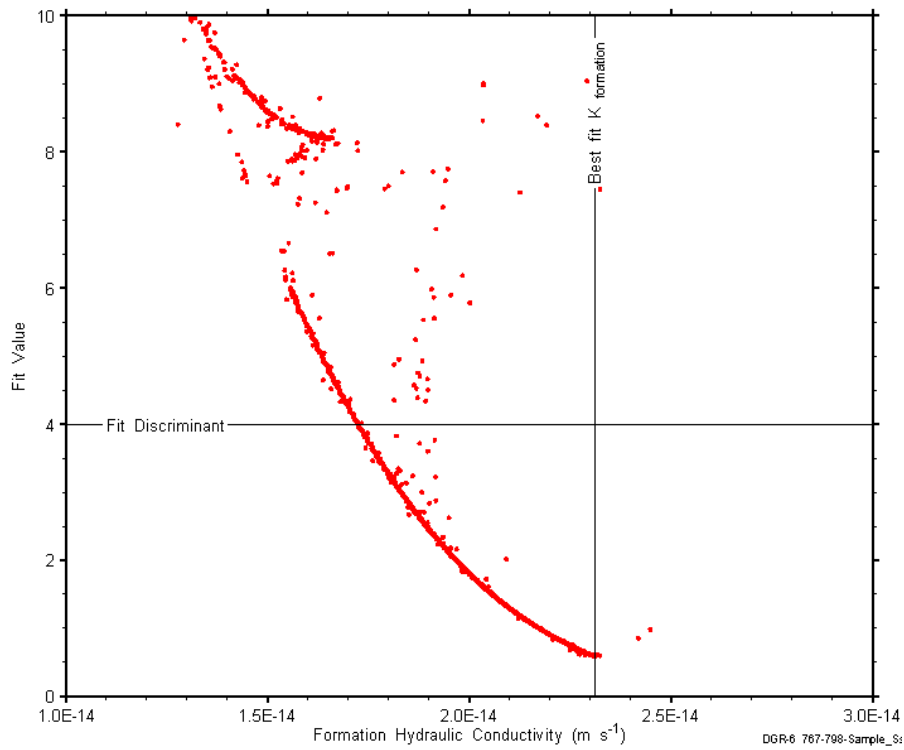


Figure E-158: XY-scatter plot showing the formation hydraulic conductivity parameter space derived from DGR5_715.94-745.48 perturbation analysis along with the fit discriminant and best fit values.

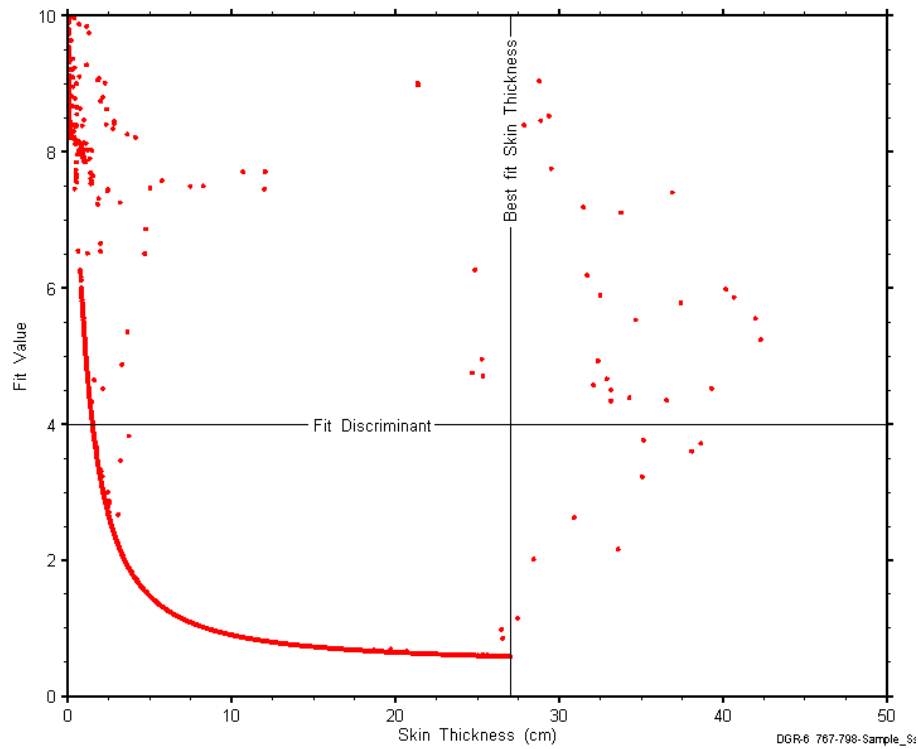


Figure E-159: XY-scatter plot showing the skin-thickness parameter space derived from DGR5_715.94-745.48 perturbation analysis along with the fit discriminant and best fit values.

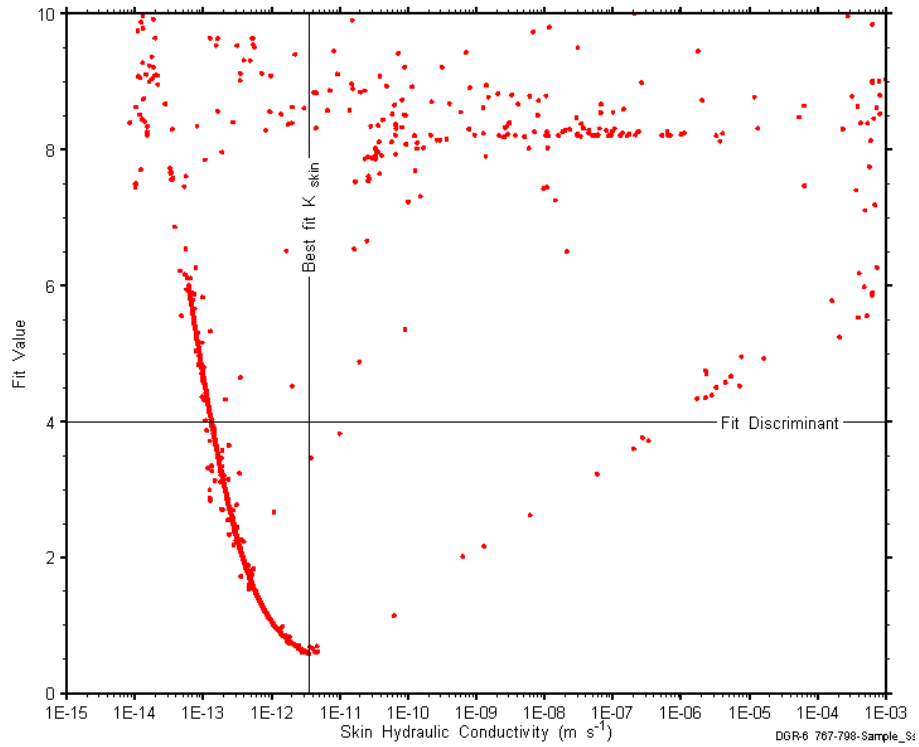


Figure E-160: XY-scatter plot showing the skin hydraulic conductivity parameter space derived from DGR5_715.94-745.48 perturbation analysis along with the fit discriminant and best fit values.

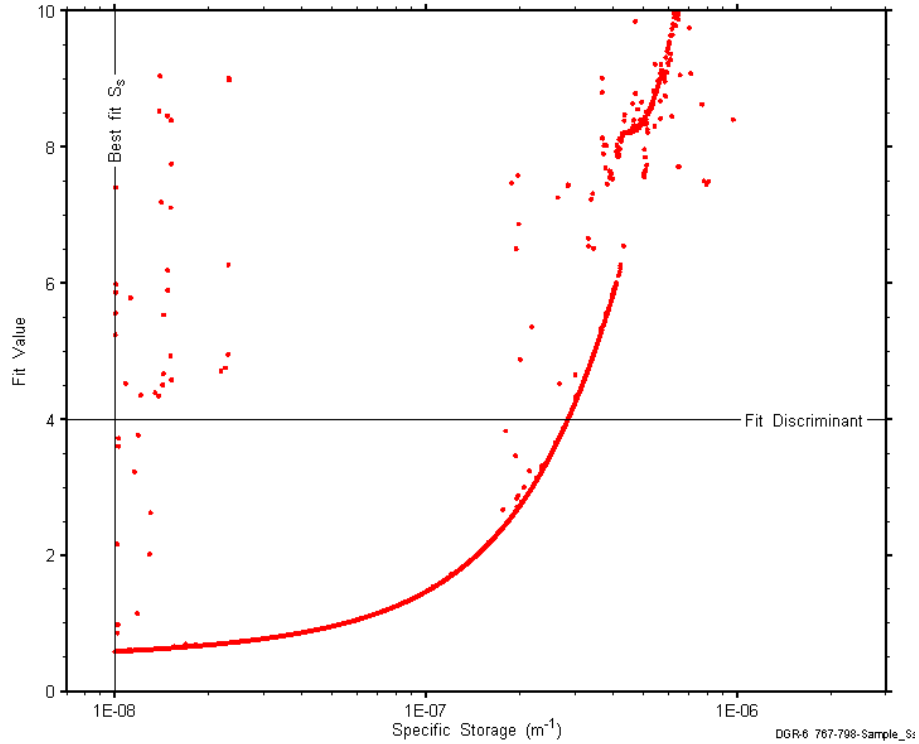


Figure E-161: XY-scatter plot showing the formation specific storage parameter space derived from DGR5_715.94-745.48 perturbation analysis along with the fit discriminant and best fit values.

Appendix F. DGR-6 Plots

Various plots of results from the DGR-6 analyses are shown below. These plots include XY-scatter plots of the fitting-parameter estimates, linear and log-log horsetail plots of the simulated pressure responses showing field-data matches, K_f , P_f , and S_s cumulative distribution functions, and parameter-space plots showing the characteristics of the minima for each of the fitting parameters.

F.1 453.30-462.80 Queenston

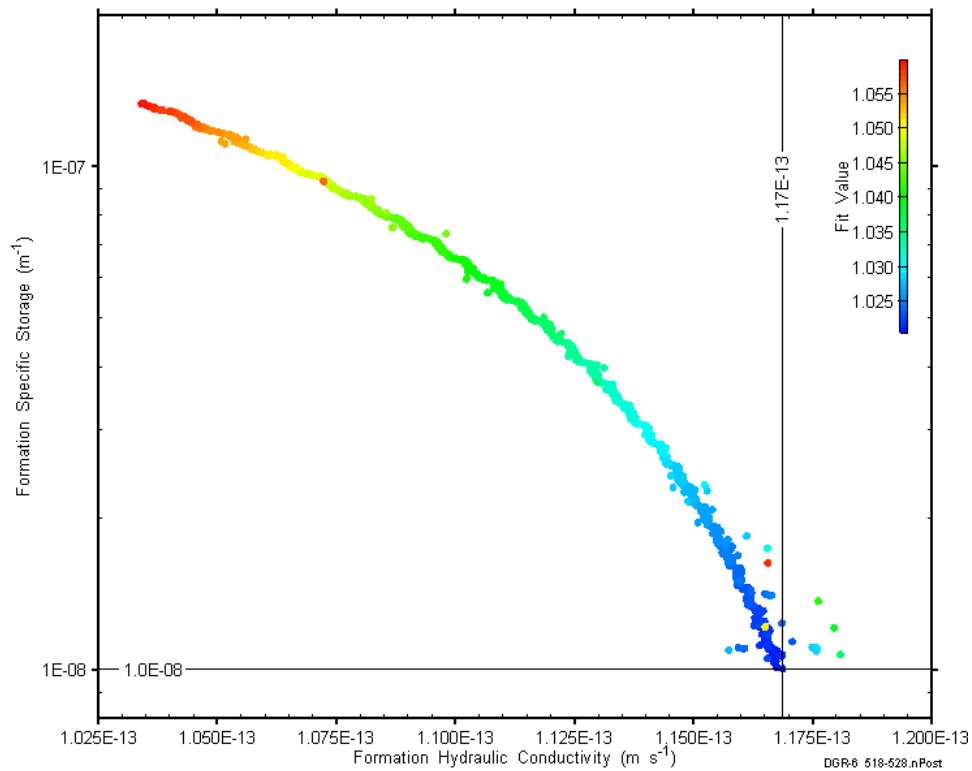


Figure F-1: XY-scatter plot showing estimates of formation hydraulic conductivity and formation specific storage derived from the DGR6_453.30-462.80 perturbation analysis.

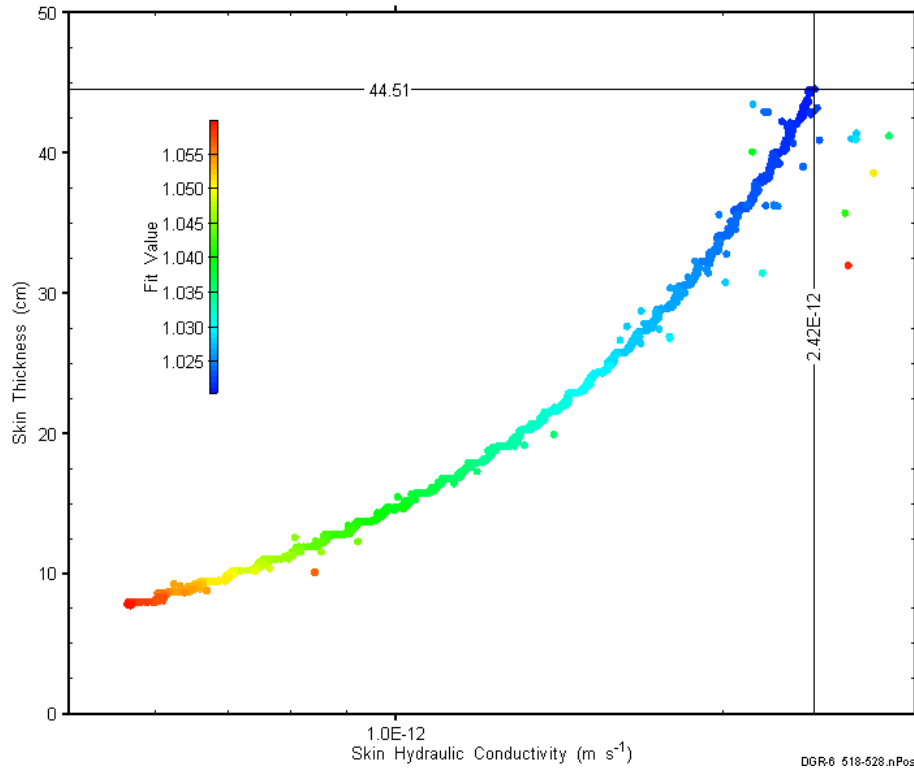


Figure F-2: XY-scatter plot showing estimates of skin hydraulic conductivity and skin thickness derived from the DGR6_453.30-462.80 perturbation analysis.

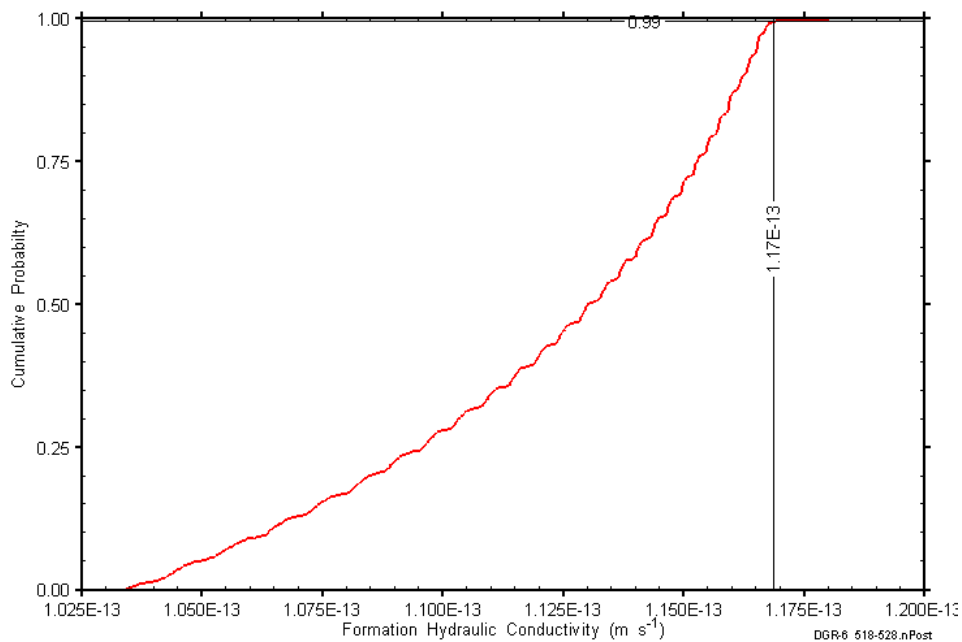


Figure F-3: DGR6_453.30-462.80 formation hydraulic conductivity cumulative distribution function.

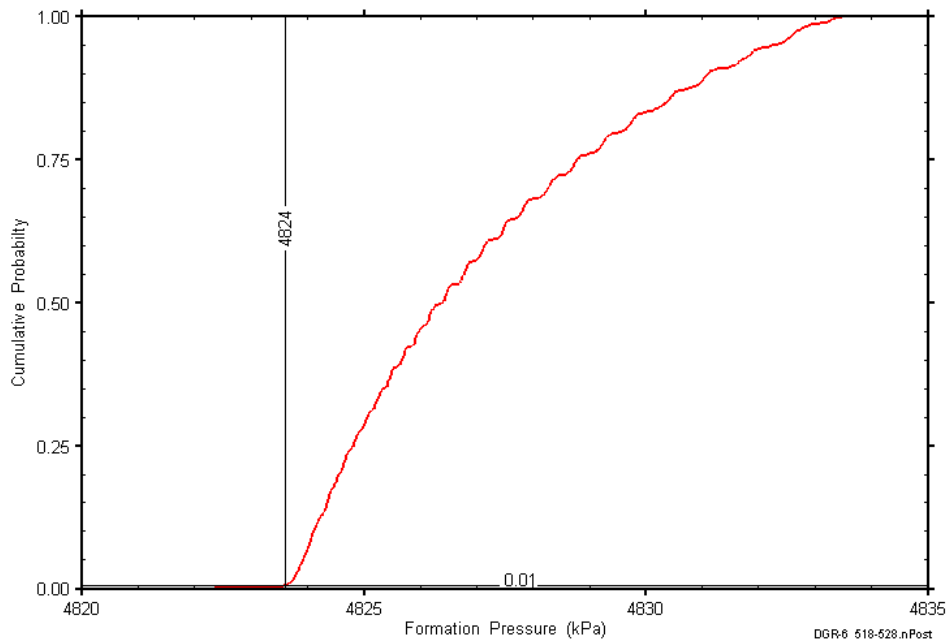


Figure F-4: DGR6_453.30-462.80 static formation pressure cumulative distribution function.

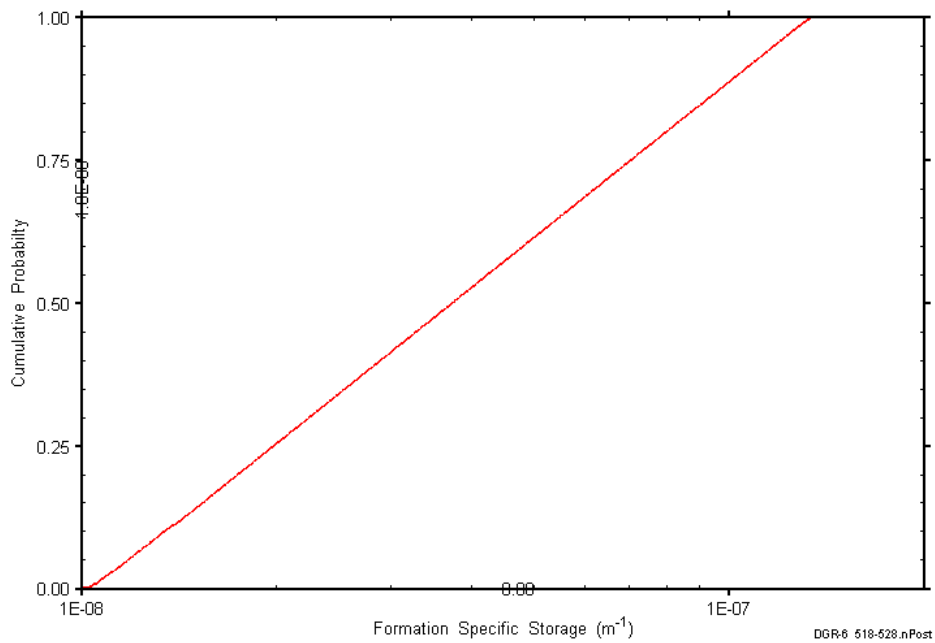


Figure F-5: DGR6_453.30-462.80 formation specific storage cumulative distribution function.

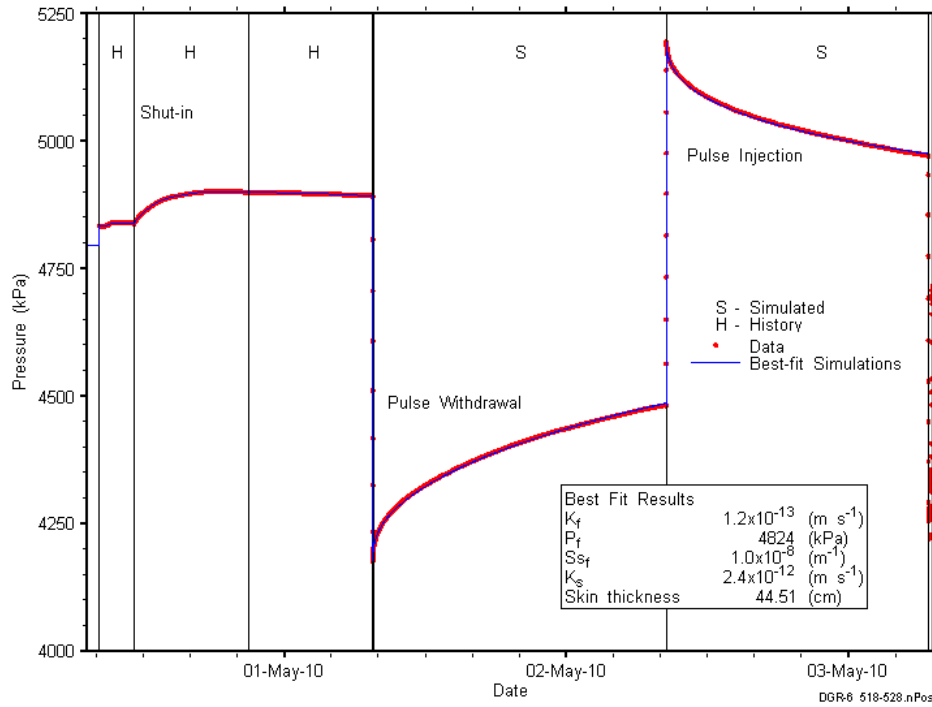


Figure F-6: Linear plot showing simulations of the DGR6_453.30-462.80 pressure response.

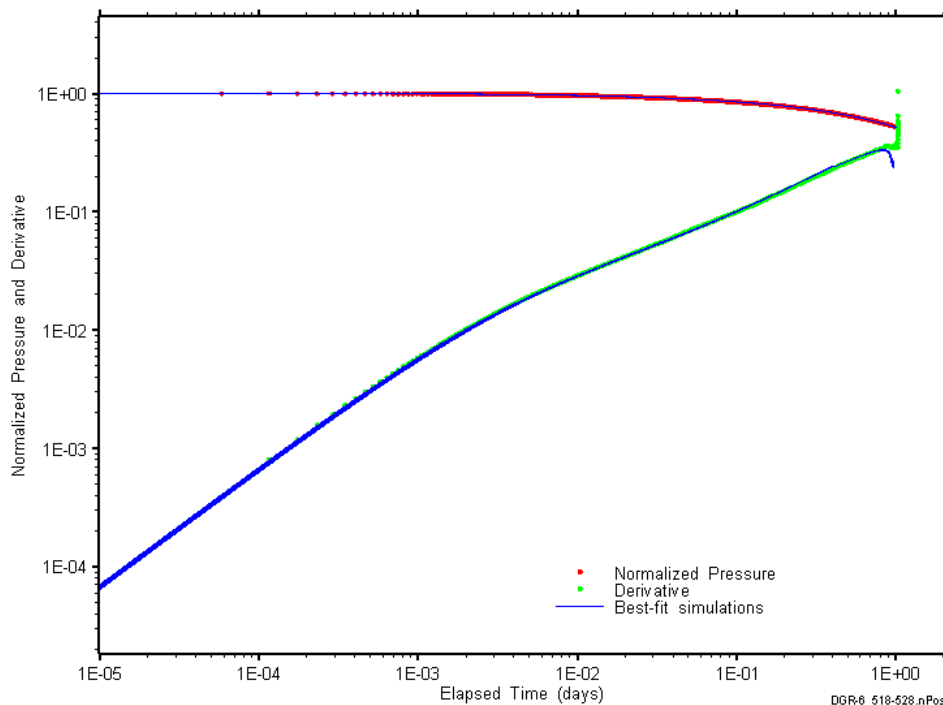


Figure F-7: Log-log plot showing simulations of the DGR6_453.30-462.80 PW Ramey B and derivative response.

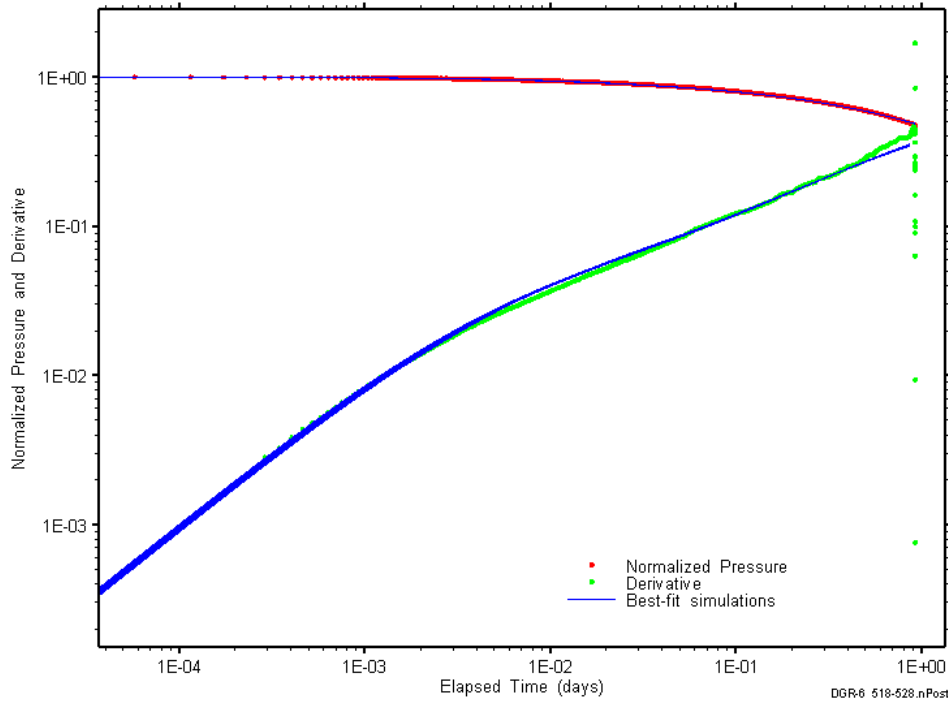


Figure F-8: Log-log plot showing simulations of the DGR6_453.30-462.80 PI Ramey B and derivative response.

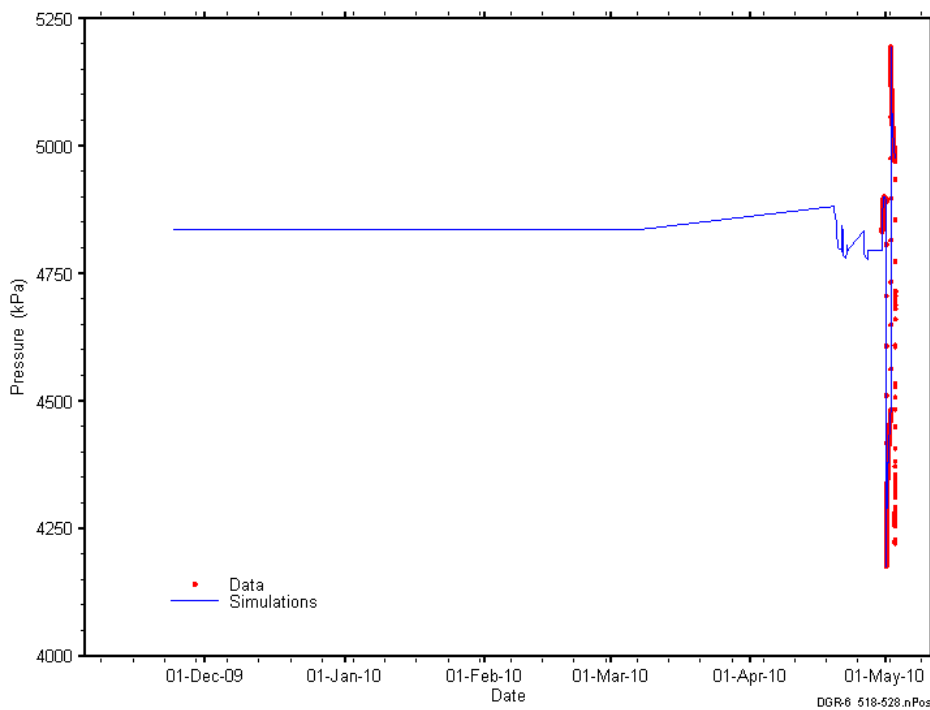


Figure F-9: Linear plot showing simulations of the DGR6_453.30-462.80 pressure response, including pre-test pressure history.

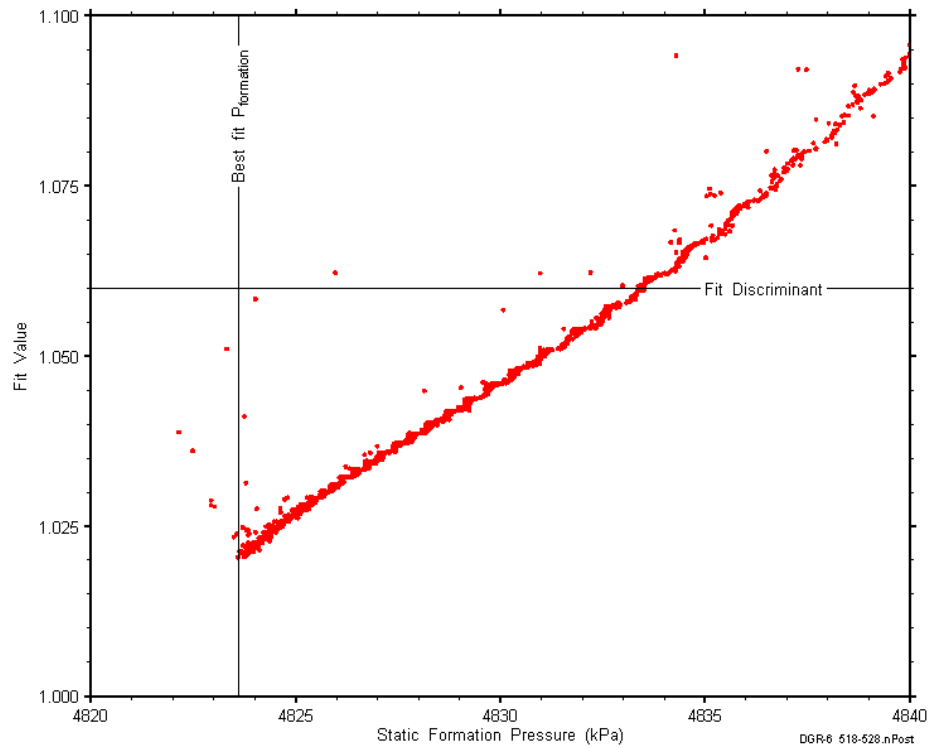


Figure F-10: XY-scatter plot showing the static formation pressure parameter space derived from DGR6_453.30-462.80 perturbation analysis along with the fit discriminant and best fit values.

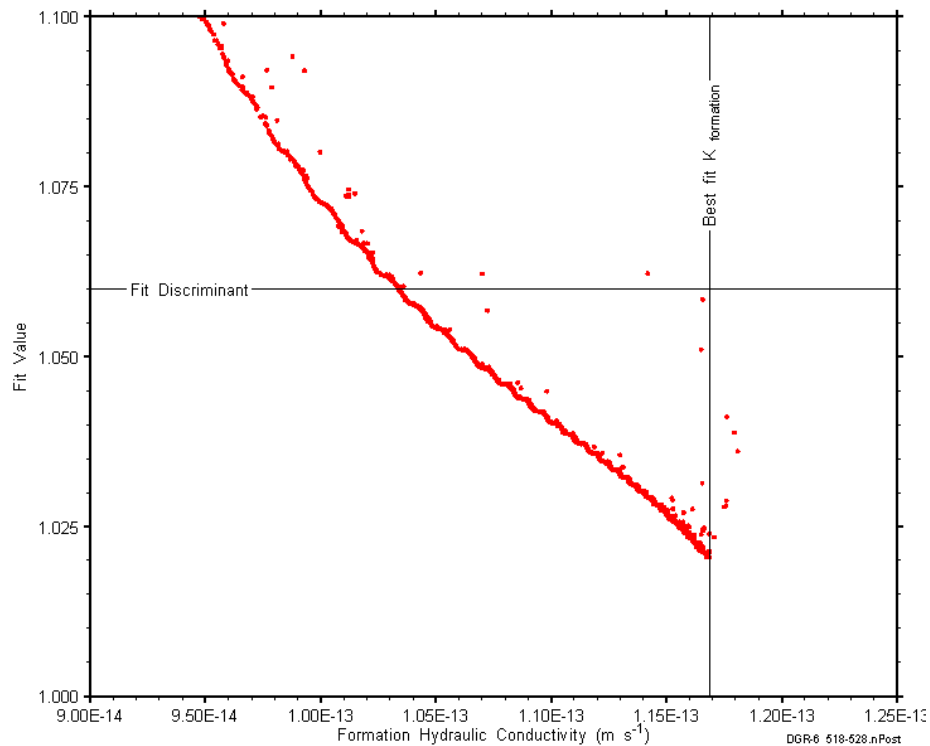


Figure F-11: XY-scatter plot showing the formation hydraulic conductivity parameter space derived from DGR6_453.30-462.80 perturbation analysis along with the fit discriminant and best fit values.

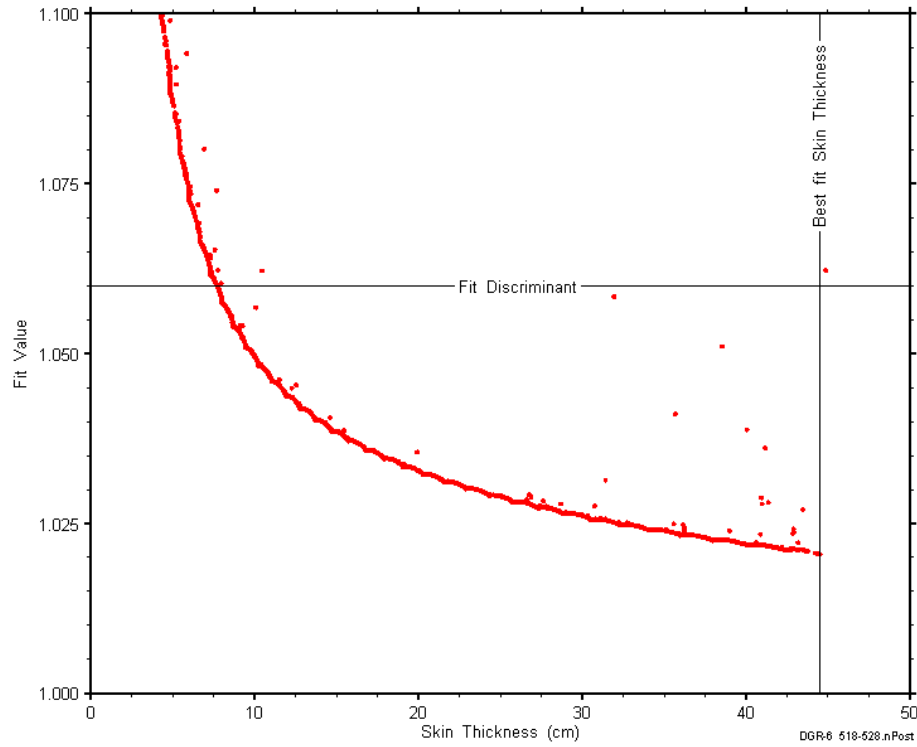


Figure F-12: XY-scatter plot showing the skin-thickness parameter space derived from DGR6_453.30-462.80 perturbation analysis along with the fit discriminant and best fit values.

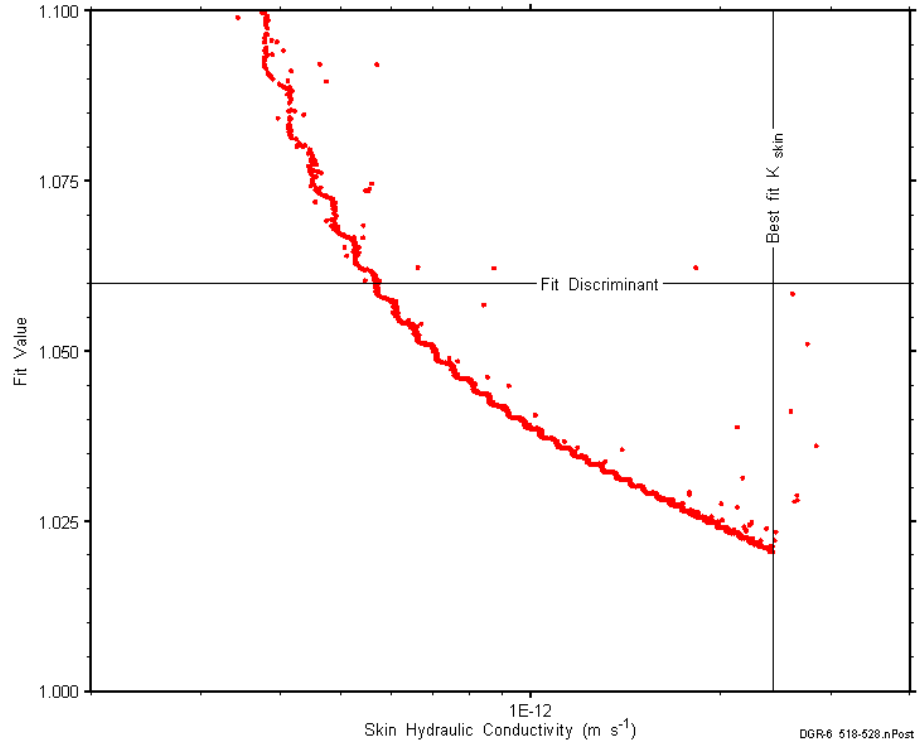


Figure F-13: XY-scatter plot showing the skin hydraulic conductivity parameter space derived from DGR6_453.30-462.80 perturbation analysis along with the fit discriminant and best fit values.

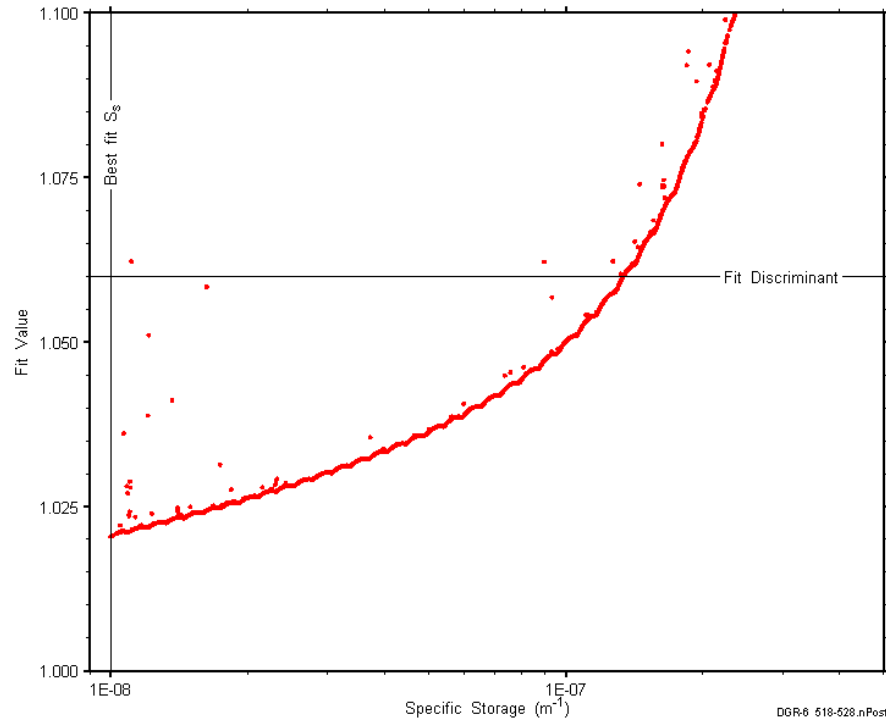


Figure F-14: XY-scatter plot showing the formation specific storage parameter space derived from DGR6_453.30-462.80 perturbation analysis along with the fit discriminant and best fit values.

F.2 572.46-581.09 Georgian Bay

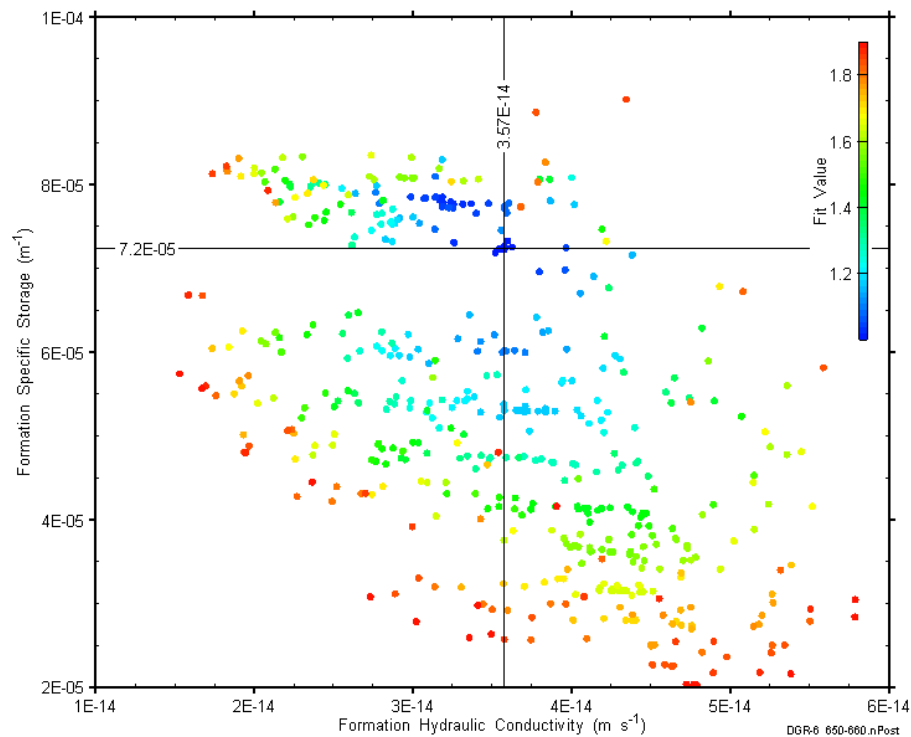


Figure F-15: XY-scatter plot showing estimates of formation hydraulic conductivity and formation specific storage derived from the DGR6_572.46-581.09 perturbation analysis.

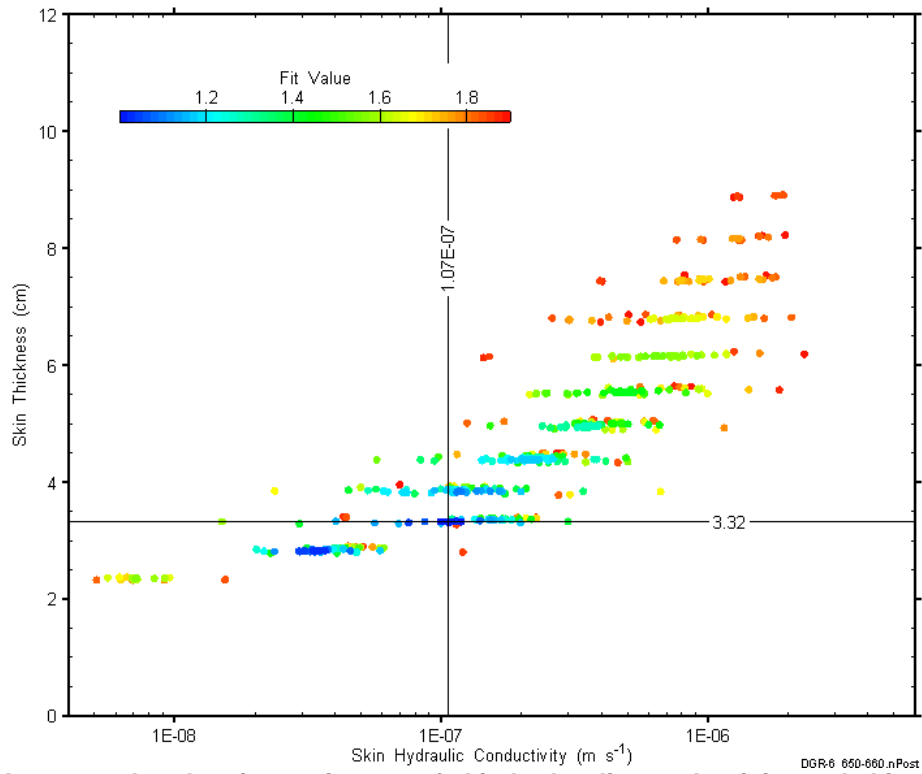


Figure F-16: XY-scatter plot showing estimates of skin hydraulic conductivity and skin thickness derived from the DGR6_572.46-581.09 perturbation analysis.

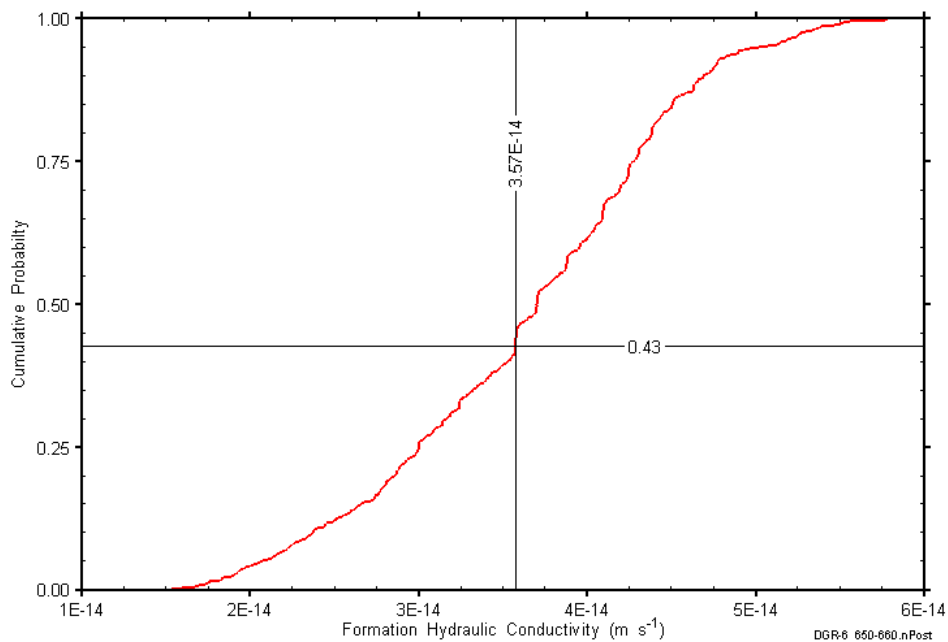


Figure F-17: DGR6_572.46-581.09 formation hydraulic conductivity cumulative distribution function.

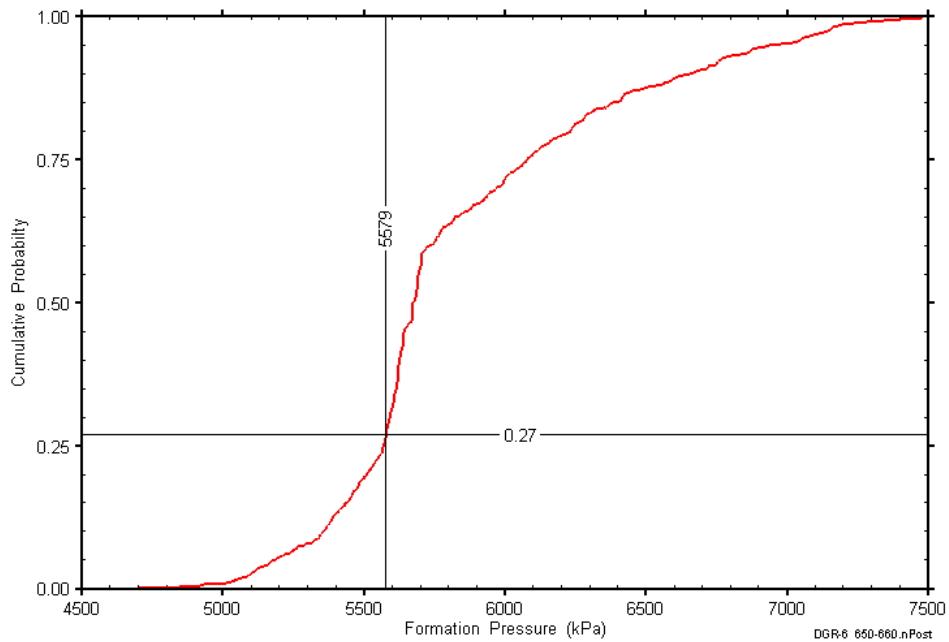


Figure F-18: DGR6_572.46-581.09 static formation pressure cumulative distribution function.

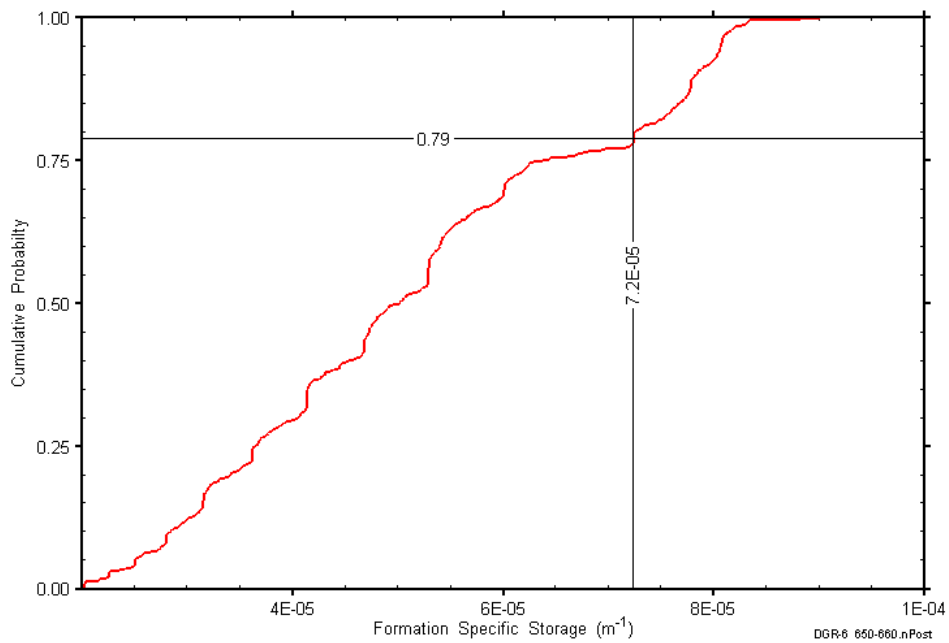


Figure F-19: DGR6_572.46-581.09 formation specific storage cumulative distribution function.

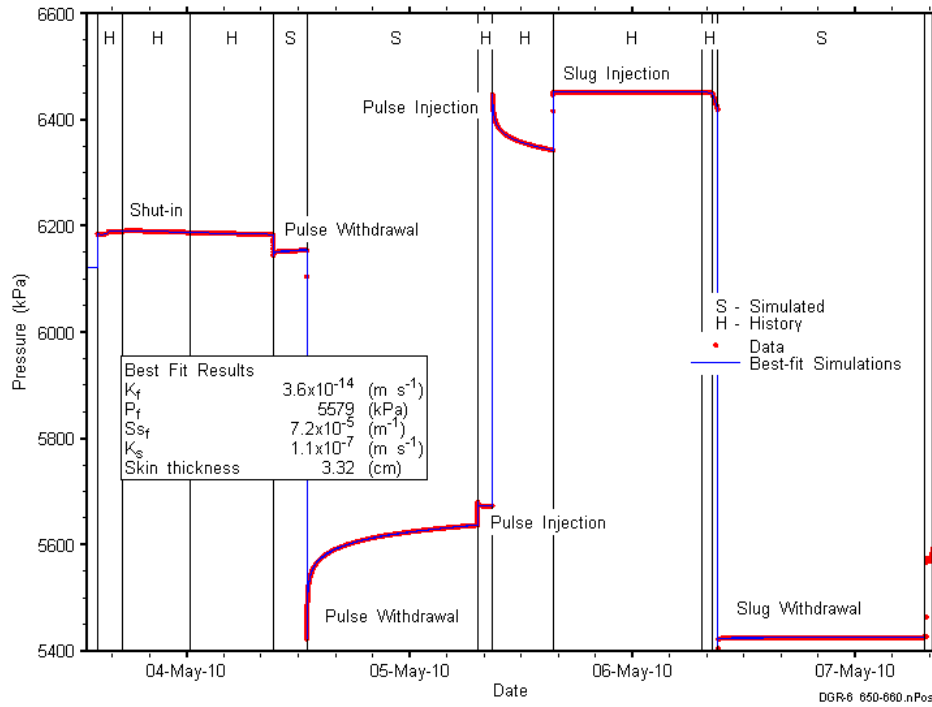


Figure F-20: Linear plot showing simulations of the DGR6_572.46-581.09 pressure response.

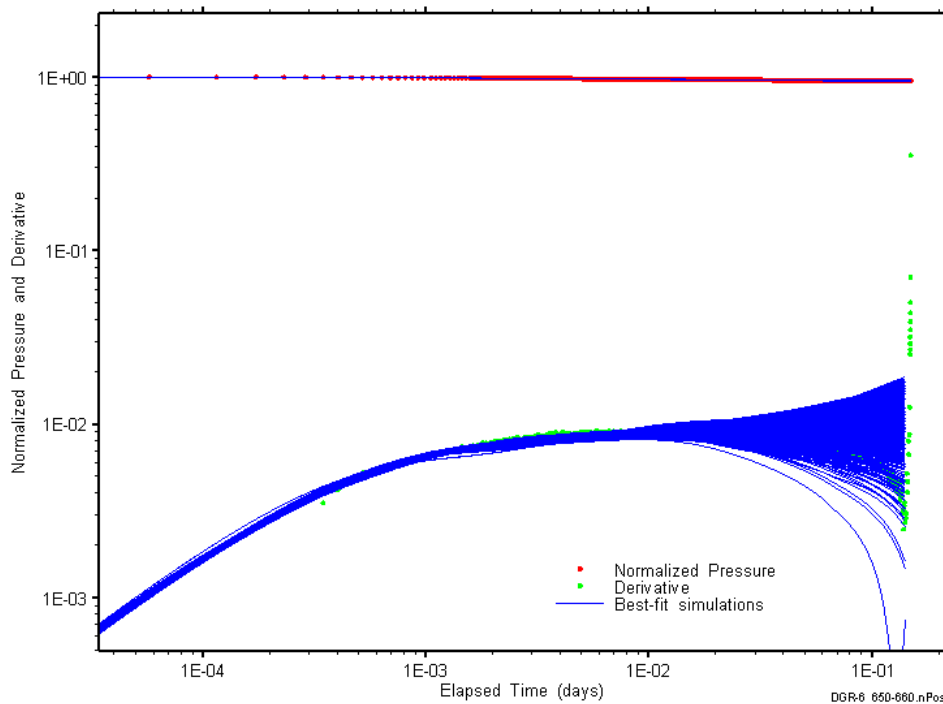


Figure F-21: Log-log plot showing simulations of the DGR6_572.46-581.09 PW1 Ramey B and derivative response.

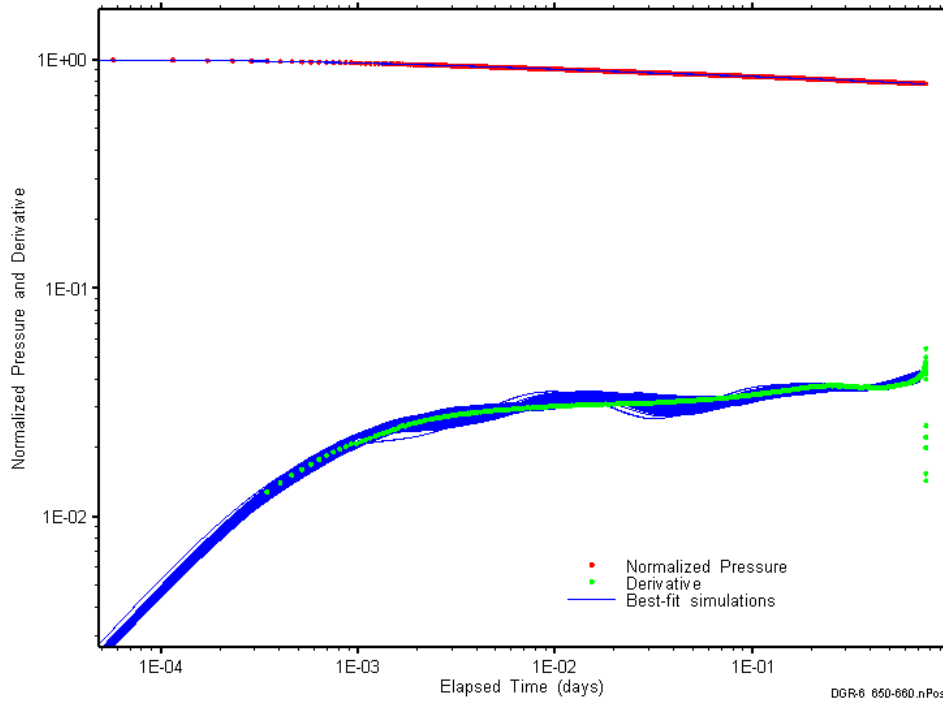


Figure F-22: Log-log plot showing simulations of the DGR6_572.46-581.09 PW2 Ramey B and derivative response.

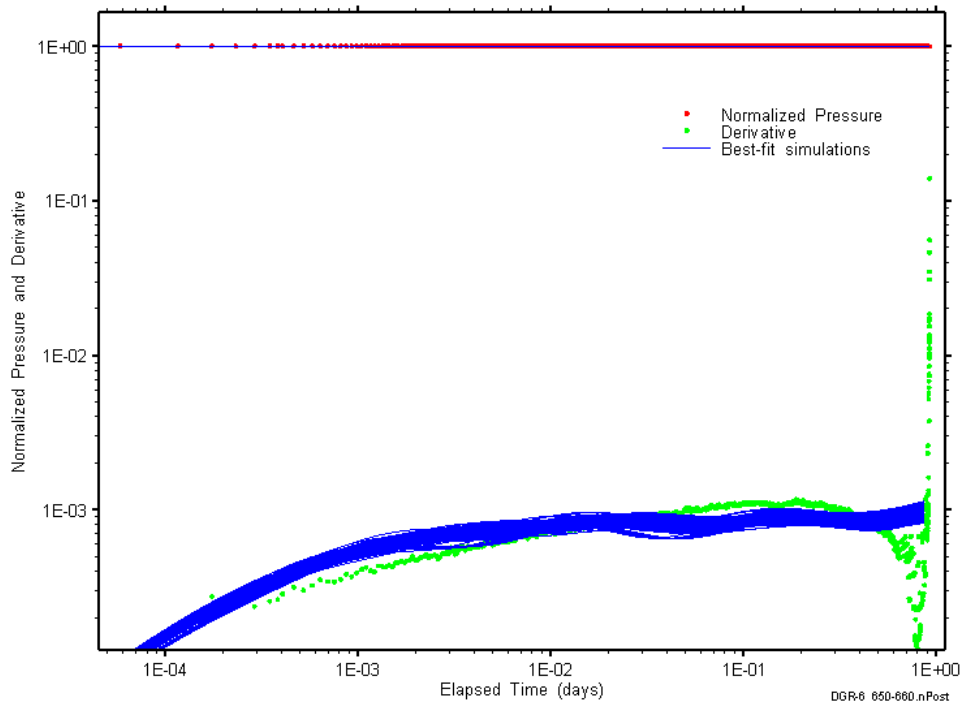


Figure F-23: Log-log plot showing simulations of the DGR6_572.46-581.09 PW Ramey B and derivative response.

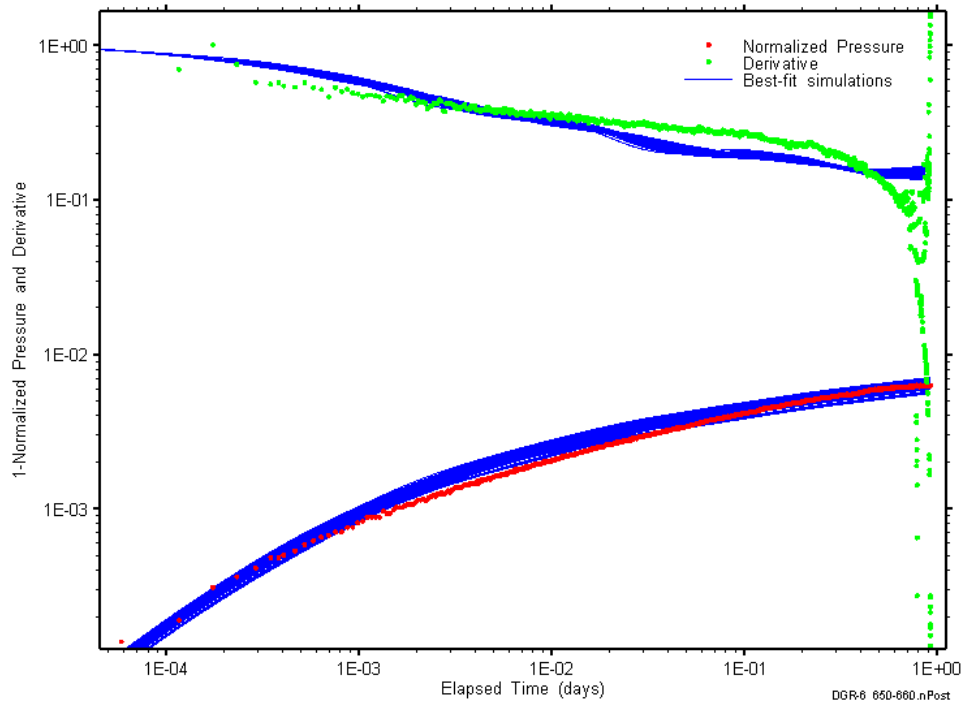


Figure F-24: Log-log plot showing simulations of the DGR6_572.46-581.09 SW Ramey C and derivative response.

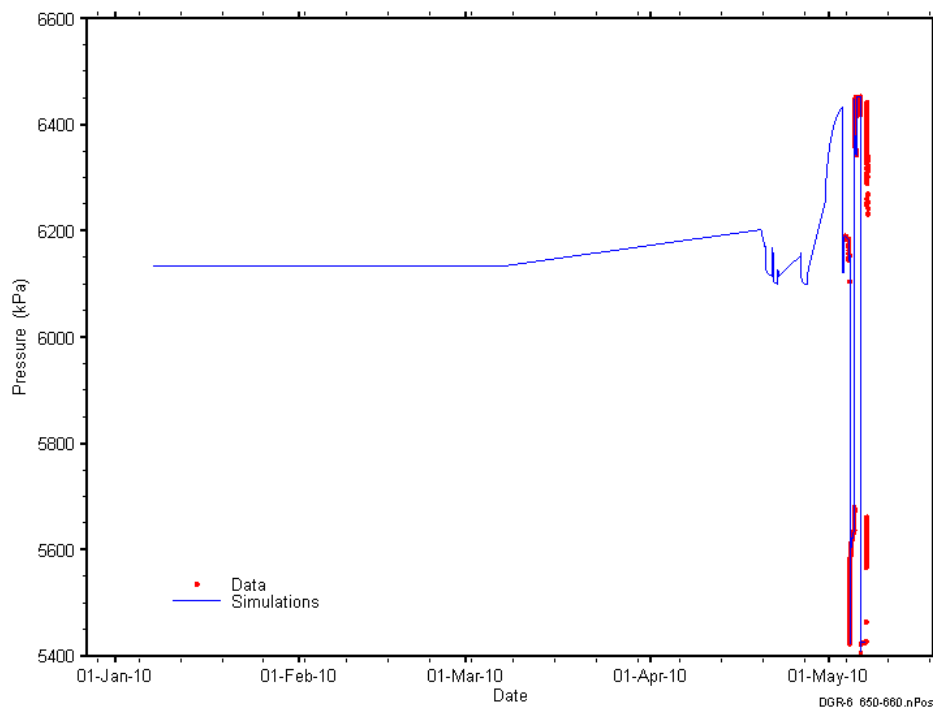


Figure F-25: Linear plot showing simulations of the DGR6_572.46-581.09 pressure response, including pre-test pressure history.

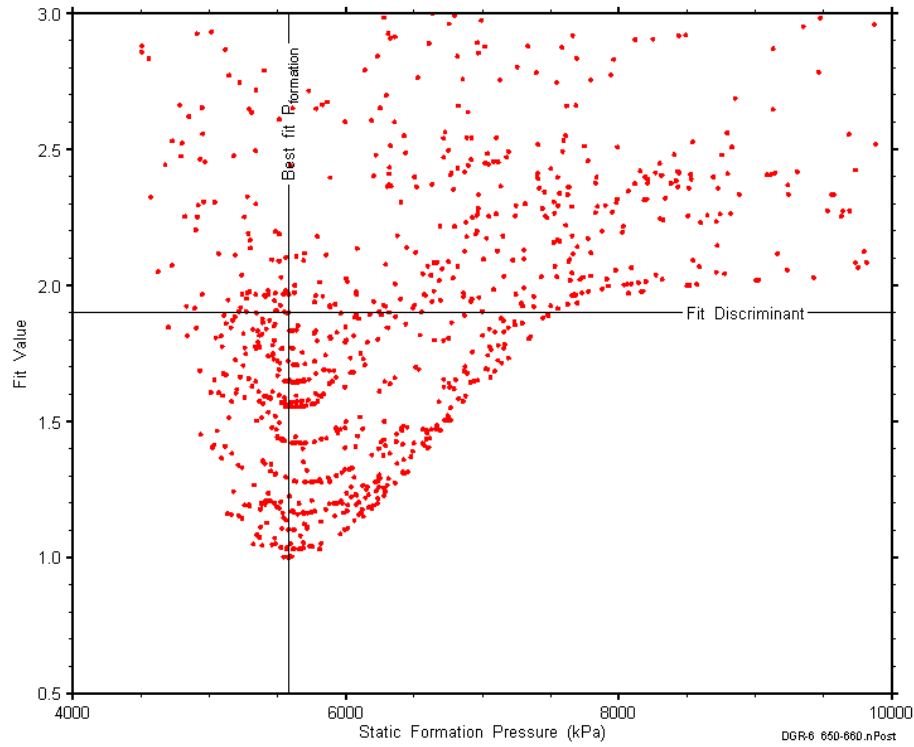


Figure F-26: XY-scatter plot showing the static formation pressure parameter space derived from DGR6_572.46-581.09 perturbation analysis along with the fit discriminant and best fit values.

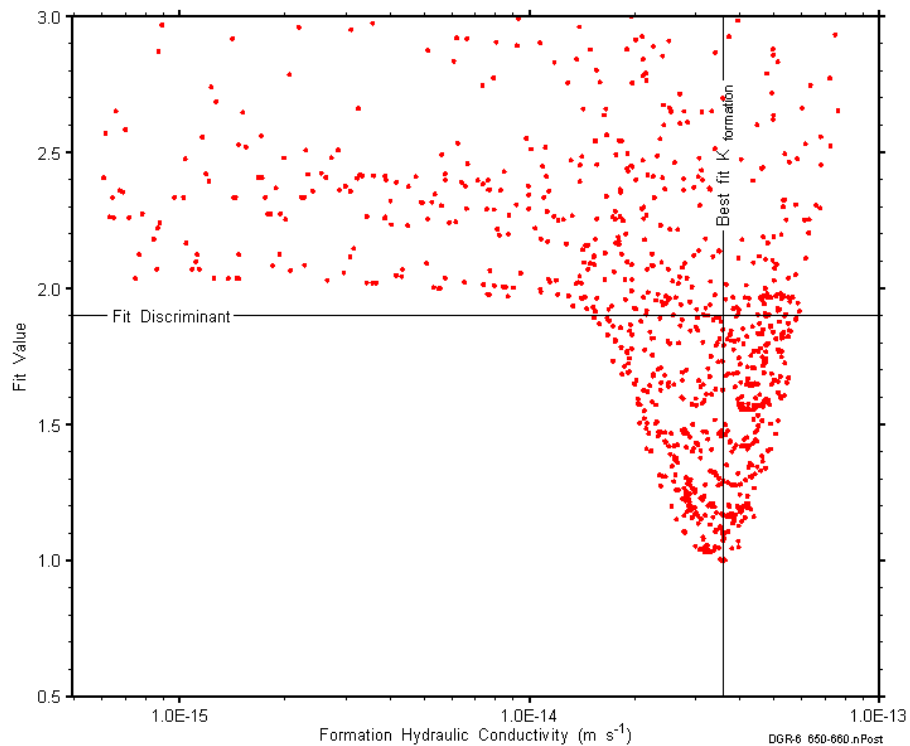


Figure F-27: XY-scatter plot showing the formation hydraulic conductivity parameter space derived from DGR6_572.46-581.09 perturbation analysis along with the fit discriminant and best fit values.

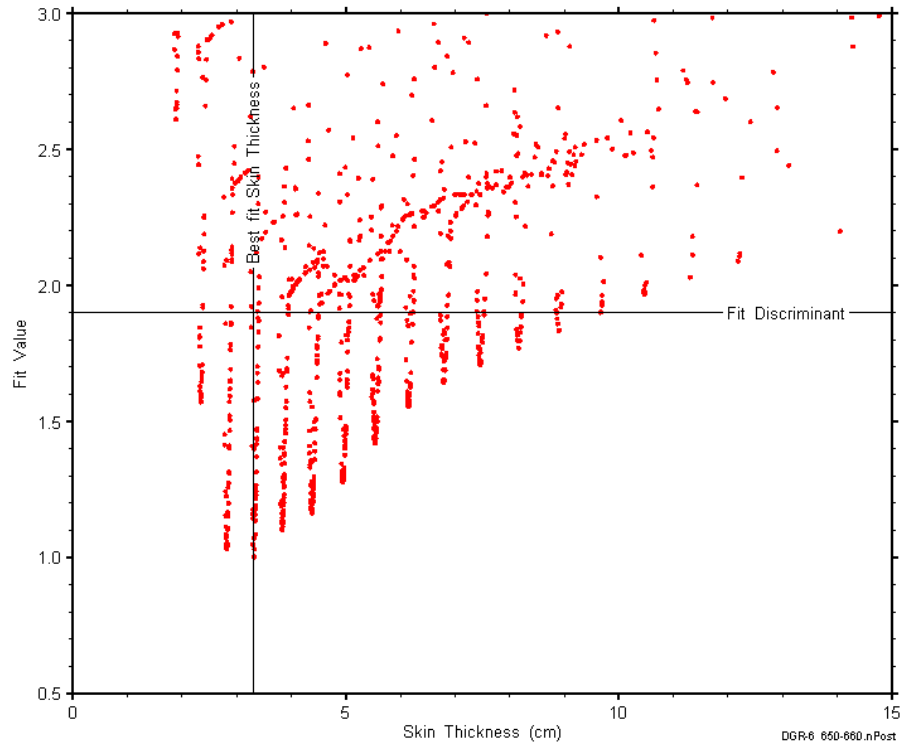


Figure F-28: XY-scatter plot showing the skin-thickness parameter space derived from DGR6_572.46-581.09 perturbation analysis along with the fit discriminant and best fit values.

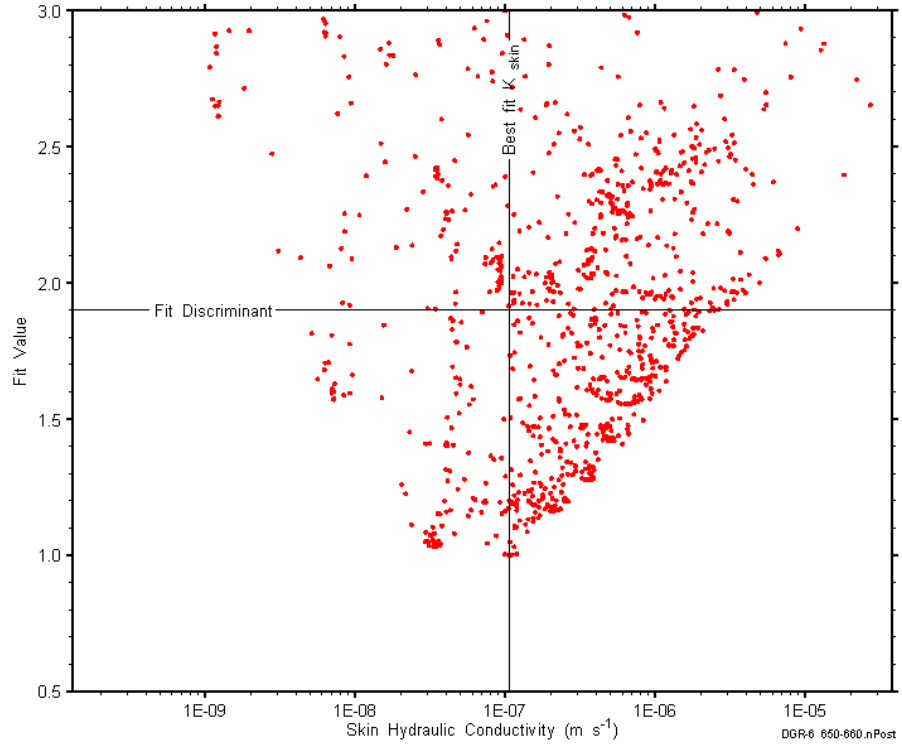


Figure F-29: XY-scatter plot showing the skin hydraulic conductivity parameter space derived from DGR6_572.46-581.09 perturbation analysis along with the fit discriminant and best fit values.

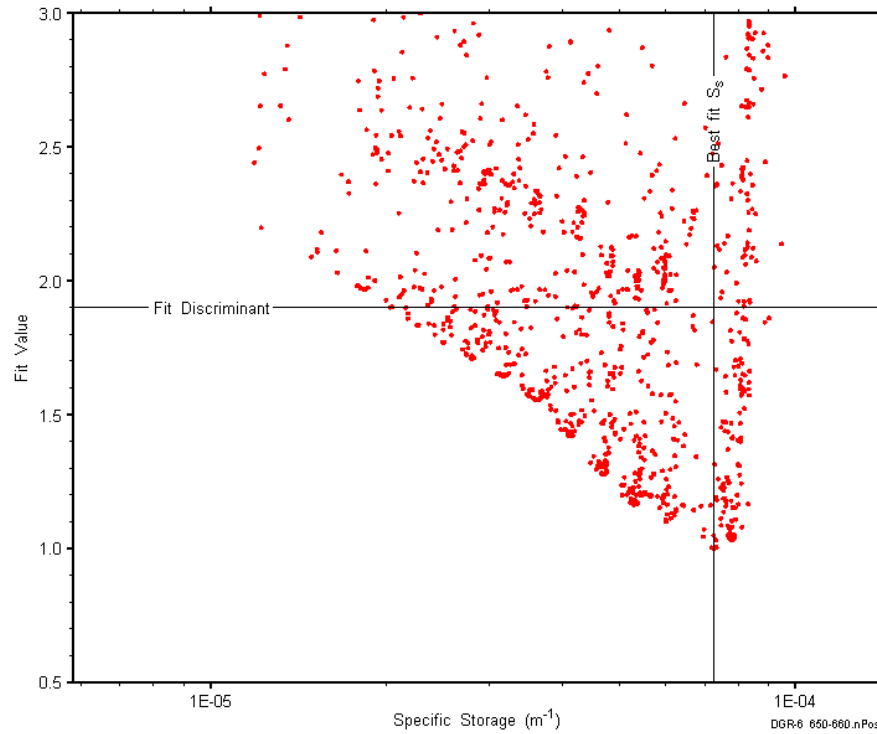


Figure F-30: XY-scatter plot showing the formation specific storage parameter space derived from DGR6_572.46-581.09 perturbation analysis along with the fit discriminant and best fit values.

F.3 596.02-604.60 Georgian Bay

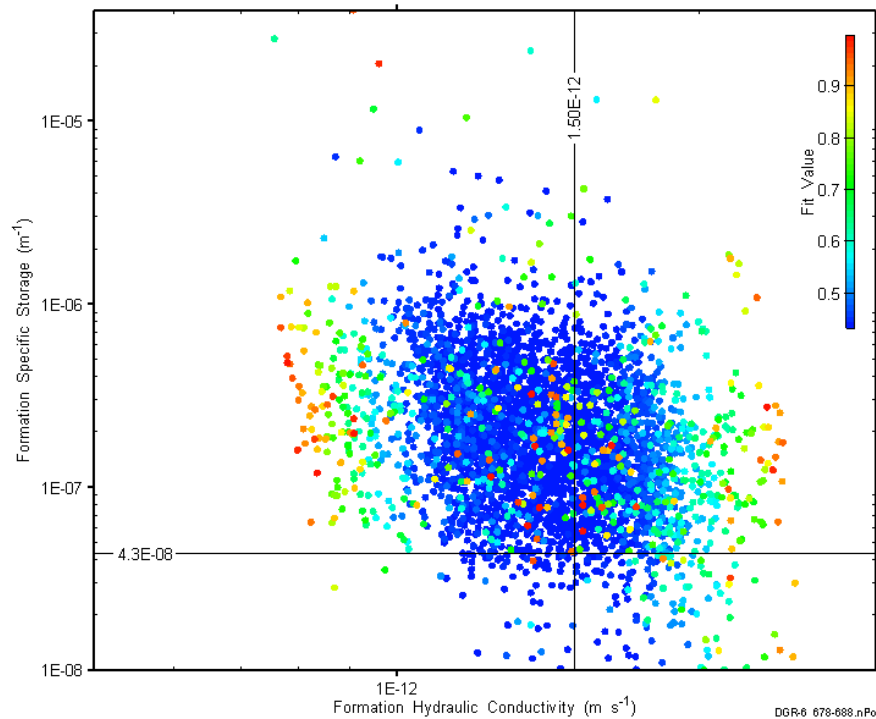


Figure F-31: XY-scatter plot showing estimates of formation hydraulic conductivity and formation specific storage derived from the DGR6_596.02-604.60 perturbation analysis.

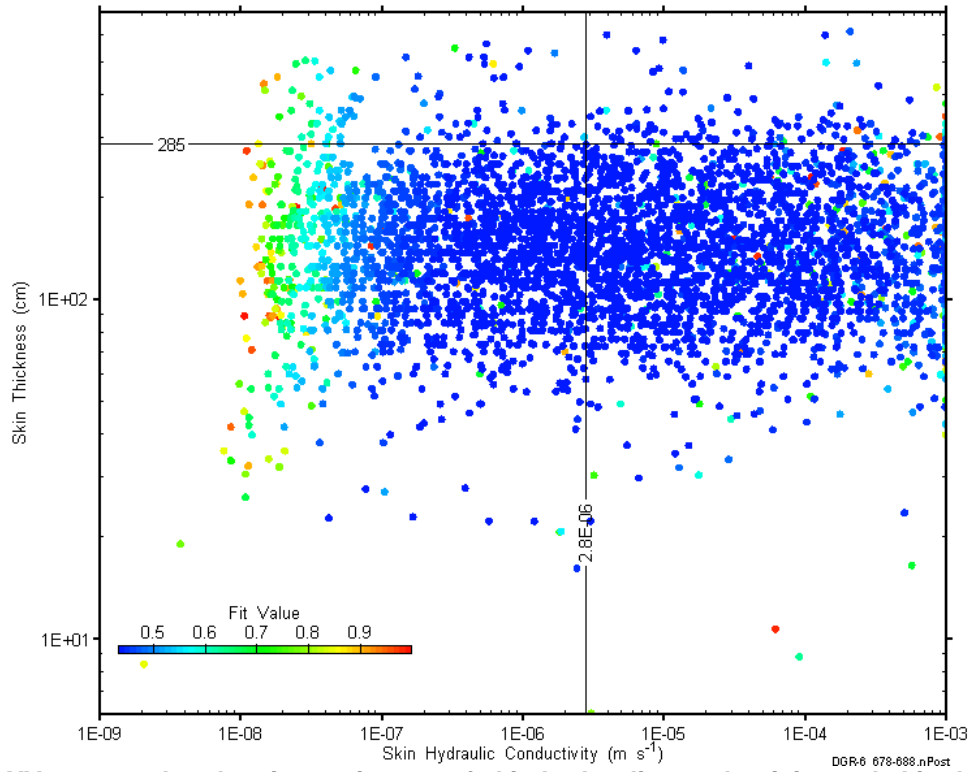


Figure F-32: XY-scatter plot showing estimates of skin hydraulic conductivity and skin thickness derived from the DGR6_596.02-604.60 perturbation analysis.

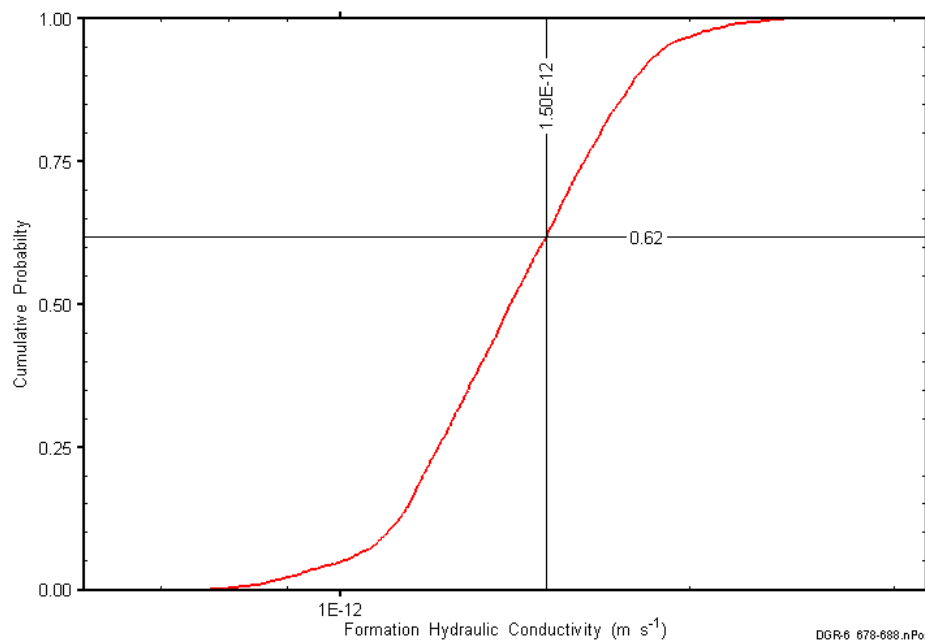


Figure F-33: DGR6_596.02-604.60 formation hydraulic conductivity cumulative distribution function.

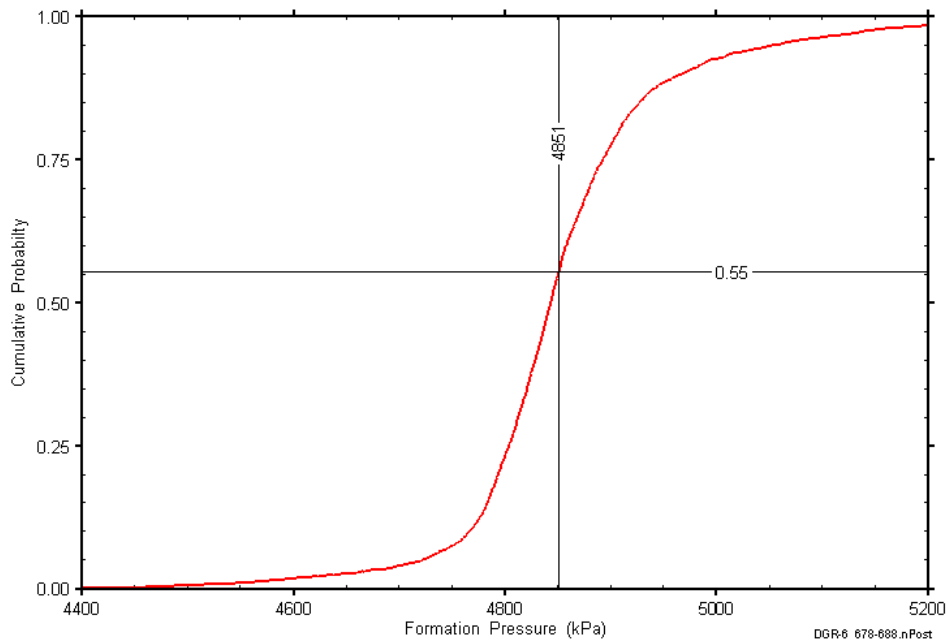


Figure F-34: DGR6_596.02-604.60 static formation pressure cumulative distribution function.

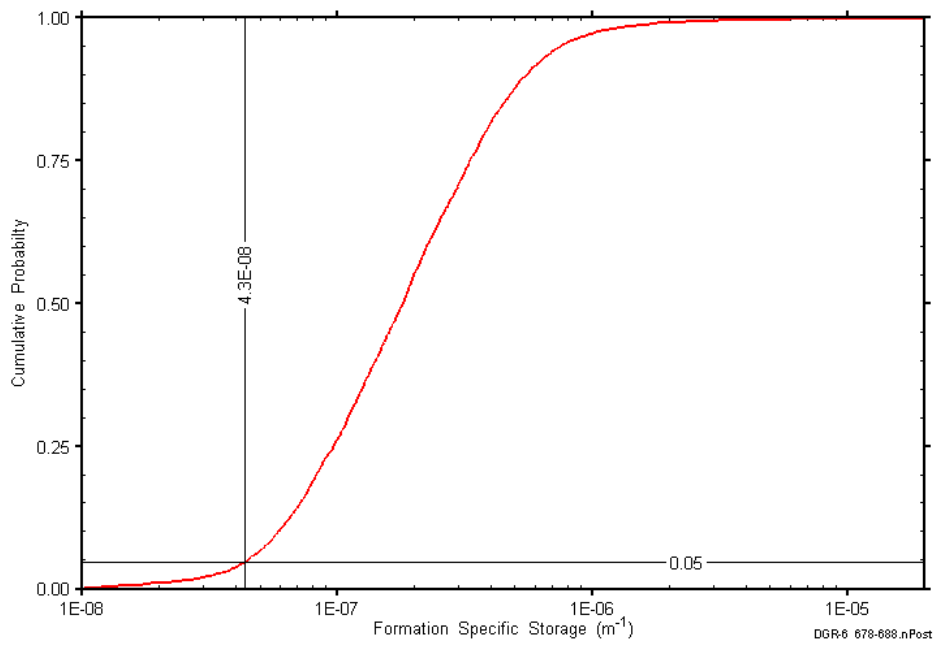


Figure F-35: DGR6_596.02-604.60 formation specific storage cumulative distribution function.

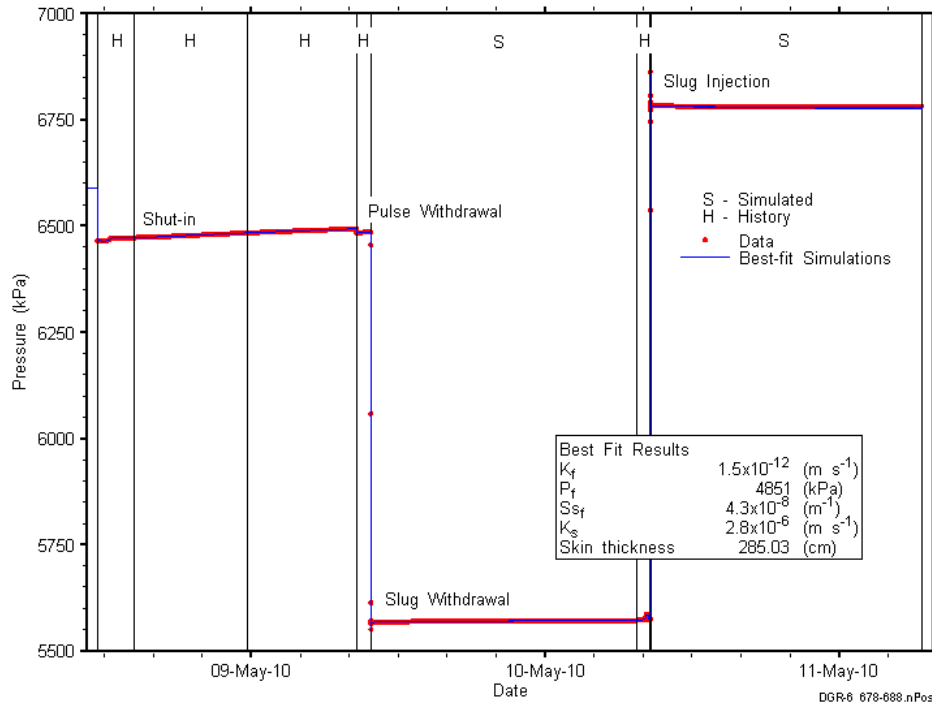


Figure F-36: Linear plot showing simulations of the DGR6_596.02-604.60 pressure response.

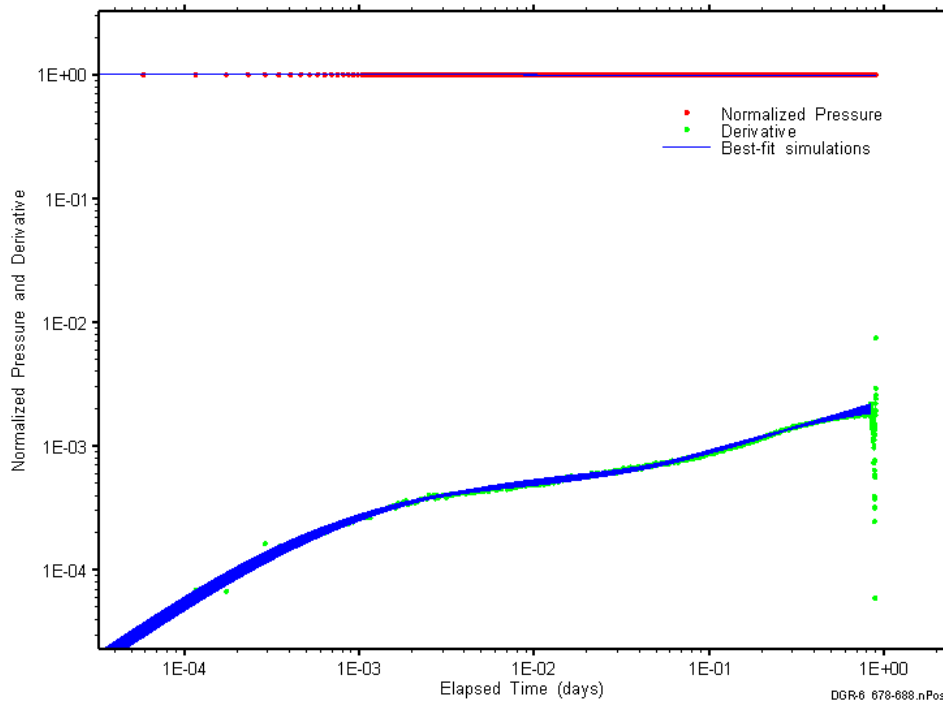


Figure F-37: Log-log plot showing simulations of the DGR6_596.02-604.60 SW Ramey B and derivative response.

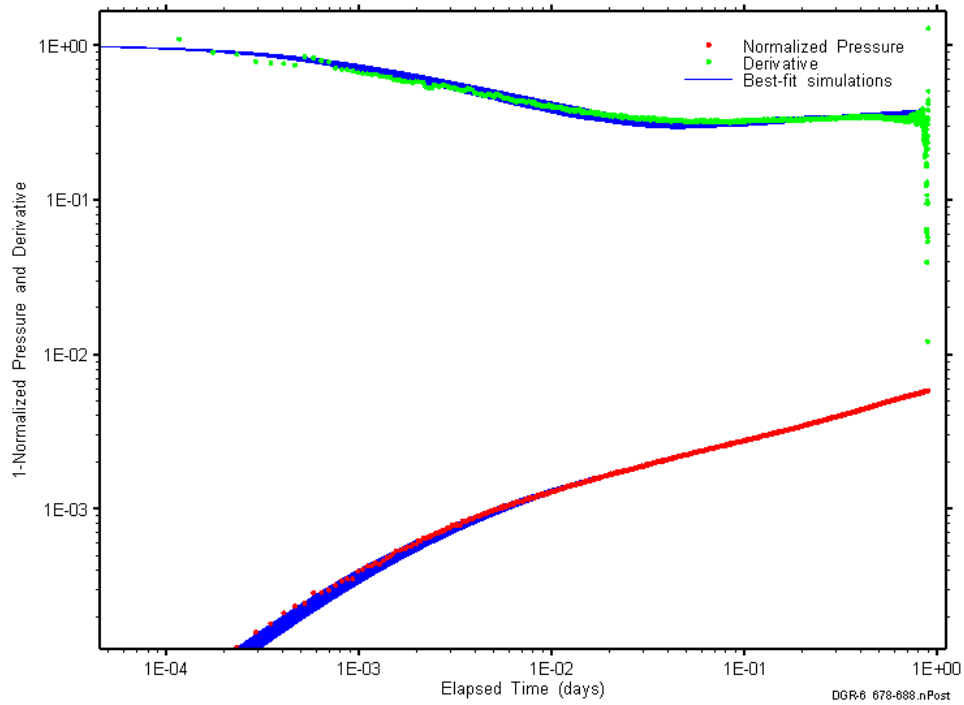


Figure F-38: Log-log plot showing simulations of the DGR6_596.02-604.60 SW Ramey C and derivative response.

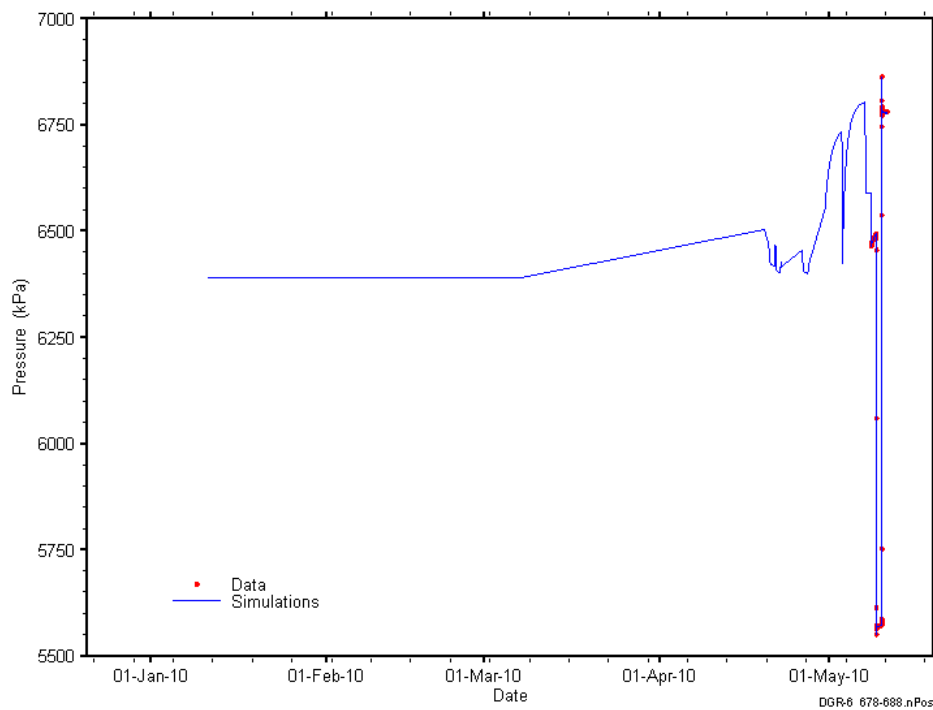


Figure F-39: Linear plot showing simulations of the DGR6_596.02-604.60 pressure response, including pre-test pressure history.

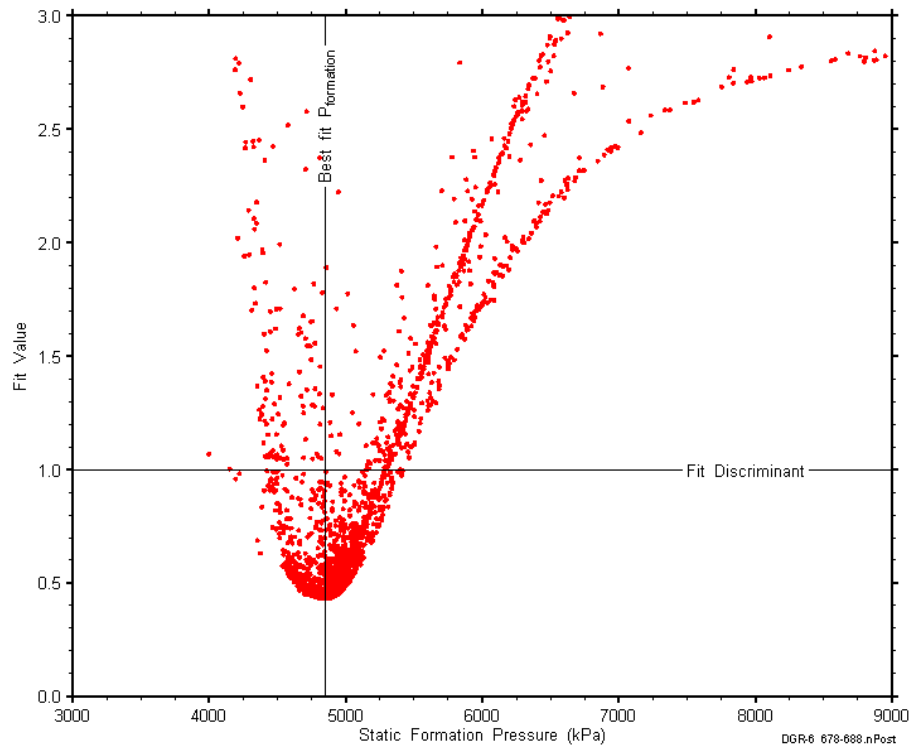


Figure F-40: XY-scatter plot showing the static formation pressure parameter space derived from DGR6_596.02-604.60 perturbation analysis along with the fit discriminant and best fit values.

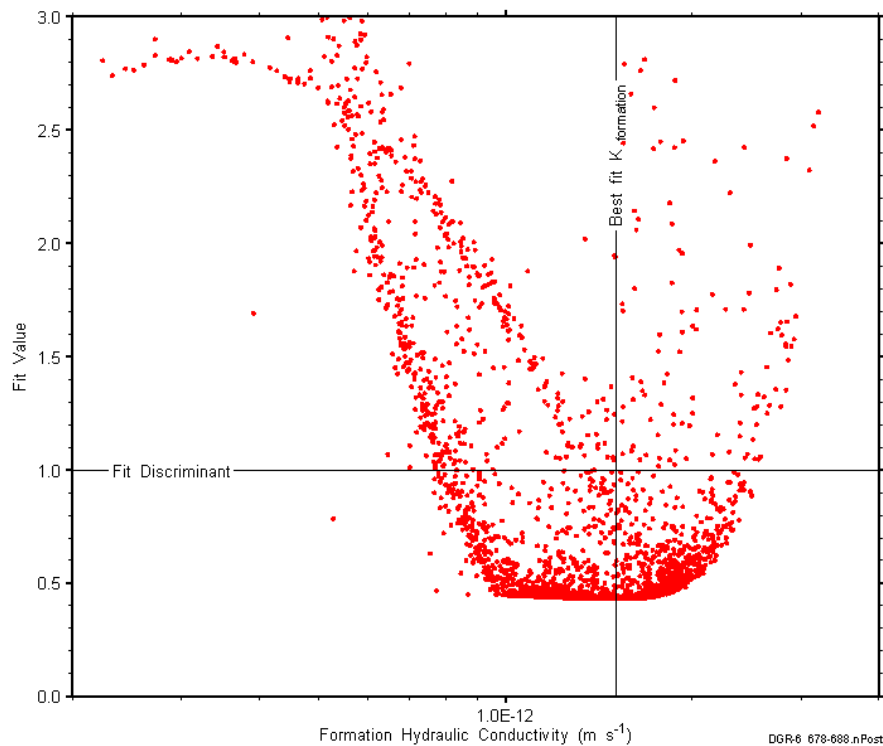


Figure F-41: XY-scatter plot showing the formation hydraulic conductivity parameter space derived from DGR6_596.02-604.60 perturbation analysis along with the fit discriminant and best fit values.

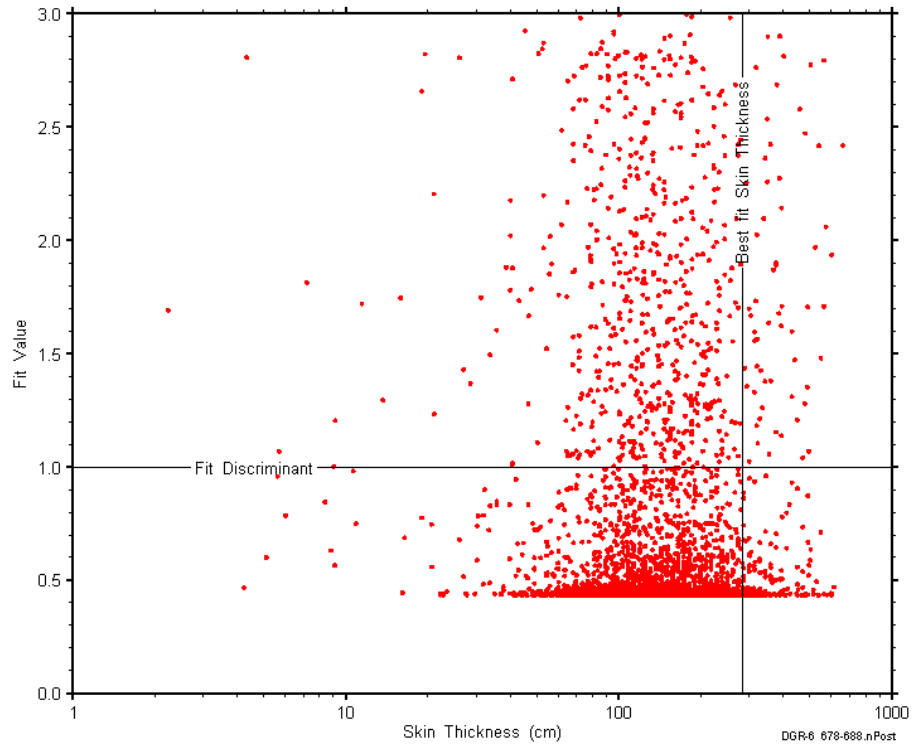


Figure F-42: XY-scatter plot showing the skin-thickness parameter space derived from DGR6_596.02-604.60 perturbation analysis along with the fit discriminant and best fit values.

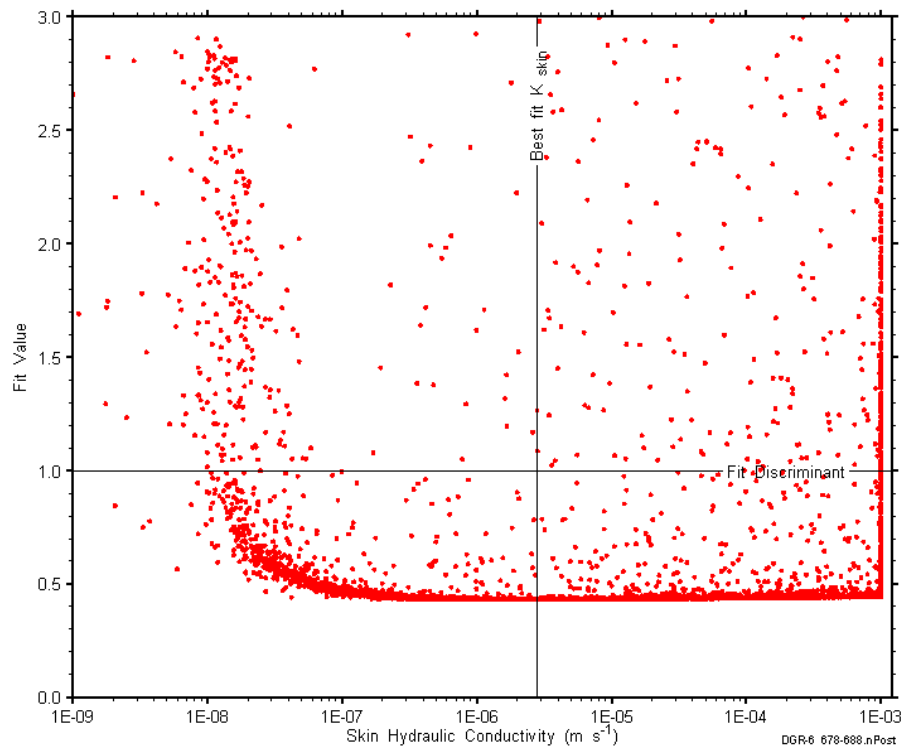


Figure F-43: XY-scatter plot showing the skin hydraulic conductivity parameter space derived from DGR6_596.02-604.60 perturbation analysis along with the fit discriminant and best fit values.

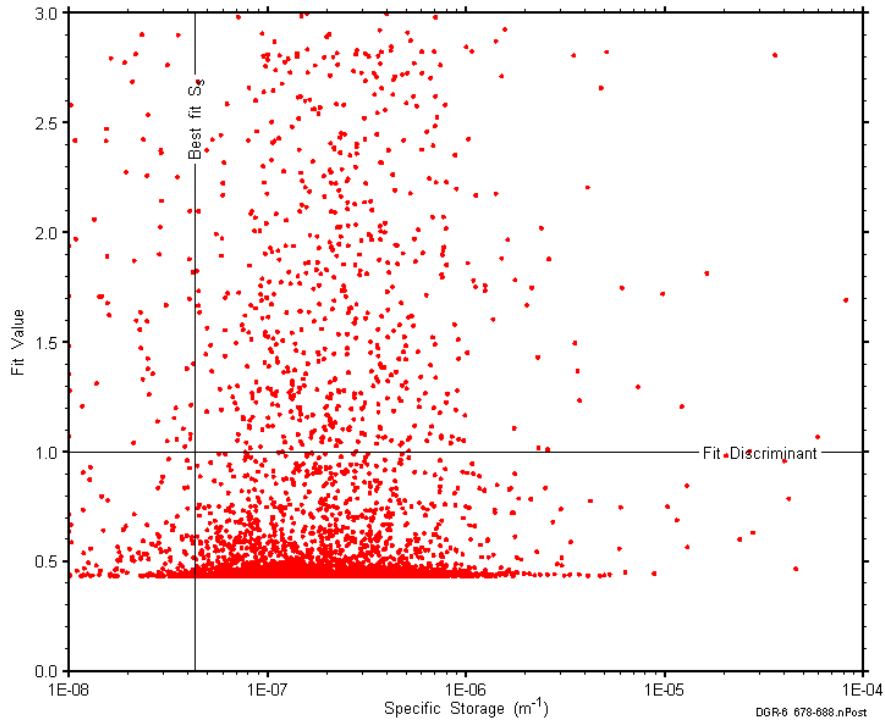


Figure F-44: XY-scatter plot showing the formation specific storage parameter space derived from DGR6_596.02-604.60 perturbation analysis along with the fit discriminant and best fit values.

F.4 614.49-623.14 Blue Mountain

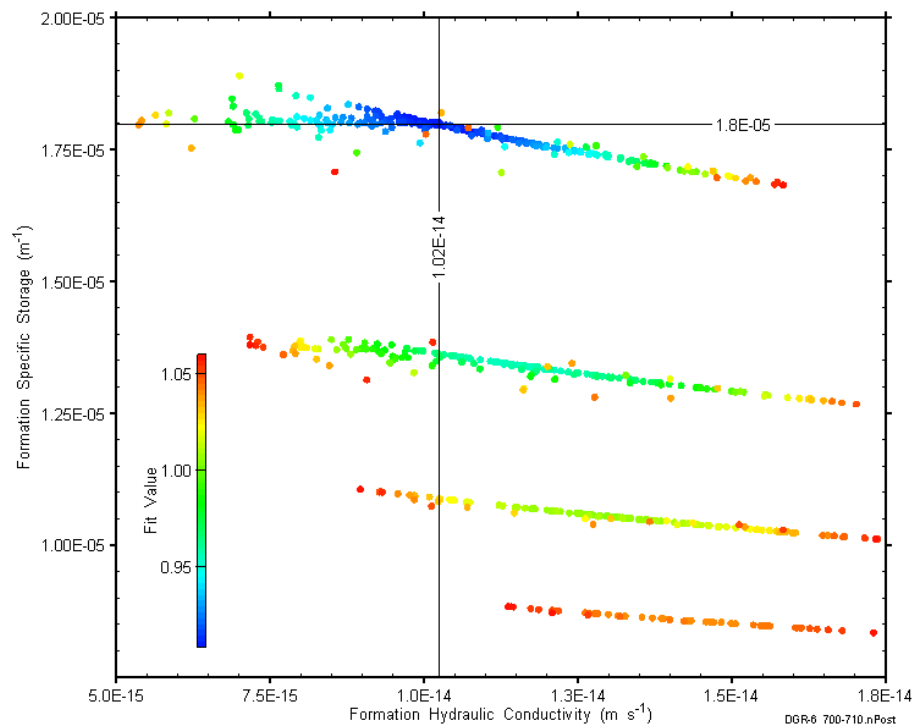


Figure F-45: XY-scatter plot showing estimates of formation hydraulic conductivity and formation specific storage derived from the DGR6_614.49-623.14 perturbation analysis.

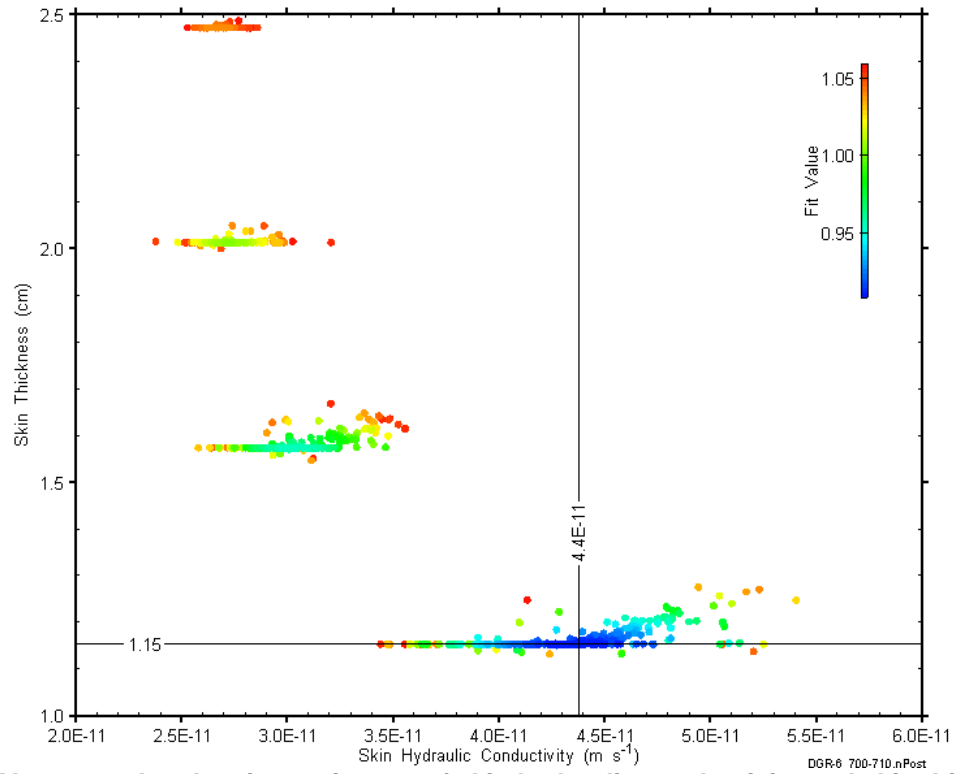


Figure F-46: XY-scatter plot showing estimates of skin hydraulic conductivity and skin thickness derived from the DGR6_614.49-623.14 perturbation analysis.

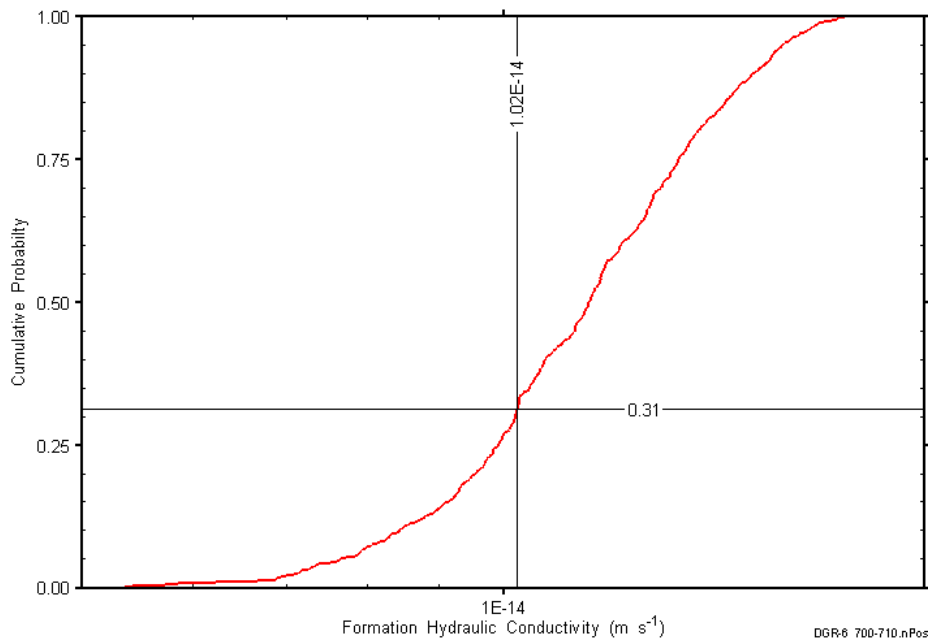


Figure F-47: DGR6_614.49-623.14 formation hydraulic conductivity cumulative distribution function.

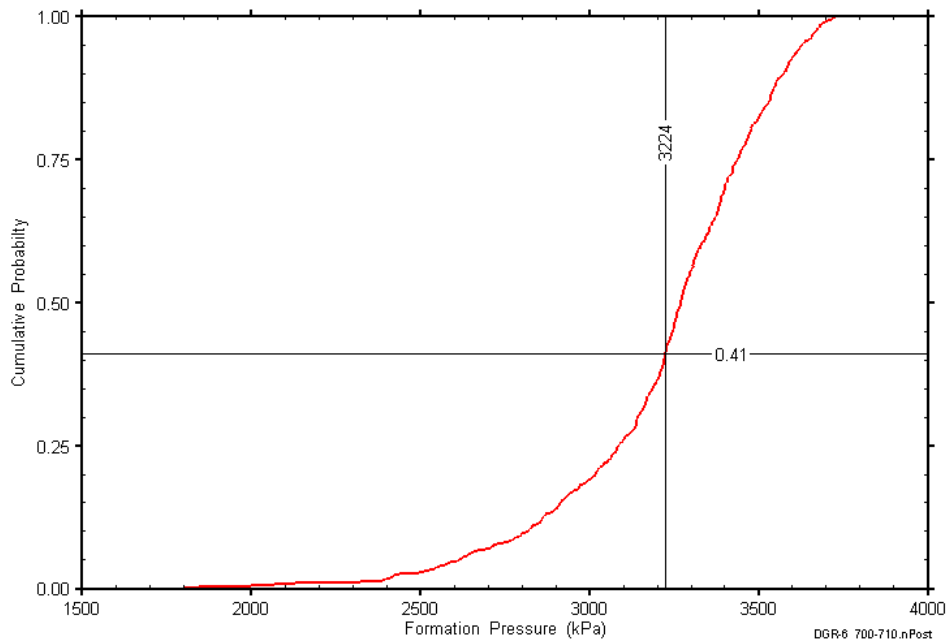


Figure F-48: DGR6_614.49-623.14 static formation pressure cumulative distribution function.

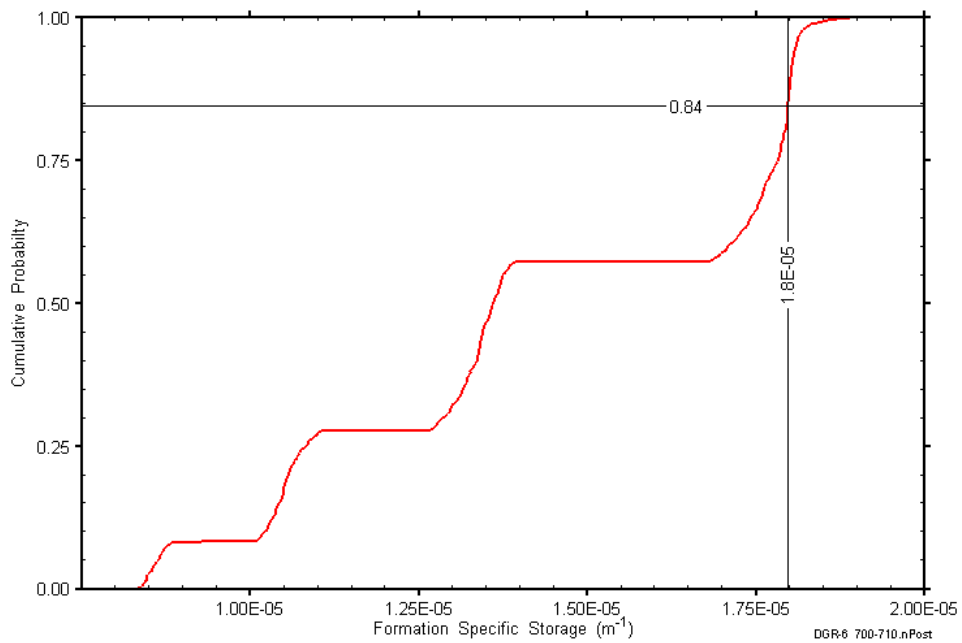


Figure F-49: DGR6_614.49-623.14 formation specific storage cumulative distribution function.

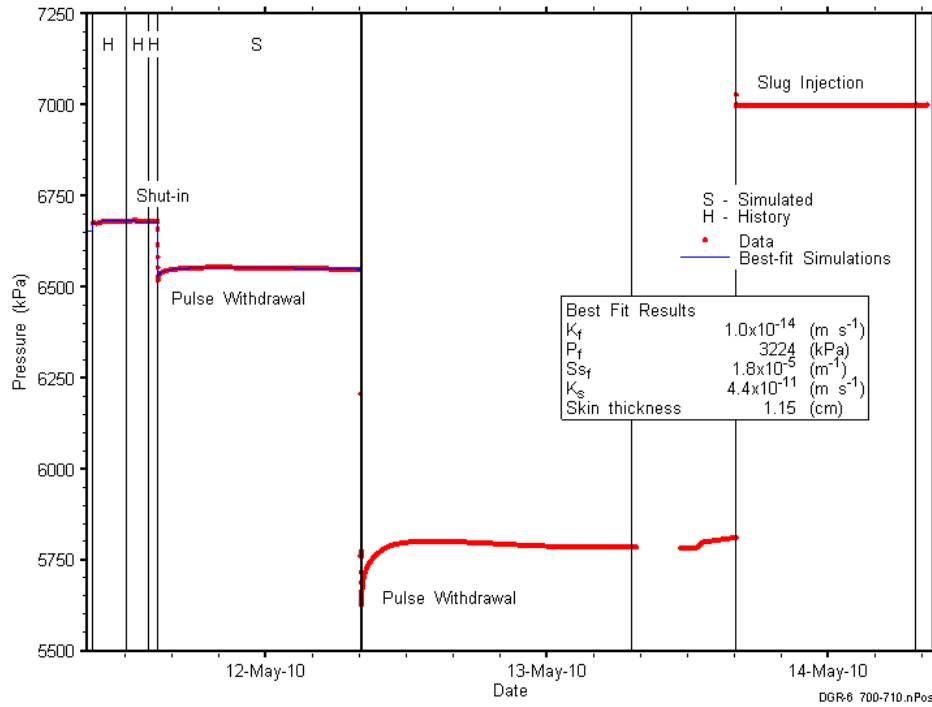


Figure F-50: Linear plot showing simulations of the DGR6_614.49-623.14 pressure response.

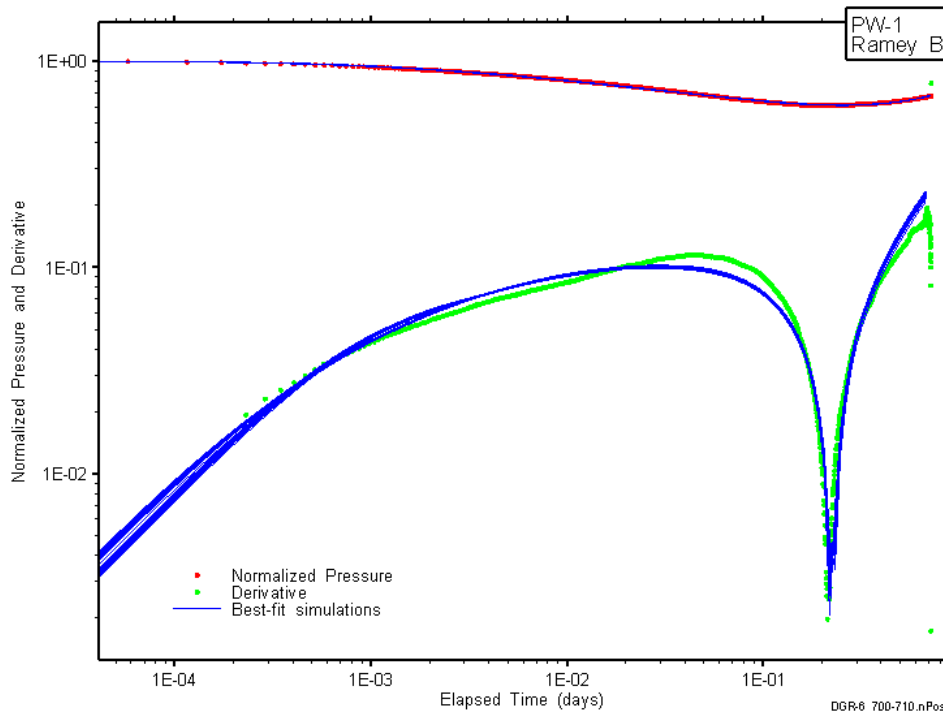


Figure F-51: Log-log plot showing simulations of the DGR6_614.49-623.14 PW1 Ramey B and derivative response.

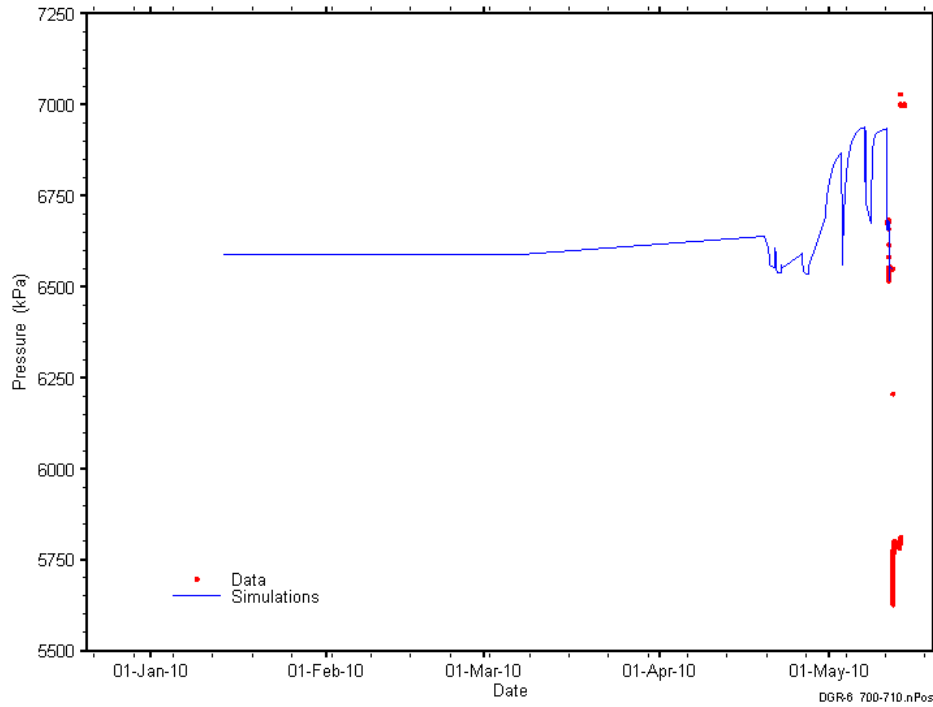


Figure F-52: Linear plot showing simulations of the DGR6_614.49-623.14 pressure response, including pre-test pressure history.

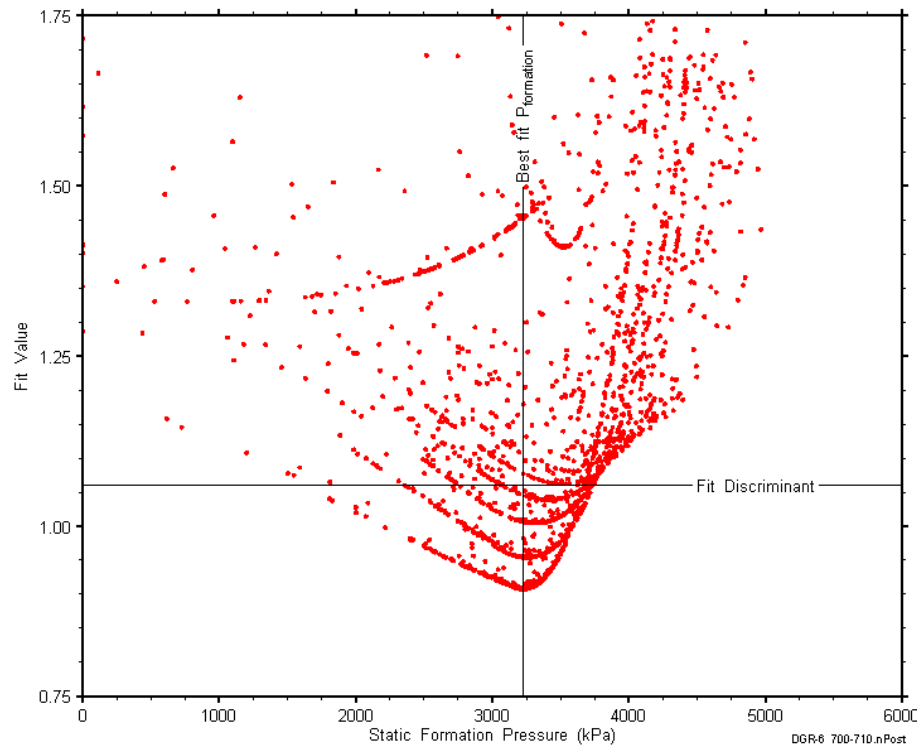


Figure F-53: XY-scatter plot showing the static formation pressure parameter space derived from DGR6_614.49-623.14 perturbation analysis along with the fit discriminant and best fit values.

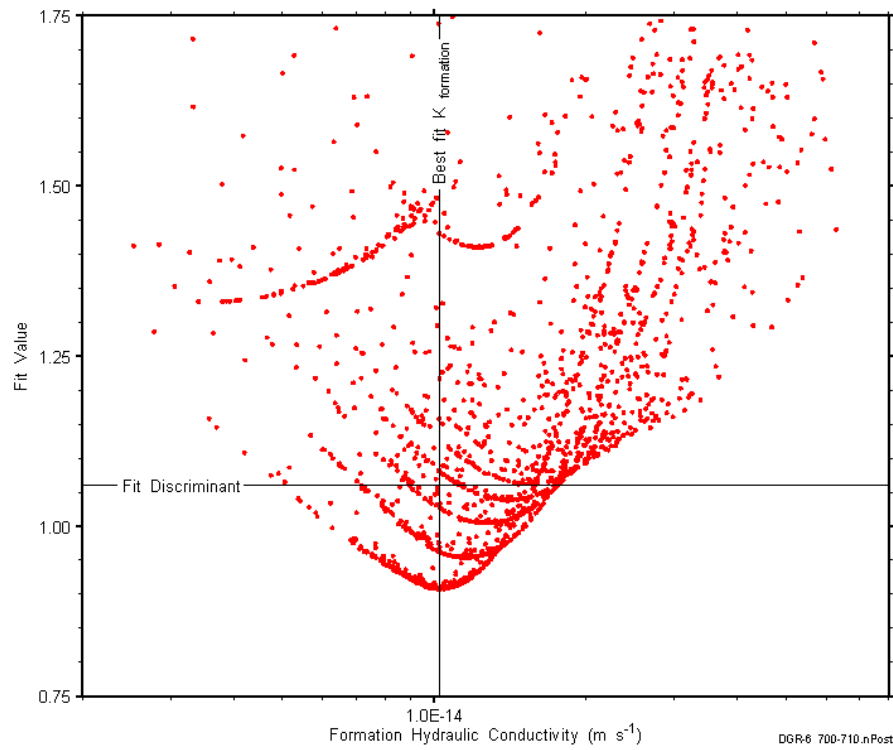


Figure F-54: XY-scatter plot showing the formation hydraulic conductivity parameter space derived from DGR6_614.49-623.14 perturbation analysis along with the fit discriminant and best fit values.

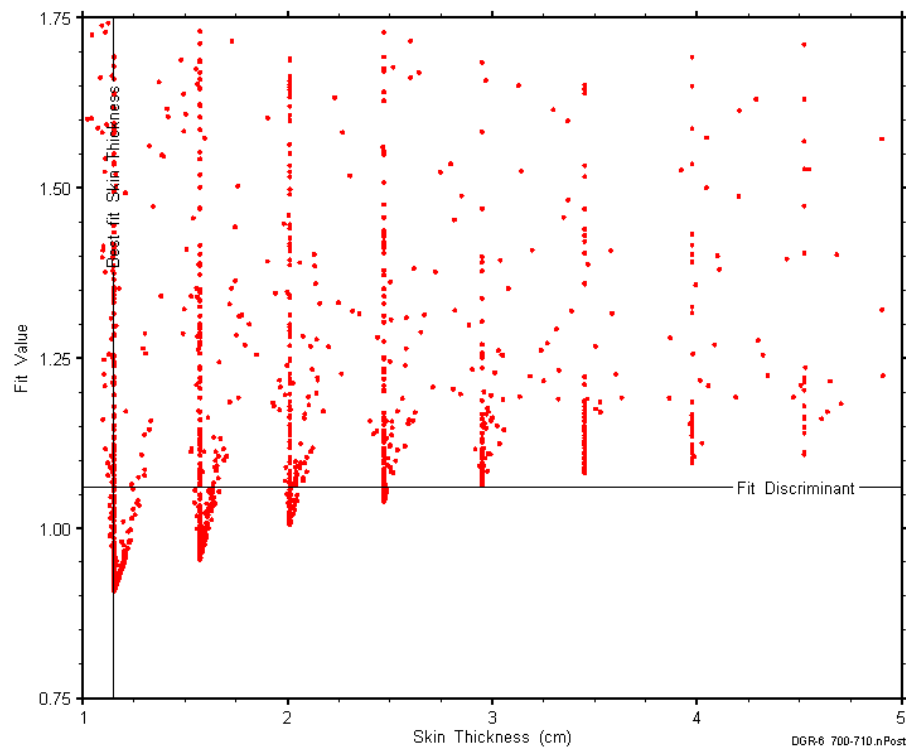


Figure F-55: XY-scatter plot showing the skin-thickness parameter space derived from DGR6_614.49-623.14 perturbation analysis along with the fit discriminant and best fit values.

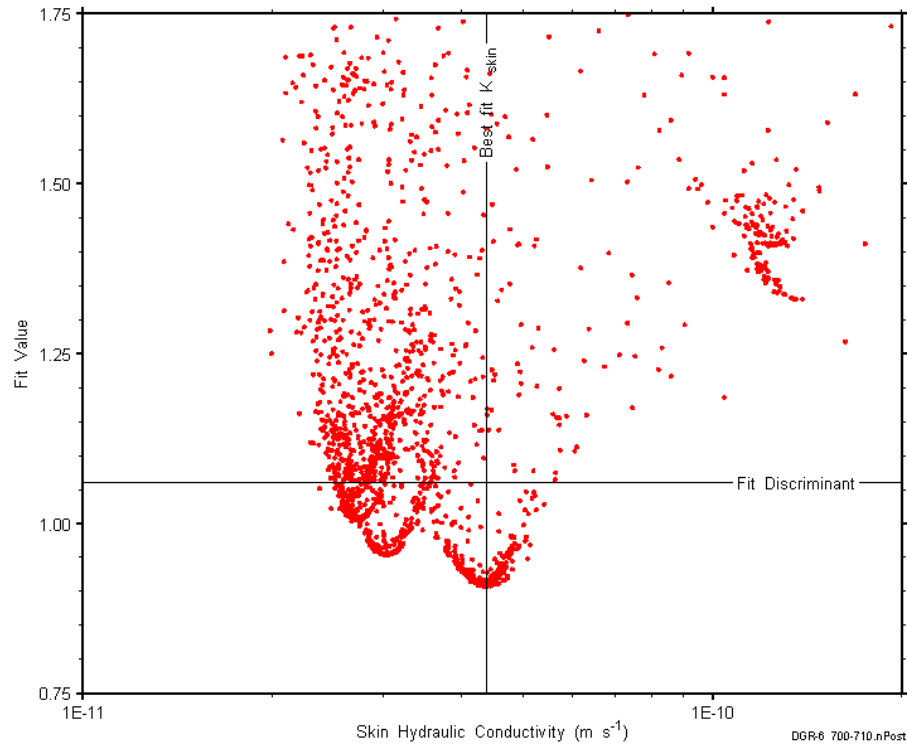


Figure F-56: XY-scatter plot showing the skin hydraulic conductivity parameter space derived from DGR6_614.49-623.14 perturbation analysis along with the fit discriminant and best fit values.

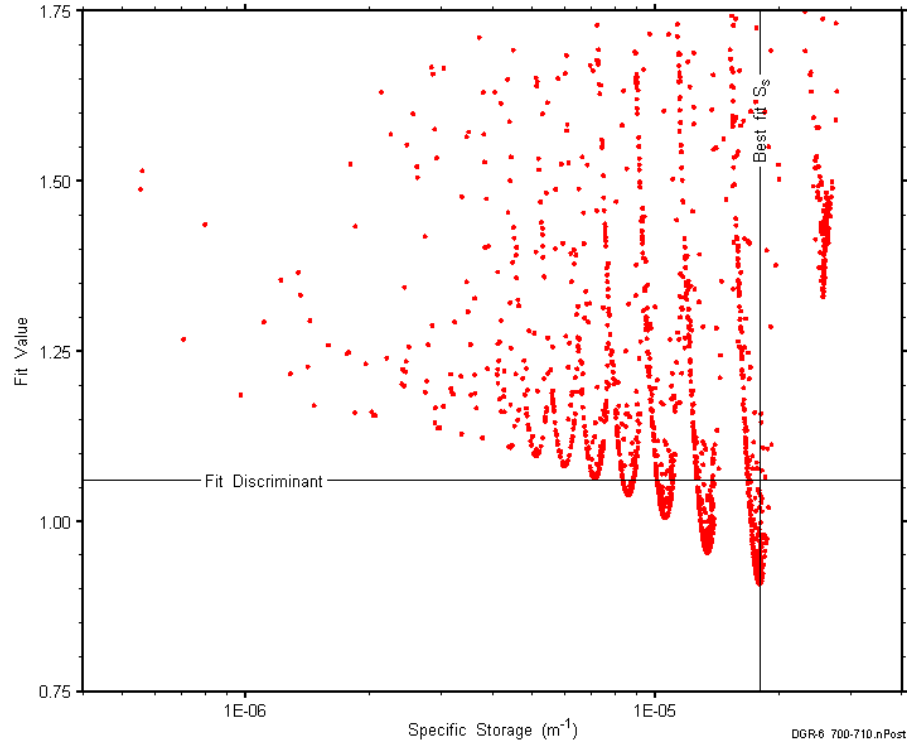


Figure F-57: XY-scatter plot showing the formation specific storage parameter space derived from DGR6_614.49-623.14 perturbation analysis along with the fit discriminant and best fit values.

F.5 635.61-644.22 Blue Mountain

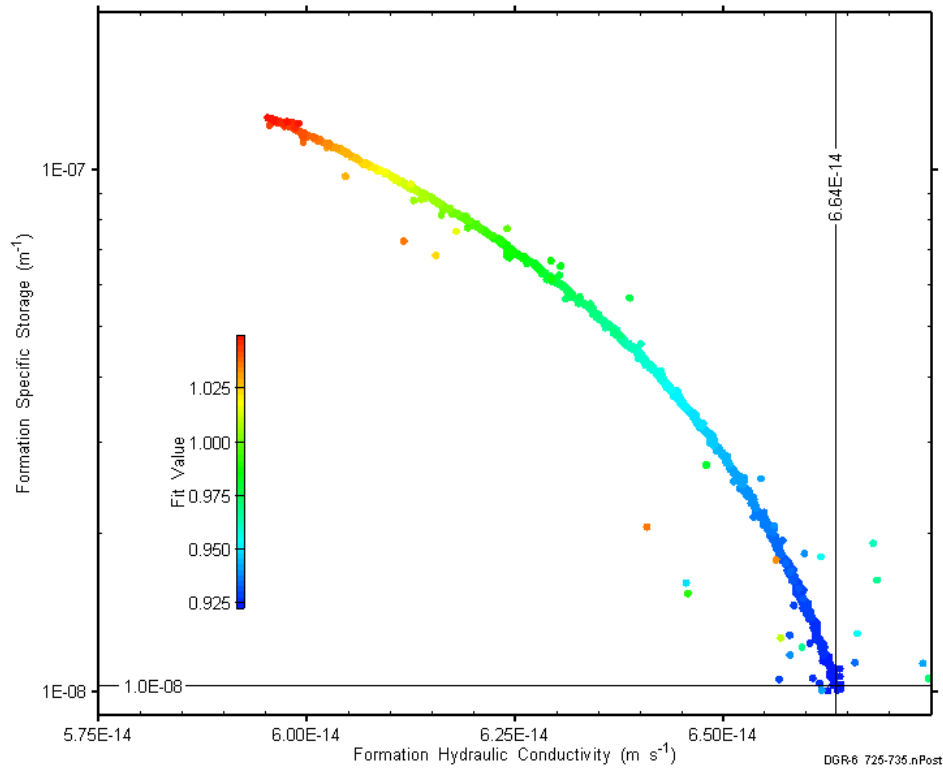


Figure F-58: XY-scatter plot showing estimates of formation hydraulic conductivity and formation specific storage derived from the DGR6_635.61-644.22 perturbation analysis.

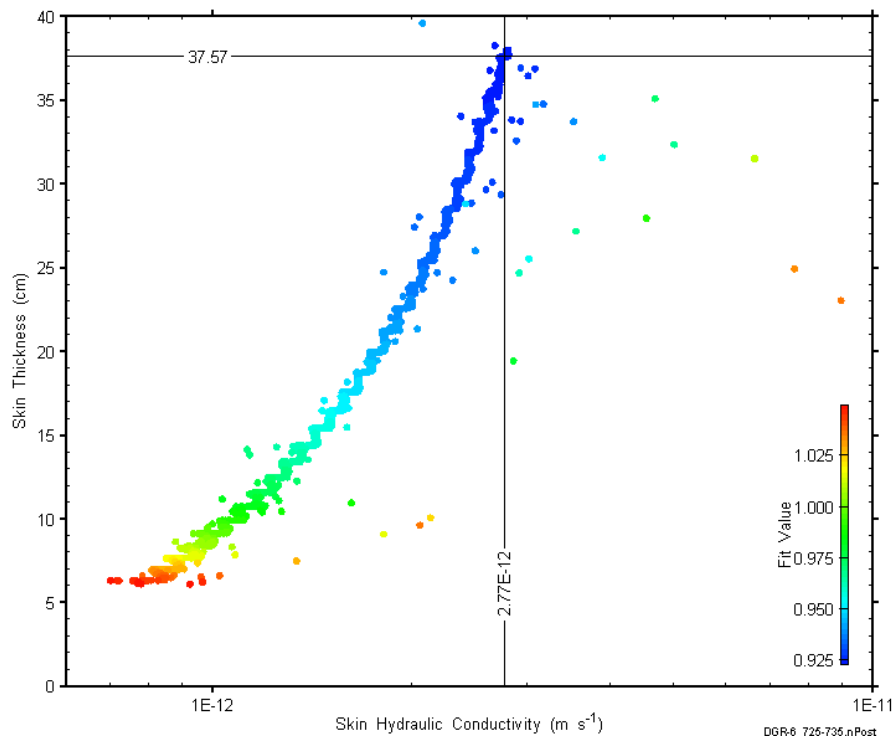


Figure F-59: XY-scatter plot showing estimates of skin hydraulic conductivity and skin thickness derived from the DGR6_635.61-644.22 perturbation analysis.

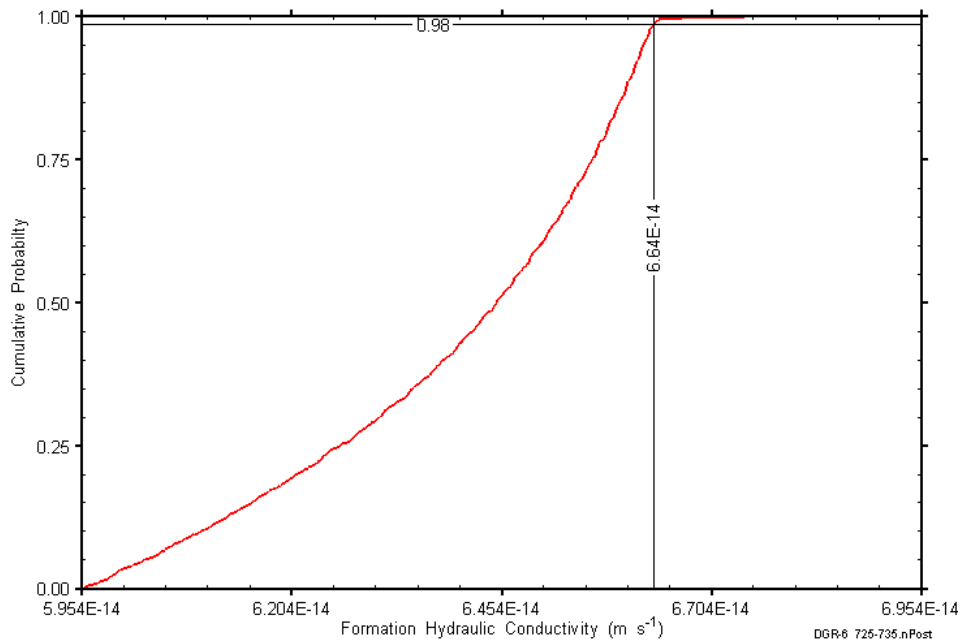


Figure F-60: DGR6_635.61-644.22 formation hydraulic conductivity cumulative distribution function.

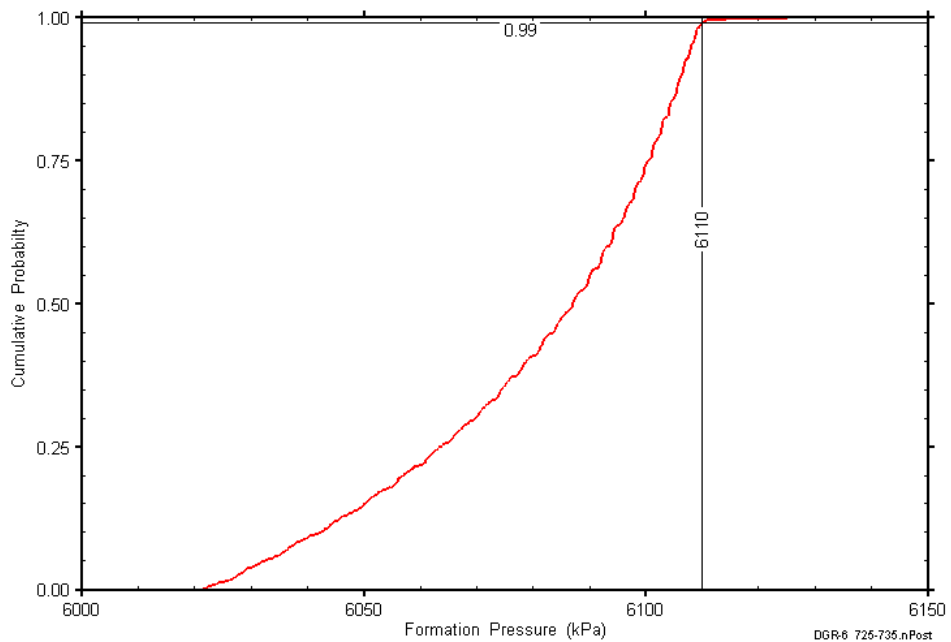


Figure F-61: DGR6_635.61-644.22 static formation pressure cumulative distribution function.

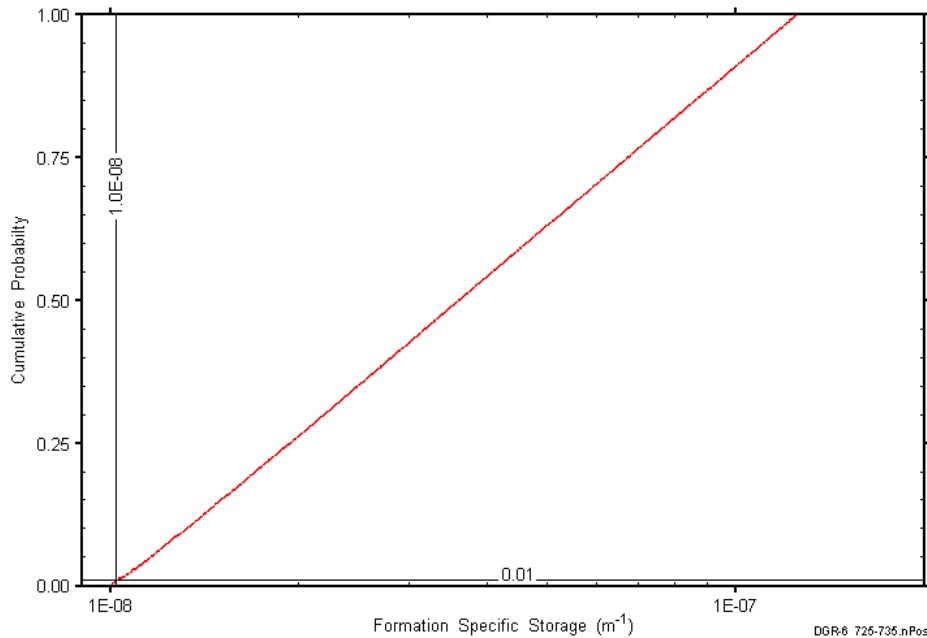


Figure F-62: DGR6_635.61-644.22 formation specific storage cumulative distribution function.

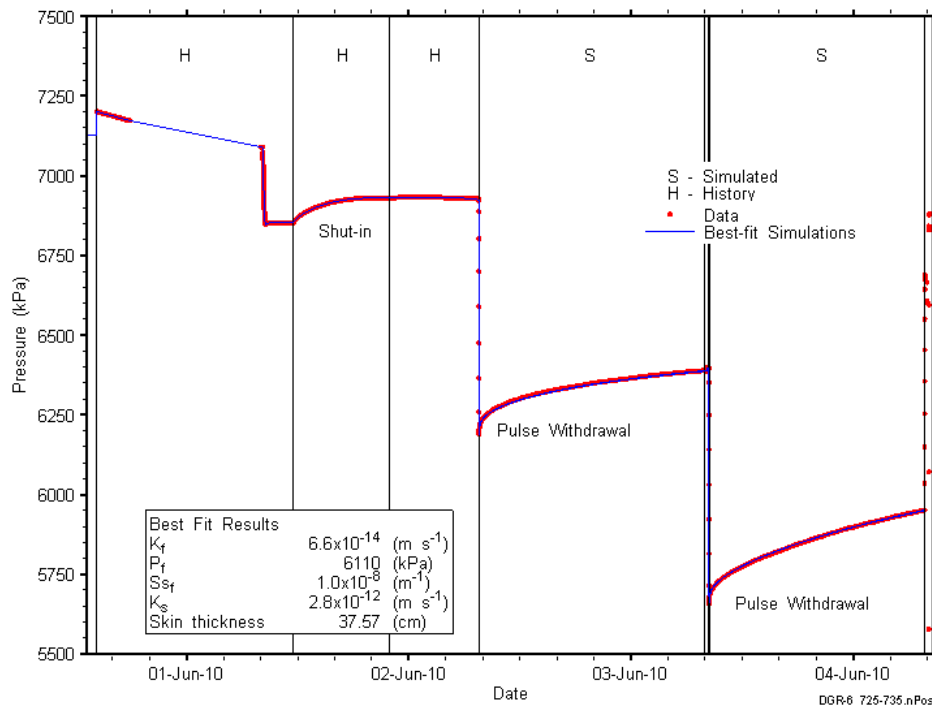


Figure F-63 Linear plot showing simulations of the DGR6_635.61-644.22 pressure response.

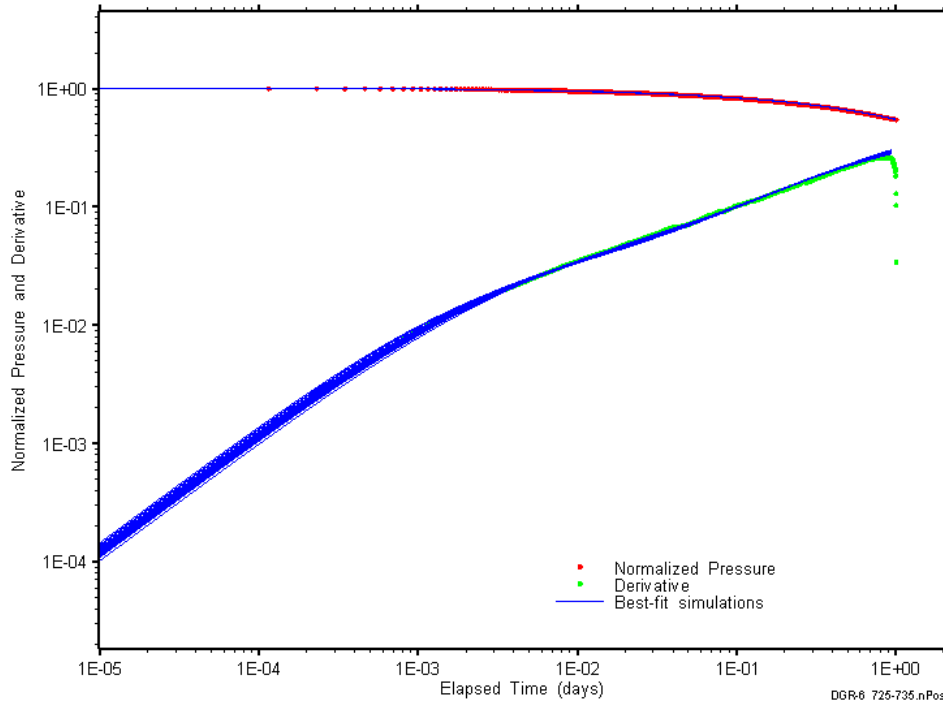


Figure F-64: Log-log plot showing simulations of the DGR6_635.61-644.22 PW1 Ramey B and derivative response.

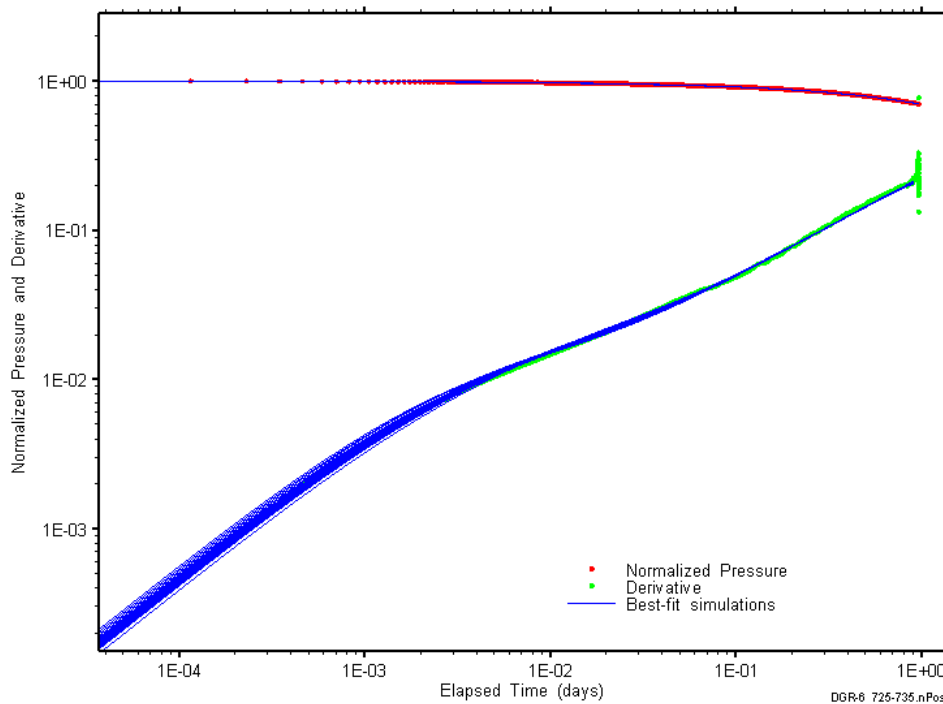


Figure F-65: Log-log plot showing simulations of the DGR6_635.61-644.22 PW2 Ramey B and derivative response.

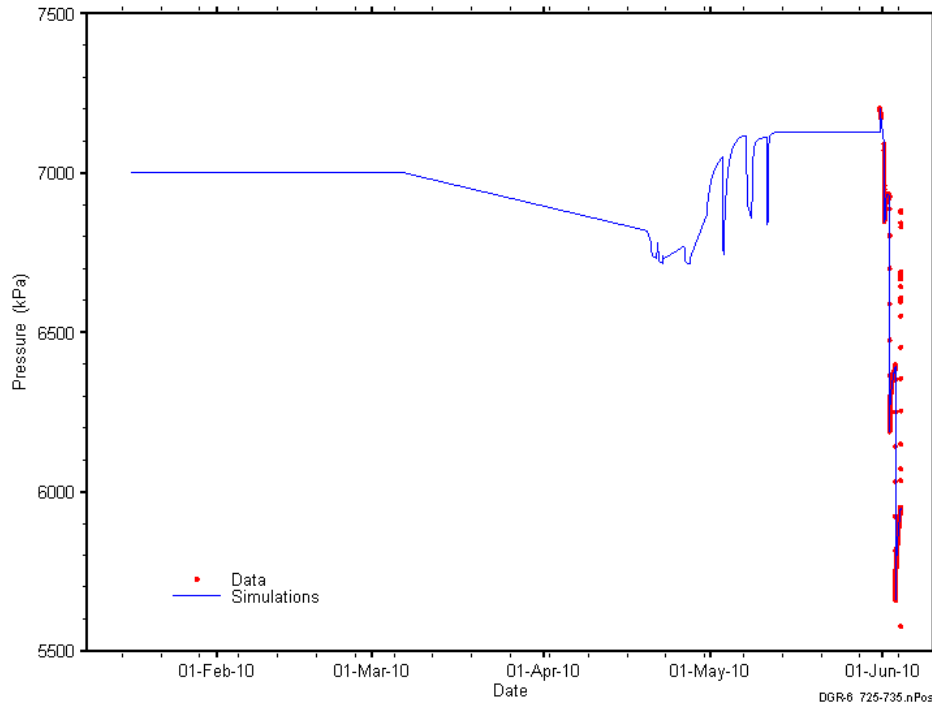


Figure F-66: Linear plot showing simulations of the DGR6_635.61-644.22 pressure response, including pre-test pressure history.

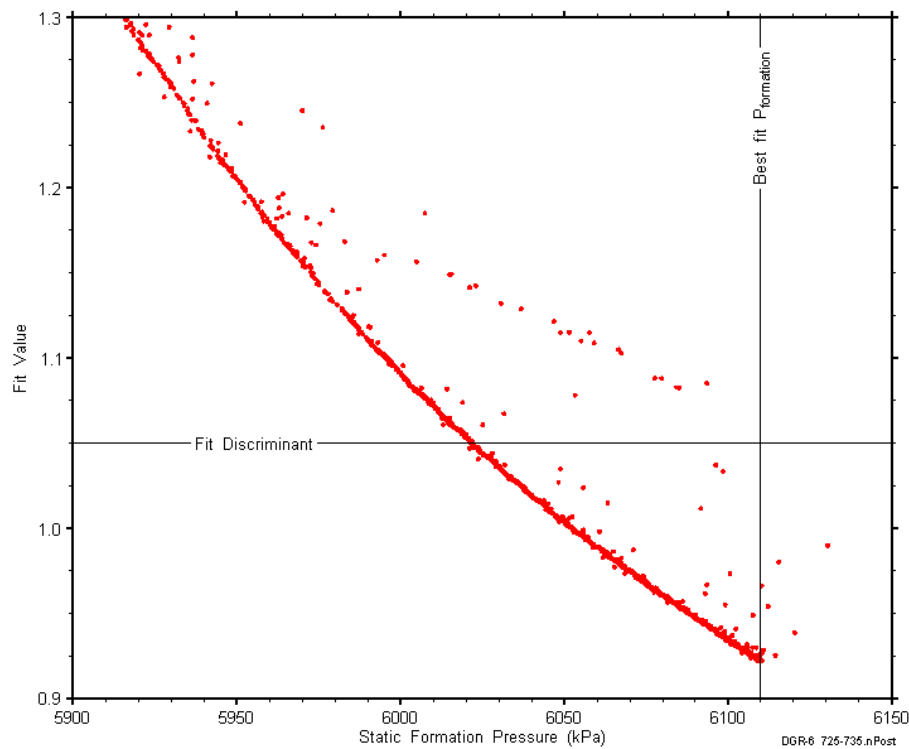


Figure F-67: XY-scatter plot showing the static formation pressure parameter space derived from DGR6_635.61-644.22 perturbation analysis along with the fit discriminant and best fit values.

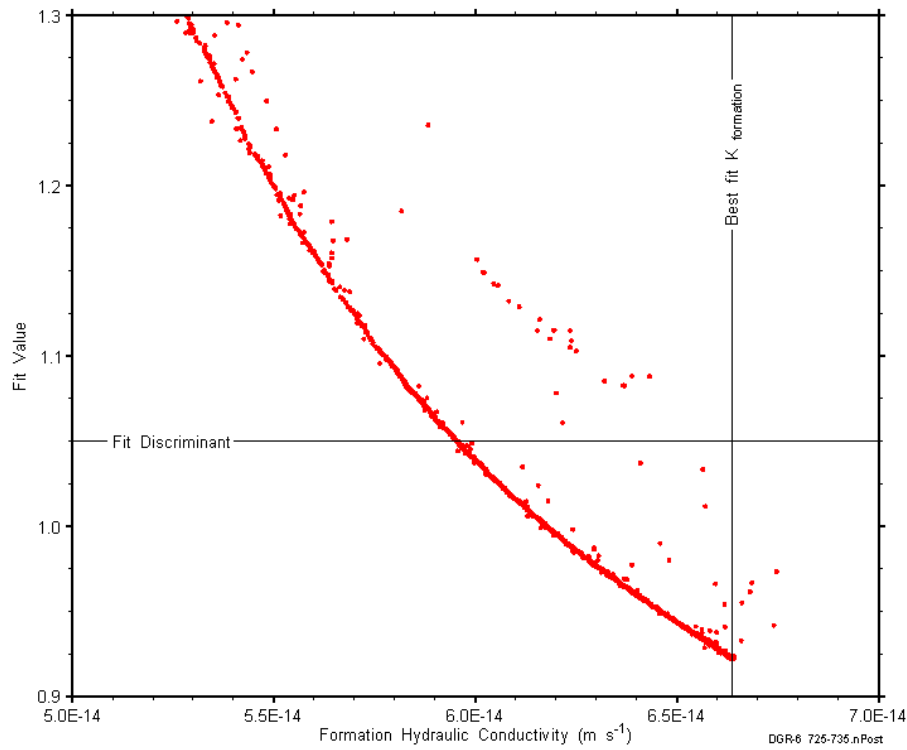


Figure F-68: XY-scatter plot showing the formation hydraulic conductivity parameter space derived from DGR6_635.61-644.22 perturbation analysis along with the fit discriminant and best fit values.

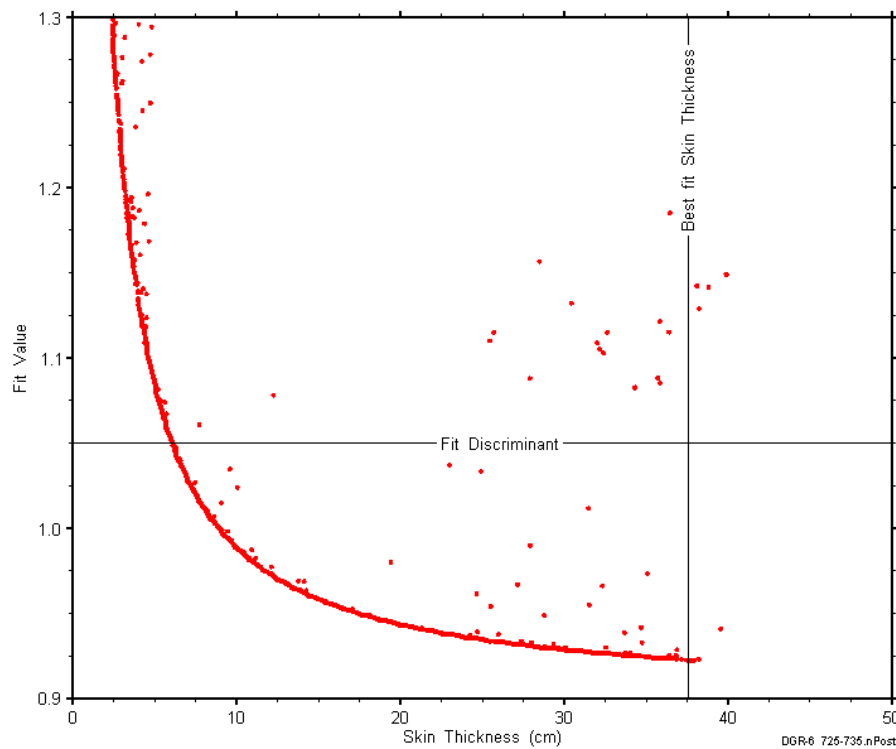


Figure F-69: XY-scatter plot showing the skin-thickness parameter space derived from DGR6_635.61-644.22 perturbation analysis along with the fit discriminant and best fit values.

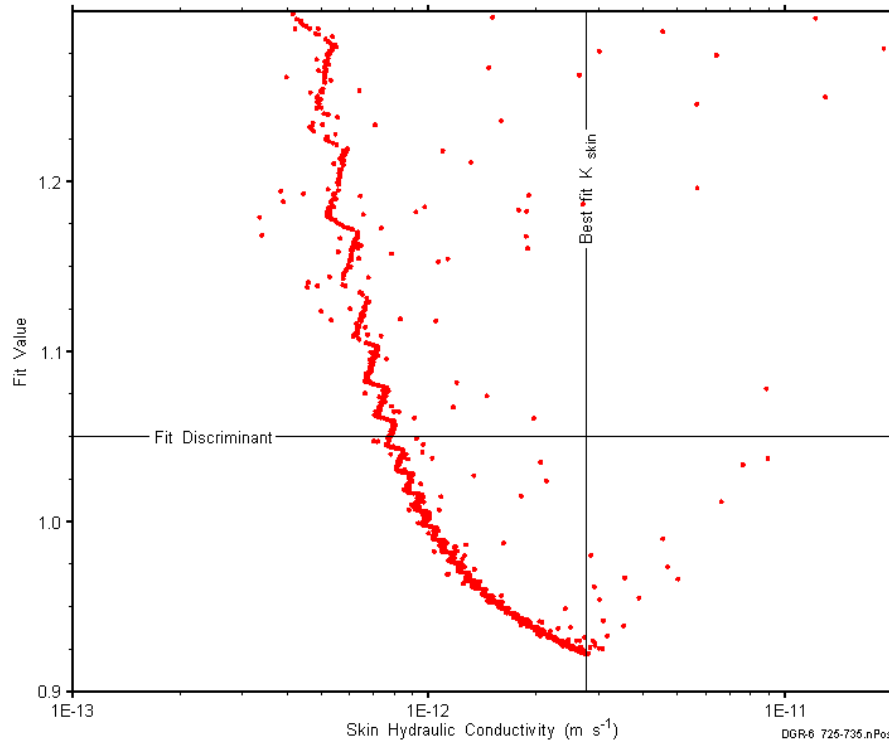


Figure F-70: XY-scatter plot showing the skin hydraulic conductivity parameter space derived from DGR6_635.61-644.22 perturbation analysis along with the fit discriminant and best fit values.

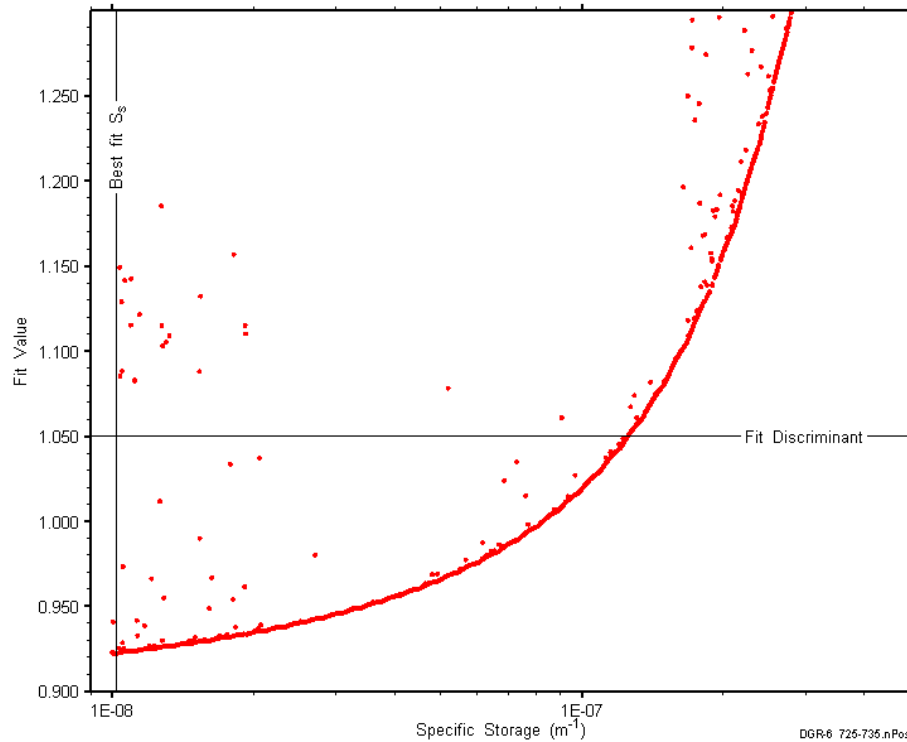


Figure F-71: XY-scatter plot showing the formation specific storage parameter space derived from DGR6_635.61-644.22 perturbation analysis along with the fit discriminant and best fit values.

F.6 645.71-654.31 Collingwood

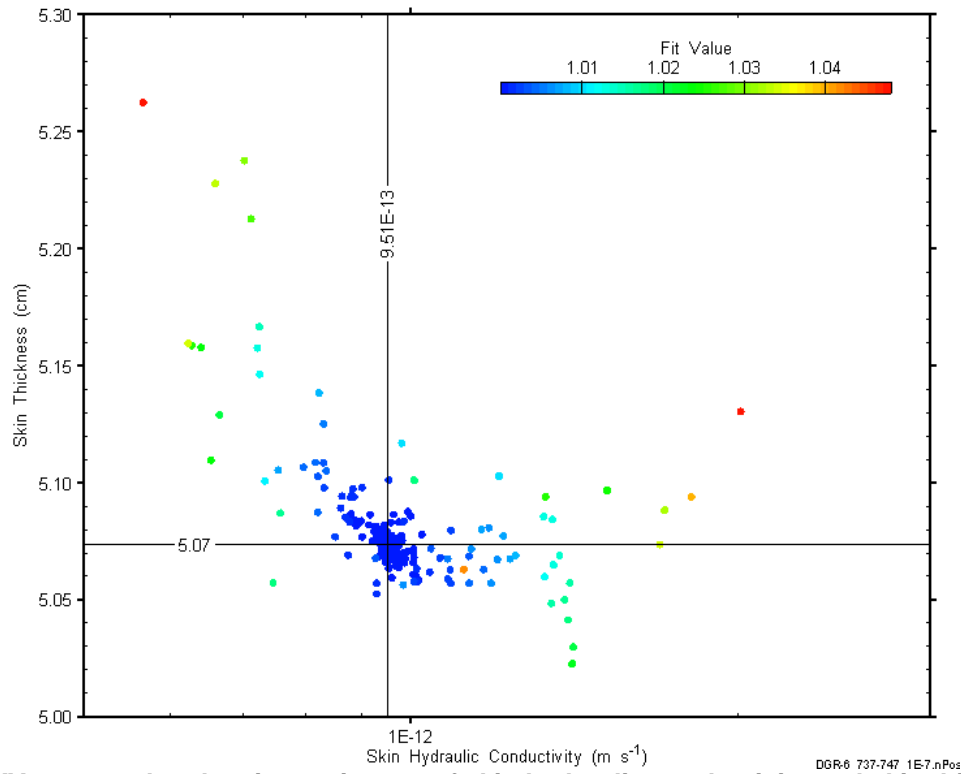


Figure F-72: XY-scatter plot showing estimates of skin hydraulic conductivity and skin thickness derived from the DGR6_645.71-654.31 perturbation analysis.

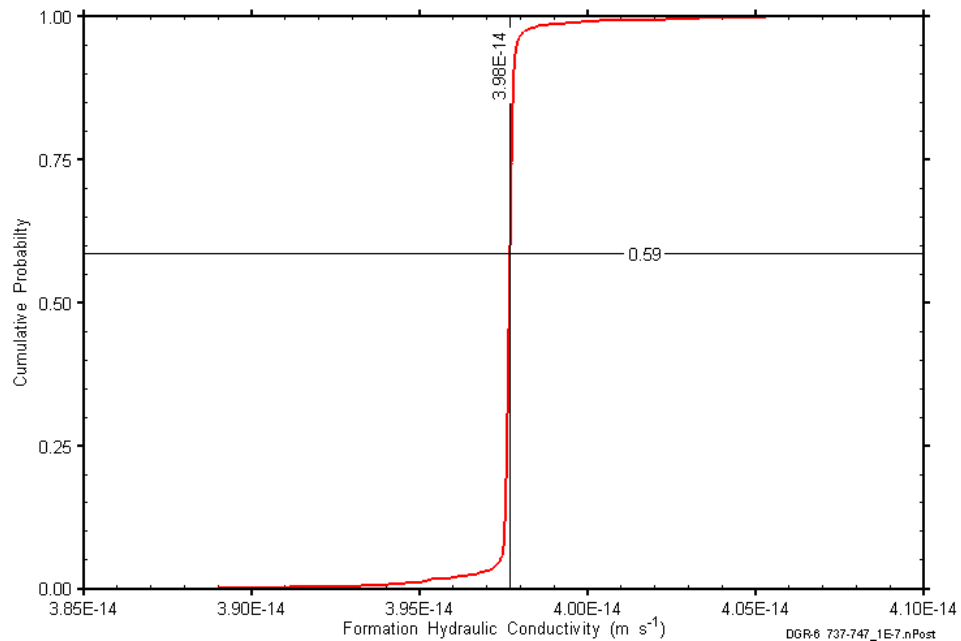


Figure F-73: DGR6_645.71-654.31 formation hydraulic conductivity cumulative distribution function.

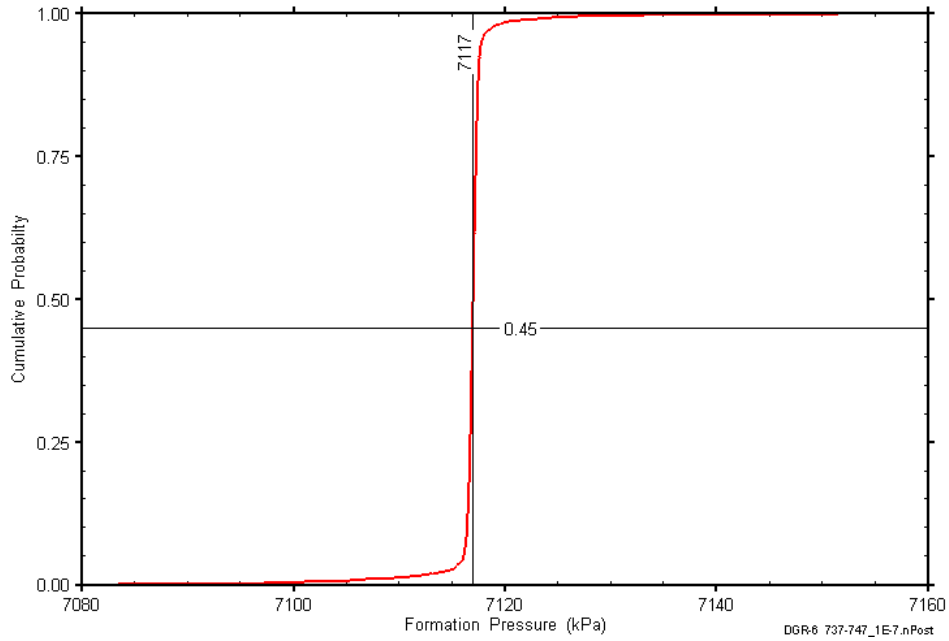


Figure F-74: DGR6_645.71-654.31 static formation pressure cumulative distribution function.

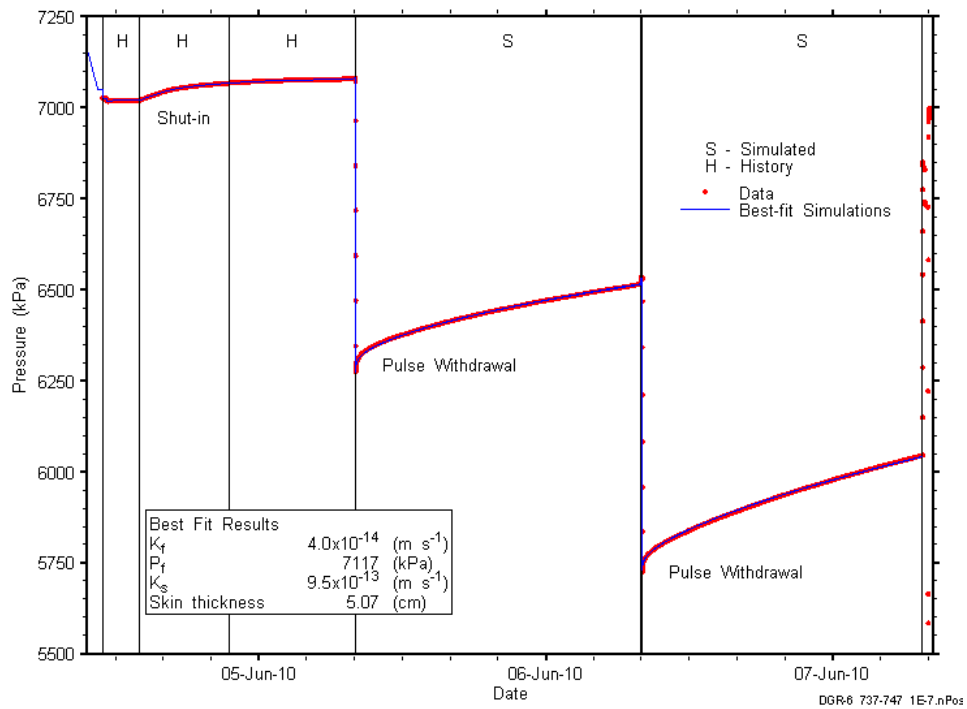


Figure F-75: Linear plot showing simulations of the DGR6_645.71-654.31 pressure response.

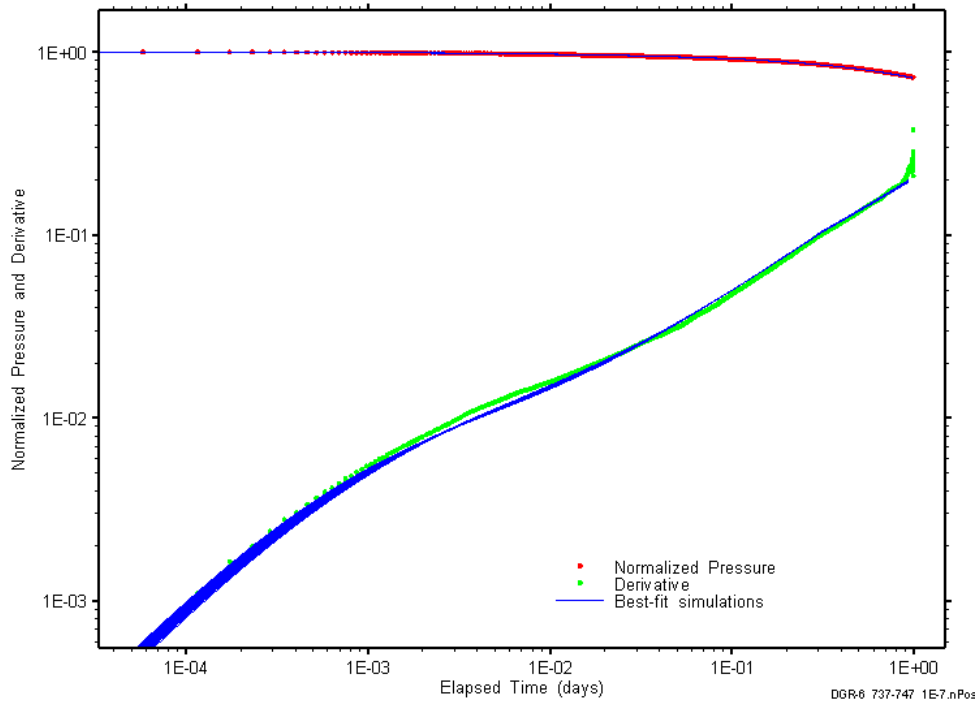


Figure F-76: Log-log plot showing simulations of the DGR6_645.71-654.31 PW1 Ramey B and derivative response.

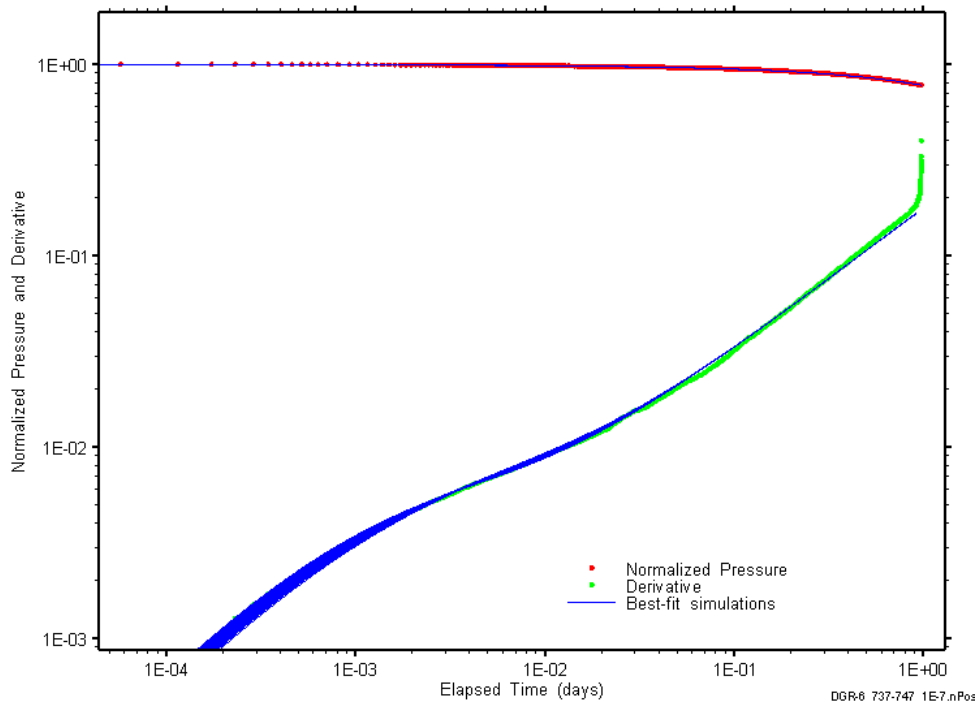


Figure F-77: Log-log plot showing simulations of the DGR6_645.71-654.31 PW2 Ramey B and derivative response.

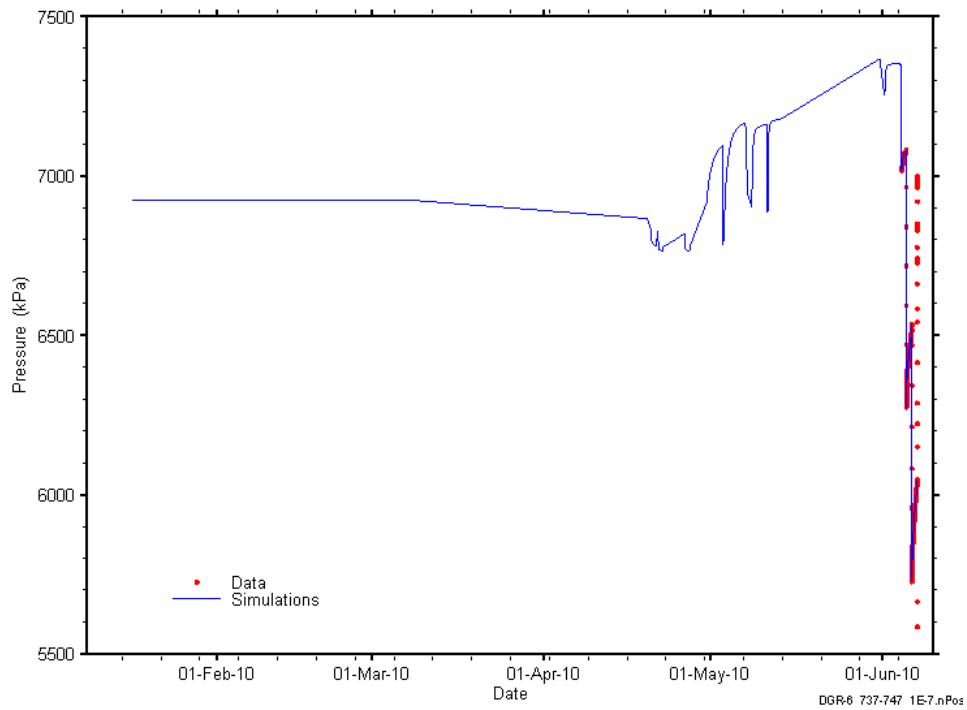


Figure F-78: Linear plot showing simulations of the DGR6_645.71-654.31 pressure response, including pre-test pressure history.

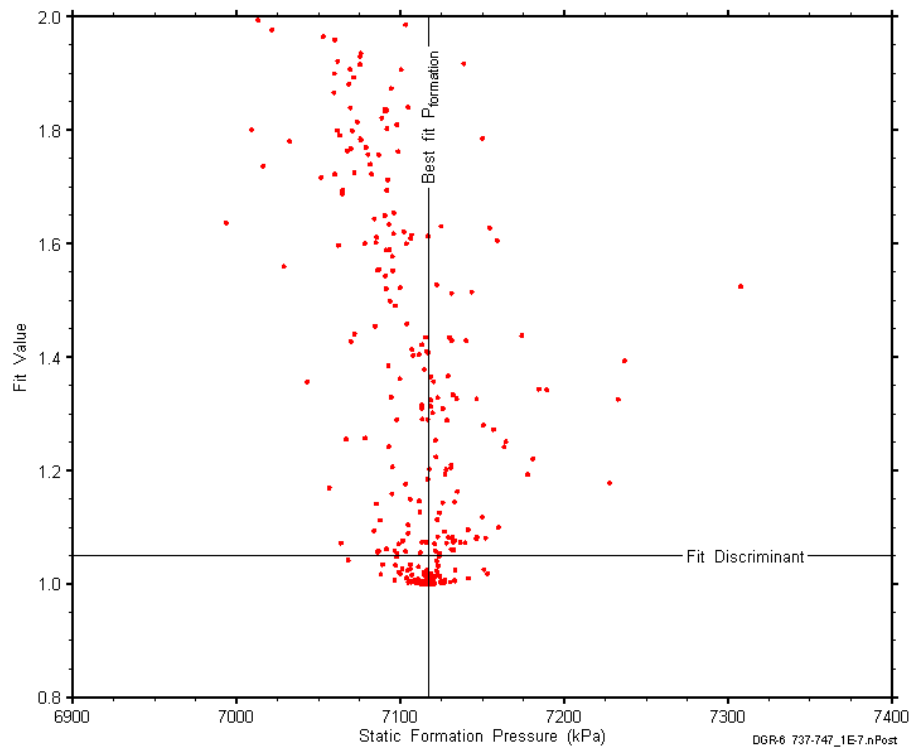


Figure F-79: XY-scatter plot showing the static formation pressure parameter space derived from DGR6_645.71-654.31 perturbation analysis along with the fit discriminant and best fit values.

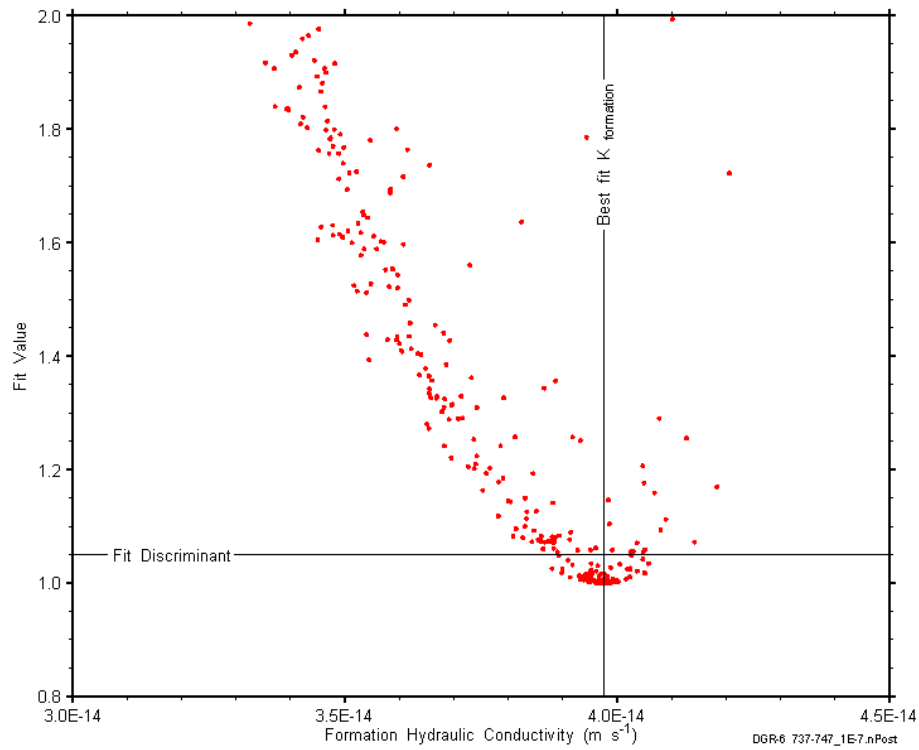


Figure F-80: XY-scatter plot showing the formation hydraulic conductivity parameter space derived from DGR6_645.71-654.31 perturbation analysis along with the fit discriminant and best fit values.

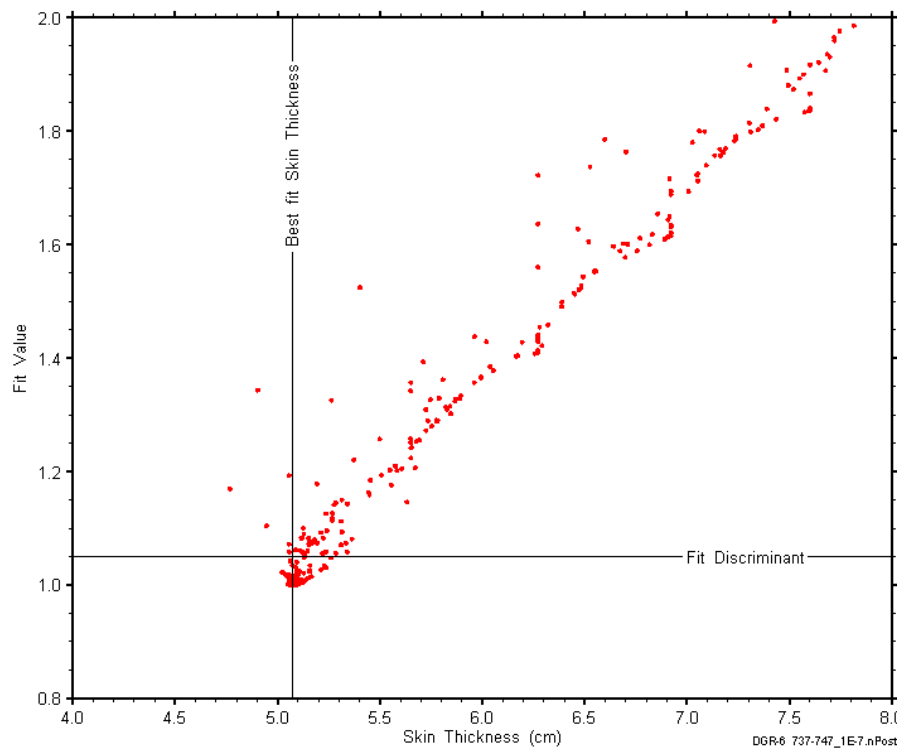


Figure F-81: XY-scatter plot showing the skin-thickness parameter space derived from DGR6_645.71-654.31 perturbation analysis along with the fit discriminant and best fit values.

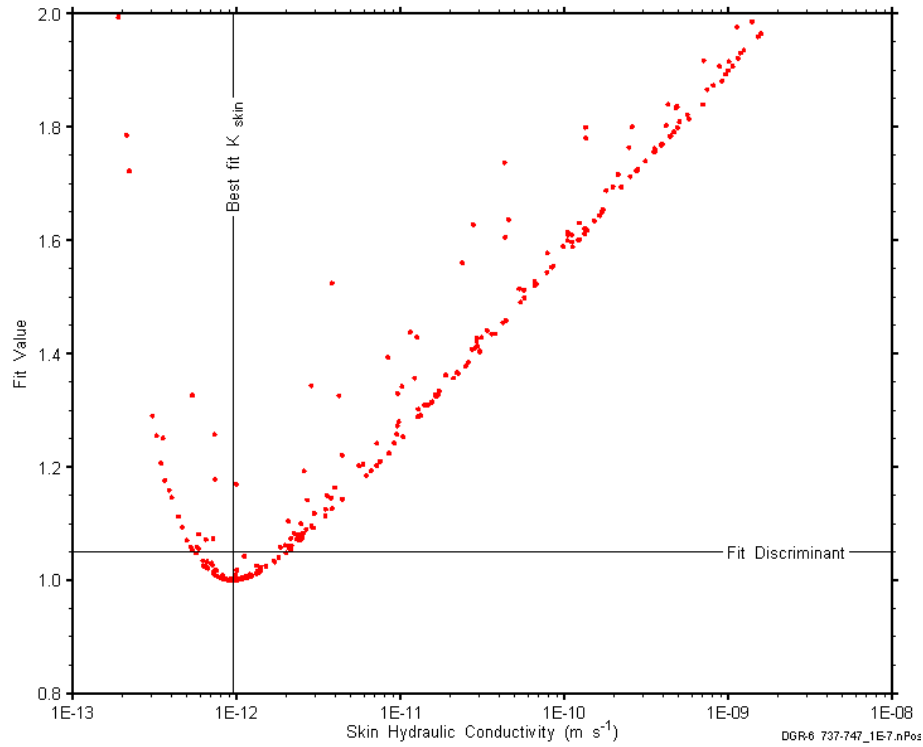


Figure F-82: XY-scatter plot showing the skin hydraulic conductivity parameter space derived from DGR6_645.71-654.31 perturbation analysis along with the fit discriminant and best fit values.

F.7 668.34-676.89 Cobourg

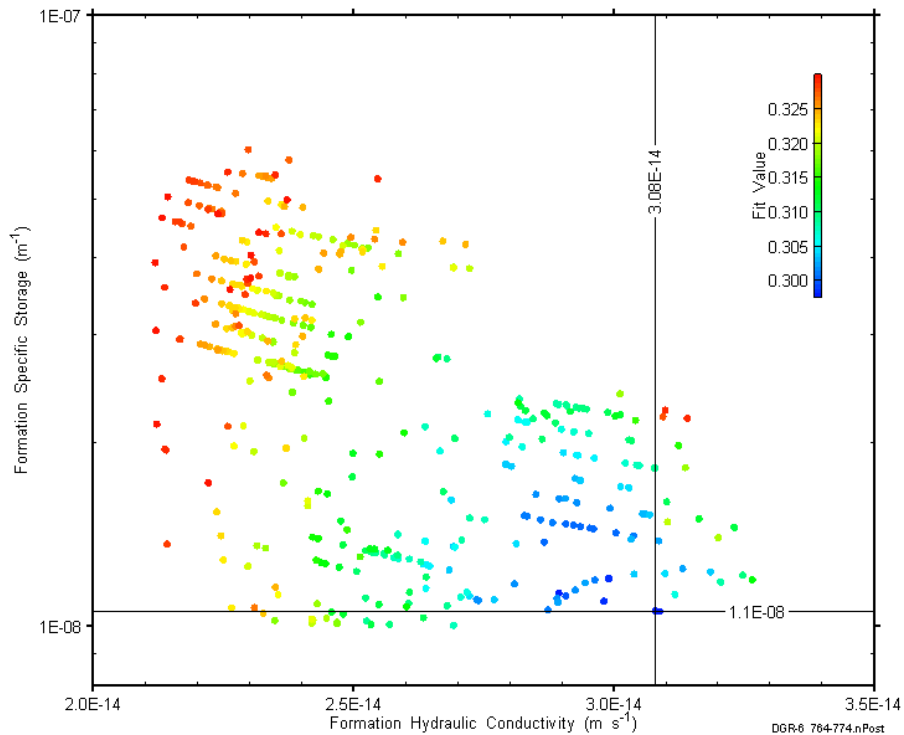


Figure F-83: XY-scatter plot showing estimates of formation hydraulic conductivity and formation specific storage derived from the DGR6_668.34-676.89 perturbation analysis.

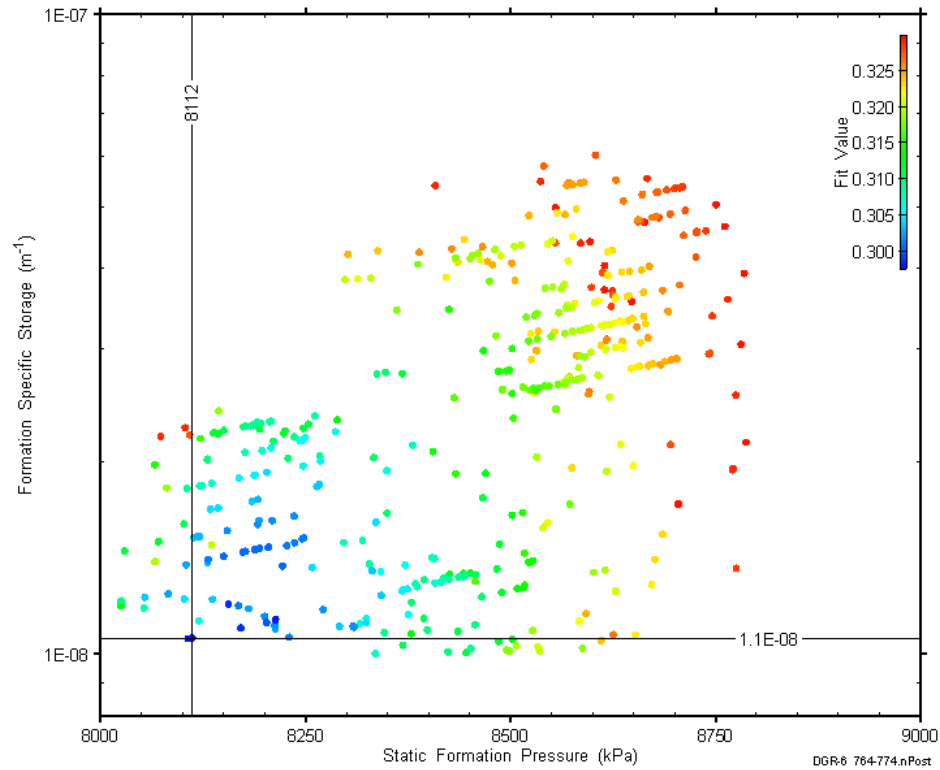


Figure F-84: XY-scatter plot showing estimates of static formation pressure and formation specific storage derived from the DGR6_668.34-676.89 perturbation analysis.

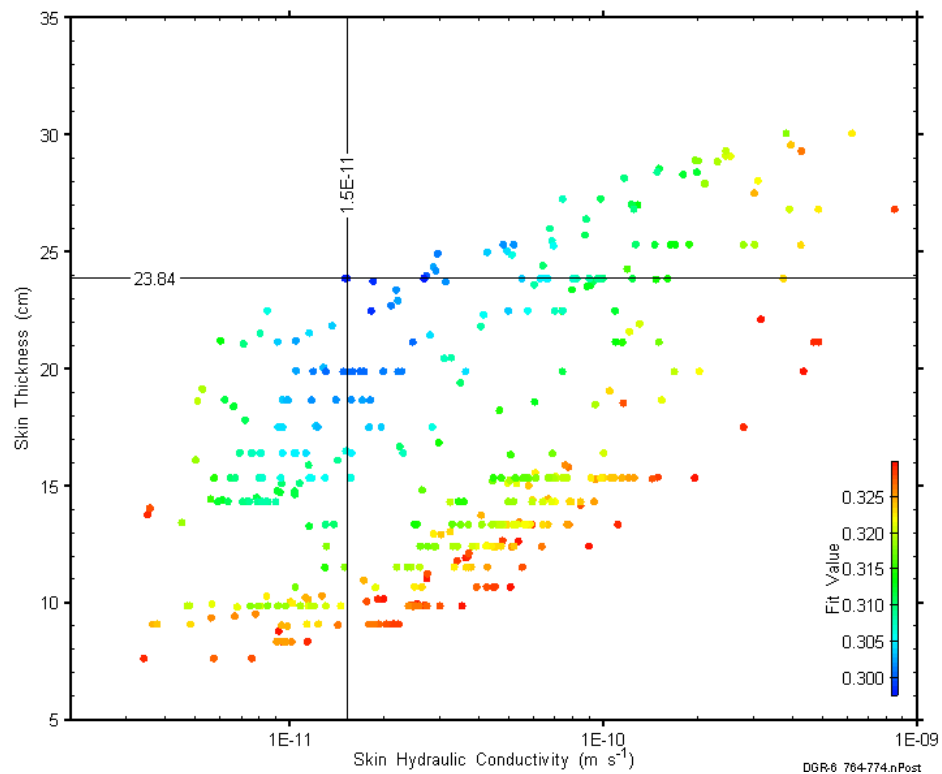


Figure F-85: XY-scatter plot showing estimates of skin hydraulic conductivity and skin thickness derived from the DGR6_668.34-676.89 perturbation analysis.

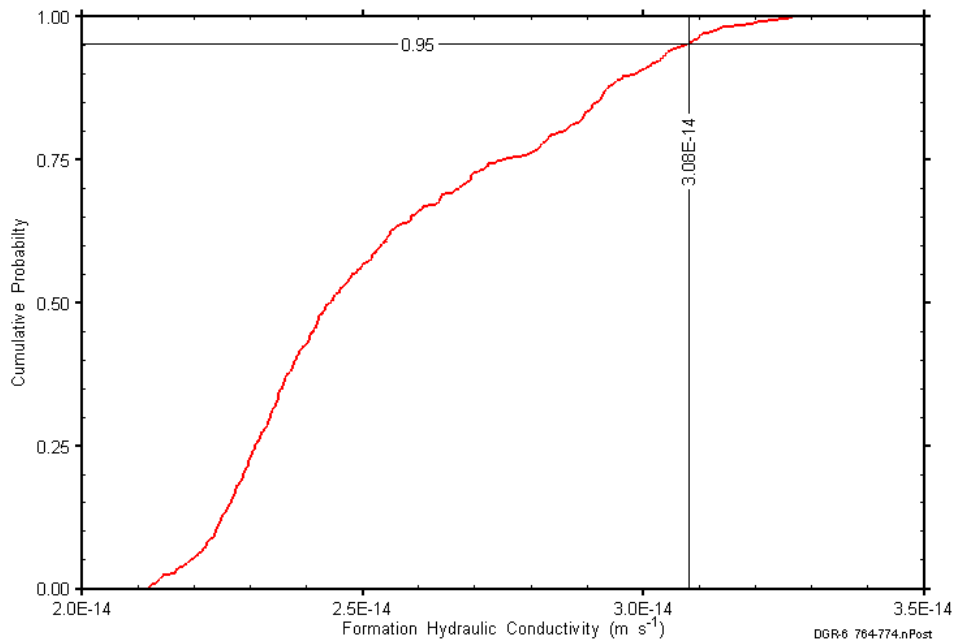


Figure F-86: DGR6_668.34-676.89 formation hydraulic conductivity cumulative distribution function.

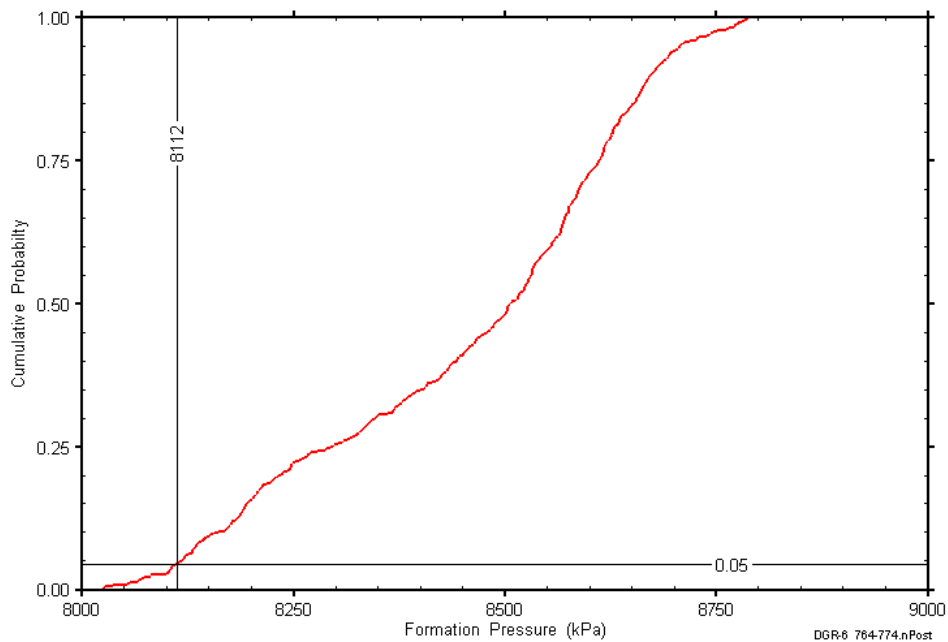


Figure F-87: DGR6_668.34-676.89 static formation pressure cumulative distribution function.

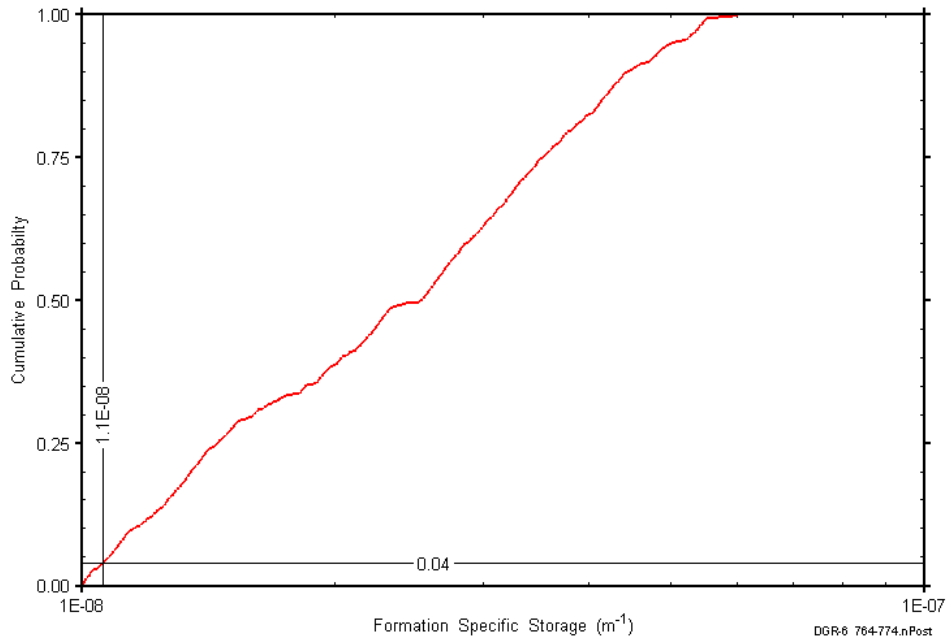


Figure F-88: DGR6_668.34-676.89 formation specific storage cumulative distribution function.

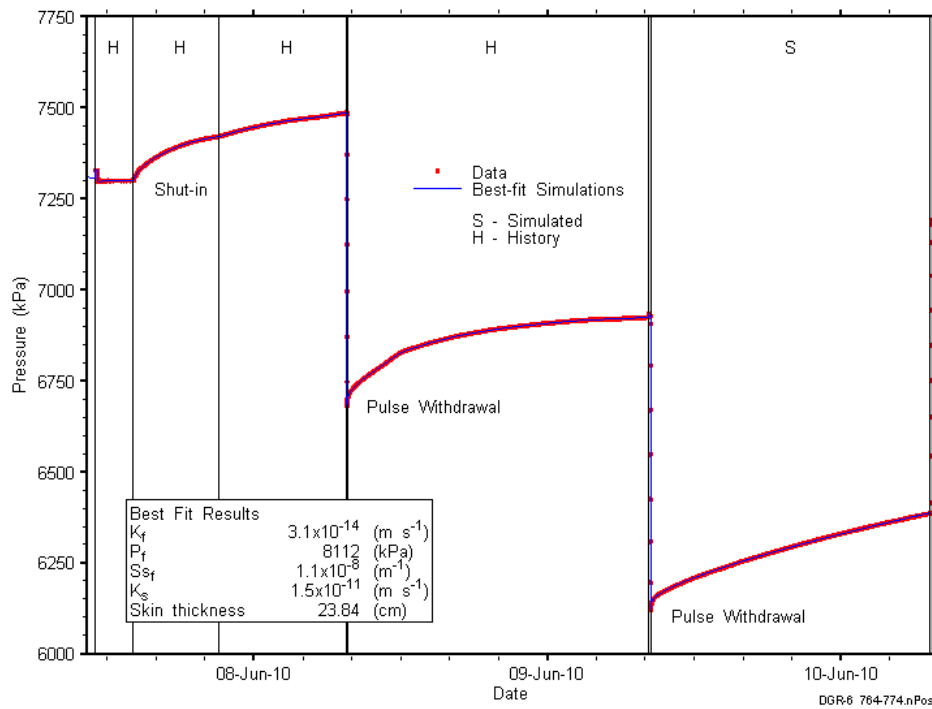


Figure F-89: Linear plot showing simulations of the DGR6_668.34-676.89 pressure response.

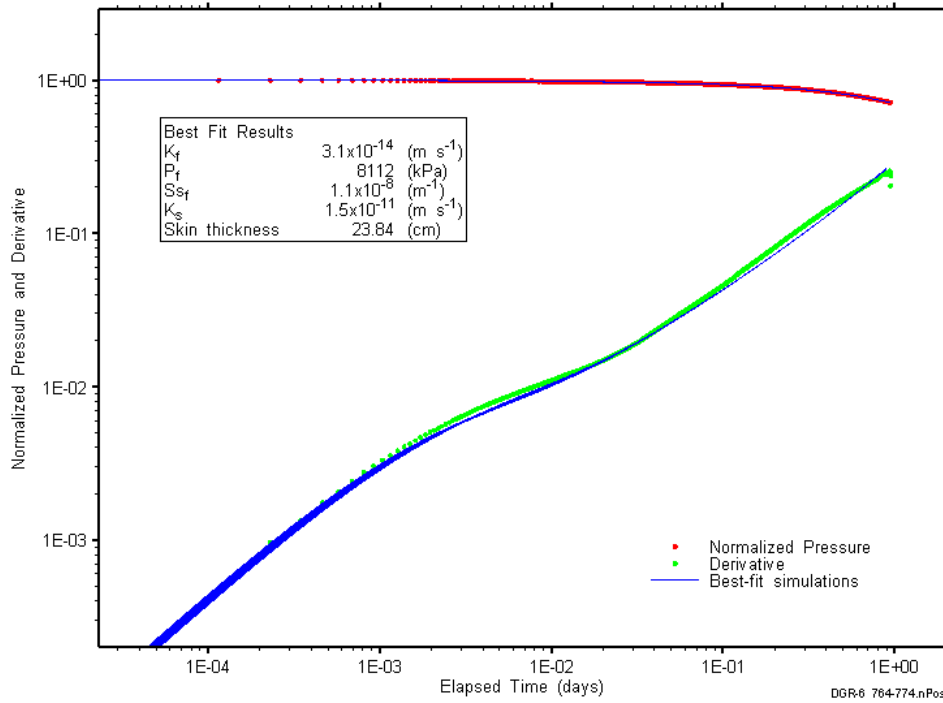


Figure F-90: Log-log plot showing simulations of the DGR6_668.34-676.89 PW2 Ramey B and derivative response.

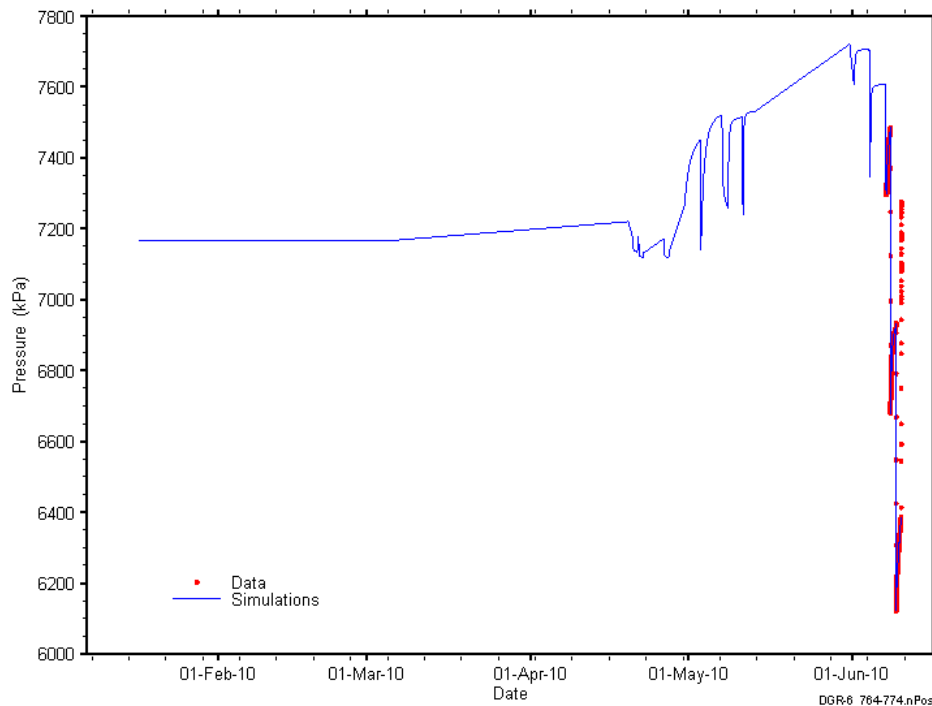


Figure F-91: Linear plot showing simulations of the DGR6_668.34-676.89 pressure response, including pre-test pressure history.

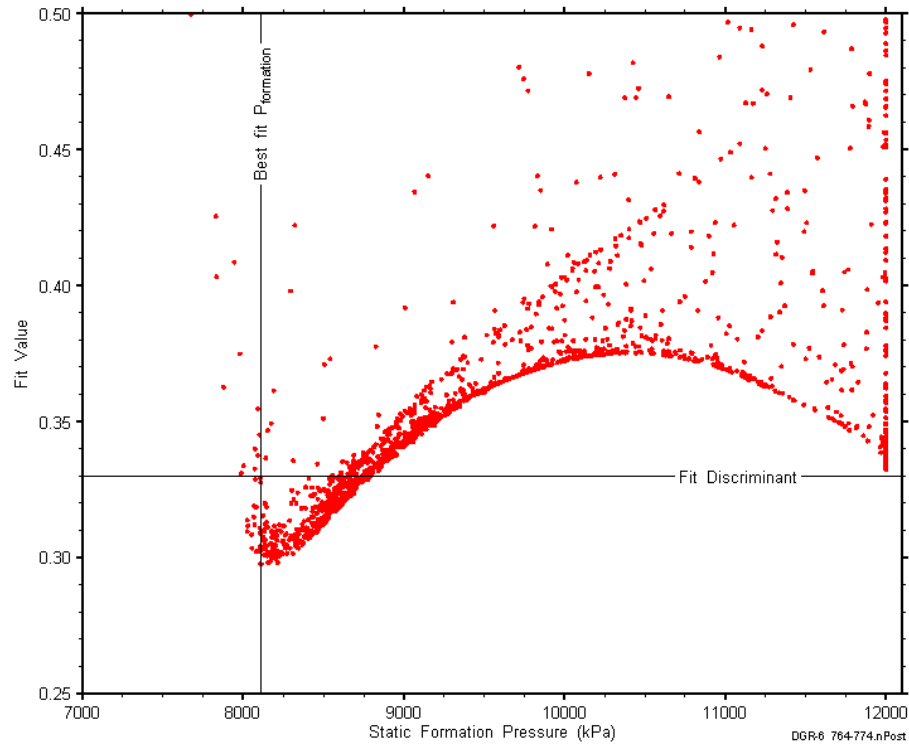


Figure F-92: XY-scatter plot showing the static formation pressure parameter space derived from DGR6_668.34-676.89 perturbation analysis along with the fit discriminant and best fit values.

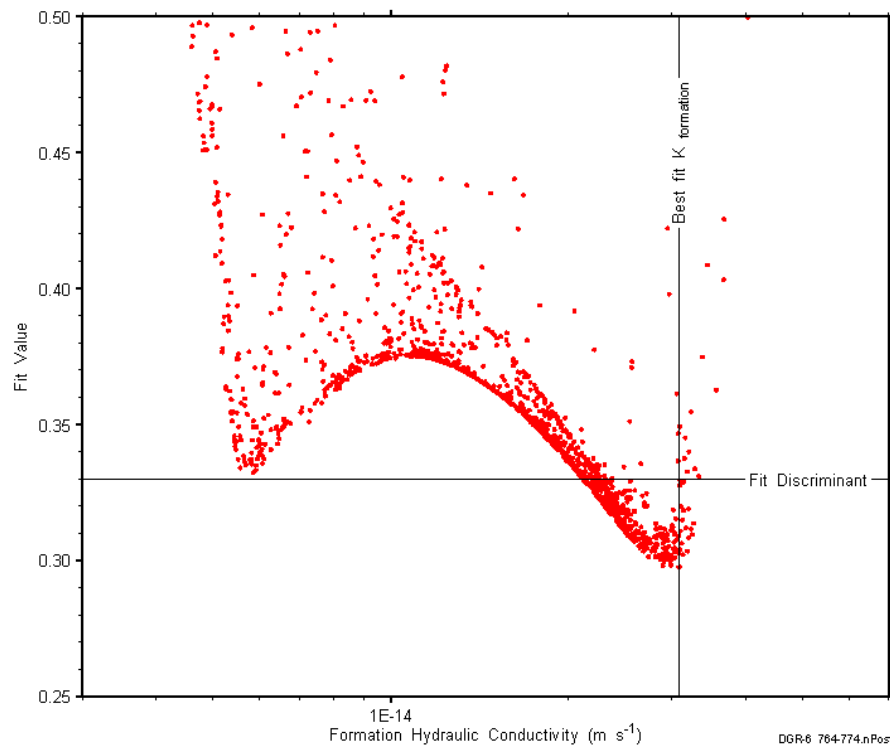


Figure F-93: XY-scatter plot showing the formation hydraulic conductivity parameter space derived from DGR6_668.34-676.89 perturbation analysis along with the fit discriminant and best fit values.

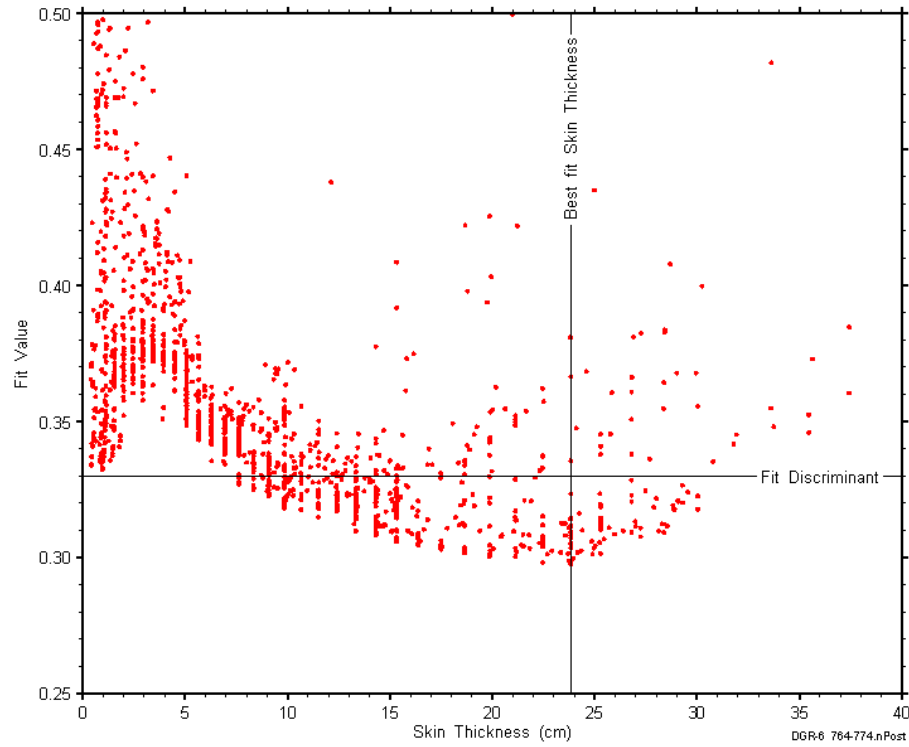


Figure F-94: XY-scatter plot showing the skin-thickness parameter space derived from DGR6_668.34-676.89 perturbation analysis along with the fit discriminant and best fit values.

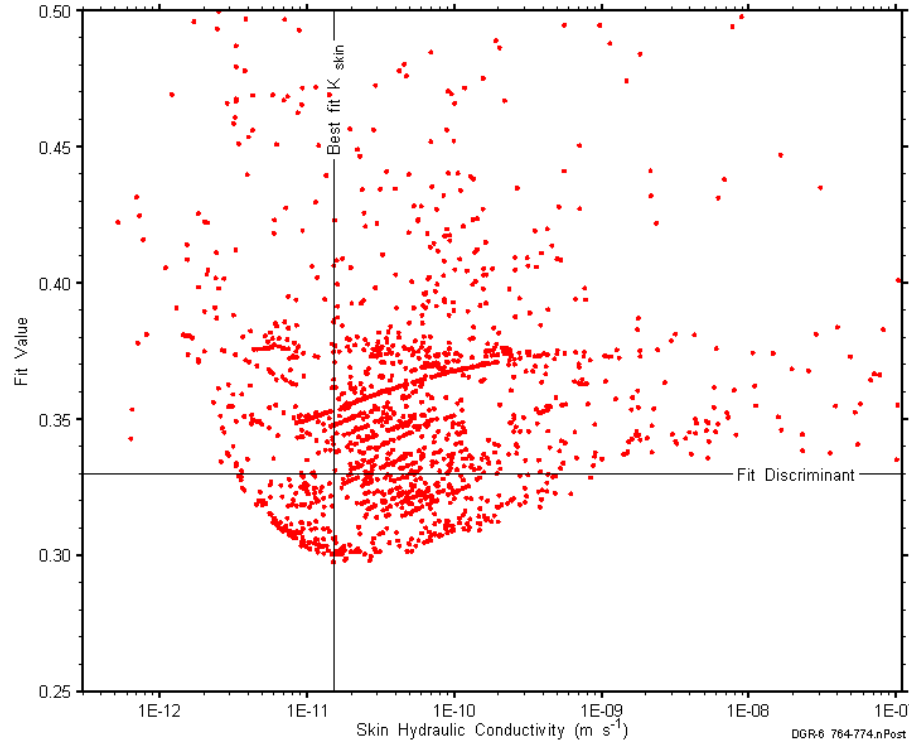


Figure F-95: XY-scatter plot showing the skin hydraulic conductivity parameter space derived from DGR6_668.34-676.89 perturbation analysis along with the fit discriminant and best fit values.

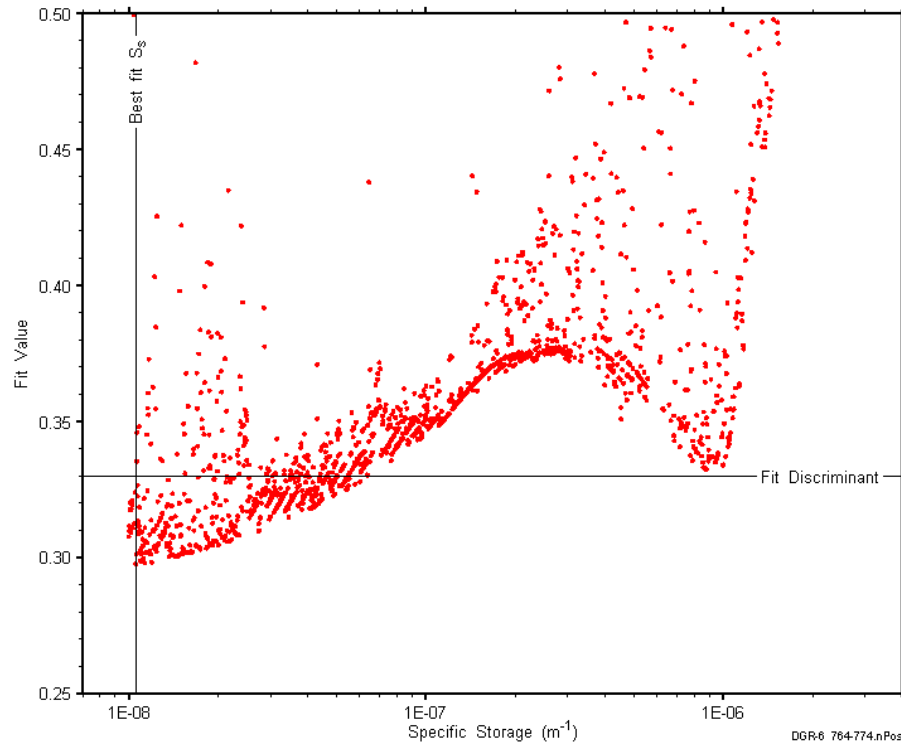


Figure F-96: XY-scatter plot showing the formation specific storage parameter space derived from DGR6_668.34-676.89 perturbation analysis along with the fit discriminant and best fit values.

F.8 683.39-691.94 Sherman Fall

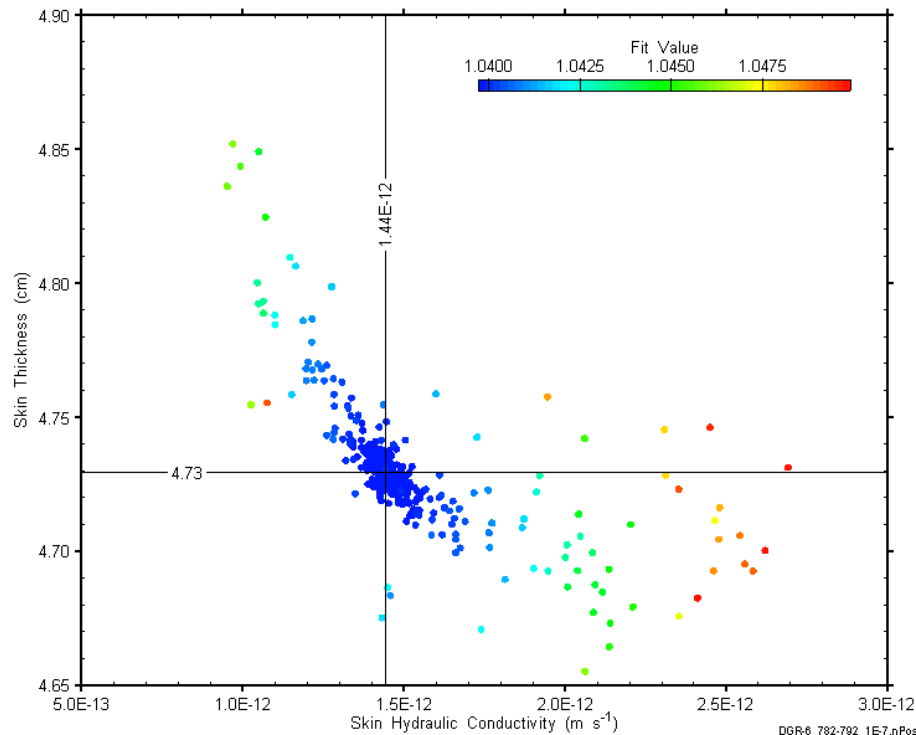


Figure F-97: XY-scatter plot showing estimates of skin hydraulic conductivity and skin thickness derived from the DGR6_683.39-691.94 perturbation analysis.

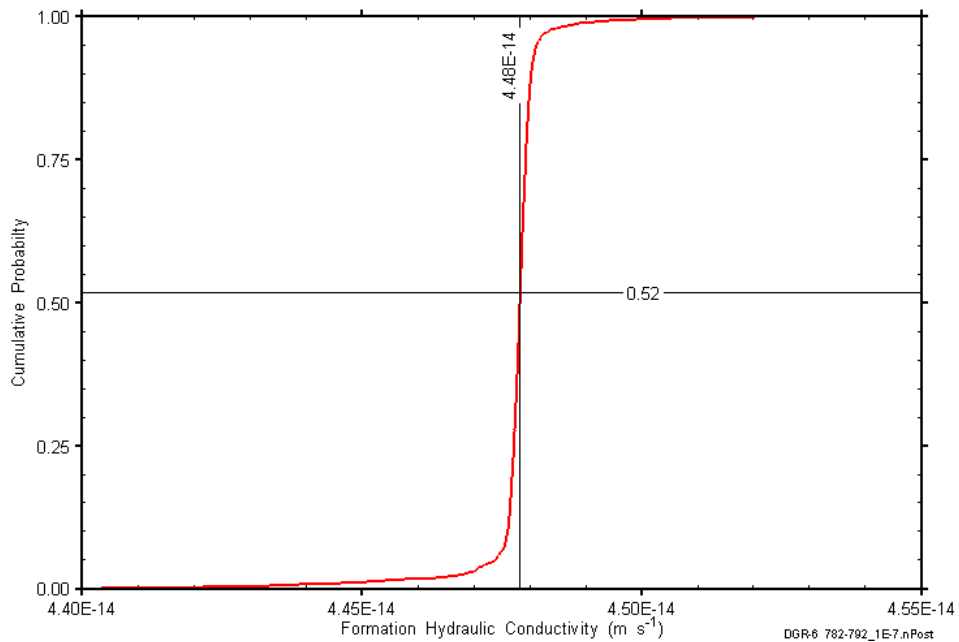


Figure F-98: DGR6_683.39-691.94 formation hydraulic conductivity cumulative distribution function.

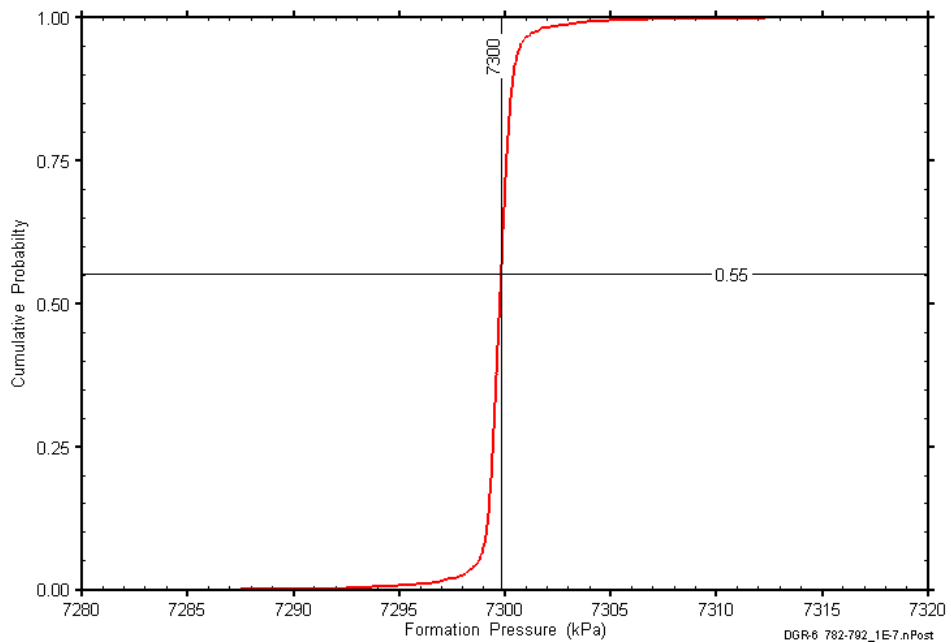


Figure F-99: DGR6_683.39-691.94 static formation pressure cumulative distribution function.

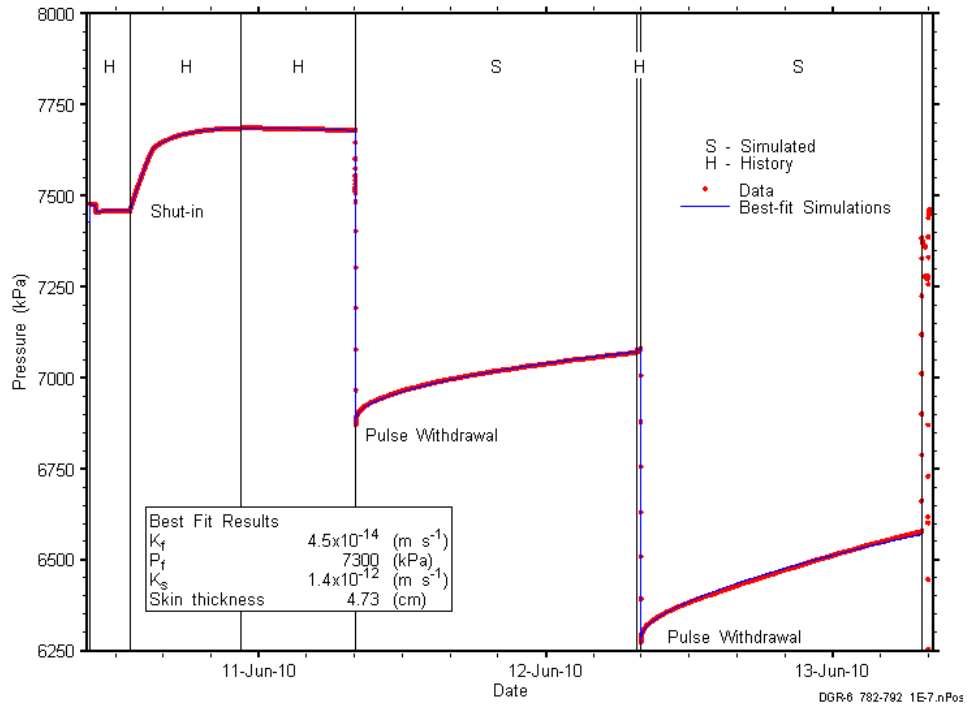


Figure F-100: Linear plot showing simulations of the DGR6_683.39-691.94 pressure response.

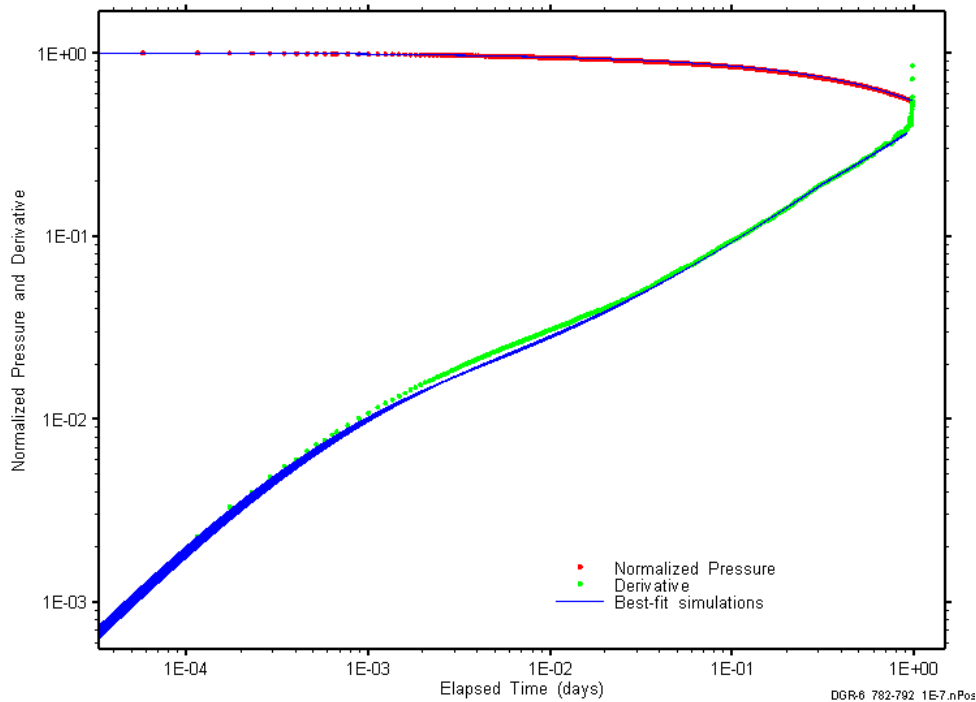


Figure F-101: Log-log plot showing simulations of the DGR6_683.39-691.94 PW1 Ramey B and derivative response.

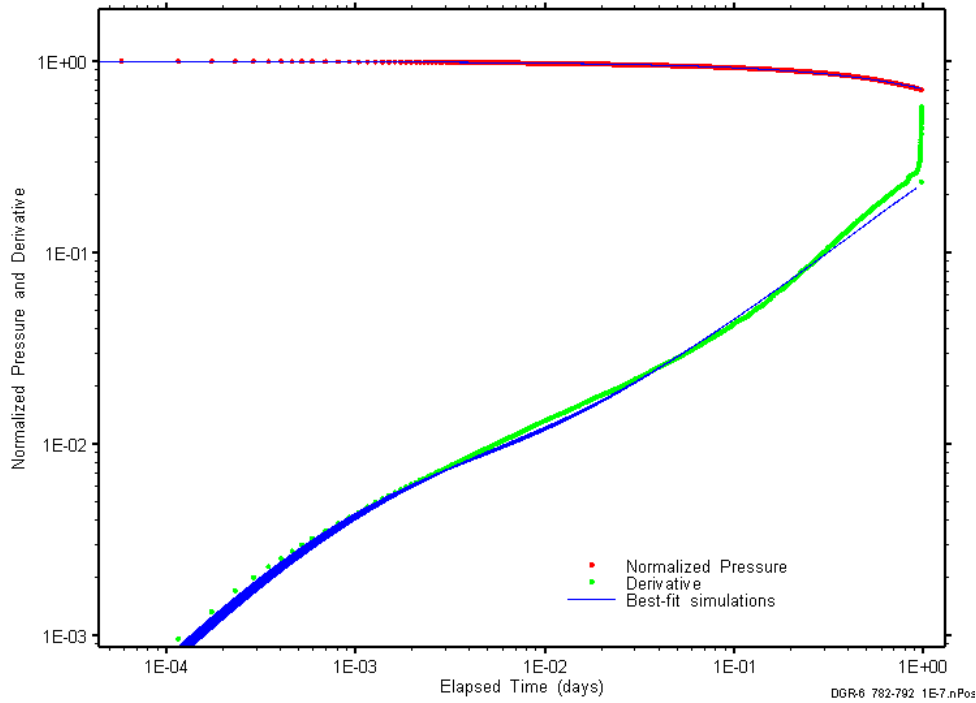


Figure F-102: Log-log plot showing simulations of the DGR6_683.39-691.94 PW2 Ramey B and derivative response.

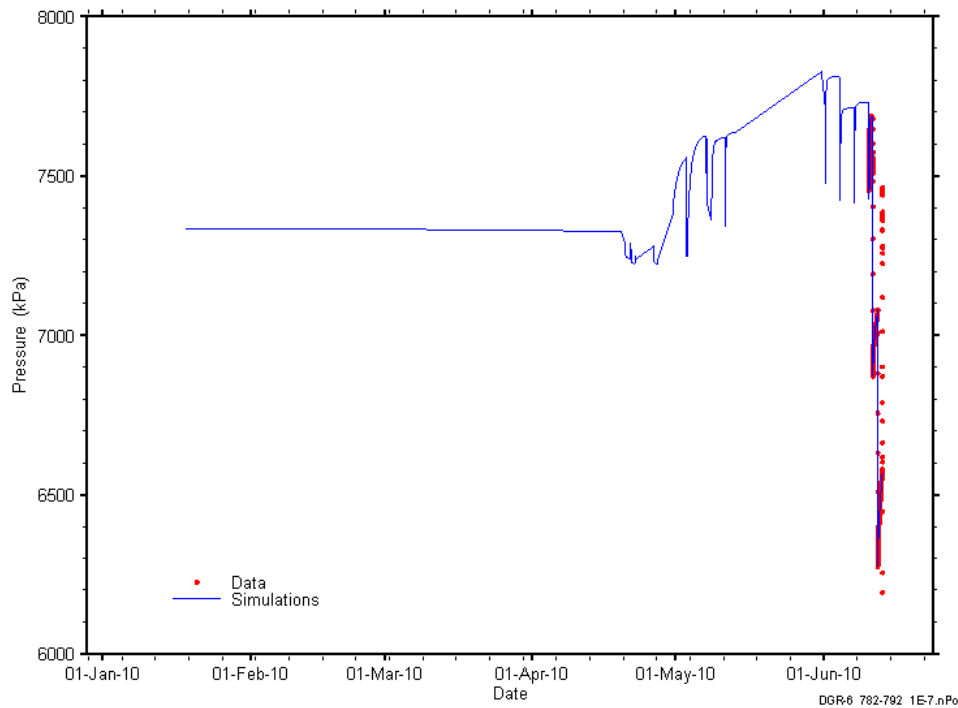


Figure F-103: Linear plot showing simulations of the DGR6_683.39-691.94 pressure response, including pre-test pressure history.

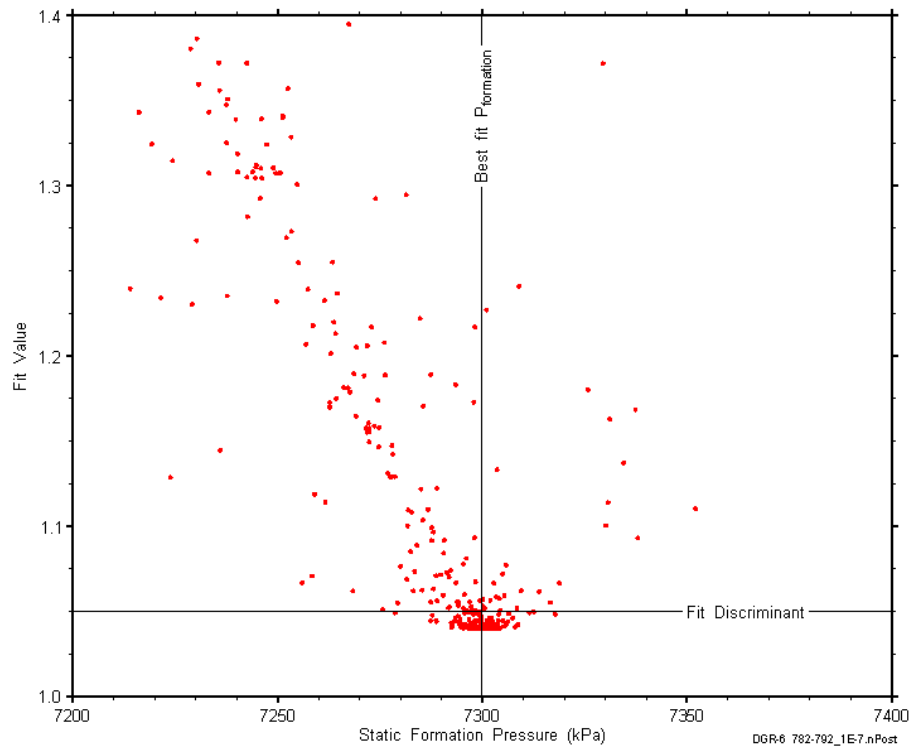


Figure F-104: XY-scatter plot showing the static formation pressure parameter space derived from DGR6_683.39-691.94 perturbation analysis along with the fit discriminant and best fit values.

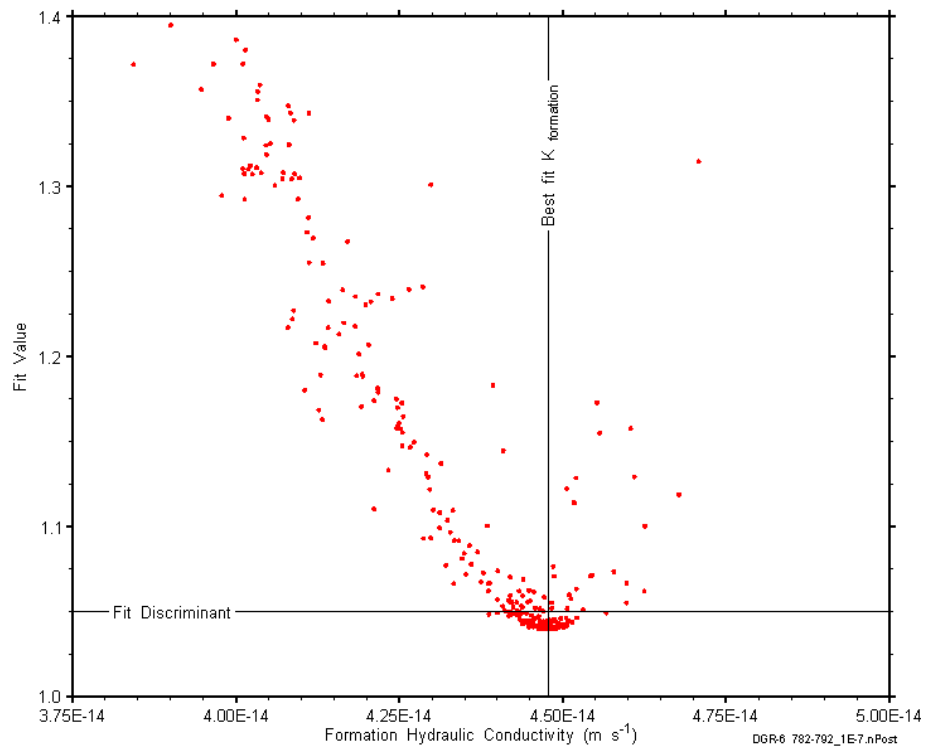


Figure F-105: XY-scatter plot showing the formation hydraulic conductivity parameter space derived from DGR6_683.39-691.94 perturbation analysis along with the fit discriminant and best fit values.

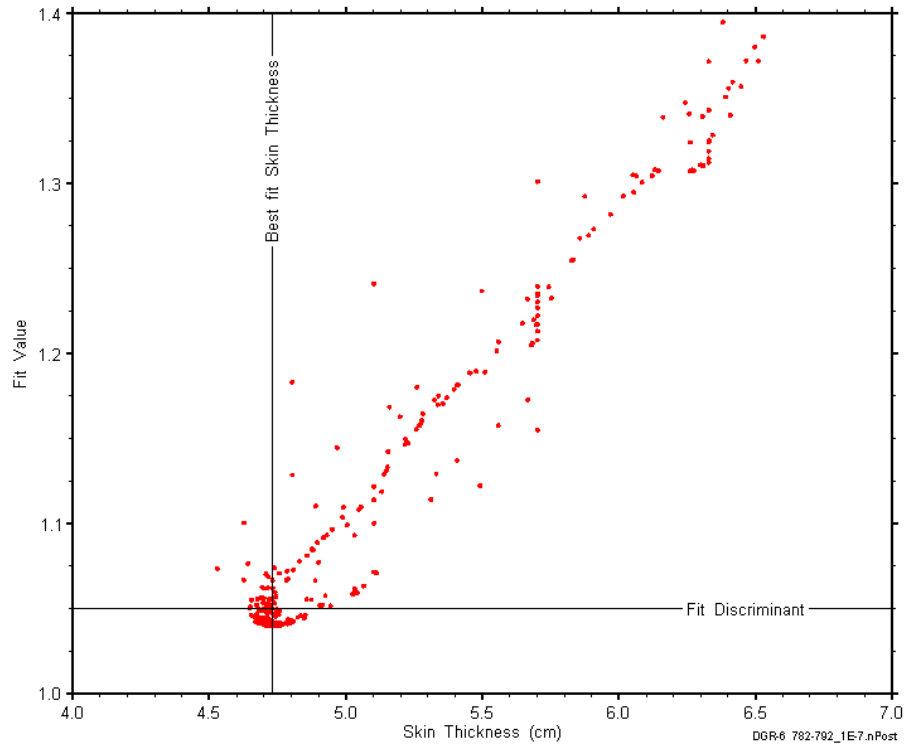


Figure F-106: XY-scatter plot showing the skin-thickness parameter space derived from DGR6_683.39-691.94 perturbation analysis along with the fit discriminant and best fit values.

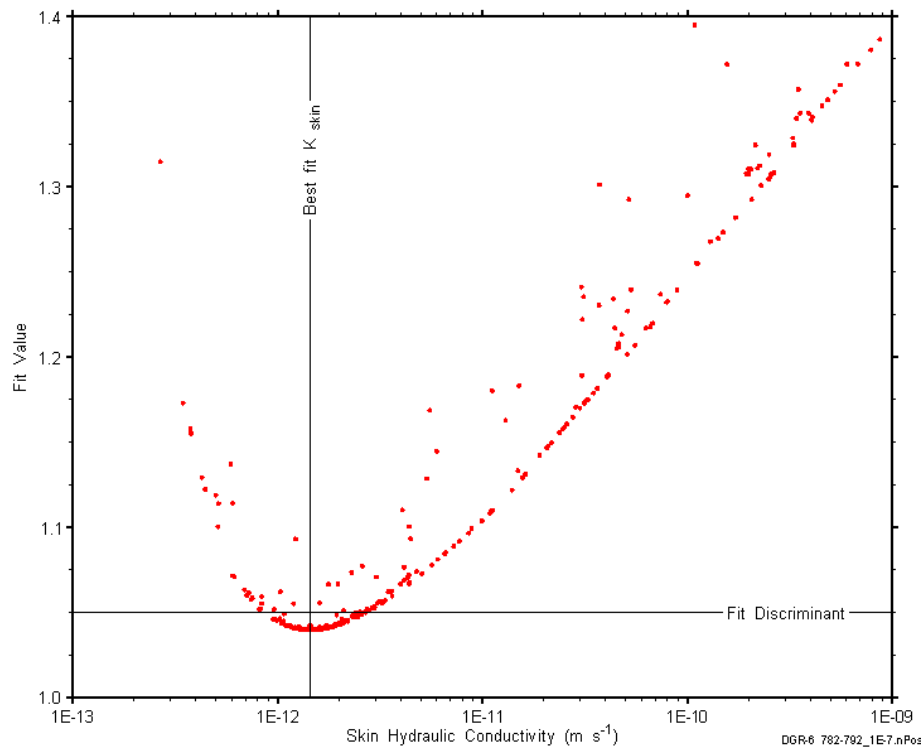


Figure F-107: XY-scatter plot showing the skin hydraulic conductivity parameter space derived from DGR6_683.39-691.94 perturbation analysis along with the fit discriminant and best fit values.

F.9 695.94-704.51 Sherman Fall

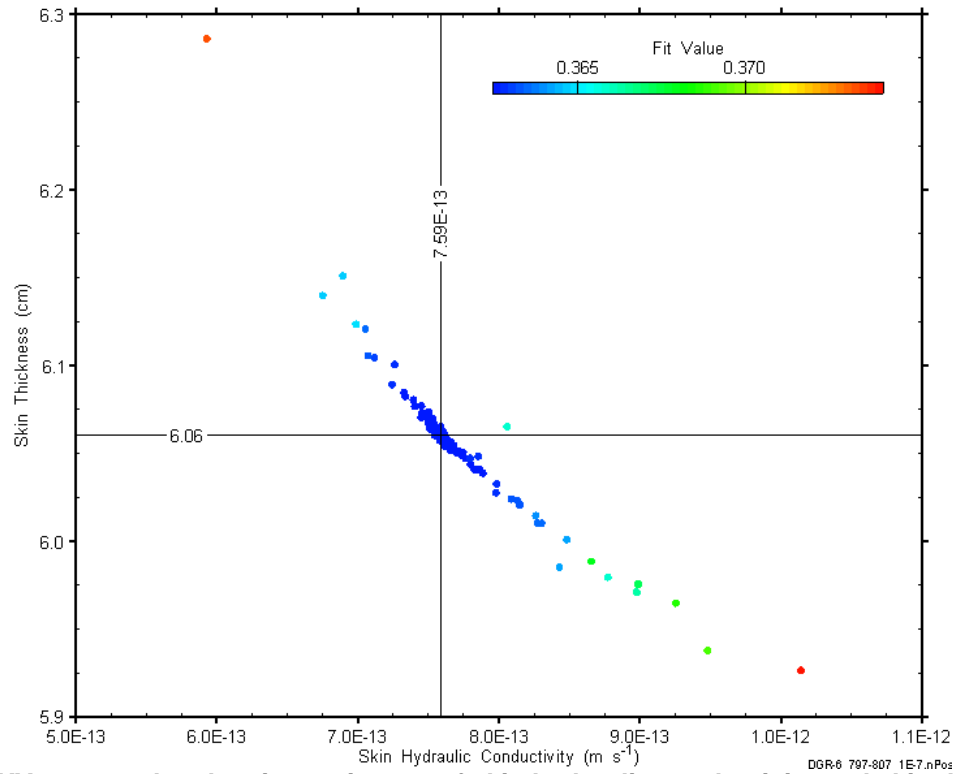


Figure F-108: XY-scatter plot showing estimates of skin hydraulic conductivity and skin thickness derived from the DGR6_695.94-704.51 perturbation analysis.

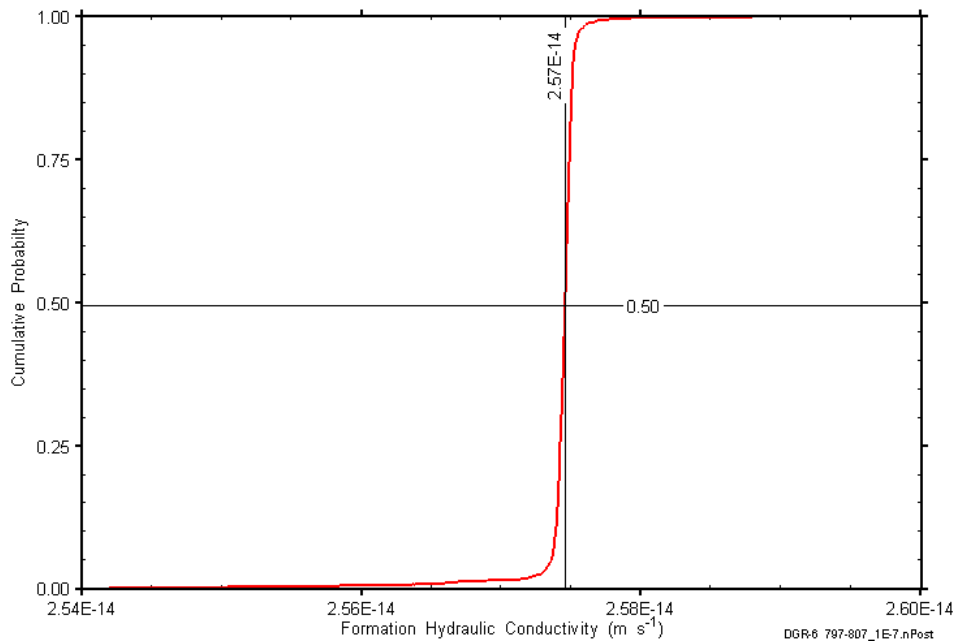


Figure F-109: DGR6_695.94-704.51 formation hydraulic conductivity cumulative distribution function.

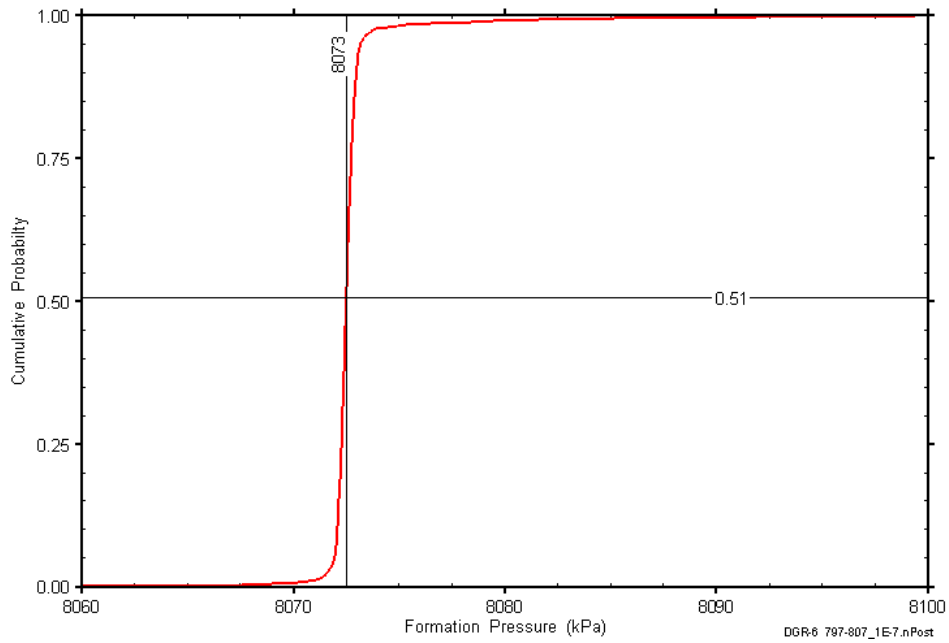


Figure F-110: DGR6_695.94-704.51 static formation pressure cumulative distribution function.

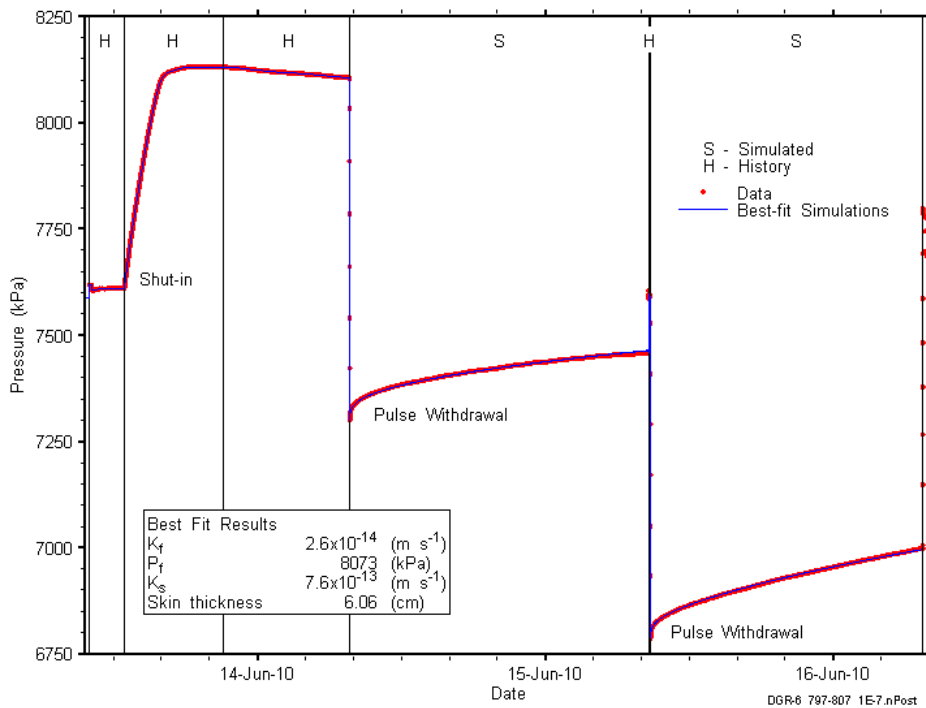


Figure F-111: Linear plot showing simulations of the DGR6_695.94-704.51 pressure response.

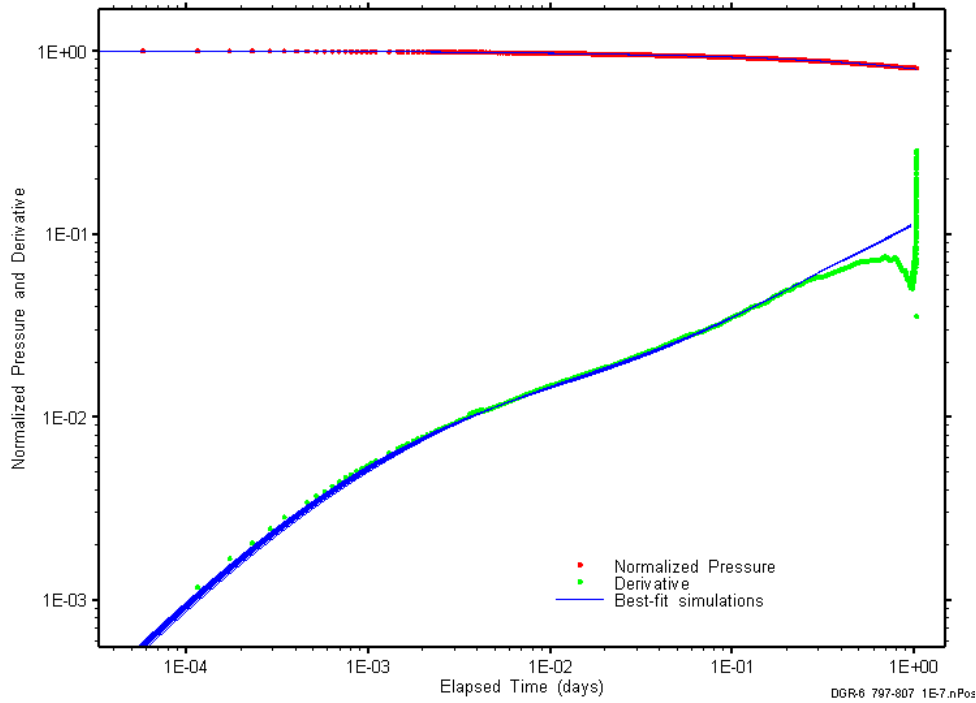


Figure F-112: Log-log plot showing simulations of the DGR6_695.94-704.51 PW1 Ramey B and derivative response.

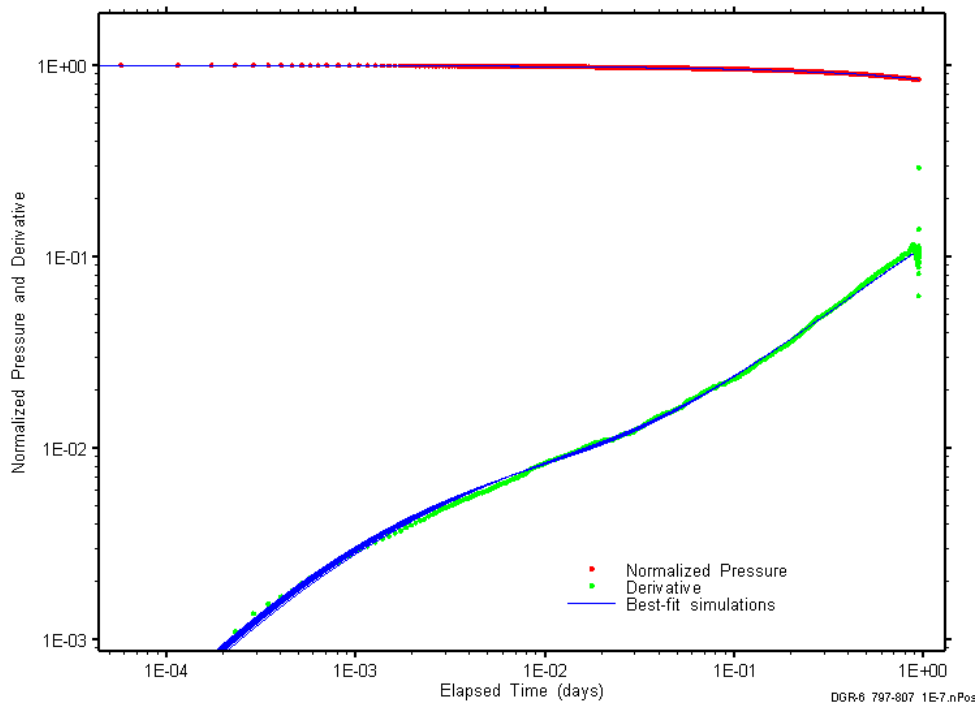


Figure F-113: Log-log plot showing simulations of the DGR6_695.94-704.51 PW2 Ramey B and derivative response.

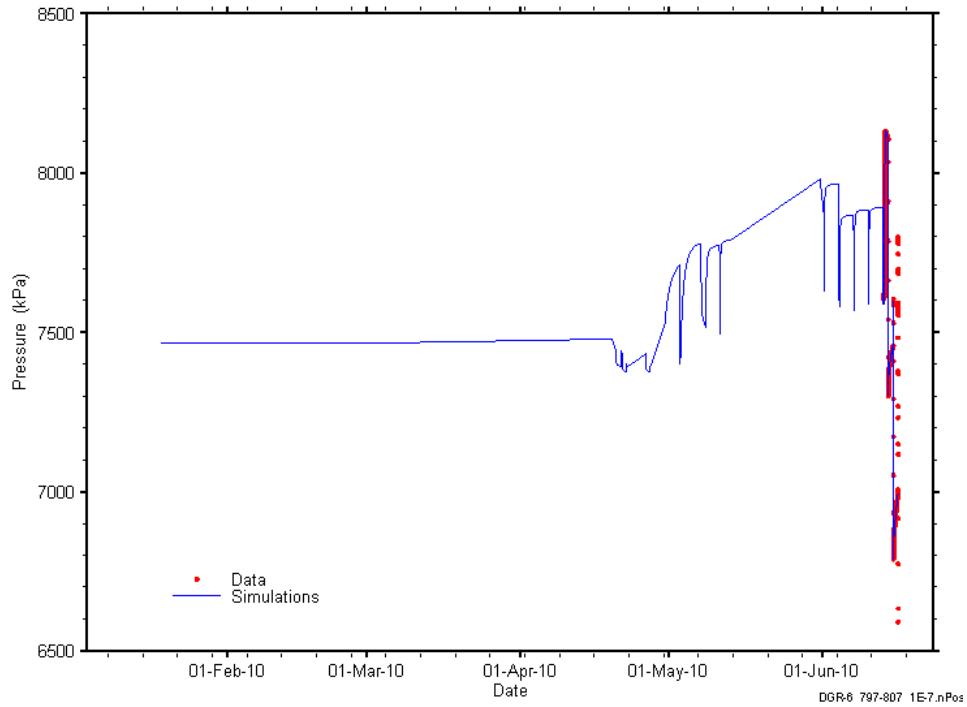


Figure F-114: Linear plot showing simulations of the DGR6_695.94-704.51 pressure response, including pre-test pressure history.

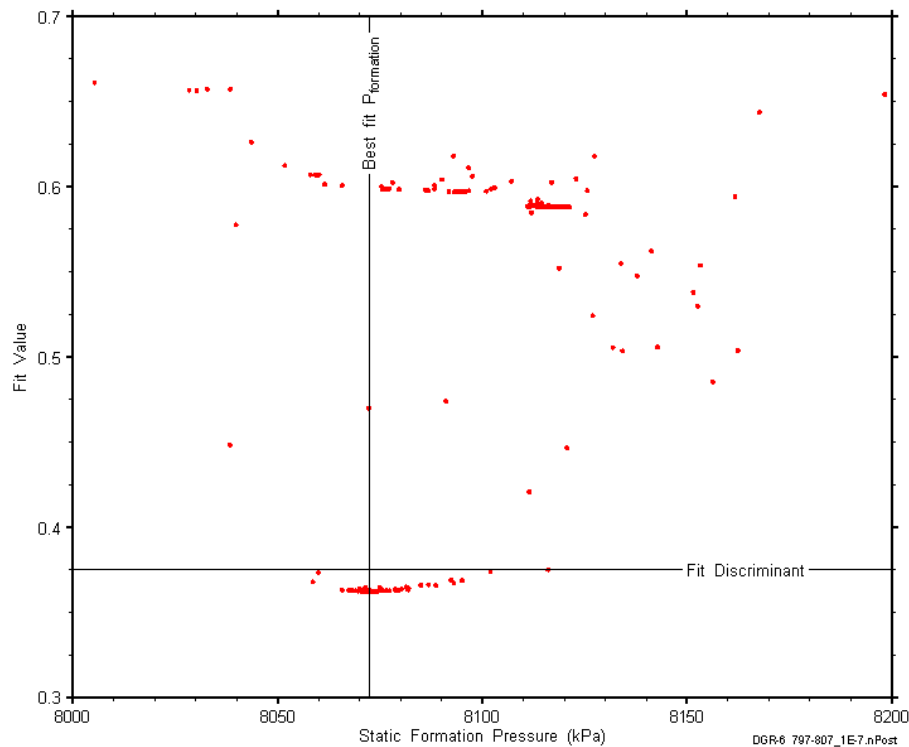


Figure F-115: XY-scatter plot showing the static formation pressure parameter space derived from DGR6_695.94-704.51 perturbation analysis along with the fit discriminant and best fit values.

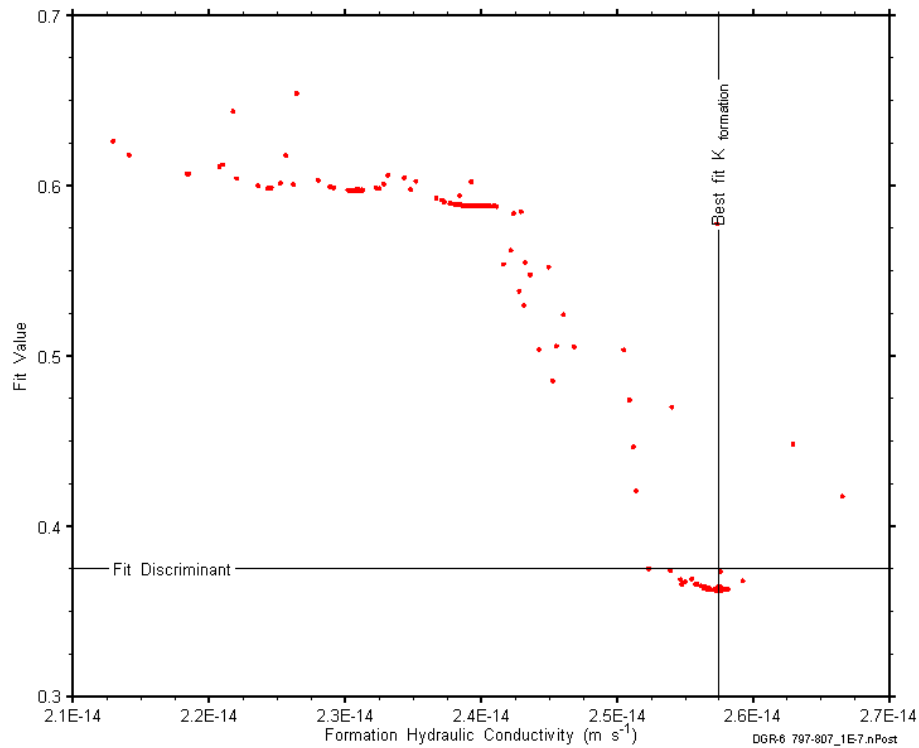


Figure F-116: XY-scatter plot showing the formation hydraulic conductivity parameter space derived from DGR6_695.94-704.51 perturbation analysis along with the fit discriminant and best fit values.

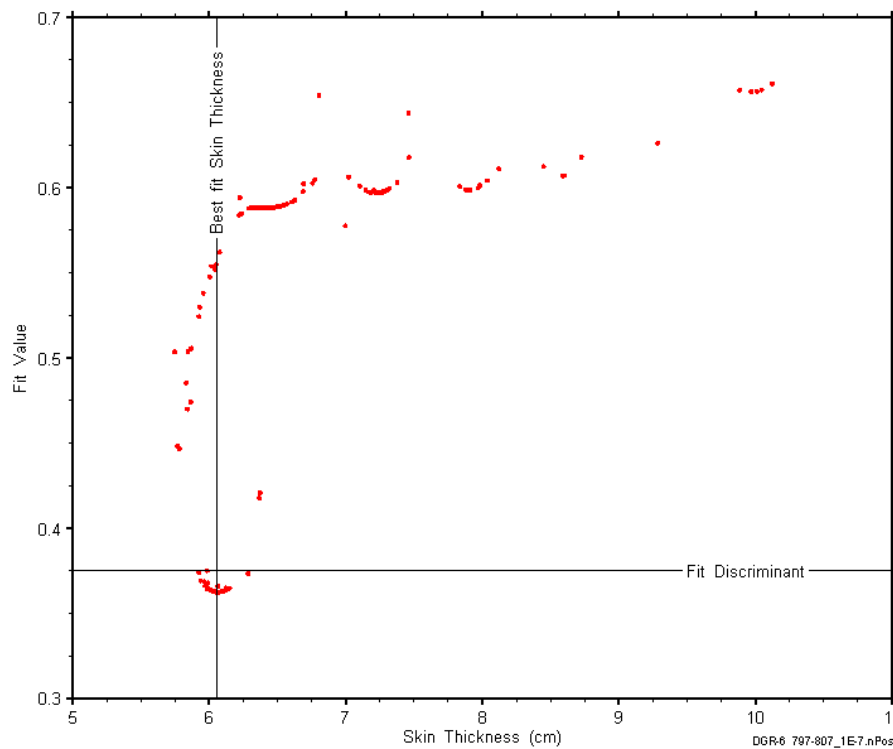


Figure F-117: XY-scatter plot showing the skin-thickness parameter space derived from DGR6_695.94-704.51 perturbation analysis along with the fit discriminant and best fit values.

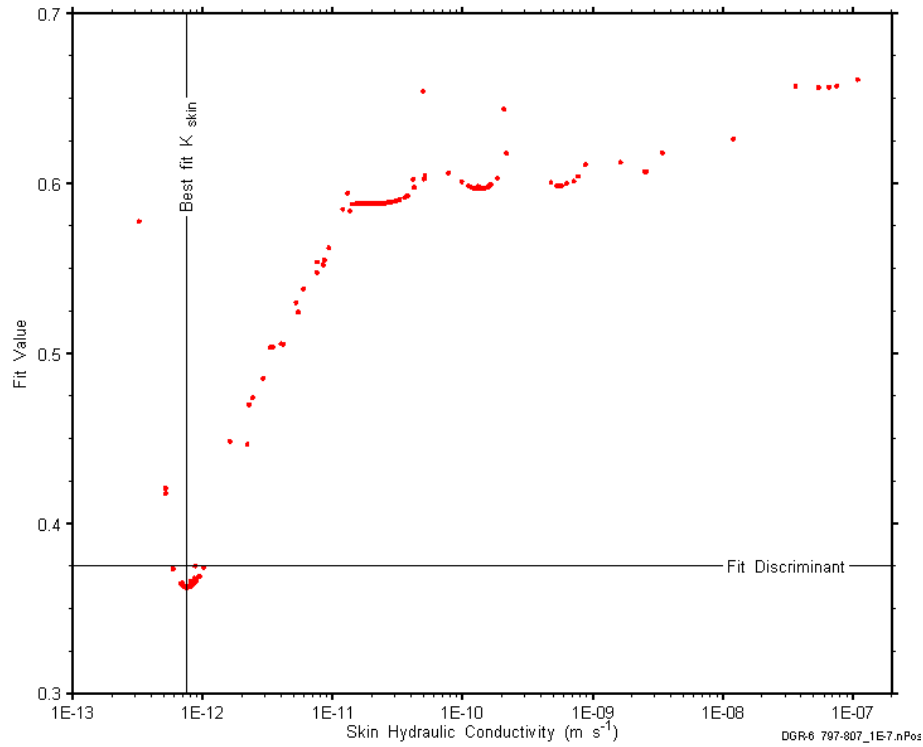


Figure F-118: XY-scatter plot showing the skin hydraulic conductivity parameter space derived from DGR6_695.94-704.51 perturbation analysis along with the fit discriminant and best fit values.

F.10 732.76-741.35 Kirkfield

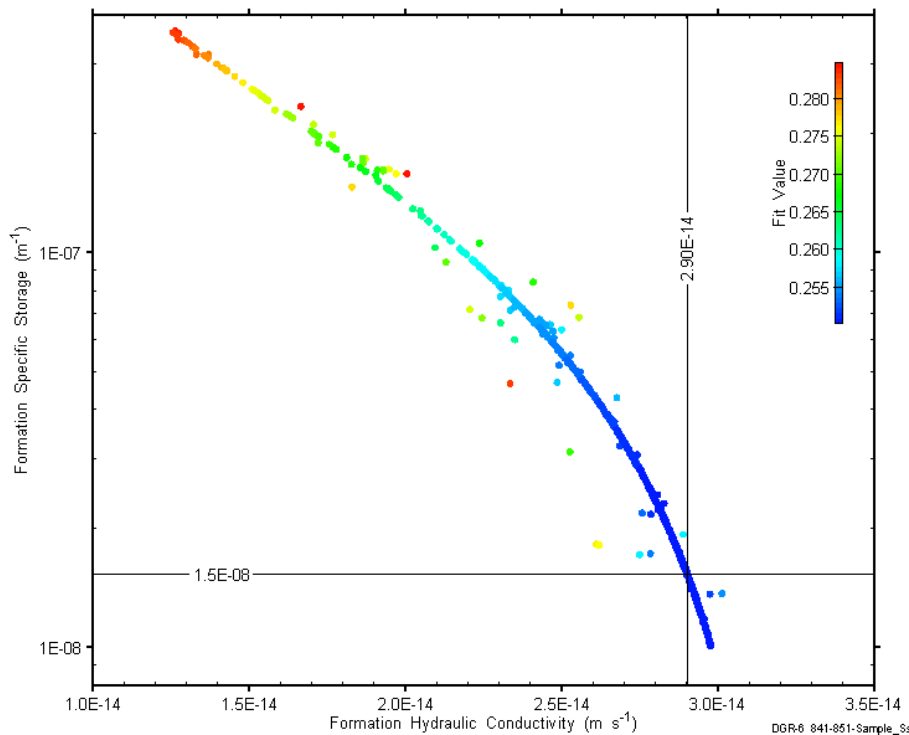


Figure F-119: XY-scatter plot showing estimates of formation hydraulic conductivity and formation specific storage derived from the DGR6_732.76-741.35 perturbation analysis.

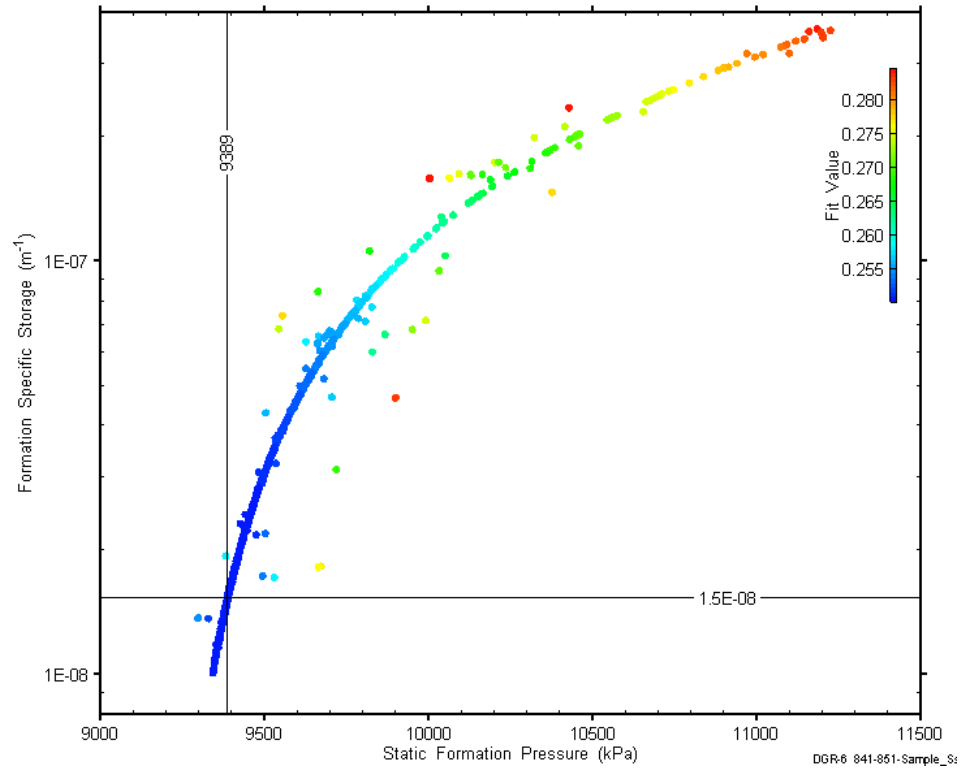


Figure F-120: XY-scatter plot showing estimates of static formation pressure and formation specific storage derived from the DGR6_732.76-741.35 perturbation analysis.

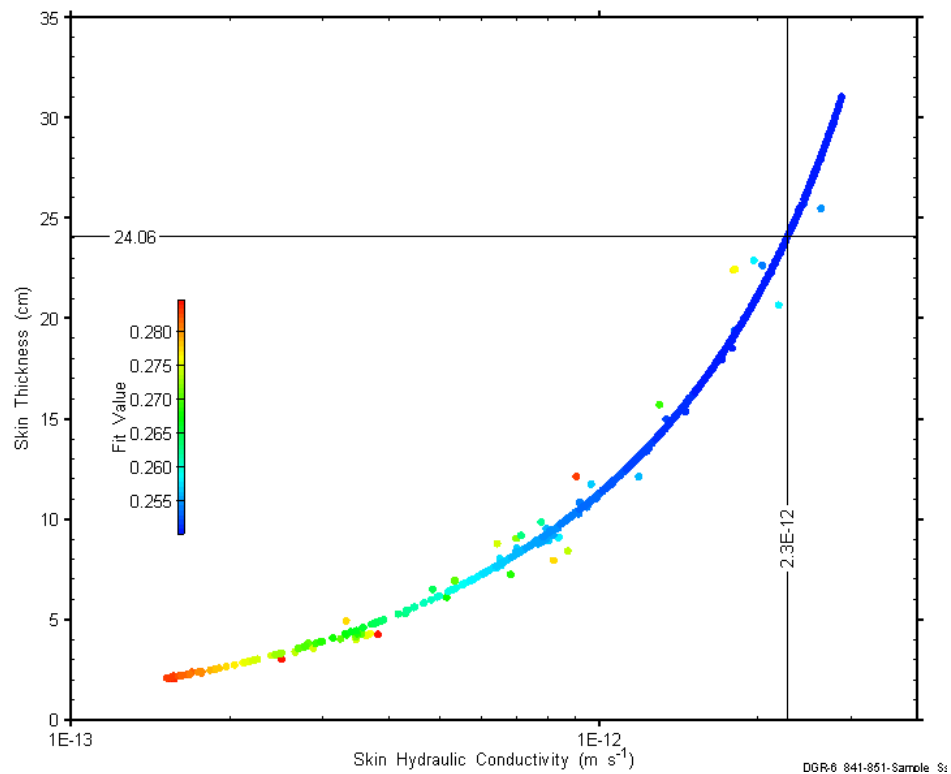


Figure F-121: XY-scatter plot showing estimates of skin hydraulic conductivity and skin thickness derived from the DGR6_732.76-741.35 perturbation analysis.

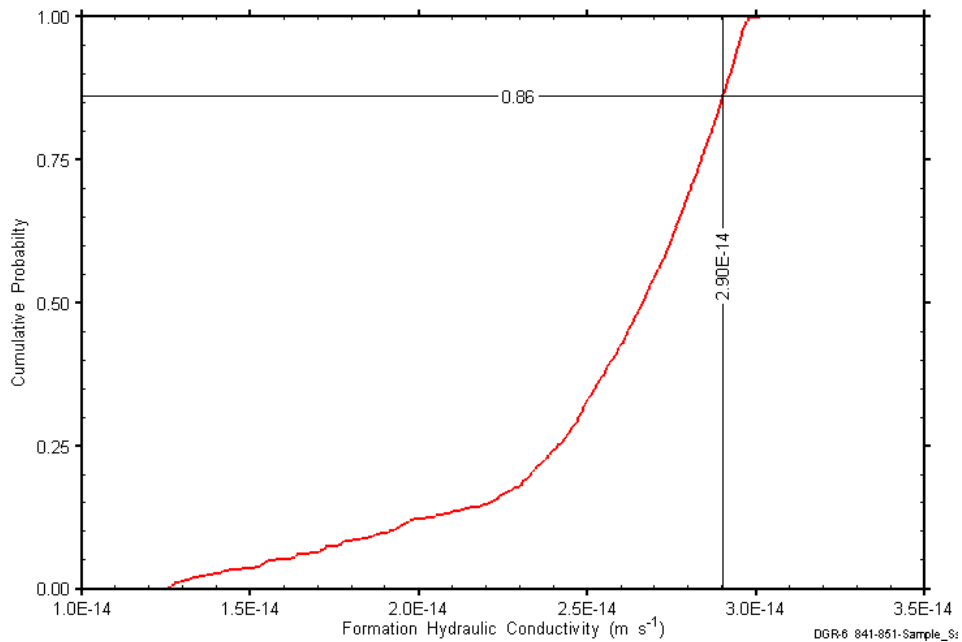


Figure F-122: DGR6_732.76-741.35 formation hydraulic conductivity cumulative distribution function.

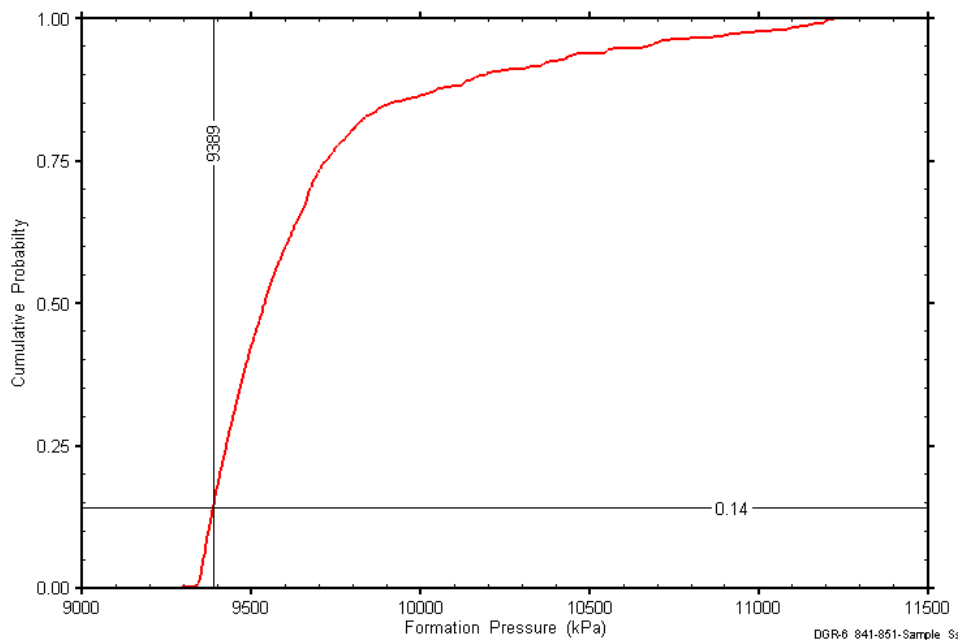


Figure F-123: DGR6_732.76-741.35 static formation pressure cumulative distribution function.

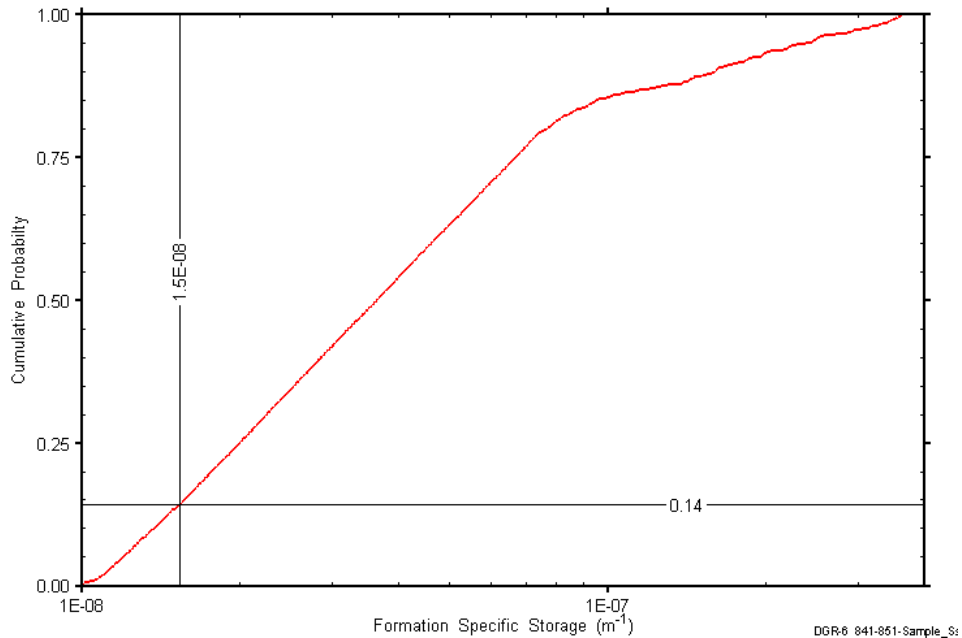


Figure F-124: DGR6_732.76-741.35 formation specific storage cumulative distribution function.

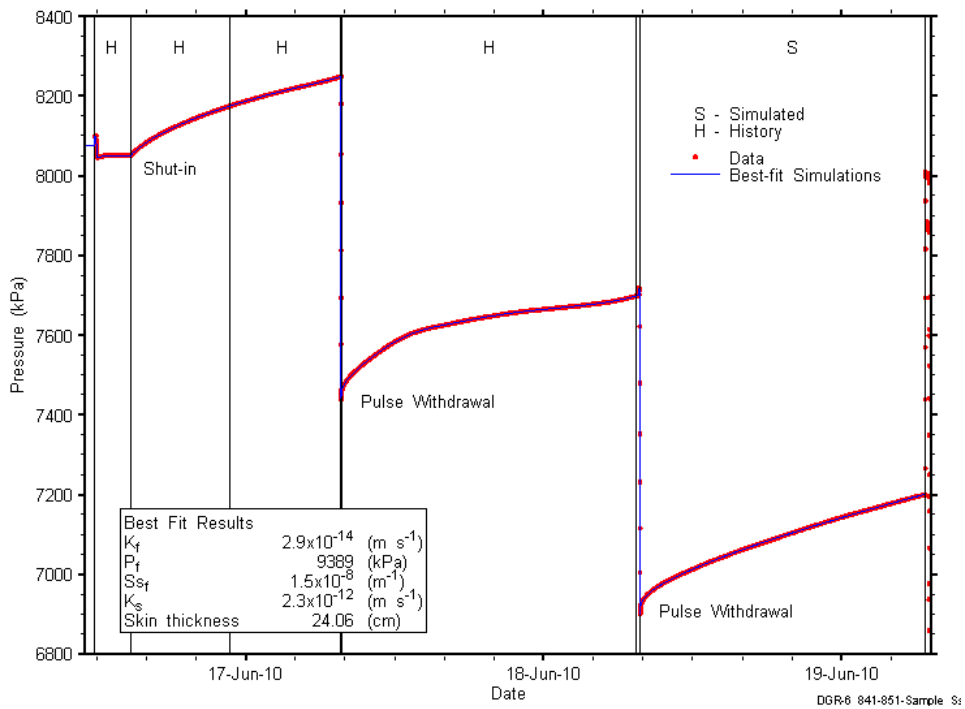


Figure F-125: Linear plot showing simulations of the DGR6_732.76-741.35 pressure response.

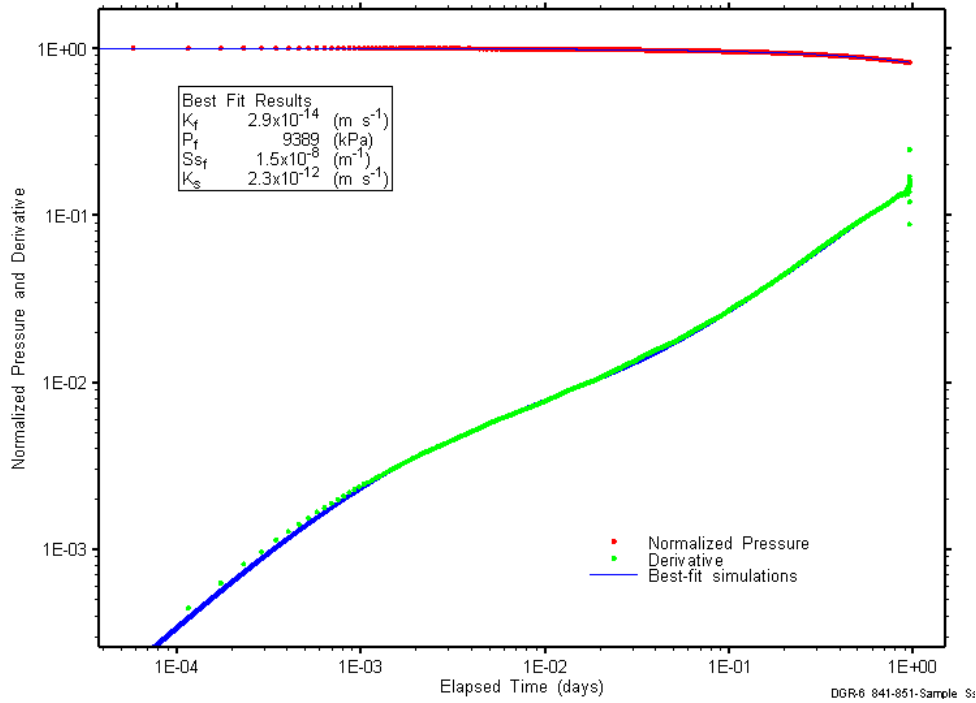


Figure F-126: Log-log plot showing simulations of the DGR6_732.76-741.35 PW2 Ramey B and derivative response.

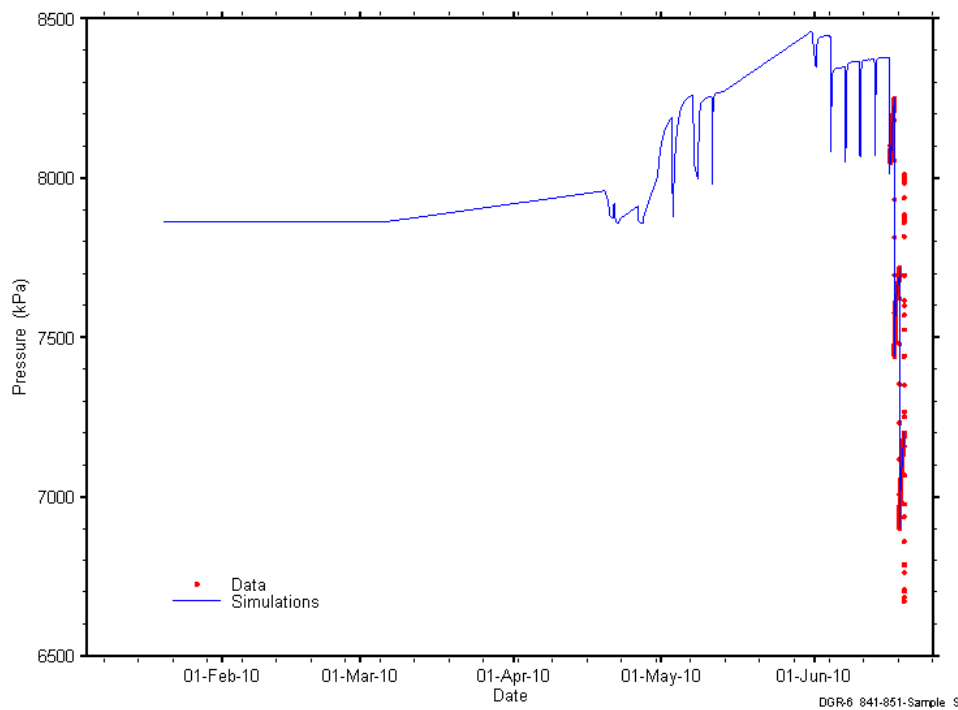


Figure F-127: Linear plot showing simulations of the DGR6_732.76-741.35 pressure response, including pre-test pressure history.

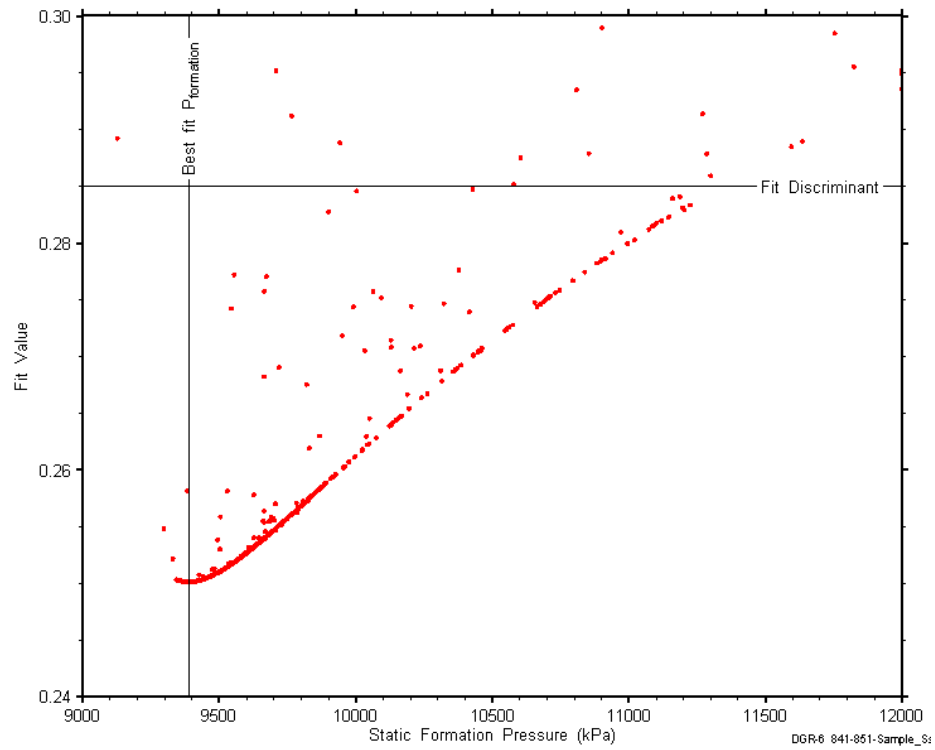


Figure F-128: XY-scatter plot showing the static formation pressure parameter space derived from DGR6_732.76-741.35 perturbation analysis along with the fit discriminant and best fit values.

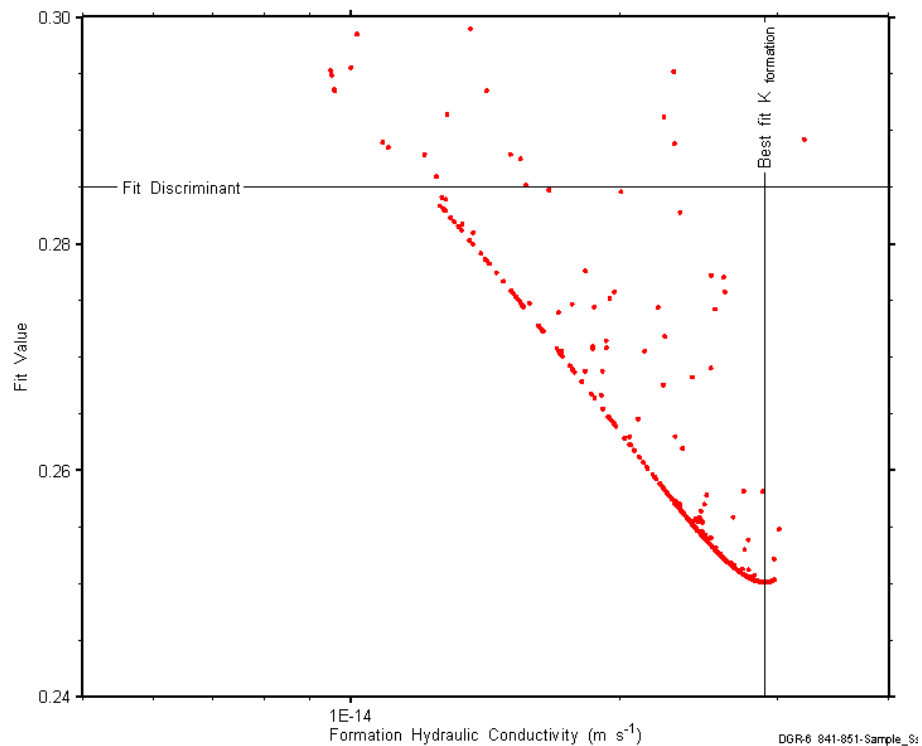


Figure F-129: XY-scatter plot showing the formation hydraulic conductivity parameter space derived from DGR6_732.76-741.35 perturbation analysis along with the fit discriminant and best fit values.

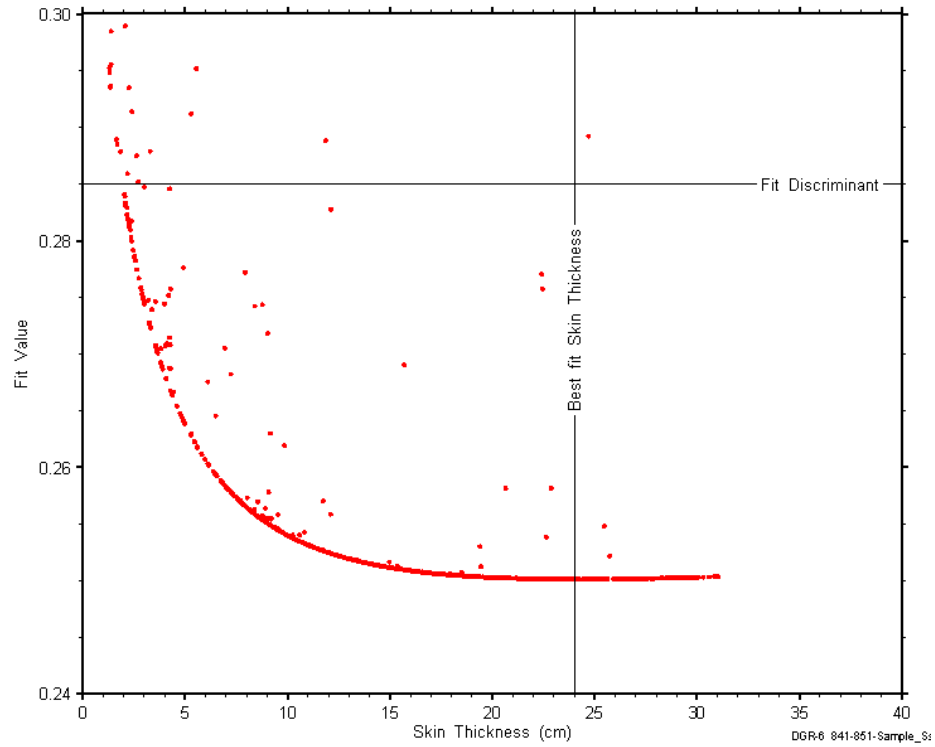


Figure F-130: XY-scatter plot showing the skin-thickness parameter space derived from DGR6_732.76-741.35 perturbation analysis along with the fit discriminant and best fit values.

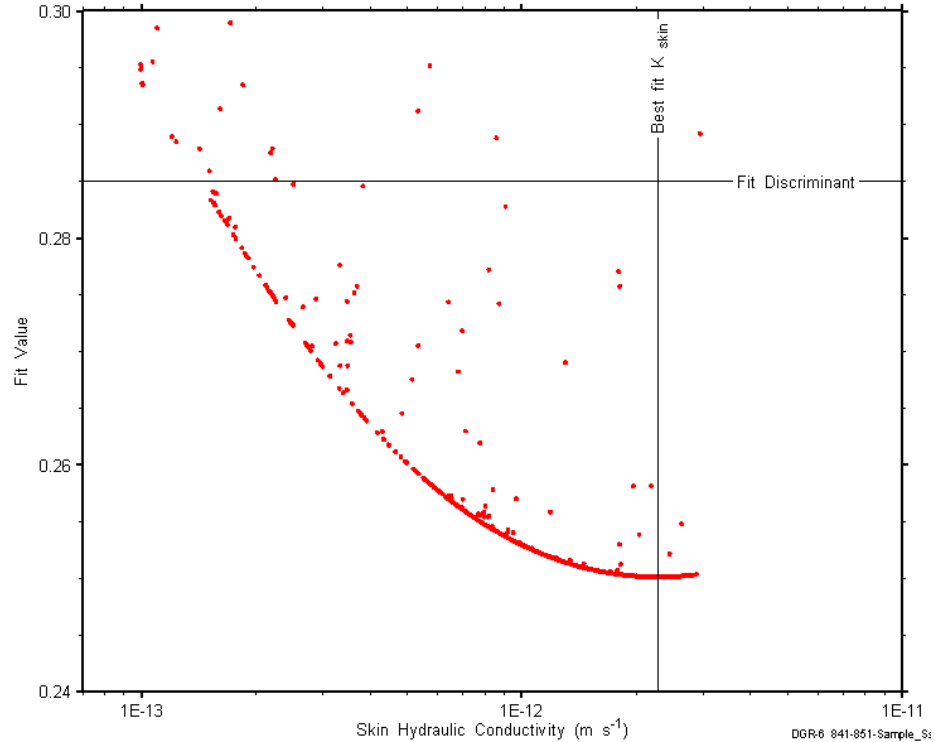


Figure F-131: XY-scatter plot showing the skin hydraulic conductivity parameter space derived from DGR6_732.76-741.35 perturbation analysis along with the fit discriminant and best fit values.

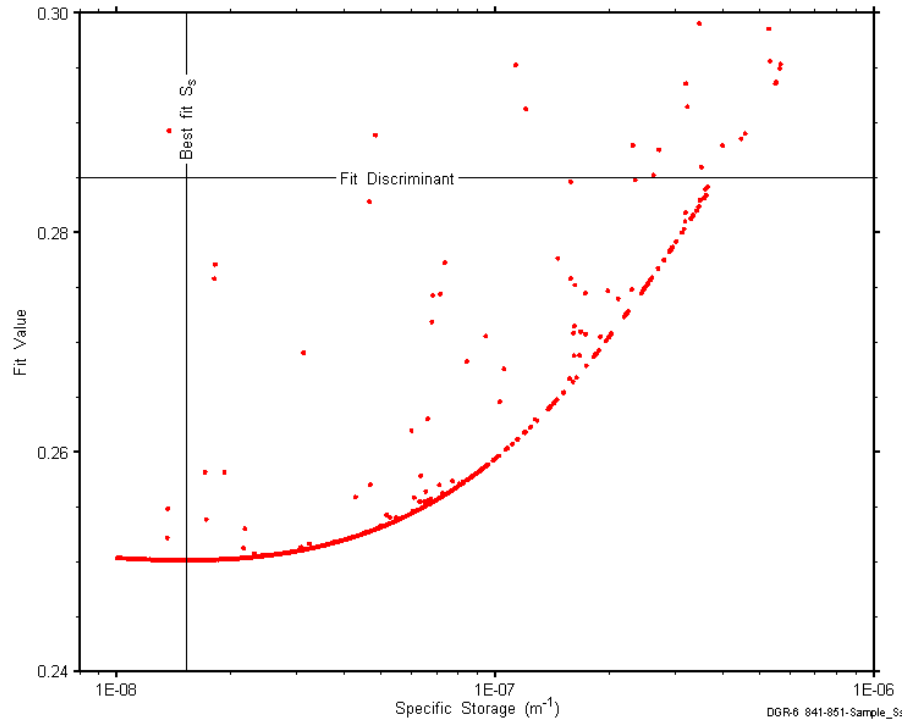


Figure F-132: XY-scatter plot showing the formation specific storage parameter space derived from DGR6_732.76-741.35 perturbation analysis along with the fit discriminant and best fit values.

F.11 756.93-765.55 Coboconk

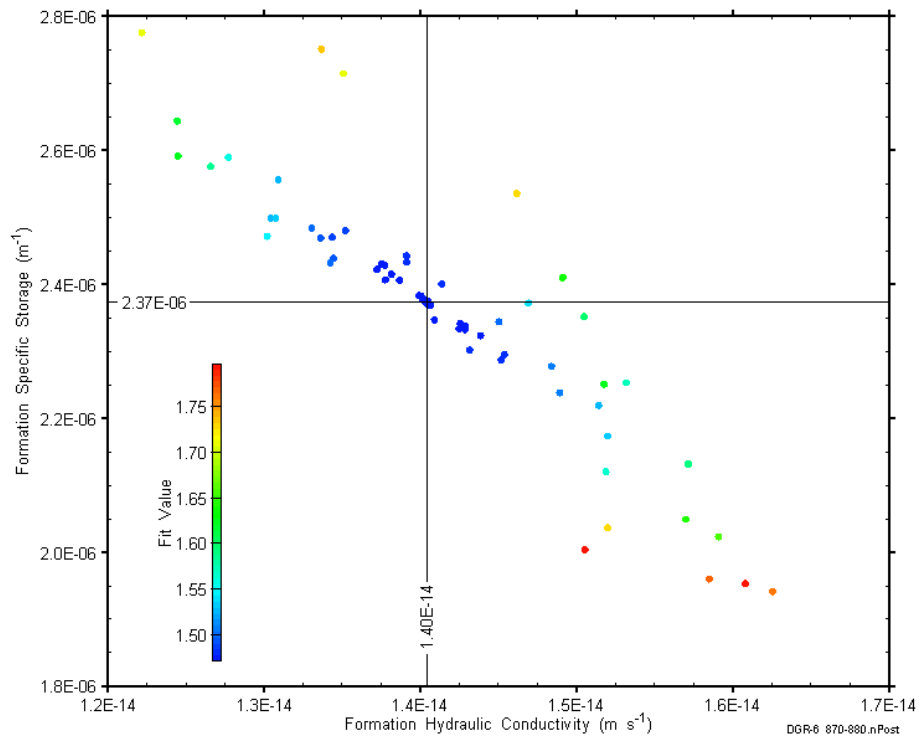


Figure F-133: XY-scatter plot showing estimates of formation hydraulic conductivity and formation specific storage derived from the DGR6_756.93-765.55 perturbation analysis.

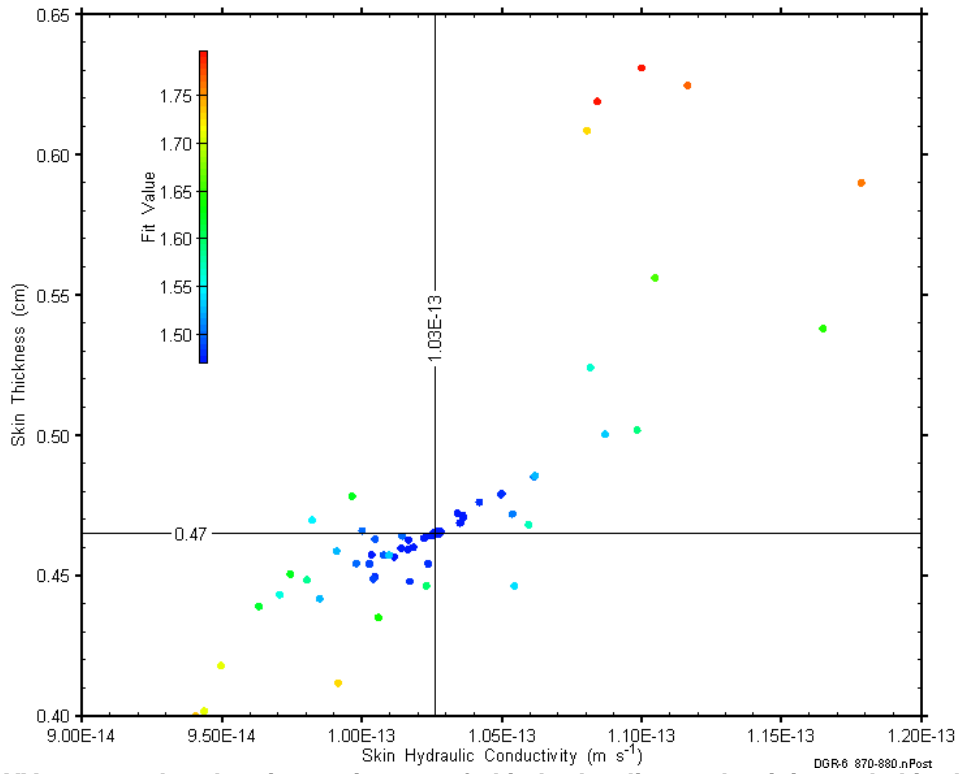


Figure F-134: XY-scatter plot showing estimates of skin hydraulic conductivity and skin thickness derived from the DGR6_756.93-765.55 perturbation analysis.

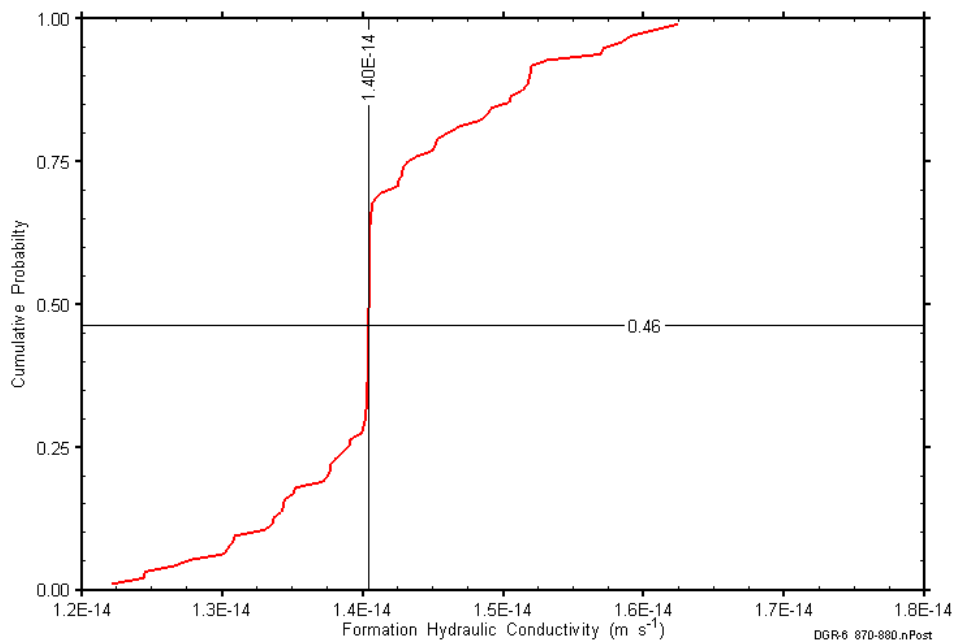


Figure F-135: DGR6_756.93-765.55 formation hydraulic conductivity cumulative distribution function.

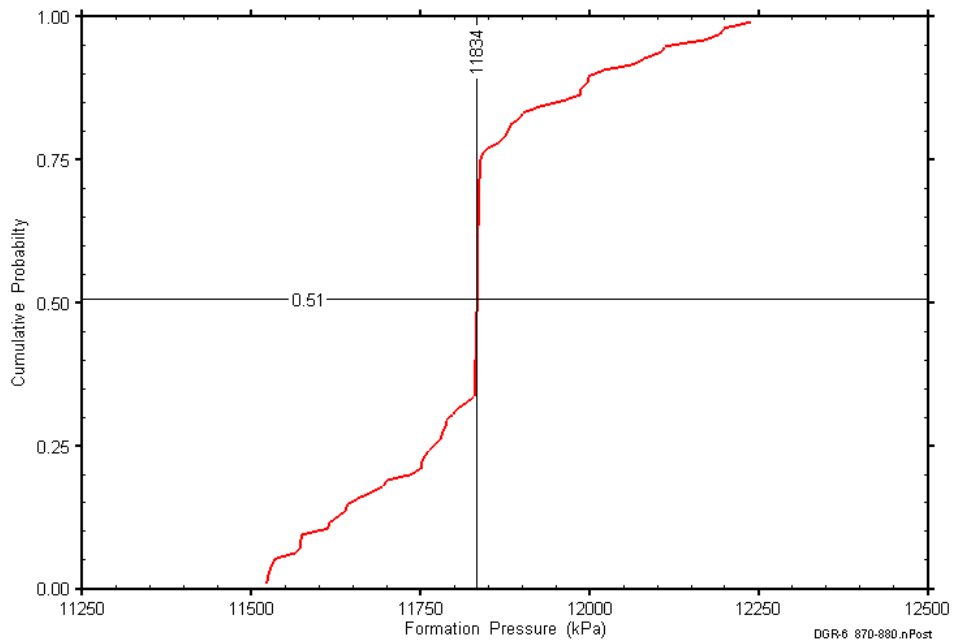


Figure F-136: DGR6_756.93-765.55 static formation pressure cumulative distribution function.

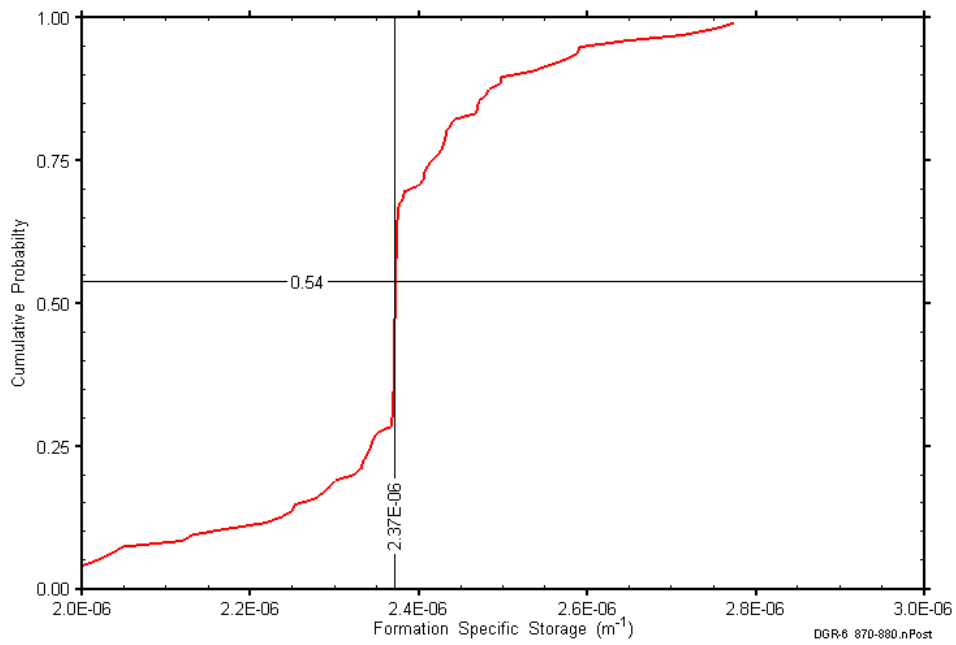


Figure F-137: DGR6_756.93-765.55 formation specific storage cumulative distribution function.

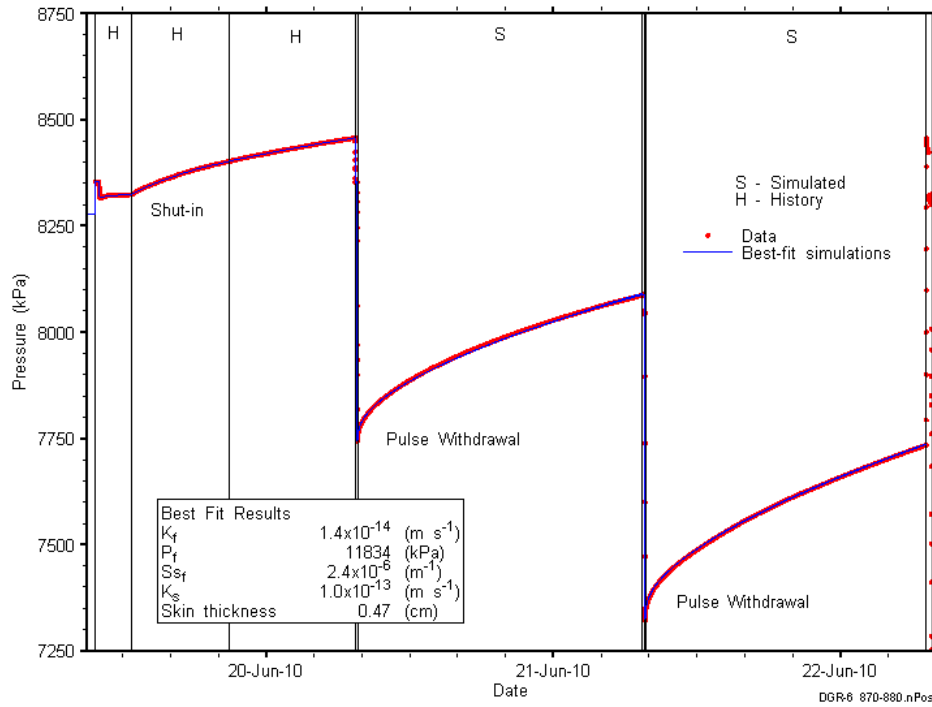


Figure F-138: Linear plot showing simulations of the DGR6_756.93-765.55 pressure response.

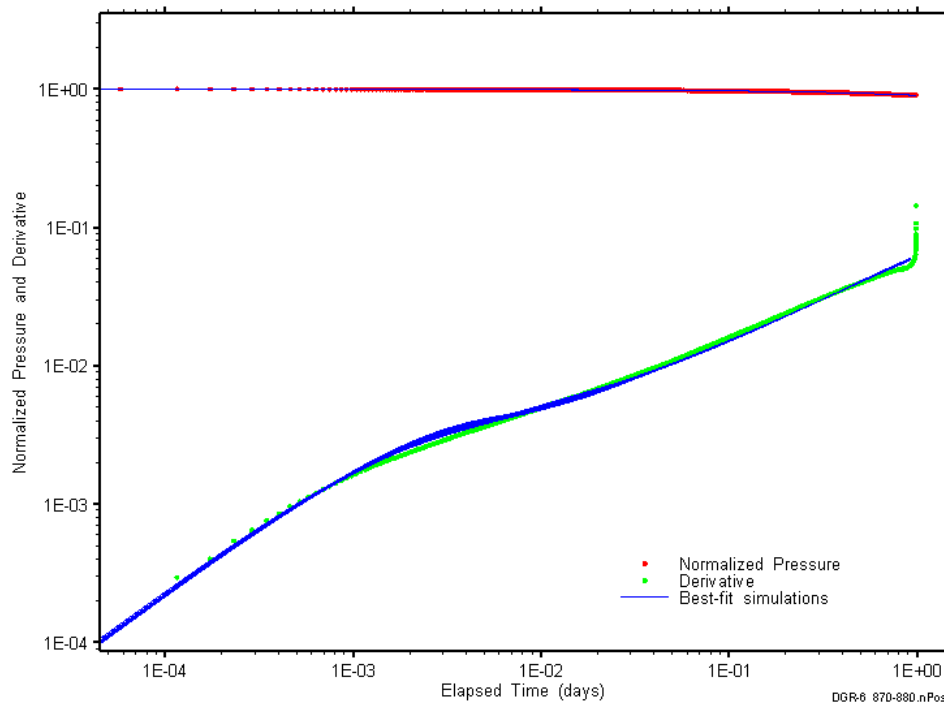


Figure F-139: Log-log plot showing simulations of the DGR6_756.93-765.55 PW1 Ramey B and derivative response.

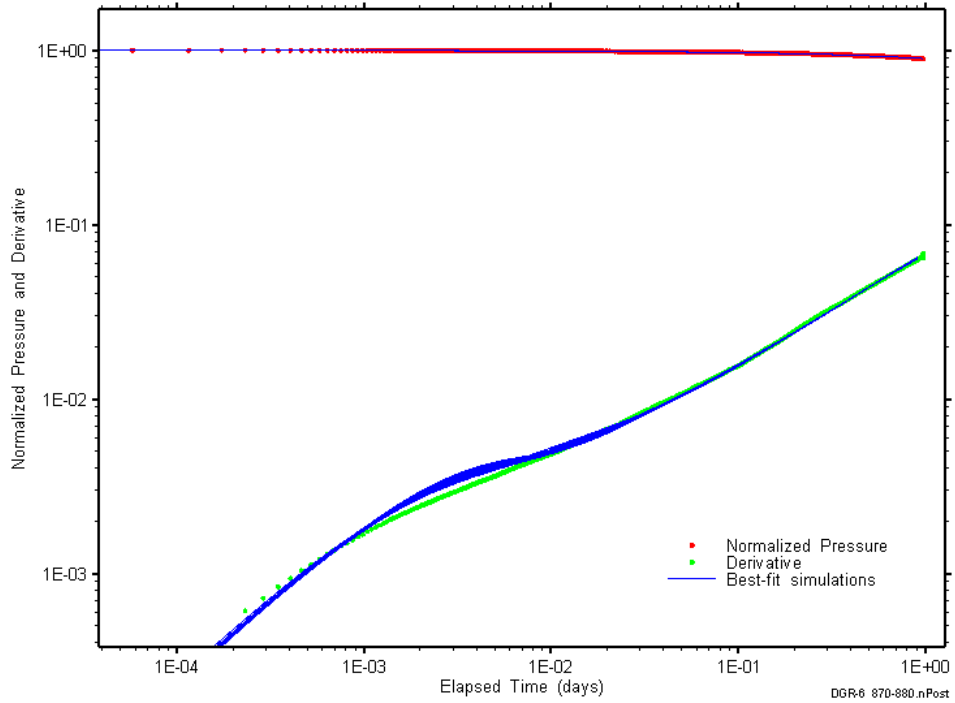


Figure F-140: Log-log plot showing simulations of the DGR6_756.93-765.55 PW2 Ramey B and derivative response.

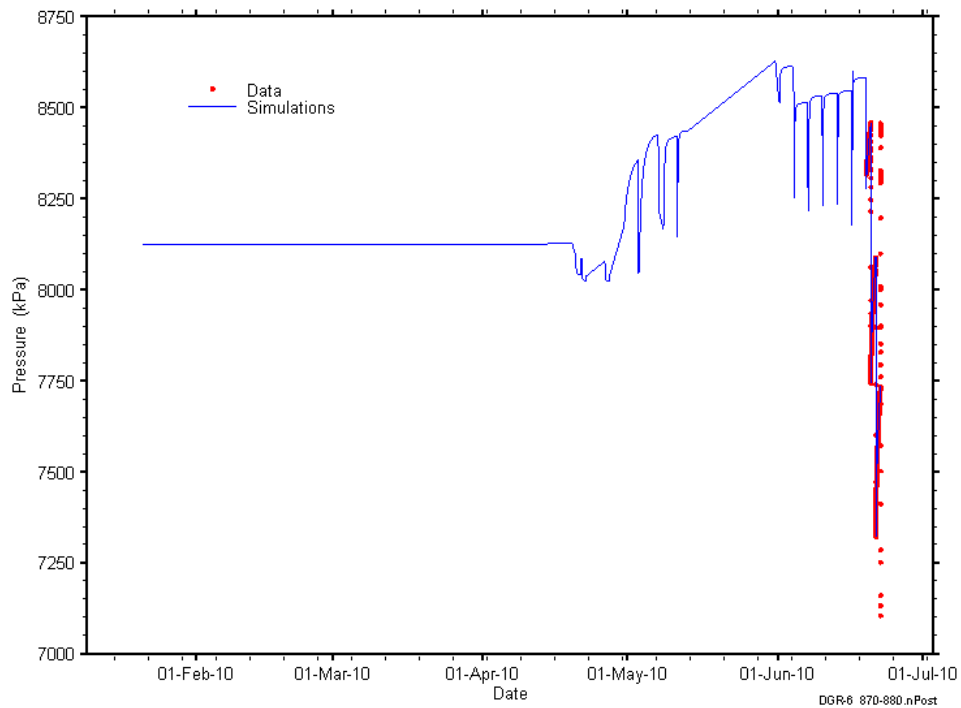


Figure F-141: Linear plot showing simulations of the DGR6_756.93-765.55 pressure response, including pre-test pressure history.

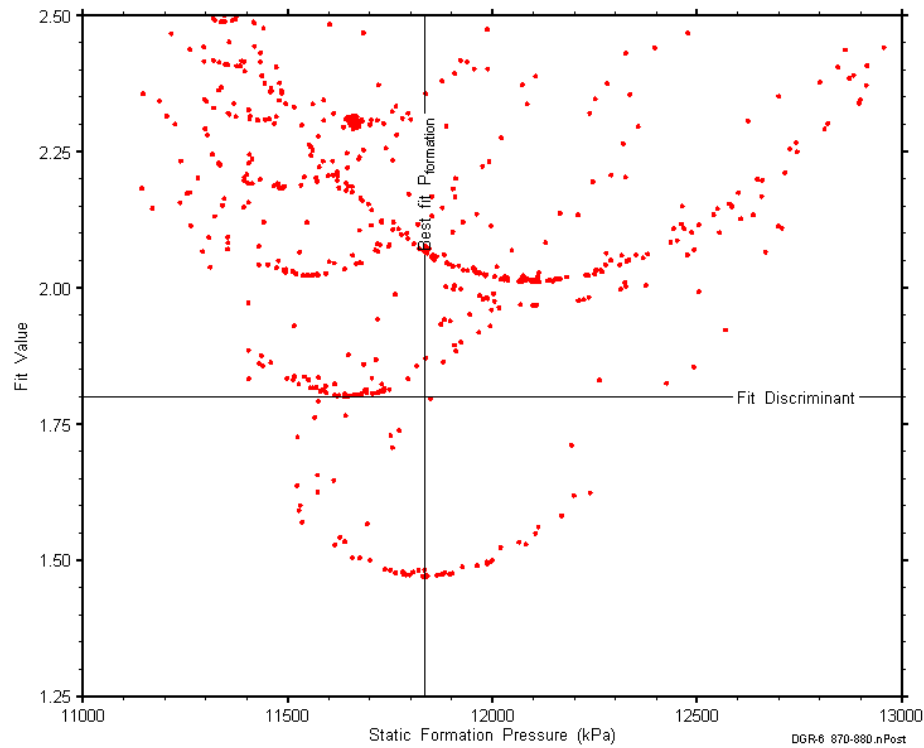


Figure F-142: XY-scatter plot showing the static formation pressure parameter space derived from DGR6_756.93-765.55 perturbation analysis along with the fit discriminant and best fit values.

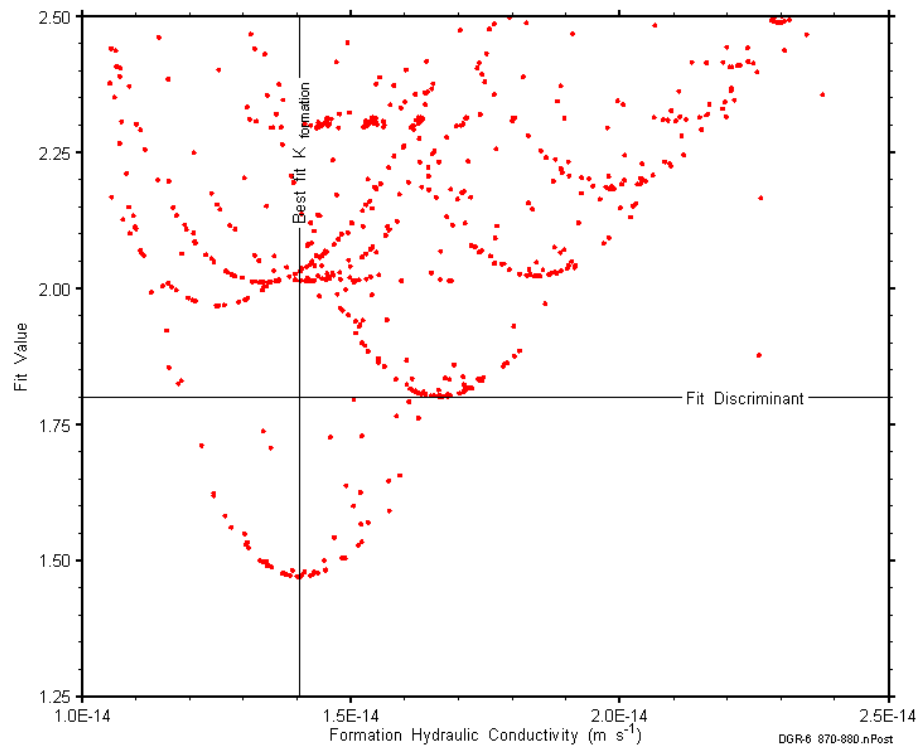


Figure F-143: XY-scatter plot showing the formation hydraulic conductivity parameter space derived from DGR6_756.93-765.55 perturbation analysis along with the fit discriminant and best fit values.

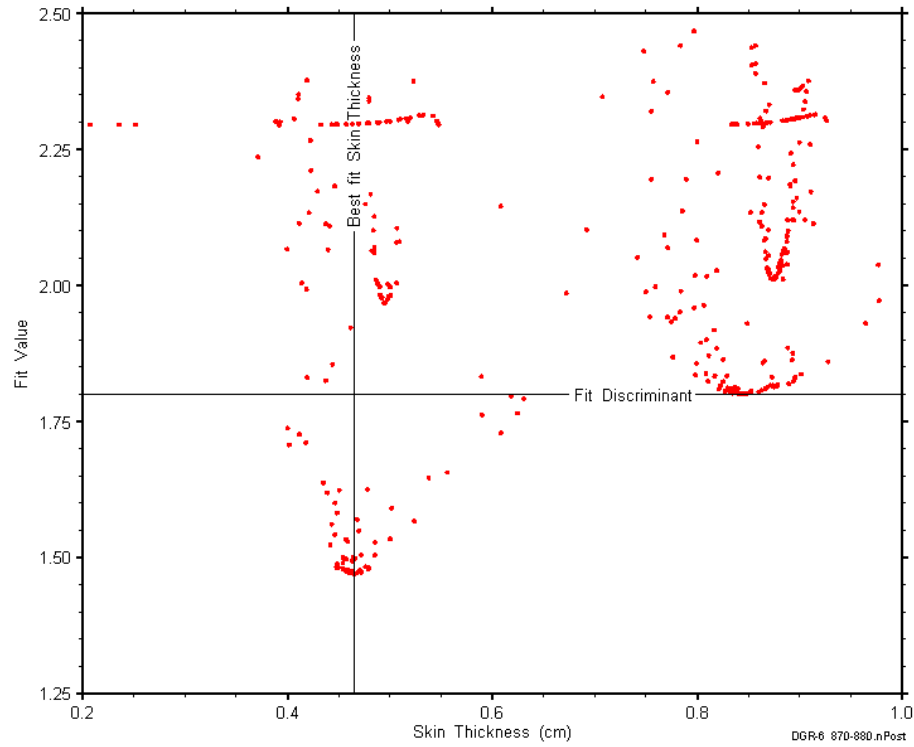


Figure F-144: XY-scatter plot showing the skin-thickness parameter space derived from DGR6_756.93-765.55 perturbation analysis along with the fit discriminant and best fit values.

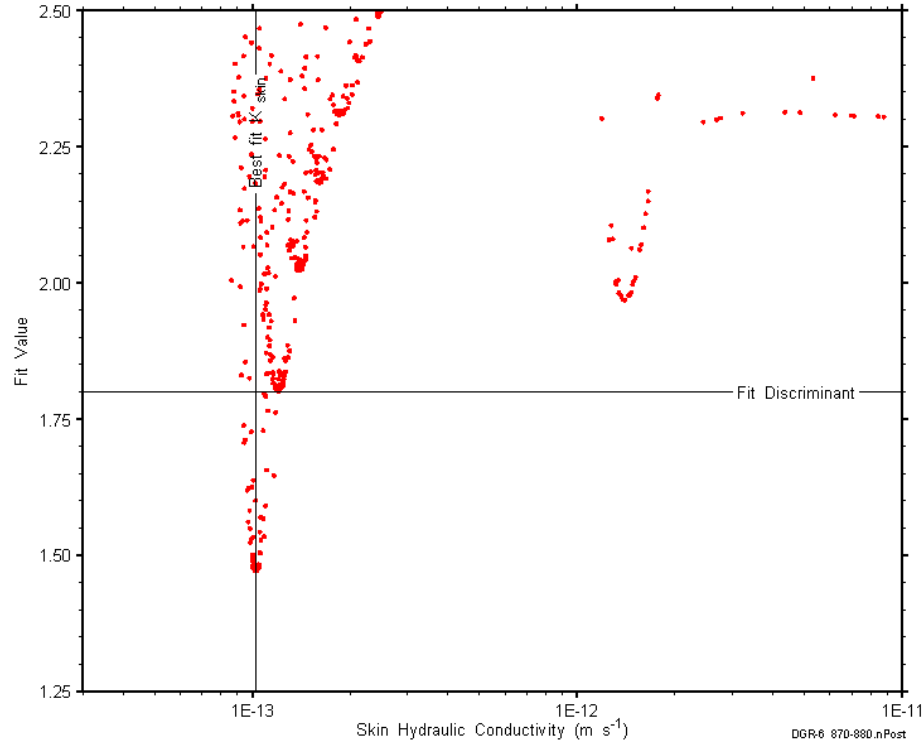


Figure F-145: XY-scatter plot showing the skin hydraulic conductivity parameter space derived from DGR6_756.93-765.55 perturbation analysis along with the fit discriminant and best fit values.

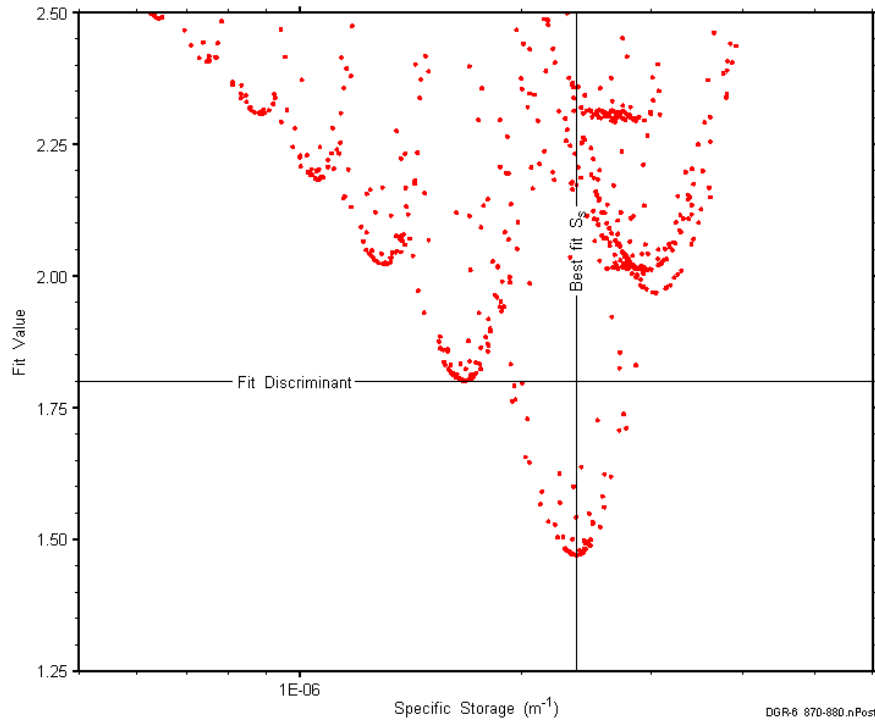


Figure F-146: XY-scatter plot showing the formation specific storage parameter space derived from DGR6_756.93-765.55 perturbation analysis along with the fit discriminant and best fit values.

F.12 765.55-774.24 Coboconk

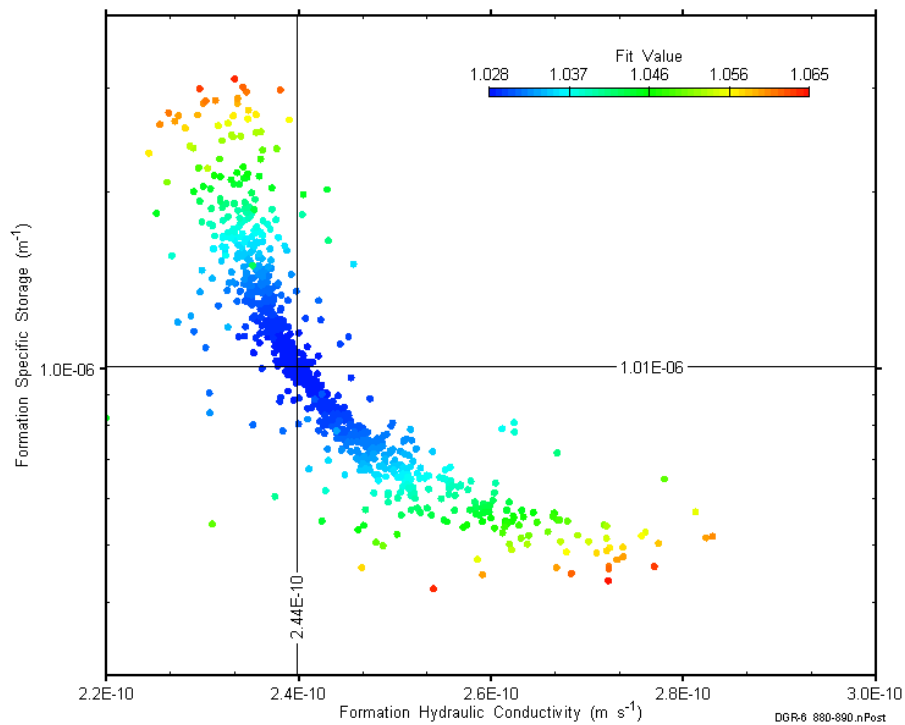


Figure F-147: XY-scatter plot showing estimates of formation hydraulic conductivity and formation specific storage derived from the DGR6_765.55-774.24 perturbation analysis.

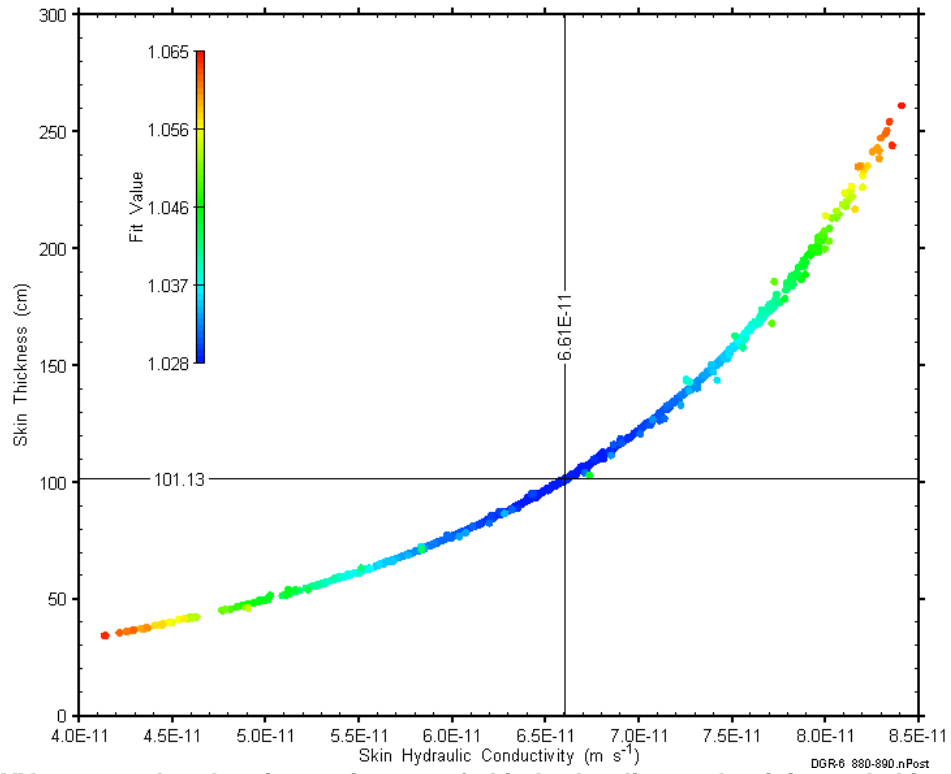


Figure F-148: XY-scatter plot showing estimates of skin hydraulic conductivity and skin thickness derived from the DGR6_765.55-774.24 perturbation analysis.

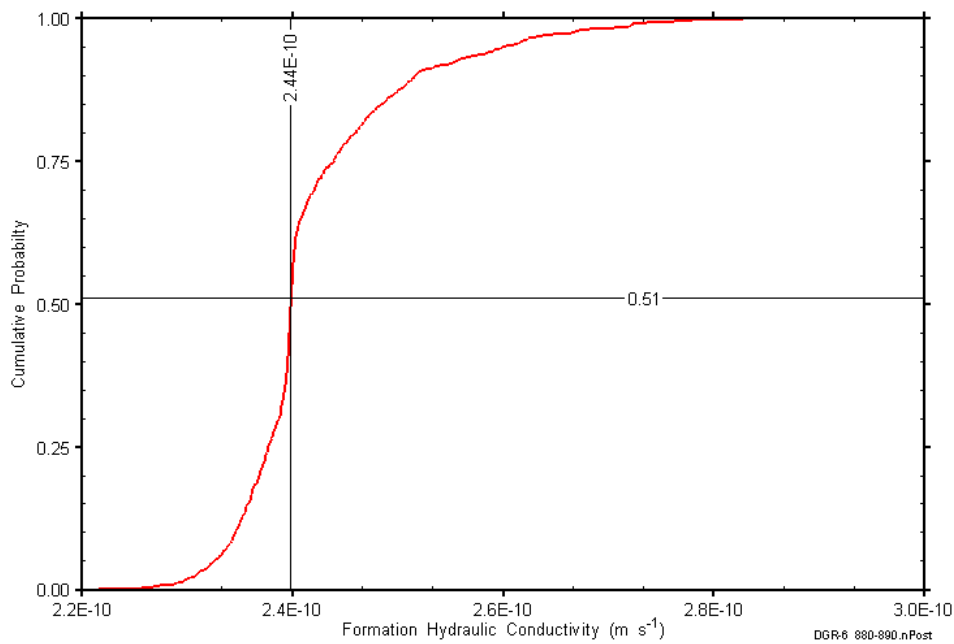


Figure F-149: DGR6_765.55-774.24 formation hydraulic conductivity cumulative distribution function.

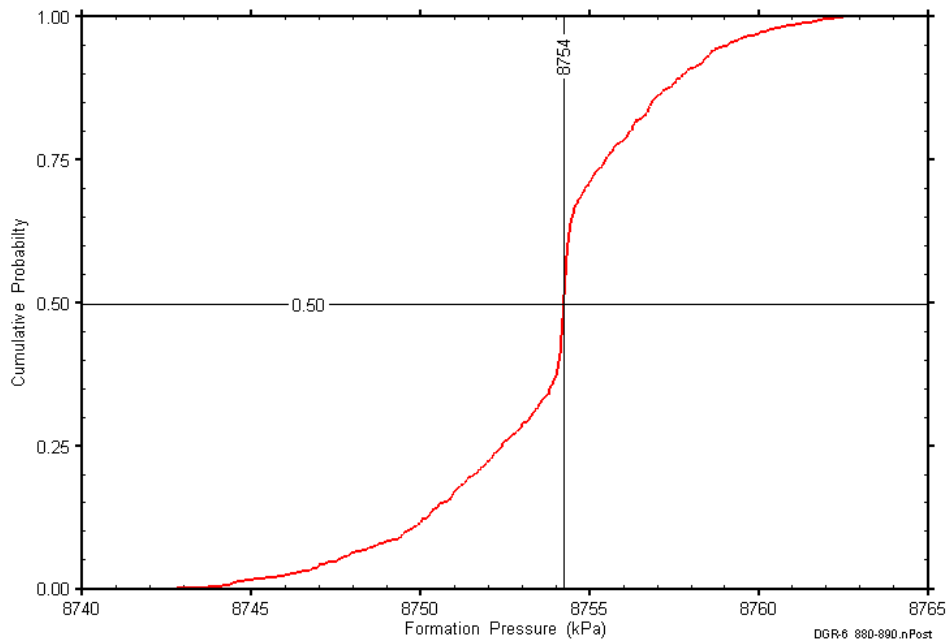


Figure F-150: DGR6_765.55-774.24 static formation pressure cumulative distribution function.

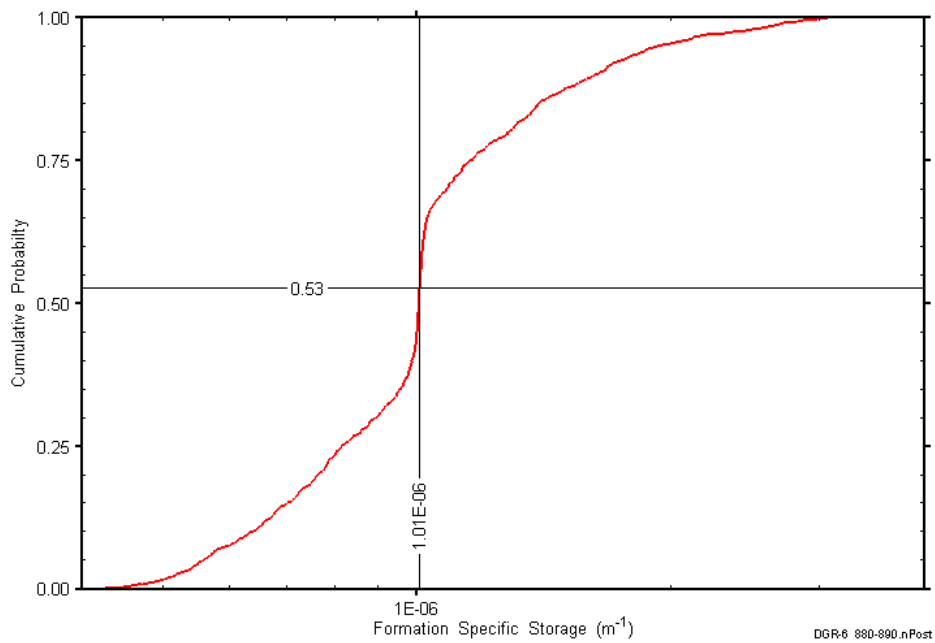


Figure F-151: DGR6_765.55-774.24 formation specific storage cumulative distribution function.

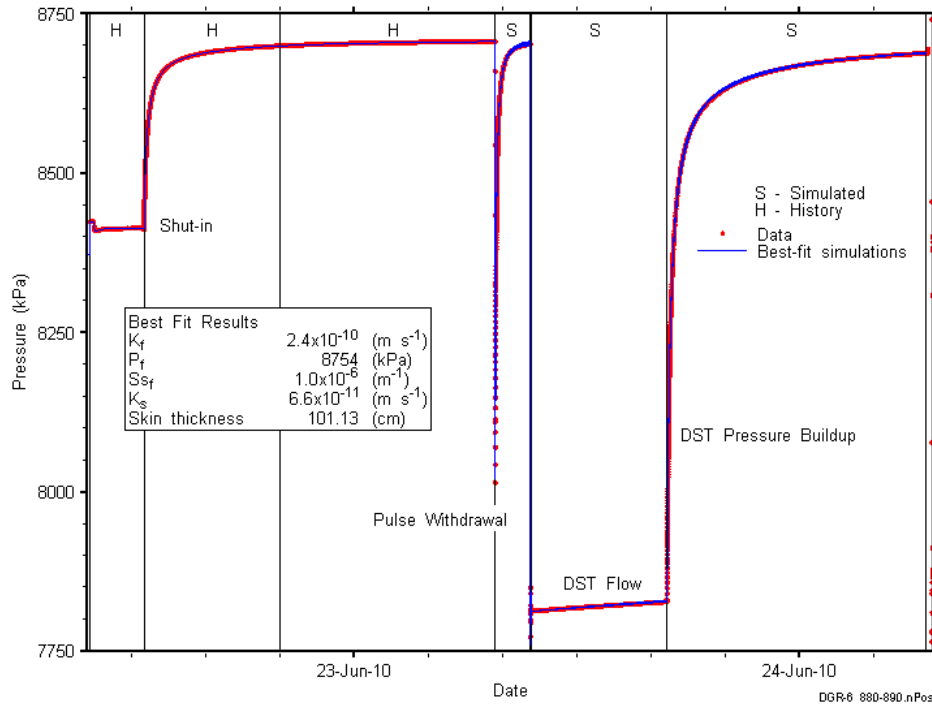


Figure F-152: Linear plot showing simulations of the DGR6_765.55-774.24 pressure response.

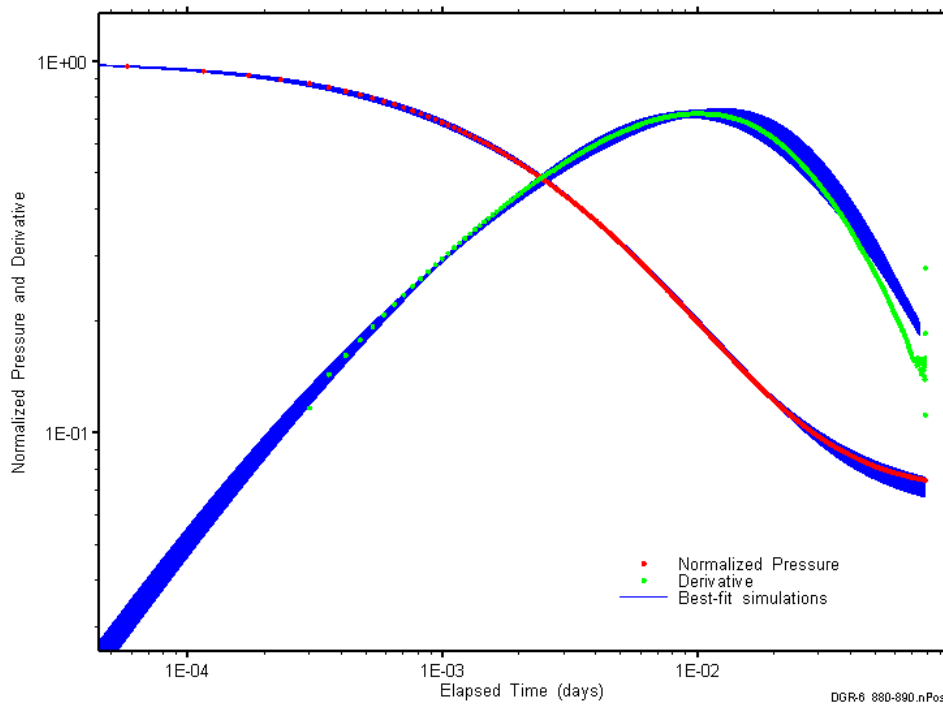


Figure F-153: Log-log plot showing simulations of the DGR6_765.55-774.24 PW Ramey B and derivative response.

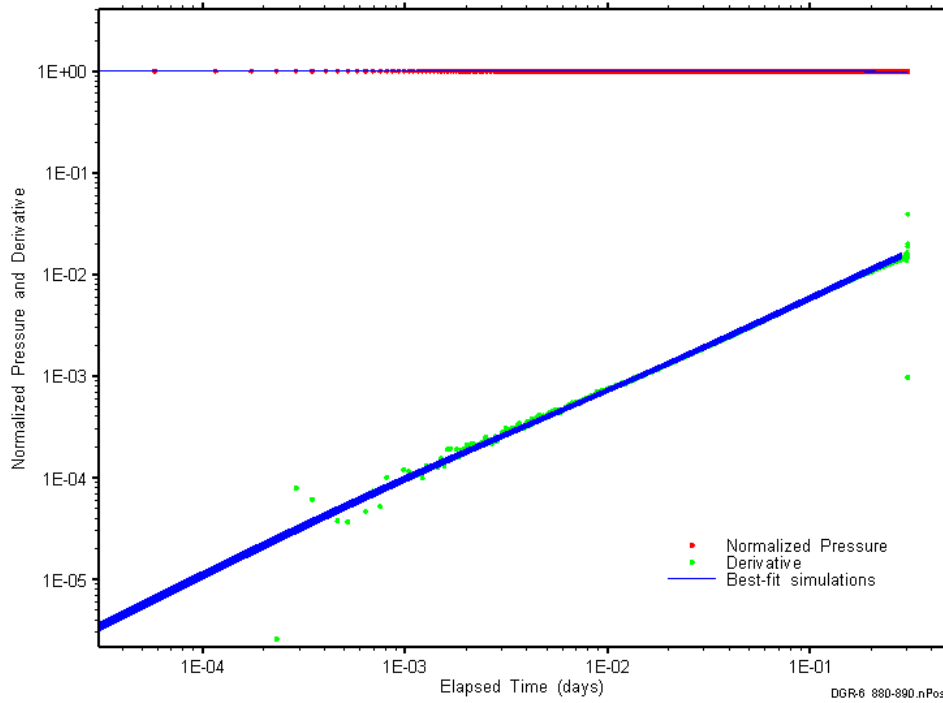


Figure F-154: Log-log plot showing simulations of the DGR6_765.55-774.24 DST flow period Ramey B and derivative response.

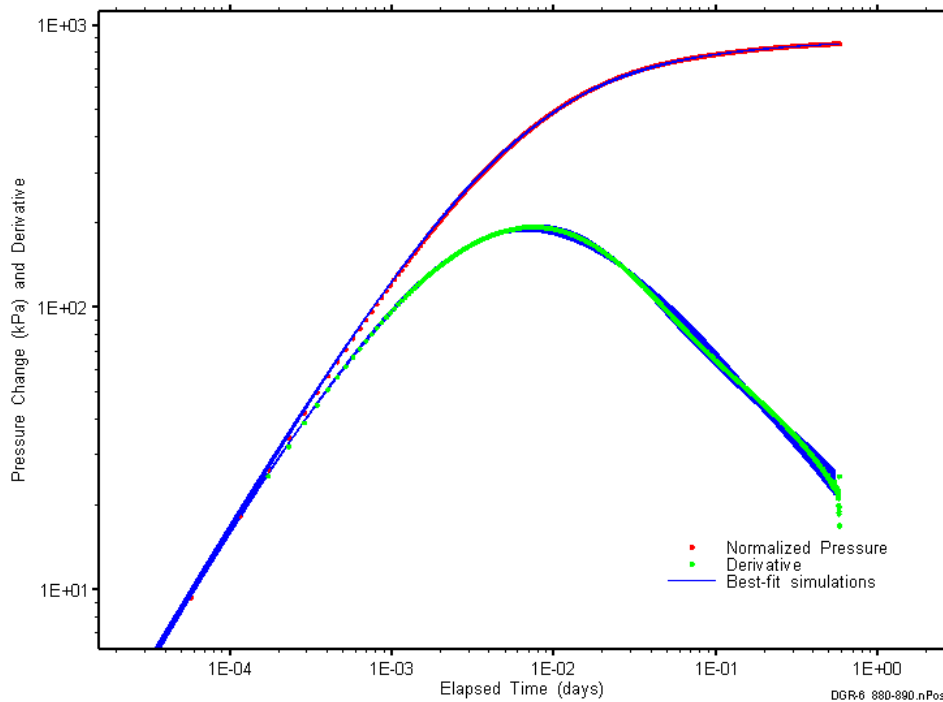


Figure F-155: Log-log plot showing simulations of the DGR6_765.55-774.24 DST pressure buildup diagnostic pressure change and derivative response.

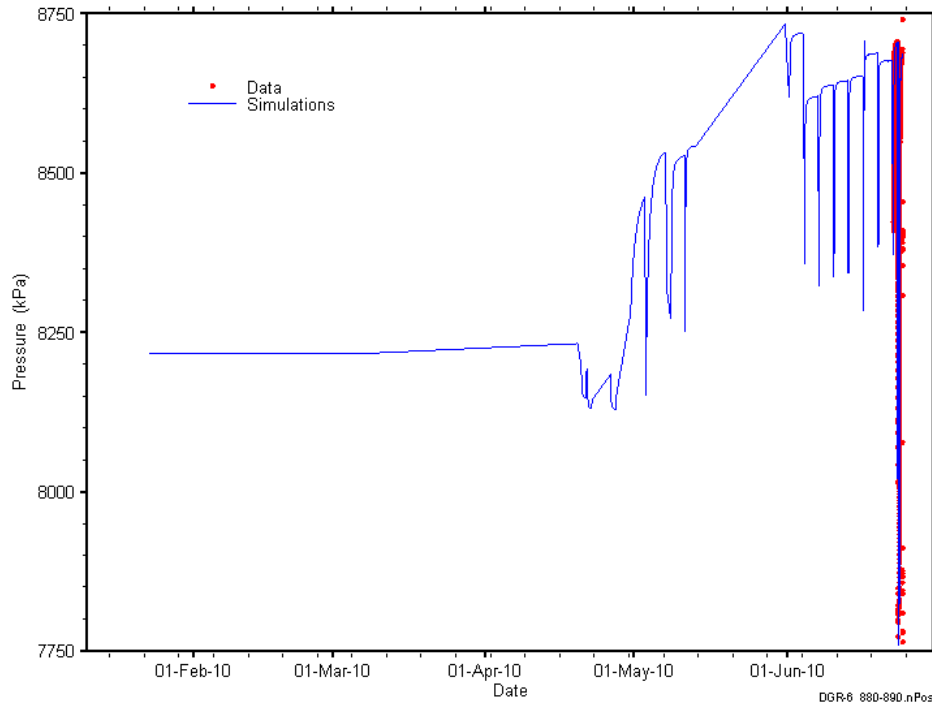


Figure F-156: Linear plot showing simulations of the DGR6_765.55-774.24 pressure response, including pre-test pressure history.

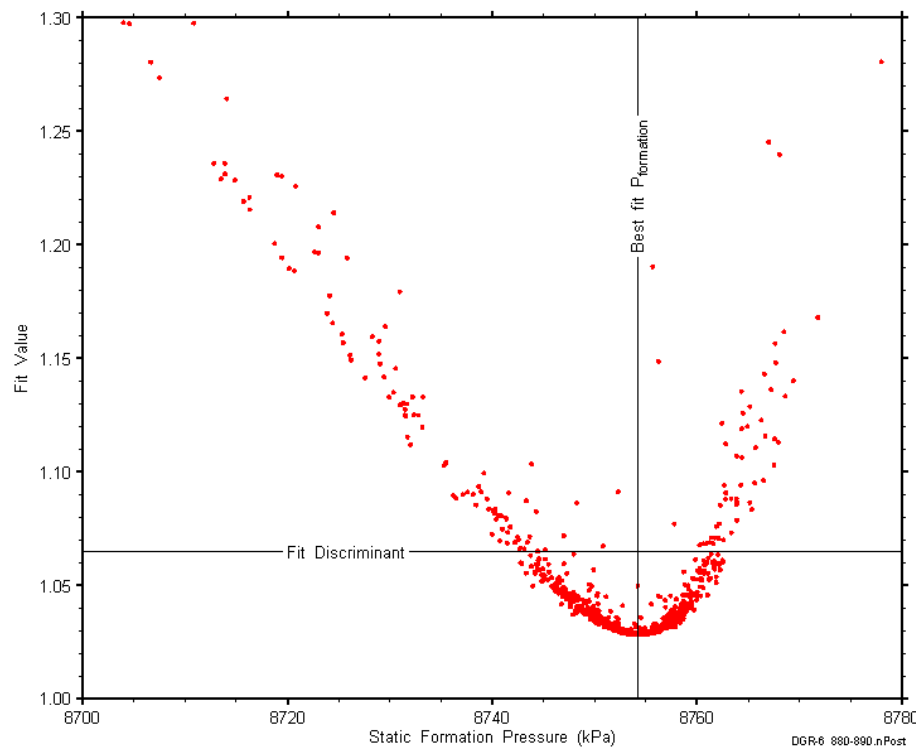


Figure F-157: XY-scatter plot showing the static formation pressure parameter space derived from DGR6_765.55-774.24 perturbation analysis along with the fit discriminant and best fit values.

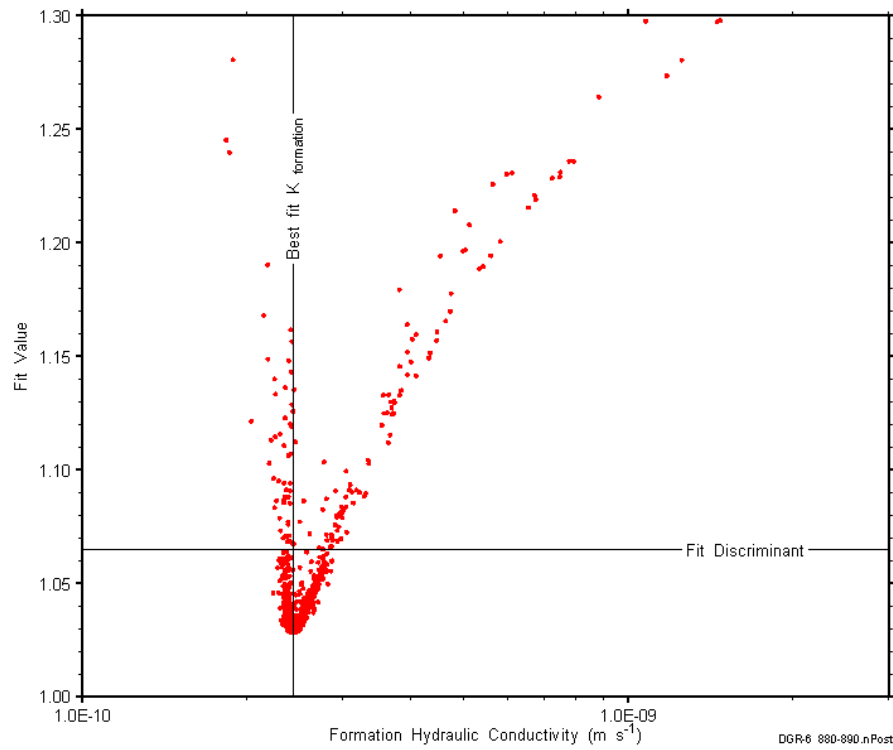


Figure F-158: XY-scatter plot showing the formation hydraulic conductivity parameter space derived from DGR6_765.55-774.24 perturbation analysis along with the fit discriminant and best fit values.

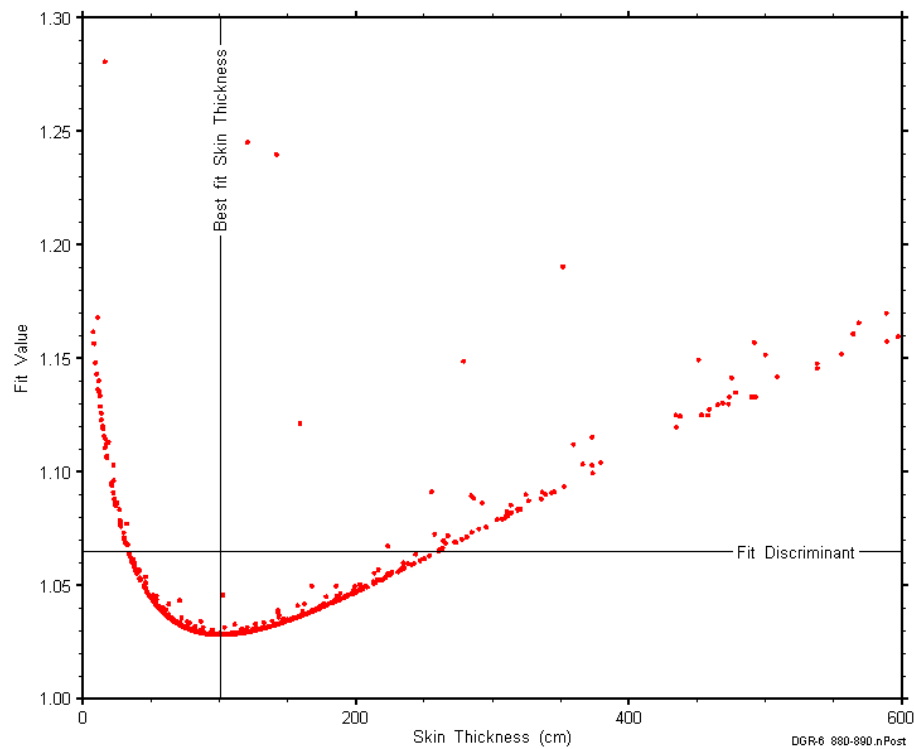


Figure F-159: XY-scatter plot showing the skin-thickness parameter space derived from DGR6_765.55-774.24 perturbation analysis along with the fit discriminant and best fit values.

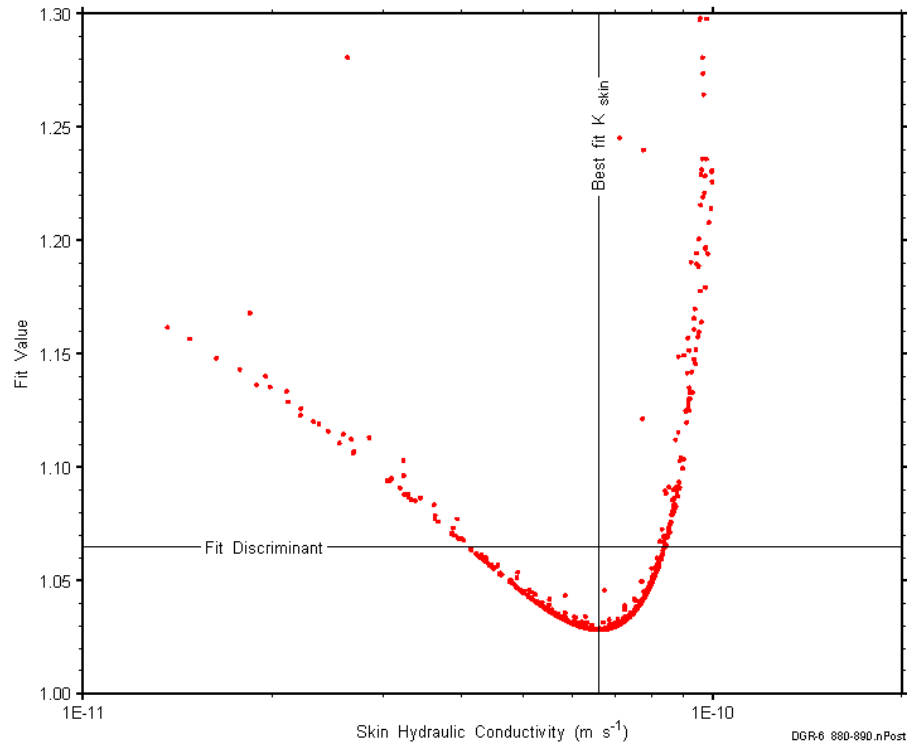


Figure F-160: XY-scatter plot showing the skin hydraulic conductivity parameter space derived from DGR6_765.55-774.24 perturbation analysis along with the fit discriminant and best fit values.

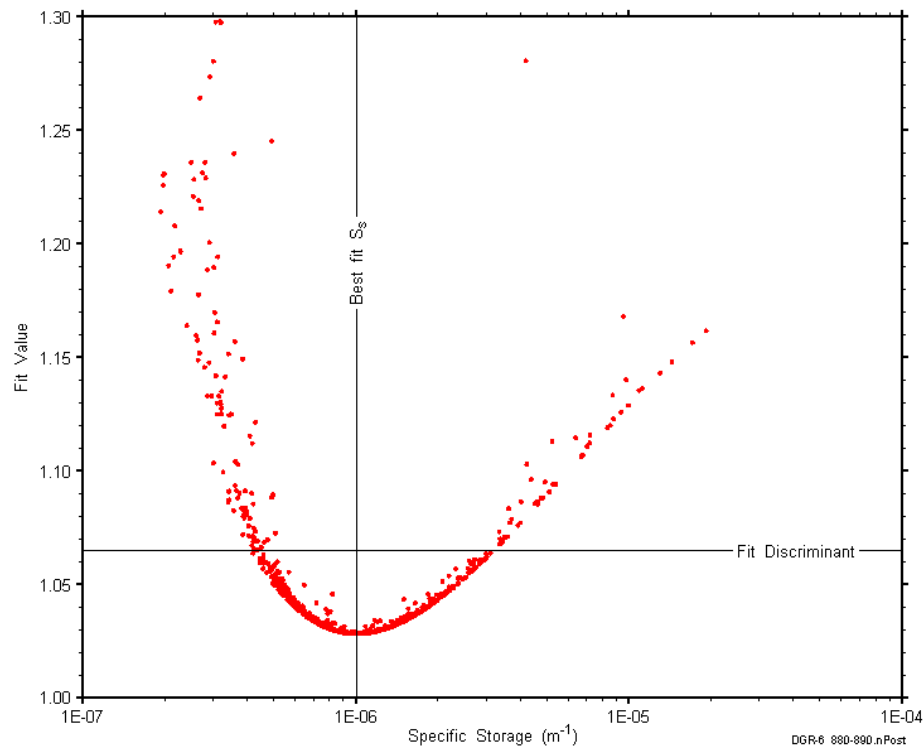


Figure F-161: XY-scatter plot showing the formation specific storage parameter space derived from DGR6_765.55-774.24 perturbation analysis along with the fit discriminant and best fit values.